U.S. DEPARTMENT OF ENERGY

Office of ENERGY EFFICIENCY & RENEWABLE ENERGY

Batteries

2020 Annual Progress Report

Vehicle Technologies Office

(This page intentionally left blank)

Disclaimer

This report was prepared as an account of work sponsored by an agency of the United States government. Neither the United States government nor any agency thereof, nor any of their employees, makes any warranty, express or implied, or assumes any legal liability or responsibility for the accuracy, completeness, or usefulness of any information, apparatus, product, or process disclosed or represents that its use would not infringe privately owned rights. Reference herein to any specific commercial product, process, or service by trade name, trademark, manufacturer, or otherwise does not necessarily constitute or imply its endorsement, recommendation, or favoring by the United States government or any agency thereof. The views and opinions of authors expressed herein do not necessarily state or reflect those of the United States government or any agency thereof.

Acknowledgements

The projects reported in this report were supported through various contracts funded by the U.S. Department of Energy, Vehicle Technologies Office. A list of contributing authors appears in the sections for specific projects in this report.

Acronyms

ABAA	Advanced Lithium Batteries for Automobile Application
ABF	Annular bright-field
ABFSTEM	Annular bright-field scanning transmission electron microscope
ABFTEM	Annular bright-field transmission electron microscopy
ABMR	Advanced Battery Materials Research
ABR	Applied Battery research
AC	Alternating current
ACS	American Chemical Society
AEI	Anode electrolyte interphase
AEM	Advanced Electrolyte Model
AER	All-electric range
AES	Atomic emission spectroscopy
AFM	Atomic force microscopy
AGG	Aggregates
AGM	Absorbent Glass Mat (batteries)
AH	Ampere hour
AI	Artificial Intelligence
AIMD	Ab initio molecular dynamics
ALD	Atomic layer deposition
ALS	Advanced Light Source (facility)
AMO	Advanced Manufacturing Office
AMP	Atomistic Machine-learning Package
AMR	Annual Merit Review
AMY	Actual meterological year
AN	Acetonitrile
ANL	Argonne National Laboratory
AOI	Area of Interest
APL	Applied Physics Laboratory
APS	Advanced Photon Source (laboratory)
AR	Auto-regressive (model)
ARC	Accelerated rate calorimetry
ARL	Army Research Laboratory
ASEI	Artificial SEI
ASI	Area-specific impedance
ASLSB	All solid lithium-sulfur battery
ASME	American Society of Mechanical Engineers
ASR	Area-specific resistance
ASSB	All solid-state battery
ATM	Asymmetric temperature modulation
ATR	Attenuated total reflection
ATRP	Atom transfer radical polymerization
BDE	Bond dissociation energy

BE	Baseline electrolyte
BERT	Bidirectional Encoder Representations from Transformers (model)
BESS	Battery energy storage system
BET	Brunauer, Emmett, and Teller (surface area analysis)
BEV	Battery electric vehicle
BL	Baseline
BLI	Beyond Lithium-ion
BM	Ball milling
BMF	Battery manufacturing facility
BMG	Ball-milled glass
BMR	(Advanced) Battery Materials Research (program)
BMS	Battery management system
BMU	Battery Management Unit
BNL	Brookhaven National Laboratory
BOL	Beginning of life
BOP	Balance of plant
BP	Budget period
BPC	Black phosphorus/Ketjenblack-multiwalled carbon nanotubes composite
BQ	1-4-benzoquenone
BSE	Backscatter and secondary electron (imaging modes)
BTC	Battery Technology Center
BTFE	Bis(2,2,2-trifluoroethyl) ether
BTMS	Behind-the-Meter-Storage
BTO	Building Technologies Office
BV	Bond valence
BYU	Brigham Young University
CAD	Computer-aided Design
CAEBAT	Computer-aided engineering of batteries
CAFE	Corporate Average Fuel Economy
CAMP	Cell analysis, modeling, and prototyping (facility)
CB	Carbon black
CBD	Conductive binder domain
CBM	Conduction band minimum
CBT	Cantilever Beam Test
CC	Constant current
CCCV	Constant current, constant voltage
CCD	Critical current density
CCEMM	Center for Complex Engineered Multifunctional Materials
CDD	Charge density difference
CDI	Cobalt Development Institute
CE	Coulombic efficiency
CEI	Cathode electrolyte interfaces
CFM	Cubic feet per minute
CG	Core-gradient
CHNS	Carbon hydrogen and nitrogen (analyzer) system

CIF	Chemical Instrumentation Facility
CI-NEB	Climbing-image nudged elastic band
CIP	Contact ion pair
CMC	Carboxymethyl cellulose
CMD	Classical molecular dynamics
CN	Coordination number
CNSSM	Carbon-nitrogen stainless steel mesh
CNT	Carbon nano-tubes
COP	Coefficient of penetrance
COTS	Commercial-off-the-shelf
CP	Co-precipitation
CPE	Constant phase element
CR	Capacity retention
CRADA	Cooperative research and development agreement
CSE	Chemical Sciences and Engineering (at ANL)
CSHS	Core-shell hollow spheres
CSM	Continuous shape measure
CSTR	Continuous stirred tank reactor
CT	Computed tomography
CUP	Constitutional underpotential plating
CV	Cyclic voltammetry
CVD	Chemical vapor deposition
CY	Calendar year
DAB	Dual active bridge (converter)
DCE	Diluted concentration electrolyte
DCFC	DC fast charging
DCIR	Direct current inner resistance
DCPC	Dicyclopentadiene compound
DDSA	Directly derived sulfur assembled
DEG	Diethylene glycol
DEMS	Differential electrochemical mass spectrometry
DES	Deep eutectic solvent
DFPT	Density functional perturbation theory
DFT	Density function theory
DFTB	Density functional tight binding (calculation)
DHB	2,5-dihydroxybenzoic (acid)
DI	De-ionized (water)
DIW	Direct Ink Writing
DMB	Dimethoxybenzene
DMC	Dimethyl carbonate
DME	Dimethyl ether
DMF	Dimethylformamide
DMSO	Dimethylsulfoxide
DMTA	Dynamic mechanical-thermal analysis
DOD	Depth-of-discharge

DOE	Department of Energy
DOL	Dioxolane
DP	Dry process
DPA	Destructive physical analysis
DPS	Dipropylulfide
DRIFTS	Diffuse reflectance FTIR spectra
DRS	Disordered rock salt
DRX	Disordered (rocksalt) transition metal oxides
DSC	Differential scanning calorimetry
DST	Dynamic stress test
DVA	Differential voltage analysis
EA	Ethyl acetate
EADL	Electrochemical Analysis and Diagnostic Laboratory (at ANL)
EAM	Electrochemically active molecules
EB	Electron beam
EBSD	Electron back-scattering diffraction
EC	Ethylene carbonate
ECI	Effective clusters interactions
ECP	(DOE) Exascale Computing Project
ECS	Electrochemical Society
EDAX	Energy dispersive x-ray spectroscopy mapping
EDP	Electron diffraction pattern
EDS	Energy dispersive spectroscopy
EDV	Electric Drive Vehicle
EDX	Energy-dispersive x-ray (spectroscopy)
EDXRD	Energy Dispersive X-ray Diffraction
EEI	Electrode/electrolyte interface
EELS	Electron energy loss spectroscopy
EERE	Energy Efficiency and Renewable Energy (DOE Office)
EIA	Energy Information Administration
EIC	Energy Innovation Center
EIS	Electrochemical impedance spectroscopy
EM	Electro-mechanical
EMC	Ethylmethyl carbonate
EO	Ethylene oxide
EOCV	End-of-relaxed charge voltage
EOD	End of discharge
EOL	End of life
EOS	Equation of state
EP	Ethylene Glycol Monopropyl Ether (solvent)
EPA	Environmental Protection agency
EPDM	Ethylene propylene diene terpolymer
EPR	Electron paramagnetic resonance
EQCM	Electrochemical quartz crystal microbalance
ESIF	Energy Systems Integration Facility

ESP	Electrostatic potential
ESS	Energy storage system
ETEM	Environmental transmission electron microscopy
ETFB	Ethyl 4,4,4-trifluorobutyrate
EV	Electric vehicle
EVI	Electric Vehicle Initiative
EVSE	Electric-vehicle supply equipment
EXAFS	Extended X-ray absorption fine structure
FA	Fumed alumina
FC	Fast-charge
FCE	First cycle efficiency
FCG	Full concentration-gradient
FCSE	Fast-charged specific energy
FDES	Fluorinated Deep Eutectic Solvent
FDM	Fused Deposition Modeling
FDMB	Fluorinated 1,4-dimethoxybutane
FEC	Fluoro ethylene carbonate
FEP	Fluorinated ethylene propylene
FF	Force field
FFT	Fast Fourier-transform
FIB	Focused ion beam
FIBSEM	Focused ion beam scanning electron microscopy
FOA	Federal opportunity anouncement
FRS	Filtered Rayleigh Scattering
FSI	(Lithium) bis(trifluoromethanesulfonyl)imide
FSP	Flame spray pyrolysis
FTC	Freeze tapecasting
FTEG	Fluorinated tetraethylene glycol
FTIR	Fourier transform infrared spectroscopy
FY	Fiscal year
GAP	Gaussian Approximation Potential
GB	Grain boundary
GBL	Gamma-butyrolactone
GC	Gas chromatography
GDOES	Glow discharge optical emission spectrometry
GEIS	Galvanostatic electrochemical impedance spectroscopy
GF	Glass fiber
GFM	Glass fiber mats
GGA	Generalized gradient approximation
GHG	Green-house gases
GITT	Galvanostatic intermittent titration
GNR	Graphene nanoribbons
GO	Graphene oxide
GOS	Grain Orientation Spread
GPC	Gel permeation chromatography

GPE	Gel polymer electrolyte
GPR	Gaussian Process Regression
GREET	Greenhouse gas regulated energy and emissions and transpiration
GROD	Grain Reference Orientation Deviation
GSE	Glassy solid electrolyte
GTP	Gibbs Thomson parameter
HA	High Active (coating technology)
HAADF	High-angle annular dark-field
HAWCS	Hybrid Alternative Wet-Chemical Synthesis
HAXPES	High energy x-ray photoelectron spectroscopy
HC	Half charged
HCE	High concentration electrolyte
HD	Half discharged
HEBM	High Energy Ball Mill
HER	Hydrogen evolution reaction
HEV	Hybrid electric vehicle
HEXRD	High-energy XRD
HF	Hydrofluoric acid
HFE	Hydrocarbon vs. fluoroether
HGA	Horizontally aligned anode
HMDS	Hexamethyl-disiloxane (additive)
HOH	Highly Ordered Hierarchical (electrodes)
HOLE	Highly ordered laser-patterned electrode
HOPG	Highly oriented pyrolytic graphite
HOR	Hydrogen oxidation reaction
HPC	Highly porous carbon
HPPC	Hybrid pulse power characterization
HRSEM	High resolution scanning electron microscopy
HRTEM	High-resolution transmission electron microscopy
HR-TEM	High-resolution transmission electron microscopy
HT	High temperature
HVAC	Heating, Ventilationg, and Air-Conditioning
HVS	High voltage spinel
HXN	Hard x-ray nanoprobe
IC	Ionic conductivity
ICE	Internal combustion engine
ICESI	International Coalition for Energy Storage and Innovation
ICEV	Internal combustion engine vehicle
ICL	Initial capacity loss
ICP	Inductively coupled plasma
ID	Internal diameter
IEA	International Energy Agency
IEEE	Institute of Electrical and Electronics Engineers
IES	Interface engineered substrate
IFC	Inorganic functional catalysts

IKB	Integrated Ketjen Black
IKBS	Integrated Ketjen Black/Sulfur
INL	Idaho National Laboratory
IPA	Isopropyl alcohol
IR	Infra-red
IS	Impedance spectroscopy
ISS	Inner-shell spectroscopy
JACS	Journal of the American Chemical Society
JT	Jahn-Teller (distortion)
KCN	Potassium cyanide
KF	Karl Fischer (titration)
KMC	Kinetic Monte Carlo (simulations)
KOH	Potassium hydroxide
KPH	Kinetic polarization hindrance
LAM	Loss of active materials
LAMMPS	Large-scale atomic/molecular massively parallel simulator
LATP	$Li_{1.17}Al_{0.17}Ti_{1.83}(PO_4)_3$
LBNL	Lawrence Berkeley National Laboratory
LBO	Li_3BO_3
LC	Liquid chromatography
LCA	Life cycle analysis
LCB	Lower confidence bound
LCF	Linear combination fitting
LCO	Lithium cobalt oxide
LCOC	Levelized cost of charging
LCOE	Levelized cost of electricity
LCV	Lower-cutoff voltage
LEDC	Lithium ethylene dicarbonate
LEMC	Lithium ethylene monocarbonate
LFP	Li-iron phosphate
LGPS	$Li_{10}GeP_2S_{12}$
LHCE	Localized high concentration electrolyte
LIB	Lithium-ion battery
LIBRA	Lithium Ion Battery Recycling Analysis
LIC	Lithium-ion conducting
LL	Layered-layered
LLI	Loss of lithium inventory
LLNL	Lawrence Livermore National Laboratory
LLS	Layered-layered spinel
LLTO	$(Li,La)TiO_3$
LLZ	$Li_7La_3Zr_2O_{12}$
LLZO	Lithium lanthanum zirconate
LLZTO	$Li_{6.75}La_3Zr_{1.75}Ta_{0.25}O_{12}$
LMA	Lithium metal anode
LMB	Lithium metal battery

LMC	Lithium methyl carbonate
LMD	lithium metal deposition
LMNO	Lithium manganese nickel oxide
LMNOF	Li-Mn-Nb-O-F
LMO	Lithium manganese oxide
LMRNMC	Lithium- and manganese-rich nickel manganese cobalt oxide
LMTOF	Li-Mn-Ti-O-F
LNCO	Lithium-Nickel-Cobalt-Oxide
LNMMO	$LiNi_{0.495}Mn_{0.495}Mo_{0.01}O_2$
LNMO	$LiNi_{0.5}Mn_{0.5}O_2$
LNMTO	$LiNi_{0.5}Mn_{1.2}TiO_{0.3}O_4$
LNO	Lithium-nickel oxide
LNTMO	$Li_{1.25}Nb_{0.15}Ti_{0.2}Mn_{0.4}O_2$
LNTMOF	$Li_{1.15}Ni_{0.45}Ti_{0.3}Mo_{0.1}O_{1.85}F_{0.15}$
LOB	Li-oxygen battery
LPS	Li_3PS_4
LPSBI	$Li_7P_2S_8Br_{0.5}I_{0.5}$
LPSCI	Lithium protected solid-state cathode interface
LSB	Lithium sulfur batteries
LT	Low-temperature
LTMO	Lithium-rich transition metal oxide
LTMOF	$Li_{1.2}Ti_{0.2}Mn_{0.6}O_{1.8}F_{0.2}$
LTO	Lithium titanate, $Li_4Ti_5O_{12}$
LUMO	Lowest unoccupied molecular orbital
LYC	Li_3YCl_6
LZO	$La_2Zr_2O_7$
MALDI	Matrix-assisted laser desorption/ionization
MAS	Magic angle spinning
MATBOX	Microstructure Analysis Toolbox
MC	Monte Carlo (simulations)
MD	Molecular dynamics
MERF	Materials Engineering Research Facility
METS	Muti-harmonic ElectroThermal Spectroscopy (sensor)
MG	Metallic Glasses
MGF	Mixed glass former
MIBC	Methyl isobutyl carbinol
MIC	Molecular ionic composites
MILP	Mixed-integer linear programming
MIT	Massachusetts Institute of Technology
ML	Machine learning
MLPC	Multi-Layer Pouch Cell
MOF	Metal Organic Framework
MOH	Metal hydroxide
MOS	Mixed oxy-sulfide
MOSFET	Metal–oxide–semiconductor field-effect transistor

MOSN	Mixed oxy-sulfide-nitride
MOSS	Multibeam optical stress sensor
MPC	Mesoporous carbon
MPO	$Mn_2P_2O_7$
MRS	Materials Research Society
MS	Molecular spectroscopy
MSD	Mean square displacements
MSMD	Multi-scale, multi-domain
MST	Mass spectrometry titration
MSU	Michigan State University
MW	Microwave (irradiation)
NASICON	(Na) Super Ionic CONductor
NAVSEA	Naval Sea Systems Command
NCA	$LiNi_{0.8}Co_{0.15}Al_{0.05}O_2$
NCM	$Li_{1+w}[Ni_xCo_yMn_z]_{1-w}O_2$
NCMAM	$LiNi_{0.85}Co_{0.05}Mn_{0.075}Al_{0.02}Mg_{0.005}O_2$
NDI	Naphthalene diimide
NEB	Nudged elastic band (method)
NECST	Nanomaterials for Energy Conversion and Storage Technology
NETL	National Energy Technology Laboratory
NFA	$LiNi_xFe_yAl_zO_2$
NG	Next-generation
NHTSA	National Highway Transportation Safety Administration
NIB	Sodium (Na)-ion battery
NLP	Natural language processing
NMA	Nickel-manganese-aluminum
NMC	Nickel manganese cobalt (oxide)
NMP	N-methylpyrrolidone
NMR	Nuclear magnetic resonance
NMT	TiMg-doped $LiNiO_2$
NN	Nearest neighbor (model)
NND	Nearest neighbor distance
NNN	Next-nearest neighbor (configuration)
NNT	Sodium nonatitanate
NO	Native oxide (layer)
NOMAD	Nanoscaled-Ordered Materials Diffractometer
NP	Nanoparticles
NPC	Net present cost
NPDF	Neutron pair distribution function
NPV	Net present value
NR	Neutron reflectometry
NREL	National Renewable Energy Laboratory
NSLSII	National Synchrotron Light Source II
OCV	Open circuit voltage
OE	Organic electrolyte

OEM	Original equipment manufacturer
OEMS	Online electrochemical Mass Spectrometry
OER	Oxygen evolution reactions
OES	Optical Emission Spectroscopy
OIM	Organic insertion material
OL	Overlithiation
OPLS	Optimized Potentials for Liquid Simulations
ORNL	Oak Ridge National Laboratory
ORR	Oxygen reduction reaction
OTE	1H,1H,5H-Octafluoropentyl 1,1,2,2-Tetrafluoroethyl ether
PAA	Polyacrylic acid
PAS	Paired anti-site (defect)
PAW	Projected augmented wave
PBDT	Poly-2,2´-disulfonyl-4,4´-benzidine terephthalamide (polymer)
PBE	Perdew, Burke, and Ernzerholf (parameters)
PBI	polybenzoimidazole
PC	Propylene carbonate
PCM	Phase change material
PDF	Pair density function
PDMS	Polydimethylsiloxane
PDOS	Projected Density of States
PE	Polyethylene
PECVD	Plasma-enhanced chemical vapor deposition
PEEK	Polyetheretherketone
PEG	Polyethylene glycol
PEGDA	Poly(ethylene glycol) diacrylate
PEGDMA	Polyethylene glycol dimethacrylate
PEI	poly ethylene imine
PEO	Polyethyleneoxide
PES	Prop-1-ene sultone
PETMP	Pentaerythritol-tetrakis(3-mercaptopropionate)
PEV	Plug-in electric vehicle
PFA	Perfluoroalkoxy
PFPE	Perfluoropolyether
PFY	Partial fluorescence yield
PG	PEO-based gel polymer
PHEV	Plug-in hybrid electric vehicle
PI	Principal investigator
PISE	Polymer-in-salt electrolyte
PLD	Pulsed laser deposition
PLIF	Planar Laser Induced Fluorescence
PNNL	Pacific Northwest National Laboratory
POSS	Poly(acryloisobutyl polyhedral oligomeric silsesquioxane)
PPT	Peak Power Test
PSD	Particle size distribution

PSO	Particle Swarm Optimization (algorithm)
PSSQ	Polysilsesquioxane
PSU	Pennsylvania State University
PTA	Polysulfide trapping agent
PTF	Post-Test Facility
PTFE	Poly(tetrafluoroethylene) (cathode)
PTO	Pyrene-4,5,9,10-tetraone
PV	Photovoltaic
PVB	Polyvinyl butyral
PVD	Physical vapor deposition
PVDF	Poly(vinylidenefluoride)
PVP	Polyvinylpyrrolidone
PYR	Pyrrolidinium
QC	Quality control
RCP	Restricted-charge protocol
RE	Reference electrode
RF	Radiofrequency
RGA	Reduced graphene oxide
RH	Relative humidity
RIXS	Resonant inelastic x-ray scattering
RM	Redox mediator
RMS	Root mean square
RP	Red phosphorous
RPC	Red phosphorus-carbon
RPM	Revolutions per minute
RPT	Reference performance test
RRDE	Rotating ring disk electrode
RS	Rocksalt
RST	Reactive Spray Technology
RT	Room temperature
RTD	Resistance thermal device
RTIL	Room temperature ionic liquid
SAE	Society of Automotive Engineers
SAED	Selected area electrode diffraction
SAM	Self-assembled molecular (film)
SAXS	Small angle X-Ray scattering
SBIR	Small Business Innovation Research
SBR	Styrene-Butadiene rubber
SCAN	Strongly constrained and appropriately normed (density functional)
SCD	surface charge density
SCP	Sulfur containing polymer
SDS	Safety data sheet
SE	Solid electrolyte
SEAD	Selected area electrode diffraction
SECM	Scanning electrochemical microscope

SEI	Solid electrolyte interphase
SEISTA	Silicon electrolyte interface stabilization
SEM	Scanning electron microscopy
SEO	Polystyrene-b-poly(ethylene oxide)
SEOS	Poly(styrene)-b-poly(ethylene oxide)-b-poly(styrene)
SETO	Solar Energy Technologies Office
SGML	Standard Generalized Markup Language
SHE	Self-healing elastomer
SIA	Structurally isomorphous alloy
SIC	Single-ion conducting (block copolymer electrolyte)
SIE	Solvation-ion-exchange
SIG	Solvate ionogel
SIL	Solvated ionic liquid (electrolyte)
SIMS	Secondary ion mass spectrometry
SLAC	Stanford acceleration laboratory
SLG	Single layer graphene
SLP	Single-layer pouch
SLPC	Single layer pouch cell
SLS	Sacrificial lithium source
SMPS	Scanning mobility particle sizing
SNL	Sandia National Laboratories
SNS	Spallation Neutron Source
SOA	State of the art
SOC	State of charge
SOH	State of health (for battery)
SOTA	State-of-the-art
SP	Spray pyrolysis
SPAN	Sulfurized polyacrylonitrile (electrode)
SPC	Solid permeability coefficient
SPE	Solid polymer electrolyte
SPM	Scanning probe microscope
SPN	Secondary pore network
SQL	Structured Query Language
SR	Surface reconstruction
SRE	Sigmoidal rate expression
SRL	Surface reconstruction layer
SRO	Short-range order
SS	Solid-state
SSB	Solid-state battery
SSE	Solid-state electrolyte
SSRM	Solvent-separated ion pair
STEM	Scanning transmission electron microscopy
STFSI	4-styrenesulfonyl(trifluoromethylsulfonyl)imide
STTR	Small Business Technology Transfer Program
SUNY	State University of New York

SWCNT	Single-walled carbon nanotube
SXAS	Soft x-ray absorption
SXRD	Surface X-ray diffraction
TAC	Technical Advisory Committee
TAMU	Texas A&M University
TAP	Technology assessment program
TARDEC	(U.S. Army) Tank Automotive Research, Development and Engineering Center
TC	Tape-cast (electrode)
TCD	Thermal conductivity detector
TCP	Technology Collaboration Program
TD	Transverse direction
TDOS	Total density of states
TEGDME	Tetraethyleneglycoldimethyl
TEGMA	Triethylene glycol methyl ether methacrylate
TEM	Transmission electron microscopy
TEMPO	(2,2,6,6-tetramethylpiperidin-1-yl) oxidanyl
TEP	Triethyl phosphate
TES	Tender-energy x-ray absorption spectroscopy
TEY	Total electron yield
TFC	Thin film constructs
TFEB	Fluorinated borate
TFEO	Fluorinated orthoformate
TFPC	3,3,3-Trifluoropropylene carbonate
TFSI	Bistriflimide (anion)
TGA	Thermal gravimetric analysis
THF	Tetrahydrofuran
TM	Transition metal
TMB	Trimethylboroxine
TMO	Transition metal oxide
TMP	Trimethyl phosphate
TMSF	Trimethylsilyl fluoride
TMY	Typical meteorological year
TNMO	$TiNbMoO_{7.5}$
TNO	Titanium niobium oxide
TNWO	$TiNbWO_{7.5}$
TOF	Time-of-flight
TRL	Technology readiness level
TTE	1,1,2,2-tetrafluoroethyl-2,2,3,3-tetrafluoropropyl ether
TTFP	Tris(2,2,2,-trifluoroethyl)phosphite
TVR	Taylor Vortex Reactor
TXM	Transmission X-ray microscopy
UAH	University of Alabama in Huntsville
UCL	University College, London
UCSD	University of California, San Diego
UCV	Upper cutoff voltage

UHV	Ultra-high vacuum
UIUC	University of Illinois, Urbana Champaign
UM	University of Michigan
UMD	University of Maryland
URDB	Utility Rate Database
USABC	United States Advanced Battery Consortium
USANS	Ultra-small angle neutron scattering
USCAR	United States Council for Automotive Research
USDRIVE	Driving Research and Innovation for Vehicle efficiency and Energy sustainability
USEPA	United States Environmental Protection Agency
USPTO	United States Patent and Trademark Office
UTA	University of Texas, Austin
UTK	University of Tennessee, Knoxville
UU	University of Utah
UV	Ultraviolet
UW	University of Washington
VASP	Vienna *ab initio* Simulation Package
VC	Vinylene carbonate
VDW	Van De Waals (scan)
VGGT	Vapor grown graphite tube
VOC	Volatile organic compounds
VTO	Vehicle Technologies Office
WAXS	Wide-angle X-ray scattering
WL	White line (energy)
WPI	Worcester Polytechnic Institute
WT	Wavelet transform
XAFS	X-ray absorption fine structure
XANES	X-ray absorption near edge structure
XAS	X-ray absorption spectroscopy
XCEL	EXtreme Fast Charge Cell Evaluation of Lithium-ion Batteries
XFC	Extreme fast charging
XFM	X-ray fluorescence microscopy
XML	Extensible Markup Language
XPD	X-ray powder diffraction
XPEEM	X-ray photoemission electron microscopy
XPEO	Cross-linked poly ethylene oxide
XPS	X-ray photoelectron spectroscopy
XRD	X-ray diffraction
XRF	X-ray fluorescence (microscopy)
XRR	X-ray reflectivity
XRS	X-ray Raman Spectroscopy
YSZ	Yttria stabilized zirconia
ZEP	Zone Entity Probability

Executive Summary

Introduction

The Vehicle Technologies Office (VTO) of the Department of Energy (DOE) conducts research and development (R&D) on advanced transportation technologies that would reduce the nation's use of imported oil and would also lead to reductions in harmful emissions. Technologies supported by VTO include electric drive components such as advanced energy storage devices (primarily batteries), power electronics and electric drive motors, advanced structural materials, energy efficient mobility systems, advanced combustion engines, and fuels. VTO is focused on funding early-stage high-reward/high-risk research to improve critical components needed for more fuel efficient (and cleaner-operating) vehicles. One of the major VTO objectives is to enable U.S. innovators to rapidly develop the next generation of technologies that achieve the cost, range, and charging infrastructure necessary for the widespread adoption of plug-in electric vehicles (PEVs). An important prerequisite for the electrification of the nation's light duty transportation sector is development of more cost-effective, longer lasting, and more abuse-tolerant PEV batteries. One of the ultimate goals of this research, consistent with the current vehicle electrification trend, is an EV which can provide the full driving performance, convenience, and price of an internal combustion engine (ICE) vehicle. To achieve this, VTO has established the following overarching goal (Source: FY2021 Congressional Budget Justification[1]):

> *…identify new battery chemistry and cell technologies with the potential to reduce the cost of electric vehicle battery packs by more than half, to less than $100/kWh (ultimate goal is $60/kWh battery cell cost), increase range to 300 miles, and decrease charge time to 15 minutes or less by 2028.*

VTO works with key U.S. automakers through the United States Council for Automotive Research (USCAR) – an umbrella organization for collaborative research consisting of Fiat Chrysler Automobiles (FCA), the Ford Motor Company, and General Motors. Collaboration with automakers through the partnership known as U.S. Driving Research and Innovation for Vehicle Efficiency and Energy Sustainability (U.S. DRIVE) attempts to enhance the relevance and the success potential of its research portfolio. VTO competitively selects projects for funding through funding opportunity announcements (FOAs). Directly-funded work at the national laboratories are awarded competitively through a lab-call process. During the past year, VTO continued R&D in support of PEVs. Stakeholders for VTO R&D include universities, national laboratories, other government agencies and industry (including automakers, battery manufacturers, material suppliers, component developers, private research firms, and small businesses).

This document summarizes the progress of VTO battery R&D projects supported during the fiscal year 2020 (FY 2020). In FY 2020, the DOE VTO battery R&D funding was approximately $110 million. Its R&D focus was on the development of high-energy batteries for EVs as well as very high-power devices for hybrid vehicles. The electrochemical energy storage roadmap (which can be found at the EERE Roadmap web page[2]) describes ongoing and planned efforts to develop electrochemical storage technologies for EVs. To advance battery technology, which can in turn improve market penetration of PEVs, the program investigates various battery chemistries to overcome specific technical barriers, e.g., battery cost, performance, life (both the calendar life and the cycle life), its tolerance to abusive conditions, and its recyclability/sustainability. VTO R&D has had considerable success, lowering the cost of EV battery packs to $185/kWh in 2019 (representing more than 80% reduction since 2008) yet even further cost reduction is necessary for EVs to achieve head-to-head cost competitiveness with internal combustion engines (without Federal subsidies). In addition, today's batteries also need improvements in such areas as their ability to accept charging at a high rate, referred to as extreme fast charging (XFC) (15 minute charge) – to provide a "refueling" convenience similar to ICEs, and

[1] https://www.energy.gov/sites/default/files/2020/04/f73/doe-fy2021-budget-volume-3-part-1.pdf, Volume 3, Part 1, Page 17.
[2] http://energy.gov/eere/vehicles/downloads/us-drive-electrochemical-energy-storage-technical-team-roadmap.

the ability to operate adequately at low temperatures. Research into "next-gen lithium-ion" batteries which would provide such functionalities is one of the R&D focus areas. VTO is funding research on both "next gen" chemistries (which employ an alloy anode and/or a high voltage cathode) and beyond lithium-ion (BLI) chemistries (which can, for example, employ a lithium metal anode). Current cycle and calendar lives of next gen and BLI chemistries are well short of goals set for EVs. To quantify the improvements needed to accelerate large-scale adoption of PEVs and HEVs, certain performance and cost targets have been established. Some sample performance and cost targets for EV batteries, both at cell level and at system (pack) level, are shown in Table ES- 1.

Table ES- 1: Subset of EV Requirements for Batteries and Cells

Energy Storage Goals (by characteristic)	Pack Level	Cell Level
Cost @ 100k units/year (kWh = useable energy)	$100/kWh*	$75/kWh*
Peak specific discharge power (30s)	470 W/kg	700 W/kg
Peak specific regen power (10s)	200 W/kg	300 W/kg
Useable specific energy (C/3)	235 Wh/kg*	350 Wh/kg*
Calendar life	15 years	15 years
Deep discharge cycle life	1000 cycles	1000 cycles
Low temperature performance	>70% useable energy @C/3 discharge at -20°C	>70% useable energy @C/3 discharge at -20°C
	*Current commercial cells and packs not meeting the goal	

The batteries R&D effort includes multiple activities, ranging from focused fundamental materials research to prototype battery cell development and testing. It includes, as mentioned above, R&D on "next-gen" and BLI materials and cell components, as well as on synthesis and design, recycling, and cost reduction. Those activities are organized into mainly two program elements:

- Advanced Battery and Cell R&D
- Advanced Materials R&D

A short overview of each of those program elements is given below.

Advanced Battery and Cell R&D

The *Advanced Battery and Cell R&D* activity focuses on the development of robust battery cells and modules to significantly reduce battery cost, increase life, and improve performance. This work mainly spans the following general areas:

- United States Advanced Battery Consortium (USABC)-supported battery development & materials R&D (5 projects)
- Processing science and engineering (13 projects)
- Recycling and sustainability (five projects)
- Extreme fast-charging (15 projects)
- Beyond batteries (one project)

- Testing and Analysis (seven projects)
- Small business innovative research (SBIR) (multiple Phase I and Phase II projects)

Chapter I of this report describes projects under the *Advanced Battery and Cell R&D* activity. This effort involves close partnership with the automotive industry, through a USABC cooperative agreement. In FY 2020, VTO supported five USABC cost-shared contracts with developers to further the development of advanced automotive batteries and battery components. The estimated DOE share of those USABC contracts (over the life of the contracts) is approximately $39M. These include high performance battery cells by Farasis Energy, high-energy anode materials by NanoGraf Technologies, high-energy EV batteries by Zenlabs Energy, low-cost fast charge battery technical assessment by Physical Sciences, Inc., and developing high-voltage electrolyte by Gotion, Inc.

In addition to the USABC projects listed above, VTO also supports multiple *processing science and engineering* projects: including 13 projects at the national labs. Most strategies for increasing the performance (and reducing cost) of lithium-ion batteries focus on novel battery chemistries, material loading modifications, and increasing electrode thickness. The latter approach is generally considered useful for increasing energy density (and in turn, the overall cell capacity). However, practical thicknesses are constrained by ionic transport limitations (which limit cell power) and processing issues. Project participants in this area include several national labs (ANL, BNL, LBNL, LLNL, and ORNL). The estimated value of those advanced processing projects (over project lifetime) is approximately $35M.

The *Recycling and Sustainability* activity involves studies of the full life-cycle impacts and costs of lithium-ion battery production/use; cost assessments and impacts of various recycling technologies; and the available material and cost impacts of recycling and secondary use. The participants include ANL, ORNL, and NREL and the associated FY20 budget was approximately $6M.

To become truly competitive with the internal combustion engine vehicle (ICEV) refueling experience, EV charging times must also be significantly shorter than at present. A research project to understand/enable extreme fast charging (XFC) in enhanced lithium-ion systems – charging an EV at power rates of up to 400 kW, began in FY 2017.

Projects on numerous XFC topics are taking place at ANL, LBNL, ORNL, SNL, SLAC, the Pennsylvania State University, the University of Tennessee, Stony Brook University, and at industry partner Microvast, Inc. A lot of this R&D takes place under the heading eXtreme Fast Charge Cell Evaluation of Lithium-ionBatteries (XCEL) by multi-lab coalitions comprised of members focusing on xix different “thrust” areas including lithium detection thrust, local heterogeneity thrust, charge protocols and life assessment thrust, anode & electrolyte thrust, lithium-ion battery cathode thrust, and the heat generation thrust. In addition, a “behind the meter” storage project is taking place by a team which includes NREL, INL, ORNL, and SNL. This area focuses on novel battery technologies to facilitate the integration of high-rate EV charging, solar power generation technologies, and energy-efficient buildings while minimizing both cost and grid impacts.

The *battery testing, analysis, and high-performance computing* activity develops requirements and test procedures for batteries (to evaluate battery performance, battery life and abuse tolerance). Battery technologies are evaluated according to USABC-stipulated battery test procedures. Benchmark testing of an emerging technology is performed to remain abreast of the latest industry developments. The *battery testing* activity includes performance, life and safety testing, and thermal analysis and characterization. It currently includes seven projects based at ANL, INL, SNL, and NREL. The testing activity also supports cell analysis, modeling, and prototyping (CAMP) projects at ANL, which include benchmarking and post-test analysis of lithium-ion battery materials at three labs (ANL, ORNL, and SNL). Projects include testing (for performance, life and abuse tolerance) of cells (for contract, laboratory-developed and university-developed cells), and benchmarking systems from industry; thermal analysis, thermal testing, and modeling; cost modeling; and other battery use and life studies. Cost assessments and requirements analysis includes an ANL project on developing the performance and cost model BatPaC. This rigorously peer-reviewed model developed at ANL

is used to design automotive lithium-ion batteries to meet the specifications for a given vehicle, and estimate its cost of manufacture. An analysis using BatPaC compared the estimated costs of cells and packs for different electrode chemistries (Figure ES- 1).

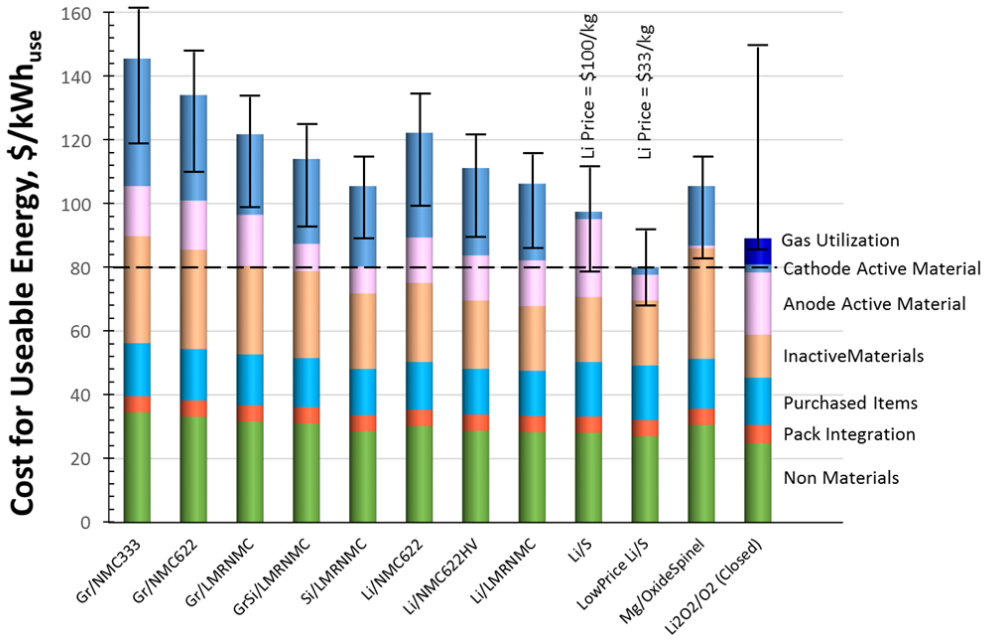

Figure ES- 1. Estimated costs of cells in automotive battery packs with different combination of electrodes. The packs are rated for 100 kWhTotal (85 kWhUseable), 300 kW, 315 V, 168 cells, and produced at a plant volume of 100K packs/year

VTO also supports several *small business innovation research* (SBIR) contracts. These SBIR projects focus on development of new battery materials and components and provide a source of new ideas and concepts. The section on SBIR projects includes a short list of recent Phase I and Phase II projects awarded during FY 2020.

Advanced Materials R&D

The *Advanced materials research & development* activity addresses fundamental issues of materials and electrochemical interactions associated with rechargeable automotive batteries. It develops new/promising materials and makes use of advanced material models to discover them, utilizing scientific diagnostic tools and techniques to gain insight into their failure modes and processes. It is conducted by various national labs, universities, and industry partners. The work is divided into two general areas –"next gen" chemistries (which can, for example, employ an alloy anode and/or a high voltage cathode) and beyond lithium-ion (BLI) chemistries (which can, for example, employ a lithium metal anode). The projects are distributed as follows:

- Next generation (next-gen) lithium-ion battery technologies (39 projects)
  - Advanced anodes (seven projects)
  - Advanced cathodes (six projects)
  - Frontier science at interfaces (seven projects)
  - No-cobalt/Low-cobalt cathodes (seven projects)
  - Diagnostics (six projects)
  - Modeling of advanced material (six projects)
- Beyond lithium-ion battery technologies (24 projects)
  - Metallic lithium (eight projects)
  - Solid-state batteries (18 projects)
  - Lithium sulfur (six projects)
  - Lithium-air Batteries (three projects)

  - Sodium-ion batteries (four projects)
  - Battery500 Consortium (five keystone projects and multiple seedling projects)

The *next generation lithium-ion battery* R&D area's goal is to advance material performances, designs, and processes to significantly improve performance and reduce the cost of lithium-ion batteries using an alloy or intermetallic anode and/or high voltage cathode. Specific areas of investigation include high-energy anodes (e.g., those containing silicon or tin), high voltage cathodes, high voltage and non-flammable electrolytes, novel processing technologies, high-energy and low-cost electrode designs, and certain other areas. This work spans a range of U.S. DRIVE activities.

- *Advanced anodes* R&D includes seven multi-lab collaborative projects. In the first project, a team consisting of ANL, LBNL, ORNL, SNL, and NREL provides research facility support for the next-generation lithium-ion anodes. The second collaborative project (NREL, ANL, ORNL, LBNL) is the silicon electrolyte interface stabilization (SEISta) project which develops a foundational understanding of the formation/evolution of the solid electrolyte interphase on silicon. Silicon is a viable alternative to graphitic carbon as an electrode in lithium-ion cells and can theoretically store >3,500 mAh/g (i.e., about ten times more than graphite). However, lifetime problems severely limit its use in practical systems – this project is focused on those problems. Five additional projects are taking place in the advanced anodes area including two at LBNL, and one each at PNNL, SLAC, and the University of Michigan.
- *Advanced cathodes* R&D includes six projects. A team consisting of ANL, LBNL, and PNNL is working on the design, synthesis, and characterization of advanced cathodes. Two collaborative projects on diagnostic testing and evaluation, including its theory and modeling, are being conducted by a team consisting of ANL, LBNL, ORNL, and NREL. Also, ANL is working on the design and synthesis of high energy, manganese rich oxides for lithium-ion batteries. In addition, there are two projects being conducted on disordered rocksalt structured cathode materials by a team which includes LBNL, ORNL, PNNL, as well as team member University of California at Santa Barbara.
- *Frontier science at interfaces R&D* includes seven projects. In one of them, SLAC is developing a molecular-level understanding of cathode-electrolyte interfaces and in another, ANL is working on developing an understanding of the stability of cathode/electrolyte interfaces in high voltage lithium-ion batteries. In another, LBNL is carrying out interfacial studies of emerging cathode materials. Additional interface projects are taking place at ANL, NREL, PNNL, and Daikin America.
- *Low-cobalt/no cobalt cathodes R&D* includes seven industry/academia-based projects. A team headed by Cabot is developing aerosol manufacturing technology for the production of low-cobalt lithium-ion battery cathodes. A UCSD project focuses on novel architectures for cobalt-free cathode materials and another at ORNL on novel lithium iron and aluminum nickelate (NFA). The University of California at Irvine is attempting to enhance the oxygen stability in low-cobalt layered oxide cathode materials by three-dimensional targeted doping and the University of Texas at Austin on developing high-nickel cathode materials for lithium-ion batteries (leading to indirect reduction of its cobalt content). In addition, Nexceris and Pennsylvania State University are also is working on cobalt-free/low-cobalt projects.
- *Diagnostics R&D* includes six projects ranging from interfacial processes to *in situ* diagnostic techniques and advanced microscopy, thermal diagnostics, and synthesis and characterization. The various researchers for these projects are based at LBNL, BNL, PNNL, and, GM.
- Of the six *modeling of advanced electrode materials* projects, one focuses on electrode materials design and failure prediction (ANL), one on the characterization and modeling of li-metal batteries: model-system synthesis and advanced characterization (LBNL), two on first-principles modeling (LBNL), one on large-scale *ab initio* molecular dynamics simulation of liquid and solid electrolytes (LBNL), and one on dendrite growth morphology modeling in electrolytes (MSU).
- There are three projects on *low-temperature electrolytes*, including one each on ethylene carbonate-lean electrolytes (LBNL), fluorinated solvent-based electrolytes (ANL), and synthesis, screening and characterization of low temperature electrolyte (BNL).

R&D on *beyond lithium-ion battery technologies*, often collectively referred to as the *Beyond Li-ion Battery Materials Research (BMR) program* includes lithium metal systems, solid-state batteries, lithium sulfur, lithium air, and sodium-ion. These systems offer further increases in energy and potentially reduced cost compared to the next-gen lithium-ion batteries. However, they also require additional breakthroughs in materials (often at a fundamental level) before commercial use is feasible.

- *Metallic lithium* R&D includes seven projects in cluding one in which ORNL is working on composite electrolytes to stabilize metallic lithium anodes. Of the remaining projects, two focus on dendrite suppression one on controlled interfacial phenomena (Texas A&M University, Purdue University), one on integrated multiscale model for design (LLNL), one on 3D printing (LLNL), and one on advanced polymer materials (SLAC).
- *Solid state batteries* R&D currently includes 18 projects – four of which are based at three national labs (ANL, LBNL, and ORNL), ten of them at nine universities (University of Maryland-College Park, Iowa State University, University of Michigan, Virginia Polytechnic Institute, Pennsylvania State University, University of Wisconsin-Milwaukee, University of Houston, Virginia Commonwealth University, and University of Louisville) and four of them at three industry partners (Solid Power, Inc., General Motors, and Wildcat Discovery Technologies).
- *Lithium sulfur R&D* includes six projects – four of them based at national laboratories and the remaining two at universities. The lab-based projects include one on lithium-selenium and selenium-sulfur couple (ANL), the development of high energy lithium sulfur batteries (PNNL), nanostructured design of sulfur cathodes (SLAC), and a new electrode binder (LBNL). The two universities for lithium sulfur projects include the University of Wisconsin at Milwaukee, and the University of Washington.
- Additional *beyond lithium-ion* projects include three on *Lithium-Air batteries* (one at PNNL and two at ANL) and four on *sodium-ion batteries* (based at ANL, BNL, LBNL, and PNNL).

The *Battery500 Innovation Center* is a combined effort by a team of four national labs (PNNL, INL, BNL and SLAC) and five universities (University of Texas-Austin, Stanford University, Binghamton University, University of Washington, and University of California, San Diego) with the goal to develop commercially viable lithium battery technologies with a cell level specific energy of 500 Wh/kg while simultaneously achieving 1,000 deep-discharge cycles. The consortium keystone projects focus on innovative electrode and cell designs that enable maximizing the capacity from advanced electrode materials. The consortium works closely with the R&D community, battery/materials manufacturers and end-users/OEMs to ensure that these technologies align well with industry needs and can be transitioned to production.

Recent Highlights

Developed Li-Ion Cell Brings 10-Minute Fast Charging Closer to Reality for Electric Vehicles. The convenience of quickly refilling a car is a major advantage that still exists for gasoline vehicles compared to fully electric alternatives. While fast charging EVs presents challenges to electricity grids and charging stations, perhaps the most difficult hurdles to overcome are from the Li-ion battery cell itself. During fast charge the high currents typically cause higher temperatures and uneven chemical reaction rates within the cells. These operating conditions in turn lead to faster cell degradation. Especially unfortunate, these degradations typically become more intense as the Li-ion cells energy density is increased.

One of the most straightforward ways to change a Li-ion cells performance and energy density is by using different materials. Cell component material properties differ based on composition and physical attributes, which in turn influences the cells performance. The cathode, the most expense cell component, is especially important to improve. Higher capacity cathodes lead to more energy density, while improved properties slow cell degradation and resistance increases. Using the full concentration gradient (FCG) cathode technology that Microvast is developing for commercialization cathodes with tailored surfaces, more stable to fast charge effects, were prepared. The FCG technology allows scientists and process engineers to change the atomic composition of metals throughout the cathode particle, allowing more desirable metal oxide combinations to

be targeted at locations most vulnerable to degradation. Also, as the nickel content of the prepared FCG was increased the prototype cells C/3 energy density could be improved.

Initially a 200 Wh/kg cell was the highest energy density cell made by Microvast that could achieve the 500 10-minute charging goals. Steadily that number has improved as the cathode was developed, eventually reaching 240 Wh/kg as the base (0.33C) energy density, a 20% improvement. In Figure ES- 2, the 10-minute charging (6C), 1-hour discharge (1C) cycle data for prototype 240 Wh/kg cell is shown compared to the project goals provided. Beyond 500 cycles the variance cell-to-cell does increase, but most cells achieve > 1,100 cycles before reaching end of life. These results, collected from automotive relevant 35 Ah pouch cells, showcase that > 1,000 10-minute fast charges is feasible for cells built with advanced components such as Microvast's designer cathode and high thermal stability separator technology.

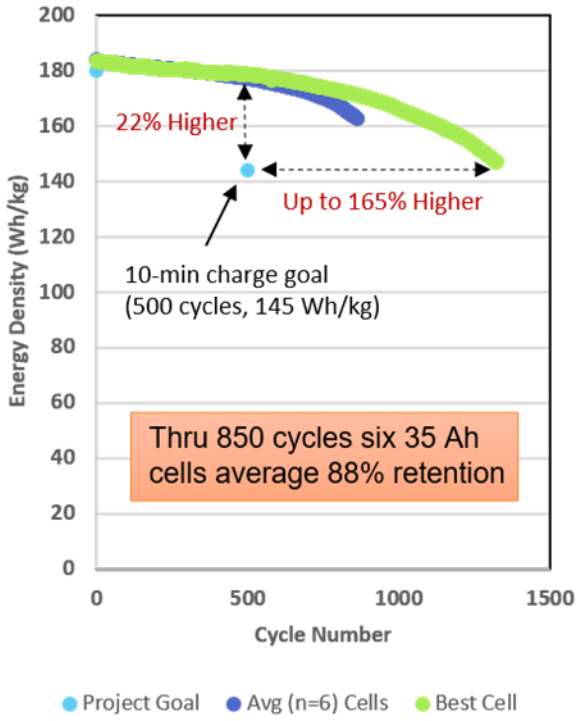

Figure ES- 2. The energy density versus cycle number of tested 10-minute charge / 1-hour discharge Li-ion cells. The project energy density goals, average for 6-duplicate cells and the best cell tested is shown.

Pushing the limit of rechargeable lithium metal batteries. The Battery500 Consortium pushes the frontier of advanced electrode and electrolyte materials and develops strategies to integrate materials science, electrochemistry, and cell engineering in high-energy rechargeable lithium metal batteries to achieve more than 400 stable cycles in prototype 350 Wh/kg pouch cells (2 Ah) (Figure ES- 3 a–b).

To decelerate the continuous side reactions in lithium metal batteries and the consumption rate of both lean electrolytes and thin lithium in realistic pouch cells, a localized concentrated electrolyte consisting of 1.54 M lithium bis(fluorosulfonyl)imide (LiFSI) in 1,2-dimethoxyethane (DME) and 1,1,2,2-tetrafluoroethyl-2,2,3,3-tetrafluoropropyl ether (TTE) has been developed to minimize the formation of "dead" lithium formed during each cycle and improve the efficiency of Li deposition/stripping. The properties of solid electrolyte interphase layers formed between the newly developed electrolyte and lithium metal are also improved, minimizing the amount of electrolyte irreversibly consumed during every cycle.

To accelerate mass transport, high mass-loading cathode architectures with controlled porosities are coupled with a modified lithium anode (Figure ES- 3c-d) to accelerate Li+ diffusion and reduce opportunities for spiky

microstructures of lithium to form during cycling. The synthesis conditions and electrochemical properties of high nickel manganese cobalt oxide cathodes are investigated to balance capacity and cycling stability.

A new, user-friendly software for designing lithium metal batteries has been developed to derive the key cell parameters needed to achieve the desired cell-level gravimetric and volumetric energy densities. Standard Battery500 coin cell testing protocols have been developed and implemented to compare and select the materials or approaches developed within the Consortium and from collaborators. Advanced in situ and ex situ characterization techniques—such as cryogenic electron microscopy and in situ X-ray diffraction—have been used by the Consortium to monitor and quantify the chemical and structural changes of electrodes, providing feedback on pouch-cell-level design.

New knowledge gathered from cell degradation mechanisms, as well as the combination of cell design, compatible interfaces, and uniform initial pressure applied on the cell, synergistically extends the stable cycling of 350 Wh/kg pouch cells with 80% capacity retention after 430 cycles.

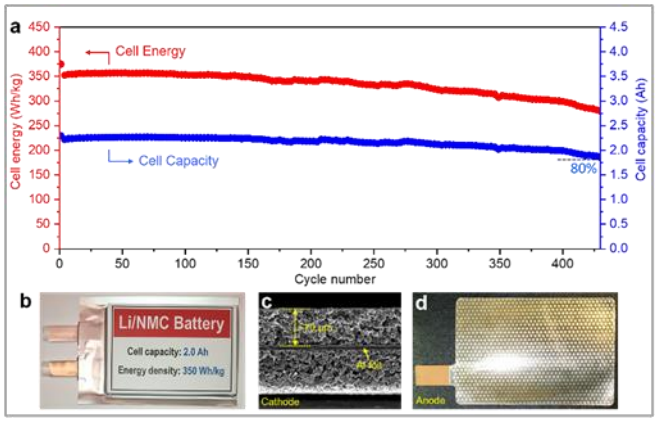

Figure ES- 3. 350 Wh/kg pouch cells achieve more than 400 cycles in research from the Battery500 Consortium. (a) Cell-level energy and capacity at different cycling. (b) Image of a 350 Wh/kg lithium metal pouch cell developed at PNNL. (c) Structure of a LiNi0.6Mn0.2Co0.2O2 cathode coated on both sides of aluminum current collector. (d) One of the lithium anodes incorporated in the pouch cell.

Scalable synthesis of high-performance single crystalline nickel-rich cathode materials for high-energy batteries. Ni-rich cathode is one of the most promising materials for next-generation, high-energy Li-ion batteries, but it suffers from moisture sensitivity, side reactions, and gas generation during cycling. A single crystalline, Ni-rich cathode may address the challenges present in its polycrystalline counterpart by reducing phase boundaries and materials surfaces; however, synthesis of electrochemically active Ni-rich single crystalline cathodes is challenging. Ni-rich cathodes require lower synthesis temperatures because of their structural instability at high temperatures, opposite to the high-temperature and time-consuming calcination process needed to grow single crystals.

Researchers at PNNL recently identified a cost-effective synthesis route to prepare high-performance single crystalline LiNi0.76Mn0.14Co0.1O2 (NMC76). Figure ES- 4 displays the cycling stability of NMC76 (Figure ES- 4 A–C) at different cutoff voltages. All material evaluations were conducted using high mass-loading (> 20 mg/cm2) single crystals in full coin cells with graphite as the anode, which is relevant for industry application. Between 2.7 and 4.2 V (vs. graphite), single crystalline NMC76 delivers 182.3 mAh/g discharge capacity at 0.1 C and retains 86.5% of its original capacity after 200 cycles (Figure ES- 4 A). Increasing the cutoff voltage improves the usable capacity, but cell degradation is faster (Figure ES- 4 B–C).

Figure ES- 4 D–F compares the corresponding morphologies of single crystals cycled at different cutoff voltages. If charged to 4.2V (Figure ES- 4 D), the entire single crystal is well maintained. Increasing the cutoff voltage to 4.3 V results in some visible gliding lines on the crystal surfaces (Figure ES- 4 E). When cut off at

4.4 V, single crystals are "sliced" (Figure ES- 4 F) in parallel. Small cracks were also discovered cycled between 2.7 and 4.4 V. Although single crystalline NMC76 as an entire particle is still intact (Figure ES- 4 D–F) even at high cutoff voltages, gliding is the major mechanical degradation mode. PNNL researchers have identified a critical crystal size of 3.5 μm, below which gliding and microcracking will not occur, providing clues to further improve single crystal performances in the future. This work has recently been published in Science (December 10, 2020).

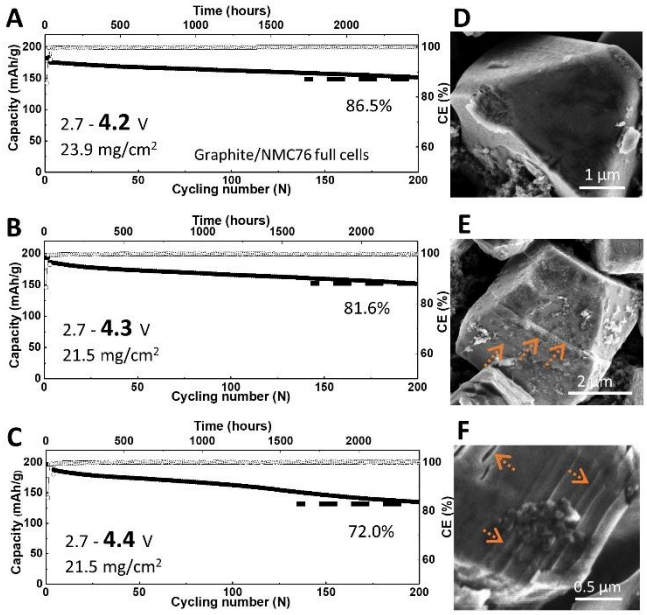

Figure ES- 4. Cycling stability of single crystalline NMC76 in full cells between 2.7 V and (A) 4.2 V, (B) 4.3 V, and (C) 4.4 V vs. graphite. (D), (E), and (F) are the corresponding Scanning Electron Microscope images of the cycled single crystals in (A), (B), and (C), respectively.

Collaborative Activities

In addition to the above, VTO has in place extensive and comprehensive ongoing coordination efforts in energy storage R&D across all of DOE and with other government agencies. It coordinates efforts on energy storage R&D with both the Office of Science and the Office of Electricity. Coordination and collaboration efforts also include program reviews and technical meetings sponsored by other government agencies and inviting participation of representatives from other government agencies to contract and program reviews of DOE-sponsored efforts. DOE coordinates such activities with the Army's Advanced Vehicle Power Technology Alliance, the Department of Transportation/National Highway Traffic Safety Administration (DOT/NHTSA), the Environmental Protection Agency (EPA), and the United Nations Working Group on Battery Shipment Requirements. Additional international collaboration occurs through the International Energy Agency's (IEA's) Hybrid Electric Vehicles Technology Collaboration Program (HEV TCP); and bilateral agreements between the U.S. and China. The *U.S. China Clean Energy Research Center* conducts collaborative research both on rechargeable lithium-ion and beyond lithium-ion battery technologies to help develop the next generation of advanced batteries to help expand electrification of vehicles and enable smart grids internationally and its main objective is to understand and develop advanced battery chemistries based on lithium-ion and beyond lithium ion that meet 300Wh/kg energy density.

Organization of this Report

This report covers all the FY 2020 projects as part of the advanced battery R&D (i.e., energy storage R&D) effort in VTO. We are pleased with the progress made during the year and look forward to continued

cooperation with our industrial, government, and scientific partners to overcome the remaining challenges to delivering advanced energy storage systems for vehicle applications.

David Howell,
VTO Deputy Director
Vehicle Technologies Office

Steven Boyd, Program Manager,
B&E Program
Vehicle Technologies Office

Tien Q. Duong, Vehicle
Technologies Office

Peter W. Faguy, Vehicle
Technologies Office

Brian Cunningham, Vehicle
Technologies Office

Samm Gillard, Vehicle
Technologies Office

Mallory Clites, Vehicle
Technologies Office

Haiyan Croft, Vehicle
Technologies Office

Simon Thompson, Vehicle
Technologies Office

Table of Contents

List of Figures

List of Tables

Vehicle Technologies Office Overview

Vehicles move our national economy. Annually, vehicles transport 11 billion tons of freight—about $35 billion worth of goods each day[3]—and move people more than 3 trillion vehicle-miles.[4] Growing our economy requires transportation, and transportation requires energy. The transportation sector accounts for about 30% of total U.S. energy needs[5] and the average U.S. household spends over 15% of its total family expenditures on transportation, making it the most expensive spending category after housing.[6]

The Vehicle Technologies Office (VTO) funds a broad portfolio of research, development, demonstration, and deployment (RDD&D) projects to develop affordable, efficient, and clean transportation options to tackle the climate crisis and accelerate the development and widespread use of a variety of innovative transportation technologies. The research pathways focus on electrification, fuel diversification, vehicle efficiency, energy storage, lightweight materials, and new mobility technologies to improve the overall energy efficiency and affordability of the transportation or mobility system. VTO leverages the unique capabilities and world-class expertise of the National Laboratory system to develop innovations in electrification, including advanced battery technologies; advanced combustion engines and fuels, including co-optimized systems; advanced materials for lighter-weight vehicle structures; and energy efficient mobility systems.

VTO is uniquely positioned to accelerate sustainable transportation technologies due to strategic public-private research partnerships with industry (e.g., U.S. DRIVE, 21st Century Truck Partnership) that leverage relevant expertise. These partnerships prevent duplication of effort, focus DOE research on critical RDD&D barriers, and accelerate progress. VTO focuses on research that supports DOE's goals of building a 100% clean energy economy, addressing climate change, and achieving net-zero emissions no later than 2050 to the benefit of all Americans.

Annual Progress Report

As shown in the organization chart (below), VTO is organized by technology area: Batteries & Electrification R&D, Materials Technology R&D, Advanced Engine & Fuel R&D, Energy Efficient Mobility Systems, and Technology Integration. Each year, VTO's technology areas prepare an Annual Progress Report (APR) that details progress and accomplishments during the fiscal year. VTO is pleased to submit this APR for Fiscal Year (FY) 2020. In this APR, each project active during FY 2020 describes work conducted in support of VTO's mission. Individual project descriptions in this APR detail funding, objectives, approach, results, and conclusions during FY 2020.

[3] Bureau of Transportation Statistics, Department of Transportation, Transportation Statistics Annual Report 2018, Table 4-1. https://www.bts.gov/tsar.
[4] Transportation Energy Data Book 37th Edition, Oak Ridge National Laboratory (ORNL), 2019. Table 3.8 Shares of Highway Vehicle-Miles Traveled by Vehicle Type, 1970-2017.
[5] Ibid. Table 2.1 U.S. Consumption of Total Energy by End-use Sector, 1950-2018.
[6] Ibid. Table 10.1 Average Annual Expenditures of Households by Income, 2016.

Organization Chart

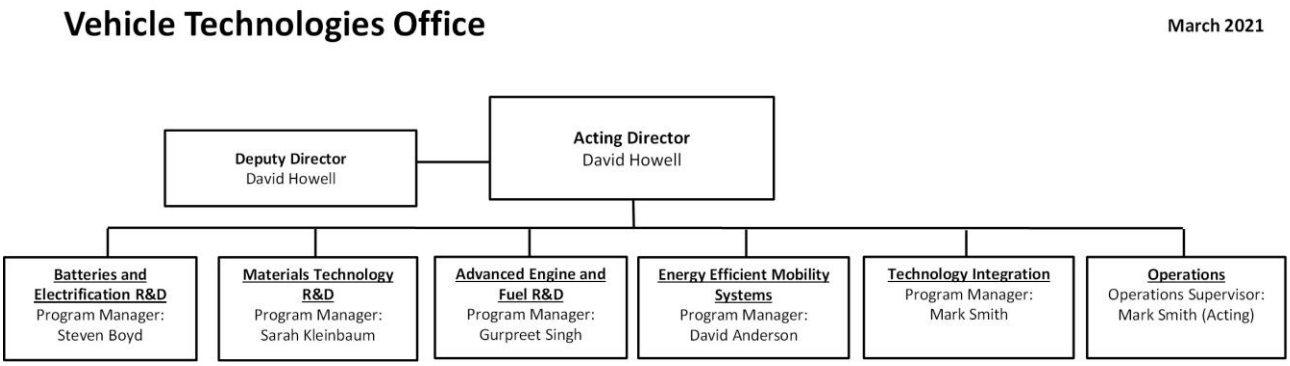

Batteries Program Overview

Introduction

During the fiscal year 2020 (FY 2020), the Vehicle Technologies Office (VTO) battery program continued research and development (R&D) support of technologies for plug-in electric vehicles (PEVs), e.g., plug-in hybrids, extended range electric vehicles, all-electric vehicles, and some hybrid electric vehicles (including 12 volt start/stop hybrid). One objective of this support is to enable U.S. innovators to rapidly develop next generation of technologies that achieve the cost, range, and charging infrastructure necessary for the widespread adoption of PEVs. Stakeholders involved in VTO R&D activities include universities, national laboratories, other government agencies and industry partners – including automakers, battery manufacturers, material suppliers, component developers, private research firms, and small businesses. VTO works with key U.S. automakers through the United States Council for Automotive Research (USCAR) – an umbrella organization for collaborative research consisting of Fiat Chrysler LLC, the Ford Motor Company, and the General Motors Company. Collaboration with automakers through the U.S. DRIVE (Driving Research and Innovation for Vehicle Efficiency and Energy Sustainability) partnership enhances the relevance and the success potential of the research platform. An important prerequisite for the electrification of the nation's light duty transportation sector is the development of more cost-effective, longer lasting, and more abuse-tolerant PEV batteries and accordingly, VTO battery R&D is focused on the development of high-energy batteries for PEVs and very high-power devices for hybrid vehicles.

Goals

The goals of this research are to address barriers to EVs reaching the full driving performance, convenience, and price of an internal combustion engine (ICE) vehicle. EVs have the advantage of a very high efficiency compared to other vehicle types, a simplified drive train, and a flexible primary energy source (i.e., the electricity needed to charge an EV can come from coal, natural gas, wind turbines, hydroelectric, solar energy, nuclear, or any other resource). Another current focus is the 12V start/stop (S/S) micro-hybrid architecture, in which the engine is shut down whenever a vehicle stops. Vehicles with the S/S functionality are being deployed worldwide. The 12V battery provides power for auxiliary equipment (e.g., the radio and air conditioning) and then restarts the engine when the vehicle moves. Current 12V S/S batteries, typically lead-acid batteries, have a poor life. Table 1 and Table 2 show a subset of the targets for high-performance EVs and 12V start/stop micro hybrid batteries that have been set by U.S. DRIVE[7], respectively.

Table 1: Subset of Requirements for Advanced High-Performance EV Batteries and Cells. (Cost and Low Temperature Performance are Critical Requirements).

Energy Storage Goals (by characteristic)	System Level	Cell Level
Cost @ 100k units/year (kWh = useable energy)	$125/kWh*	$100/kWh
Peak specific discharge power (30s)	470 W/kg	700 W/kg
Peak specific regen power (10s)	200 W/kg	300 W/kg
Useable specific energy (C/3)	235 Wh/kg*	350 Wh/kg
Calendar life	15 years	15 years
Deep discharge cycle life	1000 cycles	1000 cycles
Low temperature performance	>70% useable energy @C/3 discharge at -20°C	>70% useable energy @C/3 discharge at -20°C

[7] https://www.uscar.org/guest/article_view.php?articles_id=85

Table 2: Subset of Targets for 12V Start/Stop Micro-hybrid Batteries
(Cost and Cold Cranking are Critical Requirements)

Energy Storage Goals (by characteristic)	Under the hood	Not under the hood
Maximum selling price (@220k units/year)	$220*	$180*
Discharge pulse (1s)	6 kW	
Cold cranking power, (-30°C)	6 kW for 0.5s followed by three 4 kW/4s pulses*	
Available energy (750W acc.)	360 Wh	
Peak recharge rate (10s)	2.2 kW	
Sustained recharge rate	750 W	
Cycle life	450 k	
Calendar life	15 years at 45°C*	15 years at 30°C**
Maximum weight	10 kg	
Maximum volume	7 liters	
	*Current commercial cells do not meet this goal **Current cells almost meet this goal	

State of the Art

Battery R&D attempts to advance battery technology to help improve the market penetration of PEVs and hybrid vehicles by overcoming the current barriers. To accomplish this, it focuses on: (1) a significantly reduced battery cost, (2) increased battery performance, e.g., extreme fast charge (XFC) and low temperature performance for enhanced lithium-ion, (3) improved life advanced chemistry cells, (4) increased tolerance to abusive conditions; and (5) more cost-effective recycling and sustainability.

The current status of the broad battery chemistry types (current lithium-ion, next gen, and BLI) is summarized in Figure 1. Battery R&D spans mainly three areas:

- **Current technology (enhanced lithium-ion):** including cells with current materials (graphite anode/transition metal oxide cathode) and features like XFC compatibility, low temperature performance and improved abuse tolerance.
- **Next-gen lithium-ion:** Cells containing an alloy anode, usually silicon-based, and/or a high voltage (>4.5 V) cathode.
- **Beyond lithium-ion (BLI):** Cells containing Li metal anodes.

Over the past ten years, PEVs have become more commercially viable, with battery costs dropping over 80% since 2010. Further cost reductions in high-energy batteries for PEVs are always desirable. In addition, although today's batteries approach very attractive cost numbers, they still need the ability to accept extreme fast charging (XFC) and to perform better in low-temperature operations to compete with ICEs in all-weather performance and "refueling" convenience. Research into "enhanced lithium-ion" batteries (which would providing these functionalities) is one of the R&D focus areas. For further gains in energy density and cost reduction, research is needed in both "next gen" chemistries (which employ an alloy anode and/or a high voltage cathode) and BLI chemistries (see Figure 1). Cycle and calendar lives of next-gen and BLI chemistries fall well short of EV goals. Most cells employing a significant amount of silicon provide around 1,000 deep-discharge cycles but with less than two years of calendar life; BLI cells typically provide much less of a cycle life (250 cycles or less). In addition, the requisite low temperature performance and extreme fast charge capability are lacking in all chemistries.

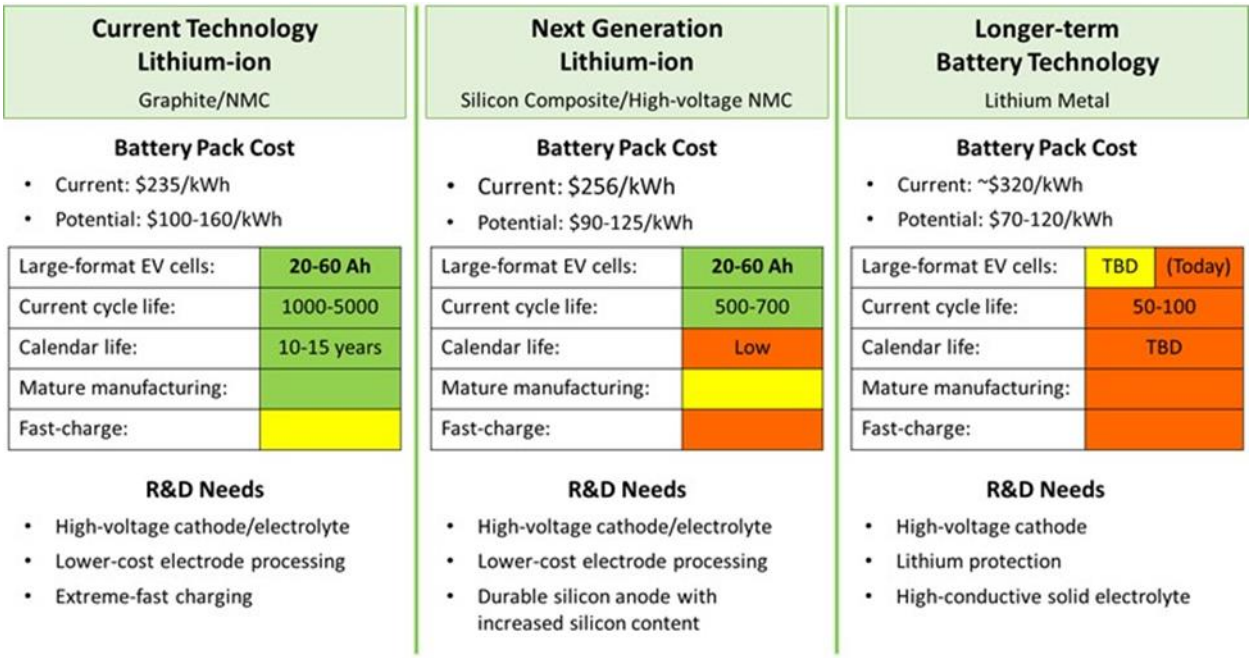

Figure 1. Chemistry classes, status, and R&D needs

An overview of the candidate battery technologies and their likely ability to meet the DOE cost goals are shown in Figure 2. Because of the large variation in different battery technologies, battery research also includes multiple activities focused to address remaining high cost areas within the entire battery supply chain.

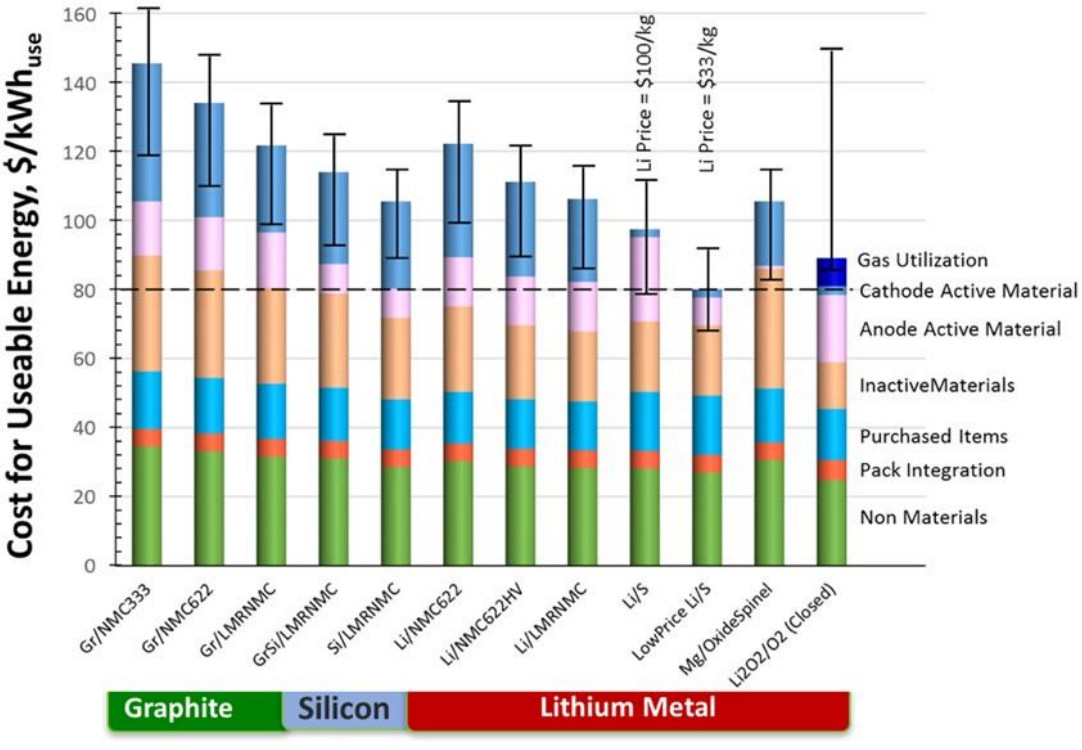

Figure 2. Potential for Future Battery Technology Cost Reductions

Battery Technology Barriers

The major remaining challenges to commercializing batteries for EVs (as well as 12V start-stop micro-hybrid batteries) are as follows:

A. Cost. The current cost of high-energy lithium-ion batteries is approximately $150 – $200/kWh (on usable energy basis), a factor of two-three times too high from where it needs to be. The cost of lithium-ion-based 12V micro-hybrid batteries (which offer significantly better life and higher capacity than conventional lead acid batteries) is approximately 50% too high compared to lead acid. The main cost drivers are the high cost of raw materials, costs associated with materials processing, the cell and module packaging, and manufacturing.

B. Performance. Historically, a higher energy density was needed to reduce the weight and volume of PEV batteries, but those weight and volume issues have been to a large degree been addressed. The use of higher energy materials is still an effective way to reduce costs further and extend driving range, but cell chemistries that provide higher energy have life and performance issues. Also, existing chemistries (e.g., graphite anodes paired with transition metal oxide cathodes) need improvement in XFC and low temperature performance to compete favorably with gas-powered vehicles in the areas of performance and customer convenience. The main performance issue with lithium-ion 12V start/stop batteries is a challenging "cold start" requirement at -30°C coupled with high or room temperature life.

C. Life. The life issue for mature lithium-ion technologies has mainly been mostly addressed. However, both next-gen and BLI cell technologies still suffer major cycle and calendar life issues. The life of lithium-ion-based 12V start/stop micro-hybrid batteries is relatively good at room temperatures. However, enhancing cold crank performance often shortens battery life at the high temperatures found in the under the hood application.

D. Abuse Tolerance. Many lithium-ion batteries are not intrinsically tolerant to abusive conditions; however, full packs have been engineered by automotive OEMs to mitigate much of the risk. The reactivity of high nickel cathodes and flammability of current lithium-ion electrolytes are areas for possible improvement. The characteristics of next-gen and BLI chemistries to abusive conditions are not well-understood. However, silicon anode cells show very high temperatures during thermal runaway and lithium metal-based batteries have a long history of problematic dendrite growth which can lead to internal shorts and thermal runaway. Thus, research into enhanced abuse tolerance strategies will continue.

E. Recycling and Sustainability. Currently, automotive OEMs pay a relatively large cost (5%–15% of the battery cost) to recycle end of life PEV batteries. The various chemistries used in lithium-ion cells results in variable backend value. Alternatively, unless they get recycled, lithium-ion batteries could lead to a shortage of key materials (lithium, cobalt, and nickel) vital to the technology. Finding ways to decrease the cost of recycling could thus significantly reduce the life cycle cost of PEV batteries, avoid material shortages, lessen the environmental impact of new material production, and potentially provide low-cost active materials for new PEV battery manufacturing.

Program Organization Matrix

VTO's energy storage effort includes multiple activities, ranging from focused fundamental materials research to prototype battery cell development and testing. The R&D activities can involve either shorter-term pre-competitive research by commercial developers or exploratory materials research generally spearheaded by national laboratories and universities. The program elements are organized as shown in Figure 3. Battery R&D activities are organized into the following program elements: Advanced Batteries and Cells R&D, Battery Materials R&D, and the current focus.

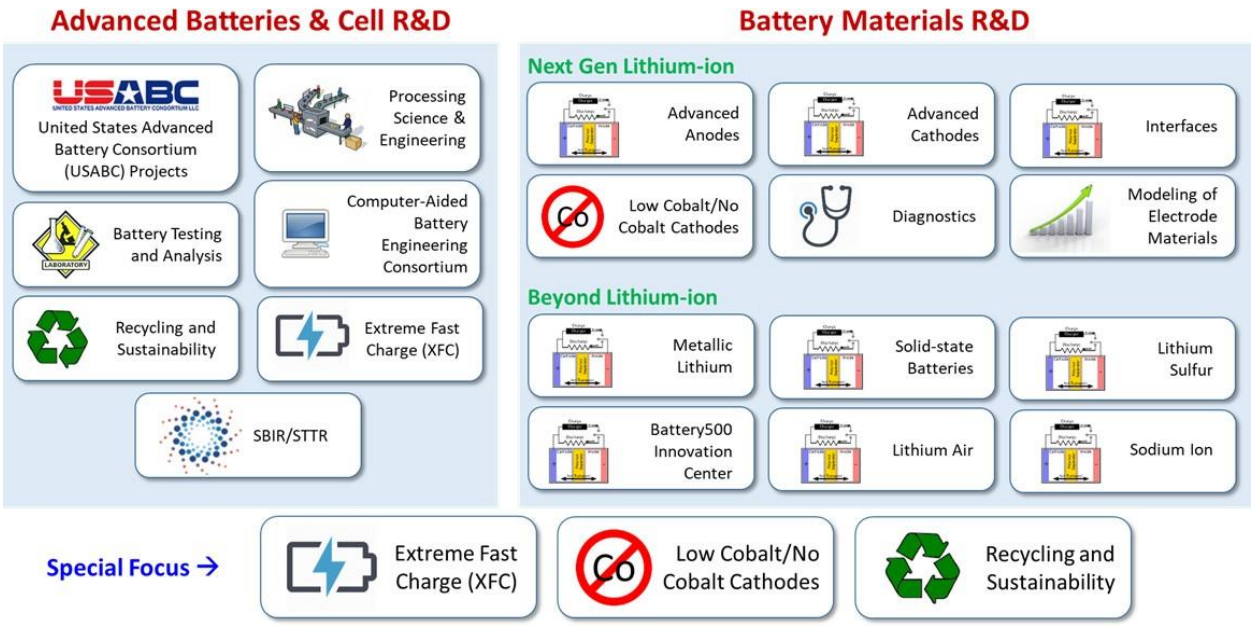

Figure 3. Battery R&D Program Structure

Advanced Cell and Battery Research and Development activity. This activity focuses on the development of robust battery cells and modules to significantly reduce battery cost, increase life, and improve performance. In this report, Part of this effort takes place in close partnership with the automotive industry, through a cooperative agreement with the *United States Advanced Battery Consortium* (USABC). In FY 2020, the USABC supported five cost-shared contracts with developers to further the development of batteries and battery components for PEVs and HEVs. In addition to the USABC projects, DOE supports battery and material suppliers via contracts administered by the National Energy Technology Laboratory (NETL). Other projects in this area include performance, life and abuse testing of contract deliverables, laboratory- and university-developed cells, and benchmarking new technologies from industry; thermal analysis, thermal testing and modeling; cost modeling; secondary usage and life studies; and recycling studies for core materials. The *processing science & engineering* activity supports the development and scale-up of manufacturing technologies needed to enable market entry of next-generation battery materials and cell components – emphasizing disruptive materials and electrode production technologies that could significantly reduce cost and environmental impact while increasing yield and process control relative to existing production technologies. Several *small business innovation research* (SBIR) projects, also supported by VTO, are focused on the development of new battery materials/components and are the source of new ideas and concepts and are covered in that chapter.

Advanced Materials Research activity. This activity addresses fundamental issues of materials and electrochemical interactions associated with rechargeable automotive batteries. It develops new/promising materials and uses advanced material models to discover them and their failure modes, as well as scientific diagnostic tools and techniques to gain insight into why they fail. This work is carried out by researchers at national labs, at universities, and at commercial facilities. It includes the *next generation lithium-ion* research activity focused on the optimization of next generation, high-energy lithium-ion electro-chemistries that incorporate new battery materials. It emphasizes identifying, diagnosing, and mitigating issues that impact the performance and lifetime of cells constituted of advanced materials. Research continues in the six areas of advanced anodes, advanced cathodes, advanced electrolytes, electrode issues, interfaces, diagnostics, and modeling. The *beyond lithium-ion* (BLI) Technology activity addresses fundamental issues associated with lithium batteries, develops new/promising materials and uses advanced material models to discover such materials using scientific diagnostic tools/techniques. It includes solid-state battery technologies, lithium

metal, lithium sulfur, lithium air, and sodium-ion systems. The newly-started VTO *Battery500* projects are also managed in conjunction with this program element.

Special Focus. The current focus targets three areas of battery research. The first area is concerned with enabling *extreme fast charging* (XFC) in enhanced lithium-ion systems. In the second area, recognizing the issues of price volatility and supply reliability with cobalt DOE recently started new projects to develop and optimize low cobalt cathode materials. The third area consists of a set of *recycling and sustainability* projects, which involve studies of full life-cycle impacts and costs of battery production and use; cost assessments and impacts of various battery recycling technologies; and the material availability for recycling and secondary usage and their cost impacts.

As a further resource, the Electrochemical Energy Storage Roadmap describes ongoing and planned efforts to develop battery technologies for PEVs and can be found at the EERE Roadmap page http://energy.gov/eere/vehicles/downloads/us-drive-electrochemical-energy-storage-technical-team-roadmap. VTO also has extensive ongoing *collaboration* efforts in batteries R&D across the DOE and with other government agencies. It coordinates efforts on energy storage with the DOE Office of Science, and the DOE Office of Electricity. Coordination and collaboration efforts include membership and participation in program reviews and technical meetings by other government agencies, and the participation of representatives from other government agencies in the contract and program reviews of DOE-sponsored efforts. DOE also coordinates with the Department of Army's Advanced Vehicle Power Technology Alliance, the Department of Transportation/National Highway Traffic Safety Administration (DOT/NHTSA), the Environmental Protection Agency (EPA), and the United Nations Working Group on Battery Shipment Requirements. Additional international collaboration occurs through a variety of programs and initiatives. These include: the International Energy Agency's (IEA's) Hybrid Electric Vehicles Technology Collaboration Program (HEV TCP); the G8 Energy Ministerial's Electric Vehicle Initiative (EVI); and bilateral agreements between the U.S. and China.

Battery Highlights from FY 2020

The following are some of the highlights associated with battery R&D funded by VTO (including highlights related to market developments, R&D breakthroughs, and commercial applications).

Developed Li-Ion Cell Brings 10-Minute Fast Charging Closer to Reality for Electric Vehicles. The convenience of quickly refilling a car is a major advantage that still exists for gasoline vehicles compared to fully electric alternatives. While fast charging EVs presents challenges to electricity grids and charging stations, perhaps the most difficult hurdles to overcome are from the Li-ion battery cell itself. During fast charge the high currents typically cause higher temperatures and uneven chemical reaction rates within the cells. These operating conditions in turn lead to faster cell degradation. Especially unfortunate, these degradations typically become more intense as the Li-ion cells energy density is increased.

One of the most straightforward ways to change a Li-ion cells performance and energy density is by using different materials. Cell component material properties differ based on composition and physical attributes, which in turn influences the cells performance. The cathode, the most expense cell component, is especially important to improve. Higher capacity cathodes lead to more energy density, while improved properties slow cell degradation and resistance increases. Using the full concentration gradient (FCG) cathode technology that Microvast is developing for commercialization cathodes with tailored surfaces, more stable to fast charge effects, were prepared. The FCG technology allows scientists and process engineers to change the atomic composition of metals throughout the cathode particle, allowing more desirable metal oxide combinations to be targeted at locations most vulnerable to degradation. Also, as the nickel content of the prepared FCG was increased the prototype cells C/3 energy density could be improved.

Initially a 200 Wh/kg cell was the highest energy density cell made by Microvast that could achieve the 500 10-minute charging goals. Steadily that number has improved as the cathode was developed, eventually

reaching 240 Wh/kg as the base (0.33C) energy density, a 20% improvement. In Figure 4 the 10-minute charging (6C), 1-hour discharge (1C) cycle data for prototype 240 Wh/kg cell is shown compared to the project goals provided. Beyond 500 cycles the variance cell-to-cell does increase, but most cells achieve > 1,100 cycles before reaching end of life. These results, collected from automotive relevant 35 Ah pouch cells, showcase that > 1,000 10-minute fast charges is feasible for cells built with advanced components such as Microvast's designer cathode and high thermal stability separator technology.

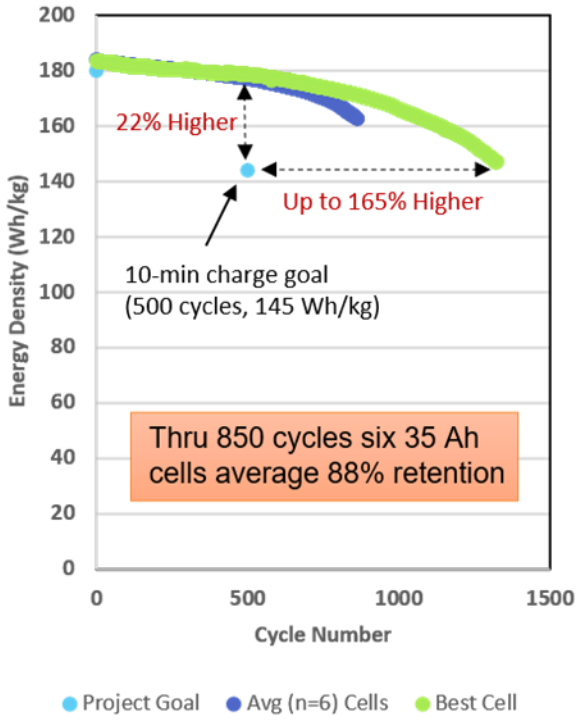

Figure 4. The energy density versus cycle number of tested 10-minute charge / 1-hour discharge Li-ion cells. The project energy density goals, average for 6-duplicate cells and the best cell tested is shown.

Pushing the limit of rechargeable lithium metal batteries. The Battery500 Consortium pushes the frontier of advanced electrode and electrolyte materials and develops strategies to integrate materials science, electrochemistry, and cell engineering in high-energy rechargeable lithium metal batteries to achieve more than 400 stable cycles in prototype 350 Wh/kg pouch cells (2 Ah) (Figure 5a–b).

To decelerate the continuous side reactions in lithium metal batteries and the consumption rate of both lean electrolytes and thin lithium in realistic pouch cells, a localized concentrated electrolyte consisting of 1.54 M lithium bis(fluorosulfonyl)imide (LiFSI) in 1,2-dimethoxyethane (DME) and 1,1,2,2-tetrafluoroethyl-2,2,3,3-tetrafluoropropyl ether (TTE) has been developed to minimize the formation of "dead" lithium formed during each cycle and improve the efficiency of Li deposition/stripping. The properties of solid electrolyte interphase layers formed between the newly developed electrolyte and lithium metal are also improved, minimizing the amount of electrolyte irreversibly consumed during every cycle.

To accelerate mass transport, high mass-loading cathode architectures with controlled porosities are coupled with a modified lithium anode (Figure 5c-d) to accelerate Li+ diffusion and reduce opportunities for spiky microstructures of lithium to form during cycling. The synthesis conditions and electrochemical properties of high nickel manganese cobalt oxide cathodes are investigated to balance capacity and cycling stability.

A new, user-friendly software for designing lithium metal batteries has been developed to derive the key cell parameters needed to achieve the desired cell-level gravimetric and volumetric energy densities. Standard

Battery500 coin cell testing protocols have been developed and implemented to compare and select the materials or approaches developed within the Consortium and from collaborators. Advanced in situ and ex situ characterization techniques—such as cryogenic electron microscopy and in situ X-ray diffraction—have been used by the Consortium to monitor and quantify the chemical and structural changes of electrodes, providing feedback on pouch-cell-level design.

New knowledge gathered from cell degradation mechanisms, as well as the combination of cell design, compatible interfaces, and uniform initial pressure applied on the cell, synergistically extends the stable cycling of 350 Wh/kg pouch cells with 80% capacity retention after 430 cycles.

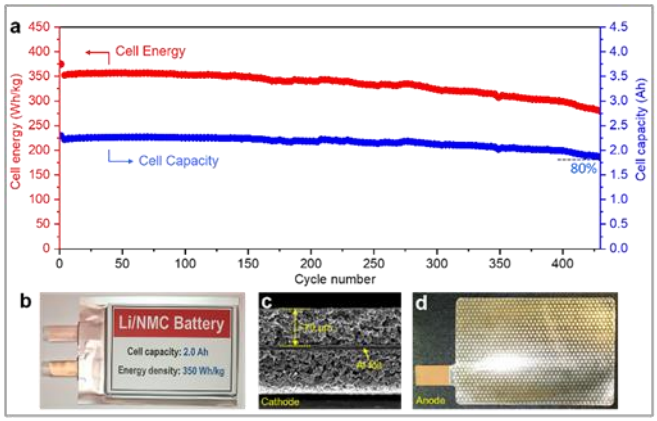

Figure 5. 350 Wh/kg pouch cells achieve more than 400 cycles in research from the Battery500 Consortium. (a) Cell-level energy and capacity at different cycling. (b) Image of a 350 Wh/kg lithium metal pouch cell developed at PNNL. (c) Structure of a LiNi0.6Mn0.2Co0.202 cathode coated on both sides of aluminum current collector. (d) One of the lithium anodes incorporated in the pouch cell.

Scalable synthesis of high-performance single crystalline nickel-rich cathode materials for high-energy batteries. Ni-rich cathode is one of the most promising materials for next-generation, high-energy Li-ion batteries, but it suffers from moisture sensitivity, side reactions, and gas generation during cycling. A single crystalline, Ni-rich cathode may address the challenges present in its polycrystalline counterpart by reducing phase boundaries and materials surfaces; however, synthesis of electrochemically active Ni-rich single crystalline cathodes is challenging. Ni-rich cathodes require lower synthesis temperatures because of their structural instability at high temperatures, opposite to the high-temperature and time-consuming calcination process needed to grow single crystals.

Researchers at PNNL recently identified a cost-effective synthesis route to prepare high-performance single crystalline $LiNi_{0.76}Mn_{0.14}Co_{0.1}O_2$ (NMC76). Figure 6 displays the cycling stability of NMC76 (Figure 6A–C) at different cutoff voltages. All material evaluations were conducted using high mass-loading (> 20 mg/cm2) single crystals in full coin cells with graphite as the anode, which is relevant for industry application. Between 2.7 and 4.2 V (vs. graphite), single crystalline NMC76 delivers 182.3 mAh/g discharge capacity at 0.1 C and retains 86.5% of its original capacity after 200 cycles (Figure 6A). Increasing the cutoff voltage improves the usable capacity, but cell degradation is faster (Figure 6B–C).

Figure 6D–F compares the corresponding morphologies of single crystals cycled at different cutoff voltages. If charged to 4.2V (Fig. 1D), the entire single crystal is well maintained. Increasing the cutoff voltage to 4.3 V results in some visible gliding lines on the crystal surfaces (Figure 6 E). When cut off at 4.4 V, single crystals are “sliced” (Fig. 1F) in parallel. Small cracks were also discovered cycled between 2.7 and 4.4 V. Although single crystalline NMC76 as an entire particle is still intact (Figure 6 D–F) even at high cutoff voltages, gliding is the major mechanical degradation mode. PNNL researchers have identified a critical crystal size of 3.5 □m, below which gliding and microcracking will not occur, providing clues to further improve single crystal performances in the future. This work has recently been published in Science (December 2020).

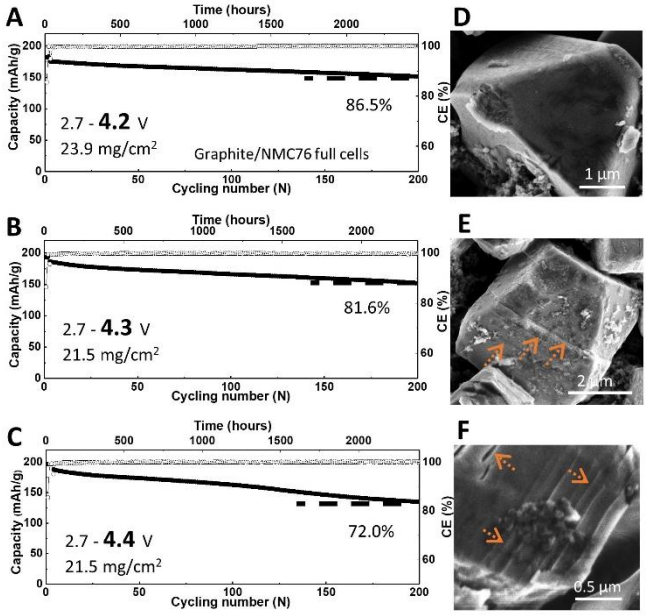

Figure 6. Cycling stability of single crystalline NMC76 in full cells between 2.7 V and (A) 4.2 V, (B) 4.3 V, and (C) 4.4 V vs. graphite. (D), (E), and (F) are the corresponding Scanning Electron Microscope images of the cycled single crystals in (A), (B), and (C), respectively.

High-Energy Cobalt-free Cathodes Enabled by Three-Dimensional Targeted Doping. Although there have been numerous efforts to develop alternative cathode materials, layered lithium transition metal (TM) oxides based on the structure of $LiTMO_2$, such as lithium nickel (Ni)-manganese (Mn)-cobalt (Co) oxide (NMC), remain the majority of cathode materials in commercialized lithium (Li)-ion batteries. As the cell chemistry of NMC811 has reached initial market penetration, a grand challenge for the field is a quest for Co-free layered cathodes to reduce the reliance on high-cost and toxic Co. However, it is well known that $LiNiO_2$ (LNO) has high capacity but is thermally unstable at charged state and has poor cycle life. To enhance its performance requires structure-stabilizing elements such as Co. Even though the instability of LNO seems to render its use in a commercial cathode bleak, it shares many of the problems of currently employed NMCs that have potential to be resolved using specialized dopants or electrolytes to target the instability of the cathode/electrolyte interfaces.

The Low/No-cobalt project led by the University of California—Irvine with team members from Virginia Tech, UC Berkeley, Pacific Northwest National Lab have developed a three-dimensional targeted doping technology that can hierarchically combines surface and bulk doping with nanometer precision. The team use computation-selected surface dopants and accurately deliver them to the surface of primary particles. They further introduce theory-rationalized bulk dopants to the interior of the particles to further enhance oxygen stability and inhibit the H2-H3 phase transition in Co-free oxides under high-voltage and deep-discharging operating conditions.

As shown in Figure 7b, the team has enabled 3D targeted doping on the surfaces of the cathode particle with nanometer precisions. In the meantime, the layered atomic structures are preserved without nearly no secondary phase on the surfaces. More importantly, the surface/bulk Ti/Mg doping significantly improve the cycling performance of the Co-free and extremely high-Ni chemistry ($LiNi_{0.96}Ti_{0.02}Mg_{0.02}O_2$) reaching a cycle life of 400 cycles (2.5 – 4.4 V vs. Li).

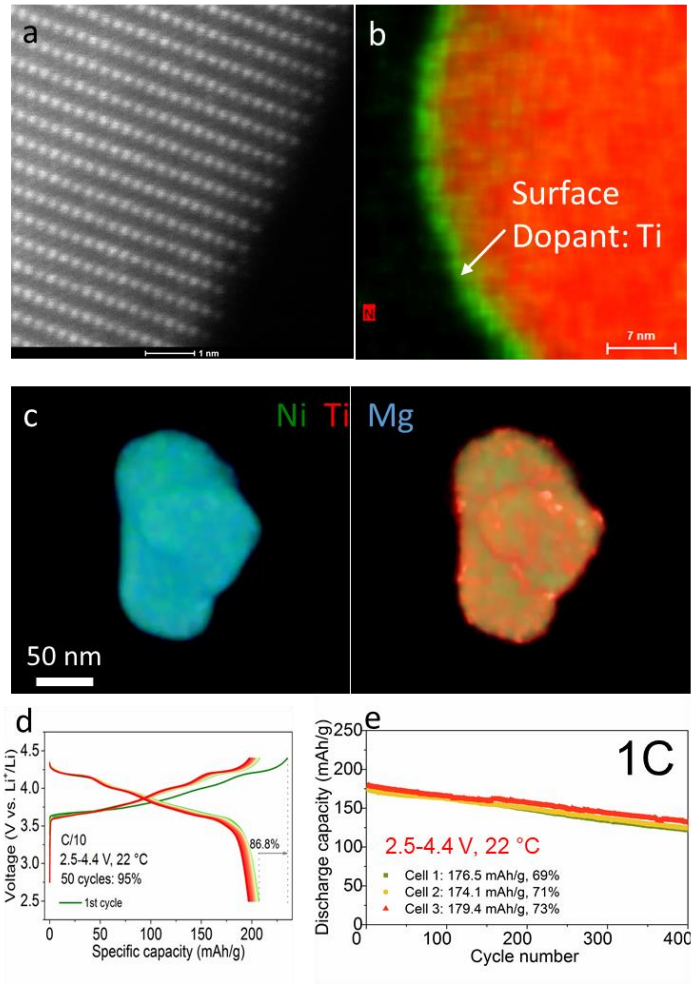

Figure 7. (a-b) Structure and chemical imaging of the Co-free cathode particles. (c) 3D nano-electron-tomography imaging of the dopant distribution. (d-e) The electrochemical performance of the Co-free cathode materials.

Laser-Patterned Electrodes for Enhanced Fast Charge Capability. Enabling lithium-ion batteries with high energy densities and fast-charging capability would accelerate public acceptance of electric vehicles. However, in order to achieve high energy densities, thick electrodes are often used, which hinder the ability to fast-charge. This leads to a tradeoff between power and energy density.

Researchers at the University of Michigan have developed a laser patterning process to precisely manufacture pore channels into graphite anodes. This process results in a highly ordered laser-patterned electrode (HOLE) architecture consisting of arrays of vertical channels through the electrode thickness, as shown in Figure 8. The pore channels facilitate rapid transport of Li-ions into the bulk electrode. As a result of the improved transport, the concentration of Li-ions throughout the electrode volume is more homogeneous, leading to a higher accessible capacity and lower propensity for irreversible lithium plating during fast charging.

The HOLE design was applied on industrially relevant cells (>2 Ah pouch cells) and electrode conditions (>3 mAh/cm^2 graphite anodes), and demonstrated significantly improved capacity retention during fast-charge cycling, compared to conventional electrodes. After 600 fast-charge cycles, the capacity retention of the HOLE cells is 91% at 4C (15-min) and 86% at 6C (10-min) charge rates, as shown in Figure 9. Moreover, the HOLE design allows for cells to access >90% of the total cell capacity during fast charging. The presented performances address both the United States Department of Energy and Advanced Battery Consortium goals

for fast-charging batteries. The improved charging performance has been further validated by Sandia National Laboratories.

The laser patterning approach is compatible with current lithium-ion battery manufacturing. The Michigan team is currently working toward scale-up and integration of their HOLE technology into roll-to-roll manufacturing lines. The HOLE architecture can enable electric-vehicle-scale batteries that can maintain long range, while simultaneously reducing charging time.

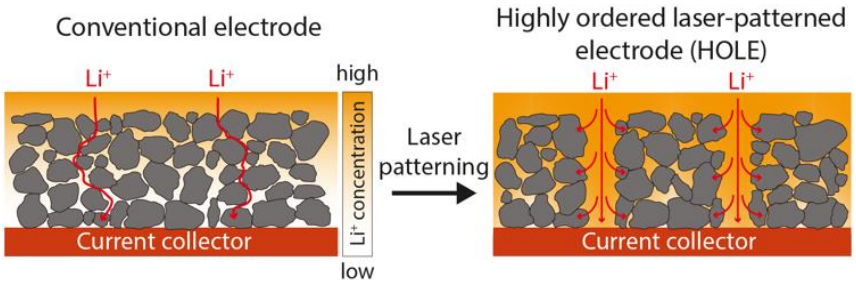

Figure 8. Schematic illustration of the conventional electrode and highly ordered laser-patterned electrode (HOLE) design.

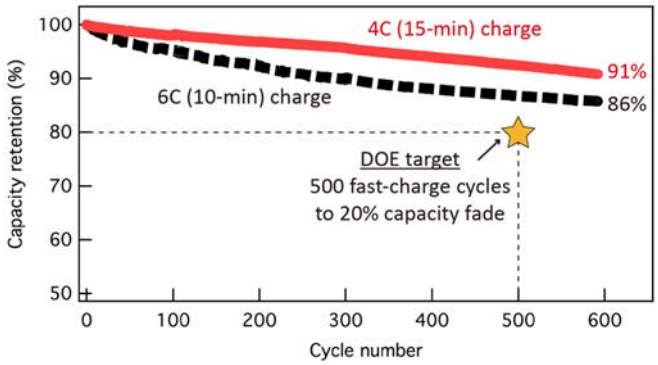

Figure 9. Capacity retention of 2.2 Ah HOLE pouch cells during long-term fast-charge cycling at 4C (15-min) and 6C (10-min) charge rates. The DOE target is labeled in the figure as a reference. Figures reproduced with permission from K.-H. Chen et al., Journal of Power Sources 471, 228475 (2020).

All Solid State Batteries Enabled by Multifunctional Electrolyte Materials. Solid Power is teaming with UCSD to develop a high energy, long life, low cost, and safe ASSB, enabled by a multifunctional solid state electrolyte (SSE). The project is enabling a scalable production of large format solid state batteries required by the vehicle market. The large-format ASSBs will ultimately be able to deliver ≥ 350 Wh/kg specific energy, ≥ 1000 cycle life, and ≤ $100/kWh cost.

The multifunctional SSE materials have been developed and met the Year 1 performance targets on both Li ion conductivity and critical current density (CCD) against Li metal as in the Table 3 below.

Table 3: Li ion conductivity and critical current density (CCD) against Li metal

Parameters	Year 1 Target	Year 1 Status
Li Ion Conductivity (mS/cm)	≥ 3.0	≥ 4.5
CCD (mA/cm2)	≥ 6.0	≥ 6.0

SSE separator coating process has been developed at pilot scale. A separator slurry was prepared by mixing the SSE powder, a binder, and a solvent by using an industrial mixer. The slurry was then cast on a carrier film or an electrode by using a pilot scale slot-die coater. Figure 10 shows the "roll-to-roll" coated separator film and the flexibility of a free-standing film.

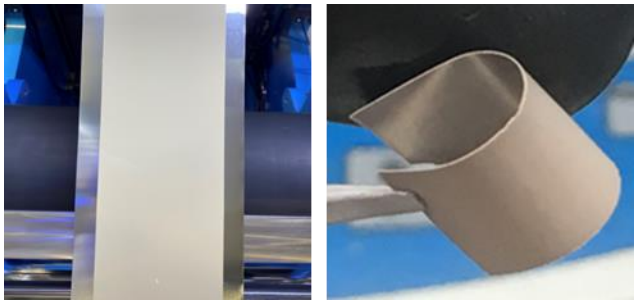

Figure 10. (left) a separator film coated by a slot-die coater; (right) flexibility of the separator

A single layer pouch cell was assembled for performance demonstration in Year 1. The pouch cell contained a NMC 622 composite cathode (at 3 mAh/cm^2), a stand-alone Li metal anode, and the multifunctional SSE separator. The cell is designed to deliver a specific energy of 300 Wh/kg if scaled to 20 Ah. When tested at C/5 - C/5, 2.8 - 4.2V, and 70°C, the cell demonstrates > 300 stable cycles as shown in Figure 11.

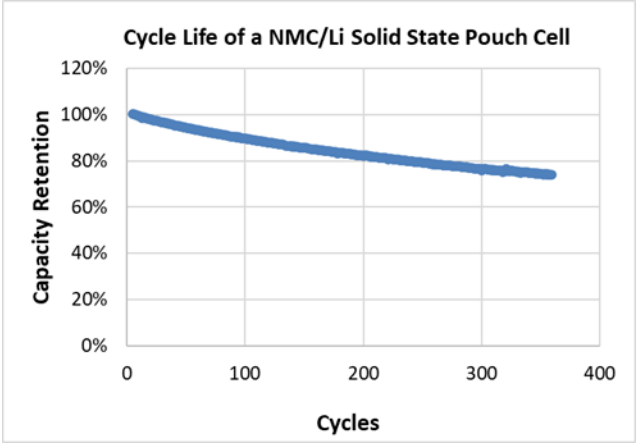

Figure 11. Cycle life of an NMC/Li metal solid state pouch cell with the multifunctional SSE

In summary, multifunctional SSE materials have been developed with high conductivity and stability. SSE separator films have been coated by using a roll-to-roll process. A solid state NMC-Li pouch cell containing the developed SSE has been assembled and tested. The cell cycle life of > 300 at 100% DOD has been demonstrated in Year 1.

A New Electrolyte Solvent Molecule Enables Realistic Lithium Metal Batteries. Lithium (Li) metal battery is highlighted as the next-generation battery yet still restrained by the poorly performing electrolytes. Conventional electrolytes fall short when confronted with Li metal anodes, let alone anode-free batteries. Previous electrolyte engineering reports improved the cycling efficiency of Li metal anodes, but fail to simultaneously address the following key parameters for enabling practical Li metal batteries: (1) high Coulombic efficiency (CE) across all cycles to minimize Li loss, including in the initial cycles; (2) practicality under lean electrolyte and limited-excess Li conditions for maximized specific energy; (3) high oxidative stability towards high-voltage cathodes; (4) reasonable salt concentration for cost-effectiveness; (5) high boiling point and non-flammability for safety and processability.

Zhenan Bao and Yi Cui at Stanford University and SLAC National Accelerator Laboratory report a new electrolyte that meets all above requirements (Nature Energy, 5, 526-533, 2020). Specifically, for the first time we synthesize fluorinated 1,4-dimethoxybutane (FDMB, Figure 12a), and pair it with 1 M lithium bis(fluorosulfonyl)imide (LiFSI) in a single-salt, single-solvent electrolyte formulation (LiFSI/FDMB) to enable stable, high energy-density Li metal batteries. The 1 M LiFSI/FDMB electrolyte reveals a high CE (~99.52%) and fast activation (Li|Cu half-cell CE ramps up to >99% within 5 cycles) for Li-metal anodes. The Li|NMC full cells with limited-excess Li retain 90% capacity after 420 cycles with an average CE of 99.98% (Figure 12b). Furthermore, anode-free Cu|NMC811 pouch cells achieve ~325 Wh kg-1 whole-cell energy density, while Cu|NMC532 pouch cells realize ~80% capacity retention after 100 cycles, which is one of the best performance among the state-of-the-art anode-free cells (Figure 12c). The 1 M LiFSI/FDMB electrolyte also enables fast discharge capability in anode-free pouch cells, which magnifies its potential application in the field of drones and wireless devices (Figure 12d). Our rational design concept for new electrolyte solvents provides a promising path to high-energy, practical Li metal batteries and anode-free pouch cells with high cyclability and processability.

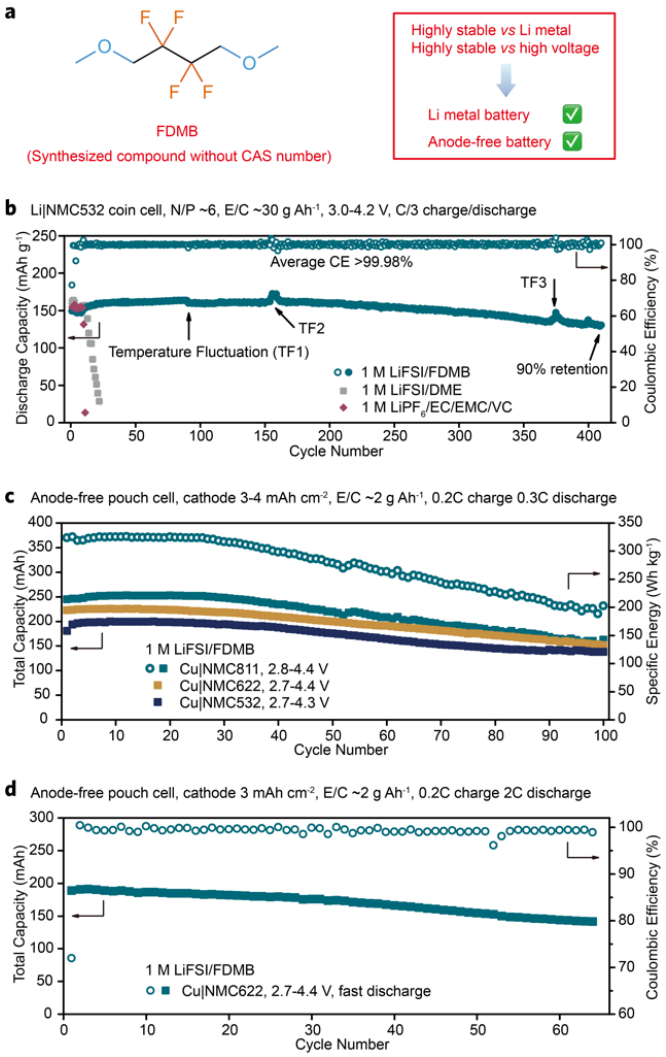

Figure 12. (a) Molecular structure of FDMB; (b-d) Cycling performance of practical Li metal batteries and industrial anode-free pouch cells.

Metal Coated Graphite Anodes Improve Capacity Retention Under Extreme Fast Charging Conditions. The development of lithium ion (Li-ion) batteries that can be charged in 10 – 15 minutes without sacrificing

driving range, cost, or cycle life is critical for the increased adoption of electric vehicles by consumers. The primary technical barrier preventing repetitive extreme fast charging (XFC) of Li-ion batteries is deposition of electrochemically isolated lithium metal on the graphite anode resulting in capacity degradation. Researchers at Stony Brook University (SBU) and Brookhaven National Laboratory (BNL) have recently invented a new approach for suppressing lithium metal deposition on the graphite anode under XFC conditions. They deliberately modify the anodes with metallic nanoscale surface films with high overpotentials unfavorable for Li metal nucleation (Figure 13). In a recently published paper (https://dx.doi.org/10.1149/1945-7111/abcaba) the effectiveness of metallic surface coatings with different areal loadings at reducing capacity fade under XFC was explored. Batteries incorporating graphite electrodes with high metal film loadings exhibited an improvement in capacity retention after 500 fast (10-minute) charge cycles of ~9% compared to uncoated anodes (Figure 14). Li metal deposition quantified by X-ray diffraction supported these findings, with higher loading metal films exhibiting enhanced Li plating suppression compared to lower loading films. Transmission electron microscopy imaging revealed that the higher loading films have more complete coverage of the graphite surface, permitting more effective overpotential control. The results from SBU and BNL highlight the use of nanoscale functional surface coatings for prevention of Li plating during battery fast charging. Future research efforts are centered on demonstrating that the metal film coated electrodes can be fabricated using a cost-effective, scalable approach that preserves the functional benefits observed for laboratory scale fabricated films.

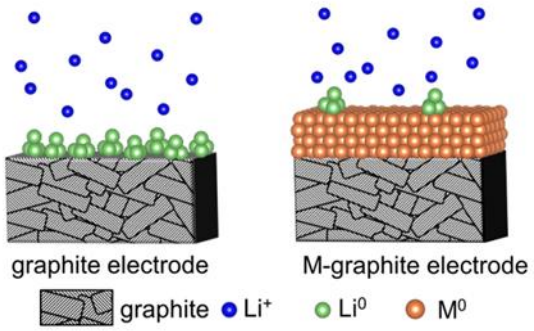

Figure 13. Schematic representation of the approach for suppressing lithium metal plating during high charging current: nanoscale metallic films applied to the upper surfaces of battery anodes increase the overpotential for the Li nucleation.

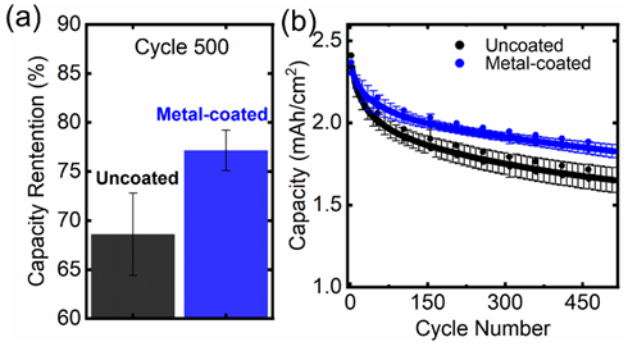

Figure 14. (a) 500 cycle capacity retention and (b) areal capacity for Li-ion pouch cells with uncoated (control) and nanoscale metal coated electrodes cycled under 10 minute charge rate.

Determination of State-of-Charge Gradients in Thick 811 Cathode Films. One generally applicable route for enhancing the energy density of Li-ion batteries (thereby increasing the range of electric vehicles) is the use of thicker cathode films. However, the specific capacity and rate performance of thick electrodes is substandard due to limitations in the transport of ions and/or electrons perpendicular to the plane of the film. If the precise origin of these transport limitations can be understood, it will be possible to rationally design

thicker cathodes that deliver higher energy densities than present battery cathodes while still meeting the other performance demands of electric vehicles. High energy synchrotron X-ray diffraction methods were used at BNL to study the top-to-bottom inhomogeneity in the state of charge (SOC) of operating battery cathode films. The height of the x-ray beam was reduced to 1/50 of a millimeter, allowing thick cathode films to be virtually 'sliced' into about ten layers (much like a stack of postage stamps), enabling the performance of each layer to within the whole to be independently followed during battery testing. The ability of the X-ray techniques to accurately measure the local SOC in a layer was confirmed by the agreement in the average response measured across all layers by X-rays (cyan line, Figure 15) to that measured conventionally using the potentiostat controlling battery cycling (black line). The next step was to compare the response from the back of the cathode layer (where the electrical contact with the current collector is made) to that of the front of the cathode (nearest to the anode). While layers in the front of the cathode behaved in the expected manner (Figure 16), it was observed that the back layers could store only about half of the capacity of the front of the cathode after a normal charging cycle, suggesting that the primary transport limitation is ionic, not electronic. Furthermore, it was observed that when the discharge of the battery starts (time = 12 hrs, green arrow), the back cathode layers unexpectedly continue to charge for another hour, and in fact increase their SOC faster than at any point during the charging of the battery. The spatially resolved diagnostic methods demonstrated here are being used to parameterize electrochemical models of cathodes that can predict how battery design modifications will affect battery performance.

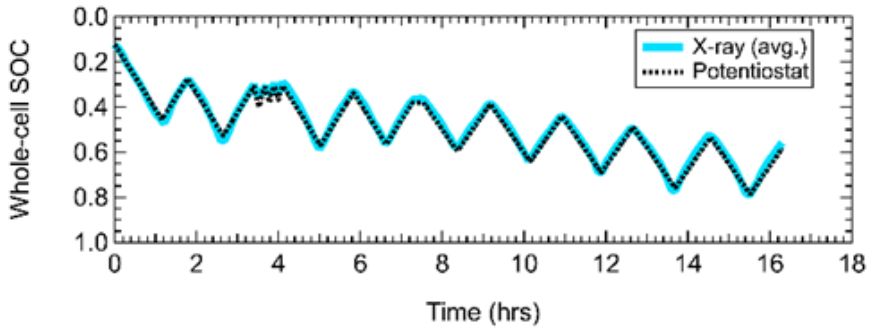

Figure 15. Comparison of the battery state of charge calculated from X-ray diffraction measurements (cyan) with that recorded using the potentiostat driving battery cycling (black)

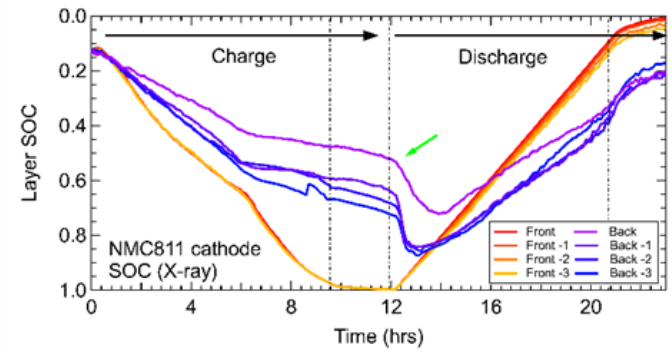

Figure 16. Comparison of the battery state of charge for 4 layers at the top of the cathode (red-orange) and 4 layers at the back of the cathode (purple-blue).

Protocol for Early Assessment of Calendar Life in Silicon Cells. The development of a short-timeframe calendar lifetime testing protocol could enable much faster feedback and development of new materials to improve the calendar lifetimes of next generation batteries. Calendar life testing of battery cells is traditionally

carried out by aging cells under open-circuit conditions for multi-month-long timeframes. These long timeframes required are a major issue and the slow tests limit the feedback loop speed and efficiency.

The new electrochemical test protocol provides a mechanism for the development of silicon (Si) electrodes that researchers and early stage developers can use to assess the progress in the development of silicon based negative electrodes within a short timeframe of two weeks. This test makes use of a constant voltage hold in a lithium (Li)-excess supplied full cell containing a lithium iron phosphate counter electrode with a flat voltage output. The current passed during the voltage hold is a measure of the reaction rate of lithium consumption at the silicon anode through parasitic and irreversible electrochemical reactions.

Figure 17 shows the current decays of three different Si test electrodes and a graphite baseline electrode. The normalization of the current data to the reversible capacity of each electrode is important because the resulting units of Amps/Ah indicate the rate at which each electrode is losing reversible capacity due to Li+ consumption at the solid electrolyte interphase or SEI. If the normalized current measured from a Si test electrode at the end of the 180 hour voltage hold is distinguishably higher than a baseline electrode, further analysis is not needed, as the electrode's SEI is clearly not sufficiently stable. This is the case for each of the Si test electrodes shown in Figure 17, thus showing the effectiveness of this simple qualitative comparison for the initial screening of Si test electrodes.

Our methodology is based on using voltage holds to measure the rate of parasitic reactions that irreversibly trap Li+ at the SEI. This approach has the advantage of recording real-time rates of side reactions, providing information about the time-dependence of such processes and potentially enabling extrapolation of behaviors observed in relatively short duration experiments. Indeed a numerical model of the parabolic-like decay of the current is under validation using long-term voltage hold measurements. The long-term validation test will allow an accurate fit traced back to 180 h of Si calendar life testing. Consequently, the numerical fit model is used to project the losses of Li+ inventory due to parasitic reactions during long-term storage.

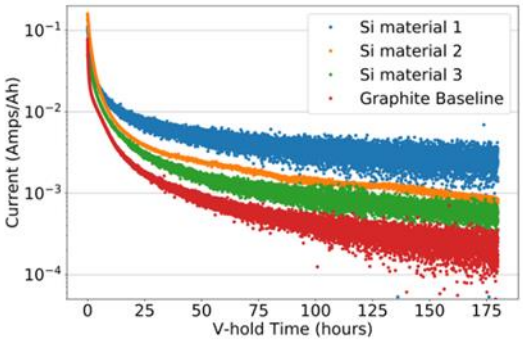

Figure 17. Current decay versus time during voltage holds of several different Si test electrodes and a graphite baseline electrode.

Linking Electrode Particle Architecture to Battery Performance. Increased demand for electric vehicles necessitates new solutions to achieve high-energy, fast-charge-capable lithium-ion batteries. At present, the performance of battery electrodes is mostly determined from electrochemical measurements, with no insight how electrochemical performance relates to the 3D architecture of the individual particles that make up the electrode. To date, techniques to create the link between sub-particle architectures and electrochemical performance have not been developed, which has hindered efforts to create structure-function relationships and guide new designs.

Under DOE's Extreme Fast Charge program (XCEL), the National Renewable Energy Laboratory (NREL) has developed a process to characterize the architecture of single electrode particles in 3D. This characterization

considers properties that influence how fast the electrode can charge or discharge while minimizing phenomena that lead to degradation. Most cathodes in commercial lithium-ion batteries consist of particles with polycrystalline grain architectures (Figure 18a,b). Within the particle, individual grains generally have mismatched crystal orientations that increase the path lithium must take to fully saturate the particle during charging. Each individual grain swells and contracts during charging and discharging, which leads to mechanical strain, cracking, and capacity loss during operation.

NREL recently developed the application of an electron diffraction technique that maps the polycrystalline architecture of single cathode particles in 3D (Figure 18c). This is the first time that the architecture of a single particle has been revealed in such detail and presents opportunities to create a link between the architecture of particles and the electrochemical performance of batteries.

Using the 3D datasets, NREL multi-physics models compare inefficiencies in how lithium moves throughout various particle architectures. Coupled with solid mechanics, the models identify where mechanical strain accumulates and predict the tendency of the particle to degrade (Figure 18d).

This capability will clarify opportunities to improve battery performance and guide novel manufacturing routes that synthesize particles with larger/oriented grain architectures more favorable for fast charging and long life. Together with 3D simulation models, the electron diffraction measurement facilitates fair comparison and benchmarking of next-generation electrode particle designs.

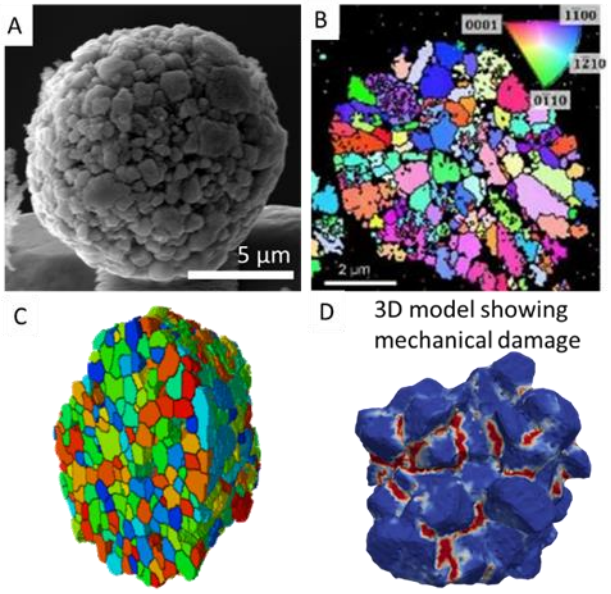

Figure 18. (a) Image of a nickel-manganese-cobalt (NMC) cathode particle. (b) Cross-section electron-diffraction image shows individual grains and their crystal orientations. (c) 3D geometry of NMC particle with anisotropic grains. (d) Multi-physics model reveals regions susceptible to damage.

Development of Si-based High-Capacity Anodes for Next Generation of Li-Ion Batteries. Porous Si has been widely used to mitigate pulverization of Si particles during battery cycling. However, the large surface area of these Si materials may lead to severe reactions between lithiated Si and electrolytes. These reactions will result in continuous growth of the solid electrolyte interphase (SEI) layer, as well as short cycle and calendar battery lives. Therefore, minimizing the surface area of Si and finding a stable electrolyte are critical for the cycling and calendar lives of Si-based lithium ion batteries (Si-LIBs).

Researchers from the U.S. Department of Energy's Pacific Northwest National Laboratory (PNNL) have developed a highly stable Si anode based on micron-sized porous Si with heterogeneous coating layers. Porous

Si is first prepared by thermal decomposition of SiO and subsequent etching with HF solution. The as-prepared porous Si has a large surface area of ~1000 m^2 g^{-1} and a large pore volume of 1.10 cc g^{-1} with nano-sized pores (~3.7 nm in diameter). For the homogeneous coating process, petroleum pitch is dissolved in toluene; the resulting pitch/toluene solution is impregnated into the porous Si under the vacuum. As shown in Figure 19a, porous Si has an average particle size of ~5 μm, which is similar to those of pristine porous Si. After carbonization of pitch at 700 °C under an Ar atmosphere, the carbon content in the composite is ~45%–48%. Using porous Si-C, Si||NMC532 coin cells have demonstrated excellent electrochemical performances with a baseline electrolyte (1.2 M $LiPF_6$ in EC/EMC [3/7 in weight] + 10% FEC). The cell retains 78% capacity after 400 cycles, with a stabilized 99.9% coulombic efficiency. The superior stability of the porous Si-C anode can be attributed to (1) mitigated volume expansion with sealed porosity; (2) improved overall conductivity of the composite; and (3) minimized electrolyte penetration into the porous Si.

To further improve the cycle life of Si-LIBs, PNNL researchers have developed several novel electrolytes based on the concept of the localized high-concentration electrolyte (LHCE). These electrolytes result in a significantly improved cycle life of Si||NMC532 cells (Figure 19b). The cycle life of the cells can increase more than 50% when PNNL's LHCEs (LiFSI-DMC-BTFE [molar ratio = 0.51:1.1:2.2] + 1.0 wt% VC + 5 wt% FEC) are used compared to that produced using baseline electrolytes. Thus, porous Si and LHCE electrolytes developed at PNNL have great potential to enable the next generation of high-energy-density LIBs.

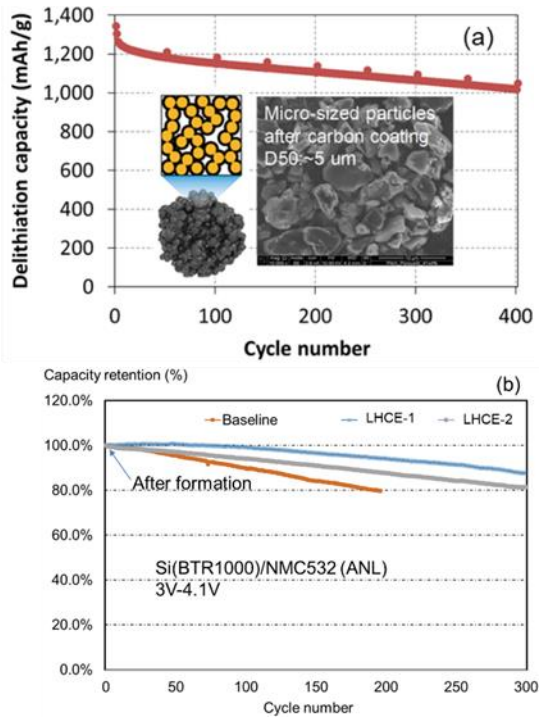

Figure 19. (a) Cycling stability of Si||NMC622 cells using a porous Si anode and baseline electrolytes. The insert shows the schematic structure and scanning electron microscope image of porous Si. (b) Cycling stability of Si||NMC532 cells using a porous Si anode and different electrolytes.

In-Operando Detection of Lithium Plating During Fast Charge with Rapid EIS and Differential Coulometry. Fast charging of lithium ion batteries is a critical enabler for mass EV adoption. Sandia National Laboratories (SNL) has been working with the University of Michigan to develop graphite anodes with novel 3D structures that facilitate faster charging while avoiding lithium plating, a main danger of unaided fast charging. Last year, SNL used its unique high precision cycling and rapid electrochemical impedance spectroscopy (EIS) capabilities to identify distinct indicators of lithium plating at increased charge rates and demonstrate the ability of improved anodes to withstand fast charge and resist lithium plating.

Figure 20 shows dQ/dV plots at increasing rates for cells with graphite anodes. At low charge rates (<1C, 1 hour charge), peaks from 3.5-3.8V indicate normal charging behavior. At higher rates (> 3C; 20 min charge), a second growing peak at 4.1V indicates a new process occurring, hypothesized to be lithium plating. Rapid EIS collected during fast charge operation is presented in Figure 21. The impedance of the graphite anode cell increased with cycle number and charge current, particularly at higher voltages (>4V), while the impedance of the 3D anode structure cell remained un-changed through the high rate cycles. Both techniques demonstrated the ability of the 3D anode structure to operate under fast charge conditions while resisting lithium plating.

The dQ/dV and rapid EIS lead us to in-operando identification of lithium plating behavior, including at what current it occurred and to what degree. This powerful tool was used to compare unimproved anodes similar to present day cells, with cells containing 3D anode structures.

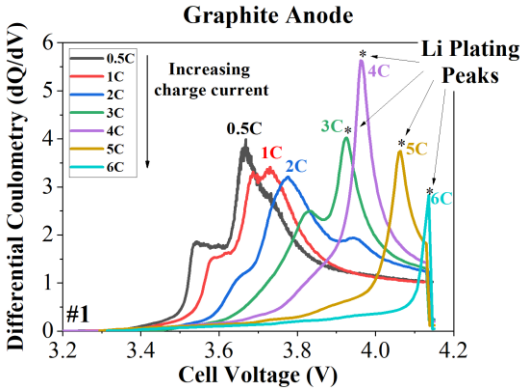

Figure 20. Differential Coulometry (dQ/dV) of a Li-ion cell with a graphite anode.

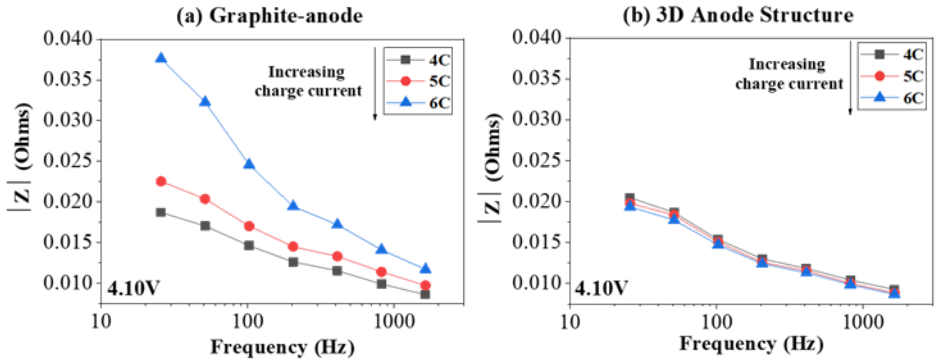

Figure 21. Rapid EIS during fast charge of a Li-ion cells with (a) graphite anode, and (b) 3D anode structure.

Battery Safety Testing. The Battery Abuse Testing Laboratory (BATLab) at Sandia National Laboratories has historically collected accelerating rate calorimetry (ARC) data to compare the safety performance of new and existing active materials. However, calorimetry methods such as this present an opportunity to explore the energetic behavior of thermal runaway due to a wide range of factors. A recent study compared cell capacity, energy density, sate of charge, and cathode chemistry to observe how they impact the severity of thermal runaway. This analysis covers four cathode chemistries, multiple form factors, and stored energy ranging from 3.5 to 122 Wh.

In a practical scenario, thermal runaway occurs when the self-heating rate of a battery failure event exceeds the heat loss rate in its current environment or installation. The logical next step is that increasing energy density will lead to increased consequences of thermal runaway occurring. With exponentially faster heat release at higher energy density it will be easier for the thermal runaway to exceed any heat dissipation to the

environment, likely leading to more severe consequences in terms of further damage or cascading failure. Figure 22 illustrates this in the data analyzed, showing exponentially increasing peak heating rates until the very highest effective specific energy. This would be considered intuitive if discussing chemical energy storage, but is a concept often avoided when considering electrochemical energy. As new technologies are developed with increased energy in mind, increasing attention will need to be paid to designing mitigation into systems that minimize consequences.

Similar comparisons of the total heat released (enthalpy of runaway in Figure 23) shows a linear tie to cell capacity. This shows that even at lower specific energies and states of charge there may be significant energy available to contribute to a failure event. This adds an additional consideration for very large systems or bulk storage, particularly when individual cells are well insulated and may be able appreciably self-heat.

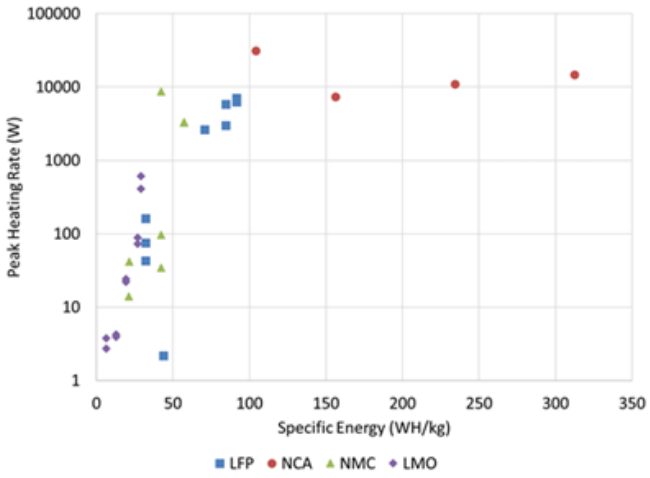

Figure 22. A comparison of different cell chemistries as a function of the effective specific energy of the device tested.

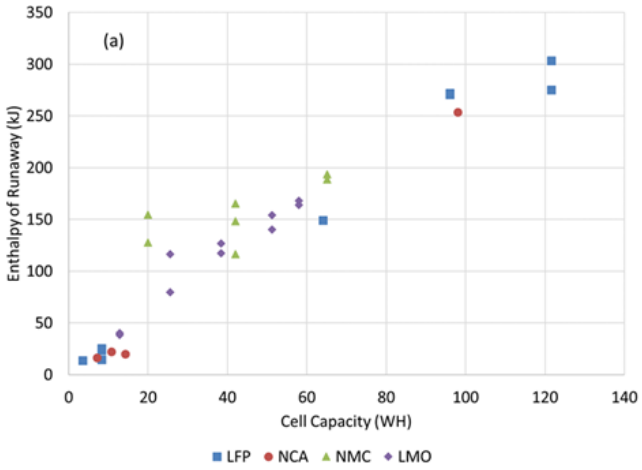

Figure 23. Cells in Figure 1 comparing the enthalpy of runaway as a function of cell capacity.

Phase II Winners for the Lithium-Ion Battery Recycling Prize Announced: As part of its efforts to facilitate a well-distributed, efficient, and profitable infrastructure for the recycling of lithium-ion batteries and to incentivize American entrepreneurs to find innovative solutions to challenges associated with collection, storage, and transportation of spent or discarded lithium-ion batteries, DOE earlier established a $5.5 Million

Battery Recycling Prize. Its goal is to develop innovative business and technology strategies to potentially capture 90% of all lithium-based battery technologies (consumer electronics, stationary, and transportation applications) and to make collecting, sorting, storing, and transporting lithium-based batteries safe, efficient, and profitable. The Prize spans three phases. In each phase, winners are determined by a panel of expert judges evaluating concepts based on feasibility, cost to implement, and potential impact. Earlier, in Phase I of the Prize, after review by industry experts and a Federal Consensus Panel, DOE had determined that 15 submissions adequately met the criteria for innovativeness, impact, feasibility, and technical approach outlined in the Prize Rules. During FY20, the Prize Administrators successfully launched Phase II, entitled "Prototype and Partnering", organizing an in-person networking opportunity in partnership with the National Alliance for Advanced Transportation Batteries (NAATBatt) National Conference in February 2020. TFourteen submissions were received in Phase II of the Prize to further the development of the winning concepts from Phase I. Expert judges reviewed the Phase II Final Submissions in late September and seven winners were announced in December advancing the winners (see Table 4) to the third and final phase of the Prize.

Table 4: Lithium-ion battery recycling prize Phase II winners

Team (Location)	Project Title
Li Industries (Blacksburg, VA)	Smart Battery Sorting System
OnTo Technologies (Bend, OR)	DISC: Deactivate, Identify, Sort, Cut
Powering the Future (Glendale, WI)	Powering the Future
Renewance (Chicago, IL)	Renewance Connect
Smartville (San Diego, CA)	Smartville Battery Reuse & Recycling HUB System
Team Portables (Seattle, WA)	Reward to Recycle – Closing the Loop on Portables
Titan Advanced Energy Solutions (Sommerville, MA)	Battago – Battery Market Intelligence Platform

I Advance EV Battery Development

I.1 USABC Battery Development & Materials R&D

I.1.A Development of High Performance Li-ion Cell Technology for EV Applications (Farasis Energy)

Madhuri Thakur, Principal Investigator
Farasis Energy
21363 Cabot Blvd, Hayward, CA 94545
Hayward, CA 94545
E-mail: mthakur@farasis.com

Brian Cunningham, DOE Technology Development Manager
U.S. Department of Energy
E-mail: Brian.Cunningham@ee.doe.gov

Start Date: February 1, 2017 End Date: December 31, 2020
Total Project Cost: $5,900,000 DOE share: $2,950,000 Non-DOE share: $2,950,000

Project Introduction

The goal of this project is to develop a high energy density, low-cost Li-ion cell technology that meets the USABC Goals for Advanced Batteries for EV's. Farasis leads the development effort which will bring together technical contributions from a large number of leaders in the Li-ion technology industry including subcontractors Argonne National Laboratory (ANL), Lawrence Berkeley National Laboratory (LBNL), material suppliers for anode, cathode, electrolyte and separator etc. The project will build on technology development efforts at Farasis and our collaborators that have been supported, in some cases, through previous Department of Energy sponsored projects. The development effort will be iterative, with an intermediate Go/No Go Milestone based on cell performance goals and progress tracked against the USABC Battery goals. The main objective of this program is to develop cell technology capable of providing 350 Wh/kg after 1000 cycles at a cost target of $100/kWh. The beginning of life (BOL) target for the cell level-specific energy is ~ 400 Wh/kg, which is approximately 12% higher than the energy needed to meet the USABC end of life (EOL) cell level targets. To achieve the desired target of 350Wh/Kg the anode needs to be pre-lithiated with a capacity ≥ 1500mAh/g and cathode with a capacity higher than 220mAh/g. The pre-lithiation of the anode done by adding sacrificial lithium source into the cathode. For the past two years, we try to optimize the amount of sacrificial lithium source added to the cathode. The addition of sacrificial lithium source (SLS) leads to a decrease in the capacity of the cathode and increase the impedance of the cells. To overcome all the problems associated with the Li source requires more work on the stabilization of this material, and would be challenging to implement in the required time frame of the program. During the Go/No Go Milestone based on cell performance, a change in the chemistry of was done to meet the deliverable energy target of 330Wh/Kg. The final deliverable must achieve specific energy of 330Wh/Kg at the beginning of life without pre-lithiation at a cost target of $100/ kWh. The main objective of this project is to develop a cell technology capable of providing 280 Wh/kg after 1000 cycles at the end-of-life. The specific energy of the cell at the beginning of life will be approximately 15% higher than the energy needed to achieve the cell level target for this program..

Objectives

- Develop an EV cell technology capable of providing 280 Wh/kg after 1000 cycles at a cost target of $0.10/Wh.
- Develop high capacity cathode and Si anode materials to meet USABC EV goals through collaborative development efforts with partner organizations.

- Develop and optimize electrolyte and conductive additives to stabilize Ni rich cathode and improve the safety
- Optimization of negative electrode formulation for maximum energy density and cycle life, calendar life, power, safety, and low/high temperature cell requirements.
- Investigate effect of Si incorporation on conductivity and mechanical stability of negative electrode relative to graphite electrodes.

Approach

Phase I of the project, which lasted for approximately 20 months, was focused on the development and characterization of materials and optimization of electrolyte technology. Initial sets of small cells (ca. 1-2 Ah) was used to evaluate different positive/negative electrode composites, material combinations and for electrolyte development in an iterative manner. During this phase, Farasis optimize the electrode compositions of anode and cathode in half coin cell as well as in single and double layer pouch cells. The materials down-selected based on these test result for the Gen1 deliverable cells. End of the phase1, the cells were built with a capacity of 41.5Ah and delivered to the National Labs. During this phase, we also work on the pre-lithiation of the anode by adding sacrificial lithium source into the cathode. We try to optimize the addition of the sacrificial lithium source to the cathode. We know that the disadvantage of adding the sacrificial lithium source (SLS) leads to a decrease in the capacity of cathode material. But during the study, we have seen that it also leads to an increase in the impedance of the cells. During the Go/No Go Milestone based on cell performance, a change in the chemistry done to meet the deliverable energy target of 330Wh/Kg.

Phase II of the project is scheduled for approximately 20 months and focus on down selecting the chemistry to achieve an energy target of 330Wh/Kg. To achieve the targeted energy of 330Wh/Kg without pre-lithiation of an anode required a high 1st cycle efficiency Si material. During this phase, we worked on high-efficiency Si material as well as on Ni-rich cathode materials from different suppliers. The materials evaluated in the coin cell as well as in single and double layer pouch cells. The down-selected optimized chemistry transferred to deliverable cells (see Table I.1.A.1). Phase II of the program will also include testing to guide system development in future applications; these tests will characterize cells in small groups to efficiently evaluate their behaviour on a large scale where thermal management, cycling-induced gradients, and failure isolation become important.

Table I.1.A.1 Phase II Down-selected cell information.

Electrode Chemistry	Electrolyte Formulation	Electrodes and Cell
• Stabilized Ni-rich NCM cathode with a capacity of (220-240 mAh/g) • Silicon Composites (400–800 mAh/g)	• Fluorinated solvents • Stabilizing additive/ salts	• Optimized, high density, composite active material formulations • Low reactivity conductive additives • Advanced binder formulations • Advanced separators: Coatings, high voltage stability

Results

Gen1: Technology Development: The Gen 1 cells build with the down-select chemistry of Ni-rich and high voltage NCM as the cathode and low-efficiency SiO/C composite as an anode. The Gen1 chemistry down-selected based on data calculated from the single and double layers pouch cells built during the phase1 of the program. Gen1 cells were built-in for the capacity of 35Ah with Ni-rich cathode and High voltage NCM523. Based on the test results and learning from these cells, we finalize the Gen1 deliverable chemistry. Figure I.1.A.1 show the dynamic stress testing (DST) cycling data for the Gen1 cells (35Ah & 41.5 Ah). Figure I.1.A.2 shows the calendar life capacity retention and DCIR for Ni-rich cathode and SiO/C anode for the Gen1 cells.

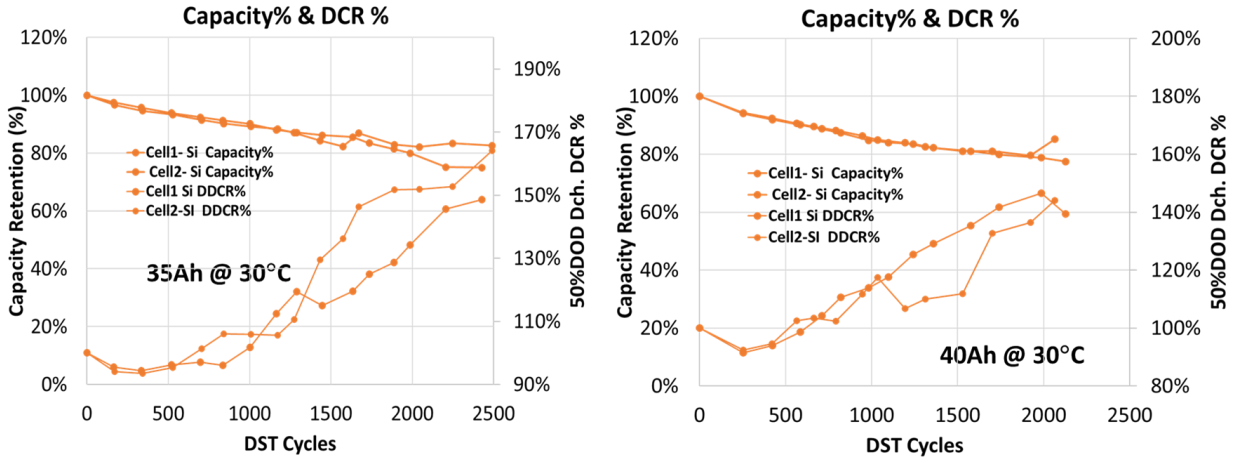

Figure I.1.A.1 the DST Cycle life for Gen1 Cells at 35Ah and 40Ah at 30°C

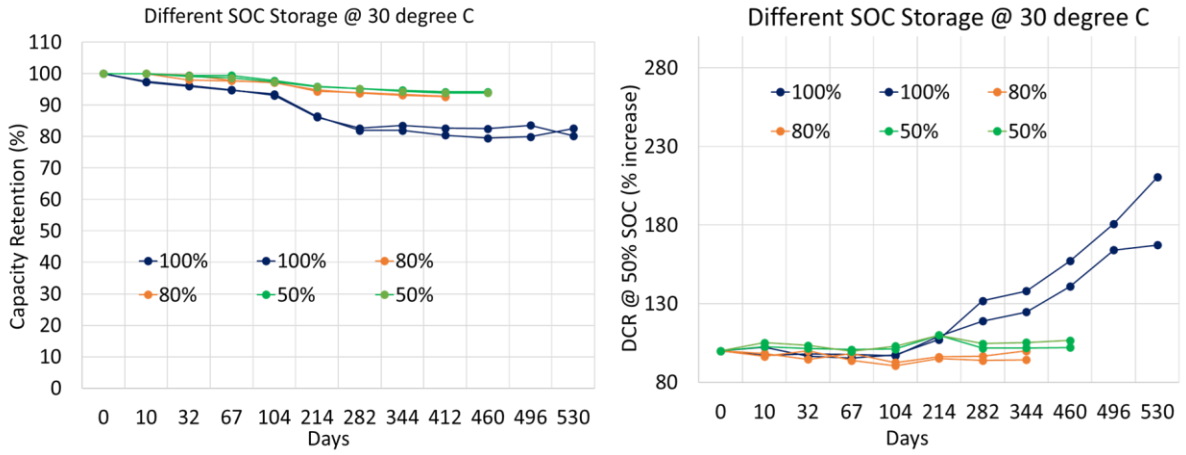

Figure I.1.A.2 Calendar life capacity retention for the Gen 1 (40Ah) deliverable chemistry & 4b) DCIR

Gen2 Deliverable

To achieve the specific energy of 330Wh/Kg needed an electrode (cathode capacity ≥200mAh/g and an anode capacity ≥450mAh/g). To achieve the targeted energy density need silicon material with higher coulombic efficiency to avoid the pre-lithiation of the anode. The 1st cycle efficiency of 100% silicon material needs to be more than 85%. Depending upon the capacity of the Ni-rich cathode, an anode needs the optimization. During the optimization, we built the cell for the cathode capacity ranging from 200-220mAh/g with different amount

of the silicon. Figure I.1.A.3 shows the cycle life for 10%–22% Si with a cathode having a capacity of 220mAh/g and cell-specific capacity, of 325 and 328Wh/Kg in the deliverable form factor.

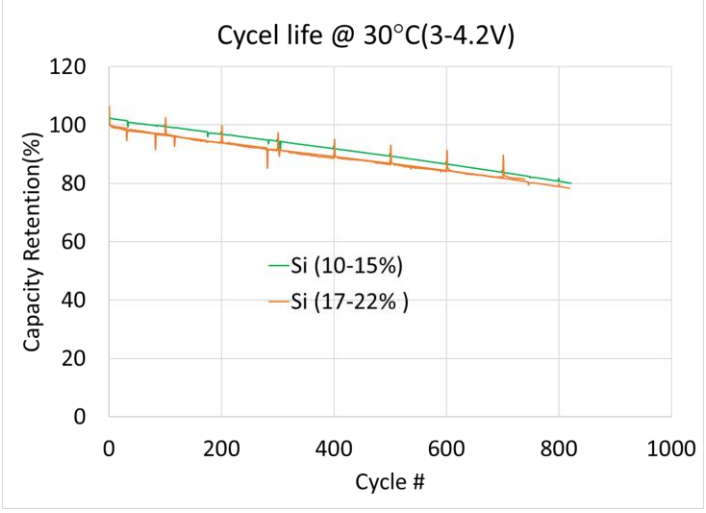

Figure I.1.A.3 shows the capacity retention of ~10%–22% %Si with Ni rich cathode

The high-efficiency Si anode of capacity ranging from 4.7-4.75mAh/cm2 was tested with Gen1 cathode in a double layer pouch cell for the targeted energy density of 330Wh/Kg in 80-87Ah form factor cells. Figure I.1.A.4 shows the cycle life and capacity of the double layers pouch cells. The final deliverable cells have the same chemistry.

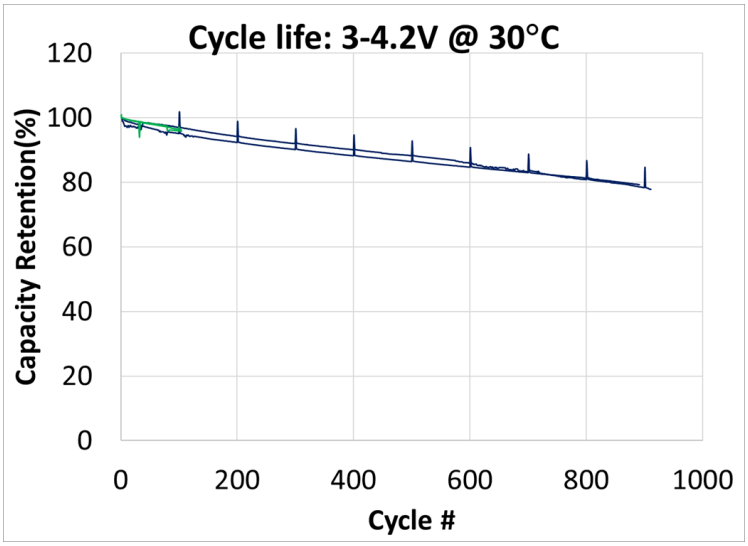

Figure I.1.A.4 shows the initial result for high efficiency anode with Gen1 cathode in double layer pouch cell

Conclusions

Farasis has shown more than 1000 cycle before reaching 80% capacity retention in 41.5Ah Gen1 cells with a specific energy of 270Wh/Kg. Farasis delivered 41.5Ah Gen1 pouch cells to National Labs for testing, abuse testing and thermal testing (INL, SNL and NREL). The Gen2 cells built for the energy density of ~ 330Wh/Kg are getting delivered at National Lab by November 2020.

Key Publication

1. “Development of High-Performance Lithium-Ion Cell Technology for Electric Vehicle Applications”, bat355_thakur_2018_p, US DOE Vehicle Technologies Program Annual Merit Review, AMR, 2018.

2. “Development of High-Performance Lithium-Ion Cell Technology for Electric Vehicle Applications”, bat355_thakur_2019_p, US DOE Vehicle Technologies Program Annual Merit Review, AMR, 2019.

3. “Development of High-Performance Lithium-Ion Cell Technology for Electric Vehicle Applications”, bat355_thakur_2020_p, US DOE Vehicle Technologies Program Annual Merit Review, AMR, 2020.

Acknowledgements

Meng Jiang (meng.jiang@gm.com) from the GM R&D Center, Battery Systems Group, CMS, in Warren, MI served as the USABC Program Manager for this project.

I.1.B Rapid Commercialization of High Energy Anode Materials (NanoGraf Technologies)

Cary Hayner, Principal Investigator
NanoGraf Corporation
3440 S. Dearborn Street, #113N
Chicago, IL 60616
E-mail: cary@nanograf.com

Brian Cunningham, DOE Technology Development Manager
U.S. Department of Energy
E-mail: Brian.Cunningham@ee.doe.gov

Start Date: May 23, 2019 End Date: June 30, 2022
Project Funding: $2,500,000 DOE share: $1,250,000 Non-DOE share: $1,250,000

Project Introduction

As global usage of electric vehicles steadily increases, so does the power/energy requirement to meet mainstream needs. Performance trajectories of traditional lithium-ion technology, despite an annual 3%–5% improvement in energy density since inception, suggest that long-term electric vehicle needs will not be met without an evolution beyond traditional energy storage materials (i.e. graphitic anodes). NanoGraf Corporation has developed a novel Si-based, negative-electrode material which can enable a quantum leap in battery energy and power density, and significantly impact battery weight and run-times that burden today's electric vehicles.

Objectives

The project entitled "Rapid Commercialization of High Energy Anode Materials" has been established with the aim of extending, benchmarking, and demonstrating the performance of NanoGraf's advanced silicon-based anode materials in battery form factors and designs relevant for electric vehicle applications.

Approach

NanoGraf Corporation has demonstrated a novel high energy density (>1,000 mAh/g) Si-based negative-electrode materials technology with a long-term potential to replace graphitic-based anodes in lithium-ion batteries. NanoGraf's technology uses a proprietary silicon alloy-graphene material architecture to achieve: i) category-leading performance and ii) solutions to long-standing Si anode technical hurdles. The proprietary combination of silicon-based alloys and a flexible 3D graphene network helps to stabilize the active material during charge and discharge by providing an interfacial barrier between the active material and the electrolyte which can accommodate large volumetric changes through a laminar graphene sliding mechanism. The 3D graphene-silicon architecture results in a minimization of capacity losses due to electrical disconnection, significantly improved active utilization (mAh/g), and partial stabilization of the SEI interface with a flexible physical barrier between electrolyte and active material (Figure I.1.B.1).

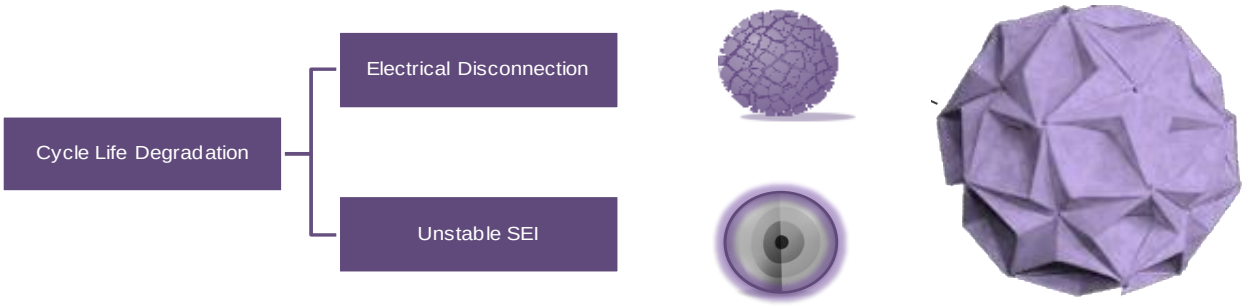

Figure I.1.B.1 Si anode failure mechanisms (left), NanoGraf graphene-wrapped silicon anode architecture (right).

NanoGraf has made continuous improvements against key USABC advanced electrode metrics over time, and has demonstrated an attractive trajectory towards USABC advanced electrode goals. The goal of the program is the advancement and commercialization of advanced silicon-based active materials for high energy and high power EV batteries. Specifically, the program aims to demonstrate that NanoGraf technologies can exceed USABC electric vehicle performance targets in USABC-recognized form factors, be produced at-scale by commercially viable methods and reach USABC cost targets at scale. To this end, a series of tasks have been developed to address the core technology gaps and their associated barriers: Task 1: Electroactive Synthetic Design & Optimization, 2. Electroactive Barrier Design & Optimization, 3. Anode/Cathode/Electrolyte/Binder Design Optimization, 4. Material Production & Process Development, 5. System Integration & Cell Production and 6. Electrochemical & Safety Testing.

NanoGraf has two strategic partners for this program. A123 Systems works with NanoGraf on Tasks 5 and 6 for the cell deliverables and PPG works with NanoGraf on Task 3 to assist with electrode design and optimization.

Results

Throughout FY20, NanoGraf made significant progress in numerous development pathways including active material development (Task 1 & 2), electrode & cell design (Task 3), materials production (Task 4), and prototype performance (Task 5 & 6). Select project advancements have been highlighted below:

Active Material Development: In FY20, NanoGraf focused on different experimental designs to improve the stability of SiOx-based anode materials by optimizing the active particle core as well as surface coatings to stabilize the SEI. For the electroactive particle core, NanoGraf has completed investigation of the SiOx microstructure to optimize the overall cycling stability and improve the energy density of the graphene-wrapped electroactive components. As shown in Figure I.1.B.2, optimized microstructural treatments (MT) materials (MT2-4) are compared against the previous best-performing MT1 material that was previously developed. As can be seen in Figure I.1.B.2C, improved MT2 and MT3 samples provide >5% energy density increase with similar cycling life in a pure anode material format, compared to MT1. Upon extended cycling (Figure I.1.B.2D), sample MT2 was determined to be the optimal material due to its combination of high energy and good capacity retention characteristics.

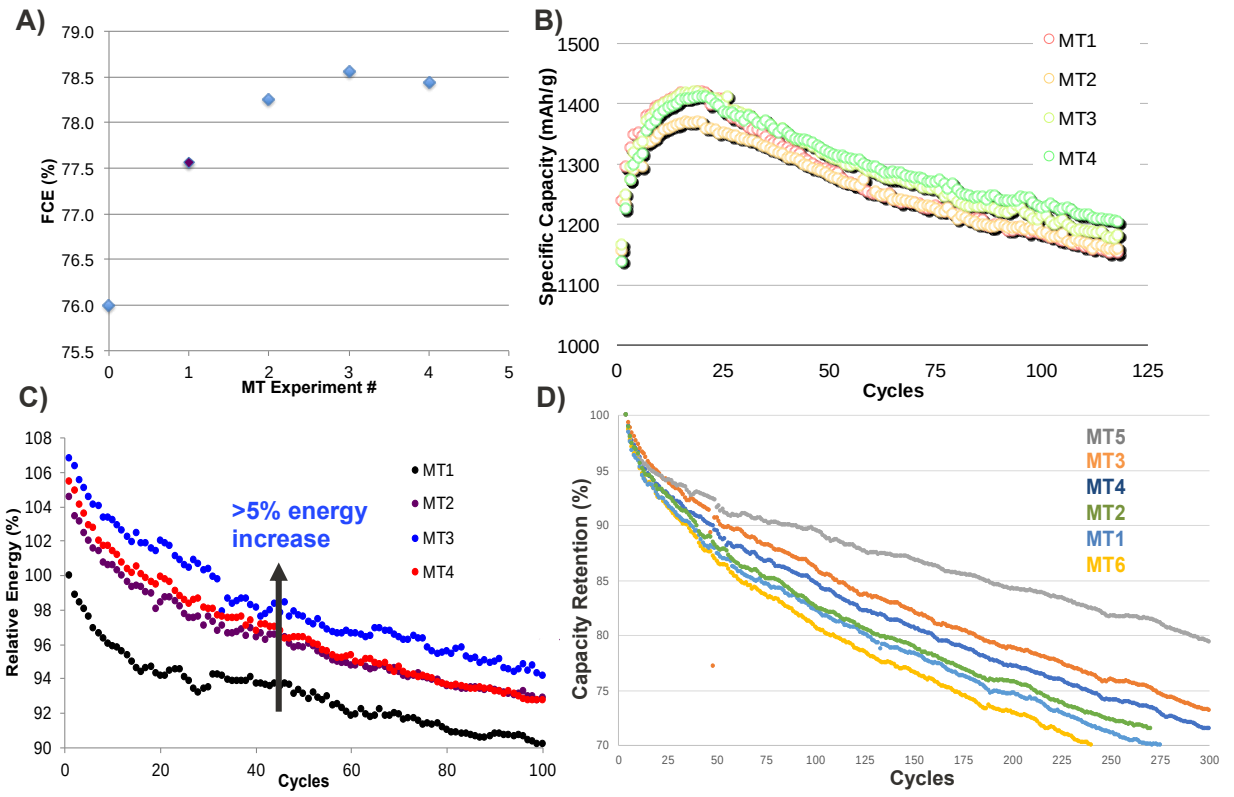

Figure I.1.B.2 A) 1st cycle Coulombic efficiency for microstructural treatment (MTx) samples B) half-cell coin cell electrochemical cycling of MTx samples C) full cell coin-cell electrochemical cycling of MTx samples in pure silicon anode formulation (no graphite blending) and D) extended full-cell cycling for MT1-MT6 samples in pure silicon anode formulation showing divergence in extended cycling.

In addition to the progress on the particle core, NanoGraf also focused on developing novel surface barrier coatings that could further improve the electrochemical performance of the SiOx material. These novel surface barriers were investigated with the intent of providing more stable SEIs and increased energy density to the optimized MTx core developed previously (see Figure I.1.B.3).

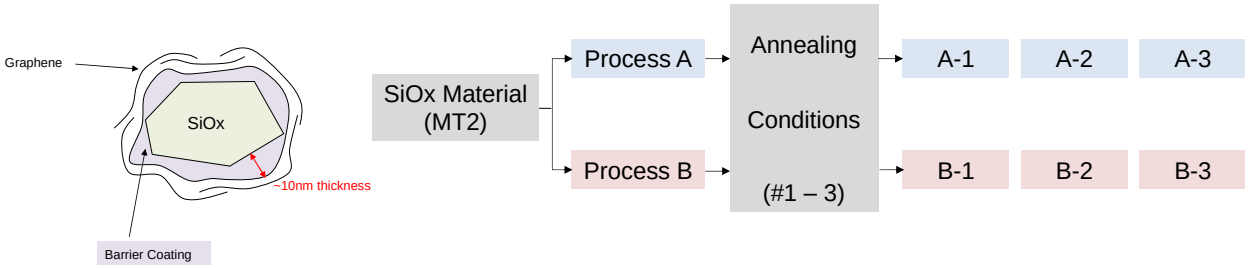

Figure I.1.B.3 (Left) Schematic of the novel surface barrier coating on top of the SiOx core particle, with graphene-coating applied to the exterior of the barrier-coated particle. (Right) Simplified flow diagram illustrating the processing (e.g. A-E) and annealing conditions (e.g. #1-3) to develop the barrier coating for the MT2 SiOx material.

These barrier coatings were investigated via various synthetic processes and annealing conditions to improve the coating coverage and decrease resistance. All barriers developed were both air- and water-stable coatings that are compatible with existing aqueous processing conditions. In addition, graphene coatings were still applied to ensure good electrical connectivity and cycle life.

As shown in Figure I.1.B.4 below, these novel barriers have resulted in significant improvement in the performance of the MT2 material. By optimizing the synthetic conditions, NanoGraf was able to apply the barrier coatings to result in an improvement in the cycling stability of the material as well as reduce the irreversible capacity loss. As seen below (Figure I.1.B.4C, D), in some instances the barrier coating could enable an increase of the 1st cycle efficiency 5% compared to the MT2 control. In addition, the increased efficiency was able to translate to an increased energy density of 7% with identical cycle life compared to the MT2 control material (Figure I.1.B.4B).

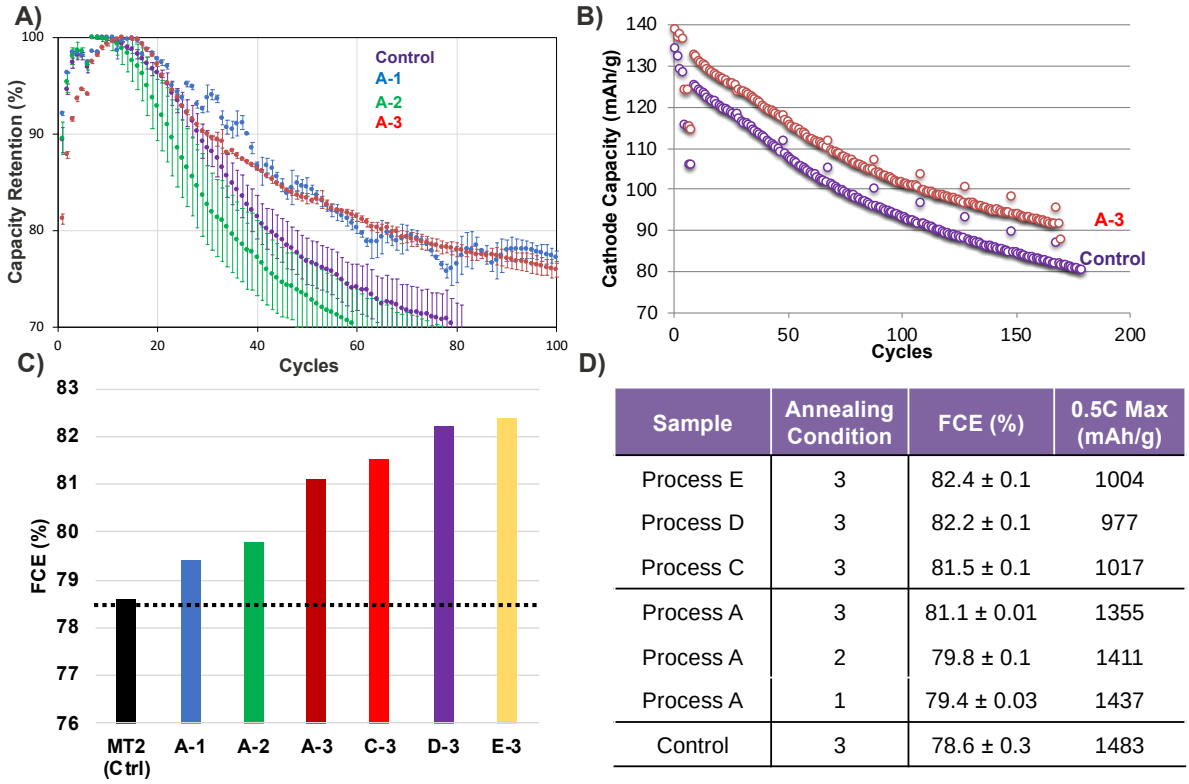

Sample	Annealing Condition	FCE (%)	0.5C Max (mAh/g)
Process E	3	82.4 ± 0.1	1004
Process D	3	82.2 ± 0.1	977
Process C	3	81.5 ± 0.1	1017
Process A	3	81.1 ± 0.01	1355
Process A	2	79.8 ± 0.1	1411
Process A	1	79.4 ± 0.03	1437
Control	3	78.6 ± 0.3	1483

Figure I.1.B.4 (A) Half-cell coin cell cycle life results for various barrier materials in pure silicon anode formulation. (B) Corresponding full-cell coin cell cycle life results for sample A-3 and the MT2 sample (Control). C) First Cycle Efficiency (FCE) values for different synthetic conditions. D) Materials electrochemical properties for various synthetic conditions.

Electrode & Cell Design: In addition to the improvements made to the active material, there were also substantial developments made to other cell components, especially the anode and cathode binder materials. In FY20, PPG focused on developing improved anode and cathode binders to enable good electrode adhesion with minimal binder content to decrease inactive components and maximize energy density. On the cathode size, PPG has developed a suite of R&D binders that offer competitive performance compared to the conventional PVDF/NMP system. As shown in Figure I.1.B.5, PPG's R&D binders are capable of providing high electrode peel strength compared to conventional PVDF materials, even at high areal loadings of 4 mAh/cm^2 and 5 mAh/cm^2. Additionally, these R&D binders provided very similar electrochemical performance, similar rheological properties, and improved slurry stability for NMC811 slurries compared to PVDF/NMP (Figure I.1.B.6).

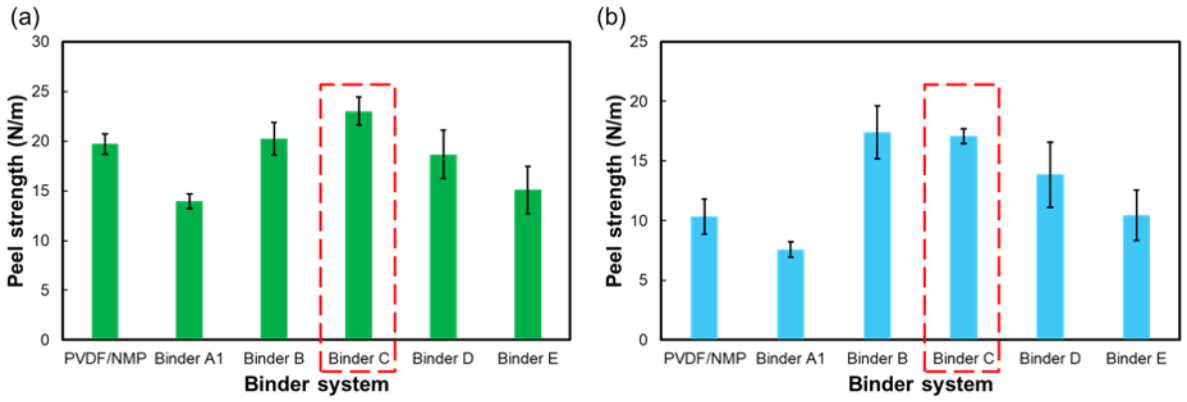

Figure I.1.B.5 Peel strength of different binders at the loading of (a) 4 mAh/cm2 and (b) 5 mAh/cm2.

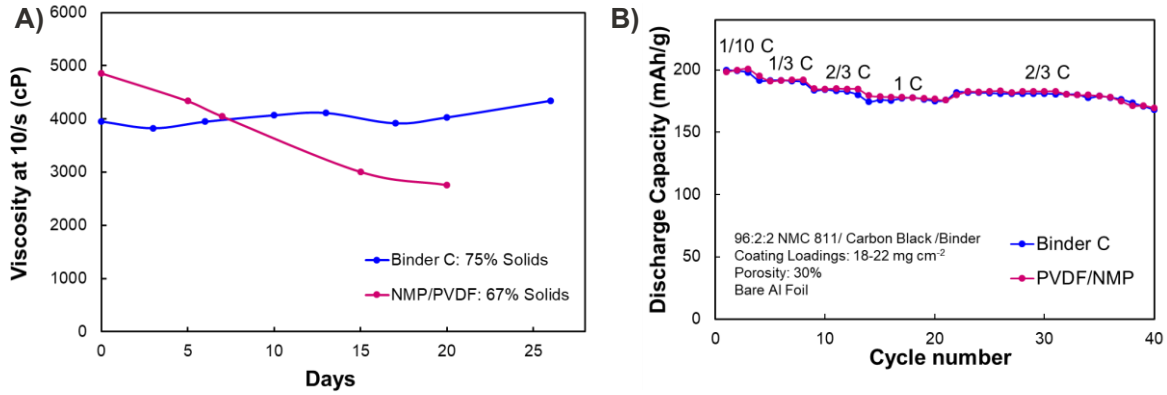

Figure I.1.B.6 (A) Viscosity change for NMC811 slurries using Binder C and PVDF/NMP as a binder. (B) Electrochemical performance of high-loading NMC811 electrodes.

PPG also commenced development of an anode binder material with promising initial results. As shown in Figure I.1.B.7, PPG's SiA-1 binder offers improved half-cell cycling stability and better Coulombic efficiency compared to a standard LiPAA (lithiated polyacrylic acid).

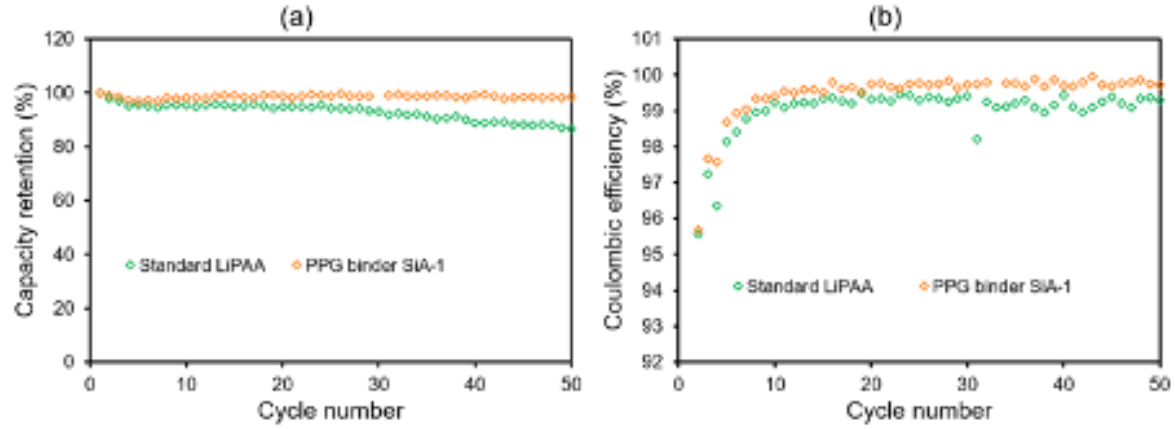

Figure I.1.B.7 (A) Capacity retention and (B) Coulombic efficiency plots of half-cell coin cells in pure anode formulation.

Prototype Performance: In addition to the improvements made to the electrochemically-active silicon anode material and the electrode binder materials, NanoGraf was also able to conduct 1 Ah prototype cell performance with A123 Systems. Since many of the demonstrated materials developments were accomplished

in parallel, much of the exhibited material improvements in the core and the barrier materials in this section have not yet been electrochemically tested in prototype cells. Therefore, in FY20, NanoGraf and A123 Systems were able to construct 1 Ah prototype cells utilizing the optimized MT2 material (without the barrier coatings or improved PPG binders). A123 Systems scaled the design that was established between NanoGraf and A123 from single-layer pouch (SLP) cells to small format pouch cells. The theoretical capacity of the cells based on design is 1.13 Ah. These anode electrodes were formulated for a silicon-dominant composition (75wt% silicon material, 10wt% graphite, 5wt% conductor 10wt% binder). Anode and cathode electrodes exhibited good physical properties including wet and dry adhesion, uniform coat weight, good resistance, and passed all mandrel tests. A123 Systems was able to construct >40 1 Ah cells, for which 15 cells were internally tested at A123 and 24 cells were externally validated by Argonne National Laboratory.

Electrochemical data obtained by A123 Systems confirms that cells were very consistent with very little cell-to-cell variation. Cells were tested at room temperature at two different voltage ranges – 4.2-3.0V and 4.2-3.25V to determine the impact on overall cycle performance. Additionally, one set of cells was cycled at a higher C-rate of 1C rather than the standard 0.5C for the other two data sets. As can be seen in Figure I.1.B.8 below, cells cycled under the 4.2-3.25V range were able to achieve ~800 cycles to 80% capacity retention. Similarly, cells cycled at the higher 1C rate also achieved the similar cycle life to the cells cycled at 0.5C. However, increasing the voltage window to 4.2-3.0V led to a decrease in cycle life, with a ~250-300 cycles to 80% capacity retention.

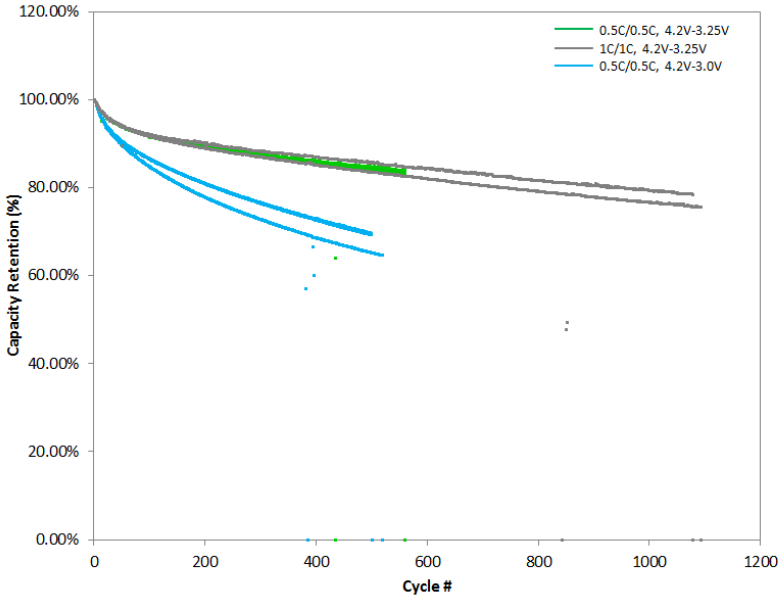

Figure I.1.B.8 Electrochemical cycling peformance for 1 Ah small format pouch cell samples utilizing NanoGraf MT2 anode and NCA cathode. Anode electrodes contained 75wt% MT2 silicon material, 10wt% graphite, 5% conductor, and 10wt% binder.

From the electrochemical testing results and the subsequent post-mortem teardown performed, NanoGraf and A123 Systems have investigated the main drivers of capacity fade, especially for the 4.2-3.0V window tests. Key learnings from the analytic tests have been used to inform and refine the cell design for the subsequent prototype build scheduled to occur in FY21.

Conclusions

NanoGraf has concluded the 16th month of the 36-month long project. The 1 Ah cell deliverables were delivered to Argonne National Laboratory in Q3 2020 for independent verification. Significant improved to the underlying silicon material has been made over FY20 in addition to the advancements that were able to be integrated into the initial 1 Ah cell build. Subsequent cells builds that will integrate the remaining

improvements and developments shown in this Progress Report are scheduled to occur in Q1 2021. Additionally, NanoGraf will investigate various cell form factors to understand its impact on electrochemical performance. A major milestone was achieved in the improved cycle life of the SiOx materials via structural changes and improved barrier properties.

Several challenges need to be surmounted over the coming year, including consistent improvements to the energy, cycle life, calendar life, scale and cost of the NanoGraf material in order to successfully surpass USABC key metrics.

NanoGraf has demonstrated a cadence of innovation and product development throughout the project, and looks optimistically towards demonstration of viable performance in commercially relevant EV cells.

Key Publications

1. ”High-Energy Anode Material Development for Lithium-Ion Batteries”, BAT240_Hayner_2020_p, US DOE Vehicle Technologies Program Annual Merit Review, AMR, 2020.

I.1.C Fast-Charge and Low-Cost Lithium Ion Batteries for Electric Vehicle Applications (Zenlabs Energy)

Herman Lopez, Principal Investigator
Zenlabs Energy
3390 Gateway Blvd.
Fremont, CA 94538
E-mail: herman@zenlabsinc.com

Brian Cunningham, DOE Technology Development Manager
U.S. Department of Energy
E-mail: Brian.Cunningham@ee.doe.gov

Start Date: February 1, 2019 End Date: August 31, 2021
Project Funding: $4,842,045 DOE share: $2,421,022 Non-DOE share: $2,421,023

Project Introduction

In order to reduce our dependence on fossil fuels and decrease greenhouse gas emissions, electric vehicles (EVs) have received intense attention as a possible solution. Electrification of automobiles is gaining momentum with the main barrier preventing widespread adoption being the lack of available low cost, high energy, fast-charging and safe energy storage solutions. Lithium ion batteries (LIBs) are presently the best energy storage solution used in current and upcoming EVs. Further improvements to the performance of LIBs by integrating high capacity active materials, novel passive components and unique cell designs will be critical for the success and mass adoption of EVs.

This project is developing novel electrolyte formulations, optimized cell designs and a scalable pre-lithiation solution that enables the use of high capacity silicon oxide anodes that will result in lithium-ion batteries capable of meeting the Low-Cost and Fast-Charge (LC/FC) USABC goals for advanced EV batteries in CY 2023. High specific capacity anodes containing high amounts of active silicon (>50%), Nickle-rich Ni-Co-Mn (NCM) cathodes and uniquely tailored electrolyte formulations will be integrated in large capacity (10-60 Ah) pouch cells targeting Fast-Charge and Low-Cost energy solutions. At the conclusion of the program, Zenlabs aims to demonstrate Fast-Charge and Low-Cost LIBs maintaining other performance requirements of EV cells, including energy, power, cycle life, calendar life, and safety.

Objectives

- Develop unique electrolyte formulations integrating commercially available organic solvents, salts and additives that will perform well with Silicon anodes and Ni-rich NCM cathodes.
- Evaluate and support the develop of a pre-lithiation solution for high capacity and high percent active silicon anodes addressing manufacturability, reproducibility, accuracy, cost and safety.
- Develop optimized cell designs to build and deliver cells that will meet the USABC EV battery goals for commercialization in calendar year 2023.
- Evaluate and integrate cost effective and high performing active and passive materials, processing steps and cell designs to meet the Low-Cost and Fast-Charge targets.
- Build, deliver and test large format (10 - 60 Ah capacity) pouch cells integrating optimized high capacity silicon-based anode, NCM cathode, electrolyte, separator and pre-lithiation to meet the USABC fast-charge, low cost, energy, power, cycle life, calendar life, safety and temperature EV goals.

Approach

Zenlabs is utilizing a system-level approach to screen, develop and optimize the critical cell components (cathode, anode, electrolyte, separator), pre-lithiation process (process, dose), cell design (N/P ratio, electrode design) and cell formation and testing protocols that will enable meeting the USABC EV cell level goals for the year 2023. The development consists in integrating pre-lithiated silicon-based high capacity anodes, high capacity Ni-rich NCM cathodes, high voltage electrolytes and composite separators into large capacity (10-60 Ah) pouch cells. The developed cells will target Low-Cost and Fast-Charge along with high energy density and power, good cycle life and calendar life, safety and low and high temperature performance. During the program, Zenlabs will utilize three cell build iterations to meet the program targets that will deliver cells to the National Laboratories for testing. Cells will be tested both at Zenlabs and independently by three National Laboratories: Idaho National Laboratory (INL), Sandia National Laboratory (SNL) and National Renewable Energy Laboratory (NREL).

During the program, Zenlabs will leverage its material, processing and cell design and development expertise to screen, engineer and optimize various electrolytes, pre-lithiation approaches and cell design solutions addressing the challenges associated with meeting the USABC Low-Cost and Fast-Charge cell targets. Zenlabs has identified development areas that will be addressed and improved during the program. Significant material and cell development in the areas of electrolyte engineering, pre-lithiation development and cell design engineering will take place. Material and cell development typically starts at the coin-cell level where initial screening, testing and optimization takes place. Zenlabs has extensive experience working with coin-cells ensuring that identical electrode formulations, specifications, cell designs, components, formation, etc. are identical to what is used in the pouch cell designs and therefore ensuring similar results are obtained. Once the critical parameters have been optimized at the coin-cell level, results are validated and fine-tuned at the pouch cell level typically in 12 Ah capacity pouch cells.

Zenlabs believes that their silicon-dominant cell technology will be able to meet the USABC program EV cell cost target of 75 $/kWh. First, the high energy density of the cells increases the kWh of a given system, which reduces the $/kWh ratio and reduces the cost target gap. In addition, by utilizing a high capacity silicon based anode, the quantity of material needed is reduced and cost decreases. While the current costs for silicon oxide and pre-lithiation can be relatively high, Zenlabs continues to evaluate and qualify cost effective options and believes that the cost of these important components and processes will continue to decrease significantly in the near future as existing suppliers scale production and additional suppliers come online. Zenlabs has identified and qualified cost effective silicon suppliers that are projecting similar costs to graphite once manufacturing production levels continue to scale. Zenlabs is also partnering with a cell manufacturing partner and equipment vendors to build pre-lithiation equipment capable of meeting the Low-Cost and manufacturing program targets.

The duration of the program is 2 ½ years where Zenlabs will meet the USABC Low-Cost and Fast-Charge cell specifications by integrating silicon-dominant anodes, unique electrolyte formulations and cell designs that will improve fast charging, cycle life and calendar life, as well as focusing on the best pre-lithiation solutions and material options to reduce cost and improve performance. At the conclusion of the program, the cells will meet the USABC EV cell goals for the year 2023.

The program has been structured in a way that as it progresses, the cell targets increase with respect to specific energy, energy density, cycle life and lower cell cost. The program consists of 3 cell builds during the 2 ½ years that include a baseline cell build at the beginning of the program (CB#1), a second cell build (CB#2) midpoint in the program and a final cell build (CB#3) at the conclusion of the program. Cells from each of the builds will be delivered and independently tested by the National Laboratories. Figure I.1.C.1 shows the projected usable BOL (beginning of life) and EOL (end of life) cycle life (a), cell cost (b), specific energy (c) and energy density (d) for the three program cell builds. The measured cell paraments and cost for the baseline cells (CB#1) are also shown

in the figure. Different cell builds will focus on different size and capacity cells, with CB#1 and CB#2 focusing on 12 Ah capacity cells while CB#3 primarily focusing on larger 50 Ah capacity cells.

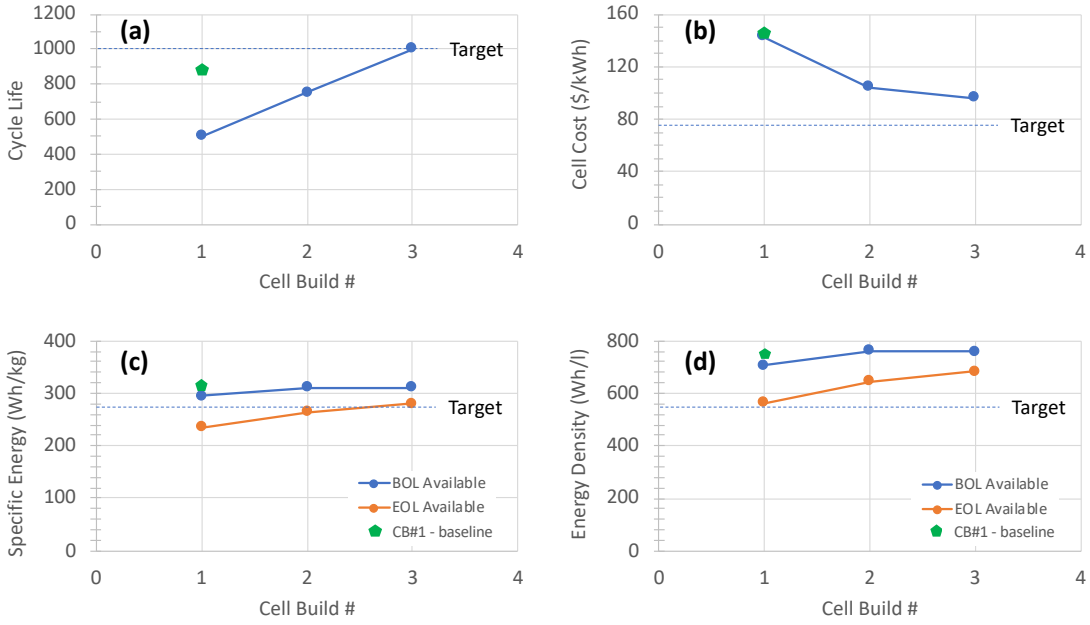

Figure I.1.C.1 Projected cell development progression throughout the USABC program and measured CB#1 values

Results

Zenlabs has demonstrated 1,000 cycles at 1C charging rate (1 hour) and 650 cycles at 4C charging rate (15 minute) from 12 Ah capacity, 315 Wh/Kg energy density pouch cells before reaching 80% capacity retention. In both cases the cells are discharged at a 1C rate and cycled at 100% of its full state of charge window consisting of 2.5V to 4.3V. The cells integrate a silicon-dominant SiO anode and Ni-rich NCM622 cathode. The same high-energy cells are highly rate capable being able to charge to 80% and 90% of its capacity in 10 minutes and 15 minutes, respectively. Figure I.1.C.2a shows the 1C rate charge and discharge cycling meeting the USABC 1,000 cycle goal. Figure I.1.C.2a also shows the 4C fast charge (15 minute total CC + CV) cycling followed by a 1C rate discharge meeting 650 cycles before reaching 80% capacity retention. The fast charge cycling also contains a 1C charge and 1C discharge capacity check every 50 fast charge cycles. Figure I.1.C.2b shows the fast charging capability of the cells being able to charge 80% of their capacity under a 10 minute charge.

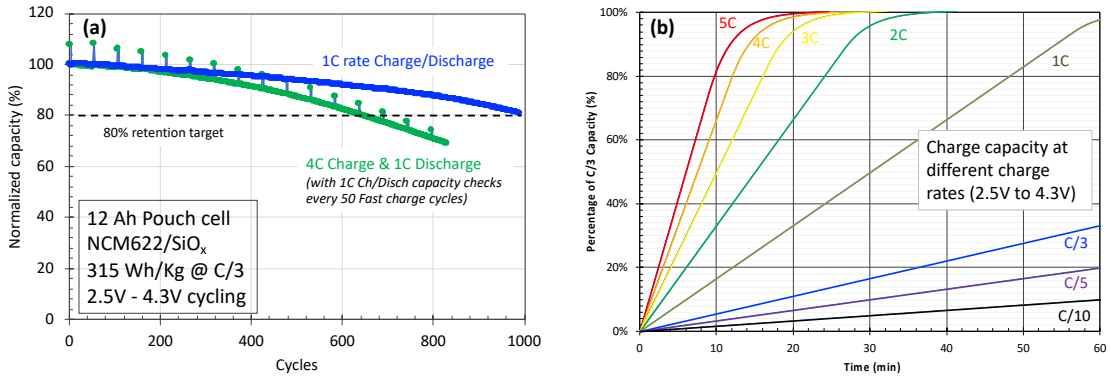

Figure I.1.C.2 Cycle life from 1C rate and 4C rate charging (a) and fast charging capability of the pouch cells (b)

Cycle life results from the 12 Ah capacity pouch cells are meeting the USABC 1,000 cycle target for 1C charging rate and showing very promising 4C rate fast charge cycling with 650 cycles. From similar baseline CB#1 pouch

cells (12 Ah, 315 Wh/Kg), Idaho National Laboratory has independently tested and obtained improved cycling results. Figure I.1.C.3 shows the Dynamic Stress Test (DST) cycling results under standard C/3 rate (3 hour) charging and under 100% fast-charging 4C rate (15 minute) conditions. After 9 reference performance tests (RPTs), each taken after 112 DST cycles, INL has obtained 1,008 DST cycles with cells still maintain 85% capacity retention under the C/3 rate charging condition. Cells continue to cycle under C/3 charging and are projecting to achieve ~1,500 DST cycles before reaching 80% capacity retention. Figure I.1.C.3 also shows the DST cycling performance from cells under 100% 4C rate fast-charging condition. After RPT8, the cells successfully completed 896 DST cycles. Cells under 100% fast-charging conditions did not complete RPT9, but overall showed excelled fast charging results nearly meeting the USABC 1,000 fast-charge cycle target.

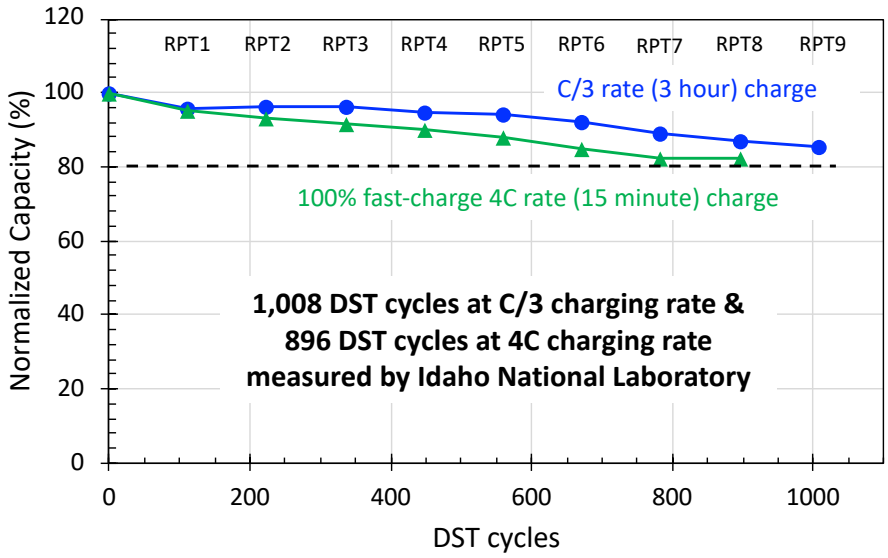

Figure I.1.C.3 DST cycling from standard C/3 rate charging and 100% fast-charging 4C rate conditions

Zenlabs continues to demonstrate that their high-energy silicon-dominant cell technology consisting of SiO anodes and Ni-rich NCM cathodes are able to cycle at full 100% usable window (4.3V to 2.5V) under standard and fast-charging conditions. Cycling results have been measured internally at Zenlabs and independently validated by various automotive OEMs and INL. Cycling results suggest that Zenlabs' cell technology is able to compensate and support the large volume expansion of silicon while avoiding fragmentation and pulverization problems. Based on cycle life, fast-charging capability, high energy and power, this technology is nearly ready from commercialization. Some of the remaining challenges of the technology are gas generation and calendar life. Both reduction of gas and improvement of calendar life are closely tied to the electrolyte formulation. Zenlabs continues to focus on the development of unique electrolyte formulations to reduce gas generation and improve calendar life performance while maintaining other critical cell parameters like cycle life, rate capability, energy, power, low/high temperature operation, cost and safety.

The stability and properties of the electrolyte are critical to ensure good cell performance with respect to calendar life and reduced gas generation while continuing to meet the fast rate charging, cycle life, low and high temperature operation, cost and safety requirements. Decomposition of the electrolyte at the negative electrode can take place under the highly reducing and oxidative high voltage environments. The only reason graphite electrodes remain dormant to the reduction process is due to the formation of a stable protective film at the interface of the anode electrode and the electrolyte which is termed as the solid electrolyte interface (SEI). Si-based materials also require an SEI, that is chemically and potentially structurally different than graphite. The chemical nature and stability of the SEI film is highly dependent on the type of electrolyte with respect to the organic solvents, additives and salts used. The SEI is electronically insulating but allows the ionic transport of lithium ions. Forming a stable SEI on the silicon surface can reduce gas generation and

improve calendar life by preventing an increase in cell resistance associated with the continual breaking and reforming of the SEI with cycles and high temperature storage.

Zenlabs continues to evaluate various electrolyte formulations containing different commercially available linear and cycling organic carbonate solvents, solvent ratios, lithium salts, salt concentrations and various additives known to perform well with silicon anodes and Ni-rich NCM cathodes. Various anti-gassing additives, anode and cathode SEI forming additives, hydrofluoric (HF) acid scavenging additives, and fire retardant additives are also being evaluated. Initially the electrolyte formulations are screened and evaluated in coin-cell full-cells under identical cell design conditions used in the pouch cells. After promising electrolyte formulations based on capacity, rate, and cycle life are identified from coin-cells, evaluation in large capacity pouch cells will follow. Figure I.1.C.4a shows the coin-cell full-cell cycle life data at 1C rate for various electrolyte formulations where different antigassing, SEI former and nonflammable additives A9 and A10 were evaluated. The results show promising cycle life at 1C rate and 4C rate (not shown) while integrating the additives into electrolyte system #29. Figure I.1.C.4b shows the gas generation from small 2 Ah capacity pouch cells. Zenlabs has developed a high-throughput protocol using small 2 Ah capacity pouch cells to quickly evaluate the gas generation and thermal stability of the cell integrating different electrolyte formulations. Reducing the gas generation is important to improve the safety and longevity of the cell. By using smaller 2 Ah pouch cells without pre-lithiation, Zenlabs can use pre-made pouch cells to easily screen different electrolyte formulations. The 2 Ah cells integrate identical Ni-rich NCM cathodes, SiO anodes, separator and cell design. Normally, the down-selected electrolytes are integrated into larger pre-lithiated 12 Ah capacity cells where similar trends to the 2 Ah capacity cells are obtained and results are validated. The thermal performance test consists of storing the cell at a temperature of 65˚C at a 100% SOC (corresponding to a charge voltage of 4.3V) and monitoring the cell thickness change versus time. Figure I.1.C.4b shows the cell thickness increase as a function of storage time for different electrolyte formulations tested in the high-throughput 2 Ah capacity cell. It can be seen that the gas generation from electrolyte #4 which is used as the build #1 baseline electrolyte, is high compared to electrolyte #29 and #39. The gassing experiments also show that gas is reduced by integrating electrolyte additive A9 and A10. Promising electrolyte formulation with additive A9 and A10 are being integrated in upcoming cell build #2 (CB#2) and gassing results will be reported in future report.

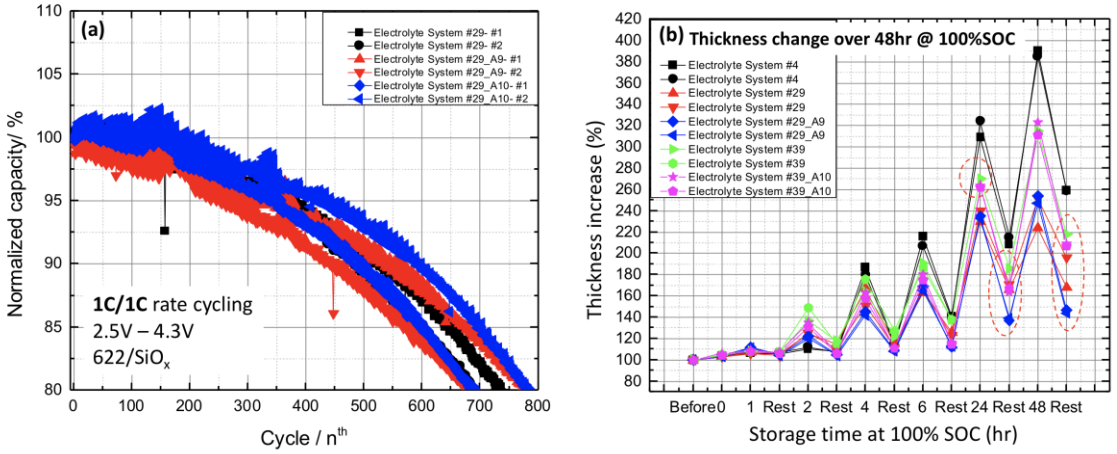

Figure I.1.C.4 1C rate cycling (a) and cell thickness increase versus storage time (b) for different electrolyte formulations

Zenlabs experienced delays with cell build #2 (CB#2) due to the ongoing COVID-19 pandemic, relocation of their cell prototyping facility and equipment problems. Zenlabs relocated its cell prototyping facility to a new location. The new space is 2.3 times larger in total area and 3 times larger in dryroom space compared to the previous facility. The new space is setup to support future growth of the company. Figure I.1.C.5 shows images of the new facility highlighting the coating and dryroom areas. Zenlabs cell prototyping facility is currently operating after completing the relocation and resolving the facility and equipment problems. The

new facility has completed building the next set of cells (CB#2) to be delivered to the National Labs. For cell build #2, Zenlabs down-selected NCM622 cathode #1, SiO_x material from vendor #1, composite separator with drying temperature T4 and electrolyte formulation #4 with additives A9 and A10. Zenlabs expects to deliver 37 – 12 Ah capacity cells to the National Labs in early January 2021 consisting of 26 cells to INL, 8 cells to SNL and 3 cells to NREL.

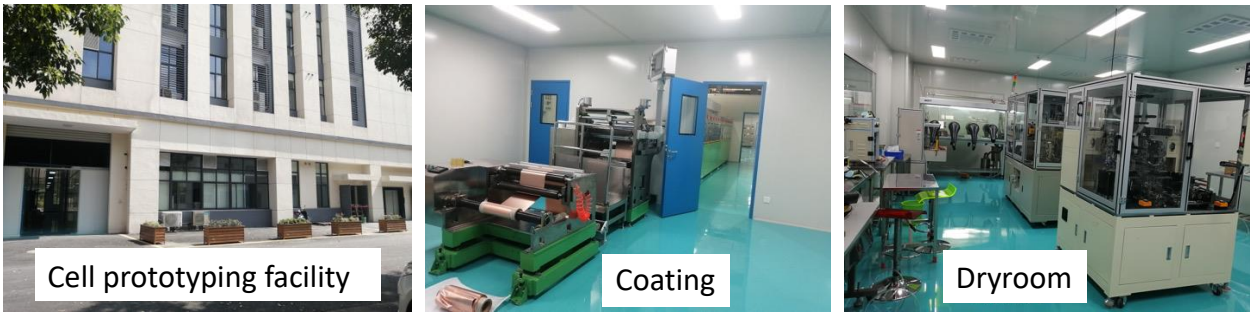

Figure I.1.C.5 Zenlabs new cell prototyping facility

Zenlabs continues its cell development focused on improving calendar life and reducing cost for the upcoming final cell build #3 (CB#3). Zenlabs has developed a protocol to evaluate calendar life from coin-cells as a screening tool, where promising conditions and designs are later evaluated in large capacity pouch cells. Additional development is ongoing to further improve the fast-charge capability and reduce cost of the final cells while continuing to meet the rest of the USABC cell specifications (energy, power, safety, calendar life, temperature, etc.). The final development of the program is focusing to down-select and integrate the best electrolyte formulation to reduce gassing and improve calendar life, a higher Ni-rich cathode capable of higher capacity at lower voltages, a water-based anode binder to simplify processing and reduce cost and a pre-lithiation approach using a newly develop deposition tool from Applied Materials that is reproducible, cost effective and able to support giga-scale production. CB#3 material and cell development continues and results will be reported in future reports.

Conclusions

Zenlabs silicon-dominant 12 Ah capacity and 315 Wh/Kg specific energy pouch cells have meet the 1,000 cycle life target from USABC and have shown excellent fast charging capability recovering >80% of its capacity under a 10 minute charge. Results have been independently validated by Idaho National Laboratory where they showed 1,008 DST cycles completed while still maintain 85% capacity retention under a C/3 rate charging condition. Identical baseline cells (CB#1) also successfully completed 896 DST cycles under 100% fast-charging 4C rate condition. The excellent cycling performance under standard and fast-charging conditions show that this high-energy silicon-dominant cell technology is mature and nearing commercialization. Final material and cell development of the program is focused on reducing gas generation and improving calendar life while continuing to meet the fast-charge, low-cost, cycle life, energy, power, low/high temperature operation and safety specifications. The down-selected materials and cell design will be integrated in the final cell build (CB#3) of the program due in mid 2021.

Key Publications

1. “Fast-Charge and Low-Cost Lithium Ion Batteries for Electric Vehicles”, ES247_Lopez_2020_p, US DOE Vehicle Technologies Program Annual Merit Review, AMR, 2020.

2. “High Energy Lithium Batteries for Electric Vehicles”, ES247_Lopez_2019_p, US DOE Vehicle Technologies Program Annual Merit Review, AMR, 2019.

Acknowledgements

This work is being performed under the guidance and support from the USABC technical work group. Oliver Gross (oliver.gross@fcagroup.com), Fiat Chrysler Automobiles, Auburn Hills, MI serves as the USABC Program Manager. Other team members include Meng Jiang, Minghong Liu, Jack Deppe, Brian Cunningham, Lee Walker, Aron Saxon and Joshua Lamb.

I.1.D Low Cost Fast Charge Battery Technical Assessment Program (Physical Sciences Inc.)

Christopher M. Lang, Principal Investigator
Physical Sciences, Inc
20 New England Business Center
Andover, MA 01810-1077
E-mail: lang@psicorp.com

Haiyan Croft, DOE Technology Development Manager
U.S. Department of Energy
E-mail: Haiyan.Croft@ee.doe.gov

Start Date: July 23, 2019 End Date: February 1, 2021
Project Funding: $1,000,000 DOE share: $500,000 Non-DOE share: $500,000

Project Introduction

Physical Sciences Inc. (PSI) recognizes the need to advance the state of the art of lithium ion battery technology for transportation uses. Two critical issues are demonstrated in this technology assessment program: Cost and Performance. PSI has developed a technology that has shown in defense applications the ability to both improve the volumetric and gravimetric energy density while also allowing for lower cost due to advantages in materials and processing. This TAP program is meant to demonstrate these advantages of the PSI innovation.

Objectives

The objective of the technology assessment program is to both deliver prototype batteries (8Ah) capacity along with an updated cost model to project how the advantages of this technology can lower the $/kWh cost. The cells with advanced cathodes and constructed utilizing know-how developed by PSI will be delivered to USABC in late 2020.

Approach

The 18 month TAP program consists of three distinct stages. In Stage 1 individual components, cathode, anode and electrolyte were optimized around the 8Ah cell design selected by USABC for this technology assessment. In State 2, smaller 2-4 Ah cells were prototyped and further optimized with an emphasis on low cost, fast charge and energy density. Finally, in Stage 3, the 8Ah cell design was frozen and cells were built for both internal testing and delivery. A cost model will be delivered as part of the final program deliverable that demonstrates anticipated costs using a process familiar to LG Chem who is the commercialization partner for PSI in this program.

The PSI innovation being demonstrated is PSI's patented High Active (HA) coating technology which puts a conductive coating on the active materials and eliminates the need for high surface area carbons in the electrode formulation. Thus, the resulting electrodes are denser and contain 99% by mass of the active material. Other key advantages of this technology are the need for much less NMP in slurry preparation, less binder, faster drying times, less overall surface area, less electrolyte and longer shelf life. All these advantages lead to both performance and cost benefits.

Results

To date, the deliverable cells are undergoing acceptance testing at PSI and are planned to be shipped prior to the end of calendar year 2020. Below is a summary of both the energy and power performance of these cells that contain cathode electrodes whose composition are 99% active material.

Table I.1.D.1 Summary 8Ah Cell Information

Cell Specification	Value	Unit
Nominal Voltage	3.72	V
Nominal Capacity, C/3	7.8	Ah
Max/Min Voltage	4.35/2.8	V
Mass	0.117	kg
Volume	54	cc
Specific Energy	247	Wh/kg
Energy Density	533	Wh/l

Table I.1.D.1 provides a summary of the 8Ah cells to be delivered to USABC. These are the actual average performance values for cells that are currently undergoing break-in testing prior to delivery. These cells are only meant to demonstrate the performance characteristics of the PSI technology and the cost models are based on much larger cell sizes that tend to improve the total cost savings and the specific energy density.

Table I.1.D.2 Detailed Cell Information

Cathode Design		
Cathode Material	HA Coated NCM-622	Unit
Active Percentage	99%	%
Electrode Loading (single side)	17.3	mg/cm2
Areal Capacity	2.9	mAh/cm2
Press Density	3.4-3.5	g/cc
Number of Pairs	22	
Foil Thickness	Bare Aluminum, 12	µm
Anode Design		
Anode Material	Articicial Graphite	
Electrode Loading Isingle side)	9.4	Mg/cm2
Areal Capacity	3.1	mAh/cm2
Press Density	1.5-1.6	g/cc
Number of Pairs	23	
Foil Thickness	Bare Copprt, 9	µm
Separator		
Type	Polypropylene	
Thickness	12	µm
Slit Width	92	mm
Electrolyte		
LiPF6	1	M
EC:DEC:EMC	4:3:3	
VC	2	Wt%

Table I.1.D.2 gives the complete bill of materials for the 8Ah cells that are to be delivered to USABC from this TAP program. For this program, HA was only applied to the cathode material (NMC-622) although work was done and will later be shown where the HA technology was also applied to the anode material.

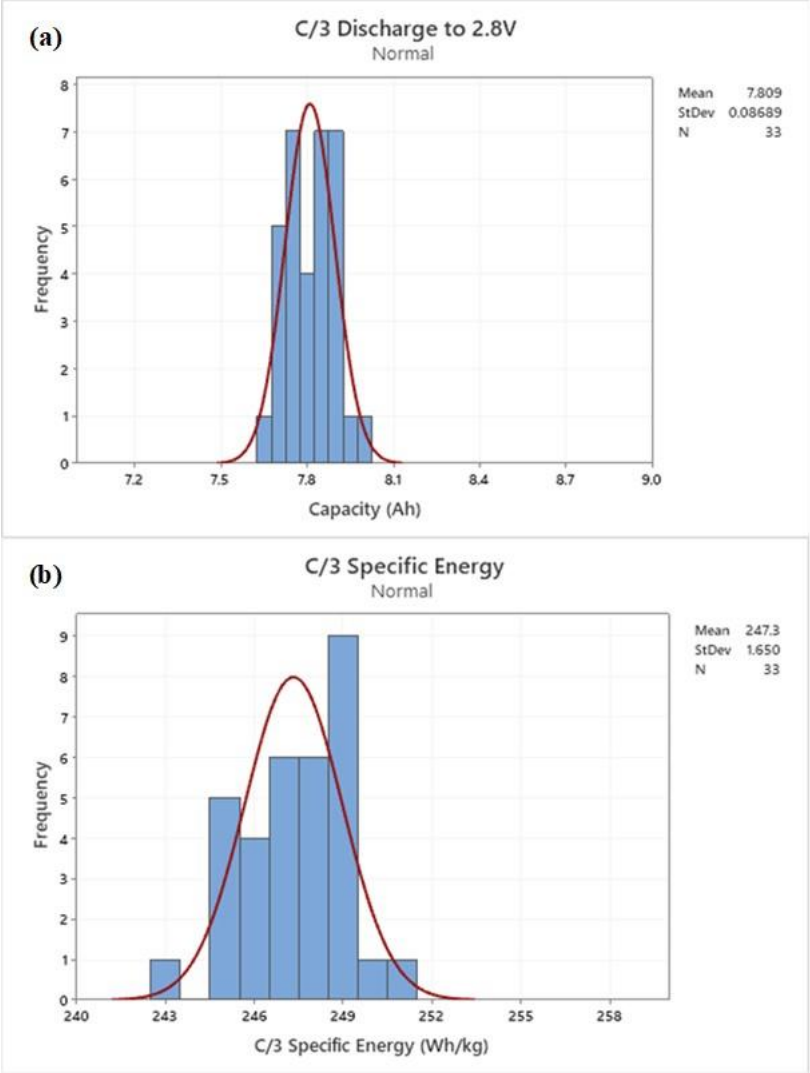

Figure I.1.D.1 (a) Frequency vs. Capacity for 8Ah Cell Build (b) Frequency vs. Energy for 8Ah Cell Build

Figure I.1.D.1 provides cycling data for the group of 8Ah cells that will be delivered to USABC at the conclusion of this TAP program. Another advantage of the HA technology is that it allows for much tighter processing conditions (higher solids in slurry, no active carbons in slurry, less binder) that results in much less spread of the performance characteristics of cells. All measured performance properties shown are within 1% of the mean. This advantage will also lead to better grading of cells to be selected for battery builds going forward, which also contributes to a lower overall cost.

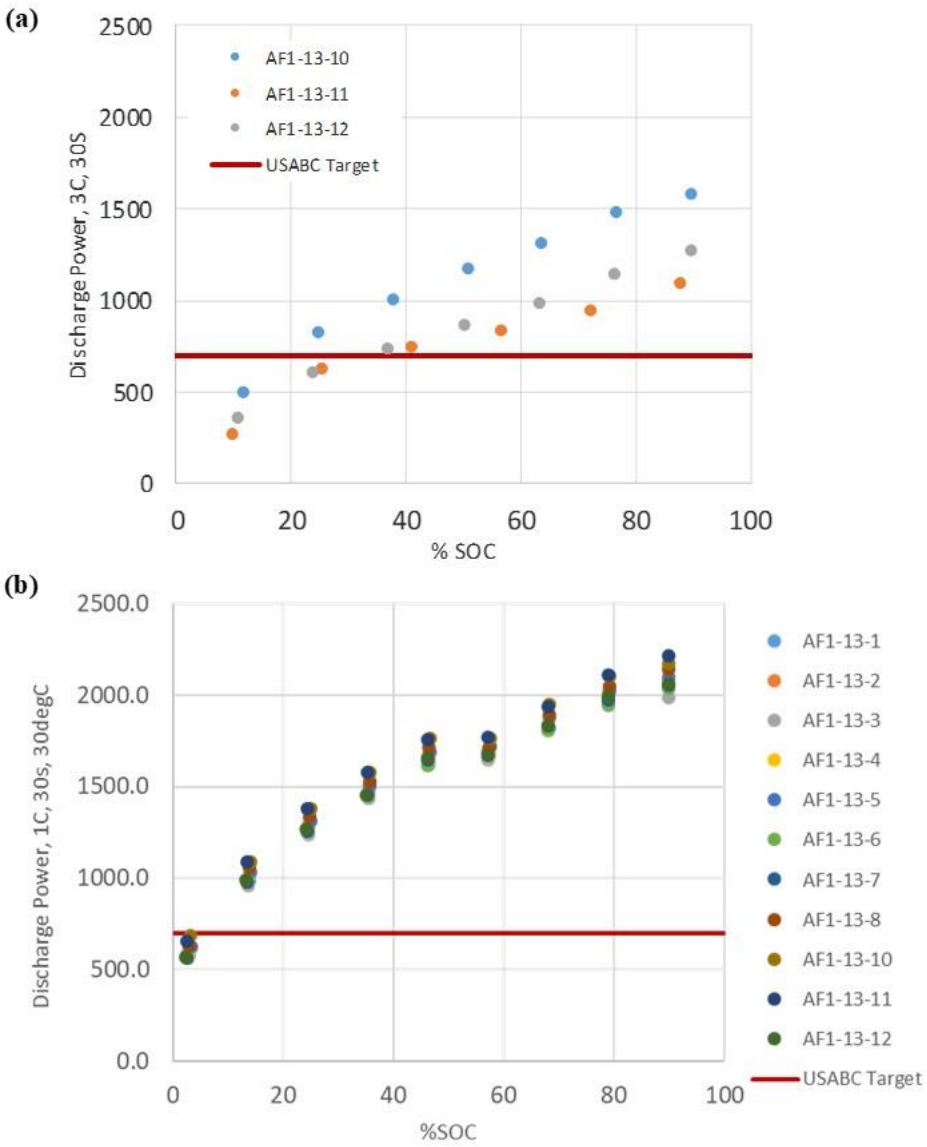

Figure I.1.D.2 (a) 3C Discharge Power vs. % SOC on HPPC Testing (b) 1C Discharge Power vs. % SOC on HPPC Testing

Figure I.1.D.2 shows the HPPC test both at the 1C and 3C rates. These cells all meet the performance requirement above 20% state of charge. PSI has also utilized this data to construct a charging protocol that allows for more than 80% of the available energy to be recharged in less than 15 minutes.

Table I.1.D.3 Projected HA Cost Impact on Process and Component Costs

Process	LG Baseline	With HA Technology
Slurry Preparation	0.025	0.02
Coating/Drying	0.1	0.075
Balance of Operations	0.075	0.075
Component	LG Baseline	With HA Technology
Cathode Material	0.25	0.22
Electrolyte	0.1	0.09
Balance of Materials	0.45	0.43

Table I.1.D.3 provides the basis of the cost model employed by PSI to determine the cost saving incurred by utilizing PSI's HA coating technology (values only represent cathode coating). In this model developed in conjunction with LG Chem, acting as a commercialization partner, the overall cost of a cell currently comes to about 80% of costs coming from materials whereas 20% comes from processing costs. This table shows how the HA technology only on the cathode can reduce the cost by 9%, from $100/kWh to $91/kWh.

Conclusions

Although this TAP program is still active, current conclusions are that 8Ah cells have been fabricated using the PSI HA technology that show performance gains over baseline technology. These cells have a higher specific energy while maintaining power performance. The scale-up and cell construction efforts demonstrate the increased active material content, 99%, and decreased processing solvent and therefore cost that the HA technology enables.

I.1.E Development of High Voltage Electrolyte (Gotion Inc.)

Dr. Jennifer Hoffmann, Principal Investigator
Research Scientist
Gotion Inc.
8001 E. Pleasant Valley Rd.
Independence, OH 44131
j.hoffmann@gotion.com

Brian Cunningham, DOE Technology Development Manager
U.S. Department of Energy
Brian.Cunningham@ee.doe.gov

Start Date: March 20, 2019 End Date: March 20, 2021
Project Funding: $3,115,015 DOE share: $1,499,456 Non-DOE share: $1,615,559

Project Introduction

As the automotive industry continues to expand into electromobility with hybrid electric vehicles and fully electric vehicles to meet emissions goals, the need for advanced materials to meet standards for safety, energy density, and cost demand technical advances in battery systems and materials. Lithium titanate ($Li_4Ti_5O_{12}$ or LTO) negative electrode material has the potential to meet or even exceed these targets. The material has lower temperature compatibility and excellent cycle life that has resulted in its application in urban electric buses. LTO has offers improved safety over other materials making it an ideal material to commercialize. The factors impeding its commercialization include low voltage potential, high temperature gas generating reactions, and increased cost over other negative electrode materials. Many of these issues stem from the cathode material most often paired with LTO, nickel cobalt manganese (NCM) cathode materials. The pairing of NCM with LTO for a lithium ion battery results in low energy density and fairly high cost. However, coupling LTO with lithium nickel manganese oxide high voltage spinel ($LiNi_{0.5}Mn_{1.5}O_4$ or LNMO or HVS) resolves those concerns given its price and voltage advantage over NCM materials. By resolving the gas generation issues of LTO and developing an electrolyte that can work with the LNMO material, advances in electromobility commercialization can be realized.

Objectives

The primary objective of this project is to develop electrolyte formulations and novel electrolyte additives to protect and improve LTO and LNMO materials. The electrolytes and additives developed for these electrode materials are targeted to have minimal gas generation, high cycle life, high power charge/discharge capabilities, wide operating temperature, and competitive cost. In addition to this primary objective, the analysis of the interactions of the electrolyte with these materials leading to the understanding of gassing and failure mechanisms is also being targeted.

Approach

The approach to this project has been broken into 6 tasks as identified below:

- Task 1: Novel Additive Design, Synthesis, Screening and Scale Up
- Task 2: NCM622 v. LTO Multi-Layer Pouch Cell (MLPC) Testing and Analysis
- Task 3: LNMO v. Carbon Anode MLPC Testing and Analysis
- Task 4: LNMO v. LTO 2Ah MLPC Testing and Optimization
- Task 5: LNMO v. LTO 10 Ah MLPC Testing and Optimization
- Task 6: LNMO v. LTO 10 Ah MLPC Scale Up and Deliverable.

In task 1, the novel additives that are targeted for solid electrolyte interface (SEI) formation, cathode electrolyte interface (CEI) formation, and manganese dissolution prevention are synthesized and screened in

coin cells before testing small batches of the best candidates in pouch cells. In addition, surface analyses that aid in development and understanding of additives with the electrode materials are also conducted. Most promising candidates are then scaled up for large batch production and selected for patent protection.

Task 2-4 are similar in testing, but different in objective. The goal of combining the LTO with NCM622 in task 2 is to isolate the LTO gas generation mechanisms from the LNMO gas generation mechanisms to understand which additives LTO responds to best. The same is true for task 3, where the LNMO is kept apart from the LTO for understanding and additive development. The hope is that this will not only provide additives for the NCM/LTO systems currently being investigate, but also provide additives and formulations for the 4.9V LNMO/C system as well. These two tasks will narrow down the novel additives and formulations with the information being used to make more intelligent electrolyte design for task 4. Task 4 will still have analyses and discoveries to be made in testing as each combination has its unique mechanisms and voltage ranges, but the need for understanding on these materials and combinations is important. Task 2 focuses on 45°C cycling and 45°C storage testing. Task 3 focuses on 25°C and 45°C cycling. Task 4 focuses on 25°C cycling, 45°C cycling, and 45°C storage. During the performance testing of each task, electrolyte will undergo property testing to measure conductivity, viscosity, vapor pressure, flash point, water and HF content, and lithium transference number. Finally, any surface analysis, gas analysis, or other analytical techniques need will be carried out.

Once the initial testing in task 4 is completed, the MLPC will be scaled up from 2Ah cells to 10 Ah cells. In task 5, the large cells will undergo -20°C, 25°C, and 45°C performance testing. The best formulations will then be selected for task 6 deliverable testing where the cells will be sent to National Laboratories for further testing.

Results

This project has undergone delays due to the COVID-19 pandemic, but many results have been able to be gathered. The findings and results will be addressed in order of the tasks as described in the approach section of this report.

Task 1 has produced small scale quantities of 12 different novel additives. Of the 12 additives, 10 have been evaluated in NCM622/LTO and LNMO/C MLPC, with 2 awaiting testing. Currently, 4 of the 10 have been selected for scale up and potential patent protection. The additives will continue to be screened in LNMO/LTO cells as development continues.

Task 2 focused on the electrolyte optimization and mechanistic understanding of the NCM622/LTO MLPC testing. The data is still being analyzed to determine best novel additive candidates, but the performance testing showed optimized, EC free formulations were successful at mitigating gas generation without sacrificing performance as seen in Figure I.1.E.1. Extensive work has been done to find suitable EC replacement solvents as well as optimization of the novel additives to improve the performance. It is expected that the results from this work will be disclosed further through publication or presentation when finalized.

Task 3 results can be categorized into three findings. The first finding has been extensive comparison of LNMO material from various suppliers. Due to unforeseen circumstances with the original material supplier, supply was obtained from two other sources. Comparison of these materials has shown a variety of differences in particle size and morphology resulting in difference performance trends. Supplier 1 showed good performance with low impedance while Supplier 2 showed improved gas generation but higher impedance. Supplier 3 showed the best capacity retention, impedance, and gas generation of the three suppliers. Even with the comparison and obvious differences, all three materials showed dismal initial cycle efficiency (ICE) , and two of the materials have shown degradation/instability in storage over time indicating the consistent commercialization, fabrication, and synthesis of this material is not yet realized.

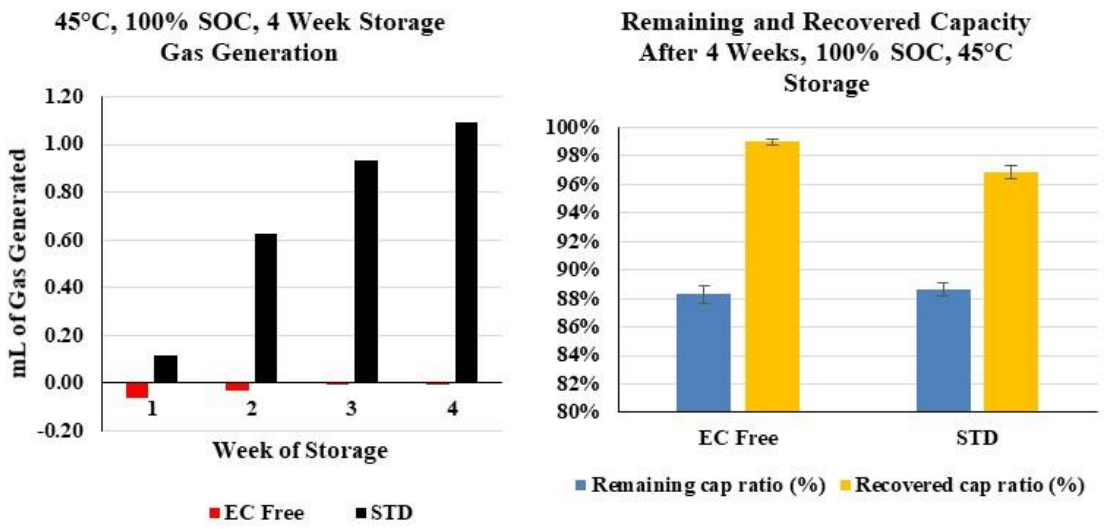

Figure I.1.E.1 Comparison of EC free formulation with a standard (STD) EC containing electrolyte formulation after 4 weeks of 45°C storage in 2 Ah NCM622/LTO MLPC. The EC free formulation shows no gas generation after 4 weeks of high temperature storage and improved recovered capacity.

Task 3 results also showed an unexpected gassing mechanism. Results of gas analysis and gas measurement showed that during cycling, generated gas was consumed. Based on gas analysis, it is likely the carbon dioxide that is being consumed. Extensive examination of this was unable to be carried out due to scope of the project, but the results and findings were collected and shared. The final results from this task included development of formulations and novel additives that improved the cycling performance of the LNMO/C 2Ah MLPC. Figure I.1.E.2 shows the cycling of formulations that showed similar or improved performance over the baseline (black curve) using novel additives and/or combinations of additives. Figure I.1.E.3 shows the corresponding gas generation of the cycled formulations with many showing decreased gas generation compared to the baseline (red bar).

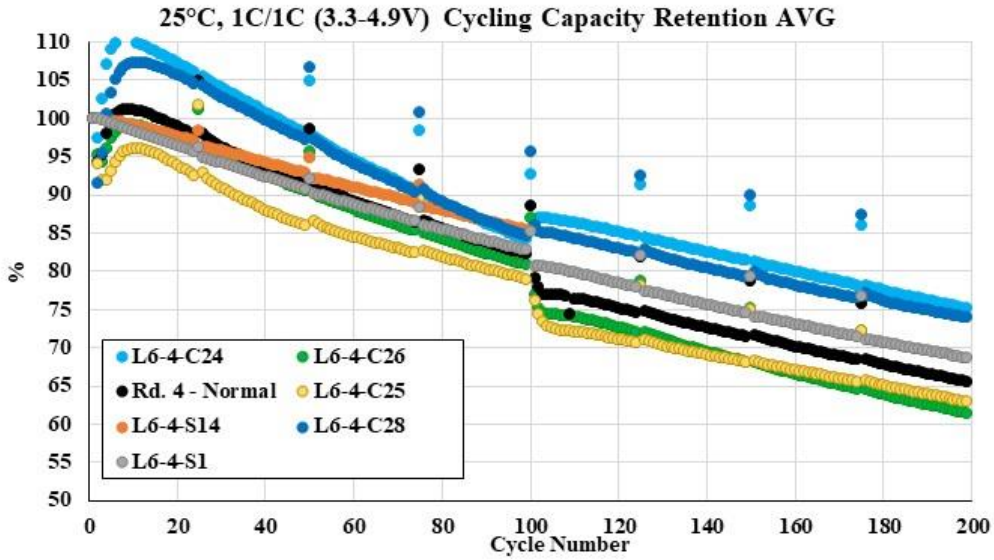

Figure I.1.E.2 Cycling at 25°C in LNMO/C MLPC showing L6-C24, L6-4-C26, and L6-4-S1 have improved performance over the baseline L6-4 (Rd. 4 - Normal, Black Curve).

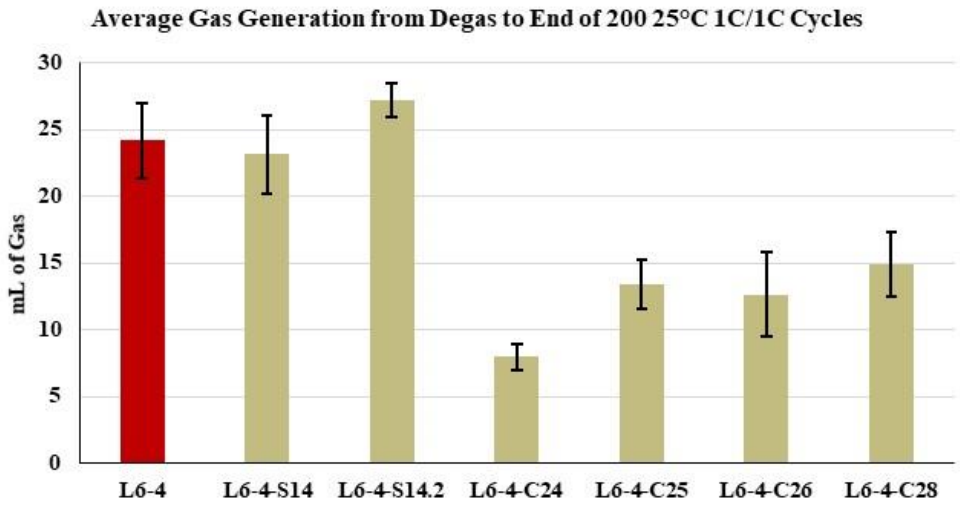

Figure I.1.E.3 Corresponding volume of gas generated by the formulations undering 200 cycles of 25 °C cycling testing in LNMO/C MLPC in the previous figure.

Task 4 is now the current focus of the project with extensive testing being carried out in LNMOLTO MLPC. No findings or results are yet prepared, but extensive work on novel additive screening as well as novel solvents is being undertaken. This is the task most delayed by COVID-19, but with operations temporarily back progress is expected to be made.

Conclusions

In this annual project write up, several conclusions can be made. The first being that NCM622/LTO pouch cells benefit greatly from EC free formulations when optimized with the appropriate EC replacement solvents and additives. This work is expected to be published as the data analysis is completed. The novel additives generated from this project show promising results with one patent being drafted, others being evaluated, and scale up of selected compounds started. The work being done on the LNMO material is exposing failure, aging, and gassing mechanisms that allow for more understanding of the electrolyte-electrode interactions. Even with this understanding, the supplier comparisons have shown the need to work towards improved synthesis and commercialization of the material. With the compounds created in task 1 of the project and the information from task 2 and 3, the LNMO/LTO MLPC work being carried out in task 4 to develop an electrolyte to meet the objectives of this project is underway.

Acknowledgements

It is important to acknowledge Dr. Brett Lucht of the University of Rhode Island and his technical group as they have been integral in the design, development, and synthesis of the novel additives in this project. Dr. Lucht and his group have carried out extensive surface analysis of the materials and been of huge assistance with the LNMO supplier comparison.

The PI of this project would also like to acknowledge Dr. Martin Payne for all his assistance in meeting project requirements and finances. His participation and support of this project has made the extensive work being carried out possible.

I.2 Processing Science & Engineering

I.2.A Towards Solventless Processing of Thick Electron-Beam (EB) Cured LIB Cathodes (ORNL)

David L Wood,III, Principal Investigator
Energy and Transportation Science Division
Oak Ridge National Laboratory
One Bethel Valley Rd, Oak Ridge, TN 37830
E-mail: wooddl@ornl.gov

Zhijia Du, Principal Investigator
Energy and Transportation Science Division
Oak Ridge National Laboratory
One Bethel Valley Rd, Oak Ridge, TN 37830
E-mail: duz1@ornl.gov

Peter Faguy, DOE Technology Development Manager
U.S. Department of Energy
E-mail: Peter.Faguy@ee.doe.gov

Start Date: October 1, 2015 End Date: September 30, 2022
Project Funding: $400,000 DOE share: $400,000 Non-DOE share: $0

Project Introduction

There are a variety of technical attributes to electron beam (EB) curing of LIB binders. EB curing uses solvent-free compositions that have low emissions (VOCs, etc.) and are recognized by federal, state and local governments as being a more desirable technology. Solvent or water-based processing requires high drying energy and results in significant CO_2 emissions. EB curing offers significant process energy savings, is ultra-high speed, and utilizes much more compact equipment than conventional drying ovens (much less plant floor space required). Furthermore, it is a relatively cool process and is compatible with heat-sensitive substrates. Conventional thermal drying of LIB electrodes is typically conducted using multiple temperature stages; however, EB can be conducted in a single step. Solvent-free electrode compositions are rated as non-flammable, which translates into lower insurance costs, less stringent storage requirements and, a reduction in handling hazards.

EB treatment is a fast, robust materials processing technology that commonly delivers low cost and excellent performance for high-volume materials production. Based on decades of development and commercial deployment, self-shielded machines routinely operate with high reliability and low maintenance in industrial roll-to-roll production environments. ORNL is developing, demonstrating, and transitioning technology for high-speed roll-to-roll EB processing of LIB electrodes (i.e. coating formation and binder curing). Further specific advantages of this processing route for LIBs are:

- Unmatched throughput – We estimate ≥ 600 m^2/min throughput can be achieved based on ≥300 m/min line speed for roll widths up to 2 m ($1.5-2.0M installed with machine footprint ~10 m^2).
- Thicker electrodes – Up to 150 microns can be achieved at the throughput rate mentioned above. Coatings of several hundred microns could be processed at higher capital cost per unit throughput, modest reduction in energy efficiency, and larger equipment footprint.
- Excellent energy efficiency – Electrical efficiencies ≥60% are possible, including voltage transformer losses (i.e., ≥60% of electrical line energy is converted to productive EB energy).

- Environmentally friendly – EB processing requires no solvent and no initiator and has low emissions.

Objectives

- Significant process energy savings
- Ultra-high electrode processing speed
- Utilize much more compact equipment than conventional drying ovens.

Approach

ORNL is working on a multiphase approach to develop, demonstrate, and transition EB processing of roll-to-roll battery materials.

Phase 1 – Demonstrate the technology's key differentiating attributes of high throughput and thick layer processing (FY15-16).

Phase 2 – Address the key challenges of EB curing parameters and resulting material performance; develop coating methods requiring little or no solvent. (FY17-18).

Phase 3 – Demonstrate an optimized curing system in conjunction with a high-speed coating line together with a key equipment partner and battery manufacturer (FY19-20).

Results

As this project moving into Phase 3, a roll-to-roll EB processing pilot line is procured, installed, and implemented at the DOE Battery Manufacturing R&D Facility (BMF). Key parameters of the pilot lines are listed in Table I.2.A.1. The highest voltage is 300 KeV, which is capable of penetrating thick electrode with 40 mg/cm^2 loading (~ 6.5 mAh/cm^2). It also comes with a "clam-shell" chamber for self-shielding and N_2 inerting to ≤ 200 ppm of oxygen.

Table I.2.A.1 Key features of the EB processing pilot line at BMF.

	Key parameters
Voltage	120-300 keV
Width	15 inches
Line speed	3-30 feet per minute
Inert	self-shielded and N_2 inerted ≤ 200 ppm of oxygen

Figure I.2.A.1a shows the completion of the framework of the EB pilot line during a progress inspection in December 2019. The factory acceptance was conducted in March 2020. Figure I.2.A.1b, c and d show the unwind front, web passing-though the chamber, and rewinding end, respectively. During the inspection, the conditioning test was conducted at a minimum requirement of 300 kV and 15 mA. Radiation survey was conducted, and the reading was less than 0.1 mR/hr at 10 cm from all surfaces and the entering/exiting slots. Four (4) hour production rate test was carried out at 300 kV, 75 kGy at a line speed of 10 meter/minute. The beam cross-web uniformity was ±6.5% as shown in Figure I.2.A.2. The equipment was then shipped and installed at BMF as shown in Figure I.2.A.3.

Figure I.2.A.1 (a) overview of the framework of the EB pilot line. (b) the unwind front, (c) web passing through the chamber, and (d) the rewind end of the pilot line during the factory acceptance.

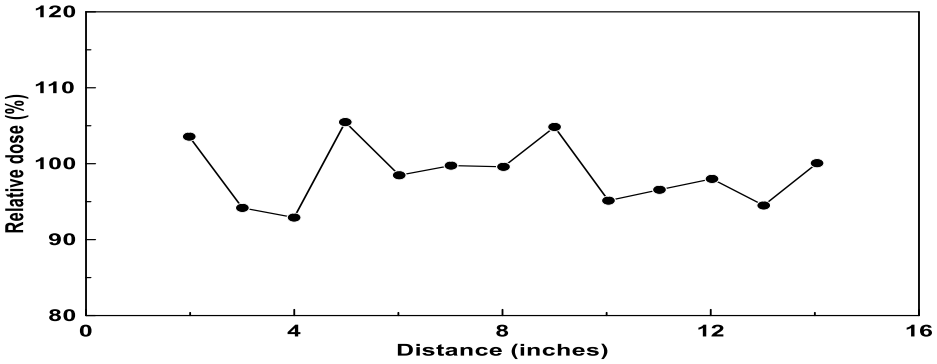

Figure I.2.A.2 Dose uniformity across the dosimeter strip.

Figure I.2.A.3 The EB pilot line installed at Battery Manufacturing R&D Facility at ORNL (BMF).

Electron beam curing were conducted on cathode electrodes using the newly installed EB curing pilot line. Four different EB curable binders were used (here and after denoted as Binder A, Binder B and Binder C). The electrodes were prepared at BMF using a doctor-blade coating bar with formulation of NMC/Binder/carbon black at 88/7/5 wt%. The loadings are about 24 mg/cm^2. The processing meters were controlled by HMI at 300 kV, 60 kGy and 2 feet-per-minute.

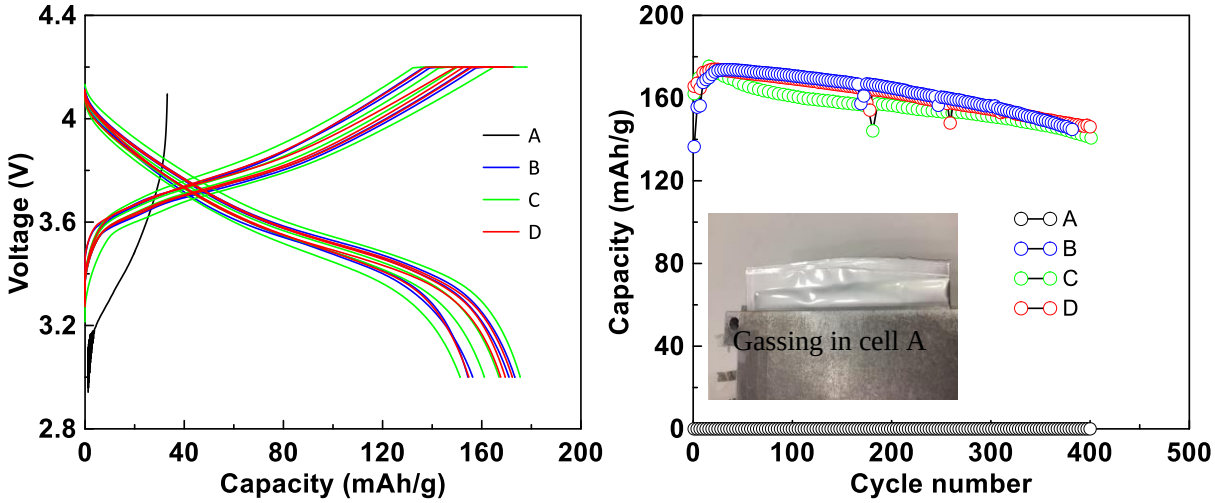

Figure I.2.A.4 (a) Voltage curves of the EB processed NMC cathode using different binders. (b) Cycling performance of EB processed NMC cathodes using different binders.

Pouch cells were assembled using EB cured NMC cathode electrodes with 4 different binders. Figure I.2.A.4a shows the voltage curves of EB processed NMC cathodes for the 2nd, 50th, 100th and 300th cycles. For binder A, the cell is unable to deliver meaningful capacity. For the other 3 binders, the voltage curves show typical features of NMC materials. Figure I.2.A.4b shows the cycling performance of EB processed NMC cathodes with 4 different binders. A phenomenon observed in cell A is enormous gassing as shown in the inset of Figure I.2.A.4b. This is an indication that this type of binder is not stable in Li-ion cell environment and leads to serious side reaction. The other 3 binders show good cycling performance with about 81% capacity retained after 400 cycles.

Several important studies have been done, which consider the pack-level cost implications of LIB electrode processing. BatPaC, Argonne's spreadsheet-based performance and cost model for automotive battery packs, has been widely used to project battery costs. In the NMP based electrode processing, the energy demand for the process can be as high as 10.2 kWh per kg of NMP vaporized. The large energy demand is because of the large quantity of air that must be heated and cooled. The main driver behind the heat demand is the large air flow rate required in the dryer to ensure that the NMP concentration is always maintained far below the flammability limits, typically an order of magnitude lower. The overall cost of the drying and NMP recovery contribute ~3% to the cost of the battery pack. Figure I.2.A.5a shows the cost breakdown distributed to materials (58%), purchased items (23%) and manufacturing (19%). In the manufacturing part, Figure I.2.A.5b shows the cost breakdown into electrode processing, cell assembly, formation, module/pack assembly and others. In the electrode processing, about half of the cost is related to NMP drying and recovering.

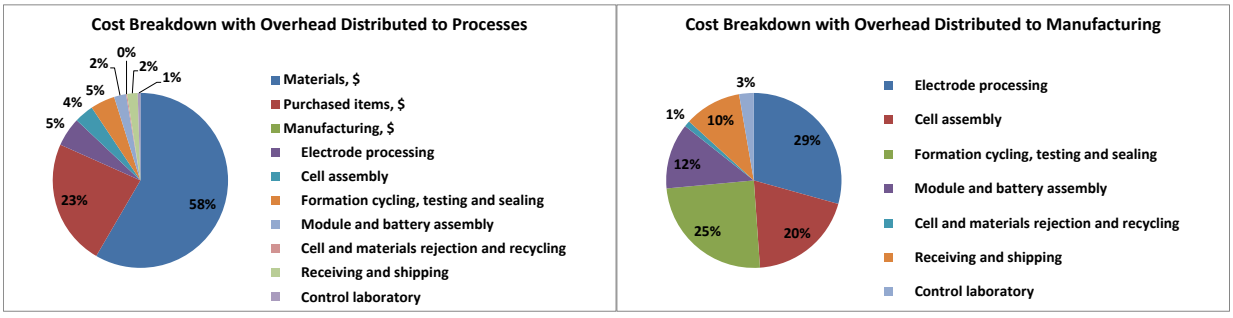

Figure I.2.A.5 (a) Cost breakdown distributed to processes, and (d) cost breakdown of the manufacturing when NMP drying and recovering are used in electrode processing.

The objective of this part of work is to study the energy demand and distribution for the EB curing of the cathode, and to estimate the cost of this process compared to the NMP drying/recovering process. Figure I.2.A.6 shows the cost reduction benefit when EB curing is used to replace the NMP drying/recovery process

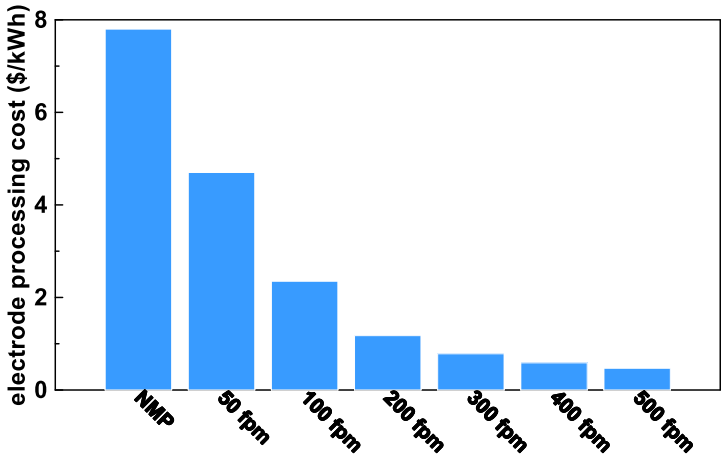

Figure I.2.A.6 Electrode processing cost reduction by using EB processing compared to NMP drying/recovering process.

in the electrode processing. The cost input values are listed in Figure I.2.A.7. When similar line speed (50 fpm) is used, EB processing can save 40% of the cost. Electron beam can enable high speed production because chemical curing takes less than 1 second compared to thermal drying. Figure I.2.A.6 shows the cost reduction benefits with the increase of the web speed in EB processing. When a high speed of 500 fpm is used, the cost can be decreased to 6% of the NMP based process.

Category	Parameter	Value	Unit		Category	Parameter	Value	Unit
Electricity	Electricity	0.1	/kW-hr		Material	Electrode	1.2	g/cc
						Weight fra	0.85	wt%
						Current co	2.7	g/cc
Nitrogen	Nitrogen c	0.13	/scm			Current co	15	microns
	Nitrogen e	20000	/yr			Active mat	150	mA-hr/g
	Nitrogen d	1.2	kg/scm					
Embodied	Primary en	3			Capital eq	275 keV si	3200000	
	Nitrogen	1700	kIJ/kg			275 keV du	4200000	
						Equipment	0.2	
Labor	Direct ope	28	/p-hr			Equipment	10	yr
	Direct mai	80000	/yr					
	Indirect lal	0.4			Building	Area	7500	sq ft
						Unit cost	200	/sq ft
Operation:	Shift durat	2000	hrs			Bldg & me	1500000	
	Total oper	7500	hrs			Facility de	30	Yr
	Annual shi	4				Startup, cc	0.2	
	Spare part	10000	/beam-shift					
					Miscellane	Insurance	0.02	
Cell	Average vc	3.5	V			Bldg utilitie	2	/sq ft/yr

Figure I.2.A.7 Cost input values for calculating the EB processing cost in electrode processing.

Conclusions

- An EB processing pilot line has been successfully purchased, installed and implemented at BMF.
- Binder evaluation found that certain type of EB curable binder can have serious side reaction in Li-ion battery. Several good binder candidates have been identified with good cycling performance.
- The benefit of using EB processing has been calculated compared to NMP drying/recovering processing. The EB processing shows 94% cost reduction when 500 fpm production rate is implemented.

Key Publications

1. Wood III, David L., Marissa Wood, Jianlin Li, Zhijia Du, Rose E. Ruther, Kevin A. Hays, Nitin Muralidharan, Linxiao Geng, Chengyu Mao, and Ilias Belharouak. "Perspectives on the relationship between materials chemistry and roll-to-roll electrode manufacturing for high-energy lithium-ion batteries." Energy Storage Materials, 29 (2020) 254-265.
2. Toward Solventless Processing of Thick Electron-Beam (EB) Cured Lithium-Ion Battery Cathodes, VTO AMR 2020.

I.2.B Performance Effects of Electrode Processing for High-Energy Lithium-Ion Batteries (ORNL)

David L. Wood, III, Principal Investigator
Oak Ridge National Laboratory
Energy & Transportation Science Division
2370 Cherahala Blvd., GRID Center, MS-6479
Knoxville, TN 37932
wooddl@ornl.gov

Jianlin Li, Principal Investigator
Oak Ridge National Laboratory
Energy & Transportation Science Division
2370 Cherahala Blvd., GRID Center, MS-6479
Knoxville, TN 37932
lij4@ornl.gov

Peter Faguy, DOE Technology Development Manager
U.S. Department of Energy
E-mail: Peter.Faguy@ee.doe.gov

Start Date: October 1, 2014 End Date: September 30, 2022
Project Funding: $400,000 DOE share: $400,000 Non-DOE share: $0

Project Introduction

This project at the DOE Battery Manufacturing R&D Facility (BMF) at ORNL builds on past research successes in the areas of battery electrode process development and optimization, cost reduction, cell energy density improvements, and manufacturability advancements, which support the Vehicle Technologies Office (VTO) and Electrochemical Energy Storage Tech Team ultimate targets of $80/kWh-usable system cost, 500 Wh/kg cell energy density, 800 W/kg cell power density, and 10-15 min extreme fast charging times. Our goal is to perform the science needed to reduce high-risk, high-payoff technologies to lower risk levels, such that U.S. industry will consider their integration in future products. Once a new material, process, or concept has demonstrated feasibility for integration and scaling, the BMF will work to make it a viable processing methodology (preferably with industry partners) with validated performance in a full pouch cell design. While doing so, the BMF will leverage a large array of complimentary projects and sponsors that will provide additional experience and a fast, efficient methodology for solving problems faced by the domestic lithium-ion battery (LIB) industry.

Objectives

To improve cell energy and power density and reduce battery pack cost by manufacturing thick electrodes with tailored electrode architecture via advanced processing and high-energy, high-voltage cathode materials:

- Apply aqueous processing to Ni-rich layer oxides (NMC811 and NCA).
- Fabricate thick (6-8 mAh/cm^2), crack-free composite NMC811 cathodes via aqueous processing.
- Create laser structured electrodes.
- Characterize electrolyte imbibition rate and understand the electrolyte imbibition-processing relationship.
- Assemble pouch cells with NMC811 and thick, tailored electrode architecture

- Demonstrate energy density ≥225 Wh/kg (BMF pouch cell level).

Approach

- Evaluate stability of high-energy and high-voltage cathodes (NMC811, LMO, NCA) during aqueous processing.
- Incorporate aqueous processing to fabricate NMC811 and NCA cathodes.
- Fabricate crack-free NMC811 cathodes with high areal loading (6-8 mAh/cm^2) via aqueous processing.
- Create laser structured electrodes to overcome Li^+ mass transport limitation
- Simulate energy and power density improvements of laser structured electrodes
- Characterize electrolyte imbibition in porous electrodes.
- Characterize electrode microstructure.
- Evaluate rate performance and long term cyclability at room temperature and high temperature in pouch cells.

Results

1. Identified gas evolution as the main reason for electrode cracking in aqueous processed NMC811 cathodes and developed strategies to improve electrode integrity

Aqueous-processed Ni-rich cathodes typically lead to formation of bubbles in the coating soon after it is casted, and these bubbles eventually lead to formation of cracks in the dried coating (Figure I.2.B.1 a,b). This bubble formation was found to be occurring primarily due to the generation of hydrogen gas from the reaction of high-pH aqueous-slurry (due to dissolution of Li ion compounds and leaching of lithium-ion from cathode into water) and the aluminum substrate. Gas generation was observed under goniometer, when a drop of NMC811 aqueous filtrate was placed on to aluminum foil. Within seconds of the contact, hydrogen bubble formation was observed that emerged from the aluminum surface (Figure I.2.B.1 c).

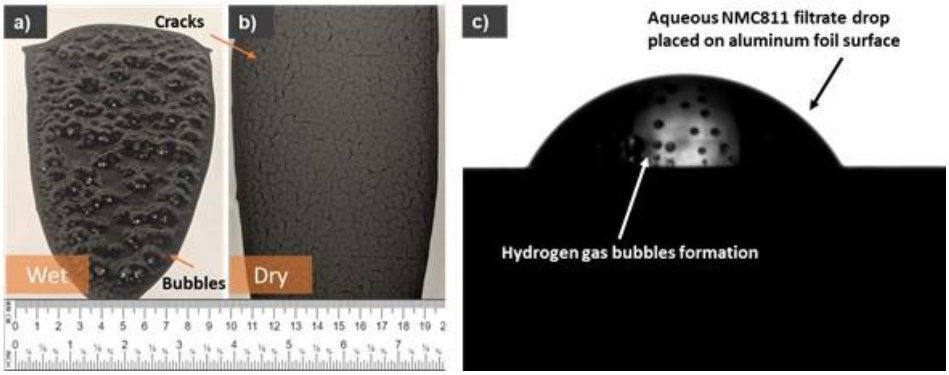

Figure I.2.B.1 Photographs of a typical thick (500 µm wet gap), aqueous-processed NMC811 cathode coating a few seconds (a) after it was cast and (b) after it had completely dried. c) A screenshot of the video recorded with a goniometer that shows gas generation due to aluminum corrosion, when a drop of the NMC811 aqueous filtrate was placed on to a piece of aluminum foil.

This was further verified by making the coatings on to copper foil substrates which does not corrode under high-pH. The severe cracking was completely eliminated for Cu foil, irrespective of the coating thickness. However, secondary cracks in the coating still remained which were more severe as the coating thickness increased. The cause of secondary crack was further investigated. All results presented next are for coatings made on Cu to eliminate hydrogen-evolution induced cracking.

First, it was discovered that if carbon black conductive additive was replaced with carbon fibers (VGGT), the amount of secondary cracks was significantly reduced for all coating thicknesses tried.

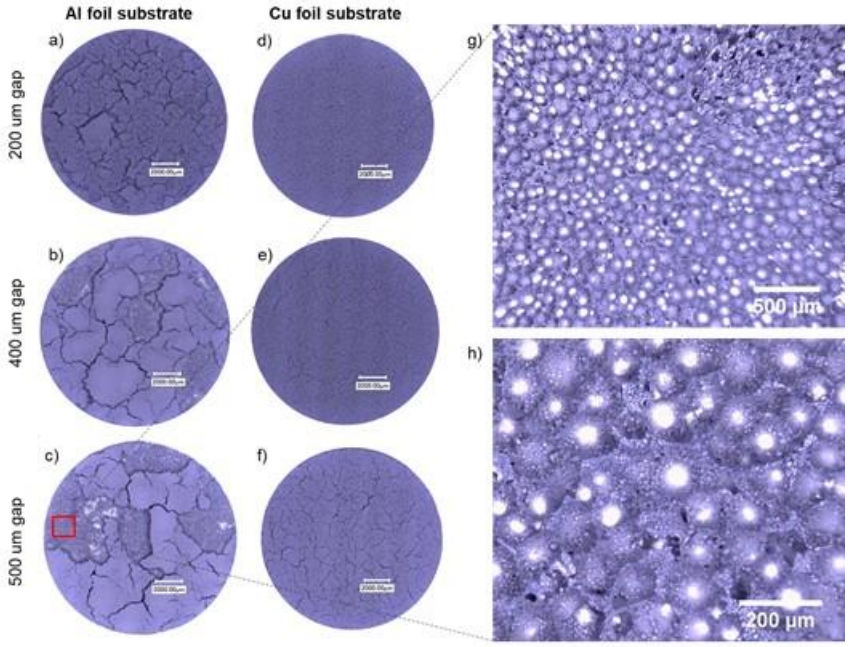

Figure I.2.B.2 Optical micrographs of aqueous-processed NMC811 coatings of different thicknesses coated on to (a–c) aluminum foil and (d–f) copper foil substrates. g,h) Higher magnification optical images of the foil underneath flaked-off coating highlighted by a red box in panel (c).

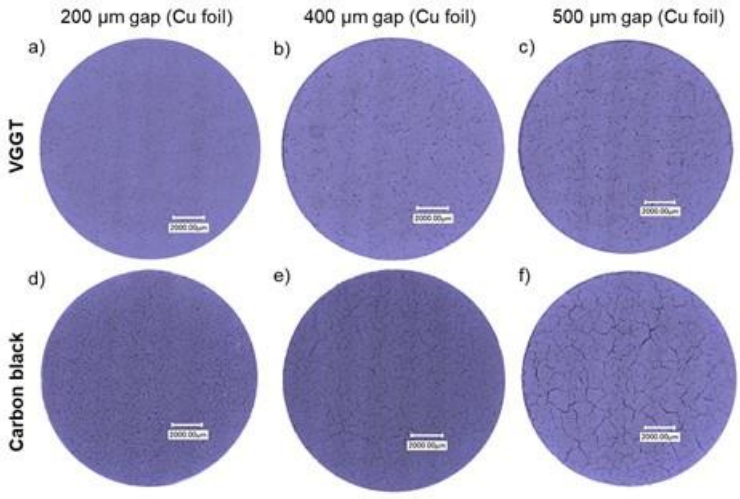

Figure I.2.B.3 Optical micrographs of aqueous-processed NMC811 coatings of different thicknesses coated on to copper foil with (a–c) VGGT or (d–f) carbon black as the conductive additive.

To understand this difference, the coatings microstructures were evaluated via SEM. The distribution of conductive additive and binder network was found to be significantly differerent for the aqueous-coatings made with VGGT compared with that of carbon black. For carbon black, this network engulfed the NMC811 particles leading to its inefficient utilization in binding the particles together. For VGGT, this network is located between the NMC811 particles, similar to how it is for PVDF-carbon black network in NMP-processed coatings which have much superiour cohesion and flexibility. We believe, when the carbon black and emulsion binder network completely coats the NMC particle surface, this leaves the less free binder in the coating to

hold the NMC particles together, causing poorer cohesion of the coating, which in turn reduced the ability of the electrode coating to absorb the residual stresses of shrinkage without cracking during drying.

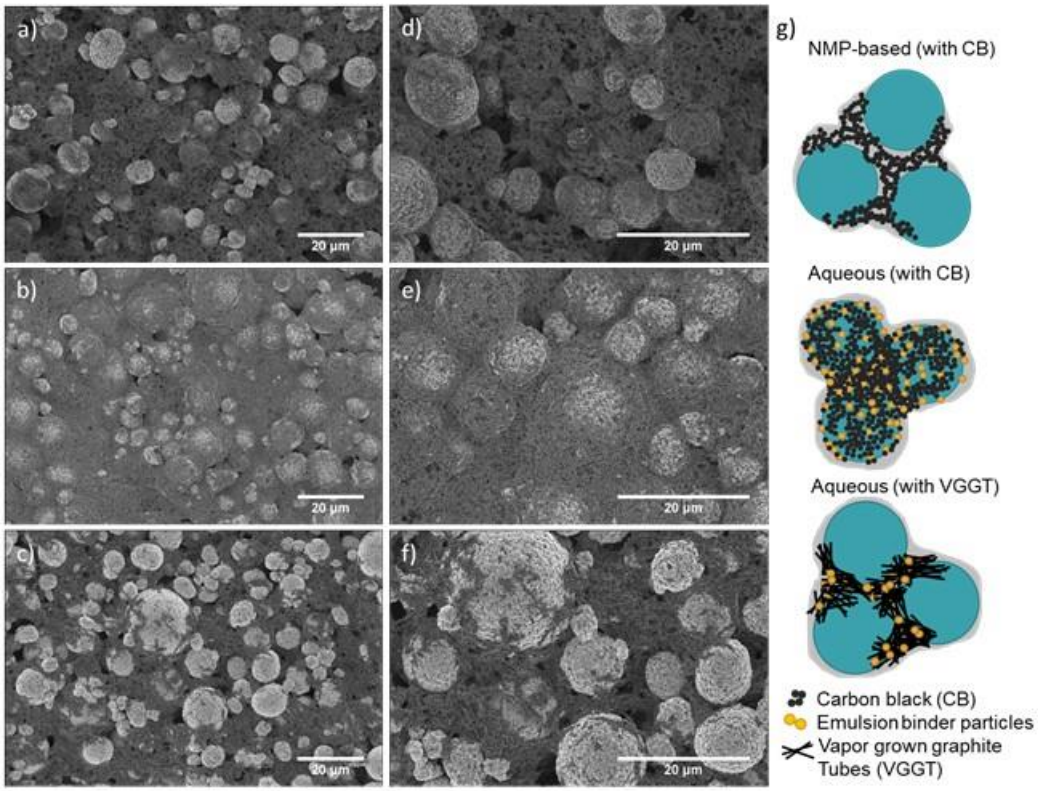

Figure I.2.B.4 SEM images of the surfaces of NMC811 cathode coatings made with (a, d) carbon black, PVDF, and NMP as solvent; (b, e) carbon black, CMC + JSR, and water as solvent; and (c, f) VGG, CMC + JSR, and water as solvent. (g) Distribution of the conductive additive and emulsion binder (if present) within the coating is shown schematically where the cyan colored spheres represent NMC811 secondary particles.

Furthermore, it was discovered that reducing the NMC811 particle from D_{50} = 13.8 µm to D_{50} =7.4 µm also significantly reduced the secondary cracks. This was explained to be due to lesser strain on the conductive additive+binder network that connect the NMC811 particles as the particle size gets reduced (shown schematically with a simplified ball and spring model in Figure I.2.B.5). For larger particles, the strain on the network is higher compared to that for smaller particles since the NMC particles themselves are nonstretchable.

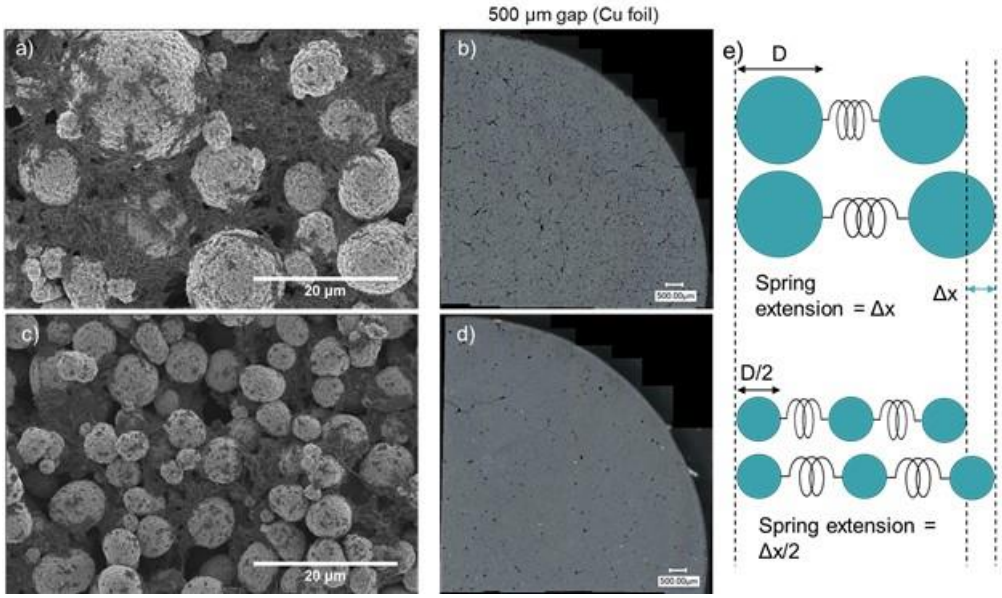

Figure I.2.B.5 SEM and optical microscope images of aqueous-processed cathode coatings (500 µm coating wet gap) on copper foil comprising a VGGT conductive additive and NMC811with particle sizes of (a, b) D50 = 13.8 and (c, d) 7.4 µm. (e) The difference in the degree of stretching of the binder + conductive additive network of the two coatings (with a different NMC811 particle size) under strain during drying is highlighted with a simplified schematic. The springs correspond to the stretchable binder and conductive additive network, and the spheres correspond to NMC811 particles.

Consistent with our groups's previous work on use of IPA as a co-solvent to reduce the surface tension of water and the consequent capillary stresses that can also contribute to cracking, we indeed found that addition of 12 wt.% IPA as co-solvent to VGGT-containining aqueous slurries almost eliminted the secondary cracks (Figure I.2.B.6). However, addition of IPA was found to not be sufficient in preventing the primary hydrogen-induced cracking in case of aluminum substrates.

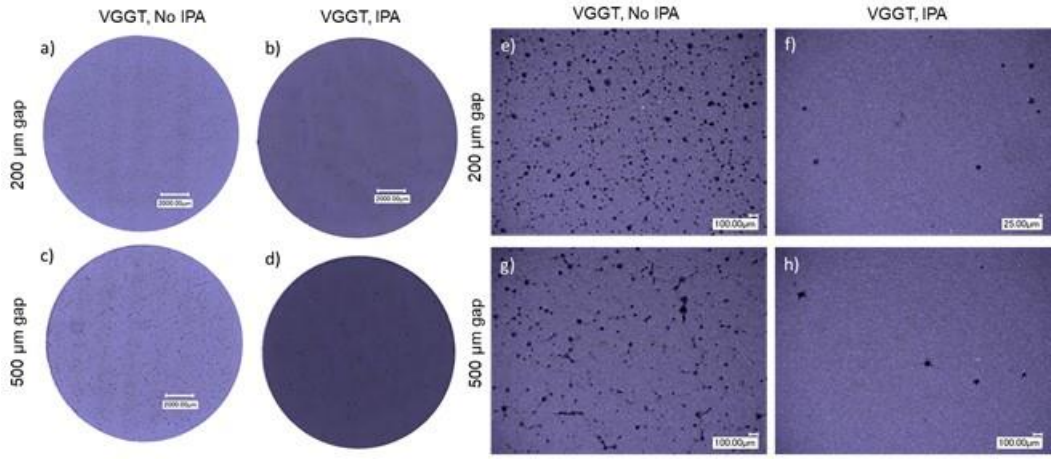

Figure I.2.B.6 Optical micrographs of aqueous-processed NMC811 coatings of different thicknesses coated on to copper foil with (a–c) 100% water as the solvent or (d–f) 12 wt % IPA as a co-solvent (IPA/water = 12/88. (e–h) Higher magnification optical micrographs of the four coatings in panels (a)–(d).

2. *Optimization of H_3PO_4 (PA) content in fabricating NMC811 cathode up to 8 mAh/cm² via aqueous processing*

To tackle the corrosion to Al foil and gas generation, phosphoric acid was introduced during the slurry preparation process in order to combat rising pH. Three differing amounts of phosphoric acid (PA) were investigated, 0.5 wt%, 1.0 wt%, and 1.5 wt%, using no acid as a control. These slurries used a 90/5/5 wt

composition of NMC 811, carbon black conductive additive, and composite binder. The composite binder was a mixture of JSR TRD202A and carboxymethyl cellulose in a 4:1 weight ratio.

Adding PA in these small amounts was shown to shift the pH back within the stability window for aluminum (Figure I.2.B.7a), suppressing corrosion to the current collector. This was confirmed by submerging aluminum foil in filtrate from active material and PA dispersions before drying and observing corrosion under an optical microscope. Electrode adhesion was evaluated with a 180-degree peel test and it was determined that adhesion decreased as acid was added (Figure I.2.B.7b), likely due to the increased surface area of corroded current collectors creating a better binding network. Although adhesion was lower with increased phosphoric acid, the adhesion was sufficient for further manipulation and production.

Slurry viscosity was also investigated and showed increased viscosity as acid concentration increased (Figure 7 c), until 1.0 wt%. Above 1.0 wt%, slurry viscosity began decreasing, suggesting phosphoric acid has a role in the colloidal chemistry of the dispersions. Although the viscosity was affected by phosphoric acid, every slurry was well withing the viscosity limits of roll-to-roll manufacturing requirements.

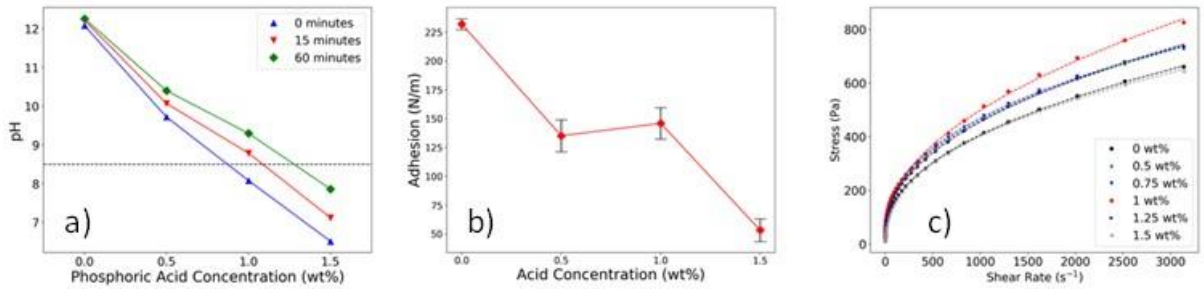

Figure I.2.B.7 PA effect on aqueous-processed NMC811: pH in slurry (a), adhesion (b), and rheological properties (c).

Along with mechanical tests, electrodes were assembled into single layer pouch cells to determine the electrochemical performance of each acid concentration. Pouch cells were matched with graphite anodes and subjected to rate capability testing to investigate the high rate performance of each configuration. Cells with both 6 mAh/cm^2 and 8 mAh/cm^2 areal loadings were produced and tested. High rate testing determined that 1.5 wt% phosphoric acid concentrations were optimal in both 6 and 8 mAh/cm^2 electrodes. Limited liquid phase mass transport in the ultra-thick electrode lead to lower discharge capacity at higher discharge rates, rendering required novel structured electrode designs in future studies. Excellent recovery from high rate cycling suggests the limited discharge capacity is in fact due to mass transport limitations and that there are no significant side reactions occurring that would lead to cell degradation.

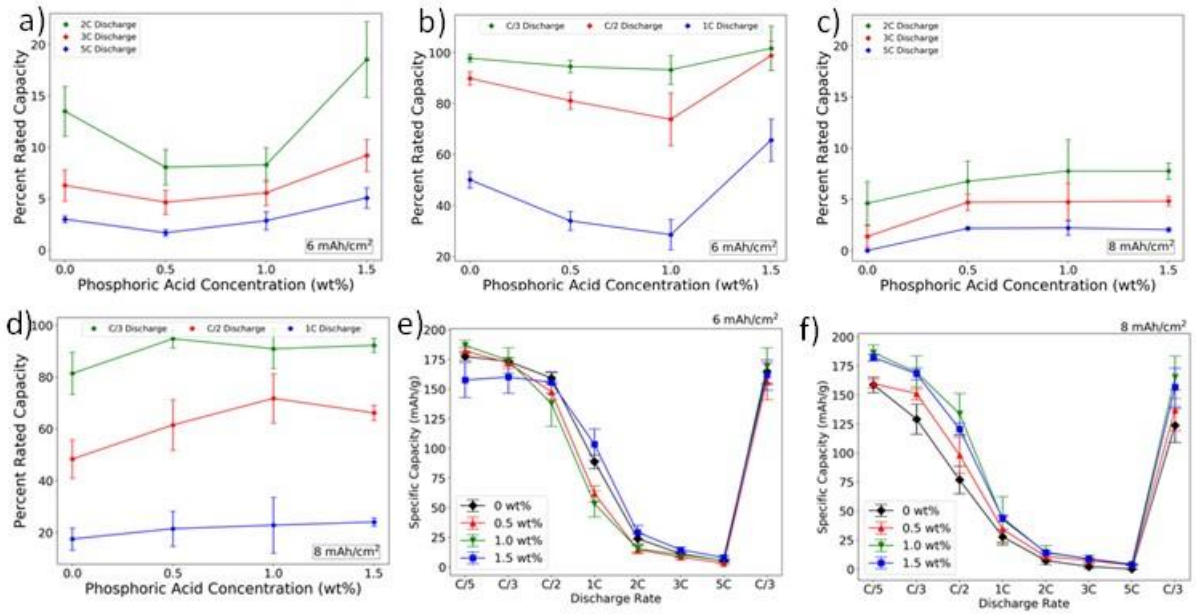

Figure I.2.B.8 PA effect on normalized discharge capacity of NMC811 (a) high rate with 6 mAh/cm², (b) low rate with 6 mAh/cm², (c) high rate with 8 mAh/cm², (b) low rate with 8 mAh/cm², and specific capacity (e) 6 mAh/cm², and (f) 8 mAh/cm².

This work concluded that the addition of phosphoric acid in a 1.5 wt% concentration was optimal for both electrochemical and mechanical reasons. Although the adhesion was diminished with increased acid, the superior electrochemical behavior and lack of corrosion provide a clear path of scalability of this technique.

3. *Characterization of lithium and transition metal dissolution in water with various cathode materials and successfully demonstration NCA cathode from aqueous processing*

Five cathode active materials were investigated and when dispersed in DI water, all exhibits basic behavior (see Figure I.2.B.9a). However, the pH tends to stabilize in LMO and LFP solutions at a value around 9, in LCO around 10.5, and in NCA and NMC532 in excess of 12. The initial rapid rise in pH for these materials is most likely ascribed to the dissolution of surface compounds into water (i.e Li_2CO_3 and/or Li_2O) as Li leaching from the active material particles involves solid diffusion and would take a longer time. The Li leaching contributes to the subsequent pH rise. Nevertheless, this would suggest that corrosion to the Al substrate would take place with an aqueous slurry for all of these active materials due to the chemical instability of Al at pH in excess of 8.5, While corrosion to the Al current collector with the LFP and LMO slurry could be minor, it is expected to be increasingly severe with LCO, NMC532 and NCA, respectively.

The XRD patterns (Figure I.2.B.9b) reveal that exposure to water for 24 h does not change the crystal structure of NCA. As shown in Figure I.2.B.9c, Drastic differences in composition are observed for NCA, with Li decreasing by nearly 50% and Ni and Co increasing by an order of magnitude after exposure to water. This indicates a thick layer of impurity (i.e. Li_2CO_3 and Li_2O) on the D-NCA sample, which blocks all the signal from bulk NCA. The dramatic reduction in the Li 1s for the D-NCA also confirms the removal of the surface layer. The elevated C content indicated that Li_2CO_3 is formed on the W-NCA similar to that of W-LCO.

As the exposure time in water is increased from 1 h to 24 h, the Li^+ concentration does not differ appreciably (see Figure I.2.B.9d). The transition metal dissolution in water is negligible, with most metals showing a concentration of less than 0.01 $\mu g \cdot mL^{-1}$ regardless of exposure time or active material. While the Li^+ dissolution is much greater in water than it is in NMP, the transition metal dissolution is much lower. This indicates that aqueous processing can alleviate transition metal dissolution during slurry preparation, though there is minimal transitional metal dissolution in both solvents.

NCA cathodes can't be fabricated with great integrity without pH control. To remedy this, long-chained polyacrylic acid (PAA) was included as a pH modifier and additional binder. NCA cathodes were successfully fabricated with minimal cracks with PAA via aqueous processing. Their electrochemical performance is shown in Figure I.2.B.9e. Initially, the discharge capacity of the PAA-processed NCA cell is only 95% of the NMP-processed cell (176.3 mAh·g^{-1} to 185.2 mAh·g^{-1}, respectively). However, as the cell cycles, the capacity retention of the PAA-processed cell is far better, retaining 84.2% of its capacity at cycle 100 compared to 78.1% for the NMP-processed cell, though the average coulombic efficiency of the NMP-processed cell (98.4%) is slightly better than that of the PAA-processed cell (98.0%). It is noted that this is only a preliminary result with limited cycle numbers. Extensive performance tests, including long-term cycle life in full cells, is required to further validate the feasibility of aqueous processing for a NCA cathode, especially when a limited Li inventory is present at the cathode. Nevertheless, these are promising results. By optimizing the slurry recipe, it is possible that better performance could be obtained from the aqueous-processed NCA cathode. This strategy could also be enacted for higher Ni-content NCA materials, whose chemistries are favorable from a cost and energy density perspective due to lower Co-content.

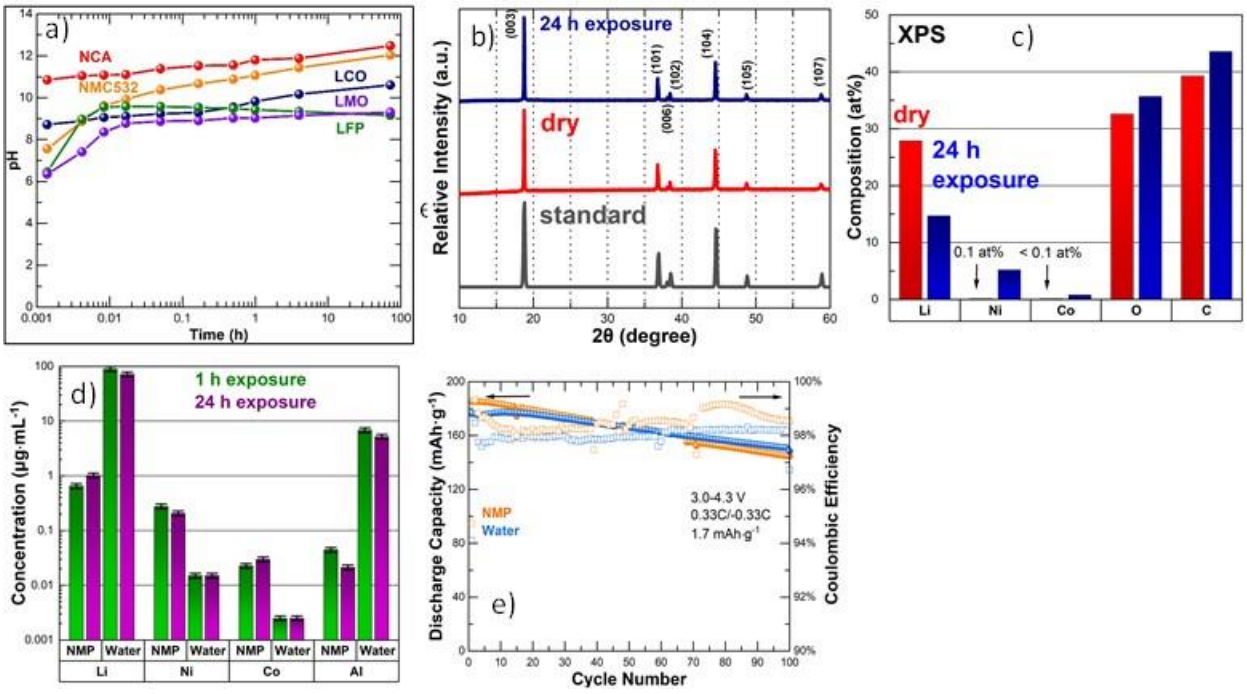

Figure I.2.B.9 (a) pH as a function of dispersion time with five cathode active materials, (b) XRD patterns of NCA, (c) Comparison in NCA surface compositions, (d) elements concentration in NCA filtrate, and (f) discharge capacity and coulobic efficiency of NCA cathode.

4. Determining the electrolyte imbibition dependence on processing conditions

Electrolyte imbibition was investigated using NMC532 and graphite electrodes, which were fabricated via conventional NMP-based processing and aqueous processing. Various parameters were evaluated for their effect on electrolyte imbibition, including salt contents in electrolyte and electrode porosity. Both electrolyte salt content and solvent compositions were varied as shown in Table I.2.B.1. We define coefficient of penetrance (COP) and solid permeability coefficient (SPC) as below:

Table I.2.B.1 Electrolyte information.

Electrolyte#	Solvent Composition	$LiPF_6$ Concentration (M)	σ (mN/m)	μ (mPa x s)
1	EC-DEC	1.2	30.992 ± 0.043	5.13 ± 0.12
2	EC-EMC	0.6	30.832 ± 0.055	2.39 ± 0.06
3	EC-EMC	1.0	31.291 ± 0.290	3.28 ± 0.08
4	EC-EMC	1.2	32.626 ± 0.107	4.60 ± 0.14
5	EC-EMC	1.5	33.194 ± 0.154	6.17 ± 0.11
$COP \equiv \sigma \cos\theta / (2\mu)$				
$SPC \equiv kB\cos\theta / (2r_e\phi)$				

where *B* is the capillary geometrical coefficient, σ is the surface tension of the electrolyte, μ is the viscosity of the electrolyte, *k* is the permeability of the electrode, ϕ is the porosity of the electrode, θ is the intrinsic contact angle of the electrolyte on the electrode, and r_e is the effective capillary radius of the electrode. The ratio σ / μ solely depends on the properties of the electrolyte, the ratio $kB/(r_e\phi)$ only depends on the properties of the electrode, and $\cos\theta$ is an electrode/electrolyte interface property.

As shown in Figure I.2.B.10a, NMP-processed graphite anodes have better wettability than aqueous-processed graphite anodes. Higher $LiPF_6$ content resulted in lower electrolyte wetting rate due to higher viscosity. Binary solvent system of ethylene carbonate and ethyl methyl carbonate increases electrolyte wetting compared to ethylene carbonate and diethyl carbonate. To investigate how the electrode wettability changes with calendering degree, Figure I.2.B.10b and c compare the *SPC* values and the $kB/(2r_e\phi)$ values of the two A12-NMP electrodes, one uncalendered and the other calendered, and the three NMC532-NMP electrodes, one uncalendered and the other two calendered, respectively. It shows that the electrode wettability decreases with increasing calendering degree.

Since *SPC* is proportional to $kB/(r_e\phi)$ and *k* is proportional to $r_e^2/(1-\phi)$, it can be concluded that *SPC* is proportional to $kBr_e/[\phi(1-\phi)]$. Due to calendering, the bulk porosity ϕ of the electrodes decreases from 55% to approximately 40% or 30%, and thus the value of $\phi(1-\phi)$ does not change much. However, the effective pore radius r_e significantly decreases due to calendering, which leads to the decreased electrode wettability.

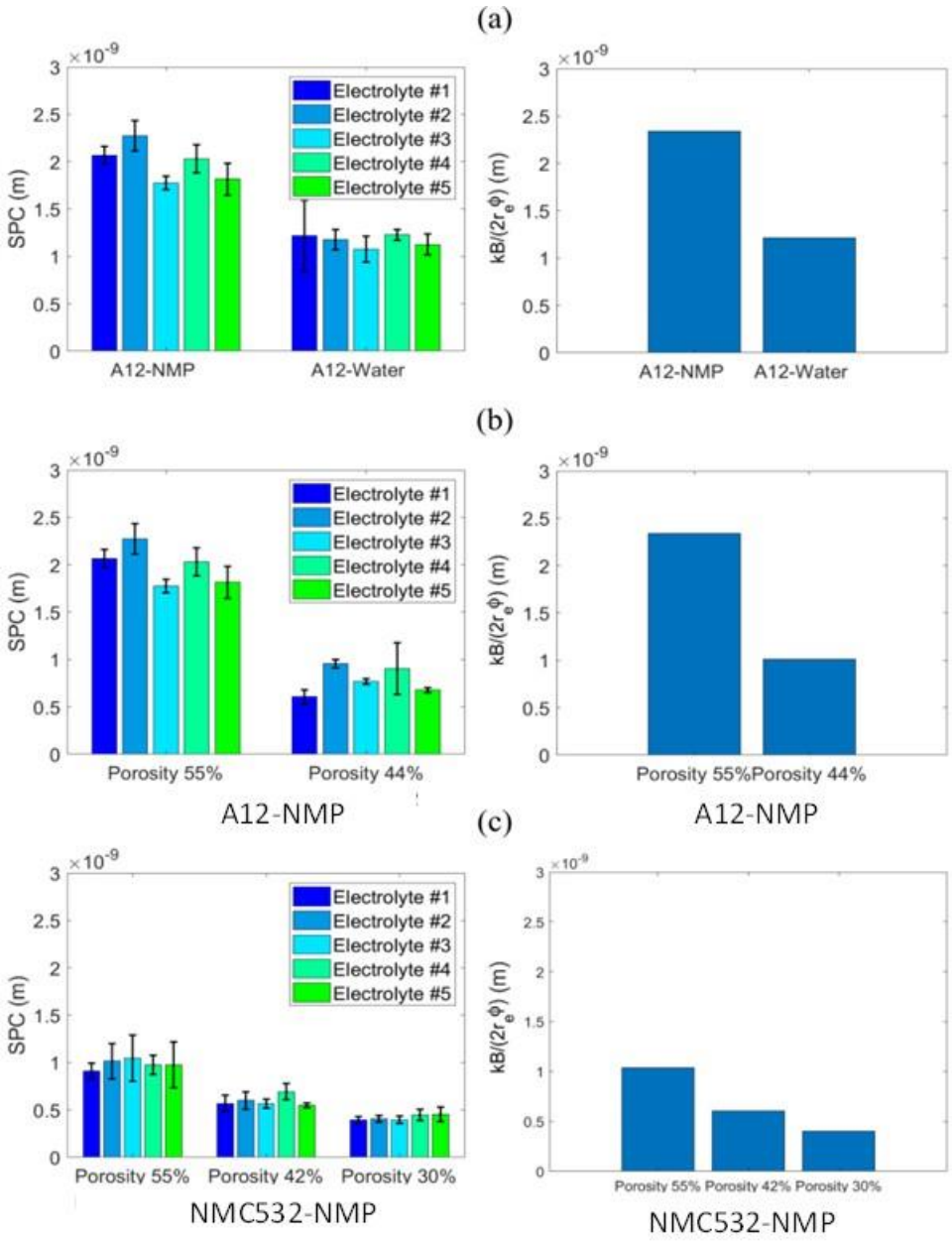

Figure I.2.B.10 . (a) Comparison between the SPC values and the $kB/(2r_e\phi)$ values of the uncalendered NMP-processed graphite anode and the uncalendered aqueous-processed graphite anode, respectively. (b) Comparison between the SPC values and the $kB/(2r_e\phi)$ values of the two A12-NMP samples, one uncalendered and the other calendered, respectively. (c) Comparison among the SPC values and the $kB/(2r_e\phi)$ values of the three NMC532-NMP samples, one uncalendered and the other two calendered, respectively

Conclusions

Lithium and transition metal dissolution in water was investigated in five cathode active materials. Both NMC811 and NCA cathodes were successfully fabricated via aqueous processing with PA and PAA as the pH modifier, respectively. Several strategies were developed to improve electrode integrity and minimize electrode cracking. Excellent initial performance was achieved. Effect of electrolyte formulation and electrode porosity on electrolyte wetting was determined.

Key Publications

1. A. Kukay, R. Sahore, A. Parejiya, W.B. Hawley, J. Li and D. L. Wood III, "Aqueous Ni-rich-cathode dispersions processed with phosphoric acid for lithium-ion batteries with ultra-thick electrodes", *Journal of Colloid and Interface Science,* 581 (2021) 635-643.

2. W.B. Hawley, A. Parejiya, Y. Bai, H.M. Meyer, III, D.L. Wood, III, J. Li, "Lithium and transition metal dissolution due to aqueous processing in lithium-ion battery cathode active materials", *Journal of Power Sources,* **466** (2020) 228315.

3. D.L. Wood, III, M. Wood, J. Li, Z. Du, R.E. Ruther, K.A. Hays, C. Mao, and I. Belharouak, "Perspectives on the relationship between materials chemistry and roll-to-roll electrode manufacturing for high-energy lithium-ion batteries", *Energy Storage Materials,* **29** (2020) 254-265.

4. J. Li, Y. Lu, T. Yang, D. Ge, D.L. Wood, III, Z. Li, "Water-based electrode manufacturing and direct recycling of lithium-ion batteries electrodes-a green and sustainable manufacturing system", *iScience,* **23** (2020) 101081.

5. Y. Liu, X. Wang, J. Cai, X. Han, D. Geng, J. Li, and X. Meng, "Enhanced electrochemical performance of $Li(Ni_{0.6}Co_{0.2}Mn_{0.2})O_2$ cathode with atomic-scale tuned interface via atomic layer deposition of zirconium oxide", *Journal of Materials Science & Technology,* **54** (2020) 77-86.

6. R. Sahore, D.L. Wood, III, A.J. Kukay, K.M. Grady, J. Li, I. Belharouak, "Towards understanding of cracking during drying of thick aqueous-processed $LiNi_{0.8}Mn_{0.1}Co_{0.1}O_2$ cathodes", *ACS Sustainable Chemistry and Engineering,* **8** (2020) 3162-3169.

7. M. Wood, J. Li, R.E. Ruther, E. Self, H.M. Meyer, III, C. Daniel, I. Belharouak, D.L. Wood III, "Chemical stability and long-term cell performance of low-cobalt, Ni-rich layer oxide cathodes prepared by aqueous processing for high-energy lithium-ion batteries", *Energy Storage Materials,* **24** (2020) 188-197.

8. A. Davoodabadi, J. Li, H. Zhou, D.L. Wood, III, T.J. Singler, C. Jin, "Effect of calendering and temperature on electrolyte wetting in lithium-ion battery electrodes", *Journal of Energy Storage,* **26** (2019) 101034-101043.

9. Z. Du, J. Li, D.L. Wood, III, C. Daniel, Manufacturing of Thick Composite Electrode Using Solvent Mixtures, US Patent 10,601,027, Issued March 24, 2020.

10. J. Li, A. Davoodabadi, C. Jin, D. L. Wood III, "Characterization of electrolyte wetting in lithium-ion batteries", 2020 International Battery Seminar, virtual meeting, July 28-30, 2020. **(Invited)**

11. J. Li, "Advanced processing for low-cost, low environmental impact and high energy density lithium-ion batteries", First Battery Manufacturing Days, ARTISTIC project webinar series 2020 (Virtual conference), July 29-July 3, 2020. **(Invited)**

12. R. Sahore, J. Li, D. L. Wood III, "A study of factors responsible for cracking during drying of thick aqueous-processed NMC811 cathodes", 236th Meeting of the Electrochemical Society, Atlanta, GA, October 13-17, 2019.

13. A. Davoodabadi, J. Li, D. L Wood III, C. Jin, "A novel technique to analyze the electrolyte wetting rate through Li-ion battery electrode", 236th Meeting of the Electrochemical Society, Atlanta, GA, October 13-17, 2019.

14. W. B, Hawley, J. Li, “Elevated mixing and coating temperatures yield beneficial processing properties of organic solvent-based lithium-ion battery cathode slurries”, 236th Meeting of the Electrochemical Society, Atlanta, GA, October 13-17, 2019.

Acknowledgements

The co-PIs are grateful to ORNL team members Ritu Sahore, Blake Hawley, Alexander Kukay, Dhrupad Parikh and Kelsey Grady, for valuable data collection and analysis, and Binghamton University for completing the electrolyte wetting experiments. We also thank Dr. Ozge Kahvecioglu at the Materials Engineering Research Facility (MERF), Argonne National Laboratory, for providing the NMC811 powder with smaller particle size, which is through project I.2.F “Process R&D for Next Generation Cathode Materials (BAT167)”.

I.2.C Processing Next Generation Li-ion Battery Cathode Materials (ANL)

Ozge Kahvecioglu, Principal Investigator
Argonne National Laboratory
9700 South Cass Avenue
Lemont, IL, 60439-4837
E-mail: okahvecioglu@anl.gov

Peter Faguy, DOE Technology Development Manager
U.S. Department of Energy
E-mail: Peter.Faguy@ee.doe.gov

Start Date: October 1, 2019 End Date: September 30, 2020
Project Funding: $1,000,000 DOE share: $1,000,000 Non-DOE share: $0

Project Introduction

Nickel-rich cathode materials with low or no cobalt content are critical for the development of less expensive batteries with higher energy densities that meet DOE goals while limit dependences of the country from foreign sources. Although, the theoretical capacity of lithium-nickel oxide ($LiNiO_2$, LNO) is high the rapid capacity fade makes the material unusable for practical application. Thermal stability and capacity fade are common issues when the nickel content in the cathode active material increases to 80% or above. The first step to understand the phenomenon and ultimately to solve the problem is to gain an understanding at atomic level what is the role of nickel substitutes (e.g., cobalt, manganese, aluminum, and the like) in pure $LiNiO_2$ (LNO) that stabilized the material. Material of various structures with a variety of percentages and combinations of elements are needed for the study. There is no reliable source of such materials available to the research community. The availability of hard-to-make, on-demand materials is critical to battery research community to explore and progress toward developing advanced LIBs chemistry. In a close collaboration with other partners in the program, the Process R&D and Scale Up Group at Materials Engineering Research Facility (MERF) at Argonne National Laboratory is utilizing non-traditional, advanced co-precipitation synthesis methods, such as the Taylor Vortex Reactor (TVR), to produce large quantity of high, uniform quality materials. Sample of the materials are distributed to collaborating research groups for investigation and performance evaluation. By evaluating new precipitation technologies, the Processing Next Generation Li-ion Battery Cathode Materials project is establishing new platform for scalable and economically feasible manufacturing of advanced cathode materials. The results presented in the report demonstrate that the MERF's developed TVR technology is capable of producing high quality materials with desired composition and morphology at scale for ultimate deployment in a full-scale manufacturing. The development and employment of the TVR platform by the project makes the advance in new materials synthesis and deployment faster than ever before.

Objectives

The multifaceted objective of the program is to provide the research community with materials they design and want to investigate and therefore ascertain the key missing link between discovery of advanced active battery materials, evaluation of these materials, and ultimately high-volume manufacturing of the selected targets to reduce the risk associated with their commercialization. We perform systematic process and material engineering research to develop cost-effective customized synthesis and to produce sufficient quantities of high-quality target materials by optimizing process parameters tailored to specific material compositions, evaluating material purity profiles, and applying emerging manufacturing technologies to address challenges associated with manufacturing of advanced materials. The technical targets of this program are the development of customized synthesis processes for each material selected, scaling up to multi-kilogram quantities with reproducibility under rigorous quality control, and evaluation of emerging manufacturing technologies to assist fundamental research and to reduce the commercialization risk of newly invented active battery materials.

Approach

Last year, the advantages of utilizing an emerging synthesis technology, the Taylor Vortex Reactor (TVR), for the production of cathode precursors for lithium-ion batteries, were demonstrated. This innovative reactor has a cylindrical rotor and tremendous Taylor vortices in the annulus. It produces homogenous micro-mixing, and high mass and heat transfer, enabling a high degree of uniform super-saturation eliminating local concentration and temperature gradient. This results in faster kinetics and denser particles with minimal optimization. The TVR continuously produces spherical precursor particles with a narrow particle size distribution, which is critical to achieve high-quality battery materials, and now it is the preferred platform for rapid production of new chemistries that are not commercially available. While supporting the Realizing Next Generation Cathode (RNGC) Materials program, a total of 10 different cathode chemistries were synthesized at a 1L TVR, more than 300 g scale each. Some of the promising candidates were then transferred to and scaled up in a 10L TVR to generate kilogram quantity of material. The advantages of TVR over the Continuously Stirred Tank Reactor (CSTR) operation are its easy scalability, unique flow pattern, and dead-zone-free design, which bypasses the scale-up issues encountered with CSTRs.

Within the scope of the project, different scales of TVR operations were used in the reporting period to produce materials in support of basic R&D groups at national laboratories, universities, and startup companies with the new or scaled up cathode chemistries from FY19, such as $LiNiO_2$ (LNO), $LiNi_{0.95}Co_{0.05}O_2$, $LiNi_{0.95}Mn_{0.05}O_2$, $LiNi_{0.95}Mg_{0.05}O_2$, and $LiNi_{0.95}Co_{0.025}Mn_{0.025}O_2$, and $LiNi_{0.60}Co_{0.20}Mn_{0.20}O_2$. Among those, LNO was further scaled up to be used extensively in coating and doping studies within the Deep-Dive program and fresh NMC622 was also scaled up in 10L TVR to be compared as the baseline with other chemistries that were done at TVR. Current research is trending toward advanced particle coatings because of the undesirable surface interaction of nickel-rich compositions with ambient atmosphere (carbon dioxide, humid) along with rapid capacity fading and thermal runaway issues. Coating technologies are seeking small but excellent performing NMC particles for conformal and efficient coatings. Based on requests from companies and other research institutions, various small NMC particles with a D50 value of ≤5 µm were generated using TVR to enable an advanced coating technology compatible with particle sizes ranging from 100 nm up to 8 µm. All preliminary syntheses were conducted at a 1L TVR and scaled up in a 10L TVR to validate a smooth transition and the scalability of this advanced reactor.

While the utilization of small secondary particles is of a growing interest (for advanced coatings, solid state batteries, fast charging, thick electrode loadings), their higher surface area creates post-processing problems which is very evident in the case of nickel-rich compositions. A post treatment is always necessary to eliminate the problem and makes the material suitable for cathode manufacturing. Within the current reporting period the surface treatment of nickel rich cathodes were also studied by applying a washing/re-calcining method.

Results

Materials in Support of "Deep-Dive into Next Generation Cathode Materials (BAT251 & BAT252)"

In FY20, the majority of our effort was devoted toward generating nickel-rich NMC chemistries for supporting the "Deep-Dive into Next Generation Cathode Materials Program". We have continued scaling up the physiochemical baseline material LNO and LNO-based materials using 10L TVR for different subgroups; (a) coating and doping studies, (b) electrode manufacturing, (c) gassing, thermal stability and surface reactivity studies. In FY20 we supported the program with higher nickel (95%) compositions such as; $LiNi_{0.95}Co_{0.05}O_2$, $LiNi_{0.95}Mn_{0.05}O_2$, $LiNi_{0.95}Mg_{0.05}O_2$, and $LiNi_{0.95}Co_{0.025}Mn_{0.025}O_2$, some of which are currently under optimization stage. The commercial NCM622 material was used as a baseline material for performance metrics (energy, power, impedance, retention); however this material has a proprietary coating. In order for a fair comparison, baseline NCM622 material was also synthesized and scaled up, using both 1L and 10L TVRs, with no dopants or coatings. Some of these chemistries were sent to Argonne's Cell Analysis, Modelling and Prototyping (CAMP) facility for electrode manufacturing and are currently stored in their electrode library to be shared across the programs and other interested parties. Advanced electrochemical characterization of the

materials produced in FY19, as well as some of the new compositions of FY20 have been done and are reported in detail in Annual Merit Review presentations BAT251 & BAT252.

In general, best performing LNO-based chemistries are obtained at high pH conditions in the co-precipitation reactions; the higher the pH the denser the material is. The secondary particle formation in continuous co-precipitation processes is well-known, and the utilization of higher pH further introduces smaller particles which creates the bi-modal particle size distribution. This, in fact, was found to improve the packing density of the powders in electrode manufacturing along with resulted in superior rate capability (see Figure I.2.C.1). The optimal calcination temperature varies depend on the Ni/Mn/Co contents. Table I.2.C.1 shows the physical properties of LNO-based materials calcined at different temperatures, including the Rietveld Refinement analysis retrieved from X-ray diffraction studies (not shown in here).

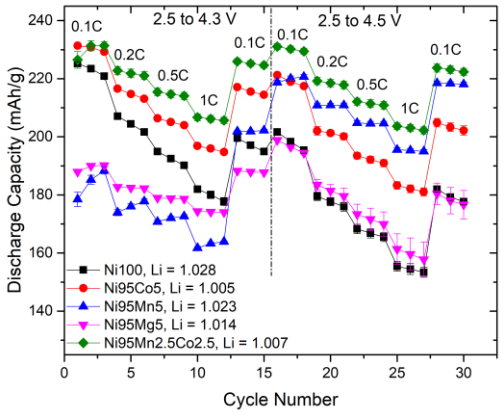

Figure I.2.C.1 Rate capability comparison of LNO-based materials with 5% dopants vs physiochemical baseline LNO material [coin half-cell vs Li, @ 30°C]

Table I.2.C.1 Physical Properties of LNO-based Materials with 5% Dopants vs LNO Baseline Material

Chemistry by ICP / Calcination Temperature	Tap Density, g/cc	PSA (µm) D10 / D50 / D90	Li^+ / Ni^{2+}, %
$Li_{1.03}NiO_2$ (725°C)	2.1	7.35 / 13.84 / 26.05	1.84
$Li_{1.00}Ni_{0.95}Co_{0.05}O_2$ (725°C)	1.9	6.49 / 11.83 / 21.84	1.96
$Li_{1.02}Ni_{0.95}Mn_{0.05}O_2$ (700°C)	2.3	6.65 / 11.98 / 21.21	7.61
$Li_{1.01}Ni_{0.95}Mg_{0.05}O_2$ (750°C)	2.0	9.56 / 17.88 / 32.98	2.93
$Li_{1.01}Ni_{0.95}Co_{0.025}Mn_{0.025}O_2$ (700°C)	2.0	4.83 / 8.60 / 15.34	3.26

The second step of synthesizing the actual active cathode material powders (calcination step) was challenging because of their sensitivity towards ambient conditions requiring high O_2 partial pressure during calcining. Besides, delicate storage conditions, free of humidity and air exposure, should be secured for these materials to eliminate the surface impurity formation. In FY20, we studied the post treatment of cathodes in an attempt to remove the surface impurities (e.g.; Li_2CO_3, LiOH and etc.). The LNO cathode materials were washed, vacuum filtered, vacuum dried and re-calcined after the first calcination step. In general, we observed the surface impurities were washed off, along with the lithium removal (~5%) from the bulk. The comparison of rate capabilities of the pristine and treated LNO material is shown in Figure I.2.C.2. This data displays a lower capacity for the treated cathode in narrow potential window which is probably due to the removal of bulk Lithium from the pristine structure; however improved rate capability at the wider potential window when cycled between 2.5 – 4.5 V.

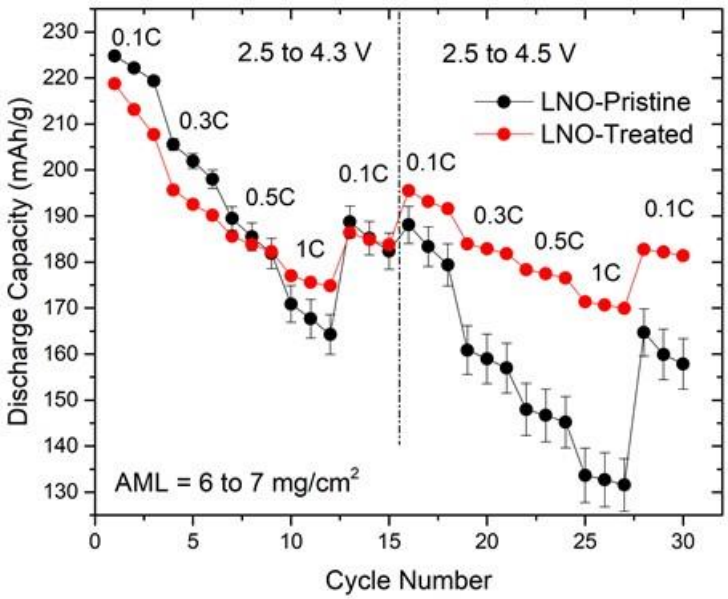

Figure I.2.C.2 RNGC specific rate testing protocols for pristine LNO and washed/re-calcined (treated) LNO material

Advanced Characterization Studies of Cobalt Free LNO-based Materials

As a part of the ongoing research we studied the X-ray absorption spectroscopy (XAS) at Ni and Mn K-edge of $LiNi_{0.9}Mn_{0.1}O_2$ cathode material using Argonne's Advanced Photon Source (APS) Facility. In-situ coin cell showed charge/discharge capacity values similar to the normal coin cell. Ni K-edge XANES (Figure I.2.C.3) showed mostly Ni in Ni^{3+} state in the OCV state and Ni^{3+}/Ni^{4+} is the main redox process for electrochemical charge storage while Mn is mostly in Mn^{4+} state and apparently doesn't participate in the redox reaction.

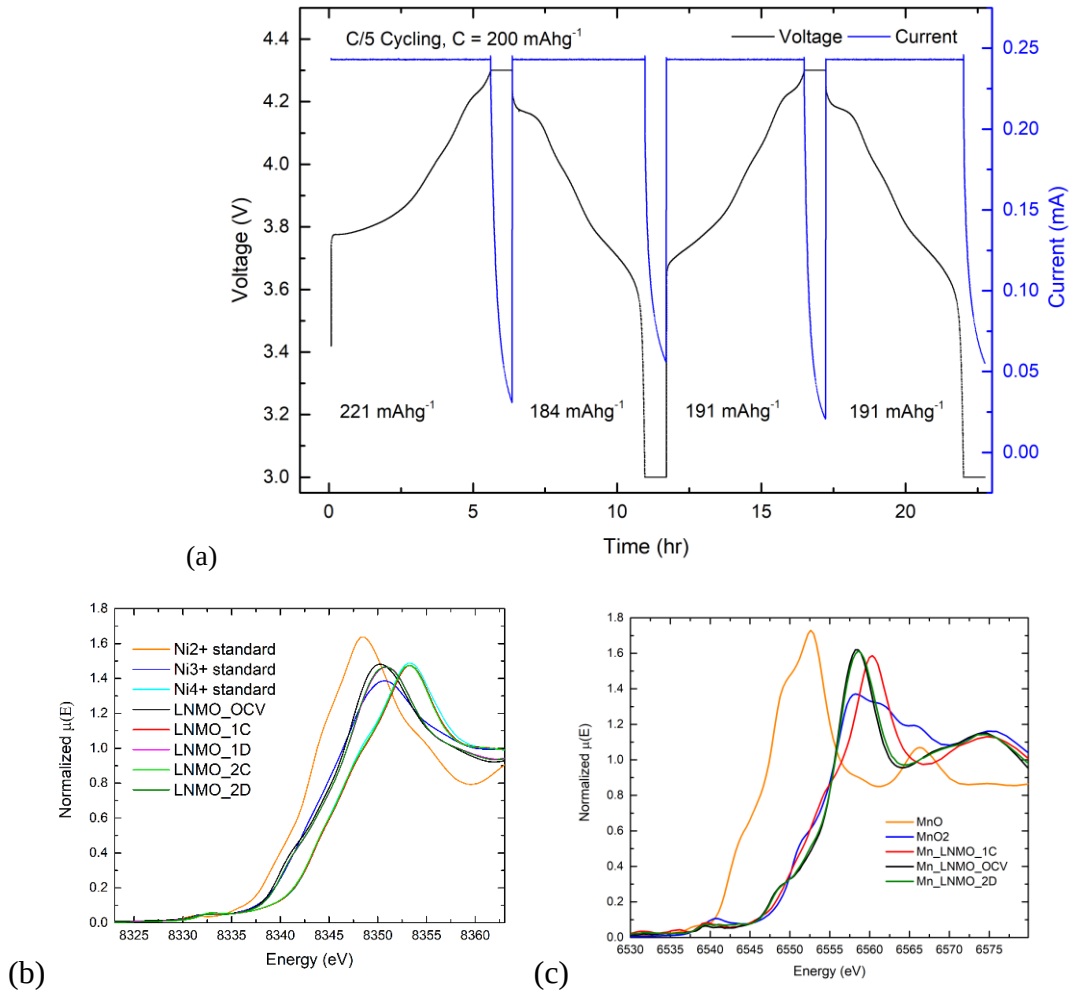

Figure I.2.C.3 (a) Electrochemical charge/discharge curve in the first two cycles of in-situ cell, (b) and (c) Ni and Mn K-edge XANES of LNMO cathodes at OCV, and 1st/2nd cycle complete charge and discharge

The EXAFS spectrum of LNMO cathode measured at Ni K-edge showed clear distinction/shift between the charged state and discharged/OCV state, indicating reversible change in Ni local environment (Figure I.2.C.4). In contrast Mn K-edge EXAFS in the charged and OCV/discharged state showed closely similar Mn-O and Mn-M peak intensity and position, indicating no Mn local environment change. Tetravalent Mn in the amount of 10% provided structural and thermal stability in this composition such that decent long term cycle life is achieved. Figure I.2.C.5 shows the Ni-O and Ni-M bond distances decreased on charging and increased back on discharging. The irreversible decrease in Ni-O and Ni-M bond distances in the 32% state of charge (SOC) of the 1st charge is due to the loss of Li during solid electrolyte interface (SEI) formation, the reversible changes in Ni-O and Ni-M distances are marked with the blue lines.

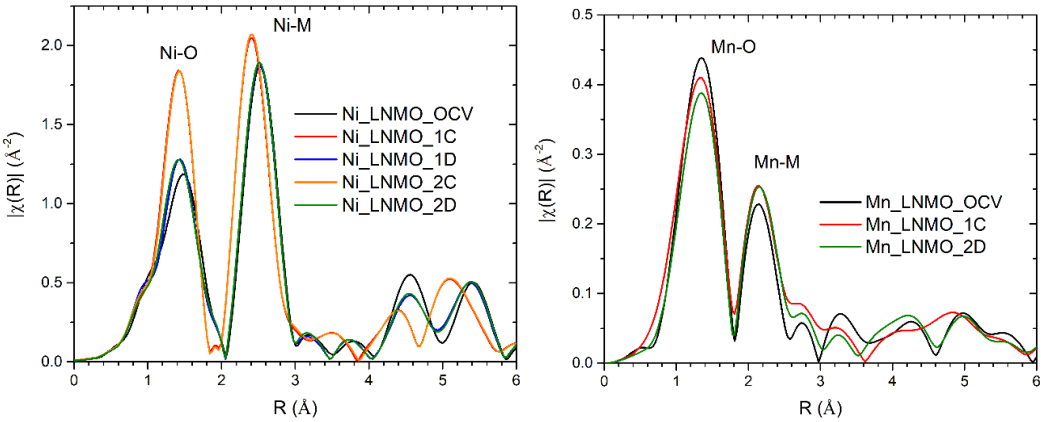

Figure I.2.C.4 In-situ EXAFS spectra in R-space measured at Ni and Mn K-edges of LNMO cathode. Mn K-edge XAS data was collected at limited representative state of LNMO cathode.

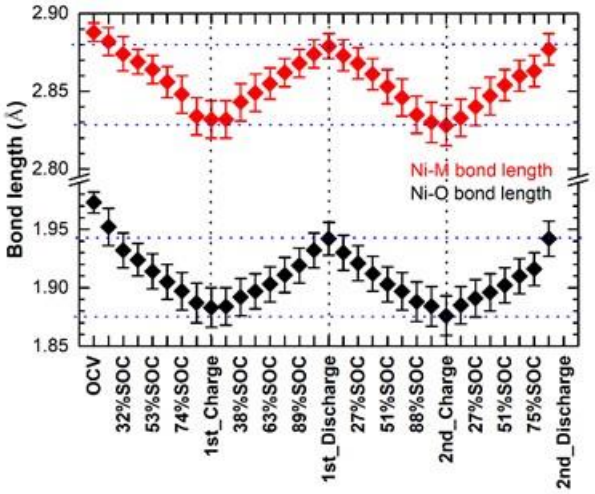

Figure I.2.C.5 Fitting results of Ni K-edge EXAFS at different states of LNMO cathode during the first 2 cycles at C/5. [Image and data credit: Dr. Shankar Aryal]

Materials in Support of "Thick, Low-Cost, High-Power Lithium-Ion Electrodes via Aqueous Processing (BAT164)"

In the previous reporting period we synthesized and provided the NCM811 small size particles (~6-7µm) to support "Thick, Low-Cost, High-Power Lithium-Ion Electrodes via Aqueous Processing" program at Oak Ridge National Laboratory. In FY20, the TVR-made material was built in electrodes for electrode cracking study which showed improved resistance against cracking (see Figure I.2.C.6, image on the left). Our collaborators at ORNL, also used the TVR-made materials to build graded bilayer cathode pouch cells and tested those for Fast Charge program (see Figure I.2.C.6, image on the right) which showed high rate performance.

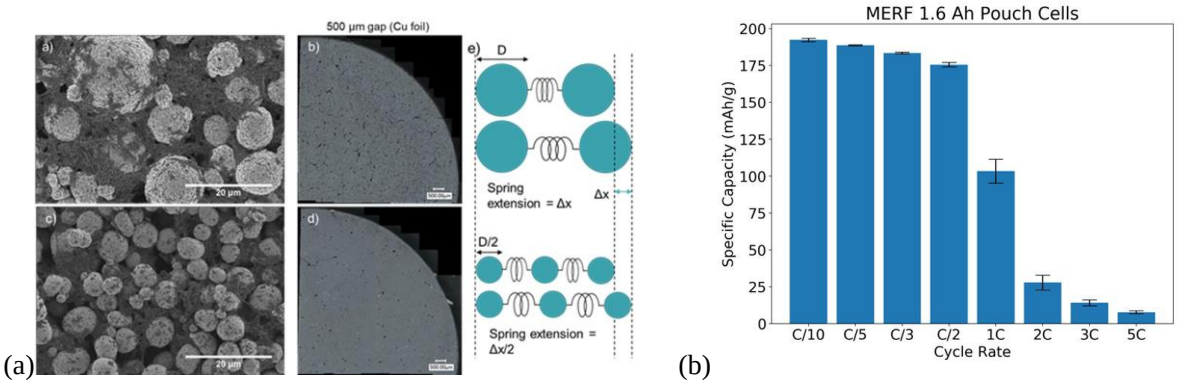

Figure I.2.C.6 Particle size effect on electrode cracking. Image on the left (a); top row (a,b) shows commercial NCM811 material, bottom row (c,d) shows TVR-made NCM811 which shows fewer cracks. Image on the right (b); shows the rate capability of graded 6 mAh/cm^2 bilayer cathode pouch cells. [Image and data credit: Dr. Jianlin Li, Dr. David Wood; ORNL].

Materials in Support of "Improving Battery Performance through Structure-Morphology Optimization (BAT402)"

Yet another program we supported in FY20 is a still an on-going collaboration with the "Improving Battery Performance through Structure-Morphology Optimization" program where the TVR made NMC811 and NMC111 hydroxide precursors were used in studying the sintering behavior of those using both Li_2CO_3 and $LiOH.H_2O$ as the lithiation source in different atmospheres. In-situ X-ray diffraction studies were conducted at 13BMC at the APS. Figure I.2.C.7 displays an example data taken from NCM811 with both Li-sources showing strong SAXS signals indicating the intense change in NMC primary particle size near its melting point.

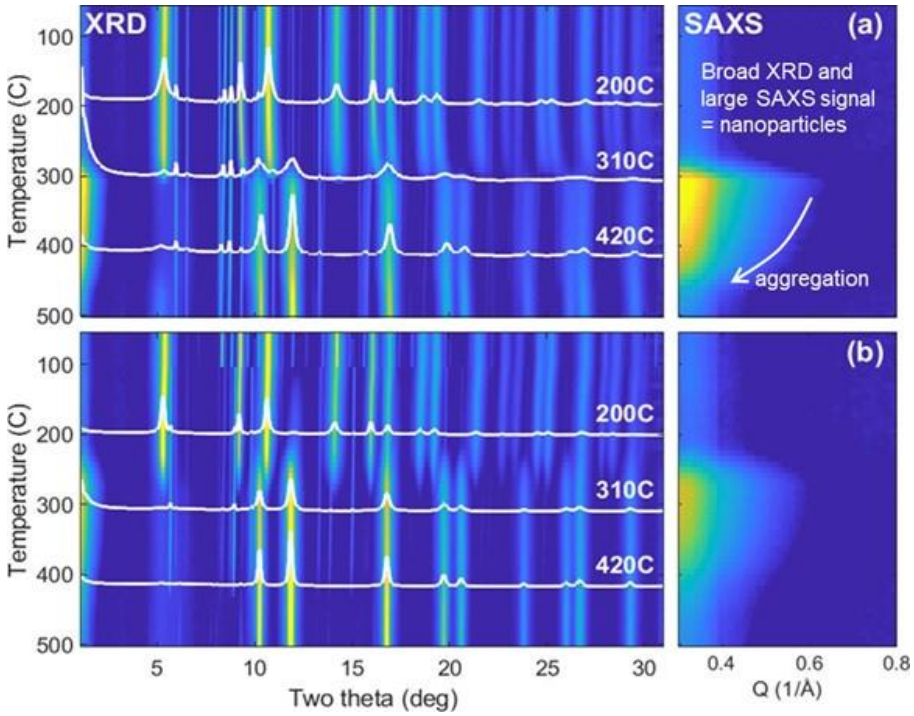

Figure I.2.C.7 In-situ calcination of NCM811-hydroxide precursor with Li_2CO_3 and $LiOH.H_2O$ shows strong SAXS signals, suggesting a dramatic change in NMC primary particle size near its melting point. With $LiOH.H_2O$, this phase change occurs at lower temperature and proceeds more slowly. [Image and data credit: Dr. Tim Fister, ANL].

Materials in Support of "In Situ Spectroscopy of Solvothermal Synthesis of Next-Generation Cathode Materials (BAT183)"

In FY20, a new collaboration was established between ANL and Brookhaven National Laboratory (BNL) under the Process Science and Engineering Program focusing on "synthesis by design". Cathode precursor materials, $Ni(OH)_2$, $Ni_{0.33}Co_{0.33}Mn_{0.33}(OH)_2$ and $Ni_{0.8}Co_{0.1}Mn_{0.1}(OH)_2$ were synthesized either at 1L or at 10L TVR and shared with the collaborators at BNL for in-situ calcination studies. An exemplary data is shown in Figure I.2.C.8, comparing the composition dependent reaction pathways where NMC111 showed gradual transformation into layered oxides with high ordering and NMC811 showed an abrupt transformation with low ordering.

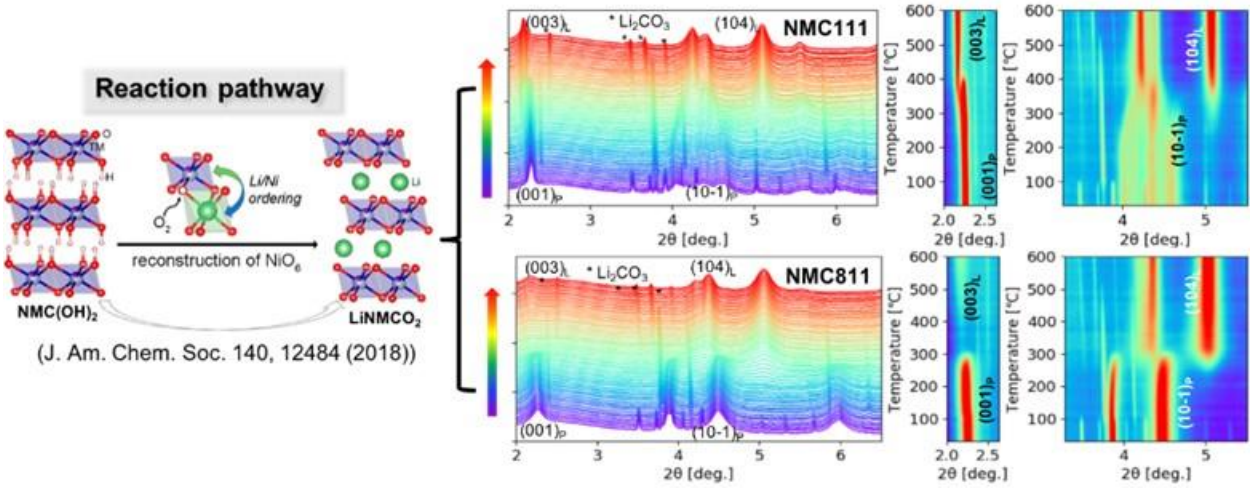

Figure I.2.C.8 In-situ calcination of NCM811-hydroxide precursor with Li_2CO_3 and $LiOH.H_2O$ shows strong SAXS signals, suggesting a dramatic change in NMC primary particle size near its melting point. With $LiOH.H_2O$, this phase change occurs at lower temperature and proceeds more slowly. [Image and data credit: Dr. Feng Wang, Dr. Jianming Bai; BNL].

Materials in Support of Northwestern University

In FY20, we continued supporting researchers at the Northwestern University. Upon request, different sizes of $LiNiO_2$ (D_{50} = 3 and 10 µm) and NCM811 (D_{50} = 6 µm) were synthesized using 1L and 10L TVRs for the proprietary graphene coating methodology (to suppress the O1-O3 stacking faults) that was invented at the Northwestern University. An overview snapshot of the work is shown in Figure I.2.C.9; SEM on top left shows the TVR-made small LNO particles (3 µm) coated with graphene. Oxygen suppression during cycle was plotted based on the amount of graphene coating and compared to the pristine material without graphene coating, showing a suppression was achieved. SEMs on the left hand side displays the removal of creep after graphene coating. Cycling data on top right and on bottom right, indicated the graphene coating (at 1-2%) can improve capacity retention up to 94%.

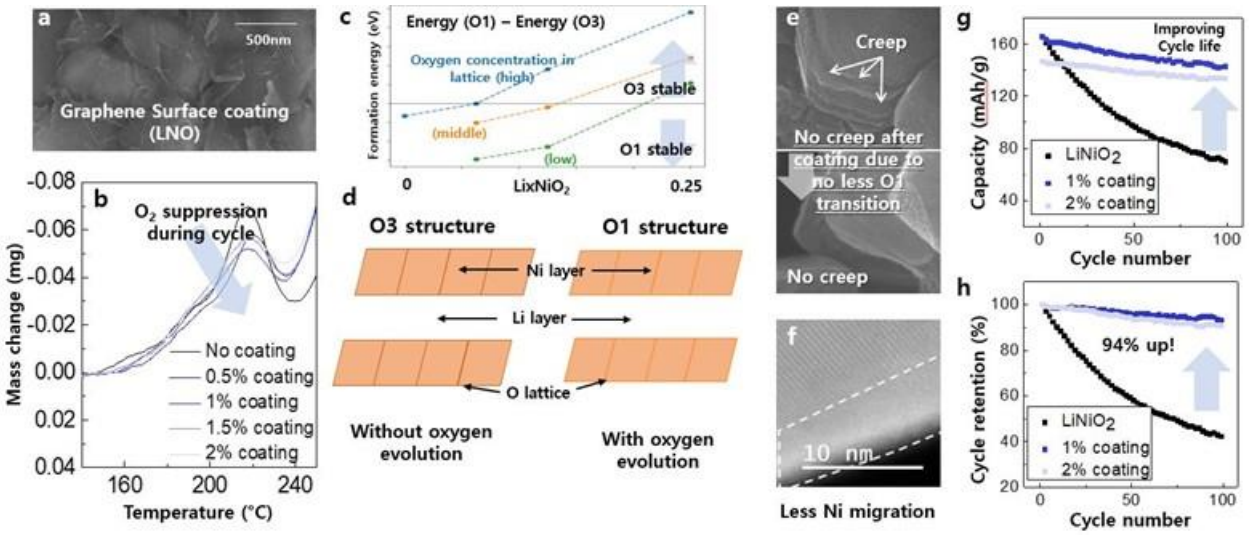

Figure I.2.C.9 Suppression of O3-O1 stacking fault in Ni-rich layered materials toward superior cycle life [Image and data credit: Dr. Kyu-Young Park, Prof. Mark Hersam Group at Northwestern University].

Conclusions

MERF's experimental active cathode materials process R&D and scale-up program assists the battery research community, allows for a comprehensive evaluation of new materials by industrial laboratories, and supports basic research. In fiscal year 2020 the program provided several new, not commercially available materials. Samples of high, uniform-quality materials were distributed for further evaluation and research. A total of 12 different cathode active material compositions have been synthesized using 1L TVR, and some of the material with higher quantity demand were scaled up in 10L TVR. All the materials produced at MERF were shared with the collaborators either in the form of precursor or active cathode material, ranging from 50 to 1,000 g per sample.

Key Publications

1. Shankar Aryal, Ozge Kahvecioglu, Jessica L. Durham, Albert L. Lipson, "Nickel-Rich Layered Oxide Cathodes for Next Generation Lithium Ion Battery" 236th ECS Meeting, October 13-17, 2019, Atlanta, GA

2. Shankar Aryal, Ozge Kahvecioglu, Jessica L. Durham, Albert L. Lipson, Krzysztof Z. Pupek, “In-situ and Operando Electrochemical Investigation of Cobalt-free, Nickel-rich Layered Oxide Cathode for Next Generation Lithium Ion Batteries” 2020 Spring/Fall Meeting and Exhibit, November 27-December 4, 2020, (Virtual)

3. Shankar Aryal, Ozge Kahvecioglu, Krzysztof Pupek, “Emerging Manufacturing Technologies and Characterization of Next Generation LIB Materials” Battery Congress 2020 Livonia, September 23-24, 2020, (Virtual)

4. Shankar Aryal, Ozge Kahvecioglu, Jessica L. Durham, Albert L. Lipson, Krzysztof Z. Pupek, “Roles of Mn and Co on Structure and Electrochemistry: Towards Designing High Ni Layered Oxide Cathodes” Ready for submission, 2019

5. Shankar Aryal, Ozge Kahvecioglu, Jessica L. Durham, Albert L. Lipson, Krzysztof Z. Pupek, “Physical and Electrochemical Studies of Cobalt Free Nickel Rich $LiNi_{0.9}Mn_{0.1}O_2$ Cathode” In preparation, 2020

6. Kyu-Young Park, Yizhou Zhu, Carlos, Carlos G. Torres Castanedo, Ozge Kahvecioglu, Michael Bedzyk, Chris Wolverton, Mark C. Hersam, "Controlling Oxygen Lattice Stacking by Suppression of O_2 for Better Cycle Life of High Ni Layered Materials", In preparation, 2020

7. Contribution in paper publication: MERF made small NMC811 particles in, ACS Sustainable Chem. Eng. 2020, 8, 3162 – 3169 by Ritu Sahore et.al.

Acknowledgements

In-situ XAS studies were done by Dr. Shankar Aryal using the resources of the Advanced Photon Source (Beamline 10 BM); an Office of Science user facility, was supported by the U.S. Department of Energy, Office of Science, Office of Basic Energy Sciences, under Contract No. DE-AC02-06CH1135.

I.2.D Novel R&D for Manufacturing of SS Electrolyte Materials (ANL)

Joseph Libera, Principal Investigator
Argonne National Laboratory
9700 S. Cass Avenue
Lemont, IL 60439
E-mail: jlibera@anl.gov

Peter Faguy, DOE Technology Development Manager
U.S. Department of Energy
E-mail: Peter.Faguy@ee.doe.gov

Start Date: October 1, 2019 End Date: September 30, 2020
Project Funding: $300,000 DOE share: $300.000 Non-DOE share: $0

Project Introduction

Aerosol manufacturing technology holds the potential of commodity scale production of energy storage materials in powder form. Reduced liquid chemical waste and suitability for continuous operation are advantages aerosol processing has over competing liquid based powder synthesis. Aerosol synthesis of powders falls broadly into several categories: (a) spray drying, (b) spray pyrolysis, (c) flame spray pyrolysis and (d) gas combustion synthesis. At the Argonne's MERF aerosol synthesis facility modalities a-c are now active for materials research into energy storage materials.

Flame spray pyrolysis (FSP) is a materials synthesis technique that uses solution of organic and/or inorganic metal salts in flammable liquids. In the gas-to-particle mode (FSP-GP), the liquid solution is atomized using oxygen and combusted to atomic species from which particles condense and are collected in the exhaust filters. If the available combustion enthalpy is insufficient, particle formation follows the droplet-to-particle modality (FSP-DP) and the produced solids retain some history of the spray droplets.

Spray pyrolysis (SP) starts as in FSP by producing liquid droplets of metal salt solutions but not using combustible solvents. The droplet solvent is removed by evaporation in a tube furnace followed by solid state reaction of the dried particle to produce the desired solid materials. Optional addition of enthalpic components such as ethylene glycol or organic acids allows for exothermic support of the solid state reactions.

In Spray Drying (SD) the drying of the droplets and subsequent solid state reactions that characterize Spray Pyrolysis are decoupled and only the dried particles are collected to be separately solid state reacted in calcination furnaces. This techniques allows for the exclusion of the spray solvent in the calcination steep and enable controlled atmosphere calcination such as inert gas or pure oxygen.

At Argonne's MERF facility, these three modalities are used synergistically to produce a single target materials and thus gain greater understanding of the material apart from the process. In, general FSP-GP produces nano sized powder, while FSP-DP produces micron sized agglomerates of nano-sized primary particles. SP produces micron sized secondary particles consisting of sub-micron primary particles. SD produces micron particles of the constituent metal salts which following a separate calcination retain their particle characteristics. For the FSP and SP techniques we seek to optimize the process to produce ready to use particles in the proper phase purity. However, this can be thermodynamically prohibited by the gaseous environment in the processing reactors requiring separate calcination and or powder refinement. In the industrial setting even these additional steps are amenable to continuous processing following continuous aerosol powder production.

Objectives

Develop Aerosol Manufacturing Technology as a manufacturing option for Li-ion battery active cathode phase and for solid electrolyte powder for use in conventional and solid state Li-ion batteries for the automotive sector. Obtain economically competitive protocols and recipes using the lowest cost precursor and solvent options. Produce optimized LLZO for separator and catholyte applications. Leverage the advantages of the atomically mixed nano-powder produced by FSP to access otherwise difficult to produce materials.

Approach

Solid state electrolyte (a) aluminum doped lithium lanthanum zirconium oxide Al-LLZO and energy storage materials (b) high Ni cathode active phases are the focus of development using multiple aerosol technologies. Aerosol synthesis is co-optimized with downstream calcination, powder refinement, and validation in battery test cells. Research is focused on the lowest cost precursors available in commodity scales, typically nitrates salts of the metals. Advanced concepts are explored that utilize unique powder morphology available only by aerosol processing.

The ANL MERF FSP reactor has features that allow for convenient and high throughput sample production. A glovebox design filter box allows for collection of nanomaterials and restoration of the filter media within 15 minutes of a run completion allowing for up to 6 generated and collected samples per workday. Material that deposits on the walls of the reactor does not significantly cross-contaminate from sample to sample. On a day to day basis, a clean-in-place brushing fixture allows for the combustion tube to be cleaned of wall deposits for changeover to new material systems further assuring no cross contamination between runs.

The ANL FSP facility has been designed to produce powder materials in an industrially relevant way using liquid spray (droplet) combustion which can produce materials at the highest possible rate compared to ultrasonic atomization or gas-fed precursor introduction. In order to best navigate the complexities of spray combustion, the ANL FSP facility has been provided with a suite of in-situ advanced diagnostics: (a) laser diagnostic system for Filtered Rayleigh Scattering (FRS) and Planar Laser Induced Fluorescence (PLIF) imaging of temperature and species distribution respectively, (b) Optical Emission Spectroscopy (OES) of the flame zone, (c) In-situ Raman spectroscopy and (d) particle size analysis using Scanning Mobility Particle Sizing (SMPS). Ex-situ diagnostics are also applied including (a) XRD and temperature programmed XRD, (b) BET-SA, (c) DSC-IR/MS, (d) electrochemical testing and electron microscopy (SEM and TEM).

Results

Aerosol Synthesis Facility Expansion

1. Added Spray Pyrolysis Reactor: Installed and recommissioned the Nomad VIII ultrasonic spray pyrolysis system donated to ANL by Cabot Corp. The system is capable of processing 500 g/hour of solution to produce 50 g/hour of powder which is collected in a bag filter. Powder is collected using a glove panel serving as permanent PPE for rapid collection and turnover. The reactor tube is a 3" ID x 42" long quartz tube centered in a tube furnace for up to 1100°C processing temperature. Nebulization takes place in a 9 transducer ultrasonic nebulizer which delivers the solution droplets to the reactor via controlled flow air carrier gas.

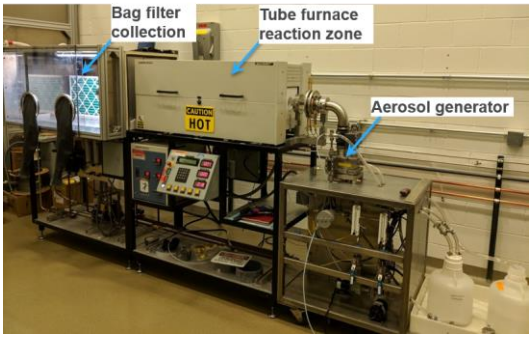

Figure I.2.D.1 NOMAD VIII Spray Pyrolysis Reactor

2. Added In-Situ UV-Raman spectroscopy for the FSP reactor (Figure I.2.D.2). Samples are collected in-situ by depositing FSP aerosol solid particles onto the back side of a quartz sample plate by particle impactor principles. Multiple wavelengths are available for Raman analysis, 266,355,512, and 633 nm excitation. Samples are

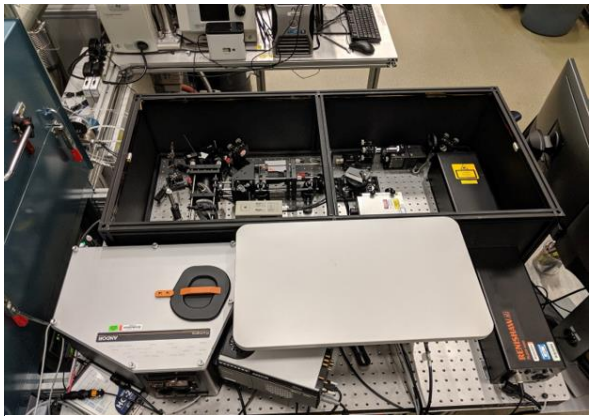

Figure I.2.D.2 Custom Raman spectrometer with in-situ sampling

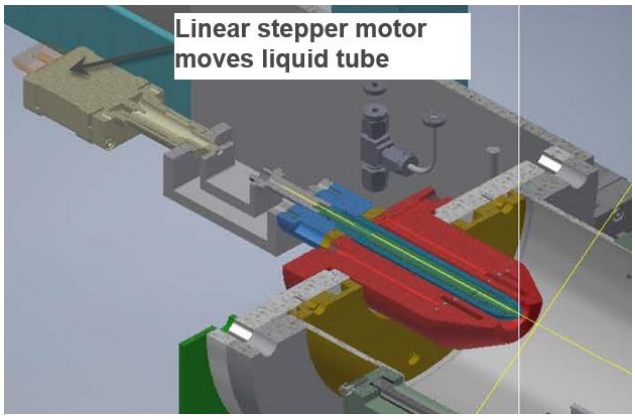

Figure I.2.D.3 GEN2 burner upgrade

sufficiently accumulated in 5 minutes and selective Raman analysis is performed in 5-15 minutes. The system is optimized to focus analysis on key relevant spectral features while permuting through FSP processing parameters.

3. Installed and commissioned GEN2 FSP burner assembly (Figure I.2.D.3). The burner upgrade features a motorized atomizing nozzle air-gap control that permits dynamic adjustment of this critical spray setting for rapid optimization of combustion settings. Burner body cooling was added for rapid process stabilization greatly improving material consistency and flame stability in short duration material runs.

4. Added a Kymera 328 medium resolution spectrograph for monitoring flame chemistry by optical emission spectroscopy. The spectrograph serves the dual purpose of providing measurement for both Raman and OES spectroscopy. An 8-to-1linear fiber array allows for simultaneous projection of 8 flame source positions through the spectrometer and onto an imaging sensor (Andor Newton and iSTAR CCD sensors). The axial array produces flame chemical signatures along the flame axis of the spray flame.

Solid Electrolyte Al-doped LLZO

The ability to produce the cubic phase of Al-LLZO at temperatures lower than 800°C is a very important advance as it permits precise targeting of Li content which otherwise is very difficult at higher calcination temperature. This is very important for implementation of production at large scale. Spray Pyrolysis was used to produce Al-doped LLZO through low-temperature calcination. It was found that the SP produced green powder more readily converted to the cubic garnet phase than for FSP green powders. This is potentially the most economic route for large scale production as the feedstocks are water and metal nitrate salts. c-LLZO was also produced using Spray Drying but a higher calcination temperature of 900°C was required since the emergent phase was tetragonal LLZO. Samples of SP

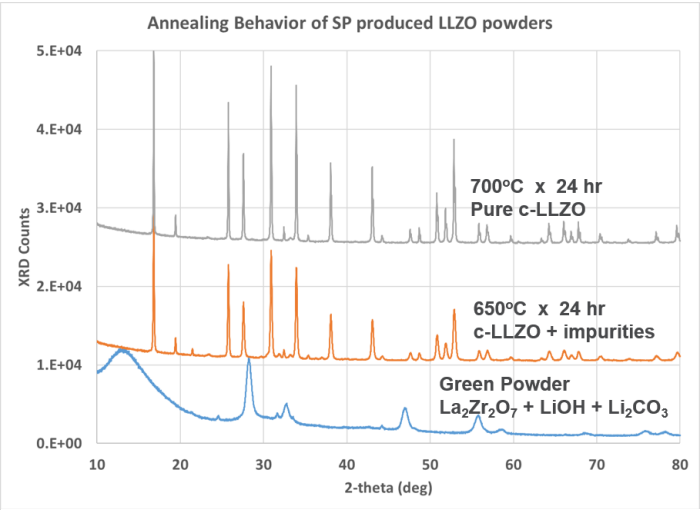

Figure I.2.D.4 Calcination properties of SP produced LLZO green powders

produced cubic LLZO were distributed to collaborators at LBNL and ORNL.

Additional experiments were performed to assess the possibility to produce LLZO using Spray Drying. A Buchi spray dryer apparatus was used to produce precursor powder using the identical solution as used in the SP LLZO shown in Figure I.2.D.4. The precursor powder lacked any crystallized phase but nevertheless could be calcined to cubic LLZO at 800°C. This material exhibited a higher tendency to form impurities which is attributed to the greater segregation of elements in the dried nitrate precursor solid particles. Apparently, process characteristics in the FSP and SP processes favor the atomic mixing of the constituent atoms to facilitate easy conversion to the thermodynamically favored LLZO phase. Future efforts in LLZO synthesis will seek to deploy Collison nebulization methods to produce similar result as obtained in the SP process. This would provide the final industrial path to large scale production using these very stable aerosol generation devices.

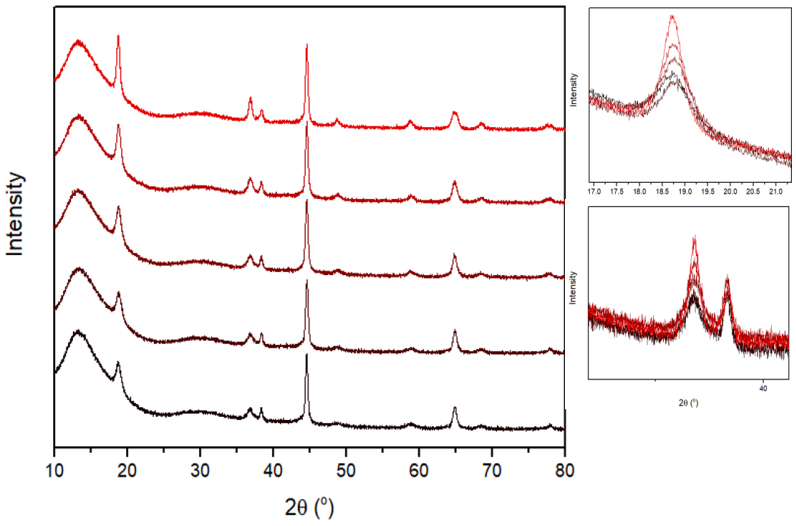

Figure I.2.D.5 Optimization of spinel ordering in NCM111 produced by FSP

Cathode Phase Synthesis

A broad sweep of NCM materials was synthesized in both SP and FSP reactors. A tendency to form the spinel phase in the NMC 111, 622, and 811, and NCA phases was observed throughout the series. The spinel phase could be pursued in its own right for certain battery applications but it also suggests the possibility to achieve the layered phase directly in aerosol synthesis since the spinel phase indicates the necessary ordering along the progression toward the layered phase. The NCM 111 spinel active phase using FSP was further explored as a battery material by post synthesis calcination (Figure I.2.D.5) This material has an initial EC capacity of 150 mA/g. This effort was performed collaboratively with E.J. Lee.

Single Crystal Particle Morphology

A unique feature or FSP and SP aerosol synthesis techniques is the inclusion of Li in the synthesis solution to make pre-lithiated green powders. This is in contrast to conventional wet-chemical synthesis routes that require Li to be added after the formation of the metal hydroxide intermediate phase. SP and FSP produce the rock salt phase and it works best when Li is also included so that some degree of pre-lithiation in the metal oxide phase is attained or at a minimum, a very uniform nano-mixture with Li carbonate and/or hydroxide phases is obtained. A tendency toward the formation of large crystal grains was observed (Figure I.2.D.6) after calcination of FSP green powder. Low enthalpy FSP solutions tend to larger primary particles that then calcine to multi-micron single crystal grains, whereas high-enthalpy solutions produce the smallest nano—

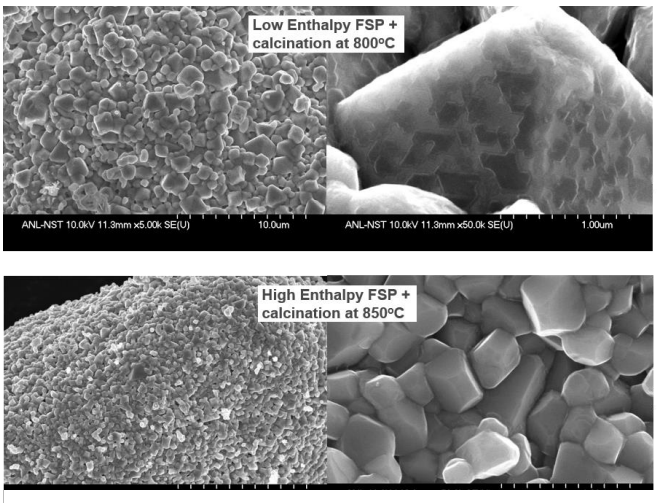

Figure I.2.D.6 Large grain single crystal morphology in FSP produced cathode materials

sized primary particles which results in smaller grain sizes as show in Figure I.2.D.6. A remaining challenge is to achieve the result as separated single crystal primary particles and avoid the high degree of sintering. The tendency to form large single crystal grains is related to the degree of rock salt crystal phase in the green powder. These phases require higher calcination temperatures to activate Li to then form the layered phase. Subsequently rock salt grain growth precedes the layered phase formation. However, when a higher degree of spinel ordering is observed in the green powders, a greater tendency to preserve the green particle morphology is observed.

Conclusions

Spray Pyrolysis and Spray Drying were added as complimentary aerosol synthesis techniques and the MERF's FSP facility received upgrades in burner technology, OES and Raman spectroscopy. SP was used to synthesis cubic LLZO using very low cost metal nitrate aqueous solution which was also used successfully in the Spray Drying technique. Materials based on these low-cost routes were distributed into the SSB research community. Routes to the spinel phases in NMC materials were discovered in FSP produced cathode materials. The tendency to produced large grained single crystal morphology in NMC layered phase cathode materials was observed in FSP produced materials.

Acknowledgements

The authors greatly acknowledges the generous donation to ANL of the NOMAD VIII research reactor by Toivo Kodas and Cabot Corporation. We also acknowledge the contributions to this research by Kyojin Ku, E.J. Lee and Yujia Liang. We greatly acknowledge the expertise of Hack-Sung Kim in the development of the custom Raman spectrometer. We also acknowledge the Manufacturing Science and Engineering Initiative at ANL for providing support for the advanced diagnostics for the FSP unit. We also acknowledge the valuable insights for LLZO applications from Marca Doeff and Nancy Dudney.

I.2.E Supercritical Fluid Processing of Battery Cathode Materials (ANL)

Youngho Shin, Principal Investigator
Argonne National Laboratory
9700 S Cass Avenue
Lemont, IL 60439
E-mail: yshin@anl.gov

Peter Faguy, DOE Technology Development Manager
U.S. Department of Energy
E-mail: Peter.Faguy@ee.doe.gov

Start Date: October 1, 2019 End Date: September 30, 2020
Project Funding: $662,500 DOE share: $662,500 Non-DOE share: $0

Project Introduction

The development of rapid and reproducible manufacturing processes for cathode active materials is important for improving performance, increasing lifespan, ensuring safety, and reducing prices of lithium-ion batteries. Supercritical fluids technology, an emerging manufacturing process, can potentially provide materials for a high electrode density due to a robust single crystal without internal void fraction, an improved rate capability due to submicron particle size, cycling stability due to suppressed particle crack and resistance layer, and a facet-controlled particle, thus enabling the production of high-performance battery cathode materials. These material properties are the result of a higher degree of supersaturation and the formation of mono-crystalline oxide particles because of the reduced solubility of metal ions under supercritical hydrothermal conditions. The supercritical hydrothermal reaction is a practical and scalable route for mono-crystalline particle production. The morphology of cathode particles can be customized by changing reactants, solvents, reaction pressure, and reaction temperature. New mono-crystalline active battery materials with tunable particle size, composition distribution, and morphology are synthesized using the installed supercritical hydrothermal reaction system. These advanced battery materials, which are not commercially available yet and not achievable by traditional co-precipitation techniques, are distributed to collaborating research groups for investigation and performance evaluation.

Objectives

The aim of the project is to establish a flexible R&D capability of supercritical fluid reactions as an emerging manufacturing process for active battery materials. It is also one of the key roles to produce and provide mono-crystalline advanced battery materials with the desired particle size, composition distribution, and shape to support basic research. This process is one of the emerging manufacturing technologies with the goal of reducing the risks associated with the discovery of advanced active battery materials, market evaluation of these materials, and their commercialization with mass production. We perform systematic research to develop a cost-effective supercritical fluids process, to produce sufficient quantities of target materials with high quality by optimizing the synthesis parameters and material composition to assist fundamental research. Our effort deepens a basic understanding of the structure-property relationship of the materials and ultimately can contribute to selecting the desired target before the material would be deemed suitable and desirable for large scale manufacturing. This approach will reduce the commercialization risk of advanced battery cathode materials.

Approach

A multipurpose supercritical fluids reaction system has been designed, built in, and is currently fully operational that allows the synthesis and surface treatment of battery cathode materials. Using the installed batch-type supercritical hydrothermal reaction system, the synthesis of various battery materials has been optimized, and materials have been produced in quantities suitable for distribution for a comprehensive

investigation. At this stage, the particle shape of the battery materials is controlled by changing reactants, solvents, additives, pH, reaction pressure, reaction temperature, reaction time, and stirring speed. Synthesis and evaluation of various battery materials are performed. The battery material selected for morphology control and optimization of synthesis conditions is nickel-rich NMC811 cathode material. 3D XRF tomography measurements are performed for the characterization of the synthesized mono-crystalline nickel-rich NMC811. In addition, research on the use of nano-indentation is conducted to measure particle strength through collaboration. We perform material characterization with particle cross-sectional mapping and Rietveld refinement of powder XRD and evaluate the electrochemical performance of the synthesized cathode particles.

Results

A mono-crystalline NMC811 cathode material was produced using the installed multipurpose supercritical fluids reaction system. The size of this mono-crystalline NMC811 particle is about 1 µm. To understand the characteristics of mono-crystalline NMC811 synthesized through the hydrothermal process, poly-crystalline NMC811 consisting of clusters of primary particles was produced by a conventional coprecipitation process for comparison. These poly-crystalline NMC811 particles range in size from 3 to 8µm.

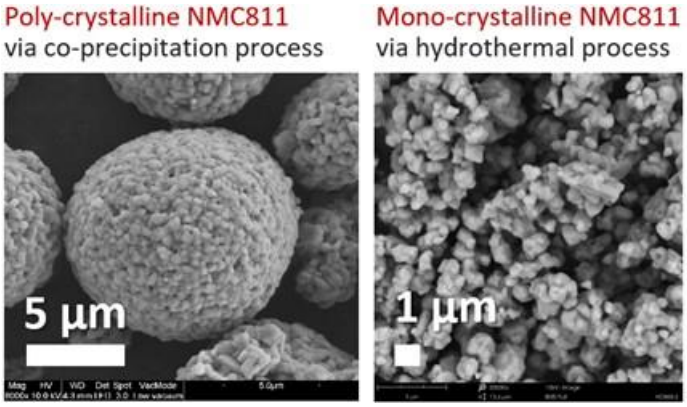

Figure I.2.E.1 Synthesized poly-crystalline NMC811 and mono-crystalline NMC811

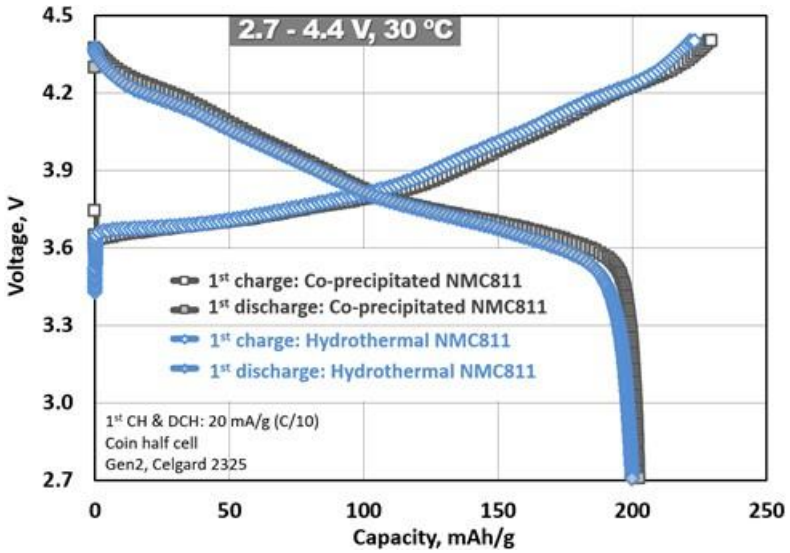

Figure I.2.E.2 Voltage profiles of poly-crystalline NMC811 and mono-crystalline NMC811

Voltage profiles of poly-crystalline NMC811 cathode via coprecipitation and mono-crystalline NMC811 cathode via hydrothermal reaction were measured. Coin-cell tests were conducted at a 0.1 C rate (20 mA g^{-1}) between 2.7 and 4.4 V at 30°C. These very similar results indicate that the poly-crystalline or mono-crystalline

particle morphology does not affect much the voltage profile. The initial discharge capacities of these two NMC811 cathode materials are about 200 mAh g^{-1} for each.

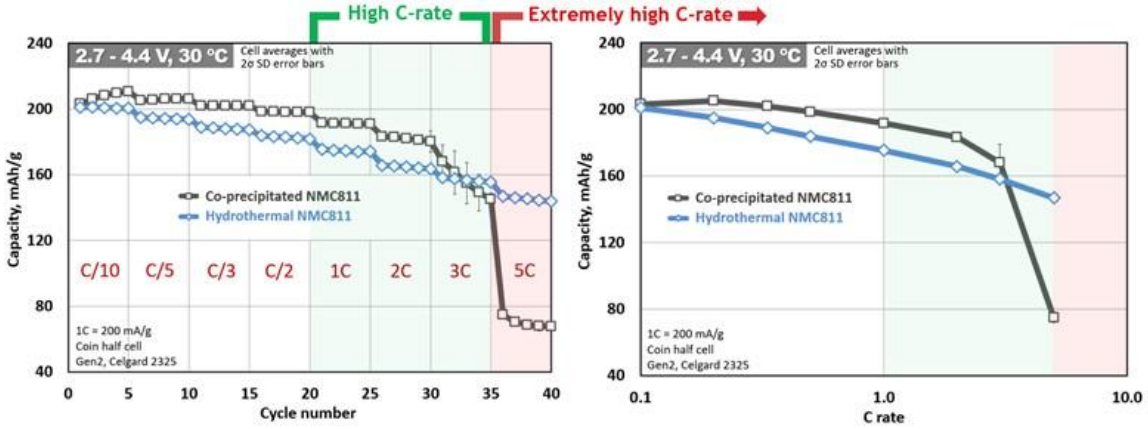

Figure I.2.E.3 Rate performance comparison of poly-crystalline NMC811 and mono-crystalline NMC811

Regarding the electrochemical cycling performance, the hydrothermal mono-crystalline NMC811 shows more than twice the discharge capacity and stable cycling performance at a high C-rate of 5 C than co-precipitated poly-crystalline NMC811. The hydrothermal mono-crystalline NMC811 exhibits improved rate performance over poly-crystalline NMC811, although its synthesis has been only partially optimized and can be further improved.

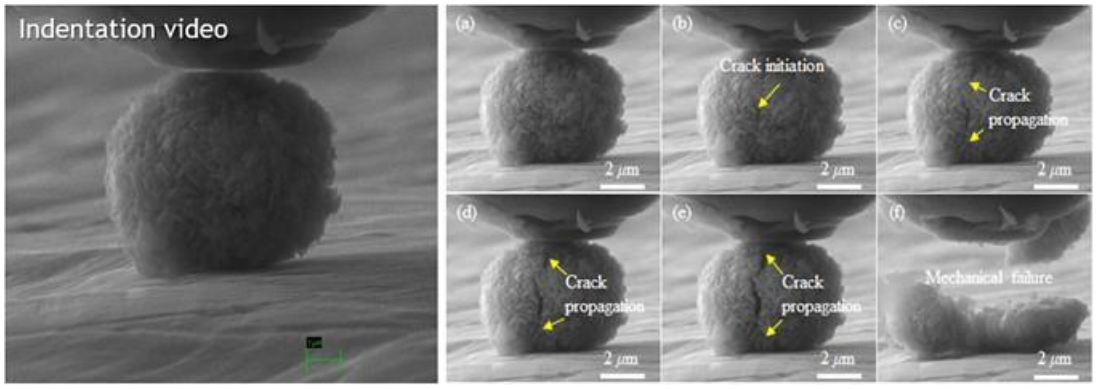

Figure I.2.E.4 Set-up of nano-indentation to measure particle breaking force

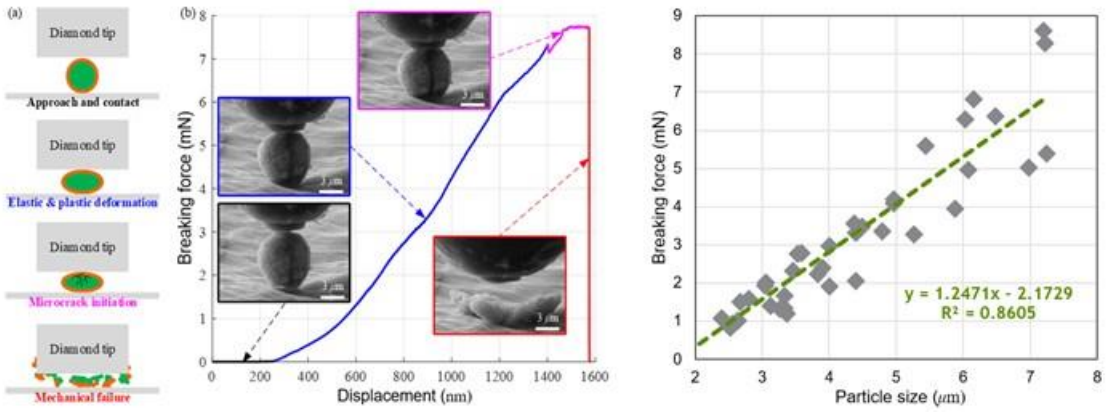

Figure I.2.E.5 Particle breaking force measurement of poly-crystalline NMC811

Nano-indentation was studied to analyze the particle strength of poly-crystalline NMC811 via coprecipitation and mono-crystalline NMC811 via hydrothermal synthesis. We first performed a nano-indentation set-up to measure the particle breaking force of poly-crystalline NMC811 with a relatively large particle size. Through this measurement, it was confirmed that the particle breaking force of poly-crystalline NMC811 decreases linearly as the particle size decreases. The nano-indentation test for the hydrothermal-synthesized mono-crystalline NMC811 is planned on the basis of the established measurement system.

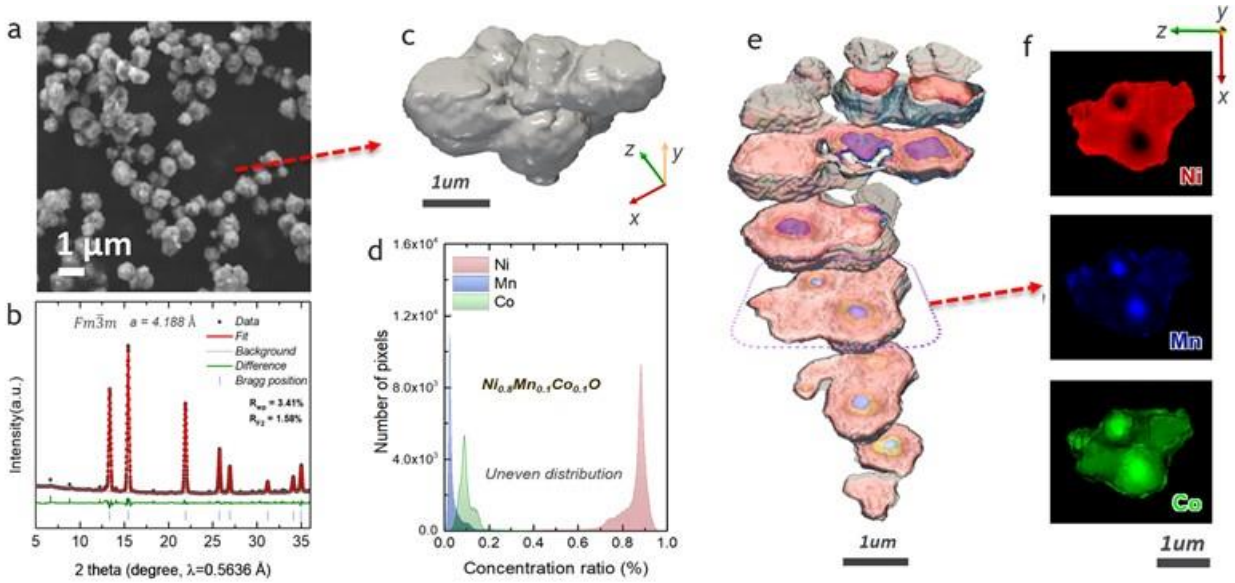

Figure I.2.E.6 Characterization of hydrothermal-synthesized NMC811 precursor

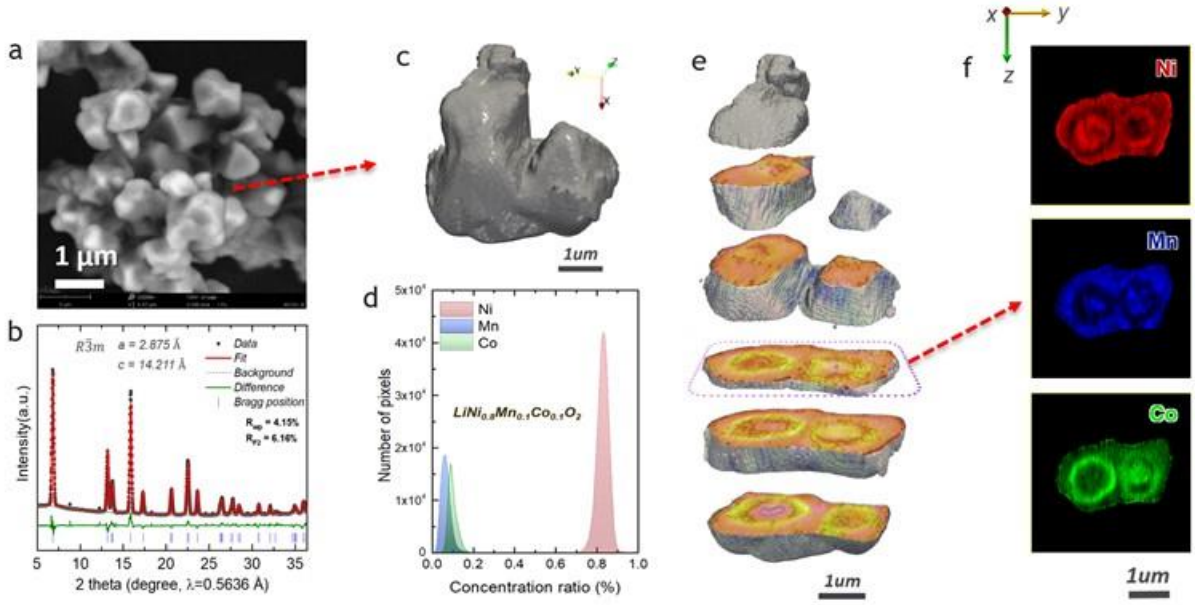

Figure I.2.E.7 Characterization of hydrothermal-synthesized NMC811 cathode

In collaboration with BNL (Dr. Seongmin Bak), we analyzed the hydrothermal-synthesized mono-crystalline NMC811 precursor and cathode using Rietveld refinement of powder XRD, composition analysis, cross-sectioned view, 2D, and 3D XRF tomography. Powder XRD results of the precursor material prepared by hydrothermal show the rock-salt structure, which indicates the precursor is $(Ni_xCo_yMn_z)O$ type oxide. After calcination (lithiation via solid-state reaction) process, $LiNi_{0.8}Co_{0.1}Mn_{0.1}O_2$ has been successfully prepared.

The elemental distribution from the XRF image shows the Mn segregation at the core region of the particles in both precursor and as-prepared NMC811. The Mn-rich core may form from the precursor level during the hydrothermal process.

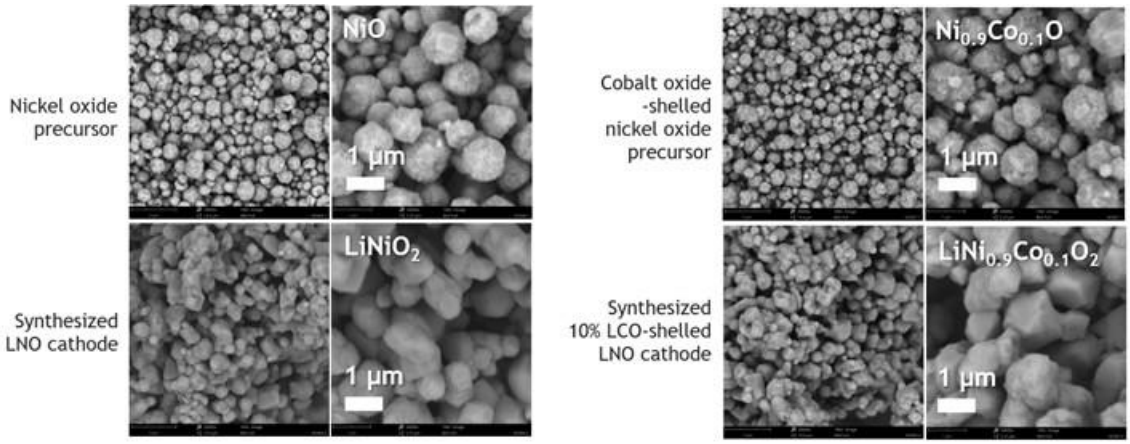

Figure I.2.E.8 Hydrothermal-synthesized LNO and LCO-shelled LNO

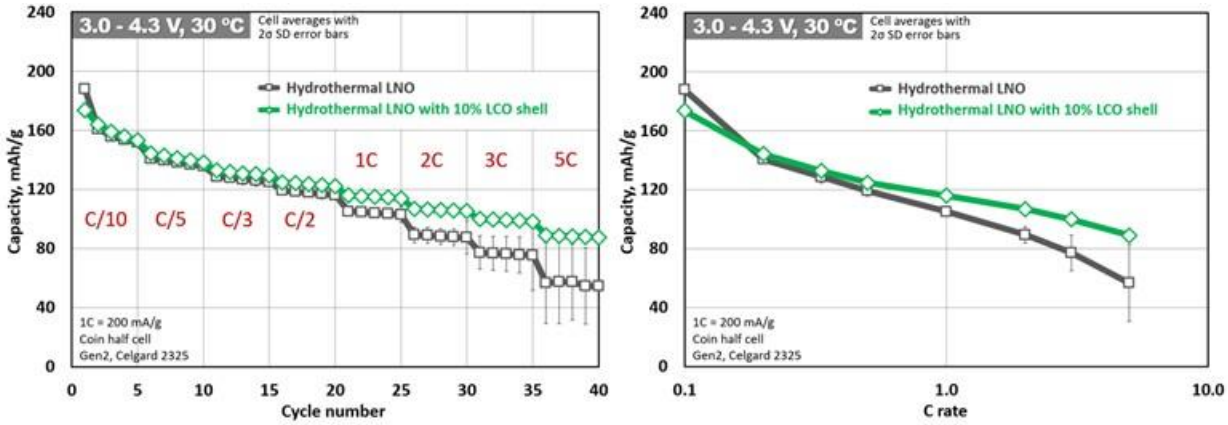

Figure I.2.E.9 Rate performance comparison of LNO and 10% LCO-shelled LNO

In a preliminary synthesis attempt, LNO and LCO-shelled LNO materials were prepared to test and validate the application of the supercritical hydrothermal synthesis process. This is an effort to understand the potential for improving material stability and rate performance versus traditionally co-precipitated material. Rate performances of the hydrothermal LNO and the 10% LCO-shelled LNO materials were compared with constant current rates of 0.1 C, 0.2 C, 0.33 C, 0.5 C, 1 C, 2 C, 3 C, and 5 C between 3.0 and 4.3 V at 30°C. The hydrothermal-synthesized 10% LCO-shelled LNO shows improved rate performance compared to LNO.

To demonstrate the flexibility of the supercritical hydrothermal process, the synthesis of pure LLZO and 0.2 Al-doped LLZO solid electrolytes were conducted and the materials were successfully produced. We confirmed the controllability of particle size and morphology of LZO precursor using additives. Pure LLZO and 0.2 Al-doped LLZO with accurate stoichiometry were synthesized. 0.2 Al-doped LLZO of about 2µm particle size with uniform Al distribution was obtained. The results of these preliminary experiments will lead to efforts to resolve high interfacial resistance caused by poor contact and interfacial reactions of the cathode composite layer of solid-state lithium batteries.

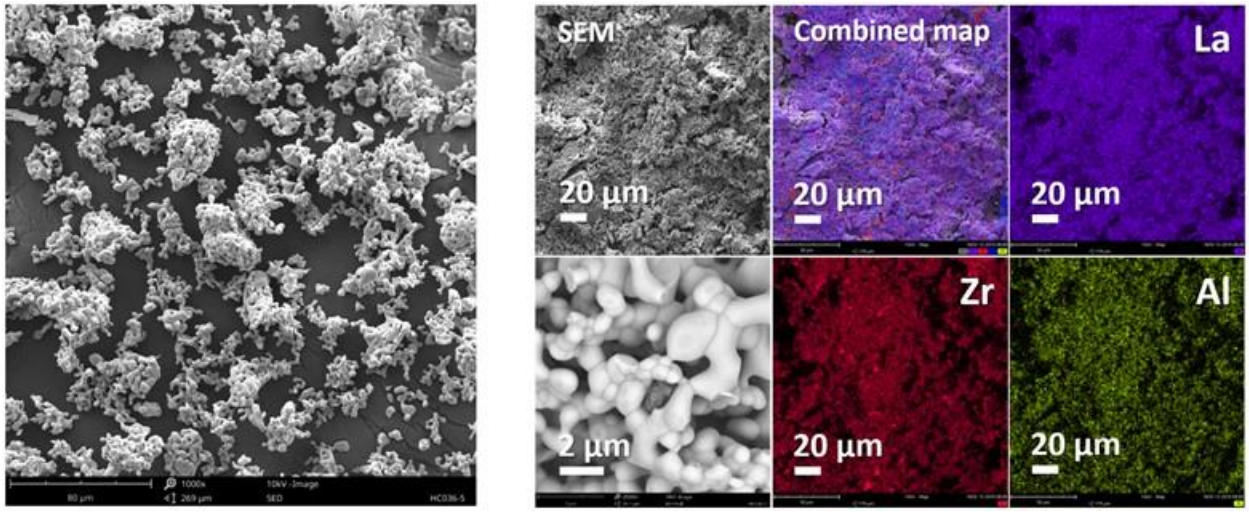

Figure I.2.E.10 Hydrothermal-synthesized 0.2 Al-doped LLZO solid electrolyte

Conclusions

A multi-purpose supercritical hydrothermal reactor system was installed and is being operated, which leads to the establishment of new capabilities to manufacture battery materials with supercritical fluid technology. This supercritical fluid system is a material synthesis platform that is able to produce mono-crystalline cathode materials with a solid structure and unique mechanical and electrochemical properties. Hydrothermal-synthesized mono-crystalline NMC811 shows promising capacity and stability at extremely high C-rate (above 5C). Nano-indentation test platform was set up using polycrystalline NMC811. The elemental distribution from 3D XRF tomography shows the Mn segregation at the core region of the particles in both precursor and as-prepared NMC811. Hydrothermal-synthesized 10% LCO-shelled LNO shows improved rate performance compared to LNO. 0.2 The system flexibility was demonstrated by producing 0.2 Al-doped LLZO solid electrolyte with accurate stoichiometry and about 2µm-size particles with uniform Al distribution. This supercritical hydrothermal process is a powerful platform for the synthesis of new battery materials with the desired particle size, composition distribution, and morphology which are not commercially available and difficult to produce using other technologies. We will continue to provide new battery cathode materials that meet the needs of the battery community.

Key Publications

1. Sangjin Maeng, Youngmin Chung, Sangkee Min, and Youngho Shin, “Enhanced mechanical strength and electrochemical performance of core–shell structured high–nickel cathode material,” Journal of Power Sources, 448 (2020).

2. Youngho Shin and Gregory Krumdick, “Tangent Gradient Concentration Material for Battery, Digital Gradient Concentration Material for Battery”, U.S. Pat. Appl. Publ. US 2020/0099045 A1.

Acknowledgements

Continuous support from David Howell and Peter Faguy of the U.S. Department of Energy’s Office of Vehicle Technologies is gratefully acknowledged.

We gratefully acknowledge the collaboration with Dr. Seongmin Bak (BNL), Dr. Sangjin Maeng, Prof. Sangkee Min (University of Wisconsin-Madison) and the use of facilities and instrumentation supported by NSF through the University of Wisconsin-Madison Materials Research Science Center (DMR-1720415).

I.2.F Process R&D and Scale Up of Critical Battery Materials (ANL)

Krzysztof Pupek, Principal Investigator
Argonne National Laboratory
9700 S. Cass Ave
Lemont, IL, 60439
kpupek@anl.gov

Peter Faguy, DOE Technology Development Manager
U.S. Department of Energy
E-mail: Peter.Faguy@ee.doe.gov

Start Date: October 1, 2019 End Date: September 30, 2020
Project Funding: $687,500 DOE share: $687,500 Non-DOE share: $0

Project Introduction

New experimental materials are constantly invented to improve the safety, energy density, cycle, and calendar life of lithium ion batteries for EV. These materials are typically synthesized in discovery laboratories in small batches providing amounts sufficient only for limited basic evaluation but not in quantities required for full scale validation and prototyping. In addition, bench-scale processes are often un-optimized, not validated, and generate materials with inconsistent purity and yield. This project aims to assist advanced battery research community by enabling access to larger quantities of high quality innovative materials.

Objectives

The objective of this project is to conduct research toward scaling up production of advanced materials for Li-ion batteries originally created in small quantities by discovery scientists at various research organizations. Scaling up the original route used by discovery scientists often requires an extensive modification of the bench-scale chemistry and systematic, science-based process research and development to allow for 1) safe and cost effective production, 2) development of an engineering flow diagram, 3) design of a mini-scale system layout, 4) construction of the experimental system, and 5) validation of the optimized process, all of which are needed for full industrial implementation. The experimental system will be assembled and the materials will be manufactured in quantities sufficient for full scale industrial evaluation and to support further research. The materials produced by the program will be fully characterized to confirm chemical identity and purity. Analytical methods will be developed for quality control. The electrochemical performance of the materials will be validated to confirm that these properties match the original data generated by the discovery scientist. Sample of the materials produced by the project will be available to the advanced lithium ion battery research community to support basic development and large scale performance validation.

Approach

New materials for experimental electrolyte formulations often have complex molecular structure that translates frequently into increased synthesis difficulties and cost. Argonne's Applied Materials Division's Process R&D group, operated in the newly expanded Materials Engineering Research Facility (MERF) is evaluating emerging production technologies to address the challenges. A comprehensive, systematic approach to scale-up of advanced battery materials has been defined. This approach starts with analyzing of the original route the new material was first made in the discovery lab and initial electrochemical evaluation. This determines if the material is to be added to the inventory database, ranked, prioritized and selected for scale up. The Applied Materials Division's Process R&D group at Argonne consults with the DOE technology manager to prioritize new materials based on level of interest, validated performance and scale up feasibility. The new candidate materials for scale up are discuss with DOE for final approval. The Process R&D group evaluates several approaches, including non-standard manufacturing technologies, to determine the best route to scale up of each particular material. One such technology is a Continuous Flow Chemical Reactor that enables the continuous

synthesis of materials from discovery through process development and production scale. Continuous flow reactor technology can be used for rapid screening of reaction conditions to better understand the fundamentals of process kinetics and thermodynamics. The technology offers a cost-effective and safer alternative to traditional batch processes by improving material and energy usage and minimize the environmental impact of the manufacturing operation. At this point, the scale-up process begins with a feasibility study, followed by proof of concept testing, first stage scale-up and, as needed, further scale-up cycles. Several Go/No Go decisions are located after feasibility determination and electrochemical validation testing. For each material, we will develop a scalable manufacturing process, analytical methods and quality control procedures. We also prepare a "technology transfer package" which includes detailed procedures of the revised process for material synthesis, materials balance, analytical methods and results (Specification Sheet) and the SDS for the material. The detailed process description allows for preliminary estimates of production cost, an important factor for decision making in industry. We apply the newly developed process to manufacture kilogram quantities of the material. We fully chemically characterize each material and make samples available for industrial evaluation and to the research community. We also provide feedback to discovery chemists helping to guide future research.

Results

Flow Chemistry Synthesis of 3,3,3-Trifluoropropylene Carbonate (TFPC).

Continuing work from the last fiscal year, we further developed the synthesis of 3,3,3-trifluoropropylene carbonate (TFPC), which has shown excellent properties for several areas of lithium ion battery design.[1] This solvent has been investigated extensively in recent years, but is not widely available due to the difficulty in its synthesis. Additional investigations on a fully continuous method of production using a different chemistry based on carbon dioxide and a catalyst to ring-expand 3,3,3-trifluoropropylene oxide (Figure I.2.F.1). This "Green chemistry" approach is highly atom-efficient and produces virtually no waste or by-product. We have extensively studied this reaction and developed an optimized procedure. Well over a kilogram of high purity material has been prepared and is available for sampling.

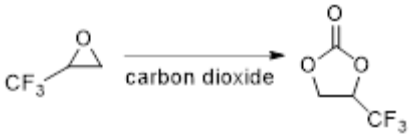

Figure I.2.F.1 Flow Chemistry Synthesis of TFPC.

Methyl bis-(Fluorosulfonyl)imide (Me-FSI)

Previously, we had supplied the Zhang group at Argonne with methyl bis(fluorosulfonyl)imide, a reagent that was originally used in a one-step synthesis of high purity ionic liquids. We have also now discovered that this material can act as a base solvent for inherently non-flammable electrolyte formulations (Figure I.2.F.2). Preliminary coin cell studies (Full cell analysis: NMC622 (C022)/Gr (A002B); 1C = 1.6 mA; 4.1-3.0 V cycled at C/3) using an electrolyte solution composed of 1M LiFSI in Me-FSI:GBL or EC (90:10) + 5 wt% VC) showed good cycle-ability. However, contrary to expectations, FEC as an additive did not result in satisfactory cell performance in coin cell experiments.

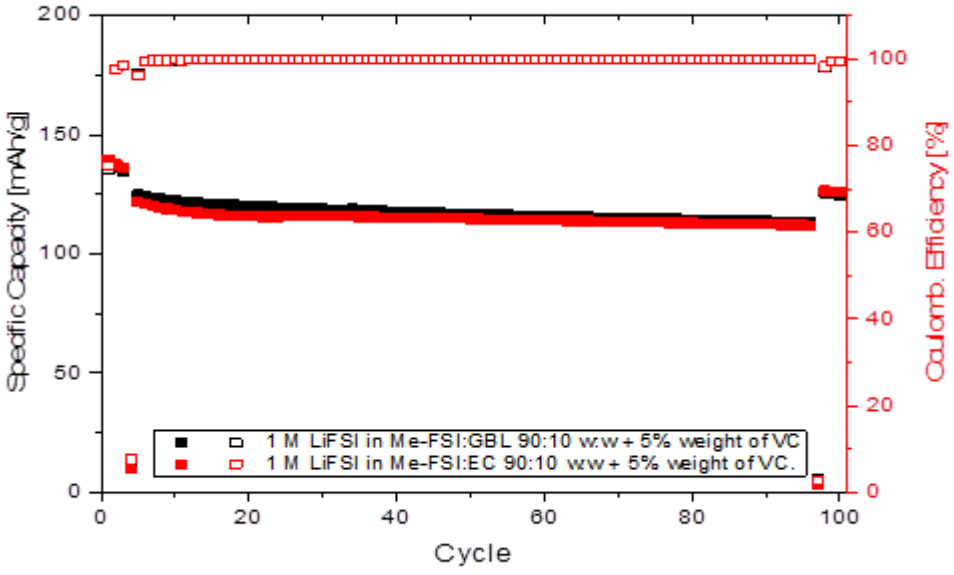

Figure I.2.F.2 Cycling profile of 1M LiFSI in Me-FSI:GBL or EC (90:10) + 5 wt% VC.

Several research groups have expressed interest in large quantities of this material as either a co-solvent, or additive, in addition to the original use as a reagent to produce high purity ionic liquids. The current literature route (Figure I.2.F.3) suffers from a large excess of highly corrosive and toxic reagents and solvents as well as unacceptable low yields (40-60%).

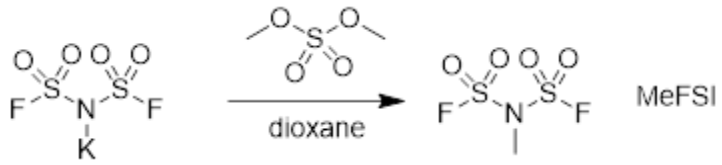

Figure I.2.F.3 Synthesis of Me-FSI using literature precedent.

While suitable for initial testing amounts, synthesis of large amounts (>100g) of Me-FSI would highly benefit from a new procedure. To this end, we have just begun investigating different and more efficient synthesis methods (Figure I.2.F.4).

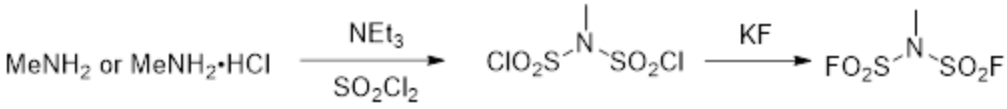

Figure I.2.F.4 Potential route for Me-FSI synthesis.

We believe this route has the potential to be more efficient and less costly than the current technology utilizing K-FSI, which is currently not readily available. It is unclear from the nature of these reactions (solids, gas removal) if they will be amenable to flow chemistry conditions.

Towards the Flow Chemical Synthesis of Li-TCI

Lithium tricyanoimidazole (Li-TCI) is a new material that has potential to prevent anodic dissolution in LiFSI-based electrolyte, similar to that reported with Li-TDI [2]. We reasoned that both Li-TCI and Li- 2- fluoro-4,5-dicyanoimidazole (Li-F-DCI) would show suitable electrochemical behavior. We have made small amounts of both, but now focus on Li-TCI due to a relatively short synthesis. Initial coin cell tests show that the

electrochemical cyclability (3.0-4.1V) of cells with electrolyte based on pure LiFSI and LiFSI/LiTCI are similar. More detailed examinations of "corrosion inhibiting" behavior are pending synthesis of suitable amounts of material.

The proposed synthesis of Li-TCI is relatively straightforward. However, the main difficulty are the hazards associated with the diazonium intermediate (Figure I.2.F.5). This material is frequently cited in the relevant literature as being a potentially explosive compound. This safety concern would stop further scale-up investigations using batch processes, which would involve accumulation of large quantities of the unstable, potentially explosive intermediate. However, one huge advantage of flow chemistry is the ability to make and use only small amounts of material at any one time. This allows the synthesis to be run safely, as the hazardous intermediate is made only in small quantities, and reacted soon after formation. Hazardous quantities are never accumulated, keeping the process safe.

Several remaining adaptations are needed, primarily to overcome the heavy presence of solid materials in the literature procedures, such as the limited solubility of the starting 2-amino-4,5-dicyanoimidazole in most solvents, precipitation of the diazonium intermediate in most procedures, and finally, finding suitable conditions for a smooth reaction with CuCN and KCN. Preliminary results indicate that a mixed solvent system of acetonitrile, dimethylsulfoxide and water are suitable for both dissolving the starting material and running the diazotization reaction.

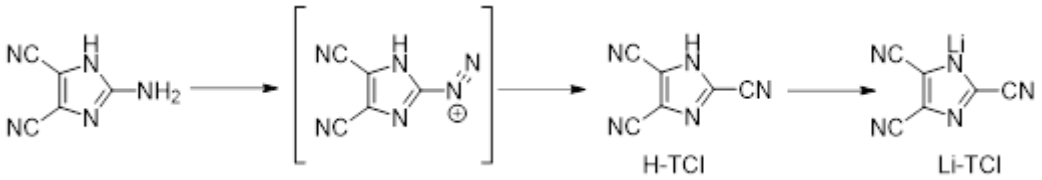

Figure I.2.F.5 Structures and proposed flow chemistry synthesis for Li-TCI.

We are projecting to optimize the flow chemistry reaction of the diazo intermediate with cyanide to form H-TCI. This is currently run by mixing the diazo intermediate solution 1:1 with a solution of KCN and CuCN in water. Isolation is complicated by low to moderate yields, high solubility of the product in water, and the large amount of copper salts present. Optimization of this step remains a challenge.

Conclusions

The Process group's experimental materials scale-up program assists the battery research community and allows for a comprehensive evaluation of new materials by industrial laboratories as well as supports basic research. In FY20 the program provided several new, not commercially available materials. Samples of high, uniform quality materials were distributed for further evaluation and research. Over 200 samples, ranging from grams to hundreds of grams of experimental battery materials have been provided to researchers since the program inception.

Evaluate emerging manufacturing technologies such as continuous flow reactors, microwave assisted reactions, acoustic mixing or reactive distillations to improve product quality while lowering manufacturing costs are all under consideration. We utilize our recently acquired, customized Syrris ASIA320 and Corning Advanced-Flow™ continuous flow chemical reactors to develop expedient manufacturing processes for new electrolyte solvents, salts and additives by improving safety, minimize waste stream and lower material and energy costs.

Key Publications

Issued Patents

1. Dzwiniel; Trevor L., Pupek; Krzysztof, Krumdick; Gregory K. "Solvent for non-aqueous battery" U.S. Patent 10,622,675 April 14, 2020.

2. Dzwiniel; Trevor L., Pupek; Krzysztof "Method for preparing bis-(silylalkyl)carbonate esters" U.S. Patent , 10,556,917 February 11,2020.

3. Patent Applications

4. Dzwiniel, Trevor L.; Pupek, Krzysztof; "Continuous method for preparing carbonate esters" filed March 09, 2020 as Application # 16/812,628.

Published Papers

1. Liu, Qian; Hsu, Chia-Wei; Dzwiniel, Trevor L.; Pupek, Krzysztof Z.; Zhang, Zhengcheng; "A fluorine-substituted pyrrolidinium-based ionic liquid for high-voltage Li-ion batteries" Chemical Communications (Cambridge, United Kingdom) (2020), 56(53), 7317-7320.

2. Liu, Qian; Jiang, Wei; Munoz, Maria Jose Piernas; Liu, Yuzi; Yang, Zhenzhen; Bloom, Ira; Dzwiniel, Trevor L.; Li, Ying; Pupek, Krzysztof Z.; Zhang, Zhengcheng; "Stabilized Electrode/Electrolyte Interphase by a Saturated Ionic Liquid Electrolyte for High-Voltage NMC532/Si-Graphite Cells" ACS Applied Materials & Interfaces (2020), 12(20), 23035-23045.

3. Liu, Qian; Dzwiniel, Trevor L.; Pupek, Krzysztof Z.; Zhang, Zhengcheng; "Corrosion/passivation behavior of concentrated ionic liquid electrolytes and its impact on the Li-ion battery performance" Journal of the Electrochemical Society (2019), 166(16), A3959-A3964.

References

1. TFPC references

1. Mueller, Guillaume; Won, Ji-Hye; Lee, So-Young; Lee, Hyuncheol; Hough, Lawrence Alan "Fluorinated liquid electrolyte for electrochemical cells having a lithium metal anode" PCT Int. Appl. (2019), WO 2019042741 A1 20190307.

2. Hu, Zhongli; Zhao, Liubin; Jiang, Tao; Liu, Jie; Rashid, Arif; Sun, Pengfei; Wang, Gulian; Yan, Chenglin; Zhang, Li "Trifluoropropylene carbonate-driven interface regulation enabling greatly enhanced lithium storage durability of silicon-based anodes" Advanced Functional Materials (2019), Ahead of Print.

3. Yun, Jiaojiao; Zhang, Li; Qu, Qunting; Liu, Hongmei; Zhang, Xianlin; Shen, Ming; Zheng, Honghe "A Binary Cyclic Carbonates-Based Electrolyte Containing Propylene Carbonate and Trifluoropropylene Carbonate for 5 V Lithium-Ion Batteries" Electrochimica Acta (2015), 167, 151-159.

4. Wang, X. J.; Lee, H. S.; Li, H.; Yang, X. Q.; Huang, X. J. "The effects of substituting groups in cyclic carbonates for stable SEI formation on graphite anode of lithium batteries" Electrochemistry Communications(2010),12(3),386-389.

5. Zhang *et.al*: *J. Electrochem. Soc.*, **162** (9) A1725-A1729 (2015).

2. TFPC synthesis

1. Tan Jin; Fang Dong; Yang Liu; Yu Lin Hu, "Novel and effective strategy of dual bis(trifluoromethylsulfonyl)imide imidazolium ionic liquid immobilized on periodic mesoporous organosilica for greener cycloaddition of carbon dioxide to epoxides" New Journal of Chemistry, 43(6), 2583-2590, 2019.

2. Yu Lin Hu, Rui Li Zhang, Dong Fang "Quaternary phosphonium cationic ionic liquid/porous metal–organic framework as an efficient catalytic system for cycloaddition of carbon dioxide into cyclic carbonates" Environmental Chemistry Letters, 17(1), 501-508, 2019.

3. Manuela Philipp; Rebecca Bernhard; Hubert A. Gasteiger; Bernhard Rieger “A Green Route: From Carbon Dioxide to Silyl Substituted Carbonate Electrolytes for Lithium-Ion Batteries” J. Electrochem. Soc. 162(7), A1319, 2015.

3. Other

1. Piotr Jankowski, Orcid, Maciej Dranka, Władysław Wieczorek, and Patrik Johansson “TFSI and TDI Anions: Probes for Solvate Ionic Liquid and Disproportionation-Based Lithium Battery Electrolytes” Journal of Physical Chemistry Letters (2017), 8(15), 3678-3682.

2. Ilya A. Shkrob, Orcid, Krzysztof Z. Pupek, James A. Gilbert, Stephen E. Trask, and Daniel P. Abraham “Chemical Stability of Lithium 2-Trifluoromethyl-4,5-dicyanoimidazolide, an Electrolyte Salt for Li-Ion Cells” Journal of Physical Chemistry C (2016), 120(50), 28463-28471.

3. An electrolyte additive for extended battery life and fast charging. Charged Magazine March 30, 2020.

4. Schmidt, Grégory, Collier, Bertrand, Bonnet, Philippe “Long-Life Lithium-Ion Batteries” World Intellectual Property Organization, WO2015136199 A1.

5. Bitner-Michalska, Anna, Poterała, Marcin, Gajewska, Agnieszka, Kalita, Michał, Żukowska, Grażyna, Piszcz, Michał, Marcinek, Marek, Wieczorek, Władysław, Nolis, Gene “Electrolyte For Metal-Ion Batteries” World Intellectual Property Organization, WO2016203390 A1.

Acknowledgements

Continuous support from David Howell and Peter Faguy of the U.S. Department of Energy’s Office of Vehicle Technologies is gratefully acknowledged.

MERF Critical Battery Materials Team

Trevor Dzwiniel, Chia-Wei Hsu, Amber Tabaka

Argonne's Collaborators

John Zhang, Daniel Abraham, Qian Liu, Wenquan Lu, Bryant Polzin, Steven Trask

I.2.G Optimizing Co-sintering of Ceramic Components for Manufacturing of All-Solid-State Lithium-Ion Battery (Lawrence Livermore National Laboratory)

Brandon C. Wood, Principal Investigator
Lawrence Livermore National Laboratory
7000 East Ave
Livermore, CA, 94550
E-mail: wood37@llnl.gov

Peter Faguy, DOE Technology Development Manager
U.S. Department of Energy
E-mail: Peter.Faguy@ee.doe.gov

Start Date: April 1, 2019 End Date: March 31, 2021
Project Funding: $300,000 DOE share: $300,000 Non-DOE share: $0

Project Introduction

The performance of solid-state batteries is greatly limited by the high interfacial impedance between the solid components of the batteries. Unlike conventional liquid electrolytes, ceramic solid-state electrolytes often form poor physical contact with the solid electrodes, which impedes Li-ion transport across the interfaces. Whereas the contact between the electrolyte and the anode can be improved by post-annealing processing, this approach is far less effective at the interface with the cathode because very high ceramic processing temperatures required to produce full densification at the interfaces. Unfortunately, at these elevated temperatures, the electrode materials are prone to decomposition and formation of ionically resistive secondary phases at the interfaces.

As a prime example, $Li_{7-x}La_3Zr_2O_{12}$ (LLZO) is (electro)chemically stable against Li metal and forms a robust LLZO|Li metal interfacial structure upon heating. Instead, the main challenge of employing LLZO in a full electrochemical cell lies in the difficulty of fabricating a densified ceramic interface against typical cathode materials. Depending on particle size and shape, LLZO is typically sintered at a temperature above 1100°C.[1] However, most cathode materials, such as $LiCoO_2$, cannot survive a temperature above 900°C, either decomposing or reacting with the LLZO electrolyte. Lowering the LLZO sintering temperature to below 900°C has therefore become a critical step toward the commercialization of LLZO-based all-solid-state batteries.

It has been reported that the sintering temperature of LLZO can be lowered by doping LLZO with different elements.[2], [3] This is a promising strategy that is based on altering fundamental materials chemistry rather than introducing an external sintering agent, which may produce unwanted side reactions or residual byproducts. Similarly, sintering conditions may be influenced by microstructure, packing density, and other physical properties of the green body particles. Finding the proper combination of chemical composition and microstructure that facilitates sintering while maintaining high ionic conductivity is time consuming and costly. Instead, this project leverages multiscale computational approaches to predict the effects of chemical and microstructural modification of LLZO on sintering temperature and densification kinetics during processing, as a first step towards enabling co-sintering of the electrolyte and cathode materials in ceramic solid-state batteries.

Objectives

This project is building computational capabilities to identify LLZO-based solid electrolyte compositions, particle microstructures, and processing conditions that could lead to sintering temperatures below 900°C while preserving suitable ionic conductivities above 0.3 mS/cm. Key descriptors of sintering temperature are computed and calibrated from atomic-scale simulations. Methodologies for direct mesoscale simulation of sintering are also being developed and deployed to predict densification kinetics.

Approach

This project utilizes *ab initio* and mesoscale simulations to provide an efficient and unbiased way of exploring the effects of composition (doping) and microstructure on the performance of LLZO based solid electrolytes. Density functional theory (DFT), *ab initio* molecular dynamics (AIMD) simulations, and custom codes being developed at LLNL for predicting densification kinetics form the cornerstone computational methodologies. Because directly predicting quantitative sintering temperatures is challenging, the team instead invokes an approach that relies on candidate descriptors that we expect to track with the sintering temperature. Candidate descriptors for sintering temperature are computed for selected LLZO compositions and calibrated against experimental sintering temperatures to evaluate effectiveness. Next, these descriptors are applied to other compositions to predict trends in sintering temperature. At the same time, the team is developing a phase field-based sintering kinetics model to probe the effects of LLZO microstructure, packing density, and particle green body formulation.

Results

Static descriptors for sintering trends from atomistic simulations

To predict sintering temperatures as a function of composition, the team is pursuing both static descriptors, which are relatively simple to compute, and dynamic descriptors, which require much longer and more cumbersome simulation techniques. In the past year, they investigated three distinct sets of static descriptors, namely (a) mechanical properties such as elastic moduli, bulk moduli and shear moduli, (b) amorphization energies and (c) surface energies for different atom-termination surfaces. For these tests, dopants were explored at three distinct sites (Al on Li sites, Ba on La sites, and Ta on Zr sites) in the cubic LLZO structure to understand the impact of doping at different sites on the sintering temperature. In addition, three different doping levels were considered. Results for some of the static descriptors evaluated from DFT (bulk modulus, shear modulus, and amorphization energy) are shown in Figure I.2.G.1. Smaller elastic constants are indicative of softening of the materials and thereby can be correlated to lower sintering temperatures. The amorphization energy is defined as the energy difference between the ground state structure and the amorphous structure (created using AIMD by the melt-and-quench method). It quantifies the energy penalty to disorder and should therefore track with sintering temperature. Both the elastic constants (bulk and shear moduli) and the amorphization energy decrease continuously with increasing Al-dopant concentration, suggesting lower sintering temperature with higher Al dopant concentration in agreement with experiments.[4] The last static descriptor pursued was surface energies for various surfaces with Li, La and Zr terminations. The team evaluated (110) and (111) surfaces with different Li, La and Zr terminations. The (110) surface with La termination shows lowest energy and therefore is the most stable surface, while the (111) surface is used to represent the higher energy surfaces to render enough surface reactivity. The results showed that Al-doping leads to higher surface energy for all the surfaces whereas the Ba-doping shows consistent decrease. Because higher surface energies promote sintering at low temperature, this implies that Al-doping would promote lower sintering temperatures, consistent with the elastic properties and amorphization energies. Overall, each of the descriptors shows promising behavior as static descriptors for predicting the impact of dopants on the sintering temperature. However, the trend is non-monotonic for the Ba and Ta cases, which demands compilation with other candidate descriptors and more sophisticated validation.

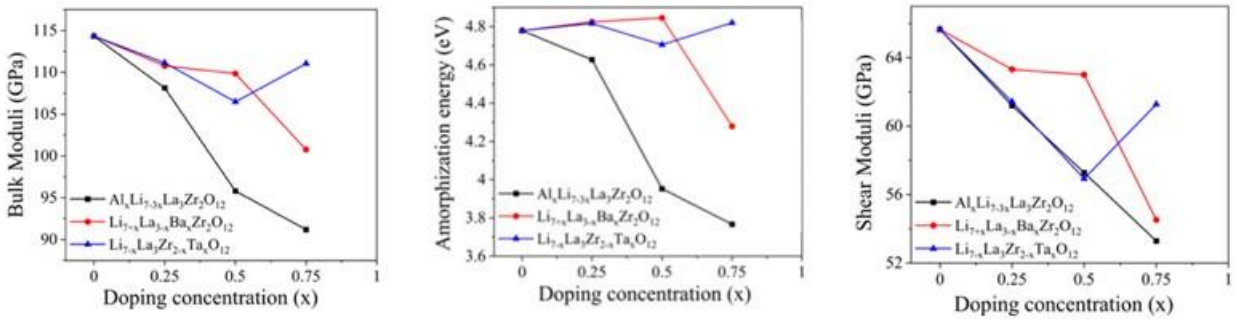

(a) (b) (c)

Figure I.2.G.1 Calculated (a) bulk and (b) shear moduli, and (c) amorphization energies for different doped-LLZO compositions we tested.

Dynamic descriptors for sintering trends from atomistic simulations

The team also evaluated different dynamic descriptors to study the impact of doping on the sintering temperature of LLZO, based on AIMD simulations run for each composition at 1500K. Select results are shown in Figure I.2.G.2. One dynamic descriptor involves the change in the symmetry of LaO_8 polyhedra, which are an important building block of the LLZO structure. A symmetry change corresponds to the softening of the material, which can be directly correlated to the sintering/melting behavior. The team evaluated the symmetry change using the continuous shape measure (CSM) metric (Figure I.2.G.2(a-c)). The CSM value is referenced to ground state configuration in fully relaxed, undoped-LLZO, with a greater CSM value indicating larger distortion. The variation in CSM for different compositions of doped-LLZO were then averaged over the AIMD trajectories. The CSM trends in Figure I.2.G.2(c) suggest that Al-doping invokes increased distortion of LaO_8 polyhedra, which should ultimately lead to lower sintering/melting temperatures. Likewise Ba also shows a increasing trend in CSM with increase in dopant concentration. However for Ta, we do not observe any significant increase in the CSM with increasing dopant concentration. A second dynamic descriptor, shown in Figure I.2.G.2(d), is the Lindemann ratio, which is often used to predict melting temperature. In particular, the Lindemann melting criterion states that melting might be expected when the root mean vibration amplitude exceeds 10%-15% of the average interparticle distance between ions. The Lindemann ratio was computed as the ratio of the these two quantities for the La ions, the disordering of which is expected to signal the premelting phenomenon during sintering. A consistent increase in the Lindemann ratio at constant temperature is indicative of material structure corresponding to more melt-like structure. Hence greater the Lindemann ratio, lower would be the melting/sintering temperature. For Al-doping, we observe very high Lindemann ratio as compared to other dopants. All three dopants show increasing trends with increased dopant concentration. The results are broadly consistent with the symmetry measure. The team is currently finalizing the descriptor analysis and calibrating against experimental sintering temperatures and simulated melting temperatures of doped LLZO to make a final selection of a compound descriptor that is maximally predictive across all compositions.

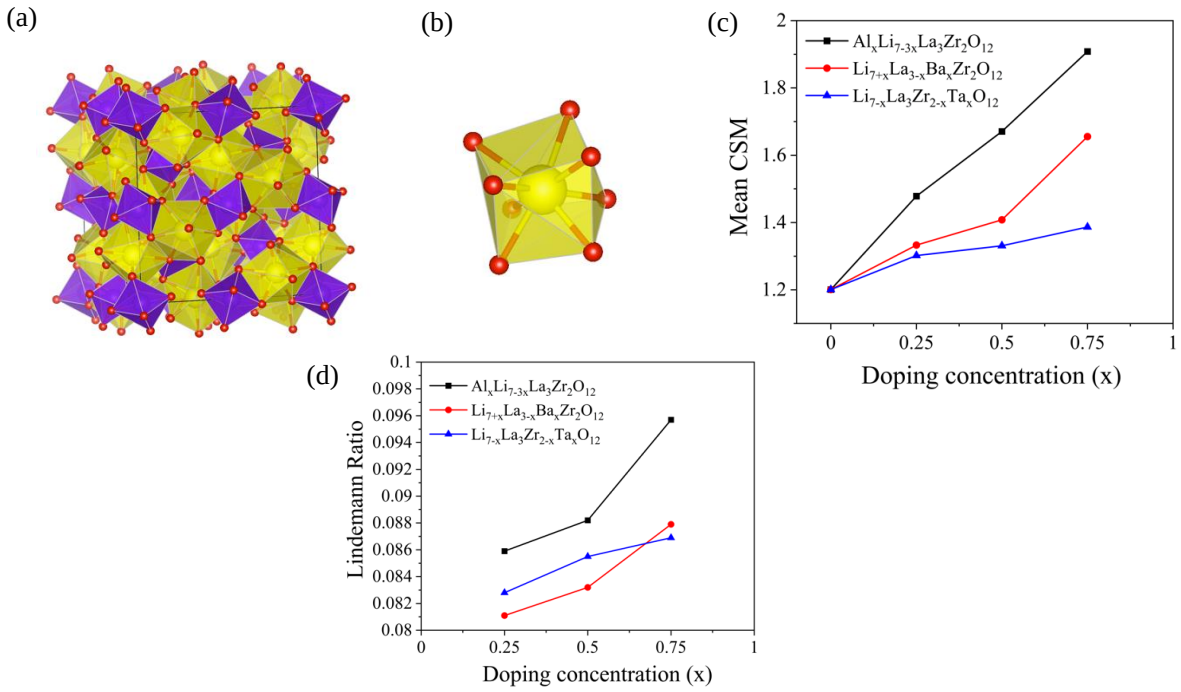

Figure I.2.G.2 (a) LLZO structure showing LaO_8 and ZrO_6 polyhedra, (b) a LaO_8 polyhedra for which the CSM values are calculated and (c) the variation of CSM for doped LLZO at 1500 K. The yellow, purple and red spheres are La, Zr and O ions respectively. (d) Calculated Lindemann ratio at 1500K for doped LLZO.

Mesoscale sintering modeling

To co-optimize the sintering conditions and the green body characteristics for reducing LLZTO sintering temperature, the team also developed a phase-field model based on the multiphase-field framework. The model is being used to gain a better understanding of the microstructure evolution during sintering, as well as the relationship between densification kinetics and processing parameters, including particle size and distribution, sintering temperature and doping species and concentrations. It accounts for multiple concurrent and coupled physical processes involved in sintering, including various diffusion paths (along the particle surfaces and grain boundaries, as well as through the bulk lattice), vapor transport (through evaporation and condensation), particle rigid-body motion, and grain growth through boundary migration. The model was first tested using three spherical particles of the same size in point contact, emulating the implicit dependence of the predicted densification kinetics as a function of particle size and temperature (Figure I.2.G.3). The dependence of the time to full densification (i.e., closure of the internal pore) on particle size was then monitored (Figure I.2.G.3(a)). To mimic the effect of temperature, the team ran a second set of simulations in which the reference bulk diffusivity was increased while maintaining the same relative ratios between all other diffusive contributions. At the same time, experimental collaborators Ye and Wood (LLNL) performed sintering densification experiments on surfactant-assisted ball milled LLZO powders with different initial particle sizes, which provided a point of comparison for the trends computed using the models. The time to full densification was found to increase rapidly with particle size and temperature, in agreement with the higher degree of densification for the smaller ball-milled particles observed in experiments. The models were also able to capture the underlying physics, demonstrating that advective flux is far more sensitive to particle size than diffusive flux, indicating that its contribution is primarily responsible for the altered densification kinetics for smaller particles (Figure I.2.G.3(b-e)). These results were recently accepted for publication.[5] The team is now pursuing more complex green body particle size distributions that are broadly representative of real LLZO powders.

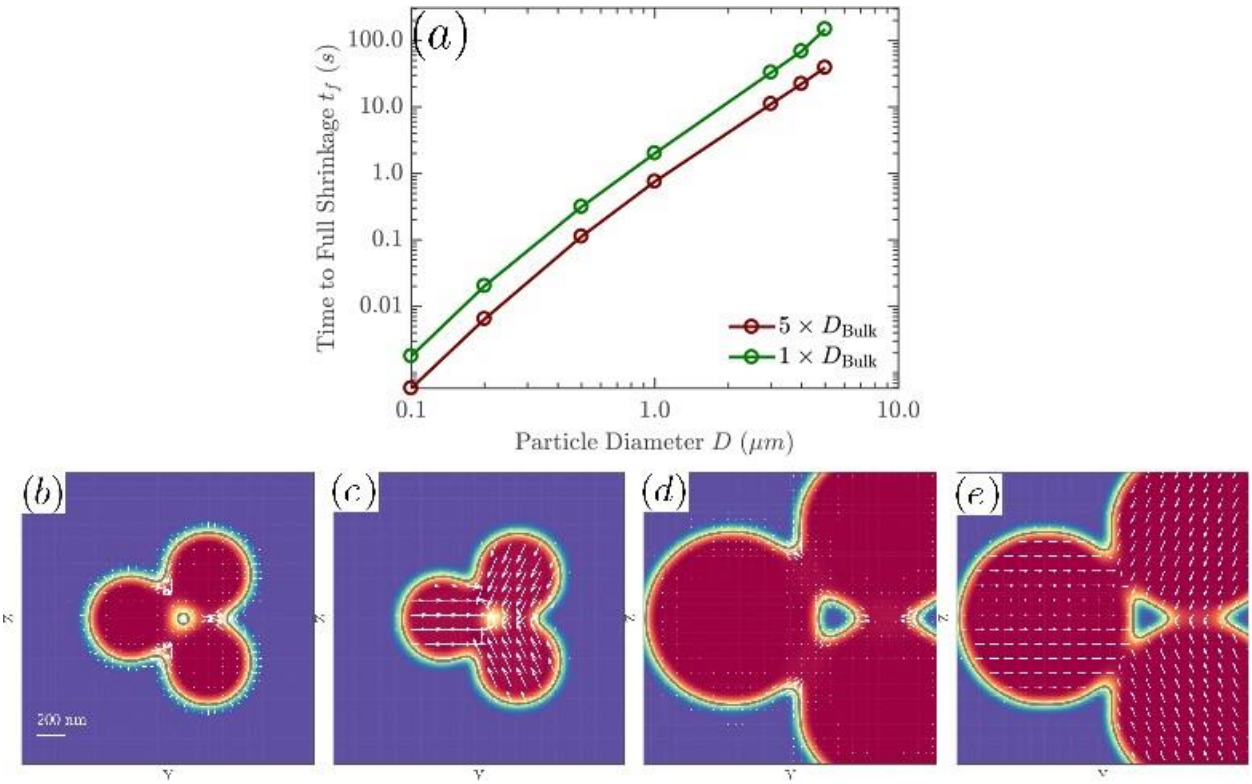

Figure I.2.G.3 Phase-field simulation of densification during sintering for a model three-particle LLZO system. (a) Predicted densification kinetics as a function of particle size and simulated temperature (as mimicked by fivefold acceleration of the diffusion kinetics). (b,d) Diffusion flux and (c,e) advective flux contributions associated with particle translational motion during sintering of three spherical particles with diameter of 0.6 μm (b and c) and 1.2 μm (d and e). The white arrow size scales with the flux magnitude. Both flux contributions increase with decreasing particle size to drive faster densification kinetics, but the advective flux term dominates.[5]

Conclusions

The goal of this project is to find appropriate chemical compositions and powder microstructures to lower the sintering temperature of LLZO while preserving the desired ionic conductivity. To efficiently screen the space of possible dopants and compositions, it is critical to identify computationally efficient and accurate descriptors based on examinations of selected dopants (Al, Ba and Ta) and doping levels. This year, the team tested a variety of atomic-scale "static" and "dynamic" descriptors, including elastic moduli, amorphization energy, surface energy, Lindemann ratio, and local symmetry fluctuation analysis. The descriptors follow similar trends, suggesting their viability as easy-to-compute proxies for sintering temperature. For instance, Al-doping should lower the sintering behavior, whereas Ba doping would increase it. Ta-doping does not show any significant impact on the sintering temperature. Although these descriptor results are highly promising, there are minor deviations in the specific ordering across the tested compositions. Further validation is underway, and a compound descriptor will soon be chosen that provides the best match to experimental data and predicted melting temperatures. For the mesoscale sintering models, the team has successfully reproduced the essential dependence of densification kinetics on particle size. This is the first step towards also incorporating the role of green body particle formulations and microstructure in sintering kinetics, in addition to composition.

Key Publications

1. M. Wood, X. Gao, R. Shi, T. W. Heo, J. A. Espitia, E. B. Duoss, B. C. Wood, and J. Ye, "Exploring the Relationship Between Solvent-Assisted Ball Milling, Particle Size, and Sintering Temperature in Garnet-Type Solid Electrolytes", *J. Power Sources*, in press (2020).

2. B.C. Wood, “Optimizing co-sintering of ceramic components for manufacturing of all-solid-state batteries,” Vehicle Technologies Office Annual Merit Review (June 2020).

References

1. R. Murugan, V. Thangadurai and W. Weppner, “Fast lithium ion conduction in garnet-type $Li_7La_3Zr_2O_{12}$”, *Angew. Chem. Int. Ed.* **46**, 2007, 7778-7781.

2. R.-J. Chen, M. Huang, W.-Z. Huang, Y. Shen, Y.-H. Lin and C.-W. Nan, “Effect of calcining and Al doping on structure and conductivity of $Li_7La_3Zr_2O_{12}$”, *Solid State Ionics* **265**, 2014, 7-12.

3. S. Ohta, T. Kobayashi and T. Asaoka, “High lithium ionic conductivity in the garnet-type oxide $Li_{7-x}La_3(Zr_{2-x},Nb_x)O_{12}$ (x=0-2)”, *J. Power Sources* **196**, 2011, 3342-3345.

4. S. Cao, S. Song, X. Xiang, Q. Hu, C. Zhang, Z. Xia, Y. Xu, W. Zha, J. Li, P. M. Gonzale, Y. H. Han and F. Chen. “Modeling, Preparation, and Elemental Doping of Li7La3Zr2O12 Garnet-Type Solid Electrolytes: A Review”, Journal of the Korean Ceramic Society, **56 (2)**, 2019, 111−129.

5. M. Wood, X. Gao, R. Shi, T. W. Heo, J. A. Espitia, E. B. Duoss, B. C. Wood, and J. Ye, “Exploring the Relationship Between Solvent-Assisted Ball Milling, Particle Size, and Sintering Temperature in Garnet-Type Solid Electrolytes”, *J. Power Sources*, in press (2020).

Acknowledgements

This work was performed under the auspices of the U.S. Department of Energy by Lawrence Livermore National Laboratory under contract DE-AC52-07NA27344.

Collaborations. The LLNL computational modeling team includes Liwen Wan, Tae Wook Heo, and Rongpei Shi. The project also collaborates with Jianchao Ye and Marissa Wood from LLNL on determining experimental sintering conditions for LLZO-cathode interfaces in solid-state batteries. Through the U.S.-Germany partnership on solid-state battery research, an additional collaboration is underway with Eric Wachsman (U. Maryland) and with Timo Danner and Arnulf Latz (DLR) on realistic microstructure formulation and analysis for LLZO.

Impact: Completion of this project will lead to improved understanding of chemical and microstructural factors that determine sintering kinetics during processing of ceramic solid-state electrolytes. The results will be used to co-optimize green body formulations, compositions, and sintering conditions that can lead to improved electrode-electrolyte contacts with retention of ionic conductivity.

I.2.H Structure-Activity relationships in the optimizing of electrode processing streams for LiBs (LBNL)

Vincent Battaglia, Principal Investigator
Lawrence Berkeley National Laboratory
1 Cyclotron Rd., MS70R0108B
Berkeley, CA 94720
E-mail: vsbattaglia@lbl.gov

Peter Faguy, DOE Technology Development Manager
U.S. Department of Energy
E-mail: Peter.Faguy@ee.doe.gov

Start Date: April 1, 2019 End Date: September 30, 2022
Project Funding: $230,000 DOE share: $230,000 Non-DOE share: $0

Project Introduction

Procedures for preparing battery slurries and processing them into composite electrodes have mostly developed through trial-and-error, yet are critical in determining component-level structure, which in turn strongly influences final product performance. Furthermore, there is typically large performance variability as one moves from material to material. Optimizing for material changes through trial-and-error can waste valuable time and resources. This project aims to produce a better understanding of component interactions and arrangement in battery slurries and slurry coatings, as well the influence of processing decisions, in order to more precisely guide composite electrode fabrication. To pursue this, we are constructing precise experimental setups and will develop mathematical models as tools for testing hypotheses against experimental results.

Objectives

The ultimate goal of this project is to create approaches to generating mathematical models that accurately describe slurry preparation and composite electrode coating processing, connecting component-level information to macroscopic characteristics. For this to happen, we must achieve multiple intermediate objectives, as these systems are not well-understood. We are creating new computer-automated experimental setups that can be combined with a variety of instruments to perform precise, reproducible experiments on mixing and coating-drying. In the process of analyzing experimental data, we are developing corresponding mathematical submodels that encode our hypotheses for testing.

Approach

We have used VTO funding through this project to supplement AMO funding in a larger effort in understanding how component-level interactions and process parameters affect outcomes for dried coating products. Our VTO work focuses on battery slurries, which differ substantially from the inks that are the focus of the AMO work. Careful planning has been required in the development of our experimental setups for use with both types of dispersions; in some cases, we have had to plan on separate setup components for the two classes of dispersions.

One important aspect of our approach is to create computer-automated sample preparation subsystems with which we can reliably recreate dispersions or coatings. This will allow us to use a variety of instruments in different locations to investigate samples, with good assurance that we are making observations of consistent states.

Since component-level interactions during slurry processing are not well-understood, we have begun by developing an experimental setup to precisely study the mixing process, combining a dispersion preparation subsystem with a high-speed particle size analyzer. Mathematical analysis of observed particle size distributions obtained from carefully controlled experiments should provide indirect information about

component interactions. As particle size analyzers typically operate through light diffraction, they are limited to dilute dispersions. While we recognize that practical slurries and inks are much more concentrated, we expect that the fundamental interactions that occur in dilute dispersions should also occur in concentrated dispersions that differ only in solvent concentration.

To transition to dispersions at practical concentrations, we plan to turn to confocal microscopy. Custom flow cells will first be used to observe the same dilute dispersions examined with the particle size analyzer. An image analysis pipeline will be used to process large amounts of image data for comparison with results from the particle size analyzer, providing context and agglomerate structure information.

Finally, to examine coating drying dynamics, we plan to construct a portable, computer-automated, miniature coating table setup intended to simulate manufacturing conditions while being physically compatible with confocal microscope observation and selected Advanced Light Source beamline hutches. This will allow us to reproducibly probe the influence of various processing decisions on drying dynamics. As with the mixing experiments, we intend to develop mathematical models in the process of understanding experimental results.

Results

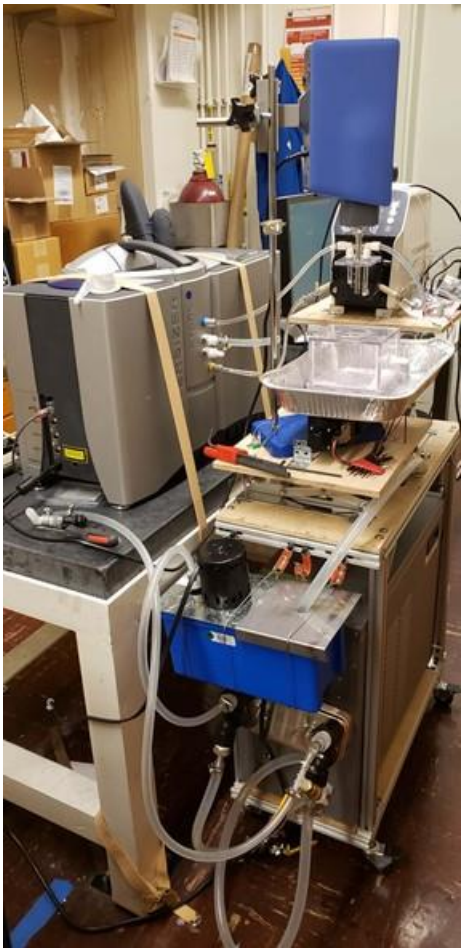

Figure I.2.H.1 Photo of precision mixing experiment

Progress on this project was limited due to the pandemic, as on-site access and services remain limited. Nevertheless, we have nearly completed the construction of a portable computer-automated mixing station (see Figure I.2.H.1) with streamlined operation for consistent sample production, connected to a high-speed particle size analyzer. The mixing station components are positioned with brackets, allowing components to be

removed for maintenance and rapidly and precisely replaced, further promoting reproducibility. This system has been designed to accommodate dilute slurries of battery components along with the dilute inks used under the AMO project. The setup additionally includes a custom temperature bath, a computer-controlled chiller, thermocouples with computer readout, a computer-controlled disperser customized to allow a lower minimum rotational speed than the stock product, and a computer-controlled peristaltic pump. We have begun collecting baseline data from single-component mixtures, which later will be used as a basis for understanding multicomponent dispersions.

We have additionally identified a confocal microscope for purchase and have been preparing our lab space for its installation (including ongoing installation of an optical table). We will use this to observe both battery slurries and catalyst inks (the latter under AMO funding), and in our planning have carefully considered the requirements for accurately and safely imaging both types of systems. These preparations have continued into FY21 as we set up a ventilation system to extract NMP vapors and build appropriate flow observation cells.

We have developed CAD models of the miniature coating table components. These will evolve as we begin the process of building the experimental setup and refine designs based on practical considerations.

In preparation for our modeling efforts, we have updated an open-source LBNL simulation package that was developed under VTO funding several years ago for a silicon particle simulation project [1], but intended as a general-purpose tool for domain scientists to easily solve complicated equations on simple spatial domains. This is a good fit for our modeling efforts, which we expect might produce ODEs and 1D PDEs that differ somewhat from the commonly solved equations built into many existing numerical packages. To accompany this extensive update of both the software and documentation, we have submitted an article describing the software to the Journal of Open Source Software; it is presently nearing the end of the review process.

Conclusions

Composite electrode performance depends on component-level arrangement, which depends on slurry preparation and coating processing. However, manufacturing processes have evolved through trial-and-error because component-level interactions and dynamics are not well-understood. We have laid out a project with an aim of developing approaches for understanding these processes and representing them through mathematical models, starting with carefully controlled experiments using custom experimental setups. Although our work in FY20 has been impacted by the COVID-19 pandemic, we have nearly completed construction of a computer-automated mixing experiment that can be applied to both battery slurries and catalyst inks, and have laid the groundwork for a wide range of planned experimental and modeling work.

Key Publications

1. Under review: Higa, Kenneth, V. Srinivasan, and V. S. Battaglia. “PyGDH: Python Grid Discretization Helper.” *Journal of Open Source Software*

References

1. Higa, Kenneth and V. Srinivasan. “Stress and Strain in Silicon Electrode Models.” *Journal of the Electrochemical Society*, Volume 162, Number 6, (2015): A1111

Acknowledgements

We gratefully acknowledge funding from DOE AMO through Technology Development Manager Brian Cunningham that we have used in conjunction with the present VTO project funding to develop capabilities that are applicable to both battery slurries and catalyst inks.

Other team members include Kenneth Higa, Zhi Huang, Bei Fan, Ravi Prasher (LBNL) and Buyi Zhang (LBNL/UC Berkeley).

I.2.I Fabricate and test solid-state ceramic electrolytes and electrolyte/cathode laminates (LBNL)

Mike Tucker, Principal Investigator
Lawrence Berkeley National Laboratory
1 Cyclotron Rd
Berkeley, CA 94720
E-mail: MCTucker@LBL.gov

Peter Faguy, DOE Technology Development Manager
U.S. Department of Energy
E-mail: Peter.Faguy@ee.doe.gov

Start Date: October 1, 2019 End Date: September 30, 2020
Project Funding: $350,000 DOE share: $350,000 Non-DOE share: $0

Project Introduction

Ceramic solid state battery technology is limited by processing constraints such as Li loss during sintering, reaction between active materials and electrolyte during processing, and non-ideal microstructure and electrochemical/mechanical properties of layers fabricated via conventional processing routes. This project will address these limitations by elucidating behavior of the key materials during processing, including sintering behavior, reactivity, and phase stability. Of particular importance is the fabrication of thin, completely dense electrolyte and thick, highly porous cathode scaffold layers using high-volume, low-cost fabrication processes. Initial work focuses on $Li_{6.25}Al_{0.25}La_3Zr_2O_{12}$ (Al-LLZO).

Objectives

The project objectives are: to determine processing methods and conditions that enable high-volume, low-cost production of solid state battery ceramic electrolyte and electrolyte-cathode bilayer structures; and, demonstrate improved electrochemical and mechanical performance for these structures.

Approach

The impact of processing conditions and precursor properties on layer structure, electrochemical performance, and mechanical properties will be determined. Diagnostic tools such as electrochemical impedance spectroscopy, scanning electron microscopy, and synchrotron techniques will be used to interrogate the relationship between processing and layer quality. Commercially-available LLZO powder is used for all experiments to eliminate batch variations and ensure experimentally observed processing improvements are not due to variation of powder properties.

Results

Al-LLZO sheet sintering optimization

Experiments on pellets in the last reporting period identified that the sintering protocol for Al-LLZO parts must be optimized for each specific sample geometry because the rate of evaporation of Li at sintering temperature is dependent on the sample surface-to-volume ratio. Additionally, the presence of a Li/Al containing liquid phase at sintering temperature promotes abnormal grain growth (AGG) which inhibits densification of the part. Nano-sized MgO can be added prevent the AGG though grain boundary pinning. In order to obtain Al-LLZO sheets with high density and conductivity both sintering time and MgO additive content were optimized (Figure I.2.I.1). These sheets were approximately 1.5cm on edge and 100µm thick. They contained 5 wt% Li_2CO_3 added as excess lithium and were sintered at 1115°C. The highest ionic conductivity, up to $4x10^{-4}$ S/cm, is found in samples sintered for 3h. With 2 h of sintering time, too much Li remains in the lattice and the sample contains the low-conductivity tetragonal LLZO phase, while with 4 h of sintering time too much Li has been lost leading to the formation of the non-conductive $La_2Zr_2O_7$. The addition of 3 wt% MgO increases conductivity 33% over pure

Al-LLZO but MgO content of 5 wt% or greater results in lower conductivity. This suggests the MgO is not chemically inert and may react with the Al-LLZO. Additionally, improved ionic conductivity comes with a trade-off in density as 3 wt% MgO samples are ~1-2 per percentage points less dense than pure Al-LLZO and up to 4 percentage points less dense than samples with 5 %wt MgO. For screening of tape casting binder systems 5 wt% MgO was chosen because of its higher density.

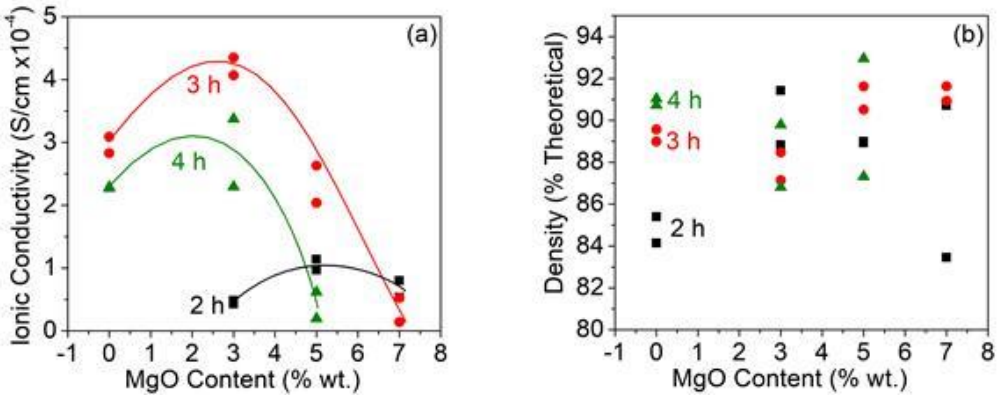

Figure I.2.I.1 Optimization of sintering additives and sintering time for LLZO sheets with 5 wt%. Li_2CO_3. (a) Ionic conductivity and (b) density for LLZO sheets with a range of MgO content sintered at 1115 °C for 2 (black), 3 (red) and 4 h (green). The lines are a guide for the eye.

Comparison of tape casting binder systems

It would be beneficial from health and safety and environmental standpoints to eliminate the use of volatile organic solvents in tape casting. To that end an aqueous tape casting system based on methycellulose binder was developed for comparison to Polymer Innovations' proprietary binder (MSB1-13) and several other aqueous and solvent-based binder systems. Table I.2.I.1 summarizes the green properties of the tape casting binder systems examined. Methycellulose did not react with Al-LLZO in contrast to the other aqueous binders, and had mechanical properties superior to the other options except for MSB1-12 (Figure I.2.I.2). When laminated the methycellulose tapes were 1.5-4.1 percentage points less dense than the solvent-based binders. After sintering, however, all binders systems achieved similar density and ionic conductivity.

Table I.2.I.1 Summary of tape casting system usability

Binder System	Solvent Health/ Safety	Usable	Foaming	Carrier Release	Mechanical Properties	Oxide-Only Density (%)
PVA	Aqueous	Gels				
PII – WB4101	Aqueous	Gels	-	-	-	-
Methyl-Cellulose	Aqueous	Yes	Yes Controllable	Controllable De-wetting	Good	40.2
PVB	Ethanol/ Acetone/ Phthalate	Yes	No	Poor	Brittle	44.3
Ethyl-cellulose	Toluene/ Ethanol	Yes	Minor	Good	Brittle	43.9
PII - MSB1-13	Toluene/ Xylene	Yes	No	Good	Very Good	41.7

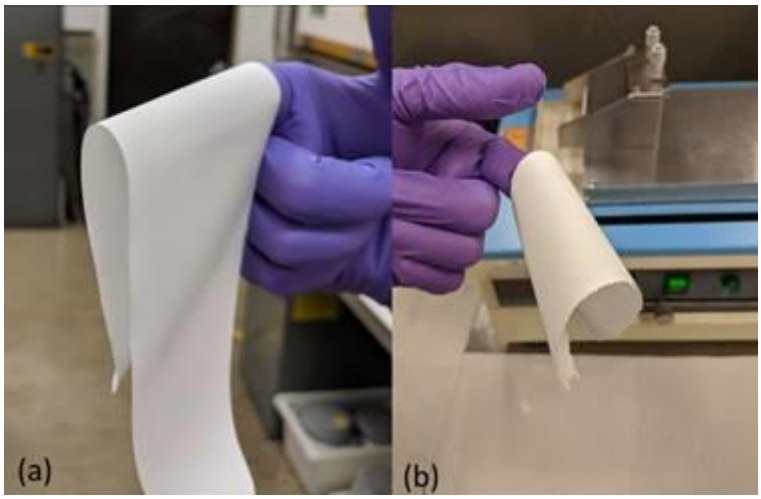

Figure I.2.I.2 Photographs of green Al-LLZO tapes using (a) MSB1-13 and (b) methylcellulose binders.

Bilayer structures

A bilayer or trilayer LLZO structure consisting of one or two porous layers bonded to a central dense layer is desirable for battery applications of the LLZO electrolyte. The porous structures provide increased surface area and paths for ion conduction for infiltrated electrode materials. The methycellulose tape casting system was used to produce a bilayer structure. Porous tapes were cast by replacing 60% of the volume of Al-LLZO in the slurry mixture with 63µm PMMA spheres. Several porous tapes were laminated to a dense methycellulose tape and then sintered. X-ray tomography was used to observe the bilayer microstructure (Figure I.2.I.3). Development of porous and bilayer structures is ongoing.

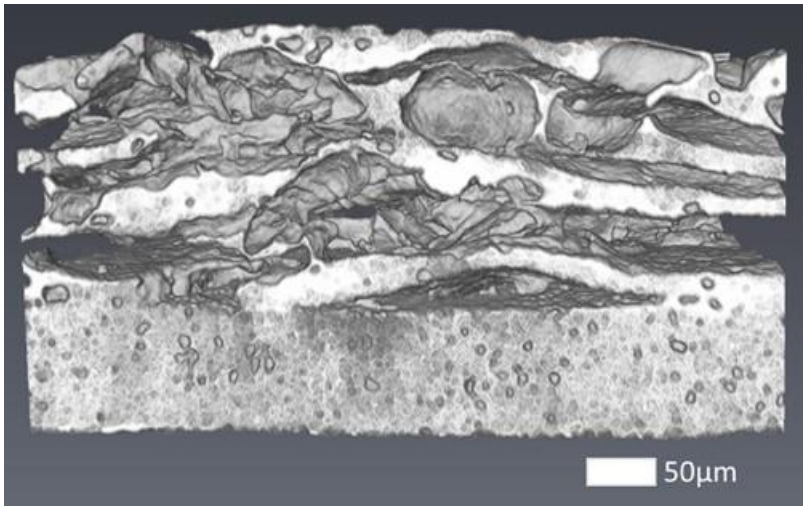

Figure I.2.I.3 Cross-section of an LLZO bilayer reconstructed by X-ray tomography. The bilayer was sintered at 1100 °C for 1 hour.

Conclusions

This project aims to prepare LLZO-based electrolyte and electrolyte/cathode scaffold structures using scalable processing techniques such as tapecasting and furnace sintering. Work in this project period focused on developing and screening tape casting slurry formulas for Al-LLZO and optimizing the sintering conditions for tape cast Al-LLZO sheets. Sintering optimization confirmed the importance of adapting the sintering process for the current sample geometry to obtain optimal Li concentration in the final part. MgO was used as a sintering additive to control AGG and enhance the conductivity and density of Al-LLZO sheets.

An aqueous tape casting system based on methylcellulose binder was developed and compared to various solvent-based binder systems. The methycellulose system had favorable health and safety properties and produced sintered Al-LLZO sheets with similar properties to the solvent-based systems.

The next project period will focus on optimizing tape cast porous Al-LLZO layers and developing bilayer and trilayer structures with high ionic conductivity and density. Solid state batteries will be constructed by infiltrating the porous layers with electrode material and the performance of the batteries will be optimized for cycle life and specific capacity.

Key Publications

1. Robert A. Jonson, Eongyu Yi, Fengyu Shen, Michael C. Tucker, "Optimization of Tape Casting for Fabrication of $Li_{6.25}Al_{0.25}La_3Zr_2O_{12}$ Sheets," Submitted.

2. Robert A. Jonson, Fengyu Shen, Michael C. Tucker, "Optimization of Lithium Content and Sintering Additives in Tape Cast Lithium Garnet Electrolyte Sheets", presented at ECS Prime 2020

Acknowledgements

All data presented in this report was generated by Robert Jonson. Thanks to Eongyu Yi who provided the samples tape cast with PVB binder. Special thanks to Dula Parkinson at the Advanced Light Source for training and support for X-ray tomography.

I.2.J Higher Energy Density via Inactive Components and Processing Conditions (LBNL)

Vincent Battaglia, Principal Investigator
Lawrence Berkeley National Laboratory
1 Cyclotron Rd., MS70R0108B
Berkeley, CA 94720
E-mail: vsbattaglia@lbl.gov

Peter Faguy, DOE Technology Development Manager
U.S. Department of Energy
E-mail: Peter.Faguy@ee.doe.gov

Start Date: October 1, 2018 End Date: September 31, 2022
Project Funding: $2,675,000 DOE share: $2,675,000 Non-DOE share: $0

Project Introduction

The "active materials" are directly responsible for the amount of energy in a battery. The cathode and anode materials can accommodate a fixed amount of a particular ion. The measure of the degree to which the electrodes accept the ions is reflected in the voltage difference of the electrodes with respect to the intercalation level of the ion. The energy density of the active materials is equal to the harmonic average of the capacity of the electrodes to hold a particular ion times the average voltage difference between the two electrodes. All other components in a battery add mass and volume without contributing additional energy resulting in a decrease in the specific energy and energy density, respectively. Thus, outside of changing the active materials, a means of increasing the energy density is by increasing the fraction of active material over the inactive material. The inactive materials include current collectors and separator and binder and conductive additive. The electrodes are produced by treating the current collectors as substrates, casting active material slurries onto them and pulling them through an oven to dry. As such, the current collectors must be of a minimum thickness (around 10 to 15 microns) to withstand the stress of being pulled through the coater without tearing. The separator consists of a porous polymer structure like polypropylene or polyethylene that must be thick enough (typically between 15 to 20 microns) to prevent the active material from pushing though and causing a short.

To discharge the battery in a time scale of hours requires the active material to have dimensions of around 10 microns. The laminates of active material therefore require a binding material to hold the particles onto the current collector and to each other. The laminates also require a conductive additive (typically a high surface area carbon) to make the active material more conductive and the laminate itself electronically conductive. Thus, the key to increasing the energy density of a battery, outside of changing the active material is by making the electrodes significantly thicker than the separator and current collectors and minimizing the fraction of polymer binder and carbon additive. The problem we are addressing is that manufacturers are unable to make thick electrodes with minimal inactive components that demonstrate high power and excellent cycle life and they have no idea of the underlying physics that is limiting this capability.

Objectives

The objective of the research is determining the proper processing conditions that lead to thick electrodes with a minimal fraction of inactive components. This objective faces a number of subproblems. The thicker electrodes are cast, the more the components of the laminate stratify during the casting and drying processes. Depending on the mixing order, the materials agglomerate differently, which changes the drying rate, the final electrode morphology, the final binder properties, and the electrodes mechanical and electrochemical performance. Reducing the binder and conductive additive requires the right mixer and the right mixing order to achieve the right morphology. An objective of this research is to understand the physics of thick electrode processing, understanding how the final electrode particle morphology impacts the electrodes performance,

and how to modify the processing conditions and binder and carbon additive properties to produce thick electrodes that perform as well as nominal electrodes.

Approach

The approach to understanding how to fabricate high-performing, thicker electrodes is to understand the impact materials of different surface and structural properties have on mixing order, mixing rate, mixing time, casting speed, drying temperature and drying rate, and how all of this manifests itself in final particle configuration and electrode performance. Specifically, we will investigate the impact of different carbon additive compounds including Ketjen black, acetylene black, carbon black, and carbon fibers on material agglomeration, electrode morphology, and electrode performance. We shall also investigate the effect of binder molecular weight and binder structure, *i.e*. linear *versus* branching on the same performance markers as the carbon. After this assessment is performed on NCM material, we will look again at a different cathode chemistries to investigate the impact of surface chemistry and conductivity on all aspects of the process. This research will be performed by: measuring the rheological properties of the slurry as a function of time and mixing speed; qualitatively assess the processability, coat ability, and compatibility of the cast slurry; use SEM to investigate the uniformity of the cast slurry; use mechanical tests to evaluate the dried coatings; and use electrochemical testing to assess overall performance. The goal is to produce thick electrodes (> 5 mAh/cm2) with less than 2% inactive material within the laminates.

Results

Drying conditions on polymer conductivity

This is the third year of the project where we continue to expand our knowledge into the intricacies of electrode fabrication. We performed some fundamental work on the polymer itself to understand the impact of drying temperature on performance. Films of PVdF were cast in the lid of the cathode side of a coin cell, a small, consistent amount of electrolyte added, and the conductivity measured using ac-impedance. The results are provided in Figure I.2.J.1. The data indicates that films formed at room temperature are significantly more conductive than films formed at 80ºC. It also shows that the ionic resistivity shows a hyperbolic dependence on drying temperature. This is unfortunate, as electrodes are dried at high temperatures to accelerate drying rate.

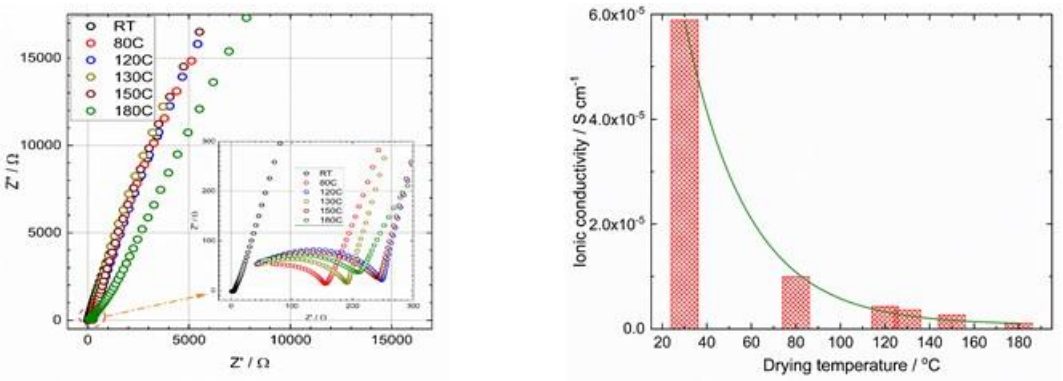

Figure I.2.J.1 Left: Impedance of PVDF films (impregnated with electrolyte) formed by drying at different temperatures. Right: the ionic conductivity calculated from the impedance data taking into consideration the films' area and thickness.

Not only does the resistivity of the polymer increase with drying temperature but so does the activation energy. This is reflected in the slope of the log of the ionic conductivity *versus* one over the temperature, as shown in Figure I.2.J.2. From the slopes of the data one estimates the activation energy of ionic transport rises from 26 to 42 kJ/mol.

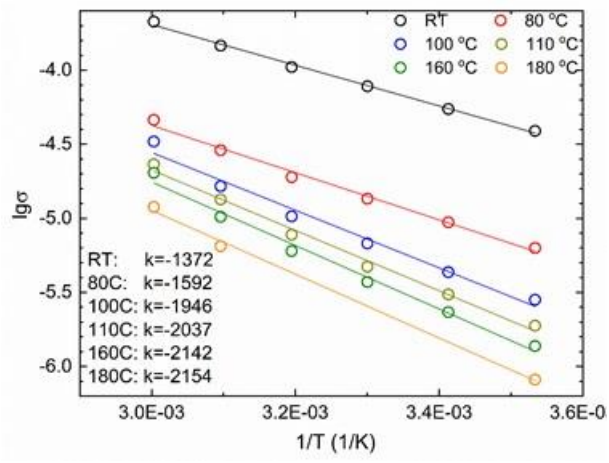

Figure I.2.J.2 Arrhenius plot of the log of the ionic conductivity versus 1/T (K). The slopes are provided on the figure as k

As has been explained in previous reports, PVdF takes on several crystallographic forms based upon the temperature it was dried at when starting from a solution in which it is dissolved. When dried below 70 °C it takes the β-form, when dried above 110 °C it takes the α-form, when dried between these two temperatures it takes on portions of α and β, and when dried near the melting temperature, 167 – 177ºC, it takes on the γ-form. We investigated the drying temperature and the amount of time spent at the drying temperature and measured the conductivity of the films. The results of x-ray measurements are provided in Figure I.2.J.3 for a drying temperature of 130ºC. The films were held at this drying temperature for 0.5, 1, 2, 5,12, and 21 hours. The figure indicates that the degree of crystallinity increased with the time at temperature and slowly shifted from β to α and the ionic conductivity decreased monotonically.

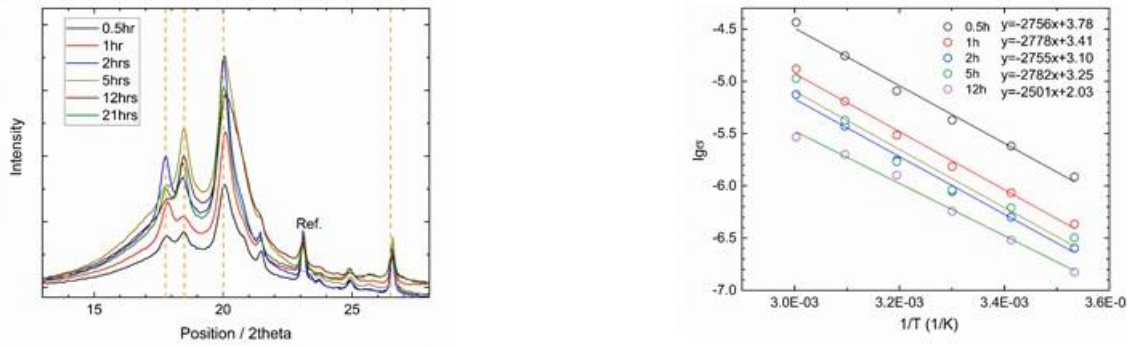

Figure I.2.J.3 Left: X-ray data of PVdF films dried at 130 °C and held at that temperature between 0,5 and 21 hours. Right: conductivity data of films measured at different temperatures after being held for various times at 130ºC

A final experiment was developed to determine if we could change the crystallographic structure if we dried it at one temperature and raised it to another temperature. Figure I.2.J.4 shows the results of producing a PVdF film at 60 ºC and holding it there for 17 hours and a film produced at 130°C and holding it there for 1 hr. The X-rays are quite different. When we increased the temperature of the 60 °C film to 130 °C and held it there for another 19 hours, the crystallinity did no change and the material still resembled the crystallinity it obtained at 60 °C.

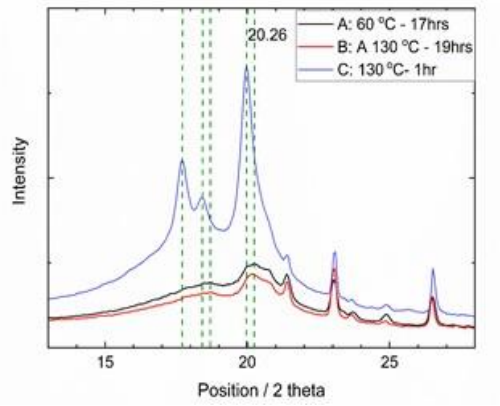

Figure I.2.J.4 X-ray data of PVdF films dried at 130°C and held at that temperature between 0,5 and 21 hours.

These data indicate that lower drying temperatures result in less crystallinity and higher conductivity, that holding the temperature for an extended period of time increases the amount of crystallinity and decreases the conductivity, and that the crystallinity cannot be changed by storing at an elevated temperature.

Some effort was put toward studying the impact of a change in temperature during the cooling process on the polymer's crystallinity. Three laminates were cast, dried, and then cooled in three different ways. All three laminates consisted entirely of PVdF and dried for 5 minutes at 180 °C. After the first 5 minutes of drying, the first laminate was cooled *via* a quenching process that dropped the temperature from 180°C to -18°C, the second laminate was removed from the oven and allowed to cool to room temperature through natural convection, and the third laminate was left in the oven and cooled to room temperature at a controlled rate that was slower than that seen for natural convection. All three laminates were evaluated for their FTIR signal once they reached room temperature (Figure I.2.J.5). Each cooling condition lead to a slightly different FTIR spectra. This suggests that if the laminates are dried starting from a high temperature, there is still an opportunity to change the structure of the binder in the cooldown stage.

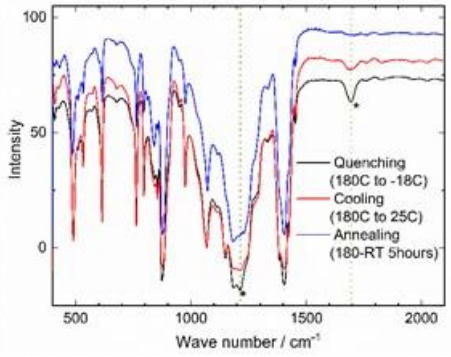

Figure I.2.J.5 FTIR spectrum of PVDF films cooled from 180 °C by three routes: quenching to -180C, natural convection cooling on a benchtop, and slow cooling in an oven at a designated cooldown rate

Carbon content on polymer properties

The next step was to understand the impact of high-surface-area-carbon content and temperature of drying on polymer crystallinity. Some of the data is presented in Figure I.2.J.6. For the three drying temperatures highlighted (80, 130, and 180 °C), the films with the tallest, sharpest peaks are those without carbon present. For the films dried at 80 °C, the one without carbon displays α and β peaks but the films with carbon show generally β peaks. For the films dried 130 °C, the films showed mostly α peaks except at the highest carbon levels where the peaks look like β. Films dried at 180 °C showed strong α peaks when no carbon was present but quickly shifted to a mix of α and β peaks for the lowest carbon content of 1:5 carbon to binder. This new shape of the x-ray data remained constant as the carbon fraction increased above 1:5.

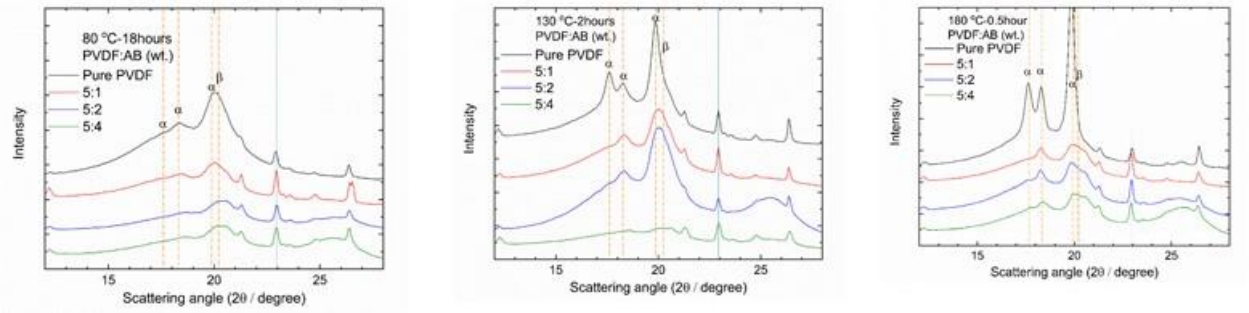

Figure I.2.J.6 Xray data of films dried at different temperatures and different levels of carbon from 0 to 5:4 PVdF to carbon. Left: dried at 80 °C for 18 hours, Center: dried at 130 °C for 2 hours, and Right: dried at 180 °C for 0.5 hours.

In the future, it would be nice to measure the adhesion and cohesion of some of these films as a function of carbon content and drying temperature, *i.e*. crystallinity.

Mixing Order

Since the earliest days of preparing electrode laminates we have found that the order in which the three components, active material, carbon additive, and polymer binder, are mixed together in a solvent of NMP impacts the final electrode performance. Research since then indicates that this is related to the irreversible interactions of the components which affects the final morphology. More recently we have also discovered that the temperature at which the electrodes are dried affects the final film morphology and electrode electrochemical and mechanical performance as well, which we attribute to, at least partially, the crystal structure of the polymer. In previous years we investigated the mixing of the carbon and active material first (Process II), the carbon and binder first (Process III), and the active material and binder first (Process IV). Results have been reported in previous yearly reports and AMRs. This year we focused on hybrid mixes where part of the binder (*ca*. 25%) is mixed with the active material and the other part with the carbon additive (*ca*. 75%) in separate solutions and then the two solutions mixed together (Process V) and where part of the carbon was mixed with the active material and the other part with the binder and the two solutions then mixed together (Process VI). Another way to think of Process V is as a hybrid of Processes III and IV; and Process VI as a hybrid of Processes II and III. All mixing was performed in solvent using a homogenizer at 3000 rpm. The final electrode composition for all electrodes was 92.8/4/3.2 active-material/binder/carbon – the binder to carbon was 5:4 for each electrode. With this level of carbon we expect the least amount of crystallinity of the binder and therefore the highest ionic conductivity but the lowest mechanical strength.

We cast films of all five processes (II – VI) and then measured the force required to separate the laminates from the aluminum current collector. We divided the force required to detach the laminate by the width of the laminate and refer to it as the adhesion stress. Once the laminates were detached from the current collector, we clamped the ends of the laminates into the same instrument and measured the tensile stress required to pull the laminates apart. This force was divided by the cross-sectional area of the laminate and is refer to as the cohesion stress. A graph of the adhesion and cohesion is provided in Figure I.2.J.7, along with the measurements obtained of laminates prepared by Process III and Process IV.

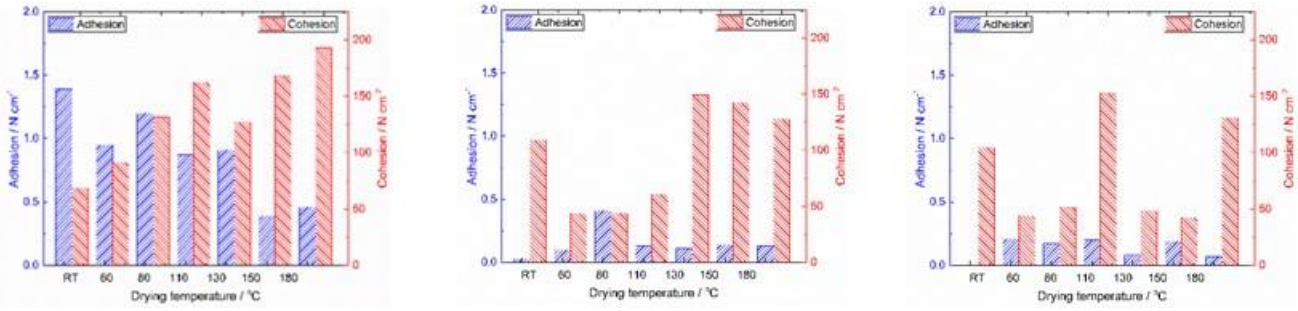

Figure I.2.J.7 Adhesion (blue) and cohesion (red) data of films prepared by Processes III (left), IV (center), and V (right) dried at different temperatures ranging from room temperature to 180°C.

Inspection of the graphs in Figure I.2.J.7 clearly show that the mechanical strength of the laminate in Process III where the carbon is first mixed with the binder exceeds that of both IV and V and that the mechanical strength of IV and V are similar and poor. This suggests that, mechanically speaking, even more than 75% of the binder should have been mixed with the carbon in Process V to improve the mechanical strength. We also measured the resistance of the laminates taken from a 30-sec pulse for a range of laminate drying temperatures. This data, acquired at 30 % DOD, is provided in Figure I.2.J.8.

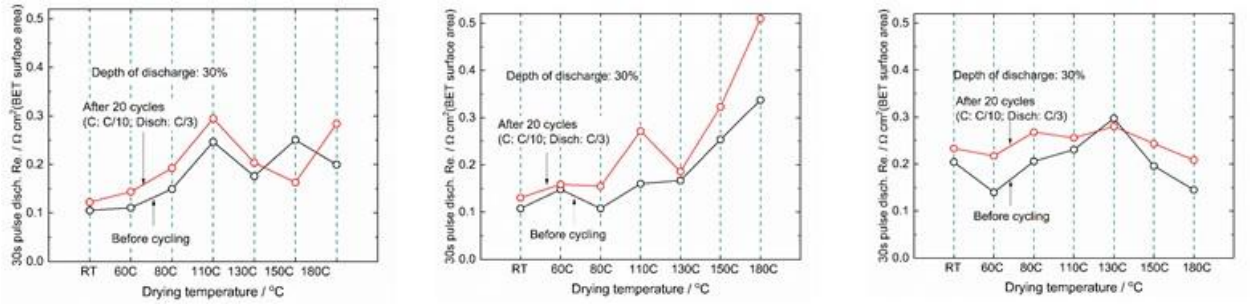

Figure I.2.J.8 The resistance of laminates produced by Processes III (left), IV (center), and V (right) as measured at 30 % DOD from a 30 sec. discharge pulse for a range of laminate drying temperatures between room temperature and 180°C

A cursory inspection of this data suggests that the resistance of the films produced by Processes III and V are very similar and that reducing to 25% of the binder with the active material is enough to get rid of the large impedance rise seen at high drying temperatures seen when all of the binder is first mixed with active material.

We then investigated the hybrid system where we split the carbon between the binder and the active material: 75% of the carbon was combined with the binder; 25% was combined with the active material. The laminates were cast and dried at discrete temperatures between room temperature and 180 °C. We did observe that films dried above 165 °C showed cracks, the higher the temperature, the higher the number of cracks. With regard to the 30-second pulse resistance, the resistance increased with temperature but was split between two ranges. For films dried under 90 °C, the resistance was between 0.1 and 0.15 ohm.cm^2; for films dried between 90 and 180 °C, the resistance was between 0.2 and 0.25 ohm.cm^2. The adhesion of these films was better than the other processes except for when all of the carbon was mixed with all of the binder. There is a maximum in the adhesion at around 130 °C.

In general, when looking at the order of mixing of the active material, binder, and carbon, one sees the following results.

1. Carbon and active material mixed together first: Displays a maximum in mechanical strength at a drying temperature around 130 °C. Above this temperature the dried film displays cracks. The resistivity starts at 0.15 Ohm.cm^2 when dried at 80 °C and monotonically increases with drying temperature to 0.22 Ohm cm^2 at 180 °C.

2. Carbon and binder mixed together first: This mixing results in films with the greatest mechanical strength overall. Their resistivity for a 30-sec pulse is rather low at 0.1 Ohm.cm^2 if dried at a temperature below 70 ^{o}C. If dried above 70 ^{o}C, the resistivity varies between 0.15 and 0.25 Ohm-cm^2. The combination of carbon and binder required 3x more time to dry at a given temperature but could be raised to 180 ^{o}C without cracking.

3. Active material and binder mixed first: This film showed good adhesion, especially at higher temperatures but poor adhesion. The resistivity of the films is rather low when dried at temperature between room temperature and 130 ^{o}C increasing from 0.1 to 0.15 Ohm.cm^2, but rising rapidly when dried at higher temperatures reaching 0.34 Ohm.cm^2 at 180 ^{o}C.

4. Hybrid mixing – 75% binder and carbon; 25% binder and active material: This mixing showed poor mechanical properties at all temperatures. The resistivity appears to have little correlation with drying temperature, varying between 0.13 and 0.28 Ohm.cm^2.

5. Hybrid mixing – 75% carbon and binder; 25% carbon and active material: The adhesion was second only to the film where all of the carbon was mixed with the binder and the resistance was low or moderate depending if the drying temperature was low or high. The resistance did not get above 0.25 ohm.cm^2. The films cracked above 165 ^{o}C. We need to measure the rate of drying for this process and compare it to the rate of drying of Process III.

In general, we saw at high temperatures poorer adhesion and better cohesion, unless the films showed cracking which impacted cohesion. The combination of carbon and binder improves cohesion even though it may reduce the crystallinity of the binder. We believe the increase in mechanical strength brought on through the agglomeration of carbon and binder more than offsets the negative impact of reduced crystallinity.

High temperature drying appears to have a number of effects: 1) it increases the rate of drying that can result in film cracking, 2) it results in crystalline phases that show reduced ionic transport, 3) if carbon is present, the carbon can inhibit the crystalline formation long enough to prevent crystalline formation before the film is dried. If the film can then be cooled quickly, one can prevent the formation of the crystal structure.

Conclusions

We conducted a number of experiments on the binder, binder and carbon, and binder, carbon, and active material under a number of different orders of mixing and hybrid forms of mixing. (To complete the analysis, we should probably look at the situation where the active material is spilt, with some mixed with carbon and some mixed with binder prior to mixing the two together.) We have a general understanding of how the interactions of these components are impacting the mechanical and electrochemical performance. It is understood that crystallinity in polymers improves their mechanical strength while also decreasing the ionic mobility through the polymer. We have seen that an increase in drying temperature or an increase in drying at temperature can lead to an increase crystallinity and a decrease in the electrolytic conductivity of polymer films. We have also seen that high levels of carbon additive can disrupt the formation of the crystalline regions which promote strength and replace it with carbon-polymer agglomerates that enhance strength. The agglomeration also slows drying that mitigates cracking. As such, there may be an opportunity to reduce the amount of carbon and improve the mechanical strength. If the mechanical strength is coming from the agglomeration of carbon and binder, there may be an opportunity to replace much of the high surface area carbon additive with carbon fiber. If we are able to adequately disperse the nanofibers it may reduce the clumping of carbon and binder which should reduce the diffusion length of trapped solvent that results in slow drying times. We will then see if the mechanical strength of the fiber and binder is strong enough to retard cracking. The addition of binder and carbon to solvent increases its viscosity which requires the additional of solvent to allow for stable film casting. Likewise, the removal of carbon and binder should reduce the need for solvent and result in a more compact film that should dry more quickly than a standard formulation.

For the coming year the plan is to take this collective information to reduce the total amount of carbon and binder to 2% or less and keep the drying time to under three minutes for a film with a loading of 5 mAh/cm^2.

Acknowledgements

The experimental work was performed entirely by Yanbao Fu of the LBNL.

I.2.K Novel data-mining and other AI approaches for synthesis and processing of cathode materials (LBNL)

Gerbrand Ceder, Principal Investigator
Lawrence Berkeley National Laboratory
One Cyclotron Rd, Bld. 33, Rm. 142B
Berkeley, CA 94720
E-mail: gceder@lbl.gov

Peter Faguy, DOE Technology Development Manager
U.S. Department of Energy
E-mail: Peter.Faguy@ee.doe.gov

Start Date: January 1, 2019 End Date: September 30, 2022
Project Funding: $200,000 DOE share: $200,000 Non-DOE share: $0

Project Introduction

A major obstacle to large-scale manufacturing and utilization of advanced materials arises from the inability to devise synthesis methods for materials in a rational manner. This is an issue for novel predicted materials, which have never been synthesized, as well as for existing materials, which often have to be synthesized in a particular particle form, with particular surface chemistry, or with very targeted structure and composition, in order to have optimized behavior in the dispersions used to cast electrodes.

To bridge the gap between materials prediction and production, we envision the following for this project:

1) An automatic materials synthesis design solution, which employs machine-learning approaches to learn synthesis concepts from scientific publications and patents, and design efficient synthesis routes for novel materials.

2) Predictive tools that can modify a synthesis method to achieve optimal particle size, shape, and surface chemistry for a given application and performance requirement.

Objectives

Use Machine Learning and First-Principles Calculations to develop the ability to predict the appropriate synthesis routes for battery cathode materials, their surface chemistry, and their interaction with solutions.

Approach

Our objective is to extract all known synthesis methods for battery cathode materials from publications and patents, organize them, make them available, and use them for machine learning of novel synthesis recipes. In order to obtain details of synthesis procedures from publications and convert them into a machine-readable format, we developed a data mining pipeline that uses machine learning techniques to retrieve “codified synthesis recipes” of inorganic compounds from available scientific publications and patents. The most important steps of the pipeline include: i) collecting journal articles and patents available online using our own web scraper; ii) extraction of experimental sections and identification of paragraphs describing ceramics synthesis, made in an unsupervised way by using topics modeling approaches; iii) extraction of so-called “codified recipes” of the synthesis procedures which include final product, starting materials, operations and conditions of synthesis, via named entity recognition methods based on Bidirectional Encoder Representations from Transformers (BERT) model [1]; iv) accumulating all recipes in the database and their subsequent mining.

Results

An updated data pipeline for extracting synthesis information from both journal articles and patents

As a continuing effort since last year, we have extended our data-mining pipeline developed for journal articles to publicly available patents. Patents are usually strictly examined by national patent offices before granted. Moreover, for patents on battery materials, R&D institutions and companies are motivated to publish details of synthesis experiments to protect their intellectual property. Hence, patents may serve as another high-quality and rich data source of synthesis information.

Besides the 4.1 million journal articles collected last year, we have recently downloaded the full text of 6.8 million patents, covering all the utility patents granted in the US since the year 1976. The United States Patent and Trademark Office (USPTO) released 3 different versions of data formats including XML, SGML, and APS, and 9 subversions of data schemas for patents in various years. We have developed a markup parser that is capable of parsing these 6.8 million patents into 606 million plain text paragraphs. By screening the paragraph text with the keywords “battery” and “batteries”, 658,725 patents potentially related to batteries were gathered for further text mining. The number of battery-related patents has been exponentially increasing almost every year as shown in Figure I.2.K.1, indicating the dramatically rising popularity of battery studies.

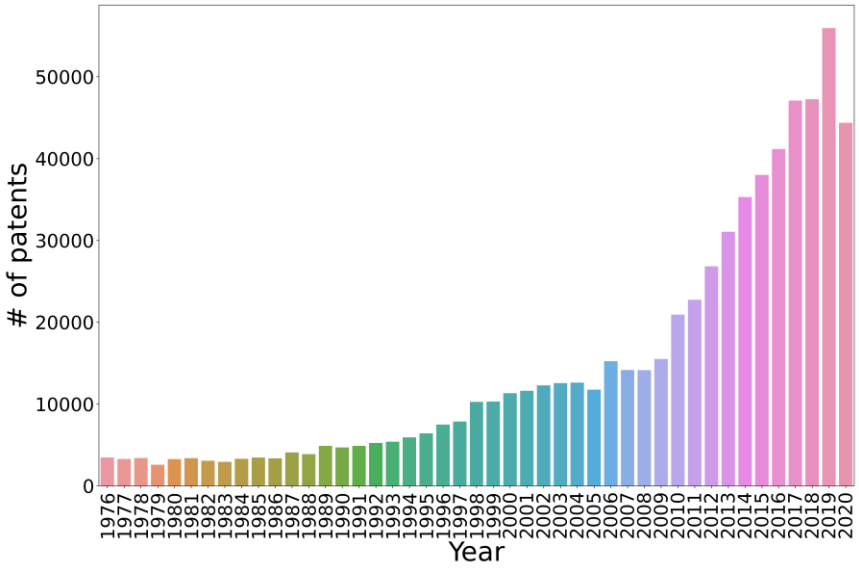

Figure I.2.K.1 The growth of battery-related patents from 1976 to 2020.

The data extraction tools developed for journal articles were applied to patents because the written styles of synthesis experiment paragraphs from these two sources are usually consistent. We also revised our machine learning models to improve extraction performance by incorporating the latest progress in the natural language processing (NLP) field. BERT [1] has emerged as the backbone of many state-of-the-art (SOTA) NLP models in the last two years, but most BERT models are trained on text corpora of book sections or Wikipedia pages for general purposes. We have trained a MatBERT model dedicated to NLP for materials science with a similar neural network structure to BERT but using 2 million materials science articles. The MatBERT model has been used to provide digitalized word embeddings to our data extraction tools. As a result, started with the 6.8 million patents, we were able to classify and identify 80,846 patents containing 205,328 synthesis paragraphs in the four most typical synthesis categories (Figure I.2.K.2): conventional solid-state synthesis (15.4%), sol-gel precursor synthesis (22.5%), precipitation synthesis (26.4%), and hydrothermal synthesis (35.7%).

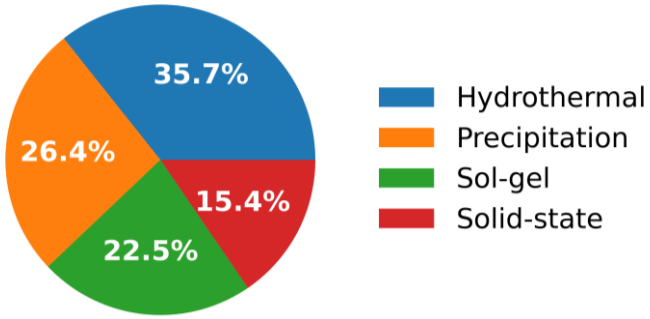

Figure I.2.K.2 The fraction of different synthesis methods in 19,839 battery-related patents with synthesis paragraphs.

A database of patents related to the synthesis of battery materials

Although our data pipeline generally extracts synthesis information for all inorganic materials, a substantial subset of the extracted data is related to battery materials. We have established a database containing 1,862 patents on the synthesis of battery materials by applying a series of filtering criteria associated with the data pipeline. Each of these patents contains at least one keywords of "battery"/"batteries" indicating the patent is related to battery studies, at least one synthesis paragraph indicating the patent is related to materials synthesis, and at least one target material that can be parsed into computer-readable chemical composition with our Materials Parser.

1,009 different target material compositions were extracted from the 1,862 patents. These supplement the 3,000 Li-ion battery related materials extracted from scientific articles last year, and also form an important data source for building machine-learning synthesis prediction models of battery materials. Table I.2.K.1 lists the 5 most and 5 least frequently synthesized materials in the patents with both keywords "battery"/"batteries" and "cathode". The top 5 ones are well-known commercial cathode materials, including $LiFePO_4$, $LiMn_2O_4$, the base materials of lithium nickel manganese cobalt oxide (NMC), and V_2O_5. In addition, we find many derivatives of these top 5 materials which are modified by doping or elemental substitution..

Synthesis parameters such as synthesis type, precursors, operations, and conditions are highly correlated with the chemistry of the target materials, providing the possibility to machine-learn predictive synthesis in the later stage. Generally, four general types of synthesis methods are used. These appear with frequency hydrothermal synthesis > precipitation synthesis > sol-gel synthesis > solid-state synthesis as shown in Figure I.2.K.2. However, when constraining the chemistry to battery materials that contain alkali/alkaline earth elements such as Li, Na, K, Mg, and Ca, the different synthesis methods are redistributed as shown in Figure I.2.K.3. Solid-state synthesis is the predominant method used, nearly three times as common as the second-frequently used method, sol-gel synthesis. Precipitation synthesis and hydrothermal synthesis are even less frequently adopted. Figure I.2.K.3 further indicates that Li-ion battery materials are the most studied, but Na- and Mg-ion batteries are emerging. K- and Ca-based batteries might be technically harder because the ionic radius and atomic mass of K and Ca are larger than Li, Na, and Mg.

Table I.2.K.1 Typical Cathode Materials Extracted from Patents Related to the Synthesis of Battery Materials. Note that this only includes the patents with these exact compositions, not derivatives.

Cathode Material	Number of Patents
$LiFePO_4$	87
$LiCoO_2$	52
V_2O_5	43
$LiMn_2O_4$	38
$LiNiO_2$	29
$Li_{0.6}Mn_{1.5}Ni_{0.5}S_{0.05}O_{3.95}$	1
$Li_{1.2}Mn_{0.534}Co_{0.123}Ni_{0.123}B_{0.02}O_2$	1
$LiMg_{0.01}Al_{0.01}Co_{0.96}O_2$	1
$LiFePO_4F$	1
V_3AgO_8	1

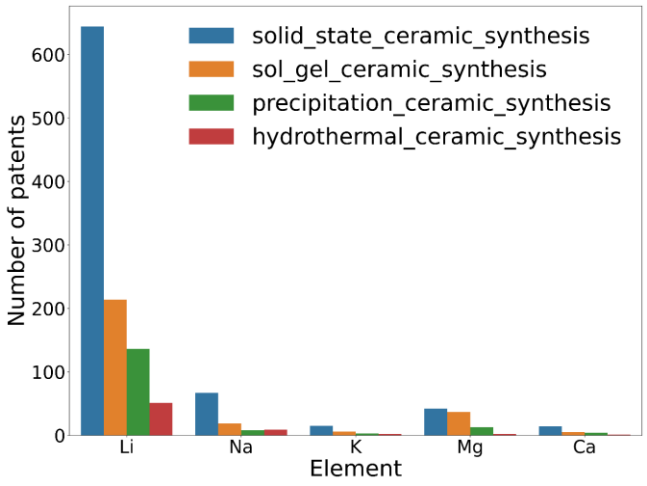

Figure I.2.K.3 The number of patents related to the synthesis of battery materials containing Li, Na, K, Mg, or Ca.

A pipeline for synthesis recipe recommendations and initial attempts to create a similarity measure fors precursors

We are building a synthesis prediction pipeline (Figure I.2.K.4) to suggest precursors and synthesis attributes for battery materials. Given a novel material to be synthesized, researchers usually refer to similar materials in the existing literature and modify the old recipes to fit the new material. Compiling the same logic into an automatic predictive pipeline, we first search similar targets from our dataset with a model for materials similarity. Then, we substitute the precursors to match the elements in the novel material and estimate the synthesis conditions such as temperature and atmosphere. At last, we recommend a ranked list of recipes for this novel material. The pipeline is under active development, but we have made the initial attempt to build a model for the similarity of precursors because a good measure of material similarity is critical for the pipeline.

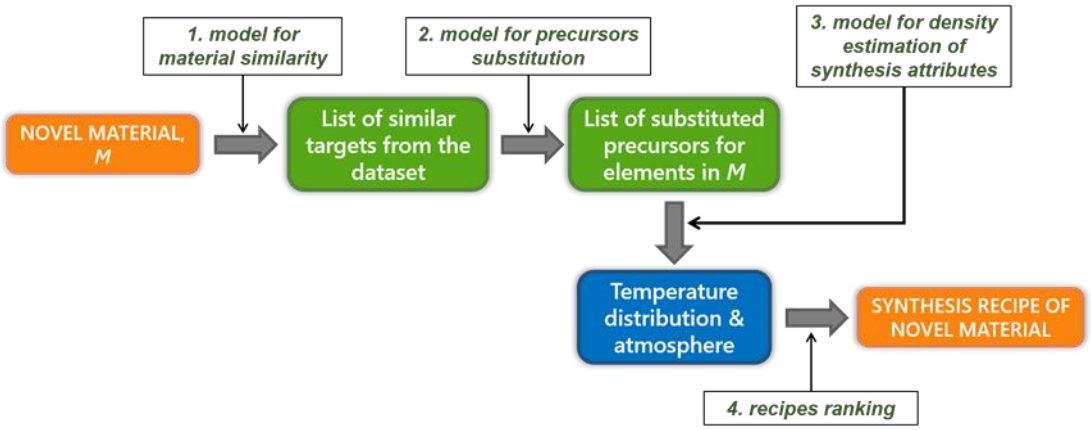

Figure I.2.K.4 Schematic representation of the pipeline for synthesis recipe recommendations.

To characterize the similarity of precursors, two features were utilized: i) the probability to substitute one precursor with another in the synthesis reaction for a common target material, and ii) the overlap between the distributions of synthesis temperatures for two precursors. With the similarity, precursors for the same elements are hierarchically clustered as dendrograms in Figure I.2.K.5. The vertical axis represents the distance between two precursors or the distance between two clusters. In general, similar precursors will be drawn closer to each other on the horizontal axis. The hierarchical clusters agree well with the “chemical similarity” used by researchers when choosing the precursors for materials synthesis. The similarity could help guide the selection of precursors when researchers alter existing recipes by replacing precursors. If many possible combinations of precursors are possible, the quantitative value of the similarity could serve as a reference to rank them. Quantifying the similarity of precursors helps provide a foundation for suggesting candidate reactants in our predictive pipeline.

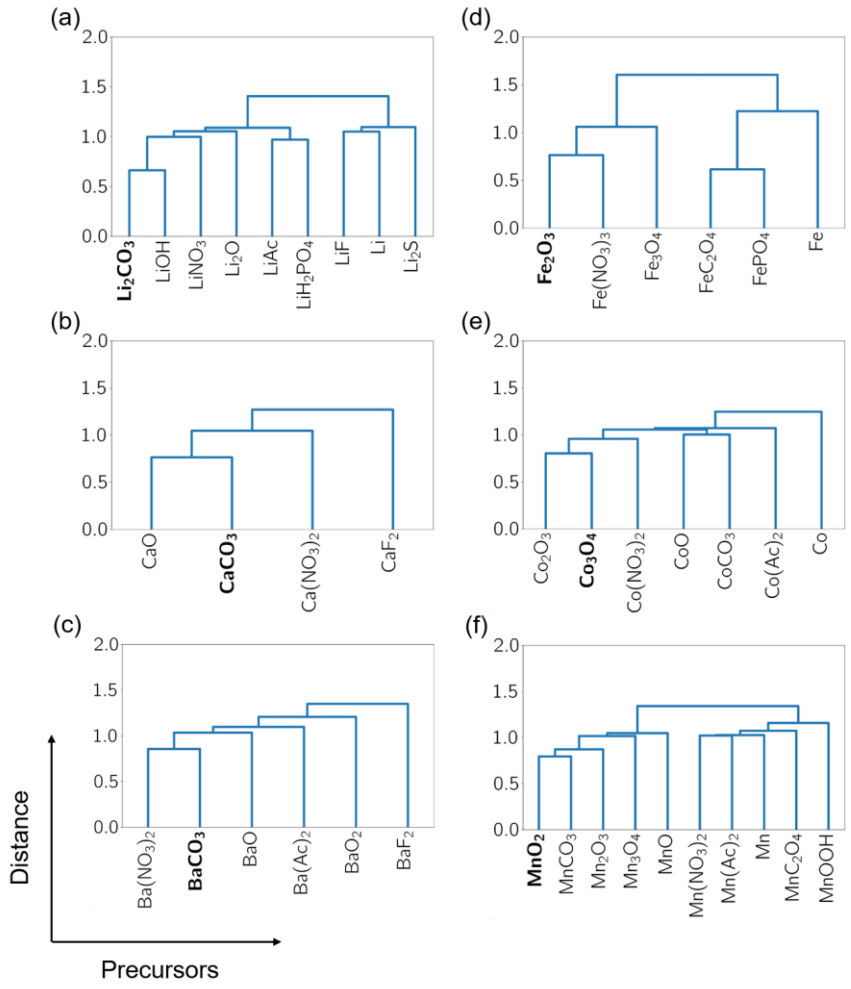

Figure I.2.K.5 Clusters of precursors for (a) Li, (b) Ca, (c) Ba, (d) Fe, (e) Co, and (f) Mn by similarity. The most frequently used precursor for each element is indicated using bold fonts

Conclusions

As a continuing effort since the first year, we have extended our data-mining pipeline developed for journal articles to mine 6.8 million publicly available US utility patents. From this corpus 1,862 patents are identified in which 1,009 distinct battery material compositions are synthesized. The preference of synthesis methods for Li-, Na-, K-, Mg-, and Ca-ion battery materials is analyzed from the patent data. The results indicate a strong correlation between synthesis parameters and the chemistry of target materials.

We propose a predictive pipeline for synthesis recipe recommendations based on material similarity and density estimation. We have made the initial attempt to build a model for the similarity of precursors, which demonstrates that the "chemical similarity" can be extracted from text data without including any explicit domain knowledge. The quantification of the similarity of precursors helps provide a foundation for suggesting candidate reactants in our predictive pipeline.

Key Publications

1. Olga Kononova, Haoyan Huo, Tanjin He, Ziqin Rong, Tiago Botari, Wenhao Sun, Vahe Tshitoyan, and Gerbrand Ceder. "Text-mined dataset of inorganic materials synthesis recipes." Scientific data 6, no. 1 (2019): 1-11.

2. Tanjin He, Wenhao Sun, Haoyan Huo, Olga Kononova, Ziqin Rong, Vahe Tshitoyan, Tiago Botari, and Gerbrand Ceder. "Similarity of precursors in solid-state synthesis as text-mined from scientific literature." Chemistry of Materials 32, no. 18 (2020): 7861-7873.

3. Olga Kononova, Tanjin He, Haoyan Huo, Amalie Trewartha, Elsa A. Olivetti, and Gerbrand Ceder. "Uncovering the Knowledge behind the Text: Text Mining and Natural Language Processing Approaches for Data-Driven Materials Discoveries". Submitted.

References

1. Jacob Devlin, Ming-Wei Chang, Kenton Lee, and Kristina Toutanova. "Bert: Pre-training of deep bidirectional transformers for language understanding." arXiv preprint arXiv:1810.04805 (2018).

I.2.L Minimizing Side-Reactions in Next-Generation Lithium Ion Battery Cathodes Through Structure-Morphology Optimization

Venkat Srinivasan, Principal Investigator
Argonne National Laboratory
9700 S. Cass Avenue,
Lemont, IL 60439
E-mail: vsrinivasan@anl.gov

Peter Faguy, DOE Technology Development Manager
U.S. Department of Energy
E-mail: Peter.Faguy@ee.doe.gov

Start Date: October 1, 2019 End Date: September 30, 2020
Project Funding: $300,000 DOE share: $300,000 Non-DOE share: $0

Project Introduction

The goal of this project is to improve the performance of next-generation Li-ion battery cathodes by synergistically tuning the structure of the cathode along with its morphology. Understanding the densification behavior of LLZO type oxide based ceramic SSEs, and how that improves its overall conductivity, is another major aim of this project. Improvement in performance will be achieved by developing multi-scale theoretical methods, coupled with *in situ* operando experimentation to create a one-of-a-kind "particles by design" framework. This framework will go beyond the traditional "materials by design" approach used today, wherein the focus is on calculating material crystal structure, by incorporating morphological features to create particles in which the exposed surfaces are tuned to maximize performance. This year, we focused on the carbonate based coprecipitation process for making cathode precursors, high temperature calcination process for understanding the lithiation mechanism into Ni-rich NMC hydroxides, and densification of LLZO solid electrolytes. NMC111-carbonate and individual Mn, Ni and Co carbonate were coprecipitated to understand the growth process of these carbonate cathode precursors. In order to investigate the lithiation of Ni-rich NMC-hydroxide precursors, in situ characterization of the high temperature calcination was conducted under both the pre-treated and non-pre-treated conditions. During calcination, extent of lithiation and particle size evolution were extracted from the x-ray diffraction data. For SSEs, dependence of particle morphology on the densification process have been simulated to determine the optimal particle size and size distributions that maximizes the relative density of LLZO pellets. Understanding the evolution of particle morphology during the synthesis of cathode precursors and SSEs will help to improve the performance of next generation lithium ion batteries.

Objectives

The overall objectives of this project can be divided into three different parts. The first component deals with the investigation of the impact of solution pH, ammonia content, and transition metal concentration on the size, shape, porosity, tap density and facet dependent reactivity of cathode precursors during the coprecipitation process. As a part of this task, we aim to determine the equilibrium Wulff shape and corresponding surface energies of cathode precursors and final lithiated oxide materials. We also aim to elucidate the impact of thermodynamic and kinetic factors in determining the size and shape of primary and secondary particles. The second task involves in situ characterization of the calcination of NMC-hydroxide precursors in the presence of LiOH using x-ray diffraction techniques. Extraction of information regarding the extent of lithiation and evolution in particle size is the major aim of this study. Understanding impact of the pre-treatment process in determining the magnitude of lithiation and particle size evolution is also a major objective of this project. In the third task of the project, the main objective is to understand the densification and grain growth mechanism observed during the sintering of LLZO pellets. To accomplish this, we will develop a phase-field based mesoscale models capable of capturing the sintering process between multiple LLZO particles. Influence of

particle morphology in determining the relative density of LLZO will also be elucidated as part of this research activity.

Approach

To understand how the structure and morphology of cathode and electrolyte particles evolve during the synthesis steps, experimental techniques as well as computational methodologies have been developed. Attempts have been made to establish good correlation between the two for proper elucidation of the physical and chemical phenomena that controls the structure and morphology of these battery particles. The computational approach involves capturing the physical phenomena observed at the atomistic length scale, as well as the mesoscale level.

The atomistic calculations are carried out using spin-polarized Density Functional Theory (DFT) as implemented in the Vienna Ab Initio Simulation Package (VASP). The exchange-correlation potentials are treated by the generalized gradient approximation (GGA) and the interaction between valence electrons and ion cores is described by the projected augmented wave (PAW) method. Moreover, the GGA+U scheme is used for applying the on-site correlation effects among 3d electrons of the transition metal.

Our approach to understanding the morphology changes during calcination of layered NMC cathodes combines chemical and physical modeling with in-situ X-ray characterization. At the meso-scale, phase field modeling was used to predict the lithiation and sintering behavior of collections of crystallites, while ab-initio molecular dynamics provided atomic-level simulations of the chemical processes driving calcination. In-situ X-ray diffraction provided experimental input and verification for the results derived from computational models. In the in situ x-ray diffraction methodology, β-$Ni_{0.8}Mn_{0.1}Co_{0.1}(OH)_2$ and $Ni_{0.8}Mn_{0.1}Co_{0.1}O$ precursors were loaded into separate quartz capillaries along with $LiOH{\cdot}H_2O$ as a lithium source. X-ray diffraction patterns were collected once per minute during heating to 800°C between 2 to 5°C per minute with a 90 minute temperature hold at 500°C. Diffraction patterns were refined using the Rietveld method to determine the relative phase fractions, unit-cell parameters, and domain sizes.

For the mesoscale analysis, mass balance equations at the continuum level are solved for the estimation of reaction kinetics as a function of solution pH, ammonia content and concentration of transition metal salt. Phase field based methodologies are adopted to capture the facet dependent growth of the transition metal carbonate precursors. A continuum based nucleation, growth and aggregation model have been developed for estimating the secondary particle size of the NMC111 carbonate precursors. Phase field based methodologies are used to predict the densification and sintering of LLZO particles. Increment in particle size during high temperature sintering is also captured in these mesoscale models. A combination of volume conserving Cahn-Hilliard equations, and non-conserving Allen-Cahn equations are solved to capture the densification and grain ripening behavior of LLZO particles.

Results

The results obtained from the research work conducted as part of this project will be divided into three categories. The first one will describe the evolution of carbonate based cathode precursors during the coprecipitation process. The second set of results will elaborate the calcination mechanism of Ni-rich NMC-hydroxides with LiOH as the source of lithium. The impact of pre-treatment on the overall calcination process will also be discussed. The third, and final, section will elaborate the influence of particle morphology on the densification behavior experienced by LLZO solid electrolytes.

Predicting Morphological Evolution during Coprecipitation of MnCO3 Battery Cathode Precursors using Multiscale Simulations Aided by Targeted Synthesis: The performance of lithium-ion batteries is intimately linked to both the structure and the morphology of the cathode material, which in-turn is critically linked to the synthesis conditions. However, few studies focus on understanding synthesis, especially during the co-precipitation of metal oxide precursors; a process that largely determines the final morphology of the material. In this work, we go beyond the typical equilibrium particle shape analysis conducted in the literature

and incorporate kinetic aspects of morphology evolution. We perform these studies using controlled synthesis on a well-defined metal salt system ($MnCO_3$) combined with multiscale simulations and high-resolution microscopy.

According to the equilibrium analysis, the solution pH has been maintained at 7.5. SEM images of the particles precipitated under Mn^{2+} concentration of 1.5mM, 4.5mM and 12.0mM are shown in Figure I.2.L.1(a), Figure I.2.L.1(b), and Figure I.2.L.1(c), respectively. It is evident that some of the precipitated particles show a rhombohedral shape, some shows cubic shape, and some looks spherical. Further investigation reveals that majority of the particles precipitated under 1.5 mM concentration of Mn^{2+} demonstrate a rhombohedral shape. Whereas particles precipitated at 4.5 mM concentration of Mn^{2+} show a cubic shape. Please note that there exist some spherical particles in these two concentrations as well. However, all the particles precipitated at 12.0 mM Mn^{2+} concentration demonstrate spherical shape when visualized using low magnification SEM images. The relative amounts of rhombohedral, cubic, and spherical particles precipitated at the three concentrations are clearly depicted in Figure I.2.L.1(d). Formation of particles with different shapes under different Mn^{2+} concentrations is not well understood and will be analyzed later using computational means.

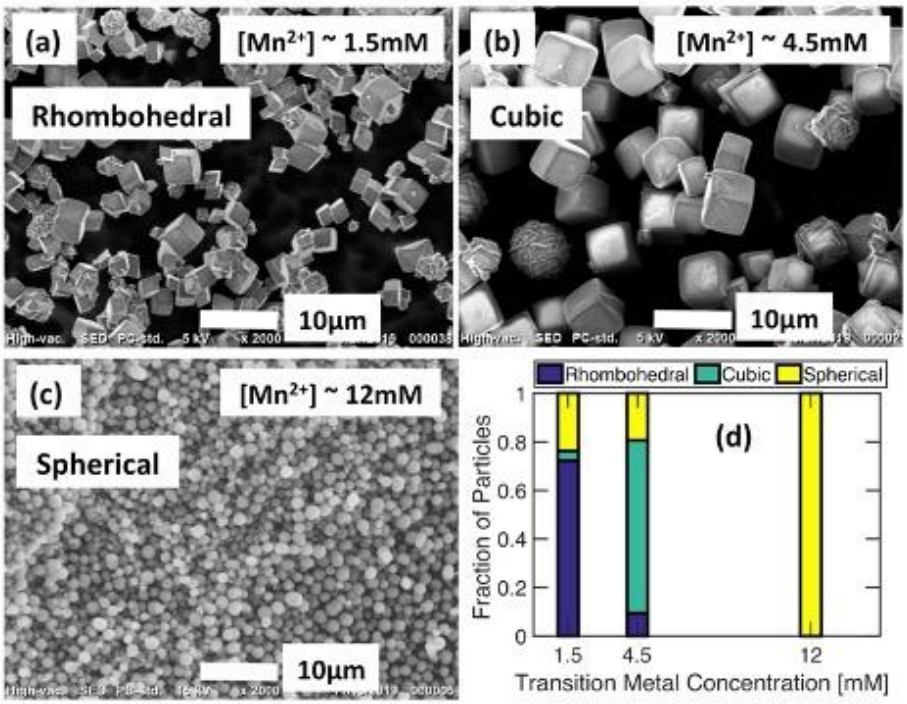

Figure I.2.L.1 (a-c) SEM image of the $MnCO_3$ particles coprecipitated at initial Mn^{2+} concentration of 1.5 mM, 4.5 mM and 12.0 mM, respectively. In all the three cases (a), (b) and (c), NH_4HCO_3 has been used as the source of carbonate ions. A ratio of 1:40 has been maintained between the concentrations of Mn^{2+} and NH_4HCO_3. pH is maintained constant at 7.5 during all the coprecipitation processes. (d) Relative amount of rhombohedral (dark blue), cubic (turquois/green) and spherical (yellow) particles, obtained during coprecipitation of $MnCO_3$ at 1.5 mM, 4.5 mM and 12.0 mM concentration. It is evident that majority of the precipitates at 1.5 mM, 4.5 mM, and 12 mM concentration shows rhombohedral, cubic, and spherical shapes, respectively. Small amount of spherical particles are observed at 1.5 mM and 4.5 mM Mn^{2+} concentration as well.

To understand the variation in particle shape with increasing concentration of $MnSO_4$ within the reaction solution, atomistic and mesoscale level calculations have been conducted. Competition between the surface diffusion and growth rate of particles in determining the final shape, have been investigated using the mesoscale modeling technique. Figure I.2.L.2(a) shows the surface energies of the most relevant facets as a function of the Mn chemical potential. For low concentration of Mn^{2+} (low Mn^{2+} chemical potential), the (104) and (102) facets are predominant. Given the similar values of their surface energies, γ_{104}= 0.98 J/m^2 and γ_{102} = 1.05 J/m^2, it is feasible that the particles adopt a shape mostly dominated by the (102) facet as shown in Figure

I.2.L.2(b) or mostly dominated by the (104) facets as shown in Figure I.2.L.2(c). Both shapes are rhombohedral with slightly different angles between the edges. This explains the appearance of rhombohedral shaped particles under low concentration of Mn (1.5 mM), which indicates precipitation occurs at equilibrium. Figure I.2.L.2(d) shows the equilibrium particle shape using all the surface energies for low Mn^{2+} chemical potential in solution. In the real system a statistical mix of these facets is expected. Furthermore, it is also clearly demonstrated in Figure I.2.L.2(a) that with increasing Mn^{2+} concentration in the reaction solution, the surface energy of the (103) facet decreases to a level even smaller than the energy of (102) and (104) surfaces. Therefore, at high Mn^{2+} concentrations, (103) facets are stabilized and eventually dominate the exposed surfaces producing a more cubic particle shape. This effect is due to the stabilization of the step defects in the (103) surface by the high concentration of Mn^{2+}. Steps and corners are favored when the concentration of Mn^{2+} in solution increases. Hence, at higher concentrations of Mn^{2+} within the reaction solution, such as 4.5 mM, cubic particles of $MnCO_3$ are observed to precipitate.

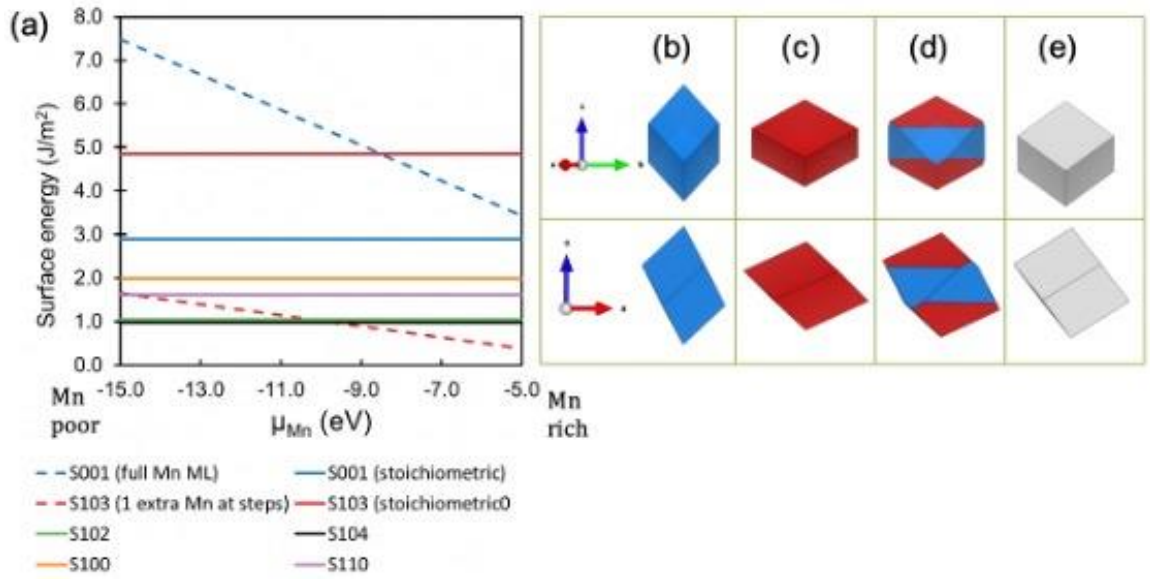

Figure I.2.L.2 (a) Change in equilibrium MnCO3 particle surface energies with Mn chemical potential. (b-e) MnCO3 predicted equilibrium shapes using the Wulff construction when: (b) Mn chemical potential is low and the surface is predominantly (102), (c) Mn chemical potential is low and the surface is predominantly (104), (d) Mn chemical potential is low using calculated (102) and (104) surface energies. (e) Mn chemical potential is high.

The equilibrium rhombohedral shape of the $MnCO_3$ particles, as predicted by the Wulff construction, has been imported into the continuum-based phase field model. Evolution of particle shape and size due to precipitation and surface diffusion have been incorporated within the mesoscale model. It should be noted that surface diffusion of the precipitates helps to form the equilibrium configuration. Shape of the particles as predicted by the phase field model at different concentrations of Mn^{2+} are shown in Figure I.2.L.3(a) – Figure I.2.L.3(c). It is evident that as the concentration of Mn^{2+} increases from 1.5 mM to 4.5 mM, and finally to 12.0 mM, the particle shape changes from rhombohedral to cubic, and finally to spherical. This observation is consistent with the particle shapes reported in the SEM images of Figure I.2.L.3(a) – Figure I.2.L.3(c). This change in particle shape is attributed to the competition between growth kinetics and surface diffusion of precipitates. As the Mn^{2+} concentration, and hence the supersaturation ratio, increases, the growth rate of the particles also increases. At $Mn^{2+} \sim 1.5$ mM, the rate of precipitation is small, and the surface diffusion is sufficient to take the particle to the equilibrium rhombohedral shape (as predicted by the Wulff construction). With increasing concentration of Mn within the solution, (103) facets become more favorable as shown in Figure I.2.L.2. Hence, at 4.5 mM Mn^{2+} concentration, the particles demonstrate a cubic shape. At the mesoscale level, for $Mn^{2+} \sim 4.5$ mM, the supersaturation ratio increases, and causes the growth rate to rise, which eventually compete with the surface diffusion mechanism. This enhanced rate of reaction at higher Mn^{2+} concentration helps in the formation of equilibrium (103) facets.

Diffusion of reactants within the solution phase have also been modeled in the present analysis. Concentration gradients of Mn^{2+} observed in the reaction solution at concentrations of 1.5 mM, 4.5 mM, and 12.0 mM are shown in Figure I.2.L.3(d) – Figure I.2.L.3(f). Due to high diffusivity of the reacting species, the concentration gradient of reactants does not contribute substantially to the shape evolution of the particles. However, the absolute concentration of the reactants determines the supersaturation ratio. The driving force for precipitation and homogeneous/heterogeneous nucleation is provided by the supersaturation ratio. It has already been discussed earlier that rhombohedral particles evolve under lower concentrations of Mn^{2+} cations, whereas, with increasing Mn^{2+} concentration, the shape of the particles changes to cubes, and very high concentrations lead to spherical particles. All these various shapes are observed due to increase in rate of precipitation, and formation of heterogeneous nuclei, at higher concentrations of transition metal salt. It is worthwhile to point out that the precipitation of $MnCO_3$ is being studied here as a model system, and the understanding developed from this system can be applied to elucidate the structure morphology relationships observed within more practical Ni-rich NMC hydroxides and Mn-rich NMC carbonate precursors.

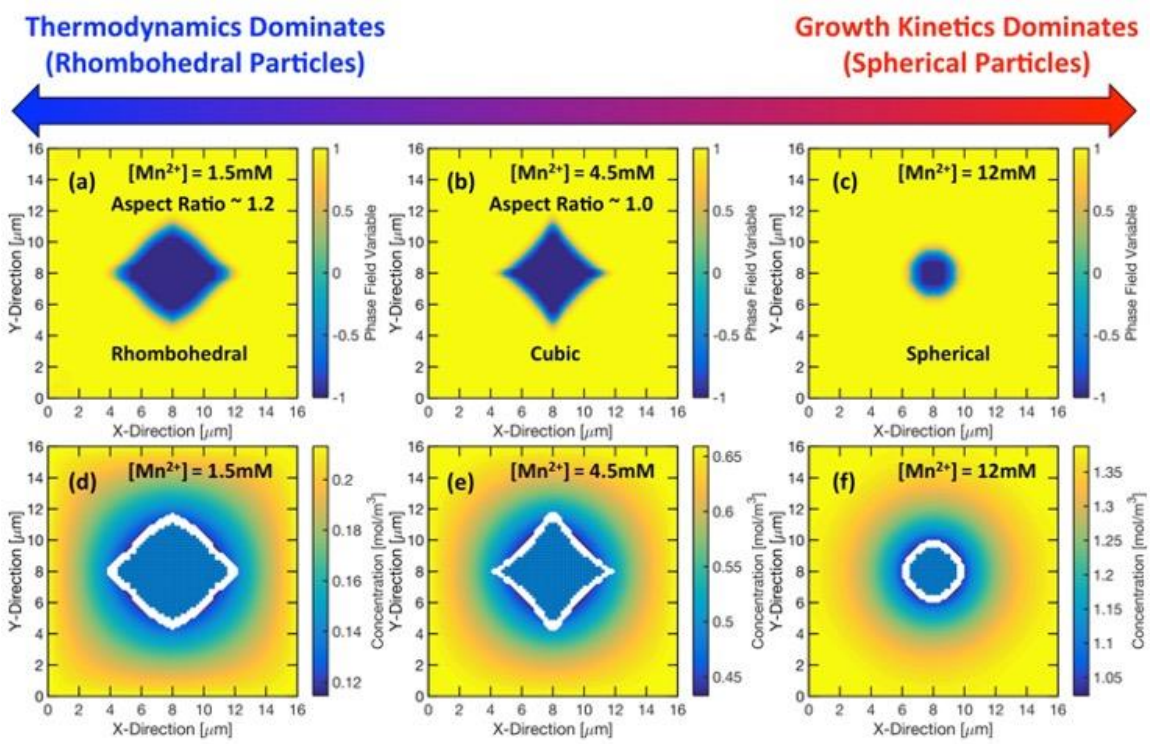

Figure I.2.L.3 Particle shape and size as predicted by the computational model at a mesoscale level. Competition between thermodynamics and growth-kinetics dictates the final shape of the particles. (a) Rhombohedral shaped particles obtained with initial $[Mn^{2+}]$ ~ 1.5 mM. (b) Cubic shaped particles obtained with initial concentration of Mn^{2+} ~ 4.5 mM. (c) Spherical shaped particles obtained with initial concentration of Mn^{2+} ~ 12.0 mM. (d-e) Evolution of concentration profile within the solution around the growing particle with rhombohedral, cubic, and spherical shapes under Mn^{2+} concentrations of 1.5 mM, 4.5 mM, and 12.0 mM, respectively. At lower Mn^{2+} concentration, growth rate is slower, and thermodynamics dictates the final shape of the particle. However, at higher supersaturation ratios, growth of the particle occurs at all the directions, and the particle takes a spherical shape, which can be characterized as the growth kinetics dominated growth of particles.

To understand the rapid growth dynamics of the precipitates, mesoscale analysis has been conducted using the phase field model. Increase in particle size with time has been plotted in Figure I.2.L.4(a) for six different initial concentrations of the Mn^{2+} ions. The initial concentration of Mn^{2+} ions considered ranges between 1.5 mM and 12.0 mM, which approximately corresponds to supersaturation ratios between 5×10^3 and 3.2×10^5. It is evident that as the concentration of Mn^{2+} ions increase, the particles start to grow faster. This can be attributed to the fact that the rate of precipitation is almost directly proportional to the supersaturation ratio, and subsequently depends on the concentration of Mn^{2+} cations within the solution. Thus, the particles form more quickly as the concentration of reactants is increased in the solution. In the present experiments, all the

reactants are added at the same time, at the beginning of the precipitation process. This eliminates the impact of the rate of reactant addition on the particle formation and growth process. Over time, as the particles grow in size, the reactants from the liquid are consumed. Hence, the available amount of Mn^{2+} and CO_3^{2-} ions in the solution decreases. Growth of the particles is dictated by the residual amount of reactants in the solution. As the particles grow with time, the ions within the liquid decreases. This lack of reactants eventually slows down the growth of the particles. As the concentration of available reactants falls below the supersaturation limit, growth of the precipitating particles ceases to occur. Hence, the flat portions that appear towards the end of the growth process, is attributed to the inability of the particle to grow due to lack of reactants in the solution.

The final particle size and the particle growth rate, as predicted by the phase field based mesoscale model, is shown in Figure I.2.L.4(b) and Figure I.2.L.4(c), respectively, for the six different initial concentrations of $MnSO_4$. It is evident from Figure I.2.L.4(b) that as the initial concentration of Mn^{2+} in the solution increases, the final particle size decreases. This inverse relationship is attributed to the different number of particles that form at each of the concentrations of Mn^{2+}. Based on classical nucleation theory, increasing Mn^{2+} concentration, and hence the supersaturation ratio, results in formation of more nuclei within the solution. Assuming that each of the nuclei has equal amount of reactants available for their growth, enhanced number of nuclei should lead to availability of less reactants for the growth of each of the particles. Hence, the size of each of the particles decreases with increasing Mn^{2+} concentration. Average size of the final particles obtained from precipitation experiments at 1.5 mM, 4.5 mM, and 12.0 mM are also demonstrated in Figure I.2.L.4(b) by the filled symbols. The trend of decreasing particle size with increasing Mn^{2+} concentration is very well captured by the phase field model. The deviation in the magnitude of final particle size at 1.5 mM and 12.0 mM can be attributed to the various unknown factors associated with the precipitation process, such as impact of stirrer size and stirring speed, local heterogeneity in concentration, etc.

In Figure I.2.L.4(c), growth rate of the particles at different Mn^{2+} concentrations, as predicted by the phase field model, is compared with the experimental observation. Computational models predict that increasing Mn^{2+} concentration, and subsequent supersaturation ratio, substantially enhances the growth rate of the precipitates. The experimentally observed growth rate of 11 µm/min at 4.5 mM concentration of Mn^{2+} is in very good agreement with the computational predictions shown in Figure I.2.L.4(c).

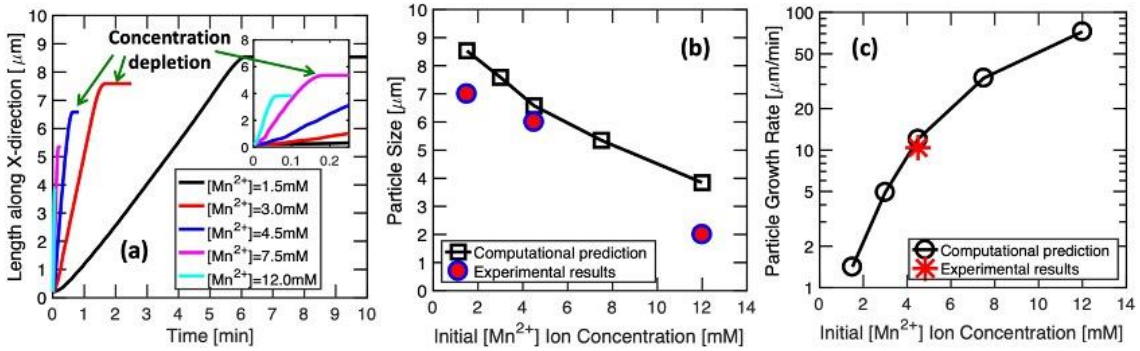

Figure I.2.L.4 Growth dynamics of the $MnCO_3$ particles as predicted by the phase field model at the mesoscale level. (a) Evolution of size of the $MnCO_3$ particles with time. Length of the particle along the x-direction have been used as the indicator of its size. The figure in the inset demonstrates the particle growth observed at higher concentration of Mn^{2+}. Growth of the particles stops due to depletion of Mn^{2+} within the bulk of the reaction solution. (b) Comparison between computationally predicted (black square) and experimentally observed (circular symbols) size of the $MnCO_3$ particles. Coprecipitation has been conducted here with different initial Mn^{2+} concentrations. (c) Comparison between the computationally predicted (black circles) and experimentally observed (red star symbol) growth rate of the $MnCO_3$ particles.

Evolution of Particle Morphology during Calcination of Ni-rich Layered NMC Cathode Precursors:
Calcination is the second of a two-step process to produce the final layered $Ni_{0.8}Mn_{0.1}Co_{0.1}O_2$ (NMC-811) cathode. The β-$Ni_{0.8}Mn_{0.1}Co_{0.1}(OH)_2$ precursor first undergoes a transformation to a cubic $Ni_{0.8}Mn_{0.1}Co_{0.1}O$ rock-salt-like intermediate phase, and then accepts lithium while forming the characteristic lithium/transition-

metal layers of the final cathode. Powder X-ray diffraction (XRD) is sensitive to the sizes of the coherent scattering domains being probed (in this case the primary particles), which are reflected in the breadths of the measured Bragg peaks. The positions and intensities of these peaks can be used to determine the identity and relative abundance of the crystallographic phases. In-situ X-ray diffraction was performed during calcination of β-$Ni_{0.8}Mn_{0.1}Co_{0.1}(OH)_2$ with $LiOH{\cdot}H_2O$. Refinement of the resulting diffractograms using the Rietveld method allows for quantification of the relative phase fractions and coherent domain sizes. Upon initial heating, the flat hexagonal β-$Ni_{0.8}Mn_{0.1}Co_{0.1}(OH)_2$ precursor decreases sharply in size along the flat dimensions until it reaches a uniform size below 10 nm matching that of the newly formed rock-salt intermediate (Figure I.2.L.5○). While holding the sample at 500°C, the newly formed rock-salt particles ripen considerably, reaching 20-30 nm (Figure I.2.L.5○). Further heating from 500°C to 750°C produces the layered cathode while also producing considerable ripening both in the cathode product (Figure I.2.L.5○) and the rock-salt intermediate.

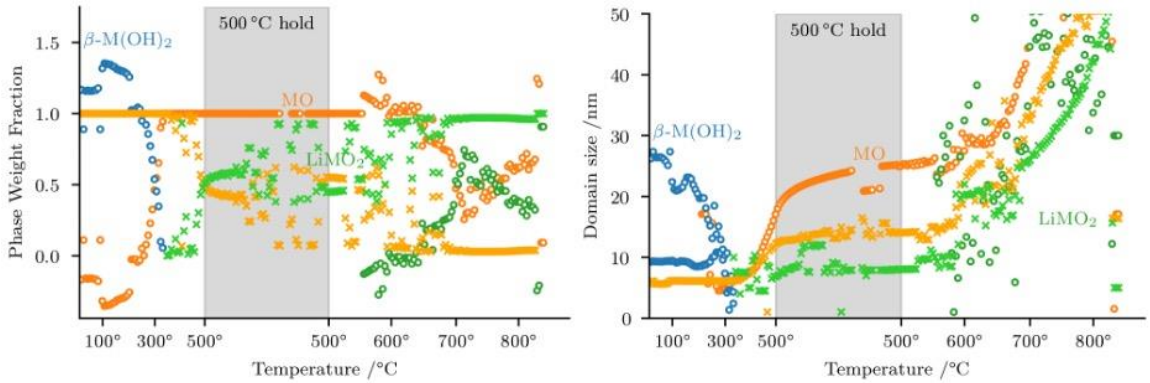

Figure I.2.L.5 Experimental domain sizes from in-situ diffraction during calcination of NMC-811. Domain sizes extracted by Rietveld refinement for hydroxide precursor (β-$M(OH)_2$), rock-salt intermediate (MO) and layered cathode product ($LiMO_2$) both with (×) and without (○) pre-treatment at 350°C.

Conversion of the initial β-$Ni_{0.8}Mn_{0.1}Co_{0.1}(OH)_2$ precursor to the rock-salt intermediate can be represented with the following reaction:

$$Ni_{0.8}Mn_{0.1}Co_{0.1}(OH)_2 \rightarrow Ni_{0.8}Mn_{0.1}Co_{0.1}O + H_2O$$

This reaction does not involve the LiOH salt, and so can be performed separately from the main calcination reaction. A pre-reacted rock-salt sample was prepared by heating the same $Ni_{0.8}Mn_{0.1}Co_{0.1}(OH)_2$ precursor to 350°C under ambient atmosphere. This pre-treated sample was then combined with $LiOH{\cdot}H_2O$ and subjected to the same heating conditions as described above during in-situ XRD for comparison to the conventional $Ni_{0.8}Mn_{0.1}Co_{0.1}(OH)_2$ precursor. The coherent domain size of 6-7 nm refined for the pre-treated rock-salt did not change during initial heating (Figure I.2.L.5×), and matched the domain size observed when the previously discussed $Ni_{0.8}Mn_{0.1}Co_{0.1}(OH)_2$ precursor was converted to the rock-salt intermediate (Figure I.2.L.5○). A further increase in domain size was again observed during the temperature hold at 500°C, however the pre-treated sample did not reach the same size as the conventional precursor (~15 nm vs. ~25 nm). Furthermore, the pre-reacted sample began forming the layered cathode phase at much lower temperatures (Figure I.2.L.5×). The cathode product and rock-salt intermediate still exhibited a sharp increase in domain sizes above 500°C, though to a lesser extent than the products formed from the conventional $Ni_{0.8}Mn_{0.1}Co_{0.1}(OH)_2$ precursor.

The addition of the pre-treatment produces smaller particles and, consequently, shorter diffusion lengths. Pre-treatment also allows the layered cathode to form at lower temperatures. While the benefits of pre-treatment are clear, the mechanism by which these benefits arise is not available from the diffraction data. With both precursors, the rock-salt intermediate begins with similar domain sizes. The obvious hypothesis that pre-treatment produces a precursor with smaller initial particle sizes is therefore incorrect.

To better understand the mechanism of lithiation of the NiO rock-salt phase, we performed Ab-Initio Molecular Dynamics (AIMD) at several temperatures (700K, 800K and 1200K) using a four-layer NiO slab with the vacuum in between filled with LiOH. The AIMD resulted in the distortion of LiOH and NiO but, without any reaction between NiO surfaces and LiOH. The reactions necessary to initiate the lithiation of NiO phase required the addition of adsorbed O on the NiO surfaces (see Figure I.2.L.6(a)). The addition of a monolayer of O on NiO surfaces triggered the reaction between LiOH and O-covered NiO, leading to the formation of H_2O in LiOH phase, and Li incorporation into NiO surface layers. The reaction continues until all of the NiO is converted to $LiNiO_2$ (see Figure I.2.L.6(b-c)). The water molecules were continuously removed from the simulation cell as they form.

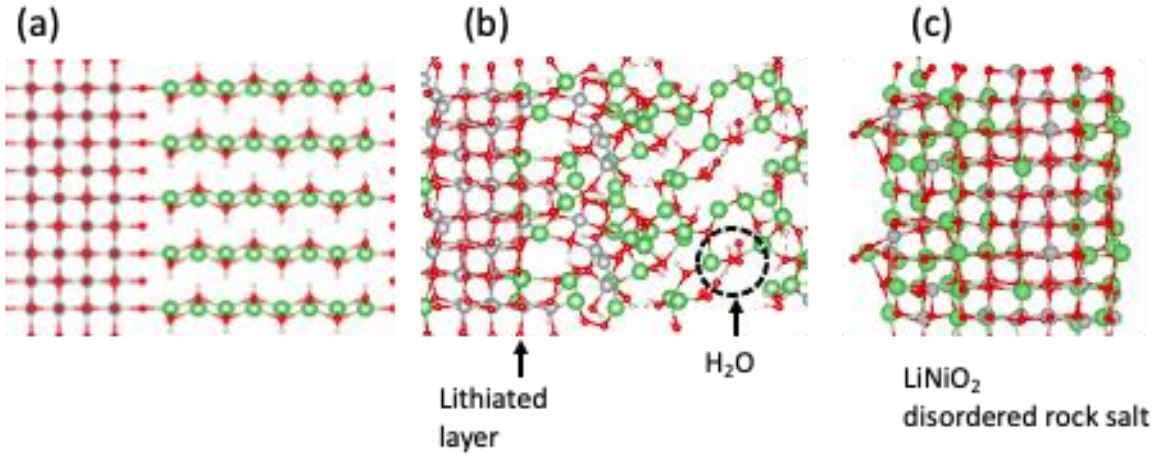

Figure I.2.L.6 NiO lithiation molecular dynamic simulation snapshots. (a) initial configuration: LiOH and a full monolayer of oxygen absorbed on the surface of NiO. (b) formation of lithiated layers in the solid and water in the solution. (c) final fully lithiated $LiNiO_2$. Green spheres represent Li, grey spheres represent Ni, red spheres represent O and white spheres represent H.

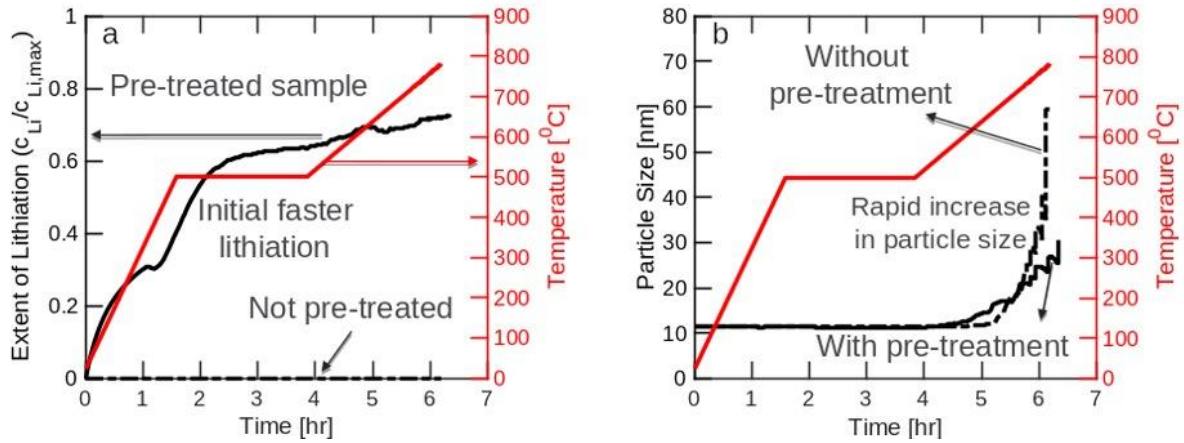

Figure I.2.L.7 Simulation of calcination reaction dynamics for layered cathode. (a) extent of lithiation and (b) particle size during calcination based on simulation by phase field modeling.

In order to further understand the mechanism by which calcination takes place, phase field models were built to capture both lithiation and sintering. The reaction to convert the rock-salt intermediate into the final lithiated cathode is:

$$Ni_{0.8}Mn_{0.1}Co_{0.1}O + LiOH + ¼O_2 \leftrightharpoons LiNi_{0.8}Mn_{0.1}Co_{0.1}O_2 + ½H_2O$$

For calcination of high-nickel cathodes, a pure oxygen atmosphere is needed to reduce cation mixing resulting from the similar ionic radii of Li^+ and Ni^{2+}. Phase field modeling reveals a secondary role for oxygen in promoting lithiation and impeding grain growth. The experimentally observed grain growth behavior is observed when the pre-treated sample is modeled with full oxygen termination on the surface of individual grains. For both precursors, no change in particle size was predicted until reaching temperatures above 500°C, above which a rapid increase in particle size should occur (Figure I.2.L.7(b)). Furthermore, grain growth was predicted to be more severe at high temperatures for the conventional precursor. These models were in agreement with the experimentally observed domain sizes (Figure I.2.L.5○,×). The extent of lithiation was also accounted for with this model. With the pre-treatment step present, lithiation was predicted to proceed quickly upon heating from room temperature and again when approaching 500°C (Figure I.2.L.7(a)). This model predicted no lithiation for the conventional precursor. This is largely in agreement with the experimental results in Figure I.2.L.5, with two differences. First, no lithiation was observed until reaching temperatures above 400°C. The melting point of LiOH is 462°C so the initial absence of lithiation was likely due to the slow kinetics of a fully solid-state reaction until the LiOH salt melted. Additionally, some formation of layered cathode was observed even in the conventional precursor at temperatures above 650°C. Further comparison of the phase field models, and experimental results may help resolve this difference.

Impact of Particle Morphology on the Densification Experienced by the LLZO Solid Electrolytes: The developed phase field based model has been used to estimate the extent of densification experienced by LLZO pellets with increasing time and temperature. In the densification process, sintering of the individual particles helped in removal of internal voids within the powder compact, and improved its relative density. Some increase in particle size may also occur during the densification process due to grain ripening mediated by grain-boundary movement, but its extent is considered to be minor.

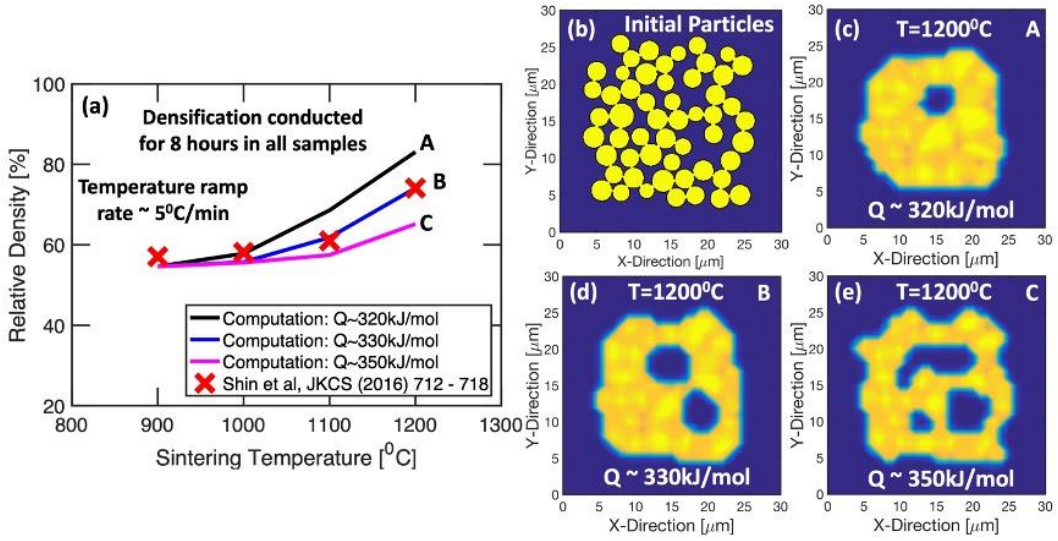

Figure I.2.L.8 After the formation of cubic-LLZO particles from the calcination process, they are densified to form pellets, which act as solid electrolytes. (a) During the sintering process, the relative density increases as the holding temperature is increased. Computational sintering was conducted for 8 hours, and the temperature was increased as a rate of 5°C/min. Final magnitudes of relative density obtained using activation energies of 320kJ/mol, 330kJ/ml and 350kJ/mol have been demonstrated by the black, blue and magenta lines, respectively. The red cross ("x") symbols indicate relative density observed in experiment. (b) Initial particle microstructure with average size around 2.75μm. (c – e) Final particle microstructures after sintering at 1200°C with activation energies of 320kJ/mol, 330kJ/mol and 350kJ/mol. It is evident that activation energy Q ~ 330kJ/mol provides the best fit with experimental results.

In order to validate the developed phase field based densification model, in Figure I.2.L.8 the relative densities obtained from the computational model have been compared with that reported in experiments. Experimentally observed relative densities for LLZO pellets after sintering at different temperatures of 900°C, 1000°C, 1100°C, and 1200°C, for 8 hours, have been extracted from existing literature. In order to be consistent with the experimental study, a temperature ramp rate of 5°C/min has been used in the present context. The initial

LLZO microstructure has been populated with multiple particles with average size around 2.75 µm, which is clearly shown in Figure I.2.L.8(b). Relative density of the initial LLZO microstructure has been maintained at around 55%. All the LLZO particles are assumed to be spherical in shape and they are connected to at least one of its neighbors. Densification simulations were run on this initial microstructure for 8 hours by setting the maximum temperature at 900°C, 1000°C, 1100°C, and 1200°C. The final relative densities after 8 hours, as predicted by the phase field model, have been plotted in Figure I.2.L.8(a) by the solid lines. Almost negligible densification, or improvement in relative density, is observed at 900°C and 1000°C. Further increase in sintering temperature demonstrates some improvement in relative density. It is evident from Figure I.2.L.8(a) that increasing temperature helps to densify the LLZO pellets, which can be attributed to the increase in surface and grain boundary diffusion coefficients at elevated temperatures.

The extent of densification depends on the magnitude of activation energy used while simulating the sintering process. Three different sets of simulations were run with three different values of the activation energies, 320 kJ/mol, 330 kJ/mol and 350 kJ/mol, and the corresponding relative densities have been depicted in Figure I.2.L.8(a) by the black, blue, and magenta lines, respectively. It is evident that decreasing the activation energy barrier helps to improve the relative density. For example, at 1200°C, only 65% relative density has been observed with activation energy of 350 kJ/mol, whereas, 83% relative density is obtained while the activation energy barrier is reduced to 320 kJ/mol. This can again be attributed to the larger diffusivities observed with smaller magnitudes of activation energy barriers. The experimentally observed data for relative densities has also been included in Figure I.2.L.8(a) and denoted by the red cross symbols. It is evident that the activation energy of 330 kJ/mol provides the best fit with the experimental observations. Hence, in all the subsequent simulations of LLZO densification, an activation energy barrier of 330 kJ/mol will be adopted.

The densified LLZO microstructure after sintering at 1200°C for 8 hours with activation energies of 320 kJ/mol, 330 kJ/mol and 350 kJ/mol, have been demonstrated in Figure I.2.L.8(c), Figure I.2.L.8(d) and Figure I.2.L.8(e), respectively. The relative densities obtained with activation energies of 350 kJ/mol, 330 kJ/mol, and 320 kJ/mol are 65%, 75% and 83%, respectively. Lower relative density with higher activation energy is also evident from the presence of multiple internal pores for the LLZO microstructure obtained by sintering with activation energy 350 kJ/mol (see Figure I.2.L.8(e)). From visual inspection, it can also be concluded that, irrespective of the activation energies, no major evolution of the particle size occurs during densification even at 1200°C for 8 hours.

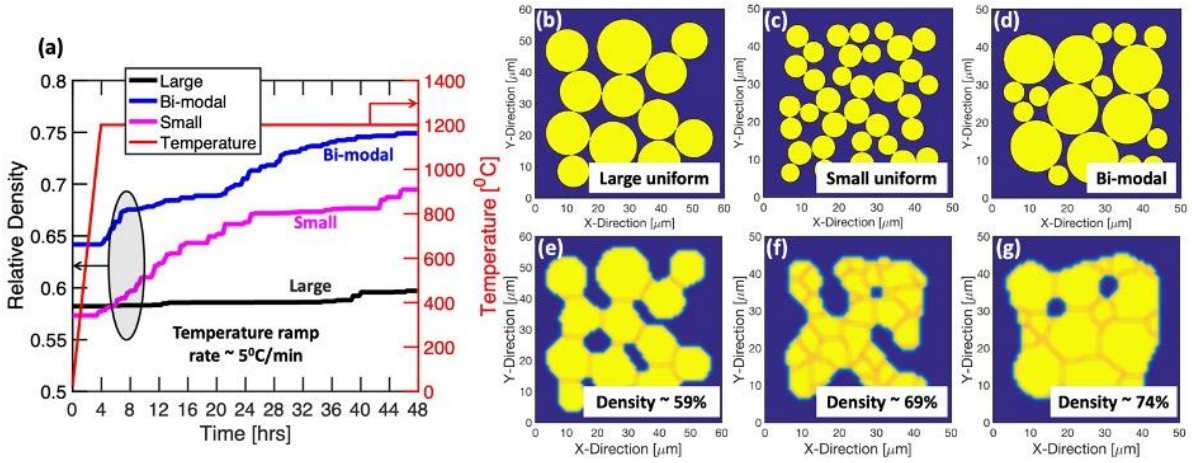

Figure I.2.L.9 (a) Computationally predicted relative densities for large (black line), small (magenta line) and bi-modal (blue) particles during sintering at 1200°C for 48 hours. The red line indicates temperature profile maintained during the sintering process. The small and bimodal particles experience substantial densification, as compared to the large particles. (b – d) Initial particle microstructure for particles with large size and uniform distribution, small size and uniform distribution, and bi-modal particle size distribution, respectively. Average sizes for the large, small and bi-modal particles are 14µm, 6µm and 9µm, respectively. (e – g) After sintering, final microstructures for the large, small and bi-modal particles along with their relative densities.

Next, the impact of particle size on the relative density of sintered LLZO will be elucidated. Three different particle sizes have been considered for this study:

i) Large particles, with average size 13 µm

ii) Small particles, with average size 6 µm

iii) Bimodal particles, with the two peaks at 6 µm and 14 µm

The sintering simulations were conducted for 48 hours at 1200°C along with a temperature ramp of 5°C/min. Increase in temperature with time has been clearly depicted by the red line and right axis in Figure I.2.L.9(a). The left axis in Figure I.2.L.9(a) denotes increase in relative density with time for the three different particle sizes of large, small, and bimodal particles. The initial particle microstructures for large, small and bimodal sizes are shown in Figure I.2.L.9(b), Figure I.2.L.9(c) and Figure I.2.L.9(d), respectively, which demonstrate initial relative densities of 58%, 57% and 64%. During the sintering and densification process, increases in relative densities experienced by the large, small and bimodal particles have been demonstrated by the black, magenta and blue lines, respectively, in Figure I.2.L.9(a). The large particles did not experience substantial increase in relative density, whereas both small and bimodal particles showed acceptable improvements. Final microstructures for the large, small and bimodal particles after densification are shown in Figure I.2.L.9(e), Figure I.2.L.9(f) and Figure I.2.L.9(g), where the final relative densities of 59%, 69% and 74%, are also clearly denoted. It is interesting to note that the absolute relative density of the bimodal particles (~ 74%) is much higher than the small and the large particles (69% and 59%). However, increase in relative density, is around 10% for the bimodal particles, and 12% for the small particles. Hence, to obtain higher relative density, bimodal particles are preferred, whereas the microstructures with small particles demonstrate maximum amount of increase in relative density during the 48 hour long sintering process.

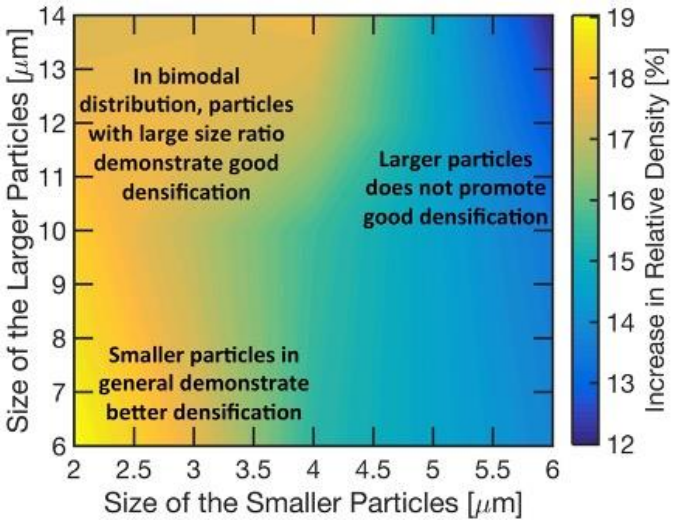

Figure I.2.L.10 Since bimodal distributions provide large relative densities, we investigate which combination of large and small particles would provide good densification behavior. A phase map has been generated here for the increase in relative density with large particle size along the y-axis and small particle size along x-axis. It is evident that: i) Smaller particles demonstrate better densification (bottom-left corner). ii) Larger particles are difficult to densify (right side of the map). iii) Bimodal size distributions with large size ratio demonstrate substantial increase in relative density. Hence, a combination of small particles and large size ratio would be ideal for dense LLZO solid-electrolytes.

In the previous paragraph it has been concluded that bimodal particle size distributions may be beneficial to attain high relative densities within the sintered LLZO pellets. However, Figure I.2.L.9(a) also depicts that smaller particles may experience better increase in relative density than the bimodal distributions. It is worthwhile to point out that the size ratio of large particles over small particles, adopted for the bimodal

distribution used in Figure I.2.L.9(a), is around 2.33, which is not the optimized size ratio for maximum increase in relative density. Accordingly, it would be interesting to determine the optimum particle size and size ratio for obtaining higher magnitudes of increase in relative density during the sintering process with bimodal particle size distributions. In this optimization study, the size of the smaller particles has been increased from 2 µm to 6 µm, whereas the size of the larger particles has been varied between 6 µm and 14 µm. Increase in relative density for these ranges of particle sizes has been demonstrated in Figure I.2.L.10 in the form of a phase map. The smaller particle size has been placed along the x-axis, and the larger particle size has been placed along the y-axis. The sintering simulations have been conducted for 48 hours at a temperature of 1200°C. The temperature has been increased from room temperature to the desired value at a rate of 5°C/min. All the microstructures demonstrate initial relative densities around 55%, among which approximately 30% are occupied by the larger particles, and the rest (~ 25%) is occupied by the smaller particles. Within the phase map in Figure I.2.L.10, the yellow domain indicates higher increase in relative density, whereas the blue region denotes smaller improvement in relative density during the sintering process. It is evident from the right blue domain of the phase map, that large size of the smaller particles is not favorable for densification processes. The left bottom corner demonstrates higher magnitudes of increase in relative density, which indicates that smaller particles are better for densification. Interestingly, the left top portion also demonstrates a large amount of increase in relative density, where the size of the larger particles is around 14 µm and the size of the smaller particles' ranges between 2 µm to 4 µm, which indicates a size ratio ranging between 3.5 to 7.0. From this observation, it appears that bimodal size distributions with higher ratio between the size of the larger and the smaller particles, demonstrates good densification. This observation is also aided by the fact that the size of the smaller particles is small, between 2 µm to 4 µm. Hence, to conclude, a combination of small particles, with size less than 4µm, and high size ratio, should lead to enhanced densification of the LLZO pellets.

Conclusions

Evolution of transition metal carbonate particle morphology during precipitation has been investigated in detail from a multiscale perspective. A better understanding of the kinetics and dynamics of particle nucleation and growth has been developed, which can be extended to understand the precipitation mechanism of Ni-rich, Mn-rich and gradient NMC precursors. In the present context, the transition metal carbonate precursors have been generated through coprecipitation reaction in a batch reactor. It has been revealed that at Mn^{2+} concentrations of 1.5 mM, 4.5 mM, and 12.0 mM, particles of rhombohedral, cubic, and spherical shape have been precipitated. Higher resolution images obtained from TEM reveal that the spherical particles obtained at 12.0 mM are *pseudo-single crystalline* in nature, which formed due to nucleation and growth of surface particles on top of the parent one.

Multiscale computational methodology has been adopted to elucidate the variation in $MnCO_3$ particle shape and size with increasing concentration of Mn^{2+}. DFT calculations reveal that the minimum surface energies are observed along (102) and (104) facets with magnitudes around 1.05 J/m^2 and 0.98 J/m^2, respectively, and both of them demonstrate rhombohedral Wulff shape. Formation of rhombohedral particles under 1.5 mM concentration of Mn^{2+} can be attributed to precipitation under equilibrium conditions. However, formation of cubic particles at higher concentration of Mn^{2+} (4.5 mM) can be attributed to stabilization of (103) facets, which has been facilitated by the enhanced growth rate at higher Mn^{2+} concentrations. The spherical particles observed at very high concentration of Mn^{2+} (12 mM), is attributed to substantially higher growth rate at very high supersaturation ratio, and its dominance over the surface diffusion process, which effectively leads to the formation and growth of surface particles. It is worthwhile to note that the supersaturation provides the required driving force for the nucleation and growth of $MnCO_3$ particles, and this supersaturation ratio is directly proportional to the concentration of Mn^{2+} ions within the solution.

Regarding the NMC calcination research, the combination of simulation at the atomic and meso scales with in-situ characterization has provided new insights in the complex lithiation and sintering mechanisms of layered NMC cathodes. The agreement between model and experiment demonstrates that oxygen plays a more important role than initially thought by promoting lithiation and slowing sintering in addition to limiting cation

mixing. The addition of a pre-heating treatment at 350°C facilitates this surface oxygen adsorption, though further investigation is needed to fully understand this relationship.

Densification of LLZO solid electrolytes have been investigated using phase field based methodology. Analysis of the densification phenomena for cubic-LLZO at different operating temperatures indicates the activation energy associated with densification of LLZO is around 330 kJ/mol. A bi-modal particle size distribution of LLZO provides the strategy to maximize relative density during the densification process. However, during densification, in order to maximize the increase in relative density adoption of smaller particles, and a large ratio between the size of the larger and smaller particles are necessary. The conclusions obtained from the present study should be applicable irrespective of the length scale, with the exception of time required to reach the desired relative densities. For example, in smaller length scales higher relative densities may be achieved in shorter times, whereas longer time is required to densify pellets of larger thickness.

Key Publications

1. Juan C. Garcia, Pallab Barai, Jiajun Chen, Arturo Gutierrez, Jianguo Wen, Ilke Arslan, Xiaoping Wang, Timothy T. Fister, Hakim Iddir, and Venkat Srinivasan. *Predicting Morphological Evolution during Coprecipitation of MnCO3 Battery Cathode Precursors using Multiscale Simulations Aided by Targeted Synthesis.* Chem. Mater. 2020, 32, 21, 9126-9139.

Acknowledgements

This research is supported by the Vehicle Technologies Office (VTO), Department of Energy (DOE), USA. Argonne National Laboratory is operated for DOE Office of Science by UChicago Argonne, LLC under the contract number DE-AC02-06CH11357. The authors also acknowledge the computing resources provided by the Laboratory Computing Resource Center (LCRC) at Argonne National Laboratory. Portions of this work were performed at GeoSoilEnviroCARS (The University of Chicago, Sector 13), Advanced Photon Source (APS), Argonne National Laboratory. GeoSoilEnviroCARS is supported by the National Science Foundation – Earth Sciences (EAR – 1634415) and Department of Energy- GeoSciences (DE-FG02-94ER14466). This research used resources of the Advanced Photon Source, a U.S. Department of Energy (DOE) Office of Science User Facility operated for the DOE Office of Science by Argonne National Laboratory under Contract No. DE-AC02-06CH11357.

Regarding the computational and experimental research, the atomistic computations were conducted by Juan Garcia and Hakim Iddir, and the mesoscale level computational modeling and subsequent analysis was carried out by Pallab Barai and Venkat Srinivasan. All the experimental research was conducted by Timothy Fister, Mark Wolfman and Xiaoping Wang. Also, Venkat Srinivasan managed the entire project, and made sure that the project follows the correct direction without deviating much from its primary goal.

I.2.M *In Situ* Spectroscopies of Processing Next-Generation Cathode Materials

Feng Wang, Principal Investigator
Brookhaven National Lab
Interdisciplinary Science Department
Upton, NY 11973
E-mail: fwang@bnl.gov

Jianming Bai, Principal Investigator
Brookhaven National Lab
National Synchrotron Light Source II
Upton, NY 11973
E-mail: jmbai@bnl.gov

Peter Faguy, DOE Technology Development Manager
U.S. Department of Energy
E-mail: Peter.Faguy@ee.doe.gov

Start Date: October 1, 2018 End Date: September 31, 2021
Project Funding: $1,500,000 DOE share: $1,500,000 Non-DOE share: $0

Project Introduction

Despite large number of promising cathode materials with high lithium-storage capacity, very few of them have been synthesized, and even fewer have realized full capacity. One major obstacle to practical deployment of new electrode materials is rooted in the difficulty of rational materials processing, *i.e.*, synthesis of certain phases with an intended control of their structure, morphology and surface properties for meeting the multifaceted performance requirements. This has been one challenge not only for a general synthesis process, but more broadly for each step of materials processing, where complex reaction may get involved, proceeding *via* kinetic pathways under *non-equilibrium* conditions, so making it hard to be predicted by theories or computations. As there are a variety of processing parameters (precursor concentration, temperature, pressure, p*H* value, reaction time etc.), materials processing for optimal performance mostly relies on trial and error.

Under this project, *in situ* spectroscopic techniques are developed and applied to studies of processing next-generation lithium-ion cathode materials, to elucidate how the processing parameters affect the kinetic reaction pathways and, consequently, the target material phase and structural properties. This capability enables probing of reactions in each step of processing at scales varying from the bulk phases to a single particle, as well as surface/interfaces. By coupling with electrochemical characterization of the final products, such studies shed light on the processing-structure-property relationship, thereby providing a science basis for rational design of novel protocols for processing cathode materials.

Currently, this project focuses on high-nickel cathode materials, in collaboration with some of the major players in the field from national laboratories, universities and industrial. Following the previous efforts on *in situ* probing and kinetic control of structural ordering in the bulk and surface, new spectroscopic techniques were developed in FY20 for probing surface changes during the sintering/cooling processes. Efforts were also made in understanding the kinetic processes during sintering and microwave-assisted hydrothermal synthesis of layered oxides, providing new insights into developing new protocols for rapid synthesis and, potentially large-scale production at low cost and minimized energy consumption.

Objectives

Use *in situ* spectroscopies to develop mechanistic understanding and novel protocols of processing next-generation lithium-ion cathode materials.

Approach

Electrode performance is largely determined by the structural properties of active materials, and so can be advanced by developing new protocols for materials processing in obtaining phase-pure materials with desired structure, morphology and surface/interface properties. One unique approach taken in this project is to develop mechanistic understanding of materials processing through *in situ* spectroscopy studies using the world-leading facilities at Brookhaven and other national laboratories. More specifically, synchrotron X-ray, neutron-based *in situ* techniques are developed and applied to studies of reaction processes and kinetic pathways during processing of cathode materials. Insights from this study provide a science basis for rational design of new protocols for materials processing in developing next-generation cathodes, and some of the results may also be used as direct input for theory, modeling and scaled-up processing through collaborations under the *Processing Science & Engineering* and other VTO programs.

Results

In situ Spectroscopies of Surface Change in High-Ni Cathodes during Sintering/Cooling Processes

Recent studies demonstrate that stoichiometric high-Ni NMC oxides with high structural ordering may be obtained through rational design of synthesis devised to control the cationic ordering as the materials are synthesized, but the surface reconstruction, shown as Ni reduction and off-stoichiometry at the particle surface (i.e. Li-deficiency), was found to be an issue. Such surface construction was observed ex situ, on the samples cooled down to room temperature, and it is still unclear how the surface reconstruction happens during synthesis. In order to understand how the surface reconstruction occurs, *in situ* synchrotron X-ray diffraction (XRD) based spectroscopy techniques were developed for tracking the whole synthesis process, to captures all of the crystalline species, not only the main layered phases, but those formed at the surface, such as Li_2CO_3 (as in Figure I.2.M.1). Through this study, we reveal, for the 1st time, the surface reconstruction during cooling process in synthesis of $LiNi_{0.70}Mn_{0.15}Co_{0.15}O_2$ (NMC71515), leading to buildup of surface Li_2CO_3, formation of a Li-deficient layer and Ni reduction at the particle surface. Such surface reconstruction occurs mainly at high temperatures (above 350 ℃), is different than that during storage or electrochemical cycling. In addition, we demonstrated that, the kinetic reconstruction process is cooling rate dependent, and can be suppressed by quenching, to improve rate performance. Findings from this study, particularly the origin of surface reconstruction, and the demonstrated solutions to alleviate the issue, may inspire new strategies for designing sintering/cooling protocols in processing high-Ni layered oxide cathodes.

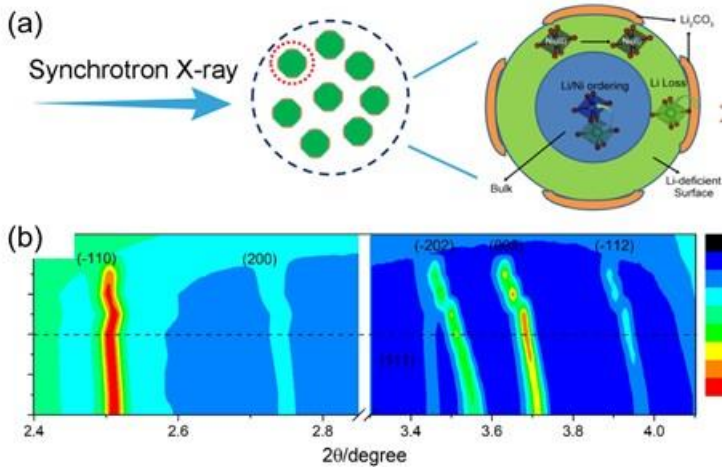

Figure I.2.M.1 (a) Schematic of the developed in situ synchrotron X-ray technique for tracking surface reconstruction during synthesis of high-Ni layered oxides. (b) Temperature resolved XRD patterns showing the gradual formation of surface Li_2CO_3 layer during the cooling process.

Kinetic Pathways of Layered Oxides During Sintering Templated by Low-Temperature Intermediates

This work was done through collaboration with Ceder Group (Berkely), involving a combined *in situ* XRD and *ab initio* study of the solid-state synthesis of layered oxides, $LiCoO_2$ (LCO), $LiNiO_2$ (LNO) and the high-Ni solid-solution, $LiNi_{0.8}Co_{0.2}O_2$ (LNCO) being chosen because of their technological relevance to the battery application (Figure I.2.M.2a).

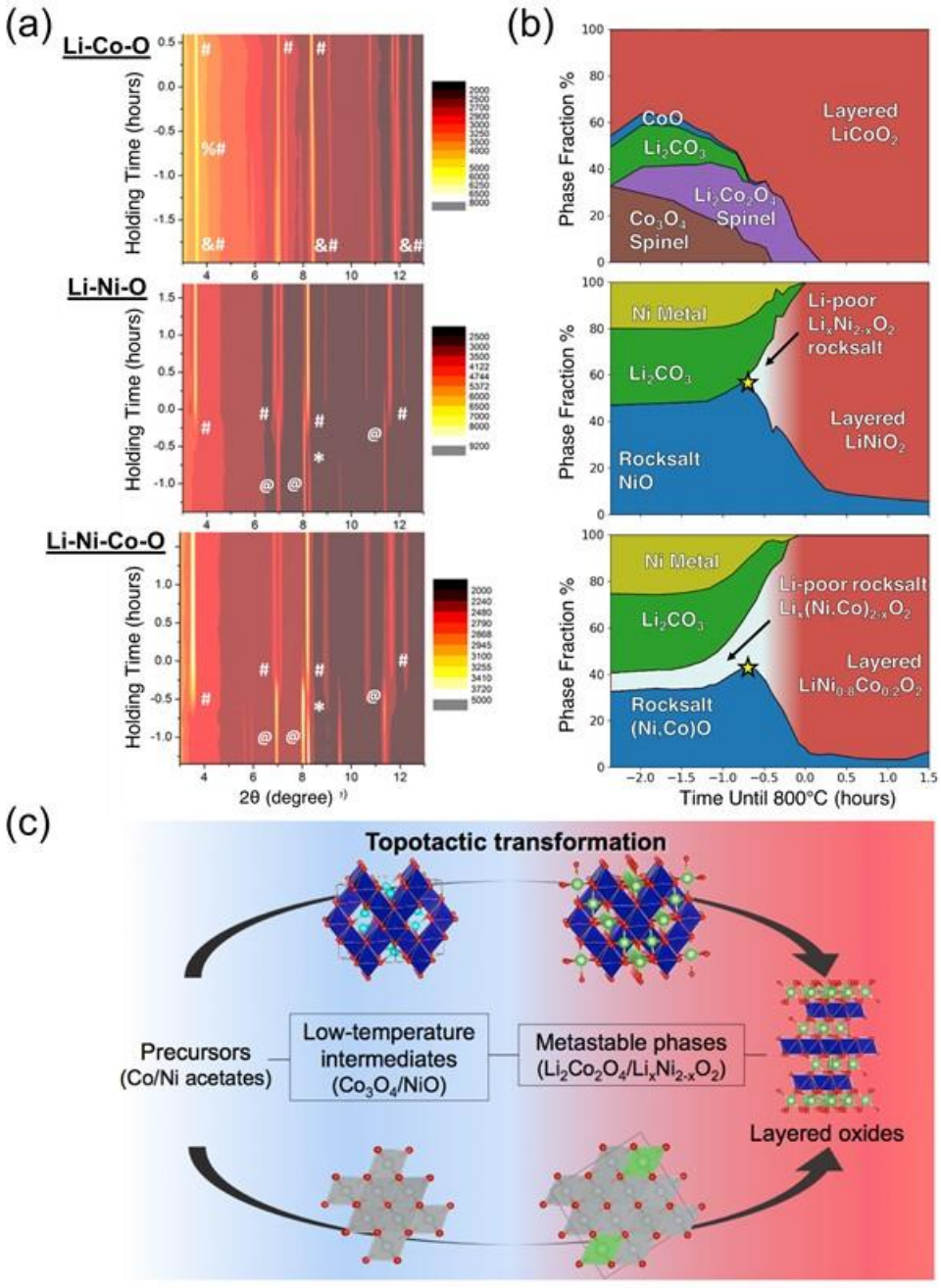

Figure I.2.M.2 (a) Contour plots of the in situ XRD patterns taken during synthesis of Li-Co-O (LCO) Li-Ni-O (LNO) and Li-Ni-Co-O (LNCO) as temperature ramps to 775 °C for LNO and 825 °C for LCO and LNCO. Bragg peaks representing the major phases are marked with symbols: # Layered oxides, & Co3O4, @ Rocksalt (Ni/Co)O, * Ni, % $Li_2Co_2O_4$-spinel. (b) Stack plots for phase fractions of the detected crystalline phases, obtained from Rietveld refinements of in situ XRD data. In the heating profile, the heating time is set as 0 at the beginning of constant-temperature holding. (c) schematic of the non-equilibrium formation pathways of Co- and Ni-based layered oxides, templated by the low temperature intermediates.

The common solid-state synthesis route was studied, whereby metal salt precursors were initially mixed into an aqueous slurry, which was then dried and calcined to high temperatures. From this study we demonstrated that, a combination of *in situ* quantitative analysis and *ab initio* calculations provides access to the kinetic pathways during sintering process, involving metastable intermediates prior to forming the final equilibrium phases (Figure I.2.M.2b). Although both Ni- and Co-based layered oxides ultimately crystallize into the same thermodynamically stable $R\bar{3}m$ layered structure, they evolve through different metastable intermediates on the way to the final equilibrium products (as illustrated in Figure I.2.M.2c).

LCO intermediate phases are primarily dominated by a metastable spinel structural motif with the same stoichiometry, whereas the LNO and LNCO intermediates proceed through a disordered rocksalt structural motif. Or put it another way, the structural evolution during high-temperature solid-state synthesis is not necessarily governed by a slow formation and further structural transformation to the reaction end-product, as is commonly assumed. Rather, materials formation proceeds through a series of well-defined phases, including phases that are thermodynamically stable in other parts of the composition space (*e.g.*, Co_3O_4), combined with kinetically-facile topotactic transformations if such pathways are available. Because the metastable spinel $Li_2Co_2O_4$ polymorph and disordered non-stoichiometric $Li_{1-x}(Ni,Co)_xO_2$ phases are kinetic lithiation byproducts from these initial binary oxides, the formation and persistence of these intermediates to high temperatures may be the origin of the well-known structural defects that plague the electrochemical performance of layered oxide cathode materials. Therefore, the observations may explain the common observations of the preferential off-stoichiometry and high Li/Ni mixing in $LiNiO_2$, and high-Ni layered oxides, but not in Co-based ones. These findings highlight new opportunities of engineering precursors to form low-temperature intermediates that template synthesis of target phases and structural properties.

By rationalizing the mechanisms driving the formation of non-equilibrium intermediates during solid-state synthesis, we can more rationally design the early-stage processing or manipulation of precursors towards targeted structural motifs.

Microwave-Enabled Rapid Hydrothermal Synthesis

Solid-state reaction, using the mixture of a Li source (LiOH or Li_2CO_3) and transition metal (TM) precursors (co-precipitated Ni-Mn-Co hydroxides or carbonates), is the mainstream synthesis of these layered oxides in both laboratory research and industrial production. The formation of desirable TM layered structures requires high temperature (750-1000 ºC), long reaction duration time (>10 hours) and heavy carbon footprint, which lead to significant energy consumption, environmental pollution and high production cost. New synthetic methods of lower cost, shorter reaction-duration and minimized energy consumptions would be of critical importance considering the rapidly increasing scale of these LIB materials needed by the future energy storage markets. Herein, we adopt the synthesis of TM layered oxide $LiNi_{1/3}Mn_{1/3}Co_{1/3}O_2$ (NMC333) as a model reaction to explore the possibility of precise energy delivery from microwave (MW) irradiation to the reactants, so that the targeted structures can be efficiently assembled with minimum energy dissipation to the environments and non-targets. Time-resolved synchrotron X-ray diffraction as a powerful *in situ* probe was employed to monitor the entire progress of forming the layered oxides, where the MW effect on both external environment and individual reactants was rigorously and quantitatively evaluated (Figure I.2.M.3).

Classic thermal syntheses of NMC333, including conventional solid-state and hydrothermal, were also studied. Our analysis reveals that, by proper selection of the reaction vessel and solvent, MW energy could be directly and precisely guided to the reactant particles/ions, i.e., TM hydroxide and hydrated Li^+. The confined energy instantly accumulated, and drove an ultrafast formation of layered oxide structures in less than 4 minutes, at a rather low temperature (<160 ℃), in contrast to the long duration (hours) and high temperature (up to 1000 ℃) needed for the conventional calcination. Compared with the requirements of long time and/or high temperatures in conventional hydrothermal and solid-state reactions, this much higher efficiency in completing the same reaction is beyond doubt of critical importance for synthetic chemistry of condensed matters. The identification of this hitherto unknown energy transmission mechanism not only enables molecular-level understanding of how energy transfers in MW synthetic chemistry; more importantly it opens up a new

perspective to design and synthesize new materials with unprecedented high energy efficiency and chemical accuracy.

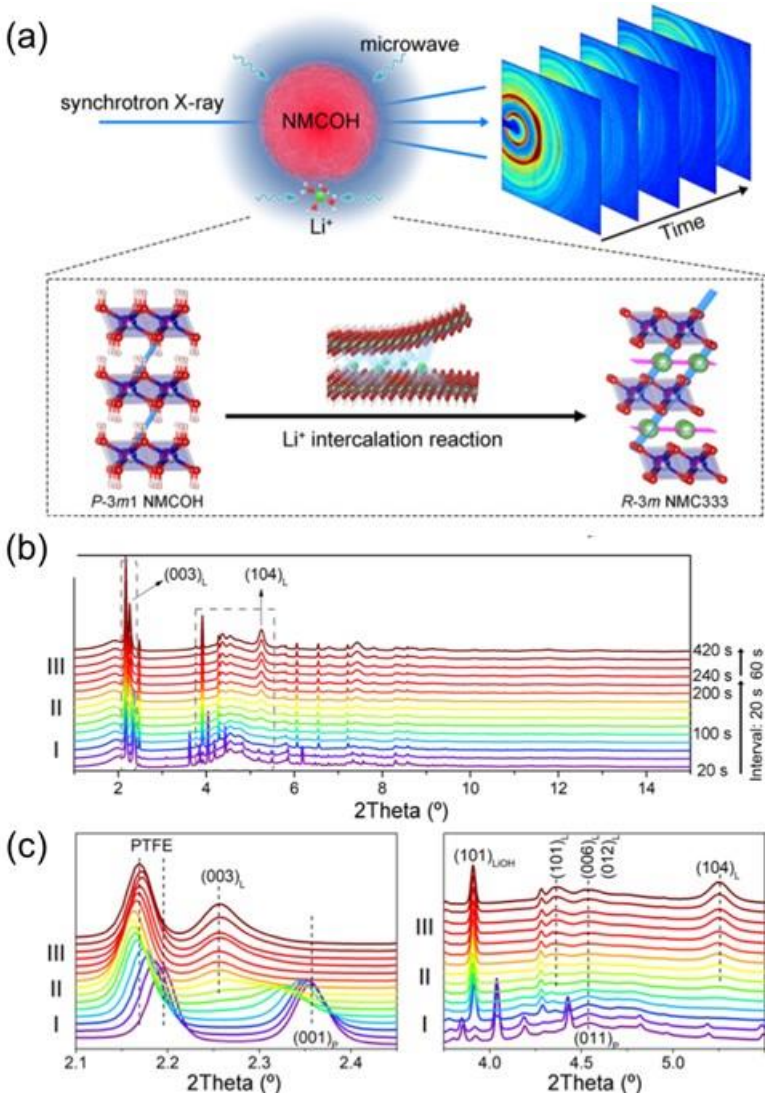

Figure I.2.M.3 Real-time monitoring of structural evolution during MW hydrothermal synthesis of the layered oxide NMC333. (a) Schematic of the fast synchrotron X-ray probing of the lithium intercalation during MW hydrothermal synthesis of NMC333 from the hydroxide counterpart (left) and the representative 2D diffraction patterns taken during the process (right). The synchrotron X-ray wavelength is 0.1885 Å. (b) Time-resolved XRD patterns recorded during in situ MW hydrothermal synthesis of NMC333. (c) Enlarged regions in the 2θ range of 2.10-2.45 degree, and of 3.75-5.50 degree (as marked in (b) to show the evolution of the $(001)_P$ peak associated with the hydroxide precursor and the $(003)_L$ peak of the layered oxide (left), and the evolution of $(104)_L$ and other peaks associated with the layered oxide (right).

Conclusions

In FY20, progress was made in the development and application of *in situ* spectroscopic techniques for fundamental understanding and rational protocol design of processing high-Ni NMC and other type of cathode materials, as briefly summarized here.

- *In situ* synchrotron X-ray techniques were developed and applied to studying surface change during synthesis of high-Ni NMC cathodes and with the findings from these studies, we developed new cooling protocols to alleviate the surface reconstruction, thereby improving electrode performance. Through such

studies, we have been developing new surface conditioning technologies for large-scale production of surface-stabilized high-Ni, low-Co cathode materials.

- Through a combined *in situ* X-ray and *ab initio* study, we revealed the role of low-temperature intermediates in templating the kinetic pathway of forming metastable disordered rocksalts $Li_xNi_{2-x}O_2$, consequently leading to the final off-stoichiometric, disordered $(Li_{1-x}Ni_x)NiO_2$ -- in contrast to the formation of stoichiometric, ordered $LiCoO_2$ as commonly observed. By rationalizing the mechanisms driving the formation of non-equilibrium intermediates during solid-state synthesis, we may rationally design the early-stage processing or manipulation of precursors towards targeted structural motifs, therefore providing new opportunities to design predictive strategies for synthesizing advanced cathode materials.

- By monitoring the structure and temperature of all the involved components during microwave-assisted hydrothermal synthesis of the layered NMC333 using X-rays, we revealed microwave-enabled rapid synthesis at low temperatures and the underlying energy delivery mechanism − *via* direct energy transmission between microwave irradiation source and the targeted reactants. This study may open a new avenue for large-scale production of cathode materials at low cost and minimized energy consumption.

With the developed *in situ* spectroscopic techniques for probing structural ordering both in the bulk and locally, this project will investigate the compositional dependence of structural ordering and surface properties in high-Ni cathode materials in FY21. Efforts will be made on studying the structural and morphological evolution during the sintering process, and the impact of some of the key parameters, such as the size/morphology of hydroxide precursors, on the process with $LiNiO_2$ and NMC811 as model systems.

Key Publications

1. M. Ge, S. Wi, X. Liu, J. Bai, S. Ehrlich, D. Lu, W-K. Lee, Z. Chen, F. Wang, Elucidating the Kinetic Limitations in Single-Crystal High-Nickel Cathodes, **Angewandte Chemie** (*accepted*).

2. M.J. Zhang, Y. Duan, C. Yin, M. Li, H. Zhong, E. Dooryhee, K. Xu, F. Pan, F. Wang, J. Bai, *Ultrafast Solid-Liquid Intercalation Enabled by Targeted Microwave Energy Delivery*, **Sci. Adv.** (*accepted*).

3. J. Bai, W. Sun, J. Zhao, D. Wang, P. Xiao, J.Y.P. Ko, A. Huq, G. Ceder, F. Wang, *Kinetic Pathways Templated by Low-temperature Intermediates during Solid-state Synthesis of Layered Oxides*, **Chem. Mater.** with a front cover (online: *https://doi.org/10.1021/acs.chemmater.0c02568)*

4. H. Lu, K. Tian, L. Bu, X. Huang, X. Li, Y. Zhao, F. Wang, J. Bai, L. Gao, J. Zhao, *Synergistic Effect from Coaxially Integrated CNTs@MoS2/MoO2 Composite Enables Fast and Stable Lithium Storage*, **J. Energy Chem.**, 55, 449 (2020).

5. M. Bianchini, J. Wang, R. Clément, B. Ouyang, P. Xiao,T. Shi, H. Kim, M. Zhang, J. Bai, F. Wang, W. Sun, G. Ceder, *The Interplay between Thermodynamics and Kinetics in the Solid-state Synthesis of P2 Layered Oxides*, **Nat. Mater.** (Online: *https://doi.org/10.1038/s41563-020-0688-6).*

6. P. Vanaphuti, J. Bai, L. Ma, S. Ehrlich, K. Kisslinger, F. Wang, Y. Wang, *Unraveling Na and F Coupling Effects in Stabilizing Li, Mn-Rich Layered Oxide Cathodes via Local Ordering Modification*, **Energy Storage Mater.,** 31, 59 (2020).

7. W. Zhang, D-W. Seo, T. Chen, L. Wu, M. Topsakal, Y. Zhu, D. Lu, G. Ceder, F. Wang, *Kinetic Pathways of Ionic Transport in Fast Charging Lithium Titanate*, **Science**, 367, 1030 (2020).

8. M.J. Zhang, G. Teng, Y.C.K. Chen-Wiegart, Y. Duan, J.Y.P. Ko, J. Zheng, J. Thieme, E. Dooryhee, X. Hu, M. Li, Y. Duan, L. Yang, C. Yin, M. Ge, X. Xiao, W-K., Lee, J.Y.P. Ko, K. Amine, Z. Chen,

J. Bai, F. Pan, F. Wang, *Cooling Induced Surface Reconstruction during Synthesis of High-Ni Layered Oxides*, **Adv. Energy Mater.**, 9, 1901915 (2019).

Acknowledgements

The work was supported by the Energy Efficiency and Renewable Energy, Office of Vehicle Technologies of the U.S. Department of Energy under contract DE-SC0012704. We thank the contribution by the team members, Yusuf Celebi, Sungun Wi, Chong Yin, Mingjian Zhang, and by collaborators, Eric Dooryhee, Steve Ehrlich, Mingyuan Ge, Andy Kiss, Wah-Keat Lee, Juergen Thieme (Brookhaven Nat. Lab), Khalil Amine, Pallab Barai, Zonghai Chen, Ozge Kahvecioglu, Krzyszt Pupek, Yang Ren, YoungHo Shin, Venkat Srinivasan, Chengjun Sun, Xiaoping Wang (Argonne National Lab), Gerdbrand Ceder, Wenhao Sun (Berkeley National Lab), Ashfia Huq (Oak Ridge Nat. Lab), Peter Ko (Cornell High Energy Synchrotron Source).

I.3 Recycling and Sustainability

I.3.A Battery Production and Recycling Materials Issues (ANL)

Jarod Kelly, Principal Investigator
Argonne National Laboratory
9700 S. Cass Avenue
Lemont, IL 60439
E-mail: jckelly@anl.gov

Samm Gillard, DOE Technology Development Manager
U.S. Department of Energy
E-mail: Samuel.Gillard@ee.doe.gov

Start Date: October 1, 2019 End Date: September 30, 2020
Project Funding: $175,000 DOE share: $175,000 Non-DOE share: $0

Project Introduction

This project examines the critical issues related to automotive battery production, from raw material extraction, through processing to usable chemicals, to assembly within battery cells and packs, all the way to potential recycling stages. Doing so allows for identification of hot spots along the supply chain with respect to energy and environmental burdens. Recycling of used automotive batteries is a critical aspect of the supply chain as it seeks to move beyond the framework of environmental stewardship of disposal and into the stage of developing a new supply base for recycled elemental and cathode materials for new batteries produced from recycled materials. We consider battery materials produced for current batteries along with battery assembly and battery recycling processes available commercially as well as those that are being developed.

Understanding raw resource recovery processes is necessary to evaluate the total energy and environmental burden associated with virgin material production and identify the benefits that may be available through battery recycling. Additionally, regional aspects of material acquisition and processing can influence total environmental effects of battery production. We evaluate battery materials, assembly, and recycling processes based on consumed energy and emissions, suitability for different types of feedstock, and potential advantages relating to economics and scale. We also consider the potential of recycling processes to displace virgin materials at different process stages, thereby preserving resources and reducing emissions from battery production. While few automotive batteries have reached their end of life, it is important to evaluate environmental impacts of the viable processes for end-of-life recycling treatments of such batteries.

This project evaluated the life-cycle performance of numerous automotive battery chemistries, considering different processing locations worldwide, considered how such batteries would be incorporated into light duty vehicles, and refined the life-cycle inventory for cathode material inputs, thereby improving understanding of vehicle battery burdens. Through this, the project also supports R&D at the ReCell Center, aimed at developing a commercially viable process.

Objectives

- Continue to follow developing and potential material issues affecting automotive lithium-ion batteries (LIB) viability
- Identify, characterize, update, and release LIB models in Argonne's life-cycle analysis model (GREET – Greenhouse gases, Regulated Emissions, and Energy Use in Technology model) to evaluate of burdens
- Engage with the international battery community to exchange battery production and recycling technologies knowledge and advance understanding of battery life cycle

- Evaluate the global supply chain of automotive battery materials through regional analyses
- Identify technical, systemic, and institutional barriers to battery recycling.

Approach

Argonne has developed and maintained models of battery materials production and updated those models with industrial insights and market changes. In addition, automotive LIBs have advanced, and this means that up-to-date analyses of such batteries must have updated models. This is especially true when identifying the energy density and battery material composition for the numerous battery chemistries. This improves temporal models of LIB recycling outputs. Life-cycle analysis (LCA) was used to evaluate the environmental burdens of battery production, and compare energy savings and emissions reductions enabled by different recycling processes. LCA was also used to investigate how regional variations in production could affect energy and environmental issues along the global supply chain. Nickel is an increasingly important material for the LIB industry with potentially significant environmental impacts depending upon both its mineral source and production technique. Argonne investigated nickel to develop multiple pathways for nickel chemicals production, considering both sulfidic and lateritic ore bodies.

Close interactions with stakeholders were sustained to remain engaged in and informed of technological and legislative developments associated with LIB production and recycling, and to maintain Argonne's position as the world's leader in battery recycling research and LCA. During FY20, Argonne staff 1) gave invited talks and presentations to government, industry, and academia; 2) interacted with international groups like the IEA and the Faraday institution to coordinate research, 3) improved understanding of the impacts of battery materials production, 4) served on SAE and NAATBatt recycling committees and the Science Advisory Board of the Responsible Battery Coalition; 5) negotiated materials production modeling studies with global battery material leaders; and 6) responded to countless requests for information.

Results

To increase adoption of electric vehicles (EV), there is a push towards increasing the specific energy of LIBs. This has a multitude of consequent effects. First, increased specific energy allows automakers to increase vehicle range within the same volumetric footprint of a current vehicle design. It also allows for lower costs of LIBs if driving range is maintained and these lower costs can lead to lower EV costs. To achieve the specific energy increase, automakers and battery manufacturers are increasing cathode active material nickel content while reducing cobalt content. The effect of the transition to higher-nickel, lower-cobalt, and higher-energy-density lithium-ion battery cathode chemistries on the environmental impacts of LIB production was investigated. Focusing on the NMC cathode chemistry, the effect of the transition to higher nickel content in the form of $LiNi_{0.6}Co_{0.2}Mn_{0.2}O_2$ (NMC622) and $LiNi_{0.8}Co_{0.1}Mn_{0.1}O_2$ (NMC811) from a baseline $LiNi_{1/3}Co_{1/3}Mn_{1/3}O_2$ (NMC111)-based LIB was investigated. The projected increase in EV adoption has also spurred an increase in the global battery manufacturing capacity with announced investments in Asia, where China is dominant, as well as a push for production in Europe. The effect of globally regional production of LIBs (and constituent materials and processes) on the environmental impact of battery production was examined as well.

The study was carried out using GREET for midsize passenger sedan EVs with 300-miles of driving range on a single charge (84 kWh LIB). The bill-of-materials for the three NMC cathode chemistries (considering increased specific energies) were obtained from the BatPac model (also developed at Argonne) and used to evaluate the life-cycle environmental impact of LIB production including the upstream extraction of raw materials. For regional variability, different global electricity profiles were employed for different LIB material acquisition and processing locations.

For the greenhouse gas (GHG) impact category, a monotonic reduction in the emission levels was observed as the nickel content was increased from NMC111 to NMC622 and NMC811 as shown in Figure I.3.C.1. The effect of regional variability associated with the nickel refining stage was investigated and indicated significant variation in SO_x emissions from different world regions, with increases as LIB nickel content increases. We

found that the use of better control technologies for SO_x, as is the case in Canada and China, leads to significantly lower SO_x compared to a location like Russia, which may not use such strong controls.

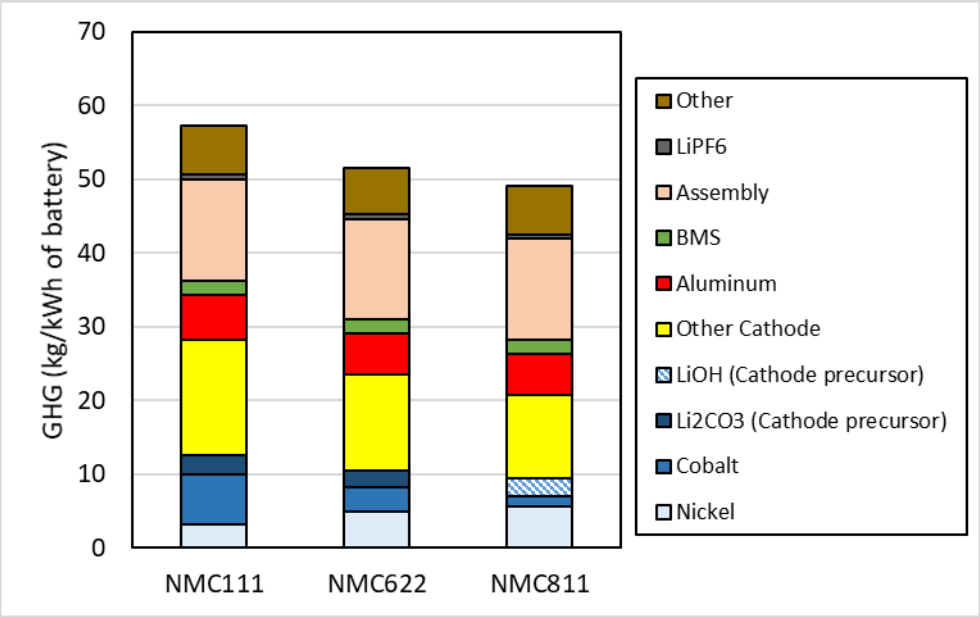

Figure I.3.A.1 The GHG emissions associated with NMC LIBs decrease as both energy density and stoichiometric nickel content increase.

Argonne conducted LCA of conventional battery recycling technologies including pyrometallurgical (pyro) and hydrometallurgical (hydro), together with direct recycling, which is an emerging technology. We compared the environmental impacts of cathode materials recovered from these three recycling technologies and compared recycled cathode materials with their virgin counterparts. Figure I.3.A.2 shows this comparison for GHG emissions of NMC111 and NMC811, respectively. The results show that for NMC111, pyro and hydro recycling can offer modest reductions in GHG emissions compared with virgin production. For NMC811, however, conventional recycling technologies do not necessarily outperform virgin production, mostly due to higher process energy requirement and the use of lithium hydroxide for NMC811 synthesis. In contrast, direct recycling can offer significant reductions in GHG emissions compared with conventional recycling technologies or virgin production regardless of cathode chemistry.

For FY20, the different cathode chemistries in the GREET model were updated based on the most recent version of the BatPac model. The update included changes to the specific energy of the cathode chemistries (with appropriate specifications for different vehicle powertrains including hybrid electric, plug-in hybrid electric, battery electric, and fuel cell vehicles) as well as the bill-of-materials of the LIBs. Additionally, for FY20 the $LiNi_{0.5}Co_{0.3}Mn_{0.2}O_2$ (NMC532 cathode chemistry was also added to the suite of EV chemistries in GREET, thereby expanding its capabilities and improving its coverage of the present-day electric vehicle market.

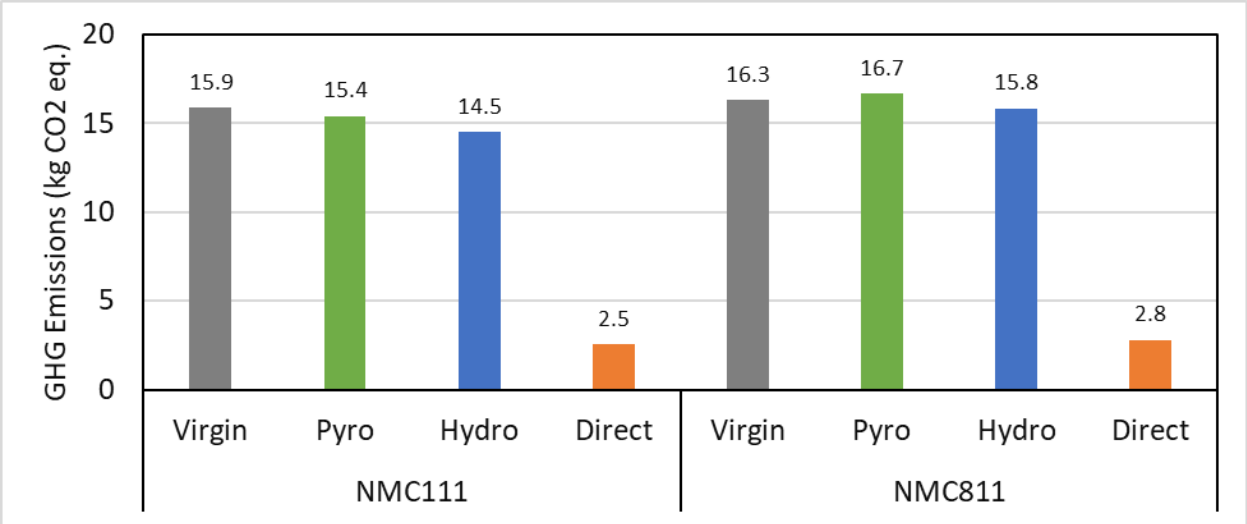

Figure I.3.A.2 GHG emissions comparison for 1kg active cathode material. Please note that the recycling processes are generic in nature and do not reflect specific companies, and results for recycled cathode materials are conservative as credits for other recycled materials are not considered.

Production of class I nickel and battery-grade nickel sulfate was also updated based on industry data compiled by the Nickel Institute, which represent 52% of global class I nickel production and 15% of global nickel sulfate production in 2017. A pathway for battery-grade nickel sulfate production from mixed hydroxide precipitate was also developed since it has recently become an important source of nickel sulfate supply, based on industry reports and literature. These efforts serve to improve Argonne's capacity to represent the energetic and environmental effects of battery nickel production.

Argonne expanded and updated the structure of lithium production pathways in the GREET model. This has created pathways for lithium extracted from spodumene ore and converted into lithium carbonate (Li_2CO_3) and lithium hydroxide (LiOH). No numerical data are yet provided for these ore-based pathways. The brine-based lithium pathways are retained. This will allow for quick integration of lithium production data that are being developed with industrial partners.

In the spring of 2020, Argonne planned to host an in-person meeting of the IEA Electric and Hybrid Vehicle Working Group's Task 40, Critical Materials for Electric Vehicles (CRM4EV), for which Dr. Gaines is the U.S. representative. This meeting was scheduled to include technical exchanges and several site tours, including one to Superior Graphite in Chicago, IL. However, due to the ongoing pandemic, the meeting was of necessity held online. Argonne successfully hosted a virtual tour of the Cell Analysis, Modeling, and Prototyping (CAMP) facility and a full 3-day technical program. The unexpected benefit of the virtual nature of the meeting was that instead of the expected attendance of around 30 researchers, nearly 130 technical experts were able to participate in the tours and research discussions.

Conclusions

The advancement of nickel-rich cathode chemistries coupled with the global effort to develop new battery material production and assembly supply chains leads to important questions pertaining to the consequent effect on both energy and environmental burdens. Through literature examination and industry engagement Argonne has improved its modeling capabilities of these conditions and disseminated the findings of this research through literature publications and technical presentations. Namely that increasing nickel content of battery cathode chemistries can reduce GHG emissions, and that the global variance in battery material production and location can have significant effects on the total burdens associated with automotive LIBs. Argonne has additionally disseminated research results in battery recycling and fostered open discussion of

technical, institutional, and economic issues therein. Importantly highlighting the potential of direct cathode recycling as a pathway that could yield overall GHG reductions in battery cathode production.

Key Publications

1. Paper: Kelly, Jarod, Qiang Dai and Michael Wang. “Globally regional life-cycle analysis of automotive lithium-ion nickel manganese cobalt batteries.” Mitigation and Adaptation Strategies for Global Change, Volume 25, Issue 8, December 2019, doi: 10.1007/s11027-019-09869-2

2. Paper: Gaines, Linda. “Profitable recycling of low-cobalt lithium-ion batteries will depend on new process developments.” One Earth, Volume 1, No. 4, December 20 2019, doi: 10.1016/j.oneear.2019.12.001.

3. Paper: Harper, Gavin, Roberto Sommerville, Emma Kendrick, Laura Driscoll, Peter Slater, Rustam Stolkin, Allan Walton, Paul Christensen, Oliver Heidrich, Simon Lambert, Andrew Abbott, Karl Ryder, Linda Gaines & Paul Anderson. “Recycling lithium-ion batteries from electric vehicles”. Nature, no. 575, November 6, 2019, doi: 10.1038/s41586-019-1682-5.

4. Presentation: Gaines, Linda. " Electric Vehicle Battery Recycling Strategies.” Transportation Research Board Annual Meeting, Washington, DC, January 11-16, 2020.

5. Presentation: Gaines, Linda. “Battery Recycling: What is the ReCell Center doing.” IEA HEV Task 40 CRM4EV: Webinar, June 9-11, 2020.

6. Presentation: Dai, Qiang. “Economics and environmental impact implications of new recycling processes vs established ones, as battery content evolves.” IEA HEV Task 40 CRM4EV: Webinar, June 9-11, 2020.

7. Presentation: Kelly, Jarod. “Lithium-ion Battery Life-cycle Analysis: Data Challenges Illustrated Through Regional Supply Chains.” UCOP MRPI Workshop, Maximizing the Environmental Utility of Battery Storage: Building a Life-cycle Assessment Framework, Davis, CA, October 25, 2019.

8. Presentation: Kelly, Jarod and Olumide Winjobi. “Life-cycle Analysis of Automotive Lithium-ion Battery Cathode Chemistry Changes.” American Council on Life-cycle Assessment Virtual Conference: ACLCA 2020, September 22 - 24, 2020.

9. Presentation: Dai, Q. and Winjobi, O., 2020. Life Cycle Analysis of Battery Materials: A Circular Economy Perspective. TMS 2020, February 23-27 2020, San Diego, CA.

10. Technical Publication: Qiang Dai and Jarod C. Kelly. “Nickel Life-cycle Analysis Updates and Additions in the GREET Model.” Argonne technical memo. September 2020.

11. Technical Publication: Kelly, Jarod¸ Qiang Dai, and Olumide Winjobi. “Lithium Pathway Updates and Additions.” Technical memo. September 25, 2020.

12. Presentation: Jarod C. Kelly. “Battery Supply Chain with GREET.” Argonne Virtual Townhall on Batteries. March 26, 2020.

13. Invited Lecture: Kelly, Jarod. “Electrified Vehicles and the Batteries they Require: Is this Sustainable?” University of Illinois at Chicago, November 12, 2019.

I.3.B Lithium-ion Battery Recycling Prize Support

Lauren Lynch, Principal Investigator
National Renewable Energy Laboratory
15013 Denver West Pkwy
Golden, CO 80401
Email: lauren.lynch@nrel.gov

Connie Bezanson, DOE Technology Development Manager
U.S. Department of Energy
E-mail: Connie.Bezanson@ee.doe.gov

Start Date: October 1, 2017 End Date: September 30, 2022
Project Funding: $6,570,000 DOE share: $6,570,000 Non-DOE share: $0

Project Introduction

Lithium-ion batteries have become the main choice for portable electronics (such as smart phones, tablets, and laptops), power tools, and electric vehicles (EV) for personal, commercial, industrial, and military applications. The demand for lithium-ion batteries for EVs is expected to grow as the cost of manufacturing and materials is reduced while performance improves. The U.S. Energy Information Administration (EIA) projects that U.S. light-duty battery EV sales will reach 1.3 million by 2025 and others project even higher sales growth. Global EV sales are expected to reach 30 million by 2030, up from 1.1 million in 2017. This growth in EV sales, as well as increased demand for consumer and stationary uses, are expected to double the demand for lithium-ion batteries by 2025 and quadruple the demand by 2030.

Demand for global production of battery materials, such as lithium, cobalt, manganese, nickel, and graphite, will grow at similar rates depending on the future changes on the composition. In fact, the growth in demand for lithium-ion batteries for EVs is expected to establish EVs as the largest end- user of cobalt and lithium and could create a particularly high supply risk for cobalt as it could be expensive, and its availability depends on foreign sources for production. To address this potential risk, the DOE Vehicle Technologies Office (VTO), within the Office of Energy Efficiency and Renewable Energy (EERE), developed a Research Plan to Reduce, Recycle, and Recover Critical Materials in Li-ion Batteries. A goal identified in the Plan is to reduce the cost of electric vehicle battery packs to less than $150/kWh with technologies that significantly reduce or eliminate the dependency on critical materials (such as cobalt) and utilize recycled material feedstocks. However, li-ion batteries are only recycled at a rate of about 5% currently. Analysis has shown that recycled material could potentially provide one-third of United States cathode material needs for Li-ion batteries by 2030. The current recycling supply chain for collecting, sorting, safe storing and transporting of lithium-ion batteries and recovery of valuable materials is limited, particularly for larger batteries used in EVs and industrial applications. Preventing the lithium-ion batteries, particularly consumer electronics not going to waste disposal facilities (as some of them has caused fires) landfills is important not for recovery of the key materials, but for the economy and environment.

To achieve the above goal and address potential critical materials issues, VTO has initiated 3 key areas of R&D: 1. Supporting laboratory, university, and industry research to develop low-cobalt (or no cobalt) active cathode materials for next-generation lithium-ion batteries, 2. Establishing the ReCell Lithium Battery Recycling R&D Center focused on cost- effective recycling processes to recover lithium battery critical materials, and 3. Launching a Lithium-Ion Battery Recycling Prize to incentivize American entrepreneurs to find innovative solutions to solve current challenges associated with **collecting, sorting, storing, and transporting** discarded lithium ion batteries safety and economically for eventual recovery of valuable materials for re-introduction to the battery production supply chain.

While the first two initiatives focus on creating next-generation cobalt-free Li-ion batteries and conducts research into recovery of critical materials and reintroduction of these materials in recycled batteries, the $5.5M Li-ion Battery Recycling Prize leverages innovative ideas from American entrepreneurs to develop and demonstrate a supply chain that safely transitions spent batteries to specialized battery recycling facilities. The Recycling Prize is a joint collaboration between VTO and DOE's Advanced Manufacturing Office with $4.5M funding support from VTO and $1.0M from AMO.

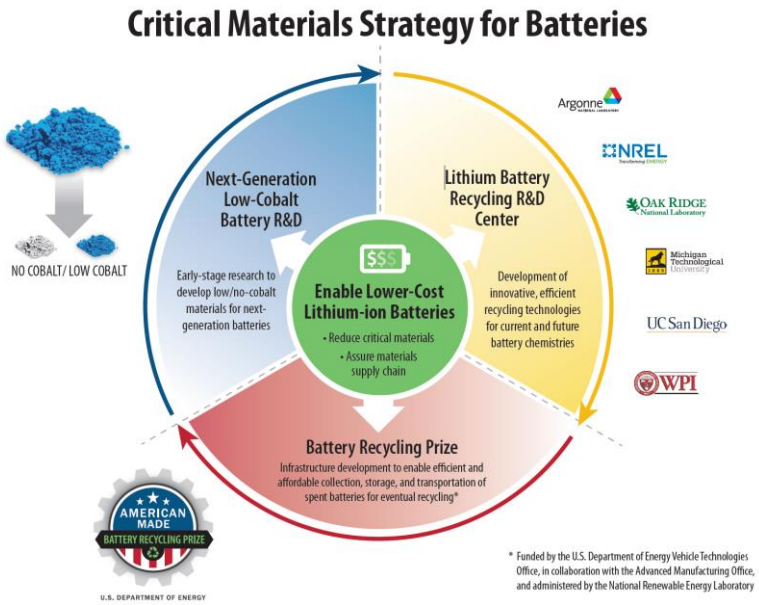

Figure I.3.B.1 The Critical Materials Research Plan with three major areas of research to address to address critical materials issues for of Lithium-ion batteries and recovery of materials for re-introduction into the supply chain.

The $5.5 million Prize is designed to be implemented in three progressive phases for three years to bring ideas from concept to prototype and partnering, through pilot validation. In each phase, submissions will be evaluated by expert reviewers and a federal consensus panel for recommendation to the DOE selection officials. DOE assigned the administration and execution of the Battery Recycling Prize to National Renewable Energy Laboratory (NREL) to use an already-established framework for American-Made Challenges that has been used to administer prizes for other EERE Offices such as Office of Solar Technologies. Figure I.3.B.2 provides an overview of the three phase of the contest and the amount of award and number of awards available in each phase.

This progress report provides summary of activities of the Prize for the second year and Phase II "Prototype and Partnering" with the aim of awarding $2.5M cash prize distributed equally among the Phase II winners, along with $100,000 in vouchers per team.

Figure I.3.B.2 Left: Logo of the Lithium Ion Battery Recycling Prize. Right: The Lithium-ion Battery Recycling Prize consists of three progressive phases from concept through pilot validation for about three years.

Objectives

The purpose of Lithium-Ion Battery Recycling Prize is to incentivize American entrepreneurs to develop and demonstrate processes that, when scaled, have the potential to capture 90% of ALL lithium-based battery technologies in the U.S. covering consumer electronics, stationary, and transportation applications. 90% recycling rate of lithium-based batteries would be a significant achievement compared to today's 5% recycling rate. It is the goal of this Prize to find innovative solutions to current challenges in safe and economical collecting, sorting, storing, and transporting discarded (or end of life) lithium-ion batteries for eventual recycling so the 90% target could be achieved.

Approach

The NREL Prize Administrators successfully launched Phase II "Prototype and Partnering" of the Lithium-Ion Battery Recycling Prize. In December 2019, the Prize Administrators developed comprehensive Phase II Prize Rules, as well as a separate in-depth Voucher Guidelines document to prepare participants for the voucher process. These rules were released alongside a 30-minute webinar by the Prize Administrators that reviewed the complete rules. The Prize Administrators later released three additional 30-minute webinars to further expand on partnering expectations and the Voucher Guidelines.

The Prize Administrators organized an in-person networking opportunity in partnership with the NAATBatt National Conference in February 2020. Phase II participating teams were invited to give a brief presentation to the NAATBatt conference attendees and battery industry experts to introduce their concepts. Twelve teams accepted the opportunity to attend and present at the event. Prize Administrators introduced the Prize and provided a print postcard to encourage the development of partnerships between Prize participants and NAATBatt attendees. The postcard connected potential partners directly to a "Partners" page on the HeroX website with brief overviews of the Phase II teams and their Phase I winning concepts.

To ensure that Phase II participating teams were on-track with the continued development of their concepts, Prize Administrators coordinated an interim "concept update" and review process. Phase II teams each submitted a 12-page update on their concept proposals and a Technical Assistance Request to outline areas of their concept that may need additional support from partners or vouchers. The Prize Administration team reviewed each proposal thoroughly and provided feedback on each of the scoring categories: end-to-end solution approach, impact, team, and partnering.

Although the "Demo Day" was initially planned as a subsection of the VTO Annual Merit Review, the Prize Administrators moved the event to a virtual format to ensure the safety of all participants. The new virtual Demo Day refocused from prototype presentations to highlighting Voucher Service Providers (VSPs) within the American-Made Challenge Network, including both businesses and national labs. The prize Administrators coordinated 27 virtual presentations from Phase II participating teams and VSPs for the event. In addition, the Prize Administrators aimed to simulate the networking that occurs at in-person events by coordinating a day of one-on-one meetings between Phase II teams and VSPs they wanted to meet with personally. A total of 39 sessions were coordinated for this event.

Here are key dates for execution of Phase II of the Prize:

- January 14, 2020: The Phase II Rules and Voucher Guidelines were released
- January 27, 2020: Phase II Rules webinar
- February 13, 2020: NAATBatt National Conference, twelve teams participated in this voluntary partnering event. The Prize Administrator made short highlight videos about each participating attendee
- March 11, 2020: Phase II Partnering webinar
- April 20, 2020: Registration for Phase II closes, fourteen teams register their intent to participate.
- May 6, 2020: Phase II Concept Update deadline, requiring teams to provide a concept status update. The Prize Administrator then provided extensive feedback to inform the development of the validation plans and overall end-to-end solution
- July 6, 2020: Voucher Overview webinar
- July 22, 2020: Virtual Demo Day
- August 28, 2020: Statement of Work and CRADA webinar
- October 13, 2020: Phase II Online Submission Deadline.

Throughout the course of Phase II, NREL maintained the website and email account for the Prize, answering questions and providing updates, and provided support for ongoing outreach efforts including the coordination of an informational webinar. NREL further promoted Phase II through social media outreach through NREL and American Made Challenges social media properties; as well as articles posted to NREL.gov that were extended through NREL e-newsletters.

Results and Conclusions

Fourteen submissions were received for Phase II of the Lithium-Ion Battery Recycling Prize. These submissions furthered the development of the winning concepts from Phase I. Numerous teams went on to partner with other nonwinning Phase I applicants, as well as voucher service providers from the American-Made Challenge network.

Expert judges began their review of the Phase II Final Submissions in late September but did not complete their review until FY21.

Key Publications

- Phase II Lithium-Ion Battery Recycling Prize Rules
- Voucher Guidelines
- Phase II Rules webinar

- NAATBatt partnering postcard
- Partnering informational flyer
- Phase II Partnering webinar
- Voucher Overview webinar
- Statement of Work and CRADA webinar.

References

1. Stone, Maddie. “Most lithium batteries end up in a landfill. A new bill aims to change that.” Grist, March 17, 2020. https://grist.org/politics/most-lithium-batteries-end-up-in-a-landfill-a-new-bill-aims-to-change-that/

Acknowledgements

DOE Battery Recycling Prize Team:

- Connie Bezanson
- Samm Gillard
- Helena Khazdozian

NREL Battery Recycling Prize Team:

- Nick Langle
- Lauren Lynch
- Sandra Loi
- Rebecca Martineau
- Julie Sodano

I.3.C ReCell Advanced Battery Recycling Center (ANL)

Jeff Spangenberger, Principal Investigator
Advanced Materials Division
Argonne National Laboratory
9700 South Cass Avenue
Lemont, IL 60439
E-mail: jspangenberger@anl.gov

Samm Gillard, DOE Technology Development Manager
U.S. Department of Energy
E-mail: Samuel.Gillard@ee.doe.gov

Start Date: October 1, 2018 End Date: December 31, 2021
Project Funding: $5,065,000 DOE share: $5,065,000 Non-DOE share: $0

Project Introduction

The use of lithium-ion batteries has steeply risen in recent years, starting with electronics and expanding into many applications, including the growing electric vehicle (EV) and grid storage industries. But the technologies to optimize recycling of these batteries have not kept pace.

The launch of the ReCell Center, U.S. Department of Energy's (DOE) first advanced battery recycling center, will help the United States grow a globally-competitive recycling industry and reduce our reliance on foreign sources of battery materials.

Objectives

DOE sees an opportunity to economically recycle lithium-ion and future batteries and accelerate the growth of a profitable recycling market for spent EV, electronics, and stationary storage batteries. This can be done by developing novel recycling techniques to make lithium-ion recycling cost-effective by using less energy-intensive processing methods and capturing more metals and other high-value materials in forms that make reuse easier.

A profit-driven battery recycling infrastructure will help meet the Vehicle Technology Office's goal of lowering the cost of new batteries and increasing the use of domestic recycled battery materials.

Approach

ReCell is a collaboration of researchers from academia and national laboratories that are working together with industry to develop new recycling processes and battery designs that will enable greater material recovery at end of life. The most promising processes and designs will be demonstrated at pilot scale at the ReCell laboratory facilities based at Argonne. Validated processes and designs will be licensed to industry for commercialization.

The center collaborators will also use modeling and analysis tools to help industry determine how to optimize end of life battery value. Argonne's EverBatt model evaluates the techno-economic and environmental impacts of each stage of a battery's life, including recycling. NREL's LIBRA model provides a birds-eye view of the interconnections between raw material availability, primary manufacture, recycling, and demand.

Despite COVID-19, work in the ReCell laboratories has continued to press forward. As we conclude our second year, we remain on our scheduled path to demonstrate a complete direct recycling process in a small pilot-scale batch operation. In FY21, we expect to complete the scale-up of all the unit processes required to turn spent end-of-life cells into functional new cells. Figure I.3.C.1 below depicts the basic operations that need to be accomplished.

We are working to determine which of the multiple concepts being evaluated at bench-scale for each recycling process step will be the most viable to scale up. Relithiation is a key step in the direct recycling process, and ReCell currently has five potential techniques under investigation: solid state, hydrothermal, ionothermal, electrochemical, and redox mediated. In the next quarter, we will compare the effectiveness of each of these techniques to process end-of-life cathode materials. Each technique will have an identical sample to process, and the products will be compared to determine the optimum path forward for the relithiation work.

In the next quarter, we will undertake a project to demonstrate the feasibility of recycling manufacturing scrap. This represents an early point-of-entry for direct recycling. The benefits of recycling can be realized with many fewer steps than needed for end-of-life material recycling. The ReCell team will collect samples of different manufacturers' scrap and subject it to the processes required to feed the recycled material back into the cell fabrication process. Successful deployment of this concept could enable significant savings on the production of new cells.

As we move into the new quarter, look for ReCell to investigate fresh ideas to cost effectively recover additional materials from end-of-life batteries. We will also continue to improve the front-end processing of batteries to produce cleaner active electrode material, and we will work to combine processes for more efficient results. Lastly, ReCell will be working hard to demonstrate the capability to modernize older cathode chemistry so that it can find a ready market.

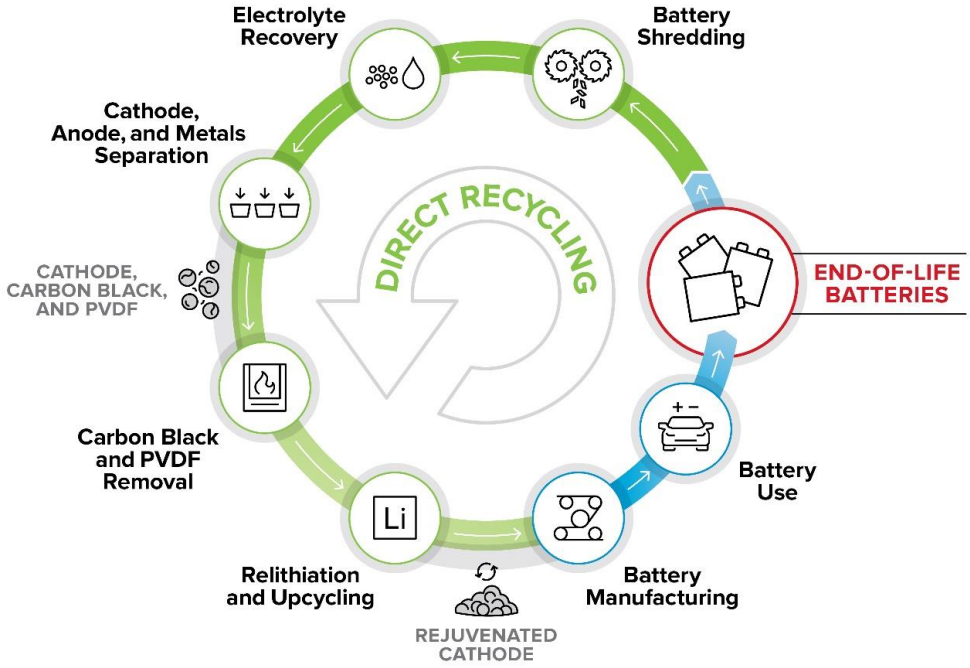

Figure I.3.C.1 Basic processing steps associated with direct recycling

Milestone FY20 Q4

The center's FY20 Q4 milestone was to demonstrate recovery of anode and cathode powders using the new pilot scale froth column.

Froth flotation has been previously shown to separate metal oxide cathodes from graphite utilizing a Denver cell with high separation efficiency. In order to scale up this method, a continuous process employing a froth column was needed. A three-inch diameter froth column was purchased from Eriez and then installed in the Materials Engineering Research Facility at Argonne National Laboratory. After installation, the first step in achieving separation of graphite from NMC111 was to determine the conditions under which graphite would

float with little-to-no graphite in the tailings. Figure I.3.C.2a shows a picture of the froth column with graphite being continuously added. Through simple visual inspection, nearly all the graphite was floated. The conditions shown in Table I.3.C.1 were then used to separate a mix of 1:1 graphite: NMC111 slurry. The resulting separation, after the initial experiments, had very poor purity of graphite in the froth (Figure I.3.C.2b) and high purity but low yield of NMC111 in the tailings (Figure I.3.C.2c).

Table I.3.C.1 Optimization of froth flotation column conditions.

Experiment	Frother (MIBC)	Collector (Kerosene)	Wash Water	Air Flow	Pump Feed Rate	Feed Solid Loading
1	300 ppm	30 ppm	0 Lpm	4 Lpm	10 rpm	5%
2	20 ppm	30 ppm	0.3 Lpm	4 Lpm	5 rpm	5%
3	10 ppm	0 ppm	1 Lpm	2 Lpm	5 rpm	5%
4	20 ppm + 2 ppm PPG400	10 ppm	1 Lpm	2 Lpm	5 rpm	5%

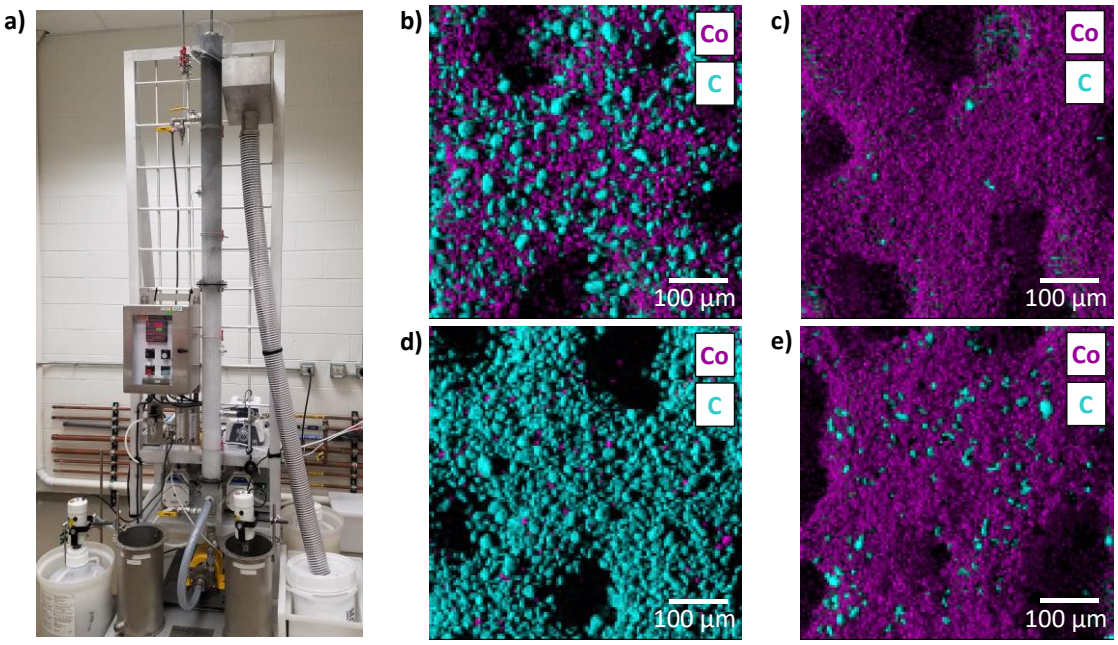

Figure I.3.C.2 a) Photograph of the froth column operating with pure graphite. EDX overlay maps for C and Co for the b) froth and c) tailings from experiment 2. EDX overlay maps for C and Co for the d) froth and e) tailings from experiment 4.

Conditions were then further optimized using pure NMC111 to determine how to get the NMC111 to sink in the column. It was determined that sufficient wash water, slower air sparging rate, and careful manipulation of frothing and collecting agents was needed to ensure that NMC111 would be pushed down the column to the tailings. The separation was then attempted again using the new conditions and this separation resulted in improved yields and purity of the froth. The resulting EDX maps are shown in Figure I.3.C.2d and Figure I.3.C.2e for the froth and tailings, respectively. The froth shows nearly pure graphite, while the tailings have more graphite than the previous conditions, which is expected due to the higher likelihood that graphite will be pushed down the column with the NMC111 under these conditions.

Several characterization methods were used to determine the purity of the froth and tailings after each optimized experiment. Analysis included inductively coupled plasma-mass spectrometry (ICP-MS), X-ray diffraction using Rietveld analysis, and thermogravimetric analysis (TGA). The results are summarized in Table I.3.C.2 and illustrated in Figure I.3.C.3. For later experiments, the increased use of wash water meant

that our 20 Liter tailings collection filled up faster, and multiple bottles ended up being required to contain the tailings output. We aimed to keep froth height consistent, around 6-8 inches, during each experiment. The parameters that were optimized for improved separation during each experiment included frother concentration, collector concentration, wash water flow, air flow, pump feed rate, and solids loading in the feed solution. The frother concentration affects the height of the froth at the top of the column, while the collector reacts with the surface of materials to increase the hydrophobicity, meaning that increased collector concentrations will lead to more material collected in the froth. Methyl isobutyl carbinol (MIBC) and kerosene were used as frother and collector agents, respectively.

Table I.3.C.2 Analysis of froth and tailings purity for each optimized experiment.

	ICP		XRD		TGA	
Sample	NMC (wt.%)	Graphite (wt.%)	NMC (wt.%)	Graphite (wt.%)	NMC (wt.%)	Graphite (wt.%)
Experiment 1						
Froth	47.7	52.3	61.8	38.2	*TBD*	*TBD*
Tailings	97.7	2.3	99.8	0.2	*TBD*	*TBD*
Experiment 2						
Froth	60.7	39.3	80.9	19.1	*TBD*	*TBD*
Tailings	97.1	2.9	100.1	-0.1	*TBD*	*TBD*
Experiment 3						
Froth	7.1	92.9	7.0	93.0	*TBD*	*TBD*
Tailings 1	56.9	43.1	65.9	34.1	*TBD*	*TBD*
Tailings 2	72.8	27.2	74.2	25.8	*TBD*	*TBD*
Tailings 3	68.8	31.2	73.1	26.9	*TBD*	*TBD*
Experiment 4						
Froth	2.0	98.0	2.2	97.8	2.2	97.8
Tailings 1	89.2	10.8	89.1	10.9	88.3	11.7
Tailings 2	88.5	11.5	89.6	10.4	86.9	14.0
Tailings 3	92.7	7.3	91.1	8.9	92.8	7.2

The characterization results in Table I.3.C.2 and Figure I.3.C.3 show the initial froth flotation conditions led to high purity tailings (e.g., >97%), however, much of the NMC cathode material was also stuck in the froth fraction leading to only about 50% purity. The experiment was optimized to include wash water, slow down feeding rate, and reduced the frothing agent, MIBC. These parameters were all targeted to help lower the entrainment of NMC in the froth to obtain higher purity graphite. The incorporation of a 0.3 Lpm wash water flow and reduced MIBC concentration improved the purity of the froth by 10%–20%, however, more optimization was still needed to reach over 90% graphite in the froth. A third experiment further increased wash water flow to 1.0 Lpm, reduced both frothing and collector reagents, and reduced air flow to 2 Lpm. Collectively, these process changes further lowered the amount material held up in the froth. This experiment showed increased purity of graphite in the froth, to over 90%, while decreasing the purity of the tailings to about 60%–70%. The last experiment gave us the highest purity of both froth and tailings. This experiment included adding a froth-stabilizing agent (i.e., polypropylene glycol as PPG400) and using a low collector concentration. Previous experiments illustrated that adding a higher concentration of kerosene as the collector

was efficient at sending graphite to the top of the column, but the material become so heavy that it would often collapse the froth; PPG400 helped us to overcome this issue. Improving the froth behavior allowed us to collect a froth with 98% graphite and tailings that contained over 90% NMC.

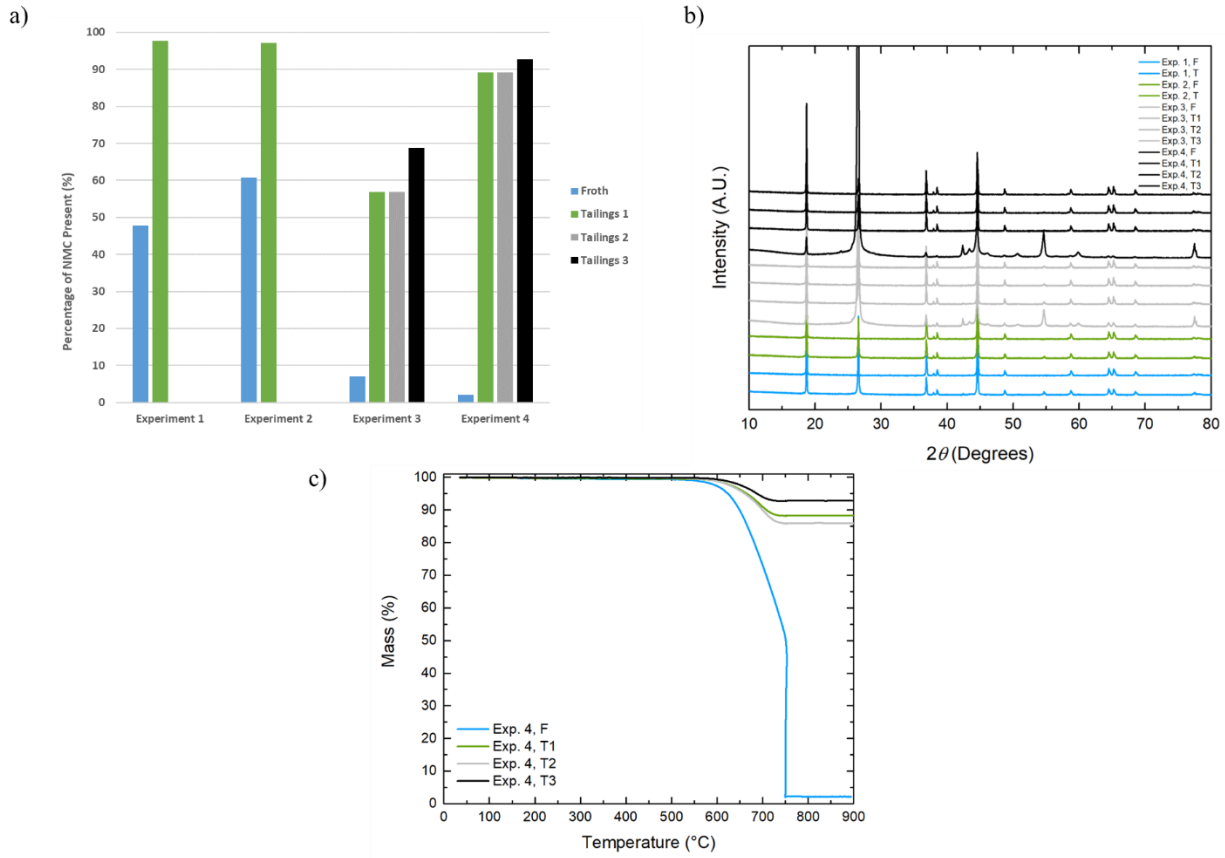

Figure I.3.C.3 a) Bar graph results estimated from ICP metals concentrations and b) XRD patterns of froth and tailings fractions for four optimized experiments. c) TGA curves of froth and tailings from experiment 4.

Next: Further optimize the froth flotation process to obtain anode and cathode materials with purities greater than 95%. Two recent froth experiments using adjusted kerosene concentration are under analysis. We will also be conducting froth flotation on black mass from Retriev to separate and collect graphite for other experiments.

Direct Cathode Recycling

In 2018, production of lithium-ion batteries (LIB) to meet the world's energy storage needs consumed over 50,000 tons of various transition metals and lithium salts. The consumption of these critical materials is at a scale that has significant impacts on the business models for materials and component suppliers, mining companies, and materials processers. This complex relationship can be seen in the production and supply of cobalt, where approximately 50% of the world's output is now used to make LIBs. This drives up prices, making more marginal sources viable for suppliers. The price of cobalt on the open market recently started showing supply and demand correlations. As a by-product of nickel and copper mining, increasing cobalt sourcing also effects the price of these metals. An alternative to increased mine output and exploration is to utilize recycled end-of-life LIBs as a source of feedstock for new low-cobalt compositions. We are exploring how to separate various types of cathode materials from each other, evaluating their end-of-life performance, and developing processes to, with minimal input, recover, rejuvenate, and reuse these materials. In this section we address the issue that at end of life, due to side reactions, salt precipitation, and corrosion, the amount of useable lithium within the cathode structure is typically about 15%–20% below the initial formulation, e.g.,

$Li_{0.8}(Ni_{0.33}Mn_{0.33}Co_{0.33})O_2$. This loss of active lithium is seen as capacity fade and loss of performance. Within Direct Recycling, there are five efforts focused on cathode separation and isolation processes (froth flotation, magnetic separation, cathode upcycling, electrode binder removal, impurity incorporation into the cathode). There are also four pathways that address relithiation of the recovered cathode (chemical relithiation, electrochemical relithiation, ionothermal relithiation, and hydrothermal relithiation). We will evaluated these in terms of relithiation extent, relithiation rate, and eventually by process cost (with Q. Dai, EverBatt Model).

Recovery of Other Materials

A lithium-ion cell is a complex device that contains a number of valuable materials. Although cathode active materials recovery is the main focus of the program, recovery of other materials is also important and offers additional benefits. For the purpose of the project, "other materials" are defined as electrolyte components, anode materials, and metals from current collectors.

It is important to design all down-stream processing and material recovery sequences in a way that preserves integrity and assures high salvage rate and quality of all recovered materials.

Cell disassembly and size reduction is the critical first step in LIB recycling. This a new ReCell project in FY 2020. We plan to investigate non-aqueous shredding methods that will preserve materials to be recovered later in the recycling process. Safety of the process needs to be the top priority. It is also important to explore the effects of size and size distribution of shredded materials on separation efficiency. A shredder will be purchased in FY 2020 to begin shredding cells at Argonne National Laboratory. In the future, battery material shredded at Argonne can be used as a baseline material for the ReCell Center.

Graphite and lithium compounds (electrolyte salt) are the two high-value materials that are present in cells besides cathode active material. These materials are defined as critical due to their limited supply or their geographical location. By recovering these materials, we will be securing a domestic source of these materials, therefore reducing our foreign dependence and increasing our national security.

In FY 2020, anode/cathode separation efforts in the ReCell Center focused on separating the anode and cathode shreds while the films of active materials are still attached to copper and aluminum foils, respectively. This would reduce black mass complexity and simplify separation processes further downstream. Ideally, the size-reduced cell components would be processed to remove electrolyte components, followed by dry separation techniques, with the most reasonable option being continuous eddy current separation. The most effective anode/cathode separation technique from FY 2019 and 2020 will be chosen and combined with processes for recovering other materials to determine which processes can be easily integrated into a battery recycling model and to identify areas for improvement.

Metals, particularly copper recovered from current collector, provide an additional revenue. By recovering additional materials, the recycling process maximizes the reuse of lithium-ion cell components and therefore tightens the closed loop, driving the overall process to profitability. In addition, costs to dispose of waste are avoided.

Design for Recycle

Millions of batteries are approaching their end of life and need to be recycled. While many efforts have been focused on recycling the elements and/or compounds from spent cells through various techniques, this project aims to create cell designs that will enable rejuvenation of a spent cell, and/or improve the ease of recycling at the end of life. The ability to regenerate a cell with an electrolyte flush/rejuvenation and restoration of lithium inventory has the potential to extend the life of a lithium-ion battery far beyond its nominal 10-year life. This will reduce the number of packs requiring recycling and/or make for easier target material extraction.

Modeling and Analysis

The modeling and analysis focus area is fundamentally different from the other three areas, which perform laboratory experiments to develop recycling processes to separate, recover, and upgrade materials from spent

batteries. Technical success is not the only hurdle ReCell processes must overcome; processes must also be economically viable, environmentally benign, and avoid exacerbating any material supply constraints. The projects in this focus area evaluate and compare processes developed in the experimental focus areas to make sure that only those that satisfy all of the required conditions are further developed and scaled up. The EverBatt model examines energy and environmental implications, as well as economics, of individual processes and the entire battery lifecycle, to identify the most promising process options. The LIBRA model places battery material supply and demand in a global context.

Results

Binder Removal via Thermal Processing

Once cathode materials are separated to be recycled, the poly(vinylidene difluoride) (PVDF) binder needs to be removed to allow for further processing. This can be done using a large quantity of n-methyl-2-pyrrolidone (NMP), but this is not cost effective for battery recycling. As an alternative to solvent-based methods, thermal decomposition can be used to eliminate the binder. This has the advantage of producing no liquid waste, and can be performed at temperatures as low as 500oC. Last year, we demonstrated processes to remove binder from both pristine materials that would be similar to manufacturing scrap, as well as delithiated materials similar to what would be found after cycling. The key to these processes is slow ramping of the temperature plus the addition of a small amount of excess lithium to prevent lithium removal from the bulk of the materials. In FY20, this project focuses on the difficulties in process scale-up, as well as testing with real materials.

Scaling up the thermal binder removal process requires better mixing than a static furnace can provide. Rotary kilns may be an option to provide the improved mixing of air and particles inexpensively. We began testing rotary kilns, in collaboration with Hazen Research, this quarter. Figure I.3.C.4 shows the resulting electrochemistry after binder removal for NMC111 black mass that has 3 wt.% PVDF and 5 wt.% carbon black. The rotary kiln used either 100 g or 200 g batch size, and the data are compared to 5 g of material in a box furnace. Both with and without added LiOH·H2O, the rotary kiln has similar initial performance to the box furnace, despite the increase of scale to 100 g or 200 g. This is a strong indication that rotary kilns will not suffer from the same scaling issues that we saw with box furnaces. However, the rotary kiln samples with added LiOH·H2O do show faster capacity fading than the box furnace sample. The rotary kiln used for these experiments utilized a quartz tube, which transferred a small quantity of one of a variety of possible silicon compounds to the cathode material. This subtle doping or impurity inclusion may be the cause of the additional capacity fade. Whatever the cause, there is clearly a need for further optimization of the process.

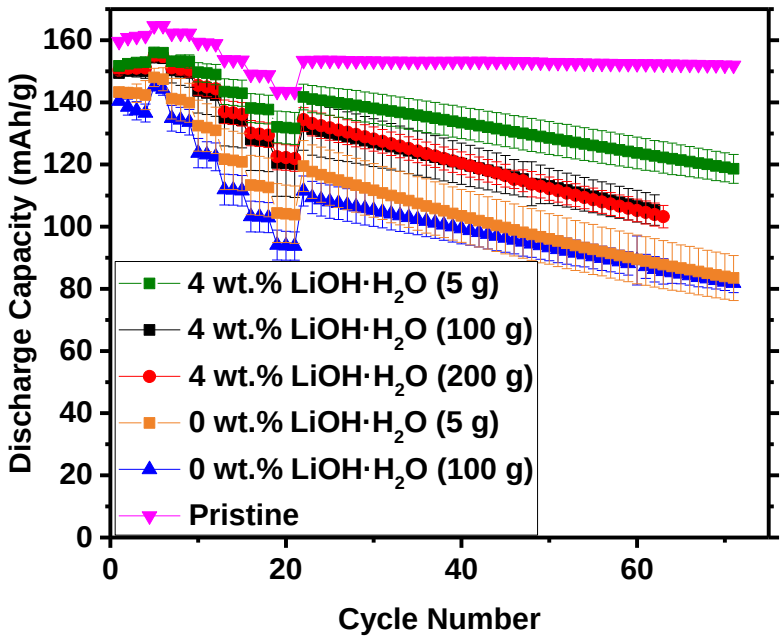

Figure I.3.C.4 Electrochemical cycling of NMC111 black mass after binder removal at 500°C in air using either a box furnace (5 g batches) or a rotary kiln (100 g/200 g batches).

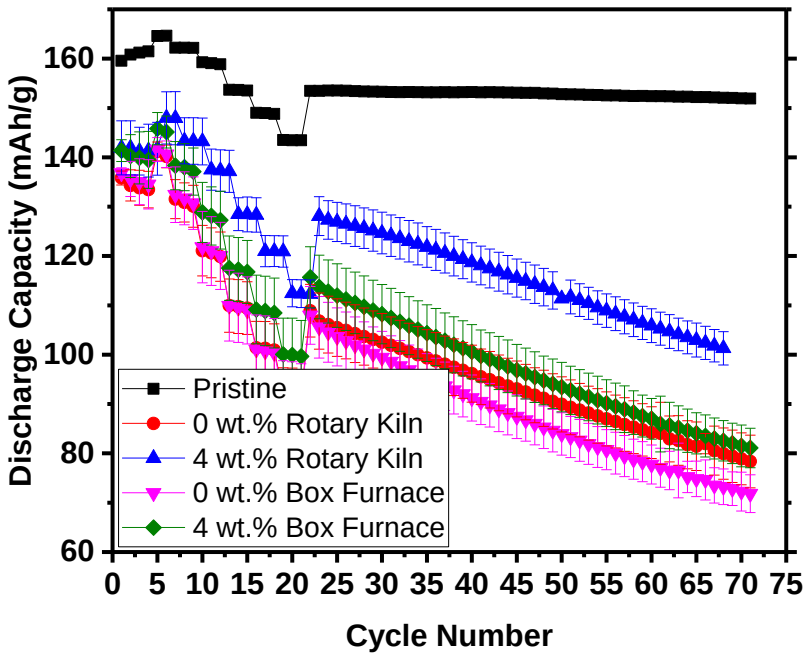

Figure I.3.C.5 Electrochemical cycling of NMC111 electrodes after binder removal at 500°C in air using either a box furnace or a rotary kiln with different quantities of LiOH·H2O added.

In addition to looking at the binder removal from delaminated black mass, we were interested in determining if rotary kilns could directly delaminate the material from the electrodes. A 500°C heat treatment in the rotary kiln was determined to remove the cathode from the Al foil. In a box furnace, the material remains loosely attached

to the foil and can easily be separated via vibratory sieving. Adding $LiOH \cdot H_2O$ in the box furnace causes only a minimal improvement, but caused a substantial improvement in the rotary kiln. This is presumably caused by the improved mixing while the material is being delaminated with the $LiOH \cdot H_2O$. However, the performance of the material from this one-step process is inferior to that from binder removal on the already-delaminated material.

Binder Removal via Soxhlet Extraction

This project will evaluate the Soxhlet extraction method to remove the polymer binder (e.g., PVDF) from EoL (End-of-Life) battery cathodes. The electrodes in Li-ion batteries use polymer binders to hold active materials and conductive carbon additives to foils. However, it is necessary to remove and/or separate the polymer binder to recycle cathode materials such as LCO and NMC. In the ReCell center, thermal decomposition of PVDF has been studied as an option, but a solution method may be better. The previous method to dissolve PVDF involves a large amount of toxic and high-boiling-point solvents (e.g., NMP), causing toxic waste, so it cannot be considered as a feasible way to remove PVDF. It is necessary to minimize the use of organic solvent and the resultant environmental impact. In the Soxhlet method, samples are repeatedly extracted with solvent, which is regenerated by distillation through a periodic siphoning process. Therefore, a minimal amount of solvent is required, and fresh solvent is repeatedly fed via distillation into the sample container. The process is suitable for scale-up to industrial scale. In FY20, this project will test the Soxhlet extraction method for PVDF removal.

In the fourth quarter, we tested a cryovap (vacuum transfer) solvent transfer method to recover PVDF and solvent from a PVDF binder solution. In the previous quarter, we examined a conventional rotovap (rotary evaporator) technique to evaporate solvent Y, but its high boiling point (b.p.) and insufficient vacuum strength made it difficult to recover the solvent from the solution. To address this issue, we moved to a lower b.p. solvent for PVDF, namely dimethylformamide (DMF). DMF is a good PVDF solvent and has a b.p. of 152~154 ^oC, producing a clear advantage for the solvent recovery process. Other well-known PVDF solvents are NMP and DMSO, which boil at 202~204^oC and 189^oC, respectively.

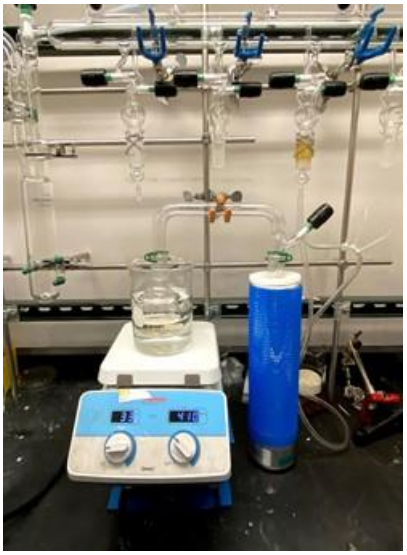

Figure I.3.C.6 PVDF binder and solvent recovery apparatus

Figure I.3.C.6 shows a cryovap solvent transfer apparatus. A flask filled with PVDF solution is located in a water bath and connected to a solvent transfer manifold. The manifold is connected to a liquid nitrogen solvent trap to collect solvent, and also connected to a Schlenk line to evacuate the whole apparatus. The starting solution in the flask includes 5 wt.% PVDF. We chose a dynamic (rather than static) vacuum by leaving the

vacuum valve open to minimize total process time. After the temperature reached ~50oC, the solvent transfer rate was sufficient, and the transfer reaction was finished within 1 hour.

Figure I.3.C.7 shows the recovered PVDF and DMF solvent. The PVDF becomes a thin membrane with a balloon shape, owing to continuous stirring and evacuation. The recovered PVDF will require testing as an electrode binder. Next, the volume of recovered DMF solvent was measured. The apparent volume recovery is ~93%, but is probably higher due to a small loss during PVDF solution transfer from a storage jar to the solvent transfer flask. Future work involves testing the process with different PVDF concentrations and water bath temperatures. Preliminary work indicates that this process may enable a near closed-loop solvent reuse system, and the recovered PVDF may be reusable in the electrode manufacturing process.

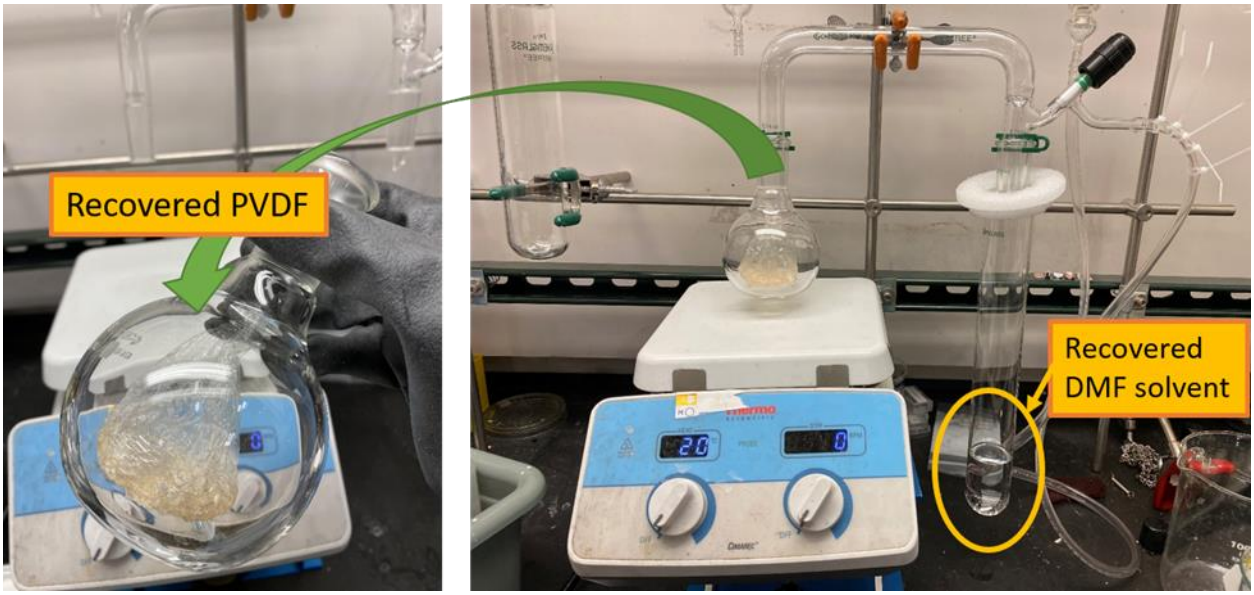

Figure I.3.C.7 Recovered PVDF and DMF solvent.

Cathode/Cathode Separation Process Development

Most direct recycling operations involve the collection of "black mass," which is a mixture of anode and cathode powders recovered from shredded cells. Even if cells are presorted before processing, it is still likely that some mixing of cathode materials will occur. Additionally, some cells contain mixtures of different cathode materials, such as lithium manganese oxide (LMO) and lithium nickel manganese cobalt oxide (NMC). While the LMO is unlikely to be reused, the NMC could be used in a modern cell. Direct recycling of lithium-ion batteries will require the ability to effectively separate different cathode chemistries. This work will focus on separation of complex mixtures of virgin cathode powders, as well as those recovered from actual cells. The ability to separate these materials based on differences in magnetic properties will be studied using various techniques.

Wet magnetic separation experiments were conducted in collaboration with RSR Corporation (Dallas, TX) on lab-created binary and ternary mixtures. Cathode mixtures were added to water to create 5% solid loading slurries. Experiments were conducted at a range of magnetic field strengths from 1-3 Tesla. Experiments were conducted and samples were taken of the material at each stage. The slurry was passed through the separator and the magnetic and non-magnetic fractions were retained. Each separated fraction was recovered and then passed through the separator again. High purity fractions were generally recovered after recycling the magnetic fraction three times. As an initial test a 50/50 mixture of LMO and NMC111 (see Figure I.3.C.8) was separated at several different field strengths to help determine baseline operating conditions. The initial separation occurred at one Tesla and the magnetic fraction that was recovered was recycled through the separator three times. This resulted in a high purity fraction with a concentration of 97% LMO. The non-magnetic fraction

which contained the bulk of the material initially passed through the separator was then passed through the separator at two Tesla. After three recycles this resulted in a fraction with a concentration of 82% LMO. This falls in line with expectations since the increase field strength renders the separator less selective for LMO. Again, the non-magnetic fraction resulting from the separation of the previous non-magnetic fraction was passed through the separator at three Tesla. This resulted in very low separation efficiency. This can be attributed to several factors the most prevalent being the high field strength. The second reason is the small amount of LMO that was left in the mixture after repeated separation steps, which is known to have some effect at lower field strengths, but is probably negligible at the highest field strengths.

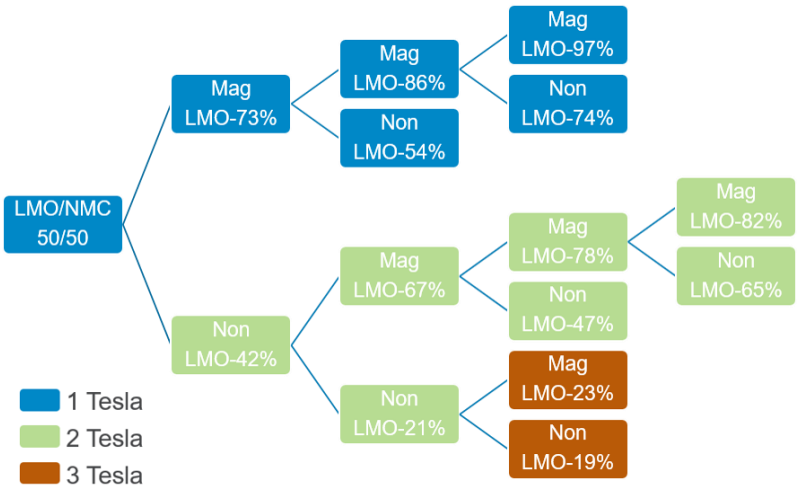

Figure I.3.C.8. Baseline separation of LMO/NMC mixture.

Tests of ternary mixtures of LMO/NMC/NCA were conducted at field strengths between one and three Tesla. The best separation of LMO occurred at 1 Tesla. As the magnetic field strength was increased to two Tesla, the proportion of NMC in the magnetic fraction increased, while NCA was marginally increased to 2%. NCA was absent from the magnetic fraction until the field strength was increased to three Tesla.

Separations of the ternary mixture at 2 Tesla were conducted under the same conditions. The additional field strength prevented highly selective separations, as shown in Figure I.3.C.8. In the case of industrial separation of complex mixtures, it may be beneficial to separate the mixture into 2 less complex mixtures. Conditions could be tailored to remove all the LMO and LFP from a mixture in a single pass. This LMO LFP fraction would certainly have other components in it, but in much smaller quantities. This would leave the higher-value cobalt and nickel cathodes in a fraction relatively free of the more magnetic and less valuable cathode chemistries.

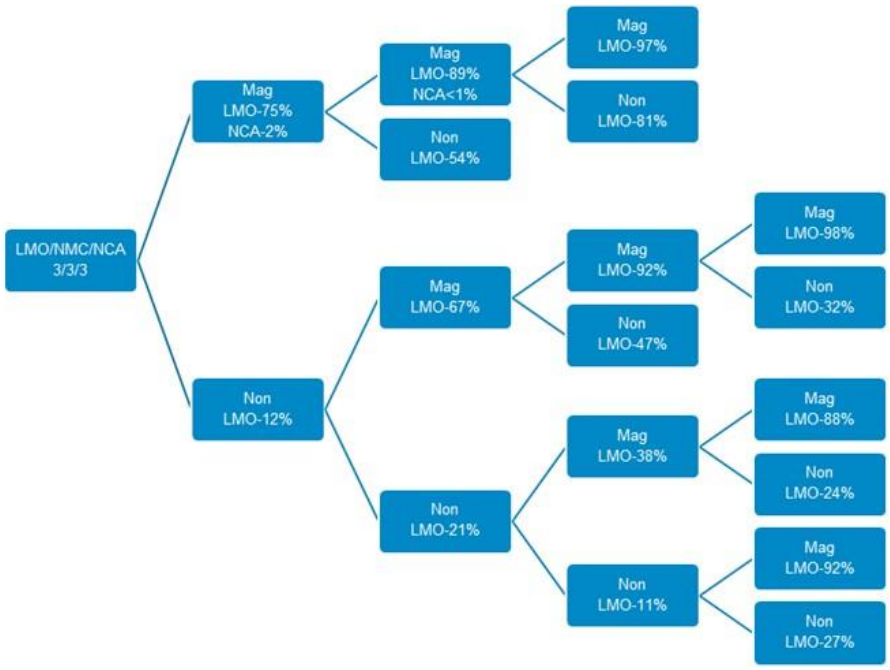

Figure I.3.C.9 Separation tree for a mixture of LMO, NMC111 and NCA separated at 1 Tesla.

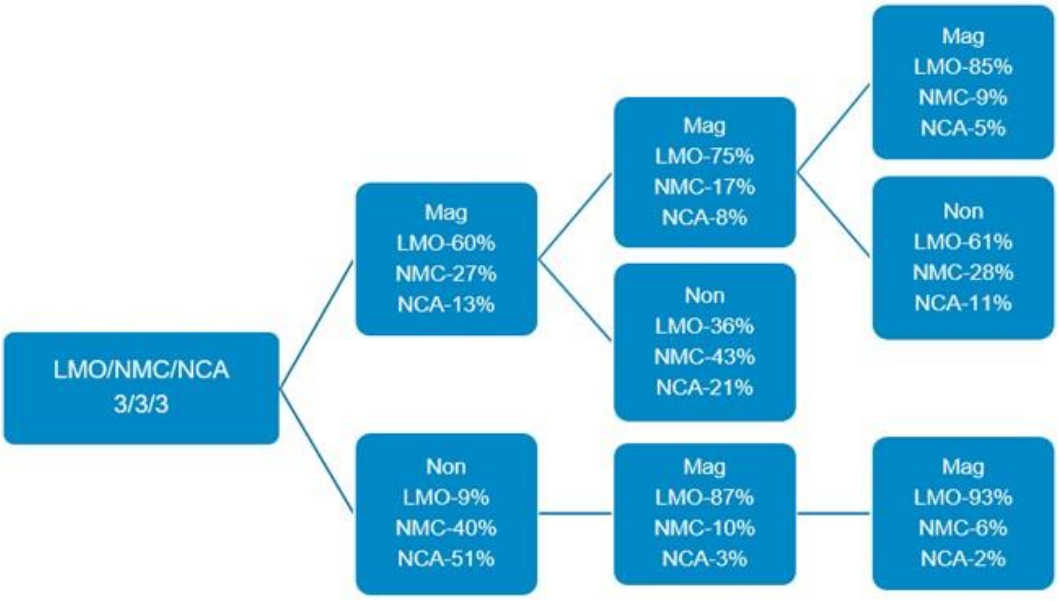

Figure I.3.C.10 Ternary mixture of LMO/NMC/NCA separated at 2 Tesla.

Cathode-Cathode Separation via Froth Flotation

Li-ion batteries may use more than one type of cathode active material in a given design, and different manufacturers use different cathode chemistries. Unlike other recycling processes, direct recycling requires single battery chemistries or compatible chemistries to produce a viable product. It is desirable to separate different types of cathode active materials prior to the follow-up relithiation and repairing processes. In FY19, we investigated the separation of a binary mixture of cathode active materials using the froth flotation process. Promising preliminary results were obtained with a number of binary mixtures; we demonstrated that we can recover 90% of cathode active materials with a grade of above 90%. In FY20, we will investigate 1) separation

of different cathode active materials from ternary and quaternary mixtures, 2) separation of cathode active materials from binder-carbon-cathode mixtures, and 3) methods to remove surface species after the froth flotation process.

Black mass is composed of a mixture of anode materials (graphite), cathode materials (a lithium metal oxide), and other battery cell components, such as PVDF binders and the conductive additive carbon black. In previous quarters, we showed that froth flotation is effective in separating anode and cathode active materials. However, the presence of PVDF binder and carbon black in cathode composites results in a loss of cathode materials during the recycling process. In this quarter, we report on a thermal pyrolysis method as a way to effectively decompose adhering PVDF binder and carbon black in the isolated materials. Our hypothesis is that anode materials remain hydrophobic, while cathode active materials become hydrophilic during the thermal pyrolysis process. As a consequence, a good separation between anode and cathode materials can be then achieved. Another objective of this study is to evaluate how the thermal pyrolysis process impacts the structure and surface chemistry of active materials.

Figure I.3.C.11 shows froth flotation results for separating a) a binary mixture of NCM111 and LMO and b) a binary mixture of NCA and LMO. We compared the results of individual materials' floatability with floatability of individual materials in a binary mixture. This data set was obtained using a 1L Denver cell. The results show that for individual materials, the recovery of cathode materials increases with increasing collector dosages. At 300 ppm dosage or above, 100% of pristine NMC111 was recovered in the froth product, while 87% of pristine LMO material was recovered in the froth product. When both cathode materials were mixed in DI water, the floatability behavior of individual cathode materials changed. As shown, at 333 ppm dosage, 100% of NMC111 was recovered, while only 8% of LMO was recovered in the froth product. The result clearly suggests that a good separation between NMC111 and LMO was achieved by the froth flotation process. It seems that there is a competitive adsorption mechanism involved between collector molecules and different cathode active materials. Surfaces of pristine NMC111 are more attractive to collector molecules. Even better results were obtained with NCA and LMO than those with NMC111 and LMO. At 300 ppm dosage, 98% of NCA was floated, and only 2% of the LMO was floated in the froth product.

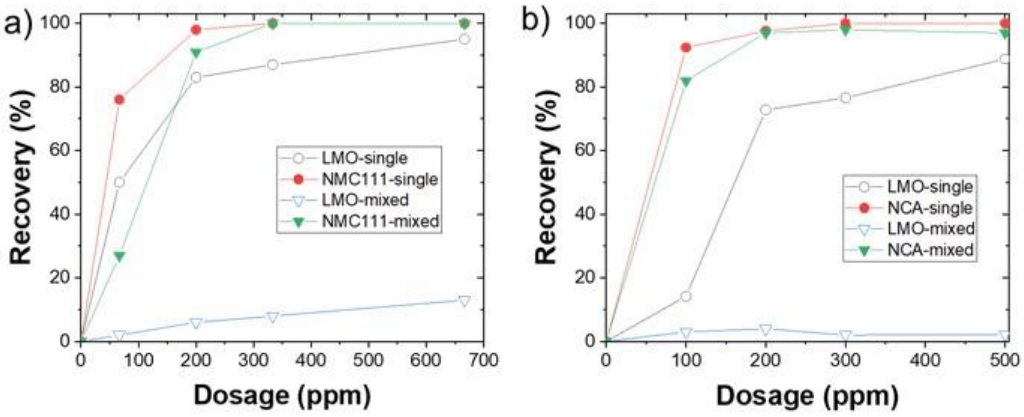

Figure I.3.C.11 a) Results of froth flotation separation between NMC111 and LMO at different collector dosages; b) Results of froth flotation separation between NCA and LMO at different collector dosages.

Figure I.3.C.12 shows the separation results for a binary mixture of pristine NMC111 and LMO. The feed was separated by a one-stage froth flotation process into two streams, i.e. a froth product and a tailing product. Individual data points labeled with 1-7 (Figure I.3.C.12a) were obtained at different collector dosages. As shown, at an optimized collector dosage, a product with 84% purity of NMC111 at a 93% recovery was obtained after a one-stage flotation experiment. The optimum collector dosage was used in the follow-up multi-stage flotation experiments. Figure I.3.C.12b shows the flotation result between NMC111 and LMO at different solid concentrations. The results were obtained after two stages of froth flotation experiments. Two-

stage separation yields a product with higher purity than one-stage (i.e., 95% or above) at a recovery of 90% or above. Both purity and grade of the separated products can be further improved through circuit design and reagent optimization. Even better separation results were obtained with a binary mixture of NCA and LMO.

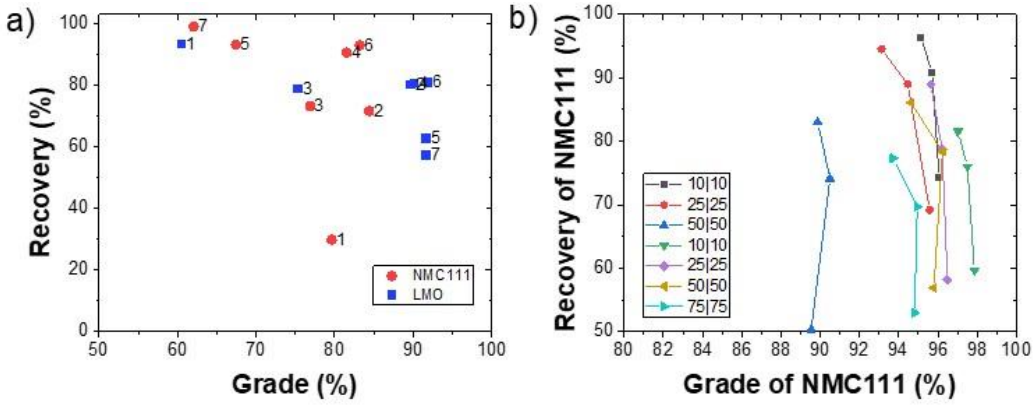

Figure I.3.C.12 a) Separation performance of a binary mixture of NMC111 and LMO at different collector dosages, and b) Recovery vs. grade of NMC111 in the froth products with different quantities of feeds.

Table I.3.C.3 shows chemical compositions as well as initial electrochemistry data of four samples. Sample 1 consisted of 98.7% NCA with 1.3% LMO, while Sample 2 consisted of 0.9% NCA and 99.1% LMO. These two samples were separated from a binary NCA/LMO mixture (1:1 by weight). The electrochemistry data show that the initial cycling capacity of recycled NCA was worse than that of pristine NCA, despite its high purity (i.e., 99%). The poor cycling capacity of NCA was due to a degradation of pristine NCA during the water-based froth flotation process. On the contrary, there was very little degradation for the recycled LMO. Samples 3 and 4 are the separated samples from a binary mixture of pristine NCA and NMC111. Sample 3 was the froth product consisting of 98.6% of NCA, while Sample 4 is a tailing product consisting of 97% purity NMC111. The electrochemical result again showed that the cycling capacity of the recycled NCA was much interior to that of pristine NCA. The MTU team is currently investigating strategies to mitigate the electrochemistry degradation issue for high-nickel cathode materials.

Table I.3.C.3 Electrochemical performance of separated cathodes materials from a binary mixture of pristine cathode materials.

Samples	Elemental Composition (ICP data)					Composition		Initial cycling capacity (mAh/g)	
	Al	Co	Li	Mn	Ni	NCA	LMO	Recycled	Pristine
R-LP2-1	0.04243	0.14995	0.96908	0.01349	0.79413	98.7%	1.3%	143	191
R-LP2-2	0.00259	0.00139	0.46507	0.98926	0.00675	0.9%	99.1%	118	120
	Al	Co	Li	Mn	Ni	NCA	NMC111	Recycled	Pristine
R-LP2-5	0.04299	0.15622	0.97344	0.00691	0.79387	98.6%	1.4%	161	191
R-LP2-6	0.00162	0.32982	1.03962	0.33243	0.33612	3.0%	97.0%	158	160

Figure I.3.C.13 compares the cycling performance of pristine, washed, and recycled NMC111. The washed sample was obtained by mixing a pristine NMC111 sample in DI water at a 2% solid concentration twice. The slurry was dried by vacuum filtration, and further dried in an oven overnight at 105oC. Both the pristine and washed NMC111 have very similar initial performance; however, starting at 30 cycles, the washed sample exhibited a slightly higher capacity fade. This result is consistent with the previous finding [1]. The recycled

NMC111 sample was obtained from a binary mixture of NMC111 and LMO (1:1 by weight) after a froth flotation process. The flotation separation was conducted at a 20% solid concentration. The final froth product consisted of approximately 92% NMC111 and 8% of LMO. The cycling performance of recycled NMC111 was about 91%–93% that of pristine NMC111. This was mainly attributed to the presence of LMO in the recycled product. Note that the capacity fading curve for the recycled NMC111 was very similar to that of pristine NMC111, suggesting that separation of NMC111 and LMO in a high-solid slurry preserves the original electrochemistry of the cathode materials.

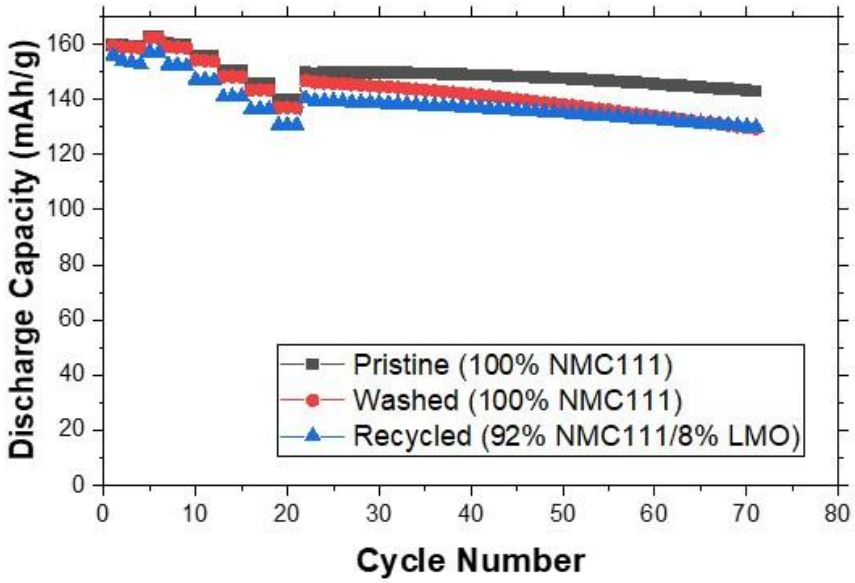

Figure I.3.C.13 Electrochemical cycling of pristine, washed NMC111, and recycled NMC111 from a binary NMC111/LMO mixture.

Chemical Relithiation of NMC Cathodes

Lithium-ion cells made using a recycled cathode are limited in the amount of active lithium they have available to the amount present at initial cell construction. Performance degradation for energy storage materials results from the gradual cycle-to-cycle loss of active lithium from the system by SEI formation, corrosion, and electronic isolation of particles, with the active lithium being irreversibly trapped in a variety of forms that diminish long-term battery performance. On cycling, the amount of lithium trapped and rendered inactive increases at a slow rate (after losses involved in the initial break-in cycling), gradually decreasing the cell's capacity until performance is noticeably affected or the commonly used 80% of initial capacity value is reached. The 80% value (stoichiometry: Li0.8(NiMnCo)O2) is associated with rises in impedance, loss of stability, and a decrease in capacity in the standard window (lifetime). The material's structure is a lithium-deficient version of the starting materials, although some further structural changes can be related to the temperature of operation, initial stoichiometry, or processing conditions. Typical structural changes include site mixing of lithium and nickel (due to similar size), oxygen loss, or degradation of the surface layers to similar (but electrochemically less desirable) materials, including various defect spinel or rock-salt structures. In this section we are establishing the conditions required to convert a lithium-deficient NMC cathode material back to a stoichiometric material using chemical relithiation by low- to mid- (< 400 ◦C) temperature annealing in the presence of a lithium source and O2-containing atmosphere. Relithiated materials will be characterized and studied for electrochemical activity, extent of anti-site mixing, and sample purity. Data and insights will be provided to the EverBatt team led by Qiang Dai (ANL) and modeled for cost and performance metrics.

In previous quarters we evaluated and devised coating methods for the relithiation process in accordance with guidance and cost estimates from the EverBatt model. The amount of ethanol used during the mixing step between the delithiated NMC and LiOH• H2O was reduced by a factor of 10 in the scaled up relithiation

process, reducing the cost per kg of recycled cathode from $23.76 to $8.81. Estimates for the complete removal of ethanol from reagent costs further reduced the recycled cathode cost to $6.95/kg. These estimates accounted for the potential need for mechanical mixing at large scale. However, initial tests of solvent-free chemical relithiation were done by hand mixing at low scale.

The investigation of a solvent-free approach to relithiation was performed at a scale of 1.5 g NMC. The delithiated NMC was mixed thoroughly with LiOH• H2O by grinding with a mortar and pestle. The combined solid was processed using both the single (650°C, 8 hours) and the two-step heating method (350°C, 4 hours followed by 650°C, 4 hours). The elemental analysis using GDOES (Table I.3.C.4) shows similar lithium contents to the previous relithiation reactions using ethanol to coat LiOH onto the delithiated NMC.

Table I.3.C.4 Elemental composition for solvent-free relithiation products measured using GDOES

Temperature (°C)	[Li]	[Ni]	[Mn]	[Co]
650	1.03	0.32	0.36	0.32
350/650	1.07	0.32	0.36	0.32

Initial half-cell tests with this material showed lower-than-theoretical capacity, though the capacity did remain stable after 4 cycles. Compared to the ethanol solution mixture, the use of the mortar and pestle could give an inferior distribution of the lithium source to the NMC particles, and the heterogeneity may require more grinding time to get a better distribution. Analysis by microscopy may indicate whether this method has resulted in notable morphological changes from the previous relithiated powders. Alternative mixing methods are being considered, notably a High Energy Ball Mill (HEBM) or an Eiger Mill.

Table I.3.C.5 Half-cell formation data for relithiated NMC (solvent-free process)

Cycle no	Charge Capacity (mAh/g)	Discharge Capacity (mAh/g)
1	165.4	134.4
2	135.7	133.8
3	135.0	133.8
4	134.7	133.7

Direct Regeneration of NMC Cathodes through Ionothermal Lithiation

This project will develop a cost-effective ionothermal lithiation process using ionic liquids (ILs) to relithiate and/or upgrade spent cathodes at ambient pressure and low temperature. ILs are a family of non-conventional molten salts that offer many advantages, such as negligible vapor pressures, negligible flammability, wide liquidus ranges, good thermal stability, and much synthesis flexibility. The unique solvation environment of these ionic liquids provides new reaction or reactive flux media for controlling the formation of solid-state materials with minimum perturbation of morphologies.1 In addition, ILs can be readily recycled and reused after the ionothermal lithiation. In year 2 of this project, we will scale up and optimize the ionothermal process, and we will continue the cost evaluation with ANL's EverBatt.

During FY20Q4, we continued our work on reducing the amount of ionic liquid required in an ionothermal reaction, since IL is the major cost factor (according to EverBatt). In these studies, the amount of IL has been reduced from initial 75 g to 25 g added to a consistent 25 g of delithiated materials (D-NMC). Scaling to 50 g was successfully achieved. The detailed experimental results are summarized in Table I.3.C.6.

Table I.3.C.6 Results of large-scale ionothermal experiments using LiBr as lithium precursor in [C2mim][NTf2]

Ionic liquid/Delithiated NMC111 ratio	Lithiated reagent	Temp. (°C)	Black powder recovered (%)	IL recovered (%) and color	TGA (%)	TGA (%) after 600°C 6 h
75g IL: 25g D-NMC	LiBr, 244-1	150	98.9	88.9, green	97.25	99.36*
50g IL: 25g D-NMC	LiBr, 247-3	150	98.4	82.5, green	98.01	99.38
25g IL: 25g D-NMC	LiBr, 247-4	150	98.4	64.5, green	98.40	99.58
50g IL: 50g D-NMC	LiBr, 247-5	150	99.1	67.1, green	98.79	99.31

From data in Table I.3.C.6 and Figure I.3.C.14, we can conclude that the reduced amount of [C2mim][NTf2] used under these experiment conditions does not affect the relithiation of the materials, although the amount of IL recovered decreased from ~90% to 65%. Thermal stability of relithiated materials can reach as high as ~99.5% when [C2mim][NTf2] was used as reaction medium and the Li ratio is ~1.03 (Table I.3.C.6). Further optimization investigations with LiBr in this IL and experimental conditions will be conducted in next quarter.

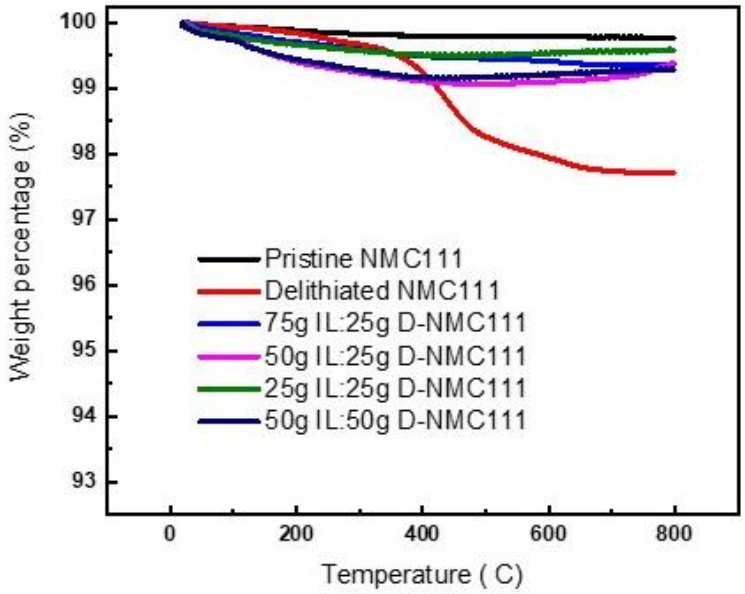

Figure I.3.C.14 Comparison of TGA plots of large scale ionothermal reactions in [C2mim][NTf2]

During FY20Q4, experimental scale up reactions were performed at the 25g scale (and once at 50 g) with LiBr in [C2mim][NTf2]. TGA and XRD indicated that the initial relithiation results are promising. TGA data of these relithiated samples showed the expected enhanced thermal stability of ~99.5% over the D-NMC (97.84%), see Figure I.3.C.14. The XRD pattern (Figure I.3.C.15), is consistent with relithiation as the peak splitting between (108) and (110) narrowed from 1.05 to 0.75 degree after ionothermal process.

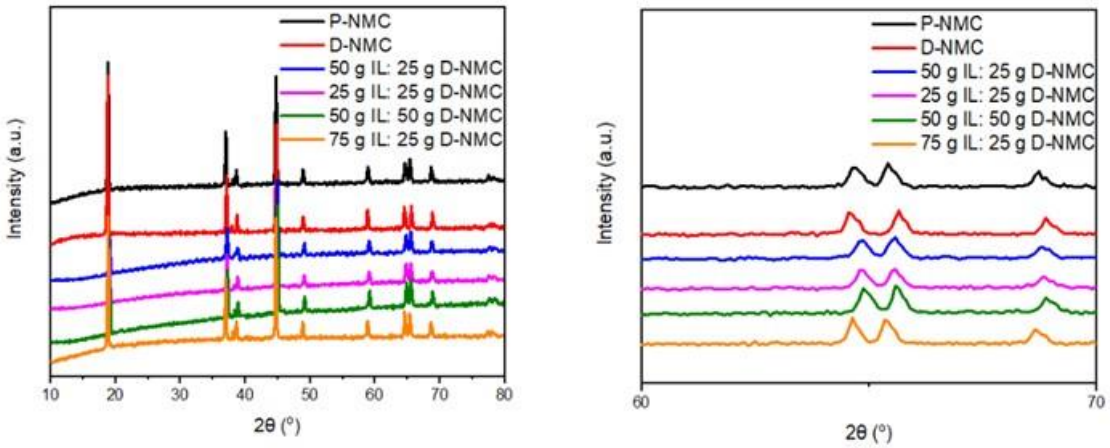

Figure I.3.C.15 XRD patterns for P-NMC, D-NMC, R-NCM from four different large-scale experiments

Elemental analysis of these samples was performed using inductively coupled-plasma optical emission spectroscopy (ICP-OES). Results are summarized in Table I.3.C.7. Besides a consistent Ni:Mn:Co ratio in either P-NMC and D-NMC, the Li mole ratio was restored going from 0.96 to ~1.03.

Table I.3.C.7 ICP-OES results for R-NCM large-scale experiments

Sample ID/IL:D-NMC ratio	Mole ratio				
	Li	Ni	Co	Mn	Al
P-NMC	1.09054	0.33098	0.33534	0.33368	--
D-NMC	0.96306	0.33202	0.33386	0.33412	--
75.2 g : 25.3 g 244-1a	1.021	0.337	0.332	0.331	
50.2 g : 25.1 g 247-3a	1.03608	0.33295	0.33447	0.33258	--
25.1 g : 25.1 g 247-4a	1.04584	0.33111	0.33506	0.33383	--
50.2 g : 50.2 g 247-5a	1.03905	0.33408	0.3341	0.33182	--

The electrochemical performance for these larger-scale materials was evaluated in a half-cell configuration. As summarized in Table I.3.C.8, the 2nd charge and discharge capacities are also very high with a similar coulombic efficiency as the pristine sample. It is worth mentioning that half-cell configuration was utilized for evaluating electrochemical performance, which is not accurate because electrochemical relithiation always occurred during the discharge processes for half-cell test due to abundant lithium in the lithium foil anode. Electrochemical relithiation is a useful approach for direct cathode regeneration. As shown in Figure I.3.C.16, the large-scale relithiated materials show similar charge capacity to that of pristine sample, with negligible differences in the discharge curves, suggesting the lithium was restored from the lithium foil. After the 1st cycle, there are no differences in the 2nd charge-discharge curves for delithiated and pristine, but much lower for relithiated samples. Full cells pairing these samples with a graphite anode will be tested in the next quarter using a more lithium-limited testing regime.

Table I.3.C.8 Summary of electrochemical performance for large scale experiments using LiBr in [C2mim][NTf2] as the reaction medium.

Sample	1st charge (mAh/g)	1st discharge (mAh/g)	Coulombic efficiency	2nd charge (mAh/g)	2nd discharge (mAh/g)	Coulombic efficiency
Pristine	159.30	140.82	88.40%	143.01	140.85	98.49%
Delithiated	107.11	104.82	97.86%	118.71	113.81	95.87%
75g IL: 25g D-NMC	176.57	162.38	91.97%	163.18	161.02	98.68%
50g IL: 25 g D-NMC	202.47	163.58	80.79%	163.98	157.20	95.87%
25g IL: 25 g D-NMC	175.97	150.00	85.24%	152.20	149.09	97.95%
50g IL: 50g D-NMC	172.69	145.52	84.27%	149.90	145.37	98.26%

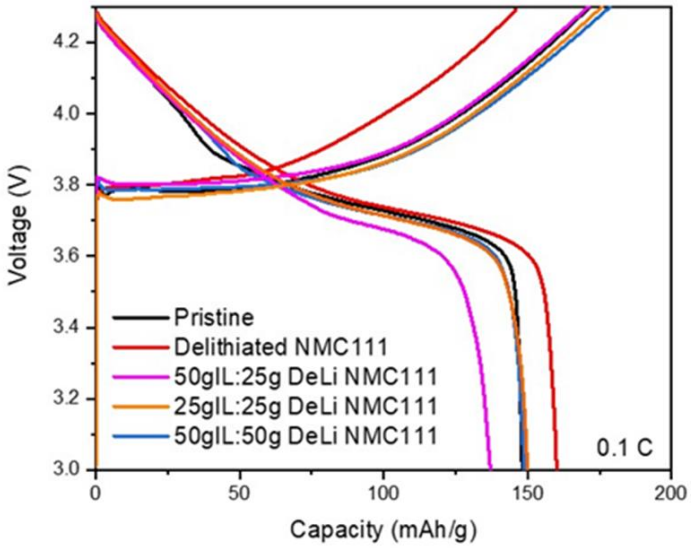

Figure I.3.C.16 Voltage profiles for the pristine, delithiated, and relithiated samples tested in half cell configuration.

Hydrothermal Relithiation of Chemically Delithiated NMC111 Cathodes

UCSD has previously demonstrated a promising hydrothermal relithiation process for the direct regeneration of spent lithium-ion battery (LIBs) cathodes using LiCoO2 as a model material. The underlying principle behind the need for relithiation in the recycling process was developed over the past two decades. Cathode degradation is attributable to Li inventory loss (corrosion), formation of the cathode-electrolyte interphase (CEI) layer, anode-electrolyte interphase (SEI) layer, and microphase changes. Although mechanical degradation has been observed, it has not been identified as a source cell-level capacity loss. In these studies, we are evaluating processes to relithiate Li-deficient cathodes without altering the transition metal framework, employing minimal heating before a short thermal annealing step to help fix the undesired microphases. In the end, the degraded cathode particles can be regenerated into fresh particles that show the same level of electrochemical performance as the pristine cathode. The advantage of a hydrothermal approach is that by retaining the transition metal framework we not only recycle valuable materials, but also reclaim the energy used to synthesize the initial material when compared to commercially used pyrometallurgical and hydrometallurgical processes. The latter two processes can be economically feasible only if expensive metals (e.g., Ni, Co) are prevalent. As the LIB industry moves towards cathodes with less and less expensive metals,

these processes may not be viable. Our direct regeneration method based on hydrothermal relithiation and short annealing requires minimal energy and chemicals, thus having the potential to recycle spent cathodes at much lower cost.

Continuous process optimization and intensification remain needed to demonstrate technological and economic feasibility for large-scale applications of the hydrothermal relithiation process. For example, we noted that the Li+ and OH- in the solution play different roles in the hydrothermal relithiation process, where a high concentration of OH- limits proton exchange (H+/Li+), and Li+ repairs the lithium deficiencies in the cathode materials. In the past quarter, the UCSD team explored different temperatures and times for both the hydrothermal and annealing steps, to identify an optimal operation window for complete regeneration of degraded NCM111. Considering the high cost of 4 M LiOH, a high concentration of KOH is proposed as an alternative to maintain a low proton concentration environment, along with diluted LiOH to complete the relithiation process. As shown in the Q2 report, the capacity of the delithiated NCM111 (Del NCM111) can be efficiently recovered to the pristine level (Toda NCM111), however, the stability is not as good as expected. We investigated the effect of an annealing step following the hydrothermal relithiation on the stability of regenerated cathode materials. In addition, we explored the recyclability of the LiOH solution.

We first explored solution compositions for hydrothermal relithiation, based on 1g reaction, and found that a highly alkaline solution (4M OH-) was important for restricting protonation of NMC111. Considering the high cost of 4M LiOH solution, a mixture of 0.1M LiOH and 3.9M KOH was proposed instead. The crystal structure of D-NMC111 relithiated with the mixture solution of 0.1M LiOH and 3.9M KOH was characterized by X-Ray diffraction (XRD). The patterns of the sample treated with 4M KOH as well as D-NMC111 and T-NMC111 were also collected and shown in Figure I.3.C.16 (a) as references. Overall, the diffraction peaks of all the samples matched well with the typical α-NaFeO2 structure with "R" "3" $\bar{3}$"m" space group, indicating that the bulk structure of NMC111 is not affected by chemical delithiation and relithiation. When the area around the (003) peak was blown-up, an obvious shift to a lower angle after chemical delithiation (D-NMC111) was observed, reflecting a small increase in the c lattice constant. This is due to increased electrostatic repulsion between the oxygen layers along the c direction when Li+ is deficient1 The (003) peak was still situated at a low angle after treatment with 4M KOH, but it obviously shifted back to the position of pristine T-NMC111 after treatment with the mixture of 0.1M LiOH and 3.9M KOH, which suggests that Li+ from the solution is intercalated into the layered crystal structure to repair the lithium deficiencies.

X-ray photoelectron spectroscopy (XPS) was performed to probe the valence state of Ni, which is tied to the concentration of lithium in the NMC particles (Figure I.3.C.17(b)). The spectra of Ni 2p of all the samples showed two main peaks corresponding to Ni 2p 3/2 and Ni 2p 1/2, accompanied by a satellite peak (labeled “Sat”) respectively. After chemical delithiation, the Ni 2p 3/2 peak shifted to 854.8 eV from the original 854.1 eV (T-NMC111), indicating a higher valence state of Ni, which is due to the balance of charge after extraction of Li+. The treatment with 4M KOH did not change the valence state of Ni. But the Ni 2p 3/2 peak shifted back to the same position of T-NMC111 after treatment of 0.1M/3.9M KOH, which indicates that Ni is reduced to 2+, further implying the insertion of Li+ to the crystal structure. Interestingly, two obvious peaks related to K 2p 3/2 and K 2p 1/2 for the sample treated with 4M KOH were noted (Figure 1(b)) which may be due to partial surface exchange of K+ and Li+. Notably, the sample treated with the mixture solution of 0.1M LiOH and 3.9M KOH showed a flat XPS spectrum in K 2p region, similar to the spectra of D-NMC111 and T-NMC111, suggesting that the exchange behavior between K+ and Li+ can be efficiently restrained with the addition of diluted LiOH (0.1M).

The concentrations of Li+ and K+ in the crystal structure were determined with inductively coupled plasma mass spectrometry (ICP-MS) measurement (Figure I.3.C.17(c)). The chemical oxidation product T-NMC111 was formed by extraction of 10% Li+ (D-NMC111). After treatment with 4M KOH, an additional 4% of Li+ in the particles was lost and ~4% of K+ was detected. This undoubtedly demonstrates the exchange behavior between K+ and Li+, which might be driven by the concentration difference of Li+ between the solid and

liquid phases. When 0.1M LiOH was introduced, the cationic exchange was completely eliminated. Moreover, the lithium content can be recovered to 1.07, close to the value of T-NMC111 (1.06).

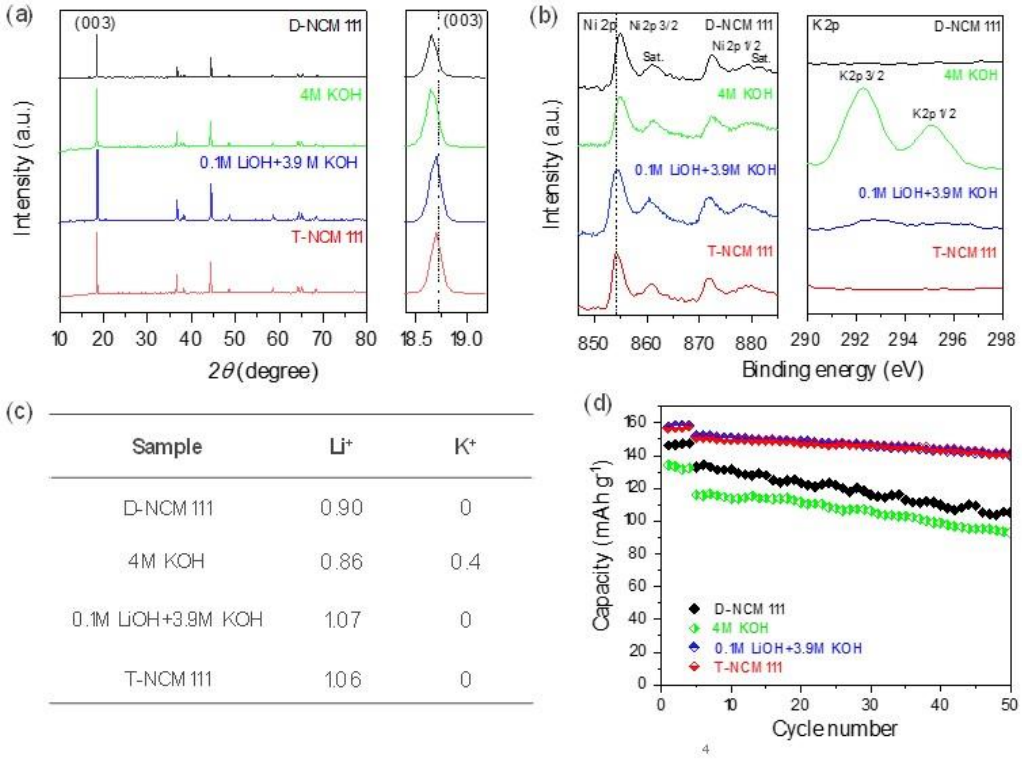

Sample	Li+	K+
D-NCM 111	0.90	0
4M KOH	0.86	0.4
0.1M LiOH+3.9M KOH	1.07	0
T-NCM 111	1.06	0

Figure I.3.C.17 XRD patterns (a), XPS spectra (b), ICP results (c), and comparison of cycling stability (d) of samples treated by the mixture solution of 0.1M LiOH and 3.9M KOH and 4M KOH as well as the control samples (D-NMC111 and T-NMC111).

The electrochemical performance was then evaluated by coin cells (half-cell) with cathode mass loading of ~10 mg cm-2 and LP40 (1M LiPF6 in EC/DEC) electrolyte. The cells were cycled in the voltage range of 3-4.3 V with activation for 4 cycles at C/10 followed by 50 cycles at C/3. All the samples after hydrothermal treatment were annealed at 850oC for 4h before making cells. The electrochemical results are shown in Figure I.3.C.17(d). After chemical delithiation, the discharge capacity at the first cycle of C/10 dropped from 157 mAh/g (T-NMC111) to 146 mAh/g (D-NMC111), which further decreased to 134 mAh/g after treatment with 4M KOH. The capacity degradation can be mainly attributed to lithium deficiencies (Figure I.3.C.17(c)). After treatment with the mixture of 0.1M LiOH and 3.9M KOH, the capacity of NMC111 was restored to 157 mAh/g, equal to T-NMC111. When the rate was changed to C/3, D-NMC111 exhibited an initial capacity of 133 mAh/g and dropped to 103 mAh/g after 50 cycles. Due to the cationic exchange, the sample treated with 4M KOH only delivered a capacity of 115 mAh/g at the first cycle of C/3, which decayed to 92 mAh/g at the end of 50th cycle. Notably, the initial capacity of the sample treated with 0.1M LiOH and 3.9M KOH was improved to 150 mAh/g with capacity maintained at 140 mAh/g after 50 cycles, which was comparable to T-NMC111. Therefore, besides the restored structural and compositional defects, the electrochemical performance can also be recovered. The effective regeneration of D-NMC111 using 0.1M LiOH and 3.9M KOH mixture solution to achieve the same level of performance as using 4M LiOH suggests that the cathode recycling cost can be reduced by replacing a majority of Li in the hydrothermal relithiation solution.

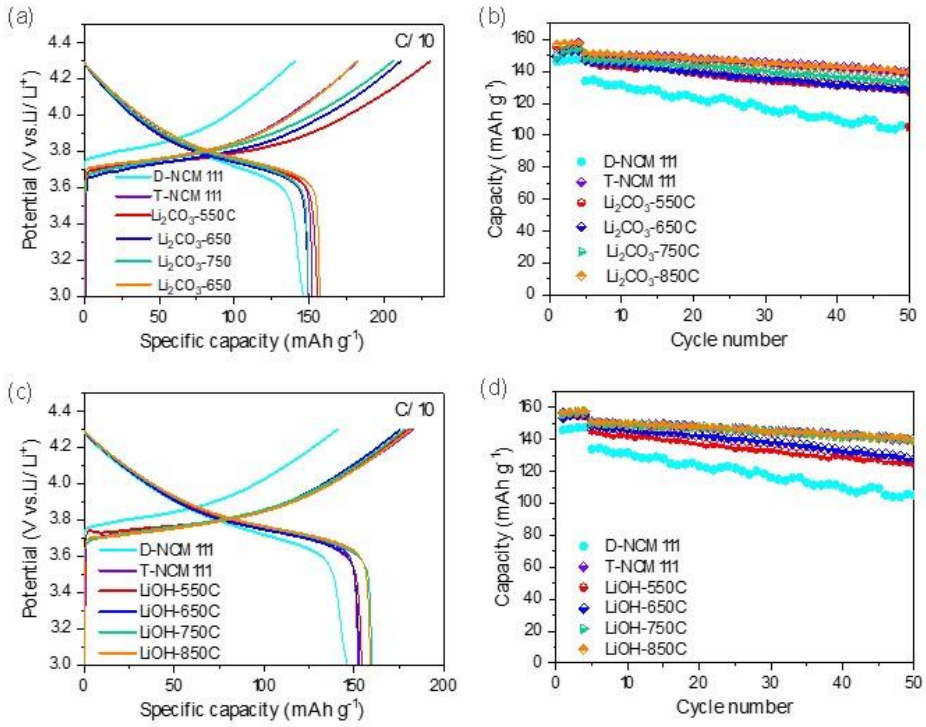

Figure I.3.C.18 Voltage profiles (a) and cycling stability (b) of relithiated NMC111 mixed with excess 5% of Li2CO3 and then annealed at different temperatures of 550°C, 650°C, 750°C and 850°C; Voltage profiles (c) and cycling stability (d) when equivalent LiOH was used instead of Li_2CO_3 in the annealing step.

To achieve desired electrochemical performance, short annealing is generally required to enhance the crystallinity of hydrothermally relithiated samples. In this step, an excess of 5% lithium was added to the relithiated NMC111 powder to compensate for lithium loss. In order to explore the relationship between annealing conditions and lower energy consumption, the relithiated samples were annealed at different temperatures, ranging from 550oC to 850oC, with Li2CO3 as a secondary lithium source. As shown in Figure I.3.C.18(a), when the relithiated sample was annealed at 550oC, the capacity of the first charging cycle at a rate of C/10 was up to 231 mAh/g, far beyond the theoretical capacity of NMC111 (150 mAh/g). Interestingly, after washing with water, the capacity dropped to 185 mAh/g (the result was not shown here), similar to R-NMC111 (183 mAh/g) before annealing. This indicates that the additional capacity originates from the residual Li2CO3 which isn't incorporated into the delithiated cathode material at these low temperatures due to its low activity up to its relatively high melting point (723oC). The discharge capacity was 154 mAh/g, corresponding to a Columbic efficiency (CE) of ~67%, owing to the irreversible lithium introduced by Li2CO3. When the annealing temperature was increased to 650oC, the charging and discharge capacities dropped to 212 mAh/g and 152 mAh/g, corresponding to a CE of ~72%, which indicates inactive Li2CO3 remaining on the cathode surface. When the temperature was further increased to 750oC, the charging capacity was 206 mAh/g but the discharge capacity fell to 149 mAh/g, delivering a CE of ~72%. When the annealing temperature was increased to 850oC, the charging capacity dropped to 182 mAh/g but the discharge capacity was increased to 157 mAh/g, achieving a CE of 86%, which is identical to pristine T-NMC111.

In the cycling stability test (at a rate of C/3), the samples annealed at 550oC and 650oC showed similar capacity degradation trends, starting with a discharge capacity of 146 mAh/g and remaining 129 mAh/g after 50 cycles, as shown in Figure I.3.C.19(b). The initial capacity was improved to 148 mAh/g when the annealing temperature was increased to 750oC, and 134 mAh/g was maintained after 50 cycles. The capacity retention was also improved from 88% to 90%. Further increasing the annealing temperature to 850oC promoted the capacity of the first cycle to 150 mAh/g, and a capacity of 140 mAh/g could still be achieved after 50 cycles, corresponding to a capacity retention of 93%. It should be noted that this performance already reached the

level of pristine T-NMC111. Therefore, we believe 850oC is the minimum required temperature for fully reviving the electrochemical performance when Li2CO3 is used as a lithium source.

As an alternative, LiOH was then proposed as a lithium source, in part due to its lower melting point (462oC) compared to Li2CO3. Similarly, different annealing temperatures were explored to identify the optimal temperature for full recovery of electrochemical performance. When the annealing temperature was 550oC, the charging capacity reached to 180 mAh/g (Figure I.3.C.18(c)), which was significantly lower than the sample annealed under the same condition with Li2CO3 (231 mAh/g) as the lithium source. The reversible capacity was 154 mAh/g, corresponding to a CE of 86%. This indicates that Li+ from LiOH can be more easily incorporated into the layered crystal structure under such low temperatures. The charging and discharge capacities were similar when the temperature was increased to 650oC. When the sample was annealed at 750oC, while the charging capacity was maintained at 180 mAh/g, the reversible capacity can be further improved to 157 mAh/g, which was close to the sample annealed at 850oC. The improved electrochemical performance can be ascribed to a more stable crystal structure and better interfacial surface being obtained by annealing at relatively high temperatures.

The cycling stability was then examined with a rate of C/3 (Figure I.3.C.18(d)). The samples annealed at 550oC and 650oC delivered capacities of 145 and 148 mAh/g at the initial cycle, respectively. After 50 cycles, capacities of 124 and 128 mAh/g were maintained respectively, corresponding to a retention of 85% and 86%. In contrast, the samples annealed at 750oC and 850oC can both achieve an initial capacity of 150 mAh/g and remained 140 mAh/g after 50 cycles, reaching a retention of 93%, similar to T-NMC111. Therefore, although a relatively low temperature may still trigger the diffusion of Li+ from LiOH into the layered structure of D-NMC111, high temperature is still required to obtain a stable phase that can withstand long-term charge/discharge cycling. It is worth noting that the optimal temperature can be decreased to 750oC when LiOH is used as a lithium source instead of Li2CO3, which can effectively shorten the regeneration period and reduce energy consumption.

In order to scale up the bench-scale regeneration process, 10 g of D-NMC111 was subjected to a direct regeneration process using the same Li-containing solution at 220oC. The composition of the product (R-NMC-10 g) was analyzed by ICP (Figure I.3.C.19(a)). The content of lithium for R-NMC-10 g can also be recovered to a value similar to T-NMC111, showing negligible difference from the sample regenerated at a scale of 1g (R-NMC-1 g). The recovery of the electrochemical performance of R-NMC-10 g was also examined (Figure 3(b)). Both the capacity and retention can be improved to a pristine level (T-NMC111) for R-NMC-10 g, suggesting the potential to further scale-up of the process.

(a)

Sample	Composition
D-NCM 111	$Li_{0.9}Ni_{0.33}Co_{0.33}Mn_{0.33}O_2$
R-NCM 111-1g	$Li_{1.05}Ni_{0.33}Co_{0.33}Mn_{0.33}O_2$
R-NCM 111-10g	$Li_{1.07}Ni_{0.33}Co_{0.33}Mn_{0.33}O_2$
T-NCM 111	$Li_{1.06}Ni_{0.33}Co_{0.33}Mn_{0.33}O_2$

(b)

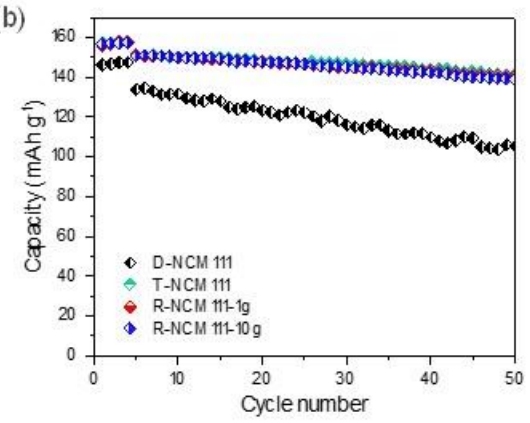

Figure I.3.C.19 The composition (a) and electrochemical performance (b) of NMC111 regenerated at scale-up to 10 g and the control samples (D-NMC111 and T-NMC111, as well as NMC111regenerated at a scale of 1g).

Relithiation via Redox Chemistry

This project will develop a direct cathode recycling method that utilizes redox mediator chemistry for EoL (End-of-Life) battery cathode materials. One of the main characteristics of EoL cathode materials is Li deficiencies due to the formation of the irreversible anode SEI layer. In FY19, the electrochemical relithiation project showed that the Li vacancies in EoL cathodes are fairly isolated and need electrochemical perturbation to be filled with Li ions at room temperature. These revelations led us to design a room-temperature electrochemical relithiation process using redox mediators that have reversible and characteristic oxidation/reduction behaviors. The redox mediators are reversible charge shuttles in an electrochemical cell that deliver lithium ions and electrons from the anode (e.g., Li atoms) to the cathode materials with Li deficiencies. The cathode materials are reduced by the Li-ions/electrons and the original Li concentration is restored. Potential advantages of this method are: (i) It's basically an autonomous process by the shuttle current, so there's no need to control any electrochemical parameters. (ii) The selection of redox mediators will determine discharge voltage, electrochemical kinetics, and materials stability. (iii) The process is expected to generate little or no wastes and be easy to scale up. In FY20, this project will test the redox mediator (RM) chemistry for cathode relithiation and develop a lab-scale reactor for the powder relithiation process.

In this quarter, we continued screening and evaluating redox mediator concentrations to get the optimal electrochemical properties. The goal is to minimize the use of redox mediators and thereby to lower the total processing cost. The previous quarterly report shows some preliminary results with 0.1 and 0.5M electrolyte data, and we also tested 0.2 and 0.3M electrolytes as well, and finished the screening at this time. The model end-of-life cathode for the test is 10% chemically delithiated NMC111 from CAMP. The Li source for the reaction is Li metal, and the electrolyte is X molar [RM] in DME solvent (X = 0.1, 0.2, 0.3, and 0.5). The reaction time was set to 1 hour, and the relithiated powder was post-annealed at 850ºC for 4 hours. To evaluate the degree of relithiation of the EOL cathode materials, coin half-cells were assembled and evaluated. Figure I.3.C.20 shows charge/discharge voltage curves of the relithiated cathode materials, and Table I.3.C.9 shows a summary of charge/discharge capacities and coulombic efficiencies during first and second cycles.

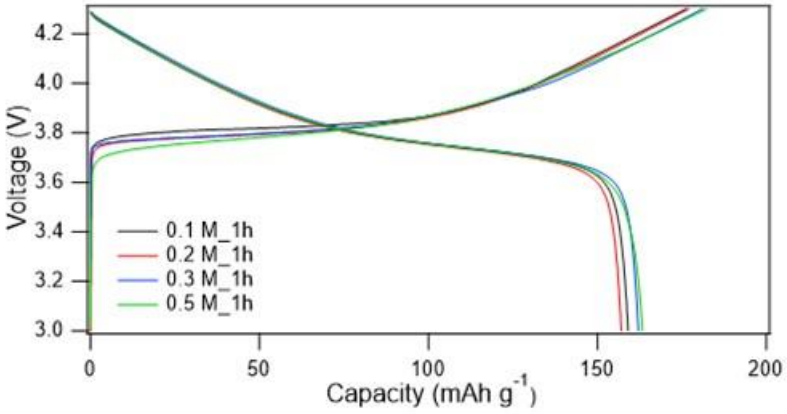

Figure I.3.C.20 Initial charge/discharge voltage profiles of the relithiated NMC111 powders using X M RM (X = 0.1, 0.2, 0.3, and 0.5) at C/10 current density.

From the coin cell test results, it was observed that 0.1 and 0.2M electrolytes are not concentrated enough to finish the relithiation reaction within 1 hour. Initial charge capacities are 176.23 and 177.04 mAh/g, respectively. The 0.3M electrolyte shows similar charge and discharge capacities to those with the 0.5M electrolyte. Both show higher than 181 mAh/g during the first charge. This suggests that a higher redox mediator concentration is required to promote the reduction at the Li metal surface and the oxidation at the cathode surface.

Table I.3.C.9 Summary of electrochemical capacities after 0.X M [RM] relithiation process for 1 hour

	1st Ch cap (mAh/g)	1st Dis cap (mAh/g)	1st Cycle efficiency (%)	2nd Ch cap (mAh/g)	2nd Dis cap (mAh/g)	2nd Cycle efficiency (%)
0.1M_1h	176.23	159.08	90.3	160.72	159.57	99.3
0.2M_1h	177.04	157.03	88.7	158.98	157.48	99.1
0.3M_1h	181.06	162.07	89.5	163.19	162.00	99.3
0.5M_1h	182.24	163.30	89.6	164.42	163.31	99.3

Moreover, the initial discharge capacities also show clear contrast between the different electrolyte concentrations. The 0.1 and 0.2M electrolyte test conditions only exhibit 159 and 157 mAh/g, respectively, but the 0.3 and 0.5M electrolyte test conditions show 162 and 163 mAh/g, respectively. The results suggest that an incomplete relithiation leaves some Li vacancies unfilled that would induce a local structural degradation during post-annealing step. From the charge/discharge capacity data, it is apparent that at least 0.3M or a higher redox mediator concentration is required to fully lithiate EOL cathode materials.

We checked powder X-ray diffraction (XRD) patterns of the cathode samples before and after relithiation, as shown in Figure I.3.C.21, in order to probe possible structural changes. All the samples exhibit a single-phased layered structure without a notable impurity phase. Although the electrochemical data in Table I.3.C.9 suggest a possible local structural degradation, XRD cannot detect the minor change, consistent with a surface reaction. We will do ICP composition analysis and confirm the degree of relithiation in the next quarter.

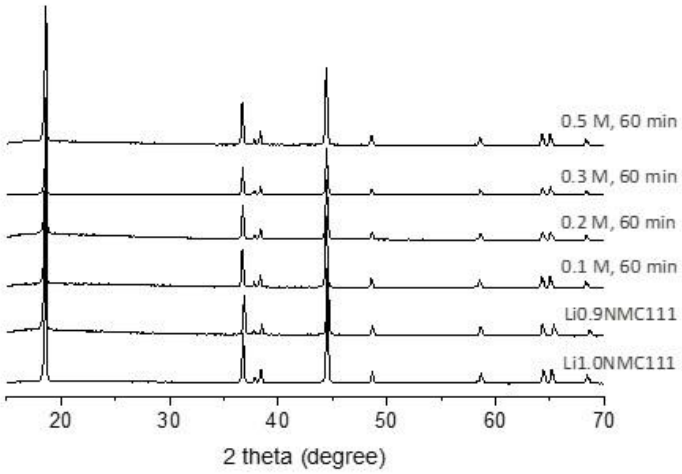

Figure I.3.C.21 Powder XRD patterns of the pristine, chemically delithiated, and relithiated NMC111 powders using X M [RM] (X = 0.1, 0.2, 0.3, and 0.5).

Electrochemical Relithiation

This project will develop a direct recycling method that utilizes electrochemical relithiation for EoL (End of Life) battery cathodes. We are developing a scalable recovery process to restore lithium loss caused by SEI formation. Our electrochemical relithiation process will be optimized for application to large-scale direct recycling, such as roll-to-roll processes. This means that it must be optimized for rapid relithiation in order to minimize the time the EoL cathodes are in an electrochemical bath during lithiation. In FY19, we identified several variables that are essential to process optimization, including relithiation temperature, application of voltage holds, and the content and character of the initial lithium-ion vacancies in the Li-deficient cathode

material. There is a kinetic limitation to relithiation for Li-deficient NMC111 materials that can be overcome by temperature application or by charging the NMC111 material before attempting to relithiate it. In FY20, this project continued to optimize electrochemical relithiation protocols by incorporating what we learned about the kinetics of the delithiated cathode materials and by further characterization of the delithiated materials themselves through aging of pouch cells. The optimized electrochemical relithiation protocols were applied to cathodes from aged pouch cells to verify successful restoration.

In FY20Q4, we verified that the initial impedance to relithiation for the electrochemically delithiated samples is an order of magnitude lower that the chemically delithiated materials, possibly as a result of surface damage during preparation or nucleation of a stable surface phase. In this quarter, the degradation mechanism of NMC 111 cathodes in full cells was analyzed and a novel discharge relithiation protocol was developed and tested. Figure I.3.C.22 is a plot of the capacity over cycling of two NMC111/graphite full cells with 30uL of 1.2M $LiPF_6$ 3:7 EC:EMC electrolyte that were formed at C/10, then cycled at 1C/1C rate for 25 cycles followed by a single C/10 charge/discharge cycle in order to evaluate the degradation mechanism of the NMC111 cathode.

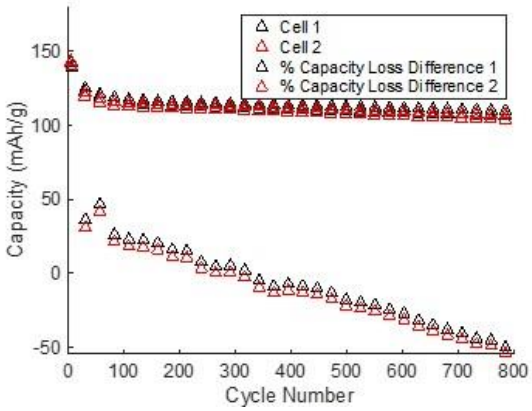

Figure I.3.C.22 Difference in capacity of loss between 1C/1C and C/10 aging of full NMC111 coin cells

This plot shows that the C/10 capacity check cycles have a higher capacity than the previous 1C/1C cycle during the initial 50 cycles and then gradually decrease with continued cycling until, after about 300 cycles, the 1C/1C cycling shows less capacity loss than the C/10, indicated by the transition from positive to negative capacity difference on the plot. This could be indicative of a transition in the capacity loss mechanism from one prevalent in earlier cycling (<300 cycles) to one prevalent in later cycling (> 300 cycles) that is dependent on the C-rate. This could be due to a combination of mechanical isolation of active materials, poor diffusion kinetics and lithium loss from SEI formation. To further examine the degradation of just the NMC111 cathode that is most relevant to this relithiation study, cross-sectional SEM images of NMC111 cathode materials that were aged to increasing extents were taken and are shown in Figure I.3.C.23.

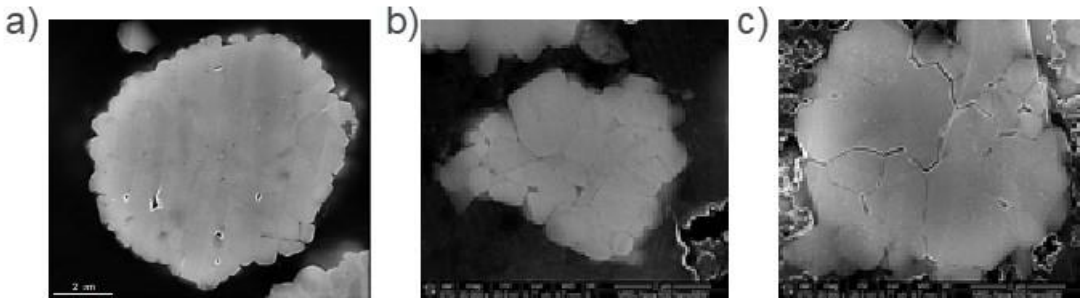

Figure I.3.C.23 NMC111 particle cross-sections for a) pristine cathode, b) cathode aged to 15% capacity loss and c) cathode aged to 25% capacity loss

These cross-sections show that with increased aging or cycling, the cracking between the primary particles is aggravated, as expected. The effect these cracks have on the ability to electrochemically relithiate the material is not immediately apparent, but it may inhibit these materials' long-term stability over extended cycling. Figure I.3.C.24 shows a scanning voltage protocol, designed on our team's previous work on fast charging anodes, implemented on two different aged NMC111 materials.

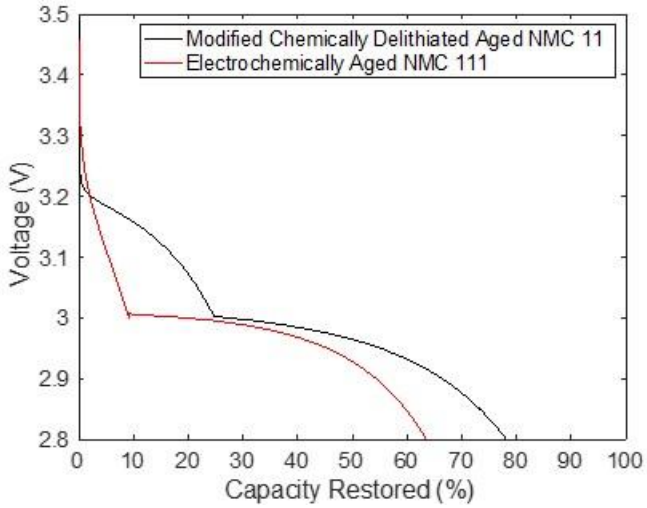

Figure I.3.C.24 Capacity restored for modified chemically delithiated NMC111 material and electrochemically aged NMC111 material using scanning voltage protocol

The scanning voltage protocol shown in Figure I.3.C.24 is composed of a $9C_r$ constant current (CC) discharged to 3.0V, followed by a .0001mV/s voltage scan to 2.8V where $1C_r$ is the C-rate calculated based on a 16mAh/g relithiation capacity, as described in previous quarterly reports for this project. The electrochemically aged NMC111 material was aged at 1C/1C until 20%of the full cell capacity was lost, and thus likely has some mechanical degradation within the primary particles of the material, based on conclusions drawn from the results in Figure I.3.C.23. A modified chemically delithiated material was cycled twice at C/10 in a full cell, disassembled, rinsed, and rebuilt to provide a more rapidly formed model delithiated material, while addressing the high impedance of the unmodified chemically delithiated material, as described in our previous reports. The modified chemically delithiated material shows a higher relithiation capacity percentage compared to the electrochemically delithiated material, as well as less over potential. Both materials were relithiated in only about 35 minutes, which is a more suitable amount of time for scalable applied electrochemical relithiation techniques. After the scanning voltage relithiation step, both samples were charged and discharged at C/10 to determine if the pristine capacity of ~161 mAh/g was restored. The results are quantified in Table I.3.C.10.

Table I.3.C.10 Comparison of relithiation, first charge and reversible charge and discharge cycles at C/10 for samples relithiated using scanning voltage protocol

	% Relithiation Capacity Restored	First Charge (mAh/g)	Reversible Charge (mAh/g)	Reversible Discharge (mAh/g)
Modified Chemically Delithiated NMC111	78.1	159.8	159.8	159.9
Elelctrochemically Aged NMC11	63.4	151.6	151.4	151.4

Both materials showed higher capacities after relithiation, with the modified chemically delithiated material showing very promising reversible relithiation capacities with continued cycling. We will continue to optimize this protocol based on computational modelling parameters.

Roll-to-Roll Reactor Design for Electrochemical Relithiation

Restoring cyclable lithium is one of the key challenges in recovering cathodes from recycled streams. This project will develop a roll-to-roll (R2R) process for electrochemical relithiation of NMC cathodes. Parameters for electrochemical relithiation, such as voltage, current profiles, and temperature of the reactor are developed under a different sub-task within this thrust area. The results from those screening tests will be used to design a prototype roll-to-roll cathode recycling reactor that pairs the aged cathode material with a lithium source. This work will determine the optimal throughput to achieve a stable cathode whose performance is comparable to a pristine-equivalent, creating the roadmap for design of an industrial-scale roll-to-roll relithiation process.

In the actual workflow, a feedstock of aged cathode material from a battery waste stream will be coated onto a fresh current collector and run through such a reactor. Using a controlled current, lithium will be driven from the anode into the cathode, restoring the cathode to its original capacity. Parameters such as the line speed and C rate will be investigated in conjunction with the relithiated cathode cycle life. The outcome from this effort includes:

1. Minimizing efficiency losses in relithiation between the screening tests that involve batch processing and the roll-to-roll reactor
2. Determining reactor parameters such as line-speed, electrode area, and spacing between the two electrodes
3. Balancing throughput targets for the process to be viable from a techno-economic perspective against performance targets such as uniformity and extent of relithiation.

Using the same NMC111 18650 cells that served as the samples for the FY20Q3 tests, a set of experiments determined the theoretical baseline relithiation performance of an aged cathode. Rather than delaminating and recasting the cathode active material, efforts were taken to preserve the quality of the cathode between extraction from the aged cell and relithiation in the reactor. Immediately after extracting the jellyroll from the 18650 case, it was submerged in DMC to ensure it would not dry. While submerged, it was unrolled, allowing for the separation of the layers. Samples were then cut from the cathode near the current collector tab, resulting in two samples with 7.8cm^2 of active material, and an uncoated area to connect current and voltage leads. Each sample was placed in an individual sealed container and submerged in DMC prior to relithiation in the reactor.

The relithiation protocol employed was based upon modeling results (Andrew Colclasure and Jaclyn Coyle performed this work), which suggested that a 9C_r discharge to 3.0V, followed by a 0.001V/s scan to 2.8V, would best optimize relithiation time (or residence time in the reactor). The cathode samples were taken from a cell that had been aged to 85.7% SOH, and had a specific capacity of approximately 152.3mAh/g_{NMC} (at C/10), equating to sample capacities of roughly 26 mAh pristine, and 22.3mAh aged. Therefore, 9C_r would be 33.3mA. Since the cathodes needed to remain submerged, it would not be possible to weld them to foil and make use of the standard reactor connections. As such, alligator clips were necessary to deliver the discharge current to the samples, and thus a more cautious protocol was employed for the relithiation tests:

1. Charge at 0.8C_a (aged capacity)/17.8mA to 4.2V
2. Hold at 4.2V for 1 hour
3. Discharge at 0.72C_a/16mA to 3.0V
4. Voltage scan of 0.001mV/s to 2.8V

Using the above protocol, the two samples demonstrated a nearly identical performance in the reactor, both receiving approximately 155mAh/g in just over two hours. The delivered capacities within the reactor closely match the pristine NMC111 sample capacity.

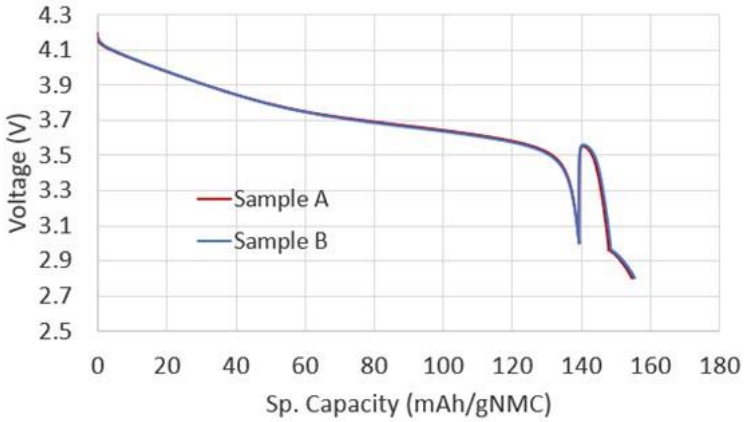

Figure I.3.C.25 Voltage vs NMC111 specific capacity of samples A and B during the discharge portion of the reactor protocol. For sample A, discharge time = 126.2min, capacity = 154.7mAh/gNMC, for sample B, discharge time = 127.6min, capacity = 155.4 mAh/gNMC

Subsequent to relithiation, the samples were once again placed in sealed containers of DMC and transferred to a separate glove box to be used in coin cells. Using the cathode from the same 18650, control samples were made which had not undergone relithiation. The relithiated full cell, an aged full cell, and an aged half-cell were then run through the same protocol to evaluate the relithiated capacity retention. On the first charge, the capacity of the relithiated cell exceeded the rest by a substantial margin, but in subsequent cycles, only the half-cell performed as expected, while both full cells dropped to approximately 100mAh/g_{NMC}. Another set of controls were then made, using off-the-shelf cathodes from the same manufacturer as the anodes. The performance of these cells closely mimicked that of the aged and relithiated full cells, including the ultimate capacity of 100mAh/g_{NMC}. This result suggested that defective anodes had been used in the full cells. The one piece of information that can be taken qualitatively from these data is that the relithiated cell had the best performance of all samples during the first charge, indicating that at least some of the relithiated capacity is retained. Any further conclusions will require repeating these experiments with different anodes.

Cathode Upcycling

Battery recycling is an overarching process used to recover materials from previous generations of energy storage materials and reverse the effects of degradation, impurity build-up, or having no relevance in the present marketplace to supply new markets, or lower the overall costs of storage. A significant issue in this fast-changing market is that batteries supplied to recyclers reflect chemistries from 5-10 years ago that may not be viable in the present. Recycled materials and materials wanted by the marketplace may not be in sync over time as new chemistries and cell designs drive changes in supply and materials choices. Besides changes in the materials stream available due to material performance improvements and emerging new chemistries, materials from non-transportation sectors may also play a role in adding anomalous materials to the waste stream, for instance LiCoO2 from consumer electronics. We are designing and evaluating methods to upcycle the metal ratios of recovered cathode materials to convert them to more current cathode formulations that are more relevant to the marketplace. This effort's focus will be on the raw materials, Li(Ni1/3Mn1/3Co1/3)O2 (NMC111) and LiCoO2 (LCO) and will establish methods to use them as feedstock material to produce other stoichiometries. Initial targets will be NMC622 and Li(CoAl)O2 [Al-doped LiCoO2], the latter being a variant that has a larger electrochemical window and higher capacity.

Upcycling cathode materials may be necessary, as recovered materials may not match those needed in the present (or future) marketplaces. EV batteries from the past decade are usually built on NMC111; however,

more nickel- rich compositions, i.e. NMC622, are now more commonly used. A two-step process involving lithiation followed by stoichiometry changes was determined to create more uniform and homogenous samples tan did a single-step process. NMC composition change reactions to target higher nickel content used precipitation of a nickel coating from nickel (II) sulfate with lithium hydroxide onto NMC111. The quantity of nickel added was stoichiometric to reach the NMC622 composition shown in the equation below.

$$\underline{\text{Target}}:\ LiNi_{0.33}Mn_{0.33}Co_{0.33}O_2 + 0.67\ NiSO_4 + 1.3\ Li(OH) \xrightarrow[\text{Air or } O_2]{\text{600-750 °C}} \xrightarrow{H_2O\ \text{wash}} LiNi_{0.6}Mn_{0.2}Co_{0.2}O_2$$

The interaction between different compositions NMCs (NMC111 and NMC811) at high temperatures was investigated to observe the diffusion of the fully formed oxides. Two different composition mixtures of NMC111 and NMC811 (45:55 and 40:60) were used in an initial test to target a final composition near that of NMC622. Both NMCs were first mixed together thoroughly using a mortar and pestle and then transferred to a crucible and heated to 700 °C for 12 hours. The XRD data for the two mixtures are shown in Figure I.3.C.26. Under these trial conditions, separate peaks for the two starting NMCs are still distinguishable, however there appears to be an intermediate shoulder forming indicating the presence of an intermediate phase. The measured GDOES compositions (Table I.3.C.11) approach the targeted transition metal content, though the 45:55 mixture is slightly nickel-poor and the 40:60 mixture is slightly nickel-rich.

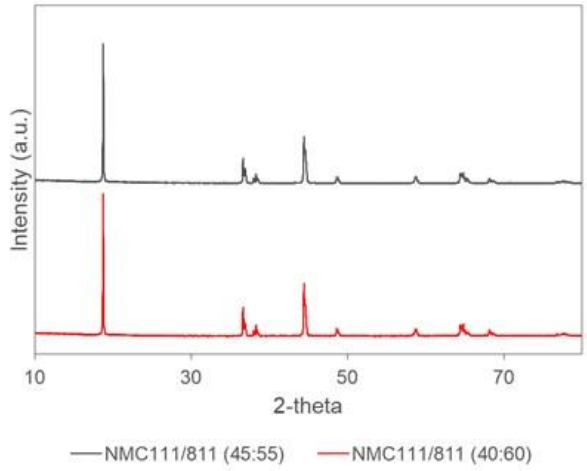

Figure I.3.C.26 XRD of NMC111/NMC811 mixtures heated at 700 °C

Table I.3.C.11 Elemental compositions of NMC111:NMC811 mixtures measured from GDOES analysis

NMC111:NMC811	[Li]	[Ni]	[Co]	[Mn]
45:55	1.12	0.56	0.19	0.25
40:60	1.05	0.65	0.15	0.20

Results from previous quarters showed the formation of (LiNi)O2 and NiO as secondary phases in the XRD, the latter case indicating there was insufficient lithium present during high-temperature heating. This was also supported by GDOES compositions, showing low Li content in the final product. Several of these reactions were retested using excess lithium to reduce the formation of these unwanted phases. Ni-only coatings and Ni/Mn/Co coatings were tested with the addition of citric acid or oxalic acid. Final annealing was at 750°C in air or oxygen atmosphere. The XRD data shown in Figure I.3.C.27 are only for powders processed in air. The additional lithium in these new reactions has eliminated the previously observed (LiNi)O2, NiO, and other

minor oxide phases. A secondary peak or weak shoulder appears for the 104 reflection from the presence of an off-stoichiometry NMC phase.

The GDOES compositions for these samples (shown in Table I.3.C.12) reach the transition metal contents. The lithium values are slightly low (1%–2%), which is improved from the lithium-deficient reactions. A supplemental relithiation step could be added if this continues to be an issue once a product that is entirely NMC622 is obtained.

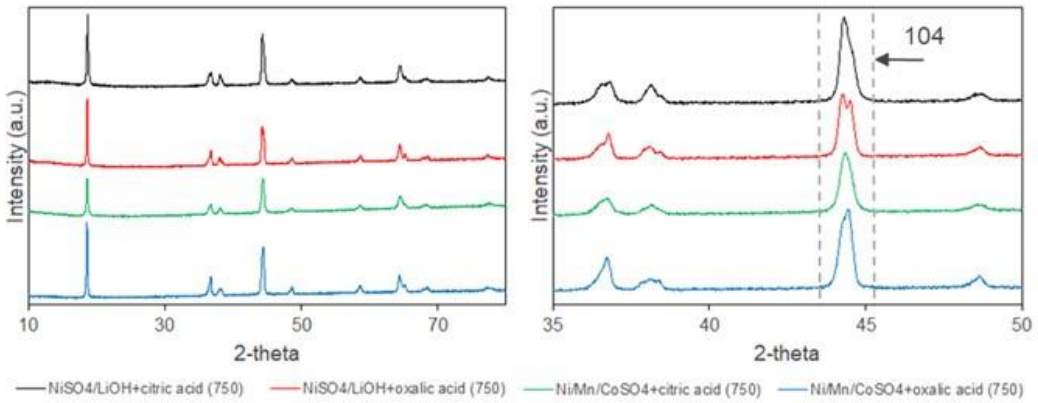

Figure I.3.C.27 XRD of products from Ni-rich coatings on NMC111 heated at 750 °C

Table I.3.C.12 Elemental compositions from Ni-rich coating reactions measured from GDOES analysis

Additives	[Li]	[Ni]	[Co]	[Mn]
$NiSO_4$+O.A.	0.98	0.64	0.17	0.19
Ni/Mn/$CoSO_4$+C.A.	0.98	0.62	0.18	0.20
Ni/Mn/$CoSO_4$+O.A	0.97	0.61	0.19	0.20

Role of Impurities in Recycled Cathodes

When identifying and developing lithium-ion battery recycling technologies, understanding the role of impurities is always a concern, as they may have an impact on electrochemical performance, material stability, or lifetime. Knowing the wide variety of impurities that may be introduced in the recycling process, the objectives of this project are to determine the possible impurities, their role in structural stability, and their impacts (during synthesis and after synthesis) on the recovered NMC622 precursor and cathode materials. The main impurities in the black mass were determined, including metallic elements (Cu, Al and Fe) and non-metallic elements (C, F and P). The impact of Cu introduced during precursor synthesis was determined in previous reports. Surprisingly, small amounts of Cu improve the electrochemical performance of synthesized NMC622. The last quarterly report described how Al introduced during precursor synthesis affects the morphology, structure, and electrochemical properties of synthesized NMC622 precursor and cathode powder.

In the past, we studied the impacts of four different cations (Cu^{2+}, Al^{3+}, Fe^{2+} and Fe^{3+}) on synthesized NMC622 precursor and cathode materials. This report mainly summarizes the impacts of carbon impurities on the synthesized NMC622 precursor and cathode materials. Unlike cations dissolved in a transition metal sulfate solution, nano-size carbon is suspended in the solution. Figure 1 is the SEM image of NMC622 precursor with 1% carbon, collected at different times. From the figure, the precursor particles are seen to become larger and more spherical with the reaction time, which is consistent with the reaction without any

impurities. The suspended carbon particles do not afFigure I.3.C.28 fect morphology of the precursor particles much. Figure I.3.C.29 is the cross-sectional image of synthesized NMC622 precursor and cathode powder with carbon impurity. It is found that some of the precursor and cathode particles exhibit a hollow structure. Nano-size carbon particles are embedded in the precursor particles, and after sintering, the carbon is burned. Therefore, for NMC622 cathode particles, there are no more carbon particles. Figure I.3.C.30 is the XRD of the precursor and cathode powder compared to the virgin materials. No impurity peaks are found, although there is slightly peak shifting, which suggests a change of lattice parameters.

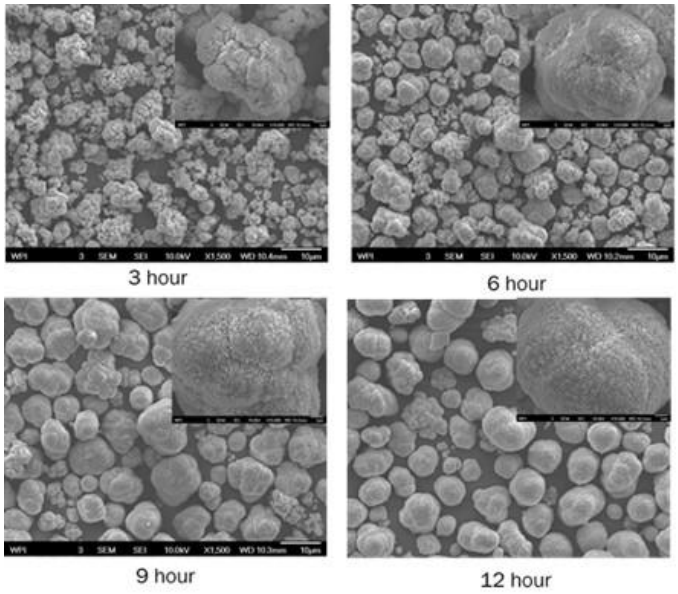

Figure I.3.C.28 Collected precursor particles at different times

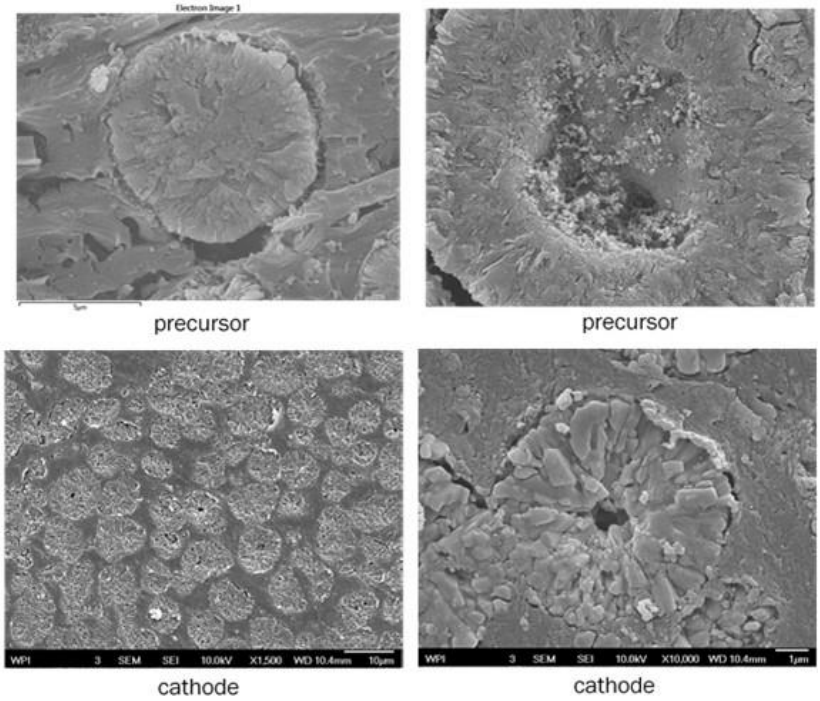

Figure I.3.C.29 Cross sectional images of synthesized NMC622 precursor and cathode particles with carbon impurity

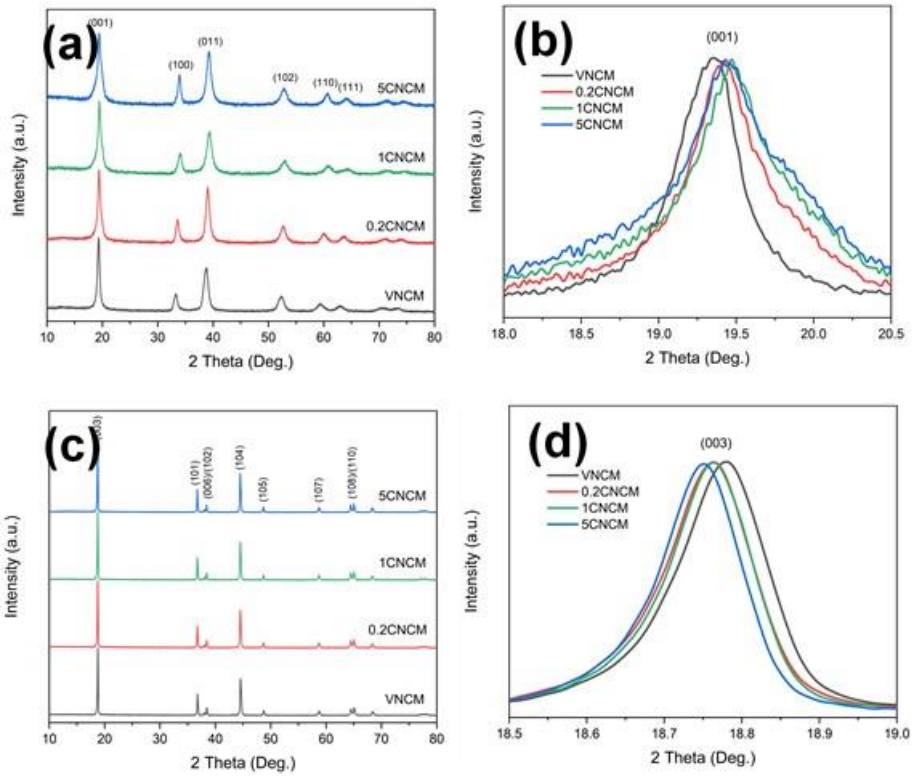

Figure I.3.C.30 XRD pattern of synthesized NMC622 precursor and cathode particles

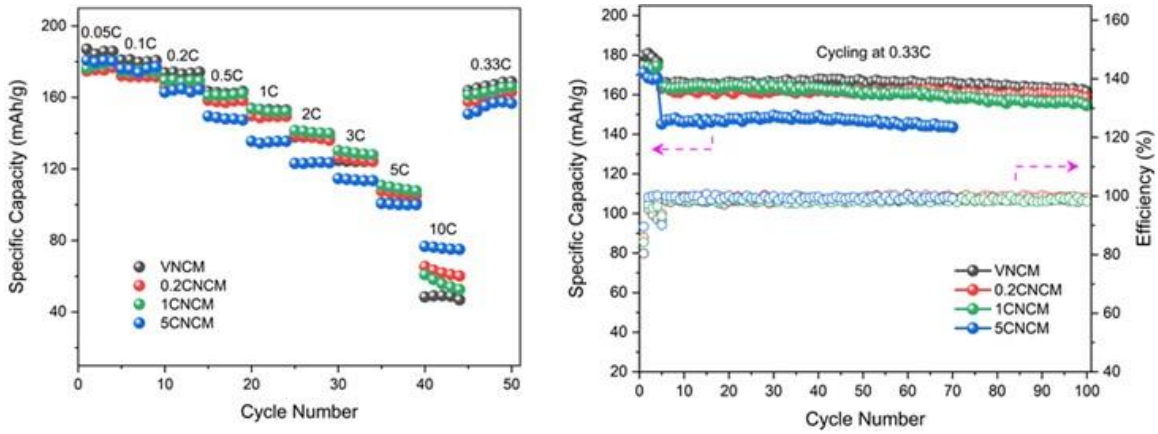

Figure I.3.C.31 Electrochemical performance of synthesized NMC622 precursor and cathode particles with carbon impurity

Figure I.3.C.31 is the rate performance and cycle life of the synthesized NMC622 with carbon impurity compared to the virgin material. NMC622 with 0.2% and 1% carbon has similar performance with virgin materials. However, it is surprising that NMC622 with 5% carbon has lower capacity than the virgin materials. Since carbon is burnt during the sintering process to form CO_2, NMC622 should not have any carbon left. Our hypothesis is that the transition metal valence could be changed due to the carbon burning, with loss of surface oxide, which affects the electrochemical performance of the cathode materials. This will be confirmed with XPS analysis.

Cell Preprocessing

Cell pre-processing is a new ReCell project in FY20. This task can encompass a variety of mechanical processes, including battery disassembly/dismantling, shredding/crushing/milling, and component separation. The primary goal is to determine scalable technologies/techniques that can safely and cost-effectively size

reduce batteries or manufacturing scrap. The separation of component materials also falls under cell pre-processing. When a battery is broken down via shredding/crushing/milling, the casing (pouch/can) material, separator, current collector foils, etc. need to be separated from the black mass or electrode laminates. It is important to explore the effects of size and size distribution of broken-down battery materials with respect to separation efficacy. The ideal end-product from cell pre-processing is contaminant-free black mass, or electrode laminates that can then be used as the starting material to recover clean black mass, cathode material, or anode material using optimized direct recycling processes within the ReCell Center.

Pre-processing cells is a critical step in ReCell's direct recycling model. The configuration of battery packs, modules, and cells varies among different electric vehicle models and presents significant challenges for disassembly and material liberation. Current commercial methods for battery shredding used by recyclers create a large amount of contamination. This contamination is an issue of great importance when direct recycling is the preferred route of recycling. Clean black mass is needed for direct recycling to be economically and technically viable. In addition, pre-processing techniques must not adversely affect separation processes further down the line (e.g., we may not want to shred with water because it will cause issues with the recovery of electrolyte salts).

Shredding Wetted Pouch Cells to Determine Effect on Fine Particle Contamination

Size reduction of dry, pristine pouch cells was demonstrated on four shredders (ST-15, ST-25, SSD, Camec) by one of our commercial partners and the results have been summarized in previous FY20 quarterly reports. The Camec and SSD shredders showed the greatest potential owing to increased liberation of cell layers and uniform size distribution of shredded material, respectively. In an attempt to replicate a more realistic approach to shredding batteries, the pouch cells were saturated with a non-flammable solvent. It was anticipated that saturating pouch cells with solution may influence shredding and fine particle contamination. Unfortunately, safety concerns and potential flammability lead us to replace the typical carbonate electrolyte with safer solvent. We chose a safe, non-flammable wetting agent, diethylene glycol, which is also a derivative of Solvent X used in other ReCell processes and known not to alter the electrode chemistry or morphology. Pouch cells saturated with diethylene glycol (DEG) were tested in the SSD (dual shaft) and Camec (single shaft) shredders (Figure I.3.C.32) and compared to results from dry, pristine cells.

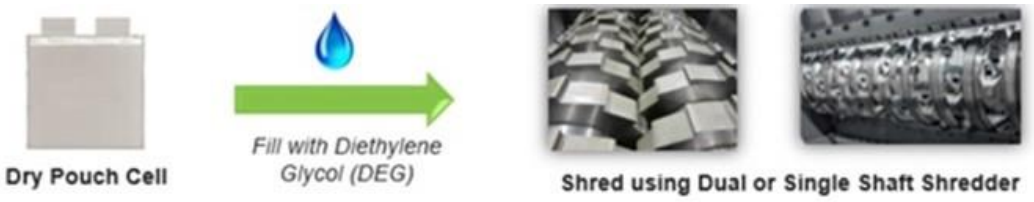

Figure I.3.C.32 Preparation of wet cells for shredding

The size and size distribution from the shredded wet cells appears to be consistent with the dry, pristine cells' (Figure I.3.C.33). Further examination of the pouch cells after shredding showed areas where the separator appeared to be wetted and other pieces of separator that were completely dry. Although DEG was added to each cell and sealed after removal from a vacuum chamber, the solvent did not seem to thoroughly and uniformly wet the cells. Sieving of the shredded wet cells (45 g of material in an 8" sieve) did not illuminate any significant differences in liberation of cells layers or fine particle contamination between dry and wet cells. These results may be due to the insufficient wetting of pouch cells using diethylene glycol or that DEG is not a suitable substitute for carbonate electrolyte in terms of wetting and penetrating pouch cell layers. This study was initially designed to be a step toward determining how cycled, end-of-life cells that are saturated with electrolyte would perform in a shredder. Cycled cells with the same electrode composition and format would provide a better comparison in future experiments.

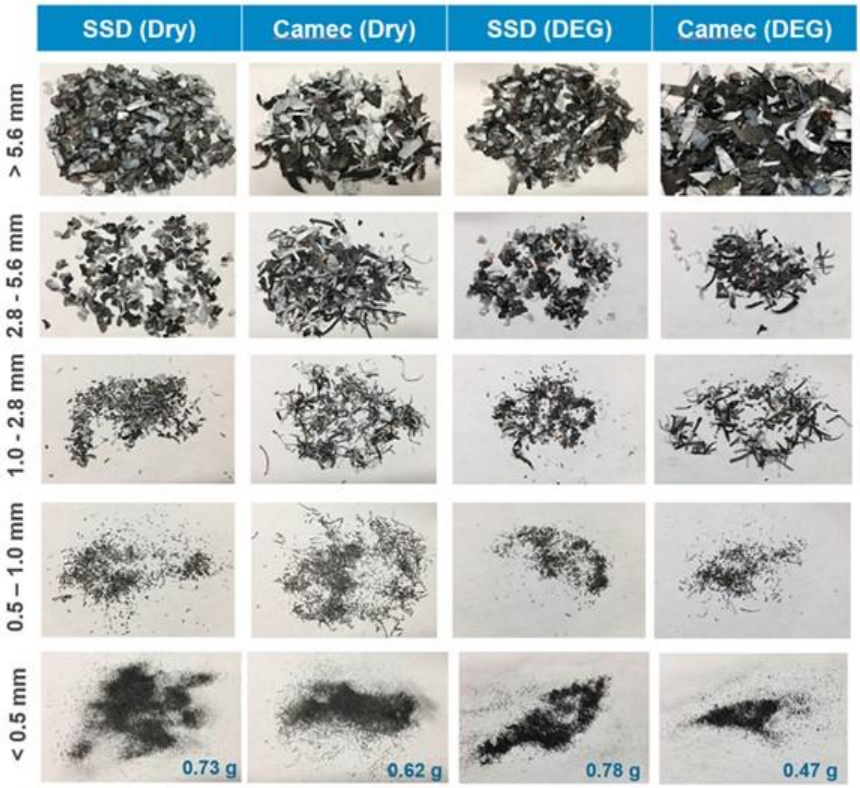

Figure I.3.C.33 Pouch cells size-reduced using SSD (dual shaft) or Camec (single shaft) shredders where the cells were either dry or wetted with diethylene glycol

Size Reduction Using a Hammermill

As a second size reduction technique, pristine, dry pouch cells were hammermilled by a commercial partner. The screen size in the unit and rotation speed were controlled during the milling process to determine the effect on fine particle contamination. The feed hopper of the hammermilling unit was not large enough to accommodate a whole pouch cell, therefore, the cells were cut in half prior to feeding (Figure I.3.C.34). Screens used during the milling process consisted of either 1" or 1.5" holes. The smaller the screen size, the more time the material will spend in the hammermill being broken down into small enough pieces that will fall through the holes in the screen and out of the bottom of the mill. This means that a smaller screen size will likely lead to more fine particle generation. The rotational speed of the hammers was also controlled at either 2,000 or 4,000 RPM. A portion of the milled pouch cell contents (45 g) was sieved through a stack of 8" sieves; results are shown in Figure I.3.C.35.

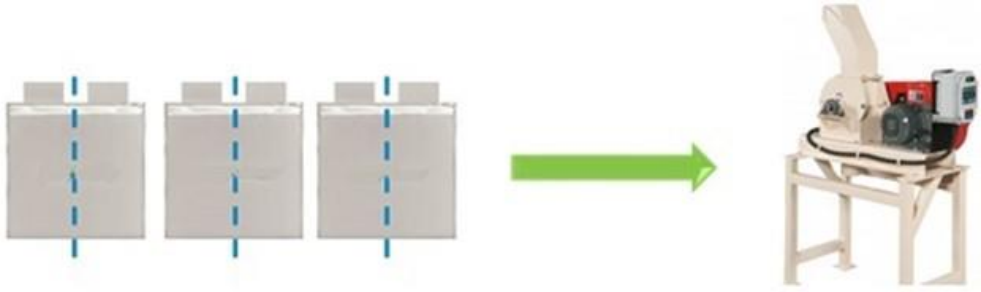

Figure I.3.C.34 Schematic showing that pristine, dry pouch cells had to be cut in half prior to feeding into the hopper of the hammermill

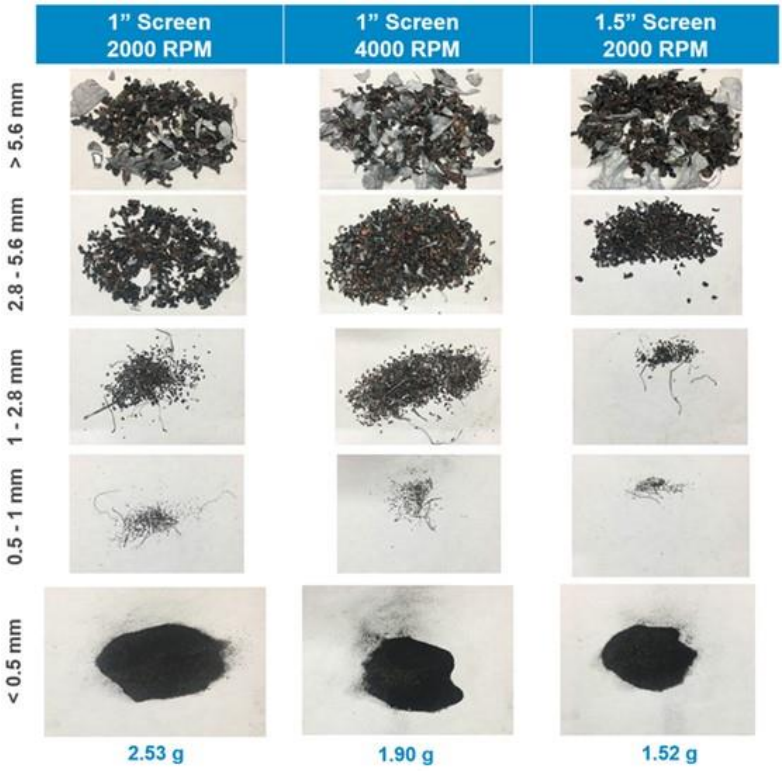

Figure I.3.C.35 Pouch cells size-reduced using a hammermill where the screen size and milling speed were controlled

From the images in Figure I.3.C.35 and Figure I.3.C.36, we can see that there is a significant difference in size between the plastic separator and electrodes in the >5.6 mm fraction. The elasticity of the plastic separator leads to reduced tearing and larger pieces after milling. In smaller size fractions, the size and shape of the plastic separator appears in ribbon-like strands and demonstrates a stark contrast to the bulk material. These characteristics may allow for easier separation of plastics from electrodes and other components further down the line.

In addition to size differences of milled pouch cell components, the quality of electrodes differs from those obtained after shredding. Compared to shredding, the integrity of the anode was considerably compromised during the hammermilling process. Images in Figure I.3.C.36 show that a majority of the graphite film is abraded from the copper current collector in the final product. Additionally, folded edges of cathode electrodes also exhibit various degrees of scuffing to the point where the aluminum foil current collector is visible. This type of abrasion during milling leads to a large amount of fine particles being produced. A smaller screen and slower rotation speed both contribute to increased fines during hammermilling.

Figure I.3.C.36 Detailed images of sieved fraction >5.6 mm after hammermilling showing size difference of separator vs. foil (left) and abrasion of graphite film from copper current collector (right)

Examination of Fine Particle Contamination after Hammermilling

The fine particle contamination from hammermilling was examined using scanning electron microscopy (SEM) imaging and energy dispersive X-ray spectroscopy (EDS) for elemental mapping. SEM imaging and EDS mapping was performed on fines that passed through a 0.5 mm sieve to determine which components of the shredded battery are present within this size regime (Figure I.3.C.37).

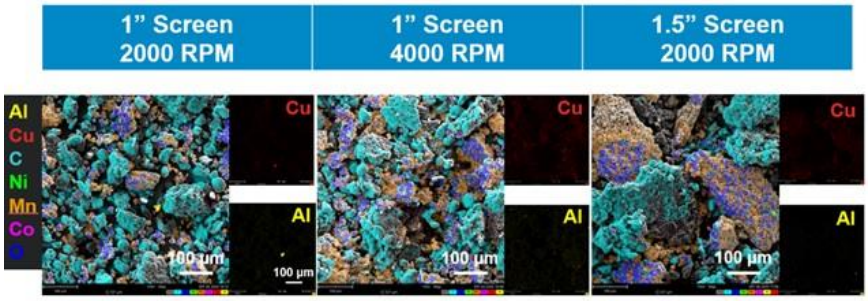

Figure I.3.C.37 SEM/EDS mapping of fine particle contamination (<0.5 mm) from hammermill experiments

The SEM/EDS images display evidence of graphite anode, NMC cathode, Al foil, and Cu foil. The small pieces of electrode in the samples are not observed to be attached to their respective metal foils. The delamination of the electrodes from foil was likely a result of the mechanical sheer force which abraded most of the anode film from the Cu current collector and the cathode from the edges of torn, folded electrodes. Pieces of Al and Cu foil were observed in both the micron and nanometer size range in mapped SEM images. This type of contamination, particular in the nanometer range, will be difficult to separate and can remain throughout the next steps of the direct recycling process. If this is the case, the metal contaminants will show up in the regenerated cathode material and may affect overall performance. The hammermill is often used by current lithium-ion battery recycling industries, such as hydrometallurgical processors, because they are looking to remove as much material as possible from the current collectors for recycling. However, for a direct recycling process the goal is to eliminate or reduce the quantity of fine particles generated during a size reduction process.

Comparison of Hammermill vs. Shredding

Pristine, dry pouch cells provided by a commercial partner were used in four different types of shredders and one hammermill. The shredders were demonstrated by an industrial vendor and they varied in the number of shafts (single vs. double), knife configuration, and the number and geometry of knife teeth. The hammermill was also demonstrated by an industrial vendor where the screen size and rotation speed were varied. The degree of material liberation, distribution of shred size, and fine particle contamination were analyzed for each piece of size reduction equipment by sieving through various sieves including 5.6 mm, 2.8 mm, 1 mm, and 0.5 mm mesh sizes. A comparison of the fines (<0.5 mm) from a 45 g batch of sieved material is shown in Figure I.3.C.38. The fines generated by hammermilling contribute to approximately 3.4%–5.6% of the total sieved material while shredding produced only 0.3%–1.6%. These numbers illustrate that hammermilling the same pristine pouch cells can lead to a substantial increase in fine particles collected as part of the bulk material.

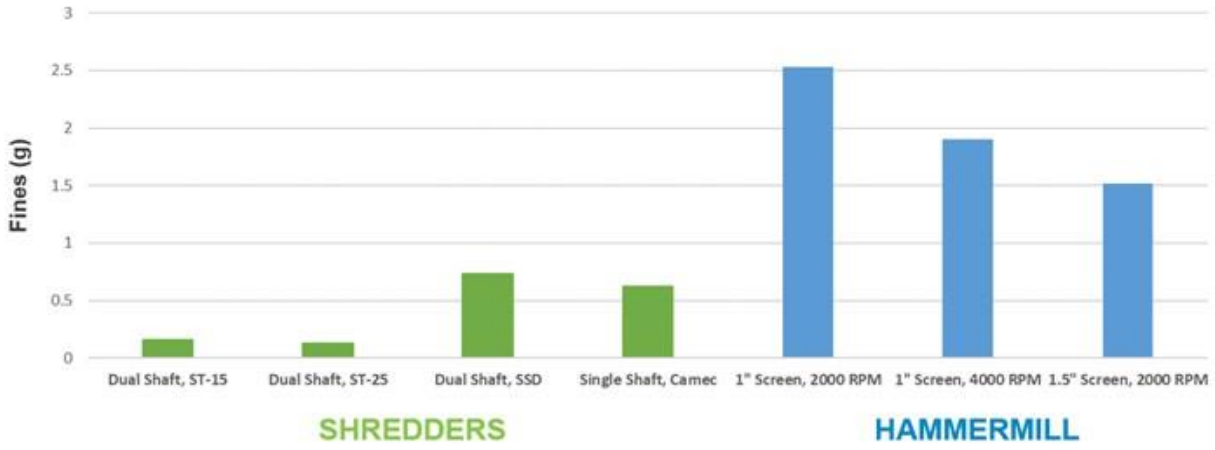

Figure I.3.C.38 Bar graph showing the fine particle contamination (<0.5 mm) produced via shredding vs. hammermilling

Size Reduction Using a Submersible Dual Shaft Shredder

In order for end-of-life battery size reduction to be conducted at scale and in a safe manner, precautions must be taken to exclude oxygen and moisture from the environment. Pristine, dry pouch cells have been shipped to another shredder manufacturer who has extensive experience in enclosed, inert shredders, and submersible shredders. The material was tested using a single-stage or two-stage approach to determine if more uniform size distribution could be achieved. Single-stage shredding means that the pouch cells were sent through the shredder and the second stage indicates that the shredded material was passed through the shredder again. The second stage appears to generate more fines; analysis of the material is in progress.

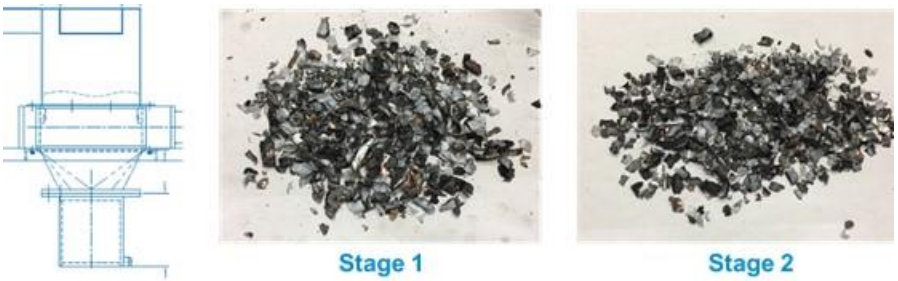

Figure I.3.C.39 Single-stage and two-stage shredding of pristine pouch cells in a submersible shredder

Future Work

Additional data (i.e., TGA and ICP) are being collected to give us insight into how much Al and Cu contamination is present in the fines and the approximate cathode:anode composition. It was observed that material shredded in the submersible dual shaft shredder fell apart more easily than material shredded by our previous industrial partner. Efforts are underway to determine the most effective method (*e.g.*, forced air, electrostatic, shear mixing) for liberating layers of pouch cell materials that are stuck together after size reduction.

Other efforts are being made to find a size reduction company that has experience with performing the operations cryogenically or at low temperatures, which would ideally deactivate the battery before it is broken open. Work is needed to determine at which temperature deactivation of the battery occurs. Determining this temperature threshold will enable us to fine-tune our processing parameters and give us insight into what type of infrastructure will be needed to create such an environment. A number of other factors must be taken into consideration when freezing batteries. These include how to approach condensation issues which could potentially add water to the process and decompose electrolyte before it is recovered, how to keep batteries

cold during the entire process, and the possibility of safety hazards if batteries are allowed to warm up to some extent before they are size reduced.

Work is also in progress to study end-of-life (EOL) EV batteries shredded in a dual shaft shredder by an industrial collaborator. This material was shredded under inert atmosphere (CO_2) and the electrolyte has been recovered. Particular attention will be paid to the integrity of the laminates and fine particle contamination during shredding of end-of-life batteries. Furthermore, collaboration is ongoing with Qiang Dai to include shredding in the EverBatt model, and we are exploring additional techniques for component separation (*e.g.*, electrostatic or forced air).

Solvent-based Electrode Recovery

This project will develop efficient recovery processes for the separation of black mass from current collectors. The separation processes use green solvents that are inexpensive, nontoxic, and do not cause water and/or air pollution, and do not incur a penalty in terms of damage to active materials and current collectors. The recovery of cathodes and anodes from spent Li-ion batteries has high peeling-off efficiency and is cost effective, scalable, energy efficient, and environmentally friendly. The work plan is based on a wet-chemical recovery approach for separating the black mass from metal foils by either solvating the PVDF binder or weakening its binding with laminates.

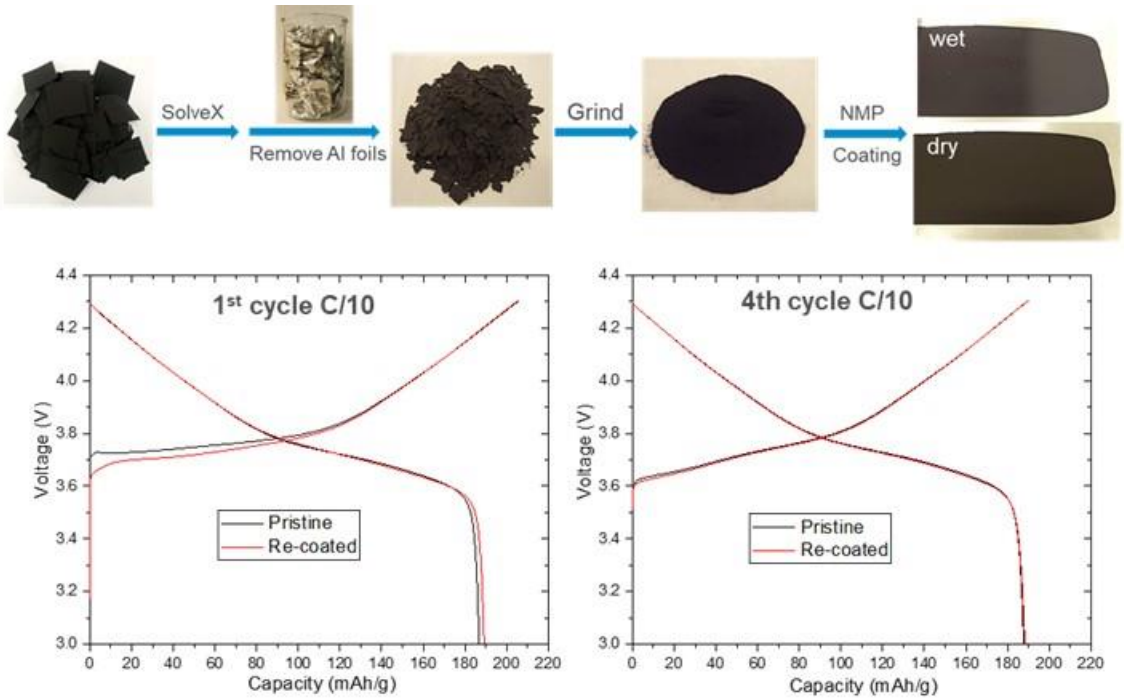

Figure I.3.C.40 Diagram with photos showing a separation and re-coating process for manufacturing cathode scraps (top) and charge/discharge voltage profiles for the pristine and re-coated NMC622 cathode (bottom).

As previously reported, cathode films could be rapidly delaminated from Al foils via a SolveX process. In this quarter, those delaminated cathode films were re-coated onto Al foils to produce new electrodes (Figure I.3.C.40). Specifically, cathode scraps of NMC622 from trimmings were treated in solvent X to form delaminated cathode films and Al foils, followed by washing with isopropanol to remove the residual solvent. After drying, those cathode films were ground into powder, as shown in Figure I.3.C.41. This powder contains NMC622, carbon black, and PVDF, with a similar weight ratio of 90:5:5 as the cathode scraps. NMP solvent was then added to produce the cathode slurry, followed by coating on the Al foil. Preliminary electrochemical testing in a half-cell shows that similar charge/discharge profiles were obtained for the re-coated electrode to those for the pristine one, as shown in Figure I.3.C.41.

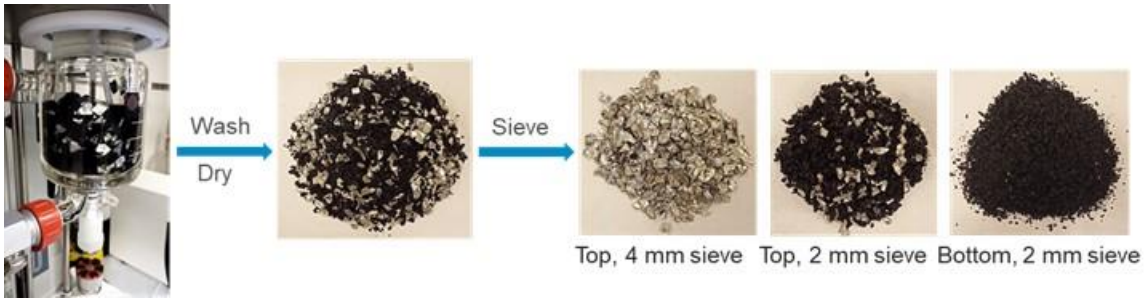

Figure I.3.C.41 Diagram with photos showing the delamination in a CSTR and separation of cathode films from Al foils through sieving.

After solvent delamination, the cathode films and Al foils need to be separated, which was previously demonstrated by hand picking. This is feasible only for lab-scale experiment. To scale up the process in an automated way, we proposed to break the cathode films to smaller pieces through mechanical stirring in solvent X so that these smaller cathode pieces can be sieved and separated from the Al foils. As shown in Figure I.3.C.42, cathode scraps were delaminated in a continuous stirred tank reactor (CSTR). Mechanical stirring was utilized to tear cathode films into smaller pieces in solvent X. The mixture of delaminated cathode pieces and Al foils was dried and passed through two sieves (4 mm and 2 mm) successively to separate them, as shown in Figure I.3.C.42. However, some of the cathode pieces were not separated due to their similar sizes to the Al foils. This is because the cathode films are quite flexible in the solvent, which makes it hard to reduce their size. In addition, mechanical stirring would break Al foils, introducing small Al pieces to the cathode films and making it hard to separate. As dry cathode films are more brittle than Al foil, breaking them under dry conditions is being explored.

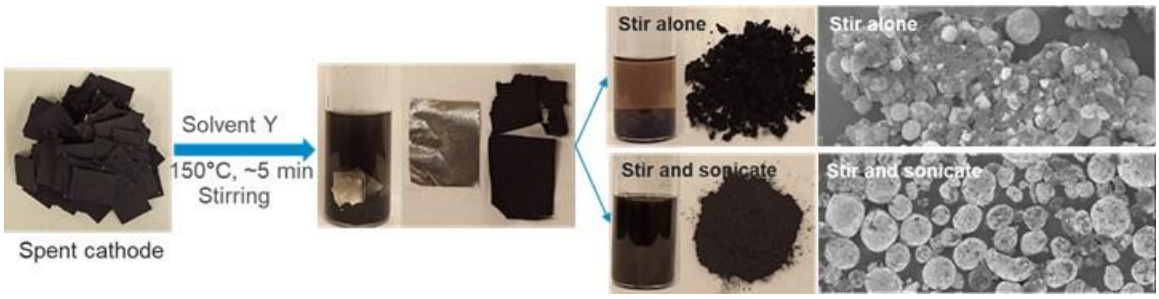

Figure I.3.C.42 Diagram with photos showing the recovery of spent cathode in the solvent Y (left) and digital images and SEM images showing the differences between stir alone and stir & sonication (right).

The solvent Y based process previously demonstrated separation of cathode particles from Al foils through dissolving PVDF. This process has been successfully utilized for recycling cathode scraps. Previous results showed that cathode powder could be recovered by stirring the cathode scraps in solvent Y at 100 °C for 1 h. In this quarter, we investigated the solvent Y based process for the recovery of spent cathode. Pouch cells made of NMC622 and graphite were fabricated at the DOE's Battery Manufacturing Facility. Those cells were charged and discharged at 1C rate for 1000 cycles and considered as spent cells. Spent cathode of NMC622 was washed with DMC to remove electrolyte, followed by cutting into small pieces. The same reaction conditions as for the recovery of cathode scraps were applied to recover spent cathode powder but failed. It was found that delamination of cathode films from Al foils occurred when the reaction temperature was increased to ~150 °C, as shown in Figure I.3.C.42. Further stirring the cathode films in solvent Y at 150 °C, however, could only break the cathode films to smaller pieces, as shown in the digital photos and SEM image in Figure I.3.C.43. In contrast, we found that sonication could help the dissolution of the PVDF binder in solvent Y. As shown in Figure I.3.C.43, isolated cathode particles were obtained after sonication. One major difference between cathode scraps and spent cathode is that a cathode electrolyte interface (CEI) layer is formed on the spent cathode, which may affect the kinetics of dissolving PVDF. Sonication may break the CEI

layer and facilitate the dissolution process. Optimization of the reaction conditions to recover spent cathode particles is being investigated.

Anode/Cathode Separation and Purification

After battery shredding, electrolyte recovery, and component separation (*i.e.* plastics, cell casing, magnetic ferrous-based metals), we are left with electrode fragments that include anode/copper foil and cathode/aluminum foil. Most recycling efforts focus on recovering the cathode materials and metals, which neglects the potential value from recovering anode material. The focus of this project is to separate and recover usable anode materials from black mass. The cost contribution of anode powder in a typical cell is approximately 10%. Being able to efficiently produce multiple clean streams of material (cathode, anode, and Al/Cu foil) and avoid waste disposal costs will make direct battery recycling more profitable.

The separation of anode, cathode, and metals can be achieved in several ways (Figure I.3.C.43). First, thermal binder removal can be performed on the anode/cathode mixture to yield one product streams consisting of mixed Al/Cu foils that can be sieved from the other, which consists of combined anode/cathode powders. The second method would produce cleaner product streams, but would require an extra processing step. This method would separate the electrode laminates while still attached to their foils. One product would be cathode on Al foil and the other, anode on Cu foil. Thermal binder removal would be performed on the two batches to produce separate streams of Al foil, Cu foil, anode powder, and cathode powder. The presence of four separate product streams at this point would significantly streamline subsequent steps in the direct recycling process.

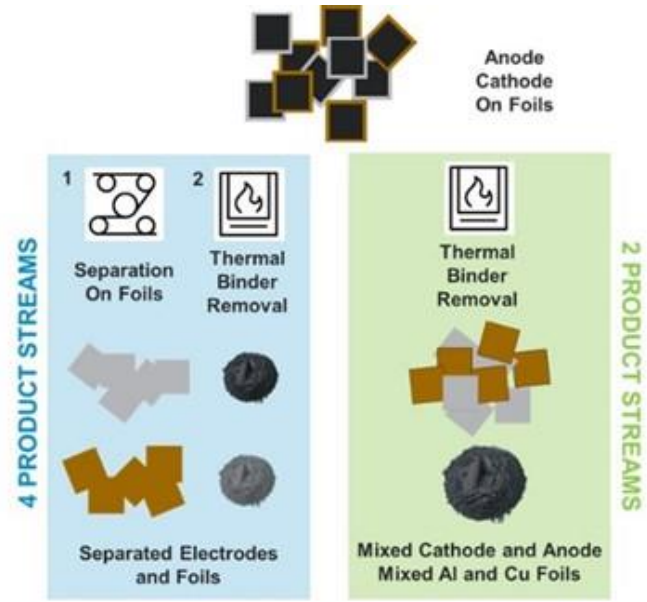

Figure I.3.C.43 Methods of separating anode, cathode, and metal foils

The properties of the powders or metals are being exploited to determine the most efficient techniques for separation (Figure I.3.C.44).

Figure I.3.C.44 Properties of cathode powder vs. metals

Magnetic Separation

Preliminary magnetic separation tests were initiated by Erik Dahl (ANL) for anode/cathode separation and conducted with the help of an industrial partner. Magnetic separation experiments were performed on an aqueous slurry consisting of a 50:50 anode/cathode powder mixture at 5% solids loading in water. The magnetic and non-magnetic fractions were collected using the methodology in Figure I.3.C.45 after 1 pass over the magnet at various magnetic field strengths (i.e., 1, 2, and 3 T).

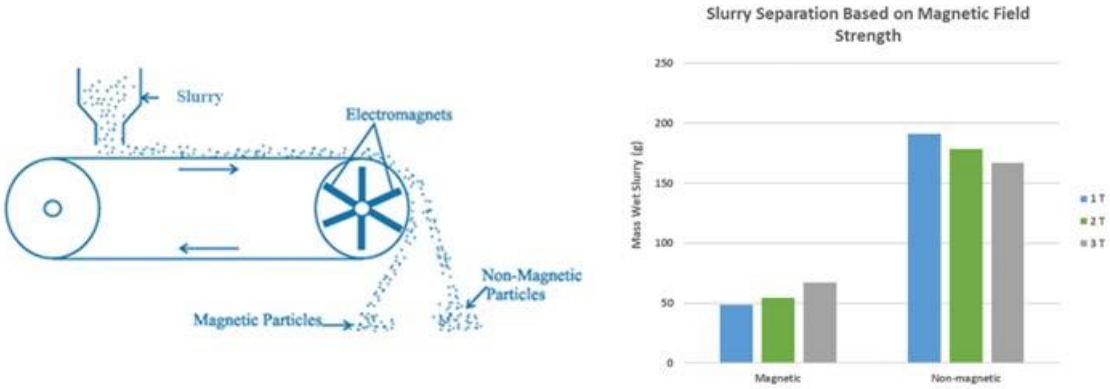

Figure I.3.C.45 Methods of separating anode, cathode, and metal foils

Several characterization techniques were used to characterize the magnetic and non-magnetic fractions at various field strengths. Samples were first examined using scanning electron microscopy (SEM) imaging and energy dispersive X-ray spectroscopy (EDS) for elemental mapping to determine the approximate anode:cathode composition of each fraction (Figure I.3.C.46 and Figure I.3.C.47).

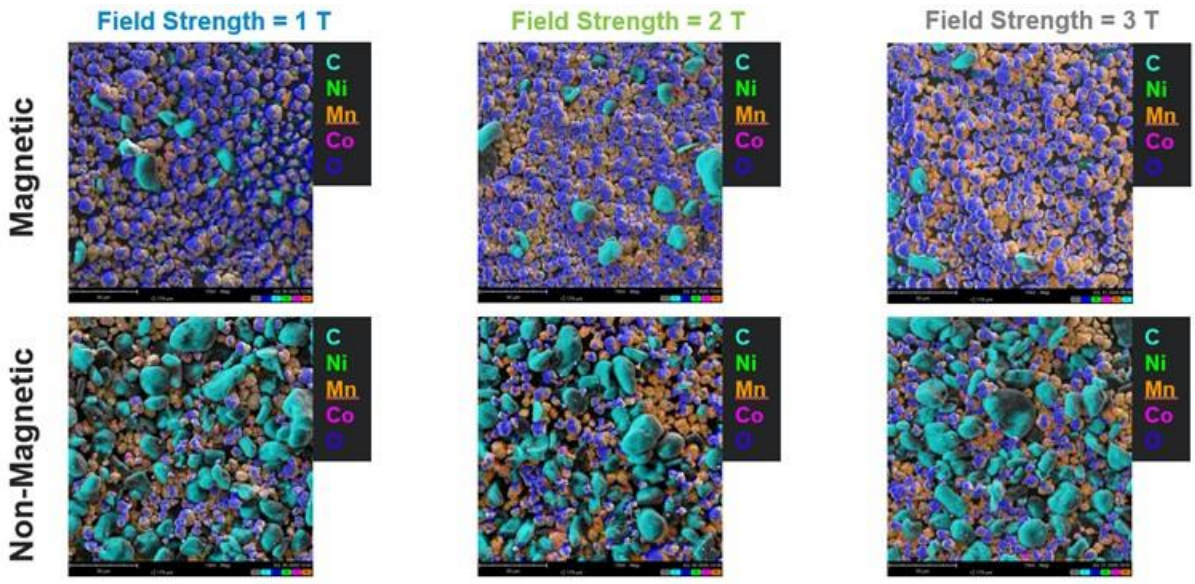

Figure I.3.C.46 SEM/EDS mapping of magnetic and non-magnetic fractions at various field strengths

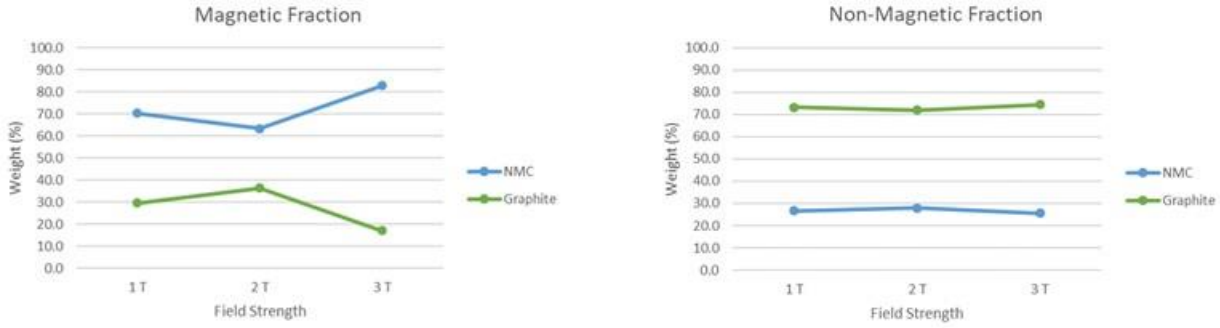

Figure I.3.C.47 Anode:cathode compositions calculated from EDS mapping for magnetic (left) and non-magnetic (right) fractions at various field strengths

SEM imaging and EDS mapping results show that the composition of the non-magnetic fractions is fairly consistent at 1, 2, and 3 T, where the mixture contains 73% graphite and 27% NMC on average. On the other hand, the separation efficiency of the magnetic fraction may increase with higher magnetic field strength. The composition of anode:cathode in the magnetic fraction was 30:70 and 17:83 for 1 T and 3 T field strengths, respectively.

The magnetically separated samples were also characterized using X-ray diffraction (XRD) and thermogravimetric analysis (TGA) with simultaneous mass spectrometry (MS) as shown in Figure I.3.C.48. The XRD illustrates the strong presence of graphite peaks in the non-magnetic samples while weaker graphite signals are observed in the magnetic fractions. These data agree with the SEM/EDS results, which show a higher concentration of graphite in the non-magnetic fraction. We plan to use Rietveld analysis to determine the ratio of graphite to NMC within each sample. Using TGA-MS we observe the decomposition of graphite within each sample as a function of temperature, up to 900°C. Within this window NMC will not decompose, which will allow us to estimate the composition of the mixture by the weight loss due to graphite. The MS confirms that CO_2 is evolved from 600-800°C and agrees with data collected for the decomposition of a pure graphite sample. The magnetic fraction collected at 2 T shows a weight loss of about 9%, which is lower than what was estimated using SEM/EDS. This run included heating the sample at 5°C/min to 900°C and didn't allow for all of the carbon to burn off. A more recent TGA run of pure graphite included a 1 h hold at 750°C

and demonstrated nearly 100% weight loss. We are in the process of recalibrating our TGA instrument after replacement of the heating elements and will re-run every sample with the optimized conditions. Additionally, a number of standards are currently being run to generate a calibration curve for analyzing the composition of anode/cathode mixtures using a variety of characterization techniques (SEM/EDS, ICP, and TGA).

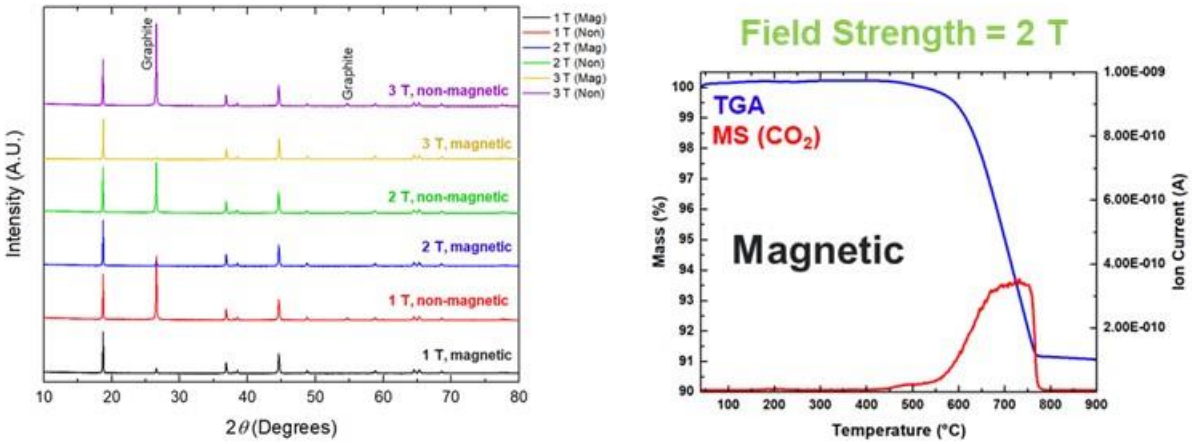

Figure I.3.C.48 XRD and TGA-MS of magnetically separated samples

In summary, the magnetic separation experiments shown here (i.e., 1 pass over the magnet at 1, 2, and 3 T) show a separation efficiency of approximately 70%–80% cathode in the magnetic fraction and about 70% graphite in the non-magnetic fraction. This separation efficiency is relatively low compared to froth flotation, another anode/cathode separation technique in the ReCell Center, which can generally achieve over 90% efficiency on the first pass. The efficiency of magnetic separation may be improved by diluting the solids content of the slurry to reduce entrapment of unwanted particles during separation, performing multiple passes, or by further optimizing magnetic field strength. In order for this technique to be competitive with froth flotation, it would need to achieve greater than 90% separation efficiency on the first pass or within a few rapid passes to maintain high-throughput in the process.

Flotation Experiments

Flotation of anode and cathode foil while still attached to their respective Cu and Al foils is of interest as the density of the metal foils and hydrophobicity of the anode can be taken advantage of. Using non-aqueous solvents for separation is of benefit for batteries with cathode compositions that are higher in Ni content than NMC111 (*e.g.*, NMC532, NMC622, and NMC811). Ni-rich cathode compositions are less stable in water, leading to Li leaching from the particle surfaces and increased pH. If Al foil is also present in the solution, high pH will liberate Al^{3+} ions from the metal, which can contaminate electrode powders in the direct recycling process. Each of these are reasons to carefully select a solvent for separation processes. Flotation experiments have been conducted to study the flotation of shredded materials in water, diethylene glycol (*i.e.*, derivative of Solvent X), carbonate, and isopropyl alcohol (IPA), and the results are shown in Figure I.3.C.49. Using a solvent like carbonate or Solvent X, that is already present in the direct recycling process may streamline the recycling model and reduce waste. Depending on which point in the process these solvents are used, the stability of electrolyte salt will be important.

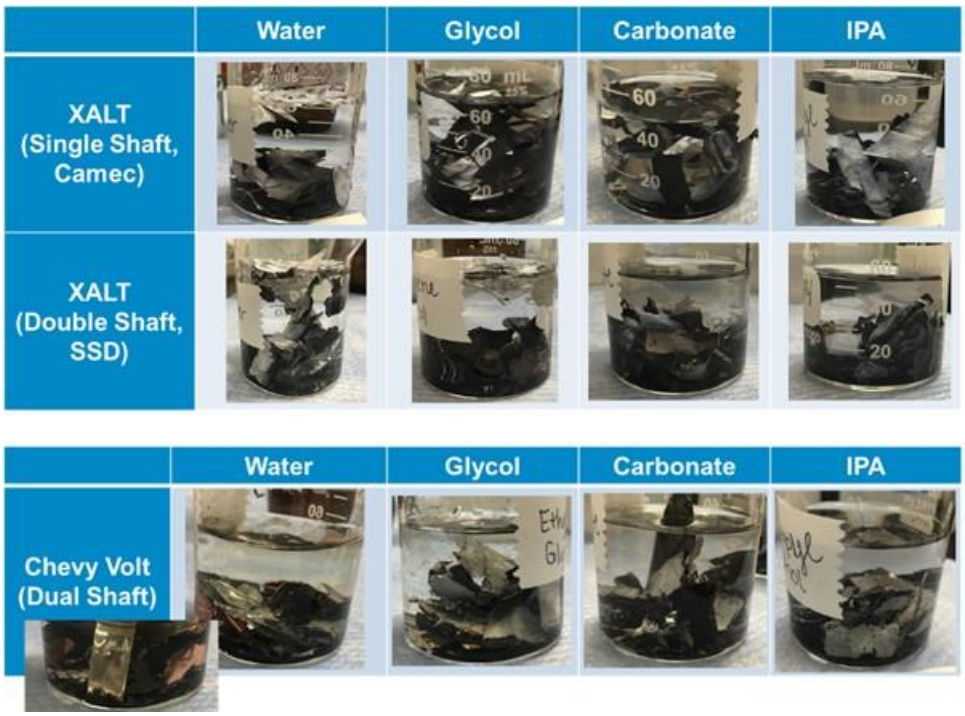

Figure I.3.C.49 Flotation experiments using water, glycol, carbonate, and isopropyl alcohol (IPA) on shredded pristine pouch cells (top) and end-of-life cells (bottom)

Three types of shredded cells were used in this experiment. Dry, pristine pouch cells that were shredding using either a single- or double-shaft shredder or end-of-life (EOL) EV batteries shredded with a dual-shaft shredder by an industrial collaborator. This EOL material was shredded under inert atmosphere (CO_2), and the electrolyte had been recovered prior to flotation experiments.

The flotation experiments for shredded pristine pouch cell materials in water and glycol show that the plastic separator has an affinity to float while the other pouch cell components sink to the bottom of the beaker. In carbonate and IPA, the pristine cell materials sink to the bottom of the beaker and no significant flotation effects are observed.

The flotations results for shredded end-of-life cells are quite different compared to pristine cells. Overall, the electrodes are more fragile in cycled cells, where more flaking of the electrodes from the current collectors after shredding is observed. When introduced to water, the graphite film readily de-laminates from the current collector. Furthermore, this water is discolored (slightly yellowish-brown) and, depending on the state of charge of the cell, may be related to the exfoliation of graphite. Another interesting observation is that the separator that was previously saturated with electrolyte in the cycled cell is less prone to floating on water or glycol. The results for carbonate and IPA are similar, with the materials sinking to the bottom of the beaker. It is important to note that the end-of-life cells had been discharged and sat on a shelf at the company for some time before shredding, so the exact state of the battery is unknown. The results, while proof-of-concept, suggest that different processes may be needed for EOL batteries *vs.* manufacturing scrap.

Future Work

Separation technologies being pursued at Argonne include froth flotation and dry separation techniques. Additional experiments are being performed with the help of an industrial partner using eddy current and electrostatic processes. The ReCell Center has recently purchased its own eddy current separator for separation experiments.

Electrolyte Component Removal and Recovery

Electrolyte must be removed from the electrode materials to allow for further recycling processes. This can be done in several ways, including supercritical CO_2, thermal drying, water washing, and solvent extraction. Of these, only supercritical CO_2 with added co-solvent or solvent extraction can recover the $LiPF_6$, which is the most valuable component of the electrolyte. Last year, we demonstrated that the electrolyte salt could be extracted by diethyl carbonate, and then reconstituted with cycling performance exceeding that of 1.2 M $LiPF_6$ in 3:7 EC:EMC electrolyte. This year, the goal is to determine a method to further purify the $LiPF_6$ salt in a cost-effective manner. We also plan to model the process cost, and to scale the process to supply cleaned cycled materials to downstream processes.

After the initial success of recovering electrolyte from cycled commercial cells from one manufacturer, we wanted to validate the recovery process for electrolyte from other cell manufacturers, so we attempted a similar process on a different manufacturer's cells. These were shredded end-of-life cells, unlike the cells from the original manufacturer, which were hand disassembled, with only the electrodes extracted. Figure I.3.C.50 shows the resulting electrochemical performance for coin cells with NCM111 cathode with graphite anodes. The initial capacity and fade of the electrolyte extracted from manufacturer #2 is poorer than that from manufacturer #1 and the baseline electrolyte. It is suspected that this electrolyte decayed during storage in the glovebox, which was demonstrated in a color change. The behavior of the extracted electrolyte could be due to differences in formulation between the two manufacturers, or to potential contamination with water during the shredding process. Although this electrolyte shows an initial poor capacity, it thereafter shows fading rates similar to the electrolyte recovered from manufacturer #1 cells. This is indicative that the main issues are likely due to handling and moisture content, and not to fundamental differences in the electrolyte composition and chemical stability.

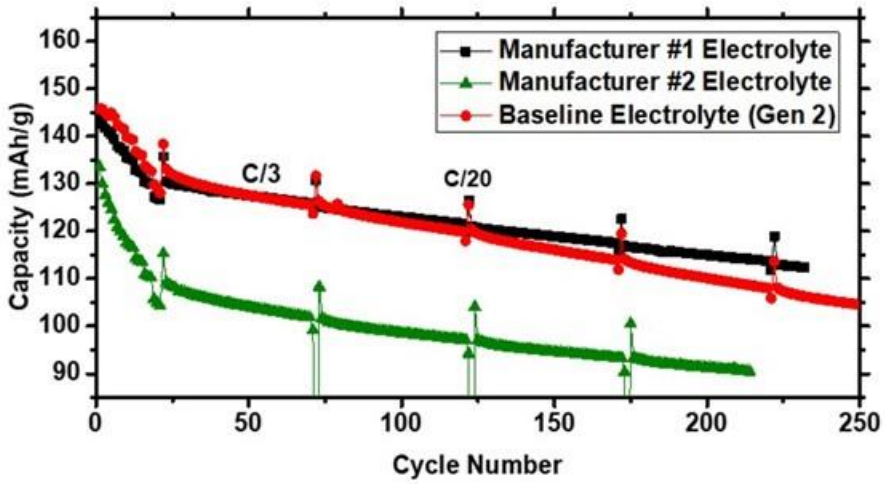

Figure I.3.C.50 Electrochemical cycling in coin-type full cells with NCM 111 cathode and graphite anode with electrolytes extracted and reconstituted from end-of-life Li-ion batteries.

We are continuing to search for an effective method of purification for extracted $LiPF_6$ to make the final product uniform and adhere to battery-grade specification. One possible method is using supercritical CO_2 extraction to purify the crude recovered salt. We had noted previously that this method cannot extract $LiPF_6$, but only carbonate solvents and other components. The concept was first demonstrated on a simple mixture of $LiPF_6$ salt with propylene carbonate (PC) added. This quarter we utilized this method on more realistic electrolytes extracted from commercial used batteries (manufacturer #2) with added PC. Before supercritical CO_2 extraction, the electrolyte contained about 11% PC with a 4.7:1 ratio of ethylene carbonate (EC) to PC. After the first extraction, this ratio increased to 10.9:1, however, the two additional supercritical CO_2 cycles did not substantially improve the ratio further. During this process a substantial amount of $LiPF_6$ was

decomposed and converted to POF_3 and HF, as seen in the NMR. This is probably due to handling, as the extractor is not in an inert atmosphere, and there was possible moisture exposure during shipping. This makes it extremely difficult to determine the actual purity of $LiPF_6$ that could be achieved if the process were run in suitable conditions.

Table I.3.C.13 NMR analysis of electrolyte extracted and crystallized from cells with PC added, which was then extracted with supercritical CO2 for different numbers of cycles

$SCCO_2$ Cycles	$LiPF_6$ (%)	EC (%)	PC (%)	EC/PC
0	36.5	52.5	11.1	4.7
1	3.5	88.3	8.1	10.9
3	1.0	90.9	8.1	11.2

Cell Design

Current lithium-ion batteries are manufactured with little consideration for recycling. Developing a new cell design that allows for cell maintenance could of great interest, as it can extend cycle life. As a result, the number of batteries to be recycled could be significantly reduced, alleviating the demand for battery materials and the pressure on battery recyclers. In FY19, we developed new cell configurations with external ports on both cylindrical and pouch cells. We investigated the flow-pressure relation when flushing liquid through the cells. Promising preliminary results were obtained, showing capacity recovery from the rinsed spent electrodes. We also used the battery technoeconomic model BatPac to estimate the energy densities in the new designs. Depending on the cell and pack design, there would be 1%–13% reduction in energy density in the new designs to accommodate the ports and tubing. In FY20, we focused on optimizing the rinsing protocol, understanding the compounds that are washed off from the spent electrodes, restoring Li to the spent cathodes, and demonstrating capacity recovery and cycle life extension.

Rinsing pouch cells with test fixture

After 550 cycles at C/3, one three-pouch cell was cut open at one side and an amount of electrolyte equal to its initial loading during cell assembly was added. The cell was resealed under vacuum and rested for six hours before going through cycles at C/3. As shown in Figure I.3.C.51(a), the cell demonstrated excellent cyclability (red curve) with 0.034% capacity fade per cycle. The blue curve shows the cycles with fresh electrolyte added. There is slight but insignificant increase in capacity. The capacity fade rate is identical to that during the previous 550 cycles. The working electrode voltage (EWE-ERE) and counter electrode voltage (ECE-ERE) increase in the first cycle after adding fresh electrolyte (Figure I.3.C.51(b) and Figure I.3.C.51(c)). As adding fresh electrolyte should not result in voltage increase in the EWE and ECE, the voltage increase may be due to the re-sealing, the reason is not yet fully understood. The EWE and ECE after 100 cycles are reduced compared to the first cycle.

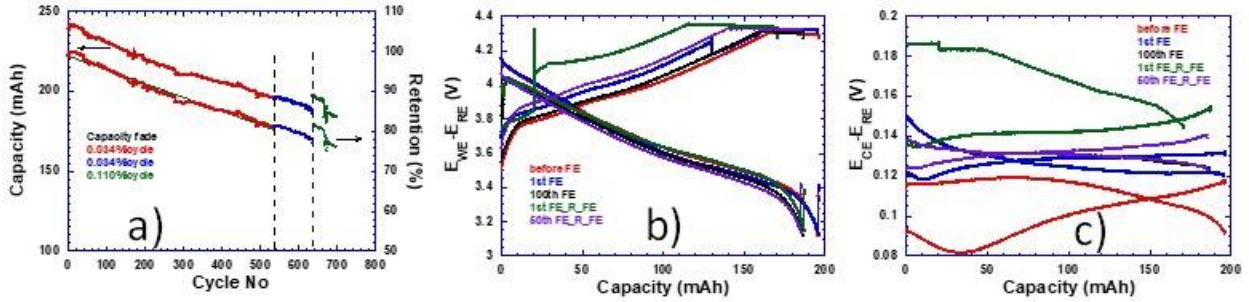

Figure I.3.C.51 Comparison of capacity (a), and voltage of the working electrodes (b) and counter electrodes (c) before and after rejuvenation.

After 100 cycles, the cell was reopened on the same side as previously and rinsed with dimethyl carbonate (DMC) twice before adding electrolyte back. The cell was sealed with DMC inside and rested for 30 min before being cut open to drain the DMC, and the rinsing process was repeated. The cell was left in a fume hood in a dry room for one hour with one side open. Then, the initial quantity of electrolyte was again added. The cell was sealed under vacuum and rested for six hours before cycling 50 times at C/3. There was a 6% capacity recovery. Based on a capacity fade rate of 0.03%/cycle, the capacity recovery could extend the cycle life by 200 cycles. However, there was a significant capacity drop after 31 cycles, reversing all the capacity gain and returning to the same capacity as at the end of 100 cycles with fresh electrolyte. Similarly, the EWE and ECE in the first cycle after treatment increase but then reduce after 50 cycles. The initial increase in ECE and EWE is likely attributed to removal of (part of) SEI on the graphite anodes and/or the aforementioned resealing. Another reason could be lithium leaching from the NMC622 cathode into DMC.

Rinsing pouch cells without test fixture

Another cell went through 600 cycles with excellent performance as shown in Figure I.3.C.52(a). The cell was removed from the test fixture, rinsed with DMC and injected with fresh electrolyte following same procedure as discussed in the previous paragraph. Compared to rinsing the cell with a test fixture, there is no capacity recovery but 6% drop instead. The cell also fails after ~50 cycles. The EWE increases quickly during first charge cycle after treatment with only 60% charge capacity (Figure I.3.C.52(b). However, the first cycle discharge capacity only drops ~6%. Similar to the treatment with a test fixture, EWE increases significantly during charge, while ECE reduces. The increase in EWE indicates significant polarization, which could be ascribed to loosening of contact between electrodes during rinsing. There are materials rinsed into the rinsing solution, including some black debris.

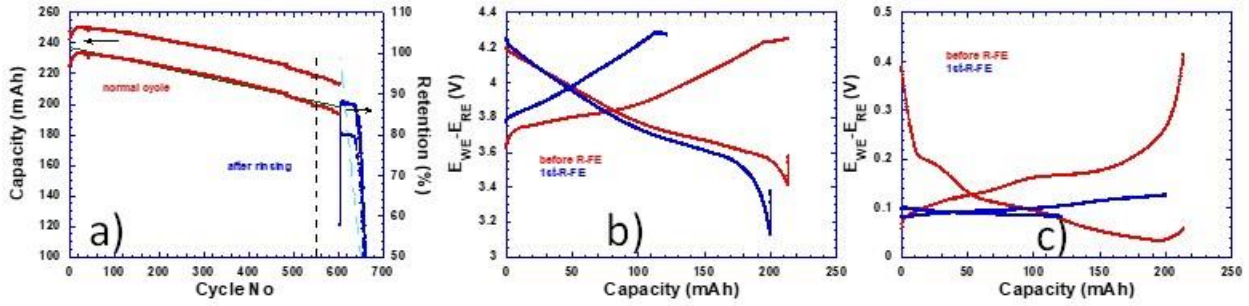

Figure I.3.C.52 Comparison of capacity (a), and voltage of the working electrodes (b) and counter electrodes (c) before and after rejuvenation.

Rinsing pouch cells with CAN and without test fixture

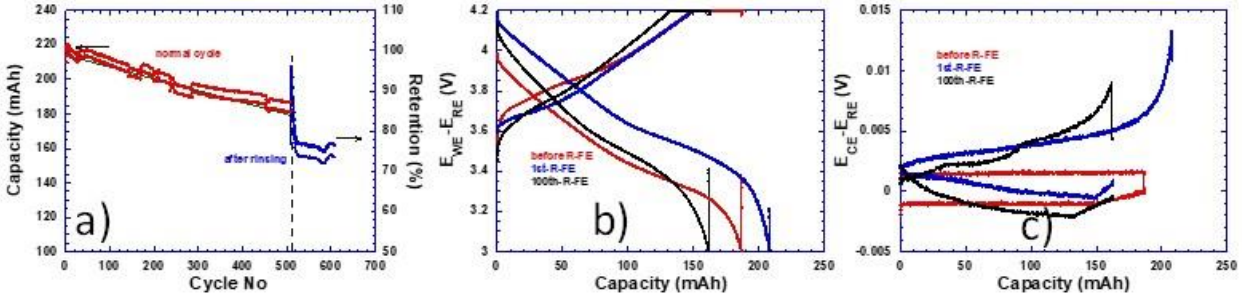

Figure I.3.C.53 Comparison of capacity (a), and voltage of the working electrodes (b) and counter electrodes (c) before and after rejuvenation.

The effect of different solvents on rinsing efficacy was investigated. The same experimental protocols were adopted, replacing DMC with acetonitrile (CAN),. The results (Figure I.3.C.53) are similar to those in Figure I.3.C.52, supporting the idea that rinsing aged cells without a test fixture may damage the electrodes, resulting in higher polarization and inducing adverse effects on cycle life.

EverBatt: Cost and Environmental Impacts Modeling

Recycling has the potential to reduce the cost and environmental footprint of lithium-ion batteries (LIBs). Argonne has developed the EverBatt model to estimate the cost and environmental impacts associated with closed-loop recycling of LIBs. We will use the model to evaluate the recycling processes and design-for-recycling (DfR) strategies developed under the ReCell Center, and help inform and direct the R&D efforts. Specifically, we will

1. Expand EverBatt to include unit processes proposed for direct cathode recycling and recovery of other battery components;

2. Increase the granularity of the battery manufacturing module and the recycling module in EverBatt to enable evaluation of DfR strategies; and

3. Develop customized versions of EverBatt for specific recycling techniques to identify cost/environmental hotspots and barriers to commercialization.

During Q4 FY2020, we focused on getting EverBatt ready for its 2020 release. Major expansions and updates in EverBatt 2020 include

1. the addition of battery pack manufacturing;

2. the addition of battery pack and module disassembly;

3. the addition of $LiNi_{0.5}Mn_{0.3}Co_{0.2}O_2$ (NMC532) as a new cathode chemistry, including NMC532 battery manufacturing and recycling, and NMC532 cathode powder production;

4. a refined logistics module that separates packaging cost from transportation cost and accounts for the impact of truck payload on transportation cost;

5. background data update based on BatPaC4.0, GREET2020, and most recent prices for materials and utilities.

Preliminary analyses with EverBatt 2020 demonstrate that logistics cost in EverBatt 2019 is likely overestimated and may not play as significant a role in total recycling cost as previously thought. In the absence of sufficient data, the logistics cost in EverBatt 2019 is calculated based on a simple linear model that

extrapolates class 9 hazardous material transportation cost by truck for all transportation distances from 2012 national data for an average transportation distance of ~70 miles. The refined logistics module in EverBatt 2020, takes into account packaging cost, truck operating cost per mile, and truck payload. As shown in Figure I.3.C.54, transporting batteries in bulk and reusing packaging materials represent great opportunities to reduce logistics cost, and should become feasible in the near future as the amount of batteries available for recycling continues to grow. Transporting batteries in bulk, however, would necessitate battery storage between transportation segments. We had originally planned to add battery storage to EverBatt 2020, but decided to address it in the next release because not enough information, especially which for the fire suppression system required at the storage facility, is available at present. Admittedly, without battery storage cost, the baseline and lower bound logistics costs shown in Figure I.3.C.54 could be too optimistic.

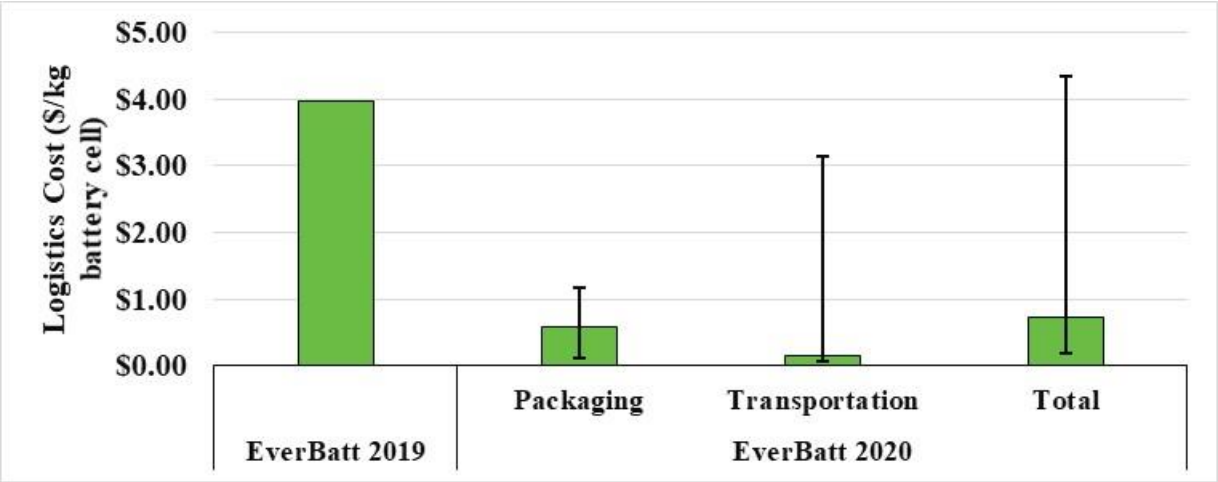

Figure I.3.C.54 Comparison of logistic cost in EverBatt 2019 and that in EverBatt 2020, for a collection transportation distance of 50 miles, and a recycling transportation distance of 500 miles. Baseline logistics cost in EverBatt 2020 assumes using the same packaging for all transportation segments, and a half-loaded truck. Lower bound assumes reusing packaging for 4 times, and a fully loaded truck. Upper bound assumes repackaging once during transportation (e.g. after disassembly) and transporting only 1 Tesla Model 3 battery pack per truck.

Preliminary analyses with EverBatt 2020 also demonstrate that battery pack and module disassembly could be quite expensive, because the processes are labor intensive but do not recover much valuable material. Figure I.3.C.55 shows that battery disassembly is a significant contributor to the total closed-loop recycling cost, only second to cathode powder production. It should be noted that EverBatt 2020 only includes manual battery disassembly. Automated battery disassembly could drastically reduce the labor requirement and thereby reducing the associated cost, and should be investigated in the next iteration of EverBatt.

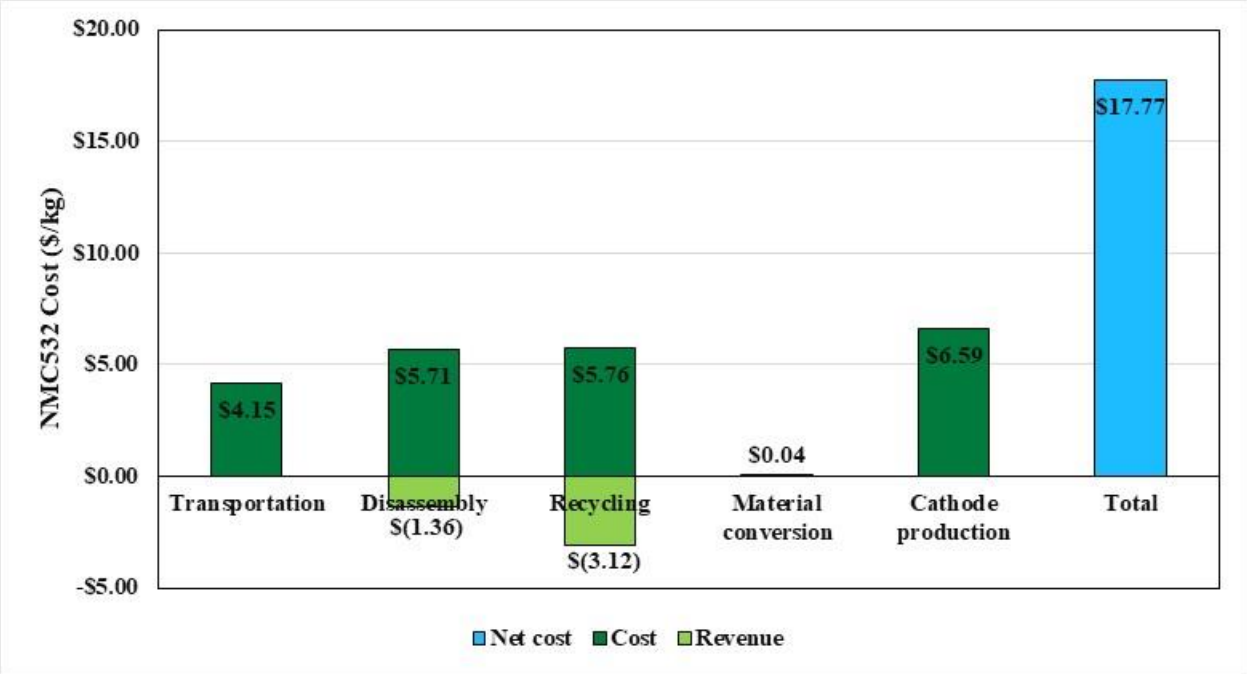

Figure I.3.C.55 Cost breakdown by closed-loop recycling stages for 1kg of NMC532 powder produced from materials recovered from a hydrometallurgical recycling plant that recycles 10,000 metric tons of NMC532 batteries per year, at a cathode production plant that produces 3,800 metric tons of NMC532 per year. No intermediate pre-treatment is assumed.

Analysis of Supply Chain Challenges for Battery Recycling

As R&D efforts to better recycle lithium ion batteries are undertaken, a birds-eye view of the interconnections between raw material availability, primary manufacture, recycling, and demand is needed. In this project, NREL is incorporating previous analysis and data in a system dynamics framework, named LIBRA (Lithium Ion Battery Recycling Analysis), to explore issues related to the global and regional impacts of the interlinking supply chains associated with battery manufacturing and recycling. Electrification of the transportation and energy storage markets is projected to result in explosive growth in the demand for batteries. In response to concern over raw material demands, increased emphasis is being placed on battery recycling capacity expansion. While some resulting impacts are anticipated, such as the shift in manufacturing costs and raw material prices, the inter-connectiveness of multiple markets, new manufacturing investments, operations, and policies could have unanticipated impacts on the success of electrification efforts. LIBRA analytically explores the technological and market feedback and feed-forward signals that could affect global supply chains for raw materials, primary and recycled batteries, and electric vehicles. The objective of this project is to help answer critical supply chain questions regarding the opportunities and challenges of lithium ion battery recycling, including insights into the impact that R&D achievements can have on the successful development of recycling capabilities, and how evolving global supply chains are affecting the projections of EV deployment.

The LIBRA (Lithium Ion Battery Recycling Analysis) system dynamics model and corresponding interface were completed. LIBRA explores the development of the lithium-ion battery (Li-ion) recycling and supporting industries (e.g., minerals supply and primary battery manufacturing). The LIBRA model uses the information in the database developed in Q3 and summarized in the last quarterly to project the build-out of the domestic Li-ion recycling industry. A detailed discussion of this complex systems dynamics model is beyond the scope of this report. Instead, this report will provide a high-level description of the model and will summarize important assumptions underlying its base case. The majority of this report will describe the model interface that allows users to evaluate different scenarios by modifying the base case.

LIBRA models the entire Li-ion supply chain from raw material extraction and refinement, to use in xEVs in the light-duty vehicle sector, in grid-connected applications in the stationary energy storage sector, and in personal electronics in the consumer sector, followed by disposal or recycling of end-of-life batteries from those sources. This supply chain is modeled each year from 1998 to 2040 using actual data and published projections. LIBRA is structured into interacting modules representing each of the existing markets, namely mineral, battery, and xEV, and a developing recycling industry. These modules individually specify the dynamics for these key segments of the Li-ion supply chain and together they provide key insights for the future of Li-ion production, distribution, and recycling.

Earlier assessments of battery supply chains make it abundantly clear that no nation currently operates without significant trade interactions with other countries. To explore the trade and competitiveness aspects of mineral supply, component (e.g., cathodes) and battery manufacturing, and battery recycling, the model is regionalized into five regions: China, Europe, U.S, Rest of Asia (ROA) and Rest of World (ROW). Information regarding the regional mineral, xEV, and other Li-ion markets are included in the model. For the sake of deeper exploration, current results focus on the U.S., however.

Selected parameters of the base case LIBRA model are shown below in Table I.3.C.14 below. Detailed documentation of the model is currently under development and is outside the scope of this report.

Table I.3.C.14 Selected LIBRA Base Case Parameters

Parameter (units)	Values
Overall	
Regions	China, Europe, ROA, ROW, U.S.
Years Modeled	1998-2040
Metals of Interest	Cobalt, Lithium, Class 1 Nickel
Battery Chemistries	LCO, LMO, LFP, NMC111, NMC442, NMC532, NMC622, NMC811, NMC955, NCA
Recycling Industry	
Facility Size (tonnes/day)	78.1
On-stream time (%)	87.8
Design and Construction Period (yrs)	3
Technologies modeled	Pyrometallurgical; Hydrometallurgical; Direct Recycling
Return on Investment	15
Dollar-Years	2017
Location	US
Government Assistance for Direct - 2022-2028 **Capital Subsidy** **Loan Guarantee**	 50% 100%
2020 Process Maturity (Fully mature = 1) **Hydrometallurgical** **Pyrometallurgical** **Direct Recycling**	 0.80 0.90 0.10
Metals Cost Increase (%/yr)	5
Value of Directly Recycled Cathodes	$10,000+Current Value of Metals

The facility size and on-stream time parameters were used in the EverBatt model by Argonne National Laboratory (https://www.anl.gov/egs/everbatt) to estimate the fixed capital investment, variable operating costs, fixed operating costs, and by-product credits for all three processes. Metal recovery rates for each process and transportation costs were also obtained from EverBatt. In addition to these selected parameters, the model has numerous datasets, both historical and projected, that are used to model factors such as xEV demand, consumer electronics demand, and battery chemistry. These datasets, including sources, were outlined in the Q3 quarterly report.

One of LIBRA's strengths is the ability to quickly run different scenarios and compare results across runs. Its online interface gives users the ability to change selected parameters and quickly see their combined impact on the model outputs.

The User Interface is composed of 12 screens grouped by Model Background and Assumptions, Model Input and Input Summaries, Model Results and Scenario Evaluation. Each of the groupings are described below and screen shots of specific screens are provided.

Model Background and Assumptions

- Table of Contents
- LIBRA Interface Instructions
- LIBRA Documentation Summary
- Base Case Assumptions

Model Inputs and Input Summaries

- Recycling Industry Assumptions
- U.S. Battery Sales Summary

Model Results

- U.S. Industry Development Summary
- U.S. Battery Recycling Summary
- U.S. Mineral Market Summary

Scenario Evaluation

- U.S. Recycling Market Scenarios
- U.S. Industry Development Scenarios
- U.S. Battery Flow Scenarios.

Model Background and Assumptions

The Table of Contents is the landing page for the interface that allows the user to jump to any other page. Next, is the LIBRA Interface Instructions page. As shown below, the page provides the user the instructions necessary to navigate the model, modify base case assumptions and view results. It also provides information for comparing results across runs (i.e., Scenario Comparisons).

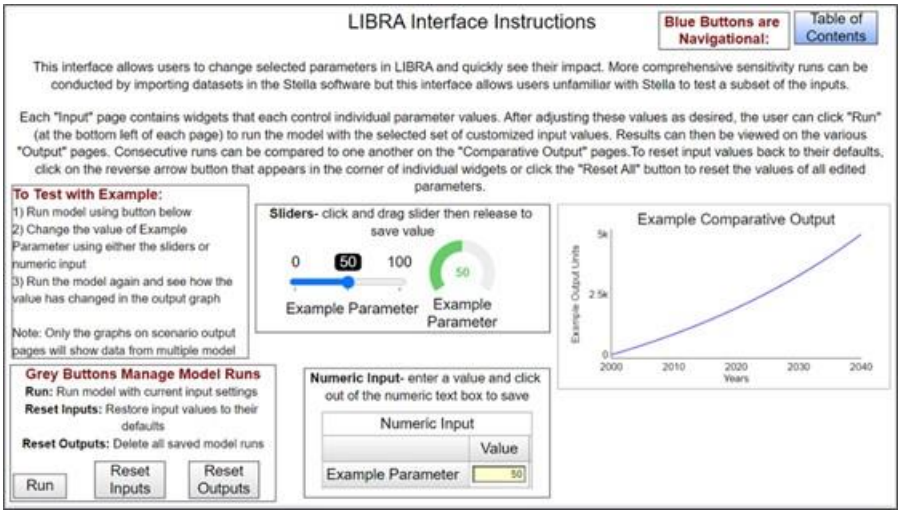

Figure I.3.C.56 LIBRA User Interface Instruction Page

A high-level summary of the LIBRA model followed by a summary table of assumptions for the base case is provided on the next two pages, respectively.

Model Input and Input Summaries

One page is provided for the user to modify base case parameters. The user may modify specific assumptions in plant economics, plant operations and battery transport. In addition, the user can add a tipping fee or modify the projected annual metal price increase and the split between rail and road transportation. Figure I.3.C.57 is a screen shot of the input page.

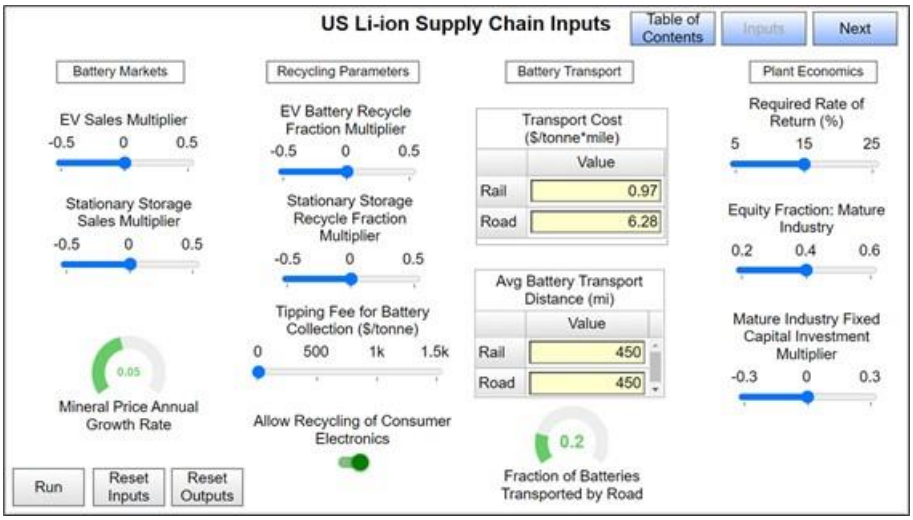

Figure I.3.C.57 LIBRA User Interface Input Screen

The second page in this section is a summary of battery sales based on input parameters. As shown in Figure I.3.C.58, the following summaries are shown:

- Battery Sales Summary
    - xEV Battery Sales (MWh) by xEV Type
    - xEV Sales (No. Vehicles) by xEV Type

- Stationary Storage Sales (MWh) by Battery Chemistry
- Consumer Electronics Sales (MWh) by Battery Chemistry.

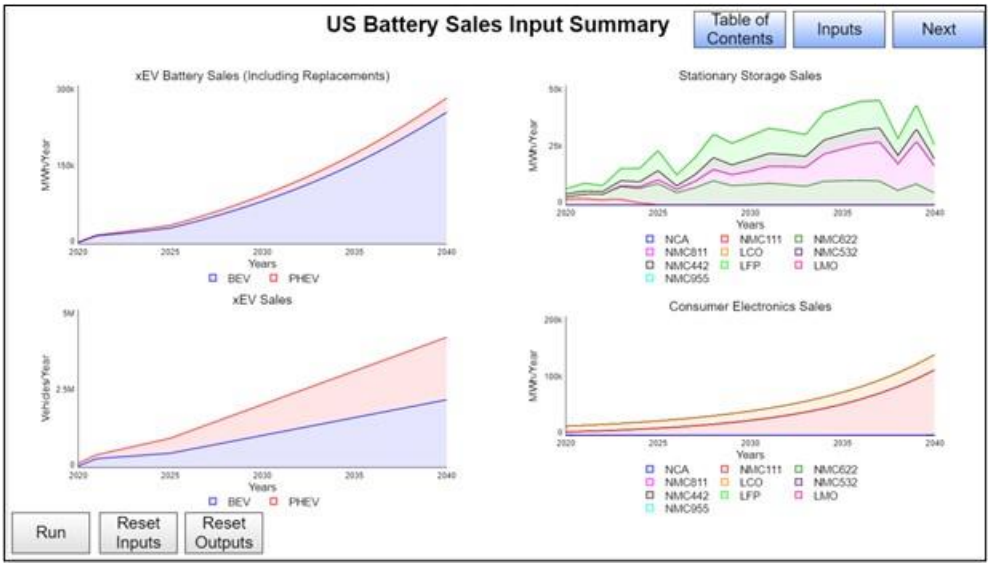

Figure I.3.C.58 LIBRA User Interface Battery Market Input Screen

Model Results

The next three pages (U.S. Industry Development Summary, U.S. Battery Market Summary and U.S. Mineral Market Summary) present the results of the model for 2020-2040. If the user makes no changes in the input sheets, the base case results are shown. If the user does make changes and runs the simulation, then the base case results are overridden. Each of the 19 graphs in this section show the current run for one or more variables as outlined below:

- U.S. Industry Development Summary – 4 graphs
  - NPV ($) of New Recycling Facility Construction by Process Type
  - Active Recycling Plants by Process Type
  - Cumulative Investment ($ million) in Battery Recycling Facilities
  - Distribution of Recycled Batteries by Chemistry (Fraction)
- U.S. Battery Recycling Summary – 6 graphs
  - Annual xEV Batteries Scrapped (MWh) by xEV Type
  - Annual xEV Batteries Recycled (MWh) by xEV Type
  - Annual Batteries in Recycling Supply (Tonnes) by Disposition
  - Annual Batteries In-Use (MWh) by Battery Type
  - Annual Stationary Storage (MWh) Recycled
  - Annual Consumer Electronics (MWh) Recycled
- U.S. Mineral Market Summary – 9 graphs

- (Cobalt, Lithium, Nickel) Collected for Recycling by Battery Chemistry – 3 graphs
- (Cobalt, Lithium, Nickel) Recycled by Battery Chemistry – 3 graphs
- (Cobalt, Lithium, Nickel) Recycled by Process – 3 graphs.

A screen shot of the Minerals Market Summary is Figure I.3.C.59.

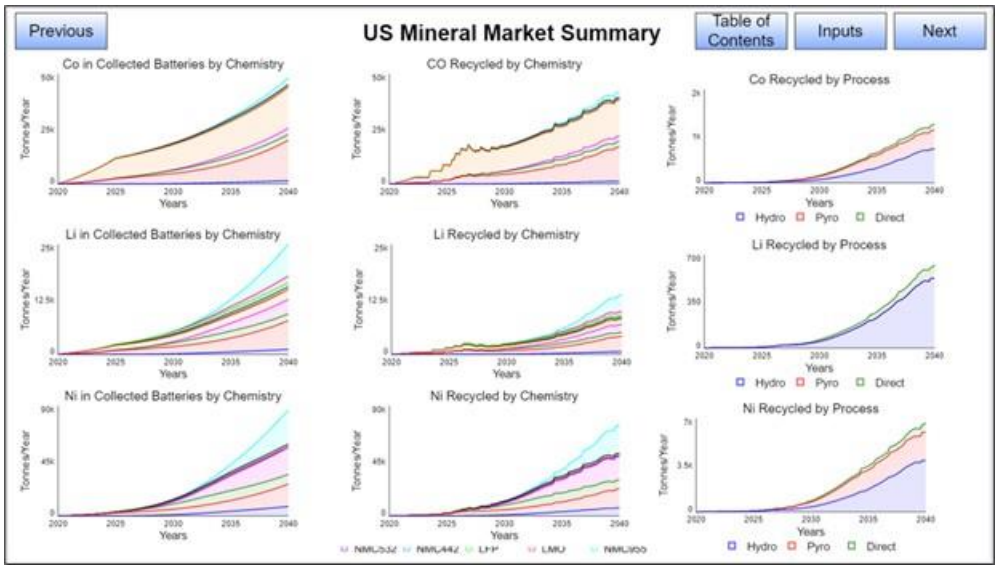

Figure I.3.C.59 LIBRA User Interface Mineral Market Summary Screen

Scenario Evaluation

In addition to looking at results for a single run, the interface allows the user to look at specific important parameters across several runs as a scenario analysis. A user can change any number of inputs on the input sheets and run the model. Each time the user runs the model, the scenario will be added to the base case scenario as well as any previous runs on the scenario comparison sheets: U.S. Recycling Market Scenarios, U.S. Recycling Industry Scenarios, and U.S. Battery Flow Scenarios. To clear the results and start on a new series of runs, the user would push the Reset All button and begin again.

The following is a summary of the three scenario comparison sheets.

- U.S. Recycling Market Scenarios – 6 graphs
  - Annual CO, Ni, Li (Tonnes/yr) Supplied by Recycling – 3 graphs
  - Annual BEV Batteries (MWh) Scrapped
  - Annual BEV Batteries (MWh) Recycled
  - Annual BEV Sales (MWh)
- U.S. Recycling Industry Scenarios – 6 graphs
  - NPV ($) of Hydro, Pyro and Direct Recycling Facility Construction – 3 graphs
  - Plants Online: Hydro, Pyro, Direct – 3 graphs
- U.S. Battery Flow Scenarios – 3 graphs

- Quantity of Batteries (Tonnes/yr) Recycled
- Quantity of Batteries (Tonnes/yr) Exported
- Quantity of Batteries (Tonnes/yr) Scrapped.

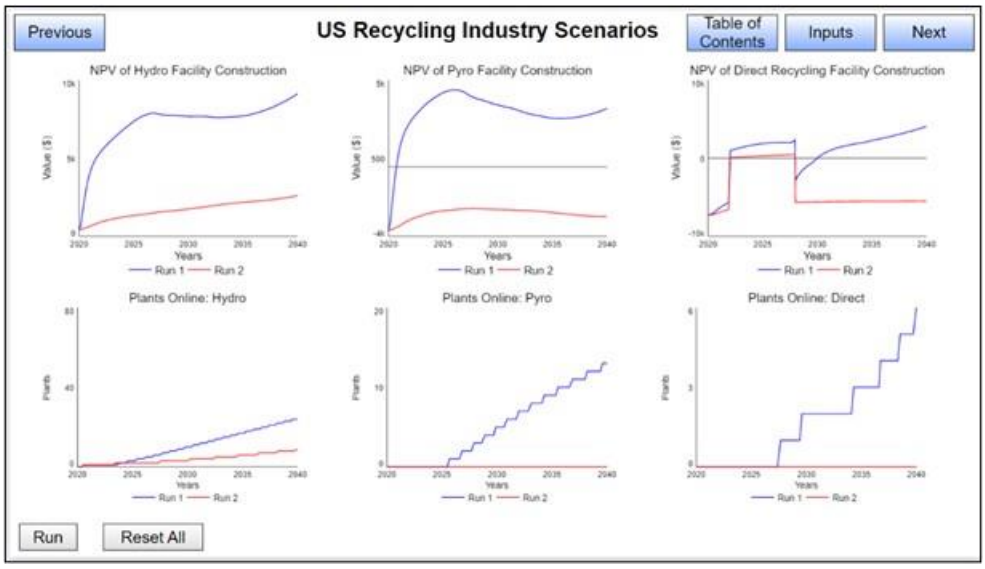

Figure I.3.C.60 LIBRA User Interface Scenario Comparison of Industry Development

Figure I.3.C.60 provides a screen shot of the Scenario Comparison of Industry Development showing 2 example runs.

CAMP Facility Support

Numerous recycled battery materials will be created in the ReCell Program that will need to be validated in prototype electrodes and pouch cells. The Cell Analysis, Modeling, and Prototyping (CAMP) Facility at Argonne will validate these materials (active cathode powders, graphite, electrolytes, etc.) and compare their electrochemical performance to baseline electrodes (and electrolyte). Validating the electrochemical performance of recycled battery materials will be critical to establishing their market viability.

The CAMP Facility will use pristine NMC111 cathode material and SLC1520P graphite as the baseline materials to use in capacity-matched electrodes and cells. All future recycled NMC111 cathode materials will be compared against this baseline electrochemical performance data, as well as other recycled battery materials that are of interest to the ReCell Center. All electrodes will first be tested in coin cells for initial validation and then tested in single-layer pouch cells for rate performance, HPPC impedance, and cycle life, if warranted.

Manufacturing Electrode Scrap

One common waste product in a lithium-ion battery manufacturing facility is electrode scrap. This consists of reject rolls of electrodes due to quality control issues or obsolescence, as well as the electrode material that is trimmed from the final electrode during the slitting or punching process. In all regards, this should be the easiest battery material to recycle because it is uncontaminated with electrolyte or cycling byproducts, is not regulated as a lithium-ion battery, is non-flammable, and comes from large single-point sources. In the beginning of FY 2020, ORNL coated a large supple of NMC622 cathode onto aluminum foil to be used as a baseline for studying solvent removal of cathode binders to enable harvesting of NMC cathode powders. This electrode had a loading near 3.0 mAh/cm^2 with a composition of 94 wt% NMC622, 3 % carbon black, and 3 % PVDF binder. Surface and cross-section images are provided in Figure I.3.C.61.

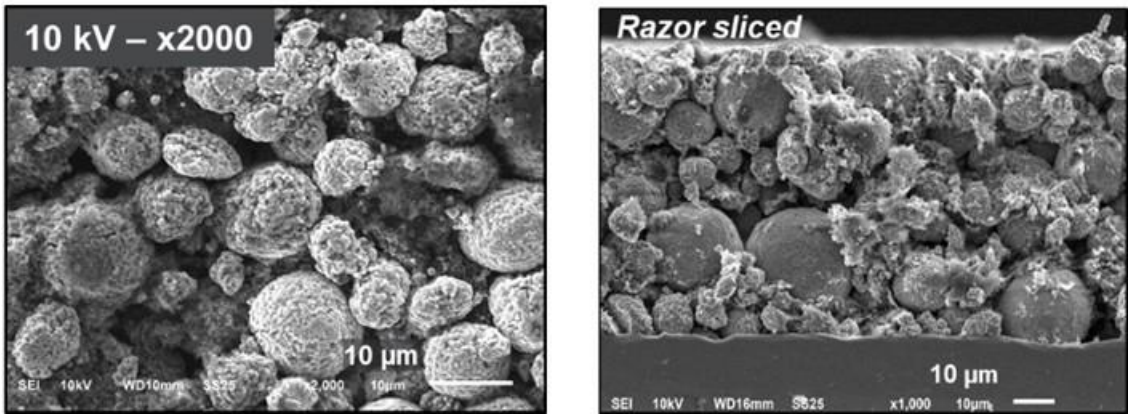

Figure I.3.C.61 Surface (left) and Cross Section (right) SEM Images of the ORNL_01-2020 NMC622 Baseline Electrode (by Nancy Dietz Rago Test (Post-Test Facility).

The CAMP Facility received a portion of these pristine electrodes in the 2nd Quarter of FY2020 for establishing a baseline that will be used for comparison against future solvent-extracted cathode NMC622 derived from this manufacturing scrap baseline. Coin cells were made from this pristine electrode scrap and tested versus lithium metal with Gen2 electrolyte. The cells were formed and tested for rate performance in a 3.0 – 4.3 V window at 30°C. Figure I.3.C.62 is a summary of the rate performance at C/20, C/10, C/5, C/2, 1C, and 2C.

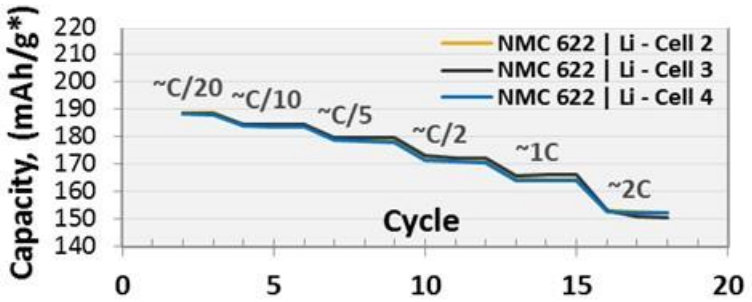

Figure I.3.C.62 Summary of the discharge capacities from the Rate Testing of NMC622 Manufacturing Scrap versus lithium metal (Gen2 electrolyte, 30oC, 3.0 – 4.3 V).

A capacity-matched graphite anode (SLC1520P) was made by the CAMP Facility. This electrode will be used as a baseline for full cell testing against the pristine NMC622 scrap electrodes from ORNL. It will also be used against electrodes made with solvent-extracted (harvested) NMC622 powders, which were received from ReCell teams in August and September. Electrodes will be made with the solvent-extracted NMC622 powder in early FY 2021 and tested in half-cells and full-cells for comparison to the pristine baseline. The CAMP Facility will use half-cell data provided by project teams to design each electrode.

Plans were made for the CAMP Facility to make a total of 16 single-layer pouch cells (~30 mAh each) with the baseline anode and the following cathode materials:

4 cells with baseline NMC622 electrodes

4 cells with Thermally Delaminated NMC622 powder

4 cells with Solvent X Recovered NMC622 powder

4 cells with Solvent Y Recovered NMC622 powder

All NMC622 cathodes were received in sufficient quantities (>30 g) for the CAMP Facility to begin electrode fabrication, with the exception of the Solvent X recovered NMC622. Preliminary testing by MERF indicated this cathode powder did not cycle well. It will most likely be dropped from present electrode and cell fabrication plans.

Post-Test Facility Support

The Post-Test Facility at Argonne performs a supporting role in the ReCell Program. Post-test diagnostics of aged batteries can provide additional information regarding the cause of performance degradation, which previously could be only inferred. The facility combines microscopy, spectroscopy, and chromatography in a controlled-atmosphere glove box to characterize materials without air exposure. These results help identify issues in the recycled materials, such as how well a given recycling process separates an initial mixture of cathode, anode, supporting foils, and casing materials.

After returning to the lab, we continue to help different groups understand the key parameters in different recycling processes. We characterized the samples given in Table I.3.C.15 by a combination of scanning-electron microscopy and X-ray photoelectron spectroscopy. Our contributions to the work are summarized below.

Table I.3.C.15 Sample information for XPS or SEM study

Institutes	Sample description
MTU (anode and cathode separation)	1. untreated anode from spent cells 2. untreated cathode from spent cells 3. treated anode at 400 °C for 1h 4. treated anode at 500 °C for 1h
WPI (impurity study)	1. Pristine NMC622 powder 2. 0.2% Fe^{2+} doped NMC622 powder 3. 1.0% Fe^{2+} doped NMC622 powder 4. 5.0% Fe^{2+} doped NMC622 powder 5. 0.2% Fe^{3+} doped NMC622 powder 6. 1.0% Fe^{3+} doped NMC622 powder 7. 5.0% Fe^{3+} doped NMC622 powder
NREL (comparison of surface and bulk composition from chemical delithiation and electrochemical delithiation)	1: pristine NMC111 laminate 2: chemically delithiated NMC111 (10% loss) 3. chemically delithiated NMC111 after 4 formation cycles 4. electrochemically delithiated NMC111 (cycled after 10% capacity loss) 5. electrochemically delithiated NMC111 (cycled after 20% capacity loss) 6. electrochemically relithiated NMC111 (relithiated at 3.0V, C/10)
WPI (recovered single crystal NMC)	1: pristine NMC111 2. etched NMC111 3. single crystal NMC111

- MTU: We used XPS to evaluate the effect of thermal pyrolysis on the surface composition during the separation of anode and cathode materials by froth flotation from MTU. Surface morphology and composition were also characterized by SEM/EDS at low magnification for many particles and at higher magnification for single particles. We analyzed the data and shared it with the MTU team to complete their manuscript preparation.

- WPI: We characterized more samples from WPI to characterize the effect of the concentration of Fe^{2+} and Fe^{3+} impurities on the surface and the bulk properties of transition metals (TMs) in NMC622 cathodes.

- WPI: Single-crystal cathode materials enable higher capacity and better rate performance by eliminating grain-boundary fractures during cycling and thus have attracted significant attention recently. WPI team started a new line of research using the recovered single crystal NMC111 materials. We received three powder samples for the preliminary surface chemistry study by XPS.

- NREL: We received six electrode samples from the NREL team to compare the effect of chemical and electrochemical delithiation on the surface and bulk chemistry of TMs for NMC111 using XPS depth profiling.

We have already shared the results with the owners and are working together on the data analysis, including XPS data fitting for potential publications.

Diagnostics of Aged Materials

There are trade-offs between keeping recycling streams separate and co-mingling materials from cells with different histories. Similarly, there is a need to balance quality of recovered material and associated recycling costs. This task evaluates the extent of material degradation in cathodes subjected to different cycling conditions and/or recycling processes. These results are then used to differentiate the quality of material recovered from different recycling methods and determine suitability of specific recycling processes to restore cathodes with varying extents of degradation.

Traditional methods to characterize recovered cathodes typically involve measurement of parameters like particle size distribution, tap density, reversible capacity, first cycle efficiency, and specific surface area. This project aims to provide statistical distributions of structural change, composition, and morphology of aged electrode materials using electron backscatter diffraction (EBSD), which enables analysis of cathode materials at the primary particle level. These measurements will be used to:

1. Identify chemical signatures corresponding to efficiency losses from calorimetry measurements

2. Inform electrochemical relithiation conditions and

3. Match the extent and type of degradation to target recycling methods, based on load profiles, cycling windows, and cost metrics.

With sample preparation and EBSD characterization methods largely optimized, this quarter's work prioritized the identification of relevant and statistically grounded parameters to inform material health metrics. Throughout the course of this project, we have been tracking grain size and grain misorientation (Grain Orientation Spread (GOS) and Grain Reference Orientation Deviation (GROD)) across spatial regions of the electrode, and have been monitoring changes to these parameters with electrochemical cycling and chemical delithiation. Our datasets now include structural information for ~10,000-30,000 primary particles per cathode sample, enabling statistical evaluation at scale.

Comparison between pristine, formed, and 80% state-of-health (SOH) samples of both NMC111 and NMC532 across three spatial regions (surface, middle, interface) suggests that mean GOS and median GROD values at the surface region are the most promising candidates for material health diagnosis. Figure I.3.C.63 quantifies these

parameters for eight of the samples analyzed in the past fiscal year. As shown, both mean GOS and median GROD values at the surface region are generally found to increase with electrochemical cycling (pristine < formed < 80% SOH). This trend is most consistent for the median GROD parameter, for both NMC111 and NMC532 chemistries. As has been described in previous quarterly reports, GROD directly measures the misorientation existing within primary particles, and thus is a proxy for intra-grain strain. The increase in GROD values observed with electrochemical cycling is consistent with electrochemical cycling data, as repeated Li (de)intercalation is anticipated to induce stress (and thus strain) within the NMC lattice at the primary particle scale. Further, electrode-scale heterogeneity in Li^+ occupancy has been attributed to solid-state diffusion limitations. This may explain the higher variation in GROD values between as-formed and cycled samples at the surface region, and offers physical justification for analyzing the surface region to assess material health. Examination of more heavily degraded materials (<80% SOH), as well as additional NMC stoichiometries, will contribute to the delineation of a quantified metric of material health. This may be applied upstream, to characterize and sort end-of-life material entering the direct recycling line, or downstream, to evaluate the success of remediation techniques.

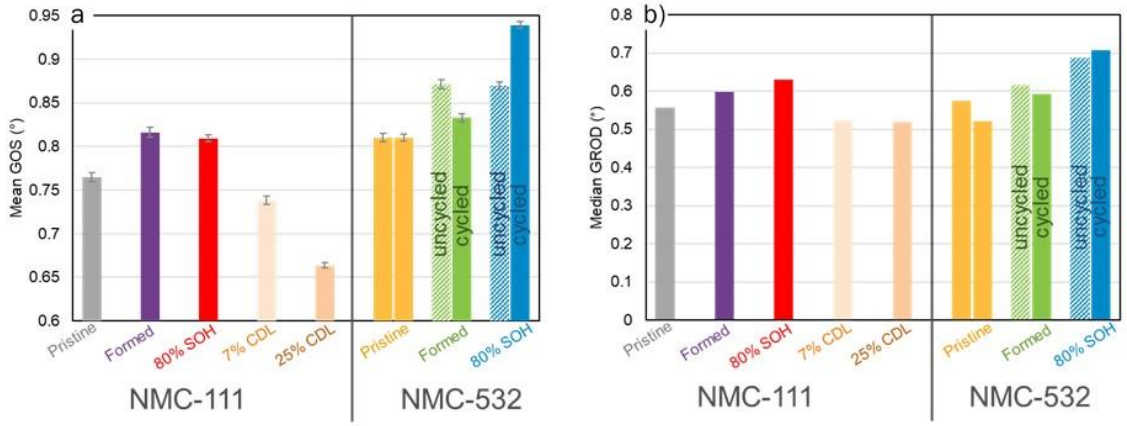

Figure I.3.C.63 Parameters for the evaluation of material health, as identified through statistical analysis of EBSD data: (a) Mean GOS; (b) Median GROD. In both (a) and (b), data for the surface region is shown. Error bars in (a) reflect a 95% confidence interval around the mean.

To further streamline the characterization of end-of-life and recycled materials, In Q4, NREL set up capabilities to enable simultaneous EBSD and electron dispersive spectroscopy (EDS) measurements. EBSD/EDS analysis of pristine NMC111 baseline samples (Figure I.3.C.64) allows for the collection of structural and chemical data on the same secondary particle, thereby allowing for the differentiation of chemically distinct phases due to aging-associated factors such as transition metal leaching or lattice oxygen loss. Efforts are underway to integrate EDS data with EBSD parameters (e.g., median GROD), as well as with electrochemical and thermal signatures.

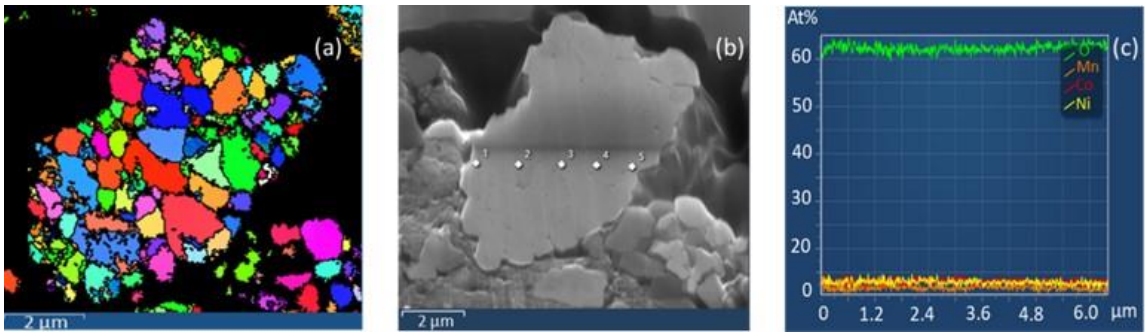

Figure I.3.C.64 Simultaneous EBSD (a) and EDS (b-c) measurements, using pristine NMC111 samples, helps relate changes in chemical composition to structural evolution within the cathode particles. Compositional variation across the secondary particle is shown as a line scan in (c).

This task is transitioning to an "on-demand" analysis technique beginning in Q1 of FY21. In addition to continued support of several other subtasks, we plan to analyze cathodes recovered from highly degraded cells (40% and 20% SOH NMC532) and to corroborate EBSD data with other advanced structural characterization techniques. Two publications are planned for FY21.

Microcalorimetry on Recycled Materials

The chemistries of advanced energy storage devices are very sensitive to operating temperature. High temperatures degrade batteries faster, while low temperatures reduce their power and capacity. NREL's equipment is sensitive enough to determine how changing the design of cell components affects the overall performance of the cell. We will use our isothermal calorimeters to develop an understanding of the life cycle effects on heat generation and determine if the recycling processes being developed under the ReCell program have a deleterious effect on cell performance. In particular, NREL will investigate the following:

1. Thermally characterize existing NMC cathode compositions to understand how the thermal signature of a battery changes from the beginning of life to the end of life. The data will be used to assess the quality of the recycled material being produced under the ReCell program.

2. Thermally characterize NMC/graphite cells with a known contaminant. For instance, we want to understand how much copper material can be tolerated in the cathode without having a negative effect on heat generation and efficiency.

3. Match the extent and type of thermal degradation to target recycling methods, based on load profiles, cycling windows, and cost metrics.

In Q1FY20, NREL received cells from Argonne National Laboratory (ANL) that had a known contaminant added to the cathode or anode. The entire list is given in Table I.3.C.16. The batteries supplied by CAMP are a combination of NMC111 and graphite – a typical chemistry used in electric vehicles today. The contaminant was added to the slurry of the cathode or anode during the coating process – the contaminants added were either iron, copper, silicon, magnesium, and aluminum at a 1% by mass ratio.

Table I.3.C.16 CAMP cells to be used for thermal Characterization. The cathode material was supplied by Toda and the anode material was supplied by Superior Graphite. Contaminants were added to the slurry before coating the current collectors

Cell	Cathode Material	Cathode Impurity	Anode Material	Anode Impurity
1	NMC111 (90%)	NA	Graphite 1520P (91.83%)	NA
2	NMC111 (89%)	Cu 1%	Graphite 1520P (91.83%)	NA
3	NMC111 (89%)	Fe 1%	Graphite 1520P (91.83%)	NA
4	NMC111 (89%)	Al 1%	Graphite 1520P (91.83%)	NA
5	NMC111 (89%)	Mg 1%	Graphite 1520P (91.83%)	NA
6	NMC111 (89%)	Si 1%	Graphite 1520P (91.83%)	NA
7	NMC111 (90%)	NA	Graphite 1520P (90.83%)	Fe 1%
8	NMC111 (90%)	NA	Graphite 1520P (90.83%)	Al 1%
9	NMC111 (90%)	NA	Graphite 1520P (90.83%)	Mg 1%
10	NMC111 (90%)	NA	Graphite 1520P (90.83%)	Cu 1%

CAMP shipped the cells to NREL dry and sealed, as we anticipated that the heat generation would be most visible during the formation process. After receiving the cells from CAMP, NREL filled and resealed the pouch material and then placed the cells within our microcalorimeter for testing. In the Q2 and Q3 quarterly

update, NREL reported on the cathode/anode contaminated cells but we had only tested one cell for each contaminant. During the most recent fiscal quarter, we wanted to understand the repeatability of using the calorimeter to detect contamination in cells. As such, we duplicated the prior Q2/Q3 tests. Figure I.3.C.65 shows the heat generation profile during the first C/10 formation charge for two cells with a copper contaminant (Figure I.3.C.65a) and two cells with a silicon contaminant (Figure I.3.C.65b)– both contaminants were introduced to the cathode. For Figure I.3.C.65, we used the technique related to dQ/dV and graphed the heat generation as a function of voltage. The graph clearly shows that when two different cells are tested with the same cathode contaminant, the heat generation vs. voltage curves are repeatable and show similar peaks/valleys at the corresponding voltage. For reference, refer to the Q2 and Q3 reports to contrast the heat signatures of the baseline and contaminated cells. Thus, the heat generation profiles during formation can reliably be used to identify contaminants within the electrode that are not normally present in the cathode material.

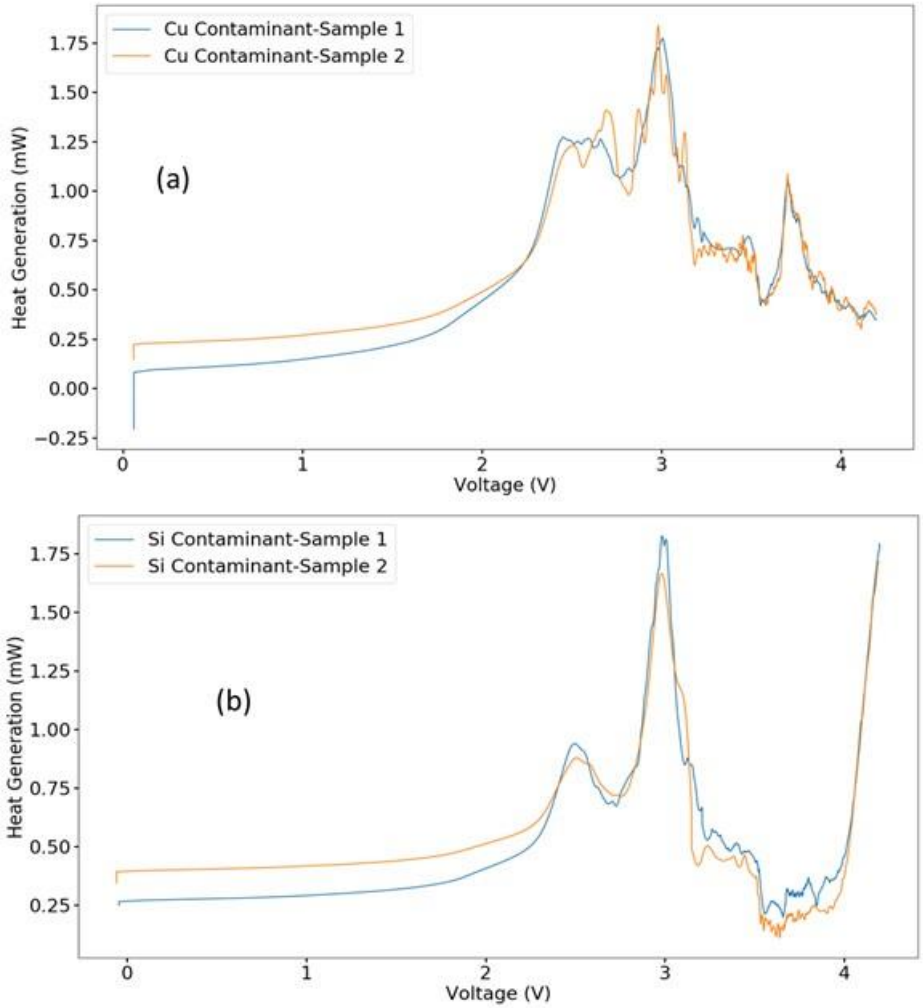

Figure I.3.C.65 Heat generation profiles of cathode contaminated with (a) copper and (b) silicon during the first C/10 formation charge of cells.

Figure I.3.C.66 shows the heat generation profile during the first C/10 formation charge for two cells with an aluminum contaminant (Figure I.3.C.66a) and two cells with an iron contaminant (Figure I.3.C.66b)– both contaminants were introduced to the anode during fabrication. As with the cathode contaminants, the heat generation vs. voltage curves for the anode contaminants are repeatable and show similar peaks/valleys at a corresponding voltage.

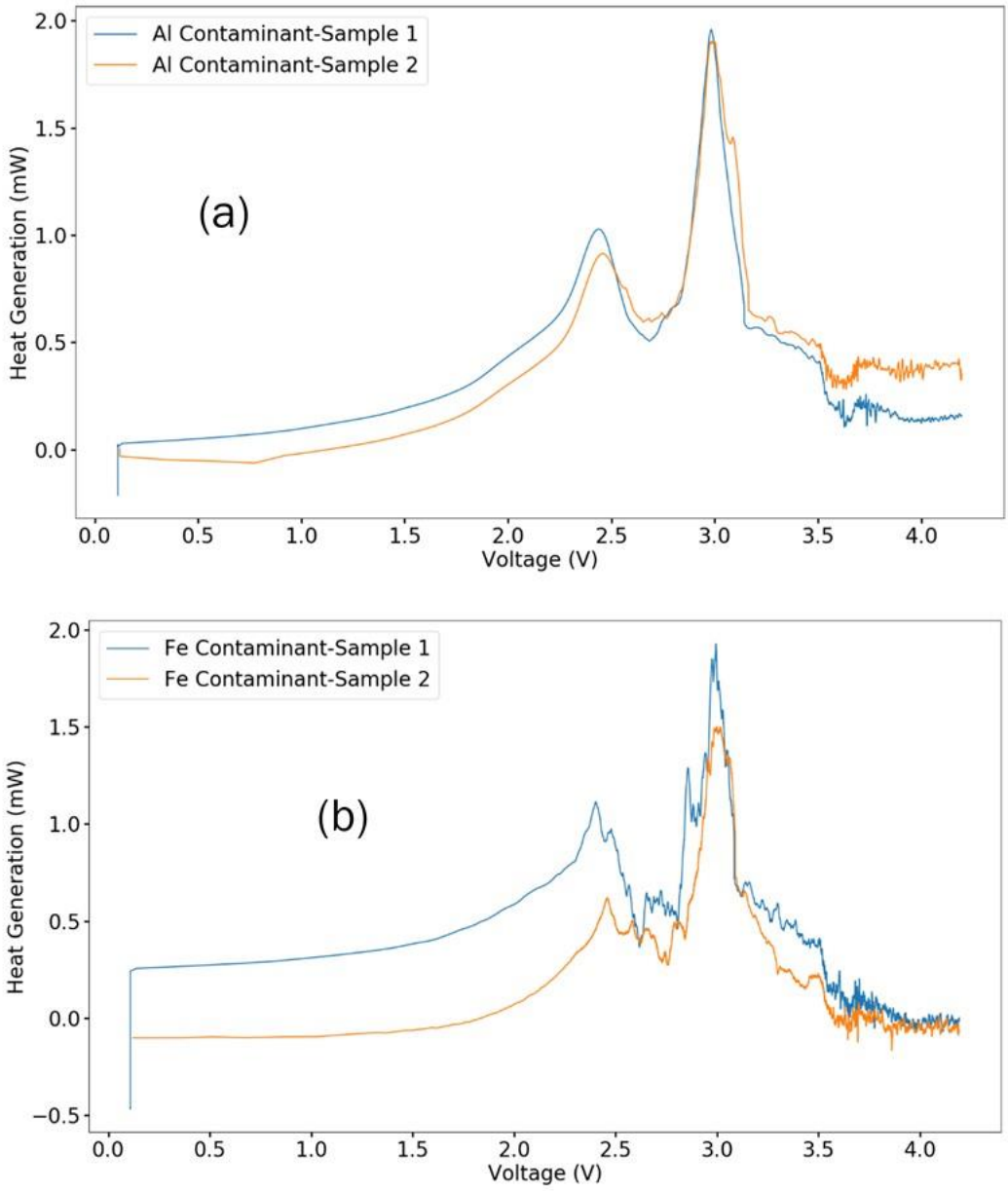

Figure I.3.C.66 Heat generation profiles of anode contaminated with (a) aluminum and (b) iron during the first C/10 formation charge of cells.

Conclusions

Binder Removal via Thermal Processing

Thermal binder removal using rotary kilns appears to be a promising path towards scaling up the binder removal process. Additional work is needed to address issues with tube contamination of the materials, as well as parameter optimization to improve capacity fading. However, even in this initial testing the rotary kiln-processed material does not show the scaling issues seen in static furnaces. In addition, this was batch testing, while a scaled-up process would be continuous. We have purchased a rotary kiln that can test the process continuously, which may provide benefits beyond throughput, due to smaller quantities of material being decomposed at a time.

Binder Removal via Soxhlet Extraction

We examined a cryovap solvent transfer method as an alternative method for removal of solvents with high b.p. The cryovap apparatus was installed in a fume hood and connected to a Schlenk line. A PVDF solution (5 wt.% in DMF) was used to separate PVDF and the solvent. The cryovap method successfully removed DMF from the solution and left PVDF in a membrane form. The recovery yield is high enough to enable a near-closed-loop solvent reuse system. In the next quarter, we will examine the sono-soxhlet (high-power ultrasound added) process for PVDF binder removal.

Cathode/Cathode Separation Process Development

Pilot scale separation of binary and ternary mixtures has been demonstrated. Results from this and previous studies show promise, with additional pathways identified for progress. Tests have been conducted using mixtures of LMO, NMC, and graphite to determine the ability of magnetic separation to remove graphite, as well as the effect of graphite contamination on further separation. A more detailed look at the separation of NMC and NCA was also conducted, as well as mixtures of NMC, NCA, and LCO. Analysis of these samples is ongoing and will be completed shortly.

Cathode-Cathode Separation via Froth Flotation

A good separation between pristine NCA and LMO as well as between NMC111 and LMO has been achieved using the froth flotation process. The electrochemistry data show that both NMC111 and LMO are less likely to be damaged electrochemically during the water-based separation process, but NCA is prone to capacity fade during the recycling process. Separation of two different cathodes in a high-solid slurry preserves their original capacity.

Chemical Relithiation of NMC Cathodes

Scale-up of the relithiation process has been modified by reducing solvent consumption to decrease material cost, as suggested by the EverBatt model. Further possible cost reduction by solvent-free methods of chemical relithiation is also being tested. Physical characterization of this material appears consistent with previous work, however electrochemical performance showed lower capacity. Further tests are being conducted, and a new acoustic mixer ordered by CAMP may also be tested as an alternative approach. The best practices for the chemical relithiation process will be tested with real battery cathode powders in the next fiscal year.

Direct Regeneration of NMC Cathodes through Ionothermal Lithiation

We reduced the amount of ionic liquid used in our ionothermal reactions because IL cost is a major factor driving total materials costs, according to ANL's EverBatt. To date we have downscaled the amount of IL used to get similar results from 75g / 25g D- NMC to 25 g/ 25g D-NMC. A larger scale (~50 g) ionothermal experiment has also been successfully completed. The recovered materials were analyzed by various characterization techniques, including TGA, XRD, and ICP-OES, which demonstrate that the ionothermal approach to restoring Li into delithiated NMC111 for direct regeneration of cathode materials can be scaled up and is promising. During this quarter, we began relithiation via ionothermal synthesis using LiBr along with the addition of an Al source in both [C2mim][NTf2] and [C2mim][OAc] as the reaction medium. Preliminary results show that upcycling seems to be working. Further investigation with a different Al source in different ILs and experimental conditions will be conducted in next quarter.

Hydrothermal Relithiation of Chemically Delithiated NMC111 Cathodes

In summary, we showed that the 4M LiOH solution can be replaced by a mixture of 0.1M LiOH and 3.9M KOH to achieve the same effectiveness of relithiation, significantly lowering the overall regeneration costs. Furthermore, the energy consumption can be further reduced by replacing Li2CO3 with LiOH as the lithium source for the annealing step to compensate Li loss at high temperature. In addition, the scale of the direct regeneration process can be up to 10 g. Further scaling up to 50 g per batch will be verified in future work.

Relithiation via Redox Chemistry

In this quarter, we examined various redox mediator concentrations to determine if process control can reduce the required amount of redox mediator. We found that a minimum 0.3M redox mediator concentration is needed to fully lithiate EOL cathode and recover a good discharge capacity. Moreover, we confirmed that the redox relithiation process does not induce structural degradations. We will study and report the reaction mechanism for the redox relithiation in the next quarter.

Electrochemical Relithiation

A scanning voltage protocol applied to electrochemically aged and modified chemically delithiated material enabled improved capacity retention and a more rapid relithiation technique. This protocol takes only about 35 minutes to effectively relithiate aged NMC111 materials. Next steps will include verifying the robustness of the protocol for different aged cathode materials and application in a scalable process.

Roll-to-Roll Reactor Design for Electrochemical Relithiation

Aged cathodes on their original current collectors, stored in DMC, were relithiated to an extent marginally exceeding that of the pristine material. Further testing is necessary to evaluate the performance of these cathodes in full cells.

Cathode Upcycling

We have evaluated the use of various temperatures and starting materials to add stoichiometric nickel to the baseline NMC111 materials. In general, the process requires metal cation diffusion which is favored at high temperature and lower oxidation states. The formation of unwanted oxide phases observed from work in the previous quarter was eliminated by the addition of excess lithium into the reaction. There is still separation and formation of intermediates between the starting NMC111 and nickel-rich phases. Reactions using Ni-rich coating in the absence of the coordinating organic additives (oxalate, citrate) are also being retested in the presence of excess lithium. Additional test reactions between NMC111 with NMC811 could give insight in optimal conditions (time, temperature, atmosphere) for the upcycling reactions using nickel-rich coatings. Future cross-cutting efforts may provide more detail on the temperature dependence of the structural changes.

Role of Impurities in Recycled Cathodes

Unlike the cations dissolved in the transition metal sulfate solution, carbon is suspended in the solution and does not significantly affect the morphology of the synthesized NMC622 precursor. However, hollow NMC622 particles are formed due to added carbon. The structures of NMC622 precursor and cathode particles do not change much with carbon impurity, although there is slightlpeak shifting. Surprisingly, NMC622 with 5% carbon has lower capacity compared to virgin materials. Since carbon is burnt during the sintering process, the NMC622 should not contain any carbon. Our hypothesis is that transition metal valence could be changed due to the carbon burning and loss of surface oxide, which affects the electrochemical performance of the cathode materials.

Cell Preprocessing

The cell pre-processing task plans to identify a size-reduction technology for breaking down cells and/or batteries, order equipment for pilot scale, and have it in place in the ReCell Center's facilities at Argonne National Lab prior to the end of FY 2021. The goal is to begin pre-processing real batteries at Argonne National Lab acquired from various sources. Several shredder and hammermill configurations have been tested to determine appropriate parameters that will increase separation efficacy of shredded battery materials. It has been shown that the number of shredder shafts (single vs. double), shredder knife configuration, the number and geometry of shredder knife teeth, the size of the hammermill screen, and rotation speed of hammers can have a significant effect on the size and size distribution of shredded material and amounts of fine particles produced.

Solvent-based Electrode Recovery

Cathode films recovered from cathode scraps via the SolveX process were re-coated and their electrochemical performance was evaluated. Preliminary results showed similar battery performance as the pristine cathode. In addition, separation of cathode films from Al foils through mechanical stirring and sieving was investigated. Finally, recovery of spent cathode particles was demonstrated with the aid of sonication through the solvent Y based process.

Anode/Cathode Separation and Purification

Separation of the anode and cathode is a critical step in the direct recycling process to purify the black mass. Techniques are being explored using reagents that are compatible with the materials being processed and with other steps in the direct recycling process chain. Separation techniques that allow us to reduce the number of processes used (e.g., separation of electrodes on foil) or utilize solvents that are already present in direct recycling are of particular interest. In addition, recently acquired equipment at Argonne National Laboratory will allow us to expand our capabilities tob explore and develop more robust separation procedures.

Electrolyte Component Removal and Recovery

Electrolyte from manufacturer #2 is believed to be more sensitive to exposure to moisture and other factors. This points out that careful handling and possibly drying is required to ensure LiPF6 does not degrade during the recovery process. Supercritical CO2 extraction appears to have some purification benefits but does not completely remove PC from the electrolyte. To truly demonstrate this process, an extractor that can be offloaded into an inert atmosphere or dry room would be needed. Other purification methodologies are being explored to see if a more efficient method to protect the sensitive electrolyte salt can be found.

Cell Design

In this project period, we evaluated cell rejuvenation in 4 conditions. The results indicated that the rinsing process should be conducted without taking cells out of their test fixture. The capacity recovery is minimal without a rinsing step, but is more significant with a rinsing step. However, the capacity gain only lasts for a short term before the capacity drops down to that prior to treatment. When taking the aged cells out of their test fixture, rinsing electrodes may loosen contacts between cell components and lead to fast capacity fade.

EverBatt: Cost and Environmental Impacts Modeling

EverBatt 2020 includes important expansions and updates that can better help inform R&D efforts under the ReCell center and battery recycling decisions in general. Analyses with EverBatt 2020 identify battery disassembly as a potential hurdle to profitable battery recycling and recognize bulk battery transportation and reusing packaging as opportunities to reduce logistics cost. In the next iteration of EverBatt, we plan to include battery storage and automated battery disassembly to make the model more comprehensive and complete.

Analysis of Supply Chain Challenges for Battery Recycling

The 2020.1 version of the LIBRA model and interface has been completed. LIBRA models the full supply chain for Li-ion batteries for 5 regions (China, Europe, ROA, ROW, U.S.) based on three metals (Co, Li, Ni) focusing on the light-duty xEV, stationary storage, and consumer electronics markets. Mining, refining, and non-Li-ion impacts are also considered. LIBRA projects the build-out of a recycling industry by process type (hydrometallurgical, pyrometallurgical, and direct recycling) based on an assessment of their economic viability (NPV). Batteries that cannot be recycled are exported.

The model interface is user-friendly and allows users to evaluate single or multiple changes to the base case across the full supply chain. It also allows users to compare runs through the development of scenarios. Users have almost 40 summary figures that display real-time results.

CAMP Facility Support

The CAMP Facility actively supports the efforts of the ReCell Center by providing baseline materials, fabricating trial electrodes and baseline electrodes, fabricating and testing numerous coin cells, and fabricating

single-layer pouch cells. It has established a thorough test matrix and protocols that have been used to conduct electrochemical evaluation of baseline active materials of interest to the ReCell Center in FY 2019-2020. These protocols and the testing results are uploaded to the ReCell Center website as they become available (started in FY 2020 2nd Quarter) for the general public's use.

Post-Test Facility Support

The Post-Test Facility will continue to provide support for the ReCell project, providing characterization expertise where needed. The planned, future work includes characterizing recycled materials that were produced as part of this project. As the recycling processes mature, cells will be constructed from the materials. Cells containing these materials will be sent to Post-Test for additional characterization data regarding causes of loss of performance.

Diagnostics of Aged Materials

The compilation of an extensive EBSD dataset of two different NMC chemistries (NMC532 and NMC111) across various life conditions and states-of-health has enabled identification of key diagnostic parameters. In particular, mean GOS and median GROD values at the surface region appear to be a consistent metric for material health for both chemistries studied. Both of these parameter values are found to increase with electrochemical cycling, consistent with physical models of stress induced by Li (de)intercalation. New analysis capabilities have also enabled the integration of chemical analysis (EDS) this quarter. These complementary techniques will further streamline the diagnostic approach for end-of-life cathodes, and may allow for the development of additional aging metrics, such as transition metal leaching and oxygen loss.

The present EBSD work is evolving to an "on-demand" analysis technique beginning in Q1 of FY21; this is the final quarterly report designated specifically to the EBSD task.

Microcalorimetry on Recycled Materials

In the next fiscal quarter, NREL plans to collate the data from the contamination studies into a Journal article. The processes developed from the calorimeter tests will be used to assess the performance of future recycled material and processes. Furthermore, NREL will thermally test various CAMP NMC/1506T graphite cells with aged cathode/anode materials. NREL previously tested the samples at their beginning of life. The data from these tests will be used to bookend the efficiency and heat generation performance of pristine materials to understand the efficacy of future recycled materials and processes.

Key Publications

1. Fink, K.; Santhanagopalan, S.; Hartig, J.; Cao, L. Characterization of Aged Li-Ion Battery Components for Direct Recycling Process Design. *J. Electrochem. Soc.* **2019**, *166* (15), A3775-A3783.

2. Gaines, L. Profitable Recycling of Low-Cobalt Lithium-Ion Batteries Will Depend on New Process Developments. *One Earth* **2019**, *1* (4), 413-415.

3. Bai, Y.; Hawley, W. B.; Jafta, C. J.; Muralidharan, N.; Polzin, B. J.; Belharouak, I. Sustainable Recycling of Cathode Scraps via Cyrene-Based Separation. *Sustainable Mater. Technol.* **2020**, *25*, e00202.

4. Bai, Y.; Muralidharan, N.; Li, J.; Essehli, R.; Belharouak, I. Sustainable Direct Recycling of Lithium-Ion Batteries via Solvent Recovery of Electrode Materials. *ChemSusChem* **2020**, *13*, 5664-5670.

5. Ross, B. J.; LeResche, M.; Liu, D.; Durham, J. L.; Dahl, E. U.; Lipson, A. L. Mitigating the Impact of Thermal Binder Removal for Direct Li-Ion Battery Recycling. *ACS Sustainable Chem. Eng.* **2020**, *8* (33), 12511-12515.

6. Tan, D. H. S.; Banerjee, A.; Chen, Z.; Meng, Y. S. From Nanoscale Interface Characterization to Sustainable Energy Storage Using All-Solid-State Batteries. *Nat. Nanotechnol.* **2020**, *15*, 170-180.

7. Tan, D. H. S.; Xu, P.; Chen, Z. Enabling Sustainable Critical Materials for Battery Storage through Efficient Recycling and Improved Design: A Perspective. *MRS Energy Sustain.* **2020**, *7*, E27.

8. Wang, T.; Luo, H.; Bai, Y.; Li, J.; Belharouak, I.; Dai, S. Direct Recycling of Spent NCM Cathodes through Ionothermal Lithiation. *Adv. Energy Mater.* **2020**, *10*, 2001204.

9. Zhang, R.; Zheng, Y.; Yao, Z.; Vanaphuti, P.; Ma, X.; Bong, S.; Chen, M.; Liu, Y.; Cheng, F.; Yang, Z.; Wang, Y. Systematic Study of Al Impurity for NCM622 Cathode Materials. *ACS Sustainable Chem. Eng.* **2020**, *8* (26), 9875-9884.

References

1. For Cathode/Cathode Separation via Froth Flotation:

2. Wood et al., 2020, Chemical stability and long-term cell performance of low-cobalt, Ni-Rich cathodes prepared by aqueous processing for high-energy Li-Ion batteries, Energy Storage Materials, 24, 188-197.

3. For Hydrothermal Relithiation of Chemically Delithiated NMC111 Cathodes:

4. Mohanty, D.; Kalnaus, S.; Meisner, R. A.; Rhodes, K. J.; Li, J.; Payzant, E. A.; Wood, D. L.; Daniel, C. Structural transformation of a lithium-rich Li1.2Co0.1Mn0.55Ni0.15O2 cathode during high voltage cycling resolved by in situ X-ray diffraction. *Journal of Power Sources* **2013,** *229*, 239.

5. For Cell Processing:

6. Harper, G.; Sommerville, R.; Kendrick, E.; Driscoll, L.; Slater, P.; Stolkin, R.; Walton, A.; Christensen, P.; Heidrich, O.; Lambert, S.; Abbot, A.; Ryder, K.; Gaines, L.; Anderson, P. "Recycling Lithium-Ion Batteries from Electric Vehicles." *Nature* **2019**, *575*, 75-86.

7. Velázques-Martínez, O.; Valio, J.; Santasalo-Aarnio, A.; Reuter, M.; Serna-Guerrero, R. "A Critical Review of Lithium-Ion Battery Recycling Processes from a Circular Economy Perspective." *Batteries* **2018**, *5*, 68.

Acknowledgements

The following individuals worked as individual task leaders/members for the tasks described in this project: Michael LeResche, Donghao Liu, Albert L. Lipson (ANL) on Binder Removal via Thermal Processing; Jaclyn Coyle, Kyusung Park (NREL) on Binder Removal via Soxhlet Extraction; Erik Dahl (ANL) on Cathode/Cathode Separation Process Development; Lei Pan, Tinu Folayan, Ruiting Zhan (Michigan Technological University) on Cathode/Cathode Separation via Froth Flotation; Tony Montoya, Jack Vaughey (ANL) on Chemical Relithiation of NMC Cathodes; Sheng Dai, Huimin Luo, Yaocai Bai, Jianlin Li, and Ilias Belharouak (ORNL) on Direct Regeneration of NMC Cathodes through Ionothermal Lithiation; Panpan Xu, Zheng Chen (UC San Diego) on Hydrothermal Relithiation of Chemically Delithiated NMC111 Cathodes; Jaclyn Coyle, Kyusung Park (NREL) on Relithiation via Redox Chemistry; Jaclyn Coyle, Kyusung Park (NREL) on Electrochemical Relithiation; Nate Sunderlin (NREL) on Roll-to-Roll Reactor Design for Electrochemical Relithiation; Jack Vaughey, Tony Montoya (ANL) on Cathode Upcycling; Yan Wang (WPI) on Role of Impurities in Recycled Cathodes; Jessica Durham (ANL) on Cell Preprocessing; Ilias Belharouak, Yaocai Bai, Jianlin Li, Rachid Essehli, Huimin Luo, Sheng Dai (ORNL) on Solvent-based Electrode Recovery; Jessica Durham (ANL) on Anode/Cathode Separation and Purification; Donghao Liu, Albert L. Lipson (ANL) on Electrolyte Component Removal and Recovery; Jianlin Li, Yaocai Bai, Sergiy Kalnus (ORNL) on Cell Design; Qiang Dai (ANL) on EverBatt: Cost and Environmental Impacts Modeling; Margaret

Mann, Vicky Putsche, Dustin Weigl, Michael Tandoh, Daniel Inman (NREL) on Analysis of Supply Chain Challenges for Battery Recycling; Alison R. Dunlop, Andrew N. Jansen (PI), Bryant J. Polzin, Stephen E. Trask (ANL) on CAMP Facility Support; Zhenzhen Yang, Ira Bloom (ANL) on Post-test Facility Support; Kae Fink, Helio Moutinho, Patrick Walker, Shriram Santhanagopalan (NREL) on Diagnostics of Aged Materials; and Matthew Keyser, Josh Major, Kae Fink, Shriram Santhanagopalan (NREL) on Microcalorimetry on Recycled Materials

I.3.D Li-Ion Cell Manufacturing Using Directly Recycled Active Materials (Farasis Energy)

Michael Slater, PhD, Principal Investigator
Farasis Energy, Inc.
Address: 21363 Cabot Blvd
Hayward, CA 94545
E-mail: mslater@farasis.com

Brian Cunningham, Technology Development Manager
U.S. Department of Energy
E-mail: Brian.Cunningham@ee.doe.gov

Start Date: February 1, 2017 End Date: December 31, 2020
Project Funding: $1,000,000 DOE share: $500,000 Non-DOE share: $500,000

Project Introduction

The rapid performance gains of Li-ion batteries in the past few decades have led to accelerating implementation of this electrochemical energy storage technology on an unprecedented scale. For this growth to be sustainable, the entire life cycle of the batteries must be accounted for, from raw material sourcing to end-of-life disposal and reuse. So far, the cost associated with end-of-life disposition of these batteries has not been included in the product price; coupled with a drive to use less costly materials in the batteries themselves we are arriving at a situation in which there is less intrinsic value in the elemental composition of the battery than it costs to recycle/dispose of them in a responsible manner. Thus, there is a need for a recycling method that goes beyond treating the battery as an ore and can harvest some of the additional value that is invested in the product during complex raw material and cell manufacturing processes.

Objectives

There are four main objectives for this project:

1. Optimize direct recovery processes at larger scale (>8 kg cell/module input)
2. Optimize electrode formulations to make best use of refurbished active materials
3. Manufacture full-size LiBs on commercial production line using direct-recycled active materials
4. Quantify impacts of using recycling active materials on technology cost.

Approach

Farasis Energy has been working on recycling technology for Li-ion batteries for a number of years. We have addressed the challenges of closing the loop of the Li-ion product life cycle by developing methods for recovery and reuse of valuable components in the batteries largely based on the direct recycling approach. “Direct Recycling” refers to battery recycling technology in which material recovery is performed using physical separation processes and active materials are reused with minimal processing, ideally without the need for extensive chemical transformation. In this way, some of the value invested in the materials (*e.g.*, synthesis process energy, particle size distribution and shape) can be recovered without the need to resynthesize these materials from their lowest value elemental form. Figure I.3.D.1 shows a flow chart for a straightforward direct recycling process used to recover the high value components of the Li-ion battery. In this approach the entire cell or module is shredded after being fully discharged and deactivated. Safety is a key requirement for this step, and therefore measures to prevent release of hazardous materials and fires are a primary consideration. The shredded material is subjected to a solvent extraction step, which removes the electrolyte while also stabilizing the cell chemistry by removing a source of hydrofluoric acid, which can damage the valuable active materials upon exposure to air and water during subsequent processing. The

shredded mass is then screened/sieved to remove other battery components from the micron-sized active materials. This leaves the "Black Mass," a mixture of active anode and cathode powders with some binder, carbon, and small amounts of other components as contaminants. Separation of the cathode and anode active materials from each other is achieved using a liquid with density between that of graphite and the metal oxide. In this state, the recovered active materials are not immediately ready for use in new lithium ion cells; the recovered cathode material is missing some lithium due to the inherent losses during the formation process and extended cycling while the graphite active material contains some lithium and surface species generated during the formation and cycling processes. Regeneration of the active materials by removing contaminants, restoring the lithium inventory, and final annealing in which the structural integrity of the materials is returned to its pristine state. Farasis has developed proprietary approaches to achieve these final steps that are chemistry independent and have demonstrated the capability to achieve good separation yields, high purity, and high performance materials.

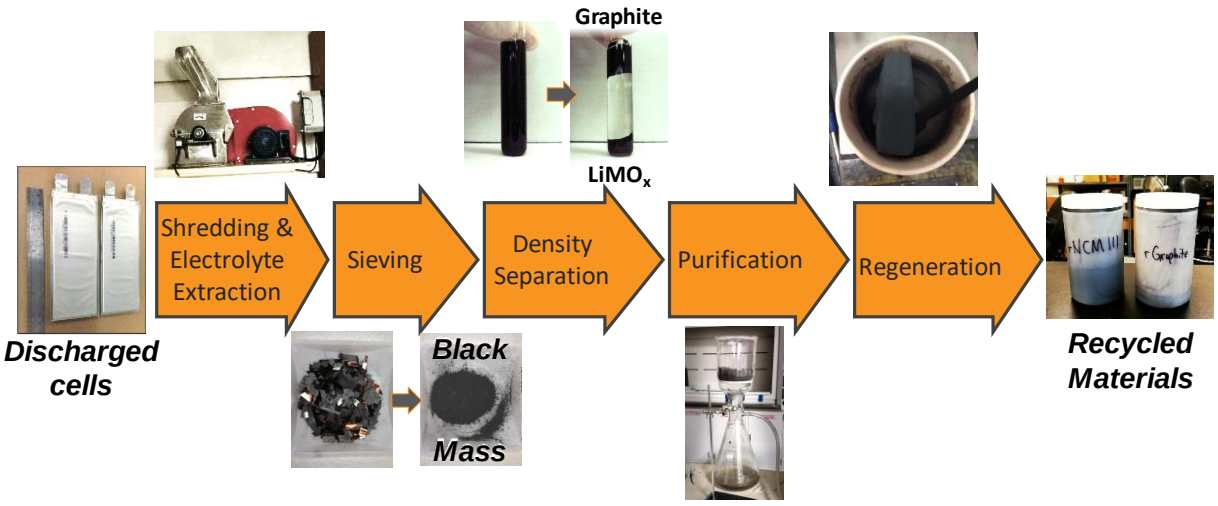

Figure I.3.D.1 Pictorial representation of the direct recycling process which largely relies on physical separation processes; compared to other recycling technologies, the positive electrode active material is recovered intact, preserving some of the value added during its synthesis.

Available evidence to-date suggests that modified surface chemistry of the isolated active materials is the primary technological challenge to address from a process perspective, while any intervention in this domain also provides an opportunity for improvements over the properties of the pristine materials. Detailed structural investigations as to the nature of material changes during recycling processes are being explored in collaboration with Robert Kostecki at Lawrence Berkeley National Laboratory. The suite of analytical tools that will be used to inform the optimization of the recycling steps include:

- High resolution X-ray instrumentation at DOE's Synchrotron User Facilities, enabling detailed investigation of structural parameters such as microstrain and lattice defects
- SEM will be used for imaging particle morphology and surface chemical analysis by EDAX
- Electrochemical Impedance Spectroscopy will be used to determine intrinsic conductivity of materials and for electrode-level characterization during formulation research with recycled materials
- Particle size distribution measurements and gas adsorption analysis will be used to determine material physical characteristics such as particle size, surface area, and internal microporosity
- Raman spectroscopy will be used to study surface and near surface changes in material structure and chemistry which are difficult to characterize by other methods

- Neutron diffraction will be employed in conjunction with XRD to more accurately characterize the structure of Li-containing materials. Due to the extremely weak scattering cross section of Li for X-rays, neutron diffraction is required to positively locate Li in the crystal structures

The direct recycled active materials will be used in iterative cell builds through which insight will be gained on how to best incorporate recycling technologies in battery manufacturing, resulting in more environmentally friendly, lower cost production of Li-ion batteries. A high-level summary of project deliverables (internal and external) may be found in Table I.3.D.1.

Table I.3.D.1 Overview of Program Hardware Deliverables and Build Strategy

Hardware Deliverable	I.3.D.2Description	Source Material	Quantity ANL/FEI*	Delivery Date
Cell Build 1 (84 x ~1 Ah cells)	Control: pristine Graphite//pristine NMC	commercial powders	9/24	Month 27
	recycled Graphite//recycled NMC	manufacturing scraps	9/24	Month 27
	pristine Graphite//recycled NMC	manufacturing scraps	0/18	Month 27
Cell Build 2 (60 x ~2 Ah cells)	Control: pristine Graphite//pristine NMC	commercial powders	9/12	Month 35
	pristine Graphite//40 % recycled NMC	BOL cells/QC rejects	9/12	Month 35
	pristine Graphite//100 % recycled NMC	BOL cells/QC rejects	0/12	Month 35
Final Build (54 x ~2 Ah cells)	Control: pristine Graphite//pristine NMC	commercial powders	15/12	Month 38
	optimized maximum recycled content in each electrode (*tbd*)	EOL cells and module parts	15/12	Month 38

* Each build will include cells for external (USABC/ANL) and internal (Farasis Energy) testing and evaluation

The measure of success of the program is being quantified by measuring the gap between recovered material and equivalent control test articles made using commercial grade active materials, which will be included with each build to allow comparative evaluation. While not included in the final deliverables, there will be development work addressing how best to handle mixed chemistry feed streams, which is an inherent challenge for direct recycling processes. Specifically, recovery of feed streams with NMC532 and mixed NMC/spinel compositions will be studied. Another important outcome of the program will be to refine current assumptions of a scaled production process (including milling, separation, purification and regeneration operations) and evaluate revenue potential against capital and energy requirements and operating costs, thus ensuring that the technology is economically relevant.

Results

Evaluation of cells built using electrode scrap-derived active materials (Cell Build 1) was completed in FY20. Cells for all three material configurations (*vide supra*) were subject to either dynamic stress testing (DST) at 30,45, and 55 ^{o}C or 100 % SOC storage at 45 or 55 ^{o}C. Monthly reference performance tests (RPTs) were performed for all cell groups at 30 ^{o}C, consisting of the C/3 static capacity and hybrid pulse power characterization (HPPC) tests as described in the USABC EV test manual. Compared to control cells that were built using only pristine active materials, cells with recycled graphite and/or recycled NMC ("rNCM") exhibited higher rates of capacity fade and impedance increase. The impacts of using the recycled active materials are most evident at higher temperature due to acceleration of the side-reactions responsible for these processes.

The results of the static capacity tests from the RPTs are summarized in Figure I.3.D.2 There is a general trend of increasing rate of capacity loss with increasing temperature across all cell groups. Cells with rNCM as the only recycled component have a higher rate of capacity loss compared to pristine controls under DST conditions, but no significant difference in capacity fade for the storage cells. The faster rate of capacity fade for the DST cells due to inclusion of rNCM is attributable to the fact that all cells are being tested at the same reference power level (630 W/kg) even though the rNCM cells have *ca.* 5 % lower lithium inventory due to the

decreased specific capacity of the rNCM. The inclusion of recycled graphite has an additive impact on capacity fade, likely due to solid electrolyte interphase instability arising from impurities that were not fully removed during the recycling process.

To simplify discussion of the impedance growth characteristics of these cells, the 40 % DOD resistance data from the HPPC test was used to create bar charts which are shown in Figure I.3.D.3. Similar to the discussion

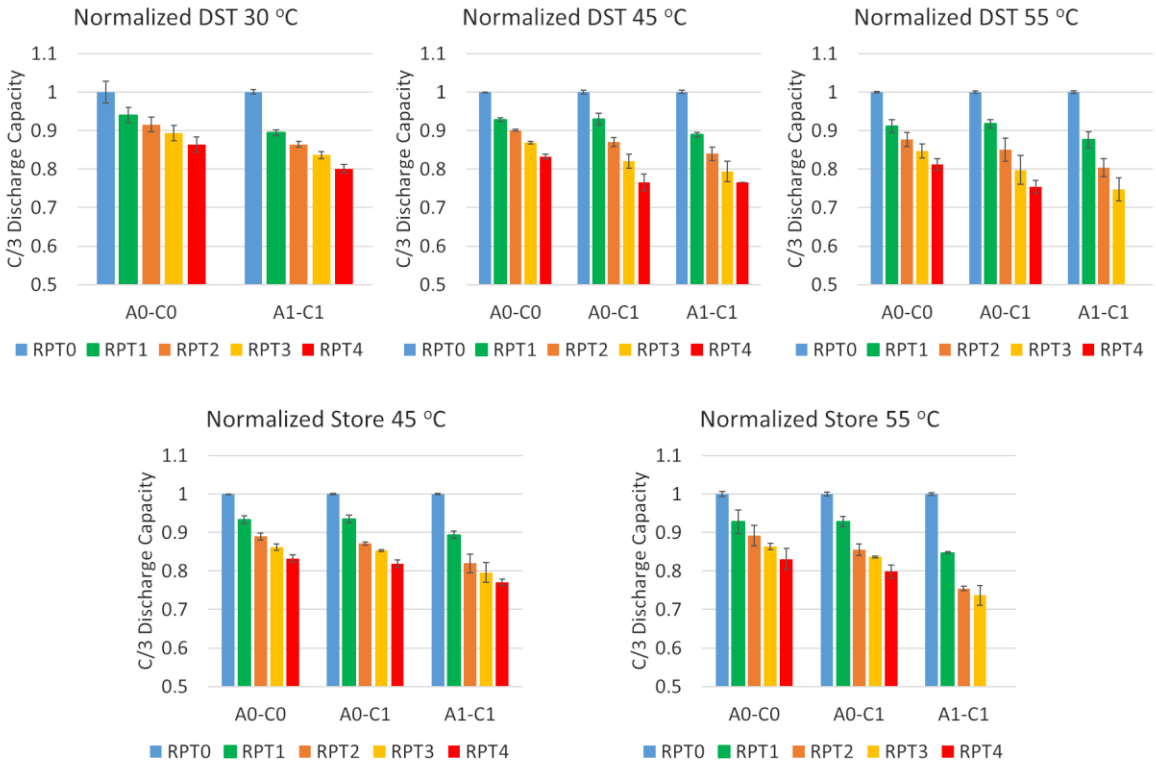

Figure I.3.D.2 Average normalized C/3 static capacity results from RPTs for Cell Build 1 testing at Farasis. Cells are normalized to RPT0 within each material configuration and test condition combination. A0 = pristine graphite, A1 = recycled graphite, C0 = pristine NMC111, C1 = recycled NMC111

of capacity loss, the use of these recycled active materials leads to higher resistance and the effects of using rNMC and rGraphite are additive. The relative rates of impedance growth are similar for all cells, although the pristine material cells start out with lower resistance. In general, the cells in the 100% SOC storage condition for a given temperature exhibited a slightly faster rate of impedance growth compared to the DST cells. The different shape of the impedance growth curve for pristine cells as compared to cells with recycled active material content suggests some differences in cell chemistry evolution.

Across Cell Build 1 testing, the differences in performance between the different material configurations can be tied to the difference in material properties as illustrated in the materials gap charts (which have been previously reported in Annual Merit Review presentations for this project). Further process refinement as the technology is developed at scale will improve material purity and allow full realization of the economic advantages of applying direct recycling to manufacturing waste feedstocks.

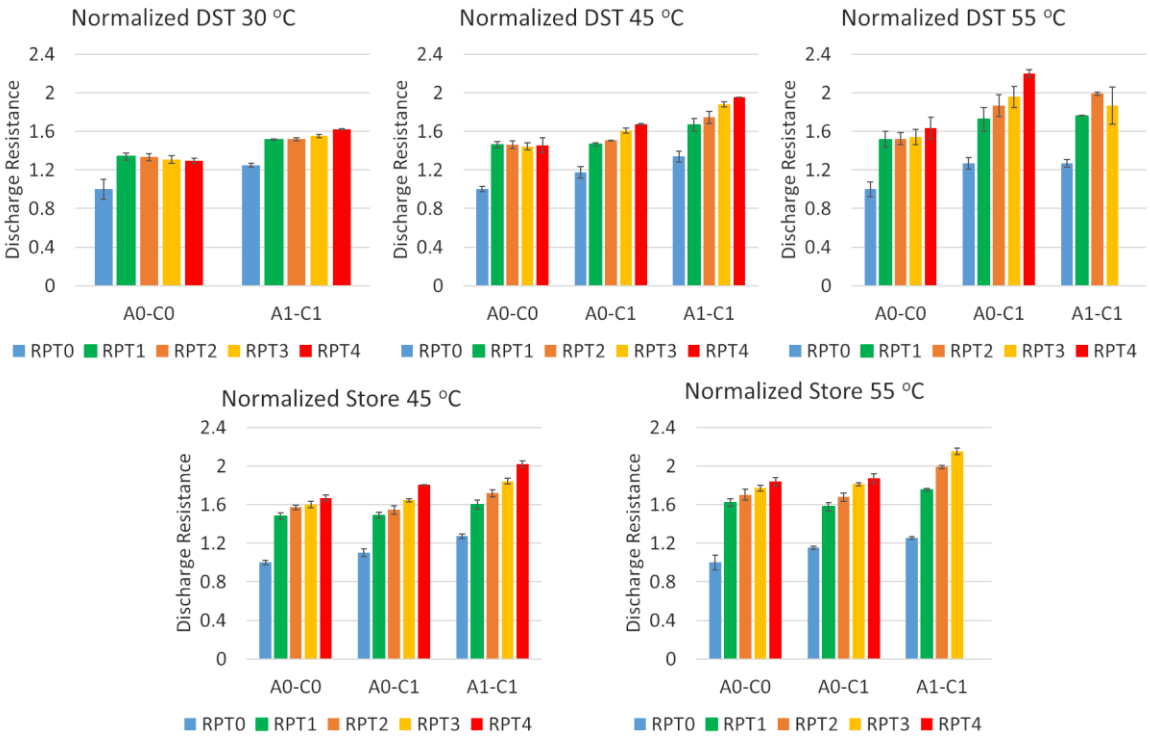

Figure I.3.D.3 Average normalized 40% DOD discharge resistance values from HPPC test for Cell Build 1 evaluation at Farasis. Data within each test condition are all normalized to the lowest impedance pristine material cells. A0 = pristine graphite, A1 = recycled graphite, C0 = pristine NMC111, C1 = recycled NMC111

Producing recycled active materials for Cell Builds 2 and 3 was the major focus of project effort in FY20. COVID-19 had a tremendous impact on this work, causing delays due to shutdowns at our manufacturing and R&D facilities, extended shelter-in-place orders, and the need for modified, less-efficient work practices. Two routes were used to directly recover kilogram quantities of NMC from whole cell feedstocks, schematically illustrated in Figure I.3.D.4. Route (a) in this figure was developed to address difficulties, which have since been resolved, that we were experiencing with the density-based separation step. In this new route, some of the graphite is mechanically separated early in the process based on differences in the mechanical degradation characteristics of the electrode coatings. This ultimately produces a “cathode-rich black mass” which contains less graphite than typical black mass; the remaining graphite is sacrificially combusted during solid state relithiation of the crude NMC. Care must be taken with this approach to avoid carbothermal reduction of the NMC. In contrast, route (b) is our originally proposed process that uses a dense media separation step to isolate NMC from graphite; the separation efficiency of this step was improved to useful levels through the addition of process control agents.

The properties of the rNMC materials recovered via the different routes are compared in Table I.3.D.2. The rNMC111 produced *via* the density-based separation route exhibited decreased particle size and tap density and increased specific surface area compared to the pristine control. There are some residual contaminants evident in the elemental analysis, most notably Cu, F, and W. These elements contribute to the decreased specific capacity by representing “dead weight” in the cathode and also by increasing interfacial impedance as dopants at the particle surfaces (*n.b.*, the metal contaminants are certainly present as oxides). In contrast, the rNMC111 produced *via* the combustion route exhibited nominally better powder characteristics and had a decreased impurity burden, however this material was inferior in terms of its electrochemical characteristics.

This is likely due to particle surface reconstruction during the combustion process that creates a high impedance topotaxial surface phase.

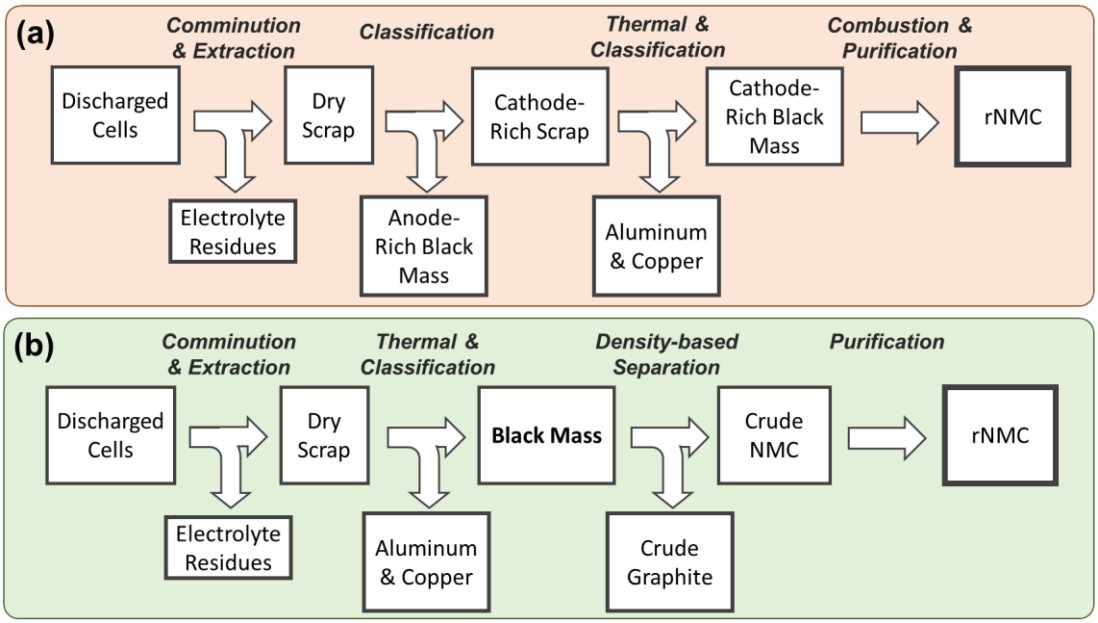

Figure I.3.D.4 Comparison of different routes to isolate rNMC from black mass: (a) Combustion of excess graphite and (b) density-based separation in liquid media.

Table I.3.D.2 Materials Properties of Direct Recycled NCM111 From Whole Cell Feedstock via Two Different Routes

Characteristic	Units	Pristine NCM111	rNMC111 *via* Combustion Route	rNMC111 *via* Density Separation Route
Particle size (d_{50})	µm	11	7.3	4.0
Tap Density	g/cm³	2.2	2.0	2.1
Reversible capacity (4.2 - 3.0 V vs. Li/Li⁺, 0.1 C)	mAh/g	150	116	132
Specific Surface Area (BET method)	m²/g	0.38	0.46	0.62
First cycle efficiency	%	90	85	86
Impurities	%w/w	0.11 < Na < 1 Mg < 0.05 Ca < 0.07 Fe = 0.024 Cu < 0.0014 Al < 0.072	Na < 0.05 Mg < 0.05 Ca < 0.05 Fe < 0.05 W < 0.05 Cu = 0.93 Al < 0.05	Na < 0.05 Mg < 0.05 Ca < 0.05 Fe < 0.05 W = 0.17 Cu = 2.6 Al < 0.05
pH assay	$-\log_{10}[H^+]$	11.0	tbd	tbd

Cell Builds 2 and 3 are aimed at evaluating different use scenarios for direct recycled active materials. Cell Build 2 examines the hypothesis that the maximum content of rNMC blended with its pristine counterpart is dictated by a linear combination assumption for critical material characteristics in the cell design. Based on the properties of the rNMC produced for Cell Build 2 it was determined that 25% rNMC would be tolerated while still meeting minimum QC standards (except for the impurity content, which will have to be addressed through

further process improvements). Cell Build 3 targets a likely use case based on estimated quantities of rNMC available due to the quantity of electric vehicles being recycled relative to expected new production. In this case the rNMC is being blended with pristine NMC at a rate of 5% (which would translate to a cell level cost reduction of 2-3 %). The properties of the blended materials for each build are reported in Table I.3.D.3. These materials were delivered to our factory and manufacturing of the Cell Build 2 and 3 deliverables is in progress.

Table I.3.D.3 Materials Properties of Recycled/Pristine NCM111 Blends for Cell Builds 2 and 3

Characteristic	Units	Pristine NCM111	CB2 Recycled Blend	CB3 Recycled Blend
Particle size (d_{50})	μm	11	6.6	*tbd*
Tap Density	g/cm^3	2.5	2.3	2.4
Reversible capacity (4.2 - 3.0 V vs. Li/Li$^+$, 0.1 C)	mAh/g	150	149	149
Specific Surface Area (BET method)	m^2/g	0.21	0.41	0.24
First cycle efficiency	%	90	90	89
Impurities	%w/w	0.11 < Na < 1 Mg < 0.05 Ca < 0.07 Fe = 0.024 Cu < 0.0014 Al < 0.072	Na < 0.05 Mg < 0.05 Ca < 0.05 Fe < 0.05 W < 0.05 Cu = 0.36 Al < 0.05 F = 0.12	Na < 0.05 Mg < 0.05 Ca < 0.05 Fe < 0.05 W = 0.009 Cu = 0.42 Al < 0.05 F = 0.04
pH assay	-log$_{10}$ [H$^+$]	11.3	11.2	11.2

Conclusions

The electrochemical testing of manufacturing scrap-derived direct recycled active materials is now complete. Between the different materials configurations, the cells in which NMC is the only recycled component perform more like the pristine material cells, though with diminished capacity. Cells in which both the NMC and graphite are both recycled have significantly higher rates of capacity fade and impedance increase. The different performance characteristics can be traced back to residual impurities that are not fully removed during the recycling process and we are confident that additional process refinement will further improve the performance characteristics of direct recycled active materials. The material recovery phase of this project was completed this year, producing direct recycled NMC111 at the kg scale through two possible pathways, developing extensive process knowledge along the way. These materials are currently being manufactured into test articles to perform electrochemical testing that will correlate the material properties of direct recycled NCM111 with device level performance.

Key Publications

1. “Li-Ion Cell Manufacturing Using Directly Recycled Active Materials,” bat356_Slater_2020_p, US DOE Vehicle Technologies Program Annual Merit Review, 2020.

Acknowledgements

The PI would like to extend special thanks to Renata Arsenault, who manages this project for USABC, for her collaboration and dedicated effort to advance Li-ion battery recycling technology, and Benjamin Little at Farasis Energy who has worked hard to keep the project moving despite the difficult circumstances of this year.

I.3.E A Closed Loop Recycling Process for End-of-Life Electric Vehicle Li-ion Batteries-Phase II (Worcester Polytechnic Institute)

Yan Wang, Principal Investigator
Worcester Polytechnic Institute
100 Institute Road
Worcester, MA 01609
E-mail: yanwang@wpi.edu

Brian Cunningham, DOE Technology Development Manager
U.S. Department of Energy
E-mail: Brian.Cunninham@ee.goe.gov

Start Date: March 26, 2018 End Date: November 30, 2020
Project Funding: $1,083,616 DOE share: $541,808 Non-DOE share: $541,808

Project Introduction

During the course of the Phase I USABC program, the team has observed that the xEV battery industry is moving to higher nickel NMCs. Although the team has successfully synthesized NMC111 which has similar performance with the commercial powder, it is considered necessary to be able to synthesize high nickel NMC (for example NMC622) from the recycling stream in order to compete in the market and successfully commercialize the technology. Therefore, in the Phase II (follow-on) of the USABC project, the team has been developing the capability to synthesize NMC622, once again striving to demonstrate both flexibility to accommodate recycling streams diverse in EV battery chemistry, and the ability to generate NMC622 with similar performance to commercial grade powder. The impacts of emerging new anode materials and adhesives is also being examined. Finally, the recycling process is being further refined and scaled, with the cost model being updated accordingly.

Objectives

The overall objective of the Phase II program is to demonstrate the recovery of NMC622 cathode materials from cycled lithium ion batteries with mixed and emergent cathode and anode chemistries, and adhesives. In comparison to NMC111, NMC622 offers higher energy density, which is increasingly demanded by the EV industry. In addition, the recycling process and cost model will be further developed based on the process update and scale-up.

Approach

Similar to the phase I program, WPI collaborated with A123 Systems and Battery Resourcers for this phase II program. WPI's primary focus was developing the recycling process and recovering NMC622 powder, A123's focus was on powder characterization, cell fabrication and testing, and Battery Resourcers' focus was on scale up and cost analysis. In addition, the cells will be delivered to Argonne National Laboratory for independent testing and evaluation. Figure I.3.E.1 shows the hardware strategy of the program. The project included 3 phases: initial scale-up, optimization and final deliverables. During the initial scale-up, the synthesis parameters of NMC622 precursor and cathode materials were determined and electrochemical testing was conducted using coin cells and single layer pouch cells. During the optimization phase, 1~2 different spent battery streams (30kg each) were utilized for recycling experiments to generate NMC622 for 1Ah cells. At the same time, virgin NMC622 was used to fabricate 1Ah control cells for side by side evaluation. For the final deliverables phase, 1 spent battery stream, with intentionally different input chemistry combinations, was

utilized for recycling experiments to generate NMC622 for 10Ah cells. At the same time, virgin (commercial) NMC622 was again used to fabricate 10Ah control cells.

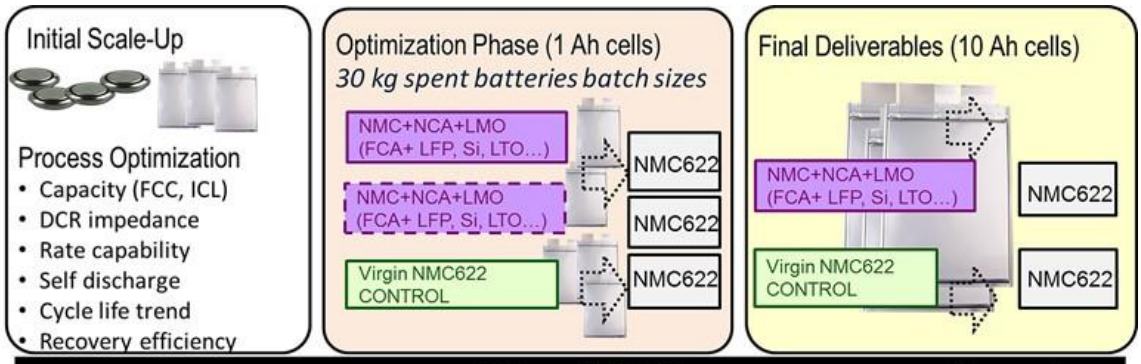

Build	Test Article	Total Made	USABC/ ANL	A123/ WPI	Kg powder per group
1	1 Ah NMC622/gr	20	12	8	6 (WPI)
1-control	1 Ah NMC622/gr	20	12	8	6 (comm.)
(2)*	(1 Ah NMC622/gr)*	(20)*	(12)*	(8)*	6 (WPI))*
3	10 Ah NMC622/gr	20	12	8	15
3-control	10 Ah NMC622/gr	20	12	8	15 (comm.)

** 2nd 1 Ah build will only be executed if required. Depends upon 1st build results.*

Figure I.3.E.1 Hardware Strategy of the Program

Results

In order to generate enough NMC622 powder for 1Ah and 10Ah cells, a 14 and 27 days co-precipitation reaction was conducted, respectively. Similar to the previous experiments, the particles are spherical shape, which is important for the electrochemical performance. With the increased time, the particles become larger and stabilize once they reach to certain size. This means that the experiment reaches to the steady state. After sintering with Lithium source, Al_2O_3 is coated on the synthesized NMC622 powder in order to stabilize its performance. Figure I.3.E.2 is the SEM and XRD pattern of the typical cathode powder delivered to A123 for cell fabrication. From the SEM image, the particles are spherical shape and the XRD shows the layered structure of NMC622 (There are no Al_2O_3 peaks due to the small amount of coating).

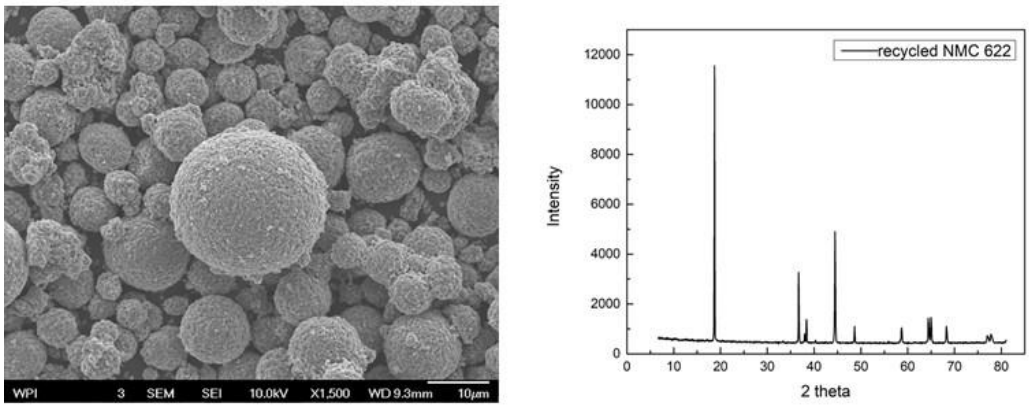

Figure I.3.E.2 SEM and XRD of final cathode materials

A123 systems has fabricated 1Ah cells (24 cells with WPI powder and 30 cells with control powder) and 24 cells (12 with WPI powder and 12 with control powder) has been delivered to Argonne National Laboratory for

testing. At the same time, A123 systems is doing some internal testing for these 1Ah cells and the results are shown in Figure I.3.E.3. From Figure, 1Ah cells with both recycled and control powder have more than 1,000 cycles while keeping the capacity above 80%, which is acceptable by industry. 1Ah cells with control powder show better cycle life than those with WPI recycled powder. There are a few reasons why the cells with recycled powder shows worse cycle life, which includes (1) residual lithium, (2) coating, (3) higher surface area.

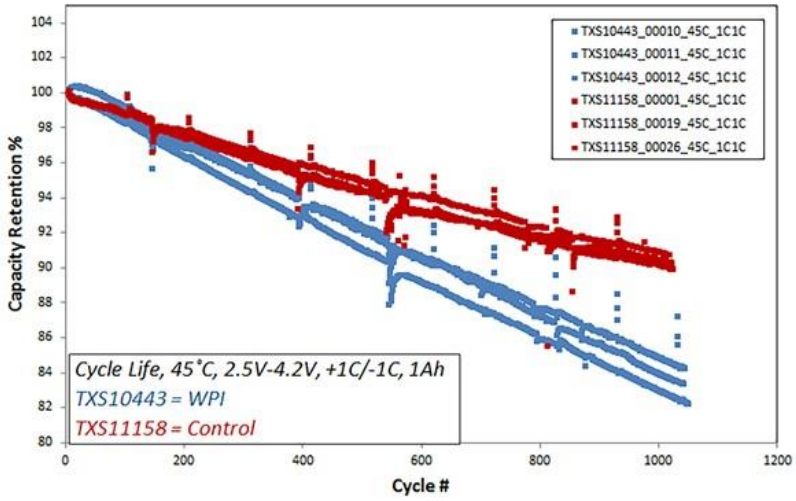

Figure I.3.E.3 Cycle life of 1Ah cells with recycled and control powder

The team has also fabricated 10Ah cells (21 cells with WPI recycled powder and 21 cells with control powder) and 24 cells (12 with WPI powder and 12 with control powder) will be delivered to Argonne National Laboratory for testing and the rest cells are being tested at A123 and some initial results are shown in Figure I.3.E.4 and Figure I.3.E.5. Figure I.3.E.4 is the first cycle charge and discharge and third cycle discharge capacity, which shows that the capacity of all cells is consistent with ~10Ah. Figure I.3.E.5 is the cycle life of 10Ah cells with WPI recycled and control powder. The cells have been cycled ~85 cycles and there is almost no different between the cells with WPI recycled and control powder. Longer cycle life is needed to see the difference between the cells with WPI recycled and control powder.

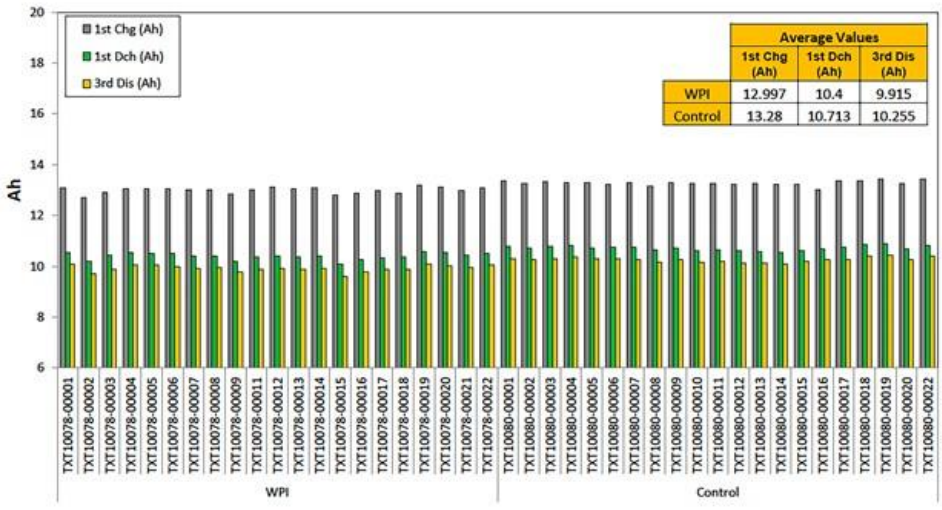

Figure I.3.E.4 The initial capacity of 10Ah cells with recycled and control powder

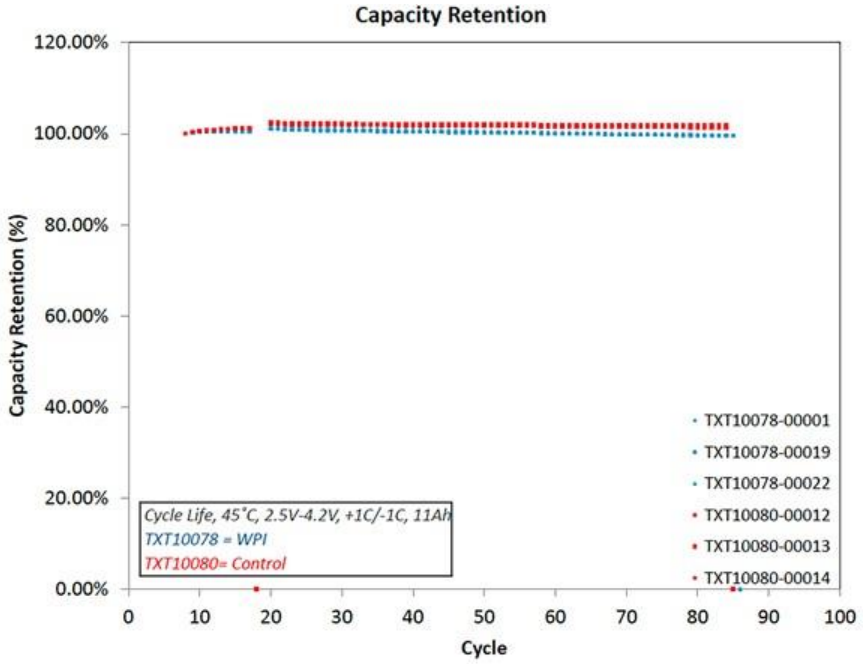

Figure I.3.E.5 The cycle life of 10Ah cells with recycled and control powder

An economic model was developed using Argonne National Laboratory EverBatt model. The model calculated the cathode material price for Battery Resourcers (BRs) material as well as the material generated via smelting batteries and making cathode materials from virgin materials. The model also calculated the emissions and total energy of each process. The model calculates the cost of BRs NMC622 cathode material to be over $6/kg cheaper than virgin cathode materials or greater than 20% cheaper.

Conclusions

In this USABC Phase II project, the team has successfully recycled end of life EV batteries consisting of different incoming cathode, anode chemistries and adhesives, and producing NMC622 powder. In addition, the team developed surface coating technique to stabilize the NMC622 active material and mitigate cycling and calendar aging-induced degradation. The team has successfully synthesized and delivered NMC622 powder to A123 Systems for 1Ah and 10Ah cell fabrication. 1Ah cells with both recycled and control powder have more than 1,000 cycles while keeping the capacity above 80%, which is acceptable by industry. 1Ah cells with control powder show better cycle life than those with WPI recycled powder. 10Ah cells have been cycled ~85 cycles and there is almost no different between the cells with WPI recycled and control powder. Longer cycle life is needed to see the difference between the cells with WPI recycled and control powder.

Acknowledgements

The development team (WPI/A123/BRs) would like to thank the following for all of the help, advice, support and suggestions: USABC program manager Renata Arsenault (Ford Motor Company) and USABC work group members Nakia Simon (FCA), Peter Karlson (GM), Brian Cunningham (DOE), and David Robertson (ANL).

COVID-19 Impacts

Due to the wide spreading of Coronavirus, WPI, BRs, A123 and Argonne were completely or partially shut down from March 2020 to June 2020, which impacts the progress of the project.

I.4 Extreme Fast Charge (XFC)

I.4.A Research advanced battery cell designs and strategies to operate and improve life and fast charging at higher temperatures (Argonne National Laboratory)

Zhengcheng (John) Zhang, Principal Investigator
Argonne National Laboratory
9700 S. Cass Ave.
Lemont, IL 60439
E-mail: zzhang@anl.gov

Brian Cunningham, DOE Technology Development Manager
U.S. Department of Energy
E-mail: Brian.Cunningham@ee.doe.gov

Start Date: July 1, 2018 End Date: June 30, 2020
Project Funding: $150,000 DOE share: $150,000 Non-DOE share: $0

Project Introduction

Widespread adoption of electric vehicles is limited by the current necessary charging times of greater than one hour. However, high charging rates are kinetically limited by lithium ion intercalation into graphite, which causes undesirable lithium plating and dendrite formation. High temperature charging could eliminate this issue.

Objectives

The objective of this subproject is to design and develop new electrolytes that are stable at elevated temperatures (>50°C) which could support the fast charging at high temperatures while maintaining excellent cycle life and calendar life.

Approach

In this project, a targeted additive approach was employed to directly address the causes of high temperature cell degradation. Electrolyte additives that stabilize the electrolyte bulk and protect the cathode surface at high temperatures will be designed and their impact on the cell performance will be evaluated. The best-performing additives will be verified in the commercial EV cells.

Results

Covid Delays

Argonne National Laboratory was in minimum safe operations between March 20th and July 20th, followed by limited operations until the present day. These modes either eliminated or restricted in-lab work, causing significant delays in research progress, particularly for strategy two.

Strategy One: Analysis of Electrolyte Solutions

Here, a novel experimental setup was proposed to observe the generation of PF_5 over time, therefore allowing us to study the effects of different perturbations on the degradation process. Using this information, electrolyte additives that can limit the reactivity or generation of PF_5 was designed, synthesized, and electrochemically tested in a lithium-ion cell with improved overall battery performance.

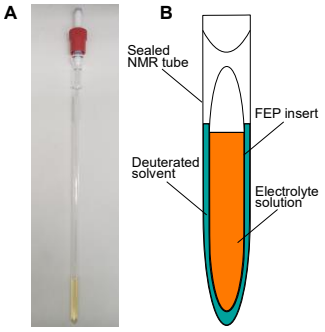

Figure I.4.A.1 NMR experimental setup. (a) Picture of NMR tube with an PTFE/FEP insertion and (b) schematics of the NMR setup

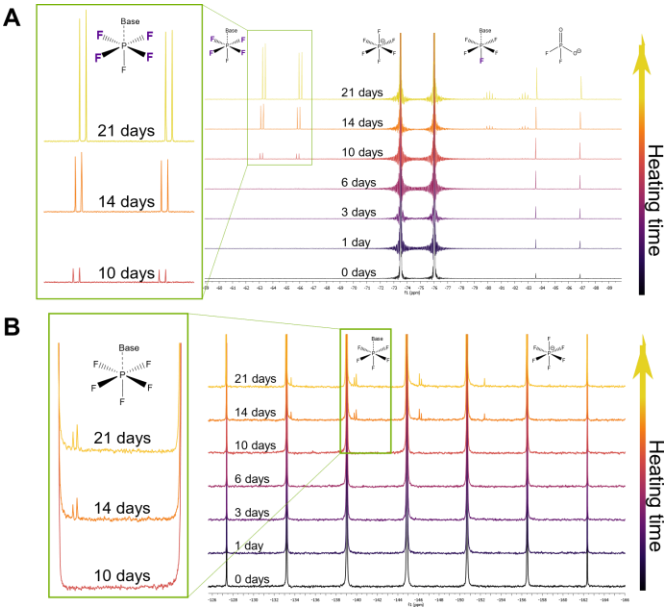

Figure I.4.A.2 (a) ^{19}F NMR and (b) ^{31}P NMR spectra of Gen 2 electrolyte heated at 80 °C for increasing lengths of time.

Discovery and characterization of new PF_5 complex

The commonly accepted mechanism for electrolyte decomposition at high temperatures was initially proposed by Campion *et al.*[1], [2], which involves PF_5 reacting with trace protic impurities to form POF_3, which can then react *via* an autocatalytic mechanism to generate CO_2, fluoroalkyl chains, and an extra equivalent of POF_3. To study the dynamic structure and chemical composition of the electrolyte at elevated temperatures, a new NMR setup was established as shown in Figure I.4.A.1. An PTFE/FPE insert design could eliminate the complication of the deuterated solvent with the subject testing electrolyte affording a more accurate information.

Testing temperatures of 50°C and 80°C were selected to represent medium and extreme temperatures for lithium-ion battery operation. When a sample of Gen 2 electrolyte was exposed to such a high temperature for an extended period in our new experimental setup, a new set of peaks was seen in both ^{19}F and ^{31}P spectra as shown in Figure I.4.A.2. This consisted of a doublet of doublets (-63.70 ppm, J= 766.9, 56.9 Hz) and a doublet of quintets (-80.84 ppm, J = 743.5 Hz, 57.0 Hz). Coincident to this was the growth of a doublet of quintets in the ^{31}P NMR (-143.0 ppm, J = 765.0, 745.0 Hz). Both ^{19}F and ^{31}P-NMR indicates the existence of a complex of PF_5 with a Lewis base. However, attempts to positively identify this complex have so far failed.

As it is widely accepted that the decomposition mechanism of Gen 2 electrolyte begins with the formation of PF_5, the potential to use this PF_5-base complex as a marker for electrolyte decomposition was explored by NMR. Many additives have been tested for the purpose of suppressing this process and improving the cell performance at high temperatures, with one of the most common one being *N*,*N*-dimethylacetamide (DMAc)[3]. In order to test our hypothesis, 2% DMAc (w/w) was chosen and added to Gen 2 electrolyte with the belief that this would limit the growth of this signal. The ^{19}F-NMR spectra shown in Figure I.4.A.3a indicate the strong coordination of PF_5 with DMAc, based on the appearance of a second set of peaks indicative of a separate PF_5 complex being formed. The overall strength of the new PF_5 signal was restricted when compared to the unmodified electrolyte (Figure I.4.A.3b), indicating that the concentration was limited as well.

Validated by the DMAc experiment, we started to test different perturbations to the electrolyte system to investigate their effects on the thermal degradation process. Figure I.4.A.4 shows the addition of different materials to Gen 2 electrolyte aged for elongated period of times at both 50°C and 80°C. It is manifest

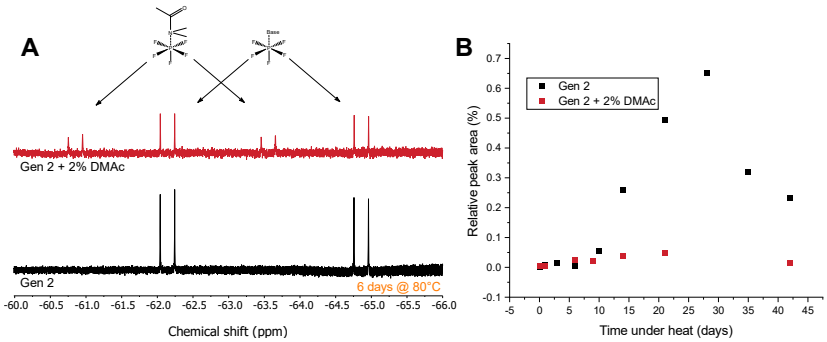

Figure I.4.A.3 (a) 19F NMR spectra of Gen 2 with DMAc (top) and Gen 2 (bottom) after 6 days of heating at 80 °C, and (b) peak area of PF_5 complex signals relative to $LiPF_6$ salt in the solution.

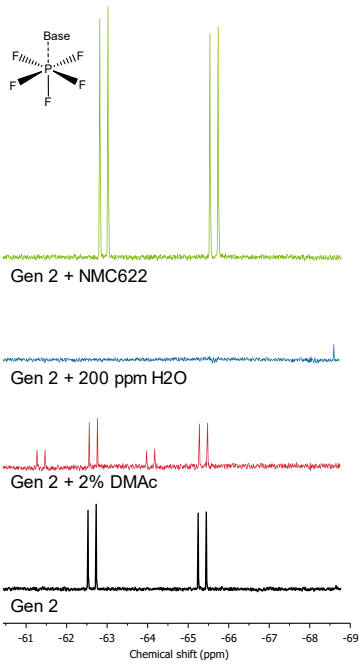

Figure I.4.A.4 ^{19}F NMR spectra after aging at elevated temperatures from bottom to top: Gen 2 @ 80°C, Gen 2 + 2% DMAc @ 80°C, Gen 2 + 200 ppm H_2O @ 50°C, and Gen 2 + NMC powder @ 50°C.

that addition of the cathode active material NMC622 actually increased the decomposition rate over the baseline electrolyte when treated at the same temperature. This could be due to the addition of a catalytic surface, or potentially the dissolution of the transition metal ions into the electrolyte solution. Water prevented any complex from forming, potentially because of the rapid reaction of PF_5 with H_2O.

One piece of evidence supporting the role of transition metals in the decomposition process is the changing peak width in electrolyte solution. While peak width is dependent on many factors, such as ionic strength, rotational averaging, 90° pulse calibration, or the quality of the magnetic shimming, it can also be affected by the addition of paramagnetic ions. As Mn^{2+} is a paramagnetic species, it is expected to see peak broadening as its concentration increased in the solution. This explains the significant peak broadening for difluorophosphate for the NMC sample as evidenced by the NMR data shown in Figure I.4.A.5. Hexafluorophosphate $PF6^-$ maintained a constant peak width, which indicates a close association between Mn^{2+} and difluorophosphate. An alternative explanation is an increase in water content leading to higher rotational averaging, however the same degree of peak broadening wasn't seen in a sample with added H_2O.

Owing to the chemical composition and morphology change of the cathode material during repeated lithiation and delithiation, the reactivity of the electrolyte with cathode at different state of charge (SOC) could be differing. Given pristine NMC622 sample is considered as 100% discharged stage, a chemical delithiation process[4] was employed to prepare an approximately 50% SOC NMC622 cathode. Surprisingly, the delithiated NMC622 sample didn't significantly affect the electrolyte decomposition process under this testing condition, which supports the theory of transition metal dissolution.

Design of advanced high-temperature electrolytes

Now that a working system was established, we undertook to use the information to design an electrolyte that could perform well at elevated temperatures. As DMAc is well understood to be effective for these purposes, we sought an alternative whose mechanism and effectiveness is less well studied. One class of compounds that has been shown to slow the decomposition of electrolyte are the cyclic phosphazenes[5], although there is considerable disagreement as to their mechanism of action[5], [6], [7], [8], [9]. In order to validate the electrochemical performance of this type of additives, a series of fluorinated phosphazenes were designed. Three substituted phosphazenes were synthesized and their chemical structure and purity were identified by NMR, FT-IR and GC-MS. When 2% hexa(trifluoroethoxy)cyclotriphosphazene [7] was added to Gen 2 electrolyte, the growth of the new PF_5-base marker was restricted, similarly to DMAc (Figure I.4.A.6a). To validate the NMR results, the lithium-ion battery was assembled and tested using the same electrolytes. First, half-cell studies were undertaken to determine how the additive was interacting with the electrodes. As can be seen from the data shown in Figure I.4.A.6b, there was no interaction evident on the cathode. On the anode, increasing concentrations of PzTFE

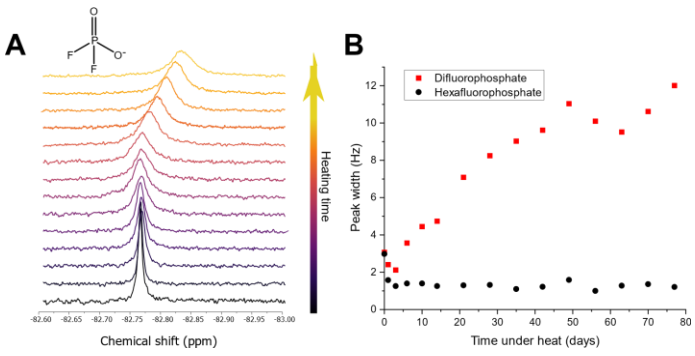

Figure I.4.A.5 (a) ^{19}F NMR spectra of Gen 2 + NMC powder after being heated for various days, and (b) peak widths for different signals vs heating time.

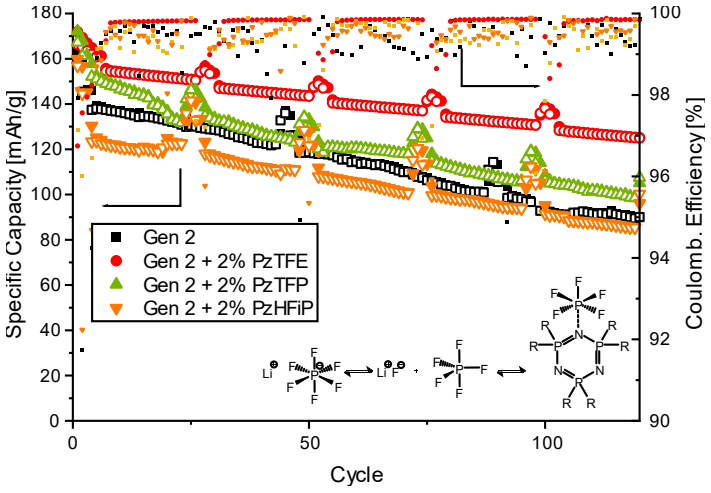

Figure I.4.A.6 Specific capacity and Coulombic efficiency of NMC622/graphite cells with various electrolytes containing 2% PzTFE, 2% PzTFP, and 2% PzHFiP as well as Gen 2 electrolyte alone cycled at 55 °C.

seemed to shift and flatten the decomposition peak of EC at 0.6 V, but no peaks were evident that would indicate a new decomposition product. This information indicates that any effect on the cycling performance could be attributed to interaction with the bulk electrolyte, rather than with cathode/electrolyte and anode/electrolyte interface.

Subsequently, NMC622/graphite full cells were assembled and cycled at 55°C with a 1 C rate for 100 cycles at 55ºC. The capacity, capacity retention and Coulombic efficiency data are shown in Figure I.4.A.7. It is clear that the PzTFE additive cell delivers a much higher capacity retention (80.8%) than the baseline Gen 2 electrolyte cell (64.7%) under the same testing conditions, along with a more consistent Coulombic efficiency. This was compared with other fluorinated ether-substituted derivatives PzTFP and PzHFiP, and while they tended to show favorable performance relative to Gen 2 electrolyte alone, PzTFE was still the overall superior additive.

The improved performance of the phosphazene derivatives are attributed to an *in-situ* interaction with the PF_5 generated under elevated temperatures from the $LiPF_6$ salt. This interaction is weak enough to prevent forming a stable adduct which can unfavorably alter the LiPF6 thermal decomposition equilibrium. However, it is enough to lower the reactivity of PF_5, thus preventing it from reacting further and accelerating the process of electrolyte degradation. This allows the electrolyte containing the fully substituted phosphazenes to maintain high stability, thus improving cycling performance of the lithium-ion battery under elevated temperature conditions.

Strategy Two: Design of Cathode-Protective Additives

Here we present a targeted cathode additive strategy based on chemical interactions. The concept is to use a chemical with a known ability to strongly interact with TMs in the positive electrode, allowing us to selectively modify its surface with a small amount of material. This strategy can be applied in the future toward the development of more additives for the stabilization of cathode materials. In this paper, we chose the hydroxamates, specifically lithium benzohydroxamate (LiBnHA). They are well known in biochemistry as enzyme inhibitors due to their strong interactions with metallic centers[10], and have been shown to have good coordination strength with a wide variety of transition metals[11]. They are untested as additives in lithium-ion batteries (LIBs), and thus would serve as an excellent illustration of our strategy.

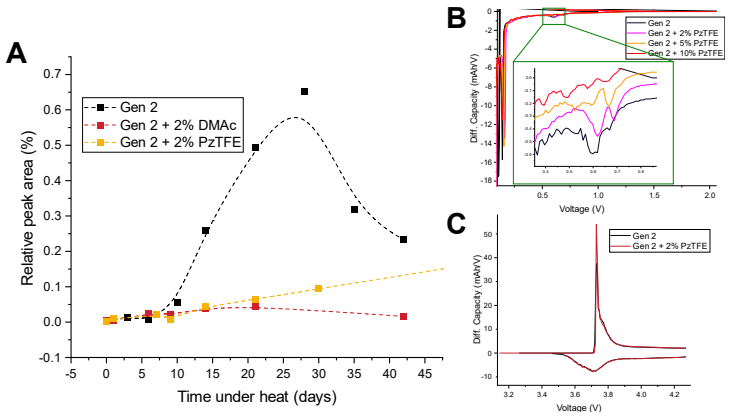

Figure I.4.A.7 (a) ^{19}F NMR peak area of PF_5 complex signals relative to $LiPF_6$, and differential capacity profiles (dQ/dV) of the 1st cycle of (b) graphite/Li half-cells and (c) NMC622/Li half-cells with increasing concentrations of PzTFE additive.

Electrochemical behavior

During the first cycle of a full cell, known as the formation cycle, the potential of the positive electrode rises slowly, while the potential of the negative electrode falls rapidly. Chemicals that are susceptible to reduction will therefore react in the early stages of this cycle, showing characteristic signals, and allowing insight into the impact of additives on the negative electrode. In the differential capacity plot (dQ/dV) shown in Figure I.4.A.8a, it can be seen that Gen 2 alone shows a broad shoulder at 2.96 V, and a sharp peak at 3.24 V. These events have been associated with the decomposition of EC, which is the main component of the Gen 2 SEI. Adding increasing amounts of LiBnHA to the electrolyte modifies this peak distribution, with an increasing strength of the shoulder and decreasing strength of the peak. However, no significant new signals are seen until the concentration reaches 2 wt%, indicating that low concentrations of LiBnHA do not have a unique reduction product in a full cell. At 2 wt%, a new sharp peak appears at 2.05 V, and no signals associated with EC are evident in the dQ/dV. This strongly indicates that high concentrations of LiBnHA will reduce on the anode, forming a unique SEI that limits the electrochemical reduction of EC.

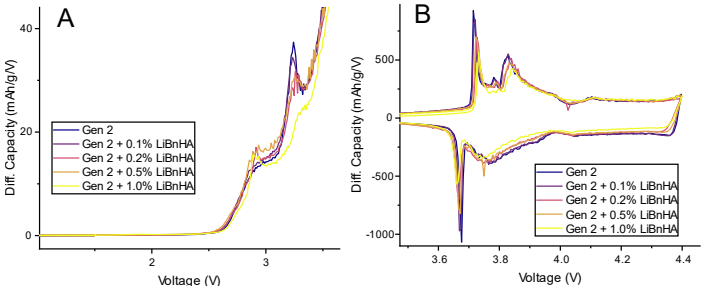

Figure I.4.A.8 Differential capacity (dQ/dV) profiles of the first cycle of LCO/graphite full cells with increasing amounts of LiBnHA, highlighting (a) interfacial reactions, and (b) (de)lithiation events.

Effects of LiBnHA can also be seen on the lithiation/delithiation events occurring in the cell. In Gen 2, these appear primarily as two peaks in the dQ/dV, appearing at 3.715 V and 3.928 V (Figure I.4.A.8b). Adding even 0.1 wt% of LiBnHA is enough to shift the potential of these peaks to higher voltages. Increasing the amount of LiBnHA will induce steadily increasing overpotentials, up to 1 wt%. Since it was previously established that low concentrations of LiBnHA don't significantly affect the negative electrode, we can conclude that this increased potential is associated with an interaction with the positive electrode. This is consistent with our hypothesis that the LiBnHA will chemisorb onto the surface of the electrode, forming a layer that would increase the impedance of the cell, inducing an overpotential on the delithiation process.

Elevated temperature behavior

The first set of cells were run at low upper cutoff voltages (UCVs) of 4.2V and room temperature in order to set a baseline level of performance for Gen 2 and Gen 2 with 0.5 wt% of LiBnHA as an additive. Under these conditions, both electrolytes performed similarly, with a small initial drop in capacity, followed by stable performance out to 100 cycles (Figure I.4.A.9a). While the capacity retention for LiBnHA was better (92.9% vs 82.2%), this is due to the lower starting capacity of 120 mAh/g vs 130 mAh/g, likely caused by the much higher impedance, as signified by the difference between the average charge and discharge voltage (ΔV) of 224 mV vs 143 mV.

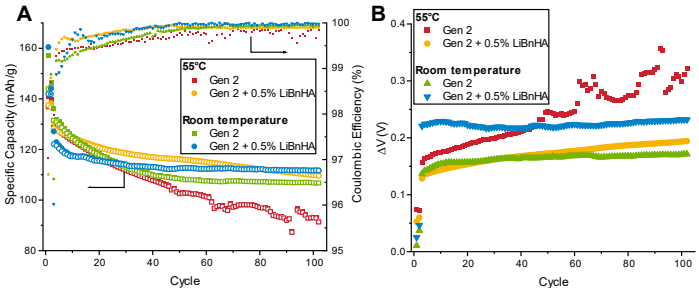

Figure I.4.A.9 (a) Specific capacity, Coulombic efficiency and (b) ΔV of electrolytes with and without LiBnHA

When increasing the cycling temperature to 55˚C, differences between the two electrolytes start to become more apparent. Here, the initial ΔV is actually lower for electrolyte containing LiBnHA, and it grows much more slowly over the next 100 cycles, for a total of 57 mV compared to 157 mV (Figure I.4.A.9b). This corresponds to better capacity retention (86.3% vs 71.9%) and improved Coulombic efficiency when cycled at elevated temperature.

Finally, EIS analysis of the cells was done after cycling was completed. Results were fit to two sequential RQ elements, plus a Warburg impedance (Figure I.4.A.10a). The high-frequency semicircle was assigned to impedance originating from the interphase, while the mid-frequency semicircle was assigned to the charge-transfer impedance. After cycling at low temperatures, the impedances were quite similar for both sets of electrolytes. However, after cycling at elevated temperatures, both electrolytes show a large increase in the R_{int}. The R_{ct} didn't show any change with added LiBnHA, while it grew to a similar extent for Gen 2 alone. Previous research has indicated that increases in the R_{ct} can be mainly attributed to the cathode[12], [13], which supports the theory that LiBnHA is forming a protective film on the surface of the cathode material.

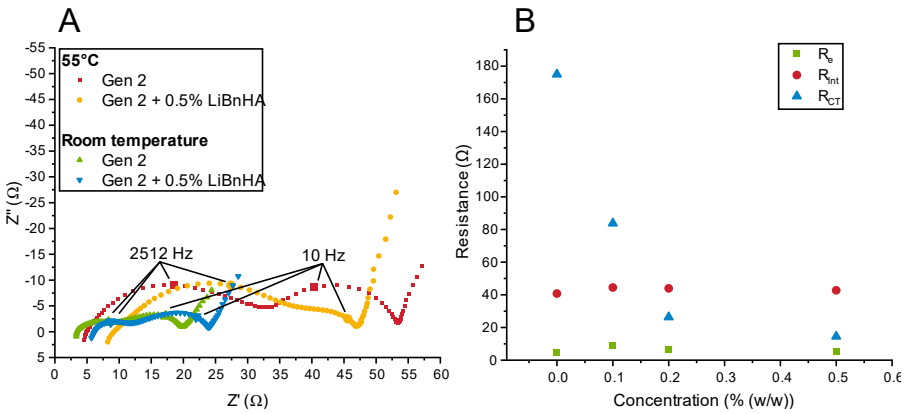

Figure I.4.A.10 (a) EIS of cells after cycling with and without LiBnHA, at elevated and room temperature, (b) resistance values from EIS by concentration of LiBnHA

To test this theory, a concentration series was cycled with a 4.4V UCV at elevated temperatures, and the EIS was then taken (Figure I.4.A.10b). While the R_e and R_{int} were relatively constant between the different cells, R_{ct} decreased rapidly as the concentration of LiBnHA was increased. This supports the hypothesis that LiBnHA isn't participating in SEI formation on the anode surface, and is instead protecting the cathode from decomposition.

4.4 V cell performance

After baseline performance was established, testing was done to determine behavior under higher voltages and elevated temperatures. Li1-$\boldsymbol{x}$CoO2 is structurally unstable when $\boldsymbol{x}$>0.5[14], [15], leading to a practical limitation for reversible capacity of around 140 mAh/g. This has shown to be attenuated by stable surface coatings, such as Al_2O_3, AlF_3, ZrO_2, and more[16], [17].

The starting discharge capacity at 1C for Gen 2 electrolyte at 4.4V and 55˚C was 146 mAh/g, compared to the slightly higher starting capacity of 153 mAh/g for electrolyte containing LiBnHA (Figure I.4.A.11). They both

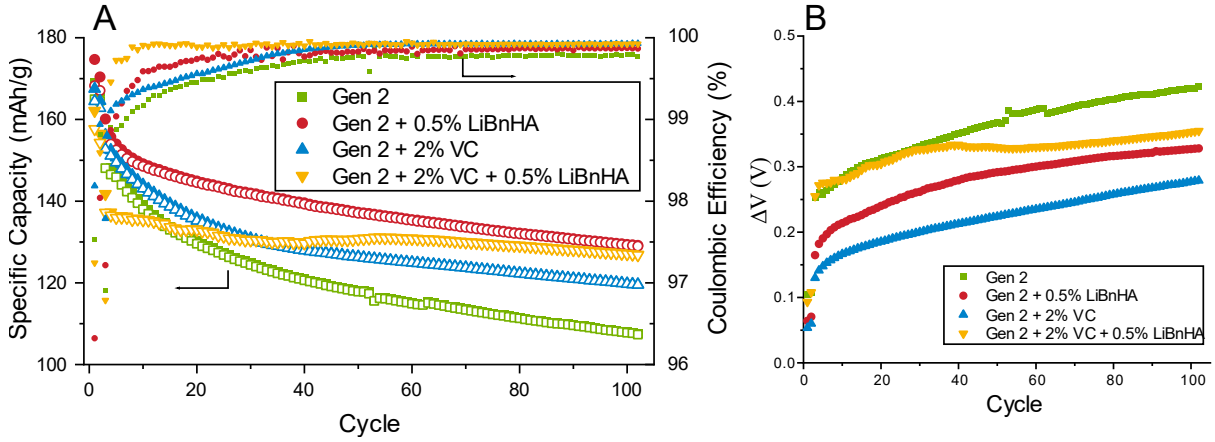

Figure I.4.A.11 (a) Specific capacity, Coulombic efficiency and (b) ΔV of electrolytes with different additives

had similar capacity retentions to the cells run at 4.2V and 55˚C (73.5% and 84.6%). However, the absolute capacity loss increased for both, from 35.7 mAh/g to 38.6 mAh/g for Gen 2, and 17.4 mAh/g to 23.5 mAh/g for LiBnHA. While this may be due to the increased UCV, it could also be related to the increased loading of graphite (5.9 mg/cm2 to 8.6 mg/cm2). As well, the increase in ΔV for both increased dramatically for higher UCV, to 165 mV for Gen 2 and 138 mV for LiBnHA. When half cells for both the low and high loading graphite electrodes were compared, it was found that ΔV increased much more rapidly and capacity dropped more quickly for the higher capacity anode, indicating that there's no structural instability of LCO evident at 4.4V.

Combination with other additives

The half cell results (not shown) indicated that the reduction product of LiBnHA is detrimental to long-term performance, through a negative interaction with the cathode. To enable the use of LiBnHA in cells, it would be helpful to combine it with an additive designed to create a stable SEI at low potentials, therefore preventing the LiBnHA from experiencing significant reduction. When prop-1-ene sultone (PES) was combined with LiBnHA, the results were nearly indistinguishable from LiBnHA alone, with PES starting at a slightly lower capacity of 121.1 mAh/g compared to 127.0 mAh/g, but maintaining a nearly identical capacity retention of 85.5% vs 86.3%. By contrast, using VC seemed to offer significant benefits. VC alone offered inferior performance to LiBnHA alone, with a capacity retention of 77.3% compared to 84.6%. However, when combined with LiBnHA the behavior drastically changed. Cells containing both additives had a capacity retention of 93.3%, along with better Coulombic efficiency and a flattened ΔV curve. This indicates that our hypothesis was correct, and an additive that can prevent the reduction of LiBnHA can offer synergistic benefits not seen with either additive alone.

Conclusions

In FY2020 we finished a project involving the NMR analysis of electrolyte decomposition at elevated temperatures and used the results to design a series of additives that could prevent the decomposition process from happening. We also began a project involving intelligent design of an additive to protect transition metal cathodes from decomposition at elevated temperatures.

Key Publications

1. Noah Johnson, Zhengcheng Zhang, *Enabling High Temperature Lithium Ion Batteries through NMR Analysis*, 236th Electrochemical Society Meeting, Oct 2019. Atlanta, GA

2. Johnson, Noah M., and Zhengcheng Zhang. *An NMR-Guided High Temperature Electrolyte Design Using a Novel PF_5 Marker.* The Journal of Physical Chemistry C, 2020. **124(**25): p. 13602–13608.

3. Johnson, Noah M., and Zhengcheng Zhang. *Electrolytes for Electrochemical Energy Storage.* US. Patent #16/828,748, filed March 24, 2020

4. Johnson, Noah M., and Zhengcheng Zhang. *Targeted Cathode Protection in Lithium Ion Batteries Using a Novel Hydroxamate Additive.* In preparation.

References

1. Ravdel, B., et al., Thermal stability of lithium-ion battery electrolytes. Journal of Power Sources, 2003. 119: p. 805-810.

2. Campion, C.L., W.T. Li, and B.L. Lucht, Thermal decomposition of LiPF6-based electrolytes for lithium-ion batteries. Journal of the Electrochemical Society, 2005. 152(12): p. A2327-A2334.

3. Smart, M.C., B.L. Lucht, and B.V. Ratnakumar, The Use of Electrolyte Additives to Improve the High Temperature Resilience of Li-Ion Cells. ECS Transactions, 2008. 11(29): p. 79-89.

4. Yin, S.C., et al., X-ray/Neutron Diffraction and Electrochemical Studies of Lithium De/Re-Intercalation in Li1-x Co1/3Ni1/3Mn1/3O2 (x= 0→ 1). Chemistry of materials, 2006. 18(7): p. 1901-1910.

5. Harrup, M.K., et al., Phosphazene based additives for improvement of safety and battery lifetimes in lithium-ion batteries. ECS Transactions, 2012. 41(39): p. 13-25.

6. Li, W.T., et al., Additives for stabilizing LiPF6-based electrolytes against thermal decomposition. Journal of the Electrochemical Society, 2005. 152(7): p. A1361-A1365.

7. Liu, J., et al., Fluorinated phosphazene derivative – A promising electrolyte additive for high voltage lithium ion batteries: From electrochemical performance to corrosion mechanism. Nano Energy, 2018. 46: p. 404-414.

8. Rollins, H.W., et al., Fluorinated phosphazene co-solvents for improved thermal and safety performance in lithium-ion battery electrolytes. Journal of Power Sources, 2014. 263: p. 66-74.

9. Zhang, Q., et al., Improved thermal stability of LiCoO2 by cyclotriphosphazene additives in lithium-ion batteries. Chemistry Letters, 2005. 34(7): p. 1012-1013.

10. Marmion, C.J., D. Griffith, and K.B. Nolan, Hydroxamic Acids− An Intriguing Family of Enzyme Inhibitors and Biomedical Ligands. European Journal of Inorganic Chemistry, 2004. 2004(15): p. 3003-3016.

11. Codd, R., Traversing the coordination chemistry and chemical biology of hydroxamic acids. Coordination Chemistry Reviews, 2008. 252(12-14): p. 1387-1408.

12. Chen, C.H., J. Liu, and K. Amine, Symmetric cell approach and impedance spectroscopy of high power lithium-ion batteries. Journal of Power Sources, 2001. 96(2): p. 321-328.

13. Amine, K., et al., Factors responsible for impedance rise in high power lithium ion batteries. Journal of power sources, 2001. 97: p. 684-687.

14. Ohzuku, T., et al., Comparative study of LiCoO2, LiNi12Co12O2 and LiNiO2 for 4 volt secondary lithium cells. Electrochimica Acta, 1993. 38(9): p. 1159-1167.

15. Ohzuku, T. and A. Ueda, Solid-state redox reactions of LiCoO2 (R3m) for 4 volt secondary lithium cells. Journal of The Electrochemical Society, 1994. 141(11): p. 2972.

16. Hwang, B.J., et al., Mechanism study of enhanced electrochemical performance of ZrO2-coated LiCoO2 in high voltage region. Journal of power sources, 2010. 195(13): p. 4255-4265.

17. Sun, Y.K., et al., Significant improvement of high voltage cycling behavior AlF3-coated LiCoO2 cathode. Electrochemistry communications, 2006. 8(5): p. 821-826.

Acknowledgements

Support from Brian Cunningham and David Howell at Vehicle Technologies Office (VTO), Office of Energy Efficiency and Renewable Energy, U.S. Department of Energy is gratefully acknowledged. Argonne, a U.S. Department of Energy laboratory, is operated by UChicago Argonne, LLC under contract DE-AC02-06CH11357.

I.4.B Research on high power, doped titanium-niobium oxide anodes (ORNL)

Sheng Dai, Principal Investigator
University of Tennessee
354/502 Buehler Hall
1416 Circle Drive
Knoxville, TN 37996-1600
E-mail: sdai@utk.edu

Brian Cunningham, DOE Technology Development Manager
U.S. Department of Energy
E-mail: Brian.Cunningham@ee.doe.gov

Start Date: July 1, 2018 End Date: June 30, 2021
Project Funding: $800,000 DOE share: $720,000 Non-DOE share: $80,000

Project Introduction

Commercial lithium ion batteries (LIBs) using graphite as the anode material can easily result in lithium plating during extreme fast charging or abuse conditions, leading to fast capacity fading and safety issues. To eliminate the lithium plating issue in LIBs during extremely fast charging, we proposed to use doped titanium niobium oxide (TNO) as anode, which has not only an operation voltage of 1.66 V *vs.* Li/Li^+ that is far from the lithium plating but also a high theoretical capacity of 387 mA h g^{-1}.

Objectives

The main objective of this project is to synthesize titanium niobium oxide (TNO) that has a nanoporous structure with porous channels for rapid lithium diffusion, enabling extreme fast charging (XFC). The focus of this project is to improve the electronic conductivity and ion diffusion coefficient in TNO to achieve high capacities under extreme fast charge conditions. In addition, electrolytes with additives will be formulated to promote stable interphase formation on the NMC cathode surface to improve long cycling stability.

Approach

- Enhance rate capability by formation of nanostructures.
- Improve electronic conductivity by doping and surface coating with carbon.
- Synthesize large scale TNO with low cost precursors.
- Evaluate rate performance and long term cyclability of coin cells with high loading TNO.
- Improve long term cyclability of coin full cells using functional additives.
- Evaluate rate performance and long term cyclability of pouch full cells.

Results

In 2019, we successfully synthesized non-template TNO with low-cost raw materials and increased the energy density of the NMC/TNO full cell from 93 to 130 Wh/kg after optimization. In 2020, our research has been focused on improving Li-ion diffusion of TNO by doping as well as enhancing the energy density of full-cells by electrolyte additives.

In the previous studies, we have proven that the carbon coating is an efficient approach to improve the electronic conductivity of the TNO material, resulting in better high-rate performance. However, the extra carbon coating step complexed the synthesis procedure of the TNO material. Therefore, the *in-situ* carbon doping strategy has been tried last year, that is, the TNO precursor was heated to a lower temperature (400 or 450 ºC) in air to

partially remove F127 and subsequently heated to 750 ºC in N_2 to obtain porous crystalline carbon doped TNO. The resulting products were denoted as TNO-400 and TNO-450. TNO-750 was also synthesized as a reference by directly heating the precursor to 750 ºC in air. According to the X-ray diffraction (XRD) results, all the products have a single phase TNO structure, indicating that TNO can also be well crystallized with *in-situ* carbon doping. The carbon content of TNO-400, TNO-450 and TNO-750, based on thermalgravimetric analysis (TGA), are 0.5 wt%, 0.2 wt% and 0 wt%, respectively. Thus, carbon doped TNO with different carbon content can be obtained by varying the preheating temperatures. In addition, carbon nanotubes (CNTs) and C45 were also chosen as the carbon source to obtain carbon doped TNO materials due to their excellent conductivities. TNO/CNTs was synthesized by adding 10% CNTs in the precursor solution, which was calcinated in air at 400 °C for 30 mins followed by treatment in N_2 at 700 °C for 3 hrs. The TGA result shows about 10 wt% CNTs remained in the final product. TNO/CNTs electrodes were casted with 90% active material, 4% C45, and 6% PVDF. For comparison, TNO-C45 and TNO-CNTs composite electrodes were also casted with compositions of 80% active material, 14% C45 or C45/CNTs (1:1), and 6% PVDF, respectively.

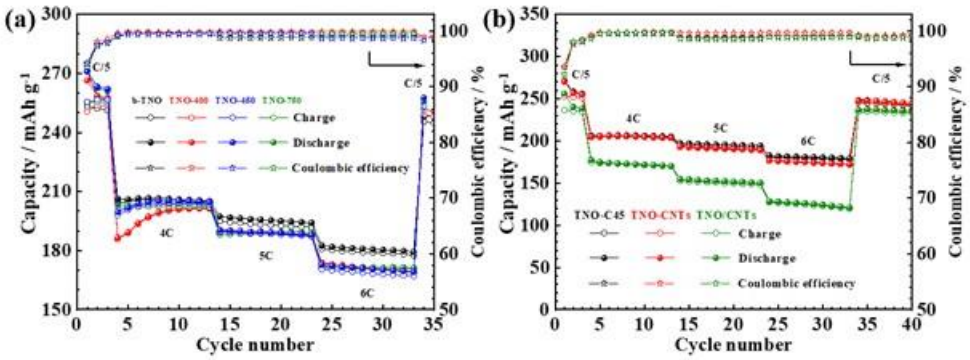

Figure I.4.B.1 High rate performance of (a) in-situ carbon doped TNO and (b) CNTs doped TNO.

As shown in Figure I.4.B.1a, all the *in-situ* carbon doped TNOs exhibit higher capacities than the pristine TNO at a low rate of C/5. However, their capacities are all lower than those of TNO at high current rates of 4C, 5C, and 6C, particularly showing deep dives when the current rate was switched from C/5 to 4C due to higher cell impedances of the carbon doped TNOs. This result indicates that residual carbons in TNO-400 and TNO-450 could not improve their electronic conductivity to achieve better rate performance than that of pure TNO. On the other hand, Figure I.4.B.1b shows that TNO-C45 has the best rate performance due to the excellent conductivity of C45. The capacity of TNO-CNTs is higher than that of TNO/CNTs, indicating the better conductivity of CNTs in the electrode than that in the TNO frameworks. Although CNTs are stable up to 600 °C in the air, the pre-oxidation process at 400 °C might have already damaged the structure of CNTs, resulting in poor electronic conductivity and thereby poor rate performance of TNO/CNTs half-cells. In addition, TNO-CNTs half-cells in which half of C45 was replaced with CNTs also failed to deliver better high rate performance than TNO-C45, confirming CNTs doping is not an ideal method to enhance high rate performance of the TNO anodes.

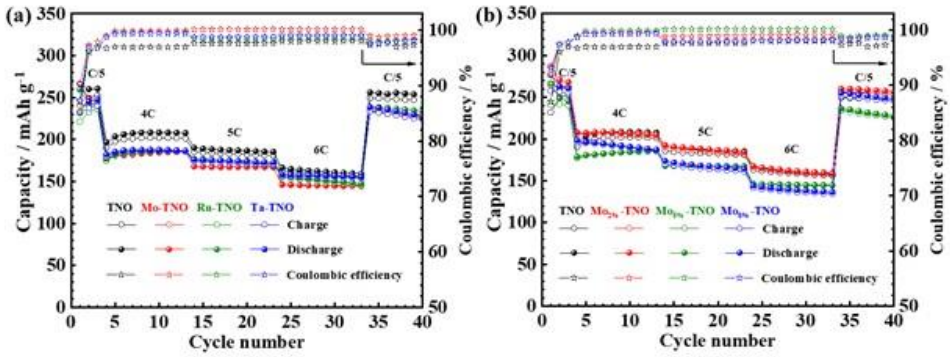

Figure I.4.B.2 High rate performance of (a) 5% molybdenum (Mo), ruthenium (Ru), or tantalum (Ta) doped TNO; and (b) Mo doped TNO with different Mo contents.

In 2020, we have also synthesized transition metal doped TNO to improve the high rate performance of TNO based batteries. Firstly, we prepared molybdenum (Mo), ruthenium (Ru), and tantalum (Ta) doped TNO using anhydrous metal chloride salts as the doping reagents. The composition of the doped TNO is $M_{0.05}Ti_{0.95}Nb_2O_7$, where M represents Mo, Ru, or Ta. As shown in Figure I.4.B.2a, although the transition metal doping hardly improves the high rate performance, it does increase the coulombic efficiencies. We further adjusted the Mo doping content to obtain $Mo_{0.02}Ti_{0.98}Nb_2O_7$, $Mo_{0.05}Ti_{0.95}Nb_2O_7$, and $Mo_{0.08}Ti_{0.92}Nb_2O_7$. Figure I.4.B.2b shows that the $Mo_{0.02}Ti_{0.98}Nb_2O_7$ half-cell with the lowest Mo doping content exhibits the best rate performance among the four TNO half cells and higher coulombic efficiencies than pure TNO. The above results show that replacing 2% Ti with Mo not only maintains the structural stability of TNO crystals but also provides more defects and distortions for fast ion diffusion. Therefore, we continued to exploreother transition metals such as manganese (Mn), iron (Fe), cobalt (Co), nickel (Ni), or copper (Cu) to obtain the doped TNO as $M_{0.02}Ti_{0.98}Nb_2O_7$, where M represents Mn, Fe, Co, Ni, or Cu. As seen from Figure I.4.B.3a, all the transition metal doped TNO materials have almost the same XRD patterns as the pristine TNO, indicating that the TNO crystal structure is barely affected by the transition metal doping. Unfortunately, all the transition metal doped TNO materials exhibit worse rate performance than pristine TNO. Although the Ni doped TNO exhibits the best rate performance among all the doped materials, it is still about 20 mAh g^{-1} lower than those of pristine TNO under different high rates (4C, 5C, and 6C). While we were working on transition metal doped TNO, we have noticed a newly published paper in the Journal of the American Chemical Society (JACS), which showed that the n-type doping of TNO by addition of Li atoms increased the electronic conductivity of the TNO host by ca. seven orders of magnitude even at low doping concentrations.[1] As the lithium doping in this paper was accomplished by pre-discharging the TNO electrode with lithium metal that is unacceptable in practical applications, we have tried to achieve the same goal with a synthetic approach. The idea is to dope TNO material with lower valance (II) transition metal precursors along with lithium (I) salt to achieve charge neutrality in the TNO structure. Therefore, a series of Li/transition metal (II) co-doped TNO materials were synthesized by adding anhydrous lithium chloride and transition metal chloride salts in the precursor solution during the synthetic process of TNO. The co-doped TNO with a composition of $Li_{0.04}M_{0.02}Ti_{0.98}Nb_2O_7$ was obtained by controlling the molar ratio of the reagents, where M represents Mn, Fe, Co, Ni, or Cu. As shown in Figure I.4.B.3c, the XRD patterns of Li/transition metal co-doped TNO are almost the same, suggesting the crystal structure of TNO is well maintained after co-doping. However, the specific capacities of the selected Li/Ni co-doped TNO half-cells suffer from severe capacity fading under high rates, which are lower than both pristine TNO and the Ni-doped TNO. Therefore, the Li/transition metal co-doping method also failed to realize pre-lithiation as well as simultaneous transition metal doping in TNO to deliver high rate performance.

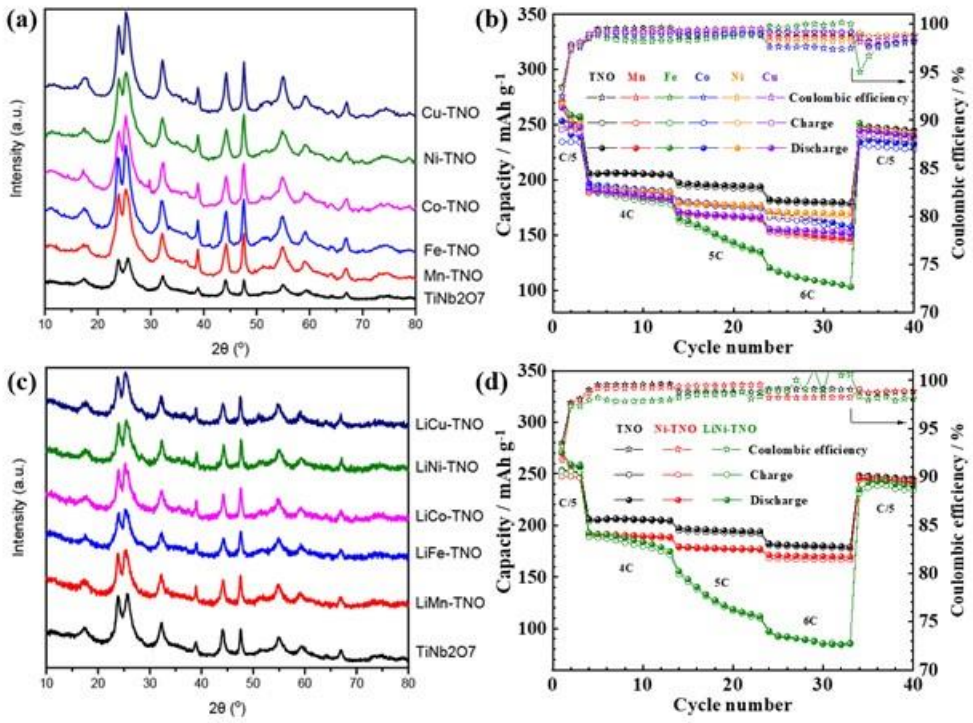

Figure I.4.B.3 (a) XRD patterns and (b) high rate performance of 2% manganese (Mn), iron (Fe), cobalt (Co), nickel (Ni), and copper (Cu) doped TNO; (c) XRD patterns of Li/transition metal co-doped TNO and (d) high rate performance of Li/Ni co-doped TNO half-cells.

After failing to improve the rate performance of TNO materials with small amount transition metal doping, we tried to partially replace Nb with other cations such as molybdenum (Mo) and tungsten (W), that is, $TiNbMoO_{7.5}$ (TNMO) and $TiNbWO_{7.5}$ (TNWO). The XRD pattern of TNWO exhibits low crystallinity but still maintains single-phase, while TNMO shows obviously phase separation. We also prepared $TiNb_{0.5}W_{1.5}O_{7.75}$ ($TN_{0.5}W_{1.5}O$) and $TiNb_{1.5}W_{0.5}O_{7.25}$ ($TN_{1.5}W_{0.5}O$) by adjusting the molar ratio of $NbCl_5$ and WCl_6. The XRD results show that both $TN_{0.5}W_{1.5}O$ and $TN_{1.5}W_{0.5}O$ materials preserve the similar single-phase of TNWO but with different intensities of the characteristic peaks. As shown in Figure I.4.B.4a, the partially Nb replaced TNO materials cannot deliver higher capacities than pristine TNO under each rate, proving partially replacing Nb by Mo or W is not an efficient approach to improve the high rate performance of TNO materials. Meanwhile, we have noticed another newly published paper in Nature on using disordered rock salt (DRS) $Li_{3+x}V_2O_5$ as a fast-charging anode, which exhibits exceptional rate capability and performs over 1,000 stable charge-discharge cycles.[2] However, the DRS $Li_{3+x}V_2O_5$ was synthesized by electrochemical lithiation of V_2O_5 with lithium metal, while the corresponding V_2O_5 electrodes were consisted of 60 wt.% active materialand 30 wt.% carbon with an active material loading about 2-3 mg cm^{-2}. Such an electrode preparation procedure is difficult for practical application regarding cost and energy density. Therefore, we tried to dope V element in our TNO materials to achieve faster Li-ion diffusion as well as better XFC performance. The low-cost Vanadyl(IV) acetylacetonate ($200 for 500g) was used as the precursor for the V doped TNO materials. In the typical synthesis, either half of Ti or Nb in TNO was replaced by adjusting the molar ratio of vanadyl(IV) acetylacetonate, $NbCl_5$, and titanium butoxide in the sol-gel process. The targeted structures of the V doped TNO would be $TiVNbO_7$ and $TiVNb_4O_{14}$, respectively. The XRD patterns of the V doped TNO materials contain no obvious miscellaneous peaks compared to pristine TNO, at least no characteristic peaks of the vanadium oxide, which can be roughly considered as a single-phase structure. Moreover, it is noted that the V doped TNO materials show a much better crystallinity than the raw TNO material, which are supposed to deliver better rate performance. As shown in Figure I.4.B.4b, both $TiVNbO_7$ and $TiVNb_4O_{14}$ fail to deliver better rate performance than pristine TNO, proving V doping is not an efficient approach to improve the high rate performance of the TNO materials either.

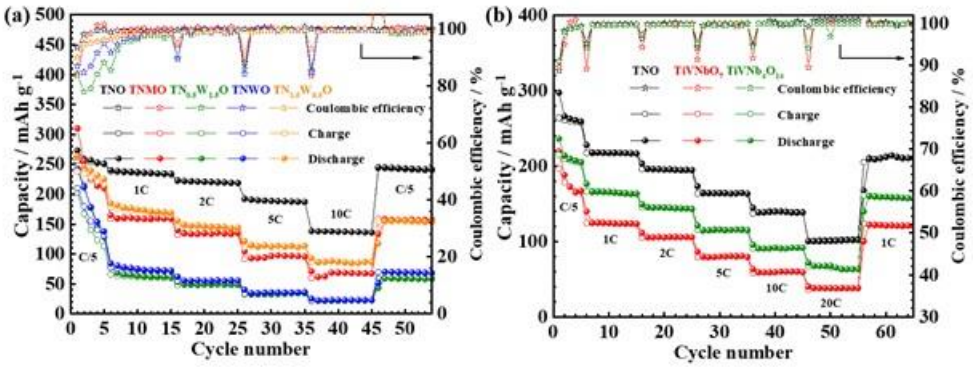

Figure I.4.B.4 Rate performance of (a) $TiNbMoO_{7.5}$ (TNMO), $TiNb_{0.5}W_{1.5}O_{7.75}$ ($TN_{0.5}W_{1.5}O$), $TiNbWO_{7.5}$ (TNWO) and $TiNb_{1.5}W_{0.5}O_{7.25}$ ($TN_{1.5}W_{0.5}O$); as well as (b) $TiVNbO_7$ and $TiVNb_4O_{14}$.

Besides doping, we also tried to improve the XFC performance of NMC/TNO full-cells using additives. Before evaluation of different electrolyte additives, the surface behavior of the TNO anode and NMC cathode after XFC cycling in the baseline $LiPF_6$ electrolyte were characterized with SEM and XPS. Although the morphologies of the pristine TNO and NMC electrodes are well maintained after 500 XFC cycles, exhibiting no obvious SEI films, the XPS data indeed show the passivation films on the cycled TNO and NMC electrodes (Figure I.4.B.5). Firstly, much higher concentrations of C-C (285 eV) and C-F (291.5 eV) from the conductive carbon C45 and the polymeric binder PVDF can be observed in the fresh NMC and TNO electrodes, whereas they are significantly lower in the cycled electrodes due to the presence of passivation layers (Figure I.4.B.5a & Figure I.4.B.5b). Secondly, the concentration of O-C=O (~533 eV) related to the decomposition of the carbonate solvents is much higher for both cycled TNO and NMC electrodes compared to pristine electrodes (Figure I.4.B.5c & Figure I.4.B.5d). Thirdly, the O1s peak at 530.2 eV assigned to the transition metal oxygen bonds becomes almost invisible in the cycled NMC cathode compared to the pristine one due to the formation of passivation layer (Figure I.4.B.5c). Similarly, the concentration of O-H (531.5 eV) in the pristine TNO is significantly decreased after cycling, 58.33% *vs.* 29.31%, due to the formation of passivation layer (Figure I.4.B.5d). Finally, the existence of LiF peaks in both cycled NMC and TNO electrodes suggests $LiPF_6$ participates in the formation of passivation layers (Figure I.4.B.5e & Figure I.4.B.5f). Particularly, the lower concentration of LiF in the cycled TNO anodes proves the formation of SEI layers is partially suppressed by the utilization of a high-voltage anode, in sharp contrast to the high concentration of LiF in cycled graphite anodes. The above results show that the formation of SEI layers could be suppressed by the relatively high-voltage anode material TNO even under XFC conditions. However, the small amount of SEI and passivation layers from interface reactions of full-cell electrodes suggest the application of electrolyte additives is still necessary.

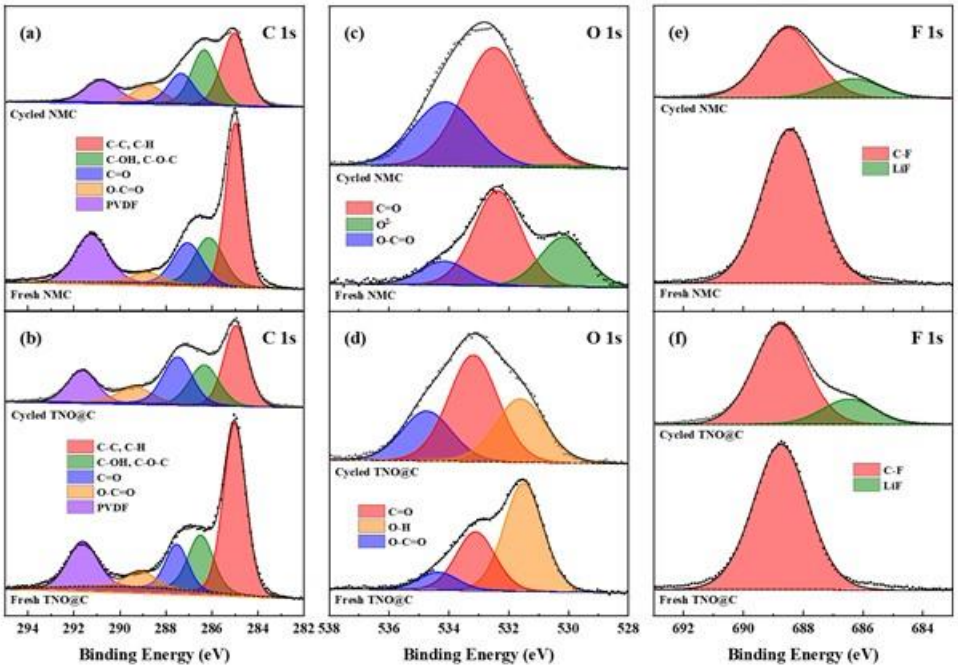

Figure I.4.B.5 X-ray photoelectron spectra (XPS) of (a & b) C1s, (c & d) O1s, and (e & f) F1s for (a, c, & e) NMC and (b, d, & f) TNO electrodes before and after XFC cycling.

Therefore, we have systematically investigated the effects of different electrolyte additives on the performance of the NMC and TNO half-cells. Figure I.4.B.6a & Figure I.4.B.6b shows the cycling performance of NMC and TNO half-cells with 1 wt.% commercial additives VC and FEC. For the NMC half-cells, 1 wt.% VC or FEC additive increases specific capacities about 10-15 mAh/g at different rates, while maintaining similar initial Coulombic efficiencies around 90%. It is noted that FEC is harmful to the cycling stability of the NMC half-cell as shown in Figure I.4.B.6a. On the other hand, 1 wt.% VC or FEC does not affect the capacities of the TNO half-cells, while slightly decreasing the initial Coulombic efficiencies. Moreover, the cycling stability of the TNO half-cells is dramatically affected by the VC or FEC additive (Figure I.4.B.6b). Overall, the 1 wt.% commercial additive VC or FEC has a positive influence on the NMC cathodes but a negative impact on the TNO anodes. In addition, we have evaluated new lithium malonatoborate salts such as lithium bis(2-methyl-2-fluoromalonato) borate (LiBMFMB)[3] or lithium difluoro-2-methyl-2-fluoromalonatoborate (LiDFMFMB)[4] as additives in the NMC and TNO half-cells as well as NMC/TNO full-cells (Figure I.4.D.6c-e). For the NMC half-cells, the lithium malonatoborate salt additives barely affected the rate and cycling performance. For the TNO half-cells, the rate performance and initial Coulombic efficiencies are slightly improved by the LiDFMFMB additive, especially with the amount of 0.5 wt.%. However, the cycling performance of TNO half-cells is negatively affected by the LiDFMFMB additive (Figure I.4.B.6d). With 0.05 M LiBMFMB additive, the specific capacities of the TNO half-cell decrease under each rate, meanwhile, the full-cell also shows much lower capacities, which may be ascribed to the high concentration of LiBMFMB additive initiating too much surface reaction that affected the ion diffusion across the interfaces. In future , the concentration of lithium malonatoborate salt additives will be further optimized to improve the performance of NMC and TNO half-cells as well as NMC/TNO full-cells.

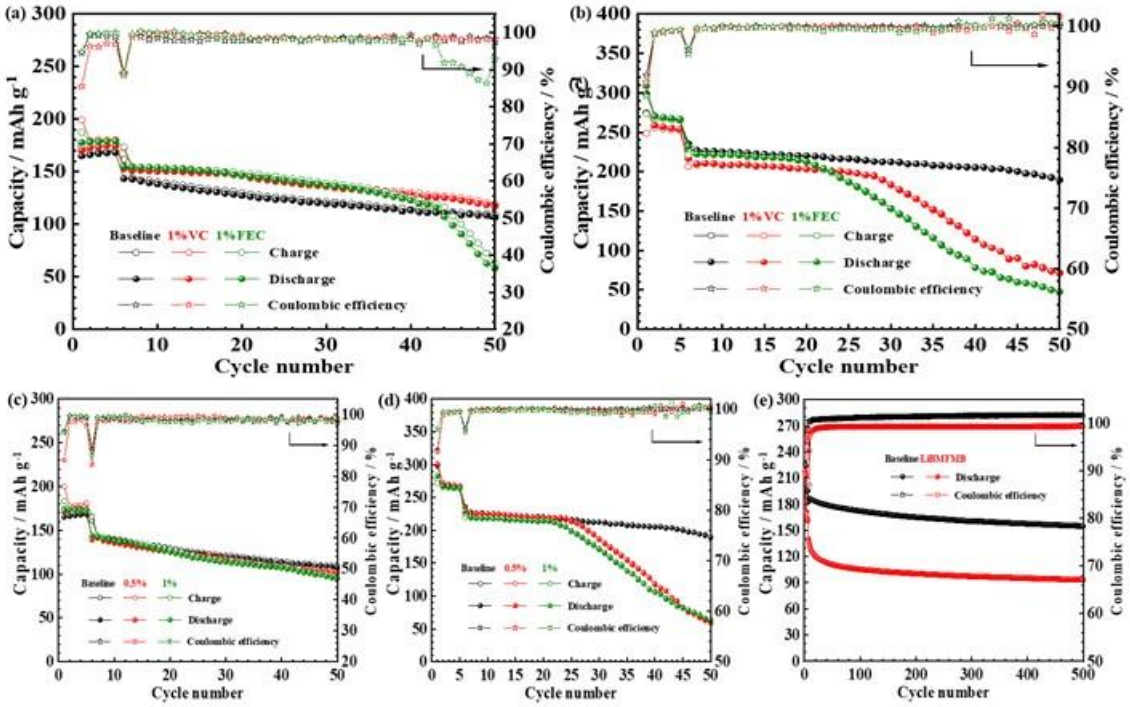

Figure I.4.B.6 Cycling performance of (a & c) NMC and (b & d) TNO half-cells with (a & b) 1% electrolyte additives VC and FEC, and (c & d) LiDFMFMB additive; (e) XFC performance of NMC/TNO full-cells with LiBMFMB additive.

At the beginning of 2020, all the experimental works in this project were forced to suspend for several months because of the severe COVID-19 pandemic. Even though the project progress was catching up under the excellent collaboration of all the team members, currently it is still delayed very much than the proposed milestones.

Conclusions

In conclusion, various doping strategies have been tried to improve the high rate performance of TNO anode materials, such as *in-situ* carbon doping, self-doping, transition metal doping, Li co-doping, anion doping, partially replacing, and high-entropy doping. The interface behavior of cycled TNO anodes and NMC cathodes studied by SEM and XPS showed that the formation of SEI layers could be suppressed by the relatively high-voltage TNO anode material, while the passivation layers from interfacial reactions of electrodes still exist. Therefore, different electrolyte additives were applied to enhance the XFC performance of NMC/TNO full-cells, including commercial VC and FEC additives, lithium malonatoborate salts LiDFMFMB and LiBMFMB, mixed bi-additives, different lithium salts, and so on. Due to the delay by COVID-19 pandemic, limited accomplishments have been achieved so far. Efforts on elemental doping and optimization of additive combination and concentration will be continued in this project to improve the XFC performance of the NMC/TNO full-cells.

Key Publications

1. Lyu, Hailong, Jianlin Li, Tao Wang, Bishnu Prasad Thapaliya, Shuang Men, Charl J. Jafta, Runming Tao, Xiao-Guang Sun, and Sheng Dai. "Carbon coated porous titanium niobium oxides as anode materials of lithium ion batteries for extreme fast charge applications." *ACS Applied Energy Materials* 3, no. 6 (2020): 5657-5665.

2. Lyu, Hailong, Jianlin Li, Xiao-Guang Sun, and Sheng Dai. " Titanium Niobium Oxide Anode-Based Lithium-Ion Batteries for 10 Minutes Fast-Charging Applications." *PRiME 2020 (ECS, ECSJ, & KECS Joint Meeting)*.

References

1. Griffith, Kent J., Ieuan D. Seymour, Michael A. Hope, Megan M. Butala, Leo K. Lamontagne, Molleigh B. Preefer, Can P. Koçer et al. "Ionic and electronic conduction in TiNb2O7." *Journal of the American Chemical Society* 141, no. 42 (2019): 16706-16725.

2. Liu, Haodong, Zhuoying Zhu, Qizhang Yan, Sicen Yu, Xin He, Yan Chen, Rui Zhang et al. "A disordered rock salt anode for fast-charging lithium-ion batteries." *Nature* 585, no. 7823 (2020): 63-67.

3. Wan, Shun, Xueguang Jiang, Bingkun Guo, Sheng Dai, John B. Goodenough, and Xiao-Guang Sun. "A stable fluorinated and alkylated lithium malonatoborate salt for lithium ion battery application." *Chemical Communications* 51, no. 48 (2015): 9817-9820.

4. Sun, Xiao-Guang, Shun Wan, Hong Yu Guang, Youxing Fang, Kimberly Shawn Reeves, Miaofang Chi, and Sheng Dai. "New promising lithium malonatoborate salts for high voltage lithium ion batteries." *Journal of Materials Chemistry A* 5, no. 3 (2017): 1233-1241.

Acknowledgements

U.S. DOE Office of Energy Efficiency and Renewable Energy (EERE) Vehicle Technologies Office (VTO)

Program Managers: Adrienne L. Riggi, Brian Cunningham, David Howell

ORNL Contributors: Xiao-Guang Sun, Jianlin Li

UTK Contributors: Hailong Lyu, Tao Wang

I.4.C Research Three-Dimensional Hierarchical Graphite Architectures for Anodes for Fast Charging (SNL)

Mohan Karulkar, Principal Investigator
Sandia National Laboratories
1515 Eubank Dr. SE, M/S 0613
Albuquerque, NM, 87185
E-mail: mpkarul@sandia.gov

Loraine Torres-Castro, Principal Investigator
Sandia National Laboratories
1515 Eubank Dr. SE, M/S 0614
Albuquerque, NM, 87185
E-mail: ltorre@sandia.gov

Brian Cunningham, DOE Technology Development Manager
U.S. Department of Energy
E-mail: Brian.Cunningham@ee.doe.gov

Start Date: October 1, 2019 End Date: September 30, 2020
Project Funding: $80,000 DOE share: $80,000 Non-DOE share: $0

Project Introduction

With current lithium ion batteries optimized for performance under relatively low charge rate conditions, implementation of XFC has been hindered by drawbacks including Li plating, kinetic polarization, and heat dissipation. This project will utilize model-informed design of 3-D hierarchical electrodes to tune key XFC-related variables like 1) bulk porosity/tortuosity; 2) vertical pore diameter, spacing, and lattice; 3) crystallographic orientation of graphite particles relative to exposed surfaces; 4) interfacial chemistry of the graphite surfaces through “artificial SEI” formation using ALD; and 5) current collector surface roughness (aspect ratio, roughness factor, etc.).

A key aspect of implementing novel electrodes is characterizing them in relevant settings. This project, ultimately led out of University of Michigan by Neil Dasgupta, includes both coin cell and 1+ Ah pouch cell testing, as well as comparison testing against baselines. Sandia National Labs will be conducting detailed cell characterization on iterative versions/improvements of the model-based hierarchical electrodes, as well as COTS cells for baseline comparisons. Key metrics include performance under fast charge conditions, as well as the absence or degree of lithium plating. Sandia will use their unique high precision cycling and rapid Electrochemical Impedance Spectroscopy (EIS) capabilities to accurately characterize performance and any lithium plating during 6C charging and beyond, coupling electrochemical observations with cell teardown. Sandia will also design custom fixturing to cool cells during rapid charge, to decouple any kinetic effects brought about by cell heating and allow comparisons between different cells and charge rates. Using these techniques, Sandia will assess Highly Ordered Hierarchical (HOH) electrodes from the University of Michigan, as well as aiding in iterative model and electrode design.

Objectives

- Work with University of Michigan to establish cadence for receiving improved-electrode cells for characterization via in-person kickoff and weekly update meetings.
- Fast charge characterization of NMC/Graphite and NMC/HOH cells.
- Demonstrate high fidelity dQ/dV measurements during 6C charging using high precision coulometry.

- Investigate the use of rapid EIS as a technique to detect Li plating during cell operation

Accomplishments

- Completed fast charge performance evaluation of NMC/Graphite and NMC/HOH cells made at University of Michigan.
- Obtained dQ/dV measurements demonstrating lithium plating for NMC/Graphite control cell.
- Potential Li plating marker identified during the initial testing of XFC coupled with in-operando rapid EIS.
- Attended weekly teleconferences with the University of MI team to discuss progress.

Approach

The fast charge performance of the UM-made NMC/HOH cells was evaluated with a combined rate capability and high rate cycling approach. Cells were cycled with increasing charge rates using a taper current of C/10, followed by a 0.5C discharge. After the rate capability portion, the cells were cycled with a 6C charge rate using 10 minutes as a termination limit in order to investigate the fast charge capability of the cells. The discharge rate was kept at 0.5C for the high rate cycling and intermittent state of health cycles were included to monitor cell degradation. (See Table I.4.C.1). The cells evaluated are 1.2 Ah UM-made NMC/Grahpite (control cell), and 1.2 Ah UM-made NMC/HOH (improved anode).

We also evaluated rapid EIS (additional experiments) as a technique to identify markers of lithium plating during fast charge operation. Control cells containing a traditional unmodified graphite anode have previously revealed severe degradation during fast charge using current rates >3C. Therefore, the rapid EIS technique was evaluated with control cells to facilitate the deposition of lithium and provide an easier path for its detection.

Cycling for all testing was performed with an Arbin high precision cycler. A rapid response cooling system was used to maintain isothermal operation and avoid complications arising from temperature rise during testing.

Table I.4.C.1 Test protocol

Cycles	Charge Current	Charge Taper Current	Discharge Current
Rate Capability			
1 - 3	0.5C	C/10	0.5C
4 - 6	1C	C/10	0.5C
7 - 9	2C	C/10	0.5C
10 - 12	3C	C/10	0.5C
13 - 15	4C	C/10	0.5C
16 - 18	5C	C/10	0.5C
19 - 21	6C	C/10	0.5C
High Rate Cycling			
22 - 125*	6C	CC+CV time = 10 min	0.5C
42, 63, 84, 105, 126	0.5C	C/10	0.5C

**Except intermittent state of health cycles*

Results

Testing on the Control and HOH cells

Control and HOH cells were cycled according to the test protocol described in Table I.4.C.1. Figure I.4.C.1 shows the electrochemical performance of the cells throughout the rate capability and high rate region (6C-10min). The control cell exhibited severe degradation during the rate capability, particularly during and after the 3C charge region. The performance during the high rate charge (6C-10min) was poor with a delivered capacity of only ~100 mAh during CCC since the voltage quickly polarized to the maximum cutoff limit and switched to a CCV. The total delivered capacity over 10 min was ~500mAh (CCC+CCV), 40% of the rated capacity. Minor changes in cell efficiency and capacity were identified during the 5C charge region as seen in Figure I.4.C.1(b), indicating minimal cell degradation. The capacity delivered during the 6C-10min charge was ~300mAh, with an overall capacity of 800mAh (67% of the rated capacity).

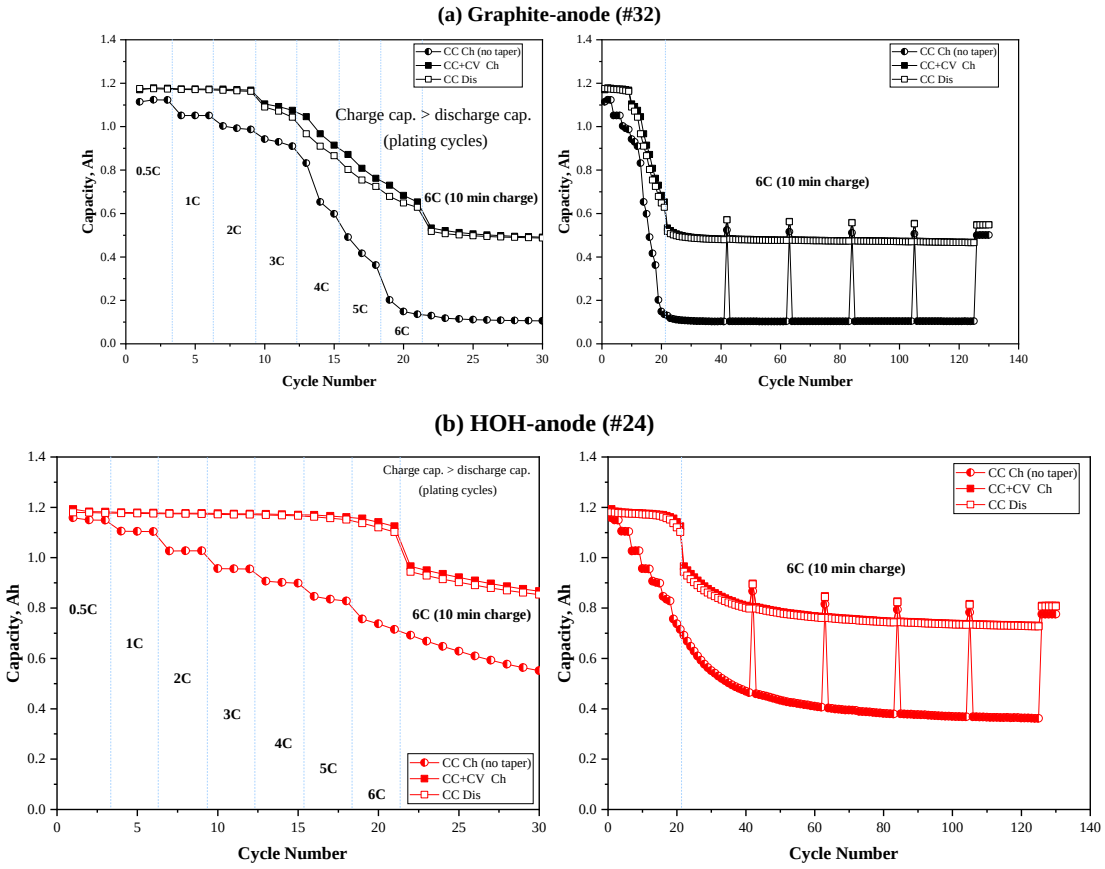

Figure I.4.C.1 Cyclability of (a) Graphite-anode, and (b) HOH-anode cells.

The improved performance of the HOH cell is further validated with a comparison of the charge polarization and efficiency, as presented in Figure I.4.C.2 and Figure I.4.C.3. The charge polarization for the rate capability region is consistent among both cells up to the 2C region. Afterward, the control cell behaves erratically, and the polarization significantly increases. During the high rate cycling, the charge polarization of the HOH cell

was 50% lower compared to the control cell. The efficiency in Figure I.4.C.3 also supports the hypothesis that the control cell plated more lithium, as evidenced by the efficiency drop between the 3C and 6C charge region.

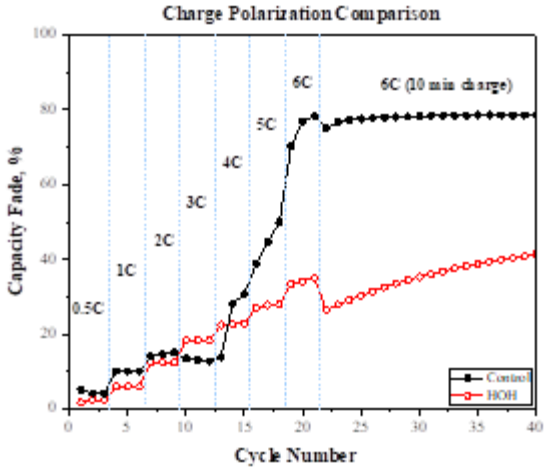

Figure I.4.C.2 Amount of polarization for the control and HOH cells. Expressed as % Capacity fade between high rate charge and total charge including taper.

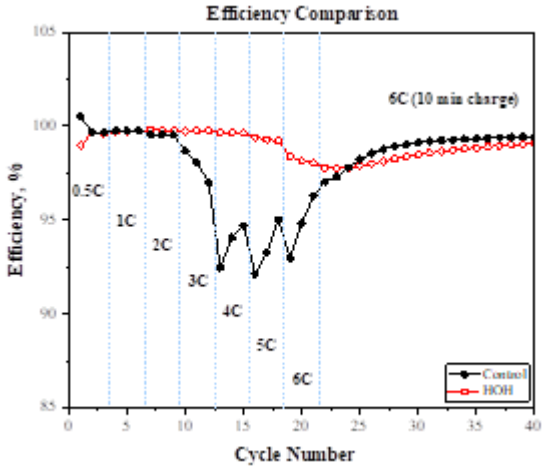

Figure I.4.C.3 Cycle efficiency comparison between the control and HOH NMC/Graphite cell.

Figure I.4.C.4 and Figure I.4.C.5 show the differential capacity plots for the rate capability cycles as well as the intermittent state of heath cycles performed during the high rate cycling. The charge dQ/dV of the rate capability region indicated a lithium plating peak developed at 2C for the control cell (Figure I.4.C.4(a) #1), vs. 5C for the HOH cell (Figure I.4.C.4(b) #1). Interestingly, the capacity and efficiency show evidence of lithium plating at 3C for the control and 6C for the HOH. This validates the use of differential capacity to detect cell degradation and lithium plating in early stages. The discharge dQ/dV shown in Figure I.4.C.4(a) #2 and Figure I.4.C.4(b) #2 exhibited two lithium stripping peaks for the 3C and 4C cycles while the HOH cell only displayed the expected delithiation profiles of discharge. Moreover, there are minimal changes among the curves, suggesting low cell degradation during the rate capability test.

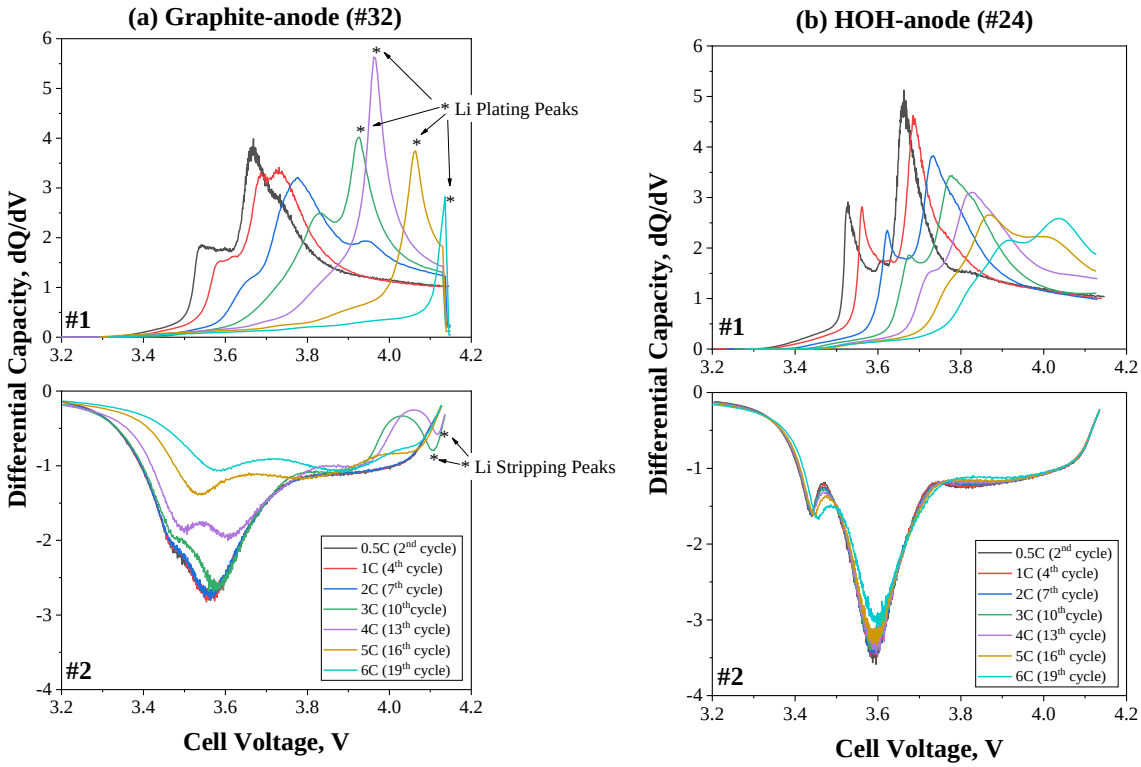

Figure I.4.C.4 Differential capacity at different c-rates for the (a) graphite-anode, and (b) HOH-anode cells.

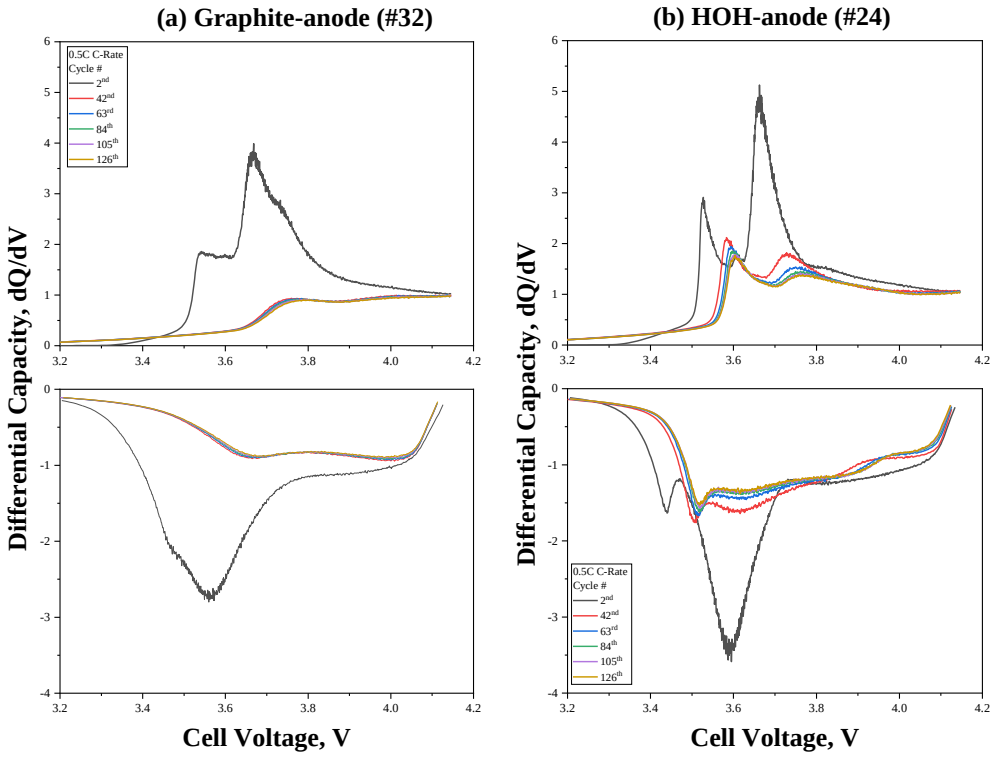

Figure I.4.C.5 Differential capacity for the capacity check cycles of the (a) graphite-anode, and (b) HOH-anode cells

The differential capacity of the state of health cycles during the high rate cycling is presented in Figure I.4.C.5(a) and Figure I.4.C.5(b) for the control cell and HOH cell, respectively. The control cell shows a major decrease in differential capacity and shifts of peak potential. The decrease in peak intensity is linked to loss of active material, while shifts of potential are associated with loss of lithium inventory, which is expected due to the plated lithium. The HOH cell also exhibits some degradation in the form of loss of active material and lithium inventory; however, the main lithium intercalation peaks are present, and the degradation is minor compared to the control cell.

Lithium Plating Identification with Fast EIS

In a separate experiment, control cells were cycled according to the test protocol described in Table I.4.C.2, and rapid EIS was collected continuously during each charging step. EIS measurements were collected continuously during fast charge operation with the intent to identify markers of plated lithium. The impedance response at 3.75V and 4.10V is presented in Figure I.4.C.6 in which each line corresponds to a different c-rate/cycle. The impedance at 3.75V displays minimal changes at mid-low frequencies, while the impedance at higher frequencies is consistent between cycles and c-rates. However, the impedance response at 4.10V shows significant changes, particularly at mid-low frequencies. Based on our experience with rapid EIS and plated lithium, we believe the impedance increase is likely a contribution of lithium plating. The reason is two-fold, (1) we have previously determined that lithium plating contributes to the rise of impedance at mid-low frequencies, and (2) the changes were identified at 4.10V, which is the voltage where lithium plating peaks are seen in the differential capacity.

Rapid EIS reveals changes in the impedance during fast charge operation. These changes could be attributed to lithium plating, however, further testing is required to validate the conclusions. Evaluating the impedance response of the HOH cell during fast charge will play a key role in determining if the changes are indeed related to plated lithium.

Table I.4.C.2 Test protocol for XFC coupled with EIS

Cycles	Charge Current	Charge Taper Current	Discharge Current
1 - 3	4C	CC+CV time = 15 min	1C
4 - 6	5C	CC+CV time = 12 min	1C
7 - 9	6C	CC+CV time = 10 min	1C
EIS Measurements (continuous during charge)			
RMS (A)		0.5	
Frequency range (Hz)		0.1 -1638.4	

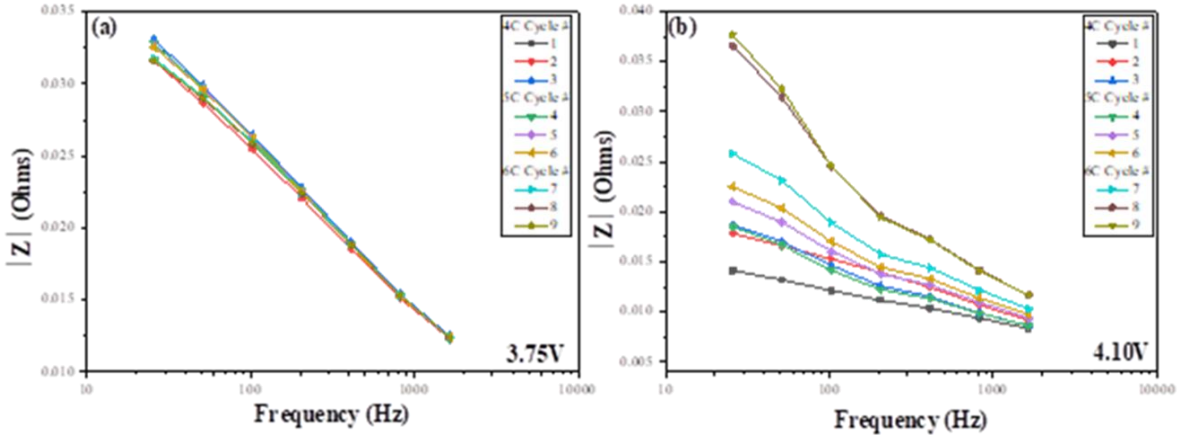

Figure I.4.C.6 Impedance response in the form of Bode Plots at (a) 3.75V and (b) 4.10V

Conclusions

The work performed in FY20 demonstrated the use of High Precision dQ/dV analysis to detect lithium plating at both the earliest stages when lithium appears to re-strip during discharge and later stages when dead lithium accumulates to reduce battery capacity and ultimately cause failure. Preliminary results with rapid EIS also confirm the low tolerance of the control cell to withstands current rates higher than 3C. Based on the results, it is clear that the HOH anode improvements have a significant effect on capacity, polarization, and lithium plating behavior at 6C charge rates.

In FY21, cells with anodes using HOH improvements will be tested with the rapid EIS technique to be compared to the control cell. The methods established during FY20 will be used to quantify the improvements as they related to lithium plating.

Acknowledgements

Sandia co-authors

Josh Lamb, Chris Grosso, Lucas Gray, Kyle Fenton, and Christopher Orendorff co-authored this report.

I.4.D Enabling Extreme Fast Charging through Control of Li Deposition Overpotential on Graphite Electrodes (Stony Brook University)

Esther Takeuchi, Principal Investigator
Stony Brook University
100 Nicolls Road, 675 Chemistry
Stony Brook, NY 11790-3400
E-mail: esther.takeuchi@stonybrook.edu

Brian Cunningham, DOE Technology Development Manager
U.S. Department of Energy
E-mail: Brian.Cunningham@ee.doe.gov

Start Date: July 1, 2018 End Date: August 31, 2021
Project Funding: $892,496 DOE share: $800,000 Non-DOE share: $92,496

Project Introduction

A major barrier facing the adoption of electric vehicles (EVs) is that currently utilized Li-ion batteries take significantly longer to recharge compared to the time necessary to refuel vehicles powered by internal combustion engines. Thus, the need to develop Li-ion batteries which can be charged in approximately 10 minutes (6 C rate) without sacrificing range, cost, or cycle life is critical for the widespread implementation of EVs. Fast charging capability of state of the art Li-ion batteries is limited by the occurrence of Li plating at the graphite anode. At fast charge rates the graphite anode is polarized below 0V, causing Li plating that results in capacity loss, increased resistance, and internal short circuits. To suppress Li plating, multiple strategies have been demonstrated with only limited effectiveness, and new approaches are needed to enable cycling at extreme fast charging rates.

Objectives

The objective of the project is to research, develop, design, fabricate, and demonstrate 2 Ah XFC cells, with an energy density ≥200Wh/kg, capable of a 10-minute fast charge protocol at ≥6 C charging rate, cost of ≤$150/KWh, and 500 cycles with <20% fade in specific energy.

Approach

The technological approach is to deliberately increase the overpotential for Li metal deposition at the graphite anode surface, thereby inhibiting Li metal deposition. This is accomplished by coating graphite electrodes with nanometer scale coatings of Cu or Ni metal, which have high overpotentials unfavorable for lithium deposition. During battery charging, the overpotentials for Li deposition on the metal coated electrode surface are greater in magnitude than the overpotential for intercalation into graphite, resulting in preferred lithiation of graphite and inhibited Li plating. The nanometer scale thickness of the metal coatings enable the function of the graphite electrode to be maintained and preserve state of the art energy density. The program represents an entirely novel and potentially transformative strategy for Li plating suppression.

Results

1. *Preparation and Characterization of Nanometer Scale Metal Coated Graphite Electrodes at Different Thicknesses*

Graphite electrodes with 5, 10, and 20 nm thick Ni or 10 nm Cu surface films were prepared using DC magnetron sputtering. At these thicknesses, the contributions of the metal coatings to the inactive mass of the electrode are insignificant: for a theoretical 1 Ah NMC622/graphite pouch cell with 20 cm^2 electrode area and 2.5 mAh/cm^2 areal capacity, the extra mass contributed by the 20 nm thick coatings on the anode would result in only a 0.03% decrease in energy density. The thicknesses of the deposited Ni and Cu films were verified via atomic force microscopy (AFM) analyses of ultra-flat SiO_2 wafers which were sputtered alongside the graphite anodes. Post-sputtering, a

portion of the sputter deposited coating was removed, creating a step between the metal coated and uncoated areas. Non-contact AFM scanning was then performed on the stepped region to determine the thickness of the deposited films. For Cu, the average thicknesses for nominal 5 nm, 10 nm, and 20 nm films were 5.3 ± 0.8 nm, 10.2 ± 0.5 nm, and 19.9 ± 0.6 nm, respectively (n=3). For Ni, the average thicknesses for nominal 5 nm, 10 nm, and 20 nm films were 5.0 ± 0.5, 9.6 ± 0.8, and 19.5 ± 0.8 nm, respectively (n=3). These findings verify that 5 nm, 10 nm, and 20 nm thicknesses of Cu and Ni could be consistently prepared under controlled conditions of sputtering power and argon pressure using the DC magnetron sputtering technique.

Energy dispersive x-ray spectroscopy mapping (Figure I.4.D.1and Figure I.4.D.2) was used to characterize the films. EDS maps collected from the top down indicate good uniformity of the deposited Cu and Ni layers on the electrode surfaces for all thicknesses prepared. EDS maps of the electrode cross sections clearly reveal that the deposited Ni and Cu are located at the upper surfaces of the graphite electrodes. Li primarily deposits at the interface between the electrode and the separator during battery charging, due to the maximum electrode overpotential in this region [1], [2] and thus the surface films target the region where Li plating is most likely to occur.

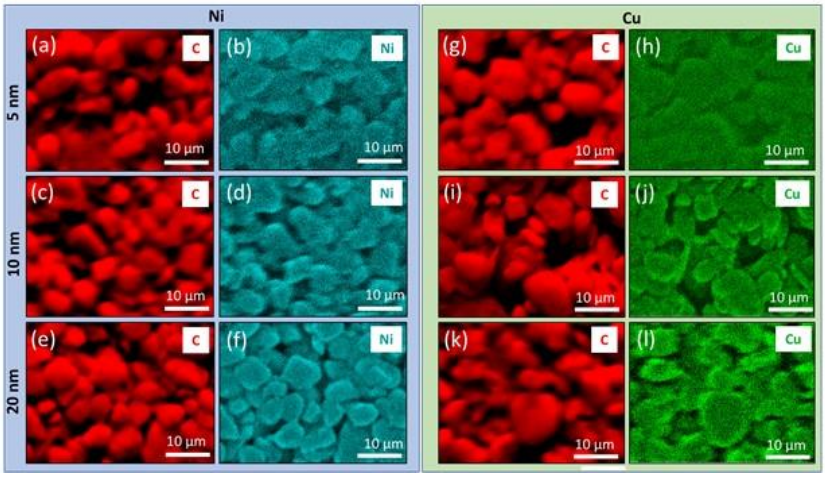

Figure I.4.D.1 EDS mapping images for the top down view of Cu and Ni deposited on graphite. (a-f) Ni deposited on graphite with thickness of 5, 10 and 20 nm. (g-l) Cu deposited on graphite with thickness of 5, 10 and 20 nm. Magnification is 3000x.

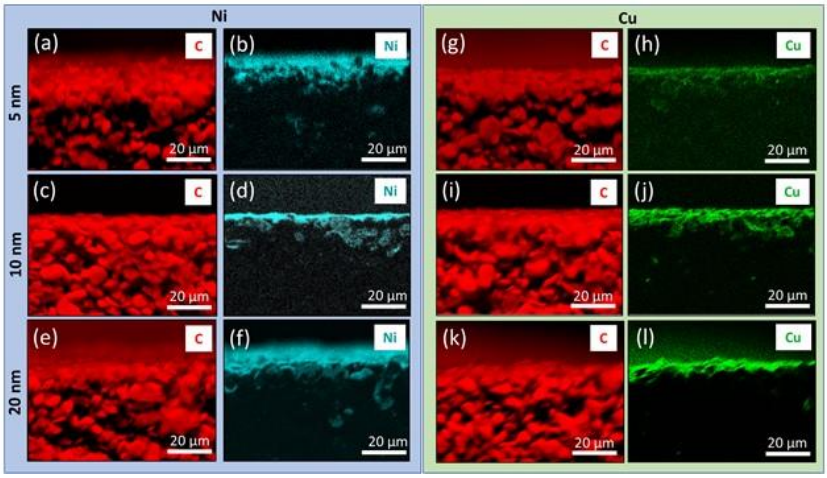

Figure I.4.D.2 EDS maps for the cross section views of Ni or Cu deposited on graphite. (a-f) Ni deposited and (g-l) Cu deposited on graphite with thicknesses of 5, 10 or 20 nm. Magnification is 1500x.

The sputter deposited graphite films were characterized using high resolution scanning electron microscopy (HRSEM) at 300kx and 800kx. Top-down HRSEM images and nanoparticle size distributions of metal coated graphite electrodes are shown in Figure I.4.D.3 and Figure I.4.D.4. As observed in the electrode images, there were some cracks in the sputtered films. Qualitatively, the cracks increased with increasing film thickness. The size of the sputter deposited nanoparticles also increased with the coated film thickness. The images were analyzed using ImageJ where quantitative values could be obtained. Ni-sputtered films on graphite were comprised of particle sizes of 4.7 ± 1.1 nm, 6.3 ± 1.3 nm, 6.5 ± 1.5 nm for film thicknesses of 5 nm, 10 nm or 20 nm respectively. The Cu-sputtered films on graphite displayed slightly larger nanoparticle sizes with 5.5 ± 0.9 nm, 8.6 ± 1.4 nm, 9.9 ± 1.2 nm for the film thicknesses of 5 nm, 10 nm or 20 nm, respectively.

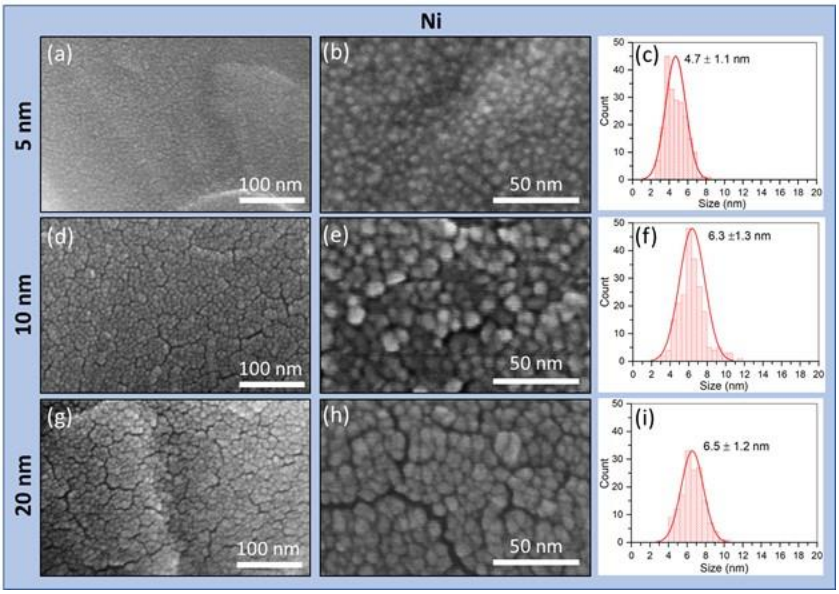

Figure I.4.D.3 High resolution SEM images and particle size distributions of Ni deposited on graphite with thickness of 5 nm (a-c), 10 nm (d-f) or 20 nm (g-i).

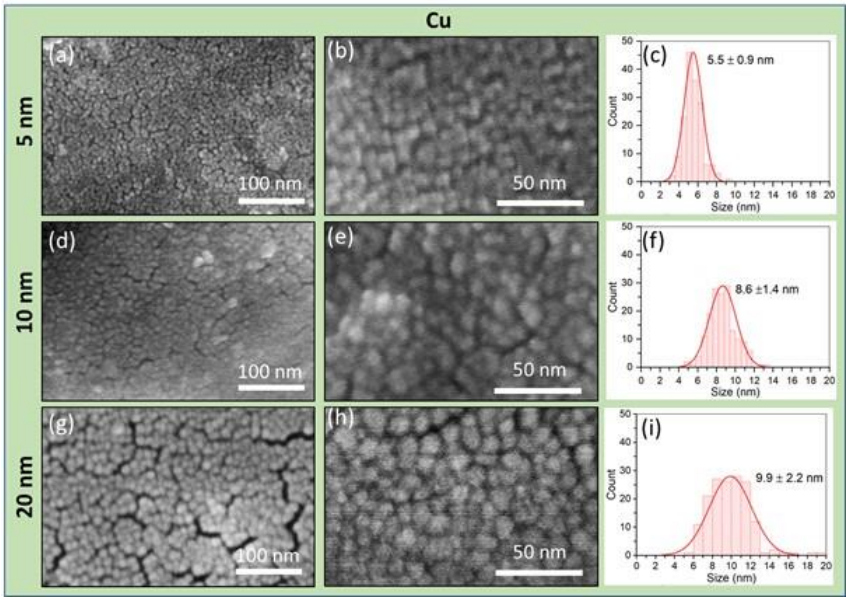

Figure I.4.D.4 High resolution SEM images and particle size distributions of Ni deposited on graphite with thickness of 5 nm (a-c), 10 nm (d-f) or 20 nm (g-i).

2. *Electrochemical Testing of Metal Coated Graphite Electrodes with Different Thickness in Full Cells*

The electrochemistry of Li-ion pouch cells containing the metal coated electrodes with different film thicknesses was tested using galvanostatic cycling under fast charge rates. Graphite electrodes were prepared with composition of 90% SLC 1506T natural graphite, 3% carbon black, and 7% KF-9300 Kureha PVDF binder. Electrode loading was 8.6 mg cm^{-2} with electrode porosity of~ 40 %. The graphite electrodes were sputter coated with Ni or Cu films at the 5 nm, 10 nm, and 20 nm. The graphite electrodes were paired with NMC 622 cathodes (90% NMC622, 5% carbon black, 5% PVDF, 16.4 mg/cm^2 loading, 35% porosity) with N:P ratio of 1.17 : 1 and were used to prepare single layer pouch cells with 1M $LiPF_6$ 30:70 ethylene carbonate (EC): dimethyl carbonate (DMC) electrolyte with 2% wt. of vinylene carbonate (VC). A cell formation protocol of 4 cycles at C/10 rate between 3 V – 4.3 V was used. After formation, the cells were fully discharged at C/10, and charged under a 10 minute charge protocol consisting of a 6C constant current step to 4.3 V followed by a constant voltage hold at 4.3V for the remainder of the 10 minute segment. The cells were then discharged at C/3 rate to 3.0 V to determine the initial discharge capacity after the 10 minute charge. Further cycling was then performed under a regime of 10 minute charge/1C discharge, where every 50 cycles the cells underwent the fast charge protocol followed by discharge at a C/3 rate.

Plots of areal capacity, capacity retention and coulombic efficiency vs. cycle number for all 6 coated electrode types vs. uncoated graphite are shown in Figure I.4.D.5 and representative voltage profiles as a function of cycling are shown in Figure I.4.D.6. Cells containing graphite electrodes with the 5 nm or 10 nm metal films had capacity retention within error of the control group (uncoated graphite anodes). However, for 20 nm metal films, reduced capacity fade was achieved compared to cells with the uncoated electrodes. During cycling the metal coated electrodes did not increase electrode polarization relative to the uncoated graphite electrode. Furthermore, coulombic efficiency plots reveal higher efficiency within the first 50-100 cycles for the metal-coated electrodes with 20 nm film thicknesses that exhibit improvement in capacity retention. Beyond 50 cycles, efficiencies increased to approach ~99.8–100.0% and were within error for the various electrode groups.

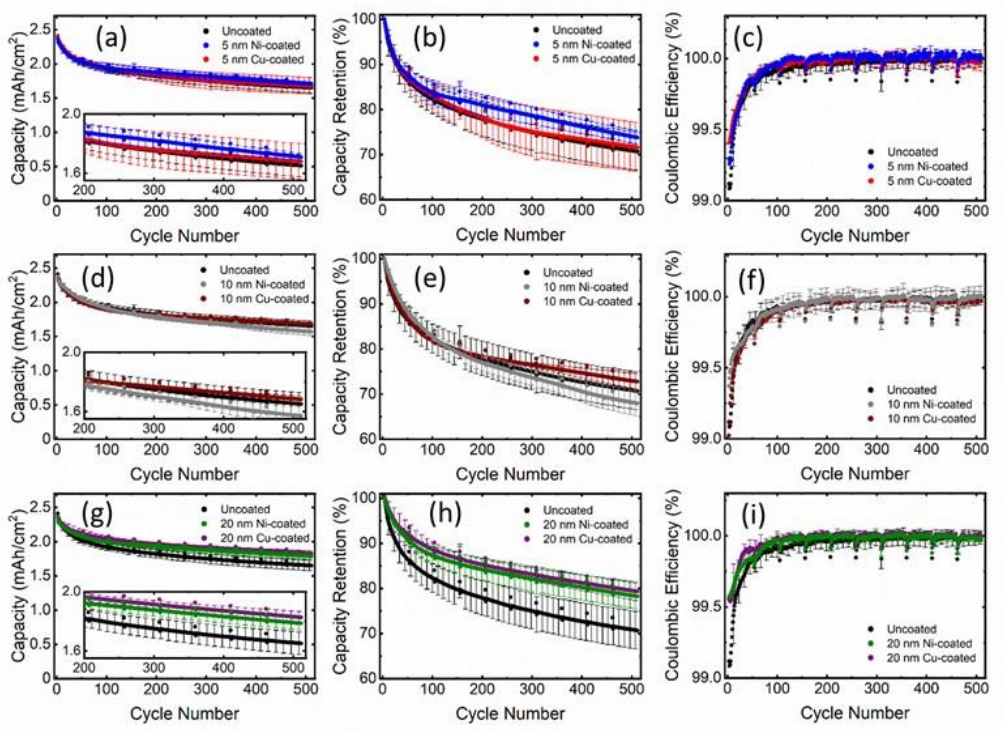

Figure I.4.D.5 (a, d, g) Areal capacities, (b, e, h) capacity retention, and (c, f, i) coulombic efficiency for single layer full cells with NMC 622 cathodes and uncoated graphite electrodes and graphite electrodes sputtered with Ni or Cu at three different electrode thicknesses: (a, b) 5 nm, (c, d) 10 nm, (e, f) 20 nm. Cells were cycled under 10 minute charge/ 1C discharge protocol with a C/3 discharge every 50 cycles. Error bars represent one standard deviation from the mean (n = 3 cells per electrode type).

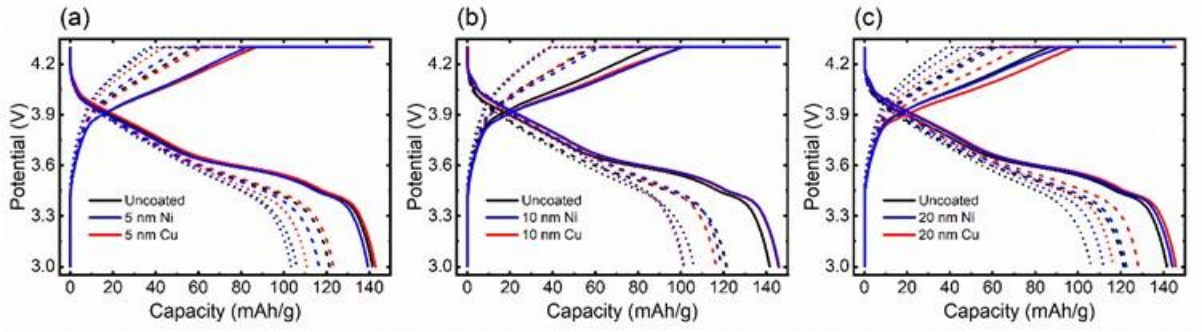

Figure I.4.D.6 Representative voltage profiles under 10 minute time limited CC CV charge (6C, 4.3 V limits), 1C discharge for single layer NMC622/graphite cells with (a) 5 nm films, (b) 10 nm films, and (c) 20 cycle 2 voltage profiles for 20 nm Cu-coated, 20 nm Ni-coated, and control graphite electrodes. Plots show cycle 2 (solid lines), cycle 100 (dashed lines), and cycle 500 (dotted lines).

A comparison of the capacity retention at various cycle numbers for all anode types tested is shown in Figure I.4.D.7. The Ni- and Cu-coated electrodes with 20 nm thickness exhibited mean improvement of 8% and 9% relative to the control group, respectively. The differences in capacity retention improvement afforded by the metal coatings of different loadings are correlated to the variation in the nanostructures of the films. Notably, the sputter deposited nanoparticles that form the 5 nm Ni or Cu loading films have diameters of 4.7 ± 1.1 nm and 5.5 ± 0.9 nm, respectively and are approximately equivalent to the 5 nm film thickness, indicating that the film is comprised of a single layer of nanoparticles. For 10 nm films, particle sizes are also on the order of the film thickness. In contrast, the 20 nm thick films have considerable overlap of nanoparticles, with particle sizes of 6.5 ± 1.5 nm and 9.9 ± 2.2 nm comprising the 20 nm Ni or Cu films, respectively. The overlap of the deposited nanoparticles in the high loading films is anticipated to enable more complete coverage of the graphite surface and may permit more effective overpotential control for suppression of Li plating during extended cycling.

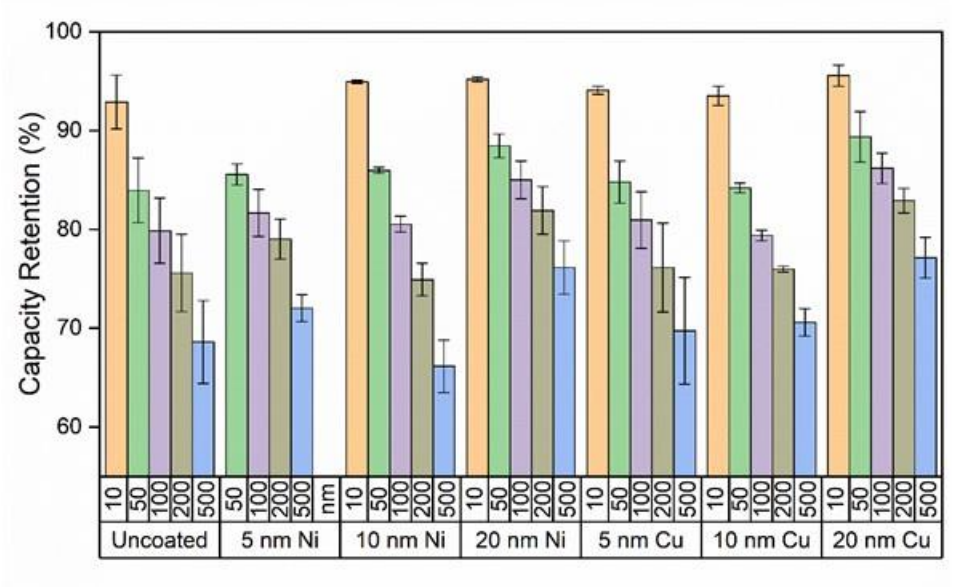

Figure I.4.D.7 Capacity retention at 10, 50, 100, 200 and 500 cycles under 10 minute time limited CC CV charge (6C, 4.3 V limits), 1C discharge protocol for single layer NMC622/graphite cells with uncoated graphite and metal coated graphite anodes. Error bars represent one standard deviation from the mean (n = 3 cells per electrode type).

3. Fast Charge Protocol Optimization

The influence of charging voltage limit and operating temperature was also evaluated with the goal of improving 500 cycle capacity retention. Testing was performed using single layer pouch cells using control graphite anodes and NMC622 cathodes using the electrode compositions, porosities, and N:P ratio detailed above. First, the influence of the constant current rate during the 10 minute CC/CV charge protocol was tested (Figure I.4.D.8). Previous testing had utilized 6C as the constant current rate and it was observed that the voltage limit was reached after ~ 5 minutes of constant current charging. To reduce the residence time at the upper voltage limit, lower constant current rates were tested. Constant current rates of 6C, 5C, 4.5C, and 4C were tested for 500 cycles at 30° C with 4.3 V upper voltage limit. While a 4C constant current was found to be too low to reach the 4.3 V limit within the 10 minute charge time, both the 4.5 C and 5C constant current rates resulted in dramatic improvement in the 500 cycle capacity retention, from < 70% to > 80% while still conforming to the 10 minute charge duration.

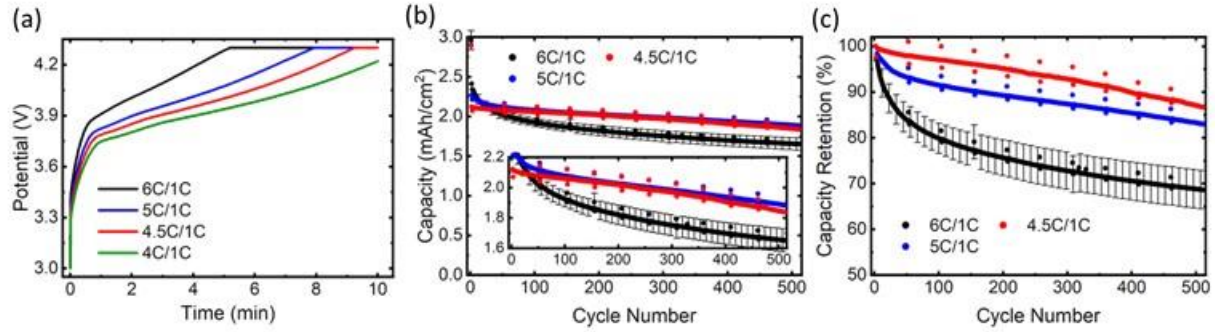

Figure I.4.D.8 Evaluating the influence of constant current charge value during 10 minute CC/CV charge protocol: (a) Voltage profiles for first charge at 4C, 4.5C, 5C, and 6C rates, (b) areal capacities, (c) capacity retention values.

The influence of charging voltage limit and operating temperature was also evaluated. A 2 x 2 design of experiments matrix of 30 °C vs. 40 °C and 4.2 V vs. 4.3 V was tested, with triplicate cells for each condition (Figure I.4.D.9). A 5C constant current rate was used for the CC/CV protocol. Results are summarized in Table I.4.D.1. The 4.3 V, 40 °C condition results in both the highest initial delivered capacity after first fast charge (2.26 ± 0.04 mAh/cm^2) as well as the highest capacity retention (93 ± 1%) after 500 fast charge cycles. The optimized charging protocol and temperature demonstrates achievement of the project capacity retention goal of 80% retention after 500 10-minute charge, 1C discharge cycles.

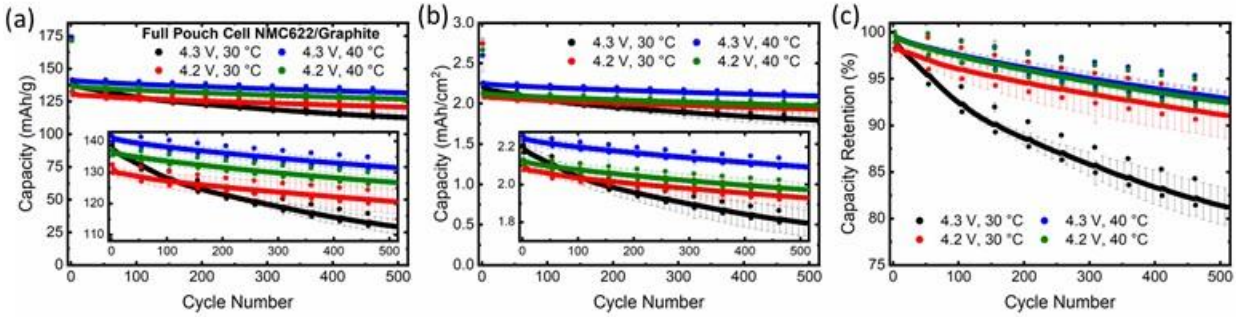

Figure I.4.D.9 Evaluating the influence of upper charge voltage limit (4.2 V vs. 4.3 V) and operating temperature (30°C vs. 40°C) during 10 minute CC/CV charge, 1C discharge protocol: (a) gravimetric capacities, (b) areal capacities, (c) capacity retention values.

Table I.4.D.1 Tabulated results of testing the effect of upper charge voltage limit (4.2 V vs. 4.3 V) and operating temperature (30°C vs. 40°C) during 10 minute CC/CV charge, 1C discharge protocol

Condition	Discharge Areal Capacity (mAh/cm²)		Capacity Retention (%)
	After 1st Fast Charge	After cycle 500	
30°C, 4.2 V	2.12 ± 0.04	1.93 ± 0.06	91 ± 3
30°C, 4.3 V	2.21 ± 0.04	1.80 ± 0.07	81 ± 2
40°C, 4.2 V	2.13 ± 0.03	1.97 ± 0.05	93 ± 1
40°C, 4.3 V	2.26 ± 0.04	2.10 ± 0.02	93 ± 1

4. Preparation of 2 Ah cells

A deliverable for the project is the delivery of multilayer pouch cells containing the optimized metal coated electrodes to DOE for testing. Due to the COVID-19 pandemic and associated loss of access to laboratories and closures of outside vendors, the development and fabrication of these cells was delayed. A 12-month no-cost extension for the project was granted to complete the deliverable.

Conclusions

Graphite electrodes with 5, 10, and 20 nm thick Ni or 10 nm Cu surface films were prepared using DC magnetron sputtering technique. The use of nanoscale metal films deposited on the surface of graphite electrodes was demonstrated to reduce capacity fade under repetitive fast charge conditions. The benefit was dependent on metal film thickness for both Ni and Cu film types. Extended galvanostatic cycling of metal-coated graphite electrodes in graphite/NMC622 pouch cells revealed that 20 nm Ni- or 20 nm Cu-coated electrodes enabled enhanced capacity retention under fast (10 minute) charge, with mean improvement of 8% and 9%, respectively, over uncoated graphite anodes after 500 cycles. Films of lower thickness did not reduce capacity fade, suggesting that there is a minimum metal loading necessary for effective overpotential control. Charge protocol and operating temperature were optimized to further improve capacity retention to above 80% retention after 500 10-minute charge, 1C discharge cycles. The development and fabrication of Ah scale pouch cells containing the optimized metal coated electrodes is in progress.

Key Publications

Publications

1. Tallman, Killian R.; Zhang, Bingjie; Wang, Lei; Tong, Xiao; Thieme, Juergen; Kiss, Andrew; Marschilok, Amy C.; Takeuchi, Kenneth J.; Bock, David C.; Takeuchi, Esther S. “Anode Overpotential Control via Surface Treatment: Inhibition of Lithium Plating.” ACS Appl. Mater. Interfaces 2019, 11, 50, 46864-46874.

2. Tallman, Killian R.; Yan, Shan; Quilty, Calvin D.; Abraham, Alyson; McCarthy, Alison H.; Marschilok, Amy C.; Takeuchi, Kenneth J.; Takeuchi, Esther S.; Bock, David C. “Improved Capacity Retention of Lithium Ion Batteries under Fast Charge via Metal-coated Graphite Anodes.” J. Electrochem. Soc, in press.

Patents

1. Takeuchi, Esther S.; Takeuchi, Kenneth J.; Marschilok, Amy C.; Bock, David C. Device and Method for Fast Charge of Batteries. Provisional Patent Application No.: 62/618,116 (2018). (filed prior to program start).

Presentations

1. Takeuchi, Esther S.; Takeuchi, Kenneth J.; Marschilok, Amy C.; Bock, David C., “Enabling Extreme Fast Charging Through Control of Li Deposition Overpotential,” Poster Presentation at 2019 Vehicle Technologies Office Annual Merit Review, Arlington, VA, June 2019.

2. Takeuchi, Esther S.; Takeuchi, Kenneth J.; Marschilok, Amy C.; Bock, David C., "Enabling Extreme Fast Charging Through Control of Li Deposition Overpotential," Oral Presentation at U.S. Drive XFC Meeting, Lemont, IL, August 2019.

3. Takeuchi, Esther S.; Takeuchi, Kenneth J.; Marschilok, Amy C.; Bock, David C., "bat 396: Enabling Extreme Fast Charging Through Control of Li Deposition Overpotential," 2020 Vehicles Technologies Annual Merit Review, virtual, June 2020.

4. Takeuchi, Esther S.; "From Medical Applications to the Environment: The Important Role of Energy Storage, Cary Lecture, Ga Tech University, Atlanta, GA, March 2020, *invited.*

5. Takeuchi, Esther S.; "Parasitic Reactions and Their Impact on Electrochemistry: Battery Gordon Conference, Ventura, CA, February 2020, *invited*.

References

1. Arora, P.; Doyle, M.; White, R. E., Mathematical Modeling of the Lithium Deposition Overcharge Reaction in Lithium-Ion Batteries Using Carbon-Based Negative Electrodes. J. Electrochem. Soc. 1999, 146 (10), 3543-3553.

2. Hein, S.; Latz, A., Influence of Local Lithium Metal Deposition in 3d Microstructures on Local and Global Behavior of Lithium-Ion Batteries. Electrochim. Acta 2016, 201, 354-365.

Acknowledgements

The co-PIs for this project include Kenneth J. Takeuchi (Stony Brook University), Amy C. Marschilok (Stony Brook University and Brookhaven National Laboratory) and David C. Bock (Brookhaven National Laboratory).

I.4.E Detecting Lithium Plating during Fast Charging, and Heterogeneity Effects during Fast Charging (LBNL)

Dr. Nitash P. Balsara, Principal Investigator
Department of Materials Sciences
Lawrence Berkeley National Laboratory
University of California, Berkeley
Berkeley, CA 94720
E-mail: nbalsara@berkeley.edu

Dr. Guoying Chen, Principal Investigator
Lawrence Berkeley National Lab
Berkeley, CA 94720
E-mail: gchen@lbl.gov

Dr. Bryan McCloskey, Principal Investigator
Lawrence Berkeley National Lab
Berkeley, CA 94720
E-mail: bmcclosk@berkeley.edu

Dr. Robert Kostecki, Principal Investigator
Lawrence Berkeley National Lab
Berkeley, CA 94720
E-mail: r_kostecki@lbl.gov

Dr. Ravi Prasher, Principal Investigator
Lawrence Berkeley National Lab
Berkeley, CA 94720
E-mail: rsprasher@lbl.gov

Dr. Wei Tong, Principal Investigator
Lawrence Berkeley National Lab
Berkeley, CA 94720
E-mail: weitong@lbl.gov

Samm Gillard, DOE Technology Development Manager
U.S. Department of Energy
E-mail: Samuel.Gillard@ee.doe.gov

Start Date: October 1, 2019 End Date: September 30, 2020
Project Funding: $900,000 DOE share: $900,000 Non-DOE share: $0

Project Introduction

The U.S. Department of Energy's Office of Energy Efficiency and Renewable Energy (DOE-EERE) has identified fast charging — with a goal of 15-min recharge time — as a critical challenge to pursue in ensuring mass adoption of electric vehicles. Present-day high-energy cells with graphite anodes and transition metal cathodes in a liquid electrolyte are unable to achieve this metric without negatively affecting battery performance. There are numerous challenges that limit such extreme fast charging at the cell level, including Li plating, lithiation heterogeneity, rapid temperature rise, and possible particle cracking. Of these, Li plating is thought to be the primary reason for limiting charging rates in lithium batteries.

Objectives

The primary goal of this project is to detect the initial nucleation event using data available in typical battery management systems. Identifying the initial onset of Li plating during fast charging is a multi-faceted, challenging "needle-in-a-haystack" problem. First, there may be a barely perceptible chemical signature of this event. For example, the presence of lithium may lead to the sudden formation of a small amount of gases due to irreversible reactions between the plated lithium and the electrolyte-soaked solid electrolyte interphase (SEI). Second, identifying the particular particle where the overlithiation and Li plating occurs can be challenging at the immediate onset of Li plating. Clearly, the particular particle that is overlithated first will depend on the state-of-charge of the electrode, as it will be governed by the amount of lithium intercalated at that time and the lithium concentration in the surrounding liquid electrolyte. The third and final challenge is identifying electrical signatures of the overlithation event so that our work can be used in practical battery management systems. We note here that the signatures may be different at different states-of-charge and that the electrical signature may be inherently non-linear, and thus not clearly evident in standard electrochemical measurements. Our objective is to address all three challenges.

Improved fast charging performance of lithium-ion batteries requires an accurate understanding of the lithium intercalation currents than can be sustained, and the conditions under which Li plating is initiated, at the graphite anode. In practical graphite anodes characterization of these processes is complicated by the three-dimensional porous composite nature of the anode and its interaction with an electrolyte whose lithium concentration at the interface with the graphite varies as a function of depth within the electrode during fast charging. The goal of our work is to determine some of the fundamental factors at play by performing experiments using planar, highly oriented pyrolytic graphite (HOPG) samples. HOPG is as close to monocrystalline graphite as is commercially available, and consists of a stack of graphite planes, with in-plane grain sizes on the order of 0.1-1mm. It is therefore possible to study the difference in lithium intercalation and plating behavior on edge and basal planes as a function of (well-defined) current density on these samples.

To perform thermal analysis of lithiation and lithium plating in graphite anodes, we are developing an anode-side 3ω sensor for *operando* measurements of anode thermal conductivity (k_{anode}). As Li^+ ions intercalate into the graphite anode, the anode thermal conductivity varies with the associated lattice change. With k_{anode} vs. state of charge (SOC) calibrated at a slow charge rate, the measured local thermal conductivity across the anode can thus be related to the local lithium distribution including for very fast charge rates. Therefore, our sensors, which live on the outside of the battery, can non-invasively measure *operando* the spatial distribution of Li ion concentration across the thickness of the anode, including during extreme fast charging.

Approach

A wide variety of methods have been utilized to address the problems mentioned earlier. Titrations with *ex situ* differential electrochemical mass spectrometry was performed on lithium plated graphite electrodes. Optical and X-ray tomography cells are being developed to study lithiation and plating *in situ*. Thermal sensors were developed for *operando* measurements of thermal resistances during fast charging. Electrochemical techniques were applied to detect the onset of plating, to investigate rate limitations of NMC and graphite electrodes, and to compare the edge and basal plans of HOPG. A 3ω sensor was developed for *operando* measurements of anode thermal conductivity.

Results

Quantification of Inactive Li and SEI on Fast-Charged Graphite Electrodes. Bryan McCloskey's group developed a mass spectrometry titration (MST) technique to quantify interphasial species on graphite electrodes that have undergone fast charging. Inactive Li, carbonate-containing SEI species, and lithium acetylide (Li_2C_2) were quantified via the amount of H_2, CO_2, and C_2H_2 gases, respectively, evolved upon exposure to acid (Figure I.4.E.1). They found that the majority of the capacity loss during fast charging is attributable to the formation of inactive Li metal, and prolonged fast charge cycling induces further capacity fade mechanisms, such as reaction of the plated Li to form additional carbonate-containing SEI species and Li_2C_2.

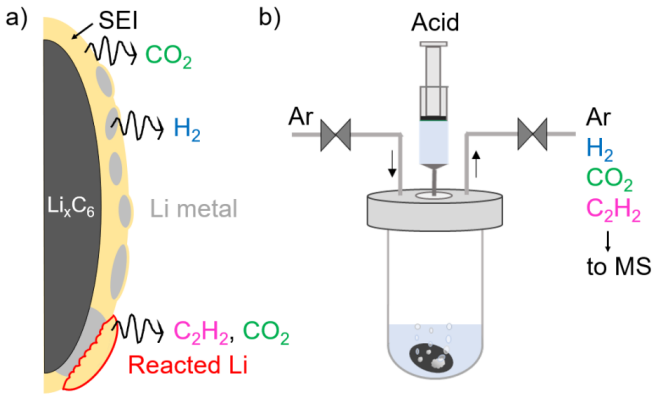

Figure I.4.E.1 a) Schematic representation of a graphite particle surface with SEI coating and inactive Li metal interspersed. Gases evolved upon acid titration are shown emanating from each species. b) Schematic representation of titration vessel apparatus with outlet gas line which is sent to the mass spectrometer (MS) for product analysis. Reproduced from [1].

Mapping the onset of lithium plating using differential OCV analysis and modeling. The McCloskey Lab has previously used a differential open-circuit voltage analysis (dOCV) after fast charge to detect the onset of Li plating at 2C, 3C, and 4C rates for Round 2 graphite/Li coin cells (Figure I.4.E.2a). For a single constant-current charge cycle at 23°C, Li plating was shown to begin at 25% SOC for 4C charge, 50% SOC for 3C charge, and 75% SOC for 2C charge. Coulombic efficiency data estimate that the Li detection limit of this technique is about 1% of the graphite electrode capacity, or 4 mAh Li/g graphite. This work has spurred ongoing collaboration with Andrew Colclasure at NREL to validate models for electrochemical Li detection and map the onset SOC of lithium plating for different c-rates and electrode thicknesses (Figure I.4.E.2b).

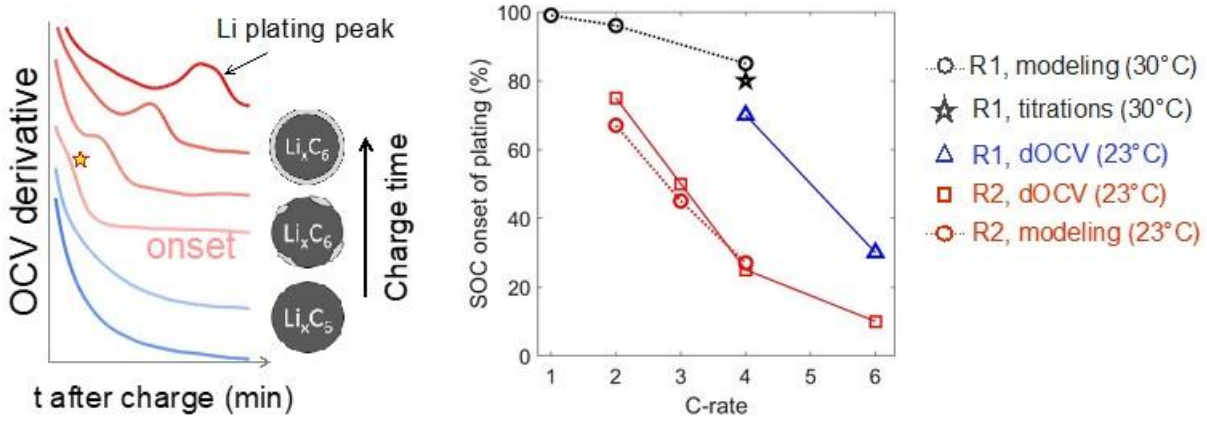

Figure I.4.E.2 Detecting the onset of Li plating with dOCV and mapping the onset of plating. a) The emergence of a peak feature in the voltage derivative can indicate the onset of Li plating. Reproduced from [2]. b) Li plating onset SOC plotted vs. c-rate for various graphite electrode thicknesses, techniques and temperatures, modeling results from NREL and titration data from [1].

In-situ X-ray tomography to measure local SOC/lithium plating. The Balsara group has performed *in situ* X-ray tomography on Li metal/101 µm Superior graphite SLC1520P (D50 = 16.94 µm) microtomography cells with a Celgard 2500 separator wetted with 1.2 M $LiPF_6$ 3:7 wt% EC:EMC. Digital volume correlation was used to calculate lithiation-induced volumetric strains within the graphite electrode resulting from C/10 intercalation to 100% state-of-charge (SOC) to obtain a calibration for strain to SOC. Another graphite half-cell was charged at 1C to 100% SOC, and Figure I.4.E.3a, b show the top and side views, respectively, of the lithium plating segmented from graphite in a portion of the cell. Figure I.4.E.3c-e shows the SOC maps of the lithiation within the same portion of the graphite electrode. A cross-section of the SOC map (y = 250 µm, Figure I.4.E.3c) shows inhomogeneous SOC across the electrode. The graphite near the separator (z = 70 µm, Figure I.4.E.3d) lithiates normally and reaches a high SOC. However, a slice of the graphite far away from the

separator (z = 20 µm, Figure I.4.E.3e) reveals a high SOC region on the left and a low SOC region on the right. The region of poor lithiation lies underneath the region of mossy lithium (Figure I.4.E.3a), below the region of high SOC, indicating transport limitations to the back of the electrode. We refer to this phenomenon as a "shadow effect". Based on the SOC maps, an estimated 6.5 µAh of Li^+ is missing from the graphite capacity. The volume of segmented lithium within the mossy lithium accounts for 6.2 µAh of missing capacity. Additional capacity is lost to reactions of lithium with electrolyte in the gaps between the lithium pebbles to form secondary SEI. However, the attenuation of this SEI is similar to that of the polypropylene separator, making segmentation difficult. Future work will involve stepwise charging at 1C to determine the onset of both lithium plating and lithiation heterogeneity in a graphite half cell, as well as a full cell with NMC. This work will contribute to quantitatively understanding effects of heterogeneity at the 1-10 micron length scale.

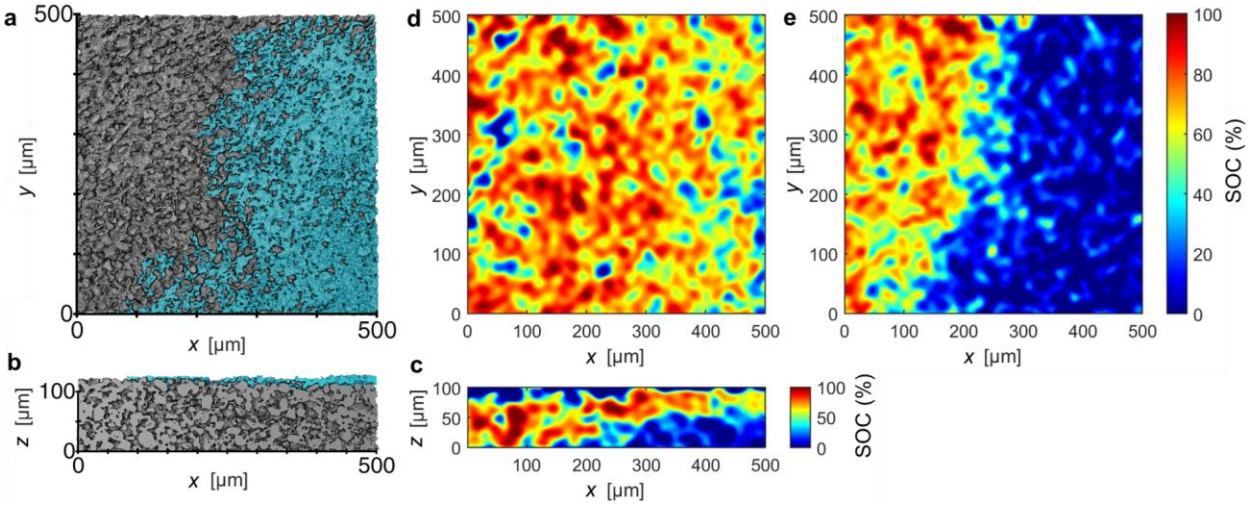

Figure I.4.E.3 Volume rendering of a portion of the segmented graphite electrode in the (a) xy-plane and (b) xz-plane after 1C intercalation to 100 % state-of-charge (SOC). The graphite is shown in gray, and the mossy lithium is shown in turquoise. SOC contour map of the same portion of the graphite electrode from the slice (c) y = 250 µm xz-plane, (d) z = 70 µm in the xy-plane, and (e) z = 20 µm in the xy-plane. Digital volume correlation was used generate volumetric strain maps, which were converted to SOC. We observe a lithium "shadow effect", where poor lithiation occurs at the back of the graphite in the region underneath the region of lithium plating.

In situ microscopic characterization of graphite lithiation and delithiation. Guoying Chen's group continued to optimize optical cell design suitable for carrying out *operando* study of Li plating on graphite. Figure I.4.E.4a shows the configuration of a modified coin cell that houses a graphite working electrode (SLC1605T, ANL), Li metal counter and reference electrodes, and a Celgard 2325 membrane separator. An optical observation window allows real-time imaging while the cell is being charged and discharged repeatedly. For example, Figure I.4.E.4b shows the 4th cycle voltage profiles at C/10 rate, which delivered a charge and discharge capacity of 328 and 322 mash g^{-1}, respectively. These cycling results are consistent with the literature reports on electrochemical performance of the graphite anode.

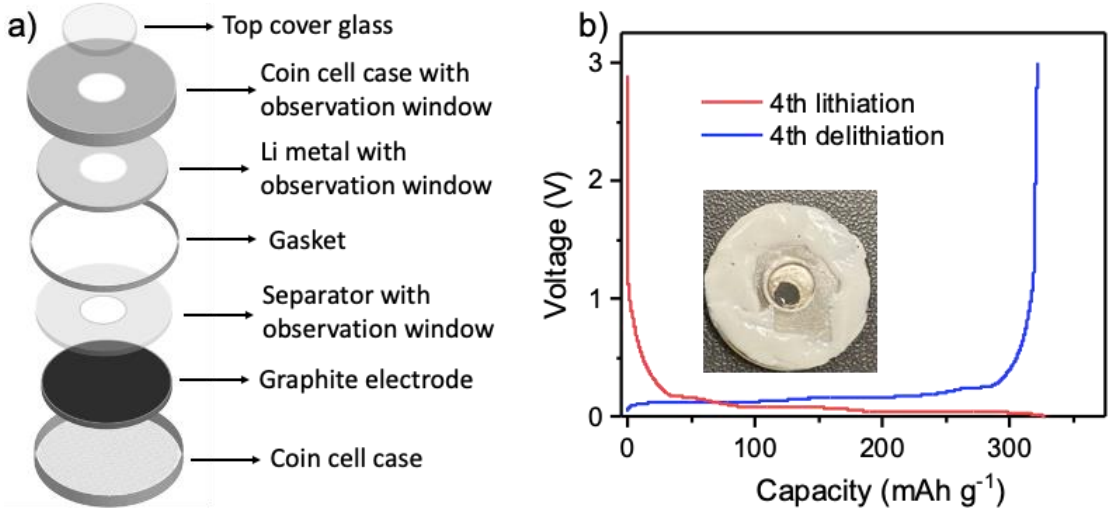

Figure I.4.E.4 a) Configuration of the redesigned in situ optical cell and b) the 4th cycle charge/discharge voltage profiles collected on the in situ optical cell cycled at C/10 rate between 0.01 and 3 V. Inset: a photo of the fabricated cell.

The *in situ* optical images taken at selected voltages on the 1st lithiation (Figure I.4.E.5a) are shown in Figure I.4.E.5b. Depending on the lithiation stage, the graphite electrode experienced color changes from grey (pristine), blue, red and gold, corresponding to C, LiC_{18}, LiC_{12} and LiC_6 phases, respectively, coinciding with the changes in band structure due to lattice spacing variation. The successful cycling of the optical cell and *in situ* observation of graphite staging validate the feasibility of using the redesigned coin cell for *in situ* studies. In the future work, we will investigate the effect of current density and cycling conditions on dendrite formation.

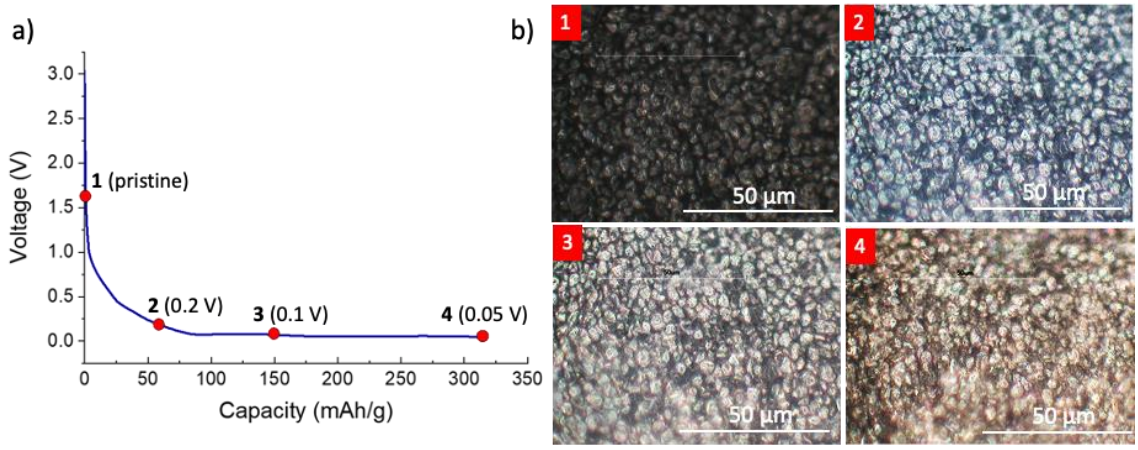

Figure I.4.E.5 a) The 1st lithiation voltage profile collected on the in situ optical cell and b) in situ optical images taken at the voltages indicated in Figure a.

Electrochemical and WAXS characterization of free-standing graphite. The Tong group's initial Li detection efforts have been devoted to connecting the early detection of plated Li metal with the electrochemical features. The electrochemical characterization was performed on the free-standing graphite electrode at various rates. After the full lithiation, the cells start to show different relaxation curves during the open-circuit potential (OCV) period at increased rates, while the cell takes the longest time to recover to its equilibrium voltage at 1C (Figure I.4.E.6a), which possibly signifies the chemical absorption of plated Li metal by the unreacted graphite. From the *ex situ* wide-angle X-ray scattering (WAXS) tests (Figure I.4.E.6b), the peaks of the lithiated graphite (LiC_{12} and LiC_6) can be clearly differentiated from those of graphite, meanwhile, the diffraction peaks related to plated Li metal is also detectable. The Li metal plating at the rates higher than 2C is

clearly visible. A closer examination reveals Li plating at C/2 and 1C likely occurs. Based on the different voltage recovery behavior, we hypothesize that Li plating possibly occurs in different morphology and mechanism at different rates (Figure I.4.E.6c). It is known that the plated Li can react with unreacted graphite, which may correlate with the morphology and amount of the plated Li. Moreover, the plated Li is likely related to the electro-dissolution reaction between the Li^+ in the electrolyte and e^- during later cycling. We aim to investigate how Li plates at different rates and whether the plated Li of different morphology and mechanism affects cycling. Similar electrochemical method was employed on the CAMP R2 graphite electrode (70 µm thick) by charging the half-cells to different SOCs at different rates to capture the varied types of Li plating. The voltage relaxation profiles clearly show the varying voltage recovery with rates (Figure I.4.E.6d). Typically, the "normal" cells show a quick and smooth voltage recovery, and it takes longer to recover to its equilibrium voltage at SOCs ≤ 90%. However, at 100% SOC, CAMP R2 electrode exhibits a similar trend with extensive voltage stabilization at 1C rate and a quick voltage recovery at higher rates. Moreover, the voltage recovery varies with SOCs. It takes longer to reach the equilibrium voltage during relaxation at high rates and SOCs. These electrochemical phenomena could be an indication of different Li plating behavior and mechanism, which will further characterized by WAXS to testify the proposed Li plating mechanism.

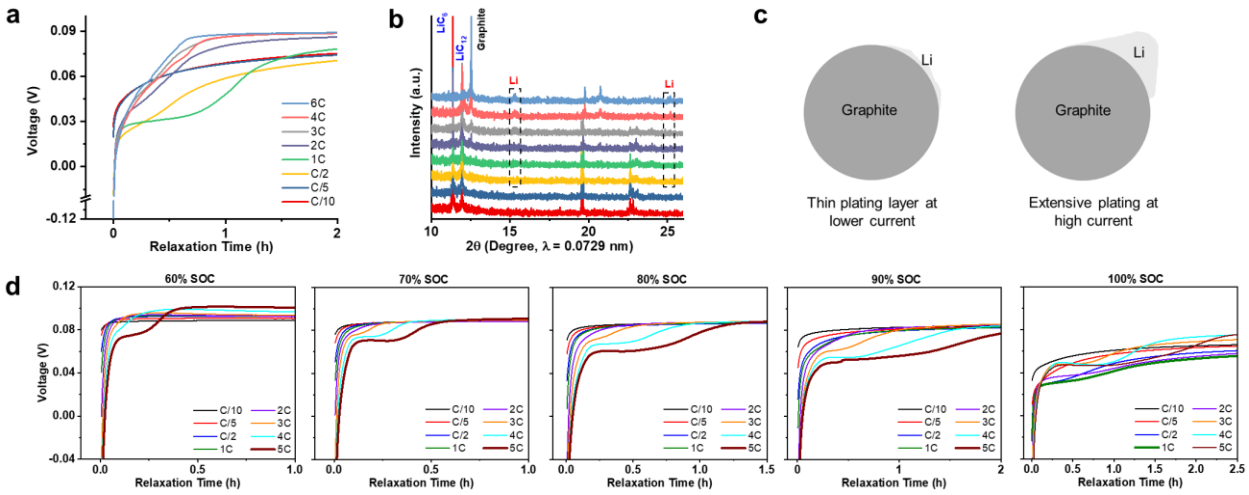

Figure I.4.E.6 (a) Voltage profiles during a relaxation process after full charge of free-standing graphite half-cells, (b) ex situ WAXS patterns collected after relaxation, (c) schematic showing different Li plating, and (d) voltage profiles during a relaxation process after charge of CAMP R2 graphite half-cells at different SOCs and C rates.

Comparing effects of lithium plating on edge and basal planes of graphite. The Kostecki group performed electrochemical experiments selectively on only basal or only edge plane graphite, using pieces of HOPG that were cleaved and mounted as shown in Figure I.4.E.7(a). A piece of HOPG with the edges covered in Kapton tape served as the basal plane sample, and a piece of HOPG conductively bonded edge-on to a Cu disc and embedded in an insulating and inert epoxy served as the edge plane sample. Basal plane samples were re-used between experiments by exfoliating a fresh layer of graphite, whereas edge plane samples were re-used by polishing the surface using sandpaper and suspensions. The optimization of the polishing process is shown in Figure I.4.E.7, indicating that a very smooth finish – and thus accurate active area – was obtained, along with a Raman spectrum indicative of a surface with pure edge character.

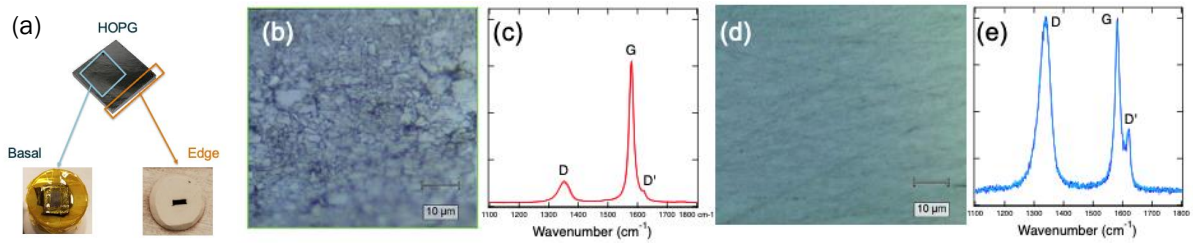

Figure I.4.E.7 (a) Photographs of HOPG, and basal and edge type electrodes. The edge electrodes were polished between experiments, and the polishing process optimized from a coarse (b,c) to a fine (d,e) finish. Microscopy images are shown in (b,d), Raman spectra in (c,e). The D' peak is a signature of edge graphite, validating the preparation process.

On both surfaces, cyclic voltammetry (CV) at 0.1 mV/s was performed for initial electrochemical characterization and to mimic the formation process applied to composite electrodes. Linearly increasing current ramps, and galvanostatic cycling at current densities near limiting values, was applied with a 0 V (vs Li/Li^+) cut-off to determine the maximum intercalation currents that can be sustained while avoiding Li plating, and cyclic voltammetry to negative voltages was performed to determine the onset of Li plating. Results are shown in Figure I.4.E.8.

Cyclic voltammograms show distinctly different behavior on edge and basal planes. Basal plane graphite sustains less than 25 µA/cm^2 and exhibits highly irreversible electrochemistry. Most likely this is electrolyte reduction, though irreversible Li insertion cannot be definitively ruled out. Conversely, edge plane graphite sustains currents of 2-3 mA/cm^2 and exhibits highly reversible electrochemistry, indicative of Li intercalation and de-intercalation. Nevertheless, the total irreversible capacity loss per cm^2 is higher for edge than basal planes. This suggests more SEI growth on edge than basal planes, in agreement with the literature.

In order to determine the current densities that can be sustained in the time frame of 0.1-1 h that is relevant for fast charging, linear current ramps were applied for about 0.5 h. Again, basal and edge planes exhibit very different behavior: basal planes sustain no more than 60 µA/cm2 above 0 V, whereas edge planes sustain more than 3.7 mA/cm^2. Galvanostatic measurements at current densities in the vicinity of these limiting currents for up to 1 h indicate that 20µA/cm^2 can be sustained above 0 V, while currents of 40 µA/cm^2 will lead to negative potentials on basal planes after 15 mins. For edge planes, measurements were applied multiple times, and the range of profiles obtained were shaded in the relevant panel in Figure I.4.E.2. It can be seen that 1 mA/cm^2 can generally be sustained for 1 h, and 2 mA/cm^2 can mostly be sustained for the time windows required for fast charging, while remaining above 0 V.

Charging at current densities that do not require negative voltages is important to avoid Li plating. The cyclic voltammograms to negative cut-off voltages show that Li plating occurs at very moderate negative voltages, -0.03V on edge planes and -0.06V on basal planes. Electrodes ought to remain entirely above these voltages to avoid Li plating.

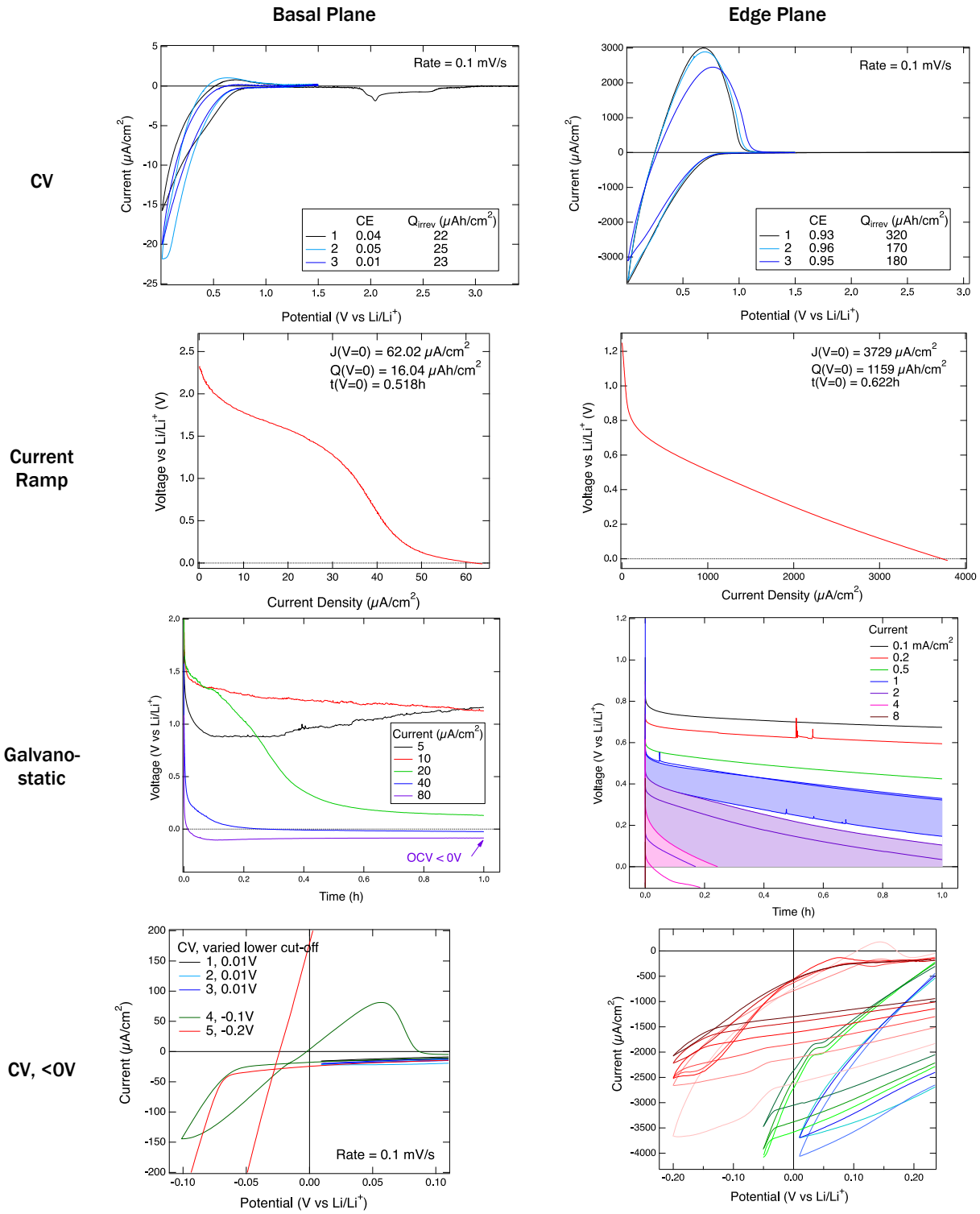

Figure I.4.E.8 Electrochemical data obtained on basal and edge plane HOPG samples shown in Figure I.4.E.1(a). Apart from the CV measurement itself, all measurements are preceded by three CV cycles (0.1 mV/s, 0.001-1.5V).

The full dataset in Figure I.4.E.8 provides invaluable input for simulations of composite electrodes containing graphite with edge and basal type surfaces. In addition, a simple estimate of what these results mean for fast charging of composite graphite anodes can be made. Taking as an example the round 2 graphite anode

manufactured by the CAMP facility within this project, with its 3 mAh/cm^2 capacity, 9.1 mg/cm^2 loading, and use of SLC 1506 T graphite with a BET surface area of 2 m^2/g and D50 particle size of 8 µm, yields an electrochemically active area of 30 cm^2 per cm^2 of electrode area assuming 8 µm graphite spheres, and 180 cm^2 per cm^2 of electrode area when using the BET area. The discrepancy indicates that the graphite particles have a tortuous surface, and good electrolyte wetting can determine which of these two bounds is more accurate. Using these values as upper and lower bounds, the limiting current of 2 mA/cm^2 translates to 60-360 mA/cm^2 on composite electrode level, or 20-120 C, assuming graphite with fully edge-like surfaces.

This work has yielded reproducible quantitative data on limiting intercalation currents and plating onset potentials on basal and edge plane graphite. It provides valuable input for the electrochemical modelling conducted within this XCEL, and has shown that graphite is compatible with charging at extremely high rates provided that potential variations within the anode are minimized and graphite with a large proportion of edge-like surface is used.

Anode-side 3ω sensor for detecting lithiation and Li plating. The Prasher group is working on new measurement and data analysis techniques to study lithiation and lithium plating in graphite anodes. After extensive theoretical modeling, sensitivity studies, and prototyping, we have developed an anode-side 3ω sensor that can be used for detecting lithiation and lithium plating (see Figure I.4.E.9a). The 3ω signal across a wide range of frequency enables measuring properties at different distances from sensors. Higher frequency data depends on material properties closer to the sensor, while lower frequency data captures material properties farther away from the sensor (i.e. deeper inside the battery). Figure I.4.E.9b-d describe the fabrication process of making anode-side sensors: b) the sensor is deposited on a passivated Cu current collector through a shadow mask; c) electrically insulated Cu wires are attached to sensor contact pads using an electrically conducting silver epoxy; d) a thick polyethylene foam is attached on top of the sensors to minimize heat loss from the sensors. Figure I.4.E.1e shows an assembled pouch cell with internal anode-side sensors connected. The trend of the data from the anode-side sensors agrees well with the previous data from cathode-side sensors (see Figure I.4.E.9f), which verifies the effectiveness of anode-side sensors for measuring thermal properties.

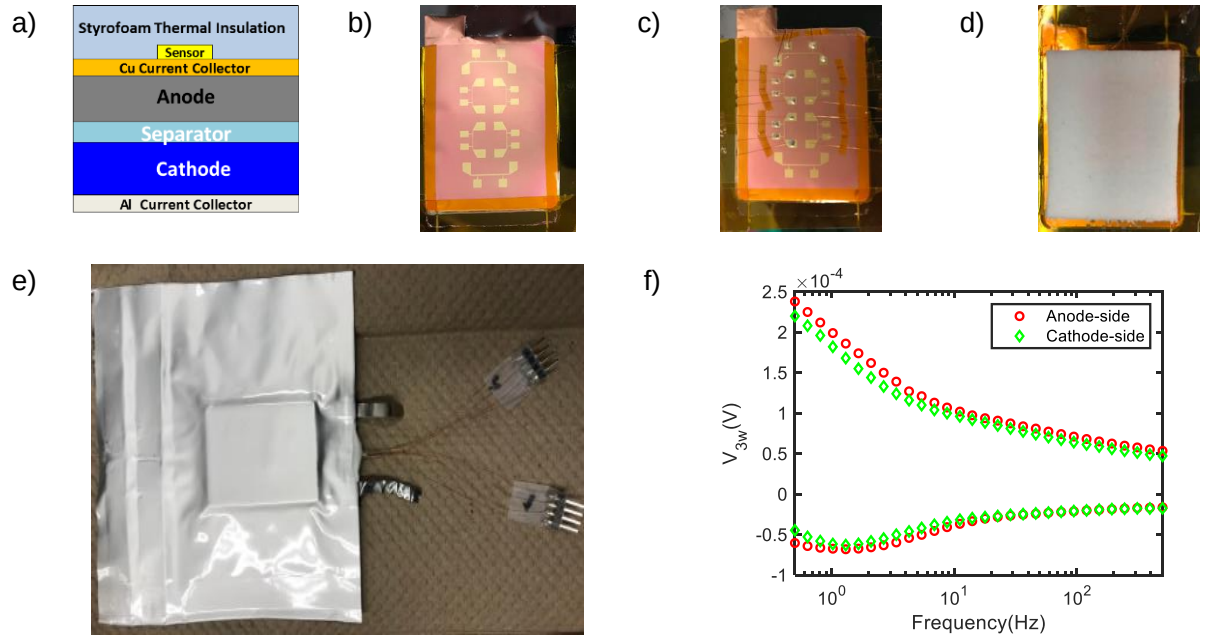

Figure I.4.E.9 a) 3ω sensor designed for lithium detection, b-d) anode-side sensor fabrication process, e) pouch cell with anode-side sensors, and f) representative data from anode-side sensor of formed pouch cell.

To detect Li distribution, thermal conductivity of the graphite anode *vs.* SOC is calibrated at a slow charge rate (C/10) after formation. Figure I.4.E.10a shows that the 3ω voltage increases as the SOC increases, which

agrees with the existing simulation and experimental results that the thermal conductivity of graphite intercalation compounds decreases as lithium ions are intercalated into graphite. By fitting to the data, we quantify the relationship k_{anode} *vs.* SOC and observe a decrease (24.9%) of the thermal conductivity in lithiated graphite anode from SOC = 0% to 100% (see Figure I.4.E.10b). At C/10, it is universally believed that Li^+ ions are uniformly distributed across the anode. As the charge rate increases, graphite particles near the separator can have a higher local SOC, which may lead to a different k_{anode} *vs.* SOC. Thus, it is possible to detect the lithium ion distribution across the anode using our 3ω sensor.

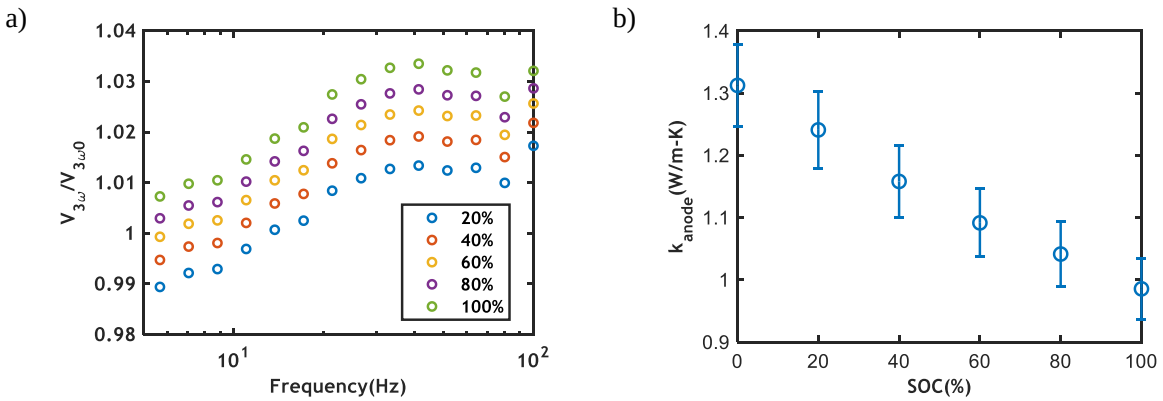

Figure I.4.E.10 a) V3ω at various SOCs calibrated at C/10 and b) operando measured kanode vs. SOC assuming uniform Li distribution across the anode at C/10 charge.

To extract the Li distribution we create a theoretical model that divides the graphite anode into 4 layers for analysis (see Figure I.4.E.11a)). Compared to 0.1C, more Li^+ ions tend to intercalate into graphite particles near the separator at faster charge rates, resulting in a gradient of lithium concentration across the anode. At charge rates greater than 0.1C, it is reasonable to assume the local SOCs with $SOC_1 > SOC_2 > SOC_3 > SOC_4$, and thus $k_1 < k_2 < k_3 < k_4$. Figure I.4.E.11b-c) shows the 3ω signal for SOC = 30% and SOC =50% after 0.1C and 1C charge rates. Note that for the same total SOC the $V_{3\omega}$ is higher at 0.1C than at 1C as more Li^+ ions intercalate into layer 4 and lead to a lower thermal conductivity in this layer, which has a higher sensitivity to the signal as it is closest to the sensor on the current collector. With the known total SOC and the relationship among local SOCs, we obtain the lithium distribution across the anode when the cell is charged to 30% and 50% SOCs (see Figure I.4.E.11d)) by fitting to the $V_{3\omega}$ data.

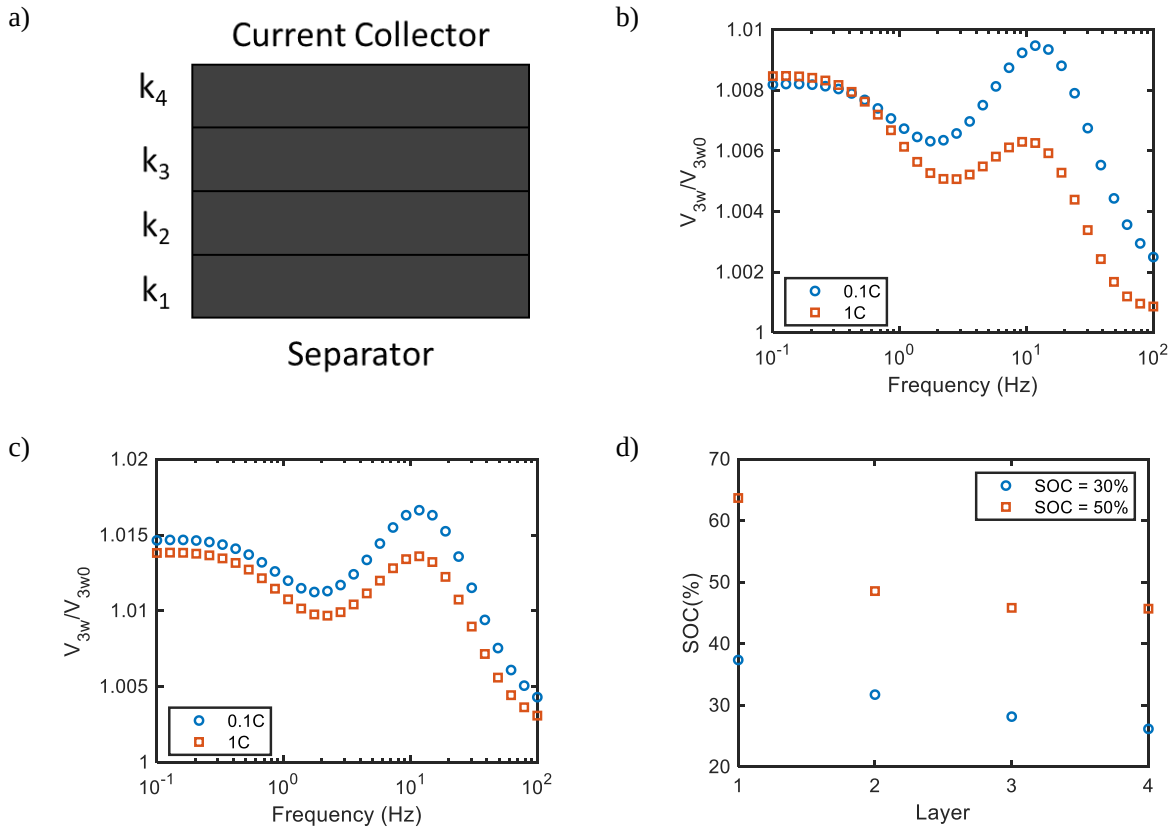

Figure I.4.E.11 a) Schematic of the 4 sub-layers (coarse mesh) in our theoretical model for the graphite anode analysis; $V_{3\omega}$ (raw measured signal) at b) SOC = 30% and c) SOC = 50% after charging at 0.1C and 1C. Note that higher frequency data corresponds to material properties closer to the sensor (i.e. closer to the current collector), while lower frequency data corresponds to material properties farther away from the sensor (i.e. closer to the separator); d) Measured Li distribution (local SOC) across the anode after 0.1C and 1C charge rates. Mesh layer 1 of the anode is adjacent to the separator, while mesh layer 4 of the anode is adjacent to the current collector.

The Prasher group is also working on understanding the critical parameters that affect heat generation of batteries during extreme fast charging (XFC), including: 1) Long time evolution of heat flux, thermal resistance, and temperature rise in cycling cells; 2) Time-resolved calorimetry of large cells during fast charge based on surface heat flux and temperature measurements; 3) An AC method to spatially resolve heat generation *operando*; and 4) Thermodynamic heat of mixing in cells during XFC. More experiments are in progress to understand the evolution of thermal properties in cells cycling at XFC.

Evolution of heat flux, thermal resistance, and temperature rise in cycling cells. The Prasher group developed a 3ω sensor inside the battery for *operando* measurements of thermal transport properties in pouch cells. The 3ω signal across a wide range of frequency enables analyzing thermal properties at different distances from sensors. Higher frequency data depends on material properties closer to the sensor, while lower frequency data captures material properties farther away from the sensor (i.e. deeper inside the battery). A main observation is that the thermal transport properties can change with cycling at different charge rates, drifting over a battery's lifetime. This indicates the increasingly significant impact to battery life from thermal resistance and the resulting variation of temperature rise. These impacts would be underestimated if based only on measurements performed on fresh batteries, before thermal properties have degraded.

The temperature rise of batteries during operation depends on heat generation, thermal transport properties, and thermal management. To understand the impact of heat generation and thermal transport properties, we developed a measurement scheme to simultaneously measure the time-resolved heat flux, thermal

conductivity, and temperature rise of operating batteries (see Figure I.4.E.12a). Note that the max temperature rise is measured by the thermocouple on the top as the top side is thermally insulated. Figure 1b shows a 3Ah pouch cell with a 3ω sensor and thermocouple on the top. Representative raw data of temperature rise, heat flux, and 3ω signal are shown in Figure I.4.E.12c-e), respectively. Note that we have 3 peaks for the temperature and heat flux in one cycle and the peak values are used to show the variation in cycling. $\Delta T = T_1 - T_2$ is the temperature difference across the cell, Q" is the heat flux from the cell to the heat sink, and $\Delta T/Q$'' represents the effective thermal resistance.

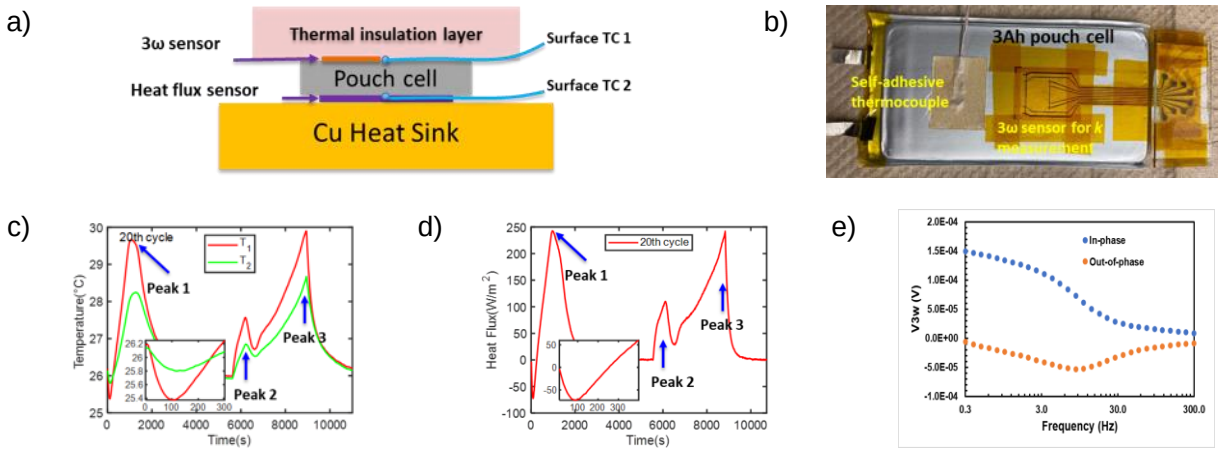

Figure I.4.E.12 Our measurement scheme designed for simultaneously measuring the heat flux, thermal transport properties, and temperature rise of operating batteries.

Figure I.4.E.13 shows the evolution of temperature difference (ΔT), heat flux (Q"), and effective thermal resistance ($\Delta T/Q$") in batteries charged at 1C and 2C. To exclude the discharge effect, the same discharge rate (1C) is used in both studies, and the values at peak 3 in each cycle are used for analysis. For the cell charged at 1C, both the temperature difference (see Figure I.4.E.2a) and heat flux (see Figure I.4.E.2b) decreases in the initial 200 cycles, and then increases due to the aging effect. Although the effective thermal resistance ($\Delta T/Q$") has a similar trend, the turning point is ~800 cycles. In contrast, for the test with 2C charge, the turning point for ΔT, Q", and $\Delta T/Q$" is ~20 cycles, which indicates a much earlier degradation of thermal transport properties in cells at fast charge rates. This data shows that the internal thermal transport properties of even commercial cells degrades with cycling, and degrades more than 10x faster from 2C charging rates than from 1C charging rates. Therefore, any lifetime estimates or performance simulations of batteries may be inaccurate if they do not account for the evolution of thermal resistance (and hence increased temperature gradients) within the cell.

In future XFC studies we plan to collect the temperature, heat flux, and thermal transport properties of cells charged at various rates (1C – 6C) and understand the degradation of thermal properties in cells during XFC. This information can be used to better understand the fundamental degradation mechanisms, and to provide more accurate predictive models for battery performance and lifetime.

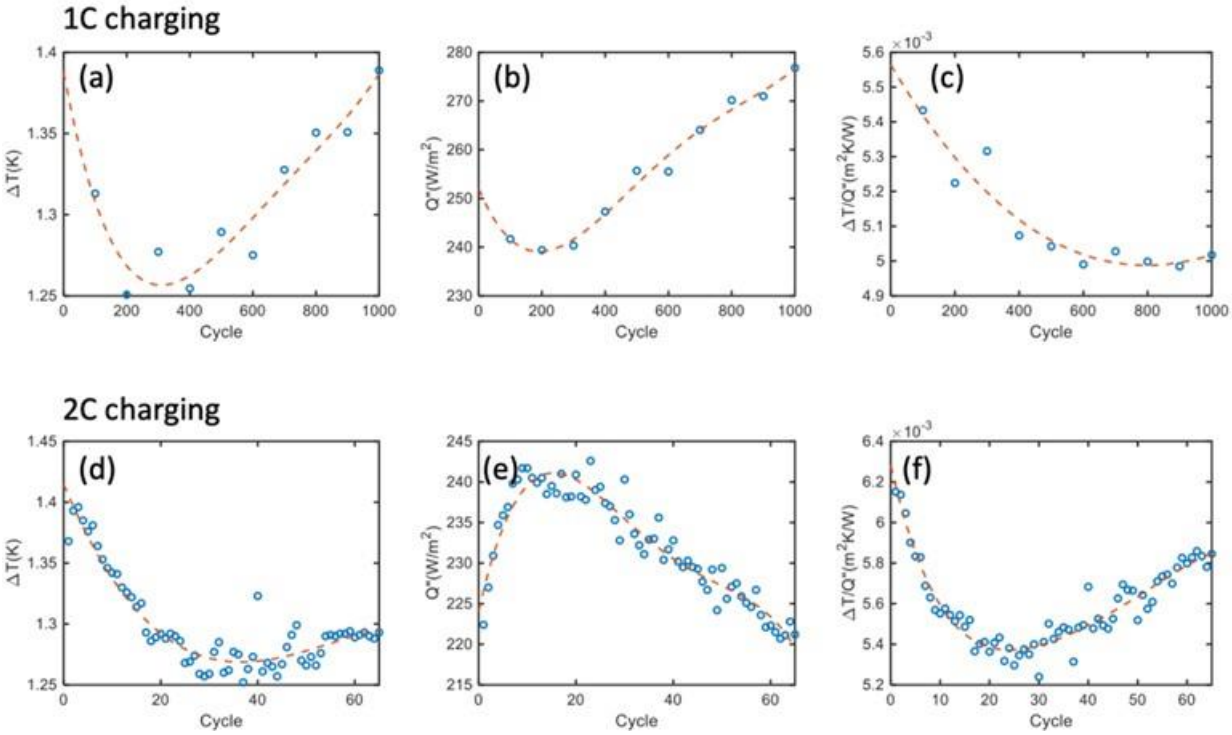

Figure I.4.E.13 The evolution of temperature difference (ΔT), heat flux (Q"), and effective thermal resistance (ΔT/Q") in batteries charged at a-c) 1C and d-f) 2C. The discharge rate is 1C in both studies and the values at peak 3 are used for analysis. Dashed lines are just a guide for the eye.

Time-resolved calorimetry of large cells in fast charge from surface heat flux and temperature measurements. The Prasher group has developed a method to perform time resolved calorimetry of the heat generated in large cells in XFC. This method is based on inverse heat transfer analysis of the cell and requires simultaneous heat flux and surface temperature measurements. Conventional calorimetry approaches such as isothermal microcalorimetry are limited by the overall cell size and therefore not applicable to large cells. Additionally, other existing approaches such as the ones based on lumped thermal analysis are limited by the thermal transport properties and the cell thickness. In contrast, the calorimetry method we have developed, based on inverse heat transfer analysis, can account for finite thermal transport properties and large cell dimensions and is therefore more accurate than the existing methods. Our approach does not need to make any assumptions about lumped capacitance, slow charging, or isothermal conditions.

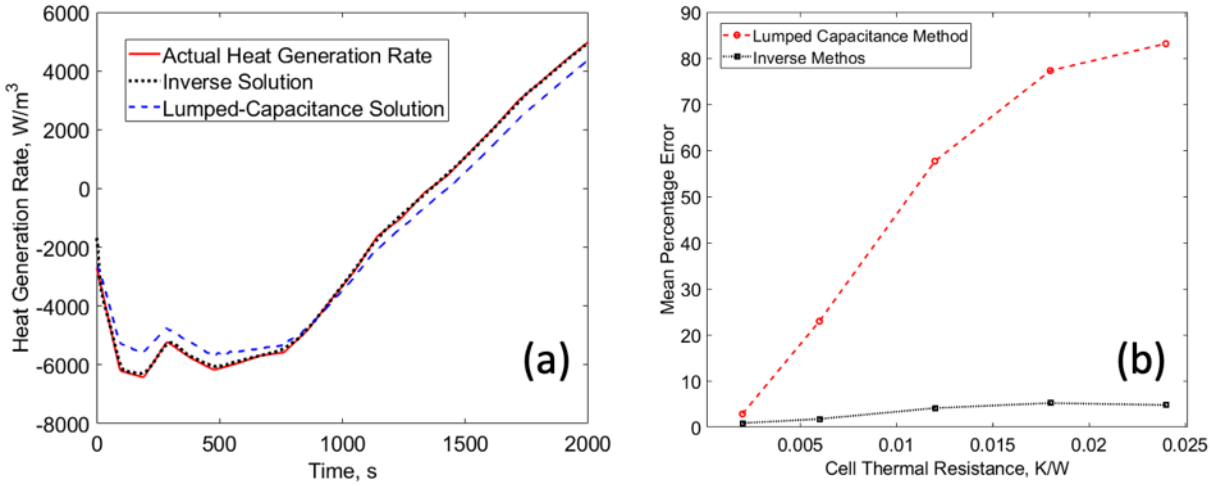

Figure I.4.E.14 a) Heat generation rate calculated from our inverse method compared with the standard lumped capacitance method. The true heat generation rate used to obtain the surface temperature and heat flux is shown for reference. b) The percentage RMS error associated with our inverse method and the standard lumped capacitance method as a function of cell thermal resistance. The error with the lumped capacitance method increases as the cell's thermal resistance increases whereas the error with the inverse remains essentially the same (< 5%).

Figure I.4.E.14(a) compares the calorimetry results from our inverse analysis with that from the standard lumped thermal analysis. Both the results are compared with a true (actual) heat generation function used to simulate the heat flux and the surface temperatures for the lumped and the inverse analysis. It is evident from the figure that the inverse analysis predicts the heat generation better than the lumped analysis. Figure I.4.E.14(b) quantifies the RMS percentage error associated with predicting the true heat generation rate using the lumped analysis instead of our inverse analysis as a function of the thermal resistance of the cell. As seen from the figure, the error associated with the standard lumped thermal analysis increases significantly with the cell thermal resistance while it levels off at ~5 % with the inverse analysis even for large cells with considerable thermal resistance. This analysis demonstrates the applicability of our inverse analysis for calorimetry of large cells and fast charge conditions.

AC method to spatially resolve heat generation. The Prasher group is developing a method to spatially resolve heat generation in a cell. A cell under an AC charge-discharge generates heat at different harmonics of the charge frequency; each associated with a different heat-generating electrochemical process. The first harmonic is related to the entropic heat generation. The fourth harmonic is determined by the kinetic overpotential resulting in irreversible heat. The second harmonic is related to the ohmic heat. By utilizing the idea of the frequency dependence of the thermal penetration depth we have devised a method to spatially resolve the different types of the heat generated inside the cell. Higher frequencies correspond to shallower thermal penetration depths, while lower frequency temperature oscillations penetrate deeper into the battery. Therefore, by monitoring the magnitude and phase of the frequency-dependent temperature oscillations on the battery's surface we can infer how much of each kind of heat was generated at what depths within the battery. We plan to exploit the frequency-domain nature of this approach and use a lock-in amplifier technique to boost signal-to-noise ratios allowing us to measure sub-millikelvin temperature oscillations. The simulated response for the complex surface temperature oscillations at each relevant harmonic are shown in Figure I.4.E.15 for one possible cell.

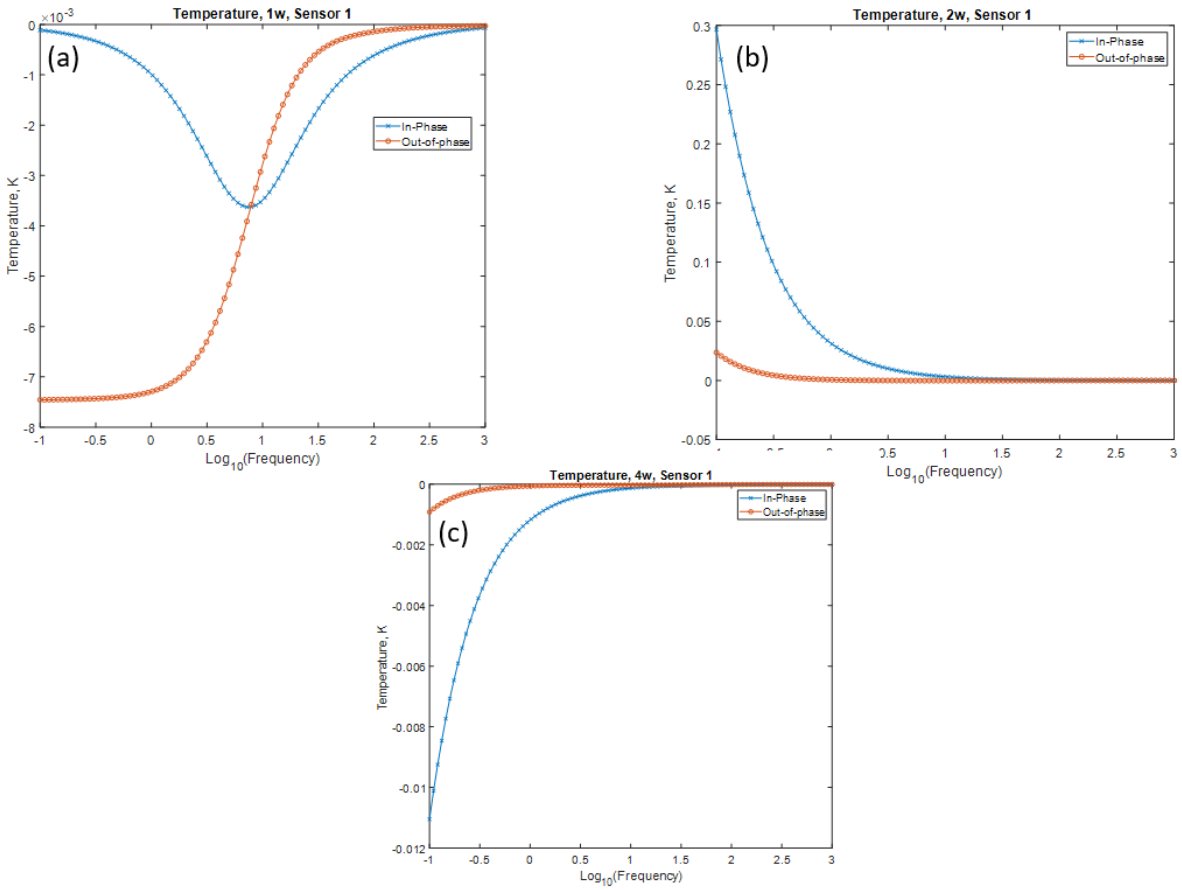

Figure I.4.E.15 Simulated magnitude of surface temperature oscillation as a function of frequency at different harmonics of the AC charging current. The temperature rise at the first harmonic (1ω) shown in (a) is due to the reversible (entropic) heart. The temperature rise at the second harmonic (2ω) shown in (b) is due to the Ohmic heating and the temperature rise at the fourth harmonic (4ω) shown in (c) is due to the kinetic overpotential for the reactions at the electrodes. These signals contain information about the magnitude and depth of each kind of heat generating process.

Heat of mixing in cells at XFC. The Prasher group investigated the importance of the heat of mixing in cells at XFC. To calculate the heat of mixing, our study utilized a fundamental thermodynamic framework independent of commonly used assumptions in other studies of heat of mixing. In particular, we calculated the expression for the rate of change of the total enthalpy of a cathode particle and the rate of change of the total enthalpy of the cell (sum of the rate of enthalpy change of all the particles). Subtracting the work done by the cell yields an expression for the overall heat generated that naturally accounts for all mechanisms of heat generation including the heat of mixing. Subtracting out the heat generation due to other mechanisms results in an isolated expression for heat of mixing. This approach avoids the assumptions of small concentration gradients or pseudo-steady state (which are generally used in other models for heat of mixing) thereby making our method applicable to cells undergoing XFC.

Our study showed that the previously used method of estimating the heat of mixing using an expression based on the method of Taylor expansion is erroneous and inapplicable at XFC. Additionally, our study showed that in a Li-ion cell with NMC cathodes and Li-metal anodes at XFC, the heat of mixing is a significant portion of the total heat generated and can contribute up to 23% of the total heat generated in a 6C discharge. This contribution is entirely neglected by the previous method.

a)

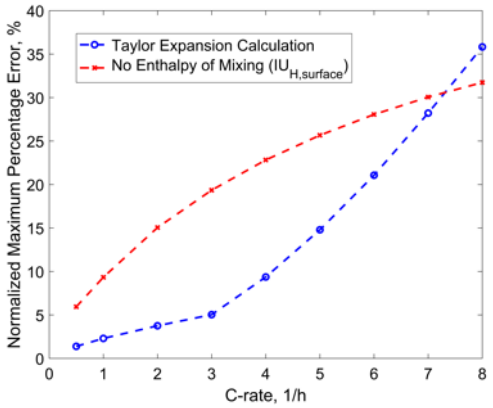

b)

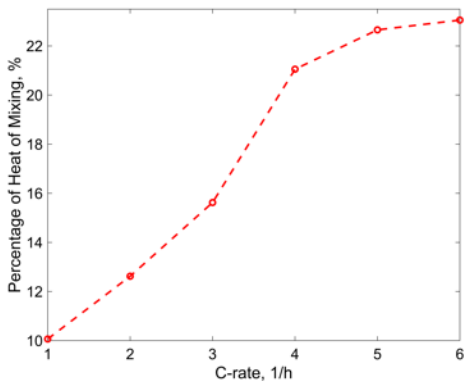

Figure I.4.E.16 a) Error associated with the method of Taylor expansion and (b) the average contribution of the heat of mixing in the overall heat generated. As the charge/discharge rate increases, the Taylor expansion approach becomes increasingly inaccurate while the overall contribution and therefore the importance of the heat of mixing in the overall heat generated also increases.

Conclusions

In the present research, detecting lithium plating during fast charging, heterogeneity effects, and graphite anodes with directional pores have been investigated. The major conclusions are summarized below:

1. *Ex situ* titrations with DEMS show that a majority of the capacity loss during fast charging is attributable to the formation of inactive Li metal, and prolonged fast charge cycling induces further capacity fade mechanisms.

2. Differential open-circuit voltage analysis (dOCV) after fast charge can detect the onset of Li plating at 2C, 3C, and 4C rates for Round 2 graphite/Li coin cells with a Li detection limit of about 1% of the graphite electrode capacity.

3. A “shadow effect” of Li plating blocking lithiation has been identified with *in situ* X-ray microtomography. Future experiments will aim to pinpoint the onset of Li plating and lithiation heterogeneity.

4. An *in situ* optical cell has been designed to track lithiation by the color changes during graphite staging and will be used to detect Li plating in future work.

5. Voltage relaxation in conjunction with WAXS has been used to probe Li plating behavior and mechanism. We aim to investigate how Li plates at different rates and whether the plated Li of different morphology and mechanism affects cycling.

6. We have determined quantitative data on limiting intercalation currents and plating onset potentials on basal and edge plane graphite. The edge plane of graphite was found to sustain a much higher current density than the basal plane.

7. We have developed a measurement scheme to measure spatially-mapped local lithium concentration distributions through the thickness of graphite anodes based on the relationship between the amount of intercalated Li^+ and the thermal conductivity. These measurements are non-invasive and can be performed on a battery while it is cycling, including at extreme fast charging (XFC) rates. A case study at 1C demonstrates reasonable lithium distribution. We plan to investigate Li distribution across the anode at XFC and study the impact of lithium plating on thermal contact resistance between the separator and anode, which can provide insightful information of lithiation and lithium plating during XFC. Further, the sensor we developed enables this type of study with a simple setup.

Key Publications

1. McShane, E. J. *et al.* Quantification of Inactive Lithium and Solid–Electrolyte Interphase Species on Graphite Electrodes after Fast Charging. *ACS Energy Lett.* 5, 2045–2051 (2020).

2. Konz, Z. M.; McShane, E. J.; McCloskey, B. D. Detecting the Onset of Lithium Plating and Monitoring Fast Charge Performance with Voltage Relaxation. *ACS Energy Lett.* 5, 1750−1757 (2020).

3. Divya Chalise et al 2020 J. Electrochem. Soc. 167 090560

4. Chalise, D.; Lu, W.; Srinivasan, V.; Prasher, R. S. In *Heat of Mixing in NMC 523 Cathode During Fast Charge/Discharge*; 020 ASME International Technical Conference and Exhibition on Packaging and Integration of Electronic and Photonic Microsystems: Anaheim, CA, 2020.

5. "Kinetics of Lithium Insertion and Plating on Basal and Edge Planes of Graphite," Manuel Schnabel, Robert Kostecki, *in preparation.*

References

1. McShane, E. J. *et al.* Quantification of Inactive Lithium and Solid–Electrolyte Interphase Species on Graphite Electrodes after Fast Charging. *ACS Energy Lett.* **5**, 2045–2051 (2020).

2. Konz, Z. M.; McShane, E. J.; McCloskey, B. D. Detecting the Onset of Lithium Plating and Monitoring Fast Charge Performance with Voltage Relaxation. *ACS Energy Lett.* **5**, 1750−1757 (2020).

I.4.F Novel Electrolyte Development with High Lithium-Ion Transference Number (Hi-LiT) for Extreme Fast Charging (ORNL))

Zhijia Du, Principal Investigator
Oak Ridge National Laboratory
One Bethel Valley Road
Oak Ridge, TN 37830
E-mail: duz1@ornl.gov

Brian Cunningham, DOE Technology Development Manager
U.S. Department of Energy
E-mail: Brian.Cunningham@ee.doe.gov

Start Date: August 15, 2018 End Date: December 31, 2020
Project Funding: $1,000,000 DOE share: $900,000 Non-DOE share: $100,000

Project Introduction

This project focuses on development of novel electrolyte to address AOI 2 (Batteries for Extreme Fast Charging (XFC)) in DE-FOA-0001808. The DOE has ultimate goals for EV batteries, which include reducing the production cost of a BEV cell to $80/kWh, increasing the range of BEVs to 300 miles, and decreasing the charging time to 15 minutes or less. Increasing electrode thickness is an effective way to achieve these goals; however, thicker electrodes present several barriers to fast charging. This project is to implement a novel high-Li-ion-transport (Hi-LiT) electrolyte and enable a 10-minute charge of 180 Wh/kg energy density with less than 20% fade after 500 cycles (144 Wh/kg). The targeted improvements in the Hi-LiT electrolyte will be increasing Li ion transference number from 0.363 to 0.7-0.75 while maintaining a relatively high conductivity of 4-10 mS/cm. The improvement in electrolyte formulation will suppress the Li plating issue during cycling. This electrolyte will be implemented into high energy density Li-ion cells.

Objectives

The objective of this project is the increase of Li ion transference number while maintaining high conductivity of non-aqueous electrolyte through novel Li salt synthesis, anion receptors additives screening and solvent systems optimization, which will significantly increase the Li ion mass transport from cathode to anode during XFC to avoid abrupt end of charging and Li plating/dendrite growth. The implementation of this novel non-aqueous electrolyte system in high energy density Li-ion cells meet the battery performance goal of delivering 180 Wh/kg of stored energy to the cell in 10-minute charging at the beginning of life and achieving less than 20% fade in specific energy after 500 cycles (144 Wh/kg).

Approach

(1) Innovative Li salts to improve Li ion mobility and increase Li ion transference number.

(2) Formulations with multiple solvent systems to provide better Li ion mobility and suppress Li plating.

(3) Anion receptor additives to further immobilize anions and dissociate cations in electrolyte.

Results

Figure I.4.F.1 shows the cycling performance of pouch cells under fast charging conditions using different electrolyte formulations discussed above. The cell with EF electrolyte shows the worst cycling performance with only ~40% of capacity retained after 160 cycles. The cells with MA and EA electrolytes show improved cycling performance compared to EF, with 66.2% and 73.6% capacity retention after 200 fast charging cycles, respectively. The use of DMC in the electrolyte shows the best cycling performance among all electrolyte formulations with 88.7% capacity retention after 200 cycles. The Li plating on graphite electrodes after

repeated fast charging cycles is also shown in Figure I.4.F.1. All the electrodes show apparent Li plating on top of graphite electrodes. However, the Li plating in electrolytes with EA, DMC and EMC is uniform and has smooth surface, while it is non-uniform in electrolytes with EF and MA. The uniformity in Li plating is phenomenally related to the cycling performance to a certain extent.

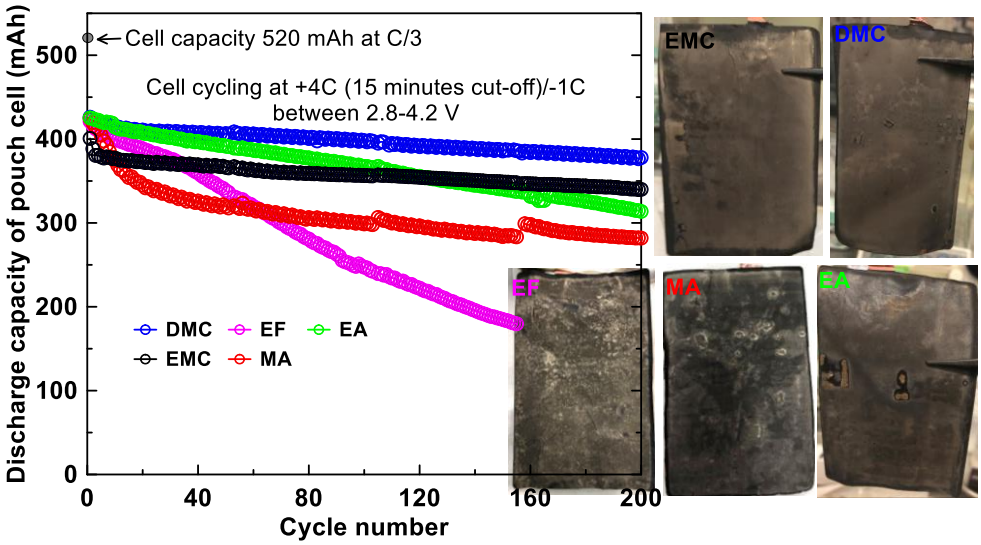

Figure I.4.F.1 The long-term cycling performance of the pouch cell under fast charging conditions with different electrolytes of 1.2 M $LiPF_6$ in EC:EMC:Co-solvent 30:50:20 wt%. Li plating on graphite electrodes after 200 fast charging cycles.

The surface chemistry on both cathodes and anodes was studied by XPS after formation and after 200 fast-charging cycles. Figure I.4.F.2 and Figure I.4.F.3 show the detailed analysis of F 1s, C 1s, O 1s and P 2p of solid electrolyte interphase (SEI) on graphite electrodes and cathode electrolyte interphase (CEI) on NMC622 electrodes. It is well known that the SEI and CEI consist mainly of organic components including $(CH_2OCO_2Li)_2$ (lithium ethylene decarbonate, LEDC), other organic carbonates (R_2CO_3), polyethylene glycol (PEO) oligomer, etc., and inorganic compounds such as Li_2CO_3, LiF, Li_2O, $LiPF_xO_y$ and Li_xPF_y.

By comparing the F1s spectra in Figure I.4.F.2a between the pristine graphite electrode and electrodes after formation, a new Li-F peak at ~685 eV evolved which is from the decomposition of $LiPF_6$ into LiF and PF_5. The C-F peak is from the PVDF binder in the electrodes. In Figure I.4.F.2b, the area ratio of Li-F/C-F is increased in all five samples compared to the counterparts in Figure I.4.F.2a, indicating the increase of SEI thickness after fast-charging cycles. In the DMC case, the area ratio of Li-F/C-F is the lowest, suggesting the thinnest SEI in this electrolyte after fast charging cycles, which can be related to its best fast charging cycling performance. In the C 1s spectra, the peaks at 286.4, 288.6 and 289.8 are assigned to CO-, CO_2- and CO_3- like carbon environments which are from the reduction of solvents at the graphite surface besides the C-C in graphite and Li-C from residual Li in graphite. This solvent reduction is also confirmed in the O 1s spectra. Compared to the pristine sample, the O1s spectra evolved with two peaks after formation and after the fast-charging cycles. The peak at ~532 eV is assigned to CO_2-like oxygen from carbonate compounds such as lithium alkyl carbonates ($ROCO_2Li$) and/or lithium carbonate; the second peak at ~533.6 eV is assigned to –C–O– bonds from $ROCO_2Li$ and/or ether derivatives. The increase of the latter one after fast charging cycles is probably due to the increase of more ether derivatives such as PEO-like oligomers. PEO formation has been suggested to occur through PF_5 catalyzed electrolyte solvent polymerization reactions. The P 2p spectra evolved after formation cycles of the cells due to $LiPF_6$ decomposition and the intensity increased after fast charging cycles. The P–F peaks are ascribed to the reduction of $LiPF_6$ on the graphite to form PF_5 and Li_xPF_y, and the P=O peaks are assigned to the $LiP_xO_yF_z$ from the hydrolysis of $LiPF_6$ with trace water in the electrolyte.

Figure I.4.F.3 shows the F 1s, C 1s, O 1s and P 2p XPS spectra of NMC622 electrodes in pristine state, after formation and after 200 fast-charging cycles. In the F 1s spectra (Figure I.4.F.3a), similar $LiPF_6$ decomposition occurred and Li-F peak evolved after formation cycles besides the C-F peak from the PVDF binder. In Figure I.4.F.3b, the intensity of Li-F increases for all five different solvent systems, indicating the increase of CEI thickness after fast-charging cycles. The area ratio of Li-F/C-F in carbonates (DMC and EMC) is lower than that in esters (EA, MA and EF), indicating a thinner and stable CEI in carbonates than esters. This is in accordance with the cycling performance. The C 1s spectra show little change between the pristine sample and the electrodes after formation in all five electrolytes. The peaks in C 1s spectra are ascribed to the PVDF binder and carbon blacks in the electrodes. The O 1s spectrum of the pristine electrode shows two peaks with the peak at 529.5 eV attributed to M-O from the lattice oxygen in NMC622 and the peak at 531.5 eV assigned to CO_x-like oxygen from the carbon black. After formation cycles, the O 1s peak from the pristine electrode at 531.5 eV is replaced by two new peaks at ~531.7 and ~533.5 eV indicating the formation of CEI layers from electrolyte decomposition. The peak at ~531.7 is ascribed to CO_2- like oxygen from carbonate compounds ($ROCO_2Li$) and/or Li_2CO_3, and the peak at ~533.5 eV is assigned to -C–O- bonds from ether derivatives and/or $ROCO_2Li$. After repeated fast-charging cycles, the intensity of CO_2-/C-O increased greatly by comparing the M-O peak, indicating the continuous decomposition of electrolyte and formation of carbonate compounds in the CEI layer. For the EF case, the M-O peak almost disappeared, indicating the CEI in this electrolyte is the thickest. This suggests the CEI may be not stable when EF is present in the electrolyte. The P-F and P=O peaks are shown after formation in P 2p spectra compared to the blank feature in pristine sample. The P-F/P=O peaks grow in intensity after fast charging cycles, which is another indication of the CEI growth from the salt decomposition.

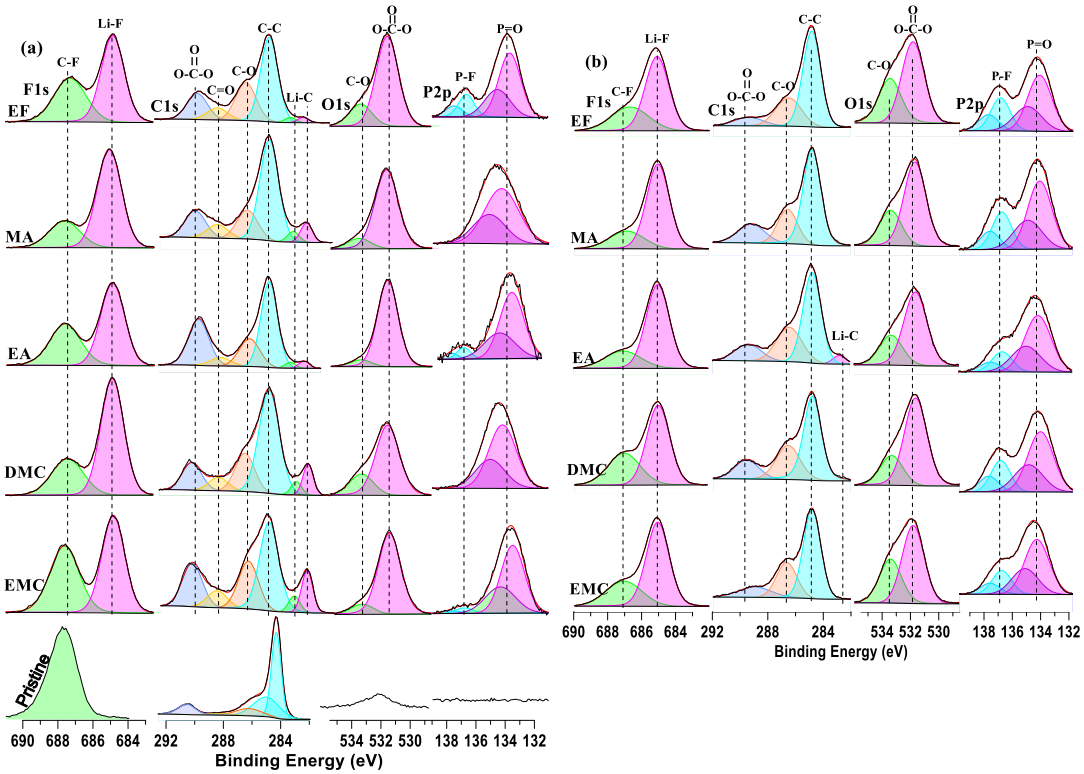

Figure I.4.F.2 XPS spectra of negative electrodes (a) after formation cycles and (b) after fast-charging cycles in cells with different electrolytes.

Figure I.4.F.4 shows the long term cycling performance of the cells with a 15 minute fast charging for over 200 cycles when different molarities are used in electrolytes. For baseline with Gen2 electrolyte, the capacity retention after 200 cycle is about 90% compared to the 1st cycle under 4C charging. A strong correlation was found between the salt molarity and the cycling performance. The cycling performance improved with

increasing salt molarity from 0.75 M to 1.5 and 1.75 M. After 200 cycles, the cells were opened at fully discharged state. Here we can clearly see the metallic lithium platting on graphite electrode in the top three pictures. They are from cells with electrolyte of 0.75, 1.0 and 1.25 M. The surface was not fully covered with Li plating, but rather with scattered Li plating areas. Interestingly, the Li plating was significantly alleviated when the molarity increases to 1.5 M. Even more interesting is the 2.0 M electrolyte, the capacity during fast charging is the lowest. However, no Li plating can be observed in this electrolyte. This demonstrates that Li plating is induced by Li ion depletion from mass transport limitation when low molarity electrolyte is used.

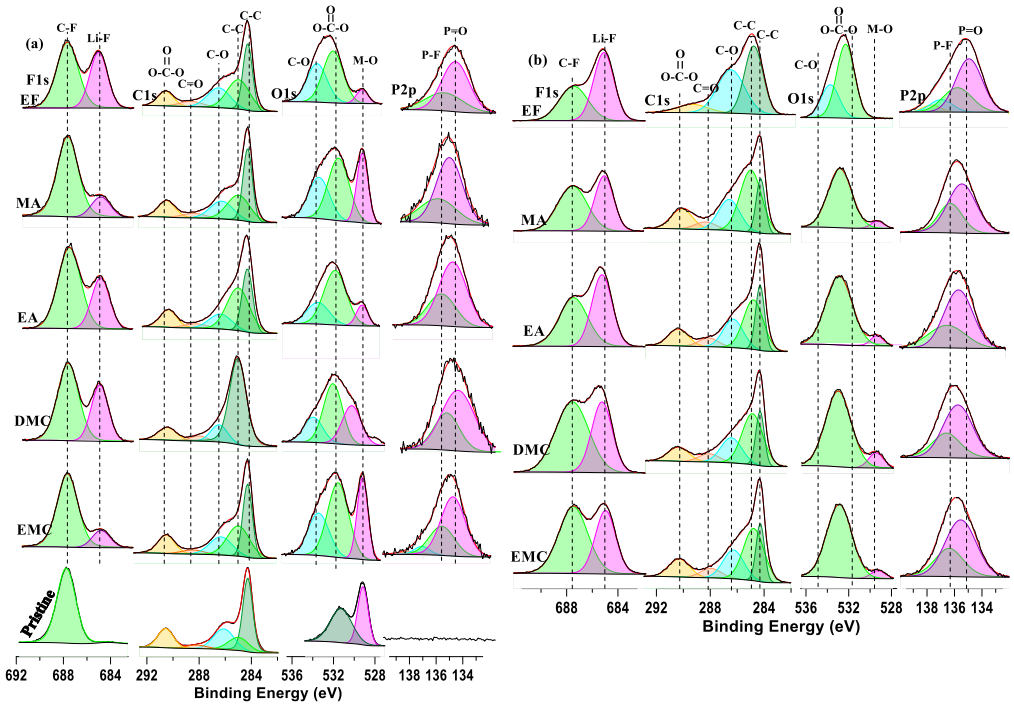

Figure I.4.F.3 XPS spectra of positive electrodes (a) after formation cycles and (b) after fast-charging cycles in cells with different electrolytes.

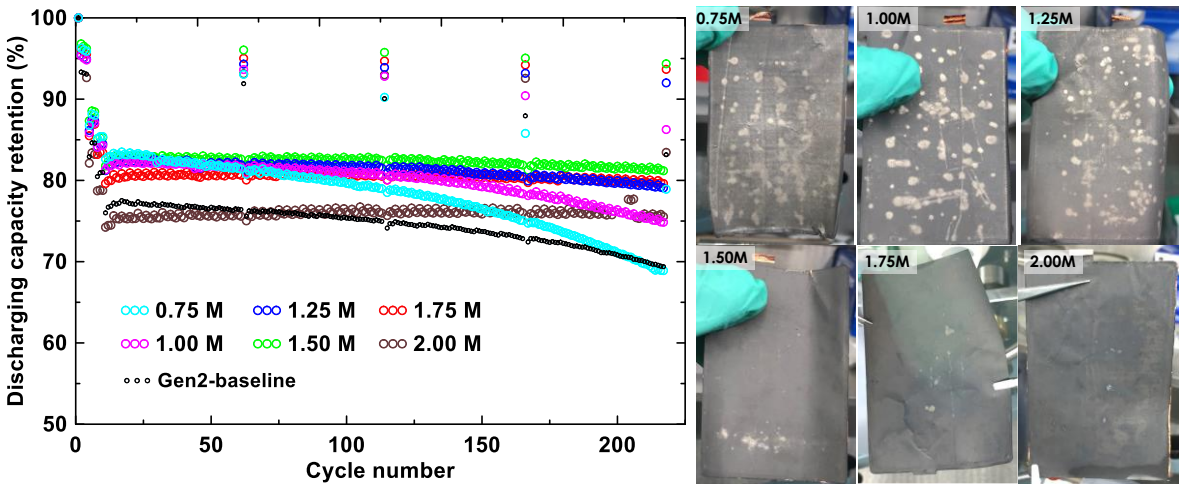

Figure I.4.F.4 Cycling performance of electrolyte with different molarity of Li salts. Post-mortem photos of the graphite anodes after 200 cycles.

Figure I.4.F.5 shows the cycling performance of 540 mAh pouch cell under 6C (10 minutes) XFC protocol and C/3 every 100 XFC cycles. The ORNL baseline electrolyte shows better XFC capacity and cycling stability compared to Gen2 baseline. With four different additive formulations, there are two formulations C and D

shows more improved performance with about 80% capacity retention after 1000 XFC cycles. The cells with C and D also show excellent C/3 cycling performance on the right. The capacity retention after 1000 cycles can be greater than 85%.

An ORNL V2 electrolyte formulation has been developed based on the optimized electrolyte salt, solvent and additives. NMC622||graphite Li-ion cells were scaled up to 1.5 Ah pouch cells and tested under 6C (10 minutes) XFC protocol in Figure I.4.F.6. The cell with ORNL V2 electrolyte has 84% capacity retained after 800 XFC cycles, which is much better than the targeted goal (80% after 500 cycles). The cell can have an energy density of ~180 Wh/Kg (if scaled up to 50 Ah), which has met the targeted goal for energy density. After 800 XFC cycles, the cell still has 148 Wh/kg energy density. When the cell was charged/discharged at C/3 after 800 cycles, it can still deliver 207 Wh/kg. This demonstrates the excellent performance of Li-ion cell using ORNL V2 electrolyte formulation for XFC capability.

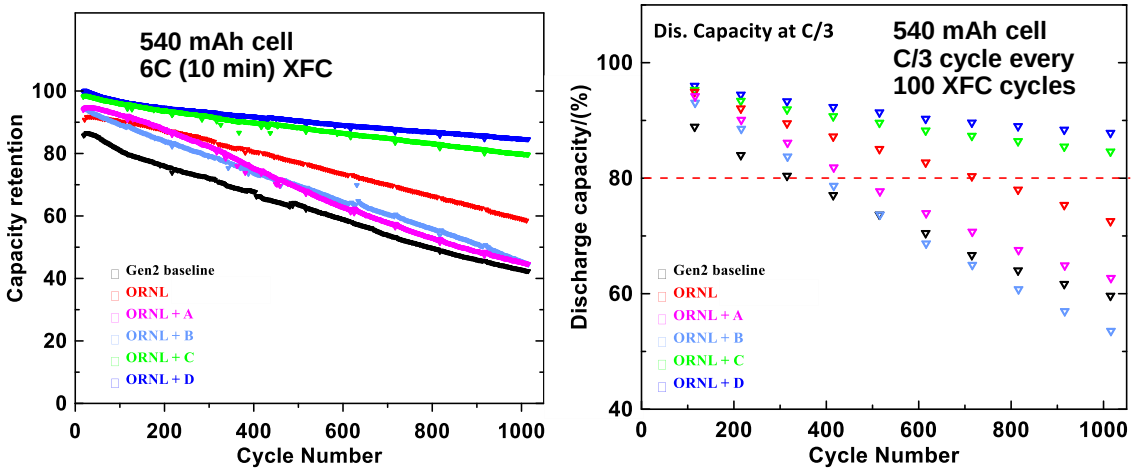

Figure I.4.F.5 Cycling performance of 540 mAh pouch cells with different electrolyte formulations under 6C (10 minutes) XFC protocol and C/3 cycle every 100 XFC cycles.

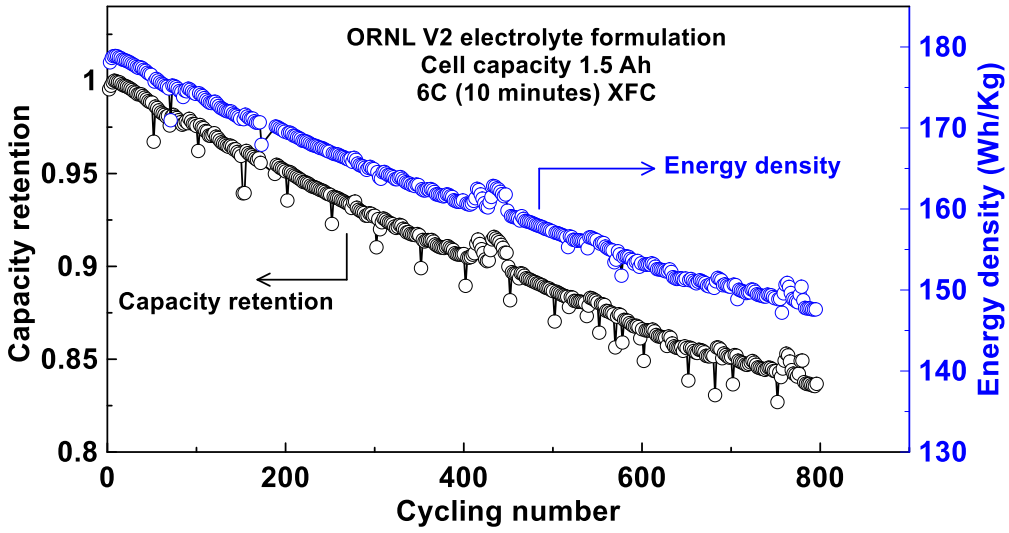

Figure I.4.F.6 Capacity retention and energy density versus cycling number under 6C (10 minutes) XFC protocol. The cell is 1.5 Ah pouch cell filled with ORNL V2 electrolyte formulation.

Conclusions

Different cycling performance was observed when different electrolyte solvents are used. The lithium plating on graphite electrodes were found to be in accordance with the cycling performance. The SEI and CEI in different electrolyte formulations were analyzed by XPS. Both the SEI and CEI in DMC are thin and stable

during fast charging cycles, compared to other solvent formulations. The present results suggest that DMC in the electrolyte formulation is encouraged in developing fast charging technologies for Li-ion cells. Electrolyte with different molarity are found to have significant impact on fast charging. With the increase of molarity, the cycling performance under fast charging is improved. An optimized molarity for fast charging is 1.5-1.75 M/L. Li plating is observed when the molarity is below 1.25 M/L. This suggest that Li plating is related to Li ion depletion in the electrolyte when mass transport is limited during fast charging. The ORNL V2 electrolyte formulation has optimized solvent, salt and additive formulation. The cell can achieve 180 Wh/Kg energy density when a 6C (10 minutes) extreme fast charging protocol is used. The cycling performance is also excellent with 84% capacity retention after 800 cycles.

Key Publications

1. Zhijia Du, Development of High Li ion Transport Electrolyte for Fast Charging of High Energy Density Li-ion Cells (Invited), 44th ICACC meeting.

2. T. Liu, Z. Du, X. Wu, et al, Bulk and surface structural changes in high nickel cathodes subjected to fast charging conditions, Chem. Commun., 2020, 56, 6973-6976.

3. Xianyang Wu, Tianyi Liu, Zhijia Du, et al. Effects of Solvent Formulations in Electrolytes on Fast Charging of Li-ion Cells, Electrochimica Acta, 353 (2020) 136453

4. Xianyang Wu, Zhijia Du, et al., Effects of charging rates on LiNi0. 6Mn0. 2Co0. 2O2 (NMC622)/graphite Li-ion cells. Journal of Energy Chemistry 56 (2020): 121-126.

Acknowledgements

We would like to acknowledge the following collaborators: Prof Guangsheng Zhang (UAH), Feng Lin (Virginia Tech), Kejie Zhao (Purdue), Jue Liu (SNS).

I.4.G New High-Energy & Safe Battery Technology with Extreme Fast Charging Capability for Automotive Applications (Microvast, Inc.)

Wenjuan Liu-Mattis, Principal Investigator
Microvast, Inc.
3259 Progress Dr. OFC132
Orlando, FL 23826
E-mail: wenjuanmattis@microvast.com

Brian Cunningham, DOE Technology Development Manager
U.S. Department of Energy
E-mail: Brian.Cunningham@ee.doe.gov

Start Date: July 3, 2018 End Date: February 1, 2021
Project Funding: $3,000,000 DOE share: $1,500,000 Non-DOE share: $1,500,000

Project Introduction

Automakers worldwide have announced plans to begin transitioning from gasoline powered vehicles to ones driven via electricity. To makes these bold adoption plans a reality the lithium-ion battery must continue to improve so electric drive trains can become competitive in cost and convenience to a traditional gasoline powered vehicle.

In this project technology is being explored to try and make lithium-ion batteries re-energize in a matter of minutes without making significant sacrifices to safety, cost or energy density of the cell. To that end, we are exploring extreme fast charge (i.e. under 10 minutes charge) in larger capacity (> 20AH) cells using a concentration gradient cathode chemistry, advanced impedance reduction additives, and Microvast's high performance separator.

Objectives

The objective of the project is to develop a redox couple that can be implemented into a large format automotive cell capable of 500 cycles of 10-minute fast charge and 1C discharge. The targeted cell will maximize the energy density while still being able to meet the > 180Wh/kg energy density target after fast charge. The final cell built will use advanced materials to offer excellent abuse tolerance for cells applied towards an electric vehicle.

Approach

To achieve the end goal two thrusts are undertaken simultaneously during the project. The first thrust is related to material development, so a higher energy redox couple can be utilized in the cell and lower impedance gain during cycling via an effective interface can be realized. The second thrust is via cell design, by going thru at least 3 generations where at least one principle material – anode, cathode or separator – will be replaced to try and stepwise improve the energy density and/or performance.

For the material work, project members Microvast and Argonne National Labs will focus on developing a high nickel content concentration gradient cathode. Higher nickel cathodes are desirable for their higher gravimetric capacity, but the safety of the materials particularly when de-lithiated is a concern. As the nickel concentration of the cathode increases the performance of the gradient cathode maybe improved by manipulating the atomic concentrations of cobalt/manganese, or via the addition of other dopants and/or coatings to the cathode. At the same time, advanced electrolyte additives will be explored by Microvast and Argonne National Labs to minimize the resistance increase that negatively effects fast charge energy density.

For cell design, there will be 3 generations (labeled as Gen#) during the project, with each generation adding at least one significant material change to the cell. Each generation is tested by Microvast and BMW for performance evaluation. The first-generation cell design started with a 220 Wh/kg pouch cell design goal. After

each cell generation the performance will be analyzed to determine if the cycling goals are met. If met, the next round of cell design will incorporate a higher electrode loading to boost the cells 0.33C Wh/kg energy density. In the event the cell is unable to successfully meet the XFC cycling requirements a material will be upgraded and the same energy density will be repeated. Cell testing procedures will follow USABC/DOE guidelines for the project, and two cell deliveries will be made to the Department of Energy for independent testing of the cell generations.

Results

As detailed in the project approach, the team this year focused on increasing the energy density of the developed XFC cell to ~240 Wh/kg after successfully demonstrating the project conditions for a 220 Wh/kg system in year 1. To boost the cells energy density the cathode nickel content was raised, and the electrode loadings for the anode were increased. The changes between Gen1 and Gen2 were compared in stacked pouch cells by Microvast and wound jelly rolls by BMW. In Figure I.4.G.1 the rate capability of Gen1 and Gen2 are compared for charge and discharge in BMW's PHEV1 hard can format. The higher areal loadings lowered the insertion rate performance for both charge and discharge, though the charge losses are more severe. This could be because the cathode chemistry changed from Ni60% to Ni80% between Gen1 and Gen2, which means the thickness gains for a balanced cell were less intense on the cathode electrode compared to the carbon based anode.

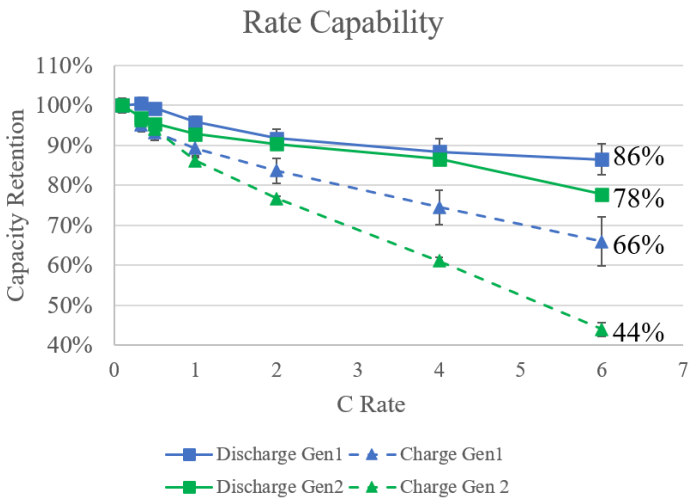

Figure I.4.G.1 High resolution TEM of cycled full concentration gradient cathode powder, with a comparison of area 1 and area 2 along a single nanorod primary particle.

The changes in rate performance from Gen1 to Gen2 correlate with higher max temperature rise recorded during fast charge in the hard can and pouch cell. Lower max temperatures are thought to be desirable for improved cell life since side reactions and material degradation are less intense.

In an effort to better understand the changes in XFC active materials as they are cycled high resolution transmission electron microscopy (TEM) and electron diffraction were collected on a cycled full concentration gradient cathode. In Figure I.4.G.2 the images collected clearly show densification of the cathode crystal structure is occurring near the particle surface. Interestingly, these TEM images clearly show that the structural phase change can proceed along a single nanorod primary particle. The densification observed may lead to overpotential rise over time, which is of special concern for XFC cells. A growing number of resources suggest this phenomena is unavoidable in the cathode, so technologies that provide a relatively more stable interface, such as full concentration gradient cathode materials, are of great interest.

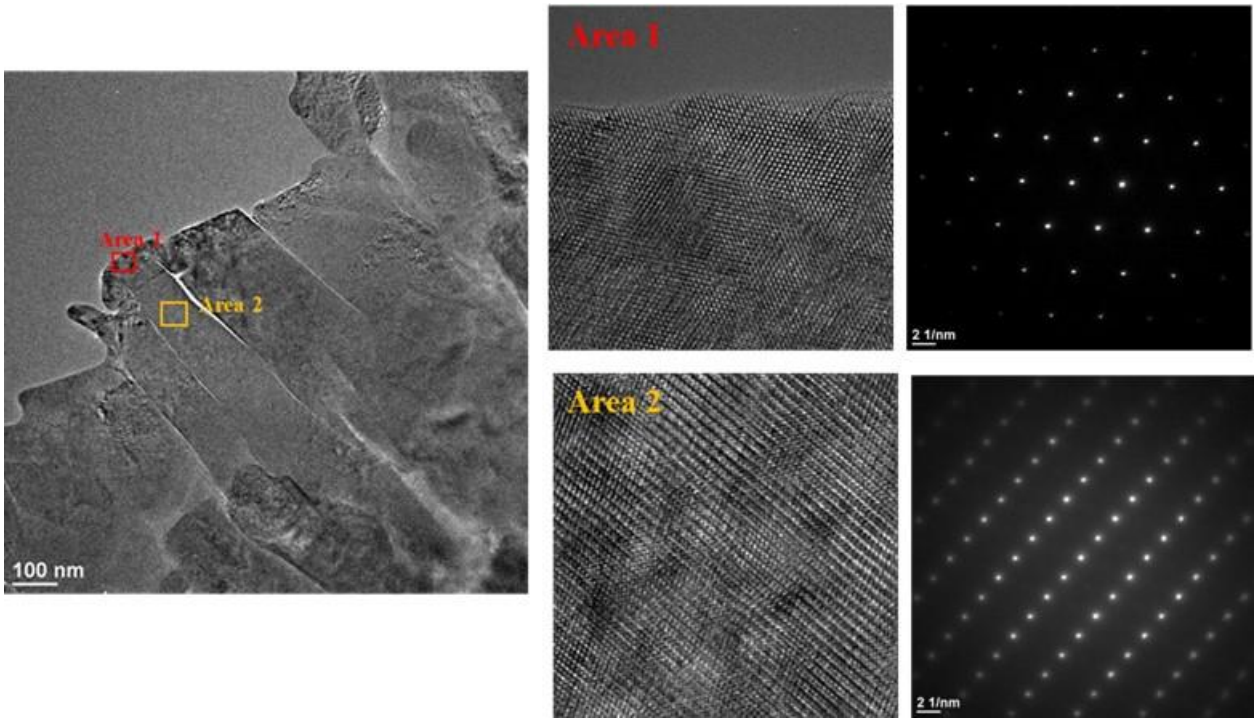

Figure I.4.G.2 High resolution TEM of cycled full concentration gradient cathode powder, with a comparison of area 1 and area 2 along a single nanorod primary particle.

As part of the project's efforts, a full concentration gradient variant was investigated, scaled to 100s of kg, and tested in pouch cells. In Figure I.4.G.3 the capacity and retention of the cathode material is evaluated at room temperature in a 5.5Ah pouch cell. The cycle life for a relatively unoptimized material and cell can reach ~1,500 cycles before 80% of cells retention is reached.

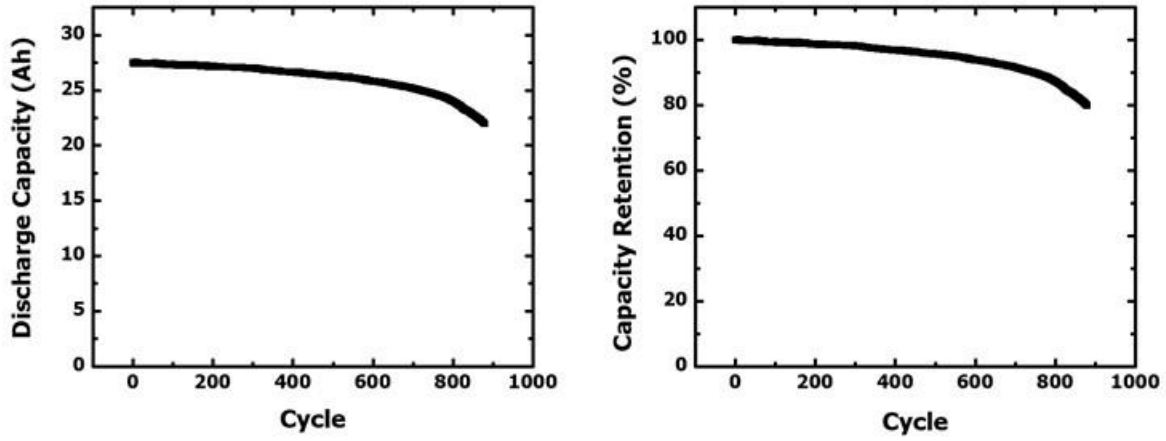

Figure I.4.G.3 Capacity and capacity retention plots for pouch cells containing a new FCG designed for XFC cells. The pouch cells were tested at 25ºC, 2.7-4.25V with 1CCCV (C/20 cut-off)/1CD and periodic 0.33C reference cycles.

Building upon knowledge and materials developed thru the project, the final Gen3 pouch cells – 240 Wh/kg at 0.33C – were built after a series of optimization iterations. In Figure I.4.G.4 the XFC cycling of the Gen3 cell is shown. It turns out for this cell design only a 5C constant current is necessary in 10-minutes to reach the 180Wh/kg fast charge energy density goal at beginning of life. Thru 500 cycles the cell still had ~94% capacity.

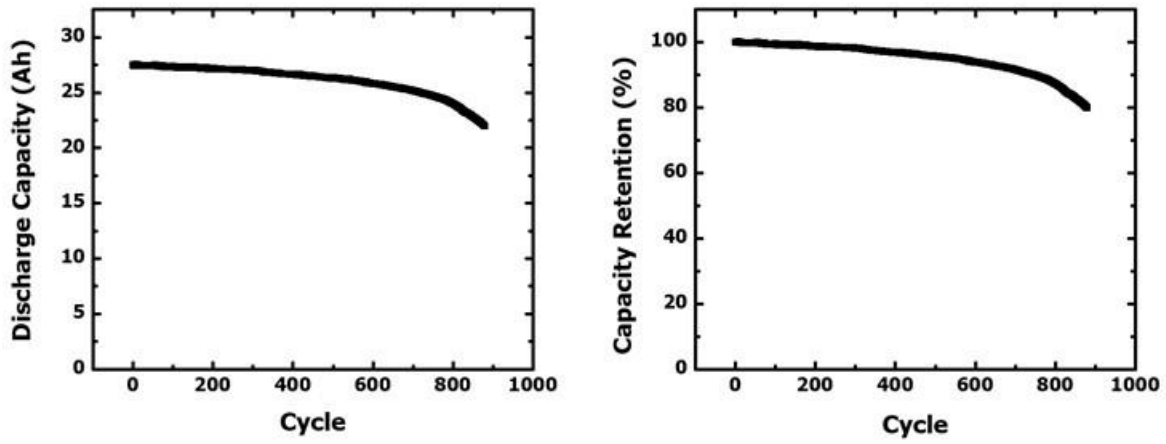

Figure I.4.G.4 XFC cell cycling capacity (left) and capacity retention (right) for the projects Gen3 pouch cells. The cells are tested from 2.7-4.2V, 5CCCV (10-min total charge cut-off) / 1CD at 30^{0}C.

Conclusions

The project has successfully demonstrated a 240 Wh/kg pouch cell that is capable of meeting the XFC cycling goals of 500 cycles while delivering a starting energy of 180 Wh/kg. Advanced materials and advanced post-op analysis were required to build the successful Gen3 cell. There are still challenges that must be addressed, but thru cutting-edge materials and advanced diagnostics it seems advancements in XFC cells energy and performance is possible.

Key Publications

1. Poster presentation, DOE Annual Merit Review, Washington D.C. June 10-13, 2019
2. Oral presentation, DOE Annual Merit Review, Online, June 1-4, 2020

Acknowledgements

Microvast would like to thank Brian Cunningham and Kimberly Nuhfer (NETL manager) for their support. This project would not be possible without the helpful discussion and contributions by our collaborators Peter Lamp (BMW), Forrest Gittleson (BMW), Khalil Amine (ANL), Tongchao Liu (ANL), Chicheung Su (ANL), and Jihyeon Gim (ANL).

I.4.H Development of an Extreme Fast Charging Battery (Pennsylvania State Univ.)

Chao-Yang Wang, Principal Investigator
The Pennsylvania State University
162 Energy and Environment Laboratory Building
University Park, PA, 16802
E-mail: cxw31@psu.edu

Brian Cunningham, DOE Technology Development Manager
U.S. Department of Energy
E-mail: Brian.Cunningham@ee.doe.gov

Start Date: July 1, 2018 End Date: June 30, 2020
Project Funding: $1,112,133 DOE share: $1,000,000 Non-DOE share: $112,133

Project Introduction

Adding a 200-mile range in 10 min, so-called extreme fast charge (XFC), is the key to the mainstream adoption of battery electric vehicles (BEVs). Governments and companies worldwide are pushing actively for a pervasive network of public direct-current fast chargers with power up to 400 kW. No BEV today, however, can withstand such high charging power due to the bottleneck in batteries. A critical barrier is Li plating in Li-ion batteries (LiBs), which drastically reduces battery life and even induces safety hazards. This project focuses on developing a battery technology that can withstand the 6C charging current without Li plating.

Objectives

Develop XFC cells capable of 10-min charging to yield a discharge (C/3) specific energy of 180Wh/kg at the beginning of life (BOL) and sustain >500 XFC cycles with less than 20% capacity loss.

Approach

We developed an asymmetric temperature modulation (ATM) method that charges a cell at an elevated temperature (e.g., 60ºC) and discharges it at ambient temperature, as sketched in Figure I.4.H.1. The elevated temperature enhances reaction kinetics and mass transport and thereby prevents Li plating. On the other end, the cell is exposed to the high temperature only during charging, which is 10 min per cycle, or 0.1% of a BEV lifetime, which prevents severe solid-electrolyte-interphase (SEI) growth.

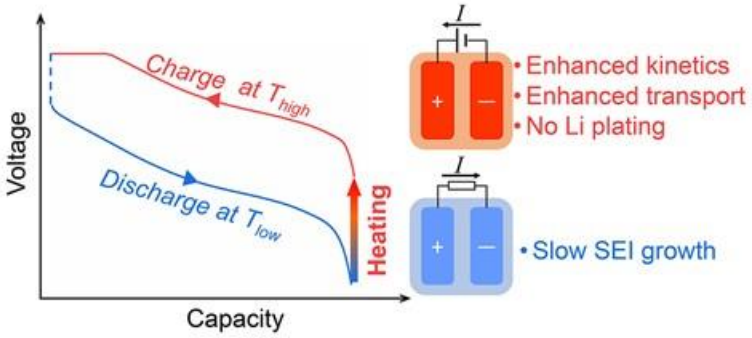

Figure I.4.H.1 The asymmetric temperature modulation (ATM) method

Results

Elimination of Li plating through elevated charging temperature

Figure I.4.H.2 shows the evolutions of cell voltage, charge C-rate, and temperature during one XFC cycle of our Gen-1 XFC cells. The Gen-1 cells have an anode areal capacity of 3mAh/cm^2, which renders a specific energy (C/3) of 209Wh/kg in 35-Ah format. As shown in the figure, the cell was heated from room temperature (RT) to 60°C before charging. The heating speed is a crucial factor because the total time of charging and heating should be within 10 min. Conventional external battery heating methods face a dilemma between heating speed and uniformity, and their heating speed is limited to <1°C/min, meaning the heating step alone already takes far over 10 min. To reduce the heating time, in this project, we adopt the self-heating structure developed by the PI's group [1], [2], which has a thin piece of nickel foil embedded inside as an internal heater and thus warrants rapid and uniform heating (>1°C/sec). After heating to 60°C, the cell was charged with the conventional constant-current-constant-voltage (CCCV) protocol with 6C and 4.15V to 80% state of charge (SOC). We note that the total time of heating plus charging is <10 min. After that, the cell rested for 10 min and then discharged with a constant current (C/3 or 1C). Cell temperature dropped rapidly in the rest and discharge processes. Hence, the cell is exposed to 60°C only during the 10-min charging period.

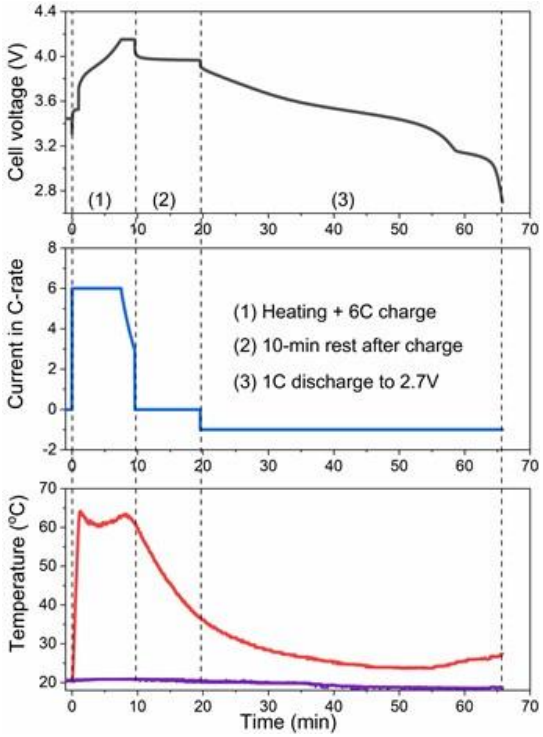

Figure I.4.H.2 Evolutions of cell voltage, current, and temperature during an XFC cycle with the ATM method.

Figure I.4.H.3 shows optical photos and SEM images of the graphite anodes taken from cells cycled with 6C charge at different cell temperatures. For the control cell charged at RT without heating, most of the anode is covered by plated Li metal (Figure I.4.H.3A), displaying a typical dendritic morphology (Figure I.4.H.3E). With the increase of temperature, we can see that the amount of plated Li decreases significantly. For the cell charged at 60°C, most of the anode shows dark-blue color (Figure I.4.H.3D), known as lithiated graphite in LiC_{18} phase, and the SEM image presents clear morphology of graphite flakes (Figure I.4.H.3F).

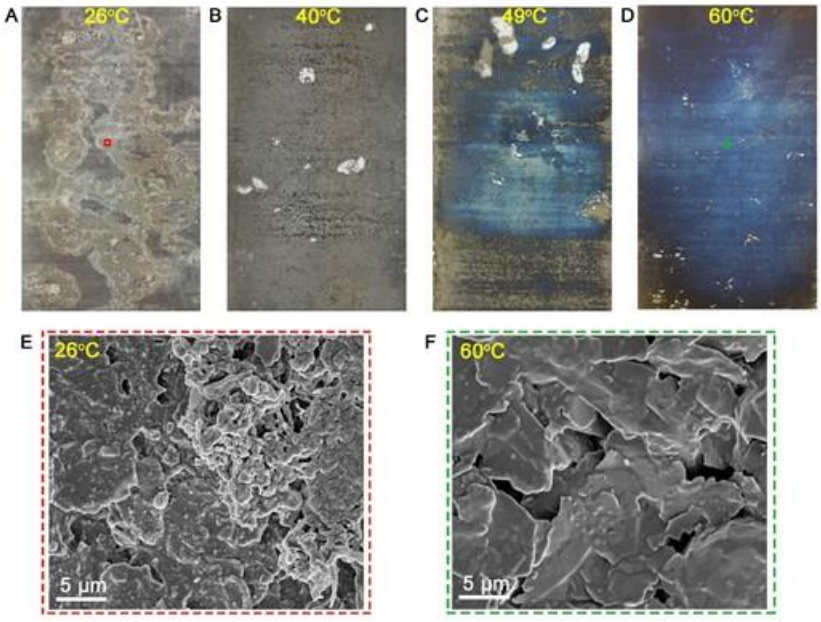

Figure I.4.H.3 Optical photos and SEM images of graphite anodes taken from cells cycled with 6C charge at different temperatures.

We then employed X-ray photoelectron spectroscopy (XPS) depth profiling to further confirm the existence of Li metal in the control cell and the elimination of Li plating in the 60°C cell, as shown in Figure I.4.H.4. The curves from top to bottom denote the Li 1s spectra acquired after puttering for 0, 2, 4, 6, 8, and 10 min at a sputtering rate of 30 nm/min based on SiO_2. The top curve in both cases shows a peak at ~55 eV which is associated with Li salts, indicating the top surface is covered by SEI. Starting from the 2nd curve, a new peak at ~51.5eV corresponding to Li metal appeared in the spectra of the 26°C cell, whereas no new peak appeared in the spectra of the 60°C cell.

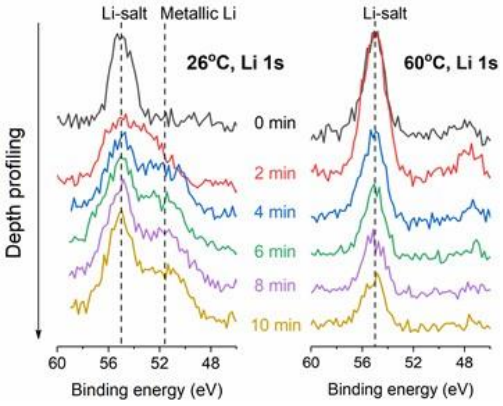

Figure I.4.H.4 XPS depth profiling of Li 1s spectra of the anodes from the cells after XFC cycling at the charge temperature of 26°C and 60°C.

From Figure I.4.H.3 and Figure I.4.H.4, we can conclude that the elevation of charging temperature can effectively alleviate or even eliminate Li plating during XFC.

Mild SEI Growth by Limited Exposure Time to High Temperatures

In the past, it is universally believed that Li-ion batteries (LiBs) should avoid operating at high temperatures due to the concern of accelerated SEI growth. A key part of the ATM method is that the cell is exposed to high temperature only during the 10-min charging period in each cycle. To identify the main aging mechanisms, we compare the capacity retention (CR) of the XFC cell cycled with the ATM method and that of a baseline cell cycled with 1C charge and 1C discharge always at 60°C. Figure I.4.H.5A compares the CR of the two cells against the time of the cell at 60°C. The ATM cell stays at 60°C for 10 min per cycle, while the baseline cell sits at 60°C throughout the cycling. It is interesting to note that the two cells' CR-curves overlap in the time domain, meaning that SEI growth is the dominant aging mechanism of both cells. Figure I.4.H.5B compares the CR of the two cells against the cycle number. As the baseline cell operates at 60°C for ~2 hours per cycle, it lost 20% capacity after only ~200 cycles due to the severe SEI growth. Despite the high charge rate (6C), the ATM cell retained 91.7% capacity after 2500 XFC cycles. From these results, we can conclude that: 1) the elevated charging temperature effectively eliminates Li plating during 6C charge; 2) the limited exposure time to 60°C prevents severe SEI growth. As such, the life of the ATM cell depends mainly on the time of the cell staying at 60°C.

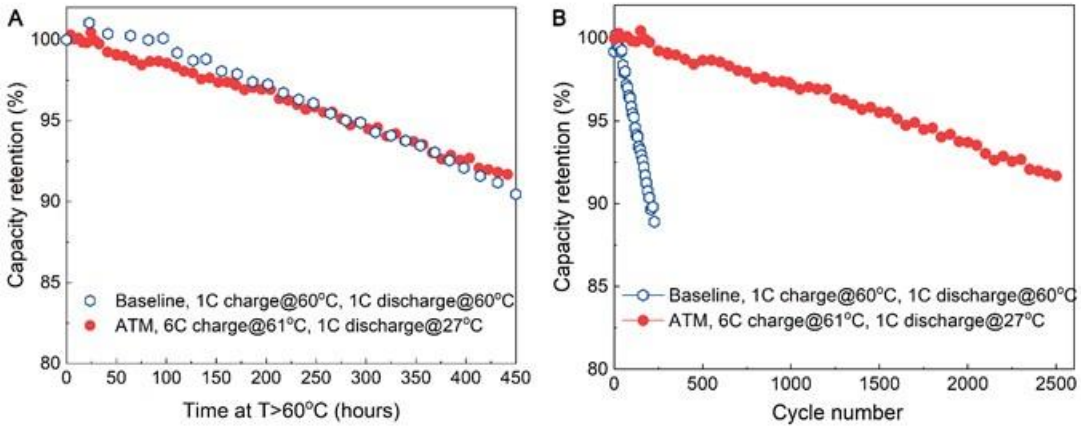

Figure I.4.H.5 Capacity retention vs (A) time at T>60°C and (B) cycle number. The baseline cell was cycled with 1C charge and discharge always at 60°C; the ATM cell was cycled with 6C charge at 60°C and 1C discharge at room tmperature.

Extraordinary Cycle life under XFC

We can note from Figure I.4.H.5B that the ATM method enables remarkable cycle life under 6C XFC. Figure I.4.H.6A further studies the effect of charge temperature on cycle life. We can note that the cell charged at

40ºC lost 20% capacity in only 300 XFC cycles, indicating severe Li plating during 6C charge at 40ºC. Thus, it is vital to fast-charge a cell at a temperature that can eliminate Li plating.

The overarching DOE target on XFC is to achieve fast-charged specific energy (FCSE) of 180Wh/kg at BOL and a life of >500 cycles at 20% loss. The FCSE refers to the C/3 discharge specific energy after a charge. Figure I.4.H.6B displays the FSCE of our Gen-1 cells during XFC cycling with the ATM method. We can see that the cell achieved a FCSE of 167Wh/kg at the BOL, which is 7% lower than the 180Wh/kg DOE target. Nevertheless, the extraordinary cycling stability of the cell makes it surpass the DOE target in 300 XFC cycles. Even after 2500 XFC cycles, the Gen-1 cell still retained a FCSE of 144Wh/kg (equal to the DOE target at 500 cycles), indicating a boost of DOE target on cycle life by 5-fold. We have delivered 9 Gen-1 pouch cells to Argonne National Lab (ANL), and our results have been successfully replicated in ANL.

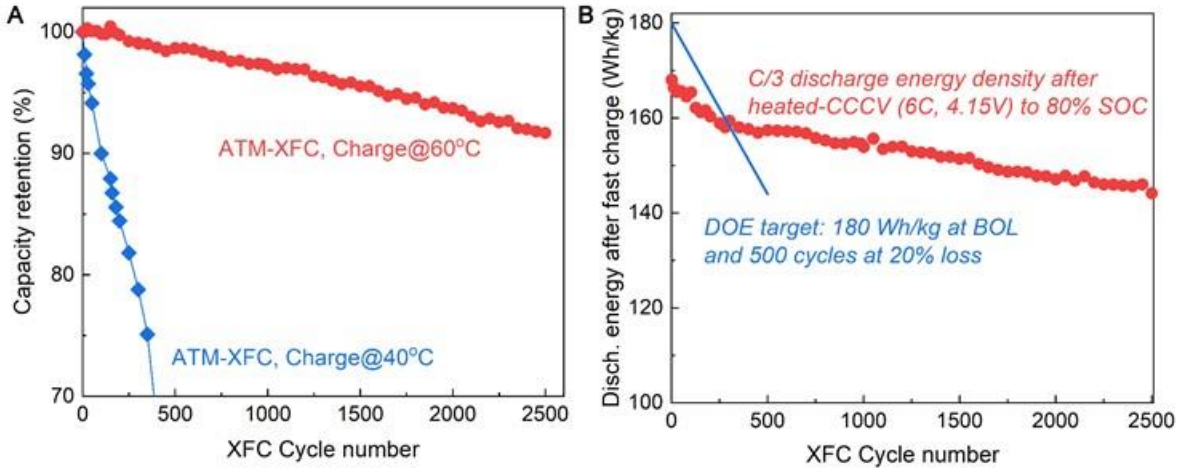

Figure I.4.H.6 (A) Capacity retention during XFC cycling with ATM charging at different temperatures. (B) Fast-charged specific energy, referring to the specific energy of the C/3 discharge subsequent to a 6C charging to 80% SOC, of our ATM cell charged at 60ºC. The blue line is the DOE target.

To meet the DOE target on FCSE at the BOL, we adopted a two-pronged strategy. One is to use the Gen-1 cell with a revised charging protocol, changing the cutoff criterion from 80%SOC to 10-min total time (heating and charging). As shown in Figure I.4.H.7A, the revised protocol includes ~1 min heating (from RT to 60ºC) followed by a CCCV (6C, 4.15V) charge for 9 min. At the BOL, the cell is able to charge to 86.8% SOC at the 10-min cutoff, which corresponds to FCSE of 181.4 Wh/kg and meets the DOE target. We performed cycling tests with this revised protocol. As shown in Figure I.4.H.7B, after 500 XFC cycles, the cell can still deliver FCSE of 155 Wh/kg, which is 7.6% larger than the DOE target (144Wh/kg). Therefore, the final objective of this project has been met.

Our second strategy is to increase the cell's specific energy by raising areal capacity. We developed Gen-2 cells using graphite anodes and NMC811 cathodes. The anode areal loading is 4mAh/cm^2, which renders the Gen-2 cells to have a specific energy of 273 Wh/kg. As such, a 10-min charging to 66%SOC of the Gen-2 cells can give 180Wh/kg FCSE. The fabrication and testing of the Gen-2 cells have been delayed due to the COVID-19 pandemic, and we will report the cycle testing results at a later time.

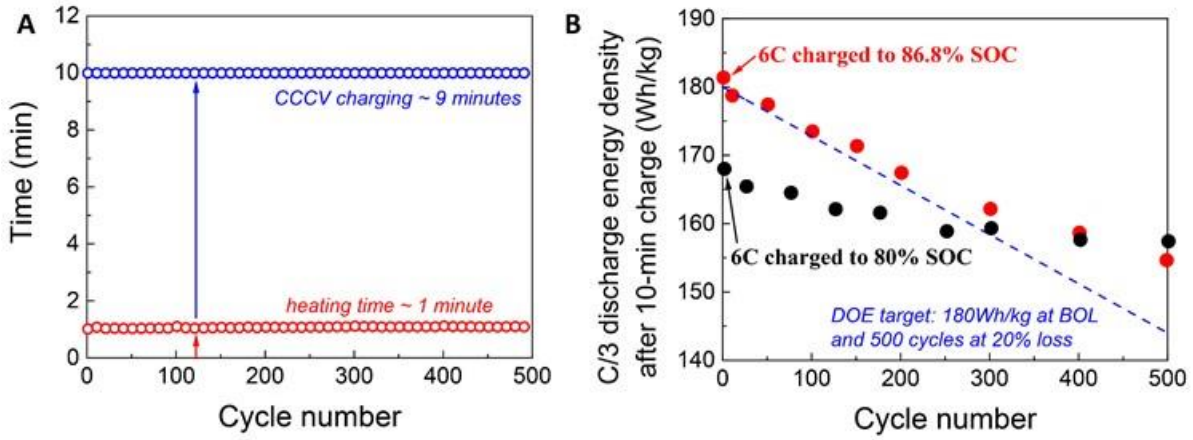

Figure I.4.H.7 (A) Revised chaging protocol for the Gen-1 cells, which changed the cutoff criterion from 80% SOC to 10-min total time (heating and charging). (B) Evolution of the fast-charged specific energy of the Gen-1 cell with two different charging cutoff criteria.

Conclusions

We have developed an asymmetric temperature modulation (ATM) method to achieve XFC of Li-ion cells. We demonstrate that elevating the charging temperature (e.g., to 60ºC) can effectively eliminate Li plating and that restricting the time of the cell at 60ºC can significantly suppress SEI growth. With the ATM method, our XFC cells delivered 181Wh/kg discharge energy after a 10-min charge at BOL and 155 Wh/kg after 500 XFC cycles, which exceeded the DOE target.

Key Publications

1. X.G. Yang, T. Liu, Y. Gao, S. Ge, Y. Leng, D. Wang, C.Y. Wang, Asymmetric temperature modulation for extreme fast charging of lithium-ion batteries. *Joule* **3**(12), 3002-3019 (2019).

2. X.G. Yang, T. Liu, C.Y. Wang, Thermally Modulated Lithium Iron Phosphate Batteries for Mass-Market Electric Vehicles. *submitted*

3. T. Liu, X.G. Yang, S. Ge, C.Y. Wang, Ultrafast Charging of Energy-dense Lithium-Ion Batteries for Urban Air Mobility. *submitted*

References

1. C.Y. Wang, G. Zhang, S. Ge, S., T. Xu, Y. Ji, X.G. Yang, Y. Leng, Lithium-ion battery structure that self-heats at low temperatures. Nature 529(7587), 515-518 (2016)

2. X.G. Yang, G. Zhang, S. Ge, C.Y. Wang, Fast charging of lithium-ion batteries at all temperatures. Proceedings of the National Academy of Sciences 115(28), 7266-7271 (2018)

Acknowledgements

This work was supported by the Department of Energy, Office of Energy Efficiency and Renewable Energy, Vehicle Technology Office, under Award Number DE-EE0008355. We appreciate the support from Colleen Butcher at National Energy Technology Laboratory.

I.4.I An Extreme Fast Charging Li-ion Cell Using Advanced Electrolyte

William Chueh, Principal Investigator
SLAC National Accelerator Laboratory
2575 Sand Hill Road
Menlo Park, CA 94025
E-mail: wchueh@stanford.edu

Brian Cunningham, DOE Technology Development Manager
U.S. Department of Energy
E-mail: Brian.Cunningham@ee.doe.gov

Start Date: October 1, 2019 End Date: September 30, 2022
Project Funding: $1,667,000 DOE share: $1,500,000 Non-DOE share: $167,000

Project Introduction

The limited range and slow recharge times of Electric and Plug-In Hybrid Vehicles (EVs and PHEVs) cause range anxiety among existing owners while limiting market adoption by potential new owners. Current state-of-the-art Li-ion battery technology addresses this problem by employing thicker and denser electrodes to achieve higher energy densities (i.e., >200 Wh/kg). However, this "thick electrode" approach, when implemented without improving other aspects of the battery, poses a significant barrier to achieving 10-minute fast charging. Our proposed effort takes a new approach by using a high rate electrolyte that eliminates ionic conductivity and slow Li^+ desolvation kinetics as barriers to fast charging. Furthermore, we will optimize the anode based on commercially available high rate graphite powders and binder, as well as an optimize charging protocols that goes beyond CC-CV.

Objectives

We will develop an advanced electrolyte and four-step charging protocols that enable extreme fast charging on thick graphite-based anodes. Together with full-cell modeling, state-of-the-art X-ray and cryogenic electron microscopy (cryo-EM) characterization, we will:

(1) Tailor an advanced electrolyte paired with commercial graphite-based anodes to enable extreme fast charging in 10 minutes to 80% state-of-charge.

(2) Optimize the charging protocol to achieve 500 cycles with less than 20% capacity fade.

(3) Understand the impact of extreme fast charging on the battery components, and understand and control Li plating/dead Li formation in full cells throughout extended cycling.

(4) Exhaustively validate results using not only through battery cycling but also in-situ X-ray and ex-situ cryo-EM characterizations of full cells.

(5) Deliver nine 2Ah cells with the incorporated extreme fast charge technology by the end of year 1, and 18 2Ah cells be the end of year 2.

The final outcome, which combines a novel electrolyte, a nanostructured graphite-based electrode, and an optimized charging protocol, is a 250 Wh/kg Li-ion cell capable of 10-minute fast charging. Importantly, because the cells will be exhaustively validated not only by conventional battery cycling but also by full-cell characterizations, this work will provide the confidence required to translate this technology to commercial products.

Approach

We will develop an extreme fast charging Li-ion battery cell featuring a novel electrolyte optimized for a complementarily designed graphite-based anode that is readily scalable in commercial high volume manufacturing. The proposed electrolyte, blended from commercially available components, exhibits high ionic conductivity and facile Li^+ desolvation kinetics across a broad temperature range, thereby enabling fast charging in thick, high-energy-density anodes. Both the anode and the electrolyte will be characterized *in-situ* at the full-cell level (to probe local state-of-charge and local Li plating) using synchrotron X-ray microscopy/diffraction as the cell is rapid charged over many hundreds of cycles. This will be the first time that such characterizations are carried out to understand the effects of electrolyte additives, graphite particle morphology, electrode composition and binders on Li plating/dead Li formation at high charge rates. Additional insights and cross-validation will come from full-cell computational models that goes beyond the Newman model. Multi-layer, 2Ah pouch cells will be built, and a four-step charging algorithm that goes beyond CC-CV (constant current-constant voltage) will be optimized using a machine-learning, optimal experimental design approach.

Results

Electrolyte development

We investigated the use of methyl acetate (MA) as a co-solvent in addition to a standard carbonate solvent formulation (EC:DMC). The reduced viscosity greatly improved the transport property of the electrolyte, reaching nearly 20 mS/cm at 20 deg. C. Temperature and salt-concentration-dependent conductivity is shown in Figure I.4.I.1 According to our porous electrode simulation, this 2.5 fold increase in conductivity lowers the concentration polarization within the porous electrode, which is a necessary condition for extreme fast charging. However, this condition is not sufficient by itself. Another crucial consideration is the impedance of the solid electrolyte interphase (SEI), which can dominate under high current. We explored several additive packages, with the objective of forming thin, conformal and self-passivating SEI). Throughout the year, we synthesized MA electrolytes with numerous additive packages, in which FEC is a standard component. Experimentally, we observed that certain additives decreased resistance and improved cycle life, while others did the opposite. Based on this optimization, we identified that a two-component additive package (for which one is FEC) produces the best results in terms of impedance and capacity fade.

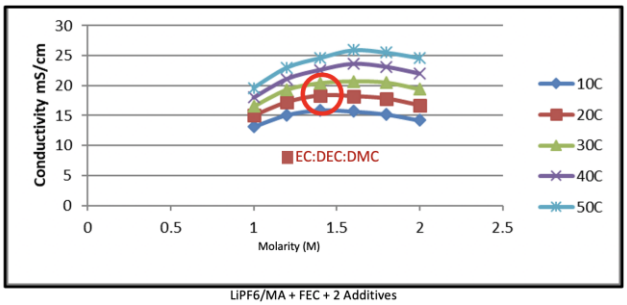

Figure I.4.I.1 Ionic conductivity of the advanced electrolyte developed in this work as a function of salt concentration and temperature. Typical conductivity of a standard electrolyte is shown for reference.

Full cell optimization

In order to evaluate electrolyte performance in a real-world setting, we fabricated and optimize single-layer (~ 120 mAh) and multi-layer (2.0 Ah) cells. These cells consists of ~ 3 mAh/cm^2 thick graphite electrode. For simplicity, we employed $LiCoO_2$ cathodes (matched to the anode) in order to hone on the effect of extreme fast charging on the anode. For the anode, we screened a large number of morphologies and observed the best results with ShanShan graphite. We also observed that carbon nanotube conductive additive was needed to minimize the anode transport resistance.

We evaluated various electrolyte formulations using single-layer pouch cells. The cycling procedure consisted of charging at 6C for 10 minutes (with a 4.2V cutoff), rest for 10 minutes, and discharging at C/3. The cycle life varied significantly between formulations, with some cells exhibiting cycle life on the order of a few tens of cycles and significant lithium plating. For the optimized electrolyte, > 500 cycles was obtained under extreme fast charging conditions before reaching 80% of initial capacity. Continued testing to 1,000 cycles showed no "knee" in the capacity fade curve (reaching 60% retention at 1,000 cycles). Interestingly, a subsequent diagnostic cycle at C/3 at the 500th cycle revealed negligible capacity loss, suggesting no significant loss of lithium inventory nor loss of active material. The results are summarized in Figure I.4.I.2. We also translated the results successfully to 2.0 Ah multi-layer cells.

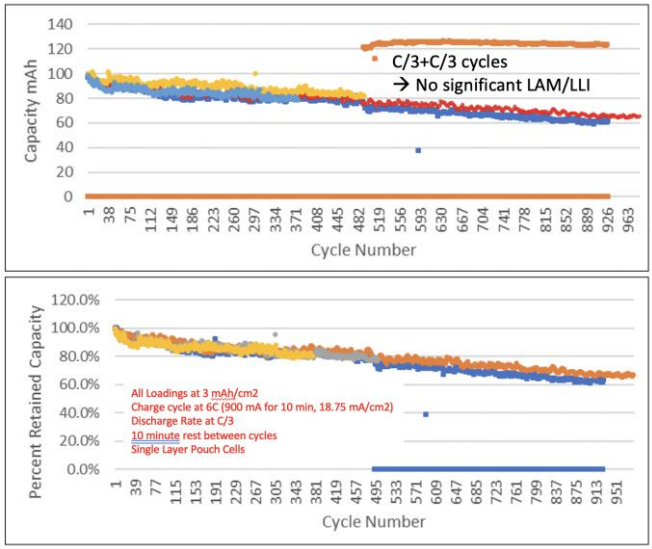

Figure I.4.I.2 Cycling performance of 120 mAh single-layer pouch cells at 3 mAh/cm^2 anode loading under extreme fast charging conditions (10 minutes to 80% SOC) and C/3 discharge.

Multimodal characterization: X-rays & cryo-EM

An important aspect is this project is to validate the electrolyte development through advanced characterization. Specifically, we employed cryogenic transmission electron microscopy to characterize the SEI and X-ray diffraction to identify lithium plating during extreme fast charging. We developed a matrix of electrodes harvested from single-layer pouch cells with 1, 2 and 3 additives, each displaying a different initial impedance and capacity fade rate. The goal of the characterization is to understand why certain additives work better than others.

Cryogenic transmission electron microscopy was carried out on the best-performing additive package. In general, we observed SEI particles are rich in F and P, coming from FEC and $LiPF_6$ decomposition. At the same time, we also detected O signal, which arises from both EC and FEC decomposition. In one additive package which contains S, we detected S in the SEI, which may be responsible for the inferior performance (especially in terms of high SEI impedance).

The X-ray characterization of this task has been delayed to the COVID-19 due to the limited access to synchrotron facilities. To mitigate this challenge, we turned to lab-based X-ray diffraction. The lower flux means that the acquisition time is longer at a given special resolution. We performed X-ray diffraction on the best-performing additive package and did not detect plated lithium after extensive extreme fast charging cycling. This is consistent with optical inspection of the electrode. Additional measurements are underway to assess the degree of lithium plating in other additive formulations.

Modeling

We developed a porous electrode model in order to understand the distribution of overpotential and polarization within the battery cell. Specifically, we posed the following questions: (1) what is the extent of electrolyte concentration polarization during extreme fast charging, and (2) what is the source of impedance? We answer these questions by fitting porous electrode models to experimental data. Transport properties of the electrolyte such as diffusivity is specified, and electrode resistances are fitting parameters. Specifically, we considered Butler-Volmer-type charge-transfer resistances as well as Ohmic contact resistances. The different current-voltage functional forms between the two types of resistances allow us to estimate the magnitudes of both. As shown in Figure I.4.I.3, the model predicts negligible concentration polarization in the MA-based electrolyte throughout extreme fast charging in the anode (< 5 mV). This is consistent with the absence of lithium plating. Surprisingly, the charge-transfer (activation) overpotential is also small, both in the cathode and in the anode (< 15 mV). The majority of the overpotential was best described using Ohm's law. Based on our observation that such overpotential is very sensitive to the composition of the additive package, we conclude that this Ohmic resistance corresponds to the transport resistance within the SEI.

Charging protocol optimization on full cells

This task has been delayed to the COVID-19.

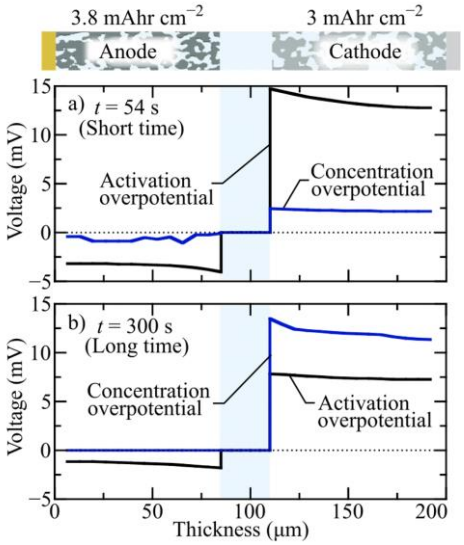

Figure I.4.I.3 Porous electrode simulation of extreme fast charging using parameters fitted to experimental data collected during 10 minute extreme fast charging.

Conclusions

We have developed a high-performance MA-based electrolyte which enables extreme fast charging (10 minutes to 80% state-of-charge). The electrolyte exhibits high conductivity approaching 20 mS/cm at room temperature. When combined with appropriate additives, the electrolyte generates low-impedance and conformal SEI on graphite, which are keys to long cycle life. We demonstrate the effectiveness of this electrolyte in single- and multi-layer pouch cells. Advanced X-ray and cryogenic electron microscopy characterization and porous electrode simulation provided mechanistic understandings on why this electrolyte is effective for extreme fast charging.

Key Publications

1. W. Huang, P. Paul, J. N. Weker, Y. Cui, W. C. Chueh. Roles of Additives to Forming a Low-Resistance Solid-Electrolyte Interphase for Extreme Fast Charging. In preparation.

2. P J. Weddle, T. Evans, P. Attia, W. C. Chueh, and R. J. Kee, "Model-based analysis of rate-limiting electrochemical and transport processes in Li-ion batteries under extreme-fast-charging conditions." In preparation.

3. P. P. Paul, C. Cao, V. Thampy, H.-G. Steinrück, T. R. Tanim, A. R. Dunlop, S. E. Trask, A. N. Jansen, E. J. Dufek, J.N. Weker, M. F. Toney. Using in-situ X-ray Diffraction to Quantify Electrode Behavior of Lithium-Ion Batteries from Extreme Fast Charging. In preparation.

4. W. C. Chueh. Advanced Automotive Battery Conference. Nov. 4, 2020. Virtual. Invited Seminar.

5. W. C. Chueh. Dalhousie University, Department of Physics & Atmospheric Sciences. Jan. 27, 2020. Halifax, Canada.

6. W. C. Chueh. American Chemical Society National Meeting. Aug. 17, 2020. Virtual. Invited Seminar.

7. W. C. Chueh. Gordon Research Conference on Nanomaterials for Applications in Energy Technology. Feb. 26, 2019. Ventura, USA. Invited Seminar.

8. M. F. Toney. PETRA IV Workshop, Materials and Processes for Energy and Transport Technology, Oct 21, 2020.

9. M. F. Toney. STFC.batteries.org Annual Meeting 2019, Cosener's House, Abingdon, UK July 1, 2019

10. M. F. Toney. 1st International conference on New Energies, Center for Innovative New Energy, University of Campinas, Brazil, March 27, 2019.

11. M. F. Toney. 2019 Silicon Valley Women in Engineering Conference, San Jose State University, March 16, 2019.

12. M. F. Toney. Prisker School of Molecular Engineering Colloquium, University of Chicago, Feb 25, 2020

13. M. F. Toney. Chemical Engineering Colloquium, University of Colorado at Boulder, Jan 23, 2020.

14. M. F. Toney. Materials Sciences seminar, Imperial College, London. July 4, 2019.

15. M. F. Toney. Materials Sciences and Engineering Seminar, Technion University, Haifa, Israel, Feb 11, 2019.

16. P. P. Paul. Gordon Research Seminar and Conference - Batteries, Feb 2020.

17. P. P. Paul. Materials Research Society Fall Meeting & Exhibit, Dec 2019.

18. P. P. Paul. Bay Area Battery Summit, Nov 2019.

19. P. P. Paul. The 40th International Conference on Vacuum Ultraviolet and X-ray Physics, July 2019.

Acknowledgements

This project was conducted by a team of researchers including William Chueh, Yi Cui, Michael Toney, Johanna Nelson Weker (SLAC National Accelerator Laboratory), James Kaschmitter (SpectraPower, LLC), and Robert Kee (Colorado School of Mines).

I.4.J XCEL R&D: Lithium Detection Thrust

Venkat Srinivasan, Principal Investigator
Argonne National Laboratory
9700 S. Cass Avenue,
Lemont, IL 60439
E-mail: vsrinivasan@anl.gov

Samm Gillard, DOE Technology Development Manager
U.S. Department of Energy
E-mail: Samuel.Gillard@ee.doe.gov

Start Date: October 1, 2019 End Date: September 30, 2020
Project Funding (FY20): $742,000 DOE share: $742,000 Non-DOE share: $0

Project Introduction

The U.S. Department of Energy's Office of Energy Efficiency and Renewable Energy (DOE-EERE) has identified fast charge — with a goal of 15-min recharge time — as a critical challenge to pursue in ensuring mass adoption of electric vehicles (EVs). Present-day configurations of high-energy cells with graphite anodes and transition metal cathodes in a liquid electrolyte are unable to achieve this metric without negatively affecting battery performance. There are numerous challenges that limit such extreme fast charging (XFC) at the cell level, including lithium (Li) plating, rapid temperature rise, and possible particle cracking. Of these, Li plating is thought to be the primary culprit. This project aims to gain an understanding of the main limitations during fast charge using a combined approach involving cell builds, tests under various conditions, characterization, and continuum-scale mathematical modeling. Researchers from five national laboratories are contributing their expertise to make progress on the eXtreme Fast Charge Cell Evaluation of Lithium-ion Batteries (XCEL) project.

Cells are built at the Cell Analysis, Modeling, and Prototyping (CAMP) Facility at Argonne National Laboratory (Argonne) using various carbons and different cell designs, in both half-cell and full-cell configurations and with reference electrodes. Cells are tested at both Idaho National Laboratory (INL) and Argonne under various operating conditions (e.g., C-rate, temperature) and under different charging protocols with the aim of identifying the onset of plating, quantifying the extent of the problem, and determining parameters and test data for mathematical models. After testing, cells are opened, and various advanced characterizations are performed at Argonne to determine the extent of plating and to determine whether other failure models, such as particle cracking, also play a role.

A critical part of the project is the use of continuum-scale mathematical models so XCEL participants can understand the limitations at high charge rates and, therefore, suggest possible solutions for researchers to pursue. Both macro-scale approaches and microstructure-based simulations are pursued and serve to complement each other. Macromodeling at the National Renewable Energy Laboratory (NREL) is used to test cell designs, accompanied by development of microstructure models to provide deeper insights into the electrochemical phenomena in the battery. This effort is complemented with development of models incorporating new physics, such as phase change and solid-electrolyte interphase growth, at Argonne.

Two exploratory projects aim to study ways to detect Li in situ during operation. NREL is pursuing the use of microcalorimetry to detect heat signatures during plating. INL is working with Princeton University to examine the use of acoustic methods to determine whether plating leads to a signature in the acoustic signal.

Finally, the Stanford Linear Accelerating Center (SLAC) National Acceleratory Laboratory is using synchrotron X-ray methods to guide the cell design and charging protocols of XFC of Li-ion battery cells, and Lawrence Berkeley National Laboratory (LBNL) is investigating the initial onset of Li plating during fast charging as well as developing a strategy to detect it.

Approach

Detecting the onset of lithium (Li) metal plating and quantifying its presences during extreme fast charging (XFC) is fundamental to understanding the role of Li plating in the degradation of cells at such high charging rates. Additionally, understanding the conditions under which Li plating occurs during fast charging is critical to taking steps to avoid plating and extending the lifetime of Li-ion cells. Our approach is to compare the strengths and weaknesses of different detection techniques to identify a set of nondestructive, quantitative techniques we will leverage to link the onset of Li plating with cell performance and aging. We will detect the onset of plating with global detection methods and understand the plating heterogeneity (through and across the anode) with local detection methods. Destructive, yet quantitative techniques with excellent detection limits will be used to confirm Li detection signatures and pin down limits on less quantitative, yet nondestructive techniques.

Results

Milestone 1 was to identify and contrast the strengths and weaknesses of global (not localized), nondestructive detection techniques to use on single-layer Round 2 pouch cells produced at the Cell Analysis, Modeling, and Prototyping (CAMP) facility at Argonne National Laboratory (Argonne). Milestone 2 was to identify and contrast the strengths and weaknesses of localized and/or destructive Li detection techniques and to identify where we can combine techniques to span length scales. This milestone has been summarized in a table that we have been updating throughout the project. Table I.4.J.1 is a subset of the full table that focuses on the techniques explored by the XCEL team. Milestone 3 was to combine at least two techniques to study when, where, and/or how Li plates on the same electrode. Finally, Milestone 4 was to link detection of the onset of Li with cell performance and other cell/cycling properties (aging) and address how that evolves with aging. Annual updates from each of these milestones are presented below.

Table I.4.J.1 Summary of Li detection techniques that were the primary focus of the XCEL team. They include observing a Li plating peak in the dQ/dV plot, observing a similar peak during open circuit voltage (OCV) that is attributed to Li intercalating into the graphite after plating, inductively coupled plasma mass spectrometry (ICP-MS), mass spectrometry titration (MST), 3ω sensor measuring thermal conductivity, measuring changes in the cell pressure, Raman mapping, and X-ray diffraction (XRD) mapping

Technique	*Operando*?	Cell type	Detection	Li type	Limit
dQ/dV	*Operando*	Full cell	Indirect	Reversible metal	2% graphite capacity
OCV	*Operando*	½ cell	Indirect	Reversible metal	1%–2% graphite capacity
ICP-MS	*Ex situ*	Full electrode	Both	Metal, solid electrolyte interface (SEI)	Few µmol
MST	*Ex situ*	Full electrode	Both	Metal, SEI	20 nmol
3ω	*Operando*	Sensors inside pouch	Indirect		Unknown
Pressure	*Operando*	Multilayer pouch	Indirect	Metal + SEI	Unknown
Raman	*Ex situ*	Coin cell electrode	Indirect	Metal	Unknown
XRD map	*In situ*	Full	Direct	Metal, intercalated	2–4 µm crystallites

Global, nondestructive Li detection techniques

Global Li detection with electrochemical signatures

At the end of third quarter (Q3) of fiscal year (FY) 2020, Idaho National Laboratory (INL) was able to test some additional lithium (Li/Gr) Round 2 (R2) half-cells to provide more understanding on the effect of rest, C-rate, and state of charge (SOC) during long-term electrochemical (EC) Li-plating detectability as shown in Figure I.4.J.1. The investigated global electrochemical signatures were coulombic efficiency (CE), dQ/dV, dV/dt, and end-of-relaxed charge voltage (EOC) under different fast-charging conditions.

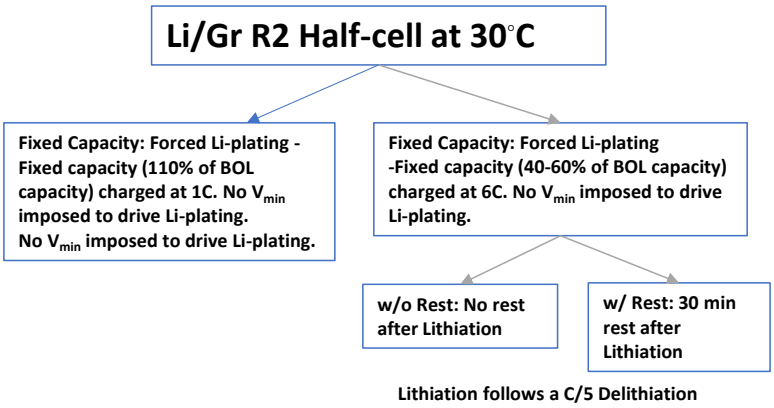

Figure I.4.J.1 Li/Gr R2 half-cells testing conditions for understanding the EC lithium detectability and reliability.

The outcome of the Li/Gr R2 half-cells study was that dV/dt signatures with 60% and 40% SOC 6C-lithiation conditions and C/5 de-lithiation conditions are not reliable. The variability of the dV/dt signatures with 40% SOC at 6C-lithiation is observed, and the peak intensity in some cells increases with cycling and then decreases (Figure I.4.J.2A). With similar cell conditions, the second peak appears at the end of cycling and the second peak moves to higher rest time (Figure I.4.J.2B). The intensity of the dV/dt peak decreases even though CE and end of-battery-life (EOL) EC signatures confirms continuous Li plating on the graphite electrode. The post testing of graphite electrodes is underway to examine the morphology and the thickness of Li metal on the graphite electrode and to correlate with EC signatures.

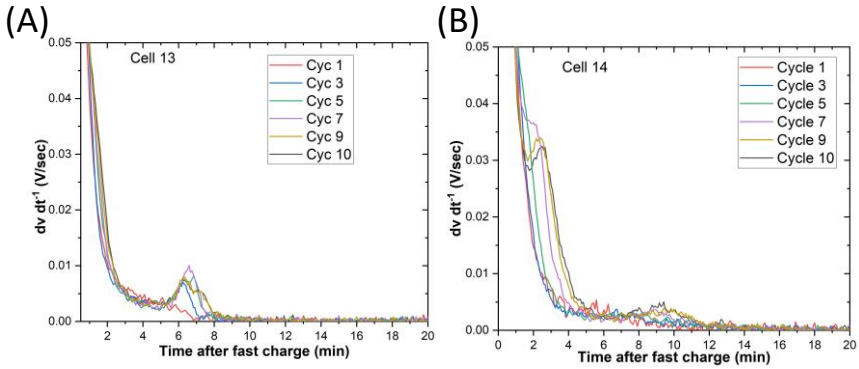

Figure I.4.J.2 (A) Differential open-circuit voltages (OCVs) corresponding to 6C lithiation (40% SOC); and (B) cell conditions similar to A (duplicate cell).

In addition to EC Li detectability, results suggest that low C-rate lithiation and reasonable (e.g., at C/5) de-lithiation increases the stripping efficiency (SE) up to 90% (Figure I.4.J.3A). The long-term cycling with similar conditions found that SE decreases after a certain number of cycles (Figure I.4.J.3B). The fact that CE and SE decrease with cycling confirms that there was dead lithium on the graphite, and eventually these cells shorted. The post testing of graphite electrodes is underway to examine the morphology, thickness of Li metal plating, and possible formation of dendrites as a reason for the cells shorting and to correlate with EC signatures.

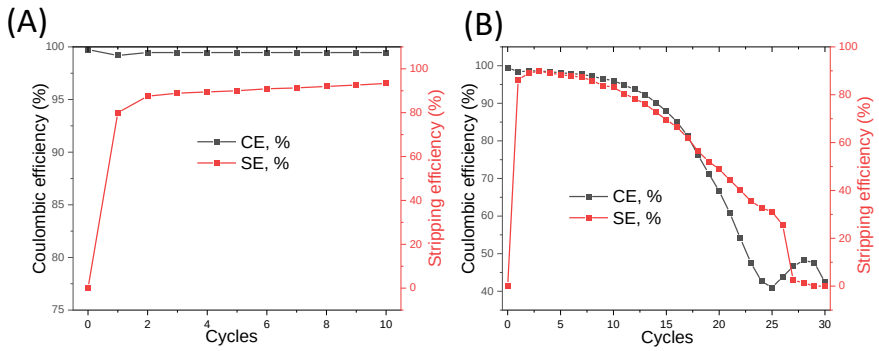

Figure I.4.J.3 (A) Comparison of CE and SE for low C-rate lithiation and C/5 de-lithiation; and (B) comparison of CE and SE for low C-rate lithiation and C/5 de-lithiation during long-term cycling (same cell conditions as A).

Based on these Li/Gr R2 half-cell testing results, INL designed and tested full coin cell tests in Q4. The investigated electrochemical signatures were CE, dQ/dV, dV/dt, and EOC under different fast-charging conditions with long-term testing and reliability of these signatures with aging, as shown in Figure I.4.J.4. The long-term testing with low 6C-rate charging and C/5 discharge shows lithium plating is detectable with CE EOC but the sensitivity of the dQ/dV and dV/dt signatures is not reliable. The discharge capacity versus voltage plateau at all testing conditions shows the reduced capability of Li^+ intercalation into graphite with aging. Moreover, the EC Li detection signatures in half-cells and full cells align with each other within the experimental error. Final analysis will be completed by FY 2021-Q1. A journal article is in preparation.

INL had three milestones to pursue in FY 2020. The first milestone, to investigate Li plating detectability in Li/Gr coin cells, was completed in Q1. The second milestone, to investigate plating detectability in full coin cell settings, was completed in Q4. The final milestone, to demonstrate EC detection in full Round 2 pouch cells, may not be needed. Its timeline was pushed to Q1 of FY 2021.

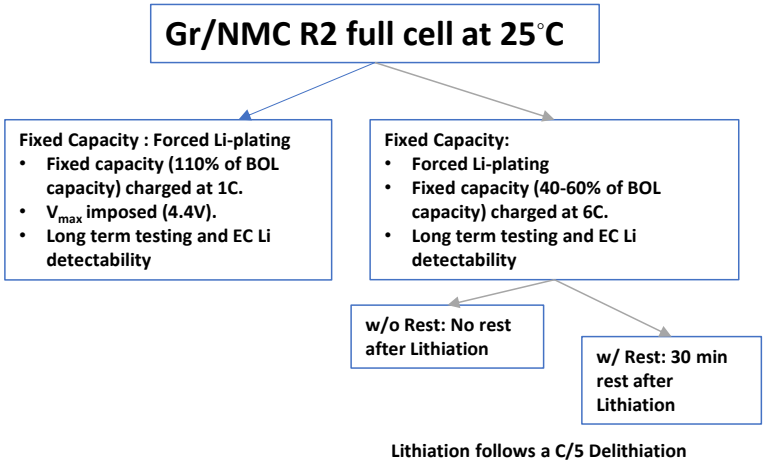

Figure I.4.J.4 Gr/NMC R2 full-cells testing conditions for understanding the EC lithium detectability and reliability.

Perform electrochemical cycling to be explored for Li detection

The object of this work is to quantify the amount of Li plating on the graphite anode and to study the evolution of Li plating with cells aging. First, cells were cycled in the $Li(Ni_{0.5}Mn_{0.3}Co_{0.2})O_2$ cathode (NMC532)/Graphite 2032 type of coin cell configuration. Figure I.4.J.5 shows the capacity retention and differential capacity (dQ/dV) curves from cells cycled at the 1-C and 6-C charging rates, which represent the normal and fast charging conditions, respectively. The 1-C charged cells show an initial, average discharge capacity around 101 and 119 mAh g^{-1} after 100 cycles, whereas the 6-C charged cells showed only an initial average discharge capacity around 80 and 37 mAh g^{-1} after 100 cycles. Capacity retention for 6-C charged cells was low, as expected, due to kinetic limitations and the lithium plating on the anode surface.

Figure I.4.J.5b–c compares the discharge-only part of the dQ/dV curves of two samples charged at the 1-C and 6-C rates. Note that both samples were discharged at a rate of C/2. While intensities and shapes of reduction peaks in the 1-C charged cell (Figure I.4.J.5b) remained similar during cycles, those peaks in the 6-C charged cell show dramatic changes upon cycling. The dQ/dV curve for the 6-C cell does not contain discharging portion higher than 3.8 V after 10 cycles. This result implies that the charging reaction above 3.8 V may be incomplete, resulting in low capacity retention. In addition, the intensities for the peaks corresponding to $LiC_x \rightarrow C_6$ in Figure I.4.J.5c also decreased with cycle count. This result indicates lithium intercalation/deintercalation of graphite is hindered by possible lithium plating on the graphite surface.

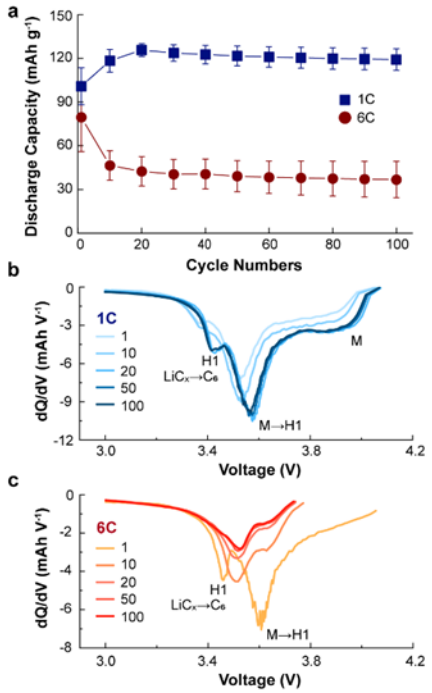

Figure I.4.J.5 Comparisons of the electrochemical cycling performance of NMC532 against a graphite full cell with charging rates of 1-C and 6-C. (a) Specific discharge capacity as a function of cycling number. Cycling stability data were plotted using three cells, with the error bar representing standard deviation. (b) dQ/dV curves for a 1-C and (c) dQ/dV curves for a 6-C charging rate cell.

Global Li detection with differential pressure sensing

The Cui group at Stanford University developed an operando technique for detection of Li-plating based on differential pressure sensing (DPS). With a low-cost sensor attaching externally to mechanically constrained multilayer pouch cells, we demonstrated that with DPS, which measures the change of cell pressure per unit of charge, Li-plating can be easily detected before the hazardous dendrite formation. This differential pressure

method is one step further compared to previous battery pressure studies. In addition, we show that by integrating DPS into the battery management system (BMS), a dynamic self-regulated charging protocol can be realized to effectively extinguish the Li-plating triggered by charging at low temperature while the conventional static charging protocol leads to catastrophic Li-plating. We anticipate that DPS will also serve as an early nondestructive diagnosis method to accelerate the development of fast-charging battery technologies.

The configuration of the operando DPS measurement is shown in Figure I.4.J.6a: the stack containing a multilayer pouch cell, metal force-distribution plate, and pressure sensor (load cell) is clamped into a fixed constraint. The setup can measure the real-time pressure change of the battery and further produce the operando dP/dQ information at the same time. When Li-plating takes place, it causes a much more dramatic thickness change in the anode compared to conventional intercalation chemistry (Figure I.4.J.6b), which leads to the dP/dQ pivoting away from the characteristic dP/dQ curve of intercalation by going beyond the Li-plating threshold (Figure I.4.J.6d). In last year's annual report, we showed that this method can detect Li-plating in its nucleation stage.

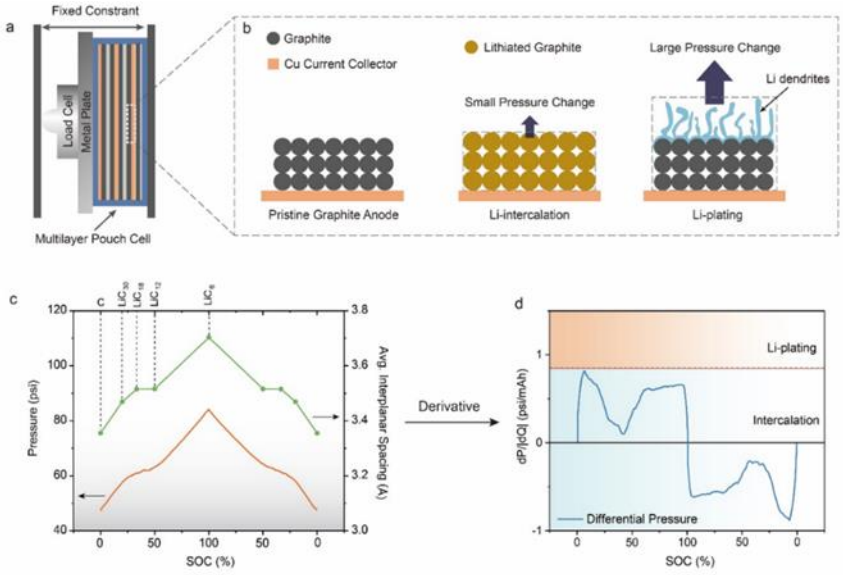

Figure I.4.J.6 (a) The configuration of operando pressure measurement: the stack contains a multilayer pouch cell and a metal force-distribution plate, and the pressure sensor (load cell) is clamped into a fixed constraint. (b) Zoomed-in schematic of a graphite anode illustrating that for the same amount of lithium ions, Li-plating induces a much higher volume/pressure than intercalation. (c) The average interplanar lattice spacing of graphite at different lithiation stage agrees with the pressure profile. (d) The differential pressure (dP/dQ) profile of the cell. The red dashed line is the upper bound of dP/dQ during intercalation, defining the Li-plating threshold. (e) Lab-made 70-mAh multilayer graphite/NMC532 with Round 2 electrodes. (f) Commercial cell with a 200-mAh capacity and artificial graphite/NMC532 electrodes. Both cells contain gasbag (blue area) to avoid gas generation interference with pressure measurement.

To validate whether the single-value threshold holds within the normal operational temperature range of lithium ion batteries (LIBs), we performed slow charge with the same cell under different temperature conditions (0°C and 60°C) as shown in Figure I.4.J.7. It shows that, although the base pressure of the cell changes due to thermal expansion, its maximum value of dP/dQ (Li-plating threshold) does not change, which indicates that DPS can serve under a wide range of temperatures with a single fixed numerical threshold for Li-plating detection. It is worthwhile to note that, although it seems that the maximum value of dP/dQ decreases in the latter two cycles under 0°C, it does not imply that the threshold changes as we can see from the first cycle of 0°C. The reason is that at 0°C, the cell cannot be fully discharged to 0% SOC in the first cycle; therefore, the charging cycles that follow have a starting SOC > 20%, which bypass the maximum value of dP/dQ, which does locate below the 20% SOC.

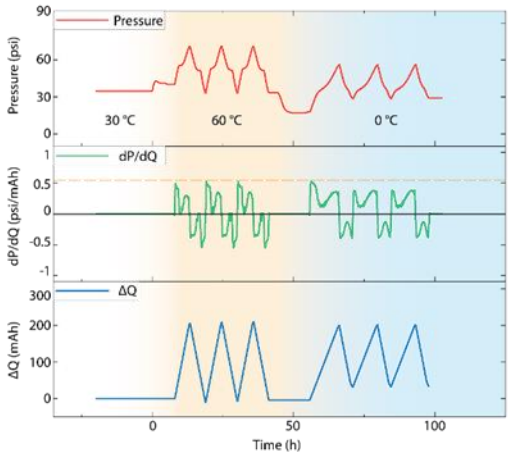

Figure I.4.J.7 A 200-mAh NMC532/Gr cell cycles under 60°C and 0°C with 0.2 C and 0.1C, respectively. The first cycle under certain temperature starts when both temperature and cell pressure are stabilized.

We further integrated this sensing technique into our in-house BMS to show that DPS can serve as on-board detection to improve battery safety by dynamically regulating the charging protocol; therefore, to extinguish the Li-plating in the early stage, we cycled a 200-mAh NMC532/graphite commercial cell built from CAMP Round 2 electrodes under 1-C at 30°C then 0°C. With a "rigid" charging protocol, although the cell cycles normally at 30°C, low temperature causes severe Li-plating (Figure I.4.J.6a). In contrast, with dynamic BMS, when dP/dQ goes beyond the threshold at 0°C, the charging current is dynamically regulated to 0.2 C; therefore, Li-plating is effectively extinguished (Figure I.4.J.8).

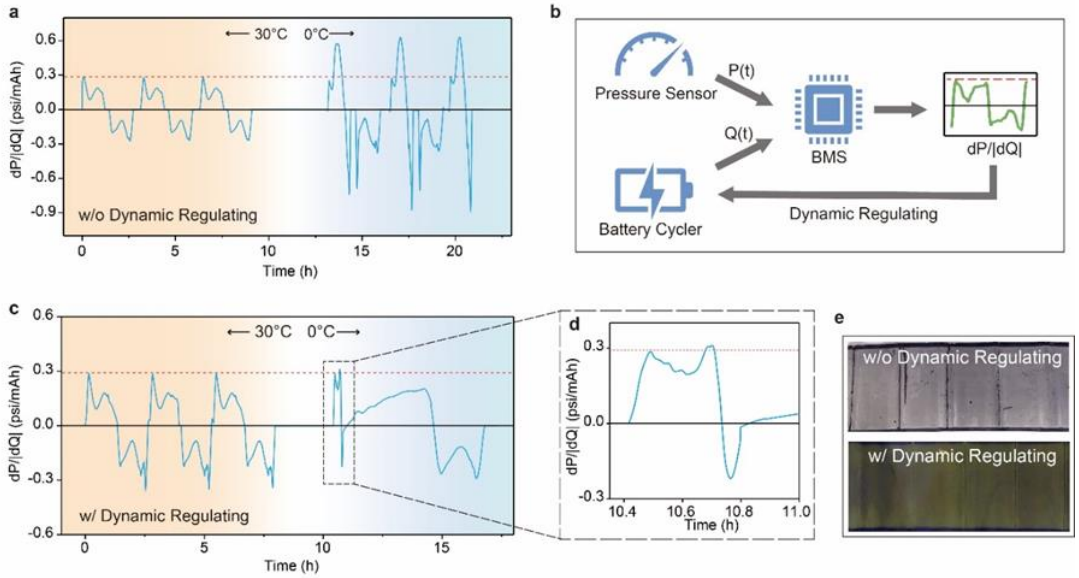

Figure I.4.J.8 Dynamic charging regulated by dP/dQ avoids catastrophic Li-plating under low temperature. (a) When a 200-mAh commercial battery with rolled graphite/NMC532 electrodes is cycled at 1-C under 30° and 0° without dynamic regulating, dP/dQ displays Li-plating triggered by low temperature. (b) Scheme for self-regulated charging. BMS calculates and monitors the real-time dP/dQ value; when it senses Li-plating, the current is modulated to extinguish the plating. (c-d) When the 200-mAh commercial cell is cycled at 1-C under 30° and 0° with the dynamic regulating of BMS, Li-plating is effectively contained. (e) Optical images of the cycled graphite anodes at charged state. Without dynamic regulating, the anode surface is covered by a thick layer of Li metal; with dynamic regulating, the anode shows a golden color, known as lithiated graphite in LiC6 phase.

Anode-side 3ω sensor for detecting lithiation and Li plating

The Prasher group (Lawrence Berkeley National Laboratory [LBNL]) is working on thermal analysis of lithiation and lithium plating in graphite anodes. We developed an anode-side 3ω sensor for *operando* measurements of anode thermal conductivity (k_{anode}). As Li^+ ions intercalate into the graphite anode, the anode thermal conductivity varies with the associated lattice change. With k_{anode} vs. SOC calibrated at a slow charge rate, the measured local thermal conductivity across the anode can thus be related to the local lithium distribution, including for very fast charge rates. Therefore, our sensors, which live on the outside of the battery, can non-invasively measure *operando* the spatial distribution of Li ion concentration across the thickness of the anode, including during extreme fast charging.

The Prasher group is working on new measurement and data analysis techniques to study lithiation and lithium plating in graphite anodes. After extensive theoretical modeling, sensitivity studies, and prototyping, we have developed an anode-side 3ω sensor that can be used for detecting lithiation and lithium plating (Figure I.4.J.9a). The 3ω signal across a wide range of frequencies enables us to measure properties at different distances from sensors. Higher-frequency data depends on material properties closer to the sensor, while lower frequency data captures material properties farther away from the sensor (i.e., deeper inside the battery). Figure I.4.J.9 b-d describe the fabrication process for making anode-side sensors: (b) the sensor is deposited on a passivated Cu current collector through a shadow mask; (c) electrically insulated Cu wires are attached to sensor contact pads using an electrically conducting silver epoxy; and (d) a thick polyethylene foam is attached on top of the sensors to minimize heat loss from the sensors. Figure I.4.J.9 e shows an assembled pouch cell with the internal anode-side sensors connected. The trend of the data from the anode-side sensors agrees well with the previous data from cathode-side sensors (Figure I.4.J.9 f), which verifies the effectiveness of anode-side sensors for measuring thermal properties.

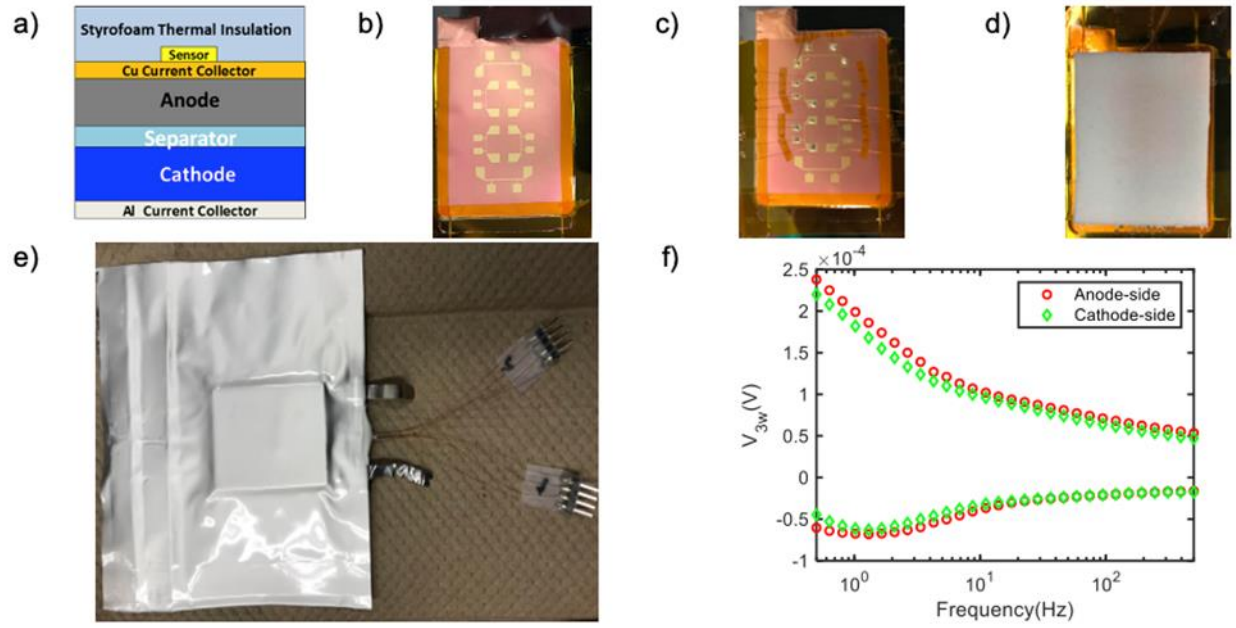

Figure I.4.J.9 (a) 3ω sensor designed for lithium detection, (b-d) anode-side sensor fabrication process, (e) pouch cell with anode-side sensors, and (f) representative data from anode-side sensor of formed pouch cell.

To detect Li distribution, thermal conductivity of the graphite anode *vs.* SOC is calibrated at a slow charge rate (C/10) after formation. Figure I.4.J.10a shows that the 3ω voltage increases as the SOC increases, which agrees with the existing simulation and experimental results indicating that the thermal conductivity of graphite intercalation compounds decreases as lithium ions are intercalated into graphite. By fitting to the data, we quantify the relationship k_{anode} *vs.* SOC and observe a decrease (24.9%) of the thermal conductivity in

lithiated graphite anode from SOC = 0% to 100% (Figure I.4.J.10b). At C/10, it is universally believed that Li^+ ions are uniformly distributed across the anode. As the charge rate increases, graphite particles near the separator can have a higher local SOC, which may lead to a different k_{anode} *vs.* SOC. Thus, it is possible to detect the lithium ion distribution across the anode using our 3ω sensor.

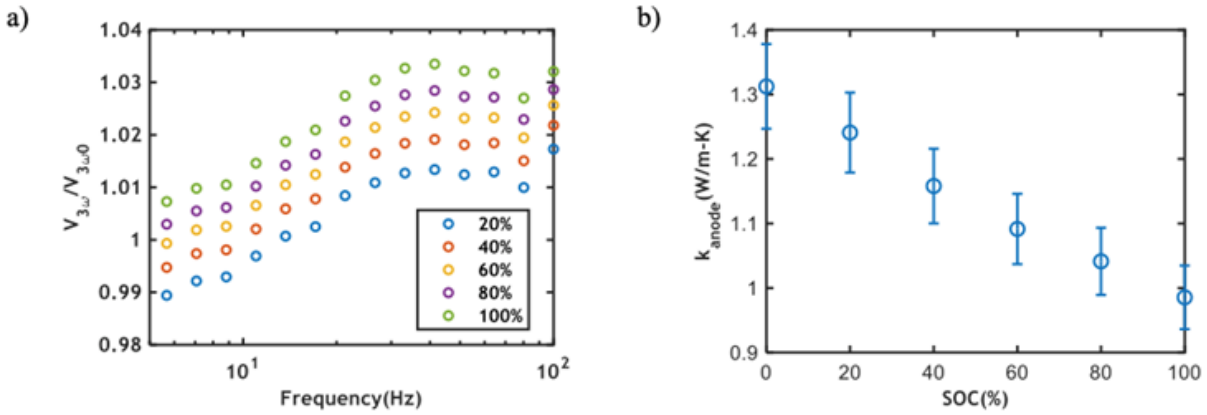

Figure I.4.J.10 (a) V3ω at various SOCs calibrated at C/10 and (b) operando measured k_{anode} vs. SOC assuming uniform Li distribution across the anode at C/10 charge.

To extract the Li distribution, we create a theoretical model that divides the graphite anode into four layers for analysis (Figure I.4.J.11a). Compared to 0.1C, more Li^+ ions tend to intercalate into graphite particles near the separator at faster charge rates, resulting in a gradient of lithium concentration across the anode. At charge rates greater than 0.1C, it is reasonable to assume the local SOCs with $SOC_1 > SOC_2 > SOC_3 > SOC_4$, and thus $k_1 < k_2 < k_3 < k_4$. Figure I.4.J.11b and Figure I.4.J.11c shows the 3ω signal for SOC = 30% and SOC = 50% after 0.1C and 1C charge rates. Note that for the same total SOC, the $V_{3\omega}$ is higher at 0.1C than at 1C as more Li^+ ions intercalate into layer 4 and contribute to a lower thermal conductivity in this layer, which has a higher sensitivity to the signal as it is closest to the sensor on the current collector. With the known total SOC and the relationship among local SOCs, we obtain the lithium distribution across the anode when the cell is charged to 30% and 50% SOCs (Figure I.4.J.11d) by fitting to the $V_{3\omega}$ data.

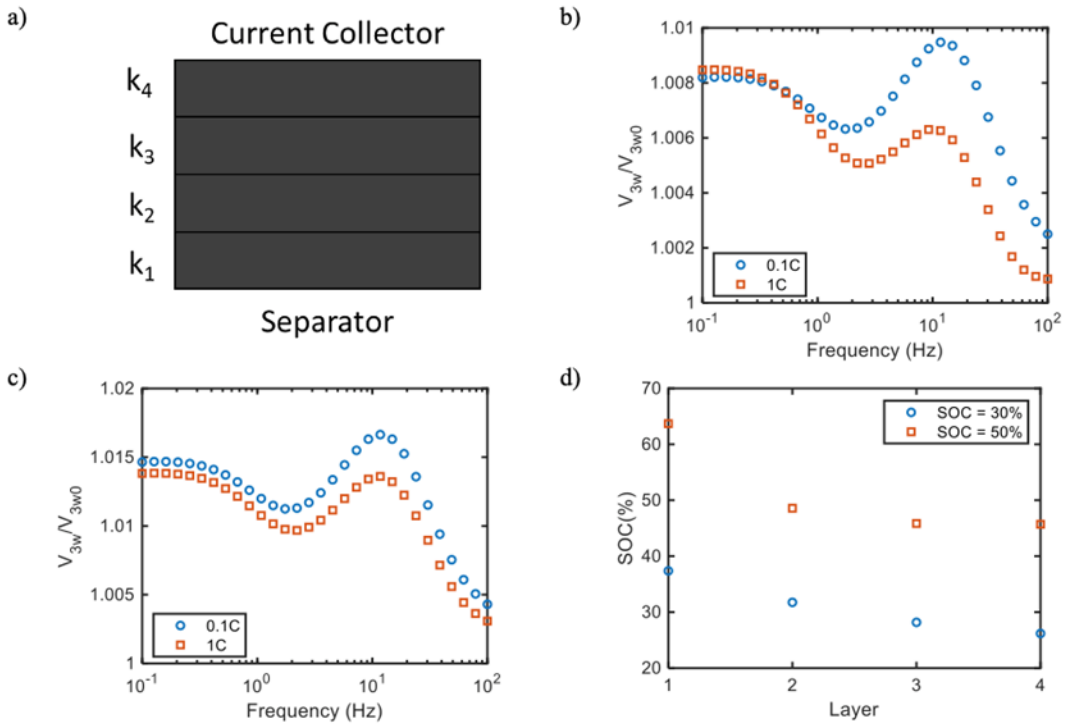

Figure I.4.J.11 (a) Schematic of the four sublayers (coarse mesh) in our theoretical model for the graphite anode analysis; $V_{3\omega}$ (raw measured signal) at (b) SOC = 30% and (c) SOC = 50% after charging at 0.1C and 1C. Note that higher-frequency data corresponds to material properties closer to the sensor (i.e., closer to the current collector), while lower-frequency data corresponds to material properties farther away from the sensor (i.e., closer to the separator). (d) Measured Li distribution (local SOC) across the anode after 0.1C and 1C charge rates. Mesh layer 1 of the anode is adjacent to the separator, whereas mesh layer 4 of the anode is adjacent to the current collector.

We have developed a measurement scheme to measure spatially mapped local lithium concentration distributions through the thickness of graphite anodes based on the relationship between the amount of intercalated Li^+ and the thermal conductivity. These measurements are non-invasive and can be performed on a battery while it is cycling, including at extreme fast charging rates. A case study at 1C demonstrates reasonable lithium distribution. We plan to investigate Li distribution across the anode at XFC and study the impact of lithium plating on thermal contact resistance between the separator and anode, which can provide insightful information of lithiation and lithium plating during XFC. Further, the sensor we developed enables this type of study with a simple setup.

Localized and/or destructive Li detection techniques

Quantification of Inactive Li and SEI on Fast-Charged Graphite Electrodes

Bryan McCloskey's group developed a mass spectrometry titration (MST) technique to quantify interphasial species on graphite electrodes that have undergone fast charging. Inactive Li, carbonate-containing solid electrolyte interface (SEI) species and lithium acetylide (Li_2C_2) were quantified via the amount of H_2, CO_2, and C_2H_2 gases, respectively, that evolved upon exposure to acid (Figure I.4.J.12). They found that the majority of the capacity loss during fast charging is attributable to the formation of inactive Li metal, and prolonged fast charge cycling induces further capacity fade mechanisms, such as reaction of the plated Li to form additional carbonate-containing SEI species and Li_2C_2.[1]

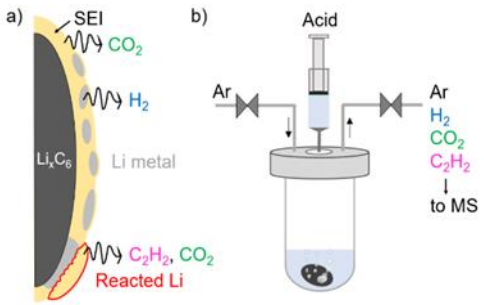

Figure I.4.J.12 (a) Schematic representation of a graphite particle surface with SEI coating and inactive Li metal interspersed. Gases evolved upon acid titration are shown emanating from each species. (b) Schematic representation of titration vessel apparatus with outlet gas line, which is sent to the mass spectrometer (MS) for product analysis. Reproduced from [1].

Quantifying amount of plated Li with ICP-MS

Figure I.4.J.13a shows optical images of the graphite anodes as a function of cycle count. Lithium plating was observed on the graphite electrode in the 6-C charged cells, and the amount of lithium plating seemed to increase with cycle count. It is interesting to see heterogeneous lithium plating on the edges of the anode after limited cycling. Lithium plating was also observed from graphite anodes in the 1-C charged cell after 10, 20, 50, and 100 cycles, but the amount was relatively small.

To quantify the lithium plating driven by fast charging, lithium concentrations in anodes from both 6-C and 1-C charged cells were analyzed with inductively coupled plasma mass spectrometry (ICP-MS). Here, the amount of lithium plated from 1-C charged cells were used as a baseline. Figure 11b shows the ICP-MS results of lithium for both charging rates as a function of cycle count. The results show that the detected amount of lithium from 6-C charged cells gradually increased with cycle number, although the relationship between lithium concentration and cycle count was not linear. In contrast to the observations from the 6-C cells, the amount of lithium in the 1-C samples did not vary notably throughout the cycling experiment. The detected lithium from the 1-C samples included a small amount of lithium plating on the graphite (Figure I.4.J.13a) and any lithium inside the graphite and SEI on its surface.

Figure I.4.J.13c illustrates the amount of fluorine ion as a function of cycle count. Because fluorine ions generally combine with lithium ions, forming LiF or Li_xPO_yF in SEI, the amount of lithium plated on the anode surface was calculated from the total moles of lithium detected, minus the moles of fluoride. There probably were additional lithiated species in the SEI; we assumed that these amounts were relatively small. The results from these calculations are given in Figure I.4.J.13d.

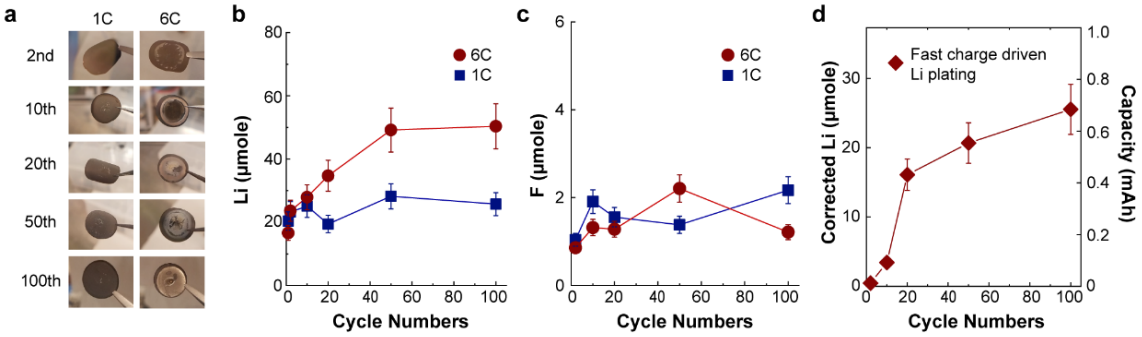

Figure I.4.J.13 (a) Optical images of graphite anode charged at the 1-C and 6-C rates with various cycle numbers. (b) ICP-MS results for lithium from graphite anode charged at the 1-C and 6-C rates with various cycle numbers. (c) Selected electrode results for fluorine from graphite anode charged at the 1-C and 6-C rates with various cycle numbers. (d) Corrected lithium amount that is driven by fast charging. The error bars represent ±14% uncertainty in the values.

We observed that the amount of lithium plating dramatically increased between the 1st and 20th cycles and gradually increased after 20 cycles. It is not clear why the slope for the amount of fast-charge-driven lithium plating vs. cycle count changed at around the 20th cycle, but it should be noted that the capacity retention for the 6-C charged sample (Figure I.4.J.5a) also showed a slope change around the 20th cycle. The amount of lithium plating after 100 cycles reached 25.59 µmole; this amount corresponded to 0.69 mAh (26.80 mAh g^{-1}cathode) of capacity lost. Considering that most of the plated lithium is electrochemically inactive, the lithium plating behavior should correlate to irreversible capacity loss, and even lithium deficiency in cathode crystal structure.

To better understand how fast charging impacts the stoichiometry of the NMC532, we plotted the stoichiometric lithium deficiency of NMC532 as a function of cycle count in Figure I.4.J.14. The overall lithium deficiency from cathode was determined by the amount of ICP-MS–detected lithium on the graphite anode (6-C results in Figure I.4.J.13b), and results in Figure I.4.J.13d were used to plot the lithium deficiency caused only by lithium plating. Figure I.4.J.14 shows that 0.19 mole of lithium ions per 1 mole of $LiNi_{0.5}Mn_{0.3}Co_{0.2}O_2$ were lost after 100 cycles, and only 0.10 mole of lithium ions participated in lithium plating on the anode surface. These results generally suggest that fast charging at the 6-C rate generates a large amount of lithium plating on the anode; however, its influence on lithium deficiency in terms of the NMC532 stoichiometry is not large. In addition, the results in Figure I.4.J.14 support the XRD analysis data (which showed only 0.59% of volumetric strain after 100 cycles) because the lattice parameter variation and volumetric strain of NMC532 are attributed to the loss of active lithium during cycling, which reveals negligible lattice parameter variation and volumetric strain.

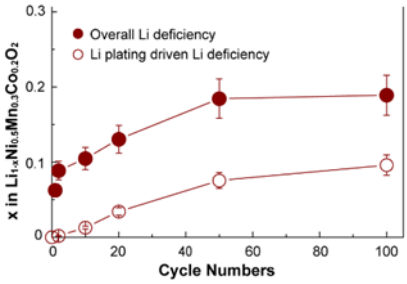

Figure I.4.J.14 Fast-charge-driven lithium plating and overall lithium deficiency of NMC532 in stoichiometric lithium deficiency of NMC532 as a function of cycle counts.

High-speed XRD for a spatial description of Li-plating dynamics

Li-plating occurs heterogeneously throughout Li-ion cells, the cause of which is not well understood. It is expected that different regions within an operating cell experience different current densities and propensities to plate Li. This work focuses on creating a link between heterogeneous activity within operating Li-ion cells and the local likelihood and dynamics of Li-plating. The objective of this work is to quantify the local response of graphite to fast charging conditions both through the depth of electrodes and across the face of a cell. We then aim to link the dynamics of graphite lithiation and delithiation to the onset of Li-plating.

High-speed XRD depth profiling was carried out on a 101-µm-thick graphite electrode to quantify the spatial and temporal state of the electrode and concurrent Li plating during high rate (up to 6-C) conditions (Figure I.4.J.15a,b). Extreme lithium concentration gradients were observed through the depth of the electrode during both 6-C and 2-C charge and discharge conditions (Figure I.4.J.15c). The evolution of the distinct lithiation stages was quantified at each depth, providing insight into the lithiation state distribution. There was extensive evidence of phase co-existence observed within single depths, and phase co-existence of Stage I and graphite was observed after the electrode was fully delithiated at regions where Li plating was present. The Stage I and graphite continued to co-exist for at least 800 s, where solid-solution models would predict that the phases relax to some intermediate concentration. Li plating was shown (Figure I.4.J.15d) to affect the equilibrium state of particles, which has raised questions for how the performance of graphite particles will be influenced

by Li plating, addressing, for example, the question of whether the plating hinders or improves further (de)lithiation and how the transport properties of graphite are affected by the presence of plating and co-existence of LiC_6 with graphite.

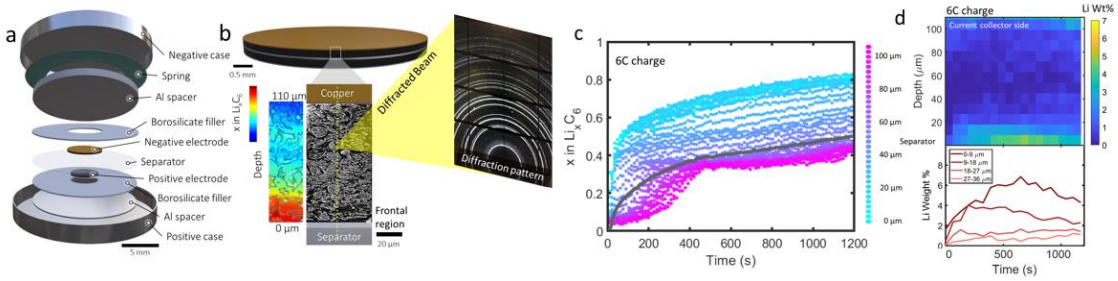

Figure I.4.J.15 (a) Illustration showing the construction of the cell and (b) the imaging method for measuring depth-dependent lithium concentrations using XRD. (c) State of graphite lithiation (LixC6) color coded with distance from the separator. (d) Weight fraction of Li-metal as a function of depth and time.

A second experiment focused on quantifying lithiation heterogeneities across the face of a pouch cell, complementing the previous depth profiling experiment by adding further insight into spatial heterogeneities within cells. This work involved doing line scans of XRD measurements from left to right across the face of a pouch cell (Figure I.4.J.16a). The state of lithiation as a function of position and time were quantified (Figure I.4.J.16b). The data showed that different regions within the cell lithiated at different rates, with as much as a 20% difference in the state of lithiation between regions after the 6-C charge step (Figure I.4.J.16c).

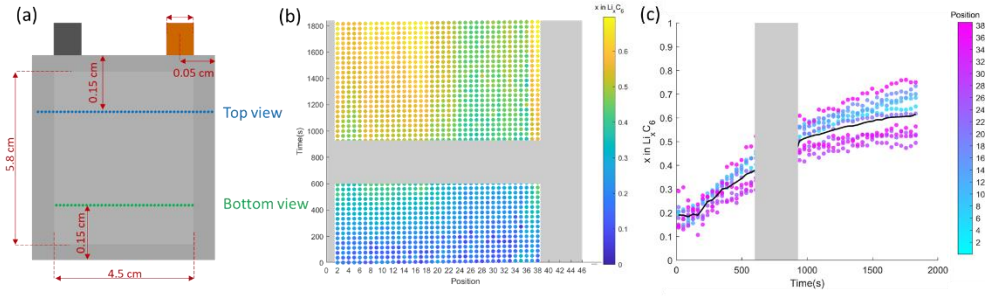

Figure I.4.J.16 (a) Illustration showing the locations of line scans of XRD across the face of a pouch cell. (b) Lithiation state as a function of position and time within the cell. (c) Lithiation state with time for color-coded positions, showing the extent of lithiation variation at each point in time.

In summary, we have provided a detailed experimental description of the response of graphite electrodes to fast charging conditions, as well as a description of the onset of Li plating. The results have shown that a high degree of variation in the rate of lithiation of graphite electrodes can occur both in the depth-direction (separator to current collector) and the in-plane direction (across the face of the pouch cell). A consequence of this is that certain regions are favored for plating more than others – highly active regions across the face of a pouch cell and then regions close to the current collector along the depth of the electrode are more prone to plating. The data presented in this work are expected to guide and validate modeling efforts for predicting fast charge and discharge behaviors. Furthermore, it shows that it is important to consider heterogeneous activity within a cell when determining suitable charge rates to avoid Li plating.

Quantification of heterogeneous, irreversible lithium plating in extreme fast charging of Li-ion batteries

Quantitative and simultaneous characterization of various components during cell degradation represent a major experimental challenge. We employ spatially resolved, high-energy XRD as a *quantitative*, *in-situ* method to study the degradation, both *locally* (mm-scale) and *globally* over the entire cell (cm-scale), in extreme fast charging of lithium-ion batteries. These cells were single-layer pouch cells, cycled 450 times

under XFC conditions (ranging from 4-C to 9-C charging) and analyzed in the discharged state using mm-scale spatially resolved XRD.

As evident in cell 6c-a (450 cycles, 6-C charge, C/2 discharge), irreversible lithium plating is observed to be spatially heterogeneous on the anode, and the regions with plated lithium on the anode are co-located with regions of trapped LiC_6 and LiC_{12} within the anode (Figure I.4.J.17a-c). Additionally, the regions of lithium plating also show a loss of active material (LAM) on the anode side, as indicated through the reduced amount of graphite in the discharged state of the cell (Figure I.4.J.17d). Finally, these regions of lithium plating also correspond to a locally reduced SOC in the NMC cathode in the discharged state, consistent with the loss of lithium on the anode side (Figure I.4.J.17e-f). Globally, the total amount of irreversibly plated lithium on the anode is directly correlated to the capacity fade of the cell across the C-rates we have studied and is the primary driver of capacity fade during XFC cycling. Furthermore, loss of lithium inventory (LLI) from trapped LiC_6 and LiC_{12} in the anode due to Li plating is a minor contributor to XFC capacity fade (Figure I.4.J.18). SEI-related losses are relatively independent of Li plating and play an increasingly minor role in loss of cell capacity as the amount of Li plating increases. Thus, an analysis on the anode side enables the separation of individual LLI mechanisms and the quantification of their relative contributions to the battery performance. On the cathode side, the overall capacity fade of the battery is directly correlated to the LLI in the fully discharged state.

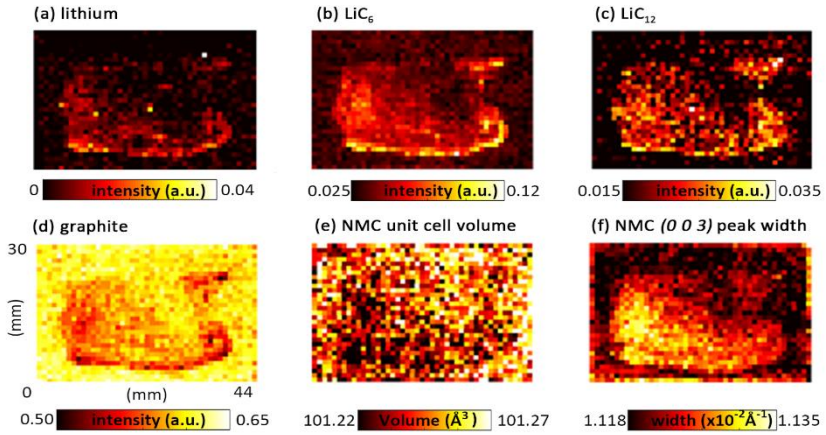

Figure I.4.J.17 Spatial maps of irreversibly plated lithium (a) and the anode (b-d) and cathode (e-f) phases, obtained through XRD. On the anode side, the regions with plated lithium directly correlate to regions of higher intensity of LiC_6 in (b) and LiC_{12} in (c) and inversely to graphite intensity (d). As explained in the text, on the cathode, the regions of plated lithium correspond to a lower average cathode SOC (shown in by the NMC unit cell volume in [e]) and higher variation in cathode SOC (shown by the width of the NMC peak in [f]). The spatial maps are for **cell 6C-b.**

Our results show that the Round 2 cells with thicker electrodes are *inventory limited* with LLI playing a primary role in the deterioration of cell performance rather than the LAM on either electrode. Therefore, analysis of the cathode side can be leveraged to keep track of the overall dominant mechanism of cell degradation. Such a simultaneous analysis of different battery components, enabled by an in-situ scan, provides a pathway toward developing a comprehensive understanding of lithium plating and its effect on local and global battery degradation under extreme fast charging conditions.

Combine multiple techniques

Raman mapping to detect Li plating

Li plating is a partially reversible process. While a fraction of the deposited Li remains isolated within SEI shells, a significant portion maintains electronic connectivity to the anode matrix and remains part of the cyclable inventory of the cell. This "connected" lithium can chemically intercalate into the partially charged graphite anodes shortly after charging is interrupted, as it possesses sufficient reducing power for the reaction to proceed spontaneously. It has been suggested that this post-charge intercalation can be observed by

inspecting the voltage relaxation profile of the cell[2] and can serve as a warning sign that plating has occurred. The occurrence of this chemical intercalation distorts the cell voltage and can be clearly seen as valleys when differentiating the rest profile with respect to time (dV/dt; see example in Figure I.4.J.19a). While such a method of detecting Li plating has practical relevance, the test to demonstrate whether it is capable of detecting the occurrence of low levels of plating remains.

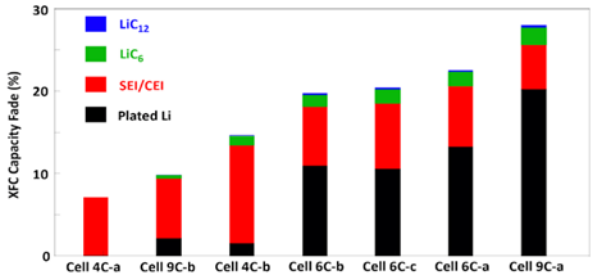

Figure I.4.J.18 Contributions from individual LLI mechanisms to the XFC capacity fade across cells. The cells are arranged horizontally in increasing order of XFC capacity fade after 450 cycles.

Figure I.4.J.19 contains information from two types of cells. While Figure I.4.J.19a shows data obtained with a conventional coin-cell, the cell used in Figure 1b employed a modified design in which the wave spring is substituted with three 0.5-mm-thick stainless steel spacers; such alteration can reduce the distortion of the electrodes in the cell, decreasing the likelihood of plating.[3] Both cells were tested by using constant current constant voltage (CCCV) charging (6-C initial rate, CV at 4.1 V until 10 minutes of total charging time), followed by one hour of rest and C/5 discharge to 3.0 V. In addition to dV/dt plots, Figure I.4.J.19 also presents the coulombic efficiencies and the false-color Raman map of the cycled anodes; the red circles in the map indicate spots where the Li_2C_2 band, which is indicative of Li, is observed.[4] While both samples show Li plating, it occurs at a much smaller extent in the cell built with the modified design. For this sample, efficiencies of ~99% could be obtained in most cycles — much higher than observed for the conventional coin-cell. Importantly, notwithstanding the occurrence of Li deposition in the former, the characteristic valleys are absent from the dV/dt curves. This preliminary analysis suggests that obvious signs of plating may be observable by the voltage relaxation method only after significant Li deposition (Figure I.4.J.19a). At low levels of plating, features are either very subtle or completely absent (Figure I.4.J.19b). Utilization of this technique to identify early stages of plating may still be possible but could require data to be acquired with much higher time resolution that can support a finer numerical analysis.

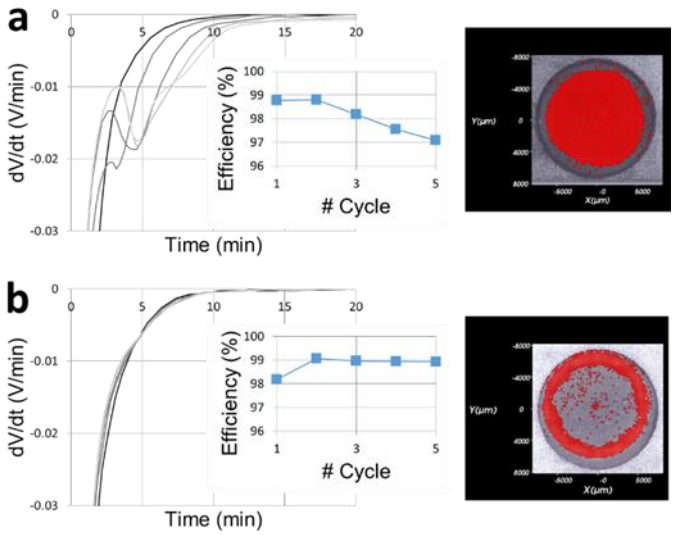

Figure I.4.J.19 Diagnostic metrics and characterization of fast charged cells using (a) typical coin-cell configuration and (b) a modified design, using three stainless steel discs in lieu of the wave spring. Differential voltage plots of the rest after charge, coulombic efficiencies, and the Raman map of "dead" Li are presented for both configurations

Mapping the onset of lithium plating using differential OCV analysis and modeling

The McCloskey Lab has previously used a differential open-circuit voltage analysis (dOCV) after fast charge to detect the onset of Li plating at 2-C, 3-C, and 4-C rates for Round 2 graphite/Li coin cells (Figure I.4.J.20a).[2] For a single constant-current charge cycle at 23°C, Li plating was shown to begin at 25% SOC for a 4-C charge, 50% SOC for a 3-C charge, and 75% SOC for a 2-C charge. Coulombic efficiency data estimate that the Li detection limit of this technique is about 1% of the graphite electrode capacity, or 4 mAh Li/g graphite. This work has spurred ongoing collaboration with Andrew Colclasure at NREL to validate models for electrochemical Li detection and map the onset SOC of lithium plating for different c-rates and electrode thicknesses (Figure I.4.J.20b).

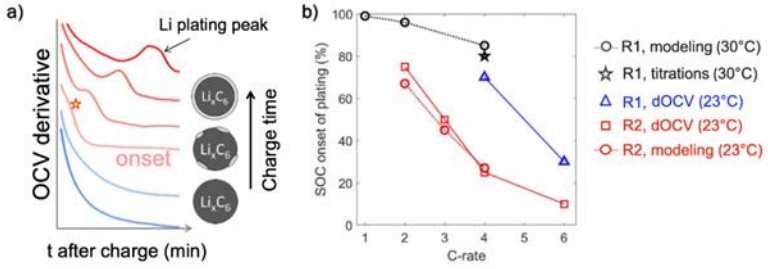

Figure I.4.J.20 Detecting the onset of Li plating with dOCV and mapping the onset of plating. (a) The emergence of a peak feature in the voltage derivative can indicate the onset of Li plating. Reproduced from [2]. (b) Li plating onset SOC plotted vs. c-rate for various graphite electrode thicknesses, techniques and temperatures, modeling results from NREL and titration data from [1].

Quantify plating Li with mass spectrometry and XRD mapping

The McCloskey Lab (in collaboration with SLAC) has used mass spectrometry titrations (MSTs) to quantify inactive Li (combined plated Li and Li_xC_6) and carbonate-containing SEI species on pouch cell graphite electrodes that have undergone 450 fast charging cycles. The goal of these experiments is to provide quantitative information about the contribution of inactive Li to the observed capacity loss after fast charging and compare the results of MST and X-ray diffraction measurements performed by the SLAC team on the same electrode. Figure I.4.J.21 and Table I.4.J.2 show the results of such titrations. We note that the total measured amount of inactive Li from MST closely matches the total observed cell capacity fade when

corrected for the baseline amount of Li contained in the graphite after formation cycling (i.e., the cell lost 22.4% capacity, and the inactive Li would account for 16.4% capacity), suggesting that the vast majority of the observed capacity fade during fast charging can be attributed to inactive Li. For reference, XRD measurements reliably quantify ~70% of the total Li+Li_xC_6 measured by MST in a given region. We also observe that, in general, regions of higher inactive Li also contain higher amounts of carbonate-containing SEI species.

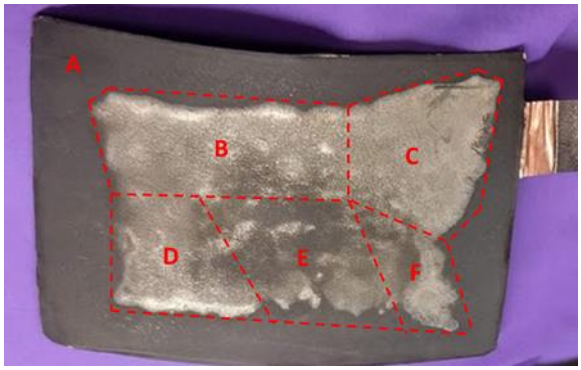

Figure I.4.J.21 Picture of an electrode extracted from a pouch cell. Regions A–F indicate how the sample was cut. Each region was separately titrated using MST.

Table I.4.J.2 MST results from electrode in the adjacent electrode picture

Region	Li+Li_xC_6 (µmol/cm²)	Titration CO_2 (nmol/cm²)
A	7.30	713
B	34.7	2300
C	61.6	3200
D	37.7	2390
E	21.6	2490
F	45.4	3760

Link onset of Li with cell performance

Influence of External Pressure in Fast-Charging Li-ion Batteries

External stack pressure is an essential factor that affects batteries' performance. In this study, we focus on the pressure-dependence of extreme fast charge batteries using an in-house designed gas bladder cell configuration. We utilized single-layer pouch cell batteries with the Round 2 graphite anode, $LiNi_{0.5}Mn_{0.3}Co_{0.2}O_2$ (NMC532) cathode, and Gen 2 organic liquid electrolyte solution. Electrode stack pressure is achieved by opposing pairs of external flexible gas bladders. These gas bladders are formed by airtight sealing of a Kapton dome against each side of the flexible battery pouch (Figure I.4.J.22a). By controlling the gas pressure within the bladders, the external pressure is precisely set, and the flexible bladders locally conform to provide uniform pressure across the electrode stack. This combination bypasses issues with rigid plates where electrode thickness variations and internal electrical connections prevent uniform pressure. Additionally, the pressure is stable during the battery cycling process regardless of material expansion/contraction or gassing. Furthermore, the X-ray transparent Kapton domes allow *operando* X-ray characterization.

Using external pressures of 10, 50, and 125 psi, and on a control group with pressure applied by rigid plates, we performed a series of electrochemical experiments. All batteries were charged at 6-C using the CCCV

protocol and discharged at C/2 at room temperature for 140 cycles with a voltage range of 3–4.1 V. We found that the capacity fade decreases with increasing pressure (Figure I.4.J.22b). Additionally, with increasing pressure, the fast charge capacity increases, while the difference between the open circuit voltages (OCVs) at the end of charge and discharge decreases, which indicates that the depth of charge/discharge of the entire cell increases while the depth of reaction of the active material decreases. Combining these two findings, we infer that there is more active material loss at lower external pressure (Figure I.4.J.22c), which is one of the causes of capacity fading.

We have revealed the correlation between externally applied electrode stack pressure and capacity fade through a systematic study. We propose that it is beneficial to control the battery's stack pressure within an optimal range to mitigate the capacity fading problem in XFC batteries. We plan to conduct *operando* X-ray diffraction experiments using the X-ray transparent gas-bladder cell to monitor the evolution of anode and cathode materials and Li plating during fast charge to investigate the underlying mechanism of the pressure-dependent behaviors.

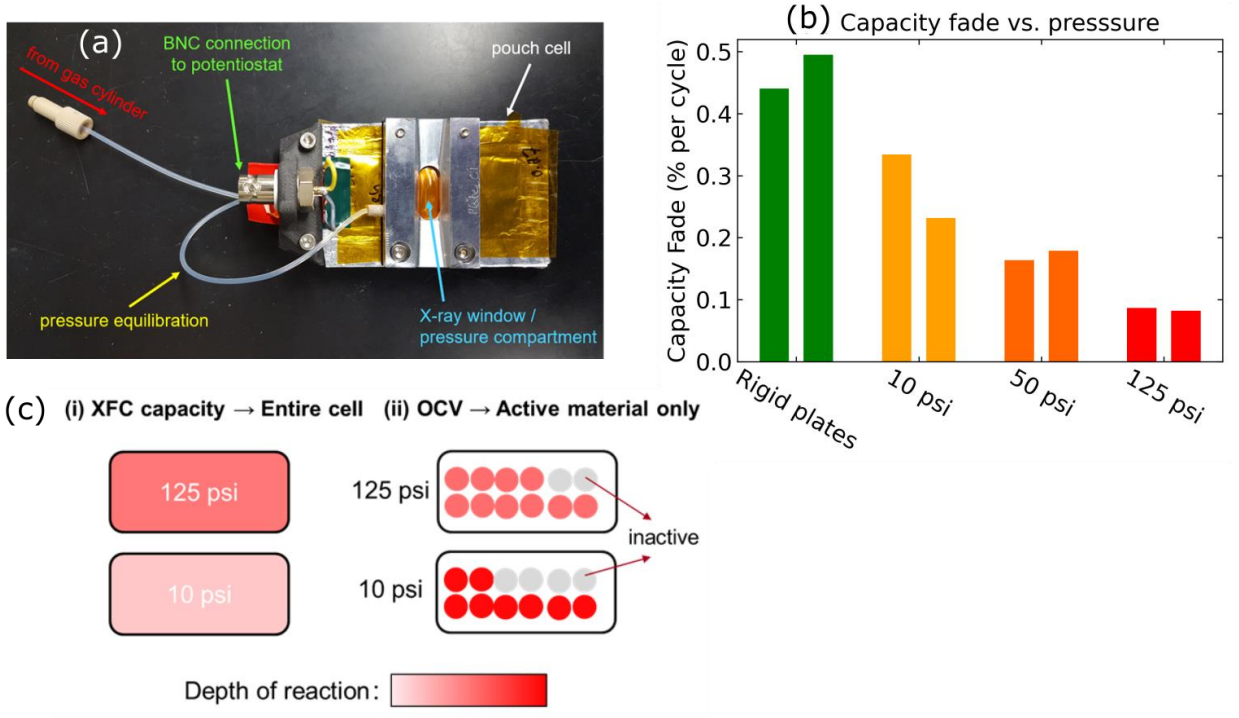

Figure I.4.J.22 (a) Photo of the gas bladder cell configuration. (b) Capacity fading at different pressure conditions. (c) Sketch illustrating more active material loss at lower pressure.

References

1. McShane, et al. ACS Energy Lett. 5, 2045–2051 (2020).
2. Konz, et al. ACS Energy Lett. 5, 1750−1757 (2020).
3. Okasinski et al., Phys. Chem. Chem. Phys. 22, 21977–21987 (2020).
4. Rodrigues et al., ACS Appl. Energy Mater. 2, 1, 873–881 (2019).

Publications

1. Tanvir R. Tanim et al., "Heterogeneous Behavior of Lithium Plating during Extreme Fast Charging," Cell Reports Physical Science, 1(7), 100114 (2020).

2. Seoung-Bum Son et al., "Fast Charge-driven Li Plating on Anode and Structural Degradation of Cathode," J. Electrochem. Soc. 167 140506 (2020).

3. Eric J. McShane et al., "Quantification of Inactive Lithium and Solid–Electrolyte Interphase Species on Graphite Electrodes after Fast Charging," ACS Energy Lett. 5, 2045–2051 (2020).

4. Zach M. Konz, et al., "Detecting the Onset of Lithium Plating and Monitoring Fast Charge Performance with Voltage Relaxation," ACS Energy Lett. 5, 1750−1757 (2020).

5. Donal Finegan et al., "Spatial Dynamics of Lithiation and Lithium Plating during High-Rate Operation of Graphite Electrodes," Energy & Environmental Science, 13, 2570–2584 (2020).

Publications in preparation

1. Partha Paul et al., "Quantification of Heterogeneous, Irreversible Lithium Plating in Extreme Fast Charging of Li-ion Batteries," Energy and Environmental Science, under review.

2. Chuntian Cao et al., "Influence of External Pressure in Fast-Charging Li-ion Batteries – A Study Using Gas Bladder Configuration to Provide Conformal and Constant Stack Pressure."

3. Partha Paul et al., "Using in-Situ X-ray Diffraction to Quantify Electrode Behavior of Lithium Ion Batteries from Extreme Fast Charging."

4. Monasterial et al., "Heterogeneous Lithiation within Li-ion Pouch Cells Measured by High Speed X-ray Diffraction."

Oral Presentations

1. "Understanding the Limitations of Fast Charging Li-ion Batteries," Finegan, UK STFC Batteries Webinar, Aug. 2020.

2. "Influence of External Pressure in Fasting-Charging Li-Ion Batteries," Chuntian Cao, Christopher J. Takacs, Hans-Georg Steinrück, Partha P. Paul, Alison R. Dunlop, Andrew N. Jansen, Vivek Thampy, Maha Yusuf, Johanna Nelson Weker, Michael F. Toney, PriME – The Electrochemical Society, Oct. 2020.

3. "Quantifying Local and Global Effects of Li Plating in Extreme Fast charging of Li-Ion Batteries," Partha P. Paul, Vivek Thampy, Chuntian Cao, Hans-Georg Steinrück, Michael F. Toney, Johanna Nelson Weker, MRS Annual Fall Meeting and Exhibit, Dec. 2020, invited presentation.

4. "Quantification of Degradation Mechanisms in Extreme Fast Charging of Li-Ion Batteries," Partha P. Paul, Vivek Thampy, Chuntian Cao, Hans-Georg Steinrück, Michael F. Toney, Johanna Nelson Weker, PriME – The Electrochemical Society, Oct. 2020.

5. "Spatial Heterogeneities of Irreversible Li Plating During Extreme Fast Charging in Lithium Ion Batteries," Partha P. Paul, Vivek Thampy, Chuntian Cao, Hans-Georg Steinrück, Michael F. Toney, Johanna Nelson Weker, Gordon Research Seminar, Feb. 2020.

6. "Challenges and Opportunities in Electrochemical Energy Storage Technologies," MF Toney, PETRA IV Workshop, Materials and Processes for Energy and Transport Technology, Oct. 21, 2020.

7. "Fast Charging of Li-ion Batteries: Aging and Diagnostics," Marco T. F. Rodrigues and Daniel P. Abraham, TMS 2020 Annual Meeting & Exhibition, invited presentation.

8. "Li Plating During Fast Charge: Detection and Prevention," Marco T. F. Rodrigues and Daniel P. Abraham, PRiME 2020, invited presentation.

Poster Presentations

1. "Quantification of Heterogeneous Degradation in Extreme Fast Charging of Li-ion Batteries," Partha P. Paul, Vivek Thampy, Chuntian Cao, Hans-Georg Steinrück, Michael F. Toney, Johanna Nelson Weker, Bay Area Battery Summit, Nov. 2020.

2. "Using X-rays to Understand Extreme Fast Charging in Li-Ion Batteries," Partha P. Paul, Vivek Thampy, Chuntian Cao, Hans-Georg Steinrück, Michael F. Toney, Johanna Nelson Weker, Gordon Research Conference, Feb. 2020.

Acknowledgements

This project was funded by the U.S. Department of Energy, Vehicle Technologies Office. The technology development manager was Samm Gillard. The project overview was prepared by Venkat Srinivasan (ANL). Other contributing team members for Thrust 1 (Lithium Detection Thrust) include Johanna Nelson Weker (SLAC) who served as the thrust coordinator; Bryan McCloskey, Ravi Prasher, and Nitash Balsara (LBNL); Donal Finegan, and Francois Usseglio-Viretta (NREL); Seoung-Bum Son (ANL); Tanvir Tanim (INL); and Yi Cui and Dan Steinrück (SLAC).

I.4.K XCEL R&D: Local Heterogeneity Thrust

Venkat Srinivasan, Principal Investigator
Argonne National Laboratory
9700 S. Cass Avenue,
Lemont, IL 60439
E-mail: vsrinivasan@anl.gov

Samm Gillard, DOE Technology Development Manager
U.S. Department of Energy
E-mail: Samuel.Gillard@ee.doe.gov

Start Date: October 1, 2019 End Date: September 30, 2020
Project Funding (FY20): $742,000 DOE share: $742,000 Non-DOE share: $0

Project Introduction

A 2017 DOE technology gap assessment report [1] established goals for next-generation electric vehicle (EV) batteries, namely, a battery cost of $80/kWh, energy density of 275 Wh/kg and 550 Wh/L, vehicle range of 300 miles, and charge time of 80% ΔSOC (state of charge) in 15 minutes. Compared to thin electrodes, thick electrodes are preferred due to their less inert material, higher energy density, and lower cost. Unfortunately, today's thick electrodes cannot tolerate fast charge rates. The thick electrodes have increased the distance for ionic transport through the liquid electrolyte. Thin electrode batteries are capable of fast charge; however, they come at a cell cost of almost 2x higher (from $103/kWh to $196/kWh) and have around 20% less energy density (180Wh/kg vs. 220 Wh/kg) [1]. In addition to polarization and low capacity, electrolyte transport limitations can lead to lithium plating, a side reaction with degradation and safety consequences. It is uncertain what graphite materials can best tolerate fast charge and why. At the system level, fast charging presents thermal management challenges to remove the heat generated during charging.

Objectives

The goal of this workgroup is to quantify how local heterogeneities result in early onset of lithium plating during extreme fast charging (XFC). Local heterogeneities being investigated span length scales from nm (graphite crystallographic orientation of edge vs. basal plane) to mm (changes in local electrode microstructure properties such as porosity, tortuosity, and conductivity). A major objective is to determine whether local lithium plating is driven by local changes in ionic transport properties. Another objective is to understand the effectiveness of electrolyte wetting/trapped gas on variation in local SOC and lithium plating. Further, more accurate models for lithium plating and graphite lithiation are needed to better understand fast-charge performance/limitations. Major milestones for the workgroup include:

- Determining a framework for the kinetic model to more accurately predict lithium plating –Q2 (Completed)
- Developing a more accurate kinetic model for lithium plating – Q4 (Completed)
- Quantifying the effect of edge/basal plane on intercalation/lithium kinetics – Q4 (Completed)
- Mapping electrode heterogeneities overlaid with lithium plating – Q4 (Delayed due to COVID to Q1FY2021).

Approach

The team has used a combination of novel experimental techniques/characterization and theoretical modeling to investigate heterogeneity at many different length scales. Experimental techniques include:

- Local mapping of MacMullin number (ionic resistance) of electrodes using novel probe/EIS – Brigham Young University (BYU)
- In-situ X-ray tomography to measure local variation in graphite SOC and lithium plating – Lawrence Berkeley National Laboratory (LBNL)
- Atomic force microscopy (AFM) and scanning electron microscopy (SEM) images used to examine where lithium plates form on graphite nano-platelets – SLAC
- High-energy, in-situ X-ray powder diffraction (XRD) to monitor local SOC and lithium plating – the Advanced Photon Source (APS) at Argonne National Laboratory (Argonne)
- Neutron imaging to measure electrolyte saturation distribution – Oak Ridge National Laboratory (ORNL)
- Highly oriented pyrolytic graphite (HOPG) samples used to examine lithium intercalation and plating on edge/basal plane– LBNL
- Combination of X-ray and neutron imaging to determine when and where lithium plates – SLAC
- Determining of characteristics of plated lithium using X-ray microdiffraction – SLAC.

Further, many modeling efforts have helped interpret experimental measurements and suggest methods to improve fast charge performance:

- First-generation lithium plating kinetic model with global Butler-Volmer plating/stripping from National Renewable Energy Laboratory (NREL)
- Second-generation lithium plating model with nucleation and growth principles from ORNL
- Electrolyte wetting modeling from Argonne
- Microstructure electrochemical model to study heterogeneity at different length scales – NREL.

Results

Development of First-Generation Li Plating Kinetic Model – NREL/LBNL

NREL continued to develop its lithium plating model by considering both lithium plating and stripping by using the framework developed by Smith et al. The plating/stripping process is simulated with the following global charge transfer reaction:

$$Li^{+}(\text{electrolyte}) + e^{-}(\text{anode}) \Leftrightarrow \beta\ Li^{rev}\ (\text{anode}) + (1-\beta)\ Li^{irr}\ (\text{anode}),$$

where β represents the fraction of lithium that can be reversibly stripped. The rate of reaction is calculated with a Butler-Volmer expression. Presently, the open circuit potential for plating is set to a fixed value of 0.0 V; and the exchange current density is constant, that is, it is not a function of local activity. The stripping reaction goes to zero when the amount of reversible plated lithium goes to zero.

The lithium plating model incorporated into NREL's macro-homogeneous electrochemical model is compared with experimental results from LBNL for gas titration and NREL's in-situ beamline XRD experiments. Figure I.4.K.1 illustrates a comparison of model results with different exchange current densities compared to half-cell measurements at LBNL for Round 1 1506 T graphite (~45-micron-thick graphite). Comparisons are shown for the amount of plated Li in nMoles after three full cycles and half-cell potential during 4C lithiation. Anodes were lithiated to their full theoretical capacity of 372 mAh/g. Thus, a significant amount of lithium plates exist at rates above 0.5C, even though in the full cell configuration, Round 1 cells did not plate lithium even at 9C. For this setup, lithium plates at only at very high lithiation level/SOC due to saturation of graphite throughout the entire electrode. Through a combination of measured amount of plated lithium and analyzing voltage curves, the best plating model parameters were determined to be an exchange current density of 10 A/m^2 and reversibility β of 60%–70%.

Next, the model was also compared with in-situ XRD beamline data for a very high loading anode with a thickness of 100 microns in a full-cell configuration. Figure I.4.K.2 shows comparison of measured current during 6C CC-CV charging and solid weight fraction of plated lithium in 10 microns of the anode closest to the separator. For this cell with a loading of 4 mAh/cm^2, a 6C current causes the cell voltage to rapidly hit the upper cutoff of 4.2V in only ~50 seconds. In-situ XRD measurements show that significant amounts of lithium had plated 100s into charging and reaches a maximum of around 5% around 700 s into charging. Interestingly, lithium begins to strip after 700 s during the continued CV charging as the applied current falls below 2C and as the solid phase potential rises above the liquid phase potential, causing stripping. Using the same plating parameters of 10 A/m^2 and 60% reversibility, the model can capture the observed lithium plating and stripping relatively well. The model predicts that both plating and stripping occur slightly before that measured experimentally. For this setup, lithium plating occurs at low SOC and is driven by insufficient lithium-ion transport in the electrolyte, causing the graphite to be preferentially used near the separator. These model results have been summarized in publications [1] and [2].

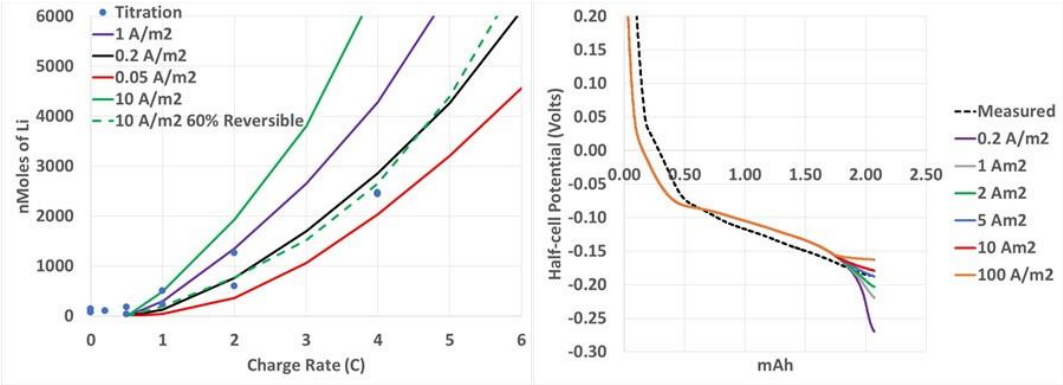

Figure I.4.K.1 Comparison of gas-titration results from LBNL and macro-homogeneous model predictions with different exchange current densities for lithium plating/stripping for (left) the amount of lithium plated during three charge/discharge cycles; and (right) voltage profile during 4C lithiation. Note solid lines are for the model, with only lithium plating and setup a half-cell configuration.

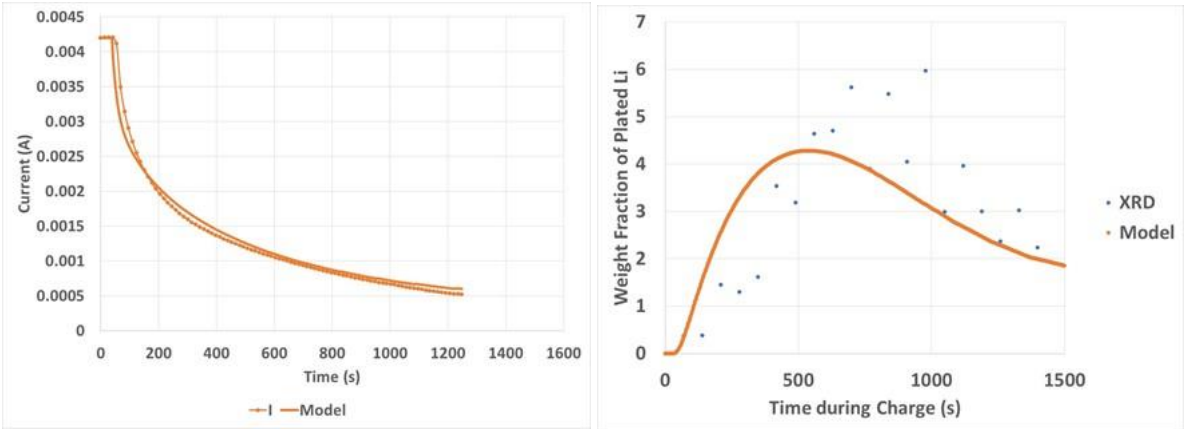

Figure I.4.K.2 Comparison of XRD results from NREL with macro-homogeneous model predictions: (left) comparison of measured and predicted current during 6C CC-CV charging, and (right) comparison of solid-weight fraction of plated lithium in 10 microns of anode closest to the separator. Full cell consists of 100-micron 1506T graphite anode and 110-micron NMC cathode.

Electrolyte Wetting Model – Argonne

Building on development of a two-phase wetting model and experiments to measure wetting characteristics, Argonne investigated Round 2 cell wetting characteristics using model parameters based on ethyl methyl carbonate (EMC). As discussed previously, the solvent mixture in the Round 2 cell electrolyte contains 70% by weight EMC, which should be an improvement over the octane-based parameters previously used to conduct the cell wetting simulation studies. Octane is considered a universal solvent (i.e., the wetting angle is zero for all materials). As in the earlier simulations, the electrolyte density, surface tension, and viscosity were provided by Kevin Gering's Advanced Electrolyte Model.

Detailed in the previous report, the permeabilities for both electrodes with EMC are significantly lower than those for octane, as estimated by the porosimetry results using the Kozeny-Carman equation. As an example, the permeability of the negative electrode using the octane-based parameters is 7.2×10^{-12} cm^2 compared to 1.5×10^{-12} cm^2 for the EMC-based parameters (i.e., about a factor of five difference). This, of course, slows the overall wetting process. The initial portion of the cell wetting process, where electrolyte is worked between the layers and the components are wetted from the face is slower, but still occurs very quickly (i.e., in tenths of seconds). The second portion of the cell wetting process, where the cell components are wetted from the edge occurs much more slowly. A direct comparison of the cell wetting simulations is given in Figure I.4.K.3 for the negative electrode saturation. For the octane-based parameters, the negative electrode reaches 90% saturation in 1.5 hours and 99% in 22.7 hours. For EMC, it takes the negative electrode about 11.0 hours to reach 90% saturation and 5.4 days to reach 99% (i.e., more than a factor of five slower).

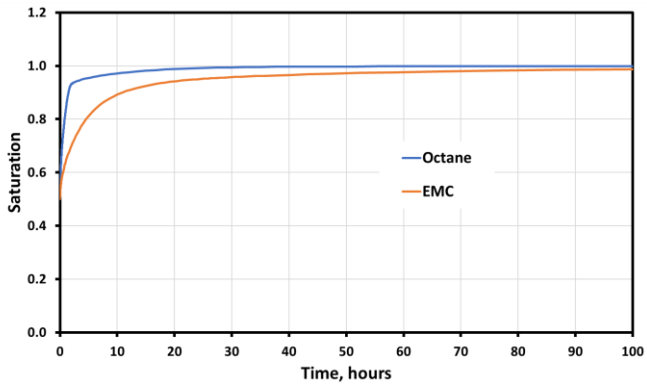

Figure I.4.K.3 Round 2 cell negative electrode saturation over time. Cell is wetted from ends and the initial saturation is at 50%.

Like the permeability, the relative permeability of each phase, ideally, should be measured, but is usually estimated. The relative permeability of the electrolyte (i.e., liquid or wetting phase) generally follows a cubic function, whereas that of the gas (i.e., non-wetting phase) is less well defined. It is often described as an s-shaped function that is approximated by a linear function. In the earlier studies, a minimum relative permeability of the gas phase at high saturation levels of the electrolyte (i.e., saturation greater than approximately 0.9) was used to approximate the s-shaped function as it approaches zero. Otherwise, if zero is used, the gas would not move at the higher saturation levels and the pores would never be completely wetted. It was found that if the minimum value was greater than about 10^{-5}, the cell would be completely wetted. It should be noted that almost any other proposed functionality of the relative permeability would result in relatively quick saturation. With the new parameter set, a second look at the relative permeability was conducted. Rather than use a fixed value at high electrolyte saturation levels, in the simulations below, a linear function was used that reduces to zero at full saturation to better approximate the functionality at high saturation levels. In general, the overall impact on the simulations is relatively small but can be significant near full saturation.

The electrolyte saturation of a Round 2 cell wetted on its ends is shown in Figure I.4.K.4 for each cell component. As with the earlier studies, the separator wets first, and both electrodes have similar wetting properties. While the electrolyte prefers to be in the separator, its relatively low permeability causes most of the electrolyte to seep in through the electrodes. In this simulation, the negative electrode reaches 90% saturation in 11.4 hours and 99% in 15.9 days. Also, there is a tendency for electrolyte to saturate all edges first, which, combined with the higher saturation level of the separator, tends to cause gas to be trapped in the electrode layers. The model predicts full saturation can take weeks, but progresses to completion providing there is an adequate quantity of electrolyte in contact with the cell edges and the gas has a path to escape. This longer time constant for full saturation when compared to the earlier studies suggests that the wetting process can extend past the formation process. Finally, at any point where the gas cannot escape, the wetting process will effectively stop.

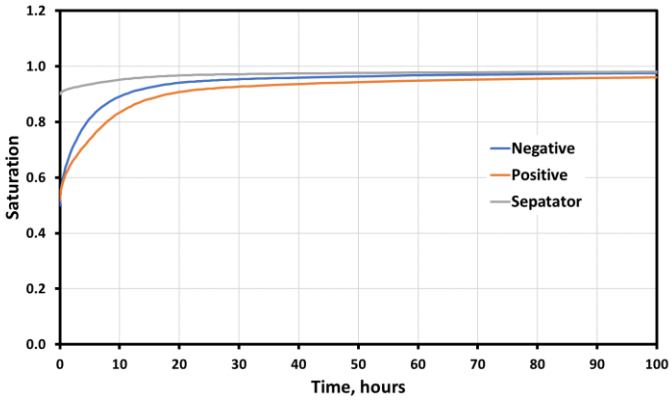

Figure I.4.K.4 Round 2 cell component saturation over time. EMC parameters, cell wetted from ends, and initial saturation at 50%.

Improved wetting of the cell can result from an electrolyte with a higher surface tension. Of course, changing the electrolyte could also modify the J-function, but if it does not, the impact on Round 2 cell wetting from increasing the electrolyte surface tension by a factor of two is shown in Figure I.4.K.5 for the negative electrode. For the higher surface tension simulation, the negative electrode reaches 90% saturation in 5.6 hours and 99% in 8.7 days (i.e., also about a factor of two faster).

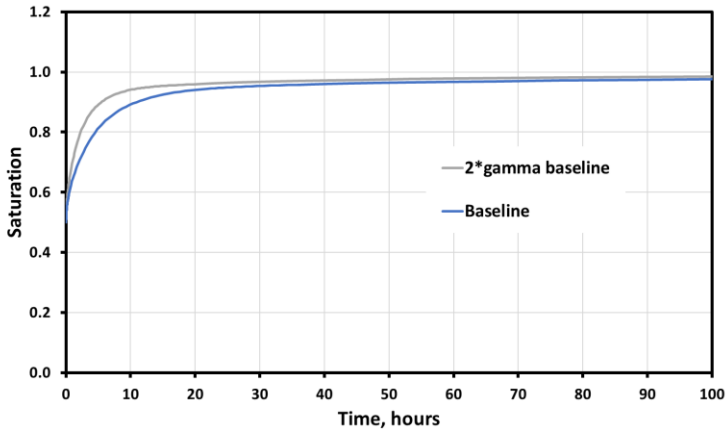

Figure I.4.K.5 Impact of electrolyte surface tension (γ) on Round 2 cell negative electrode saturation over time. EMC parameters, cell wetted from ends, and initial saturation at 50%.

Local mapping of ionic resistance of electrodes – BYU

The objective of this work is to measure localized ionic transport properties (in terms of a MacMullin number) and determine their effect on lithium plating or other degradation occurring during fast charge. Previously, a correlation between poor conductive pathways and locations of lithium plating was shown. However, it is not clear if the reduced transport preceded the plating or was a consequence of it. Therefore, a more complete study requires that the electrodes be scanned prior to assembly and cycling. The Cell Analysis, Modeling, and Prototyping (CAMP) facility at Argonne delivered a series of pre-cut, pouch-size Round 2 anodes and cathodes to BYU for analysis.

The goal this fiscal year was to achieve a reliable, high-resolution map of these pouch-size electrodes. The primary difficulty was that this requires high stability of the probe and samples during an electrochemical and mechanically invasive test that takes at least 24 hours. The test involves conducting ions into the electrode sample from an inert counter electrode through a small aperture. A blocking electrolyte (i.e., not containing Li ions) and electrochemical impedance spectroscopy (EIS) is used to perform the measurement at many locations across the sample in order to produce a map. A transport and reaction model is used to invert the experiment to produce local conductivity values.

Several improvements were made to the experimental apparatus and inversion algorithm. For the experiment, these included improved temperature and mechanical controls. A recurring problem that was observed with the Argonne-delivered anodes is that they would delaminate from the current collector during the long-running experiment. Modifications to the probe and increased mechanical stabilization of the sample appears to have ameliorated the delamination problem. In addition, the probe was changed from 3D-printed PLA polymer to machined Teflon, to improve chemical durability while in contact with the organic-based electrolyte.

To assess possible experimental drift in electrolyte properties during the long experiment, a benchmark or standard was incorporated into the test fixture. During the electrode scan, the probe periodically moves to the benchmark sample and tests it before returning to the primary sample. Stability in the Nyquist plots of the benchmark sample indicate the experiment is functioning as intended. The BYU team has now demonstrated more reliable and repeatable experimental results.

The BYU team also improved the inversion process that determines the local MacMullin number (and other parameters) from a theoretical model fit to experimental data. The inversion program uses a least-squares regression to perform the fit. Due to the nonlinearity and complexity of the model and experimental noise, the results were sensitive to the guess values used to fit the data. This problem was solved by using a stochastic ensemble of guesses and solutions to determine the most likely and reliable solution to the MacMullin number at each point in the map. Using this improved method, the inversion process is much more reproducible.

Figure I.4.K.6 and Figure I.4.K.7 show results for a full-size R2 anode and cathode, respectively, that shortly will be delivered to Argonne for assembly into a pouch cell and X-ray scanning at the APS during cycling (1Q21). The maps show variations of the MacMullin number for a first scan (left) and a subsequent fast scan with lower resolution (right). Despite the difference in resolution, the agreement between the two scans and the stability of the benchmark results and other scans (not shown) indicate much higher reliability than was achieved in the past. Interestingly, the scans show a striped horizontal pattern in the ionic properties of the anode and a localized high-resistance region of the cathode that may be due to the electrode fabrication process. These anomalies are not visible in optical pictures of the electrodes. The high and low MacMullin numbers on some edges of the maps are due to edge effects and will be corrected after adjustments are made to the model.

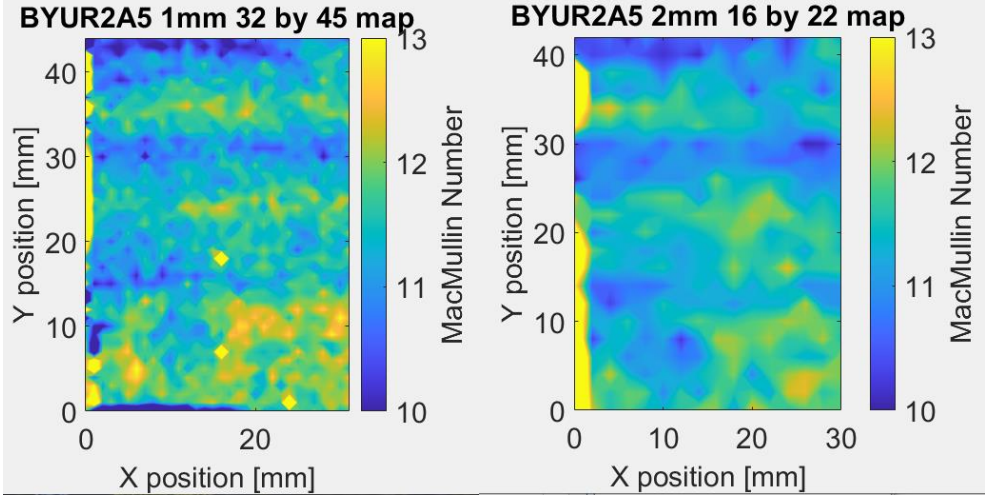

Figure I.4.K.6 Two subsequent passes of a scan on a single R2 anode at (left) higher and (right) lower resolutions.

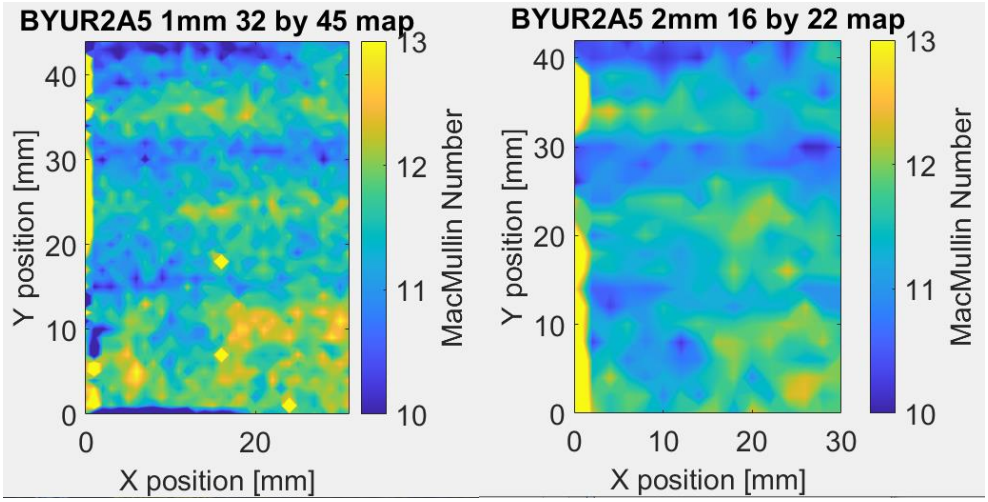

Figure I.4.K.7 Two subsequent passes of a scan on a single R2 cathode at (left) higher and (right) lower resolutions.

In-situ X-ray tomography to measure local SOC/lithium plating – LBNL

The Balsara group has performed *in situ* X-ray tomography on Li metal/101-µm Superior graphite SLC1520P (D50 = 16.94 µm) microtomography cells with a Celgard 2500 separator wetted with 1.2 M $LiPF_6$ 3:7 wt% EC:EMC. Digital volume correlation was used to calculate lithiation-induced volumetric strains within the graphite electrode resulting from C/10 intercalation to 100% SOC to obtain a calibration for strain to SOC. Another graphite half-cell was charged at 1C to 100% SOC, and Figure I.4.K.8 a,b shows the top and side views, respectively, of the lithium plating segmented from graphite in a portion of the cell. Figure I.4.K.8c-e shows the SOC maps of the lithiation within the same portion of the graphite electrode. A cross-section of the SOC map (y = 250 µm, Figure I.4.K.8c) shows inhomogeneous SOC across the electrode. The graphite near the separator (z = 70 µm, Figure I.4.K.8d) lithiates normally and reaches a high SOC. However, a slice of the graphite far away from the separator (z = 20 µm, Figure I.4.K.8e) reveals a high SOC region on the left and a low SOC region on the right. The region of poor lithiation lies underneath the region of mossy lithium (Figure I.4.K.8) and below the region of high SOC, indicating transport limitations to the back of the electrode. We refer to this phenomenon as a "shadow effect." Based on the SOC maps, an estimated 6.5 µAh of Li^+ is missing from the graphite capacity. The volume of segmented lithium within the mossy lithium accounts for

6.2 µAh of missing capacity. Additional capacity is lost to reactions of lithium with electrolyte in the gaps between the lithium pebbles to form secondary solid electrolyte interface (SEI). However, the attenuation of this SEI is similar to that of the polypropylene separator, making segmentation difficult. Future work will involve stepwise charging at 1C to determine the onset of both lithium plating and lithiation heterogeneity in a graphite half-cell, as well as a full cell with NMC. Additionally, tomography will be performed for standard R2 anodes at higher charge rates. This work will contribute to quantitatively understanding the effects of heterogeneity at the 1- to 10-micron length scale.

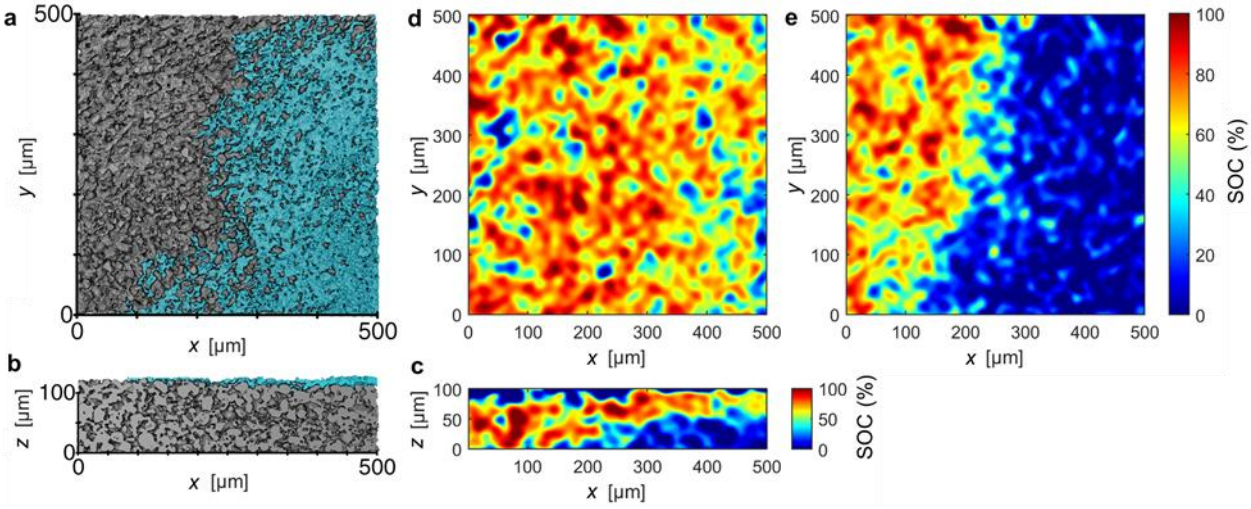

Figure I.4.K.8 Volume rendering of a portion of the segmented graphite electrode in the (a) xy-plane and (b) xz-plane after 1C intercalation to 100% SOC. The graphite is shown in gray, and the mossy lithium is shown in turquoise. A SOC contour map of the same portion of the graphite electrode from the slice has (c) y = 250 µm xz-plane, (d) z = 70 µm in the xy-plane, and (e) z = 20 µm in the xy-plane. Digital volume correlation was used to generate volumetric strain maps, which were converted to SOC. We observe a lithium "shadow effect", where poor lithiation occurs at the back of the graphite in the region underneath the region of lithium plating.

Operando imaging of lithium plating and SEI growth with electrochemistry atomic force microscopy – SLAC

The Chueh group has been developing *operando* imaging of lithium plating and solid electrolyte interface (SEI) growth in non-aqueous electrolytes using electrochemistry atomic force microscopy (EC-AFM). To verify the electrochemistry of the AFM liquid cell (Figure I.4.K.9a), we started with lithiating graphite particles under voltage control where the liquid cell was linearly scanned from open circuit voltage to 10 mV. From the I-V curve in Figure I.4.K.9b, we were able to identify a SEI reduction peak around 0.6 V (pointed by a blue arrow). Further, while the coverage of dispersed graphite nanoplatelets on the copper substrate is around 15% - 20 %, we could still identify three reduction peaks contributed from graphite lithiation under 0.3 V (pointed by red arrows). Therefore, the electrochemistry of the AFM liquid cell is confirmed, and the cell setup is feasible for *in-situ* and *operando* studies.

So far, we have successfully scanned graphite nanoplatelets in electrolyte, lithiated nanoplatelets, and plated lithium on nanoplatelets *in-situ*. Our results show that the thickness of the nanoplatelet becomes higher upon lithiation and that lithium tends to plate at the edge and the tip of the platelet (Figure I.4.K.9c). While it is time consuming to use AFM to scan each particle, we used the same AFM liquid cell setup to perform electrochemistry and observed lithium plating using SEM. This allows us to investigate the plating behavior of multiple particles in a shorter amount of time, and we could collect the statistics of plating locations through this method. The representative images of lithium plating on graphite nanoplatelets are shown in Figure I.4.K.10a-d and the collective data show that the majority of lithium plating occurred at either the edge planes or the defect sites of graphite.

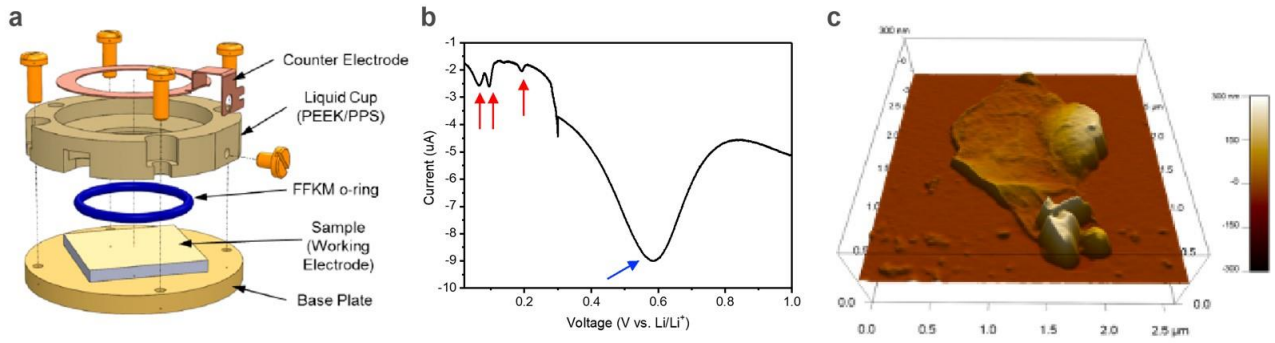

Figure I.4.K.9 (a) Illustration of the liquid cell for operando AFM experiment. (b) Linear scanning of the AFM liquid cell with dispersed graphite particles on a copper substrate as the working electrode and a lithium ring as the counter electrode. (c) Three-dimensional (3D) topography AFM image of a lithium-plated graphite nanoplatelet on a polycrystalline Cu substrate. The nanoplatelet was scanned when the potential of the working electrode was around -105 mV and the scanning was conducted in a non-aqueous electrolyte (1 M LiPF6 in 1:1 EC/DEC).

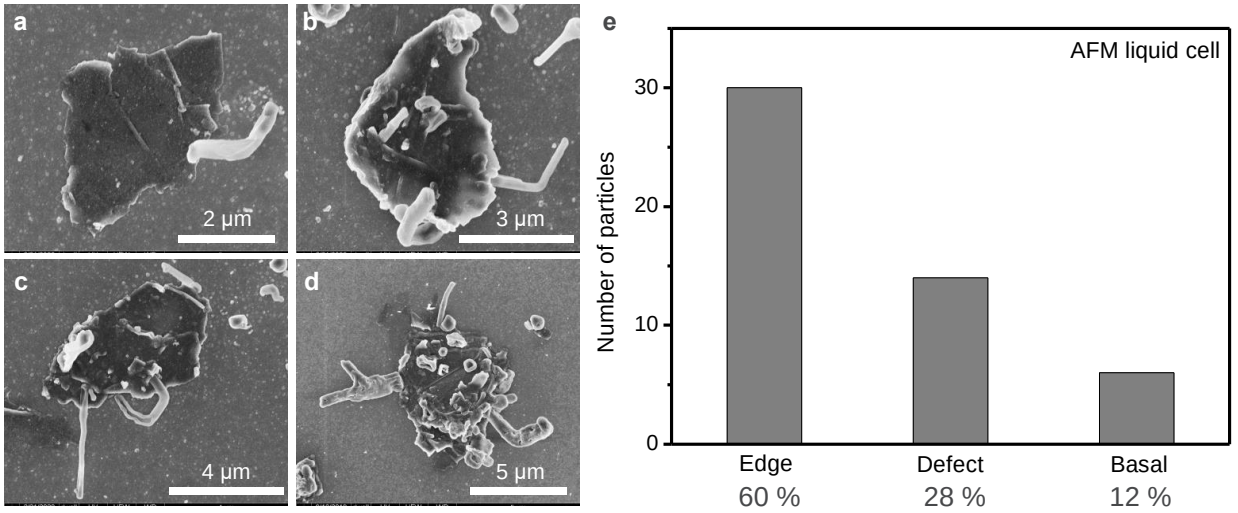

Figure I.4.K.10 (a-d) SEM images of lithium plating on graphite nanoplatelets where the samples were electrochemically lithiated and plated in an AFM liquid cell setup. (e) Histogram showing the number of particles with lithium plating at edge planes, defect sites, and basal planes.

Atomistic modeling of graphite lithiation – Argonne

During the short time scales of the initial fast-charging process, the thermodynamic system is far from equilibrium. For such non-equilibrium conditions, we found that extra electron charge near the surface layers of the graphite affects the Li diffusion process. The uncompensated electronic charge during this non-equilibrium state increases the interlayer spacing in graphite, which consequently lowers the Li diffusion barrier. A second mechanism that could explain the increase of Li diffusion during the initial stages of fast charge is related to the presence of local high Li concentrations. A concerted diffusion of Li within the graphite layers shows that the energy barrier for Li migration is reduced for Li diffusion from high concentration (near the surface layers) into low concentration domains toward the bulk layers, while it drastically increases for diffusion within the high concentration domains.

To estimate transport properties under fast charging conditions at higher length and time scales, a procedure to "average" the atomistic events is needed. One well-known method to accomplish this task is Kinetic Monte Carlo (KMC).[1] Using the migration barriers computed for several configurations of Li environments, a (KMC)

model was developed to evolve the system in time and compute a diffusion coefficient corresponding to possible fast charge scenarios and hence closer to experimental conditions. Figure I.4.K.11 shows a schematic of the software we developed. In order to describe the system, a hexagonal lattice that restricts the movement of the Li ions was built. They are allowed to hop only through the carbon-carbon (C-C) bonds (which was shown to be more favorable than along the C-C bond). Hence, for each Li ion, there are a maximum of six possible hopping events (west, east, northeast, southeast, northwest or southwest). Each hopping event is allowed if the neighboring site is empty or the Li-ion occupying the neighboring site is also moving simultaneously (concerted diffusion). The horizontal boundaries are set to periodic to emulate a large region of the surface. The vertical boundaries are closed (diffusion is not allowed beyond those borders). However, the left vertical boundary could be open (grand canonical ensemble), allowing the simulation of Li interchange with a Li reservoir (electrolyte). That could allow the simulation of Li plating conditions.

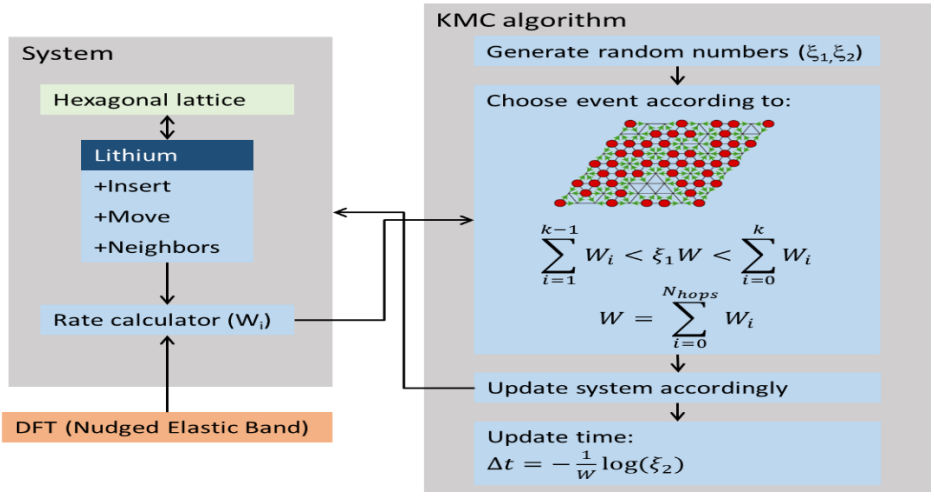

Figure I.4.K.11 Schematic of the Kinetic Monte Carlo approach to simulate the diffusion of Li in graphite under fast charging conditions using kinetic parameters from Ab Initio calculations.

Initial results are shown in Figure I.4.K.12. We tested our code using a simplified case, where the concerted diffusion of Li ions, and the effect of increased inter-layer spacing are not taken into account. Only individual Li hopping events took place. Complexity will be added in increments. Figure I.4.K.12a shows the evolution of a Li "front" from the surface (left boundary) moving into an empty graphite region. The initial condition emulates a pulse of current that produces a highly localized Li concentration region at the surface of a graphite particle. The system rapidly relaxes the high Li concentration at the surface. Afterwards, the diffusion of Li slows down until some regions reach the equilibrium LiC_6 local composition. Figure I.4.K.12b shows the concentration profile. The initial step function concentration profile relaxes into a flatter distribution.

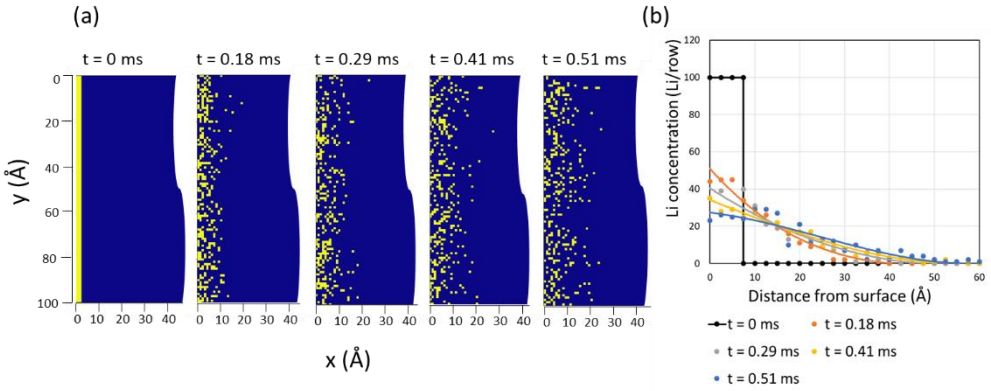

Figure I.4.K.12 Time evolution of Li concentration in the region close to the surface (x=0) of graphite. (a) Li ions (yellow pixels), coordinate change in graphite (blue pixels) with time. (b) Evolution of Li concentration profile with time.

To better understand the effect of different contributions to the overall transport properties, complexity has been added in increments. Namely, more hopping events have been incorporated in the algorithm that computes the rates in the KMC algorithm. In previous reports, we have shown (DFT)-level energy barriers computed for several different cases. Using this information, concerted diffusion is now taken into account. As an initial proof of concept, a simulation was set up with an initial very high concentration of Li ions in the surface region within the graphite layer (LiC_2). Figure I.4.K.13a shows a representation of the system and the corresponding Li profile. This simulation mimics the evolution of a Li "front" from the surface (left boundary) moving into an empty graphite region. The total amount of Li in the simulation corresponds to a global composition equivalent to LiC_6. The simulation box is closed. As a consequence, the current rate is zero at the surface (x=0). The step function-like Li concentration profile will drive the Li diffusion. Hence, the initial condition emulates a pulse of current that produces a highly localized Li concentration region (the LiC_2 region shown in yellow) at the surface of a graphite particle, relaxing into the inner empty graphite sites. The system rapidly relaxes the high Li concentration at the surface (see Figure I.4.K.13b). The KMC simulation shows that the diffusion of Li slows down when regions at the front of the new Li concentration profile reach the LiC_6 equilibrium local composition. The insets below the simulation boxes show the concentration profiles. The initial step function concentration profile relaxes into a "flatter" distribution.

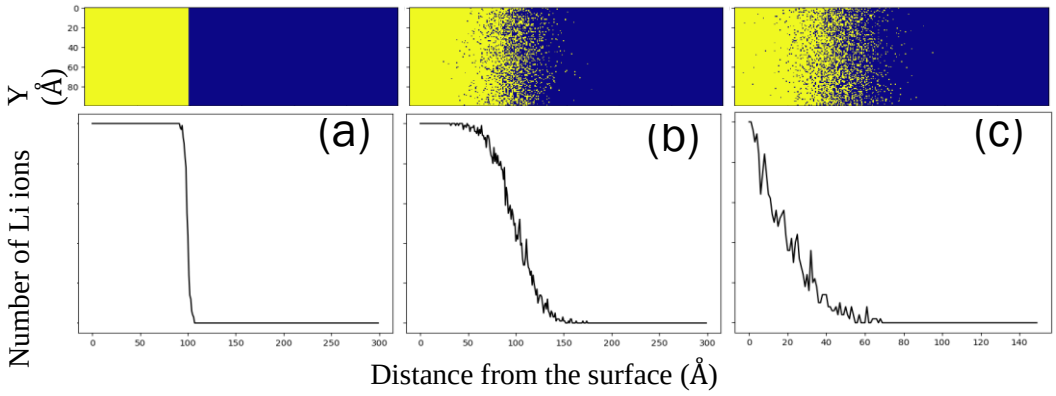

Figure I.4.K.13 Time evolution of Li concentration in the region close to the surface (x=0) of graphite. Li-ion (yellow-pixel) coordinates diffuse into graphite (blue pixels) with time. Insets represent the content of Li per column. (a) Initial state t = 0 ms, (b) t = 3.2 ms, and (c) t = 6.4 ms.

To simulate a constant current influx of Li, a simulation with an open boundary was set up. The left boundary of the simulation box (at x=0) is replenished with Li any time a vacancy is produced at that surface (at x=0

line). This situation emulates a high current rate where there is just enough Li to be "pushed" into the graphite. The initial condition, shown in Figure I.4.K.14a, has a small region (just three atomic layers) with high Li concentration while the rest of the simulation box is empty graphite. Figure I.4.K.14b shows the simulation box and Li profile after 0.5 ms. In agreement with the previous simulation, the initial movement of Li is very fast, reaching up to 30 Å from the surface in a very short time. Also in agreement with a previous simulation (relaxation), when a LiC_6 region is formed, the Li diffusion slows down.

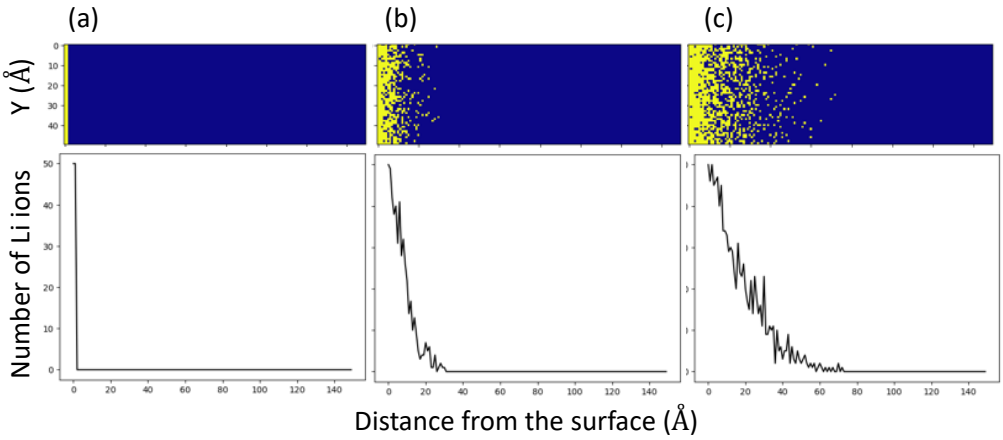

Figure I.4.K.14 Time evolution of Li concentration in the region close to the surface (x=0) of graphite. Li-ion (yellow-pixel) coordinates diffuse into graphite (blue pixels) with time. Insets represent the content of Li per column. The left boundary is open, and a current rate is set just enough to fill any vacancy at the surface. (a) Initial state t = 0 ms, (b) t = 0.5 ms, and (c) t = 5 ms.

Subsequently, the diffusivity was computed exploiting the random-walk theory using the expression:

$$\mathrm{D} = -\lim_{t\to\infty}\frac{1}{6t}\left[\sum_{t=0}^{\infty}\langle r(t+\Delta t)-r(t)\rangle\right]^2$$

where D is the diffusivity, t is the simulation time, and $r(t+\Delta t)-r(t)$ represents the change in position after a time interval Δt. The square brackets indicate an expectation value which is obtained by averaging over long-time intervals. Figure I.4.K.15 shows the change in diffusivity with time for the simulations previously described (relaxation and constant flux). The initial diffusivities are high for both scenarios, and as expected higher for constant flux case. As Li start to migrate into the empty sites of graphite within the particles, the diffusivity decreases and stabilizes at a lower value. That high concentration front favors Li hopping events with low energy barriers contributing to the initial high diffusivity values. Once LiC_6 domains form, now representing the Li new concentration front, as shown in Figure I.4.K.13b-c and Figure I.4.K.14c, the diffusivity decreases and stabilizes at a lower value. Hence, LiC_6 regions represent a bottleneck for Li diffusion in graphite.

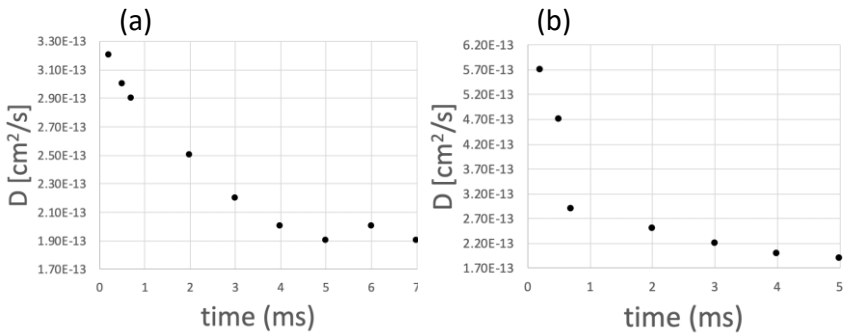

Figure I.4.K.15 Diffusivity change with simulation time for a system emulating a Li "front" diffusing into an empty graphite layer. (a) Relaxation of an initial LiC_2 surface region, and (b) high current rate keeping the surface vacancy free.

In order to reach larger length and time scales, the parallelization of the code was necessary. The python multiprocessing library was used to allow the code to run in a multicore machine. The increased performance of the code allowed the simulation of domains up to 200 nm long and times of up to 400 ms. Larger simulations are currently in progress, and we are adding more complexity to the model. For instance, the presence of defects (vacancies) in the graphite layer, allowing diffusion across the layer, increased Li diffusivity slightly (Figure I.4.K.16).

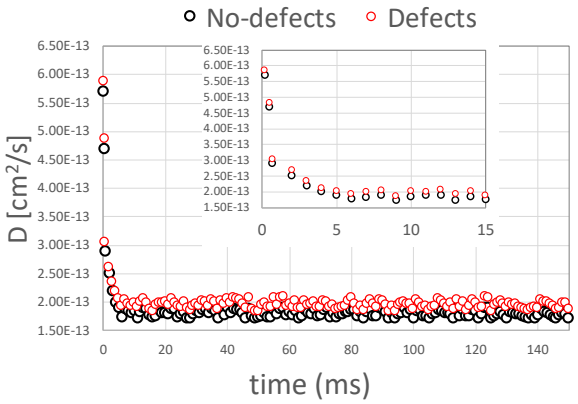

Figure I.4.K.16 Li diffusivity in graphite change with simulation time for a system with graphite defects.

The origins and heterogeneity evolution in R1 and R2 cells – via 2D high-energy XRD mapping – APS

Understanding the origin of fast charge limitations, capacity fade mechanisms, and lithium plating characteristics is critical for enabling practical fast charge technology in electric vehicles. Uneven battery performance throughout the electrode area may lead to non-uniform degradation across the cell, making it difficult to predict cell life and safety.

High-energy diffraction (59 keV), collected at the 11-ID-B beamline of the Advanced Photon Source (APS) at Argonne National Laboratory, is used to probe electrode composition and structure across the entire cell area. The reconstructed 2D maps of composition (anode) and lattice parameters (cathode) are derived based on fitting of the diffraction patterns, collected in transmission mode through the battery stack using a 1-mm, step-size grid with 0.5-mm beam size. The resulting maps visualize the development and evolution of heterogeneity in Round 1 and Round 2 electrodes at different stages of cycle life. In this study, we track NMC532 (0 0 3) and (1 0 -5) reflections, as well as Li_xC_6 (0 0 z) reflections and search for signs of lithium plating by detecting the presence of Li metal (1 1 0) reflection.

The cells were operated under fast charge conditions according to the 6-C constant current constant voltage (CCCV) 3- to 4.1- procedure. The formation step followed 1.5 V tap charge, three C/10 cycles with a 3- to 4.1-V window (Figure I.4.K.17), three C/2 cycles with a 3- to 4.1-V window, and ending with partial charge to 3.5 V. Cells were cycled under a 4 psi stack pressure. Long-term cycling was performed up to 1200 fast cycles at 6-C charge and C/2 discharge rates within a 3- to 4.1-V voltage window.

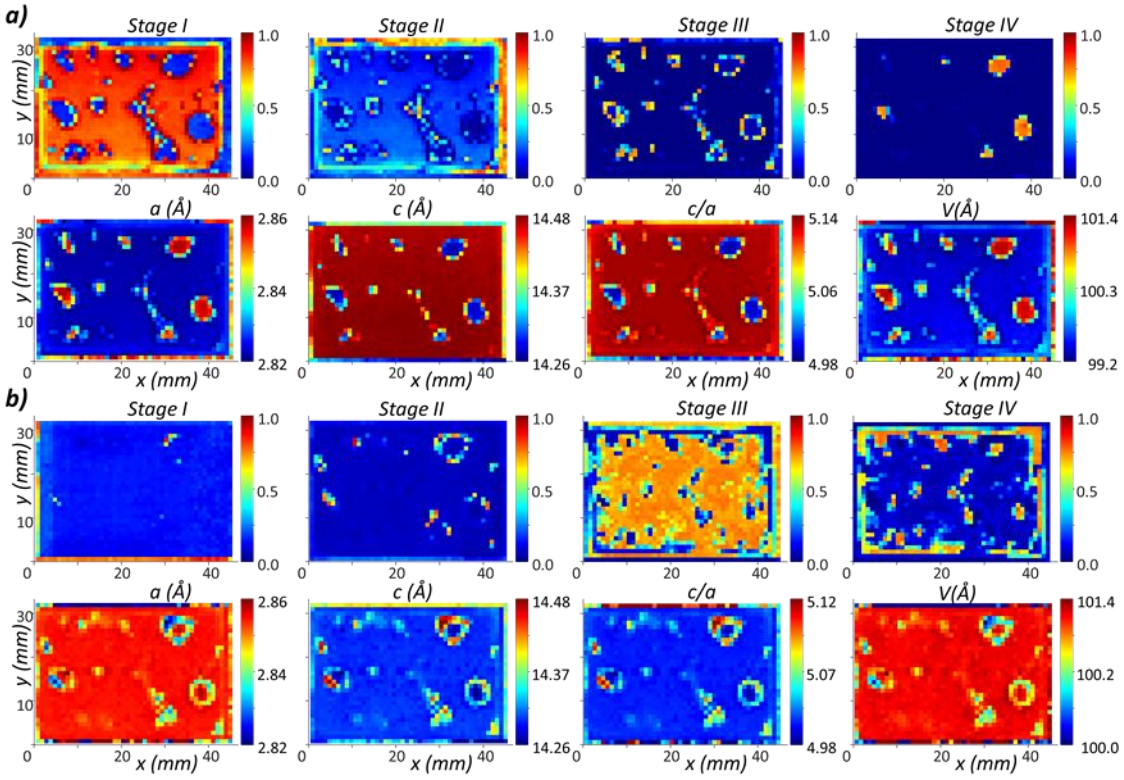

Figure I.4.K.17 Area map of fresh cell subject to (a) first formation charge to 4.1 V at C/10 rate and (b) first formation discharge to 3 V at C/10 rate. Graphite lithiation modeled according to a simplified 4-stage model, Stage I–Stage IV, relating x in Li_xC_6: x=1.

While thin (40-µm) electrode Round 1 cells are designed to maximize performance, thick electrode (70-µm), Round 2 cells are designed to maximize volumetric capacity for increased driving range. The diffraction maps track electrode uniformity through extended cell life (1200 cycles) and are used to understand the origins and significance of observed heterogeneities (Figure I.4.K.18). Previously, it has been shown that fast charging drives higher levels of heterogeneity compared to slow charging, and this may play a role in the onset of lithium plating. Through comparison of Round 1 cells, cycle 0 (C/2 charge) and cycle 6 (6-C charge), it is apparent that fast charge not only lowers average charge capacity, but also induces spatial heterogeneity across both anode and cathode. In the early stages, residual cell outgassing temporarily lowers local area cycling efficiency, resulting in areas with lower-than-expected (based on electrochemistry) anode lithiation as shown by the bubble-shaped poor performance region. However, large consolidated bubbles do not appear to be stable over the long run; and by cycle 200, there is no evidence of this initial heterogeneity element. Instead, by cycle 200, heterogeneity is dominated by a center to edge regions, with highly lithiated edges and a moderately lithiated central region of the anode (Figure I.4.K.18). The total lithium balance suggests gradual depletion of lattice-lithium (lithium stored either in anode or cathode) in the center region at a higher rate than the edges. As Figure I.4.K.19 shows, by cycle 1200, center to edge heterogeneity is still present although lattice-lithium

has been lost throughout the cell. The total lattice-lithium balance decreases steadily over cycle life, suggesting capacity fade is due to permanent loss of lithium inventory.

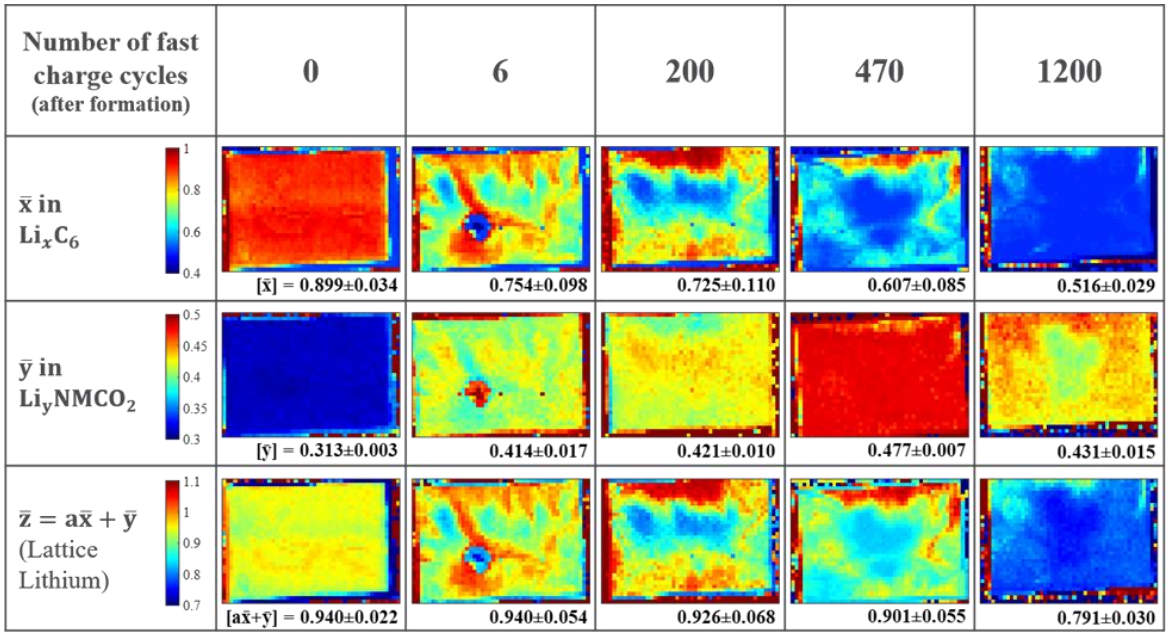

Figure I.4.K.18 Tracking of full charge lithium content and heterogeneity at cycle 0 (before fast charging), 6, 200, 470, and 1200. Anode ($\bar{x}$) and cathode ($\bar{y}$) contributions as well as total lattice-lithium balance ($\bar{z}$) maps are shown.

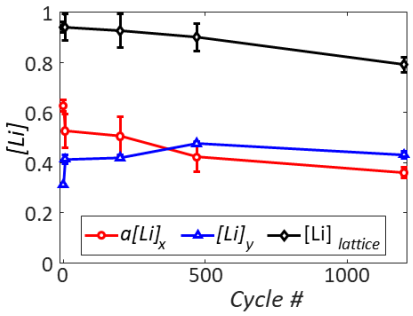

Figure I.4.K.19 Evolution of average lithium content within cell components and total balance of lattice-lithium.

A key safety concern for fast charging is identification of high-risk areas of lithium plating on the anode. Understanding the onset of plating is critical for safe operation of lithium-ion batteries with graphite anodes. A small amount of lithium plating late in cycle life was detected for Round 1 by monitoring for the Li (1 1 0) crystallographic reflection. The regions where lithium metal was located do not correlate with the earlier observed overall heterogeneity, which we attribute to cathode aging.

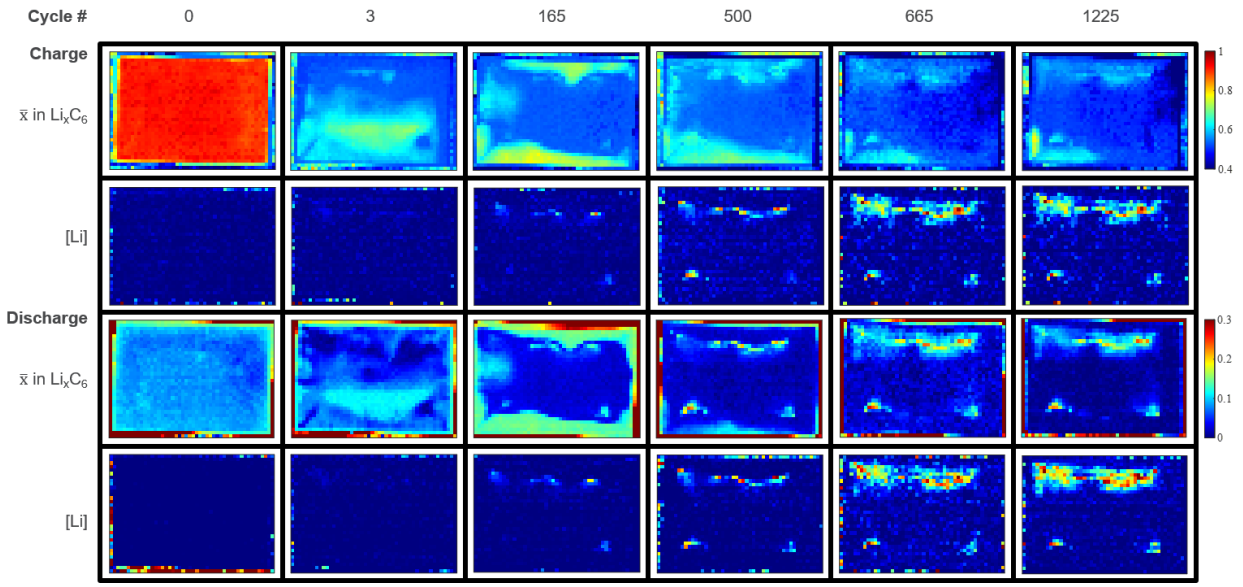

Figure I.4.K.20 Evolution of anode charge and discharge intercalated lithium heterogeneities and corresponding plated lithium concentrations for a Round 2 cell.

Round 2 cells were mapped at both charge and discharge at different points of extended cycle life (>1200 cycles). The graphite lithiation is a rough approximation based on a four-stage model with Li_xC_6 (stage I: x=1, stage II: x=1/2, stage III & IV: 1/2>x(III)>x(IV)>0). An initial baseline set of charge (C/2-CCCV) and discharge (C/2-CC) maps show a homogeneous anode. Fast charging quickly diversified the cell performance and by cycle 3, the distinct heterogeneity patterns can be recognized (Figure I.4.K.20). It should be noted that regions with more complete delithiation after only 3 cycles overlap with lithium plating regions in the later stages of battery life. By cycle 165, observable plating sites were established and with time the amount of lithium and the plating area grew; however, new plating sites were not observed, suggesting that unique nucleation sites are established only in earlier cycle life. Most of the plating appears to have formed in the first half of the 1200+ cycle life as the intensity and distribution of the Li (2 0 0) peak across the diffraction map changed little between cycle 665 and 1225 (Figure I.4.K.21). Notably, in all cases the positions where plating was observed and their relative intensity corresponded to locations and intensities of "trapped" LiC6 phase at discharge. This correlation shows that plating traps fully during the intercalated lithiated graphite phase.

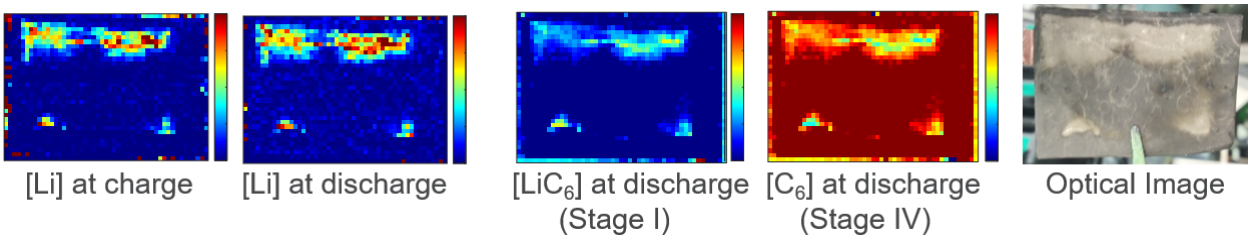

Figure I.4.K.21 Correlation of plated lithium to LiC_6 phase spatial distribution and relative intensity at cycle 1225 for a Round 2 cell.

Neutron imaging to measure electrolyte wetting – ORNL

The partial saturation of electrodes by electrolyte can contribute to the non-uniform distribution of lithium plating during extreme fast charging. It is assumed that as the electrolyte seeps and spreads in the electrodes during back filling of pouch cell under vacuum, gases are trapped as a ring toward the outer edge of the cell. Also, there is a tendency of electrolyte saturation along the edges that could cause gases generated during formation cycle to be trapped in the electrode layers causing these patterns. Though high-energy XRD experiments were conducted, they can only be used to understand the irreversible plating of the inactive lithium after the repeated fast charge cycles, whereas neutrons' radiography can be used to understand the

internal structure as they strongly attenuate light elements like hydrogen and lithium. Because the electrolyte has both lithium salt $LiPF_6$ and hydrogen groups, the distribution in the cross-sectional area with any gases trapped will generate good contrast, providing heterogeneity maps across large format cells.

A proof-of-principle work was carried out at ORNL using neutron radiography on the single-layer pouch cells to identify the electrolyte saturation and wetting of electrodes. A total of six pouch cells were imaged and studied for identifying the electrolyte saturation in the electrodes. Out of six cells, three dry cells were studied for variation in transmission signal. The 2D radiographs showed uniform distribution of signal, indicating that the electrode coating does not significantly vary the beam attenuation. The remaining three are wet cells, filled with electrolyte in excess of the pore volume and are cycled for a week, degassed, and discharged to 10% SOC. In Figure I.4.K.22a, we show the neutron transmission distribution that is normalized with open beam and dark field profiles and corrected to the dry cells. The image clearly suggests variations in transmission distributions due to electrolyte saturation along the edges of the pouch cell. Next, the profiles along three distinct locations parallel to the x and y axes are shown indicating a 20%–30% variation of the signal. Finally, in Figure I.4.K.22c, a neutron tomography(ct-scan) of the same pouch cell clearly showed 3D gas pockets in the cell that are generated during the formation process and trapped within the electrodes. Because the initial in-situ neutron imaging results clearly demonstrate electrolyte saturation distribution in the pouch cell, we planned extensive studies to correlate the neutron absorption during fast charge to quantify lithium plating next quarter.

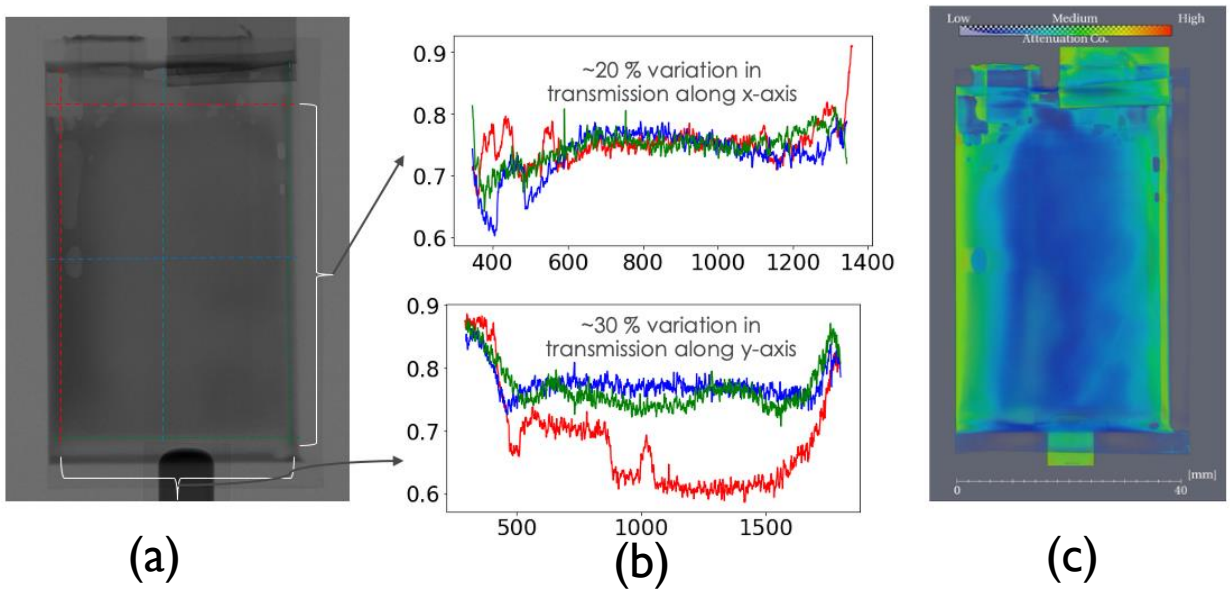

Figure I.4.K.22 In-situ neutron imaging results: inset (a) radiography imaging showing transmission distribution; inset (b) profiles showing variation of transmission along horizontal and vertical lines; and inset (c) tomography showing gas pockets and electrolyte distribution.

Second-generation lithium plating model with nucleation and plating dynamics – ORNL

One of the important challenges under fast charge conditions is the lithium plating on graphite anode, which severely degrades the performance and cycle life of the batteries. To this end, the ORNL team has developed theoretical formulation and computational framework for modeling the lithium nucleation, plating, and stripping phenomenon on the charged surfaces. To pose this problem consistently, we have to overcome many challenges, such as evaluation of the complex interplay of surface energetics of different interfaces such as electrolyte/graphite particle surfaces, graphite particle/metallic lithium, and electrolyte/metallic lithium that effects the transport of lithium ions and overall intercalation kinetics. We have developed a thermodynamically consistent variational theory to comprehensively consider the lithium plating at the electrolyte and graphite

particle interface, in addition to the intercalation of the lithium into the graphite particles. The formulation provides a rational basis to understand the nucleation and growth kinetics of lithium deposits, along with the effect of lithium plating on the lithium intercalation kinetics in graphite under fast-charge conditions. Within this framework, the sum of contributions from structural and chemical energy from different phase fractions, $\{\xi_i\} = \xi_l, \xi_e, \xi_a$: the lithium metal, ξ_l, the electrolyte region, ξ_e, and the anode graphite particles, ξ_a, the electrostatic energy density, $\rho\phi$, and the interfacial energies to the total free energy functional, is given by:

$$G[\{\xi_I\},\{c_j\},\rho;T] = \int_\Omega \left[g(\{\xi_i\}, c_j, T) + \frac{\alpha_l}{2}|\nabla\xi_l|^2 + \frac{\alpha_e}{2}|\nabla\xi_e|^2 + \frac{\alpha_a}{2}|\nabla\xi_a|^2 + \frac{\alpha_c}{2}|\nabla c_j|^2 + \rho\phi \right] d\Omega \quad (1)$$

where ρ is the electrostatic charge per unit volume, ϕ is local electrostatic potential, α_l is the gradient energy coefficient of the lithium-electrolyte interface, α_e is the gradient energy coefficient of the electrolyte-graphite interface, α_a is the gradient energy coefficient of the graphite-lithium interface, and $\alpha_{c_j}$is the gradient energy coefficient of chemical species.

The controlled reaction rates of lithium intercalation, $\overrightarrow{\Gamma_{\text{int}}}$, and lithium plating, $\overrightarrow{\Gamma_{\text{pla}}}$,, and the Butler-Volmer reactions on graphite/electrolyte interface are incorporated in the variational framework, and the resultant kinetic equations are:

$$\frac{\partial \xi_l}{\partial t} = -M_{\xi_i}\left[\frac{\partial g}{\partial \xi_l} - \alpha_l \nabla^2 \xi_l - \frac{\alpha_a}{2}\nabla^2 \xi_a + \omega_j \overrightarrow{\Gamma_{\text{pla}}} \cdot \nabla \xi_a\right]$$

$$\frac{\partial c_j}{\partial t} = \nabla \cdot M_j \nabla\left[\frac{\partial g}{\partial c_j} - \frac{Z_j F \phi}{\omega_j}\right] - \nabla \cdot M_j \alpha_{c_j} \nabla^3 c_j - \omega_j \overrightarrow{\Gamma_{\text{pla}}} \cdot \nabla \xi_a + \omega_j \overrightarrow{\Gamma_{\text{int}}} \cdot \nabla \xi_a \quad (2)$$

$$\frac{\partial \rho}{\partial t} = \nabla \cdot \kappa \nabla \phi + \frac{F}{\omega_j}\left(\nabla \cdot M_j \nabla\left[\frac{\partial g}{\partial c_j}\right] - \nabla \cdot M_j \alpha_{c_j} \nabla^3 c_j\right) - Z_j F \overrightarrow{\Gamma_{\text{pla}}} \cdot \nabla \xi_a + Z_j F \overrightarrow{\Gamma_{\text{int}}} \cdot \nabla \xi_a$$

The first row of Equation 2 corresponds to time evolution of lithium phase following a non-conserved Allen-Cahn kinetics coupled with a lithium plating interfacial reaction. The second row represents the mass transport equation following a Cahn-Hilliard kinetics due to local gradients in electrochemical potential in addition to interfacial Butler-Volmer reactions. The last row corresponds to a charge continuity equation. The resulting formulation captures all of the physical processes that are relevant during the Li plating phenomenon, that is, charge and species transport through both phases (i.e., liquid electrolyte and solid graphite particle), nucleation, and growth of the Li deposit.

Figure I.4.K.23 demonstrates the effect of nucleation and growth of metallic lithium on the lithium diffusion into the graphite particle under the fast charging condition of an applied current density of 100A/m^2. In the initial stages of charging (i.e., at t=60 s), the nucleation of the metallic lithium (see Figure I.4.K.23a) occurs on the interfacial sites on the graphite particle where the local change in potential across the interface is given by $\Delta\phi = \phi_s - \phi_e < 0$. Here ϕ_s is the local electrostatic potential in solid graphite particle, and ϕ_e is the local electrostatic potential in liquid electrolyte near the graphite/electrolyte interface. The new nucleated metallic lithium particles are highly conductive and induce a nearly zero local overpotential for lithium intercalation, which obstructs the Butler-Volmer intercalation reaction, and thus decreases the fraction of lithium intercalation at the tip of the graphite particle (see Figure I.4.K.23d). At t=180 s, the metallic lithium nucleates at new sites as show in Figure I.4.K.23b. The neighboring lithium particles coalesce to minimize the excess interfacial energy results in lithium plating, which in turn slows down the interfacial intercalation kinetics (see Figure I.4.K.23e). At t=600 s (Figure I.4.K.23,f), a thick metallic lithium strip is grown on the tip of the graphite particle along with some small isolated new lithium nuclei. The plated metallic lithium further slows down the lithium intercalation kinetics in the graphite particle.

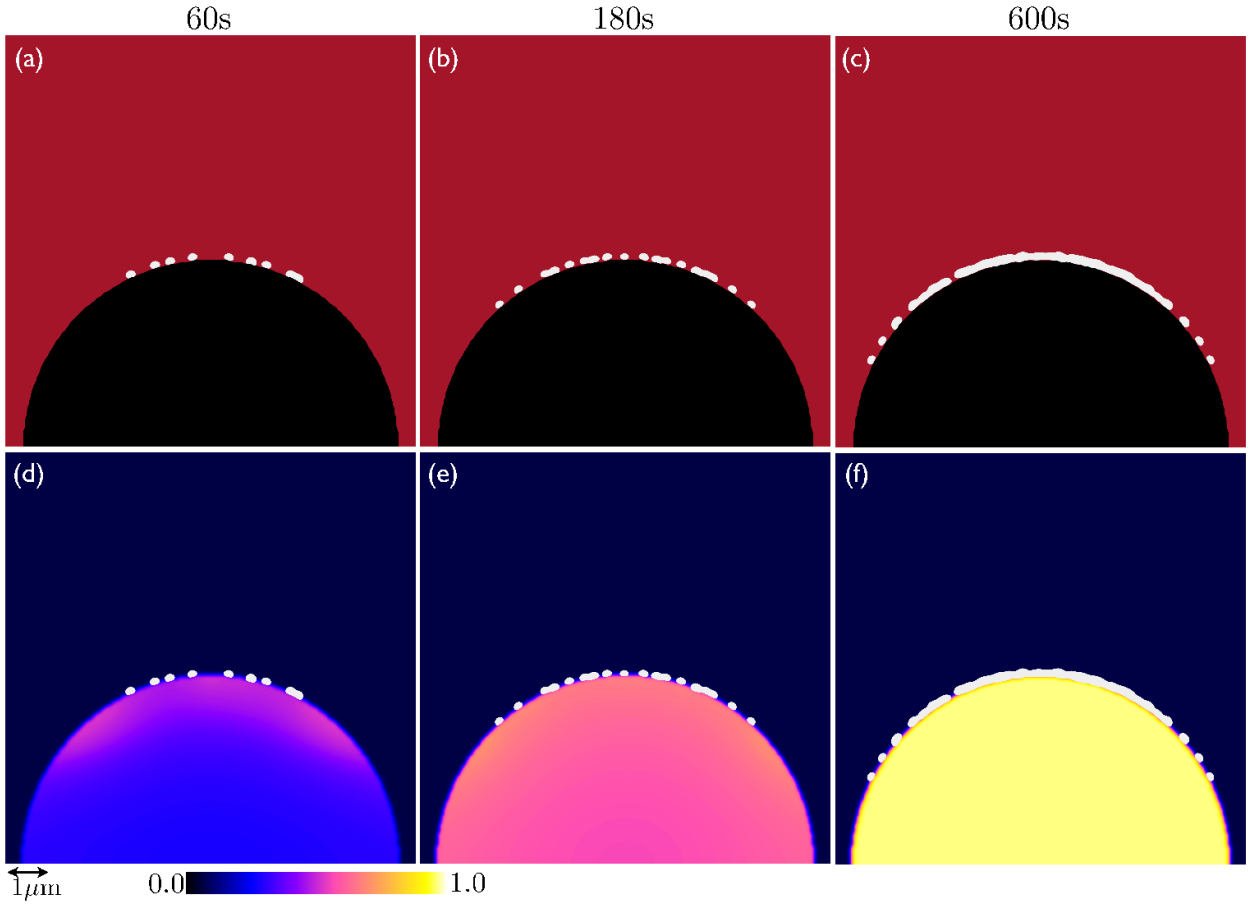

Figure I.4.K.23 Simulated metallic lithium nucleation and plating kinetics under a charging condition for an applied current density of 100A/m² at selected times: t=60 s (first column), t=180 s (second column), and t=600 s (third column). The top row shows metallic lithium phase evolution. The bottom row shows an intercalation fraction of lithium in the graphite.

The model has a capability to understand the multi-particle interfaces interaction as shown in Figure I.4.K.24a. For a fast charging condition, the interactions of surfaces affect the amount of lithium deposition on the particles due to change in local overpotential values. Also, the framework has a capability to predict the lithium plating for different physical parameters such graphite/electrolyte surface tension and molar volume of electrolyte, as shown in Figure I.4.K.24b.

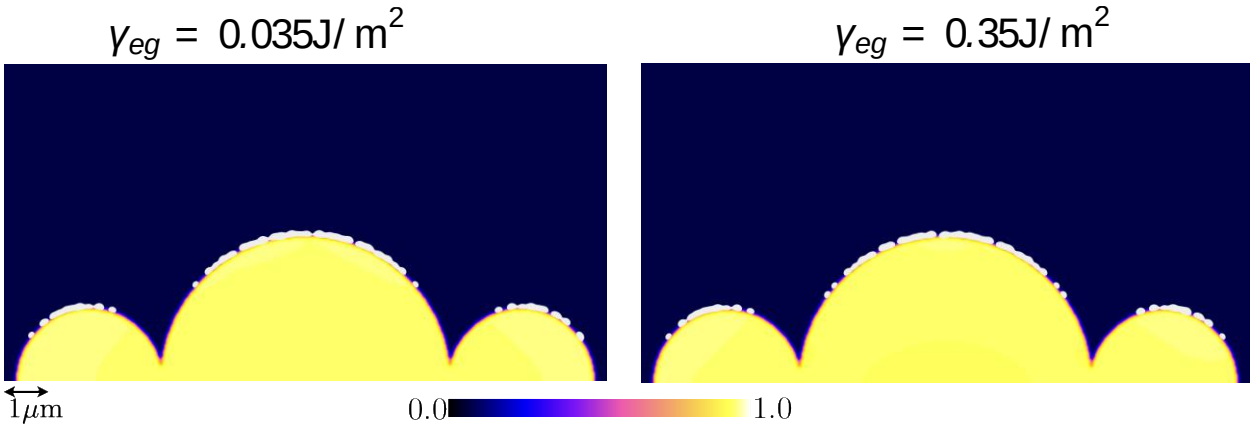

Figure I.4.K.24 Simulated metallic lithium nucleation and plating kinetics under a charging condition for an applied current density of 100A/m^2 for multi-particles graphite anode for two different surface tension properties of graphite/electrolyte interface.

Next, we studied the effect of anisotropic diffusivity properties of graphite particle in edge and basal plane directions on lithium nucleation and plating kinetics and their impact on overall lithium intercalation. In the initial stages of charging (i.e., at t=60 s), for orientation, $\theta = 0°$, the nucleation of the metallic lithium (see Figure I.4.K.25a) occurs on the tip of the particle. At t=180 s, more metallic lithium nucleates at the tip of the particle as show in Figure I.4.K.25b. At t=600 s, the neighboring lithium particles at the tip coalesce to minimize the excess interfacial energy that results in lithium plating, which, in turn, slows down the interfacial intercalation kinetics as shown in Figure I.4.K.25c. At t=60 s, for orientation, $\theta = 90°$, there is negligible nucleation (see Figure I.4.K.25d). A few lithium particles are nucleated on the lateral side of the graphite as shown in Figure I.4.K.25e. At t=600 s, more isolated lithium nuclei are observed on the graphite surface. Overall, the analysis indicate that lithium intercalation is suppressed in $\theta = 0°$because the lithium plating is large as the lithium-ion flux direction is in parallel to slow diffusion path of Z-direction. In contrast, lithium plating is small in $\theta = 90°$, and subsequently fast in intercalation kinetics. Further, we demonstrate the advanced capability of studying the nucleation and plating kinetics of a polycrystalline graphite as shown in Figure I.4.K.26.

The formulation presented herein allows to incorporate SEI effects and other interfacial electrochemical reactions, such as lithium metal/graphite re-intercalation and electrolyte/lithium metal for dendrite growth during overcharging conditions. Finally, the framework we developed is a good starting point to spatially predict the amount of plated lithium in the complex graphite anode microstructures including such effects as surface tension, particle sizes, porosity, tortuosity, etc., and allowing us to design the optimized physical electrolyte properties and operating conditions.

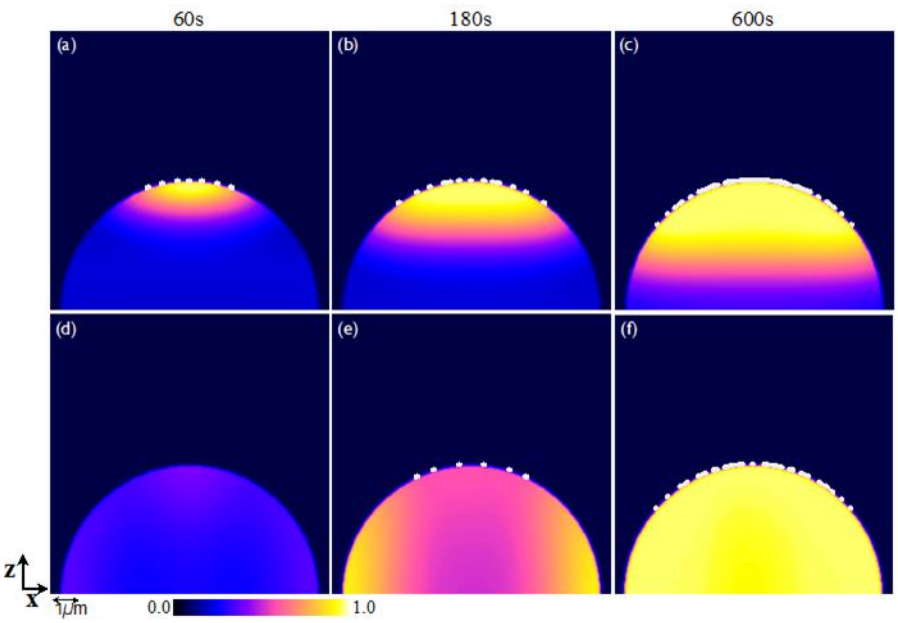

Figure I.4.K.25 Simulated metallic lithium nucleation and plating kinetics under a charging condition for an applied current density of 100A/m² at selected times: t=60 s (first column), t=180 s (second column), and t=600 s (third column). The top row shows intercalation fraction of lithium in the graphite particle in which the diffusivity in Z-direction (normal to basal plane) is six orders of magnitude smaller than the diffusivity in X-direction (parallel to basal plane), that is, with an orientation of $\theta = 0°$. The bottom row shows the intercalation fraction of lithium in the graphite particle of orientation, $\theta = 90°$, where the diffusivity in X-direction is six orders of magnitude smaller than the diffusivity in the Z-direction.

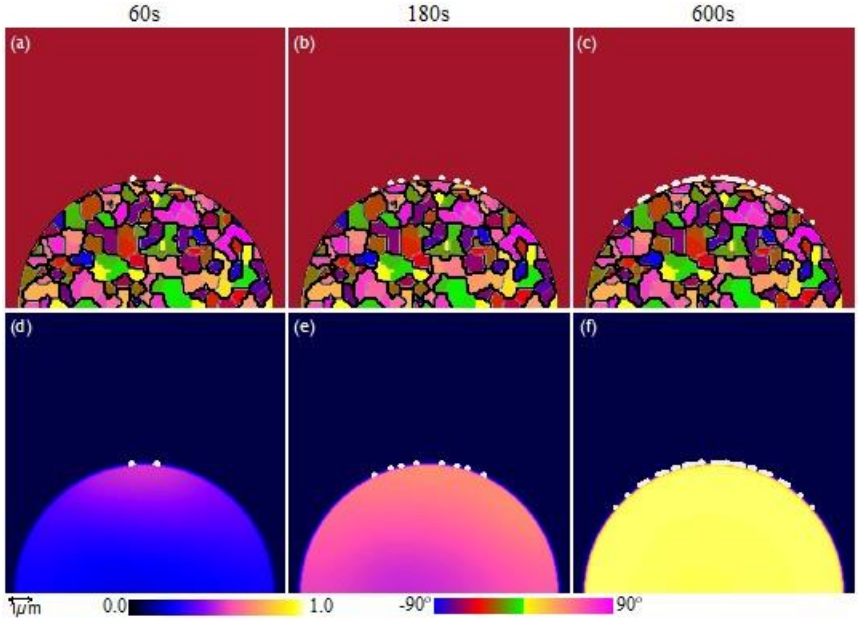

Figure I.4.K.26 Simulated metallic lithium nucleation and plating kinetics under a charging condition for an applied current density of 100A/m² at selected times: t=60 s (first column), t=180 s (second column), and t=600 s (third column). The top row shows the metallic lithium phase evolution on a randomly distributed orientation of a polycrystalline graphite. The bottom row shows the intercalation fraction of lithium in the polycrystalline graphite.

Intercalation and lithium plating kinetics on edge/basal plane graphite – LBNL

Improved fast-charging performance of lithium-ion batteries requires an accurate understanding of the lithium intercalation currents that can be sustained, and the conditions under which Li plating is initiated, at the graphite anode. In practical graphite anodes, characterization of these processes is complicated by the three-dimensional porous composite nature of the anode and its interaction with an electrolyte whose lithium concentration at the interface with the graphite varies as a function of depth within the electrode during fast charging. The goal of our work is to determine some of the fundamental factors at play by performing experiments using planar, highly oriented pyrolytic graphite (HOPG) samples. HOPG is as close to monocrystalline graphite as is commercially available, and consists of a stack of graphite planes, with in-plane grain sizes on the order of 0.1–1 mm. It is therefore possible to study the difference in lithium intercalation and plating behavior on edge and basal planes as a function of (well-defined) current density on these samples.

In order to perform electrochemical experiments selectively on only basal or only edge plane graphite, pieces of HOPG were cleaved and mounted as shown in Figure I.4.K.27a. A piece of HOPG with the edges covered in Kapton tape served as the basal plane sample, and a piece of HOPG conductively bonded edge-on to a Cu disc and embedded in an insulating and inert epoxy served as the edge plane sample. Basal plane samples were reused between experiments by exfoliating a fresh layer of graphite, whereas edge plane samples were reused by polishing the surface using sandpaper and suspensions. The optimization of the polishing process is shown in Figure I.4.K.27, indicating that a very smooth finish — and thus accurate active area — was obtained, along with a Raman spectrum indicative of a surface with pure edge character.

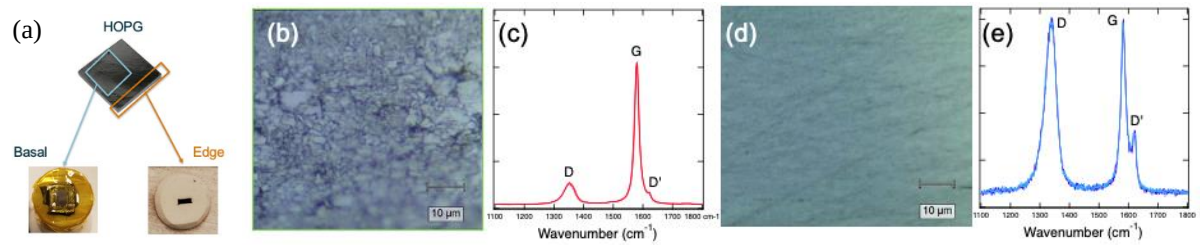

Figure I.4.K.27 (a) Photographs of HOPG and basal and edge type electrodes. The edge electrodes were polished between experiments, and the polishing process optimized them from a coarse (b,c) to a fine (d,e) finish. Microscopy images are shown in (b,d), Raman spectra in (c,e). The D' peak is a signature of edge graphite, validating the preparation process.

On both surfaces, cyclic voltammetry (CV) at 0.1 mV/s was performed for initial electrochemical characterization and to mimic the formation process applied to composite electrodes. Linearly increasing current ramps, and galvanostatic cycling at current densities near limiting values, was applied with a 0 V (vs Li/Li^+) cut-off to determine the maximum intercalation currents that can be sustained while avoiding Li plating, and cyclic voltammetry to negative voltages was performed to determine the onset of Li plating. Results are shown in Figure I.4.K.28.

Cyclic voltammograms show distinctly different behavior on edge and basal planes. Basal plane graphite sustains less than 25 $\mu A/cm^2$ and exhibits highly irreversible electrochemistry. Most likely this is electrolyte reduction, though irreversible Li insertion cannot be definitively ruled out. Conversely, edge plane graphite sustains currents of 2–3 mA/cm^2 and exhibits highly reversible electrochemistry, indicative of Li intercalation and de-intercalation. Nevertheless, the total irreversible capacity loss per cm^2 is higher for edge than basal planes. This finding suggests that there is more SEI growth on edge than on basal planes, in agreement with the literature.

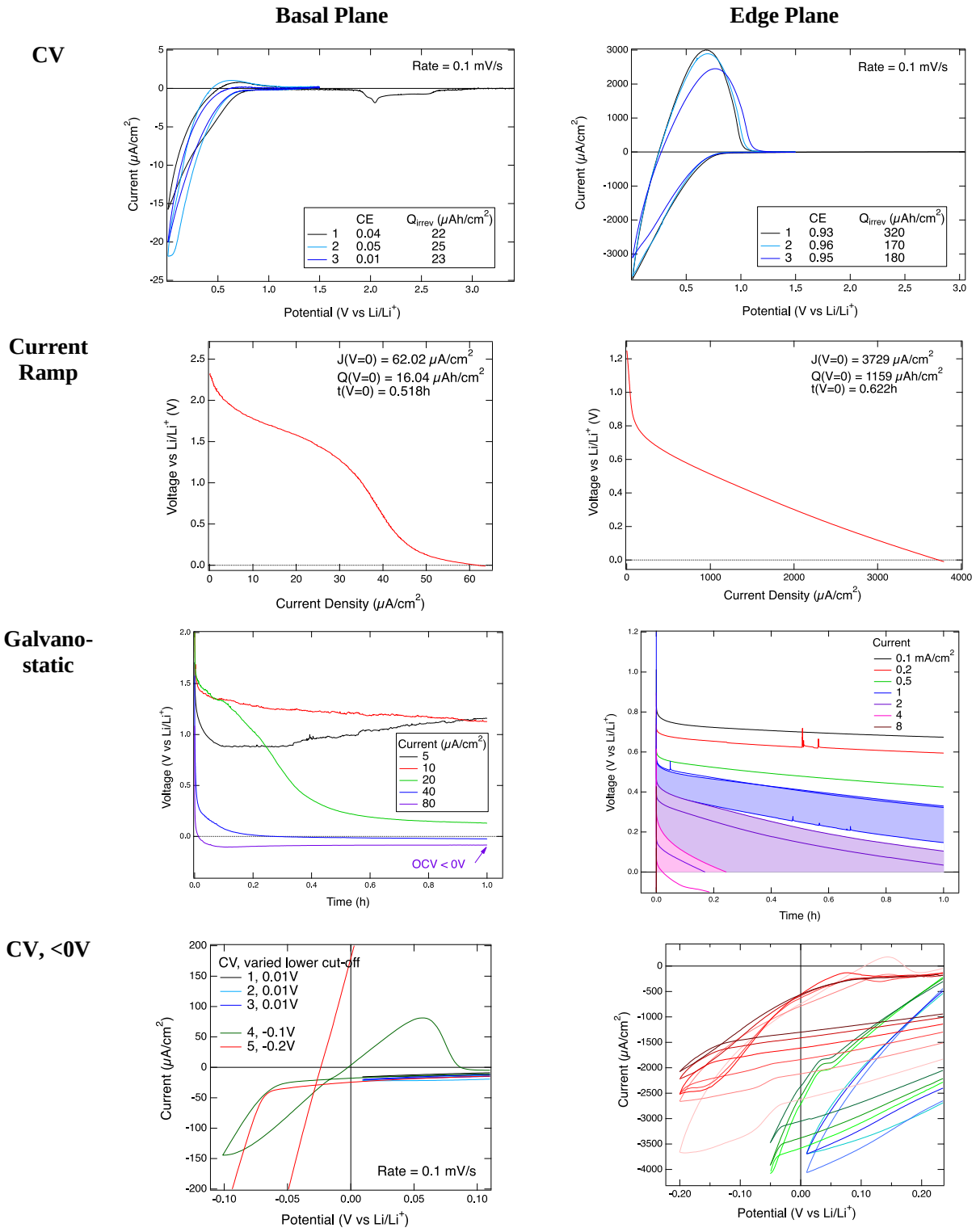

Figure I.4.K.28 Electrochemical data obtained on basal and edge plane HOPG samples shown in Figure 1(a). Apart from the CV measurement itself, all measurements are preceded by three CV cycles (0.1 mV/s, 0.001-1.5V).

In order to determine the current densities that can be sustained in the time frame of 0.1–1 h, which is relevant for fast charging, linear current ramps were applied for about 0.5 h. Again, basal and edge planes exhibit very different behavior: basal planes sustain no more than 60 µA/cm^2 above 0 V, whereas edge planes sustain more

than 3.7 mA/cm^2. Galvanostatic measurements at current densities in the vicinity of these limiting currents for up to 1 h indicate that 20 µA/cm^2 can be sustained above 0 V, while currents of 40 µA/cm^2 will lead to negative potentials on basal planes after 15 mins. For edge planes, measurements were applied multiple times, and the range of profiles obtained were shaded in the relevant panel in Figure 2, where it is evident that 1 mA/cm^2 can generally be sustained for 1 h, and 2 mA/cm^2 can mostly be sustained for the time windows required for fast charging, while remaining above 0 V.

Charging at current densities that do not require negative voltages is important to avoid Li plating. The cyclic voltammograms to negative cut-off voltages show that Li plating occurs at very moderate negative voltages, -0.03V on edge planes and -0.06V on basal planes. Electrodes ought to remain entirely above these voltages to avoid Li plating.

The full dataset in Figure I.4.K.28 provides invaluable input for simulations of composite electrodes containing graphite with edge- and basal-type surfaces. In addition, a simple estimate of what these results mean for fast charging of composite graphite anodes can be made. Taking as an example the Round 2 graphite anode manufactured by the CAMP facility within this project ― with its 3 mAh/cm^2 capacity, 9.1 mg/cm^2 loading, and use of SLC 1506 T graphite with a BET surface area of 2 m^2/g and D50 particle size of 8 µm ― yields an electrochemically active area of 30 cm^2 per cm^2 of electrode area assuming 8-µm graphite spheres, and 180 cm^2 per cm^2 of electrode area when using the BET area. The discrepancy indicates that the graphite particles have a tortuous surface, and good electrolyte wetting can determine which of these two bounds is more accurate. Using these values as upper and lower bounds, the limiting current of 2 mA/cm^2 translates to 60–360 mA/cm^2 on the composite electrode level, or 20–120 C, assuming graphite with fully edge-like surfaces.

This work has yielded reproducible quantitative data on limiting intercalation currents and plating onset potentials on basal and edge plane graphite. It provides valuable input for the electrochemical modeling conducted within XCEL, and has shown that graphite is compatible with charging at extremely high rates provided that potential variations within the anode are minimized and graphite with a large proportion of edge-like surface is used.

Microstructure electrochemical model to investigate heterogeneity at particle to electrode length scale – NREL

NREL used its suite of microstructural models to quantify microstructure heterogeneity and evaluate its impact on electrochemical performances and onset of the lithium plating degradation mechanism. Heterogeneity is either introduced directly with tomography-based electrode volumes or, for lower scale variations for which imaging is limiting, numerically generated through stochastic processes (separator heterogeneity, particle cracks and surface roughness) or deterministic process (carbon-binder heterogeneity). Heterogeneity is then quantified through microstructure characterization, for which correlations with tortuosity factors are established, and microstructure direct numerical simulation, for which the electrochemical response is calculated along with its own heterogeneity.

Particle scale morphology heterogeneity: Particle-scale heterogeneity analysis requires particles to be identified individually. NREL has developed an in-house particle identification algorithm that is more efficient than the baseline watershed algorithm commonly used in the literature [4]. The new method has been used to establish generic microstructure-tortuosity factor correlation on a large variety of electrodes and porosity, indicating that porosity and particle elongation, both tunable to a certain extent during the manufacturing process, control the tortuosity factor (Figure I.4.K.29a-b). Microstructure scale analysis also revealed that microstructure heterogeneity is increasing with the tortuosity factor: wider distribution of particle elongation, particle sphericity, and geometric tortuosity have been calculated for the higher tortuosity factor electrodes, suggesting that tortuosity and heterogeneity are linked. The result indicates that for electrodes with high tortuosity factors, the shortest ionic diffusion path from the current collector to separator interfaces, and vice-versa, is less uniform (in addition to being longer) compared with electrodes with lower tortuosity factors,

which means higher levels of in-plane heterogeneity are to be expected for the electrochemical response of high-tortuosity electrodes, in addition to being less transport-capable in general. Algorithms developed in this work have been published open source.

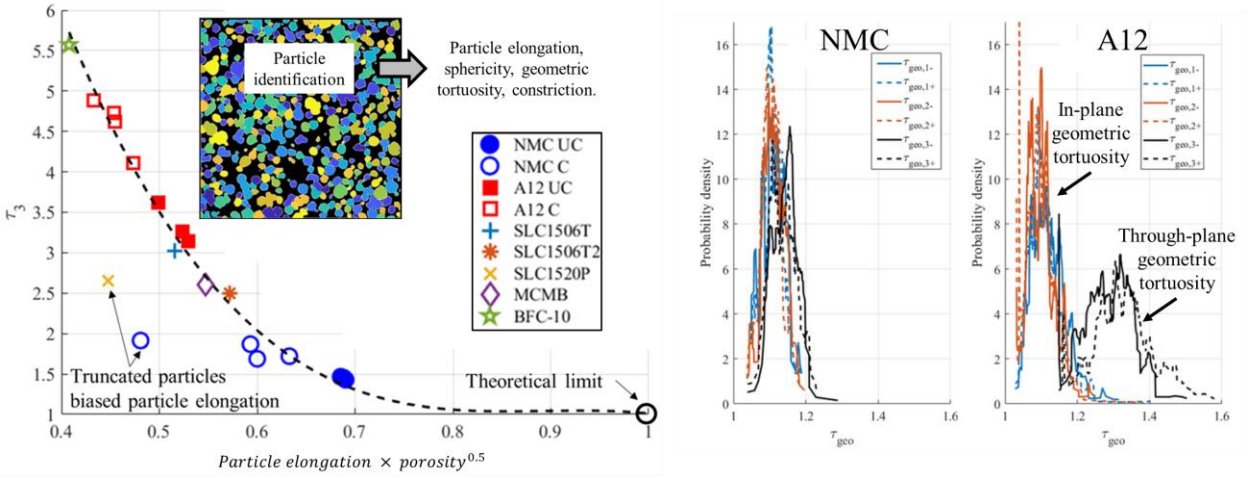

Figure I.4.K.29 (a) Tortuosity factor correlated with porosity and particle elongation for a large variety of electrode, and (b) wider diffusion path heterogeneity for the higher tortuosity electrodes.

Particle size heterogeneity: Mixing powders with different particle size (e.g., SLC1506T2 and SLC1520P) is a relevant approach to reach denser electrode and thus higher theoretical capacity. Indeed, packing density of unisize spherical particles is lower than bi-modal spherical particles as smaller particles can fill the gaps between larger particles, effectively reaching a higher density packing. Nested scale theoretical analysis indicated that a bi-modal particle size distribution could have either a positive, neutral, or negative impact on the ionic diffusion depending on the diffusion coefficients of both scales. To produce more conclusive results, NREL has calculated tortuosity factors on single and mixed NMC powder electrodes furnished by UCSD and imaged by UCL. Figure I.4.K.30 reveals that a single powder (although with a very wide unimodal size distribution) exhibits better ionic diffusion compared with a mixed powder (although with significantly narrower peaks) with effect more pronounced for the low porosity region, indicating particle size heterogeneity is to be controlled to improve ionic diffusion.

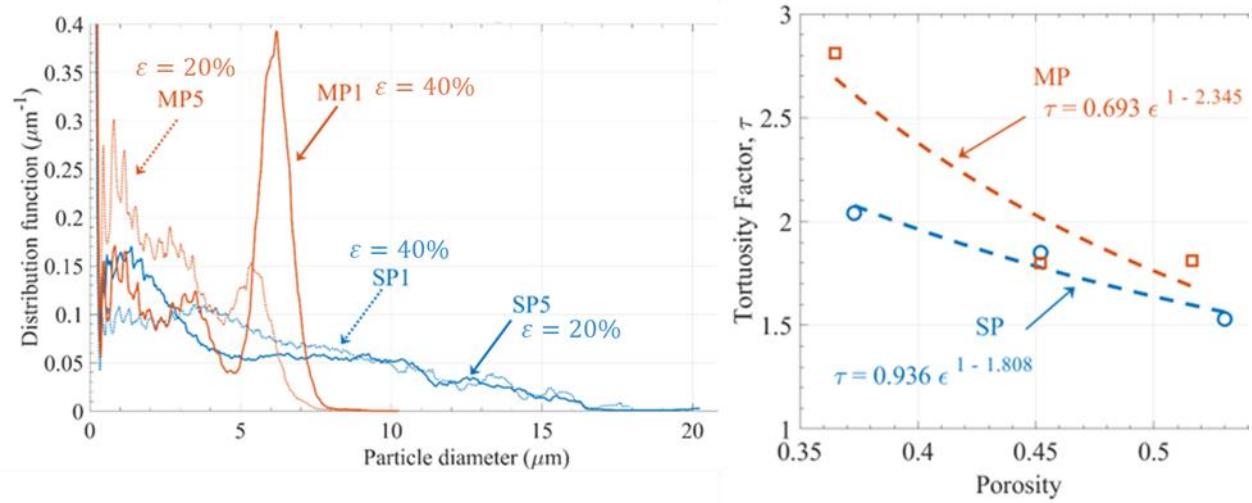

Figure I.4.K.30 (left) Particle size distribution of single (SP) and mixed (MP) powder NMC electrodes, and (right) associated tortuosity factor, neglecting CBD. Note: particle size absolute values are irrelevant for the tortuosity factor calculation, only relative size variation between particles.

Full-cell microstructure scale electrochemical heterogeneity: Electrochemical microstructure scale FEniCS model [5] has been extended to full-cell geometry (cf. Figure I.4.K.31), handling ~30 millions of degrees of freedom distributed among 300+ processes on NREL Eagle HPC. Micromodel predicts lithium-plating thermodynamically favorable condition is reached 8.5 to 14s earlier compared to macroscale model at 6C, 30°C for round 2 cell. This offset is attributed to the detrimental impact of microstructure heterogeneity. In addition, microscale model predicts the potential difference at the separator-anode interface is not uniform, with a 6-mV difference. Therefore, the separator-anode interface does not plate uniformly, as 4s is required for the whole interface to reach the lithium-plating thermodynamically favorable condition once it has started locally. During CC the potential difference in-plane heterogeneity is increasing (in-plane standard deviation increases from ~1 mV to ~7mV) with higher heterogeneity calculated in the anode bulk, suggesting lithium plating in the bulk is more heterogenous than the one initially occurring at the separator-anode interface.

Micromodel predicts significant in-plane heterogeneity, especially for the electrolyte concentration within the NMC cathode during fast charging (cf. Figure I.4.K.31). Indeed the large concentration gradient induces high electrolyte concentration at the back of the NMC electrode, close to the positive current collector, which corresponds to low ionic diffusion coefficient (~1e-11 $m^2.s^{-1}$ compared to ~1.34e-10 $m^2.s^{-1}$ at the at-rest concentration) that locally exacerbates concentration heterogeneity. Consequently, electrolyte concentration in-plane standard deviation as high as 160 $mol.m^{-3}$ are calculated. As well, Faraday current density is significantly heterogenous, with in-plane relative standard deviation reaching 35% (cf. Figure I.4.K.34). As lithiation progresses, graphite particles closed to the separator interface are getting saturated, effectively delocalizing the intercalation reaction deeper in the anode bulk inducing a heterogeneity propagation front in the anode bulk.

Electrochemical response representativeness has been quantified by adapting the representative volume element analysis approach, initially formulated for static microstructure parameters, to the dynamic electrochemical simulation. Analysis revealed that the concentration and potential mean profiles calculated along the electrode thickness for different independent subvolumes are diverging with the C-rate. This indicates the microstructure scale field of view required to accurately describe electrochemical response is increasing with the C-rate. The newly developed method enables build confidence in the model results, as well as determining a threshold doublet {tortuosity, C-rate} for which macroscale model are precise enough compared with their microscale model counterparts.

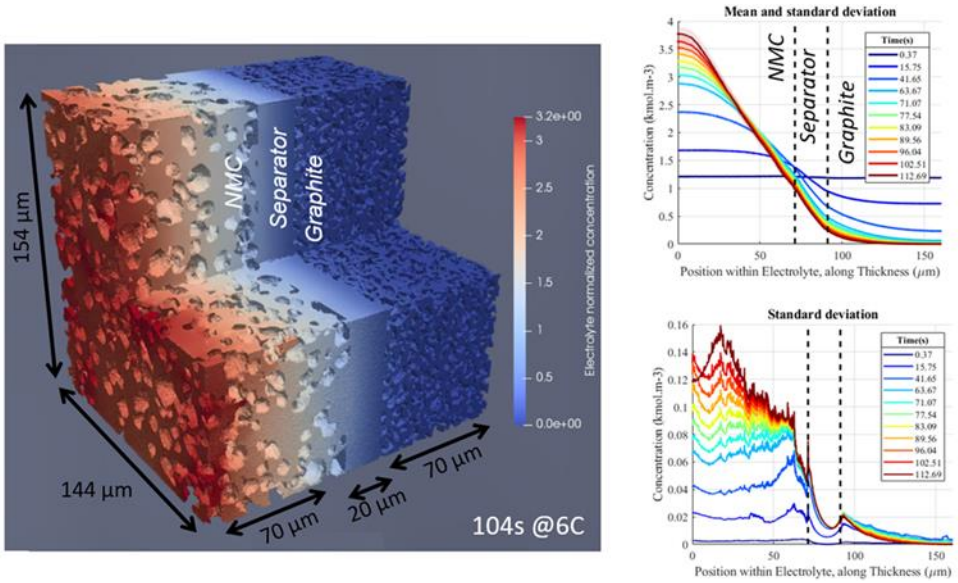

Figure I.4.K.31 (Left) Electrolyte concentration calculated for a full cell NMC LN2487-113-13C / electrolyte Gen2 / SLC1506T during 6C charging. (Right top) Electrolyte concentration mean (solid line) and standard deviation (transparent area) calculated slice per slice along the cell thickness. (Right bottom) Electrolyte concentration standard deviation calculated slice per slice along the cell thickness.

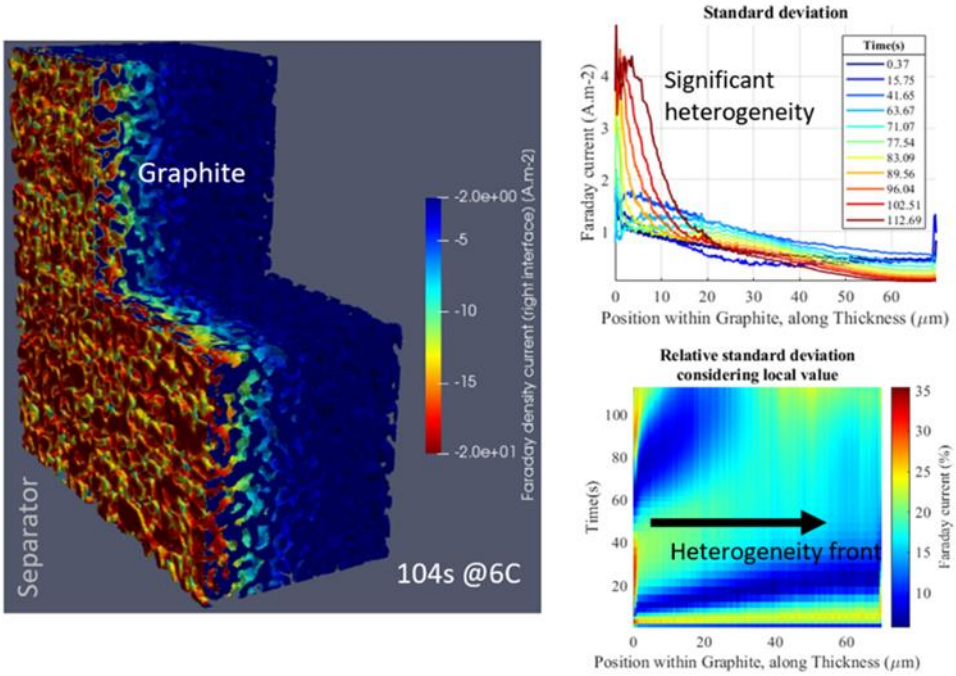

Figure I.4.K.32 (Left) Faraday current density calculated within the graphite electrode during 6C charging showing electrode is overutilized close to the separator interface. (Right top) Anode Faraday current density standard deviation calculated slice per slice along the cell thickness. (Right bottom) Anode Faraday current density relative standard deviation (normalized with the average in-plane current) calculated slice per slice along the cell thickness.

Li plating detection in extremely fast-charged lithium-ion batteries using simultaneous neutron and x-ray imaging – SLAC

Lithium-ion batteries (LIBs) have profoundly advanced the development of electric vehicles (EV). However, one of their remaining bottlenecks is the long charging times required. There is a global push towards extreme fast charging (XFC) to reduce their charging times to 10-15 minutes. However, XFC results in severe degradation in the electrochemical performance of batteries. This is mainly attributed to the loss of active Li, either as "dead" which has become electronically disconnected after plating on the anode or as "inactive" due to the irreversible reaction of Li with the electrolyte to form a solid electrolyte interphase. Since parasitic lithium plating is one of the identified major results of XFC, understanding its origin and characteristics on graphite anodes is crucial to developing fast-charged batteries.

In this work, we used simultaneous neutron and x-ray-based dual-mode micro-computed (CT) tomography, a 3D non-destructive imaging modality, to investigate the characteristics of Li plating on graphite anodes in fast-charged LIBs. Since X-rays and neutrons are sensitive to the electron and nuclear density of the material respectively, dual-mode X-ray and neutron CT offers advantageous to readily separate battery anode components such as Li, C, and Cu, due to the complementary interaction of the two imaging probes with matter. Higher energy X-rays are needed to get through the metallic components in a battery such as Cu. However, they do not provide sufficient imaging contrast to distinguish low-Z materials such as Li and C. For that purpose, neutrons are used to detect and distinguish these lighter battery components.

We performed these multi-modal imaging experiments at the Neutron and X-ray Tomography (NeXT) system located on the BT-2 imaging beamline at National Institute of Standards and Technology Center for Neutron Research. We characterized pristine and cycled graphite anode strips containing plated lithium at different regions. For cycled anode strips, we disassembled the battery pouch cells and used graphite anodes cycled under XFC (9-C rate) for 450 cycles at fully discharged condition. In addition, we characterized an uncycled single-layer battery pouch cell containing electrolyte. Our spatial resolution was ~10-15 μm, thus providing

sufficient resolution to pinpoint the location of Li plating within the thickness of the 100 μm anode. For data analysis, we used bivariate histogram phase segmentation to distinguish C, Li, and Cu from each other, and detect lithium metal plating on graphite anodes. Our current ex-situ data-set enables us to answer: "where does Li plating deposit on the battery anode during XFC in LIBs?" However, to answer when and why Li plating deposits on battery anode during XFC in LIBs, we are focusing on non-destructive in-situ imaging of full battery pouch cells at different states-of-charge (0%, 25%, 75%, 100%). Addressing these fundamental questions will inform improved battery designs, graphite anode architectures, and charging protocols that will reduce Li plating during XFC in LIBs. (See Figure I.4.K.33, Figure I.4.K.34, and Figure I.4.K.35.)

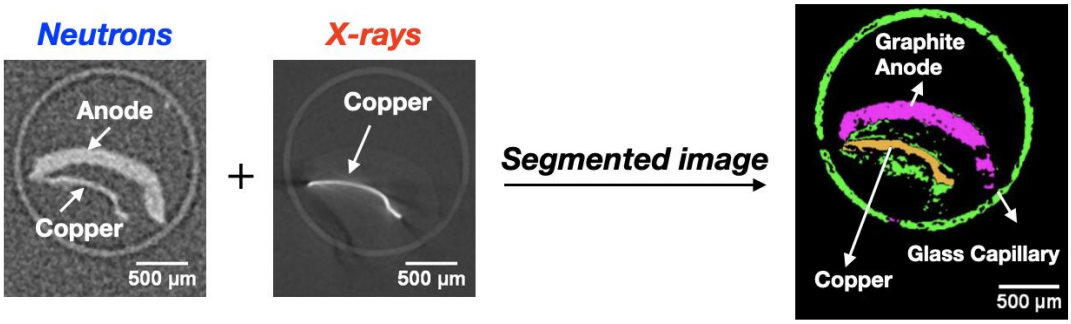

Figure I.4.K.33 **D grayscale image (neutrons and x-rays) of a cycled graphite anode showing different battery components.** Bivariate histogram phase segmentation was used to convert grayscale images to segmented colorized image as shown on the right hand side.

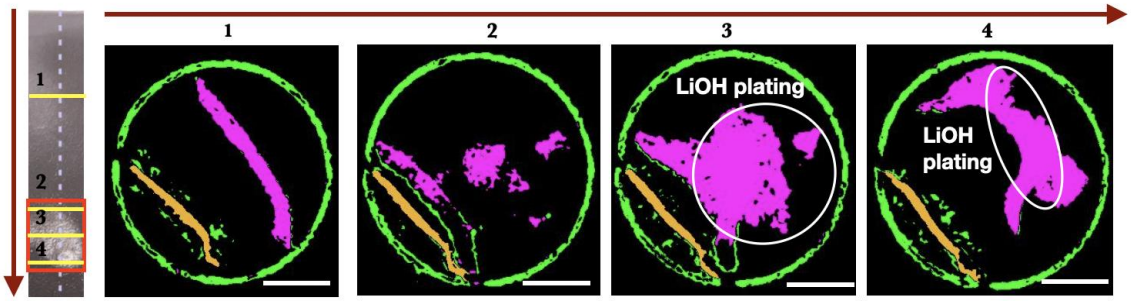

Figure I.4.K.34 **(a) Optical image of a cycled graphite strip** showing Li plating deposition inside a red highlighted box. **(b) 2D colorized segmented images** show graphite anode in different spatial dimensions that can be correlated to the optical image. E.g. Slices 3 and 4 that show growth of Li plating correspond to the yellow lines labelled 3 and 4 on the graphite strip. Note: During sample preparation, Li was exposed to air and converted to LiOH. Hence, Li plating corresponds to LiOH plating deposition in this data-set.

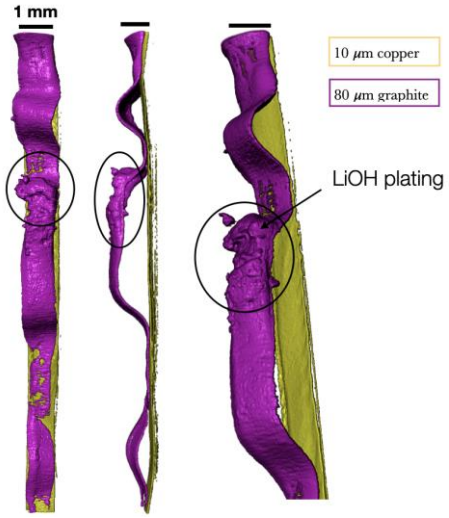

Figure I.4.K.35 3D visualizations of the cycled graphite anode showing copper current collector and thickness of LiOH plating on graphite anodes.

Revealing Heterogeneity and Grain Characteristics of Plated Li in Extremely Fast Charging Li-ion Batteries at the Microscale by X-ray Microdiffraction - SLAC

Parasitic plating of Li metals occurring during fast charging of Li-ion batteries is detrimental to the performance of the batteries, causing capacity fading, Columbic inefficiency, battery life shortening, and posing safety threat. The plating of Li particles and their subsequent fates are highly dependent on the local electrochemical potentials, and therefore heterogeneities of the cell structure greatly impact the behaviors and the batteries. In this study, we aim to reveal the heterogeneities and crystallite characteristics of the components in Li-ion batteries that have undergone many extremely fast charging cycles and have Li metals irreversibly plated on the graphite anodes. The experiment was carried out by rastering focused X-ray source over areas of pouch cell samples and recording the transmitted diffracted patterns.

We previously recorded local heterogeneity over the full area of the cell using this in situ diffraction approach with mm-scale resolution, which showed positive correlation between local amount of Li and LiC_6, but negative correlation between local Li and graphite at this length scale. The approach is extended using microdiffraction using focused X-ray beam with 300×300 nm^2 beam size so that the spatial resolution of the technique is comparable to the grain size of the associated materials. We have shown that decent signals from all important components (NMC, graphite, Li, LiC_6, LiC12) can be captured using this 300 nm beam size, with the Li (110) peak coming from a Li-rich region shown in Figure I.4.K.36a. From microdiffraction performed with 300 nm beam size and 2 µm step size, we found significant variations of Li signal intensity over total areas of 50×50 μm^2 (Figure I.4.K.36b). The Li signals are contributed from multiple individual diffraction spots coming from individual Li grans. We realized that the overall signals are dominated by a few super-bright spots, but there are many more dim spots accounting for the majority of the number of Li grains. We found that, within 300×300 nm^2 diffraction area, around four grains are typically registered on the area detector (Figure I.4.K.36c) in regions which are found to be Li-rich by mm-scale in situ diffraction. This allows estimation of individual grain characteristics (e.g. strain) and therefore grain heterogeneity analysis in the future. We also demonstrated that grain size of Li can be directly captured in real space using microdiffraction with both beam size and step size being 300 nm. The Li intensity mapping at this scale, Figure I.4.K.36d shows that the sizes of plated Li are estimated to be around 1 µm. Going forward, we plan to obtain more robust estimates on the grain size distribution, grain density, and strains of the key materials present in these fast-charged Li-ion batteries and reveal the correlations between these metrics.

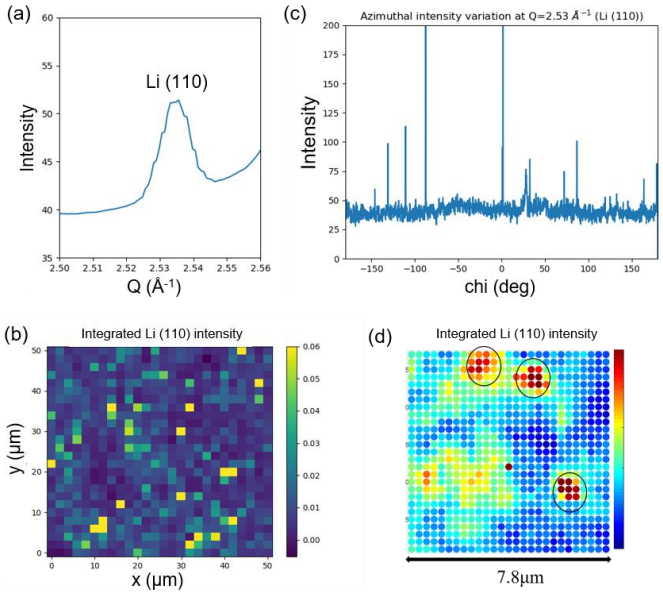

Figure I.4.K.36 (a) Example Li (110) peak captured with 300 nm beam microdiffraction. (b) Integrated Li (110) intensity spatial variations with 300 nm beam but 2 μm step size. (c) Example azimuthal dependence of Li (110) intensity from a single microdiffraction pattern. (d) Integrated Li (110) intensity spatial variations with both beam and step size being 300 nm.

Conclusions

A combination of novel characterization and modeling is used to better understand the early onset of lithium plating during extreme fast charging. The electrolyte wetting model by ANL has shown complete electrolyte wetting can take several days to weeks. Further, gas may become isolated and trapped in the center of electrodes. Initial neutron imaging performed by ORNL seems to confirm that electrolyte saturation is non-uniform/incomplete within pouch cells. Thus, electrolyte wetting may be responsible for visual lithium plating pattern observed and XCEL team should investigate methods to improve such as electrolytes with higher surface tension or formation at elevated temperature/mechanical agitation.

Other key highlights/findings include:

- Determination of exchange current density and rough estimate for lithium plating reversibility using 1st generation kinetic model and gas titration/XRD measurements
- Considerable enhancements to ability to measure local ionic properties enabling detailed/reliable mapping of pouch cell electrodes. Next, these electrodes will be assembled into cells and cycled at APS to have detailed high energy, in-situ XRD mapping performed and compared with ionic resistance map.
- X-ray tomograph has revealed a “shadow effect” of lithium plating. That is the regions of graphite under extensive lithium plating near separator charge effectively, but regions further away near current collector don’t likely due to limitations in ionic transport from deposited lithium.
- AFM and SEM imaging of graphite nanoplatelets indicate lithium tends to preferentially plate at edge and defect sites
- Atomistic modeling provides insight into the apparent increase in diffusion coefficient during fast charging
- High energy, in-situ XRD mapping reveals that fast charging increases SOC heterogeneity. Lithium plating is observed to occur at spots with high de-intercalation in the anode during discharge during initial cycling. Cyclable lithium preferentially moves to edge of cell during fast charge cycling.

- 2nd generation lithium plating model with nucleation and plating dynamics suggest surface tension doesn't significantly mitigate lithium plating. The model is also used to explore the effect of grain architecture and particle morphology on plating.
- HOPG studies show the limiting intercalation current for edge plane without plating is 2-3 mA/cm^2, while basal is only 20-60 uA/cm^2. Thus, enough exposed edge sites must be at graphite surface to support fast charge. However, excessive edge sites promote more SEI growth.
- Microstructure modeling reveals spherical, unimodal particles should be used to reduce tortuosity and in-plane heterogeneity. Lithium plating can occur 2%–3% lower SOC due to microstructure effects compared to standard Newman modeling. Amount of heterogeneity increases with C-rate.
- Size of plated lithium are revealed to be around 1 micron from X-ray microdiffraction.

Key Publications

1. D.P. Finegan, A. Quinn, D.S. Wragg, A.M. Colclasure, X. Lu, C. Tan, T.M.M. Heenan, R. Jervis, D.J.L. Brett, S. Das, T. Gao, D.A. Cogswell, M.Z. Bazant, M.D. Michiel, S. Checchia, P.R. Shearing, K. Smith, "Spatial dynamics of lithiation and lithium plating during high-rate operation of graphite electrodes," *Energy Environ. Sci.*, **13**:2570-2584 (2020).
2. EJ McShane, AM Colclasure, DE Brown, ZM Konz, K Smith, BD McCloskey, "Quantification of Inactive Lithium and Solid Electrolyte Interphase (SEI) Species on Graphite Electrodes After Fast Charging." *ACS Energy Letters*, **5**: 2045-2051 (2020).
3. Juan C. Garcia, Ira Bloom, Christopher Johnson, Dennis Dees, Hakim Iddir. "Graphite Lithiation under Fast Charging Conditions: Atomistic Modeling Insights**,"** *Phys. Chem. C* **124**, 8162-8169 (2020).
4. F. Usseglio-Viretta, D. P. Finegan, A. Colclasure, T. M. M. Heenan, D. Abraham, and K. Smith, Quantitative relationships between pore tortuosity, pore topology, and solid particle morphology using a novel discrete particle size algorithm, *J. Electrochem. Soc.*, **167** 100513 (2020).
5. J. Allen, J. Chang, F. Usseglio-Viretta, P. Graf, and K. Smith, "A Segregated Approach for Modeling the Electrochemistry in the 3-D Microstructure of Li-Ion Batteries and its Acceleration Using Block Preconditioners," *submitted to Journal Scientific Computing*
6. H. Xu, F. Usseglio-Viretta, S. Kench, S. J. Cooper, and D. P. Finegan, Microstructure reconstruction of battery polymer separators by fusing 2D and 3D image data for transport property analysis, *J. Power Sources*, **480** 229101 (2020).
7. Maha Yusuf, Jacob LaManna, Partha Paul, David Agyeman Badu, Lambertus Hesselink, Michael Toney, Johanna Nelson Weker , "Ex-situ Li plating detection on graphite anodes in fast-charged lithium-ion batteries using simultaneous neutron and x-ray tomography,"*in preparation*

Acknowledgements

This project was funded by the U.S. Department of Energy, Vehicle Technologies Office. The technology development manager was Samm Gillard. The project overview was prepared by Venkat Srinivasan (ANL). Other contributing team members for Thrust 2 (Local Heterogeneity Thrust) include Andrew Colclasure, Francois Usseglio-Viretta, Jeffrey Allen, and Kandler Smith (NREL); Che-Ning Yeh, William Chueh, Maha Yusuf, Michael Toney, Johanna Nelson Weker, Partha Paul, Zhelong Jiang, and Yi Cui (SLAC); Dennis Dees, Hakim Iddir, Juan Garcia (ANL); Kamila Wiaderek, Yang Ren, Harry Charalambous, and Uta Ruett (APS); Alec Ho, Nitash Balsara, Manuel Schnabel, and Robert Kostecki (LBNL); Srikanth Allu (ORNL); and Dean Wheeler (BYU).

I.4.L XCEL R&D: Charge Protocols and Life Assessment for Extreme Fast Charging Thrust

Venkat Srinivasan, Principal Investigator
Argonne National Laboratory
9700 S. Cass Avenue,
Lemont, IL 60439
E-mail: vsrinivasan@anl.gov

Samm Gillard, DOE Technology Development Manager
U.S. Department of Energy
E-mail: Samuel.Gillard@ee.doe.gov

Start Date: October 1, 2019 End Date: September 30, 2020
Project Funding: $742,000 DOE share: $742,000 Non-DOE share: $0

Project Introduction

Extreme fast charging (XFC) of Li-ion batteries can create life and safety issues. Among the issues are shortened battery life due to enhanced loss of lithium inventory and electrolyte degradation and enhanced safety concerns due to potential short creation by Li dendrites. The detection and monitoring of Li plating onset and evolution over aging is a significant challenge. While several cell and materials science issues exist that need to be evaluated for XFC there are also other methods which can be used to advance high rate charging. One distinct area is the use of advanced charging protocols which enable high rate charging, but which are designed to minimize or mitigate transport issues in cells and which are also meant to decrease any possible deleterious impacts from adverse temperature rise during charging.

Of the six main tasks within the XCEL program, the charge protocols and performance analysis task is focused on identifying and investigating the core scientific issues which are associated with these advanced charge protocols. The team which is composed of members from Idaho National Laboratory (INL), the National Renewable Energy Laboratory (NREL), and Argonne National Laboratory (Argonne), is tasked with developing new protocols and the methods needed to electrochemically characterize performance and life expectations for cells which undergo XFC. This report is split into three primary sections related to the computational development of charge protocols, the analysis and characterization of aspects that can enhance the scientific underpinning of charge protocols and the evaluation and assessment of how charge protocols impact the life and performance of cells undergoing fast charge.

Objectives

The key objectives of this work are to advance the scientific rationale behind advanced charge protocols which increase charge acceptance for batteries undergoing fast charge. In doing so a mix of computational and experimental tools and analysis methods have been employed to understand how the potential of anode changes as charge or environmental conditions are altered. The work also looks to enhance the ability to perform failure analysis to better inform and classify the reasons behind cell degradation during fast charge.

Approach

To achieve the objectives of the Charge Protocol and Life Assessment thrust the team used a suite of different methods. Researchers at NREL used a validated electrochemical macro-homogeneous model to screen novel charging approaches to maximize charge capacity achieved in ten minutes while avoiding lithium plating. At Argonne, researchers used a combination of three electrode studies, other electrochemical analyses and post-test characterization of cells. At INL, researchers used a combination of electrochemical analysis, life testing and secondary characterization to understand how cells evolved over extensive fast charging. The INL team also performed analysis to better understand how protocols at the single cell level would scale to full vehicle battery packs.

Across the labs research on charge protocols primarily focused on the use of Round 2 cells which include a graphite anode and NMC 532 cathode with a nominal loading of 3.0 mAh/cm^2. Some work using Round 1 cells (~2 mAh/cm^2) was also performed for comparison to understand the differentiation between material and design related degradation.

Results

During Fiscal Year 2020 (FY20) there were several significant findings that provide understanding of charge protocols and how they influence the aging pathways for cells. While plating of Li metal is a known degradation mode and cathode fade has been reported, the interaction and evolution of the two modes has not been clearly defined. Advances in understanding the cell level impacts of both degradation modes occurred during FY20 with the two modes being linked and with the key understanding that more advanced knowledge related to adaptive protocols which co-optimize to reduce Li plating and cathode fade being a key research challenge for future work. The insights and directions from work in FY20 provide a grounded understanding in how to adapt charge protocols for the graphite/NMC 532 cells currently under use, but also for other designs which may adopt higher Ni NMC and thicker electrode structures to facilitate higher energy cells.

In addition to the understanding aligned with the need to jointly focus on both anode and cathode degradation processes key areas of advancement achieved as part of the Charge Protocol and Life Assessment task include:

- Macro-homogenous model to identify charge protocols which reduce the likelihood of Li plating
- Use of 3-electrode methods to develop charge protocols that adapt based on the anode potential
- Comparative analysis of different protocols and cells showing the impact of materials and cell designs
- Impact of temperature on Li plating
- How charge protocols scale when considering different vehicle battery pack sizes.

Model-based Protocol Development

NREL used its macro-homogeneous electrochemical model to explore novel charge protocols. More specifically, the model was used to investigate strategies for maximizing capacity obtained in 10 minutes without Li plating. Model parameters were determined previously under the CAEBAT project for cells composed of graphite anodes and NMC 532 cathodes [1]. The model has been validated extensively with electrochemical data collected during the XCEL program including single layer pouch cells and custom 3-electrode setup from ANL for charging rates spanning C/20 to 9C [publications 1-6]. A detailed writeup of exercising the model to develop novel protocols to maximize fast charge capacity and limit lithium plating is written up in Publication 7.

First, the model is run several hundred times to investigate novel protocols suggested in the literature such as multi-step current with a constant transition potential and pulse charging. These multi-step strategies are found to be ineffective because the current/voltage are not adjusted based on propensity for Li plating. These protocols could be further refined to improve capacity/minimize Li plating by allowing the transition voltage to vary from 4.1V. However, this would be a large parameter space to sweep. Pulse charging may only be effective because Li stripping rapidly occurs during the short rest periods and only accounting for the Li plating potential may not capture the benefits of pulse charging. However, capturing benefits for stripping would require a model incorporating a detailed Li plating/stripping kinetics model which is beyond the scope of this work but may be considered in the future. Further, determining what an acceptable amount of Li plating is problematic.

Instead, NREL used the model to develop strategies for a novel protocol to maximize capacity while preventing any Li plating. To meet this criterion, a high current is initially applied such that the Li plating potential quickly approaches zero. The current is then reduced in small steps to keep the Li plating potential close to, but above zero. In practical operation though, the potential for Li plating is not measured and this protocol could not be directly implemented. However, after initial CC charging, we observed the voltage profile increases in a near-linear manner as the cell model follows the internal Li-plating limit. Thus, NREL

explored the performance of a "voltage ramp" protocol. This protocol is defined by 3 parameters: the initial C-rate, the voltage for switching from constant current to voltage ramping (V-switch), and ramp rate in mV/s. Results are summarized in Figure I.4.L.1. The potential for Li plating for the ramp protocol is significantly improved compared to the traditional CCCV or CPCV protocols. For the round 2 cell, the maximum plating-free capacity was found with an initial charge rate of 9.5C, V-switch of 4.02V, and ramp rate of 0.25 mV/s. With these conditions, the final charge capacity and voltage were 1.84 mA/cm^2 (11% improvement over CCCV) and 4.16V, respectively. Raising the ramp rate higher than 0.25 mV/s results in even higher capacity, but at the expense of significant amounts of Li plating.

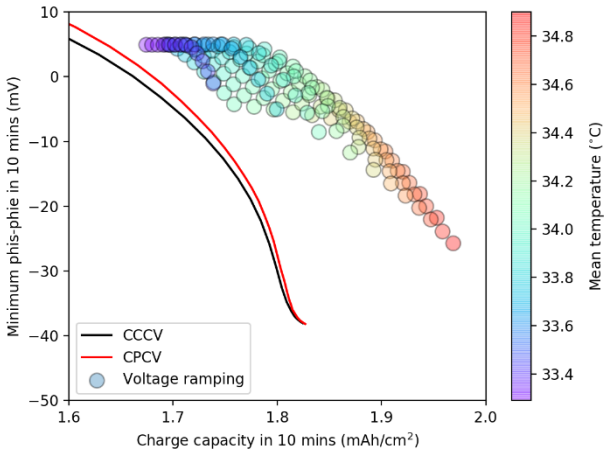

Figure I.4.L.1 Potential for lithium plating as a function of achieved capacity for A.) Novel voltage ramping protocol

NREL further investigated if the proposed protocol would be very beneficial for even higher loading cells suitable for EV use. Simulations were performed for cells with a loading of 4 mAh/cm^2 with severe electrolyte transport limitations. The proposed ramp protocol resulted in a plating-free capacity increase of around 18% both at 30°C and elevated temperature of 55°C. The charge protocol alone is not enough to enable 80% capacity in 10 minutes without plating even at 55°C (71% SOC). However, for these EV loadings, the novel protocol eases the amount of elevated temperature needed or improvements required for electrolyte transport/electrode tortuosity.

Lastly, NREL investigated the sensitivity of the proposed ramp protocol optimal values to uncertainties in model parameters. That is how, much do the 3 ramp parameters of initial rate, V-switch, and ramp rate change with differences in electrochemical model parameters. NREL determined 11 sets of model parameters that gave reasonable 6C CC charge times close to that experimentally measured 230s to hit 4.1V cutoff. Model parameters varied include tortuosities, solid-state diffusivities, and exchange current densities. The optimal ramp protocol was determined for each of these 11 scenarios. For all 11 cases, the optimum initial rate was around 7C and V-switch was around 4.0V. The optimal ramp rate is somewhat sensitive to uncertainties in electrochemical model parameters and varied from 0.1 to 0.3 mV/s. The protocols identified by NREL are currently under evaluation at INL using different ramp rates ranging between the values listed above. The proposed protocol values of (7C, 4.0V, 0.1-0.3 mV/s) is specific to Round 2 single-layer pouch cells and considers only the Li plating degradation mechanism. The model can be extended moving forward to consider cathode cracking effects and heating in large capacity cells. Note, the ramping protocol and multi-step protocol likely work well for all cathode chemistries with a significant variation in cathode open circuit potential with de-lithiation, such as NCA and all NMCs. However, the protocol likely provides little benefit to cathodes with flat open circuit potentials, such as lithium-iron phosphate.

Electrochemical analysis

Fast charging of lithium-ion batteries (LIBs) that does not compromise cell performance and durability is critical for wide adoption of electric vehicles. In a recent series of articles from Argonne the performance and

practical limits of fast charging for LiB cells built using layered oxide cathodes and graphite anodes has been reported. [2-5] The researchers had a particular interest in preventing Li plating on the anodes [6]: strong cell polarization at high currents causes the anode potential to decrease to values at which Li plating becomes competitive with Li intercalation, leading to loss in cell performance. In this annual report, we highlight some of the observations from the experimental data and electrochemical model simulations. These highlights are for cells containing the Round 2 NMC532 cathode, graphite anode and Gen2 electrolyte (1.2 M lithium hexafluorophosphate salt in a 3:7 w/w solvent mixture of ethylene carbonate and ethyl methyl carbonate).

To monitor electrode potentials during the electrochemical cycles, the experiments rely on a reference microelectrode made of a thin copper wire, lithiated in-situ. This probe is positioned between (and at the center of) two microporous separators (Celgard 2320) that are sandwiched between the 20.3 cm^2 area electrodes. In Figure I.4.L.2, let $\phi_{1,2}(z)$ be the potentials in the solid electrodes (index 1) and liquid electrolyte (index 2) at the cell depth z. Then the reference potentials for the cathode and anode vs. Li/Li^+ are given by $\phi_c = \phi_1(CC) - \phi_2(R)$ and $\phi_a = \phi_1(CA) - \phi_2(R)$ respectively. The Li plating occurs when the overpotential between the anode and liquid electrolyte at its interface becomes negative; this overpotential becomes more positive with increasing anode depth from the separator. For this reason, the overpotential at the separator is the critical indicator for Li plating, and we will refer to this quantity as the *surface* anode potential η_a. As such, it can neither be measured nor controlled directly. However, it is possible to measure a *reference* potential ϕ_a between the anode and an electrolyte-immersed microprobe electrode some distance away. In order to have fast charging without Li plating, one needs to maximize the charging current I while keeping $\eta_a > 0$ at any point in time.

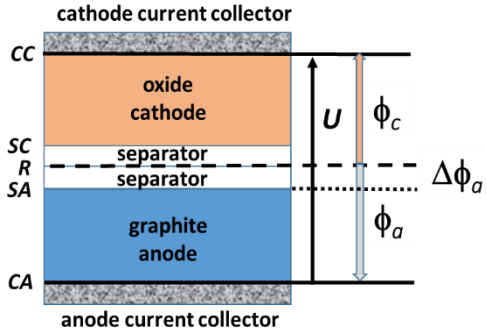

Figure I.4.L.2 Schematic of a Li-ion cell. **CC** is the cathode current collector, **CA** is the anode current collector, **SC** and **SA** are the cathode and anode electrode surfaces, respectively, U is the cell voltage, $\phi_{a,c}$ are anode and cathode reference potentials, respectively, and $\Delta\phi_a$ is the correction to obtain the anode surface potential η_a. [4]

We have conducted constant current, pulse current, and variable-rate charging on the Round 2 NCM523/Gr cells at various temperatures. By repeating the experiment for many C-rates we mapped the currents at which the anode potential (as measured by the reference electrode) reached or crossed zero vs. Li/Li^+. We used these maps, and a state-of-the art multiphase electrochemical model, to compute the currents at which anode *surface* potential reaches zero vs. Li/Li^+, thereby determining the boundary of charging regimes that cause Li plating on the graphite anode. Some of our key observations are as follows:

- Generally, the cell and electrode polarization at faster charge decreases with increasing test temperature. At all temperatures, polarization at the oxide cathode is considerably greater than polarization at the graphite anode. However, at temperatures > 45°C the gains through speeding of Li^+ ion diffusion become offset by growing resistance, especially at the oxide-cathode. Thus, increasing temperature over 45°C for extended periods is counter-productive because it degrades long-term cell performance.
- For constant current charge, higher capacities can be "safely" attained (meaning no Li plating on the graphite anode) with lower C-rates, thinner electrodes, and higher temperatures (see Figure I.4.L.3). For a 70 mm thick electrode, full cell capacity can be achieved with a 3C rate at 45 °C, whereas only

56% of the capacity can be reached at a 6C rate. In contrast, only 25% capacity can be achieved at 30°C at the 6C rate.

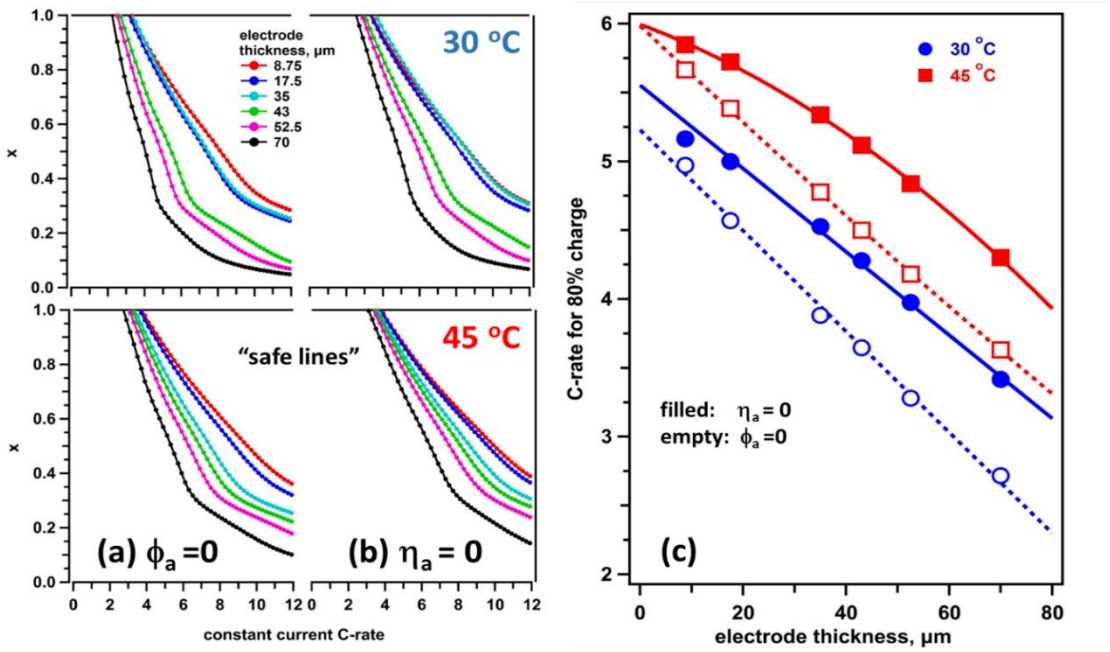

Figure I.4.L.3 (a, b) The "safe lines" computed for cells with different electrode thicknesses in which the transferred lithiations x for achieving (a) $\phi_a = 0$ or (b) $\eta_a = 0$ are plotted vs. the C-rate of constant current for 30 °C and 45 °C. Staying below the "safe lines" in panel b helps avoid Li plating during fast charge. (c) A crosscut of these plots at 80% full charge, with the critical C-rates plotted vs. the electrode thickness. The blue lines and symbols are for 30 °C and the red ones are for 45 °C. The filled circles and solid lines are for η_a=0 and the empty circles and dashed lines are for ϕ_a=0 (these two conditions become the same for an infinitely thin separator).

- At all temperatures, cell relaxation displays stretched exponential (Kohlrausch) kinetics, which includes a fast exponential component and a slow dispersive component extending over several decades in time. The electrode potentials generally follow the cell voltage trends.
- For pulsed charge, the likelihood of Li plating increases considerably with increasing rate and duration of the pulse but decreases with the increasing temperature. We have developed a general methodology of obtaining the "safe lines" for different charge regimes without crossing into the Li plating zone. [5]
- Two types of variable-rate charging protocols to mitigate Li-plating have been examined with our cells. In the *seesaw* charging experiments conducted using a Maccor cycle, the anode reference potential ϕ_a was monitored continuously and used to switch the current; the current was decreased in constant increments of 0.25C. The *potentiostatic* charging experiments were conducted with a Solartron Analytical 1470E cell test system; here, ϕ_a was maintained at a set value. Figure I.4.L.4 contains data from cells that were precharged at C/3 to 16% SOC, and had the fast charge terminated upon reaching 80% SOC: we juxtapose the potentiostatic and seesaw profiles obtained using two control conditions indicated in the plots for I_0 =6C. The profiles track each other suggesting that seesaw charging with 0.5C current stepping is nearly as efficient as the potentiostatic charging. For the seesaw charge, an average current $\langle I \rangle$ of 4.2C is obtained using $\phi_a = 0$ control (Figure I.4.L.4a) and $\langle I \rangle$ of 4.79C using ϕ_a = -25 mV control (Figure I.4.L.4b).

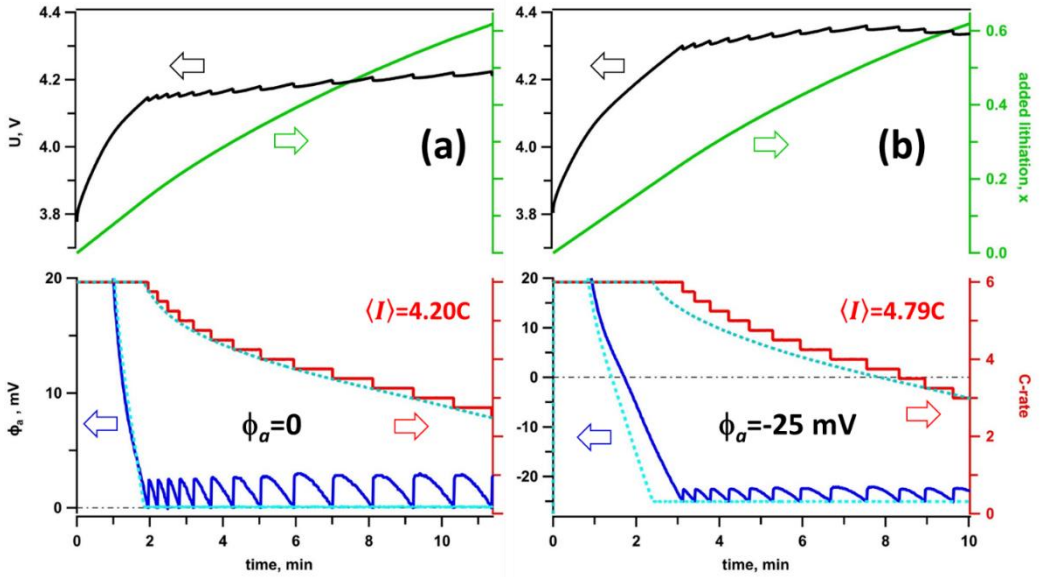

Figure I.4.L.4 Experimental demonstration of the seesaw (solid lines) and potentiostatic (dashed lines) charge for a round-2 cell at 30°C using (a) the $\phi_a = 0$ control and (b) ϕ_a = -25 mV control. The upper panels show the cell voltage U and the SOC, while the lower panels show the anode reference potential ϕ_a and the C-rate during fast charge. The black lines are the cell voltage, the red lines are the C-rate, the blue line is the anode potential, and the green line is the added lithiation x (equal to SOC change). The black dashed horizontal lines indicate the zero anode reference potential ($\phi_a = 0$).

Performance characterization and aging analysis

Understanding how changes in materials and electrode designs impact fast charge capability is vital for the advancement of XFC. At INL, researchers performed fast charge studies on multiple groups of cells with two primary electrode loadings using different charge protocols. The aim of these studies was to identify and link the differences in aging to either the materials within the cell or to the structural design of the cells. One of the first steps in identifying differences between the cells was performing overvoltage analysis as previously described in Tanim et. al. [8]. The overvoltage analysis was able to show a clear delineation for Round 2 cells above 4C where the trend in overvoltage went from a linear increase to a plateau. When looking at the performance of cells using a CCCV charging protocol (Figure I.4.L.5) it is clear that for cycling at rates below the plateau there is low cell-to-cell variation and the overall fade is significantly lower.

To better understand the differences between the cells, the team used the NREL macro-model to characterize the ion concentration in the vicinity of the electrodes during each of the different CCCV charging experiments. Using the model it became clear that once the plateau was reached that there was a severe depletion of Li-ion in the vicinity of the anode leading to wide plating of Li metal during the charging event. Post-test characterization of cells showed high levels of Li plating and at 6C early evaluation after 10 cycles indicated that the Li plating started during early cycling. The INL team also performed assessment and analysis of cycling using several other charging protocols.

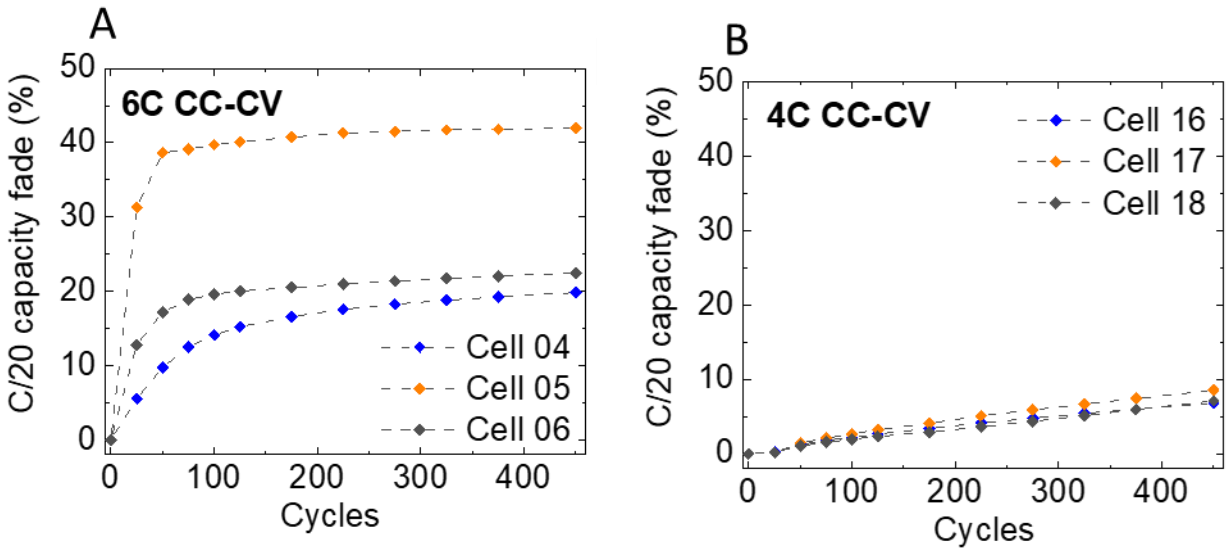

Figure I.4.L.5 A) 6C CC-CV C/20 capacity fade with respect to BOL capacity B) 4C CC-CV C/20 capacity fade with respect to BOL capacity for $L_{moderate}$ cells that underwent continued fast charging. Figure from P.R. Chinnam et al.

As part of characterizing multiple charge protocols shown in Figure I.4.L.6, the INL team performed degradation analysis to better understand how degradation modes evolved over the course of cycling. In particular the team focused on the evolution of loss of lithium inventory (LLI) and loss of active material at the cathode (LAMdePE) for both Round 1 and Round 2 cells to obtain a better grasp of the conditions that result in either fade at the anode or cathode during fast charge. Quantification of failure mode was performed using incremental capacity (IC) analysis. In Figure 6 it can be seen that Round 2 cells have a relatively constant LAMdePE across the different protocols, but wide variation in LLI occurs. In contrast the Round 1 cells show lower levels of variation inf LLI, but more extensive variation in LAMdePE. To confirm the analysis of the LAMdePE, several swatches of cathode material were characterized after testing to confirm the IC analysis.

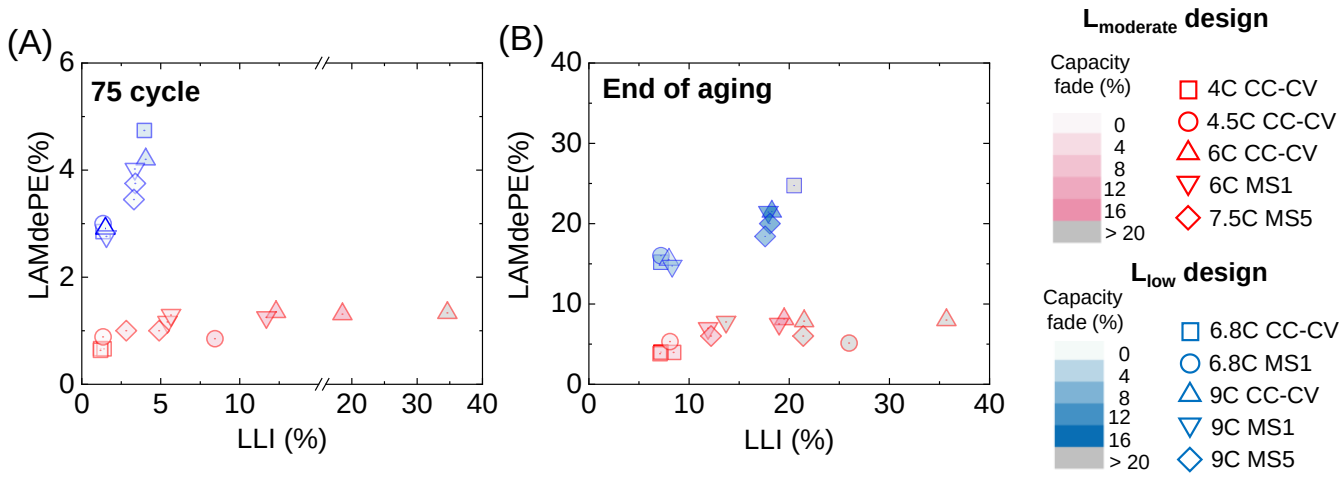

Figure I.4.L.6 Comparison of the aging phenomena between Round 2 ($L_{moderate}$) and Round 1 (L_{low}) cell designs. (A-B) The percentages of LLI and LAM for selected charging protocols for $L_{moderate}$, L_{low} loading cells at early cycle life (A) and end of cycle life (B), respectively. The capacity fade is shown by color shade for both cell designs.

The IC analysis provides information on the respective fade rates associated with the different cell designs and charge protocols. Based on the information obtained from the overvoltage analysis and the fade rates, it was determined that as energy levels of cells increase (especially due to increased electrode loading) that the failure mode is more strongly determined by the design of the electrodes and the transport within the cell and less by

the specific materials in the anode and cathode. However, in instances where low loading or high rates were observed at the positive electrode material degradation is still a distinct factor that becomes slightly more accentuated after extensive cycling. For this reason, while Li plating is a key focus there is still a need to ensure that protocols take into account both electrode aging factors.

The teams at INL and NREL also worked to better understand why there was increased cell-to-cell variability in some of the protocols. Through analysis and modeling experiments it became clear that in many instances the cells during fast charge were very close to the Li plating potential. Analysis of the impact of partial pore closure due to either electrically isolated Li or due to excessive SEI formed due to Li plating suggests that as low as 1%–3% blockage can have a distinct impact on failure mode and can either lead to the situation where Li metal cascades to excessive levels or transitions from Li plating to less proclivity to Li plating. Based on this information it is important that cell-to-cell variation be understood early in life or that adaptive protocols need to be developed.

The INL team also expanded the analysis of the charge protocols to gain understanding of what the actual power levels at the vehicle level would be for different sized battery packs using some of the experimentally evaluated and computationally identified charge protocols. Looking at packs that ranged in size from 35 kWh to 95 kWh the team was able to identify the level of electric vehicle service equipment (EVSE) that would be necessary to sustain the protocols for the different packs. As shown in Figure I.4.L.7, in some instances, especially where the initial C-rates are well above 7C it is plausible that the EVSE would need to support charging capability above 700 kW if looking to fast charge a vehicle with a large battery pack. For smaller pack sizes and for protocols that are less aggressive during the initial charging that value significantly decreases with the variation from a constant power charge being within ~20% of the mean value.

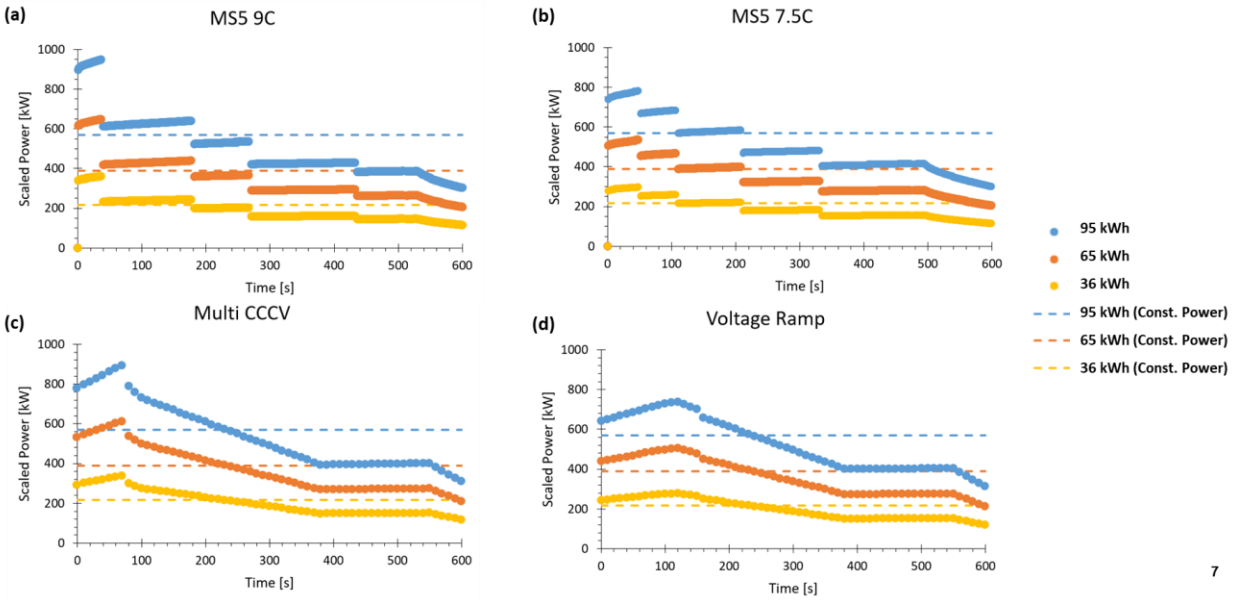

Figure I.4.L.7 Scaled charge protocols to vehicle pack sizes of 35-95 kWh based on Round 2 cell design. A) 5 step protocol with initial rates of 9C B) 5 step protocol with initial rates of 7.5 C C) Multi-CCCV protocol D) Voltage ramp profile with initial CC of 7.5C.

Effect of anode porosity and temperature on the performance and Li plating during fast-charging of lithium-ion cells.

Researchers at Argonne and NREL looked to characterize the role of porosity and temperature as contributing factors to Li plating. Twenty-four cells were tested to determine the effect of electrode porosity on Li plating. Twelve cells contained the 1506T electrode that had been calendared to 22% porosity and twelve, to 49%

porosity. Initial measurement of the C/2 capacity at 30°C showed that the cells were well-matched. The average C/1 capacity of the low-porosity cells was 32.062 ± 0.355 mAh (1-s) and that of the high-porosity cells, 32.421± 0.326 mAh. The cells were cycled using a 6-C charge (CV as needed, maintaining 10 minutes total charging time) and a C/2 discharge protocol at temperatures in the range of 20-50°C. RPTs were conducted, initially, every five cycles at the testing temperature. The RPT consisted of C/20 discharge capacity measurement and EIS.

Based on visual observations, random cell porosity had very little effect on lithium plating, as shown in Figure I.4.L.8. The results indicate that the porosity of the graphite electrode in these experiments played a relatively small role in limiting lithium deposition. Both at short and long times, temperature seemed to determine the extent of lithium plating. At high temperatures, lithium plating was not seen at short times and was limited at longer ones.

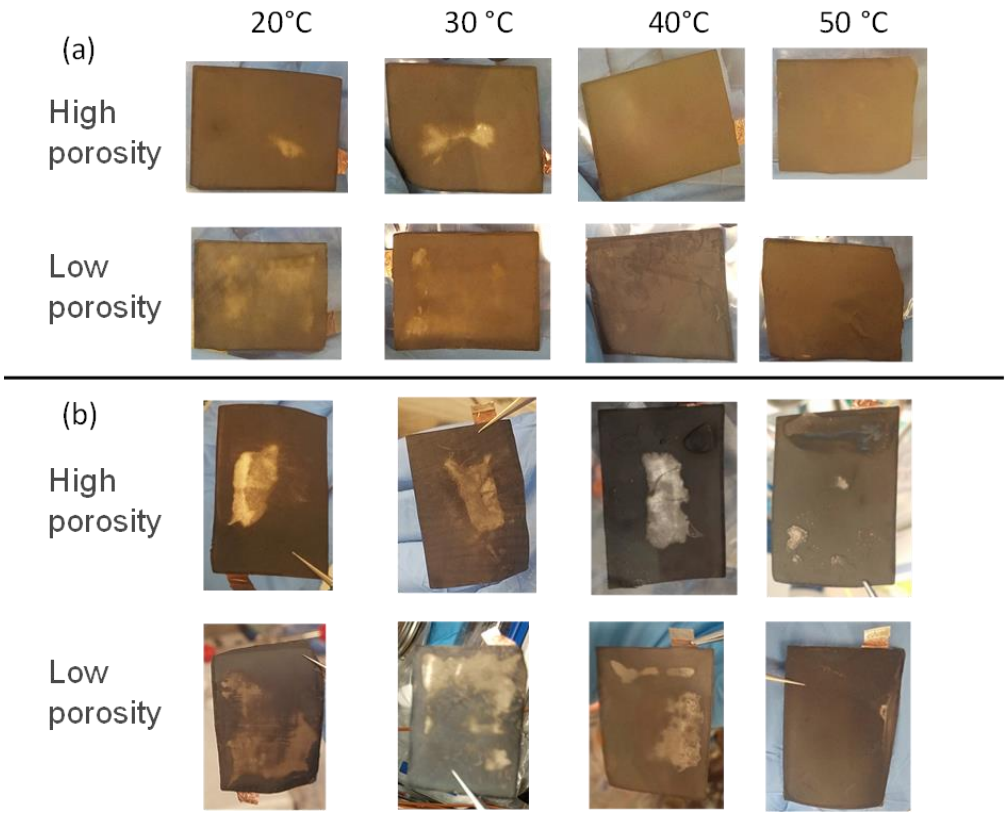

Figure I.4.L.8 Glove box images of the anodes (a) after 5 fast-charge cycles and (b) at the end of fast-charge testing as a function of temperature and porosity.

Model predictions for lithium plating during initial fast charging.

Figure I.4.L.9 illustrates the fast charge capacity added to cells with low and high porosity anodes during the 10-minute charge protocol of constant current and voltage (CC-CV), implemented for the second cycle at operating temperatures of 20-50°C. The average of measurements for three cells for each condition is plotted as open circles versus electrochemical model simulations, shown as solid lines. The capacity linearly increases with time during CC charging, and the rate of capacity addition decreases during the CV charging due to decreasing current. For the low porosity cell, the average charge capacities achieved in 10 minutes were 20.2, 23.2, 25.2, and 25.7 mAh at 20, 30, 40, and 50°C, respectively. The corresponding capacity values for the high porosity cells were slightly higher, 20.7, 23.6, 26.4, and 26.5 mAh. There was good agreement between measured capacity and the simulation results from the electrochemical model for the chosen parameter set. Increasing the porosity resulted in very little improvement in the 10-minute capacity values compared to those

at elevated temperatures. To be discussed below, this behavior seems to be due to the anode tortuosity remaining unexpectantly high even with high porosity and slightly longer solid-state diffusion distance for uncalendered particles.

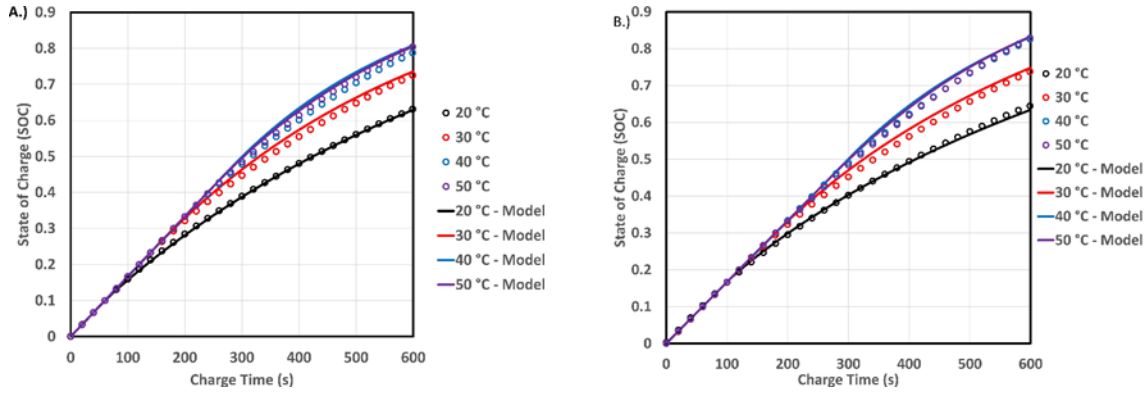

Figure I.4.L.9 Charge capacity as function of time during initial 10 minute CC-CV charging for low porosity (A) and high porosity (B). The experimental measurements are the average of three cells and are shown as circles. Model results are plotted as solid lines.

The electrochemical model was used to investigate the effect of temperature and anode porosity on lithium plating and electrolyte depletion during initial cycling. Example results are shown in Figure I.4.L.10. Commensurate with visual observations shown in Figure I.4.L.8, the model predicts significant amounts of lithium plating except for cells operating at 50°C. Increasing temperature significantly mitigates lithium plating due to improvements in the electrolyte transport properties [9-11] and graphite transport/kinetic properties. Further model development is required to better understand the reversibility of the lithium stripping process and the effect of this on cell lifetime.

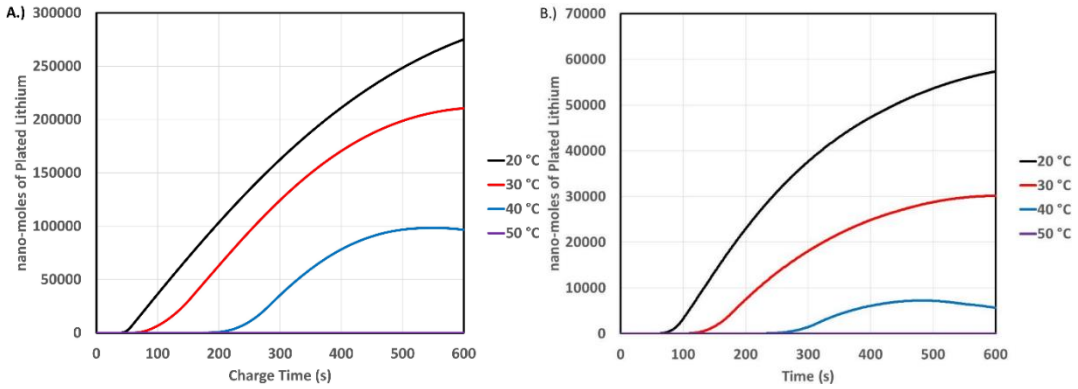

Figure I.4.L.10 Model predictions for plated lithium during 10-minute CC-CV charging for cells with low porosity (left) and high porosity (right) anodes. Note that 12,000 nanomoles of lithium capacity corresponds to 1% of the cell capacity.

A simple analytical model has been used to quantify the impact of calendering on characteristic diffusion time. Assuming calendering redistributes the location of particles without modifying their volume and does not modify Bruggeman coefficient, the characteristic diffusion time ratio between the high-porosity and low-porosity electrode have been calculated (see Figure I.4.L.11). Analytical model indicates that calendering electrodes exhibiting poor-to-intermediate ionic diffusion (such as ANL CAMP electrodes) will aggravate ionic transport limitations with a stronger negative impact for thinner electrodes (even though calendered electrode are thinner) and explains transport limitation calculated with the electrochemical model for the calendered electrodes. Microstructure-scale modeling performed with the NREL open-source Microstructure

Analysis Toolbox (MATBOX) [12] also revealed that the standard relationship between specific surface area and porosity commonly used in the literature does not stand for the low-porosity electrodes, which may induce errors if not corrected. Modeling calendered electrodes requires a more accurate estimation of the specific surface area (e.g. BET, microstructure characterization). The results highlight the fact that more research needs to be done to definitively determine how microstructure properties change with electrode porosity, especially on the low-porosity range.

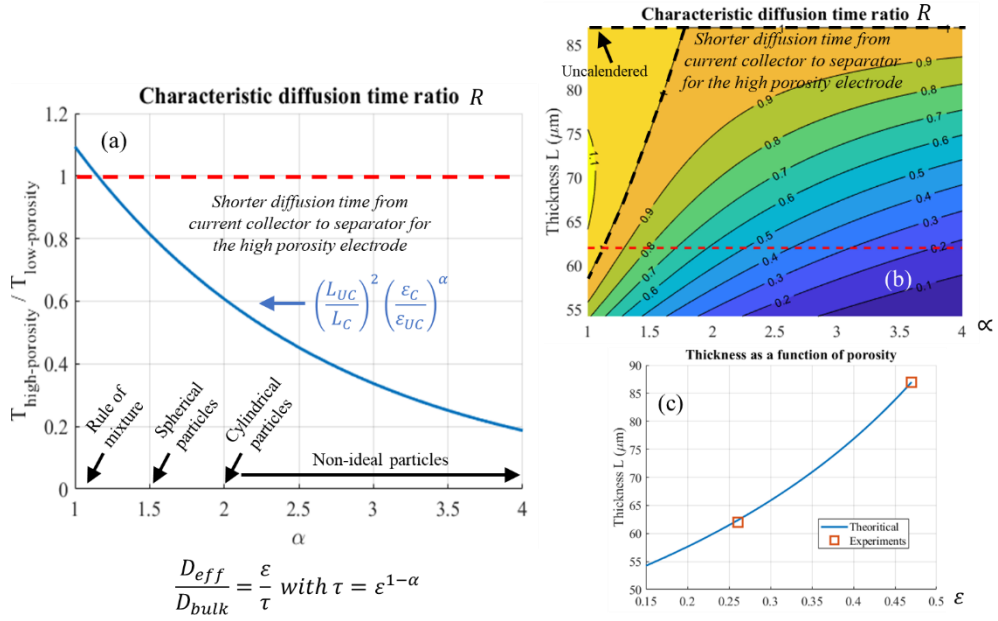

Figure I.4.L.11 Characteristic diffusion time ratio, R, between (a) the high and low porosity electrodes that were experimentally tested and (b) the high and a range of low porosity electrodes considering various calendered thicknesses (dashed black line represents the characteristic diffusion isovalue time, and the red dashed line corresponds to the thickness of the calendered electrode). (c) Electrode thickness as a function of porosity from an uncalendered electrode.

In summary, the modeling suggests that higher anode porosity should mitigate lithium plating more than experimentally observed. Continued research is needed to better understand these phenomena. Possible explanations include:

- Lithium stripping is less reversible for the higher porosity case.
- Plating for the high porosity case is driven by local heterogeneity, which is challenging to model, instead of bulk transport limitations.
- Plating is driven more by limitations in the intercalation process than liquid phase ionic transport.
- The continued growth of metallic lithium is very different than the initial plating behavior.
- Lithium plating is a highly stochastic process that is not well represented with the standard deterministic approach reported here.

Curve-fitting.

Example results from the curve fitting exercise are given in Figure I.4.L.12 and Figure I.4.L.13. The relative capacity loss is plotted in both figures for both low- and high-porosity cells. An apparent kinetic rate law of the general form, $At + Bt^{1/2}$, can be fit to the capacity loss data in Figure 11 (low porosity). This is not the case for the data from the high porosity cells. Figure I.4.L.12 shows that the $At + Bt^{1/2}$ rate law can be fit to the 20, 30 and 40°C data, but a logistics rate law was needed for the 50°C data (Figure I.4.L.13b). The $At + Bt^{1/2}$ rate indicates that a mixed mechanism was present, combining linear-with-time and parabolic elements.

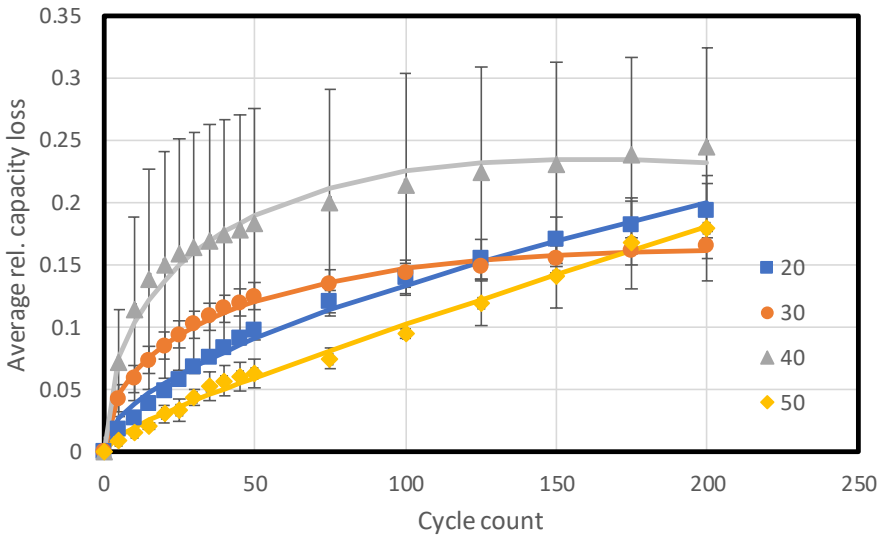

Figure I.4.L.12 Average, relative capacity loss vs. cycle count for the low porosity cells tested at temperatures of 20, 30, 40 and 50°C. The markers represent the average values and the solid curves, the results of fitting. The error bars represent the range of values; Since there were only two cells per condition in the cycling experiment, the uncertainty was calculated from |(average value)-(observed value)| for each condition; thus, average+uncertainty and average-uncertainty represent the range of the observed values.

Logistics kinetics are common where there is a reaction which has a limited amount of reaction material. When the limiting material is plentiful, the reaction rate increases with time, reaching a maximum rate about 90 cycles in this case. After that point, the amount of limiting material decreases sharply, causing a corresponding decrease in observed rate. This type of behavior is usually seen in biological systems where bacteria grow on a limited food supply. In our case, the limiting material may be the amount of active anode material. After a point, chemical and physical stress in the cell may cause binder degradation, limiting the amount available for lithium intercalation.

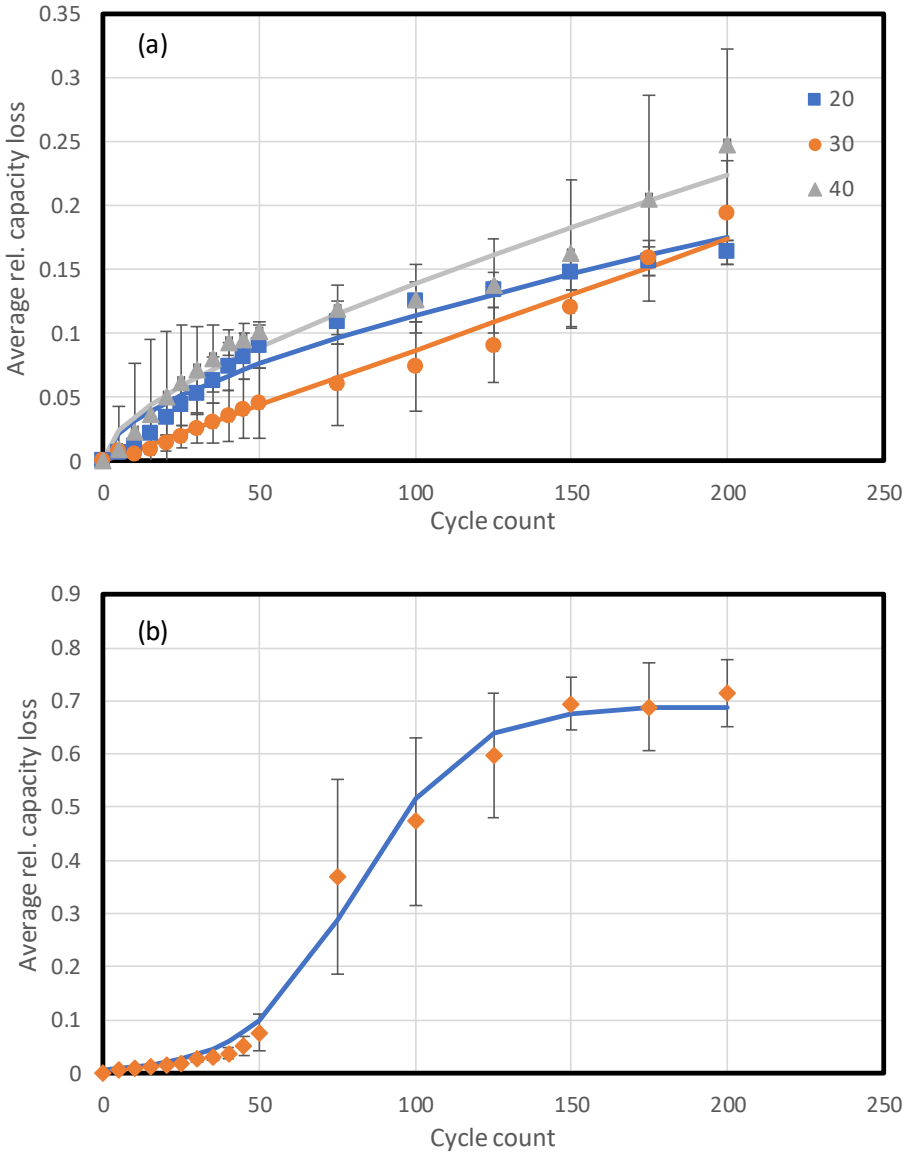

Figure I.4.L.13 (a) Average, relative capacity loss vs. cycle count for the high porosity cells tested at temperatures of 20, 30 and 40°C. (b) Average, relative capacity loss vs. cycle count for the cells tested at 50°C. The markers represent the average values and the solid curves, the results of fitting

Conclusions

During FY20 the team of researchers at INL, NREL and Argonne made several advances in understanding how advanced charge protocols impact life and performance of batteries. It was found that cycling above the transport limits of the cells leads to significant Li plating which can be somewhat lessened using different protocols. In some instances, even if the Li plating is reduced for a single cell, some protocols still displayed high cell-to-cell variability likely due to small evolutions in the structure of the anode. In complimentary work, it was found that porosity and temperature play a key role in the extent of both Li plating and Li stripping.

Based on insights from running the model, novel charging protocols are proposed that are predicted to improve 10-minute charge capacity and prevent lithium plating. A detailed summary of these model findings has been published in a recent journal article [publication 7]. The team is currently experimentally validating these new proposed protocols using Round 2 pouch cells. Models will be updated with cathode aging phenomena and used to explore protocols to minimize both lithium plating and cathode degradation. Lastly, the team will

determine how novel protocols need to be adjusted based on expected aging phenomena like reduction in anode porosity from SEI growth.

When looking at the potential of the anode in theory, the $\phi_a = 0$ control presents the safest option to reliably exclude Li plating. This measure assumes that the electrode display homogenous behavior, which is not the case especially at high rates. Furthermore, Li plating at the graphite anode is not the sole factor that governs the long-term cell behavior: cathode processes, including electrolyte oxidation and oxide structure changes can also have a deleterious effect on cell performance. [6] All these aging processes (that are still being explored) need to be considered during the design of cell charging/cycling protocols.

Key Publications

1. A. M. Colclasure, T.R. Tanim, A.N. Jansen, S.E. Trask, A.R. Dunlop, B.J. Polzin, I. Bloom, D. Robertson, L. Flores, M. Evans, E.J. Dufek, and K. Smith, "Electrode scale and electrolyte effects on extreme fast charging of lithium-ion cells," *Electrochimica Acta*, **337**, 135854 (2020).
2. A. M. Colclasure, A.R. Dunlop, S.E. Trask, B.J. Polzin, A.N. Jansen, and K. Smith, "Requirements for Enabling Extreme Fast Charging of High Energy Density Li-Ion Cells while Avoiding Lithium Plating," *J. Electrochem. Soc.*, **166**, A1412-A1424 (2019).
3. F.L.E. Usseglio-Viretta, W. Mai, A. Colclasure, K. Smith, "Enabling fast charging of lithium ion battery through Secondary/dual pore network: Part I - analytical model," *Electrochimica Acta*, **342**, 136034 (2020).
4. W. Mai, F.L.E. Usseglio-Viretta, A. Colclasure, Kandler Smith, "Enabling fast charging of lithium ion battery through Secondary/dual pore network: Part II - numerical model," Electrochimica Acta, **341**, 136013 (2020).
5. D.C. Robertson, L. Flores, A.R. Dunlop, S.E. Trask, F.L.E. Usseglio-Viretta, A.M. Colclasure, Z. Yang, I. Bloom, "Effects of Anode Porosity and Temperature on the Performance and Lithium Plating during Fast-Charging of Lithium-Ion Cells," *Energy Technology* – 2000666 (2020).
6. M.T.F. Rodrigues, I.A. Shkrob, A.M. Colclasure, and D.P. Abraham, "Fast Charging of Li-Ion Cells: Part IV. Temperature Effects and "Safe Lines" to Avoid Lithium Plating," *J. Electrochem. Soc.*, 167 130508 (2020).
7. W. Mai, A.M. Colclasure, K. Smith, "Model-instructed design of novel charging protocols for the extreme fast charging of lithium-ion batteries without lithium plating," *J. Electrochem. Soc.*, **167**, 080517 (2020).
8. T.R. Tanim, P.P. Paul, V. Thampy, C. Cao, H.G. Steinruck, J.N. Weker, M.F. Toney, E.J. Dufek, M.C. Evans, A.N. Jansen, B.J. Polzin, A.R. Dunlop, S.E. Trask "Heterogeneous Behavior of Lithium Plating during Extreme Fast Charging," *Cell Rep. Phys. Sci.* **1**, 100114 (2020).
9. P.R. Chinnam, A. Colclasure, B.R. Chen, T.R. Tanim, E.J. Dufek, K. Smith, M.C. Evans, A.R. Dunlop, S.E. Trask, B.J. Polzin, A.N. Jansen "Fast charging aging considerations: Incorporation and alignment of cell design and material degradation pathways" *in preparation*
10. S. Kim, T. Tanim, E. Dufek, A. Colclasure, M. Shirk, A. Meintz, D. Scoffield, T. Pennington "Scaling next generation charging profiles and battery designs to understand implications for future electric vehicle infrastructure" *in preparation*
11. B.R. Chen, R. Kunz, T.R. Tanim, E.J. Dufek "A Machine Learning Framework for Early Detection of Lithium Plating Combining Multiple Physics-based Electrochemical Signals" *in preparation*
12. A. Raj, M.-T.F. Rodrigues, D.P. Abraham, "Rate-Dependent Aging Resulting from Fast Charging of Li-Ion Cells", J. Electrochem. Soc. 167, 120517 (2020).
13. I.A. Shkrob, M.-T.F. Rodrigues, D.P. Abraham, "Fast Charging of Li-Ion Cells: Part III. Relaxation Dynamics and Trap-Controlled Lithium Ion Transport", J. Electrochem. Soc. 166, A4168-A4174 (2019).
14. M.T.F. Rodrigues, I.A. Shkrob, A.M. Colclasure, D.P. Abraham, "Fast Charging of Li-Ion Cells: Part IV. Temperature Effects and "Safe Lines" to Avoid Lithium Plating", J. Electrochem. Soc. 167 130508 (2020).
15. M.-T. F. Rodrigues, V.A. Maroni, D.J. Gosztola, K.P.C. Yao, K. Kalaga, I.A. Shkrob, D.P. Abraham, "Lithium Acetylide: A Spectroscopic Marker for Lithium Deposition During Fast Charging of Li-Ion Cells", ACS Appl. Energy Mater. 2, 873−881 (2019).

16. Z. Yang, J.W. Morrissette, Q. Meisner, S.B. Son, S.E. Trask, Y. Tsai, S. Lopykinski, S. Naik, I. Bloom, "Extreme Fast-Charging of Lithium-Ion Cells: Effect on Anode and Electrolyte" Energy Technology, *submitted*

References

1. F.L.E. Usseglio-Viretta, A. Colclasure, A.N. Mistry, K.P.Y. Claver, F. Pouraghajan, D.P. Finegan, T.M.M. Heenan, D. Abraham, P.P. Mukherjee, D. Wheeler, P. Shearing, S.J. Cooper, and K. Smith, "Resolving the discrepancy in tortuosity factor estimation for Li-ion battery electrodes through micro-macro modeling and experiment," *J. Electrochem. Soc.*, **165**, A3403-A3426 (2018).
2. M.-T.F. Rodrigues, K. Kalaga, S.E. Trask, Dennis W. Dees, I.A. Shkrob, D.P. Abraham, "Fast Charging of Li-Ion Cells: Part I. Using Li/Cu Reference Electrodes to Probe Individual Electrode Potentials", J. Electrochem. Soc. 166, A996-A1003 (2019).
3. I.A. Shkrob, M.-T.F. Rodrigues, D.W. Dees, D.P. Abraham, "Fast Charging of Li-Ion Cells: Part II. Nonlinear Contributions to Cell and Electrode Polarization", J. Electrochem. Soc. 166, A3305-A3313 (2019).
4. I.A. Shkrob, M.-T.F. Rodrigues, D.P. Abraham, "Fast Charging of Li-Ion Cells: Part III. Relaxation Dynamics and Trap-Controlled Lithium Ion Transport", J. Electrochem. Soc. 166, A4168-A4174 (2019).
5. M.T.F. Rodrigues, I.A. Shkrob, A.M. Colclasure, D.P. Abraham, "Fast Charging of Li-Ion Cells: Part IV. Temperature Effects and "Safe Lines" to Avoid Lithium Plating", J. Electrochem. Soc. 167 130508 (2020).
6. M.-T. F. Rodrigues, V.A. Maroni, D.J. Gosztola, K.P.C. Yao, K. Kalaga, I.A. Shkrob, D.P. Abraham, "Lithium Acetylide: A Spectroscopic Marker for Lithium Deposition During Fast Charging of Li-Ion Cells", ACS Appl. Energy Mater. 2, 873−881 (2019).
7. A. Raj, M.-T.F. Rodrigues, D.P. Abraham, "Rate-Dependent Aging Resulting from Fast Charging of Li-Ion Cells", J. Electrochem. Soc. 167, 120517 (2020).
8. T.R. Tanim, E.J. Dufek, M. Evans, C. Dickerson, A.N. Jansen, B.J. Polzin, A.R. Dunlop, S.E. Trask, R. Jackman, I. Bloom, Z. Yang, E. Lee, "Extreme fast charge challenges for Lithium-ion Battery: Variability and positive electrode issues", J. Electrochem. Soc. 166(10), A1926 (2019).
9. A. M. Colclasure, A. R. Dunlop, S. E. Trask, B. J. Polzin, A. N. Jansen, and K. Smith, *J. Electrochem. Soc.*, 166 (2019) A1412-A1424.
10. A. M. Colclasure, T.R. Tanim, A.N. Jansen, S.E. Trask, A.R. Dunlop, B.J. Polzin, I. Bloom, D. Robertson, L. Flores, M. Evans, E.J. Dufek, and K. Smith, *Electrochimica Acta*, 337 (2020) 135854.
11. X. Yang, G. Zhang, S. Ge, and C-Y Wang, *Proc. Natl. Acad. Sci. Unit. States Am*., 115 (2018) 7266-7271.
12. F. Usseglio-Viretta et al., MATBOX: Microstructure Analysis Toolbox, https://github.com/NREL/MATBOX_Microstructure_analysis_toolbox

Acknowledgements

This project was funded by the U.S. Department of Energy, Vehicle Technologies Office. The technology development manager was Samm Gillard. The project overview was prepared by Venkat Srinivasan (ANL). Other contributing team members for Thrust 3 (Charge Protocols and Life Assessment for Extreme Fast Charging Thrust) include Marco-Tulio Fonseca Rodrigues, Ilya A. Shkrob, Daniel P. Abraham, David C. Robertson, LeRoy Flores, Alison R. Dunlop, Stephen E. Trask, Zhenzhen Yang, and Ira Bloom, Francois L. E. Usseglio-Viretta, Andrew M. Colclasure, Kandler Smith, Eric Dufek, Tanvir Tanim, Bor-Rong Chen, Parameswara Chinnam Rao; Sangwook Kim and Michael Evans.

I.4.M XCEL R&D: Anode & Electrolyte Thrust

Venkat Srinivasan, Principal Investigator
Argonne National Laboratory
9700 S. Cass Avenue,
Lemont, IL 60439
E-mail: vsrinivasan@anl.gov

Samm Gillard, DOE Technology Development Manager
U.S. Department of Energy
E-mail: Samuel.Gillard@ee.doe.gov

Start Date: October 1, 2019 End Date: September 30, 2020
Project Funding (FY20): $742,000 DOE share: $742,000 Non-DOE share: $0

Project Introduction

The focus of the XCEL Program in FY 2018–2019 centered on the influence of areal capacity loading on lithium plating during extreme fast charging (XFC). Two sets of capacity-matched electrodes were designed and fabricated by the Cell Analysis, Modeling, and Prototyping (CAMP) Facility at Argonne National Laboratory (Argonne) with identical compositions — only the capacity loading was changed. The low loading electrode set (Round 1) utilized a 2-mAh/cm^2 graphite loading, and the higher loading set utilized a 3.0-mAh/cm^2 graphite loading. Numerous pouch cells were fabricated and delivered to the national laboratory and university team. These two cell builds are still considered the baselines for the XCEL Program. It became clear after extensive testing that lithium plating is rare on the Round 1 anodes, but is abundant on the Round 2 anodes during 6C charging. A multi-thrust approach was needed to solve the problems related to XFC, the chief of which is lithium plating. This section summarizes the activities of the XCEL-Anode & Electrolyte Thrust.

Objectives

The goal of the XCEL Anode & Electrolyte Thrust in FY 2020 was to develop an anode structure with a tailored electrolyte system that can enable a 6C charge for >600 cycles with no lithium-plating. Modifications of the electrode architecture have the goal of low tortuosity to enable fast lithium ion transport to and from the active material closest to the current collector, while maintaining low porosity to maintain high energy density. New electrolyte systems are targeted to have higher ionic conductivity with lithium transference numbers closer to 1, while also maintaining a robust solid electrolyte interface (SEI) on the anode (and cathode to a lesser extent).

Approach

There are several approaches underway in the area of electrode architecture as well as in the area of electrolyte development. Both of these areas involve coordinated efforts between several national labs.

1. The National Renewable Energy Laboratory (NREL) used its suite of electrochemical models and microstructure analysis tools to investigate advanced electrode architectures to improve fast charge performance and prevent lithium plating. The key to improving fast charge performance is to lower the ionic transport resistance through the entire cell including anode, separator, and cathode to prevent preferential utilization of electrodes near separator [Ref. 1]. Detailed modeling indicates three promising strategies to improve ionic transport: reducing the amount of carbon/binder in electrodes, introducing a secondary pore network, and utilizing dual-layer electrodes.
2. It is then up to the electrode fabrication teams to design and build electrodes that mimic the model-predicted ideal electrode architectures. These fabrication teams are centered at Argonne's CAMP Facility, which relies on traditional coating equipment, and Lawrence Berkeley National Laboratory (LBNL), which has developed freeze cast techniques.

3. Model predictions of ideal electrolyte systems rely heavily on the Advanced Electrolyte Model (AEM) developed at Idaho National laboratory (INL), which is used here to investigate premier electrolyte metrics that have influence on cell performance during XFC, most notably viscosity, conductivity, diffusivity (all species), lithium transference number, lithium desolvation energies, and other terms.
4. Meanwhile, the NREL team assembles electrolyte formulations using solvents screened from high throughput calculation results, evaluates the stability of these formulations across the usable electrochemical window, and measures cell-level performance. In FY 2020, six formulations containing the molecules shortlisted from calculations were assembled and subjected to experimental evaluation.

The benchmark for the start of FY 2020 remained the Round 2 electrodes (described in Figure I.4.M.1) with the "Gen2" electrolyte, which is 1.2 M $LiPF_6$ in EC:EMC (3:7 wt%, from Tomiyama). Round 2 baseline pouch cells consist of 14.1-cm^2 single-sided cathodes (0.236 grams of NMC532 per pouch cell) and 14.9-cm^2 single-sided graphite anodes (SLC1506T from Superior Graphite) using Celgard 2320 separator (20 µm, PP/PE/PP) and 0.615 mL of "Gen2" electrolyte for an electrolyte-to-pore volume factor of 4.20. The n:p ratio is between 1.07 to 1.16 for this voltage window (3.0 to 4.1 V), and the nominal C/2 capacity is 32 mAh.

New electrolyte formulations using solvents screened from calculation results, were evaluated for their stability across the usable electrochemical window within the cell using the Round 2 baseline electrodes. For candidates that appeared suitable for fast charging, pouch cells were built with the Round-2 baseline electrodes by CAMP and subject to long-term cycling according to standard protocols established for the XCEL program. Detailed characterization of the degradation mechanism and integration of these results into INL's AEM provided additional insights into electrolyte and interfacial properties that enable fast charge.

It was planned that in the third quarter of FY 2020, the best candidate electrode architecture and the best candidate electrolyte system would be selected for scale up. Coin cells and pouch cells would be assembled with the selected electrode pair and selected electrolyte and evaluated for electrochemical performance. Efforts were also directed to developing formation processes with the new electrodes and electrolytes to create a robust SEI while preventing lithium-plating during cycling. A final pouch cell build was planned for the fourth quarter of FY 2020, to be distributed to the testing labs for electrochemical performance under fast charges. (Many of these lab activities were shortened due to the COVID-19 pandemic's impact on laboratory time.) Comparisons would subsequently be made to the benchmark (Round 2 pouch cells). The techno-economic model BatPaC would also be used in the fourth quarter to determine the cost implications of the new fast charge cell system.

Anode: LN3107-190-4A
91.83 wt% Superior Graphite SLC1506T
2 wt% Timcal C45 carbon
6 wt% Kureha 9300 PVDF Binder
0.17 wt% Oxalic Acid
Lot#: 573-824, received 03/11/2016
Single-sided coating, CFF-B36 anode
Cu Foil Thickness: 10 µm
Total Electrode Thickness: 80 µm
Total Coating Thickness: 70 µm
Porosity: 34.5 %
Total SS Coating Loading: 9.94 mg/cm^2
Total SS Coating Density: 1.42 g/cm^3
Made by CAMP Facility

Cathode: LN3107-189-3
90 wt% Toda NMC532
5 wt% Timcal C45
5 wt% Solvay 5130 PVDF
Matched for 4.1V full cell cycling
Prod:NCM-04ST, Lot#:7720301
Single-sided coating, CFF-B36 cathode
Al Foil Thickness: 20 µm
Al Foil Loading: 5.39 mg/cm^2
Total Electrode Thickness: 91 µm
Coating Thickness: 71 µm
Porosity: 35.4 %
Total Coating Loading: 18.63 mg/cm^2
Total Coating Density: 2.62 g/cm^3
Made by CAMP Facility

Figure I.4.M.1 Electrode composition and design parameters for baseline Round 2 pouch cell design.

Results

Model Prediction of Ideal Electrode Architecture (NREL Focus)

NREL used its microstructure electrochemical full cell model to investigate the effect of carbon/binder domain (CBD) loading on the onset of lithium plating. The CBD is added to provide mechanical integrity and sufficient electronic conductivity. Determining the impact of CBD on hindering electrolyte transport/effective

electrode tortuosity is difficult because the domain cannot be easily distinguished from pores with conventional methods like computed tomography (CT) imaging. Also, the key feature size of the CBD is on the order of tens of nm and very small compared to active material particles or pores. In a previous Computer-Aided Engineering for Electric-Drive Vehicle Batteries (CAEBAT) program, NREL worked with Purdue University to numerically generate the CBD phase to investigate its effect on ionic transport. A wide range of CBD morphologies were explored, ranging from a film-like phase preferentially covering active particles to a spider-web-like morphology contained within pores. The standard CAMP anodes contain roughly 8 wt% CBD, and the cathodes have 10%. These relatively high CBD fractions are used by CAMP as a standard recipe designed to enable swapping of the active material for more novel materials and ensuring sufficient mechanical and electrical properties. Figure I.4.M.2 illustrates that reducing the amount of CBD in the electrodes by 50% significantly delays the onset of lithium plating during a 6C charge for Round 2 electrodes. Reducing the CBD in the cathode is particularly important because the 10 wt% occupies a considerably higher volume fraction and thus significantly hinders ion transport. CAMP has made significant progress in making Round 2 electrodes with lower CBD fractions, and initial results are promising.

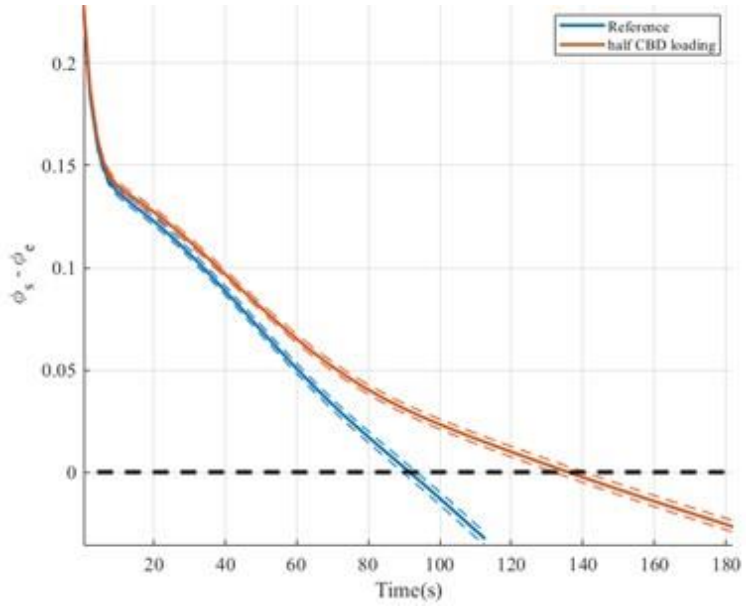

Figure I.4.M.2 Microstructure electrochemical model prediction for lithium plating potential during 6C fast charge. By reducing the CBD domain by half, the onset of lithium plating is delayed by more than 7% state of charge (SOC).

Another approach to improve ion transport through electrodes is the introduction of a secondary pore network (SPN). The SPN provides low-resistance ionic pathways and can be made through laser ablation, freeze casting, or pore formers. A combination of analytic diffusion and two-dimensional (2D) COMSOL models are used to determine how SPN architecture can be tailored to maximize fast charge performance. A detailed report of model results for SPN can be found in key [Ref 2 and 3]. As more void is introduced in the microstructure through the oriented channels, the non-channel portions of electrode active material must be densified to maintain constant theoretical capacity for a given electrode thickness. This induces an exponential decrease of the in-plane ionic diffusion while the through-plane diffusion is only increasing linearly. Within the possible design space, nonuniform in-plane utilization of the active material limits the maximum acceptable SPN channel volume. Thus, SPN feature size must be kept relatively small and SPN channel volume should be limited to around 25% or less of the total porosity to enhance extreme fast charging. For example, for straight channels, the pore channel width should be less than 10 microns, and the distance between channels should be less than the thickness of the electrode. Somewhat larger feature sizes can be used when an individual hole SPN architecture is used compared to continuous straight channels. Figure I.4.M.3 illustrates model predictions for a ~35% energy density increase for a 3-mAh/cm^2 cell after 6C CC when both

anode and cathode are structured with a 26% SPN volume ratio, a channel spacing of 8.4 µm, and a width 3 µm. NREL is providing design guidance to LBNL to manufacture such SPN architectures.

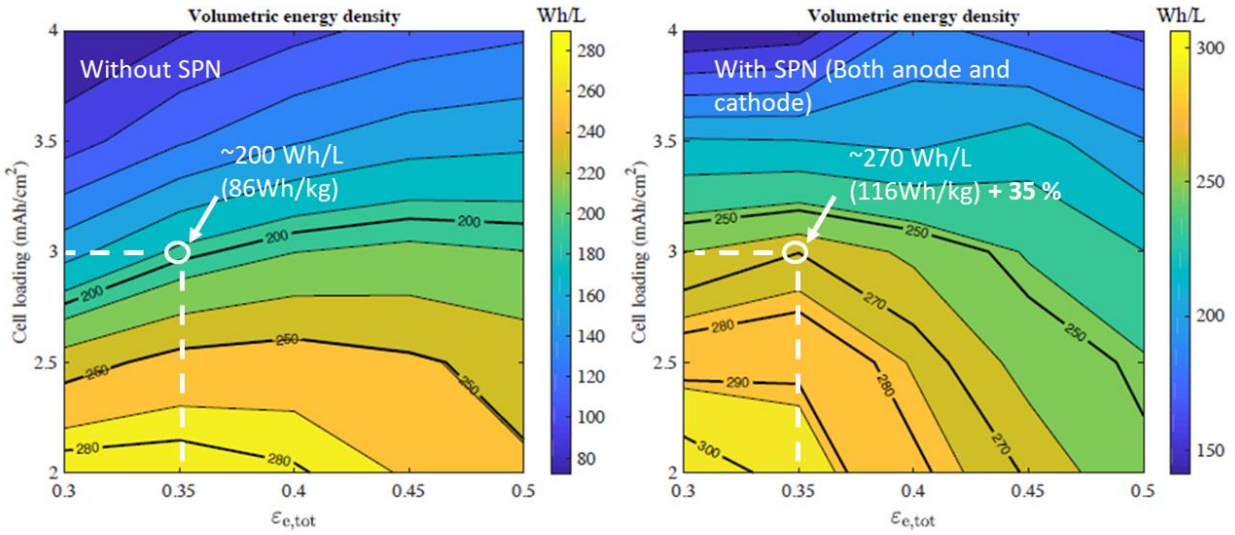

Figure I.4.M.3 Volumetric energy density calculated after 6C CC charging with a 4.2-V cutoff voltage and at 45°C. Without SPN (left) and with SPN (right) architecture, both compared at the same total porosity and electrode thickness. With SPN, 116 Wh/kg (52% of theoretical energy density) is reached after 6C CC, and 173.9 Wh/kg (77% of theoretical energy density) is reached after 10 minutes CC CV for a 3-mAh/cm² cell loading.

Last, a dual-layer electrode architecture is investigated to improve ion transport to enhance fast charge performance. NREL used its macro-homogeneous model to explore improvement in performance by using electrodes with higher porosity near separator and lower porosity near current collector as illustrated in Figure I.4.M.4. The model predicts that a 20% offset in porosity is a good baseline for dual-layer fabrication with each layer being of equal thickness. That is, the first layer coated on the current collector should be significantly calendered down to 25%, a second layer coated, and then the second layer should only be slightly calendered to 45% porosity. The cathode tortuosity is assumed to vary in the standard fashion with a slightly higher exponent than traditionally used by others at $\tau=1.4\varepsilon^{-0.7}$. This relationship has been determined with both microstructure reconstruction and experimental measurements performed by Dean Wheeler at Brigham Young University (BYU) for CAMP NMC532 electrodes. Thus, the cathode tortuosities at 25% and 45% porosity are estimated to be 3.7 and 2.5, respectively. Due to discrepancies between microstructure reconstructions for tortuosity and experimental measurements for CAMP graphite electrodes, the model is run with different values for the anode tortuosity at a given porosity.

The black line in Figure I.4.M.4 represents baseline performance for standard single-layer electrodes achieving ~40% SOC at 6C before cutoff voltage with lithium plating predicted to start around 16% SOC. The solid-gray lines represent performance using a dual-layer structure in both electrodes with anode tortuosity being 5.8 in both sections, which fits trends measured experimentally using symmetric cell with blocking electrolyte. If the anode tortuosity remains high even with high porosity, then the dual-layer setup has a similar capacity and onset of lithium plating as baseline cells. The dashed grey lines represent cases with the anode tortuosity being a function of porosity, similar to what is predicted from microstructure reconstructions. For these cases, the dual layer structure is effective at slightly improving capacity and significantly delaying lithium plating until around 30% SOC.

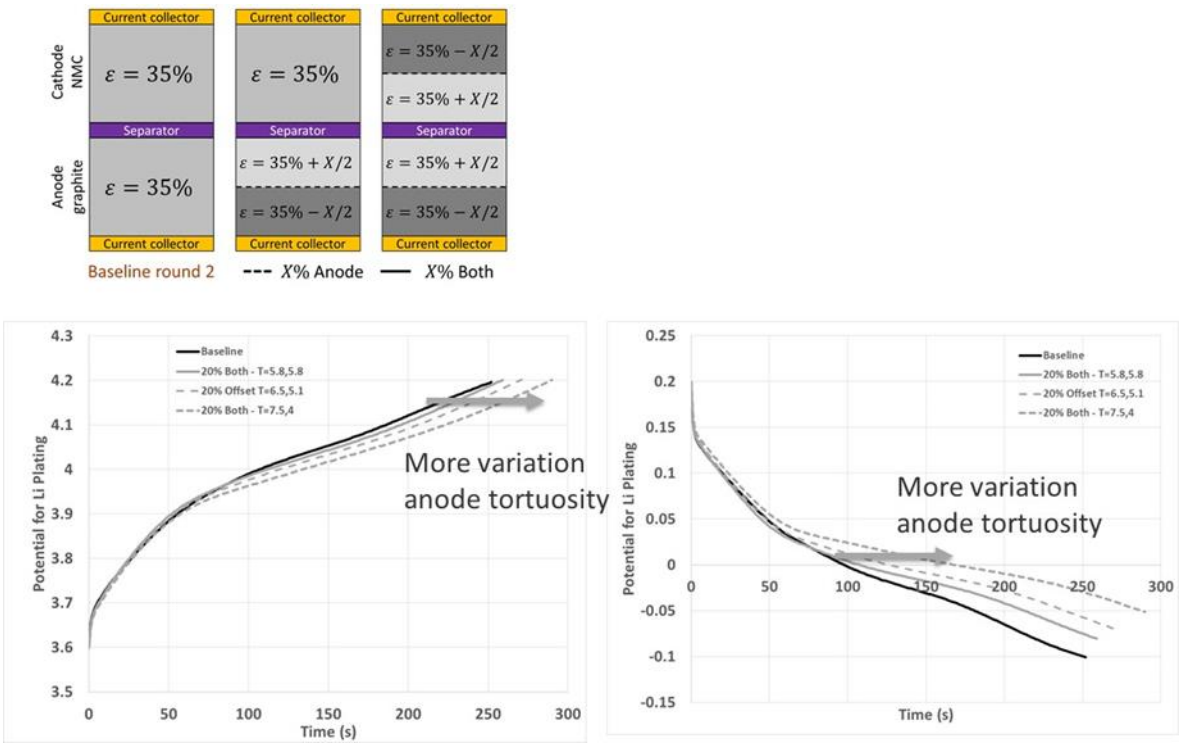

Figure I.4.M.4 Model predictions for effect of dual-layer electrode structure on fast charge performance for Round 2 loading. Note: the dual-layer structure is only beneficial if anode tortuosity changes significantly with porosity.

Structured Electrode Development Using Conventional Coating Equipment (Argonne-CAMP Focus)

The CAMP Facility at Argonne fabricated a dozen experimental negative electrodes using three morphologically different graphite powders: the baseline SLC1506T (Superior Graphite), SLC1520P (Superior Graphite), and MCMB (Gelon). The properties of these powders are described in Table I.4.M.1. In general, SLC1506T has lower tap density, ~2x surface area, and ~1/2 smaller particle size compared to SLC1520P. The MCMB is an artificial graphite that is somewhat spherical, with higher tap density and surface area compared to both SLC1506T and SLC1520P. The average MCMB particle size is like the SLC1520P.

Table I.4.M.1 Properties of Selected Graphite Powders for Anode Architecture Development

Trade Name	Company	Type	Particle Shape or Morphology	Tap Density, [g/mL]	Surface Area, [m²/g]	Particle Size D10, [µm]	Particle Size D50, [µm]	Particle Size D90, [µm]
SLC1506T	Superior Graphite	Natural graphite, coated	Spherical graphite powder	1.03	1.936	5.37	8.06	13.15
SLC1520P	Superior Graphite	Natural graphite, coated	Spherical graphite powder	1.19	0.89	11.03	16.94	26.76
MCMB	Gelon	Artificial, mesocarbon microbeads, std type-G15	MesoCarbon microBeads	1.324	2.022	-	17.649	-

Dual-layer coatings were made with large particles near the foil (small particles near the separator), which is predicted by the NREL modeling effort to be closer to the ideal architecture that minimizes lithium plating. The reverse order was also fabricated to enhance the difference in expected degrees of lithium plating. Two methods of coating were tried: reverse comma (rc), knife-over-roll (kor), and knife-over-roll with NMP pre-wetting (kor*). There was some difficulty in making the dual-layer (dual-pass) electrodes with the reverse comma method, which resulted in bubbles forming on the second layer (top layer) that caused a hole on the surface when it dried. Better results were obtained with the knife-over-roll method, but the ability to control the loading level was more difficult. These dual-layer electrodes, along with other graphite choices, are summarized in Table I.4.M.2. Scanning electron microscopy (SEM) cross-sections were made of many of the fabricated electrodes; three pertinent ones are shown in Figure I.4.M.5.

Table I.4.M.2 Anode Architectures Explored in FY 2020

Structured Anode (Sticker Electrode Information)	ID No.	NMC532 Pairing - Loading (mg/cm^2)	Anode Coating Loading (mg/cm^2)	Anode Porosity (%)	Anode Coating Density (g/cm^3)	Anode Areal Capacity (mAh/cm^2)
BASELINE SLC 1506T	#0	C0 - 18.57	9.38	38	1.34	2.74
SLC 1520P [B, rc] : SLC 1506T [T, rc]	#1	C0 - 18.57	9.77	36	1.40	2.76
SLC 1520P [B, rc] : SLC 1506T [T, kor]	#2	C1 - 21.54	11.56	33	1.46	3.41
SLC 1506T [B, rc] : SLC 1520P [T, rc]	#4	C0 - 18.57	9.63	37	1.36	2.84
SLC 1506T [B, rc] : SLC 1520P [T, kor]	#5	C1 - 21.54	11.32	31	1.49	3.29
SLC 1520P/SLC 1506T (Slurry mix)	#7	C0 - 18.57	10.04	34	1.43	2.88
MCMB	#10	C0 - 18.57 C2 - 17.20	10.29	38	1.34	2.73
MCMB/SLC1506T Mix	#11	C2 - 17.20	10.15	35	1.41	2.78
SLC 1520P	#12	C0 - 18.57	9.88	35	1.41	2.98
SLC 1506T Laser Ablated	LA	C0 - 18.57	8.53	-	1.01	2.62

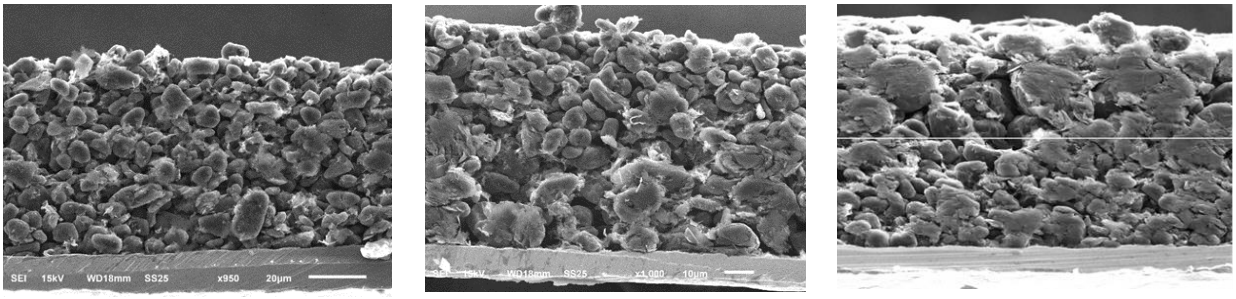

Figure I.4.M.5 Photos of the Baseline SLC1506T (left), SLC1506T on SLC1520P on foil (center), and SLC1520P on SLC1506T on foil (right).

A screening protocol was created to test several of these structured anodes in the 2032 coin cell format that required that a total of four coin cells be made for each condition. The Round 2 (NMC532) cathode was used at the counter electrode, with a Gen2 electrolyte. All cells in each electrode cell set were formed (via a C/10 tap charge for one hour, followed by a five-hour rest, then three cycles at C/10, and then three cycles at C/2). One cell was then cycled 10 times with a 6C charge (C/2 discharge), one cell was cycled 25 times with a 6C charge, and one cell was cycled 50 times with a 6C charge. The cells were then opened in the dry room, the anodes were rinsed in DMC, air dried for a couple minutes, and then photographed. A pictorial summary of the resulting harvested anodes is provided in Figure I.4.M.6.

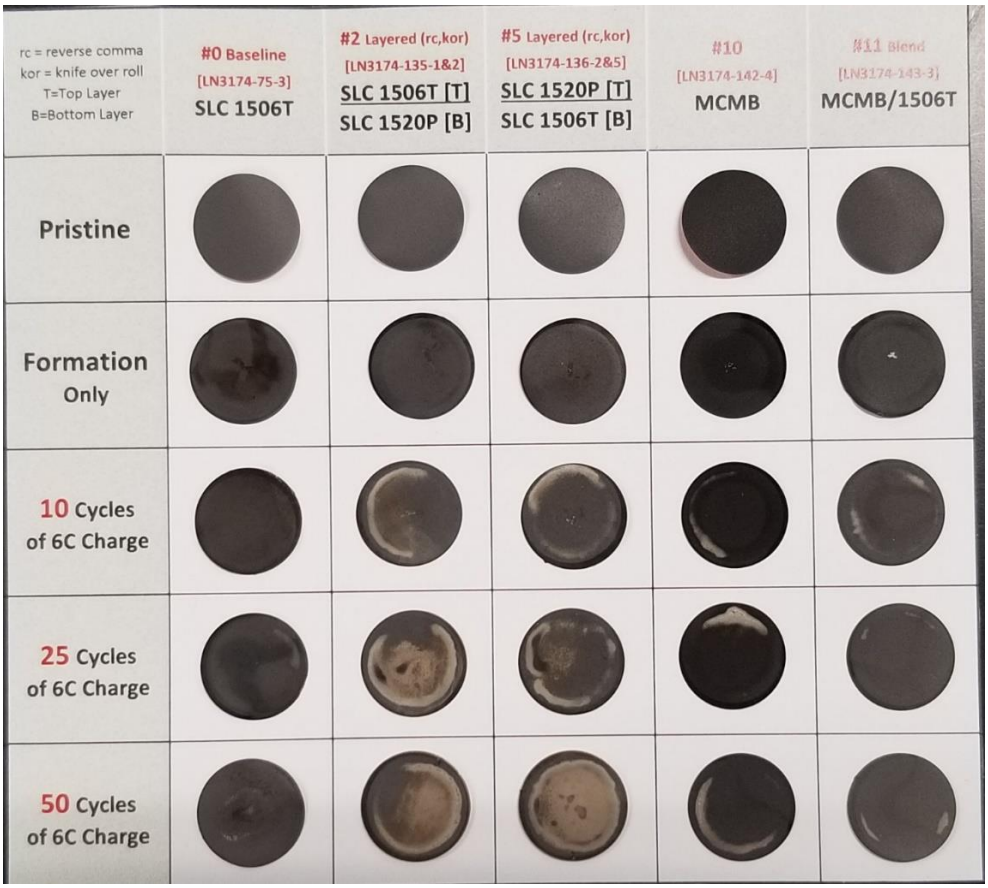

Figure I.4.M.6 Pictorial summary of harvested anodes after varying degrees of cycling and the resulting lithium plating.

The most obvious observation that can be made from an inspection of Figure 6 is that the dual-layer electrodes exhibited excessive amounts of lithium plating. This was true regardless of the layer stacking order, small graphite particles near separator (a more ideal case), or large graphite particles near the separator. This result is attributed at this time to the reduced total graphite surface area for the dual-layer electrodes that used the much larger SLC1520P (~20 microns) graphite over the smaller SLC1506T (~8 microns) graphite. In the NREL model predictions above, the more ideal particle size next to the separator is near 2 microns, with the relatively larger SLC1506T near the foil. Efforts are underway to source a graphite near 2 microns. The other graphite electrodes (MCMB & MCMB/ SLC1506T blend), as shown in Figure 6, exhibited lithium plating. The baseline SLC1506T unilayer electrode is still the best anode structure at this point in time, but will hopefully be improved upon with gradient porosity in the electrode, smaller graphite particles near the separator, and reduced carbon and binder content.

Freeze Tape-Casting of Graphite Anodes (LBNL Focus)

Graphite anode architecture, with low tortuosity open pores parallel to the ion transport direction during cycling, were developed by a freeze tape-casting method. Diverse combinations of graphite, carbon, water-soluble/dispersible binders, dispersants, and surfactants were tested and down-selected to prepare stable slurries. The slurries were then freeze tape-cast (FTC) at selected temperatures, casting speeds, and gap heights to form graphite anodes of controlled architectures.

Methods were developed to freeze tape-cast graphite anodes using a doctor blade. Prior castings were conducted using a plastic film top cover with spacers for thickness control in order to prevent surface water evaporation of the cast slurry. Without the top cover, slurry surfaces typically dried out before reaching the freezing bed due to the slow casting speed (15 cm/h), and the limited amount of solvent used (as it controls porosity), (Figure I.4.M.7a). The feasibility of graphite freeze tape-casting was demonstrated in the prior year but encountered issues with thickness control/uniformity. In order to produce large area samples with good thickness control, a doctor blade was used for casting, and an ultrasonic humidifier was introduced to suppress water evaporation. This approach resolved the surface pore blockage issue but resulted in surface binder segregation due to excessive surface water condensation from the humidifier (Figure I.4.M.7b,c).

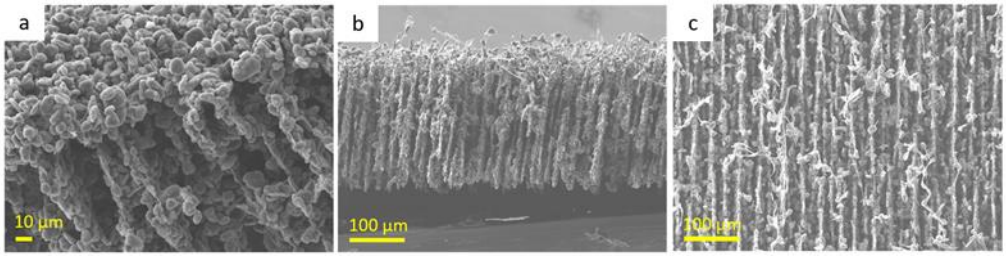

Figure I.4.M.7 (a) Fracture surface SEM image of FTC graphite electrode showing surface pore blockage as a result of surface water evaporation. (b),(c) Fracture surface and surface SEM images of FTC graphite electrode showing surface binder segregation due to surface water condensation.

Both issues could be addressed by modifying the FTC equipment such that the cast slurry immediately enters the freezing zone as soon as it exits the doctor blade gap. Through iterations of freeze tape-casting processing parameter control, graphite anodes of aligned porosity using a doctor blade could be produced (Figure I.4.M.8a). Typical electrodes' FTC were 65%–75 % porous, much higher compared to 30%–40% porous tape-cast (TC) and calendered electrodes. In order to reduce the overall electrode porosity, we investigated FTC on top of a TC electrode, forming a dual-layer structure.

Two different formulations were tested for the TC layer, which forms the bottom layer and is bonded to the Cu current collector foil. The TC electrodes are dried to remove the solvent, and an FTC slurry is then placed on the TC electrode and subsequently spread over the entire area using a doctor blade, as the electrode is pulled into the freezing bed of the freeze tape caster. Two binder systems, CMC/SBR and PVDF, representing reactive and non-reactive binder systems, respectively, were tested. The dual-layer electrode with a CMC/SBR tape-cast layer did not show any pore structure in the freeze-tape-cast layer, and the two layers also showed poor adhesion. In contrast, a dual-layer electrode with the tape-cast layer using the PVDF binder showed the desired pore structure in the freeze-tape-cast layer and good adhesion between the two layers. However, the FTC layer produced by this approach always had mixed ice domains of vertical and horizontal ice channels as shown in Figure I.4.M.8b,c,d. It is likely that the surface roughness and non-uniformity of the TC layer compared to Cu foil or Mylar film contributes to non-uniform ice growth directions.

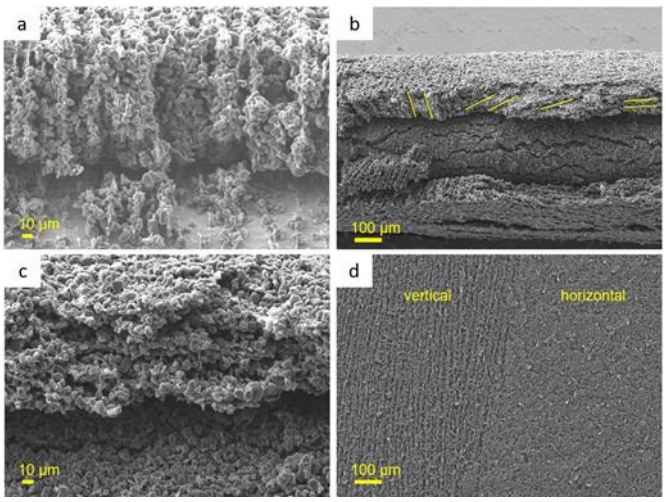

Figure I.4.M.8 (a) Fracture surface SEM image of FTC graphite electrode. (b),(c) Fracture surface SEM images of dual-layer (TC/FTC) graphite electrode showing mixed ice growth directions. (d) Surface SEM image of dual-layer (TC/FTC) graphite electrode showing vertical and horizontal ice growth regions.

An alternative approach was explored in which a freeze-tape-cast electrode was produced in a free-standing form, and the free-standing electrode was attached onto the tape cast electrode (Figure I.4.M.9). It was possible to attach the free-standing FTC electrode either onto a dried tape-cast electrode using a PVDF solution in NMP or by simply placing the free-standing electrode on top of a tape cast electrode immediately after tape casting (prior to solvent drying).

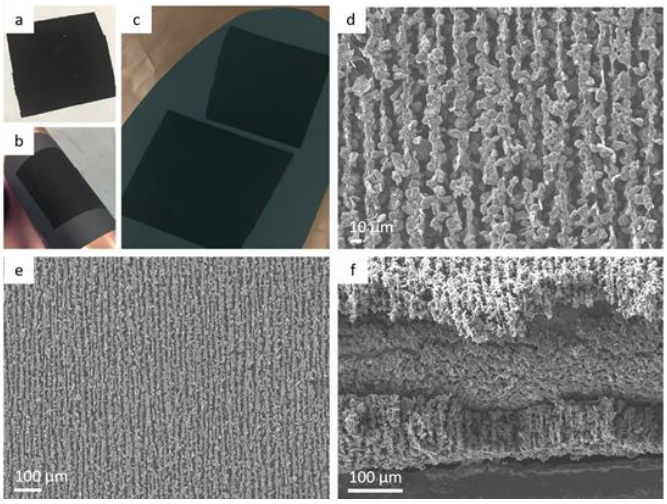

Figure I.4.M.9 (a) Photo of free-standing FTC electrode, roughly 4''×4''. (b).(c), Photo of free standing FTC electrode attached to TC electrode. (d),(e) Surface SEM image of FTC graphite electrode after attachment. (f) Fracture surface SEM image of TC/FTC dual layer electrode.

Tomographic images of the dual-layer electrodes were obtained to further analyze and visualize the architecture in 3D. Figure I.4.M.10 represents the images obtained and an exemplary 3D visualization. The brighter particulates represent the 1506T graphite particles, whereas the dark area represents pores. Per image processing through thresholding and binarization, porosities of ~71% and ~49% were obtained for the freeze-tape-cast and tape-cast layer, respectively, similar to the expected values. The overall porosity is ~69%. Due to the low thickness of the tape-cast layer (~17 µm), it had little impact on the overall porosity. The pore channels had an average width of ~13 µm.

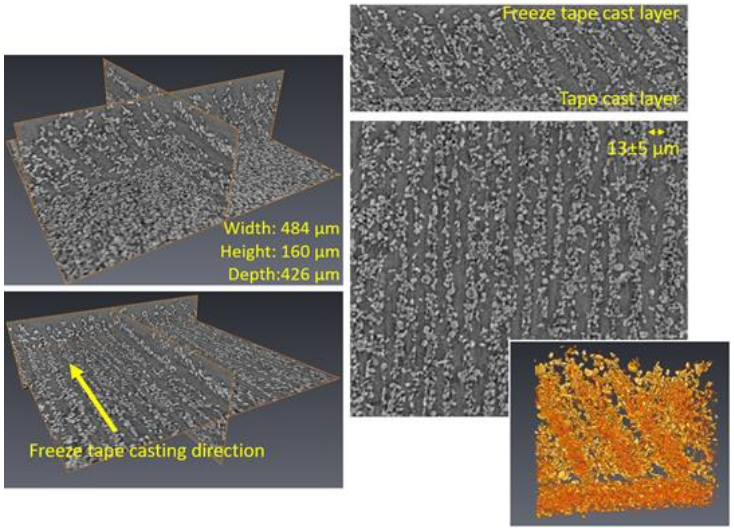

Figure I.4.M.10 2D and 3D reconstructions of micro tomographic images of the TC/FTC dual-layer electrodes.

Electrolyte Predictions from Advanced Electrolyte Model (AEM); Cell Testing (INL Focus)

INL is supporting the XCEL Anode Thrust area in terms of electrolyte modeling (characterization and screening) and cell testing to identify candidate electrolyte systems compatible with XFC conditions. Within the modeling task, the INL Advanced Electrolyte Model (AEM) is being applied to investigate premier electrolyte metrics that have influence on cell performance during fast charge, most notably viscosity, conductivity, diffusivity (all species), lithium transference number, lithium desolvation energies, and other terms related to concentration polarization (which alters local transport properties and behavior at nearby electrode surfaces). AEM is also being used to investigate terms related to the electrode wetting process, such as electrolyte surface tension and liquid permeation rates into electrode porous structures of various dimensions. In all such AEM simulations, conditions cover a wide range of salt concentration (to anticipate extent of concentration polarization in cells) and temperature. Cell testing at INL has identified viable electrolyte candidates that may replace the baseline Gen2 system (EC-EMC-$LiPF_6$). These alternative electrolyte systems are designed based on considerations of improved transport properties (past the Gen2 baseline) to mitigate concentration polarization effects; improved permeation of electrolytes through the electrode materials; and stable, low-impedance SEI films. To achieve these goals, the XFC electrolytes are multi-component formulations that have minimized ethylene carbonate (EC) content with a host of co-solvents that include linear carbonates, linear esters, nitriles, a phosphate, and key additives. In some formulations, mixed salts have been used to seek further performance enhancement. In many cases, the XFC electrolytes demonstrate conductivity and diffusivity values that are 2-3 times that of the Gen2 system. Coordination for this task area involves Argonne, INL, and NREL.

Highlights and summary of tasks within this year:

A. Initial screening through AEM produced several XFC electrolyte candidates that were tested in coin and pouch cells. Early coin cell testing with R2 NMC532/Gr produced clear cases where INL XFC electrolytes provide competitive advantage over the Gen2 baseline.
B. Electrode wetting is a practical consideration for battery electrolytes, and key terms were added to the AEM computational architecture to cover this aspect. These terms regard prediction of pure solvent surface tension, mixed solvent surface tension, as well as surface tension of their electrolytes as a function of salt concentration. Temperature dependence is also captured for these terms.
C. Quantitative metrics were defined for how a high charge rate gives a correspondingly high anode surface charge density (SCD), and how this can cause a disruptive response within the neighboring electrolyte solvent dipoles that encourages conditions for lithium metal deposition.

D. AEM outputs for two electrolytes (Gen2 BL vs INL XFC system B26) were compared through NREL cell models to determine differences in charge rate performance, with clear indications that the INL XFC electrolyte gives substantial improvements in terms of charging performance, reducing polarization and avoidance of conditions toward lithium metal deposition.
E. Multi-solvent highly concentrated electrolyte (HCE) systems were identified that satisfy many of the attributes needed for use in Li-ion cells used for fast-charge applications. Early cell tests were initiated.
F. Activation energy analysis through AEM allowed investigation of multiple property metrics over an extended salt range. For many electrolyte properties the activation energy increases with increased salt concentration, causing a profound difference in activation energies within a cell during XFC where concentration polarization is highly manifest. Using AEM, HCE systems were identified with less variance of activation energies over salt concentration.
G. Hero Cell Electrolyte: Testing of CAMP Facility Round 2 (R2) pouch cells with down-selected XFC electrolyte candidates showed where one such candidate (denoted B26) gives competitive advantage over the Gen2 baseline in every measured category. This electrolyte was distributed by INL to ANL and UC Berkeley for the hero cell build and further testing.
H. An early optimization study was done that looked at cell formation parameters and their impact on capacity and early aging trends, using B26 with the NMC532/graphite electrode couple. Our studies indicate that it is beneficial to extend the rest periods between formation cycles.
I. A scoping study was performed that confirmed good compatibility between electrolyte B26 and the NMC811 cathodes.

Examples of AEM-guided electrolyte formulations are given in Figure I.4.M.11 where they are compared to the Gen2 system in terms of conductivity, salt diffusivity and the maximum velocity of penetrance, a wetting parameter. Formulations are geared toward NREL performance recommendations of having significantly increased conductivity and diffusivity.

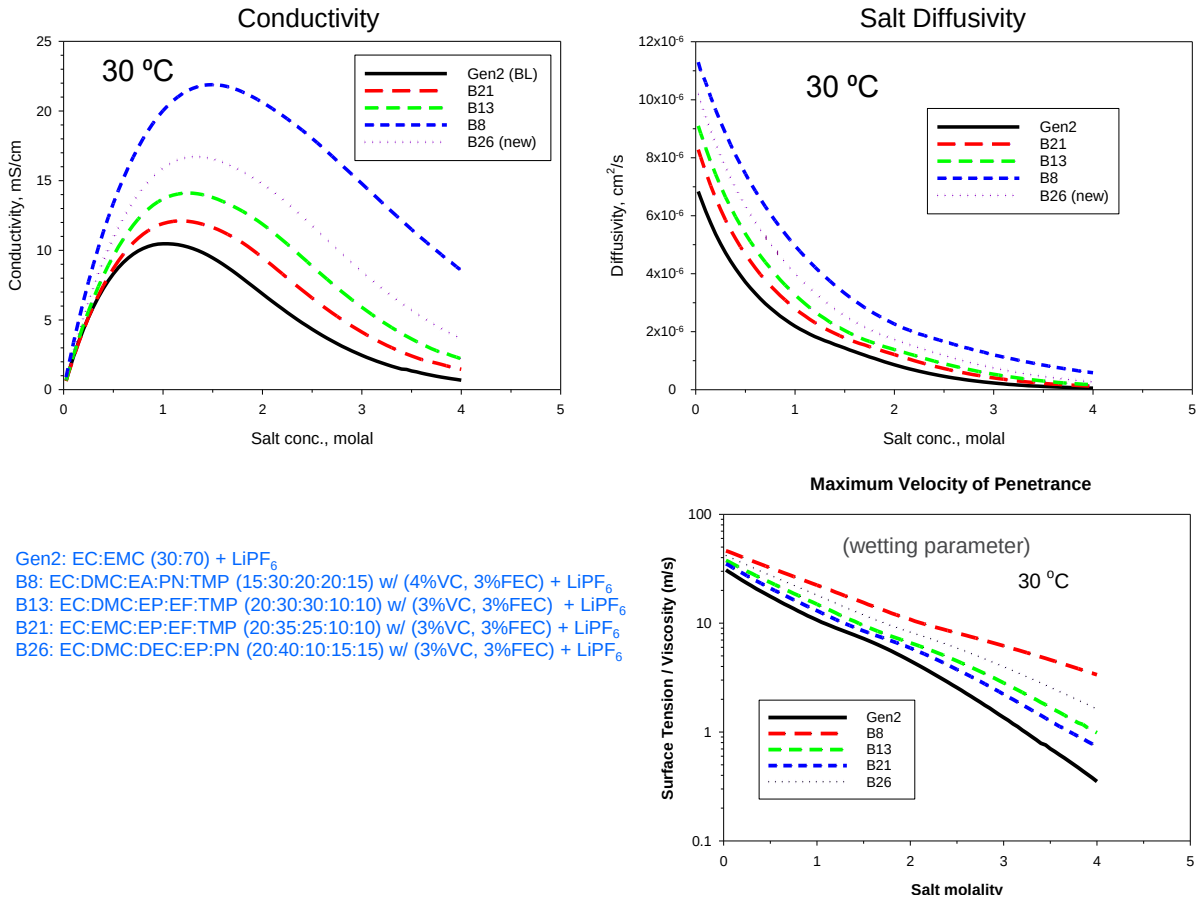

Gen2: EC:EMC (30:70) + $LiPF_6$
B8: EC:DMC:EA:PN:TMP (15:30:20:20:15) w/ (4%VC, 3%FEC) + $LiPF_6$
B13: EC:DMC:EP:EF:TMP (20:30:30:10:10) w/ (3%VC, 3%FEC) + $LiPF_6$
B21: EC:EMC:EP:EF:TMP (20:35:25:10:10) w/ (3%VC, 3%FEC) + $LiPF_6$
B26: EC:DMC:DEC:EP:PN (20:40:10:15:15) w/ (3%VC, 3%FEC) + $LiPF_6$

Figure I.4.M.11 Comparison of selected AEM-guided electrolyte systems to Gen2

Electrolyte attributes that impact electrode wetting are also captured in AEM, namely, in terms of surface tension, viscosity and density. Since the context for electrolyte permeation here is porous electrodes, the AEM considers a range of pore diameters for a chosen pore length and pore roughness to determine the liquid permeation rates. This is facilitated by the following set of equations known as the Bosanquet approach, wherein we see the importance of viscosity (η), density (ρ) and surface tension (γ), where the 'b' term can be modified to include external pressure.

$$\frac{d}{dt}\left(\pi r^2 \rho x \frac{dx}{dt}\right) + 8\pi\eta x \frac{dx}{dt} = 2\pi r\gamma\cos\theta,$$

$$x^2(t) - x^2(0) = \frac{2b}{a}\left[t - \frac{1}{a}(1 - e^{-at})\right] \qquad a = \frac{8\eta}{\rho r^2} \qquad b = \frac{2\gamma\cos\theta}{\rho r}.$$

Examples of model predictions for surface tension are given in Figure I.4.M.12a-b. B13 is a low-viscosity electrolyte blend tested for XFC conditions. Good agreement is seen in Figure 12a between AEM predictions and lab data. In both (a) and (b) AEM was allowed to run out to higher salt concentrations, where it is seen that surface tension becomes highly non-linear. This attribute will play a role in altering the effective electrolyte surface tension values resident in the electrical double layers under conditions of cell polarization, where salt concentrations can easily exceed 3 Molar on the enrichment side of the cell, impacting all properties therein.

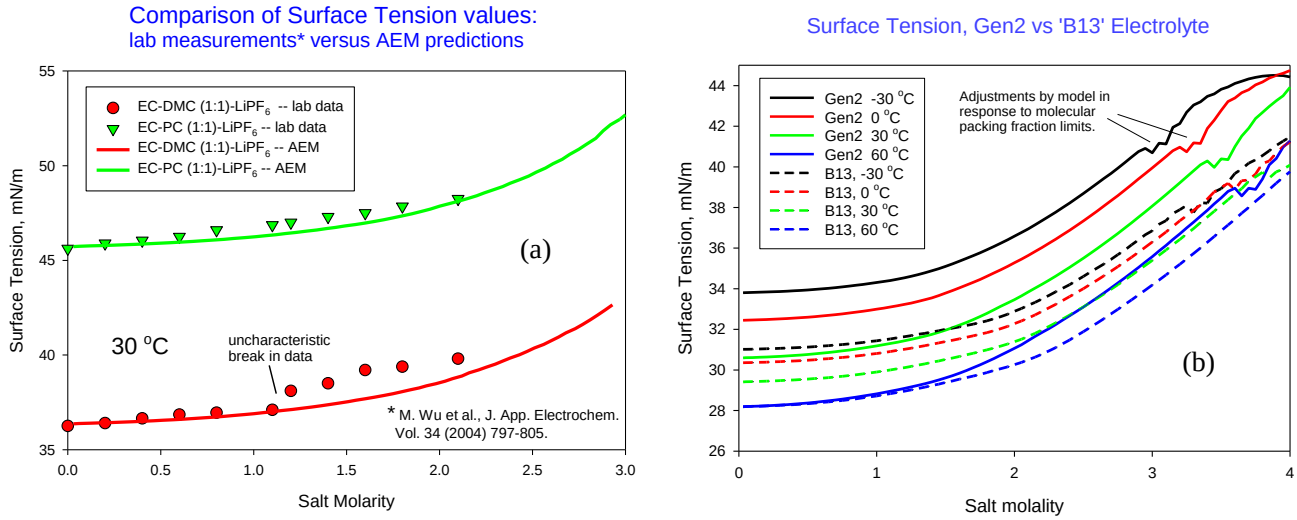

Figure I.4.M.12 Comparison of surface tension values for (a) AEM predictions versus measured values, and (b) AEM predictions for the Gen2 electrolyte versus 'B13" alternative fast charge electrolyte.

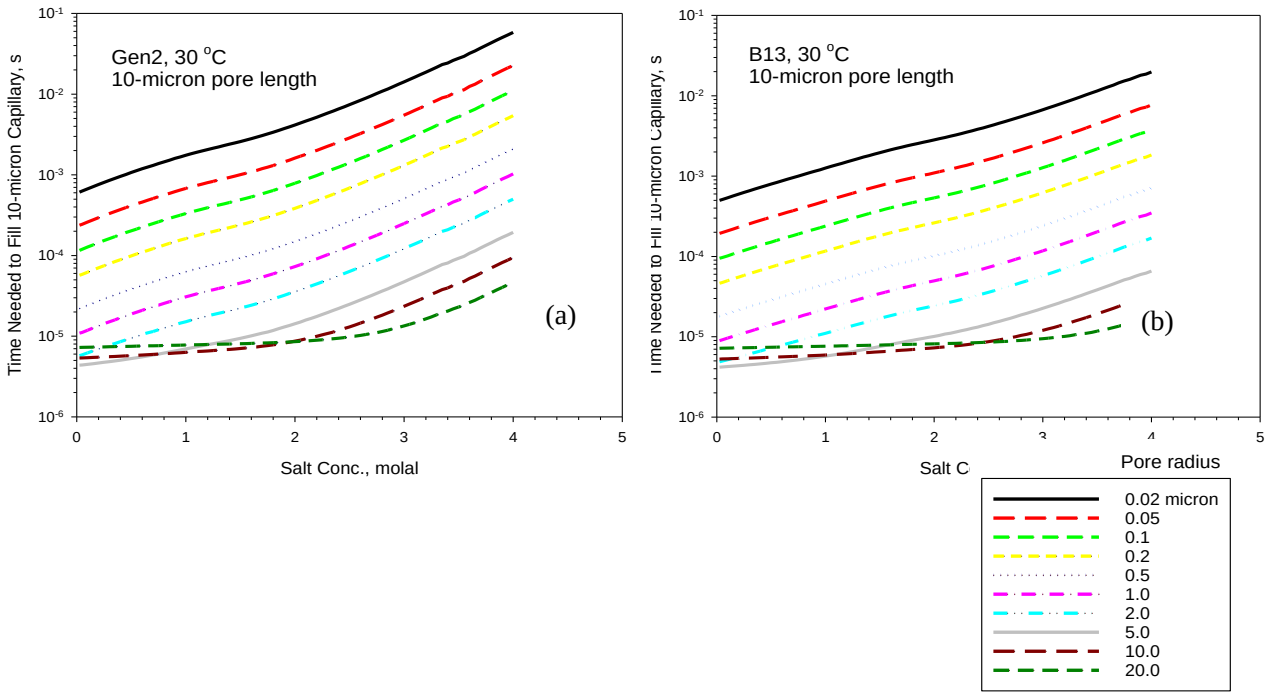

Figure I.4.M.13 Comparison of predicted electrolyte permeation time through a 10-micron pore length for (a) Gen2 and (b) B13 XFC electrolyte (better wetting). A wide range of pore radii are investigated to account for variations of porous regions in battery electrodes.

In Figure I.4.M.13a-b plots are shown from AEM simulations that capture the time required for electrolyte to fill 10-micron capillaries of various radii, considering 30°C. Please note the log scale given in the y axes. For demonstration purposes, the Gen2 electrolyte (a) is compared to B13 (b), as in Figure I.4.M.12b. The 10-micron pore length is used as an example, but its value is arbitrary and is determined through AEM user inputs. From this comparison it is seen B13 permits quicker permeation of electrolyte through porous structures than Gen2 (by ≈ 2 to 4 times), which will have a positive impact to promote more complete and timely electrode wetting. The next steps for this topic will be to mimic electrode cases: consider porous networks with differing pore dimensions, various degrees of connectivity, and trapped gas.

Electrolyte behavior under concentration polarization may well play a role in promoting lithium metal deposition. Figure I.4.M.14a,b shows predictions for the electrostatic repulsive energy caused by the anode surface charge density, SCD. This effect is a strong function of distance from the anode surface, producing a region of probable solvent disruption or repulsion (denoted 'A') from surface at the shown surface charge density, where Li^+ is acted on more by the SCD than solvent dipoles. Larger SCD produce greater regions of solvent response/reorientation/repulsion with corresponding decrease of permittivity. This creates a region of "unprotected" lithium that can encourage lithium metal deposition at the anode surface. Loci of surface heterogeneities where surface charge is locally higher will worsen this process and become initiation sites for lithium metal deposition.

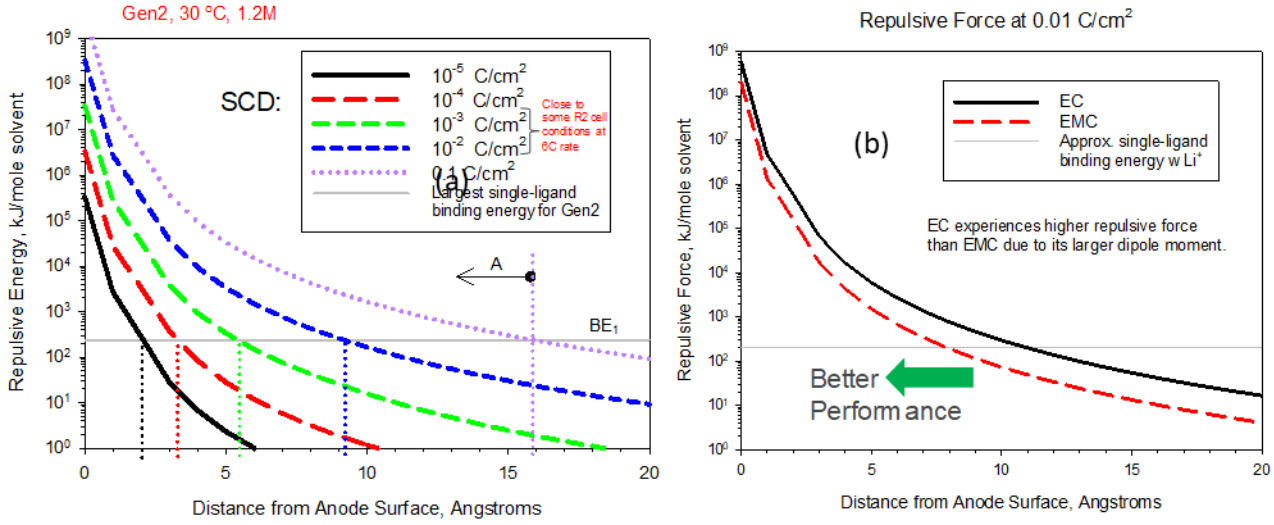

Figure I.4.M.14 Effect of surface charge density to produce electrostatic effect on solvent dipoles.

Results in Figure I.4.M.14 are shown in comparison to BE_1, the largest single-ligand binding energy for the Gen2 electrolyte at 30°C. Regions where the repulsive energy at a given SCD is greater than BE_1 represents where the lithium ions are more likely to be acted upon by the SCD rather than solvating solvent. Note also that in regions of disrupted and repulsed solvent the local impedance will become larger and the relative permittivity will become quite low, tending toward unity (→1). This is a noteworthy electronic transition point that can lead to conditions favorable for lithium metal deposition. In Figure 14b, it is seen that an electrolyte with EMC as the solvent will undergo less repulsive effect than EC due to the lower dipole moment of EMC.

Key property outputs from AEM were provided to NREL (A. Colclasure) to facilitate cell performance simulations at the conditions of 6C charge rate under a CCCV profile with the XCEL R2 electrodes (70-micron thick) at 30°C, as well as cases of 100-micron thick electrodes at 45°C. Two electrolytes were compared, Gen2 and a low-viscosity multi-solvent formulation denoted as B26. Figure I.4.M.15 shows the simulation outcomes for these conditions. For 70-micron electrodes, B26 should eliminate Li plating and increase SOC for 10-minute capacity (from ~80% to 90%). For 100-micron electrodes, B26 should reduce Li plating and increase SOC for 10 minute capacity (from ~72% to 83%). These gains in SOC and mitigation of lithium plating conditions are very encouraging in finding XFC alternatives to the Gen2 BL.

Plots courtesy of NREL (A. Colclasure)

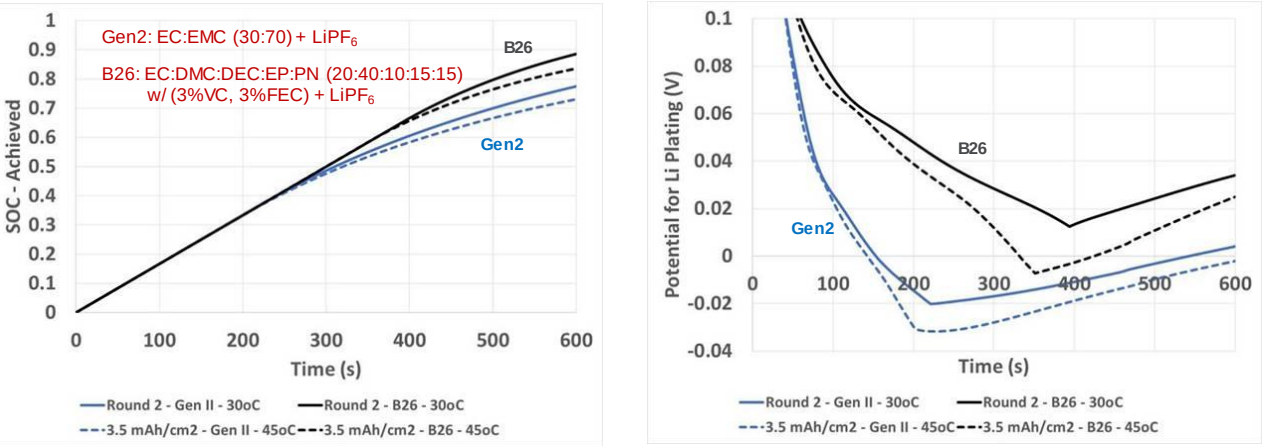

Figure I.4.M.15 Results from NREL cell model simulations for charging performance that compare Gen2 and the B26 XFC electrolyte.

Concentration polarization (CP) is another key aspect of cell performance that gains importance under XFC conditions. The level of CP at each side of the cell will determine the local impedances and these are generally much higher than that of the cell at rest. High levels of CP will cause voltage limits to be reached prematurely before charging can be completed. Thus, XFC electrolytes must alleviate a noteworthy amount of CP to improve charging performance. Figure I.4.M.16 is based on simulations at NREL for Gen2 vs B26, where CP and voltage are shown at end of CC charge segment (roughly 210-220 seconds for Gen2, later for B26). B26 reduces polarization across the cell, allowing lower resistances at the extremes, quicker recovery between cycles, and a gain of SOC delta of about 0.25 by end of CC. These gains as demonstrated by the B26 electrolyte underscore that our design approach is producing viable candidates. Further work will be done to identify candidates that will further reduce polarization, increase attainable SOC, and fully mitigate voltage conditions for lithium metal deposition. Direction and success of this work will also be tied to the final charging protocol that is adopted by the XCEL group, since methods other than 6C CCCV are likely to produce lesser polarization.

70-micron electrodes, 30 ºC

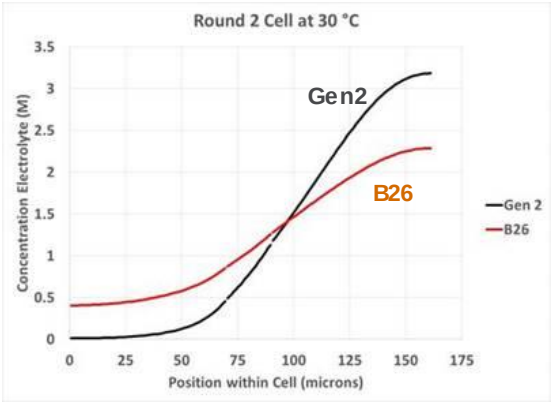

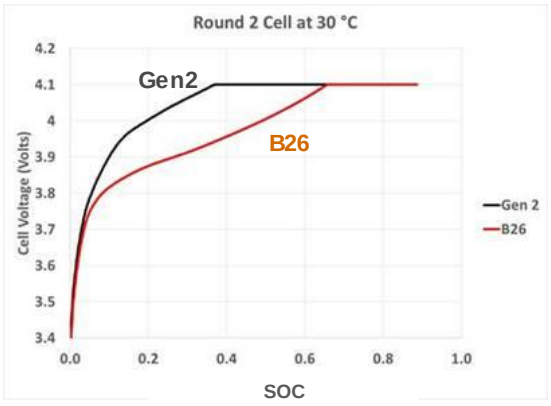

100-micron electrodes, 45 ºC

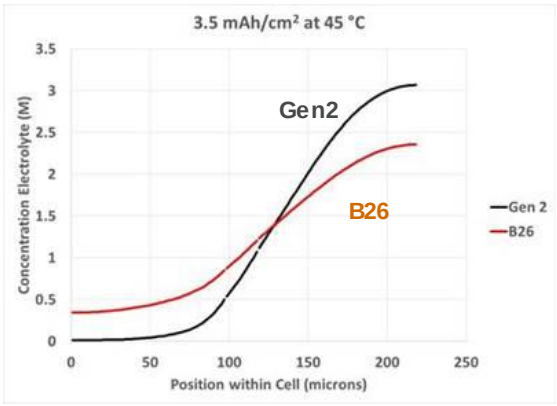

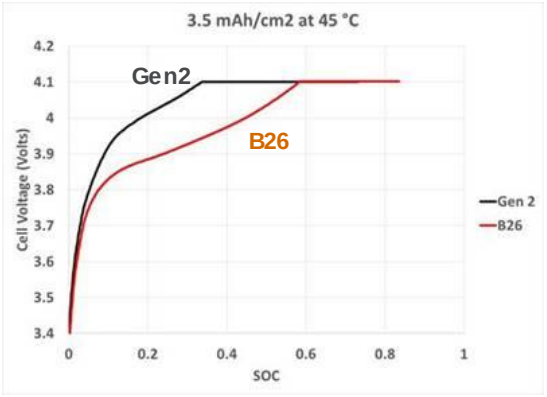

Figure I.4.M.16 Results from NREL cell model simulations for concentration polarization and cell voltage, comparing Gen2 and the B26 XFC electrolyte. Plots courtesy of A. Colclasure (NREL).

Accuracy of the AEM was improved for application to highly concentrated electrolytes (HCE), generally up through 5 Molar salt or up to about 8-10 molal for non-aqueous systems. This expanded capability also accommodates conditions of concentration polarization that can be severe during XFC. New HCE systems were identified through AEM and are currently being tested at INL.

HCE for Li-ion systems are attractive for use in higher-rate applications due to the following attributes at the high-salt region (typically 2.5 to 4 Molar (M) salt in non-aqueous systems):

- Decrease of solvation number per lithium cation,
- Corresponding drop in lithium desolvation energy requirements,
- Higher salt content helps moderate concentration polarization,
- Surface tension is greater at higher salt content, which can help mitigate Li metal deposition,
- Voltage stability is also improved through low solvent activity (nearly all solvent is coordinated with ions),
- Thermal runaway performance should be likewise improved,
- Ion hopping is more likely as a transport mechanism (very efficient),
- Will remain viable for XFC provided lithium transport through the electrolyte does not become rate limiting to a significant extent,
- Valid for current 532 and 622, 811 cathodes (high salt content drops solvent reactivity and gas formation at the surface)
- Operation at higher cell voltages is more feasible.

AEM is accurate for HCE conditions, with examples given in Figure I.4.M.17. Based on molecular packing constraints and ionic density information, AEM provides an estimate for the onset of solid phase behavior. Various prototypical HCE were investigated with AEM, with properties of interest shown in Figure 18 for four example systems, emphasizing the salt concentration range of 2.5 to 4 Molar (for these systems this would span about 3 to 7 molal). The desirable attributes given above are well met by some of these HCE, where cell testing will reveal whether they become rate limiting at XFC conditions for the Round-2 materials. Many other HCE were investigated aside from those demonstrated in Figure I.4.M.18, and other datasets were used to assess consequences in the cell environment under conditions of concentration polarization. For example, Figure 19 shows analyses of AEM-derived activation energies (E_a) for several electrolyte property metrics at 30°C, comparing Gen2, B26, HCE4 and HCE5 systems. B26, as mentioned earlier, is an electrolyte with the composition EC-DMC-DEC-EP-PN (20:40:10:15:15, mass) plus $LiPF_6$ with 3% VC and 3% FEC. Note that the activation energies are plotted versus salt molality to avoid the temperature dependence of density that is inherent with the molar scale.

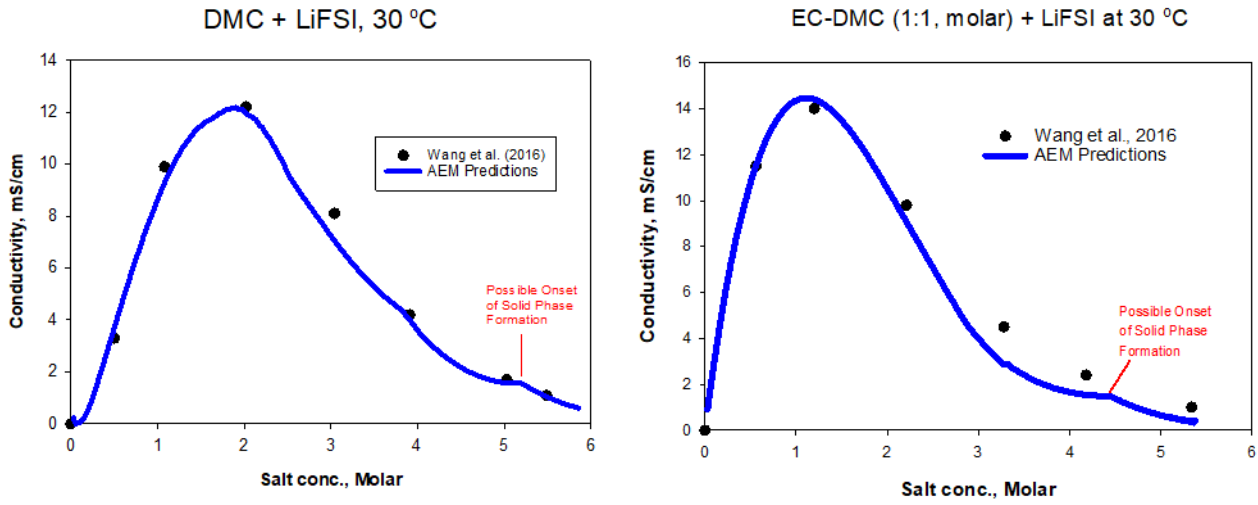

Figure I.4.M.17 Predicted versus measured electrolyte conductivity for example HCE systems.

Of the systems shown, Gen2 electrolyte has the largest variance (increase) of activation energies over salt concentration, where conductivity and diffusivity metrics show E_a that increase to over 40 and 60 kJ/mole, at around 4 Molar, respectively. Cell-level simulations at NREL have shown that the magnitude of concentration polarization for XCEL R2 with Gen2 can exceed 3 Molar (higher on the molal scale) on the cathode side under 6C CCCV conditions. There is also evidence from the AEM results that there is a possible onset of solid phase formation in Gen2 that starts around 4 Molar. Such a phase transition would have consequences for the average microstates of the liquid phase and corresponding ion solvation interactions. Thus, under concentration polarization from XFC conditions there would generally be higher activation energies for the transport properties on the cathode side, where the salt concentration is enriched, where the Gen2 system is the worst of those shown in Figure I.4.M.19. B26 shows transport related E_a that are lower and more well-behaved compared to Gen2. The HCE in Figure I.4.M.19 demonstrate transport related activation energies that are even lower and with less variance over the range of salt concentration. These results infer that HCE can provide better and more consistent cell performance under conditions of concentration polarization. Since the higher activation energies at higher salt concentrations relate to the cathode side during XFC, then these results give clues as the impact of the electrolyte on local cathode performance and fate in terms of lithium transport and other aspects.

Simple cases for demonstration purposes:

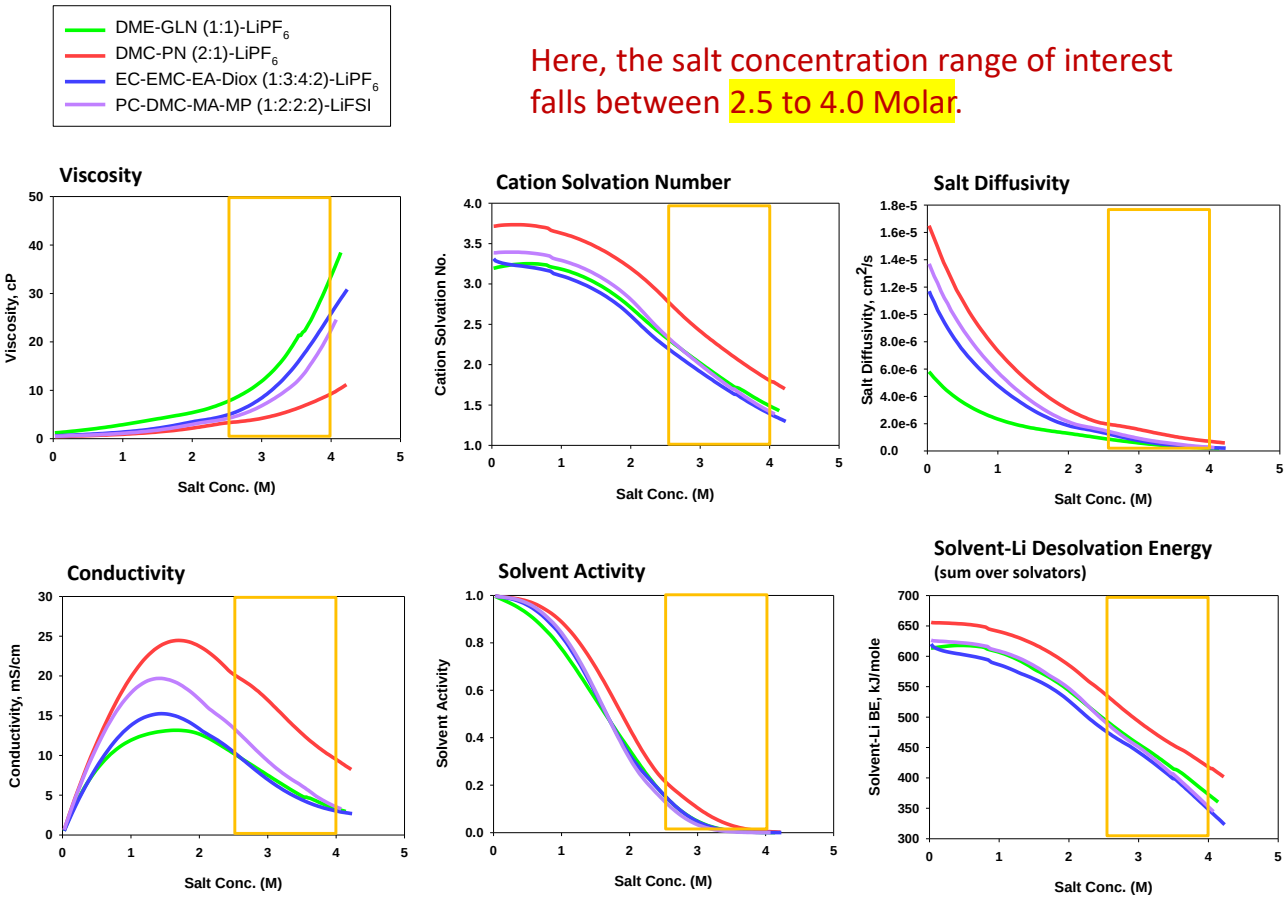

Figure I.4.M.18 Electrolyte properties of interest for HCE, showing four HCE examples for demonstration purposes. Note that the salt concentration range of interest here is 2.5 to 4 Molar (gold boxes).

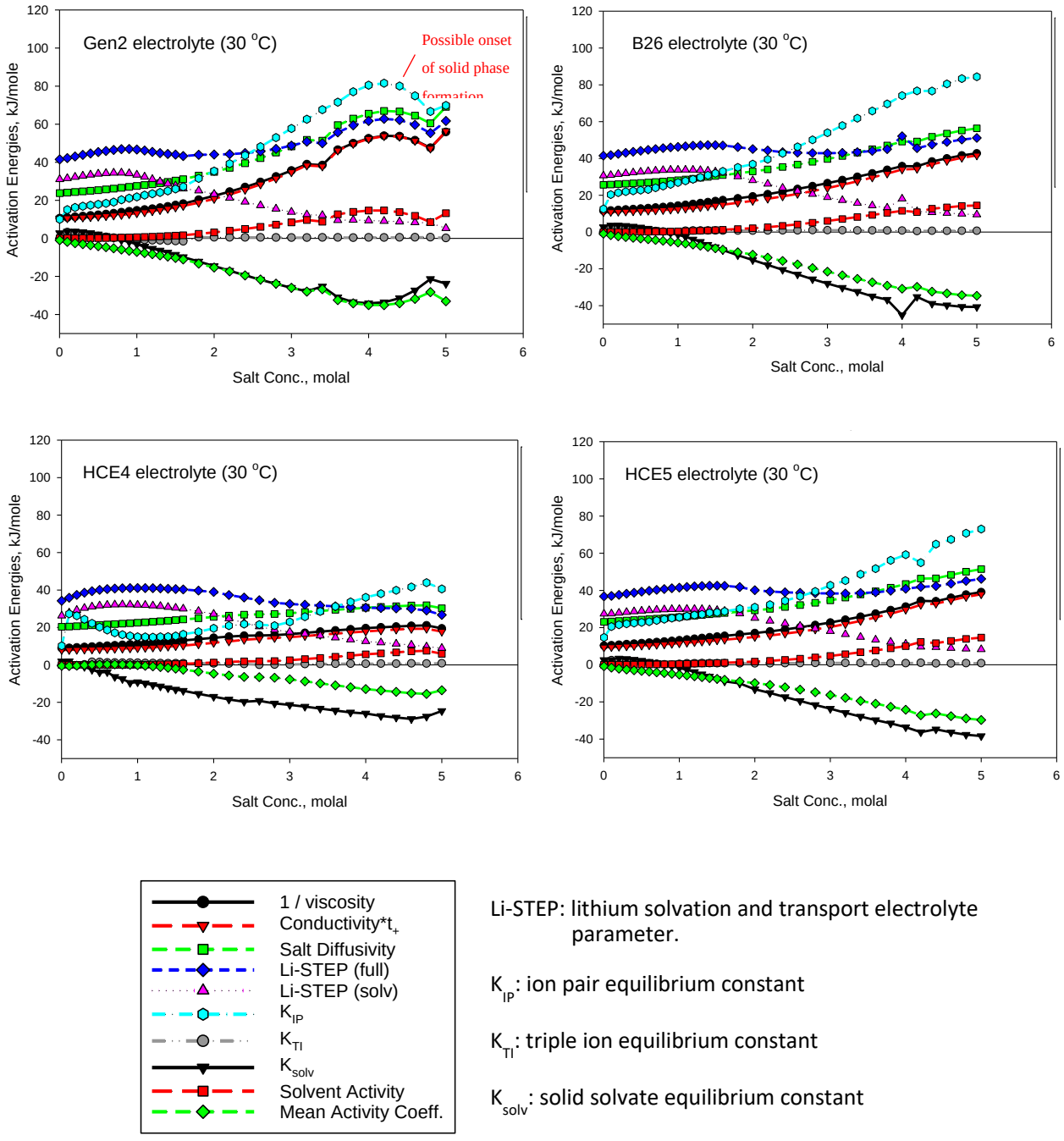

Figure I.4.M.19 Activation energies for electrolyte properties of interest for Gen2, B26, HCE4, and HCE5 electrolytes. Note that if activation energies change markedly over salt concentration (more so for Gen2), cell performance will be more problematic under concentration polarization.

Laboratory testing is indispensable in determining performance and stability of electrolytes in the intended electrochemical environment. Upfront testing at INL involved CR2032-type coin cells that have the Round 2 (R2) XCEL anode and cathode. Final testing was performed with pouch cells manufactured by Argonne's CAMP Facility. Coin cell testing has shown encouraging results in finding suitable replacements for Gen2 in fast charge applications. In general, test results have shown cases wherein the capacity and cycling efficiency CE (or, Coulombic efficiency) have met or exceeded those obtained using the Gen2 baseline. Another benefit from our fast charge candidates is reduced polarization (reduced voltage shift) that develops during charge and discharge steps. Figure I.4.M.20a,b demonstrates such early improvements seen by using fast charge electrolytes in terms of capacity and CE, interfacial impedance, and polarization during charge conditions. Many of the shown fast charge electrolytes contain one or more additives such as vinylene carbonate (VC) and mono-fluoro ethylene carbonate (FEC). A legend of the formulations is given in Figure I.4.M.21. Recent work has been to refine the wetting, formation, and post-formation cycling protocols toward arriving at a viable approach for achieving stable cell chemistries that will deliver a ten-minute charge in the pouch cells.

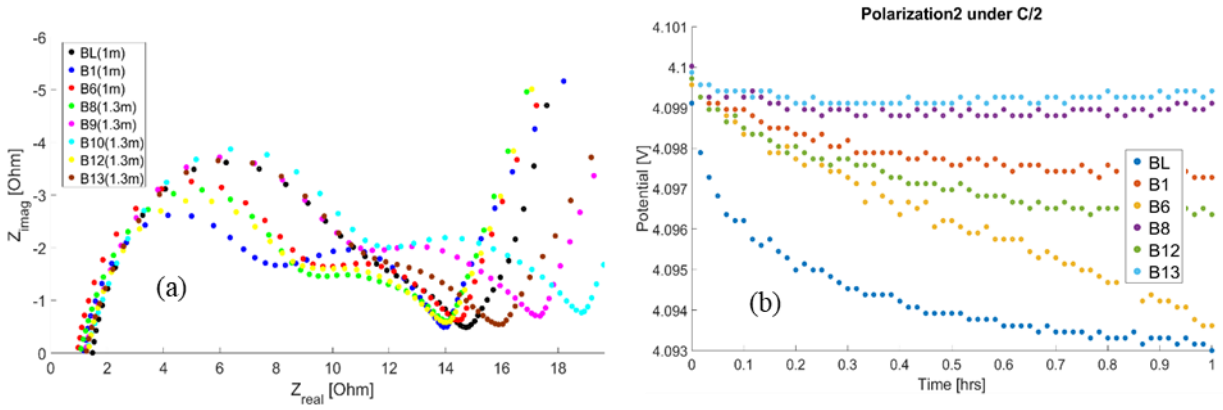

Figure I.4.M.20 Comparison of coin cell performance for selected early XFC electrolyte formulations versus the Gen2 baseline, considering (a) EIS interfacial impedance, and (b) polarization relaxation following C/2 charge conditions. Electrolytes B8, B12 and B13 show particular improvement over the Gen2 BL system.

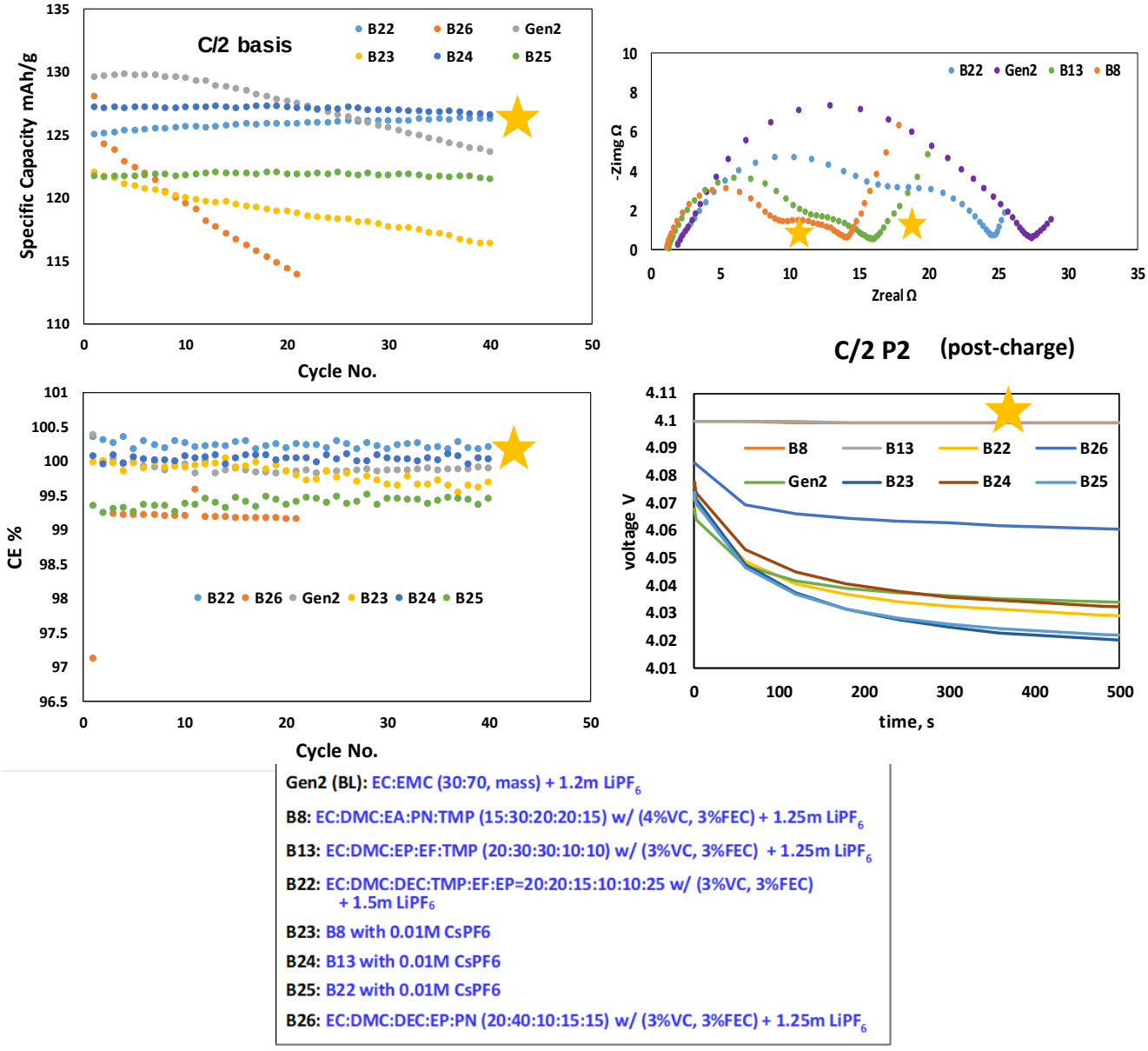

Figure I.4.M.21 XCEL R2 cell test results for various INL XFC electrolyte candidates compared against Gen2. Improvements via XFC systems are seen on many fronts. The results shown for B26 are believed to be from a poor cell or faulty test channel.

Figure I.4.M.22 shows a collection of cell test results for the CAMP Facility R2 cells having various electrolyte candidates. Here, Gen2 electrolyte serves as the baseline and testing was performed at 30°C. Overall, the XFC formulation B26 shows excellent life and reduced polarization compared to Gen2. The capacity of the B26 cells undergoes very little change over 140 cycles, whereas Gen2 cells show a downward trend. Likewise, the polarization metrics such as the voltages at end of charge (EOC), end of discharge (EOD) and the voltage changes under polarization relaxation all show improvement under B26, wherein polarization is reduced for both charging and discharging compared to Gen2 and the other cells. There was a pause of about a week in cell testing after forty (40) C/2 cycles, then cycling was resumed under identical conditions. This pause had very little effect on cell capacities but did influence some of the polarization metrics such as those tied to discharge conditions.

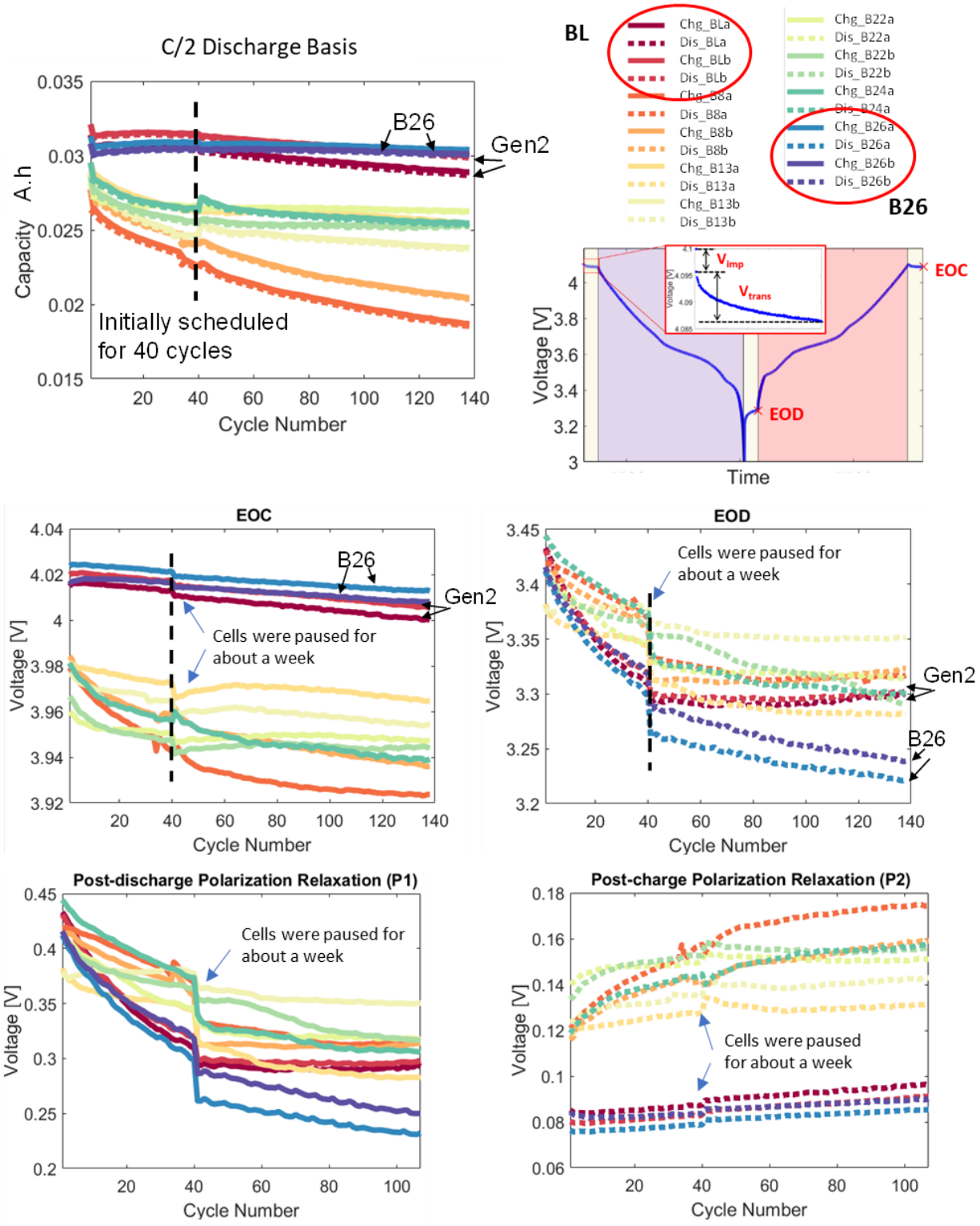

Figure I.4.M.22 Cell test data for the CAMP Facility R2 pouch cells having Gen2 (BL) versus XFC electrolytes. B26 generally outperformed Gen2 for all metrics.

In recent thermal modeling performed at NREL it was determined that B26 allowed lesser heat generation per unit capacity gained during fast charge conditions, compared to Gen2. This is largely due to the lower native resistance of B26. *From this collective work we conclude that electrolyte B26 is a suitable candidate to replace the Gen2 baseline for XFC using the XCEL R2 electrode materials.* We satisfied our deliverable of sending the hero electrolyte B26 to XCEL partners for hero cell builds and auxiliary testing.

We anticipate that the HCE work will yield additional XFC electrolyte alternatives that can provide further benefits in terms of increased rate capabilities, voltage stability and thermal runaway. By the end of this year we were testing HCE candidates within a small matrix to determine performance in a cell environment having 70-micron R2 electrodes with NMC532/Gr. It is anticipated that some aspects of cell wetting and formation procedures will need to be adapted to the HCE systems, which can be more viscous than the Gen2 electrolyte at the salt concentration range of interest. Since HCE can enable operation at higher cell voltages, we will investigate operation at up to 4.1, 4.2 and 4.3 V. HCE testing will be extended to include NMC811 cathode material.

Lastly, work was done to refine the cell formation procedure for the combination of electrolyte B26 with R2 electrodes NMC532/Gr, and to determine the compatibility between B26 and NMC811/Gr. For the cell formation study there were three parameters that were singly varied to determine their impact on cell performance:

A. BL Reference
B. Increase rest hour from 1hr to 4hr during first 3 C/10 cycles and increase rest hour from 1hr to 2hr during last 2 cycles.
C. Increase tap charge from 1.5 V to 2.5 V. Increase rest hour from 12 h to 20 h at OCV. Change Vmax from 4.1 V to 4.0 V.
D. BL formation cycles in 40°C chamber.

Figure I.4.M.23 shows that of these parameters, increasing the rest time provided the most benefit in terms of retaining capacity and lowering interfacial impedance. This outcome likely reflects two factors (1) the longer rest period allows for greater electrolyte permeation throughout the electrode porous regions during formation, and (2) self-diffusion of the solvent species to reactive surface sites is able to proceed to greater extent. Regarding B26 compatibility with NMC811, Figure I.4.M.24 shows the capacity of the third C/10 formation cycle and the first C/2 cycle, comparing results for NMC811/Gr (colored bars) versus NMC532/Gr (dashed boundary). Considering the numerous implications of how NMC811 might vary from NMC532 in formation outcomes, the results in Figure I.4.M.24 are encouraging in a practical sense in that we see only very minor difference in capacity during the third formation cycle.

We will continue to work with ANL and NREL toward XFC electrolyte selection and to optimize procedures for electrode and separator wetting, cell formation, and post-formation cycling protocols toward arriving at a viable approach for achieving stable cell chemistries that will deliver a ten-minute charge in the CAMP Facility XCEL pouch cells. Such procedures will require review as we proceed to test a greater number of HCE candidates with various types of electrode configurations.

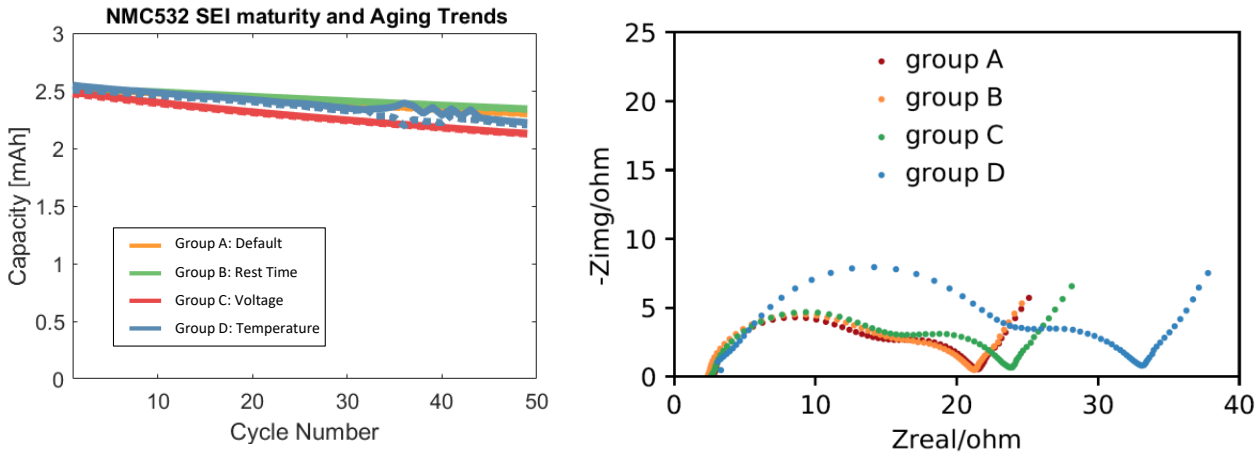

Figure I.4.M.23 Results of formation parameter study for using electrolyte B26 with XCEL R2 NMC532/Gr. Group B cells (increasing rest periods) exhibit the greatest benefit.

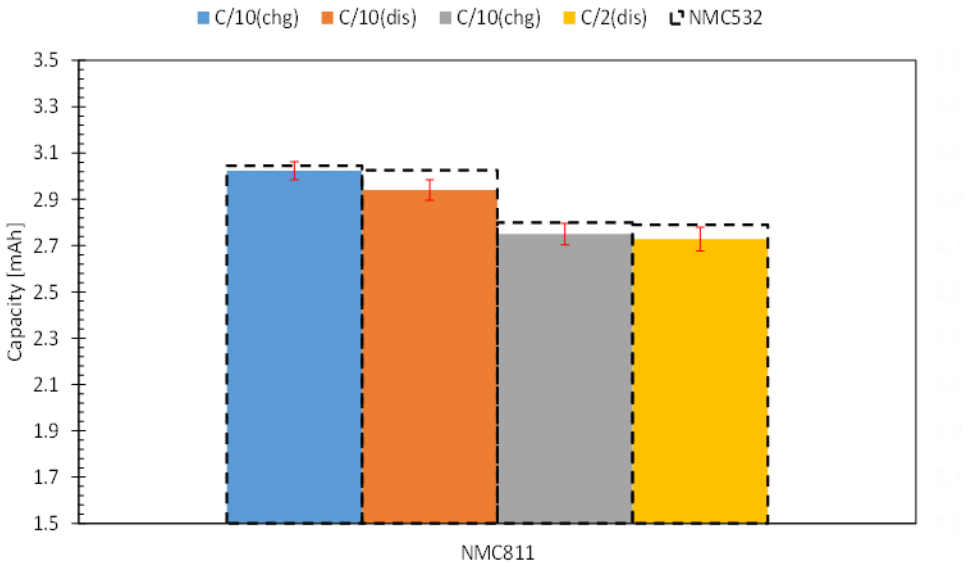

Figure I.4.M.24 Results of formation study for using electrolyte B26 with XCEL NMC811/Gr. Only slight reductions in capacity are observed compared to the NMC532/Gr system.

Electrolyte Predictions using Database of Electrolyte Properties (NREL Focus)

Cyclic voltammetry at 5 mV/s across a voltage window of 0.5 – 4.5 V using aluminum as the working electrode and lithium metal as the reference and counter, was used to screen for electrolyte stability. Details on the individual compositions were included in earlier reports. The response at multiple scan rates resembled that for typical Gen2 electrolyte. No adverse decomposition was observed (Figure I.4.M.25).

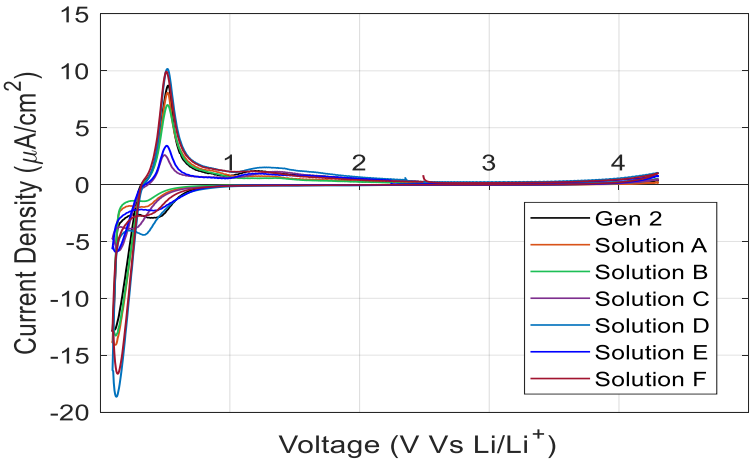

Figure I.4.M.25 Cyclic voltammogram was used to verify the stability of the electrolyte formulations across the operating voltage window.

Some of the shortlisted solvent molecules show initial discharge capacities better than the baseline electrolyte – however, long-term stability is poor (Figure I.4.M.26). One challenge in performing extensive analysis of degradation during calendar or cycle-life aging with these formulations, is the limited quantities in which these molecules have been synthesized. This also drives decisions with prioritizing measurement of cell level performance over characterizing physical properties such as viscosity measurements. As subsequent batches become available, experimental evaluation will include measurement of additional properties for these solvents. Compatibility against different electrodes was also suggested by the workgroup as a consideration for follow on work. There are other parameters to optimize (e.g., formation conditions or salt to solvent ratios). We are currently working with the Post-Test Facility at Argonne to analyze resistance build up during the first few cycles in these cells containing the other candidates.

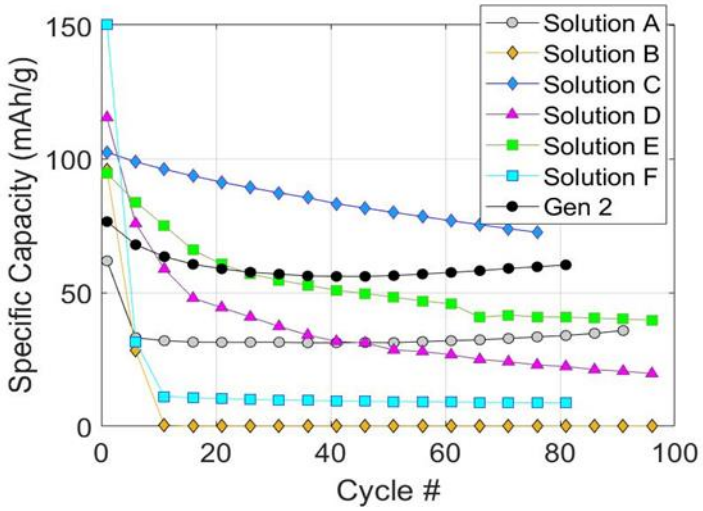

Figure I.4.M.26 Cycling performance of short-listed electrolyte additives.

Transport property calculations were performed on the electrolyte formulations containing the different additives. These results showed that at 1.2 M concentrations, the Gen-2 formulation still maintained the highest conductivities and diffusivities. However, when the salt concentrations were increased to 2 M or higher (one of the requirements identified early on in the XCEL targets) changes in solution viscosities for Sol. C and Sol. F are far less compared to that for the control (Gen-2). Thus, these solutions fare better in terms of

conductivities at higher salt concentrations. We are currently comparing stability of the different formulations at the anode surface, under fast-charge conditions.

Dry cells were also received with the Round-2 electrodes from the CAMP Facility for evaluating performance of these electrolyte formulations. These pouch cells were filled, formed, and cycled to verify the initial coin-cell results. Initial results show that the cell performance is limited by diffusion. These cells were formed using the standard XCEL formation protocol, which still need optimization.

Fabrication of Pouch Cells for FY 2020 Milestone

The key milestone at the end of FY 2020 is the delivery of 24 single-layer pouch cells to INL for testing. These pouch cells are to use the latest improvements to electrode architecture with the best candidate electrolyte system. Despite the several months of work-from-home orders due to COVID19, the Anode & Electrolyte Thrust were able to propose and produce candidate electrodes and electrolyte in the last month (September) of FY 2020. Modeling results predicted that a dual-layer anode would be beneficial for fast charging, and the CAMP Facility was able to make dual-layer anodes via double-pass coating on their pilot-scale coater. However, initial results showed that the available graphite particle choices were to large. A graphite vendor was approached by Argonne for their assistance on providing a smaller graphite particle, but this powder will not be available until late 2020.

The CAMP Facility decided to make anode and cathode with lower carbon and binder content, their composition is shown in (Figure I.4.M.27).

Anode: LN3237-70-2
(single-sided)
95.83 wt% Superior Graphite SLC1506T
0.5 wt% Timcal C45 carbon
3.5 wt% Kureha 9300 PVDF Binder
0.17 wt% Oxalic Acid
XCEL, Trial coating as part of electrode compositional study
Targeted Round 2 areal capacity. SLC1506T Lot#: 573-824
"SS" = single sided -> ***CALENDERED***
Cu Foil Thickness: 10 µm
Total Electrode Thickness: 80 µm
SS Coating Thickness: 70 µm
Porosity: 37.4 %
Total SS Coating Loading: 9.57 mg/cm²
Total SS Coating Density: 1.37 g/cm³
Estimated SS Areal Capacity: 3.03 mAh/cm²
[Based on rev. C/10 of 330 mAh/g for 0.005 to 1.5 V vs. Li]
Made by CAMP Facility

Cathode: LN3237-78-4
(single-sided)
96 wt% Toda NMC532
2 wt% Timcal C45
2 wt% Solvay 5130 PVDF Binder
XCEL, Coating used in FY20 Q4 SLP Hero Cells
Targeted Round 2 areal capacity, Prod:NCM-04ST, Lot#:7720301
"SS" = single sided -> ***CALENDERED***
Al Foil Thickness: 20 µm
Total Electrode Thickness: 80 µm
SS Coating Thickness: 60 µm
Porosity: 34.9 %
Total SS Coating Loading: 17.24 mg/cm²
Total SS Coating Density: 2.87 g/cm³
Estimated SS Areal Capacity: 2.65 mAh/cm²
[Based on rev. C/10 of 160 mAh/g for 3.0 to 4.2 V vs. Li]
Made by CAMP Facility

Figure I.4.M.27 Low carbon & binder electrode composition and design parameters for pouch cell FY 2020 Milestone.

The team met to decide on the most efficient cell design plan that would also capture the effects of key improvements regarding the separator and electrolyte choices. Two separator were selected: the baseline Celgard 2320 (PP:PE:PP trilayer) and Celgard 2500 (PP), which has higher porosity. Two electrolytes were selected: baseline Gen2 and B26 ($LiPF_6$ in EC:DMC:DEC:EP:PN (20:40:10:15:15) with 3% VC & 3% FEC), which INL was able to provide in 100's of mL quantity. It was decided to make cells with the low carbon & binder content electrodes divided as such:

8 cells with Gen2 electrolyte and Celgard 2320

8 cells with B26 electrolyte and Celgard 2320

4 cells with Gen2 electrolyte and Celgard 2500

4 cells with B26 electrolyte and Celgard 2500

Two dozen pouch cells were fabricated at the end of September 2020 and filled with the selected electrolytes. A photo of the cells is shown in (Figure I.4.M.28) They were then placed on formation using a modified

formation protocol that included longer rest times between cycles. These cells were shipped to INL to begin testing in November 2020.

Figure I.4.M.28 Photo of fabricated pouch cells using low carbon and binder electrodes and selected electrolytes and separators for FY 2020 Milestone.

Conclusions

The Anode & Electrolyte Thrust of the XCEL Program is successfully coordinating its efforts in developing the ideal structured electrode and electrolyte to enable fast charging with minimal lithium plating:

- A suite of electrochemical and microstructure tools were developed at NREL to investigate the effect of advanced electrode architectures on fast charge performance. For near term, the reduction of carbon/binder additive fraction and implementation of dual-layer electrode structures should significantly improve performance and be practically implemented in coming months. For the long term, the introduction of a secondary pore network could further improve performance if sufficiently small feature size can be achieved.
- Freeze tape-cast efforts at LBNL used the modeling results from NREL for a graphite anode. Large area (>4''×4") graphite electrodes were successfully freeze tape cast through equipment modification and processing parameter control. The graphite electrodes with oriented pore channels can either be cast on Cu foil directly or on a Mylar film for free standing electrodes. The latter can be attached to a tape cast electrode to form a porous/dense dual layer electrode for overall porosity control.
- The NREL model also predicted that a structure with higher porosity/smaller particle diameter (HP/SD) for the layer near the separator delays lithium plating by 7%. These results were used by Argonne's CAMP Facility to make dual-layer electrodes, which were tested in coin cells. Electrolyte predictions were made by INL using their Advanced Electrolyte Model (AEM).
- A database of available electrolyte properties was created at NREL and used to probe for pattern identification of functional groups to predict candidate electrolytes. Several electrolyte candidates that may replace the baseline Gen2 system are under test in coin and pouch cells.
- Electrodes were fabricated at Argonne's CAMP Facility with lower carbon and binder content. Two dozen pouch cells were fabricated with these electrodes using combinations of Gen2 and INL's B26 candidate electrolyte, and combinations of low and high porosity separators. These cells were shipped to INL to begin testing in November 2020.
- BatPaC analysis is on-going and will be finalized based on preliminary results from pouch cell testing at INL.
- Technical data and electrochemical results were provided to all team members as needed to aid in their experiments and modeling efforts.

Key Publications

1. C. Robertson, L. Flores, A. R. Dunlop, S. E. Trask, F. L. E. Usseglio-Viretta, A. M. Colclasure, Z. Yang, and I. Bloom, "Effect of anode porosity and temperature on performance and lithium plating during fast-charging of lithium-ion cells," *submitted*
2. L. E. Usseglio-Viretta, W. Mai, A. M. Colclasure, M. Doeff, Eongyu Yi, and K. Smith, "Enabling Fast Charging of Lithium-Ion Batteries through Secondary- /Dual- Pore Network: Part I - Analytical Diffusion Model, *Electrochimica Acta*," 342(10), 136034 (2020)
3. W. Mai, F. L. E. Usseglio-Viretta, A. M. Colclasure, K. Smith, "Enabling Fast Charging of Lithium-Ion Batteries through Secondary- /Dual- Pore Network: Part II - Numerical Model," *Electrochimica Acta*, 341(1), 136013 (2020)
4. M. Colclasure, T.R. Tanim, A.N. Jansen, S.E. Trask, A.R. Dunlop, B.J. Polzin, I. Bloom, D. Robertson, L. Flores, M. Evans, E.J. Dufek, and K. Smith, "Electrode scale and electrolyte effects on extreme fast charging of lithium-ion cells," *Electrochimica Acta*, 337, 135854 (2020).
5. Tanvir Tanim, Eric Dufek, Michael Evans, Charles Dickerson, Andrew Jansen, Bryant Polzin, Alison Dunlop, Stephen Trask, Ryan Jackman, Ira bloom, Zhenzhen Yang, and Eungje Lee, "Extreme Fast Charge Challenges for Lithium-ion Battery: Variability and Positive Electrode Issues," *J. Electrochem. Soc.* **166** (10) A1926 (2019).
6. A.M. Colclasure, A.R. Dunlop, S.E. Trask, B.J. Polzin, A.N. Jansen, K. Smith, "Requirements for Enabling Extreme Fast Charging of High Energy Density Li-Ion Cells while Avoiding Lithium Plating," *J. Electrochem. Soc.* **166** (8) A1412-A1424 (2019).

References

1. A. M. Colclasure, T.R. Tanim, A.N. Jansen, S.E. Trask, A.R. Dunlop, B.J. Polzin, I. Bloom, D. Robertson, L. Flores, M. Evans, E.J. Dufek, and K. Smith, "Electrode scale and electrolyte effects on extreme fast charging of lithium-ion cells," *Electrochimica Acta*, 337, 135854 (2020).
2. F. L. E. Usseglio-Viretta, W. Mai, A. M. Colclasure, M. Doeff, Eongyu Yi, and K. Smith, "Enabling Fast Charging of Lithium-Ion Batteries through Secondary- /Dual- Pore Network: Part I - Analytical Diffusion Model," *Electrochimica Acta*, 342(10), 136034 (2020)
3. W. Mai, F. L. E. Usseglio-Viretta, A. M. Colclasure, K. Smith, "Enabling Fast Charging of Lithium-Ion Batteries through Secondary- /Dual- Pore Network: Part II - Numerical Model, *Electrochimica Acta*," 341(1), 136013 (2020)

Acknowledgements

This project was funded by the U.S. Department of Energy, Vehicle Technologies Office. The technology development manager was Samm Gillard. The project overview was prepared by Venkat Srinivasan (ANL). Other contributing team members for Thrust 4 (Anode & ElectrolyteThrust) include Alison Dunlop, Andrew Jansen (Thrust Lead), Bryant Polzin, Steve Trask, Zhenzhen Yang (ANL); Kevin Gering, and Eric Dufek (INL); Marca Doeff, and Eongyu Yi (LBNL); and Ryan Brow, Andrew Colclasure, Anudeep Mallarapu, Shriram Santhanagopalan, Kandler Smith, and Francois Usseglio-Viretta (NREL).

I.4.N XCEL R&D: The Effects of Extreme Fast Charging on Lithium-ion Battery Cathode Thrust

Venkat Srinivasan, Principal Investigator
Argonne National Laboratory
9700 S. Cass Avenue,
Lemont, IL 60439
E-mail: vsrinivasan@anl.gov

Samm Gillard, DOE Technology Development Manager
U.S. Department of Energy
E-mail: Samuel.Gillard@ee.doe.gov

Start Date: October 1, 2019 End Date: September 30, 2020
Project Funding (FY20): $742,000 DOE share: $742,000 Non-DOE share: $0

Project Introduction

Extreme fast charging (XFC) of Li-ion batteries can create a host of life and safety issues. The XCEL program, in the prior two years, has worked on identifying the key bottlenecks of enabling XFC. Collaborative research has found that besides Li plating, there could be a significant impact of XFC on battery cathode performance [1]. In some instances, the fade associated with cathode aging actually exceeds losses due to Li plating. Upon finding the cathode issues, program leaders decided to pursue a deep-dive into the scientific underpinnings for the cathode fade during XFC. Key objectives of the cathode thrust include gaining a better understanding of the cathode issues and their dynamics with XFC cycling, and identification and quantification of different cathode aging mechanisms, including cracking by combining experimental, operando, and modeling efforts. The findings of this activity are deemed to be crucial for a comprehensive understanding of the extent of cathode issues and identifying key R&D efforts required to resolve those issues for enabling XFC. The cathode thrust team is composed of members from Idaho National Laboratory (INL), the National Renewable Energy Laboratory (NREL), Argonne National Laboratory (Argonne), SLAC National Accelerator Laboratory, and Lawrence Berkeley National Laboratory (LBNL).

Objectives

The key objectives of this work are to enable a better scientific understanding of the cathode aging modes and mechanisms during XFC conditions. Earlier studies have suggested that a major cause of capacity fade within the Li-ion cell is the cracking of polycrystalline nickel-manganese-cobalt (NMC) particles [1]. The cathode thrust aimed to understand the impact of charging rate and voltage on polycrystalline cathode cracking and how that evolves with cycling. In particular, the thrust is focused on gaining a better understanding on whether cracking triggers additional aging mechanisms (e.g., transition metal [TM] dissolution, rock salt formation, etc.). Gaining a better understanding of the impact of reaction heterogeneity that typically arises during XFC conditions and its correlation with cracking is another aim. Other objectives include developing tools to better classify aging including mapping polycrystalline architectures of NMC particles in 3D and implementation of the mapped architectures in multi-physics models to better capture particle-grain interactions that may limit performance and induce aging. The final objective looks to evaluate innovative particle architectures (i.e., particle size, microstructure, crystal type, etc.) under XFC conditions and identify performance improvements.

Approach

To achieve the objectives of Cathode thrust, the team used a combination of experimental (including post testing), in-operando X-ray powder diffraction (XRD), and modeling. Researchers at INL performed extensive experimental tests on 40+ single-layer pouch cells (SLPCs) assembled at the Cell Analysis, Modeling, and Prototyping (CAMP) facility of Argonne. INL tested the cells at different charging rates (1C, 4C, 6C, and 9C)

and upper charge cutoff voltages (4.1V-100% state of charge [SOC], 3.78V-60% SOC, and 3.66V-35% SOC). INL identified the dominating aging modes using electrochemical data, namely, reference performance test (RPT) and cycle-by-cycle data. Researchers at Argonne performed a comprehensive post-test characterization on a subset of INL cells for mechanism verification/confirmation. Researchers at the Advanced Photon Source (APS) at Argonne performed in-operando studies using high energy diffraction X-ray. At NREL, researchers identified and quantified sub-particle architectures of the cathode materials using electron back-scattering (EBSD) and then extended them to 3D through the application of focused-ion beam (FIB) EBSD. NREL also developed a chemo-mechanical model incorporating strain-induced damage to study the effects of particle size, grain size, and charge rate on capacity fade. Finally, LBNL researchers evaluated the effects of XFC on particles and micro-structures, identifying improvement needs and exploring synthesis approaches to produce cathode particles with different microstructures.

Across the labs, research in the cathode thrust primarily focused on the use of Round 1 cells, which include a graphite anode (1.93 mAh cm-2) and NMC532 cathode (1.65 mAh cm-2). However, research on the gr/NMC811 system has also been initiated in Fiscal Year 2020 (FY20). Tools and learnings from the work using NMC532 will be transferred over to the NMC811 system, and the key issues associated with NMC811 during XFC will be identified in FY21.

Results

While the Li-plating is a key bottleneck for XFC on the anode side, the full suite of limitations are not well understood for the cathode. During FY20, the team gained a clearer understanding of the impact of XFC on the lithium ion battery (LiB) cathode. The FY20 cathode work provides a more comprehensive understanding of the dominant aging mechanisms and their relative extent in NMC-based LiB under XFC conditions and suggests ways to mitigate them through designing better materials and usage protocols.

Identifying the key aging modes and mechanisms and their relative extent

Figure I.4.N.1 shows the test fixture, cycling protocol, and beginning of life (BOL) charge acceptance for the different charging conditions. The C-rates investigated in this study include 1C, 4C, 6C, and 9C, all up to the 4.1V (100% SOC) upper charge cutoff voltage. Two additional cells were cycled at the most aggressive charging rate, that is, 9C, but at a lower upper cutoff voltage, namely, 3.66V (35% SOC) and 3.78V (60% SOC), to test the effects of SOC on cell aging. These cells showed more than 90%+ CC-CV charge acceptance with low variability across the cells when Vmax was 4.1V. The CC fraction of charge was inversely proportional to C-rates because of higher polarization. For the lower Vmax conditions, charging was primarily dominated by the CV fraction. The 4.1V conditions completed 600 cycles. The 9C-lower voltage conditions completed 1000 cycles to achieve comparable throughput to the 4.1V conditions.

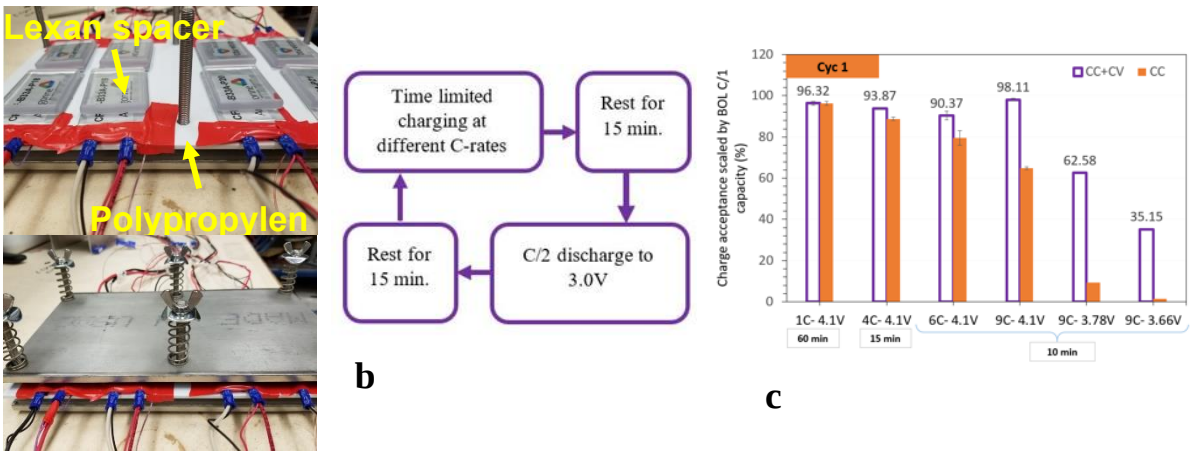

Figure I.4.N.1 Test fixture (a), cycling protocol (b), and BOL charge acceptance (c) for different cycling groups

Figure I.4.N.2a and b show the cell capacity fade with respect to cycle number and throughput for different test conditions. Cells cycled up to the 4C rate show comparable capacity fade with very low cell-to-cell variability. The 6C rate condition showed slightly lower average capacity fade with increased aging variability. Cells cycled at the 9C rate showed the highest capacity fade with the largest cell-to-cell aging variability. The lower voltage conditions, even though cycled at the aggressive 9C-rate, showed a drastic reduction in capacity fade, which is lower than the 1C rate condition at comparable cycles/throughputs. Therefore, lowering the upper cutoff voltage during charging has a positive impact on the cycle life of LiBs.

The comparison of Nyquist plots at the BOL, 225 cycles, and end of testing for the different charge protocols is shown in Figure I.4.N.2c-d. The BOL data show two distinct semi-circles, identified as SEI and current transformer (CT) in Figure I.4.N.2c. Both the SEI and CT impedances increase with cycling, but their rates are distinctly different for different conditions. SEI impedance showed a slightly higher rate of increase at early cycles, which became gradual in later cycles. Such an increase in SEI impedance throughout cycling is because of continuous formation of SEI by the consuming of lithium by the cathode and electrolyte. Unlike SEI impedance, the increase in CT impedance remained uniform and comparable up to 225 cycles, but then increased drastically in later cycles irrespective of C-rates for the 4.1V conditions. The 9C lower voltage conditions had comparable SEI growth even after 1000 cycles, but significantly reduced growth in CT impedance.

INL used RPT and cycle-by-cycle coulombic efficiency, end-of-charge rest voltage, end-of-discharge rest voltage, and EIS data to identify the dominating aging modes. An IC model was used to quantify the dominating aging modes. INL identified and quantified two dominating modes of aging modes ― loss of Li inventory (LLI) in the form of SEI layer growth and loss of active material in the positive electrode (LAM_{PE}). Figure I.4.N.3a shows the quantified LAM_{PE}, where the lines are showing the loss simulated by IC model and the markers are experimentally obtained capacity fade from harvested cathodes in coin cells (i.e., Li/NMC532). The IC model-predicted LAM_{PE} and experimental capacity fade show very good agreement. Results obtained by the IC model show a drastic increase in LAM_{PE} after 450 cycles for up to 6C-4.1V conditions. The 9C-4.1V shows a distinct break-in during early cycling and reduced loss in later cycling with significantly higher variability. Like the full cells, the 9C-low voltage conditions show less cathode issues. The half-cell EIS data mirrors the half-cell fade cathode fade trends and closely correlates CT impedance growth in full cells, indicating distinct but varying CT issues with respect to charge rate and upper cutoff voltage originating from the cathode.

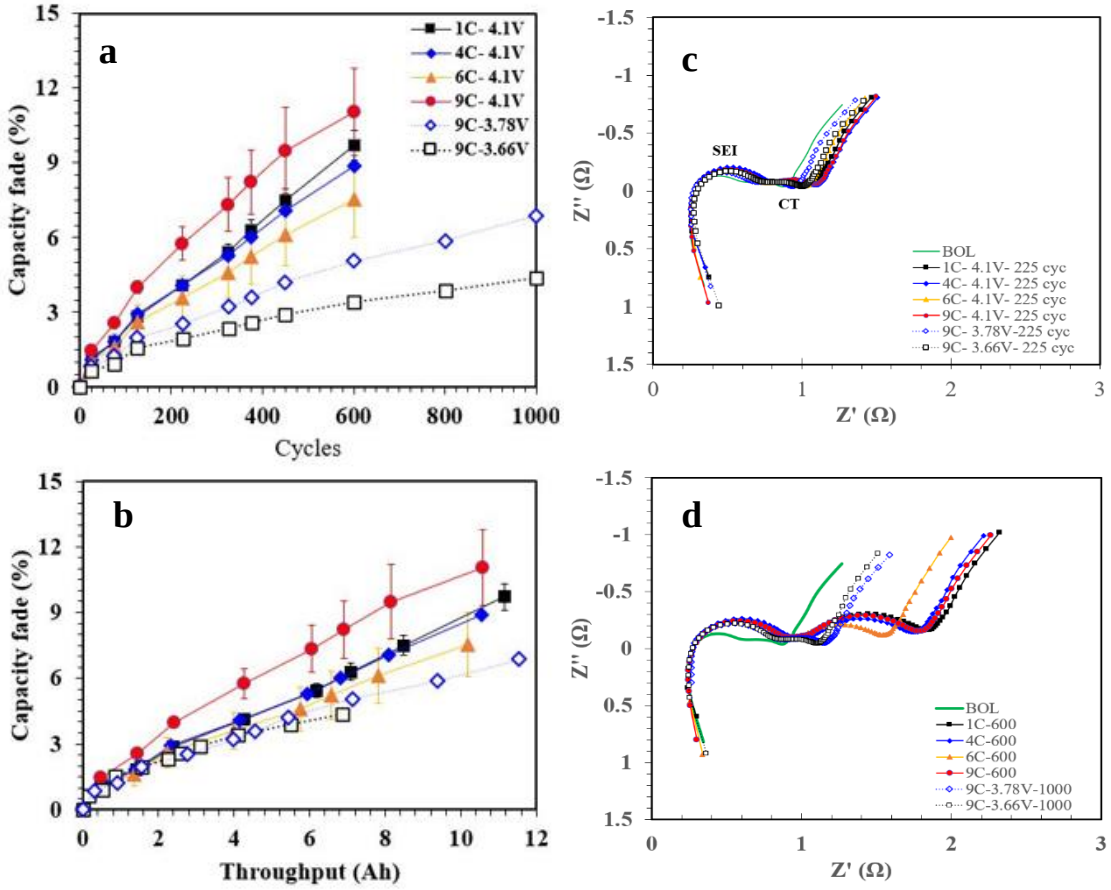

Figure I.4.N.2 Capacity fade and impedance growth. (a) C/20 average capacity fade with respect to cycle number, (b) C/20 capacity fade with respect to charge throughput, (c) EIS at 225 cycle, and (d) EIS at end of testing. Note: The error bar is showing 1σ standard deviation.

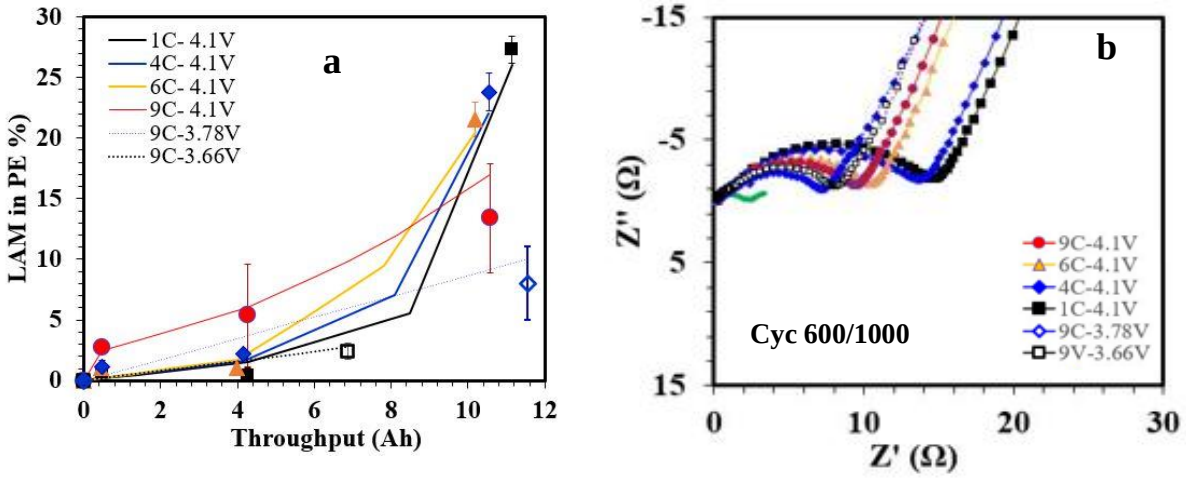

Figure I.4.N.3 Capacity fade and impedance growth in gr/NMC532 harvested coin cells from pouch cells: (a) LAM in PE, and (b) EIS at end of testing.

Post testing characterization

To gain a better understanding of the aging mechanisms, INL sent cells to different institutions at different aging states. Figure I.4.N.4 schematically shows the sample flow. Because of the COVID-19-related work curtailments at different labs, some of the post-testing results have not been completed by the end of FY20. We hope to have those completed by Q1FY21.

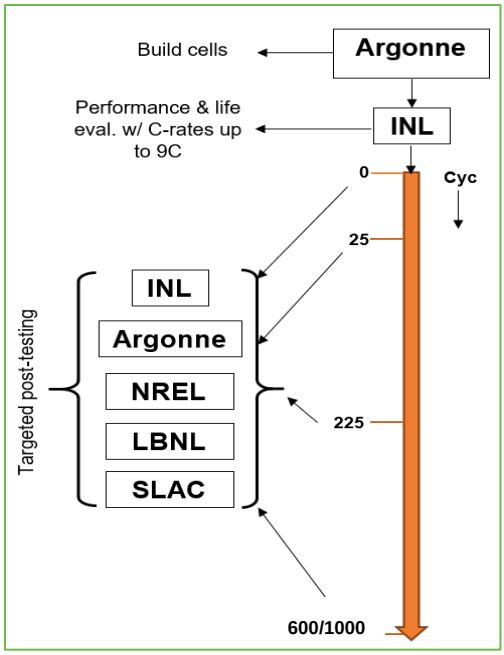

Figure I.4.N.4 Sample flow of the test cells.

Argonne focused on identifying performance degradation mechanisms and relevant characterization techniques by post-test characterization. Aged cells charged at different fast rates and cycle numbers were obtained from the INL cell testing group. Argonne opened the cells up in the glovebox. Cell parts, including cathodes and anodes, were saved for characterization. The electrolyte from the separator and cell was collected for HPLC-MS study.

Cathode cracking identification by cross section-scanning electron microscopy (SEM)

The evolution of intragranular cracks in NMC532 cathodes after different charging rate and cycle counts were characterized by ion milling and SEM, and the results are shown in Figure I.4.N.5. More cracks formed at the 6- and 9-C charge rates in the early stage of the cycle-life experiment (< 225 cycles) as compared to that seen at the 1-C rate. This result is in line with INL's conclusions on LAM_{PE} (see Figure I.4.N.3). However, extensive internal cracking in the aged secondary particles was observed at lower charge rates (1- and 6-C) after long-term cycling (600 cycles). The results clearly illustrate the effect of charge rate and cycle count on the intragranular crack formation. Cracking at the grain boundaries compromise the connectivity and the reaction kinetics of the particles in the electrodes, which reflected as increased LAM_{PE} and CT impedance growth (see Figure I.4.N.3).

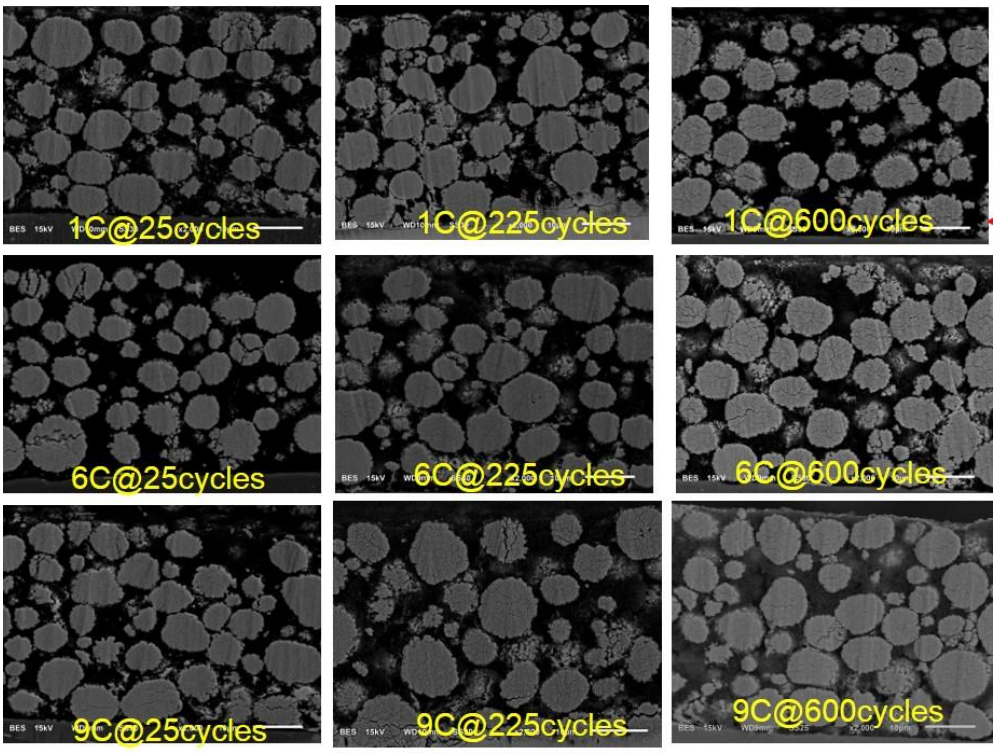

Figure I.4.N.5 Cross-sectional SEM images of the NMC 532 cathodes cycled using 1-, 6-, and 9-C charge rates after 25, 225, and 600 cycles.

Surface phase transformation of degraded cathodes by high-resolution transmission electron microscopy (HR-TEM)

The SEAD pattern at lower magnification shows that the bulk material retains the layered structure after cycling. However, at the particle surface, there are three different structural regions, as shown in Figure I.4.N.6. They are layered structure in the bulk, a mixture of layered and rock salt phases at the sub-surface, and the pure rock salt phase at the surface. The thickness of cation mixing is almost 13 nm. It appears that rock salt formation combined with cracking might have aggravated the capacity fade and CT impedance of the cathode. HR-TEM images at other charge conditions are needed for confirmation.

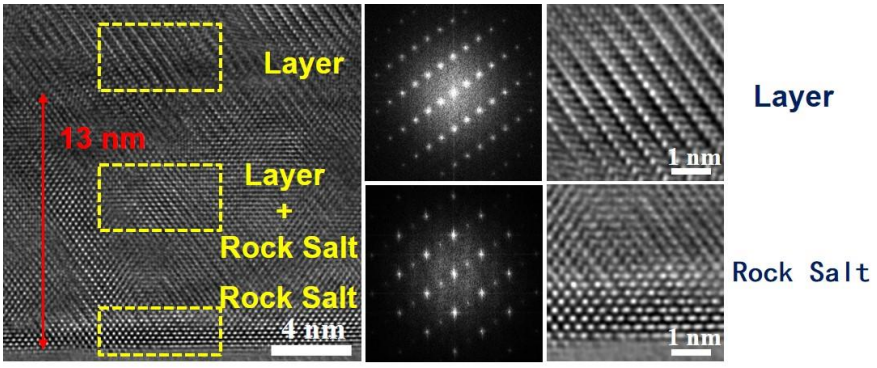

Figure I.4.N.6 HR-TEM images of NMC532 particle surface structure charged at 9-C after 600 cycles.

Transition metal dissolution and deposition and Li on anodes by inductively coupled plasma mass spectrometry (ICP-MS)

Transition metal (TM) dissolution from the cathode active material and its deposition on the anode causes significant cell aging. The concentrations of the TMs deposited and Li on anodes were measured by ICP-MS and shown as a function of charge rate in Figure I.4.N.7. At a given charging rate, the amounts of TMs and of Li on the anode increase as cycle count increases. At the same cycle count, the amount of TM remained mostly comparable with the exception of Mn. The extent of TM dissolution did not show a drastic increase in cathode capacity fade or impedance rise.

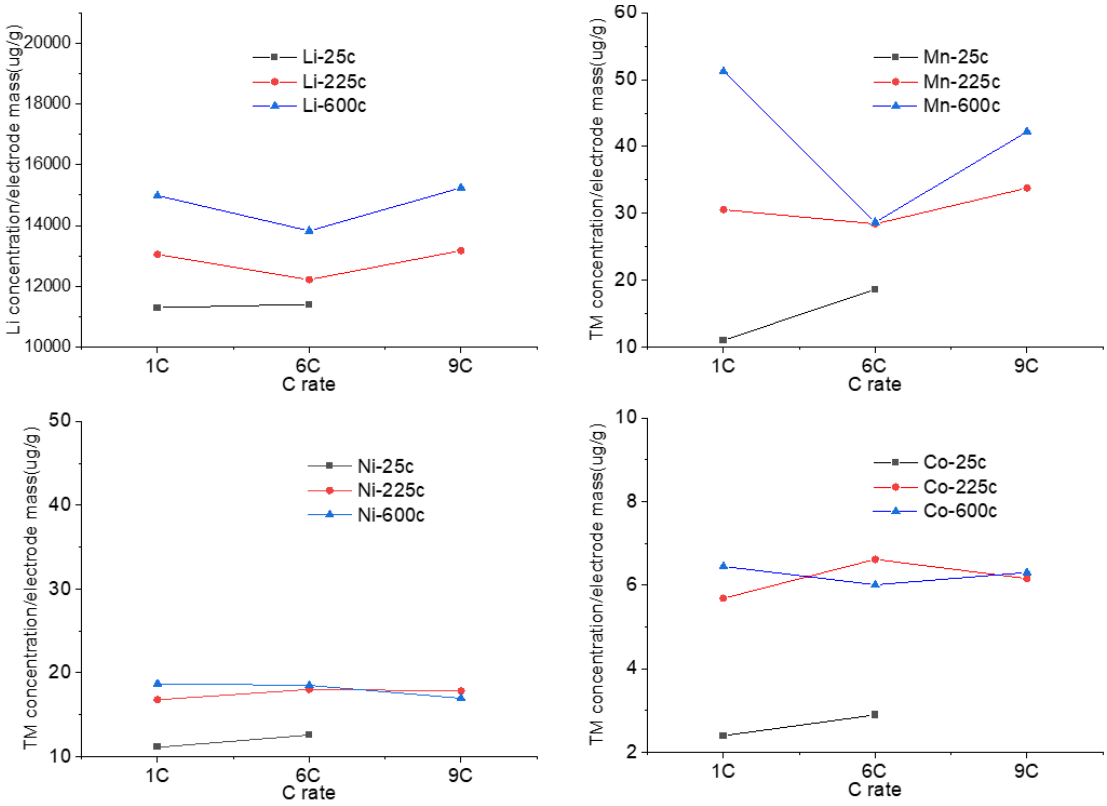

Figure I.4.N.7 The amount of TM dissolution and deposition ICP-MS results from anodes.

SEI characterization on anodes by XPS

Figure I.4.N.8 shows the XPS results collected on anodes from a BOL cell and cells after 225 and 600 cycles charged at 1-, 6-, and 9-C rates, respectively. The surface compositions (C, F, O, P, Li) on the BOL anode were different from those on the surfaces of anodes from the cells cycled at the different C-rates. For example, more LixPOyFz (at 687.3eV) formed on the BOL anode surface than LiF (at 684.8eV), but fast charging promotes the formation of LiF in the three fast-cycled cells. Cycle life impacts more on SEI composition. Ni dissolution was found on all samples, but there were no Mn and Co detected by XPS at the outermost surface (up to~10-nm thick). Depth profiling does not show Mn and Co present through a few hundred nm, which indicated that TM deposition and the distribution was inhomogeneous. The combined results of ICP-MS of the bulk anode suggest that most of the Ni may be on the surface of the anode, whereas Co and Mn diffuse through the solid-electrolyte interphase layer and, possibly, into the bulk. Due to these distinct differences in functions and composition, one might deduce that there are different aging processes at SEI layers on anodes in the fast-charged cells.

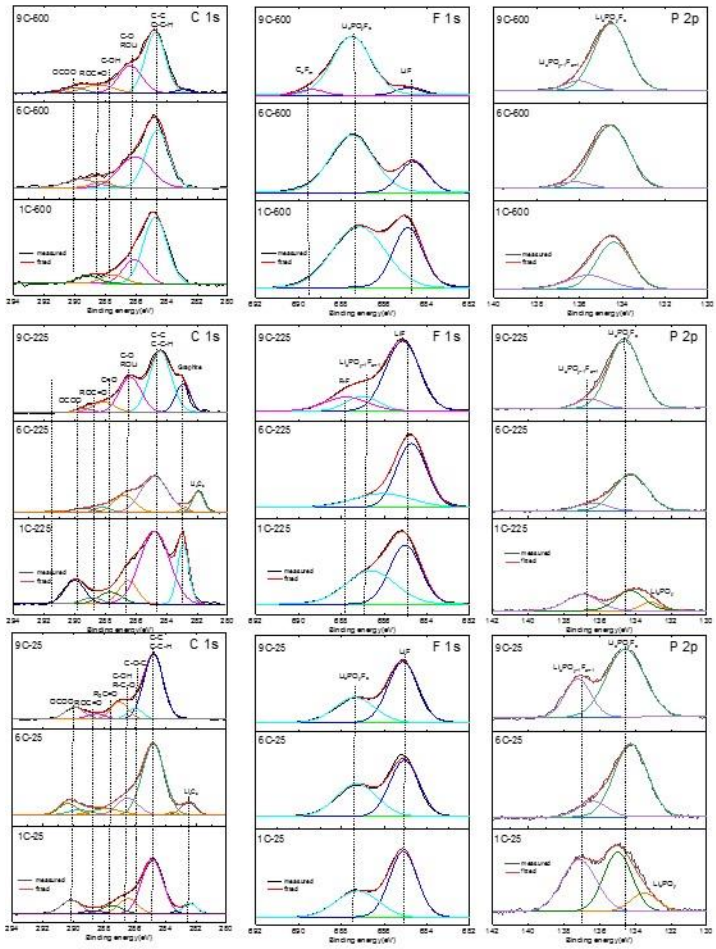

Figure I.4.N.8 XPS core spectra of C 1s, F 1s, and P 2p on graphite anodes after formation cycle, 225 cycles, and 600 cycles charged at 1-, 6-, and 9-C rates.

In-situ and operando investigation of high-rate NMC532 performance

Cathode performance limitations in gr/NMC532 full cells subjected to fast charge conditions were investigated using high energy diffraction (59 keV and 27 keV) at the 11-ID-B and 17-BM-B beamlines of the Advanced Photon Source (APS) at Argonne National Laboratory. Long-term cathode lithium storage performance was evaluated based on reconstructed 2D maps of lithium concentration in NMC material across the electrode area. The maps were derived based on fitting of the diffraction patterns collected in transmission mode through the battery stack using a 1-mm-step size grid with 0.5-mm beam size. The Li concentration within NMC was obtained based on polynomial fitting of NMC lattice volume to Li concentration from NMC532 half-cell lattice volume expansion versus electrochemistry in the first cycle.

The Round 1 cells, designed to maximize performance, were chosen for this study, to minimize potential anode limitations and electrode thickness gradient effects. Single-layer pouch cells were operated under fast charge conditions according to the 6C CC-CV 3-4.1V procedure. Long-term cycling was performed up to 1200 fast cycles.

Comparison of the electrode uniformity after cycle 0 (collected after formation step followed by C/2 charge) and cycle 6 (6C charge after cycle 0) shows that fast charge not only lowers average cathode delithiation, but also induces spatial heterogeneity across the electrode in a very short time. With time, the cell develops clear disproportionation in lithium content of the cathode between the electrode center and the edges (Figure I.4.N.9a). Upon discharging at cycle 1200, the lithium content pattern in the cathode is preserved despite the

uniform delithiation of the anode. A deep discharge by holding the cell at 3.0 V for 2 h slightly increases the lithium content in the cathode but does not noticeably reduce cathode heterogeneity, while the anode is uniformly delithiated (Figure I.4.N.8b). Residual high cathode heterogeneity suggests permanent lattice-lithium loss from the cell center or the inability of NMC532 in the center of the electrode to store lithium, which reflected as increased LAM_{PE} capacity variability in harvested coin cells as shown in Figure I.4.N.3.

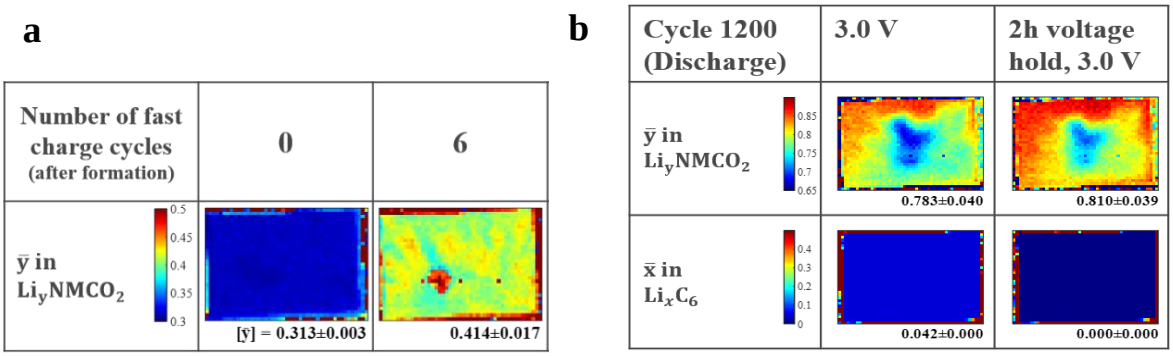

Figure I.4.N.9 (a) Spatial maps of lithium concentration within an NMC lattice under fast charging conditions (4.1V, CCCV), and (b) discharge (C/2 3.0 V CC) and deep discharge (2h, 3.0 V, CV) of the cell at 1200 cycles.

Operando studies have been conducted to search for potential signatures of cathode cracking, as well as to understand the cause of observed performance variability. Due to the presence of heterogeneity, operando studies require careful planning. The APS has established that it is a best practice to combine them with periodical spatial mapping of the battery area. Based on the maps, candidate regions for operando studies were selected covering areas with high and low performance. Consecutive cycles of in operando data were collected in parallel, and variability in electrode responses was tracked. Within the diffraction patterns, the spatiotemporal distribution in cathode performance was observed based on the broadening and splitting of NMC (0 0 3) and (1 0 -5) peaks (Figure I.4.N.10). In the following example, the battery was operated at 6C charge and C/2 discharge within a 3–4.4 V window. Operando data collected during the first 10 cycles of fast charge show cathode material stress even in the first fast charge cycle, manifested by peak broadening when the sample has reached approximately 3.7 V. In the subsequent cycles, material fatigue becomes even more evident, and noticeable peak splitting is observed for both reflections, suggesting possible reduction of particles connectivity, which is a sign pointing toward particle cracking.

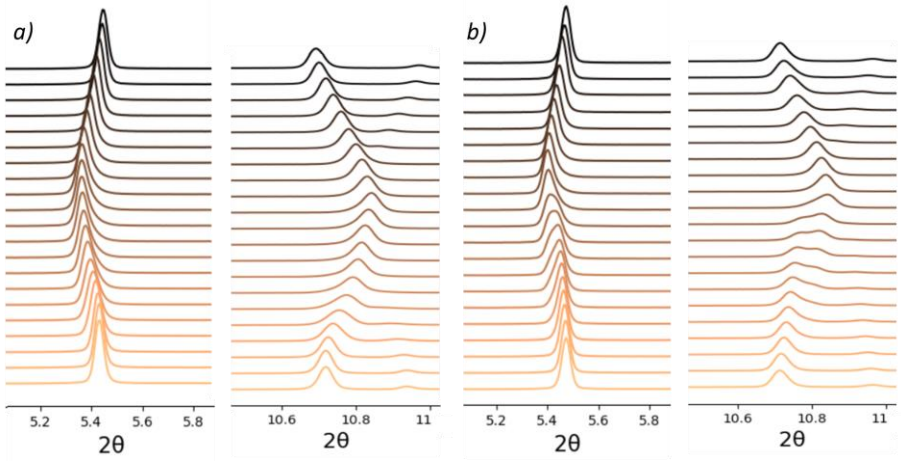

Figure I.4.N.10 Selected reflections of NMC during first and tenth 6C charge and C/2 discharge within a 3-4.4V voltage window. (Discharge data has been plotted every 12th frame for clarity.)

Understanding the cause of cracking in NMC particles

Developing EBSD as a technique for quantifying sub-particle architectures first required demonstration in 2D, which is shown in Figure I.4.N.11a. The grain boundaries and orientation of individual grains were quantified with a high degree of confidence, and software was developed to segment and distinctly label the grains. The technique was then extended to 3D through the application of focused-ion beam (FIB) EBSD and, with help from collaborators at the University of Ulm, the images were aligned and segmented using machine learning approaches before reconstructing the particle architecture in 3D (Figure I.4.N.11b, c). For the first time, the morphological properties of sub-particle grains were then quantified (Figure I.4.N.11d), and the particle's polycrystalline architecture was characterized in 3D.

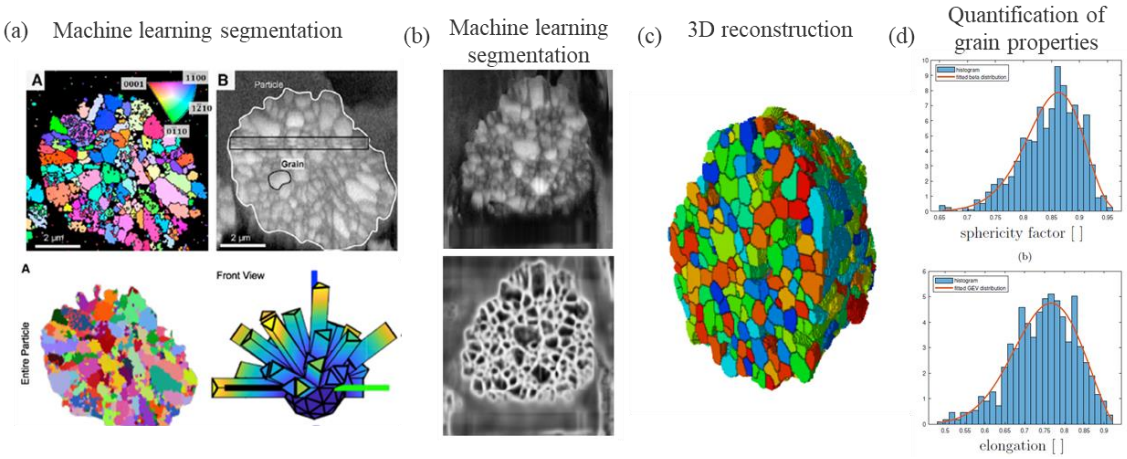

Figure I.4.N.11 (a) 2D EBSD slice clearly showing sub-particle polycrystalline architecture; (b) machine learning approach used to identify and segment grain boundaries; (c) 3D view of a reconstructed particle; and (d) quantified morphological properties of the particle grains.

To understand the influence of NMC particle architecture on fast charge performance and damage, NREL also developed a 3D electrochemical/mechanical-coupled continuum damage model that simulates the 3D anisotropic polycrystalline geometry [2]. The electrochemical portion of the model captures Li-diffusion tortuosity due to randomly oriented grain structure within the particle. Butler–Volmer boundary conditions capture non-uniform reactions at the particle surface. With just a few preferred "fast highway" transport paths within each particle, the NMC random "meatball" architecture is not ideal for fast charge. Around 30% of the particle surface has no Li pathway to the interior and is thus underutilized. The solid mechanics portion of the model captures state-of-charge-dependent anisotropic expansion and isotropic stiffness properties. Irreversible damage occurs when a hydrostatic strain threshold is exceeded. Damage impacts local diffusivity and stiffness.

Figure I.4.N.12 shows intercalation gradients, surface displacement, and damage evolution within an NMC particle of ~6-µm diameter during 6C fast charge (constant current, 4.2-V constant voltage with a 10-minute cutoff), followed by C/2 discharge. As illustrated, the particle shrinks anisotropically (left) during the first charge. The anisotropic deformation causes damage near misoriented grain boundaries. The damage factor (right) is concentrated near the primary particle (grain) interfaces, especially near the secondary particle surface. The continuum-damage model is further used to investigate the influence of primary and secondary particle size. Small particles have shorter diffusion lengths and incur less damage and are thus preferred to large particles. Large-grain particles have fewer grain-to-grain misoriented boundaries and are thus preferred to small-grain particles. Simulation of multiple charge/discharge cycles shows damage quickly occurs during the first charge cycle and then plateaus after several cycles. The same behavior is observed in experimental data. However, real batteries also show a secondary fatigue mechanism that plays out slowly over hundreds of cycles. The modeling team is working with the experimental team at INL to understand the root cause of the fatigue mechanism.

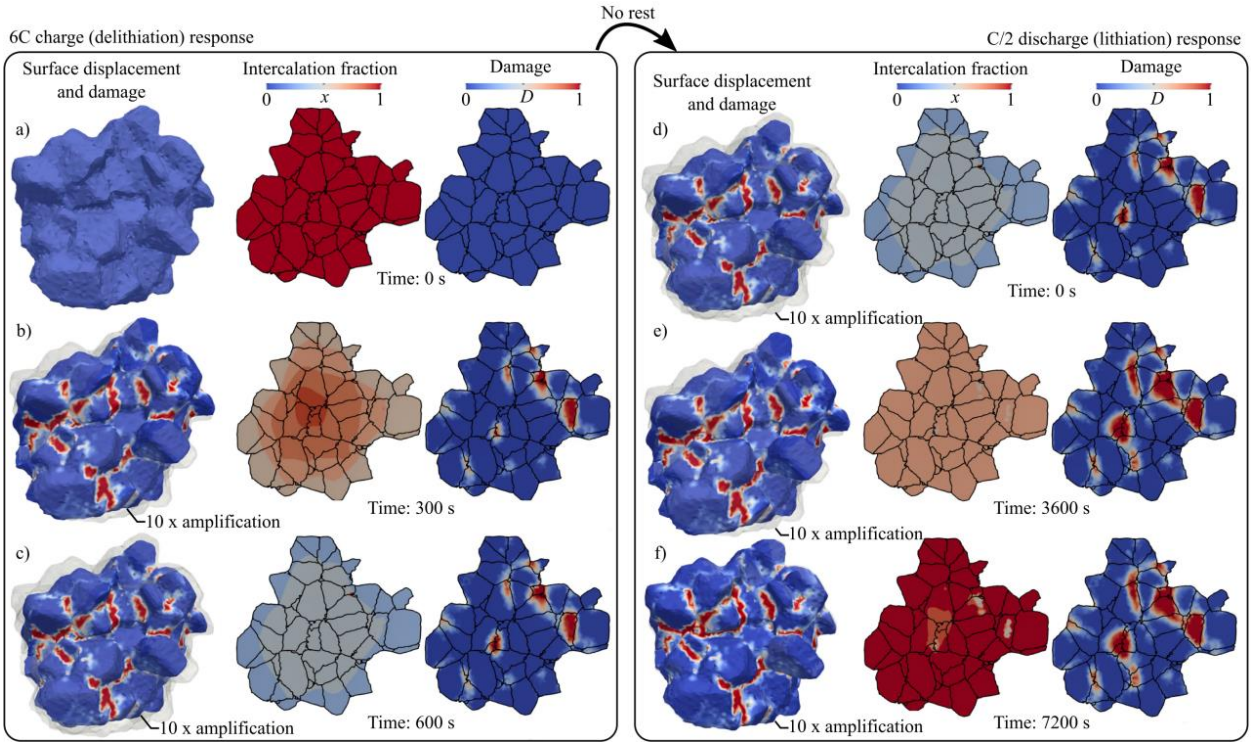

Figure I.4.N.12 Particle displacement, intercalation fraction, and damage during a 6C constant-current/constant-voltage hold and a C/2 discharge. Figure 12a-c illustrate the particle during a 6C charge, whereas Figure 12d-f illustrate the particle during a C/2 discharge.

Evaluate the effects of XFC on particles and micro-structures, identify improvement needs, and explore synthesis approaches

To evaluate the relationship between NMC particle microstructure and cathode fast charge behavior, we first investigated the effect of primary particle morphology on the rate capability. Single-crystalline (SC) NMC532 samples with the platelet shape (Figure I.4.N.13a) and truncated-octahedron (T-Oct) shape (Figure I.4.N.13b) were prepared by using a co-precipitation procedure followed by annealing and a molten-salt synthesis method, respectively. Careful analysis following a previously established procedure showed that both samples were phase-pure single crystals with an average size of ~ 200-300 nm. While the surface of the platelet particles is predominately enclosed by the (001)-family facets, the T-Oct surface is dominated by the (012)-family facets, as shown in the inset schematics in Figure I.4.N.13a and b, respectively.

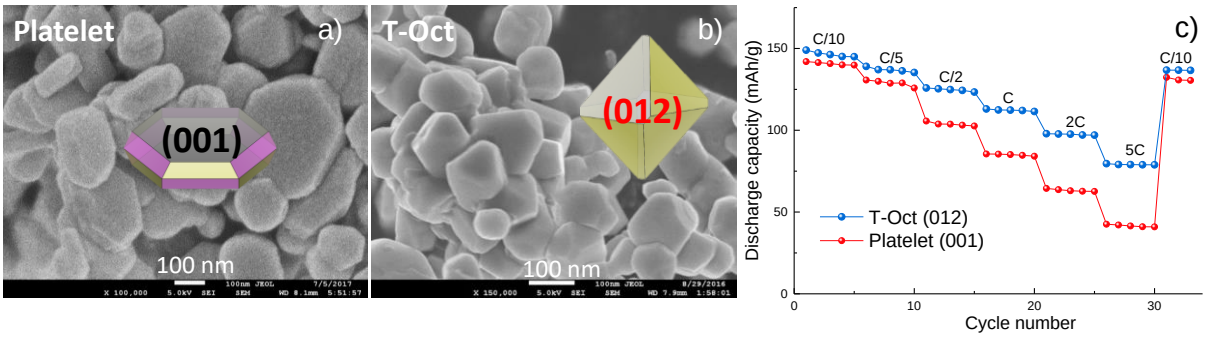

Figure I.4.N.13 Scanning electron microscopy images of NMC532 samples with the platelet- (a) and T-Oct- (b) shaped particles, and (c) comparison of the cathode discharge capacity at the indicated rate

Figure I.4.N.13c compares the capacity retention upon charging and discharging the NMC cathodes at the indicated rate. The half-cells were assembled in coin cells and cycled between 3 and 4.3 V. At all rates tested,

the T-Oct sample consistently outperformed the platelet sample. The difference is significantly more drastic at high rates, suggesting that for fast charging applications, T-Oct with the (012) surface is a more superior morphology compared to the platelet with the (001) surface. This is conceivable as the (001)-family facets are in parallel to the transition-metal layers in the oxide crystal structure and therefore, impermeable to Li ions. On the other hand, sufficient Li diffusion pathways exist on the (012)-family facets. The study suggests that primary particle morphology plays an important role in rate performance and its optimization is necessary.

During the course of FY20, the fast charging program started to transition from NMC532 to NMC811. Accordingly, we explored scalable synthesize approaches to prepare SC-NMC811 samples. In the first approach, large $Ni_{0.8}Co_{0.1}Mn_{0.1}(OH)_2$ secondary particles (~5-10 µm) consisting of sub-micron sized primary particles (Figure I.4.N.14a) were obtained from Argonne. The precursor was ground together with LiOH (an excess amount was used to compensate Li loss at high temperatures) and then calcinated stepwise at 350, 550 and 900 °C under the oxygen flow. The total heating time was about 20 h. After the reaction, T-Oct shaped SC-NMC811 particles with an average size of ~ 300-500 nm were obtained, as shown in the scanning electron microscopy image in Figure I.4.N.14b. The new process effectively eliminates the need of using a molten-salt flux in our previous synthesis approach and reduces the manufacturing cost of SC-NMC cathodes.

Electrochemical performance of the synthesized SC-NMC811 sample was evaluated in half-cell coin cells. Figure I.4.N.14c shows the charge-discharge voltage profiles of the cathode cycled between 3 and 4.3 V at 0.1C rate. The smooth profiles as well as the obtained initial discharge capacity (~ 195 mAh/g) are consistent with those reported on polycrystalline NMC811 made by the traditional co-precipitation methods. Our preliminary evaluation showed excellent capacity retention after 40 cycles (Figure I.4.N.14d).

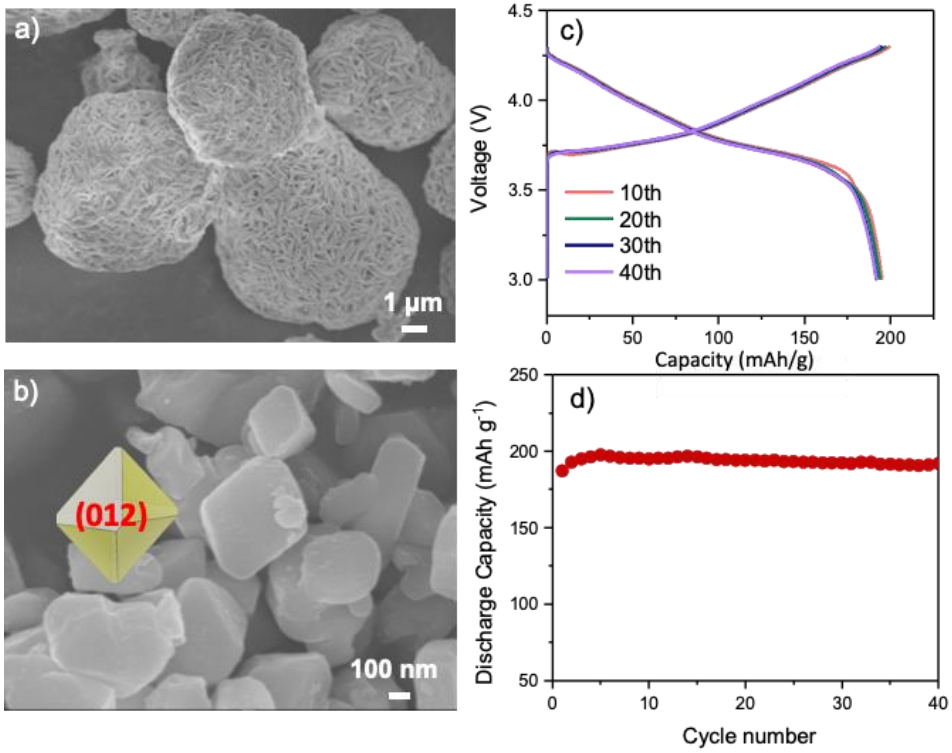

Figure I.4.N.14 Scanning electron microscopy images of (a) Ni0.8Co0.1Mn0.1(OH)2 precursor and (b) synthesized SC-NMC811, c) voltage profiles and d) discharge capacity retention of SC-NMC811 cathode during the first 40 cycles at 0.1C rate

In the second approach, a hydrothermal synthesis approach was developed to prepare $Ni_{0.8}Co_{0.1}Mn_{0.1}(OH)_2$ precursors with various microstructures. The process typically involves the dissolution of transition-metal (such as Ni, Mn and Co) salts in a solvent mixture followed by heat treatment in Teflon lined reactors at

specified temperatures. Reaction solvent was found to play a critical role in influencing the size and morphology of resulting precursor particles. Figure I.4.N.15a-d show the SEM images of $Ni_{0.8}Co_{0.1}Mn_{0.1}(OH)_2$ samples obtained by simply tuning the solvent ratio during the hydrothermal treatment. The use of water and ethanol mixtures in a ratio of 1:1, 1:2, 1:5 and 1:6 led to the formation of secondary particles with a uniform average size of 1, 1.5, 2 and 2.5 µm, respectively.

$Ni_{0.8}Co_{0.1}Mn_{0.1}(OH)_2$ precursor with a secondary particle size of 2.5 µm (Figure I.4.N.15d) was selected to prepare SC-NMC811. After grinding together with LiOH, the mixture was calcinated under an oxygen atmosphere at 550 and 900°C for a total of ~ 25 h. Phase-pure NMC811 sample with the a-$NaFeO_2$ type layered structure (space group: R-3m) was obtained with only a low degree of cation mixing. In contrast to the T-Oct SC-NMC811 particles with dominating (012) surface obtained by thermal treatment of the Argonne precursor (Figure I.4.N.15a,b), here the single crystalline sample adopted a truncated-polyhedron (T-Poly) particle morphology with an average size of ~ 1 µm (Figure I.4.N.15e). Preliminary analysis showed that the majority of the surface is composed of (104)-family facets. Our results confirm the feasibility of preparing varying SC-NMC811 samples by manipulating precursor size and morphology before the annealing step. In the future work, we will evaluate electrochemical performance and rate capability of SC-NMC811 with different morphologies and compare them to that of the polycrystalline baseline used in the program.

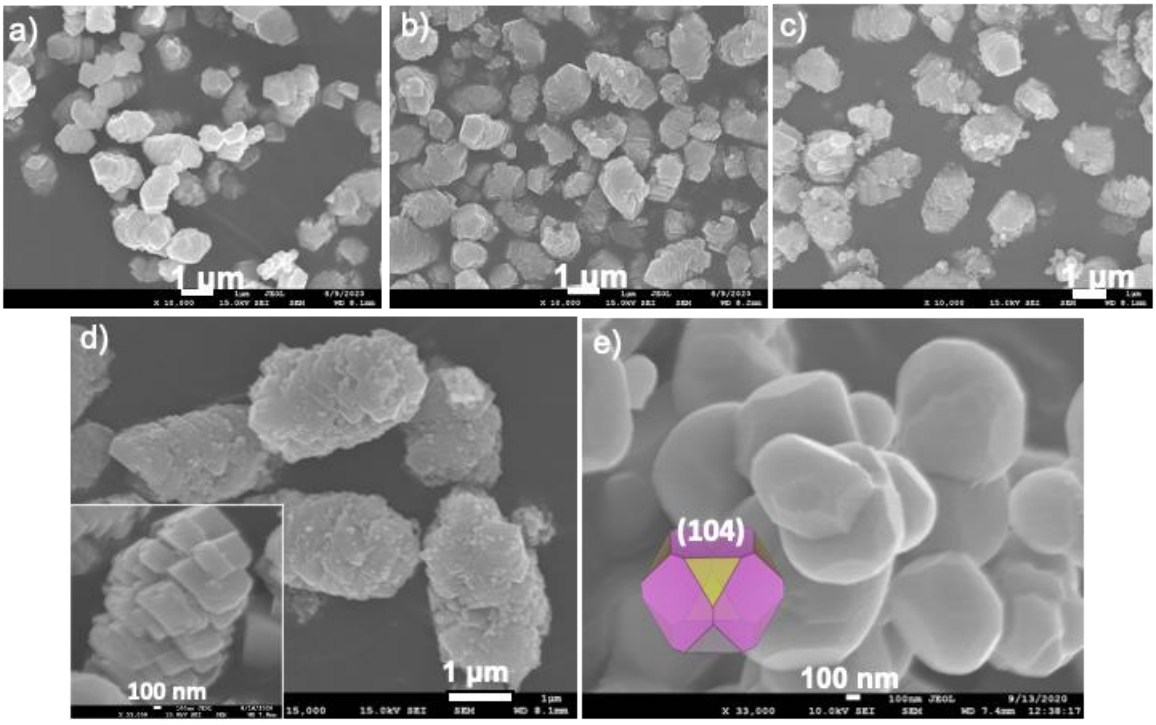

Figure I.4.N.15 SEM images of as-synthesized Ni0.8Co0.1Mn0.1(OH)2 precursors with varying average secondary particle sizes: a) 1 µm, b) 1.5 µm, c) 2 µm and d) 2.5 µm, e) SEM image of SC-NMC811 obtained after annealing the precursor shown in d).

Conclusions

During FY20, the team of researchers at different national labs made several advances in understanding the implication of XFC on NMC cathodes. On a cell level, we identified two dominating aging modes: Loss of lithium inventory (LLI) in the form of SEI growth and Loss of active material in the cathode (LAM_{PE}). The LLI dominated up to 600 cycles. While the LAM_{PE} was not the dominate mode through 600 cycles it continued to occur. Cracking in the secondary NMC particles could primarily be attributed to the cathode issues under XFC. A distinct evolution of cracking with cycling was observed for different charging protocols, i.e., more cracking during initial cycling for the aggressive C-rates which appears to reduce slightly as cycling

progressed. Quantification and correlation of the crack induced damages is under way. TM dissolution was found to be comparable for different charging rates up to 9C. Evidence of other surface issues such as rock salt formation at higher C-rates were present, however, the team is currently awaiting additional post testing data. Fast charging at aggressive rates (9C) but at lower voltage, i.e., up to 60% SOC, appears to mitigate cathode issues. Transition from NMC532 to NMC811 is underway. As part of that effort, 18 R1 gr/NMC811 cells at different charging rates and voltages are currently being evaluated. All these understandings will enable the modeling team to advance cathode cracking agnostic charging protocols to minimize cathode issues and extend life.

In-line with other experimental studies, the operando study suggested lower utilization of cathode in early fast charge cycling with significant heterogeneity, which persisted with extended cycling. The team will continue its efforts to identify potential signatures of cathode cracking and to understand the cause of observed performance variability.

Electron back-scattering (EBSD) has been demonstrated as an accessible lab-based technique that can quantify the grain architecture of NMC particles. EBSD facilitates mapping the orientation of grains in 3D and thus provides the data necessary to model lithium-transport pathways during lithiation and delithiation as well as the associated sub-particle strain during operation. The 3D data is incorporated into multi-physics models to assess transport. limitations and strain hotspots that accrue from unfavorably oriented grains. This has provided new insights into particle degradation and opportunities for optimizing single particle architectures for enhanced rate and life cell performance.

A chemo-mechanical model incorporating strain-induced damage was developed to study the effects of particle size, grain size and charge rate on capacity fade. To our knowledge, the model is the first to do so in 3 dimensions, capturing an actual particle's grain structure and anisotropic transport and expansion. Anisotropy & random-oriented crystals result in a low number of "fast highway" transport paths through the particle. Much of the particle surface is underutilized. Damage quickly accumulates near the particle surface at beginning of fast charge. To minimize damage, small particles with fewer, larger grains are preferred. Radially oriented grains further reduce the likelihood of damage. Damage criteria are being refined in the model to match experimentally observed capacity fade including a long-term fatigue mechanism. The present NMC532 models are readily extensible to NMC811, high voltages, and alternate sub-particle architectures.

Researchers at LBNL investigated the effects of primary particle morphology (polycrystalline and single crystalline) on the rate capability. They found that primary particle morphology plays an important role in rate performance, and its optimization is necessary for XFC conditions for potential crack mitigation. Scalable synthesis approaches to prepare SC-NMC811 was explored in FY20. LBNL and NREL researchers will continue to work together to identify feasible particle architectures and electrode microstructures and synthesize, baseline and validate them in coin cells.

Key Publications

1. Tanim et al., Heterogeneous Behavior of Lithium Plating during Extreme Fast Charging, Cell Reports Physical Science, 1(7) 100114
2. Quinn et al. Electron Backscatter Diffraction for Investigating Lithium-Ion Electrode Particle Architectures, Cell Reports Physical Science, 2020
3. Furat et al. Mapping the architecture of single electrode particles in 3D using electron backscatter diffraction and machine learning segmentation, Journal of Power Sources, 2020
4. Allen et al. A continuum-level damage model fro Ni0.5Mn0.3Co0.2 secondary cathode particles in Li-ion batteries, in preparation.
5. Charalambous, et al., "Evaluation of sources of macroscale heterogeneity in lithium ion pouch cells via in situ synchrotron X-ray diffraction mapping," submitted to Journal of Power Sources.
6. Tanim et al., Extended cycling life implications of extreme fast charging on lithium ion battery cathode, in preparation

7. Paul et al., Quantification of heterogeneous, irreversible lithium plating in extreme fast charging of Li-ion batteries, under review in Energy and Environmental Science.
8. Paul et al., Using in-Situ X-ray Diffraction to Quantify Electrode Behavior of Lithium Ion Batteries from Extreme Fast Charging, in preparation.
9. J. Allen, A. Verma, P.J. Weddle, A. Mallarapu, F. L.E. Usseglio-Viretta, D. Finegan, A. Colclasure, K. Smith, "A continuum-level damage model for Ni0.5Mn0.3Co0.2 secondary cathode particles in Li-ion batteries", in preparation

References

1. Tanim et al., Extreme fast charge challenges for lithium-ion battery: variability and positive electrode issues, J Electrochem Soc., 166 (10) (2019) A1926
2. http://www.neper.info/.

Acknowledgements

This project was funded by the U.S. Department of Energy, Vehicle Technologies Office. The technology development manager was Samm Gillard. The project overview was prepared by Venkat Srinivasan (ANL). Other contributing team members for Thrust 5 (The Effects of Extreme Fast Charging on Lithium-ion Battery Cathode Thrust) include Thrust Coordinator: Tanvir Tanim (INL); Task leads: Tanvir Tanim (INL), Kamila Wiaderek (Argonne), Donal Finegan (NREL), Kandler Smith (NREL), Johanna Nelson Weker (SLAC), and Guoying Chen (LBNL); and the following supporting individuals: Andrew N. Jansen, Bryant J. Polzin, Alison R. Dunlop, and Stephen E. Trask, Zhenzhen Yang, Seoung-Bum Son, Ira Bloom, Harry Charalambous, Kamila Wiaderek, Yang Ren, Uta Ruett, Kandler Smith, Donal Finegan, David Dierks, Orkun Furat, Volker Schmidt, Jeffrey Allen, Ankit Verma, Peter Weddle, Anudeep Mallarapu, Francois Usseglio-Viretta, Andrew Colclasure, Paul Gasper, Johanna Nelson Weker, Molleigh Preefer, Partha Paul, Michael Toney, Guoying Chen, Tanvir Tanim, Bor-Rong Chen, Parameswara Chinnam Rao, Sangwook Kim, Michael F. Evans, Charles Dickerson.

I.4.0 XCEL R&D: Heat Generation Thrust

Venkat Srinivasan, Principal Investigator
Argonne National Laboratory
9700 S. Cass Avenue,
Lemont, IL 60439
E-mail: vsrinivasan@anl.gov

Samm Gillard, DOE Technology Development Manager
U.S. Department of Energy
E-mail: Samuel.Gillard@ee.doe.gov

Start Date: October 1, 2019 End Date: September 30, 2020
Project Funding (FY20): $742,000 DOE share: $742,000 Non-DOE share: $0

Project Introduction

The 2022 U.S. Department of Energy's (DOE's) battery goals of 350 Wh/kg, 1,000 Wh/L, and $150/kWh(useable) require battery packs that have higher energy densities, resulting in a very compact system. To meet the specific energy goal, the electrode thickness of the battery will need to increase while decreasing the thickness of the current collectors. Furthermore, the amount of electrochemically inactive material, such as binders, will need to decrease. All of these factors will have a deleterious effect on the thermal performance of the cell. Furthermore, many of the advanced chemistries being developed to attain these goals, such as silicon and lithium metal anodes along with high-energy cathodes, have heretofore suffered from low efficiencies at low to moderate charge and discharge rates. Even if the energy efficiency of the next generation of batteries increases, more heat is being generated per unit volume with a smaller heat transfer area because of the compactness of these batteries. Thus, combining the heat transfer limitations associated with advanced chemistries with extreme fast charging (XFC) will challenge the battery designers to keep the battery temperatures in the "Goldilocks" zone that prevents acceleration of the aging mechanisms within the battery while limiting the cycle life cost. Our working group is seeking to identify the critical parameters associated with heat generation and to develop techniques to quantify temperature gradients within the cell.

Objectives

The battery thermal performance is critical to the life, cost, performance, and safety of energy storage systems. As such, the objectives of this workgroup are to:

- Provide feedback to DOE on the battery thermal challenges associated with XFC
- Understand temperature nonuniformity within the cell during XFC
- Develop techniques for operando interior temperature measurements
- Identify limitations of using high specific energy density cells
- Identify thermal areas of concern with existing battery systems
- Identify how changes to the battery chemistry and cell design affect the cells' efficiency and performance
- Identify state-of-the-art thermal management strategies and how these can be applied to future battery electric vehicles.

Approach

Develop a one- or three-dimensional (1D/3D) model capable of assessing heterogeneities, heat transport, and strategies to mitigate temperature rise under XFC conditions. During Q1FY20, we developed a 1D model to explore the critical parameters associated with heat generation within a representative pouch cell for an electric vehicle (EV). The study performed was not exhaustive, but we include an executive summary of the major findings below.

- A 100 kW-hr battery would produce 50 kW of heat during 10-minute charge, with a significant amount of heat being generated from li-ion transport/conduction within the electrolyte phase using current Gen2 formulation.
- For every 1.0 kW of heat generated during a 10-minute charge, the adiabatic temperature of the cell will rise a corresponding 1.3°C.
- If the allowable temperature rise of the cell is 20°C during charge, then 35 kW of heat must be removed to prevent the cell from exceeding the maximum operational temperature of the cell. A thermal management system of this size is substantially larger than what is in present EVs.
- Temperature difference from top to bottom of a pouch cell is proportional to the number of layers squared (N2).
- If cooling is only available from one face side, then capacity is likely limited to ~30 Ah.
- If cooling is available on both sides of the pouch cell, then 50- to 60-Ah cells could be used.
- Large amounts of heat can be removed via tab cooling. However, the temperature difference between the center and edge of the layers becomes large when >20% of heat is removed through tabs.
- Voltage drop across the cell from lateral current conduction is proportional to the square of the cell length (L2).
- Using existing 10- and 15-micron copper and aluminum foils, respectively, would limit cell length to 15 cm to prevent a large temperature spread/voltage change across the cell.
- Cells up to 23 cm in length could be made if the current collector thickness was doubled. However, the cell energy density would be reduced from 230 to 210 Wh/kg.

The 1D model gave us direction but not the required fidelity. Thus, we utilized an ANSYS/Fluent modeling framework developed under the DOE computer-aided engineering for battery (CAEBAT) program. The semi-empirical Newman, Tiedemann, Gu, Kim (NGTK) electrochemical model is suitable for thermal modeling of battery cells under constant current charge/discharge conditions. The high computational efficiency of the model allowed us to vary the numerous cell parameters to assess the temperature differences within a cell and module. The model was used to investigate temperature heterogeneities for:

- Various cooling strategies – air, liquid, and active.
- Different tab designs – opposing tabs, large/small, “standard” tab, etc.
- Alternative electrolytes proposed by the XCEL electrolyte team to increase heat transport and ionic conductivity while limiting lithium plating.
- Cell sizes between 20 and 60 Ah with an areal capacity of greater than 3.5 mAh/cm^2 for the anode.
- Various cell length/width ratios.
- Impact on cell life/degradation.

Finally, temperature inhomogeneity is often hypothesized to be a culprit in observed inhomogeneous degradation such as local Li plating, local state-of-charge variation, and local and solid electrolyte interphase (SEI) thickness variation. Measuring internal temperature will allow for correlation between hot spots for evidence of degradation. Thus, the workgroup has focused on three techniques capable of measuring the internal temperature of a battery:

- Placing a resistance thermal device (RTD) into an electrochemically active cell.
- Using X-ray diffraction/synchrotron to measure operand temperature gradients via the change in d-spacing of materials in the battery while it is cycling.
- Using an internal/external 3ω sensor to measure the thermal transport properties at different distances from the sensor. Combining the measured transport properties with a thermal model should allow for the internal temperature of the cell to be determined.

Results

Develop a 3D model that is capable of evaluating heterogeneities, heat transport, and strategies to control temperature rise under XFC conditions. (NREL)

NREL developed and validated a 3D thermal model to access heterogeneities and cooling strategies to control temperature rise under XFC conditions. The model is based on the multi-scale multi-domain (MSMD) modeling framework implemented in ANSYS/Fluent, under the DOE Computer-Aided Engineering for

Electric Drive Vehicle Batteries (CAEBAT) program. The semi-empirical NGTK model is employed to predict battery electrochemical behaviors and heat generation. With high computational efficiency, it can predict the non-uniform electrical and thermal fields within a battery cell. The modeling parameters were extracted from voltage curves of XCEL Round 2 cells in charging at varying C-rates from 1C to 7C at 30°C and 45°C. The model was validated by comparing results against measurements conducted using the National Renewable Energy Laboratory's (NREL's) microcalorimeter (details in the second quarterly report for FY20 under the heat generation thrust). As shown in Figure I.4.O.1, voltage responses and heat generation rates predicted by the model match well with experimental data. Because of the lack of experimental data, modeling parameters at 60°C were approximated using the difference of parameters at 45°C and 30°C. These parameters, as functions of temperature, are linearly interpolated among calibrated temperatures. For temperatures more than 60°C, parameters are the same as that at 60°C.

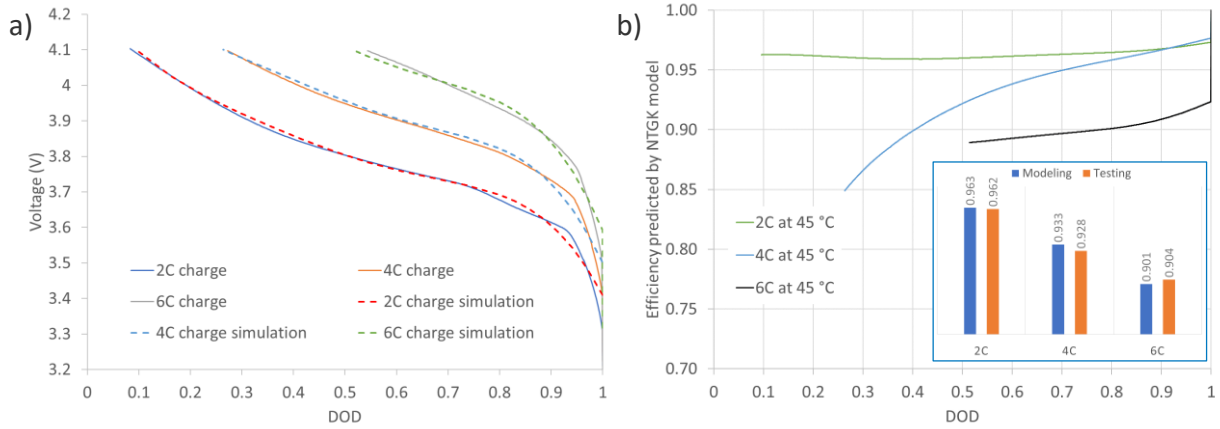

Figure I.4.O.1 NTGK model validation against calorimetry data of XCEL Round 2 single-sided cathode/anode cells at 45°C (a) charging voltage curves at 2C, 4C, and 6C; and (b) transient heat generation rates estimated by the model and comparisons of total energy efficiencies by testing and modeling.

This validated thermal model was applied for a battery module. Figure I.4.O.2 illustrates the cell and module geometries. Referring to the battery pack of a 2017 Chevy Bolt, the module consists of six large-format pouch cells connected in a 3P2S configuration, a liquid cold plate, and packing materials such as busbars, fins, forms, and gap pad. The mass ratio of the cells in the module is about 86%. The pouch cell with a capacity of 25 Ah has the identical electrode design of the Round 2 32-mAh cells. Its geometry is selected by following the guidance from the critical parameter analysis as reported in XCEL FY20 Q1 report.

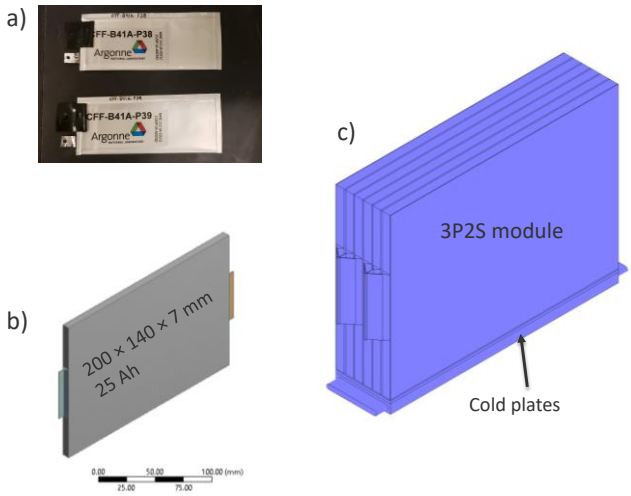

Figure I.4.O.2 Battery cells and module for 3D simulations: (a) XCEL Round 2 32-mAh Cells; (b) a large-format pouch cell with identical electrode design with the 32-mAh cell; and (c) a battery module consisting of cells, cold plates, and packing materials.

The 3D thermal model was used to address two critical concerns for fast charging. One is the needed time to cool down the 3P2S module from 60°C to about 40°C. The other is to access the heterogeneous behaviors being developed during fast charging and associated solutions to mitigate these heterogeneities. Table I.4.O.1 lists the simulation parameters for these two case studies. For Case 1 to estimate cool-down time, an electrochemical model was not included because cells were under relaxation. For Case 2 to access heterogeneities, electrochemical-thermal modeling was performed.

Table I.4.O.1 Simulation parameters of the 3D thermal modeling

Case #	Initial Temperature	Coolant Temperature	C-rates	Parameters
Case 1	60°C	30°C	N/A	Thermal resistances, coolant flow rates, and heat dissipation rates
Case 2	30°C	30°C	6C	Thermal resistances, cooling surfaces, and cell thermal conductivities

Cool-down simulation results suggest coolant flow rates and thermal resistances between cells and coolant are critical parameters. As shown in Figure I.4.O.3a, turbulent flow enhances heat transfer between coolant and cold plate compared to laminar flow. However, further increasing flow speed is unnecessary (i.e., 3 m/s). Minimizing thermal resistances is essential. The ideal gap pad case assumed that thermal contact resistance between the bottom fin and cold plate does not exist. Instead, it is estimated by the model that the cool-down time is reduced nearly half under this condition. Opposingly, improvements of these parameters result in temperature differences in the cells, as shown in Figure I.4.O.3b. Enhancing cell thermal conductivity and including fins on both sides of the cells not only increase heat dissipation rates but reduce cell temperature difference. The improvement with both-sides fins can be limited due to the thermal resistance. Moreover, it may be impractical given that it increases the weight of the module by about 6%.

The aforementioned studies were focused on heat transport within the module configuration. To estimate the cooling capacity of vehicle air conditioning (AC) systems, boundary conditions of constant heat flux/cooling power were applied. Figure I.4.O.3c presents the cool-down time with different cooling power under the ideal condition that heat is transferred from cells directly to the AC evaporator. We estimate that 100W is sufficient to cool down the module from 60°C to 40°C within about 10 minutes, corresponding to 12.1 kW to a battery pack having the same volume as the Chevy Bolt's. However, higher cooling capacity increases temperature difference (Figure I.4.O.3d). Optimization of the cooling system will be required to reduce the pack

temperature but prevent temperature differences across the cell. In a real design case, coolant may be the medium to transfer heat between the cells and AC evaporator. After addressing this in the updated boundary condition shown in Figure 3c, cool-down times are prolonged, and 200 W instead of 100 W is needed to meet the 10-minute cooling goal.

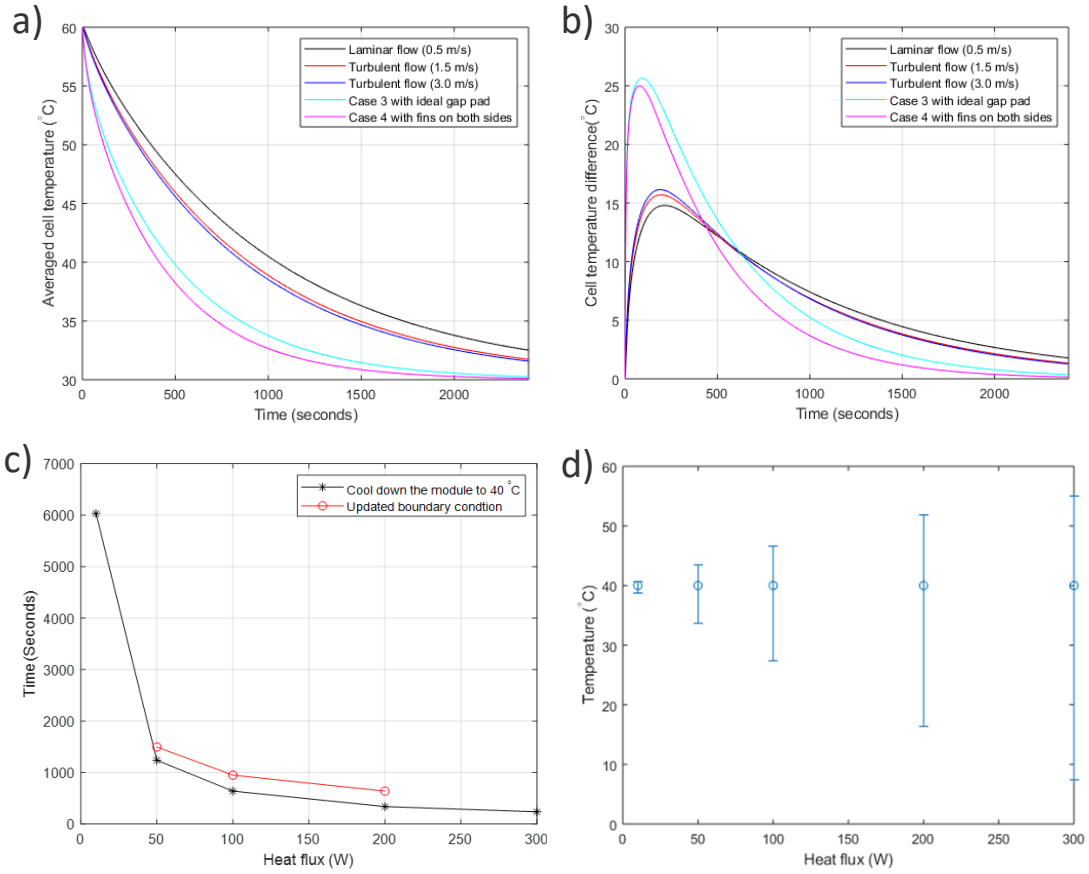

Figure I.4.0.3 Simulation results for battery cool-down studies: (a) impact of design parameters on heat transfer performance; (b) impact of design parameters on temperature distributions; (c) cool-down times as a function of AC cooling power; and (d) temperature differences within the module while average temperature of the module is 40°C.

Heterogeneous behaviors were quantified in the Case 2 study. The 3D model captures the heterogeneity caused by non-uniform electrical and thermal fields within the module. It was found that electrodes close to the tabs were preferentially used during charge. The heterogeneous behavior was increased as the charge rate increased. This result is evident in Figure I.4.O.4a, which shows a DOD contour on a cross-section of the module at 250 seconds after 6C charge. Simulation results suggest two related reasons to generate heterogeneity: one is the higher voltage of the sandwich electrode close to the tabs (Figure I.4.O.4c) and higher temperature of electrode away from cold plates leading to lower resistance of the electrode (Figure I.4.O.4b,d).

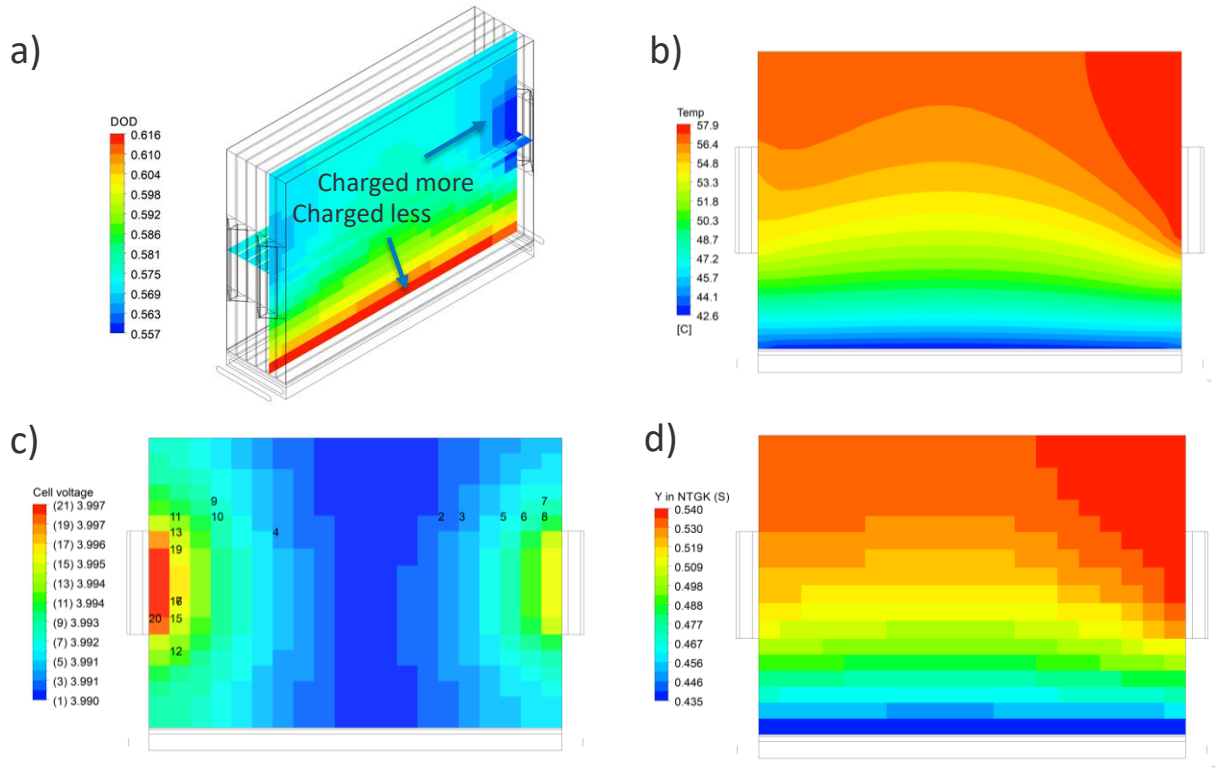

Figure I.4.O.4 Contours of modeling parameters on a cross-section surface after 250-seconds 6C charging: (a) DOD; (b) cell temperature; (c) cell voltage; (d) conductance of the cell (Y in NTGK model).

Therefore, cell electrochemical heterogeneity can be reduced by decreasing cell temperature difference. This can be achieved by enhancing cell thermal conductivity and arranging heat transfer pathway more evenly. Figure I.4.O.5 shows the improvement made by doubling thermal conductivity of the cell and using fins on both sides of the cell. It also suggested that DOD difference can be controlled by interrupting the continuous constant-current charge. Additionally, optimal design of the cooling surfaces to the cell is necessary. Cell temperature rises less by reducing thermal resistances of the module. However, temperature difference within the module is exacerbated, leading to higher resistance non-uniformity and possibly decreased charged capacity. The model suggests that a considerable amount of heat can be removed from the busbar and cell top surfaces with convective cooling, especially through cell top surfaces. These additional surfaces result in more even heat dissipation and reduce both temperature rise and difference across the module.

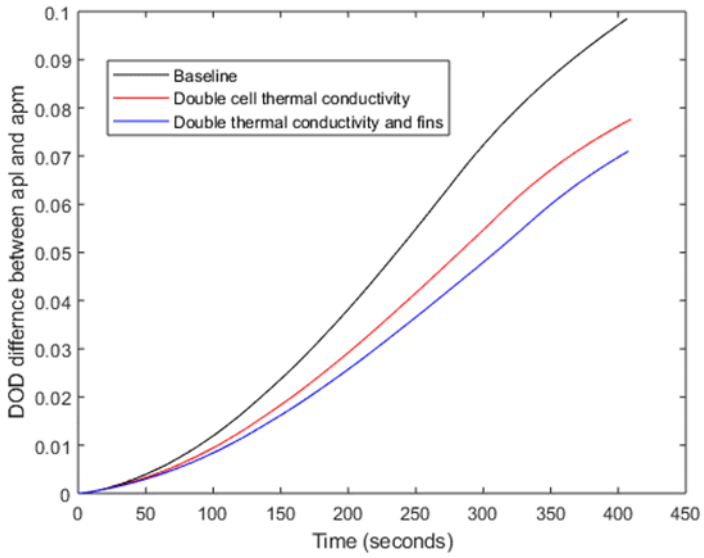

Figure I.4.O.5 Profiles of DOD difference along 6C charging for baseline case, cells with double thermal conductivity and plus fins on both sides.

Evolution of heat flux, thermal resistance, and temperature rise in cycling cells. (LBL)

The Prasher group developed a 3ω sensor inside the battery for *operando* measurements of thermal transport properties in pouch cells. The 3ω signal across a wide range of frequency enables analyzing thermal properties at different distances from sensors. Higher frequency data depends on material properties closer to the sensor, while lower frequency data captures material properties farther away from the sensor (i.e., deeper inside the battery). A main observation is that the thermal transport properties can change with cycling at different charge rates, drifting over a battery's lifetime. This indicates the increasingly significant impact to battery life from thermal resistance and the resulting variation of temperature rise. These impacts would be underestimated if based only on measurements performed on fresh batteries before thermal properties have degraded.

The temperature rise of batteries during operation depends on heat generation, thermal transport properties, and thermal management. To understand the impact of heat generation and thermal transport properties, we developed a measurement scheme to simultaneously measure the time-resolved heat flux, thermal conductivity, and temperature rise of operating batteries (see Figure I.4.O.6a). Note that the max temperature rise is measured by the thermocouple on the top as the top side is thermally insulated. Figure I.4.O.6b shows a 3-Ah pouch cell with a 3ω sensor and thermocouple on the top. Representative raw data of temperature rise, heat flux, and 3ω signal are shown in Figure I.4.O.6c-e, respectively. Note that we have three peaks for the temperature and heat flux in one cycle, and the peak values are used to show the variation in cycling. $\Delta T = T_1 - T_2$ is the temperature difference across the cell, Q" is the heat flux from the cell to the heat sink, and $\Delta T/Q''$ represents the effective thermal resistance.

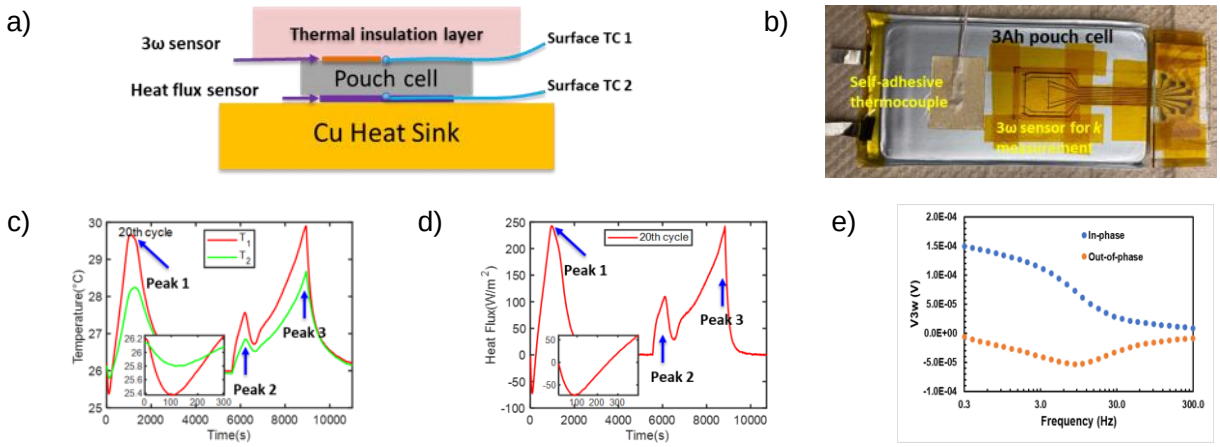

Figure I.4.O.6 Our measurement scheme designed for simultaneously measuring the heat flux, thermal transport properties, and temperature rise of operating batteries.

Figure I.4.O.7 shows the evolution of temperature difference (ΔT), heat flux (Q”), and effective thermal resistance (ΔT/Q”) in batteries charged at 1C and 2C. To exclude the discharge effect, the same discharge rate (1C) is used in both studies, and the values at peak 3 in each cycle are used for analysis. For the cell charged at 1C, both the temperature difference (see Figure I.4.O.7a) and heat flux (see Figure I.4.O.7b) decrease in the initial 200 cycles, and then increase due to the aging effect. Although the effective thermal resistance (ΔT/Q”) has a similar trend, the turning point is at ~800 cycles. In contrast, for the test with 2C charge, the turning point for ΔT, Q”, and ΔT/Q” is ~20 cycles, which indicates a much earlier degradation of thermal transport properties in cells at fast charge rates. This data shows that the internal thermal transport properties of even commercial cells degrade with cycling and degrade more than 10x faster from 2C charging rates than from 1C charging rates. Therefore, any lifetime estimates or performance simulations of batteries may be inaccurate if they do not account for the evolution of thermal resistance (and hence increased temperature gradients) within the cell.

In future XFC studies, we plan to collect the temperature, heat flux, and thermal transport properties of cells charged at various rates (1C–6C) and understand the degradation of thermal properties in cells during XFC. This information can be used to better understand the fundamental degradation mechanisms and to provide more accurate predictive models for battery performance and lifetime.

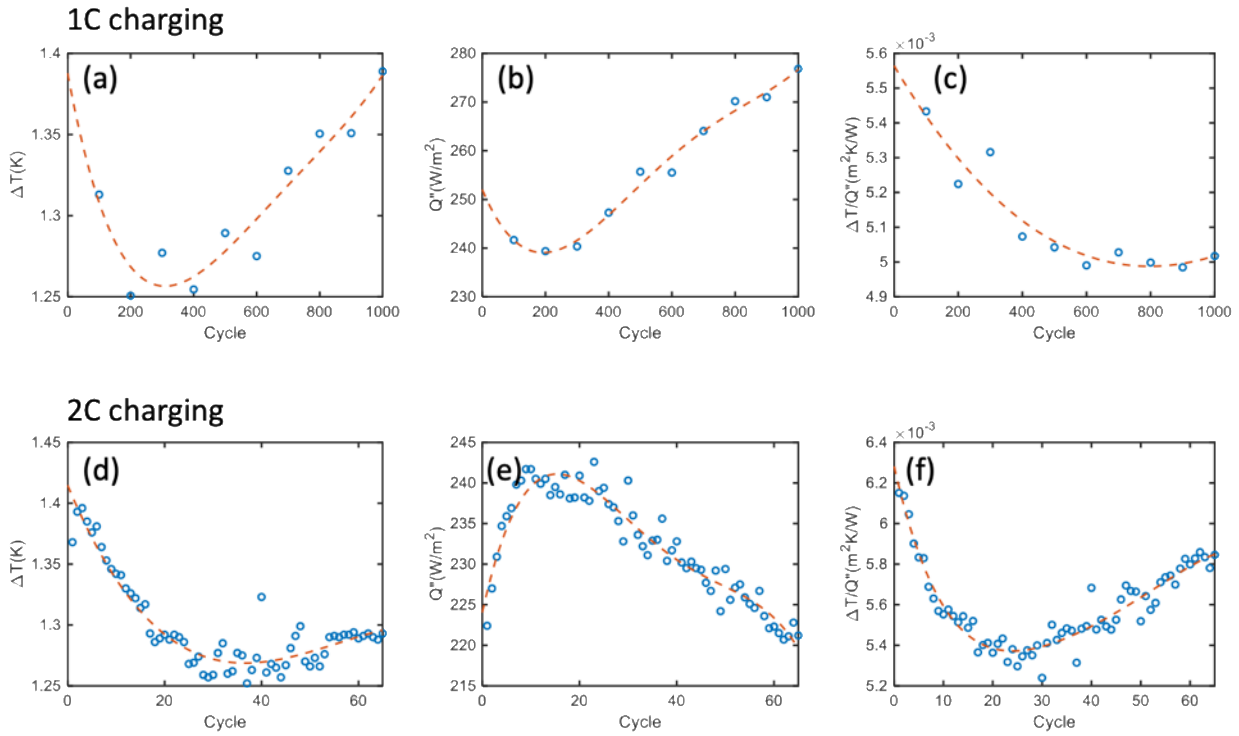

Figure I.4.0.7 The evolution of temperature difference (ΔT), heat flux (Q"), and effective thermal resistance (ΔT/Q") in batteries charged at (a-c) 1C and at (d-f) 2C. The discharge rate is 1C in both studies and the values at peak 3 are used for analysis. Dashed lines are just a guide for the eye.

Time-resolved calorimetry of large cells in fast charge from surface heat flux and temperature measurements

The Prasher group has developed a method to perform time-resolved calorimetry of the heat generated in large cells in XFC. This method is based on inverse heat transfer analysis of the cell and requires simultaneous heat flux and surface temperature measurements. Conventional calorimetry approaches such as isothermal microcalorimetry are limited by the overall cell size and therefore not applicable to large cells. Additionally, other existing approaches such as the ones based on lumped thermal analysis are limited by the thermal transport properties and the cell thickness. In contrast, the calorimetry method we have developed, based on inverse heat transfer analysis, can account for finite thermal transport properties and large cell dimensions and is therefore more accurate than the existing methods. Our approach does not need to make any assumptions about lumped capacitance, slow charging, or isothermal conditions.

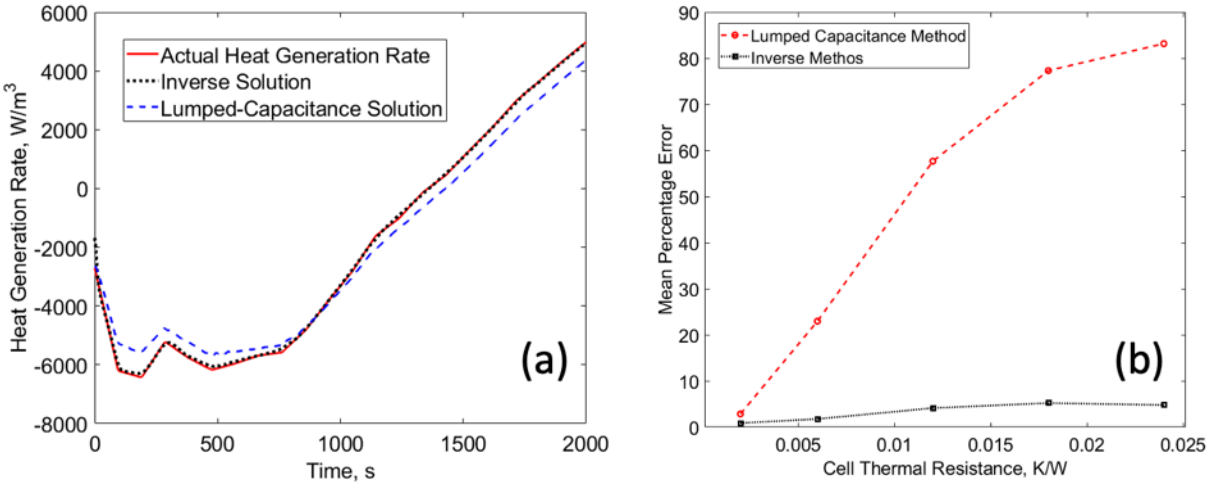

Figure I.4.O.8 (a) Heat generation rate calculated from our inverse method compared with the standard lumped capacitance method. The true heat generation rate used to obtain the surface temperature and heat flux is shown for reference. (b) The percentage root mean square (RMS) error associated with our inverse method and the standard lumped capacitance method as a function of cell thermal resistance. The error with the lumped capacitance method increases as the cell's thermal resistance increases, whereas the error with the inverse remains essentially the same (< 5%).

Figure I.4.O.8(a) compares the calorimetry results from our inverse analysis with that from the standard lumped thermal analysis. Both the results are compared with a true (actual) heat generation function used to simulate the heat flux and the surface temperatures for the lumped and the inverse analysis. It is evident from the figure that the inverse analysis predicts the heat generation better than the lumped analysis. Figure I.4.O.8(b) quantifies the RMS percentage error associated with predicting the true heat generation rate using the lumped analysis instead of our inverse analysis as a function of the thermal resistance of the cell. As evident in the figure, the error associated with the standard lumped thermal analysis increases significantly with the cell thermal resistance while it levels off at ~5% with the inverse analysis even for large cells with considerable thermal resistance. This analysis demonstrates the applicability of our inverse analysis for calorimetry of large cells and fast charge conditions.

AC method to spatially resolve heat generation

The Prasher group is developing a method to spatially resolve heat generation in a cell. A cell under an AC charge-discharge generates heat at different harmonics of the charge frequency, each associated with a different heat-generating electrochemical process. The first harmonic is related to the entropic heat generation. The fourth harmonic is determined by the kinetic overpotential resulting in irreversible heat. The second harmonic is related to the ohmic heat. By utilizing the idea of the frequency dependence of the thermal penetration depth, we have devised a method to spatially resolve the different types of the heat generated inside the cell. Higher frequencies correspond to shallower thermal penetration depths, while lower frequency temperature oscillations penetrate deeper into the battery. Therefore, by monitoring the magnitude and phase of the frequency-dependent temperature oscillations on the battery's surface, we can infer how much of each kind of heat was generated at what depths within the battery. We plan to exploit the frequency-domain nature of this approach and use a lock-in amplifier technique to boost signal-to-noise ratios, allowing us to measure sub-millikelvin temperature oscillations. The simulated responses for the complex surface temperature oscillations at each relevant harmonic are shown in Figure I.4.O.9 for one possible cell.

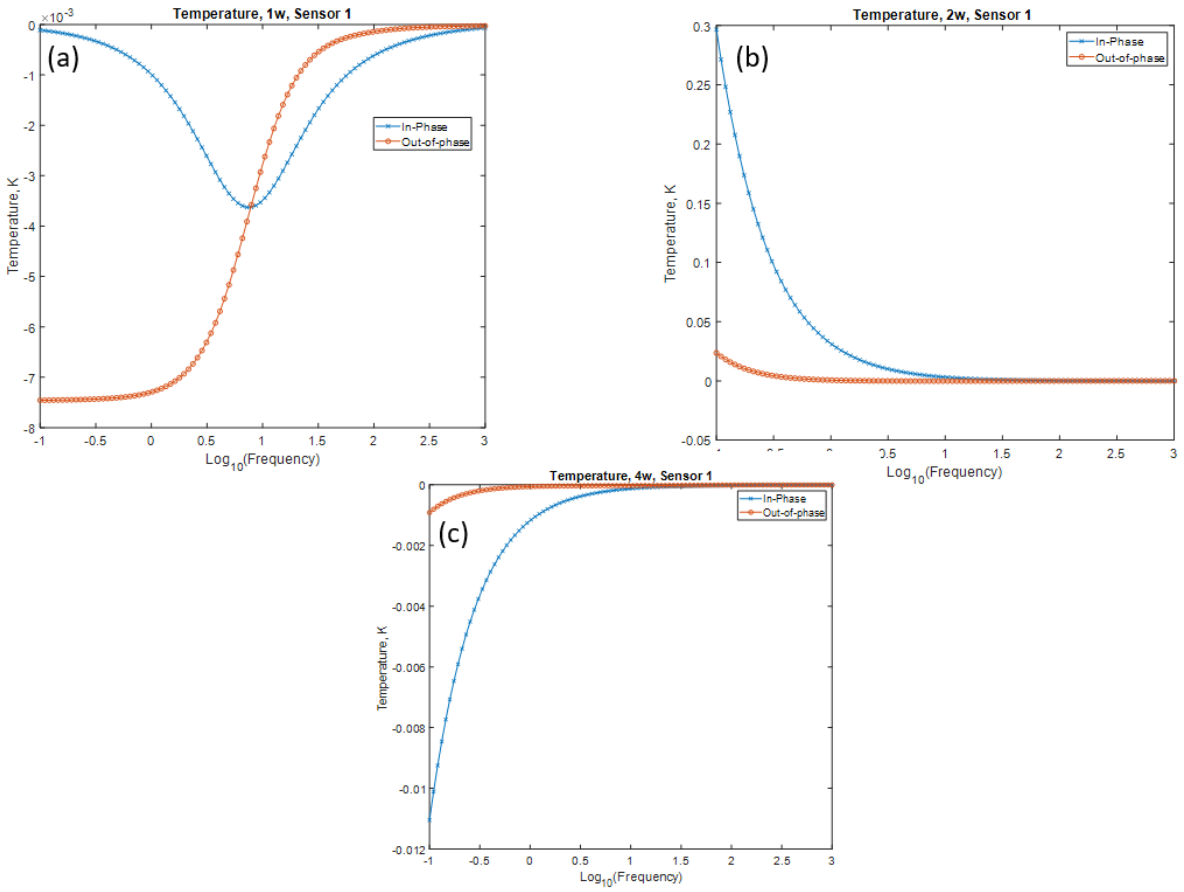

Figure I.4.O.9 Simulated magnitude of surface temperature oscillation as a function of frequency at different harmonics of the AC charging current. The temperature rise at the first harmonic (1ω) shown in (a) is due to the reversible (entropic) heart. The temperature rise at the second harmonic (2ω) shown in (b) is due to the ohmic heating, and the temperature rise at the fourth harmonic (4ω) shown in (c) is due to the kinetic overpotential for the reactions at the electrodes. These signals contain information about the magnitude and depth of each kind of heat-generating process.

Heat of mixing in cells at XFC

The Prasher group investigated the importance of the heat of mixing in cells at XFC. To calculate the heat of mixing, our study utilized a fundamental thermodynamic framework independent of commonly used assumptions in other studies of heat of mixing. In particular, we calculated the expression for the rate of change of the total enthalpy of a cathode particle and the rate of change of the total enthalpy of the cell (sum of the rate of enthalpy change of all the particles). Subtracting the work done by the cell yields an expression for the overall heat generated that naturally accounts for all mechanisms of heat generation including the heat of mixing. Subtracting out the heat generation due to other mechanisms results in an isolated expression for heat of mixing. This approach avoids the assumptions of small concentration gradients or pseudo-steady state (which are generally used in other models for heat of mixing) thereby making our method applicable to cells undergoing XFC.

Our study showed that the previously used method of estimating the heat of mixing using an expression based on the method of Taylor expansion is erroneous and inapplicable at XFC (Figure I.4.O.10). Additionally, our study showed that in a Li-ion cell with NMC cathodes and Li-metal anodes at XFC, the heat of mixing is a significant portion of the total heat generated and can contribute up to 23% of the total heat generated in a 6C discharge. This contribution is entirely neglected by the previous method.

a)

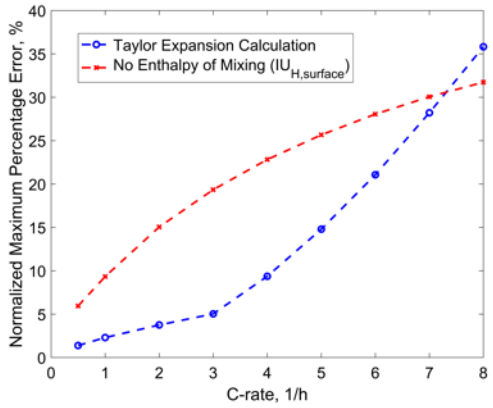

b)

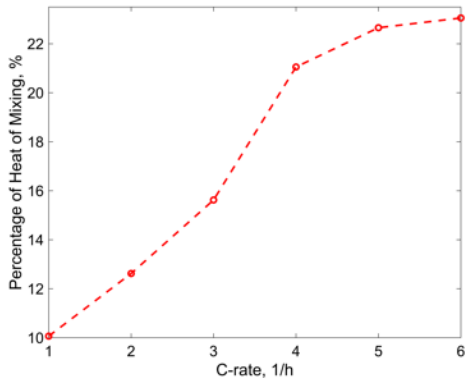

Figure I.4.O.10 a) Error associated with the method of Taylor expansion, and (b) the average contribution of the heat of mixing in the overall heat generated. As the charge/discharge rate increases, the Taylor expansion approach becomes increasingly inaccurate while the overall contribution and therefore the importance of the heat of mixing in the overall heat generated also increases.

In summary, we have developed a measurement scheme to simultaneously measure the evolution of heat flux, thermal transport properties, and temperature rise in cycling cells. Preliminary data indicates that the thermal resistance inside commercial batteries changes with cycling, ultimately becoming worse. Furthermore, the rate of degradation seems to be a strong function of charging rate. These results are consistent with our previous results showing that the thermal contact resistance between the separator and electrodes increases with cycling. These degraded thermal properties result in worse temperature gradients within operating batteries. More experiments are in progress to understand the impact of heat generation and thermal transport properties on the evolution of temperature rise.

We developed a method based on inverse heat transfer analysis for time-resolved calorimetry of large cells during fast charging. This method can be applicable in accurately quantifying the heat generation in our experiments as well as be generally applicable in the calorimetry and internal temperature prediction of high-capacity cells, accounting for their size and finite thermal resistance. Our method eliminates most of the error associated with standard calorimetry lumped capacitance methods when they are applied to cells that are large, have high thermal resistance, or are charged quickly.

We have also designed a method based on the frequency dependence of the thermal wave penetration depths to spatially resolve the different types of heat generation within a single cell during fast charging.

Finally, we have quantified the effect of heat of mixing in cells at XFC and have highlighted the importance of accurately modeling the heat of mixing at XFC. We have identified regimes where the standard Taylor-expansion model produces significant error and show that our analysis method eliminates most of this error.

Battery Diagnostic with RTDs under Extreme Fast Charging Conditions (Stanford)

Under this project, we are developing a set of resistive temperature detectors (RTDs) which potentially enables temporal/spatial resolved temperature monitoring in LIBs *in operando*. The challenge of this project is, how to build thin film RTDs that can be reliably performed in the nonaqueous electrolyte environment within a relative wide temperature range. As shown in Figure I.4.O.11, three different RTDs were fabricated/utilized for stability test in liquid electrolyte (1M $LiPF_6$, EC/DEC v:v=1:1). While Gen1 and Gen2 RTDs (Figure I.4.O.11a,b) showed drifting resistance during 20-60^{o}C temperature cycles, Gen 3 RTD demonstrated extremely stable resistance.

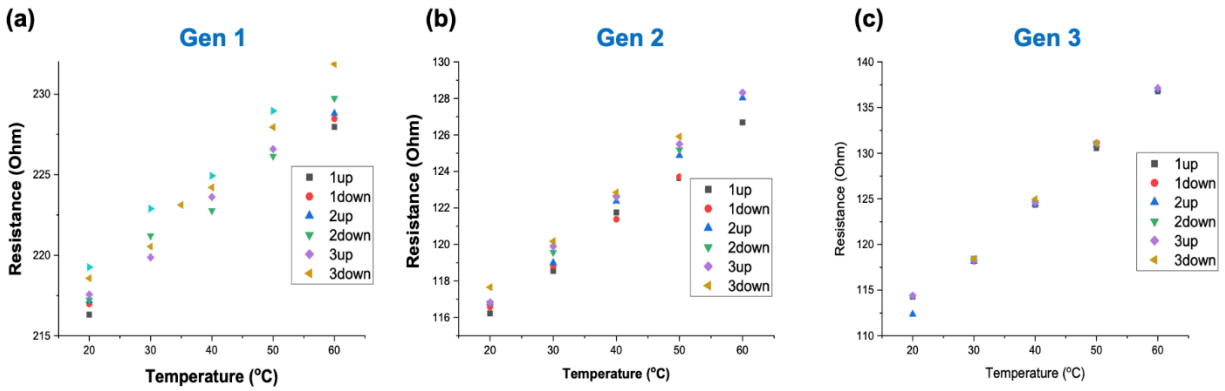

Figure I.4.O.11 RTD resistance measurement of three different RTDs with flooding 1M $LiPF_6$, EC/DEC (v:v=1:1) liquid electrolyte, at temperature cycling from 20 to 60°C.

Based on our previous success of demonstrating a stable RTD at cell environment (with nonaqueous liquid electrolyte), we build a pouch cell with RTD sensors both inside and outside the cell (Figure I.4.O.12a,b). The battery was then cycled at different charge/discharge rates, while both electrochemical performances (Figure I.4.O.12c, upper and middle panel) and RTD responses (Figure I.4.O.12c, lower panel) are recorded. We realized operando temperature measurements with RTD in real batteries. While limited temperature responses can be observed at 0.5C rate with rather flat current response, significant resistance change can already be observed at 2C rate (both black and red curve in Figure I.4.O.12c, lower panel). However, we did not observe significant temperature difference between the inside and outside the cell even at 2C rate, due to the limited capacity (200 mAh) and fast heat dissipation of the cell.

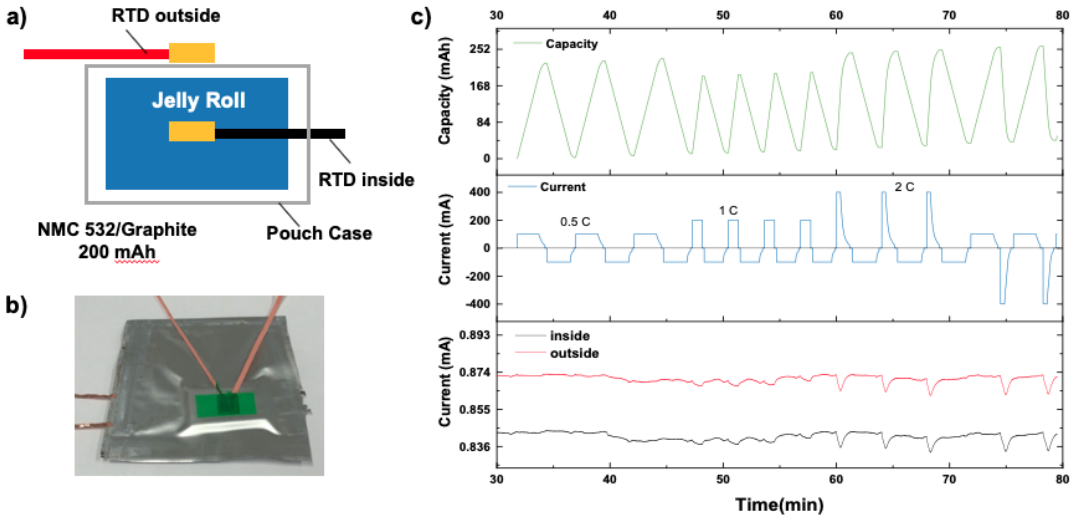

Figure I.4.O.12 Operando Temperature monitoring using RTD in pouch cells (a) schematic image; (b) photo image of the cell; (c) electrochemical performance of the cell vs. RTD responses charging at different rates.

Fast charging can lead to relatively large temperature heterogeneity in LIBs, while undesired plated Li are often times observed after prolonged cycles. Plating of metallic Li on graphite anodes is a critical reason for Li-ion battery capacity decay and short circuit. It is generally believed that Li plating is caused by the slow kinetics of graphite intercalation, but in our work, we demonstrate that thermodynamics also serves a crucial role. Surprisingly, we found that a nonuniform temperature distribution within the battery can make local plating of Li above 0 V vs. Li^0/Li^+ (room temperature) thermodynamically favorable. This phenomenon is

caused by temperature-dependent shifts of the equilibrium potential of Li^0/Li^+. (Figure I.4.O.13a,b) Supported by simulation results, we confirm the likelihood of this failure mechanism during commercial Li-ion battery operation, including both slow and fast charging conditions (Figure I.4.O.13c-f). This work furthers the understanding of nonuniform Li plating and will inspire future studies to prolong the cycling lifetime of Li-ion batteries at XFC.[1]

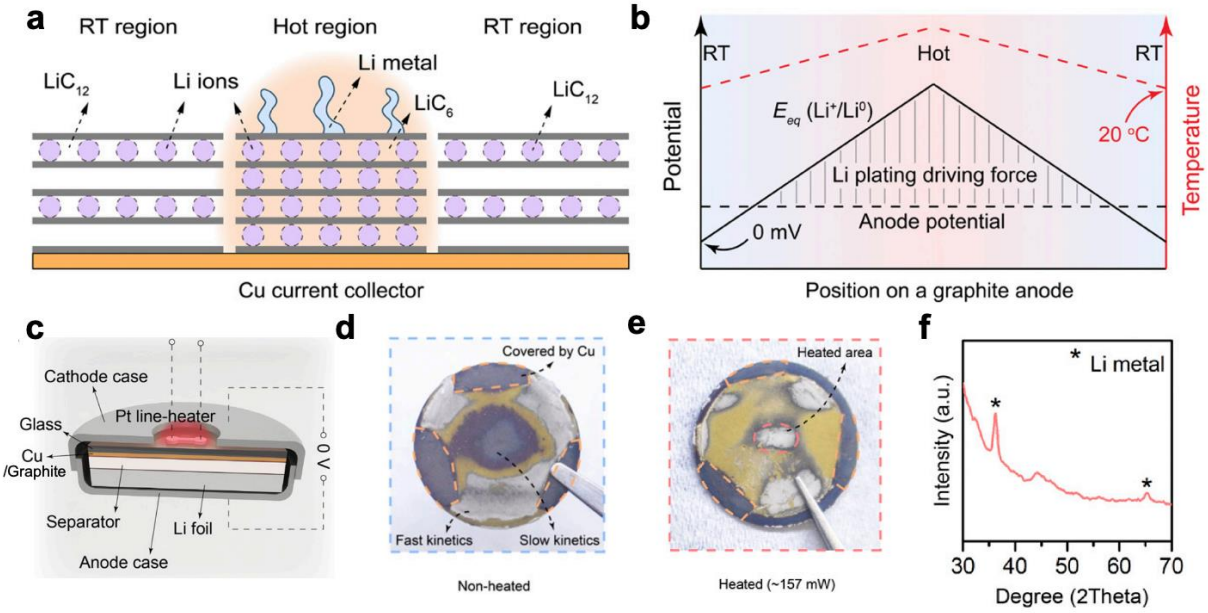

Figure I.4.O.13 (a) Schematic drawing of preferential local metallic Li plating at hot regions on a graphite anode with a nonuniform temperature distribution. (b) Schematic illustrating the mechanism for Li plating above 0V vs. Li^0/Li^+ (RT) on a graphite anode. (c) Schematic drawing that shows the configuration of the Li–graphite coin cell. (d-e) Metallic Li plating on graphite under fast charging conditions: (d) Digital photo of the graphite electrode after fast charging without local heating. Graphite particles at the center are not intercalated. (e) Digital photo of the graphite electrode after fast charging with local heating. Graphite particles are intercalated, and metallic Li is also plated at the center (f) XRD result of the silver-color material showing obvious metallic Li signal.

In summary, we investigated the temperature effect on Li plating in LIBs. Different from previous study on thermal gradient promoted Li plating through a kinetic perspective, we discover that a nonuniform temperature can cause metallic Li plating due to the temperature-dependent nature of the equilibrium potential. We demonstrate metallic Li plating on a graphite electrode above 0 V vs. Li^0/Li^+ (RT) utilizing a locally heated Li-graphite coin cell. We further demonstrate reliable *operando*, temporal/spatial temperature monitoring in pouch cells, which paves the way for monitoring and analysis 3D temperature distribution of pouch cells with practical capacity at fast charging conditions.

Operando Temperature Measurements in Pouch Cells (LBL)

The LBL group (Steve Harris and Eric McShane) performed operando XRD measurements on a modified pouch cell to measure the temperature change of the Cu and Al current collectors simultaneously during cycling via the change in d-spacing of the respective materials. The temperature change of the pouch surface was also measured via the change in d-spacing of a Mg alloy sheet placed adjacent to the pouch. The sample setup is shown in Figure I.4.O.14a. Unfortunately, the hole in the plastic holder (which was incorporated to eliminate background XRD signal from the plastic holders) likely caused electrode-separator contact issues within the cell, which were apparent from the XRD spectra obtained. Figure I.4.O.14b confirms this notion, as the LiC_6 and LiC_{12} peaks (which describe the relative ratio of LiC_6 to LiC_{12}) do not change in the expected manner during cycling, indicating that the graphite material in the hole region is underutilized due to poor contact within the pouch. This hole region also caused issues with the temperature measurement, as the current collectors likely moved slightly during cycling (due to, e.g., bubble formation or expansion/contraction of

electrode materials adhered to the current collectors), which made the measured d-spacing and thus the calculated temperature change noisy (as seen in Figure I.4.O.14c). Going forward, this study will be continued by Mike Toney's group, who will measure the d-spacing of the Cu current collector in an appropriately clamped cell during cycling. Continuing in the heat generation thrust, Eric will conduct gassing measurements for cells cycled at elevated temperature using differential electrochemical mass spectrometry (DEMS) during the next fiscal year.

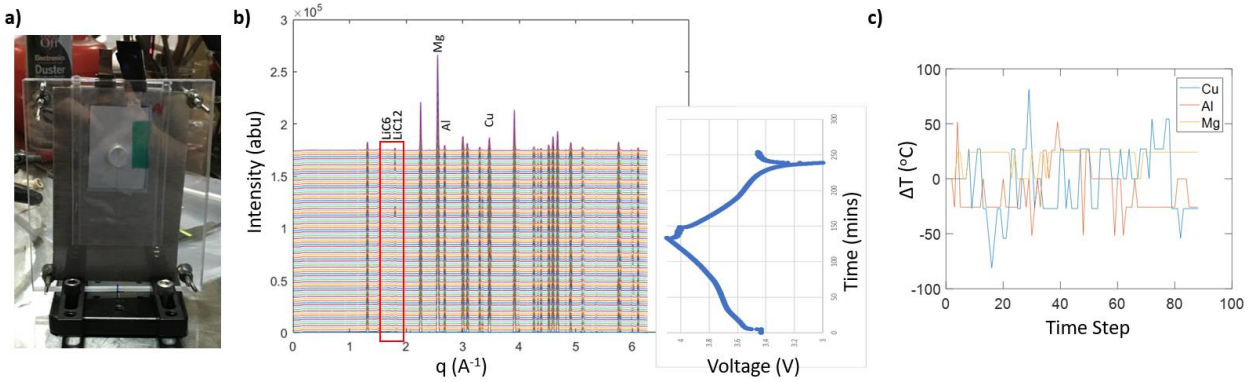

Figure I.4.O.14 a) Battery assembly with plastic block holder compressing clear pouch cell and AZ31 Mg alloy sheet, whose shift in d-spacing was used for pouch surface temperature measurement. b) Left: Stacked XRD spectra obtained during C/2 cycling. Right: Voltage profile for cell during C/2 cycling, rotated and scaled to match each spectrum with the corresponding time during cycling. c) Calculated temperature change based on d-spacing obtained from XRD for Cu, Al, and Mg as a function of time step. Acquisition time for a single spectrum was ~3 minutes, meaning each time step is ~3 minutes apart.

Conclusions

The heat generation workgroup has made significant progress towards understanding the crucial parameters that affect heat generation and how to measure temperature within a cell. During Q4FY20, we used the ANSYS/Fluent model to assess the temperature heterogeneities for different cell geometries and electrolytes. Furthermore, we successfully fabricated and tested the third generation RTD in a working 200 mAh cell. We also performed XRD experiments at ALS with a modified CAMP cell to assess the temperature distribution within the cell – the data from these experiments did not provide the desired temperature resolution in the cell. However, these initial experiments provided a roadmap for successful experiments in the future. Finally, we developed a measurement scheme to simultaneously measure the evolution of heat flux, thermal transport properties, and temperature rise in cycling cells with the 3ω sensor.

Publications

1. Divya Chalise et al 2020 J. Electrochem. Soc. 167 090560
2. Chalise, D.; Lu, W.; Srinivasan, V.; Prasher, R. S. In *Heat of Mixing in NMC 523 Cathode During Fast Charge/Discharge*; 020 ASME International Technical Conference and Exhibition on Packaging and Integration of Electronic and Photonic Microsystems: Anaheim, CA, 2020.

References

1. H. Wang, Y. Zhu, Y. Cui et al, "Underpotential lithium plating on graphite anodes caused by temperature heterogeneity", PNAS, 2020, http://doi.org/10.1073/pnas.2009221117

Acknowledgements

This project was funded by the U.S. Department of Energy, Vehicle Technologies Office. The technology development manager was Samm Gillard. The project overview was prepared by Venkat Srinivasan (ANL). Other contributing team members for Thrust 6 (Heat Generation Thrust) include Matt Keyser, Chuanbo Yang, Josh Major, Andrew Colclasure, Kae Fink, Kandler Smith (NREL); Ravi Prasher, Sean Lubner, Eric McShane, Steve Harris (LBNL); and Jiayu Wan, Wenxiao Huang, Yi Cui and Mike Toney (SLAC).

I.5 Beyond Batteries

I.5.A Behind-the-Meter Storage (NREL, INL, ORNL, SNL)

Anthony Burrell, Principal Investigator
National Renewable Energy Laboratory
15013 Denver West Parkway
Golden, CO, 80401
E-mail: anthony.burrell@nrel.gov

Samm Gillard, DOE Technology Development Manager
U.S. Department of Energy
E-mail: Samuel.Gillard@ee.doe.gov

Start Date: October 1, 2018 End Date: September 30, 2022
Project Funding: $2,400,000 DOE share: $2,400,000 Non-DOE share: $0

Project Introduction

This initiative, referred to as Behind-the-Meter Storage (BTMS), focuses on novel critical-materials-free battery technologies to facilitate the integration of electric vehicle (EV) charging, solar power-generation technologies, and energy-efficient buildings while minimizing both costs and grid impacts. For extreme fast-charging at levels of 350 kW or higher, novel approaches are required to avoid significant negative cost and resiliency impacts. However, it is reasonable to assume that BTMS solutions would be applicable to other intermittent renewable energy generation sources or short-duration, high-power-demand electric loads.

BTMS research is targeted at developing innovative energy-storage technology specifically optimized for stationary applications below 10 MWh that will minimize the need for significant grid upgrades. Additionally, avoiding excessive high-power draws will eliminate excess demand charges that would be incurred during 350-kW fast charging using current technologies. The key to achieving this is to leverage battery-storage solutions that can discharge at high power but be recharged at standard lower-power rates, acting as a power reservoir to bridge to the grid and other on-site energy-generation technologies such as solar photovoltaics (PV), thereby minimizing costs and grid impacts. To be successful, new and innovative integration treatments must be developed for seamless interaction between stationary storage, PV generation, building systems, and the electric grid.

Key components of BTMS address early-stage research into new energy-generation and building-integration concepts, critical-materials-free battery energy-storage chemistries, and energy-storage designs with a focus on new stationary energy-storage strategies that will balance performance and costs for expanded fast-charging networks while minimizing the need for grid improvements. The four main components include:

- BTMS Analysis
- BTMS Power Electronics
- BTMS Testing
- BTMS Materials Development.

This project write-up organizes its contents accordingly.

BTMS Analysis

The BTMS Analysis project is funded by the Building Technologies Office (BTO), Vehicle Technologies Office (VTO), and Solar Energy Technologies Office (SETO) within the U.S. Department of Energy (DOE)

EERE, whose mission is to create and sustain American leadership in the transition to a global clean energy economy. EV adoption is expected to grow significantly over the coming years, and could have a significant, and potentially negative, effect on grid infrastructure due to large and irregular demands. Additionally, the rapid penetration of solar PV generation installed on buildings is leading to new challenges for the electric grid. In response to these changes, utilities are evaluating multiple options for managing dynamic loads, including time-of-use pricing and demand charges. Buildings, as well as EV charging stations, can leverage energy storage, including battery and thermal energy storage (TES), coupled with on-site generation to manage energy costs as well as provide resiliency and reliability for EV charging and building energy loads. Although each of these technologies can make contributions to the U.S. economy, integrating them in ways that optimize cost and energy flows for varying energy demand and climate conditions across the country can lead to multiple benefits. BTMS research is targeted at developing innovative modeling approaches to optimize energy storage and PV system designs and energy flows for grid-interactive energy-efficient building and extreme EV fast-charging loads.

The key question in this project is the following: What are the optimal system designs and energy flows for thermal and electrochemical energy storage systems at sites with on-site PV generation and EV charging, and how do solutions vary with climate, building type, and utility rate structure?

BTMS Power Electronics

The power electronics effort for BTMS has been tasked with evaluating methods to reduce the balance-of-plant cost associated with electrical connection and power conversion components for a stationary battery system. The technology target for the entire BTMS system ranges from $295/kWh to $235/kWh, for a C/1 or C/4 charging station target. The balance of plant, including the power conversion, is roughly two-thirds of the system cost. From a power perspective, the balance of plant equates to between $0.195/W and $0.540/W between the two station designs (C/4 and C/1). In the FY 2019 analysis of current-state stationary energy storage systems considering at least a 1-MW system with a 13.8-kV connection, the balance-of-plant costs ranged from $0.40/W to $1.01/W. An investigation of the various power conversion topologies (AC-coupled, DC-coupled, and modular-based multiple DC bus) will be investigated to determine strategies for the entire site to optimize the design of the balance of plant.

BTMS Testing

Testing activities in the second year focused on completing extreme fast charging (XFC) demand-reduction testing protocols, which included validation testing on surrogate cells. Later, cells of several distinct cobalt-free chemistry types were put on test to cycle under those protocols. The couples put on test included lithium-ion manganese oxide (LMO)/LTO and lithium iron phosphate (LFP)/graphite lithium-ion cells, lead acid mono-block modules, and nickel zinc cells. In addition to the application specific testing developments, a design of experiment intended for machine-learning activities was completed and a large batch of cells was screened and placed on test. Life testing of commercial cells started in year one continued through year two for NMC/LTO cells and completed for LFP/graphite and NMC/graphite cells.

BTMS Materials Development

Battery technologies for BTMS applications require long cycle life and critical-material-free chemistry. $Li_4Ti_5O_{12}$ (LTO) anode and $LiMn_2O_4$ (LMO) cathode system, widely used as high-power chemistry [1], is a good candidate to meet such requirements. One major drawback of the LTO/LMO cells, however, is their low energy density. The energy density can be increased by using thicker electrodes—converting power chemistries to energy electrodes. As the electrodes get thicker, however, their rate capability decreases due to the high tortuosity and sluggish kinetics [2]. Such limitations can be overcome by increasing the operating temperature, which facilitates the lithium-ion diffusion within the electrode as well as their mobility in the electrolyte [3]. Thus, the temperature-dependent rate capability of LTO/LMO cells with varying electrode thickness was tested. This work is contribution to the Q3 (delayed to Q4) Milestone: Determine thickness vs. temperature limitations for non-Co electrodes.

Objectives

A cohesive multidisciplinary research effort is being undertaken to create a cost-effective, critical-materials-free solution to BTMS by employing a whole-systems approach. The focus of this initiative is to develop innovative battery energy-storage technologies with abundant materials applicable to EVs and high-power charging systems. Solutions in the 1–10-MWh range will eliminate potential grid impacts of high-power EV charging systems as well as lower installation costs and costs to the consumer.

Although many lessons learned from EV battery development may be applied to the BTMS program, the requirements for BTMS systems are unique—carrying their own calendar-life, cycle-life, and cost challenges. For example, EV energy-storage systems need to meet very rigorous energy-density and volume requirements to meet consumer transportation needs. Despite that, current stationary-storage systems use batteries designed for EVs due to high volumes that drive down costs. This creates another market demand for EV batteries, further straining the EV battery supply chain and critical-material demand.

By considering BTMS electrochemical solutions optimized for these applications with less focus on energy density in mass and volume, the potential for novel battery solutions is very appealing. Furthermore, the balance-of-plant (BOP) cost for a BTMS battery system—the cost of everything minus the battery cells—is thought to be upwards of 60% of the total energy-storage system cost. In contrast, the BOP costs of EVs make up roughly 30% of the total battery cost. Therefore, to realize desired cost targets, BTMS will also need to focus on reducing BOP cost through system optimization.

Design parameters are needed to optimize the BTMS system for performance, reliability, resilience, safety, and cost.

The main objectives of this project are to:

- Produce behind-the-meter battery solutions that can be deployed at scale and meet the functional requirement of high-power EV charging
- Use a total-systems approach for battery storage to develop and identify the specific functional requirements for BTMS battery solutions that will provide novel battery systems in the 1–10-MWh range at $100/kWh installed cost, and that are able to cycle twice per day, discharging for at least 4 hours, with a lifetime of roughly 20 years or at least 8,000 cycles.

BTMS Analysis

The primary objective function for most analyses in this project will be levelized cost of charging (LCOC). This metric, measured in $/kWh, is the minimum price that EV station owners would need to charge users in order to “break even,” or to pay back all capital and operating expenses over the lifetime of the system. Financial metrics including LCOC are crucial for determining how various details of the BTMS system affect the whole and assessing the economic value and attractiveness of BTMS. A high-level schematic depicting the various behind-the-meter systems, including stationary battery, solar PV, electric vehicle supply equipment (EVSE), and TES, is shown in Figure I.5.A.1.

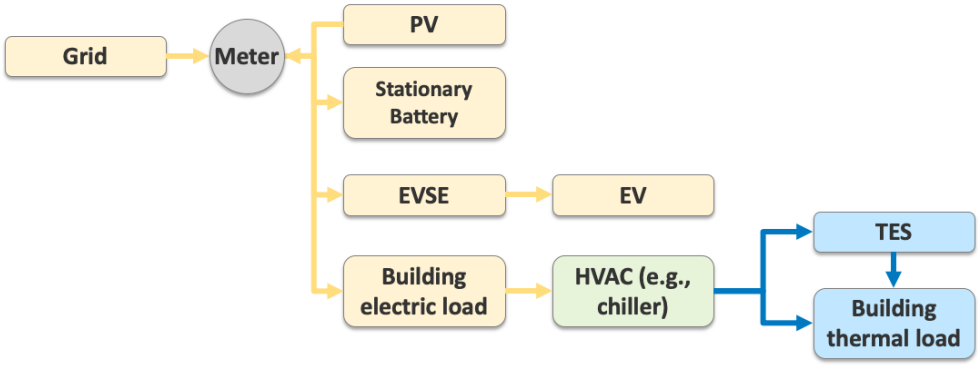

Figure I.5.A.1 Schematic depicting the default combination of technologies for BTMS analysis (HVAC: heating, ventilating, and air conditioning)

BTMS Power Electronics

The task objectives for investigation of the primary power conversion optimization are as follows:

- Explore different configurations for integrating ~2-MW DC fast charging (DCFC) loads, ~2-MW PV generation, and ~2-MW energy storage systems (ESS) with the power grid:
  - Conventional common AC bus configuration
  - New common DC bus configuration
  - Modular-based multiple DC bus
- Develop efficiency/load models for all power electronic conversion systems in each configuration:
  - DC fast chargers
  - PV converter
  - Grid energy storage system bidirectional converter
  - Grid AC/DC converter
- Work with the cost analysis team at NREL to integrate the efficiency/load models with EnStore platform for system cost analysis and optimization.

Approach

A cohesive multidisciplinary research effort—involving the National Renewable Energy Laboratory (NREL), Idaho National Laboratory (INL), Sandia National Laboratories (SNL), and Argonne National Laboratory (ANL)—will create a cost-effective, critical-materials-free solution to BTMS by employing a whole-systems approach. The focus of this initiative is to develop innovative battery energy-storage technologies with abundant materials applicable to PV energy generation, building energy-storage systems, EVs, and high-power charging systems. Solutions in the 1–10-MWh range will enable optimal integration of PV generation from a DC-DC connection, increase energy efficiency of buildings, eliminate potential grid impacts of high-power EV charging systems, and lower installation costs and costs to the consumer. (See Figure I.5.A.2.)

Many lessons learned from EV battery development may be applied to the BTMS program, but the requirements for BTMS systems are unique—carrying their own calendar-life, cycle-life, and cost challenges. For example, EV energy-storage systems need to meet very rigorous energy-density and volume requirements to meet consumer transportation needs. Despite that, current stationary-storage systems use batteries designed

for EVs due to high volumes that drive down the costs. This creates another market demand for EV batteries, further straining the EV battery supply chain and critical-material demand.

By considering BTMS electrochemical solutions optimized for these applications with less focus on energy density in mass and volume, the potential for novel battery solutions is very appealing. Furthermore, the BOP cost for a BTMS battery system, or the cost of everything minus the battery cells, is thought to be upwards of 60% of the total energy-storage system cost. In contrast, the BOP costs for EVs make up roughly 30% of the total battery cost. Therefore, BTMS will also need to focus on reducing BOP cost through system optimization to realize desired cost targets.

Integration of battery storage with PV generation, energy-efficient buildings, charging stations, and the electric grid will enable new and innovative control strategies. Design parameters are needed to optimize the BTMS system for performance, reliability, resilience, safety, and cost.

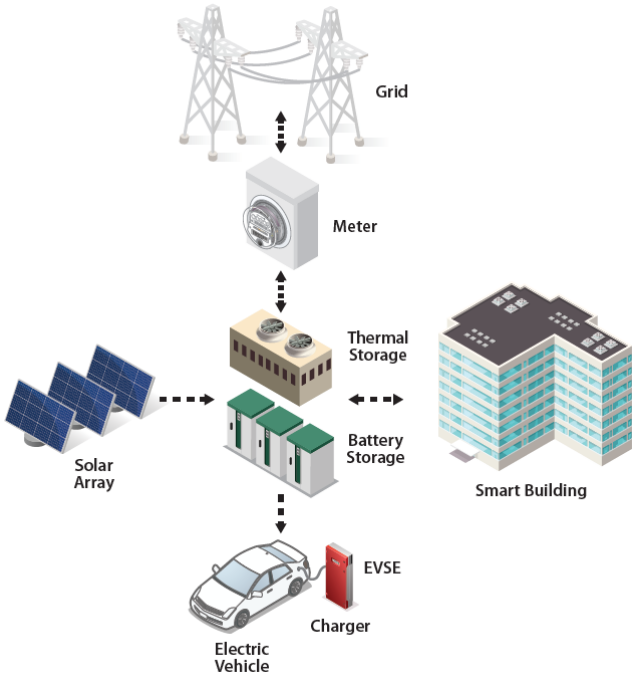

Figure I.5.A.2 Overview of BTMS relevance (EVSE: electric vehicle supply equipment)

Fiscal Year (FY) 2020 Milestones

Q1: Presentation to Technical Review committee and provided feedback from the meeting to the Office of Energy Efficiency and Renewable Energy (EERE). (100% complete)

Q2: Establish initial protocols and procedures for BTMS electrochemical energy cell evaluation that will enable feedback to the cost analysis task and the machine-learning physic-based model development tasks. (100% complete)

Q3: Go/No-Go on graphite anodes related to the BTMS EES cost and lifetime targets. Go will be determined by experimental evidence that graphite-based cells have demonstrated 1,000 cycles and the lifetime model predict can achieve at least 5,000 cycles (50% of target) and have projected cost targets of $250/KWh usable energy (2.5x target). (100% complete)

Q3: Determine thickness vs. temperature limitations for non-cobalt electrodes. (100% complete)

Q4: Thick electrode cells under test using BTMS protocols. (100% complete)

BTMS Analysis

The BTMS Analysis team has developed a multitool simulation platform called EnStore (Energy Storage) to capture performance characteristics and interactions between disparate technologies with high fidelity. In researching existing tools used in this space, the team concluded that no one existing tool could complete the multisystem, detailed analysis required for this project, but rather a combination of several existing tools would be necessary. This project utilizes the following tools to allow for detailed simulation of building energy loads, battery performance and lifetime models, and novel thermal energy storage technologies:

- REopt™ energy system optimization tool [1], [2]
- System Advisor Model (SAM) [3], [4]
- EnergyPlus™ building simulation engine [5]
- OpenStudio® suite of supporting building simulation applications [6]
- Utility Rate Database (URDB) [7]
- DOE prototype building energy models [8].

This report details many aspects of the EnStore platform, including model process flows, model inputs and outputs, detailed building and EV load profile inputs, the various financial metrics reported, and preliminary EnStore time series load profile and aggregated financial analysis results. Work in FY 2020 focused on building a functional model, assembling relevant data, and constructing methodologies for determining optimal configurations of BTMS components.

IMPORTANT NOTE: It is critical that preliminary results shown in this report not be used in developing conclusions related to the viability or application of behind-the-meter storage systems.

Results

BTMS Analysis

EnStore Process Flows

For any given application of EnStore, the simulation process can be divided into five major stages as shown in Figure I.5.A.3. In the “Pre-Process” stage, inputs required to initiate an EnStore simulation are generated. The next three stages, “Seed,” “Explore,” and “Report,” include processes managed and executed by EnStore code. In the “Post-Process” stage, output files created by EnStore are used to answer research questions for the associated application.

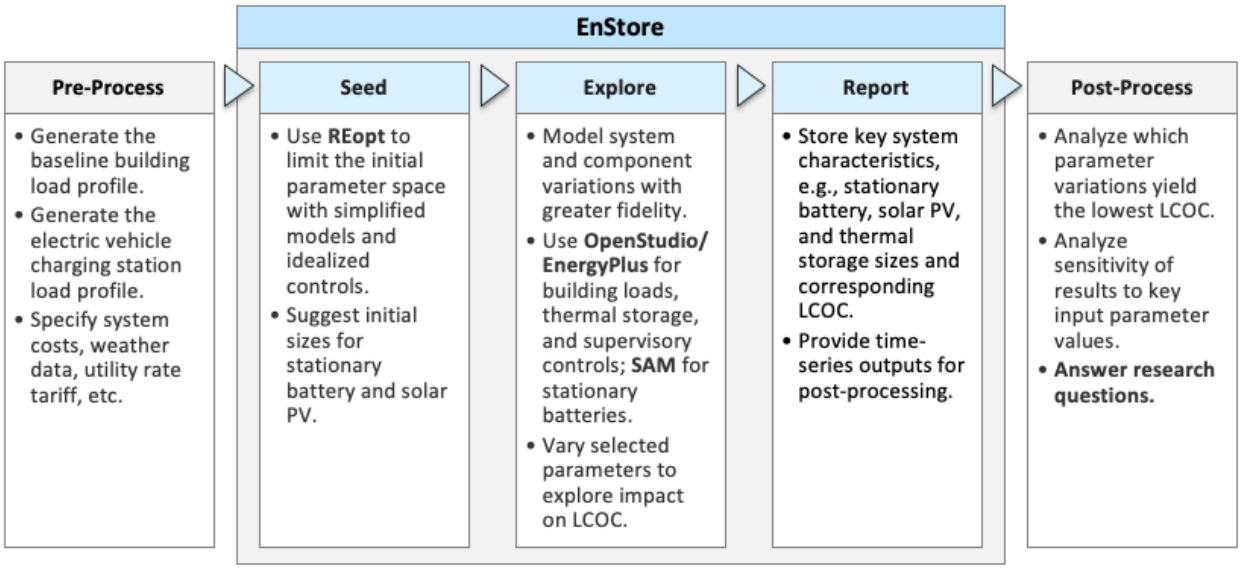

Figure I.5.A.3 Major stages of the multitool workflow

Tools utilized in the Pre-Process stage to generate inputs required for EnStore include:

- OpenStudio and EnergyPlus to generate a "seed" building model, or starter model with no solar PV, battery, TES, or EVSE, which will be modified later in the Explore stage. This may also be used to generate a load profile for REopt when combined with the EVSE load profile (alternatively, for some applications, the load profile for REopt may be generated using meter data or a combination of meter and model data).

- EV-EnSite to generate an EVSE load profile.

These and other inputs are combined into a set of standardized input files for each EnStore simulation.

In the Seed stage, EnStore uses REopt to suggest preliminary sizes for the stationary battery system and PV system that maximize the net present value (NPV) of the system. The REopt-generated system sizes are considered preliminary because REopt uses a mixed-integer linear programming (MILP) approach to calculate an absolute minimum value for cost optimization problems; this MILP approach requires simplified, linearized models and omits physical details that can affect the accuracy of electrical and thermal load profiles and storage system performance. However, these simplifications can be useful at this stage for enabling relatively rapid calculation of preliminary system sizes, which can then be permutated and explored with more detailed models in the next stage of simulation.

The Explore stage uses higher-fidelity, physics-based models of load, generation, and storage systems to increase the accuracy of electrical power and heat-transfer calculations. At this stage, OpenStudio, EnergyPlus, and SAM are used to examine how the inclusion of more detailed component performance characteristics and system interactions can affect design optimization results. EnergyPlus enables the team to capture a variety of critical electrical and thermal system interactions, such as the interactions between TES systems, space conditioning systems, internal gains (e.g., occupants, lighting, plug loads, process loads), internal mass objects, construction elements, exterior conditions, operational schedules, and control systems. OpenStudio makes it easier to modify EnergyPlus models in a replicable manner. SAM enables the team to compare stationary battery designs with different component-level characteristics such as chemistry, voltage vs. depth-of-discharge curves, temperature dependencies, and lifetime degradation. It also allows for exploration and permutation of system-level inputs such as battery replacement conditions and dispatch algorithms. To enable co-simulation and supervisory control of key component models, EnergyPlus calls the SAM battery model at

each simulation time step via the EnergyPlus Python Plugin System and a SAM Python module called PySAM [9]. For each EnergyPlus simulation in the Explore stage, permutations of the solar PV size, TES size, and stationary battery size occur. If there are 10 permutations of solar, TES, and stationary battery sizes each, decided upfront by the user, then there will be 10 × 10 × 10, or 1,000 total EnergyPlus simulations for a single REopt run.

For each of the hypothetical 1,000 EnergyPlus runs mentioned, EnStore executes the Report stage, saving select time series data from EnergyPlus runs and computing financial metrics, including net present cost (NPC), LCOC, and levelized cost of electricity (LCOE), which are further described later in this report. The run with the lowest NPC computed in financial calculations will be that which has the "optimal configuration." Because the energy usage of the EV charging station and the seed building is fixed beforehand, the configuration with the lowest NPC will match that with the lowest LCOC and LCOE. In the Post-Process stage, the run with the minimum associated NPC, LCOC, and LCOE for a given utility rate, location, building type, unit costs, etc., will be stored and its respective BTMS size configuration will be reported. A more detailed process flow diagram for pre-processing, EnStore, and post-processing is shown in Figure I.5.A.4.

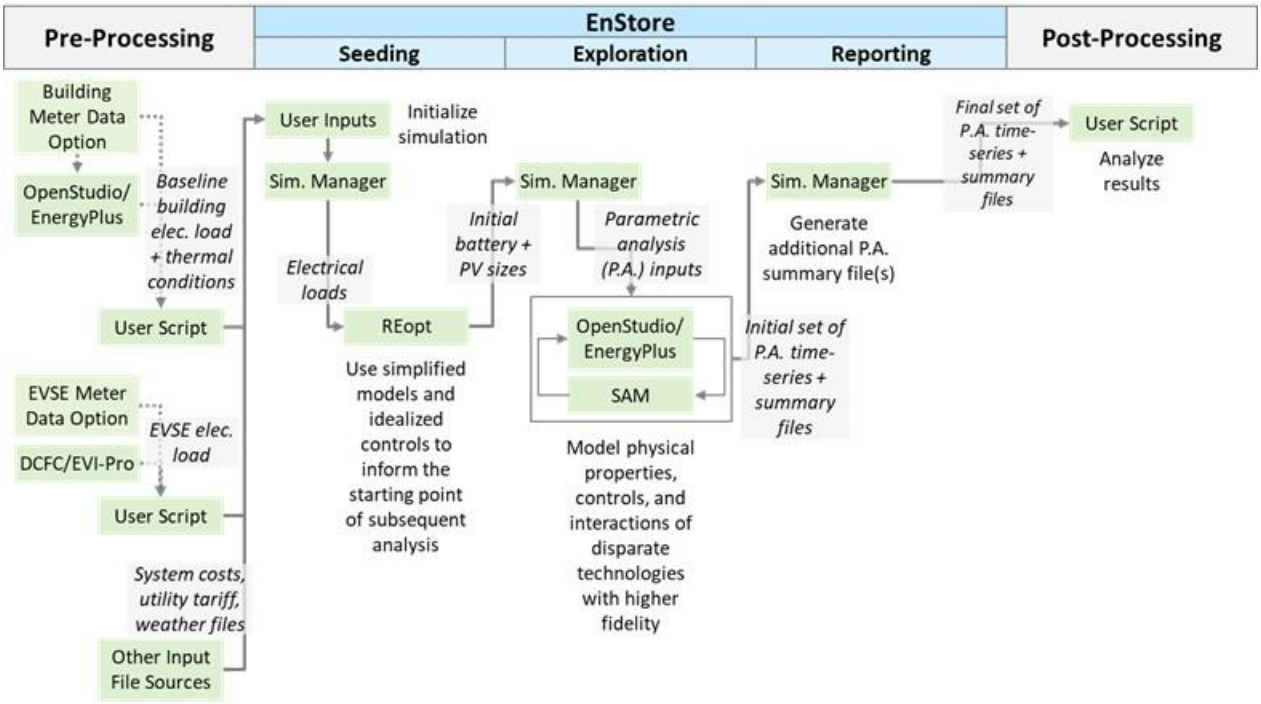

Figure I.5.A.4 Model architecture details including data exchanged between tools and stages

EnStore Inputs and Outputs

Certain categories of data are necessary to run EnStore. These include component system costs (e.g., battery installed cost per kW), utility rate tariff information, seed building models and load time-series profiles, EVSE load time-series profiles, and weather information (e.g., an .epw file). These inputs collectively include data that are either required for specific tools used within EnStore (e.g., REopt, SAM, and OpenStudio/EnergyPlus) or for higher-level EnStore operations. EnStore will pass specific inputs to constituent tools as required. The inputs and outputs of the EnStore simulation platform can be seen in Table I.5.A.1 and Table I.5.A.2.

Table I.5.A.1 Main Input Categories for EnStore

Input Category	Description
System Costs	Solar PV installed cost per kW, solar PV operations and maintenance (O&M) cost per kW, battery installed cost per kW, battery installed cost per kWh, TES cost, EVSE capital and O&M costs, interconnection cost
Electric Utility Rate Tariffs	URDB label or custom rate tariff information
Net Metering Assumptions	Presence/absence of net metering; net metering rules if applicable
Building Loads	Seed building model and load profile generated by OpenStudio in pre-processing for select building types, including big box retail grocery store, commerical office building, fleet vehicle depot and operations facility, multifamily residential, and stand-alone EV charging station
EVSE Loads	Generated using EV-EnSite with various demand scenarios
Weather Data	Typical meteorological year (TMY) (National Solar Radiation Database) or actual meterological year (AMY) data, saved in standard EnergyPlus format (.epw file)
Financial Information	Discount rate, tax incentives, etc.
Component-Level Details	For stationary battery: battery chemistry, configuration, performance specifications, and control parameters, including max. and min. allowable state of charge (SOC); For TES: TES type, configuration, and performance specifications; For solar PV: PV type, configuration, and performance specifications
Size Permutation Details	How many times and to what degree solar PV, battery, and TES sizes are varied in EnergyPlus/SAM co-simulations
Dispatch Control Logic	Supervisory dispatch control logic for dispatching stationary battery and TES
Power Electronics and BOP Information	For example, AC-coupled system vs. DC-coupled system
Ownership Model	Whether system owner has purchased all technology assets (solar PV, stationary battery, TES, EVSE) or a subset of these
Stationary Battery Conditioning	Cooling/heating system assumptions, whether battery is placed inside or outside the building
Analysis Period	For example, 1 year vs. 20 years.

Table I.5.A.2 Main Output Categories for EnStore

Output Category	Description
Financial Metrics	NPC, LCOC, and LCOE
Technology System Sizes	Solar PV size (kW), stationary battery size (kW and kWh), TES size (kWh)
Time-Series Data	Net loads from system to grid and grid to system; solar PV production, stationary battery charge/discharge rates; power from solar PV to grid, solar PV to EVSE, stationary battery to EVSE, grid to building, grid to EVSE, etc.; other system and subsystem loads and conditions.

Inputs and Outputs for Other Tools in the BTMS Analysis Workflow

1. Generating Electric Vehicle Load Profiles

The team is using the EV-EnSite tool to generate EVSE load profiles. This tool, developed by NREL and the University of Alabama [10], uses an agent-based modeling approach in which the vehicles and station are defined by a set of representative properties. For a vehicle, these properties include battery capacity, arrival time, initial SOC, energy demand, and power acceptance curve. Monte Carlo simulations determine when

vehicles arrive at the corresponding stations, wait in the queue if there is not any available port to plug into, plug in if a port is available, charge according to their power acceptance curves, and depart the port after their energy demand needs are met [10], [11]. Inputs and outputs for EV-EnSite are shown in Table I.5.A.3 and Table I.5.A.4.

Table I.5.A.3 Main Input Categories for EV-EnSite

Input Category	Description
Probability Distribution Functions	Probability distribution functions for: • Arrival time (when vehicles arrive at the station) • Initial SOC (the SOC of vehicles when they arrive at the station) • Energy demand (energy taken from the grid during each session, which is tied to initial SOC: if a vehicle arrives with a low SOC, there is a greater chance it will demand more energy)
Vehicle Battery Sizes	Battery sizes and ratio of battery sizes of vehicles charging at station (kWh)
Station Design Information	Station port capacity (kW) and number of ports at the station
Station Utilization Information	Number of events per station per day
Battery Acceptance Curve	Battery chemistry needed to generate battery acceptance curve.

Table I.5.A.4 Main Output Category for EV-EnSite

Output Category	Description
EVSE Load Profile	Minute kW time-series load profile for single EV station for 28 days, post-processed for a full year.

Post-processed results from both EVI-Pro and DirectXFC simulations can be used to produce the necessary probability distribution functions (PDFs) and other inputs needed for EV-EnSite. EVI-Pro was developed by NREL in partnership with the California Energy Commission and utilizes EV market and real-world travel data to estimate future requirements for home, workplace, and public charging infrastructure [12]. The DirectXFC project, funded by VTO Grid and Infrastructure, focuses on incentivizing plug-in electric vehicle (EV) owners to charge in locations beneficial to themselves, renewables, and utilities.

Results were first generated using EVI-Pro, but DirectXFC results are now priority. To properly post-process DirectXFC results for use in the EV-EnSite tool, Minneapolis, Minnesota, travel data were generated and the Zone Entity Probabilities (ZEP) algorithm was used to take data from real-life disparate trips and chain them into weeklong tours. In the case of DirectXFC, this generated 24 million trips and 7 million tours. The goal of the ZEP algorithm was to produce tours and preserve the transitive and spatial properties of the original data set. This large database of trips was used to create various PDFs for the EV-EnSite tool, characterizing and discretizing different locations by building type and size, such as medium office building or small apartment complex. The various scenarios and vehicle types from the DirectXFC project that correlate with the BTMS analysis project can be seen in Table I.5.A.5 and Table I.5.A.6.

Table I.5.A.5 DirectXFC Scenarios

Scenario	Level	Year	EV Population Size
1	Medium	2025	65,195
2	High	2025	120,360
3	Medium	2030	135,405
4	High	2030	330,989
5	Medium	2035	238,212
6	High	2035	654,455
7	Medium	2040	368,601
8	High	2040	975,414
9	Medium	2045	511,528
10	High	2045	1,228,670

Fleetwide parameters from research regarding the battery electric vehicle (BEV) to PHEV ratio, BEV 200+ to PHEV ratio, sedan EV share, and others were used to assign to vehicle models that match the expected vehicle types fleet for 2025 to 2045, shown in Table I.5.A.6. Vehicle fleet composition will naturally evolve over time (Gen 3 vehicles come into the market in 2035). Changes in types of vehicles in the fleet will affect EV station load profiles, especially in extreme fast-charging scenarios.

Table I.5.A.6 DirectXFC Vehicle Fleet Composition

Car Type	Model Name	EV Range (miles)	Usable Battery Capacity	Rated Battery Capacity	Fast Charging Power (kW)
Sports Car (Gen 2)	XFC250_400kW	250	87.5	92.1	400
Sports Car (Gen 1)	XFC250_300kW	250	87.5	92.1	300
XFC 300 – Truck (Gen 3)	XFC300_575kW	300	142.5	149.6	575
XFC 300 – Car (Gen 3)	XFC300_400kW	300	97.5	102.4	400
XFC 250 – Truck (Gen 2)	XFC250_350kW	250	118.75	124.7	350
XFC 300 – Car (Gen 2)	XFC300_300kW	300	97.5	102.4	300
XFC 200 – Truck (Gen 1)	XFC200_150kW	200	95	100	150
XFC 275 – Car (Gen 1)	XFC275_150kW	275	82.5	86.8	150
BEV 250 – Car	BEV250_75kW	250	75	78.9	75
XFC 150 – Car (Gen 2)	XFC150_150kW	150	45	47.4	150
BEV 150 Car	BEV150_50kW	150	45	47.4	50
PHEV 50 – Truck	PHEV50_SUV	50	23.75	25	None
PHEV 50 – Car	PHEV50	50	15.5	19.4	None
PHEV 20 – Car	PHEV20	20	5	6.3	None

PDFs for the arrival time, initial SOC, and energy demand for the various building types included in this analysis (EV fast charge station, big box retail grocery store, office, multifamily residential building, etc.) generated from post-processed DirectXFC results are used as inputs to the EV-EnSite model to generate yearlong EV load profiles. These profiles help model the effects various EV loads have on BTMS systems.

2. Inputs and Outputs for REopt

In the Seed stage of the EnStore workflow, the team will use REopt. Inputs and outputs required for using REopt in the EnStore workflow are summarized in Table I.5.A.7 and Table I.5.A.8.

Table I.5.A.7 Main Input Categories for REopt

Input Category	Description
Location	Latitude and longitude (REopt uses these to determine solar generation)
Electric Utility Rate Tariff Information	URDB label or custom rate tariff information
Cost Information	Solar PV installed cost per kW and O&M cost per kW; stationary battery installed cost per kW and installed cost per kWh; EVSE capital and O&M costs; interconnection cost
Detailed Component Information	Solar PV degradation percentage and existing kW; stationary battery replacement year, internal efficiency percentage, inverter efficiency percentage, inverter replacement year, max. kW, min. kW, initial SOC percentage, and min. SOC percentage
Load Profile	Aggregated building + EVSE load profile
Default Values	See REopt API documentation [18] for details.

Table I.5.A.8 Main Output Category for REopt

Output Category	Description
Preliminary system sizes	Solar PV size (kW), stationary battery size (kW and kWh).

3. Inputs and Outputs for EnergyPlus and OpenStudio

EnergyPlus is a whole-building energy simulation engine, and OpenStudio is a suite of complementary tools that can expand EnergyPlus capabilities. These tools will be used in both the Pre-Process stage and the Explore stage. Inputs and outputs required for using EnergyPlus and OpenStudio in the EnStore workflow are summarized in Table I.5.A.9 and Table I.5.A.10.

Table I.5.A.9 Main Input Categories for EnergyPlus and OpenStudio

Input Category	Description
Seed Building Model	Seed building model (.idf or .osm file) with no solar PV, stationary battery, or TES. A different seed building model will be created for each of the building types included in this project (big box retail grocery store, commercial office building, fleet vehicle depot and operations facility, multifamily residential, and EV charging station)
Weather Data	Standard EnergyPlus format (.epw file)
Measures	In this context, "measures" are scripts for modifying building models in a replicable manner. EnStore inputs will include measures to add solar PV, stationary battery, and TES systems of various sizes.
Content for EnergyPlus Python Plugin System	Depending on the application, examples may include: supervisory control logic for dispatching multiple energy storage systems; custom component models for novel TES technologies that differ from native EnergyPlus TES options; code for generating custom output variables.
Default Values	See the EnergyPlus Input Output Reference[a] document for details.

[a] https://energyplus.net/sites/all/modules/custom/nrel_custom/pdfs/pdfs_v9.2.0/InputOutputReference.pdf

Table I.5.A.10 Main Output Category for EnergyPlus and OpenStudio

Output Category	Description

Time-Series Data	Various time-series data will be used for post-processing, including the following:
	- Electrical power from:
	  o Full system to grid
	  o Grid to full system
	  o Grid to stationary battery
	  o Grid to EV charging station
	  o Grid to building
	  o Solar PV to grid (if applicable)
	  o Solar PV to building
	  o Solar PV to EV charging station
	  o Solar PV to battery
	  o Stationary battery to building
	  o Stationary battery to EV charging station
	  o Stationary battery to grid (if applicable)
	- Electrical input to TES systems
	- Thermal input to TES systems
	- Thermal output from TES systems
	- System losses
	- Other system and subystem loads and conditions.

4. Inputs and Outputs for the SAM StandAloneBattery Module

The SAM StandAloneBattery module is a detailed battery storage model that has detailed lifetime and degradation parameters, developed from work by Dey [13]. The SAM battery model is instantiated within EnergyPlus to model battery capacity, output, losses, and life more accurately than would be possible with

default EnergyPlus battery models. We are collaborating with the various battery teams within BTMS to improve the battery model inputs for testing different chemistries in this analysis.

Table I.5.A.11 Main Input Categories for SAM Battery Module

Input Category	Description
Stationary Battery Characteristics	- Battery size (kW and kWh) - Battery chemistry - Battery voltage curve - Battery thermal parameters - Battery control parameters (e.g., max./min. allowable SOC) - Battery replacement assumptions (e.g., replace when capacity drops to 80% of original capacity)
Default Values	See PySAM Battery documentation[a] for details.

[a] https://nrel-pysam.readthedocs.io/en/latest/modules/StandAloneBattery.html

Table I.5.A.12 Main Output Category for SAM Battery Module

Output Category	Description
Time-Series Data	Various time-series data will be used for post-processing, including: - Battery SOC - Battery kW charging/discharging rates - Battery temperature - Battery capacity fade.

5. Inputs and Outputs for the SAM UtilityRate5 Module

UtilityRate5 PySAM module is a retail electricity bill calculator that uses the URDB and can apply net metering rules to determine monthly and annual electricity bills. It receives necessary "gen" (generation) and "load" input vectors from EnergyPlus time-series outputs. The load vector is equivalent to the total load behind the meter and is the net electricity bought from the grid ("grid to system"); in EnergyPlus, this is denoted as "ElectricityPurchased:Facility [J](TimeStep)." The gen vector is equivalent to the net electricity sold to the grid ("system to grid"); in EnergyPlus, this is denoted as "ElectricitySurplusSold:Facility [J] (TimeStep)." Net loads and the utility rate information are sufficient to compute the annual electricity bill, which is one of the inputs to the CashLoan module.

Table I.5.A.13 Main Input Categories for SAM UtilityRate5 Module

Input Category	Description
Time-Series Data	- Electricity received from the grid - Exported surplus solar generation (for net metering)
Net Metering Assumptions	Presence/absence of net metering; net metering rules if applicable
Default Values	See PySAM Utilityrate5 documentation[a] for details.

[a] https://nrel-pysam.readthedocs.io/en/latest/modules/Utilityrate5.html

Table I.5.A.14 Main Output Category for SAM UtilityRate5 Module

Output Category	Description
Electricity Bill	Monthly electricity bill.

6. *Inputs and Outputs for the SAM CashLoan Module*

The CashLoan PySAM module is a financial model for residential and commercial behind-the-meter projects. Both the CashLoan module and the NumPy financial calculator [14], a calculator found in the NumPy mathematical library for the Python programming language[8] are used to compute EnStore financial metrics. These tools take in all installed costs, capital costs, and annual O&M costs, including the annual electricity bill, and use this information alongside information such as the discount rate, federal and state tax rate, and inflation rate to compute NPC. NPC is used in calculating both LCOC and LCOE. Financial metrics are discussed in more detail later in this report.

Table I.5.A.15 Main Input Categories for SAM CashLoan Module

Input Category	Description
Monthly Electricity Bill	From UtilityRate5 Module
Costs	Aggregated capital costs, aggregated additional O&M costs
Financial Information	Discount rate
Default Values	See PySAM Cashloan documentation[a] for details.

Table I.5.A.16 Main Output Category for SAM CashLoan Module

Output Category	Description
NPC	Will be used to compute LCOC and LCOE.

Preliminary Building and Electric Vehicle Input Load Profiles

As previously mentioned, building and EVSE profiles are important inputs for EnStore. Preliminary EVSE and building load profiles are shown for the following three scenarios:

- Public DC fast chargers at a big box retail grocery store
- Level 2 chargers at a medium-size commercial office building
- Level 2 chargers at a low-rise multifamily residential apartment building.

We first detail the methods used to create both the EV and building profiles for each of these scenarios, and then present the load profiles of the retail big box retail grocery store, medium-size commercial office building, and low-rise multifamily residential apartment building, detailing the following:

- EV station loads
- Building loads
- Combined loads (combination of building and EV station loads).

Note that the load profiles demonstrated are seed building and EVSE profiles, which do not yet include the effects of solar PV, battery, or TES. Seed building and EVSE profiles are necessary for each of the building types scoped in the Annual Operating Plan: big box retail grocery store, three sizes (small, medium, and large) of commercial office buildings, fleet vehicle depot and operations facility, low-rise multifamily residential, and an EV charging station.

[8] https://github.com/numpy/numpy-financial/blob/master/numpy_financial/_financial.py

Methodology for Load Profile Generation

1. EV Loads

EV load profiles for the BTMS analysis project are generated exogenously and altered to assess how EV adoption as well as changes in station design and station utilization will affect usage and sizing of BTMS systems. The EVSE profiles in this report were generated using EVI-Pro and EV-EnSite, but current EVSE profiles are generated using post-processed DirectXFC results and EV-EnSite.

2. Building Loads

For each EnStore run, a seed building model with no solar PV, stationary battery, or TES is simulated. This occurs for two reasons: to generate the necessary input for REopt and to have a base case comparative benchmark to ensure BTMS would be a worthwhile investment. A different seed building model will be created for each of building type analyzed in this project (big box retail grocery store, commercial office building, fleet vehicle depot and operations facility, multifamily residential, and an EV charging station) for each location of interest. In EnergyPlus/OpenStudio, measures will be applied to these seed models to add solar PV, stationary battery, and TES of various sizes to assess what is optimal from a financial perspective. The building load profiles seen in this report were generated from running EnergyPlus models in Tucson, Arizona, which has both high air-conditioning demands in the summer and high solar energy potential.

Big Box Retail Grocery Store: EV and Building Loads

One BTMS case is a big box retail grocery store (e.g., Walmart Supercenter, SuperTarget, Kroger Marketplace) with public EV fast-charging stations delivering 350 kW of power per plug. It is assumed that, at least in the first stage of this analysis, these EV fast-charging stations will be used by grocery store customers and not by heavy-duty delivery trucks.

1. EV Loads

Because the number of electric vehicle ports at a big box retail grocery store location will likely increase over time as EV demand increases, it was initially assumed that the number of ports in 2025 will be two. In 2035, however, there may be four, and in 2045 there may be six. These particular station design assumptions were made because current EVGo fast-charging stations often have two ports, and a typical current gas station at a big box retail grocery store has 20 ports. However, even if EVs did penetrate a significant portion of the market, 20 ports may be unreasonable because EV owners can refuel at home or work, whereas all internal combustion engine vehicles must refuel at gas stations.

Because the frequency of events, or number of events per day per plug, has high variation among sites, the following three cases will be analyzed:

- A high utilization case (16 events per day)
- An average utilization case (8 events per day)
- A low utilization case (2 events per day).

Based on initial EVGo data analysis there is no great variation in frequency of events from weekday to weekend, no weekend or weekday variation in events per plug per day was assumed for this building type [15].

Example Electric Vehicle Load Profiles: Two Monte Carlo Simulations

To generate the two daylong load profiles in Figure I.5.A.5 for a public EV fast-charge station, inputs included six total plugs at the station and eight events per plug per day. The two plots are slightly different due to the inherent Monte Carlo stochasticity, because time of arrival, energy demand, and initial SOC for each EV charging event is randomly regenerated from the input PDFs. Although the number of plugs is lower for this public fast-charge station than those for office and multifamily residential, the total station peak power levels

are significantly higher. This is not only because the frequency of events is higher, but also because the power delivered to the vehicle in DC fast charging (compared to Level 1 or Level 2 charging) is much greater.

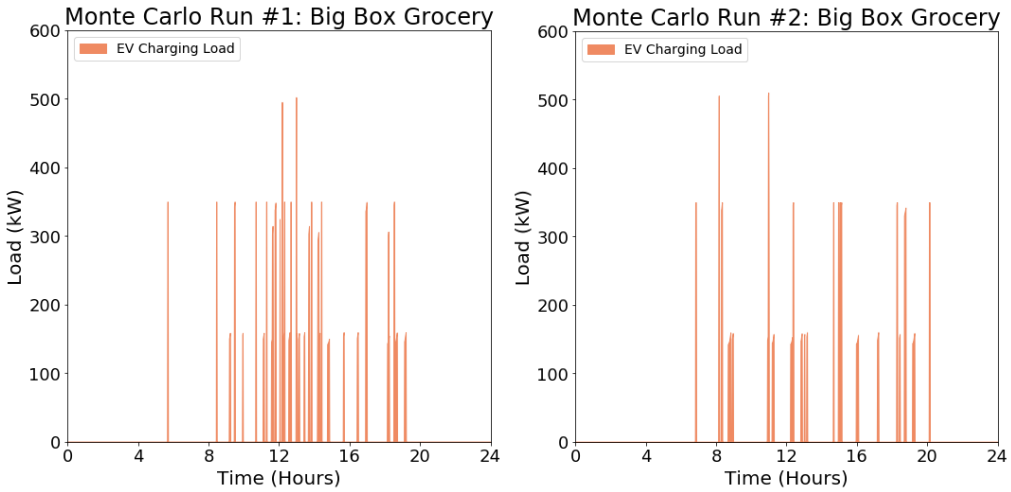

Figure I.5.A.5 Two Monte Carlo simulations generate two daylong load profiles at a big box retail grocery store

Load Profile Variance: Varying Station Design and Station Utilization

Figure I.5.A.6 and Figure I.5.A.7 show daylong electric vehicle load profile outputs, varying number of ports and number of events per day per port at a station. It is likely that the port count at an electric vehicle charging station will increase as demand increases, and that frequency of charging events per port will also increase over time. However, it may possible that stations will be initially oversized (i.e., ports initially underutilized) to accommodate the likely increasing frequency of charge events with growing EV adoption.

Six-Port Station

Figure I.5.A.6 displays load profiles with varying utilization for a six-port station. Low utilization is 2 events per plug per day; medium utilization is 8 events per plug per day; high utilization is 16 events per plug per day.

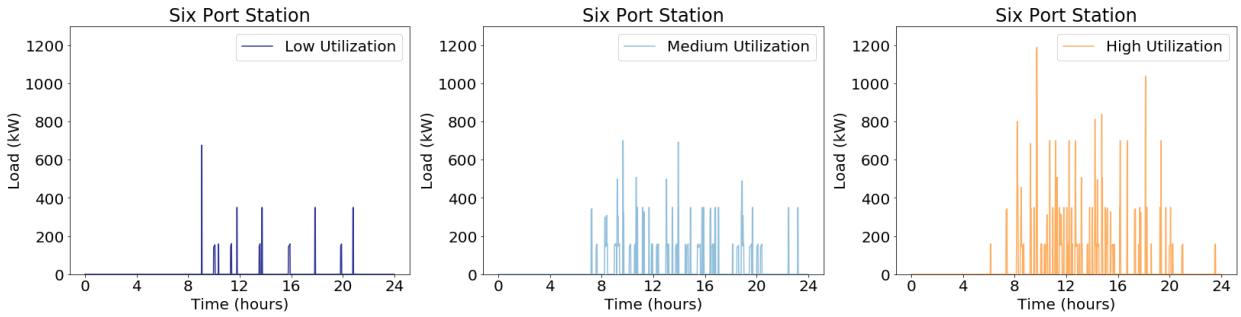

Figure I.5.A.6 How station utilization affects the load profile for a six-port station

Two-Port Station

Figure I.5.A.7 shows load profiles with varying utilization for a two-port station. Low utilization is 2 events per plug per day; medium utilization is 8 events per plug per day; high utilization is 16 events per plug per day.

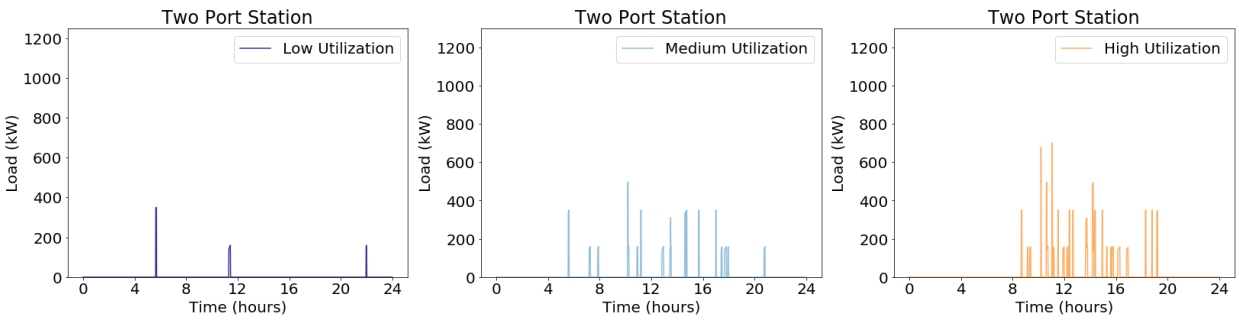

Figure I.5.A.7 How station utilization affects the load profile for a two-port station

Analysis to Determine Station Utilization: Events Per Plug Per Day

EVGo data from 2017 were used in assessing what could be reasonable input assumptions for the number of events per day per charger to the EV-EnSite model to generate the electric vehicle load profiles. The EVGo stations analyzed are 50-kW fast-charging stations spread throughout the United States in San Francisco (SF), San Diego (SD), Los Angeles (LA), Washington, D.C. (DC), and Boston (BOS). Seen in Table I.5.A.17, many stations have two chargers per site.

Table I.5.A.17 EVGo High Variance in Average Charging Events Per Day Per Port for Different Properties

Property	Market	Min.	Avg.	Max.	# Chargers	Average number of events per day per charger
Site 1	SF	0	64	99	4	16
Site 2	SD	1	24	48	2	12
Site 3	SF	0	17	38	2	9
Site 4	SD	0	16	37	2	8
Site 5	LA	0	16	39	2	8
Site 6	LA	0	12	26	2	6
Site 7	DC	0	12	51	2	6
Site 8	SF	0	11	23	2	5
Site 9	SD	0	10	25	2	5
Site 10	SF	2	17	34	4	4
Site 11	LA	0	8	27	2	4
Site 12	DC	0	3	20	2	2
Site 13	BOS	0	4	22	2	2
Site 14	BOS	0	2	18	2	1
Site 15	BOS	0	2	17	2	1

This analysis helped inform the high utilization case for the BTMS analysis of 16 events per day per plug. This utilization level is reached at the "busiest" EVGo station, or Site 1, which averages 16 events per day per charger. The low utilization case for the BTMS analysis was chosen to be two events per day per plug, seen at some of the sites in Table I.5.A.17.

2. Building Loads

The EnergyPlus model of big box retail grocery store was generated as part of a separate project for a store located in Centennial, Colorado. This model was calibrated with submetered data from the store. For this analysis, we simulated the building in Tucson, Arizona. A full-year profile can be seen in Figure I.5.A.8 (left) and a daylong time series can be seen in Figure I.5.A.8 (right), with both EV and building profiles in minute resolution. Note that load peaks in the middle of the year due to high summer air-conditioning and grocery refrigeration demands.

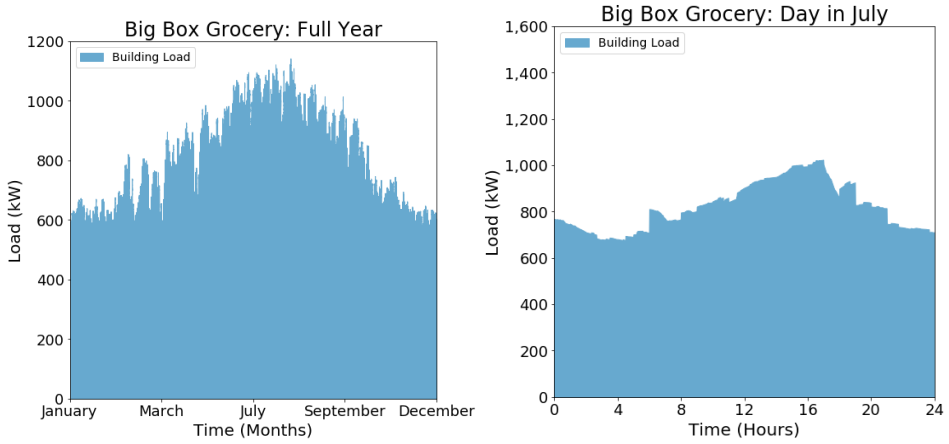

Figure I.5.A.8 Yearlong (left) and daylong (right) power time-series profiles of a big box retail grocery store

3. Combined Loads

To compare magnitudes between the electric vehicle load profiles and building load profiles, the EV and building load profiles were combined. Figure I.5.A.9 shows that for this scenario, the electric vehicle load profile is fairly significant, with similar magnitude compared to that of the electric building load profile. To obtain a year 2030 electric vehicle load profile for the big box retail grocery store, a station with two ports and 16 events per day per port was assumed. In 2030, it is likely that two ports would be in place at a station, rather than four or six ports, because many EVGo stations have two ports. However, utilization in 2030 will likely be higher than that seen today at a public EV charging station. Therefore, 16 events per port per day was selected, as seen in Table I.5.A.17 in the busiest EVGo station.

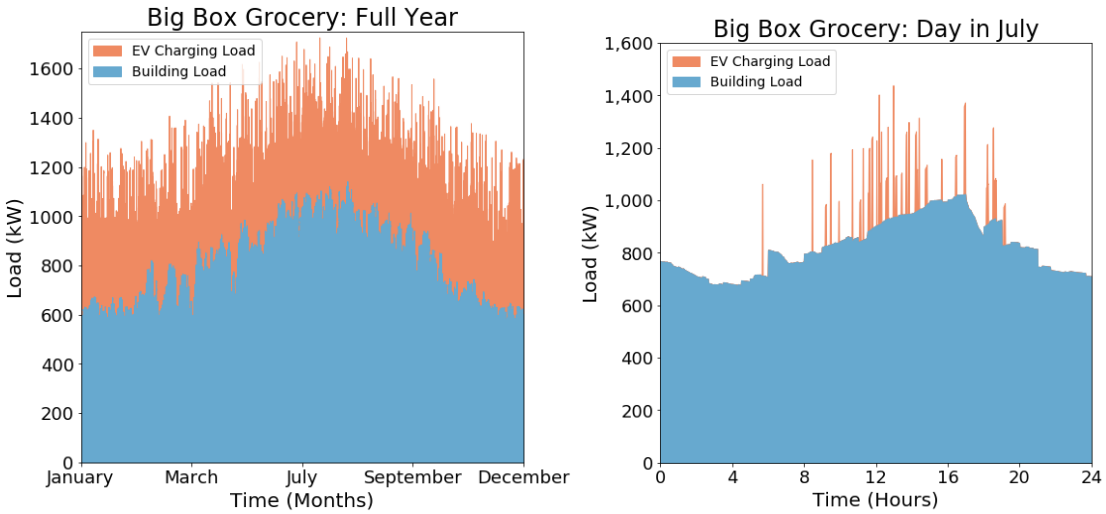

Figure I.5.A.9 Yearlong (left) and daylong (right) power time-series profiles of a big box retail grocery store and EV station

Medium Commercial Office: EV and Building Loads

A medium-size office building is modeled using the DOE prototype for medium commercial office building, with Level 2 chargers delivering 6.6 kW of power per plug.

1. EV Loads

It is assumed that the charging level will be Level 2 at 6.6 kW for this scenario, because people are generally at an office for long periods of time and therefore expensive fast-charging infrastructure is not necessary. It is also assumed that the number of events per day per plug will vary between one and two, because office workers will likely not desire to leave their office space to move their car throughout the day. There is likely variation of utilization between weekday and weekend for this case, with zero to one event per day per port on the weekends when many don't come into work.

Example Electric Vehicle Load Profiles: Two Monte Carlo Simulations

To generate these two daylong load profiles for an office building, the inputs regarding station design and station utilization are the same, with 20 total plugs at the Level 2 (6.6-kW) station and one charge event per plug per day. The two plots are slightly different due to the inherent variation teased out in Monte Carlo simulations, because time of arrival, energy demand, and initial SOC for each EV charging event is stochastically regenerated from the input PDFs. Note that for this office scenario, due to the arrival time probability distribution function input, most charging events occur at the beginning of the day when EV owners are typically at work.

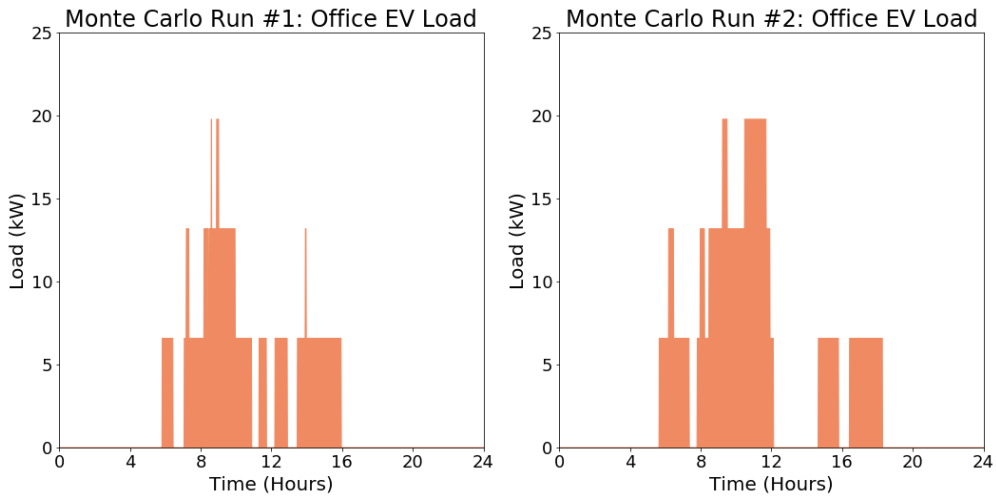

Figure I.5.A.10 Two Monte Carlo simulations generate two daylong EV profiles for an office

2. Building Loads

The DOE medium-office prototype model (ran in Tucson, Arizona) was used to represent a typical medium-sized office building. A full-year load profile can be seen in Figure I.5.A.11 (left) and a daylong time series can be seen in Figure I.5.A.11 (right). Note that the DOE prototype model has a spike at the beginning of each day due to the electric reheat terminals cycling on as the building thermostats return from nighttime setback.

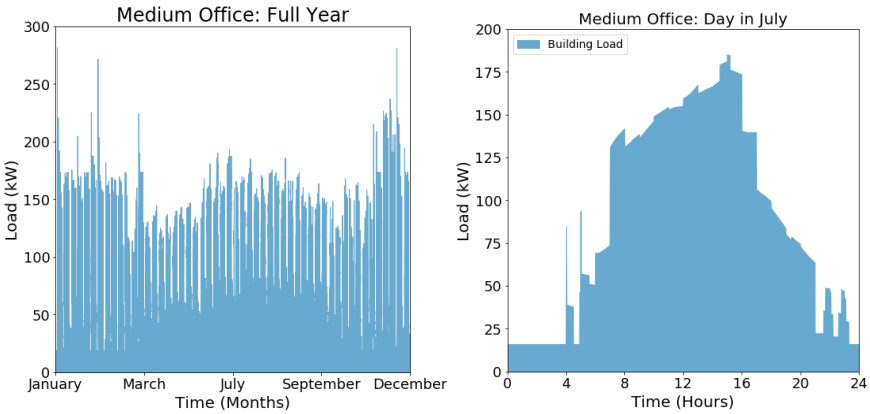

Figure I.5.A.11 Yearlong (left) and daylong (right) power time-series profiles at a medium commercial office

3. Combined Loads

To compare magnitudes between the electric vehicle load profiles and building load profiles, the EV and building load profiles were combined. As shown in Figure I.5.A.12, for this scenario, the average daily energy consumed by electric vehicles is fairly insignificant compared to that of the building. To obtain the electric vehicle load profile for the medium office building, the 2030 Electric Power Research Institute high-BEV scenario was utilized, predicting 13.2% BEV penetration. The DOE prototype medium office building assumes 268 occupants. Based on the ratio of 0.6 parking spaces per occupant (a general rule of thumb used to determine the number of spots at the NREL parking garage [16]), this results in approximately 161 parking spots for the medium office building. Assuming everyone parking at work with a BEV can and will charge at the office on a regular basis, 13.2% of all parking spots, or 22 ports, may be an appropriate estimation for the size of the station. To generate the electric vehicle load profile, it was also assumed that there would be one charge event per day per plug.

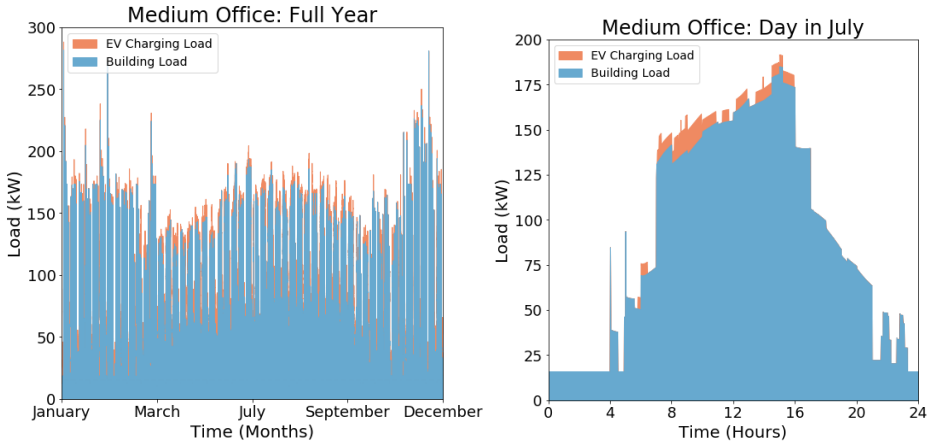

Figure I.5.A.12 Yearlong (left) and daylong (right) power time-series profiles of a medium commercial office and EV station

Apartment: EV and Building Loads

The multifamily residential (apartment) load profile is generated using the DOE prototype for the mid-rise apartment building, with Level 2 chargers delivering 6.6 kW of power per plug. The high-rise apartment DOE prototype building could also be used for this case, but the mid-rise apartment captures a larger portion of the multifamily residential population; high-rise apartments are usually found in downtown urban areas, but mid-rise apartments can be found in both urban and suburban areas.

1. EV Loads

For this building type, it is assumed that the charging level will be Level 2 at 6.6 kW, because people generally dwell at their homes for long periods, usually during the evening, and therefore expensive fast-charging infrastructure is not necessary. It is also assumed that number of events per day per plug will vary between one and two, because those living in an apartment will likely not be inclined to move their car in the middle of the night to allow for another vehicle to charge. It is uncertain whether variation of utilization between weekday and weekend occurs for this case, but it likely won't because instead of working during the day, people are likely running errands and doing activities on the weekend and will still charge primarily at night.

Example Electric Vehicle Load Profiles: Two Monte Carlo Simulations

To generate the two daylong load profiles in Figure I.5.A.13 for a multifamily residential building, the inputs regarding station design and station utilization levels are the same as that of the medium commercial office building, with 20 total plugs at the Level 2 (6.6-kW) station and one event per plug per day. These are the same station design and station utilization inputs as for the office (i.e., the number of plugs at the station and frequency of charging events per plug are identical). However, the load profiles are quite different, as more charging events occur in the evening when EV owners are home.

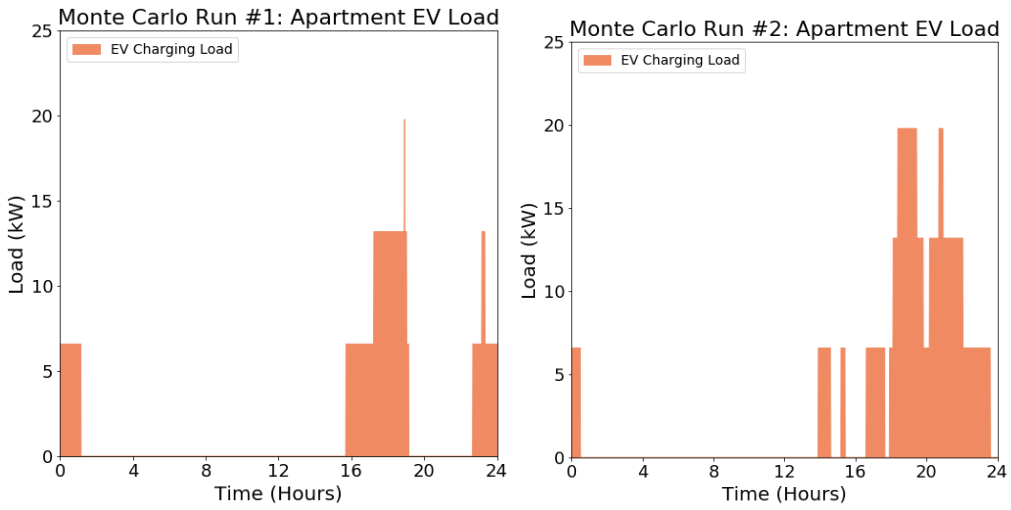

Figure I.5.A.13 Two Monte Carlo simulations generate two daylong EV profiles for a multifamily residential building

2. Building Loads

The DOE mid-rise apartment prototype model (ran in Tucson, Arizona) was used to represent a typical multifamily residential building. A full-year load profile can be seen in Figure I.5.A.14 (left) and a daylong time series can be seen in Figure I.5.A.14 (right). As seen in Figure I.5.A.14 (left), the load is very high at the beginning of the year, likely due to convergence anomalies in the simulation trying to reach steady state. Seen in Figure I.5.A.14 (right), the rapidly cycling load throughout the day is due to the 23 in-unit electric water heaters. Because this creates a highly variant power profile that may be problematic given the needs of this project to have a relatively accurate estimate of demand at minute intervals, we plan on changing the electric water heaters in the existing DOE prototype building model to natural gas heaters, which may actually be more realistic because that is the current primary heating fuel. We will take measures to remove irregularities from any existing models to generate a robust minute power load profile.

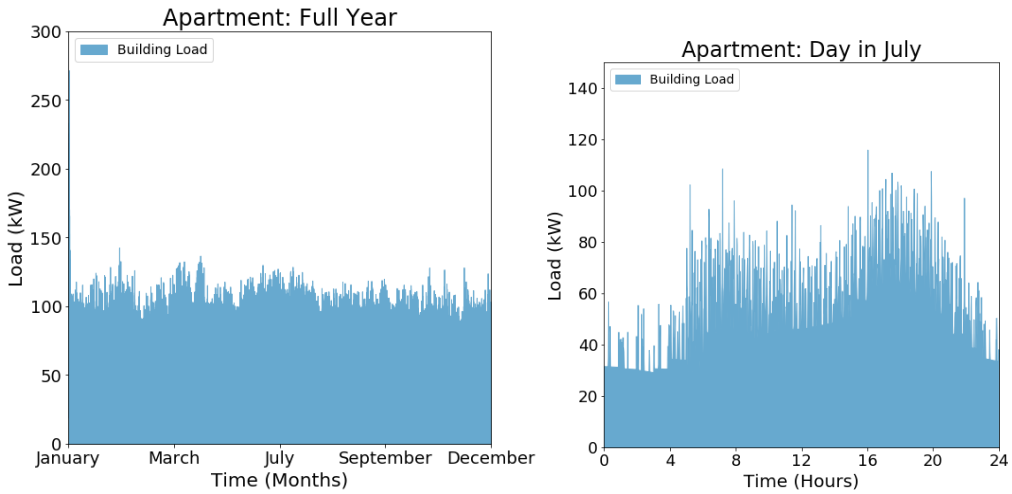

Figure I.5.A.14 Yearlong (left) and daylong (right) power time-series profiles of a multifamily residential building

3. *Combined Loads*

To compare magnitudes between the electric vehicle load profiles and building load profiles, the EV and building load profiles were combined. As shown in Figure I.5.A.15, for this scenario, the average daily energy consumed by electric vehicles is fairly insignificant compared to that of the building. To obtain the electric vehicle load profile for the multifamily residential building, the 2030 Electric Power Research Institute high-BEV scenario was again utilized, predicting 13.2% BEV penetration. Assuming the mid-rise apartment has 67 occupants, and using the parking rule of thumb, there are likely 39 parking spots at this site. Assuming 13.2% of those parking spots have electric vehicle charging options, six ports exist at this building type.

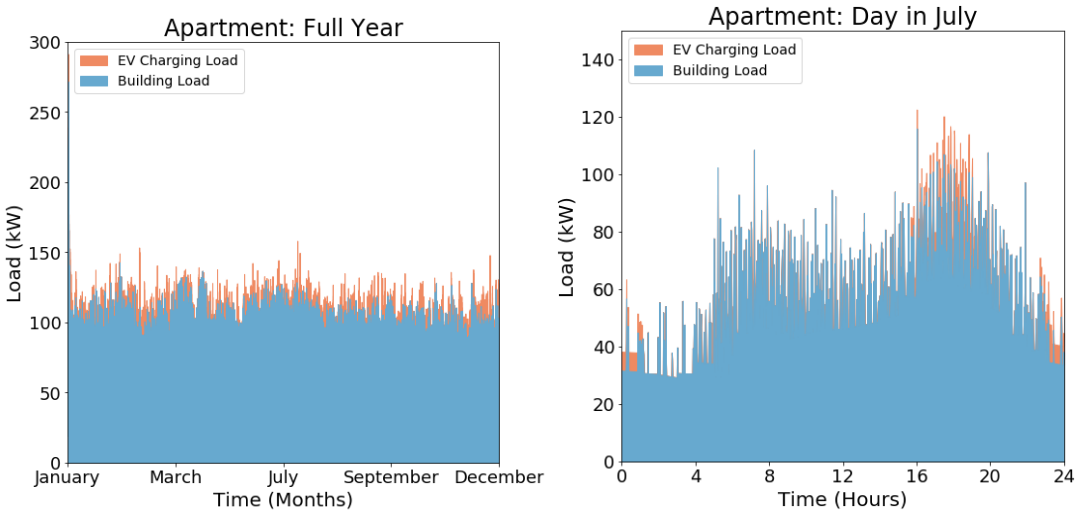

Figure I.5.A.15 Yearlong (left) and daylong (right) power time-series profiles for a multifamily residential building and EV station

Load Profiles Summary

Comparison of building and electric vehicle loads for one week in April for the big box retail grocery, medium office, and mid-rise apartment can be seen in Figure I.5.A.16. Note that the big box retail grocery and electric vehicle station use much more energy than the office or apartment building because the big box retail grocery store is very large and has high loads due to significant HVAC, refrigeration, and lighting demands.

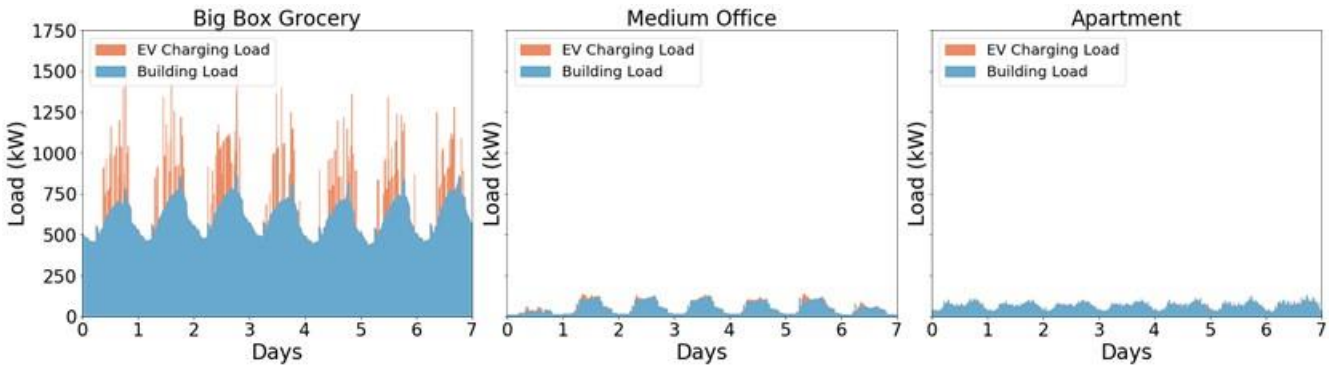

Figure I.5.A.16 Comparison of big box retail grocery store, office, and apartment EV and building load profiles

As seen in Figure I.5.A.17, when comparing just the office and apartment buildings loads for one week in April, one can see that the office loads are dramatically lower on the weekends (the first and last day of the week seen). Note also that the EV loads for the office complex are higher than that for the apartment complex because the office has higher occupancy and therefore more EV ports.

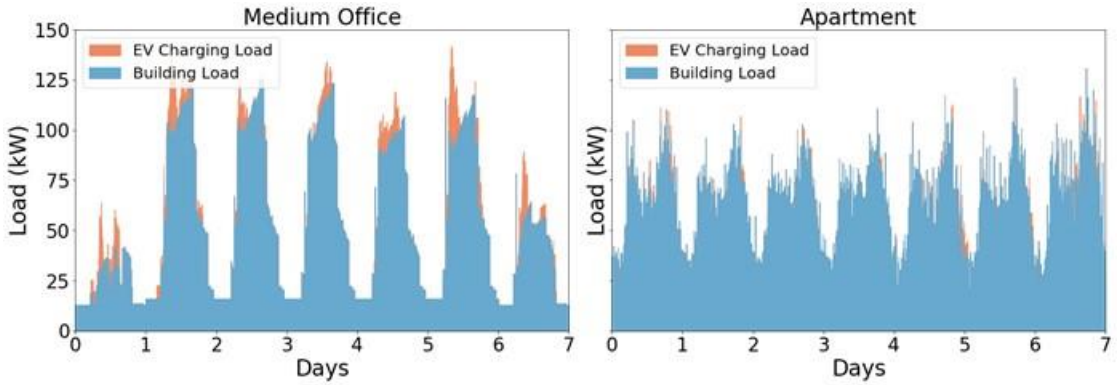

Figure I.5.A.17 Comparison of office and apartment EV and building load profiles

Figure I.5.A.18 compares the electric vehicle loads for one day for each of the three building types: big box retail grocery store, medium commercial office, and multifamily residential. The big box retail grocery store with 350-kW DC fast chargers has much shorter and higher-power charging events than the medium office and apartment.

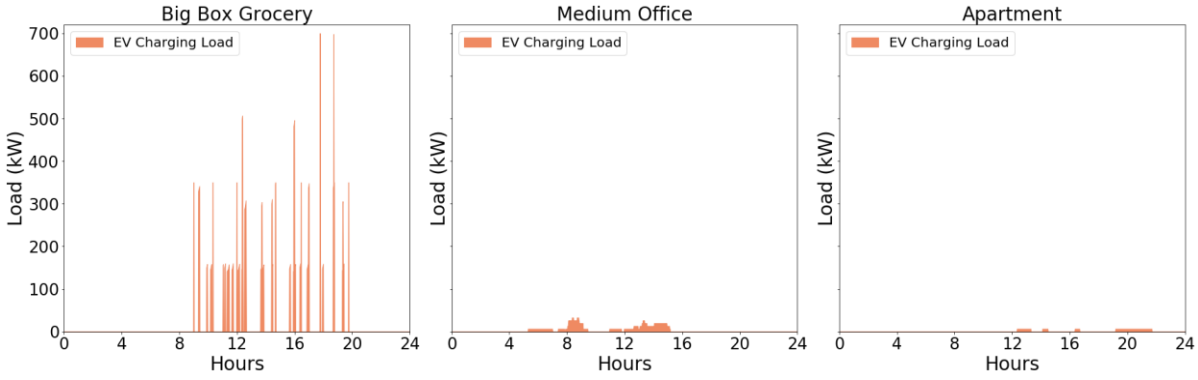

Figure I.5.A.18 Comparison of big box retail grocery store, office, and apartment EV load profiles

Seen in Figure I.5.A.19, when comparing just the office and apartment EV station loads for one day, the charging events for the office often take place in the morning and throughout the day while many are at work.

However, the charging events for the apartment complex take place largely at the evening and throughout the night, as this is when the majority of people are at home.

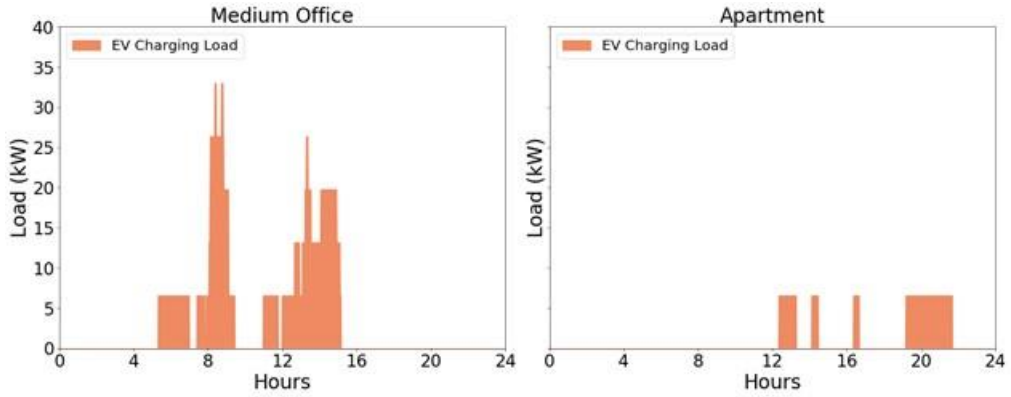

Figure I.5.A.19 Comparison of office and apartment EV load profiles

Financial Metrics Captured in EnStore

In computing key financial metrics for this project, we referenced the existing SAM cash flow calculator so that financial metrics are consistent with prior NREL and EERE research and tools [3], [17]. Initial focus for the analysis and methodology is around a single-ownership model, in which one entity owns the building, the EV charging station, and any BTMS equipment, including the stationary battery, solar PV, and TES. Therefore, all the BTMS costs and benefits accrue to a single owner. We understand that this may not be representative of the market today, as places like Walmart may have EV stations owned and operated by Electrify America that are separately metered. However, this provides a starting point for BTMS system comparisons. Throughout this project, we will continue to explore other ownership models, try to identify which are the most prevalent, and determine the appropriate financial metrics for these disaggregated ownership models in the future.

Three financial metrics will be used to understand the economic impact of BTMS to the system owner: NPC, LCOC, and LCOE.

- **NPC** is the total present cost of the system to the system owner. Note that net present value and the net present cost differ only in sign.
- **LCOC** is the minimum required selling price that the owner of the system must charge EV owners in order to "break even" after paying for the capital and operating expenses with a specified rate of return. At a high level, LCOC is computed by identifying all the system costs outside of the building electricity costs, and then determining what EV owners must pay ($/kWh) in order to achieve an NPV equal to zero. It is important to note that the LCOC is not the market price for EV charging, as the market may be willing to pay more or less than this amount and the true market value for EV charging is unknown in this analysis.
- **LCOE** is analogous to LCOC but is instead computed from the building's perspective (e.g., all marginal systems costs and benefits accrue to the building).

In this analysis, we compare each of the financial metrics of a base case (with a seed building with EV charging stations but no BTMS system) with the financial metrics of the full BTMS system, including the building and EV charging station. The base case provides the benchmark for the system owner to use when determining if the BTMS system is economically attractive. In the base case scenario, it is important to note that it is implied that the EV station and the building are under the same meter and exist before any BTMS equipment is installed. An illustrative comparison comparing the two cash flows can be seen in Table I.5.A.18,

where there are higher upfront costs with procuring and installing BTMS component, but lower annual O&M costs due to electricity bill savings.

Table I.5.A.18 Cash Flow Illustrative Example

Year	Base Case Costs	BTMS Costs
0	−$60,000	−$80,000
1	−$500	−$200
2	−$500	−$200
…	…	…
N	−$500	−$200

Net Present Cost

NPC is defined as the sum of all the discounted costs of the entire system over the lifetime of the project. NPC can be computed for a base case system (building and EVSE infrastructure) as well as the BTMS system (building, EVSE infrastructure, and the new battery, PV, and TES assets). By computing the NPC for both systems, the metric can be used to help answer a key research question: Should the system owner install the BTMS equipment or not?

NPC is the most straightforward to calculate of the three financial metrics discussed previously, because all the costs and benefits of the BTMS system are accrued to a single owner.

Understanding that the NPC for the multi-asset BTMS system will have higher upfront capital costs than that of the base case system (with no initial capital costs), the future lower operational costs from saving money on the annual electricity bill must at some point allow the system owner to "break even" and cover the initial investment costs. If the BTMS system is worth the investment, the annual electricity bill must be low enough such that the NPC of the BTMS system is lower than that of the base case system.

Mathematically, NPC includes capital costs, fixed and variable operational costs, and the monthly utility bill, which is another type of operational cost. Costs that are incurred over time are discounted back to present values using a discount rate representing the risk-adjusted time value of money.

$$NPC = Discounted\ CapEx + Discounted\ Fixed\ OpEx + Discounted\ Variable\ OpEx + Discounted\ Monthly\ Utility\ Bill \quad (1)$$

CapEx (capital expenditures) for the BTMS case include all upfront installed costs, including the battery, solar PV, TES, EVSE, power electronics, interconnection, and balance of plant. CapEx for the base case system (with building and EV charging station only) include only that of the EVSE, interconnection cost, and related power electronics components.

OpEx (operational expenditures) for the BTMS case could include the energy costs, maintenance labor, and maintenance supplies for the battery, solar PV, TES, or EVSE. The annual electricity cost is broken out in Eq. 1 for convenience with later calculations.

NPC can be written mathematically as:

$$NPC = \sum_i C_i + \sum_n \left[\frac{\sum_i (F_{i,n} + V_{i,n}) + \sum_m M_m}{(1+r)^n}\right] \quad (2)$$

where:

$i = asset\ i$

$n = period\ (e.g.,\ year)$

$m = subperiod\ (e.g.,\ month)$

$C_i = capital\ cost\ of\ asset\ i$

$F_{i,n} = fixed\ cost\ of\ asset\ i\ in\ period\ n$

$V_{i,n} = variable\ cost\ of\ asset\ i\ in\ period\ n$

$M_m = subperiod\ (e.g.,\ month)\ utility\ bill\ for\ subperiod\ m$

$r = discount\ rate\ per\ period$

Levelized Cost of Charging

LCOC is defined as the minimum required selling price of the electricity sold to the EV owners to pay back all costs associated with the project at the specified rate of return. LCOC can be computed for the base case scenario (building and EV charging station only) and the BTMS scenario (building, EV charging station, battery, PV, and TES) to help answer the research question: If BTMS equipment were installed, what would be the relative impact to the EV owner?

Example output would be similar to:

- $LCOC_{baseline}$ = \$0.15/kWh
- $LCOC_{BTMS}$ = \$0.10/kWh

which would be able to inform the system owner that the project is both economically attractive (because $LCOC_{BTMS}$ is less than $LCOC_{baseline}$) and lowers the required EV electricity selling price to break even by 33%.

In order to compute LCOC, the relative costs of the EV charging station and building must be disaggregated and allocated to each subsystem (building or EV owners). For example, in the base case scenario (building and EV charging station only), the LCOC must be computed to represent the effective cost of electricity sold to the EV owners whilst the building pays its "fair share" of the total system utility bill. Because a combined building and EV charging station utility bill may not simply be the sum of two separate utility bills (due to nonlinear demand charges), the following assumptions are made:

1. The building will pay a utility bill equal to that if the EV charging station did not exist
2. The EV owners will pay for all marginal costs associated with installing and utilizing the EV charging stations (marginal demand charges, marginal energy consumption, marginal asset costs [EVSE, controls, etc.]).

The assumption that the EV owners pay for all marginal costs is justified as vehicle owners have (1) a more inelastic demand for energy prices and (2) a higher willingness to pay for electricity than a building would. With those two assumptions, the LCOC for a base case system can be calculated by removing the building electricity costs associated with only the building and normalizing by the total energy consumption of the EVs:

$$LCOC_{base\ case} = \left(\frac{C\prime_{EVSE+building} - C\prime_{baseline\ building\ only}}{E\prime_{BEV}}\right) \quad (3)$$

where:

$C'_i = vector\ of\ discounted\ cash\ flows\ (costs) for\ system\ i$

$E'_i = vector\ of\ discounted\ energy\ flows\ going\ to\ item\ i$

Specifically, $C'_{EVSE+building}$ represents the vector of cash flows for the base case system (building with the EV charging station), whereas $C'_{seed\ building\ only}$ denotes the cash flows for the annual electricity bill of the building. By removing the building cost from the base case system, only marginal costs related to the addition of the EV charging infrastructure are left, which can be normalized by the battery EV charging to obtain an LCOC.

Expanding Eq. 3 into the summation over the periods yields:

$$LCOC_{baseline} = \left(\frac{\sum_i C_i + \sum_n \left[\frac{\sum_i \left(F_{i,n} + V_{i,n} \right) + \sum_m M_m}{(1+r)^n} \right] - \left(C_b + \sum_n \left[\frac{F_{b,n} + V_{b,n} + \sum_m M_{b,m}}{(1+r)^n} \right] \right)}{\sum_n \left[\frac{E_n}{(1+r)^n} \right]} \right) \quad (4)$$

or more succinctly:

$$LCOC_{baseline} = \left(\frac{\sum_i [C_i] - C_b + \sum_n \left[\frac{\sum_i \left(F_{i,n} + V_{i,n} \right) - F_{b,n} - V_{b,n} + \sum_m \left(M_m - M_{b,m} \right)}{(1+r)^n} \right]}{\sum_n \left[\frac{E_n}{(1+r)^n} \right]} \right) \quad (5)$$

where:
$i = asset\ i$

$n = period\ (e.g.,\ year)$

$b = building\ (subscript)$

$m = subperiod\ (e.g.,\ month)$

$C_i = capital\ cost\ of\ asset\ i$

$F_{i,n} = fixed\ cost\ of\ asset\ i\ in\ period\ n$

$V_{i,n} = variable\ cost\ of\ asset\ i\ in\ period\ n$

$M_m = subperiod\ (e.g.,\ month)\ utility\ bill\ for\ subperiod\ m$

$r = discount\ rate\ per\ period$

$E_n = BEV\ charging\ energy\ (e.g.,\ kWh)\ in\ period\ n$

As seen in Eq. 5, the removal of the seed-building-only costs can be any capital, fixed, or variable costs associated with the building. However, it is likely that only a monthly utility bill of the seed building will need to be removed to calculate the LCOC metric.

The LCOC of the BTMS system can be computed in an analogous way by replacing the base case system costs with the BTMS system costs. Mathematically, this can be expressed as:

$$LCOC_{BTMS} = \left(\frac{C\prime_{EVSE+building+BTMS} - C\prime_{base\ case\ building\ only}}{E\prime_{BEV}}\right) \quad (6)$$

By computing the LCOC metric in this way for both the base case scenario and the BTMS scenario, the metric can be used to both inform the system owner on the economic attractiveness of the project and provide information on the relative impact to the EV owners.

Also, it should be noted that impact of taxes, carry-forward tax losses, and incentives are not explicitly shown in these equations for clarity but will be accounted for in the actual computation within EnStore.

Levelized Cost of Electricity

LCOE is defined as the minimum required selling price of the electricity sold to the building owner to pay back all costs associated with the project at the specified rate of return. It answers the research question: If BTMS equipment were installed, what would be the financial benefits of the investment to the building owner?

Mathematically, this is very similar to the LCOC calculation, except it assumes all benefits of the BTMS system go to the building owner as opposed to the EV owner. Thus, the calculations for LCOE are similar to those of LCOC, but levelization is by energy usage of the building as opposed to energy usage of the EVSE. Because all marginal costs of adding the EV station accrue to the EV owners, the LCOE for the building is trivial and is effectively the levelized utility rate for the building:

$$LCOE_{baseline} = \left(\frac{C\prime_{baseline\ building\ only}}{E\prime_{building}}\right) \quad (7)$$

where:

$C'_i = vector\ of\ discounted\ cash\ flows\ (costs) for\ system\ i$

$E'_i = vector\ of\ discounted\ energy\ flows\ going\ to\ item\ i$

The LCOE of the BTMS system can be computed in an analogous way but replacing the base case system costs with the BTMS system costs. Mathematically, this can be expressed as:

$$LCOE_{BTMS} = \left(\frac{C\prime_{EVSE+building+BTMS} - [C\prime_{EVSE+building} - C\prime_{baseline\ building\ only}]}{E\prime_{building}}\right) \quad (8)$$

Thus, by defining the LCOE of the building in this way, it can be used to determine if the BTMS system is economically attractive ($LCOE_{BTMS}$ is less than $LCOE_{baseline}$) and the relative impact to the building owner assuming all benefits are accrued to the building (e.g., by what percentage LCOE was reduced due to the BTMS investment).

Using consistent accounting allows us to compute both LCOC and LCOE. These metrics provide additional information beyond the NPC metric and help answer additional research questions, such as what the relative impact is to the individual EV owners or building rate payer.

EnStore Preliminary Results

During FY 2020, we developed a functional EnStore software platform, successfully linking (1) REopt, (2) OpenStudio/EnergyPlus, and (3) SAM together to produce time-series energy flows and financial metrics of interest. We call this initial software EnStore version 1.0, and through beta testing find that it nominally functions as intended. In FY 2021, we will refine or update the initial assumptions used to develop a first

version of EnStore to improve accuracy and customize the assumptions for the BTMS analysis. Future work is elaborated later in this report.

In EnStore version 1.0, controls are simple and siloed (device-level as opposed to supervisory). The battery is controlled via the hourly dispatch schedule provided by REopt, and the TES charge/discharge start/stop times are entirely schedule-based. The battery and TES function without knowledge of one another. In FY 2021, we plan to implement hierarchical supervisory controls that better manage power flows at each time step. For instance, in EnStore 1.0, excess PV can only be sold back to the grid, meet load, or charge the battery; however, if the TES were reducing the load, optimal use of the PV system may change. Temporal resolution of power flows will also be enhanced in future iterations of the controls in EnStore, such as being able to address sub-15-minute peaks due to DC fast charging. These are examples of capabilities to be implemented in our optimal control problem.

Another major simplification in EnStore version 1.0 is related to power electronics. Devices that convert and condition power are required in many places when a building has on-site PV generation and electrochemical storage; however, in EnStore 1.0, these devices are modeled with idealized placeholders. In FY 2021, we plan to replace these proxies with more accurate models that capture functional relationships between efficiency of these devices and the operating conditions.

Lastly, in EnStore 1.0, we only incorporated a generic lithium-ion battery model in our PySAM Battery model. Although this model is relatively robust, it does not include any of the BTMS battery testing and life modeling for other battery chemistries (e.g., nickel-manganese-cobalt [NMC], lithium-titanate [LTO], lead acid). In FY 2021, we plan to replace this generic model with those that more accurately capture how other battery chemistries behave at different operating conditions.

In summary, we caveat the following results that this analysis is simply a demonstration of the functionality of the first version of EnStore. *It is critical that these preliminary results not be used in developing conclusions related to the viability or application of behind-the-meter storage systems.*

EnStore Inputs for Preliminary Runs

As seen in Table I.5.A.1, the primary EnStore inputs include system costs, electric utility rate tariffs, weather data, financial information, component-level details for battery and TES, simulation details, experiment design, and initial building and EVSE loads.

1. System Costs

System cost inputs include solar PV installed cost per kW, solar PV O&M cost per kW, battery installed cost per kW, battery installed cost per kWh, TES cost per kWh, EVSE capital and O&M costs per port, and interconnection cost. BTMS unit costs for various components can be referenced in Figure I.5.A.20. For the present analysis, solar PV and battery unit costs are taken from defaults in the REopt API [18], and TES unit costs were found in a report by Navigant [19]. EVSE capital and O&M costs for future studies will come from various sources, including a recent NREL paper about LCOC [20]. However, for the present analysis, we have made EVSE procurement and installation inexpensive at $12,000 total and ignore any interconnection cost.

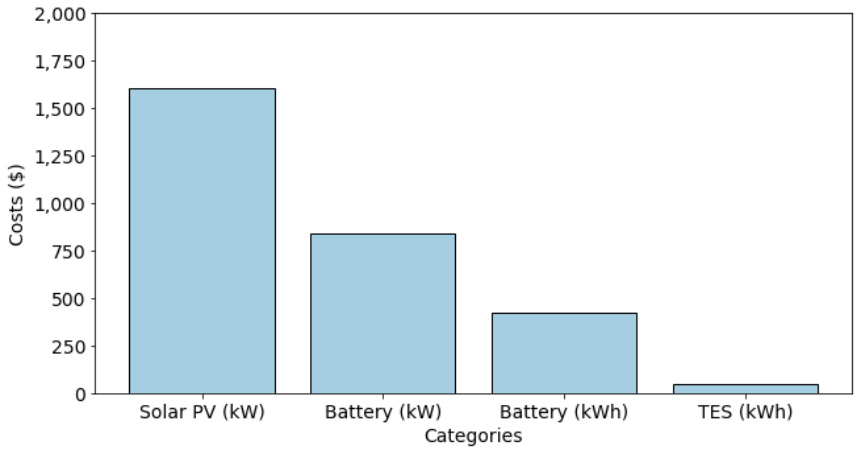

Figure I.5.A.20 Unit costs for various BTMS components

2. *Utility Rate Tariff*

For this analysis, we have chosen Pacific Gas & Electric's (PG&E's) commercial tariff [21]. Seen in Table I.5.A.19, this tariff includes both time-of-use demand and energy charges.

Table I.5.A.19 Demand Charge Schedule

Period	Rate ($/kW)
1	0
2	0.13
3	5.45
4	20.62

The periods for demand charges can be seen for the weekday and weekend schedule in Figure I.5.A.21.

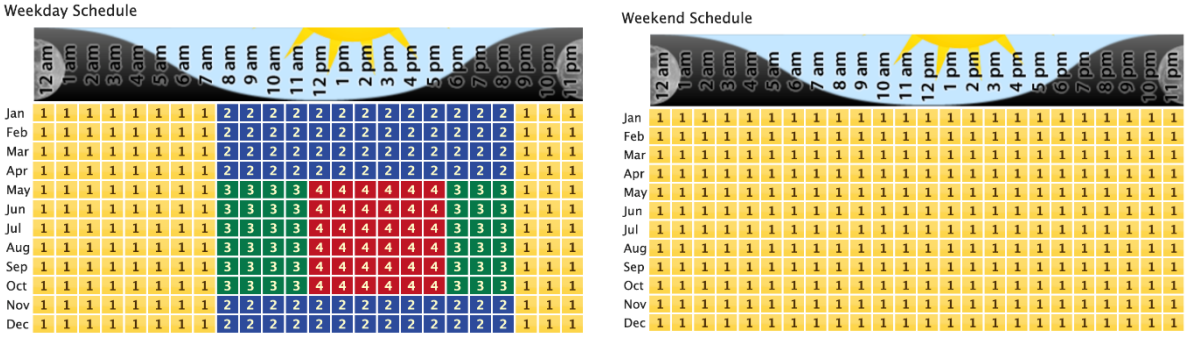

Figure I.5.A.21 Demand charge schedule for weekday and weekend

Table I.5.A.20 Time-of-Use Energy Charge Schedule

Period	Rate ($/kW)
1	0.087
2	0.102
3	0.080
4	0.107
5	0.152

The periods for time-of-use energy charges can be seen in Figure I.5.A.22.

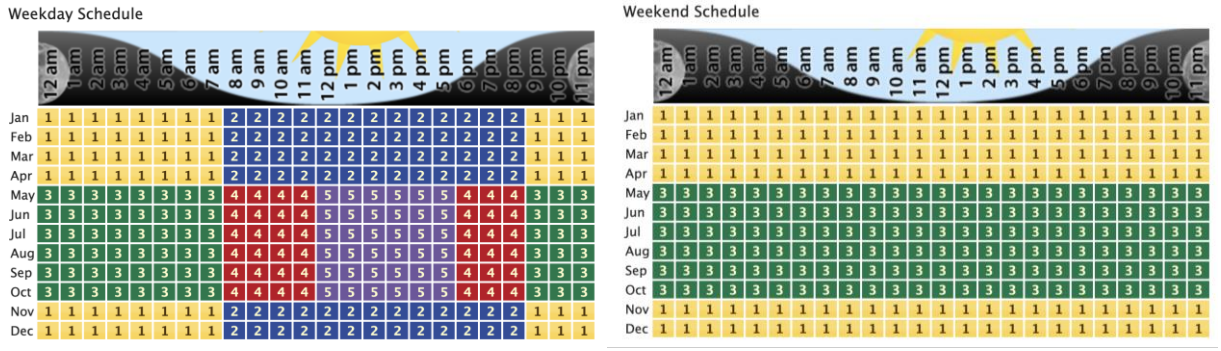

Figure I.5.A.22 Time-of-use energy charge schedule for weekday and weekend

3. *Weather Data*

Weather data are stored in an EnergyPlus Weather file (.epw). For these initial EnStore runs, we have chosen Golden, Colorado, as our area of interest and used the "USA_CO_Golden-NREL.724666_TMY3.epw" file, which contains TMY data. Because this is simply a demonstration run, we did not match the weather file location with the utility rate tariff but intend to explore matching in future runs.

One of the columns of this file is global horizontal radiation, which will affect how much electricity is generated from solar PV. Note that the solar resource availability seen for day 183 of the year in Figure I.5.A.23 corresponds well with the solar PV electricity production in Figure I.5.A.27.

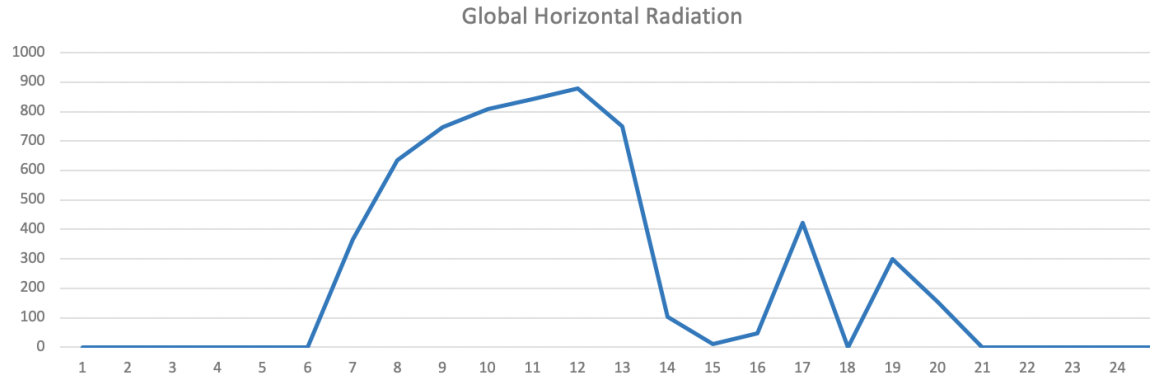

Figure I.5.A.23 Global horizontal radiation is one field in the EnergyPlus Weather input file

4. Financial Information

Many financial details will be passed into EnStore in FY 2021 development, including the discount rate, inflation rate, loan rate, loan term, state tax rate, and federal tax rate. For this demonstration, we simplified many of the financial metrics, assumed no inflation rates or federal/state tax rates, and chose a discount rate of 8.3%.

5. Component Details for BTMS Technology

Component-level details for the battery, TES, and solar PV are necessary inputs to EnStore. Battery information such as voltage vs. SOC curves, thermal parameters, life models, conversion efficiencies, and replacements can be found from data sheets, scientific articles, and BTMS testing and life modeling in future work. TES details include charge start time, charge end time, discharge start time, and discharge end time, as controls are currently schedule-based. PV parameters are currently only degradation percentage, but could be expanded to include tracking type and DC to AC ratio.

6. Simulation Details

Simulation details include relative paths to the building and EV load paths, weather file, and output directory, as well as the analysis period, which was set to 20 years for this demonstration. The analysis period input currently only affects financial computations, as all EnergyPlus/SAM runs are simulated for 1 year. In this case, our cash flow statement has 20 years assuming the same utility bill, operating costs, etc., with all upfront capital costs accounted for in year 0. Finally, useful constraints for the REopt suggested sizing, such as the min. and max. sizes of the solar PV and battery, can also be provided to EnStore.

7. Experiment Design

Permutation details are vital to understand how design variables for each of the previous categories will be varied for the experiments. For each variable, users can choose the number of permutations around a base value, as well as the positive and negative fractions from the base value. In this analysis, we limit the design variables to be sizes of the PV, battery, and TES. We assume a fixed ratio between the battery demand and energy (e.g., the battery kW to kWh ratio) and only vary the battery power (kW) from the REopt suggestion. TES will be varied around a user-selected starting base value.

8. Initial Building + EVSE Loads

Input building loads and EVSE loads can be seen in Figure I.5.A.24 and Figure I.5.A.32 for the simple building model and DOE prototype medium commercial office building model. Here, we use the same EVSE load: a station with 22 Level 2 charging events per day.

Verification with Simple Building Model

We first tested EnStore functionality using a simple one-zone building model. This allowed rapid simulation, simplified debugging, and swift analysis. The one-zone model has no fenestrations, is slab-on-grade, and has a square footprint of 100 × 100 feet with a 21-ft-tall ceiling. The floor is modeled as an 8-in insulated heavyweight concrete slab with adiabatic boundary conditions. The walls are 4-in mediumweight insulated concrete and the EPDM (ethylene propylene diene terpolymer) roof is insulated entirely above a metal deck. The internal loads consist of 1 W/ft² of lights and 0.25 W/ft² of plug loads, both on 24/7/365. The building has an infiltration rate of 0.112 cubic feet per minute per square foot (CFM/ft²) of exterior surface (wall and roof) area. Lastly, the building is conditioned via a rooftop unit with direct expansion cooling and a natural-gas-fired furnace controlled to a heating set point of 68°F and a cooling set point of 75°F. The simulations are run with data from the Weather Data section.

1. Time-Series Data

The seed building for the simple building model and EVSE load profile for day 183 of the year (early July) can be seen in Figure I.5.A.24. For remaining graphs where various combinations of solar PV, battery, and TES

are added to the building, we overlay EnergyPlus time-series output data with the seed building and EVSE loads for comparative purposes to ensure the EnStore components are functioning as expected.

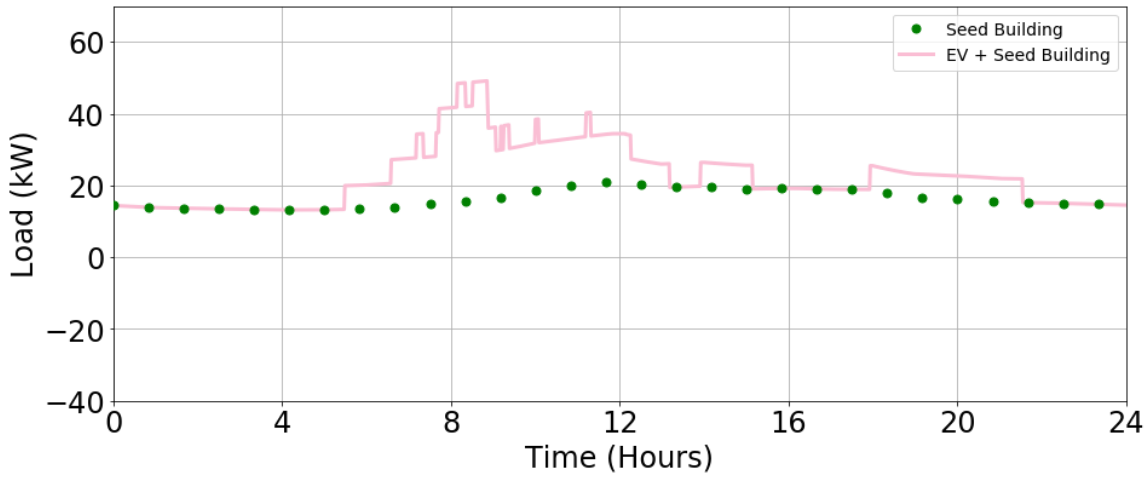

Figure I.5.A.24 Seed building and EVSE load profile for validation simulation

For the following EnStore results adding various configurations of solar PV, battery, and TES, time-series results are only shown for one EnergyPlus simulation (with one configuration of PV, battery, and/or TES) for simplicity. In cases where REopt is used to develop a preliminary sizing estimate, only runs with the REopt recommend PV and battery sizes are shown.

Test Run Adding Only Solar PV

An EnStore run was completed adding only solar PV (no battery or TES), shown in Figure I.5.A.25. Solar PV production peaks midday just before noon and varies as the global horizonal radiation varies throughout the day, seen in Figure I.5.A.23. Total electricity purchased matches the seed building and EVSE load while the sun is not shining but decreases throughout the day as solar PV electricity is generated. As solar PV production peaks around 11 a.m., one can see that some electricity is even being sold back to the grid.

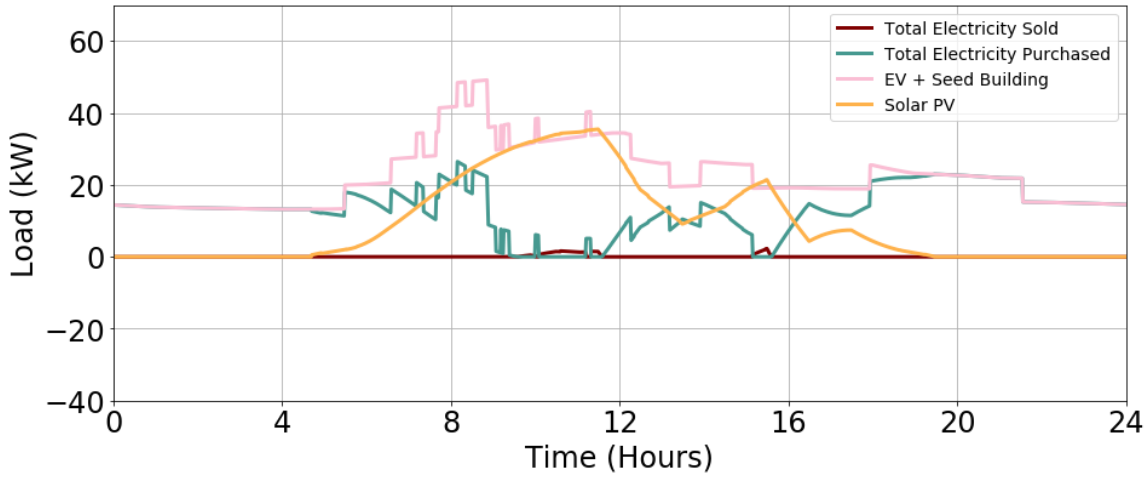

Figure I.5.A.25 Adding solar PV in validation simulation

Test Run Adding Only Battery

An EnStore run was completed adding only a battery, with results shown in Figure I.5.A.26. The battery is seen charging (negative) before 8 a.m. and after 10 p.m., when PG&E rates are cheaper, and discharging (positive) between 8 a.m. and 3 p.m., when PG&E rates are more expensive. When the battery is charging, one

can see that this adds to the total electricity purchased; when the battery is discharging, the building total electricity purchased is less than the seed building. At around 12:30 p.m., one can note that energy arbitrage is occurring as the battery is discharging and some electricity is being sold back to the grid.

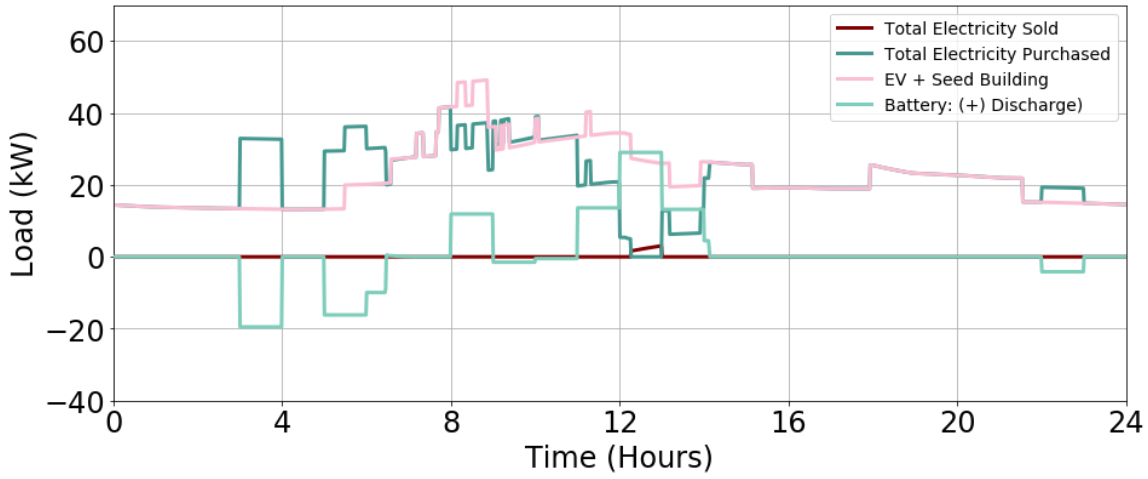

Figure I.5.A.26 Adding battery in validation simulation

Test Run Adding Solar PV + Battery

An EnStore run was completed adding solar PV and battery, with results shown in Figure I.5.A.27. Similar to what was seen in Figure I.5.A.26, the battery is charging (negative) before 8 a.m. and after 10 p.m., as this is when PG&E rates are cheaper, but also through the day to absorb excess electricity from the solar PV. In this case, the battery is discharging later in the evening, between 4–8 p.m. rather than between 8 a.m. and 3 p.m. in the battery-only case, likely because solar PV is now being produced and electricity from the battery is not necessary early in the morning but rather later in the evening when solar irradiance levels are decreasing. Much more electricity is sold back to the grid in this scenario than the prior two scenarios with just PV or just battery. Interestingly, as a cloud covers the sun and solar irradiance is down at around 2 p.m., much more electricity is purchased to supply electricity to the building.

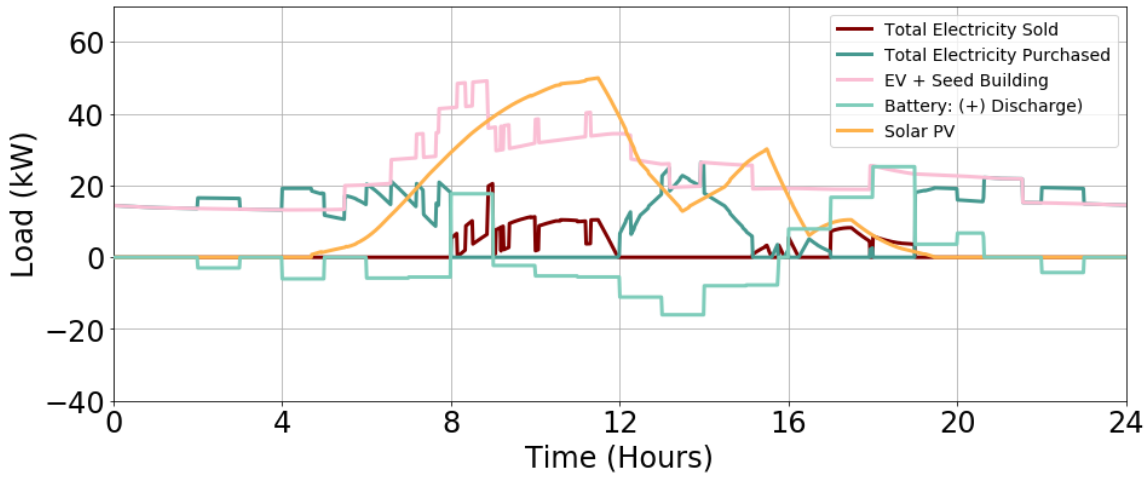

Figure I.5.A.27 Adding solar PV + battery in validation simulation

Test Run Adding Only TES

An EnStore run was completed adding TES, with results shown in Figure I.5.A.28. As mentioned previously, the TES is currently schedule-based. In the EnStore inputs, charge start time is set to 9 p.m., charge end time is

set to 7 a.m., discharge start time is set to 12 p.m., and discharge end time is set to 6 p.m. This is evident in Figure I.5.A.28, as TES is charging at night, adding to the electricity purchased for the building, and TES is discharging during the day, lowering the amount of electricity purchased during the day. In this simple case, the TES size is fixed at 100 kWh, which may not be large enough to see prominent annual electricity bill savings.

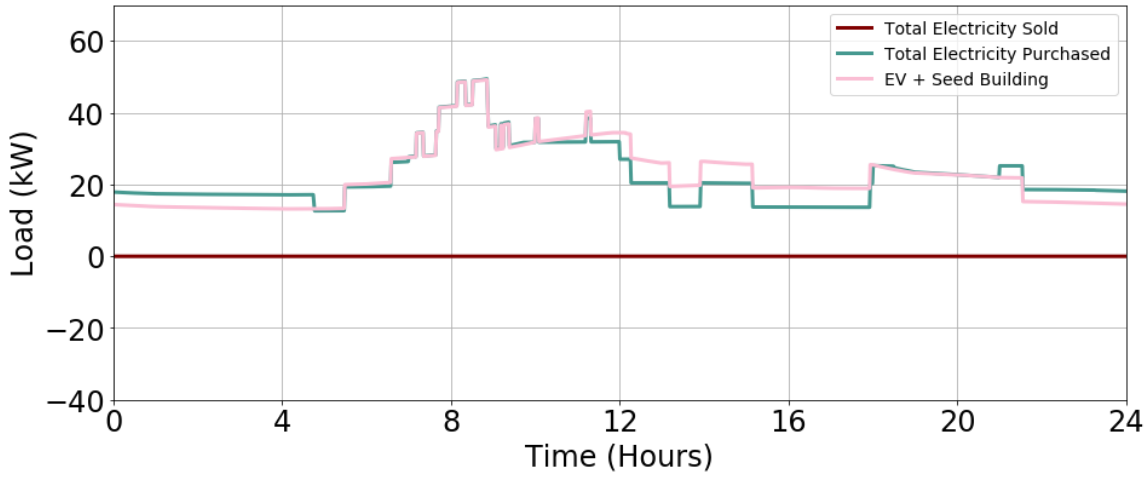

Figure I.5.A.28 Adding TES in validation simulation

Test Run Adding Solar PV + Battery + TES

An EnStore run was completed adding solar PV, battery, and TES, with results shown in Figure I.5.A.29. One can witness solar PV, whose production is highest midday; the battery, charging when electricity is cheap or solar PV is plentiful and discharging when solar PV electricity is subsiding but rates are still expensive; and the TES, charging and discharging based on the fixed schedule that can be seen more clearly in Figure I.5.A.28. In this simple case, the TES size is again fixed at 100 kWh, which may not be large enough to see prominent annual electricity bill savings.

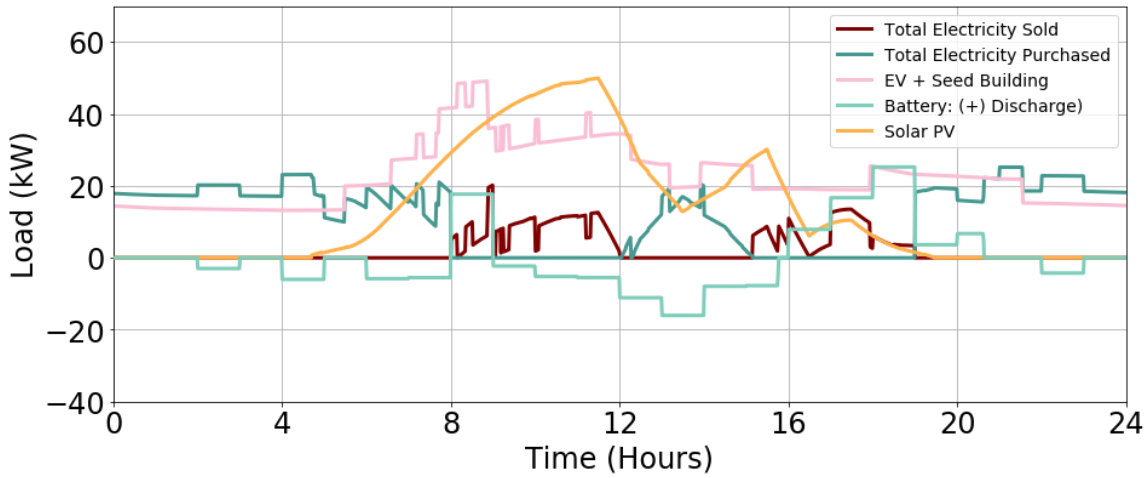

Figure I.5.A.29 Adding solar PV, battery, and TES in validation simulation

2. Financial Metrics Verification

In addition to analyzing detailed daylong time-series output data in validating EnStore functionality, we also sought to understand trends regarding the resulting financial metrics tied to each EnergyPlus run.

Test Run Adding Only Solar PV

Figure I.5.A.30 shows financial outputs for an EnStore run with five permutations of solar PV in a system with no battery or TES. Including the base case run, this creates a total of six financial runs. The simulations have been reordered from left to right by increasing PV size. Simulation 0 is the base case simulation, with EV charging stations but no BTMS system. This simulation provides the benchmark for the system owner to use when determining if the BTMS system is economically attractive. Simulation 1 is the simulation using REopt suggested sizes for solar PV and battery. One can see from this graph that adding solar PV is worth the investment, as LCOC decreases from the base case. In fact, one can see that not enough permutations of PV have been tested in this case, as we have not reached maximum where a certain amount of PV is no longer financially lucrative. At some point there must be too much PV, such that the upfront cost does not justify the incremental electricity savings and net metering profits.

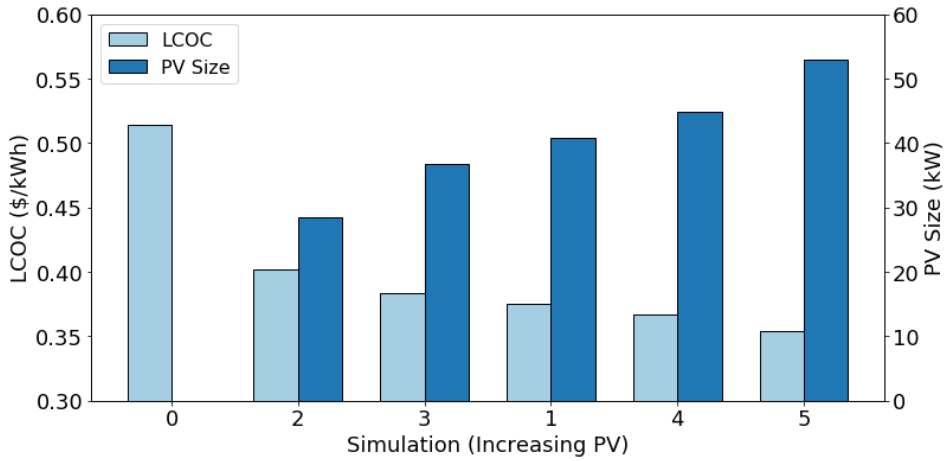

Figure I.5.A.30 Levelized cost of charging and corresponding solar PV sizes

Test Run Adding Solar PV, Battery, and TES

Figure I.5.A.31 shows financial outputs for an EnStore run with four solar PV permutations and four battery permutations, creating 16 total permutations, as well as a run the REopt base values, which accounts for 17 total EnergyPlus simulations. There are 18 total LCOC values as the base case value is also shown, with the simulation order defined by increasing PV size from left to right. Here, TES was fixed at 200 kWh. Again, simulation 0 is the base case simulation, with EV charging stations but no BTMS system, providing the benchmark for the system owner to use when determining if the BTMS system is worth the investment. Simulation 1 is the simulation using REopt suggested sizes for solar PV and battery. Here, it is difficult to see a trend between size configuration and LCOC, as both PV size and battery size are being varied. In Figure I.5.A.35 and Figure I.5.A.38, heat maps and plots with sorted information will better display relationships among the two independent variables (battery size and PV size) and the LCOC.

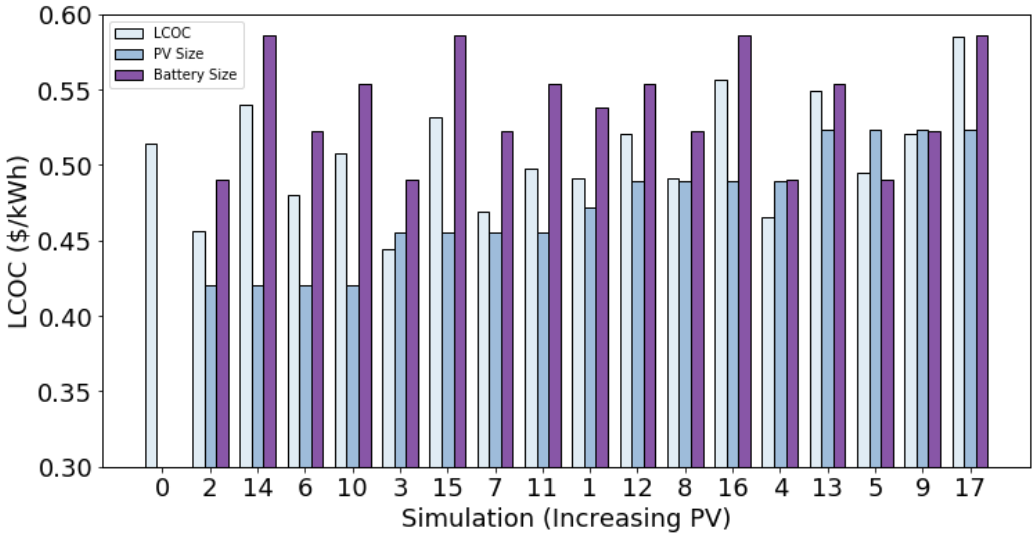

Figure I.5.A.31 Levelized cost of charging and corresponding PV and battery sizes

3. Preliminary EnStore Batch Run Results

Upon testing EnStore functionality using a simple building model, we tested EnStore using the DOE medium office prototype model to ensure EnStore functions with a building type of interest to this analysis. As previously mentioned, the EVSE load is the same as that used for the simple building model runs, a simulated station with 22 Level 2 charging events per day. A seed building + EVSE load profile for day 183 of the year (early July) can be seen in Figure I.5.A.32. Note that the peak load, around 100 kW, is significantly higher than the peak load for the simple building model (~50 kW) and the building load profile has more variation throughout the day.

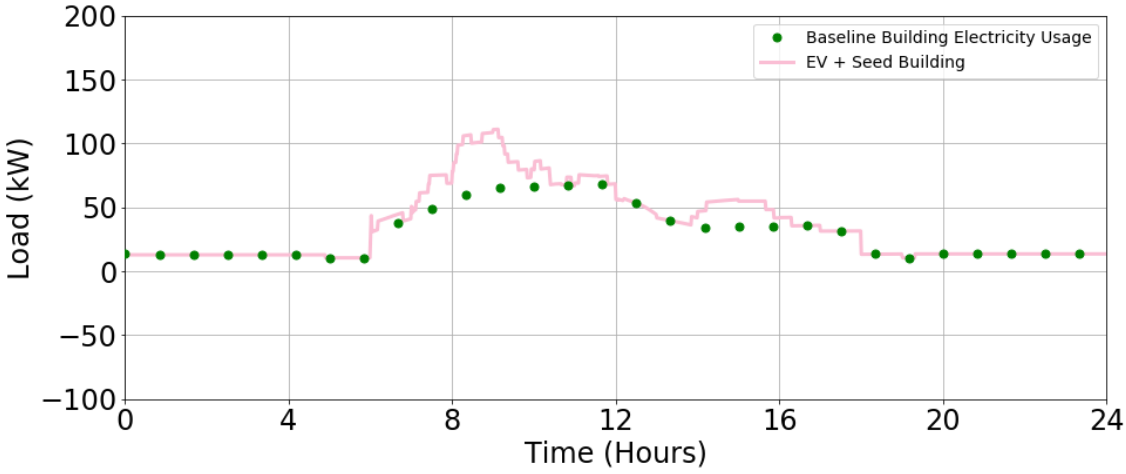

Figure I.5.A.32 Seed medium office building and EVSE load profile for batch simulation

We completed two major batch runs with 100 total EnergyPlus simulations each: one with no TES and one with 500-kWh TES. One hundred EnergyPlus simulations occurred due to user-defined inputs of 10 permutations of PV size and 10 permutations of battery size. Time-series results are only shown for the REopt recommend PV and battery size for simplicity, but aggregated financial results for all runs can be seen in Figure I.5.A.34.

Batch Run Adding Solar PV + Battery (No TES)

One major batch run included solar PV and battery without TES. Daylong time-series results for the REopt recommended size combination EnergyPlus run can be seen in Figure I.5.A.33. The battery is charging (negative) as solar PV is prevalent and discharging (positive) as solar irradiance decreases around 11 a.m. and in the late afternoon when electricity rates are higher. Electricity is sold back to the grid via net metering between 7 a.m. and 3 p.m. due to excess solar PV generation.

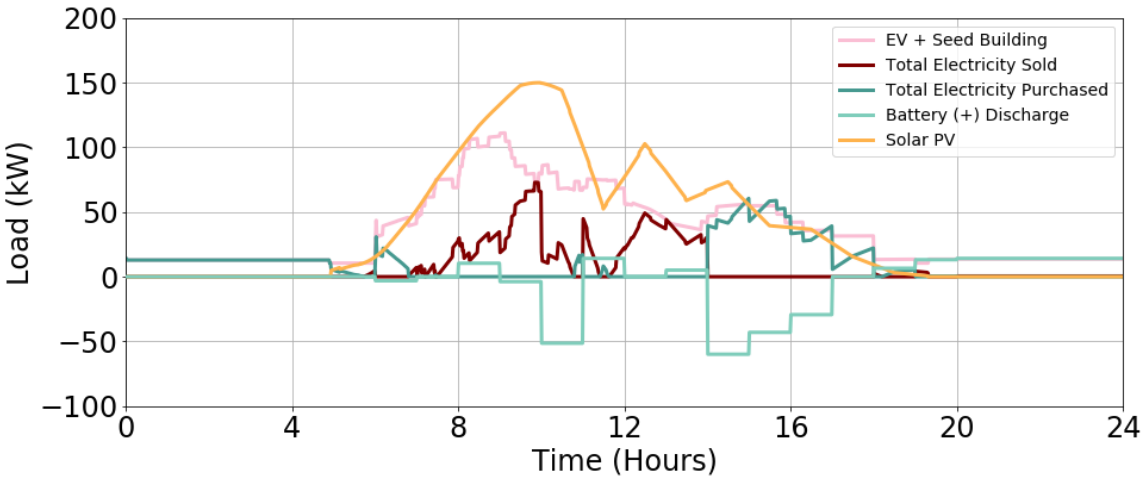

Figure I.5.A.33 Adding solar PV + battery in batch simulation

For this batch of runs, LCOC outputs varied from $0.17/kWh to $0.60/kWh. Figure I.5.A.34 and Figure I.5.A.35 show the LCOC for all simulations (x-axis) sorted by solar PV and then battery size. The top subplot of Figure I.5.A.34 shows the values of the sizes for each simulation: a set of battery sizes is run for each solar PV size for a full combination. The bottom subplot shows the LCOC for the sorted simulations, an LCOC parabolic trend corresponding to PV and battery sizes, and the LCOC for the base case. The trend line shows LCOC is lowest for PV sizes left of middle, whereas for each PV size, the LCOC is proportional to battery size. The simulations for which the LCOC line is lower than the LCOC Base Case line are where adding solar PV + battery is worth the investment. A local optimum for LCOC is prevalent, seen by the parabolic nature of the LCOC in the trendline.

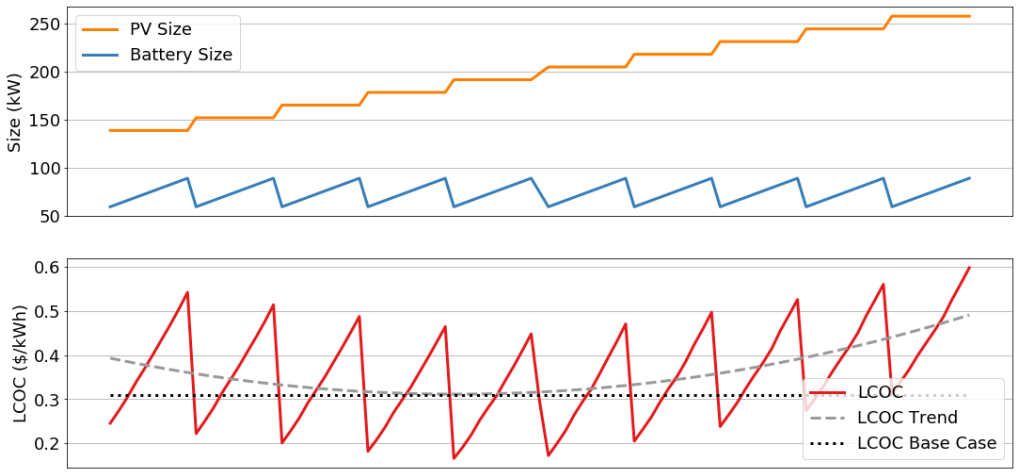

Figure I.5.A.34 Aggregated financial results for solar PV and battery run ordered by increasing PV

A heat map displaying the same information is shown in Figure I.5.A.35. The base case simulation LCOC result is shown to the right. One can see that the BTMS system is economically attractive because there are

LCOC results lower than the base case that occur with multiple PV and battery size configurations. The simulation using REopt-suggested sizes for solar PV and battery is seen in the center of the heat map; we simulate the full combination of sizes within a range for each dimension. In this run, a minimum for PV size was found near 198.2 kW; however, a minimum for battery size was not found, suggesting that a larger range for battery sizes is required in our search.

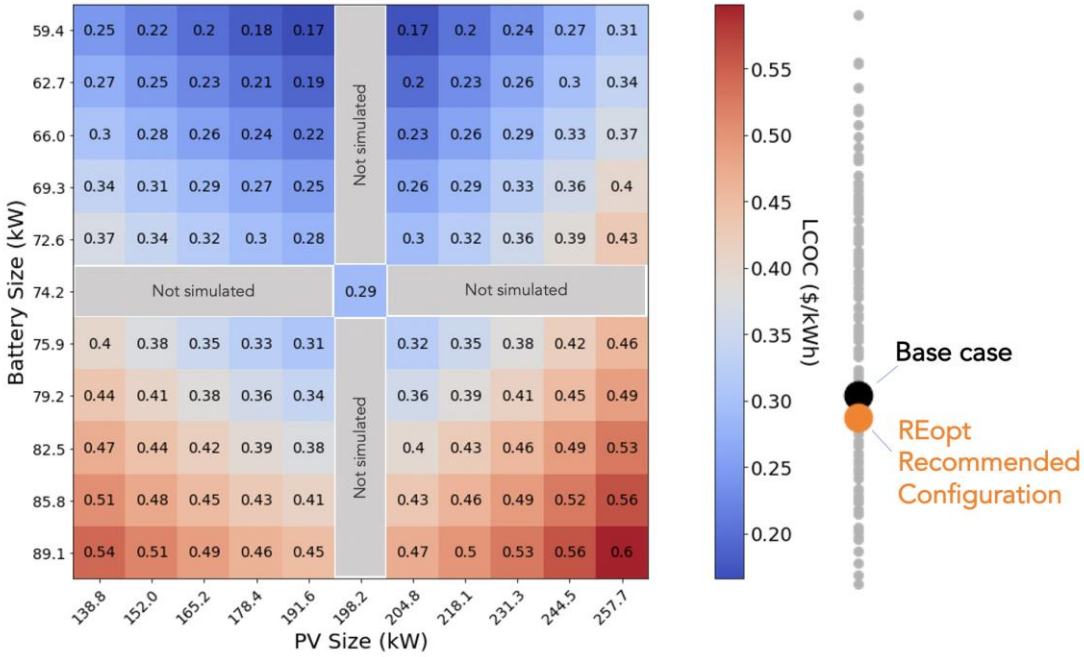

Figure I.5.A.35 Heat map with aggregated results for batch run with solar PV and battery

Caveats to these results should be emphasized: (1) the battery dispatch is borrowed from the REopt API dispatch outputs and is on an hourly basis, (2) several component models such as the battery have not been fully adapted for this use case, and (3) we are only testing a very limited range of the search space of interest. As can be observed, smaller battery sizes should have been tested because we have not reached a point where LCOCs are more expensive with "too small" battery sizes, as we have seen with "too little" PV sizes on the x-axis.

Batch Run Adding Solar PV, Battery, and TES

The second major batch run added TES to the previous experiment. The TES size was roughly estimated using the peak load and was fixed at this value for all simulations. Daylong time-series results for the REopt recommended size combinations are shown in Figure I.5.A.36. TES charges and discharges at high power levels based on the fixed schedule can be seen most clearly in Figure I.5.A.28. The medium office DOE prototype building model is a three-story model, and each story is served with its own packaged variable-air-volume HVAC system with direct expansion cooling. Each system is equipped with a packaged TES unit sized at 500 kWh.

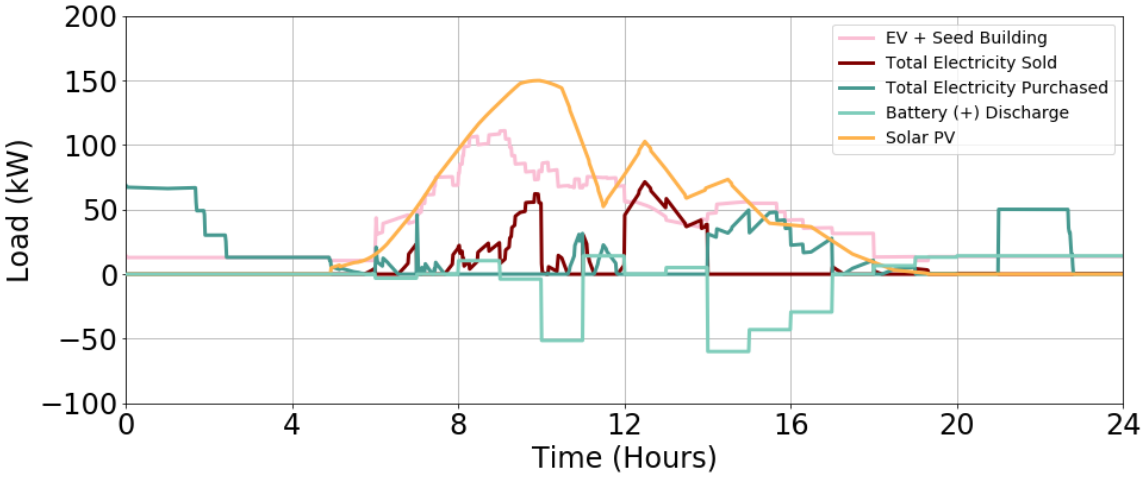

Figure I.5.A.36 Adding solar PV, battery, and TES in batch simulation

Aggregated financial results related to the sizing of the solar PV and battery components are shown in Figure I.5.A.37. The TES size is not plotted here because it is a constant size. Here, the LCOC parabolic trend corresponding to PV and battery sizes has a different minimum that has both a higher LCOC and prefers smaller PV. As opposed to the previous case of solar PV + battery, when TES is added to the mix, the red LCOC line is much higher than the base case LCOC.

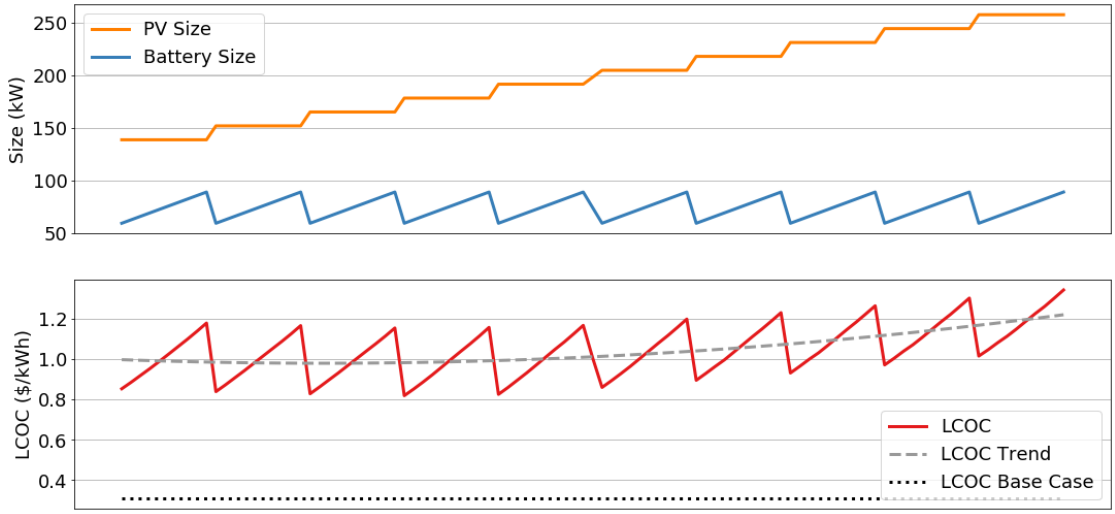

Figure I.5.A.37 Aggregated financial results for solar PV, battery, and TES run ordered by increasing PV

In Figure I.5.A.38, a heat map shows that for this batch of runs, LCOC output varied from $0.82/kWh to $1.34/kWh. The base case simulation LCOC result is shown to the right, providing a benchmark to determine if any BTMS system configuration is economically attractive. One can see that the BTMS system is not economically attractive for these runs because the LCOC results with BTMS are much higher than the base case.

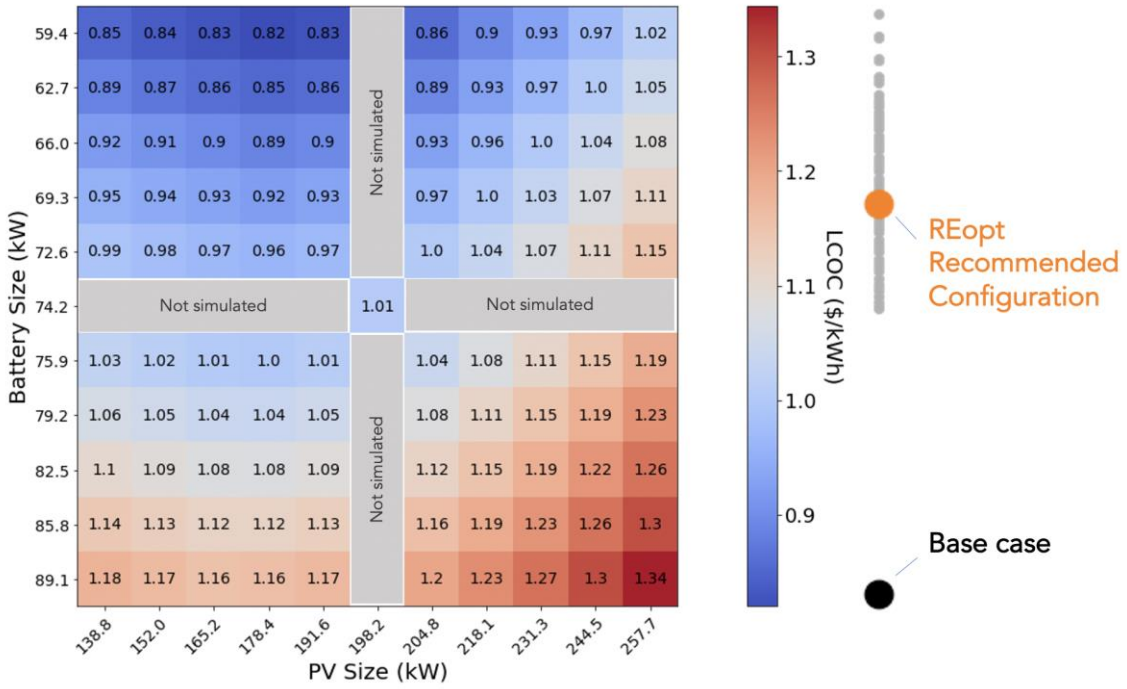

Figure I.5.A.38 Heat map with aggregated results for batch run with solar PV, battery, and TES

There are caveats to these results in addition to the ones stated for the first batch of runs: (1) the TES seed size was not rigorously estimated, much less optimized; (2) its size was fixed for the entire batch; and (3) the controls are not yet optimized to coordinate the TES and the electrochemical battery, so this BTMS mix may not be providing significant value to the consumer but have high upfront costs. The TES-based controls are only schedule-based and do not vary day by day depending on the load (charging and discharging always occurs at the same times each day). Also note that REopt makes sizing recommendations for the battery and solar PV without awareness for how TES would also be part of the system in subsequent EnergyPlus simulations.

BTMS Power Electronics

Integration Configurations

Based on the literature, the team has defined three possible configurations for a site integrated with ~2-MW DCFC loads, ~2-MW PV generation, and ~2-MW ESS with the power grid: (1) common AC bus configuration, (2) common DC bus configuration, and (3) modular-based multiple DC bus configuration.

Conventional common AC bus configuration

This is the present-day configuration considered in integrating distributed energy resources, ESS, and chargers to the grid. The utility provides a transformer that converts from distribution voltage to 480 V, though maximum single service is limited to ~2.5 MW. All elements are connected to the 480-V AC bus through an AC/DC conversion system. The main features of this configuration are:

- It is mature enough to be implemented and most of the components are available in the market
- It includes redundant AC/DC conversion stages between PV, storage, and DC charging, which may reduce the efficiency of the overall system and add to higher capital cost requirements for installation and system footprint
- Larger sites would be metered at primary voltage and own their distribution equipment.

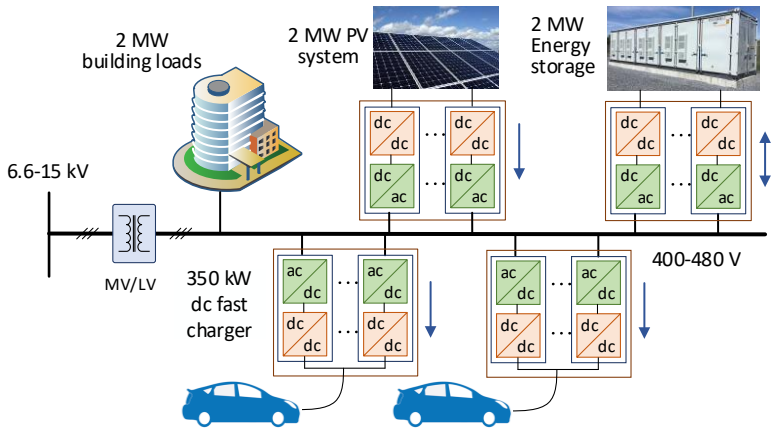

Figure I.5.A.39 Block diagram of the conventional common AC bus configuration

Common DC bus configuration

This is a futuristic configuration, which contains one AC/DC conversion stage and all elements coupled to a common DC bus. The main features of this configuration are:

- Moves isolation to higher frequency within the DC/DC
- Reduces AC/DC conversion stages between PV, battery, and charging (higher conversion efficiency)
- Improves redundancy of system with interleaved AC/DC stages
- Requires new protection devices and methods for DC breakers
- Simplifies integration with PV, EV charging, and ESS
- DC bus voltage design will influence AC/DC conversion as a trade-off with bus wire size and conductive losses.

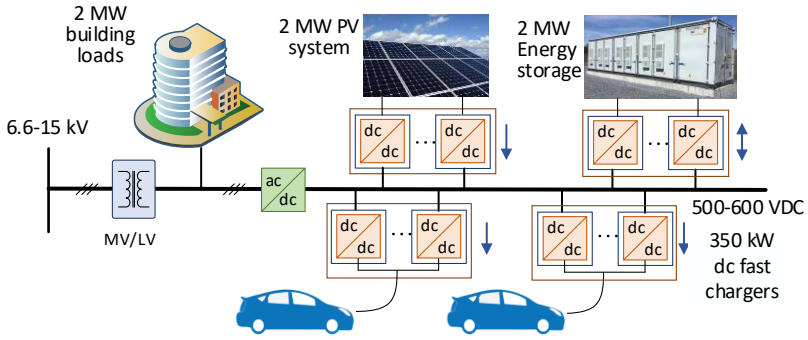

Figure I.5.A.40 Block diagram of the common DC bus configuration

Multiple DC bus configuration

This is another futuristic configuration in which the elements (PV, ESS, and chargers) are distributed for multiple DC buses. Each DC bus includes one charger and associated PV and ESS, connected to the grid through an AC/DC conversion stage. This configuration shows similar features to the common DC bus, but:

- Reduces the rating of AC/DC conversion stages
- Reduces bus capacity and protection requirements

- Segments the system, allowing for redundant operation
- Supports the scalability of the system.

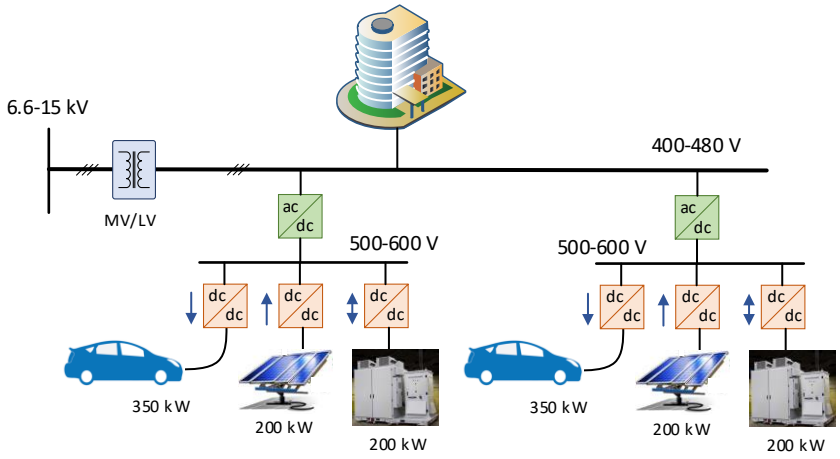

Figure I.5.A.41 Block diagram of the modular-based multiple DC bus configuration

Efficiency/Load Models

Two modeling approaches are considered in this effort based on the integration configuration. For the common AC bus, an empirical model is developed that uses data available in the manufacture datasheet and measurements. This is because the power converters for this configuration are commercial products and not much information is typically available about the converter design, switches, topology, etc. Thus, an empirical model that depends on manufacturer datasheet and measurements is needed. For common DC-bus and modular multiple DC-bus configurations, all elements are connected to DC bus though isolated DC/DC converters. These converters are not available in the market; therefore, a physics-based efficiency model is considered. This model is based on the converter topology, design, power switches, etc.

Empirical efficiency/load model (generic converter power model)

This model is developed for commercial converters to use the information available in the manufacture datasheet and measurements. It is applicable for all conversion systems in the common AC bus configuration to connect PV, ESS, and EV chargers.

For PV system, the EnStore platform incorporates SAM to model its performance. SAM includes a database for several commercially available PV inverters and uses the Sandia Inverter model to predict the PV system performance, as indicated in Figure I.5.A.42 [1], [2]. It estimates the AC output power as a function of DC input power and DC input voltage [3]. The Sandia Inverter model is applicable for PV inverter only, in which the power moves from the DC to AC side. The model is not appropriate for EV charging application, in which the power flows from AC to DC, as well as the bidirectional operation associated with ESS. Therefore, it is crucial to develop a new model that can predict the performance of DCFCs and ESS.

NREL's team developed a generic converter power model that is applicable for AC/DC, DC/AC, and DC/DC conversions, both unidirectional and bidirectional. It estimates the output power and efficiency in terms of input power and DC bus voltage. The model uses parameters from the datasheet of commercially available converters as well as actual tests. The model is generic and applicable for different converters for different applications, including PV inverter, DCFC, and bidirectional converter. The model is described in Figure I.5.A.42 and stated mathematically in Eqs. 9–11.

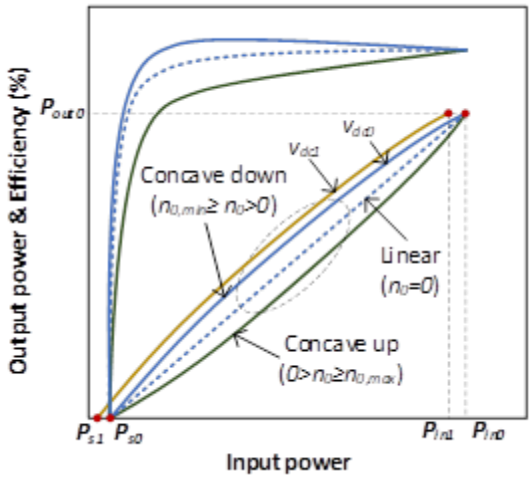

Figure I.5.A.42 Generic converter efficiency/load model

$$P_{out} = \left(\frac{P_{out0}}{P_{in0} - P_{s0}}\right)(P_{in} - P_{s0}) - \frac{n_0(P_{in0} - P_{in})(P_{in} - P_{s0})}{P_{in0}} \quad (9)$$

where:

P_{out}: Output power from the converter (W)

P_{in}: Input power to the converter (W)

P_{out0}: Maximum output power "rating" for converter at the standard test condition, assumed to be an upper-limit value (W)

P_{in0}: Input power at which P_{out0} is achieved at the standard test condition (W)

P_{s0}: Standby power at which the conversion process starts at standard test condition (W)

n_o: Nonlinearity factor defining the curvature of the relationship between input and output power at the standard test

The impact of variation of DC bus voltage (whether on the input or the output side) is considered using Eq. 10:

$$\begin{aligned} P_{in1} &= P_{in0}[1 + C_1(V_{dc1} - V_{dco})] \\ P_{s1} &= P_{s0}[1 + C_2(V_{dc1} - V_{dco})] \\ n_1 &= n_0[1 + C_3(V_{dc1} - V_{dco})] \end{aligned} \quad (10)$$

where:

C_1: empirical coefficient allowing P_{in0} to vary linearly with DC-voltage input, default value is zero (1/V)

C_2: empirical coefficient allowing P_{s0} to vary linearly with DC-voltage input, default value is zero (1/V)

C_3: empirical coefficient allowing n_0 to vary linearly with DC-voltage input, default value is zero (1/V).

Nonlinearity factor is an imperial parameter that defines the nonlinearity in the relationship between input and output power, as described in Eq. 11. For the concave up and linear models, the maximum efficiency happens

at the rated power. For the concave down model, the maximum efficiency happens before the rated power. Impact of the nonlinearity factor on the power and efficiency curve is indicated in Figure I.5.A.42.

$$n_0 = \begin{cases} n_0 = 0 & \text{Linear} \\ n_{0_{min}} \geq n_0 > 0 & \text{Concave down} \\ 0 > n_0 \geq n_{0_{max}} & \text{Concave up} \end{cases} \quad (11)$$

$n_{0,max}$ is very close to 1 (~0.9)

$n_{0,min}$ varies based on the rated and standby powers. It is very close to −0.1.

NREL's team used this model for DCFCs and bidirectional converters for ESS. In this case, a list of commercial converters, which are available at NREL's facilities (Electric Vehicle Research Infrastructure [EVRI] lab and the Energy Systems Integration Facility [ESIF]). A list of commercial DCFCs at different power levels are presented in Table I.5.A.21.

Table I.5.A.21 List of Commercial DCFCs Available at NREL's EVRI Lab

Model	P_{in0} (kW)	P_{out0} (kW)	V_{ac} (V)	P_{s0} (W)	V_{dc0} (V)	Efficiency%	
						Maximum	Minimum
ABB-Terra-HPC (1x175)	175	160	480/277	-	150–920	95.51	94% @ 20% load
ABB-Terra-HP (2x175)	350	320	480/277	-	150–920	95.51	94% @ 20% load
BTC-HP (2x50)	86.10	80	480	-	50–950	93.518	92%
BTC-350-HP (8x50)	376.7	350	480	-	50–950	93.518	92%
Tritium-50-HP	55	50	480/277	-	300–600	93.518	92%
ABB Terra 50	49.7	45.9	480	99	397	92.8	79.8

As an example, the NREL Power Electronics team levered the test data for the ABB-Terra-50 published by INL [4]. The measurements show P_{out0} = 45.9 kW, P_{in0} = 49.7 kW, η_0 = 92.3%, P_{s0} = 99 W, and η_{max}= 92.8%. These data are digitalized and used to estimate the model parameters associated with the DCFC. The model parameters are fitted to the measurements to match the curve very closely with the data. A comparison between the model output and the measurements is indicated in Figure I.5.A.43, which shows very good correlation at a nonlinearity factor of 0.0121.

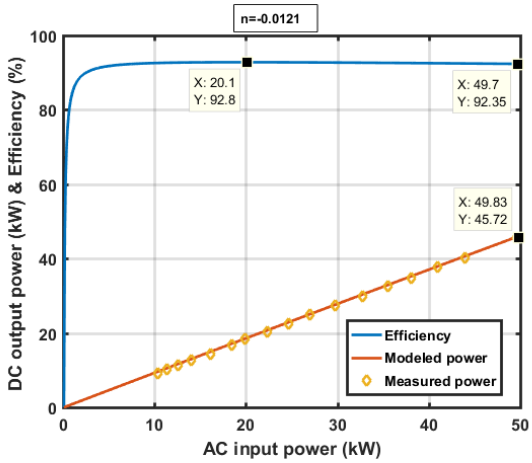

Figure I.5.A.43 Measured and modeled power and efficiency curve for ABB-Terra-50

These analyses are repeated for all DCFCs in Table I.5.A.22 and the information available in the datasheets are considered to estimate the model parameters, as presented in Table I.5.A.23. In this case, the DC bus voltage is assumed to be fixed.

Table I.5.A.22 Model Parameters for Commercial DCFCs Available at NREL's EVRI Lab

Model	P_{in0} (kW)	P_{out0} (kW)	P_{s0} (W)	V_{dc0} (V)	V_{dc0} (V)	n	$C1$	$C2$	$C3$
ABB-Terra-HPC (1x175)	169	160	338.6	400	400	−0.0208	0	0	0
ABB-Terra-HP (2x175)	339	320	677.2	400	400	−0.0208	0	0	0
BTC-HP (2x50)	86	80	172	400	400	−0.0132	0	0	0
BTC-350-HP (8x50)	376	350	752.7	400	400	−0.0131	0	0	0
Tritium-50-HP	54	50	107.8	400	400	−0.0162	0	0	0
ABB Terra 50	49.7	45.9	99	397	397	−0.0121	0	0	0

The same steps are repeated for the bidirectional converter of ESS. Two commercial converters are considered in the case Schneider XC540_ES and Caterpillar BDP250, as presented in Table I.5.A.23. In this case, two different models are associated with each converter: one for charging mode and the other for discharging mode. The model parameters for these converters are presented in Table I.5.A.24 and Table I.5.A.25.

Table I.5.A.23 List of Commercial Bidirectional Converter Available at NREL's ESIF

Model	P_{out}	Q_{out} (kVAr)	V_{ac} (V)	V_{dc} (V)	*Efficiency (%)*		
					CEC	*Max.*	*Rectifying*
Schneider XC540	±540 kVA	±540	300	440–850	98.3	98.6	>98
Caterpillar BDP250	±250 kW @ 0.8 PF	-	480	300–650	96.6	>97	-

Table I.5.A.24 Model Parameters for Commercial Bidirectional ESS Converter During Charging Mode

Model	P_{in0} (kW)	P_{out0} (kW)	P_{s0} (W)	V_{dc0} (V)	V_{dc0} (V)	n	$C1$	$C2$	$C3$
Schneider XC540	443	432	4,426	600	600	−0.0345	0	0	0
Caterpillar BDP250	262	250	2,615	600	600	−0.0338	0	0	0

Table I.5.A.25 Model Parameters for Commercial Bidirectional ESS Converter During Discharging Mode

Model	P_{in0} (kW)	P_{out0} (kW)	P_{s0} (W)	V_{dc0} (V)	V_{dc0} (V)	n	$C1$	$C2$	$C3$
Schneider XC540	438	432	4,381	600	600	−0.0175	0	0	0
Caterpillar BDP250	259	250	2,587	600	600	−0.0175	0	0	0

This model, along with the list of DCFCs and bidirectional converter with associated parameters, are provided to the cost analysis team to be included in the EnStore tool.

Physics-based, reduced-order analytical model

The common DC bus and modular-based multiple DC bus configurations require several DC-DC converters that can convert and exchange energy between the DC bus, energy storage, fast charging stations, and PV system, as shown in Figure I.5.A.40 and Figure I.5.A.41. Some of the widely used topologies for such

applications are dual active bridge converter (DAB), buck-boost converter, and resonant converter. Buck-boost converter is a non-isolated topology, whereas DAB and resonant converter are isolated topologies. Isolated topology is desired because the converter must electrically isolate from the DC bus. The most widely used converter for such applications is a DAB converter. Some of the key advantages that this topology offers are:

- High-voltage isolation
- Bidirectional power flow
- High power density
- Easy implementation of zero voltage switching
- Convenient access to cascading and parallelism.

DAB is a bidirectional DC-DC converter with a high-frequency transformer and identical full bridges on either side of the transformer. The secondary side has DC-link capacitors, and the primary side has an inductor for energy transfer. With appropriate closed loop controls, this topology can provide robust dynamic performance.

Figure I.5.A.44 shows the circuit-level topology of the DAB. The two legs of full bridges are driven with complementary square-wave pulses using gate drivers. By controlling the phase shift between the primary-side bridge and secondary-side bridge, power flow between the two bridges can be controlled. The leading bridge delivers power to the lagging bridge depending on the control algorithm. Once the switching of the full bridges is applied, a potential difference is created across the inductor, and the stored energy of the inductor is transferred based on the phase shift between the two bridges. The transformer turns ratio determines the voltage transfer ratio across the bridge. This topology can be made to operate in hard switching mode or in zero voltage switching mode.

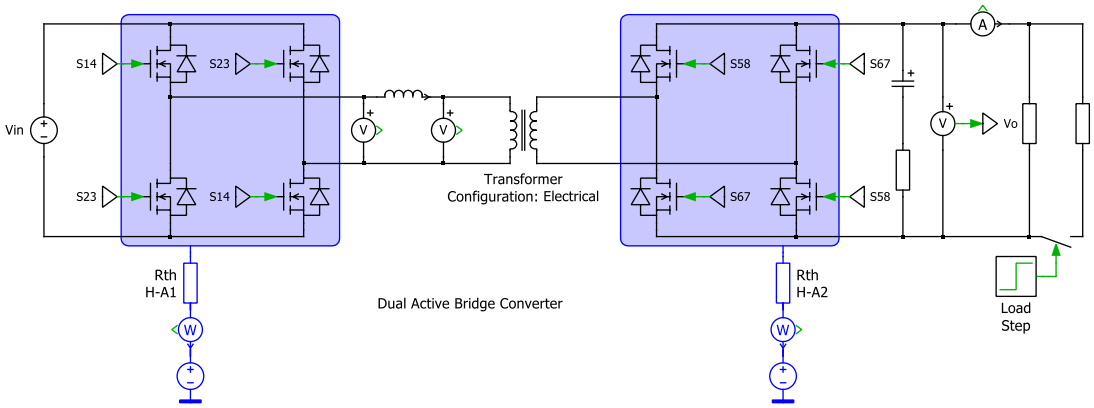

Figure I.5.A.44 Circuit topology of a dual active bridge converter

An analytical physics-based model is developed to estimate the efficiency/load curve of DAB. It involves estimating the switching and conduction losses of the switching devices and the core losses of the transformer. The phase shift between the two bridges plays an important role in the power transfer and overall efficiency of the converter. The switching and conduction losses largely depend on the characteristics of the semiconductor devices and can be estimated from the measured inductor conductor waveform [5], [6].

Switching Losses

The switching losses of the converter are mostly dependent on the switching frequency and internal device parameters of the switching devices such as an insulated-gate bipolar transistor/metal–oxide–semiconductor field-effect transistor (MOSFET)/diode used in the converter topology. From Figure I.5.A.44, the switching devices are highlighted in the purple boxes of the topology diagram. For the example used in this analysis, a

commercial SiC MOSFET device is used for directly using the device parameters from the manufacturer's datasheet.

The switching losses in a Power MOSFET can be calculated as:

$$\mathrm{P_{sw}} = \frac{1}{2} V_{ds} I_{ds} t_{on} f_{sw} \tag{12}$$

where P_{sw} is the switching loss, V_{ds} and I_{ds} are drain-source voltage and current of the MOSFETs, respectively, t_{on} is the transition on time of the MOSFET, and f_{sw} is the switching frequency. The turn-on and turn-off transition time can be estimated as:

$$\mathrm{T_{on}} = \mathrm{T_{off}} = \frac{Q_{ds}+Q_{gs}}{I_{driver}} \tag{13}$$

where Q_{ds}, Q_{gs}, and I_{driver} parameters can be obtained from the device datasheet.

Conduction Losses

The conduction losses are also associated with switching devices and are directly related to the on-resistance (R_{ds}-on) of the devices, which is a function of a device's internal charge behavior and rated electrical parameters. The conduction losses for the switch can be obtained from the following equations:

$$\mathrm{P_{MC}} = {I_{Mrms}}^2 \, R_{ds}(on) \tag{14}$$

$$\mathrm{P_{DC}} = I_{Drms} \, V_f \tag{15}$$

In these equations, the conduction losses for MOSFET and reverse conducting diode are identified by M and D subscripts, respectively. R_{ds} and V_f parameters are obtained from the device datasheet.

The RMS values for the currents in Eqs. 14 and 15 can be described as:

$$I_{Mrms} = \sqrt{\frac{D_2}{3}{I_1}^2 + \frac{D_3}{3}{I_\delta}^2 + \frac{D_4}{3}\left({I_0}^2 + I_0 I_\delta + {I_\delta}^2\right)} \tag{16}$$

$$I_{drms} = \sqrt{\frac{D_1}{3}\left({I_0}^2 + I_0 I_1 + {I_1}^2\right)} \tag{17}$$

In these equations, the magnitude of currents I_0, I_1, and I_δ can be obtained from either the measured inductor current waveform in time-domain or through circuit simulations.

Core Losses

The core losses of the transformer also affect the efficiency of the converter, which can be described by an empirical formula as:

$$P_c = k * f^{\alpha} * {B_m}^{\beta} \tag{18}$$

where f is the excitation frequency, B_m is the maximum flux density, and k, α, and β are the frequency-dependent Steinmatz parameters, which are usually available from the datasheet of the material used for the core [7]. In the analysis presented here, we have chosen ferrite core (N87), whose Steinmatz parameters are provided in Table I.5.A.26.

Total Losses

The average power flow for the DAB converter can be obtained as:

$$P_o = \frac{V_1^2 d\delta(\pi - |\delta|)}{\omega L \pi} \quad (19)$$

where V_1 is the primary-side voltage magnitude, d is the ratio of V_2 and V_1, and δ is the phase shift between the two full bridges. Based on the losses of different components, the total losses can be described as:

$$P_{Loss} = P_{sw} + P_{cond} + P_{core} \quad (20)$$

The input power to the converter can be described as:

$$P_{in} = P_{sw} + P_{cond} + P_{core} + P_O \quad (21)$$

Based on these equations, the efficiency of the converter may be described as:

$$\eta = \frac{P_o}{P_{in}} * 100 \quad (22)$$

Based on these equations, the efficiency of the converter is estimated as a function of the input power. The parameters used for the calculation of efficiency for essential model parameters are described in Table I.5.A.26. Figure I.5.A.45 shows the efficiency of the converter as a function of the normalized input power. This model can be extended for calculating efficiency of various ratings of converters.

Table I.5.A.26 Model Parameters for Dual Active Bridge Converter

Model Parameter	Parameter Value	Unit of Parameter	Parameter Details
V_1	600	V	Primary-side DC voltage
V_2	300	V	Secondary-side voltage referred to the primary side
d	1	-	Voltage ratio at inductor terminals
f_{sw}	200	kHz	Switching frequency
R_{ds}	8.2	mΩ	On-resistance of MOSFET
V_f	1.2	V	Forward voltage drop of diode
L	2.5	μH	Inductance
dT	50	ns	Dead time of switches
Q_{ds}	2.9	nC	Drain-source charge of MOSFET
Q_{gs}	5.1	nC	Gate-source charge of MOSFET
Q_{gd}	4.6	nC	Gate-drain charge of MOSFET
T_{on}	9.1	ns	Switching transistion time
α	1.13	-	Parameter related to core material
β	2.16	-	Parameter related to core material
k	0.05	kW/m³	Parameter related to core material
B_m	1	tesla	Maximum flux density

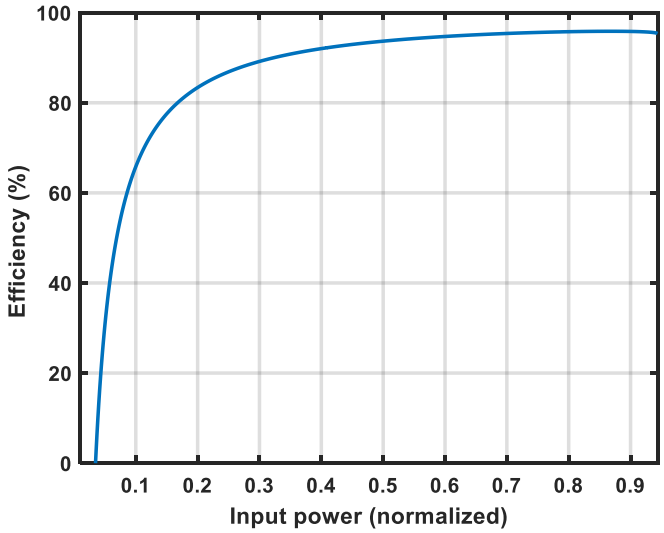

Figure I.5.A.45 Calculated efficiency of the dual active bridge converter based on the analytical model

BTMS Testing

XFC Demand Reduction Cycle Life Protocol

Overview and Methodology

A routine was developed to cycle an energy storage device as it would operate in a BTMS-assisted XFC station designed for peak shaving, operating at its maximum power capability. This edge case is designed to test the most strenuous use case, as most high-speed charging protocols are expected to have a peak-to-average power ratio greater than one. For our case, two XFC station design metrics define cycle for the ESS device. The first is XFC station continuous use time, which translates to BTMS battery continuous discharge time between recharge opportunities. The second is the XFC station usage time in a 24-hour period. This translates directly to the maximum period that must be supported by the BTMS battery in a 24-hour period. From these station design parameters, we can define two metrics used in the cycling procedure: (1) discharge time target and (2) charge time target. First, discharge time target is defined simply as the continuous XFC station use time design requirement, expressed in hours. Charge time target is defined by the amount of time in a 24-hour period that the BTMS system is not discharging, divided by the number of BTMS battery cycles needed in that 24-hour period to meet the total daily discharge time requirement. With all times expressed in hours, this results in the following equation:

$$Charge\ Time\ Target = \frac{[Discharge\ Time\ Target] * (24 - [total\ daily\ discharge\ time])}{[total\ daily\ discharge\ time]} \tag{23}$$

If a nominal XFC duration is defined, then the continuous and total daily discharge times can be expressed in number of back-to-back and daily XFC events supported, respectively. In Table I.5.A.27, a 10-minute XFC event was chosen to illustrate the number of events that could be supported at the design threshold for three different scenarios. These are not finalized design cases, but early estimations of practical station designs.

Table I.5.A.27 Relationships Between Station Design Parameters and Resulting Cell Cycling Parameters Based on Usage at Design Threshold

XFC Duration (Minutes)	*10*									
Peak-Day Station Design Parameters		**Max-Usage Results**					**Lifetime Implications**			
XFC Events per Day	Back-to-Back XFC Events	Total Discharge Hours per Day	Max BTMS Battery Cycles per Day	Discharge Time per Cycle	Max Charge Time per Cycle	BTMS Share of XFC Input Power (rough)	Minimum Years to 10,000 Cycles	Years to 10,000 Cycles if Avg usage = 0.5 Design Peak	Maximum Number of Cycles in 20 Years	Number of Cycles in 20 years if Avg usage = 0.5 Design Peak
24	6	4	4	1.0	5.0	0.83	6.8	13.7	29,200	14,600
24	12	4	2	2.0	10.0	0.83	13.7	27.4	14,600	7,300
36	18	6	2	3.0	9.0	0.75	13.7	27.4	14,600	7,300

Two cycling routines were developed to test the use case of 24 10-minute XFC events per day, with continuous discharge capability of 120 minutes (middle row in Table I.5.A.27). The first continuously discharges the device's usable energy in a 2-hour period, followed by a full recharge over a 10-hour period, resulting in two continuous cycles per day. The second routine intersperses opportunity recharges within the discharge of the BTMS system, breaking up the discharge as if vehicles arrived periodically. Both routines use the same charge and discharge power levels and result in the same energy throughput per day. These were developed to investigate the corner cases, as the real-world usage would certainly lie somewhere between the two.

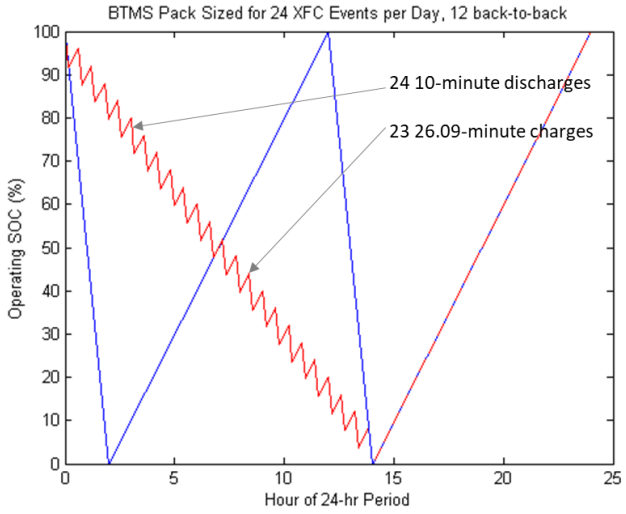

Figure I.5.A.46 Example of 24 daily XFC events per day, with device discharge power scaled to deplete usable energy target with 12 10-minute charges. Both continuous (blue) and intermittent (red) discharge/recharge cases are illustrated

The energy requirement of the BTMS system would then depend on the power delivered from the BTMS battery to the XFC station. The XFC station is receiving power from both the BTMS and the grid, and the proportion of power supplied by the BTMS system can be approximated, as shown in Eq. 24, given that the energy used to recharge the BTMS system is nearly evenly spread over the charge window as a consistent recharge power. In this approximation, system and energy storage device efficiency are not considered.

$$BTMS\ Share\ of\ XFC\ Input\ Power \sim 1 - \frac{Discharge\ Time\ Target}{Discharge\ Time\ Target + Charge\ Time\ Target} \quad (24)$$

A better approximation of the share of power delivered by the BTMS system, a measure of demand reduction capability, would be determined by also factoring in the inefficiency of the BTMS charge process and the 15-minute peak power utilized in the charge procedure, but these will not be known until characterization testing is conducted. Once the charge and discharge power requirements are determined from device characterization, Eq. 25 better represents the BTMS share of XFC power output, though it still doesn't account for unequal

power electronics system inefficiencies that could occur due to charging and discharging at disparate power levels and current flow.

$$BTMS\ Share\ of\ XFC\ Power = \frac{P_{device,dis}}{P_{device,dis} + P_{device,peak\ 15-minute\ charge}} \quad (25)$$

The BTMS share of XFC power can be multiplied by the XFC total peak power input to determine the power that must be provided by the BTMS battery. The result of this calculation is then divided by the device-level discharge power used in testing and rounded up to the next integer value to determine the minimum cell- or module-to-system scaling factor. String topology, including the number of series and parallel connections, may need to be considered to get a more realistic scaling factor; however, it is likely that the capacity of the cells tested may not be ideal for the application, so applying the logistics of full pack design may not be prudent for all devices.

It is important to note that the cycling routine presented is not likely to represent an actual usage scenario in which the arrival timing of vehicles, XFC event durations, and XFC power levels would be expected to vary significantly, affecting depth of cycling, discharge power profile, and rest periods. Rather, this tests the cycle-life capability of a device against usage at the design threshold.

NMC/graphite cells were used to shake down the cycling procedure, and several nuances were found that were incorporated into the test procedure that is being used to test the cobalt-free devices discussed in the following section.

Cobalt-Free Cell Testing

The scenario of 24 XFC events per day and 12 XFC events back-to-back was chosen as the common test to be performed when resource limitations prevented testing all of the scenarios detailed in Table I.5.A.27. The following section discusses the devices that have begun testing under the protocol laid out in the previous section.

Nickel Zinc Testing at INL

Nickel zinc cells are not a new technology, but technical solutions have been developed that claim to address some of their previous shortcomings while maintaining such attractive attributes as low cost, environmentally friendly materials, and recyclability. Eight cells were put on test and beginning-of-life tests were performed to prepare for life cycling. Ambient temperature for all tests and cycling was set at 25°C.

Rate testing and a few iterations of discharge and charge tests yielded a discharge power of 76 W and a charge power of 21.6 W. This resulted in an initial depth of discharge of about 60%, allowing for 40% fade-through cycling. The maximum operating voltage was lowered to approximately 90% to reduce the likelihood of gassing to maximize cycle life. The voltage response of one cell running the continuous discharge/charge cycle is shown in Figure I.5.A.47. The charging power used allows some time margin, about 50 minutes, as cell degradation could lead to longer charging time. Capacity will be checked after the first 100 cycles.

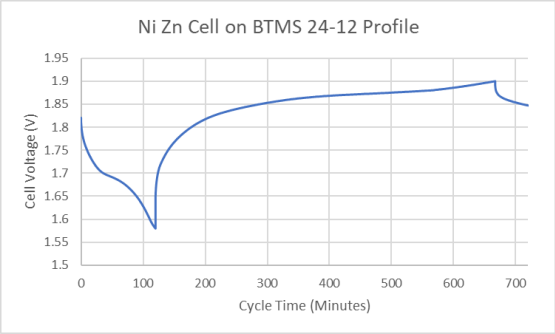

Figure I.5.A.47 Voltage response of 140-Ah Ni Zn cell running the BTMS 24-12 continuous discharge/charge cycle protocol

Lead Acid Testing at Electric Applications Incorporated

Electric Applications Incorporated developed a full test plan to guide characterization of several lead acid technologies, and cycle life testing of three of those. The test plan is designed in two parts for testing of lead acid batteries, based on test cycles developed in the last quarter: baseline performance testing and cycle life testing. Baseline performance testing includes constant-current discharge tests and constant-power discharge tests at different rates using duplicate samples of each battery type to be tested. The test results provide technical parameters of each battery type such as Peukert slope, roundtrip energy efficiency, vinyl slope, constant discharge power, and constant charge power needed for finalizing cycle life testing protocol and estimating the scale factor to a full-scale Battery Energy Storage System (BESS) pack design. The determination of these parameters ensures the candidate batteries will be cycled under conditions that will optimize their lifetime energy throughput while minimizing the grid power required for operation of the vehicle fast charger.

Cycle life testing was designed for conduct on duplicate samples of two of the commercially available lead battery types and one advanced lead battery type. Testing will determine the lifetime energy throughput of each battery type under two simulated test protocols. Reference performance tests including capacity check, weight, and impedance measurement will be performed every 99 cycles (50 calendar days). The status of test articles is detailed in Table I.5.A.28, and a summary of results from baselines testing is presented in Table I.5.A.29.

Table I.5.A.28 Status of Test Articles

1. Battery Type	Status
High Carbon AGM	Completed baseline performance testing, entered cycle life testing
Flat Plate Gel	Estimated arrival time, early October
Thin Plate Pure Lead	Completed baseline performance testing, waiting for decision on cycle life testing
Quasi Bipolar	Estimated arrival time: early October
Bipolar	Estimated arrival time: mid-October

Table I.5.A.29 Test Results Summary at End of FY 2020

Technical Characteristics					
Parameters	**HC AGM**	**GEL**	**TPPL**	**Quasi Bipolar**	**Bipolar**
Nominal Voltage (V)	12	12	12	12	48
Nominal Capacity (Ah)	50	165	210	120	30
Cycling DOD (%)	70%	50%	50%	30%	
Peukert Slope	1.18		1.10		
Energy Efficiency	87%		87%		
Vinyl Slope	1.5		1.0		
Constant Discharge Power (W)	164		480		
Constant Charge Power (W)	50		173		
Capital Estimate					
Monoblock Price ($)	$230.00	$211.69	$496.00	$239.71	
Projected Cycle Life	5,000	3,800	2,050	4,000	
CTO (kWh)	2,100	3,762	2,583	1,728	
Cost/CTO (¢/kWh)	10.95	5.63	19.20	13.87	
Scale Factor	1,640		536		
Battery Initial Cost ($)	$377,200		$265,856		

Lithium-Ion Testing at SNL

Several LFP/graphite cells and one NMC/graphite cell were characterized to determine the power levels yielding the desired discharge and charge windows outlined by the BTMS 24-12 and 24-6 testing protocols. The power for each is shown in Table I.5.A.30.

Table I.5.A.30 Optimized Power Profiles for Each Chemistry and Cell Size [a]

Chem	Size	Capacity	Average Voltage	24-6 Discharge power	24-6 Charge power	24-12 Discharge power	24-12 Charge power
LFP	26,650	3.2	3.3	10.56	2.112	5.28	1.056
LFP	26,650	2.85	3.3	9.405	1.881	4.7025	0.9405
LFP	18,650	1.1	3.3	3.63	0.726	1.815	0.363
NMC	18,650	3.5	3.635	12.7225	2.5445	6.36125	1.27225

[a] Items in yellow are currently under test for validation

Although NMC cells are not candidates for BTMS because they contain cobalt, they are included in this test matrix as a point of reference to compare other chemistries and to further test the protocol. The results for the optimized 24-6 power profiles can be found in Figure I.5.A.48.

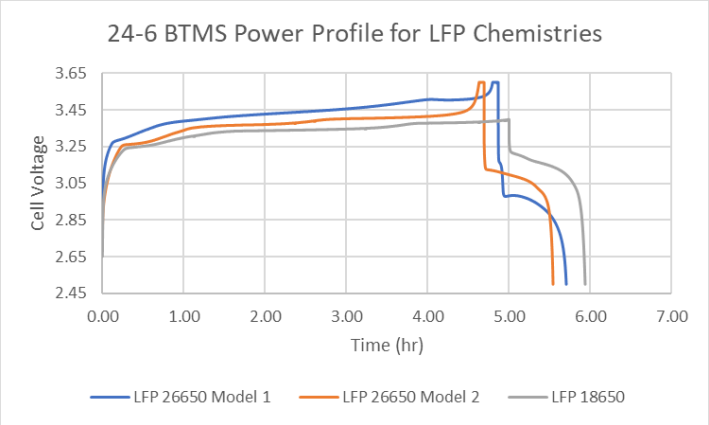

Figure I.5.A.48 24-6 constant-power profiles of LFP/graphite cells

The goal for the 24-6 profile was to have a 5-hour charge and a 1-hour discharge, ±20 min (10 minutes shorter or longer for the charge or discharge steps). All three cell types fit this criterion, but there are apparent differences in the performance of the cells. This is most likely due to cell construction/design and less with the operating chemistry. These cells have had their first reference health point taken and are currently undergoing 6 months of cycling to understand the cycling aging impact of this profile. Optimization on the 24-12 is still currently underway. The most recent results are shown in Figure I.5.A.49.

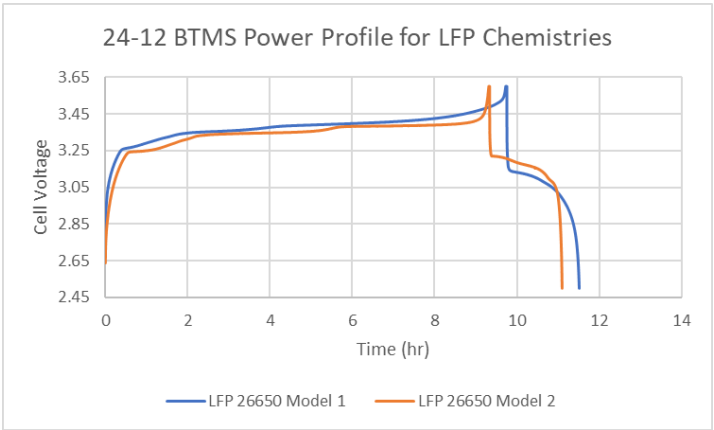

Figure I.5.A.49 24-12 constant-power profiles of LFP/graphite cells

The goal for the 24-12 profile was to have a 10-hour charge and a 2-hour discharge, ±20 min (10 minutes shorter or longer for the charge or discharge steps). We are 32 minutes from the 20-min cutoff in one case and 1 hour off in another, so power levels are still being adjusted to hit the desired metric. Once optimized such that they are within the 20-min cutoff they will be subjected to 6 months of cycling to understand the cycling aging impact of this profile.

Machine-Learning Testing

LMO/LTO cells were procured and screened to select a well-matched set of 48 cells for calendar and cycle testing in a design of experiment tailored towards feeding a machine-learning analysis approach that aims to accelerate life modeling and feature identification. The LMO/LTO is known to have a relatively long cycle life, and reducing time on test is one of the goals of the machine-learning program that is coupled with BTMS, which itself has a long cycle life goal, making testing to the goal burdensome. Temperature, SOC, and rate

were chosen as the treatment variables, with three points selected for each for cycling and three temperatures and four SOCs chosen for calendar aging. A full factorial design combing all possible permutations of the variables would have resulted in 117 cells and associated testing resources. Rather, an orthogonal approach was taken, and the combinations of testing variables chosen is shown in Table I.5.A.31.

Table I.5.A.31 All Combinations of Variables for Cycling and Calendar Aging, and Those Chosen Based on the Orthogonal Approach

Cycled Cells					Calendar Aged Cells		
Temp	DOD	Rate	Replicates		Temp	SOC	Replicates
30	8020	1	3		30	100	0
30	8020	5	0		30	90	3
30	8020	10	0		30	80	3
30	9020	1	0		30	20	3
30	9020	5	0		40	100	0
30	9020	10	3		40	90	3
30	100	1	0		40	80	3
30	100	5	3		40	20	0
30	100	10	0		50	100	3
40	8020	1	0		50	90	3
40	8020	5	0		50	80	0
40	8020	10	3		50	20	0
40	9020	1	0				
40	9020	5	3				
40	9020	10	0				
40	100	1	3				
40	100	5	0				
40	100	10	0				
50	8020	1	0				
50	8020	5	3				
50	8020	10	0				
50	9020	1	3				
50	9020	5	0				
50	9020	10	0				
50	100	1	0				
50	100	5	0				
50	100	10	3				

Thickness of the hard-sided prismatic cans was measured with a micrometer at a reference location at beginning of life (BOL), and it will be measured periodically throughout aging to capture a relative measure of gas pressure evolution within the cell. Cycling and calendar data will be continuously recorded in 100-cycle and 30-day intervals, respectively, after which reference capacity and resistance tests will be performed automatically at the aging temperature. Every 90 days, cells will be returned to 30°C, the reference temperature for this study, and all cells will perform an Hybrid Pulse Power Characterization (HPPC) with 1-hour rests, along with 20-hour charge and discharge tests, which will yield data for incremental capacity

analysis. The data warehousing structure is being built to allow the machine-learning team to have streamlined access to the data via an SQL server interface.

Ongoing Testing from Year One

Of the cells that began testing in the first year of the project, only the NMC/LTO cells remain cycling at INL, with the high-rate cells having reached more than 6,000 cycles with less than 2% capacity fade at 30°C. The high-rate cell testing at 45°C, despite retaining more than 96% capacity, failed by rupturing, likely due to gas evolution, which has been challenging to suppress for LTO cells. The cells at 30°C do not show signs of gassing. Relative capacity retention for those cells is shown in Figure I.5.A.50.

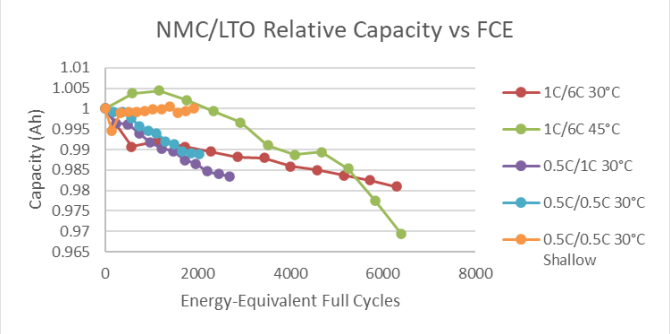

Figure I.5.A.50 NMC/LTO relative capacity of cycled cells

SNL completed testing of two models of LFP/graphite cells. These cells have undergone continuous cycling until reaching the target of 1,000 cycles. The effects of this cycling on the capacity fade of the cells can be observed in Figure I.5.A.51.

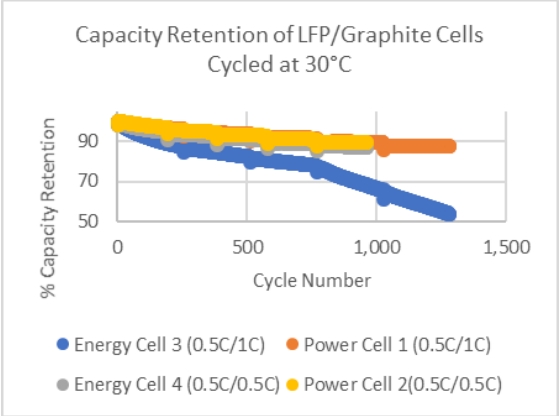

Figure I.5.A.51 LFP/graphite cycling results

Results show that, on average, the power cells have lost ~10% and the energy cells have lost close to ~50% in the worst case. It is difficult to say of the ~50% loss in the energy cell is representative without additional cells to provide statistics. If we target a 50% capacity retained at end of life after 10,000 cycles, the capacity fade rate would need to be 0.005% capacity fade/cycle. These data suggest that the capacity fade rate of this chemistry in this form factor exceed the desired decay rate by factors of ~2–5, indicating that these cells should not meet our lifetime targets. Differences in the state of health testing of these cells can also be observed in Figure I.5.A.52.

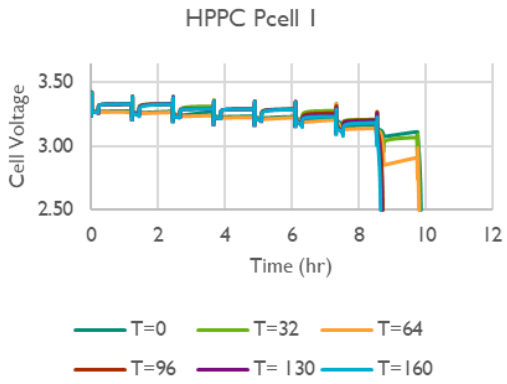

Figure I.5.A.52 Power cell 1 state of health indicated by voltage response during HPPC test

HPPC results show that as the cell continues to cycle, it loses its ability to deliver power at low states of charge. Understanding this phenomenon will be critical for predicting end-of-life behavior of these cells. The differential capacity results suggest that the loss of performance is most likely attributed to changes in the graphite anode. This is a known problem. Graphite is known to degrade from extensive cycling. As advances are made in electrolyte and electrode work, these hurdles may be overcome.

BTMS Materials Development

LTO and LMO electrodes tested in this report were provided by ANL's Cell Analysis, Modeling, and Prototyping (CAMP) facility. Detailed information on the electrodes and the rate capability test conditions are provided in Figure I.5.A.53. Three different loadings—1.7, 3.2, and 4.2 mAh/cm^2—were tested and the N/P ratios for all parings were slightly less than 1. LTO/LMO full cells were assembled in 2032-type coin cell configuration using Gen2 electrolyte (1.2-M lithium hexafluorophosphate [$LiPF_6$] in ethylene carbonate [EC]/ethyl methyl carbonate [EMC] [3:7, w/w]) or 1-M $LiPF_6$ in propylene carbonate (PC) electrolyte. Different electrolyte volumes were used for the three electrode loadings to keep the ratio of electrolyte volume to anode + cathode + separator pore volume fixed. The rate capability was tested with seven different discharge C rates—C/10, C/5, C/2, 1C, 2C, 5C, and 10C—and each discharge rate had two cycles. Charge C-rate was fixed at C/5 except for the slowest (C/10) discharge, in which the charge and discharge C-rates were the same. Cells were charged with Constant Current, Constant Voltage (CCCV) protocol (i.e., C/10 or C/5 constant current followed by voltage hold at 3.0 V until the current became smaller than C/20) and discharged with CC protocol to 1.5 V. After the rate capability test up to 10C, the cells were cycled at C/10 again. Three different temperatures were tested: 30°C, 45°C, and 55°C.

(a) Electrodes provided by CAMP

		Coating Thickness (μm)	Areal Capacity (mAh/cm^2)	Electrolyte Volume (μL)***
Paring #1	LTO*	80	1.65	40
	LMO**	66	1.67	
Paring #23	LTO	157	3.14	70
	LMO	126	3.22	
Paring #27	LTO	214	4.15	100
	LMO	172	4.21	

*87 wt% Samsung $Li_4Ti_5O_{12}$ + 5 wt% Timcal C45 + 8 wt% Kureha 9300 PVDF
**90 wt% Targray $LiMn_2O_4$ + 5 wt% Timcal C45 + 5 wt% Solvay 5130 PVDF
***(Electrolyte Volume)/(Electrodes and Separator Pore Volume) = 3

(b) Cycle conditions

	Charge CCCV, C/20 limit	Discharge CC
2 Cycles	C/10	C/10
2 Cycles	C/5	C/5
2 Cycles	C/5	C/2
2 Cycles	C/5	1C
2 Cycles	C/5	2C
2 Cycles	C/5	5C
2 Cycles	C/5	10C
2 Cycles	C/10	C/10

- 12 h rest prior to cycling
- Voltage range: 1.5 – 3 V
- Temperature: 30, 45, and 55°C

Figure I.5.A.53 (a) Coating thickness and areal capacity of the electrodes tested, and electrolyte volume used for each pairing. (b) Rate capability test protocol.

Temperature vs. Electrode Thickness

Energy (mWh) vs. power (mW) plots (i.e., Ragone plots) of 1.7-, 3.2-, and 4.2-mAh/cm^2 loading electrodes cycled in Gen2 and $LiPF_6$/PC electrolytes are presented in Figure I.5.A.54. For each electrode thickness, 30°C, 45°C, and 55°C test results are compared. Note the different scales in each plot. In these Ragone plots, cells exhibiting better rate capability will have a more gradual slope (i.e., less decrease in the energy upon increasing the power). In the Gen2 electrolyte (Figure I.5.A.54a), 30°C cells show worse performance at all C-rates tested, even with the thinnest electrodes (1.7 mAh/cm^2). Comparing the 45°C and 55°C results, the two temperatures show similar performance up to 1C at all electrode loadings, and the 55°C cells start to show better performance at 2C. At C-rates higher than 2C (i.e., 5C and 10C), only the lowest-loading electrodes show reasonable performance. In the $LiPF_6$/PC electrolyte (Figure I.5.A.54b), all cells exhibit worse rate capability (i.e., steeper slope) compared to the Gen2 electrolyte. The 45°C cells start to show worse performance compared to the 55°C cells starting from C/2, whereas in Gen2 electrolyte the two temperatures exhibited similar performance up to 1C. Such behavior can be attributed to the absence of linear carbonates in the solvent, resulting in higher viscosity and lower ionic conductivity of the electrolyte [4].

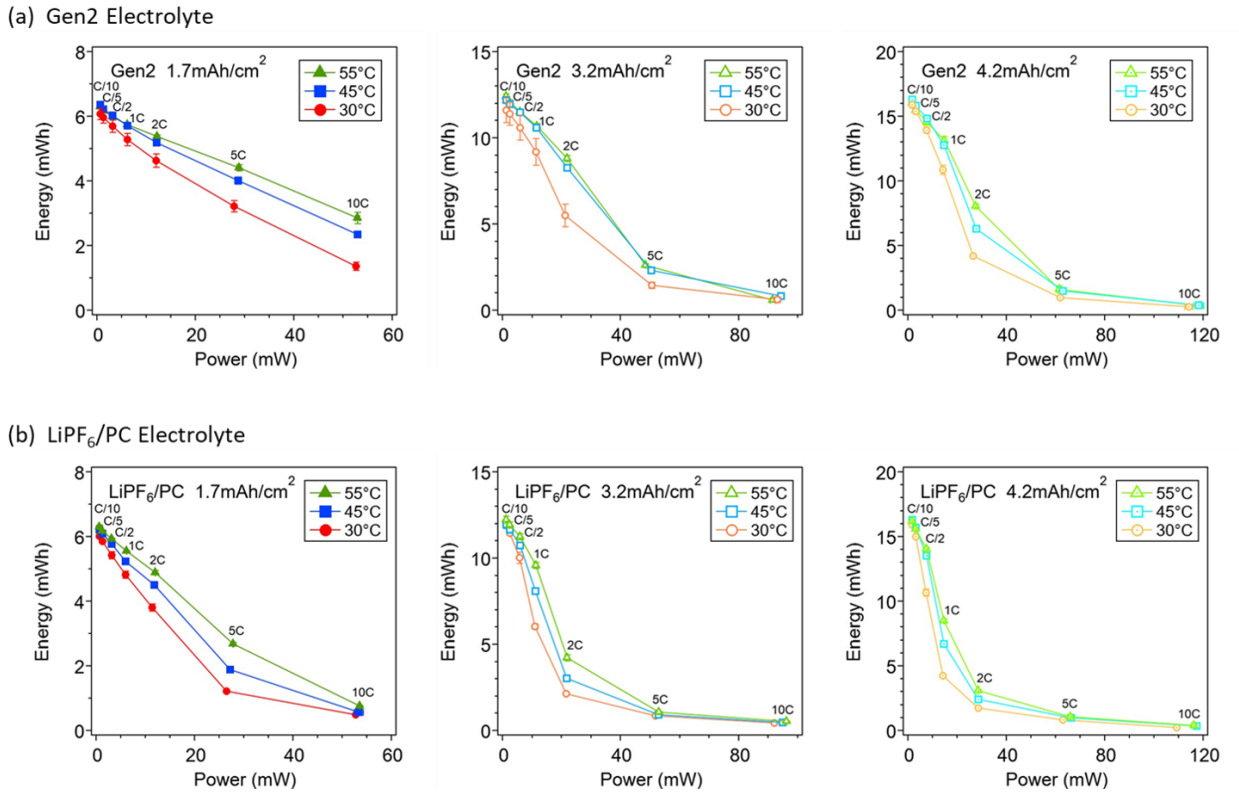

Figure I.5.A.54 Energy (mWh) vs. power (mW) plots of LTO/LMO cells tested in Gen2 electrolyte (a) and $LiPF_6$/PC electrolyte (b) at 30 °C, 45 °C, and 55 °C. Electrode parings of 1.7 mAh/cm² (left), 3.2 mAh/cm² (middle), and 4.2 mAh/cm² (right) are shown.

Gen2 vs. $LiPF_6$/PC Electrolytes

The temperature-dependent rate capability of Gen2 and $LiPF_6$/PC electrolytes at each loading is compared in Figure I.5.A.55a. As discussed, the $LiPF_6$/PC cells exhibit steeper slope compared to the Gen2 cells at all electrode loadings and temperatures tested. The two electrolytes show more comparable performance as thinner electrodes are used; at 55°C, the Gen2 and $LiPF_6$/PC cells exhibit comparable performance up to 1C, C/2, and C/5 at 1.7-, 3.2-, and 4.2-mAh/cm^2 loadings, respectively. In Figure I.5.A.55b, the electrode thickness-dependent rate capability at each temperature is compared. The 10C rate results are shown only for the lowest-loading cells (1.7 mAh/cm^2); for the other two loading cells (3.2 and 4.2 mAh/cm^2), the results up to 5C are plotted. The thickest electrode (4.2 mAh/cm^2) shows good rate capability (i.e., highest energy at a given power) up to 1C in the Gen2 electrolyte and up to C/2 in the $LiPF_6$/PC electrolyte at all temperatures tested. The results presented in Figure I.5.A.55 show that (1) the Gen2 electrolyte exhibits superior rate capability (i.e., gradual slope) compared to the $LiPF_6$/PC electrolyte at all temperatures and electrode loadings tested and (2) the Gen2 and $LiPF_6$/PC electrolyte performance show less difference when the operating temperature is increased or thinner electrodes are used. Although these are expected results considering the kinetics and electrode/electrolyte properties, the data in this report serve as a metric for designing electrodes and establishing test protocols for the BTMS cells moving forward. In addition, note that the energy and power values are not normalized as these are coin cell test results. Larger-format cells will need to be examined to obtain more accurate values.

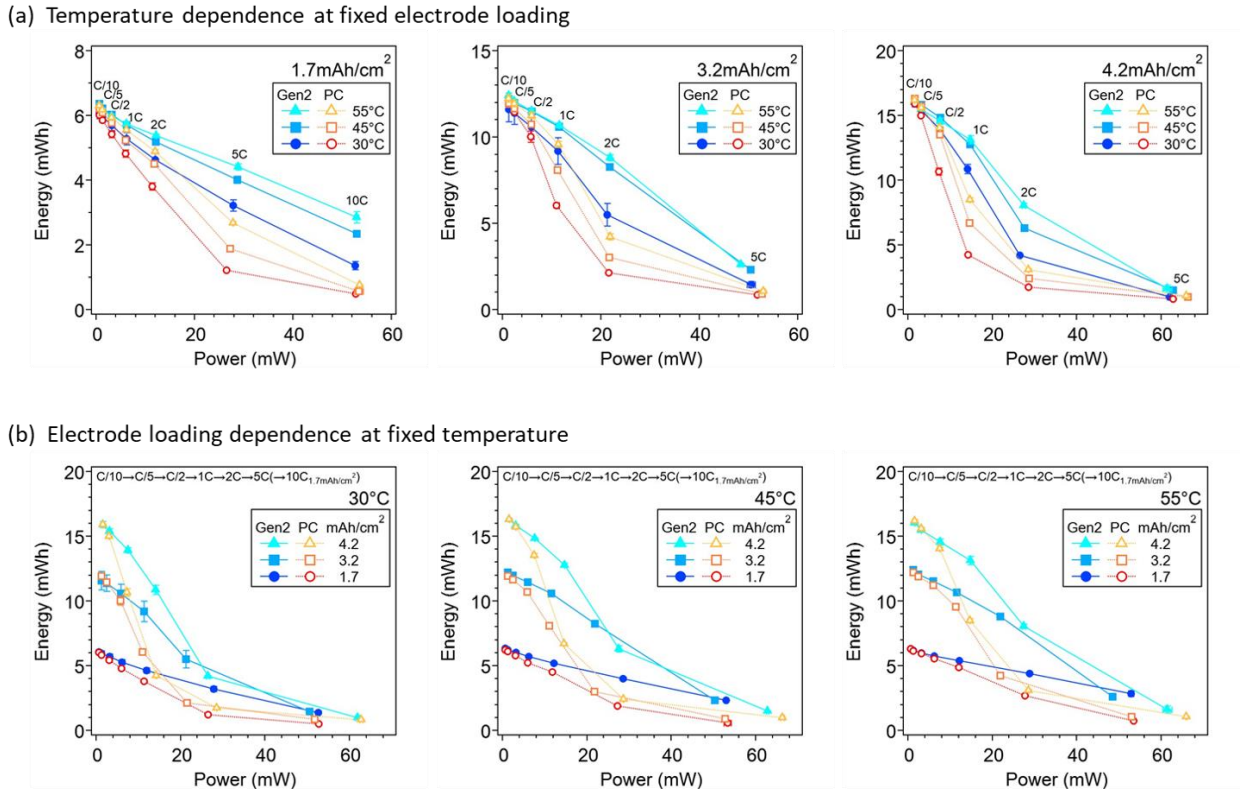

Figure I.5.A.55 Energy (mWh) vs. power (mW) plots of LTO/LMO cells tested in Gen2 and $LiPF_6$/PC electrolytes. (a) Effect of temperature at fixed electrode loading: 1.7 mAh/cm² (left), 3.2 mAh/cm² (middle), and 4.2 mAh/cm² (right). (b) Effect of electrode loading at fixed temperature: 30 °C (left), 45 °C (middle), and 55 °C (right).

Rate Capability vs. Cycle Stability.

To examine the degradation of the cells, C/10 discharge capacities before and after the rate capability test are compared (Figure I.5.A.56). In both Gen2 and $LiPF_6$/PC electrolytes, slight degradation is observed at 45°C and 55°C, with greater capacity fade at 55°C. Comparing the Gen2 and $LiPF_6$/PC electrolytes, the Gen2 electrolyte cells show larger capacity loss compared to the corresponding $LiPF_6$/PC electrolyte cells. This result indicates the Gen2 electrolyte will have worse long-term cycle performance. Indeed, the Gen2 electrolyte exhibited lower capacity retention compared to the $LiPF_6$/PC electrolyte when cycled at 45°C. The Gen2 electrolyte had ~70% capacity retention and the $LiPF_6$/PC electrolyte had ~80% capacity retention at the 1,000th cycle. Thus, while the Gen2 electrolyte is more beneficial considering the rate capability, the $LiPF_6$/PC electrolyte is favored in terms of the cycle stability.

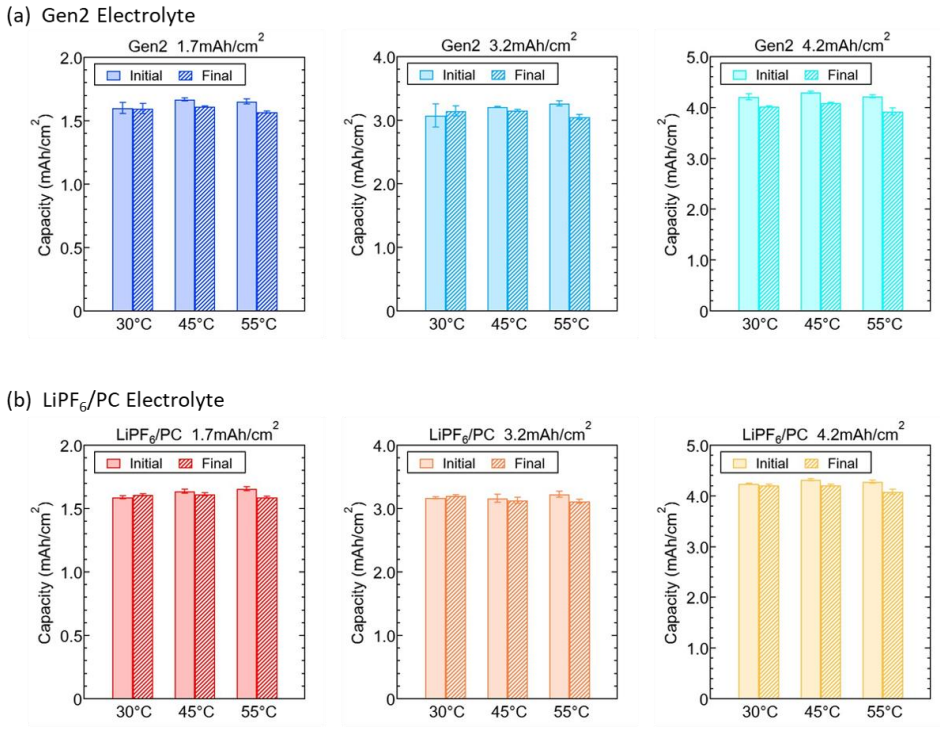

Figure I.5.A.56 Discharge capacity during the C/10 cycles before (initial) and after (final) the rate capability test in Gen2 electrolyte (a) and $LiPF_6$/PC electrolyte (b) at 30 °C, 45 °C, and 55 °C. Electrode parings of 1.7 mAh/cm² (left), 3.2 mAh/cm² (middle), and 4.2 mAh/cm² (right) are shown.

Conclusions

BTMS Analysis

In FY 2021, we plan to address the following work: developing a supervisory control algorithm for the battery and TES, integrating power electronics research from BTMS, continuing to collaborate and align research and analysis with the greater BTMS battery and TES teams, integrating the new EV load profiles that correlate with the DirectXFC project, improving the selected DOE prototype models to be more accurate at estimating demand profiles, determining and developing an EnergyPlus model and EVSE load profile for the vehicle fleet depot building type, preparing and improving the financial calculations such as incorporating federal and state tax incentives, and developing scenarios for the FY 2021 batch runs on the supercomputer using the high-performance computing (HPC) allocation. These efforts are elaborated in the following subsections.

Developing Supervisory Control Algorithm

Developing a supervisory control algorithm is critical for our BTMS analysis, as the value of the battery and TES depend on how well they are utilized and coordinated to capture value while considering operational and cost trade-offs. Flexible implementation allows for comparison of different algorithms, from schedules to advanced controls. Schedules leverage existing software and industry methods, and advanced controls with optimal control algorithms inform scenario-specific patterns and upper bounds on value. In this report, a few scenarios were run with simple, single-device control algorithms; we took from the REopt API a dispatch schedule for battery and implemented schedule-based controls for TES. In FY 2021, we plan to develop a supervisory control algorithm that uses predictive, efficient metamodels of the BTMS components and advanced control algorithms, such as model predictive control.

Integrating Power Electronics

We plan to continue to collaborate with the BTMS power electronics team to incorporate models for power electronics for EVSE, battery, and solar PV into the EnStore model, as well as understand the effects of various topologies on efficiencies of the system such as an AC vs. DC bus, or multiple DC buses.

Improving Battery Model Inputs

In initial EnStore runs we use a simple lithium-ion generic battery model in our PySAM Battery model that is not tied to a specific battery chemistry; however, in FY 2021, we plan to work with the battery team to develop inputs tied to specific battery chemistries (e.g., NMC, LTO, lead acid) to more accurately capture how those types of batteries behave at different operating conditions.

Enhancing TES Models and Capabilities

In initial EnStore runs we use a rooftop unit-coupled ice TES system with simple schedule-based controls. Plans for future work related to types of TES include adding the chiller-coupled ice TES, as well as a rooftop unit-coupled TES that uses novel phase-change materials different from ice. In addition to the different types of TES, various control strategies will be implemented, including: state-of-charge-based controls, hybrid approaches that keep a small mechanical cooling system on most of the time, and the TES cycles between charge/discharge mode to meet the cooling load and maintain occupant comfort.

Improving Electric Vehicle Load Profiles

Robust EV load profiles are vital in understanding how EV adoption and changes in station design and station utilization can affect the usage and proper sizing of BTMS systems. The EVSE profiles in this report were generated using EVI-Pro and EV-EnSite, but current EVSE profiles are generated using post-processed DirectXFC results and EV-EnSite. To properly post-process DirectXFC results for use in the EV-EnSite tool, travel data were generated, and the ZEP algorithm was used to take data from real-life disparate trips and chain them into weeklong tours. This large database of trips was used to create various PDFs for the EV-EnSite tool, characterizing and discretizing different locations by building type and size, such as “medium office building” or “small apartment complex.” We now have the code infrastructure in place to create EV-EnSite runs using DirectXFC results, but there are too many possible load profiles, and narrowing down to which EV load profiles we are interested in testing using EnStore is a necessary next step. As seen by the plethora of possible scenarios in Table I.5.A.5 and other variables not included in the DirectXFC project, including station size and station utilization, scenario definition is a critical next step in running the EV-EnSite tool to create select EV load profiles for EnStore.

Improving DOE Prototype Building Models

We plan to improve the DOE prototype models to be more accurate on a demand basis, as models that can generate a robust minute-level power load profile are important for understanding how a battery and TES system should operate. The DOE prototype models we plan to improve include the office and mid-rise apartment. The DOE office prototype model has a spike at the beginning of each day, seen in Figure I.5.A.12, due to the electric reheat terminals cycling on as the building thermostats return from nighttime setback. The DOE mid-rise apartment prototype model, seen in Figure I.5.A.14 (left), has very high loads at the beginning of the year, likely due to convergence anomalies in the simulation trying to reach steady-state. Seen in Figure I.5.A.14 (right), the rapidly cycling load throughout the day is due to the 23 in-unit electric water heaters. Because this creates a highly variant power profile that may be problematic given the needs of this project to have a relatively accurate estimate of demand at minute intervals, we plan to change the electric water heaters in the existing DOE prototype building model to natural gas heaters, which may actually be more realistic because that is the current primary heating fuel. We will take measures to remove irregularities from any existing models to generate a robust power load profile.

Developing Vehicle Fleet Depot Scenario

Because a vehicle fleet depot building type is listed as one of the building types we will explore in the Annual Operating Plan, we plan to narrow down what type of fleet depot is of most interest to both the BTMS team and DOE, as well as develop an EnergyPlus/OpenStudio model and EVSE load profile for this depot of interest to test in EnStore.

Enhancing Financial Computations

We plan to further enhance financial computations in FY 2021, implementing a more rigorous financial analysis calculator that uses generally accepted accounting principles (GAAP), which will more explicitly account for the impacts of different tax regimes and local incentives for renewable energy technologies. We also plan to explore multiple ownership models, as opposed to only a single ownership model where one single entity owns all assets behind the meter. Multiple ownership models will be evaluated in detail to better understand how asset ownership structure impacts the decision about whether to invest in this BTMS equipment. This will involve developing a better understanding of the common business models seen today or that could be used in the future, identifying how interactions and agreements between owners will be handled and determining the relative cost impacts within and across owner boundaries. We will also work to further improve the accuracy of input cost data (e.g., battery costs, power electronics, interconnection costs) and explore running future cost scenarios to see the effects on main financial metrics.

Completing Batch Runs and Visualization Using FY 2021 HPC Allocation

Finally, we plan to develop and run scenarios on the supercomputer using the HPC allocation, noting that although these runs incorporate simplified single-device controls for the battery and TES, we may be able to gather some interesting insights and trends that we can continue to build upon and test more in-depth in FY 2022. In Q1 of FY 2021, for example, we plan to deliver a summary of results and insights from more EnStore scenarios, focusing on varying the location, EV charging demand, and component costs. Initial EnStore batch runs will also aid in continuing to develop data visualization capabilities that we can further improve upon in FY 2022.

BTMS Power Electronics

The objective of this task is to support the cost analysis effort for accurately representing and modeling the power system and electronics configuration in the EnStore platform. The findings and contributions are summarized as follows:

- Different configurations for integrating PV, ESS, and EV chargers are explored
- Three configurations are chosen to represent present-day (common AC bus) and futuristic (common DC bus and modular-based multiple DC bus) scenarios
- Two efficiency/load models are developed for the energy conversion systems:
    - Empirical model for commercially available converters
    - Physics-based model for futuristic converters that are not available in the market
- List of commercial converters for DCFCs and ESS available at NREL are modeled using the empirical model
- Reduced-order analytical model for a bidirectional dual active bridge converter is implemented in MATLAB for DC-DC converters in common DC bus and modular-based configurations
- These models, along with the associated parameters, are provided to the cost analysis team to be integrated to the EnStore tool.

The estimation approach outlined will support “datasheet” conversion efforts, though the team intends to leverage other activities to refine these models for actual equipment available at the ESIF. The task objectives for investigation of the primary power conversion are expected to support a broader understanding of which scenarios (based on energy throughput, on-site equipment, etc.) will benefit from these new approaches to identify operational benefits.

BTMS Testing

The BTMS cycle life protocol developed this year is being used to evaluate several cobalt-free technologies, with more expected to be received for testing next year. Specialized testing to produce data for the interface task between BTMS and machine learning has commenced. The LTO-anode-based cells that began cycling in year one are the only cells that continue to cycle, and indicate very high cycle life, though not with a cobalt-free cathode.

BTMS Materials Development

Temperature-dependent rate capability of LTO/LMO cells with varying electrode loadings (1.7, 3.2, and 4.2 mAh/cm^2) were tested using the conventional Gen2 electrolyte and the newly developed $LiPF_6$/PC electrolyte. Using the Gen2 electrolyte, the highest-loading electrodes showed good performance up to 1C rate and the cells exhibited similar performance at 45°C and 55°C. The $LiPF_6$/PC cells showed worse rate capability compared to the Gen2 electrolyte, potentially due to the lack of linear carbonate solvents. However, in terms of cycle stability, the $LiPF_6$/PC electrolyte outperformed the Gen2 electrolyte. These results suggest 45°C is an appropriate temperature to cycle LTO/LMO cells with the electrode loadings up to 4.2 mAh/cm^2, assuming the electrolyte has a similar rate capability to the Gen2 electrolyte and the maximum C-rate is 1C. Although the Gen2 electrolyte showed superior rate capability, the $LiPF_6$/PC electrolyte exhibited better cycle stability. By tuning the electrode design and electrolyte properties, the rate capability and cycle stability of the cells will need to be balanced.

References

BTMS Analysis

1. National Renewable Energy Laboratory. 2020. “REopt: Renewable Energy Integration & Optimization.” Accessed October 1, 2020. https://reopt.nrel.gov/.
2. D. Cutler et al. 2017. “REopt: A Platform for Energy System Integration and Optimization.” Renewable Energy: 75.
3. N. Blair et al. 2018. “System Advisor Model (SAM) General Description (Version 2017.9.5).” Renewable Energy: 24.
4. National Renewable Energy Laboratory. 2020. “System Advisor Model (SAM).” Accessed October 1, 2020. https://sam.nrel.gov/.
5. U.S. Department of Energy. 2020. “EnergyPlus.” Accessed October 1, 2020. https://energyplus.net/.
6. U.S. Department of Energy. “OpenStudio.” Accessed October 1, 2020. https://www.openstudio.net/.
7. OpenEI. 2020. “Utility Rate Database.” Accessed October 1, 2020. https://openei.org/wiki/Utility_Rate_Database.
8. U.S. Department of Energy Office of Energy Efficiency and Renewable Energy. 2020. “Commercial Prototype Building Models.” Accessed October 1, 2020. https://www.energycodes.gov/development/commercial/prototype_models.
9. P. Gilman et al. 2019. “PySAM (Python Wrapper for System Advisor Model ‘SAM’).” Golden, CO: National Renewable Energy Lab. doi: 10.11578/dc.20190903.1.
10. E. Y. Ucer, M. C. Kisacikoglu, F. Erden, A. Meintz, and C. Rames. 2018. “Development of a DC Fast Charging Station Model for use with EV Infrastructure Projection Tool.” 2018 IEEE Transportation Electrification Conference and Expo (ITEC), June 2018, 904–909. doi: 10.1109/ITEC.2018.8450158.

11. X. Zhu, B. Mather, and P. Mishra. 2020. “Grid Impact Analysis of Heavy-Duty Electric Vehicle Charging Stations.” 2020 IEEE Power Energy Society Innovative Smart Grid Technologies Conference (ISGT), Feb. 2020, 1–5. doi: 10.1109/ISGT45199.2020.9087651.

12. E. Wood, C. Rames, and M. Muratori. 2018. “New EVSE Analytical Tools/Models: Electric Vehicle Infrastructure Projection Tool (EVI-Pro).” Golden, CO: National Renewable Energy Laboratory. NREL/PR-5400-70831.

13. S. Dey, Y. Shi, K. Smith, A. M. Colclasure, and X. Li. 2020. “From Battery Cell to Electrodes: Real-Time Estimation of Charge and Health of Individual Battery Electrodes.” IEEE Transactions on Industrial Electronics 67(3): 2167–2175. doi: 10.1109/TIE.2019.2907514.

14. NumPy Financial. 2019. “npv — numpy-financial documentation.” Accessed October 1, 2020. https://numpy.org/numpy-financial/latest/npv.html.

15. M. Muratori et al. 2019. “Technology solutions to mitigate electricity cost for electric vehicle DC fast charging.” Applied Energy 242(C): 415–423. doi: 10.1016/j.apenergy.2019.03.061.

16. L. Myers. 2020. “Discussing employee count to parking ratio rule of thumb for NREL.” Jan. 29, 2020.

17. W. Short, D. Packey, and T. Holt. 1995. “A Manual for the Economic Evaluation of Energy Efficiency and Renewable Energy Technologies.” Golden, CO: National Renewable Energy Laboratory. NREL/TP-462-5173, 120.

18. National Renewable Energy Laboratory. “REopt LiteTM API (Version 1).” Accessed October 1, 2020. https://developer.nrel.gov/docs/energy-optimization/reopt-v1/.

19. S. Jaffe and K.-A. Adamson. 2013. “Energy Storage in Commercial Buildings.” Navigant Research.

20. B. Borlaug, S. Salisbury, M. Gerdes, and M. Muratori. 2020. “Levelized Cost of Charging Electric Vehicles in the United States.” Joule 4(7): 1470–1485. doi: 10.1016/j.joule.2020.05.013.

21. OpenEI. 2018. “Pacific Gas & Electric Co - U.S. Utility Rate Database.” Accessed October 7, 2020. https://openei.org/apps/USURDB/rate/view/5bc91ae45457a3996e3b43ec.

BTMS Power Electronics

1. P. Gilman, A. Dobos, N. DiOrio, J. Freeman, S. Janzou, and D. Ryberg. 2018. *SAM Photovoltaic Model Technical Reference Update*. Golden, CO: National Renewable Energy Laboratory. NREL/TP-6A20-67399. https://www.nrel.gov/docs/fy18osti/67399.pdf.

2. P. Gilman. 2015. *SAM Photovoltaic Model Technical Reference*. Golden, CO: National Renewable Energy Laboratory. NREL/TP-6A20-64102. https://www.nrel.gov/docs/fy15osti/64102.pdf.

3. D.L. King, W.E. Boyson, and J.A. Kratochvil. 2004. *Photovoltaic Array Performance Model*. Albuquerque, NM: Sandia National Laboratories. SAND2004-3535. https://prod-ng.sandia.gov/techlib-noauth/access-control.cgi/2004/043535.pdf.

4. Idaho National Laboratory. 2016. “DC Fast Charger Fact Sheet: ABB Terra 53 CJ charging a 2015 Nissan Leaf.” Idaho Falls, ID: Idaho National Laboratory. INL/MIS-15-34055. https://avt.inl.gov/sites/default/files/pdf/evse/ABBDCFCFactSheetJune2016.pdf.

5. Y. H. Abraham, H. Wen, W. Xiao, and V. Khadkikar. 2011. “Estimating power losses in Dual Active Bridge DC-DC converter.” *2011 2nd International Conference on Electric Power and Energy Conversion Systems (EPECS)*, November 2011, Sharjah, United Arab Emirates, 1–5.

6. F. Krismer and J. W. Kolar. 2010. “Accurate Power Loss Model Derivation of a High-Current Dual Active Bridge Converter for an Automotive Application.” *IEEE Transactions on Industrial Electronics* 57(3): 881–891. doi: 10.1109/TIE.2009.2025284.

7. S. Yue, Q. Yang, Y. Li, and C. Zhang. 2018. “Core loss calculation for magnetic materials employed in SMPS under rectangular voltage excitations.” *AIP Advances* 8(5). https://doi.org/10.1063/1.5007201.

BTMS Materials Development

1. T. Tan, H. Yumoto, D. Buck, B. Fattig, and C. Hartzog. 2008. "Development of Safe and High Power Batteries for HEVs." World Electr. Veh. J. 2(2): 164–170.

2. Y. Kuang, C. Chen, D. Kirsch, and L. Hu. 2019. "Thick Electrode Batteries: Principles, Opportunities, and Challenges." Adv. Energy Mater 9(33): 1901457.

3. S. K. Kumar, A. A. B. M. Abduh, O. Sabih, and R. Yazami. 2018. "Temperature Effect on "Ragone Plots" of Lithium-Ion Batteries." J. Electrochem. Soc. 165: A674-A679.

4. J. M. Tarascon and D. Guyomard. 1994. "New electrolyte compositions stable over the 0 to 5 V voltage range and compatible with the Li1+xMn2O4/carbon Li-ion cells." Solid State Ion. 69: 293–305.

I.6 Testing, Analysis, High-Performance Computing, Lab-I4

I.6.A BatPaC Model Development (Argonne National Laboratory)

Shabbir Ahmed, Principal Investigator
Argonne National Laboratory
9700 S. Cass Avenue
Argonne IL 60439
E-mail: Shabbir.Ahmed@anl.gov

Brian Cunningham, DOE Technology Development Manager
U.S. Department of Energy
E-mail: Brian.Cunningham@ee.doe.gov

Start Date: October 1, 2019 End Date: September 30, 2022
Project Funding: $600,000 DOE share: $600,000 Non-DOE share: $0

Project Introduction

A performance and cost model (BatPaC [1]) was developed at Argonne to design automotive Li-ion batteries that can meet the specification of a given vehicle, and then to estimate the cost of manufacturing such batteries. It is the product of long-term research and development at Argonne through sponsorship by the U.S. Department of Energy.

Over a decade, Argonne has developed methods to design Li-ion batteries for electric-drive vehicles based on modeling with Microsoft® Office Excel spreadsheets. These design models provided all the data needed to estimate the annual materials requirements for manufacturing the batteries being designed. This facilitated the next step, which was to extend the effort to include modeling of the manufacturing costs of the batteries.

The BatPaC model has been peer reviewed and is available on the web [2]. It captures the interplay between design and cost of Li-ion batteries for transportation applications. It is used to estimate the impact of R&D advances on the mass, volume, and cost of lithium ion cells and battery packs. Moreover, BatPaC is the basis for the quantification of battery costs in U.S. EPA and NHTSA 2017-2025 Light-Duty Vehicle Technical Assessment. This assessment is then used to determine what mileage (i.e. CAFE) and CO2 emission standards are optimal from a cost-benefit analysis.

Objectives

To develop and utilize efficient simulation and design tools for lithium ion batteries to predict

- Overall and component mass and dimensions
- Cost and performance characteristics when manufactured in large volume.

Approach

The battery pack design and cost calculated in BatPaC represent projections for a specified level of annual battery production (10,000-500,000). As the goal is to predict the future (~5 years) cost of manufacturing batteries, a mature manufacturing process is assumed. The model designs a manufacturing plant with the sole purpose of producing the battery being modeled. The assumed battery design and manufacturing facility are based on common practice today but also assume some problems have been solved to result in a more efficient production process and a more energy dense battery. Our proposed solutions do not have to be the same methods used in the future by industry. We assume the leading battery manufacturers, those having successful operations in the near future, will reach these ends by some means.

For a selected battery chemistry, BatPaC solves the governing equations to determine the size of each layer, cell, and module that make up the battery pack that can meet the desired requirements for power and energy. This allows the calculation of the mass of each material, the volume of the components, and the heat removal needed during discharge. The cost of the pack is then estimated based on a predefined manufacturing process.

Current effort is directed at

- Improving the design capability by including correlations derived from continuum modeling and updating the default material properties to reflect recent experimental and industrial performance data
- Reducing the uncertainty of model predictions by setting up independent models of the manufacturing processes
- Validating the results through discussions with manufacturers and component developers.
- Updating the cost of materials used in BatPaC calculations.

Results

Key Accomplishments

- Released a new version of BatPaC
- Developed cell models to represent the electrochemical and thermal characteristics
- Developed a model of a cylindrical cell to estimate the cell specific energy and energy density
- Studied the effect of thin current collectors on specific energy and energy density.

BatPaC 4.0 Release

A new version of BatPaC was released with a variety of changes to reflect the changing state of the technology and our own understanding of the performance and cost drivers. A new Dashboard tab has been added to consolidate some of the input and output parameters that are of interest to most users. It shows the default input parameters and the option to override these values. Figure I.6.A.1 shows the input section of the Dashboard with pulldown menus for the electrode combination, the type of vehicle for which the battery is being designed, the type of coolant, and if the battery is to be capable of fast charge. BatPaC calculations determine the electrode thickness to meet the design constraints (pulse power, fast charge) and then proceeds with the cell, module, and pack level parameters. However, some researchers prefer to specify the electrode thickness to compare cell chemistries and costs. This feature has been enabled with a warning that the design constraints may not be met, especially if the user specifies the electrode to be thicker than determined from BatPaC iterations. A default set of output parameters is reported in the Dashboard and this can be customized by selecting parameters reported in the other tabs. A quick review of parametric sensitivity is enabled with a XY plot located in the Dashboard. The X and Y parameters can be selected from those available in the output tables, where the X and Y values are drawn from the columns representing Battery-1 through Battery-7, as shown in Figure I.6.A.2.

DASHBOARD

Default input values (can be changed by using Override)	Default input values (may be changed)	Required input by user	Optional override input

INPUTS

Chemistry

	Current Selection	Choose
Electrode Pair	NMC622-G	NMC622-G
Positive Electrode: Li1.05(Ni0.6Mn0.2Co0.2)0.95O2		Override
Positive active material specific capacity, mAh/g	180	
Void volume fraction, %	25	
Positive foil thickness, µm	15	
Maximum positive electrode thickness, µm	120	
Negative Electrode: Graphite		
Negative active material specific capacity, mAh/g	360	
N/P capacity ratio after formation	1.10	
Void volume fraction, %	25	
Negative current collector thickness, µm	10	
Separator thickness, µm	15	
Maximum charging current density, mA/cm²	9.00	

Costs

	Current Selection	Override
Positive Electrode, $/kg		
Active material	$20.60	
Carbon	$6.60	
Binder	$9.50	
Solvent (NMP)	$3.10	
Negative electrode, $/kg		
Active material	$12.50	
Carbon Black	$6.60	
Binder	$10.00	
Solvent (Water)	$0.00	
Al Foil, $/m²	$0.30	
Cu Foil, $/m²	$1.20	
Separator, $/m²	$1.10	
Electrolyte, $/L	$15.00	

Battery Design

	Current Selection	Choose
Vehicle Type	EV	EV
Coolant Type	EG-W	EG-W
Calculate Fast Charging?	No	No

	Override
Useable battery energy, % of total (EV)	85

Add Default # of Cells/Modules for given system

	Battery 1	Battery 2	Battery 3	Battery 4	Battery 5	Battery 6	Battery 7
Target battery pack power at 20% SOC, kW	180	220	260	300	120	400	360
Number of cells per module (total)	12	12	12	12	14	12	18
Number of cells in parallel group in module	1	1	1	1	1	1	2
Number of modules in row	5	5	5	5	5	5	6
Number of rows of modules per pack	4	4	4	4	2	4	4
Number of modules in parallel	1	1	1	1	1	1	1
Number of packs manufactured per year	100,000	100,000	100,000	100,000	100,000	100,000	100,000
Energy requirement for a UDDS cycle, Wh/mile	250	250	250	250	250	250	350
Select capacity, energy, or vehicle range, but only one.							
Pack capacity (Ah)							
Pack energy (kWh)							
Vehicle range (miles)	180	220	260	300	100	270	300

EV Charging

Time to recharge from 15% to 75% SOC, min	9.65	9.65	9.65	9.65	9.65	9.65	9.65
Optional positive electrode thickness override							

Figure I.6.A.1 Common input parameters selected or specified in the Dashboard

Summary of Results and Graphing								
Unit	Absolute	Battery 1	Battery 2	Battery 3	Battery 4	Battery 5	Battery 6	Battery 7
X =	Battery system total energy storage, kWh	53	65	76	88	29	79	124
Y1 =	Pack total mass, kg	244	287	330	373	143	343	538
Y2 =	Total cost of cells, $/kWh	$94	$90	$86	$84	$103	$86	$82

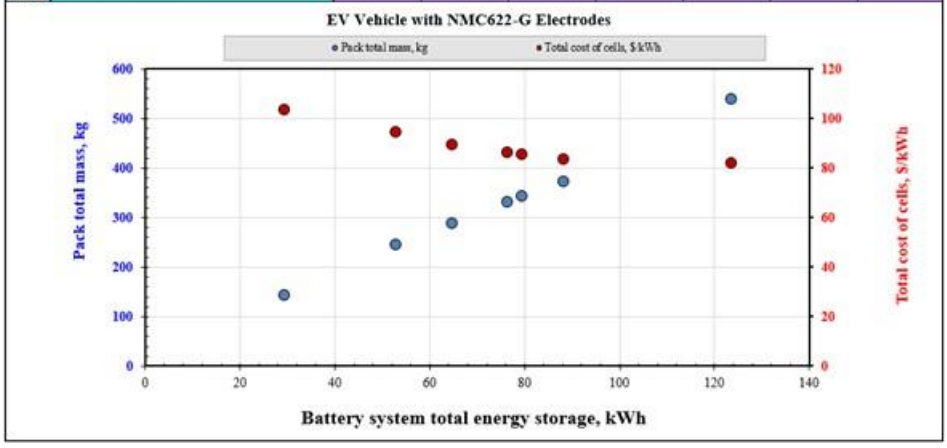

Figure I.6.A.2 Plot showing parametric sensitivity in Dashboard

A more detailed Battery Management Unit (BMU) has been incorporated into this latest version. The net effect is a greater fidelity and direct dependence on the specifics of the pack needs, such as the number of cells, modules, series-parallel connections, etc. Compared to earlier versions of BatPaC, the new BMU unit indicates a cost reduction of 30%–60%, lowering the pack/cell cost ratio, and a cost savings of about 3.5% in a $14,000 Battery Electric Vehicle (BEV) pack.

Silicon is increasingly found in the anodes of many commercial cells. BatPaC now allows the use of 5 wt.% silicon in the graphite electrode. This amount is small enough that these cells can tolerate the volume change during a cycle. The electrode couple database of cathode active materials has been expanded to include NMC532 and NMC811. The default material properties have been updated to reflect available data from the Cell Analysis, Modeling, and Prototyping (CAMP) facility and literature. The default material prices and other costs have been updated by using a combination of our NMC production model, metal prices, literature, and private communications with market experts.

Electrochemical and Thermal Model

The design calculations in BatPaC assume that no gradients exist for properties such as temperature, potential, and lithium concentrations within the cell. This approach is valid for most of the operating conditions and leads to acceptable designs when the battery has a low to moderate load. Multidimensional continuum models enable understanding of the lithium concentration, potential and temperature distribution within the cell layers. These conditions in turn affect the transport and material properties (e.g., particle size, interfacial resistance, etc.) and vice versa. These distributions help identify the regions that limit the performance of the cell, especially important under stressed conditions at the extremes of each cycle, during fast charge and discharge conditions, or regions where the transport mechanisms are limited by design features (aspect ratio, tab location, etc.).

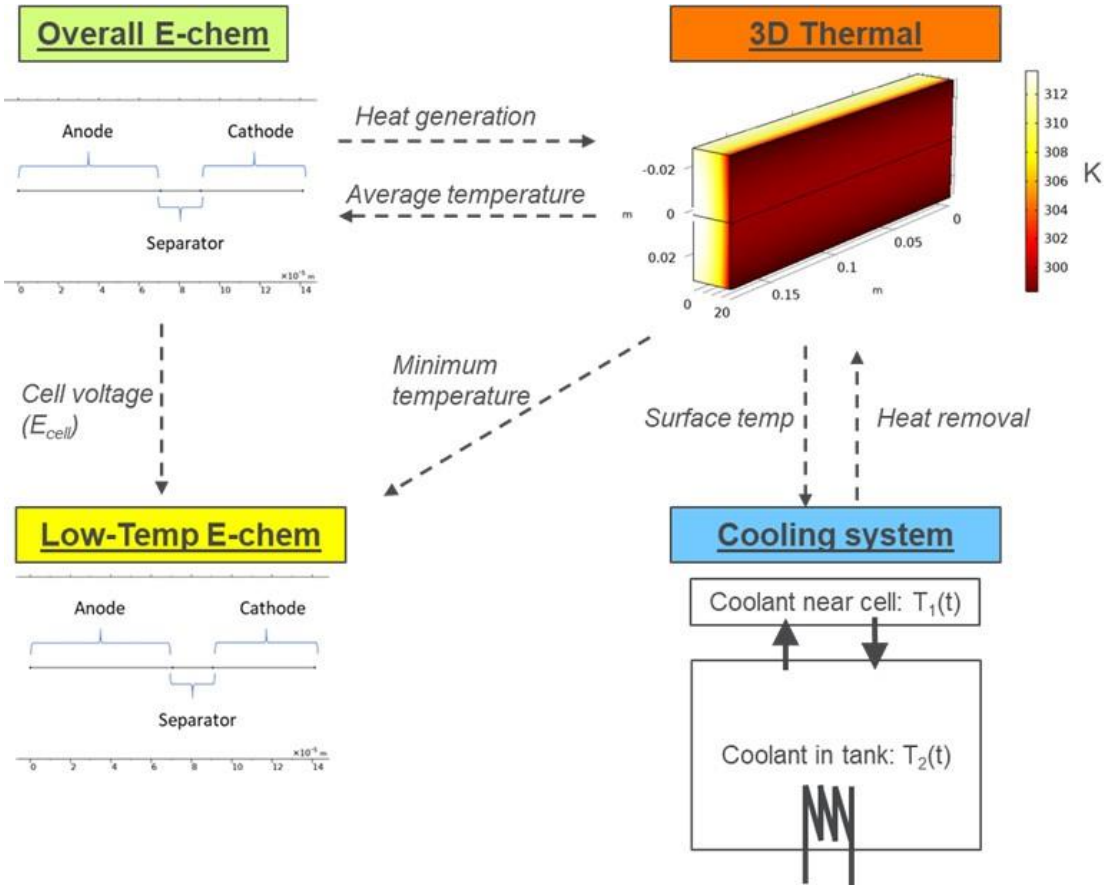

Figure I.6.A.3 Schematic of the interactions represented in models of the cell layers.

A series of continuum models have been set up to represent the distribution of potential and temperature within each cell. These models are being exercised to define the limiting conditions and to explore operating modes and their effect on material properties and performance. These results (properties, current densities, etc.) are then used in the form of simplified correlations in BatPaC to rapidly resolve the design and cost calculations.

Figure I.6.A.3 shows a schematic representation a cell and the interactive phenomena that affects the thermal and potential distributions. These distributions can then be simulated for transient operations such as during fast charge to understand and design a charging protocol (constant current, constant voltage, constant power) that prevents the anode potential to drop into lithium plating conditions. Figure I.6.A.4 shows an example of the current and voltage profiles during charging, and its effect on the potential and cell temperature. These simulations allow the exploration and optimization of charging protocols and to identify the conditions that limit fast charging.

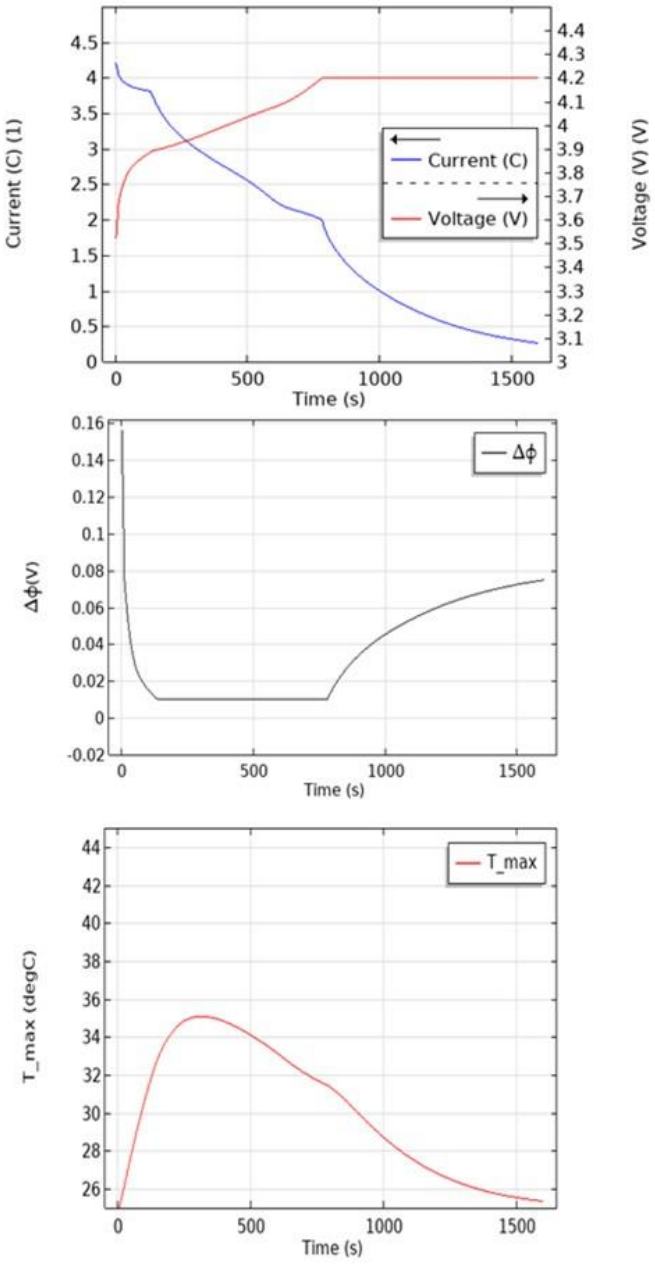

Figure I.6.A.4 Effect of current on the cell voltage, the anode potential (Φ) and the maximum temperature (T) in the cell during fast charging

Cylindrical Cell Model

One of the key benefits of BatPaC to researchers is the ability to extrapolate the material properties to cell-level performance metrics such as specific energy and energy density. Considering that commercial battery packs are available in both rectangular (pouch) and cylindrical (can) geometries, a spreadsheet tool for the cylindrical cell has been set up to compare the effect of the two geometries. Figure I.6.A.5 shows the five layers (positive current collector, positive electrode, separator, negative electrode, and the negative current collector) rolled to fit into a cylindrical shell or can.

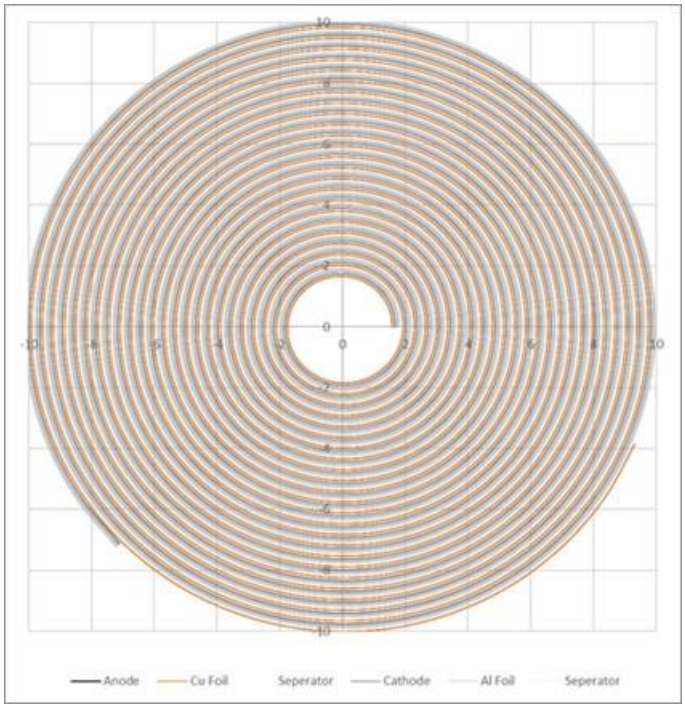

Figure I.6.A.5 Diagram showing the rolled cell layers in a cylindrical cell.

Table I.6.A.1 shows a comparison of a pouch cell with two cylindrical cells that are commercially available. The pouch cell has nearly 20X larger capacity (Ah) than the 18650 cell, and 13X the capacity of the 21700 cells. The pouch cell has a useable specific energy of 283 Wh_{use}/kg while the cylindrical cells yield 211 and 220 Wh_{use}/kg. The pouch format yields 28%–34% higher specific energy than the cylindrical cells. On the other hand, the cylindrical cells have slightly higher useable energy densities (625 and 637 Wh_{use}/L) than the pouch cell (601 Wh_{use}/L). This is due to extra volume at the ends of pouch cells needed for tabs and current collector welding. However, since rectangular cells can be packed more closely than cylindrical cells, it is anticipated that the difference in pack-level energy densities will be smaller for the two forms.

Table I.6.A.1 Comparing the useable specific energy and useable energy density of rectangular and cylindrical cells with NMC622-Graphite electrodes [Useable Energy = 85% of Rated Energy]

Cell Design	Rectangular Pouch	Cylindrical 18650	Cylindrical 21700
Positive electrode thickness, μm	80	80	80
Negative electrode thickness, μm	86	86	86
Cell Capacity, Ah	63	3.2	4.8
Cell energy, Wh	235	12	18
Cell energy, $Wh_{Useable}$	200	10	15
Mass of Cell, g	832	49	70
Volume of Cell, cm^3	333	17	24
Cell specific energy, $Wh_{Useable}$/kg	283	211	220
Cell energy density, $Wh_{Useable}$/L	601	625	637

Effect of Thinner Copper Current Collectors

Mass and cost reduction efforts have driven a trend to reduce the mass of copper that is used as current collectors through the production of thinner copper foils. The foil thicknesses are being reduced from the more common 10 microns to as thin as 4 microns [3], [4] which are produced by electrodeposition. The obvious lower mass and reduced demand for expensive copper are obvious attractions, but the feasibility of this change depends on how much reduction can be accomplished without increasing the cell resistance. On the production side, there is the question of whether they can be produced in large volume, without risking imperfections and structural strength during roll-to-roll processing. On the cost question, much will depend on whether the electrodeposited copper foil can end up being less expensive than the current production method of hot rolling.

A study was conducted to estimate the effect of the current collector thicknesses on the cell's area specific impedance (ASI). Table I.6.A.2 shows the input conditions and the calculated results. Reducing the copper current collector thickness from 10 µm to 4 µm increases the cell current collector ASI from 2.3 to 3.8 Ω-cm^2 (by 70%) and the total cell ASI from 17.8 to 19.4 Ω-cm^2 (by 9%). The cell specific energy would increase from 250 to 273 Wh/kg (by 9%).

Table I.6.A.2 Effect of current collector thickness on cell area specific impedance and cell specific energy

	4-micron Cu	10-micron Cu
Negative current collector thickness, microns	4	10
Positive current collector thickness, microns	15	15
Battery system total energy storage, kWh	88.2	88.2
Required battery system power, kW	300	300
Cell capacity, Ah	98.51	98.48
Cell current collector ASI, ohms-cm^2	3.84	2.27
Total cell ASI for energy (C/3 rate), ohm-cm^2	22.48	20.90
Cell specific energy, Wh/kg	273	250

As illustrated in Figure I.6.A.6, the specific energy of the cell increases by about 14.2% when the copper current collector is decreased in thickness from 10 microns to 4 microns if the positive current collector thickness is decreased correspondingly from 15 to 6 microns. Even if the aluminum positive is maintained at 15-micron thickness, the improvement for reducing the negative electrode from 10 microns to 4 microns is 9.4% in the specific energy of the cell. The corresponding improvements in the specific energy of the entire pack are 11.5% and 7.6%. We believe that this technology could improve high-energy cells but would be a hindrance if fast charge is desired, due to the increased resistance.

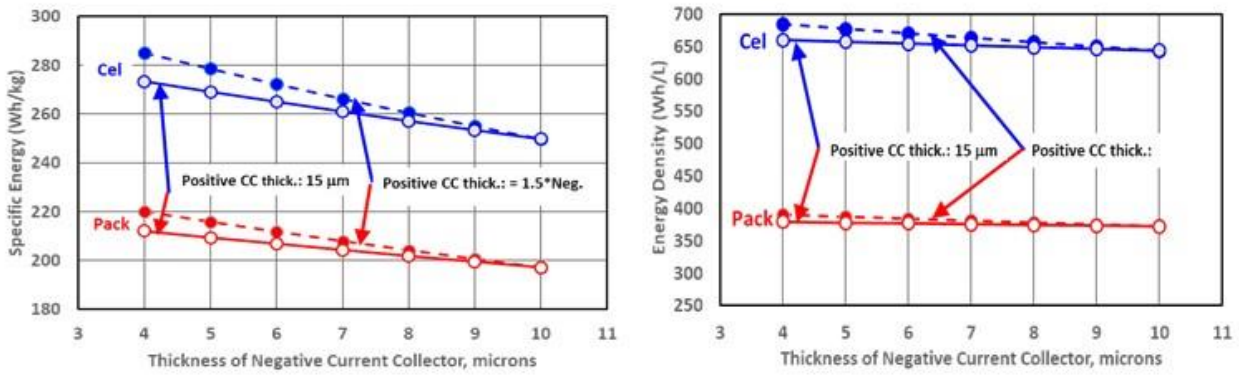

Figure I.6.A.6 Effect of the current collector thicknesses on the specific energy and energy density of the cell

Conclusions

A new version of BatPaC has been released with expanded electrode options, revised constraints used for electrode designs, a detailed component count of the battery management unit, updates on material properties and prices, and a consolidated user interface.

Several continuum cell models of the electrochemical and thermal characteristics have been set up to look at the 2D and 3D distributions of current, potential and temperature variations under steady state and transient conditions. Results from these models will be used to support performance and design calculations in BatPaC.

A version of BatPaC for cylindrical cells has been set up to enable performance comparison of cylindrical cells with pouch cells. The specific energy of the typical automotive rectangular pouch cells is found to be higher than with the 18650 or 21700 cylindrical cells.

The effect of thin current collectors on the cell area specific impedance, specific energy, and energy density were established. The thinner current collectors increase the impedance and the specific energy. The integrity and robustness of the thinner foils are still being demonstrated by industry. It is expected that the cell costs will come down as the price of the electrodeposited 4-6 micron foils become competitive with the rolled 8-15 micron foils available today.

Key Publications

1. Modulating electrode utilization in lithium-ion cells with silicon-bearing anodes, Journal of Power Sources 477 (2020), https://doi.org/10.1016/j.jpowsour.2020.229029
2. Impact of U.S. DOE R&D on Potential Future Battery Material Demand, EVS 33, June 2020
3. Estimating the cost and energy demand of producing LMO for Li-ion batteries, Report ANL/CSE-20/1

References

1. P. Nelson, S. Ahmed, K. Gallagher and D. Dees, "Modeling the Performance and Cost of Lithium-Ion Batteries for Electric-Drive Vehicles, ANL/CSE-19/2, DOI:10.2172/1503280," 2019.
2. "BatPaC Model Software," Chemical Science and Engineering Division, Argonne National Laboratory, 2020. [Online]. Available: https://www.anl.gov/cse/batpac-model-software.
3. Roskill, "Copper: Korea's KCFT begins mass production of 4-micron copper foil for EV batteries," 2019. [Online]. Available: https://roskill.com/news/copper-koreas-kcft-begins-mass-production-of-4-micron-copper-foil-for-ev-batteries/.

4. Targray, "High-performance Cu Foil Rolls for LiB Manufacturing," [Online]. Available: https://www.targray.com/li-ion-battery/foils/copper.

Acknowledgements

P. Nelson, J. Kubal, J. Song, Z. Liu, Cell Analysis Modeling and Prototyping Facility (CAMP), D. Robertson, G. Henriksen

Acronyms

ASI	Area specific impedance
BEV	Battery electric vehicle
BMU	Battery management unit
CAFE	Corporate average fuel economy
CAMP	Cell Analysis Modeling and Prototyping
NHTSA	National Highway Traffic Safety Administration
NMC	Lithium nickel manganese cobalt oxide
USEPA	United States Environmental Protection Agency

I.6.B Battery Performance and Life Testing (ANL)

Ira Bloom, Principal Investigator
Argonne National Laboratory
9700 South Cass Avenue
Lemont, IL 60439
E-mail: ira.bloom@anl.gov

Samm Gillard, DOE Technology Development Manager
U.S. Department of Energy
E-mail: Samuel.Gillard@ee.doe.gov

Start Date: October 1, 2019 End Date: September 20, 2020
Project Funding: $1,000,000 DOE share: $1,000,000 Non-DOE share: $0

Project Introduction

Batteries are evaluated using standard tests and protocols that are transparent to technology. These protocols are based on those developed by the USABC [1], [2], [3], [4].

Objectives

- Provide DOE, USABC, and battery developers with reliable, independent and unbiased performance and life evaluations of cells, modules and battery packs.
- Benchmark battery technologies that were not developed with DOE/USABC funding to ascertain their level of maturity.

Approach

The batteries are evaluated using standardized and unbiased protocols, allowing a direct comparison of performance within a technology and across technologies. For those tested using the USABC methods, the performance of small cells can be compared to that of larger cells and full-sized pack by means of a battery scaling factor [1], [2].

Results

Batteries, which were fabricated during programs with developers, are sent to Argonne for evaluation. Here, the purpose of evaluation is two-fold: to provide confirmation of other test information and to provide an independent assessment of the state of the given battery technology, that is, how does it compare to the USABC [1], [2], [3], [4] and/or project goals. A list of program deliverables associated with Argonne is given in Table I.6.B.1, along with their status.

Table I.6.B.1 Status of Deliverables for Testing

Developer	Sponsor	Quantity x System Level	Application	Status
WPI	USABC	40 x Cell	Recycling/PHEV-20	complete
WPI	USABC	30 x cell	Recycling/PHEV-20	complete
WPI	USABC	24 x 1-Ah cell	Recycling/PHEV-20	On-going
WPI	USABC	TBD x 100-AH cell	Recycling/PHEV-20	Expected
WPI	USABC	TBD x 1-Ah	Low-cost, fast-charge	Expected
SiNode/Nanograf	USABC	18 x 8.9 Ah	EV	On-going
Nanograf	USABC	24 x 1-Ah	EV	On-going
24-M	USABC	11-, 52-Ah	EV	Complete
Penn State	DOE	9 x 5 Ah	XCEL	Complete
Microvast	DOE	9 x 20.6 Ah	XCEL	Complete
ORNL	DOE	9 x 2.33 Ah	XCEL	Complete
Stonybrook	DOE	9 x 2.1 Ah	XCEL	Complete
University of Michigan	DOE	9 x 2.1 Ah	XCEL	Complete
University of Tennessee	DOE	9 x TBD Ah	XCEL	On going
ORNL	DOE	15 x 2 Ah	EV (low cobalt)	Expected
Penn State	DOE	20 x 20 Ah	EV (low cobalt)	Expected

Refilling an automobile with gasoline typically takes ten minutes or less. Decreasing the charging time of a battery to something that today's drivers are accustomed represents a technical challenge. To do this, the battery must be charged at very high rates. Here, not only does the technology have to avoid lithium deposition at the high charge rate, the technology must avoid life-shortening degradation caused by i^2R heating from the high current/power. There are, in principle, many ways to do this, including increasing the pack voltage so that the current at high power is relatively low. This is an engineering solution. Perhaps, a better way to overcome these issues is to develop or adapt lithium-ion technology to tolerate or avoid the problems.

There were many different solutions proposed to the fast-charge problem under the XCEL Project. The target for the project is to be able to discharge 180 Wh/kg after in a 10 min charge at the beginning of life and not exhibit more than 20% energy loss after 500 cycles. Some results from one of these projects is shown in Figure I.6.B.1.

Figure I.6.B.1 shows that the initial, C/3 discharge energy for this group of cells met the beginning-of-life goal of 180 Wh/kg. Indeed, with continued cycling, the average energy fade was 7.8% after 500 cycles, clearly exceeding the project goal. One cell (green curve) was taken off test; the remaining two cells continued cycling until 20% decline was observed. After 800 cycles, one cell (blue curve) displayed 25.8% decrease in energy and the final cell, 23.2% after 1000 cycles. These results indicate that solutions to the XFC are possible and that project goals can be met (and, in some cases, exceeded).

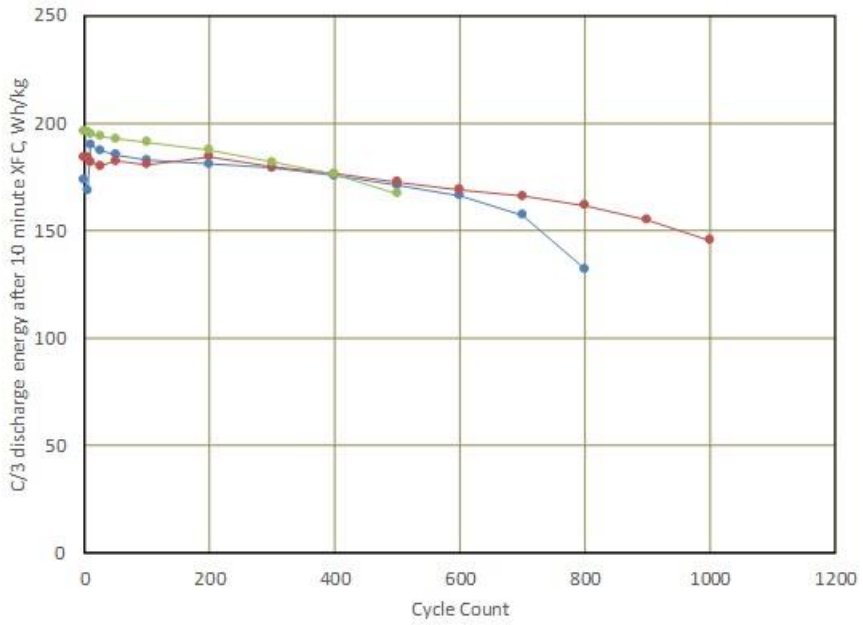

Figure I.6.B.1 C/3 discharge energy vs. cycle count for cells undergoing XCEL charging.

Conclusions

We will continue to support DOE's and the USABC's cell development efforts by providing unbiased evaluation of cell performance. In the case cited above, there appears to be at least one solution to the general fast-charging problem.

Acknowledgments

David Robertson, Panos Prezas and LeRoy Flores contributed significantly to this project.

References

1. FreedomCAR Battery Test Manual for Power-Assist Hybrid Electric Vehicles, DOE/ID-11069, October 2003.
2. FreedomCAR Battery Test Manual for Plug-In Hybrid Electric Vehicles, June 2010.
3. Electric Vehicle Battery Test Procedures Manual, Revision 2, January 1996.
4. Battery Test Manual for 12 Volt Start/Stop Vehicles, Rev. 1, May 2015, INL/EXT-12026503.

Abbreviations

USABC : United States Advanced Battery Consortium

HPPC : hybrid pulse power characterization test

PHEV-20 : plug-in hybrid electric vehicle, 20-mi electric range

12-V S/S : 12-V start/stop

XCEL, XFC : extreme fast charging

EV : electric vehicle

I.6.C Battery Safety Testing (SNL)

Joshua Lamb, Principal Investigator
Sandia National Laboratories
1515 Eubank Dr. SE, M/S 0613
Albuquerque, NM, 87185
E-mail: jlamb@sandia.gov

Samm Gillard, DOE Technology Development Manager
U.S. Department of Energy
E-mail: Samuel.Gillard@ee.doe.gov

Start Date: October 1, 2019 End Date: September 30, 2020
Project Funding: $400,000 DOE share: $400,000 Non-DOE share: $0

Project Introduction

Abuse tests are designed to determine the safe operating limits of HEV\PHEV energy storage devices. Testing is intended to achieve certain worst-case scenarios to yield quantitative data on cell\module\pack response, allowing for failure mode determination and guiding developers toward improved materials and designs. Standard abuse tests with defined start and end conditions are performed on all devices to provide comparison between technologies. New tests and protocols are developed and evaluated to more closely simulate real-world failure conditions. While robust mechanical models for vehicles and vehicle components exist, there is a gap for mechanical modeling of EV batteries. The challenge with developing a mechanical model for a battery is the heterogeneous nature of the materials and components (polymers, metals, metal oxides, liquids).

Materials characterization to better understand batteries that have undergone abusive conditions is of interest. Our partnerships with Argonne National Lab (ANL) and Oakridge National Lab (ORNL) through the Post Test Analysis Program for ABR, spans the building of cells with known materials (ORNL), overcharge testing to various states (SNL), and the posttest analysis of the cells (ANL). Abuse testing of advanced high energy materials has also revealed limits of existing test hardware, particularly regarding the maximum observed temperatures during thermal runaway. Continuous development of capabilities is necessary to ensure the most relevant data is collected. This has included the stand up of a small number of high temperature thermocouples that are able to detect these extreme temperatures.

Sandia has a record of a wide variety of Accelerating Rate Calorimetry (ARC) data that have been used to evaluate the relative safety of various materials. A new analysis compares the evaluation of different cells on the basis of specific energy. This has found that thermal runaway risk may be heavily tied to the specific energy of a battery system and should be factored in any safety evaluation.

The ability to fast charge electric vehicles addresses two major points of consumer EV adoption: range anxiety and convenience. However, fast charging also introduces new degradation mechanisms in the battery, and may contribute to new failure mechanisms. In fact, adverse effects seen during fast charge resemble battery abuse in several ways. In the cathode, fast charging is known to cause localized heating, which can lead to breakdown of active materials, electrolyte, and binder.

It can also cause localized over-delithiation, damaging the cathode structure. In the anode, the primary danger is lithium plating, which occurs if lithium diffusion into the cathode can’t keep pace with high rate Li+ delivery to the anode. The anode can also be host to Li+ depletion in the adjacent electrolyte, causing unexpected electrolyte changes and double layer effects. To study this cells were built in Sandia’s prototyping facility at varying n:p ratios, with the low n:p ratios used as conditions highly likely to plate lithium. After charging to induce lithium plating, cells were analyzed with DPA and ultimately subjected to abuse testing to observe changes in thermal runaway severity after significant lithium plating.

Objectives

- Provide independent abuse testing support for DOE and USABC
- Abuse testing of all deliverables in accordance with the USABC testing procedures
- Evaluate the impact of high quantities of lithium plating on abuse response of cells. Evaluate control and test cells with forced lithium plating to observe the impacts to failure.
- Improve the ability of calorimetry and other test methods to withstand and provide relevant data for high energy materials, particularly their ability to withstand high temperature failure. Begin evaluations of impacts of high energy materials.
- Provide testing data to support failure propagation model (NREL)
- Provide testing support for Post Test program (ORNL/ANL).

Accomplishments

- Completed testing of all USABC deliverables to date and reported results to the USABC TAC
- Test cells at varying n:p ratios built in Sandia prototyping facility and cycled to induce plating in low n:p ratio cells. Cells were analyzed using DPA and abuse testing. Results published in JES Safety special issue.
- Accelerating rate calorimetry data from programs at SNL were collected into a study covering the impact of increasing capacity and energy density. Publication submitted and awaiting review.
- Further supported publications of material from post-test efforts collected at Sandia with new publications released in FY20.
- Extended failure propagation modeling efforts with NREL by providing propagating thermal runaway testing data. This resulted in newly published work using direct test data to establish validated models.

Approach

Abuse tolerance tests evaluate the response to expected abuse conditions. The goals of abuse and safety testing include a) testing to failure of energy storage devices and documentation of conditions that caused failure, b) systematic evaluation of failure modes and abuse conditions using destructive physical analysis (DPA), c) provide quantitative measurements of cell/module response, d) document improvements in abuse response, and e) develop new abuse test procedures that more accurately determine cell performance under most probable abuse conditions. Electrical (overcharge/overvoltage, short circuit, over discharge/voltage reversal, and partial short circuit), mechanical (controlled crush, penetration, blunt rod, drop, water immersion, laser induced short circuit, mechanical shock and vibration) and thermal abuse (thermal stability, simulated fuel fire, elevated temperature storage, rapid charge/discharge, and thermal shock cycling) cover the main categories of possible conditions evaluated. These techniques are applied to USABC deliverables and the results reported to DOE and USABC.

Research and development batteries used for new test development, including stand up of the drop tower, studies to render batteries inert, and testing of temperature hardened calorimetry test cells use commercial off the shelf (COTS) 18650 and pouch format cells. Generally, NMC-graphite cells were used for testing due to the general relevance to EV applications. The testing of the hardened calorimetry test cells used high energy density materials, particularly NCA-graphite cell as the cells in question had been previously observed to exhibit a severe runaway event. Testing of lithium plating effects on abusive battery failure used cells built within Sandia's battery prototyping facility to build NMC-graphite cells.

Results

Testing of deliverables was performed for USABC development programs, including testing deliverables from 24M, Farasis, Microvast, Gotion, and Zenlabs. Test results have been reported to the USABC Technical Assessment Committee. Sandia continues to make functional improvements to battery testing to enable the testing of new high energy materials. This included the procurement of high temperature sensors that are able to adequately measure the potentially high temperatures observed during the thermal runaway of advanced battery materials.

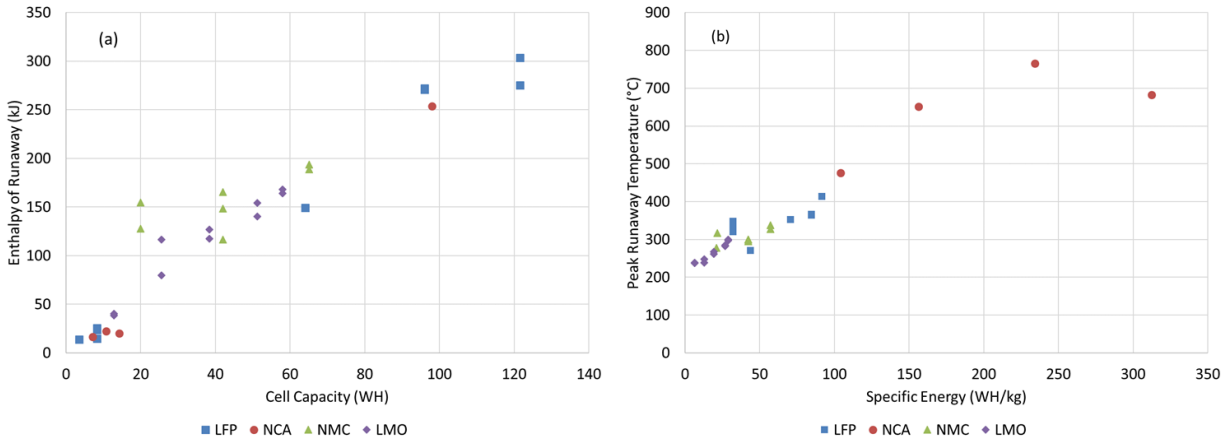

Figure I.6.C.1 Collected analyzed ARC data showing the impact of cell capacity on runaway enthalpy (a) and the impact of specific energy on peak observed runaway temperatures (b).

The data presented in Figure I.6.C.1 consider cells charged to 1.08-38 Ah (3.5-122 Wh) and chemistries including LFP, NMC, and NCA taken from historic data previously collected at Sandia. These data were limited to results collected in open-air testing using the EV ARC, and the physical constraints used varied based on the cell construction and geometry. This variation in mass is accounted for in the overall energy density of the cells shown in Figure I.6.C.1b. The raw ARC data are provided in supplemental information. These data show the total enthalpy of thermal runaway as a function of stored energy, and the peak thermal runaway temperatures as a function of the specific energy, calculated as using the overall temperature change during thermal runaway and accounting for the mass of any inactive material. This effectively corrects for the relatively high mass of the test apparatus when testing low capacity cells, as well as cells of similar chemistries with different specific energies.

Figure I.6.C.1a tracks how the heat released during thermal runaway is impacted by the total energy storage of the cell. The enthalpy of the thermal runaway event tracks linearly with the total stored energy. This indicates safety implications for even low-specific energy cells or cells at lower states of charge. The stored energy is still available to potentially initiate events like cell venting and fire. If the cells in question are well insulated (similar to the adiabatic environment of the present study), even a low rate of energy release is able to drive the cells to high temperatures.

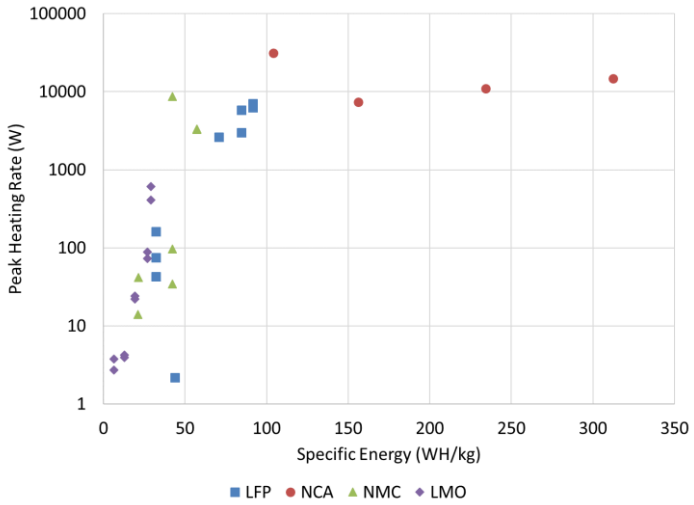

Figure I.6.C.2 Collected analyzed ARC data showing the effect of specific energy of cells on the peak heating rate.

More qualitatively, it can be useful to evaluate the ARC measurements in terms of the maximum temperatures of the high rate region. These data are shown in Figure I.6.C.1b with the peak temperature as a function of specific energy. These data show in stark terms the increase in potential risk as specific energy increases. As higher energy density cells are fielded, it should be generally expected that peak temperatures observed in thermal runaway will increase. This becomes of particular concern if thermal runaway temperatures increase to a point where typical structural materials within battery systems are affected (including aluminum, copper, and steel), increasing the likelihood of propagation to other cells.

Meanwhile, peak heating rates follow an exponential curve (shown as linear on the log scale of Figure I.6.C.2) until very high specific energies, where the rate becomes roughly flat. This flattening at high peak heating rates may be a limitation of the equipment used, as at these high heating rates the ARC is well outside of adiabatic control. The exponential slope of the peak heat release rate as a function of the specific energy in Figure I.6.C.2, together with the related peak temperatures in Figure I.6.C.1b, suggest an Arrhenius approximation might be appropriate for analyzing the peak heating rates.

Conclusions

Development and testing of higher energy, larger format cells and modules continues for USABC developers in hopes to meet the EV Everywhere 2022 goals. We provide a means to field the most inherently safe chemistries and designs to help address the challenges in scaling up lithium-ion technologies of interest. This has required careful control and monitoring of tests with the potential of high energy release as well as standing up a larger facility at SNL to support module level testing this FY. This has provided critical information to cell developers to aid in the development of increasingly abuse tolerant cell chemistries and module designs. This independent testing is also necessary to perform objective evaluations of these various designs and chemistries by the DOE and US automobile manufacturers. SNL has completed abuse testing support for all USABC deliverables to date.

An evaluation of ARC data presented here, when normalizing for energy density, indicates that peak runaway temperatures in adiabatic environments tend to be linearly proportional to the cell specific energy. These data cover four cathode chemistries, multiple form factors, and stored energy ranging from 3.5 to 122 Wh. This follows from ARC measurements that show the heat released is also linearly proportional to the stored energy. More importantly, perhaps, ARC measurements of the heat-release rate suggest that the kinetics of cell failure display an exponential relationship with increasing energy density. This compares well to a materials level analysis of oxygen release presented for layered metal oxide cathodes.

In a practical scenario, thermal runaway occurs when the self-heating rate of a battery failure event exceeds the heat loss rate in its current environment or installation. The logical next step is that increasing energy density will lead to increased consequences of thermal runaway occurring. With exponentially faster heat release at higher energy density it will be easier for the thermal runaway to exceed any heat dissipation to the environment, likely leading to more severe consequences in terms of further damage or cascading failure. This would be considered intuitive if discussing chemical energy storage, but is a concept often avoided when considering electrochemical energy. As new technologies are developed with increased energy in mind, increasing attention will need to be paid to designing mitigation into systems that minimize consequences.

Work has been performed this FY to expand the capabilities at SNL. High temperature failure analysis has been expanded, and further modernization of mechanical abuse equipment has been performed. Cell holder equipment for accelerating rate calorimetry has also been temperature hardened to better accommodate the high temperature failures that have been observed with high energy active materials. On going testing will evaluate the impact of increasing levels of silicon in the failure response of 18650 cells.

Key Publications

1. Torres-Castro, L., et al., *Passive Mitigation of Cascading Propagation in Multi-Cell Lithium Ion Batteries.* Journal of the Electrochemical Society, 2020. **167**(9): p. 9.

2. Rago, N.D., et al., *Effect of binder on the overcharge response in LiFePO4-containing cells.* Journal of Power Sources, 2020. **450**.

3. Rago, N.D., et al., *Effect of overcharge on Li(Ni0.5Mn0.3Co0.2)O-2/Graphite cells-effect of binder*. Journal of Power Sources, 2020. **448**.

4. Deichmann, E., et al., *Investigating the Effects of Lithium Deposition on the Abuse Response of Lithium-Ion Batteries.* Journal of the Electrochemical Society, 2020. **167**(9).

5. Li, Q., et al., *Numerical investigation of thermal runaway mitigation through a passive thermal management system.* Journal of Power Sources, 2019. **429**: p. 80-88.

6. Bloom, I., et al., *Effect of overcharge on lithium-ion cells: Silicon/graphite anodes.* Journal of Power Sources, 2019. **432**: p. 73-81.

7. Lamb, J et Al. “Mitigating thermal runaway propagation” International Battery Seminar, June 2020

8. Lamb, J. et Al. “Evaluating the Impact of Energy Density on Thermal Runaway” Battery Safety Summit 2019, October 2019

9. Lamb, J. et Al. “Battery Safety and Abuse Testing Overview” Stanford Battery Seminar Series, October 2019

10. Stanley, J. et al. “Li-ion Battery Impact Testing” AMSE InterPACK Conference, October 2019

11. Deichman, E. e al. “Analyzing the effect of lithium plating on the safety performance of lithium-ion batteries” Fall ECS Meeting, October 2019

Acknowledgements

Sandia Contributors

Loraine Torres-Castro

June Stanley

Christopher Grosso

Mohan Karulkar

Lucas Gray

Eric Deichmann

Kyle Fenton

National Lab and Industry Partners

USABC TAC Team

Ira Bloom (ANL)

Matt Keyser (NREL)

Shriram Santhanagopalan (NREL)

Eric Dufek (INL)

Lee Walker (INL)

Sandia National Laboratories is a multi-mission laboratory managed and operated by National Technology and Engineering Solutions of Sandia, LLC., a wholly owned subsidiary of Honeywell International, Inc., for the U.S. Department of Energy's National Nuclear Security Administration under contract DE-NA0003525.

I.6.D Battery Thermal Analysis and Characterization Activities (NREL)

Matthew Keyser, Principal Investigator
National Renewable Energy Laboratory
15013 Denver West Parkway
Golden, CO 80401
E-mail: Matthew.Keyser@nrel.gov

Samm Gillard, DOE Technology Development Manager
U.S. Department of Energy
E-mail: Samuel.Gillard@ee.doe.gov

Start Date: October 1, 2019 End Date: September 30, 2021
Project Funding: $500,000 DOE share: $500,000 Non-DOE share: $0

Project Introduction

Battery Thermal Testing, Analysis and Characterization: While EDVs promise to curb America's need for imported oil, designing high-performance, cost-effective, safe, and affordable energy-storage systems for these cars can present challenges, especially in the critical area of battery thermal control. As manufacturers strive to make batteries more compact and powerful, knowing how and where heat is generated becomes even more essential to the design of effective thermal-management systems. NREL's thermal characterization activities provide developers, manufacturers, and OEMs with the knowledge necessary to assure that batteries are designed to perform strongly, last a long time, and operate at maximum efficiency.

The Vehicle Technologies Office has a goal to reduce the cost of electric vehicle battery packs by 2022 to less than $\$150/kWh_{useable}$ with technologies that significantly reduce or eliminate the dependency on critical materials (such as cobalt) and utilize recycled material feedstocks. To meet these metrics, the battery packs will need to have higher energy densities resulting in a very compact system. Even if the energy efficiency of the next generation of batteries increases, because of the compactness of these batteries more heat is being generated per unit volume with less heat transfer area. Thus, more advanced heat rejection systems are needed to keep the battery temperatures in the "goldilocks" zone that prevents acceleration of the aging mechanisms within the battery.

The chemistries of advanced energy-storage devices—such as lithium-based batteries—are very sensitive to operating temperature. High temperatures degrade batteries faster while low temperatures decrease their power and capacity, affecting vehicle range, performance, and cost. Understanding heat generation in battery systems—from the individual cells within a module, to the inter-connects between the cells, and across the entire battery system—is imperative for designing effective thermal-management systems and battery packs.

Inadequate or inaccurate knowledge of the thermal characteristics of batteries makes it difficult to design effective thermal-control systems. This can negatively affect lifespan, safety, and cost, ultimately resulting in negative consumer perception and reduced marketability. In 2012, Nissan had to address problems with the battery for its Leaf fully electric vehicle (EV) losing capacity in the hot Arizona climate. Many attributed this issue to inadequate battery-thermal management.

Accurately measuring battery thermal performance under various electrical loads and boundary conditions makes it possible for battery-system engineers to design effective thermal-management systems. NREL, with the funding from DOE VTO, has developed unique capabilities to measure the thermal properties of cells and evaluate thermal performance of active, air, and liquid cooled battery packs. Researchers also use electro-thermal finite element models to analyze the thermal performance of battery systems in order to aid battery developers with improved thermal designs. In addition, our lumped capacitance multi-node battery-vehicle-ambient model can predict the temporal temperature of batteries as a function drive cycle, ambient

temperature, and solar radiation. These one-of-a-kind tools allow NREL to work with the battery manufacturers and OEMs to meet stringent EDV life, performance, cost, and safety goals

Physic Based Machine Learning with High Performance Computing (HPC): Algebraic models predicting battery SOH are often used to extrapolate results from accelerated aging test to real-world use cases; however, it is often difficult to identify accurate models, and manually analyzing model sensitivity or evaluating the quality of model extrapolation is extremely time consuming. To address these challenges, NREL has developed a machine-learning based model identification algorithm coupled with quantified uncertainty of model predictions. This tool dramatically accelerates the model identification process and aids analysis, enabling researchers to understand how the duration or number of test cases during accelerated aging studies influences the quality of model predictions in a rigorous and repeatable manner.

Objectives

- Thermally characterize battery cells and evaluate thermal performance of battery packs provided by USABC developers.
- Provide technical assistance and modeling support to USDRIVE/USABC and developers to improve thermal design and performance of energy storage systems.
- Evaluate extreme fast charging effects on battery thermal performance.
- Quantify the impact of temperature and duty-cycle on energy storage system life and cost.
- Address high energy storage cost due to battery packaging and integration costs
- Reduce the cost, size, complexity, and energy consumption of thermal management systems
- Optimize the design of passive/active thermal management systems—explore new cooling strategies to extend the life of the battery pack.
- Demonstrate ML to automate identification of degradation mechanisms within NREL's existing life model framework. Add model predictive uncertainty using bootstrap resampling technique.
- Apply automated life model identification and uncertainty quantification algorithms to study the dependence of life model predictive accuracy versus calendar duration of experimental testing and the number and type of tested aging conditions.

Approach

Battery Thermal Characterization/Testing: NREL has measured the thermal properties of the cells and batteries with many different chemistries (lead acid, NiMH, and many versions of lithium cells) through heat generation, heat capacity, and infrared thermal imaging; conducted performance thermal testing of battery and ultracapacitor modules and packs; analyzed the thermal performance of cells and modules; and developed thermal models. Researchers perform thermal testing, analysis, and modeling (1) to assist DOE/USABC battery developers in designing cells/modules/packs for improved thermal performance, and (2) to evaluate and validate the thermal performance of cell/module/pack deliverables from DOE/USABC battery developers and suppliers.

NREL's equipment can benchmark how changing the design of the cell using a different cathode, anode, current collector, electrolyte, additive, or separator affects the overall performance of the cell. The information garnered from these tests helps battery and advanced vehicle manufacturers improve their designs, while providing critical data for the development of thermal management systems that will reduce the life-cycle cost of battery systems. Using NREL's unique R&D 100 Award-winning calorimeters and infrared thermal imaging equipment, we obtain thermal characteristics of batteries and ultracapacitors developed by USABC

battery developers and other industry partners. NREL supports the Energy Storage Technical Team by participating in various work groups such as the Zenlabs, Farasis, 24M, and USABC Working Groups.

Physic Based Machine Learning with High Performance Computing (HPC): The identification of algebraic battery life models is automated using the machine learning technique of symbolic regression. Symbolic regression is conducted by using a sparse regularization algorithm to down select from hundreds of model features to just a few, resulting in a single model with a small number of parameters, out of potentially millions of options. Competing models are compared using the statistical method of cross-validation, which tests the ability of models to extrapolate to new conditions. Model uncertainty is quantified using the bootstrap resampling technique. Model uncertainty from training on accelerated aging test data can be forwarded to simulations of real-world use cases. These tools are being used by NREL to develop aging models for the NREL technoeconomic simulation, EnStore, using both data acquired under the BTMS project, as well as open-source data sets. NREL also uses these techniques to analyze testing data and develop predictive life models for a variety of other industry and government partners.

Results

Calorimeter Testing: Figure I.6.D.1 shows the efficiency of cells tested in FY18/FY19/FY20 at NREL at a calorimeter temperature of 30°C. The lithium ion cells were fully discharged from 100% SOC to 0% SOC under a C/2, C/1, and 2C currents. One of the high energy graphite cells tested at NREL in FY20 was power limited. That cell was compared at C/3 and C/4. The cells in this figure have been developed under the HPEV and LCFC programs within USABC. These cells are designed for mainly high energy applications (the LCFC program maintains aggressive energy level targets). It should be noted that as the specific energy of these graphite systems increases, the efficiency decreases. This is primarily due to the impact of thicker electrodes have on the thermal performance. In contrast, the efficiency of the silicon blend cells is increasing due to chemistry optimization. Silicon containing cells can maintain high energy content with lower electrode thickness due to the much greater material energy potential when compared to graphite. The general trend still shows that silicon containing systems need improvement in performance to reach the heat efficiency of graphite cells with similar electrode thickness. DOE and USABC are investigating both graphite and silicon to improve energy density, power density, cycle life and/or cost benefits. NREL's calorimeters provide the fundamental understanding of whether the inefficiencies shown below are due to chemistry or cell design.

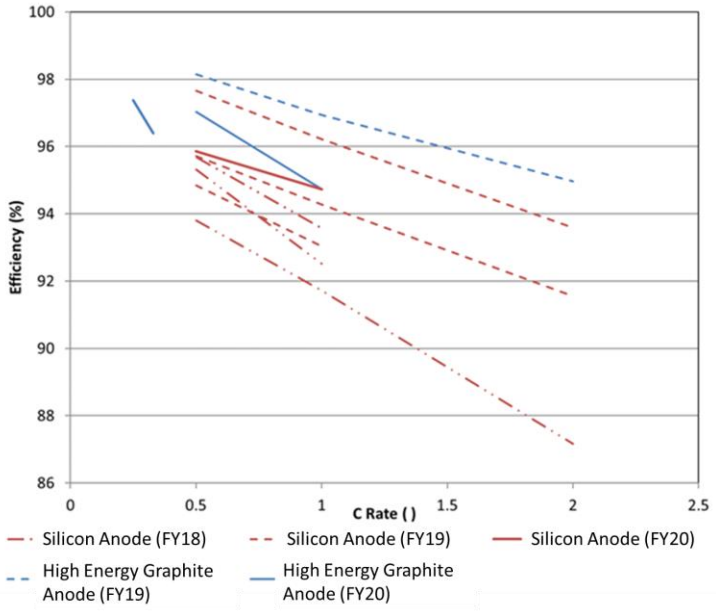

Figure I.6.D.1 Efficiency summary of cells tested in NREL's calorimeters. Caption Credits/Source: NREL-Aron Saxon

NREL's calorimeters were designed to be accurate enough to measure the electrochemical response from batteries under test – this capability allows NREL to understand benefits associated with design and chemistry changes to the cell. Figure I.6.D.2 shows the entropic heat generation rates normalized to the Ah capacity of two cells – one cell has a graphite anode and the other has a graphite/Si anode – under a C/10 charge and discharge at 30°C. The cells in this figure were cycled over their entire state-of-charge range – minimizing the current decreases the joule heating of the cell and allows for the entropic heat signature to be assessed. From the figure, the cell entropic signature undergoes a phase shift following the introduction of Si into the cell chemistry. This phase shift correlates to observation that the silicon inside the cell undergoes lithiation first under charge and de-lithiation last under discharge. Testing at low currents allows for us to understand how architecture and additive/chemistry changes affect the cells performance.

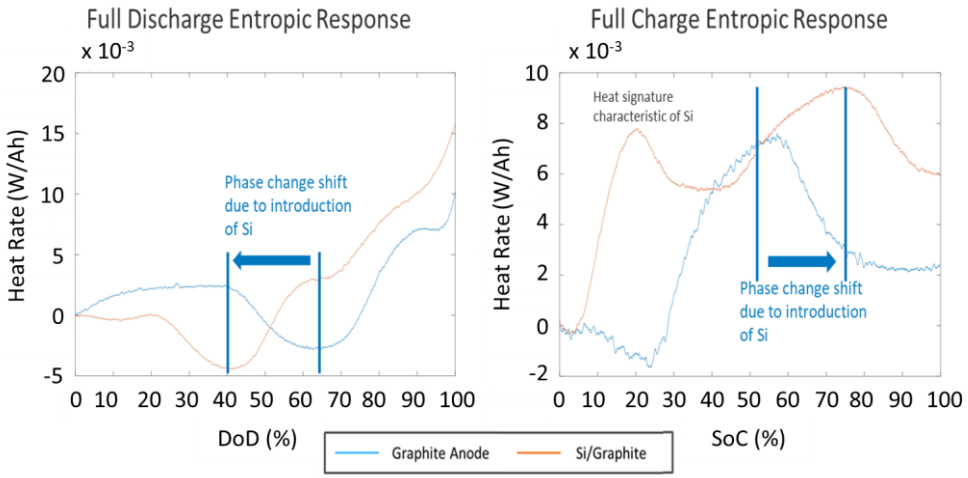

Figure I.6.D.2 Calorimeter normalized heat rate for graphite and graphite/Si NMC cells under C/10 charge and discharge.
Caption Credits/Source: NREL-Aron Saxon

NREL has also been involved with testing cells under fast charge conditions. The USABC test procedure consists of a fifteen-minute fast charge from the minimum operational voltage to the maximum operational voltage. If the maximum operational voltage is reached during the charge, then the current is tapered to complete the charge. Figure I.6.D.3 illustrates the heat generation results of a cell that was tested at NREL under this condition under three different charge rates – 3C, 3.5C, and 4C. The results indicate that the 3.5C charge case was the most efficient of the three cases. The 3.5C case generated 1.26W/Ah whereas the 3C and 4C case generated 1.3 W/Ah and 1.36 W/Ah. Under the 3C charge rate, the heat generated did not provide enough of a temperature benefit as to the 3.5C case (higher temperatures promote greater ionic transport and thus greater efficiency). By contrast, the 4C charge case had a higher heat generation rate due to the increased ohmic heating within the cell. This simple case shows that charge algorithm optimization as a function of temperature is needed in addition to chemistry optimization to provide the most return for fast charge cases. NREL is continuing research into charge algorithm optimization to lessen the deleterious effects of fast charging on the cells lifetime while minimizing the thermal management system.

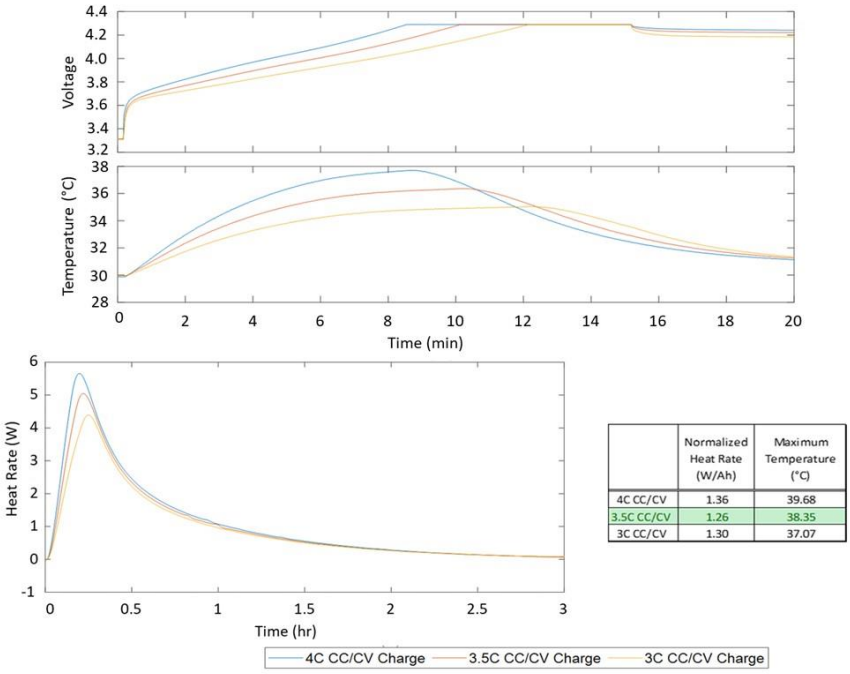

	Normalized Heat Rate (W/Ah)	Maximum Temperature (°C)
4C CC/CV	1.36	39.68
3.5C CC/CV	1.26	38.35
3C CC/CV	1.30	37.07

Figure I.6.D.3 Cell under 3C, 3.5C, and 4C fast charge. The calorimeter test temperature was 30°C. Caption Credits/Source: NREL-Aron Saxon

Infrared Imaging of Cells: NREL performs infrared (IR) thermal imaging of battery manufacturer's cells to determine areas of thermal concern. We conduct IR thermal imaging under a set of prescribed procedures and environments to minimize the error from different sources such as reflective cell surfaces, radiation from surrounding surfaces, and cooling from the power cables attached to the cell. NREL combines the IR imaging equipment with a battery cycler to place the cells under various drive cycles, such as a US06 charge depleting cycle for a PHEV, to understand the temperature differences within the cell. We then make recommendations to the battery manufacturers and USABC on how to improve the thermal design of the cell to increase its cycle life and safety.

Figure I.6.D.4 shows a lithium battery (Graphite/High Nickel Content NMC) at the end of a 3.2C charge. Each IR image has a temperature spread associated with it – by decreasing the temperature spread a visual reference can be used to determine where the heat is preferentially being generated within the cell. For this cell. the heat generation is biased towards the positive terminal of the battery. In this case, the high electrode thickness exhibits poor thermal conduction and prevents the heat from dissipating from the center of the cell. During the IR imaging, we also assess the temperature uniformity across the cell surface When the cell temperature is not uniform and consistent, individual cells within modules and packs age differently affecting the cycle life of the module. NREL is working with battery developers to understand how temperature non-uniformities affect the efficiency and cost of the cell over its life.

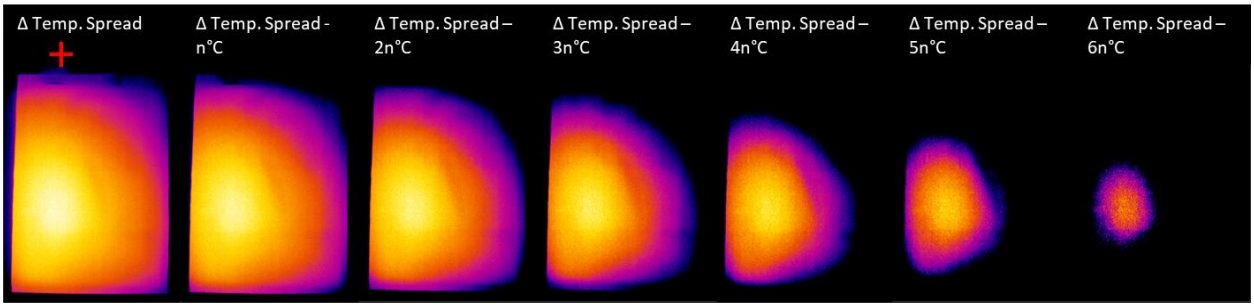

Figure I.6.D.4 Infrared image of lithium battery cell (graphite-silicon/high nickel content NMC) at the end of a C/3 discharge. Caption Credits/Source: NREL- Aron Saxon

Physic Based Machine Learning with High Performance Computing (HPC): During FY20, a procedure for the automatic identification of reduced-order models by machine-learning was developed. In Q4FY20, further analysis of capacity fade was performed for the calendar aging of Sony 3 Ah LFP/Gr cells [1] and the results prepared into a manuscript, which will be submitted to the Journal of the Electrochemical Society during Q1FY21. These results were presented at the ECS PRiME virtual conference in October, 2021. Some key takeaways from this manuscript are reported below. Also, during this quarter, the automatic identification procedure was used to construct a full life model, describing both the calendar and cycling degradation of Kokam 75 Ah NMC/Gr cells. The automatically identified life model is compared with a previously published baseline model [2].

As reported last quarter, a procedure for automatically identifying reduced-order models involving bi-level (e.g., nested) optimization and symbolic regression has been developed, and used to model the capacity fade during calendar aging of Sony 3 Ah LFP/Gr cells (data from [1]). Some key takeaways from this work include:

- Automatic identification results in a range of possible models with substantially lower error than a baseline model published for this data set [1] (see Table I.6.D.1 and Figure I.6.D.5)
- Known physical relationships can be ‘rediscovered’ by machine-learning
    - Symbolic regression consistently converges on simple variations of the Arrhenius and Tafel equations, demonstrating that the procedure can accurately identify underlying physical behaviors
    - Bi-level optimization finds that the variation of the power exponent of time for capacity fade is consistent with recently published first-principles analysis of SEI growth on graphite [3] (see Figure I.6.D.6)
- Statistical comparisons reveal that the common square-root of time model structure is not empirically validated for this data set
    - Value of 0.5 is never within the 90% confidence interval of the power exponent of time for power law model during training, indicating that the square-root of time assumption is not valid
    - Comparison of model extrapolations from the 8 months of training data to 20 years of aging show that the square-root of time model may be overpredicting capacity fade by almost 100% in certain conditions (see Figure I.6.D.7)
- Quantified uncertainty and automatic model identification via machine-learning may help guide more effective experimental design and management
    - Machine-learned models show good convergence after only 70 days of aging, while the baseline model does not obviously converge after even 235 days

- Aging tests may be conducted more efficiently by removing cells from testing channels if they can be modeled with high accuracy, and testing a new cell

- Quantified uncertainty highlights regions of high model uncertainty, which can be used to determine the highest value experiment to conduct next

Table I.6.D.1 Mean absolute error of the capacity fade of LFP/Gr cells from [1], and a comparison of the error from the baseline model vs. the machine-learned models

Model type	Model structure	Mean Absolute Error	Change vs. Baseline
Baseline (manually defined)	Square-root (from [1])	0.261%	n/a
Machine-learned	Square-root	0.192%	-26%
	Power Law	0.203%	-22%
	Stretched Exponential	0.207%	-21%
	Sigmoidal	0.125%	-52%

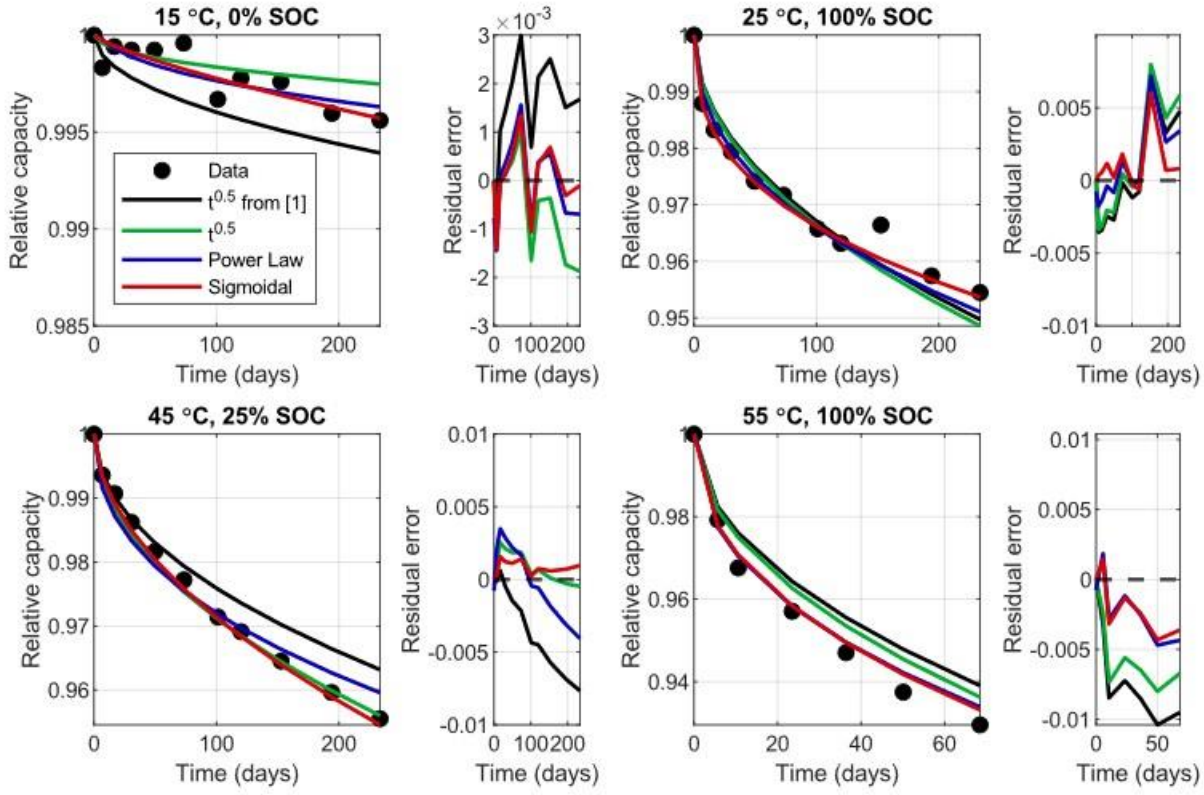

Figure I.6.D.5 Capacity fade predictions of LFP/Gr cells by the baseline model from [1], which is a square-root model, compared with the machine-learned square-root, power law, and sigmoidal models on a subset of the 16 cells used for training all models. Residual errors from each prediction are shown to the right of each plot. Stretched exponential model is not shown, as it is nearly identical to the power law model.

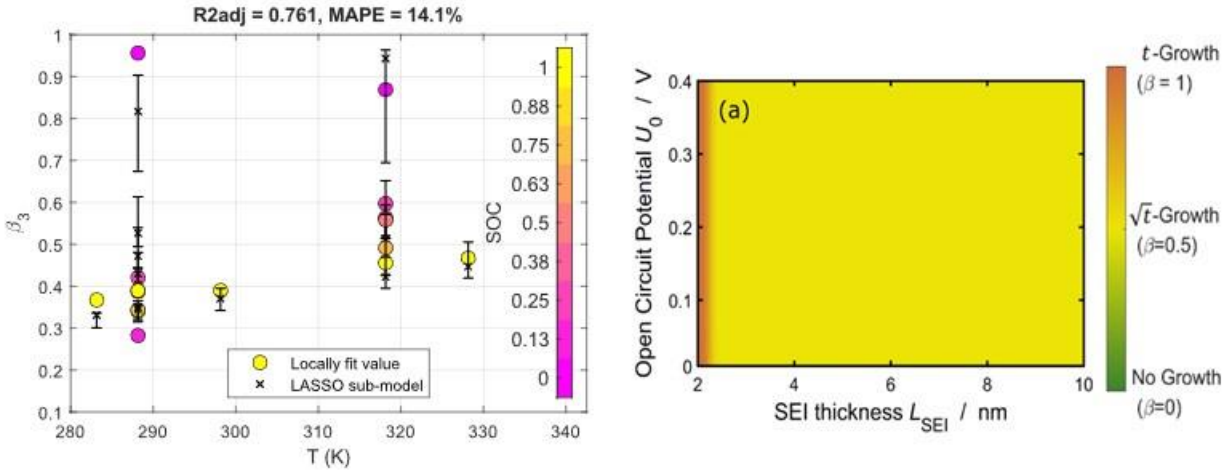

Figure I.6.D.6 (Left) Power exponent of time (β_3) for capacity fade of LFP/Gr cells as identified by bi-level optimization of the sigmoidal model vs. temperature. Solid markers are the values locally fit to each cell by bi-level optimization, and the black crosses denote predicted values by a machine-learned equation. Locally fit values are near 1 at low SOCs, which correspond to cells with almost no capacity fade (see Figure 1, 15 °C and 0% SOC, which has only 0.45% capacity fade after 8 months), and thus have not experienced much SEI growth. (Right) This result may be compared with a recent first-principles study of the SEI growth rate on graphite anodes [3], which determined that the power exponent of time for SEI growth is near 1 when the SEI is very thin, and approaches 0.5 as the SEI grows thicker.

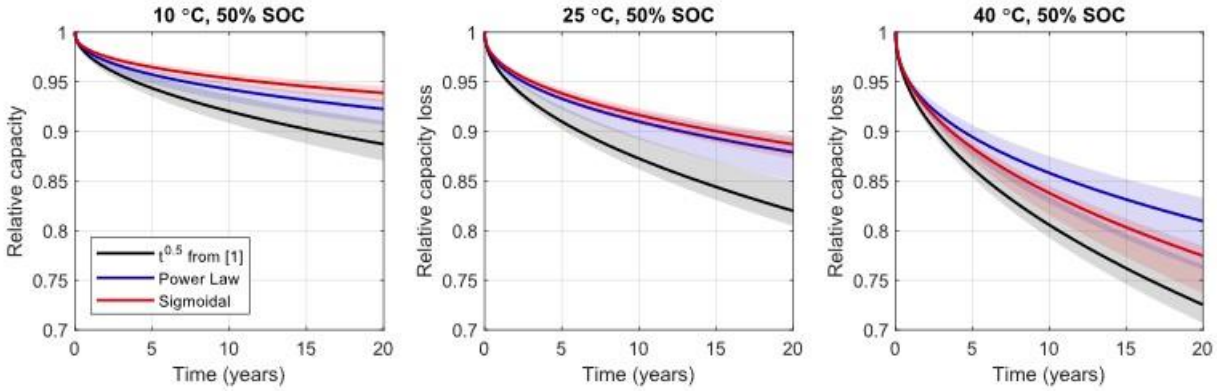

Figure I.6.D.7 Capacity fade predictions of LFP/Gr cells extrapolated to 20 years of aging for the baseline model from [1] and the machine-learned power law and sigmoidal models. While all models are being extrapolated well past the 8 months of training data available, the implication from this extrapolation is that the $t^{0.5}$ model commonly used in the literature to predict capacity fade may be substantially overpredicting cell degradation when extrapolated to long times. Compared to the sigmoidal model, which is the most accurate model during training, as well as to the power law model, which identified an optimal power exponent of time of 0.42 (rather than 0.5, as assumed by the $t^{0.5}$ model), the $t^{0.5}$ model consistently overpredicts cell degradation in all simulated conditions.

The automatic identification procedure was also used to construct a 'full' degradation model for a cell, modeling both the calendar and cycling degradation of Kokam 75 Ah NMC/Gr cells (NREL study, previously published in [2]). The previously published model serves as a baseline to compare against. The fit quality of the baseline and machine-learned models are compared in Table I.6.D.2. In this case, the machine-learned model did not improve upon the accuracy of the manually identified model, however, it still has several advantages. For instance, the manually identified model was found to be extremely sensitive, diverging to infinities when attempting cross-validation or uncertainty quantification. However, the machine-learned model can be cross validated / bootstrapped for uncertainty quantification without diverging, which is crucial for ensuring that models are tolerant to noise, can be safely extrapolated, and are more likely to be stable if retrained on new data. The machine-learned model also has far fewer parameters, 16 compared to 23 for the

baseline model, while maintaining similar predictive performance, demonstrating that the automatic identification procedure is able to identify parsimonious models (i.e., balancing model complexity with accuracy) more effectively than through manual effort.

Table I.6.D.2 Number of parameters and fit metrics of the baseline and machine-learned reduced-order capacity fade models of Kokam 75 Ah NMC/Gr cells. Baseline model previously published in [2]

Model type	Parameters	R^2_{adj}	MAPE	MSE	MSE_{cv}
Baseline from [2] (manually defined)	23	0.983	1.16%	1.26 Ah^2	n/a
Machine-learned	16	0.968	1.58%	2.36 Ah^2	17.62 Ah^2

A comparison of the predictions made on each cell of the data set is shown in Figure I.6.D.8 below. The baseline model from [2], plotted by black lines, is referred to as the 'ACC 2017 Model', and the machine-learned model, plotted by red lines, is referred to as the 'Bilevel+Lasso Model'. Both models have issues fitting the calendar fade at 30 °C and 55 °C, but with only 4 cells tested, there is not enough available data to identify a parsimonious model, manually or automatically. The automatically identified model performs noticeably worse than the manually identified model on only 2 of the 11 cells. The predictions of the automatically identified model with quantified uncertainty are shown in Figure I.6.D.9. In general, model uncertainty seems high, but this data set is extremely small for the variety of degradation behaviors observed, so high uncertainty was expected.

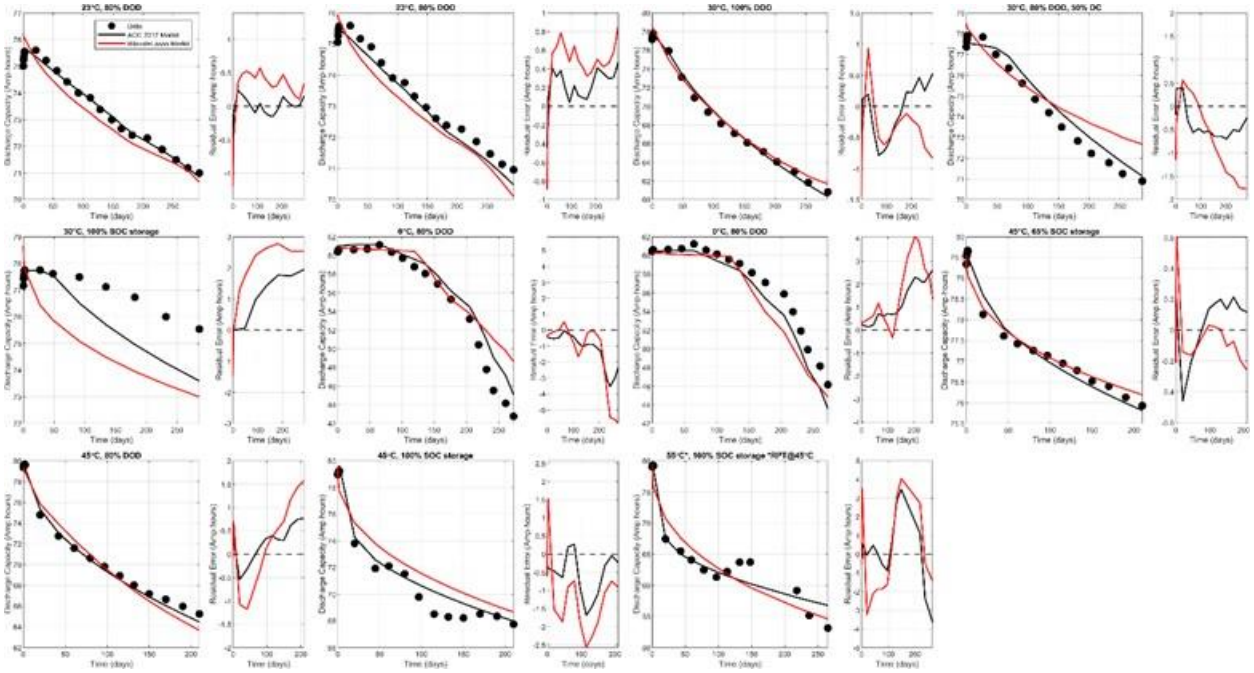

Figure I.6.D.8 Predictions of the capacity fade of Kokam 75 Ah NMC/Gr cells during calendar and cycling aging, made by the baseline model from [2] (ACC 2017 Model) and a machine-learned model (Bilevel+Lasso Model).

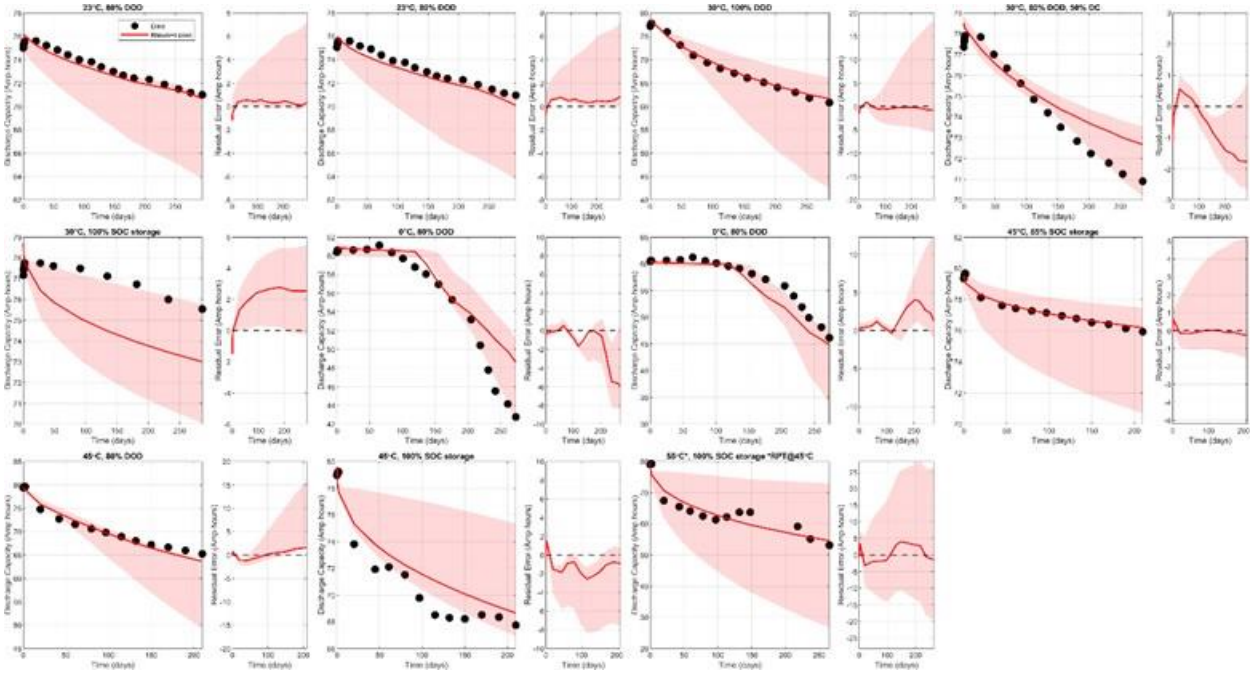

Figure I.6.D.9 Predictions of the capacity fade of Kokam 75 Ah NMC/Gr cells during calendar and cycling aging by the machine-learned model (Bilevel+Lasso Model), plotted with 90% confidence intervals. Confidence intervals are determined by retraining the model 1000 times on data sets where individual cell data series have been bootstrapped.

Conclusions

NREL has thermally tested cells and modules from Zenlabs, Farasis, 24M, and the Chevy Bolt during FY20. We have provided critical data to the battery manufacturers and OEMs that can be used to improve the thermal design of the cell, module, pack, and their respective thermal management systems. The data included heat generation of cells under typical profiles for HEV, PHEV, and EV applications, which is essential for designing the appropriately sized battery thermal management system. In FY20, NREL will continue to thermally characterize cells and modules for USABC, DOE, and USDRIVE but the focus will shift to fast charging applications and the heat generation differences between advanced battery chemistries.

In FY20, several key milestones were met concerning the development of machine-learning based identification of physics-informed battery life models:

- Quantifying model uncertainty by bootstrap resampling, and extending model uncertainty into predictions of battery lifetime
- Identifying algebraic models for battery lifetime via symbolic regression, and machine-learning method for autonomously identifying new equations from data.

Future work involves efforts to update the code base with a focus towards automating all steps of the model identification workflow. This will enable researchers to rapidly identify and compare life models from both BTMS data sets and open-source aging data sets. So far, the machine-learning approach developed in FY20 has been utilized mostly for developing calendar aging models. Developing best practices for identifying physics-informed degradation models for cycling data using machine learning will be done by collecting BTMS, NREL, and an open-source aging data sets, and identifying models. Later in FY21, efforts will be made to automate the work of simulating life models on arbitrarily complex duty cycles, which is currently a manual procedure that is slow and error prone.

Key Publications

1. Conference Presentation: Aron Saxon, “Battery thermal analysis and characterization activities”, InterPack, California, 2019.

2. Quarterly meeting presentations to the battery working group and manufacturers.

References

1. Schimpe, M., Von Kuepach, M. E., Naumann, H., Hesse, H. C., Smith, K., and Jossen, A., Comprehensive Modeling of Temperature-Dependent Degradation Mechanisms in Lithium Iron Phosphate Batteries, JES, Volume 165, Number 2.

2. Smith, K., Saxon, A., Keyser, M., Lundstrom, B., Cao, Z., Roc, A., Life prediction model for grid-connected Li-ion battery energy storage system, IEEE, American Control Conference, 2017

3. Von Kolzenberg, L., Latz, A., Horstmann, B., Solid-Electrolyte Interphase During Battery Cycling: Theory of Growth Regimes, ChemSusChem, 2020 May 18; 13(15):3901-3910. doi: 10.1002/cssc.202000867.

Acknowledgements

We wish to acknowledge Samm Gillard, Haiyan Croft, and DOE for sponsoring these efforts. We would also like to acknowledge the co-authors of this report – Aron Saxon, Paul Gasper, Kandler Smith, and Thomas Bethel.

I.6.E Cell Analysis, Modeling, and Prototyping (CAMP) Facility Research Activities (ANL)

Andrew N. Jansen, Principal Investigator
Argonne National Laboratory
9700 S. Cass Ave, CSE-200
Lemont, IL 60439
E-mail: Jansen@anl.gov

Peter Faguy, DOE Technology Development Manager
U.S. Department of Energy
E-mail: Peter.Faguy@ee.doe.gov

Start Date: September 30, 2018 End Date: September 29, 2021
Project Funding: $950,000 DOE share: $950,000 Non-DOE share: $0

Project Introduction

The "valley of death" is a phrase often used to describe the path a new discovery must traverse to become a commercial product. This is especially true for novel battery materials invented in research laboratories around the world. Often researchers are resource limited and are only able to make gram quantities of their new material. The CAMP Facility is appropriately sized to enable the design, fabrication, and characterization of high-quality prototype cells using just a few hundred grams of the latest discoveries involving high energy battery materials. Prototype cells made in the CAMP Facility generally have 400-mAh capacity, which straddles the gap between coin cells and industrially-sized cells nicely – two orders of magnitude from each end point. Thus, a realistic and consistent evaluation of candidate chemistries is enabled in a time-effective manner with practical quantities of novel materials in cell formats commonly used in industry.

The CAMP Facility is an integrated team effort designed to support the production of prototype electrodes and cells, and includes activities in materials validation (benchmarking), modeling, and diagnostics. It is not the aim of this facility to become a small battery manufacturer, but instead to be a laboratory research facility with cell production capabilities that adequately evaluate the merits and limitations of new lithium-ion chemistries in a close-to-realistic industrial format. The source of these materials (anodes, cathodes, electrolytes, additives, separators, and binders) may originate from DOE Battery Programs, as well as from other domestic and foreign organizations such as universities, national labs, and industrial vendors. Electrochemical couples with high power and energy density are given extra priority.

The CAMP Facility has the capability to make three prototype cell formats in their 150 m² dry room: pouch cells (xx3450 format, with capacity around 0.5 Ah; and xx6395, with capacity around 2 Ah) and 18650 cells (with capacity around 2 Ah). Pouch cells are generally easier to assemble, and are a great indicator of gassing problems in a cell during cell aging and cycling. Central to this effort is a pilot-scale coating machine that operates with slurry sizes that range from 20 mL to 2 L. This is a key feature of the CAMP Facility that enables a professional evaluation of small quantities of novel materials. If needed, the Materials Engineering Research Facility (MERF) is available for scaling up materials for these prototype cell builds.

Objectives

The objective of this core-funded effort is to design, fabricate, and characterize high-quality prototype electrodes and cells that are based on the latest discoveries involving high energy anode and cathode battery materials. Using this multi-disciplined facility, analytical diagnostic results can be correlated with the electrochemical performance of advanced lithium-ion battery technologies for electric vehicle (EV) applications.

- Link experimental efforts through electrochemical modeling studies.

- Identify performance limitations and aging mechanisms.
- Support lithium-ion battery projects within the DOE-EERE-VTO.

Approach

The general approach used in this effort is to start small and grow large in terms of cell size and amount of resources devoted to each novel battery material. At various points in the development process, decisions are made to either advance, modify, or terminate studies to maximize utilization of available resources.

Coin cells (2032 size) are used for materials validation purposes with initial studies performed at 30°C. After formation cycles, the coin cells go through rate capability testing, HPPC testing, and limited cycle life testing. Additional temperatures and test conditions are employed if warranted.

Using the results obtained by the materials validation of promising materials, single-sided electrodes are fabricated on the larger dry-room coater for diagnostic study. The new cell chemistries are studied in detail using advanced electrochemical and analytical techniques, including the employment of micro-reference electrode cells. Factors are identified that determine cell performance and performance degradation (capacity fade, impedance rise) on storage and on extensive deep-discharge cycling. The results of these tests are used to formulate data-driven recommendations to improve the electrochemical performance/life of materials and electrodes that will be incorporated in the prototype cells that are later fabricated in the dry room. This information also lays the foundation for electrochemical modeling focused on correlating the electrochemical and analytical studies, in order to identify performance limitations and aging mechanisms.

If the results from diagnostics and modeling still look promising, full cell builds are conducted using double-sided electrodes. The electrodes are then either punched in the case of pouch cells, or slit in the case of 18650 cells and assembled into full cells in the dry room using semi-automated cell assembly equipment. Formation procedures are conducted on the cells to encourage electrolyte wetting and uniform solid-electrolyte-interface (SEI) formation. These cells undergo rigorous electrochemical evaluation and aging studies under the combined effort of the CAMP Facility team, and Argonne's Electrochemical Analysis and Diagnostic Laboratory (EADL) and Post-Test Facility. After testing, select cells are destructively examined by the Post-Test Facility to elucidate failure mechanisms. This information is then used to further improve the new chemistry, as well as future electrode and cell builds.

Results

The CAMP Facility is designed to work closely with materials researchers across the many electrochemical energy storage programs throughout the DOE-EERE-VTO. In addition to its own yearly R&D tasks, it actively coordinates its efforts to provide support to other national lab team Programs such as: Realizing Next Generation Cathodes, Next Generation Anodes, Fast Charge (XCEL), ReCell Center, and Behind The Meter Storage (BTMS). The Materials Benchmarking Activities (Section I.6.F) is a segment of the CAMP Facility. The CAMP Facility also complements the capabilities of other DOE support facilities such as: the Materials Engineering Research Facility (MERF - Argonne), the Post-Test Facility (PTF - Argonne), the Battery Abuse Testing Lab (BATLab - SNL), and the Battery Manufacturing Facility (BMF - ORNL). More information about these programs can be found in the relevant chapters and sections of this annual report. The remainder of this CAMP Facility section will discuss the results of the CAMP Facility deliverables for FY20, and include results of related topics. It should be noted that several of the planned tasks for FY20 were modified or delayed because of reduced laboratory time due to the COVID19 pandemic.

Develop Methods to Direct Coat Hybrid Polymer Ceramic Coatings/Electrolyte Membranes onto Electrodes

In continuation of FY19 efforts for developing direct coat methods of promising hybrid polymer ceramic coatings and electrolyte membranes onto electrodes, the CAMP Facility finalized the purchase of a new multi-functional roll-to-roll coating system in FY20. The new coating line has begun the production-phase process at

the vendor and is planned to be completed and installed by the end of Q4 FY21. The advanced features of the coater will significantly increase the CAMP Facility's capabilities for investigating novel electrochemical energy storage systems by enabling uniform thin ceramic coatings and electrolyte membranes.

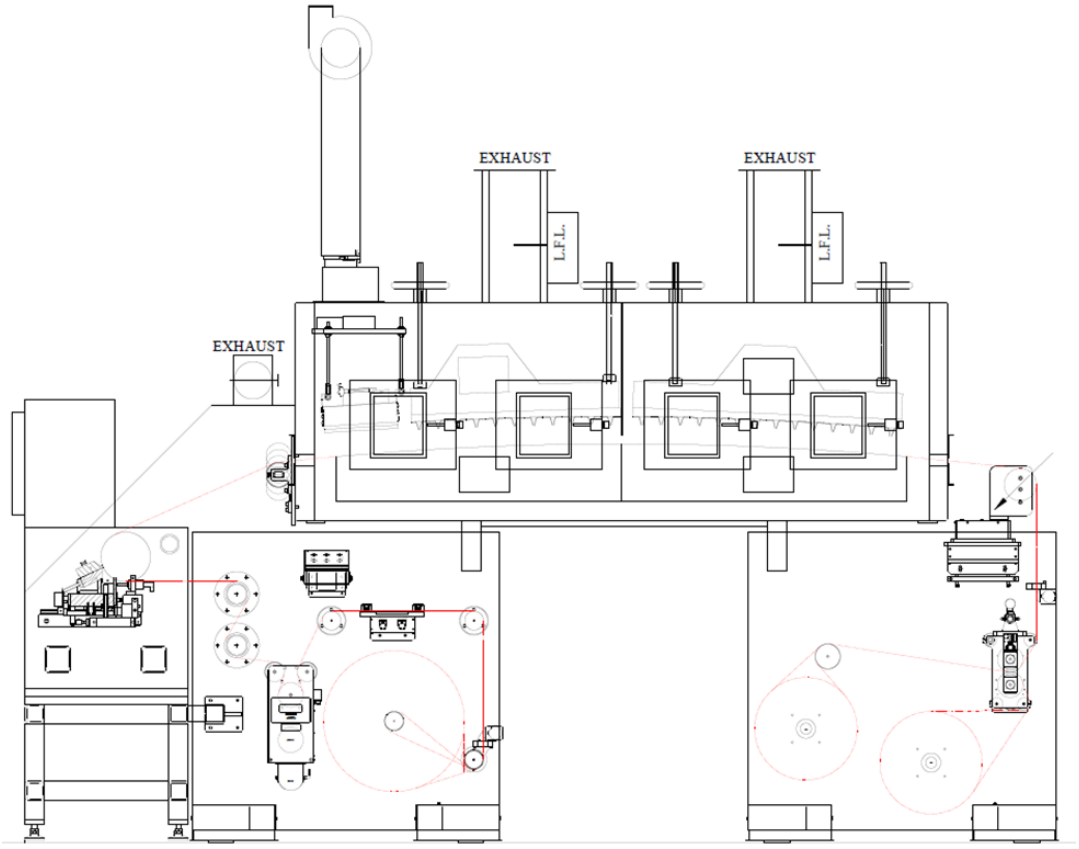

Figure I.6.E.1 Diagram of the multi-functional coating system featuring an interchangeable coating head station.

The multi-functional coating system (Figure I.6.E.1) will include:

- Interchangeable coating heads
    - Gravure (forward/reverse)
    - Single-slot die
- Corona treatment
- IR drying zone
- Progressive cavity pump

Additional capabilities available that may be purchased as needed (and as funds provided) include:

- Interchangeable coating heads
    - Knife-over-roll
    - Reverse comma

- Dual slot die

- Thermal laminate module
- Dry thickness gauge.

Develop Methods to Direct-Coat Ceramics onto Lithium-Ion Electrodes

The CAMP Facility continues to develop the capability to coat specialty films onto electrodes (preferably the anode). The techniques being learned will be valuable to the adaptation of processing solid electrolyte electrode systems. The effort remains on ceramic-based films, but may later include active materials or polymer films, that could serve a variety of applications: replace polymer separator with ceramic separator (added safety); getter undesirable decomposition products with ceramic/functional film; suppress formation of lithium dendrites with novel electrode architecture; replace liquid/polymer electrolytes with solid state electrolyte. A schematic of the cell design approaches being considered are shown in Figure I.6.E.2.

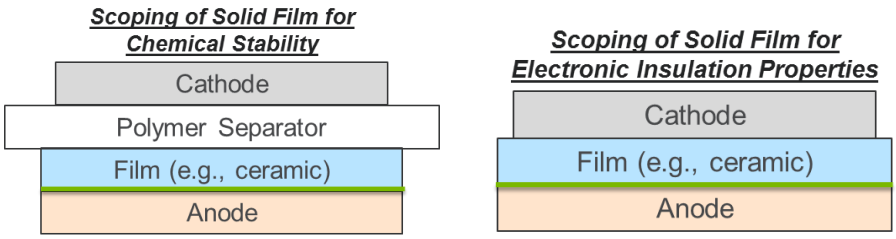

Figure I.6.E.2 Cell design options for coating materials onto an existing electrode. The green lines indicate the interface of film coating on to the anode.

The CAMP Facility has demonstrated that reverse comma coating, using existing equipment, results in uniform coatings when coating on to a foil substrate at moderate to high slurry wet gaps (between approximately 20 to 700 µm). When coating on a porous substrate, such as an electrode, the comma method provided more coating uniformity than reverse comma. In a scoping study, ceramic slurry comma-coated graphite electrodes that had intriguing electrochemical results (refer to FY18 & FY19 annual reports), where the ceramic coating was the sole electronic insulator, were provided to the Post-Test Facility for evaluation. Ion-milled (Gatan) electrodes viewed by cross section SEM displayed distinct layering of ceramic slurry coatings on graphite electrodes, and not filling the anode porosity (Figure I.6.E.3).

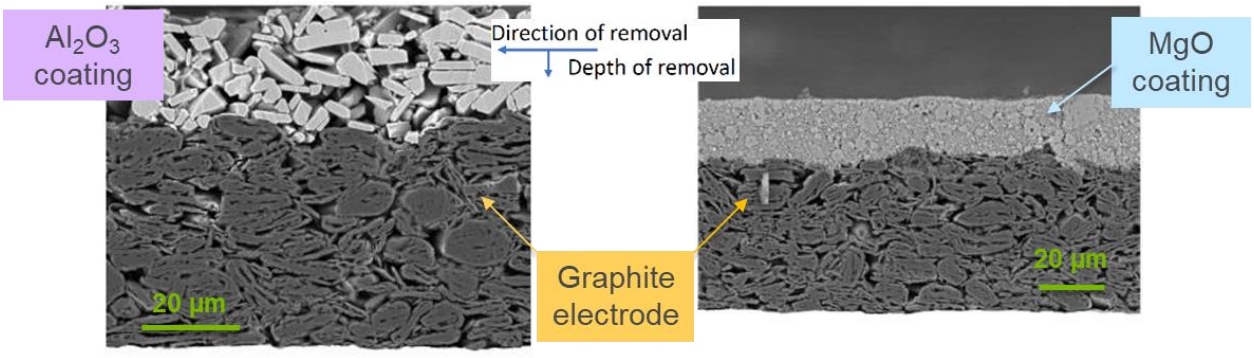

Figure I.6.E.3 Cross section SEM images of 95 wt% ceramic powder and 5 wt% PVDF slurries coated on graphite electrodes; Al_2O_3 (left), MgO (right). Images courtesy of Nancy Dietz-Rago (Post-Test Facility).

The electrochemical results and SEM observations set the stage for continued efforts to apply uniform thin (~20 µm) ceramic coatings by acquiring ceramic materials with more favorable particle sizes and morphologies, and leveraging the gravure and slot die coating methods, which can use thinner wet gaps (between 1 to 40 µm). Foil substrates and porous electrodes (*e.g.*, graphite anodes) are better suited to be coated using the gravure or slot die

coating methods. The new multi-functional coater with the noted interchangeable coating heads addresses this need and others (free-standing films, electrolyte membranes, etc.).

5V Spinel LMNO Cathode Cycled Against Ceramic-Coated Anode

The ability to coat a "protective" coating on a graphite electrode can provide opportunities to explore new cell systems. One thought was to determine if a ceramic coating on an anode could prevent manganese from 4 V and 5 V Mn-spinels from depositing on the graphite underneath. (Manganese dissolution is a common problem for Mn-spinels, particularly above room temperature, where the deposited Mn causes further electrolyte decomposition on the graphite SEI layer).

The CAMP Facility used samples from graphite (Conoco Phillips CGP-A12) electrodes that were previously coated with MgO, Al_2O_3, and AlN (Figure I.6.E.4) in a coin cell study with 5 V Mn-spinel ($LiMn_{1.5}Ni_{0.5}O_2$ or LMNO). These cells were made with Gen2 electrolyte and Celgard 2320 separator. Duplicate cells were made for each system and cycled between 3.5-4.7 V at 30°C (4 Cycles at C/10 for Formation followed by 200 Cycles at C/3). The results from these tests are summarized in Figure I.6.E.5, where initial results indicate that the ceramic coatings have a slightly higher capacity, but little impact on the capacity retention of the 5 V Mn-spinel. It remains to be seen (cells still on test) if the ceramic was able to block the Mn from depositing on the graphite underneath. If so, this would suggest that the capacity fade of the 5 V Mn-spinel is not solely due to the Mn reaching the graphite anode.

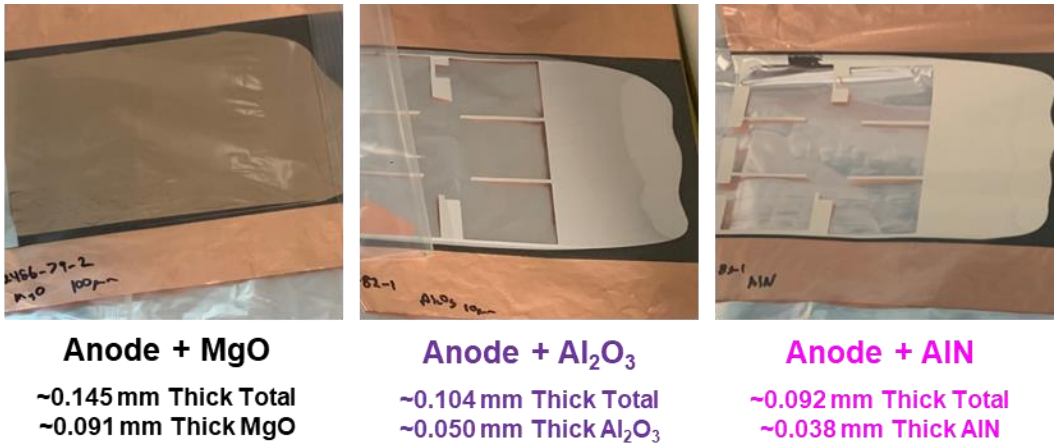

Figure I.6.E.4 Ceramic-coated graphite electrodes used to test impact on Mn cross-over from 5 V Mn-spinel cathode.

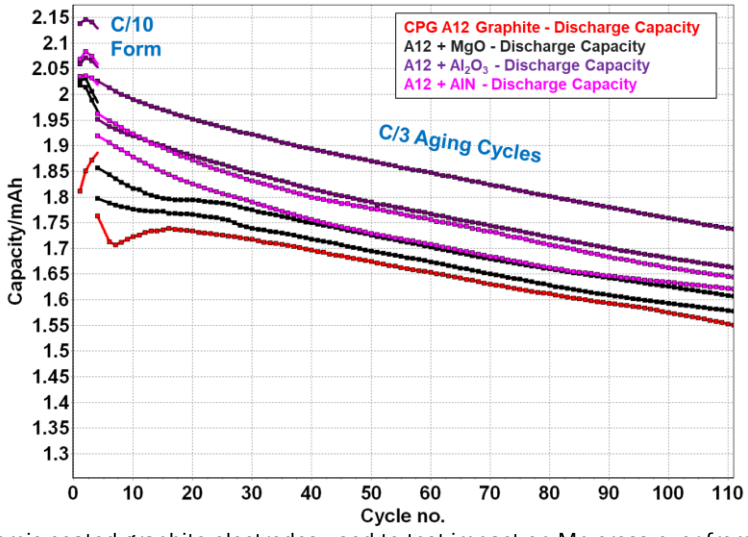

Figure I.6.E.5 Ceramic-coated graphite electrodes used to test impact on Mn cross-over from 5 V Mn-spinel cathode.

Support of Behind the Meter Storage Program

One new project that the CAMP Facility was tasked to support is the Behind the Meter Storage (BTMS), which has a goal of developing low-cost energy storage technologies on a large scale to better enable electric vehicle charging at commercial buildings/residential communities. Advanced battery systems that use earth-abundant elements are of key interest. Electrodes based on titanium (LTO), manganese (LMO), and iron (LFP) are obvious choices. One goal is to investigate the impact of electrode thickness on performance for each of these electrode/cell systems so that this data can be used to estimate cost using modeling calculations from BatPaC. The CAMP Facility fabricated electrodes with LTO, LMO, and LFP at several electrode mass loadings. These electrodes were cycled versus lithium in coin cells to validate their capacity utilization before providing them to the BTMS teams.

Figure I.6.E.6 is a summary of the capacity versus current rate for LTO and LFP versus lithium metal in coin cells. It is observed that the electrodes with high areal capacities can only yield the expected capacity at slower rates; faster rates for the thicker coatings resulted in loss of electrode utilization. Similar observations were found for the LMO electrodes. Several other DOE programs soon incorporated these electrodes into their projects. In particular, the electrodes with high loadings were desired because of their ability to provide or accept lithium at nearly constant potentials; they can function as a pseudo Reference-Counter Electrode.

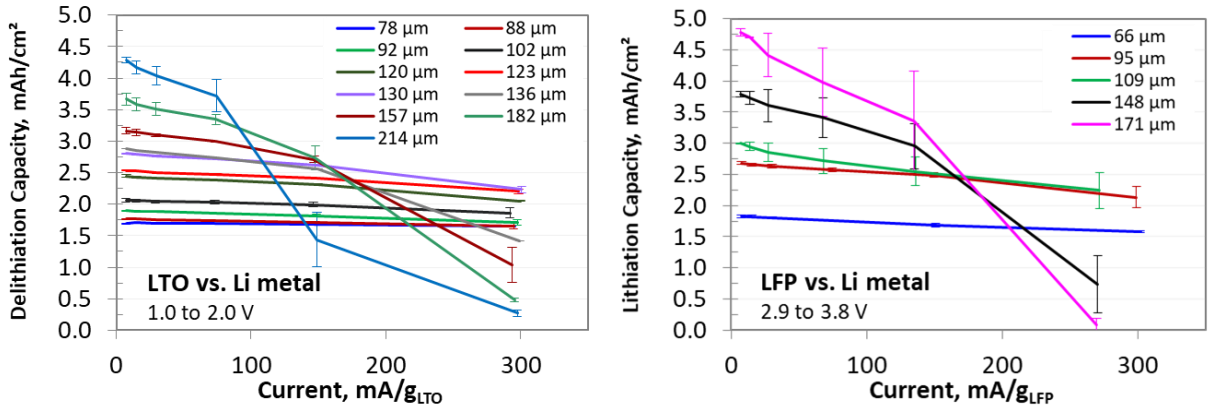

Figure I.6.E.6 Delithiation capacity for LTO (left) and lithiation capacity for LFP (right) versus lithium over a wide range of electrode mass loadings (average coin cell data, 2σ SD, 30 °C, Gen2 electrolyte, legends indicate coating thickness).

Lateral Heterogeneity Arising from Coin Cell Architecture

The CAMP Facility has been developing diagnostic methodologies for in-situ and operando measurements of lithium-ion batteries. The present focus is on coin cells as they are the most frequently used test devices for research and development in the battery sciences because of their affordability, ease of use, and robust design. In these cells, flat electrodes sandwich a microporous separator infused with a liquid electrolyte. This assembly is pressed together by two stainless steel (SS) spacers loaded from the top by a wave spring. The assembly is housed inside a SS case that is crimp-sealed through a gasket. The design mitigates concerns with electric and heat conductivity in the leads, and there is sufficient internal volume to accommodate gases generated during electrode-electrolyte reactions. The spring loading and thick SS spacers provide compression and alignment of the electrodes.

To peer into the coin cells while they are cycling, a combination of X-ray radiography and energy dispersive X-ray diffraction (EDXRD) techniques are used. The studies are conducted at beamline 6BM-A of the Advanced Photon Source at Argonne. The radiography is used to image the various components in the cell, as shown in Figure I.6.E.7.

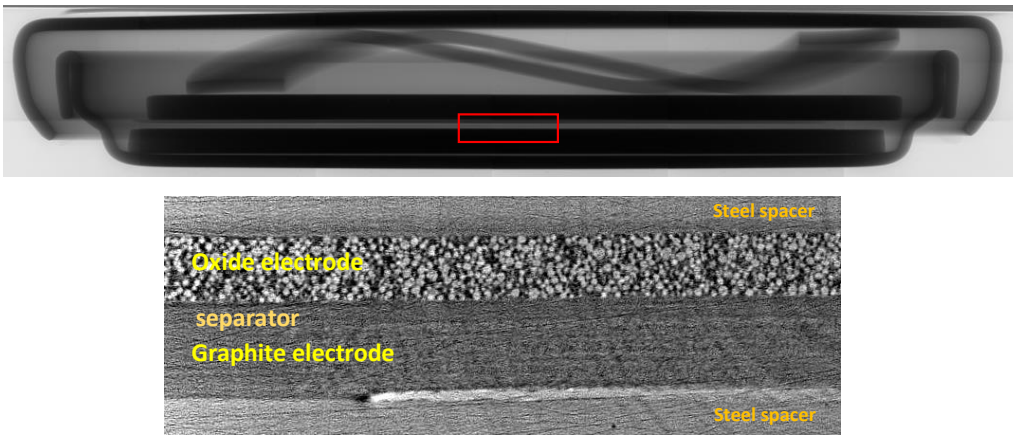

Figure I.6.E.7 Top panel shows radiograph of a conventional coin cell, which includes the top can (case), spring, electrode assembly between two stainless steel spacers and the bottom can (cap). The rectangular area marked in red is enlarged in the bottom panel which provides a close-up of the electrode/separator assembly.

In EDXRD, narrowly focused polychromatic ("white light") beams of synchrotron photons are used to obtain diffraction patterns at a fixed angle θ, so the Bragg condition, $2d \sin\theta = n^*\lambda$, is satisfied for some wavelengths λ in the light continuum; the high-energy X-rays can penetrate the casings of coin cells, so no special cell design is needed. This method is complementary to the commonly used angle-dispersive XRD method, which uses monochromatic X-ray beams and scans the angle θ to satisfy the Bragg condition. Using this technique, the phase and lattice parameter changes in the oxide cathode and graphite anode can be examined; the positions and amplitudes of the diffraction peaks depend on the lithium content of the active materials, allowing *in situ* profiling with ~ 2-5 μm precision.

In the course of these studies, strong inhomogeneity was noted both along the radial direction (in the *xy* plane of the laboratory frame) and across the electrode thickness (which is the *z*-axis of this frame); see Figure I.6.E.8a. This observation has major consequences, as such inhomogeneity can affect the current flow causing large lithium concentration gradients in the electrodes. Parasitic reactions along these gradients accelerate localized aging of the cell materials. Furthermore, such inhomogeneity makes it harder to predict cell life, as such forecasts are based on electrochemical models that typically assume lateral uniformity.

To determine causes of the inhomogeneity, detailed X-ray diffraction profilometry was obtained of the electrodes in coin cells. This showed that there is radial deformation in the electrode assembly and that this deformation can cause pinching of the porous separator; see Figure I.6.E.8b, which shows that the bottom electrode is strongly curved compared to the top one. This curvature causes a gap between the electrodes, which is smaller near the edge and greater at the center of the cell. This analysis shows that when the simply-supported bottom spacer is under load (because of the spring), it deforms slightly, becoming concave, and the bottom (but not the top) electrode follows the surface of this spacer, also becoming concave. The top spacer and the top electrode both remain almost flat: the top can is not deformed because the pressure during crimping is absorbed by the spring. Electrochemical modeling simulations indicate that variable porosity, resulting from the non-uniform separator compression, can contribute to the radially inhomogeneous lithium distribution observed in the solid electrodes. This awareness is important for battery researchers, as the effects of nonuniform separator compression can become significant during high rate cycling.

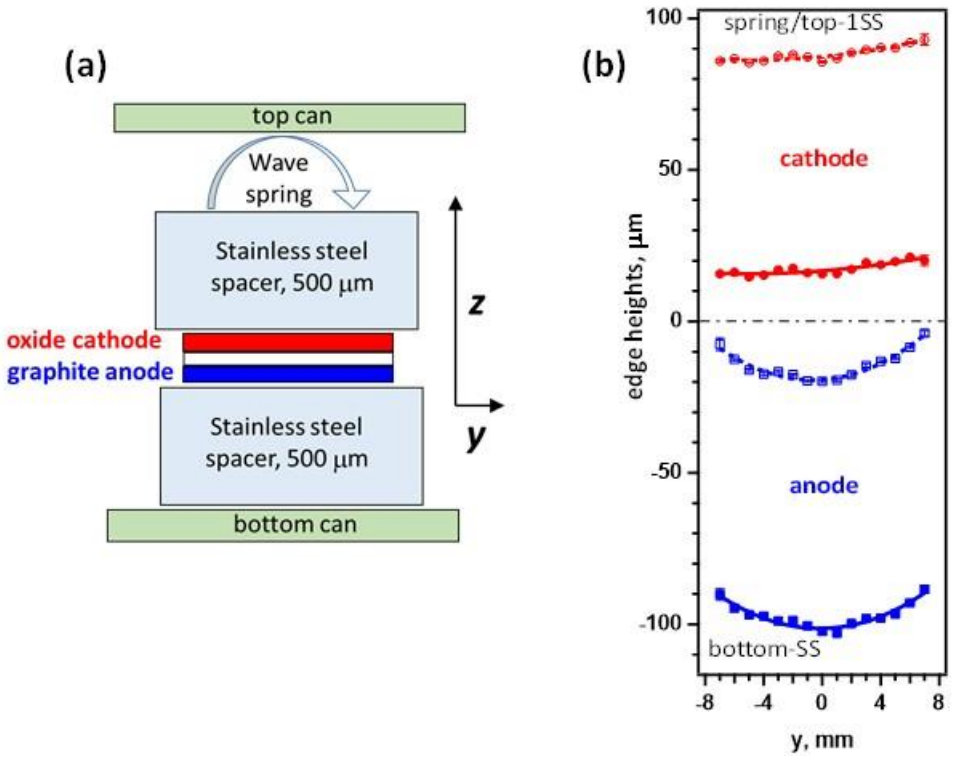

Figure I.6.E.8 Left panel (a) gives a schematic of the coin cell, with the nomenclature adopted in this study. The arrows indicate the laboratory frame axes. The right panel (b) symbols show hard edge heights of the electrodes plotted vs. the radial position y of the X-ray beam. The vertical bars in the plot give uncertainties in edge positions for each measurement and the solid lines are linear or quadratic fits.

Summary of Electrode Library Activities

Table I.6.E.1 shows the distribution of electrodes from the Electrode Library, which is maintained by the CAMP Facility. The Electrode Library serves as a supply of standard electrode samples that are designed to be interchangeable with one another (capacity matched). Electrodes can be made with as little as 50 g of experimental material, and can be made to match an existing counter electrode. From October 1, 2019 to September 30, 2020, 998 sheets of electrode were fabricated and distributed by the CAMP Facility, which is ~24 square meters of electrodes. These electrodes were supplied by the CAMP Facility in support of DOE's many activities in advanced battery R&D. In addition to these electrodes, the CAMP Facility fabricated ~188 pouch cells for these DOE projects (many unique combinations of electrodes, electrolytes, and separators).

Table I.6.E.1 Summary of Electrode Library Distributions

Electrodes Delivered	FY17		FY18		FY19		FY20	
Argonne	142	9 %	140	14 %	160	15 %	245	25 %
Other National Labs	172	11 %	172	18 %	224	21 %	299	30 %
Universities	151	10 %	175	18 %	296	28 %	333	33 %
Industry	1083	70 %	495	50 %	388	36 %	121	12 %
Total:	**1548**		**982**		**1068**		**998**	

Conclusions

The CAMP Facility purchased a multi-functional coating system that will provide coating method flexibility (i.e. single slot die, dual slot die, gravure, knife-over-roll), enhancing our ability to create uniform solid-state-

electrolyte and ceramic separator films/coatings onto electrodes. This coater is expected to be installed in summer of 2021.

Ceramic-coated anodes continued to be developed and evaluated. The interface layer between the graphite electrode and the top ceramic layer was shown to be distinct, which alleviates the worry that the ceramic particles would clog the anode pores. Overcoating with a ceramic and/or hybrid composite polymer will be greatly enhanced when the new coater is installed and operational.

X-ray radiography and diffraction studies of conventional coin cells show that there is a small gap between the flat bottom spacer and the concave wall of the cell can. Under spring-loading, this spacer deforms and becomes concave. The bottom electrode follows this curvature, while the top electrode remains relatively flat; this causes nonuniform compression of the electrode assembly. This compression is inconsequential at low rates but could become a problem when cycling rates increase over the 1C rate.

The CAMP Facility continues to support numerous DOE programs, much of which was performed through the CAMP Facility's Electrode Library. Numerous experimental electrodes and pouch cells were fabricated and delivered to DOE-EERE programs.

Key Publications

1. M.-T.F. Rodrigues, C. Liao, K. Kalaga, I.A Shkrob, D.P Abraham, "Dehydration Rather Than HF Capture Explains Performance Improvements of Li-Ion Cells by Ceramic Nanoparticles", *ACS Appl. Energy Mater.* **2**, 5380-5385 (2019).

2. R.T. Haasch, S.E. Trask, M.-T.F. Rodrigues, D.P. Abraham, "Si powders and electrodes for high-energy lithium-ion cells", *Surf. Sci. Spectra* 27, 016801 (2020); doi: 10.1116/1.5130764

3. J.S. Okasinski, I.A. Shkrob, A. Chuang, M.-T.F. Rodrigues, A. Raj, D.W. Dees, D.P. Abraham, "In situ X-ray spatial profiling reveals uneven compression of electrode assemblies and steep lateral gradients in lithium-ion coin cell", *Phys. Chem. Chem. Phys.* 22, 21977 (2020).

4. CAMP Facility contributions to other papers are acknowledged in numerous other sections of this report and peer-reviewed scientific manuscripts.

Acknowledgements

Key contributors to this work include: Daniel Abraham, Shabbir Ahmed, Ira Bloom, Dennis Dees, Nancy Dietz-Rago, Alison Dunlop, Chen Liao, Kewei Liu, Wenquan Lu, Bryant Polzin, Yan Qin, Andressa Prado Rodrigues, Marco Rodrigues, Ilya Shkrob, Seoung-Bum Son, Steve Trask, Zhenzhen Yang, and Sanpei Zhang.

I.6.F Materials Benchmarking Activities for CAMP Facility (ANL)

Wenquan Lu, Principal Investigator
Argonne National Laboratory
9700 S. Cass Ave.
Lemont, IL 60439
E-mail: luw@anl.gov

Andrew Jansen, Principal Investigator
Argonne National Laboratory
9700 S. Cass Ave.
Lemont, IL 60439
E-mail: jansen@anl.gov

Peter Faguy, DOE Technology Development Manager
U.S. Department of Energy
E-mail: Peter.Faguy@ee.doe.gov

Start Date: October 1, 2018 End Date: September 30, 2021
Project Funding: $550,000 DOE share: $550,000 Non-DOE share: $0

Project Introduction

High energy density electrode materials are required in order to achieve the requirements for electric vehicle (EV) application within the weight and volume constraints established by DOE and the USABC. One would need a combination of anode and cathode materials that provide 420 mAh/g and 220 mAh/g, respectively, as predicted by Argonne's battery design model (BatPaC), if one uses a 20% margin for energy fade over the life of the battery assuming an average cell voltage of 3.6 volts. Therefore, the search for new high energy density materials for lithium ion batteries (LIB) is the focus of this material benchmarking project. In addition to electrode materials, other cell components, such as separators, binders, current collectors, etc., are evaluated to establish their impact on electrochemical performance, thermal abuse, and cost.

This benchmarking effort is conducted as part of the Cell Analysis, Modeling, and Prototyping (CAMP) Facility (Refer to Chapter I.6.E) to identify and support promising new materials and components across the "valley of death", which happens when pushing a new discovery towards a commercial product. The CAMP Facility is appropriately sized to enable the design, fabrication, and characterization of high-quality prototype cells, which can enable a realistic and consistent evaluation of candidate chemistries in a time-effective manner. However, the CAMP Facility is more than an arrangement of equipment, it is an integrated team effort designed to support the production of prototypes electrodes and cells. In order to utilize the facility more efficiently and economically, cell chemistries are validated internally using coin type cells to determine if they warrant further consideration. In addition, the bench marking will advance the fundamental understanding of cell materials and facilitate advance the technology development.

Objectives

- The primary objective is to identify and evaluate low-cost materials and cell chemistries that can simultaneously meet the life, performance, and abuse tolerance goals for batteries used in EV applications.
- The secondary objective is to enhance the understanding of the impact of advanced cell components and their processing on the electrochemical performance and safety of lithium-ion batteries.
- This project also provides the support to the CAMP Facility for prototyping cell and electrode library development, and the MERF facility for material scale up.

Approach

Though there are an overwhelming number of materials being marketed by vendors for lithium-ion batteries, there are no commercially available high energy materials that can meet the requirements for all-electric-range (AER) within the weight and volume constraints established for EVs by DOE and the USABC. Identification of new high-energy electrode materials is one of the challenges for this project.

Under materials benchmarking activities, we constantly reach out to, or are approached by, material developers to seek opportunities to test their advanced or newly released products. By leveraging Argonne's expertise in electrode design and cell testing, we can provide not only a subjective third opinion to material suppliers, but also deeper understanding on their materials, which can aid their material development. This deep understanding becomes even more important when the material developers are small companies or new players, who often overlook overall requirements of battery materials.

In addition to industrial partners, we also work closely with scientists from various research institutes, such as universities and research laboratories. They often come up with novel materials with advanced electrochemical performance, but small quantities, which is only enough for validation purpose. These test results help us to determine how much effort should be expanded to explore the material potential.

In general, we will validate any potential cell material, which has impact on the cell performance, mainly in terms of electrochemical performance, electrode optimization, and thermal stability. The electrochemical performance is the centerpiece of the materials benchmarking activities, which will be tested using 2032-sized coin-type cells under test protocols derived from USABC PHEV 40 requirements [Battery Test Manual For Plug-In Hybrid Electric Vehicles, Idaho National Laboratory]. The freshly made coin cells will undergo three formation cycles at a C/10 rate. The cells are then tested for the rate performance. For the rate test, the charging rate is set at C/5, while the discharge rate varies from C/5, C/3, C/2, 1C to 2C. Three cycles are performed for each discharge rate. After the rate test, the cells then undergo cycling test at C/3 rate. During the cycling test, we change the current rate to C/10 every 10th cycle to check the rate effect. Also, Hybrid Pulse Power Characterization (HPPC) is conducted every 10th cycle, which will be used to calculate the Area Specific Impedance (ASI).

This fiscal year, we have investigated various battery materials, such as cathode, anode, conductive additives, and solid-state electrolyte. In this report, selective work, including SiO anode and electrode optimization using single-wall carbon nano-tube, nickel-rich cathode material, and lithium lanthanum zirconium oxide (LLZO) solid-state electrolyte, will be presented.

Results

Optimization of Graphite–SiO Blend Electrodes

Silicon oxide materials (SiO_x) are very promising anode materials and have been the subject of recent review articles [1], [2]. SiO_x is generally prepared by co-evaporation of Si and SiO_2, resulting in a composite material with nano-Si domains within an SiO_2 matrix. During initial lithiation, the SiO_2 domains irreversibly react, likely forming Li_2O and Li_4SiO_4 and thus result in significant irreversible capacity loss, while the Si domains can cycle reversibly. Therefore, SiO_x can be considered an active−inactive alloy material, resulting in lower volume fluctuation with cycling than pure Si. This, in turn, can allow for the use of larger SiO_x particles without pulverization (as compared to the nanoparticles often employed for pure Si materials) and therefore less surface area for lithium-consuming solid electrolyte interface (SEI) formation reactions. Even so, SiO_x can expand by up to 160%, which is likely too much for practical electrodes.

A common strategy to mitigate both volume fluctuation and the relatively low conductivity of silicon-based materials is to prepare composite or blended electrodes with carbon materials such as graphite [3]. In this work, we explore graphite–silicon monoxide (Gr–SiO) blended electrodes prepared by simple planetary slurry mixing. We tune slurry formulations with the goal to optimize energy density and capacity retention and find

that a commercial single-walled carbon nanotube (SWCNT) product as conductive additive shows very promising results relative to traditional carbon black.

Table I.6.F.1 SiO electrode composition with various amount of carbon black and binder

(Gr:SiO)-binder-CB	XL20	SiO	LiPAA	PVDF	C45
(1-0)-6-2	92%	0%		6%	2%
(9-1)-10-2	79%	9%	10%		2%
(7-3)-14-3	58%	25%	14%		3%
(5-5)-18-4	39%	39%	18%		4%
(0-1)-20-10	0%	70%	20%		10%

Initial Graphite–SiO blend formulations using carbon black: The graphite material chosen for study has flake-like morphology with relatively large particle size. As a starting point, Gr–SiO blend formulations were prepared with LiPAA binder and carbon black (CB) conductive additive. Our previous work demonstrated that the best cycling performance for SiO-LiPAA-CB electrodes with weight ratios of 70-20-10. Initial Gr–SiO blend formulations were chosen somewhat arbitrarily, with increasing weight percent of binder and CB conductive additive to compensate for increasing weight fraction of SiO relative to graphite, because the SiO material has a smaller particle size and higher surface area. These initial electrode compositions are provided in Table I.6.F.1.

Figure I.6.F.1a displays the half-cell voltage profiles during the first 3 formation cycles obtained from each Gr–SiO electrode formulation in Table I.6.F.1 (note, specific capacities are calculated from the combined mass of graphite and SiO). Increasing SiO content yields significant increase in specific capacity, but also increases the first-cycle irreversible capacity loss. The latter is generally attributed to the conversion of SiO_2 domains to lithium silicates and/or lithium oxide. Figure I.6.F.1b displays normalized voltage profiles during the 3rd formation cycle for the Gr–SiO (1-0), (7-3), and (0-1) formulations, demonstrating that increasing SiO content also results in a more positive average cycling potential and larger voltage hysteresis between charge and discharge. The corresponding differential capacity plots are shown in Figure I.6.F.1c.

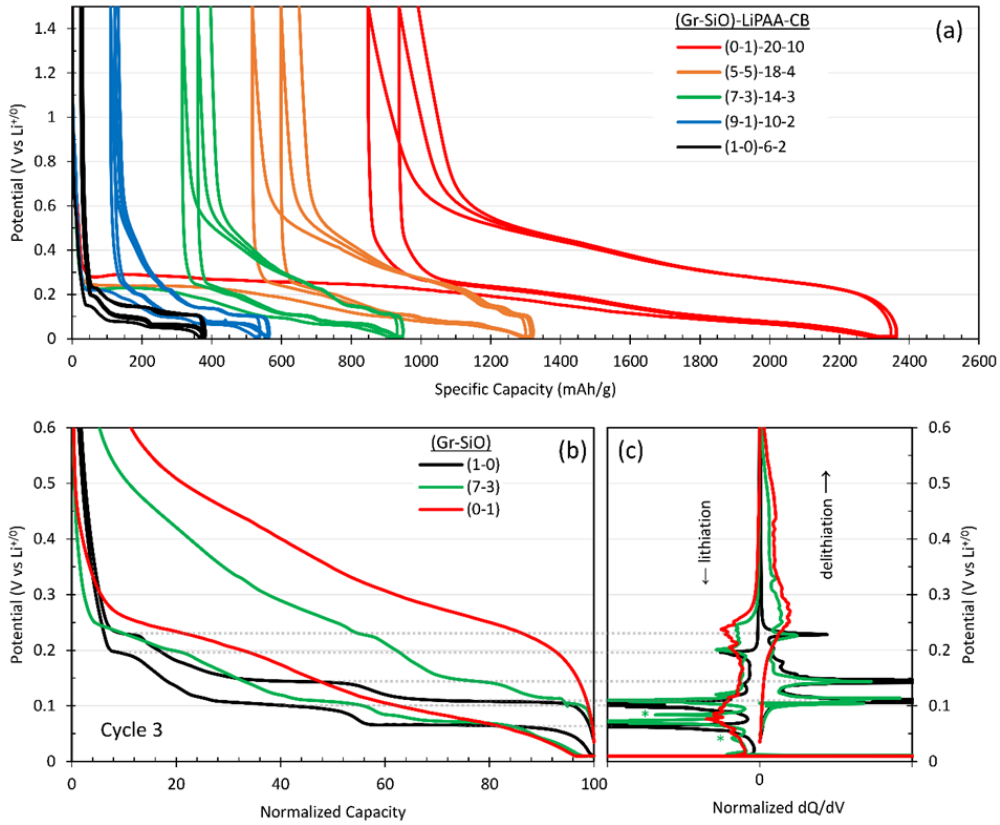

Figure I.6.F.1 (a) Half-cell voltage profiles during C/10 formation cycles from Gr–SiO blended electrode formulations. (b) Normalized voltage profiles illustrating higher average voltage and hysteresis with increasing SiO content, and (c) corresponding differential capacity plots for selected electrode formulations from the 3rd C/10 formation cycle. Cells contained 1.2M $LiPF_6$ in EC/EMC (3/7) (Gen2) electrolyte with 10 wt% FEC (Gen2 without FEC was used for the (1-0) formulation). Cycling was 1.5–0.01 V at 30 °C.

Figure I.6.F.2a displays the half-cell specific capacity for each formulation as a function of cycle number and charge (delithiation) rate, as obtained from electrodes with areal capacities between 1.5–2.0 mAh/cm². The capacity of the graphite-free SiO electrode is well-below the 1710 mAh/g theoretical capacity of SiO, demonstrating that the electrode formulation is likely not optimized. Furthermore, the capacity fade during the first three formation cycles increase significantly with increasing SiO content, which suggests non-ideal mechanical integrity and/or poor electrical conductivity for the electrodes. Figure I.6.F.2b shows the delithiation capacities normalized to the first cycle. It can be seen that reasonably good performance is obtained when the Gr-SiO weight ratio is only 10 wt.% SiO (9-1) (blue line). Interestingly, electrodes with (5-5) and (7-3) weight ratios (orange and green lines, respectively) display greater relative capacity fade than the graphite-free formulation (red line), suggesting a non-synergistic behavior between the graphite and SiO for these particular formulations. We note that both rate capability (i.e., polarization) and irreversible capacity loss with cycling contribute to the observed capacity fading in these experiments. Capacity loss with cycling can be observed as continuous capacity decay even during 3 repeat cycles at the same rate.

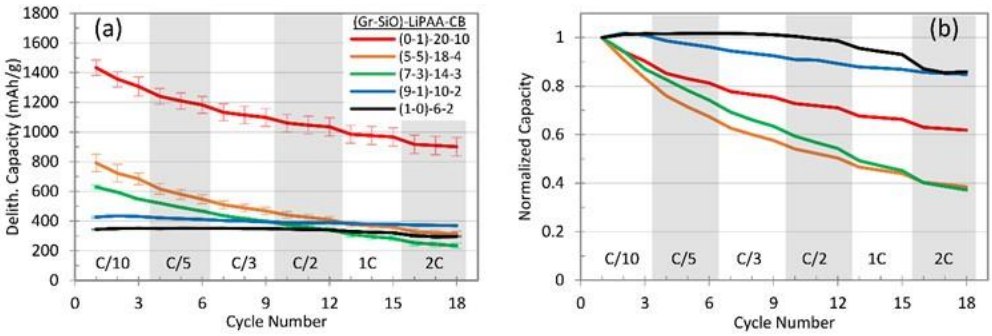

Figure I.6.F.2 (a) Delithiation Specific Capacity (per mass of graphite + SiO) as a function of cycle number and delithiation rate compared for several Gr–SiO blend formulations in half-cells. (b) Capacities normalized to the 1st formation cycle delithiation capacity.

Graphite–SiO blend formulation optimization using SWCNT: Carbon nanotubes (CNTs) and carbon nanofibers (CNFs) are often studied for their high conductivity and mechanical strength. Indeed, many have reported the use of CNTs and CNFs with graphite and SiO to make composite materials. In this work, we chose to screen a selection of commercial SWCNT conductive additive products added with a minimal loading and prepared by simple planetary mixing procedures.

Pre-mixed dispersions of SWCNTs (Tuball Batt, OCSiAl) were available in either NMP or water, and with different dispersants. Initial screening studies demonstrated minimal improvement in capacity retention for Gr–SiO blends prepared with PVDF binder and SWCNTs dispersed in NMP. Aqueous dispersions of SWCNTs were available with either polyvinylpyrrolidone (PVP) or carboxymethyl cellulose (CMC) dispersant. The PVP-stabilized SWCNT slurries did not mix well in electrode slurries with LiPAA binder, while CMC-stabilized slurries formed a homogeneous mixture and demonstrated the first breakthrough for improving capacity retention in our Gr–SiO electrodes.

Table I.6.F.2 SiO electrode composition with various amount of SWCNT and binder

(Gr:SiO)-LiPAA-SWCNT	XL20	SiO	LiPAA	CMC	SWCNT	mg SWCNT per m2 active SA
(7-3)-6-0.3	65%	28%	6.2%	0.5%	0.3%	1.7
(5-5)-10-0.4	45%	45%	9.7%	0.6%	0.4%	1.7
(3-7)-12-0.5	26%	61%	11.8%	0.7%	0.5%	1.7
(0-1)-15-0.6	0%	84%	15.0%	0.9%	0.6%	1.7

Further optimization of slurry formulations with SWCNT conductive additive was approached more systematically by controlling the loading of binder on the surface of SiO and SWCNT as shown in Table I.6.F.2. In the case of alloying anode materials, which have much higher volume fluctuation during cycling than intercalating cathode materials, it is expected that a thicker binder layer may be necessary for stable cycling. Our early screening studies with varied loadings of SWCNT showed best results with a loading of at least 1.7 mg SWCNT per m^2 of active materials (data not shown). The optimized Gr–SiO blend formulations containing SWCNT conductive additive are listed in Table I.6.F.3. It can be seen that the loading of both SWCNT and LiPAA increase with increasing weight ratio of SiO due to the larger surface area of SiO relative to graphite.

Figure I.6.F.3a shows the half-cell specific capacity for each formulation in Table I.6.F.2 as a function of cycle number and charge rate. For comparison, control data are included from SiO-free graphite electrodes with PVDF binder and CB conductive additive, and which were cycled without FEC (i.e., a standard graphite anode formulation used in the Argonne CAMP Facility). Figure I.6.F.3b shows delithiation capacities normalized to the 3rd formation cycle. It is immediately apparent that capacity retention of the Gr–SiO blend electrodes with SWCNT conductive additive are significantly improved relative to the previous formulations with CB conductive additive. Furthermore, the rate capability (as approximated by the normalized capacity at 2C charge rate) for all Gr–SiO blended electrodes with SWCNT conductive additive appear to be superior even to the SiO-free graphite electrode.

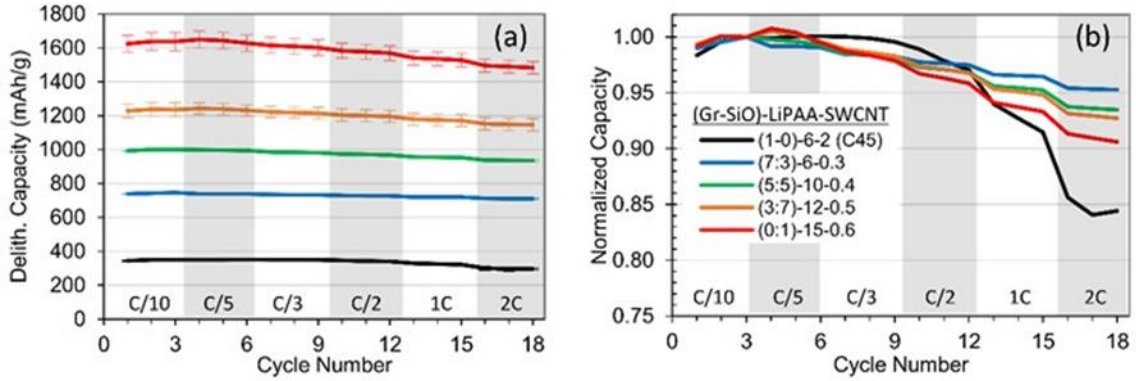

Figure I.6.F.3 Delithiation specific capacity (a) and delithiation capacity normalized to the third C/10 formation cycle (b) as a function of cycle number and delithiation rate compared for several graphite-SiO blend formulations using SWCNT conductive additive in half-cells. Cells contained 1.2M $LiPF_6$ in EC/EMC (3/7) (Gen2) electrolyte with 10 wt% FEC (except for the SiO-free cells). Cycling was 1.5–0.01 V at 30 °C.

Graphite–SiO blend electrode performance in full-cells: In order to get a better understanding of cycling stability, full-cells were assembled with NMC532 cathodes. In order to address the significant first-cycle irreversible capacity loss, on the order of 25%, we chose to 'pre-form' the Gr–SiO blend anodes by performing two cycles in a half-cell configuration with lithium metal counter electrode, then disassembled the cells and recovered the anodes for assembly in full-cells. The SiO-free graphite electrode with PVDF binder and CB conductive additive, (1-0)-6-2, was not 'pre-formed'. Electrodes were paired so that the expected first-cycle areal capacities for the anodes were ~1.2 times that of the cathode (N:P ratio = 1.2, see Figure I.6.F.4). Note that all full-cells are expected to be cathode-limited, and should therefore exhibit the same capacities and first-cycle irreversible capacity loss.

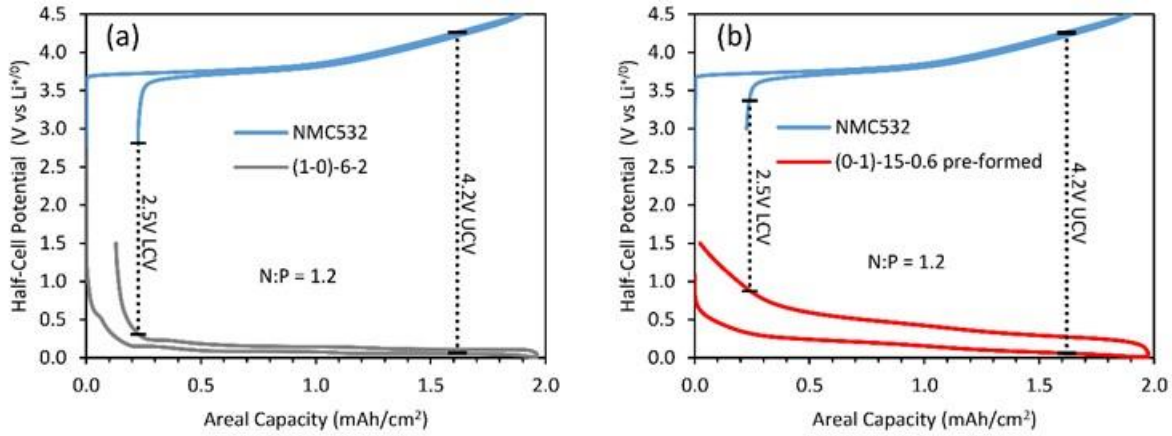

Figure I.6.F.4 Half-cell data (C/10) to show full-cell electrode pairings between NMC532 cathodes and (a) graphite anodes with formulation (1-0)-6-2 (plotting half-cell first-cycle data), and (b) pre-formed SiO anodes with formulation (0-1)-15-0.6 (plotting half-cell second-cycle data).

Full-cell cycling results are shown in Figure I.6.F.5. All full cells with Gr–SiO + SWCNT anode formulations exhibit comparable rate capability to the standard graphite anode with CB conductive additive, as indicated by the normalized capacity retention during varied discharge rate testing (cycles 4–18). Previous studies have shown that the capacity retention of graphite–silicon blended electrodes generally degrades as the silicon content is increased. Surprisingly, out results show that our full-cell capacity retention of all cells containing the optimized Gr–SiO anodes is superior relative to the control graphite anodes with CB additive. What's more, capacity retention seemed to improve with increasing SiO content.

Current understanding is that the introduction of more silicon material into blend electrodes decreases capacity retention by two mechanisms, both related to the larger volume fluctuation of lithium-alloying silicon materials. First, (i) volume fluctuation of the silicon particles causes SEI to fracture and reform, leading to continual Li^+ consumption through electrolyte reduction reactions. Second, (ii) volume fluctuation leads to bulk electrode degradation, for example by electronic isolation of the active materials. It is possible that the effects of (i) are minimized in these full-cells due to the use of micron-sized SiO materials, which will have significantly less surface area for SEI growth than the nano-silicon used in previous studies. Furthermore, the full-cells in this study included excess "flooded" electrolyte with FEC additive. FEC is known to postpone sudden capacity fade associated with rapid consumption of carbonate solvents. Therefore, it is possible that future studies with electrolyte-starved full-cells may yield a different result. Additionally, we hypothesize that (ii) is prevented by the use of the SWCNT conductive additive, allowing continued electrical and mechanical integrity of the electrodes despite the expected volume expansion and contraction. Furthermore, it appears that, if the SWCNTs alone are sufficient to maintain electrical and mechanical integrity, the presence of graphite in the electrode is not necessary for stable cycling.

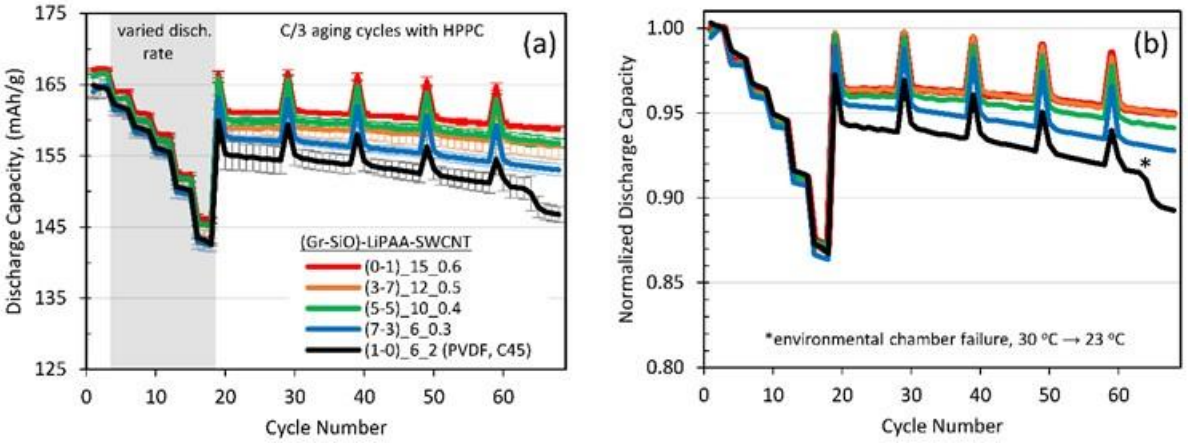

Figure I.6.F.5 Discharge capacities as a function of cycle number for full-cells with the indicated anode formulation vs NMC532 cathodes. Anode formulations containing SiO were 'pre-formed' in half-cells in order to overcome first-cycle irreversible capacity loss prior to full-cell assembly. (b) Discharge capacities normalized to the third C/10 formation cycle. All full-cells contained 1.2M $LiPF_6$ in EC/EMC (3/7) (Gen2) electrolyte with 10 wt% FEC. Cycling was 2.5–4.2V at 30 °C. The protocol included 3 formation cycles at C/10, 3 cycles each with charge rate of C/5 and discharge rate varied from C/5 to 2C, followed by C/3 ageing cycles with intermittent C/10 and HPPC testing.

NMC622 from 6K Inc.

Nickel-rich $LiNi_xMn_yCo_zO_2$ (NMC) is becoming as high-energy cathode materials for electric vehicle applications due to its high performance and low cost. 6K Inc produced NMC622 powder using their patented UniMelt® system; a high frequency microwave-based plasma process that allows for low cost, continuous flow, quick production of highly sustainable engineered advanced high-performance material for Li-ion batteries. CAMP received 6K Inc NMC622 powder [d50=28 µm; Li=0.99; uncoated material], coated an electrode from the powder, and assembled half and full coin cells with it for electrochemical testing and performance validation. The electrode composition was 89.9 wt% 6K Inc. NMC622, 5.05 wt% Timcal C-45, and 5.05 wt% Solvay 5130 PVDF. Half cells were fabricated and the voltage profiles of 4 identical cells are shown in Figure I.6.F.6. According to the figure, the cells are very reproducible. The calculated reversible

specific capacity of the NMC622 is 177 mAh/g (see Table I.6.F.3), which is comparable to the NMC622 from vendor A under the same testing conditions.

Table I.6.F.3 Specific capacity of half cells at various rage

Averaged Half Cell Data	Formation C/10 Cycles				Rate Study			
	1st Cycle Charge mAh/g	1st Cycle Efficiency	3rd Cycle Discharge mAh/g	Capacity Loss mAh/g	C/24	C/5	C/2	1C
6K Inc, 2.8-4.3V	194	92%	177	17	179	168	161	155
Vendor A, 3.0-4.3V	197	89%	179	18	182	173	166	160

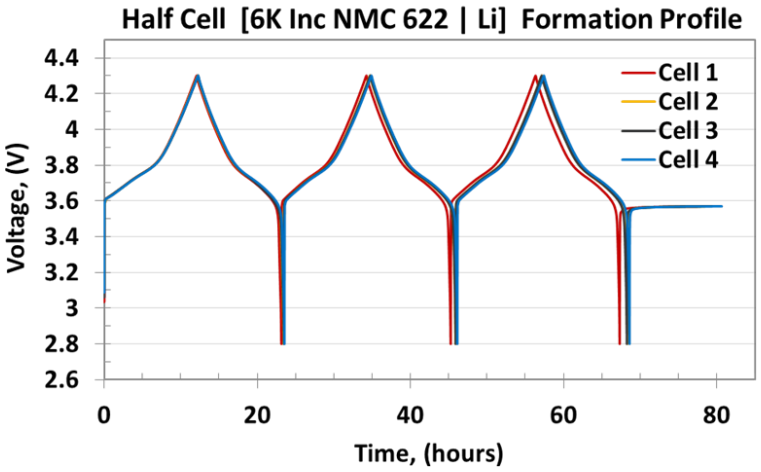

Figure I.6.F.6 Voltage profile of Li/NMC622 half cells during formation cycles. All cells contained 1.2 M $LiPF_6$ in EC/EMC (3/7) (Gen2) electrolyte cycled at 30°C between 2.8V and 4.3V with C/10 rate.

In order to investigate the cycle performance of NMC622 from 6K Inc., three full cells of 6K Inc NMC622 cathode with matched graphite anode were fabricated and tested at 30°C between 2.8V and 4.2V. CAMP electrochemically cycled the full cells through a series of tests: Formation, Rate Study, HPPC, and Life Cycle. The cycle performance of NMC622 full cells are shown in Figure I.6.F.7. 6K Inc NMC622 material showed a discharge capacity retention of ~82.6% which is on par with Vendor A's performance of ~86.9% after ~250 cycles in a coin cell.

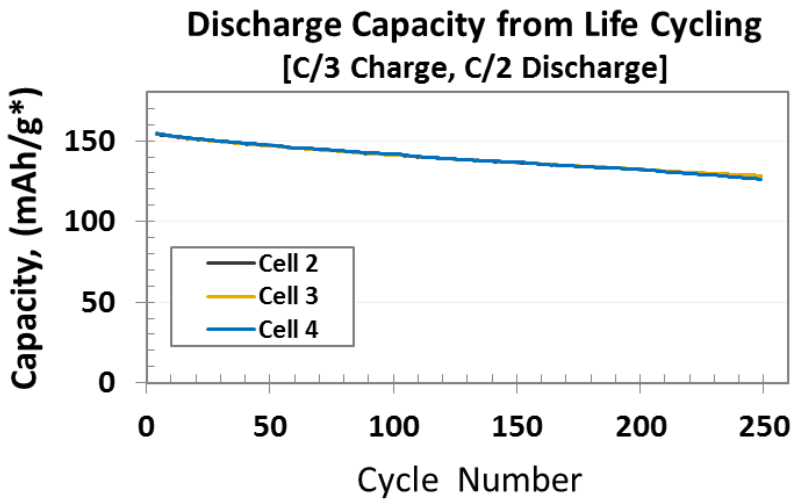

Figure I.6.F.7 Life cycling of NMC622 in full cells. All cells contained 1.2M $LiPF_6$ in EC/EMC (3/7) (Gen2) electrolyte cycled at 30°C between 2.8V and 4.2V. CAMP electrochemically cycled the full cells through a series of tests: Formation, Rate Study, HPPC, and Life Cycle

Conductivity of LLZO solid state electrolyte

To achieve the high energy outputs and eliminate the risk of thermal runaway and potential rapid discharge due to a short circuit, a solid-state approach is being investigated in the design of many advanced Li-ion batteries [4]. The high chemical, electrical, and mechanical stabilities possessed by solid-state materials make them ideal candidates for storage systems. However, the suitability of any crystalline material to act as an electrolyte hinges on its ionic conductivity and wide voltage and temperature ranges. The lithium-stuffed garnet known as $Li_7La_3Zr_2O_{12}$ (LLZO) is one of the most promising materials for this and has attracted a great deal of attention. Under benchmarking activity, we started to investigate this material to get better understanding on its performance and handling.

A 2 mm thick LLZO pellet was internally prepared by a scientist at Material Science Division at ANL. The Li/LLZO/Li assembly process was very challenging. The pellet was very brittle and easy to break. We first tried to weld the lithium metal onto the surface of the LLZO pellet. The pellet cracked probably due to the uneven heat stress. We then instead placed a lithium foil gently on the side of a new LLZO pellet without breaking the pellet. The Li/LLZO/Li cell was assembled (Figure I.6.F.8a) and sealed in pouch in the dry room at the CAMP Facility. The conductivity measurement of Li/LLZO/Li was tested at 75°C. Constant voltage (4 V) was applied to the pouch cell and current response was recorded, as shown in Figure I.6.F.8b. Though it is very noisy, the current is averaged around $2e^{-8}$ A (20 nA). The measured low conductivity of LLZO is due to very thick pellet and poor connection between the pellet and Li foil. We are working to address these deficiencies.

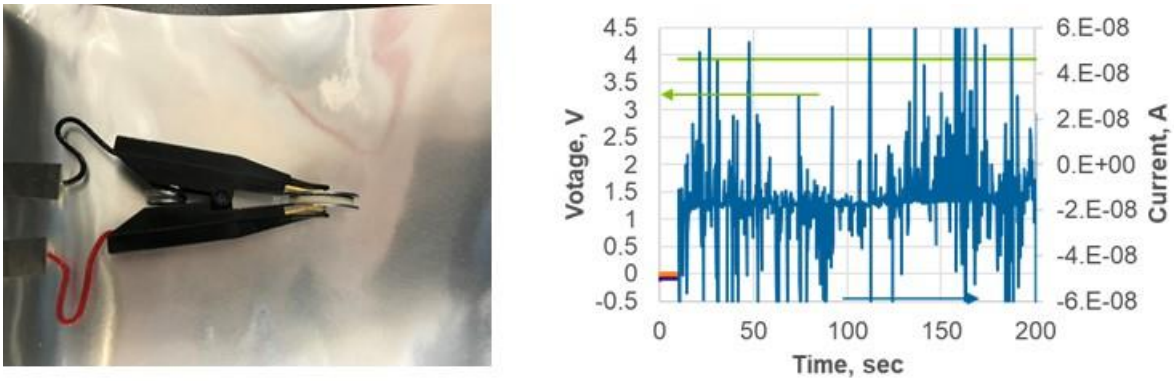

Figure I.6.F.8 (a) Li/LLZO/Li sandwich and (b) condutivity measurement of LLZO

Conclusions

We have shown that replacing carbon black conductive additive with a commercial SWCNT allows for graphite-SiO electrodes with highly stable cycling by simple planetary mixing procedures. Increasing the mass ratio of SiO relative to graphite increases the volumetric energy density for all formulations, despite the higher de-lithiation potential and volume expansion of SiO compared to graphite.

Nickel-rich transition metal oxide (NMC622) from 6K Inc. was electrochemically characterized. According to half-cell test results, including specific capacity and first cycle coulombic efficiency, 6K Inc NMC622 looked aligned with expected capacity. In full-cell couple with graphite electrode, NMC622 from 6K Inc. showed a discharge capacity retention of ~82.6%, which is on par with Vendor A's performance of ~86.9% after ~250 cycles in a coin cell.

Ionic conductivity of LLZO pellet was investigated in Li/LLZO/Li assembly at 75°C. Very low conductivity was obtained, which may be due the poor interface between the lithium foil and LLZO pellet. During Li/LLZO/Li assembly process, we noticed that the LLZO pellet was brittle and difficult to handle. In order to utilize LLZO as solid-state electrolyte, either strong and thin solid state electrolyte pellet/dics or flexible electrolyte film needs to be developed for its practical application.

Key Publications

1. Dry-Pressed, High Mass Loading, Lithium Nickel Cobalt Manganese Oxide (NCM) Cathodes Enabled by Holey Graphene Host, Brandon A Walker; Christian O Plaza-Rivera, Sam-Shajing Sun, Wenquan Lu, John W Connell; Yi Lin, Electrochimica Acta, Vol 362 (2020), 137129.

2. Heat of mixing during fast charge/discharge of a Li-ion cell: A study on NMC523 cathode, Divya Chalise, Wenquan Lu, Venkat Srinivasan, Ravi Prasher, J. Electrochem. Soc., 2020, 167, 090560.

3. Materials benchmarking activities for CAMP Facility, Wenquan Lu, Joel Kirner, Yan Qin, Steve Trask, Sanpei Zhang, Alison Dunlop, Bryant Polzin, and Andrew Jansen, 2020 DOE Vehicle Technology Office Annual Merit Review and Peer Evaluation Meeting, Washington D.C., 06/02/2020

4. Optimization of Graphite–SiO blend electrodes for lithium-ion batteries: Stable cycling enabled by single-walled carbon nanotube conductive additive, Joel Kirner, Yan Qin, Linghong Zhang, Andrew Jansen, Wenquan Lu, J. Power Sources, 2020, 450, 227711

5. Modeling framework for multiphysics-multiscale behavior of Si–C composite anode, Xiang Gao, Wenquan Lu, Jun Xu, J. Power Sources, 2020, Vol. 449, 227501

6. Conductivity, Cushioning, and Improving Lithium Ion Battery Performance, M. Lyons, J. Kirner, W. Lu, 2019 AIChE Annual Meeting, Orlando, FL, US, Nov. 10-15, 2019.

References

1. M.N. Obrovac, V.L. Chevrier, Chem. Rev., 114 (2014) 11444–11502

2. T. Chen, J. Wu, Q.L. Zhang, X. Su, J. Power Sources, 363 (2017) 126–144

3. R. Dash, S. Pannala, Sci. Rep., 6 (2016) 27449

4. W. Lan, H. Fan, V. Lau, J. Zhang, J. Zhang, R. Zhao, and H. Chen, Sustainable Energy Fuels, 2020,4, 1812-1821

Acknowledgements

We greatly acknowledge the contribution from Joel Kirner, Alison Dunlop, Yan Qin, Steve Trask, Bryant Polzin, and Sanpei Zhang.

I.6.G Electrochemical Performance Testing (INL)

Lee Walker, Principal Investigator
Idaho National Laboratory
2525 Fremont Ave
Idaho Falls, ID 83402
E-mail: lee.walker@inl.gov

Samuel Gillard, DOE Technology Development Manager
U.S. Department of Energy
E-mail: Samuel.Gillard@ee.doe.gov

Start Date: October 1, 2019 End Date: September 30, 2020
Project Funding: $4,000,000 DOE share: $4,000,000 Non-DOE share: $0

Project Introduction

The advancement of battery technologies that can meet the emerging demands for vehicle electrification requires in-depth understanding of the performance of early stage pre-commercial batteries, state-of-the art commercial cells and the ability to adapt evaluation methods as mobility needs change. The Battery Test Center (BTC) at Idaho National Laboratory (INL) has been supporting the evolution of electrified transportation through high-quality, independent testing of electrical energy storage systems for more than 30 years. Independent testing provides data for quantitative assessment of the fundamental technology gaps that exist in early stage battery development. Test methods and techniques are continuously improved to offer data on relevant metrics as vehicle applications evolve and as new core gaps are identified. Advancing electrified powertrain transportation including understanding both high-energy battery chemistries and high power, extreme fast charging needs, is a top priority in advancing how people and goods are transported in the United States. As a designated core capability and lead test facility for the Vehicle Technologies Office (VTO), the BTC at INL directly supports the US Advanced Battery Consortium (USABC) and other VTO programs by providing discrete information on failure modes, mechanisms and shortfalls in emerging technologies. Gaps in performance relative to targets are used as a metric to guide future R&D priorities.

The development and deployment of batteries in new, diverse applications requires both that the batteries function in the necessary environment as well as a deep understanding of their performance, life and expected failure mechanisms. In the past the primary means to advance knowledge on performance and life was to test batteries for extended periods of time under a range of different scenarios. Testing of batteries in this manner can take upwards of a year to make reasonable estimations of life and to clearly identify failure modes and rates. The need to shorten the design and testing cycle if critical to bringing new battery chemistries and cell designs into emerging applications such as in stationary energy storage to support electric vehicle charging stations capable of extreme fast charging. Connection of physics-based life models and machine learning (ML) provides the opportunity to enable more robust assessment of battery aging, failure mechanism identification and understanding as new use case scenarios are proposed. The current project is focused on means to apply ML to enhance the estimation of life while also identifying key failure pathways. During the first portion of the project existing data sets will be used for both training and validation of ML approaches to better characterize expected battery life. The work also looks to link ML with existing physics-based life models at INL and NREL.

Objectives

The activities at the INL BTC are focused on providing high fidelity, science-based performance and life testing, analysis, modeling, and reporting. To ensure the alignment with future industry and government needs, it is a key objective to update test and analysis procedures as new concepts and design space become

achievable. Refined procedures help identify promising future research paths and identify key fundamental gaps that need to be addressed.

Approach

With 20,000 square feet of laboratory space, the INL BTC is equipped with over 800 test channels for advanced energy storage testing at the cell-level (e.g., up to 7V, 300A), module-level (e.g., up to 65V, 1200A), and pack-level (e.g., 500-1000V, 500A). Test equipment is programmed to perform distinct test profiles while simultaneously monitoring for compliance with operating limits such as voltage, current and temperature. The output from such tests enables principles-based analysis to be performed that can aid in identification of key technology gaps.

To ensure high quality, repeatable and dependable data is used for analysis, batteries and other energy storage devices are typically subjected to specific test sequences while housed inside precision thermal chambers. To enhance performance testing across a wide range of thermal conditions, driven by automotive usage scenarios, the thermal chambers can be operated across a broad temperature range (e.g., -70 to 200°C). This temperature range enables key information to be extracted by modifying the chemical kinetic degradation rates within the evaluated items and enables accelerated aging analysis.

Successful performance testing and accurate life modeling are highly dependent on the fidelity of the acquired test data. The INL BTC has developed advanced calibration verification and uncertainty analysis methodologies to ensure that voltage, current, and temperature measurements are within the tolerance specified by the test equipment manufacturer (e.g., 0.02% of the full scale). These measured test parameters are subsequently used in various mathematical combinations to determine performance capability (e.g., resistance, energy, power, etc.). INL has also quantified the error associated with these derived parameters using the accuracy and precision of the relevant measured parameter (e.g., voltage) to ensure high-quality and repeatable results and meaningful presentation.

The INL BTC is also equipped with facilities that enable the characterization of batteries in aggressive use cases. One such use case is vibration that mimics what would be seen over the life of a battery in a typical automotive setting. Analysis of vibration on batteries at INL utilizes a high capacity vibration table to perform non-destructive tests to understand reliability and safety of new cell topologies to mechanical vibration and shock. Emerging cell designs that vary from current state of the art cell designs are the main focus of mechanical vibration and shock testing at INL.

Adjacent to the vibration table are two fire-rated isolation rooms that can be used for tests that push the known limits of battery operation. These aggressive use cases include extreme fast charging, subtle over- or under-charging, high-temperature thermal characterization for under-hood systems, among many others. The isolation rooms allow for safe testing of emerging cell technologies at or near the design limits and help characterize future use cases. The rooms also enable identification of key changes in performance fade that may emerge in aggressive use cases that can directly inform future rounds of early stage material and cell development activities. These complimentary non-destructive evaluation capabilities comprise INL's Non-Destructive Battery Evaluation Laboratory.

Results

The INL BTC continues to test articles of various sizes and configurations using standardized test protocols developed by INL with industry partnerships for different electric drive vehicle application. Table I.6.G.1 and Table I.6.G.2 summarize the testing activities under the USABC and Benchmarking programs, respectively, for FY-20. Technologies developed through USABC contracts are aged and tested against the appropriate application target (HP-EV, LC/FC-EV, HEV, PHEV, 12V S/S, 48V HEV) and, where applicable, they are compared to previous generations of test articles from the same developer. 157 articles were tested for USABC in FY-20, including 1module and 156 cells. The purpose of the Benchmark program is to evaluate device technologies that are of interest to VTO within DOE, but are not deliverables developed under a contract. In

some cases, Benchmark devices are used to validate newly developed test procedures and analysis methodologies. Benchmark activities also are used to understand which gaps need to be fundamentally addressed to improve cell performance. 131 cells were tested for the Benchmark program in FY-20. A new testing program was started in FY-20 to evaluate deliverables from the VTO Low Cobalt FOA programs. The purpose of the program is to find Li-Ion battery chemistries that have little to no cobalt content. 60 cells were tested for the Low Cobalt program in FY-20.

Analysis was performed for all articles tested, and results were presented regularly at quarterly review meetings and USABC Technical Advisory Committee (TAC) meetings to USABC representatives from different automotive manufacturers, DOE VTO representatives, developers, and national laboratory staff. INL worked with the USABC test methods committee to develop the methodology and update the manual for testing EV batteries.

Table I.6.G.1 Articles Tested for USABC

Developer	Application	System	Number of Articles Tested	Status at Year End
A123	12V Stop/Stop	Module	1	Completed
Amprius	HP-EV	Cell	24	Completed
Farasis	HP-EV	Cell	10	Completed
Farasis	HP-EV	Cell	18	Completed
Saft	12V Stop/Start	Cell	15	Completed
Zenlabs	HP-EV	Cell	5	Completed
Amprius	HP-EV	Cell	13	Ongoing
Farasis	Recycle	Cell	18	Ongoing
Saft	HEV	Cell	13	Ongoing
Zenlabs	HP-EV	Cell	17	Ongoing
Zenlabs	LC/FC-EV	Cell	23	Ongoing

Table I.6.G.2 Articles Tested for Benchmark

Developer	Application	System	Number of Articles Tested	Status at Year End
Cuberg	EV	Cell	10	Completed
Cuberg	EV	Cell	12	Completed
Diakin	EV	Cell	30	Completed
Toshiba	EV	Cell	3	Completed
Toshiba	EV	Cell	18	Completed
University of Washington	EV	Cell	13	Completed
LG/CPI	EV	Cell	15	Ongoing
Microvast	EV	Cell	6	Ongoing
Microvast	EV	Cell	6	Ongoing
PPG	EV	Cell	18	Ongoing

Table I.6.G.3 Articles Tested for Low Cobalt

Developer	Application	System	Number of Articles Tested	Status at Year End
Nextech-Nexceris	Low Cobalt	Cell	12	Completed
ORNL	Low Cobalt	Cell	12	Ongoing
Penn State	Low Cobalt	Cell	12	Ongoing
UT – Austin	Low Cobalt	Cell	12	Ongoing
UC - Irvine	Low Cobalt	Cell	12	Ongoing

New collaborative work began in FY-20 between the 21st Century Truck Partnership (21CTP) and INL. This work has focused on developing battery specifications for commercial trucks with electric drives. Targets were established for class-8 line-haul battery electric trucks across many different use scenarios. 21CTP consists of OEM companies across the commercial vehicle market, DOE-VTO, and National Labs.

A key focal area for FY-20 at INL was expanded fade analysis as part of the Benchmark and USABC activities. The analysis was focused on more directly quantifying different levels of performance fade associated with more aggressive use cases, developing the ability to accurately capture non-electrochemical data including pressure evolution during cycling and alternative ways to ensure thermal equilibrium during cycling. Many of these methods were part of a refinement to enhance the utility of the Non-destructive battery evaluation laboratory (NOBEL). In several instances, especially in the benchmark program, enhanced electrochemical analysis was performed to further isolate performance degradation pathways. In line with this work new activities using advanced data analytics were also initiated in FY-19. This work in conjunction with the National Renewable Energy Laboratory (NREL) seeks to shorten the time to characterize batteries while still providing useful, physics-backed information on performance fade and cell failure. The data analytics activity started during the last quarter of FY-19 is looks to have expanded impact in FY-21 and beyond. After refinement, it is expected that the outcomes from this project will be broadly applicable to testing and research activities alike.

Physics-based Machine Learning: Sensitivity Analysis of the Transient Analysis model (TAA/SP)

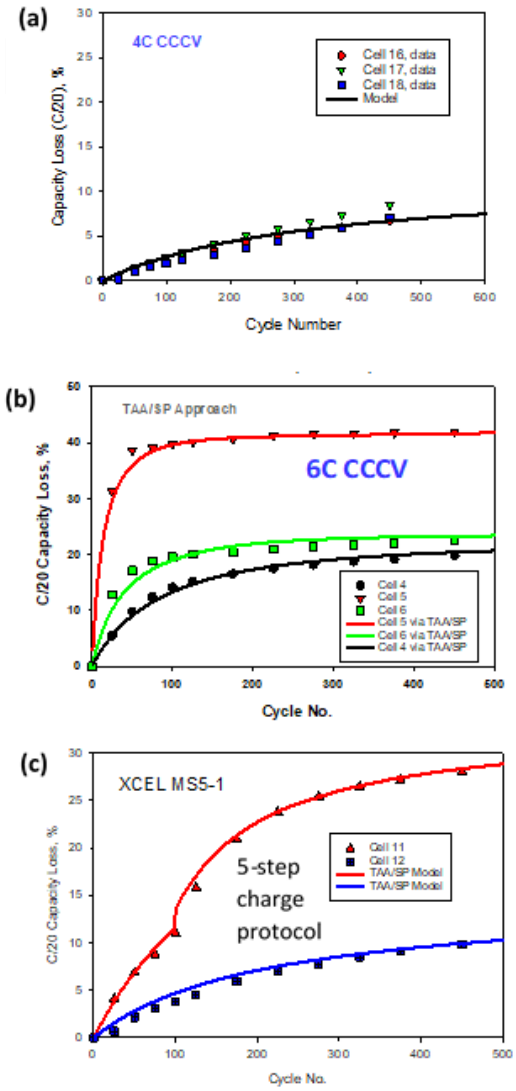

Figure I.6.G.1 Comparison of TAA/SP model and experimental data for different charge protocols

Using XCEL round-two cells as a basis, application of transient analysis modeling was extended to multiple off-matrix conditions. This sensitivity analysis gives insights into which stress factors or cell design attributes contribute most to cell aging. Stated otherwise, the results given here can help guide cell design and the choice of usage conditions to alleviate some extent of cell aging. Herein, loss of lithium inventory (LLI) is the focus, since it is generally known that LLI is the predominant early aging route in XCEL cells. LLI has connection to various surface-driven processes at the electrode, including but not limited to SEI growth, lithium metal deposition (LMD) and gas formation and related pore blockage. From such early mechanisms one or more secondary mechanisms such as loss of active material (LAM) can be promoted that impact the three-dimensional space of the electrodes.

For the sake of TAA/SP background, electrode surfaces provide a catalytic-type surface with sites that react with electrolyte species. The presence of cycling conditions provides an environment of electro-catalysis that is captured by the model. Cell design attributes regarding particle sizes, rheological terms, electrode and electrolyte loadings, etc. set the context for understanding the physical environment under which aging will

proceed. The fraction of available surface is primarily impacted by the effective electrode wetting, LMD and gas formation. Lesser available electrode surface area will increase the effective local current densities through the available area regions, raise impedance, cause increased polarization, and cause the rate of LLI to increase. The TAA/SP model can also determine if particle fracturing influenced the capacity loss rate during the cycling history.

Early model validation was performed using XCEL R2 cells having different charging protocols. Figure I.6.G.1 (a,b,c) shows selected XCEL R2 cells that have been modeled through TAA/SP. Overall good agreement is seen for the various conditions.

A sensitivity analysis was performed based on around 30 conditions of deviation from a baseline cell test condition, considering XCEL round 2 materials. Herein, the baseline (BL) is 6C CCCV charging and 0.5C discharging collectively for 9 total cycles per day, with a temperature of 30 ºC and an electrode wetting fraction of 0.99. This is represented by cell 4 in Figure I.6.G.1(b). Single-parameter variations were performed from the BL looking at temperature, particle diameter, available electrochemical surface, porosity, electrolyte properties, charge rate and daily use.

Near-term future work will investigate variance of multiple parameters per simulation. Selected conditions will be presented in future reports. Another benefit of the TAA/SP approach is the determination of aging per each of the various cycling components (charging, discharging and calendar-life). This information is not presented herein due to the large volume of material it represents, but will be selectively presented in future materials according to prioritized cell and cycling conditions.

Lastly, in general Cellsage analyses cover two independent methods to describe battery aging processes: (A) sigmoidal rate expressions (SRE) that quantify kinetic behavior, and (B) transient analysis (TAA/SP) that is a materials-centric method that treats the electrolyte-to-electrode interactions per each cycling event (as discussed herein). These two modules are highly complementary and provide cross-talk between the material design and formulation of a cell and the aging kinetics thereof as linked to the conditions of use. Diagnostics of underlying aging mechanisms and aging prediction under arbitrarily-chosen conditions can be approached by these methods. This provides a consistent physics-informed platform for advising machine learning architectures.

Classification of cells with Li Plating

Using a suite of electrochemical signals early detection of cells which had experienced Li plating during fast charging was advanced Using an auto-regressive (AR) model and elastic net model makes it possible to account for the derivative with respect to cycle number, to treat potential stationarity issues in the data, and to account for the numerical derivative. The autoregressive component determines the fraction of effect the previous cycle has on the next measurement. Using ΔQ, CE, and EOCV extracted from 31 cells it was possible to construct a training, test and validation set with varying degrees of Li plating from no plating to extensive plating. When compared with optical images of the electrodes to confirm Li plating, human-based evaluation of the electrochemical data provided the opportunity to classify Li plating or lack thereof correctly in all but one instance.

By assigning a probability (Eqn. 1) using the elastic net framework it was possible to use the same data to classify the same data using 25 cycles worth of information as shown in Figure I.6.G.2. Cells assigned a $P > 0.5$ were classified as having Li plating. The ability of the elastic-net method to reach the same conclusion on plating using ¼ of the data and with less ambiguity or human judgement provides the potential to expand extraction of electrochemical signatures to identify and eventually quantify the extent of failure modes. To achieve this goal, a larger pool of data (at least 80 cells for the training and test datasets) with known Li plating conditions will be required. Currently additional cells that will meet this requirement are under test.

$$P(Li\ Plating) = \frac{1}{1 + e^{-(0.98_{int} - 0.05CE_{\mu} + 0.35CE_{\phi} - 1.49EOCV_{\mu} + 0.21EOCV_{\phi})}} \quad (1)$$

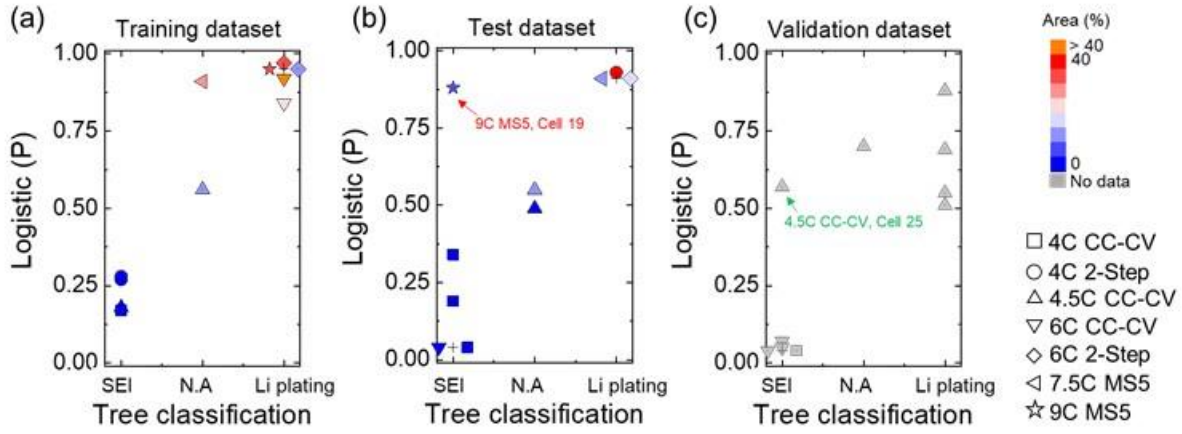

Figure I.6.G.2 Results from logistic ridge regression are provided as a probability (P) of being Li plated and compared to the user-based decision-tree classification results (N.A. means ambiguous cases) for the (a) training, (b) test, and (c) validation datasets. The various rates and protocols are represented as data points with different shapes. The color inside the data points in (a) and (b) presents the percentage of Li-plated area, when applicable. Data points overlapping with each other (marked by +) are shifted for clear visualization.

Generation and deep learning analysis of Synthetic Data (INL)

Incremental capacity model based on the battery degradation model developed by Dubarry generates synthetic data including incremental capacity curves, capacity fades, and N/P ratios under different aging conditions, e.g. LLI, LAM(PE), and LAM(NE). The synthetic data (Figure I.6.G.3) has been utilized to train and construct two categories of deep learning models, which serve as two consecutive steps in the developed hierarchical learning framework. A classification model as the first step has been designed and trained using synthetic incremental capacity curves to identify dominated aging modes, e.g. LLI + LAM(PE) or LLI + LAM(NE). The corresponding regression model as the second step has been developed and trained using synthetic data to quantify the percentages for dominated aging modes, e.g. percentages of LLI and LAM. All developed deep learning models are built using 1-D convolutional neural network structure. The deep learning models have been validated using XCEL Round 1 and Round 2 (i.e., different thicknesses of Graphite and NMC532) under different C-rates. It is demonstrated that the classification model can identify dominated aging modes successfully for current experimental validation set and the quantification model can further determine their percentages of LLI and LAM under aging modes less than 15%.

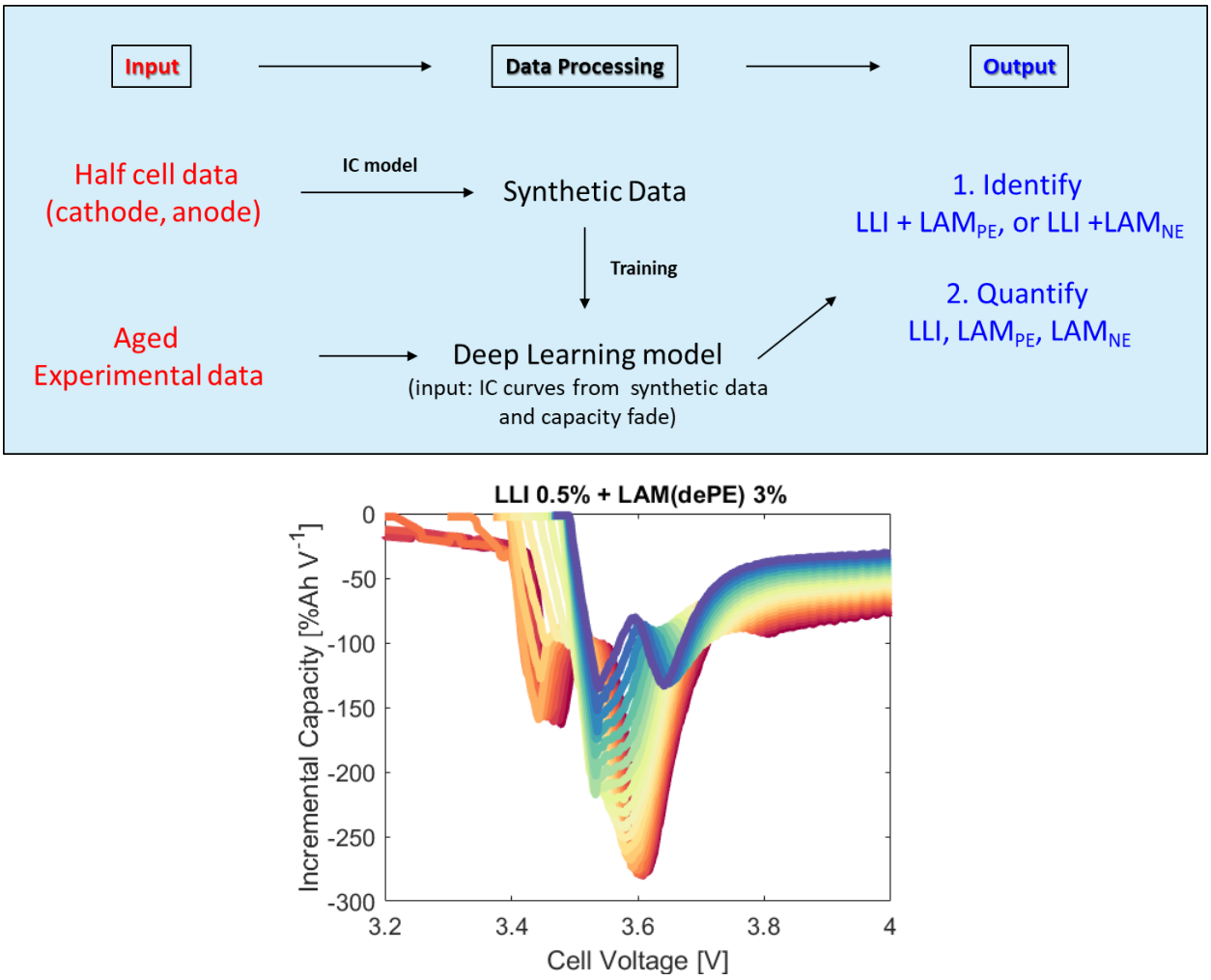

Figure I.6.G.3 Schematic for the processing and generation of synthetic data for use in Deep learning models used to identify and quantify the extent of LLI and LAM in either the positive or negative electrode and example synthetic data (bottom).

Conclusions

The ability to perform discrete performance and life evaluation of emerging technologies in an independent, reliable manner is a direct aid to the identification of key technology gaps. Over the course of FY-20, the INL BTC was able to directly support many different endeavors within VTO with a keen focus on advancing battery technologies for emerging trends in electrified transportation. As a core capability in performance and life analysis for VTO, INL has identified key performance fade modes that exist in cells used for fast charging and has advanced the understanding of performance and evaluation protocols for multiple programs funded by VTO and USABC. 348 devices were tested in FY-20. The work also continues to develop the update of the USABC EV test manual and the submission/acceptance of 2 peer reviewed manuscripts. In FY-21, INL plans to continue this level of support for multiple programs with broad support for the USABC and Benchmark programs. FY-21 activities will also look to more discretely probe key failure modes and how they relate to cell design and evaluation. Additional testing and data analytics activities will be started to support XCEL and BTMS activities. INL will also continue developing and refining standard test protocols and analysis procedures in collaboration with USABC and on providing information on core fundamental performance gaps that need to be addressed across VTO programs. Also, in FY-21, INL will continue to work with the 21st Century Truck Partnership to build battery targets for next generation electric commercial vehicles.

Key Publications

1. B.R. Chen, R. Kunz, T.R. Tanim, E.J. Dufek, "A Machine Learning Framework for Early Detection of Lithium Plating Combining Multiple Physics-based Electrochemical Signatures" *submitted*

2. M. Aykol, S. Babinec, D.A.C Beck, B. Blaiszik, B.R. Chen, G. Crabtree, V. De Angelis, P. Dechent, M. Dubarry, E.J. Dufek, E.E. Eggleton, I. Foster, C. Gopal, P.K. Herring, D.A. Howey, V.W. Hu, J. Kubal, N.H. Paulson, Y. Preger, D.U. Sauer, K. Smith, S.W. Snyder, S. Sripad, T.R. Tanim, L. Teo, V. Viswanathan, L. Ward, "Principles of a Battery Data Genome" *in preparation*

Acknowledgements

The following staff at INL supported this work Matthew Shirk, Tanvir Tanim, Sergiy Sazhin, Eric Dufek, Boryann Liaw, Randy Bewley, Charles Dickerson, Chinh Ho, Jordan Todd, Ryan Jackman, Michael Evans, David Jamison, Bor-Rong Chen, Ross Kunz, Kevin Gering, Reddy Police, Qiang Wang, Paramesh Chinnam and Sangwook Kim.

I.7 Small Business Innovation Research

Simon Thompson, DOE Technology Development Manager
U.S. Department of Energy
E-mail: Simon.Thompson@ee.doe.gov

Project Introduction

The advanced batteries effort of the Vehicle Technologies Office supports small businesses through two focused programs: Small Business Innovation Research (SBIR) and Small Business Technology Transfer (STTR). Both programs are established by law and administered by the Small Business Administration. Grants under these programs are funded by set aside resources from all Extramural R&D budgets; 3.0% of these budgets are allocated for SBIR programs while 0.45% for STTR grants. These programs are administered for all of DOE by the SBIR Office within the Office of Science. Grants under these programs are awarded in two phases: a 6-9 month Phase I with a maximum award of $200K and a 2 year Phase II with a maximum award of $1.1M. Both Phase I and Phase II awards are made through a competitive solicitation and review process.

Objectives

Use the resources available through the Small Business Innovation Research (SBIR) and Small Business Technology Transfer (STTR) programs to conduct research and development of benefit to the advanced batteries effort within the Vehicle Technologies Office.

Approach

The advanced batteries team participates in this process by writing a topic which is released as part of the general DOE solicitation. Starting in FY12, the advanced batteries team decided to broaden its applicant pool by removing specific subtopics and allowing businesses to apply if their technology could help advance the state of the art by improving specific electric drive vehicle platform goals developed by the DOE with close collaboration with the United States Advanced Battery Consortium.

Results

The advanced batteries team participates in this process by writing a topic which is released as part of the general DOE solicitation. Starting in FY12, the advanced batteries team decided to broaden its applicant pool by removing specific subtopics and allowing businesses to apply if their technology could help advance the state of the art by improving specific electric drive vehicle platform goals developed by the DOE with close collaboration with the United States Advanced Battery Consortium.

Phase II Awards Made in FY 2020

Under the SBIR/STTR process, companies with Phase I awards made in FY 2019 were eligible to apply for a Phase II award in FY 2020. The following two Phase II grants were awarded:

The Development of a Stabilized SEI Layer for Si-Containing Lithium-Ion Battery Anodes (Coulometrics, Chattanooga, TN)

This project focuses on the development of new lithium ion battery (LIB) electrolyte/cathode combinations that enable stabilized solid electrolyte interphases (SEI) on Si- based materials. This effort focuses on negative electrodes that include Si-based materials, where Si contributes at least 30% of the reversible capacity of the electrode. This effort will result in significantly longer cycle life and calendar life for LIBs that feature Si-containing negative electrodes. Recent work has shown that the capacity fade seen in well-designed Si and Si-based negative electrodes is a consequence of an increase in surface area with cycling as the Si-based material expands and contracts. The increased surface area results in an increase in parasitic side reactions and accelerated electrolyte consumption. High precision calorimetry combined with high precision coulometry

allows an early identification of the increasing parasitic thermal power that accompanies the increasing surface area. The volume changes of Si-based materials can be diluted but they cannot be suppressed. The path forward for truly enabling Si-based materials therefore lies in targeted electrolyte chemistry. Electrolyte constituents that lead to the formation of carbon dioxide (CO2) or CO2 precursors have recently been shown to be effective in extending the cycle life of Si. It is believed the presence of CO2, or readily reducible intermediates, leads to the formation of an inorganic carbonate Si SEI and has a remarkable effect on extending cycle life. Our Phase I results show that proprietary electrolytes and cell designs developed by Coulometrics & Cyclikal increase cycle life from 500 cycles for control cells to over 900 cycles. This indicates excellent initial results and the merit of this approach to stabilize the SEI on Si-contain LIBs. Coulometrics, LLC and Cyclikal, LLC have partnered to provide an excellent balance of cell assembly and cell testing capabilities with state-of-the-art microcalorimetry. This combination has proven successful in recent years and is based on the encouraging results of our Phase I effort in which over 260 cylindrical LIBs were produced and tested in just 6 months. The combined team has excellent equipment, facilities, and 20 trained staff that have over 100 years of experience. Dr. Edward Buiel has over 25 years of experience as CTO of two advanced energy storage companies and now CEO of Coulometrics, LLC. Joe Turner has 15 years of LIB development experience and recently was R&D director of K2 Energy before joining Coulometrics. Dr. Larry Krause has over 30 years of industrial energy storage experience, especially relating to Si. The team also benefits from Coulometrics' consulting business that has been profitable since 2008 and provides significant revenue to support this effort and any commercialization effort that may arise from this program.

Cobalt-Free, High-Energy Cathodes for Electric Vehicle Batteries (TexPower, Austin, TX)

State-of-the-art lithium-ion cathodes use significant amounts of cobalt, a vital component with a supply chain controlled by China. TexPower aims to commercialize the first cobalt-free, high-energy Li-ion battery cathodes that replace current cathodes Power-for-Powder without changes to other components, using only abundant metals, manufactured by standard industrial processes.

Phase I Awards Made in FY 2020

Seven Phase I grants were awarded in the Summer of FY 2020.

Manufacturing Cost Reduction Strategies for High-Performance Metal Oxide Cathode Materials (CAMX Power, LLC, Lexington, MA)

This DOE award will enable CAMX Power to substantially reduce the cost of the high-performance lithiumion battery active materials, which is key to reducing the overall cost of batteries for Electric Vehicles.

A High-Energy-Density Vehicle Battery with Drop-In Lithium Anode Enabled by a Stable Liquid Electrolyte (Automat Solutions, Inc., Fremont, CA)

The nations' energy system calls for innovations on vehicle batteries to improve transportation energy efficiency. Here, the key electrolyte component is being rapidly developed to enable a desired high- energy-density, low-cost battery, by leveraging breakthrough machine learning and robotic experimentation

Tailored Cathode Chemistry for Next-Generation Lithium-ion Batteries (NexTech Materials, Ltd. dba Nexceris, LLC, Lewis Center, OH)

This project aims to advance the commercial adoption of electric vehicles by improving battery performance. A new coating strategy will be developed to improve the durability of cell materials used in next-generation batteries.

Direct recycling of nickel-manganese-cobalt cathode materials from lithium batteries using an all-in-one rotary kiln reactor (Hazen Research, Inc., Golden, CO)

The Hazen Research-ANL team will develop and demonstrate a low-cost and scalable method for the direct recycling of the cathode materials used in state-of-art LiBs. Accelerating and advancing direct recycling will facilitate the growth of a globally competitive direct recycling industry in the US, thereby reducing our

reliance on foreign sources for materials and reducing the cost of LiBs. The project will result in multi-faceted benefits, including a positive effect on the US economy.

Nanostructured Composite Foil Anodes for High-Energy Electric Vehicle Cells (Vulcan Alloys, Inc., Austin, TX)

The importance of high-energy batteries as a strategic energy resource is continuing to skyrocket. Vulcan Alloys, Inc. domestically developed anode technology offers a transformative improvement to this critical device.

Direct separation, purification and regeneration of cathode materials for aged lithium ion battery using a novel low-temperature plasma assisted separation (LPAS) process (Princeton NuEnergy Incorporation, Princeton, NJ)

The vigorous development of lithium-ion battery production will lead to a significant increase in the number of used LIBs. Recycling plays an important role in the overall sustainability of future batteries. This project will develop a novel plasma process to recycle and regenerate aged lithium ion batteries.

Conductive Carbons by Design: Electrochemically Tailored Carbon Nanotube Conductive Additives for High Rate Battery Electrodes (SkyNano, LLC, Knoxville, TN)

SkyNano will team with Dr. David Wood's laboratory at Oak Ridge National Laboratory to develop a cathode architecture that employs advanced carbon additives to increase energy density and lower charging time for batteries that have a direct impact on the deployment of electric vehicles.

II Advanced Materials R&D

II.1 Next Generation Lithium-Ion Batteries: Advanced Anodes R&D

II.1.A Next Generation Anodes for Lithium-Ion Batteries: Silicon (ANL, LBNL, ORNL, SNL, NREL)

Jack Vaughey, Principal Investigator
Argonne National Laboratory
9700 South Cass Avenue
Lemont, IL 60439
E-mail: vaughey@anl.gov

Brian Cunningham, DOE Technology Development Manager
U.S. Department of Energy
E-mail: Brian.Cunningham@ee.doe.gov

Start Date: October 1, 2016 End Date: September 30, 2020
Project Funding: $2,150,000 DOE share: $2,150,000 Non-DOE share: $0

Project Introduction

Silicon has received significant attention as an alternative active component to the graphitic carbon in a lithium-ion battery negative electrode due to its much higher capacity and general availability. Compared to graphitic carbons, silicon has nearly an order of magnitude higher capacity (~3600 mAh/g silicon vs 372 mAh/g graphite), however, several problems that limit its utility in commercial cells have been identified including large crystallographic expansion upon lithiation (~320%), slow lithium diffusion, and high reactivity with electrode constituents at high states of charge. Combined, these materials properties can result in particle cracking, particle isolation, electrolyte reactivity, and electrode delamination issues. These chemical reactivity and volume changes are manifested in SEI stability and cycling efficiency issues for the cell. Keeping this in mind, the large number of studies focused on silicon-based electrodes is a testament to the opportunity it presents but also the size of the challenge and innovation it inspires on multiple fronts. BatPaC, a techno-economic program designed to model lithium-ion battery performance and cost, was utilized to establish program relevance by connecting DOE/USABC pack performance targets to anode targets. BatPaC analysis of the needs for LIB anode (see Figure II.1.A.1) indicated that anode volumetric capacities greater than 1000 mAh/cm^3 generally minimizes battery cost when coupled to an advanced NMC cathode.

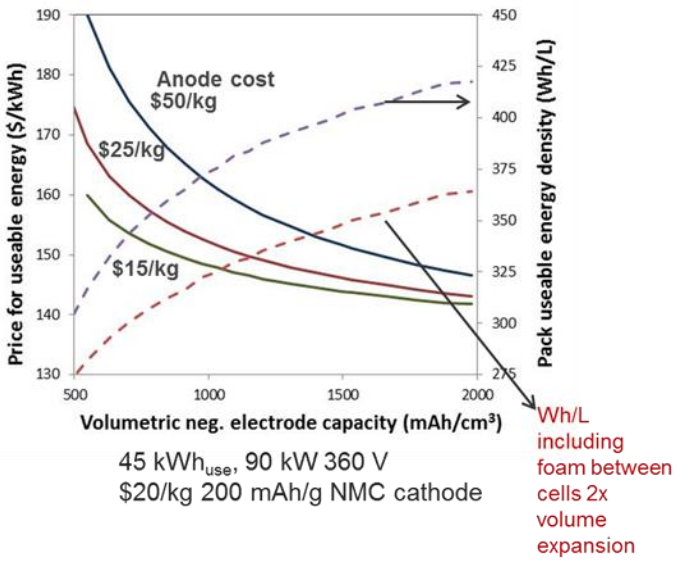

Figure II.1.A.1 Battery Performance and Cost (BatPaC) model utilized to establish relevance by connecting pack to anode targets.

The Next Generation Anodes for Lithium-Ion Batteries Program, also referred to as the Silicon DeepDive Program, is a consortium of five National Laboratories assembled to tackle the barriers associated with development of an advanced lithium-ion negative electrode based on silicon as the active material. The program goals include establishing baseline silicon materials for the multi-lab research program, executing full cell development strategies that leverage DOE-EERE-VTO investments in electroactive materials and characterization, and identifying electrode-based limitations that effect full cell performance. The primary objective of this program is to understand and eliminate the barriers to implementation of a silicon-based anode in a lithium-ion cell. The five National Laboratories work as a single program with continuous interaction, established protocols for analysis, and targets for developing both an understanding and a cell chemistry associated with advance negative electrodes for lithium-ion cells. This undertaking is a full electrode/full cell chemistry project leveraging common baseline electrodes prepared at the consortium facilities. All efforts are directed to understanding and developing the chemistry needed for advancing silicon-based anodes operating in full cells. Team focus areas include active material development, binder synthesis, electrode formulations, and electrolyte additives. Efforts include modeling and a wide range of electrochemical, chemical, and structural characterization of the system across length- and timescales. Specialized characterization techniques developed with DOE-EERE-VTO funding, include neutron diffraction studies, MAS-NMR, optical spectroscopy methods, and X-ray based techniques. The project is managed as a single team effort spanning the Labs, with consensus decisions driving research directions and toward development of high-energy density lithium-ion batteries. A detailed list of participants is given in Figure II.1.A.2.

Figure II.1.A.2 Program participants including Laboratories, research facilities, and individual contributors.

Objectives

- Understand and overcome the science and technology barriers to the use of silicon-based anodes in high-energy density lithium-ion batteries for transportation applications.
    - Stabilize the SEI
    - Stabilize the electrode structure
- Demonstrate functional prototype lithium-ion cell chemistries that include a silicon-containing anode which meet the DOE/USABC performance targets.

Milestones

FY20Q1 Evaluate two new binder - slurry – silicon laminate combinations that lead to improved stability and a 15% improvement in performance compared to baseline for a high silicon-loading (>60%) electrode. (*Completed 01/2020*)

FY20Q2 Assess and evaluate multiple surface driven coatings that utilize a multivalent surface substitution. Develop an understanding of the formation mechanism on the cycling stability of the underlying silicon electrode, propose a mechanism of formation. (*Completed 03/2020*)

FY20Q3 Assess the stability of electrode level silicon baseline materials on cycling and determine the range of species that solubilize and leach into the electrolyte. (*Completed 09/2020*)

FY20Q4 Combine the advancements made over various aspects of the silicon electrode by the Silicon Deep Dive team evaluate them at the full system level and optimize a best full cell with a commercial cathode that using BatPaC can be determined to deliver > 350 Wh/kg for 120 cycles, Evaluate the energy fade on standing for 2 mos and demonstrate an improvement over baseline of 20%. (*Completed 10/2020*)

FY20Q4 Have published a document that will enable other research and development groups to analyze stability of the SEI on a silicon-based anode, thus enabling developers or researchers to continually improve silicon cell stability (joint milestone with the SEISta). (*Completed 09/2020*)

Approach

Oak Ridge National Laboratory (ORNL), National Renewable Energy Laboratory (NREL), Pacific Northwest National Laboratory (PNNL), Lawrence Berkeley National Laboratory (LBNL), and Argonne National Laboratory (ANL) have teamed to form an integrated program dedicated to identifying, understanding, and proposing solutions to the problems associated with the commercialization of silicon as an active component of a lithium–ion electrochemical cell. Technical targets have been developed and regular communications have been established across the team through weekly meetings and quarterly face to face meetings. Throughout the program, the focus is on silicon-based materials, electrodes, and cells. Advancements will be verified based on cycle and calendar life and performance of full cells. Toward that end, baseline silicon-based materials, electrodes, and cells have been adopted, along with uniform full cell testing protocols.

With improvements, the baseline cell technology will be updated to reflect advances, new suppliers, and treatments based on the data and assessments from team members. Cycling and calendar life studies for baseline systems have adopted a testing protocol (based on literature reports) that has worked well for silicon-containing lithium-ion cells. The test consists of (1) three slow (C/20) formation cycles, (2) an HPPC cycle, (3) a set number of C/3 aging cycles, and finished with (4) another HPPC cycle, and (5) three slower (C/20) cycles. All constant current cycling is symmetric between charge and discharge rates. The tests are run at 30°C. This protocol effectively examines capacity, impedance, and aging effects in about a month's worth of testing. Our baseline silicon was produced by Paraclete Energy (Chelsea, MI) and has been made available to all participants on demand. The silicon was purchased in bulk from Paraclete to minimize batch to batch issues and electrode fabrication was done using consistent materials, compositions, and conditions. The cathode used (i.e. NMC, LMR-NMC) is matched to the silicon by CAMP, the baseline electrolyte is 1.2M $LiPF_6$ in a 3:7 ratio of EC/EMC by weight (Gen2) plus 10 wt% FEC. Based on FY19 data, although it noticeably improved performance, a determination was made not to mandate the addition of $Mg(TFSI)_2$ as an electrolyte additive to the baseline system due to researcher concerns about battery grade salt availability and uncertainty of optimized concentrations at this time. The baseline research facilities include the Battery Abuse Testing Laboratory (BATLab), the Cell Analysis, Modeling, and Prototyping (CAMP), and the Post-Test Facility (PTF).

The fundamental understanding developed as part of the silicon DeepDive is based on extensive electrochemical and analytical studies of the components, electrodes, and cells conducted by researchers in the program. This effort contains in-situ and ex-situ studies on full and specialty cells, including reference electrode cells. Overall, the diagnostic studies are intended to help establish structure-composition-property relationships, including lithium-rich surface compounds, bulk transport, and kinetic phenomena. Together they form the basis for accurately assessing component and electrode failure modes and sets a path for advancements. Supported by the diagnostic studies, materials development on silicon-based materials, electrodes, and cells has been focused on enhancement of interfacial stability, accommodation of volume changes on lithiation, improvements in overall performance and life. A key avenue of research for this goal is the development and testing of electrolyte additives designed to modify and stabilize the dynamic silicon-electrolyte interface. In this past year we added more effort focused on soluble SEI species, alternative conductive additives, Zintl electrolyte additives, and calendar life testing and de-emphasized binder development and pre-lithiation developmental studies. Keeping with the goals of using full cell for the DeepDive effort, we increased efforts in the area of slurry and electrode formulation properties as a multi-Lab pathway to improve the baseline electrodes.

Communication of programmatic progress to battery community is critical. This will generally be accomplished through publications, presentations, reports, and reviews. Further, the program is open to industrial participation and/or collaboration that does not limit program innovation or the free flow of

information. Finally, the DeepDive is highly integrated with the anode focused BMR researchers and the SEISta program, a sister program focused on stabilization of the silicon SEI layer. Generally, SEISta is focused on the development and characterization of model systems, surface analysis, well-defined thin film electrodes, and interfacial silicate phases and phenomena.

Results

Results: Silicon Electrodes: Components

Silicon

In the DeepDive Silicon effort, the baseline silicon was purchased from Paraclete Energy (Chelsea, MI) in a large batch as needed by the program to ensure minimal baseline drift over the time of the program. This is partly to help offset some of the known batch to batch variability (i.e. surface areas and crystalline to amorphous materials ratio) and aging issues associated with silicon as it oxidizes and interacts with its storage environment. In part to better understand these phenomena and create a baseline material with a longer shelf-life for testing, we have been developing a mechanochemical mixing/grinding technique to convert low surface area and high purity silicon boules to silicon powders. The technique also allows us to directly functionalize the surface during size reduction to obtain starting materials which will optimize electrode formulation and SEI formation

In order to understand the processing parameters and mixing variables, a series of new high kinetic ball milling experiments were performed to evaluate the role of polyethylene glycol (PEG) concentration on the resulting Si particle sizes, morphology and reproducibility. Nine ball milling experiments were conducted at 700 RPM milling speed for various times and with two different ball media to powder ratios of 10/1 and 20/1. Concentrations of 0.5, 1 and 5 wt.% PEG (2,000 MW) were added to intrinsic silicon boules (~ 1-2 cm cubes) and ball milled with 2 kg of 440c milling media in ball-to-powder ratios of 10/1 or 20/1 for times ranging from 1 minute to 5 hours. The milling media was reused for each experiment to evaluate aging and chemical contamination. The particle size analysis detected bimodal distribution of particles in all the ball milling experiments, which is similar to the results reported previously from the first set of milling experiments. A very noticeable effect was the volume expansion of the Si powder ball milled with the PEG additions, which correlates with a decrease in the specific density of Si. Experimentally, using 200 g of powder consisting of 95% Si + 5% PEG resulted in a volume expansion that exceeded 500 cm^3. The estimated density of the Si powder was 0.40 g/ml, or ~5.8 times lower than the 2.33g/ml density of bulk Si, demonstrating the strong interaction between PEG and the Si during ball milling.

As noted earlier, the samples isolated have a bi-modal distribution of particle sizes. Analysis of the data showed that the Si particles were continuously being fractured into smaller particles followed by agglomeration into larger particles by fusing of fractured particles during ball milling, resulting in the bimodal populations of Si particles. It was also observed that increasing the milling time led to larger agglomerated particles. Interestingly, the initial ball milling experiment at 700 RPM for 90 min. that was conducted on Si boule with ~0.5% PEG addition showed that the polymer did not have a significant effect on reducing the Si particle size compared to the Si boule ball milled with the same conditions without polymer. This result may indicate that interaction of PEG with the Si particles does not prevent the fusing of fractured Si particles during milling. Therefore, the effect of ball to powder ratio on Si particle size reduction was explored. Results comparing the ball milling of 200 g (10/1 ratio) and 100 g (20/1 ratio) of Si +1% PEG powder for 60 min. at 700 RPM are shown in Figure II.1.A.2. The plot shows the size and volume fraction of particles in the lower size population (LP) and upper size population (UP) of the bimodal size distributions. Although the 20/1 ball to powder ratio did not change the size of the LP particles there was an increase in the volume fraction of these particles compared to the UP particles. There was also a significant increase in the size of the UP particles with the larger 20/1 ball to powder ratio, strongly supporting the idea that Si particles agglomeration occurs.

The effect of milling time on the particle size was explored in another ball milling experiment. This experiment started with ball milling 200 g of powder consisting of 99% Si and 1% PEG at 700 RPM for 90

minutes. A bimodal particle size distribution resulted with one peak having an average size of 434 nm and volume fraction of 24.4% and the other peak having an average size of 3.58 μm and volume fraction of 74.3%. From the experiments comparing the ball to powder ratio, it was decided to separate the 200 g of ball milled Si + 1% PEG powder into 100 g batches for additional milling times covering the range of 1, 10 and 60 min. at 700 RPM using a ball to powder ratio of 20/1. The ball milling run for 60 min. was stopped after 1 min. to extract a powder sample for size distribution analysis followed by ball milling the powder the remainder time of 59 min. The size distribution results obtained from these ball millings are shown in Figure II.1.A.3. There is a steady increase in volume fraction of the LP particles with increasing time even though no appreciable decrease in particle size occurred. This corresponds with a decrease in volume fraction of the UP particles, but as observed in previous experiments, there is a steady increase in the particle size. These results demonstrate that increasing the frequency of ball to powder collisions by increasing the ball to powder ratio improves the yield of nano-size Si particles but does not prevent the increase in size of the larger Si particles that occurs with increasing milling time.

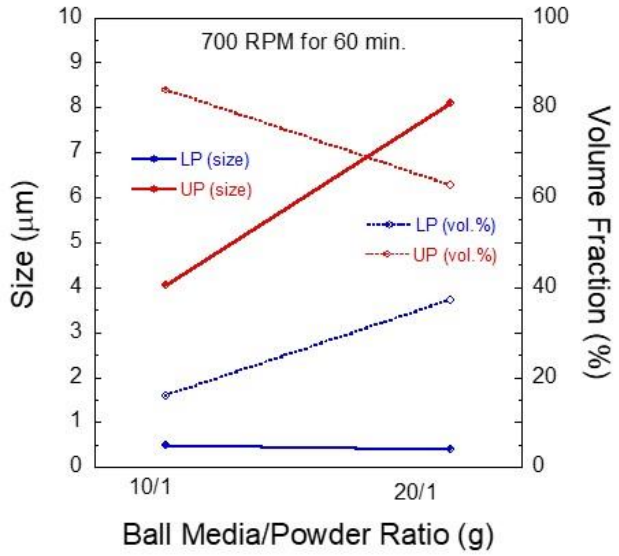

Figure II.1.A.3 Ball milling experiment comparing the effect of ball to powder ratio with particle size distribution.

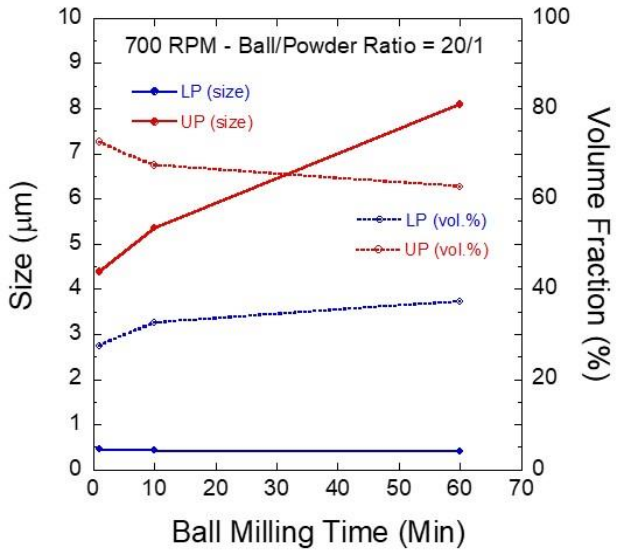

Figure II.1.A.4 Ball milling experiment comparing the effect milling time with particle size distribution.

The results of the ball milling experiments show the fracturing of Si particles exposes fresh surfaces that are extremely reactive and will reform bonds with other freshly cleaved Si particles or to surface active polymers, as demonstrated by the significant volume expansion of Si powder that was ball milled with PEG. The fusing of fractured Si particles causes the formation of larger size agglomerates with increasing milling time and higher ball to powder ratio. Further ball milling experiments will explore cooling the ball mill chamber as a means to promote more fracturing processes and less fusing that may lead to a higher volume fraction of Si particles in the 200-400 nm size range.

Milling silicon boules with additions of PEG polymers promoted significant reduction in the specific density of Si with concomitant volume expansion while increasing the ball to powder ratio to 20/1 helped to increase the volume fraction of Si particles in the ~400 nm size range. Ball milling experiments using a cooled milling chamber will be explored for keeping the Si powder from agglomerating into larger sizes. Further optimization of ball milling conditions for obtaining nano-size Si particles and additions of polymers during milling to create a uniform surface on the silicon powder will take place. These polymers may act like an artificial SEI. Consistent with this hypothesis, the best results to date have come from inert fluoropolymers, i.e. perfluorooctane (see Figure II.1.A.5) where the reactivity with the exposed silicon surfaces may be mediated by the stronger C-F bonds or the inert nature of the polymer itself to breakdown.

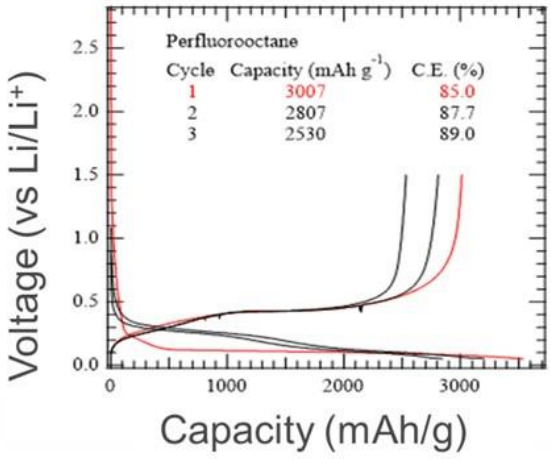

Figure II.1.A.5 Electrochemical performance of a silicon sample balled milled in the presence of perfluorooctane.

Besides the program baseline silicon from Paraclete Energy (Chelsea MI), development of alternative silicon materials has progressed in an effort to address issues not easily covered by the baseline material requirements, notably variation of passivation layer (i.e. silicon oxide) thickness and crystallite particle growth on cycling. One pathway has been designing and optimizing synthetic methods to create highly porous and nanostructured silicon materials that possess a thin oxide passivation created by an HF-based surface dissolution process. Once the oxide is removed, the surface is stabilized by a carbon coating. [1] While the large surface area can enhance kinetic issues, the continuous reaction between lithiated silicon and electrolyte still results in surface degradation and performance issues related to SEI growth. This was investigated extensively by Key, et al., as part of the DeepDive Silicon effort. [2] It is generally believed that minimizing the surface area of the active silicon structure can help minimize electrolyte reactivity and is critical for long term stability of the cells components.

With this electrolyte reactivity, the surface area of the silicon has strong implications for the silicon electrode calendar life. In an evaluation of carbon-coated porous silicon studies noted previously, Si||LFP full cells utilizing a pitch-coated porous etched silicon in baseline electrolyte and an LHCE (Figure II.1.A.6). Before full cell assembly, the porous silicon anode was characterized for its electrochemical properties in half-cells. The calendar-life studies for the pitch-coated porous silicon anode were tested using a protocol where it was

cycled at a C/10 rate in the voltage window between 0.01 to 3.0V and a CV step at 0.01V. For this ~3 V window, the 1st cycle reversible capacity was found to be 1820 mAh/g (Si-C) with 88.3% of first cycle Coulombic Efficiency. Consistent with earlier CAMP results, the capacity of silicon is dependent on its voltage window. For the pitch-coated porous silicon, approximately 60% of the capacity is below 100mV (vs Li) on charge, while on discharge approximately 80% of the reversible capacity was found to be above 700mV (Figure II.1.A.6). More restricted windows, including one proposed for the SCP silicon half-cell electrochemical cells, would need to have gone thru a series of electrode conditioning cycles in order to fully activate the silicon, to be meaningful. Studies of this material continue as part of the SCP stage-gate process and seedling effort.

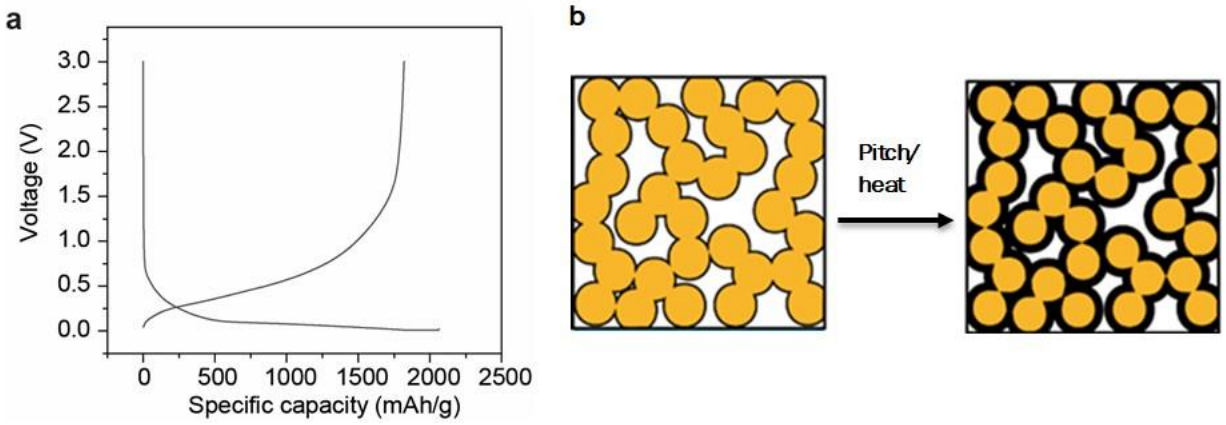

Figure II.1.A.6 (a) Electrochemical properties of pitch coated porous Si-C in the half-cell. The voltage profile of pitch coated porous Si anode at the first cycle under a 3V window testing protocol (b) cartoon showing synthesis of the porous silicon

For calendar life full cell testing, the Silicon Consortium Protocols were used. A pitch-coated porous Si anode (~1.1 mAh/cm^2 at 0.1V), the anode was matched to an LFP cathode (~2.5 mAh/cm^2) provided by Argonne's CAMP facility were utilized. The areal capacities of the electrodes were chosen to ensure enough Li^+ inventory was available to supply the Si-containing test electrode during the aging protocol. The Silicon Consortium Protocol was based on (1) three formation cycles at a C/10 rate between 2.7 and 3.35V, the full cells are charged to 3.35V at a C/10 rate, followed by voltage hold at 3.35V for a set period (360, 720, 1440, and 2160 hours). During the voltage hold at 3.35V, the parasitic current and capacity are normalized by the charge capacity before voltage hold is obtained (Figure II.1.A.7). As shown in Figure II.1.A.7, the role of the electrolyte and its subsequent voltage hold stability is noted. Overall, the parasitic current of the full cells with LHCE was found to be much smaller than that of the full cells using Gen2+FEC. The observation is consistent with the lower reactivity of the LHCE systems (due in part to its inherent limited free solvent) when compared to the baseline Gen2+FEC electrolytes.

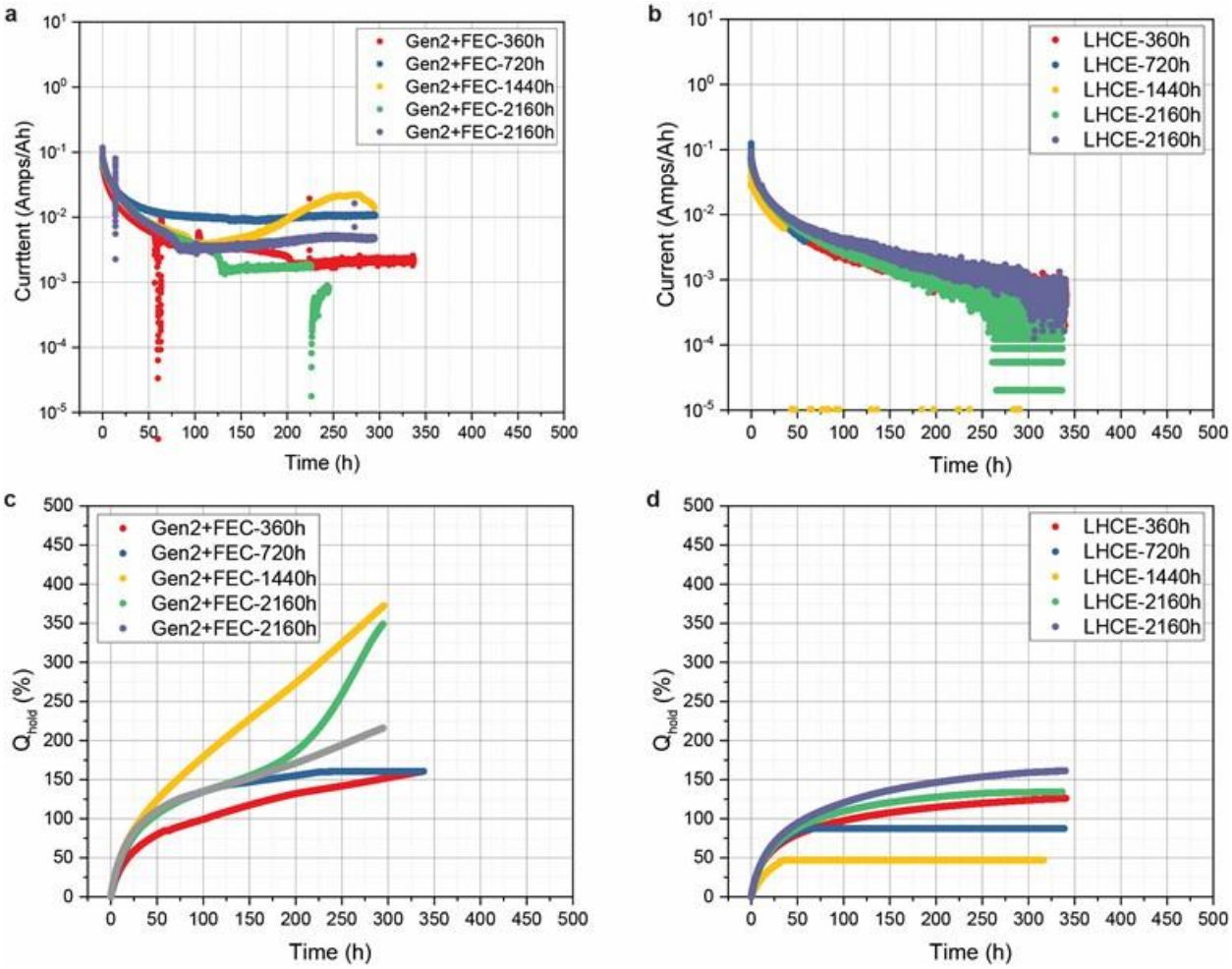

Figure II.1.A.7 Parasitic currents and accumulated capacities of Si||LFP full cells using Gen2+FEC (a, c) and LHCE (b, d) during the voltage hold at 3.35 V.

As an alternative to the C-coated porous silicon where the use of an LHCE electrolyte was effective in limiting parasitic reactions at higher states of charge, the embedding of electroactive silicon in a Li-Sn matrix was also investigated. The Li-Sn material acts as both a solid lithium ion conductor and a matrix buffer to inhibit particle growth. The amorphous Si and Si-Sn composite thin film materials were synthesized by magnetron sputtering of the elements on Cu foils. The materials were tested in half-cells using in Gen2 electrolyte (1.2 M $LiPF_6$ in ethylene carbonate-ethyl methyl carbonate (3:7 by weight)). The cells were galvanostatically discharged and charged between 1.5 and 0.01 V at C/20 based on the experimental capacity. As shown in Figure II.1.A.8, the 180 nm a-Si film delivers an initial lithiation and delithiation capacity of 0.1697 and 0.1385 mAh cm^{-2}, respectively, while the 140 nm Si- Sn film exhibits a corresponding capacity of 0.1140 and 0.099 mAh cm^{-2}. Based on the theoretical density of Si and Sn, the calculated specific capacities are 4064 and 1782 mAh g^{-1}, respectively. These correspond to full lithiation for the Si and Si-Sn, respectively, with additional capacity attributed to SEI formation and electrode break-in processes. With similar degrees of initial lithiation, these two binder and carbon additive free electrodes exhibit different cycling behaviors (Figure II.1.A.8). The Si-Sn film exhibit quite stable cycling, even without the use of fluoroethylene carbonate (FEC) additive. The Li-Sn matrix, formed on lithiation, appears to stabilize the silicon cycling performance.

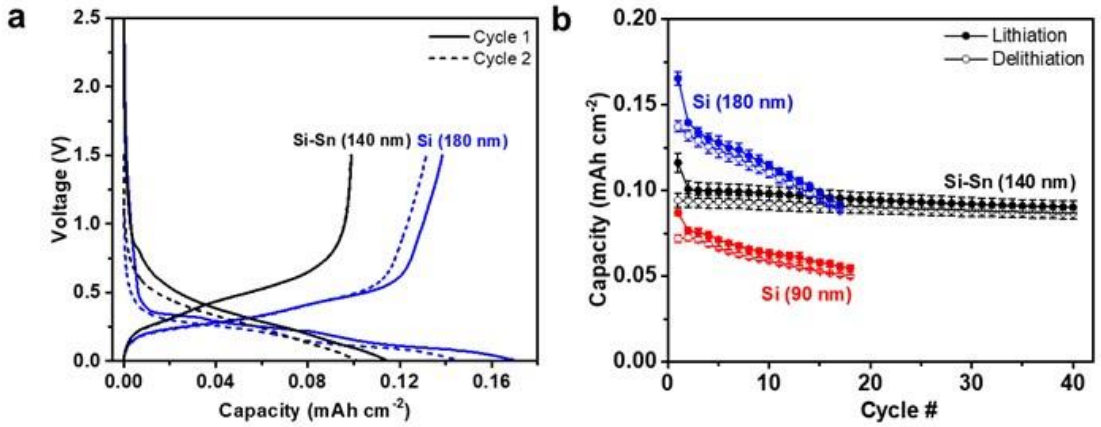

Figure II.1.A.8 (a) Charge-discharge voltage profiles and (b) cycling performance of the Si-Sn and Si films. Error bar shows the standard capacity deviation from three replicate cells.

We examined the morphological/structural changes upon lithiation to understand the impact of volume change, which is believed to contribute to the poor capacity retention. Figure II.1.A.9 shows the cross-sectional *in situ* TEM/STEM images captured at selected reaction time for the Si film. The large thickness increase along time can be clearly seen, whereas the increase for the Si-Sn film from *in situ* TEM time-sequence images (Figure II.1.A.9) is visually less pronounced. The volume expansion of Si is 140% (264 s) and 240% (893 s), while the value for Si-Sn is 158% (136 s) and 230% (408 s). In comparison, it takes around half the time for Si-Sn vs. Si to reach similar expansion, indicating a much faster reaction kinetics in the Si-Sn film. At the end of lithiation (2285 s for Si and 1360 s for Si-Sn), Si and Si-Sn expand to 400% and 266% of its original volume, respectively, suggesting a 34% smaller volume expansion of the fully lithiated Si-Sn film. This is in good agreement with our previous result that the Si-Sn film displays less cracking than the Si film under the same cycling conditions. However, it is worth noting that the Si-Sn film cracks after a few cycles, but it still shows quite stable cycling.

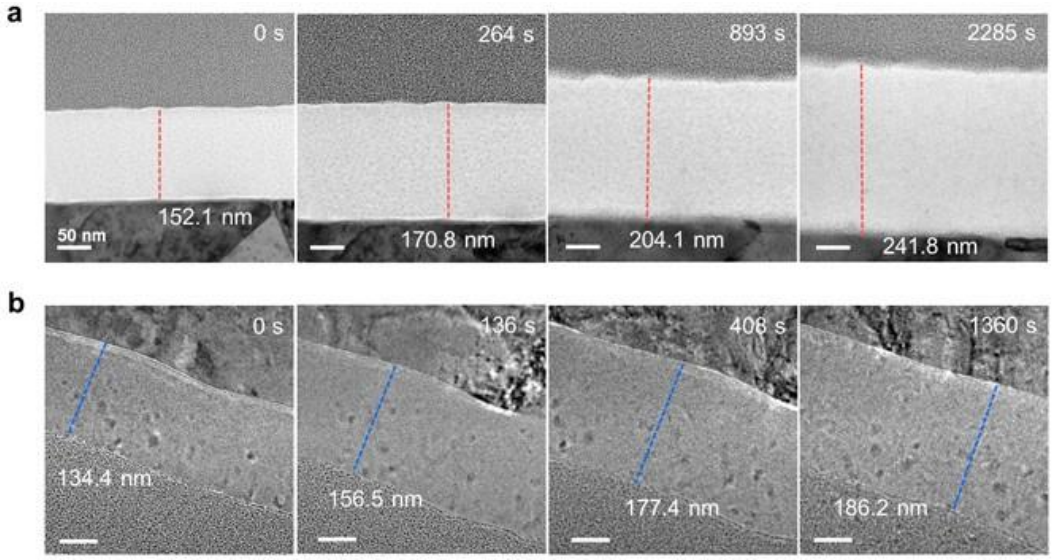

Figure II.1.A.9 (a) Cross-sectional In situ STEM images of Si film and (b) cross-sectional in situ TEM images of Si-Sn film captured at different time series during lithiation.

Figure II.1.A.10 presents the EELS mapping of the microstructure and elemental distribution of the Si-Sn film at its pristine and fully lithiated states. Before lithiation, the Si-Sn film displays a morphology with branch-like network (Figure II.1.A.10), where the separation between Si and Sn elements is revealed at nanometer scale. This is expected due to the immiscibility between these two elements. Interestingly, after lithiation, the branch-

like morphology disappears and uniform elemental distribution of Si and Sn is seen in Figure II.1.A.10**,** again consistent with the isostructural nature of the fully lithiated endmembers. Our EELS mapping results reveal the dynamic rearrangement of Sn and Si atoms after the intake of Li atoms, which can be further facilitated given the higher Li diffusivity in lithiated Sn than that in lithiated Si, resulting in the homogeneous elemental distribution after lithiation.

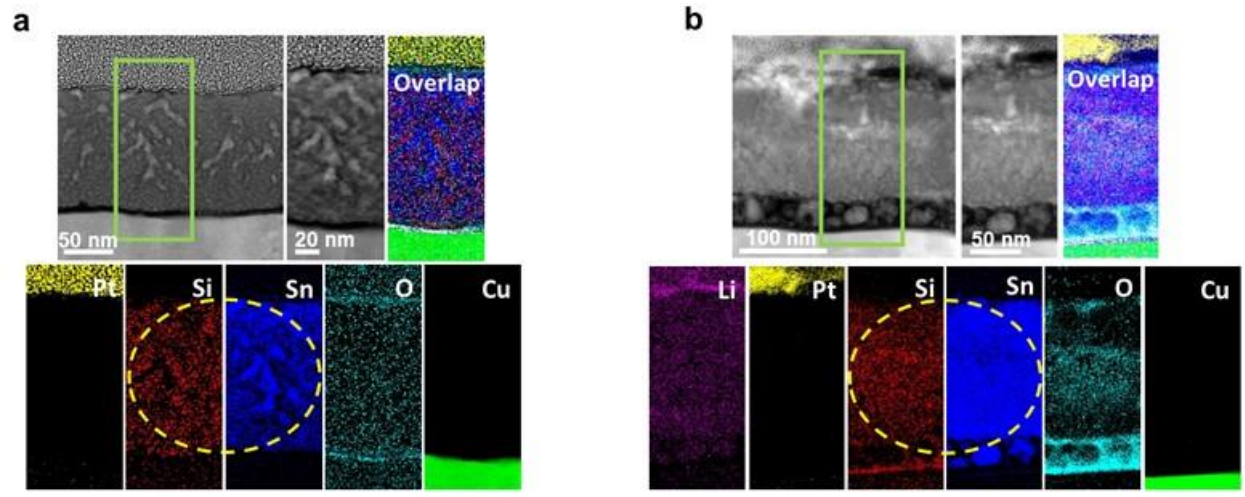

Figure II.1.A.10 EELS mapping of Si-Sn thin film at (a) pristine and (b) fully lithiated states, showing the microstructures and elemental distributions.

As noted by the alternative silicon studies, interfacial control (amorphous carbon, Li-Sn) both yield more stable cycling and appear to have attributes that favor longer calendar life via the addition of species that help maintain electrode homogeneity (lithiation). Based on new research priorities and scaling issues, this film effort is not continuing as part of the Silicon Consortium Program.

Conductive Additives

Numerous efforts in the CAMP Facility were directed to optimizing the silicon composite electrode with conductive additives, such as carbon black (*e.g.* Timcal C45), hard carbon, and graphite (flaky vs. round). In the case of Timcal C-45 carbon, the first cycle Coulombic efficiency of the C45 alone is only 62%, which is also similar to the hard carbon and flaky graphite (SFG-6-L). Another unfortunate side effect of many of these high surface area additives is that they require the use of additional binder to make a robust electrode and may have some catalytic activity towards the electrolyte. In this year the CAMP Facility explored the idea of using inert conductive additives to replace all carbon-based additives. It is hoped that this approach could also enable the use of other binders, and perhaps better control the degree of electrode expansion.

Table II.1.A.1 Volume Resistivity of Alternative Electrode Conductive Additives

Material	Volume Resistivity at 20 °C (Ohm-cm)
Cu	10^{-6}
Carbon	< 0.1
B_4C	0.1 – 10
SiC	10^{2}-10^{5}
SiO_2	10^{18}

One materials class to consider for inert conductive additives are semiconductors with low band gaps (and low resistivity) that are comprised of earth-abundant elements. Some natural choices include boron carbide and silicon carbide. A comparison of resistivities for common materials are seen in Table II.1.A.1.

Boron carbide has a resistivity that is only slightly higher than carbon & graphite, which are themselves almost five orders of magnitude more resistive than copper metal. In addition, if the semiconductor materials are doped or have crystal defects, their effective resistivity can be made even lower. A range of carbon-free additive materials were selected in this study to scope the effect of resistivity, which include boron carbide, silicon carbon, and silica. Ideally, a metal powder (such as copper or nickel) could be used in this study, but there is a concern that these metal powders could become pyrophoric during processing in the dry room. Silica was selected as a worse-case baseline, where it is expected that the silica additive would block all electrical pathways to the copper foils. Electrodes were designed with an initial concentration of 50 wt.% Si and 40 wt.% inert additives (B_4C, SiC, or SiO_2). Later, an additional boron carbide electrode was designed with 2 wt.% carbon black to create a baseline with higher electrical conductivity. These electrodes were made on the CAMP Facility's pilot-scale reverse-comma coater (A-Pro) with a target capacity of 2 mAh/cm^2.

Coin cells were made with these electrodes using lithium metal as the counter electrode and "Gen2F" electrolyte (1.2 M $LiPF_6$ in EC:EMC (3:7 wt) +10 wt.% FEC). The cells were cycled 3 times at a C/20 rate between 1.5 and 0.01 V for formation, followed by rate tests between 1.5 and 0.05 V, then cycle life test at CAMP Library.

By far, the most surprising observation from this scoping study is that all the cells performed surprisingly well, regardless of the conductive additive. This was especially surprising for the cells that used silica as the inert additive, which were cells made to set the absolute lower boundary for electrically conductive cells. Ironically, the silica cells had the best capacity utilization at all rates, as can be seen from Figure II.1.A.11 – even better than the cells made with boron carbide plus carbon black.

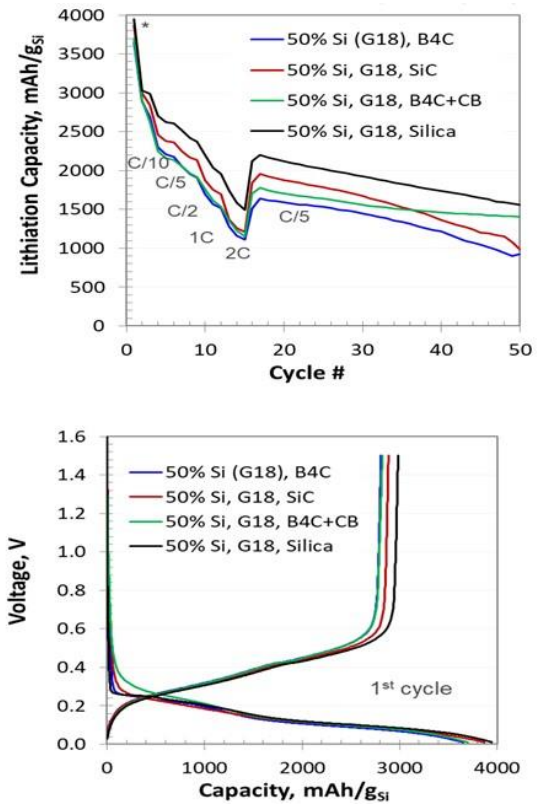

Figure II.1.A.11 Formation cycles (bottom) and Rate & Life cycles (top) for Inert Conductive Additive Study, versus Lithium.

Further testing was done in full cell coin-cells using NMC532 as the counter electrode. These coin cells were tested using the Silicon Deep Dive test protocol (3x C/20, HPPC, C/3 cycling, HPPC, 3x C/20) in a voltage window of 3.0 to 4.1 V (Gen2F electrolyte, 30°C). HPPC protocol used consisted of a charge to 4.1 V, remove

10% capacity, 10 s 3C discharge, 40 s rest OCV, 10 s 2.25C charge pulse, repeat pulse sequence for each 10% DOD. The results of these tests are summarized in Figure II.1.A.12, which includes data from baseline electrodes that consisted of 15 wt.% Si and 80 wt.% Si for comparison. Here too, it is apparent that the choice in conductive additive had little effect on the capacity utilization and retention during cycling. However, the Coulombic efficiency of the inert additive cells were found to start at a higher level and then decrease toward that of the 15 & 80 wt.% silicon cells.

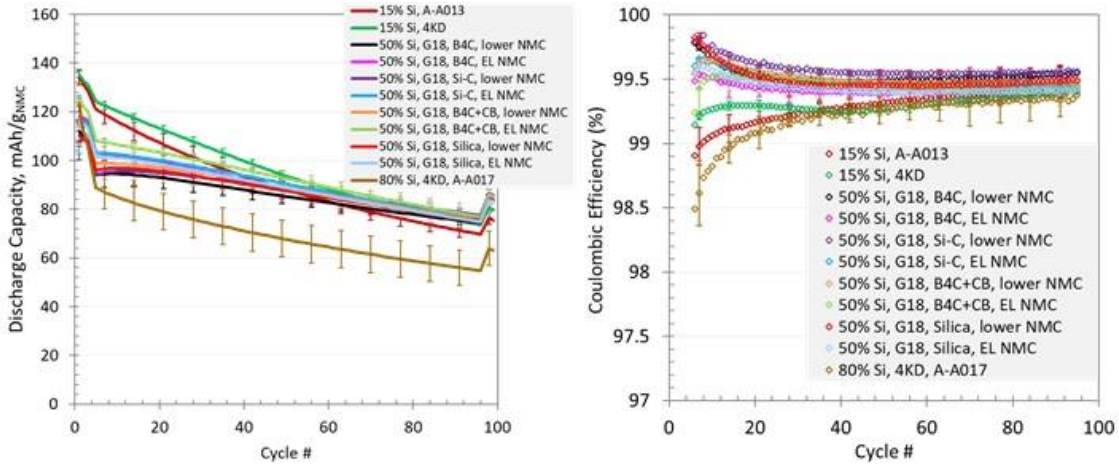

Figure II.1.A.12 Discharge capacities (left) and Coulombic efficiencies (right) for Inert Conductive Additive Study, versus NMC532.

The half-cell and full cell coin cells were opened, along with other older silicon-based coin cells with similar cycling history and similar capacity loading (near 1.9 mAh/cm^2). The silicon electrodes were harvested, rinsed with DMC, and the thickness was measured. During the harvesting of many of these cells, it was observed that silicon-based anodes that experienced lithiation near or below 10 mV usually suffered from severe delamination – a situation that often occurred in half cell tests. This was especially true for anodes with high silicon content. Whereas, full cells were designed around a 50 or 100 mV lithiation cutoff, and reference electrode data indicates that the true lithiation potential is over 100 mV for majority of the cycle life. Table II.1.A.2 is a compilation of the thicknesses of the pristine anodes and the harvested anodes (ones that did not show signs of delamination). The harvested (cycled) thicknesses shown in Table II.1.A.2 are focused on anodes from full cells cycled for 100 cycles under the Silicon Deep Dive Protocol (100 cycles) between 3 - 4.1 V at 30ºC, with similar n:p ratio.

While it is promising that the initial thickness of electrodes with inert additives (50 wt.% Si) are on par with the electrodes made with 80 wt.% Si, it is clear these cells still swell with cycling. On an optimistic note, the final thickness of the high silicon anodes is still half the thickness of the cycled graphite-only anodes. If the cycle life and calendar life problems can be solved, battery hardware can be designed to accommodate the swelling of the silicon-based cells – although the extra hardware needed will most likely lower the volumetric and mass-specific energy density (and probably increase cost).

Table II.1.A.2 Electrode Thickness of Variety of Pristine & Cycled Anode Electrodes made by the CAMP Facility

Negative Electrode from Full cells (3-4.1V, 100 cycles)	Initial thickness, calendered, ☐m	Cycled thickness, calendered, ☐m	% Increase
0% Si, 92% Graphite, 2% C45	41	44	7
5% Si, 83% Graphite, 2% C45	49	54	10
10% Si, 78% Graphite, 2% C45	33	41	24
15% Si, 73% Graphite, 2% C45	28		
30% Si, 58% Graphite, 2% C45	16		
50% Si, 40% B4C	11	21	91
50% Si, 40% B4C, 2% CB	12	20	67
50% Si, 40% SiC	11	21	91
50% Si, 40% SiO2	12	22	83
60% Si, 23% Graphite, 2% C45	18		
71% Si, 0% Graphite, 10% C45	9	20	122
80% Si, 0% Graphite, 10% C45	9		

Data in Table II.1.A.2 indicates that there is a dependence of anode swelling on silicon content. This was explored further by plotting the thickness increase (%) versus silicon content, which is shown in Figure II.1.A.13 It was interesting to see a strong linear relationship exists between thickness increase and silicon content, despite the "minor" variations in particle size, morphology, capacity loadings, porosity, binders, and n:p ratio that occurs across these cells over the years. This was not a controlled study, but merely an effort to glean preliminary correlations from existing data. Ideally, this study needs to be redone in a controlled manner where all components are fixed and the counter electrode is lithium metal, with lithiation of the silicon-based anode limited to a fixed voltage (*e.g.*, 100 mV) or capacity (*e.g.*, 1000 mAh/g).

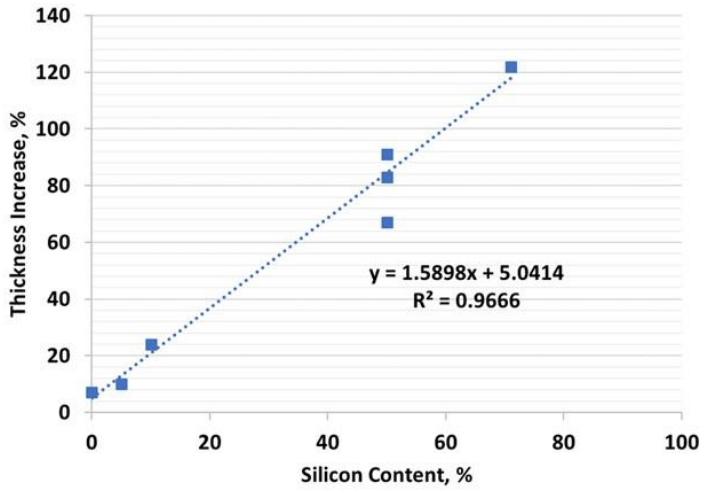

Figure II.1.A.13 Thickness of harvested anodes from full cells cycled under Si Deep Dive Protocol as a function of silicon content.

In summary, it was determined that a new class of composite silicon electrodes made with inert additives such as semiconductor materials (B_4C, SiC) and insulators (SiO_2) performed surprisingly similar to silicon electrodes made with graphite and carbon black - despite the wide range of electrical resistivity. These electrodes were mechanically robust and had thicknesses almost identical to other high-silicon content electrodes. It is time to rethink the importance (or need) of carbon & graphite additives in silicon electrodes. Preliminary investigations also indicate that the anode thickness increase during cycling shows clear linear dependence on silicon content.

PAA Binder Processing

Silicon DeepDive and baseline SEISTA electrodes in most cases use a LiPAA-based binder system. It was initially chosen from a survey study based on performance, electrode quality, and consistency. Various adhesive polymers, such as poly(vinyl alcohol), sodium alginate, sodium carboxymethyl cellulose, polyimide, and poly(acrylic acid) (PAA), were evaluated as binders to mitigate the issues associated with the volume expansion of Si during lithiation process. These polymeric binders firmly hold the electrode components together and keep them in electrical contact during electrochemical cycling. After evaluation, a lithium hydroxide (LiOH) titrated PAA (PAA-Li) was chosen as the standard binder for the Silicon Deep Dive program. Although PAA-Li binder has been widely used in laboratory development of Si anodes, multi-lab studies have indicated that protonated PAA had better cycling performance. Discussions have noted that the need for lithiation of the PAA was a conclusion from earlier studies that it was beneficial to the rheological properties of the slurries, such as viscosity and shear thinning (see Figure II.1.A.14), were beneficial to stabilizing electrode slurries and fabricating high-quality electrode laminates, whereas electrodes based on PAA-H showed better performance but had issues associated with homogeneity. This difference is based on that the higher pH preparation (with LiOH addition) accelerates side reactions at the silicon surface due in part to dissolution of passivating silica. In association with CAMP and ORNL, a method was developed to create a reversible neutralization process that uses using ammonia (NH_3/NH_4OH) as the neutralizing agent instead of LiOH. Ammonia (NH_3) is a weak base that effectively neutralizes PAA polymer effectively promoting the positive rheological properties of the higher pH processing without degrading the silicon surface.

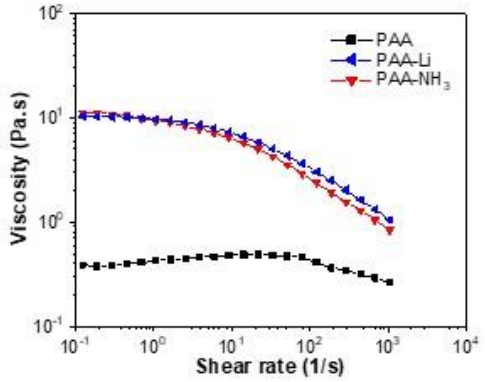

Figure II.1.A.14 Plots of apparent viscosity vs. shear rate for 10 wt% aqueous solutions of PAA, PAA-Li, and PAA-NH_3.

Characterization of pH adjusted PAA samples was undertaken to assess the role of pH and viscosity, as appropriate viscosity is critical for the electrode manufacturing side to control thickness and loading. [3], [4], [5], [6], [7] In these studies, the viscosity of PAA-NH_3 solution was raised to 11.15 Pa·s at 0.2/s, an approximate 30-fold enhancement over protonated (pristine) PAA solution (0.37 Pa·s). The viscosity of PAA-NH_3 solution decreases to 0.84 Pa·s as shear rate increases to 1057/s, indicating strong shear thinning effect. Both the high viscosity and the shear thinning effect are beneficial to the slurry processing as they can contribute to slurry stability and facilitate the mixing process, respectively. In addition, unlike the irreversible LiOH-based neutralization protocols, NH_3 neutralization (as NH_4^+ cations) provides a critical feature that restores -COOH groups. During the standard drying process of the electrodes (e.g., 80 ºC, in vacuo), PAA-NH_3

binder can be thermally reversed back to protonated-PAA with removal of NH_3. Using this technique, the advantages of the higher pH processing can be merged with the benefits of the binding as the protonated PAA form. This unique process is particularly beneficial to maintaining the binding strength of PAA binder for improved cycling performance. ATR-FTIR analysis of electrodes fabricated using PAA, PAA-NH_3, and PAA-Li binders confirmed the proposed thermal decomposition of PAA-NH_3 binder. The carbonyl peak of PAA-NH_3 electrode overlaps with that of PAA electrode (1750 cm^{-1}). On the other hand, the carbonyl peak of PAA-Li electrode showed at 1630 cm^{-1} due to the irreversible conversion of -COOH groups to -COO^- groups. In addition, the adhesive strength of PAA-NH_3 binder is also restored to almost identical to that of pristine PAA binder as evidenced by 180º peeling tests.

Initial proof-of-concept work was demonstrated on 15% Si / 73% graphite formulations. For 70 % silicon electrodes, the electrodes utilized either 20 wt% PAA-Li or PAA-NH_3 binder, or both used 10 wt% C45, conductive additive Figure II.1.A.15 summarizes capacity retention and columbic efficiency profiles of half cells, which are subjected to three formation cycles between 0.01 V and 1.50 V at C/20 rate, followed by 100 aging cycles at C/3 rate. As with the 15% silicon cells, the PAA-NH_3 cell formulation outperforms the PAA-Li cell formulation with higher initial capacity, higher average capacity, and better capacity retention. For instance, the average capacity of PAA-NH_3 cell is 1924 mAh/g during the 100 cycles at C/3, which is a 29% increase compared to PAA-Li baseline (1495 mAh/g). The capacity retention of PAA-NH_3 cell (73%) is also significantly higher than that of PAA-Li cell (64%). The PAA-NH_3 cell shows higher CE than that of PAA-Li cell, especially during the early state of aging cycling. For example, the initial CE of PAA-NH_3 cell is 94% while the initial CE of PAA-Li cell is only 89%. Overall, the reversible PAA-NH_3 binder system provides both enhanced rheological properties as well as significant improvements in cycling performance for high silicon-loading electrodes.

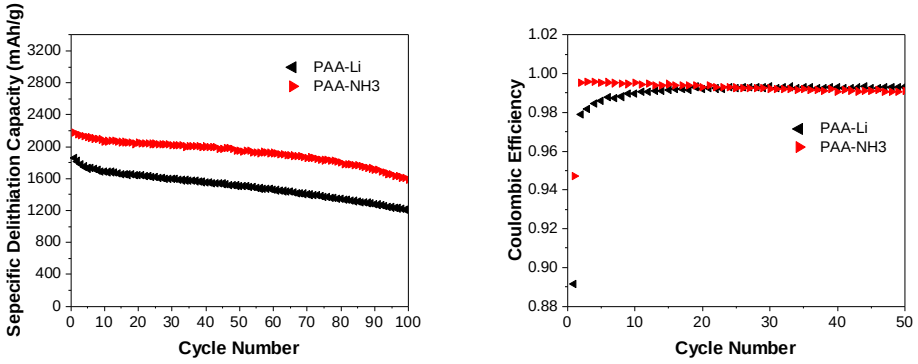

Figure II.1.A.15 Specific delithiation capacity (left) and coulombic efficiency profiles (right) of Li half-cells using electrodes containing 70 wt% Si, 20 wt% PAA-Li or PAA-NH_3 binder, and 10 wt% C45 over 100 cycles at C/3 rate.

Additionally, the reversibility feature can also be utilized to construct the **in-situ cross-linkable binders** for high silicon-content electrode that should be more robust and better able to withstand the cycle upon cycle volume changes. While mixtures of PAA and PEI (poly(ethylene imine), a linear polymer with nitrogen atoms in the backbone) immediately crashes out from solution upon mixing due to the ionic cross-linking reaction, this precipitation can be inhibited by the PAA-NH_3 reversible neutralization process that blocks the cross-linking. This compatibility allows one to create PAA-NH_3 / PEI solutions. After the thermal decomposition of PAA-NH_3 species during the drying process, the restored PAA binder then cross-links with the PEI via physical cross-linking as well as covalent cross-linking. The in-situ cross-linking mechanism between PAA and PAA-PEI films was confirmed by ATR-FTIR analysis.

The cross-linked material, a reinforced version of the standard PAA system used, was evaluated using 70% Si electrodes fabricated using PAA-Li and PAA-PEI binder systems against matched NMC622 cathodes. Half-cells were cycled between 0.01 V and 1.50 V for three formation cycles at C/20 rate, followed by 100 cycles at C/3 rate. The full cells were cycled between 3.0 V and 4.2 V using a standard cycling protocol including three

formation cycles at C/20 rate, a Hybrid Pulse Power Characterization (HPPC), 92 cycles at C/3 rate, another HPPC, and finally three cycles at C/20 rate. As shown in Figure II.1.A.16 PAA-PEI cell shows dramatic improvements in cycling performance compared to PAA-Li baseline. In a half-cell, the average capacity of PAA-PEI cell during is 2091 mAh/g, a 40% increase to our baseline PAA-Li cell (1495 mAh/g) after 100 cycles. PAA-PEI cell also delivered a remarkable 90% capacity retention, 26% higher than PAA-Li baseline. For full cell evaluation, PAA-PEI –based electrodes yielded an average capacity of 125 mAh/g at C/3 rate with a capacity retention of 70%, a 52% increase in average capacity and a 14% increase in capacity retention compared to the PAA-Li baseline system.

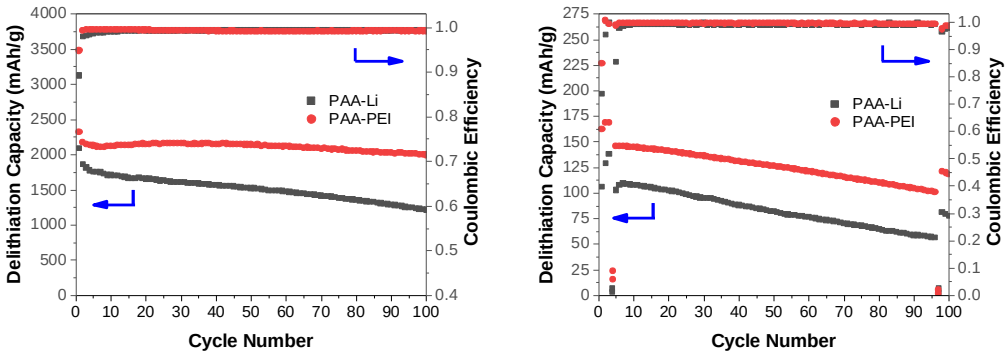

Figure II.1.A.16 Specific delithiation capacity and coulombic efficiency profiles of Li half-cells (left) and NMC622/Si full cells (right) using electrodes containing 70 wt% Si, 20 wt% PAA-Li or PAA-PEI binder, and 10 wt% C45 over 100 cycles.

The morphology of Si electrodes fabricated using PAA-Li and PAA-PEI binders was studied by scanning electron microscopy (SEM). Figure II.1.A.17 summarizes the surface SEM and cross-sectional SEM images of PAA-Li and PAA-PEI electrodes before and after aging cycles. All cycled electrodes were fully delithiated before collecting for SEM measurements. After aging cycles, obvious cracks were found on the surface of PAA-Li electrode. The integrity of PAA-PEI electrode is much better than that of PAA-Li electrode with no obvious surface cracks. The cross-section SEM images of these electrodes before and after aging cycles were collected to investigate the volumetric changes of these electrodes. As shown in Figure II.1.A.17, PAA-Li electrode shows a 52% increase in thickness after aging cycles, while PAA-PEI binder had a volume expansion of only 10%. The SEM analysis indicates the excellent binding performance of PAA-PEI binder compared to PAA-Li baseline.

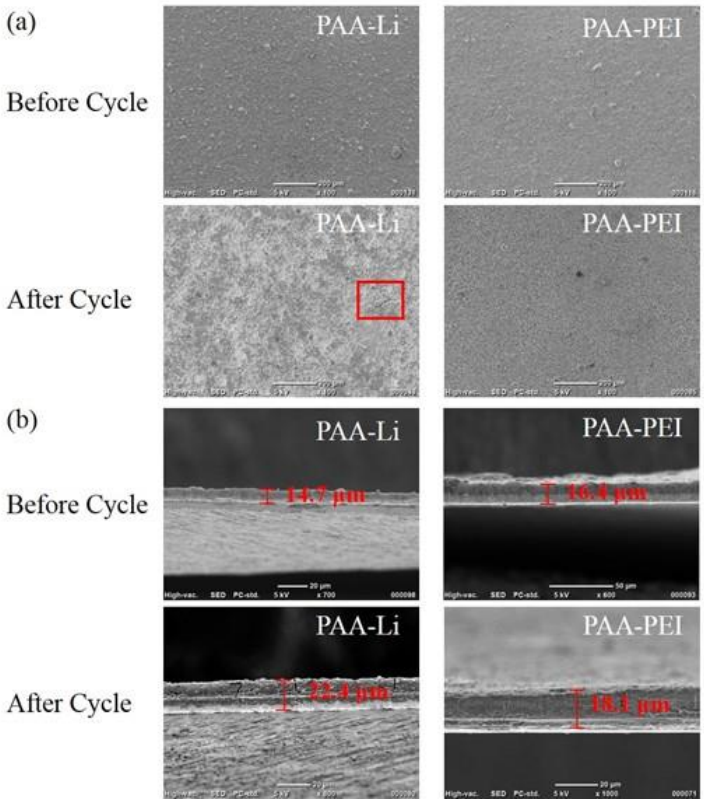

Figure II.1.A.17 (a) Surface SEM images of Si electrodes fabricated using PAA-Li or PAA-PEI binder before and after aging cycles. (b) Cross-sectional SEM images of these electrodes before and after aging cycles.

PAA Binder Modifications

While the modified PAA-NH_3 or PAA-PEI systems both show improvement over baseline based on a mechanism that modifies the binding of the polymer to the surface of the silicon. In both cases the binding is mainly thru the carboxylic acid group, while in the case of the PAA-PEI system the added PEI plays the role to constrain the volume expansion of the polymer to help maintain internal contacts. A different pathway to modifying the surface-polymer interaction is to partially esterify the PAA to make an esterified PAA (termed E-PAA) as seen in Figure II.1.A.18. Specifically, the inclusion of bulky pentyl ester groups that have a minimal ability to hydrogen-bond to the silica surface hydroxyl groups was investigated to tune the surface energy by mediating the number of polymer-surface bonding interactions.

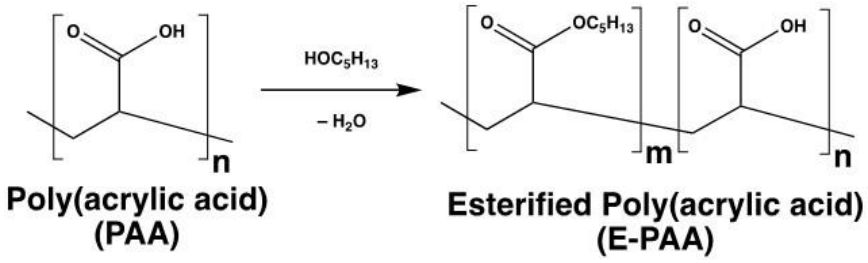

Figure II.1.A.18 Esterification of polyacrylic acid (PAA) using a condensation reaction between PAA and n-pentanol (HOC_5H_{13}) to generate Esterified PAA (E-PAA). E-PAA with 90% COOH acid groups (m = 10%, n = 90%) and 80% COOH acid groups (m = 20%, n = 80%) were prepared

Using a polished silicon wafer as a model substrate, the measured de-bond energies between Si and PAA were measured using both the native-oxide SiO_x-termination surface and an SiH_x-terminated surface. The de-bond energies were measured using the cantilever beam test (CBT) methodology. The data (in Figure II.1.A.19)

show that the SiO_x-terminated Si wafers have a higher de-bond energy than the SiH_x-terminated wafer surfaces, consistent with the stronger surface bonding interaction expected for the hydroxyl terminated surface in contrast to the weaker hydrogen bonding forces that dominate for the hydride terminated silicon.

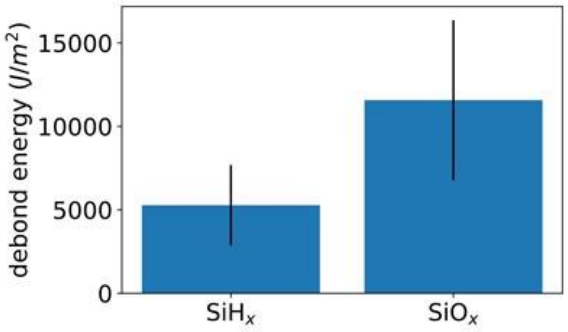

Figure II.1.A.19 Calculated de-bond energy between PAA and Si wafers with either SiH_x-termination or SiO_X termination based on CBT (cantilever beam test) experiments. The vertical black lines represent the standard deviation in the data.

The characterization of these modified PAA systems was then extended to the DeepDive baseline Paraclete silicon with a SiO_x-termination layer, like the Si wafers used in the CBT analysis. Multiple cells were evaluated with a variation in the percent of E-PAA (0%, 10%, and 20%) used in the system. Analysis of the cycling data indicated that the performance was slightly improved as the % E-PAA was increased. It was postulated that as the percent of E-PAA increases, the binder becomes more compliant and thus is more able to compensate for the volumetric changes that occur with the Si NP on cycling. This correlation between the de-bond energy (CBT measurement) and electrochemical cycling highlights the importance of being able to tune the surface – polymer interaction.

Further processing studies were then performed to conform to the CAMP lamination protocols for the Paraclete silicon using various percentages of esterified PAA binder with a single solvent (water) and two temperatures (120 °C, 150°C). At CAMP the ~150 nm diameter Paraclete Si NP samples are processed in water solvent and dried at 150 °C, which sets the high temperature for this evaluation.

To understand the mechanism of the drying process, an FTIR spectra-based technique was developed that allows investigation of the temperature-dependent chemistry of the E-PAA and correlate these data with mechanical and electrochemical results, see Figure II.1.A.20. To collect the spectra, a solution of the (E-)PAA polymer binder was deposited on a heated ATR-FTIR diamond crystal under vacuum, which replicates slurry drying conditions used to dry 3D composite electrodes and therefore provides chemical information on changes to the Si-binder chemistry during this process. In the first experiment, spectra were collected while the temperature was increased from 25 to 100 ºC (Figure II.1.A.17, left column). In the second experiment, spectra were collected while the E-PAA was held at 100 ºC for 24 h (Figure II.1.A.20, right column). We have made two key observations:

1. *Esterification alters the conformation of the polymer, increasing stability* The *cis* polymer backbone chain conformation reacts and breaks down while the *trans* conformation not undergo thermally induced reactions.

2. *PAA crosslinking occurs via both dehydration and decarbonylation to from ether groups* the reaction products from two *cis* carboxylic acids (–COOH) that combine are one ether linkage (C–O–C) formed via dehydration and decarboxylation.

This PAA reactivity under drying conditions has mechanistic implications for the optimizing the binding strength to the Si surfaces as well as the mechanical properties of composite electrodes. Since previous studies had shown that the wafer studies were an acceptable surface model for Paraclete systems, similar reactivity

between Si–OH groups that terminate SiO_2 surfaces results in similar reactivity to give bound silyl ether moieties.

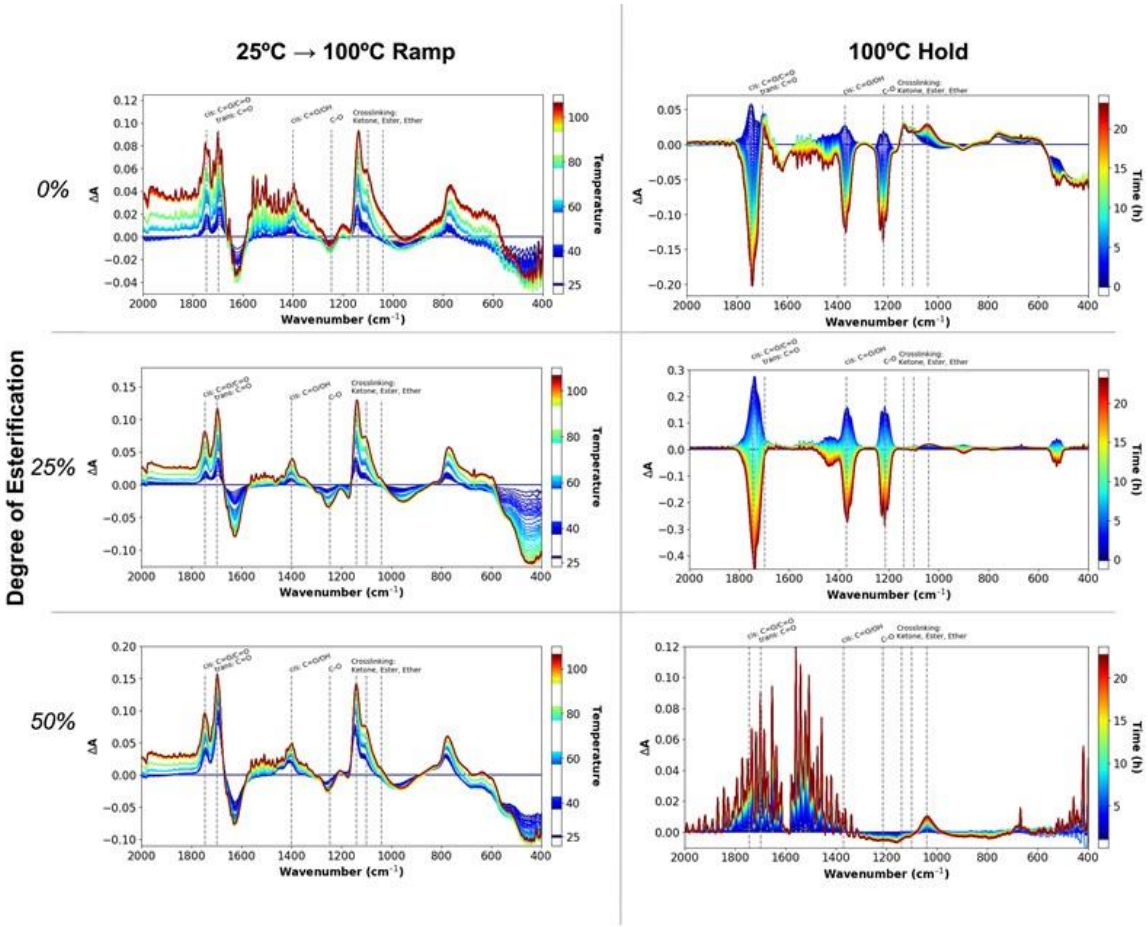

Figure II.1.A.20 Temperature-dependent FTIR measurement of the esterified polyacrylic acid (E-PAA) binder drying. The left column panels show the spectra while heating from 25 °C to 100 °C while the right column panels depict spectra while holding at 100 °C for 24 j. The top, middle, and bottom panels correspond to 0, 25 and 50% ester sidechain, respectively. The first spectrum (25 °C, atmospheric pressure) is subtracted from each spectrum to produce the difference spectra shown.

As the addition of pentyl groups to the polymer backbone weakens the overall binder polymer-surface bonding strength, we evaluated the effects of weakening this interfacial interaction on the electrochemical performance using materials beyond the 20% esterification previously evaluated. Figure II.1.A.21 shows the electrochemical cycling performance of electrodes made with PAA, E-PAA esterified to 25% and 50% pentyl groups. This differs from the PAA-PEI studies noted previously in that that study focused not on the binder-silicon interface but the flexibility and volume expansion limits of the polymer after surface bonding. The PAA-pentyl modified electrodes were fabricated using Paraclete Si NPs, the (E-)PAA binder, and Timcal C65 conductive carbon in an 80:10:10 wt% ratio, respectively. The slurry was processed in water and deposited on copper mesh foil and assembled into half-cells using Gen2F electrolyte. Three formation cycles at C/20 were performed, following by cycling at C/5. As is shown in Figure II.1.A.21, the capacity of the PAA electrodes is lower than that of the electrodes made with higher content E-PAA, although all of the samples in the study have capacities significantly below theoretical capacity, indicative of poor utilization and may reflect issues with electrode processing and formation.

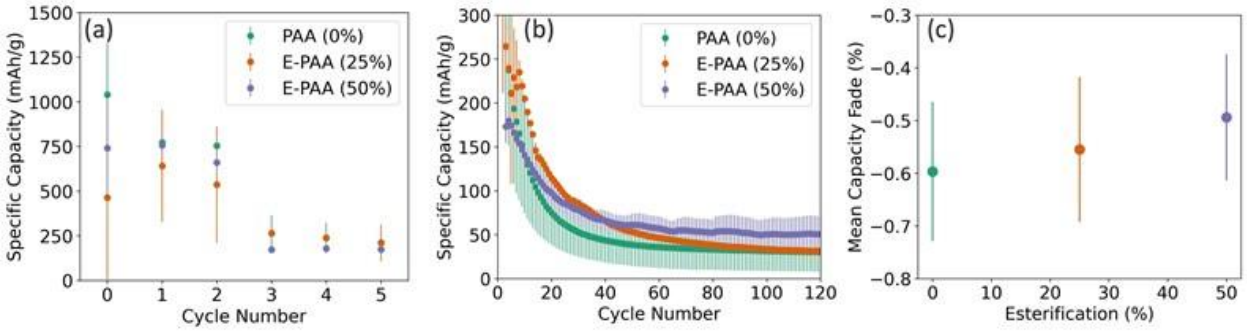

Figure II.1.A.21 Electrochemical cycling performance for Paraclete Si, (E-)PAA binder, and Timcal C65 conductive carbon electrodes (80:10:10 by wt%) in half-cell configuration with Gen2F electrolyte. (a) First 6 cycle specific capacity, (b) full cycle specific capacity, and (c) mean capacity fade as a function of degree of esterification, where 0% esterification is PAA.

The corresponding calendar lifetime test on the same electrodes also was conducted. A voltage hold at 100 mV vs. Li/Li^+ was conducted following the three formation cycles. Figure II.1.A.22 shows that the different binders had the opposite effect on performance where the electrode made with E-PAA 50% exhibits a larger parasitic current than that with PAA. As previously noted, since the E-PAA binder has a lower binding strength to the SiO_2 surface of Si, we hypothesize that this provides more pathways for the electrolyte to react with the charged Si surface and that PAA-PEI denser polymers may be a better additional pathway to enhance electrochemical properties at the electrode level. In summary we find that the bonding of the binder polymer to the silicon surface needs to be strong and enhanced for both cycle and calendar life studies, especially in instances where the surface may be unstable towards gradual interfacial dissolution or the build-up of breakdown products.

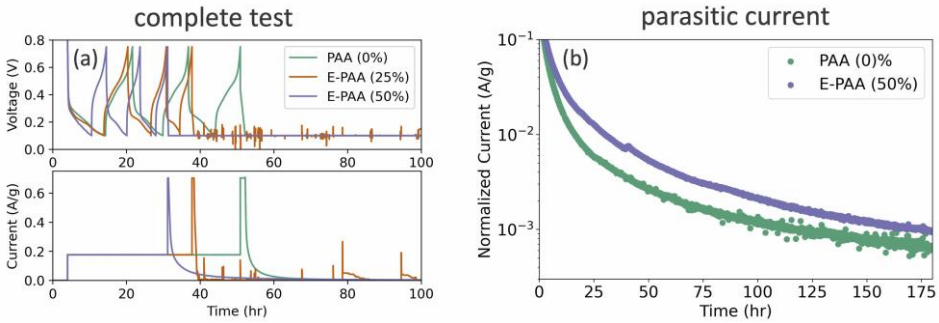

Figure II.1.A.22 Calendar lifetime test for Paraclete Si, (E-)PAA binder, and Timcal C65 conductive carbon electrodes (80:10:10 by wt%) in half-cell configuration with Gen2F electrolyte. (a) Voltage and current profiles as a function of time for PAA, 25% E-PAA, and 50% E-PAA samples. Note data beyond 100 h is not show. The 25% E-PAA sample did not exhibit meaningful cycling data and was removed from analysis. (b) Normalized parasitic current for the 100 mV voltage hold portion of the data following the 3 formation cycles shown in (a).

Using in-situ spectroelectrochemistry, the PAA and E-PAA polymer interactions were probed with respect to cell cycle and calendar lifetime. Here, we used the same Paraclete/(E-)PAA/C65 electrodes as above deposited on a Cu mesh electrode and placed this electrode directly onto an attenuated total reflectance Fourier transform infrared (ATR-FTIR) diamond crystal. Gen2 electrolyte, a Celgard separator, and lithium metal counter electrode were placed successively onto the Si NP/Cu mesh electrode. The stack was compressed with a stainless-steel plate and sealed from air. A 9-h OCV hold was performed, followed by 3 formation cycles at C/20, and either a C/5 sweep to 100 mV vs. Li/Li^+ (cycle lifetime test) or a voltage hold at 100 mV vs. Li/Li^+ for 160–180 h. An astounding amount of insight can be gained from the spectroscopic data over the course of these experiments.

FTIR data for the 9-h OCV hold is shown in Figure II.1.A.23 for electrodes made from PAA and E-PAA (50%) samples. The spectra are markedly different, with the E-PAA (50%)-based electrode swelling with significant amounts of electrolyte throughout the entire OCV hold. In contrast, the PAA-based electrode

exhibits a minor amount of electrolyte swelling. Further, the PAA-based electrode appears to preferentially exclude free EMC solvent (i.e., not coordinated to a Li^+) while at the same time showing infiltration of PF_6^- anions. These results are consistent with the solvated $Li^+[PF_6^-]$ salt as calculated by the Persson group calculations that shedding *some* of its carbonates that help solvate the salt in bulk electrolyte, and indicate that the number of carbonates coordinating each Li^+, typically between 4-6 in solution [8], [9] is reduced substantially upon entering the PAA-based film. Similar conclusions are obtained from the first cycles between 100 and 750 mV vs. Li/Li^+ (data not shown). We conclude that PAA, because of its decarbonylation-induced polyether moieties behave like an ionically conducting material. In contrast, E-PAA behaves as an electrolyte-conducting material.

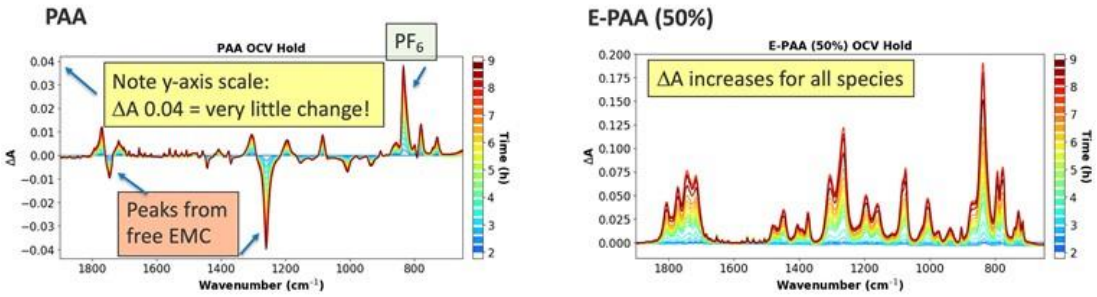

Figure II.1.A.23 Spectroelectrochemical data using in situ ATR-FTIR spectroscopy of 9-h OCV hold. Electrode is made from Paraclete/(E-)PAA/C65 deposited on a Cu mesh electrode with Gen2 electrolyte in half-cell configuration.

Next, we present FTIR data for 100 mV vs. Li/Li^+ voltage hold experiments that mimic the calendar life test for electrodes made from PAA and E-PAA (50%) samples. These 160–180 h voltage holds reveal the electrolyte and SEI speciation that is changing under prolonged polarization at lithiation potentials. As shown in Figure II.1.A.24, spectra for both electrodes exhibit broad, new peaks at 1650–1600 cm^{-1} and 1450–1400 cm^{-1} (dashed vertical lines) that grow in over the course of the experiments and are assigned to a heterogeneous mixture of lithium alkylcarbonates. Despite this similarity in the organic SEI component, significant differences also are found. The electrolyte in the E-PAA (50%)-based electrode changes in composition slightly, but the overall electrolyte volume in the film (i.e., the degree of liquid electrolyte present from swelling) does not change significantly. In contrast, the PAA-based electrode shows that all electrolyte peaks decrease dramatically during the voltage hold as the electrode expunges significant electrolyte during the voltage hold possibly due to phases formed during the parasitic reactions clogging electrode pores. This overall picture agrees with the higher parasitic current that is found with the E-PAA-based electrode (Figure II.1.A.24), where it's more compliant nature and proclivity to swell with electrolyte results in an easier pathway for electrolyte to access the Si surface, resulting in a higher parasitic current and, ultimately, a shorter calendar lifetime. This is consistent to the PAA-PEI study where crosslinking induced densification of the binder at the interface appeared to be beneficial to the cells performance.

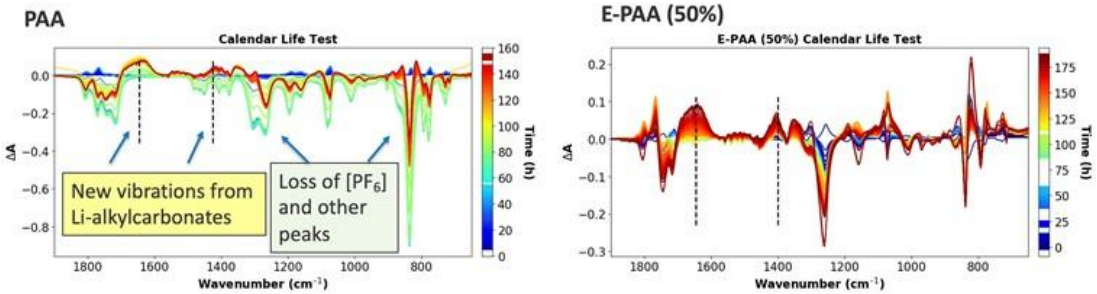

Figure II.1.A.24 Spectroelectrochemical data using in situ ATR-FTIR spectroscopy of 100 mV vs. Li/Li^+ that mimics the calendar life test. Electrode is made from Paraclete/(E-)PAA/C65 deposited on a Cu mesh electrode with Gen2 electrolyte in half-cell configuration.

For these three PAA studies, we can conclude that 1) the processing pH is important for maintaining the integrity of the silicon surface as too high a pH is likely to dissolve the interfacial silicon surface, (2)

maximizing the connectivity of the PAA to the silicon surface has been found to enhance calendar life studies, and (3) increasing the conductivity and density of the polymeric PAA binder by addition of a PEI polymer at time of surface attachment was found to limit electrode volume expansion and lead to enhanced performance.

BatPaC Model

Our calculations have shown that achieving the project-wide Si Deep Dive Q4 Milestone to: "Combine and assess the advancements made over various aspects of the silicon electrode by the Silicon Deep Dive team (Binder/Silicon/Electrode Formation/in-situ Coatings/Electrode-level Failure Mechanisms) and optimize a best full cell with a commercial cathode that using BatPaC can be determined to deliver > 350 Wh/kg" will require a silicon-based anode >500 mAh/g and ideally approaching 1000 mAh/g capacity (data not shown). We have made significant progress toward this goal using a new, surface engineered Si active material with a multivalent surface substitution. Combining the knowledge from the binder studies with optimized solvent and drying temperature conditions with this new surface engineered Si, we have achieved high >99.5% coulombic efficiencies after the first few cycles and stabilized specific capacities of ~800 mAh/g in half-cell configuration. The data are presented in Figure II.1.A.25 (red and black data points) not only meet the Q4 Milestone, but critically point a pathway toward further electrode optimization using surface engineering strategies.

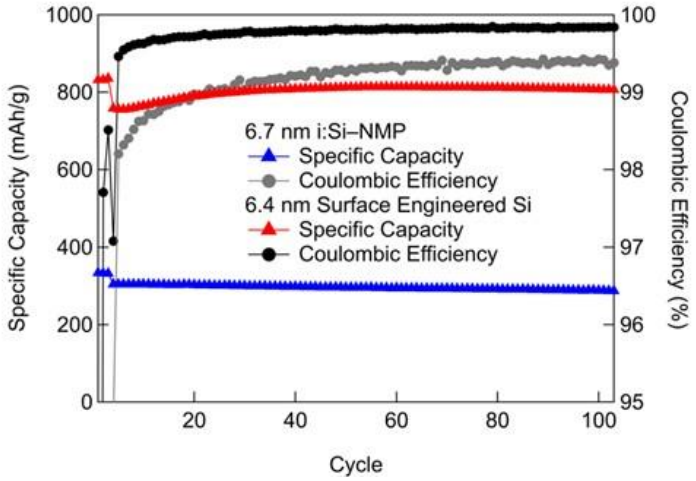

Figure II.1.A.25 Comparison of half-cell electrochemical performance of the baseline electrode containing intrinsic Si NPs coated with N-methylpyrrolidone (i:Si–NMP) active material and PAA binder (blue and grey) with an electrode containing a new, surface-engineered Si active material and PAA binder.

Electrode Formation

While often investigated as individual components, electrochemical cells are a complex balancing act of numerous materials in the form of electrodes, electrolytes, and balance of plant issues (i.e. cell stack pressure). A critical multi-component piece of an electrochemical cell is the actual electrode. The electrode is a complex mixture of engineered active materials, binders, conductive additives and metal foil current collectors. The processing of these pieces to make a porous and active electrode is an art requiring trials and conditions. At many levels electrode processing is a crucial component of materials evaluation as understanding the various surface-interfacial interactions may not always be known ahead of time. Composite silicon- graphite anodes, fabricated with poly(acrylic acid) or lithium neutralized poly(acrylic acid) (LiPAA), were shown to have preferential adsorption of PAA or LiPAA on graphite or silicon due to surface interactions. With this information, the processing requirements and optimization parameters for PAA and LiPAA polymeric binders were explored for high silicon content anodes where both PAA and LiPAA-based electrodes were fabricated. Within this effort, we sought to identify and characterize the role of electrode processing since the fabrication method directly effects electrode architecture, homogeneity, and performance. Our research pathway was to add small molecular weight polymers as dispersants into the slurry to probe their utility to stabilize the slurry structure and see how that translates to a more homogeneous silicon/ graphite electrode architecture.

The mixing and processing protocols used were developed and characterized in conjunction with the CAMP facility at Argonne. With this data, the influence of slurry homogeneity on the physical and structural chemistry (from nano to micron length scales) of the binder system was ascertained. The goal of these studies is to develop Si-based slurries that lead to higher levels of electrode homogeneity not only on the surface of the electrode, but throughout the bulk. The binder-processing combinations were selected as these baseline materials and methods are currently utilized in the CAMP facility at Argonne. The PAA used was processed with either planetary centrifugal mixing (PCM) or a ball milling (BM) method to increase the surface area and speed dissolution. Because these two mixing methods have different energies associated with them, they could alter the binder structure and electrode slurry interactions, leading to variability in electrode homogeneity (i.e. sedimentation) after casting. [10], [11], [12], [13], [14], [15] Additionally, the sedimentation rates and the flow behavior of the slurry produced can be altered by the addition of a low molecular weight dispersant to the electrode slurry. To understand the role that chemistry and processing have on the PAA binder-Si laminate combinations and eventual electrode architecture, two characterization techniques that are sensitive to the length scales and porosity produced were utilzed, namely x-ray nano-tomography and ultra-small angle neutron scattering (USANS). X-ray nano-tomography was used to probe the electrode architecture of high silicon content anodes. Given that the signal strength from X-ray techniques is tied to the atomic number of the sample, traditional binders like PAA and LiPAA will provide poor contrast against the electrode silicon. To enhance the signal strength, Cs was substituted for Li in the mixture resulting in a binder with significant electron density suitable for X-ray nano-tomography.

X-ray nano-tomography data were collected on a cast electrode without exposure to electrolyte. A triangular shaped portion of the electrode, shown in Figure II.1.A.26 (column 1), was removed from the center of the cast and used for the experiment. Figure II.1.A.26 shows an intensity color map of the electrode made with planetary centrifugal mixing (PCM) mixed CsPAA without dispersant (Figure II.1.A.26, row 1), ball milled (BM) CsPAA without dispersant (Figure II.1.A.26, row 2), PCM mixed CsPAA with dispersant (Figure II.1.A.26, row 3), and BM CsPAA with dispersant (Figure II.1.A.26, row 4). Red indicates the densest areas of Cs^+, while blue indicates the most dilute areas of Cs^+, which are assumed to be silicon-rich areas. It should be noted that carbon black is likely mixed in these areas, which would further dilute any signal from Cs^+ or silicon. However, the extent of carbon black mixing is difficult to probe since it cannot be imaged in the X-ray due to its low atomic number and low crystallinity. This is because silicon produces a detectable signal in the X-ray while carbon black does not, thus, the blue areas are assumed to be silicon rich. There appears to be “black holes” in some areas of the electrode. This is attributed to the surface roughness of the electrode. Comparisons can be made between electrodes due to the same normalization process applied to all electrodes.

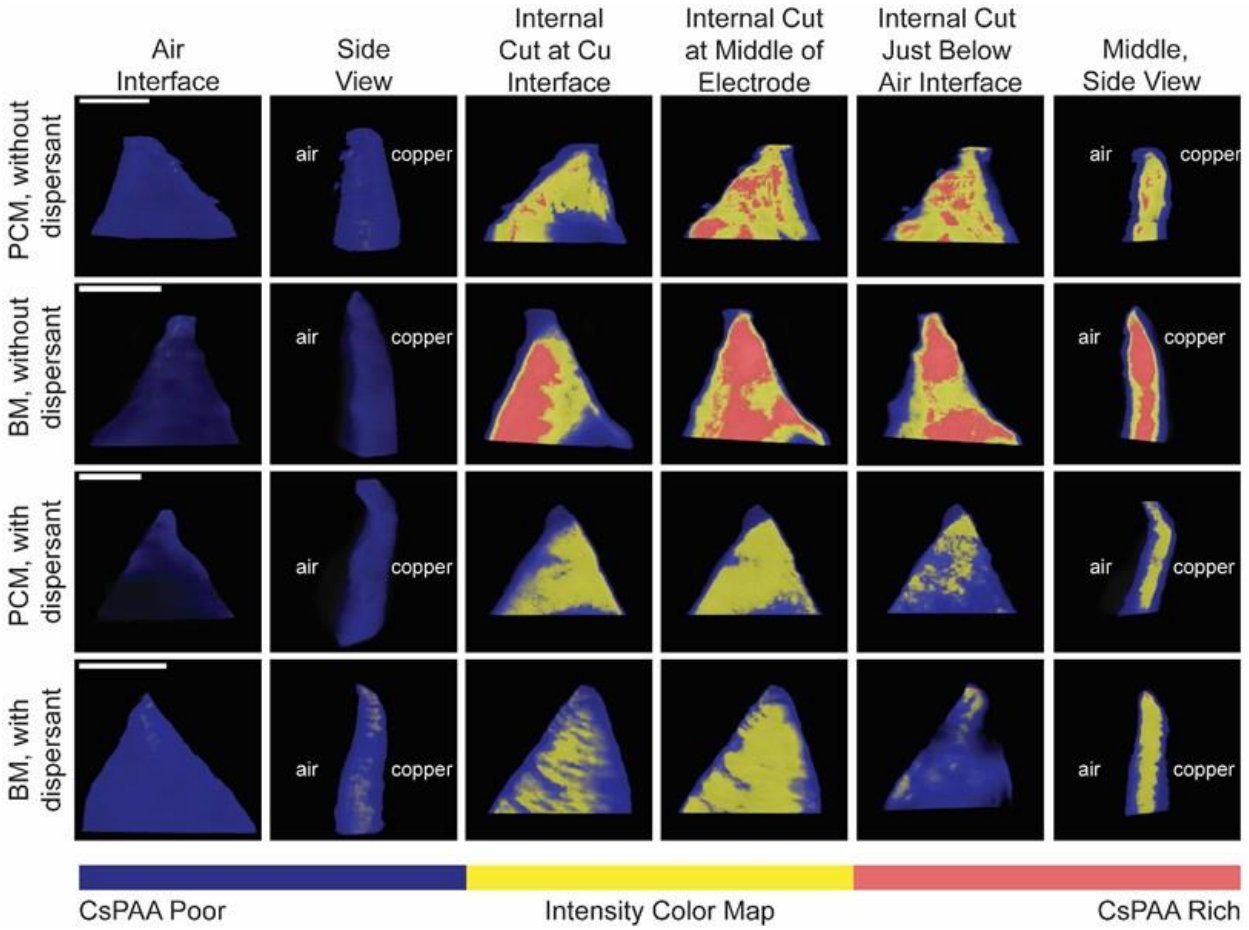

Figure II.1.A.26 X-ray nano-tomography slices of electrodes made with PCM binder without dispersant (row 1), BM binder without dispersant (row 2), PCM binder with dispersant (row 3), BM binder with dispersant (row 4). Each column represents a slice of the electrode at a certain location from left to right: (1) surface of the intact electrode at the air interface, (2) side view of the surface of the intact electrode where the air interface is the on the left and the copper interface is on the right, (3) internal structure as the electrode is sliced at the copper interface toward the air interface, (4) internal structure at the middle of the electrode, (5) internal structure at the air interface, (6) side view of the internal electrode sliced at the middle of the electrode. The color intensity map at the bottom of the figure shows that CsPAA poor areas are depicted by blue while CsPAA rich areas are depicted by red. All scale bars are 100 μm and located in the top left corner.

To quantify the electrode homogeneity as a function of depth in the electrode, 37.4 nm slices were analyzed and the concentrations of silicon and Cs^+ determined. Qualitative analysis reveals clear evidence for Cs^+ segregation in the electrode with PCM blended binder with no dispersant added as indicated by the blue regions on the surface of the electrode and yellow and red regions on the interior of the electrode. Since silicon has a longer attenuation length than Cs^+ (approximately 100 μm compared to 22 μm for Cs), the blue areas are assumed to be silicon rich and consequently CsPAA binder poor regions. Yellow regions are due to more dilute areas of Cs^+ where silicon is mixed with CsPAA thus diluting the signal from the Cs^+, while the red region corresponds to the highest Cs^+ concentration. The electrode depth was plotted as a fraction of the most prevalent species, based on the area within each slice corresponding to the different CsPAA concentrations and is presented in Figure II.1.A.26, insets, when the data show two or more species in each layer, this indicates increasing lateral heterogeneity, the percent of each species is represented as percentage in the horizontal axis. The top of the vertical axis corresponds to the air interface while the bottom (deeper) corresponds to the copper (current collector) interface.

From these data analysis the electrode appears heterogeneous as the binder contains a different distribution of electron density as a function of depth. This is an artifact of the analysis as silicon, and potentially carbon

black is likely intermixed throughout the entire electrode since it comprises 80 wt% (71.5 vol%) of the total electrode albeit again with varying concentrations of CsPAA. Blue pixels correspond to areas with the least amount of CsPAA, appearing as bands from the air interface at 0 μm to 13 μm and from 42 μm to 50 μm. The majority of the red pixels occur at a depth of 24 μm and corresponds to areas with the most (or highest concentrations) CsPAA. The yellow pixels occur between 10 μm and 42 μm where the majority occurs at 21 μm and 29 μm. From 21-29 μm, the yellow area comprises approximately 60% of the electrode, which indicates that there is more intermixing of silicon in these areas, causing the signal from CsPAA to be dampened. This clearly shows that the most concentrated areas of the binder reside in the middle of the electrode. Additionally, there is probably less silicon in the red areas than in the yellow areas because the Cs signal is not diluted by the lower absorbing silicon.

Representative tomography data for the BM without dispersant electrode is shown in Figure II.1.A.26 (second row). The BM electrode without dispersant contained 50%–60% CsPAA rich area (red areas) from approximately 22-34 μm compared to the PCM electrode without dispersant, which contained approximately 22% CsPAA rich area from 22-28 μm. The BM electrode without dispersant likely has ~40% more CsPAA rich areas due to the BM CsPAA having a larger molecular weight or a different polymer chain conformation (i.e. shape) when compared to the PCM CsPAA.

Similar to the PCM electrode without dispersant, the CsPAA rich areas reside in the middle of the electrode (red). However, it is now at a depth of 28 μm (versus 24 μm for the PCM electrode). The silicon/CsPAA intermixed region (yellow) starts at a depth of 6 μm and has a concentration of 15% at 10 μm. This is compared to the PCM electrode without dispersant in which the intermixed silicon/CsPAA areas start at a depth of 10 μm with a concentration of less than 5%. As such, these areas appear as CsPAA rich. The yellow areas are closer to the air interface by 4 μm, the yellow areas only make up 45% of the total concentration of the slice at depths of 18-23 μm and 36-40 μm for the BM CsPAA without dispersant electrode versus approximately 60% at depths of 18-38 μm for the PCM CsPAA without dispersant electrode. This coupled with the 40% increase in the CsPAA areas for the BM CsPAA without dispersant electrode versus its PCM counterpart, indicate that the BM CsPAA electrode is less homogeneous in both the lateral (i.e. along the slice) and z-direction (i.e. thickness) of the electrode. From these analyses we can conclude that the polymer solution preparation and mixing stages strongly influence the final electrode architecture.

Dispersants

have been used in these slurries for battery materials to create a more homogeneous distribution of components. [16], [17], [18], [19] To explore this effect, an 1,800 g/mol MW CsPAA (i.e. dispersant) was blended with a 450,000 g/mol CsPAA (i.e. binder). This addition to the slurry formulation has a major impact on the resulting electrode homogeneity and cycling performance as shown from the internal images of the electrode in Figure II.1.A.23, row 3. Unlike the electrodes without dispersants, the middle of the PCM electrode with dispersant is dominated (77%) by the well mixed Si/CsPAA (yellow region) with less than 2% of the regions originating the high CsPAA (red) zones. Second, with the exception of a small fraction of the silicon/CsPAA intermixed region (yellow pixels) between 5 μm and 14 μm, the well mixed Si/CsPAA zone does not materialize until 25 μm versus 15 μm for the PCM without dispersant case (Figure II.1.A.27, inset) with the remainder of the electrode dominated by the Si-rich/CsPAA poor species. Since all electrodes were fabricated with the same amount of CsPAA, dispersant causes a laterally more homogeneous distribution of silicon intermixed with binder as evidenced by the absence of the CsPAA-rich region. This shows that, while dispersant causes a laterally more homogeneous electrode, it does not necessarily result in an electrode that is more homogeneous in the z-direction (i.e. thickness of the electrode). This may indicate that dispersant is interacting more with the CsPAA binder and breaking it up rather than cleaving the silicon aggregates. In addition, the PCM electrode with dispersant has a different depth profile when compared to the other electrodes: none of the other electrodes have CsPAA mixed with silicon (yellow) in two distinct bands. These two different CsPAA mixed with silicon bands are likely due to differences in degree of entanglement of the polymer chains.

The results from the BM blended binder with dispersant are shown in Figure II.1.A.26 (last row) and 2D inset. Similar to the previous samples, the highest concentration of Cs is at the center of the electrode (Figure II.1.A.27). However, the slices from 24-44 μm are comprised of approximately 60%–80% CsPAA intermixed with silicon (yellow regions), compared to 60% of CsPAA intermixed with silicon from 18-38 μm for the PCM CsPAA without dispersant electrode, 40% of CsPAA intermixed with silicon from 18-24 μm for the BM CsPAA without dispersant electrode, and 75% of CsPAA intermixed with silicon from 32-38 μm for the PCM CsPAA with dispersant electrode. There are limited CsPAA rich areas and there is a broad band of CsPAA intermixed with silicon making up 60-80% of the slices from 20-44 μm, which indicates that the BM CsPAA with dispersant electrode is the most homogeneous electrode laterally. Similar to the PCM electrodes, adding dispersant to the silicon electrode slurry causes the CsPAA rich regions to become almost non-existent, however, adding dispersant to the electrode causes the majority of the yellow regions to be pushed deeper into the electrode. This also indicates that electrodes made with dispersant are less homogeneous in the z-direction, while being more homogeneous in the lateral direction. This supports the hypothesis that the dispersant is interacting with the binder chains and breaking up those agglomerates rather than interacting with the silicon and cleaving those bound aggregates.

Regardless of whether the electrode contained dispersant or not, there is clear evidence that the binder segregates to middle of the electrode, leaving a silicon rich, binder poor skin on both the air and copper interfaces. This may be contributing to the observed delamination issues noted by the CAMP and Post-Test Facilities in several of the postmortem analysis studies of the program cells. However, the degree of binder segregation depends on if the electrode was constructed using a slurry that contained dispersant and how the binder was fabricated. The data in Figure II.1.A.27 indicates that adding dispersant increases the homogeneity of the electrode causing the CsPAA rich region (red) to disappear, at the expense of driving the majority of the yellow regions deeper into the electrode and away from the air surface. Therefore, adding dispersant to the electrode slurry causes a laterally more homogeneous electrode by better distributing the binder and the silicon (i.e. little to no red regions in the electrodes made with dispersant). However, adding dispersant causes the electrode to be more heterogeneous in the z-direction, meaning that the silicon and silicon/binder areas have separated into a layered-like structure. One of the main questions that this data relates to the possibility of achieving homogeneity in both the lateral and z-direction and its role in electrochemical performance. In order to better probe the silicon/binder and silicon/carbon black interaction and explore the electrode homogeneity in all directions and its effect on electrode properties Raman mapping, X-ray photoelectron spectroscopy (XPS), galvanostatic cycling, and rheology are utilized.

The first lithiation cycle voltage profile is instrumental in understanding the effect the electrode architecture has on electrochemical properties. The voltage versus capacity lithiation and delithiation curves are presented for all electrodes discussed in Figure II.1.A.27. The BM CsPAA without dispersant electrode has a first lithiation voltage profile that resembles a crystalline silicon lithiation profile and shows the crystalline silicon to amorphous silicon transition indicated by the plateau at around 150 mV.[19], [20], [21] The PCM CsPAA without dispersant electrode has a similar profile in that it also reaches a crystalline to amorphous silicon transition plateau at 150 mV. However, the capacity of the PCM CsPAA without dispersant electrode is approximately 850 mAh/g compared to the BM CsPAA capacity of 1300 mAh/g. An additional 100 mAh/g is achieved for the BM CsPAA without dispersant electrode upon the voltage hold, bringing its total capacity to approximately 1400 mAh/g. The BM CsPAA with dispersant electrode only a capacity of 400 mAh/g is achieved before 50 mV is reached. However, during the voltage hold at 50 mV, an additional 1225 mAh/g in capacity is achieved, making the total first cycle capacity 1625 mAh/g. The PCM CsPAA with dispersant electrode has the worst first lithiation voltage profile in that only a capacity of 75 mAh/g is achieved until the electrode reaches 50 mV. The final capacity of the PCM CsPAA with dispersant electrode is 1600 mAh/g, indicating that an additional 1575 mAh/g in capacity is achieved during the 50 mV voltage hold. Some of this capacity is likely related to Cs reduction at 0.05V (vs. Li/Li^+). These last two electrodes don't have the characteristic voltage profile of crystalline silicon indicating poor transport of electrons and/or Li^+.

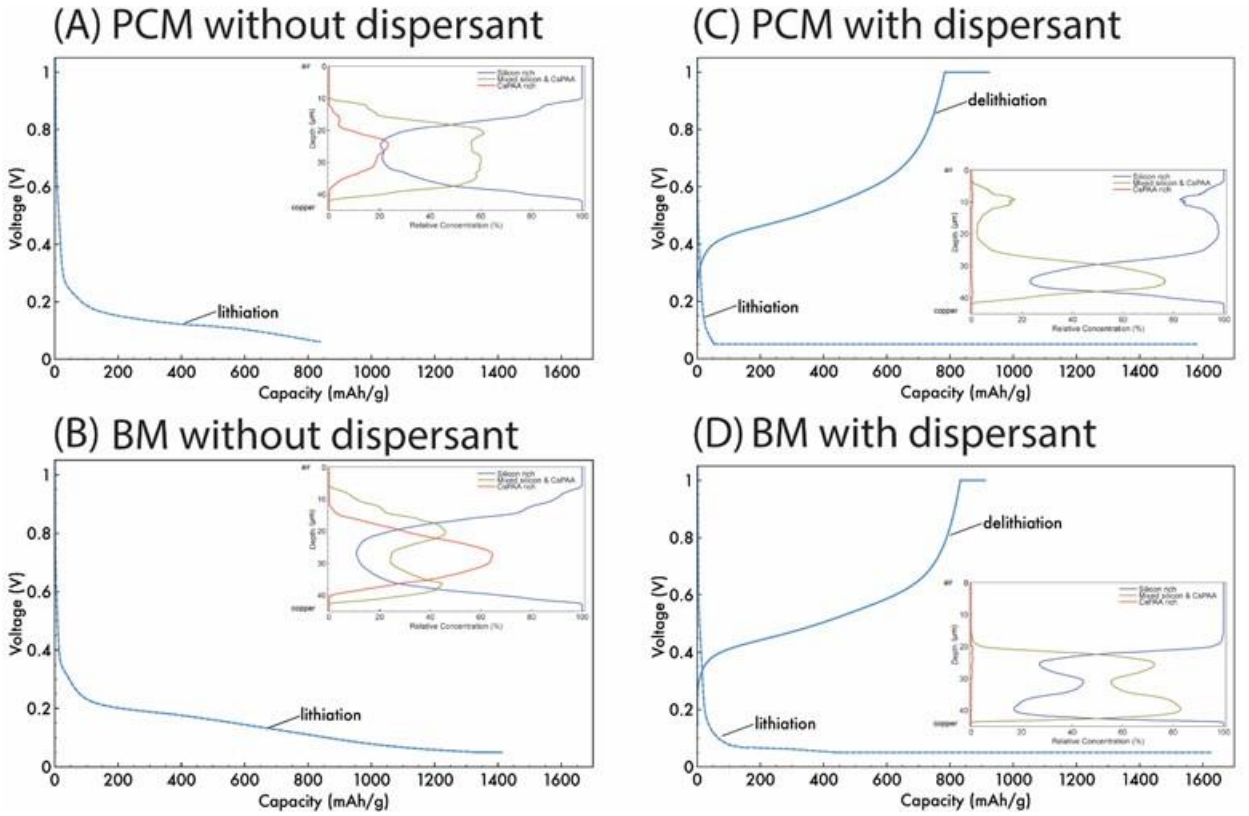

Figure II.1.A.27 First galvanostatic cycle presented as voltage versus gravimetric capacity for electrodes made with Planetary Mille (PCM) blended CsPAA (A) without and (C) with dispersant and Ball-Milled (BM) CsPAA (B) without and (D) with dispersant. Electrodes made with dispersant (C and D) completed a full lithiation/delithiation cycle while electrodes made without dispersant (A and B) only completed a lithiation cycle. Insets are the relative concentration of silicon-rich/CsPAA binder poor regions (blue), intermixed silicon and CsPAA binder regions (yellow), and CsPAA binder rich/silicon-poor (red) as a function of depth in the electrode where the two extremes are at the electrode-air interface and at the silicon-copper interface for electrodes made with (A) PCM CsPAA without dispersant, (B) PCM CsPAA with dispersant, (C) BM CsPAA without dispersant, and (D) BM CsPAA with dispersant.

From Figure II.1.A.27, it seems that adding dispersant to the electrode causes an enhancement of the layered aspects of the electrode structure, which results in an electrode with more lateral homogeneity. This is consistent with the homogeneity (z-direction) through the thickness of the electrode is more important than lateral homogeneity (x-y plane) in determining how ideal the voltage profile is and may be related to connectivity to the current collector or overall stability to delamination. While the electrodes with dispersant had higher overall capacity coming from the voltage hold, 75% for the BM CsPAA with dispersant or 95% for PCM CsPAA with dispersant electrode, respectively. This shows that there is a fundamental lithium and/or electronic transport problem in the electrodes with dispersant. Since Cs^+ has a reduction potential of 100 mV vs. Li^0/Li^+, and the minimum cut off voltage was 50 mV, the focus of the electrochemical study was on the first cycle lithiation/delithiation voltage profile. [22]

To investigate the possible change in binder structure, a series of dilute (0.25-2 wt%) solutions of each binder were used to determine the intrinsic viscosity, and thus the molecular weight, using an Ostwald viscometer. [23]-[43] Viscometer measurements showed that the molecular weight of the BM and PCM CsPAA had average molecular weights of 59,208 g/mol and 56,638 g/mol, respectively (Table II.1.A.3). Note, Ostwald viscometry provides average molecular weight, not molecular weight distribution.

The higher molecular weight BM CsPAA can explain why the electrode slurries made with BM CsPAA have higher viscosities (26.58 Pa*s and 33.01 Pa*s for slurries with and without dispersant, respectively) than that of PCM CsPAA electrodes (19.27 Pa*s and 24.10 Pa*s for slurries with and without dispersant, respectively).

However, the electrodes, irrespective of mixing method, made with dispersant consistently have a lower viscosity (difference between with and without dispersant being 6.4 Pa*s and 4.8 Pa*s for BM and PCM mixed CsPAA electrodes) than their counterparts made without dispersant (Figure II.I.A.27 and Table II.1.A.3). While all electrode slurries shear thin, the shear flow index shows the effect of molecular weight of binder and the presence of dispersant on the degree of shear thinning. The shear flow indices of electrodes made with BM CsPAA with and without dispersant or with PCM CsPAA with and without dispersant are 0.324, 0.343, 0.355, and 0.372, respectively (Table II.1.A.3). The BM CsPAA slurries with and without dispersant are more shear thinning than their PCM counterparts by approximately 14%. Again, this is likely because higher molecular weights cause a more pronounced shear thinning effect, but changes in polymer conformation could also contribute to these effects. The shear thinning behavior is mitigated when dispersant is present in the slurry because the dispersant likely helps reduce the agglomerates of CsPAA, as indicated in the X-ray tomography data, which promotes lateral homogeneity within the electrode.

From the depth profile, it seems that the dispersant is interacting with the CsPAA binder molecules and disentangling them. This is somewhat counterintuitive in that dispersants are expected to improve the overall homogeneity of the slurry. However, CsPAA may be more strongly interacting with silicon surface as both are hydrophilic whereas carbon black is hydrophobic. Therefore, the dispersant may be causing silicon to be broken into smaller aggregates, while carbon black remains as large agglomerates. This particle size discrepancy may result in a slurry that is less homogeneous than it would be without dispersant counterpart. Essentially, the slurries without dispersant have large agglomerates, but the overall agglomerate size is more similar than that of the dispersant slurries.

From these processing and tomography studies, electrodes fabricated with binder solutions that were mixed by BM or PCM showed that the molecular weight distribution of the polymeric binder chains differed and led to unique architectures. Rheology and viscometry results revealed that different mixing methods caused a drastic decrease in molecular weight of the binder. BM blended binder has a higher average molecular weight (59,208 g/mol) and produced a laterally more uniform electrode in the presence of dispersant. PCM mixed binder suffered from the largest decrease in molecular weight (56,638 g/mol) and resulted in a more heterogeneous electrode laterally in the presence of dispersant. Regardless of the binder mixing method or the presence of dispersant, the binder segregated to the middle of the electrode, which suggests that PAA is not performing as a typical binder is not holding silicon and the carbon black in intimate contact with one another.

Table II.1.A.3 Molecular weight, initial viscosity, shear flow index, initial gravimetric capacity, and number of cycles for each electrode made with PCM blended binder with and without dispersant and BM blended binder with and without dispersant

Binder, dispersant	Ostwald Molecular Weight of Binder (g/mol)	Initial Viscosity (Pa*s)	Shear Flow Index	Initial Capacity (mAh/g)	Number of Cycles
Starting PAA	450,000	---	---	---	---
PCM without dispersant	56,638	24.19	0.372	1142	1
BM without dispersant	59,208	33.01	0.343	1584	1
PCM with dispersant	---	19.27	0.355	1412	20
BM with dispersant	---	26.58	0.324	1630	20

Results: Silicon Electrode: Testing Protocols

Calendar Aging Screening Protocol

This protocol document provides a framework for the development of silicon (Si) electrodes for high capacity lithium ion batteries by providing standardized test protocols that researchers and early stage developers can use to assess the progress of silicon modifications, cell designs, electrolytes, or additives. Overall while full cell cycling for silicon anodes has progressed significantly over the past several years, similar progress in the area of calendar life remains a major challenge. The procedures detailed below have been developed out of a major scientific effort, funded by the Vehicles Technology Office, to understand the formation and evolution of the silicon solid electrolyte interphase (SEI). This first generation of procedures is designed to enable a reasonably well-equipped research laboratory to assess early research progress towards improving calendar aging issues in silicon cells in a reasonable timeframe. These generation-one procedures will be updated, modified and expanded as the research team obtains feedback from stakeholders and as our understanding of the SEI evolves.

Traditional approaches to investigate calendar aging often involve experiments that take as long as the period they investigate, the aging inflicted by months of storage is evaluated by exposing the charged cell to controlled conditions for that same number of months. More specifically, such tests age the cells under open-circuit conditions (no current or load applied), with periodic reference performance tests (RPTs) that measure the cell degradation as a function of aging time. The RPTs directly measure the metrics of interest, such as reversible capacity and energy/power retention. While providing extremely useful information, such approaches are clearly time-consuming and are likely to slow down the development of Si-based cells [44]

The testing protocol described in this document is designed to provide semi-quantitative insights on the quality of the SEI in approximately ~2 weeks. Rather than tracking cell capacity losses over very long times, the protocol presented relies on measuring, in real time, the currents associated with reactions that form or decompose the SEI as the anode is held at a constant state-of-charge (SOC). The evolution of these currents over time provides a basis to understand how the state of passivation of the anode evolves over longer time scales. We note that calendar aging is a complex process that involves not only loss of Li^+ inventory, but also active material loss, electrolyte degradation and power fade. While the testing protocol being developed by our team will *not* predict all these aspects of calendar aging, it will nonetheless provide information about the rates of Li^+ inventory losses to the SEI, which is a main factor limiting the calendar life of silicon-based anodes.

The testing protocol described herein departs from traditional calendar aging tests in that *it does not provide absolute calendar lifetime predictions*. Instead, the results should be compared against those of standard electrodes like graphite with calendar lifetimes well characterized by other methods. Future versions of this protocol may provide the ability to quantitatively predict calendar lifetime as the analysis methods are further developed and the lifetime predictions are validated by independent tests. Until such capabilities are available, this protocol can be used to quickly and easily screen electrolyte compositions and silicon electrodes. After this initial investigation, the most promising systems can be studied under more resource intensive experiments, such as traditional calendar life tests that use long rests with intermittent RPTs.

Protocols

The procedure to test the calendar life of Si anode materials is extremely sensitive to the test cell setup, especially the geometric size and areal capacities of both the test electrode and the counter electrode. Therefore, for reliable comparisons between tests, the testing procedures should adhere to the following requirements:

Cell Design: Size 2032 stainless steel coin cells are used as the electrochemical test vehicle. The electrodes consist of the Si anode material (the test electrode) against a thick high-capacity lithium iron phosphate (LFP) cathode. When an LFP electrode of sufficiently high areal capacity is not available a Li counter electrode can be used instead, we warn that the chemical reactivity of lithium can alter the electrolyte composition and can affect the generality of observations obtained for some systems. The diameters are 14 mm for the cathode

(LFP) when it is paired with the 15 mm diameter Si-containing test anode. When the Si-containing electrode is paired with a Li counter electrode then the Si electrode is 14 mm diameter with a 15 mm diameter Li foil (less than 1 mm thick).

The areal capacities of the electrodes are chosen to ensure that there is enough Li^+ inventory to supply the Si-containing test electrode with capacity during the aging protocol. The LFP electrode is greater than or equal to 2.5 mAh/cm^2, while the Si-containing test electrode is less than or equal to 1.3 mAh/cm^2 at the state-of-charge (SOC) at which aging will be assessed. This additional Li^+ inventory is meant to guarantee that the cathode would still retain excess capacity even after the large irreversibility that is typical of Si electrodes in the first few cycles. If electrodes with loadings other than those designated are used, it is imperative that the total utilized capacity of the Si electrode (reversible capacity + accumulated irreversible capacity) not exceed the capacity of the counter electrode during the test. This design ensures that the counter electrode can effectively supply the Li^+ needed to (re)form the SEI at the Si test electrode.

Table II.1.A.4 Requirements of test and counter electrodes

Electrodes	Chemistry	Capacity	Diameter
Test Anode:	Si material	<1.3 mAh/cm^2	15 mm diameter (14 mm vs. Li)
Preferable cathode:	Lithium iron phosphate (LFP)	>2.5 mAh/cm^2	14 mm diameter
Acceptable counter electrode:	Lithium metal	>2.5 mAh/cm^2	15 mm diameter

Cell assembly: The 2032 stainless steel coin cell is built following an assembly process, summarized in Table II.1.A.4, that has been well established at Argonne National Laboratory [45] and is summarized below:

1. Electrodes should be dried under dynamic vacuum for at least 14 h at 120 ºC for PVDF binder (LFP cathode) containing electrodes, and 150 ºC for PAA or LiPAA binder containing electrodes. Other binders that are used should be dried appropriately so as not to affect the cell chemistry.

    a. Note that thick single sided LFP electrodes can curl when wet with the electrolyte. Thus, we recommend assembling LFP containing cells from the anode side up in the following order: cell cap with attached polypropylene gasket, 0.5 mm thick stainless steel spacer, 15 mm Si test electrode, 20 µL electrolyte, 19 mm diameter layer of 2325 Celgard separator or equivalent, 20 µL electrolyte, 14 mm LFP counter electrode, 0.5 mm thick stainless steel spacer, stainless steel wave spring, cell case.

    b. Li half-cells should be assembled in the following order: cell case, 14 mm Si test electrode, 20 µL electrolyte, 19 mm diameter separator layer, polypropylene gasket (oriented to properly mate with cell cap), 20 µL electrolyte, 15 mm diameter Li metal foil (< 1 mm thick), 0.5 mm thick stainless steel spacer, stainless steel wave spring, cell cap.

2. The assembled cell stack should then be crimped together with a hydraulic crimper, preferably an automatic crimper for consistency.

C-rate determination

The C-rate is defined as the current necessary to drive the Si test electrode from one voltage cut-off to the other in 1 hour (a C/10 rates takes 10 hours to drive the electrode from one voltage cutoff to the other). This value is determined using half-cell data of the second cycle of the Si test electrode. Because the LFP electrode delithiates at ~3.45 V vs. Li/Li^+, and relithiates at ~3.40 V vs. Li/Li^+, the cutoff potentials correlate as follows:

- 2.7 V vs. LFP (discharge) = 0.7 V vs. Li/Li^+

- 3.35 V vs. LFP (charge) = 0.1 V vs. Li/Li^+

LFP-based full cell:

1. Rest cell at OCV for 4 hours to allow electrolyte wetting
2. At a C/10 rate, charge to 3.35 V, discharge to 2.7 V, repeat 3 times, data acquisition should be $\Delta V = 5$ mV
3. Hold cell at 2.7 V until i < C/100 to fully lithiate test electrode, data acquisition should be $\Delta t = 1$ min, $\Delta i = 10$ µA at a C/10 rate, data acquisition should be $\Delta V = 5$ mV
4. Hold potential at 3.35 V for 180 hours, data acquisition should be $\Delta t = 1$ min, $\Delta i = 10$ µA
5. Discharge to 2.7 V at a C/10 rate, data acquisition should be $\Delta V = 5$ mV
6. Hold cell at 2.7 V until i < C/100 to fully lithiate test electrode, data acquisition should be $\Delta t = 1$ min, $\Delta i = 10$ µA
7. At a C/10 rate, charge to 3.35 V, discharge to 2.7 V, repeat 2 times, data acquisition should be $\Delta V = 5$ mV

Lithium Half-cell (same procedure as LFP full cell with potential cutoffs substituted as follows):

- 0.1 V instead of 3.35 V
- 0.7 V instead of 2.7 V

The preliminary efforts described in this report are limited to studying SEI passivation at the SOC achieved by the anode at ~0.1 V vs. Li/Li^+, for a graphite electrode, this would correspond to ~55% of lithiation. Most Si-based electrodes can remain mechanically stable when cycled to this potential, and thus permanent losses of active material are less likely to occur during the tests discussed here. Our team recognizes that SOC is an important variable when investigating calendar aging and modeling SEI growth [46] and future studies will expand the scope of this report.

Data Collection

Verifying the current response of the cell during the voltage hold is critical to guarantee that the data analysis will be meaningful. Figure II.1.A.28 shows the current that is measured during the hold, normalized to the capacity (lithiation capacity measured during the charge immediately before the voltage hold) of a test silicon electrode and a graphite baseline electrode. The expected behavior for the current measured in both systems are shown in Figure II.1.A.28, where the continuous decay exhibited by the traces indicates that the counter electrode is supplying sufficient Li^+ inventory. This plot also qualitatively demonstrates that the currents that arise from parasitic reactions on the graphite electrode, seen long after the initial decay, are roughly an order of magnitude smaller than those observed for the silicon, demonstrating its better passivating behavior and longer calendar lifetimes, as expected. The results displayed in this type of plot should serve as a gate to determine if further analysis should be performed using the testing protocols described in this document. *If the residual current (i) does not approach that of a baseline electrode such as graphite (necessarily within an order of magnitude), then further analysis is not warranted, as the SEI is clearly not sufficiently stable*. It is recommended that the data acquisition parameters discussed in the previous section are used in the voltage hold test, to ensure enough resolution.

A major pitfall of this experimental protocol occurs when the Li^+ inventory of a test cell is exhausted (counter electrode is completely delithiated). The sudden decline of the current responses to diminishingly small and indistinguishable values as seen in Figure II.1.A.28 (after ~40h of voltage hold) indicates that the Li^+ inventory

supplied by the counter electrodes has been exhausted during the V-hold. Under these conditions, the external current no longer provides a direct measure of the rate of parasitic reactions, yielding inaccurate information about the electrode's calendar lifetime. This is another critical reason why the current response of the collected data needs to be evaluated before performing the analysis described in the next section. If the current response displays a similar behavior to that shown in Figure II.1.A.28, the test cell should be remade with a higher capacity counter electrode or a lower capacity test electrode.

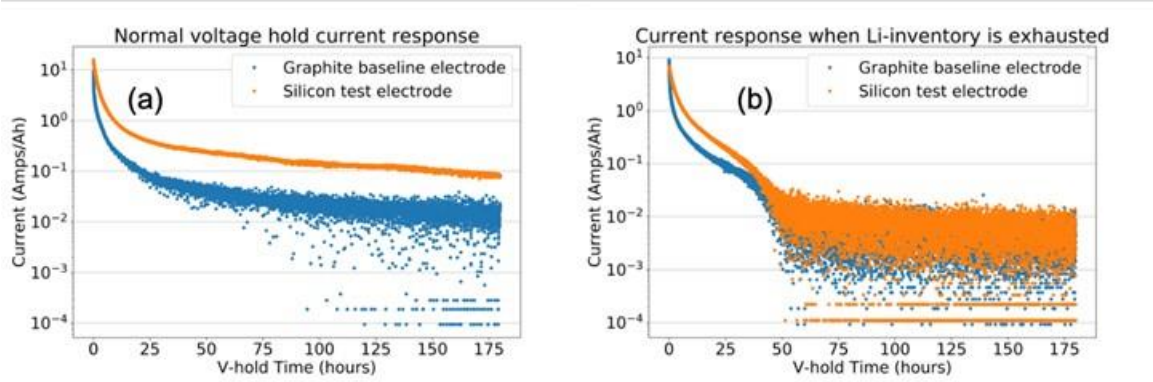

Figure II.1.A.28 Current decay versus time during voltage holds of (blue) graphite baseline anode and (orange) 80 wt% Si test anode. The current has been normalized to the capacity of the test electrode measured during the lithiation immediately before the voltage hold. Panel **(a)** shows the current response where there is an excess of Li^+ inventory supplied by a counter electrode with a flat voltage profile, as is the scenario marked (a) in Figure 3. Panel **(b)** shows how the current suddenly declines as the Li^+ inventory supplied by the counter electrode is exhausted, polarizing the electrodes to high potentials. Under these conditions, the measured current underestimates the actual rate of parasitic reactions experienced by the test electrode.

Data Analysis

Analysis of the data should first be done by qualitative visual inspection and comparison between the test electrodes and a baseline electrode. Figure II.1.A.29 shows the current decays of three different Si test electrodes and a graphite baseline electrode. The normalization of the current data to the reversible capacity of each electrode is important because the resulting units of Amps/Ah indicate the rate at which each electrode is losing reversible capacity due to Li^+ consumption at the SEI. If the normalized current measured from a Si test electrode at the end of the 180-hour voltage hold is distinguishably higher than the baseline electrode, further analysis is not needed, as the electrode's SEI is clearly not sufficiently stable. This is the case for each of the Si test electrodes shown in Figure II.1.A.29, thus showing the effectiveness of this simple qualitative comparison for the initial screening of Si test electrodes.

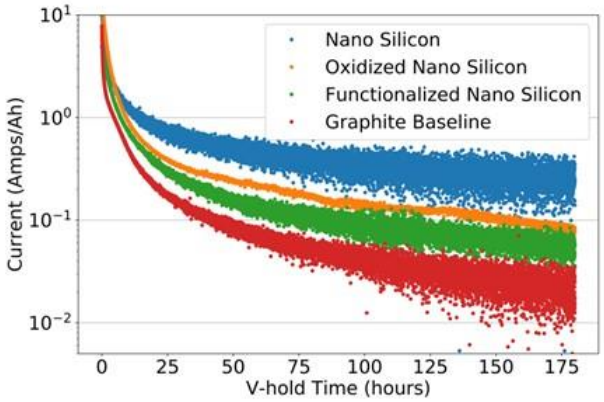

Figure II.1.A.29 Current decay versus time during voltage holds of several different Si test electrodes and a graphite baseline electrode. The rate of parasitic reactions of the Si test electrodes can be qualitatively distinguished by visual inspection, and all exhibit greater aging rates than the graphite baseline electrode.

The average current after 180 hours of voltage hold can be used as a metric to rank the rate of parasitic reactions at each electrode and is reported below for the examples shown in Figure II.1.A.29. This information should be complemented by details about electrode composition, areal capacity, and electrolyte used in the tests. Additionally, because there can be variability between tests for a given electrode and electrolyte pair, we recommend that a sample size of at least three test cells for each test electrode type be reported.

Example reporting:

Graphite baseline electrode

1.17 mAh/cm^2

91.83 wt% Superior Graphite SLC1520P

2 wt% Timcal C45 carbon

6 wt% Kureha 9300 PVDF Binder

0.17 wt% Oxalic Acid

Electrolyte: 1.2 M $LiPF_6$ in ethylene-carbonate:ethyl-methyl-carbonate 3:7 + 10 wt% FEC

Mean terminal current = 0.023 mA/Ah

Nano Silicon

0.3 mAh/cm^2

20 wt% 3.9 nm diameter Si nanoparticles

65 wt% Timcal C65 carbon

15 wt% PAA Binder

Electrolyte: 1.2 M $LiPF_6$ in ethylene-carbonate:ethyl-methyl-carbonate 3:7 + 10 wt% FEC

Mean terminal current = 0.262 mA/Ah

Oxidized Nano Silicon

1.24 mAh/cm^2

80 wt% Surface oxidized 150 nm diameter Si nanoparticles

10 wt% Timcal C45 carbon

10 wt% LiPAA Binder

Electrolyte: 1.2 M $LiPF_6$ in ethylene-carbonate:ethyl-methyl-carbonate 3:7 + 10 wt% FEC

Mean terminal current = 0.092 mA/Ah

Functionalized Nano Silicon

0.7 mAh/cm^2

40 wt% 4-phenylphenol surface functionalized 30 nm diameter Si nanoparticles

40 wt% Timcal C65 carbon

20wt% PAA Binder

Electrolyte: 1.2 M $LiPF_6$ in ethylene-carbonate:ethyl-methyl-carbonate 3:7 + 10 wt% FEC

Mean terminal current = 0.059 mA/Ah

These examples highlight the capabilities of the screening protocol described in the current version of this document. Because it is currently limited to qualitative analysis, it is especially important to use a baseline electrode with a calendar life well characterized by other methods under the conditions of interest. Future versions of this report may include a semi-quantitative model to describe the rate of parasitic reactions in the electrodes of interest, which is currently under validation by long-term experiments, this model is outlined in general terms at the end of the discussion section.

Our methodology is based on using *voltage holds* to measure the rate of Li^+ trapping at the SEI in Si-containing cells. *This approach has the advantage of recording real-time rates of side reactions, providing information about the time-dependence of such processes and potentially enabling extrapolation of behaviors observed in short duration experiments*. Its working principle is since parasitic *reduction* reactions (such as the ones involved in SEI formation) effectively consume electrons from the anode, which decreases the anode SOC. The instantaneous voltage of a cell is the difference between the potentials of the positive and negative electrodes, so a change in the anode SOC yields a change in cell voltage. If the anode SOC is "pinned" by holding the cell voltage constant, electrons must flow from the cathode to the anode to replenish the charge consumed by side reactions, in order to keep the anode SOC invariant, i.e., the *current* flowing through the cell and measured by an external circuit is equal to the rate of these parasitic processes. This ideal equivalence between the parasitic and measured currents is achieved when the anode has a sloped potential and is most sensitive to SOC and the cathode is insensitive to SOC (the voltage profile is "flat"). We can approximate these conditions by using $LiFePO_4$ (LFP) as a cathode (which can provide most of its capacity while at ~3.45 V vs. Li/Li^+), and by performing the voltage hold at potentials in which the anode cycling profiles are notably sloped to maximize sensitivity.

For these tests, it is important that the LFP counter-electrode have a capacity in excess of what is used by the reversible and irreversible reactions occurring at the Si test electrode. The importance of this condition is demonstrated by the simulated voltage profiles shown in Figure II.1.A.30, where the LFP voltage profiles are shown in blue. Profiles for pristine (solid line) and aged (dashed line) Si anodes are displayed in black with the corresponding full cell voltage profiles displayed in red. The intersecting lines marked **(a)** in Figure II.1.A.30 represent the pristine full cell being held at 3.35 V, where the potential at the pristine Si anode would be roughly equivalent to ~100 mV vs. Li/Li^+. In this pristine cell at 3.35 V, the LFP voltage profile is insensitive to SOC (voltage profile is flat), and thus any changes of the Si SOC would require a change in cell voltage i.e., the Si SOC is "pinned". As electrons and Li-ions are consumed at the Si electrode during aging, they are replenished by the LFP cathode, as additional Li^+ extraction is possible at that same electrode potential. Nevertheless, if enough capacity is lost, the aged cell may no longer be able to keep the Si SOC constant. This Li^+ inventory exhaustion scenario is represented by the intersecting lines marked **(b)** in Figure II.1.A.30, where the aged cell is still held at 3.35 V. In the aged cell with an exhausted Li^+ inventory, the LFP voltage profile is polarized above its plateau potential and is sensitive to SOC (highly sloped), resulting in the Si electrode no

longer being held at the desired potential of 100 mV vs. Li/Li$^+$. When that happens, additional Li$^+$ extraction from LFP to counter parasitic reactions at the anode would cause an increase in the potential of both electrodes, this would involve a net decrease in anode SOC, and thus the currents measured by an external circuit would underestimate the extent of side-reactions in the cell.

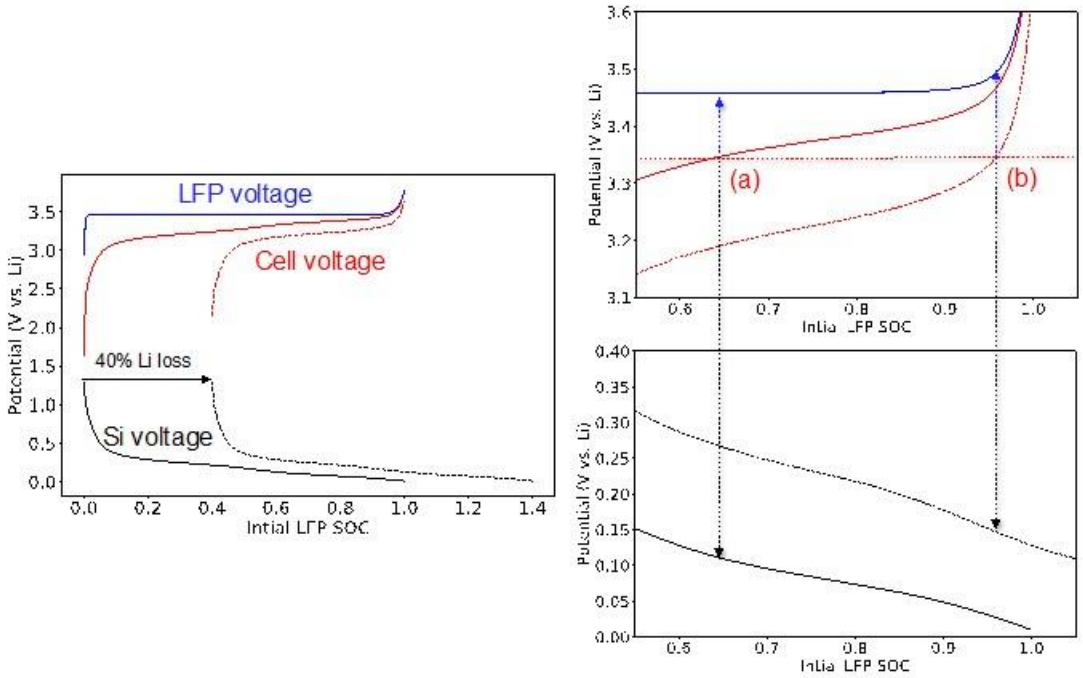

Figure II.1.A.30 **(left)** Simulated voltage profiles for an LFP cathode (blue), Si anode (black), and the 2-electrode cell combining those two electrodes (red). The dashed black line represents Si electrode aging by the loss of Li$^+$ inventory, which effectively shifts the Si voltage profile relative to the LFP voltage profile, and results in the aged cell having the dashed red voltage profile. **(right)** Zoomed in portions of the voltage profiles where the dotted horizontal red line represents a voltage hold potential of 3.35 V for pristine (a) and aged (b) Si electrode containing cells.

The use of LFP as a counter-electrode has additional advantages. One is that the cathode can be assumed to be an essentially inert electrode, since its low potentials will lead to little changes in electrolyte composition and are unlikely to generate oxidative currents that could affect the analysis. Additionally, the extremely flat voltage plateau of LFP over its entire capacity range allows it to be used as a reliable pseudo-reference electrode in a two-electrode coin cell. Thus, the absolute potential of the anode can be well controlled, facilitating studies on the effect of SOC on passivation. The test protocol specifics and an example voltage profile are shown in Figure II.1.A.31, where a 180-hour long voltage hold is preceded by three formation cycles and followed by two additional diagnostic cycles. The total test time is ~290 hours (less than two weeks).

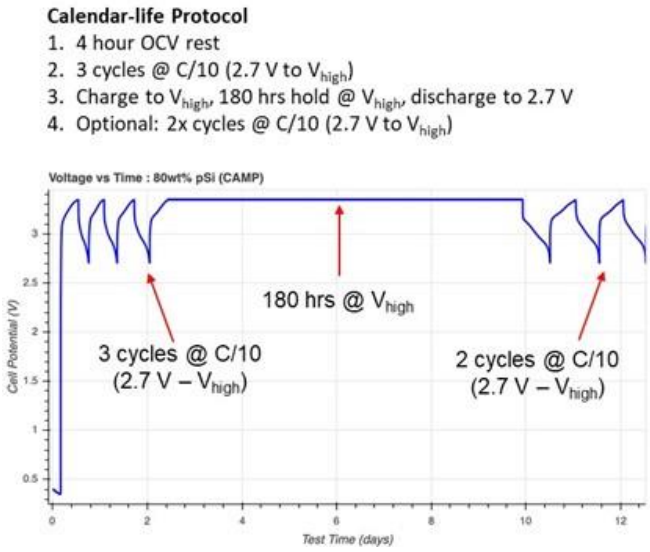

Figure II.1.A.31 The test protocol to estimate the rate of parasitic reactions of Si-based electrodes. The example voltage profile is from a cell coupling a 80% Si electrode vs. an LFP cathode.

Although this experimental approach is a logical pathway to derive information about electrode passivation from short term tests, it also presents challenges. In practice, electrodes present a finite impedance and lithiation processes are incomplete by the time the voltage hold initiates. Hence, the current measured during the early periods of voltage hold is a combination of reversible lithiation processes (lithiation of Si) and irreversible electrochemical reactions (SEI formation and concomitant Li^+ consumption). As the voltage is held for longer and longer times, the proportion of the current driving reversible reactions diminishes relative to the current driving the irreversible reactions, and the measured current becomes a more reliable descriptor of parasitic processes. For these component contributors, *the challenge exists to validate that the analyses can differentiate between both these contributions to the measured current.* The reversible capacity that is passed during the voltage hold can be experimentally quantified by inspecting cell discharge after the hold, and these values are used to help differentiate the time dependent contributions from the reversible and irreversible processes.

The purpose of the 180-hour long voltage hold is to determine the rate of Li^+ inventory consumption, as measured by the current, due to irreversible side reactions at the anode surface. Using this method, the current measured during the voltage hold is due to a combination of the reversible lithiation reactions and the irreversible side reactions. Figure II.1.A.28 shows the typical current responses during the voltage hold of example electrodes. The current densities decrease more than an order of magnitude during the first ~20 hours of the voltage hold as the reversible lithiation reactions near completion. In contrast, towards the end of the voltage hold, the current densities stabilize at diminishingly small values that are primarily due to irreversible Li^+ consuming reactions. The lower current density of the graphite electrode at the end of the voltage hold compared to the Si electrode is good confirmation that the measurement is qualitatively capturing the expectedly better SEI stability (and lower Li^+ inventory consumption rate) of the graphite electrode. Figure II.1.A.28 shows the current response during the V-hold where the Li^+ inventory of the cell becomes exhausted. This occurs when the cathode is unable to supply additional electrons and Li-ions to keep the anode pinned at a fixed SOC, as outlined by marker **(b)** in Figure II.1.A.30. In this case, the full cell is maintained at a fixed voltage with a net decrease in anode SOC, resulting in the measured currents underestimating the parasitic reaction rates. This can be seen in Figure II.1.A.28 by the sudden decrease in current to vanishingly small values and highlights the importance of performing these experiments in cells with excess counter electrode capacity.

Integrating the measured current over time during the voltage hold and normalizing to the electrode's reversible capacity yields time dependent capacity, $Q_{hold}(t)$. In order to deconvolute the irreversible and reversible contributions to the capacity, the following function can be fit to the normalized capacity data:

$$Q_{hold}(t) = Q_{irrev}(t) + Q_{rev}(t)$$

The numerical forms of these functions are still being determined using long term voltage hold validation experiments. As the validation data becomes available, future versions of this report may include numerical models that can be used to semi-quantitatively describe the rate of SEI-related side-reactions. Preliminary results suggest that $Q_{rev}(t)$ has an asymptotic time dependency as the reversible capacity approaches a maximum value at long times, whereas $Q_{irrev}(t)$ may be proportional to the square-root of time. The square-root of time dependency of $Q_{irrev}(t)$ is well supported by empirical observations in the literature, and is believed to capture the general behavior of SEI growth. [46], [47] This particular functional form arises from the hypothesis that the irreversible side reactions occurring at the electrode surface due to SEI formation are diffusion limited, and thus their rates are inversely proportional to the square root of time.

Notwithstanding, the Si SEI stability will naturally fluctuate as a function of numerous internal and external factors. The present report is just the beginning of an exploration of the Si calendar life behavior embedded in a current response, the measurement probe of choice. In an electrochemical process, electrode kinetics and their reaction rates are tied to a current value. The parasitic reactions in Si electrodes are exceedingly complex and, as a first pass, it is affiliated with (1) the Li ion conductivity in the SEI, (2) the mechanical stability of SEI, (3) chemical stability (solubility) of the SEI, and (4) the electronic conductivity within the SEI. What factors dominate thus begs the question: how can one slow down this degradation phenomena and create 'immunity'?

Results: Silicon Electrodes: Additives

Stability issues associated with silicon anodes have hampered the widespread their use in commercial lithium-ion batteries. A critical aspect, especially as it relates to calendar life issues, is their reactivity when charged (lithiated) due to formation of highly reactive lithium silicide binary Zintl phases, i.e. Li_7Si_3. This reactivity against cell components and the electrolyte causes major inefficiencies and loss of lithium and electrons, which severely reduces cycle life and long-term performance of the silicon electrode. Our FY19 efforts showed that, the addition of small amounts of soluble alkaline earth salts (Mg,Ca etc.) to the programmatic baseline Gen2 electrolyte + FEC led to a significant improvement in cycle and calendar life for silicon-containing anode materials for LIBs, a focus of the DeepDive program in association with the SEISTA Si effort. This stabilization is achieved by replacing the reactive and redox active lithium silicide with more stable surface Li-Mg-Si ternary Zintl phases. As shown by Han, et al., the incorporation of Mg was not done by heating or an external process but by inclusion from the electrolyte in an in-situ electrochemical fashion via an ion-exchange reaction at low cell voltage. Spectroscopically, data collected indicated that the Mg^{2+} from solution was incorporated into the surface of the silicon electrode, replacing 2 Li^{+} with Mg^{+2}. Of the metal salts tested in 2032-coin cells, the added electrolyte salts with either magnesium (Mg^{2+}) or calcium (Ca^{2+}) cations proved to work the best over hundreds of charge — discharge cycles. For instance, in cells with pure silicon anodes coupled with lithium-rich cathodes, the energy densities surpassed those for comparable cells having graphite chemistry by up to 50%, as long as a compatible silicon source is used to allow for multivalent ions to diffuse through the anode.

In a continuation of this effort, the DeepDive expanded the multivalent electrolyte additive study to pouch cells fabricated by ANL CAMP facility and evaluate various cell configurations with different electrolyte systems. Stabilization and optimization of silicon electrode studies have focused on electrode composition optimization and calendar life studies.

Silicon Pouch Cells with Multivalent Electrolyte Additives

The CAMP Facility completed the first round of testing the magnesium and calcium electrolyte additives in single-layer pouch cells that were fabricated in the fourth quarter of FY2019. The high silicon content electrodes

used in this project were from the CAMP Facility's Electrode Library and used a LiPAA binder paired with NMC532 or HE5050 cathodes – these cell configurations cycling protocols are described in Table II.1.A.5.

Two NMC532 cathodes were selected with different capacity loadings to test the effect of n:p ratio. Magnesium and calcium containing electrolytes were provided to the CAMP Facility before the pouch cells were assembled. These electrolytes (including the baseline electrolyte) are described as follows:

- Gen2F= Gen2 + 10% FEC (baseline electrolyte)
- GenFM = Gen2F+ 0.1M $Mg(TFSI)_2$
- Gen2FC = Gen2F+ 0.1M $Ca(TFSI)_2$

Under evaluation, the additive cells showed superior cyclability and higher coulombic efficiencies in both half-cell and full cell configurations than the cell tests using Gen2F electrolytes (Figure II.1.A.32). The pouch cells with the higher capacity NMC532 cathodes (A-C013B) lost capacity at a faster than expected rate, regardless of the electrolyte. The pouch cells with the lower capacity cathodes (HE5050 (A-C017) and NMC532 (A-C015B)) had better capacity retention and that was found to be independent of the additive electrolyte used, with the exception that the baseline electrolyte test ("GenF") pouch cells teamed with a lower capacity NMC532 electrodes (A-C015B). These results were not in total agreement with the earlier coin cell studies where the Ca^{+2} and Mg^{+2} additives had a clear advantage, in these pouch cells the Ca^{+2} stood out as the better performer and are still under evaluation (~70% retention after 300 cycles). Cells from these evaluations are being evaluated at the Post-Test Facility. As with last year's larger scale studies, the pouch cells that used the higher capacity NMC532 cathode (A-C013B) showed excessive signs of delamination in the pouch cells with NMC532 at the higher capacity (A-C013B cathode).

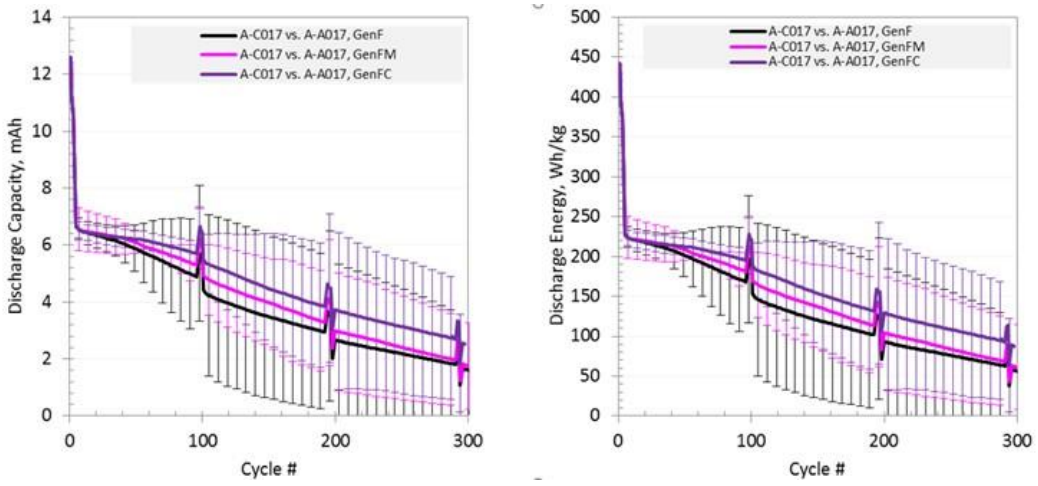

Figure II.1.A.32 Cycle life discharge capacity and energy comparison for baseline and multivalent electrolytes

The cathode cell sets with lower capacity cathodes: HE5050 (A-C017) and NMC532 (A-C015B) were also checked for signs of anode delamination. It was observed that the NMC532 low-loading cathode cells (at 4 psi) only showed anode delamination for the Gen2F electrolyte case (see Figure II.1.A.33). In FY19 this was also observed and coincided with the cell pressure applied. Work by CAMP has found that the higher constant (spring) pressure in coin cells had more stable cycling performance that the pouch cells. Adding pressure to the testing protocol (up to 76 PSI) enhanced the performance, initial analysis by CAMP researchers indicated that shrinking the lower cutoff in the testing may be beneficial after formation cycling to magnesiate the surface in order to minimize the crystallization of $Li_{13}Si_4$, the point silicon in the electrode goes from an amorphous state to a crystalline one.

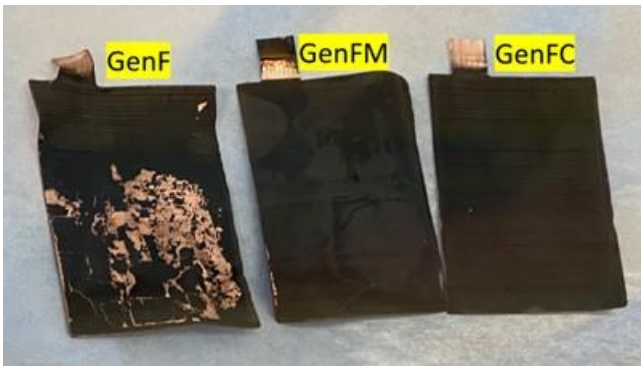

Figure II.1.A.33 Figure II.I.A.33. Harvested anode electrodes from single-layer pouch cells (at 4 psi) with baseline “Gen2F” electrolyte (left), “Gen2FM” electrolyte (center), and “Gen2FC” electrolyte (right) using the lower capacity NMC532 cathode (A-C015B). Unexpected delamination seen only on anode with Gen2F electrolyte.

Optimization of Electrode Composition

The program has been using two kinds of Si anode compositions, 80% silicon or 10%–20% silicon with graphite. The electrodes with 80% silicon show inferior stability while the Si/graphite electrodes had low specific capacity in which the performance gradually became graphite only. Therefore, we focused on optimization of silicon anode composition. This ANL effort then focused on the optimum composition for baseline systems but also helps to improve performance by understanding the working

Table II.1.A.5 Cell configurations and Cycling Protocols

Cathode	Anode	Electrolyte	Protocol
CAMP C015 NMC532 Electrode	CAMP A017 Graphite-free Si Electrode (4kg-batch)	Gen2F, Gen2FM, Gen2FC, Gen2FA	First at C/20 from 3.0 to 4.1 V for 3 formation cycles, then at C/3 from 3.0 to 4.1 V for 92 aging cycles, with voltage holding at the end of each charging stage.
CAMP C015 NMC532 Electrode	CAMP A016 Graphite-free Si Electrode (4kg-batch)	Gen2	
CAMP C015 NMC532 Electrode	CAMP A013 15%Si+73%Graphite	Gen2F, Gen2FM	
CAMP C017 HE5050 Electrode	CAMP A017 Graphite-free Si Electrode (4kg-batch)	Gen2F, Gen2FM, Gen2FC, Gen2FA	First at C/20 from 3.0 to 4.5 V for 3 formation cycles, then at C/3 from 3.0 to 4.1 V for 92 aging cycles, with voltage holding at the end of each charging stage.
CAMP C017 HE5050 Electrode	CAMP A016 Graphite-free Si Electrode (4kg-batch)	Gen2	

As shown in Figure II.1.A.34, six compositions with different silicon contents, conductive additive (C45), and binder (LiPAA) were studied. Each composition is denoted by three numbers representing the components. For instance, 811 indicates 80% Si, 10% C45, and 10% LiPAA. Since C45 is much lighter and more porosity than Si powders, the higher content of C45 automatically reduces the areal loading of electrode materials. Therefore, the areal Si loading of 442/433 anodes is 71% lower than 811 anodes (Figure II.I.A.34). Such lower areal loading would decrease the deliverable capacity of the electrodes.

Figure II.1.A.34 shows the cyclic performance of typical cells with different Si anodes, showing specific capacity normalized by the weight of silicon. Most of the initial capacities are higher than the theoretical capacity of silicon, indicating that C45 also contributes to the capacity. More conductive additive and binder

clearly enhanced the performance and stability of silicon, which is reflected by the highest specific capacity and capacity retention of the 442 electrodes while the lowest specific capacity and rapid capacity decay of the 811 electrodes. However, if the specific capacity is normalized by the weight of the electrode (Si+C45+LiPAA), 442 and 433 cells have the lowest specific capacity due to the low electrode areal loading and silicon content (Figure II.1.A.34). Except for the 811 cells, the coulombic efficiency of other cells exhibits a similar tendency without notable differences (Figure II.1.A.34). Based on Figure II.1.A.34, the 712 cell and the 622 cells have the best balance between the silicon performance and electrode performance.

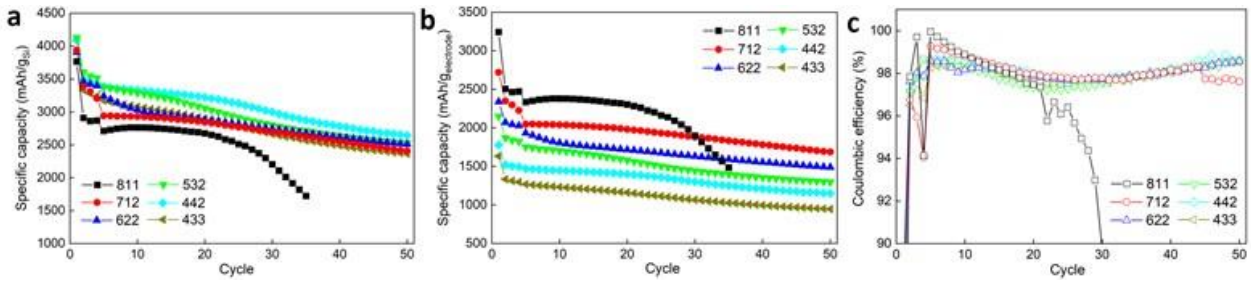

Figure II.1.A.34 Cyclic performances of typical cells with different Si anodes. (a) Specific capacity normalized by the weight of silicon. (b) Specific capacity normalized by the weight of electrode (Si+C45+LiPAA). (c) Coulombic efficiency of the cells.

Figure II.1.A.35 is the average lithiation specific capacity of three 622 cells and three 712 cells up to 60 cycles. The lithiation capacity of 622 cells surpassed that of 712 cells after 58 cycles. Moreover, from the error bars, 712 cells start losing their lithiation stability after 46 cycles. The cyclic performance of delithiation exhibited a similar tendency with an even earlier start point of 712 cells losing stability (Figure II.1.A.35). The coulombic efficiency plot indicates that 712 cells have a higher irreversible capacity loss after 40 cycles (Figure II.1.A.35). Further tests revealed that 622 cells can stably operate over 100 cycles without notable capacity fluctuation. Therefore, 622 Si anodes have a good combination of capacity and stability, which have the potential to be used in full cells.

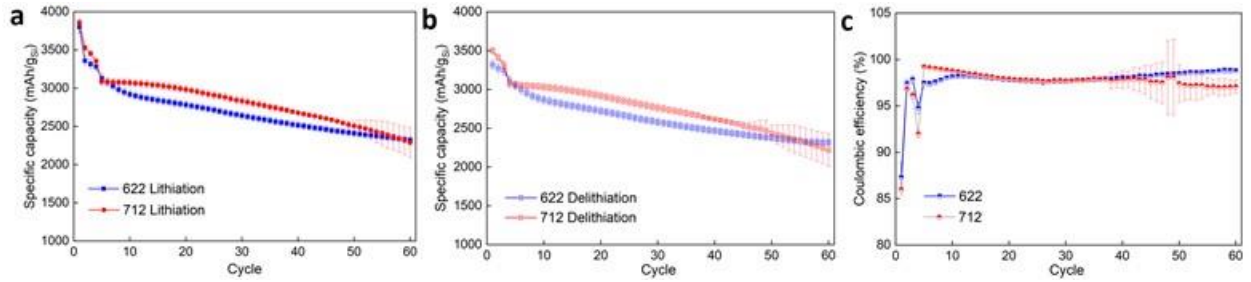

Figure II.1.A.35 Cyclic performance of 622 and 712 cells. (a) Lithiation specific capacity. (b) Delithiation specific capacity. (c) Coulombic efficiency.

Calendar Life Studies with Multivalent Electrolyte Additives

As previously discussed in detail, Li-M-Si (M=Mg, Ca, Al) Zintl phases form in-situ formed around Si particles can stabilize the electrode-electrolyte interface and improve cyclic lifespan as well as capacity retention. However, for Si anodes calendar life is also critical for practical applications. Here, a preliminary study was carried out on Si622/NMC532 cells. When assembling the cells, $Mg(TSFI)_2$ and $Ca(TSFI)_2$ were added into the baseline Gen2F electrolyte, forming Gen2FM and Gen2FC electrolytes, respectively. The cells were held at 4.1 V for 1 week (168 h) after three formation cycles at C/20 and three aging cycles at C/3. Figure II.1.A.36 is the current/time profile during constant voltage holding. The data points of the Gen2FC cell appear to be more concentrated. Accordingly, the capacity/time profiles show that the cell with the Gen2FC electrolyte had less capacity loss when holding (Figure II.1.A.36). Consistent with the current and capacity profiles, the specific capacity change of aging cycles before and after holding showed that the Gen2FC cell had the least capacity loss indicating that the Li-Ca-Si Zintl phase may also stabilize the interface while constant voltage holding, leading to better calendar life for the full cells (Figure II.1.A.36).

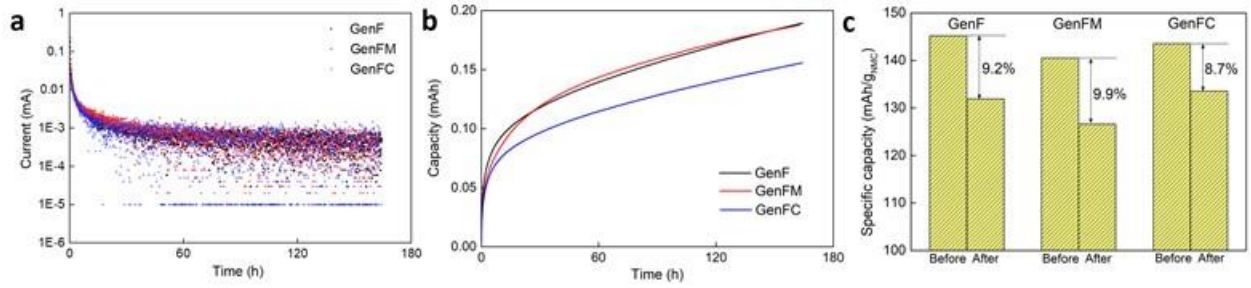

Figure II.1.A.36 Calendar life tests of Si622/NMC532 cells with GenF, Gen2FM, and Gen2FC electrolytes. (a) Current/time profile. (b) Capacity/time profile. (c) Comparison bar chart of aging cycle specific capacity before and after constant voltage holding.

Si622/LFP full cells were used to further identify the influences of Zintl phase on the calendar life due to the outstanding stability and small voltage variation of LFP when charging/discharging. For this study we used the Silicon Deep Dive Calendar Aging Electrochemical Screening Protocol. Specifically, the cells with GenF, Gen2FM, and Gen2FC electrolytes were held at 3.35 V for 1 month (720 h) after three formation cycles at C/10. The current/time clearly shows that the data points of the Gen2FC cell are highly concentrated comparing with the other two cells (Figure II.1.A.37), indicating the interphase enabled by the Li-Ca-Si ternary Zintl phase is more stable than the other two electrolytes. A similar conclusion can be concluded from the capacity/time profile (Figure II.1.A.37), which shows the cell with Gen2FC electrolyte had lower capacity loss after 720 h holding. Although more characterizations are needed, it is safe to say that Gen2FC enabled Li-Ca-Si Zintl phase stabilized the interface and has positive influences on the calendar life of Li-ion batteries with Si anodes.

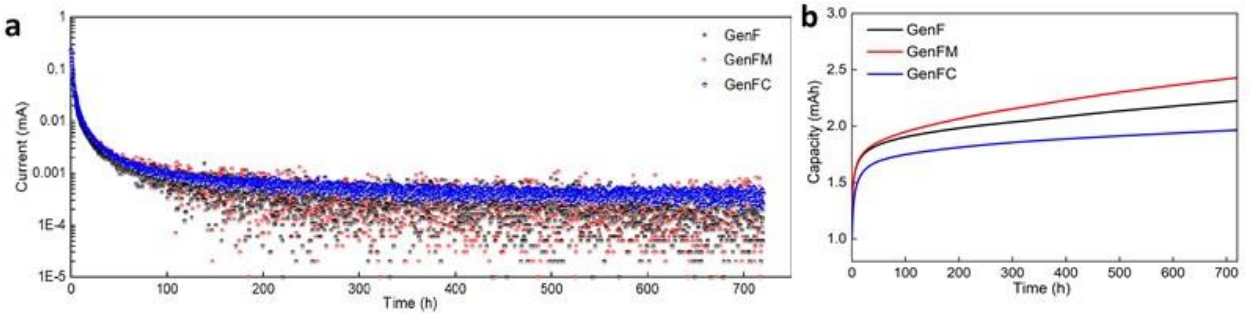

Figure II.1.A.37 Calendar life tests of Si622/LFP cells with GenF, Gen2FM, and Gen2FC electrolytes. (a) Current/time profile. (b) Capacity/time profile

Study of multivalent electrolyte additives (ternary Zintl chemistries) on CAMP pouch cells where we achieved better cyclability, higher coulombic efficiencies when compared to baseline electrolytes. An evaluation of electrode delamination identified as a major limitation on the long-term cycling effort which was partially overcome by higher pressure pouch cell design and lower cathode loadings. Examining silicon composition optimization studies (varying silicon, carbon and binder content) significantly improved capacity retention, cyclability, and calendar life. Lastly, with these optimized electrode compositions, silicon electrode calendar life studies showed significant improvements versus baseline with the advanced electrolyte additives with the Ca^{+2} system only showing a 6% increase in capacity over 700 h versus 28% increase for the baseline Gen2F electrolyte. Evaluation continues however data collected to date indicates that the growth in capacity lost to parasitic reactions will not eclipse the milestone guideline of 20% in the remaining time (goal ~1400h).

The active surface phase has been investigated by TEM, NMR, and XPS in order to better understand the formation mechanism of the Zintl phases. In this case an *in-situ* analytical technique, the Electrochemical Quartz Crystal Microbalance Measurement with Dissipation (EQCM-D), mode is applied to better understand the formation/growth of the SEI as a function of state of charge and additive. A Si thin film anode (50 nm) free of binder and conductive carbon is sputtered on a resonator and used as the working electrode with

electrochemical signals referenced with Li metal. The frequency shift coupled with the electrochemical voltages in two electrolyte environments, Gen2F (Gen2+10%FEC) and Gen2FM (Gen2+10%FEC+0.2 M $Mg(TFSI)_2$) are presented in Figure II.1.A.38, where simultaneous electrochemical lithiation voltage from OCV = 2.5 V to 0.015 V is coupled with the corresponding frequency difference at the 3rd overtone. Two lithiation stages are monitored, the pre-lithiation process for SEI formation from 2.5 V to 350 mV and the post-lithiation stage from 350 mV to 15 mV. Results suggest before lithiation occurred (>350 mV), the frequency shift for the Gen2FM electrolyte is less significant than for the Gen2F electrolyte suggesting the SEI formation is less protuberant with the Mg addition in comparison with the Gen2F electrolyte. Frequency shift is mainly contributed from the electrolyte reduction as well as lithium insertion into surface SiO_2. For the post-lithiation stage (100 mV to 15 mV), frequency shift for the Gen2FM electrolyte at lowered voltage range from 100 mV to 50 mV is more significant than the Gen2F electrolyte and this trend is opposite in contrast to the pre-lithiation stage. Lithiation of Si into $Li_{3.75}Si$ gives a mass increase of 48% of the reaction, however, formation of the Zintl phase and the magnesiation of $Li_{3.75}Si$ into $Li_{3.55}Mg_{0.1}Si$ phase merely gives a mass increase of 1.9%. Consequently, the apparently decreased frequency shift with the Mg addition occurring at lowered voltage range from 100 mV to 50 mV clearly suggests that a partial inclusion of Mg and formation of the Li-Mg-Si ternary taking place in parallel in addition to the lithiation of Si at these low voltages. At these points the silicon network has been broken down from a three dimensional solid to a molecular solid and appears to be capable of ion exchange and incorporating the magnesium ions.

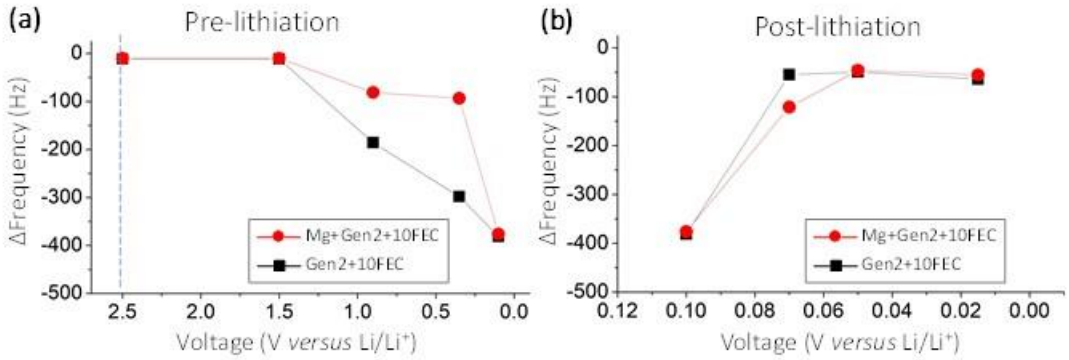

Figure II.1.A.38 Correlation of the lithiation voltage versus the frequency difference from the in-situ EQCM measurement on a 50 nm Si thin film referenced with lithium metal in Gen2F(black square) and Gen2FM (red circle) electrolyte. **(a)** pre-lithiation stage at V>350 mV, **(b)** post-lithiation stage at V < 350 mV.

Electrochemical performance of Si thin film anode with a 0.2 M $Zn(TFSI)_2$ and a 0.2 M $Mg(TFSI)_2$ as the electrolyte additives in the baseline electrolyte Gen2+10%FEC are studied and compared, presented in Figure II.1.A.39. Early stage SEI formation was more prominent with the Zn^{2+} additive in Gen2F electrolyte and SEI is suppressed with Mg^{2+} additive in the baseline electrolyte. Specifically, with the Zn^{2+} additive, no obvious current signal is detected for the first 2 electrochemical cycles suggesting no lithiation of Si. From OCV to lithiation at 0.4 V, capacitive current is detected without lithium intercalation. However, a mass accumulation is observed at the Si electrode indicative of the electrolyte reduction contributed SEI. Lithiation of Si started at lithiation potential from 0.4 V to 0.115 V, where clear intercalation and de-intercalation of Li is observed which correspond to reversible mass change. On the other hand, with the Mg^{2+} additive in the baseline electrolyte, it essentially prevents further SEI development at Si anode which is clearly indicated by the shift of the frequency. Thickness of the SEI in the $Mg(TFSI)_2$+Gen2+10%FEC electrolyte is about 50% of the SEI in a conventional Gen2+10%FEC electrolyte.

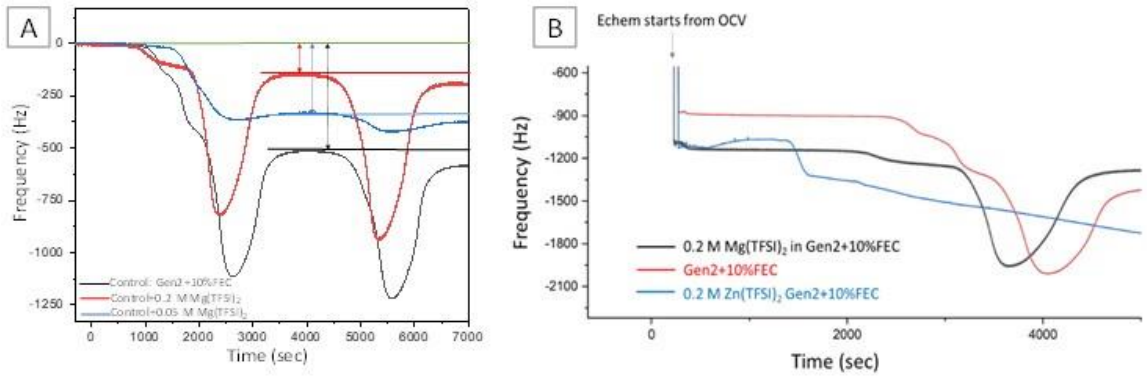

Figure II.1.A.39 In-situ early SEI formation at a Si thin film anode in different electrolytes based on the frequency shift (3rd overtone). **(a)** Gen2+10%FEC (black), 0.2 M $Mg(TFSI)_2$ in Gen2+10%FEC (red), and a 50 mM $Mg(TFSI)_2$ in Gen2+10%FEC (blue), **(b)** Frequency shift for the early SEI formation of a 0.2 M $Zn(TFSI)_2$ and a 0.2 M $Mg(TFSI)_2$ as electrolyte additives to the baseline electrolyte (Gen2+10%FEC) on a Si thin film anode. Lithiation depth is 0.115 V.

Coulombic efficiency, an indication of the reversibility of lithiation, is evaluated at different lithiation depth at 5 mV, 10 mV, 40 mV, 115 mV to 400 mV in three different electrolytes, the baseline Gen2+10%FEC electrolyte (black square), a 50 mM $Mg(TFSI)_2$ in the baseline (red circle) and a 200 mM $Mg(TFSI)_2$ in the baseline (green triangle), presented in Figure II.1.A.40. Results suggest two important findings: (1) a higher CE is favored by the existence of Mg^{2+} in the electrolyte at low lithiation voltages, (2) a higher Mg concentration enables a higher CE at low lithiation voltages. These data are consistent with the testing studies reported earlier.

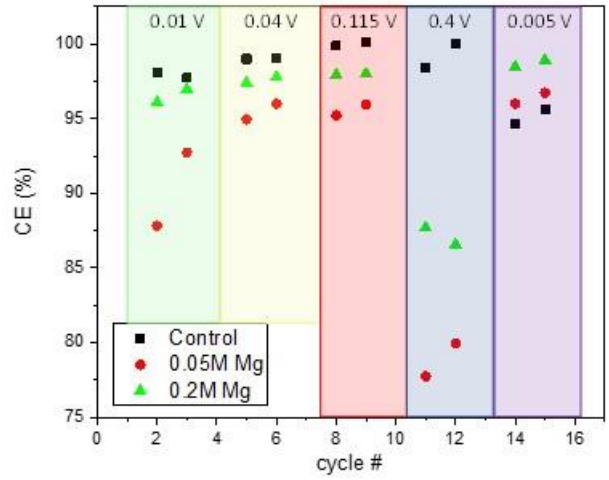

Figure II.1.A.40 Coulomic efficiency at lithiation depths of 5 mV, 10 mV, 40 mV, 115 mV, 400 mV in different electrolytes: baseline electrolyte Gen2+10%FEC (black), 50 mM Mg addition in baseline(red) and 200 mM Mg additive in baseline electrolyte (green).

These EQCM-D studies allow us to quantify the early SEI formation for a Si thin film electrode with electrolytes with multivalent ion additives. Results suggest a suppressed early SEI with the presence of Mg^{2+} additive in electrolyte, and an enhanced SEI formation with the presence of Zn^{2+} additive in electrolyte. This is consistent with earlier studies by Han et al., where Zn was found to be electrochemically active (reduced to metal at 0.65V) and be more easily removed from the system. Results from the EQCM-D present an electrolyte dependent SEI formation mechanism with the Mg^{2+} additive in electrolyte stabilizing the Si interface upon formation of a compact SEI layer and enables a higher coulombic efficiency of Si anode at low lithiation voltages.

FEC & Temperature

In addition to the Zintl additives, temperature is known to have a significant impact on the performance and cycle lifetime of lithium-ion batteries (LiB) in the baseline electrolyte system. In the past year we have studied the effects of temperature on SEI formation and stability with and without 10wt% FEC additive in the Gen 2 electrolyte within the temperature range of 25 °C to 55 °C.

In FY20, we focused on the post-test analysis of Li-Si cells after the initial five cycles and compared the SEI properties at different temperatures with and without the FEC additive. Figure II.1.A.41 shows the XPS data from the cycled Si rich anodes within the temperature range we tested.

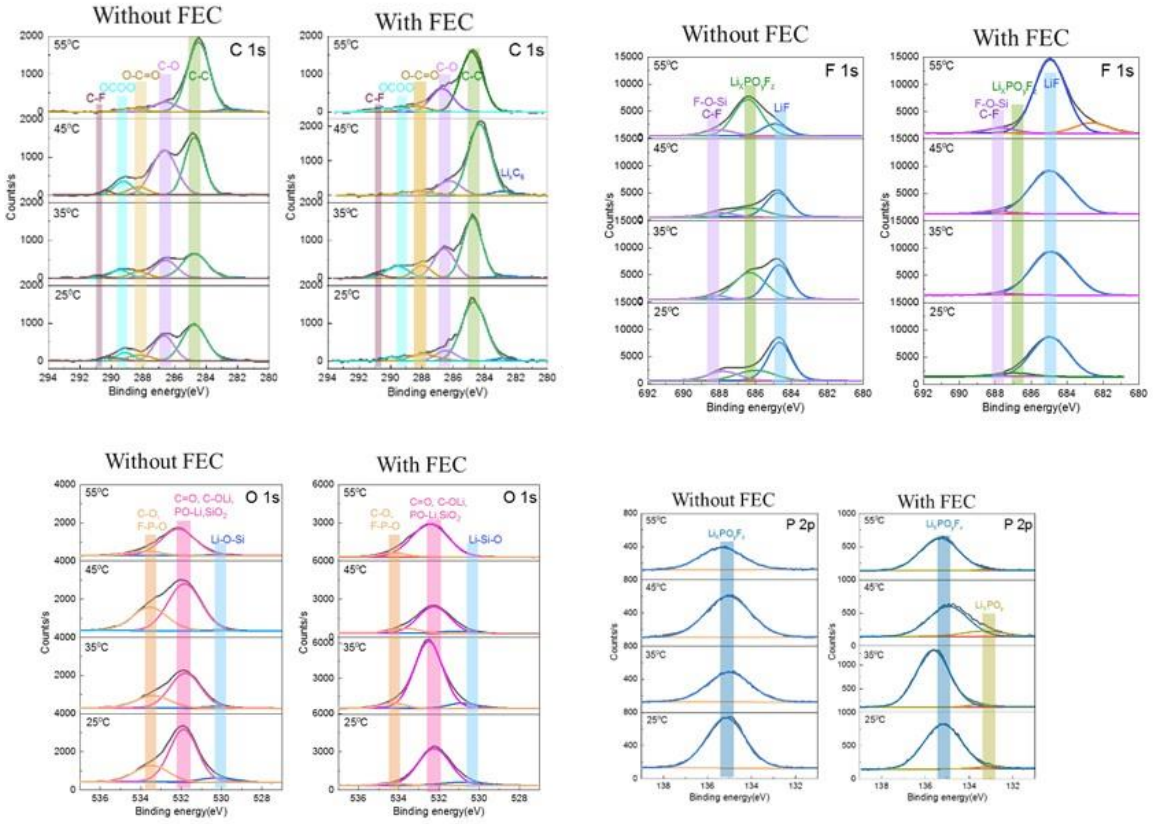

Figure II.1.A.41 C1s, F1s, O 1s, and P2p XPS spectra of Si anodes after 5 cycles in the temperature range from 25 °C to 55 °C with and without 10 wt% FEC in Gen 2 electrolyte.

The C1s spectrum at the surface consists essentially of five signals after peak deconvolution at all temperatures in both electrolytes. The line at 284.8eV corresponds to aliphatic carbon (C-C). The signal at 286.6eV can be assigned to carbon atoms in a one-oxygen environment (C-O). Based on the binding energy, it is more likely to consist of carbon atoms bound to an electron withdrawing group, as in R-C-OH (alcohols), R-C-O-C=O (esters) and C-O-COO (organic carbonate). Their presence is confirmed by the corresponding oxygen signals in the O1s spectrum. The peak at 287.8eV is assigned to a carbon atom doubly bound to one oxygen, as in ketones and aldehydes ($R_2C=O$, H-C=O) according to the literature. The peak at 289.6eV can be attributed to a carbon atom in a three-oxygen environment, such as Li_2CO_3 and organic carbonates. The signal at higher bonding energy, i.e., 290.5eV, might be related to the formation of polymeric fluoro-organic species (C_nF_m). The compound is also detected in the corresponding F1s spectrum. Overall, based on the decomposition reactions in EC/EMC system, we can assume the assigned SEI components at Si surface (C-O-C, C-OH, C-O-C=O, $R_2C=O$, C-OC(=O)O and C_nF_m) are most likely to be polymeric. These organic units can be connected to form aliphatic chains, as indicated by a relative higher contribution of aliphatic carbons in the C1s spectrum.

This is supported by the results that the trend of contribution of CO_x species is similar in O1s spectra as that in the C1s emission.

The F1s spectrum of the Si surface shows three peak positions in both electrolytes. The first line at 684.5eV is assigned to LiF in agreement with most references. The peak appearing at 686.2eV can be attributed to $Li_xPO_yF_z$, based on the component assigned in the P2p spectra. The peak at 687.8eV is related to the formation of R-F (fluoro-organic species: C_nF_m, F-O-Si). XPS analysis shows the contribution of each component is quite different with/without the presence of FEC. SEI layer on anodes with FEC is primarily composed of LiF because the fluorinated ethylene carbonate (FEC) decomposes before EC and EMC. Overall, we can observe less temperature-sensitivity of SEI chemistry in the Si-rich cell with FEC, implying the SEI is more stable with the additive.

Figure II.1.A.42 shows the atomic percentage (at%) of the major SEI components, C, O, and F, on the Si surface that were calculated from XPS survey scans. The results clearly show less carbonate (C, O) and more F species formed on the surface with FEC, confirming FEC can suppress EC/EMC decomposition to some extent at the first 5 cycles. It is interesting to note that surface content of C, O, and F increases as temperatures increases from 25º to 45ºC, but at 55ºC, the values drop. This also is confirmed by lower peak intensity of C-O and C=O in C1s spectra in Figure II.1.A.39, indicating fewer organic carbonates were formed at 55ºC, particularly for the anode without FEC. In addition, there is an increase in fluorophosphates at this temperature. It might be due to the kinetics of SEI formation were enhanced and the partial decomposition of SEI components at this high temperature.

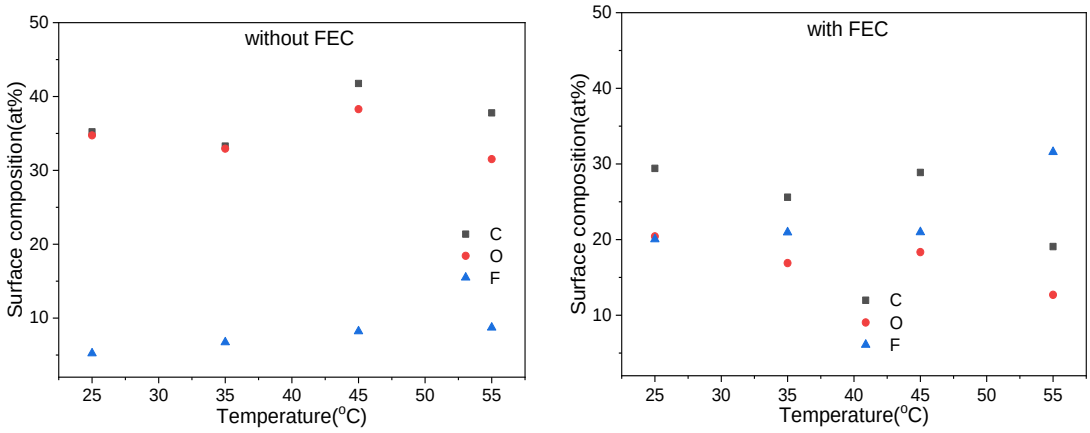

Figure II.1.A.42 The atomic percentage (at%) of the major SEI components at the Si surface after 5 cycles

From these studies**,** SEI formation and stability with and without FEC additive at different temperatures was investigated in high-Si content half cells by XPS and showed different SEI chemical species formed in the FEC-containing cells. Notably fewer organic species and more LiF observed in Si-rich with FEC addition. As result, cells with FEC showed less temperature-sensitivity of SEI chemistry when compared to the cells in Gen 2 only.

SEI Solubility

When assessing the stability of the SEI layer, previous efforts have identified dissolution and reformation as a components of silicon chemistry not seen in graphitic systems. This has been highlighted in the year using EQCM, XPS, and SECM studies who have assessed the stability of electrode level silicon baseline materials on cycling and determine the range of species that solubilize and leach into the electrolyte. To assess the dissolving materials, new analytical tools were adapted to determine the types of species that are found in the electrolyte as solubilized SEI products. For the solid silicon SEI components identified in the literature, research efforts have identified several polymerized ring-opened solvents (FEC, EC), various salts including

inorganic (Li_2CO_3) and coordination salts (i.e. LiEDC). Notably the latter, identified by the Ross Group at LBNL, has been seen to be a significant component that appears to have spectroscopic handles that allow its identification in the solid SEI films. LiEDC was later synthesized and found to form readily and, once purified, be insoluble in the solvents commonly used on out electrolytes. The insoluble nature of the materials makes identification and isolation more straightforward. However, in the silicon systems under study, it has been noted that the SEI layers on the anode are not dimensionally stable. On cycling the height, thickness, and weight of the SEI have been observed to change as a function of state of charge (SOC). Using Rotating Ring Disk Electrochemistry (RRDE), it has been seen that the SEI appears to show the most dramatic changes in volume above 450 mV (vs Li) while has seen dramatic weight and density shifts using EQCM-D. As the weight is changing as a function of state of charge, the conclusion drawn is that species in the SEI are oxidizing near those voltages and becoming soluble. Identification of these species is important as soluble species in the electrolyte may re-reduce on charge, and precipitate on the anode, transfer to the cathode and further react, or possibly change the transfer kinetics of the lithium cations in the electrolyte. In this case EC (or FEC) was seen to degrade as it accepted electrons from the reduced silicide on contact. Although made in a controlled environment, the exact nature of the reduced species was not identified, although the C-F bond in the FEC was maintained. A similar observation was seen with PVDF binders, where C-F bonds were stable and degradation reactions occurred at polymerization defects ($-CH_2-CH_2-$) rather than at random spots.

RRDE methods have been applied to solubilized species coming off as degradation products using a Si thin film cell. Earlier work (FY19) highlighted technique development efforts using redox mediators to track SEI conductivity vs SOC, the role of surface charge carrier, and FEC electrolyte additives. Work with FEC noted that measurable redox active species are coming off of 70% Si drop-cast electrode at SEI formation and during simultaneous sweep at the Pt ring electrode, in addition the FEC (via its film formed) was playing a role of surface passivation to these species, suggesting classic pre-passivation of the Si SEI.

For solubilized species, LBNL has been focused on the development of techniques to isolate and identify soluble SEI species. The work has two focus areas – a post-cycling gradient wash technique that uses polarity to solubilize and separate species formed but trapped in the SEI and FTIR, a spectroscopic technique useful for identification of organic species. The gradient solvent wash was developed with his group to isolate and identify species that formed but due to isolation techniques were often mixed. Using mixtures of ethyl acetate and hexane, he was able to create a gradient of polarity that selectively dissolved out species in the SEI by their relative iconicity, salts, to alcohols, to simple oligiomeric species. MALDI data is shown in Figure II.1.A.43. Earlier work (FY19Q2-FY20Q2) reported on its utility for test cells (Cu with Gen2, VC), with future work using FEC species and assessing the differences in SEI between species generated in Gen2, Gen2/FEC, and Gen2/FEC/Zintl additives.

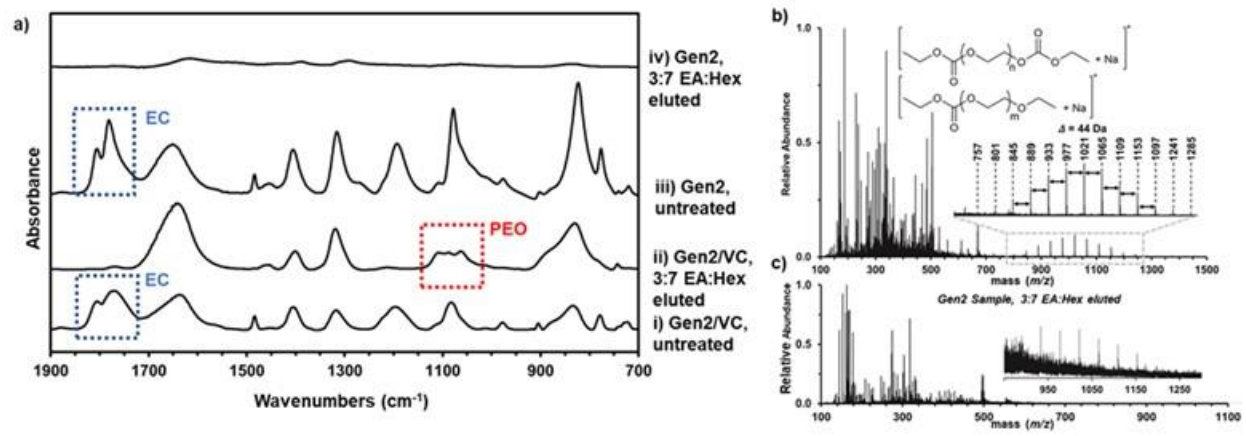

Figure II.1.A.43 a) FTIR spectra of untreated and treated electrodes cycled with and without VC. b) MALDI spectrum of electrode cycled with Gen2/VC after 3:7 EA:Hex treatment. c) MALDI spectrum of electrode cycled with Gen2 after 3:7 EA:Hex treatment. (Inserts are zoom-in spectra of PEO regions.)

The feasibility of this methodology has been fully demonstrated with Cu model electrodes, and the decomposition reaction of both electrolyte and additive molecules have been unambiguously characterized. In addition, these techniques have also been applied to actual SiO_2 and graphite composite electrodes, which delivered comparable results as those on Cu model electrodes, thus endorsing the universality of on-electrode chromatography and MALDI techniques.

Crossover

As well as species related to SEI dissolution being added to the electrolyte on cycling, crosstalk between cathode and anode in full cell system can have a significant impact on performance and cycle life for lithium-ion batteries (LIB). While this has been investigated for graphite anode systems where issues with catalytic decomposition of the SEI by the transported transition metal species are noted, similar studies for the Si-SEI in a full cell have not been investigated. To better understand if the Si SEI reacts differently than the graphite SEI to transition metal impurities, cells using a Si-rich (Si 80%/Graphite 20%) anode coupled with one of the following cathodes, $LiCoO_2$ (LCO), $LiNi_{0.5}Mn_{0.3}Co_{0.2}$ (NMC532), or $LiFePO_4$ (LFP) in a full cell were investigated. We analyzed electrolyte decomposition products by HPLC/ESI-MS and SEI chemistry of the aged Si anodes by XPS. Finally, we compared the different aging properties of the Si anodes in each full cell.

We focused on the post-test analysis of Si-rich full cells after initial 5 cycles (3 formation cycles at C/20, an HPPC cycle, 2 aging cycles at C/3, an HPPC cycle). Three full cells were used: LCO-Si, NMC532-Si, LFP-Si cells were prepared. The voltage window was 3.0-4.1V for LCO-Si and NMC532-Si cells, and 2.7-3.7V for LFP-Si cell. Gen2 electrolyte was used. After 5 cycles, we compared electrolyte decomposition products by HPLC/ESI-MS analysis, the SEI chemistry of each aged Si anode by XPS, and electrochemical properties of each aged Si anode.

Figure II.1.A.44 shows total ion chromatograms (TICs) of fresh Gen2 electrolyte and aged electrolytes extracted from three different full cells after 5cycles. Compared with TICs of Gen2 electrolyte, many different peaks are observed in TICs of the three aged electrolytes. This indicates the detection of multiple decomposition species from Gen2 electrolyte. Overall TICs of each aged electrolyte look similar, but several unique peaks are also visible in each electrolyte. This means that there are different decomposition species in each aged electrolyte. Table II.1.A.6 shows most intense ions in each electrolyte detected by HPLC/ESI-MS. Each electrolyte has many kinds of unique organic species, and there are a few organic species which are commonly observed in all samples (marked by blue) or in all aged electrolytes (marked by orange). Compared with the aged electrolytes from LCO-Si and NMC532-Si, the LFP-Si electrolyte has more organophosphate or organo(fluoro)phosphate species, indicative of more reactions involving PF_5 (in $LiPF_6$) in Gen2 electrolyte. Together, the results indicate that each of the electrolytes followed different decomposition routes, depending on cathode materials.

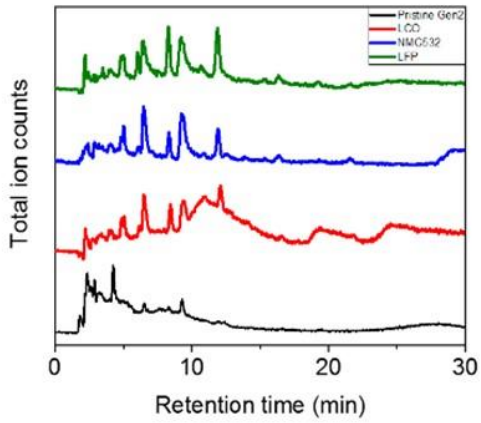

Figure II.1.A.44 TICs of fresh Gen2 electrolyte and aged electrolytes extracted from three full cells, obtained via HPLC/ESI-MS.

Different electrolyte decomposition mechanisms can lead to different SEI chemistry on the aged Si anodes in each full cell. Figure II.1.A.45 shows XPS results of the aged Si anodes in three full cells after the initial five cycles. The results clearly show that SEI chemistry on each aged Si anode is also different.

The C1s spectrum of the aged electrolyte from LCO-Si full cell consist of 4 signals. The peak at 284.8eV corresponds to aliphatic carbon (C-C). The peak at 283.2eV is assigned to lithiated carbon as a result of lithiation of graphite in the Si-rich electrode. Small peaks at 286.3eV and 288.4eV can be assigned to carbon atoms in a one-oxygen environment (C-O) and carbon atoms bound to an electron withdrawing group, like R-C-O-C=O (esters). While the C1s spectra of the both aged electrolytes from NMC532-Si and LFP-Si are quite different from that of LCO-Si. In both electrolytes, the C-O peak at 286.3eV is significantly stronger, and a new peak at 289.7eV that can be assigned to organic carbonate species (C-O-COO) is observed. Overall, the results show that SEI chemistry of aged Si anode from NMC532-Si or LFP-Si full cells consists of more organic species than the LCO-Si full cell.

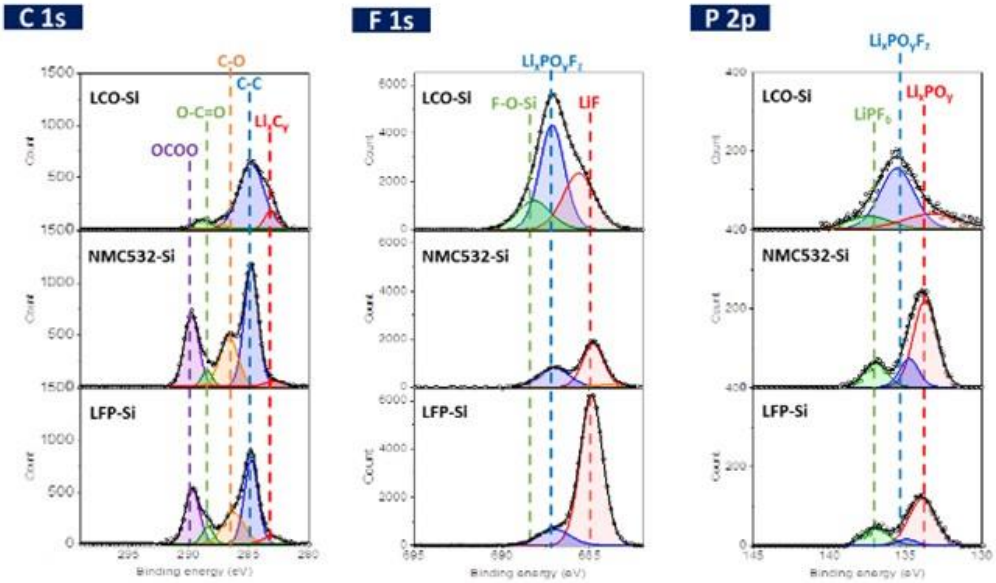

Figure II.1.A.45 C1s, F1s, and P2p XPS spectra of aged Si anodes from three full cells, after 5 cycles.

The F1s spectra of each aged Si anode are also different. In the aged Si from LCO-Si full cell, three peaks were observed. The peak at 684.9eV is assigned to LiF, in agreement with most references. The most intense peak at 687eV can be attributed to $Li_xPO_yF_z$. This could be supported by P2p spectrum. The peak at 688.2eV is related to the formation of R-F (fluoro-organic species: C_nF_m, F-O-Si). While the F1s spectra of aged electrolytes from NMC532-Si and LFP-Si are primarily composed of LiF. The peak assigned to $Li_xPO_yF_z$ is smaller, and the peak related to fluoro-organic species was not observed in both electrolytes. The smaller amount of $Li_xPO_yF_z$ could indicate that hydrolysis of $LiPF_6$ was suppressed in NMC532-Si or LFP-Si full cells.

The different crosstalk behavior in each full cell can lead to different degradation of each Si anode after 5 cycles. We prepared the aged Si anode/Li half-cell and compared their electrochemical properties. Figure II.1.A.46 shows the 1st cycle voltage profiles of the half-cells. The three half-cells show very similar 1st discharge capacities but show different coulombic efficiency (CE) and irreversible capacity. The half-cell rebuilt from the aged silicon anode from the LCO-Si full cell shows the lowest CE at 67%, while the rebuilt half-cell from the LFP-Si full cell shows a very high CE at 93%. This, at this point in the analysis, infers that the stability of the LFP/Si SEI is higher than that seen for NMC532 or LCO cells as each cell was found to have different electrolyte chemistry within five cycles.

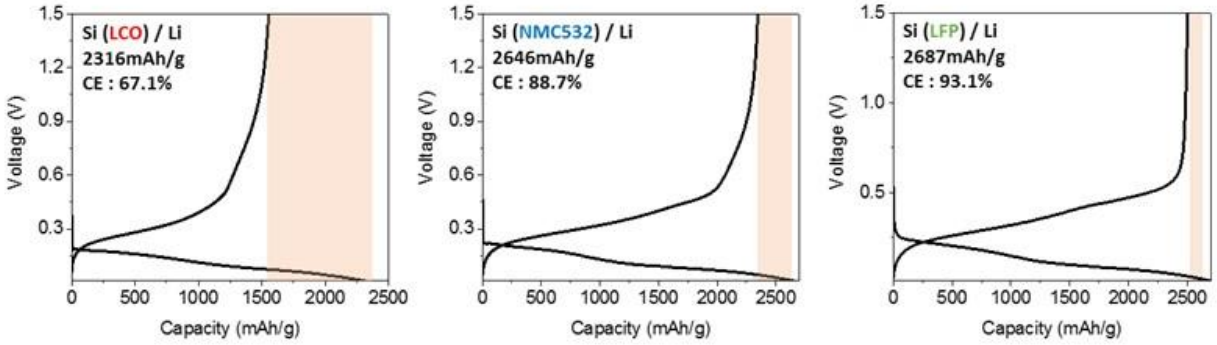

Figure II.1.A.46 The 1st cycle voltage profiles of each aged Si (from LCO-Si, NMC532-Si, LFP-Si) /Li half-cells. Red square means irreversible capacity of each half-cell.

Table II.1.A.6 Most intense ions detected via HPLC/ESI-MS

		m/z	M.W
Gen2 electrolyte	$[C_2H_6O]Na^+$	69	46
	$[C_3H_4O_3]H^+$: EC	89	88
	$[C_2H_5O_4P]H^+$	125	124
	$[C_6H_{10}O_4F_2]H^+$	185	184
	$[C_7\ H_{12}O_6]Na^+$	215	192
	$[C_9H_{13}O_8P_1]Na^+$	303	280
Aged electrolyte (LCO-Si)	$[C_3H_4O_3]H^+$: EC	89	88
	$[C_7\ H_{12}O_6]Na^+$	215	192
	$[C_6H_{11}O_7P_1F_2]H^+$	265	264
	$[C_9H_{11}O_8P_1]H^+$	279	278
	$[C_8H_9O_5P_1F_4]H^+$	293	292
	$[C_9H_{13}O_8P_1]Na^+$	303	280
	$[C_9H_{11}O_9P_1]Na^+$	317	294
Aged electrolyte (NMC532-Si)	$[C_3H_4O_3]H^+$: EC	89	88
	$[C_4H_6O_3]H^+$	103	102
	$[C_8H_7O_6F_3]H^+$	257	256
	$[C_9H_{11}O_8P_1]H^+$	279	278
	$[C_8H_{11}O_7P_1F_2]H^+$	289	288
	$[C_9H_{11}O_9P_1]H^+$	295	294
	$[C_9H_{13}O_8P_1]Na^+$	303	280
	$[C_{10}H_{14}O_{10}P_1F_1]Na^+$	367	344
Aged electrolyte (LFP-Si)	$[C_5H_7O_4P_1F_2]H^+$	201	200
	$[C_7H_4O_4F_4]H^+$	229	228
	$[C_8H_7O_6F_3]H^+$	257	256
	$[C_9H_{11}O_8P_1]H^+$	279	278
	$[C_8H_{11}O_7P_1F_2]H^+$	289	288
	$[C_8H_9O_5P_1F_4]H^+$	293	292
	$[C_9H_{11}O_9P_1]H^+$	295	294
	$[C_9H_{13}O_8P_1]Na^+$	303	280
	$[C_{13}H_{13}O_9P_1F_2]Na^+$	405	382

Conclusions

Silicon Electrodes: Components

These components, namely baseline PAA substitutional variants, alternative conductive additives, and low-oxide coated silicon materials, in combination with Zintl- electrolyte additives discussed later in the testing section, were evaluated. While data indicates that the exact conductive additive was not an important performance variable, low oxide content silicon had more stable electrochemical performance (i.e. gradual SiO_2 dissolution may disrupt the binder-solid interfaces), increasing PAA density at the electrode surface, and maximizing the bonding of the binder to the silicon surface (note dissolution issues) were critical to extending calendar life. Additionally, slurry and electrode formation studies using conventional PAA–based systems found that the binder preferentially segregates to the center of the electrode, which may be an important observation as delamination has been found to be an issue with several cell build runs where cell pressure is not controlled. Combined with BatPaC modeling efforts led by NREL, the best combination of materials available to the program, including a low oxide (hydride –terminated) silicon, a surface Ca-ion Zintl electrolyte additive, Gen2F electrolytes, and a densified PAA produced a very high CE cell that meets the Q4 milestone. Alternatives to the low oxide silicon samples are being considered once scale up issues are resolved. Notably

samples with bonded surface coatings or reactive species have shown promise but have not made it to the point where a specific material has been identified as superior and scaled to the needed amounts using the stage-gate process. While several observations of stability and performance issues have been noted, alternatives to PAA (or LiPAA), mainly rely on water-based processing that can introduce water into the electrolyte leading to gassing, surface passivation issues, and salt hydrolysis. For the SCP program, baseline binder choices will be made by agreement between the Cell Build and the Science of Manufacturing teams.

Silicon Electrodes: Testing Protocols

A method to qualitatively compare the calendar aging rates of silicon anodes has been developed using full cells with an excess amount of electrolyte and of Li^+ supplied by an LFP counter electrode. After formation cycles, the voltage of a test cell is held for 180 h, and the current response measured during the voltage hold can be used to qualitatively compare the rates of Li^+ consumption at the SEI of silicon test electrodes to a baseline electrode. Long term voltage hold aging experiments are underway to determine numerical models that can be used to derive aging parameters for silicon test electrodes. Once the numerical models developed by our team are fully validated, they can be used to support developments of cell, material, and interfacial designs that minimize calendar aging rates of Si electrodes. This protocol study, produced by a joint effort between the SEISTA and DeepDive teams, is a work in progress and will be updated on the SCP program as new updates are available and agreed upon by the SCP team.

Silicon Electrodes: Additives

In this section, calendar life and cycle testing were judged based on various electrolyte additives and SEI decomposition products, materials that may cause film formation or organic coatings within the cell. From the analysis of the data, significant improvements in calendar life were seen upon addition of alkaline earth cations to the cell's electrolyte. Previous work had highlighted that the insertion mechanism occurs at low voltage and that the extent of Ca or Mg addition was time dependent based on time at the pertinent voltages and diffusion of the metals from the electrolyte to form a ternary Li-M-Si surface phase. As noted by the SEISTA LBNL team (AMR, June 2020) this surface coating severely restricts the parasitic currents associated with charged silicon electrodes. This was consistent with the model that showed that the surface was deactivated for redox processes by the formation of the ternary phase. In this year we were able to show that for a calendar life study, the addition of Ca salts to the electrolyte with formation of a Li-Ca-Si ternary Zintl phase decreased capacity losses by 80% after 700h of evaluation compared to a Gen2F baseline. EQCM data from the Sa group at UMass-Boston was consistent with those results and highlighted their conclusion that the SEI in those ternary systems was thinner and more compact than baseline. For full cell cycling evaluation, Zintl additive testing was shown to raise the CE in cells tested and optimization of the Si to C ratio was found to have a strong correlation with cycling life, with cells < 80% Si cycling better using the SCP protocol, but with a best performance (highest stable capacity) seen for a 70% Si/ 10% C45 / 20% LiPAA binder design.

In terms of SEI stability, while the EQCM data showed the SEI to be more compact with Zintl salt addition, previous studies had shown the Si SEI to be unstable towards dissolution. This may be related to catalytic effects of the cathode towards the electrolyte (or Si SEI) where we showed LCO actively altered the electrolyte, gradual dissolution of species that polymerize in solution (or on the cathode), or loss of species to oxidative breakdown as the cell voltage cycles. RRDE studies highlight that the Si SEI thins out significantly near 400 mV (vs Li) leaving most of the inorganic species on the anode but losing some of the small molecule organic components.

Key Publications

1. *Hays, KA, Armstrong, B, Veith, GM* "Ending the Chase for a Perfect Binder: Role of Surface Chemistry Variation and its Influence on Silicon Anodes" *ChemElectroChem*, **7**, 3790 (2020).

2. *Burdette-Trofimov, MK, Armstrong, BL*, Rogers, AM, Heroux, L, Doucet, M., Yang, G, Phillip, ND, Kidder, MK, *Veith, GM* "Understanding Binder-Silicon Interactions during Slurry Processing" *J. Phys Chem C.*, **124** 13479 (2020).

3. Liu, Q., Jiang, W., Munoz, MJ, Liu, Y., Yang, ZZ, Bloom, I., Dzwiniel, T., Li, Y., Pupek, K., *Zhang, ZC* "Stabilized Electrode/Electrolyte Interphase by a Saturated Ionic Liquid Electrolyte for High-Voltage NMC532/Si-Graphite Cells" *ACS Appl Mat Interfaces*, **12**, 23035 (2020).

4. *Coyle, J.*, Brumbach M., *Veith G.*, Apblett C., "Investigating the Chemical Reactivity of Lithium Silicate Model SEI Layers" *J. Phys Chem C*., **124**, 8153 (2020).

5. Seitzinger, CL, Sacci, RL, Coyle, JE, Apblett, CA, Hays, K., Armstrong, RR, Rogers, AM, *Armstrong, BL*, Bennet, TH, *Neale, N., Veith, G*. "Intrinsic Chemical Reactivity of Silicon Electrode Materials: Gas Evolution" *Chem Material*s, **32**, 3199 (2020).

6. *Jiang, S.S., Hu, B., Shi, Z., Chen, W., Zhang, Z., Zhang, L.* "Re-Engineering Poly(Acrylic Acid) Binder toward Optimized Electrochemical Performance for Silicon Lithium-Ion Batteries: Branching Architecture Leads to Balanced Properties of Polymeric Binders" *Adv Functional Mat* **30,** 1908558 (2020).

7. *Kirner, J.*, Qin, Y., *Zhang, L., Jansen, A., Lu, WQ* "Optimizition of Graphite-SiO blend electrodes for lithium ion batteries: Stable cycling enabled by single-walled carbon nanotube conductive additive" *J. Power Sources*, **450**, 227711 (2020).

8. Browning, K., Sacci, R., Doucet, M., Browning, J., Kim, J., *Veith G*. "The Study of the Binder Poly(acrylic acid) and Its Role in Concomitant Solid-Electrolyte Interphase Formation on Si Anodes" *ACS Appl Mat Interfaces*, **12**, 10018 (2020).

9. *Piernas-Munoz, M., Trask, SE*, Dunlop, A., Lee, E., *Bloom, I.* "Effect of temperature on silicon-based anodes for lithium-ion batteries*" J. Power Sources,* **441**, 227080 (2020).

10. Rago, N., Basco, J., Vu, A., Li, J., Hays, K., Sheng, Y., Wood, D., *Bloom, I*. "Effect of formation protocol: Cells containing Si-Graphite composite electrodes" *J. Power Sources***., 435** 126548 (2019).

11. *Jiang, SS, Hu, B*, Sahore, R, Liu, HH, Pach, GF, Carroll, GM, Zhang, L , Zhao, B, *Neale, NR, Zhang, ZC* "Tailoring the Surface of Silicon Nanoparticles for Enhanced Chemical and Electrochemical Stability for Li-Ion Batteries" *ACS Appl Energy Mat*, **2** 6176 (2019).

12. *Hu, B.*, Jiang, S., Shkrob, I., Zhang, S., *Zha*ng, J., *Zhang, Z., Zhang, L*. "Poly(4-vinylbenzoic acid): A Re-Engineered Binder for Improved Performance from Water-Free Slurry Processing for Silicon Graphite Composite Electrodes" *ACS Appl Energy Mat*, **2**, 6348 (2019)

13. *Bloom, I.*, Rago, N., Zheng, Y., Li, J., Wood, D., Steele, L., Lamb, J., Spanger, S., Grosso, C., Fenton, K. "Effect of overcharge on lithium-ion cells: Silicon/graphite anodes" *J. Power Sources*, **432**, 73 (2019).

14. *Han, B.*, Liao, C., *Dogan F., Trask, S*., Lapidus, S., *Vaughey J., Key, B*. "Using Mixed Salt Electrolytes to Stabilize Silicon Anodes for Lithium-Ion Batteries via in Situ Formation of Li-M-Si Ternaries (M = Mg, Zn, Al, Ca)" *ACS Appl Mat Interfaces*, **11**, 29780 (2019)

15. Gao, X., *Lu, WQ*, Xu, J. "Modeling framework for multiphysics-multiscale behavior of Si-C composite anode" *J. Power Sources*, **449**, 227501 (2020).

References

1. Haiping Jia, Xiaolin Li, Junhua Song, Xin Zhang, Langli Luo, Yang He, Binsong Li, Yun Cai, Shenyang Hu, Xingcheng Xiao, Chongmin Wang, Kevin M. Rosso, Ran Yi, Rajankumar Patel, Ji-Guang Zhang "Hierarchical porous silicon structures with extraordinary mechanical strength as high performance lithium-ion battery anodes" Nature Communications 11 1474 (2020).

2. Binghong Han, Maria Jose Piernas-Muñoz, Fulya Dogan, Joseph Kubal, Stephen E. Trask, Ira D. Bloom, John T. Vaughey, Baris Key "Probing the Reaction between PVDF and LiPAA vs Li7Si3: Investigation of Binder Stability for Si Anodes" Journal of The Electrochemical Society, 166 A2396-A2402 (2019).

3. H. Wu, Y. Cui" Designing nanostructured Si anodes for high energy lithium ion batteries" Nano Today 7, 414-429 (2012)

4. Bing Hu., I. Shkrob, S. Zhang, L. Zhang, J. Zhang, Y. Li, C. Liao. Z. Zhang, W. Lu, L. Zhang "Understanding of pre-lithiation of poly(acrylic acid) binder: Striking the balances between the cycling performance and slurry stability for silicon-graphite composite electrodes in Li-ion batteries" J. Power Sources 416, 125-131 (2019)

5. F. Erogbogbo, T. Lin, P. Tucciarone, K. LaJoie, L.Lai, G. Patki, P. Prasad, M. Swihart "On-Demand Hydrogen Generation using Nanosilicon: Splitting Water without Light, Heat, or Electricity" Nano Lett, 13(2), 451-456 (2013)

6. M. Olszak-Humienik "On the Thermal Stability of some Ammonium Salts" Thermochimica Acta 378, 107-112 (2001).

7. Allen, C. L., Chhatwal, A. R., Williams, J. M. J.," Direct amide formation from unactivated carboxylic acids and amines" Chemical Communications 48 (5), 666-668 (2012)

8. Pekarek, R. T., Affolter, A., Baranowski, L. L., Coyle, J., Hou, T., Sivonxay, E., Smith, B. A., McAuliffe, R. D., Persson, K. A., Key, B., Apblett, C., Veith, G. M., Neale, N. R., "Intrinsic chemical reactivity of solid-electrolyte interphase components in silicon–lithium alloy anode batteries probed by FTIR spectroscopy" J. Mater. Chem. A, 8, 7897-7906 (2020)

9. Hou, T., Yang, G., Rajput, N. N., Self, J., Park, S.-W., Nanda, J., Persson, K. A. "The influence of FEC on the solvation structure and reduction reaction of LiPF6/EC electrolytes and its implication for solid electrolyte interphase formation" Nano Energy, 64, 103881 (2019)

10. Flores-Zamora, M. I., Martinez-Perez, C. A., Garcia-Guaderrama, M., Estrada-Guel, I., Espinosa-Magana, F., Martinez-Sanchez, R. "Comparative Study of Al-Ni-Mo Alloys Obtained by Mechanical Alloying in Different Ball Mills" Rev. on Adv. Mater. Science 18 (3), 301-304 (2008)

11. Hernandez-Martinez, S. E., Cruz-Rivera, J. J., Garay-Reyes, C. G., Martinez-Sanchez, R., Estrada-Guel, I., Hernandez-Rivera, J. L., Comparative Study of Synthesis of AA 7075-ZrO2 Metal Matrix Composite by Different Mills. J. Alloys Compd. 643, S107-S113 (2015).

12. Krycer, I., Hersey, J. A., A Comparative-Study of Comminution in Rotary and Vibratory Ball Mills Powder Technol. 27 (2), 137-141 (1980).

13. Martinez, Y. R., Alcazar, G. A. P., Rodriguez, H. B., Lozano, D. O., Comparative Study by MS and XRD of Fe50Al50 Alloys Produced by Mechanical Alloying, Using Different Ball Mills. Hyperfine Interact. 161, 191-195 (2005)

14. Westphal, B. G., Kwade, A., Critical Electrode Properties and Drying Conditions Causing Component Segregation in Graphitic Anodes for Lithium-Ion Batteries. J. Energy Storage 18, 509-517 (2018)

15. Kasinathan, R., Marinaro, M., Axmann, P., Wohlfahrt-Mehrens, M., Influence of the Molecular Weight of Poly-Acrylic Acid Binder on Performance of Si-Alloy/Graphite Composite Anodes for Lithium-Ion Batteries. Energy Technol. 6, 2256-2263 (2018)

16. Li, C. C., Lee, J. T., Peng, X. W., Improvements of Dispersion Homogeneity and Cell Performance of Aqueous-Processed LiCoO2 Cathodes by Using Dispersant of PAA-NH4. J. Electrochem. Soc. 153 (5), A809-A815 (2006)

17. Li, J. L., Armstrong, B. L., Daniel, C., Kiggans, J., Wood, D. L., Optimization of Multicomponent Aqueous Suspensions of Lithium Iron Phosphate (LiFePO4) Nanoparticles and Carbon Black for Lithium-Ion Battery Cathodes. J. Colloid Interface Sci. 405 118-124 (2013)

18. Li, J. L., Armstrong, B. L., Kiggans, J., Daniel, C., Wood, D. L., Optimization of LiFePO4 nanoparticle suspensions with polyethyleneimine for aqueous processing. Langmuir 28(8), 3783-3790 (2012)

19. Li, J. L., Armstrong, B. L., Kiggans, J., Daniel, C., Wood, D. L., Lithium ion Cell Performance Enhancement Using Aqueous LiFePO4 Cathode Dispersions and Polyethyleneimine Dispersant. J. Electrochem. Soc.160 (2), A201-A206 (2013).

20. Hatchard, T. D., Dahn, J. R., In situ XRD and Electrochemical Study of the Reaction of Lithium with Amorphous Silicon. J. Electrochem. Soc.151 (6), A838-A842 (2004).

21. Obrovac, M. N., Christensen, L., Structural Changes in Silicon Anodes During Lithium Insertion/Extraction. Electrochem. Solid-State Lett. 7 (5), A93-A96 (2004).

22. Obrovac, M. N., Krause, L. J., Reversible Cycling of Crystalline Silicon Powder. J. Electrochem. Soc. 154 (2), A103-A108.(2007)

23. Burdette-Trofimov, M. K., Armstrong, B. L., Rogers, A. M., Heroux, L., Doucet, M., Yang, G., Phillip, N. D., Kidder, M. K., Veith, G. M., Understanding Binder-Silicon Interactions During Slurry Processing. J. Phys. Chem. C 124 (24), 13479-13494 (2020).

24. Debye, P., The Intrinsic Viscosity of Polymer Solutions. J. Chem. Phys. 14 (10), 636-639 (1946).

25. Krigbaum, W. R., Flory, P. J., Molecular Weight Dependence of the Intrinsic Viscosity of Polymer Solutions .2. J. Polym. Sci. 11 (1), 37-51 (1953).

26. Staikos, G., Bokias, G., The Intrinsic-Viscosity of Poly(acrylic acid) and Partially Neutralized Poly(acrylic acid) by Isoionic Dilution. Polym. Int. 31 (4), 385-389 (1993)

27. Busse, W. F., Longworth, R., Effect of Molecular Weight Distribution and Branching on the Viscosity of Polyethylene Melts. J. Polym. Sci. 58(166), 49-69 (1962)

28. Schreiber, H. P., Bagley, E. B., The Newtonian Melt Viscosity of Polyethylene: An Index of Long-Chain Branching. J. Polym. Sci. 58, 29-48 (1962)

29. Hammouda, B., Solvation Characteristics of a Model Water-Soluble Polymer. J. Polym. Sci. Pol. Phys. 44 (22), 3195-3199 (2006).

30. Hammouda, B., Ho, D. L., Kline, S., Insight into Clustering in Poly(ethylene oxide) Solutions. Macromolecules 37 (18), 6932-6937 (2004)

31. Huang, B. S., Zhang, Y., Shu, X., Liu, Y., Penumadu, D., Ye, X. P., Neutron Scattering for Moisture Fetection in Foamed Asphalt. J. Mater. Civil Eng. 25(7), 932-938 (2013)

32. Hule, R. A., Nagarkar, R. P., Altunbas, A., Ramay, H. R., Branco, M. C., Schneider, J. P., Pochan, D. J., Correlations Between Structure, Material Properties and Bioproperties in Self-Assembled Beta-Hairpin Peptide Hydrogels. Faraday Discuss. 139, 251-264 (2008).

33. Lee, J. H., Ruegg, M. L., Balsara, N. P., Zhu, Y. Q., Gido, S. P., Krishnamoorti, R., Kim, M. H., Phase Behavior of Highly Immiscible Polymer Blends Stabilized by a Balanced Block Copolymer Surfactant. Macromolecules 36(17), 6537-6548 (2003)

34. Yang, Z., Hemar, Y., Hilliou, L., Gilbert, E. P., McGillivray, D. J., Williams, M. A. K., Chaieb, S., Nonlinear Behavior of Gelatin Networks Reveals a Hierarchical Structure. Biomacromolecules 17 (2), 590-600 (2016).

35. Pagac, E. S., Tilton, R. D., Prieve, D. C., Depletion Attraction Caused by Unadsorbed Polyelectrolytes. Langmuir 14 (18), 5106-5112 (1998)

36. Laguecir, A., Ulrich, S., Labille, J., Fatin-Rouge, N., Stoll, S., Buffle, J., Size and pH Effect on Electrical and Conformational Behavior of Poly(acrylic acid): Simulation and Experiment. Eur. Polym. J. 42 (5), 1135-1144 (2006).

37. Liu, L. J., Chen, J. Z., An, L. J., Individual Circular Polyelectrolytes Under Shear Flow. J. Chem. Phys. 149 (16) (2018)

38. Lin, S. H., Wiesner, M. R., Theoretical Investigation on the Interaction Between a Soft Particle and a Rigid Surface. Chem. Eng. J.191, 297-305 (2012)

39. Szilagyi, I., Trefalt, G., Tiraferri, A., Maroni, P., Borkovec, M., Polyelectrolyte Adsorption, Interparticle Forces, and Colloidal Aggregation. Soft Matter 10 (15), 2479-2502 (2014).

40. Radhakrishnan, R., Underhill, P. T., Influence of Shear on Globule Formation in Dilute Solutions of Flexible Polymers. J. Chem. Phys. 142 (14) (2015).

41. Hidber, P. C., Graule, T. J., Gauckler, L. J., Competitive Adsorption of Citric-Acid and Poly(vinyl alcohol) onto Alumina and its Influence on the Binder Migration During Drying. J. Am. Ceram. Soc. 78 (7), 1775-1780 (1995).

42. Zhang, Y., Suga, T., Kawasaki, M., Tang, X. X., Uchida, N., Uematsu, K., Effect of Poly(vinyl alcohol) Adsorption on Binder Segregation During Drying. J. Am. Ceram. Soc. 79 (2), 435-440 (1996)

43. Hoda, N., Kumar, S., Brownian Dynamics Simulations of Polyelectrolyte Adsorption in Shear Flow: Effects of Solvent Quality and Charge Patterning. J. Chem. Phys. 128 (16) (2008).

44. United States Advanced Battery Consortium Battery Test Manual For Electric Vehicles, 2015.

45. Long, B. R., Rinaldo, S. G., Gallagher, K. G., Dees, D. W., Trask, S. E., Polzin, B. J., Jansen, A. N., Abraham, D. P., Bloom, I., Bareño, J., Croy, J. R. "Enabling High-Energy, High-Voltage Lithium-Ion Cells: Standardization of Coin-Cell Assembly, Electrochemical Testing, and Evaluation of Full Cells". 35th Annu. Int. Batter. Semin. Exhib. 2018 1 (14), 112–122. (2018)

46. Single, F., Latz, A., Horstmann, B. "Identifying the Mechanism of Continued Growth of the Solid–Electrolyte Interphase" ChemSusChem 11 (12), 1950–1955 (2018)

47. Attia, P. M., Chueh, W. C., Harris, S. J. Revisiting the t 0.5 Dependence of SEI Growth . J. Electrochem. Soc. 167(9), 090535.(2020)

II.1.B Silicon Electrolyte Interface Stabilization (SEISta) (NREL, ANL, ORNL, LBNL, SNL)

Anthony Burrell, Principal Investigator
National Renewable Energy Laboratory
15013 Denver West Parkway
Golden, CO, 80401
E-mail: anthony.burrell@nrel.gov

Brian Cunningham, DOE Technology Development Manager
U.S. Department of Energy
E-mail: Brian.Cunningham@ee.doe.gov

Start Date: October 10, 2017 End Date: September 31, 2020
Project Funding: $3,800,000 DOE share: $3,800,000 Non-DOE share: $0

Project Introduction

This report documents the Silicon Electrolyte Interface Stabilization (SEISta) team's approach in (1) characterizing the early-stage silicon solid-electrolyte interphase (SEI), including progress on identifying the specific reaction pathways present in the formation of the SEI layer, and (2) establishing a procedure for measuring SEI growth rate at fixed potentials and different cycling regimes.

Silicon is a viable alternative to graphitic carbon as an electrode in lithium-ion cells and can theoretically store >3,500 mAh/g. However, lifetime problems have been observed that severely limit its use in practical systems. The major issues appear to involve the stability of the electrolyte and the uncertainty associated with the formation of a stable SEI at the electrode. Recently, calendar-life studies have indicated that the SEI may not be stable even under conditions where the cell is supposedly static. Clearly, a more foundational understanding of the nature of the silicon/electrolyte interface is required if we are to solve these complex stability issues. A new multi-lab consortium has been formed to address a critical barrier in implementing a new class of materials used in lithium-ion batteries that will allow for smaller, cheaper, and better-performing batteries for electric-drive vehicles. This consortium, named the Silicon Electrolyte Interface Stabilization (SEISta) project, was formed to focus on overcoming the barrier to using such anode materials. Five National Laboratories are involved: the National Renewable Energy Laboratory (NREL), Argonne National Laboratory (ANL), Lawrence Berkeley National Laboratory (LBNL), Oak Ridge National Laboratory (ORNL), and Sandia National Laboratories (SNL).

The SEISta project was specifically developed to tackle the foundational understanding of the formation and evolution of the solid-electrolyte interphase on silicon. This project will have as its primary goal an understanding of the reactivity of the silicon and lithiated silicon interface with the electrolyte in lithium-ion systems. It consists of researchers from NREL, ANL, LBNL, ORNL, and SNL working toward clear, unified goals. The Silicon Deep-Dive team, which focuses on the science and technology barriers in functional electrodes, is a critical partner in this work. Many of the researchers are shared between both teams, and we hold joint meetings to ensure effective communication between the teams.

The current goals of SEISta are:

1. Demonstrate ability to make model electrodes of Mg-Si Zintl compounds and compare SEI chemistry to silicon using X-ray photoelectron spectroscopy (XPS), scanning transmission electron microscopy–energy-dispersive X-ray spectroscopy (STEM-EDS), and Fourier-transform infrared spectroscopy (FTIR)/Raman. **Q1 (100% Complete)**

2. Establish experiments and protocols for understanding the factors that affect safety in silicon anodes, with a specific focus on highly exothermic reactions that occur at silicon electrodes. **Q1 (100% Complete)**

3. Determine the effect that CO_2 has on the stability of SEI formation on model electrodes, but examine the changes in the nature of the SEI (XPS, FTIR/Raman, and quantitative electrochemical measurement) as a function of CO_2 concentration. **Q2 (100% Complete)**

4. Determine Zintl phase formation mechanism and its effect on SEI with model systems including Si nanoparticles, Si wafer, amorphous silicon (a-Si) thin film using XPS, atomic force microscopy/scanning spreading resistance microscopy (AFM/SSRM), STEM-EDS, and FTIR/Raman. **Q2 (100% Complete)**

5. Go/No-Go on production of tin-silicon alloys to be determined by the ability of the alloys to be prepared in 1-gram quantities and a demonstration that the alloys exhibit greater cyclic life than the pure metals alone. **Q2 (100% Complete, Decision = GO)**

6. Determine the chemistry and interfacial properties (e.g., nature of the chemical bonding at the surface of Si and the organic material) of lithium polyacrylate (LiPAA)/Si interfaces as a function of charge (open circuit voltage [OCV], 0.8 V, 0.4 V, 0.15 V, 0.05 V) and drying temperature (100°C, 125°C, 150°C, 175°C, 200°C). **Q3 (100% Complete)**

7. Determine how binder changes the stress/strain on silicon electrodes as a function of state of charge by varying Si nanoparticle size and surface functionally using both 2D and 3D model systems. **Q3 (100% Complete)**

8. Implement protocols that enable comparisons of safety responses in silicon anodes as a metric for improving safety in silicon cells. **Q3 (100% Complete)**

9. Publish a document that will enable other research and development groups to analyze stability of the SEI on a silicon-based anode, thus enabling developers or researchers to continually improve silicon cell stability (joint milestone with the Silicon Deep-Dive team). **Q4 (100% Complete)**

10. Understand how the nature and amount of formed/soluble SEI species varies with electrolyte, binder, and Si anode (with surface functionalization) using gas chromatography–mass spectrometry, (in situ) FTIR/Raman, and XPS. **Q4 (100% Complete)**

Approach

The SEISta team works to ensure that protocols for sample preparation, experimental design, and implementation as well as data reporting are consistent across the whole team. Each laboratory is working toward the same set of quarterly milestones using its own specific talents and capabilities in a concerted effort with the other team members. This joint focus results in multiple researchers interacting to produce and analyze data to ensure that individual experimental variations will not lead to erroneous results. Critical to the success of this effort is the use of standard samples that can be shared by all parties. In addition to weekly whole-team video presentations, we have held on-site face-to-face meetings each quarter for all team members and other interested parties to brainstorm and sort out issues with existing experiments and jointly develop new experimental plans.

Objectives

The critical issues that SEISta is attempting to address are:

- What are the properties of the lithiated silicon/electrolyte interface?
- What is the silicon SEI actually made of and what reactions are contributing to it?

- How fast does the silicon SEI grow?
- Does it stop growing?
- Is it soluble?
- Can it be stabilized?

For fiscal year (FY) 2020, the team continues to focus on three broad tasks:

Materials Standardization—This task is critical to developing and deploying standardized samples and experimental procedures across the team. We will continue to provide full characterization to any new sample that is to be used for SEI studies to ensure reproducibility and full understanding of the material.

Model Materials Development and Characterization—The nature of the electrode-electrolyte interaction in silicon electrodes is at the heart of the formation and stability of the SEI. The synthesis of well-defined silicon nanoparticles and the different chemical markups of lithiated silicon surfaces is being probed by preparing model compounds and thin films that may/can exist in silicon anodes. Lithium silicides, silicates, and other inorganic material (LiF, Li_2O) are being prepared, and their reactivity with electrolytes is being determined. These materials also act as standard spectroscopy samples for the researchers who are looking at the formation of the SEI on different silicon materials.

SEI Characterization—The overall objective for SEISta is to understand the nature and evolution of the SEI on silicon anodes. The materials standardization and model compounds will enable the researchers to systematically investigate the formation of the solid-electrode interphase using a wide variety of spectroscopy techniques—from different optical, microscopy, and electrochemistry techniques—to determine how the SEI forms based on the nature of the silicon surface and how it evolves over time. This section of work will continue to grow in scope as we move beyond the sample-characterization phase of the project and toward understanding the nature and evolution of the SEI.

Results

Science of Safety: Evaluating Temperature-Dependent Degradation Mechanisms of Silicon-Graphite Electrodes

Silicon (Si) is a promising next-generation anode material as its alloying chemistry allows high specific capacity (~3,500 mAh/g_{Si} vs. 372 mAh/$g_{graphite}$) and its abundance satisfies the cost-effectiveness. However, the large volume change of Si during its lithiation and delithiation as well as the reactive nature of lithiated Si (Li_xSi) results in mechanical failure and continuous evolution of the solid–electrolyte interphase (SEI) at the anode. In addition, the high reactivity of Si-based anodes possesses intrinsic safety concerns. Thus, understanding the thermal behavior of Si-based electrodes and evaluating the degradation mechanisms at elevated temperatures is critical to develop successful, safe, long-lasting Si-based electrodes. Although differential scanning calorimetry (DSC) and accelerated rate calorimetry (ARC) are widely used to examine the thermal stability of electrode and electrolyte materials [1],[2] electrochemical testing of Si-based electrodes at elevated temperatures needs to be further established. Here, we report the electrochemical protocols developed to test the thermal behavior of Si-graphite (Gr) electrodes. The performance of baseline electrolyte (Gen2, 1.2 M lithium hexafluorophosphate [$LiPF_6$] in ethylene carbonate [EC]/ethyl methyl carbonate [EMC] [3:7, w/w]) as well as the effect of fluoroethylene carbonate (FEC) additive, which is known to enhance the thermal stability of Si-based electrodes [1], are tested. This work is contribution to the Q3 (delayed to Q4) Milestone: "Implement protocols that enable comparisons of safety responses in silicon anodes as a metric for improving safety in silicon cells."

The Si-Gr electrode was provided by the Cell Analysis, Modeling, and Prototyping (CAMP) Facility at Argonne National Laboratory. A mixture of 15 wt % Si, 73 wt % Gr, 2 wt % conductive carbon, and 10 wt % lithium polyacrylate binder (LiPAA) was coated on a 10-µm copper (Cu) foil current collector with a coating

loading of 3.0 mg/cm^2. The thickness of calendered electrode was 27 µm, excluding the Cu foil thickness, and the porosity was 45.6%. 2032-type coin cells were assembled to test the electrochemical performance of Si-Gr/Li half-cells and Si-Gr/Si-Gr symmetric cells at 25°C, 45°C, and 70°C. All cells were cycled at C/20 for the initial 3 cycles, followed by 100 cycles at C/3, and finally at C/20 for 3 cycles. The current corresponding to 1C was 3.68 mA. Half-cells and symmetric cells were cycled between 0.05–1.5 V vs. Li/Li$^+$ and −0.5–0.5 V, respectively.

Half-cells. Figure 1a shows the cycle performance of Si-Gr/Li cells in Gen2 and Gen2 + 10 wt % FEC electrolytes. Discharge capacity per gram of active material (Si+Gr) and coulombic efficiency (CE) are plotted as a function of cycle number. In the absence of FEC in the electrolyte, the first cycle lithiation capacity is greater at higher temperatures. However, the CE shows the opposite trend (i.e., lower first cycle CE at higher temperatures) and the capacity fades significantly faster in the following cycles at elevated temperatures. When FEC is present as an additive in the electrolyte, the first cycle lithiation capacity is relatively temperature-independent, although the CE is still lower at higher temperatures. Upon cycling at C/3 rate, greater discharge capacity is observed at higher temperatures and the cell cycled at 70°C shows best capacity retention after 100 cycles, albeit lower initial CE. As the cells are cycled at C/20 again after the C/3 cycles, less capacity is recovered at higher temperatures in both Gen2 and Gen2+FEC electrolytes. The capacity loss and temperature dependence are much greater in the Gen2 electrolyte.

To deconvolute the effect of Li metal on the performance of half-cells, Li/Li symmetric cells were tested using same electrolyte compositions (Gen2 and Gen2+FEC) and temperature conditions (25°C, 45°C, and 70°C) as in the Si-Gr/Li cells. A 0.7-mA/cm^2 constant current was applied for 2-h half-cycle to match the areal capacity observed at C/3 rate in half cells (~1.5 mAh/cm^2). The voltage evolution as a function of time is presented in Figure II.1.B.1b. In the Gen2 electrolyte, the overpotential increases considerably faster at higher temperatures, whereas in the Gen2+FEC electrolyte, the Li/Li cell cycled at 70°C shows markedly stable performance. Enhanced Li metal performance at elevated temperature in the presence of FEC in the $LiPF_6$/carbonate-based electrolyte has been previously reported by Wang et al. [3]. The Li/Li cell performance closely resembles the temperature-dependent cycle performance of the Si-Gr/Li cells in Gen2 and Gen2+FEC electrolytes, indicating half-cells cannot be used to study the thermal behavior of Si-based electrodes.

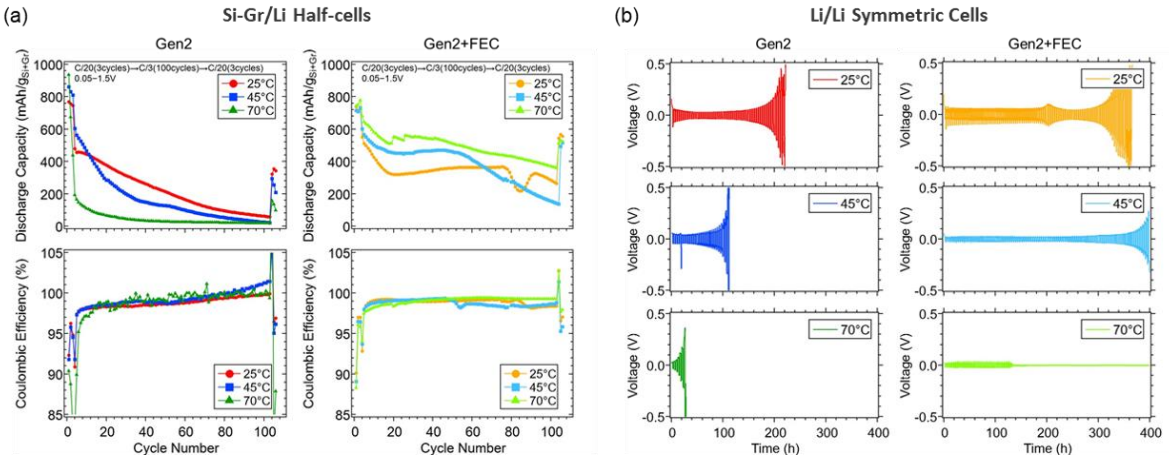

Figure II.1.B.1 (a) Discharge capacity per gram of active material (Si+Gr) (top) and coulombic efficiency (bottom) of Si-Gr/Li cells tested at 25°C, 45°C, and 70°C in Gen2 (left) and Gen2+FEC (right) electrolytes plotted as a function of cycle number. (b) Voltage evolution of Li/Li cells upon plating and stripping in Gen2 (left) and Gen2+FEC (right) electrolytes at 25°C, 45°C, and 70°C plotted as a function of time.

Symmetric cells. To exclude the effect of Li metal, a different cell configuration needs to be utilized to test the thermal behavior of Si-based electrodes. Whereas full cells reflect the cell environment closer to the commercial batteries, cathodes may introduce artifacts, such as transition metal dissolution and excess electrolyte decomposition at the cathodes, resulting in cross talks. By using symmetric cells, which consist of a

pair of lithiated and delithiated anodes, the performance of Si-Gr electrodes can be studied without getting interference from foreign materials. Symmetric cells are fabricated by following the two-step process described in Figure II.1.B.2a. First, Si-Gr electrode is lithiated in a half-cell configuration by applying constant current (C/20) followed by voltage hold at 0.05 V with C/100 limit. Then, the half-cell is carefully disassembled and the lithiated electrode is retrieved. The lithiated electrode is paired with a delithiated Si-Gr electrode to make a symmetric cell. The comparison between the half-cell and symmetric cell configurations is summarized in Figure 2b. Although the capacity fade due to the loss of active material will be detected in both half-cells and symmetric cells, the loss of Li inventory will be visible only in the symmetric cell configuration as half-cells have semi-infinite Li source. In addition, whereas the cell resistance will have contributions from both Si-Gr and Li electrodes in half-cells, the symmetric cell resistance can be correlated with the Si-Gr electrode performance.

The cycle performance of Si-Gr/Si-Gr cells at 25°C, 45°C, and 70°C in Gen2 and Gen2+FEC electrolytes are presented in Figure II.1.B.2c. In the Gen2 electrolyte, the cell cycled at 70°C shows best capacity retention and highest CE, whereas in the Gen2+FEC electrolyte, the cell cycled at 70°C shows worst performance. This observation is opposite from the half-cell results, manifesting once again the effect of Li metal on the half-cell performance. The enhanced performance of Si-Gr electrode in Gen2 electrolyte at 70°C is surprising, considering the low thermal stability of $LiPF_6$ and high reactivity of Li_xSi. Such observation can be correlated with a previous DSC study by Profatilova et al. [1] in which the presence of PF_6^- anion enhanced the thermal stability of Li_xSi as it created LiF upon decomposition, which has an excellent thermal stability. In the Gen2+FEC electrolyte, the capacity retention is enhanced compared to the Gen2 electrolyte and the 25°C cell shows best performance. Although the presence of FEC is known to enhance the thermal stability of Si-based electrodes from the DSC studies [1], the main exothermic peak appears at temperatures well above 100°C, and hence at 70°C its positive effect may not be clearly observed. Instead, greater parasitic reactions at 70°C, which was observed as the lower CE in half-cells with the Gen2+FEC electrolyte, may lead to faster Li inventory consumption and corresponding capacity fade when the symmetric cells are cycled.

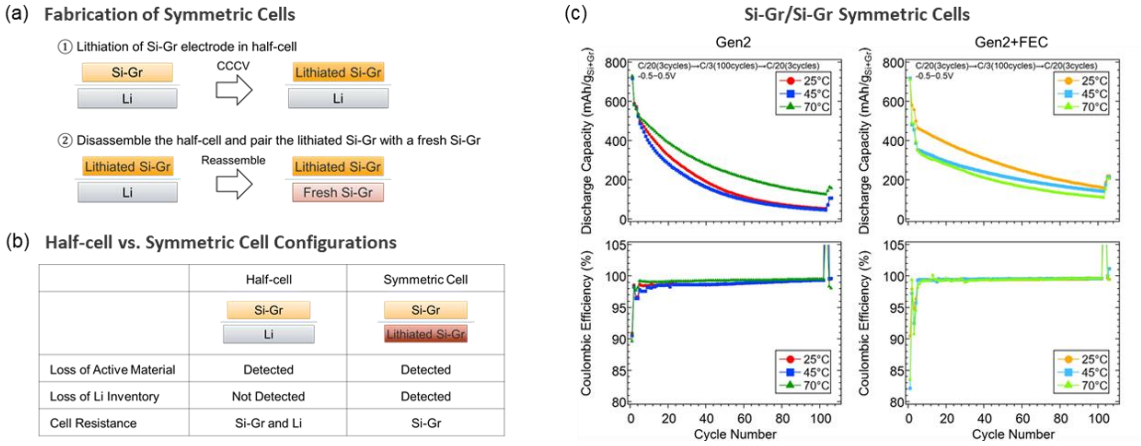

Figure II.1.B.2 (a) Schematic diagram of symmetric cell fabrication process. (b) Comparison of half-cell and symmetric cell configurations. (c) Discharge capacity per gram of active material (Si+Gr) (top) and coulombic efficiency (bottom) of Si-Gr/Si-Gr cells tested at 25 °C, 45 °C, and 70 °C in Gen2 (left) and Gen2+FEC (right) electrolytes plotted as a function of cycle number.

Deconvoluting the Degradation Mechanisms. While Si-Gr/Si-Gr symmetric cells can exclude the effect of Li metal, their degradation results from a combination of two different loss mechanisms—loss of active material and loss of Li inventory. To further deconvolute the degradation mechanisms at each temperature, symmetric cell and half-cell configurations were combined. The experimental design is presented in Figure II.1.B.3a. Steps 1 and 2 describe the fabrication and cycling of symmetric cells. At the end of the symmetric cell cycling, a half-cycle is added to delithiate the initially lithiated electrode (color coded as yellow). Then, in Step 3, the cycled symmetric cell is disassembled and the delithiated electrode is reassembled into a half-cell, where it is

lithiated again. By comparing the lithiation voltage profiles during Steps 1 and 3 (i.e., before and after the symmetric cell cycling), information on the loss of active material during the symmetric cell cycling can be obtained.

Figure II.1.B.3b shows the capacity loss (%) in half-cells, symmetric cells, and reassembled cells. For the half-cells and symmetric cells, lithiation capacity of the 2nd and the 104th cycles (i.e., C/20 cycles before and after the C/3 aging cycles) are compared. For the reassembled cells, lithiation capacity during Steps 1 and 3 are compared as described previously. In half-cells, both Gen2 and Gen2+FEC electrolytes show increasing capacity loss at higher temperature, with much less degree in the presence of FEC in the electrolyte. If Li metal were behaving like an ideal electrode, the capacity loss would be close to half of that of the symmetric cells, which have two Si-Gr electrodes. However, in the Gen2 electrolyte, the capacity loss in half-cells is more than half of that in symmetric cells due to the adverse effect of Li metal—at 70°C, the capacity loss is even larger in half-cells. In symmetric cells, smallest capacity loss is observed at 70°C in the Gen2 electrolyte and at 45°C in the Gen2+FEC electrolyte. At all temperatures, the capacity loss is smaller in the Gen2+FEC electrolyte, demonstrating the enhanced performance of the Si-Gr electrode in the presence of FEC. In the reassembled cells, less capacity loss is observed at higher temperatures in both Gen2 and Gen2+FEC electrolytes, indicating less active material loss at elevated temperatures. One possible explanation of such behavior is the soluble nature of the SEI, which is facilitated at higher temperatures [4], allowing the Li^+ ion transport network within the electrode to be maintained. The SEI composition at elevated temperatures may also play a role. By comparing the capacity loss in symmetric cells and reassembled cells, capacity loss due to the loss of Li inventory can be obtained. The difference between the capacity loss in symmetric cells and reassembled cells increase at higher temperatures, indicating that the loss of Li inventory is the major degradation mode contributing at elevated temperatures, rather than the loss of active material.

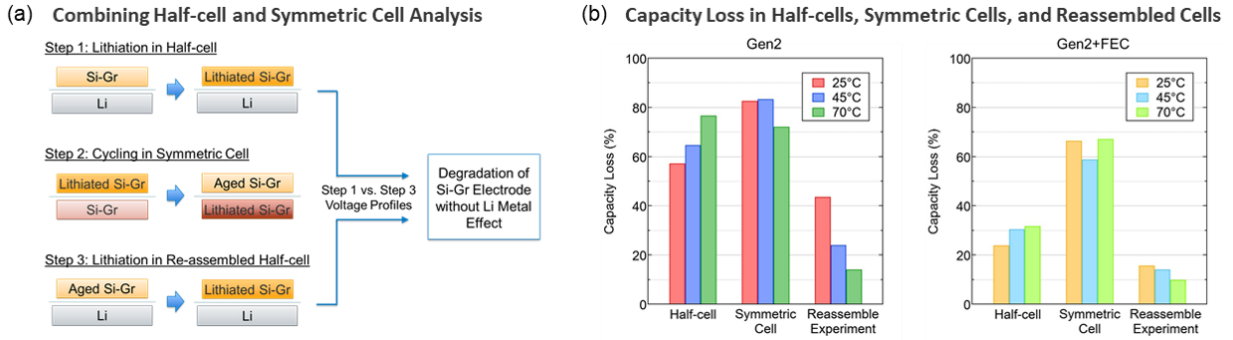

Figure II.1.B.3. (a) Schematic diagram of experimental design combining half-cell and symmetric cell configurations to deconvolute the degradation mechanisms of Si-Gr electrodes at different temperatures. (b) Capacity loss in half-cells, symmetric cells, and symmetric cell cycled electrodes reassembled into half-cells. Capacity of the C/20 cycle before (2nd) and after (104th) the C/3 cycles are compared.

Zintl Phase Formation Mechanism and its Effect on SEI

In 2018–2019 a significant advance in silicon surface stability was reported in the SEISta program. The advance was based on the addition of a Mg-ion source to the electrolyte and its eventual incorporation into the silicon surface on cycling. Spectroscopically, the Mg ion was found to be incorporated into the lattice to form a ternary Li-Mg-Si phase of an approximate refined composition $Li_{14}M_gSi_4$, a lithium-ion conductor with a stable electron configuration. Model compounds of this and related stoichiometries (same phase diagram tie-line) showed dramatically lower reactivity with electrode components and active materials, notably the electrolyte. In FY 2020, work was initiated to better understand this phenomenon and differences with other electrolytes and better characterize the phases formed and their lifetimes in the cell environment. As part of the SEISta effort, the formation mechanism of ternary Zintl phase formation on Si thin film electrodes were characterized in their as-prepared pristine state, after first lithiation, after first delithiation half cycles, and after 500 full cycles. The different possible formation pathways for the ternary Zintl phase were investigated through lithiation/delithiation of Si thin film in program electrolytes with $Mg(TFSI)_2$ salt in mixed carbonate

Gen2 (or Gen2F) electrolytes. For comparison, direct deposition of Mg vapor on Si thin films was used to create a fully surface magnesiated (lithium-free) Mg_2Si coating on the film as a model compound to evaluate lithium diffusion, and a series of silicon wafers were used to evaluate the additives on a larger scale for spectroscopic studies. The electrodes and electrode surfaces were characterized by STEM-EDS and SSRM was employed to investigate the electrode structures. Samples and electrodes based on nanocrystalline silicon were investigated by magnetic-angle spinning nuclear magnetic resonance (MAS-NMR) and X-ray diffraction.

Characterization Results

Silicon Thin Films

Amorphous silicon (a-Si) thin films were prepared via magnetron sputtering. In these cases, 50-nm a-Si was deposited on a Cu foil substrate, in addition to a second series of electrodes with an additional deposition layer of 20-nm elemental Mg (Figure II.1.B.4). For the Mg/Si samples, transmission electron microscopy (TEM) cross sections were prepared of both the pristine and cycled samples using focused ion beam (FIB) milling and were then transferred in an air-free environment to the STEM system. STEM-EDS studies were used to investigate the chemistry and morphology of the initial surface Zintl phase formation as well as after 500 cycles in GenF electrolyte. STEM-EDS was used to create elemental maps of the pristine electrode (Figure II.1.B.5) and it indicated an approximately 60-nm-thick, 2D structure with Mg covering the Si thin film. Some intermingling of the Mg and Si was observed, indicating probable diffusion of some Mg into the Si structures prior to cycling. This use of Mg/Si layered thin films helps better define the amount of Mg at the electrochemical interface. Preliminary work reported last year indicated that the probable mechanism of ternary phase formation was Mg^{+2} ion exchange with $Li_{13}Si_4$ at low voltage. These studies explored the stability of the phases formed, investigating if, mechanistically, Li^+ ions exchanged with fully reduced Mg_2Si or Li-Mg alloys should be considered intermediaries in the process. On initial cycling, these Mg/Si film model anodes did demonstrate formation of a ternary Li-Mg-Si Zintl phase by lithiation of the binary Mg/Si film.

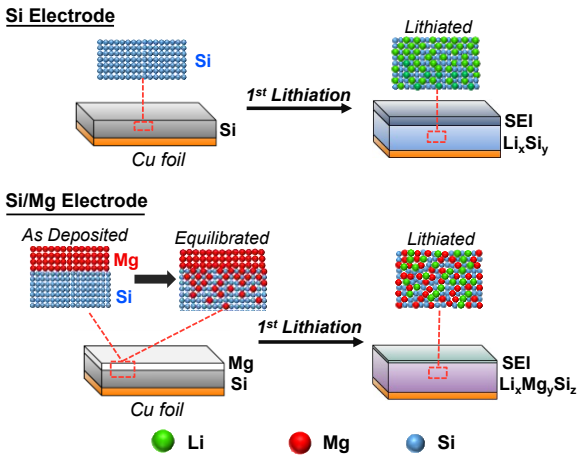

Figure II.1.B.4 Conceptual diagram illustrating pristine and lithiated amorphous Si and Si/Mg thin film electrodes.

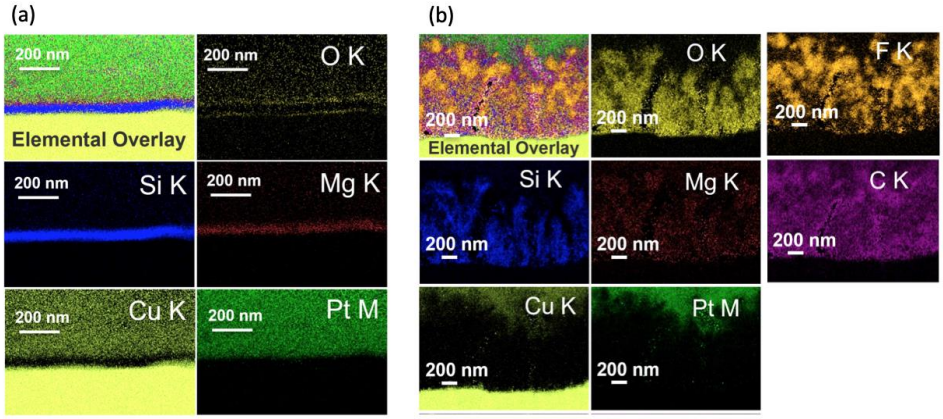

Figure II.1.B.5 STEM-EDS elemental maps of: (a) a pristine thin film electrode prepared by deposition of 20-nm Mg on 50 nm of a-Si and (b) after 500 cycles in Gen2F.

To better understand the buried interfaces, SSRM resistivity vs. depth experimental profiles were carried out on the three model systems: (1) a-Si in GenF electrolyte (Mg-free reference), (2) a-Si in GenFM electrolyte (Mg added via $Mg(TFSI)_2$ salt as an electrolyte additive), and (3) a 20-nm Mg deposited on a-Si in GenF electrolyte (metallic Mg added to the surface of the Si electrode). These three systems were each investigated (1) in their pristine condition, (2) after the first lithiation half cycle, and (3) after the first full electrochemical cycle (Figure II.1.B.6).

In comparison to the pristine Mg-free Si, the 20-nm Mg on Si pristine electrode shows a superficial resistive oxide (MgO) coating on top of a very conductive layer of metallic Mg. This is consistent with other measurements performed on these systems and the high oxophilicity of magnesium metal. The Si in this sample exhibits a lower resistivity compared to Si in the Mg-free system, suggesting that some diffusion of Mg into Si occurs during the Mg deposition process, resulting in an enhancement in the conductivity of Si. This evidence of diffusion prior to cycling is consistent with the STEM-EDS results. After the first lithiation, a resistive SEI forms on all samples. In the Si in GenF (Mg-free) system, the SEI layer is thin (~8 nm), and the resistivity of Si is halved due to lithiation of Si. In the Si in GenFM system, the SEI layer was found to be thicker (~18 nm), whereas the structure beneath the layer was measured to be very conductive (100 Ω·cm vs. 103 Ω·cm for the pristine Si), suggesting localized or heterogenous Mg reduction at the site of the resistivity vs. depth profile measurement. Lastly, the 20-nm Mg on Si sample shows a highly resistive SEI film, a disappearance of the metallic Mg, and a similar resistivity decrease for Si as that observed in the Mg-free sample due to lithiation of the Si. After a full electrochemical cycle (lithiation then delithiation), all electrodes showed similar resistivity-depth profiles; high resistivity due to an SEI layer was not detected and a 2–3 order of magnitude increase in resistivity compared to the pristine electrodes was measured in all electrodes. Results are summarized in Figure II.1.B.6, with observed trends summarized in Table II.1.B.1. Based on these data, analysis indicates that the SEI is likely unstable and changes as a function of state of charge, decomposing during the delithiation half cycle with the Si thin film electrode becoming porous and more resistive after Li and Mg migration back into the electrolyte.

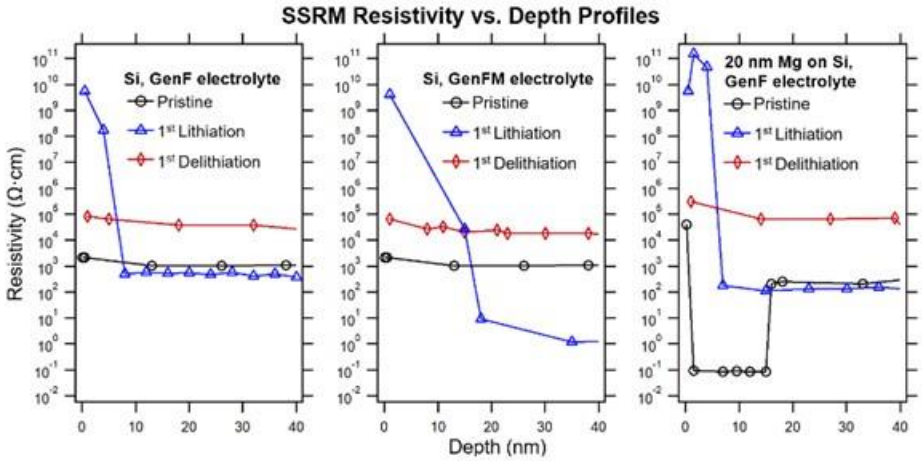

Figure II.1.B.6 SSRM resistivity vs. depth profiles of pristine, lithiated, and delithiated electrodes for Si in Gen2F electrolyte, Si in Gen2FM, and Mg/Si Gen2F.

The phases lost have provided some insights on the electrochemical activity and instability of the interface and also have the action of enriching the interface in inorganic phases (i.e., LiF) that cannot be easily solubilized and transported in the electrolyte, as noted in Figure II.1.B.5b.

The diffusion of Mg into bulk Si layer was also examined via STEM-EDS elemental maps of an FIB-prepared cross-sectional sample of the Si/Mg electrode (Figure II.1.B.5). STEM-EDS results include high-angle annular dark-field (HAADF) imaging and EDS maps for Si, Mg, Cu, and Pt. As observed in these results, there is a layered structure of Mg on Si, with some elemental overlap between the two species at their interface. This suggests that after Mg deposition, although the surface Mg layer remains, a nontrivial amount of the deposited Mg diffuses into the bulk Si layer. This elemental mapping shows agreement with the reduction of resistivity of the bulk Si in the Si/Mg electrode measured with SSRM resistivity vs. depth profiling (Figure II.1.B.5).

Table II.1.B.1 Summary of Initial Zintl Phase Formation on Si Thin Film

	Si, GenF electrolyte (Mg-free reference)	Si, GenFM electrolyte (Mg as electrolyte salt)	Mg on Si, GenF electrolyte (Mg as metal)
Pristine Electrode	a-Si: ~10^3 Ω·cm	a-Si: ~10^3 Ω·cm	Superficial MgO, metallic Mg (10^{-1} Ω·cm), a-Si: ~3 × 10^2 Ω·cm (decrease in resistivity likely due to Mg diffusion into Si)
1st Lithiation: SEI	Thin, resistive SEI (~8 nm)	Resistive SEI, thicker than Si in GenF (~18 nm)	Thin, highly resistive SEI (~7 nm
1st Lithiation: Si	Resistivity halved from pristine electrode (due to conductivity enhancement of Li_xSi_y compared to a-Si)	Resistivity decreased by three orders of magnitude, likely due to heterogenous reduction of Mg from electrolyte	Resistivity halved from pristine electrode (due to conductivity enhancement of Li_xSi_y compared to a-Si), no metallic Mg detected
1st Delithiation: SEI	Little to no SEI detected	Little to no SEI detected	Little to no SEI detected
1st Delithiation: Si	~2 orders of magnitude increase in resistivity from pristine electrode	~2 orders of magnitude increase in resistivity from pristine electrode, Mg likely migrates to electrolyte	~3 orders of magnitude increase in resistivity from pristine electrode, Mg likely migrates to electrolyte

Literature reports indicate that the interface between the Si and Mg layers consists of a thin layer of Mg_2Si (~1 nm), where the only stoichiometric Mg silicide reported may form [1]. In these reports, the lithium reactivity of Mg_2Si has been investigated with formation of a ternary Zintl phase noted using powder X-ray diffraction. Due to the high magnesium content, poor cycling performance in part due to phase separation and expulsion of Mg during cycling was reported [2]. In this evaluation, we prepared Mg_2Si film as a reference by depositing Si and then Mg film on copper foil through annealing of the deposited films. The formation of Mg_2Si was validated by X-ray diffraction (XRD) (Figure II.1.B.8). These materials allowed us to have a reference for the fully reduced and magnesiated endmember. Samples were investigated with Raman spectroscopy (see Figure II.1.B.8d) and two sharp peaks were observed at 256 and 344 cm^{-1}, which are assigned to the F_{2g} and F_{1u} phonon bands of Mg_2Si, respectively [3]. The pure Si film shows only a broad band centered around 469 cm^{-1}, assigned to a-Si [4]. In the case of the Si/Mg electrode, two minor peaks are observed at 254 and 344 cm^{-1}, along with a broad peak at 469 cm^{-1}, indicating the presence of both Mg_2Si and Si in the Si/Mg electrode. The experimental evidence posed by the SSRM, EDS, and Raman spectroscopy analysis suggests that some of the metallic Mg coating diffuses into the Si layer, coincident with a minor amount of Mg_2Si formed at the interface of the Mg and Si films. Cyclic voltammetry (CV) studies of the Si and Mg/Si electrodes were used to gain insights about the Mg coating on Si during the lithiation/delithiation processes. In the first CV cycle, the pure Si electrode shows two large cathodic peaks and two corresponding anodic peaks in the low potential region, representing the Li-Si lithiation, respectively (Figure II.1.B.7). In contrast, the Si/Mg electrode showed only one broad cathodic peak and one anodic peak associated with Li-Si reactivity, with a larger overpotential when compared to the pure Si electrode. This may reflect the lithiation of magnesium (Li-Mg) as an energy barrier to reacting with the underlying silicon, the difficulty in lithiating the Mg_2Si interface, or the broad redox peaks of the Si/Mg electrode, possibly resulting from the large polarization of surface MgO with slower lithiation kinetics. The Si/Mg electrode also displays an additional anodic peak at 0.18 V, which is attributed to the Li-Mg de-alloying process.

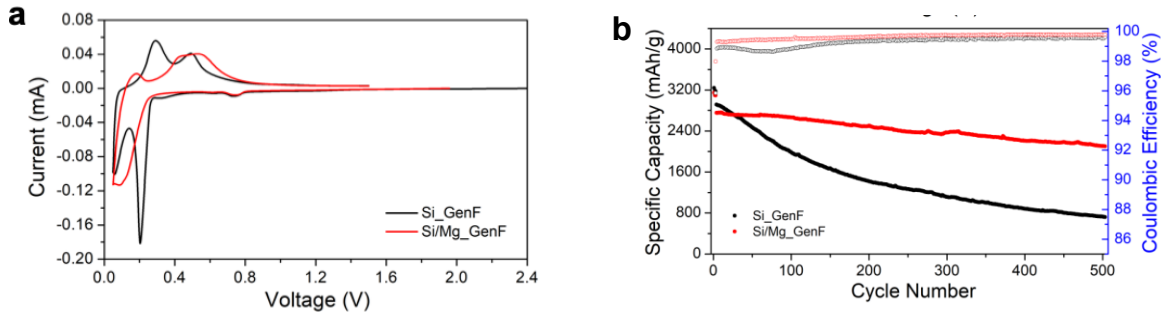

Figure II.1.B.7 Electrochemical performance evaluation of the Si and Si/Mg electrodes with GenF electrolyte in the potential range of 0.05–1.5 V. (a) The first CV cycle under scan rate of 0.1 mV/s. (b) The extended cycling performance with the first three cycles under a current density of 0.1 C and the subsequent cycles carried out at 1 C.

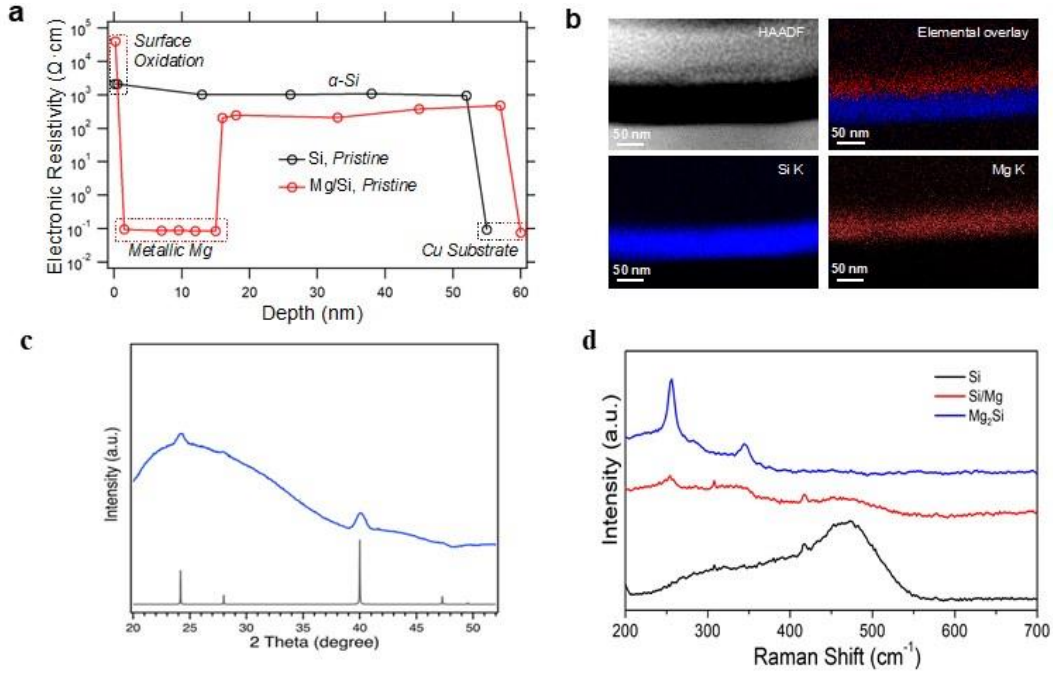

Figure II.1.B.8 (a) SSRM resistivity vs. depth profile of pristine Si and Si/Mg electrodes. (b) STEM cross-sectional HAADF image and EDS elemental maps of Si K, Mg K, and elemental overlay of Si and Mg maps of the pristine Si/Mg electrode. (c) Raman spectra of pristine Si, Mg2Si, and Si/Mg electrodes. (d) XRD pattern (blue trace) is of Mg2Si deposited on glass substrate and the gray pattern is from the Mg2Si standard.

The impact of the Mg coating on the cycling stability of the Si electrode was also evaluated by galvanostatic long-term cycling tests. The electrochemical cycling performance of Si and Si/Mg electrodes was tested at 0.1 C (3.9 μA/cm^2) for three formation cycles and then at 1 C for remaining cycles. The capacity retention of the Si electrode was measured to be 25% after 500 cycles at 1 C, in sharp contrast to the 76% capacity retention of the Si/Mg electrode (Figure II.1.B.6b). Moreover, the CE of the Si/Mg electrode was higher than that of the Si electrode during the entire cycling process, indicating less parasitic side reactions and a more stable SEI.

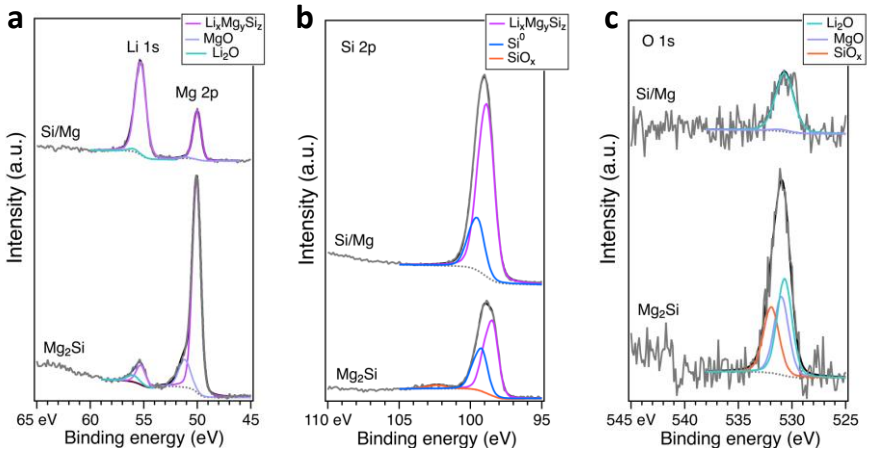

Figure II.1.B.9 Characterization of the electrodes after the first lithiation at 0.1 C in GenF. (a) SSRM resistivity vs. depth profiles of Si and Si/Mg electrodes. (b) ATR-FTIR spectra of Si and Si/Mg electrodes.

STEM-EDS of a similar electrode after 500 cycles in GenF (Fig. 4b) revealed a 3D intermixed layer of active material and SEI with an approximate thickness of >1 μm that was found to contain significant amounts of C, O, and F in addition to the Si and Mg active materials. STEM-electron energy loss spectroscopy (EELS) and transmission electron diffraction (not shown) revealed significant amounts of crystalline LiF present in the SEI region. This result illustrates the large expansion of Si active material and significant ingress of SEI into the active material by the cycling.

To understand the interfacial origins of the enhanced cycling stability observed for the Si/Mg electrode, ex situ SSRM resistivity depth profiles for Si/Mg and Si electrodes after the first lithiation were performed. Compared with their pristine electrodes (Figure II.1.B.8a), the electronic resistivity of the surface layer of the lithiated electrodes sharply increased for both Si and Mg coated Si electrodes due to the formation of SEI (Figure II.1.B.9a). The resistivity drops dramatically after approximately 8 nm, which corresponds to the thickness of the SEI layer. The surface resistivity of the SEI formed on the Si/Mg electrode is greater than that formed on the Si electrode, suggesting that the Mg coating may promote an SEI with different surface composition that is more electronically resistive, and therefore more effective in the suppression of further electrolyte decomposition. In addition, the SEI formed on the Si electrode may be slightly thicker than that of Si/Mg, as indicated in SSRM vs. depth profiles (Figure II.1.B.9).

In addition, the attenuated total reflection (ATR)-FTIR spectra of the lithiated Si and Si/Mg electrodes also reveal differences between the SEI of these two electrodes (Figure II.1.B.9b). The FTIR spectra of the lithiated Si and Si/Mg electrodes exhibit similar features in general, but close examination of the spectra reveals differences. The large peak at approximately 633 cm^{-1}, which is assigned to Si-H bond, is observed only from the lithiated Si electrode [5]. This peak is suppressed in Si/Mg, indicating that there is little free Si on the surface of lithiated Si/Mg electrode as the pristine Si/Mg electrode was covered with Mg. The lithiated Si/Mg electrode has a large peak around 700 cm^{-1} that we attribute to MgO, which can be readily formed from magnesium on the surface reacting with residual oxygen in the glovebox [6]. Furthermore, the Si sample exhibits several peaks associated with the formation of surface lithium carbonate (Li_2CO_3)—1490, 1450, and 875 cm^{-1}—and lithium alkyl carbonate ($ROCO_2Li$)—1667 and 1320 cm^{-1} [7]-[9]. Most of these peaks are significantly diminished in the Si/Mg sample, corroborating the idea that Mg coating reduces the reactivity of the anode with the electrolyte and leads to thinner SEI with fewer decomposition products on the surface.

The Li 1s, Mg 2p, and Si 2p spectra from the bulk layer after 14 sputtering cycles were further analyzed to study the possible formation of Zintl phase (Figure II.1.B.10). In both Si/Mg and Mg_2Si electrode, most of the Li 1s is associated with ternary Zintl phase with some minor contribution from Li_2O. It is worth noting that after the same sputtering cycles, the Si/Mg contains more Li than the Mg_2Si electrode, which should be due to the slow lithiation (and magnesium displacement) kinetics of Mg_2Si. For Mg 2p, both of the electrodes display

sharp Mg 2p peak, where the main component is associated with Zintl phase with minor contribution from MgO. The Si 2p peaks for both electrodes consist of Si metal and Si from Zintl phase. The existence of Si metal suggests that the electrode have not been fully lithiated after the first lithiation. As the O 1s peak of Mg_2Si is much higher than that of Si/Mg, there is more oxygen at this depth for Mg_2Si, which is related to Li_2O, MgO, and SiO_x. Overall, both the Mg 2p and Si 2p results suggest the formation of Li-Mg-Si ternary Zintl phase of the Si/Mg anode upon lithiation, even though its composition is different from that of the Mg_2Si anode. Therefore, the XPS depth profiling with the reference Mg_2Si electrode clearly demonstrates that the introduction of Mg coating on the surface of Si anode could lead to the formation of Li-Mg-Si ternary Zintl phase upon lithiation, which alters the surface SEI and improves the cycling stability of the Si anode.

Silicon Wafers

Commercially sourced silicon wafers were used to evaluate the surface reactions of the multivalent electrolyte additives, as they present a relatively flat and homogenous surface for spectroscopic studies. In these studies, XPS experiments were performed on Si wafer model electrodes that were lithiated (cycled) in either GenF or GenFM electrolytes. Depth analysis of the data demonstrated that a thinner SEI layer was formed in the GenFM electrolyte compared to the system without the additive. The results are consistent with a Mg-containing modified surface passivation formed in the presence of $Mg(TFSI)_2$. To establish the role of surface oxide contamination, we hydrofluoric acid (HF) etched the surface oxides and electrochemically treated the wafer samples to change the electrode surface to a hydrogen-terminated Si wafer. Samples were characterized using XPS depth profiling and the results were compared with the spectra for the native oxide Si wafer electrodes. In both H-terminated and baseline native oxide Si wafer electrodes lithiated using GenFM, no clear spectroscopic evidence for a Li-Mg-Si ternary Zintl phase formation was seen, although the low surface area of the silicon wafer and limited contact time may have resulted in very thin film due to a limited electrolyte penetration depth. Consistent with the oxophilicity of solubilized Mg ions, MgO was detected in the SEI layer, which may block active sites at the electrochemical interface. Analysis of the Li-Mg-Si system indicates that although the wafer model is useful for several different spectroscopic studies, its low surface area and relatively defect-free interface probably limits the penetration depth of the solubilized Mg ions, and thus significant formation of any binary (Li-Si) or ternary (Li-Mg-Si) reduced phases. Reduction of the wafer surface oxide thickness by HF etching was found to have limited effect on the experimental observations.

Nanocrystalline Powders

Although thin films and wafer have advantages, their low surface area and low defect concentration can make them difficult substrates for mechanisms that rely on surface diffusion at the interface. Powders, due to processing, synthesis, and history, have a more heterogeneous surface, which should lend itself to these electrolyte-mediated surface reactions. In fact, the samples that magnesiated most uniformly were those with the least organized and organized silica coating. Whereas traditional diffraction techniques are especially sensitive to heavy atoms and work best with materials with long-range order, the Li-related structures associated with amorphous Si phases after cycling require a local probe. NMR is a powerful tool to determine the local structural environments of nuclei such as ^{7}Li, ^{31}P, and ^{19}F. In FY 2020, we studied the electrochemical lithiation of a baseline Paraclete Energy Si anode at multiple charge states to gain insights into Zintl phase formation mechanisms.

In the first-cycle electrochemical profiles, high-resolution ^{7}Li NMR spectra and the corresponding spectral simulation from unwashed pouch cells are shown in Figure II.1.B.11. Four main Li resonances are observed and analyzed: the black peak around 0 ppm is from the residual diamagnetic Li salts in electrolyte, as well as electrolyte decomposition products; the relatively sharp and narrow component at −1 ppm is assigned to Li^+ in surface Si-O layer; Li^+ in isolated Si is at 8 ppm; and Li^+ in Si clusters resonates over 13 ppm. These peak assignments are consistent with our previous ex situ ^{7}Li NMR studies on coin cells. The electrochemical profiles are very similar for both Gen-2 + FEC (GF) and Gen-2 + FEC + Mg (GFM) electrolytes when the cells are only discharged to 100 mV, while GF shows slightly higher (~30 mAh/g) specific capacity. As a result, most Li ions are inserted into isolated Si (and/or extended silicon clusters) with 97.1% in GFM and 97.8% in

GF. When completely discharged to 10 mV, as seen in Figure II.1.B.13(a), although GF and GFM share the similar discharging profile, the GF cell holds more Li ions (~140 mAh/g) than GF. At this stage, Li insertion into Si clusters, as well as possible migration from isolated Si, eventually forms over-lithiated Si phases. Upon charge, Li extraction preferentially take place in over-lithiated Si phases, then Si clusters and finally isolated Si, which correlates well with the coin cell data. When charged to 400 mV, GF and GFM series represent Li removal hysteresis to different extents. There is still 24.7% Li in Si clusters and 57.7% Li in isolated Si in GFM cell, compared with almost all Li in isolated Si in the GF cell. At the fully charged state, spectra shift toward lower frequency, indicating reversible Li dynamics.

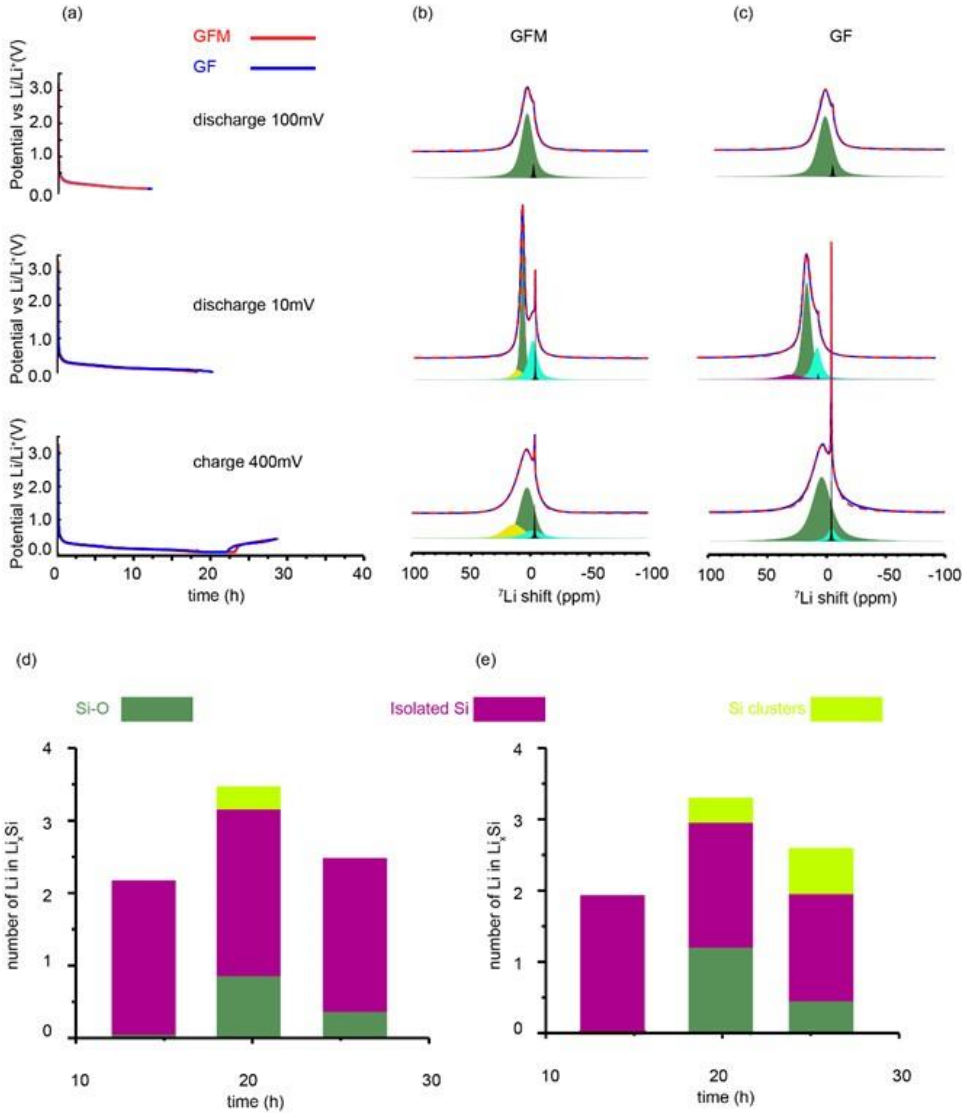

Figure II.1.B.10 Electrochemical performance of GF and GFM at 100 mV, 10 mV, and 400mV. (a) Experimental data (solid line) and simulation (dash line) of GFM (b) and GF (c), Li quantification with GF (d), and GFM (e) electrolytes.

^{7}Li NMR spectra comparison between pouch cells and half cells is shown in Figure II.1.B.12. At the early state (above 100 mV), there is no significant difference except broader line shape for pouch cells, which is due to the relatively lower MAS rate (20 kHz) of the NMR experiment when compared with that of coin cells (60 kHz). However, at the fully discharged state, both GF and GFM spectra show significant differences compared to the results for the coin cells. More Li content was found to be in the SEI and Si-O layer in pouch cells, which is likely due to the fact that pouch cells have significantly more electrolyte and larger surface areas,

leading to more side reactions on the surface and SEI formation. As shown in Figure II.1.B.10b, Figure II.1.B.11, and Figure II.1.B.12, 52.9% Li in isolated Si and 10.8% Li in Si clusters indicate that ternary phase formation may require more Li insertion into Si clusters as well as over-lithiated Si. In contrast, with additional 140-mAh/g discharge capacity, GF pouch cell spectrum shifts to lower field and shows over-lithiated Si at 22 ppm. Longer voltage hold at 10 mV may be accelerating co-insertion of Mg^{2+} and Li-Mg-Si ternary formation in GFM cells.

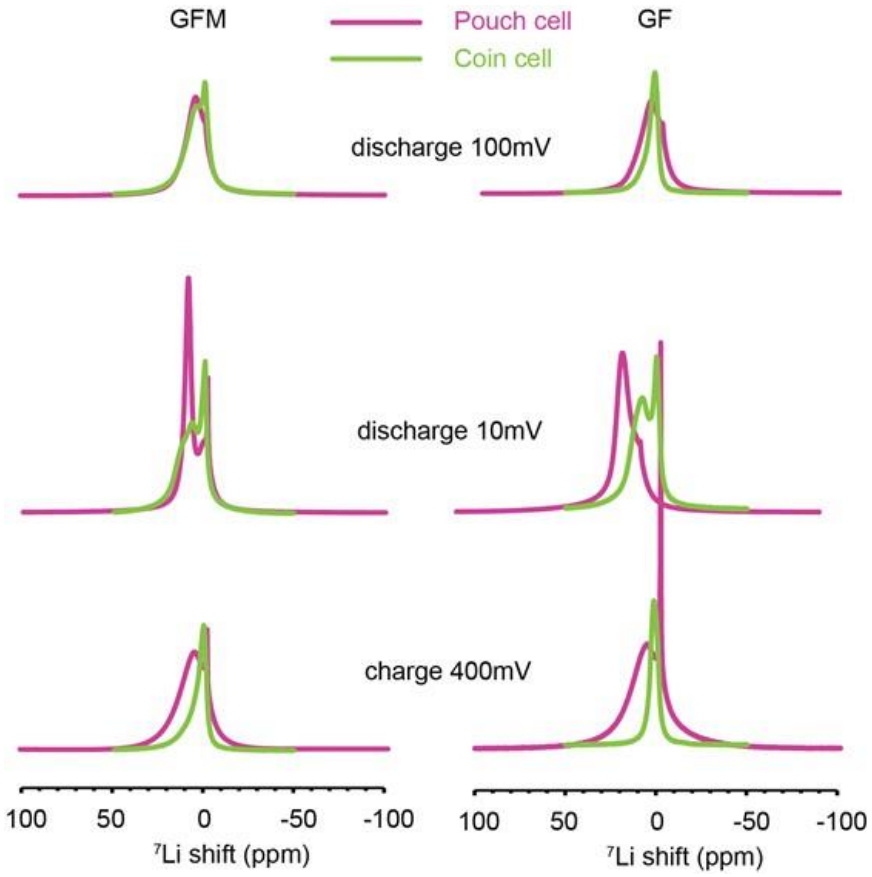

Figure II.1.B.11 ^{7}Li NMR spectra comparison between pouch cells (purple) and coin cells (green) for GFM and GF.

In Figure II.1.B.12, the discharge electrochemistry of baseline Paraclete Si is characterized by two distinct voltage plateaus at 230 mv and 100 mV, which correspond to a two-phase reaction: an irreversible dissociation of amorphous Si and a crystalline phase formation of $Li_{15}Si_4$. Voltage hold at 10 mV before delithiation is designed to break up all crystalline $Li_{15}Si_4$ and form amorphous Li_xSi upon charge, representing a broad voltage peak at 280 mV. Note that although GF and GFM share similar voltage profiles, subtle shift towards lower voltage at 100 mV is most likely a sign of Mg co-insertion. During deeper discharging process below 100 mV, Mg^{2+} could participate in lithiation to form Li-Mg-Si ternary by two possible mechanisms:

(1) $Li_{3.75}Si + 0.1Mg^{2+} => Li_{3.55}Mg_{0.1}Si + 0.2Li^{+}$

Li ions continue coordinating with Si and form crystalline $Li_{3.75}Si$ first; ion exchange between Li^{+} and Mg^{2+} is driven by low potential.

(2) $Li_{3.55}Si + 0.1Mg^{+2} => Li_{3.5}Mg_{0.1}Si$, which is more likely from electrochemical perspective due to slighly lower overall lithiation capacities observed during the discharge for GFM.

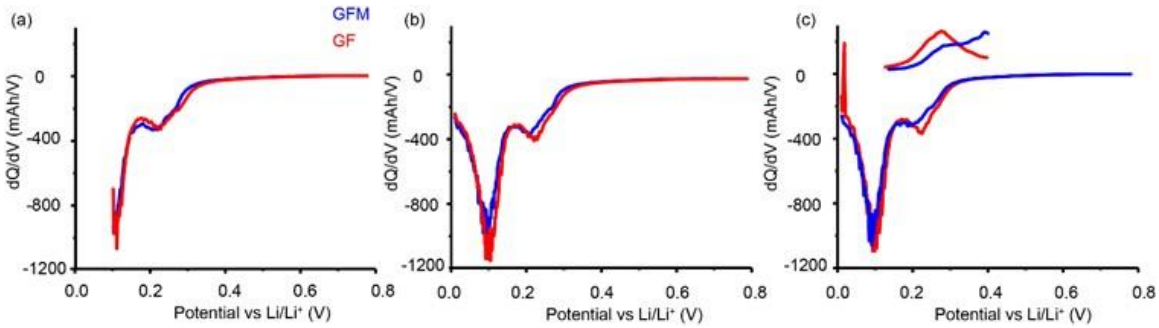

Figure II.1.B.12 Differential capacity vs. voltage plots of GF and GFM at (a) 100 mV, (b) 10 mV upon discharge, and (c) 400 mV upon charge.

The evolution of Li and Si local environments for pure Si anode in two different electrolytes were investigated using electrochemical quartz crystal microbalance (EQCM), ex situ ^{7}Li, and ^{29}Si MAS NMR. Li-Mg-Si ternary phase formation requires large amounts of Li insertion into Si clusters; it could be accumulated by holding the voltage at sufficiently low voltage, such as 10 mV. A more even Li distribution and lower electrochemical hysteresis were promoted by Li-Mg-Si ternary phase formation at the interface. Electrochemistry performance from scale-up pouch cells are consistent with lab-scale coin cells. We propose that upon discharge, Li-Mg-Si ternaries form uniformly, preferably by competition between Li and Mg only at deeply lithiated stages (below 100 mV). Upon charge, Mg remains in the bulk, possibly at a metastable Mg solubility limit in amorphous silicon, forming Li-poor or completely lithium-deficient $Li_xMg_{0.1}Si$ phases and contribute to stable ternary phases in subsequent cycles. The promising potential for scale-up applications examined by pouch cell testing offers more stable passivation at high states of charge in full cells, which should yield to longer calendar life for optimized electrodes.

Silicon Consortium Project Calendar Aging Electrochemical Screening Protocol

The purpose of this document is to provide a framework for the development of silicon (Si) electrodes for high-capacity lithium-ion batteries by providing test protocols that researchers and early-stage developers can use to assess the progress of silicon modifications, cell designs, electrolytes, or additives. Overall, whereas full-cell cycling for silicon anodes has progressed significantly over the past several years, similar progress in the area of calendar life remains a major challenge. The procedures detailed in the following sections have been developed out of a major scientific effort, funded by the Vehicle Technologies Office, to understand the formation and evolution of the silicon solid-electrolyte interphase. This first generation of procedures is designed to enable a reasonably well-equipped research laboratory to assess early research progress toward improving calendar aging issues in silicon cells in a reasonable timeframe. These generation-one procedures will be updated, modified, and expanded as the research team obtains feedback from stakeholders and as our understanding of the SEI evolves.

Traditional approaches to investigate calendar aging often involve experiments that take as long as the period they investigate; the aging inflicted by months of storage is evaluated by exposing the charged cell to controlled conditions for that same number of months. More specifically, such tests age the cells under open-circuit conditions (no current or load applied), with periodic reference performance tests (RPTs) that measure the cell degradation as a function of aging time. The RPTs directly measure the metrics of interest, such as reversible capacity and energy/power retention. Although providing extremely useful information, such approaches are clearly time-consuming and are likely to slow down the development of Si-based cells with robust SEI layers [1].

The testing protocol described in this document is designed to provide semi-quantitative insights on the quality of the SEI in under ~2 weeks. Rather than tracking cell capacity losses over very long times, the protocol presented relies on measuring, in real time, the currents associated with reactions at the SEI as the anode is held at a constant state of charge (SOC). The evolution of these currents over time provides a basis to understand how the state of passivation of the anode evolves over longer time scales. We note that calendar

aging is a complex process that involves not only loss of Li^+ inventory, but also active material loss, electrolyte degradation, and power fade. Although the testing protocol being developed by our team will *not* predict all these aspects of calendar aging, it will nonetheless provide information about the rates of Li^+ inventory losses to the SEI, which is a main factor limiting the calendar life of silicon-based anodes.

The testing protocol described herein departs from traditional calendar aging tests in that *it does not provide absolute calendar lifetime predictions*. Instead, the results should be compared against those of standard electrodes like graphite with calendar lifetimes well characterized by other methods. Future versions of this protocol may provide the ability to quantitatively predict calendar lifetime as the analysis methods are further developed and the lifetime predictions are validated by independent tests. Until such capabilities are available, this protocol can be used to quickly and easily screen electrolyte compositions and silicon electrodes. After this initial investigation, the most promising systems can be studied under more resource-intensive experiments, such as traditional calendar life tests that use long rests with intermittent RPTs.

Calendar Life Screening Protocol

The procedure to test the calendar life of Si anode materials is extremely sensitive to the test cell setup, especially the geometric size and areal capacities of both the test electrode and the counter electrode. Therefore, for reliable comparisons between tests, the testing procedures should adhere to the following requirements:

Cell Design

Table II.1.B.2 Requirements of Test and Counter Electrodes

Electrodes	Chemistry	Capacity	Diameter
Test Anode	Si material	<1.3 mAh/cm2	15 mm (14 mm vs. Li)
Preferable cathode	Lithium iron phosphate (LFP)	>2.5 mAh/cm2	14 mm
Acceptable counter electrode	Lithium metal	>2.5 mAh/cm2	15 mm

Size 2032 stainless steel coin cells are used as the electrochemical test vehicle. The electrodes consist of the Si anode material (the test electrode) against a thick high-capacity lithium iron phosphate (LFP) cathode. When an LFP electrode of sufficiently high areal capacity is not available, a Li counter electrode can be used instead; we warn that the chemical reactivity of lithium can alter the electrolyte composition and can affect the generality of observations obtained for some systems. The diameters are 14 mm for the cathode (LFP) when it is paired with the 15-mm-diameter Si-containing test anode. When the Si-containing electrode is paired with a Li counter electrode, the Si electrode has a 14-mm diameter with a 15-mm-diameter Li foil (less than 1-mm thick).

The areal capacities of the electrodes are chosen to ensure that there is enough Li^+ inventory to supply the Si-containing test electrode with capacity during the aging protocol. The LFP electrode is greater than or equal to 2.5 mAh/cm^2, whereas the Si-containing test electrode is less than or equal to 1.3 mAh/cm^2 at the SOC at which aging will be assessed. This additional Li^+ inventory is meant to guarantee that the cathode would still retain excess capacity even after the large irreversibility that is typical of Si electrodes in the first few cycles. If electrodes with loadings other than those designated are used, it is imperative that the total utilized capacity of the Si electrode (reversible capacity + accumulated irreversible capacity) not exceed the capacity of the counter electrode during the test. This design ensures that the counter electrode can effectively supply the Li^+ needed to (re)form the SEI at the Si test electrode.

Cell Assembly

The 2032 stainless steel coin cell is built following an assembly process that has been well established at Argonne National Laboratory [2]:

1. Electrodes should be dried under dynamic vacuum for at least 14 h at 120°C for polyvinylidene fluoride (PVDF) binder (LFP cathode) containing electrodes, and 150°C for polyacrylic acid (PAA) or LiPAA binder-containing electrodes. Other binders that are used should be dried appropriately so as not to affect the cell chemistry.

    a. Note that thick single-sided LFP electrodes can curl when wet with the electrolyte. Thus, we recommend assembling LFP-containing cells from the anode side up in the following order: cell cap with attached polypropylene gasket, 0.5-mm-thick stainless steel spacer, 15-mm Si test electrode, 20-µL electrolyte, 19-mm diameter layer of 2325 Celgard separator or equivalent, 20-µL electrolyte, 14-mm LFP counter electrode, 0.5-mm-thick stainless steel spacer, stainless steel wave spring, and cell case.

    b. Li half-cells should be assembled in the following order: cell case, 14-mm Si test electrode, 20-µL electrolyte, 19-mm diameter separator layer, polypropylene gasket (oriented to properly mate with cell cap), 20-µL electrolyte, 15-mm-diameter Li metal foil (<1 mm thick), 0.5-mm-thick stainless steel spacer, stainless steel wave spring, and cell cap.

2. The assembled cell stack should then be crimped together with a hydraulic crimper, preferably an automatic crimper for consistency.

Electrochemical Protocol

C-rate determination: The C-rate is defined as the current necessary to drive the Si test electrode from one voltage cutoff to the other in 1 hour (a C/10 rate takes 10 hours to drive the electrode from one voltage cutoff to the other). This value should be determined using half-cell data of the second cycle of the Si test electrode. Because the LFP electrode delithiates at ~3.45 V vs. Li/Li^+ and relithiates at ~3.40 V vs. Li/Li^+, the cutoff potentials correlate as follows:

$$2.7\ V \text{ vs. LFP (discharge)} = 0.7\ V \text{ vs. } Li/Li^+$$

$$3.35\ V \text{ vs. LFP (charge)} = 0.1\ V \text{ vs. } Li/Li^+$$

LFP full-cell:

1. Rest cell at OCV for 4 hours to allow electrolyte wetting
2. At a C/10 rate, charge to 3.35 V, discharge to 2.7 V, repeat 3 times, data acquisition should be $\Delta V = 5$ mV
3. Hold cell at 2.7 V until i < C/100 to fully lithiate test electrode, data acquisition should be $\Delta t = 1$ min, $\Delta i = 10$ µA./10 rate, data acquisition should be $\Delta V = 5$ mV
4. Hold potential at 3.35 V for 180 hours, data acquisition should be $\Delta t = 1$ min, $\Delta i = 10$ µA
5. Discharge to 2.7 V at a C/10 rate, data acquisition should be $\Delta V = 5$ mV
6. Hold cell at 2.7 V until i < C/100 to fully lithiate test electrode, data acquisition should be $\Delta t = 1$ min, $\Delta i = 10$ µA

7. At a C/10 rate, charge to 3.35 V, discharge to 2.7 V, repeat 2 times, data acquisition should be $\Delta V = 5$ mV.

Li half-cell (same procedure as LFP full-cell with potential cutoffs substituted as follows):

- 0.1 V instead of 3.35 V
- 0.7 V instead of 2.7 V.

The preliminary efforts described in this report are limited to studying SEI passivation at the SOC achieved by the anode at ~0.1 V vs. Li/Li^+; for a graphite electrode, this would correspond to ~55% of lithiation. Most Si-based electrodes can remain mechanically stable when cycled to this potential, and thus permanent losses of active material are less likely to occur during the tests discussed here. Our team recognizes that SOC is an important variable when investigating calendar aging and modeling SEI growth [3], and future studies will expand the scope of this report.

Data Collection and Presentation

Verifying the current response of the cell during the voltage hold is critical to guarantee that the data analysis will be meaningful. Figure II.1.B.13 shows the current measured during the hold, normalized to the capacity (lithiation capacity measured during the charge immediately before the voltage hold) of a test silicon electrode and a graphite baseline electrode. The expected behavior for the current measured in both systems are shown in Figure II.1.B.13a, where the continuous decay exhibited by the traces indicates that the counter electrode is supplying sufficient Li^+ inventory. This plot also qualitatively demonstrates that the currents that arise from parasitic reactions on the graphite electrode, seen long after the initial decay, are roughly an order of magnitude smaller than those observed for the silicon, demonstrating its better passivating behavior and longer calendar lifetimes, as expected. The results displayed in this type of plot should serve as a gate to determine if further analysis should be performed using the testing protocols described in this document. *If the residual current (i) does not approach that of a baseline electrode such as graphite (necessarily within an order of magnitude), then further analysis is not warranted, as the SEI is clearly not sufficiently stable*. It is recommended that the data acquisition parameters discussed in the previous section are used in the voltage hold test to ensure enough resolution.

A major pitfall of this experimental protocol occurs when the Li^+ inventory of a test cell is exhausted (counter electrode is completely delithiated). The sudden decline of the current responses to diminishingly small and indistinguishable values as seen in Figure II.1.B.13b (after ~40 h of voltage hold) indicates that the Li^+ inventory supplied by the counter electrodes has been exhausted during the voltage hold. Under these conditions, the external current no longer provides a direct measure of the rate of parasitic reactions, yielding inaccurate information about the electrode's calendar lifetime. This is another critical reason why the current response of the collected data needs to be evaluated before performing the analysis described in the next section. If the current response displays a similar behavior to that shown in Figure II.1.B.13b, the test cell should be remade with a higher-capacity counter electrode or a lower-capacity test electrode.

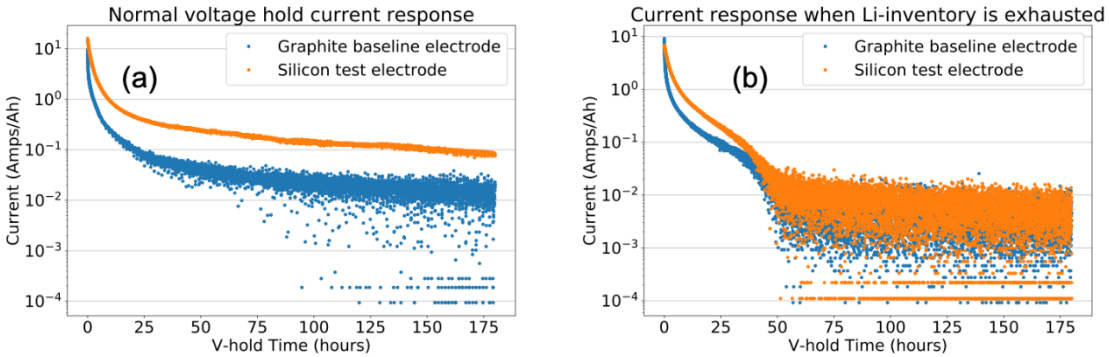

Figure II.1.B.13 Current decay versus time during voltage holds of (blue) graphite baseline anode and (orange) 80 wt % Si test anode. The current has been normalized to the capacity of the test electrode measured during the lithiation immediately before the voltage hold. Panel (a) shows the current response where there is an excess of Li^+ inventory supplied by a counter electrode with a flat voltage profile, as is the scenario marked (a) in Figure II.1.B.15. Panel (b) shows how the current suddenly declines as the Li^+ inventory supplied by the counter electrode is exhausted, polarizing the electrodes to high potentials. Under these conditions, the measured current underestimates the actual rate of parasitic reactions experienced by the test electrode.

Data Analysis and Result Reporting

Analysis of the data should first be done by qualitative visual inspection and comparison between the test electrodes and a baseline electrode. Figure II.1.B.14 shows the current decays of three different Si test electrodes and a graphite baseline electrode. The normalization of the current data to the reversible capacity of each electrode is important because the resulting units of amps/Ah indicate the rate at which each electrode is losing reversible capacity due to Li^+ consumption at the SEI. If the normalized current measured from a Si test electrode at the end of the 180-hour voltage hold is distinguishably higher than the baseline electrode, further analysis is not needed, as the electrode's SEI is clearly not sufficiently stable. This is the case for each of the Si test electrodes shown in Figure II.1.B.14, thus showing the effectiveness of this simple qualitative comparison for the initial screening of Si test electrodes.

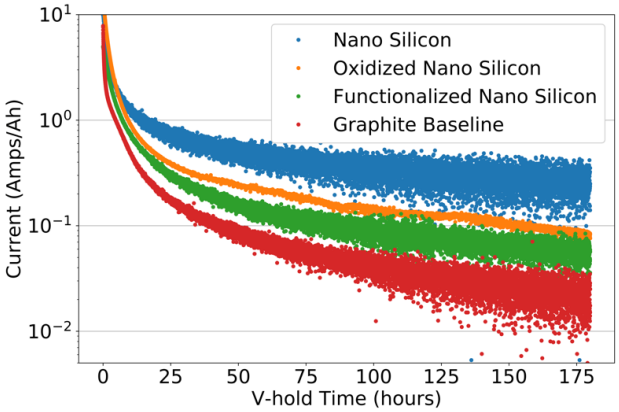

Figure II.1.B.14 Current decay versus time during voltage holds of several different Si test electrodes and a graphite baseline electrode. The rate of parasitic reactions of the Si test electrodes can be qualitatively distinguished by visual inspection, and all exhibit greater aging rates than the graphite baseline electrode.

The average current after 180 hours of voltage hold can be used as a metric to rank the rate of parasitic reactions at each electrode, reported in this section for the examples shown in Figure II.1.B.14. This information should be complemented by details about electrode composition, areal capacity, and electrolyte used in the tests. Additionally, because there can be variability between tests for a given electrode and

electrolyte pair, we recommend that a sample size of at least three test cells for each test electrode type be reported.

Example reporting:

Graphite baseline electrode

1.17 mAh/cm^2

91.83 wt % Superior Graphite SLC1520P

2 wt % Timcal C45 carbon

6 wt % Kureha 9300 PVDF binder

0.17 wt % oxalic acid

Electrolyte: 1.2 M $LiPF_6$ in ethylene-carbonate:ethyl-methyl-carbonate 3:7 + 10 wt % FEC

Mean terminal current = 0.023 mA/Ah

Nano Silicon

0.3 mAh/cm^2

20 wt % 3.9-nm-diameter Si nanoparticles

65 wt % Timcal C65 carbon

15 wt % PAA binder

Electrolyte: 1.2 M $LiPF_6$ in ethylene-carbonate:ethyl-methyl-carbonate 3:7 + 10 wt % FEC

Mean terminal current = 0.262 mA/Ah

Oxidized Nano Silicon

1.24 mAh/cm^2

80 wt % surface-oxidized 150-nm-diameter Si nanoparticles

10 wt % Timcal C45 carbon

10 wt % LiPAA binder

Electrolyte: 1.2 M $LiPF_6$ in ethylene-carbonate:ethyl-methyl-carbonate 3:7 + 10 wt % FEC

Mean terminal current = 0.092 mA/Ah

Functionalized Nano Silicon

0.7 mAh/cm^2

40 wt % 4-phenylphenol surface-functionalized 30-nm-diameter Si nanoparticles

40 wt % Timcal C65 carbon

20 wt % PAA binder

Electrolyte: 1.2 M $LiPF_6$ in ethylene-carbonate:ethyl-methyl-carbonate 3:7 + 10 wt % FEC

Mean terminal current = 0.059 mA/Ah

These examples highlight the capabilities of the screening protocol described in the current version of this document. Because it is currently limited to qualitative analysis, it is especially important to use a baseline electrode with a calendar life well-characterized by other methods under the conditions of interest. Future versions of this report may include a semi-quantitative model to describe the rate of parasitic reactions in the electrodes of interest, which is currently under validation by long-term experiments; this model is outlined in general terms at the end of the discussion section.

Discussion

Our methodology is based on using voltage holds to measure the rate of Li^+ trapping at the SEI in Si-containing cells. This approach has the advantage of recording real-time rates of side reactions, providing information about the time dependence of such processes and potentially enabling extrapolation of behaviors observed in relatively short-duration experiments. Its working principle is based on the fact that parasitic reduction reactions (such as the ones involved in SEI formation) effectively consume electrons from the anode, which decreases the anode SOC. The instantaneous voltage of a cell is the difference between the potentials of the positive and negative electrodes, so a change in the anode SOC yields a change in cell voltage. If the anode SOC is "pinned" by holding the cell voltage constant, electrons must flow from the cathode to the anode to replenish the charge consumed by side reactions in order to keep the anode SOC invariant (i.e., the current flowing through the cell and measured by an external circuit is equal to the rate of these parasitic processes). This ideal equivalence between the parasitic and measured currents is achieved when the anode has a sloped potential and is most sensitive to SOC and the cathode is insensitive to SOC (the voltage profile is "flat"). We can approximate these conditions by using $LiFePO_4$ (LFP) as a cathode (which can provide most of its capacity while at ~3.45 V vs. Li/Li^+), and by performing the voltage hold at potentials in which the anode cycling profiles are notably sloped to maximize sensitivity.

For these tests, it is important that the LFP counter-electrode has a capacity in excess of that used by the reversible and irreversible reactions occurring at the Si test electrode. The importance of this condition is demonstrated by the simulated voltage profiles shown in Figure II.1.B.15, where the LFP voltage profiles are shown in blue. Profiles for pristine (solid line) and aged (dashed line) Si anodes are displayed in black with the corresponding full-cell voltage profiles displayed in red. The intersecting lines marked (a) in Figure II.1.B.15 represent the pristine full-cell being held at 3.35 V, where the potential at the pristine Si anode would be roughly equivalent to ~100 mV vs. Li/Li^+. In this pristine cell at 3.35 V, the LFP voltage profile is insensitive to SOC (voltage profile is flat), and thus any changes of the Si SOC would require a change in cell voltage (i.e., the Si SOC is "pinned"). As electrons and Li-ions are consumed at the Si electrode during aging, they are replenished by the LFP cathode, as additional Li^+ extraction is possible at that same electrode potential. Nevertheless, if enough capacity is lost, the aged cell may no longer be able to keep the Si SOC constant. This Li^+ inventory exhaustion scenario is represented by the intersecting lines marked (b) in Figure II.1.B.15, where the aged cell is still held at 3.35 V. In the aged cell with an exhausted Li^+ inventory, the LFP voltage profile is polarized above its plateau potential and is sensitive to SOC (highly sloped), resulting in the Si electrode no longer being held at the desired potential of 100 mV vs. Li/Li^+. When that happens, additional Li^+ extraction from LFP to counter parasitic reactions at the anode would cause an increase in the potential of both electrodes; this would involve a net decrease in anode SOC, and thus the currents measured by an external circuit would underestimate the extent of side reactions in the cell.

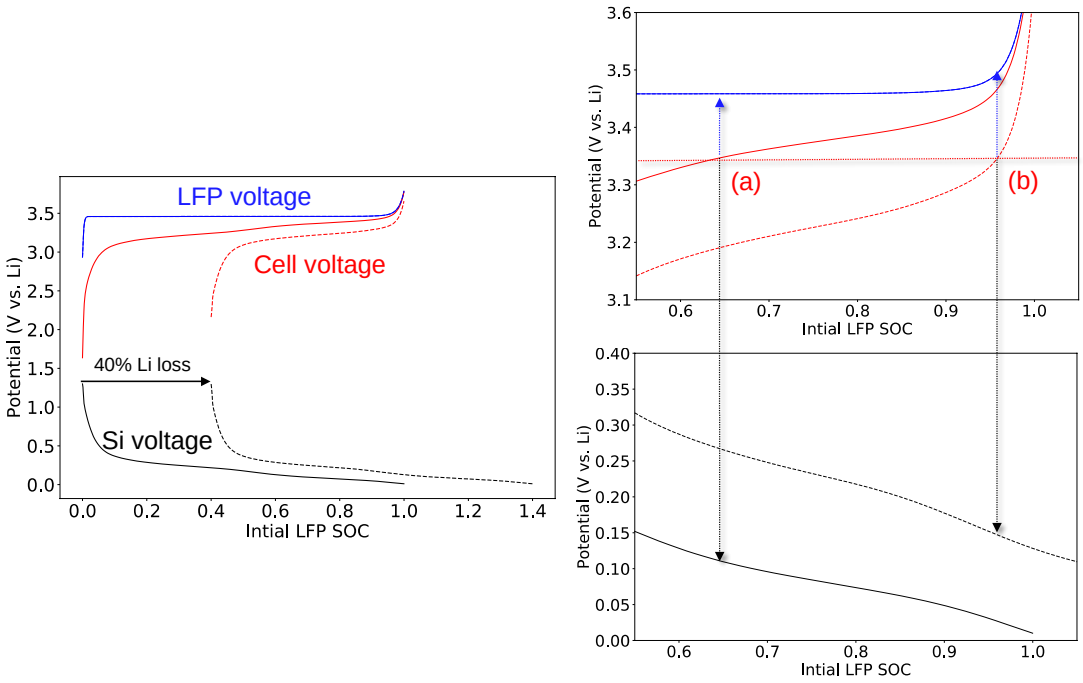

Figure II.1.B.15 (left) Simulated voltage profiles for an LFP cathode (blue), Si anode (black), and the two-electrode cell combining those two electrodes (red). The dashed black line represents Si electrode aging by the loss of Li^+ inventory, which effectively shifts the Si voltage profile relative to the LFP voltage profile and results in the aged cell having the dashed red voltage profile. (right) Zoomed-in portions of the voltage profiles where the dotted horizontal red line represents a voltage hold potential of 3.35 V for pristine (a) and aged (b) Si electrode-containing cells.

The use of LFP as a counter-electrode has additional advantages. One is that the cathode can be assumed to be an essentially inert electrode, because its low potentials will lead to little changes in electrolyte composition and are unlikely to generate oxidative currents that could affect the analysis. Additionally, the extremely flat voltage plateau of LFP over its entire capacity range allows it to be used as a reliable pseudo-reference electrode in a two-electrode coin cell. Thus, the absolute potential of the anode can be well controlled, facilitating studies on the effect of SOC on passivation. The test protocol specifics and an example voltage profile are shown in Figure II.1.B.16, where a 180-hour-long voltage hold is preceded by three formation cycles and followed by two additional diagnostic cycles. The total test time is ~290 hours (less than two weeks).

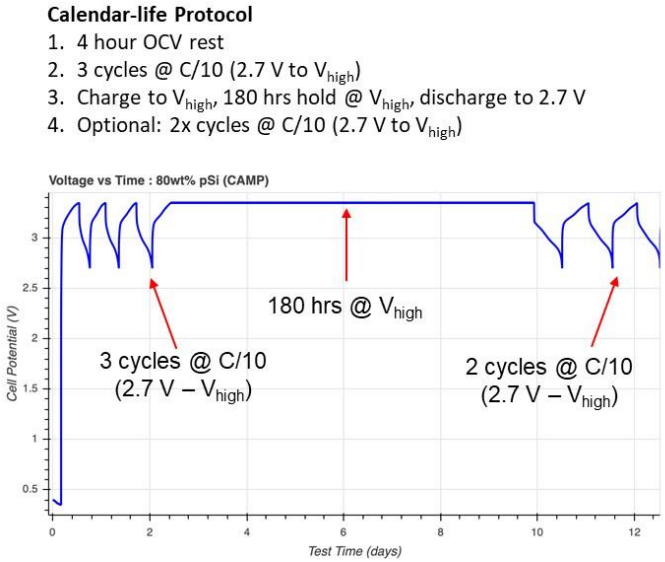

Figure II.1.B.16 The test protocol to estimate the rate of parasitic reactions of Si-based electrodes. The example voltage profile is from a cell coupling an 80% Si electrode vs. an LFP cathode.

Although this experimental approach is a logical pathway to derive information about electrode passivation from short-term tests, it also presents challenges. In practice, electrodes present a finite impedance, and lithiation processes are incomplete by the time the voltage hold initiates. Hence, the current measured during the early periods of voltage hold is a combination of reversible lithiation processes (lithiation of Si) and irreversible electrochemical reactions (SEI formation and concomitant Li^+ consumption). As the voltage is held for longer and longer times, the proportion of the current driving reversible reactions diminishes relative to the current driving the irreversible reactions, and the measured current becomes a more reliable descriptor of parasitic processes. For these component contributors, *the challenge exists to validate that the analyses can differentiate between both these contributions to the measured current.* The reversible capacity passed during the voltage hold can be experimentally quantified by inspecting cell discharge after the hold, and these values are used to help differentiate the time-dependent contributions from the reversible and irreversible processes.

The purpose of the 180-hour-long voltage hold is to determine the rate of Li^+ inventory consumption, as measured by the current, due to irreversible side reactions at the anode surface. Using this method, the current measured during the voltage hold is due to a combination of the reversible lithiation reactions and the irreversible side reactions. Figure II.1.B.13a shows the typical current responses during the voltage hold of example electrodes. The current densities decrease more than an order of magnitude during the first ~20 hours of the voltage hold as the reversible lithiation reactions near completion. In contrast, toward the end of the voltage hold, the current densities stabilize at diminishingly small values that are primarily due to irreversible Li^+-consuming reactions. The lower current density of the graphite electrode at the end of the voltage hold compared to the Si electrode is good confirmation that the measurement is qualitatively capturing the expectedly better SEI stability (and lower Li^+ inventory consumption rate) of the graphite electrode. Figure II.1.B.13b shows the current response during the voltage hold where the Li^+ inventory of the cell becomes exhausted. This occurs when the cathode is unable to supply additional electrons and Li ions to keep the anode pinned at a fixed SOC, as outlined by marker (b) in Figure II.1.B.15. In this case, the full cell is maintained at a fixed voltage with a net decrease in anode SOC, resulting in the measured currents underestimating the parasitic reaction rates. This can be seen in Figure II.1.B.13b by the sudden decrease in current to vanishingly small values, and highlights the importance of performing these experiments in cells with excess counter-electrode capacity.

Integrating the measured current over time during the voltage hold and normalizing to the electrode's reversible capacity yields time-dependent capacity, $Q_{hold}(t)$. In order to deconvolute the irreversible and reversible contributions to the capacity, the following function can be fit to the normalized capacity data:

$$Q_{hold}(t) = Q_{irrev}(t) + Q_{rev}(t)$$

The numerical forms of these functions are still being determined using long-term voltage hold validation experiments. As the validation data become available, future versions of this report may include numerical models that can be used to semi-quantitatively describe the rate of SEI-related side reactions. Preliminary results suggest that $Q_{rev}(t)$ has an asymptotic time dependency as the reversible capacity approaches a maximum value at long times, whereas $Q_{irrev}(t)$ may be proportional to the square root of time. The square root of time dependency of $Q_{irrev}(t)$ is well supported by empirical observations in the literature, and is believed to capture the general behavior of SEI growth [3], [4] This particular functional form arises from the hypothesis that the irreversible side reactions occurring at the electrode surface due to SEI formation are diffusion-limited, and thus their rates are inversely proportional to the square root of time.

Notwithstanding, the Si SEI stability will naturally fluctuate as a function of a plethora of internal and external factors. The present report is just the beginning of an exploration of the Si calendar life behavior embedded in a current response, the measurement probe of choice. In an electrochemical process, electrode kinetics and their reaction rates are tied to a current value. The parasitic reactions in Si electrodes are exceedingly complex and, as a first pass, it is affiliated with (1) the Li-ion conductivity in the SEI, (2) the mechanical stability of SEI, (3) chemical stability (solubility) of the SEI, and (4) the electronic conductivity within the SEI. What factors dominate thus begs the question: How can one slow down this degradation phenomena and create "immunity"?

Understanding Silicon Alloy Effects on the SEI

Si has garnered tremendous interest as a replacement for graphite in lithium-ion battery technology due to its potential to enable lighter-weight and lower-cost battery packs for large-scale applications such as electric vehicles and grid-scale storage. Si is primarily attractive due to its large capacity (4,200 mAh/g, which is 10 times higher than graphite) and low market price. However, commercial devices with high Si content are limited by the following pitfalls: (1) Si undergoes significant structural reconstruction and volume change during charge/discharge. This results in substantial strain within the material and leads to the propagation of cracks and material loss, resulting in a rapid capacity fade. (2) The Si–electrolyte interface is unstable during electrochemical cycling. SEI that consists of various electrolyte decomposition products does not fully passivate the Si surface. Consequently, electrolyte and the lithium inventory are consumed continuously, and this results in poor calendar life. To date, only a limited fraction of Si (~15 wt %) has been incorporated in graphite anodes to increase the energy density without sacrificing the lifetime. Significant efforts must be made to achieve further improvements.

This project's objective is to overcome the Si anode issues, such as intrinsic non-passivating surface and low electrical conductivity. Our approach to achieving the goals is to develop Si-based metallic alloys with surface properties favorable to form a stable SEI, improved kinetic properties, and conductivity.

A combination of four experimental techniques and computational techniques are adopted to develop practical Si-based metallic alloys: (1) magnetron (co-)sputtering reliably produces thin-film-type amorphous Si-Sn electrodes; (2) nonthermal plasma-enhanced chemical vapor deposition (PECVD) provides a unique pathway for metastable material synthesis, such as Si-Sn alloys, in the form of nanoparticles (NPs); (3) splat quenching enables rapid quenching of a Si-based metal alloy molt to form amorphous metallic glasses by preventing long-range reorganization of the atoms; and (4) density functional theory and ab initio molecular dynamics simulations are well suited for predicting proper Si alloy compositions among numerous combinations, thus effectively guiding the time-intensive experimental efforts.

Incorporation of Sn in Si-based anode is expected to improve the electrode conductivity and may help the formation of a stable SEI layer while maintaining the high specific capacity. Furthermore, the group IV alloys can allow us to study more fundamental material properties such as the effect of NP strain caused by the larger size of Sn atoms relative to Si during lithiation and delithiation. Being free of binder and carbon additive, the Si-Sn thin-film electrodes formed by sputtering are devoted to investigating Si-Sn alloy's interfacial properties. The results reveal that Si-Sn shows stable long-term cycling and dramatically different morphology/composition compared to the pure Si counterpart. Si-Sn NPs synthesized by PECVD are constructed into composite electrodes to investigate the electrochemical characteristics and cycling performance. The effort is conducted toward these ends that achieved the Go/No-Go Q2 FY 2020 Milestone: "Production of tin-silicon alloys to be determined by the ability of the alloys to be prepared in 1-g quantities and a demonstration that the alloys exhibit greater cyclic life than the pure metals alone."

Silicon Metallic Glasses (Si-MG) is an attractive category of materials for lithium-ion batteries due to its homogeneously distributed Si content at an atomic level, which can eliminate the two-phase coexistence and materials pulverization during electrochemical cycling through solid-solution alloying. Thus, in comparison to polycrystalline intermetallic compounds, they present the advantage of lacking phase boundaries. Multicomponent Si-MGs can also provide a pathway to address the major issues associated with Si-based electrodes by carefully selecting the elements to be introduced. First, a proper choice of Li-inert element can become a buffer or reduce the magnitude of volume change during Li alloying/dealloying, which is the source of electrode-scale mechanical instability. Second, the use of elements that favor the formation of stable SEI (e.g., Ni) may tune the SEI on Si-MG to achieve full passivation. We have successfully developed a Si-MG ($Al_{64}Si_{25}Mn_{11}$ at. %) using a splat quenching system. The investigation carried out to date shows that $Al_{64}Si_{25}Mn_{11}$ glass is electrochemically active and forms a stable SEI, unlike elemental Si. Insights from this study provide properties desired in an SEI interface and can guide future SEI design rules for Si-based anodes.

Although the experimental approaches are attempted on plausible Si-based alloy combinations, there are nearly infinite variations on elements and stoichiometry of the potential binary and ternary Si-based alloys. High-throughput computational studies are uniquely suited for such a combinatorial problem. As such, we use density functional theory and ab initio molecular dynamics to conduct a high-throughput study of the lithiation behavior of a large subset of these binary and ternary Si alloys, investigating the structural changes and lithiation potential of these alloys. The outcomes from the computational studies are expected to help selectively choose Si alloy composition and ratio with high practicality.

Investigation on Si-Sn Thin-Film Model Electrodes Prepared by Magnetron Sputtering

As previously reported, the Si_xSn_{1-x} composite thin films were directly deposited onto Cu foils by co-sputtering separated Si and Sn targets simultaneously, with the film composition tuned by controlling the deposition power level. All the as-deposited films were subsequently stored under vacuum to prevent air exposure. 2032-type coin cells were assembled using the as-produced films (1.6 cm^2) directly as the working electrodes, Li metal foil as the counter electrode, and 1.2 M $LiPF_6$ in ethylene carbonate-ethyl methyl carbonate (3:7 by weight) as the electrolyte (Gen2). For electrochemical cycling test, the cells were galvanostatically discharged and charged between 1.5 and 0.01 V at C/20 based on the experimental capacity. For scanning electron microscopy (SEM) and EDS, the cells were galvanostatically cycled between 0.01 and 1.5 V at C/20 at selected cycles. The cycled electrodes were harvested by opening the cells, rinsing with dimethyl carbonate, and natural drying inside an Ar-filled glovebox. The electrode samples were quickly transferred to the SEM chamber for morphological and compositional studies.

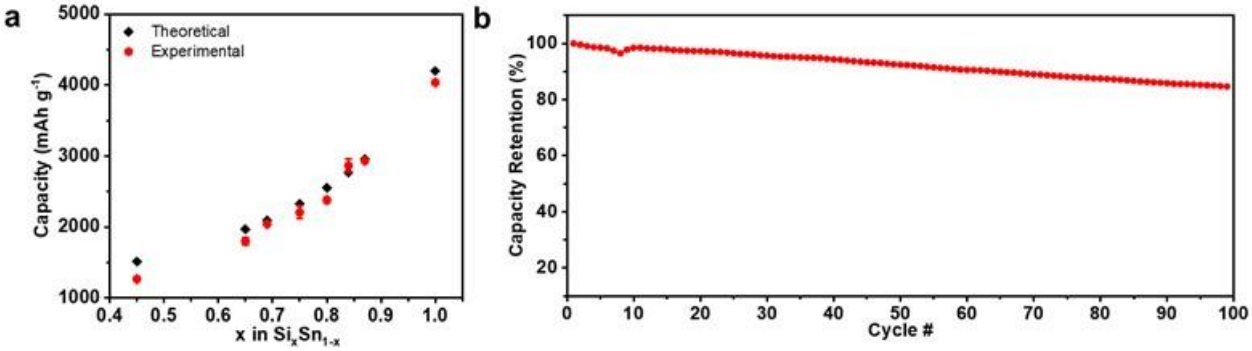

Figure II.1.B.17 (a) Theoretical and experimental capacities of SixSn1-x (0.45 ≤ x ≤ 1) films during the first lithiation. (b) Long-term cycle performance of an optimal SixSn1-x thin film (x = 0.8).

The specific capacities of Si_xSn_{1-x} ($0.45 \leq x \leq 1$) during initial lithiation are estimated based on the measured film thickness and theoretical densities of Si and Sn. The theoretical and estimated capacities during the first lithiation are plotted in Figure II.1.B.17a. It can be seen that the films with $x \geq 0.69$ all attain a high capacity of over 2,000 mAh g^{-1}. The largest gap between the theoretical and experimental values is found for the film of x = 0.45. This may be attributed to the inhomogeneous Li insertion occurring in the crystalline film (as previously revealed by X-ray diffraction), leading to the incomplete lithiation reaction. The capacities of the other X-ray amorphous films ($x \geq 0.65$) exhibit a capacity close to their theoretical values, independent of composition. It can be inferred that the amorphous nature is beneficial to more complete reactions (i.e., a higher utilization of the active material).

Although the cycling stability can be achieved by controlling the cyclable capacity of Si anode, we demonstrate that the Si-Sn composite film can cycle well in the long term at the optimal compositions, while

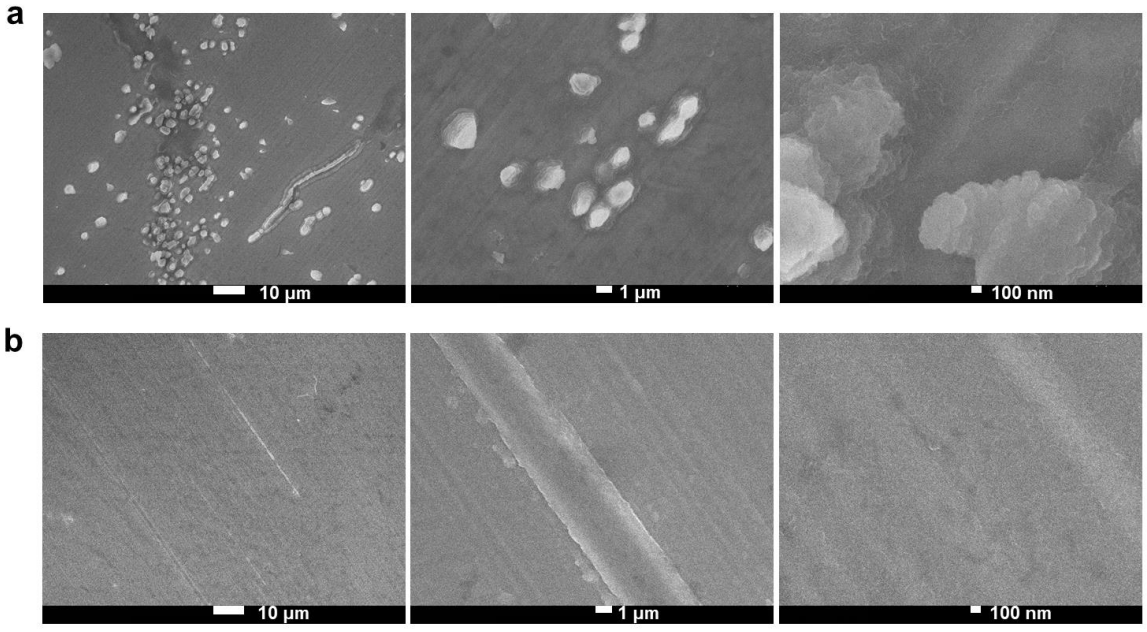

Figure II.1.B.18. Representative SEM images of (a) Si and (b) Si-Sn films after the first lithiation.

approaching nearly full lithiation. As shown in Figure II.1.B.17b, the Si-Sn film of x = 0.8 is capable of retaining 84% of its initial capacity after 100 cycles, corresponding to an average capacity loss of around 0.17% per cycle. It is worth noting that the excellent cycling of amorphous Si-Sn film is obtained without the use of any binder, carbon, or electrolyte additive.

Figure II.1.B.18 shows the SEM images of the Si and Si-Sn films after the first lithiation. As shown in Figure II.1.B.18a, after the initial lithiation of the Si film, scattered islands up to a few micrometers are clearly visible on the electrode surface, some of which are connected to form continuous structures. In stark contrast, the initially lithiated Si-Sn film displays a uniform morphology without the presence of such peculiar structures (Figure II.1.B.18b). Note the stripping feature in Figure II.1.B.18b originates from the Cu substrate. The EDS mapping of the island morphologies on the lithiated Si (Figure II.1.B.19a) reveals they are rich in O, whereas the Si-Sn film (Figure II.1.B.19b) shows uniform elemental distribution without any sign of O-enriched heterogeneity. This suggests the dramatically different SEI surface layer on the lithiated Si and Si-Sn thin film electrodes. Note that no FEC was used throughout the study to investigate the intrinsic SEI properties of Si anode in Gen 2 carbonate electrolyte.

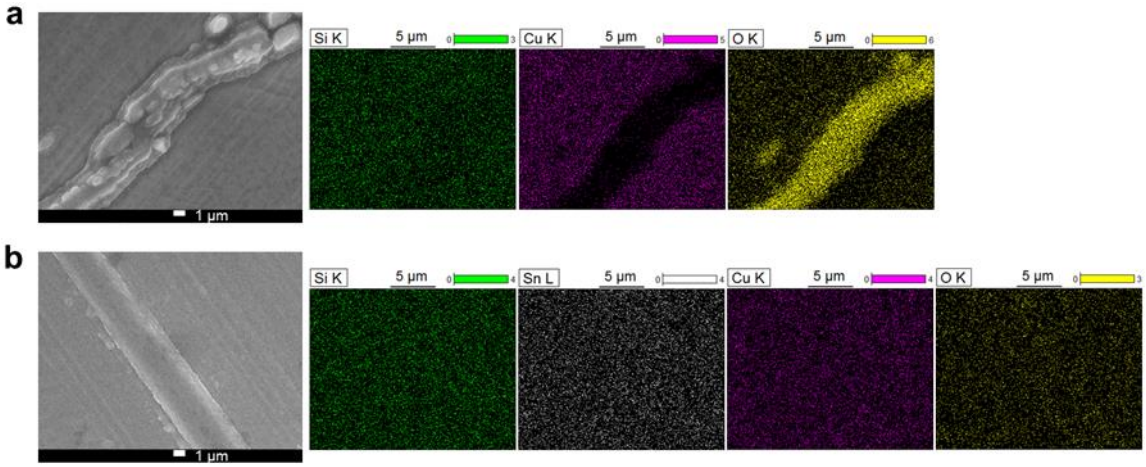

Figure II.1.B.19. EDS mapping of (a) Si and (b) Si-Sn films after the first lithiation.

The elemental distribution on the Si and Si-Sn films at pristine state and after the first charge (lithiation) and first, second and fifth discharge (lithiation) are plotted in Figure II.1.B.20. For both samples, a drastic increase in O content is observed upon the first lithiation, likely due to the electrolyte decomposition and SEI formation. Moreover, the O content for the lithiated Si is almost double compared to that for the lithiated Si-Sn film. Upon the first delithiation, the O level decreases for both films, indicating the possible dissolution or

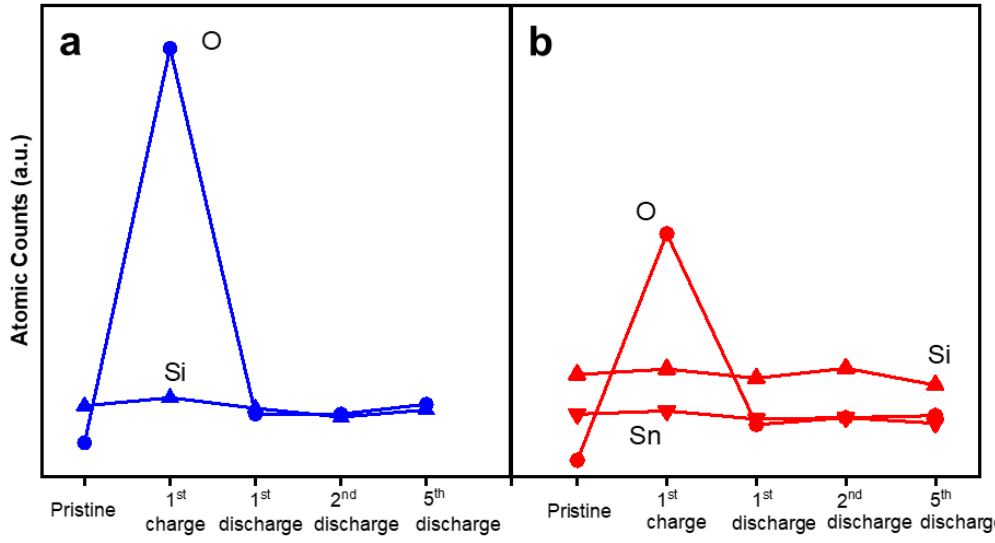

Figure II.1.B.20. Elemental distribution on (a) Si and (b) Si-Sn films at pristine state and after the first charge (lithiation) and first, second, and fifth discharge (delithiation).

decomposition of some SEI components (resulting in O loss) upon delithiation. The O content remains low for Si and Si-Sn electrodes after the second and fifth delithiation, but still higher than their pristine states (Table II.1.B.3). Such phenomena regarding the change of the O content upon initial lithiation/delithiation and distinct morphologies between the Si and Si-Sn, along with their different electrochemical performance, deserve further in-depth investigation.

Table II.1.B.3 Elemental Composition of Si and Si-Sn Films at Pristine State and After the 1st Lithiation and 1st, 2nd, and 5th Delithiation.[a]

State of Charge	Si film (V)		Si-Sn film (V)		
	Si	O	Si	Sn	O
Pristine	0.20	0.09	0.28	0.17	0.04
1st lithiation	0.22	1.18	0.30	0.18	0.67
1st delithiation	0.19	0.17	0.27	0.16	0.14
2nd delithiation	0.16	0.17	0.30	0.16	0.16
5th delithiation	0.18	0.20	0.25	0.15	0.17

[a]All elements normalized to Cu

Investigation on Si-Sn Nanoparticle Model Electrodes Prepared by PECVD

We have demonstrated the incorporation of small amounts <10 at. % of Sn into Si-Sn alloy NPs using the nonthermal PECVD approach. Tin incorporation is confirmed using a suite of chemical and structural characterization techniques, including diffuse reflectance infrared Fourier transform spectroscopy (DRIFTS), XRD, TEM, and EDS mapping. We have also incorporated these materials in composite lithium-ion battery anodes and studied their cycling performance in a half-cell architecture for >100 cycles.

The nonthermal plasma synthesis process for the production and characterization of Si-Sn alloy NPs is described in our Q2 FY 2020 report. Here, we reproduce Figure II.1.B.21 from our Q2 report, which shows the DRIFTS spectra and XRD patterns from three different NP samples: pure intrinsic Si, 5 at. % Sn ($Si_{0.95}Sn_{0.05}$), and 10 at. % Sn ($Si_{0.9}Sn_{0.1}$). The absorption feature at 1,790 cm^{-1} is attributed to *SnH_x stretching vibrations, where the * denotes a surface Sn atom, and is noticeably absent in the pure Si NP sample. Additionally, the *SiH_x stretching region (2,000–2,200 cm^{-1}) for the alloyed NPs becomes less well-defined with a broader peak that has a maximum intensity at higher energies and a lower energy tail extending below 2,000 cm^{-1}. The shift in peak maximum intensity toward higher wavenumbers suggests a higher proportion of the silicon trihydride group *SiH_3, and, combined with the lower energy tail, is characteristic of an amorphous, more highly strained surface resulting from Sn incorporation into these alloyed NPs. Figure II.1.B.21b shows the corresponding XRD patterns, with the well-defined peaks corresponding to the (111), (220), and (311) facets pointing to mostly crystalline NPs; however, the elongated aspect of the (220) peak is indicative of some amorphous character.

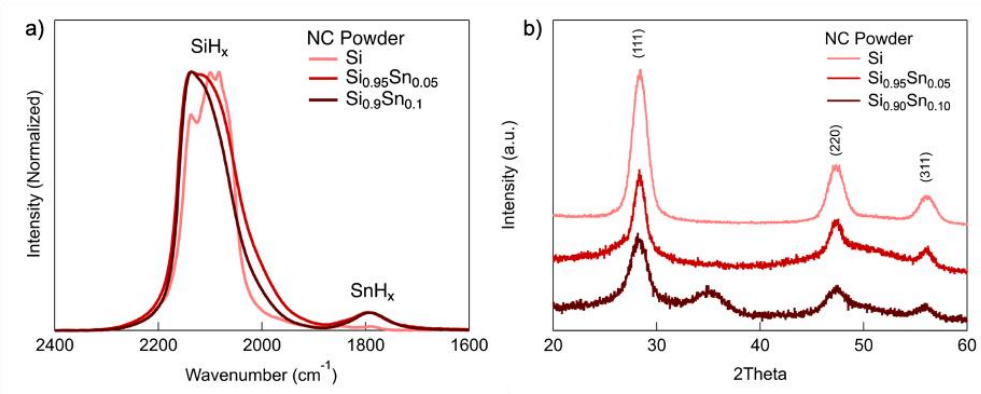

Figure II.1.B.21 (a) DRIFTS spectra for pure Si, 5 atomic % Sn ($Si_{0.95}Sn_{0.05}$), and 10 atomic % Sn ($Si_{0.9}Sn_{0.1}$) NPs. Si-Sn alloys show a peak at 1,790 cm^{-1}, characteristic of SnH_x. (b) XRD patterns for Si, $Si_{0.95}Sn_{0.05}$, and $Si_{0.9}Sn_{0.1}$ NPs. The well-defined peaks point to the formation of a crystalline alloyed material.

As shown in the Q2 report, characterization on Si-Sn alloys was also done using TEM and EDS to examine the crystalline and elemental composition of the Si-Sn NPs. Figure II.1.B.22 shows a TEM image of a cluster of $Si_{0.9}Sn_{0.1}$ NPs in which the NPs appear highly monodisperse. The right-hand side of Figure II.1.B.22 displays EDS data. The bottom-left and bottom-right images map Si and Sn, respectively, within the NP sample. Importantly, the Sn signal is observed to track the Si signal, which provides evidence of alloy formation, whereas Sn hotspots would be indicative of phase segregation or pure-phase Sn particles. From the EDS, the Si:Sn ratio is calculated to be 85:15 at. %, which compares well with our Si:Sn 90:10 gaseous precursor ratio.

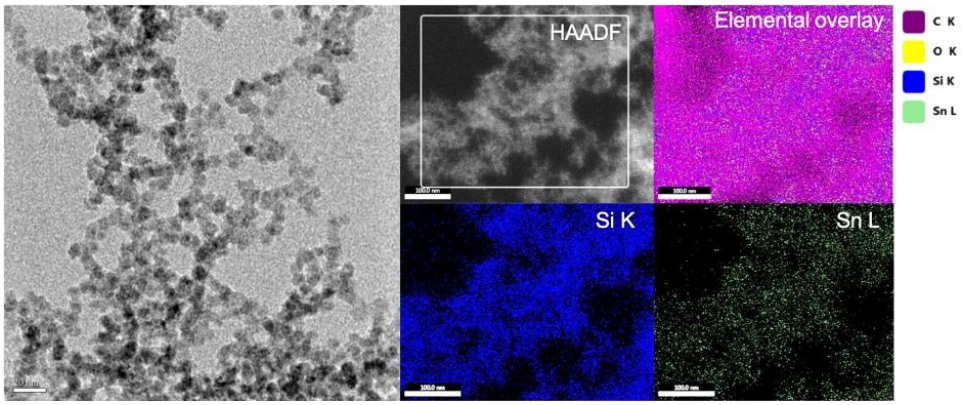

Figure II.1.B.22 Left: TEM image of a cluster of $Si_{0.9}Sn_{0.1}$ NPs. Scale bar is 20 nm. Right: EDS elemental analysis of the same NP sample shown on the left. Top left shows the HAADF image, whereas the bottom left and bottom right show Si and Sn mapping, respectively. The Si and Sn are seen to track each other, showing evidence of alloy formation. The top right shows the elemental map overlay including C, O, Si, and Sn.

These Si-Sn alloy NPs were constructed into composite anodes using our air-free methodology slurry and electrode fabrication processes described in other SEISta reports. In brief, two different compositions and sizes—7.4-nm $Si_{0.95}Sn_{0.05}$ and 5.1-nm $Si_{0.9}Sn_{0.1}$. Si-Sn NPs—were first blended into N-methylpyrrolidone (NMP) slurries with PAA binder and Timcal C65 conductive carbon. Si-Sn NPs and C65 conductive carbon were added at a 1:1 mass ratio, yielding anodes of ~33 wt % active material. Coin cells were then fabricated using a Li metal cathode and Gen2 electrolyte with 10 wt % FEC (Gen2F electrolyte). Cells were cycled at C/20 for three formation cycles and then C/5 for all additional cycles.

Figure II.1.B.23 displays plots of the electrochemical cycling data for the Si-Sn NP composite anodes and compares these directly to our intrinsic Si baseline electrodes. Specific capacity is quite reasonable for both alloy anodes, which retain greater than 90% of their original (fourth-cycle) capacity after 100 cycles. This

value compares well with that of pure intrinsic Si@NMP NP-based anodes, as both alloys and pure-phase particle exhibit about the same capacity retention (Figure II.1.B.23c). Particularly noteworthy is the rapid stabilization of the CE in the first four cycles. Anodes made using $Si_{0.95}Sn_{0.05}$ NP anodes reach their maximum CE on the fifth cycle, whereas $Si_{0.95}Sn_{0.05}$ NP anodes are within 0.1% of their maximum CE by the fifth cycle (i.e., essentially stabilized by the fifth cycle). As part of our durability study, we have come up with a new metric for evaluating half-cell and full-cell data that can be used to quantify cycle life of anodes by plotting $CE_{cycle\ n}$ vs. cycle number (i.e., the cumulative CE over all cycles). For these Si-Sn alloy NP-based anodes, the cumulative CE over all cycles is just below 40% after 100 cycles, which is a vast improvement compared with that of intrinsic Si anodes with the same NMP surface coating (~15%, Figure II.1.B.23d).

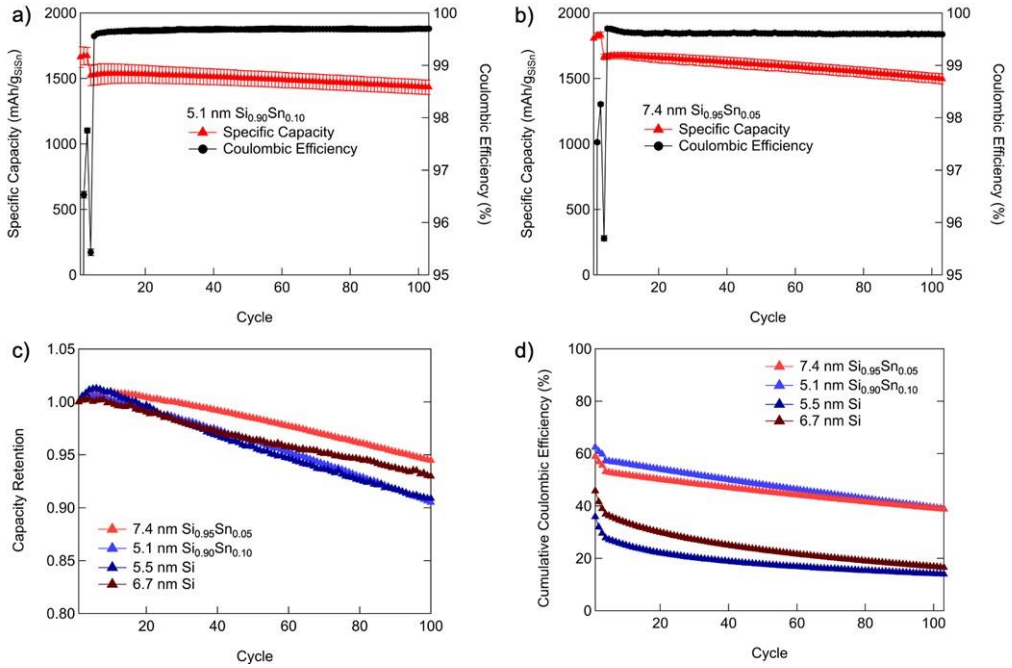

Figure II.1.B.23 Cycling performance for Si-Sn composite anodes. Specific capacity and coulombic efficiency over 103 cycles (3 forming cycles at C/20 and 100 cycles at C/5) are shown for (a) 5.1-nm $Si_{0.9}Sn_{0.1}$ and (b) 7.4-nm $Si_{0.95}Sn_{0.05}$-based NP anodes. Error bars are a one sigma deviation from a set of three anodes. (c) Capacity retention with respect to the fourth cycle and (d) cumulative coulombic efficiency over 103 cycles, including the forming cycles for the electrodes for both Si-Sn alloys and pure-phase Si NP-based anodes.

Finally, Figure II.1.B.24 shows differential capacity curves for the first three formation cycles at C/20 for Si-Sn NP composite anodes. Both plots show characteristic features during the first lithiation cycle at 1.2, 0.9, and 0.1 V vs. Li^+/Li that are attributed to SiH_x reduction, SEI formation, and crystalline Si lithiation, respectively. Subsequent lithiation cycles show features at 0.21 and 0.07 V vs. Li^+/Li that are indicative of amorphous Si lithiation, as expected for the second cycle and beyond. Interestingly, both the 5.1-nm $Si_{0.9}Sn_{0.1}$ and the 7.4-nm $Si_{0.95}Sn_{0.05}$ anodes exhibit a reduction feature at ~0.45 V vs. Li^+/Li during lithiation and a corresponding oxidative process as a shoulder on the delithiation peak centered at ~0.7 V vs. Li^+/Li. In previous SEISta reports, we have discussed this feature occurring with increasing intensity with decreasing Si NP size and believe it is related to surface strain at smaller NP sizes that may enhance Li-ion diffusion through the Si-SEI-electrolyte interface. Here, this feature appears to be about the same intensity for anodes made from both the 5.1-nm $Si_{0.9}Sn_{0.1}$ and the 7.4-nm $Si_{0.95}Sn_{0.05}$ NPs, and thus appears to be independent of size. We posit that the size independence of this feature for both 5.1- and 7.4-nm Si-Sn NP-based anodes is evidence of a strain-related effect due to Sn incorporation.

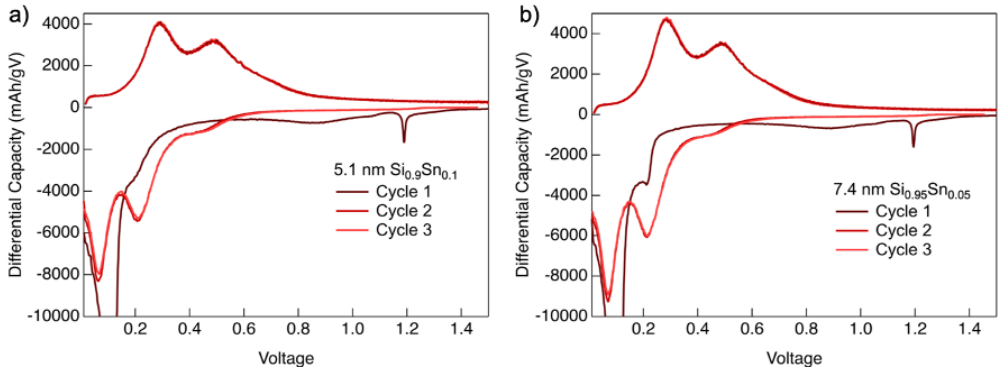

Figure II.1.B.24 Differential capacity plots for Si-Sn composite anodes. Differential capacity is shown for the first three cycles (C/20) for (a) 7.4-nm $Si_{0.95}Sn_{0.05}$ and (b) 5.1-nm $Si_{0.9}Sn_{0.1}$ anodes.

Investigation on Si-Based Metallic Glass Prepared by Splat Quenching

Materials synthesis and characterization

Metallic glasses are amorphous alloys produced from rapid cooling of a liquid melt to suppress the nucleation and growth of the crystalline phase. These rapid cooling rates can be achieved by several techniques, including sputtering, mechanical milling, melt spinning, and splat cooling [1]. Splat cooling is advantageous because practical sample sizes can be synthesized and high cooling rates can be achieved [2].

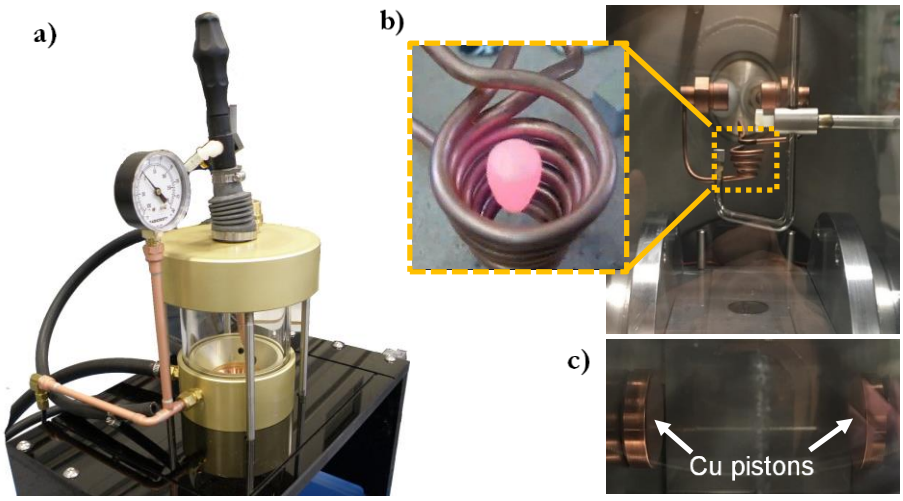

Figure II.1.B.25 Photographs of the arc-melter and the splat cooling system. (a) The parent $Al_{64}Si_{25}Mn_{11}$ alloy is fabricated by arc-melting Al, Si, and Mn powders. (b) The parent alloy is liquified by the induction levitation technique. (c) The two copper pistons splat cools the melt at a rate of ~10^5–10^6 K/s.

A splat cooling system heats an alloy inductively through the levitation melting technique. In the levitation melting technique, an alternating high current is applied through a levitation copper coil. The alternating current generates a high-frequency electromagnetic field, which produces the eddy current in the alloy. The eddy current plays two important roles: (1) melting the alloy by induction heating (typically above 1,000ºC) and (2) generation of electromagnetic body force, which makes the molten droplet levitate by balancing the gravimetric force. After a sufficient melting and homogenizing of an alloy, the levitation force is removed by stopping the alternating current. Subsequently, the molten metal is dropped at free fall, which is captured by a laser detection module. The laser detection activates the high-speed motion of two copper pistons to "splat" the molten droplet. This process quickly quenches molten metals using cold metal surfaces at the cooling rate ranging from 10^5 to 10^8 Ks^{-1}. The entire synthesis is conducted in a high-purity Ar-filled environment, which

allows minimal contamination of the alloy. However, the technique enforces at least one of the alloy components to have a ferromagnetic property for the electromagnetic levitation.

Among all Si-MGs, Al-Si-X (Cr, Ni, Fe, Mn) alloys are of particular interest because they have good glass-forming ability and large composition ranges can be fabricated through economical techniques [3]. Manganese is chosen as the third element due to its lower melting point and low cost. $Al_{64}Si_{25}Mn_{11}$ glass is prepared by rapidly cooling a liquid metal melt of a parent alloy using a splat cooling system. The parent alloy, which has the same composition as the glass ($Al_{64}Si_{25}Mn_{11}$), was prepared by melting stoichiometric amounts of Al, Si, and Mn powder in an arc melter under Ar (Figure II.1.B.25a). The parent alloy was then melted at ~1,100ºC in the splat cooling system through an induction levitation technique (Figure II.1.B.25b) and cooled by copper pistons at the rate of 10^5–10^8 K/s (Figure II.1.B.25c). The crystallinities of the parent alloy and the resulted rapid-cooled glass are measured by XRD (Figure II.1.B.26a). The parent alloy consists of three phases: crystalline Si (Fd-3m, JCPD No. 00-003-0549), Al (Fm-3m, JCPD No. 00-001-1179), and intermetallic $Al_{4.01}MnSi_{0.74}$ (Pm-3, 01-087-0528). After splat cooling, all crystalline peaks resolved into two broad bands at 20º and 42º, which suggests that the resulting material has an amorphous structure.

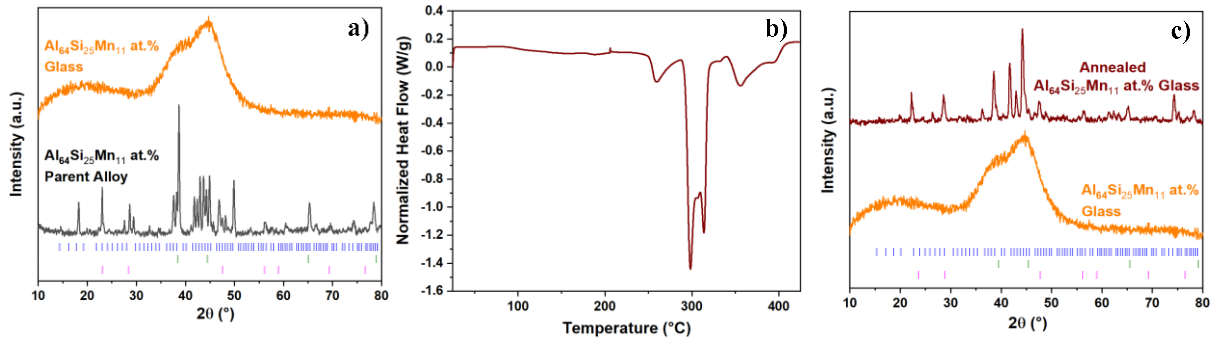

Figure II.1.B.26 (a) Powder XRD of the parent $Al_{64}Si_{25}Mn_{11}$ parent alloy (gray) and the amorphous analogue after rapid quenching (orange). (b) DSC curve of $Al_{64}Si_{25}Mn_{11}$ glass. (c) XRD of $Al_{64}Si_{25}Mn_{11}$ glass after DSC (red) in comparison to the pristine amorphous $Al_{64}Si_{25}Mn_{11}$ alloy (orange).

The amorphicity of the glass is further confirmed by DSC. The DSC curve (Figure II.1.B.26b) shows clear exothermic peaks, related to the crystallization process that the amorphous splat-quenched materials undergo at around 300ºC. Thus, these peaks correspond to the crystallization temperature, Tc, of the metallic glass. This crystallization is confirmed by XRD (Figure II.1.B.26c); the amorphous XRD pattern (the two broad humps) turn into sharp peaks, indicating the glass becomes a crystalline material after the DSC test.

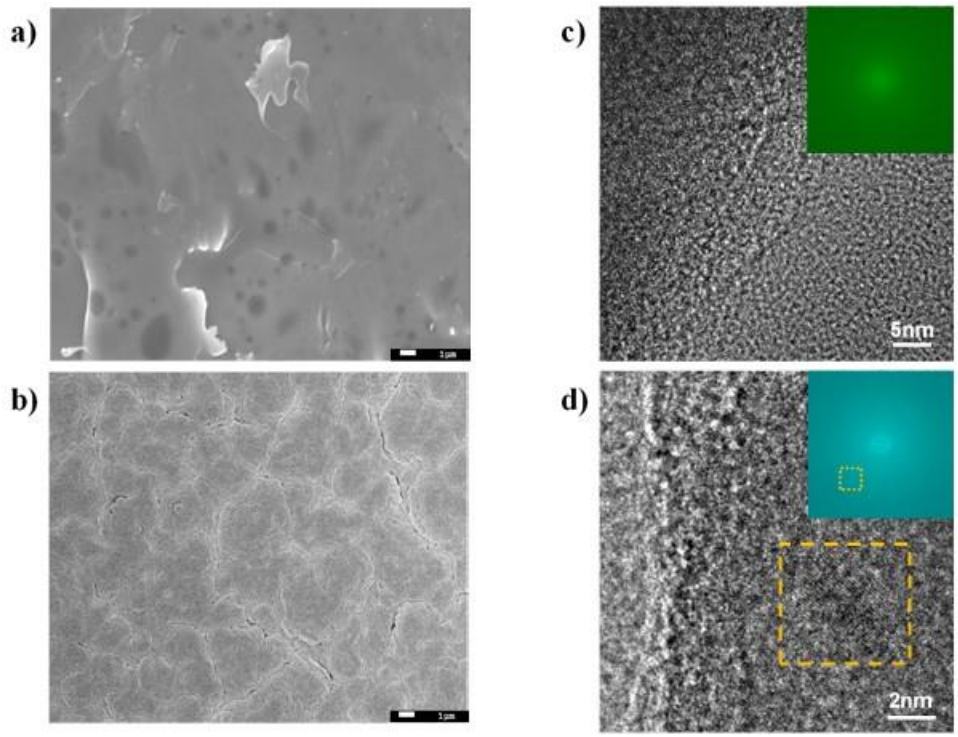

Figure II.1.B.27 (a) An SEM image of $Al_{64}Si_{25}Mn_{11}$ glass. (b) An SEM image of Si thin-film model electrode. (c) High-resolution TEM image of $Al_{64}Si_{25}Mn_{11}$ glass showing amorphous structure. (d) High-resolution TEM image of $Al_{64}Si_{25}Mn_{11}$ glass showing a nanocrystal grain with the size of ~4 nm (highlighted by a yellow box). The insets in (c) and (d) show the corresponding selected area electron diffraction (SAED).

The as-synthesized metallic glass is also analyzed using SEM and TEM. The SEM image of the metallic glass (Figure II.1.B.27a) shows dense and smooth surface topography in comparison to the Si thin-film model electrode counterpart prepared by sputter deposition (Figure II.1.B.27b). The TEM images and the corresponding SAED patterns show that the metallic glass predominantly has an amorphous phase (Figure II.1.B.27c). We conducted extensive TEM imaging and discovered that the only region of non-amorphicity are rare and isolated spots, with a maximum diameter of about 4 nm (yellow square in Figure II.1.B.27d).

Electrochemical characterization

The electrochemical characteristics of the metallic glass ($Al_{58}Mn_{12}Si_{30}$) is examined using various electrochemical methods: CV, galvanostatic cycling (GC), and electrochemical impedance spectroscopy (EIS). The metallic glasses are cycled using the standard three-electrode Swagelok cells against lithium in the Gen 2 electrolyte (1.2 M $LiPF_6$ EC:EMC (3:7 wt %)).

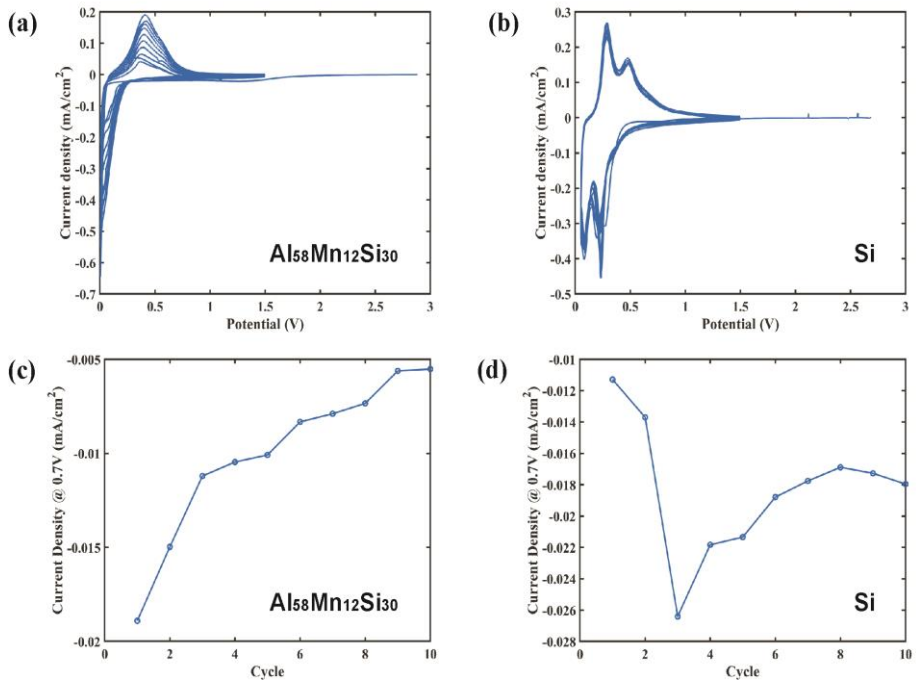

Figure II.1.B.28 Cyclic voltammograms of (a) $Al_{58}Mn_{12}Si_{30}$ and (b) Si at 0.1 mV/s for 10 cycles. The evolution of current density at the potential value of 0.7 V for (c) $Al_{58}Mn_{12}Si_{30}$ and (d) Si.

First, $Al_{58}Mn_{12}Si_{30}$ glass and the 500-nm Si model electrode are subjected to 10 CV cycles at the voltage sweep rate of 0.1 mV/s (Figure II.1.B.28a,b). The voltage sweep ranges are set to be 5 mV to 1.5 V and 50 mV to 1.5 V for the metallic glass and the Si model electrode, respectively. The cyclic voltammogram of $Al_{58}Mn_{12}Si_{30}$ shows a sharp cathodic peak during the first lithiation, which may be attributed to the slow diffusion of Li in the metallic glass. The lithiation peak broadens, and the magnitude of the anodic peak increases as the cycling number increases, indicating gradual activation of the metallic glass (Figure II.1.B.28a). Figure II.1.B.28c,d presents the current density values at 0.7 V during the lithiation process extracted from the cyclic voltammogram. The reasoning for choosing 0.7 V is because it is lower than the EC reduction potential and higher than the lithiation potential. Thus, the current density at 0.7 V can serve as a representation of interfacial instability. The metallic glass shows the current density of ~19 $\mu A/cm^2$ in the first cycle, which progressively decreases to 5 $\mu A/cm^2$ in the tenth cycle (Figure II.1.B.28c). The Si thin-film counterpart shows the current density of ~11 $\mu A/cm^2$ in the first cycle, which fluctuates in the range of 15–27 $\mu A/cm^2$ in the subsequent cycles (Figure II.1.B.28d). The overall magnitude of the current density of Si at 0.7 V is three- to fourfold higher than that of $Al_{58}Mn_{12}Si_{30}$.

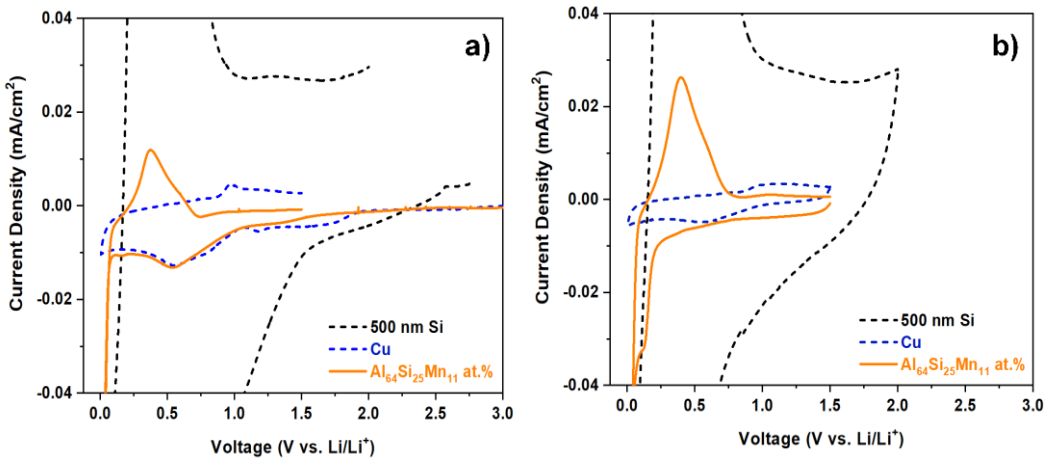

Figure II.1.B.29 Cyclic voltammogram of 500-nm Si model electrodes (dash/black), Cu foil (dash/blue), and $Al_{64}Si_{25}Mn_{11}$ glass (orange) during the (a) first and (b) second cycle.

Figure II.1.B.29 presents the CV curves of a 500-nm Si model electrode, $Al_{58}Mn_{12}Si_{30}$ glass, and a Cu foil obtained from a separate set of CV experiments. The CV curve of the $Al_{58}Mn_{12}Si_{30}$ shows the substantially lower current density at around the SEI formation potential (~0.6 V) compared to the Si model electrode; the current density in the potential region is comparable to that of Cu, which is known to form a stable passivation layer. This set of CV investigations suggests the stable formation of SEI on the $Al_{58}Mn_{12}Si_{30}$ surface.

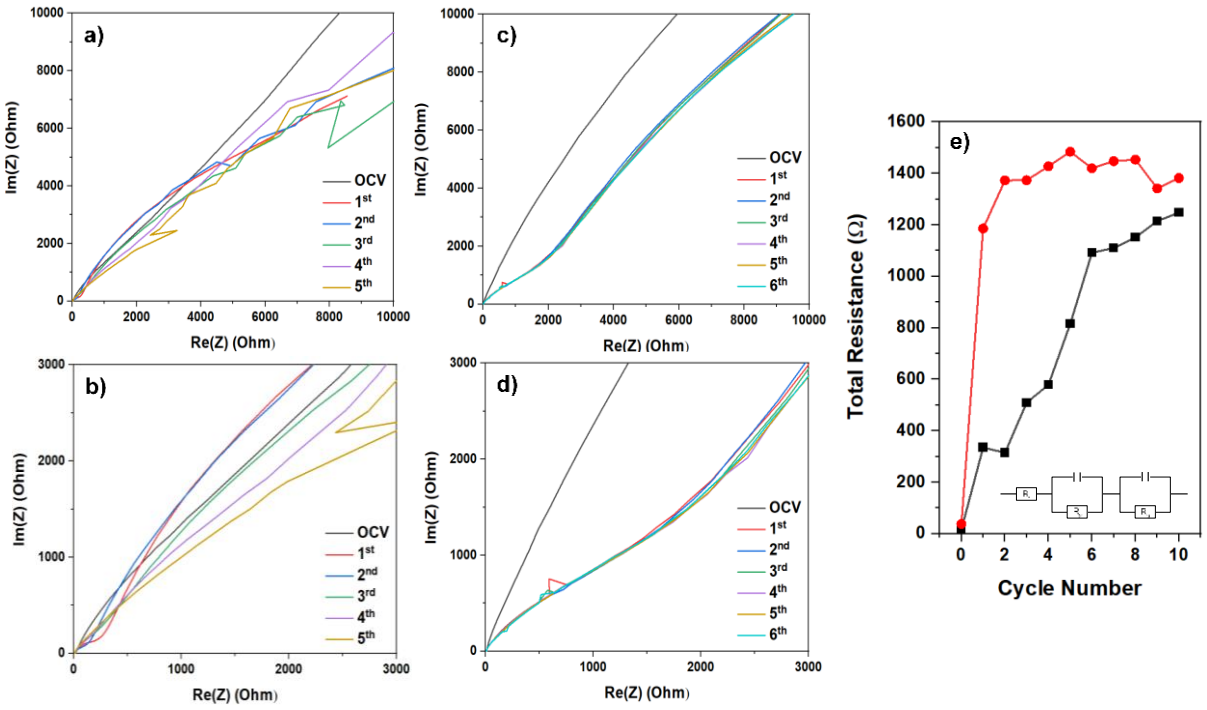

Figure II.1.B.30 (a) Nyquist plots of Si model electrode and (b) their magnified view. (c) Nyquist plots of $Al_{58}Mn_{12}Si_{30}$ glass and (d) their magnified view. (e) The total resistance evolutions of the metallic glass and the Si model electrode with increasing cycle number.

We further confirm the improved interfacial stability of $Al_{58}Mn_{12}Si_{30}$ by EIS. EIS is measured after each CV cycle to compare the stability of SEI between the Si model electrode (Figure II.1.B.30a,b) and the $Al_{58}Mn_{12}Si_{30}$ glass (Figure II.1.B.30c,d). The total resistance accounting for the electrode, electrolyte, and the interface is calculated from the Nyquist plot and presented in Figure II.1.B.30e. It is clear from the total

resistance evolution that the $Al_{58}Mn_{12}Si_{30}$ glass formed a stable SEI during initial cycles, whereas Si forms continuously evolving SEI.

To assess the specific capacity, three independent $Al_{58}Mn_{12}Si_{30}$ pellets are galvanostatically cycled at a current density of ~50 μA/cm^2. It should be noted that the metallic glass is in a foil form with the lateral dimensions in millimeter scale and the thickness of 2–4 mm. With the enormous volume change of both Al and Si, the foil form of metallic glass is expected to undergo severe mechanical degradation. Thus, only the first discharge capacity is selected to evaluate the specific capacity. Figure II.1.B.31 shows the potential profiles of three $Al_{58}Mn_{12}Si_{30}$ during one galvanostatic cycling. The average specific discharge capacity of $Al_{58}Mn_{12}Si_{30}$ is ~950 mAh/g, with the maximum value of 1,150 mAh/g. The measured capacity is already comparable to its theoretical capacity of ~1,490 mAh/g. It is found that the galvanostatic cycling causes severe pulverization (inset of Figure II.1.B.31). Thus, optimizing the electrode structure is expected to improve the practical capacity close to its theoretical capacity.

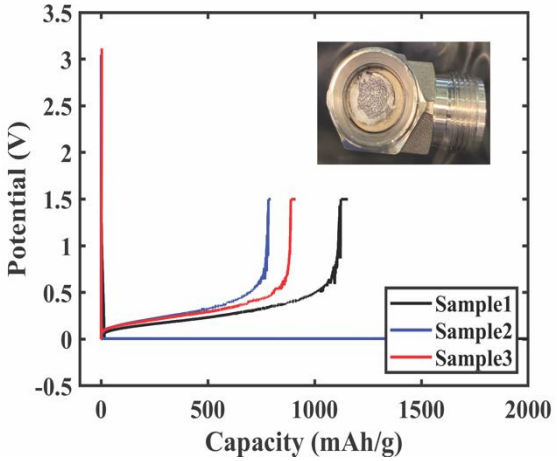

Figure II.1.B.31 Galvanostatic cycling of three $Al_{58}Mn_{12}Si_{30}$ glass samples. One GV cycling causes a drastic pulverization of the metallic glass (inset).

For XPS characterization, the $Al_{58}Mn_{12}Si_{30}$ film is subjected to a linear voltage sweep from the open circuit potential to 5 mV (half CV cycle) vs. Li at a sweep rate of 0.1 mV/s. Both this sample and pristine MG were analyzed. In the pristine sample (Figure II.1.B.32), all the constituent elements are detected but in slightly different concentrations than the nominal stoichiometry. The composition at the surface is $Al_{84}Mn_{01}Si_{15}$. Further, the more oxyphilic elements—Al and S—are in part oxidized. It is unclear if this is just a small amount of surface oxidation or if it is a property of the bulk, due to the fact that the pristine powders were exposed to an ambient atmosphere.

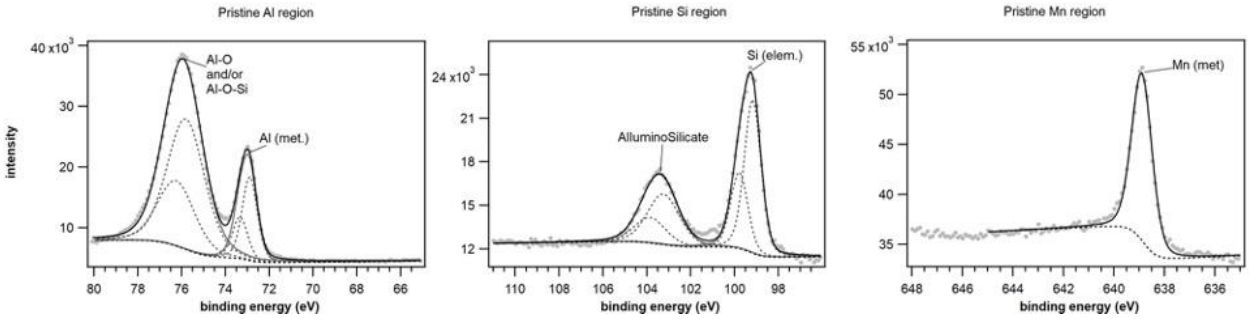

Figure II.1.B.32 XPS spectra of the glasses in pristine state. A small amount of oxides was detected in addition to the elements in their unreacted metallic state.

The BM glasses were further analyzed after the first lithiation step. The constituent elements of the MG do not show much evolution except for the oxide's components (Figure II.1.B.35). The aluminosilicate phase in part

converts to the binary oxides and the silicon peak further shows a component attributed to fluorinated silica. A small amount of manganese oxide is also formed.

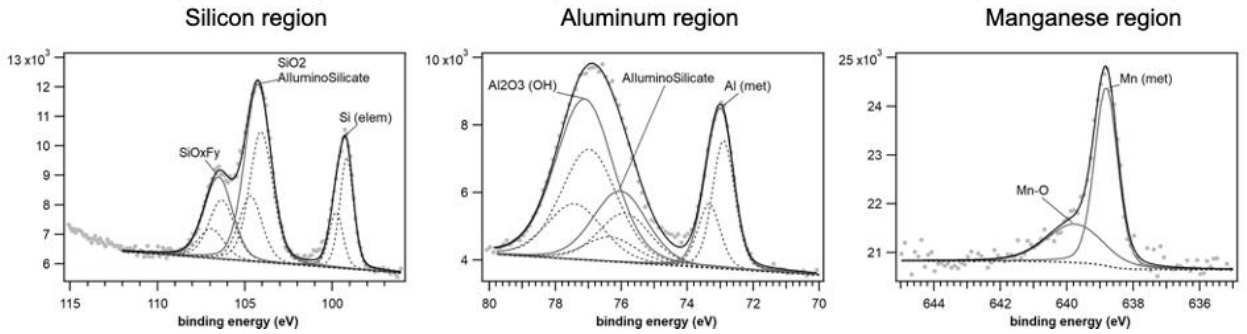

Figure II.1.B.33 XPS spectra of the BM glasses in pristine state. A small amount of oxides was detected in addition to the elements in their unreacted metallic state.

In terms of the SEI formed during the lithiation steps, we can claim that this is a very thin layer, in agreement with the CV data showing very limited charge consumption. This statement is based on the fact that all the constituent elements of the metallic glasses' electrode can be easily detected—Al, Si, and Mn—which means that the SEI is much thinner than the probing depth of these measurements (4–6 nm). This is the opposite of what happens for the Si anode, where a thick SEI is formed on the electrode surface. The composition of the SEI is also different from the one usually observed in silicon (Figure II.1.B.34). The most noticeable difference is the complete absence of carbonate decomposition products. The C1s core levels shows some compounds that contain oxygen, but at the moment it is not possible to determine the exact nature of these species and FTIR will have to be performed to be conclusive. The main SEI components are the decomposition products of the salt, namely LiF and fluorophosphates.

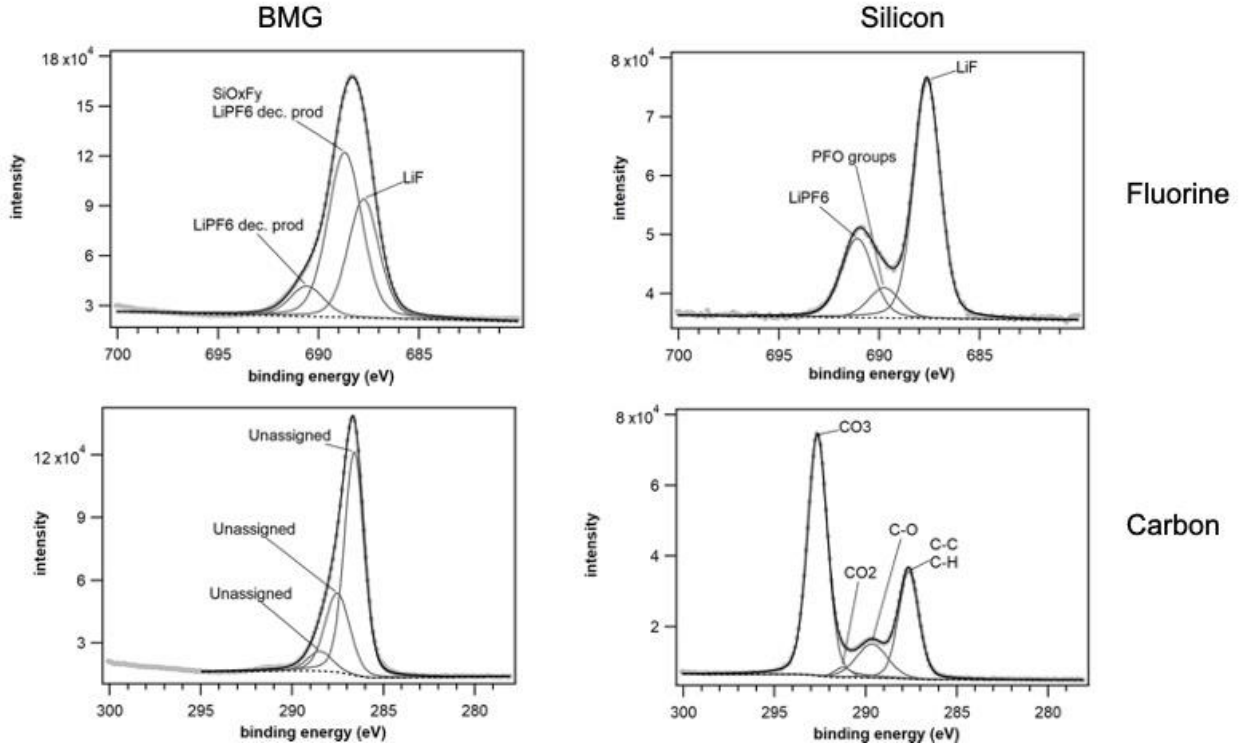

Figure II.1.B.34 XPS spectra of the BM glasses (BMG) SEI components compared to the SEI formed on Si anodes. A much thinner SEI is observed, which is also compositionally different.

Overall, the metallic glasses show an improved surface passivation in comparison to Si as demonstrated by a lower-charged consumption in electrochemical test and much thinner SEI as determined by spectroscopic methods, consisting primarily of inorganic species.

Alloying mechanisms

In order to maintain structural integrity and avoid pulverization, the glass should remain amorphous throughout electrochemical cycling. In this regard, it is essential to investigate whether $Al_{64}Si_{25}Mn_{11}$ glass phase separates into crystalline phases as it alloys with Li. Ex situ XRD (Figure II.1.B.35a) is performed on $Al_{64}Si_{25}Mn_{11}$ glass at the lithiated (0.005 V) and delithiated (1.5 V) states to investigate the possible phase change during cycling. At the lithiated state, a broad-band emerged at higher 2θ, at 62°, indicating a formation of a new amorphous phase. The broad-band observed at ~42°, which also presents in the XRD pattern of the as-synthesized, can be explained by incomplete lithiation of the glass foil. The additional peak visible in the XRD pattern of the lithiated stage is attributed to LiF and Li_2CO_3 electrolyte decomposition products, as films were only dried but not washed off prior to the XRD measurements. At the delithiated state, the intensity of the broad peak at 2θ = 62° decreased. The peak is not expected to fully disappear based on the irreversibility observed in the CV and galvanostatic cycling curves. The increased intensity of the 2θ = 42° peak and the reemergence of the broad-band at lower 2θ indicates the formation of the original $Al_{64}Si_{25}Mn_{11}$ phase observed in the pristine samples. Most importantly, no crystalline phases were observed, suggesting $Al_{64}Si_{25}Mn_{11}$ glass remains amorphous throughout the cycling. For further confirmation, ex situ TEM analysis was conducted on the lithiated glass (Figure II.1.B.35b). The high-resolution TEM and the SAED pattern of the lithiated glass show no sign of a crystalline phase, which agrees with the results from the ex situ XRD measurements.

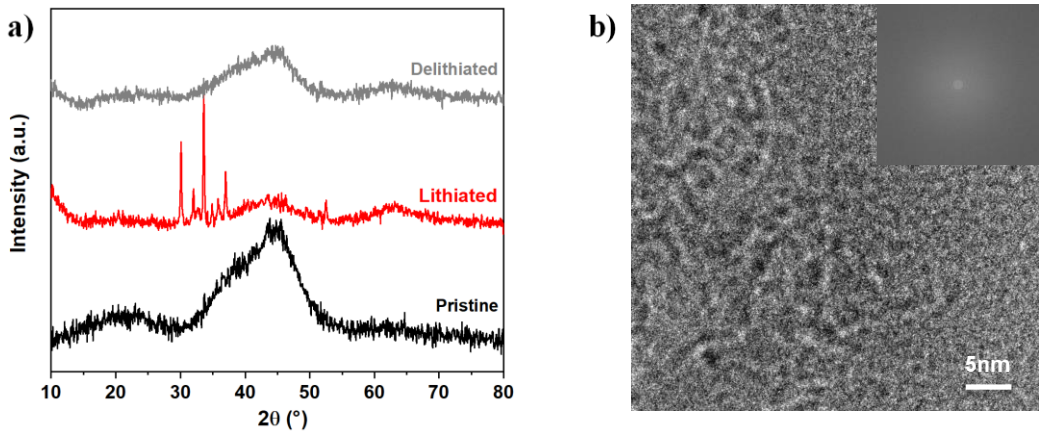

Figure II.1.B.35 (a) Ex situ XRD of the $Al_{64}Si_{25}Mn_{11}$ glass at the pristine state (black), lithiated state (red), and delithiated state (gray). (b) Ex situ TEM of the $Al_{64}Si_{25}Mn_{11}$ glass at the lithiated state.

Density Functional Theory and Ab Initio Molecular Dynamics Studies on Various Si-Based Alloys

Volumetric expansion is perhaps the most crucial factor in the cycling stability of an electrode, as evidenced by the wide body of published research surrounding morphological tuning of Si to mitigate electrode cracking from volumetric expansion. Obrovac et al. previously claimed that the volumetric expansion of Si electrodes cannot be mitigated through the use of alloyed components, because the volumetric expansion is linearly proportional to the number of Li atoms alloyed [4]. Although this is generally true in crystalline alloys, we find that this is not the case for amorphous alloys. The Li partial molar volume in crystalline silicides is constant, 14.8 $Å^3$ per Li atom; however, in amorphous silicides, it can vary between ~12 and 21 $Å^3$ per Li atom, as seen in Figure II.1.B.36. The effects of Li partial molar volume can be seen when comparing MnSi and SiNi, both of which have nearly identical initial molar volumes; however, the Li partial molar volume is lower in SiNi. Although the Li partial molar volume is 14% lower than MnSi, the volumetric expansion at $x_{Li} = 0.5$ is nearly the same. Additionally, a low Li partial molar volume is most prevalent in compositions that have a low unlithiated molar volume.

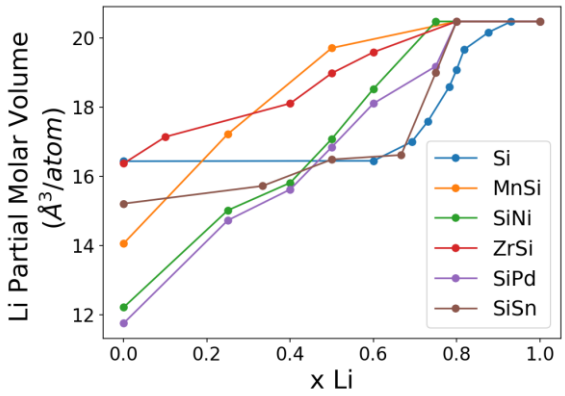

Figure II.1.B.36 Li partial molar volumes of Si alloy electrodes.

More impactful to the volumetric expansion is the initial molar volume of the electrode. As illustrated in Figure II.1.B.37, the Si alloys with the highest initial molar volume (Si-Sn) have the lowest volumetric expansion. Likewise, MnSi and SiNi have the lowest molar volumes and in turn have the largest volumetric expansions. With this in mind, we conclude that alloyed components, although capable of mitigating volumetric expansion, do so at the expense of volumetric energy density.

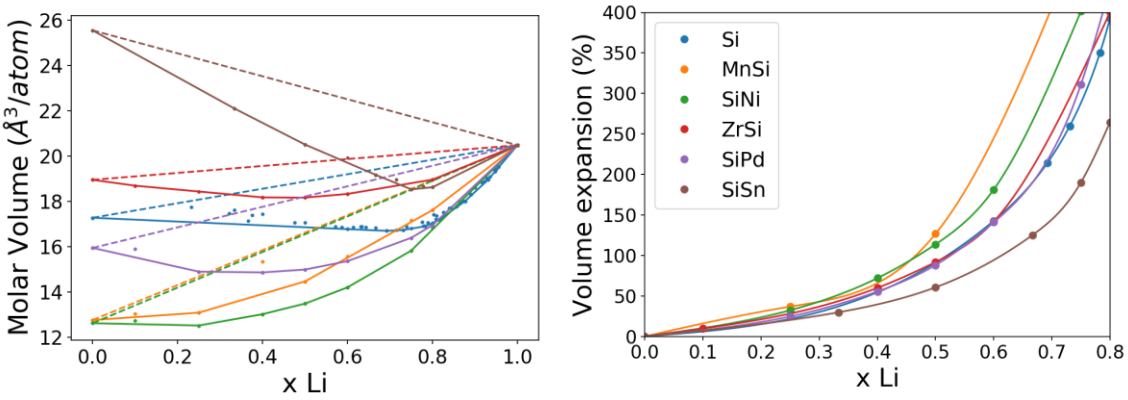

Figure II.1.B.37 (a) Molar volumes and (b) volumetric expansion of Si alloy electrodes. The dotted lines in (a) indicate the volume of ideal mixtures.

In addition to the volumetric expansion, we have investigated the Si clustering and networking behavior in the Si alloys upon lithiation. We have previously reported on the clustering of Si, finding a quick decline in the amount of networked Si as Li is alloyed, eventually breaking up into aggregates of 2, 3, 4, and 5 atoms. We have extended this analysis, converting each structure into graph representations, where each atom and bond is represented by a node and edge, respectively. By including periodic boundary conditions, we can easily identify aggregates as connected components; all other Si atoms are considered networked. This is used to explicitly identify Si networks and track their breakup. In the case of pure Si, the Si becomes half-networked at $x_L \approx 0.28$. When alloyed with active elements, the Si networks persist longer than in the base case. This is generally due to the active element lithiating before Si, allowing larger Si aggregates/networks to remain. Conversely, inactive elements result in a breakup of the network at lower lithiation levels. This is primarily the result of more uniform distribution due to the favorable bonding between Si and the inactive elements.

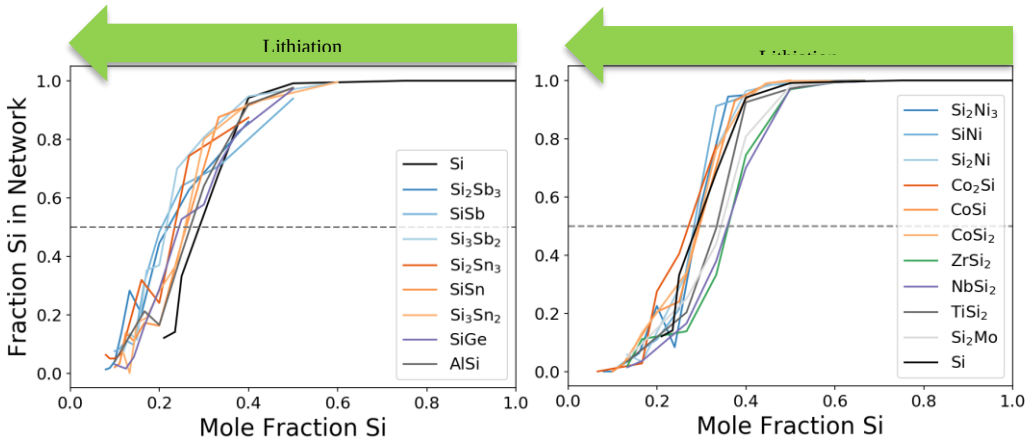

Figure II.1.B.38 Si connectivity/networking in binary Si alloys with active (left) and inactive elements (right). Dotted line is a reference line indicating the point at which half the Si atoms are not clustered.

Understanding SEI Chemistry

It has become abundantly clear that the solid–electrolyte interface on a silicon electrode is unstable, resulting in a poor calendar life. We have coined this effect "breathing" due to the continuous decomposition and reformation of the SEI with cycling and at various states of charge along with the commensurate growth of a thick or thin SEI structure at these various states of charge. What is not clear is how changes in the surface chemistry and electrolyte chemistry may affect this SEI stability and breathing. This fundamental lack of knowledge prompted the areas of inquire detailed here.

The first focus area revolved around identifying what the role is of a silicon oxide surface versus a pure silicon or silicon sub-oxide surface. Previous work in FY 2019 revealed that the choice of silicon surface chemistry resulted in drastic changes in electrolyte decomposition at open circuit voltage. This year, we explored the possibility of the change in surface chemistry directing the formation of a more (or less) stable SEI layer.

Another focus area involved understanding how a binder changes the SEI. In composite cells, the binder covers all or some of the available surface area, likely indicating that this will directly mediate SEI formation. Indeed, in FY 2019, neutron reflectivity work revealed that a binder may act as an ion- or solvent-selective membrane, enabling the transport of one or more species to the surface where they may form an SEI layer. Could this effect be used more extensively to control and direct the SEI formation and improve stability by driving specific ions or molecules to the surface or preventing them from leaving?

The third area focuses on new electrolyte formulations. It has become clear that the standard 1.2 M $LiPF_6$ ethylene carbonate/ethyl methyl carbonate electrolyte (commonly described as Gen 2) is not stable in direct contact with most silicon-based surfaces over extended calendar lifetimes. The SEISta team previously identified that one of the stable species on a silicon electrode was an ether functionality. Based on this result, the team explored glyme-based electrolytes (ether functionality).

The fourth area of focus was on the use of gaseous additives (CO_2) as a way to promote the SEI formation reaction. This approach differs from the traditional use of additives like vinylene carbonate or FEC. This approach also offers the opportunity to explore what happens to the gasses produced when the electrolyte decomposes with cycling.

In a fifth area, the team focused on understanding the mechanical properties of the SEI. The hypothesis was that the mechanical stability of the SEI could play a role in stabilizing the silicon at extended periods of time and low voltages (<0.1 V). To explore this hypothesis, we undertook various mechanical and optical experiments to evaluate the mechanical stability of the SEI as a precursor to changing the electrolyte composition in a way to introduce improved mechanical stability.

Finally, we explored how both size and surface chemistry of silicon nanoparticles grown via nonthermal PECVD synthesis affect the performance and stability of Si NP-based composite anodes. Specifically, we compared how the SEI growth and dissolution differs in 3.9-nm vs. 30-nm-diameter Si NPs. We also explored hydrophobic vs. hydrophilic molecular coating on the Si surfaces to test the influence of the differing ionic and electron properties of the formed coatings.

Role of surface oxides in SEI formation and chemistry – vapor deposited films

To alleviate the large volume change, silicon oxides have been considered as alternatives to pure silicon electrodes. There have been some mechanistic studies about the lithiation process of SiO as anodes in lithium-ion batteries; however, it is not yet fully understood how different levels of oxygen in the SiO_x electrodes affect the lithiation behavior and the SEI formation. The presence of oxygen is almost inevitable in Si anodes, where the surface of Si forms a native oxide layer when exposed to air; different preparation processes for Si electrodes may also lead to different levels of oxygen content in the bulk Si. To investigate the role of oxygen in Si anodes, we prepared model Si thin-film electrodes with different levels of oxygen to study their lithiation behaviors and the SEI formation. We have demonstrated the impact of oxygen on the electrochemical behavior of the Si electrodes, where Si electrodes with higher oxygen level in the bulk exhibit a longer irreversible plateau at around 0.6 V during the first lithiation process. In this report, we present the chemical and physical characterization of pristine and cycled electrodes to clarify the impact of oxygen on the SEI formation and the lithiation/delithiation behaviors of Si anodes.

In this study, SiO_x anode with minimum oxygen content (referred to as Si) was prepared by magnetron sputtering of Si target under low base pressure (~2×10^{-7} torr), low deposition pressure (5 mtorr), and short work distance (8 cm). This Si anode was assembled into coin cells after the deposition and did not expose to air in the process. We intentionally expose this Si anode in air to obtain Si with native oxide layer (Si_NO). To prepare SiO_x anodes with higher oxygen level, we performed Si and SiO_2 co-sputtering with different power combinations (90-30 W, 90-60 W, 90-90 W, 60-90 W) for the Si and SiO_2 target and obtained SiO_x anodes with four different oxygen levels.

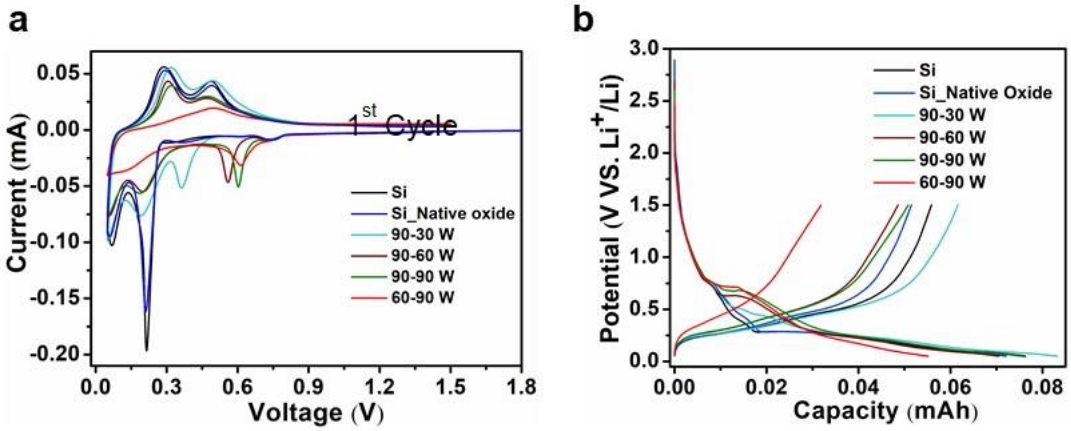

Figure II.1.B.39 The CV and first-cycle galvanostatic charge-discharge profiles of Si, Si with native oxide layer, and four SiO_x anodes with different oxygen levels tested in the potential range of 0.05–1.5 V (a) CV and (b) galvanostatic charge-discharge.

The obtained Si, Si_NO, and SiO_x anodes with different levels of oxygen content were first evaluated with CV. As shown in Figure II.1.B.39a, all the Si, Si_NO, and SiO_x anodes exhibit a small reduction peak at around 0.7 V, which should be due to electrolyte reduction. By comparing Si, Si_NO, and SiO_x anodes, a distinct difference is observed in the first CV cycle. All the SiO_x anodes prepared by co-sputtering show an extra reduction peak in the potential range of 0.3–0.6 V, where the peak position shifts to lower potential with lower oxygen content. The galvanostatic charge-discharge profiles of all Si, Si_NO, and SiO_x anodes (Figure II.1.B.39b) agrees well with the CV data, where the Si and Si_NO show similar shape during the first discharge and the SiO_x anodes with higher oxygen content have a much longer plateau in the potential range of 0.5–0.7 V. The potential of the plateau is higher for SiO_x with higher oxygen level, which again agrees with the potential of the reduction of SiO_x during the first cathodic CV cycle. This potential range should correspond to the reduction of SiO_x by lithium. As the Si anode has very low oxygen content, it did not show this plateau. Even for Si_NO with surface native oxide layer, the oxygen level is still not high enough to exhibit this plateau.

Table II.1.B.4 Summary of SSRM Findings on the Pristine and Cycled Thin-Film Samples

Sample	Original Pristine Film Resistivity	Resistivity Change After Lithiation to 0.55 V	Resistivity Change After Lithiation to 0.05 V	SEI Thickness After Lithiation to 0.05 V
Si (Si/SiO_2 90/0)	~10^3 Ω·cm	Slight decrease	Three order of magnitude decrease	Thickest
Si_NO (Si/SiO_2 90/0)	~10^3 Ω·cm	Slight decrease	Three order of magnitude decrease	Thicker
SiO_x_1 (Si/SiO_2 90/30)	~10^5 Ω·cm	Order of magnitude decrease	Five order of magnitude decrease	Thicker
$SiO_{0.6}$ (Si/SiO_2 90/60)	~10^6 Ω·cm	Order of magnitude decrease	Five order of magnitude decrease	Thin
$SiO_{0.7}$ (Si/SiO_2 60/90)	~10^8 Ω·cm	Greater than order of magnitude decrease	Five order of magnitude decrease	Thin

To understand the cause of the irreversible plateau of the co-sputtered electrodes and the impacts of oxygen on the SEI formation of the Si anodes, we characterized the pristine electrodes and electrodes after their first lithiation to 0.55 V (vs. Li^+/Li, hereafter) and held at that potential for 1 h, with duplicate samples lithiated to a lower potential of 0.05 V. The cycled cells were disassembled in an Ar-filled glovebox and rinsed with dimethyl carbonate (DMC) with no exposure to air in the sample transfer process. The samples were first characterized using the SSRM resistivity vs. depth profiling technique [1]. Results summarizing the electronic resistivity of the pristine films, resistivity change from the pristine samples to the 0.55-V lithiated samples, resistivity change from the pristine samples to the 0.05-V lithiated samples, and formed SEI thickness after full lithiation are depicted in Table II.1.B.4. The pristine samples show the expected result of higher electronic resistivity with higher O content. The change in resistivity from pristine to after lithiation to 0.55 V shows an interesting trend: the two thin films with the lowest O content have a minor decrease in resistivity, whereas the three thin films with nontrivial O content display a significant decrease in resistivity, proportional to the original O content. This result suggests that at 0.55 volts, Si electrodes with oxygen in the bulk undergo a lithiation, whereas lithiation of Si with only surface oxygen does not proceed, resulting in a conductivity enhancement proportional to the original O content. Lithiation to 0.05 V shows a more significant conductivity enhancement for all samples, with a greater conductivity decrease for samples with higher O content. This measured conductivity increase from SiO_x to $Li_xSi_yO_z$ is consistent with experimental results established in the literature [2], [3]. SEI thickness after lithiation to 0.05 V was shown to decrease with increasing O content of the pristine electrode.

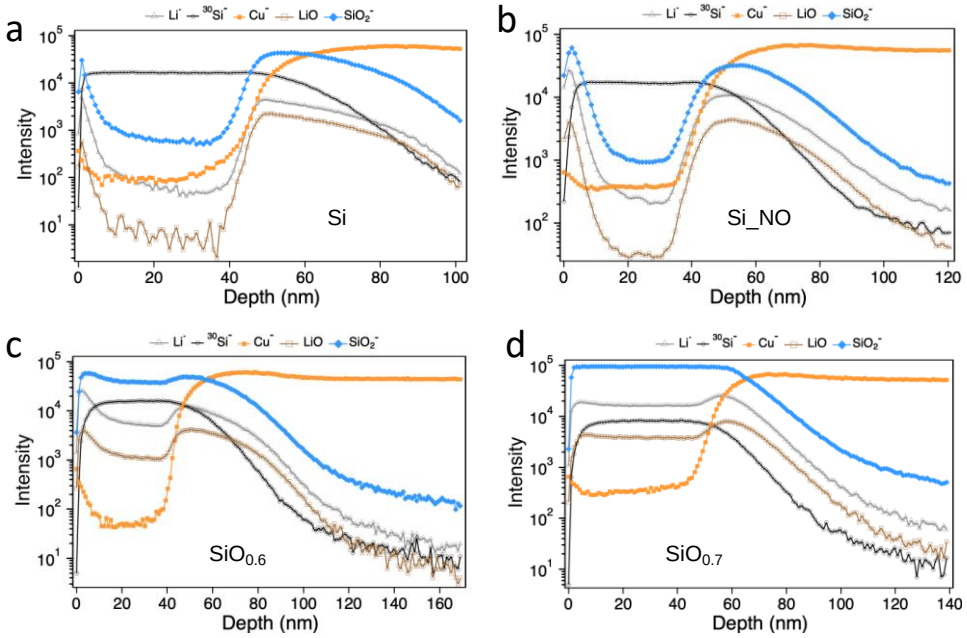

Figure II.1.B.40 TOF-SIMS profiles of the Si, Si_NO, SiO_x (90-60 W) and SiO_x (60-90 W) electrodes after being lithiated to 0.55 V.

Time-of-flight secondary ion mass spectrometry (TOF-SIMS) profiles of the cycled electrodes after lithiation to 0.55 V were collected to further investigate the possible lithiation of electrodes with oxygen in the bulk. As shown in Figure II.1.B.40, the Si and Si_NO electrodes only show Li^-, LiO, and SiO_2^- signal on the surface, which drop quickly along the depth of the samples, revealing that only the surface of these two electrodes contains Li, lithium oxides, and silicon oxides, which should be attributed to SEI. In contrast, both the SiO_x (90-60 W) and SiO_x (60-90 W) electrodes exhibit Li^-, LiO, and SiO_2^- signal throughout the bulk, especially the SiO_x (60-90 W) electrode, which shows steady Li^-, LiO, and SiO_2^- signal along the depth of the sample. This result confirms the lithiation of these two electrodes at 0.55 V, whereas the Si and Si_NO electrodes only contain lithium at the surface, agreeing with the SSRM results. In addition, the presence of LiO signal in the

bulk of the SiO_x (90-60 W) and SiO_x (60-90 W) electrodes indicates that the lithiation of silicon oxides would produce lithium oxides.

We further examined the surface properties of the cycled electrodes via XPS. The surface composition of the electrodes after the first lithiation to 0.55 V and 0.05 V is summarized in Table II.1.B.5. In general, the electrodes lithiated to 0.55 V show lower carbon and oxygen content but higher F, P, and Si content. The much higher Si content suggests a thinner SEI on the electrodes at this potential than those lithiated to 0.05 V as XPS is a surface-sensitive technique, with a sampling depth of 5–10 nm. Because the only source of phosphorous is $LiPF_6$, the relatively high P content of the electrodes at 0.55 V than at 0.05 V indicates that there are more decomposition products from $LiPF_6$ on the surface of the electrodes. After lithiating the electrodes to 0.05 V, the thickness of the SEI increases with a decrease in P and F content and an increase of the C and O content. As the C and O composition is expected to originate from the decomposition of the electrolyte solvent molecules, the change in thickness and composition of the SEI suggests that there is more $LiPF_6$ decomposition in the higher potential range and more electrolyte solvent decomposition in the lower potential range.

Table II.1.B.5 Surface Composition of Cycled Electrodes Obtained from XPS

Atomic composition (%)	C	O	F	P	Si
Si, 0.55 V	19.9	18.3	41.2	2.2	18.4
Si_NO, 0.55 V	36.8	17.0	23.2	2.8	20.2
SiO_x (90-60 W) 0.55 V	37.2	20.1	24.7	1.8	16.2
SiO_x (60-90 W) 0.55 V	25.9	17.0	41.7	1.7	13.7
Si, 0.05 V	56.0	25.4	15.4	0.79	2.47
Si_NO, 0.05 V	41.6	20.1	31.7	1.2	5.5
SiO_x (90-60 W) 0.05 V	36.9	21.8	35.0	1.2	5.1
SiO_x (60-90 W) 0.05 V	64.3	19.6	12.7	1.2	2.2

Furthermore, in the electrodes lithiated to 0.55 V, the P content decreases as the oxygen content of the electrode increases, indicating that oxygen may help suppress the decomposition of $LiPF_6$. When being lithiated to 0.05 V, the electrodes with lower oxygen content show lower Si content but higher C content, except the $SiO_{0.7}$ electrode. The lower Si content again suggests a thicker SEI of the lithiated electrodes, and the higher C content should be due to more electrolyte solvents decomposition. The deviation of the trend for the $SiO_{0.7}$ electrode indicates that it may have quite different lithiation behaviors from other electrodes. Overall, the surface composition of these electrodes lithiated to different potentials reveals the impact of oxygen content on electrolyte decomposition and formation of SEI.

Role of oxides – silicon wafers

In addition to these studies, we also fabricated custom wafer samples for the whole SEISta multi-institutional team, including wafer samples with specialized formfactors (e.g., rotating disc electrodes), and produced diffused dopant profiles and oxide overlayers. In addition, we designed an O-ring cell, distributed it to other SEISta project labs, and demonstrated the methodology to use it for electrochemistry studies. The research effort of our team focused on the role of SiO_2 overlayers, particularly as possible means to stabilize the SEI formation and evolution during cycling [4], [5].

In our contribution to the SEISta project, we performed two systematic studies to elucidate the effect of SiO_2 overlayers on Si anode performance. In the first study, we used thermally grown SiO_2, which is dense and stoichiometric when grown at high T > 700ºC, and varied its thickness over a wide range. We established a thickness range of 1–2 nm of thermal oxide as optimal for the Si anode performance boost—in particular, a more stable SEI and good cyclability. Based on this, in the second study, we compared two thin oxides—high-quality thermal oxide and native oxide—to show that the dense, stoichiometric thermal oxide is far superior for Si anode performance boost via controlled SEI and excellent cyclability. These studies resulted in two journal papers published in 2020 [4], [5].

Importance of isolation of the Si wafer edges by O-ring cells for accurate electrochemical characterization

Si wafers with SiO_2 coatings must be tested in cells that isolate the wafer edges or rear from the electrolyte. Defining the active area by an O-ring is crucial because the edges are not coated with SiO_2 and are thus initially much more electronically conductive. We designed such a cell (Figure II.1.B.41) and showed that it yields an electrochemical response as expected from the 100-nm-thick, insulating SiO_2 (Figure II.1.B.41a)—a purely capacitive response—whereas the coin cell with exposed wafer edges exhibits electrochemistry as expected from a bare Si wafer (Figure II.1.B.41b). However, a cell with an O-ring uses a larger electrolyte volume, and we found that this can lead to more pronounced side reactions. When only cleaning cell parts in dimethyl carbonate between experiments, galvanostatic cycling at 20 μAcm^{-2} yields continuous electrolyte reduction at voltages far above the lithiation potential. Through a series of experiments, it was found that using fresh Li metal for reference and counter electrodes, using fresh electrolyte, and cleaning cell parts in organic solvents as well as water between experiments was crucial to suppress electrolyte reduction. With this procedure, we are able to achieve lithiation at current densities down to 5 μAcm^{-2}, with ~1.4 mL electrolyte used per cm^2 of anode area, as opposed to ~20 μLcm^{-2} in a typical coin cell. With this approach, we used 20 $\mu A/cm^2$ in our experiments.

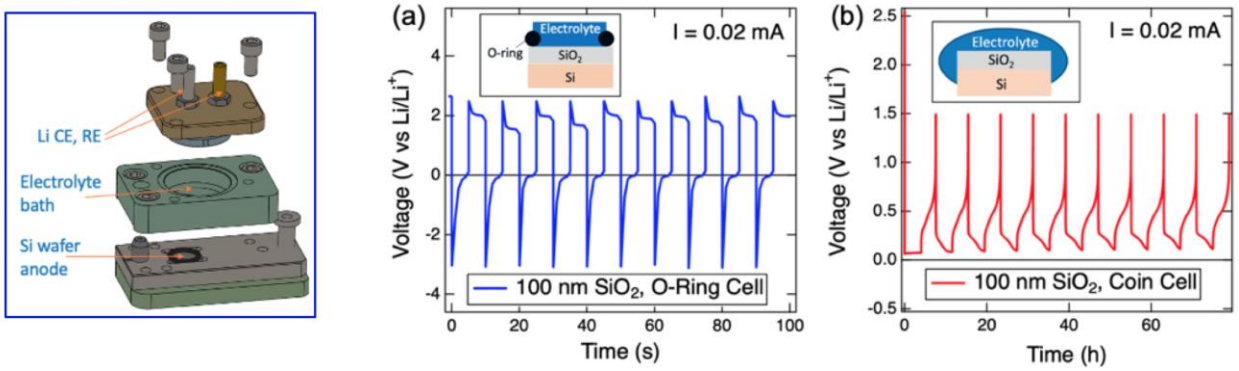

Figure II.1.B.41 Left: a detailed schematics of the O-ring cell used in our experiments. Galvanostatic cycling of a Si wafer with 100-nm SiO_2 in (a) a custom cell with an O-ring on the SiO_2 and (b) a coin cell. The O-ring is essential to ensure that only the oxidized surface of Si is lithiated; in a coin cell, the electrode edges can be lithiated (see insets in (a,b)) [4], [5].

Effect of high-quality, thermally grown SiO_2 of different thickness

Figure II.1.B.42 shows that there is a striking difference between the oxide thicknesses below 3 nm and above 3 nm. In this experiment, galvanostatic cycling was performed at 20 μAcm^{-2} in Gen2 electrolyte against Li metal counter and reference electrodes with no lower voltage cutoff. In samples with less than 3.0-nm SiO_2, their cycling curves essentially overlap, their coulombic efficiencies are over 99% from the second cycle onwards, and photographs of cycled samples show uniform lithiation. For oxides thicker than 3 nm, we observe localized (pinhole) lithiation and coulombic efficiencies well below 90%.

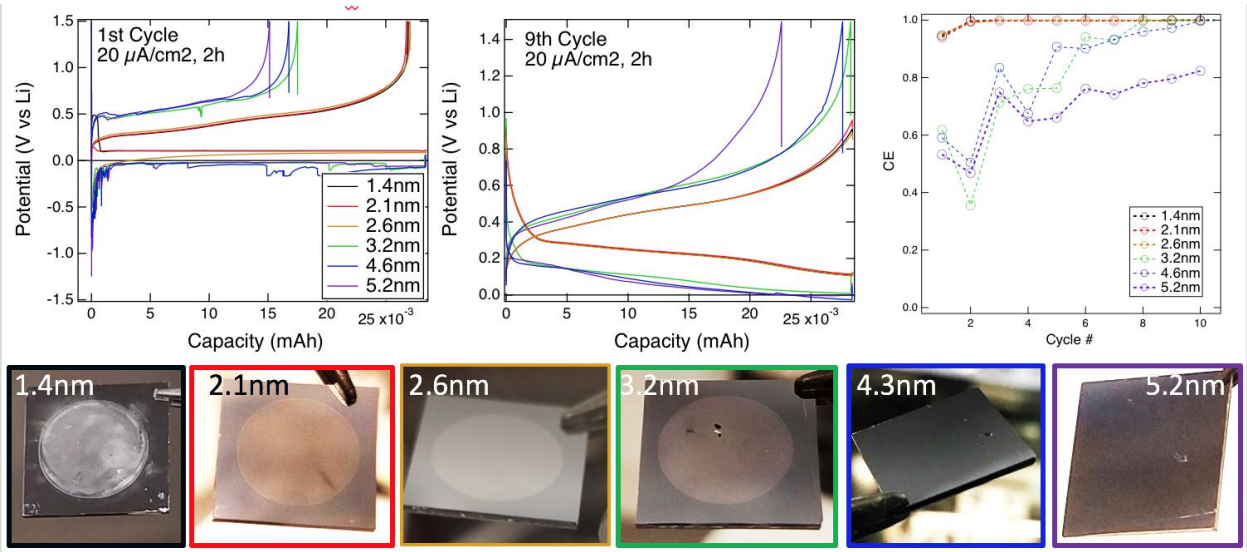

Figure II.1.B.42 Cycling of Si wafer anodes with variation of SiO_2 coating thickness at 20 μAcm^{-2} with no lower voltage cutoff. Top: first and ninth cycles as a function of SiO_2 thickness (left, middle), and coulombic efficiency as a function of cycle number (right). Bottom: Photographs of Si wafers after 10 cycles [4], [5].

The pinhole character of lithiation was confirmed and explored by SSRM, TOF-SIMS, and XPS. In this experiment, the anodes were lithiated in half-cells for 70 h at 10 mV up to a current of 200 nA/cm^2 and a total charge of 2.6 μAh/cm^2. Figure II.1.B.43 summarizes the microscopic findings and presents our model of pinhole lithiation regime based on the following experimental observations. First, the TOF-SIMS map (Figure II.1.B.43b) shows round, uniformly and heavily lithiated near-surface regions (Figure II.1.B.43c) in the Si wafer, extending ~10 nm deep and ~70 μm in radius. These regions are also seen optically as lighter contrast (Figure II.1.B.43a). These findings indicate that Li^+ ions enter the Si wafer via pinholes, then propagate radially. Surprisingly, the radial propagation is very fast and long-range and consists of two stages: (1) the heavily, uniformly lithiated region ~70 μm in radius and (2) interfacial diffusion of Li over even longer radii ~200 μm. The latter is evidenced by the Li SIMS profile (Figure II.1.B.43d) showing Li present outside the heavily lithiated region (Figure II.1.B.43c). Further evidence comes from the XPS maps (lower left panel of Figure II.1.B.43). There, shifts of O1s peaks consistent with near-interfacial lithiation and n-type doping of the wafer surface causing band bending, extend to over 200-μm radius. This is illustrated by our SIMS maps of Li^+ taken over narrow depth intervals (Figure II.1.B.44; positions shown in Figure II.1.B.43c by gray bands). Figure II.1.B.44e shows that Li signal in these maps largely disappears at depths deeper than 13 nm. At shallower depth, Li is strongly present in the Li silicide region of ~70-μm radius (see 1-nm depth map).

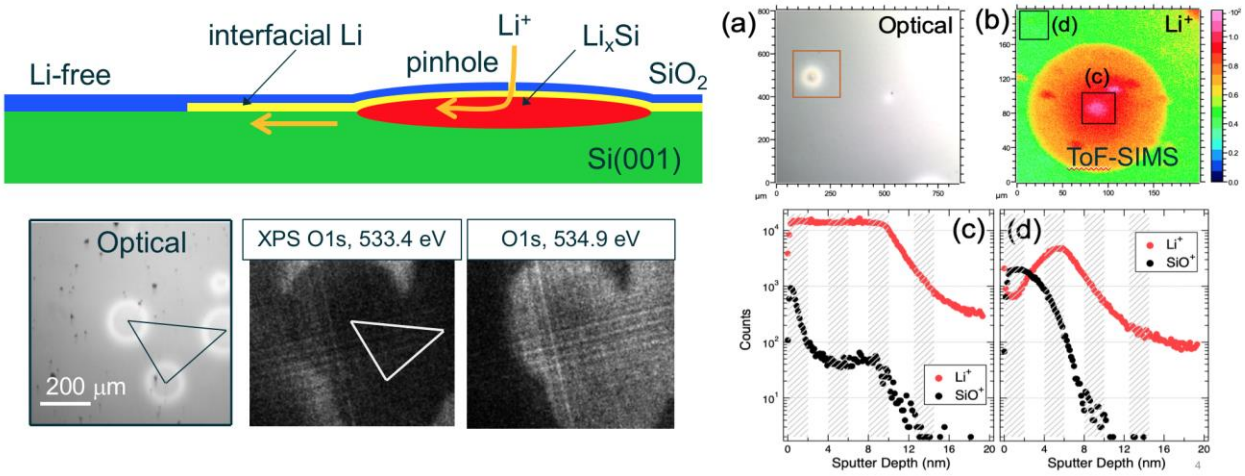

Figure II.1.B.43 Right panel: TOF-SIMS map (b) from the vicinity of a heavily lithiated region shown by a square in the optical image (a) for the 5-nm-thick thermal oxide layer on Si wafer. Bottom right: TOF-SIMS depth profiles from wafer locations (c) near the pinhole center and (d) outside the heavily lithiated region. Note that despite the weak integrated Li signal in SIMS map in location (d), there is a sharp Li peak at the wafer/SiO_2 interface (at a depth of 5 nm). Bottom left: XPS maps of O1s peak at two different electron energies on either side of the peak. The contrast indicates shift of this peak due to interfacial Li. Top left: our model schematics of Li penetration via pinhole in SiO_2 (blue), its rapid interfacial diffusion to ~200 µm (yellow) and formation of Li silicide region ~70 µm in radius (red). TOF-SIMS data from [4], [5].

However, at a specific depth of 5 nm (our oxide thickness), Li signal fills the whole map, indicating its rapid interfacial propagation to distances well beyond 70 µm. We observe a similar long-range Li propagation in SIMS maps taken over larger sample size (Figure II.1.B.44, right panel). There, a different sample location was mapped over longer distances. Ones notices different sizes for the optical contrast regions (corresponding to Li-rich regions of Figure II.1.B.43, which we attribute to Li silicide, evidenced by low O content), most likely due to different preexisting pinhole sizes or pinholes being continuously formed upon lithiation. The integrated Li maps over the 500-µm sample area clearly shows Li propagation to distances a few times longer than the Li silicide regions, >100 µm, in agreement with O1s peak shift XPS maps of Figure II.1.B.43. Notably, the C- and P-related signals corresponding to the formed SEI and are restricted to near the center (c) of the lithiated region near the pinholes. On other hand, SiO^+ signal associated with SiO_2 appears relatively intact across the sample, indicating that the integrity of the oxide is preserved except for the near the larger pinholes.

To summarize the oxide thickness effect, we observe two distinct regimes. At thermal SiO_2 thickness below 3 nm, the lithiation proceeds uniformly with coulombic efficiency close to 100% and stable cycling performance. As the oxide thicknesses increases over 3 nm, lithiation electrochemistry occurs via pinholes in the oxide. The origin of these pinholes is still not fully understood, but they are likely associated with electric breakdown and “weak” spots in the oxide layer. Li ion penetration also might play a role in pinhole formation. In the pinhole regime, Li exhibits remarkably fast interfacial diffusion, forming thin, circular Li-containing “platelets” up to hundreds of microns in diameter, whereas the $LiSi_x$ region extends only ~10 nm deep into the wafer. These platelets consist of two distinct phases: a $LiSi_x$ region ~50 microns in radius, lithiated uniformly down to ~10 nm in 70 h, and interfacial Li-containing outer regions, where Li is at the wafer/oxide interface. The latter interfacial Li extends as far as ~200 µm from the pinhole center, far beyond the $LiSi_x$ platelet. As Li

spreads radially along the Si/SiO_2 interface, ~100 microns in 70 h, its effective interfacial diffusion coefficient is ~10^{-9} cm^2/s, which is 10^3–10^4 times greater than the bulk diffusion of Li in Si and SiO_2.

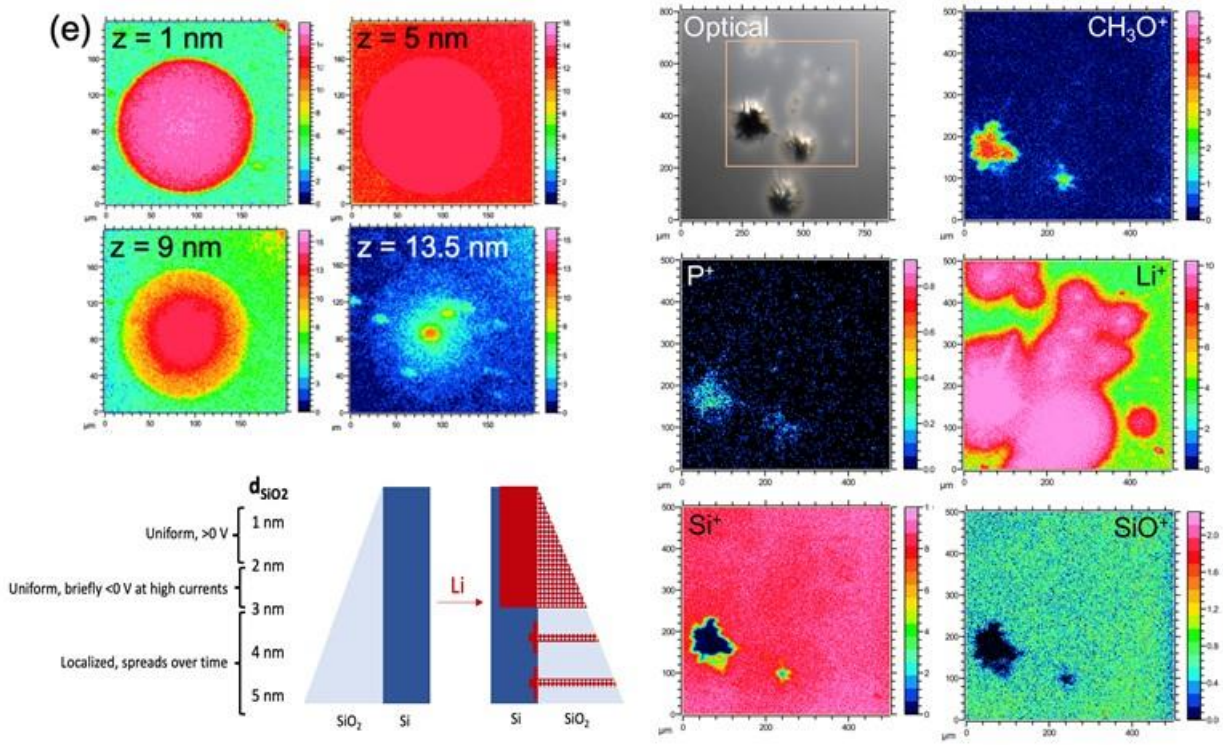

Figure II.1.B.44 Left panel: TOF-SIMS Li^+ maps from the sample of Figure 2, integrated over narrow depth intervals shown in Figure 2 depth profiles (c) and (d) by gray bands. Right: TOF-SIMS maps of several species from a different sample location than Figure 2, showing several pinholes with Li silicide regions formed around them (optical image). Bottom: brief summary of our observations of Si lithiation mechanism as a function of thermal SiO_2 overlayer thickness [4], [5].

Thin thermal oxide layer improves the performance of Si anode

To examine the oxide layer protective properties further, we focused on the uniform lithiation regime and chose thermal oxide thickness 1.4 nm, thermally grown at 850°C in a tube furnace. This was compared with 1.3-nm native oxide and "no oxide" on the Si wafer (the preexisting SiO_2 was removed by an HF dip). Figure II.1.B.45 compares their electrochemical responses.

The oxide-free Si wafer performs the worst: it has low coulombic efficiency of about 94% that does not improve with cycling, and large overpotentials for lithiation. The wafer with native oxide has lower overpotentials and significantly higher coulombic efficiency starting from the second cycle; however, the CE drops beyond the fifth cycle. With more detailed analysis, we identified two types of electrolyte reduction processes in the first cycle: A and B for the two oxidized wafers, and A' and B' for the oxide-free wafer (see the inset in Figure II.1.B.45).

Thermal and native oxide have similar processes A, B. Cao et al. [7] associated process A with LiF formation, B with Li_2O. Yin et al. [6] also assigns A to LiF, whereas B is associated with C-O groups. To correlate these processes with particular electrolyte reduction chemistries, we used XPS. Our XPS study did not detect any Li_2O signal in the early-stage SEI formation (es-SEIs), so we identify process B with solvent reduction, most likely the EC reduction. As for process A, we see clear LiF signal and P-F signals in the SEI layer. Therefore, we assigned A to the $LiPF_6$ reduction. Processes A' and B' are essentially the same as A and B (supported by the same evidence from the XPS), but occur at higher potentials than A, B. A' and B' occur at the theoretical

reduction potentials for these processes, and the oxide layers suppress the electrolyte reduction potential values significantly.

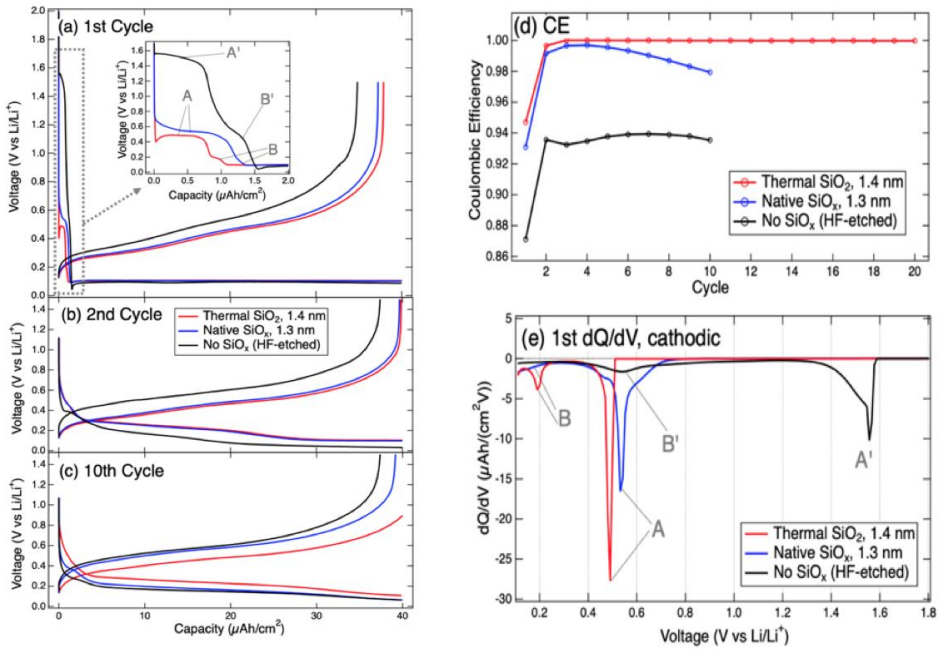

Figure II.1.B.45 Galvanostatic cycling of Si wafers with three states of surface oxidation. (a) First cycle, with enlarged start of the cathodic half-cycle at the inset; its differential capacity dQ/dV is shown in (e). (b) Second cycle. (c) Tenth cycle. (d) Coulombic efficiency [4], [5].

The electrolyte reduction is strongly suppressed for the thermal oxide wafer in the second and subsequent cycles, while it continues for the non-oxide wafer and the native oxide wafer. In Figure II.1.B.46 (left), we show the integrated charge (from the differential capacity plots dQ/dV) consumed by the electrolyte reduction as a function of cycle number. The charge approaches nearly zero for the thermal oxide by the tenth cycle, but stays high for no-oxide and native oxide wafers. This correlates with the low CE for those wafers in Figure 5. Furthermore, the XPS shows, by the height of the substrate Si peak, that the SEI grows thick on the non-oxidized wafer (see Figure II.1.B.46, right) but thinner for the oxidized wafer.

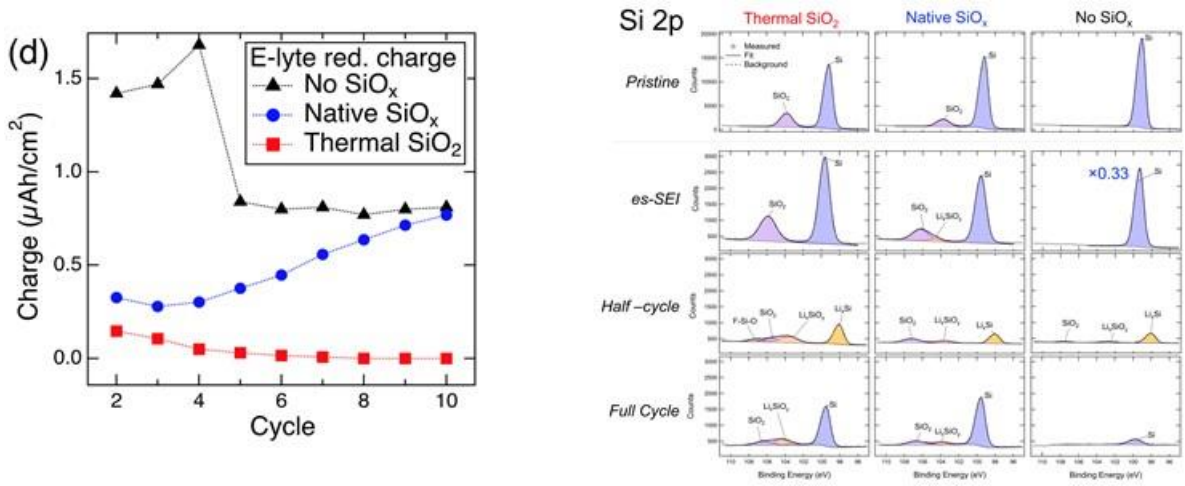

Figure II.1.B.46 Left: The charge consumed by the electrolyte reduction process in cycles 2–10, determined by peak integration in dQ/dV curves. Right: Si peak reduction measured by XPS, due to SEI formation in three stages of the first cycle: early-stage SEI, half-cycle, and full cycle. Strong and irreversible reduction of Si peak, associated with formation of a thick SEI, is evident in the non-oxidized wafer [4], [5].

To summarize our work on the different oxide comparison, we found that 1.4-nm-thick, dense, stoichiometric thermal oxide significantly improves the Si anode performance. Its coulombic efficiency remains ~99% over 20 cycles, and the electrolyte reduction is suppressed by a stable, well-formed SEI. The native oxide initially exhibits high CE, but the electrode reduction is not suppressed with cycling, likely indicating poorer and less stable SEI. Finally, the oxide-free Si performs the worst, exhibiting persistently low CE ~94%, large charge consumption due to electrode reduction upon cycling, and uncontrolled growth of the SEI.

Electron microscopy of the SEI over silicon oxides

Five samples with the different O content were characterized using the SSRM resistivity vs. depth profiling technique (profiles not shown): the pure Si electrode contains low surface oxygen (9.3 at. % O, referred as Si), a native oxide layer formed on the Si thin film (Si_NO) by exposing the film in air, SiO_x films prepared by co-sputtering under the power combinations of 90 W for Si target and 30 W for SiO_2 (SiOx_1), 90 W and 60 W ($SiO_{0.6}$), and 60 W and 90 W ($SiO_{0.7}$). Different power ratios between targets result in roughly proportional concentrations in the sputtered material. Table II.1.B.4 summarizes the electronic resistivity of the pristine films, resistivity change from the pristine samples to the 0.55-V lithiated samples, resistivity change from the pristine samples to the 0.05-V lithiated samples, and the formed SEI thickness after full lithiation. The pristine samples show the expected result of higher electronic resistivity with higher O content. The change in resistivity from pristine to after lithiation to 0.55 V shows an interesting trend: the two thin films with the lowest O content have a minor decrease in resistivity, whereas the three thin films with nontrivial O content display a significant decrease in resistivity, proportional to the original O content. This result suggests that at 0.55 volts, Si electrodes with oxygen in the bulk undergo lithiation, whereas lithiation of Si with only surface oxygen does not proceed, resulting in a conductivity enhancement proportional to the original O content. Lithiation to 0.05 V shows a more significant conductivity enhancement for all samples, with a greater conductivity decrease for samples with higher O content. This conductivity measurement is consistent with the increase from SiO_x to $Li_xSi_yO_z$. SEI thickness after lithiation to 0.05 V was shown to decrease with increasing O content of the pristine electrode.

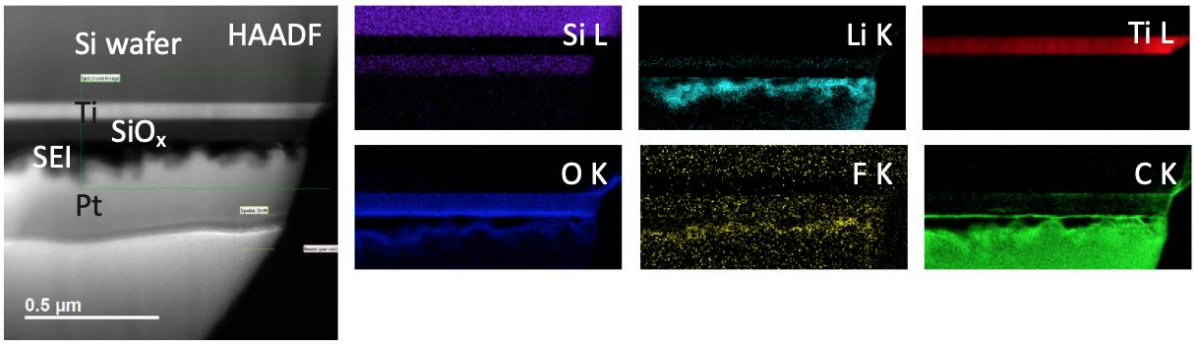

Figure II.1.B.47 STEM HAADF image and EELS edge elemental maps showing the layer structure and distribution of Si, Li, Ti, O, F, and C in a model SiO_x electrode lithiated to 0.05 V.

STEM analysis has been performed on both the pristine $SiO_{0.7}$ and after lithiation to 0.05-V $SiO_{0.7}$ electrodes. The pristine sample showed the expected deposited layer structure. After lithiation to 0.05 V, STEM EDS and EELS elemental mapping revealed the formation of a non-planar SEI layer of thickness 70–140 nm. The SEI layer was found to contain Li, O, C, and F as observed by EELS elemental mapping (Figure II.1.B.47).

Role of binder and formation of the SEI

Binders are one critical component that works directly with Si particles and plays an important role of providing strong adhesion/cohesion between the active materials (graphite and/or Si), conductive additives, and the current collector [6], [7], [8]. Whereas the traditional PVDF binder does not work well with Si-based electrodes due to its relatively low stiffness and poor adhesion [9], [10], hydroxy-containing polymers including sodium alginate [11], sodium carboxymethyl cellulose [9], poly(vinyl alcohol) [12], xanthan gum [13], and PAA [14] have demonstrated promising cycling performance for silicon anodes [15]. These polymers appear to have stronger binding strength, possibly because they tend to form hydrogen or even covalent bonding with the siloxyl groups (Si-OH) that are often found on the surface of Si particles [7], [8], [16]. Among these binders, PAA-based polymers are particularly attractive due to their low cost, facile synthesis, and excellent cycling performance [14], [17]-[19]. Pre-lithiation of PAA (PAA-Li) binders is an important yet not fully understood process that brings in contradicting effects on Si-based anodes, such as improved rheology properties and undermined cycling performance. Although we have established the cycling metrics over Si anodes using various pre-lithiated PAA binders [18], a still better understanding of the impacts on SEI formations is highly desired to inspire possible solutions toward the critical challenges of Si anodes, such as cycling life and calendar life. To this end, we revisited our systematical studies of pre-lithiation of PAA binders and identified previously overlooked correlations between binders and SEI formations. It is noted that a Si-Gr composite electrode containing 73 wt % graphite, 15 wt % silicon (70–130-nm NanoAmor), 10 w t% binder, and 2 wt % C45 is used in this report.

As shown in Figure II.1.B.48a, the pre-lithiation of PAA binders not only causes dramatic fluctuation of pH values, but also results in huge differences in cycling performance of the fabricated cells. Specifically, the dependence of PAA-Li is reminiscent of the textbook strong base–weak acid titration curve, and the added LiOH affords much more ionized binders that bear less protons but more Li^+. Such changes prodoundly affect the overall properties of the binder solutions and slurries. As shown in Figure II.1.B.48b and Figure II.1.B.48c, the fabricated cells demonstrate very different cycling perfomrance. The pre-lithiation leads to more aggressive capacity fading. As preliation of PAA becoms dominating and pH (indicated in notations [e.g., PAA-2.1 is the sample with pH 2.1]) increases, the cell performance underperforms with less initial capcity, worse capacity rententions, and lower coulombic effciencies. Such observation implies there are underlying causes asscociated with the PAA pre-lithiation process.

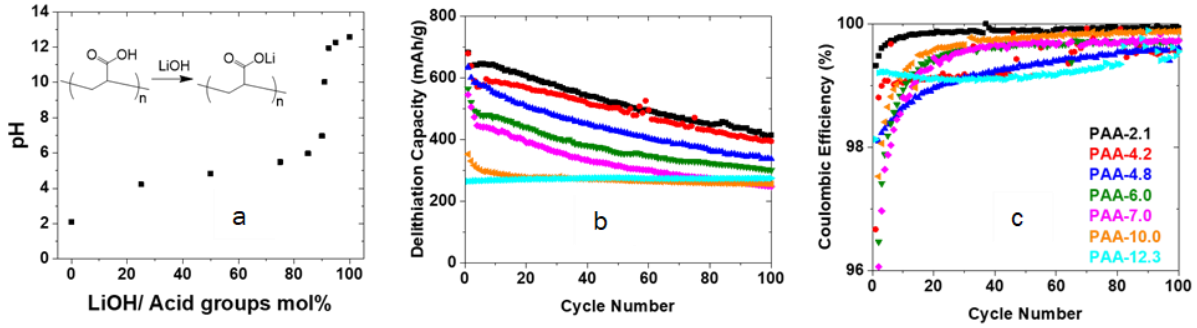

Figure II.1.B.48 (a) pH profiles of PAA-LiOH titration, (b) specific discharge capacity profiles, and (c) coulombic efficiency profiles of half cells using the pre-lithiated PAA binders over 100 cycles at C/3 rate.

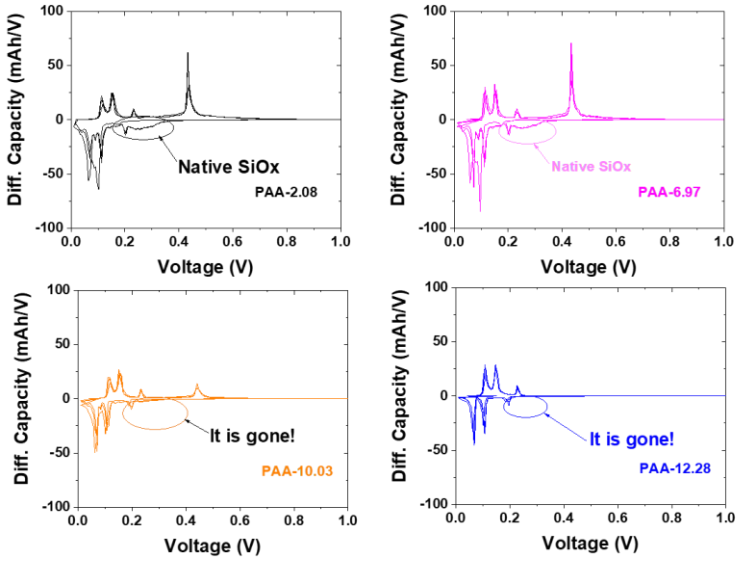

Figure II.1.B.49 Differential capacity (dQ/dV) profiles of half cells containing Si-Gr composite electrodes using PAA-Li binders during the formation cycles at a C/20 rate. The pH of the PAA solutions in Figure II.1.B.48 is indicated in each panel.

As shown in Figure II.1.B.49, differential capacity profiles of half cells fabricated using lithiated PAA binders reveal the changes of the electrochemical reactions during formations. While peaks associated with graphite are presented in all the plots, certain peaks show huge differences. With less lithiated PAA binders bearing pH < 7, we observe a broad peak at approximately 0.23–0.33 V, indicating a layer of SiO_x formed on the Si anode surfaces. However, as lithiation increases and pH reaches 10 and above, the SiO_x peak becomes absent, implying the more lithiated PAA binders may help to erode the native SiO_x.

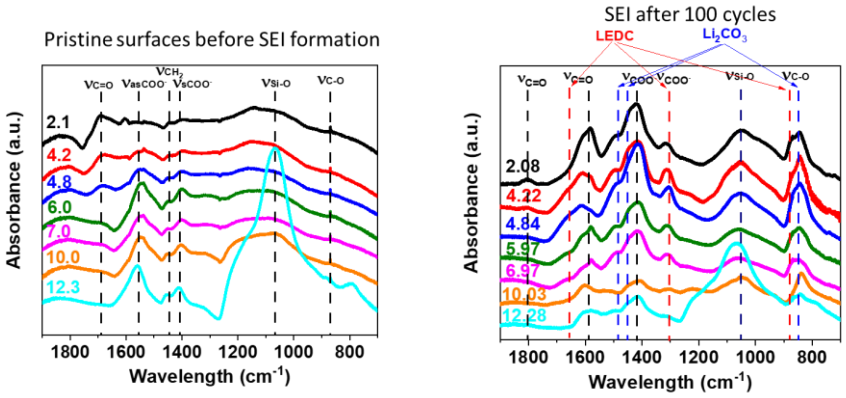

Figure II.1.B.50 SEI species evaluation: FTIR spectra of pristine (left) and cycled (right) electrodes.

FTIR spectra further reveal such changes with more in-depth information. Figure II.1.B.50 complies the FTIR spectra of the pristine and cycled electrodes (after 100 cycles) from half cells using various lithiated PAA binders. The pristine electrodes show a huge SiO_2 peak with binders bearing basic conditions (pH > 10), indicating such binder conditions promote SiO_2 formation as Si is more readily to react with water under basic conditions [6]. On the other hand, on the surface of cycled electrodes, lithium ethylene dicarbonate (LEDC) (1,490, 1,451 and 875 cm^{-1}) and Li_2CO_3 (1,653, 1,400, 1,315, 1,100 and 825 cm^{-1}) are more pronounced at acidic or neutral conditions with pH ≤ 7.

Differential capacity profiles indicate the acidic conditions with less lithiation of PAA may help to preserve the native SiO_x layers of Si particles, whereas FTIR spectra imply basic conditions with pH >10 promote the SiO_2 formation. After extensive cycling, FTIR reveals less pre-lithiation with acidic condition (pH < 7) of binders favors LEDC and Li_2CO_3 formations, two components that are required for stable SEI layers. Although many efforts are needed toward understanding, these findings reveal strong correlations between binder alternation and SEI formation.

Surface sensitive microscopy and influence of binder

SSRM 3D resistance mapping was conducted on two Si nanoparticle-based composite electrodes: one is a surface-engineered Si (SE-Si) containing Si, carbon nanotubes as the conductive carbon material, and PAA binder. The intrinsic Si (i:Si) electrode contains i:Si, graphite, and PAA. SE-Si and i:Si electrodes were lithiated/delithiated to 100 and 500 cycles, respectively. The results (Figure II.1.B.51) show highly nonuniform resistivity due to the multiple phases in the electrode. Individual Si nanoparticles could not be resolved because of their small sizes of ~6 nm. Instead, larger agglomerates of the particles were probed. Figure II.1.B.51e shows a histogram of the resistivity distribution in the four pristine and cycled anodes. The resistivity of pristine SE-Si in the analyzed area shows primarily two distinguishable phases, probably due to carbon nanotubes and SE-Si. In the pristine i:Si sample, the graphite phase dominates the analyzed area, along with the i:Si and PAA phases, likely contained in the long tail on the right of the histogram. With cycling, the resistivity maps show significant increases of high-resistivity phases on both the anode surface and in the bulk, indicating the formation and ingress of SEI. This resistivity increase occurs much more in the SE-Si sample than the i:Si sample, although SE-Si had been cycled (100 cycles) much less than i:Si (500 cycles), likely due to the much more Si phase present that resulted in more volume expansion and more subsequent SEI ingress and active material fouling.

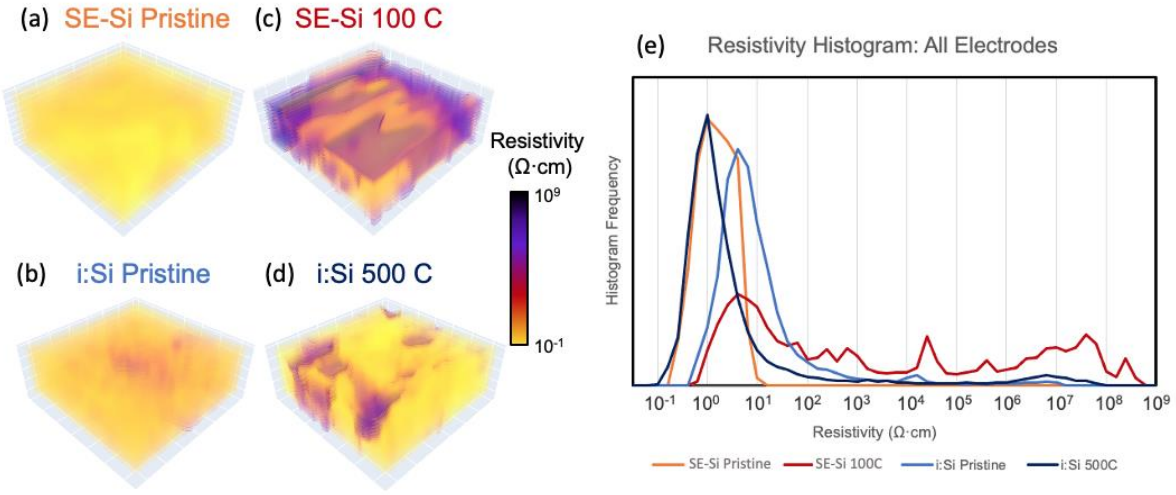

Figure II.1.B.51 3D resistance mapping on (a),(c) SE-Si and (b),(d) i:Si anodes at (a),(b) pristine and (c),(d) cycled states. (e) Histograms of resistance of the four samples.

By approximately defining the resistivity range of the different phases (Figure II.1.B.52a), 3D distribution of the phases can be identified from the resistivity mapping. One example of cycled SE-Si is shown in Figure II.1.B.52b, where the more- and less-resistive phases were drawn with significant weights of all the phases (Figure II.1.B.52).

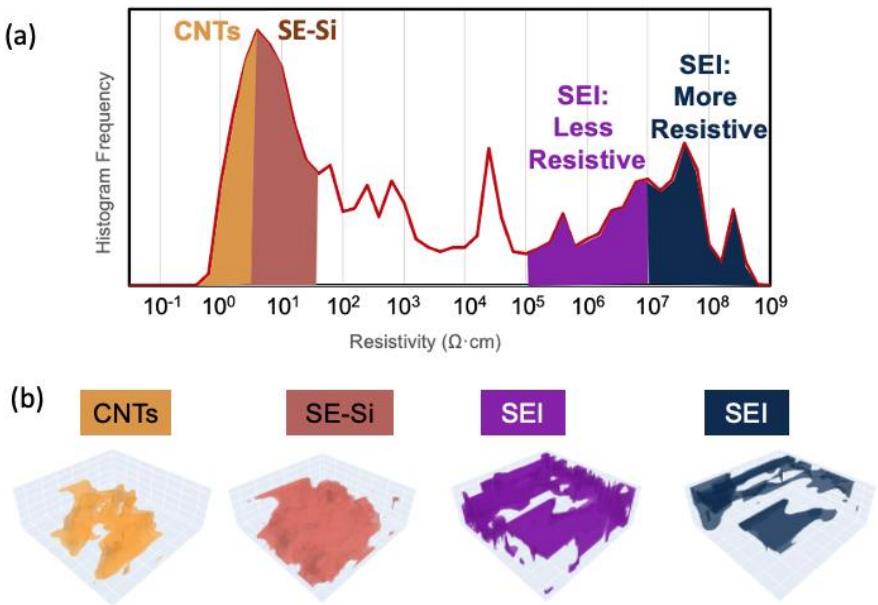

Figure II.1.B.52 (a) A histogram of the SE-Si after 100 cycling and related resistivity definition of the phases; (b) 3D identification of the multiple phases derived from the 3D resistance mapping.

New electrolytes and understanding the SEI formation

Glyme electrolytes

The conversion type of Si anode shows almost 10-times larger specific capacity than the conventional graphite anode. However, the commonly used carbonate-based electrolytes (e.g., standard Gen2 electrolyte—$LiPF_6$ in an EC/EMC mixture) that have been widely used to stabilize the carbonaceous anodes have been found incapable of stabilizing the Si anodes. It is partially ascribed to the non-passivation behavior of carbonate-

based electrolytes. Even with the best-performing carbonate electrolyte with addition of a fluorinated carbonate additive, FEC, a finite parasitic or leakage current always exists per our previous corrosion-related reports on a-Si anodes. One possible explanation is that due to the severe volumetric change of Si upon lithiation/delithiation, the sustained reaction between the electrolytes with freshly exposed silicon surface leads to an unstable SEI with the thickness increasing. One method to solve this issue is to explore solvents and salts other than commonly used carbonate-based electrolytes for Li-ion batteries that could potentially demonstrate better passivating properties on Si. Earlier study by our team investigating SEI formation on amorphous silicon (a-Si) thin film indicates that polymeric ether components such as poly(ethylene oxide) (PEO) are formed during the first couple of GCs [20], enabling certain viscoelasticity of the SEI to buffer the volumetric change of the Si anodes. Glyme is a type of under-evaluated electrolyte solvent for Si anode. The rational of using glyme is it has similar chemical structure as the PEO in SEI. A series of glyme-based electrolytes are thus being explored for their effects on the SEI formation using a model a-Si thin film anode at ORNL. We have shown in our previous reports that a type of glyme electrolyte containing lithium bis (fluorosulfonyl) imide LiFSI-DME, and a fluoroadditive, 1,1,2,2-tetrafluoroethyl-2,2,3,3-tetrafluoropropyl ether (TTE) can better stabilize the a-Si thin-film anode after extended GC. We show that the a-Si thin-film anode with a certain combination of the LiFSI, dimethoxyethane (DME) and fluorinated ether, fluoroether, 1,1,2,2-tetrafluoroethyl-2,2,3,3-tetrafluoropropyl ether (TTE) (denoted as LiFSI-3DME-3TTE) outperforms the best-performing carbonate electrolyte (Gen2 + 10 wt % FEC). A 50-nm amorphous (a-Si) thin-film anode was used as the model anode and lithium metal was used as a counter electrode. When using 1C equivalent rate GC test, the capacity retention for Gen2 in first 110 GC cycles was around 30%, whereas this value of the glyme electrolyte reached close to 89%. Preliminary characterization based on infrared spectroscopy indicates that the SEI on a-Si surface possibly has rich polymeric ether-based species. However, chemical details of thus-formed SEI and the role the polymeric ethers to stabilize the a-Si anode still remain largely elusive. We further consolidate the surface chemistry of the cycled a-Si using energy dispersion EDS and XPS. The topography of the a-Si cycled in different electrolytes is evaluated by the SEM micrographs.

Here, Gen2 electrolyte was used as a benchmark. The surface morphology of both early-stage cycling (denoted as 5 cyc) and prolonged cycling (110 cyc) are of interest. For the first 5 cycles, a-Si cycled in both Gen2 and 1-3-3 (LiFSI-DME-TTE molar ratio as 1:3:3) electrolytes exhibits cracks on the SEI, as shown by both the SEI micrographs and the EDS mapping of oxygen and carbon in Figure II.1.B.54. Further investigation on the EDS mapping of Si shows that those cracks may stem from the volumetric change of the a-Si thin film upon (de)lithiation. The EDS mapping of the Cu substrate provides complementary proof toward this point. After prolonged GC, a-Si in Gen2 electrolyte exhibits more distinguished crack pattern, as demonstrated by both the SEM micrographs and the O and Si EDS mappings.

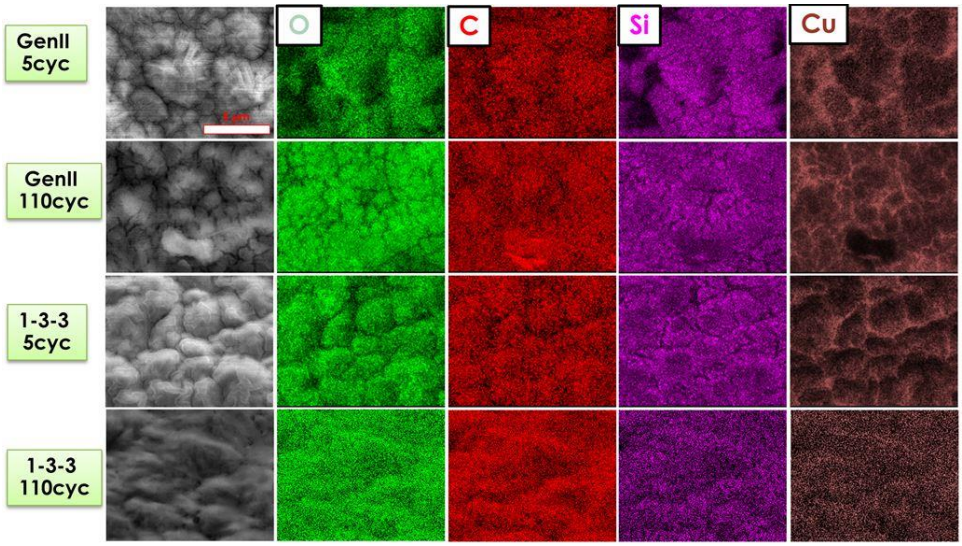

Figure II.1.B.53 SEM micrographs (left column) of cycled a-Si in different electrolytes for various cycle numbers. The EDS mapping of several elements on the corresponding scanned area by SEM are shown on right columns.

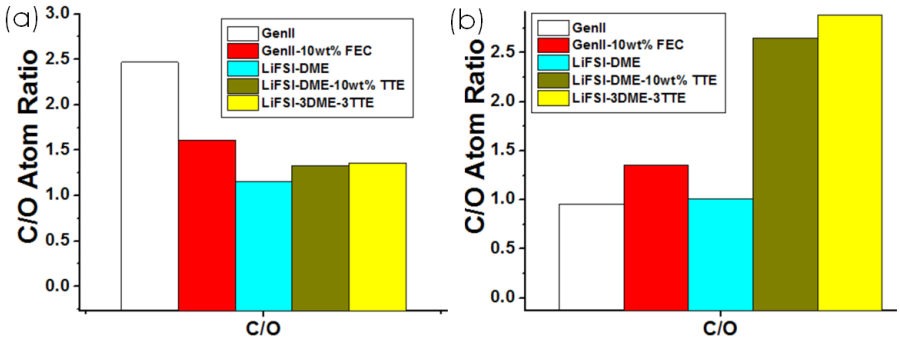

Figure II.1.B.54 The elemental molar ratio of the C/O analyzed based on the EDS mapping on a-Si anodes for various electrolytes after (a) 5 cycles and (b) 110 cycles.

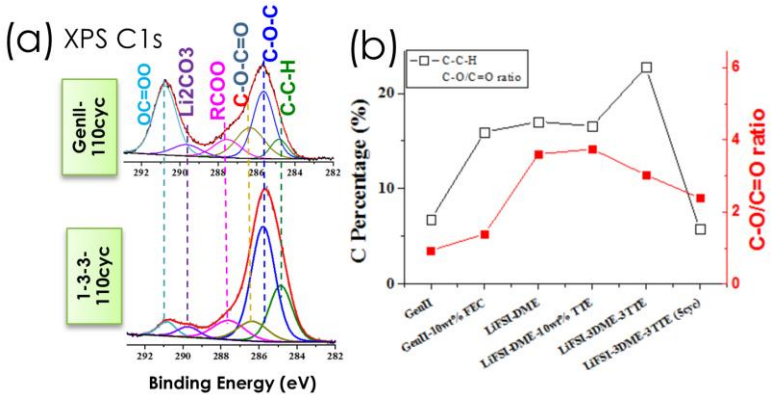

Figure II.1.B.55 (a) C 1s XPS spectra of the a-Si anodes cycled for 110 cycles in Gen2 and 1-3-3 glyme electrolytes. (b) The concentration of the C—C-H and the molar ratio of the C-O/C=O for various electrolytes.

The C/O ratio is important because two main polymeric species in SEI, namely polymeric carbonate (-COO) and polymeric ether (-COC) have different C/O ratios. This ratio serves as an initial indication of the concentrations of the carbonate and ether functional groups. Seen from Figure II.1.B.55, a-Si in Gen2 electrolytes exhibits high C/O ratio in the early GC stage, whereas the C/O ratio of the a-Si anodes cycled in glyme electrolytes with TTE additive outperforms those cycled in carbonate electrolytes, indicating the

increase of the polymeric ether species in SEI. To further solidify this statement, XPS measurements were performed on a-Si cycled in different electrolytes (Figure II.1.B.55). It is manifest from the C 1s core-level XPS spectra after prolonged GC cycling that ether carbon dominates over other species in the SEI with 1-3-3 glyme electrolyte. In contrast, the SEI of the a-Si anode from Gen2 electrolyte enriches in carbonate species. The C-O/C=O on a-Si surface with the 1-3-3 glyme is 3.2 times that with Gen2 electrolyte. The aliphatic chains (C-C-H) have the highest concentration for a-Si with 1-3-3 glyme electrolyte at 22.8%, whereas it was only 6.7% for a-Si cycled in Gen2 electrolyte. Taken together, the SEI on a-Si anode with 1-3-3 glyme electrolyte has rich polymeric ether species, which are quite possibly PEO oligomers. It is also interesting to notice that at early GC stage (5 cyc), the abundance of the ether function group is low on a-Si with 1-3-3 glyme electrolyte, agreeing very well with the EDS analysis in Figure II.1.B.5. It also corresponds to the observation that when cycled in glyme electrolytes, a-Si anode was much less stable due to the large parasitic current (corrosion test using LBNL's protocol shown in a previous quarterly report) compared with Gen2 electrolyte.

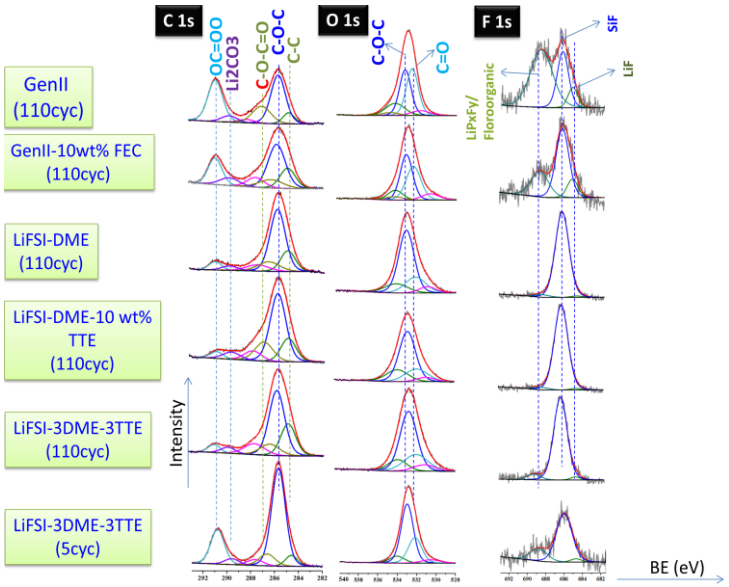

Figure II.1.B.56 Variation of XPS spectra of the a-Si thin-film anodes cycled in carbonate and glyme electrolytes at three different core levels.

A more comprehensive comparison of the surface chemistry among a-Si anodes cycled in various electrolytes characterized by XPS is shown in Figure II.1.B.56. The SEI formed on a-Si from both carbonate and glyme electrolytes have complicated chemical conformations. The first chemical difference between the carbonate SEI (denoted as c-SEI) and the glyme SEI (denoted as g-SEI) worth noting lies in the peak at 290.8 eV. This peak represents the C 1s core level of the carbonyl carbon in carboxylate compounds (OCOO) [21]. The intensity of this peak is noticeably larger in c-SEI from both Gen2 and Gen2 10 wt % FEC after 110 GC cycles than in the g-SEI counterparts. Interestingly, g-SEI on a-Si cycled for 5 times (5 cyc) in LiFSI-3DME-3TTE electrolyte exhibits higher carboxylate abundance than its 110 cyc counterpart. Regardless, the C 1s core level of the ether oxygen centered at 285.7 eV [21] shows a larger intensity than the carbonyl carbon peak for all g-SEIs. This statement is further corroborated by the O 1s core level. The ether oxygen O 1s at 533.0 eV has a comparable intensity with the carbonyl oxygen at 531.9 eV for c-SEI of the Gen2 (110 cyc) sample. Whereas the ether oxygen O 1s peak intensity of the c-SEI is only slightly larger than carbonyl O 1s peak for the Gen2-10 wt % FEC (110 cyc), the former overweighs the latter for all g-SEI samples. Taken together, it clearly demonstrates that the g-SEI has more ether functional groups than its c-SEI counterparts. Fluorinated species is another group of SEI compounds worth exploring. Shown in the right column in Figure II.1.B.55, the c-SEI for Gen2 (110 cyc) has enriched LiP_xF_y components stemmed from the

decomposition of the $LiPF_6$ salt [22]. The resultant fluorinated species has been found responsible for instability of the c-SEI [23] Addition of the 10 wt % FEC decreased the abundance of the LiP_xF_y component (F 1s core level at 688.7 eV) [24], agreeing with other studies in which the FEC reductive decomposition at the Si surface aids in forming a better and more stable SEI layer [25], further mitigating the $LiPF_6$ salt reduction. Lacking $LiPF_6$ salt, the intensity of the 688.7 eV F 1s core level peak for g-SEI drops significantly. Notably, when cycled in LiFSI-3DME-3TTE electrolyte for 5 cycles, there is a shoulder at 688.7 eV for F1s core level. This may be ascribed to the aliphatic fluoroorganic species derived from the polymerization of the glyme electrolyte components. According to [26], the peak centered at 686.3 eV is ascribed to Si-F moieties. This indicates that both c-SEI and g-SEI contain abundant fluorinated silicon species. However, for glyme-based electrolytes, the abundance of the fluorinated species was not increased upon adding more TTE. This suggests that the resource of the fluorinated species in the SEI layer on a-Si may stem from the decomposition of the LiFSI salt instead of the TTE additive.

Figure II.1.B.57b details the relative abundance of a few polymeric moieties in the SEI layer stemmed from both carbonate and glyme electrolytes. The aliphatic C-C backbone counts for 7% for Gen2 electrolyte, but it is more than doubled for Gen2 10 wt % FEC, LiFSI-DME, and LiFSI-DME 10 wt % TTE, suggesting the existence of more than doubled polymeric species. For LiFSI-3DME-3TTE, this value is further increased to 23%, demonstration that even more polymeric components are derived for g-SEI in this case. Focusing on the C-O/C=O ratio (r), the g-SEI exhibits >12.5% r value, whereas r is <5% for c-SEI. Taken together, the g-SEI contains more than twice as much CH_2-CH_2-O repeating unit with respect to inorganic carbonate or carboxylate (C=O) compounds compared to c-SEI counterparts.

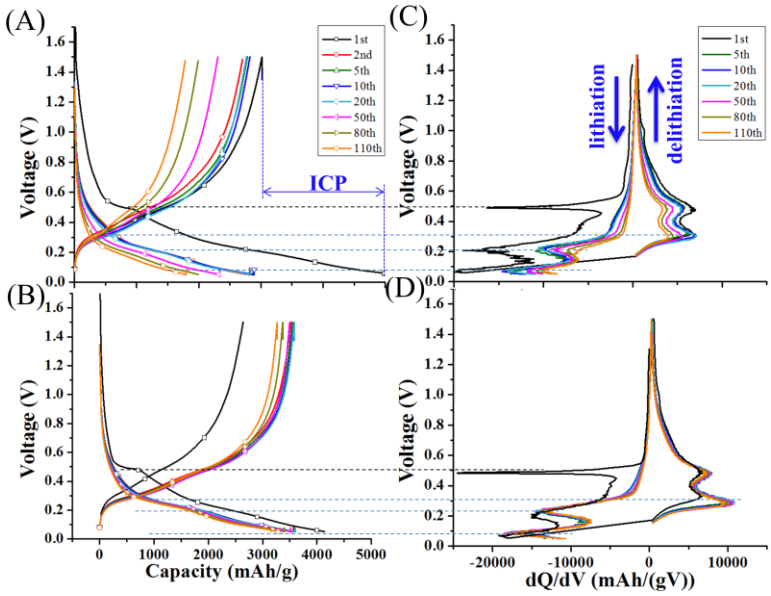

Figure II.1.B.57 Galvanostatic charge/discharge curves for a-Si anodes cycled in (A) LiFSI-DME and (B) LiFSI-3DME-3TTE. The corresponding differential capacity plots are shown in (C) and (D), respectively.

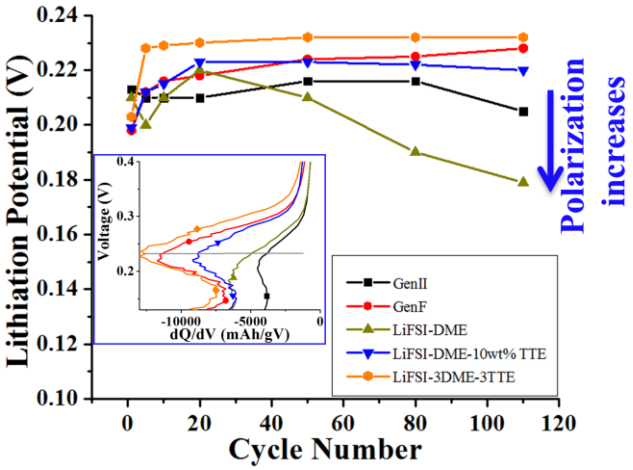

Figure II.1.B.58 The lithiation potential as a function of cycle numbers for a-Si anodes cycled in various electrolytes.

Electrochemical evaluations were further performed to evaluate the a-Si anodes cycled in carbonate and glyme electrolytes. Two types of representative long-term charge-discharge profiles of the glyme electrolytes with and without TTE are shown in Figure II.1.B.59 (A-B). Notably, the lithiation capacity of the initial cycle for LiFSI-DME is 4,975 mAh/g, larger than its Gen2 counterpart. These values are even higher than the theoretical lithiation capacity of Si (4,200 mAh/g), indicative of the side reaction occurrence during the first lithiation. This observation is further evidenced by the partial differential capacity curve shown in Figure II.1.B.57(C-D), where a sharp irreversible lithiation peak shows at ~0.49 V vs. Li^+/Li in the first cycle, >0.2 V above the a-Si lithiation potential, ascribed to the electrolyte reduction to form initial SEI layer and reduction of the surface SiO_x species [27]. These side reactions result in a large initial irreversible capacity loss of 39.7% for LiFSI-DME and 27.6% for Gen2. The initial inductively coupled plasma (ICP) value is important to estimate additional lithium loss to unveil a more accurate n/p ratio for practical design of Li-Si batteries. For glyme electrolytes, addition of TTE additive decreases the ICP to 36.4% for the LiFSI-3DME-3TTE electrolyte. On the contrary, addition of 10% FEC leads to ICP increasing to 32.8% versus Gen2 for carbonate electrolyte, agreeing with the higher parasitic current at early cycles for GenF in GC-CA test (2019 Q2 report). After the first cycle, the delithiation capacity is slightly increased and stabilized until around tenth cycle, followed by continuous fading to a certain value at the ending cycle, indicating the SEI layer constantly evolving as cycling prolongs. The primary difference upon TTE cosolvent addition is the drastically improved capacity and capacity retention as cycles progress (2019 Q4 report), manifested by the stable partial capacity peaks in Figure II.1.B.57D after the first cycle. Whereas the lithiation capacity of the LiFSI-DME is only 1,787 mAh/g, it is increased to 3,266 mAh/g for LiFSI-3DME-3TTE at 110^{th} cycle, 15% larger than its best-performing carbonate counterpart (at 2,841 mAh/g for GenF).

LiFSI-3DME-3TTE also enables the lowest polarization effect, ensuring lower energy barriers for lithiation and delithiation of a-Si. Such an observation is based on detailed exploration on the differential capacity profiles as a function of the cycle number for various electrolytes. After the first cycle, two lithiation peaks at ~0.07 V and ~0.20 V are observed (Figure II.1.A.35). For LiFSI-DME, the intensity of these two peaks continuously decreases as cycling prolongs, in accordance with the lithiation capacity fade as cycling prolongs in Figure II.1.B.59A. The similar trend is observed for two delithiation peaks at around 0.30 V and 0.49 V. Whereas decrease in intensity of these four peaks is >40% for LiFSI-DME from Cycle 5 to Cycle 110, it is less than 12% for LiFSI-3DME-3TTE. Another benefit LiFSI-3DME-3TTE distinguishes itself from the other electrolytes is its highest lithiation potential after 5 cycles, shown in Figure II.1.B.58, indicative of its lowest polarization effect in prolonged cycles. This in turn allows for ease of a-Si lithiation in prolonged cycling. The passivation on the Si anode is generally considered the major driving force to increase the polarization effect upon cycling [28]. Research on EIS of the a-Si cycled in different electrolytes for various cycle numbers are

ongoing to unveil the relation between the surface resistance due to SEI growth and the polarization effect for the glyme electrolytes.

Ongoing research in collaboration with the NREL team includes elucidating and consolidating the surface chemistry heterogeneity on both of the in-plane and through-plane of the a-Si surface using depth-profile XPS and TOF-SIMS, exploring glyme SEI mechanical property by nano-indentation and local electrochemical and electronic properties of SEI formed in glyme-based by AFM- Scanning Probe Microscopy (SSRM).

XPS depth profiles (3-keV Ar^+ ions) were performed on each sample to reveal compositional changes throughout the SEI layers. Curve-fitting analysis was performed on the initial XPS spectra collected prior to the onset of sputtering to identify species present in the SEI.

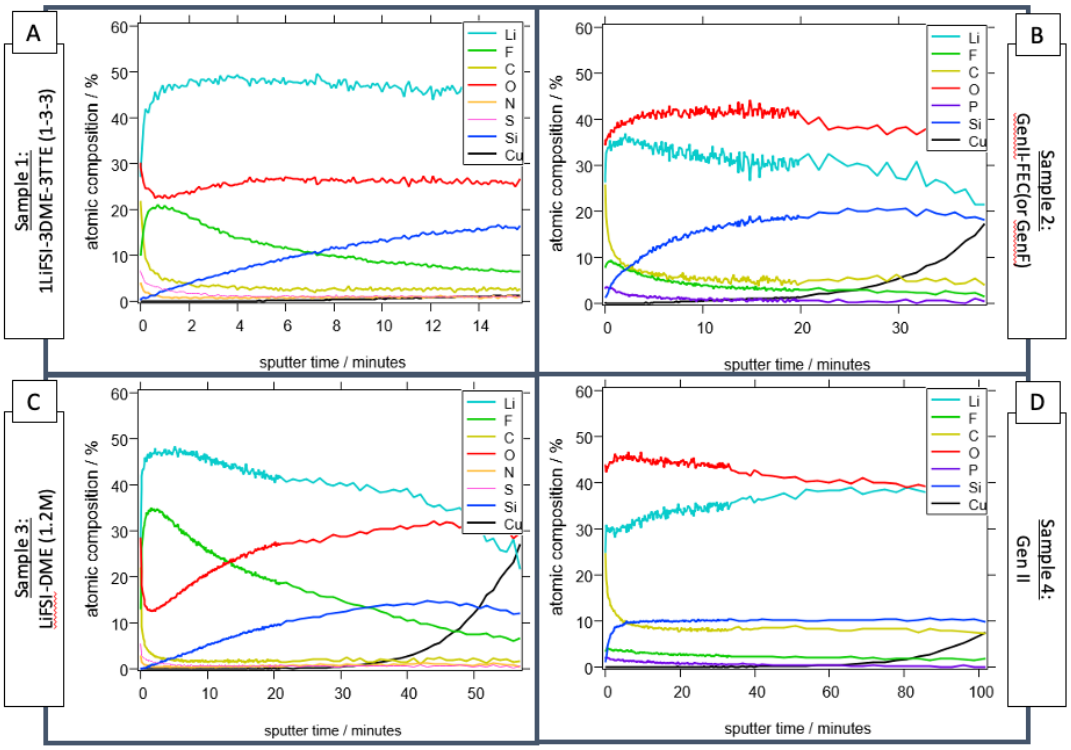

Figure II.1.B.59 XPS depth profiles of each sample, plotting atomic % composition as a function of sputter time for (A) sample 1 - 1LiFSI-3DME-3TTE (1-3-3) electrolyte, (B) sample 2 - Gen F electrolyte, (C) sample 3 - 1.2 M LiFSI in DME electrolyte, and (D) sample 4 - Gen 2 electrolyte.

Figure II.1.B.59 shows that the samples cycled in glyme-based electrolytes (samples 1 and 3) are dominated by lithium content, whereas the Gen F and Gen 2 reference samples show higher oxygen concentrations. Curve-fitting analysis of the XPS core-level spectra (Figure II.1.B.60–Figure II.1.B.64) further reveal that the glyme-electrolyte sample SEIs were composed of carbon-free inorganic compounds (e.g., Li_2SO_3 and LiF) to a greater extent than those of the carbonate-based electrolyte samples. Conversely, the Gen F and Gen 2 samples contain significantly higher amounts of Li_2CO_3.

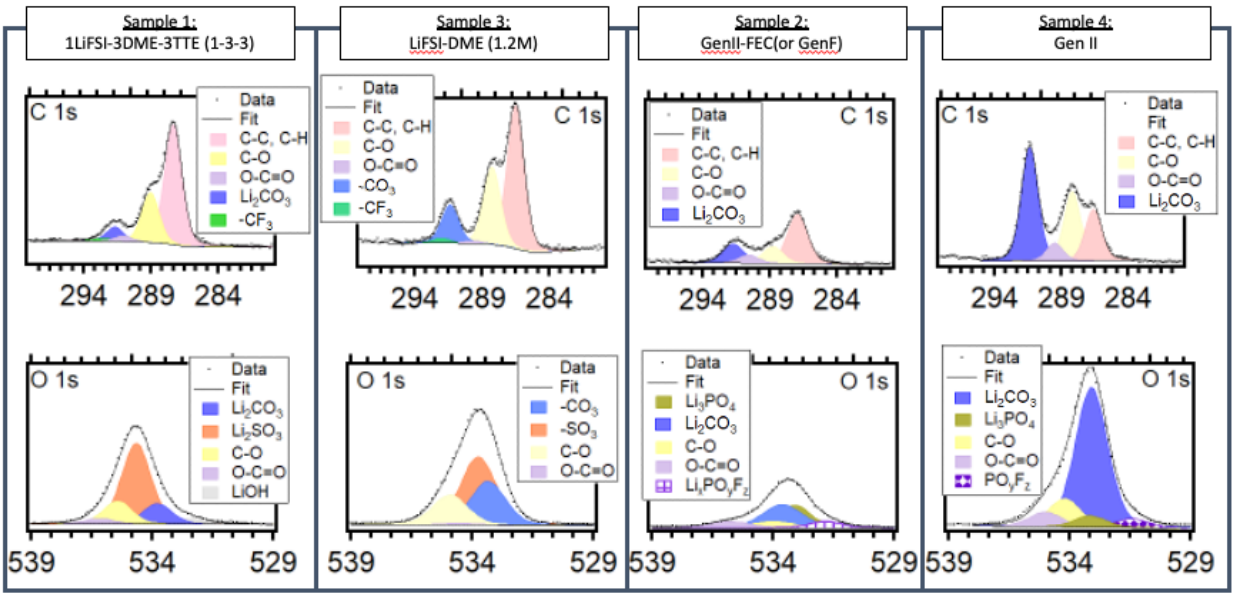

Figure II.1.B.60 C 1s and O 1s XPS core-level spectra for samples 1, 3, 2, and 4.

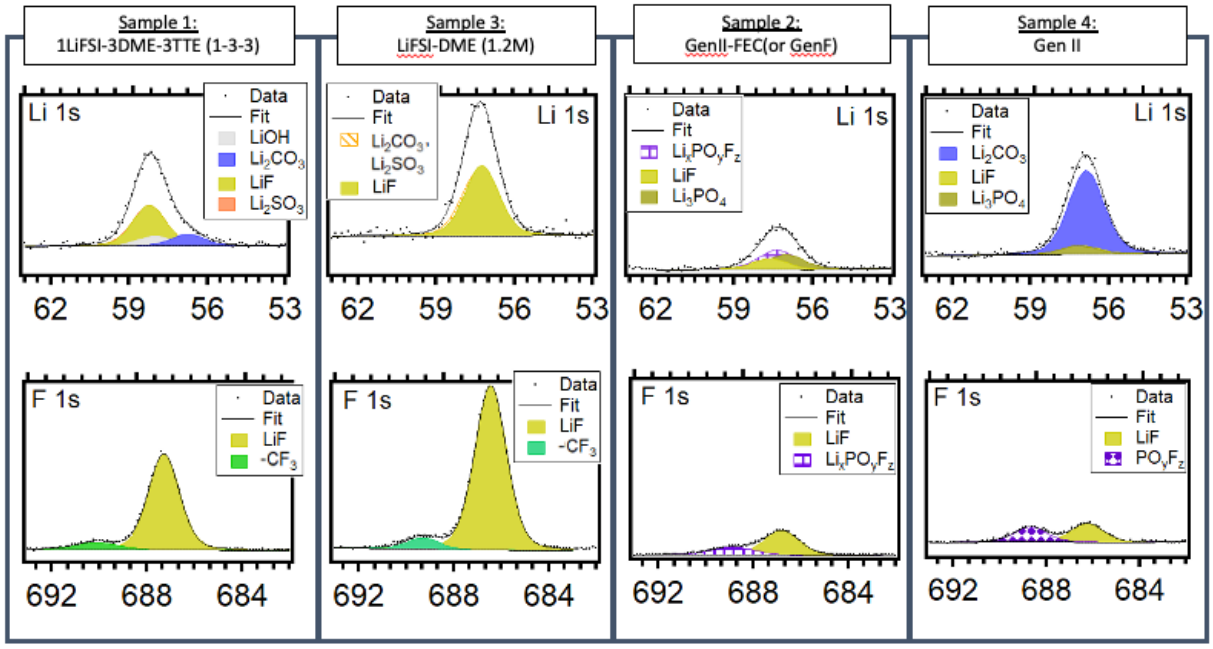

Figure II.1.B.61 Li 1s and F 1s XPS core-level spectra for samples 1, 3, 2, and 4.

Figure II.1.B.60 and Figure II.1.B.61 identify SEI species associated with the core levels that have been most widely studied in previous lithium battery SEI studies (C 1s, O 1s, Li 1s, and F 1s). All spectra for particular core levels are plotted in the same intensity range so relative signals can be directly compared across samples. Phase assignments are made via a curve-fitting analysis where suitable constraints between binding energies and sensitivity-factor-weighted peak areas are simultaneously applied to relevant core-level peaks [29]. For instance, sample 1 was determined to likely contain Li_2SO_3 due to the fact that the sensitivity-factor-weighted oxygen intensity was three times that of the correlated sulfur intensity. The $(SO_3)^{2-}$ features were then tentatively assigned to Li_2SO_3 based on the presence of unassigned intensity in the Li 1s core level at the expected binding energy and at roughly the expected stoichiometric ratio. In the case of sample 2, the lithium

intensity is not high enough to confidently report that all of the carbonate and sulfite species are lithiated, and so it is more likely a mixture of lithiated and organic carbonate and sulfite species. The other major component of the glyme species is LiF, with sample 2 having more than sample 1. This is in agreement with the depth profiles in Figure II.1.B.59, where sample 2 shows a higher fluorine signal.

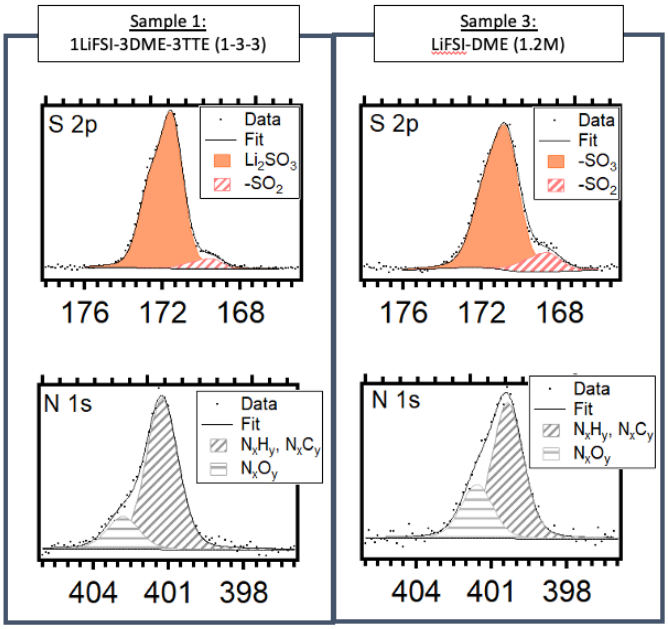

Figure II.1.B.62 S 2p and N 1s XPS core-level spectra for samples 1 and 3.

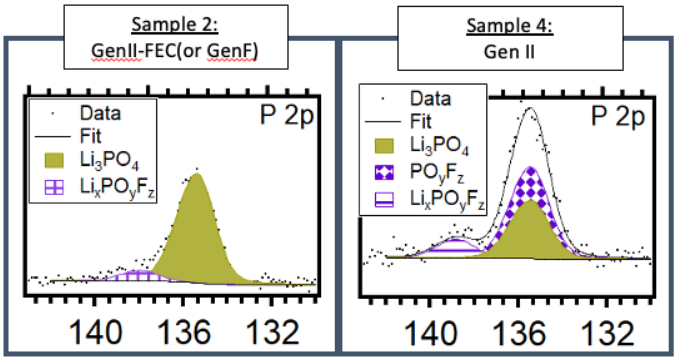

Figure II.1.B.63 P 2p XPS core-level spectra for samples 2 and 4.

Figure II.1.B.62 and Figure II.1.B.63 show the XPS core-level spectra of the elements specific to the salts used in the glyme-electrolyte samples (S 2p and N 1s in Figure II.1.B.62), and carbonate-based electrolyte samples (P 2p in Figure 25). Few quantitative XPS studies have been conducted in the precise identification of these species. In the case of the glyme samples, it is clear that similar amounts of sulfur- and nitrogen-based salt byproduct are deposited on the surface of the electrode. The sulfur species were determined to likely be SO_x compounds when considering the O 1s signal intensities, as discussed previously. For the nitrogen compounds, additional XPS data sets on reference materials would be acquired to confidently report specific species. In the case of the carbonate-based samples, NREL researchers have previously collected reference spectra on lithium phosphate, and can therefore identify its presence in the SEI with confidence. The remaining signal intensity is likely various fluorophosphate compounds.

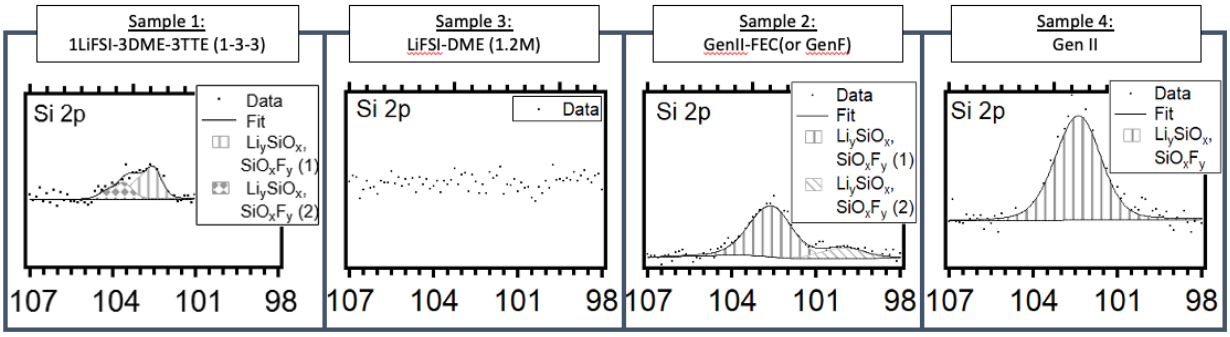

Figure II.1.B.64 Si 2p XPS core-level spectra for samples 1, 3, 2, and 4.

Figure II.1.B.64 shows that all samples except for sample 2 have some silicon signal that can be observed. Either the silicon-based species exist only at the surface of the original Si film, in which case the SEI would have to be less than 10 nm in order for there to be detectable XPS signal, or some of the silicon species are incorporated into the SEI further from the Si surface. The signal is strongest in sample 4, but it is still dwarfed by the intensity of the other core-level spectra. In Si-anode-based SEIs, silicon can exist in a variety of oxygenated, fluorinated, and lithiated species, but due to the very low Si 2p signal intensities, it is not possible to make definitive assignments for these samples.

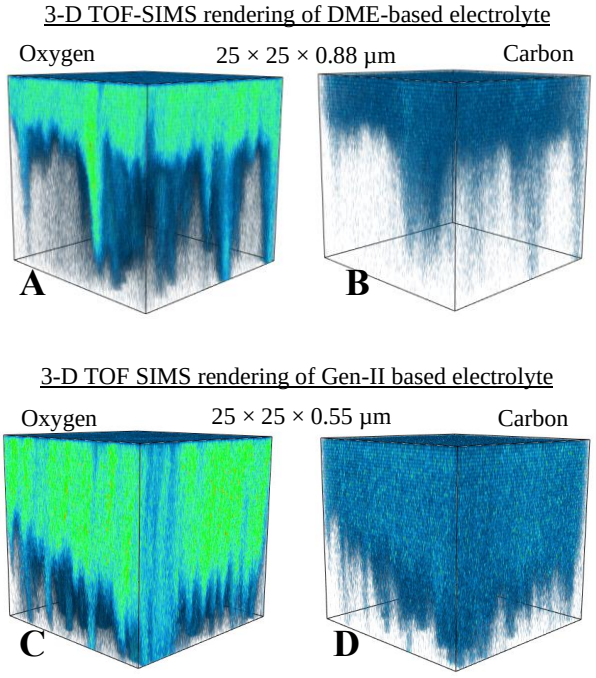

Figure II.1.B.65 TOF-SIMS tomography data for the cycled Si anodes in glyme-based (top row) and Gen 2 (bottom row) electrolytes. The formed SEI is much thinner with the cycled Si anode in glyme-based electrolyte, and more oxygen and carbon are noted in the cycled anode in Gen 2 electrolyte. 3D rendering of oxygen in the electrodes cycled in (A) glyme-based and (C) Gen 2 electrolytes. 3D rendering of carbon in the electrodes cycled in (B) glyme-based and (D) Gen 2 electrolytes.

TOF-SIMS results on the glyme-based electrolytes were consistent with XPS results, and the samples cycled in the glyme-based electrolytes had much less carbon and oxygen in the SEI compared to a sample cycled in Gen 2 electrolyte. This is consistent with the XPS results, which showed less carbonate species in the SEI for the glyme-based electrolyte cycled samples. A higher content of sulfur and fluorine in the glyme-based electrolyte

was also noted. The TOF-SIMS 3D tomography results, as shown in Figure II.1.B.65, also visually show the SEI was much thinner with the glyme-based electrolyte, also in agreement with the XPS results.

Understanding the chemical properties of the SEI in the glyme-based electrolytes using AFM-SSRM

AFM imaging was conducted to determine roughness and morphology of the electrodes. At larger scales, the sample roughness was dominated by the texture of the copper substrate, so the roughness was determined by an average of the root mean square roughness of four randomly selected 1 × 1-µm sites. These results can be seen in Figure II.1.B.66. The roughness of all cycled samples increased as compared to the pristine sample, which is expected, and is due to the formation of SEI and the expansion and contraction that Si undergoes during lithiation (discharge) and delithiation (charge). Out of the cycled samples, sample 1 is the least rough, followed by sample 2 and sample 3. Sample 4 is the roughest. A greater increase in roughness is associated with a thicker SEI, and these relative roughnesses correspond with the SEI thicknesses discussed in the following section.

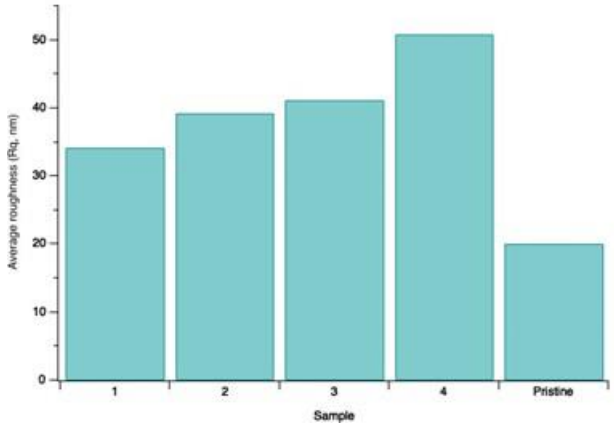

Figure II.1.B.66 Average root mean square roughness determined from 1 × 1-µm AFM scans.

SSRM resistivity vs. depth profiling was conducted for each sample. In this technique, successive SSRM scans are performed with a high enough probe force that material is milled away with each scan while resistivity is also measured. A low-force overview scan is then done after the milling to determine the depth of the resulting crater, which allows one to determine the resistivity as a function of depth. These resistivity vs. depth profiles are shown in Figure II.1.B.67. Samples 1, 2, and 3 all have thin SEIs formed on the surface, whereas sample 4 has a much thicker SEI, as well as a much greater active material depth before the Cu substrate is reached, indicating a larger volume increase. Samples 1–3 also show significant thickness increase of Si active material compared to the pristine sample, but in a less degree than sample 4. Additionally, the α-Si in samples 1 and 2 showed decreased resistivity as compared to the pristine sample. This resistivity decrease is expected as a result of Li incorporation during cycling. Sample 4 showed increased resistivity of the active material, which is consistent with previous SEISta SSRM work with Si cycled in Gen2 electrolyte. Resistivity increase can be the result of SEI ingrowth, fouling from electrolyte species, or mechanical fatigue due to volume expansion and contraction.

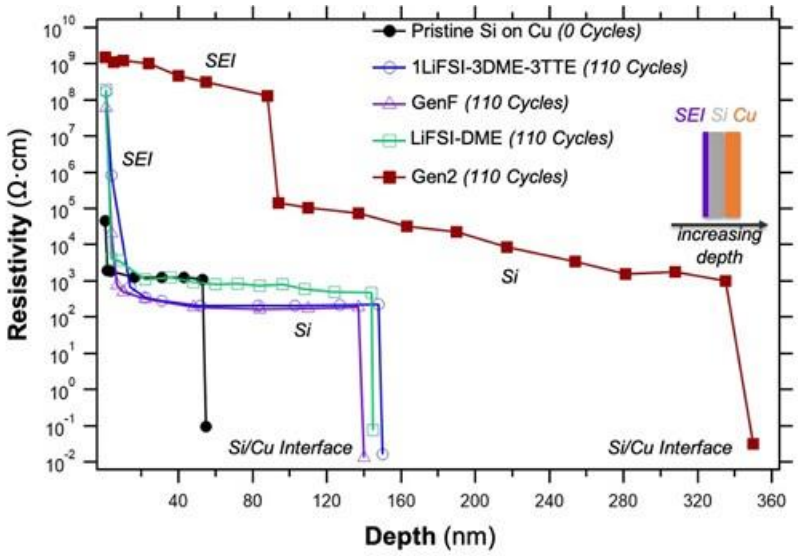

Figure II.1.B.67 Resistivity vs. depth profiles for all samples.

Additionally, 3D resistivity maps for each sample were created by interpolating the series of 2D resistivity scans along the depth direction that were generated during the milling described previously. These 3D maps, as shown in Figure II.1.B.68, provide a clear 3D visualization of the SEI and the underlying Si. Both the SEI and active Si can be seen by the difference in resistivity. For samples 1 and 2, SEI is mostly formed on the surface region with little amount ingress into Si, whereas for sample 3, SEI ingresses largely into Si, and for sample 4 SEI dominates through the milled depth. Due to the volume changes, the Si surface becomes rough, and as a result, the formed SEI is also rough.

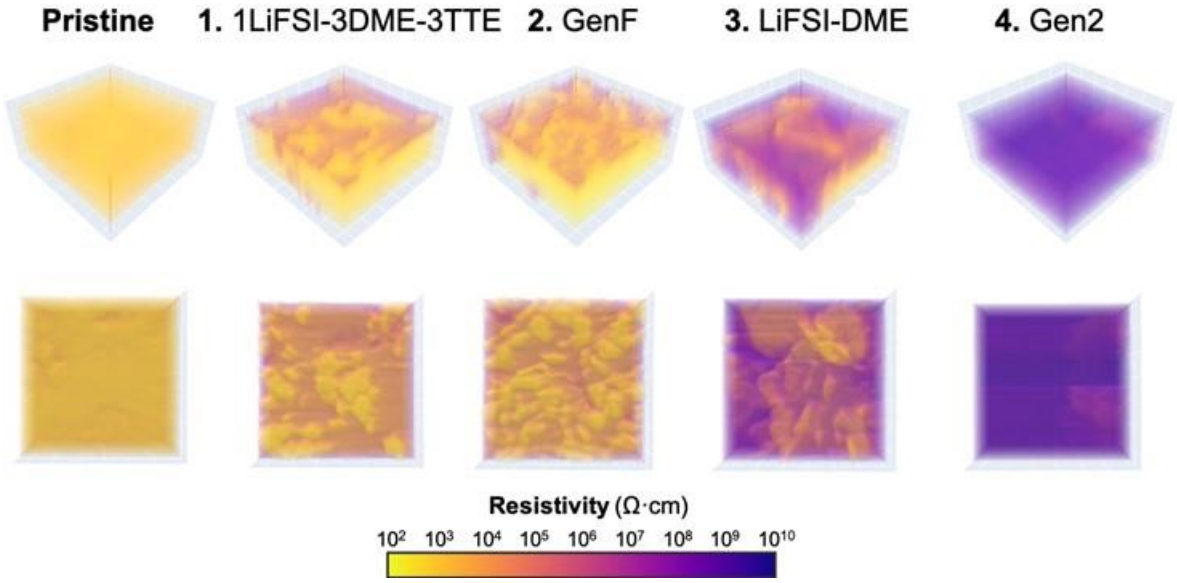

Figure II.1.B.68 3D resistivity volume interpolations for all samples. Yellow regions are low resistivity and correspond to Si, whereas purple is higher resistivity and corresponds to SEI. The upper row presents a 3D view and the lower row represents a top-down view.

Theoretical understanding of the electrolyte

We use the reaction network approach to extract decomposition pathways of the electrolyte molecules relevant to the Si system. FEC is a common electrolyte additive found to mechanically stabilize the Si anode SEI. The presence of FEC increases LiF content at the SEI, and there is still no clear consensus on the exact pathway that the LiFEC molecule takes to decompose and produce LiF. To understand FEC decomposition mechanisms, a reaction network was constructed using over 9,000 molecules and 180,000 reactions. The network was able to capture four different ways the LiFEC molecule can ring open, and its respective pathways leading to LiF formation, as shown in Figure II.1.B.69. The green path in Figure II.1.B.69 is the shortest pathway predicted by the network, and it is also one of the most frequently expert proposed paths [1]. Although the blue path may seem the best path thermodynamically, it requires an additional LiFEC molecule and Li ion to assist in LiF. Similarly, the purple pathway requires an additional Li-ion to bond with the fluorine in LiFEC to form LiF. The green path does not require any additional species for LiFEC to decompose into LiF, CO_2, and C_2H_3O. This work not only validates our network-based approach but also highlights the value of the automated framework. Our approach can predict mechanistic pathways that took years for the community to identify manually.

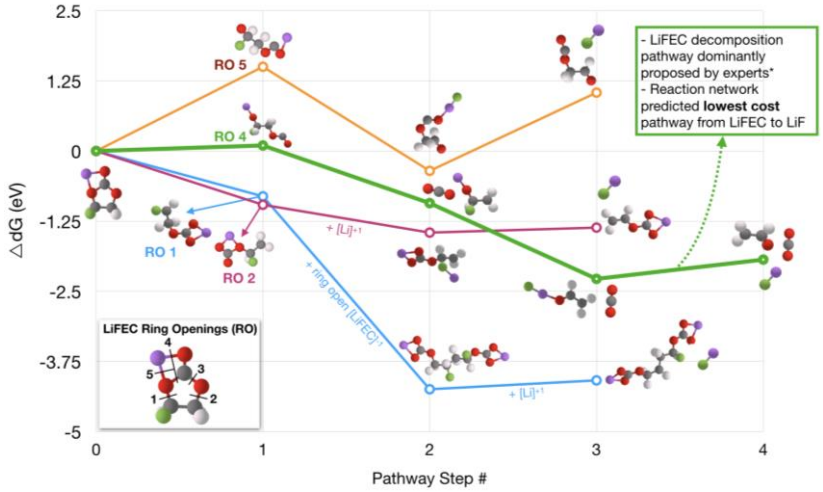

Figure II.1.B.69 Thermodynamic pathways from LiFEC to LiF found using the reaction network.

Furthermore, LiF also forms through $LiPF_6$ salt decomposition, which is commonly used in the Si system. The competing pathways from LiFEC and $LiPF_6$ leading to LiF formation are being investigated using the reaction network. An additional 3,000 $LiPF_6$-related molecules were added to the aforementioned network to form a network with over 12,300 molecules. Path search results from LiFEC and $LiPF_6$ to the four common $LiPF_6$ byproducts at the SEI ($LiPF_4$, PF_3, LiF, and LiF_2PO) are presented in Figure II.1.B.70. The network predicts the shortest path to LiF is for F-ion to leave FEC via FEC reduction and Li-ion to separate from $LiPF_6$. In other words, it is much easier to obtain fluorine from FEC and Li from $LiPF_6$. Moreover, LiF_2PO is formed by a fragment of FEC (CO_2 removed) bonding to PF_2.

The network is still in its preliminary stages of development and does not capture water reactions or energy change due to phase change. Many of the uphill steps in the initial stages of $LiPF_6$ decomposition can be lowered in thermodynamic cost with the assistance of water. Moreover, kinetics are not currently integrated into the network, but will soon be in the future.. Future work will continue the development of the reaction network tool and effectively use it to clarify the LiF formation mechanism at the SEI as a function of electrolyte content.

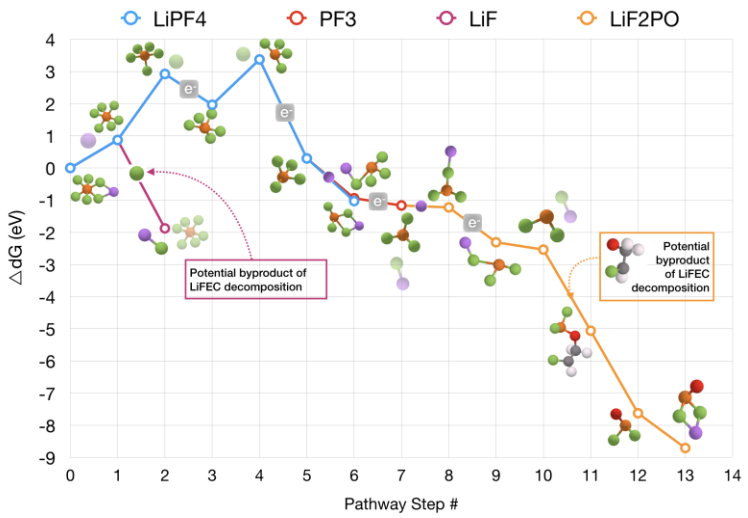

Figure II.1.B.70 Decomposition pathways of $LiPF_6$ in the presence of LiFEC.

Role of CO_2 additives

The goal of this work was to determine the effect of CO_2 on the stability of SEI formation on model electrodes, but examining the changes in the nature of the SEI (XPS, FTIR/Raman, and quantitate electrochemical measurement) as a function of CO_2 concentration. To accomplish this, a team of scientists from multiple laboratories collaborated to evaluate the resulting SEI chemistry from pouch cell-type batteries, with and without gaseous CO_2. The cells were built and cycled at ORNL using our standard Gen2 electrolyte with 50-nm amorphous silicon electrodes and lithium metal counter electrodes with Dreamweaver separator to ensure electrolyte wetting and CO_2 transport. Samples were sent to the partner laboratories for FTIR (NREL), matrix-assisted laser desorption/ionization (MALDI) (LBNL), Raman (ORNL), XPS (ORNL), TOF-SIMS (NREL), NMR (ANL), and SSRM (NREL) analysis.

We found the following results:

1. The SEI chemistry changed significantly when using CO_2, resulting in an SEI layer that has significantly more inorganic component
2. The irreversible capacity losses were constant regardless of the presence of CO_2
3. Fabrication of the cells is important, and still an unresolved issue, which we believe is due to air or water infiltration
4. Air or moisture infiltration has a larger impact on cell performance than CO_2.

As part of this set of experiments, we prepared multiple test cells cycled under the same conditions. These test cells involve the formation of pouch cell-type batteries. The electrodes were 2 by 2 in. in area (Figure II.1.B.71). We used three pieces of Dreamweaver separator. This material was chosen because it wets extremely well with electrolyte (almost instantaneous); because of this wettability, we believe it will allow gas infiltration and transport. The cells were sealed in a glovebox under argon. Samples were removed to air and the CO_2 was dosed to the cell using a gastight syringe. Cells were stacked under a 500-gram copper plate to provide stack pressure. The cells were cycled at a C/10 rate for 9.5 cycles (10 lithiations). The cycled cells were loaded into the glovebox and disassembled. Portions of the cells were washed with 2 mL of dimethyl carbonate (dropwise addition) and dried under vacuum. Other parts were unwashed for MALDI or NMR experiments. The advantage of this approach is that all the characterization was performed on the same set of samples instead of samples made at different laboratories. This is important for this work as the dosing process affects cycling.

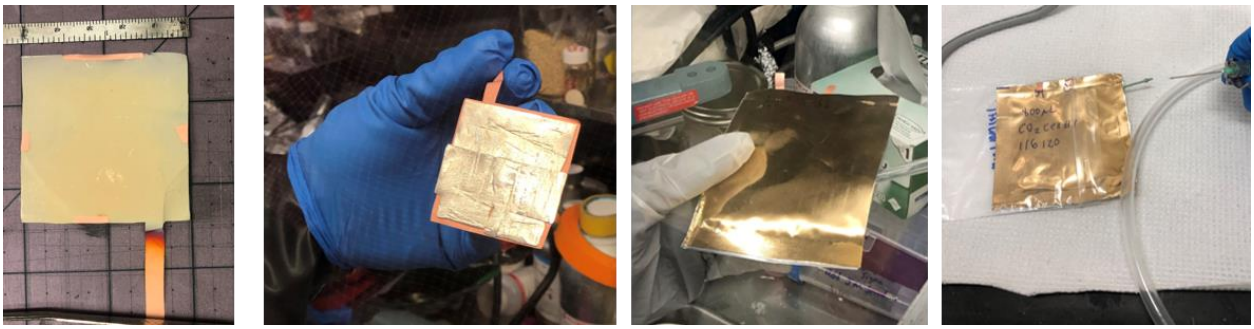

Figure II.1.B.71 Images of the Si electrode (left), Li electrode (center left), pouch cell being injected with electrolyte (center right) and pouch cell injected with CO_2 (right).

During the course of these experiments, we observed that dosing and cell preparation had a major influence on reproducibility. Figure II.1.B.72 shows a collage of data collected for different cell fabrication and dosing protocols. As can be seen in these data, the pie charts show the average elemental composition for at least two samples measured by XPS along with the cycling data. In Round 1, cells were sealed after bringing to air, with or without dosing with CO_2. Under this process, the XPS data looked the same (composition and cycling). In Round 2, the cells were sealed in a glovebox and then the leads were coated in epoxy, as this was viewed as a source of gas leakage. In Round 3, the CO_2 gassing protocol was revised to use a gastight syringe to dose the samples with 2 mL of CO_2 through the smallest hole possible. As can be seen from the experiments in Rounds 2 and 3, the SEI compositions were similar, but varying significantly from Round 1.

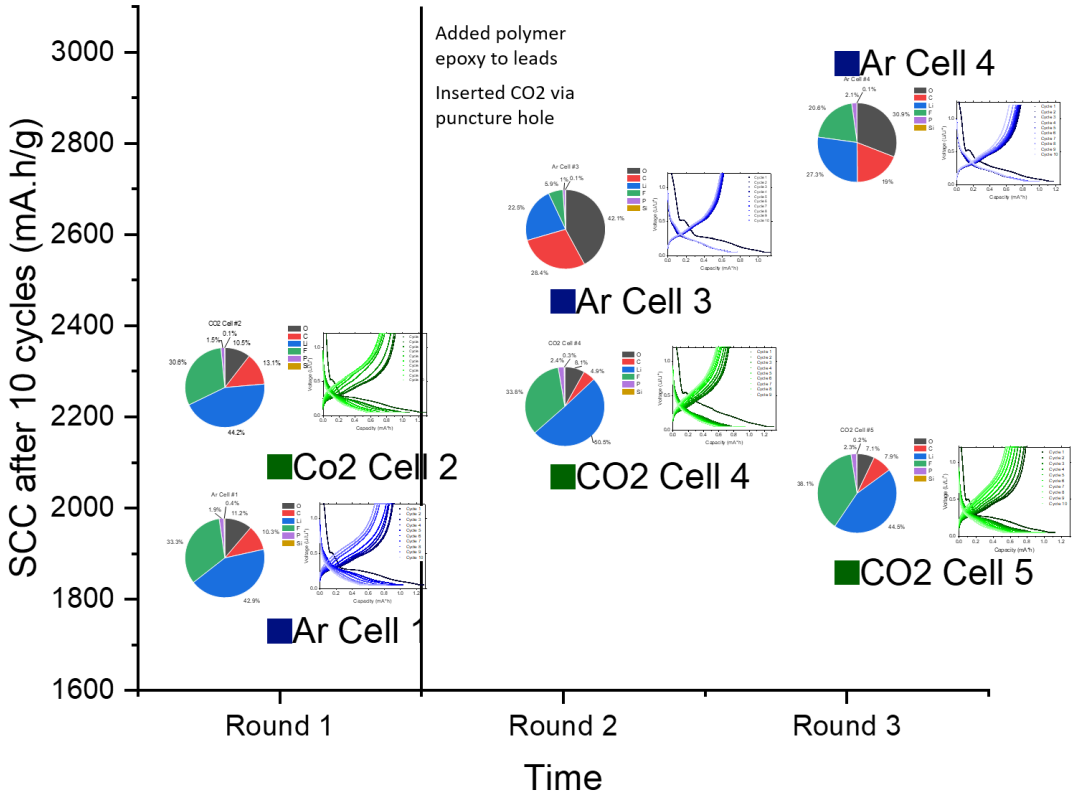

Figure II.1.B.72 Collage of SEI capacity and capacity retention as a function of fabrication method. Left axis is the capacity retention after 10 lithiations for the standard 50-nm electrode.

From these data, it is clear that the SEI becomes more inorganic-like with the introduction of CO_2, as evident by the increase in F and Li content (green and blue data, respectively). Note we use F as a marker for inorganic LiF-type SEI layers. In contrast, the SEI with Ar cells has higher concentrations of carbon (red) and oxygen (black). The higher concentrations of carbon and oxygen is consistent with a more "organic-like" SEI layer. Interestingly, these results mimic what was observed using neutron reflectivity data to follow the SEI formation with and without FEC. The FEC-containing electrolyte resulted in a more F-rich SEI, whereas the FEC-free one was more organic in nature. This points to the CO_2 promoting the inorganic SEI components.

The second observation that is clear from the data is that the CO_2 has no apparent benefit to the cycling performance of the electrodes over a standard argon configuration. Figure II.1.B.73 shows average cycling data collected for at least three cells, along with error bars for these measurements. The left data show the cells measured in argon, whereas the right data show cells dosed with CO_2. Both cells show large irreversible capacity losses with the first cycle and a slow but steady decline in capacity retention with cycles. These data indicate that CO_2 is not the cure to an unstable SEI.

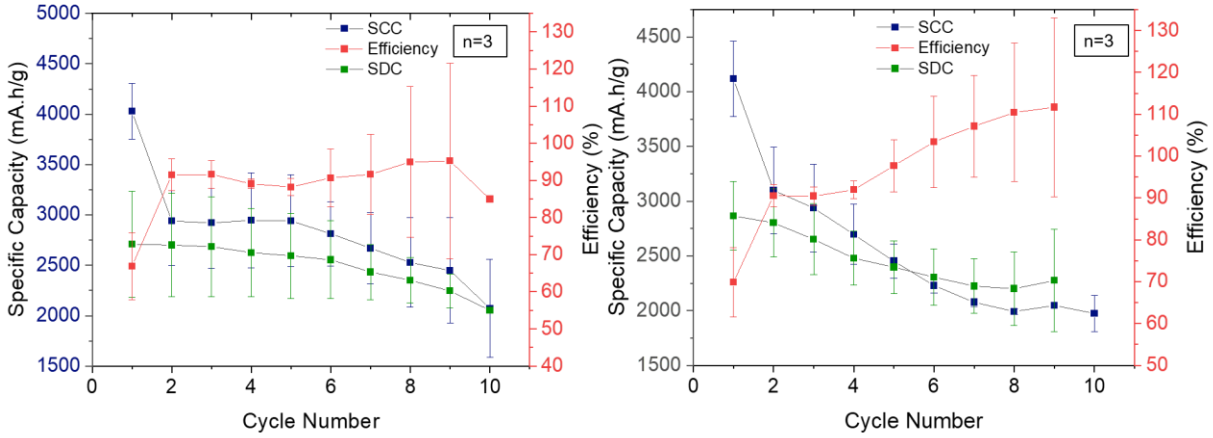

Figure II.1.B.73 Average cycling data for cells cycled in argon (left) and CO_2 (right).

To explore the organic components of the SEI, unwashed electrode samples were subjected to gradient wash and MALDI experiments. Figure II.1.B.74 shows representative FTIR spectra collected during the gradient washing process (after each elution step). In this work, progressively larger fractions of ethyl acetate (EA) are added to a hexane (Hex) solution, which gradually increases the elution intensity in terms of polarity. The electrode is evaluated as a function of EA:Hex ratio. The hexane is a "less" aggressive solvent to remove SEI components, whereas EA dissolves more carbonate and polymer species. After each wash, the electrode surface was probed with FTIR spectroscopy. Figure II.1.B.74 demonstrates that the more aggressive wash removes more and more of the residual EC (marked on the spectra) and $LiPF_6$ (~825 cm^{-1}) both for electrodes cycled with argon and CO_2. It was found that 3:7 EA:Hex elution can fully remove EC and most of $LiPF_6$ from the electrode surface.

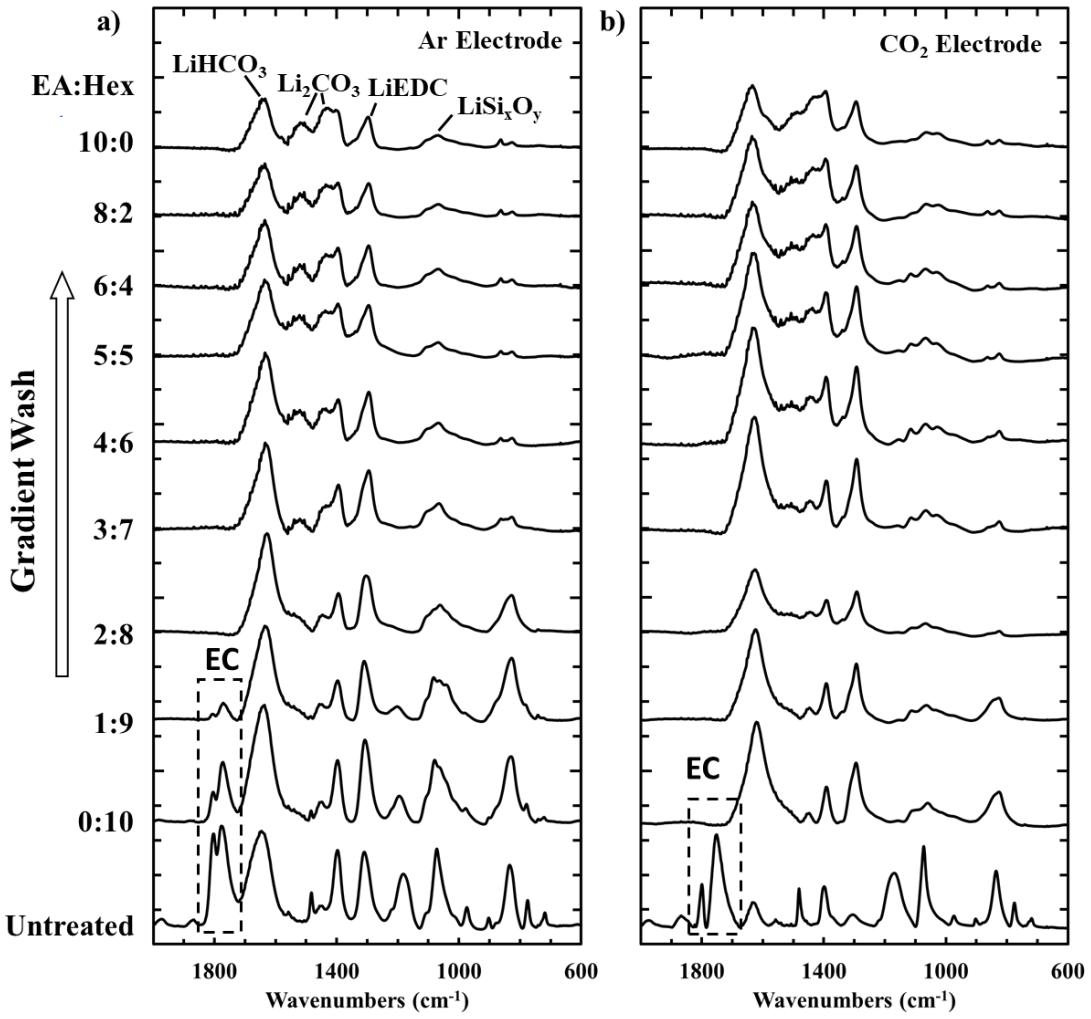

Figure II.1.B.74 FTIR spectra of electrodes after each gradient wash step (a) cycled with argon and (b) cycled with CO_2.

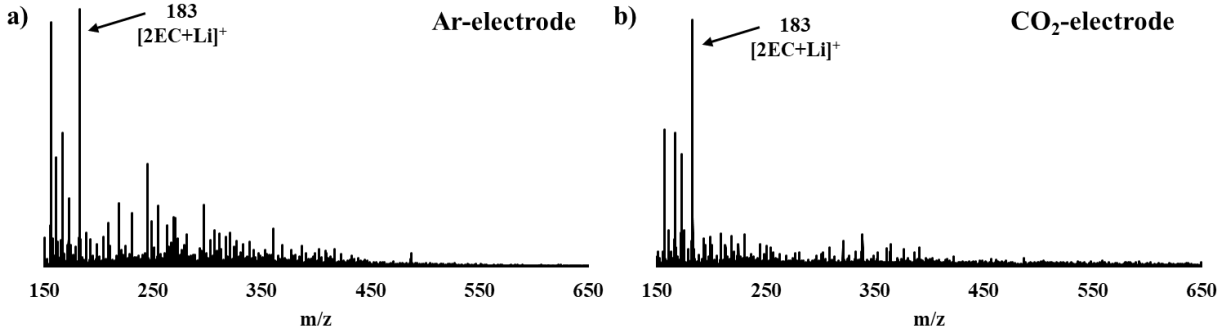

Figure II.1.B.75 MALDI spectra of electrode cycled with (a) argon and (b) CO_2.

The freshly retrieved electrodes (no elution performed) were measured by MALDI as well, and the representative data are shown in Figure II.1.B.75. For both of the electrode samples cycled with argon and CO2, only EC signal was observed with strong noise in the higher-mass regions. This result demonstrates that residue EC on the electrode surface hinders MALDI measurement of the organic species in SEIs.

When the electrodes were subjected to on-electrode chromatography with 3:7 EA:Hex elution to remove the residual EC and $LiPF_6$, PEO species were found as shown in Figure II.1.B.76 (a and b). The assignment of PEO is based on the repeating pattern of 44 m/z. The same type of PEOs were found for electrodes cycled with argon and CO_2, as evidenced by their identical distribution of PEO masses. On the other hand, PEO formation seems to be promoted by CO_2 additive as the relative PEO signal intensities in the case of CO_2 is significantly higher.

To further investigate the difference in PEO formation, the electrode samples that have gone through the entire gradient wash process (0%–100% EA:Hex), namely treated with stronger elution conditions, have also been characterized by MALDI. As shown in Figure II.1.B.76c, the argon-cycled electrode presents no PEO signals but only matrix signals (2,5-dihydroxybenzoic acid or DHB is the matrix). In contrast, the CO_2-cycled electrode still presents the high-mass PEO species (~1,000 m/z) with the same mass distribution. Notably, a new series of PEO masses were found in the lower mass range (~600 m/z) with a different pattern of mass distribution. These results demonstrate that the PEOs generated with CO_2 additives are higher in quantity in SEIs and are more robust against solvent elution. It is possible that the PEOs formed with CO_2 are generated in the inner sections of the SEIs.

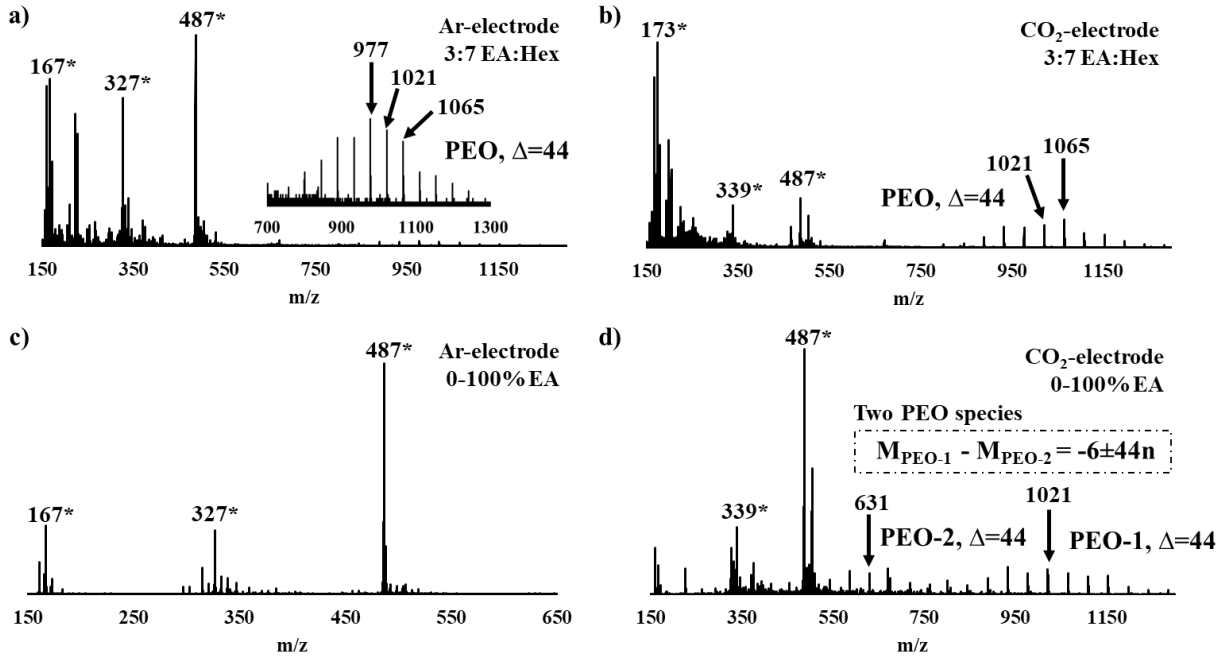

Figure II.1.B.76 MALDI spectra of electrodes cycled with argon after (a) 3:7 EA:Hex elution and (c) 0%–100% EA:Hex elution. MALDI spectra of electrodes cycled with CO2 after (b) 3:7 EA:Hex elution and (d) 0%–100% EA:Hex elution. *Signals originated from lithiated DHB clusters: m/z 167 = [DHB-H+2Li]+, 173 = [DHB-2H+3Li]+, 327 = [2DHB-2H+3Li]+, 339 = [2DHB-4H+5Li]+, 487 = [3DHB-3H+4Li]+.

AFM was utilized to examine the DMC-washed surfaces of the formed SEIs after 9.5 cycles, revealing distinctly different surface morphologies for the Ar and CO_2 electrolyte samples (Figure II.1.B.77a). Although the roughness and size of features on the CO_2 sample appear to be representative of the underlying Cu substrate, finer features were detected on the surface of the Ar control sample (Figure II.1.B.77b), suggestive of additional SEI formation.

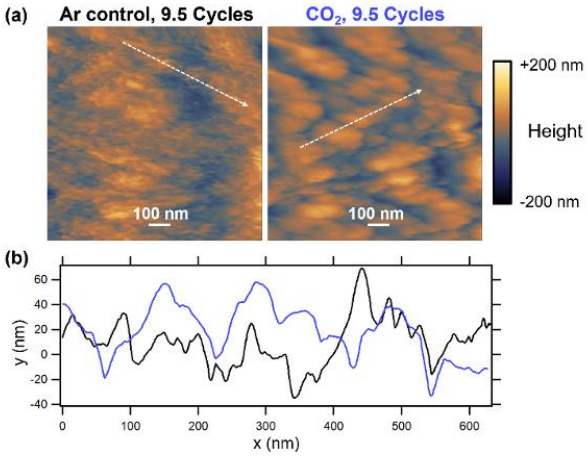

Figure II.1.B.77 1 × 1-µm AFM images of SEI formed on 50-nm a-Si on Cu after 9.5 cycles. (a) Comparison of the characteristic surface morphologies. (b) Line scans extracted from each image depicting the comparatively smaller surface features on the surface of the Ar control sample (black trace) than the CO_2 sample (blue trace).

Resistivity vs. depth profiles were obtained using SSRM to investigate the thicknesses of the layered structures and the electronic contrast between them (Figure II.1.B.78). The SEI formed from the Ar-containing electrolyte control sample was measured to be thicker and more resistive than the SEI formed from the CO_2-containing electrolyte. The underlying lithiated Si thin film in the Ar sample was 1–2 orders of magnitude more resistive, perhaps due to a more porous SEI formed from the Ar electrolyte, permitting additional fouling by species that contribute to an increase in resistivity. SEI thickness was measured to be 14 nm on the CO_2 sample and 21 nm on the Ar sample. The thickness of the lithiated Si thin film was measured to be approximately 75 nm in the CO_2 sample and 100 nm in the Ar sample.

Further analysis of the unwashed electrodes as well as electrolyte samples was performed via NMR using $^{13}CO_2$ dosed cells vs. undosed cells (Figure II.1.B.79). Solids ^{13}C MAS NMR data for these *electrode* samples are shown in Figure II.1.B.79. New peaks (marked with arrow) in the high-frequency region ~200 ppm due to aldehyde/ketone-type organic solid species were observed, indicating changes in SEI chemistry. However, no clear new soluble species in the solutions ^{13}C NMR of the *electrolyte* samples of $^{13}CO_2$ dosed cells have been found. The results suggest CO_2 dosing altering the solid SEI speciation of the electrodes.

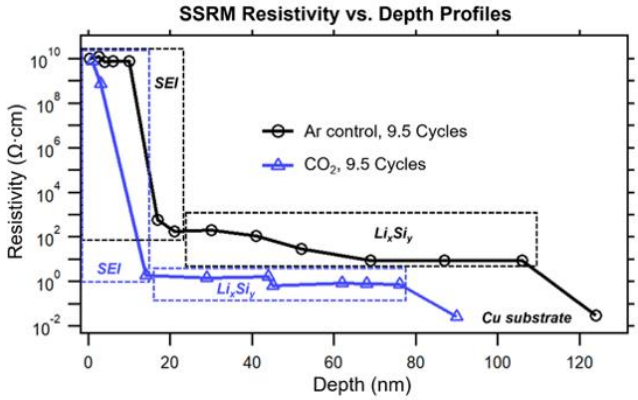

Figure II.1.B.78 SSRM resistivity vs. depth profiles obtained from samples after 9.5 cycles with Ar and CO_2 electrolytes. Composition is labeled for each profile, showing SEI at the surface, the lithiated Si thin film (Li_xSi_y), and the copper substrate beneath.

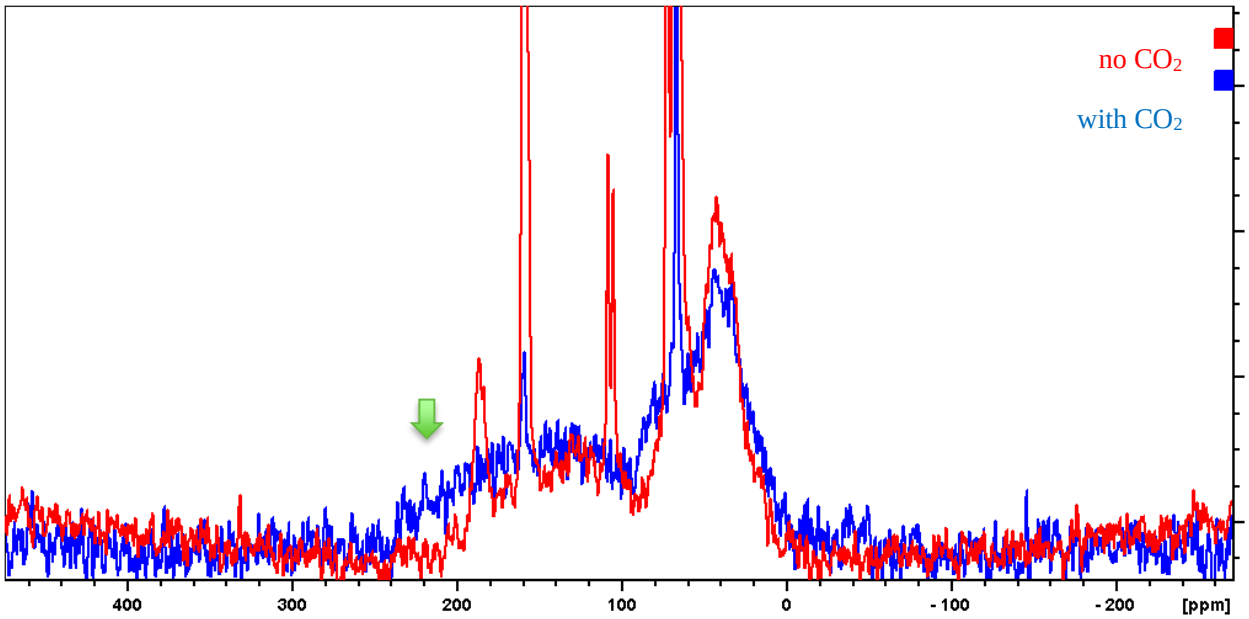

Figure II.1.B.79 NMR data collected for cells with (blue) and without (red) CO_2.

Mechanical properties of SEI and impacts

To investigate the quantitative influence of the mechanical degradation of SEI, we designed the following comparative study: A test sample allows lateral expansion of Si thin-film electrode by using a polymeric substrate (polydimethylsiloxane—PDMS), while a control sample does not allow the lateral expansion by using a rigid substrate (fused silica). The lateral expansion of Si thin-film electrodes directly translates to mechanical stretching of SEI (i.e., the SEI formed on the test sample is expected to undergo mechanical deformation, whereas that formed on the control sample does not). Comparing the cycling performance and the SEI compositions of the two types of samples is expected to unveil the influence of the mechanical deformation effect. As the first step, we conducted preliminary experiments to establish a proof of concept of this approach. Both studies contribute to a comprehensive understanding of the decomposition reactions at the Si-electrolyte interface.

As recently reported, one of the main manifestation of the electrolyte chemical and electrochemical instability is the so-called “breathing effect” (i.e., the continuous growth and shrinking of the SEI thickness upon lithiation and delithiation, respectively [30]). We have further confirmed this effect by XPS, being able to determine that during the first delithiation step, the insoluble components of the SEI are removed to a large extent, exposing the underlying Si core levels. This process repeats itself during the second delithiation, but to a lower extent, as a larger fraction of the SEI components are able to remain on the surface. This constant dissolution or detachment of the SEI from the Si surface anode during delithiation and its formation again during the lithiation steps are the source of severe charge consumptions. The use of thin (50-nm) electrode, enabled us to exclude the contribution of cracking to the problem, leaving the intrinsic (electro)chemical or possibly mechanical instability of SEI as the cause of the breathing effect and related charge consumption.

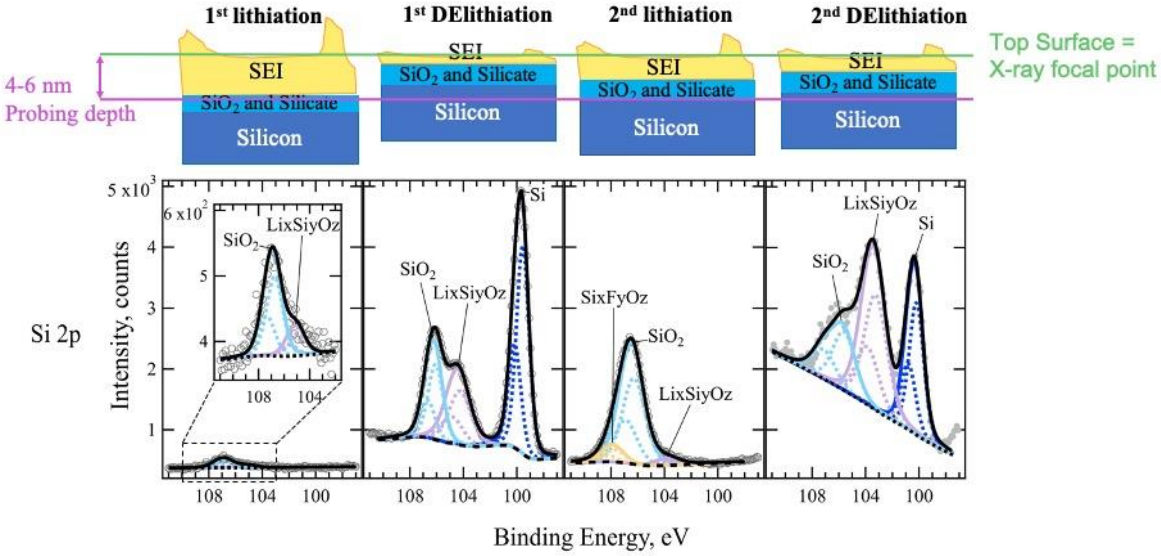

Figure II.1.B.80 The breathing effect revealed through the analyses of the Si core levels.

In order to study the composition of the SEI as a function of state of charge and cycle number, the a-Si/n-SiO_x thin films were galvanostatically cycled, rinsed, and transferred into the XPS system through airtight systems. For each sample, XPS spectra were acquired and peaks were fitted to determine the species present and their relative concentration. An example of the fitting procedure for some relevant core levels is shown in Figure II.1.B.80, whereas the results of the quantitative analysis are shown in Figure II.1.B.81.

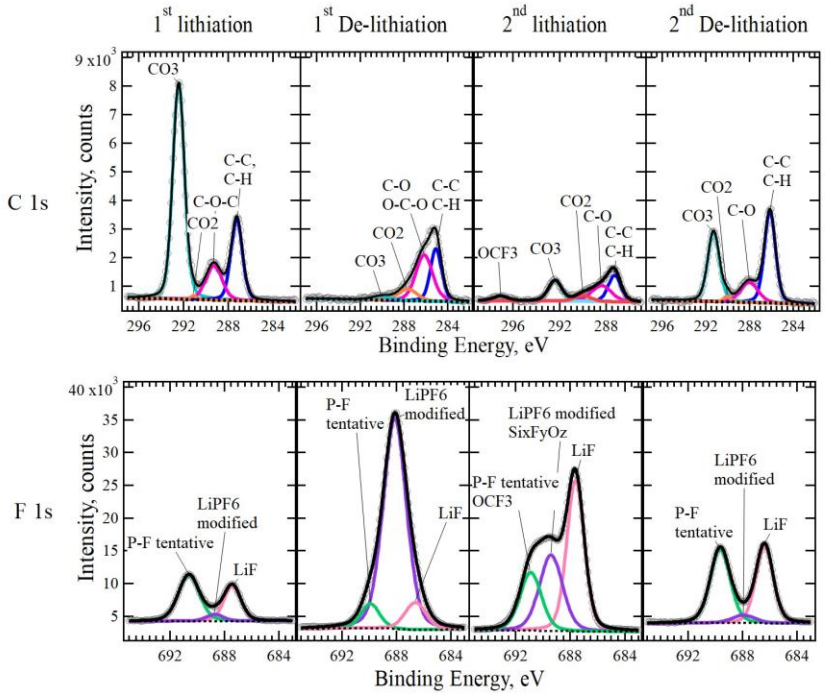

Figure II.1.B.81 An example of the fitting routine used for the phase identification applied to the C 1s and F1s core levels.

Upon the first lithiation, the SEI is rich in the decomposition product of the solvent (overall C signal is ~20 at. %, of which 10 at.% is due to carbonate alone). The salt-derived decomposition products are far less, about 10 at. % based on fluorine, of which only a small fraction (~2 at. %) is due to LiF.

Upon delithiation, the composition of the SEI changes drastically. The amount of carbonate species after delithiation is extremely low (0.4 at. % based on C), a reduction by a factor of 30 with respect to the carbonate content present in the lithiation stage. Surprisingly, the decomposition product of $LiPF_6$ is the major inorganic component, whereas LiF does not vary by much in comparison to the previous measurements.

During the second lithiation, the SEI forms again but with a composition different than the one formed during the first lithiation. Carbonate is the main C-containing species, but they are present in a much lower concentration (1.36 at. % in the second lithiation vs. 11.6 at. % for the first lithiation, thus about an order of magnitude lower). This means that the surface has been largely passivated with respect to the decomposition of the organic solvents and only a tenth of the decomposition of the organic solvent is still happening during the second lithiation. Conversely, the amount of salt-decomposition products is still quite considerable. Indeed, LiF is the major SEI component formed during the second lithiation, with a relative at. % 4–5 times higher than in previous samples (first lithiation and first delithiation). Finally, during the second delithiation, the SEI dissolves or detaches again. LiF is still the main component of the SEI, although its at. % is lower than before. Carbonate is present too, but in much lower quantities with respect to fluorinated compounds.

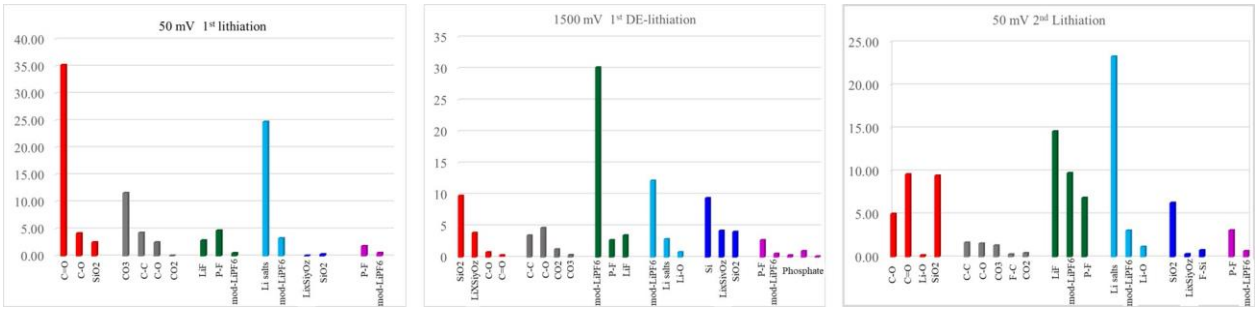

Figure II.1.B.82 XPS quantitative analysis shown for the first lithiation, first delithiation, and second lithiation process.

Regarding the experiments on the mechanical instability of SEI, the lateral expansion of the Si electrode on the polymer substrate (test sample) appears in the form of surface wrinkling. A mechanics analysis suggests that the wrinkles have a uniform wavelength to minimize the total strain energy [2]. Thus, the amplitude and the wavelength of the wrinkles can provide a quantitative level of SEI stretching. Figure II.1.B.82 summarizes the results from our preliminary experiments where we observed this phenomenon. First, a thin-film electrode consisting of Ti (~10 nm)/Ni (~50 nm) current collecting layer and Si (~60–70 nm) layer was created by sputter deposited on a PDMS substrate (Figure II.1.B.83a). Second, we designed/fabricated a custom electrochemical cell for in situ optical microscopy (Figure II.1.B.83b). The sample was assembled to the custom cell and integrated into an optical microscope setup. Next, the Si thin-film electrode was electrochemically cycled while the optical microscope captured the surface topography evolution in real time. Figure II.1.B.83c–e show three representative optical microscopy images taken at as-prepared, lithiated, and delithiated state of the Si electrode, respectively. Also shown is the 2D fast Fourier transform (FFT) images, which visualize the characteristics of the wrinkled patterns. The electrode was initially flat without any pre-wrinkles; thus, the corresponding FFT image shows no particular pattern (Figure II.1.B.83c). After the first lithiation, the lateral expansion of Si spontaneously formed surface wrinkling (Figure 45d). Distinctive high-power location was observed in the FFT image (highlighted in dashed squares); this indicated that there was a characteristic wavelength of the wrinkles of approximately 24 μm. The wrinkles mostly disappeared after the subsequent delithiation due to the contraction of the Si electrode (Figure II.1.B.83e). A minor wrinkled patter may be attributed to irreversible Si volume change. The corresponding FFT image also showed a drastic decrease of power, which confirms the fading of the wrinkles. This series of observations implied that the thin-film electrode on a polymer substrate can apply cyclic strain on the SEI.

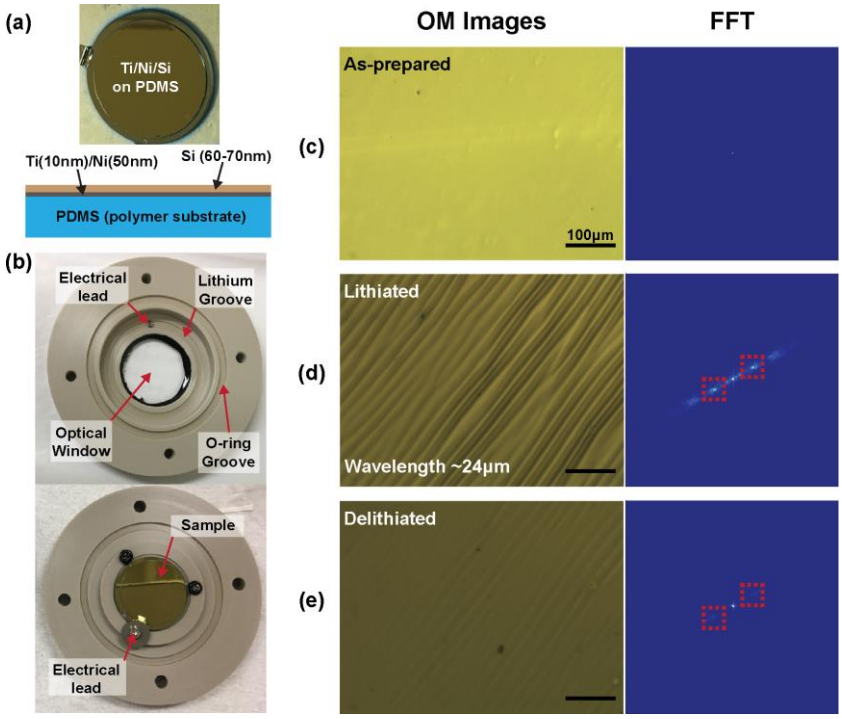

Figure II.1.B.83 Summary of key results from the investigation on the mechanical deformation of SEI. (a) A photograph of Si thin-film electrode consisting of Ti (10 nm)/Ni (50 nm)/Si (60–70 nm) layers on a PDMS substrate. Also shown is a schematic of the electrode structure. (b) A photograph of a custom electrochemical cell for in situ optical microscopy. (c–d) Optical microscopy images of the sample surface at as-prepared, lithiated, and delithiated states. Also shown are corresponding 2D FFT images.

Moiré microscopy continued to be developed and improved for the in situ study of in-plane strain in the SEI and silicon electrode during FY 2020.

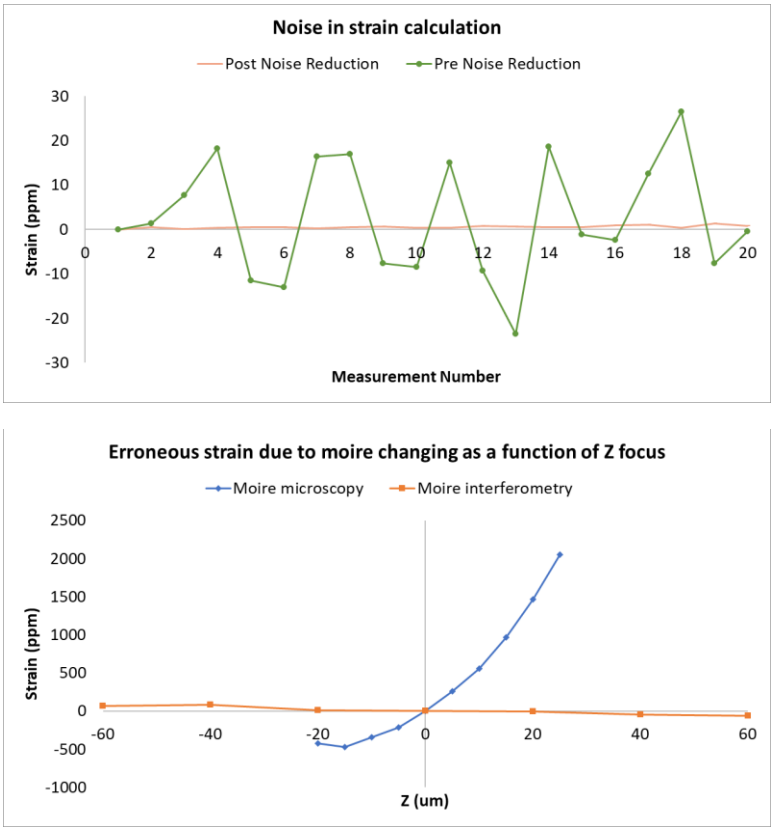

Figure II.1.B.84 Decrease in noise while static imaging by changing cameras and employing more sophisticated data analysis programming (top) and decrease in sensitivity to Z-position when switching from moiré microscopy to moiré interferometry (bottom).

Sample preparation and the in situ cell design were improved. The model electrodes were 50-nm E-beam evaporated silicon on 2-µm copper foils. On the copper side of the electrode, 61-nm silicon gratings were created lithographically. The thickness of the silicon was designed to act as an anti-reflection coating. However, it was discovered that this coating did not provide sufficient contrast to create an adequate amplitude grating. New samples had an improved anti-reflection coating for an improved signal-to-noise ratio. Furthermore, thinner samples were fabricated to improve strain sensitivity. By decreasing the thickness of the copper foil, the strain in the SEI and silicon will increase, decreasing the required strain resolution. Lastly, the use of oversampling techniques was investigated to further improve strain resolution.

The moiré microscope was also improved. The first version used structured illumination as the reference grating and was found to be too sensitive to changes in the Z-focus of the microscope. Various approaches were attempted to compensate for changes in Z-position but were not consistent enough to merit further development. The second version was a moiré interferometer where the reference grating was created through the interference of two beams. To take advantage of the previous setup, the grating used in structured illumination was used to create the ±1 diffraction orders that were recombined at the sample surface, resulting in a more stable reference grating. A filter was used to block all other diffraction orders created by the grating. The interference pattern for the reference grating, and therefore the moiré pattern, was much less sensitive to changes in focus.

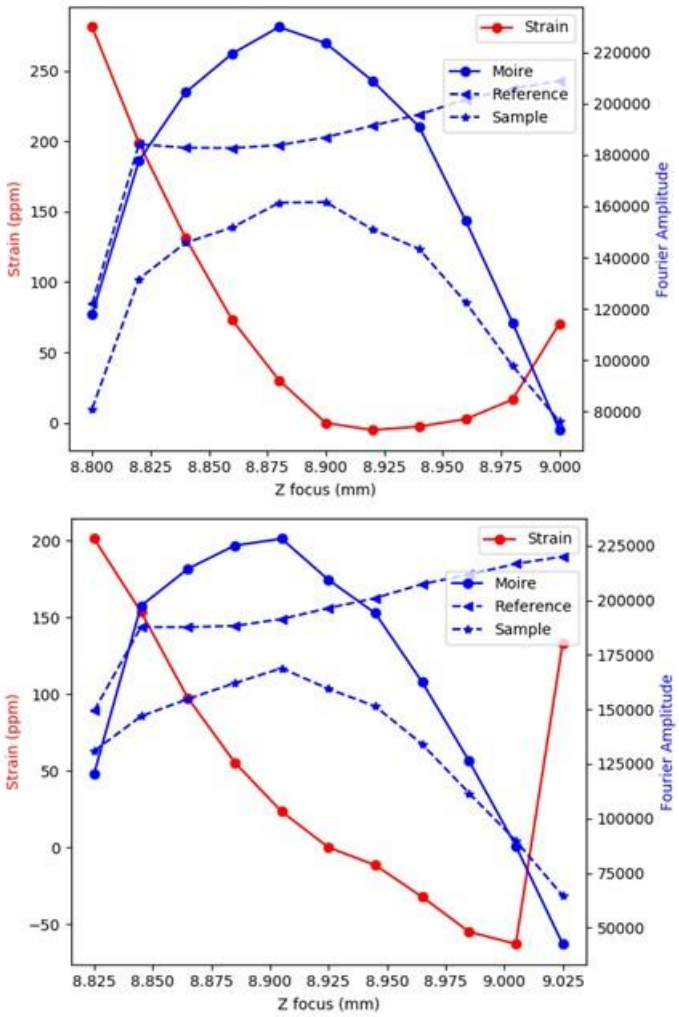

Figure II.1.B.85 Erroneous strain behavior on a silicon control wafer as a function of Z-position for a well-aligned system (top) with a relatively flat region of the strain curve and the strain behavior for the same sample tilted 0.036° (bottom).

Another issue with the setup was a large (on the same order as the desired measurement) error when static imaging. By changing cameras and writing new data analysis programs, the noise was decreased tenfold. The reduction in noise of the measurement (top) as well as the decreased sensitivity of Z of the moiré pattern (bottom) are shown in Figure II.1.B.84.

Currently, troubleshooting of the moiré interferometer is underway. Earlier in the year, we addressed difficulties with erroneous changes in strain with Z-position of the microscope relative to the sample as well as noise during static imaging. This quarter, we observed large changes in the perceived strain behavior depending on the tip/tilt of the sample. An example of this is shown in Figure II.1.B.85 for a control silicon wafer sample that was well-aligned vs. the same sample that had been purposefully tilted by 0.036°. This was further demonstrated when performing calibration experiments to calculate the coefficient of thermal expansion of silicon. Although controlling the tilt of ex situ control wafers is relatively straightforward, high sensitivity of the tilt of the sample is worrisome for in situ foil electrodes where the tip/tilt of the electrode is much more difficult to control while the cell is operating.

Gaussian beam simulations support the sensitivity of the measurement to changes in tilt of the sample observed experimentally. A differential measurement is being considered to try to address changes in tip/tilt as well as further improve changes due to Z-position.

Also in FY 2020, LiPAA solutions varying in lithium content and polymer molecular weight were used to create thin (less than 0.13 mm thick) films by spreading the polymer solution onto a glass plate, drying, and peeling the film off. EIS measurements were attempted between blocking copper electrodes in coin cells. However, most films shattered upon sealing the coin cell, preventing the collection of reliable data.

Effects of silicon nanoparticle size and surface chemistry on SEI

Our work during FY 2020 shows that the nature of the SEI is highly dependent on the initial Si NP surface chemistry. This is reflected in electrochemical cycling data, as well as postmortem characterization using techniques such as ATR-FTIR. To probe the impact of the initial surface chemical environment on the electrochemical cycling properties of Si NP-based electrodes, we have explored several different surface coating chemistries. These pre-coated Si NPs not only provide control over engineering the SEI components, but also act as a probe of the impact on SEI formation of a particular organic or inorganic molecule. Moreover, we also investigate the role of surface area and surface curvature on the SEI formation by varying the size of the Si NPs.

The baseline electrode chemistry from PECVD-synthesized Si NPs has been detailed in previous reports and we summarize briefly here. We first form a covalent bond between the surface of crystalline Si and NMP, which doubles as the slurry solvent. Electrochemical cycling data from Si NP-based electrodes of two different sizes of Si NPs with this NMP surface coating in a half-cell configuration are shown in Figure II.1.B.86. From the cycling data, the smaller (d = 3.9 nm) Si NP electrodes display a superior cycling performance compared to Si NPs with an average d = 30 nm, where the capacity retention of the smaller size exceeds the larger by hundreds of cycles. This is consistent with our prior reports. To quantify the effect of the SEI-stabilizing additive, FEC, we perform side-by-side measurements of both Si NP sizes with and without the FEC. From Figure II.1.B.86, the coin cell with the FEC additive shows an improved capacity retention for both Si NP sizes. The 3.9-nm Si NP size again displays the most robust capacity retention where the value of the 500th cycle is still 80% of that of the first, where the larger particle size displays a retention of only ~20%. The difference between the FEC-stabilized Si and non-FEC-stabilized Si points to the important conclusion that the SEI in these two electrodes is likely composed of different species.

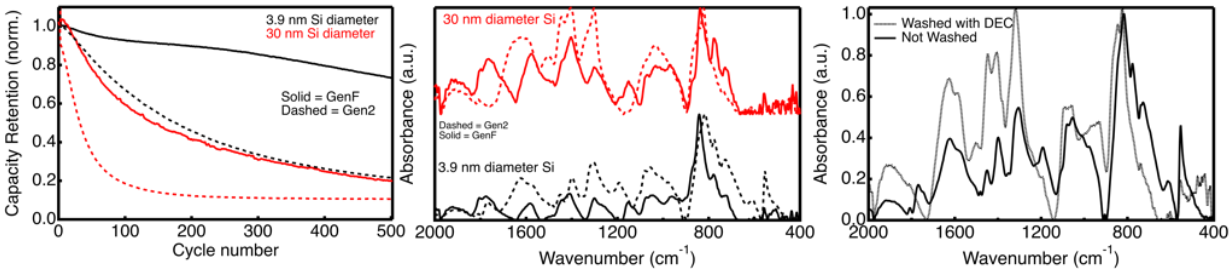

Figure II.1.B.86 (Left) Capacity retention of half-cell coin cells using 30-nm (red) and 3.9-nm (black) Si NP-based electrodes in Gen2 (dashed) and GenF (solid) electrolyte. (Middle) ATR-FTIR data collected on the same washed electrodes as the left panel after 500 cycles. The colors correspond to the same NP size. (Right) ATR-FTIR of the 3.9-nm Si NP electrode after 500 cycles in GenF electrolyte before (solid black) and after (dashed grey) rinsing in dimethylcarbonate.

To inspect how the size and presence of FEC affect the contents of the SEI, we performed ATR-FTIR spectroscopy on the washed composite electrodes, shown in the middle panel of Figure II.1.B.86 after completion of their 500 cycles. The spectra of the two different-sized Si NPs are nearly identical for each electrolyte (Gen2 or GenF) used for electrochemical cycling. Moreover, despite the increase in the relative surface area with smaller d = 3.9 nm particles (greater than tenfold compared to d = 30 nm), no new SEI components are apparent in this sample. Though this result is not too surprising considering that both Si NP

sizes have identical initial surface chemistries (NMP molecular coating), the fact that their capacity retentions are so different indicates that the effect of NP size on capacity retention is a dominant effect. Therefore, we attribute the capacity retention differences between these two Si NP sizes to mechanical (swelling/deswelling) properties during lithiation/delithiation and *not* to SEI-related effects. Comparing the two SEI components of electrodes measured in Gen2 vs. GenF, signatures of all of the same components are present, but in different proportions. For example, the electrodes cycled in Gen2 display stronger absorptions at ~1,630 cm^{-1} and ~1,420 cm^{-1} (assigned to lithium alkylcarbonates) compared to the same electrodes cycled in GenF. This observation suggests that the components making up the Gen2 SEI are more organic in nature, and those in GenF are more inorganic in nature. We hypothesize that the organic-rich SEI from Gen2-based electrolyte may be less stable compared with that of the insoluble, inorganic-rich SEI that forms in GenF electrolyte. These conclusions suggest that an organic-rich SEI may be partially responsible for the reduced capacity retention in Gen2-based electrodes.

To confirm the presence of insoluble components largely making up the GenF SEI, we measured ATR-FTIR of the same cycled silicon electrodes before and after rinsing with DMC. The data from this experiment are shown in the right panel in Figure II.1.B.86. From these spectra, the contents of the SEI do not change to any significant degree after being rinsed in DMC, where the same spectroscopic signatures for each component are present and approximately at the same relative intensities. The most striking difference in these data is that the absorption feature at ~800 cm^{-1} decreases following washing. As this absorption is due to the P–F stretch and is likely residual PF_6^- salts, it is not surprising that the feature is diminished upon rising with a polar solvent (PF_6^- salts are expected be soluble). Overall, however, the SEI of GenF cycled 3.9-nm Si NP electrodes appears to remain largely intact after DMC rinsing, consistent with our previous conclusion that it is composed primarily of insoluble, inorganic components.

We next moved beyond our "baseline" NMP-coated Si NP to understand how varying the chemistry of the surface coating on the Si NPs affects the nature and amount of the SEI formed during cycling. We begin by grafting various organic molecules to the surface of d = 30 nm Si NPs. The surface molecules are chosen to test how the coating's ionic and electronic conductivity affects the formation of the SEI in operando. We react 1-dodecene with the as-grown, SiH_x-terminated Si NPs prior to electrode fabrication, which produces an alkyl (dodecyl) coated Si electrode (Si@C_{12}). This alkyl surface coating is both ionically and electronically insulating. Binding polyethyleneoxide (PEO_n) oligomers via similar reaction chemistry to the Si NP surface produces Si@PEO_n electrodes with surface coatings that are ionically conducting but electronically insulating. Figure II.1.B.87a shows cycling data that compares the baseline Si@NMP electrode to Si@C_{12} and Si@PEO_n electrodes. The Si@C_{12} electrode rapidly (within 5–10 cycles, Figure II.1.B.87a) stabilizes at ~0 mAh/g of reversible capacity and ~100% coulombic efficiency, indicating that the ionically and electronically insulating nature of the alkyl surface coating completely arrests both the reversible lithiation/delithiation reactions as well as the irreversible SEI-forming reactions. In contrast, the Si@PEO_3 electrode shows higher capacity retention and coulombic efficiency than the baseline Si@NMP electrode. This result is consistent with the observation that oligoethers are known to conduct Li ions and, as such, have been proposed to be beneficial components of artificial and in operando formed SEI [31]-[34]. The ionically conducting and electrically insulating properties of coatings formed by the oligoethers promote facile lithiation/delithiation of the underlying Si while minimizing SEI formation by suppressing electrochemical side reactions between lithiated Si and the electrolyte. However, the electronic insulation of oligoether-derived coatings can also be detrimental to an electrode's performance. Figure II.1.B.87b shows the relative delithiation capacities of Si@PEO_n electrodes with varying lengths of oligoethers. The relative capacities decline to smaller steady-state values with increasing oligomer length. This electrochemical behavior suggests that sufficiently thick oligoether coatings electronically insulate the Si and begin to isolate a portion of the active material from the electron percolation network.

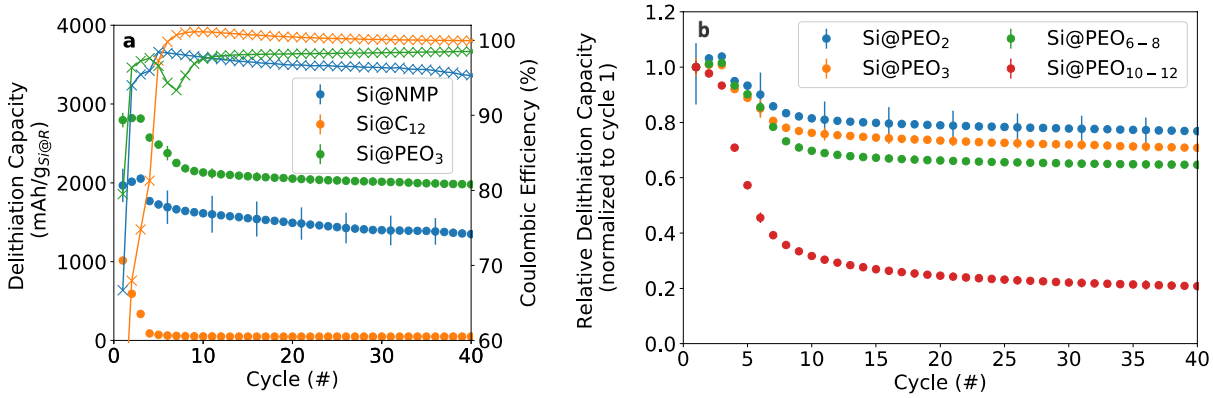

Figure II.1.B.87 (a) Delithiation capacities and coulombic efficiencies of the Si@NMP baseline, Si@C_{12}, and Si@PEO_3 electrodes. (b) Relative delithiation capacities of Si@PEO_n electrodes functionalized with different PEO_n oligomer lengths (n = 2, 3, 6–8, and 10–12).

We also performed surface coating of the Si NPs with polyaromatic molecules that can be both ionically and electronically conducting. Specifically, 4-phenyl-phenol was tethered to Si NPs that were then fabricated into Si@PP electrodes. Electrodes made with Si@PP NPs maintain reversible electrochemistry for many hundreds of cycles, as is shown by the Si@PP electrode cycled in the half-cell (Figure II.1.B.88, left panel). However, despite enabling a stable reversible capacity, the polyaromatic surface coating does not passivate against side reactions with the electrolyte and allows for continuous SEI formation. This is shown by the accumulated irreversible capacity (dotted line) in the left panel of Figure II.1.B.89, which increases continually over the entire cycle lifetime experiment. The consequences of continuous SEI formation are shown in the right panel of Figure II.1.B.89, where the Si@PP electrode is cycled vs. a $LiFePO_4$ cathode (LFP) that supplies a limited Li inventory. The immediate and continual decline of the charge/discharge capacity is a result of the SEI consuming the useable Li inventory of the full-cell, despite the benefits of the SEI formed on the polyaromatic functionalized surface of the Si NPs in half-cell configuration. This result highlights the importance of the in operando formed SEI's ability to passivate the Si active material against further SEI formation, a property that can be achieved by targeting parameters that result in measured coulombic efficiencies reaching values >>99%, especially early in an electrode's cycle lifetime.

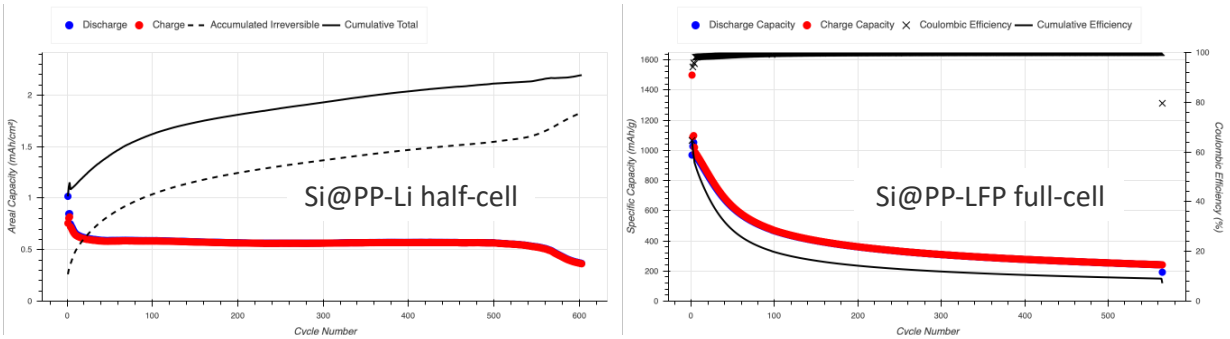

Figure II.1.B.88 Cycling data of Si@PP electrodes fabricated from Si NPs functionalized with 4-phenyl-phenol, and cycle in a (left) half-cell configuration vs. a Li metal foil and a (right) full-cell configuration vs. an LFP cathode.

Additionally, we have explored modifying the Si NP active material as a strategy for improving the performance of Si-based anodes. Related work in the SEISta and Si Deep Dive programs has shown that surface-engineered Si NPs can aid in rapidly forming a relatively stable SEI layer on the Si surface [35]. We have also pursued Si with surface engineering (Si-SE), and find this approach is viable for rapid stabilization of the coulombic efficiency. The first three formation cycles of a Si-SE NP composite anode are shown in Figure II.1.B.90. Compared with all other surface chemistries in this report, the first cycle shows a much sharper onset as the lithiation potential of crystalline Si is reached (~0.1 V vs. Li/Li^+, Figure II.1.B.89, left). The flat nature of the dQ/dV plots at potentials above lithiation is indicative of less charge consumed in

parasitic side reactions in the first formation cycle, which is direct evidence that Si-SE electrodes require a thinner SEI to passivate (equivalently, an SEI that consumes less Li). This facile passivation provided by Si-SE is reflected in the high early-cycle CEs observed not only in the first cycle, but also subsequent early cycles (Figure II.1.B.89, right). In sum, these anodes made with Si-SE NPs demonstrate first cycle CEs of over 70% and reach near-peak CE of 99.5% by the fifth cycle, an impressive result that points to surface engineering as a viable pathway to stabilize Si-based anodes.

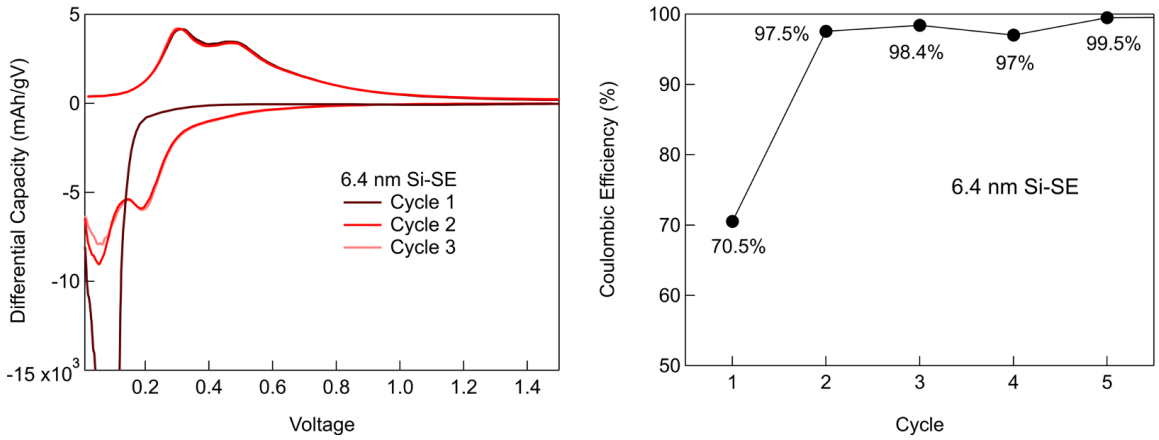

Figure II.1.B.89 Left: dQ/dV data of the first three cycles of an Si-SE composite anode in a half-cell configuration. Right: Coulombic efficiency of the first 5 cycles for the Si-SE composite anode.

Finally, we used ATR-FTIR spectroscopy to probe the nature and amount of formed/soluble SEI species of Si-SE NP composite anodes after 100 cycles in a half-cell configuration and present these data in Figure II.1.B.90. When compared with Si@NMP composite anodes (Figure II.1.B.88, right), the nature of the SEI components in the Si-SE NP-based electrode are clearly distinct. Several peaks between 1,500 and 1,000 cm^{-1} resulting from SEI formation on Si@NMP Si NP-based anodes are absent in Si-SE anodes. This result concurs with the electrochemical data presented in Figure II.1.B.90, which show that Li-consuming SEI formation reactions in Si-SE electrodes are vastly reduced relative to those in Si@NMP baseline electrodes.

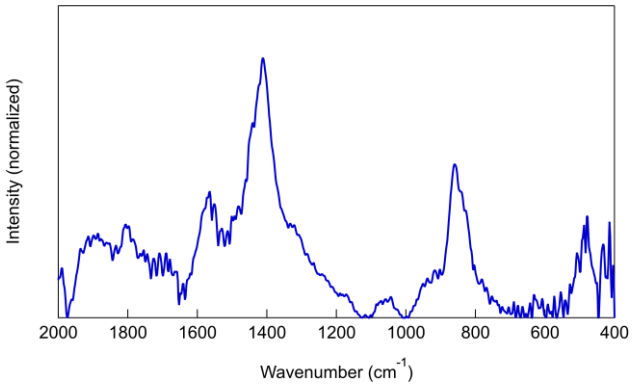

Figure II.1.B.90 ATR-FTIR data collected on an Si-SE composite anode washed with DMC after 100 cycles.

Conclusions

Science of Safety: Evaluating Temperature-Dependent Degradation Mechanisms of Silicon-Graphite Electrodes

Thermal behavior of the Si-Gr electrode was electrochemically tested using different cell configurations. The Si-Gr/Li half-cell results combined with the Li/Li symmetric cell results demonstrate that the Li metal effect obscures the Si-Gr electrode performance and hence half-cells are not ideal for testing thermal behavior of Si-

based electrodes. By utilizing Si-Gr/Si-Gr symmetric cells, the true Si-Gr performance can be studied. However, the capacity fade in symmetric cells is a combination of the loss of active material and the loss of Li inventory. By reassembling the symmetric cell cycled electrodes into half-cells and comparing the lithiation voltage profiles before and after the symmetric cell cycling, the information on loss of active material can be obtained. The results demonstrate that the major degradation mode at elevated temperature is the loss of Li inventory, rather than the loss of active material. To further understand the temperature dependent degradation mechanisms, chemical and morphological evolution of the electrodes will need to be evaluated via spectroscopic and microscopic analyses on the cycled electrodes.

Moving forward, the thermal stability of the SEI at elevated temperatures and how it relates to the reactivity of the cell as it enters thermal runaway will be studied by utilizing DSC and ARC measurements in combination with the electrochemical testing. The intrinsic reactivity of Si and Li_xSi as well as the high surface area of nanometer-sized Si particles in the electrode possess greater challenges compared to the Gr anodes. In addition, the electrolyte components, such as carbonate solvents and $LiPF_6$ salt, readily react with Si, further complicating the system. The thermal stability of different electrode formulations and electrolyte chemistries will be examined to gain insight into the factors affecting the safety of Si-based batteries.

Zintl Phase Formation Mechanism and its Effect on SEI

Thin film, wafer, and nanocrystalline model Zintl phase systems were characterized with STEM, NMR, FTIR, Raman, and SSRM spectroscopies and compared to a Mg-free reference system. For thin films, the role of magnesium was investigated, and it was shown that magnesium (as a coating or in the lattice) formed a binary Mg_2Si interface with the silicon. This material was found to be kinetically slow in lithiating to form a ternary Zintl phase (Li-Mg-Si), although it was detected in the studies. The controlled deposition gave a more uniform distribution and was found to correlate with better electrochemical performance. For the SEI, the samples that had Mg inserted at the interface were found to have much thinner SEI layers that were more resistive. Delithiated electrodes for the two Mg-containing thin film systems as well as the Mg-free system are relatively similar to one another, indicating that Mg returns to electrolyte in both systems. This is consistent with the model that utilizes Mg_2Si in that the mechanism is most likely a kinetically slow ion exchange between Mg and solution lithium cation to gradually form $(Mg_{2-x}Li_{2x})Si$. Measured differences in capacity retention between the two systems suggest that the initial Zintl phase formation mechanism is deterministic for subsequent electrochemical efficiency. Further results on the 500 cycled anode illustrated a large expansion of the Si active material and significant ingress of SEI causing the material fouling. The wafer studies highlighted the role of surface oxide species and the need for defects. In these studies, the intrusion of Mg into the bulk was minimized as the electrochemical activity was found to be low as MgO was observed on the surface of the wafers. In contrast to the near-defect-free SiO_2 rich wafers, the nanocrystalline Si powders showed the highest activity and NMR data were used to identify that the surface of the silicon did not magnesiate until low voltage. In conjunction with the other data shown and previous studies, the mechanism of ternary Zintl phase formation was identified as an ion exchange reaction between a $Li_{15}Si_4$ charged silicon anode phase and electrolyte-derived Mg cations. The species $Li_{14}MgSi_4$, noted earlier in our TEM and XRD studies, was found to be formed at the surface by an ion exchange reaction. On discharge, the lithium and some of the magnesium are removed, leaving a metastable Mg-containing, Si-rich endmember phase.

Silicon Consortium Project Calendar Aging Electrochemical Screening Protocol

A method to qualitatively compare the calendar aging rates of silicon anodes has been developed using full cells with an excess amount of electrolyte and of Li^+ supplied by an LFP counter electrode. After formation cycles, the voltage of a test cell is held for 180 h, and the current response measured during the voltage hold can be used to qualitatively compare the rates of Li^+ consumption at the SEI of silicon test electrodes to a baseline electrode. Long-term voltage hold aging experiments are underway to determine numerical models that can be used to derive aging parameters for silicon test electrodes. Once the numerical models developed by our team are fully validated, they can be used to support developments of cell, material, and interfacial designs that minimize calendar aging rates of Si electrodes.

Understanding Silicon Alloy Effects on the SEI

Various combinations of Si-based alloys were thoroughly explored using microscopy, spectroscopy, electrochemical, and computational methods.

First, Si-Sn thin-film electrodes prepared by magnetron co-sputtering were studied and compared with Si thin-film model electrodes. The calculated experimental capacities of the Si_xSn_{1-x} thin films suggest nearly full lithiation at a high capacity of over 2,000 mAh g^{-1} for the films with $x \geq 0.69$. The optimal composition ($x = 0.8$) achieves stable cycling without the use of any binder, conductive carbon, or electrolyte additive. Interfacial studies on Si vs. Si-Sn by SEM and EDS reveal dramatically different morphology/composition for the Si and Si-Sn thin-film electrodes upon initial lithiation. The Si film surface is teeming with O-rich microstructures, whereas the Si-Sn surface shows uniform morphology and elemental distribution. This observation deserves further investigation on the interphase species formed on the Si-Sn vs. Si during (de)lithiation in an air-free environment.

Second, the nonthermal PECVD synthesis method was used successfully to produce Si-Sn alloy NPs. Si-Sn NPs were incorporated into composite anodes using our air-free process and demonstrate excellent capacity retention and cumulative coulombic efficiency over 50 cycles. Future work will explore the origin of the redox wave in the dQ/dV plots with respect to strain induced by Sn and by modifying our synthetic procedures to increase the Si-Sn NP size. Additionally, we plan on exploring whether the surface chemistries that result in higher performance for intrinsic Si NP-based anodes also translate to better performance in Si-Sn-based composites.

Third, Si-based metallic glass, $Al_{64}Si_{25}Mn_{11}$, was successfully synthesized through a splat cooling system by rapidly cooling the liquid melt alloy and suppressing the nucleation and growth of the crystalline phase. $Al_{64}Si_{25}Mn_{11}$ glass exhibits good specific capacity and has demonstrated superior interfacial stability in comparison to elemental Si. EIS shows a drastic increase in the total resistance of the 500-nm Si electrode after 10 cycles. On the contrary, the total resistance of the glass stayed almost constant, suggesting the formation of a stable SEI layer. This was further confirmed by both electrochemical and XPS analysis, which shows a lower amount of charges consumed during the lithiation process resulting in a very thin SEI. These findings strongly support the validity of our approach: a stabilization of electrode–electrolyte interface by using amorphous multicomponent metallic glass as an anode material.

Finally, the computational studies revealed the impacts of alloying on volumetric expansion: (1) electrodes with large initial molar volumes yield lower volumetric expansion, at the expense of volumetric capacity, and (2) decreasing Li partial molar volume produces a decreased volumetric expansion, although its impact is far less pronounced than the initial molar volume. Thus, we conclude that although alloying can help decrease volumetric expansion, due to the inverse relationship between initial molar volume and volumetric expansion, a trade-off must be made. The Si networking/clustering in the amorphous alloys can be tuned through (1) the addition of active components to promote network retention and (2) the use of inactive components to promote a more homogeneous single-phase lithiation.

To sum up, the investigated Si-Sn alloys and Si-based metallic glasses were commonly showing improved electrochemical characteristics and physical properties compared to pure Si electrodes. Further optimization of elements and stoichiometry of Si-based alloy guided by the computational studies has the potential to resolve the problems associated elemental Si and serve as the next-generation lithium-ion battery anode materials.

Understanding SEI Chemistry

As the aforementioned data demonstrate, the SEI on silicon anodes is highly dynamic and changes with electrolytes and surface chemistry. These data also point to avenues to improve stability through Si NP size reduction, surface modification, and selective electrolyte chemistry. These avenues will be pursued in future studies.

References

Science of Safety: Evaluating Temperature-Dependent Degradation Mechanisms of Silicon-Graphite Electrodes

1. Profatilova, I. A.; Stock, C.; Schmitz, A.; Passerini, S.; Winter, M., Enhanced thermal stability of a lithiated nano-silicon electrode by fluoroethylene carbonate and vinylene carbonate. J. Power Sources (2013) 222, 140–149.

2. Wang, Y.; Dahn, J., Comparison of the Reaction of LixSi or Li0.81C6 with 1 M LiPF6 EC:DEC Electrolyte at High Temperature. Electrochem. Solid-State Lett. (2006) 9, A340–A343.

3. Wang, J.; Huang, W.; Pei, A.; Li, Y.; Shi, F.; Yu, X.; Cui, Y., Improving cyclability of Li metal batteries at elevated temperatures and its origin revealed by cryo-electron microscopy. Nat. Energy (2019) 4, 664–670.

4. Stetson, C.; Yin, Y.; Jiang, C.-S.; DeCaluwe, S. C.; Al-Jassim, M.; Neale, N. R.; Ban, C.; Burrell, A., Temperature-Dependent Solubility of Solid Electrolyte Interphase on Silicon Electrodes. ACS Energy Lett. (2019) 4, 2770–2775.

Zintl Phase Formation Mechanism and its Effect on SEI

1. An, K. S.; Park, R. J.; Kim, J. S.; Park, C. Y.; Lee, S. B.; Abukawa, T.; Kono, S.; Kinoshita, T.; Kakizaki, A.; Ishii, T. Initial interface formation study of the Mg/Si(111) system. J. Appl. Phys. 1995, 78, 1151.

2. Moriga, T.; Watanabe, K.; Tsuji, D.; Massaki, S.; Nakabayashi, I. Reaction Mechanism of Metal Silicide Mg2Si for Li Insertion. J. Solid State Chem. 2000, 153, 386.

3. Schmuelling, G.; Winter, M.; Placke, T. Investigating the Mg-Si Binary System via Combinatorial Sputter Deposition As High Energy Density Anodes for Lithium-Ion Batteries. ACS Appl. Mater. Interfaces 2015, 7, 20124.

4. Volodin, V.; Koshelev, D. Quantitative analysis of hydrogen in amorphous silicon using Raman scattering spectroscopy. J. Raman Spectrosc. 2013, 44, 1760.

5. Fujiwara, H.; Kondo, M.; Matsuda, A. Depth profiling of silicon–hydrogen bonding modes in amorphous and microcrystalline Si: H thin films by real-time infrared spectroscopy and spectroscopic ellipsometry. J. Appl. Phys. 2002, 91, 4181.

6. Nieroda, P.; Mars, K.; Nieroda, J.; Leszczyński, J.; Król, M.; Drożdż, E.; Jeleń, P.; Sitarz, M.; Koleżyński, A. New high temperature amorphous protective coatings for Mg2Si thermoelectric material. Ceram. Int. 2019, 45, 10230.

7. Brown, Z. L.; Jurng, S.; Nguyen, C. C.; Lucht, B. L. Effect of fluoroethylene carbonate electrolytes on the nanostructure of the solid electrolyte interphase and performance of lithium metal anodes. ACS Appl. Energy Mater. 2018, 1, 3057.

8. Yoon, T.; Chapman, N.; Seo, D. M.; Lucht, B. L. Lithium salt effects on silicon electrode performance and solid electrolyte interphase (SEI) structure, role of solution structure on SEI formation. J. Electrochem. Soc. 2017, 164, A2082.

9. Etacheri, V.; Haik, O.; Goffer, Y.; Roberts, G. A.; Stefan, I. C.; Fasching, R.; Aurbach, D. Effect of fluoroethylene carbonate (FEC) on the performance and surface chemistry of Si-nanowire Li-ion battery anodes. Langmuir 2012, 28, 965.

Silicon Consortium Project Calendar Aging Electrochemical Screening Protocol

1. United States Advanced Battery Consortium Battery Test Manual For Electric Vehicles; 2015.

2. Long, B. R.; Rinaldo, S. G.; Gallagher, K. G.; Dees, D. W.; Trask, S. E.; Polzin, B. J.; Jansen, A. N.; Abraham, D. P.; Bloom, I.; Bareño, J.; Croy, J. R. Enabling High-Energy, High-Voltage Lithium-Ion Cells: Standardization of Coin-Cell Assembly, Electrochemical Testing, and Evaluation of Full Cells. 35th Annu. Int. Batter. Semin. Exhib. 2018 2018, 1 (14), 112–122. https://doi.org/10.1149/2.0691614jes.

3. Single, F.; Latz, A.; Horstmann, B. Identifying the Mechanism of Continued Growth of the Solid–Electrolyte Interphase. ChemSusChem 2018, 11 (12), 1950–1955. https://doi.org/10.1002/cssc.201800077.

4. Attia, P. M.; Chueh, W. C.; Harris, S. J. Revisiting the t 0.5 Dependence of SEI Growth . J. Electrochem. Soc. 2020, 167 (9), 090535. https://doi.org/10.1149/1945-7111/ab8ce4.

Understanding Silicon Alloy Effects on the SEI

1. Khan, M. M.; Nemati, A.; Rahman, Z. U.; Shah, U. H.; Asgar, H.; Haider W. Recent Advances in Bulk Metallic Glasses and Their Applications: A Review. Critical Reviews in Solid State and Materials Sciences 43, 233–268 (2018).

2. Nair, B.; Priyadarshini, B. G. Process, Structure, Property and Applications of Metallic Glasses. AIMS Materials Science 3, 1022–1053 (2016).

3. Fleischauer, M. D.; Dahn, J. R. Combinatorial Investigation of the Si-Al-Mn System for Li-Ion Battery Applications. Journal of The Electrochemical Society 151, A1216–A1221 (2004).

4. Obrovac, M. N.; Christensen, L.; Le, D. B.; Dahn, J. R. Alloy design for lithium-ion battery anodes. J. Electrochem. Soc. 154, 849–855 (2007).

Understanding SEI Chemistry

1. Stetson, C.; Yoon, T.; Coyle, J.; Nemeth, W.; Young, M.; Norman, A.; Pylypenko, S.; Ban, C.; Jiang, C.-S.; Al-Jassim, M.; Burrell, A., Three-dimensional electronic resistivity mapping of solid electrolyte interphase on Si anode materials. *Nano Energy* **2019**, 55, 477–485.

2. Charles, R. J., Some Structural and Electrical Properties of Lithium Silicate Glasses. *Journal of the American Ceramic Society* **1963**, 46, 235–243.

3. He, L.-N.; Xua, J., Properties of amorphous SiO2 films prepared by reactive RF magnetron sputtering method. *Vacuum* **2003**, 68, 197–202.

4. Schnabel, M.; Harvey, S. P.; Arca, E.; Stetson, C.; Teeter, G.; Ban, C.; Stradins, P., Surface SiO2 Thickness Controls Uniform-to-Localized Transition in Lithiation of Silicon Anodes for Lithium-Ion Batteries. *ACS Applied Materials & Interfaces* **2020**, 12 (24), 27017–27028.

5. Schnabel, M.; Arca, E.; Ha, Y.; Stetson, C.; Teeter, G.; Han, S.-D.; Stradins, P., Enhanced Interfacial Stability of Si Anodes for Li-Ion Batteries via Surface SiO2 Coating. ACS Appl. Energy Mater. 2020, 3 (9), 8842–8849.

6. Nguyen, C. C.; Yoon, T.; Seo, D. M.; Guduru, P.; Lucht, B. L., Systematic Investigation of Binders for Silicon Anodes: Interactions of Binder with Silicon Particles and Electrolytes and Effects of Binders on Solid Electrolyte Interphase Formation. ACS *Appl. Mater. Interfaces* **2016**, 8 (19), 12211–12220.

7. Chen, H.; Ling, M.; Hencz, L.; Ling, H. Y.; Li, G.; Lin, Z.; Liu, G.; Zhang, S., Exploring Chemical, Mechanical, and Electrical Functionalities of Binders for Advanced Energy-Storage Devices. *Chemical Reviews* **2018**, 118 (18), 8936–8982.

8. Kwon, T.-w.; Choi, J. W.; Coskun, A., The Emerging Era of Supramolecular Polymeric Binders in Silicon Anodes. *Chemical Society Reviews* **2018**, 47 (6), 2145–2164.

9. Li, J.; Lewis, R. B.; Dahn, J. R., Sodium Carboxymethyl Cellulose. *Electrochemical and Solid-State Letters* **2007**, 10 (2), A17.

10. Farooq, U.; Choi, J.-H.; Atif Pervez, S.; Yaqub, A.; Kim, D.-H.; Lee, Y.-J.; Saleem, M.; Doh, C.-H., Effect of Binder and Composition Ratio on Electrochemical Performance of Silicon/Graphite Composite Battery Electrode. *Materials Letters* **2014**, 136, 254–257.

11. Kovalenko, I.; Zdyrko, B.; Magasinski, A.; Hertzberg, B.; Milicev, Z.; Burtovyy, R.; Luzinov, I.; Yushin, G., A Major Constituent of Brown Algae for Use in High-Capacity Li-Ion Batteries. *Science* **2011**, 334 (6052), 75.

12. Park, H.-K.; Kong, B.-S.; Oh, E.-S., Effect of High Adhesive Polyvinyl Alcohol Binder on the Anodes of Lithium Ion Batteries. *Electrochemistry Communications* **2011**, 13 (10), 1051–1053.

13. Jeong, Y. K.; Kwon, T.-w.; Lee, I.; Kim, T.-S.; Coskun, A.; Choi, J. W., Millipede-Inspired Structural Design Principle for High Performance Polysaccharide Binders in Silicon Anodes. *Energy & Environmental Science* **2015**, 8 (4), 1224–1230.

14. Magasinski, A.; Zdyrko, B.; Kovalenko, I.; Hertzberg, B.; Burtovyy, R.; Huebner, C. F.; Fuller, T. F.; Luzinov, I.; Yushin, G., Toward Efficient Binders for Li-Ion Battery Si-Based Anodes: Polyacrylic Acid. *ACS Applied Materials & Interfaces* **2010**, 2 (11), 3004–3010.

15. Hu, B.; Jiang, S.; Shkrob, I. A.; Zhang, S.; Zhang, J.; Zhang, Z.; Zhang, L., Poly(4-vinylbenzoic acid): A Re-Engineered Binder for Improved Performance from Water-Free Slurry Processing for Silicon Graphite Composite Electrodes. *ACS Applied Energy Materials* **2019**, 2 (9), 6348–6354.

16. Bridel, J. S.; Azaïs, T.; Morcrette, M.; Tarascon, J. M.; Larcher, D., In Situ Observation and Long-Term Reactivity of Si/C/CMC Composites Electrodes for Li-Ion Batteries. *Journal of The Electrochemical Society* **2011**, 158 (6), A750.

17. Jiang, S.; Hu, B.; Shi, Z.; Chen, W.; Zhang, Z.; Zhang, L., Re-Engineering Poly(Acrylic Acid) Binder toward Optimized Electrochemical Performance for Silicon Lithium-Ion Batteries: Branching Architecture Leads to Balanced Properties of Polymeric Binders. *Advanced Functional Materials* **2020**, 30 (10), 1908558.

18. Hu, B.; Jiang, S.; Shkrob, I. A.; Zhang, J.; Trask, S. E.; Polzin, B. J.; Jansen, A.; Chen, W.; Liao, C.; Zhang, Z.; Zhang, L., Understanding of pre-lithiation of poly(acrylic acid) binder: Striking the balances between the cycling performance and slurry stability for silicon-graphite composite electrodes in Li-ion batteries. *Journal of Power Sources* **2019**, 416, 125–131.

19. Hu, B.; Shkrob, I. A.; Zhang, S.; Zhang, L.; Zhang, J.; Li, Y.; Liao, C.; Zhang, Z.; Lu, W.; Zhang, L., The existence of optimal molecular weight for poly(acrylic acid) binders in silicon/graphite composite anode for lithium-ion batteries. *Journal of Power Sources* **2018**, 378, 671–676.

20. Nanda, J.; Yang, G.; Hou, T.; Voylov, D. N.; Li, X.; Ruther, R. E.; Naguib, M.; Persson, K.; Veith, G. M.; Sokolov, A. P., Unraveling the Nanoscale Heterogeneity of Solid Electrolyte Interphase Using Tip-Enhanced Raman Spectroscopy. *Joule* **2019**, 3 (8), 2001–2019.

21. Yang, J.; Liu, H.; Martens, W. N.; Frost, R. L., Synthesis and characterization of cobalt hydroxide, cobalt oxyhydroxide, and cobalt oxide nanodiscs. *The Journal of Physical Chemistry C* **2010**, 114 (1), 111–119.

22. Aurbach, D.; Markovsky, B.; Shechter, A.; Ein-Eli, Y.; Cohen, H., A comparative study of synthetic graphite and Li electrodes in electrolyte solutions based on ethylene carbonate-dimethyl carbonate mixtures. *Journal of the Electrochemical Society* **1996**, 143 (12), 3809.

23. Yan, J.; Xia, B.-J.; Su, Y.-C.; Zhou, X.-Z.; Zhang, J.; Zhang, X.-G., Phenomenologically modeling the formation and evolution of the solid electrolyte interface on the graphite electrode for lithium-ion batteries. *Electrochimica Acta* **2008**, 53 (24), 7069–7078.

24. Schulz, N.; Hausbrand, R.; Dimesso, L.; Jaegermann, W., XPS-surface analysis of SEI layers on Li-Ion cathodes: part I. Investigation of initial surface chemistry. *Journal of The Electrochemical Society* **2018**, 165 (5), A819–A832.

25. Hou, T.; Yang, G.; Rajput, N. N.; Self, J.; Park, S.-W.; Nanda, J.; Persson, K. A., The influence of FEC on the solvation structure and reduction reaction of LiPF6/EC electrolytes and its implication for solid electrolyte interphase formation. *Nano Energy* **2019**, 64, 103881.

26. Hantsche, H., High resolution XPS of organic polymers, the scienta ESCA300 database. *Advanced Materials* **1993**, 5 (10), 778–778.

27. Wu, Q.; Shi, B.; Bareño, J.; Liu, Y.; Maroni, V. A.; Zhai, D.; Dees, D. W.; Lu, W., Investigations of Si thin films as anode of lithium-ion batteries. *ACS applied materials & interfaces* **2018**, 10 (4), 3487–3494.

28. Yoon, T.; Chapman, N.; Seo, D. M.; Lucht, B. L., Lithium salt effects on silicon electrode performance and solid electrolyte interphase (SEI) structure, role of solution structure on SEI formation. *Journal of The Electrochemical Society* **2017**, 164 (9), A2082–A2088.

29. Wood, K. N.; Teeter, G., XPS on Li-Battery-Related Compounds: Analysis of Inorganic SEI Phases and a Methodology for Charge Correction. *ACS Appl. Energy Mater* **2018**, 1 (9), 4493–4504.

30. Hasa, I.; Haregewoin, A. M.; Zhang, L.; Tsai, W.-Y.; Guo, J.; Veith, G. M.; Ross, P. N.; Kostecki, R., Electrochemical Reactivity and Passivation of Silicon Thin-Film Electrodes in Organic Carbonate Electrolytes. *ACS Applied Materials & Interfaces* **2020**, 12 (36), 40879–40890.

31. Wu, M.; Xiao, X.; Vukmirovic, N.; Xun, S.; Das, P. K.; Song, X.; Olalde-Velasco, P.; Wang, D.; Weber, A. Z.; Wang, L.-W.; Battaglia, V. S.; Yang, W.; Liu, G., Toward an Ideal Polymer Binder Design for High-Capacity Battery Anodes. *Journal of the American Chemical Society* **2013**, 135 (32), 12048–12056.

32. Wang, W.; Yi, E.; Fici, A. J.; Laine, R. M.; Kieffer, J., Lithium Ion Conducting Poly(ethylene oxide)-Based Solid Electrolytes Containing Active or Passive Ceramic Nanoparticles. *The Journal of Physical Chemistry C* **2017**, 121 (5), 2563–2573.

33. Jiang, S.; Hu, B.; Sahore, R.; Liu, H.; Pach, G. F.; Carroll, G. M.; Zhang, L.; Zhao, B.; Neale, N. R.; Zhang, Z., Tailoring the Surface of Silicon Nanoparticles for Enhanced Chemical and Electrochemical Stability for Li-Ion Batteries. *ACS Applied Energy Materials* **2019**, 2 (9), 6176–6183.

34. Jin, Y.; Kneusels, N.-J. H.; Marbella, L. E.; Castillo-Martínez, E.; Magusin, P. C. M. M.; Weatherup, R. S.; Jónsson, E.; Liu, T.; Paul, S.; Grey, C. P., Understanding Fluoroethylene Carbonate and

Vinylene Carbonate Based Electrolytes for Si Anodes in Lithium Ion Batteries with NMR Spectroscopy. *Journal of the American Chemical Society* **2018**, 140 (31), 9854–9867.

35. Han, B.; Liao, C.; Dogan, F.; Trask, S. E.; Lapidus, S. H.; Vaughey, J. T.; Key, B., Using Mixed Salt Electrolytes to Stabilize Silicon Anodes for Lithium-Ion Batteries via in Situ Formation of Li–M–Si Ternaries (M = Mg, Zn, Al, Ca). *ACS Appl. Mater. Interfaces* **2019**, 11 (33), 29780–29790.

Acknowledgements

The following team members participated in this project:

Science of Safety: Evaluating Temperature-Dependent Degradation Mechanisms of Silicon-Graphite Electrodes

Contributors: Yeyoung Ha, Donal Finegan, Bertrand Tremolet de Villers, Andrew Colclasure, Matthew Keyser (NREL)

Zintl Phase Formation Mechanism and its Effect on SEI

Contributors: Andrew Norman, Andriy Zakutayev, Anthony K. Burrell, Baris Key, Binghong Han, Bertrand J. Tremolet de Villers, Caleb Stetson, Chun-Sheng Jiang, Fulya Dogan, Glenn Teeter, Jack Vaughey, Max Schulze, Mowafak Al-Jassim, Nathan Neale, Niya Sa, Ritesh Uppuluri, Saida Cora, Sang-Don Han, Steve Trask, Xiang Li, Yeyoung Ha, Yunya Zhang, Zhifei Li, Zoey Huey

Silicon Consortium Project Calendar Aging Electrochemical Screening Protocol

Contributors: Max Schulze (National Renewable Energy Laboratory), Marco Tulio Fonseca Rodrigues (Argonne National Laboratory), Josey McBrayer (Sandia National Laboratory), Ira Bloom (Argonne National Laboratory), Andrew Colclasure (National Renewable Energy Laboratory), Gabriel Veith (Oak Ridge National Laboratory), Daniel Abraham (Argonne National Laboratory), Nathan Neale (National Renewable Energy Laboratory), Anthony Burrell (National Renewable Energy Laboratory), Jack Vaughey (Argonne National Laboratory) and Christopher Johnson (Argonne National Laboratory)

Understanding Silicon Alloy Effects on the SEI

Contributors: Elisabetta Arca, Insun Yoon, Terri Lin, Kang Yao,Hetal Patel, Eric Sivonxay, Wei Tong, Kristin Persson, Robert Kostecki (LBNL), Greg Pach, Fernando Urias, Andrew Norman, Nathan Neale (NREL)

Understanding SEI Chemistry

Gabriel Veith (ORNL), Nathan Neale (NREL), Elisabetta Arca (LBNL), Chunmei Ban (NREL), Chen Fang (LBNL), Sarah Frisco (NREL), Yeyoung Ha (NREL), Sang-Don Han (NREL), Steve Harvey (NREL), Emma Hopkins (ORNL), Bin Hu (ANL), Zoey Huey (NREL), Chun-Sheng Jiang (NREL), Baris Key (ANL), Robert Kostecki (LBNL) Xiang Li (ANL), Zhifei Li (NREL), Gao Liu (LBNL), Mowafak Al-Jassim (NREL), Jagjit Nanda (ORNL), Andrew Norman (NREL), Kristin Persson (LBNL), Manuel Schnabel (LBNL), Zhangxing Shi (ANL), Paul Stradins (NREL), Caleb Stetson (NREL), Glenn Teeter (NREL), Guang Yang (ORNL), Insun Yoon (LBNL), Andriy Zakutayev (NREL), Zhencheng Zhang (ANL), Lu Zhang (ANL).

II.1.C Probe the Relationships between Functional Electrolytes Structure and SEI Property for Si Materials (Lawrence Berkeley National Laboratory)

Gao Liu, Principal Investigator
Lawrence Berkeley National Laboratory
1 Cyclotron Rd.
Berkeley, Berkeley, CA 94720
E-mail: gliu@lbl.gov

Brian Cunningham, DOE Technology Development Manager
U.S. Department of Energy
E-mail: Brian.Cunningham@ee.doe.gov

Start Date: October 1, 2019 End Date: September 30, 2020
Project Funding: $400,000 DOE share: $400,000 Non-DOE share: $0

Project Introduction

Electrolyte decomposition products play a critical role in stabilization of the negative electrodes in lithium-ion batteries, as the negative electrode is operated outside the stability window of the electrolyte. The electrolyte decomposition products form insoluble SEI layer, which stabilizes the electrode and electrolyte interface. Silicon alloy material has large volume expansion and surface reactions with the electrolyte when it is electrochemically lithiated (charge). When delithiated (discharge), the Si alloy volume shrinks and surface area also decreases. This dynamic surface area changes during charge and discharge cause increased side reactions with the electrolyte. Moreover, some of the electrolyte decomposition products are soluble in the electrolyte rather than solid precipitates, further increasing side reactions. There are numerous byproducts produced in the electrolyte decomposition process. Some of the byproducts are insoluble or sparsely soluble in the electrolyte. These types of byproducts precipitate on the surface of the electrode. The insoluble byproducts form an SEI layer at the electrode and electrolyte interface, limiting or altering further reactions of the electrode with the electrolyte. Other byproducts are soluble in the electrolyte. Soluble byproducts can diffuse to the counter electrode and further react at the counter electrode to form new species. This diffusion and reaction process will continue until more stable byproducts are formed or a reversible shuttle is formed. This project will investigate both the insoluble species on or near the surface of the electrode, and analyze the soluble by-products in the electrolyte.

Objectives

The key objective of this project is to understand the electrolyte decomposition products in a Si anode-based Lithium-ion battery. The conventional analytical methods often lack the sensitivity of identifying SEI components that exist in trace amount or lack the capability of retrieving SEI component information from a complicated chemical environment of SEI layers. Therefore, this project aims to develop sample processing and measurement techniques specifically suitable for identification of organic and polymeric species in SEIs that are produced by electrolyte decomposition. In particular, controlled solvent elution strategy will be developed for pre-treatment of the electrode samples, and electrode-compatible mass spectrometry techniques will be established for SEI composition investigation. The decomposition products of base carbonate electrolyte and sacrificial additives will be demonstrated.

Approach

Usually, the organic and polymeric components in SEI layers are mixed with many other species like residual electrolyte. Consequently, the direct identification of the organic and polymeric SEI elements are often challenging. It is a common practice to wash the electrode with solvents to remove the organic upper layers [1], [2] but there has been few reports exploring well-controlled washing protocols.[3], [4], [5] Here, we propose to utilize on-electrode chromatography method for fractionating different organics in SEI and near-

SEI layers, and to employ matrix assisted laser desorption ionization-time of flight mass spectrometry (MALDI-TOF-MS) technique for identification of the electrolyte decomposition products in the SEI layers.

External chromatography, such as liquid chromatography (LC), can be used for SEI component separation upon sample extraction from the electrode surfaces, but concerns have been raised regarding the chemical compatibility of external chromatography methods.[6] Therefore, instead of solvent extraction of SEIs for external chromatography, on-electrode chromatography is employed to utilize the electrode surface as the stationary phase to realize controlled separation of the molecules on the electrode surfaces. Elution in on-electrode chromatography is carried out with experimentally selected solvent combinations. The screening of elution solvent is achieved with gradient polarity solvent wash (gradient wash) technique that subjects the electrode surfaces to a series of solvent elution treatments with progressively higher polarities. MALDI measurement of SEI is carried out with electrodes attached to the standard MALDI sample plate.[7] Conventional MALDI instrumentation and parameters are employed in MALDI experiments.

Results

Our work primarily focused on development of gradient wash technique that allows screening of proper solvent elution conditions for characterization of SEIs, based on which, on-electrode chromatography approach was successfully established to facilitate MALDI measurement of the organic and polymer species in SEIS.

Gradient wash technique was developed to examine the SEIs and near SEIs produced by methacrylate additives under a series of electrochemical conditions. Copper (Cu) electrodes were electrochemically cycled with LiPF6 ethylene carbonate/ethyl methyl carbonate (EC/EMC) electrolyte containing methacrylate additives to reveal additives' impacts on SEIs. With a binary, polarity-tunable solvent system, it was possible to selectively remove different SEI components by successive washing steps to realize precise SEI characterization. The electrode surfaces before and after each wash steps were analyzed with Fourier-transform infrared spectroscopy (FTIR).

The polymerization reaction of triethylene glycol methyl ether methacrylate (TEGMA) additive was revealed by gradient wash technique. Firstly, Cu electrode was discharged with LiPF6:EC/EMC base electrolyte via linear sweep voltammetry from the open-circuit voltage to 50 mV vs Li/L+ at 60 mV min−1, at which point the voltage was held at 50 mV for 2 hours for completion of electrochemistry. The gradient wash steps were carried out with 0:10 to 10:0 volume ratio ethyl acetate (EA) in hexane (Hex) solutions with 10-percent intervals (i.e. 0:10, 1:9, 2:8, 3:7 EA/Hex, etc). After rinsing, the electrodes were immediately dried and stored under vacuum until FTIR characterization.

As shown in Figure II.1.C.1(a), the unwashed surface of the Cu electrode cycled with base electrolyte presented strong peaks for EC:LiPF6 (1801, 1769, 1482, 1405, 1197, 1084, and 831 cm−1) and LiHCO3 (1641 cm−1). These species were gradually rinsed off with 0%–30% EA/Hex (Spectrum II–IV), showing that the washing process was polarity-controlled. TEGMA additive was found able to polymerize on Cu surface. As shown in Figure II.1.C.1(b), the unwashed Cu surface was found to be mainly covered with dried electrolyte (EC:LiPF6) while the gradient wash of 0%–30% EA/Hex could sequentially wash off EC (1805, 1778 1481, 1401, 1187, 1088 cm−1), LiHCO3 (1630 cm−1) and LiPF6 (840 cm−1), exposing the underlying poly(TEGMA). The identity of poly(TEGMA) in SEI is confirmed with synthetic reference sample, as evidenced by the characteristic carbonyl peak at 1726 cm-1. The red shift of carbonyl group by solvation effect of lithium salt was observed with presence of the residual lithium salt. More polar elution seemed to have resulted in partial removal of the poly(TEGMA) species.

In addition, the same experiments were carried with slower linear sweep voltammetry at 1 and 10 mV min−1, and similar results were observed, namely that TEGMA additive can polymerize on electrode surfaces but the poly(TEGMA) products are covered with residual electrolyte, which can be removed by gradient wash of 0%–30% EA/Hex to realize FTIR observation of the polymers. Therefore, 3:7 EA:Hex mixed solvent is a reliable condition for removal of residual EC electrolyte for characterization of the underlying organic species in SEI

layers. This condition is the minimum polarity for fractionating residual EC electrolyte, and the SEI components of interest are not significantly removed under this elution polarity.

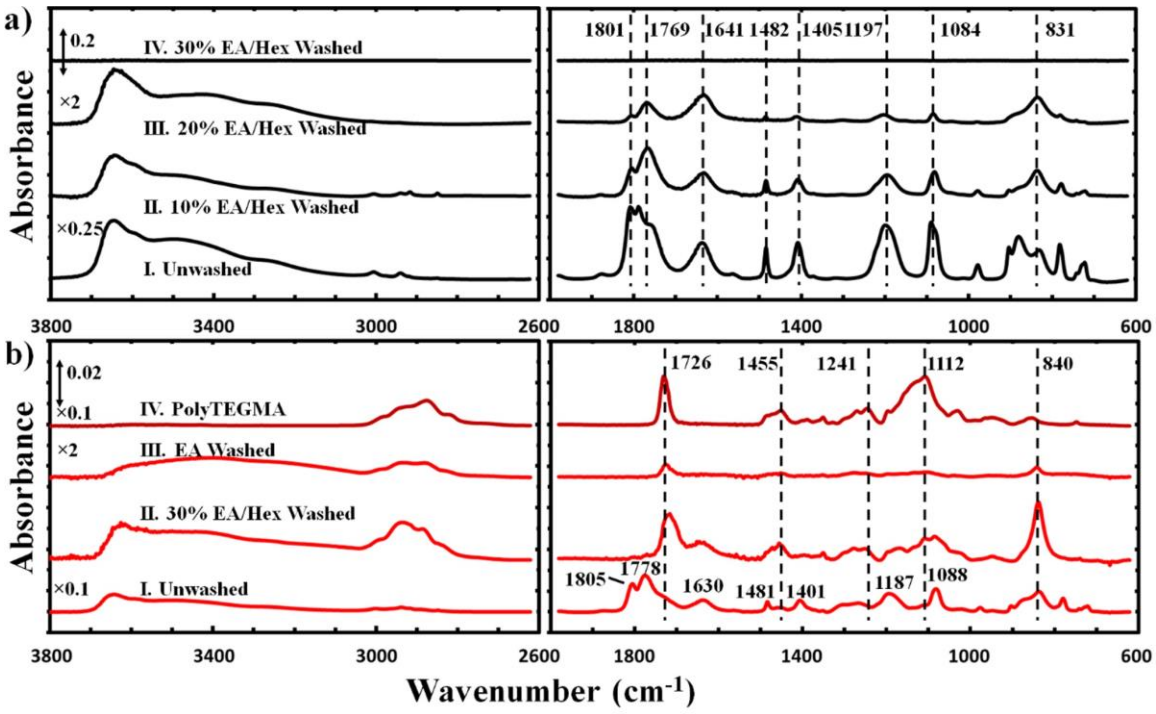

Figure II.1.C.1 FTIR spectra of electrode surface after gradient wash. (a) Cu electrode cycled with $LiPF_6$:EC/EMC base electrolyte. (b) Cu electrode cycled with TEGMA additive in $LiPF_6$:EC/EMC electrolyte in comparison with synthetic poly(TEGMA) reference. From Fang et al. Journal of the Electrochemical Society, 167 020506 (2020).

The gradient wash study successfully identified a practical solvent elution condition for removal of residual EC electrolyte from electrode surface. This laid the foundation of on-electrode chromatography technique, which has proved critical for effective MALDI measurement of polymeric SEI components on the electrode surfaces. The key concept is that on-electrode chromatography can be applied to electrode surfaces prior to MALDI measurement, which facilitates detection of polymeric species in SEIs because the interfering residual electrolyte is removed. The details of on-electrode chromatography and MALDI analysis are presented in the following sections.

As shown in Figure II.1.C.2(a), Cu electrode cycled with LiPF6:EC/EMC base electrolyte presented residual EC:LiPF6 solvate (1804, 1780, 1191, 1077, 822 cm-1), LiHCO3 (1649 cm-1), and lithium ethylene di-carbonate (LEDC, 1404, 1314 cm-1), while on-electrode chromatography of 3:7 EA:Hex elution removed residual EC from the electrode surface, as evidenced by the disappearance of EC's characteristic FTIR signals at 1804 and 1780 cm-1. Next, MALDI measurements were carried out for the untreated and eluted Cu electrodes as shown in Figure II.1.C.2(b). The major peaks associated with MALDI matrix 2,5-Dihydroxybenzoic acid or DHB (grey) and EC electrolyte (black) have been marked (assignments in Table II.1.C.1). The DHB matrix can form clusters, and can thus generate background signals in MALDI measurements. As the DHB clusters are often highly lithiated, they can be readily distinguished with the unique -1 Da isotope pattern of lithium element. Without on-electrode chromatography elution, strong EC signals were identified on the untreated electrode surface; on the other hand, upon 3:7 EA:Hex elution, EC was removed and no longer observed in MALDI measurement. The high-mass region of 3:7 EA:Hex eluted sample is shown in Figure II.1.C.2(c), where a set of weak peaks separated by 44 Da was found between 900 and 1200 Da. Such a pattern is attributed to polyethylene oxide (PEO), the decomposition product of EC-based electrolytes. In parallel tests, elution of the electrode samples with more polar solvents, namely EA and DMC, led to no outstanding MALDI signals other than DHB matrix. These results demonstrate the importance of polarity-controlled solvent elution for SEI analysis.

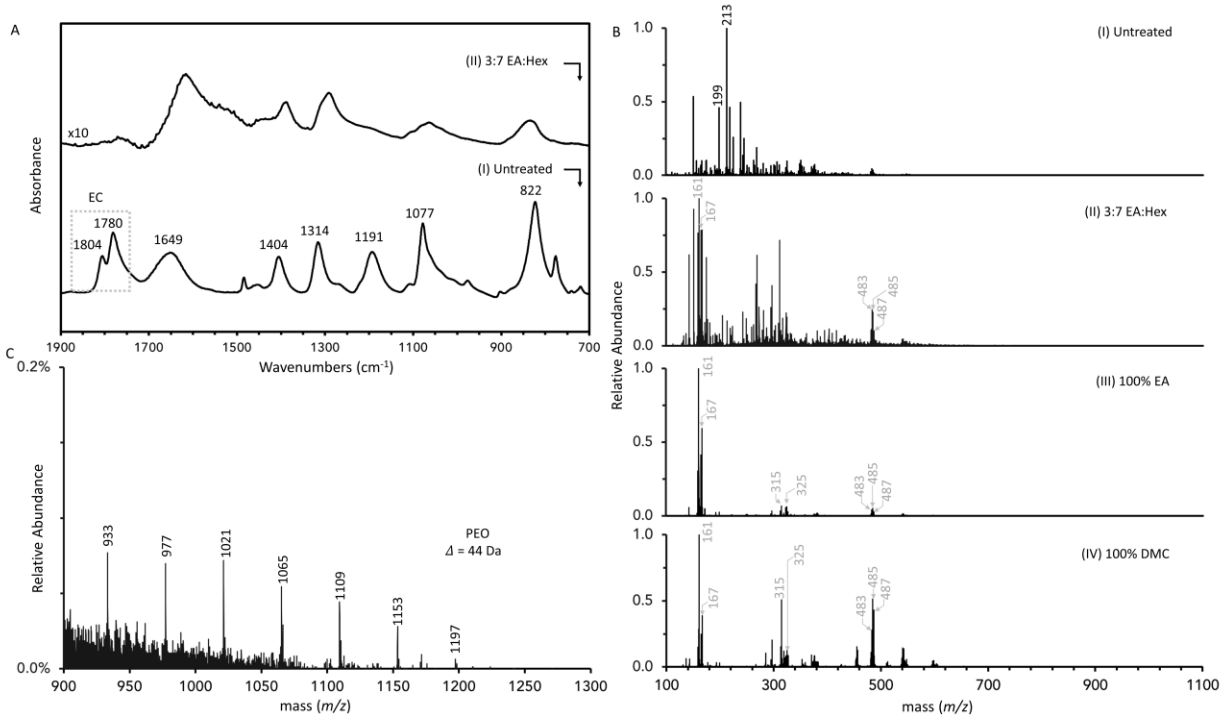

Figure II.1.C.2 On-electrode chromatography and MALDI measurement of Cu electrode cycled with base LiPF6:EC/EMC electrolyte. (a) FTIR measurement of electrode surface before and after on-electrode chromatography of 3:7 EA:Hex. (b) MALDI measurement of Cu electrode after different on-electrode chromatogram conditions. (c) Expended high-mass region of MALDI spectrum of the 3:7 EA:Hex elution sample.

Separately, the impact of vinlene carbonate (VC), a common electrolyte additive, on decomposition of EC electrolyte was investigated as well. The results from on-electrode chromatography and MALDI analysis are similar to the case of LiPF6:EC/EMC base electrolyte. Without on-electrode chromatography, the untreated electrode presented EC signals while 3:7 EA:Hex elution removed EC and exposed PEO molecules in the ~1000 Da region, which has significantly higher relative intensities compared to those produced with LiPF6:EC/EMC base electrolyte. Therefore, VC is possibly a promoter for the formation of high-mass PEOs.

In addition to carbonate electrolyte decomposition, the reaction of sacrificial additive TEGMA was also investigated by MALDI. In the previous study of gradient wash technique, the polymerization of TEGMA was confirmed by FTIR but the polymer masses were not known, which are now revealed by MALDI technique.

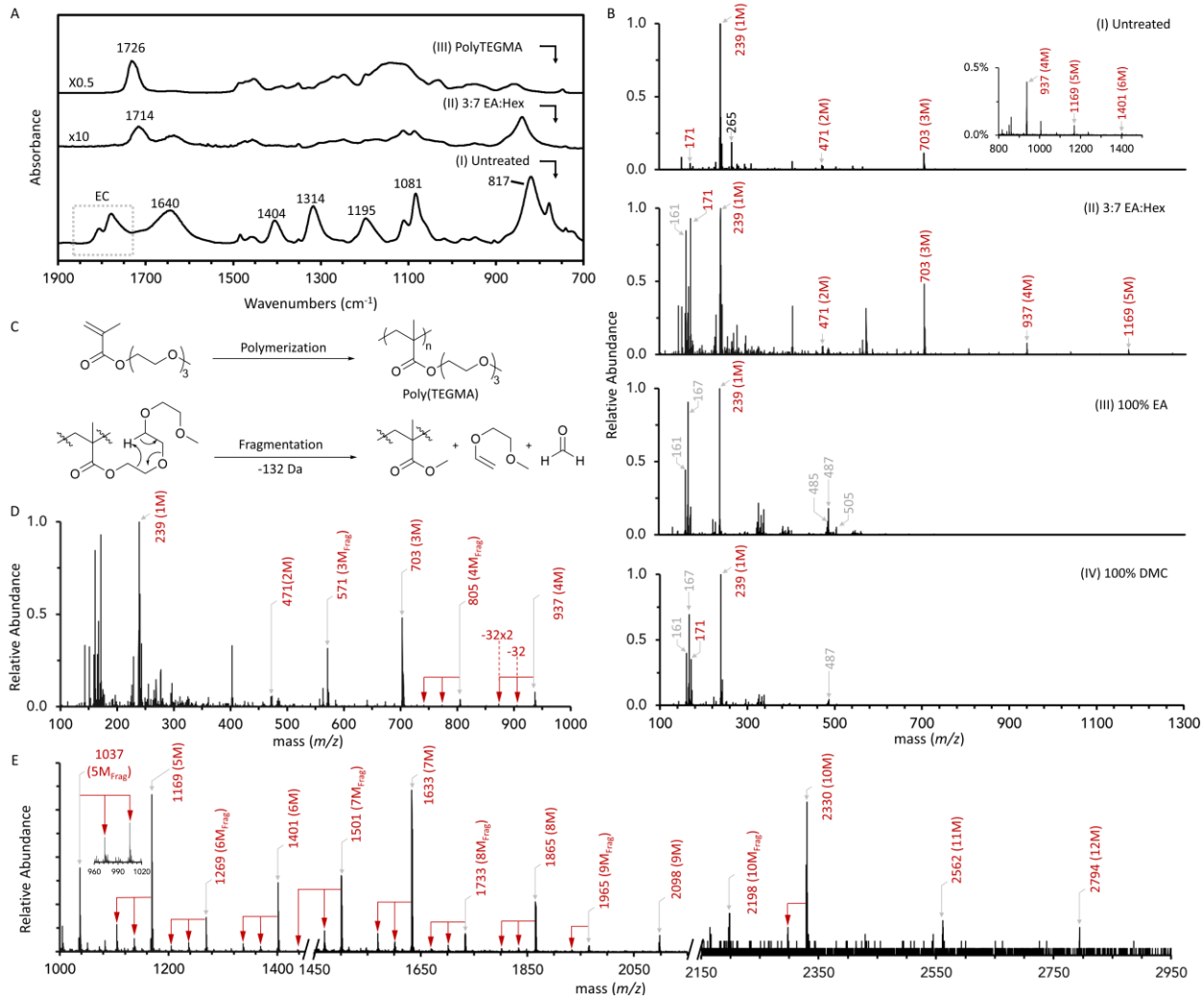

Figure II.1.C.3 On-electrode chromatography and MALDI measurement of Cu electrode cycled TEGMA additive. (a) FTIR measurement of electrode surface before and after on-electrode chromatography of 3:7 EA:Hex in comparison with synthetic poly(TEGMA) reference. (b) MALDI measurement of Cu electrode after different on-electrode chromatography conditions. (c) TEGMA polymerization reaction and fragmentation reaction of poly(TEGMA). (d-e) Expended high-mass region of MALDI spectrum of the 3:7 EA:Hex eluted sample. (1M through 12M refer to poly(TEGMA) monomer through dodecamer; annotation of 'frag' refer to fragments losing 132 Da mass.)

Firstly, FTIR measurements of the electrodes cycled with TEGMA after on-electrode chromatography treatments showed results consistent with the previous gradient wash study. As shown in Figure II.1.C.3(a), the untreated electrode surface was covered with residual EC electrolyte, which could be removed by 3:7 EA:Hex elution, exposing underlying poly(TEGMA) species as confirmed with synthetic reference. Next, the molecular weight of the poly(TEGMA) molecules was investigated by MALDI. As shown in Figure II.1.C.3(b), the untreated electrode surface presented EC and poly(TEGMA) species up to hexamer. The 171 Da peak is attributed to the lithium adduct of methyl triethylene glycol ether (TEGMA fragment). Upon 3:7 EA:Hex elution, residual EC was removed and the TEGMA oligomers were identified by MALDI. The complete spectrum of this 3:7 EA:Hex eluted sample is provided in Figure II.1.C.3(d-e), illustrating up to TEGMA dodecamers. Two common fragmentation pathways of the poly(TEGMA) species have been identified. The pronounced fragmentation pattern involves the rearrangement of the triethylene glycol side chain of the

poly(TEGMA) molecules presumably through a six-member-ring mechanism that leads to loss of 132 Da mass (Figure II.1.C.3(c)). Another minor fragmentation pathway involves the loss of the methanol mass (-32 Da) presumably by fragmentation of the terminal methoxy group of TEGMA. Loss of one or two methanol masses have been observed for all the major TEGMA species as marked by red arrows linked to the corresponding parent peaks (see the 4M peak as an example). These well-defined fragmentation pathways identified with high-quality spectra helped to endorse the assignment of poly(TEGMA) molecules.

Table II.1.C.1 Assignment of EC and DHB species in MALDI measurements

m/z	Assignment	m/z	Assignment
161	DHB+Li	325	2DHB-H2O-2H+2Li+Na
167	DHB-H+2Li	483	3DHB-2H_2O-3H+2Li+2Na
199	2EC+Na	485	3DHB-H2O-3H+3Li+Na
213	EC+DHB-2H2O+Li	487	3DHB-3H+4Li
265	EC+DHB+Na	505	3DHB-6H+7Li
315	2DHB+Li		

Conclusions

Gradient wash technique is a convenient strategy for sequential extraction of different components from the electrode surface to reveal the SEI and near SEI compositions by FTIR. The removal of residue electrolyte species by gradient wash has proven to be a consistent, polarity-controlled process. It is worth noting that selective removal of targeted species such as electrolyte molecules can be readily achieved with gradient wash technique. Based on gradient polarity wash study, on-electrode chromatography technique was employed to facilitate MALDI analysis of organic and polymeric species in SEIs by fractionating different components on the electrode surfaces. High-mass PEO and poly(TEGMA) molecules have been identified as electrolyte and additive decomposition products. This work demonstrates that conventional MALDI technique in conjunction with on-electrode chromatography is a powerful method for identification of organic and polymer components in SEIs. As the only prerequisite for MALDI approach is the moderate electrical conductivity of the electrode sample, MALDI could be applied to various battery systems for characterization and rational design of the SEIs.

Key Publications

1. Fang, Chen, Zhimeng Liu, Jonathan Lau, Mahmoud Elzouka, Guangzhao Zhang, Piyachai Khomein, Sean Lubner, Philip N. Ross, and Gao Liu. "Gradient Polarity Solvent Wash for Separation and Analysis of Electrolyte Decomposition Products on Electrode Surfaces." *Journal of The Electrochemical Society* 167, no. 2 (2020): 020506.

2. Fang, Chen, Jonathan Lau, Dion Hubble, Piyachai Khomein, Eric A. Dailing, Yi Liu, and Gao Liu. “Large molecule decomposition products of electrolytes and additives revealed by on-electrode chromatography and MALDI.” *Joule*, in press.

References

1. Dedryvère, R., S. Laruelle, S. Grugeon, L. Gireaud, J-M. Tarascon, and Danièle Gonbeau. "XPS identification of the organic and inorganic components of the electrode/electrolyte interface formed on a metallic cathode." Journal of The Electrochemical Society 152, no. 4 (2005): A689.

2. Michan, Alison L., Michal Leskes, and Clare P. Grey. "Voltage dependent solid electrolyte interphase formation in silicon electrodes: monitoring the formation of organic decomposition products." Chemistry of Materials 28, no. 1 (2016): 385-398.

3. Cresce, Arthur V., Selena M. Russell, David R. Baker, Karen J. Gaskell, and Kang Xu. "In situ and quantitative characterization of solid electrolyte interphases." Nano letters 14, no. 3 (2014): 1405-1412.

4. Zhuang, Guorong V., Hui Yang, Berislav Blizanac, and Philip N. Ross Jr. "A study of electrochemical reduction of ethylene and propylene carbonate electrolytes on graphite using ATR-FTIR spectroscopy." Electrochemical and Solid State Letters 8, no. 9 (2005): A441.

5. Xiao, Ang, Li Yang, Brett L. Lucht, Sun-Ho Kang, and Daniel P. Abraham. "Examining the solid electrolyte interphase on binder-free graphite electrodes." Journal of The Electrochemical Society 156, no. 4 (2009): A318.

6. Sahore, Ritu, Fulya Dogan, and Ira D. Bloom. "Identification of Electrolyte-Soluble Organic Cross-Talk Species in a Lithium-Ion Battery via a Two-Compartment Cell." Chemistry of Materials 31, no. 8 (2019): 2884-2891.

7. Fang, Chen, Hua Zhu, Ou Chen, and Matthew B. Zimmt. "Reactive two-component monolayers template bottom-up assembly of nanoparticle arrays on HOPG." Chemical communications 54, no. 58 (2018): 8056-8059.

II.1.D Development of Si-based High-Capacity Anodes (Pacific Northwest National Laboratory)

Ji-Guang Zhang, Principal Investigator
Pacific Northwest National Laboratory
902 Battelle Boulevard
Richland, WA 99354
E-mail: jiguang.zhang@pnnl.gov

Xiaolin Li, Principal Investigator
Pacific Northwest National Laboratory
902 Battelle Blvd, Mail Stop K2-44
Richland, WA 99354
E-mail: Xiaolin.li@pnnl.gov

Brian Cunningham, DOE Technology Development Manager
U.S. Department of Energy
E-mail: Brian.Cunningham@ee.doe.gov

Start Date: October 1, 2018 End Date: September 30, 2020
Project Funding (FY20): $450,000 DOE share (FY20): $450,000 Non-DOE share: $0

Project Introduction

Porous Si has been widely used to mitigate pulverization of Si particles during battery cycling. However, the large surface area of these Si materials may also lead to severe reactions between lithiated Si and electrolyte. These reactions will lead to continuous growth of SEI layer and higher cell impedance. On the other hand, the cross talk between Si anode and cathode (including diffusion of solvable species in SEI/CEI layers and dissolving of transition metal element in in cathode) may also lead to degradation of Si based Li ion batteries (LIBs). FEC additive, which is highly effective in forming a stable SEI layer on Si, may also form a detrimental CEI layer on the cathode surface and increase cell impedance. Therefore, minimizing the surface area of Si and finding a stable electrolyte are critical for long-term stability of Si-based LIBs.

Objectives

The objectives of this project are to enhance the cycle life and calendar life of Si-based LIBs by designing a stable porous Si structure to accommodate the volume change and new electrolytes with finely tuned salts, solvents, and additives to form a stable SEI layer on the Si anode and a stable CEI layer on the cathode to enable long-term cycling of Si-based LIBs. The degradation mechanism of Si anodes during shelf storage will be systematically investigated. New insight on these mechanisms and the new approaches developed in this work will speed up the deployment of high energy LIBs with Si-based anodes and increase market penetration of EVs and PHEVs, as required by DOE/EERE.

Approach

- Optimize omicron sized porous Si for long term stability of Si based anodes. Develop scalable carbon coating on porous Si with wet chemical method using low cost pitch, which is well known as the precursor of artificial graphite.
- Develop carbonate-based localized high concentration electrolyte (LHCE) for stabilization of Si anodes in wide temperature range.
- Explore new LHCE design for high temperature performance; 1H,1H,5H-octafluoropentyl 1,1,2,2-tetrafluoroethyl ether (OTE) will be used as a new diluent, and the electrolyte formula will be optimized.

Results

1. Optimization of micron size porous Si for long term stability of Si based anodes

Among various strategies to tackle the large volume change of Si anode, use of porous Si has been regarded as one of the most promising solutions. However, there are several intrinsic drawbacks for the use of a porous Si material: 1) the high surface area could lead to formation of large amount of SEI, causing low coulombic efficiency (CE); 2) the large pore volume requires more electrolyte to wet active materials which in turn decreases the energy density of LIBs, and it also makes the electrode preparation more difficult as more binder and solvent is needed; 3) low electrical conductivity of Si limits its rate capability during fast charge/discharge.

To address these challenges, porous Si has been coated with carbon materials with various methods such as CVD. In this work, we developed a scalable method to coat porous Si (Figure II.1.D.1a). Petroleum pitch (which is a well-known precursor for artificial graphite and various carbon materials) was used as the precursor to coat Si in a low temperature, wet chemical approach. Porous Si is first prepared by thermal decomposition of SiO and subsequent etching with HF solution. The as-prepared porous Si has a large surface area of ~1000 m2 g-1 and large pore volume of 1.10 cc g-1 with nano-sized pores (~3.7 nm in diameter). For homogeneous coating process, petroleum pitch is dissolved in toluene, and the pitch/toluene solution is impregnated into the porous Si under the vacuum. As shown in Figure II.1.D.1b, the pitch coated porous Si has average particle size of ~ 5 mm (D50) which is similar to those of the pristine porous Si. After carbonization of pitch at 700°C under the inert Ar atmosphere, the carbon content in the composite is ~45%–48%. High resolution STEM and TEM images in Figure II.1.D.1c-d indicate that nanosized primary Si particles in the porous Si are well reserved after carbonization at high temperature and nanopores are sealed by carbon.

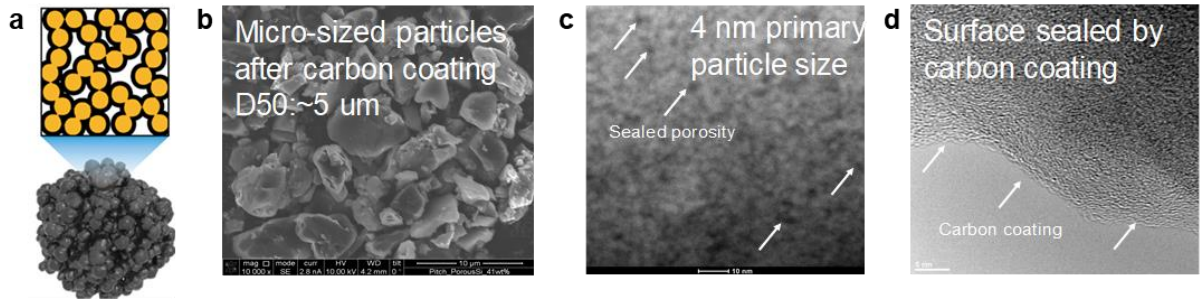

Figure II.1.D.1 Development of pitch-coated porous Si. a) schematic of pitch-coated porous Si, b) SEM image of pitch-coated porous Si, c) STEM image of pitch-coated porous Si, d) High-resolution TEM image of pitch-coated porous Si.

Figure II.1.D.2 and Figure II.1.D.3 show the electrochemical performances of the porous Si-C composite in half cells and full cells, respectively. Electrolyte used in these tests is Gen2+FEC (1.2M $LiPF_6$ in EC/EMC (3/7 in weight) + 10% FEC). The specific capacity of Si-C composite is 1708 mAh g^{-1} and the first cycle CE is 87% (Figure II.1.D.2a). During the cycling, the capacity retention is stabilized within 15 cycles and CE reaches 99.9% after 50 cycles (Figure II.1.D.2b). The full cell comprising of porous Si-C and NMC532 retains ~78% capacity after 400 cycles (Figure II.1.D.3a). The stabilized CE of ~ 99.9% is consistent with the great cycle life of porous Si-C (Figure II.1.D.3b). The superior stability of porous Si-C graphite could be ascribed to 1) the mitigation of volume expansion with sealed porosity, 2) improved overall conductivity of the composite and 3) the prevention of electrolyte penetration into the porous Si.

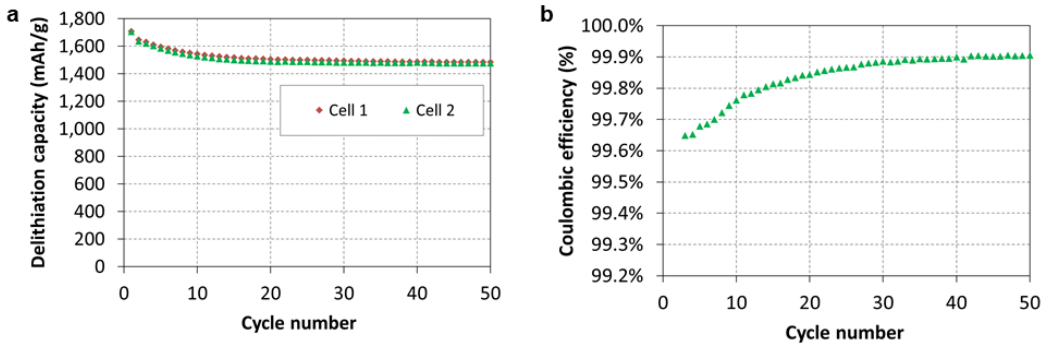

Figure II.1.D.2 Cycle life (a) and coulombic efficiency (b) of pitch-coated porous Si in a Li||Si-C half-cell.

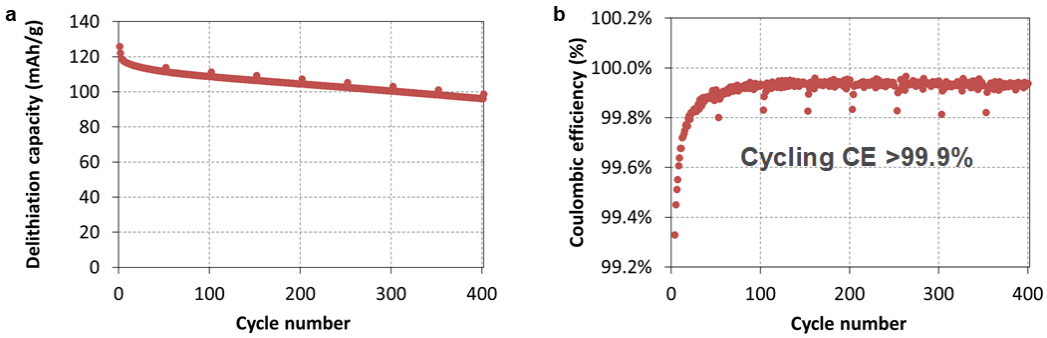

Figure II.1.D.3 Cycle life (a) and coulombic efficiency (b) of pitch-coated porous Si in a Si-C||NMC532 full cell.

The calendar life of the pitch-coated porous Si-C composite anodes were further investigated. The Si-C||LFP full cells in baseline electrolyte (Gen2+FEC: 1.2M $LiPF_6$ in EC/EMC (3/7 in weight) + 10% FEC) and LHCE electrolyte (LiFSI/DMC/TTE (0.51/1.1/2.2 in molar ratio) +5% FEC + 1% VC) were tested according to the testing protocol established by the Si consortium. Before the full-cell assembly, the electrochemical properties of anode were first characterized in half-cells (Figure II.1.D.4) at 0.1C rate between 0.01 to 3.0V with a CV step at 0.01V (0.025C cut-off). The reversible specific capacity of the cell is 1820 mAh g^{-1} with the first cycle CE of 88.3%. However, it shows a reversible capacity of only 276 mAh/g and coulombic efficiency of 33.1% (Figure II.1.D.4b) when the testing voltage window in the half cell is controlled between 0.1 to 0.7V (vs. Li/Li^+) corresponding to the anode voltage window in a full cell using consortium testing protocol. As shown in Figure II.1.D.4c, the cell shows stable cycle life at 0.2C for 100 cycles in this narrow voltage window.

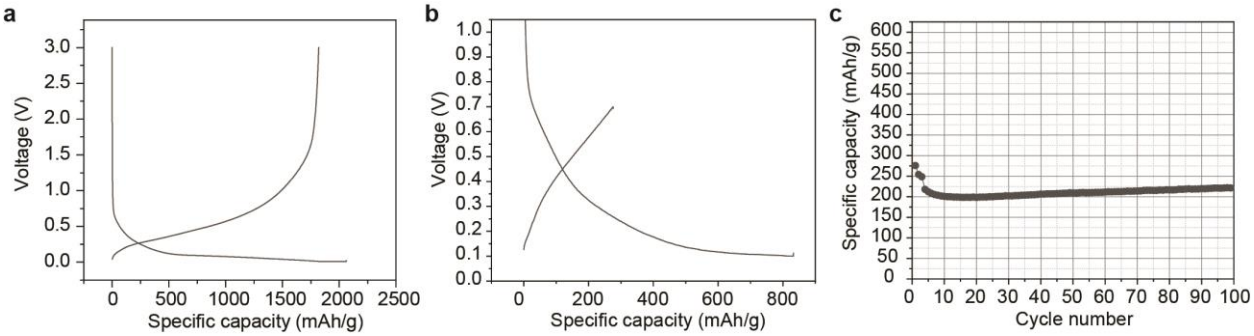

Figure II.1.D.4 Electrochemical properties of pitch coated porous Si in the half-cell. a) the voltage profile of pitch coated porous Si anode during the first cycle (0.01 V to 3 V) b) the voltage profile of porous Si anode during the first cycle where de-lithiation voltage of Si anode is 0.7 V corresponding to the Si voltage in fully discharged Si-C||LFP full cells using Si consortium's protocol for calendar life screening. c) Cycle life at 0.2C in the voltage window between 0.1 and 0.7 V.

Porous Si-C anode (~1.1 mAh cm^{-2}) is selected to match with LFP cathode (~2.5 mAh cm^{-2}) provided by Argonne's CAMP facility for the calendar life study in the full cell. Herein, the areal capacities of the

electrodes are chosen to ensure that there is enough Li^+ inventory to supply the Si-containing electrode with enough Li^+ ion during the aging protocol. It is a precaution that the parasitic current test in long-term period may cause significant consumption of Li ion with side reactions, which could exhaust usable capacity of the counter cathode. After three formation cycles at a C/10 rate between 2.7 and 3.35V, the full cells are charged to 3.35V at a C/10 rate, followed by voltage hold step at 3.35V for 720 hours. During the voltage hold at 3.35V, the parasitic current normalized by the charge capacity before voltage hold are obtained. As shown in Figure II.1.D.5a, the parasitic current of the full cells with LHCE is much smaller than that of the full cells using Gen2+FEC (the spikes in the figure is due to the instrument resolution). As a result, the accumulated capacity of the full cells using Gen2+FEC during voltage hold increases quickly compared to the full cells using LHCE (Figure II.1.D.5b). This result demonstrates improved stability on calendar life aging enabled by LHCE over Gen2+FEC.

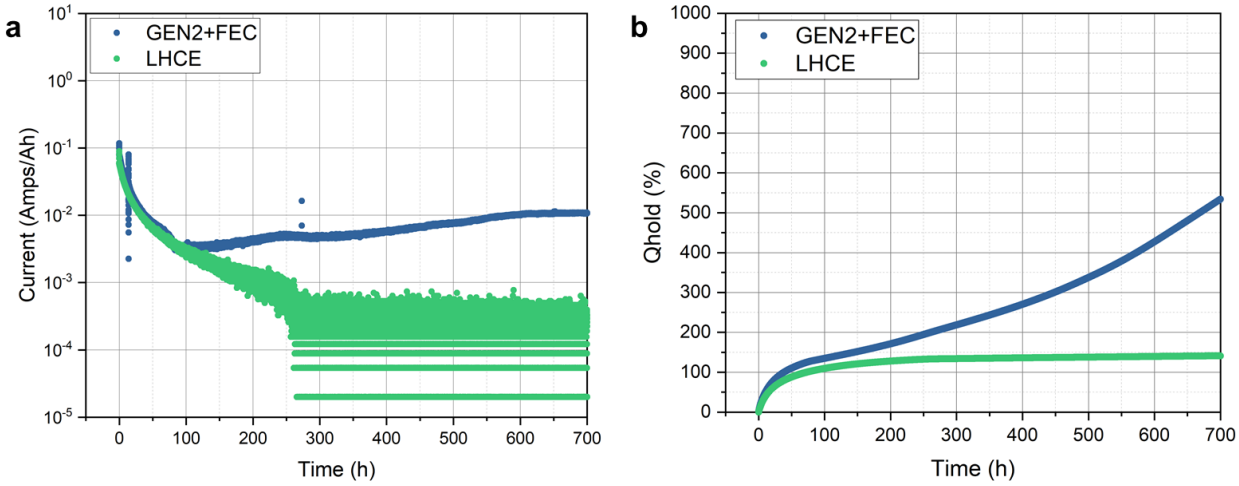

Figure II.1.D.5 Parasitic currents and accumulated capacities of Si||LFP full cells using Gen2+FEC (a) and LHCE (b) during the voltage hold at 3.35 V.

2. *Develop carbonate-based localized high concentration electrolyte (LHCE) for stabilization of Si anodes in wide temperature range*

Our early generations of LHCEs (such as 1.2 M LiFSI in TEP/FEC/BTFE (1.2:0.13:4 by mol)) uses bis(2,2,2-trifluoroethyl)ether (BTFE) as diluent.[1,2] However, BTFE exhibits a low boiling point (62°C) which is detrimental for practical applications. This year, we developed a more stable LHCE using a new diluent (1H,1H,5H-Octafluoropentyl 1,1,2,2-tetrafluoroethyl ether (OTE)) with a high boiling point of 133 °C to replace BTFE. In order to find the optimized electrolyte formula of LHCE with OTE diluent, we systematically adjusted the electrolyte salt concentration and the solvent-to-diluent ratio in LHCE. Figure II.1.D.6a show the salt concentrations of initial high concentration electrolytes (HCEs) before dilution, 3.7M, 4.5M, and 6.2M. These HCEs were then diluted with OTE to form LHCEs (OL) with an OTE to DMC molar ratios of 3:1, 2:1, 1.5:1, 1:1, 1:0.5, and 1:0.25 (Figure II.1.D.6b) and electrolytes (OL1 to OL7) having final molar concentrations from 0.6 to 3.1M were obtained Figure II.1.D.6c). OL8, -9, and -10 electrolytes which were over diluted from high concentration of 6.2M suffered the salt precipitation after dilution, rendering them not suitable as electrolytes.

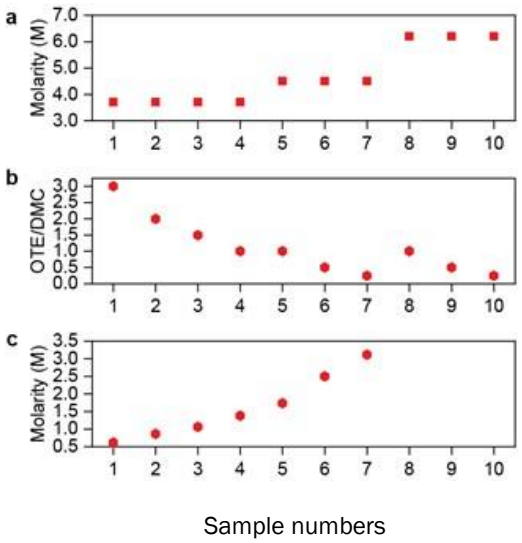

d

Electrolyte list	
Name	**Composition**
OL1	LiFSI-DMC-OTE (0.51/1.1/3.3 in molar ratio) + 5% FEC and 1% VC
OL2	LiFSI-DMC-OTE (0.51/1.1/2.2 in molar ratio) + 5% FEC and 1% VC
OL3	LiFSI-DMC-OTE (0.51/1.1/1.65 in molar ratio) + 5% FEC and 1% VC
OL4	LiFSI-DMC-OTE (0.51/1.1/1.1 in molar ratio) + 5% FEC and 1% VC
OL5	LiFSI-DMC-OTE (0.51/0.84/0.84 in molar ratio) + 5% FEC and 1% VC
OL6	LiFSI-DMC-OTE (0.51/0.84/0.42 in molar ratio) + 5% FEC and 1% VC
OL7	LiFSI-DMC-OTE (0.51/0.84/0.21 in molar ratio) + 5% FEC and 1% VC

Figure II.1.D.6 Systematical evaluation of LHCE electrolytes with OTE diluent. **a**, Initial salt molarity of HCEs. **b**, The ratio between OTE and DMC. **c**, Final salt molarity of various OL electrolytes. The electrolyte compositions in **c** are listed in d.

All OL electrolytes shown in Figure II.1.D.6d were tested in coin-type half cells and Si-Gr||NMC532 full cells. Figure II.1.D.7 compares the cell performance using the baseline electrolyte (Gen2+FEC) at 30 ºC. The composition of anode is 88 wt% Si-Gr composite (BTR New Energy Materials Inc.), 10 wt% polyimide (P84, HP POLYMER GmbH) and 2 wt% carbon black (C65, Imerys). The anode loading is 2.7 mg cm^{-2}. The composition of cathode is 90 wt% $Li[Ni_{0.5}Mn_{0.3}Co_{0.2}]O_2$ (NMC532, Toda), 5 wt% carbon black (C45, Imerys), and 5 wt% polyvinylidene fluoride (Solef 5130, Solvay), provided by CAMP facility in ANL. The loading of each anode and cathode is controlled to have the full cell N/P ratio of ~1.2. The anodes were pre-cycled 3 times in half-cell against Li metal at 0.1C (1C=1000 mA g^{-1}) and disassembled for full-cell assembly. The operational voltage window for pre-cycling is 0.02 V to 1.5 V. The full-cells were cycled for 3 cycles at 0.05C, then cycled at 0.33C. The voltage window is between 3.0 V to 4.1 V.

The cycle life in the half cell test (Figure II.1.D.7a) demonstrates that OL5, -6, and -7 electrolyte enable superior capacity retention than OL1, 2, 3, and 4 electrolytes. After 50 cycles, the capacity retention is 84.6%, 91.5% and 79.9% for OL5, 6, and 7, respectively, much better than that of OL1, 2, 3, and 4 electrolytes (19.5%, 19.3%, 28.3% and 50.1% capacity retention) and the baseline electrolyte (50.4% capacity retention). Figure II.1.D.7b compares the CE obtained from the half-cell cycled in different electrolytes. CE of the cells using OL5, 6, and 7 electrolytes quickly increased to more than 99.7% within 10 cycles. While CE of the cell using baseline electrolyte reached 99.7% only after 30 cycles. Long-term cycle life of Si-Gr||NMC532 full cells at 30 ºC using different electrolytes are shown in Figure II.1.D.7c**.** The full cells using OL5 and OL6 electrolytes remained 80% of capacity after 500 cycles, whereas the cells using baseline electrolyte retained only 52% of initial capacity. OL3 and OL4 cells also exhibit better capacity retentions than those of the baseline cell after 140 cycles. The superior capacity retentions of the LHCEs are consistent with the rapid increase and stabilization of CE (>99.8%). CE for the cell with baseline electrolyte increases slowly and cannot exceed over 99.75% even after long term cycling.

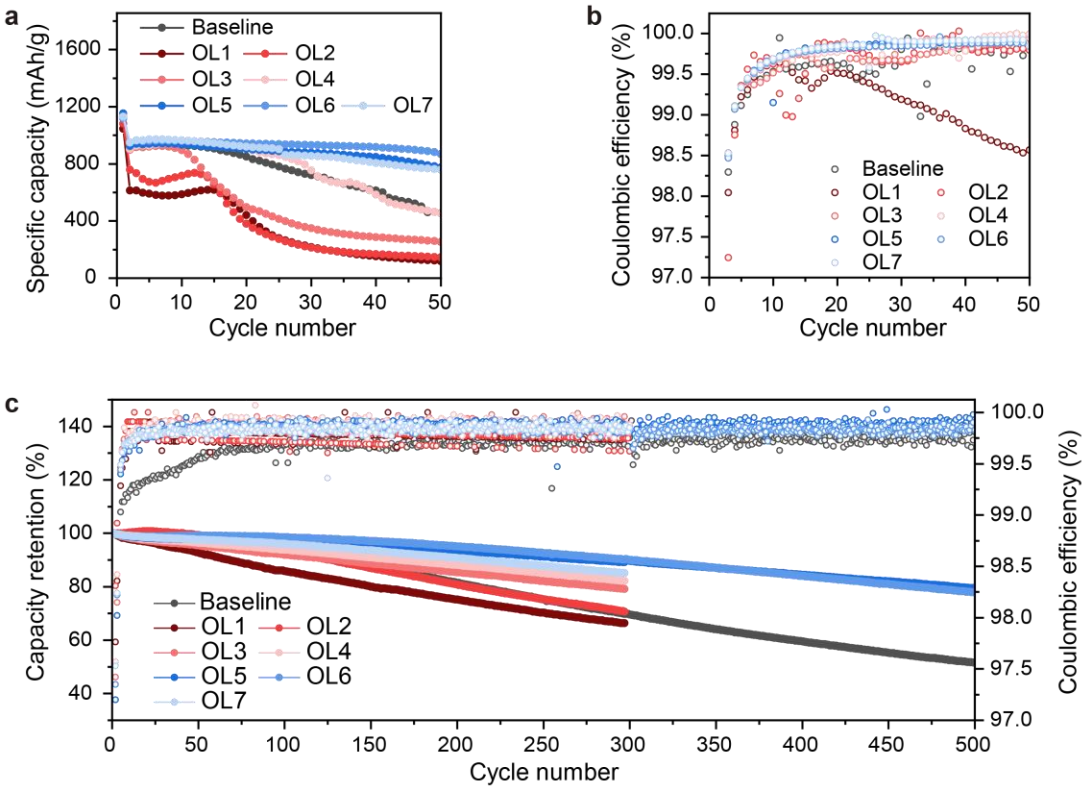

Figure II.1.D.7 Specific capacity (a), coulomic efficiency (b) and capacity retention (c) of Si-Gr||NMC532 full cells cycled in various electrolytes.

To validate the potential of OL electrolyte towards practical application, cells using various electrolytes were tested at 45 ºC. Figure II.1.D.8 compares the results of the storage test at charged state (4.1 V) and the long-term cycling of Si-C||NMC532 full cells with different electrolytes at 45 ºC. The LHCE with BTFE diluent was also used here as another control electrolyte. The cell with the baseline electrolyte suffers severe OCV drop (down to 3.22 V) after 30 days of storage at 45 ºC. While the cells with LHCEs (diluted by either BTFE or OTE) still maintained high OCV (3.88V) after 30 days. Capacity check after storage at 0.1C shows that the full cells using the LHCEs retain ~81% of the initial capacity, while the full cell using the baseline electrolyte retained only 27.6% of the capacity (Figure II.1.D.8b). These results clearly demonstrate that the LHCEs can enable high stability of the lithiated Si anode at high temperature. While the storage test does not show clear difference between BTFE and OTE diluents, large difference between these two electrolytes was observed in long term cycling test.

As shown in Figure II.1.D.8c, the cells using OL5 electrolyte show much better capacity retention (76.5%) after 300 cycles at 45 ºC than those using BTFE-based LHCE (46.6%) and the baseline electrolyte electrolytes (50.5%). Owing to the low boiling point of BTFE diluent, the degradation of full cell using BTFE-based LHCE is accelerated after 110 cycles, eventually leading to the low capacity retention after 300 cycles. It manifested that the adoption of stable diluent for LHCE is essential to achieve desired battery performance in more stringent environment.

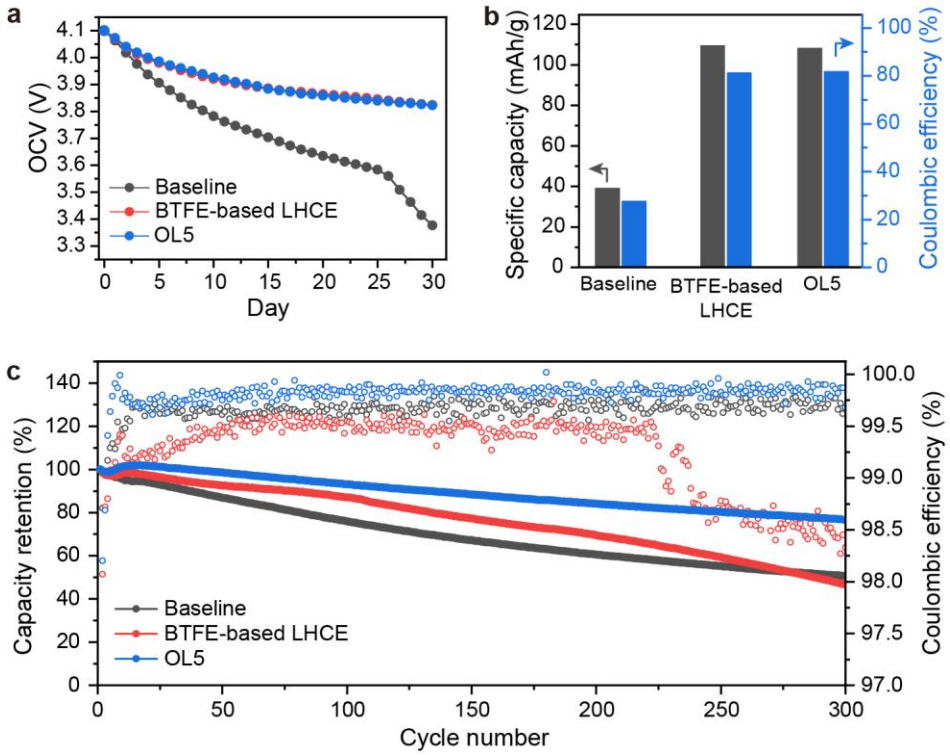

Figure II.1.D.8 Storage and cycling performance of Si-C||NMC532 full cells at 45 °C. a) OCV drop of Si-C||NMC532 full cells during storage at 45 °C. b) Discharge capacity and Coulombic efficiency after 30 days of storage at 45 °C. c) Long-term cycling performance of Si-C||NMC532 full cells at 45 °C

In order to elucidate the failure mechanism of Si-Gr anode in baseline electrolyte and OL electrolyte, SEM postmortem analysis was carried out on Si-Gr anodes cycled in OL electrolyte and Gen2+FEC baseline electrolyte. Figure II.1.D.9 shows that the Si-Gr electrodes using the baseline and OL5 electrolytes have substantially different morphologies after 500 cycles. As shown in Figure II.1.D.9a and d, the pristine Si-graphite anode is made up graphite flakes, Si nanosheets, and carbon. After 500 cycles in the full cell with baseline electrolyte, the SEI layer on the electrode is thick (Figure II.1.D.9b and Figure II.1.D.9e). The fatigued Si also became fluffy and entangled with accumulated SEI layer in the composite. On the other hand, OL5 electrolyte enables the Si-Gr anode to have only a thin SEI layer on the surface and to avoid SEI accumulation in its inner structure (Figure II.1.D.9c and Figure II.1.D.9f). The dense Si framework after 500 cycles in the cross-section SEM image supports the improved cycle life of the cells with OL5 electrolyte.

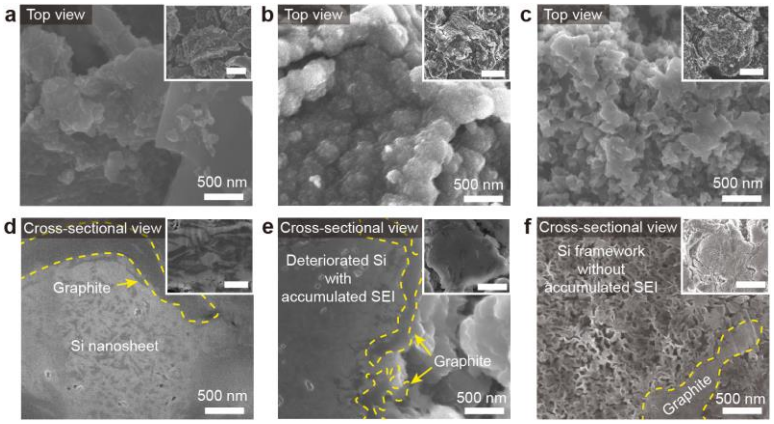

Figure II.1.D.9 SEM images of graphite/Si anodes before (a, d) and after cycling with the baseline (b, e) and OL5 electrolytes (c, f).

Conclusions

- We have developed porous Si-C composite by utilizing petroleum pitch as carbon precursor. The impregnation of petroleum pitch into porous Si enables a porous Si-C composite without aggregation of nanosized Si primary particles after carbonization at 700 ºC. It demonstrates excellent electrochemical performances in the full cell (78% capacity retention after 400 cycles) using Gen2+FEC electrolyte.

- The porous Si-C composite developed in this work exhibits much smaller (~10%) parasitic current during aging test using LHCE (LiFSI/DMC/TTE (0.51/1.1/2.2 in molar ratio) +5% FEC + 1% VC)) compared to those using Gen2+FEC electrolyte.

- OTE has been identified as a more stable diluent for LHCE that can enable high performance of commercial Si-Gr anodes. The optimized OL electrolyte, 1.74 M LiFSI in DMC/OTE (LiFSI/DMC/OTE = 0.51/0.84/0.84 in molar ratio) improves cycling performance of Si based LIBs at room temperature as well as at elevated temperature (45 ºC) by suppressing SEI formation and retaining Si nanostructure against large volume change.

Key Publications

1. Haiping Jia, Xiaolin Li, Junhua Song, Xin Zhang, Langli Luo, Yang He, Binsong Li, Yun Cai, Shenyang Hu, Xingcheng Xiao, Chongmin Wang, Kevin M. Rosso, Ran Yi, Rajankumar Patel, Ji-Guang Zhang, Hierarchical porous silicon structures with extraordinary mechanical strength as high-performance lithium-ion battery anodes, Nature Communications, 2020, 11, 1474, DOI: 10.1038/s41467-020-15217-9.

2. Haiping Jia, Peiyuan Gao, Lianfeng Zou, Kee Sung Han, Mark H. Engelhard, Yang He, Xin Zhang, Wengao Zhao, Ran Yi, Hui Wang, Chongmin Wang, Xiaolin Li, Ji-Guang Zhang, Controlling Ion Coordination Structure and Diffusion Kinetics for Optimized Electrode-Electrolyte Interphases and High-Performance Si Anodes, Chemistry of Materials, 2020, 32, 20, 8956-8964.

References

1. Cao X., Y. Xu, L. Zhang, M.H. Engelhard, L. Zhong, X. Ren, and H. Jia, et al. 2019. "Nonflammable Electrolytes for Lithium Ion Batteries Enabled by Ultraconformal Passivation Interphases." ACS Energy Letters 4, no. 10:2529-2534. PNNL-SA-145269. doi:10.1021/acsenergylett.9b01926

2. Haiping Jia, Peiyuan Gao, Lianfeng Zou, Kee Sung Han, Mark H. Engelhard, Yang He, Xin Zhang, Wengao Zhao, Ran Yi, Hui Wang, Chongmin Wang, Xiaolin Li, and Ji-Guang Zhang, Controlling Ion Coordination Structure and Diffusion Kinetics for Optimized Electrode-Electrolyte Interphases and High-Performance Si Anodes, Chemistry of Materials, DOI: 10.1021/acs.chemmater.0c02954.

Acknowledgements

Key contributors include Sujong Chae, Ran Yi, and Qiuyan Li.

II.1.E Pre-Lithiation of Silicon Anode for High Energy Li Ion Batteries (Stanford University)

Yi Cui, Principal Investigator
Stanford University
Department of Materials Science and Engineering, Stanford University
Stanford, CA 94305
E-mail: yicui@stanford.edu

Tien Duong, DOE Technology Development Manager
U.S. Department of Energy
E-mail: Tien.Duong@ee.doe.gov

Start Date: October 1, 2019 End Date: September 30, 2020
Project Funding: $500,000 DOE share: $500,000 Non-DOE share: $0

Project Introduction

Silicon (Si) is a high-capacity anode material promising to meet the ever-growing energy density demands of the lithium-ion battery industry. However, one of the main challenges of Si anodes is the low initial Coulombic efficiency (CE), which is an important parameter for lithium ion batteries (LIBs) performance as it indicates the effectiveness of active material usage and closely links to battery energy density. In a conventional Si-anode based battery, with limited lithium(Li^+) ions all originally stored in cathode sides, the solid-electrolyte interphase (SEI) formed in the initial cycle will irreversibly consume some active Li^+ ions and cause fractional utilization of active materials, limiting the energy density of a battery [1]. As Si anode exhibits a low initial CE of 50%–80% [2], which means 20%–50% of active Li^+ ions will be lost after first cycle, in other words, only 50%–80% of active materials can be utilized in later cycles. Therefore, there is a strong motivation to develop prelithiation approach, to compensate the initial active Li^+ loss and prevent battery energy density degradation.

Objectives

This study aims to design novel prelithiation approaches based on Si-anode to compensate the first cycle irreversible active lithium loss and prevent energy density degradation. With a comprehensive understanding and exploiting of prelithiation mechanisms, including new prelithiation reagents, direct contact between Li and Si, and electrochemical prelithiation, various prelithiation approaches have been designed. Besides improving initial CE, other considerations include fabrication easiness, controllable prelithiation amount, heat-free, solvent-free, environmental friendliness have also been included in order to develop facile and practical prelithiation approaches. After demonstrating the effective improvement of initial CE in half cells, full batteries are also fabricated to demonstrate the alleviated energy density degradation by prelithiation.

Approach

Three main approaches have been developed for prelithiation: 1) Synthesizing lithium alloying Li_xM particles as novel prelithiation reagents to provide a low-cost and general strategy for prelithiation. 2) Developing new prelithiation process based-on pressure-induced prelithiation. By direct contact with Li and Si under pressure, heat-free and solvent-free prelithiation can be achieved and prelithiation amount can be controlled by the contact time. 3) Developing new in-situ prelithiation process based on shorting-mechanism. A layer of thin lithium is inserted above Si anode in cell fabrication to achieve in-situ prelithiation during battery resting period. Besides prelithiation step, a series of morphological and chemical composition characterizations including SEM, TEM, XPS, Raman spectroscopy, XRD, etc. and electrochemical testing are conducted for performance characterization.

Results

A new in-situ prelithiation approach is demonstrated in the Figure II.1.E.1. This prelithiation approach takes one step to insert lithium mesh above Si anode in fabrication. With Li mesh insertion, prelithiation can in-situ take place in battery resting period based on shorting mechanism, which does not cost extra reaction time. Benefited from the in-situ nature of this prelithiation approach, there is no other action including cell disassembling and electrode washing, and thus there is no need to concern solution compatibility problem and waste management of large amount of prelithiation solution existed in other prelithiation approaches.

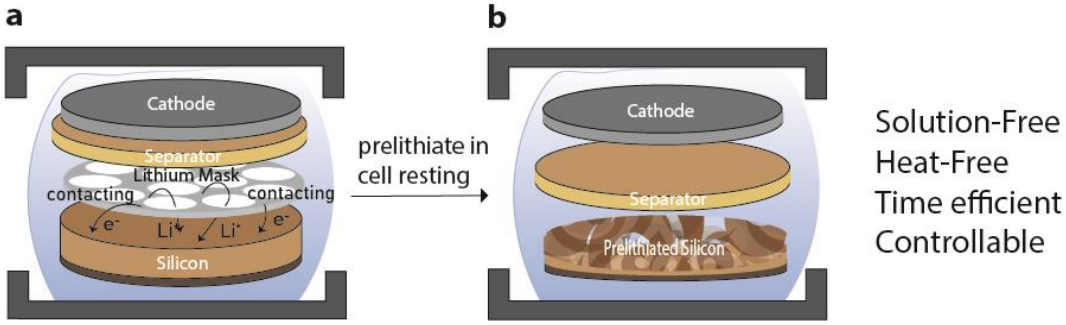

Figure II.1.E.1 **Schematic of pressure-induced prelithiation.**(a) Configuration of the prelithiation set-up and conditions. (b) Schematic showing the status after press-prelithiation and Li foil removal.

The in-situ prelithiation takes place based on shorting mechansium. A layer of lithium mesh is inserted above Si anode in cell fabrication and after assembling, Li mesh is in direct contact with Si anode with electrode around. Therefore, electrons can transport from Li mesh directly to Si anodes by the Si/Li contact points while Li^+ ions can flow from Li to Si through electrolyte to complete prelithaition. Considering battery is conventionally required a resting period after assembling for electrolyte wetting, our prelithiation approach utilizes this resting period to achieve in-situ prelithiation during battery resting. To confirm the prelithiated state of Si anode after battery resting, the cell was disassembled after 10-hour rest, and Si electrode film was taken out, washed and dried for SEM characterization. As shown in Figure II.1.E.2, before prelithiation, silicon nanoparticles were well dispersed, showing a size around 100 nm. After prelithiation, the size of silicon nanoparticles increased obviously, while the integrity of the structure was well maintained which is due to the initial size of silicon nanoparticle is below the critical crack size (150 nm). It's worth noting that solid electrolyte interface (SEI) film can also be observed at the top of the prelithiated Si film, which is due to the decomposition of electrolyte solvent along with the prelithiation.

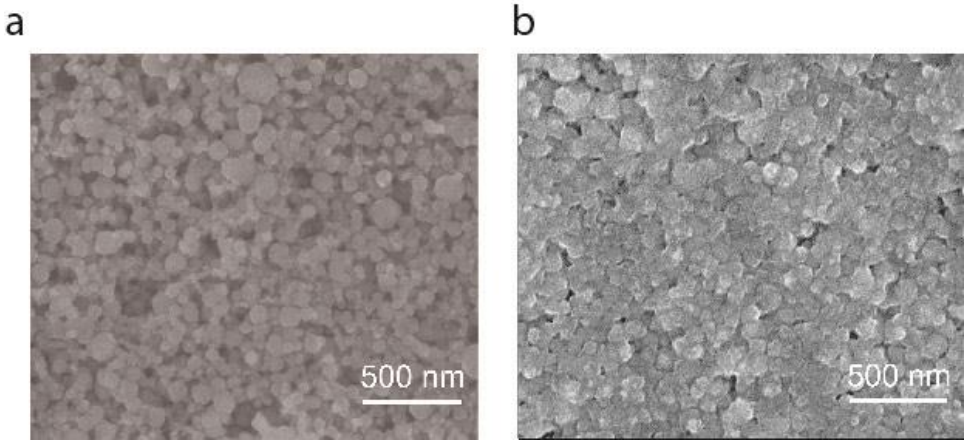

Figure II.1.E.2 **Top-view SEM images of Si anode.**(a) Before prelithiation. (b) After prelithiation.

The controllable prelithiation amount in in-situ prelithiation approach is achieved by Li mesh capacity tuning through its porosity. A series of Li meshes with varied porosity of 50%(p-50), 60% (p-60), 70% (p-70), and 80% (p-80) were designed (Figure II.1.E.3a), which store corresponding capacity of around 2.5 mAh/cm^2, 2 mAh/cm^2, 1.5 mAh/cm^2, and 1 mAh/cm^2, respectively, based on 25 μm lithium foil used in this project (Figure II.1.E.3b). To notice, considering a Si anode with initial CE of ~70% and a reasonable mass loading of 1-2 mg/cm^2, the desired prelithiation amount would be in the range of 1-2.5 mAh/cm2 based on Si theoretical capacity of 3600 mAh/g. Therefore, the above porosities were chosen to prepare Li meshes with desired prelithiation amount. The linear relationship between porosity and stored capacity (Figure II.1.E.3c) supports achievable precise capacity control in Li meshes through tuning porosity, which enables Li mesh as a promising prelithiation reagent to exactly match the desired prelithiation amount of Si anode.

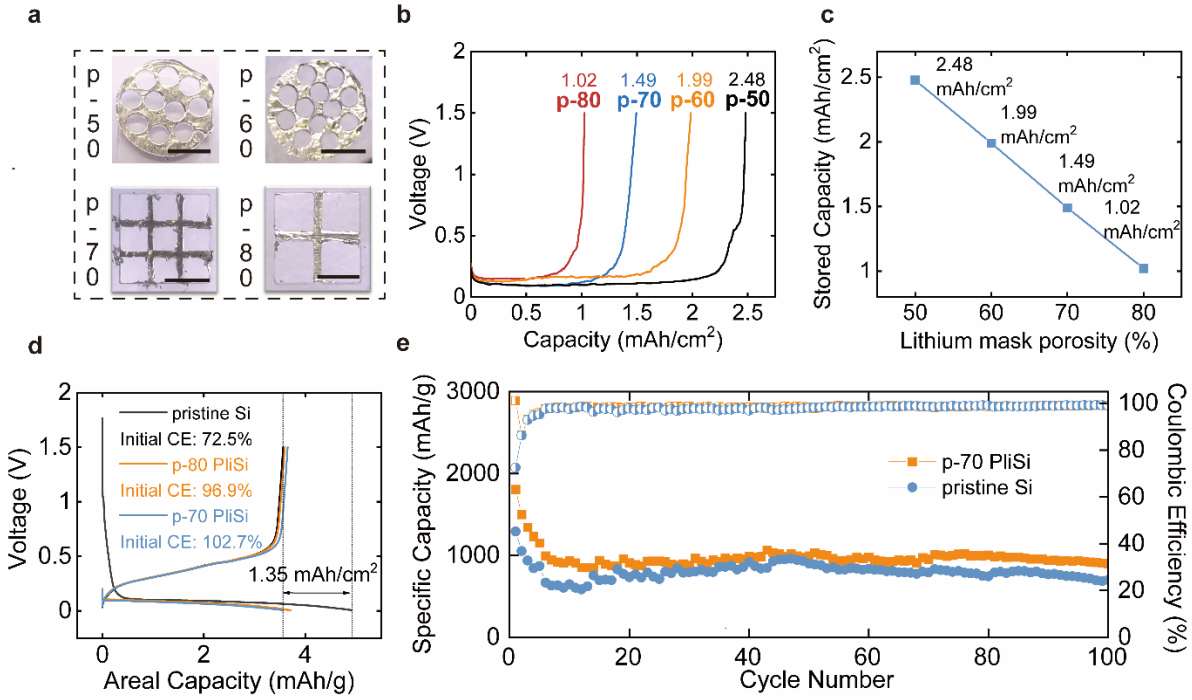

Figure II.1.E.3 **Controllable prelithiation through lithium mesh porosity.** a, Digital photos of lithium meshes with different porosity varied from 50% to 80%, scale bar = 5 mm. b, Voltage-capacity profiles of lithium meshes, showing the stored Li dose in these meshs. c, Linear relationship between stored capacity vs lithium mesh porosity, d, First-cycle voltage profiles of Si anodes of pristine Si, and p-70, p-80 lithium mesh prelithiated Si, respectively. e, Cycling performance of pristine Si anode and Si prelithiated by p-70 lithium mesh (rate = 0.05 C, 1C = 3.6 A g-1).

To prove the controllability of our in-situ prelithiation approach, Si||Li metal half cells were fabricated to test initial CE improvement using the method. The mass loading of Si electrodes were controlled 1.4±0.1 mg/cm^2 with an desired prelithiation amount of 1-1.5 mAh/cm^2. Therefore, p-70 and p-80 lithium mesh with 1.5 mAh/cm2 and 1 mAh/cm2 stored capacity respectively, were chosen here for prelithiation. As shown in Figure II.1.E.3d, in pristine Si anode, the capacity difference between 1st cycle charge and discharge was around 1.35 mAh/cm^2, indicating the amount of irreversible Li loss in the first cycle, which was the desired prelithiation amount. After prelithiation with p-80 (1 mAh/cm2) lithium mesh, whose capacity was little below the desired prelithiation amount, the initial CE of Si anode was improved from 72.5% to 96.9%. Meanwhile, when prelithiation with p-70 (1.5 mAh/cm^2) lithium mesh, whose capacity was little above prelithiation amount, initial CE was improved to 102.7%. This result well supports the corresponding relationship between desired prelithiation amount and Li mesh capacity, based on which, precise prelithiation through our in-situ prelithiation can be achieved by exactly matching Li mesh capacity with desired prelithiation amount. Additionally, it is worth to notice that delithiation curves of pristine and prelithiated Si anode presented similar trend, indicating that our prelithiation approach does not alter the electrochemical behavior of Si anodes. The

slightly more stable cycling behavior of prelithiated Si anode compared to pristine Si (Figure II.1.E.3e) further confirmed our in-situ prelithiation method does not deteriorate the cycling performance of Si anode.

In in-situ prelithiation method with Li mesh as prelithiation reagent, prelithiation amount can be delicately controlled over Li mesh capacity through tuning porosity. However, the thickness of lithium foil (~25 μm) and the technical difficulties in increasing porosity limits the range of designed prelithiation capacity (1-5 mAh/cm^2). In order to further broaden the lower limit to widen the prelithiation application, here, we develop thin lithium foils as another novel prelithiation reagent and controllable prelithiation can be achieved by varying the Li foil capacity by thickness.

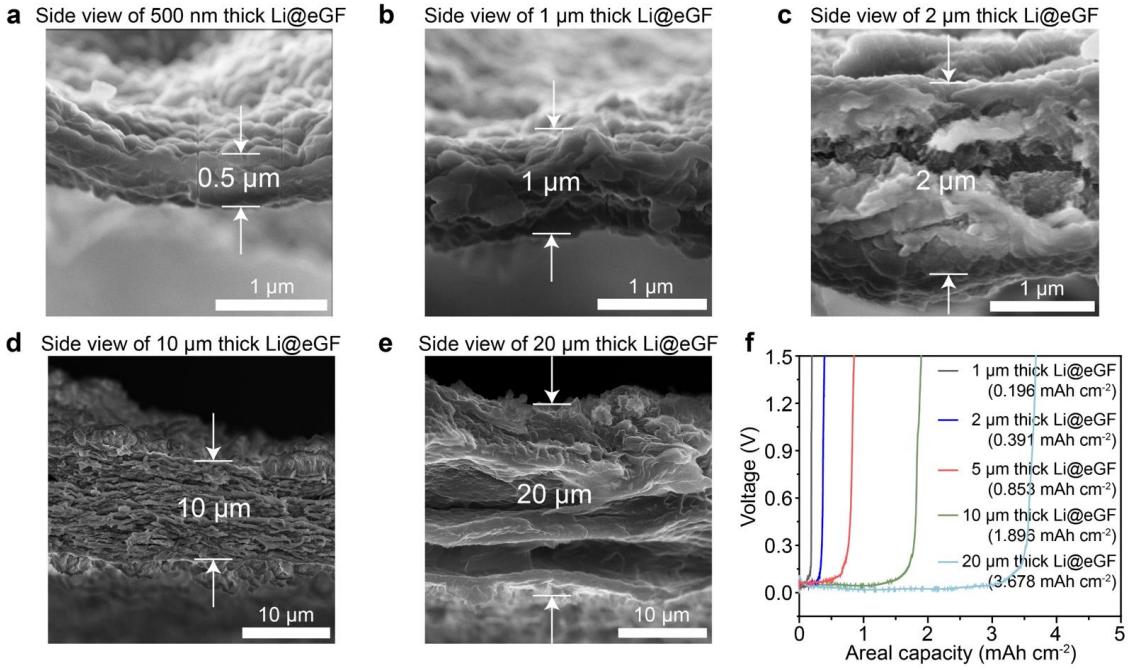

Figure II.1.E.4 **Thin Li@eGF foil as new prelithiation reagent.** a-e, Cross-sectional SEM images of Li@eGF films with tunable thickness from 500 nm to 20 μm. f, Voltage-capacity profiles of Li@eGF films with different thickness, showing the capacities exhibited in them.

Currently, the thinnest commercially available Li foils have the thickness of 20 μm, holding theoretical capacity of 4 mAh/cm^2, which is too high for prelithiation. In our design, we introduced the hosted structure into Li metal foil design to reduce the thickness. A series of lithium foils with thickness (0.5 to 20 μm) were fabricated by using reduced graphene oxide (rGO) as the host. First, we controllably calendared the a rGO to a few microns (0.5 to 20 μm). After an edge-containing molten Li absorption procedure, the rGO host loaded metallic Li inside its internal channels and retained the micron-level thickness. As a result, a hosted Li metal film (Li@eGF) with tunable micron-level thickness (0.5 to 20 μm) were successfully fabricated. The cross-sectional SEM images of Li@eGF (Figure II.1.E.4a-e) demonstrates most of the original submicron-wide void channels in fabricated Li@eGF were filled with metallic Li, supporting the successful fabrication of lithium foils hosted by rGO with different thickness. This wide range of thickness (500 nm, 1 μm, 2 μm, 10 μm, and 20 μm) enables the Li@eGF to exhibit wide range of designed prelithiation amount (0.089 mAh/cm^2, 0.196 mAh/cm^2, 0.391 mAh/cm^2, 1.896 mAh/cm^2, and 3.678 mAh/cm^2), which is verified by the voltage-capacity profiles of Li@eGF (Figure II.1.E.4f) measured in lithium stripping test. Therefore, this series of Li@eGF foils with varied thickness broadens the lower limit of designed prelithiation capacity to ~0.1 mAh/cm^2, expanding the application of one-step dry prelithiation method to Si batteries with lower designed capacities and even making it possible to be applied to relatively high initial CE anode material like graphite.

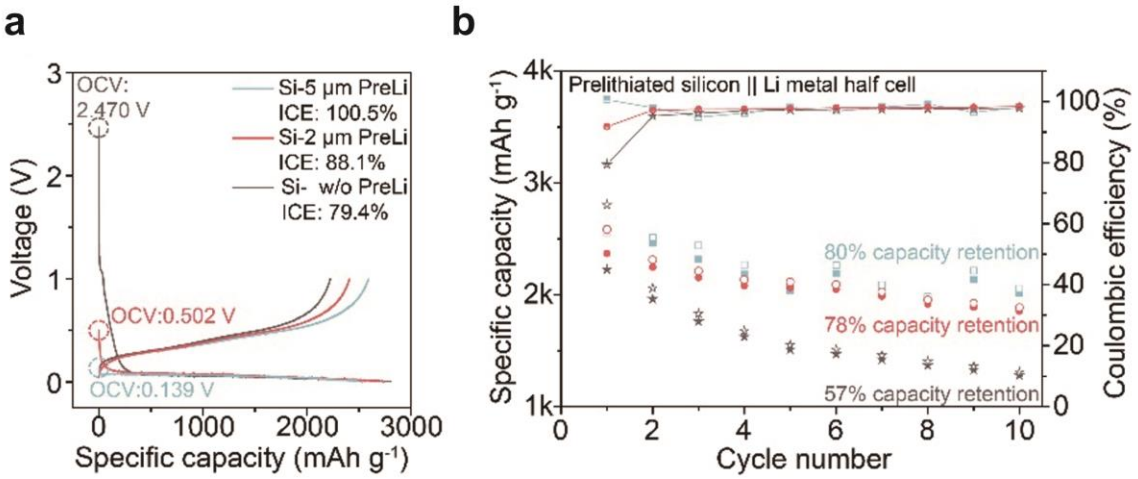

Figure II.1.E.5 **Electrochemical performance of Si anode using Li@eGF as prelithiation reagent.** a, Voltage profiles of Si electrodes using different thickness of Li@eGF film in the first cycle. b, Galvanostatic cycling of Si electrodes at 0.05 C using different thickness of Li@eGF films for prelithiation.

To prove the effectivity of Li@eGF as prelithiation reagent, Si||Li metal half cells were fabricated here to show initial CE of Si electrode improved from ~80% to ~100% with delicate. The mass loading of Si electrodes were controlled around 1.2 mg/cm^2 with an expected desired prelithiation amount of 0.8-1 mAh/cm^2. 2-μm-thick and 5-μm-thick Li@eGF with designed 0.4 mAh/cm^2 and 1 mAh/cm^2 prelithiation capacity respectively, were applied for prelithiation. As shown in Figure II.1.E.5a, pristine Si anode exhibited low initial CE ~80%. The 2-μm-thick Li@eGF (0.4 mAh/cm^2) partially compensated the first-cycle irreversible loss and improved initial CE to 88.1%. The 5-μm-thick Li@eGF, which has the well matched stored capacity (1 mAh/cm^2) with the desired prelithiation amount (0.8-1 mAh/cm^2), successfully improved the initial CE of Si anode to 100.5%. This result supports that Li@eGF is capable of finely controllable prelithiation to improve initial CE to ~100% by tuning the thickness to match stored capacity with the desired prelithiation amount. Besides initial CE improvement, Li@eGF also plays a role to enhance Si anode cycling ability (Figure II.1.E.5b). With 2-μm-thick and 5-μm-thick Li@eGF prelithiation, ~80% capacity retention was achieved after 10 cycles compared to 57% retention of pristine Si anode after cycling. As Li@eGF prelithiation will leave a layer of conductive graphene sheet above Si anode in battery cycling, the graphene film can act as a secondary current collector for active material utilization. Therefore, Li@eGF provides not only tunable prelithiation capability, but also a protection layer for Si cycling stabilization, making it a promising strategy towards applicable high-energy-density Si electrodes.

Conclusions

In the past year, we have develop a novel in-situ prelithiation method for Si anode to compensate the irreversible active Li loss in the 1st cycle and alleviate energy density degradation caused by it. Our in-situ prelithiation approach only takes one step to insert a layer of lithium mesh above Si anode in battery fabrication and prelithiation can happen simultaneously with the battery resting period based on shorting mechanism. Benefited from the in-situ nature of this prelithiation approach, there is no other action including cell disassembling and electrode washing, and thus there is no need to concern solution compatibility problem or waste management of large amount of prelithiation solution. To achieve controllable prelithiation, porous lithium mesh is first designed as prelithiation reagent. Delicate control over prelithiation amount is achieved through Li mesh capacity tuning by porosity. By matching the stored capacity in Li mesh and the desired prelithiation amount of a Si anode, initial CE can be controllably improved to ~100%. To further broaden the lower limit of the prelithiation amount, a series of rGO hosted lithium foils (Li@eGF) with thickness (0.5 to 20 μm) are developed, holding capacity as low as 0.1 – 4 mAh/cm^2. This Li@eGF prelithiation layer can successfully improve initial CE to ~100% by tuning the thickness to match stored capacity with the desired prelithiation amount. Besides providing tunable prelithiation capacity, Li@eGF also acts as a protection layer

for Si cycling stabilization by its conductive nature. This dual-function makes Li@eGF and in-situ prelithiation a promising strategy towards applicable high-energy-density Si electrodes.

Key Publications

Manuscript under preparation.

References

1. Li, Xin, Xiaohong Sun, Xudong Hu, Fengru Fan, Shu Cai, Chunming Zheng, and Galen D Stucky. "Review on Comprehending and Enhancing the Initial Coulombic Efficiency of Anode Materials in Lithium-Ion/Sodium-Ion Batteries." *Nano Energy* (2020): 105143.

2. Zhao, Jie, Zhenda Lu, Nian Liu, Hyun-Wook Lee, Matthew T McDowell, and Yi Cui. "Dry-Air-Stable Lithium Silicide–Lithium Oxide Core–Shell Nanoparticles as High-Capacity Prelithiation Reagents." *Nature communications* 5, no. 1 (2014): 1-8.

II.1.F High Performance Computing and Machine Learning for Lithium-Ion Batteries

Kristin A. Persson, Principal Investigator
Lawrence Berkeley National Laboratory
1 Cyclotron Rd
Berkeley, CA 94720
E-mail: kapersson@lbl.gov

Jean-Luc Fattebert, Principal Investigator
Computational Sciences and Engineering Department
Oak Ridge National Laboratory
One Bethel Valley Rd
Oak Ridge, TN 37831
E-mail: fattebertj@ornl.gov

Andrew Colclasure, Principal Investigator
National Renewable Energy Laboratory
Center for Integrated Mobility Sciences
Golden, CO 80401
E-mail: andrew.colclasure@nrel.gov

Brian Cunningham, DOE Technology Development Manager
U.S. Department of Energy
E-mail: Brian.Cunningham@ee.doe.gov

Start Date: October 1, 2019 End Date: September 30, 2022
Project Funding: $4,500,000 DOE share: $4,500,000 Non-DOE share: $0

Project Introduction

Silicon is a viable alternative to graphitic carbon as an electrode in lithium-ion cells and can theoretically store >3500 mAh/g. However, current lifetime limitations impact its practical use. The major issues include the stability of the electrolyte and the uncertainty associated with the formation of a stable solid electrolyte interphase (SEI). In this effort, we aim to apply computational models, leveraging DOE high-performance (HPC) computing and machine learning, to capture the chemical reaction paths and species of SEI growth on Si, coupled together with the Si electrode's surface and phase structure evolution with cycling. The resulting electrolyte stability insights, SEI phase evolution, and microstructure analysis will provide valuable data for feedback and close integration with the existing DOE SEISta program to ultimately advance our understanding of the Si anode reactivity and the development of novel Si electrolyte formulations.

Objectives

With the overall goal of understand the underlying instability of the SEI formed on silicon-based anodes in order to identify strategies to improve stability and thus cycling lifetimes, the LBNL, ORNL, and NREL teams pursue three distinct and complementary objectives:

The LBNL team seeks to use a first principles data-driven approach, leveraging both high-throughput workflows and a machine learning model of reactivity, to construct and analyze massive chemical reaction networks that include all of the thousands of species and millions of reactions that may participate in the SEI formation cascade in order to identify the reaction paths most likely to form key SEI species with minimal imposed bias. The thermodynamics and kinetics of the identified pathways are then provided to the ORNL and NREL teams.

The ORNL team seeks to simulate SEI growth on a Si anode atomistically. By supplementing classical molecular dynamics (MD) with the most important reactions identified by the LBNL team, ORNL aims to capture approximate *ab initio* reactivity on much longer timescales than are tractable for fully *ab initio* MD while accounting for atomistic interphase growth and molecular diffusion in order to obtain novel atomistic insight.

The NREL team seeks to build a continuum model of Si anode SEI growth / dissolution at the 100s of nanometers length scale where transport and mechanics have a significant impact on SEI dynamics. By avoiding atomistic descriptions and including only the most important reactions identified by the LBNL team, NREL aims to reach sufficiently long timescales to understand the large SEI thickness variations that can limit cycle lifetimes.

Approach

LBNL

In order to construct massive chemical reaction networks that can include all possible species and reactions that may participate in the SEI formation cascade, we developed three foundational tools:

- A high-throughput molecular simulation framework with on-the-fly error correction
- A novel chemically consistent graph architecture for massive reaction networks
- A graph neural network for the prediction of bond dissociation energies of charged molecules, which we named BonDNet.

The high-throughput framework was critical for data generation both to populate reaction networks and in order to have sufficient data on which to train BonDNet. In order to minimize imposed bias, we sought to simulate every molecule that has been previously proposed to participate in the EC/EMC SEI formation cascade in literature as well as every unique subfragment of each of the principle molecules. However, the resulting charged, open-shell, metal-coordinated, and solvated species are particularly difficult to simulate, with calculations encountering some sort of error or problem requiring by-hand intervention over 25% of the time. Such a high error rate precludes a straightforward simulation pipeline. To facilitate the large-scale simulation of such complex species, our high-throughput framework includes extensive autonomous on-the-fly error correction procedures which reduce our error rate to 1.2%. These capabilities allowed us to perform tens of thousands of calculations on principle molecules and their unique fragments from which we were able to construct a preliminary chemical reaction network with nearly 6000 species and 4.5 million reactions, orders of magnitude larger than any previously reported reaction network. However, standard approaches to reaction network analysis and pathfinding were intractable on this scale, necessitating our development of a novel chemically consistent graph architecture that allows optimized pathfinding algorithms to be applied to general reaction networks for the first time. We were then able to identify the best reaction paths to key SEI components, including lithium ethylene dicarbonate (LEDC), to which we recovered both expected mechanisms and novel unintuitive pathways. All relevant reactions have been provided to the NREL and ORNL teams, where the identity of the Si anode was enforced through the electron chemical potential.

Despite the immense size of our preliminary network, the nearly 6000 species include only principle molecules previously proposed to participate and their unique fragments. A more thorough and unbiased approach would allow all of these molecules and fragments to recombine in order to access unexpected molecules that are larger than any of the initial species. However, large species are substantially more computationally expensive, and recombination yields a combinatorial explosion of molecules which are intractable to all simulate from first principles. Tackling recombination was one of the main motivations behind our development of BonDNet, a graph neural network for the prediction of bond dissociation energies (BDEs) of charged molecules. While simulating larger molecules is substantially more expensive than simulating smaller molecules, chemically we expect that the thermodynamics of bond formation is in large part determined by the local environment of a

bond, which would suggest that a machine learning model trained on BDEs of small and medium-sized molecules should be able to predict BDEs of larger molecules with good accuracy. However, while a previous graph neural network model was able to predict BDEs of neutral molecules within chemical accuracy, [1] it was fundamentally limited to neutral molecules and homolytic bond breakage, which thus yields two neutral fragments. Since the reactions that occur during SEI formation involve bond breaking of charged species as well as heterolytic bond breakage, we needed to construct a new graph neural network architecture that could handle these more complex reactions.

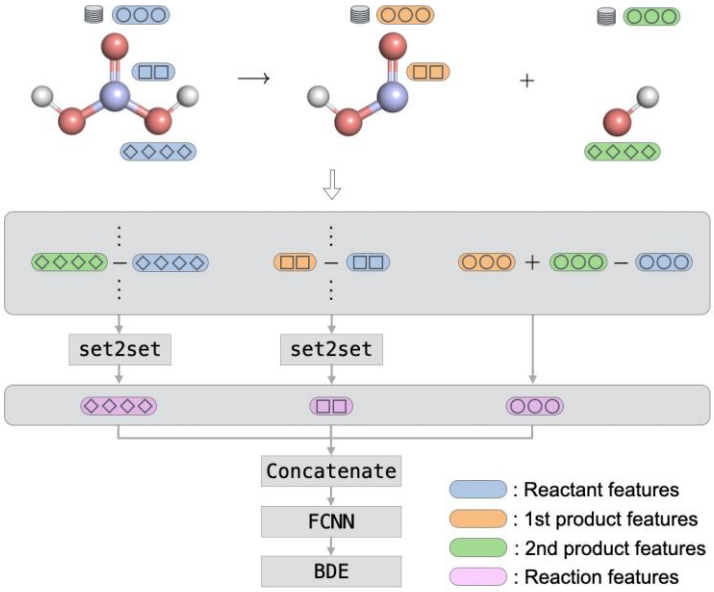

Figure II.1.F.1 Reaction difference features that allow BonDNet to predict charged and heterolytic BDEs.

As outlined in Figure II.1.F.1, BonDNet introduces global features, such as the total charge of a molecule, and represents a reaction as the difference of the reactant and product features. This allows the charge of each species participating in the reaction to be specified, thereby allowing for both homolytic and heterolytic BDEs of both neutral and charged species to be learned and predicted.

ORNL

To achieve very fast and long time-scale MD simulations, we consider molecular dynamics based on analytical expressions of interatomic forces. This approach is often referred to as “classical” molecular dynamics since it is based on a description of atoms as classical particles, without any “quantum” electrons. It typically includes energy terms that depend on distances between bonded atomic pairs, angles between triplets of atoms, as well as some “non-bonded” terms that depend on atomic distances only to describe Coulomb and Van-der-Waals interactions. These interatomic forces can be evaluated very quickly, and MD timesteps can be carried out very rapidly using such techniques, enabling computations with millions of timesteps and reaching propagations of several nanoseconds. Since classical MD does not account for the actual electronic structure responsible for the atomic interactions, a force field (FF) that describes the atomic forces needs to be parameterized to match reality as closely as possible. While no model is perfect, several FF parameters proposed in recent years give accurate results and lead to very valuable insights into atomistic phenomena. In this project we chose to use the OPLS (Optimized Potentials for Liquid Simulations) FF. [2]

However, one strong limitation with classical MD simulations is that force fields do not allow chemical reactions to happen since atomic bonds are hardcoded into the model. They cannot break, and no new bonds can be formed. Further, bonds do not change based on their environment. To overcome this restriction, one can modify the FF model each time a chemical reaction happens. In this case, after identifying when a chemical

reaction is about to happen, one needs to explicitly restart the MD with a different FF, with modified atomic bonds, to describe the products of the reaction as different molecules.

This capability was recently developed for and implemented in the LAMMPS code. [3] LAMMPS is a very popular open source classical molecular dynamics software with a focus on materials modeling (https://lammps.sandia.gov). It is supported by the DOE Exascale Computing Project (ECP) and runs very efficiently on various platforms from desktops to DOE leadership HPC resources. It not only implements the OPLS FF used in this project, but it also offers a large variety of options to specify external forces, attach specific properties to groups of atoms, split computational domains into subdomains with different properties, and more. Based on all these aspects, LAMMPS is the software that we decided to use for all our MD simulations.

To identify reactions in our simulations and generate products as a result of these reactions using LAMMPS, we need to specify a set of "reaction templates" that describe all the chemical reactions we want to model. For each reaction, we also need to specify some geometrical features of the reactants and products, as well as some tolerance that determines how closely the template and the actual geometry have to match. A reaction probability can also be assigned to each template, but we have not used that option yet. Note that a "reactant" geometry does not need to be strictly a reactant but can, for instance, be chosen as the geometry of a transition state. An example of one of the reactions considered so far in this project is shown in Figure II.1.F.2.

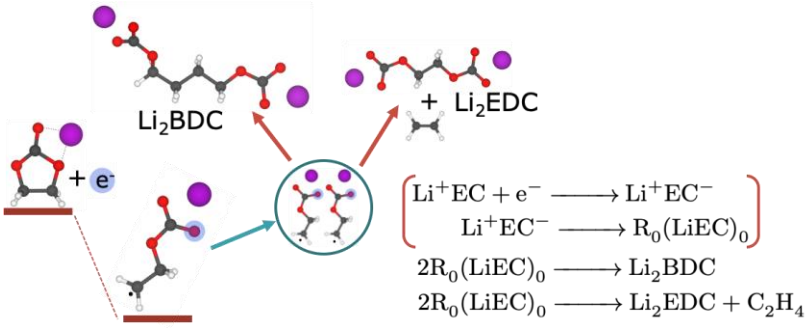

Figure II.1.F.2 One of the reactions considered in the electrolyte.

The approach described above can lead to reaction rates that are unphysically fast: while in reality reactants may be close to each other many times before a reaction actually occurs, in our simulation we can make it happen much faster. This is a good approach, since we cannot afford to simulate physical timescales much longer than nanoseconds using MD. On the other hand, we can run into issues of Li^+ depletion. Indeed Li^+ can be considered the fuel that feeds many of the reactions happening within the electrolyte. But since Li^+ diffuses slowly through the electrolyte, we found that accelerated chemical reactions led to Li^+ depletion in the region where reactions occur. To remedy to this problem, we add a fictitious external force that drives the free Li^+ in the solution towards the anode. We tune this force to a value small enough not to affect the pair correlation functions involving Li^+ but large enough to avoid the Li^+ depletion issue and increase Li-ion diffusivity along one direction.

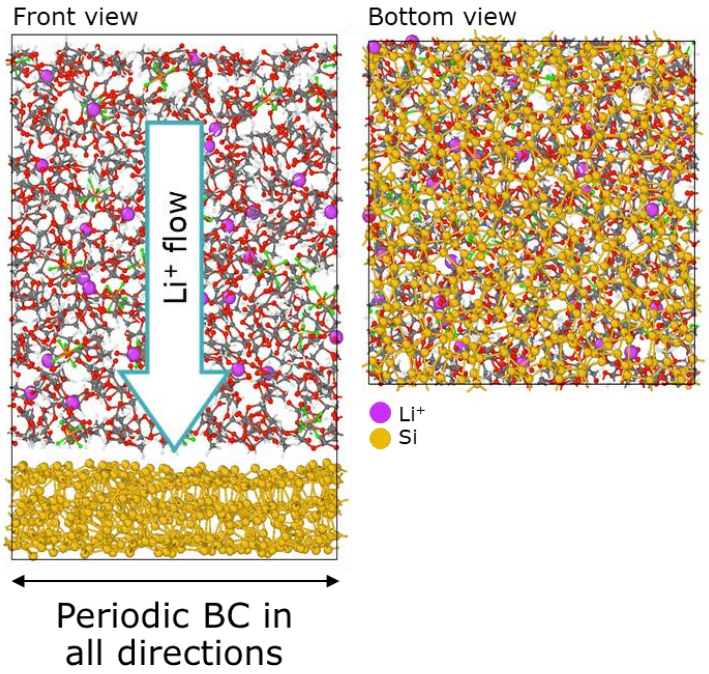

Figure II.1.F.3 Electrolyte model system with a Si anode. Li^+ flows from top to bottom and reacts with EC molecules near the anode. Periodic conditions are used in all three directions, so Li^+ ions that make it through the anode reappear at the top as if they were coming from the cathode.

NREL

The continuous evolution of the solid electrolyte interphase (SEI) on silicon anodes exhibits several defining characteristics that are poorly understood, including considerable SEI thickness variation over a single cycle, referred to generally as "breathing" of the SEI. Furthermore, the constituents of the SEI solid phase shows significant variation with cycling, dependent on the electrolyte components (salt: Li^+, PF_6^-; solvents: EC, DMC, FEC, H_2O) which reduce to subsequently form the degradation products. Furthermore, these degradation mechanisms are sensitive to silicon anode surface termination (silicon oxide, hydrogen). It is not well understood why electrolyte reduction on standard graphite anodes results in a robust/passivating SEI while the reduction products formed on Si based anodes results in continuous reactions and loss of lithium. A multiscale effort merging atomistic (ORNL+LBNL) and continuum-scale modeling (NREL+CSM) is required to unravel the fundamental mechanisms for SEI dynamics.

NREL is developing a continuum-level, physics-based, multiphase-multispecies SEI model framework informed by atomistic calculations for species thermodynamics and kinetics with the goal of deconvoluting the degradation mechanisms and aimed at reaching predictability to help delineate strategies for stabilizing the silicon SEI. Representative SEI species include Li^+, PF_6^-, EC, DMC, Li_2EDC, LiMC, Li_2O, LiF, FEC etc. while silicon can host lithium. The proposed model features include:

- Heterogeneous electrochemical reactions and homogeneous chemical reactions occurring throughout SEI volume.
- Electrolyte (ions and solvent) transport through SEI pore phase
- Ion transport through SEI solid phase
- Charge transport through the SEI electrolyte and solid phase

- Species and charge transport through the silicon anode
- Silicon and SEI growth during cycling
- Stress-based mechanics considerations to adequately treat large Si deformation

For FY20, NREL reviewed relevant experimental data collected under SEISta to better understand SEI characteristics. Based on this review, a model framework was developed to capture observed behavior. This model framework was converted into a series of conservation equations described below. The governing conservation equations are discretized using the finite volume method. The open-source software Cantera is utilized for species thermodynamics and kinetics. The flexibility of Cantera allows for incorporation of additional species and reactions without modification to underlying code. Lastly, initial model predictions are reported illustrating the capabilities of the model to capture SEI behavior.

Summary of Representative Equations

We use dilute solution theory to describe species and charge transport throughout the SEI. [4], [5], [6] Ions can flow due to diffusion and migration while neutral species can move under diffusion in the electrolyte phase. Diffusion is described using Fick's law. In the solid phase, most of the reaction products are immobile while accounting for transport of the charged species.

Species Conservation in SEI Electrolyte Phase

$$\frac{\partial(\varepsilon c_{e,k})}{\partial t} = \frac{\partial}{\partial x}\left(D_{e,k}^{eff}\left[\frac{\partial c_{e,k}}{\partial x} + \frac{z_{e,k}Fc_{e,k}}{RT}\frac{\partial \phi_e}{\partial x}\right] - c_{e,k}u\right) + a_s\dot{s}_{e,k} + \dot{\omega}_{e,k},\ k = \mathrm{Li^+}, \mathrm{PF_6^-}, \mathrm{EC}, \mathrm{EMC}, \mathrm{FEC}, \mathrm{H_20}\ \ldots$$

Here, ε is the porosity of the SEI, $c_{e,k}$ is the concentration of species *k* in the electrolyte phase, $D_{e,k}^{eff}$ is the effective diffusivity of electrolyte species, $z_{e,k}$ is the charge number, ϕ_e is electrolyte potential, u is electrolyte advection velocity and $\dot{s}_{e,k}$, $\dot{\omega}_{e,k}$ are the heterogeneous and homogeneous species production rates. For the nanoporous SEI, the effective properties differ from Bruggemann correlations for porous electrodes with much higher tortuosity expected in the nanoporous SEI. Effective diffusivity is defined as $D_{e,k}^{eff} = \varepsilon^p D_{e,k}$, with the exponent '$p$' taking much larger values ~10 as opposed to 1.5 for porous electrodes.

Species Conservation in SEI Solid Phase

$$\frac{\partial(\varepsilon_s c_{s,k})}{\partial t} = \frac{\partial}{\partial x}\left(D_{s,k}^{eff}\left[\frac{\partial c_{s,k}}{\partial x} + \frac{z_{s,k}Fc_{s,k}}{RT}\frac{\partial \phi_s}{\partial x}\right] - c_{s,k}v\right) + a_s\dot{s}_{s,k} + \dot{\omega}_{s,k},\ \ k = \mathrm{Li_2CO_3}, \mathrm{LiF}, \mathrm{LiEDC}, \mathrm{LiF}, \mathrm{Li^+}\ldots$$

The subscript 's' denotes the corresponding species in the solid phase and *v* is the solid phase advection velocity. It is to be noted here that most reaction products are immobile (like Li_2CO_3, LiF...), and hence solid phase species conservation can be further reduced to remove the diffusion and migration terms. Here effective diffusivity is defined as $D_{s,k}^{eff} = (1-\varepsilon)^p D_{e,k}$. We intend to work with the silicon consortium to determine the nominal species transport properties, especially for ion motion in the solid-phase.

Mass Conservation of Solid Phase

$$\frac{\partial \varepsilon_{s,k}}{\partial t} = V_{s,k}a_s\dot{s}_{s,k} + V_{s,k}\dot{\omega}_{s,k} - \frac{\partial}{\partial x}\left(\varepsilon_{s,k}v\right)\ ,\ \varepsilon = 1 - \sum_i \varepsilon_{s,k}$$

Here, a_s is the interfacial active area while $V_{s,k}$ is the molar volume of species *k*. Solid phase species can grow into the pore phase resulting in porosity reduction due to the generation from electrochemical and chemical reactions. The solid phase can grow until the porosity reduces to a critical limit (0.1/0.2) to allow for concurrent solid phase and electrolyte species transport to occur throughout the bulk of the SEI during the film growth as well as numerical stability. In further model development, we intend to relax this assumption to account for lower porosity inner SEI as compared to outer SEI.

Charge Conservation in Electrolyte Phase

$$\frac{\partial}{\partial x}\sum_{ions}\left(z_{e,k}D_{e,k}^{eff}\left[\frac{\partial c_{e,k}}{\partial x}+\frac{z_{e,k}Fc_{e,k}}{RT}\frac{\partial \phi_e}{\partial x}\right]\right)=-\sum_{ions}\left(z_{e,k}a_s\dot{s}_{e,k}\right)$$

Charge Conservation in Solid Phase

$$\frac{\partial}{\partial x}\sum_{ions}\left(z_{s,k}D_{s,k}^{eff}\left[\frac{\partial c_{s,k}}{\partial x}+\frac{z_{s,k}Fc_{s,k}}{RT}\frac{\partial \phi_s}{\partial x}\right]\right)=-\sum_{ions}\left(z_{s,k}a_s\dot{s}_{s,k}\right)$$

Reaction Kinetics

$$\dot{q}_i=k_{fi}\prod_k {a_k}^{\nu_{ki}}-k_{bi}\prod_k {a_k}^{\nu_{ki}}$$

$$k_{fi}=k_{fi}^0 exp\left(\frac{nF\beta\Delta\phi}{RT}\right), k_{fi}=k_{bi}^0 exp\left(\frac{nF(1-\beta)\Delta\phi}{RT}\right)$$

Here, k_{fi} and k_{bi} are the forward and reverse reaction rates, n is the number of e^- in the charge transfer reaction and β is the charge transfer coefficient. We can compute one rate from the other based on the species thermodynamics (enthalpy, entropy) data.

Silicon Anode Species and Charge Conservation

$$\frac{\partial c_{Li}}{\partial t}=\frac{\partial}{\partial x}\left(D_{Li}\frac{\partial c_{Li}}{\partial x}\right),\ \sigma_{Si}\frac{\partial^2 \phi_s}{\partial x^2}=0$$

Here, c_{Li} is the concentration of intercalated Li, while D_{Li} and σ_{Si} correspond to Li diffusivity and electronic conductivity of Si.

Implementation

The model equations are discretized using the Finite Volume Method with spatial discretization performed using central differencing for the diffusive terms and upwind differencing for any advective terms that arise due to electrolyte flow and solid film growth. A backward Euler implicit scheme is used for temporal discretization which ensures unconditional stability. All the model equations are implemented in MATLAB. Reaction data is specified through an appropriate library like Cantera. [7] All species thermodynamic (enthalpy, entropy) data and reaction rate is specified in Cantera which outputs the homogeneous and heterogenous reaction species production/generation rates. This enables modular development of the framework which can be used to add any subsequent species and reactions in the SEI and silicon phase. An example of the reaction mechanism implementation is provided in the following section, where we have taken the reaction data from LBNL and incorporated it into the Cantera file which is read by MATLAB. Extensive grid independence and time independence checks as well as conservation checks have been implemented to ensure accuracy of the solution. Our model framework accounts for three major physics: species thermodynamics and reaction kinetics (Cantera), solid and electrolyte phase species and charge transport (MATLAB), and solid mechanics. Currently, reaction and transport mechanisms have been implemented; solid mechanics integration will be performed at a later stage.

In literature, current state of the art SEI modeling by Single *et al.* [8], [9] incorporates solvent transport and three parasitic electrochemical reactions occurring throughout the bulk of the SEI phase which are detailed here: $2EC + 2Li^+ + 2e^- \rightarrow Li_2EDC + R$; $DMC + Li^+ + e^- \rightarrow LiMC + R$; $0.1Li_2EDC + Li^+ + e^- \rightarrow 0.6Li_2O + R$. Here, ion transport in the solid phase is neglected. Further, the electrochemical potential of lithium ions in the electrolyte is considered to be in equilibrium and constant (obviating the need for tracking Li^+ species in solid, electrolyte and solving the electrolyte potential). We perform an initial comparison of our model with the results published in literature to ensure correct model implementation. We note that our model is developed in

a much more flexible computational framework that allows for comprehensive development accounting for multiple species and reactions which are seen in the silicon SEI system.

Results

LBL

Training on a dataset consisting of over 60,000 unique homolytic and heterolytic bond dissociations of neutral and charged molecules and their unique fragments, BonDNet can learn and predict complex BDEs with a mean absolute error of 0.022 eV, significantly below the often referenced "chemical accuracy" benchmark of 0.043 eV. We are now working to leverage BonDNet to identify only the thermodynamically favorable recombinant molecules which will then be computed with our high-throughput framework and added to our massive reaction network in order to increase its coverage of chemical space and reduce the imposed bias.

We have additionally been supplementing our preliminary network with thousands of species relevant to FEC decomposition and PF_6^- decomposition. FEC is a common electrolyte additive found to mechanically stabilize the Si anode SEI. The presence of FEC increases LiF content at the SEI, and there is still no clear consensus on the exact pathway that the LiFEC molecule takes to decompose and produce LiF. To understand FEC decomposition mechanisms, we constructed a reaction network with 9000 molecules and 180,000 elementary reactions. We note that we are still working to supplement this network with two-bond reactions, the addition of which increased our preliminary network from 116,000 reactions to 4.5 million reactions. Our 9000 species network was able to capture four different ways that the LiFEC molecule can ring open, and its respective pathways leading to LiF formation, as shown in Figure II.1.F.4.

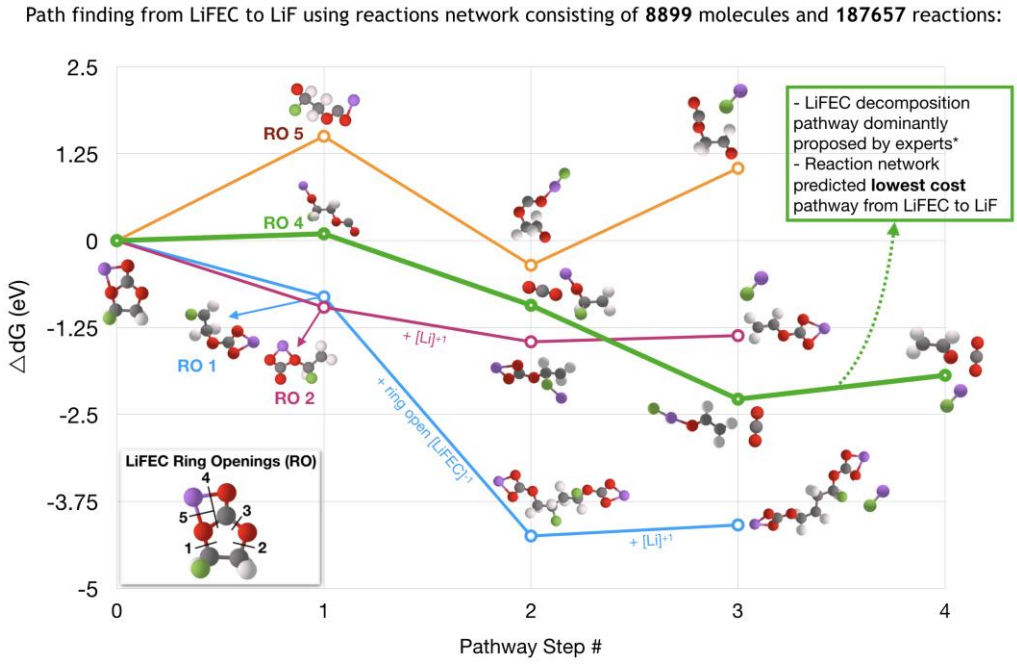

Figure II.1.F.4 Thermodynamic pathways from LiFEC to LiF found using the reaction network.

The green path in Figure II.1.F.4 is the shortest pathway predicted by the network, and it is also one of the most frequently expert proposed paths. [10] While the blue path may seem the best path thermodynamically, it requires an additional LiFEC molecule and Li-ion to assist in LiF formation. Similarly, the purple pathway requires an additional Li-ion to bond with the fluorine in LiFEC to form LiF. The green path does not require any additional species for LiFEC to decompose into LiF, CO_2, and C_2H_3O. This work not only validates our network-based approach but also highlights the value of the automated framework. Our approach can predict mechanistic pathways that took years for the community to identify manually. We expect that additional paths of low cost will be identified once two-bond reactions are added to the network. However, at present, the over

50 million additional reactions that are contributed introduce substantial technical difficulties that we are working to resolve in order to facilitate more complex pathfinding.

LiF also forms through decomposition of the $LiPF_6$ salt which is commonly used in the Si system. Therefore, we have been investigating the competing pathways from LiFEC and $LiPF_6$ leading to LiF formation using the reaction network. An additional 3000 $LiPF_6$ related molecules were added to the aforementioned network to form a network with over 12,300 molecules. Path search results from LiFEC and $LiPF_6$ to the four common $LiPF_6$ byproducts thought to be in the SEI ($LiPF_4$, PF_3, LiF, LiF_2PO) are presented in Figure II.1.F.5. The network predicts the shortest path to LiF is for an F^- to leave FEC via FEC reduction and for an Li^+ to separate from $LiPF_6$. In other words, it is easier to obtain fluorine from FEC and Li^+ from $LiPF_6$. Moreover, LiF_2PO is formed by a fragment of FEC (with CO_2 being removed) bonding to PF_2 obtained from PF_6 decomposition, again showing an FEC – PF_6 connection.

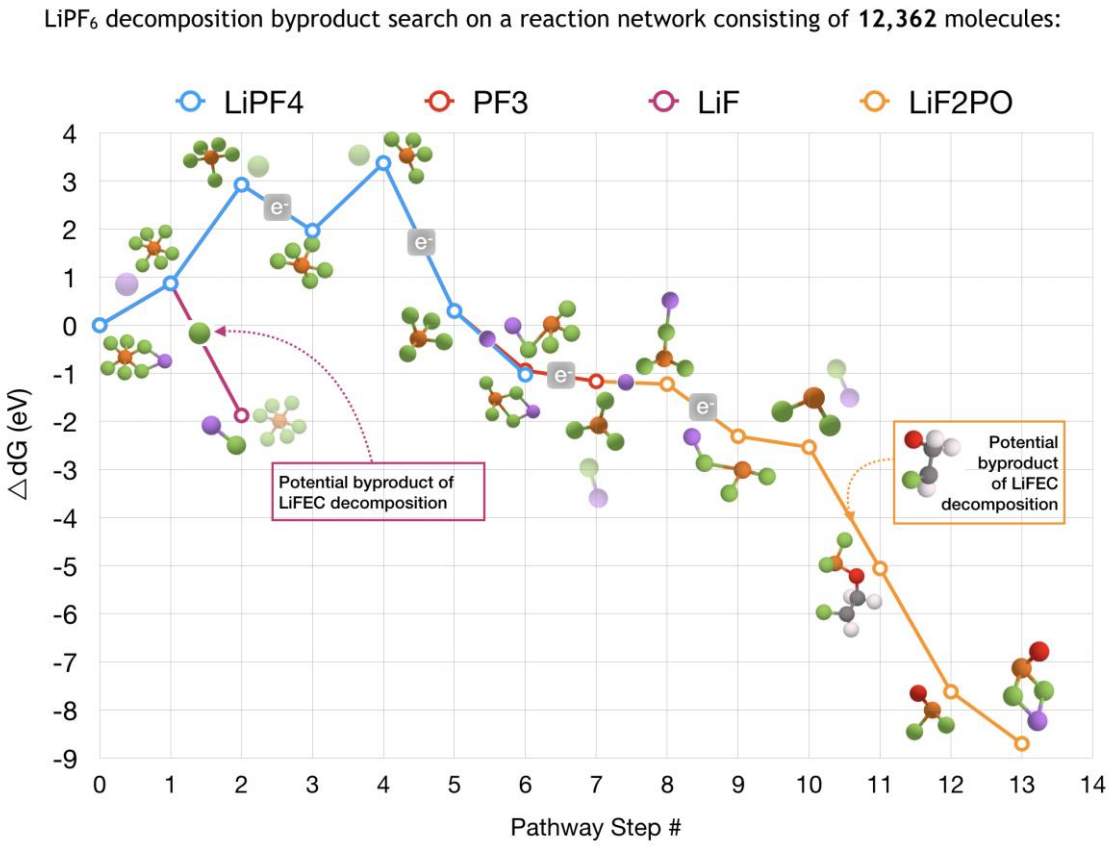

Figure II.1.F.5 Decomposition pathways of $LiPF_6$ in the presence of LiFEC.

This network is still in its preliminary stages of development and does not capture water reactions or the energetic impact of phase changes. Many of the uphill steps in the initial stages of $LiPF_6$ decomposition can be lowered in thermodynamic cost with the assistance of water. Moreover, currently, kinetic barriers are not integrated into the network, but we are working to include them in the future. Regardless, the network can already capture mechanistic interactions between LiFEC and $LiPF_6$. Future work will continue the development of the reaction network tool and effectively use it to clarify the LiF formation mechanism at the SEI as a function of electrolyte content.

ORNL

The methodology described in the previous section was implemented using LAMPPS. An initial small atomistic system which is general enough for an atomistic model of SEI initial conditions was developed for

rapid testing, debugging and performance evaluation. The simulation domain is 3 nm x 3 nm x 4 nm and contains 350 ethylene carbonate molecules, 26 Li^+ ions and 26 PF_6^- molecules, corresponding to a 1M concentration of $LiPF_6$ in EC. Then the simulation domain was doubled in the z-direction along the Li^+ flow to reduce size effects we were seeing in the initial system.

We started by carrying out some validation runs without chemical reactions to verify our force field parameterizations were correct. We showed that Li-P, Li-F, Li-O pair-correlation functions and self-diffusion coefficients for Li^+ were in good agreement with previously published results. To simulate the electrolyte in the presence of an anode, we added an amorphous silicon anode at one end of our simulation box. Even though we are currently ignoring possible chemical reactions at the anode surface, this allows us to define a "distance" from the anode on which redox reactions depend, as well as a separation wall between two periodic images of the electrolyte in the direction of the Li^+ flow.

Our current model includes 11 reactions including EC decomposition reactions and a cascade of three reactions for the decomposition of PF_6^-. The exact choice of these reactions, as well as the frequency for template matching search and the template matching tolerance, are still evolving. Substantial tuning remains to be done based on the MD results since some of the simulation parameters have no corresponding direct physical values or have not been parametrized in the force field. In Figure II.1.F.6 we show results for one example simulation. We can clearly observe the formation over time of some of the species believed to be the core components of SEI: LiF, LEDC, and, Li_2CO_3.

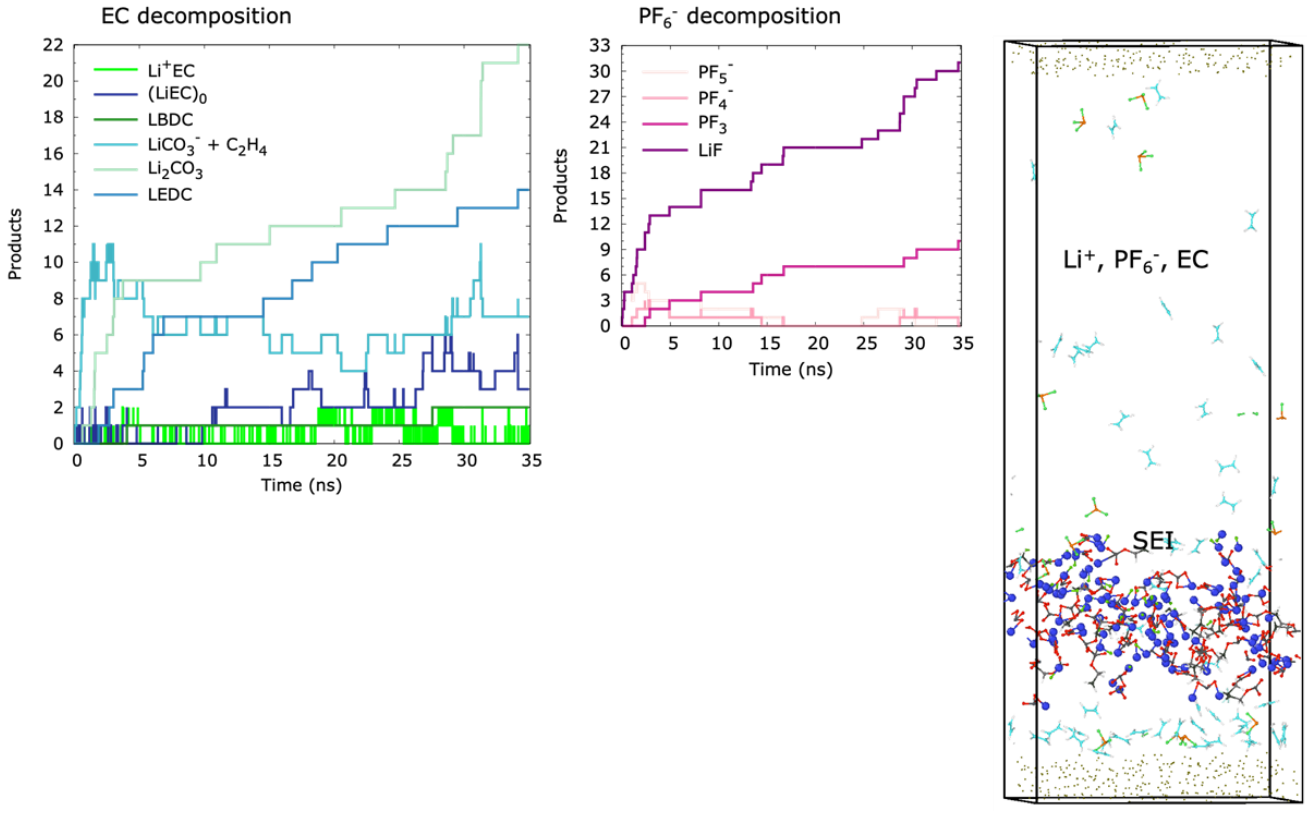

Figure II.1.F.6 Reaction product quantities produced over a 35 ns simulation (left two plots) and molecular products in the computational domain (right).

NREL

Figure II.1.F.7(a) shows the lithiation behavior of a pristine silicon nanoparticle without an SEI (initial radius 30 nm) cognizant of its expansion as the lithiation occurs. The concentration and voltage profiles during the lithiation are shown below. Lithiation of the nanoparticles causes a rise in the local state of charge and a significant increase in particle radius due to large partial molar volume of lithium in silicon. As lithiation progresses, the concentration gradients inside the particle flatten. This somewhat unintuitive result is a consequence of the surface area increase of the particle resulting in reduced surface flux which outweighs effects from an increasing diffusion length. High C-rate operation is possible because of the use of nano-silicon. Note that stress and damage have not been incorporated since the size of the nanoparticle considered is much below the critical limit for fracture (~150 nm). This model can be extended to nanorods and thin films.

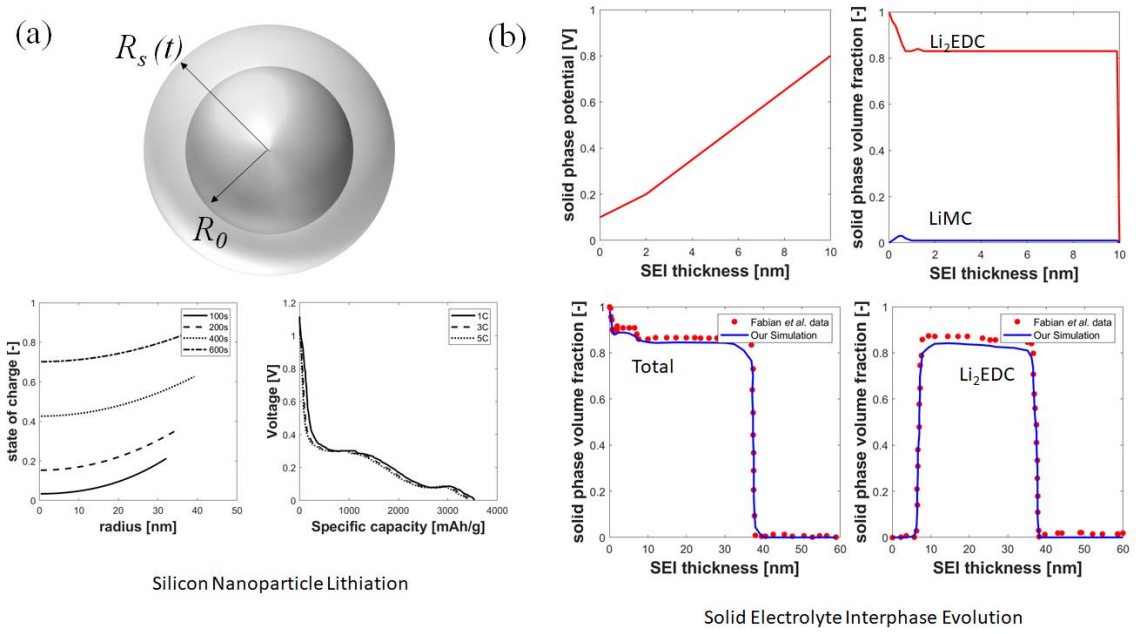

Figure II.1.F.7 (a) (Top) Lithiation of a silicon nanoparticle. (Bottom) Evolution of concentration and voltage profiles in a silicon particle with initial radius 30 nm as lithiation progresses. The concentration profiles shown are for a 5C current rate. (b) (Top) SEI solid phase potential and solid phase volume fraction evolution with EC and DMC decomposition in the SEI after constant voltage held at 100 mV. (Bottom) Comparison of total solid volume fraction and Li_2O volume fraction with Single et al. for EC decomposition and Li_2EDC to Li_2O conversion reactions after a constant voltage hold.

Figure II.1.F.7(b) shows the evolution of a multispecies SEI on the anode based on the solvent reduction mechanisms and conversion reactions of Single *et al.* [8] For the top two figures, EC and DMC reduction reactions are considered. The SEI electronic conductivity is 1pS/m, allowing for large potential gradients to develop throughout the system. There is a need to determine the electrical conductivity of SEI on silicon and its evolution with composition through scanning spreading resistance microscopy measurements. Initially, the entire SEI is at the reduction potential for EC (0.8V), and the anode potential is subsequently decreased to 0.1V and held. Consequently, solid phase potential gradients develop inside the system allowing for EC decomposition and Li_2EDC formation as well as DMC reduction at 0.3V. We see that Li_2EDC formation dominates LiMC formation in the SEI. This is also the subject of much debate in the literature, and LBNL is investigating with their atomistic simulations. The bottom figures show a comparison of the total and Li_2O volume fractions reported by Single *et al.* and our simulations. EC reduction at 0.8V and conversion of Li_2EDC to Li_2O at 0.3V are considered. After a long voltage hold, Li_2EDC converts to Li_2O close to the anode-SEI interface. We obtain a good match between the literature and our simulation, demonstrating the validity of our model implementation and its ability to model multiple reactions.

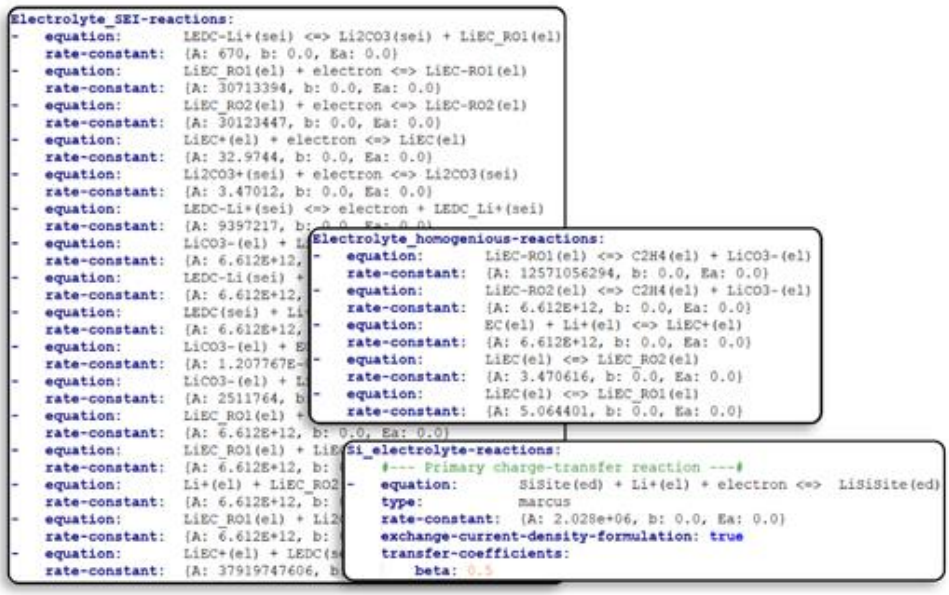

Figure II.1.F.8 Excerpts from CANTERA mechanism input file (YML format)

A primary objective is to extract quantitative thermodynamic and kinetic data developed using atomistic modeling (developed by LBNL) and upscale these insights into continuum-level models. Continuum-scale modeling is informed by atomistic-scale insights through a reaction mechanism. The reaction mechanism requires 1) phase equations of state, 2) species thermodynamics, and 3) reaction pathway kinetics. [8] Once developed, the reaction mechanism informs the continuum-level model of species production rates and electrochemical potentials (i.e. voltages). Hooking the reaction mechanism into continuum-level models requires compatible software. [4], [7]

The continuum-level, particle-scale model has three phases (silicon, solid-electrolyte-interface, and electrolyte). The silicon phase equation-of-state and species thermodynamics is modeled using tabulated non-ideal thermodynamics. [11] These non-ideal thermodynamics are calibrated to experimentally measured silicon open-circuit voltages. [12] The solid-electrolyte-interface phase and electrolyte phase are assumed to have ideal solid-solution thermodynamics whose species thermodynamics are informed by LBNL's *ab initio* calculations.

The reaction mechanism requires dominant reaction pathways for electrolyte decomposition and Li intercalation and forward/backward reaction rates for each reaction. For the present mechanism, the Eyring equation is used to predict the forward reaction rates. The Eyring equation can be expressed as

$$k_f = \frac{k_B T}{h} exp\left(\frac{-\Delta G^*}{R T}\right),$$

where k_f is the forward rate constant, k_B is the Boltzmann constant, h is Planck's constant, ΔG^* is the change in Gibbs free energy between the reactants and the transition-state species, R is the universal gas constant, and T is temperature. Figure II.1.F.8 illustrates reaction excerpts from the CANTERA mechanism. The mechanism considers homogeneous reactions in the electrolyte and SEI, and heterogeneous chemical and electrochemical reactions between phases.

The reaction mechanism and continuum-level model are under development. Presently, the model has been validated using a much simpler reaction mechanism (two irreversible reactions) available in the literature. The model is considerably expanded by implementing the new mechanism developed using the reaction pathway approach. For example, by just considering dominant Li_2CO_3 and LEDC decomposition pathways, the reaction

mechanism includes 25 electrochemical/chemical reactions and 22 total species. The SEI mechanism will be extended to consider fluorine reactions that are currently under development at LBNL. The continuum-scale model is written such that the mechanism predicted by the more fundamental reaction-pathway model can be any number of species and any number of reactions. Such capabilities will critically extend the state-of-the-art in solid-electrolyte-interface modeling.

Conclusions

LBNL

- Built a high-throughput framework for complex molecular simulations with on-the-fly error correction in order to reduce error rates from 25% to nearly 1%. Used the framework to simulate tens of thousands of molecules and fragments that may participate in the SEI formation reaction cascade.
- Developed a novel chemically consistent graph architecture for massive chemical reaction networks. Constructed and analyzed reaction networks with thousands of species and millions of reactions in order to identify optimal reaction paths to key SEI components including LEDC and LiF. Now working to tractably account for more complex reaction mechanisms which will be particularly important for LiF pathways.
- Developed the BonDNet graph neural network, the first machine learning model that can predict homolytic and heterolytic bond dissociation energies of neutral and charged molecules. Obtained a mean absolute error less than half of the standard chemical accuracy benchmark. Now using BonDNet to tractably identify the most important recombinant species to include in the network.

ORNL

- Assembled reactive molecular dynamics simulations of the Si anode and electrolyte, preliminarily including reactions that describe EC and PF_6 decomposition. Now working to add more reactive complexity in collaboration with LBNL.
- Validated force field parameters and identified an appropriate external driving force to avoid Li^+ depletion and increase reaction frequency such that the SEI formation cascade can be observed on timescales that are tractable to simulate.

NREL

- Developed a continuum scale SEI model framework based on experimentally observed phenomena from the SEISta program. Implemented a series of appropriate conservation equations.
- Validated the initial model using a reduced kinetic mechanism from the literature and demonstrated agreement with previous results. Now working to increase kinetic mechanistic complexity in collaboration with LBNL.
- In the coming year, the continuum SEI model will be further validated against current-decay data provided by the “Calendar Life Group”, scattering-length density/film thickness measurements from neutron reflectometry, and SEI elemental composition profiles from electron energy loss spectroscopy (EELS) and XPS.

Key Publications

LBNL

1. Blau, Samuel M., Evan Walter Clark Spotte-Smith, Brandon Wood, Shyam Dwaraknath, and Kristin A. Persson. “Accurate, Automated Density Functional Theory for Complex Molecules Using On-the-fly Error Correction.” *Under review*.

2. Blau, Samuel M., Hetal D. Patel, Evan Walter Clark Spotte-Smith, Xiaowei Xie, Shyam Dwaraknath, and Kristin A. Persson. “A chemically consistent graph architecture for massivereaction networks applied to solid-electrolyte interphase formation.” *Under review*.
3. Wen, Mingjian, Samuel M. Blau, Evan Walter Clark Spotte-Smith, Shyam Dwaraknath, and Kristin A. Persson. “BonDNet: a graph neural network for the prediction of bond dis-sociation energies for charged molecules.” *Under review*.

ORNL: None

NREL: None

References

1. St. John, Peter C., Yanfei Guan, Yeonjoon Kim, Seonah Kim, and Robert S. Paton. “Prediction of organic hemolytic bond dissociation enthalpies at near chemical accuracy with sub-second computational cost.” *Nat. Comm.* 11 (2020): 2328.

2. Jorgensen, William L and Julian Tirado-Rives. "The OPLS Force Field for Proteins. Energy Minimizations for Crystals of Cyclic Peptides and Crambin." *J. Am. Chem. Soc.* 110, no. 6 (1988): 1657–1666.

3. Gissinger, Jacob R., Benjamin D. Jensen, and Kristopher E. Wise. “Modeling chemical reactions in classical molecular dynamics simulations.” *Polymer* 128 (2017): 211-217.

4. Bizeray, Adrian M., David A. Howey, and Charles W. Monroe. “Resolving a Discrepancy in Diffusion Potentials, with a Case Study for Li-ion Batteries.” *J. Electrochem. Soc.* 163 no. 8 (2013): E223.

5. DeCaluew, Steven C., Peter J. Weddle, Huayang Zhu, Andrew M. Colclasure, Wolfgang G. Bessler, Gregory S. Jackson, and Robert J. Kee. “On the Fundamental and Practical Aspects of Modeling complex electrochemical kinetics and transport.” *J. Electrochem. Soc.* 165 no. 13 (2018): E637.

6. Colclasure, Andrew M., Kandler A. Smith, and Robert J. Kee. “Modeling detailed chemistry and transport for solid-electrolyte-interface (SEI) films in Li–ion batteries.” *Electrochim. Acta* 58 (2011): 33-43.

7. Goodwin, David G., Raymond L. Speth, Harry K. Moffat, and Bryan W. Weber. “Cantera: An object-oriented software toolkit for chemical kinetics, thermodynamics, and transport processes.” www.cantera.org. Caltech, Pasadena, CA (2009).

8. Single, Fabian, Birger Horstmann, and Arnulf Latz. “Revealing SEI Morphology: In-Depth Analysis of a Modeling Approach.” *J. Electrochem. Soc.* 164 no. 11 (2017): E3132.

9. Single, Fabian, Birger Horstmann, and Arnulf Latz. “Dynamics and morphology of solid electrolyte interphase (SEI).” *Phys. Chem. Chem. Phys.* 18 no. 27 (2016): 17810-17814.

10. Leung, Kevin, Susan B. Rempe, Michael E. Forster, Yuguang Ma, Julibeth M. Martinez del la Hoz, Na Sai, and Perla B. Balbuena. “Modeling Electrochemical Decomposition of Fluoroethylene Carbonate on Silicon Anode Surfaces in Lithium Ion Batteries.” *J. Electrochem. Soc.* 161 (2013): A213.

11. Mayur, Manik, Steven C. DeCaluwe, Benjamin L. Kee, and Wolfgang G. Bessler. “Modeling and simulation of the thermodynamics of lithium-ion battery intercalation materials in the open-source software Cantera.” *Electrochem. Acta* 323 (2019): 134797.

12. Mai, Weijie, Andrew Colclasure, and Kandler Smith. “A Reformulation of the Pseudo2D Battery Model Coupling Large Electrochemical-Mechanical Deformations at Particle and Electrode Levels” *J. Electrochem. Soc.* 166 no. 8 (2019): A1330.

Acknowledgements

The co-principal Investigators included Jean-Luc Fattebert (ORNL), and Andrew Colclasure (NREL). Other team members participating in this project included Samuel M. Blau, Mingjian Wen, Hetal D. Patel, Evan Walter Clark Spotte Smith, and Xiaowei Xie (LBNL); Lorena Alzate Vargas (ORNL); and Ankit Verma, Peter Weddle, Kandler Smith, Steven DeCaluwe, and Jake Atkins (NREL).

II.1.G Highly-Ordered Hierarchical Anodes for Extreme Fast Charging Batteries (University of Michigan, Ann Arbor)

Neil Dasgupta, Principal Investigator
University of Michigan, Ann Arbor
2350 Hayward Street
Ann Arbor, MI, 48109-2125
E-mail: ndasgupt@umich.edu

Jeff Sakamoto, Principal Investigator
University of Michigan, Ann Arbor
2350 Hayward Street
Ann Arbor, MI, 48109-2125
E-mail: jeffsaka@umich.edu

Katsuyo Thronton, Principal Investigator
University of Michigan, Ann Arbor
2300 Hayward Street
Ann Arbor, MI, 48109-2136
E-mail: kthorn@umich.edu

Jyoti Mazumder, Principal Investigator
University of Michigan, Ann Arbor
2350 Hayward Street
Ann Arbor, MI, 48109-2125
E-mail: mazumder@umich.edu

Mohan Karulkar, Principal Investigator
Sandia National Laboratories
1515 Eubank Dr. SE, M/S 0613
Albuquerque, NM 87185
E-mail: mpkarul@sandia.gov

Brian Cunningham, DOE Technology Development Manager
U.S. Department of Energy
E-mail: Brian.Cunningham@ee.doe.gov

Start Date: July 1, 2018 End Date: June 20, 2021
Project Funding: $1,667,000 DOE share: $1,500,000 Non-DOE share: $167,000

Project Introduction

While today's electric vehicle (EV) batteries can be charged at increasingly fast rates, enabling extreme fast charging (XFC) in < 10 min will require battery cells compatible with 400 kW charging stations.[9] This becomes particularly challenging in high energy density cells, which typically require thick electrodes. As charging rates increase in thick electrodes, several fundamental challenges arise, including 1) electrolyte concentration gradients 2) kinetic overpotentials 3) metallic Li plating 4) excess heat generation and 5)

[9] Shabbir Ahmed et al., "Enabling Fast Charging – A Battery Technology Gap Assessment," *Journal of Power Sources* 367 (November 2017): 250–62, https://doi.org/10.1016/j.jpowsour.2017.06.055.

accelerated electrolyte decomposition and capacity fade. It is therefore critical to re-think the design rules for XFC anode performance.

There have been significant efforts in both modeling and experimental investigation of the tradeoffs in electrode and electrolyte properties to design high-energy-density and high-power anodes. Recently Gallagher *et al.* quantified the physical limits of energy to power density ratio in thick graphite anodes, and demonstrated that Li plating is driven by a combination of electrolyte transport and interfacial kinetics.[10] It was concluded that an upper limit of 4 mA/cm^2 current density could be maintained before Li plating occurs, which would restrict areal capacity to 0.66 mAh/cm^2 at 6C. Therefore, to simultaneously achieve XFC charging and maintain energy density requires new approaches to address mass transport and interfacial kinetic effects.

Objectives

The main objective of this project is to enable XFC of Li-ion batteries through a combination of 1) rational design and manufacturing of hierarchically structured anode architectures; 2) computational modeling of coupled transport, kinetic, and electrochemical phenomena; and 3) improved fundamental understanding of lithium plating through electrochemical analysis. This project integrates 3-D modification of graphite anodes, multi-physics modeling of ion transport, surface modifications, advanced strategies to detect Li plating, and semi-automated roll-to-roll cell assembly. The unique facilities at the University of Michigan and Sandia National Lab are leveraged to manufacture, prototype, and characterize commercially relevant > 2Ah and > 180 Wh/kg cells with a target of charging at 6C rates with < 20% capacity fade over 500 cycles.

Approach

- Design, prototyping, and manufacturing of highly ordered laser-patterned electrodes (HOLE).
- Systematically vary HOLE geometric parameters and characterize electrochemical performance.
- Demonstrate scale-up of HOLE anodes to > 2 Ah pouch cells.
- Perform electrochemical dynamics simulations of HOLE anodes during fast charging.
- Perform high precision Coulometry and dQ/dV analysis on pouch cells during fast charging.

Results

To establish a baseline graphite anode for high-energy-density Li-ion batteries, graphite anodes were prepared using a pilot-scale roll-to-roll processing facility at the University of Michigan Battery Lab. A total areal mass loading of 9.48 mg/cm^2 (3.2 mAh/cm^2 capacity loading) was used as the baseline loading to study Li plating under fast-charge conditions. The electrode porosity was controlled to be 32%. HOLE architectures with aligned pore channels were fabricated by performing laser patterning on calendered graphite anodes.[11] A high-precision laser patterning platform was constructed to perform HOLE modifications on anodes for pouch cells. This is achieved by combining a pulsed laser source and a scanning optics system.

To examine the morphology of graphite anodes before/after laser patterning, scanning electron microscopy (SEM) was performed. Figure II.1.G.1e-g show the baseline (unpatterned) graphite anode. The graphite particles have an ellipsoidal shape with an average particle size of 8 μm. The cross-sectional image further shows the densely packed graphite particles throughout the thick anode.

---

[10] Kevin G. Gallagher et al., "Optimizing Areal Capacities through Understanding the Limitations of Lithium-Ion Electrodes," *Journal of The Electrochemical Society* 163, no. 2 (2016): A138–49, https://doi.org/10.1149/2.0321602jes.

[11] Kuan-Hung Chen et al., "Efficient Fast-Charging of Lithium-Ion Batteries Enabled by Laser-Patterned Three-Dimensional Graphite Anode Architectures," *Journal of Power Sources* 471, no. June (September 2020): 228475, https://doi.org/10.1016/j.jpowsour.2020.228475.

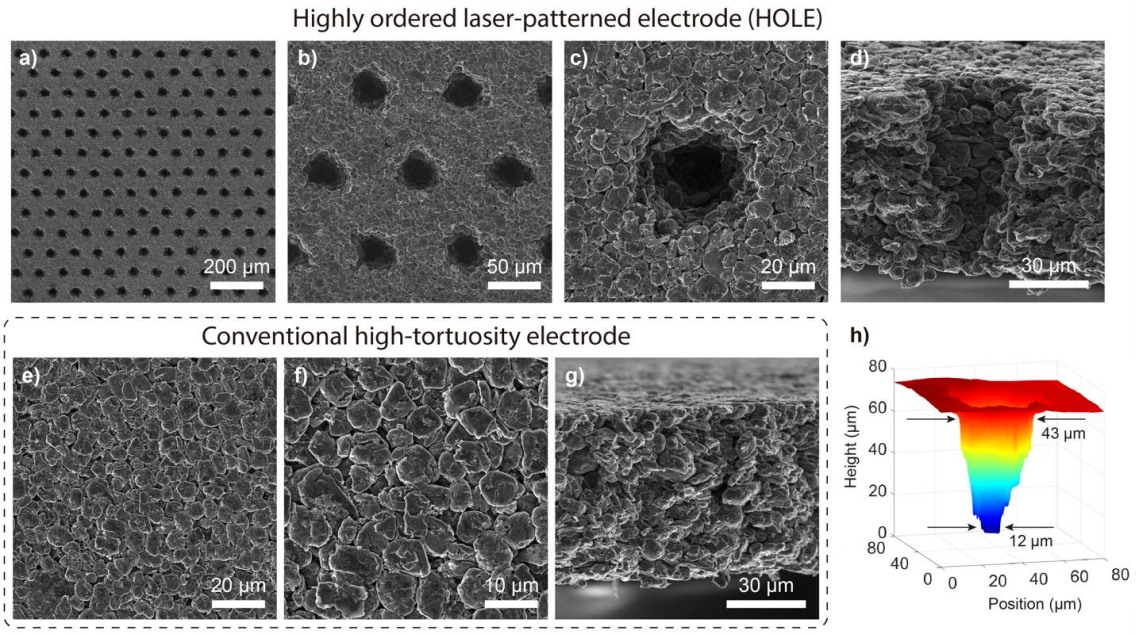

Figure II.1.G.1 Top-down and cross-sectional SEM images of the (a-d) HOLE graphite anodes and (e-g) baseline graphite anodes. (h) 3-D surface reconstructions from high-resolution optical microscope images showing the shape of tapered pore channels.

Figure II.1.G.1a-b show the HOLE anode after laser-patterning from the same control anode. As shown in the figures, uniform and close-packed hexagonal arrays of pore channels were formed. The electrode surface remained clean with no debris or residual particles after patterning. Higher magnification imaging (Figure II.1.G.1c-d) demonstrates that laser ablation results in the sublimation of entire graphite particles rather than cutting through particles. In addition, it is also shown that the pore channels are slightly tapered toward the bottom of the electrode, which results from the laser-graphite interactions. The average diameter of the channels was measured to be 42.7 µm at the top and 12.4 µm at the bottom of the electrodes. To further verify this frustum shape of the pore channels, 3-D surface reconstructions were performed using a focal series of high-resolution optical microscopy images (Figure II.1.G.1h).

To evaluate the fast-charge performance of the baseline unpatterned graphite anodes (control) and HOLE anodes, multi-layer pouch cells were assembled. Control and HOLE graphite anodes were assembled with NMC-532 cathodes with N/P ratios fixed between 1.1-1.2. The pouch cells have a capacity of 2.2 Ah and were cycled between a 3-4.15 V voltage window. A CC-CV charge protocol with a charge time cutoff was used. For 6C fast charging, pouch cells were first charged at a constant current (CC) 6 C-rate until reaching the upper voltage cutoff (4.15 V), then charged at constant voltage (CV) until a total charge time (CC+CV) of 10 minutes is reached. For the 4C charging protocol, the applied current was 4C and the total charge-time cutoff was 15 minutes. The discharge process also followed a CC-CV protocol, where cells were first discharged CC at 0.5C rate, followed by CV hold at 3.0 V until the current reached a value < 0.1C to fully discharge the cells.

Figure II.1.G.2 shows the discharge capacity of the control and HOLE cells that were charged at 4C. The cells were first charged/discharged at a 0.5C rate for 3 cycles to measure the total cell capacity (2.2 Ah), followed by 100 cycles of 4C charge/0.5C discharge. In addition, 3 cycles of 0.5C charge/discharge were repeated after every 50 fast-charge cycles to quantify the capacity fade of the cells. The y-axis shows the cell capacity normalized to the initial cell capacity to facilitate a direct comparison.

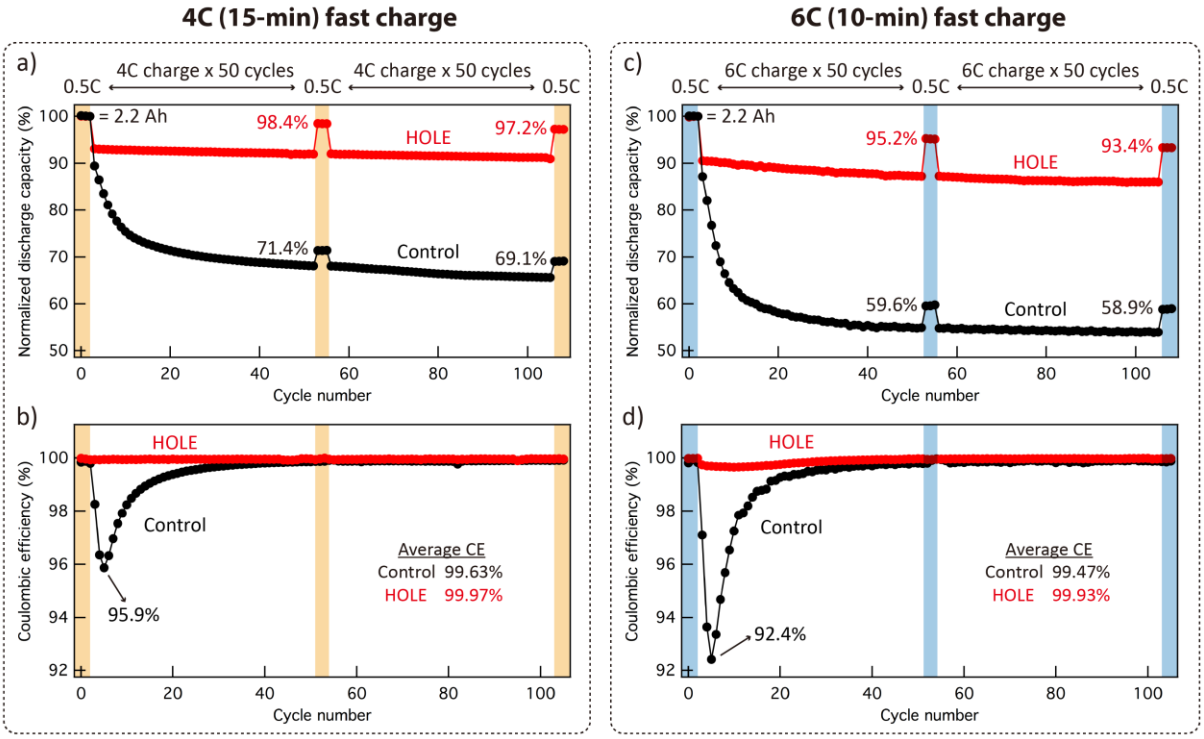

Figure II.1.G.2 Normalized discharge capacity and (b) Coulombic efficiency vs. cycle number under 4C fast-charge conditions. (c) Normalized discharge capacity and (d) Coulombic efficiency vs. cycle number under 6C fast-chareg conditions.

As shown in Figure II.1.G.2a, both the control and HOLE cells exhibit stable cycling at a 0.5C charge rate. However, upon fast charging at 4C, the control cell exhibits significant capacity fading within the first 40 cycles, which can be attributed to irreversible Li plating. From cycle 40 to 100, the capacity reaches a plateau. By comparing the charge/discharge capacities at 0.5C, it is shown that the capacity retention is 69.1% after 100 fast-charge cycles (capacity fade of 30.9%). Figure II.1.G.2b shows the Coulombic efficiency (CE) plotted vs. cycle number, providing further evidence that Li plating occurs during 4C charging of the control anode. The efficiency quickly drops to 95.9% within the first 3 cycles of 4C charging, and then slowly recovers back to > 99.5% after cycle 40. This initial decrease in CE can be attributed to Li plating during fast charging, which causes severe Li inventory loss over time.

In contrast to the control, the HOLE cell shows a significantly improved capacity retention and CE during 4C charging. As shown in Figure II.1.G.2a, stable 4C charging was achieved, allowing for 92% of the total cell capacity to be charged within 15 minutes (from 0% to 92% state-of-charge (SOC)). This large accessible capacity is maintained throughout the cycling, demonstrating that the HOLE anode design can effectively improve the fast-charge performance. The capacity retention of the HOLE cell is 97.2% after 100 cycles of 4C charging (capacity fade of 2.8%). In addition, Figure II.1.G.2b shows a stark difference in efficiency when compared to the control cell, as the HOLE cell maintains an average CE of 99.97% throughout the course of the fast-charge test. Overall, we observe > 97% capacity retention after 100 cycles at a 4C charge rate with the HOLE design, compared to 69% capacity retention of unpatterned control electrodes that were fabricated from the same batch of calendered electrodes with identical processing conditions.

To further show the effectiveness of the HOLE design, another batch of control and HOLE cells were cycled at a 6C charge rate (10-min charge time cutoff). Figure II.1.G.2c shows the cell capacity plot, where the control cell displays a more dramatic drop in capacity from 6C charging than was observed for 4C charging. The capacity retention was 58.9% after 100 cycles of 6C charging (41.1% capacity fade). The CE plot also shows a similar dip during the initial fast-charge cycles, followed by a gradual recovery to > 99.5% after 40 cycles (Figure II.1.G.2d).

Compared to the control, the HOLE cell shows a significantly improved rate performance (Figure II.1.G.2c-d). Although mild capacity fade was observed during the initial fast-charge cycles, the HOLE cell was still able to access 90% of the total cell capacity within the 6C 10-min charge (from 0% to 90% SOC). In addition, the HOLE cell shows a capacity retention of 93.4% after 100 fast-charge cycles (capacity fade of 6.6%). The average CE is 99.93% throughout the course of the test. Overall, we demonstrate the HOLE design can achieve > 93% capacity retention over 100 fast-charge cycles at 6C, compared to 59% capacity retention for unpatterned electrodes.

To confirm that the capacity fade during fast charging is due to Li plating, post-mortem SEM analysis was performed on the cycled graphite anodes of both the control and HOLE cells after 100 cycles of 6C charging. Pouch cells were fully discharged to 3.0 V before disassembly. Figure II.1.G.3a and Figure II.1.G.3f show photographs of the cycled control and HOLE anodes. As expected, a considerable amount of Li plating is observed on the control graphite anodes, where Li dendrites cover the entire anode surface.

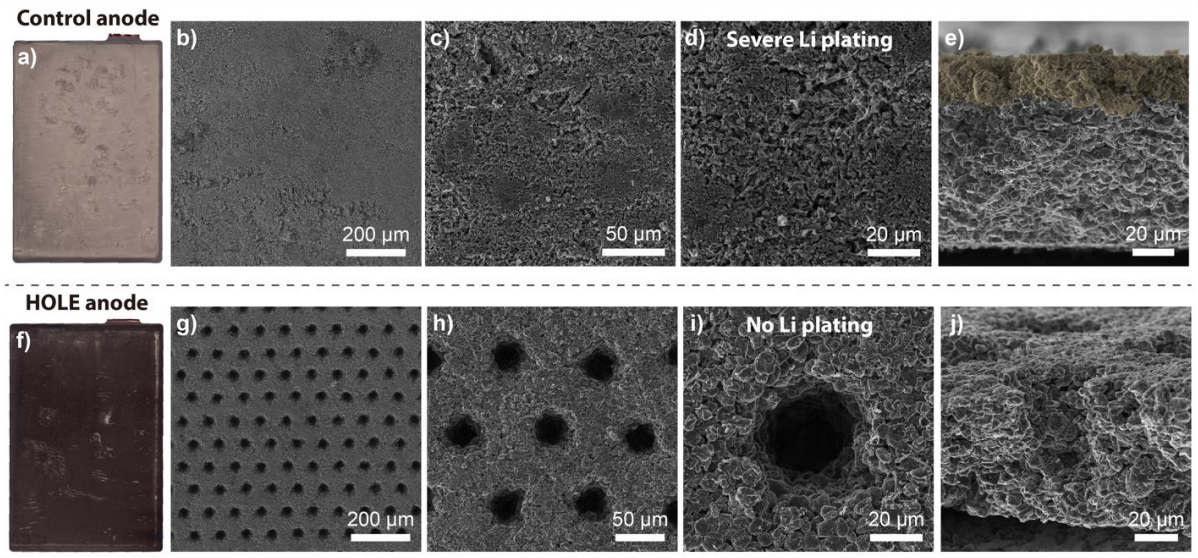

Figure II.1.G.3 Photographs of (a) control and (f) HOLE graphite electrodes from pouch cell teardown after 100 cycles of 6C charging. Li plating can be observed on the surface of the graphite. SEM images further show the (b-e) severe Li plating on control anodes and (g-j) absence of Li plating on HOLE anodes.

SEM analysis (Figure II.1.G.3b-d) further shows the extent of Li plating on the control graphite anode, where the entire surface is covered with Li deposits and no underlying graphite particles can be observed from the top-down perspective. Cross-sectional SEM imaging (Figure II.1.G.3e) shows a compact interphase of Li deposits on top of the graphite anode. In contrast, the HOLE graphite anode cycled at 6C maintains a clean surface with minimal traces of Li plating. SEM images (Figure II.1.G.3g-i) show that the HOLE architecture remains intact after fast-charge cycling, and the pore channels can be clearly observed in the images. Cross-section SEM analysis (Figure II.1.G.3Figure II.1.G.3j) further confirms the absence of Li plating on the anode surface as well as along the inner surface of the pore channels.

A 3-D continuum-scale model based on porous electrode theory was further developed to simulate the electrochemical dynamics during charging. The model describes mass and charge transport in the solid graphite particle and liquid electrolyte phases, coupled with the electrochemical reaction that occurs at the solid/liquid interface. The model was first parameterized by matching the simulated anode voltage vs. capacity profiles of the control anodes at different C-rates from 0.1C-6C using experimental results from three-electrode measurements. The same parameter set was then applied to simulate the three-electrode cell with the HOLE graphite anode, and the results matched well with the corresponding measurements. The parameterized model was then used to simulate the electrochemical performance of pouch cells during 4C fast charging.

Figure II.1.G.4c compares the simulated voltage (vs. a Li reference) vs. time curves for the control and HOLE anodes during 4C charging. The simulation for each cell was terminated when the anode voltage reached 0 V (vs. Li/Li^+). As expected, the HOLE anode was able to maintain a voltage above 0 V for a longer period of charging time than the control anode. In other words, the polarization at the HOLE anode is lower than that in the control anode. This decrease in the polarization is facilitated by improved access of Li ions to graphite particles in the bulk of the HOLE anode through the HOLE design.

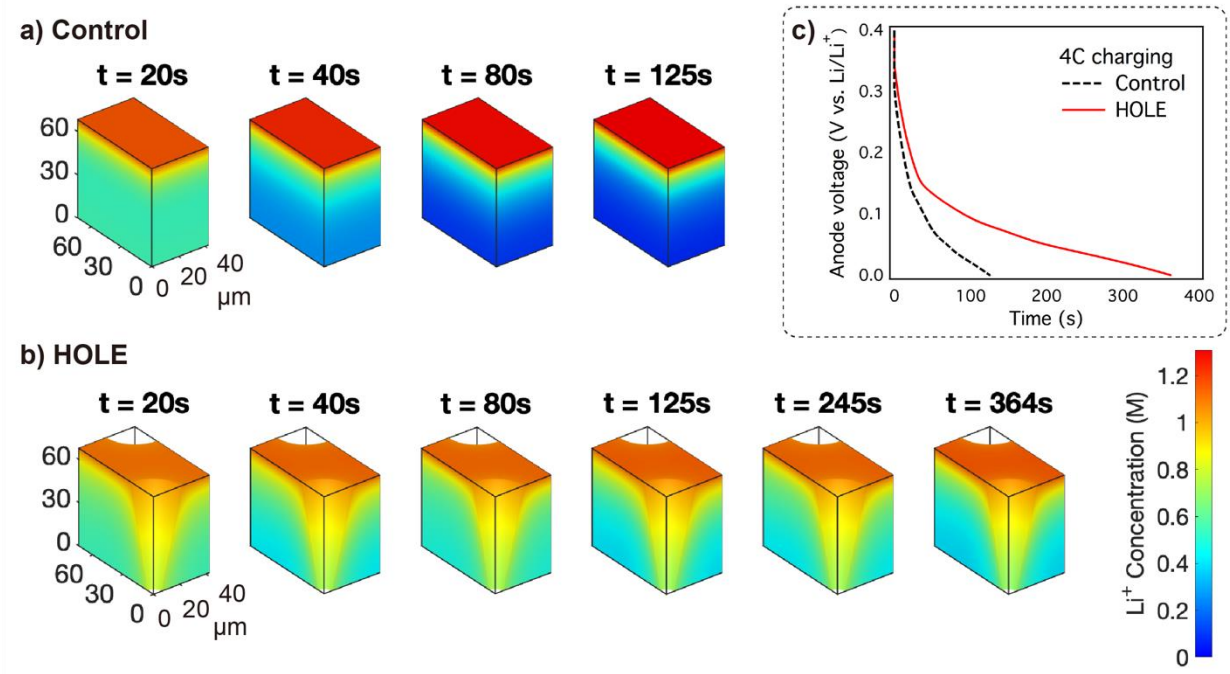

Figure II.1.G.4 Evolution of Li-ion concentration in the electrolyte phase of the (a) control graphite anode at t = 20, 40, 80, and 125 s, (b) HOLE graphite anode at time t = 20, 40, 80, 125, 245, and 364 s during 4C charging. The color indicates the Li-ion concentration according to the color bar on the right. (c) Simulated voltage response of the anode in the control cell (dashed, black line), and in the HOLE cell (solid, red line).

Figure II.1.G.4a and Figure II.1.G.4b further compare the Li-ion concentration evolution in the electrolyte phase of the control and HOLE anodes. As shown in the figures, the Li-ion concentration far from the separator/anode interface in the HOLE anode is higher than that in the control anode at all times. As a consequence of the improved Li-ion transport, a reduction in the local Li-ion concentration near the separator/anode interface can be seen in the HOLE anode compared to the control anode. The more homogenous concentration of Li ions in the HOLE anode enables a more uniform distribution of the local electrochemical reaction rate in the bulk of the HOLE anode as compared to the control anode. A more homogeneous reaction rate throughout the electrode bulk in the HOLE anode results in reduced local current density, and consequently lowers the driving force for Li plating at the separator/anode interface as compared to the control anode during fast charging.

To further identify evidence of Li plating, differential capacity (dQ/dV) analysis was performed. Figure II.1.G.5 shows the dQ/dV vs. cell voltage plots on 0.5C discharge (after 0.5C charge). Under this current density, Li plating should not occur during charging. As a result, the discharge dQ/dV plot shows similar behavior between the Control and HOLE cells.

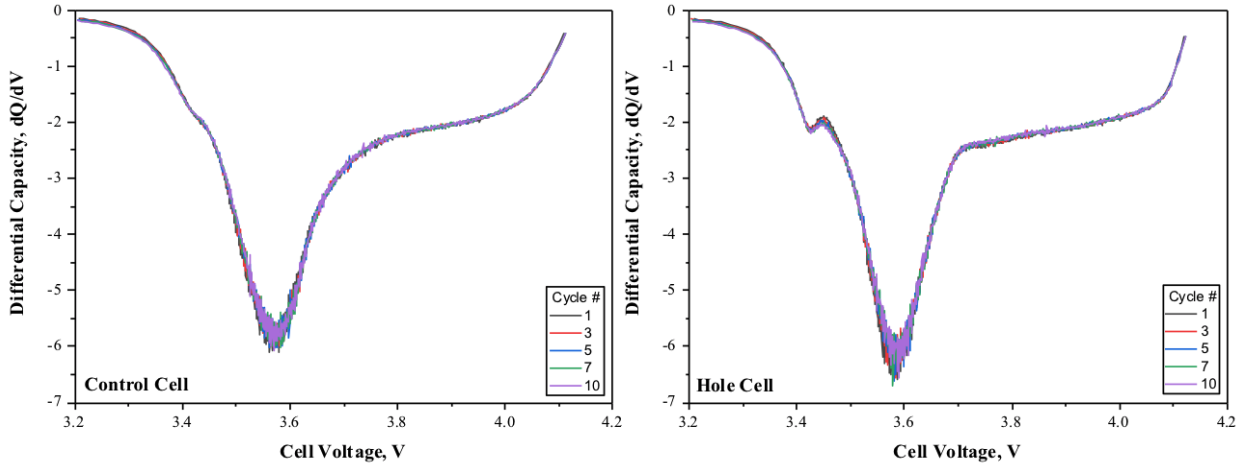

Figure II.1.G.5 Differential capacity during 0.5C discharging cycles (after 0.5C charging) for the 2.2 Ah Control and HOLE cells.

Figure II.1.G.6 further shows the dQ/dV analysis on 1C discharge after 6C charge. During fast charging, the Control cell is expected to have severe Li plating. From the discharge dQ/dV analysis, an additional peak can be clearly identified at ~4V that is distinct from the regular delithiation peaks. We attribute this dQ/dV signature to Li re-intercalation process during early discharge. On the other hand, the HOLE cell does not display this dQ/dV signature, and only the expected delithiation peaks can be observed. It is thus concluded that the HOLE architectures have a significant effect on the capacity retention, cell polarization and Li plating behavior during fast charging.

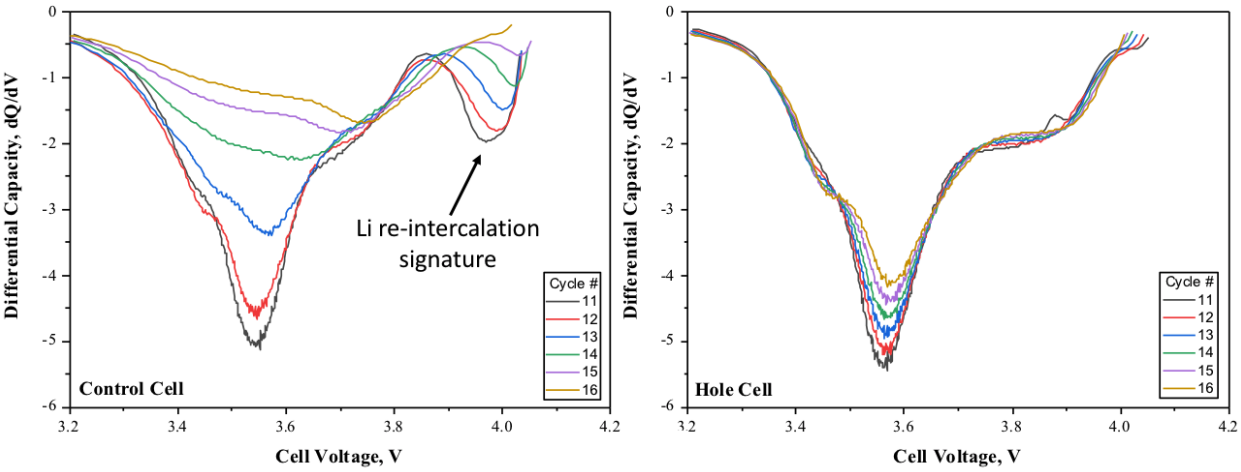

Figure II.1.G.6 Differential capacity during 1C discharging cycles (after 6C charging) for the 2.2 Ah Control and HOLE cells.

Conclusions

In this DOE XFC project, the University of Michigan team has collaborated with Sandia National Laboratory to demonstrate efficient fast-charging of Li-ion batteries (> 4C charge rate) by fabricating highly ordered laser-patterned electrode architectures. High-loading graphite anodes (> 3 mAh/cm^2) and an industrially relevant cell format (> 2 Ah pouch cells) were used to show the feasibility of using laser-patterned graphite anodes for high-energy-density Li-ion cells. The through-thickness, laser-ablated pore channels facilitate Li-ion transport into

the bulk electrode, thus reducing concentration gradients during fast charging. Consequently, a higher accessible capacity and low propensity to Li plating was achieved.

A continuum-scale model was developed and implemented to simulate electrochemical dynamics during fast charging and provide further insights into the mechanism of the improved mass transport. Using the laser-patterned electrode architecture, we observed > 97% and > 93% capacity retention over 100 cycles of 4C and 6C fast-charge cycling respectively, compared to 69% and 59% for unpatterned electrodes. After 600 cycles of fast-charging, the capacity retention of the HOLE cells remained as high as 91% at 4C and 86% at 6C charge rates. Moreover, the HOLE design allows for cells to access > 90% of the total cell capacity during fast charging.

We also employed high-precision Coulometry at the Sandia National Laboratory to identify Li plating signatures in differential capacity analysis. The dQ/dV analysis shows that due to severe Li plating in the control cell during fast charging, a Li re-intercalation peak can be identified during the subsequent early discharging. In contrast, the HOLE cell did not display this re-intercalation peak in the dQ/dV plot. The presented fast-charge performances in this project address both the U.S. Department of Energy and U.S. Advanced Battery Consortium goals for fast-charging batteries.

Key Publications

1. K.-H. Chen, M. J. Namkoong, V. Goel, C. Yang, S. Kazemiabnavi, S. M. Mortuza, E. Kazyak, J. Mazumder, K. Thornton, J. Sakamoto, and N. P. Dasgupta, "Efficient Fast-charging of Li-ion Batteries Enabled by Laser-patterned Three-dimensional Graphite Anode Architectures" *Journal of Power Sources* 471 (2020) 228475.

2. K.-H. Chen, V. Goel, M.J. Namkoong, M. Wied, S. Muller, V. Wood, J. Sakamoto, K. Thornton, N.P. Dasgupta, "Enabling 6C Fast Charging of Li-ion Batteries with Graphite/Hard Carbon Hybrid Anodes" (under review)

References

1. Ahmed, Shabbir, Ira Bloom, Andrew N. Jansen, Tanvir Tanim, Eric J. Dufek, Ahmad Pesaran, Andrew Burnham, et al. "Enabling Fast Charging – A Battery Technology Gap Assessment." *Journal of Power Sources* 367 (November 2017): 250–62. https://doi.org/10.1016/j.jpowsour.2017.06.055.

2. Chen, Kuan-hung, Min Ji Namkoong, Vishwas Goel, Chenglin Yang, Saeed Kazemiabnavi, S.M. Mortuza, Eric Kazyak, et al. "Efficient Fast-Charging of Lithium-Ion Batteries Enabled by Laser-Patterned Three-Dimensional Graphite Anode Architectures." *Journal of Power Sources* 471, no. June (September 2020): 228475. https://doi.org/10.1016/j.jpowsour.2020.228475.

3. Gallagher, Kevin G., Stephen E. Trask, Christoph Bauer, Thomas Woehrle, Simon F. Lux, Matthias Tschech, Peter Lamp, et al. "Optimizing Areal Capacities through Understanding the Limitations of Lithium-Ion Electrodes." *Journal of The Electrochemical Society* 163, no. 2 (2016): A138–49. https://doi.org/10.1149/2.0321602jes.

II.2 Next-Gen Li-ion: Advanced Cathode R&D

II.2.A Design, Synthesis, & Characterization of Low-Cobalt Cathodes (ANL, ORNL, LBNL, NREL, PNNL)

Jason R. Croy, Principal Investigator
Argonne National Laboratory
9700 S. Cass Avenue
Lemont, IL 46039
E-mail: croy@anl.gov

Peter Faguy, DOE Technology Development Manager
U.S. Department of Energy
E-mail: Peter.Faguy@ee.doe.gov

Start Date: October 1, 2018 End Date: September 30, 2021
Project Funding: $4,000,000 DOE share: $4,000,000 Non-DOE share: $0

Project Introduction

State-of-the-art Li-ion batteries (LIBs) for transportation applications contain transition metal (TM) oxide cathodes consisting of $Li_{1+x}Ni_aCo_bAl_cO_2$ (NCA) or $Li_{1+x}Ni_aMn_bCo_cO_2$ (NMC-abc) oxides, where x = ~0-0.05 and a+b+c = 1. Both oxide chemistries contain Co, which has been recognized over many years of research as an important component in terms of structure, stability, and electrochemical performance. Currently, however, geopolitical concerns associated with Co mining, availability, and cost have caused the LIB community to pursue the development of low- to no-cobalt layered oxides as next-generation cathodes. The goal of this work is to show progress towards the realization of low/no-cobalt oxides having acceptable performance (energy/power densities), safety, and cycle/calendar life by way of new insights into cathode design and synthesis as they pertain to the critical roles of Co in layered oxides.

Objectives

- Understanding of local ordering as a function of Co and dopant/substitution content.
- Synthesis of new, low- to no-cobalt cathodes showing promise with respect to an NMC-622 baseline.
- Synthesis and understanding of $LiNiO_2$-based oxides with low- to no-cobalt compositions.
- Atomic-scale characterization, understanding, design, and synthesis of NiMn-based cathodes.

Approach

- Advanced characterization of Ni-rich, low- and no-cobalt cathodes including synchrotron techniques, solid-state NMR, electron microscopy, and theory/modeling.
- Advanced characterization of MnNi-based, low- and no-cobalt cathodes including synchrotron techniques, solid-state NMR, electron microscopy, and theory/modeling.
- Development of novel surface modifications for low/no-cobalt oxides
- Large batch co-precipitation synthesis of model and new compositions for practical evaluation.
- Synthesis of standardized materials for distribution and study across multiple teams.

Results

Synthesis of low cobalt oxides – The materials approach taken in this program is based in two categories of oxides. Namely, oxides based in $LiNiO_2$ (LNO) and lower nickel-content MnNi compositions based in $LiMn_{0.5}Ni_{0.5}O_2$. Each of these categories has advantages and shortcoming but each offer the possibility of enabling high-energy, low- to no-cobalt cathodes. The first part of the program placed particular emphasis on LNO-based oxides, working across the five laboratories, to investigate select low/no cobalt compositions.

Figure II.2.A.1 shows a compositional diagram (left) highlighting the compositions of interest encompassing 90% or greater Ni content while varying the balance of Co and Mn. Taylor vortex reactors (TVR, middle), housed in the Materials Engineering Research Facility (MERF) at ANL, were used to study optimization of precursor compositions and morphologies (right). Subsequent calcination/lithiation studies were conducted and cathodes were vetted under standardized protocols developed within the program for use with lithium metal anodes (see chapter II.2.B). Final materials were fabricated into cathode-electrodes by ANL's Cell Analysis, Modeling, and Prototyping (CAMP) facility, matched to graphite anodes for full-cell testing and diagnostics. The cathode team produced 12 LNO-based compositions for distribution and study across the program which serve as the basis for all studies as presented herein and in chapters II.2.B and II.2.C.

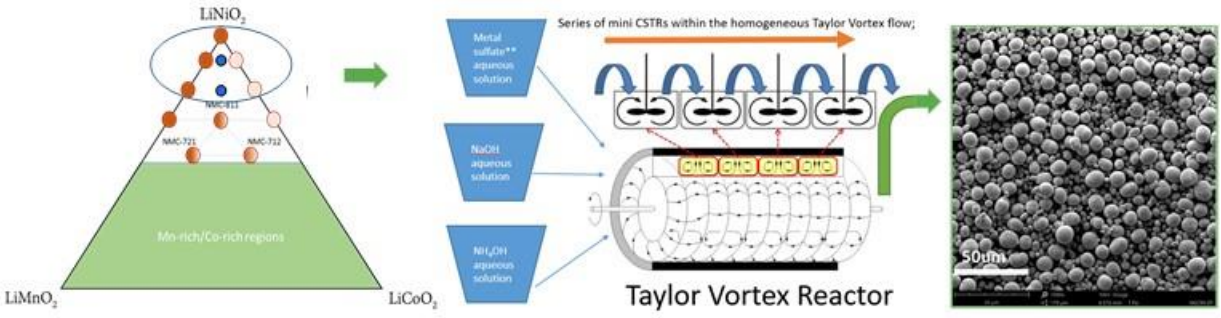

Figure II.2.A.1 Compositional phase diagram (left) of the high nickel compositions of interest. Diagram of a Taylor vortex reactor used in the synthesis of materials. SEM images of pure Ni-hydroxide precursor particles.

High nickel-content compositions are known to be extremely sensitive to synthesis and processing conditions and the availability of high-quality powders and electrodes, from the same source, to such a large project is critical. Figure II.2.A.2 shows data from initial studies on pure $LiNiO_2$ as a physiochemical baseline cathode. As shown in (a), the Li/Ni ant-site exchange is optimized in a window of just ~15°C calcination temperature and a drastic improvement in performance is observed on going from 650 to 665°C as shown in (b). Figure (c) reveals that the subtle differences in exchange and voltage profiles between the 665 and 680°C samples lead to different cycling stabilities, with the 665°C sample performing very well (green diamonds/blue circles). The cycling conditions of figure (c) were chosen to mimic data from the best performing LNO reported to data in the literature [1] (purple hexagons) and it can be seen that the LNO produced herein noticeably outperforms that sample. In fact, the LNO reported here appears to outperform, at least under these tests, many of the doped and modified versions reported as promising in the literature. This data reveals the critical importance that synthesis, processing, and standardization plays in truly understanding modifications to such nickel-rich oxides and highlights the necessity of the detailed efforts undertaken in this program in such regards.

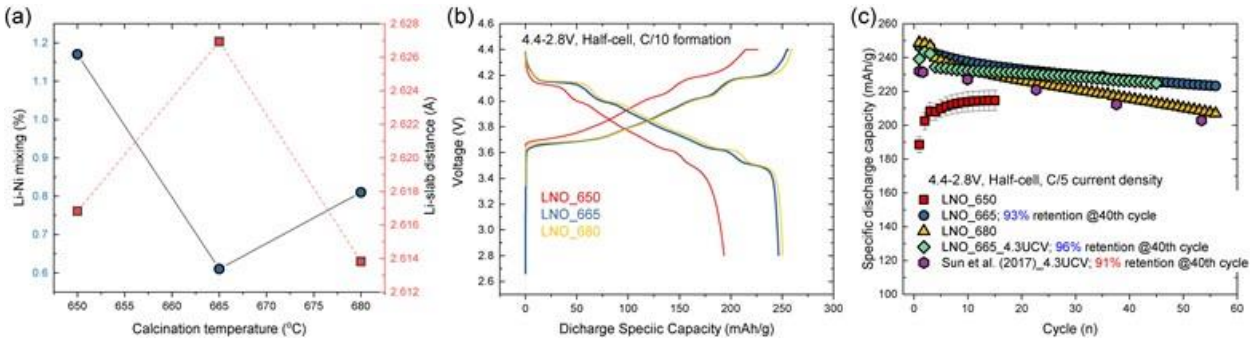

Figure II.2.A.2 (a) Li/Ni exchange as a function calcination temperature for pure $LiNiO_2$. (b) Initial charge/discharge profiles of the first cycle for $LiNiO_2$ after calcination/lithiation at 650, 665, and 680°C. (c) Discharge capacity vs. cycle number for $LiNiO_2$ at various temperatures compared to cycling performance of the best performing LNO reported to date in the literature (purple hexagons).

Figure II.2.A.3 shows results of similar studies on 6 compositions within the phase space highlighted in Figure II.2.A.1. Rietveld refinements of synchrotron X-ray diffraction data from samples synthesized under optimized conditions, (a), reveal that all substitutions resulted in an apparent increase of Li/Ni exchange with cobalt containing samples (red circles) remaining very similar to the pure LNO. However, a systematic increase of exchange was observed with increasing Mn contents (blue squares). This might be attributed to the induced formation of Ni^{2+} from the incorporation of Mn^{4+} and/or the higher calcination temperatures that were found necessary to optimize the performance of the Mn containing oxides, more than 100°C higher than pure LNO for the 10% Mn (90-10-0). All optimized samples show 3% or less exchange, however, the combination of 90% Ni, 5% Mn, and 5% Co (90-5-5) was found to perform the best electrochemically (see chapter II.2.B).

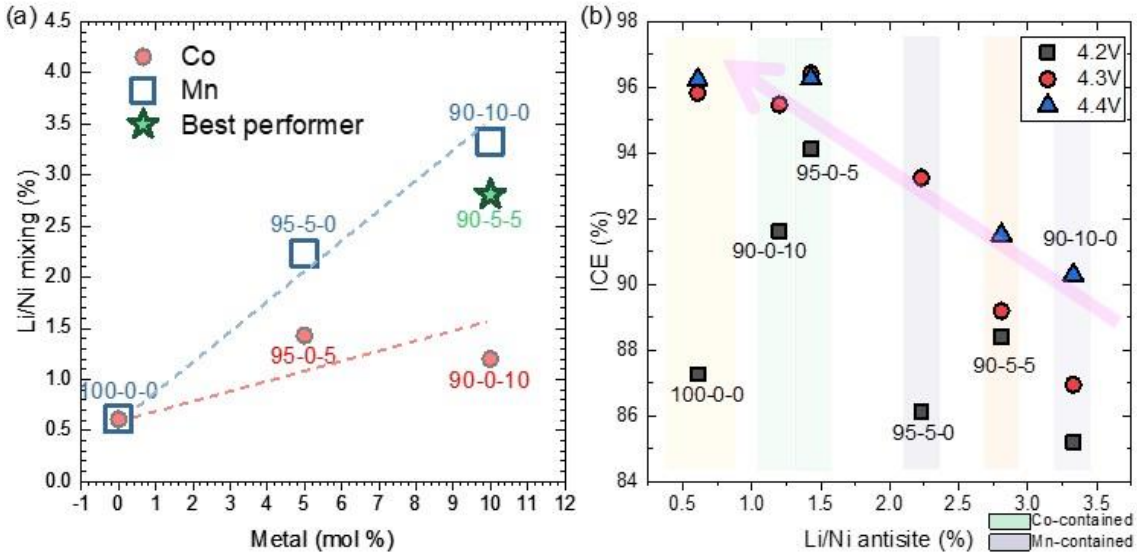

Figure II.2.A.3 (a) Li/Ni exchange as a function of Mn and Co content in cathodes with 90% or more Ni. (b) First-cycle irreversible capacity loss for the samples in (a) as a function of Li/Ni exchange at various upper cutoff voltages.

Another interesting phenomenon observed for LNO and its substituted derivatives is the first-cycle behavior. Specifically, first-cycle efficiencies (FCE) were observed to increase with increasing upper cutoff voltages, (c). This is contrary to typical FCEs of lower Ni-content NMCs where a fairly constant loss is observed regardless of upper cutoff. In figure (c) it is observed that the pure LNO increases in FCE from 87% to 96% when going from 4.2V on first charge to 4.3V on first charge. Similar effects are observed to varying degrees for all other samples. 4.1-4.3V are the SOCs where gas evolution is typically observed. Studies are ongoing to evaluate the

effect of composition on these phenomena and how they may be related to Li stoichiometry, surface impurities, processing and overall cathode performance.

Methods of elemental substitutions – It is clear that pure LNO possesses attractive qualities as a high-energy cathode, but also clear that modifications must be made to enable adequate practical performance. One of the most well-known strategies is to use substitutions such as Al^{3+} to help stabilize the lattice through, for example, strong Al-O bonding. While this strategy has shown promise, more improvements are needed. Because Al is one of the most attractive candidates it was chosen in this project as a baseline for studying synthesis methods of Al incorporation. Control over content and distribution of secondary elements is critical to controlling and tailoring oxide properties. Common wet-chemical methods, while having shown some promise, do not allow full control over site distribution, and secondary phases are often formed.

Figure II.2.A.4 shows ^{27}Al magic angle spinning nuclear magnetic resonance (MAS-NMR) spectroscopy results taken on two cathode oxides having the same composition of $LiNi_{0.92}Co_{0.06}Al_{0.02}O_2$. The oxides were prepared from the same $Ni_{0.94}Co_{0.06}$-hydroxide precursors synthesized using a 4L CSTR. However, one oxide was 'doped'' with Al after extensive studies aimed at optimizing wet-chemical processing and subsequent electrochemical performance. These studies included processing the NiCo-hydroxide before and after calcination/lithiation, as well as various solvents and Al precursors. The other oxide was doped by optimization of Al deposition on the metal-hydroxide precursor via atomic layer deposition (ALD) followed by calcination/lithiation. The major difference between the NMR data of figure (a) is that the oxide doped with the optimized wet-chemical process shows that ~20% of the Al has been incorporated as surface Al in phases such as Al_2O_3 and $LiAlO_2$ while the ALD-doped sample shows that all Al has been incorporated into fully coordinated, bulk-like sites. As shown in the figure, the ALD-treated oxide shows Al coordinated entirely to nickel (Al- 6Ni) with an Al peak at ~ - 1250 ppm. The oxide prepared by the wet method, shows both surface and bulk Al with peaks around 0-70 ppm and -250 to -1250 ppm, respectively, as well as a distribution of environments (Al-1Ni, Al-2Ni, Al-3Ni and Al-6Ni). Furthermore, high-resolution scanning transmission electron microscopy – energy dispersive spectroscopy – (HR-STEM-EDS) images reveal a uniform distribution of Al within the oxide particles (see also chapter II.2.B). Interestingly, while the optimized wet-chemical treated oxide did show improved performance over the non-doped sample, the ALD-doped oxide showed further performance enhancements [2].

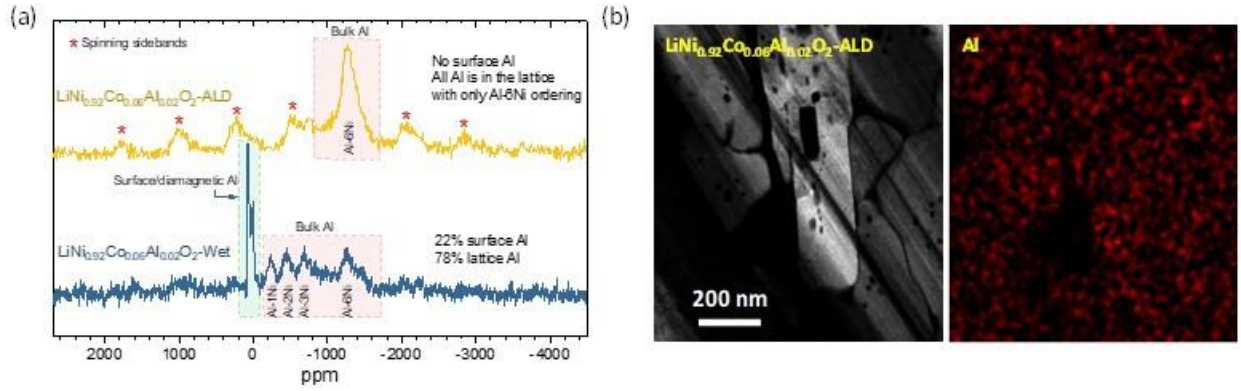

Figure II.2.A.4 (a) ^{27}Al-MAS NMR spectroscopy results of $LiNi_{0.92}Co_{0.06}Al_{0.02}O_2$ prepared by ALD (Atomic Layer Deposition) method and $LiNi_{0.92}Co_{0.06}Al_{0.02}O_2$ prepared by a wet coating method, and (b) HR-STEM-EDS (High-Resolution Scanning Transmission Electron Microscopy – Energy Dispersive Spectroscopy) images showing Al-distribution within primary particles of $LiNi_{0.92}Co_{0.06}Al_{0.02}O_2$–ALD.

Figure II.2.A.5 shows the electrochemical performance of the baseline $LiNi_{0.94}Co_{0.06}O_2$ and the ALD-doped $LiNi_{0.92}Co_{0.06}Al_{0.02}O_2$. Cathode electrodes were cycled against Li metal anodes between 4.4-3.0V using 3 formation cycles at C/10 followed by 100 cycles at C/5. Both electrodes achieve similar capacities during the first cycles with the Al-doped sample achieving just ~5 mAh/g less on the first charge, as might be expected due to the presence of inactive Al. dQ/dV features related to phase transitions are also slightly smoother in the

Al sample as is typical of doped/substituted LNO-based oxides. However, several important differences can be observed in the plots on extended cycling including strikingly stable dQ/dV profiles and less overpotential development for the $LiNi_{0.92}Co_{0.06}Al_{0.02}O_2$ as compared to the $LiNi_{0.94}Co_{0.06}O_2$. The ALD-doped cathode-electrode also achieved 92% capacity retention over the 100 cycles compared to 83% for the Al-free baseline. Furthermore, HRTEM studies showed that the surfaces of the $LiNi_{0.92}Co_{0.06}Al_{0.02}O_2$ prepared via the ALD method underwent minimal reconstruction after the 100 cycles on test (see chapter II.2.B).

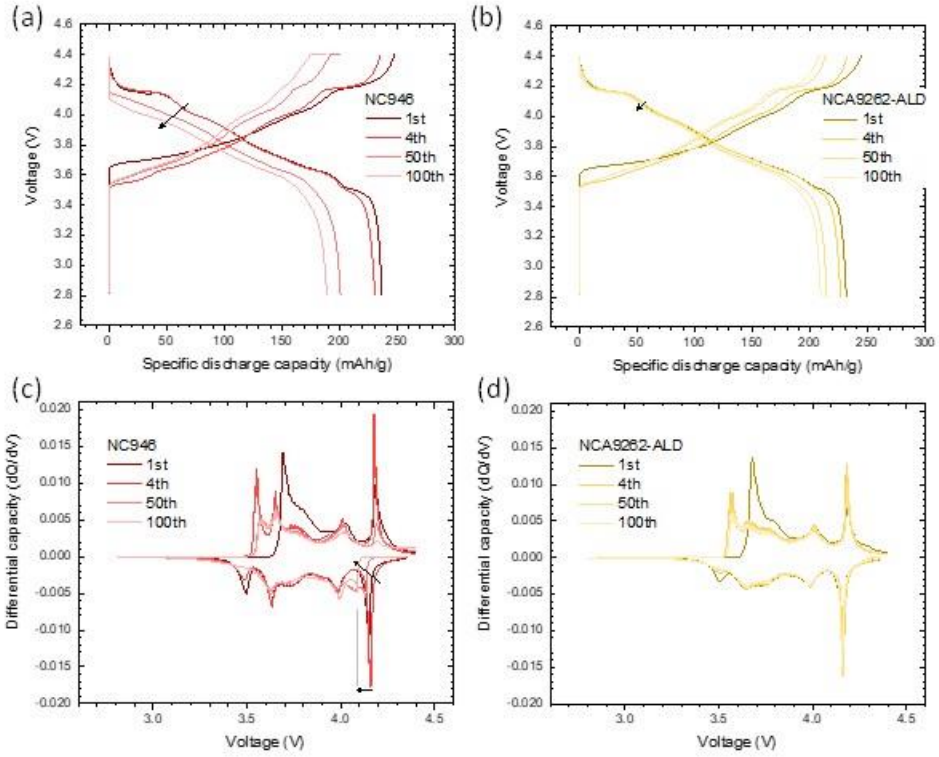

Figure II.2.A.5 1st, 4th, 50th and 100th charge/discharge profiles for (a) $LiNi_{0.94}Co_{0.06}O_2$ and (b) $LiNi_{0.94}Co_{0.06}Al_{0.02}O_2$-ALD. (c) and (d) the corresponding differential capacity plots.

To study the effect of Al substitution on thermal stability, active materials of the $LiNi_{0.92}Co_{0.06}Al_{0.02}O_2$ and $LiNi_{0.94}Co_{0.06}O_2$ were recovered from cells after 90% delithiation during the initial cycle. The collected powders were packed into an air-sealed aluminum holder and synchrotron XRD measurements were conducted by increasing the temperature from RT to 550ºC under a He carrier gas, Figure II.2.A.6. Thermal decomposition related to the phase transition from layered (R-3m) to M_3O_4-type spinel for the $Li_{0.1}Ni_{0.92}Co_{0.06}Al_{0.02}O_2$ is clearly delayed as compared to $Li_{0.1}Ni_{0.94}Co_{0.06}O_2$, implying some advantage for the Al-containing sample.

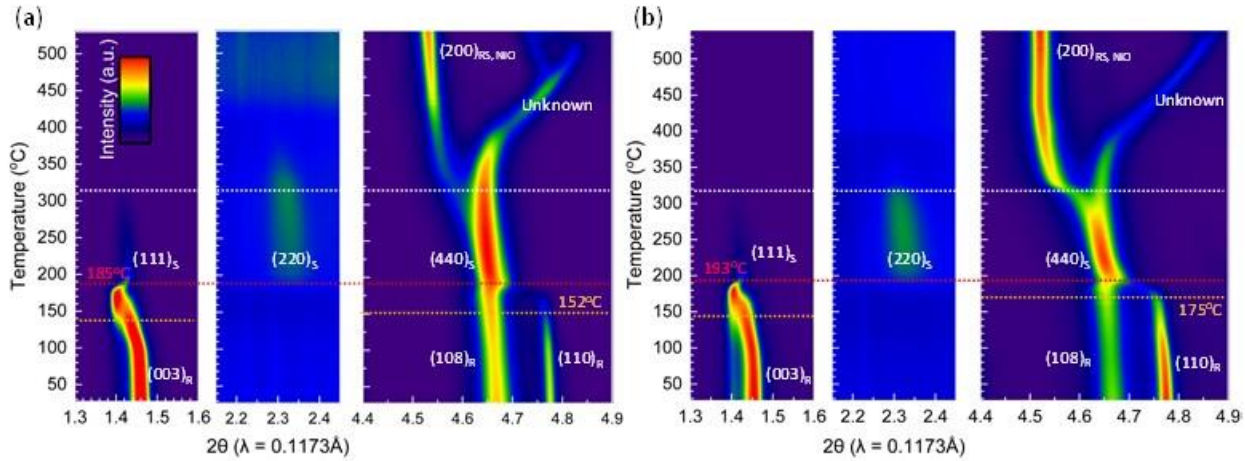

Figure II.2.A.6 Contour plots of in-situ X-ray diffraction patterns for (a) $Li_{1-x}Ni_{0.94}Co_{0.06}O_2$ and (b) $Li_{1-x}Ni_{0.92}Co_{0.06}Al_{0.02}O_2$–ALD, where x = 0.9 as the charged state.

Following electrochemical evalutaion, the evolution of Al local environments with cycling was studied by ^{27}Al MAS-NMR. The $LiNi_{0.92}Co_{0.06}Al_{0.02}O$ sample prepared via ALD was cycled between 4.4-2.8V against Li metal anodes for 100 cycles and studied in the discharged state (cycled), as well as after a low voltage hold to overcome impedance issues and recover all cyclable lithium (relithiation). As shown in Figure II.2.A.7, a major component of the ^{27}Al peak for Al-6Ni environments remain with the formation of a broad shoulder towards lower frequencies observed after cycling. The reduction of hyperfine shift suggests the presence Ni^{+4} (diamagnetic) due to lithium loss or Al reordering (e.g., coordination to diamagnetic cobalt or aluminum). However, as these ^{27}Al NMR peaks disappear with full relithiation, the changes in Al local environments are mostly reversible, revealing the relative stability of these local structures. In addition, no surface aluminum oxide formation is observed with cycling and relithiation. ^{6}Li MAS-NMR data comparisons (data not shown) for pristine, cycled, and relithiated samples revealed similar results, corroborating largely reversible local changes with delithiation/lithiation on cycling.

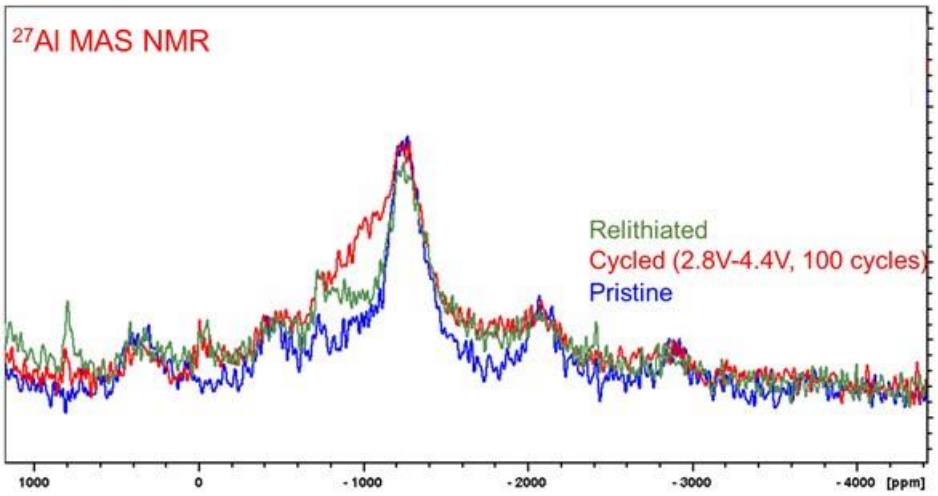

Figure II.2.A.7 Evolution of aluminum local environments in $LiNi_{0.92}Co_{0.06}Al_{0.02}$ with cycling and relithiation via ^{27}Al MAS NMR

These results presented above indicate that Al^{3+} cations incorporated into fully coordinated lattice sites have a larger impact on cathode stability than surface Al phases, in agreement with previous results showing little benefit of coatings such as Al_2O_3 when cycling to high states of charge [3]. In addition, it is clear from this work that achieving the greatest benefit from elemental substitutions requires a high degree of control over

distribution and site occupancies and novel strategies, such as the ALD processing developed herein, need to be further explored.

MnNi-based cathode oxides – Recent work from this program has focused on understanding local ordering and its relation to composition, the results of which have led to high-energy, MnNi-based compositions [4]. For example, newly developed cathodes consisting of ~60% Ni, ~35% Mn, and ~5% Co, in the presence of a small excess of Li, performed on par with an NMC-622 commercial counterpart. This represents a substantial decrease in cobalt from state-of-the-art, NMC-622 without sacrificing energy. In addition, such compositions represent a substantial increase in Mn content. Following the work presented above, co-precipitation methods were explored to study Al^{3+} incorporation into these types of oxides in an attempt to further decrease Co content and increase stability. Al-containing hydroxides with 1% and 4% Al were synthesized by way of a study aimed at optimization of CSTR processing parameters to produce ~$LiNi_{0.6}Mn_{0.35}Co_{0.04}Al_{0.01}O_2$ and ~$LiNi_{0.6}Mn_{0.35}Co_{0.01}Al_{0.04}O_2$ cathode oxides. Studies were also conducted to optimize calcination/lithiation under air and oxygen atmospheres to produce final cathode-oxides.

Figure II.2.A.8 shows the voltage profiles of the best-performing sample, out of a total of 8 studied, compared with a baseline NMC-622. The Al-containing oxide has a composition of ~$LiNi_{0.6}Mn_{0.35}Co_{0.04}Al_{0.01}O_2$ and was calcined/lithiated under an oxygen atmosphere. As observed, this sample, having just 4% Co and 35% Mn performs very well compared to the commercial NMC-622. The low cobalt electrode delivered an oxide-specific energy of ~780 Wh/kg_{oxide} at a slightly higher average potential than the NMC-622 that gave ~770 $Whkg_{oxide}$. These low-cobalt oxides, as well as more advanced variations, are scheduled to be tested against project protocols under full-cell cycling in FY21.

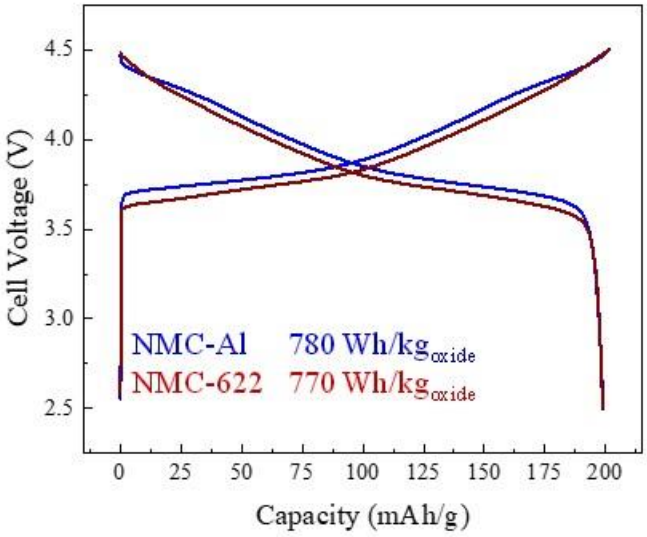

Figure II.2.A.8 First-cycle voltage profiles of NMC-622 (red) and a newly developed 4% Co, 1% Al cathode-oxide utilizing 35% Mn (NMC-Al, blue).

The design of these low-cobalt, relatively high Mn compositions, enabled through an understanding of composition, local ordering, and processing conditions bodes well for future advances and current studies are aimed at eliminating cobalt while further increasing Mn. These cathodes represent a potentially significant opportunity to broaden the portfolio of high-energy materials beyond the current focus of LNO-based oxides.

Coatings for stabilization of low-cobalt cathode-oxides – In addition to studies on composition, local ordering, elemental substitutions, and processing methods, the cathode group within this project is exploring novel materials for stabilization of low-cobalt oxides. Efforts in this project to develop fluoride-based materials have led to promising results in decreasing impedance rise, increasing thermal stability, and decreasing gassing. Such materials are promising in terms of ALD processing methods and work is ongoing in this area.

Late in FY20 a new research direction was initiated related to the non-ALD coatings efforts and moved into closer alignment with the ongoing ALD work [5]. Previously this project placed focus on coating (doping) main group metal oxides (e.g. alumina) using either aqueous or non-aqueous methods to coat nickel-rich cathodes. Using a combined NMR-DFT-Synthesis effort, the diffusion of Al(III) versus temperature and performance was tracked. While the stability increased [6], [7], increases in parasitic heat flow [8] and gas evolution [4] was also noted to increase with alumina. A way around this issue, notably gas evolution at higher voltages, is to use more complex oxides that may not be as catalytic to the electrolyte [7]. Gas evolution studies, in collaboration with ORNL, are in progress and will be a key outcome for this, as well as ALD, coating efforts. Preliminary, benchmark studies from the study of more complex Li metal oxides have shown that;

- LMO coatings on NMC-333 showed the ability to remain separate phases to 400°C before evidence of diffusion was evident (peak coalescence)
    - Lithiated oxide coatings form from constituents and diffuse > 400°C typically
- Insoluble sulfate salts sequester lithium in organic solvents and can throw off stoichiometries.
    - Ethanol can dissolve appropriate amounts of lithium salts and has the advantage of keeping the cathode surface 'drier'
    - Doping anion can become an impurity source
- Surface degradation (i.e. reduction) disrupts the coating interface (temperature, solvent). Differences in structure favor coating integrity.
    - Proton/Li exchange can lead to surface breakdown on heating (with water release)
    - Atmosphere should be controlled to avoid surface reduction during coating process, i.e. O_2 favors oxidized materials (i.e. Ni(III) in LNO).

Studies are ongoing to investigate and develop nove lithiated oxides, phosphates, and fluorides as coatings and surface treatments that have lower catalytic activity and higher lithium cation diffusion. Various solution-based strategies are under investigation for the modification of program LNO-based cathode materials as presented above. $LiNiO_2$ and $Ni_{90}Mn_5Co_5$ compositions are the first programmatic targets. Methodology work initially focused on commercial NMC-333 from ANL's CAMP facility so as not to effect program inventory of materials during this development stage.

Conclusions

Two categories of oxides are being explored towards drastically mitigating or eliminating the use of cobalt in next-generation cathodes. The most straightforward in appearance are those based in $LiNiO_2$ as they can be made well-layered with little-to-no cobalt and deliver high energy. However, important modifications to these systems, enabled by novel materials and processing methods that allow for a high level of control, are critical to success. The work herein has shown that ALD processing of Al substitution in cathodes containing ~95% Ni resulted in a more homogeneous distribution of Al in fully coordinated bulk-like sites. This distribution, confirmed by NMR and electron spectroscopy, is found to be improved as compared wet-chemical routes. Furthermore, the uniform distribution of Al in lattice sites, as opposed to both lattice and surface (e.g., $LiAlO_2$, Al_2O_3), led to superior electrochemical performance, better thermal stability, and stable local environments on cycling. These results help to delineate the role of lattice vs. surface Al phases and the importance of understanding processing conditions related to the physiochemical properties of final products. Other substitutions are being explored according the results of calculations (see chapter II.2.C).

The second category of oxides studied were those based in MnNi compositions; specifically, with lower Ni contents, higher Mn contents, and minimal Co. The work reported in this program has shown that controlling local ordering through compositional design and synthesis conditions can lead to high-energy oxides that use little cobalt and substantially less Ni than LNO-based cathodes. It was shown in this report that compositions consisting of ~35% Mn, ~60% Ni, and less than ~5% Co can achieve the energy densities of commercial NMC-622. These oxides represent potentially significant opportunities in expanding the portfolio of cathode materials beyond LNO-based oxides and further advances along these lines are expected in FY21.

In parallel to the efforts described in cathode design and synthesis, novel materials and processing routes are being explored to further stabilize the surfaces of these materials. Results from this team have shown that typical oxide materials, such as Al_2O_3, are not sufficient for improving the performance of high-energy NMCs during long-term cycling over high SOCs. Efforts are underway in the development of new fluoride-, oxide-, and phosphate-based materials and will be applied and tested on both categories of oxides presented above.

Key Publications

1. **Invited** J. R. Croy, J. Garcia, H. Iddir, S. E. Trask, M. Balasubramanian. 2020. *Harbinger of Hysteresis in Lithium-Rich Oxides: Anionic Activity or Defect Chemistry of Cation Migration*, Journal of Power Sources, June, 228335.

2. **Invited** D. Darbar, E.C. Self, L. Li, C. Wang, H.M. Meyer III, C.-W. Lee, Jason R. Croy, M. Balasubramanian, N. Muralidharan, I. Bhattacharya, I. Belharouak, and J. Nanda, J. Power Source, New Synthesis Strategies to Improve Co-Free LiNi0.5Mn0.5O2 Cathodes: Early Transition Metal d0 Dopants and Manganese Pyrophosphate Coating, 479, 228591 (2020).

3. L. Zou, W. Zhao, H. Jia, J. Zheng, L. Li, D.P. Abraham, G. Chen, Jason R. Croy, J.-G, Zhang, and C. Wang, Chem. Mater., The Role of Secondary Particle Structures in Surface Phase Transitions of Ni-Rich Cathodes, 32, 2884 (2020).

4. J. Zhu, S. Sharifi-Asl, J.C. Garcia, H. Iddir, Jason R. Croy, R. Shahbazian-Yassar, and G. Chen, Appl. Energy Mater., Atomic-Level Understanding of Surface Reconstruction Based on Li[NixMnyCo1-x-y]O2 Single-Crystal Studies, 3, 4799 (2020).

5. *High-Valent Lithiated Surface Structures for Lithium Ion Electrode Materials*, U.S. Patent 10,431,820 B2

6. *METAL FLUORIDE PASSIVATION COATINGS PREPARED BY ATOMIC LAYER DEPOSITION FOR LI-ION BATTERIES*, U.S. Patent 10177365.

7. J. R. Croy, *Lithium-Ion Cathode Development at Argonne National Laboratory*, Technical University of Munich, Munich, Germany, November 2019.

8. B. Han , B. Key, J. T. Vaughey, *Characterization Assisted Lithium Ion Cathode Design: Application of Solid-State NMR to Understand Bulk and Interface Relation of Aluminum Coated and Doped NMC Cathodes*, ECS PRIME, virtual meeting, 2020.

9. W. Shin, A.Vu, J. Garcia, H. Iddir, F. Dogan, *Impact of Annealing Time on Lithium Local Environment of $LiMn_{0.5}Ni_{0.5}O_2$: DFT-Supported 6 Li Solid-State NMR Study*, ECS PRIME, virtual meeting, 2020.

References

1. C.S. Yoon, D.-W Jun, S.-T. Myung, Y.-K. Sun, ACS Energy Lett., 2, 1150−1155 (2017).

2. Jason R. Croy, Cathode Materials for Next Generation Lithium-Ion Batteries: Design, Synthesis, and Characterization of Low-Cobalt Cathodes, DOE/VTO Annual Merit Review, BAT251, virtual, (2020).

3. Jack Vaughey, Cathode Materials for Next Generation Lithium-Ion Batteries: Materials Characterization, DOE/VTO Annual Merit Review, BAT254, Arlington, VA, (2020).

4. J. R. Croy, B. R. Long, M. Balasubramanian, A Path Towards Cobalt Free Lithium-Ion Cathodes, J. Power Sources, 440, 227113 (2019).

5. (a) Binghong Han, Baris Key, Andrew S. Lipton, John T. Vaughey, Barbara Hughes, James Trevey, Fulya Dogan J. Electrochem. Soc , 166 (15) A3679-A3684 (2019); (b) Jason R. Croy, Daniel C. O'Hanlon, Soroosh Sharifi-Asl, Michael Murphy, Anil Mane, Chang-Wook Lee, Stephen E. Trask, Reza Shahbazian-Yassar, Mahalingam Balasubramanian Chem. Mater, 31, 3891−3899 (2019)

6. David S. Hall, Roby Gauthier, Ahmed Eldesoky, Vivian S. Murray, J.R. Dahn ACS Appl. Mater. Interfaces, 11, 14095−14100 (2019)

7. J. Xiong, T. Hynes, L. D. Ellis, J. R. Dahn J. Electrochem. Soc , 164 A3174-A3181 (2017).

8. S. L. Glazier, K. J. Nelson, J. P. Allen, J. Li, J. R. Dahn J. Electrochem. Soc , 164 (6) A1203-A1212 (2017).

Acknowledgements

Anh Vu, Ozge Kahvecioglu, Jihyeon Gim, Fulya Dogan, Arturo Gutierrez, Jack Vaughey, Shankar Aryal, Eungje Lee, Mahalingam Balasubramanian, Adam Tornheim, Kris Pupek, Khalil Amine, Chongmin Wang, Lianfeng Zou, Yang Ren, Harry Charalambous, Jinhyup Han, Pragathi Darapaneni, Anil Mane, Jeff Elam, Tony Montoya, Yunya Zhang. Support from the U. S. Department of Energy (DOE), Vehicle Technologies Office, Peter Faguy, and David Howell is gratefully acknowledged.

II.2.B Diagnostic Testing and Evaluation (ANL, ORNL, NREL, PNNL, LBNL)

Daniel P. Abraham, Principal Investigator
Argonne National Laboratory
9700 S. Cass Avenue
Lemont, IL 60439
E-mail: abraham@anl.gov

Peter Faguy, DOE Technology Development Manager
U.S. Department of Energy
E-mail: Peter.Faguy@ee.doe.gov

Start Date: October 1, 2019 End Date: September 30, 2020
Project Funding: $4,000,000 DOE share: $4,000,000 Non-DOE share: $0

Project Introduction

State-of the-art lithium-ion batteries (LIBs) being developed for transportation applications contain a transition metal (TM) oxide cathode and a graphite anode; both serve as host-matrices to house lithium ions during battery operation. The cathode typically contains $Li_{1+x}Ni_aCo_bAl_cO_2$ (NCA) or $Li_{1+x}Ni_aMn_bCo_cO_2$ (NMC) oxides, where x ~0-0.05 and a+b+c = 1. Both oxide chemistries contain Co, which is known to preserve the layered structure during lithium extraction/insertion reactions. However, the possibility of a global Co shortage and soaring costs has galvanized the LIB community to seek and explore layered oxides with lower Co contents and eventually develop Co-free cathodes, while maintaining cell performance (energy/power densities), safety and cycle/calendar life. The goal of the diagnostic testing and evaluation team within this program is to identify constituents and mechanisms responsible for cell performance, performance degradation and safety. Various diagnostic tools (electrochemical, physicochemical, mechanical, etc.) are used to characterize the behavior of materials (both active and inactive) contained in the electrodes and cells; this characterization may be conducted before, during, and after electrochemical cycling. Understanding the fundamental mechanisms allows the development of rational solutions to minimize performance degradation and thermal instability in the materials and electrodes, leading to safer, long-life and battery cells.

Objectives

- Establish electrochemical half-cell test protocols to characterize multiple performance aspects (capacity, rate, high voltage stability) of various cathode active materials.
- Use standard cycling protocols to examine performance of full cells with the low (or zero) cobalt oxides
- Obtain insights on aging behavior on full cells containing a reference electrode.
- Identify additives, which when incorporated into our baseline electrolyte (Gen2), consisting of 1.2M $LiPF_6$ in EC:EMC (3:7 w/w), reduces cell degradation.
- Develop standard protocols to determine the onset potential and scale of gas generation and investigate the impact of cell operation temperature on gassing behavior.
- Determine if Li^+/H^+ ion exchange occurs during aqueous rinsing of lithium nickel oxide ($LiNiO_2$, LNO) powder using time-of-flight secondary ion mass spectroscopy (TOF-SIMS) elemental analysis.
- Conduct microscopy and spectroscopy studies on pristine and cycled electrodes and electrolytes to better understand the new oxides that are being developed.

- Utilize transmission electron microscopy (TEM) to examine evolution of the surface reconstruction layers on the various oxides during electrochemical cycling.
- Apply solid state nuclear magnetic resonance (NMR) to directly observe bulk and surface lithium environments within different oxide compositions and determine changes that occur during cycling.
- Develop differential scanning calorimetry (DSC) protocols to minimize variability in the thermal stability data of various cathode active materials.
- Develop in-situ spectroscopic techniques to examine transition metal (TM) redox chemistry, formation and evolution of the cathode-electrolyte interphase (CEI) and electrolyte solution structures.

Approach

The approach pursued to meet the above objectives is summarized in Figure II.2.B.1 (below).

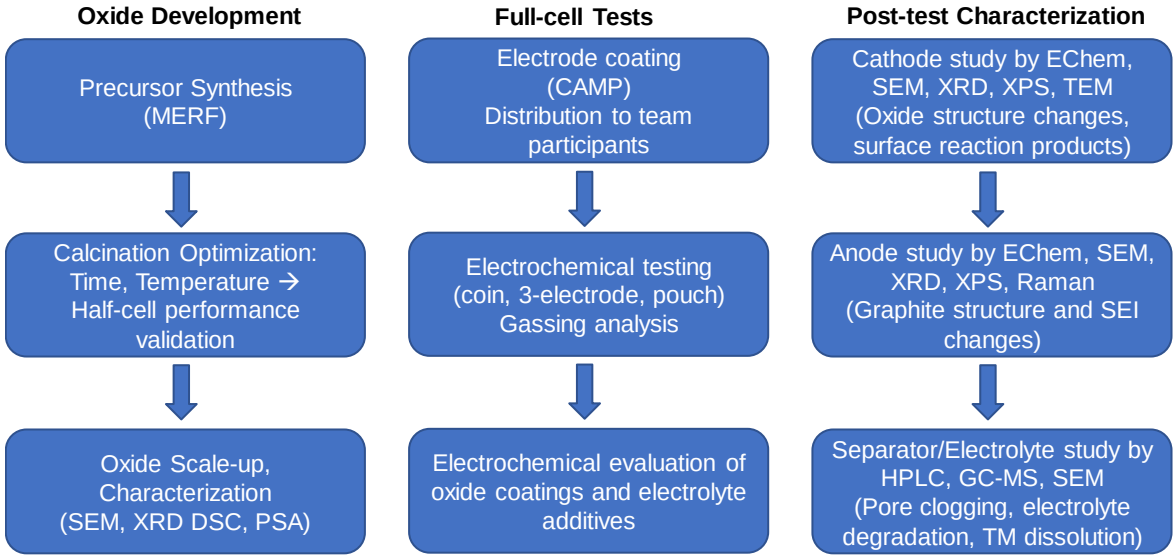

Figure II.2.B.1 Diagnostic tests are conducted at various stages of the oxide development process.

Results

Electrode Fabrication using Oxide Powders: *Steve Trask et al., CAMP, ANL*

Various low-cobalt oxide powders were synthesized in the past year. Scanning electron microscopy (SEM) images of some of these oxide powders, obtained at the ANL post-test facility, are shown in Figure II.2.B.2.

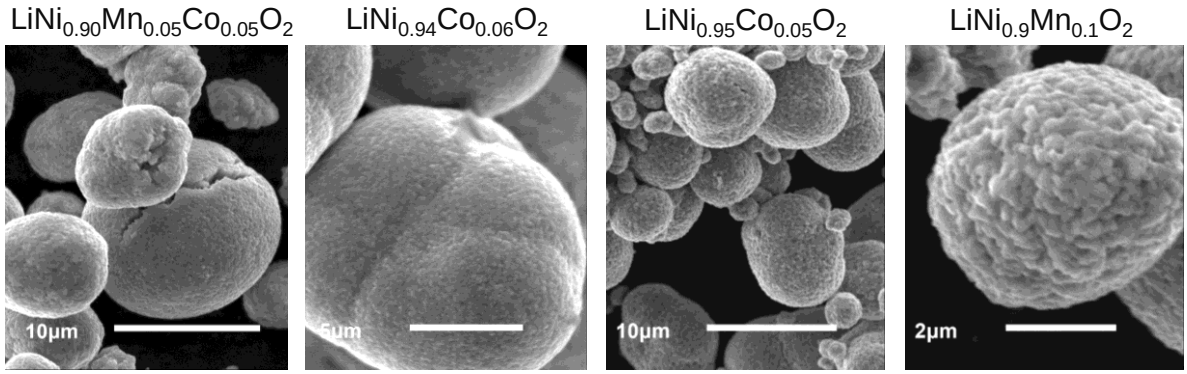

Figure II.2.B.2 SEM images of various pristine oxides synthesized in the program (courtesy – N. Dietz, ANL).

The pH of each powder is measured to determine the slurry preparation conditions; the measurement uses 1 g of powder in 10 g of de-ionized water. The pH values for some of the oxides are as follows: 12.65 ($LiNiO_2$), 12.63 ($Ni_{0.94}Co_{0.06}$), 12.65 ($Ni_{0.9}Mn_{0.05}Co_{0.05}$), 12.64 ($Ni_{0.9}Co_{0.1}$), and 12.7 ($Ni_{0.9}Mn_{0.1}$). For each of these oxides, a tendency for gelation was observed during slurry preparation with NMP/PVDF, which made it difficult to achieve consistent and uniform electrode coatings. Some oxides, such as NMC-622 (pH 12.41) and $LiNi_{0.95}Mn_{0.05}O_2$ (pH 12.75), did not show a tendency for slurry gelation; the latter is especially surprising because of the high pH value measured. Thus, it appears likely that the slurry gelation is a consequence of the surface characteristics of the oxide; residuals such as Li_2CO_3 may promote the tendency for gelation. Various oxide synthesis conditions (e.g., calcination temperature) are being examined to identify conditions that minimize slurry gelation.

Examining Li^+/H^+ ion exchange during aqueous rinsing of oxide powders: ***Kyusung Park et al., NREL***

A significant challenge to the production of Ni-rich cathode materials is the reactivity of these materials with air to form surface byproducts such as Li_2CO_3 and LiOH. These surface contaminants affect the processability of the cathode material into a slurry, as shown above, and can also affect the performance of the fabricated cell by causing outgassing reactions during cycling. Rinsing the cathode material in water to remove surface contaminants has been shown to decrease cycling performance, particularly if the powder is dried at elevated temperatures after rinsing. It has been hypothesized that this decreasing performance is due to Li^+/H^+ exchange at the cathode surface that occurs during rinsing. In order to track possible ion exchange that occurs purely between the cathode material and the rinsing solvent, deuterated water (D_2O) was used and tracked to reveal if the deuterium signal increased in the rinsed samples as opposed to the reference samples. The reference samples used here were (1) a $LiNiO_2$ (LNO) powder that was aged in a glovebox for several months, which was also the baseline material used in all rinsing studies, and (2) LNO powder that had been rinsed in MilliQ deionized water with the same conditions as the D_2O rinsed samples.

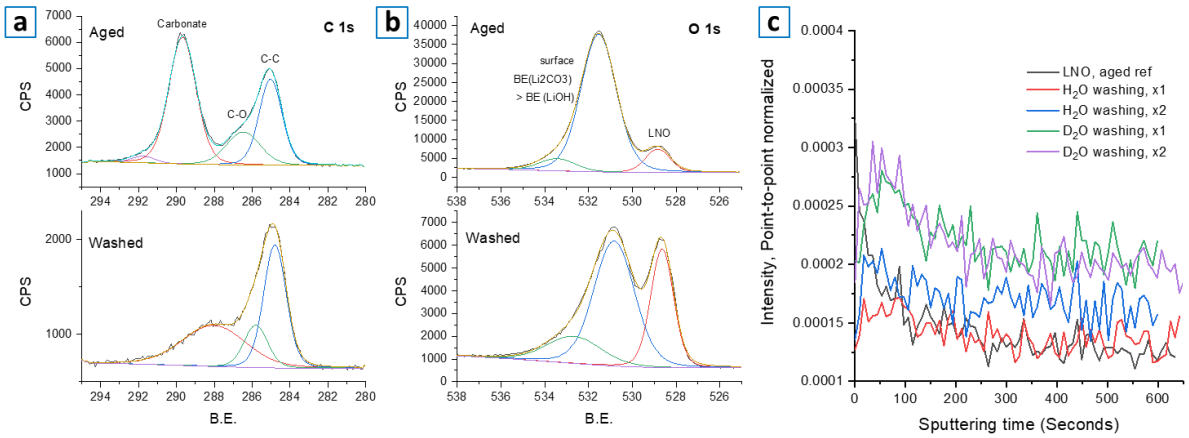

Figure II.2.B.3 (a) C 1s, (b) O 1s XPS core-level spectra for the aged LNO sample (Aged) and the sample rinsed twice with DI H_2O (Washed). (C) TOF SIMS intensity of the deuterium signal as a function of sputtering time for the unwashed and washed LNO samples.

Figure II.2.B.3a, Figure II.2.B.3b show the changes that occur on the surface composition of the LNO after rinsing with H_2O. One can see the contaminant species of Li_2CO_3 and LiOH are diminished after the rinsing by looking at the carbonate peak at ~290 eV in the C 1s spectrum and the associated peak at ~531.5 eV in the O 1s spectrum. There is a significant decrease in both of these peaks relative to the other components shown in these core levels after washing, in addition to an overall decrease in intensity for all oxygen and carbon containing components.

Figure II.2.B.3c shows the intensity of the deuterium signal from the unwashed (aged ref.), H_2O- and D_2O-rinsed samples as a function of sputtering time in TOF-SIMS analysis. From the aged reference powder, one

can see there is some D_2-O signal at the surface. This surface signal is reduced in intensity for the H_2O-rinsed samples, indicating that the original signal was possibly present in surface contaminants that were washed off during the rinsing process. In contrast, the washed samples show a persistent increase in the deuterium signal, not only at the surface but also within the bulk. From this, it is concluded that *there is Li^+/H^+ ion exchange* between the solvent and the LNO powder that occurs during rinsing.

Electrochemical testing in coin cells using standard protocols: ***Adam Tornheim et al., ANL***

To evaluate properties and performance of newly-synthesized oxides, half-cell (Li metal anode) cycling tests are conducted using various test protocols. The test data help optimize synthesis conditions and validate electrochemical performance. The *standard* protocol uses two upper-cutoff voltages (UCV) of 4.2 and 4.5 V, as well as two potentiostatic holds, with 2.5 V used as the lower-cutoff voltage (LCV). Charge and discharge capacity, kinetic losses, and high voltage instability/damage are evaluated with this protocol. The *rate* protocol comprises 20 mA/g charge cycles with discharge rates of 20, 60, 100, 200, and 20 mA/g for 3 cycles each, at a UCV of 4.3 V, for a total of 15 cycles. This protocol is then repeated with an increased UCV of 4.5 V; the LCV is 2.5 V in both cases. Figure II.2.B.4 shows the rate performance of four oxide cathode-electrodes: $Li(Ni_{0.95}Co_{0.05})O_2$, $Li(Ni_{0.94}Co_{0.06})O_2$, $Li(Ni_{0.9}Mn_{0.05}Co_{0.05})O_2$, and $Li(Ni_{0.9}Mn_{0.1})O_2$. In the 2.5-4.3 V range, there is a large capacity difference between the oxides; the higher Ni oxides display higher capacities. The capacity differences between oxides is smaller in the 2.5-4.5 V range; of note is that the Mn-containing oxides have better stability in this higher-voltage range.

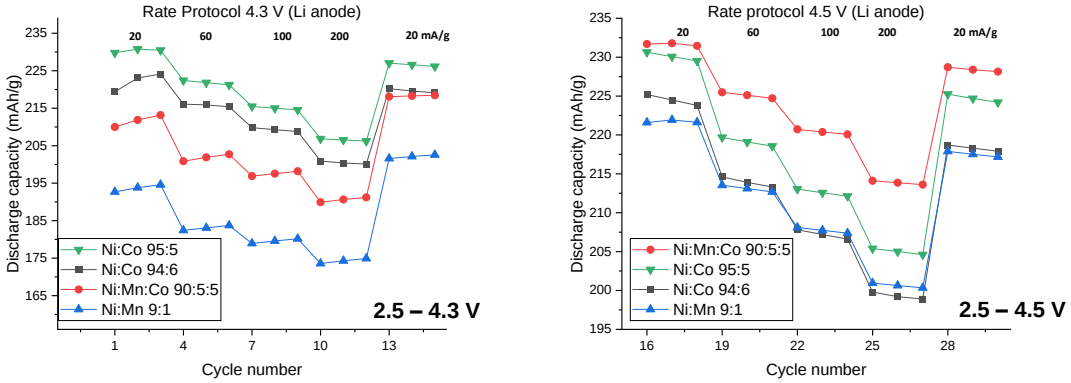

Figure II.2.B.4 Average rate performance of oxide cathode-electrodes indicated in the legend. Discharge current (mA/g) is indicated in each 3-cycle subdivision, 20 mA/g was used for all charge cycles.

For full-cell tests, the oxide cathodes are paired with matched graphite anodes fabricated at Argonne's CAMP facility. The standard protocol includes four formation cycles at a ~C/10 rate, followed by aging cycles at a ~C/3 rate that included a 3-h constant voltage hold at the UCV (4.2 V). This constant current-constant voltage (CC-CV) test is interrupted periodically to obtain reference performance data, which included impedance measurements using a modified hybrid pulse power characterization (HPPC) protocol and capacity measurements at low rates (~C/20) to determine the true loss of cyclable lithium. There are ~119 cycles in a standard protocol, and it can be repeated as necessary to accelerate cell aging.

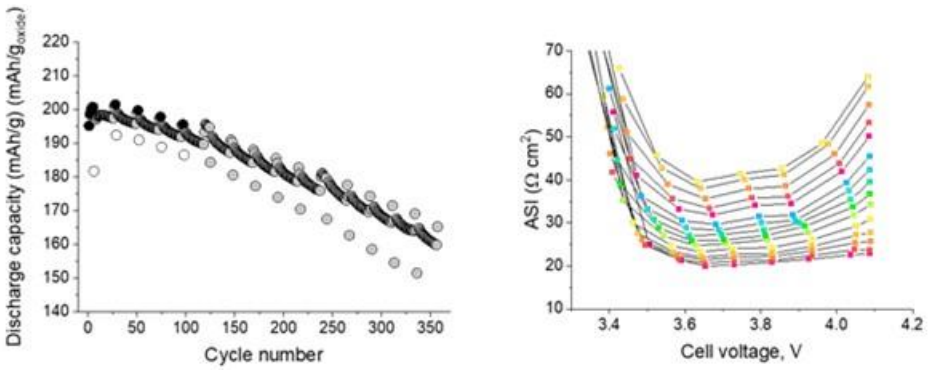

Figure II.2.B.5 Electrochemical performance of an $LiNi_{0.9}Mn_{0.05}Co_{0.05}O_2$//Gr cell: 3.0-4.2 V, 30°C, >350 cycles. Discharge capacity vs. cycle number (left) and ASI vs. state-of-charge throughout the cycling protocol (right).

Figure II.2.B.5 shows the electrochemical performance of $LiNi_{0.9}Mn_{0.05}Co_{0.05}O_2$//Gr full cells subjected to three full protocols (~357 cycles, >900 h at top of charge, 4.2 V). While the electrode couple achieves 750 mWh/g-oxide discharge energy in the first cycle, the cell exhibits ~80% capacity retention over the course of the cycling (left). On the right, the area-specific-impedance (ASI) is shown, with measurements every 20 aging cycles. The ASI increase monotonically with cycle number and roughly doubles over the cycling period. Figure II.2.B.6 shows data from a $LiNi_{0.9}Mn_{0.1}O_2$//Gr full-cell tested over one standard protocol (~119 cycles). Note that Co in the cathode-oxide has been replaced by Mn. This cell shows slightly lower initial discharge energy (~730 mWh/g) because of the higher Mn content in the oxides; however, it has excellent capacity retention and low ASI increase.

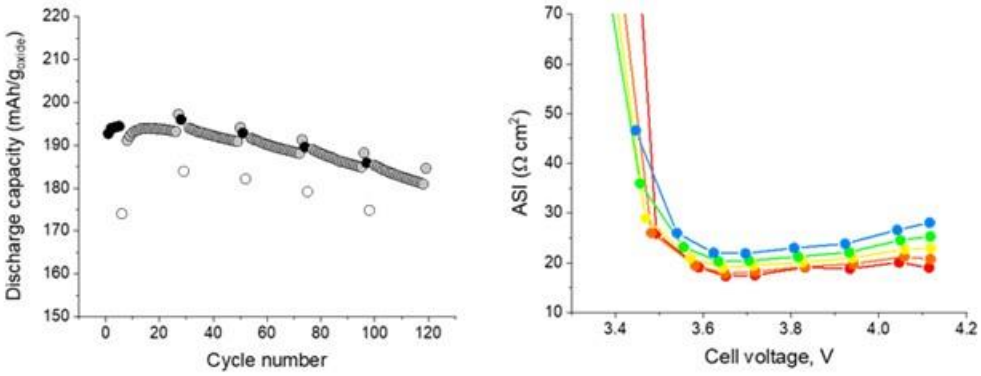

Figure II.2.B.6 Electrochemical performance of $LiNi_{0.9}Mn_{0.1}O_2$//Gr cell: 3.0-4.2 V, 30°C, ~119 cycles. Discharge capacity vs. cycle number (left) and ASI vs. cell voltage (right).

Decoupling electrode behavior from full-cell response: ***Marco Rodrigues et al., ANL***

Information about the state of the electrodes and sources of capacity loss can be inferred from the full-cell cycling data using differential voltage analysis (DVA). DVA is an analytical framework commonly applied to the study of commercial Li-ion batteries, based on the assumption that the behavior of the full-cell can be approximated by the behavior of cathode and anode half-cells. While 3-electrode cells can directly measure electrode potentials, DVA relies on the mathematical transformation of half-cell data to simulate the electrode response that is necessary to reproduce the observed full-cell characteristics. Such transformations are associated with specific performance fade mechanisms and can provide information about cell aging. For example, losses of Li^+ inventory and the subsequent slippage of electrode potentials are represented by the relative lateral translation of the half-cell data used to calculate the full-cell profile. Similarly, the inactivation of portions of the active material in a given electrode can be modeled by scaling (i.e., "squeezing") half-cell profiles appropriately. The extent to which these operations are applied to the half-cell data can help separate the contributions of each of them to the overall capacity loss exhibited by the cell.

DVA was applied to data from full-cells containing $LiNi_{0.90}Mn_{0.05}Co_{0.05}O_2$ (NMC-90-5-5) cathode, graphite anode and Gen2 electrolyte, and tested using 3.0 and 4.2 V as lower and upper cutoff voltages. The protocol involved four cycles at C/10, followed by HPCC, 92 aging cycles at C/2, and HPCC followed by two diagnostic cycles at C/10; this sequence was repeated ten times for a complete test of 1,000 full-cycles. Figure II.2.B.7a shows the capacity retention of a typical cell during the entire test. The symbols presenting higher capacity correspond to cycles carried out at C/10; loss of 20% of the C/10 capacity only occurs after 500 cycles are completed. The cumulative percentual capacity loss measured at C/10 is shown in Figure II.2.B.7b (orange symbols), indicating that capacity fade is almost linear during cell aging. The amount of capacity loss due to Li^+ inventory losses as modeled by DVA is shown in blue symbols. Inspection of Figure II.2.B.7b shows that, up to cycle 500, the Li^+ losses to the SEI can account for nearly all the capacity fade exhibited by the cell (within ~2%). From that point onwards, diversion of the trend lines exhibited by each curve indicate that losses of active material in the cathode become significant at the later portions of cell life. Such losses are likely caused by the electronic or ionic isolation of cathode domains, as indicated by an increase in cell impedance.

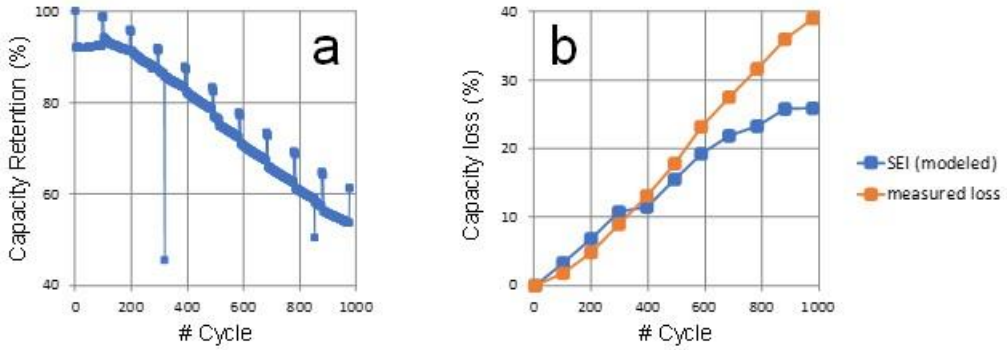

Figure II.2.B.7 a) Capacity retention of a typical NMC-90-5-5//graphite cell, indicating that 20% of capacity loss occurs only after 500 cycles. b) cumulative capacity loss (orange) and losses indicated by DVA to originate from Li^+ trapping at the SEI (blue). After 500 cycles, loss of accessibility of active sites in the cathode starts to contribute to capacity fade.

The behavior of electrodes can also be examined in a 3-electrode cell. Experiments were conducted in cells containing the oxide cathodes, graphite anodes, Gen2 electrolyte and a reference microelectrode, which is a Cu wire with lithium deposited at its tip. Typical data from the cells are shown in Figure II.2.B.8. The full impedance rise in all of the cells examined could be attributed to the positive electrodes, where impedance rise at the negative electrodes was minimal.

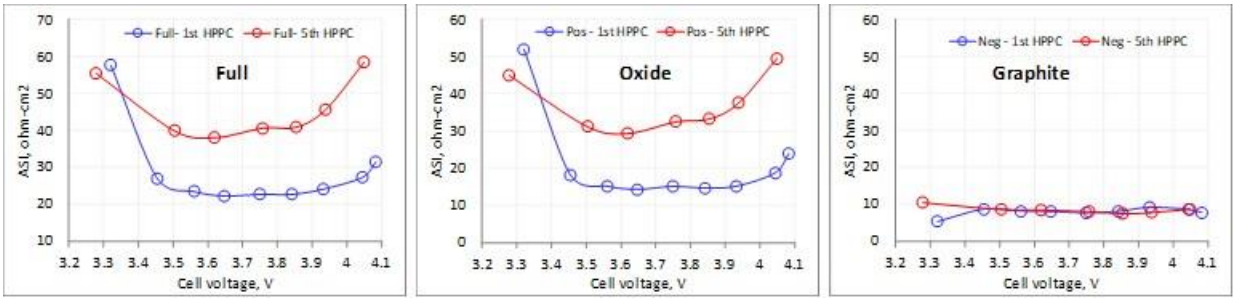

Figure II.2.B.8 Area specific impedance (ASI) vs. cell voltage for a $LiNi_{0.94}Co_{0.06}O_2$//Gr cell cycled between 3.0-4.2 V at 30°C. Data are for the full cell, oxide cathode and graphite anode. The 1st HPPC sweep is soon after formation cycling and the 5th HPPC sweep is after ~100 cycles.

Development and implementation of novel electrolyte additives: ***Chen Liao et al. ANL***

Two different strategies for new additive development was demonstrated during the past year: (1) a dual salt electrolyte, using a combination of $LiPO_2F_2$ (LiDFP) and $LiPF_6$ to form a 1.2M salt concentration in EC/EMC (3/7, w/w) mixture, and (2) 1-(Dimethylamino)pyrrole (PyDMA) as an electrolyte additive.

Electrochemical performances of $Li(Ni_{0.94}Co_{0.06})O_2$//Gr cells with the Gen2 electrolyte and dual salt electrolytes (with varying salt ratios) are shown in Figure II.2.B.9 (left panel, top). The cells are denoted as Gen2 (1.2 M $LiPF_6$), 1.15M + 0.05M, 1.1 M + 0.1 M cells, 1.0 M + 0.2 M cells, and 0.9 M + 0.3 M cells, where the former is the $LiPF_6$ salt concentration and the latter is the LiDFP salt concentration. As seen in the figure, cells with < 0.2M LiDFP display better capacity retention while increasing LiDFP to 0.3M leads to inferior performance. Cells with 1.1M $LiPF_6$ + 0.1M LiDFP have the highest capacity retention. The ASI as a function of cell voltage is shown in the right panel of Figure II.2.B.9. Compared to Gen2 cells, the dual-salt cells display lower impedance rise with 1.1 M + 0.1 M cells and 1.0 M + 0.2 M cells showing the lowest impedance rise. It is presumed that there may be less oxidation of the dual-salt electrolyte. To examine this hypothesis, a potentiostatic-hold experiment was performed. When the cells are fully charged and held at high potential, the resulting leakage currents during the hold reflect parasitic reactions on the cathode surfaces. $Li(Ni_{0.94}Co_{0.06})O_2$//Gr cells with various electrolytes were fully charged and held at 4.2 V for 60 hours and the leakage currents are shown in Figure II.2.B.9 (left panel, bottom). Clearly, cells with dual-salt electrolyte display lower leakage currents than cells with baseline electrolyte, suggesting less decomposition of the electrolyte and more stable interphase formation. The 1.1 M + 0.1 M cells had the lowest leakage currents, consistent with the lowest impedance rise and best cell performance.

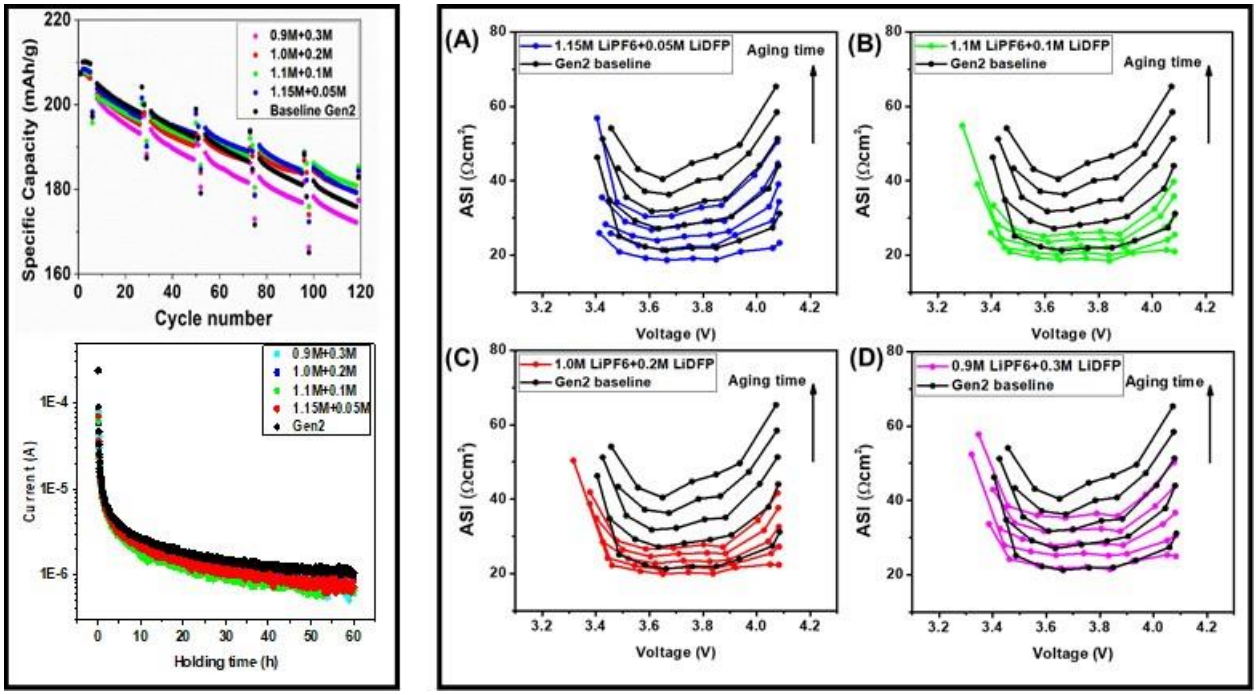

Figure II.2.B.9 Electrochemistry of $Li(Ni_{0.94}Co_{0.06})O_2$//Gr cells with dual salt electrolytes of various compositions. Left panel. (Top) Specific capacity vs. cycle number; Bottom – Leakage current during voltage hold. Right panel. ASI rise during cycling.

The idea for using PyDMA stems from combining the capability of the amino group for scavenging HF and the pyrrole group for oxide protection through the formation of a conjugated polymer. Even a small amount of PyDMA is capable of scavenging HF and stabilizing the electrolyte. To test this, 2 vol% water was added intentionally to the Gen2 electrolyte, with or without 1.0 wt% PyDMA. The electrolyte samples were stored inside a fume hood for a period of time before examination by ^{19}F NMR spectra. As shown in Figure II.2.B.10 (left panel), the hydrolytic products HF, Li_2PFO_3, and $LiPF_2O_2$ appeared in the Gen2 electrolyte with 2 vol% water after 2 days storage, however, no such products were observed in the sample with 1.0 wt% PyDMA. The latter electrolyte was examined again after 4 weeks of storage, and again, no signals from HF and Li_2PFO_3 were observed in the spectra; only a negligible amount of $LiPF_2O_2$ was seen. These results confirm that PyDMA's can scavenge HF and stabilize the Gen2 electrolyte for several weeks.

The electrochemical behavior of NMC-622//Gr cells containing electrolytes with 0.0 -2.0 wt% PyDMA in Gen2 is illustrated in Figure II.2.B.10a (right panel): the cells are denoted as Gen2 cells, 0.5 wt% PyDMA, 1.0 wt% PyDMA and 2.0 wt% PyDMA. As seen in the figure, cells with PyDMA have better capacity retention and higher average coulombic efficiency than Gen2 cells. The differential capacity (d*Q*/d*V*) profiles of the first charge cycle are plotted in Figure II.2.B.10b (right panel). In these profiles, the prominent peak at 3.0 V is observed for all cells and is from the reduction of ethylene carbonate (EC) on the graphite anode. Two new peaks around 2.5 V were found in PyDMA cells having increased intensities increased for increased wt. ratios of the additive. In general, cells containing the additives showed improved capacity retention after 119 cycles with the 0.5, 1.0, and 2.0 wt% PyDMA cells displaying 90.0%, 89.4%, and 86.1% capacity retention, respectively, while the Gen2 cells showed 84.5% capacity retention.

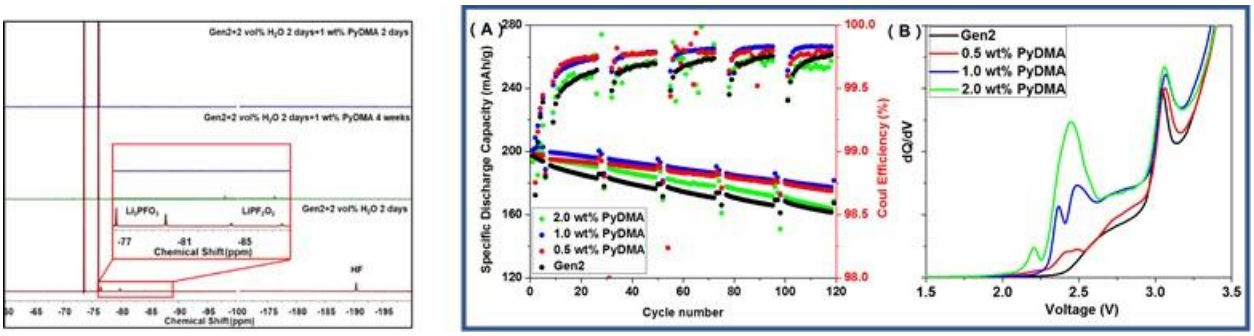

Figure II.2.B.10 Left Panel: ^{19}F NMR spectra of Gen2 electrolytes containing 2 vol % water, with and without PyDMA. Right Panels:- (a) Specific capacity of NMC622//Gr cells containing 0.5-2.0 wt% PyDMA additive in Gen2 electrolyte (black line) ; (b) Differential charge (dQ/dV) vs. cell voltage for the first charge showing electrolyte reduction peaks.

The purpose of introducing the pyrrole unit in our additive design is to utilize the film-forming property of pyrrole via oxidative polymerization. A high-quality protective layer on the cathode should not significantly increase the impedance of cells. The addition of PyDMA slightly increased the initial impedance of cells compared to Gen2 cells, which also increased as the amount of additive increased, Figure II.2.B.11. Interestingly, a lower concentration of PyDMA also leads to higher impedance than that of the Gen2 cells. This is commonly seen in cells containing film-forming additives, confirming the formation of a surface film on cathode. Previous publications revealed that the surface film formed by conjugated polymers usually render higher initial impedance, owing to the hydrophobic backbone of polymers, which is non-ionically conductive. The optimal concentration of PyDMA is in this study was found to be 0.5 wt% and its long-term effects are under investigation.

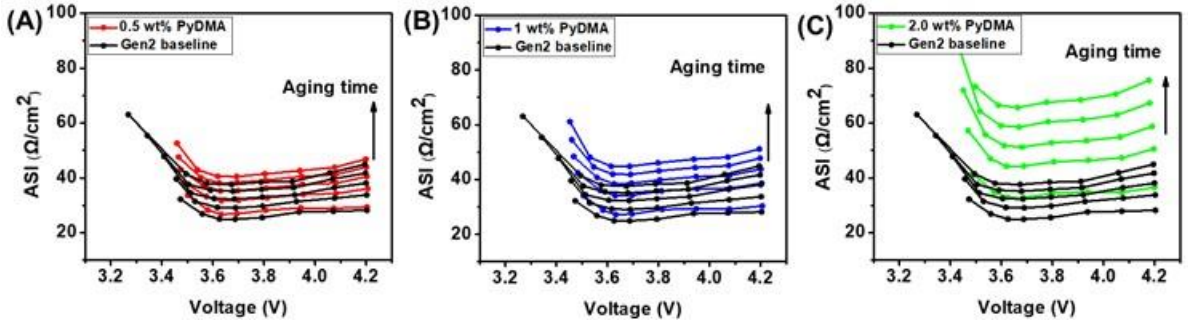

Figure II.2.B.11 ASI of NMC-622//Gr cells containing electrolytes with 0.5-2.0 wt% PyDMA in the Gen2 composition. The traces in graph correspond to 7, 30, 53, 76, and 99 cycles (from bottom to the top), respectively.

In-situ mass spectroscopy (MS) for gas analysis during cell cycling: ***Linxiao Geng et al., ORNL***

Pouch cells with LNO-based cathodes and graphite anodes made by CAMP were assembled at the Battery Manufacturing Facility (BMF), ORNL. In-situ gas analysis was performed while first charging the pouch cells galvanostatically to 3.5V and holding for 10 h followed by charging galvanostatically to 4.1V and holding for

5 h then repeating by increasing the potential by 50mV until 4.3V. The first charge to 3.5V and hold for 10 hours is to observe gas generation during SEI formation on the anode, with the long hold to make sure all the gases generated during the SEI formation reduce back to baseline levels and do not interfere with the detection of gases generated at high voltages at the cathode side. The results using this novel gassing protocol to determine the onset potential and scale of gassing are summarized in Figure II.2.B.12.

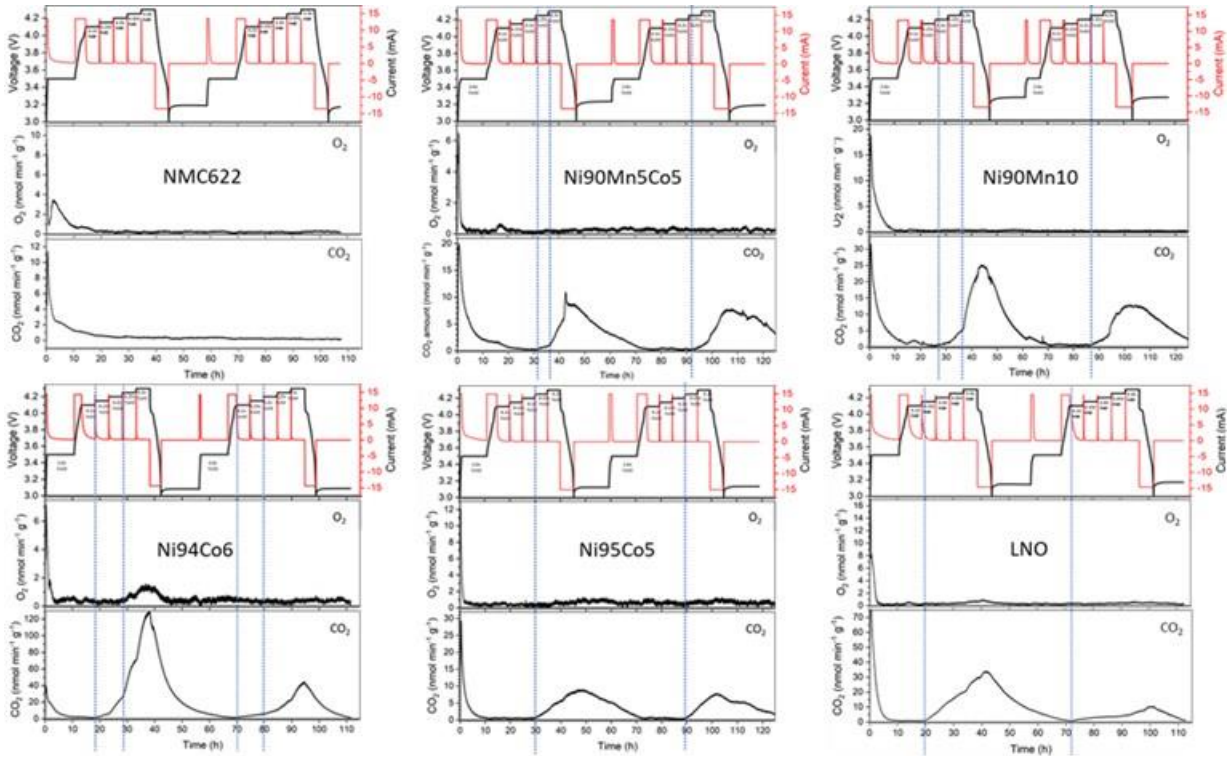

Figure II.2.B.12 Gas generation onset potential and scale from various LNO-based oxide materials in full cells.

The cathodes tested included the baseline NMC-622, $LiNi_{0.9}Mn_{0.05}Co_{0.05}O_2$ (NMC9055), $LiNi_{0.9}Mn_{0.1}O_2$ (Ni90Mn10), $LiNi_{0.94}Co_{0.06}O_2$ (Ni94Co6), $LiNi_{0.95}Co_{0.05}O_2$ (Ni95Co5) and $LiNiO_2$ (LNO). Baseline NMC-622 is shown not to generate detectable O_2 and CO_2 gases up to 4.3V. As observed from the figure, all LNO-based cathodes with Ni-contents ≥ 90% show gas generation up to 4.3V but the onset potential and scale vary considerably.

NMC9055 starts to generate low amounts of CO_2 at 4.25V and the rate of CO_2 generation quickly increases upon reaching a voltage of 4.3V as indicated by the steeper slope. During the voltage hold of 4.3V, the CO_2 generation rate continues to increase and the maximum rate is around 9 nmol/min/g. However, no sign of major O_2 generation was detected. It is hypothesized that O_2 released from the oxide crystal lattice reacts with electrolyte before it reaches the MS. Ni90Mn10 has a similar gassing behavior to the Ni90Mn5Co5. Again, no O_2 was detected during the high voltage operation. In the first cycle, a low rate of CO_2 is detected starting at 4.2V and the CO_2 generation rate significantly increases after reaching 4.3V with a peak rate around 25 nmol/min/g. In the second cycle, the cathode/electrolyte interface of Ni90Mn10 seems to stabilize and the onset potential for CO_2 generation shifts higher to 4.25V and the peak rate of CO_2 generation at 4.3V is reduced to around 12 nmol/min/g. Ni94Co6 has the most intense gassing among all the LNO-based electrodes. In the first cycle, small amounts of O_2 are detected (~2 nmol/min/g) and CO_2 generation begins at a much earlier onset potential, and at a much higher scale. CO_2 generation begins to pick up at the low potential of 4.15V and increased generation rate of CO_2 is seen during the voltage hold. The maximum generation rate of CO_2 at 4.3V is at around 125 nmol/min/g, which is much higher than other LNO-bases cathode materials. In the second cycle, the amount of CO_2 generated is reduced, presumably because of the stabilized interface.

However, the onset potential for CO_2 generation starts as early as ~4.1V and the maximum rate is around 40 nmol/min/g, which is significantly higher than that of the other LNO-based oxides.

It is interesting to compare the results of Ni94Co6 and Ni95Co5 due to the similar composition. Note that the Ni95Co5 has much milder gas generation compared with Ni94Co6. The onset potential for CO_2 generation for Ni95Co5 is around 4.25V and the peak generation rate of CO_2 at 4.3V is around 10 nmol/min/g, putting it on par with Ni90Mn5Co5 and Ni90Mn10. It is hypothesized that not only Ni content but surface impurities are a key factor affecting gas generation, since these materials were synthesized under different conditions. For LNO, the gassing in the first cycle is significant. It is shown that CO_2 is generated starting at ~4.15V during the first cycle and the peak rate is as high as 40 nmol/min/g. In the second cycle, the gassing diminishes. However, small amounts of CO_2 start to generate as early as 4.1V and the maximum rate of CO_2 generation is around 10 nmol/min/g at 4.3V for LNO.

The effect of temperature on gas generation during battery operation was also probed on pouch cells containing the NMC9055//graphite chemistry. In-situ gas analysis was performed on the same pouch cell that was cycled at four different temperatures in four consecutive cycles. In each cycle, the pouch cell was charged to 4.3V at a C/6 rate, held at 4.3V for 3h and then discharged to 3V. As seen in Figure II.2.B.13, the charge-discharge curves at the four different temperatures almost overlay completely. At 30°C, very small amounts of O_2 and CO_2 are detected during the 4.3V voltage hold: 227 nmol of O_2 and 2493 nmol of CO_2 are generated during the cycle at 30°C. At 40°C, the onset potential for O_2 and CO_2 generation remains the same as at 4.3V. The amount of O_2 generated during the 40°C cycle is 213 nmol and the amount of CO_2 generated is 14902 nmol; the latter is significantly higher when compared with the 30°C data. When the temperature is further increased to 50°C, both the onset potential and the amount of gas generated changes significantly. For O_2, the total amount generated during the 50°C cycle increases slightly to 273 nmol. For CO_2, the onset potential of gas generation reduced significantly to around 4.1V and the total amount of CO_2 generated increased to 35532 nmol. Comparing the results of gas generation at 30°C, 40°C, and 50 °C, the response of O_2 in terms of onset potential and scale to temperature is not as much as CO_2. It is hypothesized that the highly reactive O_2 reacts with electrolyte, hence only a small amount is detected. At the highest temperature of 60°C the gas generation further intensifies. The onset potentials for both O_2 and CO_2 generation decrease to around 4.0V. The amount of O_2 and CO_2 generated during the 60°C cycle are 515 nmol and 39529 nmol, respectively, which is significantly higher than that at the other temperatures.

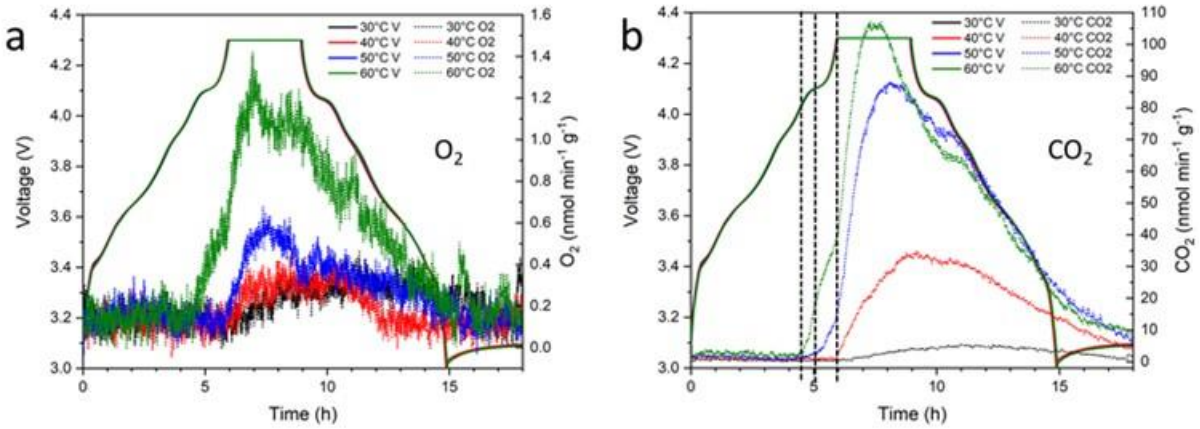

Figure II.2.B.13 O_2 and CO_2 generation rate in the Ni90Mn5Co5 cells at various temperatures.

Diagnostic studies at the post-test facility: ***Seoung-Bum Son et al., ANL***

SEM observation and XPS analysis, conducted on the pristine Ni94Co6 oxide is shown in Figure II.2.B.14. The SEM observation reveals that the powders have a non-globular powder morphology (red arrow), which would be due to lack of time for Ostwald ripening of precursors during the calcination. Particle size

distribution is bimodal (~ 2 and 15µm) to effectively increase the materials density (as well as the energy density) of the electrode.

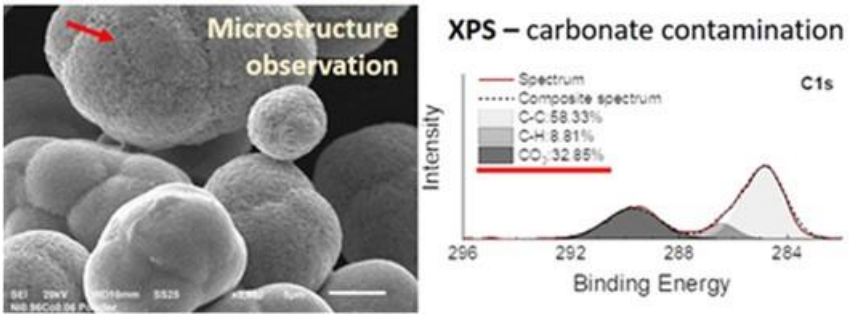

Figure II.2.B.14 Pristine $Li(Ni_{0.94}Co_{0.06})O_2$ oxide. SEM observation on the left and XPS data on the right.

The XPS results with peak fitting show the surface chemistry of the pristine powders. In the C1s region, existence of the carbonate species is revealed. Formation of the lithium carbonate on surface needs to be controlled otherwise the carbonate species would keep building up and readily aggravate issues of electrode gelation and battery swelling. In particular, the Li_2CO_3 is mainly responsible for the battery swelling as it can be oxidized to O_2 accompanied by CO_2 evolution at potentials near to 4.3 V vs. Li/Li^+.

Figure II.2.B.15 shows how the surface chemistry of the Ni94Co6 evolves depending on storage environment. The oxide powders were intentionally exposed to air for one week and two months and XPS results were compared to the samples stored in Ar-atmosphere for a week. It is clearly seen that carbonate species in C1s (290.0 eV) and O1s (531.5 eV) increased when the Ni94Co6 was stored under air compared to the Ar-storage. The increase of carbonate species in air with increasing time is likely due to the moisture and CO_2 in air. Figure II.2.B.15 also shows that the TM-oxygen peak at 528.7 eV is diminished in the air-stored Ni94Co6. This is due to the dense carbonate species blocking the XPS signal from the metal oxide.

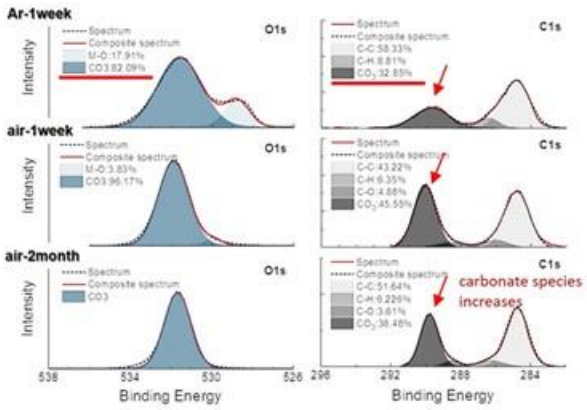

Figure II.2.B.15 XPS data from the Ni94Co6 oxide under various storage conditions. The arrow indicates carbonate species.

Diagnostic studies were also conducted on components harvested from cycled cells that were disassembled in an Ar-filled glove box. XPS data from the oxide cathodes are shown in Figure II.2.B.16, left panel. In the C1s region, the ratio of C-O and C-H bonding shows an increase between 1 and 3 standard protocol cycles (as described above). Increases in the $Li_xPO_yF_z$ species are also seen in the F1s region. Both the C1s and F1s regions indicate changes in the oxide surface species. The relationship of these species with cell capacity-retention and resistance increases will be studied further to understand the role of the cathode-electrolyte interface.

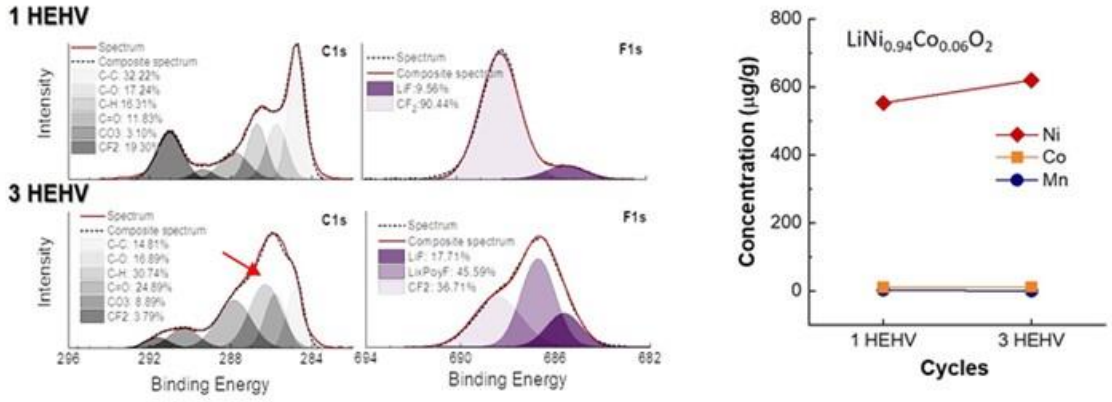

Figure II.2.B.16 XPS analysis on the cycled cathodes (left) and ICP-MS detection of TM on the graphite anode (right).

ICP-MS was used to detect TM deposition on the graphite anode. While cobalt contents were negligible, notable amounts of nickel were detected on the anode which increased with cycling, Figure II.2.B.16, right panel. The TM dissolution is believed to result from HF attack on the oxide materials.

Analytical electron microscopy studies: ***Chongmin Wang et al., PNNL***

Dopants play a crucial role in the stability of cathodes, especially for the case of high Ni concentrations. The structure and chemistry of an Al-doped, Ni-rich cathode, $LiNi_{0.92}Co_{0.06}Al_{0.02}O_2$ (See chapter II.2.A), were investigated using scanning TEM high angle annular dark field (STEM-HAADF) imaging and energy-dispersive spectroscopy (EDS) mapping as shown in Figure II.2.B.17. In the pristine state, a surface reconstruction layer of ~2 nm in thickness is formed on the particle surface (Figure II.2.B.17a). The Al dopant distribution, examined by the EDS mapping as shown in Figure II.2.B.17b, revealed that the Al is well-incorporated into the bulk lattice and is uniformly distributed. Upon cycling of the battery, the surface reconstruction layer thickness shows no significant change as representatively shown in Figure II.2.B.17c for the case of 100 cycles. EDS elemental mapping clearly reveals that the dopant Al also remains uniformly distributed in the cycled cathode particles, Figure II.2.B.17d. At the same time, a thin CEI layer is uniformly formed on the cathode particle surface as indicated by the distribution P shown in Figure II.2.B.17d. The present observation indicates that the dopant Al plays a critical role in stabilizing the layered structure upon battery cycling. Fundamentally, the function of Al can be associated with two factors: 1) the formation of a stable CEI layer, and 2) Al distributed in the lattice will lead to robust surface lattice oxygen, therefore helping to prevent Ni migration to Li layers through the octahedral-tetrahedral-octahedral pathways at the surface.

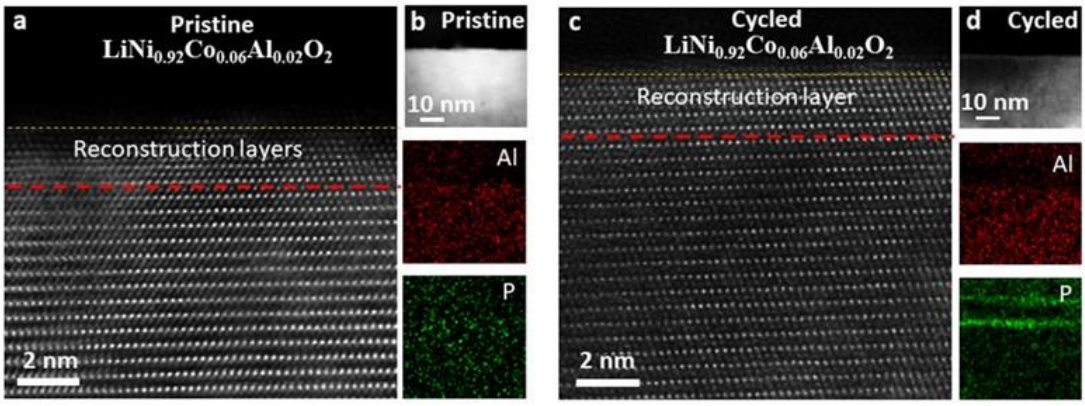

Figure II.2.B.17 Al dopant distribution, surface reconstruction, CEI layer. (a) STEM-HAADF image surface reconstruction layer on the pristine sample. (b) EDS maps of uniform distribution of Al. (c) STEM-HAADF of the surface reconstruction layer following 100 cycles. d. EDS maps of Al following 100 cycles and formation of a stable cathode electrolyte interphase layer.

For NMC oxides, subtle changes of each component can lead to significant performance modifications. For the case of Ni-rich compositions, the role of Mn and Co becomes significantly vital. In order to isolate the role of Mn and Co, the electrochemical properties of $LiNi_{0.90}Mn_{0.05}Co_{0.05}O_2$ (NMC955) and $LiNi_{0.94}Co_{0.06}O_2$ (NC9406) were compared. Upon cycling, NMC955 shows an area specific impedance of 31ohm-cm^{-2} and a capacity retention of 85% after 350 cycles, while NC9406 shows a specific impedance of 57 ohm-cm^{-2} and a capacity retention of 65% under identical cycling conditions. This electrochemical data indicates that the addition of Mn may lead to better electrochemical performance as shown above.

In order to decipher the factors that contribute to the significant differences in the electrochemical properties, we probed the structural and chemical information of the cathodes by using STEM-HAADF imaging and EDS. In particular, as the cathode-electrolyte interface is the typical site that undergoes degradation and affects to the overall performance, several interface-related properties are examined at atomic scale. The STEM-HAADF imaging shows that the pristine samples of both cathodes possess a thin surface reconstruction layer of ~2-3 atomic layers as shown in Figure II.2.B.18a and Figure II.2.B.18d. Upon cycling, the surface reconstruction layers of both cathodes becomes thicker as illustrated in Figure II.2.B.18b and Figure II.2.B.18e; ~8.5 nm for NC9406 and 4.4 nm for the NMC955. Upon relithiation, the surface reconstruction layer thickness is not changed, Figure II.2.B.18c and Figure II.2.B.18f. Based on the surface reconstruction layer thickness measurement, it is apparent that the addition of 5% Mn is beneficialdd to hindering TM mixing with Li.

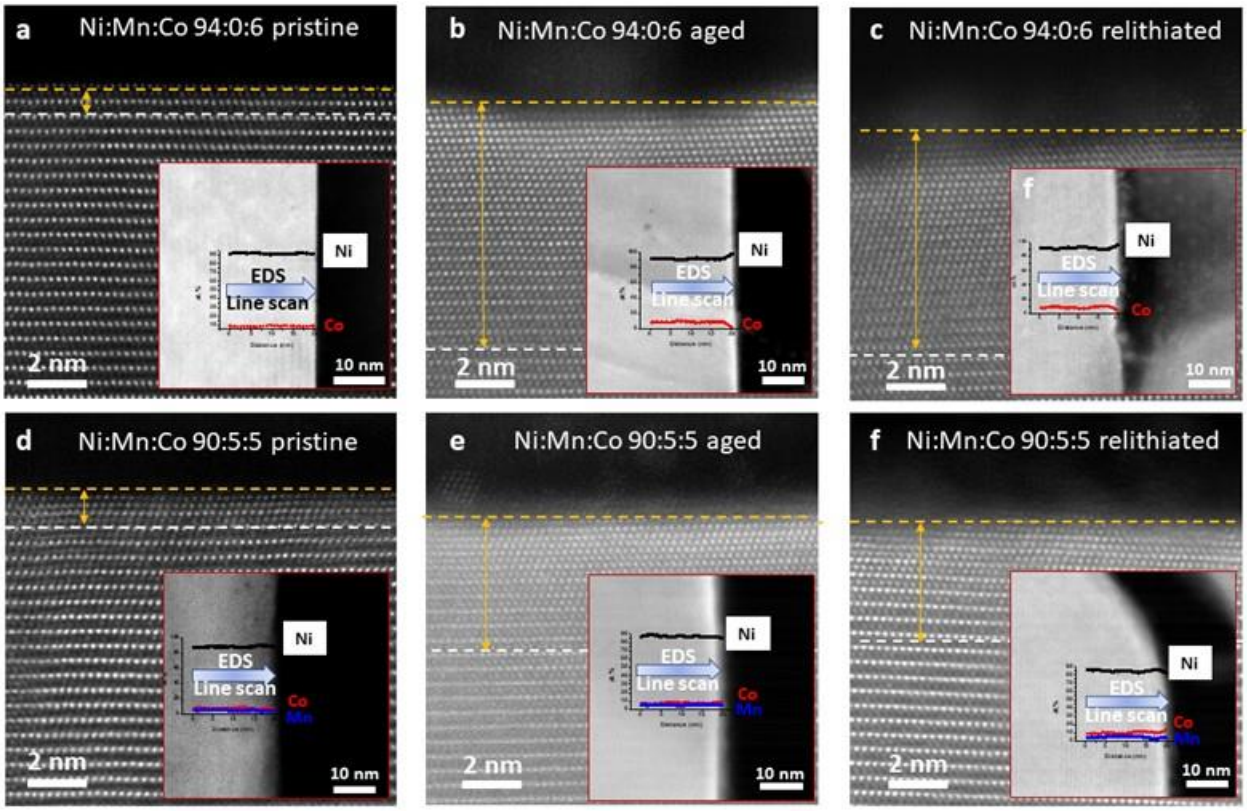

Figure II.2.B.18 **Role of Mn on the surface reconstruction layer thickness and transition metal segregation.** STEM-HAADF image showing the surface reconstruction layer thickness. a. pristine $LiNi_{0.94}Co_{0.06}$. d. pristine $LiNi_{0.90}Mn_{0.05}Co_{0.05}$. b. aged $LiNi_{0.94}Co_{0.06}$. e. aged $LiNi_{0.90}Mn_{0.05}Co_{0.05}$. c. relithiated $LiNi_{0.94}Co_{0.06}$. f. pristine $LiNi_{0.90}Mn_{0.05}Co_{0.05}$. The inset at each image is the quantified EDS line scan profile. Note the change of the Ni and Co on the particle surface.

Another prominent feature is the dependence of the surface enrichment/depletion of transition metals (TMs) on the Mn concentration upon battery cycling. The TMs are noticed to be uniformly distributed from bulk to surface for both compositions at pristine state as illustrated by the quantified EDS line scan profile and the line scan quantification (Figure II.2.B.18a and d). Upon battery cycling, the NC9406 surface shows an increase in

the Ni content from 91.6% to 97.9%, while decrease in the Co content from 8.4% to 2.1% (18b). By contrast, upon battery cycling, the NMC955 surface shows a slight reduction in the Ni content from 87% to 85%, while slight increase in the Co content from 7.5% to 9.2% (18e). Upon relithiation, both cathode surfaces show a similar TMs compositional profile as in the aged samples, with increasing Ni concentration and decreasing concentration of Co at the surface for NC9406 (Figure II.2.B.18c), contrasting the case of decreasing Ni and increasing Co at the surface for NMC955 (Figure II.2.B.18f). It should be noted that for both cases, a thin cathode electrolyte interphase was formed on the cathode particle surface. It appears that addition of 5 at% Mn dramatically modifies the interaction between the cathode and liquid electrolyte, presumably preventing oxygen loss from the surface region, thereby reducing the cation mixing with the Li ions.

Solid-state NMR characterization of oxide cathodes: ***Fulya Dogan et al., ANL***

The goal of the solid-state NMR characterization is to understand the atomic-level structural changes with various oxides compositions and to correlate the observed electrochemical behavior with local structural changes during electrochemical cycling. ^{6,7}Li nuclear magnetic resonance (NMR) spectroscopy is a structural probe that can qualitatively and quantitatively characterize and "see" lithium local environments in the bulk and on the surface, of pristine and cycled samples. In the past year the NMR effort focused on ^{6}Li and ^{7}Li solid-state NMR characterizations of pristine and cycled nickel-rich cathodes, $LiNi_{0.90}Mn_{0.05}Co_{0.05}O_2$, $LiNi_{0.90}Mn_{0.10}O_2$, and $LiNi_{0.94}Co_{0.06}O_2$ to study surface lithium bearing species due to synthesis impurities and composition differences, bulk lithium environments, TM distribution and their evolution upon cycling.

Figure II.2.B.19 (left panel) shows ^{6}Li MAS NMR data from three oxide samples with various Ni, Co, and Mn ratios. Due to the hyperfine shift mechanism observed in paramagnetic oxide systems, bulk lithium environments (coordinated to Ni and Mn in 1st and 2nd coordination shell) results in ^{6}Li peak in the 200-1000 ppm region, whereas surface Li-bearing species or segregated $LiCoO_2$ domains display in peaks in the diamagnetic, 0 ppm region. Comparison of data for the various oxides reveals that introduction of Mn in the oxide bulk broadens ^{6}Li NMR peaks, suggesting more structural disorder, partial randomization of the TM distribution and the possible presence of mixed Ni oxidation states. No preferential ordering is observed when Mn content is increases to 10% in the oxide lattice. Quantitative study of the species shows that $LiNi_{0.94}Co_{0.06}$ has the highest surface Li content of 8%, whereas $LiNi_{0.90}Mn_{0.05}Co_{0.05}$ has ~5% surface Li (Figure II.2.B.19, right panel).

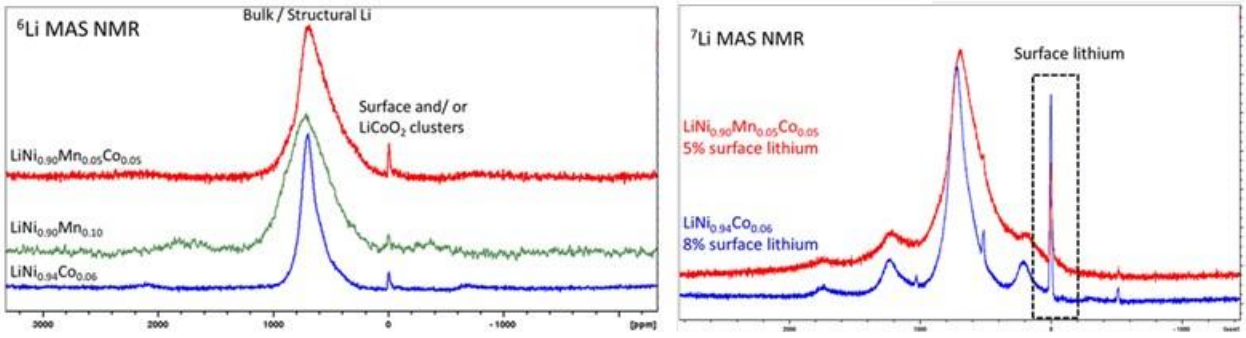

Figure II.2.B.19 ^{6}Li MAS NMR of oxide with various compositions showing local ordering differences (left figure). Quantitative ^{7}Li MAS NMR showing spectra from surface lithum bearing species on two oxide samples.

The evolution of local Li-environments on cycling was studied by ^{6}Li NMR. As shown in Figure II.2.B.20, when compared to the pristine cathode, cycled samples show shifts in the ^{6}Li NMR peak due to increase in the average TM oxidation state because of Li depletion from the oxide. Decrease in peak width for the $LiNi_{0.90}Mn_{0.05}Co_{0.05}$ composition suggests higher Li mobility, presumably due to Li loss from the lattice.

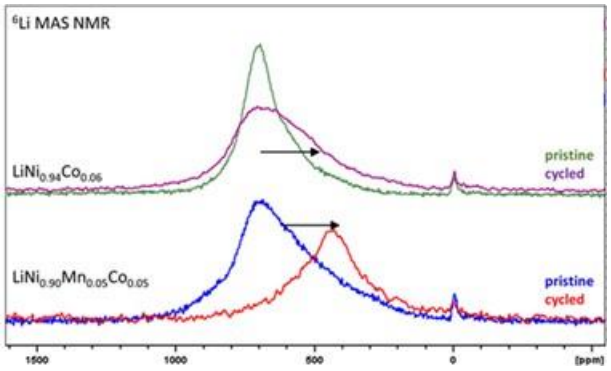

Figure II.2.B.20 Quantitative ^{7}Li MAS NMR of the oxide cathodes showing changes in Surface Li-species from cycling.

Differential scanning calorimetry (DSC) experiments: ***Wenquan Lu et al., ANL***

In order to investigate thermal stability, four oxide materials, $LiNi_{0.9}Mn_{0.05}Co_{0.05}O_2$, $LiNi_{0.9}Mn_{0.1}O_2$, $LiNi_{0.94}Co_{0.06}O_2$, $LiNi_{0.95}Co_{0.05}O_2$, were studied using DSC. From a previous study in this project, it was shown that the amount of active material, electrolyte, SOC, and temperature scan-rate play a significant role in reproducibility of the DSC data. In order to make meaningful comparisons between the materials, all the oxides were charged to 4.3V to ensure the same SOC. A controlled amount of active materials (around 3 mg) was placed in the DSC sample holder followed by addition of the electrolyte. The weight ratio of electrolyte to active material was 1:1. The temperature was scanned from RT to 400 ºC at 10 ºC/min scan rate. Figure II.2.B.21 shows the DSC results where multi-exothermic peaks were observed for all 4 samples. The first major exothermic peak and onset temperature appears to decrease with increasing Ni content. However, the total heat generation of all the samples are similar being about 1800 J/g.

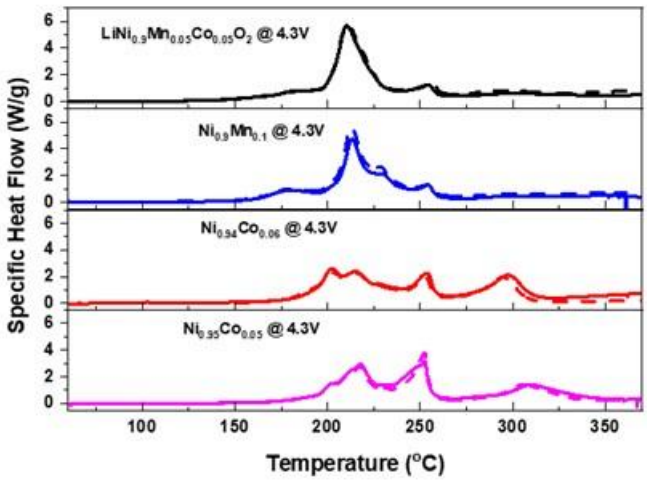

Figure II.2.B.21 DSC results of four oxide samples with various amount of Ni, Mn and Co, as indicated.

The effect of a fluoride coating on the thermal stability of $LiNi_{0.90}Mn_{0.05}Co_{0.05}O_2$ (NMC955) was also investigated. Both bare and AlF_3-coated (by ALD) electrodes were charged to 4.3V. Then electrode coatings were scraped off the current collectors and mixed with the electrolyte, as described above. The heat flow profiles of the materials are shown in Figure II.2.B.22, left panel. It is seen that the heat flow profiles of the oxide samples, with and without AlF_3 coating, are similar. The onset temperature is ~150ºC, and the first peak is at ~210ºC; however, the total heat generated, between 130ºC and 340ºC, is slightly smaller for the AlF_3-coated sample (Figure II.2.B.22, right panel). The results suggest that the electrode coating will not change the intrinsic thermal properties of the oxide but could reduce the total heat generation.

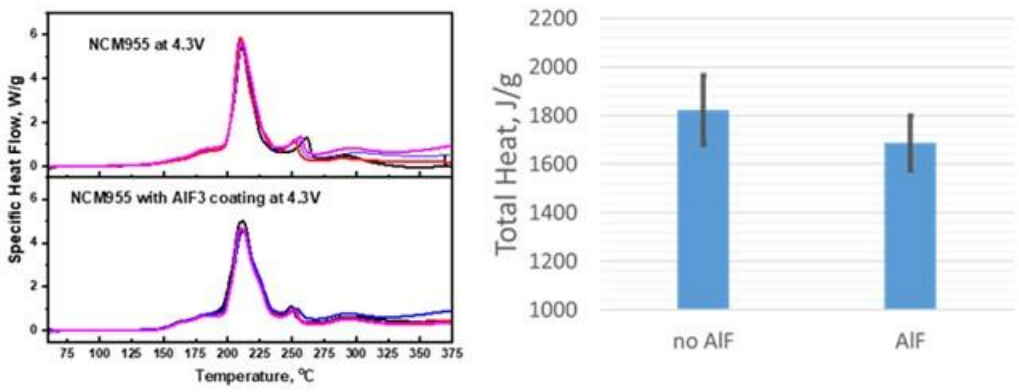

Figure II.2.B.22 Heat flow profiles (left) and total heat generation (right) from NMC955 electrodes, with and without AlF_3 coating

In-situ spectroscopic analysis of the cathode-electrolyte: ***Sang-Don Han et al., NREL***

A custom cell was designed and built for *in situ* collection of ATR-FTIR spectra while enabling reliable electrochemical battery cycling. As an example, this projected has demonstrated how the technique can be used to monitor the cathode/electrolyte interfacial interactions for $LiNi_{0.9}Mn_{0.05}Co_{0.05}O_2$ (NMC9055) during galvanostatic charging and discharging (Figure II.2.B.23). In these studies, Gen2 electrolyte (1.2 M lithium hexafluorophosphate ($LiPF_6$) in ethylene carbonate (EC):ethyl methyl carbonate (EMC), 3:7 wt%) was used. The measurements can distinguish between solvent molecules (EC and EMC) coordinating to a Li^+ ion (solvation) and free solvent molecules that do not interact with a Li^+ ion (desolvation) in the electrolyte within the CEI. Thus, it can be shown how the solvent environment surrounding the Li^+ ion in the electrolyte near the cathode surface changes during charging (oxide delithiation) and discharging (oxide lithiation) of the battery, respectively. Furthermore, it is observed that the FTIR absorptions change due to local structural variations (based on the redox behaviors of the TMs) in the oxide during cycling. In addition, it is demonstrated how the surface sensitivity of the FTIR measurement enables monitoring of CEI formation and evolution during cell cycling beginning after the first few electrochemical cycles.

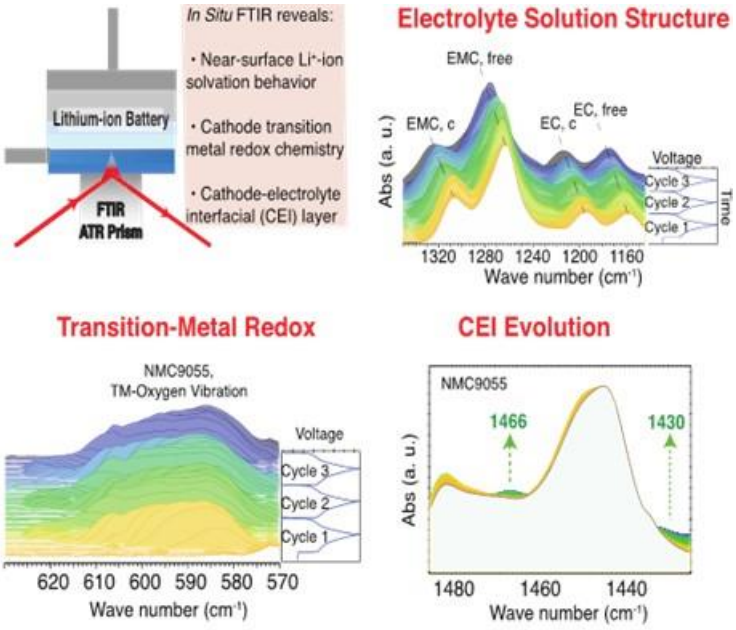

Figure II.2.B.23 In-situ ATR-FTIR is used to study the voltage-dependent electrolyte solution structure changes at the interface, transition metal redox chemistry, and cathode/electrolyte interfacial layer evolution of $LiNi_{0.9}Mn_{0.05}Co_{0.05}O_2$ during cycling.

Various NMC oxide compositions are under study to elucidate how changes in Ni content affect the Raman spectrum (Figure II.2.B.24a). In addition, an *in situ* Raman cell based on a modified 2032 coin cell that provides excellent Raman scattering signal from the cathode (i.e., $LiNi_{0.9}Mn_{0.05}Co_{0.05}O_2$ in Figure II.2.B.24b) has been developed. However, in this cell, a large broad fluorescence background appears during cycling. Advanced spectral analysis is being employed to check if meaningful signal changes can be extracted despite the large background.

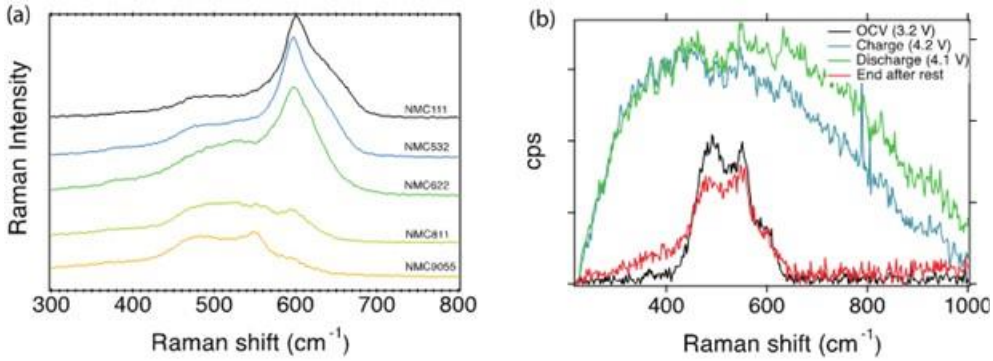

Figure II.2.B.24 (a) ex situ Raman spectra of $LiNi_xMn_yCo_zO_2$ with increasing relative Ni content, and (b) preliminary in situ Raman spectra of $LiNi_{0.9}Mn_{0.05}Co_{0.05}O_2$ during the first galvanostatic charge and discharge which shows how a large increase in fluorescence background when the electrodes are polarized complicates analyzing the NMC contribution to the signal.

Conclusions

- Low Co oxides that are variants of $LiNiO_2$ have been synthesized and scaled up to ~100 g levels. Diagnostic tests have been conducted on CAMP-fabricated electrodes containing $LiNi_{0.94}Co_{0.06}O_2$, $LiNi_{0.95}Co_{0.05}O_2$, $LiNi_{0.9}Mn_{0.1}O_2$, and $LiNi_{0.90}Mn_{0.05}Co_{0.05}O_2$.

- XPS analysis revealed the existence of carbonate species on the surface of $LiNi_{0.94}Co_{0.06}O_2$. Concentrations of the carbonate species increased when the oxides were exposed to air.

- XPS was used to confirm the removal of surface contaminants from the surface of LNO after aqueous rinsing. TOF SIMS tracking of deuterium presence in rinsed and unrinsed samples showed a significant increase both at the surface and in the bulk of the D_2O-rinsed sample compared to the unwashed and H_2O-rinsed samples. This indicates that Li^+/H^+ exchange occurred during the conventional aqueous rinsing.

- Half-cell and full-cell standardized cycling protocols developed to examine these oxide materials. Electrochemical cycling data from full cells indicate that $LiNi_{0.90}Mn_{0.05}Co_{0.05}O_2$ and $LiNi_{0.9}Mn_{0.1}O_2$ show higher capacity retention and lower impedance rise than $LiNi_{0.95}Co_{0.05}O_2$ and $LiNi_{0.94}Co_{0.06}O_2$.

- Tests in Reference-electrode cells indicate the source of impedance rise. Oxide-positive electrodes are the dominant contributors with negligible ASI rise found at the graphite-negative electrodes.

- Differential voltage analysis (DVA) has been applied to determine the sources of capacity loss from the full-cell cycling data.

- New electrolyte compositions show promise for improving capacity and power retention. Tests have been conducted using *in situ* synthesized compounds, HF getters, and dual salt electrolytes.

- Standard gassing protocol to determine the onset potential and scale of gas generation have been developed. The onset potentials for gas generation for NMC9055, Ni90Mn10, Ni94Co6, Ni95Co5 and LNO are 4.25V, 4.25V, 4.1V, 4.25V, and 4.1V respectively in full-cells. The onset potential generally decreases with increasing Ni content. The amount of gas generated, on the other hand, generally

increases with increasing Ni content. However, surface impurities also impact gassing behavior. Temperature has a direct impact on the gassing behavior. Increasing temperature reduces onset potential for gas generation and increases the total amount of gas generated for the various oxides.

- ^{6,7}Li solid-state NMR data show differences in the bulk local Li environment and surface Li content within different oxide compositions and their evolution upon cycling. Preliminary results suggest the presence of Mn introduces disorder and a random TM distribution.

- In-situ studies reveal three important aspects of the cell evolution during cycling: (i) solvation of the Li^+ ions by the solvent molecules near the cathode interface is related to the extent of electrode polarization and the (de)insertion of Li^+ ions from/into the cathode during charging/discharging of the cell, (ii) oxide lattice vibrational modes are correlated to local structural changes of the crystals, and possibly affected by the degree of Li^+ vacancies which eventually leads to a phase change, and (iii) formation and evolution of the cathode-electrolyte interface can be monitored, which is important for evaluating the cell cycle lifetime and the nature of the cathode surface.

Key Publications

1. A. Tornheim, D.C. O'Hanlon, J. Electrochem. Soc. 167 (2020) 110520.

2. L. Geng, D.L. Wood III, S.A. Lewis Sr., R.M. Connatser, M. Li, C.J. Jafta, I. Belharouak, "High Accuracy In-situ Direct Gas Analysis of Li-ion Batteries" Journal of Power Sources (2020) 466, 228211.

3. L. Geng, J. Liu, D L. Wood, III, Y. Qin, W. Lu, C.J. Jafta, Y. Bai, I. Belharouak, "Probing Thermal Stability of Li-ion Battery Ni-rich Layered Oxide Cathodes by Means of Operando Gas Analysis and Neutron Diffraction" ACS Applied Energy Materials (2020) 7058-7065.

4. D.L. Wood III, M. Wood, J. Li, Z. Du, R.E. Ruther, K.A. Hayes, N. Muralidharan, L. Geng, C. Mao, I. Belharouak, "Perspectives on the relationship between materials chemistry and roll-to-roll electrode manufacturing for high-energy lithium-ion batteries" Energy Storage Materials (2020) 254-265.

5. J. Yang, I. Shkrob, K. Liu, J. Connell, N.L. Dietz Rago, Z. Zhang, C. Liao, J Electrochem. Soc. 167 (2020) 070533.

6. J. Yang, I. Shkrob, Q. Liu, N.L. Dietz Rago, Y. Liu, K. Liu, Z. Zhang, C. Liao, Journal of Power Sources, 438 (2019) 227039.

7. I.A. Shkrob, B. Han, R. Sahore, A.P. Tornheim, L. Zhang, D.P. Abraham, F. Dogan, Z. Zhang, C. Liao, Chemistry of Materials, 31 (2019) 2459-2468.

8. C. Liao, J. Yang, I.A. Shkrob, Z. Zhang, A. Gutierrez, J.R. Croy, in: Meeting Abstracts, The Electrochemical Society, 2019, pp. 262-262.

9. H.R. Morin, D.G. Graczyk, Y. Tsai, S. Lopykinski, H. Iddir, J.C Garcia, N. Dietz-Rago, S. Trask, L. Flores, S.-B. Son, Z. Zhang, N.M Johnson, I. Bloom, ACS Appl. Energy Mater. (2020) 2565-2575.

10. S.-B. Son, D. Robertson, Y. Tsai, S. Trask, A. Dunlop, I. Bloom, "Systematic Study of the Cathode Compositional Dependency of Cross-talk Behavior in Li-ion Battery" J. Electrochem. Soc. Under review.

11. B.J. Tremolet de Villers, Y. Ha, S.-D. Han, "Investigating Electrode-Electrolyte Interphase Formation, Reactivity and Evolution in Lithium-Ion Batteries with Operando Spectroscopic Techniques" Oral presentation, 236th ECS Meeting, Atlanta, GA (2019).

12. B.J. Tremolet de Villers, S.-M. Bak, J. Yang, S.-D. Han, "In Situ ATR-FTIR Spectroscopic Analysis of NMC622 Cathode: Correlating Specific Chemistries within the Cathode-Electrolyte Interface to FTIR Signatures" Oral presentation, ECS PRiME Meeting (2020).

13. B.J. Tremolet de Villers, S.-M. Bak, J. Yang, S.-D. Han, "In situ ATR-FTIR Study of Cathode-Electrolyte Interphase: Electrolyte Solution Structure, Transition Metal Redox, and Surface Layer Evolution", Batteries & Supercaps, Under Review.

14. J.R Jokisaari, J. Guo, J. Bareno, D.P. Abraham, R.F. Klie, "Meso to Atomic Scale Microstructural Changes During Ageing of NCM Li-ion Battery Materials", Microscopy and Microanalysis 25 (2019) pp. 764-765.

15. A. Tornheim, J. Garcia, R. Sahore, I. Bloom, H. Iddir, Z. Zhang, "Decomposition of phosphorus-containing additives at a charged NMC surface through potentiostatic holds", J. Electrochemical Society 166 (2019) pp. A440-A447.

16. K. Kalaga, M.T.F. Rodrigues, J. Bareño, I.A. Shkrob, D.P. Abraham, "Insights from incorporating reference electrodes in symmetric lithium-ion cells with layered oxide or graphite electrodes", Journal of Power Sources 438 (2019) p. 227033.

Acknowledgements

Adam Tornheim, S.J. An, J. Bareño, I. Belharouak, I. Bloom, J.R. Croy, Y. Cui, L. David, Z. Du, J.C. Garcia, J.A. Gilbert, D.J. Gosztola, M. He, H. Iddir, A.N. Jansen, K. Kalaga, F. D. Key, J. Li, C. Liao, C. Mao, V. A. Maroni, H.M. Meyer, D.C. O'Hanlon, C. Peebles, B.J. Polzin, M.-T.F. Rodrigues, R.E. Ruther, R. Sahore, Y. Sheng, I. A. Shkrob, A. Tornheim, S.E. Trask, G. Veith, M. Wood, D.L. Wood, Z. Zhang, Pragathi Darapaneni, Steve Harvey, Anil Mane, Jeff Elam, Support from the U. S. Department of Energy (DOE), Vehicle Technologies Office, Peter Faguy, and David Howell is gratefully acknowledged.

II.2.C Theory and Modeling (ANL, LBNL, PNNL, NREL, ORNL)

Hakim Iddir, Principle Investigator
Argonne National Laboratory
9700 South Cass Avenue
Lemont, IL 60439
E-mail: Iddir@anl.gov

Guoying Chen, Principal Investigator
Lawrence Berkeley National Laboratory
1 Cyclotron Road
Berkeley, CA 94720
E-mail: gchen@lbl.gov

Peter Faguy, DOE Technology Development Manager
U.S. Department of Energy
E-mail: Peter.Faguy@ee.doe.gov

Start Date: October 1, 2018 End Date: September 30, 2021
Project Funding: $4,000,000 DOE share: $4,000,000 Non-DOE share: $0

Project Introduction

Geopolitical concerns over critical resources, and in particular cobalt, as well as market demand have instigated new efforts to improve the sustainability of lithium-ion cathode technologies. This project will use first-principles modeling applied to prototypical cobalt free cathode oxides including $LiNiO_2$ (LNO), $LiNi_{0.5}Mn_{0.5}O_2$, and newly developed derivatives thereof in order to advance cathode design in accord with DOE targets for cost, performance, and sustainability.

Objectives

- Identify promising surface and bulk dopant elements and provide a fundamental understanding of their efficacy in modifying the properties of low/no cobalt oxides with respect to cobalt as a counterpart.
- Improve cathode design by understanding and elucidating the mechanisms and tendencies of facet-dependent degradation, stability, and dopant segregation.
- Narrow the gap in understanding between structure-property relationships by elucidating the effects that local phenomena (e.g., cation ordering) have on measured, physical and electrochemical data.

Approach

The calculations required to accomplish the project goals were performed within the spin polarized density functional theory (DFT) methodology as implemented in the Vienna Ab Initio Simulation Package (VASP) [1], [2]. The generalized gradient approximation (GGA) is used to model the exchange-correlation potentials as developed by Perdew, Burke, and Ernzerhof (PBE) [3]. The interaction between valence electrons and ion cores is described by the projected augmented wave (PAW) method [4]. Furthermore, the GGA+U scheme is used for applying the on-site correlation effects among 3d electrons of the transition metals, where the parameter of (U−J) is set to 5.96, 5.00, and 4.84 eV for Ni, Co, and Mn, respectively [5]. The magnetization was used to assign the oxidation state of the ions. Therefore, in order to get a better representation of the electronic structure, a single point calculation with a screened hybrid functional (HSE06) is performed after each geometry optimization [6].

Total energy and hyperfine shift calculations were accomplished using the Vienna Ab initio Simulation Package (VASP) under the projector augmented wave (PAW) pseudopotentials with the generalized gradient

approximation (GGA) of the Perdew-Burke-Ernzerhof (PBE) exchange-correlation function. Two types of $LiMn_{0.5}Ni_{0.5}O_2$ supercells were used: 2x2x1 unit cell (192 atoms) and 2x2x2 (384 atoms) as circumstances demanded. Random distribution of transition metals (TM) was conducted by the assistance of Pymatgen codes. An energy cutoff of 500 eV with a Monkhrost-Pack reciprocal space grid of 1 x 1 x 1 KPOINT scheme was used for the supercell structure. Spin-polarized calculations were performed and pseudopotential of Li (1s,2s), O (2p), Ni (3p,3d,4s), and Mn (3p,3d,4s) were chosen. In order to correct the self-interaction of electrons, Hubbard correction terms were applied to Ni (6.2 eV) and Mn (3.9 eV). Atomic coordinates were fully relaxed until the forces on each atom were below 0.02 eV/Å. Theoretical Fermi contact shifts were calculated by: equation (1) below:

$$\delta_{contact} = \frac{\chi_M * A_{iso} * S(tot)}{3 * S * N_A * \gamma_N} \qquad (1)$$

where χ_M, A_{iso}, $S(tot)$, S, N_A, and γ_N represent magnetic susceptibility, the hyperfine coupling constant, a total magnetic moment of the unit cell, nuclear spin quantum number, Avogadro's number, and gyromagnetic ratio, respectively. χ_M was obtained from the literature [7], [8]. A_{iso} and $S(tot)$ were collected from the VASP output as "A_{tot}" and "total magnetic moment", respectively.

Results

Understanding the role of Co through modeling and model systems

In order to understand the role of Co on layered cathode materials, a ($LiMn_xNi_xCo_{1-2x}O_2$) model systems have been designed such that Ni resides in a layered structure and exists only as Ni^{2+}. The model allows to investigate the minimum amount of Co needed to maintain a layered structure against Li/Ni exchange and Ni/Mn migration. Furthermore, the effect of Co clustering, domain size, and local configuration effects on structural stability was studied. Additionally, NMR shifts as a function of local ordering, using DFT, have been calculated and compared to the experimental spectrum.

Starting from the zigzag structure, the DFT the total energy is calculated for several random configurations generated by random swapping of Ni with Mn. The process is repeated for hundreds of structures. The final goal is to understand the effect of metal-metal interactions on the overall energies. Figure II.2.C.1. shows the energy distribution and the correlation for metal-metal bonds with energy. The trends clearly show a dependency of the energy on the amount of Ni-Mn bonds: More Ni-Mn bonds decrease the total energy of the system. Hence, the interactions favor Ni-Mn bond formation while Mn clustering is not favorable.

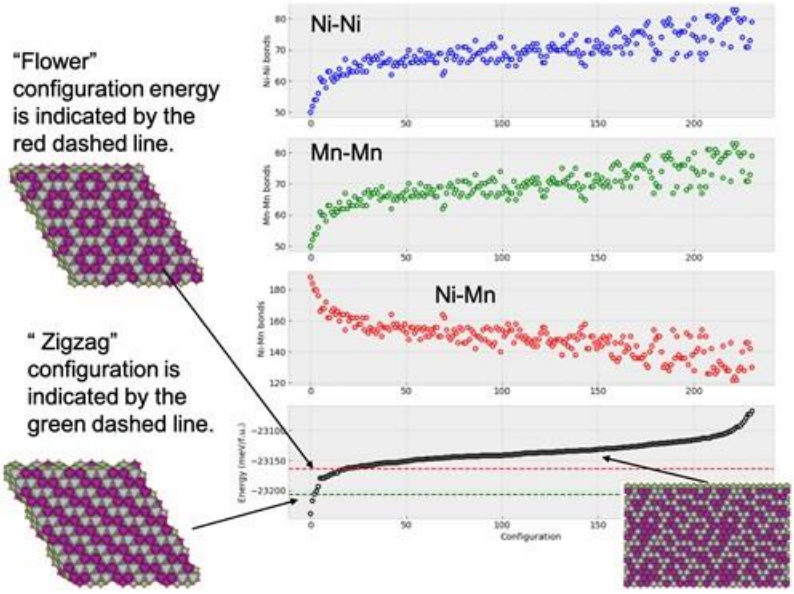

Figure II.2.C.1 Total energy as a function of the number of metal-metal bonds in $LiNi_{0.5}Mn_{0.5}O_2$.

In order to better understand NMR experimental results, DFT Fermi contact shifts have been computed. DFT is suitable to explore a large configurational space and compute the NMR shifts of select low energy structures. DFT calculated ^{6}Li NMR shifts capture the main structural features reflected in the experimental NMR spectra. Examples of local Li environments are shown in Figure II.2.C.2. Cation mixing (Li/Ni exchange) produces new NMR shifts. Also, variations in Li-O-TM angles and distances affect the computed NMR shifts, contributing to further broadening of the overall spectra.

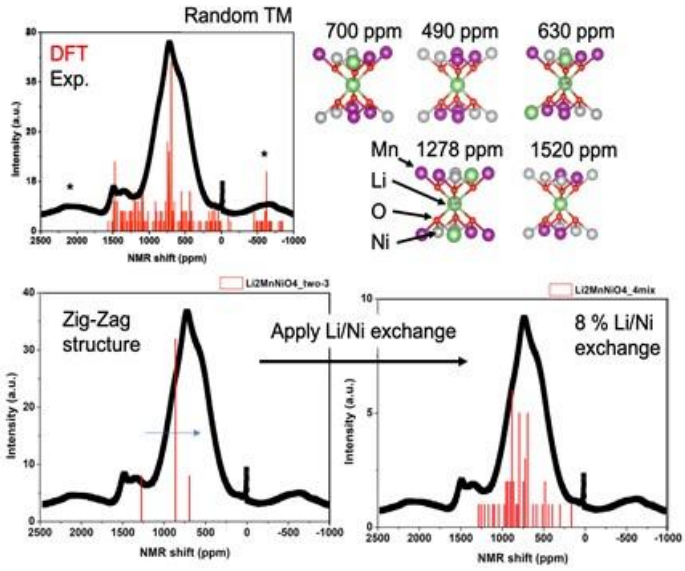

Figure II.2.C.2 Computed NMR shifts and comparison with experimental spectra for $LiMn_{0.5}Ni_{0.5}O_2$. Examples of local ordering and the effect of Li/Ni exchange on the computed NMR shifts for the low-energy zig-zag configuration are shown.

Strain-driven surface reconstruction and cation segregation in layered cathode materials

It has been found before that cobalt within the TM layer shows a driving force for segregation towards the (104) surface. On the other hand, Ni within the TM layer does not show any driving force for Ni to segregate to the surface. The total energy of the system increases with the increase of Ni within the top three TM surface layers. In fact, slabs with non-uniform Ni concentration profiles are energetically unfavorable. Although the

supercell models used here are rather large for DFT calculations (9 TM layers, 384 atoms), such segregated slabs cannot represent actual systems accurately, given the strain produced in the cell due to the constant overall stoichiometry constraint.

Since there is no evidence of a driving force for the segregation of Ni within the TM layer, a different mechanism must be responsible for the experimentally observed Ni-rich surfaces. Ni is known to produce Li-Ni anti-site defects. Such defects can actually migrate to, or favorably form, near to the surface given the mobility of Ni^{2+} ions which have a similar size to Li ions. In fact, it has been shown that Ni can readily diffuse to the surface once it is in the Li layer given the lower energy barrier for Ni diffusion in the Li layer compared to that of Li [9]. In order to get some insights into this process, the energy of formation of Li-Ni anti-site defects in the bulk of NMC-111 was computed and found to be E_f = 0.3eV/f.u. Using the energy of formation, the concentration (C) of a defect can be estimated as: $C = Aexp(-Ef/k_BT)$. Where the pre-exponential factor accounts for the total number of defect configurations, k_B is the Boltzmann constant and T is the temperature [10]. Such energy of formation corresponds to a concentration of about 1.3%. This value is in agreement with experimental values (1.6%) for NMC-111 [11]. Our results show that the probability of a single Ni anti-site defect formation is insensitive to its distance to the surface. A schematic of the Ni anti-site location is shown in Figure II.2.C.3.

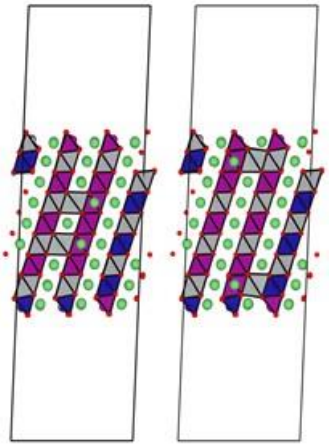

Figure II.2.C.3 Slab polyhedral model for pristine $LiNi_{1/3}Mn_{1/3}Co_{1/3}O_2$ (NMC-111) surface (012) with cation disorder (a) Li/Ni exchange in the bulk region, (b) Li/Ni exchange in the surface region. The NiO_6 octahedra are represented in grey, CoO_6 octahedra are represented in blue and MnO_6 octahedra are represented in purple. The Li ions are indicated by green spheres.

Since a Ni-rich surface reconstruction (SR) has been found experimentally, initial analysis was conducted considering the extreme case of complete Ni segregation to the (012) surface of fully lithiated NMC-111. In particular, the relative stabilities of the possible $Li_2Ni_2O_4$ (over-lithiated spinel) and $LiNiO_2$ (layered) surface phases were considered. Figure II.2.C.4. shows the total energy of the system when the layered and spinel phases are pinned to the (012) facet of NMC-111 as a function of the C/C_0 ratio. The parameter C_0 represents the unstrained reference SR phase. In the unrelaxed system, where C/C_0 equals 1.00, the strain caused by pinning the SR phase to the NMC unit cell increases the energy of the $Li_2Ni_2O_4$ SR phase (S-LNO/NMC, Figure II.2.C.4a) over the layered phase (L-LNO/NMC), which is slightly more stable at this point. However, if the SR is considered as a thin film that is allowed to relax in the direction perpendicular to the surface, the surface film would shrink in response to the applied tensile strain. The energy would then decrease, and the spinel phase would be more stable than the layered. However, for pure $Li_2Co_2O_4$ the result is opposite, and the total energy of the layered phase is always lower than that of the spinel phase (see Figure II.2.C.4b).

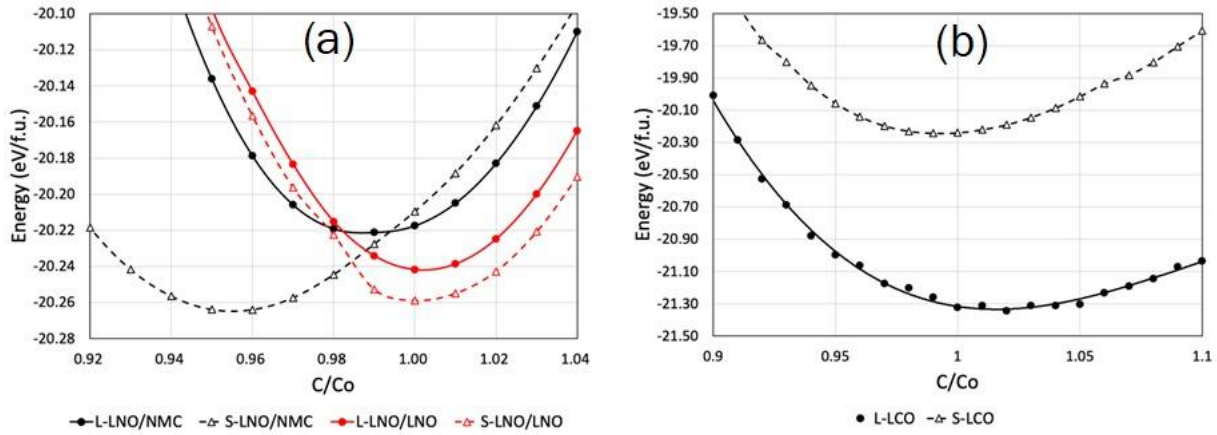

Figure II.2.C.4 Energy change with c direction expansion for (a) layered and overlithiated spinel $LiNiO_2$ ($Li_2Ni_2O_4$) pinned to NMC-111 and layered $LiNiO_2$, (b) layered and overlithiated spinel $LiCoO_2$ ($Li_2Co_2O_4$) pinned to NMC-111 (012) surface.

In summary, a complex mechanism for Ni segregation is put forward, where the presence of a thermodynamic driving force for the segregation of Ni to the surface via Li-Ni exchange near the (012) surface, and strain-driven stabilization of the $LiNi_2O_4$ spinel thin film pinned to NMC and $LiNiO_2$ lattices are revealed. This is an indication of a driving force for the inter-dependence of Ni segregation and surface reconstruction in the (012) facet. The elemental segregation and SR layer formation are intimately linked and facet dependent phenomena. The global composition and strain affect the nature and the thickness of the SR, which impacts the impedance and also necessarily the chemical stability of the cathode/electrolyte interface as well.

Transition-Metal Dissolution from NMC Oxides: A Case Study

The static reactions of highly delithiated $Li(Ni_{1/3}Mn_{1/3}Co_{1/3})O_2$, $Li(Ni_{0.5}Mn_{0.3}Co_{0.2})O_2$, $Li(Ni_{0.6}Mn_{0.2}Co_{0.2})O_2$, and $Li(Ni_{0.8}Mn_{0.1}Co_{0.1})O_2$ positive electrodes were investigated with 2,3-butanedione and with tetrabutylammonium bifluoride as model leaching agents. The response of charged, positive electrode materials in the Li(Mn, Ni, Co)O2 family was tested experimentally by using two leaching agents, biacetyl and bifluoride, in static tests. These agents represent species that might be found in an operating lithium-ion cell and that may be responsible for the increased rate of corrosion at high voltages. The response to biacetyl was statistically weak, but it was more selective for Ni than for the other metals, as expected. The response to the bifluoride salt was statistically stronger, allowing for modeling of the process. We found that [Ni] was proportional to $X_{Co}(X_{Ni})3$ and inversely proportional to $(X_{Mn})2$; [Mn] to$X_{Co}(X_{Ni})$; and [Co] toX_{Co}, which suggests that nickel as a next-nearest neighbor can make dissolution more favorable in some instances. These expressions can be related to possible configurations of atoms on the surface of the charged positive electrode. Different de/stabilizing next-nearest neighbor (NNN) configurations were found for the two leaching agents, implying that the free energy of formation of the product should also be included.

The energy needed to form a complex using a TM from the surface was calculated using a slab model with 12 Å vacuum space (see Figure II.2.C.5). Surface facets (104) and (012) were simulated because they have been found to be the most predominant in NMC positive electrodes. Each slab has 8 layers, formed by TMs and Li ions in octahedral sites, containing a total of 72 TM ions. The first three layers are delithiated in order to simulate a charged positive electrode. An implicit solvation model was used to describe the interactions between the metal complex and the solvent, as implemented in DFT code VASP. The dielectric constant for this continuum medium was chosen to be 18.5, as recommended for an EC/EMC (3:7 by weight) binary mixture at room temperature.

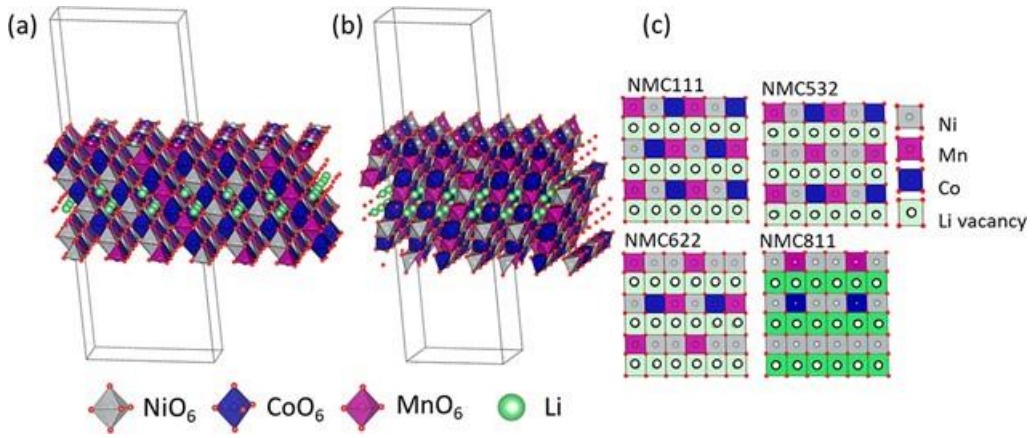

Figure II.2.C.5 Schematic representation of the charged NMC-111 slab model surface for (a) facet (104) and (b) facet (012). (c) top view of the surfaces for the four studied compositions.

Revisiting the Mechanism Behind TM Dissolution from Delithiated $LiNi_xMn_yCo_zO_2$ (NMC) Cathodes

Dissolution of TMs from lithium-ion battery cathodes under high-voltage conditions is a major issue affecting battery performance that is not well understood mechanistically. Here, this phenomenon is studied by chemically aging pristine and charged $LiNi_{0.5}Mn_{0.3}Co_{0.2}O_2$ (NMC-532) cathodes in the presence of different solutions. The solution compositions were varied by 1) adding water to a standard electrolyte, 2) replacing $LiPF_6$ salt with lithium acetylacetonate (Li-acac), 3) and/or adding oxidatively unstable tris(2,2,2-trifluoroethyl) phosphite (TTFP) as an electrolyte additive. Results demonstrate that while TM dissolution from *pristine* NMC-532 cathodes is dominated by HF-attack, TM dissolution from *charged* NMC-532 cathodes is affected by many other factors apart from HF-attack. It is suggested that reduction of TMs due to chemical/electrochemical oxidation of the electrolyte at the cathode/electrolyte interface, followed by formation of soluble TM-complexes with concomitant Li^+ intercalation into the cathode, is the dominant mechanism of TM-dissolution at high voltage.

Computational studies of isolated and solvated molecules and ions were carried out using a DFT method with the B3LYP functional and 6–31+G(d,p) basis set from the Gaussian 09 suite. All calculations of the cathode material were carried out using spin-polarized DFT as implemented in the Vienna Ab initio Simulation Package (VASP). The exchange-correlation potentials were treated by the generalized gradient approximation (GGA) parametrized by Perdew, Burke, and Ernzerhof (PBE). The interaction between valence electrons and ion cores was described using the projected augmented wave (PAW) method. Furthermore, the GGA+U scheme was used for applying the on-site correlation effects among 3d electrons of the TM ions, where the parameter of (U-J) was set to 5.96, 5.00, and 4.84 eV for Ni, Co, and Mn, respectively.

Figure II.2.C.6a shows the DFT-calculated projected d-band density of states on the TMs in a fully-lithiated, pristine NMC cathode. The lowest-lying unoccupied states belong to the Mn ions; these states are more susceptible to accepting extra electrons resulting from electrolyte/additive oxidation. However, in the charged state, it is the unoccupied Ni d-states that are closer to the Fermi level (see Figure II.2.C.6b). Therefore, in the charged state Ni ions will be more susceptible to reduction. Theoretically, the partial charges of the various TM metals in the cathode should depend only on the cathode's state of charge (SOC). Hence, the nature of the solution is not expected to affect which TMs are reduced at a given SOC. As such, at a given SOC, differences between the relative proportions of dissolved metals likely result from different interactions between the three TMs and the available anions and ligands, causing preferential solubilization.

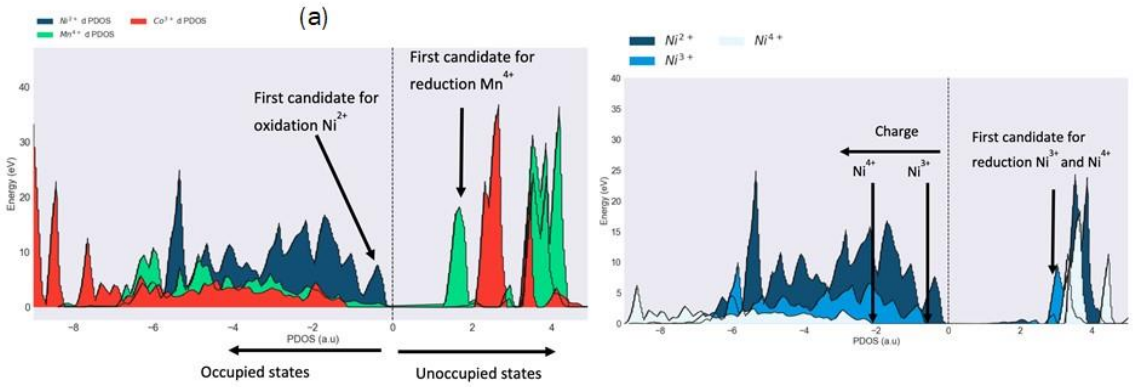

Figure II.2.C.6 Projected density of states (PDOS) on the transition metals on (a) fully lithiated (pristine) NMC and (b) partially delithiated (charged) NMC. The dashed lines indicate the Fermi level.

The role of dopants in Ni-rich cathode materials

To limit the cathode surface reactivity with the electrolyte, a high throughput screening for dopants is performed to understand the role of dopants on the reactivity of Ni-rich layered cathode surfaces. Dopants destined to reduce surface reactivity should prefer to segregate to the surface, while dopants destined to improve bulk stability (such as pillars) should prefer bulk sites. The preliminary results show that the TMs prefer to stay in the TM layer when the oxidation state is 3+ or higher. Also, decreasing by one period in the periodic table decreases the stability of the dopant in the TM layer, while decreasing by a group increases the stability in the TM layer. As expected, larger TMs exhibit larger driving force to move to the Li layer. Metalloids (As, Sb) also prefer to be in the TM layer, but the ion size does not affect location significantly. Post TMs do not present strong preference for either layer (TM or Li). Alkaline earth metals (Mg, Ca) have a small tendency to migrate to the Li layer and the driving force increases with size. In general, the preference to sit in either the TM layer or the Li layer depends on the crystal field stabilization energy of the dopant and its ionic radius. More detailed simulations are underway.

The formation energy of an oxygen vacancy has been used as a proxy for reactivity. How much energy is needed to remove an oxygen from the surface is a good indication of how easy is to reduce the surface. Figure II.2.C.7. Shows the reactivity and tendency of a select group of dopants to migrate (or stay) at the surface. Dopants in the second quadrant decreased the reactivity and stay at the surface. Those dopants are potentially beneficial for the electrochemical performance of the cathode. For example, Al prefers to be on the surface and decreases surface reactivity significantly. Pd, Y, Mo, Zr and Sn prefer the surface and decrease reactivity. In, Sb, Ga, and Mg prefer to stay in the bulk region. Furthermore, dopant segregation for $LiNiO_2$ is found to be facet-dependent with data from (104) and (001) facets currently being analyzed (not shown). This indicates that the reactivity of doped $LiNiO_2$ can change with particle shape.

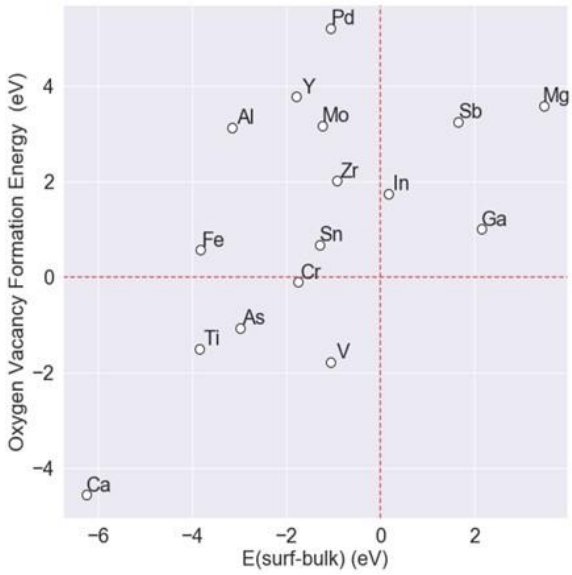

Figure II.2.C.7 Reactivity of doped $LiNiO_2$ (012) facet as a function of the dopant site preference.

Hysteresis in Lithium Rich Oxides: Anionic Activity or Defect Chemistry of Cation Migration

Novel systems, beyond layered LNO-based cathodes, are also of importance for next-gen advancements. Li-excess materials in particular offer the possibility of expanding the portfolio of energy storage materials through a deeper understanding of their unique physicochemical properties. A model, Li-rich cathode-oxide, $Li_{1.2}Ti_{0.4}Cr_{0.4}O_2$, was probed via DFT calculations and detailed analysis of operando XAS data in order to gain insights on the possible mechanisms associated with hysteresis in Li-rich oxides. Calculations show that neither oxygen nor Ti contribute to the electrochemical capacity of this material. Furthermore, oxidation of Cr^{3+} to Cr^{6+} is concomitant with both Cr and Ti migration from octahedral to tetrahedral sites, enhanced by a d^0 configuration. Subsequent re-lithiation of the oxide is subject to an energy penalty due to the unfavorable occupation of lithium surrounding the tetrahedral sites. XAS and electrochemical analysis on the experimental system are in good agreement and corroborate these findings.

The results presented in this work (*see Key Publication 2*) clearly demonstrate that anion redox in Li-rich oxides is not a prerequisite for hysteresis and energy inefficiency. Chemical inhomogeneities (e.g., local ordering and short-range order) as well as electronic structure can have a significant impact on defect formation and the subsequent electrochemical properties, in the absence of anion redox or loss. Such defects, being local phenomena, are expected to play an important role in all classes of Li-rich oxides, including disordered rock salts. In particular, promising strategies that take advantage of double-redox in disordered oxides in order to mitigate anion activity might be greatly improved if further explored with these considerations in mind.

Understanding reactivities of Ni-rich Li[NixMnyCo1-x-y]O2 single-crystal cathode materials

While LNO-based, Ni-rich $Li[Ni_xMn_yCo_{1-x-y}]O_2$ (NMC, $x \geq 0.8$) compounds are considered the most promising cathode materials for high-energy lithium-ion batteries (LIBs), a significant challenge is the higher reactivities caused by the increased Ni content, especially under SOC operation conditions. Here, NMC samples with well-controlled physical attributes and varied compositions were used to evaluate the role of each TM on stabilities. Three single-crystal (SC) samples, $LiNi_{0.8}Mn_{0.1}Co_{0.1}O_2$ (NMC-811), $LiNi_{0.80}Mn_{0.15}Co_{0.05}O_2$ (NMC-80155) and $LiNi_{0.85}Mn_{0.10}Co_{0.05}O_2$ (NMC-85105), were synthesized in the same particle size and same truncated-octahedron shape with the (012)-family surface (Figure II.2.C.8a). X-ray diffraction (XRD, Figure II.2.C.8b) analysis confirms the well-layered phase with a hexagonal α-$NaFeO_2$-type structure ($R\bar{3}m$ space group) in all samples, whereas the hard X-ray absorption spectroscopy (XAS) *K*-edge spectra (Figure II.2.C.8c) shows that the chemical oxidation states of Mn, Co and Ni are consistent with the theoretical values.

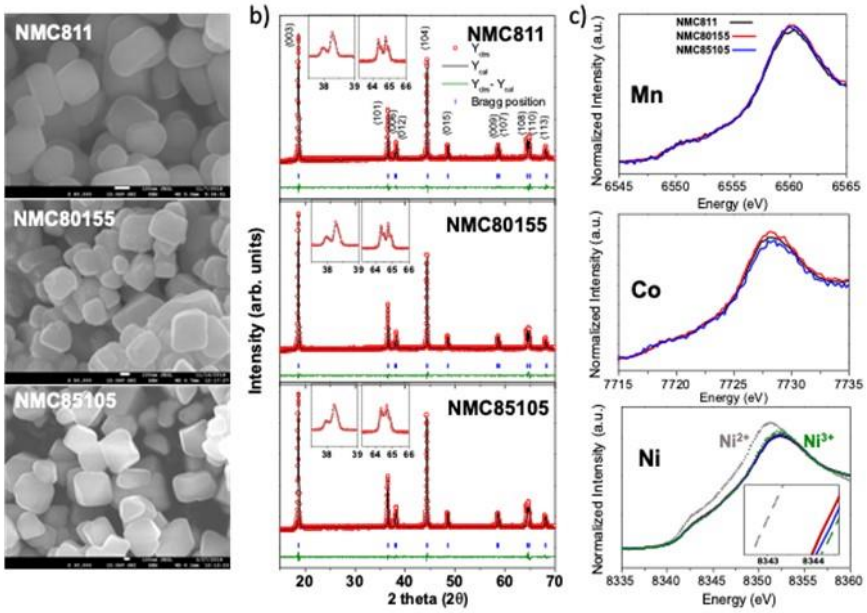

Figure II.2.C.8 a) SEM images, b) Rietveld refinement of X-ray diffraction patterns and c) hard XAS K-edge spectra of Mn, Co and Ni collected on as-synthesized single-crystal NMC-811, NMC-80155 and NMC-85105 samples. Insets in b): expanded Bragg peaks of (006)/(012) at ~ 38.2° and (108)/(110) peaks at ~ 64.5°.

Air stability was investigated by exposing the crystal samples in ambient air for 3 weeks, after which the changes in crystal structure and surface chemical compositions were analyzed by XRD and soft XAS, respectively. As the exposure time was relatively short, the layered crystal structure was largely preserved in all NMCs, as shown in the XRD patterns (Figure II.2.C.9a). Although crystalline Li_2CO_3 or LiOH phases were not detected, the enhanced XRD background indicates the possible presence of amorphous materials. Careful examination of the (006)/(012) and (108)/(110) doublets at ~ 38.2° and 65° (2Θ), respectively, also showed a reduction in the quality of peak splitting in air-exposed NMCs. These changes are most significant in NMC-85105, confirming the correlation between higher Ni content and air sensitivity. Figure II.2.C.9b-d show Mn, Co and Ni L-edge soft XAS spectra collected on pristine and air-exposed NMCs in the fluorescence yield (FY) mode. Compared to the pristine state, the intensity ratio of the Ni L_3 peaks (I_{high}/I_{Low}) decreased in all air-exposed samples (Figure II.2.C.9b), indicating reduction of surface nickel after exposing to air for 3 weeks. This is consistent with previous reports where spontaneous reduction of Ni^{3+} in air was shown. In the Mn *L*-edge spectra (Figure II.2.C.9c), the intensity of the L_2 edge increased while the ratio of the L_3 peaks (I_{high}/I_{Low}) decreased after air exposure, indicating that Mn reduction also occurs in the air-exposed NMCs. The cobalt *L*-edge spectra, on the other hand, maintained the same Co^{3+} profile before and after air exposure (Figure II.2.C.9d), confirming its superior chemical stability. We note that spontaneous reduction of surface Ni^{3+} is likely the origin of NMC degradation in air, which leads to the release of lattice O and subsequent reduction of Mn^{4+}. The resulting Mn^{3+} and Ni^{2+} have higher mobility and tendency to move towards the octahedral sites in lithium layers, rendering the gradual transformation of the layered structure to spinel-like or rocksalt-type structures, known as surface reconstruction (SR). The stability of NMC materials, therefore, are strongly dependent on nickel content. These results reveal the mechanisms necessitating that precautions be taken to avoid exposure of as-synthesized Ni-rich NMCs to air.

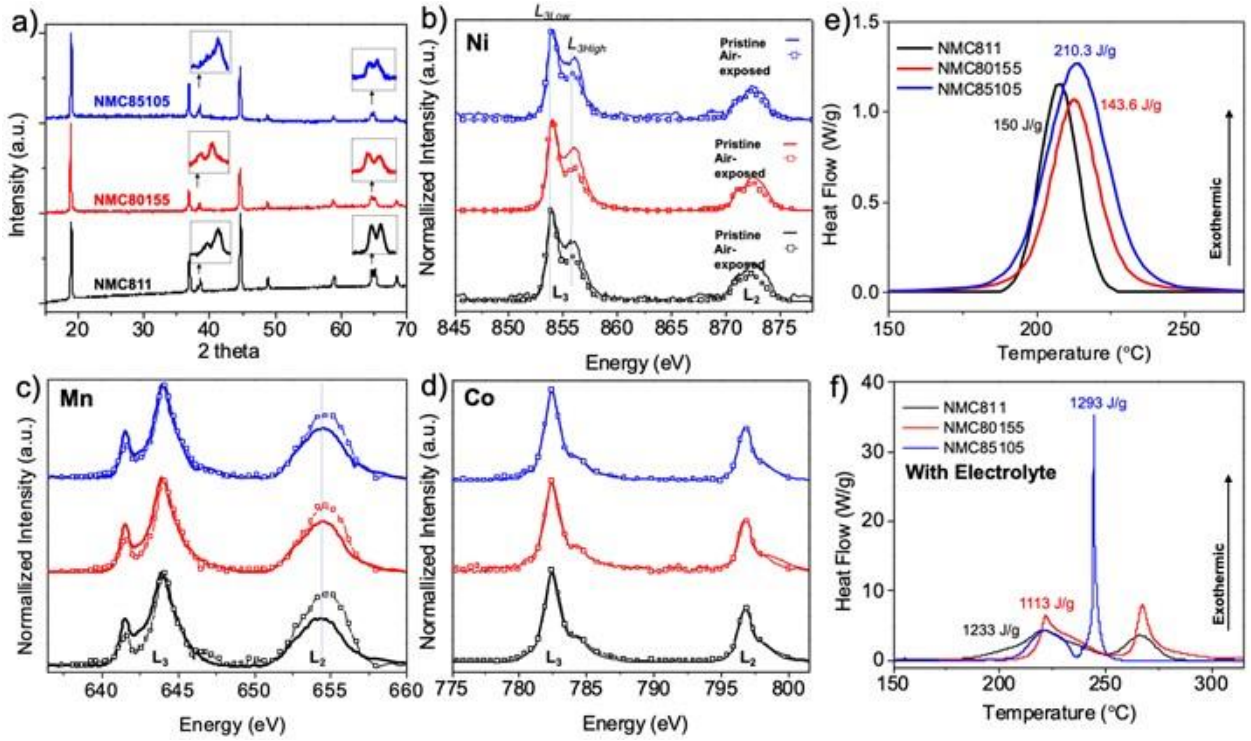

Figure II.2.C.9 a) X-ray diffraction patterns and b-d) FY soft XAS spectra of Ni L-edge, Mn L-edge and Co L-edge collected on pristine and air-exposed SC-NMCs, DSC profiles of: e) chemically-delithiated SC-NMC powder and f) chemically-delithiated SC-NMC powder in the presence of the Gen 2 electrolyte.

Thermal stability is directly related to gas evolution, heat generation and battery safety. Here intrinsic factors controlling thermal stabilities were evaluated on chemically delithiated SC-NMCs to eliminate the interference from carbon and PVDF binder commonly present in electrochemically prepared samples. The analyzed residual Li contents in all delithiated-NMC samples (denoted as CD-NMC hereafter) were 0.1, equivalent to 90% SOC upon electrochemical charging. Heat evolution during the thermal decomposition of both CD-NMC powder only and a mixture of CD-NMC and a liquid electrolyte, 1.2M $LiPF_6$ in EC + EMC (3:7 weight ratio, Gen 2), were evaluated by using differential scanning calorimetry (DSC). At a heating rate of 10 °C /min, an exothermic peak with onsets temperatures of 193, 195, and 190°C centered at 208, 212, and 213°C were observed on NMC-811, NMC-80155 and NMC-85105, respectively (Figure II.2.C.8e). The total amount of heat released was 150, 143.6, and 210.3 J/g. Increasing Ni content lowers the onset temperature while increases heat evolution. On the other hand, increasing Mn content increases the onset temperature while decreases the total heat generation, demonstrating the positive effect of Mn on thermal stability, even in SC oxides. In the presence of the Gen 2 electrolyte, two exothermic peaks were observed on all CD-NMC samples (Figure II.2.C.8f), as both oxygen release and the reactions between the released O_2 and organic solvents contribute to heat generation. For NMC-811, NMC-80155 and NMC-85105, the onset temperature of the first peak was ~ 194, 195, and 192°C, respectively, all centered at a similar temperature of ~ 221°C. This thermal signature arises from O_2 release from the crystal structure of CD-NMC. A second peak centered at 266, 267, 244°C was observed on NMC-811, NMC-80155 and NMC-85105, respectively, leading to a corresponding total heat generation of 1233, 1113, and 1293 J/g. The second exothermic peak is associated with heat generation accompanying the oxidation reaction between the released O_2 gas and organic solvents in the electrolyte. A much lower peak temperature and significantly higher heat generation was found on NMC-85105, consistent with a lower onset temperature and a larger amount of O_2 released during the initial heating, as shown in Figure II.2.C.9e.

STEM-HAADF imaging analysis was used to evaluate changes in SC-NMC surface properties before and after cycling. These images provide brightness contrast that is proportional to the atomic number ($\sim Z^{1.7}$) of the

atoms present, enabling the differentiation between heavy atoms such as TMs and light atoms such as Li. In the perfectly layered structure, no bright spots can be detected in the Li layers. Upon the migration of TMs into the Li layers, for example during surface reconstruction, the appearance of brightness in the Li layers increases. Naturally, the brightness intensity in the Li layers will then depend on the level of Li/TM mixing. Figure II.2.C.9 compares the STEM-HAADF images collected on the pristine and recovered Ni-rich SC-NMC particles after 50 cycles between 3 and 4.6 V. For the pristine series (Figure II.2.C.10a), while bright spots were not observed in the lithium layers in the bulk, their presence is clearly seen in the particle surface region (left), indicating SR on the as-synthesized SC-NMC particles. Further quantification was achieved by averaging the STEM images using a cross-correlation method and evaluating the corresponding intensity line profiles of averaged images. In the line profiles, the number of atomic layers (ALs) with enhanced Li/TM mixing near the surface can be counted, allowing the SR in different samples to be compared. Careful analysis shows the presence of a reconstruction layer on top of the original layered structure in all pristine SC-NMCs. The layer thickness was ~ 18, 15, and 20 ALs on NMC-811, NMC-80155, and NMC-85105, respectively. With all other properties remaining the same, Li/TM mixing on the pristine surface appears to increase with the increase in nickel content and decrease with the increase in Mn content, suggesting a stabilizing effect of Mn on surface crystal structure. This is consistent with previous studies where the results showed Mn^{4+} stabilizing Ni^{2+} in the layered structure. The physical barrier from the presence of Mn^{4+} cations largely impedes the occurrence of surface reconstruction from the layered to rocksalt-type or spine-like structures.

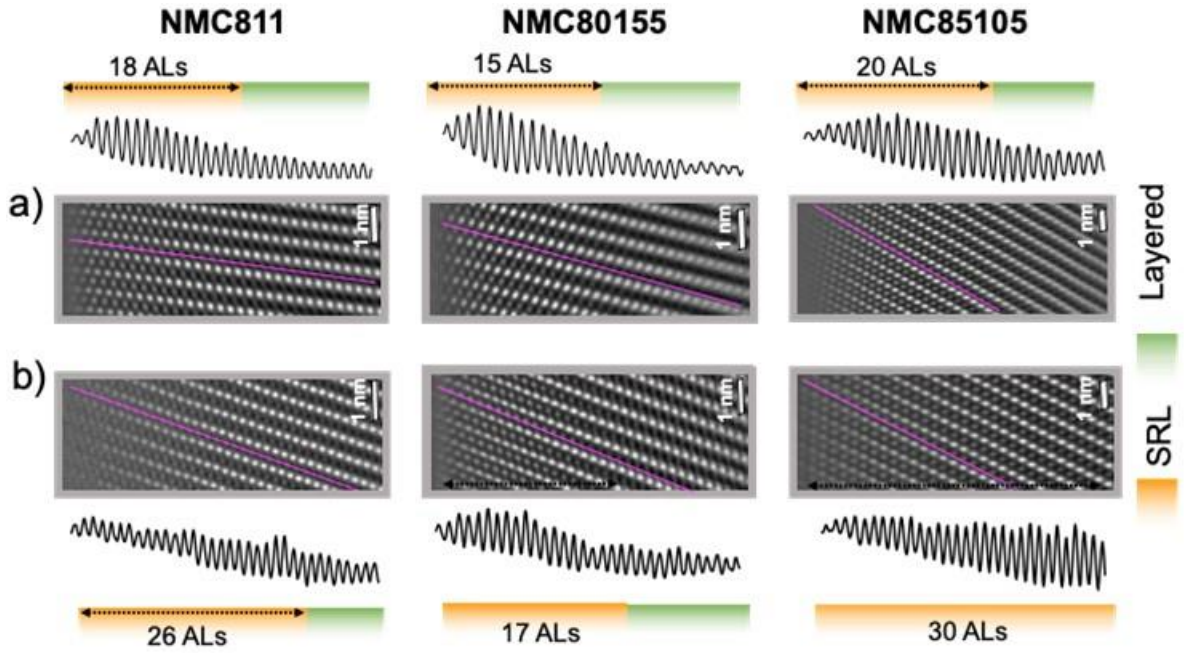

Figure II.2.C.10 STEM-HADDF images and the corresponding intensity line profiles of the pristine a) and cycled b) SC-NMCs: SC-NMC-811 (left), SC-NMC-80155 (middle) and SC-NMC-85105 (right). Cycled samples were recovered at discharged state after 50 cycles to an UCV of 4.6 V. Line profiles show image intensity distribution along the magenta lines in the STEM images. Orange and green bars represent the fractions of SRL and original layered structure, respectively. Number of atomic layers (ALs) in each SRL is as indicated. Surface to bulk direction is from left to right.

After cycling, it is evident that all SR layers became thicker. The net increase in thickness was ~ 8, 2, and 10 ALs on NMC-811, NMC-80155, and NMC-85105, respectively. This trend is similar to what was observed on the pristine SR thickness, confirming the role of Ni and Mn content in surface reconstruction. The observed differences in overall SR layer thickness, ~ 26, 17, and 30 ALs on NMC-811, NMC-80155, and NMC-85105, respectively, is also consistent with their cycling stability. NMC-80155 with the least surface reconstruction showed the best stability, whereas NMC-85105 with the most surface reconstruction was also the least stable. The results suggest that when cycled to an UCV of 4.6 V, the dominating factor that leads to capacity fade in single-grain, high-Ni NMC cathodes is likely the development of Li/TM mixing with surface layers. As the

presence of TMs in Li sites blocks Li diffusion pathways, SR layers are expected to impede lithium transport through particle surfaces and lead to increased impedance and poor utilization of NMC active materials, as shown in previous studies.

Conclusions

Conclusions - Theory

- The overall energy of NiMn, layered oxide structures depends on the number of Ni-Mn bonds, where more Ni-Mn bonds decrease the total energy of the system. Hence, the interactions favor Ni-Mn bond formation while Mn clustering is not favorable.
- A thermodynamic driving force for the segregation of Ni to the surface via Li-Ni exchange near the (012) surface, and strain-driven stabilization of $LiNi_2O_4$ spinel pinned to NMC and $LiNiO_2$ lattices are revealed. Elemental segregation and surface reconstruction are intimately linked and facet dependent phenomena.
- HF is not the only factor governing TM dissoluiton. Different interactions between the TMs and the available anions and ligands, can cause preferential solubilization of these metals in electrolyte solutions.
- Dopant elements have been studied for their tendencies for TM or Li layer occupancy as well as surface and bulk stabilities/reactivities. Dopant segregation is found to be facet-dependent.
- Preliminary studies of complex, overlithiated oxides demonstrate that anion redox is not a prerequisite for hysteresis and energy inefficiency.

Conclusions - Single Crystal Cathodes

Ni-rich NMC-811, NMC-80155, and NMC-85105 single-crystal samples were synthesized with the same particle size and the same truncated-octahedron morphology using a molten-salt method. Use of these samples allowed insights and understanding on the intrinsic reactivities of Ni-rich NMCs and the specific role that each TM plays, without the interference from other less controlled variables such as grain boundaries and porosities in conventional secondary particles. It was shown that increasing Ni content reduces air, thermal, and cycling stabilities due to Ni^{3+} instability, whereas increasing Mn content improves structural, chemical, thermal, and cycling stabilities. This is likely because the presence of Mn stabilizes reduced Ni in the crystal structure. Co appears to improve structural stability during air exposure. In the absence of cycling-induced cracking in primary particles, the dominating contributor to capacity fade was found to be SR. Upon cycling to high voltages/SOCs, the extent of SR is largely determined by the Ni content. These studies provide critical insights needed to further the design of Ni-rich NMC cathodes with improved performance.

Key Publications

1. J. C. Garcia, J. Bareño, G. Chen, J. R. Croy, and H. Iddir. 2020. "Strain-Driven Surface Reconstruction and Cation Segregation in Layered $Li(Ni_{1-x-y}Mn_xCo_y)O_2$ (NMC) Cathode Materials." Physical Chemistry Chemical Physics, **2020**, 22, 42, 24490–97.
2. J. R. Croy, J. Garcia, H. Iddir, S. E. Trask, and M. Balasubramanian. "Harbinger of Hysteresis in Lithium-Rich Oxides: Anionic Activity or Defect Chemistry of Cation Migration.", Journal of Power Sources, **2020**, 228335.
3. H. R. Morin, D. G. Graczyk, Y. Tsai, S. Lopykinski, H. Iddir, J. C. Garcia, N. Dietz, S. Trask, L. Flores, S. Son, Z. Zhang, N. M. Johnson, I. Bloom. "Transition-Metal Dissolution from NMC-Family Oxides: A Case Study." ACS Applied Energy Materials, **2020**, 3, 3, 2565–75.
4. R. Sahore, D. O'Hanlon, A. Tornheim, C. Lee, J. C. Garcia, H. Iddir, Mahalingam Balasubramanian, and Ira Bloom. "Revisiting the Mechanism Behind Transition-Metal Dissolution from Delithiated $LiNi_xMn_yCo_zO_2$ (NMC) Cathodes." Journal of The Electrochemical Society, **2020**, 167, 2, 020513.

5. J. Zhu, S. Sharifi-Asl, J. C. Garcia, H. Iddir, J. R. Croy, R. Shahbazian-Yassar and G. Chen, ¨Atomic-Level Understanding of Surface Reconstruction Based on $Li[Ni_xMn_yCo_{1-x-y}]O_2$ Single-Crystal Studies," *ACS Applied Energy Materials*, **2020**, 3 ,5, 4799.

6. M. Kim, J. Zhu, L. Li, C. Wang and G. Chen, "Understanding Reactivities of Ni-rich Li[NixMnyCo1-x-y]O2 Single-Crystal Cathode Materials," *ACS Applied Energy Materials* (**2020**). DOI: 10.1021/acsaem.0c02278

7. M. Kim, J. Zhu and G. Chen, "Study of Interfacial Reactivities Based on Facet-Specific NMC Crystals," 2019 Bay Area Battery Summit, Berkeley, CA, November **2019**.

8. J. Zhu, M. Kim and G. Chen, "Understanding Surface Reactivities on Layered Oxide Cathodes," The 236th ECS Meeting, Atlanta, GA, October **2019**.

9. J. C. Garcia, H. Iddir, J. R. Croy. *"Effect of Co Content on Li-Ni Exchange in NMC Cathode Materials: Atomistic Modeling Insights".* **2020** Pacific Ring Meeting on Electrochemical and Solid-State Science. Honolulu, HI, USA (on-line)

References

1. G. Kresse and J. Furthmüller, "Efficiency of ab-initio total energy calculations for metals and semiconductors using a plane-wave basis set," Comput. Mater. Sci., 1996, 6, 1, 15–50, doi: 10.1016/0927-0256(96)00008-0.

2. G. Kresse and J. Hafner, "Ab Initio molecular dynamics for liquid metals," Phys. Rev. B, 1993, 47, 1, 558–561, doi: 10.1103/PhysRevB.47.558.

3. J. P. Perdew, K. Burke, and M. Ernzerhof, "Generalized Gradient Approximation Made Simple," Phys. Rev. Lett., 1996, 77, 18, 3865–3868, doi: 10.1103/PhysRevLett.77.3865.

4. P. E. Blöchl, "Projector augmented-wave method", Phys. Rev. B, 1994, 50, 24, 17953–17979, doi: 10.1103/PhysRevB.50.17953.

5. J. C. Garcia, J. Bareno, J. Yan, G. Chen, A. Hauser, J. R. Croy, H. Iddir, "Surface Structure, Morphology, and Stability of Li(Ni1/3Mn1/3Co1/3)O2 Cathode Material," J. Phys. Chem. C, 2017, 121, 15, 8290–8299, doi: 10.1021/acs.jpcc.7b00896.

6. A. V. Krukau, O. A. Vydrov, A. F. Izmaylov, and G. E. Scuseria, "Influence of the exchange screening parameter on the performance of screened hybrid functionals," J. Chem. Phys., 2006, 125, 22, 224106, doi: 10.1063/1.2404663.

7. A. Abdel-Ghany, K. Zaghib, F. Gendron, A. Mauger, and C. M. Julien, "Structural, magnetic and electrochemical properties of LiNi0.5Mn0.5O2 as positive electrode for Li-ion batteries," Electrochimica Acta, 2007, 52, 12, 4092–4100, doi: 10.1016/j.electacta.2006.11.044.

8. J. Serrano-Sevillano, D. Carlier, A. Saracibar, J. M. Lopez del Amo, and M. Casas-Cabanas, "DFT-Assisted Solid-State NMR Characterization of Defects in Li2MnO3," Inorg. Chem., 2019, 58, 13, 8347–8356, doi: 10.1021/acs.inorgchem.9b00394.

9. M. Gu, I.Belharouak, A. Genc, Z. Wang, D. Wang, K. Amine, F. Gao, G. Zhou, S. Thevuthasan, D. R. Baer, J. Zhang, N. D. Browning, J. Liu, and C. Wang, "Conflicting Roles of Nickel in Controlling Cathode Performance in Lithium Ion Batteries," Nano Lett., 2012, 12, 10, 5186–5191, doi: 10.1021/nl302249v.

10. G. H. Vineyard and G. J. Dienes, “The Theory of Defect Concentration in Crystals,” Phys. Rev., 1954, 93, 2, 265–268, doi: 10.1103/PhysRev.93.265.

11. Y. Xiao, T. Liu, J. Liu, L. Heb, J. Chen, J. Zhang, P. Luo, H. Lu, R. Wang, W. Zhu, Z. Hu, G. Teng, C. Xin, J. Zheng, T. Liang, F. Wang, Y. Chen, Q. Huang, F. Pan, H. Chen, “Insight into the origin of lithium/nickel ions exchange in layered Li(NixMnyCoz)O2 cathode materials,” Nano Energy, 2018, 49, 77–85, doi: 10.1016/j.nanoen.2018.04.020.

Acknowledgments

Juan Garcia, Fulya Dogan, Woochul Shin, Anh Vu, Minkyung Kim, Jason R. Croy, Mahalingam Balasubramanian, Ritu Sahore, Ira Bloom. Support from the U. S. Department of Energy (DOE), Vehicle Technologies Office, Peter Faguy, and David Howell is gratefully acknowledged.

II.2.D Design and Synthesis of High Energy, Manganese Rich Oxides for Lithium-ion Batteries (ANL)

Jason R. Croy, Principal Investigator
Argonne National Laboratory
9700 S. Cass Avenue
Lemont, IL, 60439
E-mail: croy@anl.gov

Peter Faguy, DOE Technology Development Manager
U.S. Department of Energy
E-mail: Peter.Faguy@ee.doe.gov

Start Date: October 1, 2018 End Date: September 30, 2021
Project Funding: $775,000 DOE share: $775,000 Non-DOE share: $0

Project Introduction

This project seeks to advance the performance of Mn-rich cathode chemistries as alternatives to Ni-rich NMCs, thereby creating inexpensive, safe, energy-dense, competitive options capable of meeting DOE cost and energy targets for next-generation batteries. Manganese is one of the earth's most abundant elements, is known for its safety characteristics in Li-ion chemistries and is ~5-30 times as inexpensive as Ni and Co, respectively, depending on current prices. Therefore, significant economic opportunities will exist, including the creation of new markets, if such chemistries can achieve performance parity with Ni-rich counterparts. In order to achieve this goal, targeted engineering of nano-scale surface and bulk structures within novel, Mn-rich cathodes, developed at Argonne National Laboratory, will be pursued.

Objectives

- Develop low-cost, high-energy and high-power Mn-oxide-based cathodes for lithium-ion batteries that will meet the performance, safety, and cost requirements of electric vehicles
- Improve the design, composition, and performance of advanced electrodes with stable architectures and surfaces, facilitated by an atomic-scale understanding of electrochemical degradation processes
- Characterization of novel, end-member compositions as tailored components of integrated electrodes structures
- Explore co-precipitation reaction variables of constant stirred-tank reactors (CSTR) in order to understand critical parameters related to the synthesis of well-controlled (morphology, size, density), Mn-Rich, cathode oxides and the subsequent effects on electrode performance.

Approach

1. A bottom-up approach to fabricate Mn-rich cathodes is taken whereby x, in $xLi_2MnO_3•(1-x)LiNMCO_2$ 'layered-layered' (LL) electrodes, is limited to less than ~0.30 and the composition modified by reducing the lithium content slightly to integrate spinel domains in the LL structure, thereby creating composite, 'layered-layered-spinel' (LLS) structures with Mn contents of ~50% or more. This approach represents a comprehensive strategy to address the known limitations of LL cathodes by:
    - Inherently limiting the extent of Li/Mn ordering (i.e., $x<0.30$) and, therefore, damaging effects (e.g., voltage fade) of the electrochemical activation process whereby lithium and oxygen are removed from the Li_2MnO_3 component, while still allowing for substantial capacities (>200 mAh g^{-1});
    - Introducing spinel domains (especially at surfaces) to help improve rate capability and stability; and

- Introducing vacant lithium sites, by way of the spinel component, that can take up lithium on the first discharge after the activation of the Li_2MnO_3 component, thereby reducing first-cycle, irreversible capacities

2. Utilize CSTR reactors to gain insights on the critical parameters influencing co-precipitation synthesis of Mn-rich cathode-oxides as practical alternatives to Ni-rich NMCs

3. Utilize novel, spinel-based materials as stabilizing components of LLS electrode materials

4. Explore novel materials and processes for stabilization of Mn-rich cathode surfaces under extended electrochemical cycling with verification in graphite cells under standardized electrochemical protocols.

Results

Argonne National Laboratory was shut down in March of FY20 as a response to COVID-19. The team associated with this project returned to limited operations in August at only 30% capacity. Because the project relies heavily on synthesis and subsequent characterization of materials, the project is estimated to have lost ~40% of FY20 effort and some results have been delayed.

The goal for FY 20 was to explore and gain insights on the physiochemical properties of Mn-rich oxides that most heavily influence impedance characteristics. These properties are critically related to composition, synthesis and processing, and the subsequent bulk, surface, and local structures and ordering that result.

Processing Effects – State-of-the-art, CSTRs were used to synthesize a variety of Mn-rich compositions, and processing conditions such as reaction parameters, calcination temperature, calcination atmosphere, and particle coatings were studied. Previous results, shown in Figure II.2.D.1, reveal how subtle changes to processing parameters greatly affect the properties of Mn-rich, integrated cathode-oxides. Important findings show that varying calcination temperatures over a range of just 75°C increased first cycle coulombic efficiency by 6%, reversible capacity by 20 mAh/g, and reduced impedance by more than 50%. These enhancements could be attributed to the effect that temperature had on primary particle sizes. These studies revealed that while secondary particle sizes remained the same across the range of synthesis temperatures, primary particles sizes increased systematically with increasing temperature, Figure II.2.D.1b. Differential scanning calorimetry (DSC) results of these cathodes (1c) showed that the Mn-rich oxide with optimized primary particle sizes had an onset temperature of ~275°C, 50°C higher than a commercial NMC-622 (~225°C) tested under the same conditions.

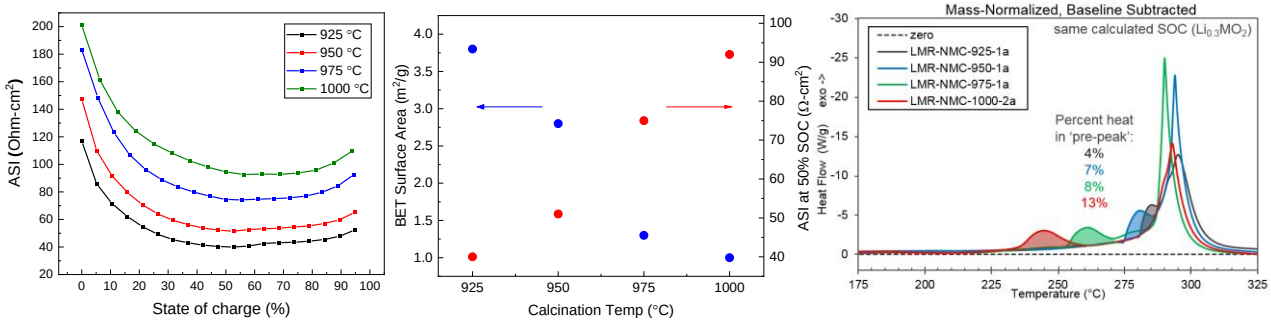

Figure II.2.D.1 (a) ASI data from LLS//graphite cells for various cathode calcination temperatures. (b) BET surface areas and ASI values at 50% SOC as for the cathodes in (a) as a function of calcination temperature. (c) DSC results at 70% delithiation on charge for the LLS cathodes of figure (a).

A follow up study on how the atmosphere under which the Mn-rich cathodes are calcined/lithiated affects final performance was also conducted. Figure II.2.D.2(a) shows the voltage profiles of cycles 1 and 2 from cathodes having a ~60% Mn content undergoing calcination in oxygen followed be either natural cooling in the furnace or quenching. While the voltage profiles are quite similar on the first charge, the slow cooled sample gives less capacity with an overpotential visible on the second cycle charge with respect to the quenched sample.

Figure II.2.D.2(b) shows area specific impedance (ASI) data derived from hybrid pules power characterization (HPPC) for the two oxides show in 2(a), collected using graphite full-cells, during discharge. While the flat portion of the ASI data above ~35% state of charge (SOC) is similar between the two cells, the low SOC impedance is considerably different. Interestingly, as discussed below, the flat portion of the ASI is mainly affected by electrolyte interactions with the cathode surface during cycling while the low SOC ASI is very sensitive to structural changes. These results emphasize the importance of continued study into the mechanisms that govern Mn-rich cathode synthesis towards better control over particle properties that can enhance electrochemical performance.

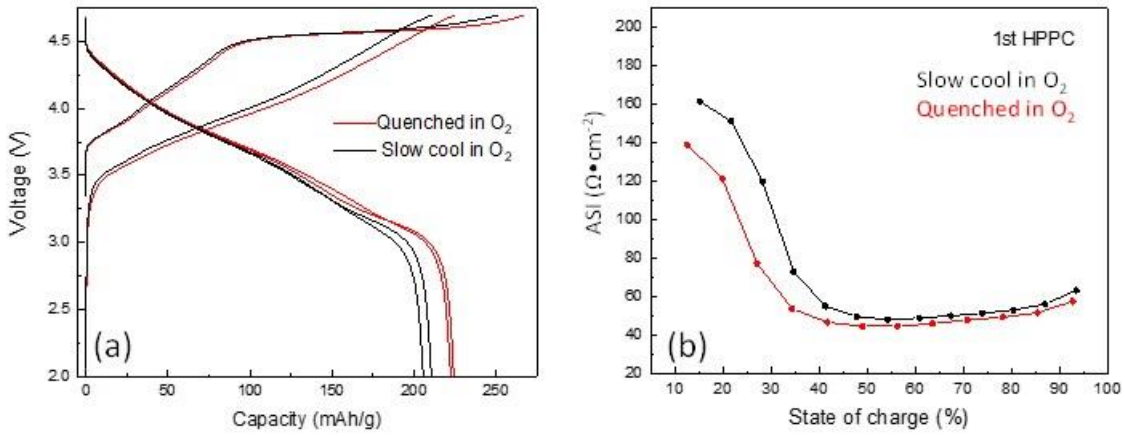

Figure II.2.D.2 (a) Voltage profiles from cycles 1 and 2 of a ~60% Mn content cathode after calcination in oxygen followed by slow cooling or quenching. (b) ASI data derived from HPPC tests for the oxides in (a).

Surface Treatment Effects – The low SOC impedance noted above is an important characteristic of Li- and Mn-rich materials and its mechanisms must be elucidated in order to enable new designs that can improve low SOC performance. However, very few studies exist that probe this unique behavior, and little is understood. This project is currently conducting a detailed study of Li- and Mn-rich, as well as other model, cathode-oxides in order to benchmark key features of ASI and its response to electrochemical cycling. Figure II.2.D.3 shows discharge ASI data for a cobalt-free, Li- and Mn-rich cathode in graphite full-cells as a function of cell voltage. The data was collected under standardized DOE protocols [1]. Notably, the cells are exposed to 4.4V vs. graphite for three hours at the top of every charge for 120 cycles in order to exacerbate high-voltage/SOC damage, and ASI data are collected every ~20 cycles. From Figure II.2.D.3(a) it can be seen that the ASI values continuously increase over the 120 cycles. Of note is that the ASI response at low voltages becomes lost in the overall impedance rise and the entire curve becomes almost linear throughout the voltage range tested. Work from this project has shown that this behavior is a consequence of severe cathode/electrolyte interactions that lead to significant Mn dissolution and cathode-surface damage [2] and these studies have led to the development of a synergistic surface treatment consisting of a low temperature (~110°C) deposition of surface Al followed by interactions with LiDFOB additives during formation cycles, as first reported in [3]. This treatment was applied to the system shown in Figure II.2.D.3(a) and retested in full-cells under the same protocols. The data is shown in Figure II.2.D.3(b) and it is immediately apparent that protecting the surface of the Mn-rich cathode leads to a substantially more stable ASI behavior, even under the harsh testing conditions. Importantly, the low voltage ASI response remains clear. This system is now being used as a benchmark to probe the various aspects of ASI response under different electrochemical protocols. Subsequent designs and modifications to the cathode-oxide that may influence ASI response can now be studied without loss of information due to the effects of surface impedance rise.

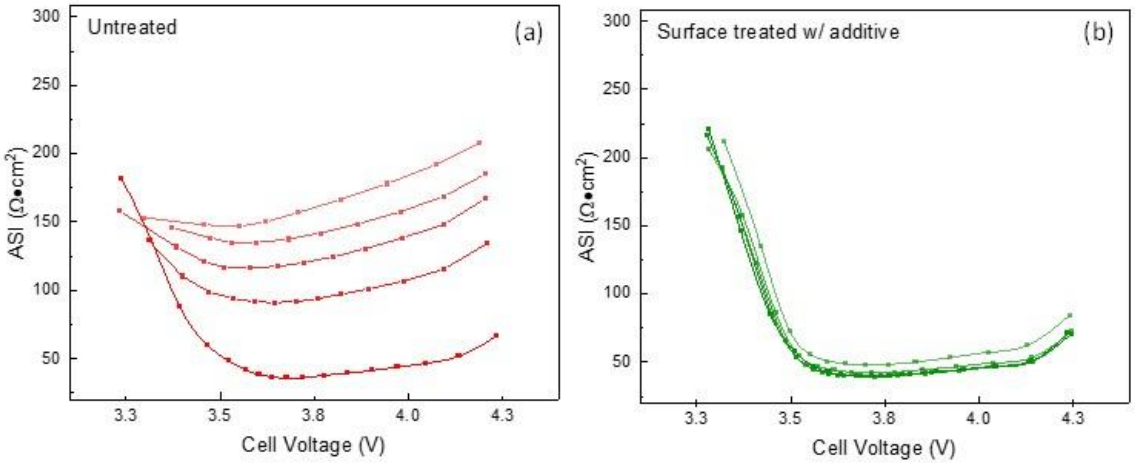

Figure II.2.D.3 (a) ASI data of a Mn-rich cathode-electrode//graphite full cell during ~120 cycles. (b) ASI data of the same cathode//graphite in (a) after undergoing a surface-treatment plus LiDFOB as an electrolyte additive as reported in [2].

The surface-treatment discussed above greatly mitigates surface damage, Mn dissolution, and impedance rise in Li- and Mn-rich electrodes. In addition, Mn-rich cathodes can be made with little to no cobalt. The promise of these surface-treated/Mn-rich systems was evaluated in graphite full-cells and is shown in Figure II.2.D.4. Here, a cathode-electrode containing ~60% Mn (~$Li_{1.13}Mn_{0.57}Ni_{0.30}O_2$) is tested and compared to NMC-622 under the same harsh protocols shown in Figure II.2.D.3. The Mn-rich electrode outperforms the NMC-622 in delivered capacity and capacity retention. The energy delivered for the NMC-622 was 707 Wh/kg_{oxide} at the beginning of test and 591 Wh/kg_{oxide} after ~120 cycles. Impressively, the Mn-rich cathode delivered a higher energy of 726 Wh/kg_{oxide} at the beginning of test and 619 Wh/kg_{oxide} after ~235 cycles. Cleary, such systems which are rich in Mn and contain no cobalt are of great interest for further development and advanced variations are currently under study in this program.

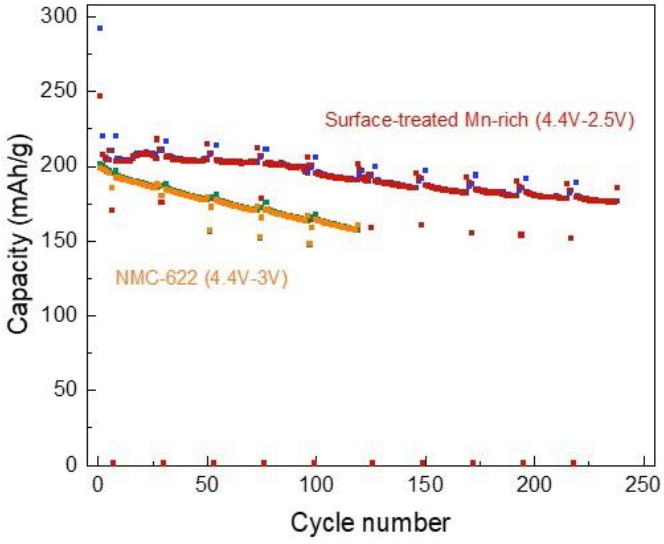

Figure II.2.D.4 Full-cell cycling behavior of a surface-treated, Mn-rich cathode compared to NMC-622.

Stabilization of surfaces, as shown above, is critical for Li- and Mn-rich oxides and will be a necessary part of successful technologies. Surface structures have been explored in this program associated with the possibility of stabilizing the oxygen lattice under a restricted-charge protocol (RCP) in the presence of a stable, semi-coherent coatings. RCP implies that the upper cutoff voltage V_c is constrained to be less than ~4.6 during cycling; specifically, less than the SOC where metal-oxygen bond-breaking occurs. First-principles DFT

simulations were performed to estimate (a) the ideal performance for Li_2MnO_3•$LiMO_2$, where $M = Ni_{0.5}Mn_{0.5}$, and (b) the compatibility of possible coating materials with the cathode. The simulations indicate that the mean voltage during charge is approximately 4V. During discharge, most Li ions occupy lattice sites vacated during the charge, however some point defects (Frenkel pairs) remain at the end of discharge, the density of which is proportional to the discharge rate. Voltage fade is minimal in the simulation and the energy density is ~ 800 Wh/kg. Such ideal behavior presumes that reaction of the near surface oxygen is minimized by a semi-coherent coating. The most desirable candidate coating materials have cubic close packed oxygen sublattices. Simulations indicate that the O-O separations of several oxides, particularly the high-voltage MnNi spinel, would be small, which would promote near coherence of the coating-substrate interface.

Preliminary experiments have been conducted to implement the RCP concept, with MnNi spinel coatings applied by wet chemistry procedures. Electrochemical cycling measurements, with V_c in the range 4.5 to 4.6, showed incremental activation on cycling, which indicates that the surface oxygen reaction was not fully suppressed in the tested materials. SEM observation indicated that coating coverage was not uniform. Other coating methods, and other coatings are under investigation to achieve a more uniform coating and a more stringent test of the RCP.

Local Ordering, Cation migration, and Anion Redox - In Li- and Mn-rich oxides the phenomena of hysteresis and voltage fade have been correlated and both processes are intimately linked to cation migrations; reversible and irreversible [4]. It is natural to assume that these processes, in turn, have an influence on low SOC behavior which is sensitive to structural changes. Anion redox is often cited as the cause of hysteresis in over-lithiated oxides but no studies to date have shown causation, only correlation; specifically, studies that prove the absence of either cation migration or anion redox have not been reported. In order to gain a deeper understanding of hysteresis in Li-rich oxides, a model system of $Li_{1.2}Ti_{0.04}Cr_{0.4}O_2$ was investigated. This system was specifically chosen as it contains 20% excess lithium, accommodates 3-electron redox conversion of $d^3\ Cr^{3+} \leftrightarrow d^0\ Cr^{6+}$ during cycling and incorporates a high-valent, $d^0\ Ti^{4+}$ element as the inactive metal. This material, by design, should not involve anion redox and will give insights on the mechanisms of hysteresis.

Figure II.2.D.5 shows data from the first two cycles of the model $Li_{1.2}Ti_{0.4}Cr_{0.4}O_2$ cathode electrode, in coin-cells (vs. Li metal), at a current rate of 9 mA/g between 4.0-2.0V (30°C). As demonstrated, this material possesses a large first-cycle inefficiency as well as a significant hysteresis between charge and discharge that persists even at slow rates and low upper cutoff voltages. As outlined above, anion redox is not expected for this system, particularly at such low SOCs.

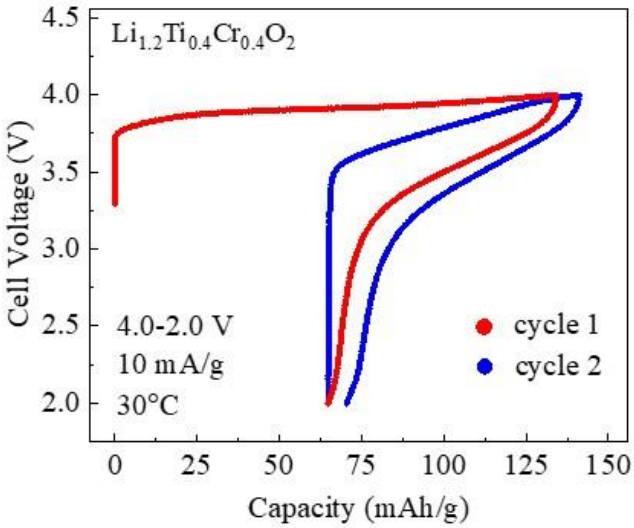

Figure II.2.D.5 First two cycles of $Li_{1.2}Ti_{0.4}Cr_{0.4}O_2$ cathode electrode in coin-cells (vs. Li metal) at a current rate of 9 mA/g between 4.0-2.0V (30°C).

In order to understand the mechanisms underlying the observed hysteresis, detailed simulations were performed as described in ref [5]. In brief, the calculations show that neither oxygen nor Ti contribute to the electrochemical capacity of this material. Furthermore, oxidation of Cr^{3+} to Cr^{6+} is concomitant with both Cr and Ti migration from octahedral to tetrahedral sites, enhanced by a d^0 configuration. Subsequent re-lithiation of the oxide is subject to an energy penalty due to the unfavorable occupation of lithium surrounding the tetrahedral sites.

Figure II.2.D.6 shows X-ray absorption near edge spectroscopy (XANES) data for $Li_{1.2-x}Ti_{0.4}Cr_{0.4}O_2$ electrodes at various SOCs during the first-cycle charge. Of note are the pre-edge features shown in figures (c) and (d). A continual increase in the Cr pre-edge, 6(c), beginning immediately on charge, occurs until x~0.5 and drastically slows, or stops, thereafter. This phenomenon is a well-known indicator of Cr^{3+} to Cr^{6+} oxidation, accompanied by Cr^{6+} occupation of tetrahedral sites. The tendency to create three- lithium vacancy clusters, seen in the computational study, is likely key for the early occupancy of tetrahedral sites near the vacancy cluster with highly oxidized chromium. The Ti pre-edge peaks, Figure II.2.D.6(d), also show a continuous increase in intensity until x~0.5 and do not change upon further charge. However, contrary to Cr, an oxidation state increase of Ti is not possible. Interestingly, the pre-edge region does show a shift in energy with lithium extraction; the main peak of the Ti pre-edge shifting by ~0.4 eV to lower energies. It has been previously reported using a series of 4 to 6-coordinate Ti compounds, that indeed, as the Ti-O bonding goes from 6 to 4 in these model systems a concomitant increase and shift to lower energies is observed for the main peak of the Ti K pre-edge.[59] Detailed analysis of the extended X-ray absorption fine structure (EXAFS) data corroborates a decrease of Ti-O coordination, indicating Ti migration to tetrahedral sites [5]. Interestingly, a similar behavior of the Mn K pre-edge of the Li- and Mn-rich compounds has recently been identified, likely related to Mn undercoordination and migration as well.[30]

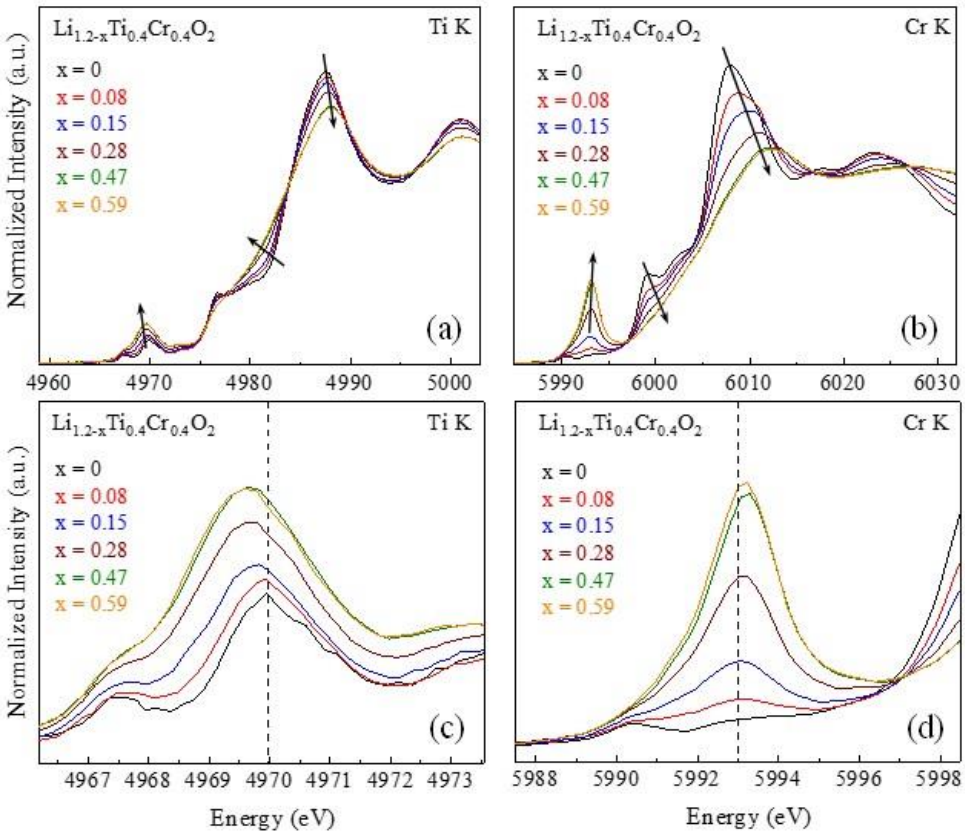

Figure II.2.D.6 (a) and (b) show the Ti K- and Cr K-edge XANES, respectively, taken at SOC points, x, as labeled. (c) and (d) show magnified views of the corresponding pre-edge regions. Dashed lines in (c) and (d) are guides to the eye.

The results presented in this work clearly demonstrate that anion redox in Li-rich oxides is not a prerequisite for hysteresis and energy inefficiency. Chemical inhomogeneities (e.g., local ordering and short-range order) as well as electronic structure can have a significant impact on defect formation and the subsequent electrochemical properties, in the absence of anion redox or loss. Such defects, being local phenomena, are expected to play an important role in all classes of Li-rich oxides.

Conclusions

Lithium- and manganese-rich electrodes still offer significant opportunities in terms of sustainable and economical options for next-generation cathode-oxides. The work conducted in this program has shown, under standardized DOE cycling protocols, that novel compositions and surface modifications can enable performances of Mn-rich cathodes that are on par, or better, than currently used NMC-622 while using little to no cobalt. Improving impedance characteristics, specifically at low states of charge, has been identified as an area of significant opportunity in moving Mn-rich technologies forward. Work from this program has shown that synthesis and processing considerations can heavily influence impedance through the particle morphologies that result, including primary particle properties. Continued studies on, and a better understanding of, these synthesis-structure-property relationships will be critical. In addition, local, atomic-scale mechanisms have been probed in connection with lithium-rich materials as they very likely play an important role in impedance behavior. The study presented herein sheds new insights on the mechanism of hysteresis in these oxides. Importantly, it was shown, contrary to current models, that anion redox in Li-rich oxides is not a prerequisite for hysteresis and energy inefficiency. These results will be important for design consideration related to all categories of over-lithiated oxides.

Key Publications

1. A. Gutierrez, M. He, B.T. Yonemoto, Z. Yang, J. Wang, H.M. Meyer III, M.M. Thackeray, and J.R. Croy, *Advancing Lithium- and Manganese-Rich Cathodes through a Combined Electrolyte Additive/Surface Treatment Strategy*, J. Electrochem. Soc., **166**, A3896 (2019).

2. J.R. Croy, J.C. Garcia, H. Iddir, S.E. Trask, and M. Balasubramanian, *Harbinger of Hysteresis in Lithium-Rich Oxides: Anionic activity or defect chemistry of cation migration*, J. Power Sources, **471**, 228335, (2020).

3. S. Sharifi-Asl, V. Yurkiv, A. Gutierrez, M. Cheng, M. Balasubramanian, F. Mashayek, J. R. Croy, and R. Shahbazian-Yassar, *Revealing Grain-Boundary-Induced Degradation Mechanisms in Li-Rich Cathode Materials*, Nano Letters, **2**, 1208 (2020).

4. ***Invited*** Eungje Lee, *Tailoring integrated layered and spinel electrode structures*, The 5th International Conference on Advanced Electromaterials, Jeju, Korea, November 5-8, 2019.

5. ***Invited*** *A*. Gutierrez, *Probing the Impedance at Low States-of-charge for Li- and Mn-rich Cathodes*, Argonne National Laboratory, Lemont, IL, September 28, 2020).

6. **Invited** Eungje Lee, *Next Generation Cathode Development at Argonne National Laboratory*, Samsung SDI, Suwon, South Korea, November 12, 2019.

7. Jinhyup Han, Bob Jin Kwon, Fulya Dogan, Jason Croy, and Michael M. Thackeray, *Cobalt-Based Lithiated Spinel Oxide as a Novel Zero-Strain Cathode*, Electrochemical Society Meeting, Atlanta, GA, October 13-17, 2019.

8. **Invited** J. R. Croy, *Lithium-Ion Cathode Development at Argonne National Laboratory*, Technical University of Munich, Munich, Germany, November 2019.

References

1. B.R. Long, S.G. Rinaldo, K.G. Gallagher, D.W. Dees, S.E. Trask, B.J. Polzin, A.N. Jansen, D.P. Abraham, I. Bloom, J. Bareño, and Jason R. Croy, *Enabling High-Energy, High-Voltage Lithium-ion Cells: Standardization of Coin-Cell Assembly, Electrochemical Testing, and Evaluation of Full Cells*, J. Electrochem. Soc., **163**, A2999 (2016).

2. A. Gutierrez, M. He, B.T. Yonemoto, Z. Yang, J. Wang, H.M. Meyer III, M.M. Thackeray, and J.R. Croy, *Advancing Lithium- and Manganese-Rich Cathodes through a Combined Electrolyte Additive/Surface Treatment Strategy*, J. Electrochem. Soc., **166**, A3896 (2019).

3. J.R. Croy, A. Gutierrez, M.M. Thackeray, and M. He, *Surface treatment for lithium battery electrode materials*, U.S. patent 10,741,839.

4. J.R. Croy, M. Balasubramanian and A.K. Burrell, *Review of the U.S. Department of Energy's "Deep Dive" Effort to Understand Voltage Fade in Li- and Mn-rich Cathodes*, Acc. Chem. Res., **48**, 2813 (2015).

5. J.R. Croy, J.C. Garcia, H. Iddir, S.E. Trask, and M. Balasubramanian, *Harbinger of Hysteresis in Lithium-Rich Oxides: Anionic activity or defect chemistry of cation migration*, J. Power Sources, **471**, 228335, (2020).

Acknowledgements

Mahalingam Balasubramanian, Roy Benedek, Jiajun Chen, Juan Garcia, Arturo Gutierrez, Hakim Iddir, Joel Kirner, Eungje Lee, Wenquan Lu. Support from the U. S. Department of Energy (DOE), Vehicle Technologies Office, Peter Faguy, and David Howell is gratefully acknowledged.

II.2.E Disordered RockSalt Structured Cathode Materials: Electrochemistry and Synthesis (LBNL, ORNL, PNNL, UC Santa Barbara)

Guoying Chen, Principal Investigator
Lawrence Berkeley National Laboratory
1 Cyclotron Road
Berkeley, CA 94720
E-mail: GChen@lbl.gov

Peter Faguy, DOE Technology Development Manager
U.S. Department of Energy
E-mail: Peter.Faguy@ee.doe.gov

Start Date: October 1, 2018 End Date: September 30, 2021
Total Project Cost: $2,500,000 DOE share: $2,500,000 Non-DOE share: $0

Project Introduction

The projected growth of Li-ion battery (LIB) production towards multiple TWh/year will require several million tons of Co/Ni combined, which constitutes a very sizeable fraction of the annual production of these metals. The recent development of Li-excess cation-disordered rocksalts (DRX) provides an alternative to develop high energy density LIB cathodes that use more abundant and less expensive elements, and can respond to the industry need for lower cost, less resource intensive cathode materials. DRX materials have been shown to deliver energy densities over 1000 Wh/kg, and its cation disordered nature allowing for a wide range of chemistry free of Co and/or Ni. The ability to substitute some of the oxygen by fluorine in locally Li-rich environments provides an extra handle to optimize performance through increasing transition-metal (TM) redox capacity. As this class of cathodes are relatively new, further materials design and development are needed in order to properly evaluate their promise and challenges towards eventual commercialization. To do so, fundamental understanding of what controls DRX performance characteristics, particularly rate capability, cycling stability and voltage slope, is critical. This project has assembled necessary research expertise in modeling, synthesis, electrochemistry and characterization to tackle these challenges. The current chapter reports on the synthesis and electrochemistry components of the project.

Objectives

The goals of this project are as follows:

- Understand the factors that control DRX cycling stability, particularly to what extent cycle life is controlled by impedance growth on the surface and by bulk changes in the material
- Understand what controls the rate of DRX materials, particularly rate limitation posed by bulk transport and surface processes
- Investigate the root of voltage profile slope in DRX
- Develop Co-free high energy density DRX cathodes.

Approach

This project originally focused on three representative baseline systems and their analogues: 1) Mn-redox based $Li_{1.2}Mn_{0.625}Nb_{0.175}O_{1.95}F_{0.05}$ (LMNOF), Ni-redox based $Li_{1.15}Ni_{0.45}Ti_{0.3}Mo_{0.1}O_{1.85}F_{0.15}$ (LNTMOF), and 3) a high F-content $Li_2Mn_{1/2}Ti_{1/2}O_2F$ (LMTOF) that utilizes the $2e^-$ Mn^{2+}/Mn^{4+}redox couple. The team operates in six thrusts areas representing the challenges and opportunities with DRX materials:

1. Characterization of the local and global structure of the bulk material before and during cycling, including detailed characterization of TM and O redox processes in the bulk and on the surface.
2. Characterization and manipulation of short-range cation order (SRO) to enhance rate capability.
3. Characterization and modeling of the DRX surface chemistry and processes during cycling to high voltage
4. Electrolyte/cathode interface issues and impedance growth due to surface processes
5. Fluorine solubility limits and synthesis of highly fluorinated compounds with scalable methods
6. Electrochemistry and testing in coin and pouch cells.
   Items (1) to (4) are discussed in the companion report.

Results

1. Synthesizing Mn2+-based DRX

Synthesis of the third baseline material based on the Mn^{2+}/Mn^{4+} redox, $Li_2Mn_{1/2}Ti_{1/2}O_2F$ or $Li_{1.333}Mn_{0.333}Ti_{0.333}O_{1.333}F_{0.667}$ (LMTOF), was achieved by using a high-energy ball milling method. Various synthesis parameters were optimized in order to improve phase purity. Rietveld refinement of the XRD pattern shows a good fit for the cubic rocksalt with an *a* lattice parameter of 4.1740(5) Å (Figure II.2.E.1a). EDS analysis reveals uniform elemental distribution of Mn, Ti, O and F in the final product (Figure 1b). The optimal electrochemistry of the LMTOF cathode wasy obtained after the optimization of carbon processing condition. The LMTOF cathode delivered a high initial specific capacity of 293 mAh/g, with 279 mAh/g maintained after 20 cycles, corresponding to 95% capacity retention (Figure II.2.E.1c-d).

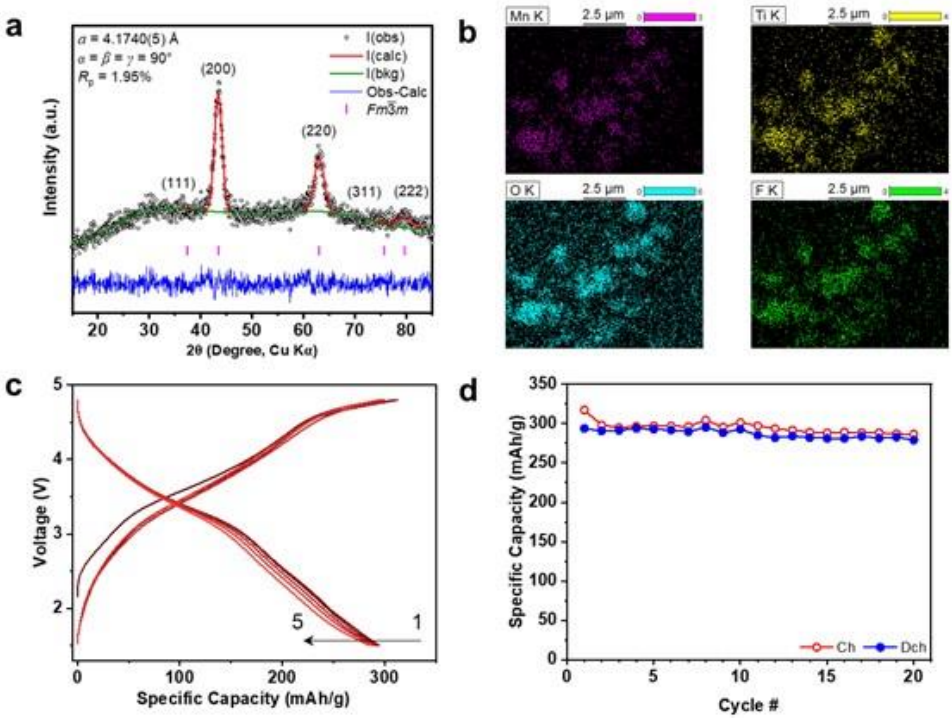

Figure II.2.E.1 a) Rietveld refinement of the XRD pattern collected on as-synthesized LMTOF, b) EDS elemental distribution maps of Mn, Ti, O and F, c) voltage profiles and d) capacity retention of LMTOF cathode when cycled at C/20 in the voltage window of 1.5-4.8 V.

Other DRX oxyfluorides utilizing the $2e^-$ Mn^{2+}/Mn^{4+} cationic redox process were also explored. Figure II.2.E.2a shows the capacity contribution in a series of samples with a general formula of $Li_{1.2}Mn^{2+}_{0.4+z/3}Nb^{5+}_{0.4-z/3}O_{2-z}F_z$. The theoretical capacity from Mn increases with F content, while the total capacity based on the Li content remains nearly constant. After optimizing the solid-state synthesis parameters previously used for Mn^{3+}-Nb^{5+} DRX (the first baseline material), including the excess Li content, precursor mixing and annealing conditions, phase-pure Mn^{2+}-Nb^{5+} DRX compounds with F content of 0.1 and 0.15 were obtained, labelled as $Mn^{2+}_{0.4333}F_{0.1}$ and $Mn^{2+}_{0.45}F_{0.15}$, respectively (Figure II.2.E.2b). Preliminary electrochemical characterization shows the characteristic charge-discharge profiles for Mn^{2+}/Mn^{4+} redox reaction (Figure II.2.E.2c-d). Initial capacities of 250 and 225 mAh/g are obtained for $Mn^{2+}_{0.433}F_{0.1}$ and $Mn^{2+}_{0.45}F_{0.15}$, respectively, with a better capacity retention achieved for the higher fluorine content material. Further improvement in electrochemical performance is anticipated through optimization of electrode formulation and testing condition.

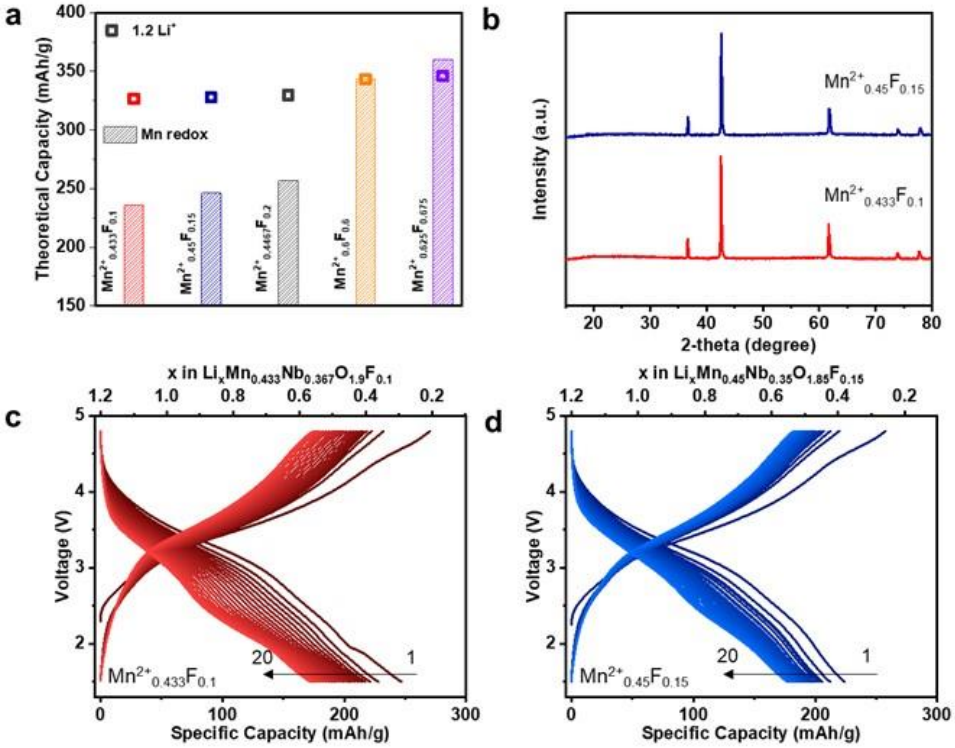

Figure II.2.E.2 a) Theoretical capacities based on Li content and Mn^{2+}/Mn^{4+} redox as a function of F content z in $Li_{1.2}Mn_{0.4+z/3}Nb_{0.4-z/3}O_{2-z}F_z$, labelled with Mn and F contents, b) XRD patterns of DRX compounds prepared by a solid-state reaction, voltage profiles of c) $Mn^{2+}_{0.4333}F_{0.1}$ and d) $Mn^{2+}_{0.45}F_{0.15}$ cathodes cycled at C/20 in the voltage window of 1.5-4.8 V.

2. *Increasing F solubility in DRX*

Modeling and initial experimental data indicate that increasing the fluorine content of DRX materials leads to better stability, better rate performance, and higher theoretical transition metal redox capacity. F incorporation in DRX is typically achieved by introducing a LiF precursor during synthesis. As LiF is highly stable, this approach limits the overall solubility. In general, samples synthesized through a prolonged high-energy ball-milling process can incorporate more F compared to those from solid-state synthesis. The ball milling process, however, presents significant challenges for commercial production and scale-up.

Methods of using inexpensive fluorinated polymeric precursor as an alternative F source during solid-state synthesis were explored. A series of fluorinated DRX (F-DRX) with the chemical formula of $Li_{1.2}Mn_{0.6+0.5x}Nb_{0.2-0.5x}O_{2-x}F_x$ (LMNOF, $0 < x \leq 0.4$) were synthesized from poly(tetrafluoroethylene) (PTFE) precursor. While LiF has a melting point of 848.2 °C, PTFE melts at a much lower temperature of 327 °C and

decomposes before 500 °C. Phase-pure DRX with the cubic rocksalt crystal structure and a $Fm\bar{3}m$ space group were obtained when $x < 0.25$, representing F substitution up to 12.5 at.%. This largely exceeds the 7.5 at. % limit when LiF was used as F precursor, suggesting that PTFE is a superior fluorination precursor compared to LiF.

Figure II.2.E.3a shows the X-ray absorption near-edge structure (XANES) spectroscopy of Mn *K*-edge collected on the pristine $Li_{1.2}Mn_{0.6}Nb_{0.2}O_2$ (F0), $Li_{1.2}Mn_{0.625}Nb_{0.175}O_{1.95}F_{0.05}$ (F2.5), $Li_{1.2}Mn_{0.65}Nb_{0.15}O_{1.9}F_{0.1}$ (F5), $Li_{1.2}Mn_{0.7}Nb_{0.1}O_{1.8}F_{0.2}$ (F10). The *K*-edge energy positions are nearly constant at ~ 6548 eV, suggesting that bulk Mn remains at the trivalent state in all pristine DRX samples. On Mn *L*-edge soft X-ray absorption spectroscopy (XAS) profiles collected in total electron yield (TEY) and total fluorescence yield (FY) modes (Figure II.2.E.3b), demonstrate Mn^{3+} cations both in the bulk and surface in all three F-DRX providing further evidence for the successful incorporation of F into the DRX. The presence of Nb^{5+} cation is evidenced by the Nb *M*-edge peaks through the low energy scan (Figure II.2.E.3c). The O pre-edge peaks for F0 and F2.5 are nearly identical (Figure II.2.E.3d), whereas the intensity of the shoulder peak at ~ 533 eV increases significantly with F content over 5 at. %, leading to the splitting peak feature centered at about 531 eV. This suggests that the presence of a larger amount of F disrupts O electronic structure in the rocksalt lattice. Further investigation of the F *K*-edge spectra (Figure II.2.E.3e and Figure II.2.E.3f) confirms the presence of F species in all F-DRX. Comparison with the standard spectrum of LiF (Figure II.2.E.3e) reveals that the TEY and FY F signals detected on F2.5, F5 and F10 are different from those of LiF, confirming the incorporation of F in the DRX lattice both in the subsurface region as well as on the surface. On the other hand, distinct LiF-like features are observed in both TEY and FY spectra collected on F15 and F20 samples with higher F contents (Figure II.2.E.3f).

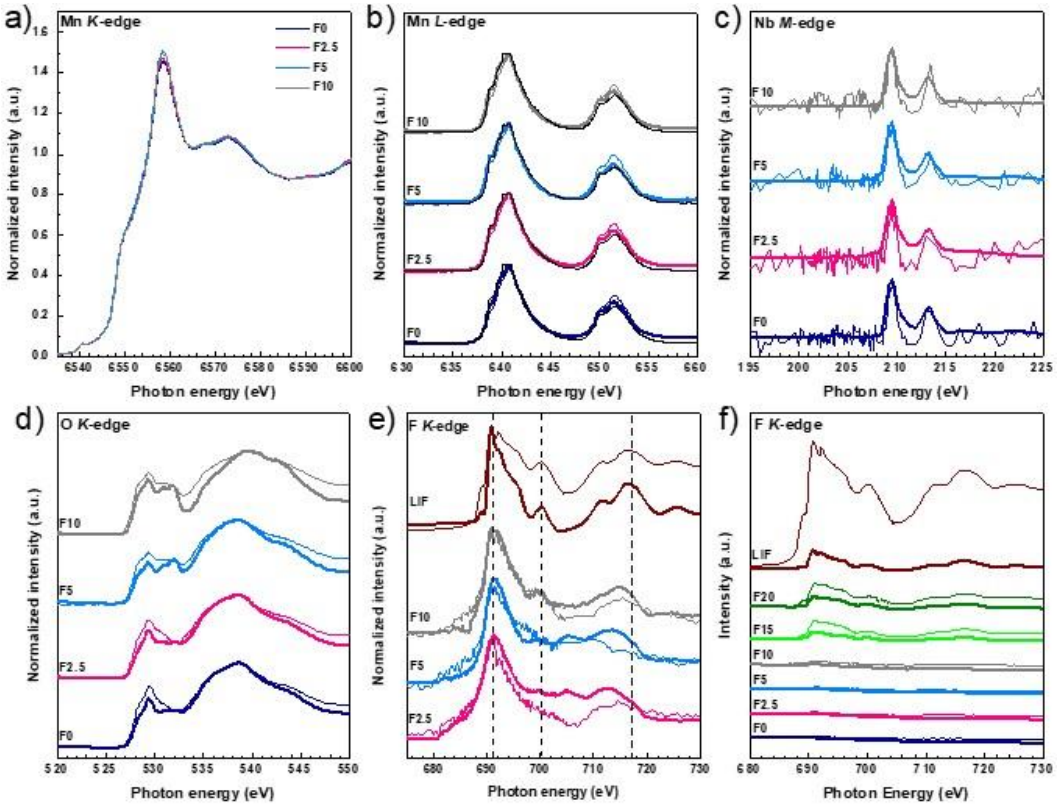

Figure II.2.E.3 Hard and soft XAS profiles of F0, F2.5, F5 and F10: (a) Mn K-edge XANES spectra and normalized soft XAS spectra of: (b) Mn L2- and L3-edges, (c) Nb M4- and M5-edges, (d) O K-edge, (e) F K-edge and (f) F K-edge including all synthesized DRX materials. TEY spectra are shown in thick lines while FY spectra are shown in thin lines.

Figure II.2.E.4 compares half-cell electrochemical performance of the DRX cathodes when cycled between 1.5-4.8 V at a current rate of 10 mA/g. The theoretical capacities based on the total Li content (1.2 mole of Li per formula unit) are 350, 353, 356 and 363 mAh/g for F0, F2.5, F5 and F10, respectively, of which 175, 184, 193 and 212 mAh/g comes from the contribution of the Mn^{3+}/Mn^{4+} redox couple. The initial voltage curve (Figure II.2.E.4a) of the non-fluorinated F0 displays a sloping region at low voltages (A) and a distinct "flatter" region at high voltages (B). which are attributed to the cationic Mn redox and anionic O redox, respectively. The latter is known to involve oxidation of lattice O^{2-} to O^{n-} ($0 < n < 2$). The two regions are also indexed as A' and B' in the dQ/dV plot (Figure II.2.E.4b). Careful comparison shows that O redox activity in the B' region tends to decrease with increasing F content in DRX, with the changes between F5 and F10 particularly significant. In the case of F10, the decrease in the O redox peak is in a remarkable contrast to the sharper and more intense Mn redox peak at region A', confirming that an increasing fraction of the capacity comes from the Mn redox. The capacity of the F-DRX materials decreases with an increase in F substitution, with an initial discharge capacity of ~ 269, 270, 241 and 207 mAh/g obtained on F0, F2.5, F5 and F10 cathodes, respectively. Figure II.2.E.4c summarizes the 1st, 2nd and 3rd cycle charge capacity contribution as a function of F content. Assuming the contribution from the Mn^{3+}/Mn^{4+} redox couple remain constant in all three cycles, the capacity contribution from the O oxidation varies with F content as well as cycle number. With the increase in F content from 0 to 2.5, 5 and 10 at. %, O redox capacity contribution in the first cycle (grey bar) decreases from ~ 136 to 130, 100 and 59 mAh/g, respectively. These values correspond to 44%, 42%, 34% and 22% of the initial charge capacity. The O oxidation capacity contribution in the second cycle (blue bar) becomes much lower, with 37%, 33%, 21% and 5% of the charge capacities for F0, F2.5, F5 and F10, respectively. While O capacity appears to stabilize after the second cycle in F-DRX, evidenced by the same contribution between the second and third cycle (magenta bar), the value in F0 continues to decrease. The results suggest that fluorination leads to an overall lower O capacity contribution but more reversible oxygen redox.

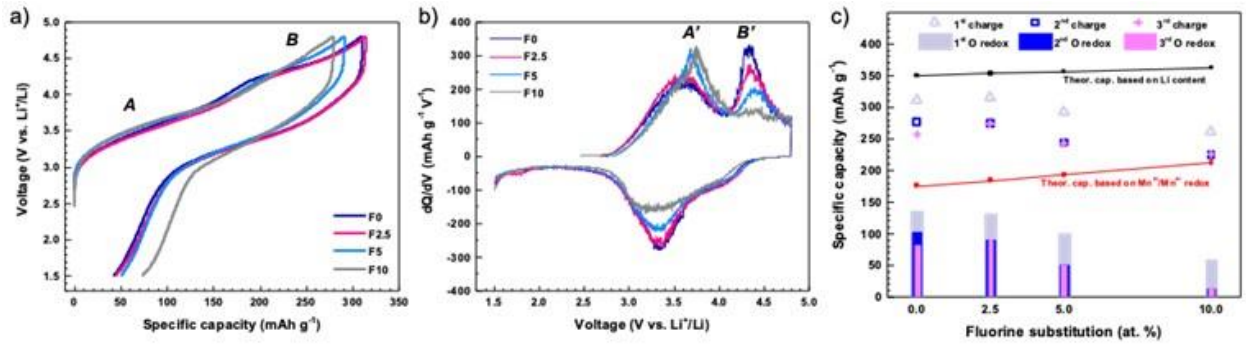

Figure II.2.E.4 Electrochemical performance evaluation of the DRX half-cells: a) voltage profiles and b) the corresponding differential capacity vs. voltage plots during the first cycle, and c) capacity origin as a function of F content in the first three cycles.

Figure II.2.E.5a and Figure II.2.E.5b compare the cycling stability of the cathodes. While the initial capacity is lower in F-DRX, the capacity retention is much improved. After 30 cycles, the remaining discharge capacities were 226, 247, 226, 254 mAh/g for F0, F2.5, F5 and F10, respectively, corresponding to a capacity retention of 84%, 92%, 94% and 123%. The unusual increase in capacity along with cycling in F10 indicates possible structural changes and is currently under investigation. Performance comparison on F-DRX samples made with PTFE and LiF precursors are also shown in Figure II.2.E.5c-d. After 30 cycles, the discharge capacity was 247 and 225 mAh/g for PTFE and LiF samples, respectively, corresponding to capacity retention of 92% and 85%. We believe the introduction of a small amount of carbon, resulting from the decomposition of the PTFE polymer, may play a role in the enhanced electrochemical performance in the former. Assuming no C loss during the heat treatment, the calculated added carbon content is 0.46, 0.92 and 1.88 wt. % for F2.5, F5 and F10, respectively.

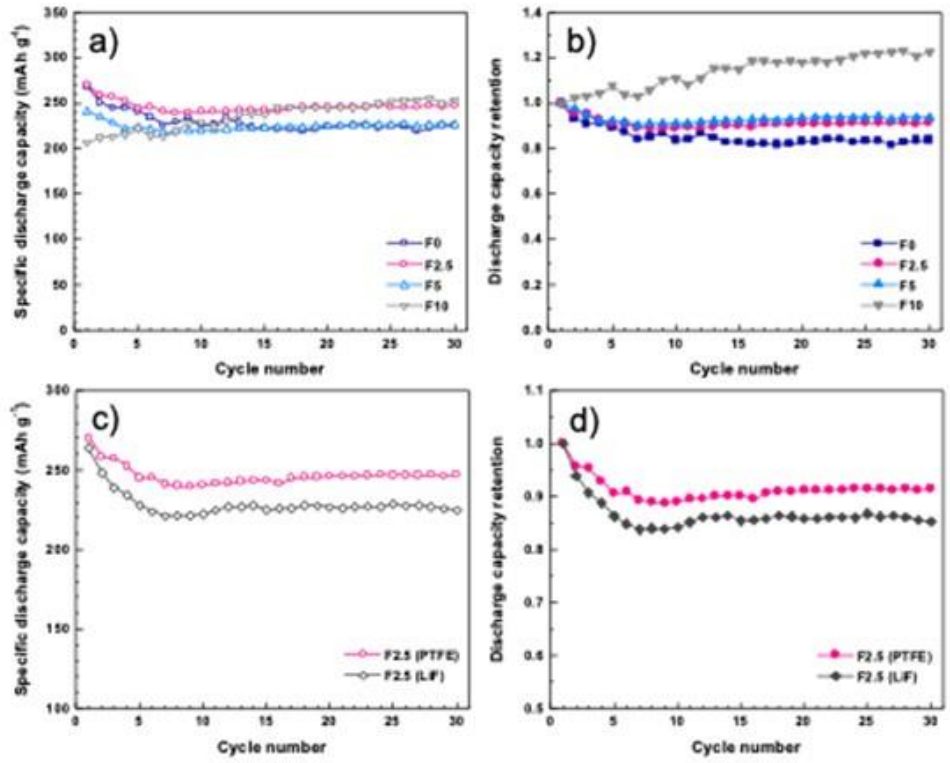

Figure II.2.E.5 (a, b) Comparison of discharge capacity and capacity retention of F0, F2.5, F5 and F10 cathodes and (c, d) comparison of discharge capacity and capacity retention of F2.5 prepared with PTFE and LiF precursors during the first 30 cycles.

3. *Improving cycling stability*

In order to evaluate intrinsic stability of the DRX materials, proper electrode fabrication and the development of an appropriate testing protocol are required. In the first year of the project we learned that the materials selected for study possessed inherent challenges such as poor electron conductivity. From this early assessment it was clear that an engineering improvement in electrode performance could be achieved by adding more carbon black and breaking down the agglomerates of secondary particles. This was achieved by ball milling carbon with the active material and by grinding that material with additional carbon with mortar and pestle. Previous experimental research also indicated that the majority of the capacity of this material is active between 1.8 and 4.6 V, however, to access this capacity, the material is cycled between 1.5 and 4.8 V. 4.8 V is fairly aggressive for most Li-ion electrolytes and leads to possible oxidation of electrolyte. To minimize this potentially negative outcome, it is important that we find ways to increase electronic conductivity and decrease lithium diffusion distances without excessively increasing surface area.

Figure II.2.E.6 shows the cycling capacity of three materials with the ratio of active material to carbon additive to polymer binder listed directly on the figure. All three electrodes were cycled between 1.5 and 4.7 V at 20 mA/g (*ca*. C/10), interrupted every 50 cycles with 5 cycles at 10 mA/g. The electrode with the highest carbon content (34 wt.%) shows the highest initial capacity of 265 mAh/g and the lowest capacity fade rate of 0.3 mAh/cycle at 20 mA/g. The cycling results demonstrate for the first time that we could access a high level of capacity without sacrificing cyclability. The improvement in impedance is also minimizing the effect of impedance rise on the cell.

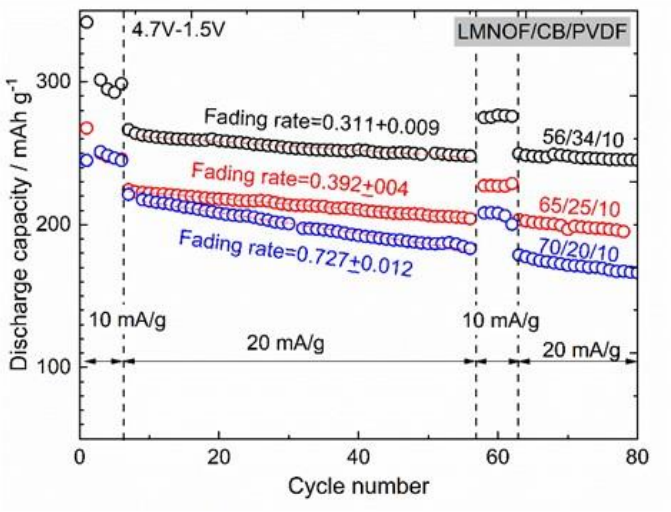

Figure II.2.E.6 Discharge capacity of LMNOF vs. cycle number for three different carbon levels. The electrode content is identified on the figure as A/C/B, where A is the weight fraction of active material, C is the weight fraction of carbon additive, and B is the weight fraction of binder.

An investigation of cycling protocols was also carried out. Figure II.2.E.7 shows results of cycling to an upper voltage of 4.7 V and a lower voltage of either 1.5 or 1.8 V. The result of this study showed that cycling with a constant voltage hold at the top of charge and the lower cutoff voltage not only achieved the highest capacity per cycle of 290 mAh/g but the least amount of capacity fade per cycle. **The capacity fade for this condition was just 0.03 mAh/g. The CV hold at the top of charge almost eliminates the capacity fade indicating that this DRX compound does not suffer intrinsic capacity loss, but that impedance growth may be responsible for the apparent fade in purely galvanostatic tests.** The study demonstrates the importance of materials engineering and cycling protocol optimization in order to properly evaluate DRX performance.

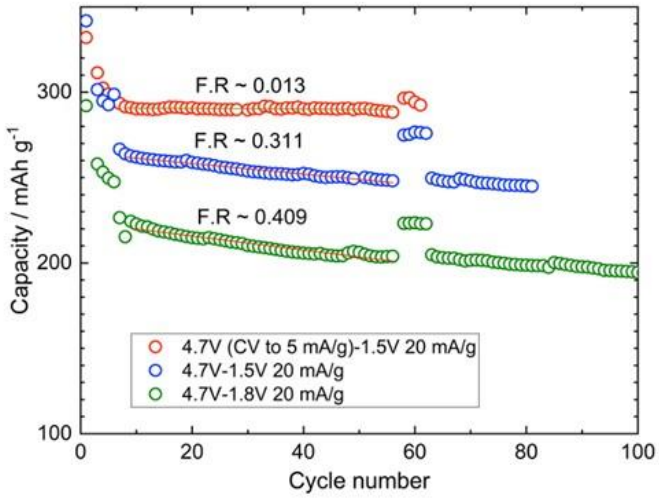

Figure II.2.E.7 The cycling results of different charge and discharge protocols. The red circles are for a cell cycled between 1.5 and 4.7 V with a constant voltage hold at 4.7 V until the current dropped to 5 mA/g, the blue circles for a cell cycled between 1.5 and 4.7 V without a voltage hold at the top, and the green circles are for a cell cycled between 1.8 and 4.7 V. All cells contained 34 wt.% carbon.

Conclusions

DRX are energy dense and Co-free cathode materials with flexible cation and anion chemistry. In FY20, reliable synthesis procedures based on mechanochemical and solid-state reactions were successfully developed to prepare Mn^{2+}-based DRX materials that utilize the $2e^-$ redox couple Mn^{2+}/Mn^{4+} to further increase capacity

and reduce cost. Synthesis methods were also developed to maximize F content in a scalable solid-state process. The use of fluorinated polymers instead of LiF as F precursor not only increases F solubility in DRX but also reduces the manufacturing cost as they are significantly cheaper. The higher F content enables an increase in redox-active TM content, resulting in oxyfluoride compounds with excellent rate capability and cycling stability. Engineering approaches and cycling protocols were optimized to reduce impedance and improve DRX cycling stability. Increasing carbon content largely improves stability while maintaining high capacity. Cycling with a constant voltage hold at the top of charge and a lower cutoff voltage enables the highest capacity and the least amount of capacity fade. In the future work, we will further explore different reaction precursors, dopants and after-synthesis treatment to maximize F content in solid-state synthesis. Processing conditions will be explored to tailor and control short-range ordering (SRO) which is expected to influence Li-ion mobility and voltage profiles of the DRX cathodes. Materials engineering strategies will be further explored, electrode fabrication variables such as binder and carbon contents as well as coating method optimized, pouch cell testing protocols developed and baseline performance will be established.

Key Publications

1. J. Ahn, D. Chen and G. Chen, "A Fluorination Method for Improving Cation-Disordered Rocksalt Cathode Performance," *Advanced Energy Materials* 2001671 (2020). DOI: 10.1002/aenm.202001671

2. D. Chen, J. Wu, J. K. Papp, B. D. McCloskey, W. Yang and G. Chen, "Role of Redox-Inactive Transition-Metals in the Behavior of Cation-Disordered Rocksalt Cathodes," *Small* 2000656 (2020). DOI: 10.1002/smll.202000656.

3. D. Chen, J. Zhang, Z. Jiang, C. Wei, L. Li, C. Wang, Y. Liu and G. Chen, "Unraveling Chemomechanics of Cation-Disordered Rocksalt Cathode Materials," submitted (2020).

4. D. Chen, J. Ahn, E. Self, J. Nanda and G. Chen, "Design Strategies for Improved Cation-Disordered Rocksalt Cathodes," submitted (2020).

5. Y. Yue, N. Li, L. Li, E. E. Foley, Y. Fu, V. S Battaglia, R. J. Clément, C. Wang and W. Tong, "Redox Behaviors in Li-Excess Cation-Disordered Mn-Nb-O-F Rocksalt Cathode," *Chemistry of Materials* **32** (11), 4490-4498 (2020).

Acknowledgements

Juhyeon Ahn, Vincent Battaglia, Tyler Bennet, Jordan Burns, Zijian Cai, Gerbrand Ceder, Dongchang Chen, Guoying Chen, Raphaele Juliette Clement, Matthew Crafton, Emily Foley, Yanbao Fu, Raynald Giovine, Yang Ha, Kenny Higa, Tzu-Yang Huang, Huiwen Ji, Robert Kostecki, Linze Li, Zhengyan Lun, Bryan McCloskey, Jagjit Nanda, Kristin Persson, Rohit Satish, Ethan C. Self, Wei Tong, Chongmin Wang, Wanli Yang, Yuan Yue, Yiman Zhang, Peichen Zhong

II.2.F Disordered RockSalt Structured Cathode Materials: Characterization and Modeling (LBNL, ORNL, PNNL, UC Santa Barbara)

Gerbrand Ceder, Principal Investigator
Lawrence Berkeley National Laboratory
1 Cyclotron Road
Berkeley, CA 94720
E-mail: gceder@berkeley.edu

Peter Faguy, DOE Technology Development Manager
U.S. Department of Energy
E-mail: Peter.Faguy@ee.doe.gov

Start Date: October 1, 2018 End Date: September 30, 2021
Total Project Cost: $2,500,000 DOE share: $2,500,000 Non-DOE share: $0

Project Introduction

The projected growth of Li-ion battery (LIB) production towards multiple TWh/year will require several million tons of Co/Ni combined, which constitutes a very sizeable fraction of the annual production of these metals. The recent development of Li-excess cation-disordered rocksalts (DRX) provides an alternative to develop high energy density LIB cathodes that use more abundant and less expensive elements, and can respond to the industry need for lower cost, less resource intensive cathode materials. DRX materials have been shown to deliver energy densities over 1000 Wh/kg, and its cation disordered nature allowing for a wide range of chemistry free of Co and/or Ni. The ability to substitute some of the oxygen by fluorine in locally Li-rich environments provides an extra handle to optimize performance through increasing transition-metal (TM) redox capacity. As this class of cathodes are relatively new, further materials design and development are needed in order to properly evaluate their promise and challenges towards eventual commercialization. To do so, fundamental understanding of what controls DRX performance characteristics, particularly rate capability, cycling stability and voltage slope, is critical. This project has assembled necessary research expertise in modeling, synthesis, electrochemistry and characterization to tackle these challenges. The current report reports on the Modeling and Characterization components of the project and has a companion report on Synthesis and Electrochemistry of the materials.

Objectives

The goals of this project are as follows:

- Understand the factors that control DRX cycling stability, particularly to what extent cycle life is controlled by impedance growth on the surface and by bulk changes in the material
- Understand what controls the rate of DRX materials, particularly rate limitation posed by bulk transport and surface processes
- Investigate the root of voltage profile slope in DRX
- Develop Co-free high energy density DRX cathodes.

Approach

This project originally focused on three representative baseline systems and their analogues: 1) Mn-redox based $Li_{1.2}Mn_{0.625}Nb_{0.175}O_{1.95}F_{0.05}$ (LMNOF), Ni-redox based $Li_{1.15}Ni_{0.45}Ti_{0.3}Mo_{0.1}O_{1.85}F_{0.15}$ (LNTMOF), and 3) a high F-content $Li_2Mn_{1/2}Ti_{1/2}O_2F$ (LMTOF) that utilizes the $2e^-$ Mn^{2+}/Mn^{4+}redox couple. The team operates in six thrusts areas representing the challenges and opportunities with DRX materials:

1. Characterization of the local and global structure of the bulk material before and during cycling, including detailed characterization of TM and O redox processes in the bulk and on the surface.
2. Characterization and manipulation of short-range cation order (SRO) to enhance rate capability.
3. Characterization and modeling of the DRX surface chemistry and processes during cycling to high voltage
4. Electrolyte/cathode interface issues and impedance growth due to surface processes
5. Fluorine solubility limits and synthesis of highly fluorinated compounds with scalable methods
6. Electrochemistry and testing in coin and pouch cells.
   Items (5) and (6) are discussed in the companion report.

Results

1. Role of fluorine

While DRX materials show less oxygen loss in DEMS than high-Ni NMC materials, they still show some surface densification when charged to high voltage. The presence of local transition-metal (TM)-poor, Li-rich environments in the rocksalt crystal structure, however, allows for substantial levels of F substitution into the O sublattice which significantly reduces oxygen loss and impedance growth. The role of F in the performance of DRX materials is studied with a combination of modeling, nuclear magnetic resonance (NMR), transmission electron microscopy (TEM), differential electrochemical mass spectrometry (DEMS) to characterize the material and correlate it to electrochemical performance. Modeling has given us significant insight into how fluorination enhances the stability of the DRX materials. A ***novel method was developed to model the surfaces of a disordered prototype DRX compound Li_2MnO_2F***. Ab initio calculations were combined with the cluster expansion technique and Monte Carlo to create and equilibrate surface structures of the DRX materials. A total of 177 separate surface energies were calculated from bulk and slab calculations. These energies were then used to calculate the Boltzmann weighted surface energies to obtain the equilibrium particle shape (Figure II.2.F.1). The dominant facets are of type {100} and {110}, creating a slightly chamfered cube shape, consistent with the particle shapes that have been observed in molten salt synthesis. In general, it was found that increasing surface manganese increased the surface energy, while increasing surface fluorine content decreased the predicted surface energy. These results indicate that ***surface enrichment of lithium and fluorine are likely energetically favorable, and the low energy surfaces of Li_2MnO_2F are likely lower in manganese content***. By demonstrating fluorine enrichment on the surface, this study directly relates to the experimental DMES observation that the loss of surface oxygen is considerably reduced in fluorinated DRX. Having less Mn on the surface may also help with the common issue of Mn dissolution during cycling for Mn-containing compounds.

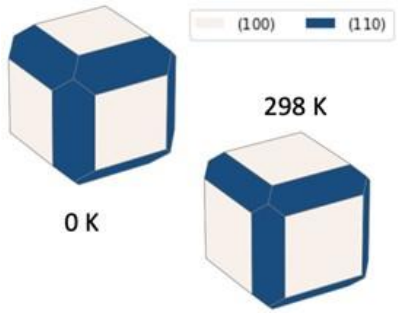

Figure II.2.F.1 The equilibrium particle shape of disordered Li_2MnO_2F is shown for 0K and 298K. The dominant facet is of type {100} followed by {110}. The particle assumes a slightly chamfered cube shape.

To experimentally investigate the effect of fluorination on DRX bulk electrochemistry and surface reactivity, a DRX oxide ($Li_{1.2}Mn_{0.6}Nb_{0.2}O_2$) and a similar DRX oxyfluoride ($Li_{1.2}Mn_{0.625}Nb_{0.175}O_{1.95}F_{0.05}$) were studied and

compared using DEMS and titration mass spectrometry (TiMS). Combining these techniques is a first in the Li-ion battery field and allows for a very quantitative accounting of the various processes that contribute to the electrochemical response of the cathode material. DEMS was used to quantify the formation of gaseous surface degradation products from the DRX material *in situ*, while TiMS was used to measure the formation and consumption of bulk oxidized oxygen and surface carbonate species in the DRX material *ex situ*. Results from DEMS and TiMS were combined with knowledge about transition metal reactivity from the literature to fully map the first-charge electrochemistry for a DRX oxide and a similar DRX oxyfluoride. This analysis allowed for the successful accounting of the experimentally observed capacity as the sum of the estimated contributions from each of the primary electrochemical reactions (TM redox, oxygen redox, carbonate oxidation, oxygen loss). The results of this analysis demonstrated that ***fluorination increases the available transition metal capacity and reduces the available oxygen redox capacity***. These two effects influence the total material capacity in opposite ways, shifting the balance between transition metal redox and oxygen redox without strongly affecting the total charge capacity. But because oxygen redox tends to lead to more capacity fade, fluorination enhances the cycle life. DEMS was also coupled with an electrolyte additive that scavenges fluoride in the electrolyte, showing small amounts of dissolved fluoride when charging to high potentials. Finally, all of these techniques were also extended over the first several cycles to study the reversibility of the redox processes and the stability of the materials during cycling. It was shown that while oxygen redox remains mostly reversible from cycle to cycle, electrolyte degradation and fluoride dissolution also continue to occur to a diminishing extent during cycling.

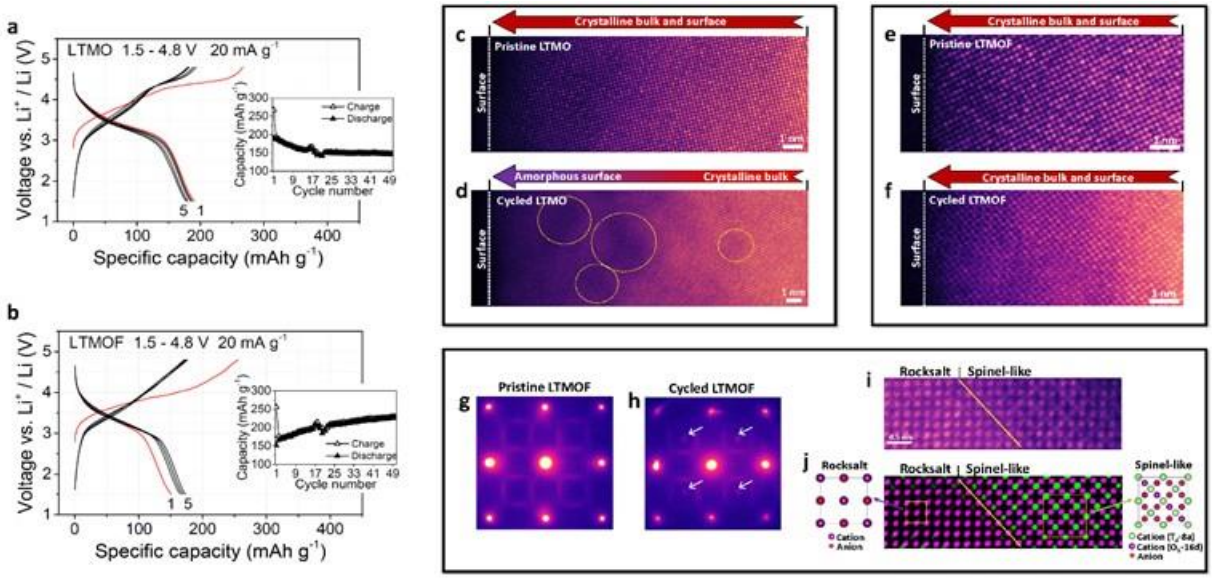

Figure II.2.F.2 Electrochemical performance and cycling-induced structural evolution in LTMO and LTMOF particles. (a,b) Charge and discharge voltage profiles for the first 5 cycles and specific capacity as a function of cycle number (inset) for LTMO (a) and LTMOF (b) cathodes in half-cells cycled between 1.5 and 4.8 V at a current density of 20 mA g−1. (c,d) Atomic-resolution STEM HAADF images of nanoscale surface regions in LTMO in the pristine state (c) and in the discharged state after 50 cycles (d). The yellow circles in (d) mark voids formed below the surface. (e,f) Atomic-resolution STEM HAADF images of nanoscale surface regions in LTMOF in the pristine state (e) and in the discharged state after 50 cycles (f). (g,h) Electron diffraction patterns for pristine LTMOF (g) and discharged LTMOF after 50 cycles (h). The white arrows in (h) mark the 4 additional spots corresponding to the spinel-like lattice. (i) Magnified STEM HAADF image of a boundary across rocksalt and spinel-like structures in cycled LTMOF. (j) Corresponding filtered image of the magnified STEM HAADF image in (i), showing the spatial distribution of rocksalt (purple) and spinel-like (green) structures. 2D atomic models of rocksalt and spinel structures are shown on the left and right sides of the filtered image, respectively.

Using atomic-resolution scanning transmission electron microscopy (STEM) we were able to investigate how fluorination improves cathode cyclability with atomistic-level detail. The structural evolution induced by electrochemical cycling was investigated in a DRX oxide cathode, $Li_{1.2}Ti_{0.4}Mn_{0.4}O_{2.0}$ (LTMO), and its fluorinated variant, $Li_{1.2}Ti_{0.2}Mn_{0.6}O_{1.8}F_{0.2}$ (LTMOF). The cathodes were cycled between 1.5 and 4.8 V *vs.*

Li/Li$^+$ at a current of 20 mA/g for 50 cycles (Figure II.2.F.2a and b). Both LTMO and LTMOF showed a uniform rocksalt structure from the inner bulk to the outer surface. After 50 cycles, an amorphous surface region of ~ 10 nm, populated with nanosized voids, was identified in LTMO (Figure II.2.F.2c and d). In contrast, LTMOF exhibited no cycling-induced surface degradation, as shown in the STEM images collected before and after cycling (Figure II.2.F.2e and f). The fact that the ***surface degradation is much less prominent in cycled LTMOF particles indicates the crucial role of fluorination in enhancing the structural stability and improving cycling stability of DRX cathodes***. Another prominent feature, evidenced by identified electron diffraction (Figure II.2.F.2g and h) and the STEM-HAADF, is the partial cycling-induced transformation from rocksalt to a spinel-like phase in the bulk of LTMOF particles. The nanosized spinel-like domains are well-dispersed in the rocksalt matrix. Such structural evolution is presumably associated with the gradual capacity increase in LTMOF (Figure II.2.F.2b). In contrast to the traditional belief that such an irreversible structural change would lead to capacity degradation, we found that this transformation surprisingly results in a capacity increase in LTMOF upon cycling. We also speculate that a partial spinel transformation at the surface may lend further protection against surface degradation and capacity loss.

Soft X-ray resonant inelastic X-ray spectroscopy (RIXS) is capable of providing the most direct and quantitative probes of the cationic and anionic redox activities in various DRX materials. Additionally, X-ray absorption spectroscopy (XAS) can be collected either simultaneously with RIXS experiments, or as a byproduct of RIXS maps, providing a separation of the chemical states in surface *vs*, bulk. The combination of these spectroscopic studies has revealed an understanding of the effects of stoichiometry and fluorination on the composition-dependent redox mechanisms in DRX materials. Figure II.2.F.3 displays the RIXS analysis of TM and oxygen states in three DRX materials, $Li_{1.2}Mn_{0.7}Nb_{0.1}O_{1.8}F_{0.2}$, $Li_{1.15}Ni_{0.45}Ti_{0.3}Mo_{0.1}O_{1.85}F_{0.15}$ and $Li_2Mn_{1/2}Ti_{1/2}O_2F$, upon electrochemical cycling. Bulk Mn states are extracted through the RIXS map and quantitatively compared with surface states (not shown). This provides the electron charge transfer number of the TM redox and defines the voltage range of the cationic redox reactions. In particular, $Li_2Mn_{1/2}Ti_{1/2}O_2F$, O-*K* RIXS shows that significantly ***higher fluorination level leads to a much suppressed oxidized oxygen state compared with other systems, along with the enhanced contributions from bulk Mn^{2+}/Mn^{4+} redox***.

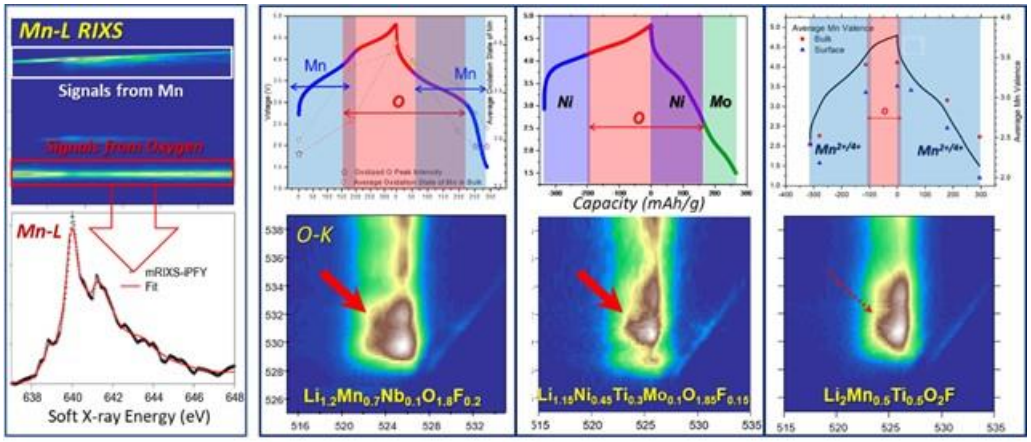

Figure II.2.F.3 A comparative study of both TM cationic and oxygen anionic redox activities in three representative DRX materials, $Li_{1.2}Mn_{0.7}Nb_{0.1}O_{1.8}F_{0.2}$, $Li_{1.15}Ni_{0.45}Ti_{0.3}Mo_{0.1}O_{1.85}F_{0.15}$ and $Li_2Mn_{1/2}Ti_{1/2}O_2F$, using high-efficiency soft X-ray RIXS. The three materials display some common behaviors, especially at the high voltage range, but contrast in various bulk and surface chemical evolutions upon cycling is also shown.

2. High-voltage issues and mitigating approaches

While DRX materials cycle with almost no capacity fade at 4.4V, the extremely high capacities achievable with them requires charge to higher voltage (4.7 or 4.8V) which may lead to electrolyte and cathode surface issues. A combination of Fourier transform-infrared (FT-IR), solid-state NMR and DEMS was used to probe the LMNOF electrodes that were cycled up to 4.8 V in two electrolyte systems containing $LiPF_6$ and $LiClO_4$, respectively. $LiClO_4$ was used as an alternate salt to specifically identify which F-containing reaction products

originated from the cathode/binder. FT-IR Attenuated Total Reflection (ATR) measurements (Figure II.2.F.4) show the presence of LiF on the electrode surface in both systems, indicating that when charged higher than 4.7 V *vs*. Li^+/Li, either the DRX powder or the F-based binders undergo side reactions with the electrolyte.

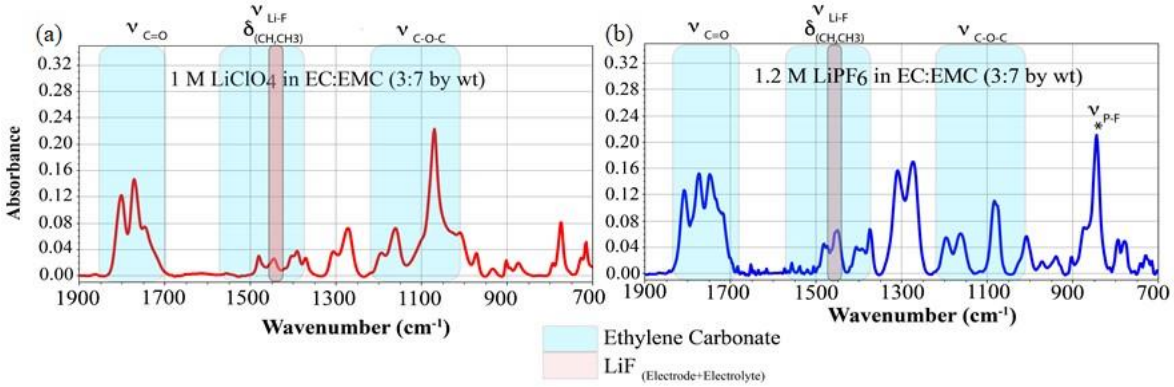

Figure II.2.F.4 FT-IR spectra of LMNOF cathode cycled in (a) 1M $LiClO_4$ and (b) 1.2 M $LiPF_6$ in EC:EMC.

Further understanding was obtained from a modified DEMS measurement. The technique uses trimethyl silyl phosphate(TMSPa) as an F scavenger which reacts with any F species in the electrolyte to form trimethylsilyl fluoride(Me_3SiF) gas that can then be quantified. The experiment was carried out on LMNOF electrodes *operando* in both electrolyte systems. Results from the $LiClO_4$ system indicate the formation of F species when charged to 4.7 V (Figure II.2.F.5a), whereas those with the $LiPF_6$ salt indicate degradation products being formed as early as 3.75 V and in a much larger quantity (Figure II.2.F.5b). This suggests that F-containing species are formed in the electrolyte with both salts but the presence of $LiPF_6$ leads to a significantly larger quantity and onset at lower potential.

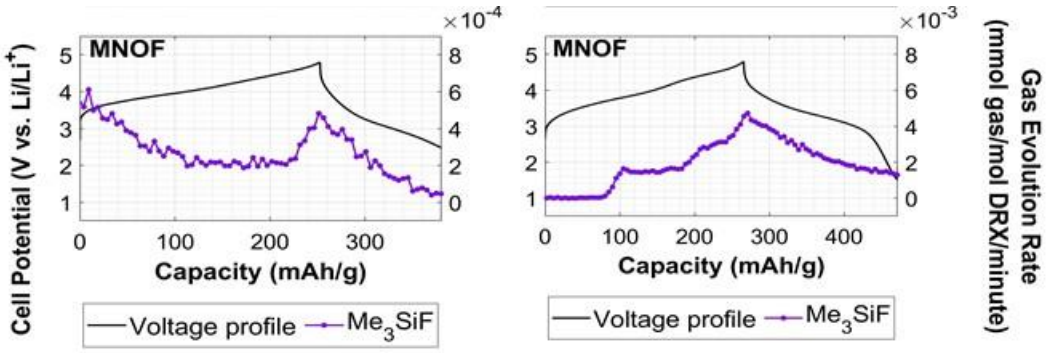

Figure II.2.F.5 DEMS profiles collected on LMNOF electrodes tested in (a) $LiClO_4$ electrolyte and (b) $LiPF_6$ electrolyte.

To understand the structural nature of the $\bar{F}$ species, ^{19}F and ^{7}Li NMR were conducted on electrodes cycled to 4.8 V for 20 cycles (Figure II.2.F.6). ^{19}F NMR data indicates that a very low amount of LiF impurity is formed upon cycling with $LiClO_4$, while ^{7}Li NMR results indicates a large fraction of Li_3CO_3 after 20 cycles. Conversely, samples cycled with $LiPF_6$ exhibit a large accumulation of LiF, along with PF_6^-, while the fraction of Li_2CO_3 decreases upon cycling. These results provide preliminary evidence that ***F incorporation into the DRX cathode is stable upon cycling but the $LiPF_6$ – containing electrolyte decomposes at high voltage (4.8 V), forming both LiF and PF_6^-.***

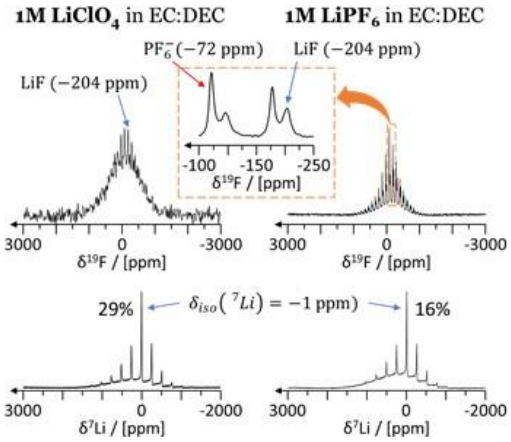

Figure II.2.F.6 Ex situ ^{19}F (top) and ^{7}Li (bottom) MAS NMR spectra of LMNOF cathode after 20 cycles using either $LiPF_6$ or $LiClO_4$. An expansion of the ^{19}F NMR spectra of the LMNOF cathode cycled in $LiPF_6$ highlights the presence of PF_6^- and LiF.

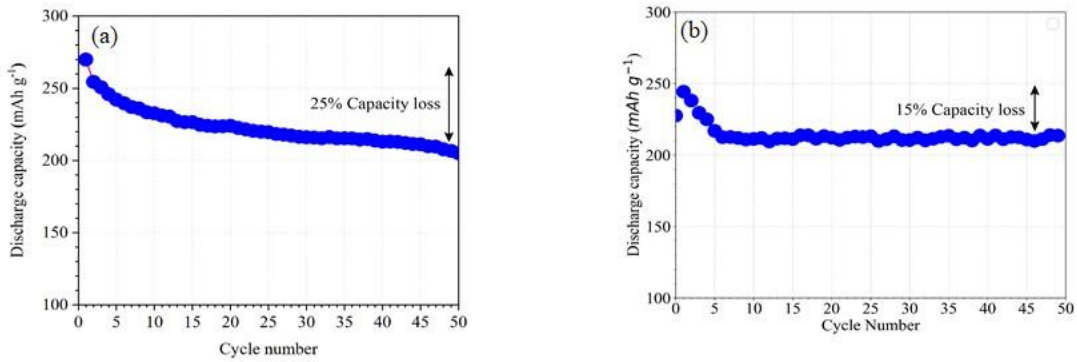

Figure II.2.F.7 Discharge capacity as a function of cycle number for (a) pristine LMNOF and (b) 3-day treated LMNOF.

Pretreatment of DRX cathodes was explored as way to establish a stable interface. Pristine LMNOF powder was immersed in the electrolyte (1.2M $LiPF_6$ 3:7 EC: EMC by wt.) and heated to 60 ˚C for varying periods of time ranging from 1 to 10 days. The powder after treatment was washed repeatedly with dimethyl carbonate (DMC) to remove remaining electrolyte, and dried at 80 ˚C in vacuum. The powder was then assembled into electrodes to quantify changes in electrochemical performance. It was found that 3 days is the optimum treatment duration. ***LMNOF samples treated for 3 days showed a drastic improvement in terms of capacity retention, with less than 15 % decay in 50 cycles as compared to 25% decay observed in untreated samples*** (Figure II.2.F.7). We believe that treatment with electrolyte at elevated temperatures may simulate the process of accelerated ageing and facilitate *apriori* surface modifications that stabilize the LMNOF cathode. This hypothesis was supported by STEM imaging coupled with electron energy loss spectroscopy (EELS). The pristine LMNOF sample was crystalline with a ~ 2 nm thick mostly amorphous surface region (Figure II.2.F.8a). EELS spectra (Figure II.2.F.8b) indicate a local enrichment of F at the surface layer. The intensity of the O *K* pre-peak is suppressed at the surface layer, suggesting a possible accumulation of O vacancies. Correspondingly, reduction of Mn valence, as evidenced by the shift of the Mn L_3 peak to lower energies (Figure II.2.F.8b), was limited to the surface layer (~ 5 nm thick). After the 3-day surface treatment in the electrolyte, the rocksalt crystalline structure is uniform from the inner bulk to the outer surface (Figure II.2.F.8c). The EELS spectra (Figure II.2.F.8d) indicate F enrichment at the surface layer. On the other hand, the intensity of the O *K* pre-peaks is gradually suppressed from the inner region to the surface, suggesting an increased accumulation of O vacancies. Correspondingly, a gradual shift of Mn L_3 peaks to lower energies from the inner bulk region toward the surface was observed, which corresponds to a gradual reduction of Mn oxidation state.

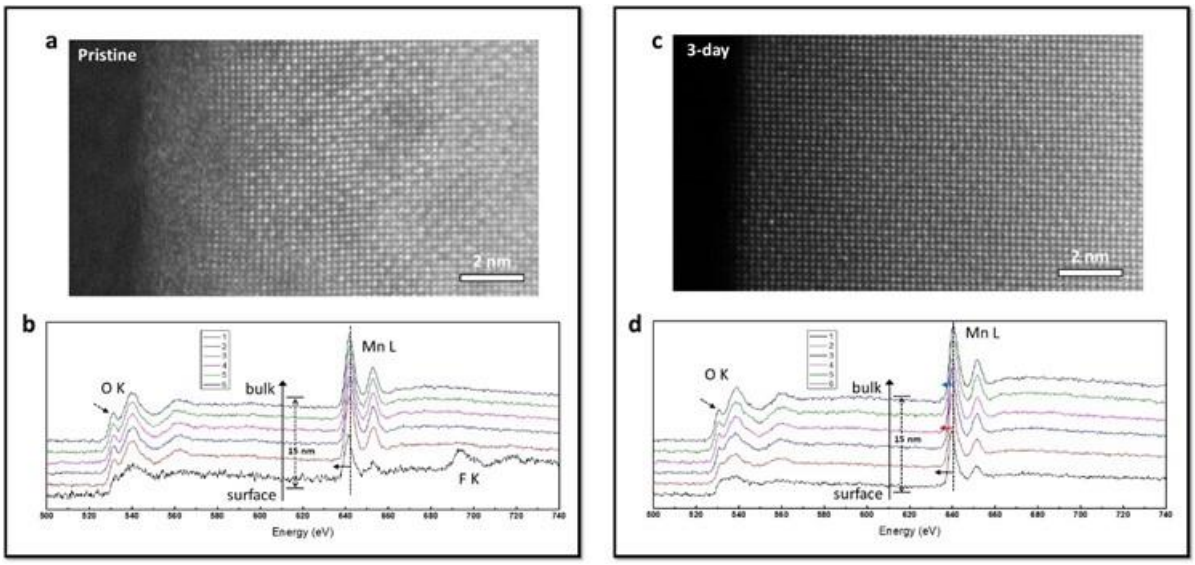

Figure II.2.F.8 (a) Atomic-scale STEM HAADF image of the pristine LMNOF sample, in which the 2 nm thick surface layer is amorphous, (b) EELS spectra collected at 6 different locations in the pristine LMNOF sample, from the surface to 15 nm deep into the bulk, (c) Atomic-scale STEM HAADF image of the LMNOF sample after 3-day treatment and (d) EELS spectra collected at 6 different locations in the surface-treated LMNOF sample, from the surface to 15 nm deep into the bulk.

3. Local structure and rate capability improvement

It is now well established that while DRX materials have no long-range cation order, they display significant short-range cation order (SRO). The nature of this SRO is often such that it reduces the number of Li transport paths, and hence degrades rate capability. A major task of this team has therefore been to develop computational and experimental approaches to characterize the SRO, and synthesis and compositional designs that minimize it. Neutron diffraction (ND) is a powerful tool for elucidating structural details of lithium-containing compounds because of the higher sensitivity of neutrons to low-atomic number elements as compared to x-rays. ND also has good scattering contrast between different transition metal cations. Pair distribution function (PDF) analysis has emerged as a powerful tool to probe short-range chemical features in disordered crystalline materials because it uses both the Bragg and diffuse scattering signal. The latter often contains important information about short-range cation/anion ordering but has been routinely ignored in the conventional Rietveld analysis.

Figure II.2.F.9a shows the ND pattern of $Li_{1.3}Mn_{0.4}Ti_{0.3}O_{2-x}F$. While Rietveld refinement using the disordered rocksalt model works well for the average structure, the expanded view (Figure II.2.F.9b) shows the presence of broad and diffuse peaks/bumps (green arrows), indicating short-range cation ordering or clustering. This is most visible in the low Q region. PDF (Figure II.2.F.9c) shows a clearer picture of the local cation ordered scheme. The average structure (disordered rock salt) fit the PDF well above 5 Å but the structure fit the short-range PDF very poorly (below 5 Å). The first PDF peak splits into two peaks indicating two drastically different M-O/F bond distances, and the split of the peak around 4 Å indicates nearest M-M or anion-anion distances). The average structure fits the intermediate range PDF data (> 6 Å) well, suggesting that the cation ordering is limited to very short distances, probably within the first one or two cation-cation shells.

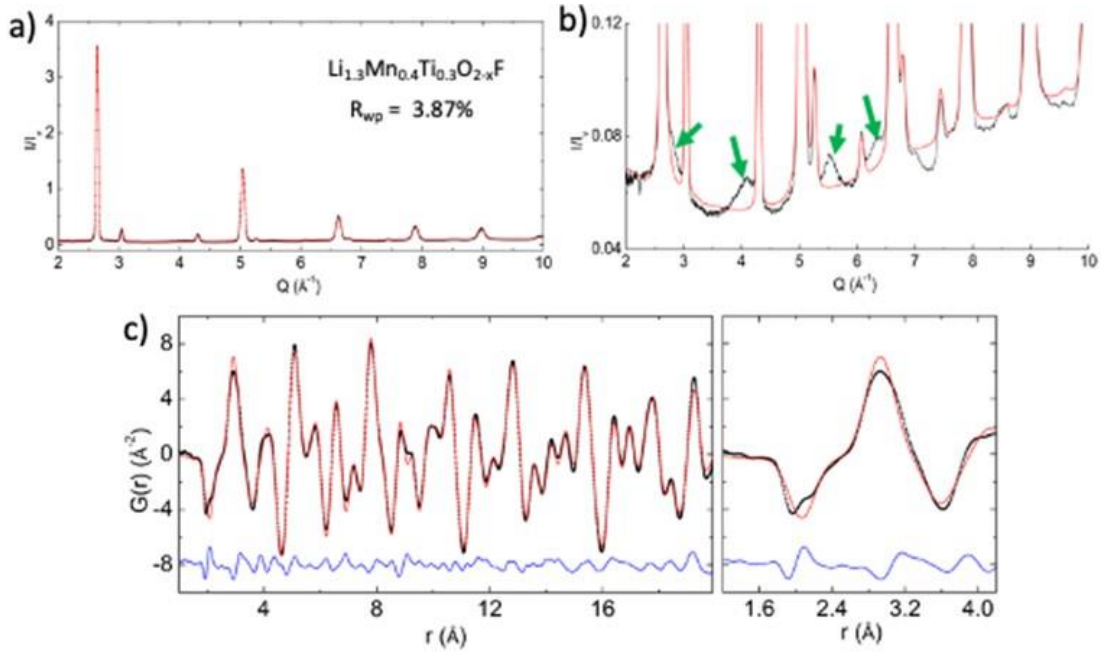

Figure II.2.F.9 a) Experimental and simulated ND of $Li_{1.3}Mn_{0.4}Ti_{0.3}O_{2-x}F_x$. Red line is the fit and black line is the experimental data, b) scaled up region to show the disagreement between fit and experiment, and c) PDF analysis showing the discrepancy between model fit.

Our team has been developing various strategies to reduce cation short-range order and thereby enhance rate capability. One concept that has already led to higher rate capable materials is the use of High-Entropy (HE) DRX materials: by using multiple metals ordering frustration is created which reduces SRO. This concept is demonstrated in Figure II.2.F.10. A material with 6 metal components (6TM) displays almost no SRO as demonstrated by the TEM diffraction (middle panel). As a result, the material shows high rate performance enabling discharge up to 2A/g. **Our work has now shown multiple approaches to create high-rate DRX cathode materials.**

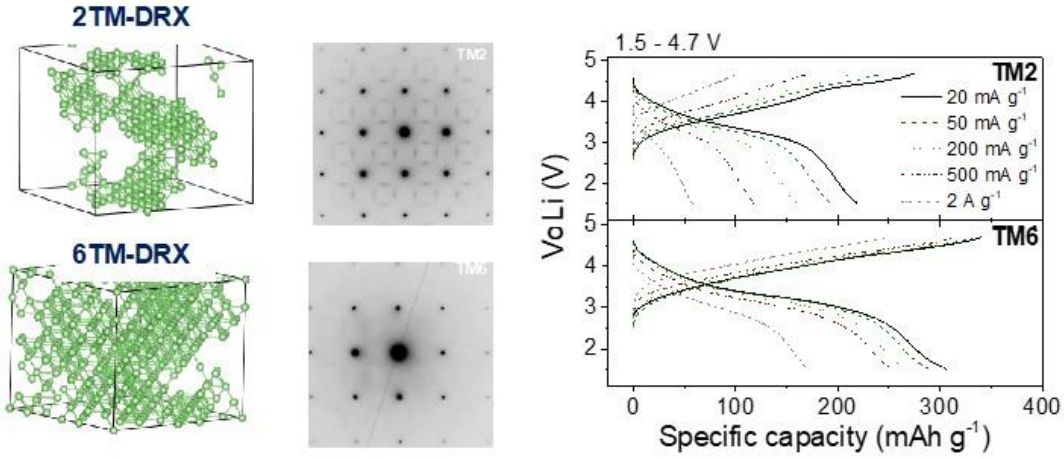

Figure II.2.F.10 High-rate performance achieved by high-entropy mixing. The left graphs show the increase Li-percolation network as one goes from a DRX with two transition metals (2TM) to one with 6 transition metals (6TM). Middle TEM graphs show reduced SRO in 6TM system. Right graphs: The 6TM compound is able to discharge at up to 2A/g.

Conclusions

DRX are energy dense, Co-free cathode materials with flexible cation and anion chemistry. Many of the promising compositions are also free of Ni, providing an inexpensive and resource-unconstrained path towards

growth of Li-ion technology. This part of the "deep-dive" program has assembled the technical strengths in theory as well as bulk, local and surface characterizations to investigate the key issues in DRX cathodes. We have demonstrated with various techniques that fluorination is an effective strategy to enhance cycle life, and operates by reducing O-redox, increasing TM redox, and stabilizing the surface chemistry of DRX materials. Our future work will focus on determining what the optimal F-content is as a function of metal chemistry and establishing the synthetic approaches to achieve it. We have also established that high voltage charging leads to degradation of $LiPF_6$ and possible reaction of the electrolyte with the DRX surface, creating impedance growth. Finally, by combining modeling and multiple characterization techniques cation SRO has been established as a controlling factor for the rate capability of DRX materials. Previously, we had demonstrated partial spinel-like ordering to create high rate DRX-like materials. This year we have added the strategy of high-entropy design to enhance the rate capability of DRX materials. Our "deep-dive" into the mechanisms by which DRX materials operate and degrade have provided the insights needed to further optimize these promising cathode materials towards potential commercialization.

Key Publications

1. H. Ji, J. Wu, Z. Cai, J. Liu, D.-H. Kwon, H. Kim, A. Urban, J. K. Papp, E. Foley, Y. Tian, M. Balasubramanian, H. Kim, R. J. Clément, B. D. McCloskey, W. Yang and G. Ceder, "Ultrahigh power and energy density in partially ordered lithium-ion cathode materials," Nat. Energy 5 (3), 213-221 (2020).

2. Z. Lun, Z. B. Ouyang, D. H. Kwon, Y. Ha, E. E. Foley, T. Y. Huang, Z. Cai, Z. H. Kim, M. Balasubramanian, Y. Sun, J. Huang, Y. Tian, H. Kim, B. D. McCloskey, W. Yang, R. J. Clement, H. Ji and G. Ceder, "Cation-disordered rocksalt-type high-entropy cathodes for Li-ion batteries," Nat. Mater. (2020).

3. M. J. Crafton, Y. Yue, W. Tong, B. D. McCloskey, "Anion reactivity in cation-disordered rocksalt cathode materials: the influence of fluorine substitution." Advanced Energy Materials 10(35), 2001500 (2020).

4. L. Li, Z. Lun, D. Chen, Y. Yue, W. Tong, G. Chen, G. Ceder, C. Wang, "Fluorination-Enhanced Surface Stability of Cation-Disordered Rocksalt Cathodes for Li-Ion Batteries," submitted (2020).

5. R. J. Clément, Z. Lun, and G. Ceder, "Cation-disordered rocksalt transition metal oxides and oxyfluorides for high energy lithium-ion cathodes", Energy Environ. Sci., 13, 345–373 (2020).

6. Y. Zhang, E. C. Self, B. P. Thapaliya, R. Giovine, L. Li, Y. Yue, D. Chen, H. M. Meyer III, W. Tong, G. Chen, C. Wang, R. J. Clément, S. Dai and J. Nanda, "Direct Fluorination of High Capacity Co-Free Disordered Rock-Salt Cathodes", submitted to ACS App. Mater. & Interfaces (2020).

7. P. Zhong, Z. Cai, Y.-Q. Zhang, R. Giovine, B. Ouyang, G. Zeng, Y. Chen, R. J. Clément, Z. Lun and G. Ceder, "Increasing capacity in disordered rocksalt cathodes by Mg doping", submitted to Chem. Mater. (2020).

Acknowledgements

Juhyeon Ahn, Vincent Battaglia, Tyler Bennet, Jordan Burns, Zijian Cai, Dongchang Chen, Guoying Chen, Raphaele Juliette Clement, Matthew Crafton, Emily Foley, Yanbao Fu, Raynald Giovine, Yang Ha, Kenny Higa, Tzu-Yang Huang, Huiwen Ji, Robert Kostecki, Linze Li, Zhengyan Lun, Bryan McCloskey, Jagjit Nanda, Kristin Persson, Rohit Satish, Ethan C. Self, Wei Tong, Chongmin Wang, Wanli Yang, Yuan Yue, Yiman Zhang, Peichen Zhong

II.3 Next-Gen Lithium-Ion: Frontier Science at Interfaces

II.3.A Molecular-level Understanding of Cathode-Electrolyte Interfaces (SLAC National Accelerator Laboratory)

Michael F. Toney, Principal Investigator
Stanford Synchrotron Radiation Lightsource, SLAC National Accelerator Laboratory
2575 Sand Hill Rd
Menlo Park, CA 94025
E-mail: mftoney@slac.stanford.edu

Peter Faguy, DOE Technology Development Manager
U.S. Department of Energy
E-mail: Peter.Faguy@ee.doe.gov

Start Date: October 1, 2018 End Date: September 30, 2021
Project Funding: $450,00 DOE share: $450,000 Non-DOE share: $0

Project Introduction

Understanding the underlying reaction mechanism accounting for cathode-electrolyte interphase formation is crucial to overcome present limitations and develop stabilization strategies for next-generation lithium-ion batteries (NG-LIBs). To tackle this challenge, we combine theoretical modeling with advanced X-ray surface scattering studies in conjunction with spectroscopic and electrochemical characterization using model thin-film cathode electrodes and high purity electrolytes. The collaboration team consists of researchers from SLAC National Accelerator Laboratory, U.S. Army Research Laboratory/ARL, and Lawrence Berkeley National Laboratory/LBNL, and Oregon State University/OSU. Molecular-level modeling of cathode-electrolyte reactions are combined with diagnostics of cathode interphase evolution. This approach allows sufficient in-depth theoretical modeling and experimental probes to develop the necessary level of understanding into the interface degradation mechanisms and cathode stabilization strategies and it builds on our past success in related interfacial research [1]-[8]. To achieve our goals, we have employed high-voltage epitaxial thin film cathodes and carbonate-based and advanced fluorinated electrolytes. We have conducted comprehensive synchrotron x-ray studies to elucidate underlying mechanism on the interfacial degradation of cathode surfaces in carbonates-based electrolytes and the rationalization on cathode stabilization strategies through electrolyte design. To determine cathode interphase evolution pathways, we use *in situ* and *ex situ* synchrotron x-ray measurements that characterize the structural and chemical transformation process of model cathodes in different electrolytes. These feature simultaneous *in situ* surface x-ray scattering, and *ex situ* x-ray spectroscopies, as well as the mass spectroscopies. Our approach will provide fundamental knowledge about how electrode surface and electrolyte design dictate interfacial reaction pathway and will help enable stabilization strategies for cathode interfaces.

Objectives

High-energy NG-LiB electrochemistry requires the utilization of high capacity and high voltage cathode materials. Their full potential has to date been hampered by the paucity of understanding the underlying chemistry and physics on the cathode-electrolyte reaction and the directed interphase. In particular, the practical implementation of NG-LIBs is to a large extent obstructed by the absence of a suitable electrolyte. While typical carbonate-based electrolytes have been reliable in commercial LiBs, there is degradation of electrolyte at higher potentials. In combination with highly reactive cathode surface and defects, this creates an unstable cathode-electrolyte interface, which results in gas evolution, transition metal dissolution active material consumption, and increased battery impedance. This is even more problematic at elevated temperatures and/or during the fast charging process. Significant progress in mitigating these issues has been reported by using different electrolytes, such as nitriles [9], sulfones [10], [11], ionic liquids, and fluorinated carbonates [12]. However, stabilization of high voltage cathode-electrolyte interface (CEI) is still unresolved due to a lack in mechanistic understanding of

the degradation mechanism and stabilization strategy [13], [14]. Our objective is to provide a detailed understanding on the interfacial reaction between cathode and electrolyte. This includes a detailed elucidation on the interphase evolution pathway and the changes on cathode morphology and composition. We anticipate that our results will fill the gap in current understanding on the underlying chemistry and physics of cathode-electrolyte reactions and will be disseminated through impactful publications. This knowledge can be utilized to guide the design of advanced electrolyte and the development of cathode stabilization strategy and will help to accelerate the development and deployment of NG-LIBs for various applications.

Approach

Our approach is to combine density functional theory (DFT) calculations and molecular dynamics (MD) simulations with advanced x-ray studies and precision electrochemical characterization using model thin-film electrodes. It starts with the purification of electrolytes and the controlled growth of NMC thin films by Pulsed laser deposition (PLD). The reactivity and stability of cathode in electrolyte are probed by synchrotron-based X-ray scattering and spectroscopy studies. PLD-derived epitaxial lithium nickel-manganese-cobalt-oxide (NMC) thin-film are used as well-defined, high voltage cathode materials. Utilization of epitaxial NMC532 thin films as model systems enables high resolution x-ray experiments and well-controlled electrochemical experiments that only contain contributions from the cathode of interest rather than the parasitic reactions from the conductive additive or binder material. In order to reach our proposed objectives on identifying the key cathode-electrolyte reactions, we plan a multimodal surface-sensitive probes, involving synchrotron-based x-ray scattering techniques (x-ray reflectivity/XRR & surface X-ray diffraction/SXRD, as well as x-ray spectroscopy (x-ray absorption spectroscopy/XAS) measurements. XRR/SXRD will yield information on the structural transformation of cathodes when they react with electrolyte. X-ray spectroscopy will unravel complementary chemical information and composition on cathode interphase. The obtained experimental results are compared with the molecular-scale modelling on the cathode-electrolyte interfacial reactions.

Results

In general, progress was slowed due to the coivd-19 restrictions and lab-based research and on access to synchrotron sources. This delayed several experiments at the Advanced Photon Source and the Stanford Synchrotron Radiation Lightsource and limited access to labs at SLAC and the ARL. From the experimental side, we focused on data analysis, some remote experiments and planning.

We first focus on the reactivity and stability of cathode thin-films in carbonate-based electrolyte. Here, NMC532 thin films with controlled surface structure and film thickness have been developed through PLD growth. Surface X-ray characterization showed that single-crystal 10 nm $LiNi_{0.5}Mn_{0.3}Co_{0.2}O_2$ (NMC532) thin-films have been succefully deposited on $SrTiO_3$ substrate with 15 nm $SrRuO_3$ as conductive buffer layer (Figure II.3.A.1). Non-specular Phi scans confirmed the epitaxial relationship between NMC film and $SrTiO_3$ substrate (Figure II.3.A.1B). In order to probe the chemical reaction between cathode and carbonate-based electrolyte, the thin-film is subject to the solvent of ethylene carbonate (EC) - ethyl methyl carbonate (EMC) and electrolyte LP57 (1 M $LiPF_6$ in EC-EMC) for chemical soaking in glovebox for 2 hours. There are almost no changes on the SXRD peak position and profile of NMC films before/after chemical soaking (Figure II.3.A.1C), indicating negligible influence of chemical soaking on the out-of-plane structure of the NMC thin films.

Although there are negligible structural transformations of NMC films upon chemical soaking, there are significant chemical transformation of NMC thin films. Total-reflection X-ray absorption near edge structure (XANES) of NMC thin-films has been utilized as a surface-sensitive probe to study the valence evolution of transition metals before and after the exposure to EC-EMC solvent and LP57 electrolyte. Ni K-edge XANES showed that compared to the pristine films, there are significant negative shifts of spectra toward lower energy after an exposure to LP57 electrolyte (Figure II.3.A.2A). This indicated a dramatic reduction of Ni sites in NMC thin films after soaking in carbonate electrolyte. Such reduction phenomena can be also evidenced using EC-EMC solvent. After EC-EMC solvent soaking, the NMC thin-films showed similar spectra shifts at Ni K-edges, indicating the main contribution from carbonate solvent for Ni reduction. Instead, $LiPF_6$ salt is believed to play a negligible role. Solvent-induced transition metal reduction is further evidenced in Co sites in NMC thin-films by

the peak shifts after chemical soaking of NMC thin-films in EC-EMC solvent and LP57 electrolyte, while the peak shifts are smaller than Ni sites, indicated a decreased reduction degree for Co sites. Interestingly, there are negligible changes on the absorption peak position for Mn sites after the exposure to LP57 electrolyte and EC-EMC solvent under the same condition. Therefore, this shows the transition-metal-dependent degradation of NMC thin-films in carbonate-based electrolyte, and the EC-EMC solvent is believed to play a dominant role. Observation of different behaviors for transition metal reduction in carbonate-electrolyte is found to be consistent with the current understanding on the key contribution from Ni redox and partial contribution from Co redox in NMC cathode capacity, while Mn sites is believed to play a stabilization effect.

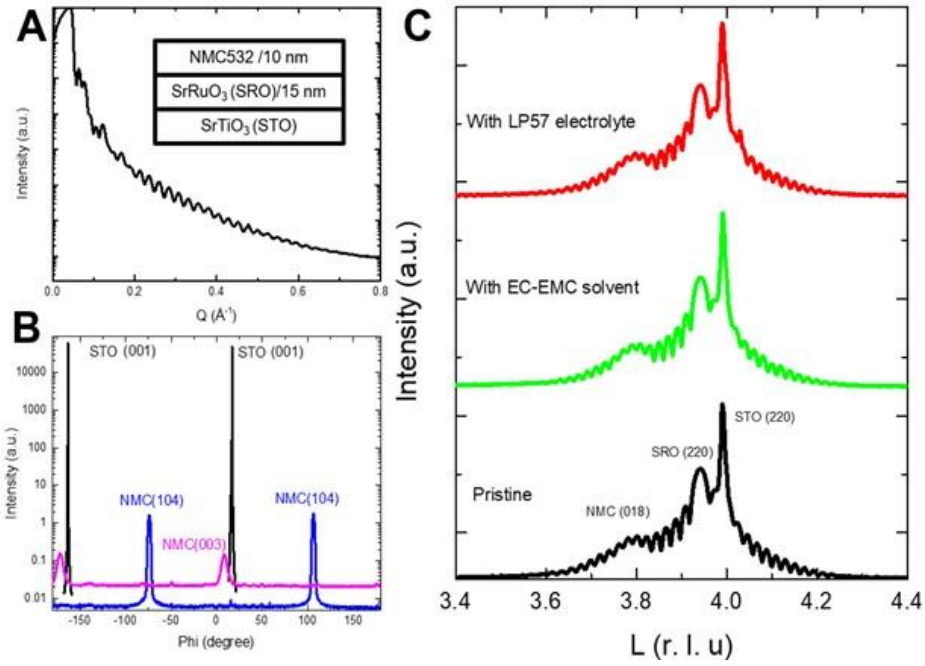

Figure II.3.A.1 Structural evolution of cathode thin-film with/without carbonate-based electrolyte (A) XRR of 10 nm NMC532 films grown on SrTiO3 substrates with 15 nm SrRuO3 buffer layers; (B) Off-specular phi-scans of STO {001}, NMC {104}, and NMC {003} of the film; C) SXRD of NMC532 films before and after exposure to EC-EMC solvent and LP57 electrolyte

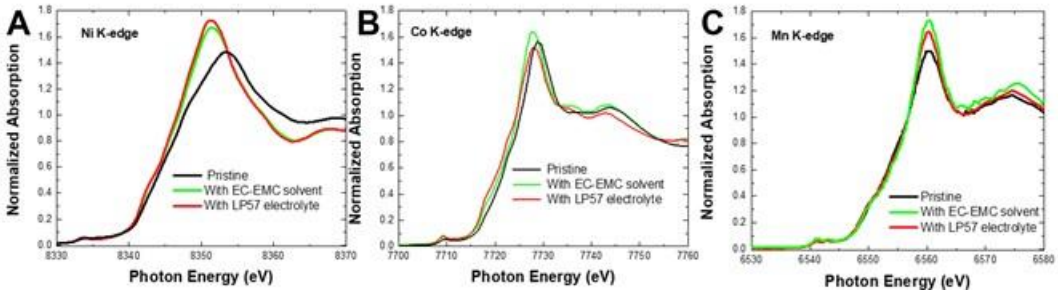

Figure II.3.A.2 **Transition metal-dependent degradation of NMC cathode in carbonate-based solvent and electrolyte**. Total-reflection X-ray absorption near edge structure (XANES) of NMC thin-films before and after exposure to EC-EMC solvent and LP57 electrolyte at Ni, Co, and Mn K-edges

To understand the chemical reaction between cathode and carbonate-based electrolyte, density functional theory (DFT) calculations have been conducted using the Li_xNiO_2 model cathode surface at different stages of lithiation that mimics different battery state of charge. The LiFSI and $LiPF_6$ salts decomposed on the $LiNiO_2$ surface forming LiF [15], [16]. Carbonate solvents EC, EMC, fluoroethylene carbonate (FEC), propylene carbonate (PC) and additives 3,5-bis(trifluoromethyl)-1H-pyrazole, 1-methyl-3,5-bis(trifluoromethyl)-1H-pyrazole underwent H-transfer from solvent to the oxygen of Li_xNiO_2 surface [16], [17]. Solvent fluorination, complexation of the

solvent with a Li^+ and increasing lithiation of Li_xNiO_2 cathode surface made this H-transfer reaction less favorable (Figure II.3.A.3). Cyclic carbonates undergo ring opening reaction after H-transfer and evolve CO_2. Further DFT calculation showed the possible proton transport pathways in layered structure.

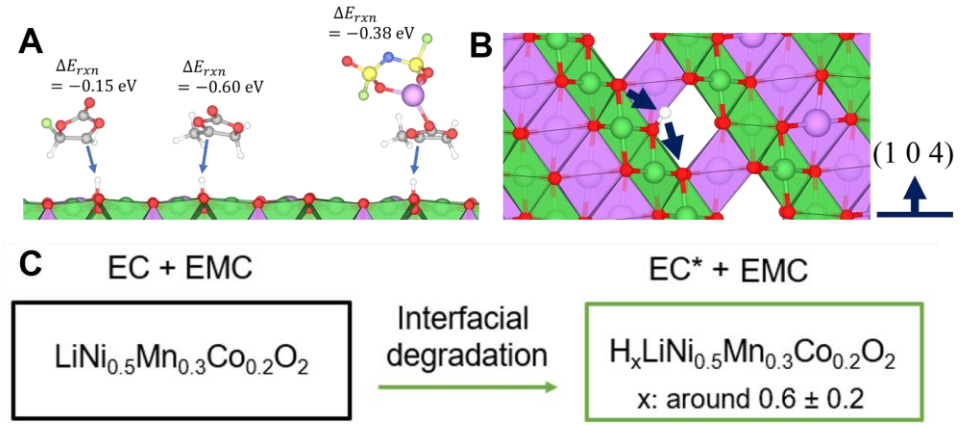

Figure II.3.A.3 Protonation reaction pathway between cathode and carbonate-based electrolyte. A) DFT calculation of EC and LiPF6 salt decomposition reactions and their reaction activation energy on standard cathode Li0.5NiO2 surface; B) Illustration of the possible proton transfer pathways inside layered structure in cathode; C) Illustration of the interfacial degradation of NMC cathodes through surface protonation due to the deprotonation reaction of EC solvent on cathode surface

Therefore, when NMC thin-films are subject to carbonate-based electrolyte, there are interfacial protonation reactions accounting for the degradation of cathode surface. The deprotonation of EC solvent at cathode can produce protons which would be transported in layered cathode, therefore reducing both Ni and Co sites, and generating radicals. Such hypothesis is found to be consistent with our x-ray studies on the chemical transformation of NMC thin-films in carbonate-based electrolyte. Due to a fact that proton is in small, there are expected to be negligible changes on the out-of-plane structure in layered NMC. However, because of the positive charge that proton carries, the charge compensation mechanism will lead to significant reduction of Ni and Co sites. Therefore, SXRD showed the negligible structural changes after chemical soaking of NMC thin film in carbonate electrolyte and solvent, however, significant chemical transformation of both Ni and Co sites have been evidenced by XAS. Since Ni and Co reduction origins from proton trapping, an estimation of proton numbers in the NMC thin film has been conducted through a quantification of Ni and Co reduction degree (Figure II.3.A.3). More importantly, our hypothesis on the protonation degradation in NMC is found to be consistent with early theoretical prediction on the possibility of layered cathode hydrogenation [18], [19].

Such hypothesis is be further supported by solvent fluorination effect on cathode stabilization. Based on the physical chemistry understanding, the fluorination of carbonate solvent leads to advanced solvent and electrolyte with enhanced chemical stability, therefore this can suppress the deprotonation reactions. NMC thin-film is then subject to carbonate-based solvent (EMC) and electrolyte (LP57), and the fluorinated electrolytes 1 M $LiPF_6$ in fluoroethylene carbonate (FEC)-EMC (labeled as 1F electrolyte) and 1 M $LiPF_6$ in fluoroethylene carbonate/3,3,3-fluoroethylmethyl carbonate/1,1,2,2-tetrafluoroethyl-2, 2, 2′-trifluoroethyl ether (FEC:FEMC:HFE, 2:6:2 by weight, labeled as 3F electrolyte) and HFE solvent. Soft-XAS collected in total electron yield with high surface sensitivity has been utilized to study the oxidation state of Ni and electronic properties of O when NMC thin-film is subject to different solvent and electrolyte (Figure II.3.A.4). As evidenced in Ni L_3-edge XAS, as compared to pristine sample, there is negative shift of spectra toward lower energy after NMC is exposed to LP57 electrolyte (1 M $LiPF_6$ in EC-EMC solvent), indicating a Ni reduction (Figure II.3.A.4A). However, such reduction is absent in NMC thin films after soaking in EMC solvent, indicating that the main deprotonation source comes from EC solvent. This result is found to be consistent with our theoretical modelling on EC deprotonation on cathode surface (Figure II.3.A 3A). Besides EMC, fluorinated solvent (HFE) and electrolytes (1F and 3F) are also found to be able to stabilize Ni sites in NMC, indicating the key contribution from solvent fluorination on cathode stabilization. The effect of solvent on

cathode reactivity can be further confirmed by O K-edge soft-XAS (Figure II.3.A.3B). The pre-edge peaks in O K-edge soft-XAS are a good indicator of transition metal oxidation states in NMC cathode since it come from the hybrid orbital of transition metal 3d orbital and oxygen 2p orbital. As clearly showed, as compared to NMC films exposure to the fully fluorinated electrolyte 3F, there is slightly decreased intensity for pre-edge peak located around 530.2 eV for NMC films exposure to half-fluorinated 1F electrolyte, while the carbonate-based electrolyte LP57 leads to significant weakening in pre-edge peak intensity. This showed that carbonate-based electrolyte tended to lead to NMC reduction, while the fluorinated solvents help to stabilize the cathode surface. The soft-XAS studies further support our hypothesis on interfacial degradation of NMC cathode by EC deprotonation reaction, since a replacement of hydrogen in solvent molecule by fluorine lead to fluorinated solvent with enhanced chemical stability toward deprotonation. Therefore, with an absence of solvent deprotonation, the stability of NMC cathode in electrolyte is enhanced.

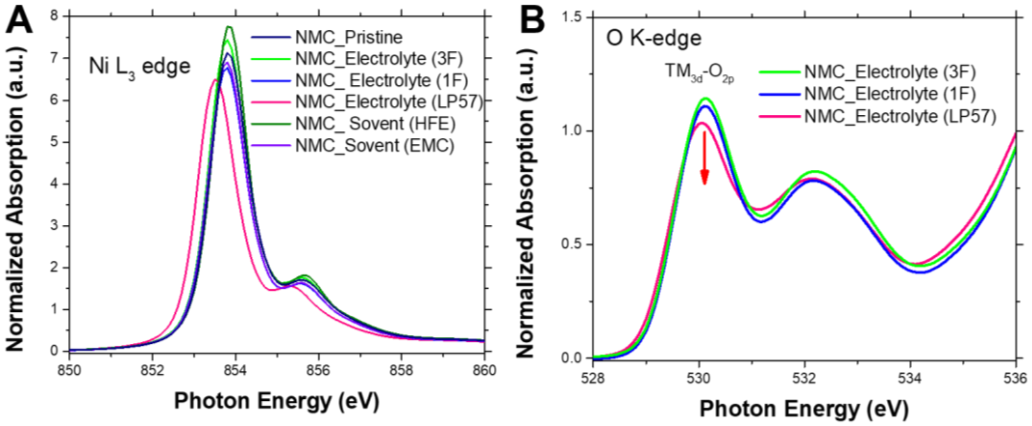

Figure II.3.A.4 **Solvent effect on cathode degradation and stabilization.** **A**) Ni L-edge XAS of NMC thin-film before and after exposure to carbonate electrolyte LP57, fluorinated electrolytes 1F and 3F; **B**) O K-edge XAS of NMC thin-films after exposure to carbonate electrolyte LP57 and fluorinated electrolytes 1F and 3F

In summary, combining advanced x-ray surface scattering and x-ray spectroscopy studies with molecular modelling, we showed that the protonation reaction is the key to understand the cathode-electrolyte reaction. The degradation of NMC cathode shows transition-metal dependent reduction behaviors in carbonate-based electrolyte, where the deprotonation from the solvent EC on cathode surface is believed to play a dominate role. We further show the rationalization for advanced electrolyte design to suppress such deprotonation reactions, therefore offering molecular-level insights into the degradation mechanisms of cathode in carbonate-based electrolyte and providing fundamental understanding for the development of cathode stabilization strategies.

We are currently working on time-of-flight secondary ion mass spectrometry (ToF-SIMS) analysis to provide the direct evidence for proton trapping in NMC thin-films that degraded in carbonate-based electrolyte. The results would be compared to the systematic study on NMC particles. More importantly, with an identification of the key interfacial degradation pathways of NMC protonation at open circuit voltage, we would move to the in-situ x-ray studies to probe the structural and chemical transformation of NMC thin-films under potentials and have the correlative analysis between CEI formation and the reactivity and stability of NMC cathodes in different electrolytes.

Conclusions

Understanding the evolution and stabilization of the cathode interphase in electrolyte is of great significance for the development of NG-LiBs. In this project, we conducted the surface X-ray scattering and spectroscopy studies using model epitaxial thin film cathodes in conjunction with theoretical modeling to probe key interfacial chemistry between thin-film cathodes and electrolytes. The structural and chemical evolutions of NMC cathode thin film in electrolyte have been experimentally and theoretically explored. As revealed by surface X-ray scattering and different x-ray spectroscopy probes, NMC thin films show transition metal

dependent degradation behaviors in carbonate-based electrolyte and solvent, which we attribute to the interfacial protonation reaction between cathode and EC solvent. We further provide the molecular-level rationalization for advanced electrolyte design to suppress solvent deprotonation on cathode surface. We anticipate that our combined x-ray, electrochemistry, and molecular scale modeling approach will provide scalable insights into the understanding of the chemical and electrochemical stability of cathode surface in electrolyte, therefore promoting the rational design of advanced high-energy batteries.

Key Publications

1. Cho, S.-J.; Yu, D.-E.; Pollard, T. P.; Moon, H.; Jang, M.; Borodin, O.; Lee, S.-Y., Nonflammable Lithium Metal Full Cells with Ultra-high Energy Density Based on Coordinated Carbonate Electrolytes. *iScience* 2020**,** 23, 100844-100855.

2. Von Aspern, N.; Grünebaum, M.; Diddens, D.; Pollard, T.; Wölke, C.; Borodin, O.; Winter, M.; Cekic-Laskovic, I., Methyl-group functionalization of pyrazole-based additives for advanced lithium ion battery electrolytes. *J. Power Sources.* 2020**,** 461, 228159-228169.

3. Ko, J. S.; Paul, P. P.; Wan, G.; Seitzman, N.; DeBlock, R. H.; Dunn, B. S.; Toney, M. F.; Nelson Weker, J., NASICON $Na_3V_2(PO_4)_3$ Enables Quasi-Two-Stage Na^+ and Zn^{2+} Intercalation for Multivalent Zinc Batteries. *Chem. Mater.* 2020**,** 32, 3028-3035.

References

1. Cao, C., H. G. Steinruck, B. Shyam, K. H. Stone, and M. F. Toney. "In Situ Study of Silicon Electrode Lithiation with X-Ray Reflectivity." Nan. Lett. 16, no. 12 (Dec 14 2016): 7394-401. https://doi.org/10.1021/acs.nanolett.6b02926.

2. Cao, C. T., H. G. Steinrck, B. Shyam, and M. F. Toney. "The Atomic Scale Electrochemical Lithiation and Delithiation Process of Silicon." Adv. Mater. Inter. 4, no. 22 (Nov 23 2017): 1700771. https://doi.org/ARTN 1700771.

3. Horowitz, Y., H. G. Steinruck, H. L. Han, C. Cao, Abate, II, Y. Tsao, M. F. Toney, and G. A. Somorjai. "Fluoroethylene Carbonate Induces Ordered Electrolyte Interface on Silicon and Sapphire Surfaces as Revealed by Sum Frequency Generation Vibrational Spectroscopy and X-Ray Reflectivity." Nano. Lett. 18, no. 3 (Mar 14 2018): 2105-11. https://doi.org/10.1021/acs.nanolett.8b00298.

4. Steinrück, Hans-Georg, Chuntian Cao, Yuchi Tsao, Christopher J. Takacs, Oleg Konovalov, Jenel Vatamanu, Oleg Borodin, and Michael F. Toney. "The Nanoscale Structure of the Electrolyte–Metal Oxide Interface." Ener. Environm. Sci. 11, no. 3 (2018): 594-602. https://doi.org/10.1039/c7ee02724a.

5. Franklin, J. B., B. Zou, P. Petrov, D. W. McComb, M. P. Ryan, and M. A. McLachlan. "Optimised Pulsed Laser Deposition of Zno Thin Films on Transparent Conducting Substrates." J. Mater. Chem. 21, no. 22 (2011): 8178-82. https://doi.org/10.1039/c1jm10658a.

6. Hartung, S., N. Bucher, J. B. Franklin, A. M. Wise, L. Y. Lim, H. Y. Chen, J. N. Weker, et al. "Mechanism of Na+ Insertion in Alkali Vanadates and Its Influence on Battery Performance." Adv. Ener. Mater. 6, no. 9 (May 11 2016): 1502336. https://doi.org/ARTN 1502336 10.1002/aenm.201502336.

7. Wang, H. W., Y. Zhang, H. X. Ang, Y. Q. Zhang, H. T. Tan, Y. F. Zhang, Y. Y. Guo, et al. "A High-Energy Lithium-Ion Capacitor by Integration of a 3d Interconnected Titanium Carbide Nanoparticle Chain Anode with a Pyridine-Derived Porous Nitrogen-Doped Carbon Cathode." Adv. Funct. Mater. 26, no. 18 (May 10 2016): 3082-93.

8. Gauthier, M., T. J. Carney, A. Grimaud, L. Giordano, N. Pour, H. H. Chang, D. P. Fenning, et al. "Electrode-Electrolyte Interface in Li-Ion Batteries: Current Understanding and New Insights." J Phys. Chem. Lett. 6, no. 22 (Nov 19 2015): 4653-72. https://doi.org/10.1021/acs.jpclett.5b01727.

9. Zhi, H., L. Xing, X. Zheng, K. Xu, and W. Li. "Understanding How Nitriles Stabilize Electrolyte/Electrode Interface at High Voltage." J Phys. Chem. Let. 8, no. 24 (Dec 21 2017): 6048-52. https://doi.org/10.1021/acs.jpclett.7b02734.

10. Alvarado, J., M. A. Schroeder, M. H. Zhang, O. Borodin, E. Gobrogge, M. Olguin, M. S. Ding, et al. "A Carbonate-Free, Sulfone-Based Electrolyte for High-Voltage Li-Ion Batteries." Mater. Today 21, no. 4 (May 2018): 341-53. https://doi.org/10.1016/j.mattod.2018.02.005.

11. Su, Chi-Cheung, Meinan He, Paul Redfern, Larry A. Curtiss, Chen Liao, Lu Zhang, Anthony K. Burrell, and Zhengcheng Zhang. "Alkyl Substitution Effect on Oxidation Stability of Sulfone-Based Electrolytes." ChemElectroChem 3, no. 5 (2016): 790-97. https://doi.org/doi:10.1002/celc.201500550.

12. Suo, L., W. Xue, M. Gobet, S. G. Greenbaum, C. Wang, Y. Chen, W. Yang, Y. Li, and J. Li. "Fluorine-Donating Electrolytes Enable Highly Reversible 5-V-Class Li Metal Batteries." Proc. Natl. Acad. Sci. U. S. A. 115, no. 6 (Feb 6 2018): 1156-61. https://doi.org/10.1073/pnas.1712895115.

13. Borodin, O., and D. Bedrov. "Interfacial Structure and Dynamics of the Lithium Alkyl Dicarbonate Sei Components in Contact with the Lithium Battery Electrolyte." J. Phys. Chem. C 118, no. 32 (Aug 14 2014): 18362-71. https://doi.org/10.1021/jp504598n.

14. Borodin, O., Guorong V. Zhuang, Philip N. Ross, and Kang Xu. "Molecular Dynamics Simulations and Experimental Study of Lithium Ion Transport in Dilithium Ethylene Dicarbonate." J. Phys. Chem. C 117, no. 15 (April 18 2013): 7433-44. https://doi.org/10.1021/jp4000494.

15. Cho, S. J., D. E. Yu, T. P. Pollard, H. Moon, M. Jang, O. Borodin, and S. Y. Lee. "Nonflammable Lithium Metal Full Cells with Ultra-High Energy Density Based on Coordinated Carbonate Electrolytes." iScience 23, no. 2 (Feb 21 2020): 100844. https://doi.org/10.1016/j.isci.2020.100844.

16. Huang, Q., T. P. Pollard, X. Ren, D. Kim, A. Magasinski, O. Borodin, and G. Yushin. "Fading Mechanisms and Voltage Hysteresis in Fef2 -Nif2 Solid Solution Cathodes for Lithium and Lithium-Ion Batteries." Small 15, no. 6 (Feb 2019): e1804670. https://doi.org/10.1002/smll.201804670.

17. Von Aspern, Natascha, Mariano Grünebaum, Diddo Diddens, Travis Pollard, Christian Wölke, Oleg Borodin, Martin Winter, and Isidora Cekic-Laskovic. "Methyl-Group Functionalization of Pyrazole-Based Additives for Advanced Lithium Ion Battery Electrolytes." Journal of Power Sources 461, (461 (2020/06/15/ 2020): 228159. https://doi.org/10.1016/j.jpowsour.2020.228159.

18. Benedek, R., M. M. Thackeray, and A. van de Walle. "Free Energy for Protonation Reaction in Lithium-Ion Battery Cathode Materials." Chem. Mater. 20, no. 17 (Sep 9 2008): 5485-90. https://doi.org/10.1021/cm703042r.

19. Fang, C. M., and G. A. de Wijs. "Local Structure and Chemical Bonding of Protonated LixMn2O4 Spinels from First Principles." Chem. Mater. 18, no. 5 (March 1 2006): 1169-73. https://doi.org/10.1021/cm051564a.

II.3.B Stability of cathode/electrolyte interfaces in high voltage Li-ion batteries (ANL)

Dusan Strmcnik, Principal Investigator
Argonne National Laboratory
9700 S Cass Ave
Lemont, IL 60439
E-mail: strmcnik@anl.gov

Peter Faguy, DOE Technology Development Manager
U.S. Department of Energy
E-mail: Peter.Faguy@ee.doe.gov

Start Date: October 1, 2018 End Date: September 30, 2021
Project Funding: $500,000 DOE share: $500,000 Non-DOE share: $0

Project Introduction

Li-ion batteries have become very important in the last two decades and represent the power source of choice for most portable electronic devices. However, an improvement of this technology is still necessary to be durably introduced onto new markets such as electric vehicles (EVs) and hybrid electric vehicles (HEVs). One of the viable options to meet the high energy density demands of the new Li-ion technology are the high voltage Li-ion batteries, which utilize the cathode materials that can operate at voltages higher than 4.5 V vs. Li/Li+. A major problem with these high voltage cathode materials is the incompatibility with "conventional" Li-ion electrolytes, which commonly consist of a combination of lithium hexafluorophosphate (LiPF6) salt with a binary solvent mixture of cyclic and linear alkyl carbonates such as ethylene carbonate (EC) and ethyl methyl carbonate (EMC). These electrolytes undergo severe degradation at high voltages which is often remedied by cathode passivation additives. Another approach is to develop new solvents which are intrinsically stable at high voltages. Both approaches, however, demand a much better fundamental understanding of the underlying degradation mechanisms of the Li-ion cathode/electrolyte interfaces, which would be on par with understanding of aqueous electrochemical interfaces.

Objectives

The main goal of this proposal is to establish fundamental mechanistic understanding of the principles that govern the decomposition and properties of cathode/electrolyte interfaces and relate them to the performance of high voltage Li-ion cells.

In order to achieve this goal, we will divide our work into five objectives:

- *Investigate the chemistries of individual electrolyte components of a Li-ion battery on a variety of materials, from well-defined metal single crystals to realistic TMO samples at high potentials, relevant for high voltage LiB. These individual components will range from different solvents, electrolyte salts to impurities that can either be present in the electrolyte from the beginning or contaminate the system during battery operation (e.g. metals from the cathode side).*
- *Investigate how the experimental conditions influence these individual chemistries or how they enhance or diminish individual processes in the case of overlapping chemistries.*
- *By utilizing both theoretical as well as experimental tools, establish thermodynamic and kinetic windows of stability of individual components. Furthermore, an attempt will be made to include mass transport effects into the understanding of the interface stability in various electrochemical environments.*
- *Combine the thermodynamic, kinetic and mass transport properties of a certain chemistry under specific experimental conditions to build an EEI with specific properties.*

- *Test the performance of the EEI in coin cells.*

Approach

The number one priority of this proposal is to extend the state of the art of understanding how individual components of the cathode/electrolyte interface behave at potentials relevant for high-voltage Li-ion batteries and how these individual components interact with each other. A long-term goal, however, is to implement this knowledge into next generation high-voltage cathode materials and electrolytes. While there are many studies available in the literature exploring the electrolyte as well as cathode material decomposition, most of the attempts focused on real materials in real cells. Although such complex phenomena can be 'tested' in real systems, the only way to resolve, apply and connect the underlying fundamental processes with real cell performance would be possible with unique experimental-computational approach. To the best of our knowledge, a deeper fundamental understanding about the structure and properties of cathode side electrode-electrolyte-interphase at the atomic/molecular level is still lacking and would be of high importance for the development of next generation LiBs.

Our approach differs significantly from the well-established testing approach, incorporating three critical steps: (i) utilization of model well-defined systems to assess fundamental descriptors for the decomposition of the electrolyte as well as cathode components; (ii) probing more complex electrolytes and electrode materials with different morphologies; and (iii) exploring the properties of cathode materials that are currently, or are potential candidates, to be used in LIB.

Results

Covid-19 Impact

Due to the pandemic, Argonne National Laboratory was shut down roughly from March to July. Since July, we have been in limited operations mode, i.e. at 40% working capacity. Our output has been affected and we are experiencing delays in reaching our milestones.

Approach development - Bridging the gap between model and real systems

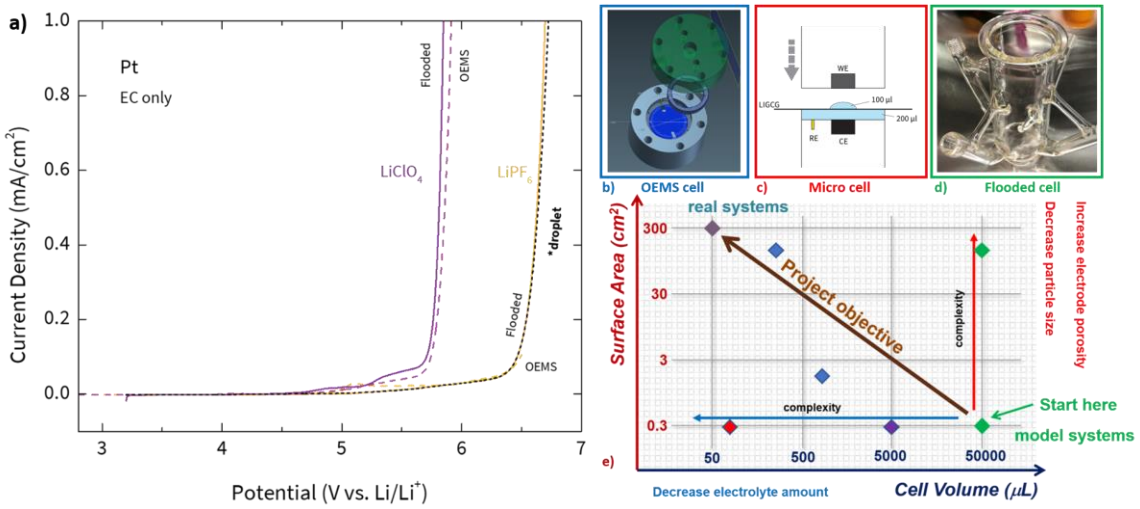

Figure II.3.B.1 Overview of our systems with substantially different surface to volume ratios and their electrochemical responses. a) Electrochemical response of Pt electrodes in flooded, OEMS and micro(droplet) cell in $LiClO_4$ and $LiPF_6$ electrolyte. b) OEMS cell. c) micro cell. d) flooded cell. e) Schematic of increasing system complexity with lowering the cell volume and raising the electrode surface area, one of the potential disconnects between model and real systems.

Oftentimes, it is challenging to connect and apply results obtained on model systems to real systems and we recognize this as one of the major risk factors in this project. This is in part due to the enormous difference in electrode surface to electrolyte volume ratios these systems operate at. Figure II.3.B.1e depicts, how the

complexity of the system increases with decreasing electrolyte volume and increasing surface area of the electrode. The inventory of individual components becomes much more important in real systems, and with that the mass transport effects.

To address this issue, we are collecting data from a number of cells with substantially different volumes as well as on electrode materials with vastly different surface areas. Figure II.3.B.1b, c and d show our OEMS cell, that operates with electrolyte volumes 250 µL – 1 mL, our micro cell, that operates with electrolyte volumes of 100-200 µL and the flooded cell that operates with electrolyte volumes of 30-50 mL. In these cells, we use electrodes with surface areas 0.3-200 cm^2, giving us 5-6 orders of magnitude range in surface to volume ratio. In Figure II.3.B.1a, we show results for Pt electrode in $LiClO_4$ and $LiPF_6$ electrolytes in OEMS, micro and flooded cells. The surface to volume spread is almost 3 orders of magnitude, the electrochemical response in the individual cells, however, is nearly identical, giving us confidence, that we are indeed observing the same chemistry over the different experimental setups.

Analytical tools and methods development

In the previous reporting cycle, we have shown preliminary results for our method for in-operando proton detection. The method is based on rotating ring-disk electrode RRDE electrochemical detection using Pt ring as an amperometric detector (Figure II.3.B.2c). The protons, generated on the disk during electrolyte/solvent oxidation, are "collected" on the ring via hydrogen evolution reaction HER (Figure II.3.B.2d). The method was validated using hydrogen oxidation reaction (HOR) to produce protons on the disk, which were then detected on the ring. The validation included measurements of polarization curves at 4 different rotation rates on the disk and the corresponding response on the ring (Figure II.3.B.2a). The ring collection efficiency η was measured to be close to 20%, an expected value for the geometry of our RRDE (Figure II.3.B.2b). The same value was confirmed with Fc/Fc^+ couple. These findings confirmed that i) it was possible to use RRDE for proton detection and ii) the protons or protonated species were stable for long enough to travel from the disk to the ring in order to be detected. We published the method in Electrochemistry Communications.

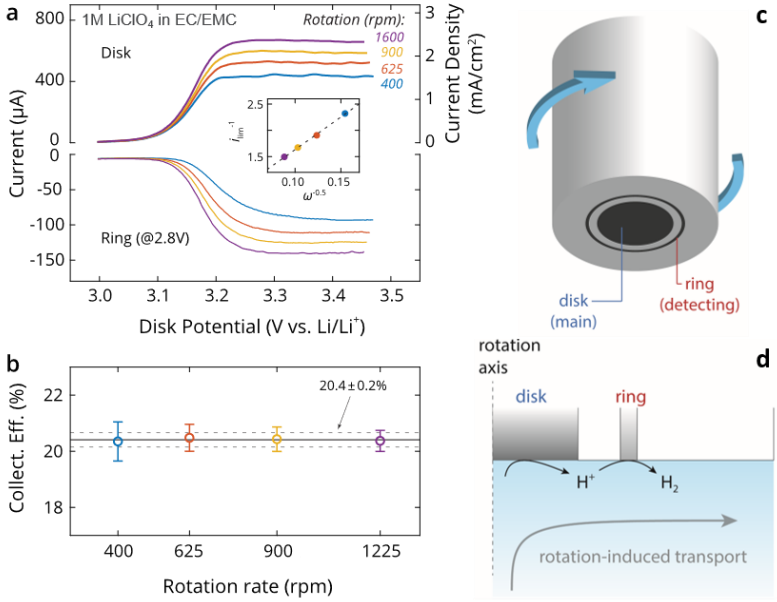

Figure II.3.B.2 Rotating ring disk proton detection method. a) Polarization curves for HOR at different rotation rates on the Pt disk and the measured responses on Pt ring. b) Collection efficiency of the ring-disk setup at different rotation rates. c) Schematic of a ring-disk electrode d) Principle of RRDE operation – protons are generated on the disk during electrolyte oxidation and then collected on the Pt ring via HER.

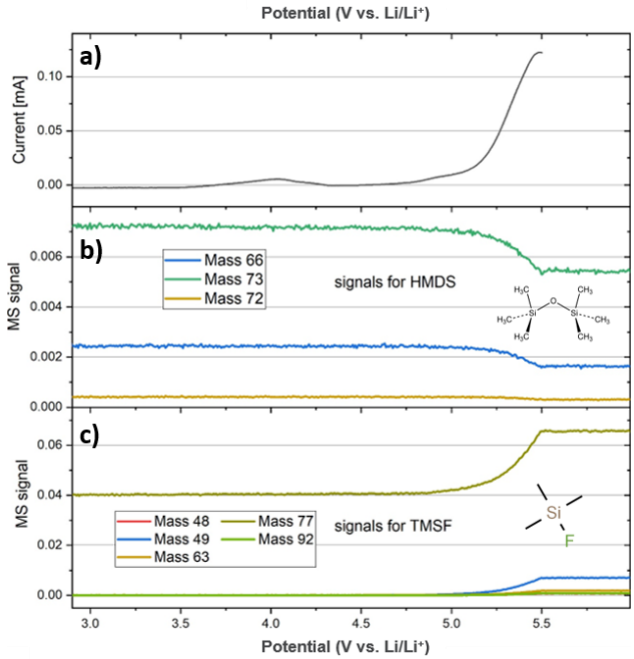

Figure II.3.B.3 Validation of our OEMS setup through a known reaction of HF with HMDS. a) Electrochemical response in 1 M $LiPF_6$/EC/EMC electrolyte – HF is formed during electrolyte oxidation. b) HMDS m/z signals showing a decrease in concentration with current increase. c) TMSF m/z signals showing an increase in concentration with current increase.

A very important analytical tool for the realization of this project is the Online electrochemical Mass Spectrometry (OEMS), which allows us to follow gaseous products during the decomposition of the electrolyte. In FY19 cycle we have built the OEMS capability, which was close to operational. All remining issues have since been resolved.

To validate the operation of our OEMS setup, we performed electrochemical oxidation of 1M LiPF6/EC/EMC electrolyte with Hexamethyl-disiloxane (HMDS) as additive. HMDS is known to react with HF produced during electrolyte oxidation, forming trimethylsilyl fluoride (TMSF) and trimethyl silanol:

$$HMDS + HF \rightarrow SiF(CH_3)_3 + Si(CH_3)_3OH$$

HMDS and TMSF both have very distinct m/z signals, different from any possible m/z signal from the matrix components. Figure II.3.B.3 shows both the decrease in HMDS and increase in TMSF signals, which were found to exactly follow the current response, giving us great confidence in proper operation of our setup.

The electro-chemistry of EC and EMC decomposition

In Figure II.3.B.4, we investigate the decomposition of EC/EMC solvents in $LiClO_4$ electrolyte by tracking the production of protons. Electrochemical responses of the disk and ring are shown. Although an extensive electrolyte decomposition is only observed above 5 V, small currents can be measured already around 4 V. The fact that we observe matching currents on the ring as well, indicates that the process starting at ~ 4 V is indeed generating protons, linked to oxidation of the solvent. Interestingly, and in contrast to the HOR measurements, the numbers of transferred electrons and measured protons do not match. Instead, in the potential range between 4.5 and 5.7 V, we can detect approximately 1 H^+ on the ring per 2 electrons transferred on the disk. This suggests that in addition to generating a proton in the oxidation process, we also consume an additional electron for a second oxidation process. At this point, our assumption is that a carbocation is created either as

an intermediate or as a more stable product species (see reaction schematic in Figure II.3.B.7 below), but more work is needed to confirm this assumption.

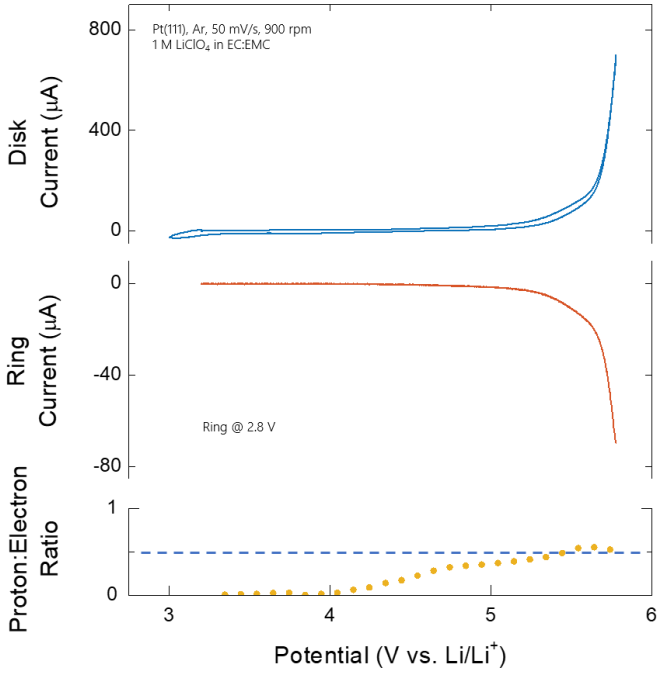

Figure II.3.B.4 RRDE proton detection on Pt disk electrode in $LiClO_4$/EC/EMC electrolyte. Disk response is shown in blue and the corresponding ring response is shown in red. The orange dots represent proton to electron ratios at differnrent potentials, obtained from ring to disk current ratio. Note that the data is more reliable at higher potentials where currents are higher. There, the proton:electron ratio approaches 1:2.

On the flipside, proton enters its own chemical reactions with the solvent, electrolyte and electrode. We first investigated its reaction with EC. In order to do that, we passed 3C of charge through our platinum disk electrode in 5 mL of $LiClO_4$/EC electrolyte. Figure II.3.B.5a shows a gradual color change of the solution in the hours/days after the experiment. The analysis of the electrolyte using GC-MS with headspace sampler revealed, in addition to CO_2, 3 products of the same family, ethylene oxide (oxirane), 1,4-dioxane and 2-methyl-1,3-dioxolane (Figure II.3.B.5b). To further corroborate these results, we monitored the volatile decomposition products during the reaction in our OEMS cell using Pt mesh. We confirm a substantial evolution of CO_2 (m/z signal 44) as well as small but clearly discernable appearance of ethylene oxide (m/z signals 44, 29 and 15) as shown in Figure II.3.B.5c. To get the correct quantification, a calibration with a standard is necessary, a part of our future work. These results suggest, that in the presence of protons, ethylene carbonate undergoes ring opening and CO_2 evolution, leaving C_2H_4O building block to form ethylene oxide as a monomer or dioxane and methyl-dioxolane as a dimer. The reaction mechanism of the proton attack on EC is shown in the schematic in Figure II.3.B.7.

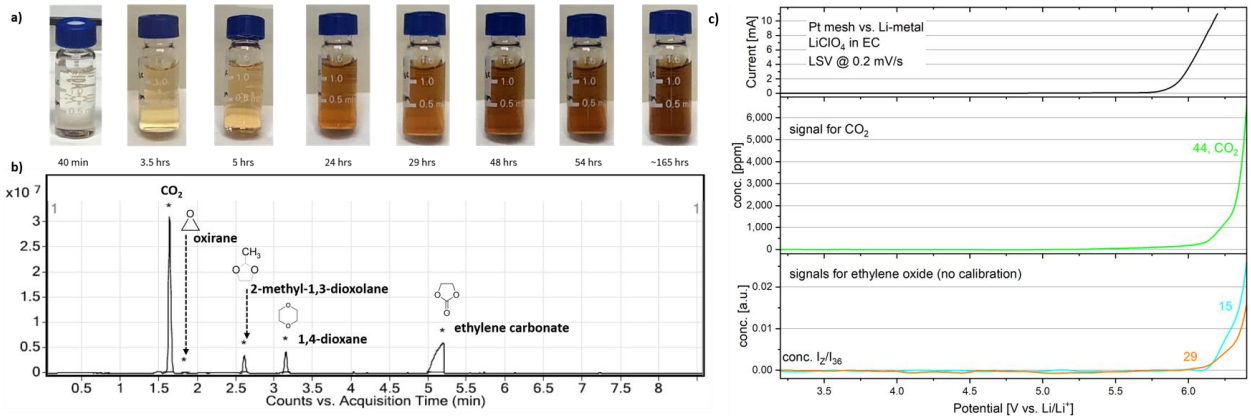

Figure II.3.B.5 Reaction of electrochemically produced protons with EC. a) Gradual color change of 1 M $LiClO_4$ electrolyte after passing 3 C of charge through the system. b) GC-MS analysis after headspace sampling of the electrolyte after 72 hours. Presence of CO_2, oxirane (ethylene oxide), methyl-dioxolane and dioxane is confirmed. c) OEMS measurement in same electrolyte during electrooxidation. Evolution of CO_2 and production of ethylene oxide is confirmed.

In the case of $LiPF_6$ as electrolyte, the proton chemistry is drastically different, as the proton readily attacks PF_6^- anion to form HF and PF_5. Typical OEMS response is shown in Figure II.3.B.6, showing HF signal (m/z 20) along with other decomposition product signals of PF_6^-.

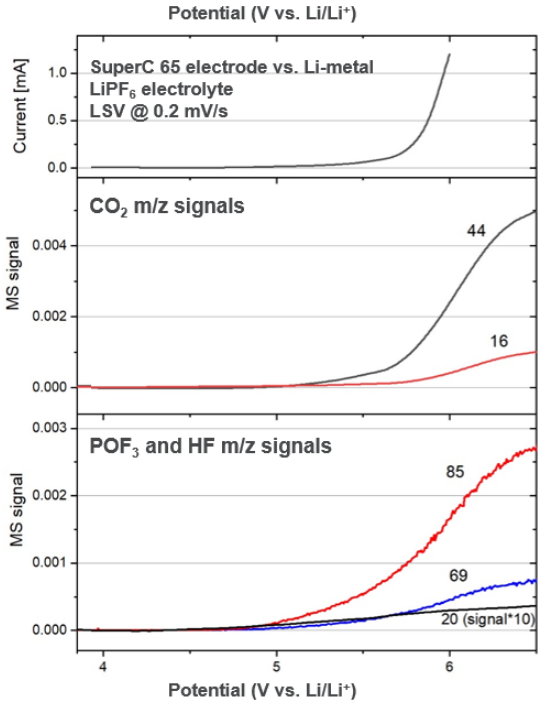

Figure II.3.B.6 Reaction of electrochemically produced protons with PF_6^- containing electrolyte. Electrochemical response as well as typical m/z signals for CO_2 as well as HF and POF_3 signals are shown.

Finally, the proton can react with the electrode material, especially relevant in the case of oxide electrodes, producing water and metal cations. Further work is planned on this topic.

Figure II.3.B.7 shows a schematic of electro-chemical decomposition of EC and the possible resulting proton interactions with solvent, electrolyte and electrode. Note that a very similar rection scheme can be written for EMC.

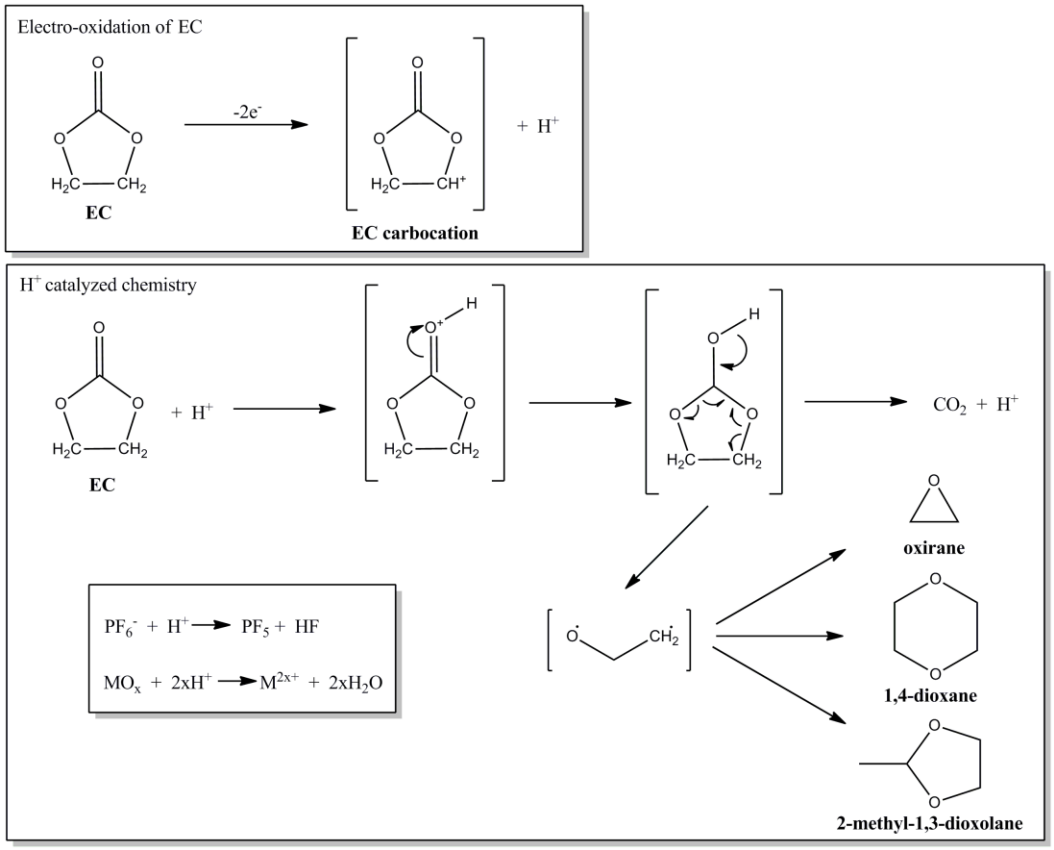

Figure II.3.B.7 Reaction schematic for electrochemical oxidation of EC and the resulting chemical attack of the generated proton on the solvent, electrolyte, and/or electrode material.

Conclusions

In the last funding cycle, we were able to refine and validate two of our analytical tools, RRDE for proton detection and OEMS for gas evolution during electrolyte composition. Moreover, we have found the electrochemical responses over wide range of systems, with ~3 orders of magnitude different electrode surface to electrolyte volume ratio, to be almost identical, signaling that the application of information, gathered on model systems, will be possible on real systems.

This, in turn, has allowed us to deepen our understanding of individual processes that occur during the electrochemical electrolyte degradation. For the first time, we experimentally confirmed the production of protons during electrolyte oxidation. Furthermore, we investigated the chemical reaction of the formed protons with the solvent and electrolyte. When proton reacts with EC, it initiates the opening of the ring with concomitant evolution of CO_2. The remaining part of the molecule can form several products, including ethylene oxide, dioxane and methyl-dioxolane. In $LiPF_6$ containing electrolytes, proton reacts with the anion, producing HF and PF_5. In addition, electrochemically produced protons can enter the reaction with oxide electrode materials.

We conclude that protons are the most detrimental species for the cathode electrolyte interface of lithium-ion-batteries.

Key Publications

Toru Hatsukade, Milena Zorko, Dominik Haering, Nenad M Markovic, Vojislav R Stamenkovic, Dusan Strmcnik, *Detection of protons using the rotating ring disk electrode method during electrochemical oxidation of battery electrolytes*, Electrochem. Comm. 2020, **120**, 106785

II.3.C Interfacial Studies of Emerging Cathode Materials

Marca Doeff Principal Investigator
Lawrence Berkeley National Laboratory
1 Cyclotron Road
Berkeley, CA 94720
E-mail: mmdoeff@lbl.gov

Peter Faguy DOE Technical Development Manager
U.S. Department of Energy
E-mail: Peter.Faguy@ee.doe.gov

Start Date: Oct. 1, 2018 End Date: Sept. 30, 2021
Project Funding: $300,000 DOE share: $300,000 Non-DOE share: $0

Project Introduction

At present, commercialized cathode materials for high-energy lithium ion batteries (LIBs) are based on transition metal oxides such as NMCs (LiNixMnyCozO2). These are intercalation electrodes, in which transition metals such as Ni and Co undergo redox as lithium is inserted or removed from the structures. The theoretical capacities of these electrodes are about 280 mAh/g based on the transition metal redox, but, typically, only a portion of this capacity can be accessed due to practical limitations such as oxidative stability limits of the electrolytic solutions and structural stability of the electrodes. Practical capacities range from about 140-200mAh/g depending on exact composition and usage (rates, voltage limits, etc.). Recently, the discovery that reversible or partly reversible oxygen redox processes can occur in a variety of structures has opened up a new design space for cathode materials, with the tantalizing possibility of attaining capacities well beyond the 280 mAh/g theoretical limit of traditional intercalation layered oxides. These materials include Li2MnO3, [1] lithium and manganese rich NMCs (LMR-NMCs) [2] and Co-free analogs, [3] other types of lithium-rich layered oxides with structures similar to Li2MnO3 [4] , three-dimensional structures such as β-Li2IrO3, [5] and cation-disordered rock salts [6], including variants of Li3NbO4 [7], [8] and Li3IrO4. [9] Many of these materials exhibit capacities of 300 mAh/g or more, but suffer from poor rate capability, voltage hysteresis, and fading. [10] In these cases, irreversible oxygen loss, [11] morphological [12] and structural changes [13], [14] are to blame for the performance issues. Other materials appear to cycle more stably, [5], [9] at least for a limited time, and strategies such as partial fluorine substitution for oxygen [15] appear to mitigate irreversible oxygen loss and result in improved behavior. Because oxygen loss tends to occur at particle surfaces, and is associated with the deleterious structural and morphological changes that are responsible for poor cycling and rate characteristics of some of these materials, it would be extremely useful to understand the fundamental processes occurring at the cathode/electrolyte interface and on particle surfaces better. While LMR-NMCs have been intensively characterized, [16] few studies to probe interfacial characteristics have been carried out on most of the other materials mentioned above. We now propose to study candidate materials, both those that perform well and those that perform badly, using an array of surface-sensitive, depth-profiling, and bulk techniques. These include synchrotron X-ray absorption spectroscopy (XAS), X-ray photoelectron spectroscopy (XPS), X-ray Raman (XRS) and transmission X-ray microscopy (TXM) as well as STEM/EELS (scanning transmission electron microscopy/electron energy loss spectroscopy). Materials will be investigated as a function of composition, particle size and surface area, state-of-charge, and cycling history. By the end of the project, there should be sufficient information to allow a set of recommendations to be made regarding the best way to ensure stable and robust cycling of electrodes that undergo both transition metal and oxygen redox.

Objectives

Reports of oxygen redox activity in materials with unusually high capacities are intriguing, but fairly little is known about how these materials actually work. There are a number of unanswered questions to which the

work proposed here is designed to answer. First, how deep into the bulk does oxygen redox occur? Is it primarily a surface reaction? When does oxygen release occur, as opposed to reversible redox? Does the oxygen redox or oxygen release contribute to the structural instability that is often seen, and can this be prevented by, e.g., cationic or anionic substitutions, coatings, or other strategies? How do the surfaces of particles of charged or partially charged materials interact with the electrolytic solutions, and how does this contribute to capacity fading, rate limitations, and other performance issues? Once these questions are answered, strategies such as substitutions, coatings and particle morphology/size engineering can be considered to ensure robust cycling.

Approach

To answer the above questions, we will synthesize selected materials with differing particle sizes/surface areas, subject them to electrochemical charge, discharge, and cycling or chemical delithiation, and study them using an array of surface and bulk sensitive techniques including synchrotron X-ray absorption spectroscopy (XAS), X-ray photoelectron spectroscopy (XPS), transmission X-ray microscopy (TXM), X-ray Raman (XRS), and microscopy. Materials of interest include $Li_4Mn_2O_5$, [17] $Li_2Ru_xM_yO_3$ (M=Sn, Fe, Ti)$_4$ and Li_4FeSbO_6. [18] Although not all of these materials are practical, the objective is to obtain information that can ultimately be used to design high capacity materials from low cost and earth-abundant elements.

Results

Due to the pandemic, we were not able to access the synchrotron facilities needed to carry out the surface characterization that forms a critical part of the proposed work. Instead, we decided to focus on synthesis and characterization of $Li_4Mn_2O_5$, with plans to carry out surface analysis of the most promising samples as facilities become available in the future. Our focus this year was exclusively on $Li_4Mn_2O_5$ due to its potentially low cost and the earth-abundance of Mn, making it of extreme interest for vehicle applications.

Initial reports of the synthesis of $Li_4Mn_2O_5$ [17] described a two-step process: first a high-temperature reaction of $LiOH{\bullet}2H_2O$ with MnO and MnO_2 to form $LiMnO_2$, followed by reactive ball-milling of $LiMnO_2$ and Li_2O [17]. We successfully repeated this procedure and were able to reproduce results reported in the literature. While discharge capacities well over 300 mAh/g can be obtained, the first cycle inefficiencies are high. Electrode engineering improves both the first cycle efficiency and the reproducibility of the results. Specifically, using a PTFE binder instead of PVdF reduces inefficiencies (Figure II.3.C.1a), and increasing carbon content improves reproducibility (Figure II.3.C.1b and c).

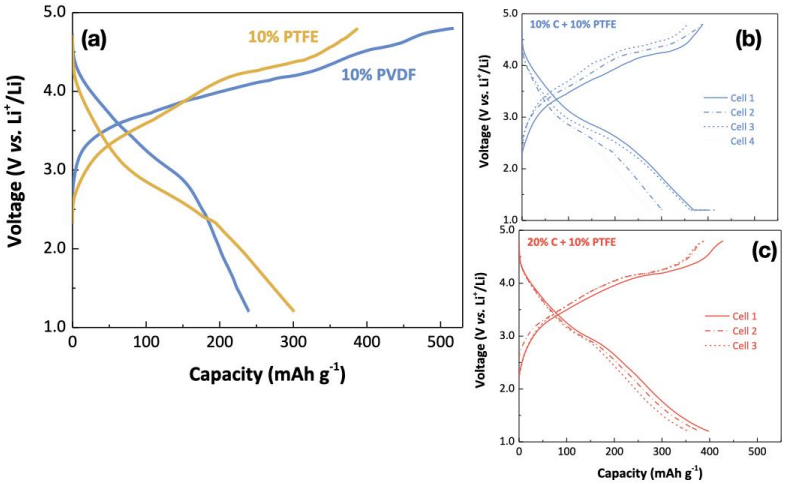

Figure II.3.C.1 (a) First cycles of cells containing $Li_4Mn_2O_5$ electrodes made with PVdF or PTFE binders. First cycles of several cells containing cathodes with PTFE binders and 10% C (b) or (c) 20% C.

Figure II.3.C.2 shows six cycles of a cell containing a $Li_4Mn_2O_5$ cathode. The initial charge appears different from subsequent cycles. This is more readily apparent in the dQ/dV plots, where a large irreversible peak at about 4.25V is observed on the first charge, but is absent in later ones. This feature may be indicative of oxygen loss and/or electrochemical decomposition of Li_2CO_3 present from the synthesis. A peak attributable to either Li2O or Li_2CO_3 was detected in pristine materials using O K-edge XRS. Li_2O reacts with CO_2 in air to form Li_2CO_3. This peak disappears on charge indicating that it decomposes electrochemically. Li_2CO_3 decomposes electrochemically at around 4V [19]. Considerable hysteresis is also apparent from the dQ/dV plots over the wide voltage window used for this cell. Hysteresis is reduced when the amount of lithium extracted is limited; i.e. the upper charge limit is reduced (Figure II.3.C.3).

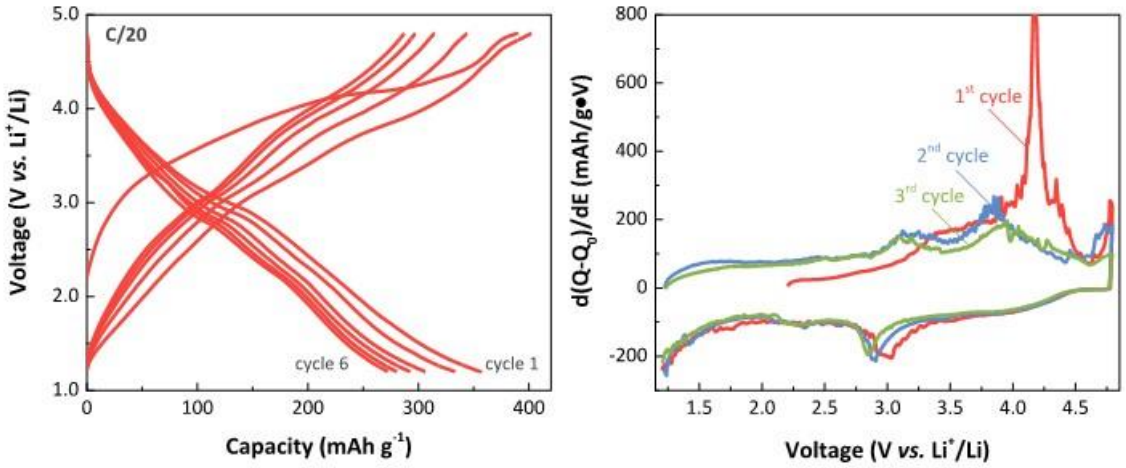

Figure II.3.C.2 (Left) cycling of a cell containing $Li_4Mn_2O_5$ and (right) dQ/dV plots of the same cell.

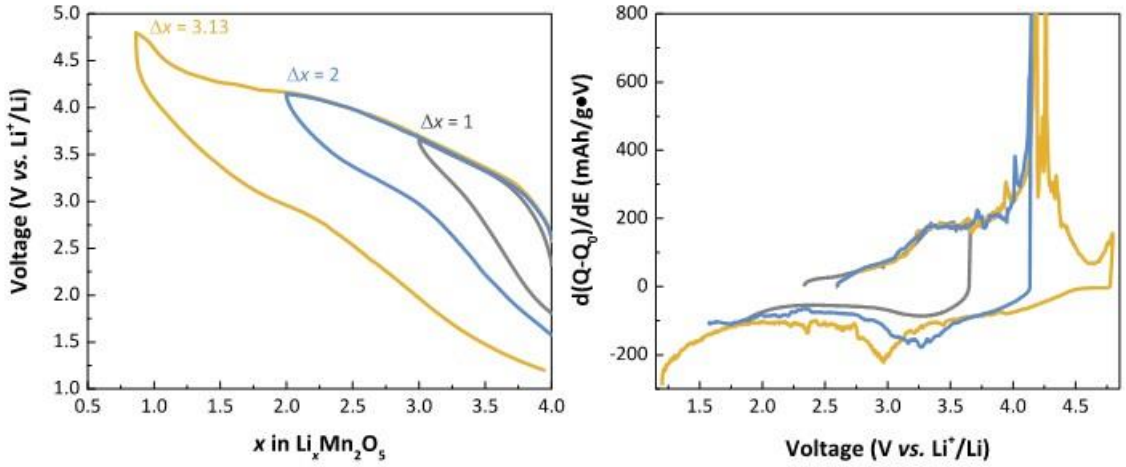

Figure II.3.C.3 (Left) Voltage window opening experiments on cells containing $Li_4Mn_2O_5$ and (right) dQ/dV plots of the same cells.

In general, it is difficult to remove all the lithium from this material at room temperature. The kinetics below about 4.2V is fairly rapid, as this is primarily due to Mn^{3+}/Mn^{4+} redox (as evidenced by XRS experiments conducted last year); this corresponds to extraction of about 1.5 Li^+ per formula unit. At room temperature, an additional 1.5 Li^+ ions can be extracted if currents are sufficiently low. If the temperature is raised to 50°C, nearly all the Li^+ is apparently extracted at low rates, but only about 2.5 Li^+ ions can be re-inserted (Figure II.3.C.4). Limiting the extraction to 3Li^+/formula unit when cells are cycled at 50°C improves reversibility. The appearance of an additional plateau at about 4.5V in the cell cycled at 50°C past the extraction of 3 Li^+

(corresponding to a second large irreversible peak in the dQ/dV plot) may be due to additional loss of oxygen, decomposition of Li_2CO_3, or irreversible oxidation of electrolyte. Preliminary ICP-OES data show that about 0.77 Li^+/formula unit remains in the sample fully charged at 50°C. This implies that the peak around 4.4V in the dQ/dV data is attributable primarily to side reactions (e.g., electrolyte oxidation).

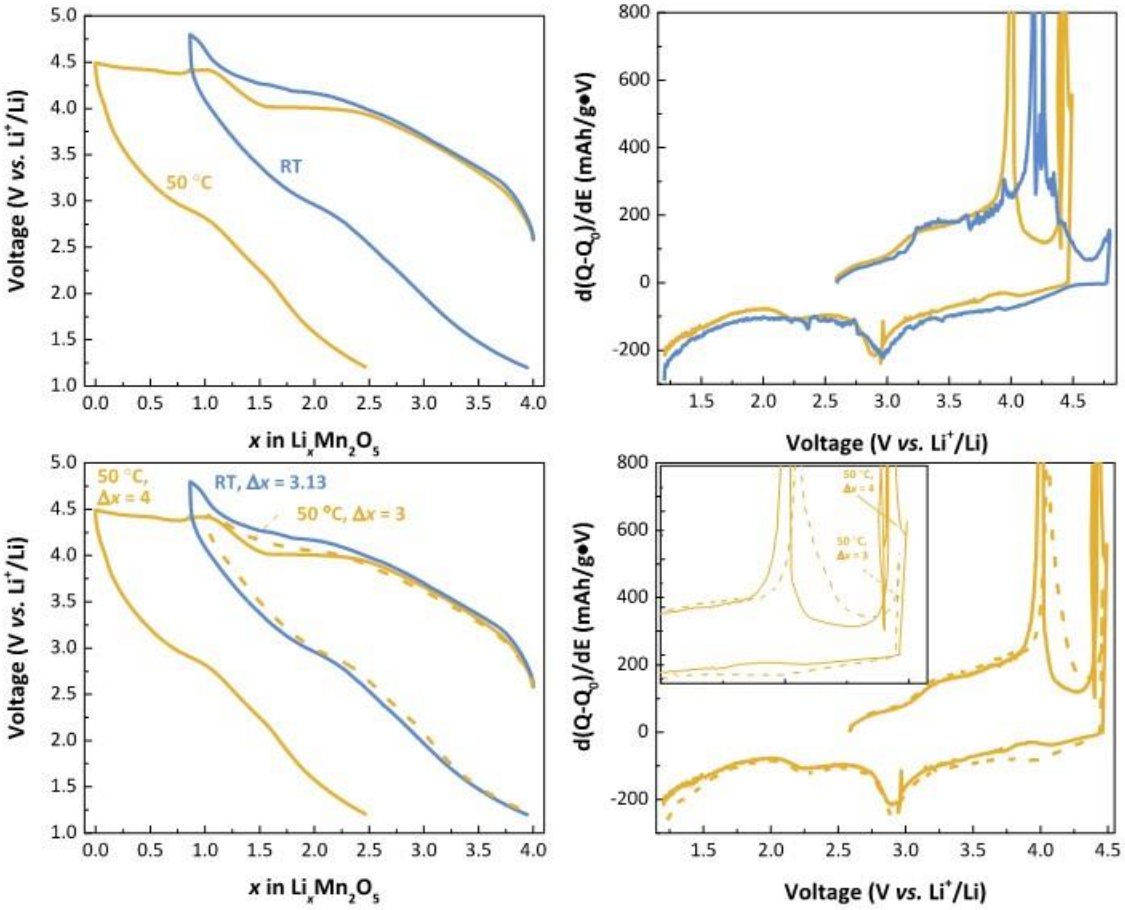

Figure II.3.C.4 (Upper left) comparison of first cycles of cells containing $Li_4Mn_2O_5$ at room temperature and 50°C. (Upper right) dQ/dV plots of the same cells. (Lower left) similar to the figure in the upper left, but with the addition of a cell cycled at 50°C in which lithium extraction is limited to 3 Li^+/formula unit, and (lower left) dQ/dV plots.

Some effort this year was directed towards improving the synthesis of $Li_4Mn_2O_5$. Towards this end, we investigated the effect of varying the amount of Li_2O from 0% to 10% excess for the second step of the procedure (reactive ball-milling). The XRD patterns of the products are all consistent with phase-pure $Li_4Mn_2O_5$; however, it is difficult to detect Li_2O, LiOH, or Li_2CO_3 (likely reaction products of excess Li_2O with air) using this method. (We have previously detected Li_2CO_3 or Li_2O in as-synthesized $Li_4Mn_2O_5$ in O K-edge XRS and soft XAS experiments). Interestingly, the degree of lithium extraction and re-insertion was highest for the material made with no excess Li_2O (about 3.25 Li^+/formula unit could be removed at room temperature and re-inserted). Materials made with excess Li_2O delivered less capacity upon discharge, although there seemed to be little correlation with the amount of excess used. Analysis of the first cycle dQ/dV plots (not shown) reveal that the position of an irreversible peak upon charge is at a lower potential for $Li_4Mn_2O_5$ made without excess Li_2O compared to those made with excess (about 4V compared to 4.2V). It is not yet known what redox processes contribute to these peaks; however, it is possible that the higher potential process is electrochemical Li_2CO_3 decomposition. This suggests that the presence of Li_2CO_3 in pristine powders has a somewhat complicated effect on the electrochemistry but is overall deleterious to performance.

Alternative synthesis routes were also explored, as the two-step process involving reactive ball-milling is tedious to perform and probably not scalable. High temperature solid-state routes have not yet proven successful. However, it was possible to carry out reactive ball-milling using Mn_2O_3 as a precursor rather than $LiMnO_2$, removing one step from the procedure. The electrochemical properties of $Li_4Mn_2O_5$ made in a single step are somewhat inferior to that made by the two-step process (Figure II.3.C.5a and c), although the former procedure has not yet been optimized.

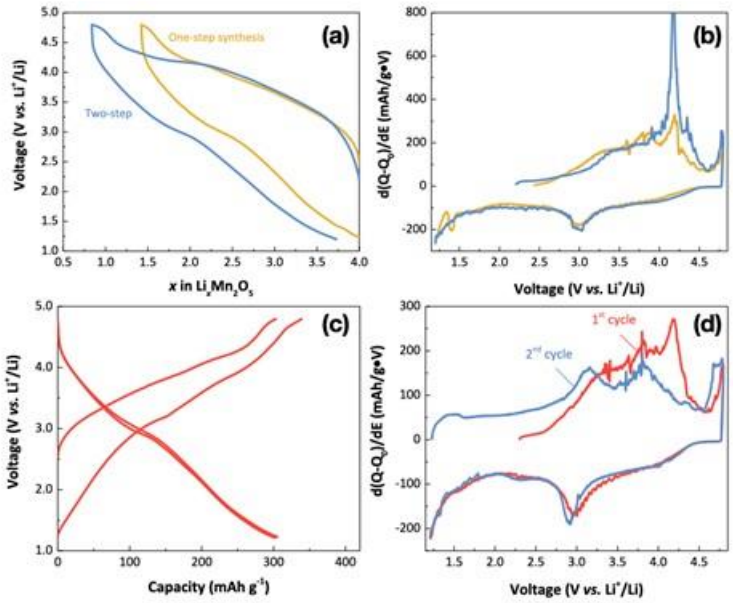

Figure II.3.C.5 (a) comparison of first cycles of cells containing $Li_4Mn_2O_5$ made by either a one-step or two-step process and (b) dQ/dV plots of the same cells. (c) two cycles of a cell containing the material made in one step and (d) dQ/dV plots of the first and second cycles of the same cell.

The first cycle dQ/dV plots show a less intense irreversible peak near 4.2V in the cell with the material made in one-step compared to the two-step material, suggesting that there may be less Li_2CO_3 present in the former. ICP-OES results confirm this hypothesis; a Li/Mn ratio of 0.28 was determined for the sample made in two steps, compared to a value of 0.24 for the one made in one step (0.25 is the expected ratio). This peak is absent in the second cycle dQ/dV plot (Figure II.3.C.5d) and is replaced by one near 4.0V.

Partial substitution of fluorine for oxygen in pristine Li-excess rock salt electrodes appears to suppress irreversible oxygen evolution and improve reversibility [15]. Preliminary attempts to produce $Li_4Mn_2O_{5-y}F_y$ by incorporating LiF during the reactive ball-milling process appear to have succeeded. A comparison of the first cycles of cells containing either $Li_4Mn_2O_5$ or $Li_4Mn_2O_{4.2}F_{0.8}$ is shown in Figure II.3.C.6. The electrochemical properties are slightly different with the main difference being the absence of the large irreversible peak near 4.2V upon initial charge in the dQ/dV plot of the fluorinated sample. It is replaced by a smaller irreversible peak at 4.0V. It is not clear at present whether this difference is simply due to varying amounts of Li_2CO_3 in these two samples.

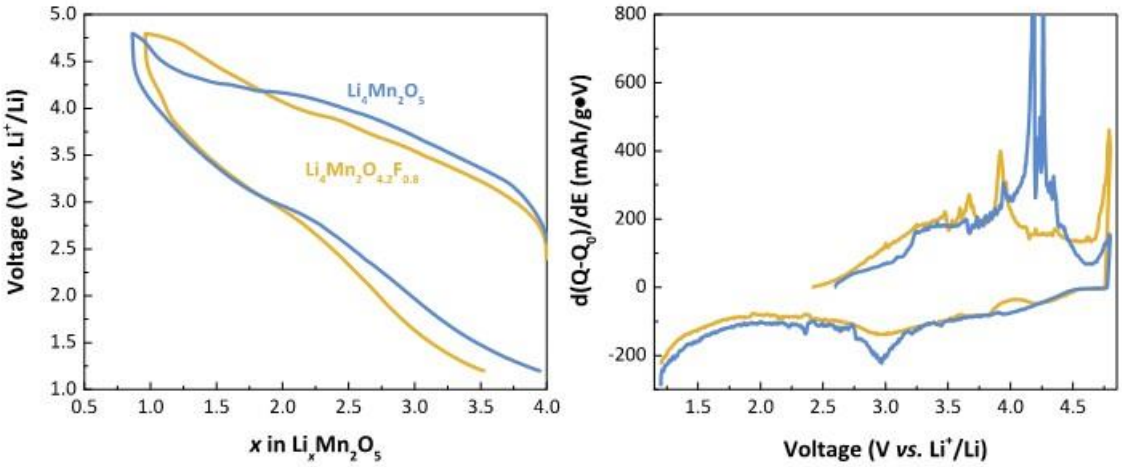

Figure II.3.C.6 (Left) comparison of first cycles of cells containing $Li_4Mn_2O_5$ or $LiMn_2O_{4.2}F_{0.8}$ and (right) dQ/dV plots of the same cells.

We will continue to optimize synthesis procedures and explore the effect of metal substitution for Mn and F substitution for O in the $Li_4Mn_2O_5$ system. As synchrotron facilities become available, we plan to use both surface (XPS, soft-XAS) and bulk (hard XAS, XRS) techniques to understand what redox processes are responsible for features in the voltage profiles of this material and how they affect cycling behavior.

Conclusions

This year, we concentrated on optimization of $Li_4Mn_2O_5$ synthesis, electrochemical characterization and electrode engineering. Improved first cycle coulombic efficiency was obtained when a PTFE binder was used in place of PVDF. Initial discharge capacities in excess of 350 mAh/g can be obtained for this material, although it is dependent on details of the synthesis, voltage limits and other experimental parameters. Redox processes that occur below about 4.2V (corresponding to extraction of about 1.5 Li^+/formula unit, and Mn^{3+}/Mn^{4+} redox) appear to be kinetically facile, but are more sluggish above this potential. At room temperature, extraction of lithium is limited to about 3-3.25 Li^+/formula unit, but nearly all can be removed at higher temperatures. Better reversibility, however, is obtained when charge is limited to 3 Li^+/formula unit. In terms of synthesis, best results were obtained for a material made without excess Li_2O, and a simpler one-step process was discovered, although it still needs optimization. Partial fluorination also appeared to be successful. Future effort will be directed towards surface and bulk synchrotron characterization to understand both the irreversible redox processes that occur on the first cycle and what limits cycle life in this system.

Key Publications

1. Besli, M., Usubelli, C., Metzger M., Hellstrom S., Sainio, S., Nordlund D., Christensen, J., Schneider, G., Doeff M. M., and Kuppan, S., "Long-Term Chemothermal Stability of Delithiated NCA in Polymer Solid-State Batteries" J. Mater. Chem. A, (2019) DOI: 10.1039/C9TA11103D.

2. Tian, C., Xu, Y., Kan, W. H., Sokaras, D., Nordlund, D. Shen, H., Chen, K., Liu, Y., and Doeff, M., "Distinct Surface and Bulk Thermal Behaviors of $LiNi_{0.6}Mn_{0.2}Co_{0.2}O_2$ Cathode Materials as a Function of State-of-Charge" ACS Appl. Mater. & Interfaces, (2020) DOI: 10.1021/acsami.

3. Alvarado, J., Wei, C., Nordlund, D., Kroll, T., Sokaras, D., Tian, Y., Liu, Y., and Doeff, M. M. "Thermal Stress-Induced Charge and Structure Heterogeneity in Emerging Cathode Materials", Mater. Today, (2019) https://doi.org/10.1016/j.mattod.2019.11.009.

References

1. Chen, H., and Islam, M. S., "Lithium Extraction Mechanism in Li-Rich Li2MnO3 Involving Oxygen Hole Formation and Dimerization" Chem. Mater. 28, (2016): 6656-6663.

2. Croy, J. R., Balasubramanian, M., Gallagher, K. G., and Burrell, A. K., "Review of the U.S. Department of Energy's "Deep Dive" Effort to Understand Voltage Fade in Li- and Mn-Rich Cathodes" Acc. Chem. Res. 48, (2015): 2813-21.

3. Luo, K., Roberts, M. R., Guerrini, N., Tapia-Ruiz, N.,Hao, R., Massel, F., Pickup, D. M., Ramos, S., Liu, Y. S., Guo, J., Chadwick, A. V., Duda, L. C., and Bruce, P. G., "Anion Redox Chemistry in the Cobalt Free 3d Transition Metal Oxide Intercalation Electrode Li[Li0.2Ni0.2Mn0.6]O2" J. Am. Chem. Soc. 138, (2016): 11211-11218.

4. Sathiya, M., Rousse, G., Ramesha, K., Laisa, C. P., Vezin, H., Sougrati, M. T.,Doublet, M. L., Foix, D., Gonbeau, D.,Walker, W.,Prakash, A. S.,Ben Hassine, M., Dupont, L., and Tarascon, J. M., "Reversible Anionic Redox Chemistry in High-capacity Layered-oxide Electrodes" Nature Mater. 12 (2013): 827-835.

5. Pearce, P. E., Perez, A. J., Rousse, G., Saubanere, M., Batuk, D., Foix, D., McCalla, E.,Abakumov, A. M.,Van Tendeloo, G., Doublet, M. L., and Tarascon, J. M., "Evidence for Anionic Redox Activity in a Tridimensional-ordered Li-rich Positive Electrode beta-Li2IrO3" Nature Mater. 16 (2017): 580- 586.

6. Seo, D. H., Lee, J., Urban, A., Malik, R., Kang, S., and Ceder, G., "The Structural and Chemical Origin of the Oxygen Redox Activity in Layered and Cation-disordered Li-excess Cathode Materials" Nature Chem. 8 (2016): 692-697.

7. Yabuuchi, N.,Takeuchi, M., Nakayama, M., Shiiba, H., Ogawa, M., Nakayama, K., Ohta, T.,Endo, D., Ozaki, T., Inamasu, T., Sato, K., and Komaba, S., "High-capacity Electrode Materials for Rechargeable Lithium Batteries: Li3NbO4-based System with Cation-disordered Rocksalt Structure" Proc. Natl. Acad. Sci. USA 112, (2015): 7650-7655.

8. Yabuuchi, N., Nakayama, M., Takeuchi, M., Komaba, S.,Hashimoto, Y., Mukai, T., Shiiba, H., Sato, K., Kobayashi, Y., Nakao, A., Yonemura, M., Yamanaka, K., Mitsuhara, K., and Ohta, T., "Origin of Stabilization and Destabilization in Solid-state Redox Reaction of Oxide Ions for Lithium-ion Batteries" Nature Commun. 7, (2016): article no. 13814.

9. Perez, A. J., Jacquet, Q., Batuk, D., Iadecola, A., Saubanère, M., Rousse, G., Larcher, D., Vezin, H., Doublet, M.-L., and Tarascon, J.-M., "Approaching the Limits of Cationic and Anionic Electrochemical Activity with the Li-rich Layered Rocksalt Li3IrO4" Nature Energy 2, (2017): 954-962.

10. Assat, G., Delacourt, C., Corte, D. A. D., and Tarascon, J.-M., "Practical Assessment of Anionic Redox in Li-Rich Layered Oxide Cathodes: A Mixed Blessing for High Energy Li-Ion Batteries" J. Electrochem. Soc. 163, (2016): A2965-A2976.

11. Xu, J., Sun, M., Qiao, R., Renfrew, S. E., Ma, L., Wu, T., Hwang, S., Nordlund, D., Su, D., Amine, K., Lu, J., McCloskey, B. D., Yang, W., and Tong, W., "Elucidating Anionic Oxygen Activity in Lithium-rich Layered Oxides" Nature Commun. 9, (2018): article no. 947.

12. Kan, W. H., Chen, D., Papp, J. K., Shukla, A. K., Huq, A., Brown, C. M., McCloskey, B. D., and Chen, G., "Unravelling Solid-State Redox Chemistry in Li1.3Nb0.3Mn0.4O2 Single-Crystal Cathode Material" Chem. Mater. 30, (2018): 1655-1666.

13. Mikhailova, D., Karakulina, O. M., Batuk, D.,Hadermann, J., Abakumov, A. M.,Herklotz, M.,Tsirlin, A. A., Oswald, S., Giebeler, L., Schmidt, M., Eckert, J, Knapp, M., and Ehrenberg, H., "Layered-to-Tunnel Structure Transformation and Oxygen Redox Chemistry in LiRhO2 upon Li Extraction and Insertion" Inorg. Chem. 55, (2016): 7079-7089.

14. Gent, W. E., Lim, K., Liang, Y, Li, Q., Barnes, T., Ahn, S. J., Stone, K. H., McIntire, M., Hong, J.,Song, J. H., Li, Y., Mehta, A., Ermon, S., Tyliszczak, T., Kilcoyne, D., Vine, D., Park, J. H.,Doo, S. K, Toney, M. F., Yang, W., Prendergast, D., and Chueh, W. C., "Coupling between Oxygen Redox and Cation Migration Explains Unusual Electrochemistry in Lithium-rich Layered Oxides" Nature Commun. 8, (2017): article no. 2091.

15. Lee, J., Papp, J. K., Clement, R. J., Sallis, S., Kwon, D. H., Shi, T.,Yang, W., McCloskey, B. D., and Ceder, G., "Mitigating Oxygen Loss to Improve the Cycling Performance of High Capacity Cation Disordered Cathode Materials" Nature Communications 8, (2017): article no. 981.

16. Wei, W., Chen, L., Pan, A., and Ivey, D. G., "Roles of Surface Structure and Chemistry on Electrochemical Processes in Lithium-rich Layered Oxide Cathodes" Nano Energy 30, (2016): 580-602.

17. Freire, M., Kosova, N. V., Jordy, C., Chateigner, D., Lebedev, O. I., Maignan, A., and Pralong, V. "A New Active Li-Mn-O Compound for High Energy Density Li-Ion Batteries" Nature Mater. 15, (2016): 173–177.

18. McCalla, E., Abakumov, A., Rousse, G., Reynaud, M., Sougrati, M. T., Budic, B., Mahmoud, A., Dominko, R., Van Tendeloo, G., Hermann, R. P. et al. "Novel Complex Stacking of Fully-Ordered Transition Metal Layers in Li4FeSbO6 Materials" Chem. Mater. 27, (2015):1699–1708.

19. Renfrew, S.E., and McCloskey, B. D. "Residual Lithium Carbonate Predominantly Accounts for First Cycle CO2 and CO Outgassing of Li-Stoichiometric and Li-rich Layered Transition Metal Oxides" J. Am. Chem. Soc. 139, (2017): 17853-17860.

II.3.D Understanding and Modification of High-Energy Cathodes and Their Interfaces with Electrolytes for Next-Generation Li-Ion Batteries (Pacific Northwest National Laboratory)

Jie Xiao, Principal Investigator
Pacific Northwest National Laboratory
902 Battelle Blvd
Richland, WA, 99352
E-mail: jie.xiao@pnnl.gov

Ji-Guang Zhang, Principal Investigator
Pacific Northwest National Laboratory
902 Battelle Blvd
Richland, WA, 99352
E-mail: jiguang.zhang@pnnl.gov

Peter Faguy, DOE Technology Development Manager
U.S. Department of Energy
E-mail: Peter.Faguy@ee.doe.gov

Start Date: October 1, 2019 End Date: September 30, 2020
Project Funding: $400,000 DOE share: $400,000 Non-DOE share: $0

Project Introduction

Ni-rich cathodes, with their >200 mAh/g capacity, high voltage and low cost, are the most promising cathodes for next generation high-energy Li-ion batteries for electrical vehicles [1], [2]. Traditional $LiNi_{1/3}Mn_{1/3}Co_{1/3}O_2$ (NMC) cathodes are prepared using a co-precipitation method which yields agglomerated nanosized NMC particles. This aggregated particle structure shortens the diffusion length of the primary particles and increases the number of pores and grain boundaries within the secondary particles, which accelerate the electrochemical reaction and improves the rate capability of NMC. However, pulverization along the weak grain boundaries is generally observed during cycling [3]. This intergranular cracking exposes more surfaces to electrolyte and drives side reactions on the newly exposed surfaces [4], [5]. Accordingly, cell degradation is accelerated once cracks form within secondary NMC particles.

As Ni content becomes ≥ 0.8 in NMC, the major challenge in Ni-rich NMC cathodes becomes quite different from those in conventional NMC. For example, NMC811 is very sensitive to moisture, which creates challenges for manufacturing, storing and transporting the Ni-rich NMC [6]. After extensive cycling, gas generation by the side reactions raises safety concerns [7]. While the detailed mechanism of gas generation and moisture sensitivity of NMC811 are still arguable, all these side reactions initiate from materials surfaces. Therefore, reducing the surface areas by synthesizing micron-sized single crystals becomes an important direction to address the materials challenges in Ni-rich NMC. Similarities can be found in $LiCoO_2$ [8].

Objectives

The objective of this project is to advance the fundamental understanding of the interfaces between electrolyte and Ni-rich and low-cobalt NMC cathode (i.e., $LiNi_xMn_yCo_{1-x-y}O_2$, x > 0.6) by using high-performance single crystalline $LiNi_{0.76}Mn_{0.14}Co_{0.1}O_2$(referred as NMC76 hereafter) as a platform. A scalable synthesis approach (Patent application #: 31837) has been developed in FY19 to prepare electrochemically active single crystalline (~ 3μm) NMC76 with >200 mAh/g capacity [9]. In FY20, we further utilize single crystalline $LiNi_{0.76}Mn_{0.14}Co_{0.1}O_2$ (NMC76) as a model material to study how the potential triggers the structural changes of single crystals from the atomic to micron scale and its implications to the electrochemical properties of cathodes.

Approach

- Examine the surface properties and stoichiometry of as-prepared single crystalline NMC76
- Validate the electrochemical performances and stability of single crystalline NMC76 at relevant scales and within different electrochemical windows
- Summarize and compare as-prepared single crystalline NMC76 with all previously published Ni-rich NMC76 single crystals.

Results

The synthesized NMC76 has an average particle size of 3 µm (Figure II.3.D.1A). A cross-section view (Figure II.3.D.1B) shows that NMC76 has a dense structure without cavities or grain boundaries. Pure phases of α-$NaFeO_2$-type layered structures are confirmed by both selected area electron diffraction (SAED, Figure II.3.D.1C) and X-ray Diffraction (XRD, Figure II.3.D.1D). Lattice parameters *a* and *c* are 2.8756(1) Å and 14.2221(1) Å, respectively, from Rietveld refinement. For comparison, polycrystalline NMC76 are found to contain many internal pores and intergranular boundaries along with surface films (data not shown here) formed from the reactions between NMC and air. The surface of single crystalline NMC76 is very uniform and clean (Figure II.3.D.1E-F). Elemental mapping (Figure II.3.D.1G-H) indicates a homogeneous distribution of Ni, Mn and Co with a stoichiometric ratio as designed.

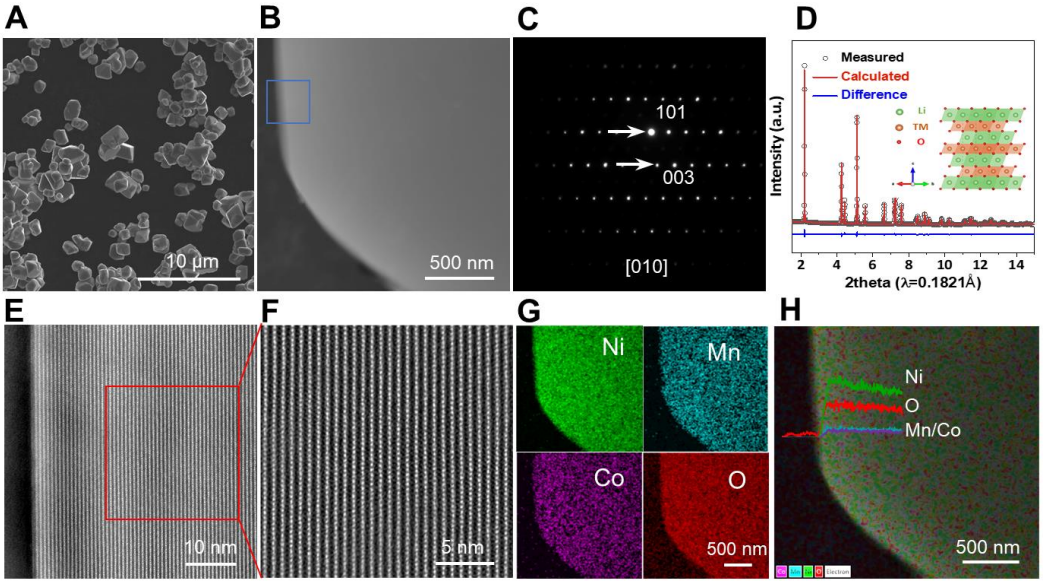

Figure II.3.D.1 Characterization of single crystalline $LiNi_{0.76}Mn_{0.14}Co_{0.10}O_2$. (A) SEM image of single crystalline NMC76. (B) Cross-section image of single crystalline NMC76. (C) Selected area electron diffraction pattern of single crystalline NMC76. (D) Synchrotron XRD and Rietveld refinement pattern. (E) High resolution HAADF-STEM image of single crystalline NMC76 (corresponding to blue color square in B). (F) Higher magnification corresponding red color-coded region in E. (G) EDS elemental mapping of Ni, Mn, Co and O. (H) EDS overlapped image and line scanning shows the elemental distribution intensity (the inset).

Single crystalline NMC76 is further tested in graphite/NMC full cells at conditions that are relevant to practical applications. The typical loading of NMC76 cathodes is ca. 20 mg/cm^2 (=4 mAh/cm^2) with ca. 32% porosity, which is needed to build a 250 Wh/kg Li-ion cell [9]. Between 2.7 and 4.2 V (*vs.* Graphite), single crystalline NMC76 delivers 182.3 mAh/g discharge capacity at 0.1C, and retains 86.5% of its original capacity after 200 cycles (Figure II.3.D.2A1). With a cutoff of 4.3 V, single crystalline NMC76 delivers 193.4 mAh/g capacity with 81.6% capacity retention after 200 cycles (Figure II.3.D.2A2). Further increasing to 4.4 V, 196.8 mAh/g discharge capacity is seen (Figure II.3.D.2A3) along with a 72.0% capacity retention after 200 cycles.

Note that 200 cycles at C/10 charge rate and C/3 discharge rate mean 2600 hours of cycling. The total testing time is equal to a cell undergoing 1300 cycles at 1C. To evaluate the electrochemical properties of materials, it is important to use a relatively slow rate rather than a very fast rate which produces seemly "longer" cycles but may "hide" critical electrochemical information. It is the total time of charge/discharge matters instead of cycling number [10]. Increased polarization (Figure II.3.D.2B1-B3) is observed when the cutoff voltage increases which is presumably assigned to the intensified electrolyte decomposition at elevated voltages and thus increased impedance resulting from cathode passivation films.

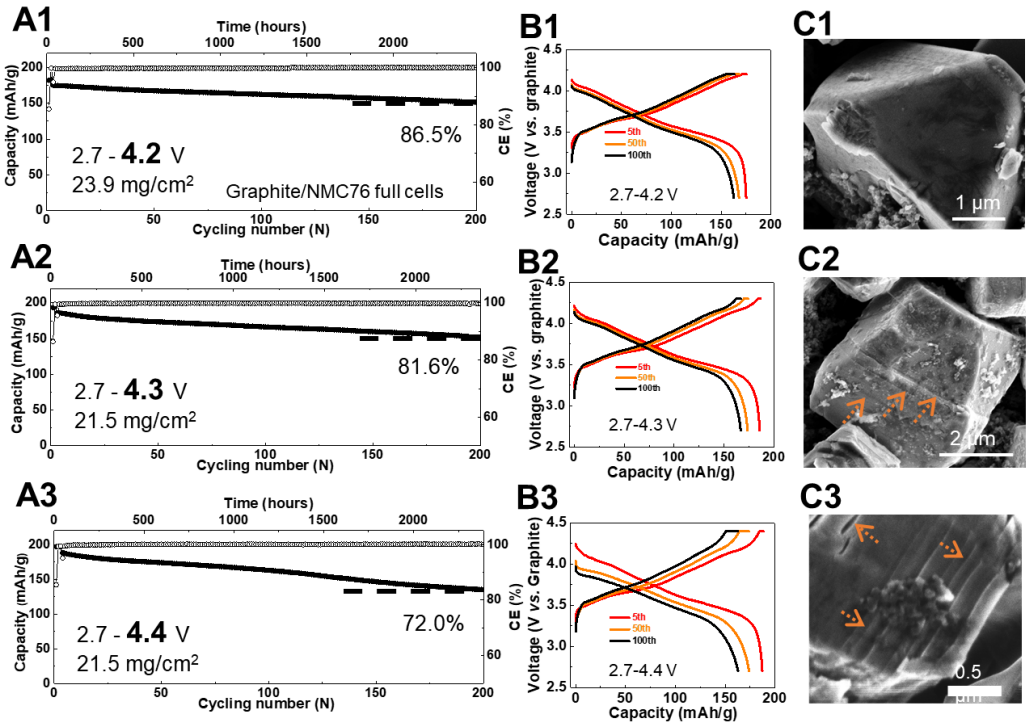

Figure II.3.D.2 Electrochemical performance of single crystalline $LiNi_{0.76}Mn_{0.14}Co_{0.10}O_2$ and SEM images after cycling stability tests. (A1)(A2)(A3) Cycling stability of single crystalline NMC76 in full cells within different electrochemical windows. (B1)(B2)(B3) The corresponding charge-discharge curves of cells in (A1)(A2)(A3). (C1)(C2)(C3) SEM images of single crystal after 200 cycles in (A1)(A2)(A3).

Table II.3.D.1 summarizes the electrochemical performances and testing conditions of all previously published single crystalline Ni-rich NMC (Ni > 0.6) cathode materials. In addition to this work, [14] reported a mass loading at a practically usable level which is also higher than our cathodes. However, the cathode in [14] was tested at 45°C instead of room temperature. Of note, although Ni content is higher in [14], the reversible capacity is lower than that of NMC76 reported here. The rest related publications on Ni-rich NMC (Ni>0.6) single crystals in Table II.3.D.1 are using very low mass loadings of single crystals and/or in half cells. Jeff's earlier work presented a wide range of testing results of Li-ion batteries based on graphite/$LiNi_{0.5}Mn_{0.3}Co_{0.2}O_2$ chemistry [17], which can serve as benchmarks for academic research. The electrode properties in terms of loading etc. in Jeff's work are similar to ours. Note that the single crystals tested by Jeff is NMC532 which has lower content of Ni.

Lattice gliding is clearly observed in single crystalline NMC76 at high voltages. Between 2.7 and 4.2 V (*vs.* Graphite), the entire single crystal is well maintained after 200 cycles (Figure II.3.D.2C1). Increasing cutoff voltage to 4.3 V, there are some gliding lines seen on the crystal surfaces after 200 cycles (Figure II.3.D.2C2). Cycled to 4.4 V, single crystals appeared to be "sliced" (Figure II.3.D.2C3) in parallel, which indicates a model II type crack (in-plane shear) in fracture mechanics. Additionally, small cracks that indicate a model I type fracture (opening) are also discovered at 4.4 V (Figure II.3.D.2C3). All characterizations have been done

by selecting various regions of NMC76 electrodes and the same phenomenon is repeatedly found. Although single crystalline NMC76 as an entire particle is still intact (Figure II.3.D.2C1-C3), gliding is the major mechanical degradation mode especially when cutoff voltage is above 4.3 V.

The scientific questions arising from the observed gliding phenomenon include: (1) what is the driving force of the lattice gliding in single crystals at elevated voltage? (2) How to compare such "gliding" in single crystals with "cracking" in polycrystalline Ni-rich NMC and its implications in long-term cycling of Ni-rich NMC? (3) Is there any strategy to prevent forming such "gliding" in single crystals from synthesis modification? All these questions will be further examined and answered in the next year.

Table II.3.D.1 Comparison with Single Crystalline Ni-rich NMC (Ni>0.6) Reported in Literature

Ref	Composition	Initial capacity			Loading	Cycling			
		Capacity(mAh/g)	Rate	Voltage		No.	Retention (%)	Rate	Total Cycling time/hr*
This work	$LiNi_{0.76}Mn_{0.14}Co_{0.1}O_2$	196.8	0.1C	4.4 V vs. Gr.	20 mg/cm^2	200 (full cell)	72	0.1/0.33 C	2389
[11]	$LiNi_{0.8}Mn_{0.1}Co_{0.1}O_2$	185	0.1C	4.3 V vs. Li	3 mg/cm^2	25	50	0.1/0.1C	~500
	$LiNi_{0.8}Mn_{0.1}Co_{0.1}O_2$	240	0.1C	4.6 V vs. Li	-	25	50	0.1/0.1C	
[12]	$LiNi_{0.88}Co_{0.09}Al_{0.03}O_2$	192	0.2C	4.3 V vs. Li	12 mg/cm^2	100 (full cell)	88	0.2/0.2C	~1000
[13]	$LiNi_{0.8}Mn_{0.1}Co_{0.1}O_2$	190	0.1C	4.3 V vs. Li	3 mAh/cm^2	100	~90	1/1C	~200
[14]	$LiNi_{0.83}Mn_{0.06}Co_{0.11}O_2$	184.1	1C	4.2 V vs. Gr/SiO	47 mg/cm^2	600 (tested at 45^{o}C, full cell)	84.8	1/1C	~1200
[15]	$LiNi_{0.92}Mn_{0.01}Co_{0.06}Al_{0.01}W_xMo_xO_2$ **	221.4	0.1C	4.3 V vs. Li	7.8 mg/cm^2	100	95.7	0.5/1C	100
[16]	$LiNi_{0.8}Mn_{0.1}Co_{0.1}O_2$	-	-	-	14 mg/cm^2	1200	98	1/1C	2400

Conclusions

High-performance single crystalline NMC76 has been successfully synthesized, tested at relevant scales and compared with all previously reported Ni-rich NMC single crystals. More than 200 mAh/g reversible capacity and a stable cycling have been demonstrated from as-prepared NMC76 single crystals in full cells. The fundamental relationship among structure-potential-properties of single crystal NMC76 has been further studied by increasing the cutoff voltage of the full cells. It is found that planar gliding and microcracking are induced when charged to greater than 4.3 V (*vs.* Graphite), although the single crystal still maintains its entire structure.

Key Publications

1. Y. Bi, J. Tao, J. Hu, L. Li, Y. Xu, C. Wang, J.-G. Zhang and J. Xiao, "Reversible planar gliding and microcracking in single crystalline Ni-rich cathode for advanced Li-ion batteries", *Science*, accepted.

2. J. Hu, L. Li, E. Hu, S. Chae, H. Jia, T. Liu, B. Wu, Y. Bi, K. Amine, C. Wang, J.-G. Zhang, J. Tao, J. Xiao, "Mesoscale-architecture-based crack evolution dictating cycling stability of advanced lithium ion batteries", *Nano Energy*, 2021, 79, 105420.

3. J. Hu, B. Wu, X. Cao, Y. Bi, S. Chae, C. Niu, B. Xiao, J. Tao, J-G. Zhang, J. Xiao, "Evolution of the rate-limiting step: From thin film to thick Ni-rich cathodes", *J. Power Sources (invited)*, 2020, 454, 227966.

4. J. Xiao, "Integrating Materials Science, Electrochemistry and Engineering in Energy Storage Technologies", ECS PRiME Virtual Meeting, October 4, 2020.

5. J. Xiao, "Energy Storage: Integration of Materials Chemistry, Electrochemistry and Engineering", Virtual Seminar for University of Washington/Clean Energy Institution, April 2020.

6. J. Xiao, "Ni-rich Cathode for Advanced Li-ion Batteries, 236th ECS meeting, Atlanta, GA, October 15, 2019.

References

1. Goodenough, John B., Youngsik Kim. 2010. "Challenges for Rechargeable Li Batteries." 2010. *Chem. Mater.* 22:587-603. https://doi.org/10.1021/cm901452z.

2. Goodenough, John B., Kyu-Sung Park. 2013. "The Li-ion Rechargeable Battery A Perspective." *J. Am. Chem. Soc.* 135:1167-1176. https://doi.org/10.1021/ja3091438.

3. Yan, Pengfei, Jianming Zheng, Meng Gu, Jie Xiao, Ji-Guang Zhang, Chong-Min Wang. 2017. "Intragranular cracking as a critical barrier for high-voltage usage of layer-structured cathode for lithium-ion batteries." *Nat. Commun.* 8:14101. https://doi.org/10.1038/ncomms14101.

4. Xu, Zhengrui, Muhammad Mominur Rahman, Linqin Mu, Yijin Liu, Feng Lin. 2018. "Chemomechanical behaviors of layered cathode materials in alkali metal ion batteries." *J. Mater. Chem. A* 6:21859-21884. https://doi.org/10.1039/C8TA06875E.

5. Besli, Munir M., Sihao Xia, Saravanan Kuppan, Yiqing Huang, Michael Metzger, Alpesh Khushalchand Shukla, Gerhard Schneider, Sondra Hellstrom, Jake Christensen, Marca M. Doeff, Yijing Liu. 2019. "Mesoscale Chemomechanical Interplay of the $LiNi_{0.8}Co_{0.15}Al_{0.05}O_2$ Cathode in Solid-State Polymer Batteries." *Chem. Mater.* 31:491-501. https://doi.org/10.1021/acs.chemmater.8b04418.

6. Jung, Roland, Robert Morasch, Pinar Karayaylali, Katherine Phillips, Filippo Maglia, Christoph Stinner, Yang Shao-Horn, Hubert A. Gasteiger. 2018. "Effect of Ambient Storage on the Degradation of Ni-Rich Positive Electrode Materials (NMC811) for Li-Ion Batteries." *J. Electrochem. Soc.* 165:A132-A141. https://doi.org/10.1149/2.0401802jes.

7. Nam, Kyung-WanNam, Seong-Min Bak, Enyuan Hu, Xiqian Yu, Youngning Zhou, Xiaojian Wang, Lijun Wu, Yimei Zhu, Kyung-Yoon Chung, Xiao-qing Yang. 2013. "Combining in situ synchrotron X-Ray diffraction and absorption techniques with transmission electron microscopy to study the origin of thermal instability in overcharged cathode materials for lithium-ion batteries." *Adv. Funct. Mater.* 23, 1047-1063. https://doi.org/10.1002/adfm.201200693.

8. Jo, Minki, Young-Sik Hong, Jaebum Choo, Jaephil Cho. 2009. "Effect of $LiCoO_2$ Cathode Nanoparticle Size on High Rate Performance for Li-Ion Batteries." *J. Electrochem. Soc.* 156:A430-A434. https://doi.org/10.1149/1.3111031.

9. Xiao, Jie. 2019. “Understanding and Modifying Cathode / Electrolyte Interfaces.” DOE VTO AMR. https://www.energy.gov/sites/prod/files/2019/06/f64/bat407_%20xiao_2019_p_4.25_1.45pm.pdf.

10. Pinson, Matthew B., Martin Z. Bazant. 2012. “Theory of SEI Formation in Rechargeable Batteries: Capacity Fade, Accelerated Aging and Lifetime Prediction.” *J. Electrochem. Soc.* 160:A243-A250. https://doi.org/10.1149/2.044302jes .

11. Zhu, Jian, Guoying Chen. 2019. “Single-crystal based studies for correlating the properties and high-voltage performance of $Li[Ni_xMn_yCo_{1-x-y}]O_2$ cathodes.” *J. Mater. Chem. A* 7:5463-5474. https://doi.org/10.1039/C8TA10329A.

12. Li, Hongyang, Jing Li, Nafiseh Zaker, Ning Zhang, G. A. Botton, J. R. Dahn. 2019. “Synthesis of Single Crystal $LiNi_{0.88}Co_{0.09}Al_{0.03}O_2$ with a Two-Step Lithiation Method.” *J. Electrochem. Soc.* 166:A1956-A1963. https://doi.org/10.1149/2.0681910jes .

13. Qian, GuannanQian, Youtian Zhang, Linsen Li, Ruixin Zhang, Junmeng Xu, Zhenjie Cheng, Sijie Xie, Han Wang, Qunli Rao, Yushi He, Yanbin Shen, Liwei Chen, Ming Tang, Zi-Feng Ma. 2020. “Single-crystal nickel-rich layered-oxide battery cathode materials: synthesis, electrochemistry, and intra-granular fracture.” *Energy Storage Mater.* 27:140-149. https://doi.org/10.1016/j.ensm.2020.01.027.

14. Fan, Xinming, Guorong Hu, Bao Zhang, Xing Ou, Jiafeng Zhang, Wengao Zhao, Haiping Jia, Lianfeng Zou, Peng Li, Yong Yang. 2020. “Crack-free single crystalline Ni-rich layered NCM cathode enable superior cycling performance of lithium-ion batteries.” *Nano Energy* 70, 104450. https://doi.org/10.1016/j.nanoen.2020.104450.

15. Yan, Wuwei, Xiaobo Jia, Shunyi Wang, Youyuan Huang, Yong Yang, Guohui Yuan. 2020. “Synthesis of single crystal $LiNi_{0.92}Co_{0.06}Mn_{0.01}Al_{0.01}O_2$ cathode materials with superior electrochemical performance for lithium ion batteries.” *J. Electrochem. Soc.* 167, 120514. https://doi.org/10.1149/1945-7111/abacea.

16. Liu, Yulong, Jessie. Harlow, Jeff. Dahn. 2020. “Microstructural Observations of “Single Crystal” Positive Electrode Materials Before and After Long Term Cycling by Cross-section Scanning Electron Microscopy.” *J. Electrochem. Soc.* 167:020512. https://doi.org/10.1149/1945-7111/ab6288.

17. Harlow, Jessie E., Xiaowei Ma, Jing Li, Eric Logan, Yulong Liu, Ning Zhang, Lin Ma, Stephen L. Glazier, Marc M. E. Cormier, Matthew Genovese, Samuel Buteau, Andrew Cameron, Jamie E. Stark, J. R. Dahn. 2019. “A Wide Range of Testing Results on an Excellent Lithium-Ion Cell Chemistry to be used as Benchmarks for New Battery Technologies.” *J. Electrochem. Soc.* 166, A3031-A3044. https://doi.org/10.1149/2.0981913jes.

Acknowledgements

We thank the contributions from Dr.Yuing Bi and Dr.Chongmin Wang at PNNL and our collaborator Dr. Enyuan Hu at Brookhaven National Laboratory.

II.3.E Fluorinated Deep Eutectic Solvent (FDES)-Based Electrolytes (ANL)

Zhengcheng (John) Zhang, Principal Investigator
Argonne National Laboratory
9700 S. Cass Ave., B200
Lemont, IL 60439
E-mail: zzhang@anl.gov

Peter Faguy, DOE Technology Development Manager
U.S. Department of Energy
E-mail: Peter.Faguy@ee.doe.gov

Start Date: October1, 2018 End Date: September 30, 2021
Project Funding: $350,000 DOE share: $350,000 Non-DOE share: $0

Project Introduction

The lithium-ion battery (LIB) is widely used in the devices supporting our digital and mobile lives; however, the LIB's adoption in electric vehicles (EVs) and more strategically smart grid applications has been limited by its energy density, high cost, and safety concerns.[1]-[4] Battery electrode materials with high theoretical capacity and high voltage are critical components and always desired for advancing the technology, and such battery materials for next-generation applications in electric vehicles have been reported in recent years.[5]-[7] However, new challenges arise from the non-aqueous electrolytes because the carbonate-based electrolytes are thermodynamically instable on charged cathode at voltages higher than 4.3 V *vs* Li^+/Li,[8]-[10] and these electrolytes are extremely reactive with the conversion–type, high-capacity anode such as silicon (Si), which leads to rapid deterioration in battery cycling performance.[11]-[13] Furthermore, there is severe safety concern of this highly flammable electrolyte due to the presence of highly volatile organic carbonate solvents. Due to its many advantages such as high conductivity, high electrochemical stability, and good passivation of the Al current collector, lithium hexafluorophosphate ($LiPF_6$) is still the dominating electrolyte salt in state-of-the-art electrolytes despite its thermal and chemical instability. Transition metal (TM) dissolution in the electrolyte and crosstalk with the anode have been widely reported for the high-voltage system; the reasons for these to occur have been ascribed to the cathode surface structure transformation and reconstruction. Nevertheless, even the pristine oxide cathode is in contact with the electrolyte, TM ions, for example Mn^{2+} dissolves simultaneously in the electrolyte due to the reaction of the weak acid HF, the hydrolysis product of $LiPF_6$ with a trace amount of moisture in the electrolyte, with oxide surface layer.[14]-[18] In both cases, diffusion and deposition of TM (mainly Mn^{2+}) on the anode side catalyzes the parasitic reactions, leading to active lithium loss and rapid capacity fade of the cell.[17], [19]-[21] Therefore, demand is great for a new electrolyte that could enable the reversible and rapid positive/negative redox reactions and thus advance next-generation, high-voltage, high-energy LIB technology.

Objectives

The objective of this project is to develop fluorinated deep eutectic solvent (FDES, also called fluorinated ionic liquid-based aprotic electrolytes)-based electrolytes as new high voltage electrolytes to address the high reactivity of conventional organic electrolyte at the surface of the charged cathode and the safety concern associated with the organic electrolyte. The FDES are designed to provide thermodynamic stability on the charged cathode surface affording a stabilized cathode/electrolyte interface, and should be highly compatible with anode including graphite and Si. The FDES is a new room-temperature molten salt comprising of new fluorinated organic cations and new fluorinated organic anions with a wide liquid window. FDES has superior thermal stability with no vapor pressure even heated to 300-400°C, and excellent fluidity at temperature lower than -20°C. Not only high performance, the FDES are non-flammable with significantly enhanced safety characteristic.

Approach

We have been focusing on development of super concentrated fluorinated deep eutectic solvents (FDES) or fluorinated ionic liquids. As an alternative non-aqueous electrolyte candidate, room-temperature ionic liquids (RTILs) have attracted tremendous interest due to their negligible vapor pressure, nonflammability, thermal stability, high-oxidation tolerance, and sufficient ionic conductivity.[22]-[24] ILs with the bis(fluorosulfonyl)imide (FSI^-) anion coupled with LiFSI salt are widely studied in the field due to their relatively low viscosity, high conductivity, and, more importantly, ability to form a robust solid-electrolyte-interface (SEI) on several high-energy electrode materials.[25], [26] Previous work has reported that, with low salt concentration, RTILs containing pyrrolidinium (PYR^+), or imidazolium (IM^+) cations paired with bis(trifluoromethanesulfonyl)imide ($TFSI^-$) or FSI^- anions, are kinetically stable with popular negative electrode materials,[27]-[30] even for lithium metal and Si anode.[31]-[33] However, there are several technical concerns including low C-rate capability and metal corrosion issues. Recently, research related to high-concentration electrolytes has attracted wide attention because of the benefits demonstrated from having additional salt in various organic solvents and ionic liquids.[34]-[43] While the performance improvement of the high concentration electrolyte over the dilute one has been identified, the real reason for the improvement over the conventional electrolyte remains unknown, especially for the high-voltage, high-energy LIB comprising a high-voltage NMC cathode and Si anode. Furthermore, little work has been dedicated to gaining a fundamental understanding of the underpinning mechanism of the highly concentrated ionic liquid-based electrolytes. We studied a LiFSI-saturated, 1-methyl-1-propylpiperidinium bis(fluorosulfonyl)imide (PMpipFSI) electrolyte, which is Al current collector corrosion free and shows remarkable voltage tolerance at 4.7 V on the NMC532 cathode as demonstrated in NMC/Li half-cells. More notably, this electrolyte is remarkably stable at both the Si and graphite anode owing to the formation of a resilient SEI, thus enabling the superior performance of the NMC/Si-graphite full cell cycled to 4.6 V. The underpinning transport mechanism of this saturated ionic liquid electrolyte was proposed based on the MD simulations, as well as the electrochemical, spectroscopic, and microscopic data.

Moreover, the physical and electrochemical properties could be systematically tuned by changing the structures of cations or anions. We have synthesized and evaluated two new ILs with fluorine and fluorinated alkyl functionalized cations, i.e. 1-methyl-1-propyl-3-fluoropyrrolidinium bis(fluorosulfonyl)imide ($PMpyr_f$-FSI) and 1-methyl-1-(2,2,3,3,3-pentafluoropropyl)pyrrolidinium bis(fluorosulfonyl)imide (P_fMpyr-FSI). Solvent purity is also critical for good cycling performance of Li-ion batteries. Different from the traditional synthesis method for ionic liquid, a facile one-step route was adopted for the FDES synthesis, which affords these materials with extremely high purity.

Results

Physical properties and ion conformation of super concentrated FDES

Table II.3.E.1 summarizes the viscosity, ionic conductivity, and Li^+ transference number of LiFSI-PMpipFSI electrolytes with different concentrations of salt; Figure II.3.E.1a depicts the conductivity at various temperatures (further discussion follows). The viscosity and conductivity for the neat IL PMpipFSI is 87.25 cP and 3.50×10^{-3} Scm^{-1}, respectively, which are comparable to previously reported results.[25] The viscosity increases and the conductivity decreases when the LiFSI salt concentration increases from 1 M to 5 M, indicating the strong electrostatic interactions between Li^+, the $PMpip^+$ cation, and the FSI^- anion. The highest viscosity and the lowest conductivity were observed for the saturated salt (5 M) — that is, 936.6 cP and 0.353×10^{-3} Scm^{-1}, respectively. As reported by other groups,[43], [44] although the overall conductivity decreases, the Li^+ transference number ($t_{Li}{}^+$) is significantly increased from 0.164 for 1 M to 0.475 for 5 M. A high $t_{Li}{}^+$ is beneficial for fast Li^+ transport, yielding high power capability of the Li-ion battery. Interestingly, when the concentration increases from 3.0 M to 4.0 M, $t_{Li}{}^+$ reaches a plateau of 0.34. Indeed, such a transference plateau corresponds to the similarity of ion-ion spatial coordination between 3 M and 4 M concentration, exhibited by all pairwise radial distribution functions g(r) (red and green line), as shown in Figure II.3.E.2. Of note is that the strong spatial correlation of Li^+-FSI^- quantified by MD simulations demonstrates the special role of FSI^- in Li^+ transport and will be further invoked, along with these coordination

numbers (see the caption for Figure II.3.E.2a–d) in the next two subsections to investigate the transport mechanism of Li^+.

Table II.3.E.1 Summary of Physical Properties, Ionic Conductivity, and Li^+ Transference Number of PMpipFSI with Different LiFSI Concentrations

Denoted concentra-tiona	Molarity of LiFSI (mol/L)	Molality of LiFSI (mol/kg)	Mole ratio of each ion			Viscosity (cP)	Conductivityb (x10^{-3} Scm^{-1})	tLi^+ (Li^+ trans. No.)
			Li^+	$PMpip^+$	FSI^-			
–	0	0	0	0.50	0.50	87.25	3.50	-
1 M	0.93	0.76	0.10	0.40	0.50	133.5	2.24	0.164
2 M	1.7	1.5	0.16	0.34	0.50	249.0	1.25	0.185
3 M	2.4	2.3	0.21	0.29	0.50	396.0	0.819	0.340
4 M	2.9	3.0	0.25	0.25	0.50	601.3	0.555	0.344
5 M	3.4	3.8	0.28	0.22	0.50	936.6	0.353	0.475

[a] Denoted concentration of LiFSI is determined by the millimoles LiFSI dissolved in 1.0 mL PMpipFSI; b Measured at room temperature.

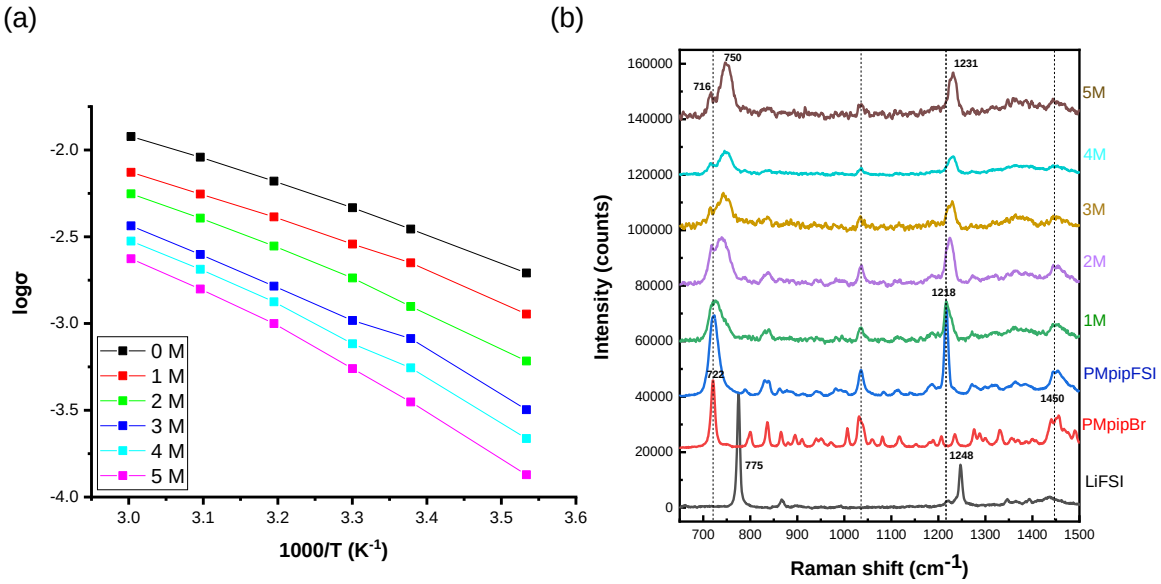

Figure II.3.E.1 (a) The dependence on temperature of the PMpipFSI/LiFSI electrolyte's conductivity measured by EIS, and (b) Raman spectra (600–1500 cm^{-1}) for the PMpipFSI/LiFSI electrolyte with different concentrations of LiFSI salt.

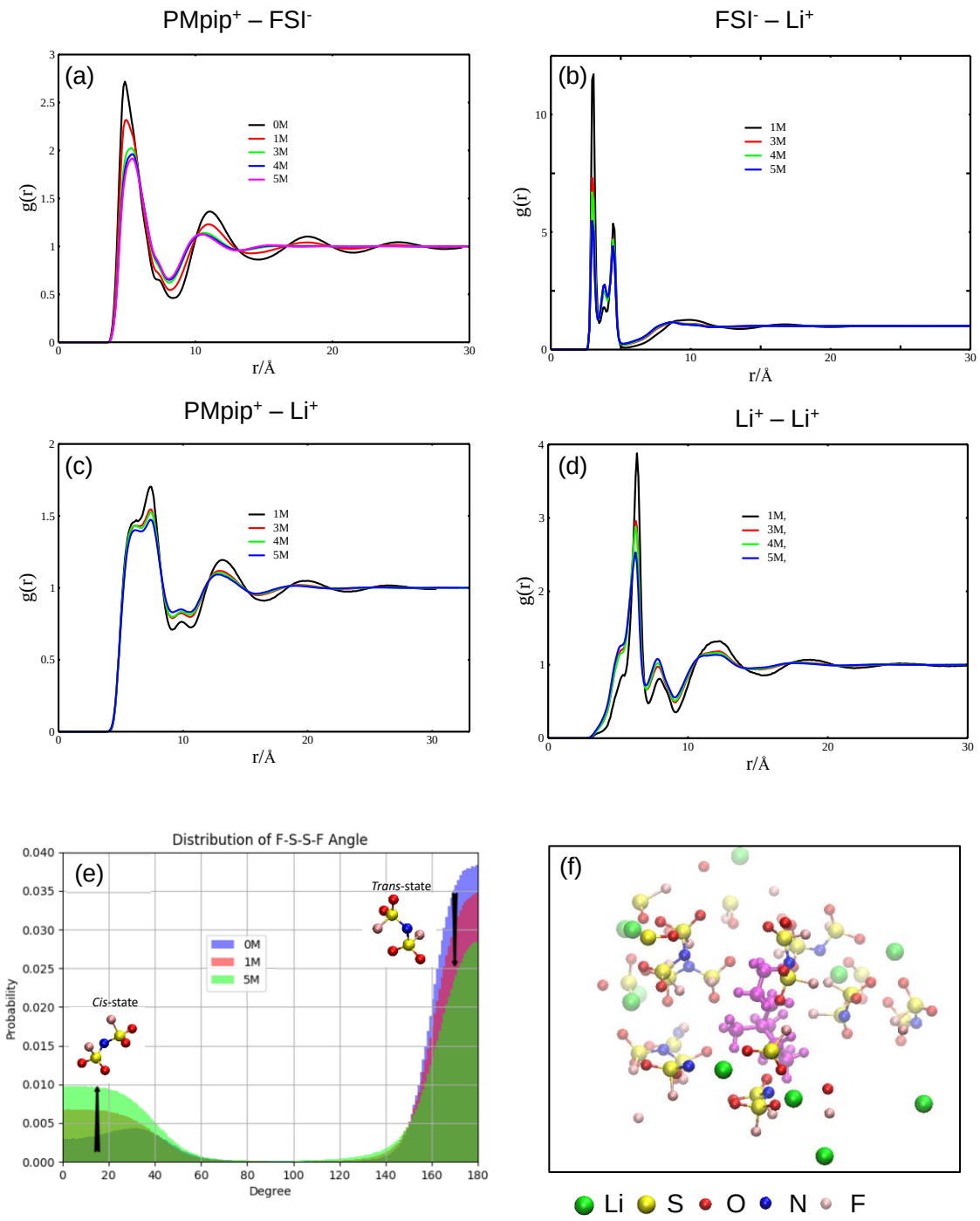

Figure II.3.E.2 (a–d) Pairwise radial distribution functions g(r) computed from MD simulations. (Strong spatial coordination between Li^+ and FSI^- within 5Å can be observed. In contrast, the coordination shells of other types of ion-ion pairs extend to 10Å and exhibit significantly weaker spatial coordination than Li^+- FSI^-. The coordination numbers of Li+ around FSI- are 0.8, 1.8, 2.1, and 2.4 under LiFSI concentration 1 M, 3 M, 4 M, and 5 M, respectively; the coordination number of FSI^- around Li^+ is 4.4 under all concentrations. The coordination numbers of Li^+ around another Li+ are 1.1, 3.0, 3.5, and 4.0 under LiFSI concentration 1 M, 3 M, 4 M, and 5 M, respectively. Another structural feature is that at high concentrations, the ion-ion spatial coordination exhibits similarity, especially between 3 M and 4 M. (e) Cis-state of FSI- and trans-state of FSI- distribution of F-S-S-F dihedral angles at 0, 1 M, 3 M, 4 M, and 5 M concentrations of LiFSI, and (f) a snapshot randomly selected from an equilibrated MD trajectory at a 5 M LiFSI concentration. (The tight Li^+(green)-FSI^- pairing centered at $PMpip^+$ [purple] can be clearly seen).

Figure II.3.E.1a shows the relationship of conductivity to temperature. The curvature feature of log(σ) *vs.* 1000/T (T is temperature in Kelvin) for the high-concentration electrolytes (>3 M) indicates that the ion transport mechanism differs from the dilute electrolytes, which follows the Arrhenius equation. This mechanism change is supported by strong interaction between Li^+ and the FSI^- anion as evidenced by Raman spectra (Figure II.3.E.1b). The substantial Raman peak change occurs in the region from 650–1500 cm^{-1}, whereas no difference was observed in the regions of 200–650 cm^{-1} and 1500–3200 cm^{-1}. The υ_sS-N-S band in the FSI^- shows a characteristic peak at 722 cm^{-1} for the neat PMpipFSI solvent, and this peak shifts to 775 cm^{-1} for solid LiFSI salt due to the tight Li^+ and FSI^- coordination. When LiFSI was added, this peak broadens and gradually shifts to a high wavenumber with increasing concentration from 1 M to 5 M. This shift reaches the maximum of 750 cm^{-1} for the 5 M electrolyte, which is close to the value for solid LiFSI.

Figure II.3.E.2a–d summarize the pairwise radial distribution functions computed from MD simulations. With the increase of the Li^+ concentration, the correlation peak of $PMpip^+$-FSI^- pairs slowly shifts to the right, and the long-range correlation completely disappears when the LiFSI concentration reaches 3 M and higher. Meanwhile, the coordination distance between Li^+ and $PMpip^+$ exhibits a corresponding slow shift while the coordination shell between Li^+ and FSI^- does not shift, revealing that the strong electrostatic attraction of Li^+-FSI^- pairs significantly influences the binding configuration between $PMpip^+$ and FSI^-. In contrast, the band at higher wavenumber blue shifted to 750 cm^{-1}, indicating the formation of Li^+ and FSI^- ion pairs as evidenced by the significantly increased coordination number of Li^+ around FSI^- (see caption for Figure II.3.E.2a–d). Concurrently, the $\upsilon_s SO_2$ band in the Raman spectrum is also blue-shifted from 1218 cm^{-1} to 1231 cm^{-1} (Figure II.3.E.1b), which is consistent with the results for the υ_sS-N-S band. In addition to the direct Raman measurement, we also observed considerable conformational transition of FSI^- with increasing Li^+ concentrations by MD simulation. Figure II.3.E.2e presents the population change of the *cis*- and *trans*-state of the F-S-S-F "dihedral" structure in the FSI^- anion with increasing LiFSI concentration. Here the *cis*-state denotes a conformation where the two fluorine atoms stand on the same side of the S-S axis, whereas in the *trans*-state, the two fluorine atoms stand on the opposite side along the S-S axis. The co-existence of the two conformations is also reflected by the dual coordination peaks in the Li^+-FSI^- radial distribution (Figure II.3.E.2b). However, with increasing Li^+-FSI^- interactions, considerable shifting from the *trans*-state (>90°) to the *cis*-state (<90°) occurred. Figure II.3.E.2f illustrates a snapshot of Li^+-FSI^--$PMpip^+$ complexes at the 5 M LiFSI concentration, centered with a $PMpip^+$ cation. Tight Li^+-FSI^- pairing can be clearly observed.It can naturally be expected that the strong electrostatic repulsion between Li^+ and $PMpip^+$ expels the $PMpip^+$ from FSI^- and screens the long-range interactions of $PMpip^+$ and FSI^- — and thus downgrades the role of $PMpip^+$ in Li^+ transport.

Oxidation stability and Al current collector passivation of super concentrated DES

Cyclic voltammetry was performed to study the oxidation stability of ILEs. Li stripping and plating peaks are also observed below 0 V during the cathodic scan and below 0.5 V during the anodic scan, respectively. Two peaks that observed in the anodic scan around 0.7 V and 1.4 V are assigned to be the stripping peaks of Li-Pt alloy.[45]-[47] When the ILEs were anodically scanned to 6 V *vs.* Li^+/Li, large oxidation currents appeared with an onset voltage of 5.5 V; and a corresponding reduction peak at 3 V appeared during the cathodic scan (Figure II.3.E.3a). However, when the scan window was narrowed down to 5 V, no oxidation current was observed, and the corresponding reduction peak at 3 V also disappeared (Figure II.3.E.3b), indicating that the ILEs are thermodynamically stable up to 5 V, which can support the redox of most high-voltage, high-energy cathodes. Although voltage stability is a critical property for an electrolyte, the ability to passivate the Al current collector is equally indispensable. It is widely accepted that carbonate electrolytes with an amide salt, such as LiTFSI and LiFSI, could not passivate Al. On the contrary, $LiPF_6$ salt could very well passivate Al by forming insoluble AlF_3 and LiF.[48]-[53] The passivation behavior for ILEs with amide salt is controversial.[54]-[62] Our group recently reported a corrosion/passivation behavior of ILEs and demonstrated that the PMpipFSI with various LiFSI concentrations could sufficiently passivate the Al current collector; however, they all show corrosion effects towards stainless-steel coin cell parts, with corrosion significantly suppressed for the high-concentration ILEs.[63] Therefore, to eliminate the high-voltage exposure of ILEs to

the stainless steel in the standard 2032-coin cells, the Al-coated 2032-coin cells shown in Figure II.3.E.3c were used for all of the cell testing.

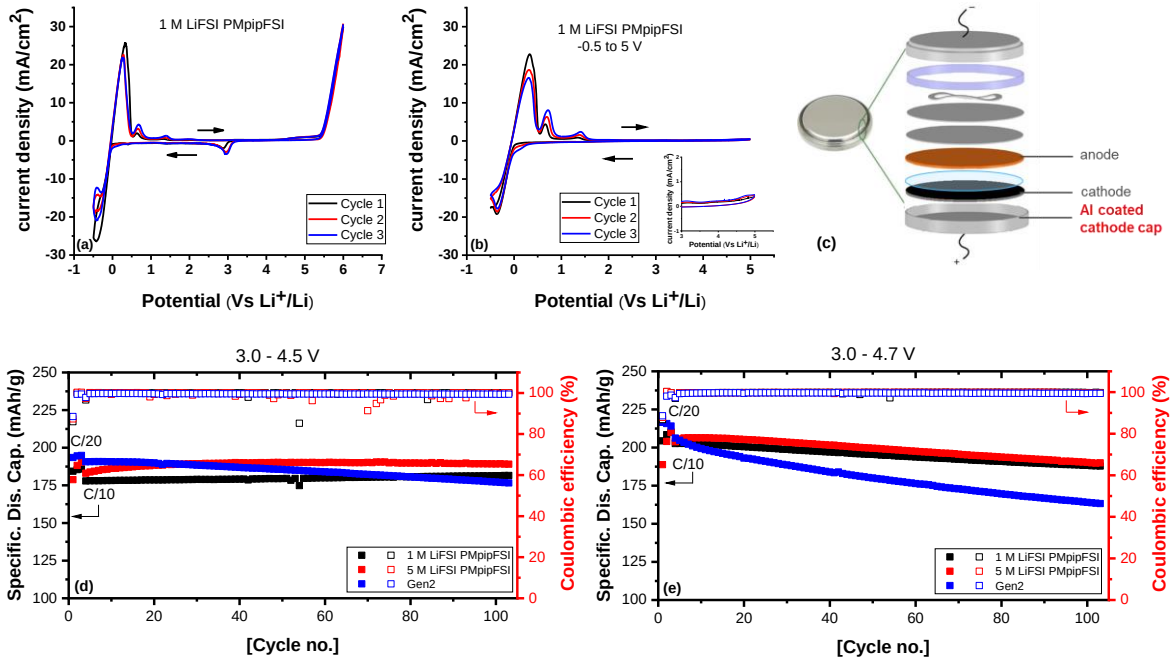

Figure II.3.E.3 (a) Cyclic voltammograms of ILEs scanned to 6.0 V vs. Li^+/Li and (b) scanned to 5.0 V vs. Li^+/Li using Pt as a working electrode and Li as a counter and reference electrode; (c) Al-coated 2032-coin cell configuration with two stainless-steel spacers placed on the anode side;[63] (d) capacity retention and Coulombic efficiency of NMC532/Li cells with 1 M and 5 M ILE with a cutoff voltage 4.5 V–3.0 V, and (e) 4.7–3.0 V.

Cycling performance of DES at high voltages in NMC532 half- and full cell

The Li salt concentration significantly affects the ion conformation as revealed by Raman spectroscopy and MD simulation. To investigate its impact on high-voltage stability, NMC532/Li half-cells were examined first. Figure II.3.E.3d-–e show the specific discharge capacity and Coulombic efficiency using a 1 M and 5 M electrolyte, as well as a conventional Gen 2 electrolyte cycled between 4.5–3.0 V and 4.7–3.0 V. For 4.5-V half cells, the Gen 2 electrolyte cell delivers the highest initial capacity of 190.6 mAh/g; however, it decays cycle by cycle with only 92% capacity retention for 100 cycles. In contrast, although both PMpipFSI ILEs deliver lower initial capacity (177.9 mAh/g for 1 M and 183.1 mAh/g for 5 M), no obvious capacity fading is observed within 100 cycles. The 5 M cell capacity slowly increased during the first 25 cycles, indicating a sluggish electrode wetting due to the increased viscosity. Surprisingly, a remarkable difference in cycling performance was achieved when the cycling upper cutoff voltage was elevated to 4.7 V. The initial specific discharge capacity is comparable for all three electrolyte cells: 206.2 mAh/g for the Gen 2, 202.6 mAh/g for the 1-M, and 203.8 mAh/g for the 5 M ILEs. At this high voltage, Gen 2 shows the fastest fading rate and delivers only 79% capacity retention. In contrast, both ILEs outperform the Gen 2. It is worth noting that the 5 M cell has a comparable or slightly better performance in terms of initial capacity and cycling stability than the 1 M cell regardless of its extremely high viscosity. More surprisingly, the C-rate test in NMC/Li cells showed that the 5 M cell has a higher power capability than the 1 M cell regardless of the upper cutoff voltage, as shown in Figure II.3.E.4a and b.

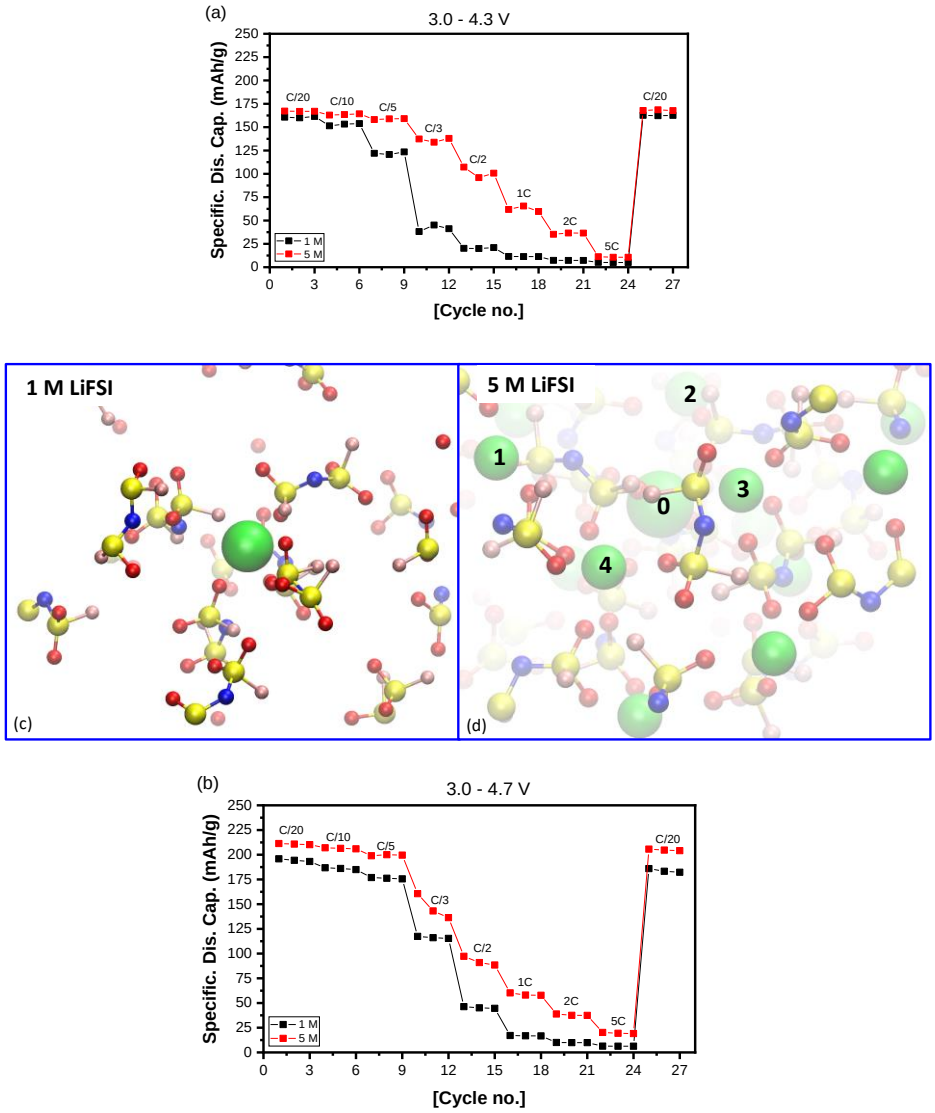

Figure II.3.E.4 C-rate capability of NMC532/Li cells with a 1 M and 5 M LiFSI PMpipFSI electrolyte cycled between (a) 4.3–3.0 V, and (b) 4.7–3.0 V; snapshots randomly selected from equilibrated MD trajectory for (c) the 1 M and (d) the 5 M LiFSI concentration, respectively. (The two concentrations exhibit sharply different coordination structure, where one Li^+ and four FSI^- constitute an isolated Li^+ solvation structure at the 1 M concentration; whereas at the 5 M concentration, a deadlocked Li^+-FSI^--Li^+-FSI^-... coordination network is established. For a center Li^+ [labeled with 0], each of its four coordinated FSI^- is also paired with another Li^+ [labeled by 1, 2, 3, 4]).

This somewhat counter-intuitive C-rate result, together with the curvature feature of log(σ)~1000/T plots and the high t_{Li^+}, all indicate that in a superconcentrated IL, Li^+ adopts a different transport mechanism. Generally, at low Li^+ salt concentrations, Li^+ adopts a "diffusive" transport mechanism, that is, the motions of Li^+ accompanied with fluctuations of local solvation (coordination) structure. As evident in Figure II.3.E.4c, for a 1 M concentration LiFSI electrolyte, each Li^+ statistically has only 0.8 neighboring Li^+ within a distance of two Li^+-FSI^- coordination shells (10 Å), and thus the transport of Li^+ completely results from structural changes of its coordination shell. In contrast, for a 5 M concentration, statistically speaking, each Li^+ has 4.0 neighboring Li^+ and 4.4 neighboring FSI^- within a distance 10 Å; alternatively, each FSI^- owns 2.4 of the closest Li^+. As illustrated by Figure II.3.E.4d, the seamlessly coupled Li^+-FSI^- pairs establish a "deadlocked" network of solvation shells. As a result, to a large degree, the motions of FSI^- are inhibited due to the dissymmetric conformation and large mass. Within the nearly static coordination shells, "hopping" between

neighboring solvation sites, namely, high potential energy-barrier crossing of Li^+ from one local minimum to another, turns out to be the only route for Li^+ transport. Figure II.3.E.4d also illustrates the four solvation sites (1, 2, 3, 4) that are nearest to a randomly selected center Li^+ (0). In such a highly concentrated Li^+ electrolyte, collective Li^+ hopping among neighboring coordination sites, such as 0⇔1, 3⇔0, 2⇔1, etc., dominates the ion transport and can achieve a high Li^+ transference number and C-rate capability.

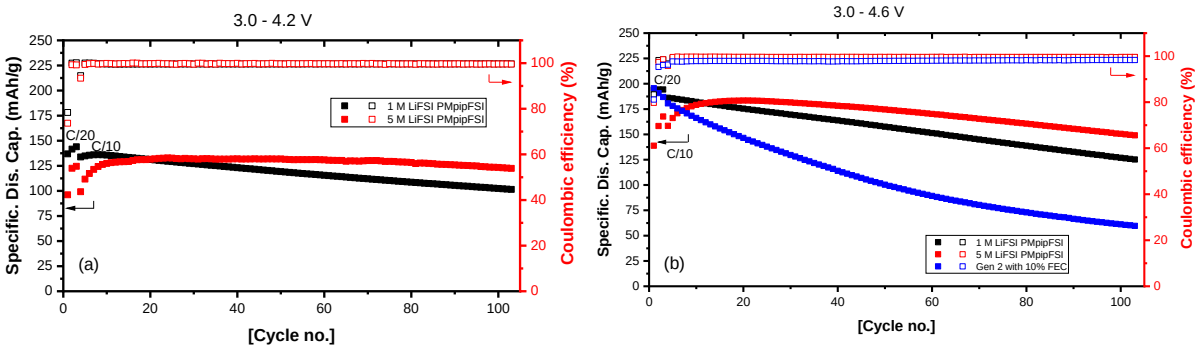

Figure II.3.E.5 Cycling performance of NMC532/Si-graphite cells using 1 M and 5 M LiFSI-PMpipFSI electrolytes with cutoff voltage (a) 4.2–3.0 V and (b) 4.6–3.0 V.

Encouraged by the NMC532/Li half-cell data, the cell performance in a high-voltage NMC532/Si-graphite full cell was assembled with Al-coated 2032-coin cells. Figure II.3.E.5a and Figure II.3.E.5b displays the specific discharge capacity and Coulombic efficiency using a 1 M and 5 M ILE with a cutoff voltage of 4.2–3.0 V and 4.6–3.0 V, respectively. Both ILE cells showed good cycling stability at normal cutoff voltage, indicating that these electrolytes are highly compatible with both Si and graphite as anode active materials due to robust SEI formation, as reported previously by Piper *et al.*[32] Surprisingly, the 5 M LiFSI-PMpipFSI shows the best performance among Gen 2+10wt% FEC and low concentration ILE cells at both cutoff voltages. At 4.6 V cut-off voltage, the capacity retention after 100 cycles for 5 M ILE, 1 M ILE and Gen 2+10wt% FEC cells is 82%, 65% and 32%, respectively. Moreover, the average Coulombic efficiency over 100 cycles (C/10) is 99.6% for 5 M ILE, which is higher than 99.5% for 1 M ILE and 98.0% for Gen 2+10wt% FEC.

SEM/EDS of cycled electrode and transition metal dissolution/deposition for super concentrated DES

It is generally accepted that the poor cycling performance of high-voltage lithium-ion cells (either NMC/graphite cells with charging voltage >4.4 V and $LiNi_{0.5}Mn_{1.5}O_4$/graphite cells at 5.0 V) originates with the electrolyte decomposition and the subsequent severe transition metal dissolution into the electrolyte. SEM images of the cycled anodes with ILE (Figure II.3.E.6a–b) showed a different morphology compared with that cycled in Gen 2 (Figure II.3.E.6c), with a more corroded surface for the latter (EDS shows negligible amounts of Mn, Ni, Co, and Al on the harvested anode surface cycled with a 5 M IL-based electrolyte compared with that of the Gen 2 electrolyte in Figure II.3.E.6e, which is consistent with the lowest average CE being observed for Gen 2 electrolyte). Furthermore, the ICP-MS data for the cycled anodes showed similar results as shown in Figure II.3.E.6f. These results are consistent with the TEM analysis of the cycled NMC532 cathodes, namely, the cycled cathodes with an IL-based electrolyte preserve the surface structure and bulk crystallinity even after high-voltage cycling, whereas those cycled in Gen 2 show severe surface reconstruction and structure transformation accompanied by TM dissolution. Because LiFSI was used in the IL-based electrolytes, we note the following: first, the HF-caused Mn^{2+} and Ni^{2+} dissolution evidenced in Gen 2 is primarily eliminated; second, the IL-electrolytes are oxidatively more stable than Gen 2 on the charged cathode surface, which inhibits the root of the generation of soluble TM ions; last, if TM ions are generated on the surface of the cathode, the highly ordered Li^+-FSI^- solvation structure in the 5 M ILE kinetically prevents the dissolution of any TM ions if present, owing to the same function for the inhibition of stainless steel and the Al current collector. Nevertheless, a low-concentration electrolyte has been proved to provide enough solvation force or space from free-state “solvents” to accelerate the dissolution of transition metal ions from the cathode, diffusion through the electrolyte, and deposition onto the anode surface, therefore significantly reducing the

lifetime of the battery.[34] As evidenced by the simulation data shown in Figure II.3.E.2 and Figure II.3.E.4, the tightly coupled Li^+-FSI^- pairing inhibits the motions of FSI^- by "doping" Li^+ to all possible coordination sites associated with FSI^-. The nearly full occupancy of Li^+ coordination sites also inhibits the space for transition metal ions to solvate and dissolve into the electrolyte. For example, without the interference of Li^+, an Mn^{2+} TM ion needs ~6.0 FSI^- to make a stable solvation shell (Figure II.3.E.6h), in contrast to the 4.4 FSI^- needed in a Li^+ solvation shell (Figure II.3.E.6g).

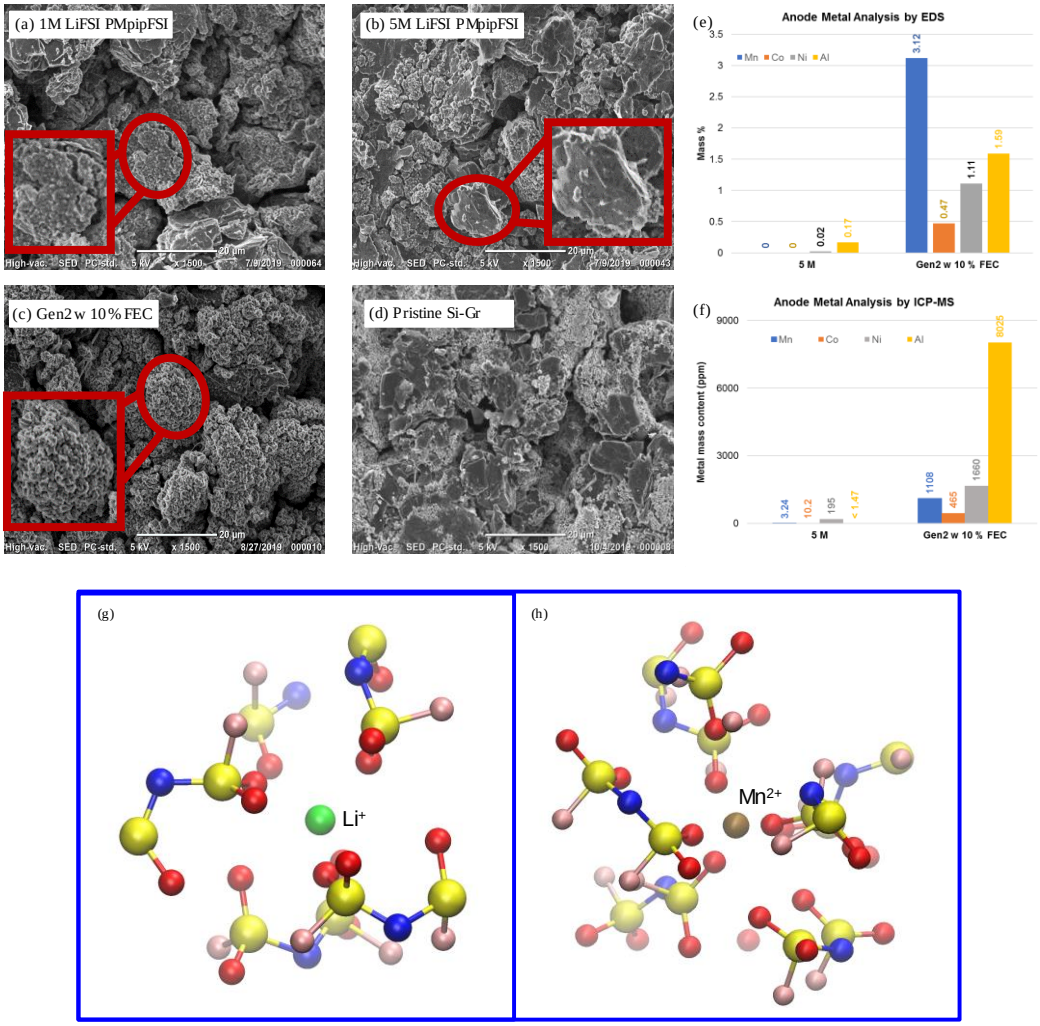

Figure II.3.E.6 (a–d) SEM images for the harvested Si-graphite anodes in the NMC532/Si-graphite cells cycled between 4.6–3.0 V using (a) a 1 M LiFSI-PMpipFSI, (b) a 5 M LiFSI PMpipFSI, (c) Gen 2, and (d) the pristine Si-graphite anode. The transition metal amount deposited on the cycled Si-graphite anodes in the NMC532/Si-graphite cells cycled between 4.6–3.0 V were determined by (e) EDS and (f) ICP-MS; the coordination shells for (g) Li^+ and (h) Mn^{2+} were randomly selected from the equilibrated MD trajectory.

One-step synthesis of Fluorinated FDES

Traditional method of ionic liquid synthesis includes two steps as shown in Figure II.3.E.7a.[64]-[66] (1) Quaternization of a tertiary amine with alkyl halide to form quaternary ammonium salt and (2) anion metathesis of the quaternary ammonium salt with Li salt that contains target anions to form the target ionic liquid. For the Li-ion battery applications, solvent purity is critical for good cycling performance. This method introduces potential halide contaminations through the quaternization step.[67]-[69] Additionally, the purification at the end of the second step requires extensively aqueous wash/extraction and the determination of complete removal of halide impurities is based on the disappearance of precipitation formation when mixed with $AgNO_3$ solution, an arbitrary operation for high purity IL preparation. Furthermore, the availability and

purity of the Li salt in the second metathesis step determine the accessibility and purity of the final ionic liquid. We synthesized the new IL with a fluorinated cation using a facile one-step synthesis as generalized in Figure II.3.E.7b.[70] This method affords extremely high purity IL-based electrolytes which is pivotal for the long-term stability of LIB. Both precursors are organic compounds which could be synthesized and purified individually beforehand easily. When mixed together, the reaction occurs and forms the target IL with high purity. In this paper, two fluorinated pyrrolidines designed and synthesized and were treated with methyl bis(fluorosulfonyl)imide (CH_3FSI) to form the target ionic liquid in one-step. As the usage of alkyl halide was eliminated, no halide impurity exists.

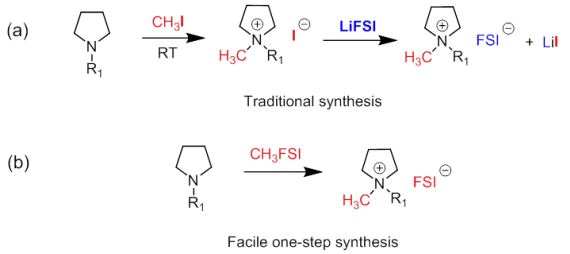

Figure II.3.E.7 (a) Representative synthesis of ionic liquids by traditional method and (b) facile one-step synthesis.

1-Methyl-1-propyl-3-fluoropyrrolidinium bis(fluorosulfonyl)imide ($PMpyr_f$-FSI) and 1-methyl-1-(2,2,3,3,3-pentafluoropropyl)pyrrolidinium bis(fluorosulfonyl)imide (P_fMpyr-FSI) were successfully synthesized using the one-step synthesis (Figure II.3.E.8). 1-Boc-3-hydroxypyrrolidine was first reacted with fluorinated reagent Xtalfluro-E [71], [72] to convert the hydroxyl group to fluoro group and the Boc protecting group was then removed by HCl. The resulting 3-fluoropyrrolidine hydrochloride reacts with 1-bromopropane to form the 1-propyl-3-fluoropyrrolidine, which was purified by distillation. 1-Propyl-3-fluoropyrrolidine was then treated with CH_3FSI to form $PMpyr_f$-FSI (Figure II.3.E.8) at room temperature with 100% conversion by NMR and 85% isolation yield. The -F group on the pyrrolidine ring backbone and methyl group on the pyrrolidine N atom can be on the same side or different side of the pyrrolidine ring. Correspondingly, two sets of pyrrolidine N-CH_3 group resonances and N-propyl group resonances are observed in ^1H NMR. The ^{19}F NMR (^1H decoupled) of $PMpyr_f$-FSI contains one resonance of FSI at δ 51.4ppm and two resonances of -F on the pyrrolidine ring backbone at δ -168.9 ppm and -172.4 ppm, respectively, indicating that PMpyrf-FSI is formed as a mixture of diastereomers.

1-(2,2,3,3,3-Pentafluoropropyl)pyrrolidine was synthesized by reacting pyrrolidine with 2,2,3,3,3-pentafluoropropyl trifluoromethanesulfonate, where three equivalent of pyrrolidine was used to serve as reactant, solvent and quenching reagent for the triflic acid to form pyrrolidinium triflate.[73] The resulting triflate salts were then removed by filtration and the excess pyrrolidine was removed by HCl wash. The fluorinated pyrrolidine was purified by distillation and then treated with CH_3FSI to yield P_fMpyr-FSI with 83% isolation yield (Figure II.3.E.8).

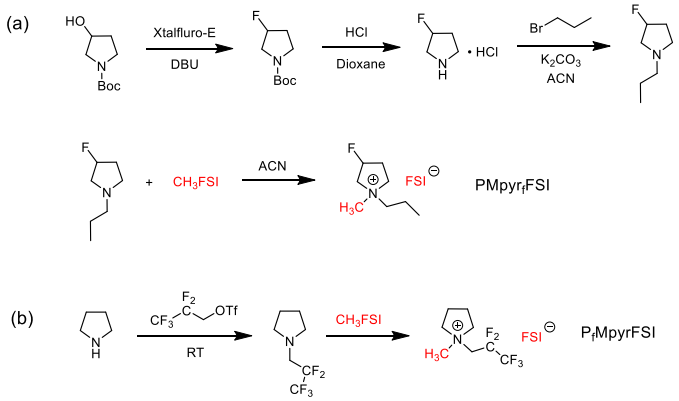

Figure II.3.E.8 (a) Synthesis of fluorine-substituted ionic liquid $PMpyr_f$-FSI and (b) P_fMpyr-FSI.

Electrochemical and physical properties of Fluorinated FDES

Electrochemical stability of the fluorinated ILs dissolved with 1 M LiFSI salt was measured by cyclic voltammetry. 1 M LiFSI $PMpyr_f$-FSI electrolyte shows a wide electrochemical window and high anodic stability up to 5.5 V vs Li^+/Li (Figure II.3.E.9a), which is slightly higher than the non-functionalized pristine IL electrolyte (about 5.4 V vs Li^+/Li). A reductive peak is observed around 3 V during the cathodic scan which is correlated to the oxidative decomposition product generated at potential > 5.5 V during the anodic scan. As the scan upper voltage was limited to 5 V, no such a reduction peak was observed. The oxidation peak around 0.5 V and reduction peak below 0 V are assigned to be Li stripping and plating peaks, respectively. Two more oxidation peaks that observed in the anodic scan around 0.7 V and 1.4 V are assigned to be the stripping peaks of the Li-Pt alloying. After introducing fluoride onto the cation structure, the viscosity shows dramatic difference. The single fluorine substitution on the cyclic ring leads to a lower viscosity of 83 mPa·s, where the fluorinated side alkyl chain substitution significantly increases the viscosity (261 mPa·s). As expected, the conductivity for $PMpyr_f$-FSI is higher than P_fMpyr-FSI. Furthermore, the conductivity of $PMpyr_f$-FSI and P_fMpyr-FSI decrease and viscosity increase with the increased LiFSI salt concentration, which is consistent with previous literature on the impact of salt concentration on the conductivity and viscosity of ionic liquids.[43], [74] Specifically, for $PMpyr_f$-FSI, with 1 M LiFSI, the conductivity deceases nearly half to 2.58 $mScm^{-1}$ and viscosity nearly doubles to 150 mPa.s at 25°C. When the LiFSI salt concentration increases to 4 M, the ionic conductivity further decreases to 0.55 $mScm^{-1}$ and viscosity increases to 528 mPa.s. Due to the intrinsic high viscosity of P_fMpyr-FSI, with 4 M LiFSI salt concentration, the viscosity increases to over 1000 mPa.s and conductivity drops to 0.36 $mScm^{-1}$.

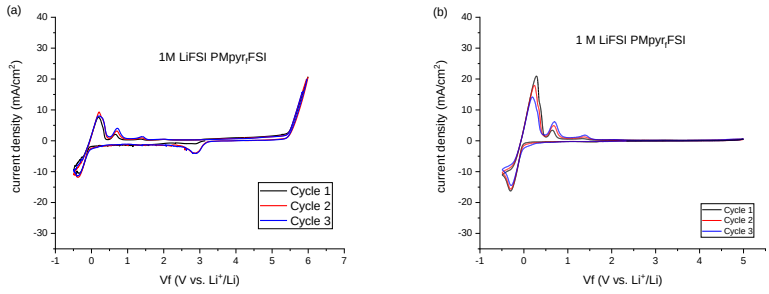

Figure II.3.E.9 Cyclic voltammetry profiles of 1 M LiFSI $PMpyr_f$-FSI. (a) Scan potential vs Li^+/Li from -0.5 to 6 V, and (b) from -0.5-5.0 V using a Pt/Li/Li three electrochemical cell (scan rate 10 mVs^{-1}).

Cycling performance of Fluorinated FDES in NMC532/Li cells and NMC532/Gr full cells

Figure II.3.E.10a shows the cycling performance of 1 M LiFSI $PMpyr_f$-FSI electrolyte and 4 M LiFSI $PMpyr_f$-FSI electrolyte in a NMC532/Li cell with a cutoff voltage of 4.3-3.0 V. To avoid the corrosion reaction of stainless-steel, aluminum-coated coin cells are used for all the electrochemical testing. The cells were formed with C/20 for 3 cycles followed by 100 cycles at C/10 rate. 145 $mAhg^{-1}$ initial specific discharge capacity and

147 mAhg^{-1} at cycle 100 were obtained for 1 M LiFSI PMpyr$_f$-FSI electrolyte cell. The reasons for the slightly increased capacity were two-fold: (1) PMpyr$_f$-FSI has high electrochemical stability resulting in nearly no capacity fading in the first 100 cycles, and (2) the intrinsic high viscosity of the ionic liquid causes a slow wetting process. As super-concentrated IL has shown improved cyclability and rate capability compared to dilute system in previous studies, we further test the ionic liquids with increased LiFSI salt concentration. For 4 M LiFSI PMpyr$_f$-FSI, the initial specific discharge capacity slightly increases to 148 mAhg^{-1}, and the slow wetting was observed for this electrolyte as the specific discharge capacity slowly increases during cycling and reaches to 159 mAhg^{-1} at cycle number of 100. The first cycle Coulombic efficiency for 1 M LiFSI PMpyr$_f$-FSI and 4 M LiFSI PMpyr$_f$-FSI are 82.2% and 83.7%, respectively. Encouraged by the excellent cycling performance with upper cutoff voltage of 4.3 V, we further evaluated this ionic liquid at high voltage condition using a 4.7 V upper cutoff voltage. As shown in Figure II.3.E.10b, initial specific discharge capacity is 206 mAhg^{-1} and first cycle Coulombic efficiency is 88.6% for 1 M LiFSI PMpyr$_f$-FSI and the capacity retention at cycle 100 is 87%. With increased the salt concertation, the initial specific discharge capacity is 207 mAhg^{-1} and first cycle Coulombic efficiency is 89.3% for 4 M LiFSI PMpyr$_f$-FSI. The capacity retention increases to 89% at cycle 100.

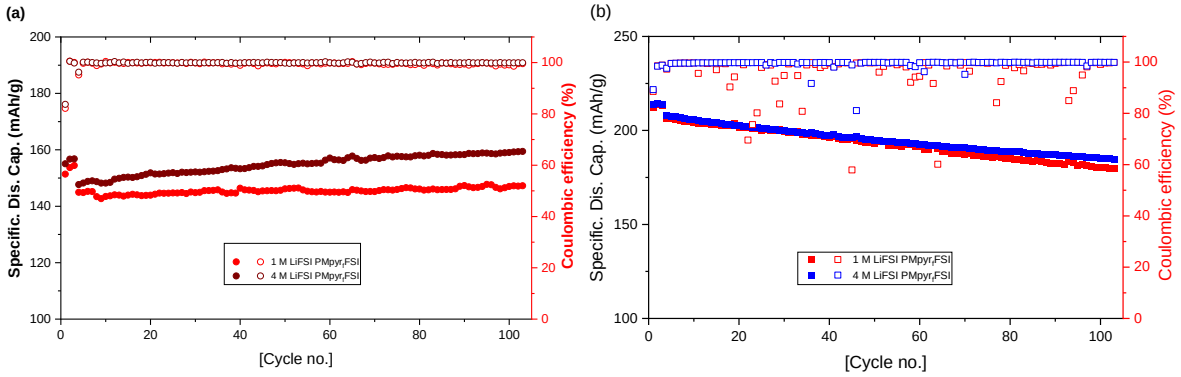

Figure II.3.E.10 (a) NMC532/Li cell cycling performance with a cutoff voltage 3.0-4.3 V and (b) 3.0-4.7 V.

PMpyr$_f$-FSI electrolyte was then evaluated in the NMC532/graphite full cells cycled between 3.0-4.2 V, with 3 formation cycles at C/20 and 100 cycles at C/10 rate. For 1 M LiFSI PMpyr$_f$-FSI, the first cycle specific discharge capacity is 96 mAhg^{-1} with Coulombic efficiency only 51.3%, while for 4 M LiFSI PMpyr$_f$-FSI, the first cycle specific discharge capacity is increased to 142.7 mAhg^{-1} and Coulombic efficiency increases to 78.4% as shown in Figure II.3.E.11. Furthermore, the capacity decreases rapidly for 1 M LiFSI PMpyr$_f$-FSI cycle by cycle, and the Coulombic efficiency, although slowly increases from the 1st cycle, is only below 99.5% during majority of cycles. These results suggest that the SEI formed on the graphite anode is more resistive in 1 M LiFSI PMpyr$_f$-FSI, therefore Li plating might occur during cycling causing low Coulombic efficiency. However with increased LiFSI salt concentration, regardless of its low ionic conductivity, a more conductive SEI forms,[34] which facilitates the Li^+ transport during cycling and up to 99.9% Coulombic efficiency is obtained.

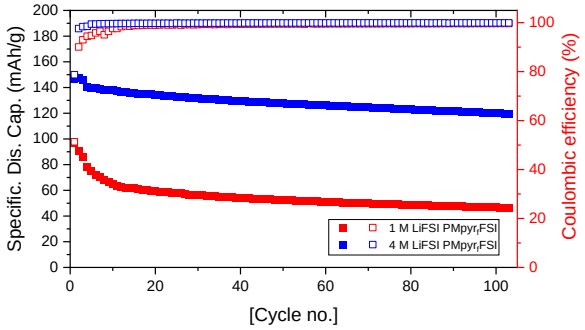

Figure II.3.E.11 Cycling performance of NMC532/graphite cells with 1 M and 4 M LiFSI PMpyr$_f$-FSI cycled between 3.0-4.2 V.

Conclusions

A systematic study of a piperidinum-FSI based FDES electrolyte was performed using a high-voltage NMC532 cathode and a high-capacity Si-graphite anode in a full cell format. The superior high-voltage cycling performance in 4.6 V NMC/Si-graphite cells originates from the stabilized electrode/electrolyte interphase. Electrode surface protection via the formation of cathode-electrolyte-interphase and solid-electrolyte-interphase was established. Furthermore, MD simulations reveal additional protection mechanism *i.e.* the dissolution of the transition metals is significantly suppressed due to the Li^+ and FSI^- solvation structure change in the ILE when LiFSI salt concentration increases. Future research should be focused on the improvement of the Li^+ conductivity to enhance its power capability. Two new fluorinated FDES (PMpyr$_f$-FSI and P$_f$Mpyr-FSI) were successfully synthesized by reacting fluorinated alkyl pyrrolidine with CH_3FSI in a facile one-step reaction. The new reaction completely eliminates the halide contamination existing in the traditional anion metathesis method. The synthesized PMpyr$_f$-FSI shows high oxidation stability (> 5.5 V vs Li+/Li) as revealed by the cyclic voltammetry and good high voltage cyclability up to 4.7 V in NMC532/graphite full cells. Further formulation with increased LiFSI salt concentration to 4 M has shown increased deliverable capacity and cycling stability in both NMC532/Li and NMC532/graphite cells. This simplified synthesis for functional ionic liquid opens up the opportunities for large scale, extremely high purity, and low cost IL-based electrolytes for safe electric vehicle application.

Key Publications

1. **Liu, Q.**; Hsu, C. W.; Dzwiniel, T. L.; Pupek, K. Z.; Zhang, Z. C. "A fluorine-substituted pyrrolidinium-based ionic liquid for high-voltage Li-ion battery" *Chem. Comm.* 2020, *56*, 7317-7320.

2. **Liu, Q.**; Jiang, W.; Piernas-Muñoz, M. J.; Liu, Y. Z.; Yang, Z. Z.; Bloom, I.; Dzwiniel, T. L.; Li, Y; Pupek, K. Z.; Zhang, Z. C. "Stabilized Electrode/Electrolyte Interphase by a Saturated Ionic Liquid Electrolyte for High-Voltage NMC532/Si-Graphite Cells" *ACS Appl. Mater. Interfaces.* 2020, *12*, 23035.

References

1. Tarascon, J. M.; Armand, M., Issues and challenges facing rechargeable lithium batteries. *Nature* **2001,** *414* (6861), 359-367.

2. Armand, M.; Tarascon, J. M., Building better batteries. *Nature* **2008,** *451* (7179), 652-657.

3. Goodenough, J. B.; Park, K.-S., The Li-Ion Rechargeable Battery: A Perspective. *J. Am. Chem. Soc.* **2013,** *135* (4), 1167-1176.

4. Nitta, N.; Wu, F.; Lee, J. T.; Yushin, G., Li-ion battery materials: present and future. *Mater. Today* **2015,** *18* (5), 252-264.

5. Myung, S.-T.; Maglia, F.; Park, K.-J.; Yoon, C. S.; Lamp, P.; Kim, S.-J.; Sun, Y.-K., Nickel-Rich Layered Cathode Materials for Automotive Lithium-Ion Batteries: Achievements and Perspectives. *ACS Energy Lett.* **2017,** *2* (1), 196-223.

6. Sun, Y.-K.; Myung, S.-T.; Park, B.-C.; Prakash, J.; Belharouak, I.; Amine, K., High-energy cathode material for long-life and safe lithium batteries. *Nat. Mater* **2009,** *8* (4), 320-324.

7. Hwang, S.; Kim, S. M.; Bak, S.-M.; Kim, S. Y.; Cho, B.-W.; Chung, K. Y.; Lee, J. Y.; Stach, E. A.; Chang, W., Using Real-Time Electron Microscopy To Explore the Effects of Transition-Metal Composition on the Local Thermal Stability in Charged LixNiyMnzCo1–y–zO2 Cathode Materials. *Chem. Mater.* **2015,** *27* (11), 3927-3935.

8. Xu, K., Nonaqueous Liquid Electrolytes for Lithium-Based Rechargeable Batteries. *Chem. Rev.* **2004,** *104* (10), 4303-4418.

9. Chen, S.; Wen, K.; Fan, J.; Bando, Y.; Golberg, D., Progress and future prospects of high-voltage and high-safety electrolytes in advanced lithium batteries: from liquid to solid electrolytes. *J. Mater. Chem. A* **2018,** *6* (25), 11631-11663.

10. Yang, L.; Ravdel, B.; Lucht, B. L., Electrolyte Reactions with the Surface of High Voltage LiNi0.5Mn1.5O4 Cathodes for Lithium-Ion Batteries. *Electrochem. Solid-State Lett.* **2010,** *13* (8), A95-A97.

11. Kennedy, T.; Brandon, M.; Laffir, F.; Ryan, K. M., Understanding the influence of electrolyte additives on the electrochemical performance and morphology evolution of silicon nanowire based lithium-ion battery anodes. *J. Power Sources* **2017,** *359*, 601-610.

12. Nguyen, C. C.; Lucht, B. L., Comparative Study of Fluoroethylene Carbonate and Vinylene Carbonate for Silicon Anodes in Lithium Ion Batteries. *J. Electrochem. Soc.* **2014,** *161* (12), A1933-A1938.

13. Jin, Y.; Kneusels, N.-J. H.; Magusin, P. C. M. M.; Kim, G.; Castillo-Martínez, E.; Marbella, L. E.; Kerber, R. N.; Howe, D. J.; Paul, S.; Liu, T.; Grey, C. P., Identifying the Structural Basis for the Increased Stability of the Solid Electrolyte Interphase Formed on Silicon with the Additive Fluoroethylene Carbonate. *J. Am. Chem. Soc.* **2017,** *139* (42), 14992-15004.

14. Leung, K., First-Principles Modeling of Mn (II) Migration above and Dissolution from LixMn2O4 (001) Surfaces. *Chem. Mater.* **2017,** *29*, 2550.

15. Aurbach, D.; Markovsky, B.; Salitra, G.; Markevich, E.; Talyossef, Y.; Koltypin, M.; Nazar, L.; Ellis, B.; Kovacheva, D., Review on Electrode–Electrolyte Solution Interactions, Related to Cathode Materials for Li-ion Batteries. *J. Power Sources* **2007,** *165*, 491.

16. Zheng, H.; Sun, Q.; Liu, G.; Song, X.; Vincent, V. S., Correlation between Dissolution Behavior and Electrochemical Cycling Performance for LiNi1/3Co1/3Mn1/3O2-based Cells. *J. Power Sources* **2012,** *207*, 134.

17. Gilbert, J. A.; Shkrob, I. A.; Abraham, D. P., Transition Metal Dissolution, Ion Migration, Electrocatalytic Reduction and Capacity Loss in Lithium-ion Full Cells. *J. Electrochem. Soc.* **2017,** *164*, A389.

18. Zhan, C.; Wu, T.; Lu, J.; Amine, K., Dissolution, Migration, and Deposition of Transition Metal Ions in Li-ion Batteries Exemplified by Mn-based Cathodes–a Critical Review. *Energy Environ. Sci.* **2018,** *11*, 243.

19. Zhan, C.; Lu, J.; Kropf, A. J.; Wu, T.; Jansen, A. N.; Sun, Y. K.; Qiu, X.; Amine, K., Mn(II) Deposition on Anodes and its Effects on Capacity Fade in Spinel Lithium Manganate–Carbon Systems. *Nat. Commun.* **2013,** *4*, 2437.

20. Shkrob, I. A.; Kropf, A. J.; Marin, T. W.; Li, Y.; Poluektov, O. G.; Niklas, J.; Abraham, D. P., Manganese in Graphite Anode and Capacity Fade in Li Ion Batteries. *J. Phys. Chem. C* **2014,** *118*, 24335.

21. Banerjee, A.; Shilina, Y.; Ziv, B.; Ziegelbauer, J. M.; Luski, S.; Aurbach, D.; Halalay, I. C., On the Oxidation State of Manganese Ions in Li-ion Battery Electrolyte Solutions. *J. Am. Chem. Soc.* **2017,** *139*, 1738.

22. Lewandowski, A.; Świderska-Mocek, A., Ionic liquids as electrolytes for Li-ion batteries—An overview of electrochemical studies. *J. Power Sources* **2009,** *194* (2), 601-609.

23. Balducci, A.; Jeong, S. S.; Kim, G. T.; Passerini, S.; Winter, M.; Schmuck, M.; Appetecchi, G. B.; Marcilla, R.; Mecerreyes, D.; Barsukov, V.; Khomenko, V.; Cantero, I.; De Meatza, I.; Holzapfel, M.; Tran, N., Development of safe, green and high performance ionic liquids-based batteries (ILLIBATT project). *J. Power Sources* **2011,** *196* (22), 9719-9730.

24. Eftekhari, A.; Liu, Y.; Chen, P., Different roles of ionic liquids in lithium batteries. *J. Power Sources* **2016,** *334*, 221-239.

25. Matsumoto, H.; Sakaebe, H.; Tatsumi, K.; Kikuta, M.; Ishiko, E.; Kono, M., Fast cycling of Li/LiCoO2 cell with low-viscosity ionic liquids based on bis(fluorosulfonyl)imide [FSI]−. *J. Power Sources* **2006,** *160* (2), 1308-1313.

26. Guerfi, A.; Duchesne, S.; Kobayashi, Y.; Vijh, A.; Zaghib, K., LiFePO4 and graphite electrodes with ionic liquids based on bis(fluorosulfonyl)imide (FSI)− for Li-ion batteries. *J. Power Sources* **2008,** *175* (2), 866-873.

27. Fernicola, A.; Croce, F.; Scrosati, B.; Watanabe, T.; Ohno, H., LiTFSI-BEPyTFSI as an improved ionic liquid electrolyte for rechargeable lithium batteries. *J. Power Sources* **2007,** *174* (1), 342-348.

28. Lee, K.-H.; Song, S.-W., One-Step Hydrothermal Synthesis of Mesoporous Anatase TiO2 Microsphere and Interfacial Control for Enhanced Lithium Storage Performance. *ACS Appl. Mater. Interfaces* **2011,** *3* (9), 3697-3703.

29. Markevich, E.; Sharabi, R.; Borgel, V.; Gottlieb, H.; Salitra, G.; Aurbach, D.; Semrau, G.; Schmidt, M. A., In situ FTIR study of the decomposition of N-butyl-N-methylpyrrolidinium bis(trifluoromethanesulfonyl)amide ionic liquid during cathodic polarization of lithium and graphite electrodes. *Electrochim. Acta* **2010,** *55* (8), 2687-2696.

30. Hassoun, J.; Fernicola, A.; Navarra, M. A.; Panero, S.; Scrosati, B., An advanced lithium-ion battery based on a nanostructured Sn–C anode and an electrochemically stable LiTFSi-Py24TFSI ionic liquid electrolyte. *J. Power Sources* **2010,** *195* (2), 574-579.

31. Song, J.-W.; Nguyen, C. C.; Song, S.-W., Stabilized cycling performance of silicon oxide anode in ionic liquid electrolyte for rechargeable lithium batteries. *RSC Adv.* **2012,** *2* (5), 2003-2009.

32. Piper, D. M.; Evans, T.; Leung, K.; Watkins, T.; Olson, J.; Kim, S. C.; Han, S. S.; Bhat, V.; Oh, K. H.; Buttry, D. A.; Lee, S.-H., Stable silicon-ionic liquid interface for next-generation lithium-ion batteries. *Nat. Commun* **2015,** *6* (1), 6230.

33. Baranchugov, V.; Markevich, E.; Pollak, E.; Salitra, G.; Aurbach, D., Amorphous silicon thin films as a high capacity anodes for Li-ion batteries in ionic liquid electrolytes. *Electrochem. Commun.* **2007,** *9* (4), 796-800.

34. Yamada, Y.; Wang, J.; Ko, S.; Watanabe, E.; Yamada, A., Advances and issues in developing salt-concentrated battery electrolytes. *Nat. Energy* **2019,** *4* (4), 269-280.

35. Yamada, Y.; Yamada, A., Review—Superconcentrated Electrolytes for Lithium Batteries. *J. Electrochem. Soc.* **2015,** *162* (14), A2406-A2423.

36. Yoshida, K.; Nakamura, M.; Kazue, Y.; Tachikawa, N.; Tsuzuki, S.; Seki, S.; Dokko, K.; Watanabe, M., Oxidative-Stability Enhancement and Charge Transport Mechanism in Glyme–Lithium Salt Equimolar Complexes. *J. Am. Chem. Soc.* **2011,** *133* (33), 13121-13129.

37. Suo, L.; Borodin, O.; Gao, T.; Olguin, M.; Ho, J.; Fan, X.; Luo, C.; Wang, C.; Xu, K., "Water-in-salt" electrolyte enables high-voltage aqueous lithium-ion chemistries. *Science* **2015,** *350* (6263), 938.

38. He, M.; Lau, K. C.; Ren, X.; Xiao, N.; McCulloch, W. D.; Curtiss, L. A.; Wu, Y., Concentrated Electrolyte for the Sodium–Oxygen Battery: Solvation Structure and Improved Cycle Life. *Angew. Chem. Int. Ed.* **2016,** *55* (49), 15310-15314.

39. Wang, J.; Yamada, Y.; Sodeyama, K.; Chiang, C. H.; Tateyama, Y.; Yamada, A., Superconcentrated electrolytes for a high-voltage lithium-ion battery. *Nat. Commun* **2016,** *7* (1), 12032.

40. Takada, K.; Yamada, Y.; Watanabe, E.; Wang, J.; Sodeyama, K.; Tateyama, Y.; Hirata, K.; Kawase, T.; Yamada, A., Unusual Passivation Ability of Superconcentrated Electrolytes toward Hard Carbon Negative Electrodes in Sodium-Ion Batteries. *ACS Appl. Mater. Interfaces* **2017,** *9* (39), 33802-33809.

41. Zheng, J.; Lochala, J. A.; Kwok, A.; Deng, Z. D.; Xiao, J., Research Progress towards Understanding the Unique Interfaces between Concentrated Electrolytes and Electrodes for Energy Storage Applications. *Adv. Sci* **2017,** *4* (8), 1700032.

42. Ashley Heist, S.-H. L., Improved Stability and Rate Capability of Ionic Liquid Electrolyte with High Concentration of LiFSI. *J. Electrochem. Soc.* **2019,** *166* (10), A1860-A1866.

43. Yoon, H.; Howlett, P. C.; Best, A. S.; Forsyth, M.; MacFarlane, D. R., Fast Charge/Discharge of Li Metal Batteries Using an Ionic Liquid Electrolyte. *J. Electrochem. Soc.* **2013,** *160* (10), A1629-A1637.

44. Forsyth, M.; Girard, G. M. A.; Basile, A.; Hilder, M.; MacFarlane, D. R.; Chen, F.; Howlett, P. C., Inorganic-Organic Ionic Liquid Electrolytes Enabling High Energy-Density Metal Electrodes for Energy Storage. *Electrochim. Acta* **2016,** *220*, 609-617.

45. Abraham, D. P.; Poppen, S. D.; Jansen, A. N.; Liu, J.; Dees, D. W., Application of a lithium–tin reference electrode to determine electrode contributions to impedance rise in high-power lithium-ion cells. *Electrochim. Acta* **2004,** *49* (26), 4763-4775.

46. Matsumoto, H.; Sakaebe, H.; Tatsumi, K., Preparation of room temperature ionic liquids based on aliphatic onium cations and asymmetric amide anions and their electrochemical properties as a lithium battery electrolyte. *J. Power Sources* **2005,** *146* (1), 45-50.

47. Sun, X.-G.; Dai, S., Electrochemical investigations of ionic liquids with vinylene carbonate for applications in rechargeable lithium ion batteries. *Electrochim. Acta* **2010,** *55* (15), 4618-4626.

48. Kanamura, K.; Okagawa, T.; Takehara, Z.-i., Electrochemical oxidation of propylene carbonate (containing various salts) on aluminium electrodes. *J. Power Sources* **1995,** *57* (1), 119-123.

49. Krause, L. J.; Lamanna, W.; Summerfield, J.; Engle, M.; Korba, G.; Loch, R.; Atanasoski, R., Corrosion of aluminum at high voltages in non-aqueous electrolytes containing perfluoroalkylsulfonyl imides; new lithium salts for lithium-ion cells. *J. Power Sources* **1997,** *68* (2), 320-325.

50. Wang, X.; Yasukawa, E.; Mori, S., Inhibition of anodic corrosion of aluminum cathode current collector on recharging in lithium imide electrolytes. *Electrochim. Acta* **2000,** *45* (17), 2677-2684.

51. Kanamura, K.; Umegaki, T.; Shiraishi, S.; Ohashi, M.; Takehara, Z.-i., Electrochemical Behavior of Al Current Collector of Rechargeable Lithium Batteries in Propylene Carbonate with LiCF3 SO 3 , Li (CF 3 SO 2) 2 N , or Li (C 4 F 9 SO 2) (CF 3 SO 2) N *J. Electrochem. Soc.* **2002,** *149* (2), A185-A194.

52. Zhang, X.; Devine, T. M., Factors That Influence Formation of AlF3 Passive Film on Aluminum in Li-Ion Battery Electrolytes with LiPF6. *J. Electrochem. Soc.* **2006,** *153* (9), B375-B383.

53. Myung, S.-T.; Sasaki, Y.; Sakurada, S.; Sun, Y.-K.; Yashiro, H., Electrochemical behavior of current collectors for lithium batteries in non-aqueous alkyl carbonate solution and surface analysis by ToF-SIMS. *Electrochim. Acta* **2009,** *55* (1), 288-297.

54. Cha, E.; Mun, J.; rang Cho, E.; Yim, T.; Kim, Y.; M. Oh, S.; A Lim, S.; Wook Lim, J., The Corrosion Study of Al Current Collector in Phosphonium Ionic Liquid as Solvent for Lithium Ion Battery. *J. Korean electrochem. soc.* **2011,** *14*, 152-156.

55. Dominik Moosbauer, S. Z., Marius Amereller, and Heiner J. Gores, Effect of Ionic Liquids as Additives on Lithium Electrolytes: Conductivity, Electrochemical Stability, and Aluminum Corrosion. *J. Chem. Eng. Data* **2010,** *55*, 1794–1798.

56. Cho, E.; Mun, J.; Chae, O. B.; Kwon, O. M.; Kim, H.-T.; Ryu, J. H.; Kim, Y. G.; Oh, S. M., Corrosion/passivation of aluminum current collector in bis(fluorosulfonyl)imide-based ionic liquid for lithium-ion batteries. *Electrochem. Commun.* **2012,** *22*, 1-3.

57. Evans, T.; Olson, J.; Bhat, V.; Lee, S.-H., Effect of organic solvent addition to PYR13FSI + LiFSI electrolytes on aluminum oxidation and rate performance of Li(Ni1/3Mn1/3Co1/3)O2 cathodes. *J. Power Sources* **2014,** *265*, 132-139.

58. Allen, J. L.; McOwen, D. W.; Delp, S. A.; Fox, E. T.; Dickmann, J. S.; Han, S.-D.; Zhou, Z.-B.; Jow, T. R.; Henderson, W. A., N-Alkyl-N-methylpyrrolidinium difluoro(oxalato)borate ionic liquids: Physical/electrochemical properties and Al corrosion. *J. Power Sources* **2013,** *237*, 104-111.

59. Goldman, J. L.; McEwen, A. B., EMIIm and EMIBeti on Aluminum Anodic Stability Dependence on Lithium Salt and Propylene Carbonate. *Electrochem. Solid-State Lett.* **1999,** *2* (10), 501-503.

60. Garcia, B.; Armand, M., Aluminium corrosion in room temperature molten salt. *J. Power Sources* **2004,** *132* (1-2), 206-208.

61. Han, H.-B.; Zhou, S.-S.; Zhang, D.-J.; Feng, S.-W.; Li, L.-F.; Liu, K.; Feng, W.-F.; Nie, J.; Li, H.; Huang, X.-J.; Armand, M.; Zhou, Z.-B., Lithium bis(fluorosulfonyl)imide (LiFSI) as conducting

salt for nonaqueous liquid electrolytes for lithium-ion batteries: Physicochemical and electrochemical properties. *J. Power Sources* **2011,** *196* (7), 3623-3632.

62. Yamada, Y.; Chiang, C. H.; Sodeyama, K.; Wang, J.; Tateyama, Y.; Yamada, A., Corrosion Prevention Mechanism of Aluminum Metal in Superconcentrated Electrolytes. *ChemElectroChem* **2015,** *2* (11), 1687-1694.

63. Liu, Q.; Dzwiniel, T. L.; Pupek, K. Z.; Zhang, Z., Corrosion/Passivation Behavior of Concentrated Ionic Liquid Electrolytes and Its Impact on the Li-Ion Battery Performance. *J. Electrochem. Soc.* **2019,** *166* (16), A3959-A3964.

64. Gwan-Hong Min, T. Y., Hyun Yeong Lee, Dal Ho Huh, Eunjoo Lee, Junyoung Mun, Seung M. Oh, and Young Gyu Kim, Synthesis and Properties of Ionic Liquids: Imidazolium Tetrafluoroborates with Unsaturated Side Chains. *Bull. Korean Chem. Soc.* **2006,** *27* (6), 847-852.

65. Celso, F. L.; Appetecchi, G. B.; Simonetti, E.; Keiderling, U.; Gontrani, L.; Triolo, A.; Russina, O., Mesoscopic structural organization in fluorinated pyrrolidinium-based room temperature ionic liquids. *J. Mol. Liq.* **2019,** *289*, 111110.

66. Gurung, E.; Meng, D.; Xue, L.; Tamas, G.; Lynden-Bell, R. M.; Quitevis, E. L., Optical Kerr effect spectroscopy of CS2 in monocationic and dicationic ionic liquids: insights into the intermolecular interactions in ionic liquids. *Physical Chemistry Chemical Physics* **2018,** *20* (41), 26558-26569.

67. Vander Hoogerstraete, T.; Jamar, S.; Wellens, S.; Binnemans, K., Determination of Halide Impurities in Ionic Liquids by Total Reflection X-ray Fluorescence Spectrometry. *Anal. Chem.* **2014,** *86* (8), 3931-3938.

68. Seddon Kenneth, R.; Stark, A.; Torres, M.-J., Influence of chloride, water, and organic solvents on the physical properties of ionic liquids. In *Pure Appl. Chem.*, 2000; Vol. 72, p 2275.

69. Villagrán, C.; Deetlefs, M.; Pitner, W. R.; Hardacre, C., Quantification of Halide in Ionic Liquids Using Ion Chromatography. *Anal. Chem.* **2004,** *76* (7), 2118-2123.

70. Jourdain, A.; Antoniuk, I.; Serghei, A.; Espuche, E.; Drockenmuller, E., 1,2,3-Triazolium-based linear ionic polyurethanes. *Polym. Chem* **2017,** *8* (34), 5148-5156.

71. Beaulieu, F.; Beauregard, L.-P.; Courchesne, G.; Couturier, M.; LaFlamme, F.; L'Heureux, A., Aminodifluorosulfinium Tetrafluoroborate Salts as Stable and Crystalline Deoxofluorinating Reagents. *Org. Lett.* **2009,** *11* (21), 5050-5053.

72. L'Heureux, A.; Beaulieu, F.; Bennett, C.; Bill, D. R.; Clayton, S.; LaFlamme, F.; Mirmehrabi, M.; Tadayon, S.; Tovell, D.; Couturier, M., Aminodifluorosulfinium Salts: Selective Fluorination Reagents with Enhanced Thermal Stability and Ease of Handling. *J. Org. Chem* **2010,** *75* (10), 3401-3411.

73. Mantani, T.; Shiomi, K.; Konno, T.; Ishihara, T.; Yamanaka, H., A Convenient Preparation of 3,3,3-Trifluoro-1-propynylamines and Their Lewis Acid Catalyzed Reaction with Carbonyl Compounds Leading to (Z)-α-(Trifluoromethyl)-α,β-unsaturated Amides1. *J. Org. Chem* **2001,** *66* (10), 3442-3448.

74. Yoon, H.; Best, A. S.; Forsyth, M.; MacFarlane, D. R.; Howlett, P. C., Physical properties of high Li-ion content N-propyl-N-methylpyrrolidinium bis(fluorosulfonyl)imide based ionic liquid electrolytes. *Phys. Chem. Chem. Phys* **2015,** *17* (6), 4656-63.

Acknowledgements

Support from Peter Faguy and David Howell at Vehicle Technologies Office (VTO), Office of Energy Efficiency and Renewable Energy, U.S. Department of Energy is gratefully acknowledged. Argonne, a U.S. Department of Energy laboratory, is operated by UChicago Argonne, LLC under contract DE-AC02-06CH11357.

II.3.F Developing In situ Microscopies for the Model Cathode-Electrolyte Interface (NREL)

Robert Tenent, Principal Investigator
National Renewable Energy Laboratory
16253 Denver West Parkway
Golden, CO 80401
E-mail: robert.tenent@nrel.gov

Peter Faguy, DOE Technology Development Manager
U.S. Department of Energy
E-mail: Peter.Faguy@ee.doe.gov

Start Date: October 1, 2019 End Date: September 30, 2020
Project Funding: $825,000 DOE share: $825,000 Non-DOE share: $0

Project Introduction

The work presented here focuses on the development of new diagnostic techniques based on the scanning electrochemical microscope (SECM) to examine cell degradation processes occurring at the cathode/electrolyte interface. While lithium-ion batteries have developed significant market traction, key issues remain to be resolved for more broad adoption including developing a better understanding of degradation processes that limit cell life. Many commonly used cathode materials are known to degrade through various processes (transition metal dissolution and oxygen evolution, as examples). Products of this degradation are also known to diffuse through the cell and deposit at the anode SEI leading to performance loss. While these processes are known to occur, many open questions remain regarding the exact mechanisms by which they take place. As an example, while dissolution of manganese from cathode materials has been extensively studied, debate still remains even regarding the oxidation state of Mn generated in the dissolution process.[1] This effort focuses on using the SECM format paired with complementary analytical techniques to detect and characterize cathode degradation products at and near to an active cathode/electrolyte interface.

Objectives

This project seeks to employ SECM paired with complementary analytical techniques to study degradation processes occurring at the cathode/electrolyte interface. Specifically, we study Mn dissolution occurring from a model LiMn2O4 (LMO) cathode. We examine the impact of varied parameters on the dissolution process as well as the properties of the resulting dissolution products. This will help develop understanding not only of how these degradation processes occur, but how degradation products may react elsewhere in the cell driving overall performance degradation.

Approach

As mentioned previously, this effort uses the SECM as an in-situ tool for the electrochemical characterization of cathode degradation products in an active cell. The SECM is a scanning probe microscope which uses a small electrode to conduct electrochemical experiments near an active electrode/electrolyte interface. Figure II.3.F.1 shows a schematic of a typical SECM instrument which includes two working electrodes consisting of the small “tip” electrode as well as the underlying substrate sample. In the case of this work, the substrate would be a model cathode material under study. All electrodes are contained in an active electrochemical cell containing an electrolyte of interest. The tip and substrate electrode voltages are controlled by a bi-potentiostat using the same reference and counter electrodes. This configuration allows independent control of electrode voltages for both the substrate sample and the “sensing” tip electrode. This allows the tip to be used to conduct a variety of electrochemical experiments either in bulk electrolyte or near the substrate which can be held at a variety

of voltages. A three-axis positioning system is used to place the tip electrode at various locations in the cell and across the substrate surface for measurements as required.

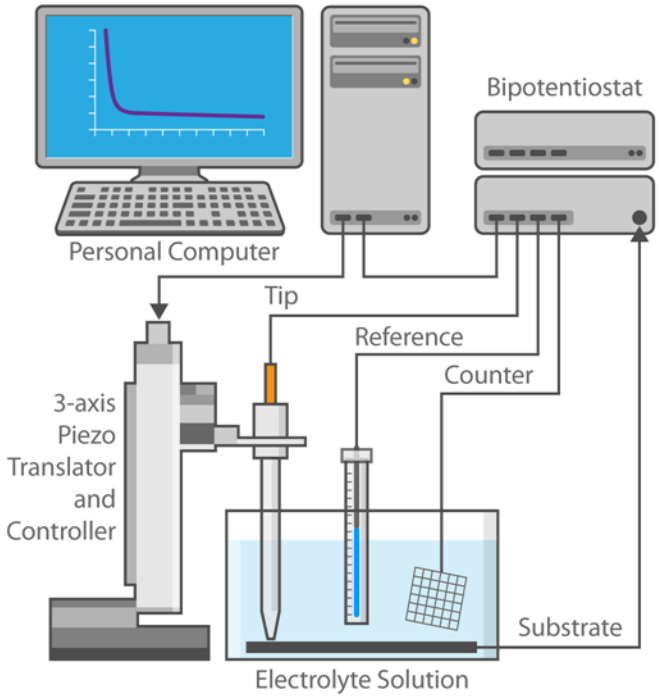

Figure II.3.F.1 Schematic of a typical scanning electrochemical microscopy / Al Hicks, NREL

The SECM can be employed in a variety of so-called "modes" which can be categorized broadly as imaging modes (as implied by the name of the technique) or as measurement modes. The work here focuses on applying SECM measurement modes to better understand cathode degradation products and their reactivity. In our particular case, we work with the "generation/collection" (GC) mode of SECM in which a species generated at the substrate is detected or "collected" at the tip electrode. This approach is conceptually similar to the rotating ring disk electrode (RRDE) method commonly used in electrochemical characterization in which a species is generated at a disk electrode and then hydrodynamically driven to a surrounding ring electrode for detection and characterization. The key differentiator between the GC-SECM and RRDE methods is increased flexibility in the experimental conditions that can be used for detection at the tip electrode. In the case of this work, we employ cyclic voltammetry measurements made at the tip to characterize the electrochemical properties of cathode degradation products occurring both near the active cathode/electrolyte interface as well as in bulk electrolyte.

In addition to SECM, we have also employed companion analysis using Inductively Coupled Plasma (ICP) and Electron Paramagnetic Resonance (EPR) spectroscopies to study the concentration and oxidation state of transition metal dissolution products, respectively. We use this combination of techniques to focus on developing a better understanding of the chemistry and electrochemistry associated with Mn dissolution from a model LMO cathode material. This allows us to study cathode degradation without the complication of conductive additives or binder systems that will explored further in a later stage of the project. Details of model cathode material synthesis was detailed in earlier reports on this work.

Results

In fiscal year 2020, our work has focused on using the combined SECM/ICP/EPR methods to characterize Mn dissolution from LMO as a function of electrolytes containing different anions. LMO

dissolution was studied in 1M solutions of $LiClO_4$, $LiPF_6$ and LiTFSI in propylene carbonate (PC). PC was chosen as our solvent due to lower volatility when compared to more commonly used EC/EMC (Gen2) carbonate blends. This allowed us to conduct longer term experiments needed to study the cathode degradation process over time. This also helped to isolate the impact of lithium salt anion in the electrolyte. Further studies on additional carbonate materials are on-going and will be reported at a later date. As an initial demonstration of our analysis protocols, Figure II.3.F.2 (a) shows GC-SECM tip voltammetry as well as ICP and EPR data for the $LiClO_4$:PC system before and after a 4.5V hold at our LMO model cathode substrate. Figure II.3.F.2 (a) shows cyclic voltammetry (CV) collected at the 25 mm tip electrode prior to and immediately after holding the substrate electrode at 4.5V for 5 hours. The scan rate for all voltammograms shown in this work is 1V/s. The initial scans shown in black were collected to establish a baseline response and identify any electrochemically active species that may be present in the fresh electrolyte. An identical CV was collected at the tip immediately after the 4.5V hold. Data from before and after the high voltage hold at the substrate were compared to identify electrochemically active products of the substrate degradation. Two companion experiments were performed, one with our LMO materials deposited on a stainless-steel substrate and a second control using only the stainless-steel substrate that was processed identically to the LMO model cathode materials. The two voltammograms shown in the top portion of Figure II.3.F.2 (a) are collected before and after the high voltage hold of the stainless-steel control sample. Note that no significant change in the voltammetric response is observed. This confirms that no electrochemically active degradation products are generated strictly from the stainless-steel substrate. The voltammograms shown on the bottom of Figure II.3.F.2 (a) are collected for our model LMO cathode material on an identical stainless-steel substrate. In this case, multiple obvious electrochemical signatures are observed following the high voltage hold of the LMO substrate. Specifically, oxidation processes are observed at 3.4V as well as an apparent increase in current above 4.5V. Multiple reduction processes are observed including at ~3.9V, ~3.2V and ~2.7V. As these signatures are only seen with the LMO substrate, we attribute these to Mn complexes formed upon dissolution from the LMO substrate. The presence of Mn in our electrolytes is also confirmed in Figure II.3.F.2 (b) and (c) which show ICP and EPR data, respectively, collected for both fresh electrolyte as well as the cell electrolyte following the high voltage hold. ICP clearly shows an increase in Mn concentration following the high voltage hold. EPR can be used not only to detect the presence of Mn, but can also detect the oxidation state of Mn present. The structure shown in Figure II.3.F.2 (c) is consistent with the presence of Mn^{2+} in solution following Mn dissolution at high voltage. It is important to note that while EPR is capable of detecting Mn^{2+}, Mn^{3+} is not detectable by EPR. Therefore, the possible presence of Mn^{3+} cannot be ruled out although Mn^{2+} is clearly present. Based on the ICP confirmation of the presence of Mn as well as the EPR confirmation of the presence of Mn^{2+} we tentatively assign the oxidation observed at ~ 3.4V to the oxidation of Mn^{2+} to Mn^{3+} with the less defined process above 4.5V to the oxidation of Mn^{2+} to Mn^{4+}

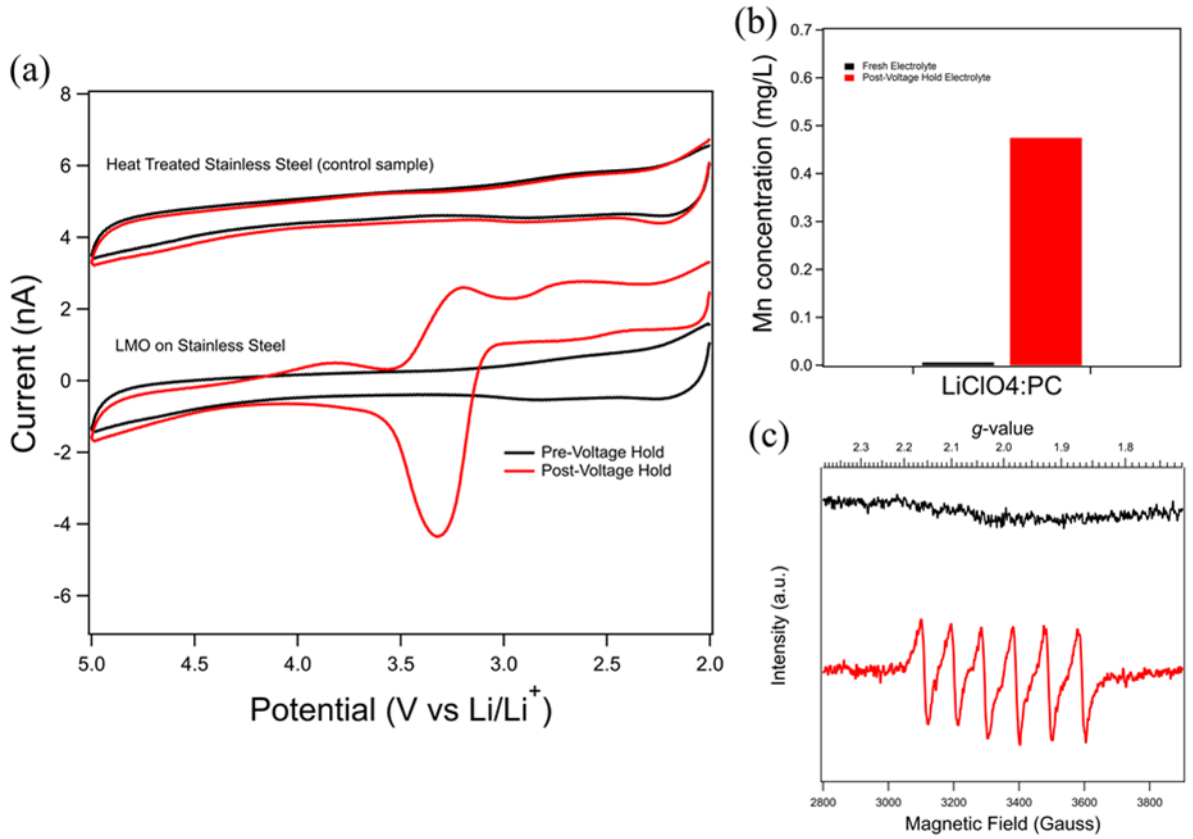

Figure II.3.F.2 (a) G/C SECM tip voltammograms collected with a 25 mm Pt embedded disk electrode in 1M LiClO4:PC before and after a 5 hour, 4.5V hold at the substrate for both a model LMO cathode on stainless steel as well as on a stainless steel disk without LMO present. (b) ICP data showing the concentration of Mn in the electrolyte solution both before and after the high voltage hold. (c) EPR spectra collected in electrolyte samples before (black trace) and after (red trace) the high voltage hold.

A further examination of the voltammetric data in the lower portion of Figure II.3.F.2 (a) can yield insight into the reactivity of LMO degradation products. As an example, note the oxidation peak observed at ~ 3.4V, which we believe is associated with the observed reduction peaks seen at ~ 3.2V and ~2.7V. The oxidation current observed at 3.4V is substantially greater than the reduction currents seen at ~3.2V and ~2.7V. This likely indicates that the species generated in the process at ~3.4V rapidly undergoes additional solution phase reactions. The strong asymmetry in the currents observed for the oxidation and associated reduction peaks could be caused by the rapid degradation of the product formed at ~ 3.4V that precludes its detection on the reverse voltage sweep. The presence of at least two reduction peaks also likely indicates that multiple distinct products are generated in the process at ~ 3.4V. It is also feasible that the apparent amplification of the oxidation current at ~3.4V could be caused by a solution phase reduction of the reaction product leading to an increased flux of the reduced species to the electrode surface. While multiple potential mechanisms may explain the observed asymmetric voltammetric response, the present data cannot clarify exactly which mechanism may be taking place. However, the data shown in Figure II.3.F.2 (a) makes two observations clear. Firstly, that the SECM/ICP/EPR combination can yield insight into both the presence and characteristics of LMO degradation products. Secondly, a high-level interpretation of the shape of the observed voltammetric response shows that the LMO degradation products undergo likely multiple reaction paths in solution. Further analysis of voltammograms collected at a variety of scan rates as well as tip to substrate distances will be used to clarify these mechanisms.

In addition to the initial experimental results reported above, we have examined the impact of electrolyte anion on the Mn dissolution process from LMO as well as the impact on the reactivity of dissolution products. Figure II.3.F.3 shows G/C SECM as well as ICP and EPR data for 1M $LiClO_4$, $LiPF_6$ and LiTFSI in PC before and after a five our 4.5V hold at the LMO substrate. The data presented for the $LiClO_4$:PC system is the same as that reported in Figure II.3.F.3 and is shown here again for direct comparison. Note that the voltammetric signature observed for the $LiPF_6$:PC system shows a similar response to that seen earlier for the $LiClO_4$:PC system in that one process is observed at~ 3.4V and a second, less defined process is seen >4.5V. In the case of the $LiPF_6$:PC system the redox process seen at 3.4V appears to show less asymmetry than seen in the $LiClO_4$:PC system. This appear to imply that the LMO degradation products formed in the $LiPF_6$:PC system are significantly less susceptible to additional solution phase reactions than degradation products generated in the $LiClO_4$:PC system.

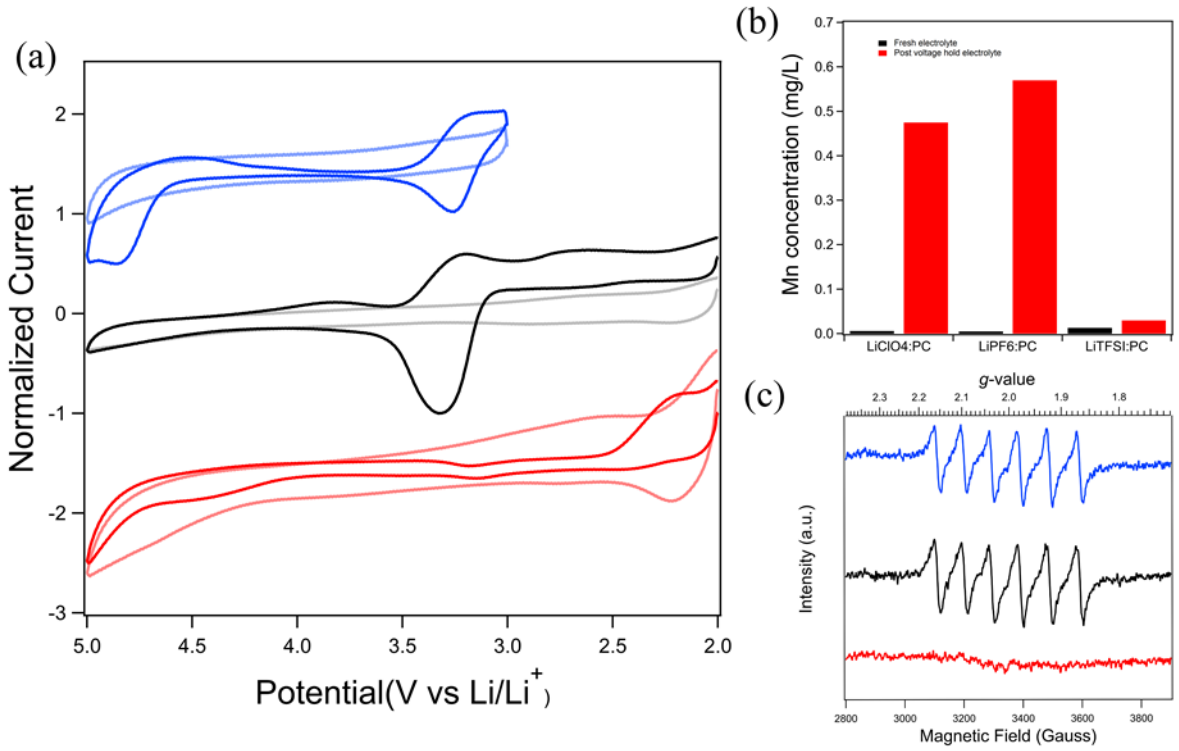

Figure II.3.F.3 (a) G/C SECM tip voltammograms collected with a 25 μm Pt embedded disk electrode in 1M $LiClO_4$:PC, 1M $LiPF_6$ and 1M $LiClO_4$ before and after a 5 hour 4.5V hold at the LMO substrate (b) ICP data showing the concentration of Mn in each electrolyte solution both before and after the high voltage hold. (c) EPR spectra collected in electrolyte samples before and after the high voltage hold for the $LiClO_4$:PC (black), $LiPF_6$:PC (blue) and LiTFSI:PC (red) systems.

Interestingly a dramatically different response is observed for the LiTFSI system. In this case, the earlier observed peaks attributed to the Mn^{2+}/Mn^{3+} and/or Mn^{3+}/Mn^{4+} redox couples are not detected. ICP also shows limited Mn present following the high voltage hold in the case of the LiTFSI:PC electrolyte, however, the detected Mn levels are higher than previously measured background levels. This appears to indicate that Mn dissolution still occurs in the case of TFSI, however at a significantly slower rate. EPR data for the three salt systems studied are shown in Figure II.3.F.3 (c). Note that in the case of the $LiClO_4$ and $LiPF_6$ systems a clear signature is seen for the presence of Mn^{2+}, however, no signature for Mn^{2+} is observed in the case of the LiTFSI:PC system. The lack of an EPR signature for Mn^{2+} as well as the dramatically different voltammetric data appear to indicate that Mn dissolution from LMO in the the LiTFSI:PC system may be following a distinct mechanism as compared to the $LiClO_4$:PC and $LIPF_6$:PC electrolytes.

In order to probe differences in the Mn dissolution process from LMO for the LiTFSI:PC electrolyte, a longer term voltage hold experiment was conducted. This was done in order to see if some of the observed differences were simply due to a lower concentration of Mn following the high voltage hold. Figure II.3.F.4 (a) shows Mn concentrations from ICP collected after varying length voltage holds with the three electrolyte salts system studied. While measurable Mn is present following the initial 5hr voltage holds, the amount of Mn dissolution in the case of the $LiPF_6$ and $LiClO_4$ salts appear to increase much more rapidly than for the LiTFSI salt. After a 60 hour, 4.5V hold at the LMO substrate the amount of Mn present in the LiTFSI containing electrolyte has risen to values that are clearly detectable by SECM, ICP and EPR based on comparison to earlier data. Figure II.3.F.4 (b) shows EPR data collected before and after the 60 hr high voltage hold in the LiTFSI:PC system. Despite the ICP confirmed Mn presence, Figure II.3.F.4 (b) shows no apparent signature for Mn^{2+}. In order to confirm if Mn^{2+} was actually detectable by EPR in the LiTFSI:PC system, Figure II.3.F.4 (c) compares the EPR signature observed after the 60 hr high voltage hold (black trace) with that seen following deliberate addition of a $Mn(TFSI)_2$ salt (red trace) to the LiTFSI:PC electrolyte. Note that the deliberately added Mn^{2+} salt yields an extremely prominent signature for the presence of Mn^{2+} as compared to the data from the 60 hr high voltage hold experiment. The fact that ICP confirmed a measurable quantity of Mn present following the 60 hr high voltage hold in the Li:TFSI:PC electrolyte while EPR shows no apparent signature for Mn^{2+} likely shows that any Mn present following LMO dissolution in this system is present in the Mn^{3+} state. This appears to confirm that either the Mn dissolution process or solution phase reactions following dissolution occur through disparate pathways in the TFSI containing electrolyte as compared to the PF_6 and ClO_4 containing electrolytes.

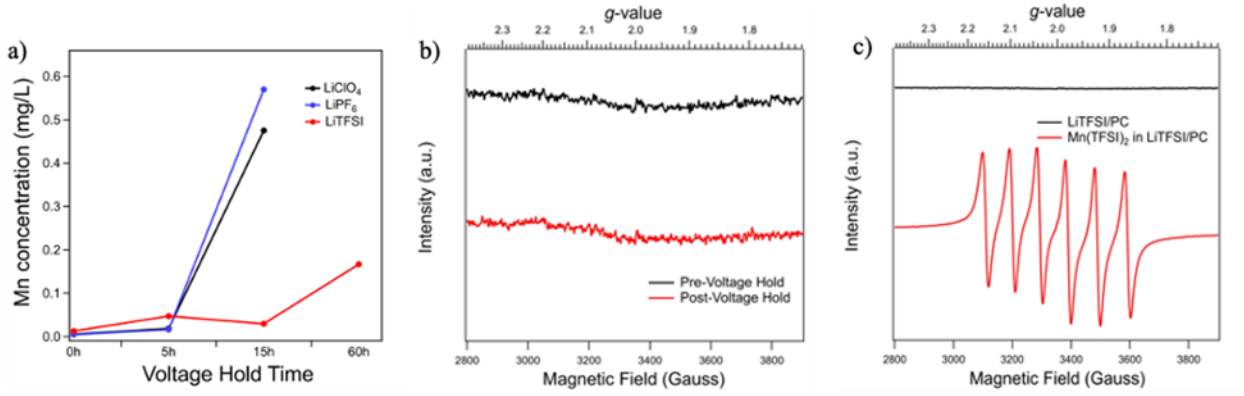

Figure II.3.F.4 (a) ICP data showing Mn concentration as a function of time of 4.5V hold at the LMO substrate in all electrolyte systems studied. (b) EPR data collected in 1M LiTFSI in PC both before and after a 60 hr, 4.5V hold of the LMO substrate. (c) Comparison of EPR spectra collected following the 60 hr 4.5V hold in LiTFSI:PC with that of deliberately added $Mn(TFSI)_2$ in 1M LiTFSI:PC.

The origin of the apparent differences between LMO degradation products in the PF_6 and ClO_4 systems as compared to TFSI is not completely understood at this time. The PF_6 and ClO_4 anions are known to potentially generate acid in the electrolyte either through hydrolysis of PF_6 or oxidation of ClO_4 while the TFSI anion is not a known acid generator.[2-4] Earlier work on Mn dissolution has shown that the presence of acid can lead to a disproportionation reaction that converts Mn^{3+} to Mn^{2+} and Mn^{4+}.[5] It is possible that this reaction occurring in the potential acid generating electrolytes leads to the presence of Mn^{2+} in the PF_6 and ClO_4 containing electrolytes while the absence of this process leads to the presence of Mn^{3+} in the case of TFSI salts. The results presented here are not presently able to confirm this hypothesis which is currently under further investigation.

Conclusions

The key finding of our results from FY20 is the dependence of Mn dissolution product properties on the anion present in our electrolyte. Comparison of electrolytes containing $LiClO_4$, $LiPF_6$ and LiTFSI in

propylene carbonate revealed that the oxidation state of Mn following dissolution changes. In the case of $LiClO_4$ and $LiPF_6$ we observe Mn^{2+} following dissolution. For the LiTFSI sample, we appear to observe Mn^{3+}.

Furthermore, the electrochemical properties of the resulting Mn complexes vary based on the involved anion as well. Notably, in the case of the $LiClO_4$ electrolyte it appears that the Mn^{2+} complexes observed appear to undergo further rapid solution phase reactions upon oxidation to Mn^{3+}. This result has significant implications for how these Mn complexes may react upon reaching the anode SEI where they are known to deposit leading to cell degradation by yet to be elucidated mechanisms.

Key Publications

1. Di Huang, Chaiwat Engtrakul, Sanjini Nanayakkara, Bobby To, Rong He, Meng Zhou, Hongmei Luo, Robert C. Tenent; Cathode electrolyte diagnostics based on scanning probe microscopy; Proceedings Volume 11387, Energy Harvesting and Storage: Materials, Devices, and Applications X; 113870D (2020) https://doi.org/10.1117/12.2559415

2. Di Huang, Chaiwat Engtrakul, Sanjini Nanayakkara, David W. Mulder, Sang-Don Han, Meng Zhou, Hongmei Luo and Robert C. Tenent; Understanding Degradation at the Lithium-Ion Battery Cathode/Electrolyte Interface: Connecting Transition Metal Dissolution Mechanisms to Electrolyte Composition; (2021) *ACS Applied Materials and Interfaces* (accepted)

References

1. Banerjee, A.; Shilina, Y.; Ziv, B.; Ziegelbauer, J. M.; Luski, S.; Aurbach, D.; Halalay, I. C., On the Oxidation State of Manganese Ions in Li-Ion Battery Electrolyte Solutions. *J. Am. Chem. Soc.* **2017,** *139* (5), 1738-1741.
2. Plakhotnyk, A. V.; Ernst, L.; Schmutzler, R., Hydrolysis in The System $LiPF_6$—Propylene Carbonate—Dimethyl Carbonate—H_2O. *J. Fluorine Chem.* **2005,** *126* (1), 27-31.
3. Arora, P.; White, R. E.; Doyle, M., Capacity Fade Mechanisms and Side Reactions in Lithium-Ion Batteries. *J. Electrochem. Soc.* **1998,** *145* (10), 3647-3667.
4. Cattaneo, E.; Ruch, J., Anodic Stability of Propylene Carbonate on Manganese Dioxide Electrodes. *J. Power Sources* **1993,** *44* (1-3), 341-347.
5. Hunter, J. C., Preparation of a New Crystal Form of Manganese Dioxide: λ-MnO_2. *J. Solid State Chem.* **1981,** *39* (2), 142-147.

Acknowledgements

This work was authored in part by the National Renewable Energy Laboratory, operated by Alliance for Sustainable Energy, LLC, for the U.S. Department of Energy (DOE) under Contract No. DE-AC36-08GO28308. Funding provided by the U.S. Department of Energy Office of Energy Efficiency and Renewable Energy Vehicles Technologies Office. The views expressed in the article do not necessarily represent the views of the DOE or the U.S. Government. The U.S. Government retains and the publisher, by accepting the article for publication, acknowledges that the U.S. Government retains a nonexclusive, paid-up, irrevocable, worldwide license to publish or reproduce the published form of this work, or allow others to do so, for U.S. Government purposes. The authors would like to thank Peter Faguy and David Howell of the U.S. Department of Energy Office of Energy Efficiency and Renewable Energy Vehicles Technologies office for their continued support of this work. The authors would also like to thank Alfred Hicks in the NREL communications department for generating many of the graphics in this manuscript.

II.3.G Advanced Lithium Ion Battery Technology – High Voltage Electrolyte (Daikin America, Inc.)

Ron Hendershot, Principal Investigator
Daikin America, Inc.
2749 Hwy 20, Suite A
Decatur, AL 35601
E-mail: hendershot@daikin-america.com

Alec Falzone, Principal Investigator
Daikin America, Inc.
2749 Hwy 20, Suite A
Decatur, AL 35601
E-mail: afalzone@daikin-america.com

Joe Sunstrom, Principal Investigator
Daikin America, Inc.
2749 Hwy 20, Suite A
Decatur, AL 35601
E-mail: sunstrom@daikin-america.com

Tien Duong, DOE Technology Development Manager
U.S. Department of Energy
E-mail: Tien.Duong@ee.doe.gov

Start Date: September 22, 2016 End Date: March 31,2020
Project Funding: $1,826,895 DOE share: $1,250,000 Non-DOE share: $576,895

Project Introduction

The use of electrolytes containing small fluorinated molecules to enable stable high voltage (> 4.3 V) battery operation is the focus of this project. Previously, Daikin has shown that it is possible to operate lithium ion batteries utilizing several different cathode chemistries up to 4.5 V. This is accomplished by reducing the gas generation originating from electrolyte decomposition at high voltage. The primary mechanism for this is not completely understood, but the hypothesis is that the fluorinated molecules form a film on the highly oxidizing cathode. It is known that battery cycle performance above 4.5 V drops significantly, however the source of the observed performance loss is not yet understood. The target for this project is to achieve 300 cycles above 80% capacity retention at 4.6 V. A better understanding of gas evolution, which happens above 4.3 V and the failure mode above 4.5 V, is sought in order to propose mitigation strategies which will facilitate better high voltage performance in lithium ion batteries.

The battery industry trend for cathode materials is toward reducing the overall cobalt content (i.e. higher nickel) for a variety of reasons some of which include: increasing cost, loss of supply, and human rights issues. The experiments proposed for this project will encompass a range of cathode materials with successfully higher nickel content in order to understand how fluorinated electrolyte interacts with various cathode surfaces. This is with the anticipation that the lithium ion battery industry will move towards nickel-rich cathodes, which can operate at higher voltage in order to achieve more energy-dense batteries.

Objectives

The three-year project can be divided into three main milestone topics, each spanning one fiscal year: 1) understanding of gassing mechanisms and kinetics, 2) examining physical and chemical aspects of film formation, and 3) observation of chemical and structural evolution of electrode surfaces at various operating

conditions. The FY2019 focus is the characterization of thickness changes in the cell (non-gassing), along with quantifying metal dissolution of the cathode as a function of different operating conditions. In addition, the absolute thickness of standard carbon films reported in FY2018 were obtained. While the qualitative understanding of gaseous components in tested cells was performed in FY2017, the capability to quantify all discovered components is established in FY2019. Quantifying these components will help develop an understanding of electrolyte decomposition at high voltage (> 4.5 V) and potentially mitigate this degradation mechanism.

Cycling cells at high voltage results in changes to the crystal structure of the $LiNi_xMn_yCo_zO_2$ (NMC_{xyz} = 111, 532, 622, 811) and $LiNi_{.80}Co_{.15}Al_{.05}O_2$ (NCA) cathodes, which leads to dissolution of transition metals and irreversible capacity loss of the cell. We aim to determine which electrolyte formulation/cell chemistry limits transition metal dissolution of the cathode. Developing methods to measure cell thickness changes will aid in the understanding of relationships between cell thickness changes (non-gassing), metal dissolution, and electrochemical performance. Additional analyses of films derived from different electrolytes (i.e. hydrocarbon vs. fluoroether (HFE) vs. HFE/FEC) will correlate chemical composition at the cathode-electrolyte interface to electrolyte formulation.

Approach

The evolving composition of the electrolyte in the battery will be examined by various analytical instruments to study volatiles [gas chromatography – mass spectrometry (GC-MS)/thermal conductivity detector (TCD)], liquid [liquid chromatography MS (LC-MS)], and solid [time-of-flight secondary ion mass spectrometry (TOF-SIMS), thermogravimetric analysis MS (TGA-MS), X-ray photoelectron spectroscopy (XPS), and Auger electron spectroscopy (AES)] electrolyte decomposition products during battery operation. In the first year, the team addressed the gas composition and kinetics for both hydrocarbon and fluorocarbon as a function of several charge/discharge conditions. In the second year, the project transitioned into analysis of the solid-state electrolyte (SSE) decomposition components of its tested batteries to obtain valuable information about SEI layer formation and how it manifests change in both the anode (graphite) and cathode (LCO and NMC). The third year is focused on measuring changes in the solid state structure of the cathode following high-voltage operation along with investigating the swelling of the solid-state components (non-gassing). Quantification of any dissolved metal ions originating from the cathode (transition metals), and deposited on the anode will be obtained using inductively coupled plasma – mass spectrometry (ICP-MS). We will also study changes in the cathode structure using powder X-ray diffraction (XRD).

Results

Changes to the bulk crystalline structure in lithium ion battery cathodes have been reported with both *in situ* and *ex situ* methods.[1], [2] The project aims to identify and correlate any observed crystalline changes to different operating conditions and/or cell chemistries. More specifically, the aim is to identify either voltage, electrolyte formulation, or a combination thereof as the major contributor to any observed crystalline phases not attributed to the layered cathode structure. Previous reports have identified minor crystalline impurities at different states of charge (SOC). Electrolyte formulation and number of cycles performed are additional factors which may or may not contribute to any observed variances in crystalline phases post-mortem. The method utilized to probe crystalline phases of the cathode is powder XRD, with all data obtained on tested cells post-mortem.

Due to their current commercial relevance, high-Ni containing cathodes such as NMC622 and NMC532 paired with artificial graphite anodes with the targeted cell chemistries for powder XRD analysis. Initial measurements were obtained on NMC622 cathodes in collaboration with the Dr. Julia Chan group at UT-Dallas and reported in FY19. Additional work was obtained at an external analytical laboratory and primarily focused on NMC532 cathodes. NMC532/AG cell chemistries with the optimized fluorinated electrolyte have shown the best performance at high-voltage (4.6V).

Powder XRD data was obtained on tested full-cells with NMC532 as the cathode (200 cycles, 0.7C, CC/CC), and analyzed at the respective upper cutoff voltage. Cells were deconstructed in an Ar-filled glovebox. The NMC532 cathodes were washed with dry dimethyl carbonate (DMC), dried *in vacuo* at room temperature, then sealed with an air-tight material prior to analysis. The initial aim is to determine effects on cathode structure at the upper cutoff voltage as a function of electrolyte in NMC532 cells (4.2V vs. 4.6V). In addition, any discernable differences in the cathode structure from portions taken from the edge and middle areas of the cathode ribbon are targeted. Three different electrolyte formulations were also investigated to probe any effects the cathode/electrolyte interphase might have on bulk property characteristics of the crystalline structure. The baseline Hydrocarbon (1.2M $LiPF_6$, 80:20 EMC:EC + 1% PS), HFE (1.2M $LiPF_6$, 60:20:20 EMC:HFE:EC+ 1% PS), and HFE/FEC (1.2M $LiPF_6$, 60:20:20 EMC:HFE:FEC + 1% PS) were the formulations studied.

Localized effects on Li-ion transport kinetics could be possible contributors to observed structural changes as seen in rock salt/mixed rock salt and/or spinel phase growth,[1] therefore an edge versus middle portion from the cathode could exhibit these differences. Figure II.3.G.1 depicts NMC532 cathodes at 4.2V from each region of the cell.

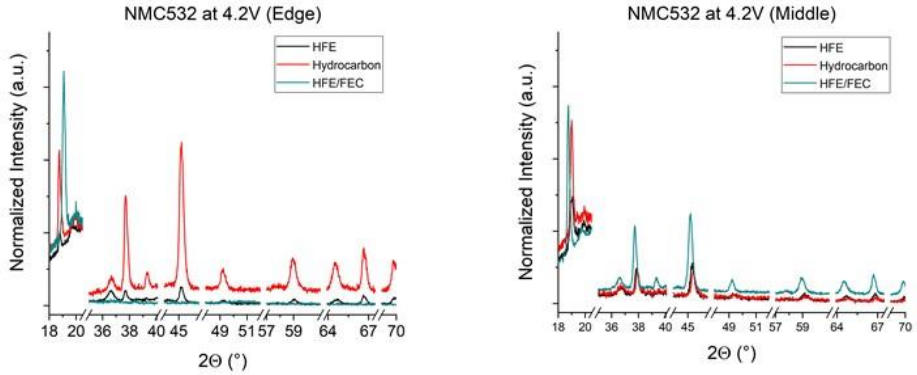

Figure II.3.G.1 Edge portion of the cathode (left) and middle region of the cathode (right). Electrolyte formulation does not appear to have an effect on the bulk crystalline phase of the NMC532 material as analyzed post-mortem.

Diffraction patterns from the edge and middle portions of the NMC532 cathodes at both 4.2V and 4.6V (Figure II.3.G.2) did not show much variance. The observed slight variations of peak location can be attributed to differing sample height. However, this could also be due to slight differing lattice parameters as a result of electrochemical testing. To probe this, it would require Reitveld refinement, which was not performed. It has been shown that voltage has the largest effect on changes to the layered structure with electrolyte composition having little to no effect.[1], [2] Results from these measurements are consistent with previous findings in NMC cathodes.

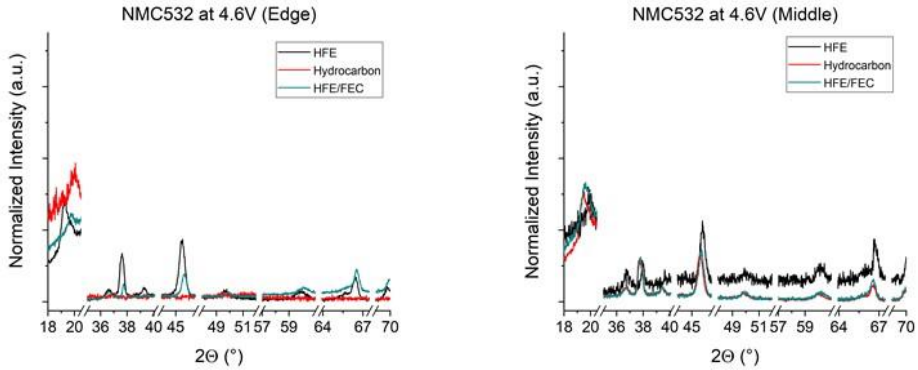

Figure II.3.G.2 Edge portion of the cathode (left) and middle region of the cathode (right). As seen in the 4.2V cathode, electrolyte formulation does not appear to have an effect on the bulk crystalline phase of the NMC532 material as analyzed post-mortem.

Additional NMC532 cells were submitted to a third party analytical laboratory for analysis post-mortem. These cells were from the interim cell test batch submitted to the DOE (Idaho National Laboratory) to gauge project progression as the Go/No-Go milestone in FY2019. Four groups of NMC532 cells were submitted, of which two electrolytes were utilized. The baseline Hydrocarbon (**EMC:EC**), and optimized Fluorinated (**EMC:FEC:HFE**) formulation (1.2M $LiPF_6$, 60:20:15:5 EMC:HFE:FEC:EC + 1% PS). Cells underwent 600 symmetric charge/discharge cycles between either 3.0 and 4.5V or 3.0 and 4.6V, at 0.7C. To prepare cells for analysis, they were either charged, or discharged at C/20 to their respective voltage. They were then deconstructed in an Ar-filled glovebox. The NMC532 cathodes were washed with dry dimethyl carbonate (DMC), dried *in vacuo* at room temperature. They were then sealed in an air-tight container to ship externally. After arriving at the third party test lab, samples were stored and prepared in a N_2 purge box. All samples were prepared just prior to XRD analysis by placing the entire folded cathode film onto low background mounts that were then sealed used Kapton® film. Co-Kα served as the X-ray source, and as such peaks are shifted to a slightly higher angle than what would be expected with Cu-Kα. Panalytical HighScore+ v4.8 was used to determine the background for each dataset and identify diffraction peaks. Diffraction peaks were then matched to the reference patterns for Li-Ni-Mn-Co-O phases from the ICDD PDF-4+ 2020 database.

Powder XRD results obtained from the initial batch of cells at UT-Dallas suggested there were no discernable differences between the edge and middle portions of the cathode. However, this method requires a high concentration of crystalline phase to be detected, so it is possible that local defect sites exist (i.e. rock salt) but not observable due to their low concentration. Broad features in the irregular background are due to the Kapton® films used to seal the samples. Table II.3.G.1 lists the voltage of each cell prior to disassembly and cell preparation post-mortem. Table II.3.G.1 lists description of each cell for data comparison.

Table II.3.G.1 NMC532 Cell Characteristics and OCV Prior to Disassembly

Battery Number	Electrolyte	UCV (V)	Test Voltage (V)
1	EMC:EC	4.50	4.42
2	EMC:EC	4.50	3.40
3	EMC:EC	4.60	4.48
4	EMC:EC	4.60	3.49
5	EMC:FEC:HFE	4.50	4.43
6	EMC:FEC:HFE	4.50	3.40
7	EMC:FEC:HFE	4.60	4.50
8	EMC:FEC:HFE	4.60	3.45

Diffraction patterns from these tested NMC532 cells as a function of voltage and electrolyte formulation are depicted in Figure II.3.G.3. Cells discharged to nominally the same SOC cycled at both UCV's (Upper Cutoff Voltages) show no differences in the layered structure post-mortem.

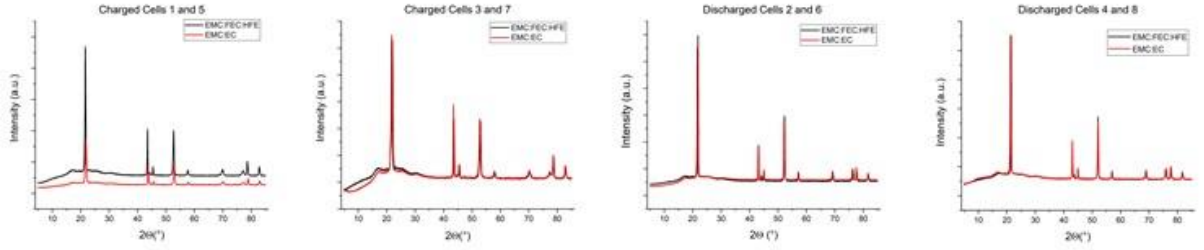

Figure II.3.G.3 Charged and discharged diffraction patterns of NMC532 cathodes displayed as a function of electrolyte and voltage.

Diffraction Pattern Match to Library Result. Cells discharged to the same SOC cycled at both voltages (4.5 and 4.6V) show no differences in the layered structure post-mortem. Although there was obvious cell failure at 4.6V with the EMC:EC electrolyte during interim cell analysis this is likely not a result of cathode structure collapse. There is no difference in the bulk crystalline structure as a function of electrolyte at either voltage suggesting the driving force behind these changes cannot be altered with electrolyte formulation. Figure II.3.G.4 overlays the obtained diffraction patterns with database matches to know reference patterns of layered $Li_{1-x}(NiMnCo)O_2$ structures.

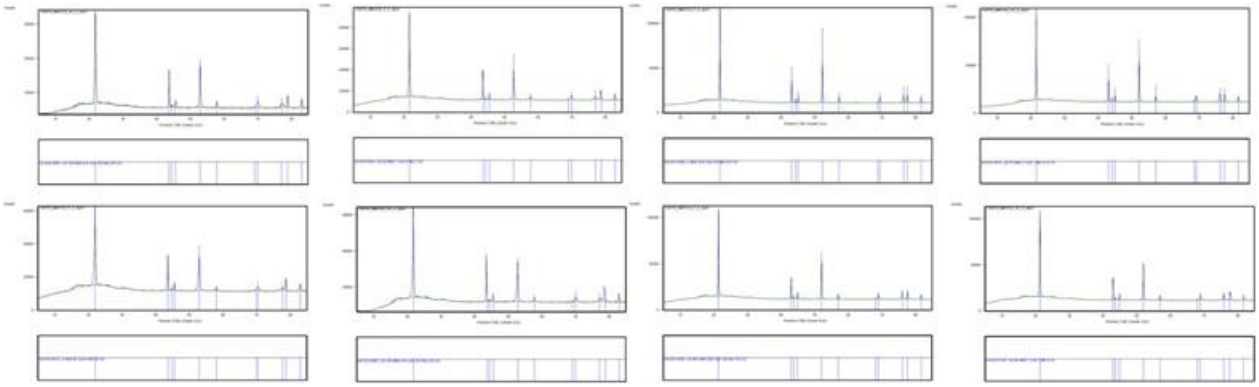

Figure II.3.G.4 Reference matched diffraction patterns from charged and discharged NMC532 cathodes. Spectra are matched to the battery description outlined in Table II.3.G.1

Discharged NMC532 cathodes do fit to a $Li_{1-x}(NiMnCo)O_2$ stoichiometry which is more lithiated than the charged cathodes. No additional bulk crystalline phases were detected in the diffraction pattern. This suggests that the interim NMC532 cells tested at INL retained their crystallinity, and are good candidates for high-voltage cycling. Diffraction peak positions are shifted between all samples suggesting differences in sample heights from how the films were folded or unit cell parameter differences that may be due to stoichiometric variability between samples. No other crystalline phases were detected. Rietveld refinement was not performed to separate these effects, but may be done using the existing data in the future.

Battery Thickness (non-gas) vs. Time/Voltage

One degradation mechanism in lithium ion batteries, especially at high voltage (> 4.5V), is the irreversible swelling of the solid components of the cell. More specifically, swelling of the anode can be correlated to irreversible capacity loss. In FY19 a method was reported that utilized a sensor requiring physical contact with the pouch cell to measure thickness changes, as measured by swelling in the z-direction, as a function of cycle number. This method for thickness change determination has been reported previously,[3] however does have limitations. The new approach to measuring thickness changes of pouch cells as a function of cycle number/SOC utilizes a pseudo-interferometer method which tracks the reflected laser position to changes in position along the z-axis. This change in the location of the reflection plane, or z-axis, is correlated to swelling of the pouch cell. Information obtained can be analyzed on a micro scale being the cycle-by-cycle comparison or as the macroscopic trend of overall thickness changes of the cell over the duration of the experiment. Figure II.3.G.5 depicts a schematic of the instrumental components, along with representative photos of a typical experiment during setup prior to starting the cycle life data acquisition.

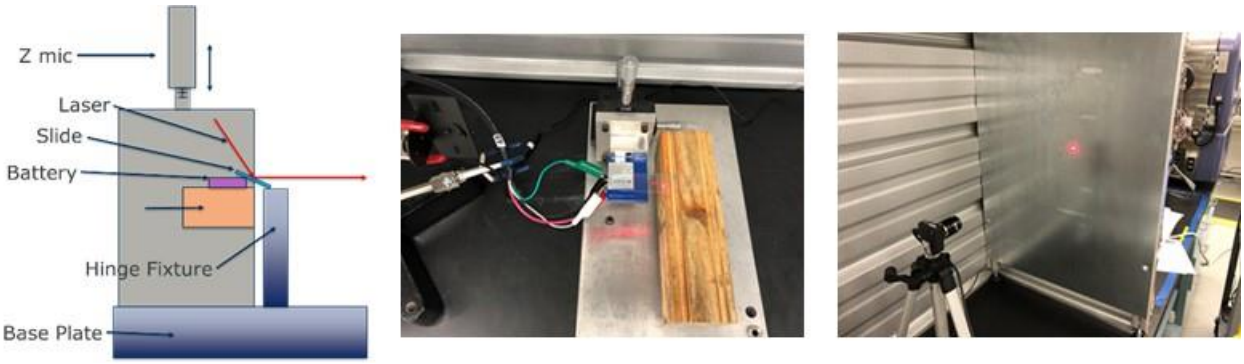

Figure II.3.G.5 Schematic of pseudo interferometer apparatus to correlate pouch cell swelling with laser position (left). Representative photo of a pouch cell with reflected laser point off the glass slide (middle). Reflected laser point is tracked with a time-lapsed photo program.

Prior to start-up, the battery undergoes formation and is discharged to 3.0V. Manual thickness measurements are obtained using a handheld micrometer to cross-check the acquired data and to confirm the thickness following the cycle life test. Seven separate regions of the pouch cell are measured to obtain an understanding of the cell as a whole. Thickness measurements post-testing are obtained in the same areas, and at the same SOC (3.0V) to minimize discrepancies due to Li ion intercalation effects in the graphite anode. Once the physical measurements are made, the pouch cell is affixed to the apparatus to generate a laser position vs. z-height calibration curve for data comparison. Figure II.3.G.6 depicts the calibration curve generated for the NMC532 cell reported herein.

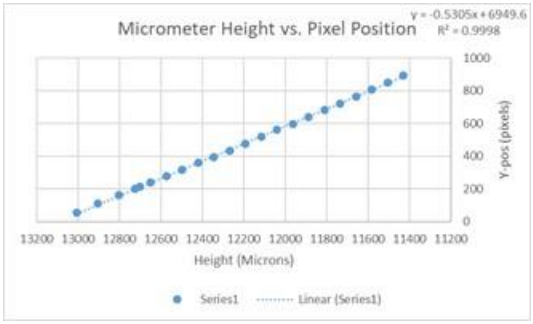

Figure II.3.G.6 Pixel position vs. changes in height of the pouch cell are compared to the calibration curve depicted above. From this, Δ thickness from the starting point (%) is calculated.

The NMC532 cell reported contained the project baseline hydrocarbon electrolyte, and cycled at C/2 between 3.0 and 4.6V, with a CC-CV charge cycle performed every 10 cycles (C/20). Both electrochemical and pixel position data was recorded every 10 seconds, with the overlay of both data sets being comparable. When at a 100% SOC, the pouch cell is at its greatest thickness due to the amount of Li intercalated within the graphite anode. When discharged, the pouch reverts back to its minima, provided the thickness change avoids hysteresis. The macro-trend in the Δ thickness vs. cycle number/SOC can be attributed to irreversible changes to the pouch cell's thickness, and not gas generation. Figure II.3.G.7 depicts the electrochemical data of the cell throughout the duration of the experiment, along with the thickness change (non-gas) vs. cycle number.

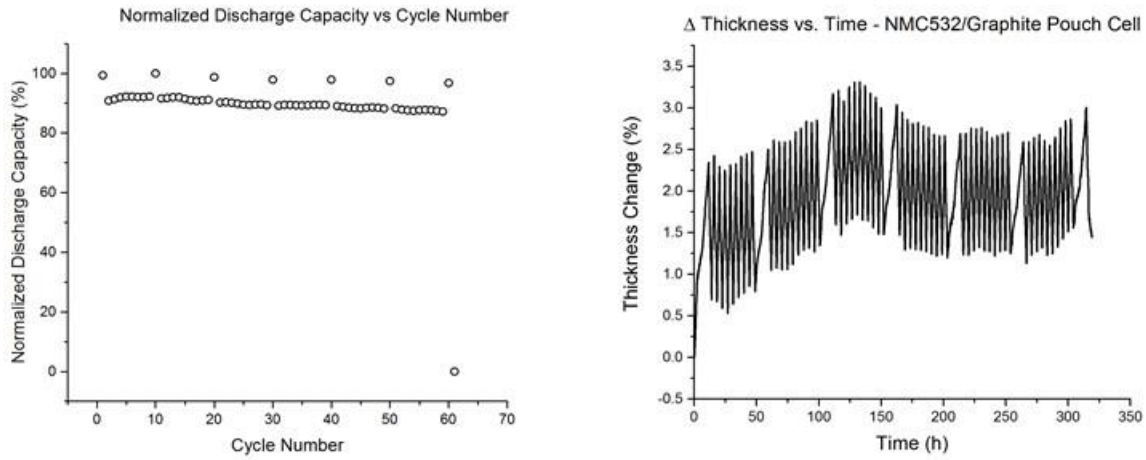

Figure II.3.G.7 After 60 cycles, the NMC532 cell exhibits minimal capacity loss (left). Δ thickness versus time (right). The CC-CV cycles are represented by the longer charge durations.

On a cycle-by-cycle basis, the NMC532 cell displays a reversible thickness change of approximately 1.5% which is consistent with what has been reported from other methods.[3], [4] This is nominally repeated throughout the 60 cycles reported, with minimal variation between cycles. When looking at the macroscopic trend as seen in Figure II.3.G.7 (right), there appears to be two periods of irreversible thickness growth in the cell. The first of which can be seen between cycles 0 and 25, with the second arising around cycle 50 and continuing on until the end of the test. A potential explanation for the initial thickness change could be the continual build-up of the SEI layer on the graphite anode early on in the test. It is known that the majority of the SEI evolves throughout formation, however can continuously grow depending operating conditions (C-rate, voltage, etc.) and chemistry (cathode, anode, electrolyte) of the cell. Since this cell was cycled up to 4.6V, a continuous build-up due to high voltage operation could occur beyond formation. The second thickness growth region identified can be correlated to a slight acceleration of capacity loss near the conclusion of the test. This irreversible trend in the Δ thickness is minimal, but must be noted. It is also important to note that although observable, these minor trend observations are within the method's experimental error.

Figure II.3.G.8 depicts the regions of the pouch cell's jelly roll where the physical micrometer measurements were obtained. Table II.3.G.2 depicts the obtained values, and aims to correlate the before and after dimensions of the cell.

Figure II.3.G.8 Regions of the pouch cell where external micrometer measurements were obtained

Table II.3.G.2 NMC532 Pouch Cell Thickness

Spot Location	Thickness Before (mm)	Avg Thickness Before (mm)	Thickness After (mm)	Avg Thickness After (mm)	% Increase
1	3.618	3.687	3.808	3.823	3.68 %
2	3.743		3.769		
3	3.776		3.819		
4	3.724		3.840		
5	3.691		3.814		
6	3.675		3.945		
7	3.583		3.765		

The external micrometer measurements indicate an overall growth of 3.68% when all regions of the cell are taken into account. This correlates to an actual change of 135 ± 50μm. It is important to note that the cell underwent 60 symmetric charge/discharge cycles, and a longer duration of electrochemical testing may potentially lead to accelerated thickness growth upon the onset of cell failure. The pixel position vs. D thickness indicates a change of approximately 3.0% at a 100% SOC, and half of that upon discharge. When comparing identical states of charge, the physical micrometer measurements suggest a marginally thicker growth (3.68%) than the optical data suggests (≈1.50%). However, these measurements are well within the experimental limitations of the reported pseudo interferometer method (± 50 μm). In summary, the reported method is a viable approach to measuring *in operando* swelling of lithium ion battery pouch cells, and avoiding physical compression of the jelly roll.

Cell Gassing Quantitation vs. Time/Voltage

Additional improvements to quantifying gaseous components in high voltage pouch cells were made in FY20. Major components were previously identified, however challenges remained to separate the low molecular weight species in the GC/MS method. In order to rectify this, a liquid nitrogen cryogenic valve (Agilent) and a corresponding 50L liquid nitrogen dewar was implemented to lower the initial temperature in the separation method to -10 °C. Without using cryogenic liquids, the separation/quantification of the lowest molecular species proved problematic (CO, CH_4, and O_2). To obtain the highest degree of accuracy in calibration curves for quantification, five or more calibration points were used. In lieu of purchasing standard gas mixtures from a supplier, the previously reported custom gas manifold was utilized in order to provide flexibility when creating compositions of the standards. Mixtures including five different concentrations of each component (CH_3F, C_2H_5F, CH_4, C_2H_4, CO, CO_2, C_2H_6, H_2) were created and injected three times to confirm reproducibility. CHF_3 was used as the internal standard to gauge performance of the mass spectrometry detector (MSD) due to its similar structure to the components of interest, but without being present in the evolved gas in the cell.

In addition to improving the analytical method for gas quantification using GC/MS, modifications to the pouch cell were performed in order to improve the gas extraction process. Previous reports have used airtight extraction chambers for pouch cells,[5], [6] however significantly dilute the gas composition. A method was introduced to apply a 2-part coating to the outside of the pouch cell. This coating serves two purposes: 1) To form a better seal around the needle when extracting gas using a gastight needle/syringe and 2) Enable multiple extractions/injections of gas extracted from a single pouch cell. Batteries were initially coated with a thin layer of adhesion promoter to prime the Mylar pouch, then hung freely to dry in a fume hood. The pouch cells were then submerged in solvent-based rubberized coating and hung to dry overnight. All injections were obtained using the same injection site from where the initial injection occurred to demonstrate the repeatability of this method compared to the uncoated analog. No residual solvents were detected by the MSD from the coating process (i.e. Xylenes), supporting the required overnight cure time.

Figure II.3.G.9 Representative 200 mAh pouch cell following calendar life test (left). The top rubberized coating layer is visible post-calendar life test (right)

Figure II.3.G.9 depicts uncoated (left) and coated (right) 200 mAh pouch cells prior to analysis. NMC622/Graphite cells underwent an extended 55 °C calendar life test at 4.6V to generate the swelling observed. In order to test the sealing improvement around the needle compared to the uncoated pouch cell, the degree of atmospheric contamination was studied. No battery was known to generate N_2, the major component of air. As a result, the concentration of N_2 detected with the MSD can be correlated to the amount of atmospheric contamination in the method. Extractions were performed at the same location on the pouch cell. Figure II.3.G.10 depicts the volume change throughout the calendar life test (left) and the amount of air introduced during a manual extraction/injection from a pouch cell (right).

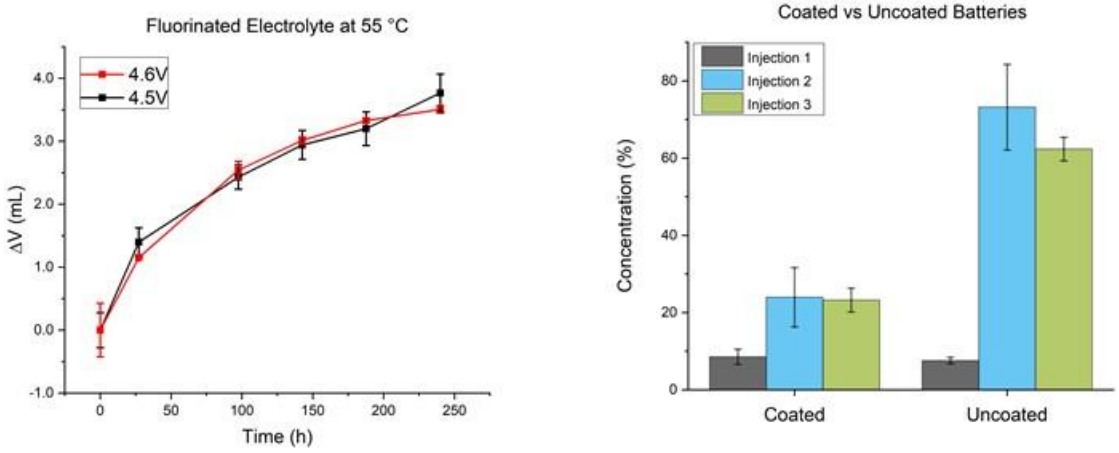

Figure II.3.G.10 NMC622 pouch cells at 4.5 and 4.6V (left) with the fluorinated electrolyte (1.2M $LiPF_6$ 60:20:20 (EMC:HFE:FEC) + 1% PS). Atmospheric concentration when extracting/injecting gas manually using a gastight syringe (right). Data was obtained from coated and uncoated NMC622 cells with the fluorinated electrolyte at 4.6V

In both methods of sample introduction, the first injection introduces approximately the same amount of air contamination. However, the two-layer coating reduces the amount of air introduced into the GC/MS if multiple injections from the pouch cell are targeted. Multiple gas injections allow for a more thorough understanding of the gassing kinetics and compositional information in cells as a function of time/voltage/electrolyte. Figure II.3.G.11 depicts the concentration of identified and quantifiable components in NMC622 pouch cells at 55 °C, which contained the fluorinated electrolyte. It is important to note that H_2 and C_2H_4 were also detected in these cells, however the concentrations were below the limit of detection (LOD) used herein. Three extractions were analyzed from each coated pouch cell, and performed immediately after one another with minimal dwell time between injections.

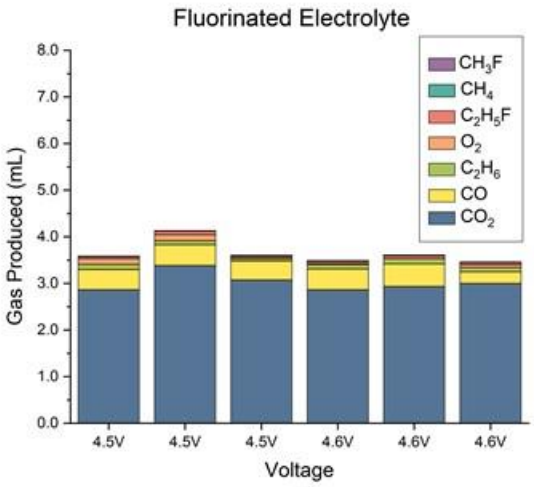

Figure II.3.G.11 Gas quantitation data from two sets of three independent NMC622/Graphite cells are depicted containing the fluorinated electrolyte.

At both 4.5V and 4.6V, CO_2 is the major component in extracted gas from the pouch cell. CO is also present in significant quantities, with the remaining gases comprising a small percentage. This is consistent with the breakdown of carbonates in electrolyte, especially at high voltage. FEC starts to break down at high voltage, which leads to the formation of fluoromethane and fluoroethane. There is no discernable difference between gas compositions at 4.5V and 4.6V, suggesting the degradation mechanisms of electrolyte components between these two voltages follows a similar pathway in the analyzed NMC622 cells.

Conclusions

In summary, changes in crystalline phases are observed in high-Ni containing cathodes as a function of voltage. This is consistent with what has been reported previously, and no defect phases were observed in tested cells post-mortem. It is likely micro defect sites exist, especially at 4.6V, however could not be detected with *ex-situ* powder XRD. There did not appear to be a difference in crystalline structure as a function of electrolyte formulation at the same SOC. While fluorinated electrolytes are necessary to achieve high energy density at 4.6V and with a long cycle life, they do not have any observable influence on crystalline phase presence.

A non-contact method using a pseudo interferometer instrument was optimized and implemented to monitor thickness changes in NMC532 pouch cells. Reversible swelling of the solid components is expected as lithium intercalates into the graphite anode, however irreversible changes can lead to premature cell failure. In the NMC532 battery studied, there was an observable ≈1.5% thickness change upon reaching 100% SOC. At the conclusion of 60 symmetric charge/discharge cycles, the pouch cell gained approximately 135 ± 50μm in thickness. This demonstrates that when cycled at 4.6V, NMC532/Graphite cells do exhibit a small amount of irreversible swelling of the jelly roll which can be monitored using a non-contact method.

Gas quantitation of NMC622 pouch cells containing the fluorinated electrolyte (1.2M $LiPF_6$, 60:20:20 (EMC:HFE:FEC) + 1% PS (w/w))was reported in FY20. Cells at both 4.5 and 4.6V had similar compositions, with all components present at similar concentrations. The majority of gas evolved during the calendar life test resulted from the breakdown of the carbonate solvents, with the majority being converted into CO_2 and CO. Fluorinated gases (CH_3F and C_2H_5F) were also quantified by creating custom mixtures containing these components. The fluorinated components are likely to result from the degradation of FEC at high voltage (≥4.5V), leading to the formation of these small fluorinated gases.

References

1. Tian, C.; Nordlund, D., et al., "Depth-Dependent Redox Behavior of $LiNi_{0.6}Mn_{0.2}Co_{0.2}O_2$," *J. Electrochem. Soc.* 165 (2018): A696-A704

2. Buchberger, I.; Seidlmayer, S., et al., "Aging Analysis of Graphite/$LiNi_{1/3}Mn_{1/3}Co_{1/3}O_2$ Cells Using XRD, PGAA, and AC Impedance," *J. Electrochem. Soc.* 162 (2015): A2737-A2746

3. Grimsmann, F.; Brauchle, F., et al., "Hysteresis and current dependence of the thickness change of lithium-ion cells with graphite anode," *J. Energy Storage* 12 (2017): 132-137

4. Siegel, J. B.; Stefanopoulou, A. G., "Expansion of Lithium Ion Pouch Cell Batteries: Observations from Neutron Imaging," *J. Electrochem. Soc.* 160 (2013): A1031-A1038

5. Peitbon, R.; Rotermund, L. M.; Dahn, J. R., "Evaluation of phenyl carbonates as electrolyte additives in lithium-ion batteries," *J. Power Sources* 287 (2015) 184-195

6. Xiong, D. J.; Ellis, L. D., et al., "Studies of gas Generation, Gas Consumption and Impedance Growth in Li-Ion Cells with Carbonate or Fluorinated Electrolytes Using the Pouch Bag Method," *J. Electrochem. Soc.* 164 (2017) A340-A347

Acknowledgements

We would like to thank Dr. Julia Chan, Trent Kyrk, and Juan Ortega (UT-Dallas) for initial powder XRD measurements of cathode materials.

II.4 Next-Gen Lithium-Ion: Low-Cobalt/No Cobalt Cathodes

II.4.A Aerosol Manufacturing Technology to Produce Low-Cobalt Li-ion Battery Cathodes (Cabot Corporation)

Toivo Kodas, Principal Investigator
Cabot Corporation
157 Concord Road
Billerica, MA, 01821
E-mail: Toivo.Kodas@cabotcorp.com

Peter Faguy, DOE Technology Development Manager
U.S. Department of Energy
E-mail: Peter.Faguy@ee.doe.gov

Start Date: October 1, 2018 End Date: June 30, 2020
Project Funding: $2,749,057 DOE share: $1,989,057 Non-DOE share: $760,000

Project Introduction

Although considerable progress has been made with battery materials over the last 5-10 years, the cathode remains a major performance-limiting material in Li-ion battery (LIB) technology. New materials and battery chemistries will overcome some of the remaining challenges, but cathode materials must also be manufactured at a lower cost and with a smaller environmental footprint using new processes that can also enable improved control over stoichiometry, morphology and compositional homogeneity. Cabot, Argonne National Laboratory and SAFT research teams are combining their extensive expertise in particle synthesis, battery materials and cell design to develop a low-cost, flexible aerosol manufacturing technology for production of high-performance Li-ion battery cathodes. This project will develop low-Co cathode materials via Reactive Spray Technology (RST) and Flame Spray Pyrolysis (FSP) to reach performance targets of < 50 mg Cobalt/Wh.

Objectives

The objective of this project is to research, develop, and demonstrate RST and FSP for production of low-Cobalt active cathode materials for use in next-generation LIBs capable of the following:

Table II.4.A.1 Project performance targets for cathode active material and cell made with this material

Beginning of Life Caharacteristics at 30°C	Cell Level	Cathode Level
Useable Specific Energy @ C/3	---	≥60 Wh/kg
Calendar Life (< energy fade)	15 years	---
Cycle Life (C/3 deep discharge with <20% energy fade)	1,000	---
Cobalt Loading	<50 mg/Wh	---
Cost	≤$100/kWh	---

Approach

To achieve the above targets, we are working towards demonstrating the production of low-Cobalt particle compositions. Cabot has shown the feasibility of $LiNi_{0.8}Mn_{0.1}Co_{0.1}O_2$ (NMC811) by RST; for this project we are extending this to even lower Co amounts. This requires us to identify approaches to solve key problems of phase stability, water sensitivity, interface degradation and others. The team is exploring particle doping, coating, morphology, and size control on a robust platform that can be extended to other material configurations. We are leveraging the flexibility of RST and FSP to produce key low-Co cathode compositions relevant for achieving a scale up pathway. Cabot and ANL are identifying the most suitable aerosol platform and process conditions to synthesize low-Co cathode active material compositions. The optimization of low-

Co electrodes includes new conductive additive formulations and improved low-Co cathode pastes that ensure percolation and mechanical stability of the film.

The performance goals in Table II.4.A.1 drive us to new compositions, lower Cobalt than NMC811 (such as $LiNi_{0.9}Co_{0.05}Mn_{0.05}$ and $Ni_{0.9}$-$xCo_{0.06}Al_x$ x=0.005-0.03), along with other materials systems comprising fluorine (Li-excess disordered rock salt, LxDRS). Composition must be optimized for performance, cycling, stability and operation, among others. Our proposed RST/FSP route will address these issues and allow doping, coating, gradients, and novel particle morphologies which can solve these problems.

Results

NCM811 by Flame spray pyrolysis (FSP)

At the beginning of FY2020, the team produced ~ 2kg NCM811 by FSP with a tap density of 2.2 mg/cm^3, and particle size distribution (PSD) of D10 =3µm, D50= 6µm and D90 = 19 µm. This powder met all BP1 technical targets summarized in Table II.4.A.2. Though, we encountered difficulties processing slurries at larger scale (SAFT, 1-galon mixer) and were not able to coat enough good quality electrodes to assemble 2.Ah cells. We believed the causes of the poor-quality slurry were the existence of isolated large aggregates, and gelation associated with surface species on the cathode particles and temperature increase during mixing. Particle aggregation could have been created during the second thermal treatment by the sintering fines (nano scale particles), which are commonly produced by FSP. In addition, fines could lead to binder polymerization during mixing (due to temperature increase) also creating polymer-powder agglomerates.

Table II.4.A.2 BP1 Go/No-Go technical targets

Parameter	Target	Actual
Tap density (g/cm^3)	>2.0	2.2
Voltage window (V vs. Li/Li$^+$)	≤2.3V to >4.25V	2.7-4.3
Specific capacity (mAh/g)	>185	188

Double layer pouch cells (150mAh) were made with recovered electrode films. These cells have the same footprint as the planned 2.Ah cells. The NCM811 cathode electrodes were matched with graphite anodes and the cells were filled with SAFT selected electrolyte. Cycle life was performed at C/3 charge/discharge rate from 2.7 to 4.2V, and at 25 and 60°C. (Figure II.4.A.1) shows the cells (assembling steps) and cycle life data. Cells have reached ~80% after 400 and 100 cycles at 25 and 60°C, respectively.

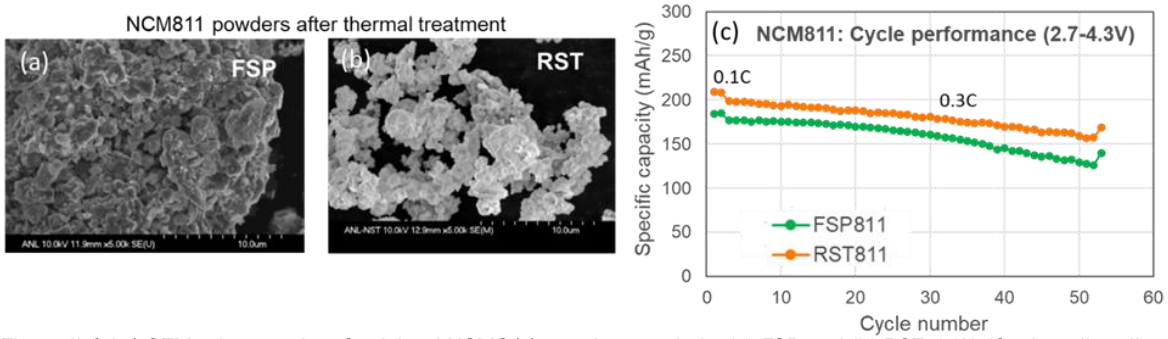

Figure II.4.A.1 SEM micrographs of calcined NCM811 powders made by (a) FSP and (b) RST. (c)Half coin cell cycling data, the initial capacity of the NCM8111 by RST is significantly higher than the FSP made powder.

High-Nickel NCMs by reactive spray technology (RST)

While the RST and FSP are similar in some respects (aerosol continuous processes using liquid precursors), they are distinct technologies. The RST process enables easier generation of micron-size particles that can contain nano-domains and it allows broader range of particle coating approaches. On the other hand, the FSP

process has higher reactor temperatures and shorter reactor times and it can produce nano-sized particles with variety of morphologies. Due to the nature of our systems, the RST yield is higher than the FSP unit.

ANL produced different NCM formulations (622, 811 and 9055) using the RST system. Half coin cell data (Figure II.4.A.1) shows better electrochemical performance for the NCM811 produced by RST compared to that by FSP. The 1st discharge capacity and coulombic efficiency (C.E.) were 208mAh/g and 88% for the RST powder in contrast to the 185mAh/g and 84% CE for the powder made by FSP. Based on this evidence, we decided to produce Hi-Ni NCMs by RST system for the fabrication of cell deliverables.

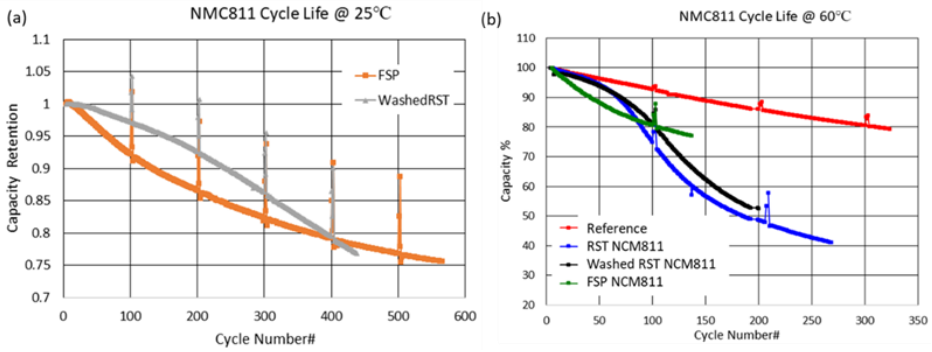

Figure II.4.A.2 Cycling data for pouch cells made with NCM811 samples made by FSP and RST. The RST powder was water washed. Cell were tested at (a) 25°C and (b) 60°C, using 1C/1C rates and 2.7-4.3 V voltage cut off.

Post processing NCM811 made by RST

High Ni-content NCM materials readily absorbs water and CO_2 when exposed to ambient air. Both, H_2O, and CO_2 react with NCM creating surface hydroxides and carbonates, which later affect powder processability and electrode performance. To this end, Cabot and ANL explored powder washing (i.e. DI water) to remove surface contaminants with the hope to reduce/eliminate slurry gelation and improve cell life. After washing, the powders are subjected to a mild recovery thermal treatment. In some cases, small amounts of Li (as LiOH) are added during recovery thermal process. Half coin and pouch cells have been made with water-washed powders and the results are showed in Figure II.4.A.2. Cycle life testing was carried out at 25 and 60°C. The washed powder shows slightly better capacity retention and ~7mAh/g higher capacity than the unwashed powder, specially at 60°C. We also compared these results with cycling data obtained earlier using NCM811 made by FSP. Cycle life at both temperatures showed similar behavior for both materials reaching 400 and 100 cycles at 25 and 60°C respectively before falling below 80% capacity retention.

Further, Cabot developed a wet mill process using anhydrous alcohols obtaining very good particle size distribution (PSD). Process parameters were transferred to ANL for scale up. Experiments at ANL with 200-g show similar PSD and tap density data as the Cabot results (2.02 mg/cm^3, D10 21μm, D50= 4.8μm and D90 = 9 μm). Surface contaminant (pH, Li_2CO_3 and LiOH content) were measured at different stages of the process and are summarized in Table II.4.A.3.

Table II.4.A.3 Impurity measurements for NCM811 by RST samples at different post processing stages

NCM811 sample	Sample (g)	pH	Li_2CO_3 (wt%)	LiOH (wt%)	Engineering decision
250-g batch dry mill	4.0086	11.6	0.264	0.191	OK
500-g bacth wet mill-wash	4.0072	11.4	0.175	0.143	Good
Commercial reference	2.0031	11.2	0.050	0.157	Good

During scale up, ANL decided to combine processes into a one-step milling-washing with water injection using a Pope filter system. After removing the milling solvent, water was injected to the still wet powder. This

step allowed for the easier and simpler removal of solvent and surface contaminant. SAFT has qualified (4kg) of this NCM811 powder using 150-g small slurry trials (impurity levels were also measured, Table II.4.A.3).

Slurry quality check has passed SAFT standard inspection and pilot-scale coating was completed without any issues (Q4FY20). 2Ah cell assembly and testing will continue during Q1FY21, and 30 cells will be sent to Idaho National Lab and TARDEC for further testing (completing M1.5).

Selection of other cell components and electrode design

SAFT has continued working to select the best options for electrolyte and binder. A new electrolyte formulation with less toxicity and flammability has been selected. The electrolyte formulation has showed very good performance in 5Ah cells (Figure II.4.A.3) at 25°C and 45°C (C/2 rate). The binder content in the electrode formulation was adjusted to consider the higher surface area of the RST NCM811 powder compared to commercial cathode materials. Cabot LTXHP is being used as baseline conductive additive. As described below, Cabot has been working to develop conductive additive formulations during BP2.

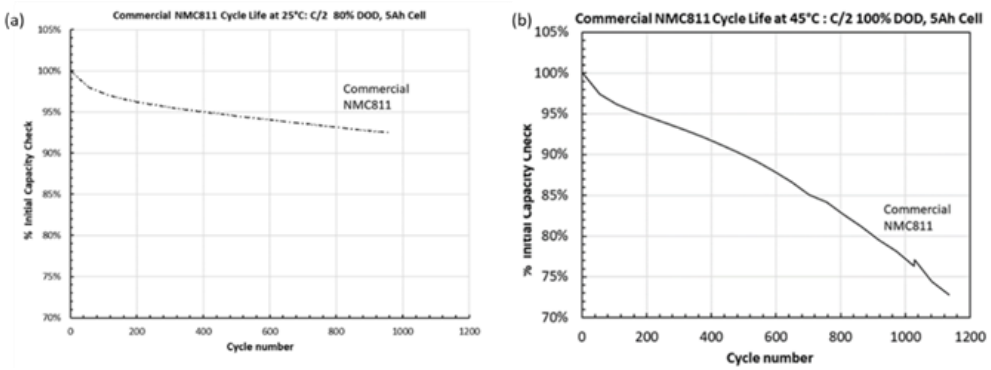

Figure II.4.A.3 Cycle life of 5Ah cells made with commercially available NCM811 and SAFT selected binder and electrolyte formulation (a) 25°C C/2 discharge rate (b) at 45°C C/2 discharge rate.

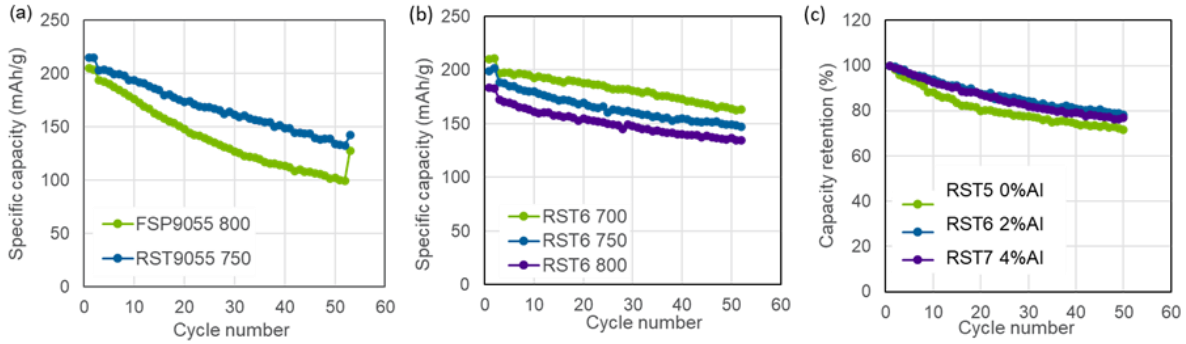

Figure II.4.A.4 Half coin cell cycle life for electrodes fabricated with (a) NCM9055 by FSP and RST; (b) NCA with 2% Al NCA at calcined at 700, 750 and 800°C; and (c) NCA with three different Al concentrations.

Higher-Nickel content cathode active material

The focus of this task is to further reduce Cobalt content in the cathode active material while improving cycle life. To this end, cathode compositions with lower Co such as NCM9055 and NCAs with Co ≤ 6% have been made by RST and FSP in small quantities (20-50g batches).

Figure II.4.A.4 (a) shows cycling data for NCM9055 made by RST and FSP. The initial capacity and C.E. were 205 mAh/g, 86% and 215 mAh/g, 89% for electrodes made by FSP and RST, respectively. After 50 cycles (1C/1C half cells) capacity retentions were higher for cells made with RST (68%) powder compared to that by FSP (56%). During the rest of BP2, we will apply particle surface modification to improve NCM9055 cycle performance at full coin and pouch cell level.

Further, the ANL team has produced NCA ($LiNi_{0.9-x}Co_{0.06}Al_x$ x=0.005-0.03) cathode active materials using the RST system and with different Al contents. Initial formation and cycling data show promising results for 2wt% Al as shown in Figure II.4.A.4 (b) and (c). We will continue with this investigation to increase initial capacity (targeting co-precipitation powder results) and improve cycle life.

Cathode active material surface modification

Surface modification of Low-Co cathode active materials has continued at Cabot during FY20. Samples were made using Cabot's nano aluminum oxide (fumed alumina) and Li-metal oxides (by FSP).

Figure II.4.A.5 shows full coin cell data for commercial NCM811 core (BET = 0.5 m^2/g) coated with fumed alumina (FA). Cycle life was initial done at 25°C and 0.3C and 1C (2.7-4.2V), at these conditions and after 200 cycles no noticeable differences were seen between coated and uncoated samples. The chamber temperature was increased to 45°C and the upper voltage cut-off was initially increased to 4.4 and then 4.5V. At the latter conditions, data clearly suggest that the metal oxide coating effectively improves cycle life performance. These learnings were transfer to the RST NMC811 (BET= 2.5 m^2/g) system, initial work using FA has started. Full coin cells were tested for cycle life at 45°C (1C/1C, 2.7-4.2V) as well as 10 days of hot storage at 60°C (Figure II.4.A.6(a)). The data clearly shows the advantage of using FA coating for both improving cycle life and reducing cell impedance (Figure II.4.A.6 (a)).

Further, nano-NCM was used to coat the same core (commercial NCM811). Full coin cells were made to test cycle life at 25°C and 1C charge/discharge (Figure II.4.A.6(b)), at these conditions and after almost 500 cycles no noticeable differences were seen between coated and uncoated samples. Further particle surface and electrochemical characterization are ongoing to continue with this investigation.

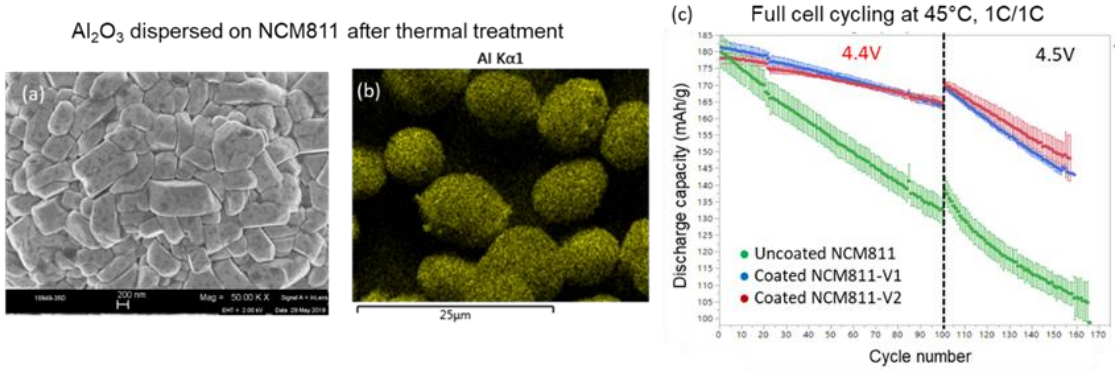

Figure II.4.A.5 (a) SEM micrograph of NCM 811 coated with FA after thermal treatment. (b) EDS Al mapping of NMC811 coated particles. (c) Full coin cell data for FA coated and uncoated NCM811.

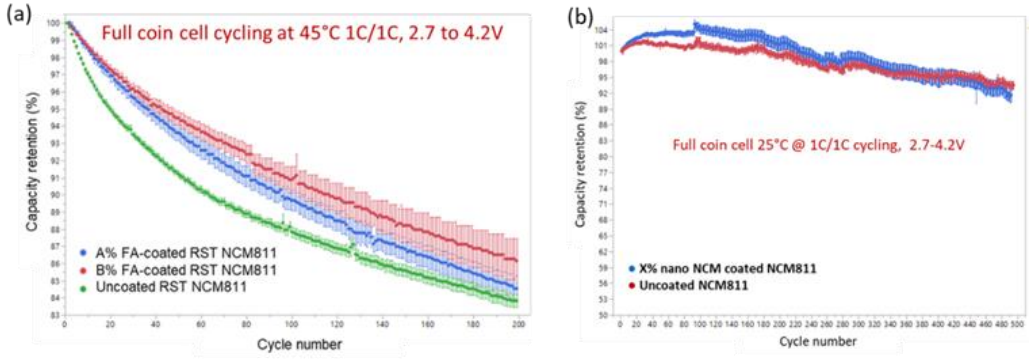

Figure II.4.A.6 Full coin cell cycle life for (a) RST NCM811 particle coated with FA and tested at 45°C; (b) nano-size NCM coated NCM811 (commercial core) tested at 25°C.

Carbon conductive additives for Low-Co cathode materials

The impact of carbon conduction additives (CCAs) on energy retention was investigated using commercial NCM811. The goal was to minimize overall contents of CCA, and to maximize the energy retention during cycling. Our previous work with NCM622 has indicated that blends of carbon black (CB) and carbon nanotubes (CNTs) are very synergistic because CB provides short-range connection of the particles for full capacity utilization and electrolyte adsorption, while CNTs provide long-range and durable conductivity, which benefits cycle-life (Figure II.4.A.7 (a)). The electrode formulations depicted in Figure II.4.A.7(b) were tested in full coin-cells for cycle-life at 45°C, 1C/1C from 2.7-4.2V. The Opt. 3 formulation was selected based on best energy retention and lowest DC-IR increase during cycling (Figure II.4.A.7 (c) and (d)). This CCA formulation will be used with surface coated Hi-Ni NCMs (by RST) to build BP2 interim cells.

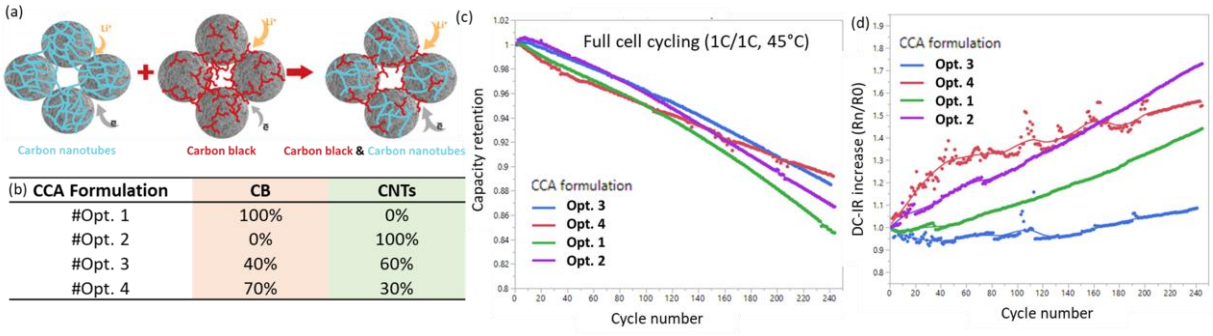

Figure II.4.A.7 (a) Synergistic conduction effects in CB and CNT blends. (b)CCA formulations tested with NCM811. (c) Energy retention and (d) DC-IR retention versus CNT contents in LITXHP:CNT.

Table II.4.A.4 Cathode energy densities for full cells made with coated and uncoated NCM811 (by RST)

RST NCM811 sample	Cathode Energy Density (Wh/kg)					
	0.1C Initial		1C, Cycle #1, 45°C		1C, Cycle # 200, 45°C	
SOC	100%	80%	100%	80%	100%	80%
Uncoated	730	620	718	595	620	515
A% FA coated	705	606	716	594	618	512
B% FA coated	681	592	692	572	605	508

Interim Pouch Cell Build and Test: to target higher energy density

Cathode energy densities (at discharge) were calculated for cells made with RST NCM811 with and w/o surface coating. Cell cycling plots are presented in Figure II.4.A.6. Table II.4.A.4 summarizes energy densities calculated at the beginning of life (0.1C) and after cycling (1C) at 100 and 80% SOC. Cathodes with surface coated particles show energy values of ~510 Wh/kg (at 80% SOC after 200 cycle at 1C and 45°C) which is 85% of 600 Wh/kg target (at 80% SOC after 300 cycles at C/3 and 25°C). It is worth nothing, that the cathode surface modification and electrode formulation were not fully optimized to make these cells. To meet the energy targets, we will switch to higher capacity CAMs (i.e. NCM9055); and apply improved particle surface coating, newly selected electrolyte, enhanced electrode composition and optimized CCA formulations.

Conclusions

Our team has employed a reactive spray technology (RST) and a flame spray pyrolysis (FSP) processes synthesize low-Co cathode active materials and down select candidate compositions for further development in a pouch cell optimization cycle. ANL and Cabot scientists have optimized the synthesis process and postprocesses to obtain NCM811 with the right electrochemical and physical properties for SAFT to fabricate PPC deliverables. Using nano-size metal oxides, Cabot has further advanced particle surface treatments to

improve high Low-Co cathode processing characteristics, environmental stability, and cycle life. The team has selected other cell components such as electrolyte and binder to improve cell performance. In addition, Cabot has started to develop conductive additive formulations to enhance electronic conduction on Hi-Ni NCMs. The current performance in full cells (pouches and coins) shows ~620 Wh/kg and ~510Wh/kg at 100% and 80% SOC after 200 cycles at 45°C and 1C/1C charge/discharge using RST NCM811 with surface medication.

Key Publications

1. "Aerosol Manufacturing Technology to Produce Low-Cobalt Li-ion Battery Cathodes", BAT411_Kodas_2020_o, US DOE Vehicle Technologies Program Annual Merit Review, AMR, 2020.

Acknowledgements

We would like to acknowledge Dr. Joseph Libera and Dr. Eungje Lee at ANL; Mrs. Carine Steinway, Mrs. Serena Peterson, and Dr. Joong Sun Park at SAFT for their valuable contribution to this project.

II.4.B Co Free Cathode Materials and Their Novel Architectures (UCSD)

Ying Shirley Meng, Principal Investigator
University of California, San Diego
9500 Gilman Dr.
La Jolla, CA 92093
E-mail: shmeng@ucsd.edu

Peter Faguy, DOE Technology Development Manager
U.S. Department of Energy
E-mail: Peter.Faguy@ee.doe.gov

Start Date: October 1, 2019 End Date: September 30, 2020
Project Funding: $1,043,000 DOE share: $834,000 Non-DOE share: $209,000

Project Introduction

Since its discovery [1], $LiNi_{0.5}Mn_{1.5}O_4$ (LNMO) spinel-type cathode materials have long intrigued the transportation industry due to their high operating voltage (4.7 V) and capability to handle high charging rates. More recently, the strong desire to eliminate cobalt in cathode materials has sparked a renewed interest in this class of oxides. Various attempts to create LNMO/graphite batteries that exhibit high voltage, relatively high energy density, and high charging capabilities have been carried out worldwide, but they all have suffered from excessive degradation and short cycle life, especially when stored or cycled at elevated temperatures (55°C or higher) [2]. Our proposed work will solve the long-standing issues by 1) novel architecture of LNMO thick electrodes to enable 4-6 mAh/cm^2 loading, 2) new electrolyte formulation to suppress degradation in LNMO/Gr full cells, and 3) close collaboration among university-national lab-industry to demonstrate the feasibility of a Co free Li-ion cell with energy density exceeding 600 Wh/kg at cathode level. The main focus of this research is to solve the structural stability of LNMO and the interphase problems with electrolytes, including adopting an appropriate surface coating for the cathode; the development of a novel electrolyte (electrolyte additive, sulfone-based electrolyte); and the advancement of a new dry electrode processing method. In the past five years, our research team has made great progress on developing innovative synthesis techniques of high tap density cathode materials; conformal coating methods on powder samples; advanced characterization techniques on the atomic scale, electrode scale, and at the cell level; we have also made significant inroads on thick-electrode-architecture cell prototyping. **UT Austin** has extensive experience in the co-precipitation synthesis of LNMO cathode materials with a batch tank reactor at above the kilogram scale. **UCSD** has achieved conformal coatings on cathode particles through polymer assisted deposition. **UCSD** has also demonstrated that cryo-(S)TEM is crucial for interphase studies as it can effectively preserve cathode electrolyte interphase (CEI) structure/chemistry from beam damage. **LBNL** has effective diagnostic methods for full cells at both the coin cell and pouch cell level. **Tesla, Inc.** possesses a unique dry battery electrode coating technology that offers extraordinary ionic and electronic conductivity for extremely thick electrodes. It is through these successful experiences and fundamental understanding of these high voltage cathode materials that we can successfully formulate strategies to optimize LNMO-based battery system.

Objectives

The proposed research aims to deliver a Co free Li-ion battery with energy density exceeding 600Wh/kg at the cathode active material level. More specifically, the main goal of this project is to develop a high-performance and low-cost spinel-type $LiNi_{0.5}Mn_{1.5}O_4$ electrode and novel electrolyte formulation to suppress full cell degradation at high voltage and temperature. The best combination of high voltage electrode and electrolyte will achieve higher cell energy density, better safety performance, longer battery life, and greatly reduce the overall cost of the battery. The critical success factors in achieving that goal include:

1. Electrolyte stability and compatibility for both the cathode and anode materials under high charge and discharge voltage;

2. LNMO bulk and surface stability at high working temperature 55-60°C;

3. High areal cathode loading with new polymer binder and a dry-processing method to ensure adequate electronic and ionic transport for fast rates.

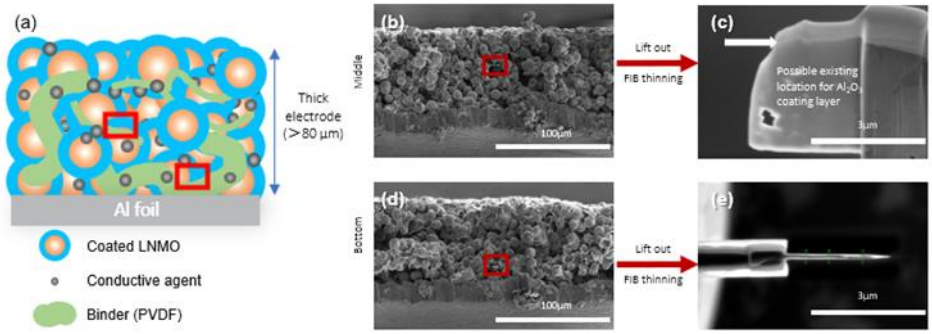

Figure II.4.B.1 (a) Schematic of the thick electrode coating by ALD process; (b) selected FIB lift-out position from the middle (b) and bottom (d) of the thick electrode with the corresponding thinned lamella (c, top view and e, side view).

Approach

The main focus of this research is to solve the structural stability of LNMO and the interphase problems with electrolytes, including adopting an appropriate surface coating for the cathode; the development of a novel electrolyte (electrolyte additive, sulfone-based electrolyte); and the advancement of a new dry electrode processing method. In addition, to guide our research to determine which electrolyte system is more stable and compatible for LNMO electrode materials under high voltage cycling, we will develop a series of characterization techniques such as ex-situ X-ray photoelectron spectroscopy (XPS), ex-situ cryogenic transmission electron microscopy (cryo-TEM), ex-situ cryogenic focused ion beam microscope (cryo-FIB), in-situ Fourier-transform infrared spectroscopy (FTIR) and in-situ time-of-flight secondary-ion mass spectrometry (TOF-SIMS).

Results

The following progress has been achieved in FY20:

Evaluation of surface modified LNMO thick cathode (3 mAh/cm^2) in full coin cell

The degradation of the LNMO/graphite full cell is caused by cross-talk between cathode and anode. Mn and Ni elements can be detected on the graphite side through TOF-SIMS and XPS. These deposited Mn and Ni can further trigger side reactions in the full cell, leading to lousy cycle performance. To prevent the dissolution of these transition metal elements from the cathode material, the surface coating can be one of the most effective ways. Herein, we employ the atomic layer deposition ALD as the coating strategy. A 3 nm thick Al_2O_3 coating layer was designed and performed. Yet, its uniformity layer needs to be verified since the precursor gas (e.g., trimethylaluminum gas as the precursor for Al_2O_3 coating) during the ALD process may not penetrate the entire thick electrode (up to 80 μm). As shown in Figure II.4.B.1, FIB was applied to slice two particles from the ALD coated electrode, one from the middle part, the other from the bottom. Then the slices were thinned down to electron transparent lamella for energy dispersive spectroscopy (EDS) test based on scanning transmission electron microscope (STEM). The EDS mapping results are illustrated in Figure II.4.B.2. Based on the element mapping, the Al element on the surface of the LNMO particle is 1.5 nm thick from the middle part, and 3 nm is obtained from the bottom part. These STEM-EDS mapping results show the uniformity of the coating layer throughout the entire electrode, although the thickness from the middle part varies from the designed value. To check the bonding information of the coating layer, XPS was applied before and after coating, as shown in Figure II.4.B.2(c). The Al 2p spectra from the coated sample demonstrate the Al-O bonding type at 74.2 eV. Thus, the chemical environment of the Al can be determined as Al_2O_3.

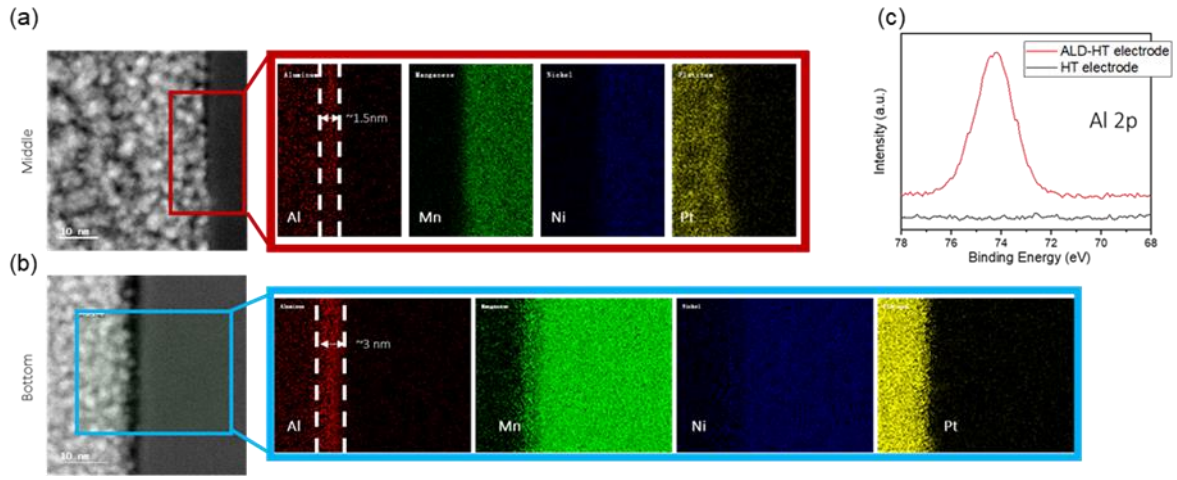

Figure II.4.B.2 STEM-EDS mapping of lamella from (a) top and (b) bottom part of electrode; (c) Al 2p XPS spectra of the thick electrode.

We further applied the coated cathode in the full coin cell test. The areal capacity of the cathode was around 3 mAh/cm^2, the N/P ratio was controlled as 1.2, the glass fiber was used as the separator, and the filled electrolyte amount was 150 µL. The discharge capacity and the coulombic efficiency (CE) of the coated and uncoated full cells are shown in Figure II.4.B.3. The full cells with Al_2O_3 coated cathode display rapidly ramped CE values up to more than 99.5%, which implies some of the side reaction has been impeded by the ALD coating layer. The cycle stability can thus be improved during the first tens of cycles remarkably. After 100 cycles at C/3 (1C = 147 mA/g), the CE values of cells with coated electrode reach 99.9%, while the uncoated cell can only achieve 99.75%. The capacity retention of the coated cells reaches 80.2% after 250 cycles, while the uncoated one only delivers less than 60%. Therefore, the coated cathode can effectively improve the cycle stability in the full cell level. The post-mortem STEM-EDS test results in Figure II.4.B.4 shows that the Al signal can still be observed on both the top and bottom parts of the electrode even after long-term cycling. Although, compared to the pristine state, the Al signal is less conformal and more dispersive to the particle bulk. The existence of Al demonstrates the robustness of the interphase, which could prevent Mn and Ni dissolution during cycling. Further investigation proving the dissolution of these two transition metal elements will be conducted by single layer pouch cells.

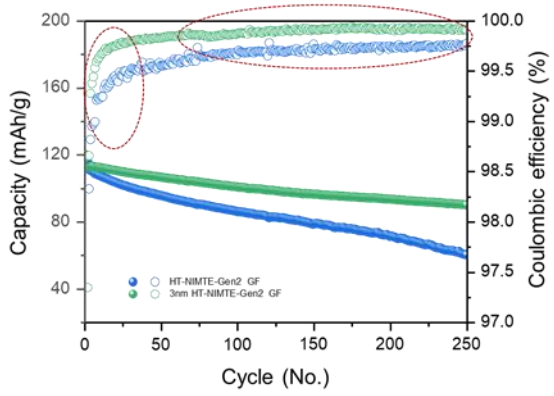

Figure II.4.B.3 Full cell testing performance with/without Al_2O_3 coating on the cathode side.

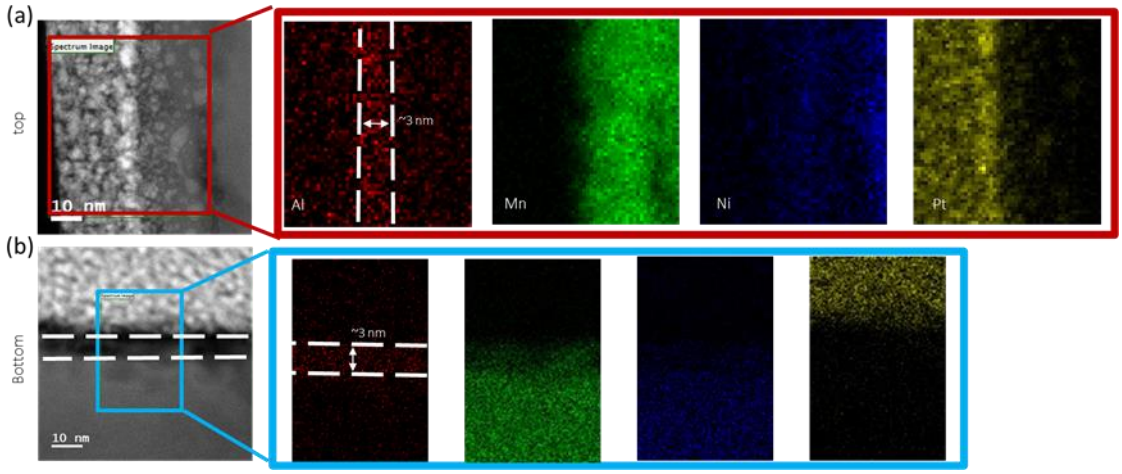

Figure II.4.B.4 STEM-EDS mapping of lamella from (a) top and (b) bottom part of the cycled cathode electrode.

Graphite coating with Al_2O_3 via ALD for improving full coin cell cycling stability

Based on the understanding of graphite degradation, UT Austin focused on graphite surface modification to stabilize the LNMO/graphite full cell. ALD technique was used to deposit an Al_2O_3 layer on graphite, which may serve as a uniform artificial AEI film on the graphite electrode. The pristine Al_2O_3-free graphite electrode with an areal capacity of ~ 2 mAh/cm^2 was purchased from MTI Corp. Figure II.4.B.5(a) presents the SEM image, and EDS elemental mapping of the cross-section of the graphite electrode with Al_2O_3 coated. As shown, the C, O, and Al elements are uniformly distributed throughout the electrode, indicating that the Al_2O_3 layer is homogeneously coated on the graphite particles.

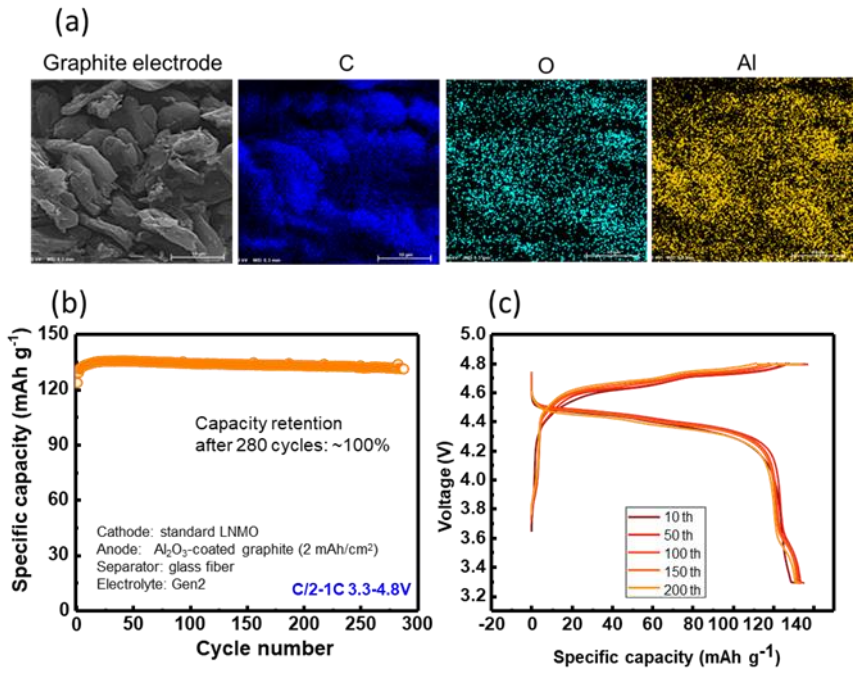

Figure II.4.B.5 (a) SEM-EDS mapping of ALD coated graphite; (b) Cycling performances and (c) voltage profiles of the full cell using ALD coated graphite.

LNMO/Graphite full cells were assembled with the standard LNMO synthesized by the UT Austin team and the ALD Al_2O_3-coated graphite with an N/P ratio of 1.1 - 1.15. Gen 2 was used as the electrolyte, and the

cycling voltage window was set between 3.3 - 4.85 V with a constant voltage during the charge. A rate C/10 was applied to the initial two formation cycles, and a C/3 rate was used for the following long-cycling test. As displayed in Figure II.4.B.5(b), the LNMO/graphite full cell with Al_2O_3-coated graphite shows superior cycling stability. The capacity retention after more than 280 cycles is around 100%. The improvement demonstrates that the Al_2O_3 layer acts as an artificial anode electrolyte interphase (AEI), preventing the formation of high-resistance AEI on the graphite surface and helping stabilize the graphite upon cycling. The ALD Al_2O_3-coated graphite sample will be sent to USCD for further testing.

LNMO thick electrode full cell evaluation with novel electrolytes

To aid in identifying a novel electrolyte formulation that can enhance thick electrode (~3 mAh/cm^2 areal capacity loading) full cell cycling retention and performance, an FEC-based electrolyte with the additive TMB (Trimethylboroxine) was proposed and tested last year by the ARL team. The same recipe was reproduced by the UCSD team.

Table II.4.B.1 Electrolyte Formulations

Name/ Supplier	Formulation
Gen2 / Gotion	1M $LiPF_6$ in EC/EMC = 3:7 wt%
FEC-based + TMB / ARL	1M $LiPF_6$ in FEC/DMC = 1:4 wt% with 0.25% TMB

The details of the recipes are shown inTable II.4.B.1, where Gen2 is a commercial product from the Gotion company, and the FEC+TMB is offered by the ARL team. The cycling performances of these two electrolytes with a 3 mAh/cm^2 level electrode are shown in Figure II.4.B.6(a)-(c). The FEC+TMB electrolyte results in a ~8% increase in cycling retention versus the Gen2 baseline, and the coulombic efficiencies show a more stable trend than Gen2. The cycled graphite samples were collected for further SEM-EDS and XPS analyses, as shown in Figure II.4.B.6(d) and (e), respectively. It was found that the FEC-TMB electrolyte could prevent the redeposition of Mn and Ni on the graphite side, which could be the result of performance improvements. Further designed experiments are ongoing to reveal the related mechanism.

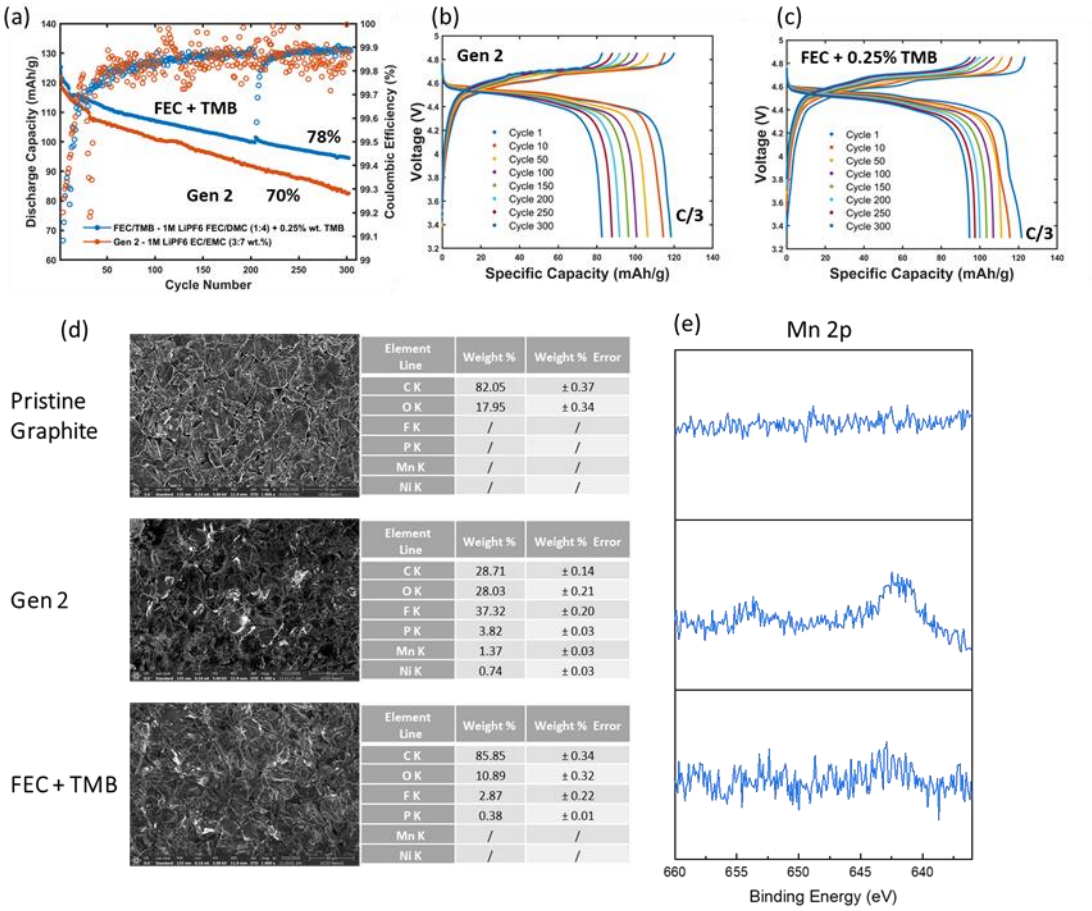

Figure II.4.B.6 (a) Cycling performances of cells using Gen2 and FEC+TMB electrolyte; Charge-discharge profiles of cells using (b) Gen2 and (c) FEC+TMB; (d) SEM-EDS and (e) XPS of graphite comparison.

Degradation mechanism study of LNMO-Gr cell comparing with NMC111-Gr cell

Single-layer pouch cells were assembled for mechanism studies, where the NMC111 cathode material was brought in as a reference. Four pouch cells were prepared using Gen2 electrolyte and disassembled after different cycles, two for LNMO-Graphite and two for NMC111-graphite. The photos of the disassembled cathode, separator, and the collected electrolyte from these four single layer pouch cells are shown in Figure II.4.B.7(a) with the electrochemical performances shown in Figure II.4.B.7(b). Delamination of the LNMO electrode from the Al current collector occurred after 1 cycle at C/3, with the electrolyte color changed to a darker brown with continued cycling. Meanwhile, the electrolyte retrieved from the NMC111 pouch cell was visibly unchanged for both short and long-term cycling compared to the pristine state. Electrolyte moisture test results and the Mn/Ni ICP results of four electrolyte samples are shown in Figure II.4.B.7(c) and (d), respectively. LNMO-graphite electrolyte shows the increasing moisture level trend and dissolved Mn/Ni amount, which indicates the instability of both electrolyte and cathode electrolyte interphase. The cycled graphite anodes from both NMC111 and LNMO pouch cells were collected and reassembled into half cells using a Li chip as the counter electrode. The related electrochemical performances are shown in Figure II.4.B.7(e), showing the cycled graphite from LNMO cells achieving lower coulombic efficiency values when compared to either pristine graphite or cycled graphite paired with NMC111. This conveys that the anode electrolyte interphase inside the LNMO-Graphite pouch cell is not stable as well. Both cathode and anode interphases in the LNMO-graphite cell are not stable during cycling, which may be due to the presence of moisture, accelerating the overall degradation of the cell.

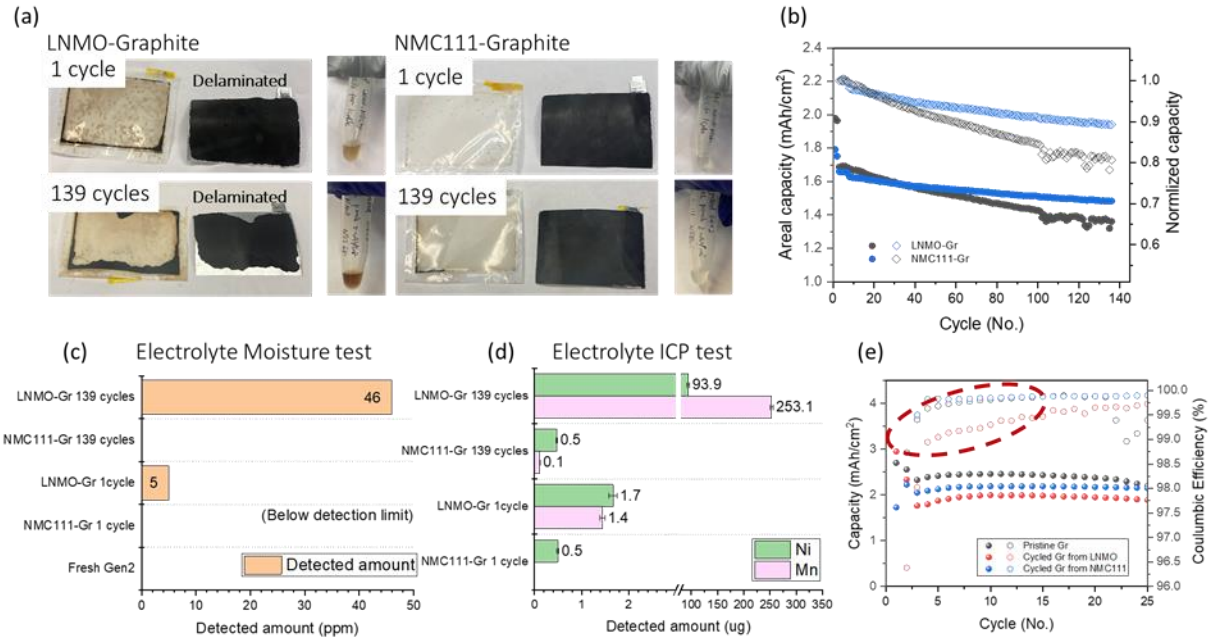

Figure II.4.B.7 (a) Disassembled single layer pouch cells using LNMO or NMC111 as cathode with different cycles; (b) Cycling performances of the single layer pouch cells; (c) electrolyte moisture test and (d) ICP test of electrolytes from single layer pouch cells; (d) Graphite electrodes harvested from different pouch cells reassemble test.

The porosity effect of high loading LNMO cathode on the electrochemical performance

Porosity control of the electrode is beneficial to increase the volume capacity and energy of the cells. However, the electrodes with too low porosity may suffer insufficient electrolyte wetting, broken secondary particles bringing extra side reactions. Thus, the high loading LNMO electrode was calendared to controlled porosity from 26% to 48% for electrochemical tests, as shown in Figure II.4.B.8. Based on both coulombic and energy efficiencies, discharge capacity, and energy density, it can be concluded that the porosity of the LNMO electrode had a negligible impact on the cycling performances except when the low value dropped to 26%. The optimized value would be around 37%.

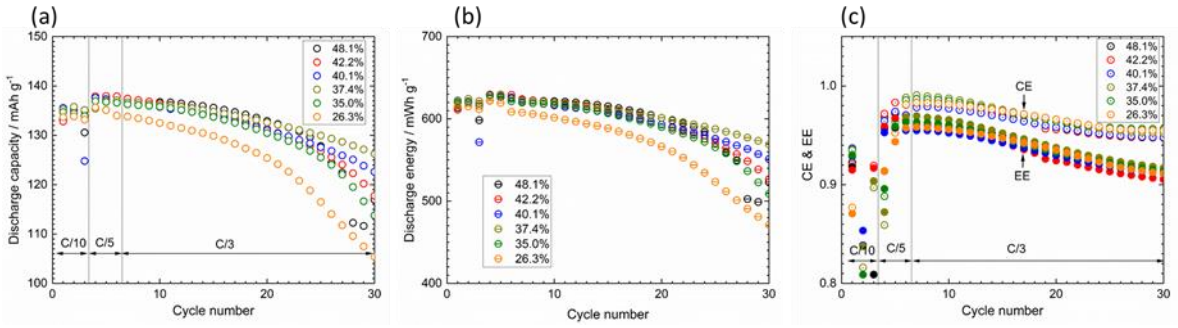

Figure II.4.B.8 The electrochemical performance of electrodes with varied porosity. (a) Coulombic and energy efficiencies; (b) discharge capacity and (c) energy density.

3 Ah multi-layer pouch cells delivery (2 mAh/cm²)

The multi-layer cell photo is shown in Figure II.4.B.9(a), and the cell with the stacking pressure controlling fixture during electrochemical cycling is in Figure II.4.B.9(b). One cell as a reference was tested internally at UCSD. The related charge-discharge profiles and the cycling performances are shown in Figure II.4.B.9(c) and (d). The cycling retention reached 95.7% after 50 cycles at C/3, and the cell impedance is well controlled, as shown in the voltage profile. The corresponding cell level energy densities, including volume and mass, are

shown in Table II.4.B.2. The prototype shows over 150 Wh/kg mass energy density and near 400 Wh/L as the volume energy density. Further increasing the areal capacity and decreasing the electrolyte amount will contribute to a higher energy density to meet commercialization demands. Eighteen cells with the same conditions have been delivered to Idaho National Laboratory (INL) for cycling and calendar life tests.

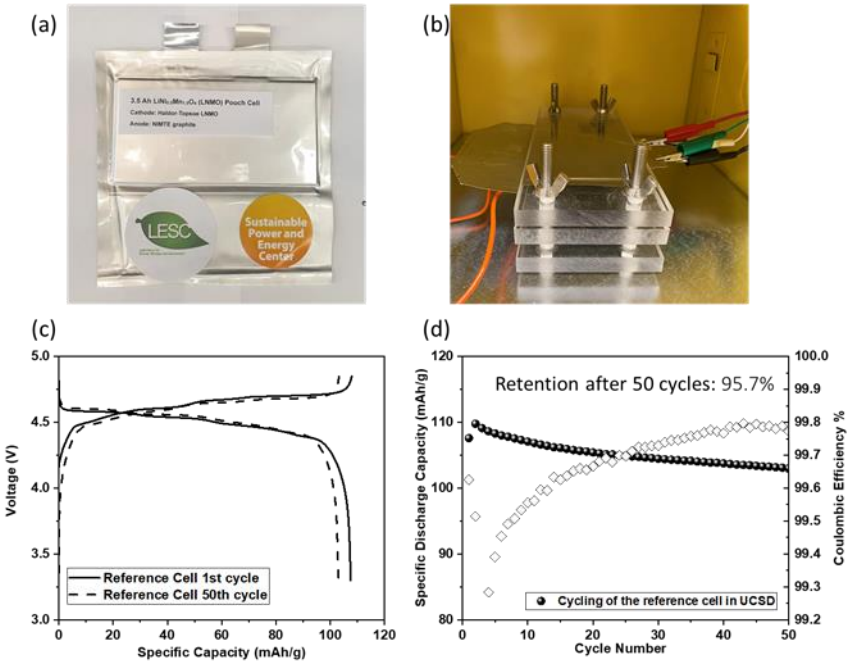

Figure II.4.B.9 3 Ah multi-layer pouch cell (a) with the LESC mark and (b) during cycling with a stacking pressure controlling fixture inside the safety box; (c) charge-discharge profiles and (d) cycling performances of the reference multi-layer pouch cell.

Table II.4.B.2 The Energy Density of the 3 Ah Multi-layer Pouch Cell

	Total mass of the cell (Wh/kg)	Cell without gas bag (Wh/kg)	Total volume of the cell (Wh/L)	Cell volume without gas bag (Wh/L)
Using C/20 energy (14.28 Wh)	151.9	156.2	393.6	421.5
Using 1st 3-hour energy (13.46 Wh)	143.2	147.2	371.0	397.3

Dry coated LNMO/graphite full pouch cell performance at 3 mAh/cm2 level

Both the coin cell and single-layer pouch cell at 3 mAh/cm^2 level were fabricated using the dry-coated LNMO (active mass loading ~22.5 mg/cm^2) provided by Tesla and wet-coated graphite (~9.5 mg/cm^2). Figure II.4.B.10(a) shows the advantage of using the dry-coated method. The active material can be well preserved on the Al current collector after long-term cycling, while the wet-coated electrode shows serious delamination issues after the same cycles. The discharge capacity is lower than our previous results in wet-coated LNMO /graphite pouch cells (101 mAh/g versus 120 mAh/g). Figure II.4.B.10 (b) shows the long-term cycling performances of both the coin cell and single layer pouch cell using the dry-coated electrode, with 66% and 60% as the capacity retentions after 118 cycles, respectively.

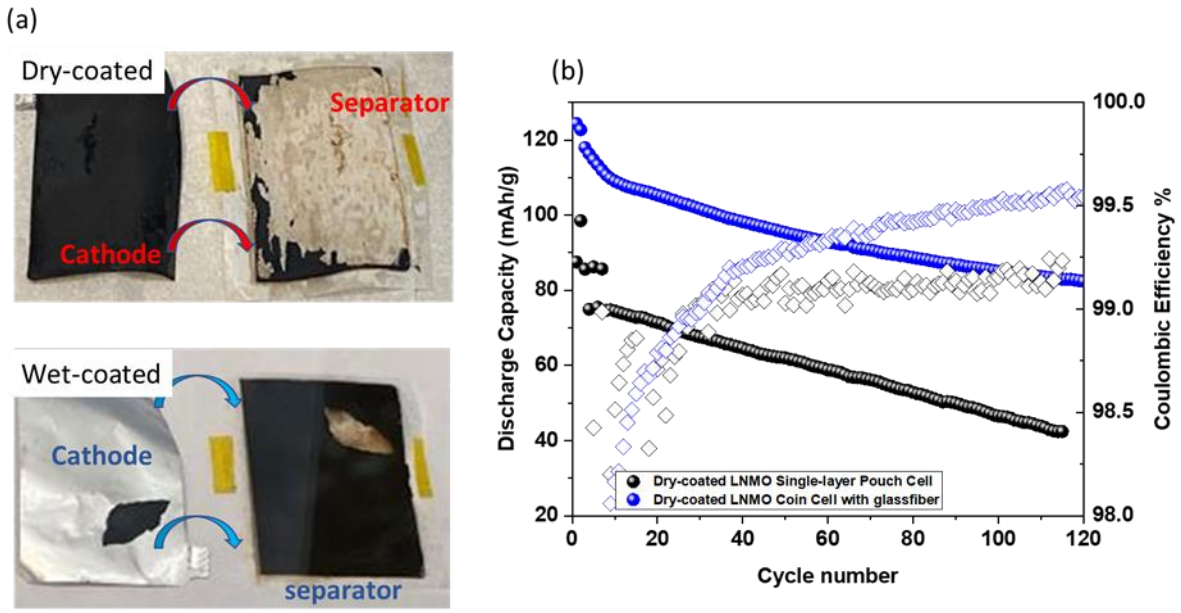

Figure II.4.B.10 (a) Dry-coated and wet-coated delamination issue comparison after cycling; (b) Electrochemical performances of single-layer pouch cell and coin cell using dry-coated electrode.

LNMO/graphite full cell performance at 4 mAh/cm² level

Haldor Topsoe LNMO (active mass loading ~28 mg/cm^2) and graphite electrode (active mass loading ~11.5 mg/cm^2) were prepared. The ratio of LNMO, PVDF, and the conductive agent is designed to be 90:5:5. The areal capacity of the cathode is calculated as the active mass loading multiplied by its initial charge capacity (~140 mAh/g) in the half cell. The porosity of the cathode was controlled to 40% through calendaring. The N/P ratio of the LNMO/graphite full cell, which is calculated using the areal capacity of the anode divided by that of the cathode, is controlled at around 1.10. LNMO and graphite electrodes were then assembled in CR2032 coin cells. During the cell assembly, a glass fiber separator was used, and 150 µL of Gen2 electrolyte was applied onto the separator to ensure complete wetting.

Figure II.4.B.11 (a) shows the cycling performance of LNMO/Graphite full cells. This cell delivers a 66% capacity retention after 500 cycles. Note that the inconsistency of the cells at the 4 mAh/cm^2 level is larger than the thinner loading version, which could be attributed to the difficulties during coin cell making. The glass fiber separator indeed improves the electrode wetting and offers an optimum internal stack pressure. However, the thick and porous nature of glass fiber makes cathode/anode alignment much more challenging since the wetted glass fiber is not as transparent as the Celgard separator. In summary, the successful cycling of 4 mAh/cm^2 level LNMO/graphite full cells will require complete wetting of both cathode and anode under an optimum stack pressure to improve the ionic conductivities of both ends. The future plan will be utilizing the single-layer pouch cell to enable the 4 mAh/cm^2 level thick electrode since stack pressure can be well controlled in the pouch cell setup.

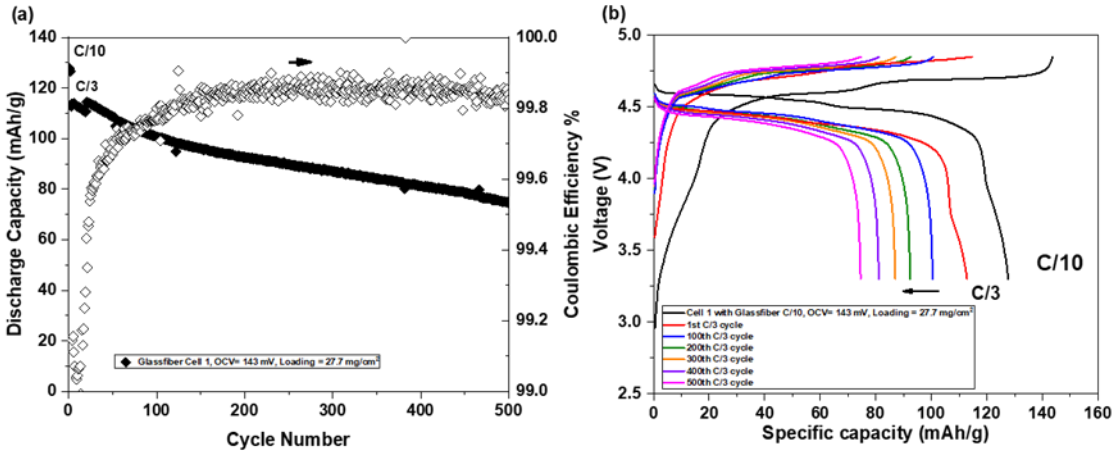

Figure II.4.B.11 (a) Cycling performance and (b)voltage profiles of LNMO/graphite full cells at 4 mAh/cm2 level.

Conclusions

The uniform Al_2O_3 coating layer was successfully applied to both the LNMO cathode and graphite anode by atomic layer deposition to improve electrochemical performances. Even after hundreds of high voltage cycles, the deposited Al_2O_3 coating layer remained. The best cell with 2mAh/cm^2 coated graphite shows no degradation after more than 280 cycles. The FEC based electrolyte with TMB as the additive offers improved cycle stability in 3mAh/cm2 electrode full cell. The post-mortem SEM-EDS and XPS revealed that the novel electrolyte could prevent the redeposition of Mn/Ni on the graphite. Cycled electrolyte samples from single layer pouch cells were collected and tested. The increasing amount of moisture in the LNMO-graphite cell could trigger the degradation of both CEI and AEI, which would be the major reason for fast capacity decay. The porosity of thick LNMO cathode was optimized carefully; either too small or too large would lead to lousy cycling performance, and the optimized value was around 37%. 3 Ah multi-layer pouch cells were prepared using the optimized recipe, delivering 95.7% cycling retention after 50 cycles. Eighteen of these cells were shipped to INL for further testing. Dry-coated LNMO electrode shows better adhesion after high voltage cycling than wet-coated electrode. Thick LNMO cathode with 4 mAh/cm^2 areal loading have been prepared, and the electrochemical performance has been evaluated with cycling retention of 66% after 500 cycles.

Key Publications

1. W. Li, M. Zhang, Y. S. Meng, et al., Enabling High Areal Capacity for Co-free High Voltage Spinel Materials in Next-generation Li-ion Batteries. *Journal of Power Sources*, **2020**, *473*, 228579.

References

1. Ohzuku, T.; Takeda, S.; Iwanaga, M. Solid-State Redox Potentials for Li[Me1/2Mn3/2]O4 (Me: 3d-Transition Metal) Having Spinel-Framework Structures: A Series of 5 Volt Materials for Advanced Lithium-Ion Batteries. *J. Power Sources* **1999**, *81-82*, 90–94.

2. Lu, J.; Lee, K. S. Spinel Cathodes for Advanced Lithium Ion Batteries: A Review of Challenges and Recent Progress. *Mater. Technol.* **2016**, *31* (11), 628–641.

Acknowledgements

This project was conducted by a team whose other partners included Arumugam Manthiram (University of Texas at Austin), Hieu Duong (Tesla, Inc.), Vince Battaglia (Lawrence Berkeley National Laboratory), and Kang Xu and Marshall Schroeder (Army Research Laboratory). We also thank Dr. Aaron D. Yocum (NETL manager), Dr. Yi Ding (TARDEC manager), Dr. Ahmad Pesaran (NREL manager), Dr. Jack Deppe (INL manager) for supporting our work.

II.4.C Novel Lithium Iron and Aluminum Nickelate (NFA) as Cobalt-Free Cathode Materials (ORNL)

Dr. Ilias Belharouak, Principal Investigator
Distinguished R&D Scientist & Section Head - Electrification
Electrification and Energy Infrastructures Division
Oak Ridge National Laboratory,
2370 Cherahala Blvd.
Knoxville, Tennessee, 37932
E-mail: belharouaki@ornl.gov

Peter Faguy, DOE Technology Development Manager
U.S. Department of Energy
E-mail: Peter.Faguy@ee.doe.gov

Start Date: October 1, 2018 End Date: September 30, 2021
Project Funding: $2,100,000 DOE share: $2,100,000 Non-DOE share: $0

Project Introduction

US DOE's cost and performance targets for electric vehicles includes lowering the production cost of modern batteries to less than $80/kWh, increasing the range of EVs to 300 miles and decreasing charging times to 15 minutes or less. Realization of the cost target, requires the focus of current battery research to be reframed towards the reduction of cobalt content in modern battery cathode materials to less than 50 mg/Wh at the cell level.[1] Achieving this target, however, poses unique challenges as the present-day mainstream commercial battery cathode materials; $LiNi_xMn_yCo_zO_2$ (NMC) and $LiNi_{0.8}Co_{0.15}Al_{0.05}O_2$ (NCA), contain substantial amounts of cobalt in their compositions. Additionally, compounding this problem, price of the cobalt raw material has been constantly fluctuating with an increasing trend over the past half-decade with prices almost tripling in the recent years. The Cobalt Development Institute (CDI) published a recent report which indicated that nearly 58% of global cobalt production is currently used in critical industrial and military applications to manufacture super alloys, catalysts, magnets, pigments, etc.[2] The companies that are engaged in this sector can sustain the cobalt price fluctuations even in the case of severe shortages as it currently constitutes only a negligible part of their material costs. However, in the case of battery manufacturing industry with tighter profit margins, this scenario exacerbated by a supply chain constraint would pose a crippling threat. The forecasted burgeoning projections for EV markets would remain a distant dream if an economically viable alternative to this cobalt problem is not immediately found. This project tackles this problem through a paradigm shifting approach that examines the question of whether cobalt is needed at all in modern battery cathodes. The primary objective here is to research, develop and scale a novel class of cobalt free battery cathode material – lithium, iron, and aluminum nickelate, $LiNi_xFe_yAl_zO_2$ (NFA: Ni, Fe, Al) class of cathodes. These new cathodes are expected to facilitate a seamless transition in the battery manufacturing industry, moving away from expensive cobalt while maintaining or exceeding the benefits offered by cobalt containing NCAs and NMCs.

Objectives

The overall research goal for this project is to implement $LiNi_{0.8(0.9)}Fe_{0.2(0.1)-x}Al_xO_2$ (NFA) as novel cobalt-free cathodes in large format Li-ion cells achieving the following performance and cost targets:

1. Zero (0) cobalt loading as NFA cathodes only have nickel (80%–90%), and the balance (10%–20%) is a combination of iron and aluminum.

2. 650-750 Wh/kg usable specific energy at C/3 rate at the material level at the beginning of life.

3. Thousand (1000) deep charge and discharge cycles at the C/3 rate with less than 20% capacity fade in 2.3 Ah cells.

4. Less than $100 per kWh at the cell level.

Approach

Three major approaches at the material level will be implemented in this work:

1. Optimization of the amounts of Al^{3+} which favors the stabilization of nickel in the 3+ oxidation state, which ensures the dual dimensionality and oxygen stability in the cathodes. *(good for reversibility and cycle life)*

2. Introduction of controlled amounts of Fe^{3+} (equal or less than 10%) to improve the electronic conductivity in the Ni-Al slab. *(good for power)*

3. Fine-tuning of the synthesis conditions and processes to yield highly-ordered layered NFA cathodes with higher packing densities to achieve higher energy densities without compromising cycling performance. *(good for translating the material properties and performance from bench scale to pilot scale)*

Results

Technical accomplishments for the previous fiscal year include successful investigation of the compositional landscape, scale-up and fabrication of cobalt free batteries enabled by generation 1 NFA cathode material (≥80% nickel), $LiNi_{0.8}Fe_xAl_yO_2$ (x+y=0.2). Figure II.4.C.1 shows the fabrication process and electrochemical performance of cobalt free lithium ion batteries using a Gen-1 NFA cathode material developed at ORNL. The co-free batteries fabricated using conventional protocols optimized for nickel rich cobalt containing batteries (Figure II.4.C.1(A)), demonstrated reasonable cycling stabilities at C/3 in the voltage window 3V – 4.4V (Figure II.4.C.1(B)). For the current fiscal year, the task flow of the project comprises of investigating the compositional landscape followed by the scale-up of best performing composition in the Gen-2 NFA space (≥90% nickel), $LiNi_{0.9}Fe_xAl_yO_2$ (x+y=0.1), for evaluation in full cell Gen-2 cobalt free lithium ion batteries. Initially, the sol-gel process was employed to investigate the compositional landscape which was followed by scale-up using the co-precipitation process in large continuous stirred tank reactors (CSTR). Figure II.4.C.2(A) shows the microstructure of Gen-2 NFA cathode particles synthesized using sol-gel method. For the sol-gel process, the transition metal reagents (Ni, Fe) along with lithium and aluminum reagents in appropriate molar concentrations were dissolved in DI water. The resulting solution mixture was then heated at 60 ^oC under continuous stirring to obtain a clear gel which was then evaporated to obtain the precursor powders. The precursor powders were then subjected to heat treatment initially at <600 ^oC to burn off organics followed by calcination in oxygen atmospheres (700 – 800 ^oC). The calcined powders were ground using a mortar and pestle to obtain the final NFA cathode powders. Scanning electron micrographs for the sol-gel synthesized Gen-2 NFA cathode powders are shown in Figure II.4.C.2(A) and (B). The SEM micrographs show primary particles of NFA forming secondary aggregates which is a characteristic of such powders synthesized using the Sol-Gel process[3]-[6]. The sol-gel process enables quick exploration of the compositional landscape of the NFA Gen-2 class even though morphological control of the powders was challenging. Crystallographic evaluation of the Gen-2 NFA variant was performed using the X-Ray Diffraction technique. The X-Ray diffractogram shown in Figure II.4.C.2(C) showed phase purity with well-ordered crystal structures in the R-3m space group. The observed diffraction patterns are consistent with the layered pure phase α-$NaFeO_2$ [6]-[8]. Cation mixing characterized by the intermixing of some Ni^{2+} ions and Li^+ ions between the two layers is an important parameter for nickel rich class of cathodes. The extent of cation mixing directly affects the electrochemical performance of the cathode material as the intermixing of ions causes ion migration bottlenecks thereby lowering the capacity delivered [9]. This parameter can be assessed using the ratio between the intensities of (003) and (104) peaks observed in the diffractograms. It was observed that the Gen-2 NFA cathode material synthesized using the sol-gel process had minimal cation mixing characterized by the high (003)/(104) ratio (>1.5).

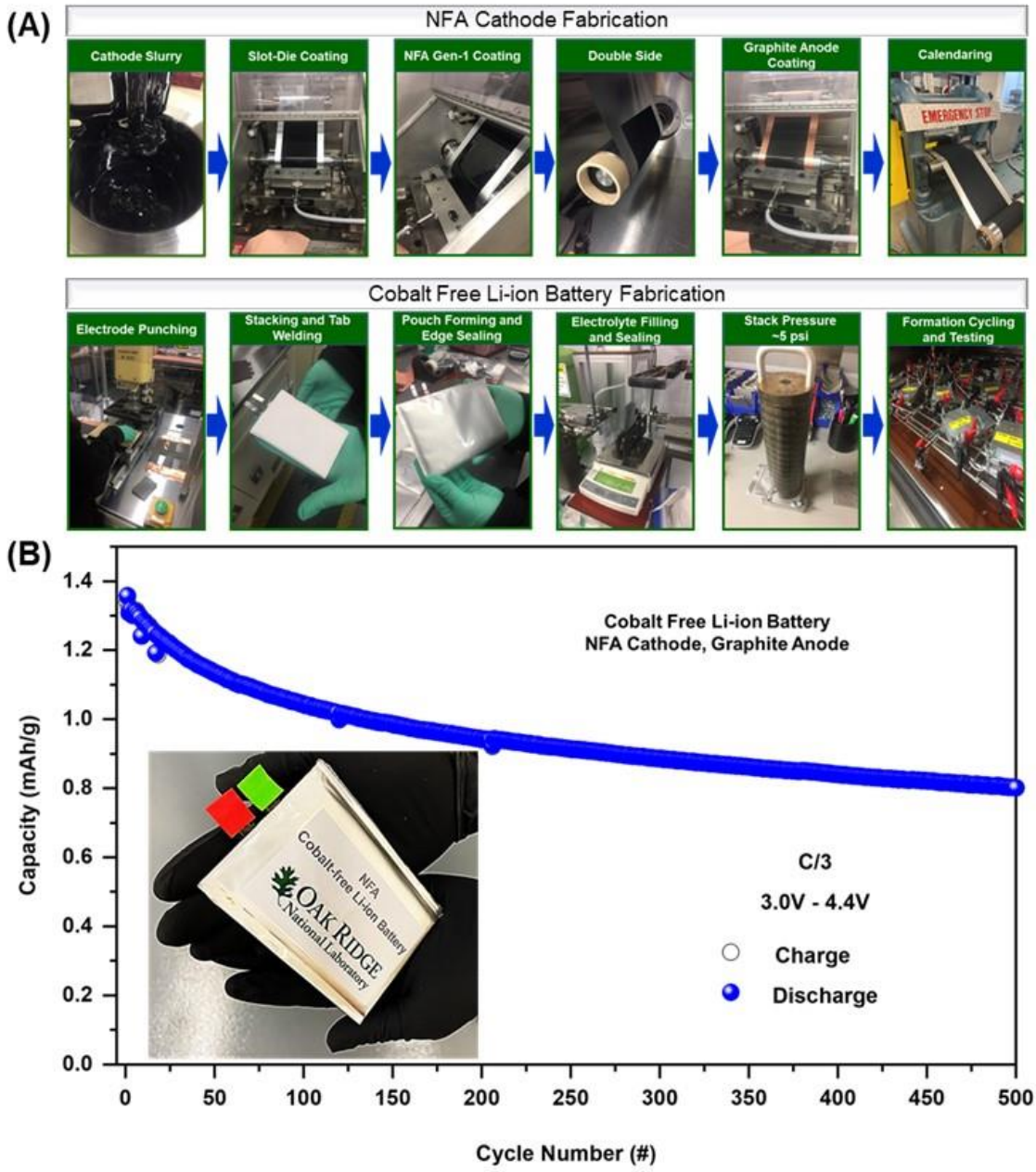

Figure II.4.C.1 (A) Fabrication process flow for NFA electrode and cobalt free battery enabled by the NFA cathode material and (B) Electrochemical charge/discharge cycling performance of the cobalt free Li-ion battery at C/3 between 3.0V – 4.0V

Electrochemical performance evaluation of the sol-gel synthesized Gen-2 cathode material was performed in half-cell configurations against lithium metal anodes. 2032-coin cells with the Gen-2 NFA material as the cathode (80 wt. % as synthesized powder, 10 wt. % PVDF binder and 10 wt% conductive carbon additive (Denka)), Gen-2 electrolyte and Li metal as the anode were assembled and evaluated. The material delivered ~230 mAh/g at 0.1C in the voltage window 3V – 4.5V as observed from the galvanostatic charge/discharge profiles (Figure II.4.C.2(D)). When the upper cut off voltage was lowered to 4.3V, the material still delivered a high capacity of 192 mAh/g at 0.1C. Galvanostatic charge/discharge cycling performance evaluation of the cathode material was performed at a c-rate of C/3 in three voltage windows; 3V-4.5V, 3V-4.4V and 3V-4.3V (Figure II.4.C.2(E)). In the voltage window 3V-4.5V and 3V-4.4V, the material exhibited greater capacity fade with continuous charge/discharge cycling. In the voltage window 3V-4.3V, the material showed minimal

capacity fade when cycled at a high c-rate of C/3 even after 500 continuous cycles. Overall, these electrochemical assessments emphasize the feasibility of the Gen-2 NFA class of cathodes in achieving the overall project objectives.

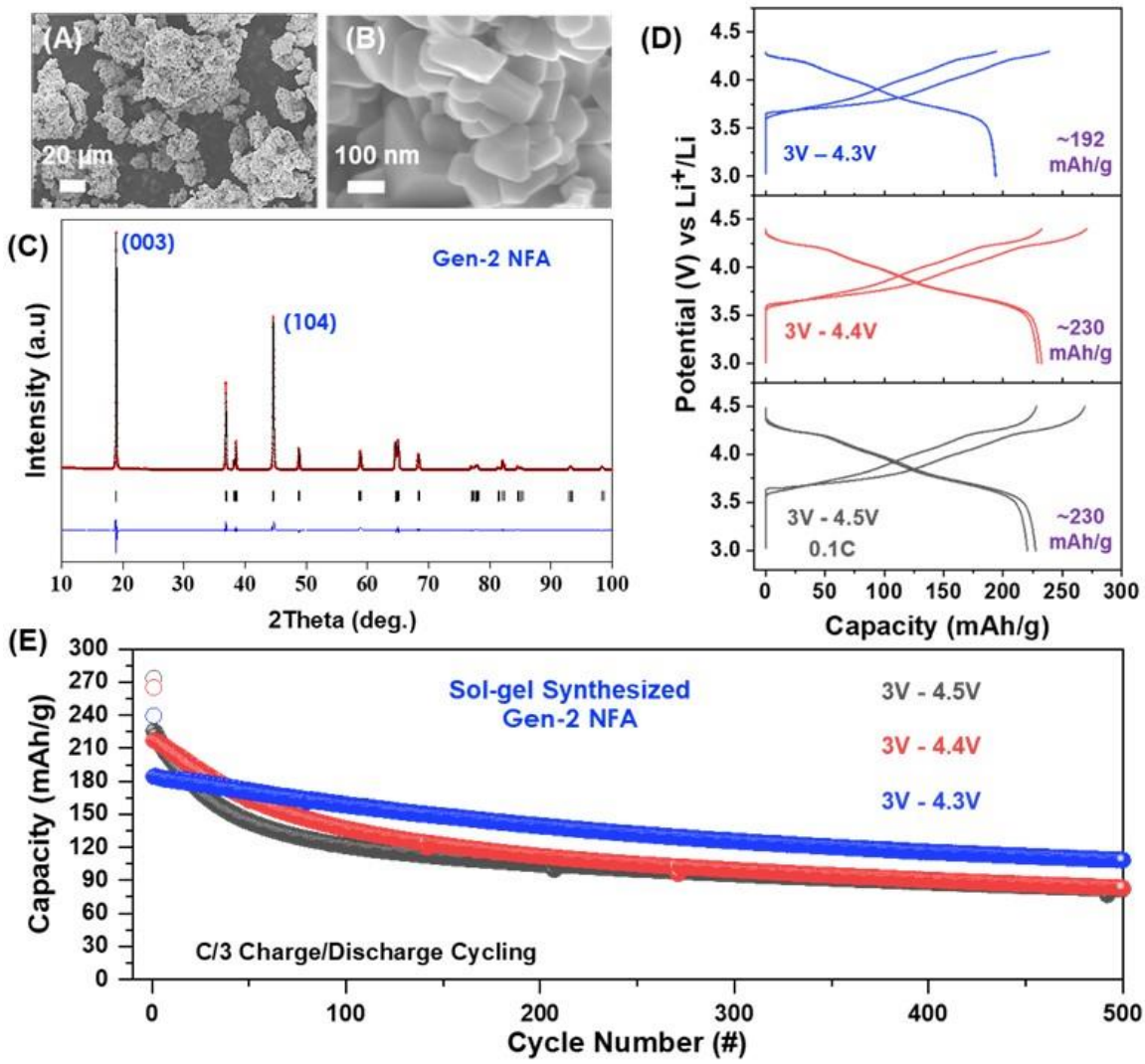

Figure II.4.C.2 Sol-gel synthesized Gen-2 NFA cathode material: (A) and (B) SEM micrographs, (C) X-Ray Diffractogram, (D) Galvanostatic charge/discharge profiles and (E) Galvanostatic charge/dishcarge cycling performance assessment at various upper cut off voltages

The best performing composition in the Gen-2 NFA landscape was chosen for upscaling using the co-precipitation process in a large continuous stirred tank reactor (CSTR). A major advantage of the co-precipitation process is that large quantities of good morphologically controlled spherical Gen-2 NFA cathode powders can be obtained. Figure II.4.C.3(A) shows a schematic representation of the process where the material is first synthesized in the form of a spherical precursor ($Ni_{0.9}Fe_xAl_y(OH)_2$) starting from the transition metal sources in the form of sulfates which are pumped into the reaction vessel containing a solution of ammonia and water at a pH >11. The base solution containing appropriate amounts of NaOH and ammonia are added to precipitate the Gen-2 NFA hydroxide precursor. PH of the process and stirring speed was maintained at a constant value and was continuously monitored throughout the process. Figure II.4.C.3(B) and (C) show SEM micrographs of the synthesized Gen-2 NFA precursor in the hydroxide form. Morphological assessment reveals good spherical morphologies with good homogeneities. Over 1kg batches at a given time per co-precipitation run can be synthesized through this process. The synthesized precursors were then mixed with

appropriate amounts of lithium source followed by heat treatments. The heat treatment protocols involve a pretreatment step (400-600 ºC) to burn off the organics followed by calcination in oxygen atmospheres at elevated temperatures (>700 ºC). Figure II.4.C.3(D) and (E) show SEM micrographs of the calcined and lithiated Gen-2 NFA powders. The calcined powders maintained their good spherical morphologies and homogeneities. Preliminary electrochemical evaluations of the scaled-up Gen-2 NFA cathode material was performed in half cell configurations. The Gen-2 NFA electrode (80 wt. % as calcined powder, 10 wt. % PVDF binder and 10 wt% conductive carbon additive (Denka)), Gen-2 electrolyte and Li metal as the anode were assembled in 2032-coin cells and were electrochemically evaluated. The Gen-2 material delivered a high capacity of ~227 mAh/g at C/3 in the voltage window 3V-4.5V. When the upper cut off voltage was lowered to 4.3V, the material still delivered a high capacity of ~222 mAh/g, which was lowered to 171 mAh/g when the upper cut off voltage was set at 4.2V. These preliminary electrochemical investigations indicate that the Gen-2 version of the NFA cathode material can successfully meet the overall project objectives and goals. Additionally, further systematic studies into the charge storage mechanisms and post-mortem analysis of cycled electrodes using advanced operando and in-situ characterization techniques are presently underway. Overall, these results highlight the potential of the NFA class of cobalt free cathodes for the development of next generation battery systems for electric vehicle applications.

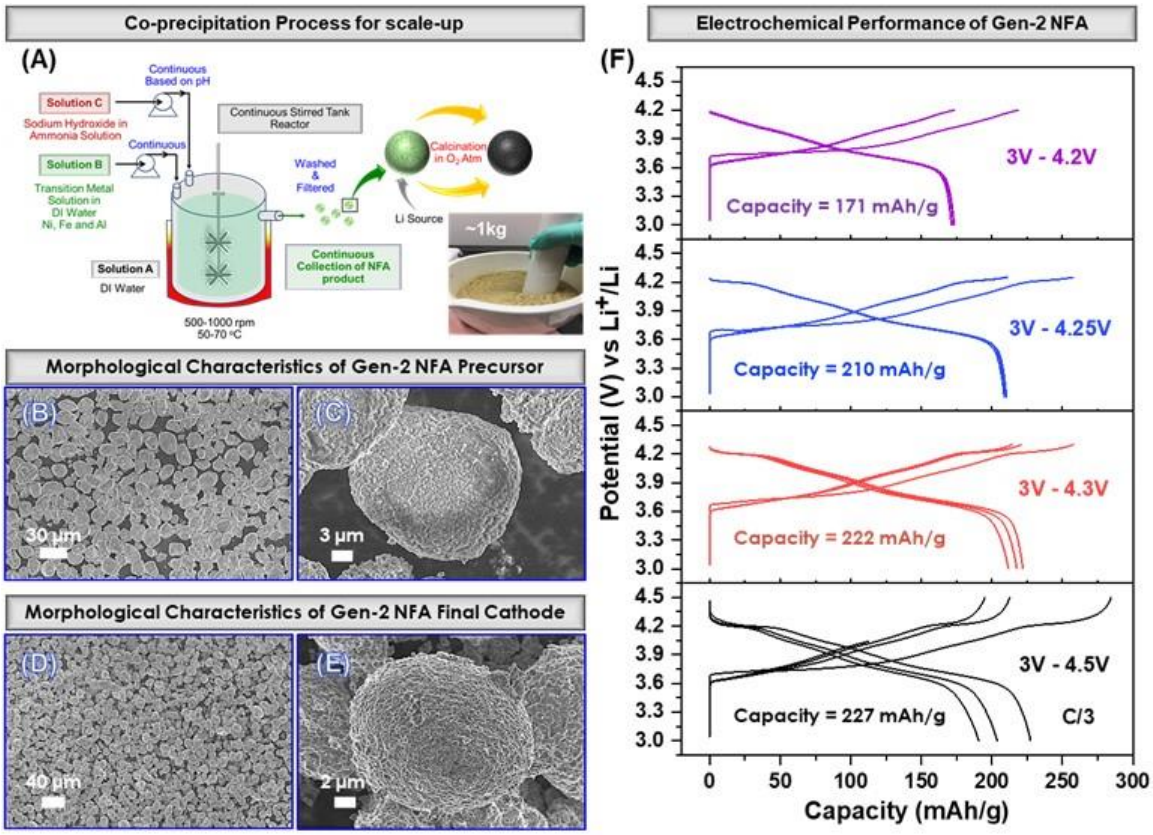

Figure II.4.C.3 Co-precipitation synthesized Gen-2 NFA cathode material: (A) Shcematic representation of the co-precipitation process (B) and (C) SEM micrographs of the Gen-2 NFA Precursor, (D) and (E) SEM micrographs of the Gen-2 NFA final cathode material (F) Galvanostatic charge/discharge profiles at various upper cut off voltages at C/3

Conclusions

To summarize, this research effort was directed towards the development of a novel class of cobalt free cathode lithium ion battery cathode, the NFA class, to target the latest US DOE's battery cost and performance targets. Technical accomplishments achieved so far include successful synthesis, evaluation and scale-up of Gen-1 NFA compositions (≥80% nickel) and, fabrication and electrochemical performance assessment of cobalt-free lithium ion batteries enabled by the Gen-1 NFA cathodes. Building off these successes, during the

current fiscal year, Gen-2 NFA compositions comprising ≥90% nickel were initially synthesized using the sol-gel process for a thorough evaluation of the compositional landscape of this system. Following which, compositional and phase purity, crystallographic stability and electrochemical performance of the synthesized material were evaluated. The best performing Gen-2 NFA cathode material was then scaled-up in large CSTRs using the co-precipitation process. Microstructural characterization revealed Gen-2 NFA precursors with spherical morphology which was maintained even after high temperature calcination processes. Electrochemical assessments indicate that the material delivers high capacities (>200 mAh/g) and demonstrates good cycling stabilities that warrant further investigations, thus highlighting the potential of the Gen-2 NFA class of cathodes in meeting the overall project objectives. Overall, the systematic approaches described in this work provide several key directions and insights on the NFA system which shows immense promise for the development of next generation li-ion batteries.

Key Publications

1. Muralidharan, Nitin, Rachid Essehli, Raphael P. Hermann, Anand Parejiya, Ruhul Amin, Yaocai Bai, Zhijia Du, and Ilias Belharouak. "LiNixFeyAlzO2, a new cobalt-free layered cathode material for advanced Li-ion batteries." Journal of Power Sources 471 (2020): 228389.

2. Muralidharan, Nitin, Rachid Essehli, Raphael P. Hermann, Ruhul Amin, Charl Jafta, Junjie Zhang, Jue Liu et al. "Lithium Iron Aluminum Nickelate, LiNixFeyAlzO2—New Sustainable Cathodes for Next-Generation Cobalt-Free Li-Ion Batteries." Advanced Materials 32, no. 34 (2020): 2002960.

3. Belharouak, Ilias, Marissa Wood, Chengyu Mao, Jianlin Li, Jagjit Nanda, and Nitin Muralidharan. "Cobalt-free layered oxide cathodes." U.S. Patent Application 16/750,171, filed July 23, 2020.

4. Belharouak, Ilias, and Nitin Muralidharan. "Battery Materials Scale-up and Processes." U.S. Patent Application 16/781,063, filed August 6, 2020.

5. Muralidharan, Nitin, Rachid Essehli, Ethan Craig Self, Jagjit Nanda, and Ilias Belharouak. "Investigating the Origin of Cation Mixing in Nickel Rich Cathodes." In 236th ECS Meeting (October 13-17, 2019). ECS, 2019.

References

1. D. Howell, Vehicle Technologies Office Merit Review 2017: Overview of the DOE VTO Advanced Battery R&D Program, https://www.energy.gov/eere/vehicles/downloads/vehicle-technologies-office-merit-review-2017-overview-doe-vto-advanced

2. Sebastien Gandon, No cobalt, no Tesla?, https://techcrunch.com/2017/01/01/no-cobalt-no-tesla/

3. Ilango, P. Robert, T. Subburaj, K. Prasanna, Yong Nam Jo, and Chang Woo Lee. "Physical and Electrochemical Performance of LiNi 1/3 Co 1/3 Mn 1/3 O 2 Cathodes Coated by Sb 2 O 3 Using a Sol–gel Process." Materials Chemistry and Physics 158 (2015): 45-51.

4. Lee, Suk-Woo, Hyungsub Kim, Myeong-Seong Kim, Hee-Chang Youn, Kisuk Kang, Byung-Won Cho, Kwang Chul Roh, and Kwang-Bum Kim. "Improved electrochemical performance of LiNi0. 6Co0. 2Mn0. 2O2 cathode material synthesized by citric acid assisted sol-gel method for lithium ion batteries." Journal of Power Sources 315 (2016): 261-268.

5. Xiang, Yanhong, Zhen Sun, Jian Li, Xianwen Wu, Zhixiong Liu, Lizhi Xiong, Zeqiang He, Bo Long, Chen Yang, and Zhoulan Yin. "Improved electrochemical performance of Li1. 2Ni0. 2Mn0. 6O2 cathode material for lithium ion batteries synthesized by the polyvinyl alcohol assisted sol-gel method." Ceramics International 43, no. 2 (2017): 2320-2324.

6. Muralidharan, Nitin, Rachid Essehli, Raphael P. Hermann, Ruhul Amin, Charl Jafta, Junjie Zhang, Jue Liu et al. "Lithium Iron Aluminum Nickelate, LiNixFeyAlzO2—New Sustainable Cathodes for Next-Generation Cobalt-Free Li-Ion Batteries." Advanced Materials 32, no. 34 (2020): 2002960.

7. Belharouak, I., Y-K. Sun, J. Liu, and K. Amine. "Li (Ni1/3Co1/3Mn1/3) O2 as a suitable cathode for high power applications." Journal of Power Sources 123, no. 2 (2003): 247-252.

8. Belharouak, Ilias, Wenquan Lu, Donald Vissers, and Khalil Amine. "Safety characteristics of Li (Ni0. 8Co0. 15Al0. 05) O2 and Li (Ni1/3Co1/3Mn1/3) O2." Electrochemistry Communications 8, no. 2 (2006): 329-335.

9. Myung, Seung-Taek, Filippo Maglia, Kang-Joon Park, Chong Seung Yoon, Peter Lamp, Sung-Jin Kim, and Yang-Kook Sun. "Nickel-rich layered cathode materials for automotive lithium-ion batteries: achievements and perspectives." ACS Energy Letters 2, no. 1 (2016): 196-223.

Acknowledgements

We would like to acknowledge Dr. Nitin Muralidharan, Dr. Rachid Essehli, Dr. Jagjit Nanda, Dr. Ruhul Amin, Dr. Jue Liu, Dr. Ethan Self, Dr. Sergiy Sazhin and Dr. Raphael Hermann for their involvement with the synthesis, characterization, and useful discussions regarding this work.

II.4.D Enhancing Oxygen Stability in Low-Cobalt Layered Oxide Cathode Materials by Three-Dimensional Targeted Doping (UC Irvine)

Huolin Xin, Principal Investigator
University of California, Irvine
4129 Frederick Reines Hall
Irvine, CA, 92697-4575
E-mail: huolin.xin@uci.edu

Feng Lin, Principal Investigator
Virginia Tech
Department of Chemistry
Blacksburg, VA, 24061
E-mail: fenglin@vt.edu

Kristin Persson, Principal Investigator
University of California Berkeley,
210 Hearst Mining Building
Berkeley, CA, 94720
E-mail: kristinpersson@berkeley.edu

Wu Xu, Principal Investigator
Pacific Northwest National Laboratory
902 Battelle Boulevard
Richland, WA 99354
E-mail: wu.xu@pnnl.gov

Jiang Fan, Principal Investigator
American Lithium Energy Corporation
2261 Rutherford Rd
Carlsbad, CA 92008
E-mail: jfan@americanlithiumenergy.com

Peter Faguy, DOE Technology Development Manager
U.S. Department of Energy
E-mail: Peter.Faguy@ee.doe.gov

Start Date: November 1, 2018 End Date: October 31, 2021
Project Funding: $3,250,000 DOE share: $2,625,000 Non-DOE share: $625,000

Project Introduction

In this project, we propose to develop a new concept and a generic platform that can lead to the greatly enhanced stabilization of all high-energy cathode materials, and in particular high-nickel (Ni) and low-cobalt (Co) oxides. The new concept is a 3D doping technology that hierarchically combines surface and bulk doping. We will use surface doping to stabilize the surface of primary particles and also introduce dopants in the bulk to further enhance oxygen stability, conductivity, and structural stability in low-Co oxides under high voltage and deep discharging operating conditions. This new concept not only will deliver a low-cost, high-energy cathode but also will provide a generic method that can stabilize all high-energy cathodes. The proposed novel 3D doping approach is poised to resolve some longstanding challenges in fundamental doping effects on battery materials as well as to reduce Li-ion batteries' cost and improve their safety, energy density, and lifetime.

To tackle this problem, we have formed a highly complementary multi-university/national labs/industry team to enable a doping-central and systematic investigation of low-Co materials and create a knowledge base for many electrode materials to be used in advanced electric vehicles. The successful execution of the proposed project relies on five components that can be carried out by the complementary team members: (1) a theoretical investigation of surface and bulk stabilizing dopants (Persson), (2) precise synthesis of materials with targeted doping (Lin and Xin), (3) development of electrolytes for high-Ni low-Co oxides (Xu), (4) multi-scale characterization of the structures and their interfaces by scanning transmission electron microscopy (SEM) and synchrotron X-ray imaging and spectroscopy tools (Xin and Lin), and (5) pouch cell-level integration (Fan). The UCI-led project will enable a doping-central and systematic investigation of low-Co materials and create a knowledge base for many electrode materials to be used in advanced electric vehicles.

Objectives

The primary objectives of this project are:

- Displace Co while maintaining high-Ni content and high energy density: Cobalt concentration < 50 mg/Wh or No-Co, Energy density > 750 Wh/kg (C/3, 2.5-4.4 V) at cathode level, Cost ≤ $100/kWh
- Improve cycle and calendar life by retaining oxygen through a 3D doping technology: Capacity retention > 80% at 1,000 cycles, energy retention > 80% at 1,000 cycles, calendar life: 15 years
- Deliver a theoretical model: High-throughput DFT calculations that rationalize the selection of oxygen-retraining surface and bulk dopants
- Develop electrolytes with functional additives to form high-quality surface protection layers on both high-Ni/low-Co layered oxides and graphite anode to help the whole project achieve the proposed energy and capacity retention target, i.e. >80% at 1,000 cycles. The FY19 work will focus on electrolyte formulating for NMC811 baseline cathode and graphite anode.
- Offer a knowledge base by performing proactive studies of thermal stability, oxygen loss, and the degradation of the cathode/electrolyte interfaces.

Approach

- We utilize a three-dimensional (3D) doping technology that is a hierarchical combination of surface and bulk doping: (1) Surface doping stabilizes the interface between the primary particles and the electrolyte. (2) Introduction of dopants to the bulk enhances oxygen stability, conductivity and structural stability in low-Co oxides under high voltage and deep discharging operating conditions. (3) A composition controlled and thermodynamics driven synthesis will be used to accurately achieve the desired 3D doping structures.
- Using first-principle calculations to predict surface dopants for oxygen retention at surface of LiNiO2 and rationalize the effectiveness of dopants.
- Formulate new electrolytes that stabilize the cathode/electrolyte interfaces at deep charging conditions: (1) Coin cell testing of commercial baseline materials. Perform coin cell electrochemical studies of baseline commercial NMC811 cathode and graphite (Gr) anode using the baseline electrolyte to establish coin cell-level benchmarks. (2) Coin cell testing of NMC-D. Evaluate the capacity and cycle life of the synthesized 3D doped cathode materials at the coin cell level using the baseline electrolyte. The results will be compared with the commercial NMC811 baseline. (3) Electrolyte formulating. Formulate functional localized high-concentration electrolytes (LHCEs) to improve cycle life and safety of baseline commercial NMC811 cathode and Gr anode at coin cell level, optimize electrolyte formulation for NMC-D-90532, and compare with electrolyte baseline for >200 cycles in Gr||NMC full cells at 4.4 V cutoff.

- Advanced computational and characterization techniques are developed to study: (1) dopant environment and chemistry. (2) thermal stability, oxygen loss, and the degradation of the cathode/electrolyte interfaces.

Results

1. *Synthesis with BP1 Predicted Dopants (Zr, Nb, Mo, etc.)*

Sb-doped chemistry

In BP2, we successfully synthesized a Sb doped $LiNiO_2$. The small amount of Sb dopant decreases the discharge capacity (Figure II.4.D.1a, both 1% Sb doped and 2% Sb doped $LiNiO_2$ only deliver a reversible capacity about 203 mAh/g, whereas the pure $LiNiO_2$ can reach around 225 mAh/g). However, as many studies pointed out, many dopants can effectively smoothen the charge/discharge profiles, the Sb dopant also alleviates the multiple phase transitions. In addition, compared with the pure $LiNiO_2$ at C/5 (Figure II.4.D.1b), the cell containing the 2% Sb doped $LiNiO_2$ cathode delivered an initial reversible capacity of 202 mAh/g and a capacity retention of 90% after 60 cycles, which largely surpasses the $LiNiO_2$. In addition, we can obtain a specific energy over 750 Wh/kg at the material level for the 2% Sb doped $LiNiO_2$ cathode.

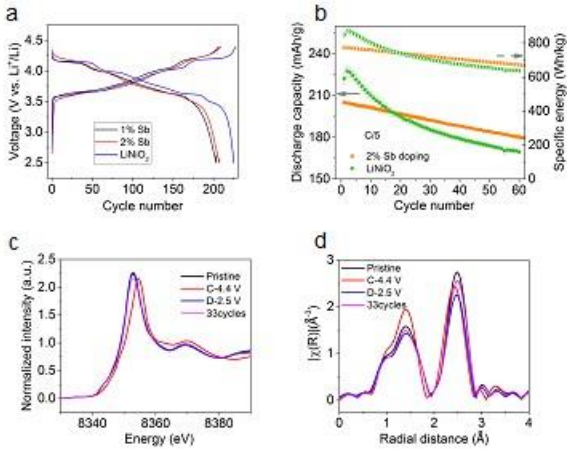

Figure II.4.D.1 (a) Comparison of the charge/discharge profiles of the cells containing the pure $LiNiO_2$, 1% Sb doped, and 2% Sb doped $LiNiO_2$, within 2.5–4.4 V at the current of C/10. (b) The discharge capacity and specific energy retentions of the cells containing the pure $LiNiO_2$ and 2% Sb doped $LiNiO_2$, within 2.5–4.4 V at the current of C/5. (c) ex-situ Ni K-edge XANES of the 2% Sb doped $LiNiO_2$ upon charging and discharging and after 33 cycles; (d) ex-situ Ni K-edge EXAFS of the 2% Sb doped $LiNiO_2$ at various states.

MgMn-doped chemistry

In BP2, we have developed a MgMn co-doped $LiNiO_2$ chemistry. The electrochemical performance of the MgMn-$LiNiO_2$ cathode vs. a lithium metal anode was evaluated. For comparison, we also added the performance of the cells containing the $LiNiO_2$ cathode. It is worth noting that the MgMn dopants can effectively smoothen the charge/discharge profiles (Figure II.4.D.2a), which is consistent with many other elemental dopants. In addition, the starting discharge voltage of MgMn-$LiNiO_2$ cathode was around 4.36 V, 76 mV higher than that of $LiNiO_2$, indicating the mitigated hysteresis with MgMn dopants at high voltages. At a scan rate of 0.1 mV/s, there were three typical oxidation peaks upon charging and three main reduction peaks upon discharging, with a high overlapping characteristic in the first 5 cycles (Figure II.4.D.2b). Note that the difference between the first cycle and following cycles might be associated with carbonate species decomposition upon the initial charging (Figure II.4.D.2b). The low initial Coulombic efficiency of 86% at C/10 (Figure II.4.D.2c) may be another indication for the carbonate decomposition. In the initial cycles, the discharge capacity slightly increased, and slowly faded in the following cycles, resulting in a capacity retention of 90% after 50 cycles. The dQ/dV curves were plotted based on the voltage profiles at C/10 in the voltage range of

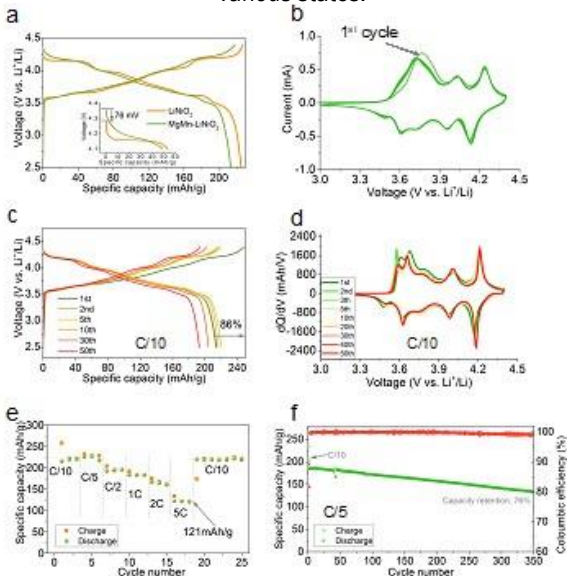

Figure II.4.D.2 Electrochemical performance of the MgMn-$LiNiO_2$ cathode. (a) The second charge/discharge profiles of the two cathodes cycled at C/10 within 2.5–4.5 V; (b) Cyclic voltammetry curves at a scan rate of 0.01 mV/s within 2.5–4.5 V; (c) Charge/discharge profiles at C/10; (d) dQ/dV curves derived from the voltage profiles at C/10; (e) Rate capability; (f) Long-term cycling performance at C/2 with the formation cycle at C/10.

2.5–4.4 V (Figure II.4.D.2d). Compared with the $LiNiO_2$ (from the reference), the intensity of each peak was lower, particularly within 4.1–4.3 V. These peaks overlapped well from first cycle to 50 cycles, suggesting the good structure reversibility of the MgMn-$LiNiO_2$ cathode, which might be the main reason for improved cycle life. The discharge capacity (Figure II.4.D.2e) at C/10, C/5, C/2, C, 2C, and 5C was 220, 225, 190, 180, 160, and 121 mAh/g, respectively. The long-term cycling performance was evaluated at C/2 (Figure II.4.D.2f). An initial discharge capacity of 185 mAh/g was obtained, and it maintained 76% of the original capacity after 350 cycles.

2. *X-ray and TEM diagnostics*

Investigation of Ni dissolution by XFM

gNickel dissolution is one of the major challenges for the $LiNiO_2$ based materials. In BP2, we conducted X-ray fluorescence microscopy (XFM), a highly sensitive technique to quantitate trace elements at the sub-ppm level, on the lithium anode to analyze the Ni concentration (Figure II.4.D.3). The range of the Ni concentration was 0-0.8, 0-1.3, and 0.8-2.6 μg/cm^2 for the anodes after 1 cycle, 100 cycles, and 200 cycles, respectively. Correspondingly, the mean value was 0.4, 0.56, and 1.66 μg/cm^2 (i.e., 6.8, 9.6, and 28.6 nmol/cm^2) of the Ni element. Therefore, one can safely conclude that Ni dissolution took place at the very beginning and deposited on the anode, which is consistent with our previous XAS analysis. Additionally, the Ni re-deposited concentration accumulated with electrochemical cycling, particularly with 100 to 200 cycles. It is noted that the Ni concentration after 100 cycles (9.6 nmol/cm^2) in the present work was still lower than a previous study using the $LiNiO_2$ cathode after 50 cycles (10.45 nmol/cm^2), which suggests that the dual dopants play a positive role in suppressing nickel dissolution. We also noticed that the Ni distribution was homogenous except for several sporadic high-concentration regions (Figure II.4.D.3b-d).

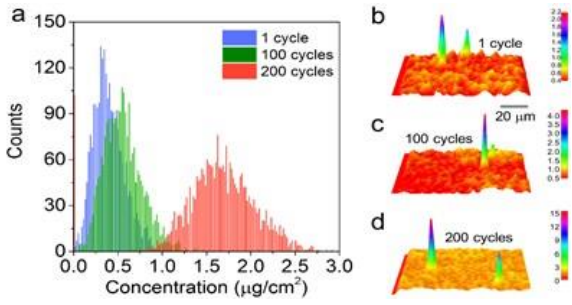

Figure II.4.D.3 X-ray fluorescence microscopy on the lithium metals countered with the Mg/Mn-$LiNiO_2$ cathode after electrochemical cycling at C/3 within 2.5–4.4 V. (a) Histograms of the Ni concentration (based on the pixel-by-pixel quantification) on the lithium metal anodes after 1, 100, and 200 cycles; (b-d) Ni distribution on the lithium metals after 1, 100, and 200 cycles, where the colors represent Ni concentration (μg/cm^2).

In-situ study of synthesis by XANES and EXAFS

The battery performance is determined by the ensemble-averaged, collective behavior of many electrode particles. Therefore, probing the bulk-sensitive, ensemble-averaged electronic and chemical environments is essential to improve the statistical relevance of the analytical results and to provide atomistic insights into the local coordination changes. Here, we performed XANES and EXAFS to investigate the electronic structure and chemical environment. As shown in Figure II.4.D.4a, the edge shifting toward higher energy implies the Ni oxidation. The overall trend of edge energy shift shows that the Ni oxidation in the bulk is not completed at 460 °C, and the prominent Ni oxidation is observed from 460 °C to 700 °C (Figure II.4.D.4b). To quantify the Ni oxidation state evolution, a calibration curve composed of estimated oxidation state as a function of edge energy was made based on standard spectra (Figure II.4.D.4c).

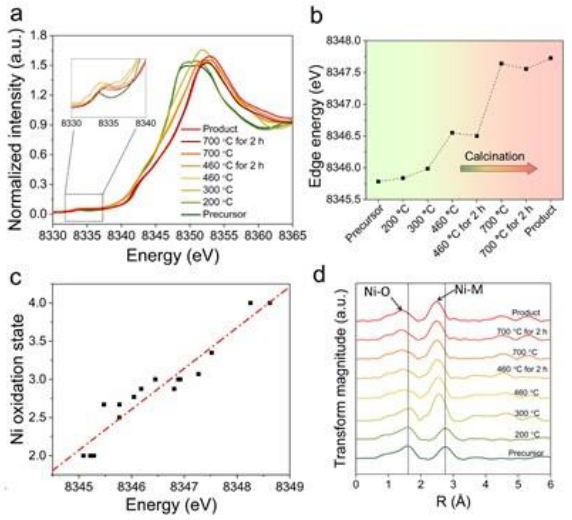

Figure II.4.D.4 Ensemble-averaged characterization of electronic structure and local environment upon calcination. (a) Ni K-edge XANES spectra at different stages of calcination; (b) Evolution of edge energy calculated from the Ni K-edge XANES spectra, where the dashed line shows the trend upon calcination; (c) Estimated Ni oxidation state as a function of edge energy defined by the integration method. The standard data points are based on the spectra of various cathode materials from measurement and in the literature. (d) Ni K-edge Fourier transformed EXAFS at different stages of calcination.

To comprehensively understand the cathode formation regarding the correlation between electronic structure evolution and elemental diffusion, we further performed EXAFS to explore the local coordination change at the atomistic scale. The Fourier-transformed Ni K-edge EXAFS indicates that the precursor shows the characteristic of $Ni(OH)_2$, while the product shows the characteristic of $LiNiO_2$ (Figure II.4.D.4d). In the intermediate stages, multiple changes are captured, including interatomic distance changes between Ni and the surrounding elements, and increasing Ti concentration surrounding Ni. An apparent shift of both Ni−O and Ni−metal (M) shells to lower R values is observed at 300 °C, indicating a decrease in the Ni−O and Ni−M interatomic distances. This decrease is associated with the dehydration of the $Ni(OH)_2$ below 300 °C. The dehydration reaction produces a NiO-based rocksalt phase that has shorter Ni−O and Ni−M interatomic distances. Next, we performed Ni K-edge EXAFS wavelet transform (WT) analysis to decompose the k-space and R-space to separate the backscattering atoms that are overlapped in the R-space. As shown in Figure I.1.A.5a-h, the WT maximum referring to Ni-metal in the second shell at ~2.5 Å (R+α) splits in the k-space. The left maximum at ~6 $Å^{-1}$ (k) is assigned to Ni-Ti scattering and the right maximum at ~8 $Å^{-1}$ (k) is assigned to Ni-Ni scattering. The decrease of R distance for Ni-Ti scattering from 200 °C (Figure II.4.D.6b) to 300 °C (Figure II.4.D.6c) implies the decreasing Ni-Ti interatomic distance and thus the Ti^{4+} diffusion into the matrix. The Ni-Ti interatomic distance remains nearly unchanged after 300 °C (Figure II.4.D.6d-h). In summary, the XANES and EXAFS results demonstrate that Ni oxidation in the bulk ensemble is not completed until 700 °C, and that the Ti dopant diffuses into the matrix predominantly between 200 °C and 300 °C.

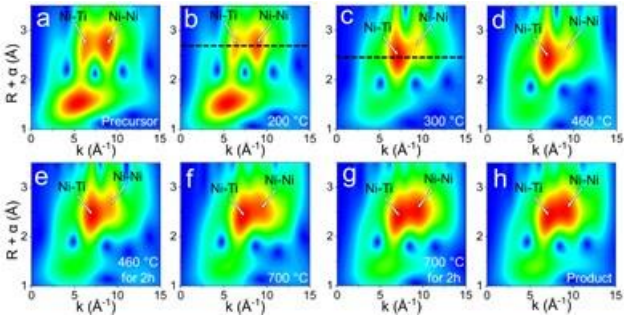

Figure II.4.D.5 Wavelet transformation of Ni K-edge EXAFS for the samples (a) at the pristine state; (b) calcined at 200 °C; (c) calcined at 300 °C; (d) calcined at 460 °C; (e) calcined at 460 °C for 2 h; (f) calcined at 700 °C; (g) calcined at 700 °C for 2 h; (h) complete calcination.

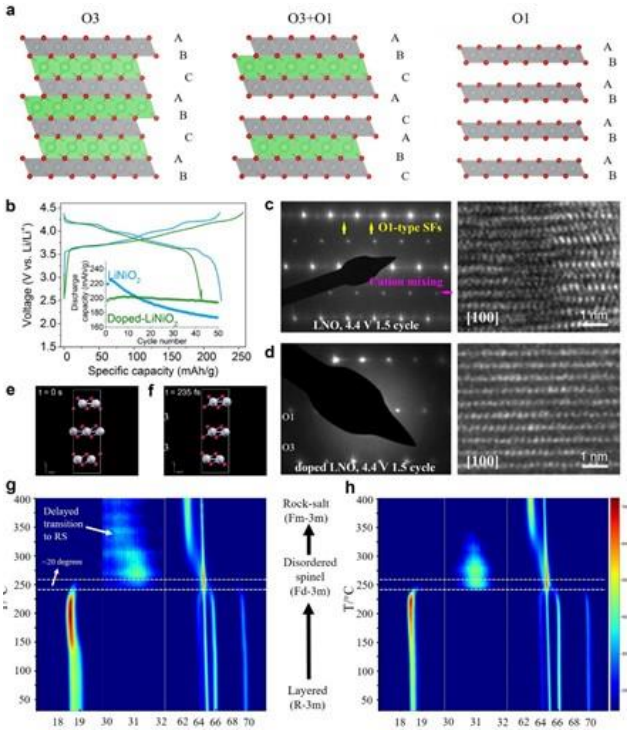

Figure II.4.D.6 Structure of delithiated nickel-rich layered oxides and its evolution during oxygen loss. (a) Atomic models of O3, O3+O1 and pure O1 phases. (b) The second charge/discharge profiles of LNO and doped LNO cycled at C/5. (c) EDP and HRTEM image of LNO charged to 4.4 V (vs. Li/Li+) at 1.5 cycle. (d) EDP and HRTEM images of doped LNO charged to 4.4 V (vs. Li/Li+) at 1.5 cycles. (e,f) ab initio MD simulation (T = 300 K) showing the transition from O3 to O1 in fully delithiated LNO. (g,h) In-situ synchrotron X-ray diffractions of delithiated doped LNO and LNO with increase of oxygen loss.

In-situ study of the thermal stability and degradation of LNO and TiMg-doped LNO

In-situ heating was carried out in TEM to directly visualize the degradation of delithiated, i.e. charged, particles. Figure II.4.D.6a shows the atomic models of pristine layered structure O3, O3+O1 and pure O1 phases that form at charged states. Electrochemical performances (Figure II.4.D.6b) show that the doped LNO has evidently smooth er charge/discharge profiles compared with that of LNO, in particular within the 4.0-4.4 and 3.7-3.5 V ranges, indicating that the two phase transformations are mitigated. Figure II.4.D.6c shows representative EDP and HRTEM image of a delithiated LNO particle. The unidirectional streaking of the Bragg reflections along the <003> direction in the EDP is present due to the formation of planar type

defects parallel to the (003) planes. In LNO, they are indicative that there are considerable amounts of randomly distributed O1 stacking faults (SFs) in the O3 lattice. The extra Bragg spots (marked by magenta arrows) indicate alternating stacks of O1 and O3 phases. HRTEM image in Figure II.4.D.6c also shows distorted layered structure with O1 phases in local regions. Besides that, cation mixing was observed to occur in delithiated LNO according to the Bragg spots indicated by the magenta arrow. Figure II.4.D.6d shows that in contrast to LNO, doped LNO preserves nearly uniform layered structure with significantly reduced cation mixing and O1 SFs after delithiation. In agreement with experimental observations, ab-initio MD simulations (Figure II.4.D.6e and f) confirm that O1 SFs are readily formed in fully delithiated LNO. Moreover, in-situ synchrotron XRD experiments were carried out to obtain an overall understanding of the structural evolution induced by oxygen loss under thermal abuse conditions. During the in-situ experiment, as the temperature increases, rapid oxygen release was activated. Both delithiated LNO and doped LNO show a similar oxygen-loss induced structural transformation pathway from layered → disordered spinel → rock-salt (RS) during oxygen loss (Figure II.4.D.6g and h). Notably, owing to the doping effect, the disordered spinel → RS transformation is clearly mitigated. That is, owing to the doping of Ti, Mg atoms, the degradation process of doped LNO is remarkably delayed compared with LNO. From the above results, the benefit of doping is two-fold: reduction of O1 SFs formation and enhancement of oxygen retention (delaying the structural degradation of layered structure). Interestingly, O1 phase was directly observed to preferentially transform into RS upon oxygen loss. Atomic-scale *in-situ* dynamics (Figure II.4.D.7a and b) show a two-step transformation from the O1 phase (yellow symbols) to RS (orange symbols), i.e., cation mixing followed by shear displacement along (003) planes. In the meantime, the region with perfect O3 layered structure remains stable although with small amounts of cation mixing. A similar transformation was also observed in doped LNO particles. To understand the rationale behind the new transformation pathway, first-principles calculations were carried out to compare the kinetic barriers of a Ni ion migrating from oxygen surrounding octahedral site in the TM layer to the nearest octahedral site in the Li layer, in O1 and O3 phases respectively. In agreement with the experimental observations, the nudged elastic band (NEB) calculations reveal that the barrier for Ni migrating into the Li layer is lower in O1 phase (Figure II.4.D.7c). It means it is kinetically faster for cation mixing to happen in O1 phase. This again, from a theoretical point of view, confirms that O1 stacking faults provides a highway for structural degradation of LNO and its derivatives including all high-Ni content materials.

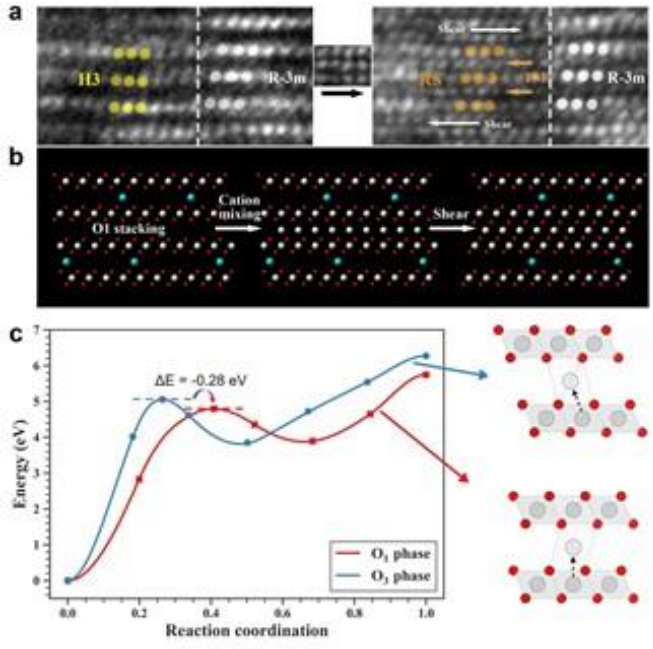

Figure II.4.D.7 Preferential transformation from O1 phase to RS. (a) In-situ HRTEM images showing the transformation from O1 phase to RS. (b) Schematic illustration of the two-step transformation pathway. (c) The minimum energy path calculation of moving Ni from TM layer to Li site in R-3m (O3) and H3 (O1) phase, respectively.

3. Refining computation, improving dopant selection

In BP2, we have made significant progress in refining the prediction of surface/ bulk dopants. For surface dopants, we are targeting the dopants that have a surface enrichment in $LiNiO_2$. Figure II.4.D.8 illustrates the calculated the total energy difference (ΔE) between the configurations of the dopant in the i^{th} layer and in the 5^{th} layer. We find that W, Sb, Ta, Ti, Y, and B have a strong tendency to segregate to the surface, while Mg

prefers to reside in the bulk. To make sure the total energy difference is substantial enough such that the dopant segregation behavior is thermodynamically driven, we estimated the mixing temperature, above which entropic effects become significant. $LiNiO_2$ synthesis temperature is around 900 K, which corresponds to $\Delta E = \Delta H = 7\ meV/f.u.$ Thus, $|\Delta E|$ should be higher than $7\ meV/f.u.$ to ensure the mixing temperature is above the synthesis temperature such that the dopant segregation behavior is thermodynamically driven. For Al, $T = 755\ K$ with $|\Delta E| = 6\ meV$ between Al doping in the 1st and 5th layer. Therefore, we conclude that $|\Delta E|$ is large enough to drive dopant segregation behavior for W, Sb, Ta, Ti, Y, Mg and B, while Al exhibits weak preference for the bulk which is re-enforced by the entropic temperature effects, and hence we expect Al to uniformly distribute from the surface to the bulk. For the bulk dopants, we are targeting the dopants that can suppress the detrimental H3 phase formation at the high charge states. We start by investigating the equilibrium Li-vacancy ordering in Li_xNiO_2, dopant-Ni ordering in $LiNi_{1-y}M_yO_2$ and Li-vacancy ordering in $Li_xNi_{1-y}M_yO_2$ hosts. In each host system, we use cluster expansion to determine the energy dependence of different ordering arrangement. The cluster expansion is parametrized by the total energies of different atomic arrangements, which are calculated from first-principles simulations. Finally, we use cluster expansion in Monte Carlo (MC) simulations to calculate thermodynamic properties, equilibrium phase boundaries and sample Li_xNiO_2, $LiNi_{1-y}M_yO_2$ and $Li_xNi_{1-y}M_yO_2$ configurations. We extract ion interaction features from the parametrized cluster expansion and in Figure II.4.D.9a, we demonstrate the favorable Li^+-Li^+ interaction through a Ni^{3+} ion in Li_xNiO_2, along with the effective clusters interactions (ECI) values used in the cluster expansion. For Li-Ni interaction, Li^+ interacts favorably with its first nearest neighbor (NN) Ni^{4+}, with a second NN Ni^{3+}. There is also an attractive interaction between Li^+ ions in different planes. Figure II.4.D.9b illustrates the attractive interactions in Li-O-Ni-O-Li configurations through the Ni^{3+} center, while the rest of Ni being Ni^{4+}. Figure II.4.D.9c shows that when two vertices of a Ni-O octahedral are occupied with Li^+, Ni-O bonds are elongated along d_{z^2} orbital, which is the occupied lower-energy orbital. When four Li^+ ions are around the Ni-O octahedral, $d_{x^2-y^2}$ becomes the occupied lower-energy orbital and leads to a negative Jahn-Teller (JT)distortion (four long and two short Ni-O bond). These favorable Li-O-Ni-O-Li configurations and JT distortions exist in all equilibrium Li_xNiO_2 structures and explain the Li-vacancy ordering during delithiation. Following similar procedure, we investigate equilibrium dopant-Ni ordering in $LiNi_{1-y}M_yO_2$ and Li-vacancy ordering in $Li_xNi_{1-y}M_yO_2$ configurations. Equilibrium $LiNi_{1-y}M_yO_2$ configurations at a 900 K synthesis condition are obtained from MC simulations. Three different doping concentrations between 5% to 15% are considered for Ti- and Al-doped $LiNi_{1-y}M_yO_2$. To illustrate the dopant distribution, we plot the radial distribution functions of Ti-Ti and Al-Al pairs in Ti- and Al-doped $LiNi_{1-y}M_yO_2$, respectively.

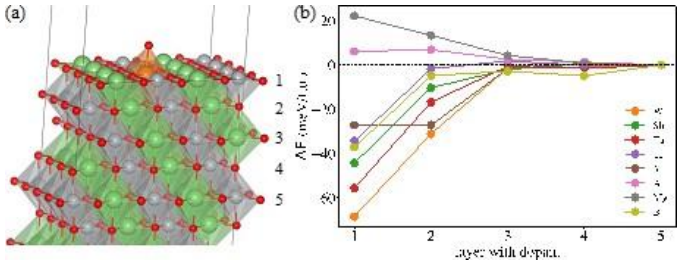

Figure II.4.D.8 (a) The total energy difference (ΔE) between the dopant in the ith layer and 5th layer as a function of the dopant position in LiNiO2. (b) A slab model of LiNiO2. The orange atom represents the doping element and substitutes one Ni atom in the 1st, 2nd, 3rd, 4th, and 5th layer.

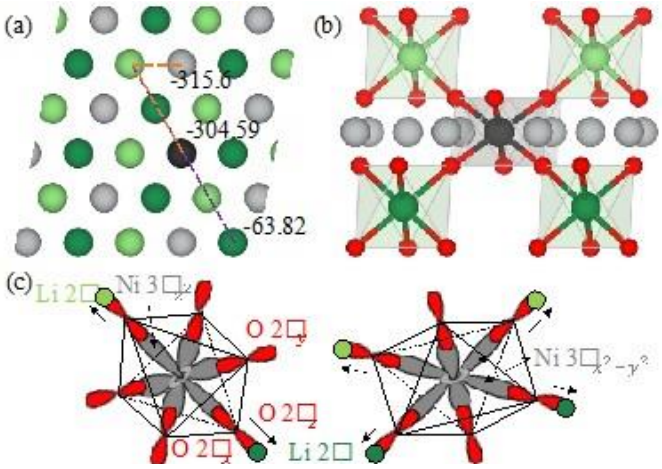

Figure II.4.D.9 (a) Pair interactions for Li^+-Li^+ and Li^+-Ni^{3+} from cluster expansion. (b) Attractive interactions between Li^+ ions in 180° Li-O-Ni-O-Li configurations. (c) Overlapping of atomic orbitals involved in the Li-O-Ni-O-Li configuration.

4. Battery testing and electrolyte formulation

In BP2, the electrochemical performance of our Gen 2 chemistry (TiMg-doped $LiNiO_2$ denoted as NMT) system was evaluated against graphite anodes (Gr||NMT) in coin cell set-up with comparison to Gr||NMC811 system. The first developed localized high-concentration electrolyte (LHCE) with code of AE003 and the baseline electrolyte of 1 M $LiPF_6$ in EC-EMC (3:7 by wt.) + 2 wt.% VC (with the abbreviation of E268) were used. The NMT cathode was homemade with an areal capacity of 1.50 mAh cm^{-2}. The NMC811 electrode (1.50 mAh cm^{-2}) and the Gr electrode (1.84 mAh cm^{-2}) were obtained from ANL CAMP. The Gr||NMT and Gr||NMC811 coin cells were assembled inside the argon-filled glovebox. 75 µL electrolyte was injected into each coin cell. Three parallel cells were assembled for each electrolyte. The formation cycles include one charge/discharge cycle at C/20 and two charge/discharge cycles at C/10, where 1C = 1.50 mA cm^{-2}. After the formation cycles, the cells were charged and discharged at C/3 rate for 100 cycles. The entire cycling performance evaluation was conducted under a constant temperature of 25 ℃ in the voltage range of 2.5-4.4 V for all cells. It can be observed from Figure II.4.D.10a that the reversible capacities of Gr||NMC811 using E-baseline and AE003 after 100 cycles at C/3 are 175.0 and 180.3 mAh g^{-1}, corresponding to capacity retentions of 97.4% and 98.0 %, respectively. When the cathode is changed to NMT, the reversible capacities of Gr||NMT in both electrolytes are obviously higher in the initial several cycles than those of Gr||NMC811. After 100 cycles at C/3, the reversible capacities of Gr||NMT using E268 and AE003 are 169.8 and 193.6 mAh g^{-1}, corresponding to capacity retentions of 90.4% and 100.0 %, respectively. Figure II.4.D.10b shows the corresponding specific energy density of the two cell systems in Figure II.4.D.11a. Obviously, the Gr||NMT cell with AE003 has the highest reversible specific energy density during the 100 cycles at C/3, which is averaged at ~720 Wh kg^{-1} during the cycling. While for Gr||NMC811 using AE003, the average energy density of the 100 cycles at C/3 is ~655 Wh kg^{-1}. As for E268, both Gr||NMT and Gr||NMC811 cell systems exhibit lower specific energy after 100 cycles at C/3 cycling than those for AE003. After that, a new LHCE was used to evaluate the electrochemical performance of Gr||NMT system with comparison to Gr||NMC811 system. E268 was employed as the baseline electrolyte again. In these coin cells, 50 µL electrolyte was injected into each coin cell and three parallel cells were assembled for each electrolyte. After three formation cycles at C/20 for the first cycle and C/10 for the rest two cycles (where 1C = 1.50 mA cm^{-2}), the cells were charged at C/3 and discharged at 1C for 500 cycles, at 25°C in the voltage range of 2.5-4.4 V. Figure II.4.D.11 summarizes the average specific discharge capacity and average specific discharge energy of Gr||NMT and Gr||NMC811 cells using two electrolytes. After formation cycles, the average specific discharge capacity and the average specific discharge energy of Gr|E268|NMT cells amount to 176.8 mAh g^{-1} and 655.4 Wh kg^{-1}, respectively. After 500 charge/discharge cycles, these values decreased to 108.1

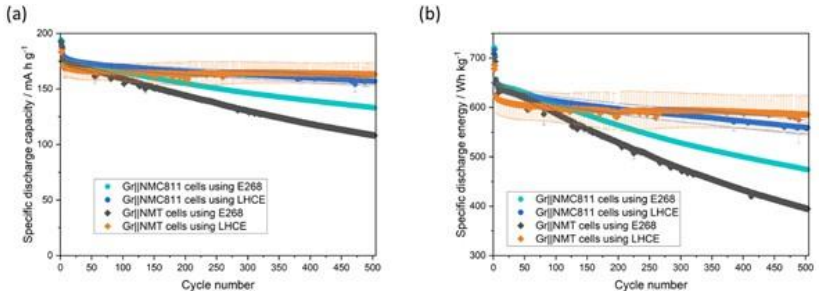

Figure II.4.D.11 Comparison of cycling performance of Gr||NMT and Gr||NMC811 coin cells with new LHCE and E268 at C/3 charge and 1C discharge in the voltage range of 2.5-4.4 V. (a) Average specific discharge capacity and (b) average specific discharge energy.

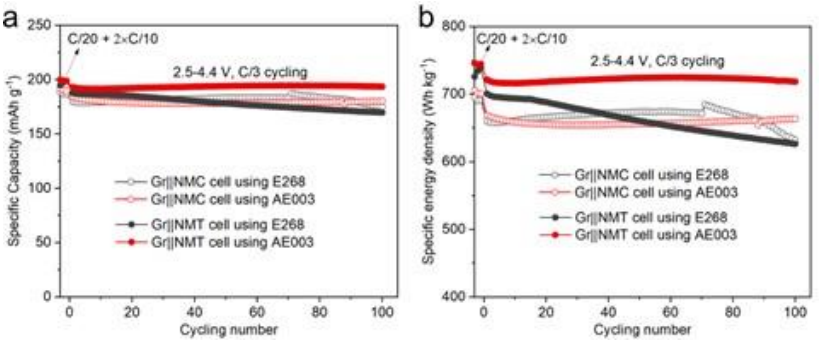

Figure II.4.D.10 Comparison of cycling performance of Gr||NMT and Gr||NMC811 coin cells with AE003 and E268 at C/3 cycling rate in the voltage range of 2.5-4.4 V. (a) Discharge capacity, and (b) specific energy.

mAh g^{-1} and 394.7 Wh kg^{-1}, corresponding to the capacity and energy retentions of 61.1% and 60.2%. Evidently, the conventional $LiPF_6$/organocarbonate based electrolyte (E268) exhibits incompatibility with the Gr||NMT cell chemistry. In contrast, the Gr|LHCE|NMT cells achieved significantly better cycling performance over the long-term cycling evaluation. After formation cycles, the average specific discharge capacity and the average specific discharge energy of Gr|LHCE|NMT cells are determined to be 171.2 mAh g^{-1} and 622.3 Wh kg^{-1}, both of which are slightly lower than those of Gr|E268|NMT cells. However, after 500 charge/discharge cycles, these values only decreased to 163.2 mAh g^{-1} and 585.7 Wh kg^{-1}, resulting in the excellent capacity and energy retentions of 95.3% and 94.1%. With this, it can be concluded that, by adopting the new LHCE, a high energy Li-ion battery based on high-Ni and Co-free cathode material (i.e. NMT) can achieve extraordinary cycle life and energy retention. In addition, the applicability of the new LHCE in Gr||NMC811 cells was investigated in a similar way to that in Gr||NMT cells. In the Gr||NMC811 cell chemistry, the new LHCE also achieved higher capacity and energy retention upon long-term cycling of 500 cycles. After formation cycles, the specific discharge capacity and energy of the Gr|E268|NMC811 cells reached 177.0 mAh g^{-1} and 657.6 Wh kg^{-1}. After 500 charge/discharge cycles, those values decreased to 132.8 mAh g^{-1} and 474.0 Wh kg^{-1}, corresponding to the capacity and energy retentions of 75.0% and 72.1%, respectively. In the Gr|LHCE|NMC811 cells, the initial specific discharge capacity and energy amount to 180.8 mAh g^{-1} and 650.9 Wh kg^{-1}. After long-term evaluation, these values decreased to 156.9 mAh g^{-1} and 559.2 Wh kg^{-1}, resulting in the capacity and energy retentions of 86.8% and 85.9%. Comparing the data between Gr||NMC811 and Gr||NMT cells, it can be concluded that Gr||NMC811 cells exhibit slightly higher specific energy than their Gr||NMT counterparts after formation cycle. The possible reason could be probably assigned to the higher active Li loss in the formation cycles in Gr||NMT cells, which leads to the slightly lower initial specific discharge capacity. It also should be noted that, after formation cycles, all the cells were discharged at 1C, being much higher than C/3 rate. The increased C-rate usually leads to higher polarization and lower energy output. Optimizations on the electrolyte formula and modification on the testing procedure are expected to further improve the initial specific energy of the Gr||NMT cells. The work completed in BP2 at the 2Ahr-3.5Ahr pouch cell level including testing of the PNNL electrolyte, AE-003, in comparison to the results collected for the baseline PPC cells. All cell materials except the electrolyte were the same for both batches of cells. Formation and testing procedures were also kept the same for both batches. The baseline electrolyte is LiPF6 in organic carbonate solvent with VC additive. In previous tests, the AE-003 localized high-concentration electrolyte (LHCE) electrolyte did not cycle well (<10 cycles), however the electrolyte mass was kept constant for the baseline and AE-003 electrolyte. In the results shown below, the electrolyte volume was kept constant, so an additional 2g (7.5g baseline and 9.4g AE-003) of AE-003 was filled to account for the difference in electrolyte densities (1.2 g/mL and 1.5 g/mL for baseline and AE-003, respectively). Cells with nominal capacity about 3.5 Ah were galvanostatically discharged at 0.7 A (C/5), 1.167 A (C/3), 1.75 A (C/2), 3.5 A (1C), and 7 A (2C) from 4.4 V to 2.5 V. Cells were recharged using a CC-CV protocol with a C/20 cutoff. Figure II.4.D.12 shows the discharge and charge rate capability at RT under various currents. For the baseline cell, the nominal (C/5) capacity is 3.58 Ah and 3.47 Ah at C/3. At 1C and 2C, the discharge capacity is 3.29 Ah and 3.08

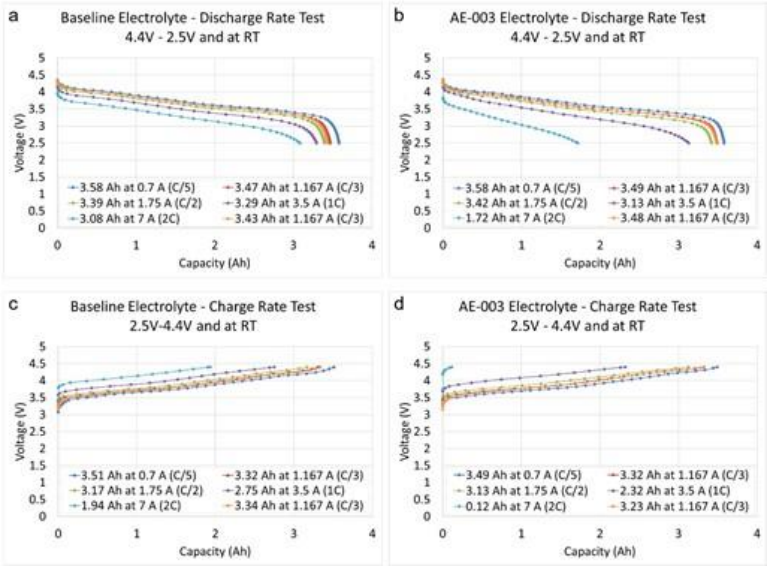

Figure II.4.D.12 Discharge rate test at RT for cells with (a) baseline and (b) AE-003 electrolyte. Charge rate test at RT for cells with (c) baseline and (d) AE-003 electrolyte.

Ah, 94.8% and 88.8% of the C/3 capacity. After the rate test, the cell was discharged at C/3 and the capacity was 3.43 Ah, suggesting a capacity loss of 1.1%. For the AE-003 cell, the nominal (C/5) capacity is 3.58 Ah and 3.49 Ah at C/3. At 1C and 2C, the discharge capacity is 3.13 Ah and 1.72 Ah, 89.7% and 49.3% of the C/3 capacity. After the rate test, the cell was discharged at C/3 and the capacity was 3.48 Ah, suggesting a capacity loss of 0.3%. The AE-003 electrolyte appears to have similar performance up to 1C, but at 2C rate, the discharge capacity is significantly lower than the baseline electrolyte. The charge rate capability at RT of the baseline and AE-003 electrolyte were also assessed. The cells were galvanostatically charged at RT at C/5, C/3, C/2, 1C, and 2C rates from 2.5 V – 4.4 V. Again, the AE-003 electrolyte showed significantly lower capacity than the baseline electrolyte at 1C and 2C rates. Moreover at 2C, the cell was not capable of accepting current at 7 A, suggesting higher charging polarization for the AE-003 electrolyte. These results are different from the results obtained the PNNL team in coil cell testing which suggests electrolyte viscosity could be a limiting factor here. Figure II.4.D.13 shows the cycle life of cells filled with the AE-003 LHCE electrolyte. Cycle life results at both RT and 45 ˚C outperform the baseline electrolyte. At RT, the initial discharge capacity is 3.554 Ah and after 100 cycles, the discharge capacity decreases to 3.211 Ah, a loss of about 10%. After 200 cycles, 82% of the initial discharge capacity is retained. Still, no divergence is observed between the charge and discharge capacity, and the average coulombic efficiency is 99.8%. At 45 C, the initial discharge capacity is 3.745 Ah and after 72 cycles the capacity decreases to 3.560 Ah, a loss of about 5%. After 172 cycles, the capacity retention is more than 88%. The average coulombic efficiency is 99.9%, and cycling is ongoing. Interestingly, the efficiency increases with higher temperature. This is counter-intuitive but reasonable, since the LiFSI salt is more thermally stable and any issues with viscosity and wetting of the LHCE can be mitigated at higher temperatures. Already, the benefit of the LHCE electrolyte is demonstrated at RT and 45 C as shown in Figure II.4.D.13e and 13f. The cycle life of these cells will be evaluated until EOL (80% of initial capacity or efficiency < 96%), and then impedance spectroscopy will be taken to understand the degradation.

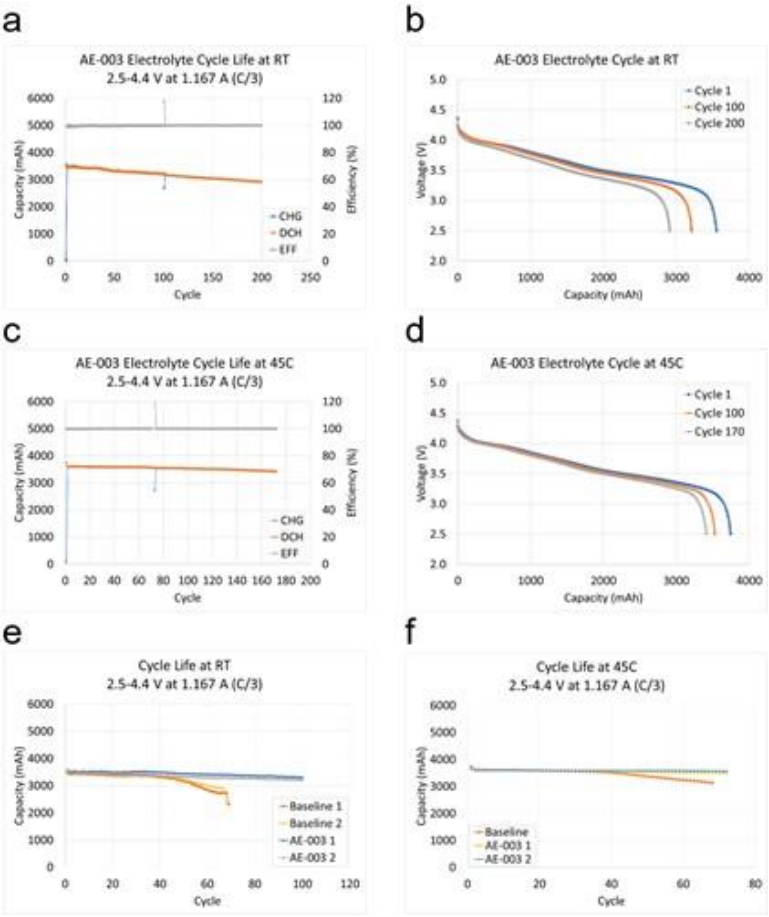

Figure II.4.D.13 Cycle life and discharge voltage profiles of NMC811|Gr cells filled with AE-003 LHCE electrolyte.

5. Scale-up of synthesis 20 g to 100 g

The synthesis of NMT precursor has been successfully scaled up to 100 g per batch. As shown in Figure II.4.D.14a, the XRD pattern of the scaled-up precursor (100 g/batch) is similar to that of the small batch one (9 g/batch). With optimized calcination parameters, the NMT from the scaled-up precursor exhibits even slightly higher reversible capacity and better cycling stability than the NMT from the small batch precursor in Li||NMT coin cells with baseline electrolyte in the voltage range of 2.5-4.4 V (Figure II.4.D.14b).

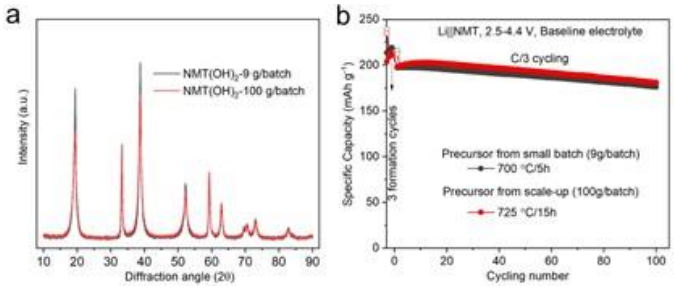

Figure II.4.D.14 (a) XRD of the precursor from scaled-up (100 g/batch) and small batch (9 g/batch). (b) Comparison of the NMT cathodes from scaled-up and small batch in Li||NMT coin cell with baseline electrolyte in the voltage range of 2.5-4.4 V.

Conclusions

- Developed two new Co-free chemistries with Ni content >95%.
- Comprehensively characterized the formation process, including dopant distribution, electronic structure change and local chemical environment evolution of VT Gen 2 material at different length scales.
- Performed extensive TEM and X-ray diagnostic studies for Gen-2 and BP2 materials to understand their thermal stabilities and formation mechanisms.
- Refined the computational model for the prediction of surface dopants and performed the computational screening of bulk dopants for $LiNiO_2$. Studied the dopant-Ni ordering in $LiNi_{1-y}M_yO_2$ and Li-vacancy ordering in $Li_xNi_{1-y}M_yO_2$ systems by using first-principles calculations.
- Tested the PNNL electrolyte, AE-003, in comparison to the results collected for the baseline PPC cells. The benefit of the LHCE electrolyte is demonstrated at RT and 45 ℃.
- Performed extensive electrochemical evaluation of the Gen-2 materials in conjunction with newly developed electrolytes. The cycle life performance meet BP1 Go target.
- NMT precursor synthesis was successfully scaled up to 100g/batch. The scaled-up precursor exhibits even slightly higher reversible capacity and better cycling stability than that from small batch precursor.

Key Publications

1. Mu, L.; Yang, Z.; Tao, L.; Waters, C. K.; Xu, Z.; Li, L.; Sainio, S.; Du, Y. ; Xin, H. L.; Nordlund, D.; Lin, F., The Sensitive Surface Chemistry of Co-Free, Ni-Rich Layered Oxides: Identifying Experimental Conditions that Influence Characterization Results Journal of Materials Chemistry A 8, 17487-17497. This paper has been collected into Journal of Materials Chemistry A HOT Papers

2. Rahman, M. M.; Chen, W.; Mu, L.; Xu, Z.; Xiao, Z.; Li. M.; Bai, X.-M.* and Lin, F.* (2020) Defect and Structural Evolution under High-Energy Ion Irradiation Informs Battery Materials Design for Extreme Environments. Nature Communications 11, 4548. [Note: The Li cathode used in this paper is developed through the DE-EE000844]

3. Tao, L.; Hu, A.; Yang, Z.; Xu, Z.; Wall, C. E.; Esker, A. R.; Zheng, Z.; **Lin, F.*** (2020) A Surface Chemistry Approach to Tailoring the Hydrophilicity and Lithiophilicity of Carbon Films for Hosting High-Performance Lithium Metal Anodes. *Advanced Functional Materials 30, 2000585.* [Note: The Li cathode used in this paper is developed through the DE-EE000844]

4. Jianli Cheng, Linqin Mu, Chunyang Wang, Zhijie Yang, Huolin L. Xin, Feng Lin, and Kristin A. Persson. "Enhancing Surface Oxygen Retention through Theory-guided Doping Selection in Layered Ni-rich Cathodes for Next-generation Lithium-ion Batteries." Journal of Materials Chemistry A, in press. This paper has been collected into Journal of Materials Chemistry A HOT Papers

5. Mu, L.*; Kan W. H.; Kuai, C.; Yang, Z.; Li, L.; Sun, C.-J.; Sainio, S.; Avdeev, M.; Nordlund, D.; Lin, F.* (2020) Structural and Electrochemical Impacts of Mg/Mn Dual Dopants on the LiNiO2 Cathode in Li-Metal Batteries. ACS Applied Materials & Interfaces. 11, 12874-12882.

6. Xianhui Zhang, Lianfeng Zou, Yaobin Xu, Xia Cao, Mark H. Engelhard, Bethany E. Matthews, Lirong Zhong, Haiping Wu, Hao Jia, Xiaodi Ren, Peiyuan Gao, Zonghai Chen, Yan Qin, Christopher Kompella, Bruce W. Arey, Jun Li, Deyu Wang, Chongmin Wang, Ji-Guang Zhang, and Wu Xu*, “Advanced Electrolytes for Fast-Charging High-Voltage Lithium-Ion Batteries in Wide-Temperature Range”, Advanced Energy Materials, 2020, 10(22), 2000368. This paper has also been selected as cover image.

7. Xianhui Zhang, Hao Jia, Yaobin Xu, Lianfeng Zou, Mark H. Engelhard, Bethany E. Matthews, Chongmin Wang, Ji-Guang Zhang, Wu Xu*, “Unravelling high-temperature stability of Li-ion battery with Li-rich oxide cathode in localized high-concentration electrolyte”, Journal of Power Sources Advances, 2020, in press.

II.4.E High-Nickel Cathode Materials for High-Energy, Long-Life, Low-Cost Lithium-Ion Batteries (University of Texas at Austin)

Arumugam Manthiram, Principal Investigator
University of Texas at Austin
Texas Materials Institute
Austin, TX 78712
E-mail: manth@austin.utexas.edu

Shriram Santhanagopalan, Principal Investigator
National Renewable Energy Laboratory
Golden, CO 80401
E-mail: Shriram.santhanagopalan@nrel.gov

Peter Faguy, DOE Technology Development Manager
U.S. Department of Energy
E-mail: Peter.Faguy@ee.doe.gov

Start Date: October 1, 2018 End Date: March 31, 2022
Project Funding: $3,000,000 DOE share: $2,400,000 Non-DOE share: $600,000

Project Introduction

Lithium-ion batteries occupy a privileged position in the energy storage landscape due to their high energy density. Despite this success, energy and cost requirements of lithium-ion batteries are extremely stringent, especially for electric vehicle (EV) applications. Therefore, there is a need to further enhance the energy density of state-of-the-art nickel-based layered oxide cathodes ($Li[Ni_aCo_bMn_c]O_2$ with $a + b + c = 1$, denoted as NCM-*abc* and $Li[Ni_{1-x-y}Co_xAl_y]O_2$, denoted as NCA). Moreover, the substantial dependence on the scarce and costly cobalt in these cathodes (*e.g.*, 12 wt.% Co in NCM-622) needs to be lowered for sustained mass market penetration of EVs. With the currently employed cathode formulations, demand for Co could outstrip supply by 2030 with surging global EV production, setting the stage for far higher prices. Although Co-free cathodes, such $LiFePO_4$ and $LiMn_2O_4$ exist, their energy density cannot meet the requirements of next-generation EVs.

This project is focused on developing low-cobalt and cobalt-free, high-nickel layered $LiNi_{1-x}M_xO_2$ (M = Mn, Al, Mg, Zr, Ta, *etc.* and $x \leq 0.15$) oxide cathode materials for lithium-ion batteries for EVs. With these high-nickel cathodes, high energy, high power, long lifetime over a wide temperature range, as well as excellent safety under abuse can be prioritized for varying market needs through careful compositional tuning. These efforts will also reduce or even eliminate the dependence of lithium-ion batteries on cobalt, thus leading to more secure supply chains, lower cost, and less adverse impacts on the environment. The cathode materials and understanding developed in this project will contribute to advancing the designs of low-cobalt or cobalt-free, high-energy-density lithium-ion batteries.

Objectives

The overall goal of this project is to produce lithium-ion cells with the following performance targets:

Table II.4.E.1 Performance Targets

Beginning of Life Characteristics at 30°C	Cell Level	Cathode Level
Useable Specific Energy @ C/3		≥ 600 Wh/kg
Calendar Life (<. energy fade)	15 Years	
Cycle Life (C/3 deep discharge with < 20% energy fade)	1,000	
Cobalt Loading		≤ 50mg/Whr
Cost	≤ $100/kWh	

Approach

Both low-cobalt and cobalt-free high-nickel layered $LiNi_{1-x}M_xO_2$ (M = Mn, Al, Mg, Zr, Ta, *etc*. and $x \leq 0.15$) oxides are developed and assessed as cathodes in lithium-ion batteries with graphite anode. Low-cobalt, high-nickel $LiNi_{1-x-y}Co_yM_xO_2$ ($y < 0.06$ and $x \leq 0.15$) compositions are screened as cathodes. The total content of Mn and other dopants (*e.g*., Al, Mg, Zr, Ta, *etc*.) can reach up to 15 % through either hydroxide co-precipitation or lithiation annealing to maintain good thermal and cycling stability while achieving the 600 Wh kg^{-1} energy goal. Selected compositions are also subjected to atomic layer deposition (ALD) coatings at NREL and assessed with compatible ethylene carbonate (EC)-free electrolyte systems. Based on the results, an optimal cathode material is selected to produce twenty-one 2 Ah pouch cells to deliver to DOE for independent evaluation/validation. Detailed experimental approaches for Year 2 are below:

1. Cell Results (Go/ No Go). ≥ 2 Ah pouch cells, capable of 600 W h kg^{-1} (cathode level) and ≥ 80 % energy retention after 1,000 cycles with cobalt content below 50 mg Co/Wh

2. Dopant Survey: Investigation and screening of various dopants in $LiNi_{1-x-y}Co_yM_xO_2$ ($y < 0.06$ and $x \leq 0.015$, M = Mn, Al, Mg, *etc*.) compositions and their effects on the electrochemical performance, air-storage stability, and safety

3. Electrode Study: Effect of electrode loading and calendaring on $LiNi_{1-x-y}Co_yM_xO_2$ ($y < 0.06$ and $x \leq 0.015$, M = Mn, Al, Mg and more) compositions.

Results

A cathode material with the composition $LiNi_{0.85}Co_{0.05}Mn_{0.075}Al_{0.02}Mg_{0.005}O_2$ (designated as NCMAM-85) was identified as the best performing candidate out of a series of coprecipitated $LiNi_{1-x-y}Co_yM_xO_2$ ($y < 0.06$ and $x \leq 0.015$, M = Mn, Al, Mg) compositions. ~ 1.7 kg of Ni-85 was synthesized at UT Austin and shipped to Tesla Inc. for fabrication of twenty-one 2 Ah pouch cells. Fourteen of those 2 Ah cells were shipped to INL for cycle and calendar life testing. The average cathode-level specific energy of the cells is approximately 630 Wh kg^{-1} at the designated rate of C/3. Four of the 2 Ah cells were also cycled at Tesla Inc. at a charge discharge rate of C/2 (1 A current) between 2.5 and 4.2 V. One cell was cycled at 25°C and three cells were cycled at 40°C (Figure II.4.E.1). The cell cycled at 25°C retained 81.8% capacity after 1,000 cycles at C/2 rate. Overall, the low-cobalt cathode material displayed high capacity with good cycle life in the 2 Ah cells fabricated by Tesla Inc.

Figure II.4.E.2 displays the evolution of the capacity of the 2 Ah cells currently undergoing cycle life (CycLT) and calendar life (CalLT) test at INL. Cycle life testing is performed at a rate of C/3 between 2.5 and 4.25 V at a temperature of 30°C. Capacity fade is largest during the first 100 cycles but slows down substantially during each subsequent 100 cycles. The cells are currently at approximately 81% capacity retention. We estimate that the cells will reach 80% capacity at roughly 650 cycles. While this falls short of the project goal of 1000 cycles above 80% capacity retention, we do not believe this is a cause for concern. Given that our in-house cycling tests and cycling performed by Tesla Inc. both show > 80% capacity after 1000 cycles at C/3 rate, and that we have already met the project goals of > 600 Wh kg^{-1} and < 50 mg kg^{-1} of cobalt quantity, we are optimistic that we will meet the final project target of 1,000 cycles with our work in Budget Periods 2 and 3.

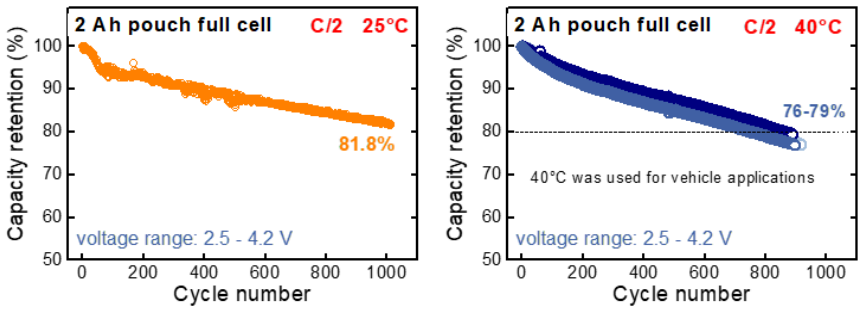

Figure II.4.E.1 Performance of NCMAM-85 in 2 Ah pouch-cell format at (left) 25°C and (right) 40°C, cycled at Tesla. Inc. between a voltage window of 2.5 to 4.2 V at C/2 rate.

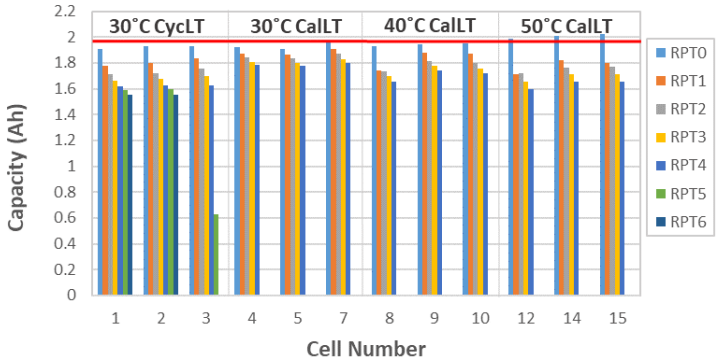

Figure II.4.E.2 Capacities of 2 Ah cells cycling at INL at C/3 rate between 2.5 and 4.25 V. Capacities were measured during Reference Performance Tests (RPTs) conducted every 100 cycles with cycle life testing (CycLT) cells. For calendar life testing (CalLT) cells, RPTs were performed every 32 days.

We have also explored methods of improving the cycle life and stability of high-nickel, low-cobalt layered oxide cathodes through doping. We have identified that a co-doping of Mg and Cu improves the specific energy and cycle life of $LiNiO_2$. Figure II.4.E.3 displays the cycling performance of undoped $LiNiO_2$, 0.5% Mg-doped (M5-$LiNiO_2$), and 0.5% Mg and 0.3% Cu co-doped (MC53-$LiNiO_2$) pouch-type full cells cycled between 2.5 and 4.3 V at a rate of C/2. After 200 cycles at C/2 rate, the undoped $LiNiO_2$ retains 73% capacity, while single-doped M5-$LiNiO_2$ and co-doped MC53-$LiNiO_2$, respectively, retain 75% and 78% capacity. Interactions between Mg and Cu produce a synergistic effect in stabilizing $LiNiO_2$. Mg dopes into Li sites in the $LiNiO_2$ lattice, improving the bulk crystal stability, but increasing the proportion of surface residual Li_2CO_3 to total residual lithium. We found that this variation aggravates parasitic side reactions during battery cycling, which necessitates additional surface protection. Single doping with Cu is highly detrimental, as Cu doped in the bulk structure severely impedes Li diffusion, causing higher polarization in the cathode and exacerbating the H2 to H3 phase transition, prompting mechanical degradation of the cathode particle. Dual-incorporation of Mg and Cu produces a complimentary effect, whereby Mg prevents Cu from doping into the bulk, causing Cu to reside on the surface in the form of Li_2CuO_2, which protects the Mg-doped $LiNiO_2$ bulk to maximize the positive effect of Mg doping. During the initial formation cycles, Li_2CuO_2 is irreversibly delithiated to form a surface CuO layer that has much higher electronic conductivity than common surface residual lithium species, such as LiOH and Li_2CO_3. The conducting CuO layer reduces voltage polarization growth and enhances energy efficiency retention (Figure II.4.E.3b-d).

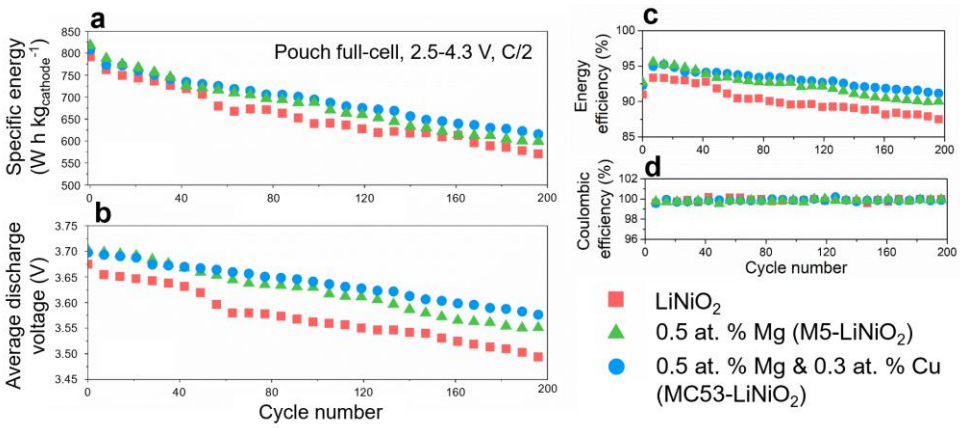

Figure II.4.E.3 Cycling performance of $LiNiO_2$ with various levels of Mg and Cu incorporation in pouch-type full-cells paired against a graphite anode, cycled between 2.5 and 4.3 V at C/2 rate. Evolution of (a) cathode level specific energy, (b) average discharge voltage, (c) energy efficiency, and (d) coulombic efficiency.

We further focused on improving the electrode fabrication process to raise the specific capacity and cycling stability of our high-nickel, low-cobalt layered oxide cathodes. Cathode formulations have been changed to include 94% active material and only 3% each of conductive carbon and polymer binder form the previously used 90% active material and 5% each of carbon and binder formulations. The new formulation more closely matches industry standards and will improve energy density at the electrode level. Furthermore, we have performed a study on the effects of calendaring on the performance of LiNi0.9Mn0.05Al0.05O2 (NMA-900505) to further improve our electrode fabrication capabilities. We calendared NMA to various levels of porosity to optimize electrode fabrication for enhanced electrical conductivity, energy density, and cycling stability. Figure II.4.E.4a displays the cycling performance of uncalendared NMA (55% porosity) and NMA calendared to 45%, 35%, and 25% porosity in coin-type full cells cycled between 2.5 and 4.3 V. Calendaring to any level improves the capacity of the NMA cathodes. This effect is small at slow current densities but is far more pronounced at a 1C discharge rate; At 25% porosity, NMA delivers 186 m Ah g-1 at 1C rate while uncalendared NMA delivers only 173 m Ah g-1. The increase in capacity with calendaring level, particularly at higher discharge rates, is due to an increase in the conductivity of the electrode brought on by the calendaring, which compresses the cathode particles in the electrode, increasing interparticle connectivity. The 45% and 35% porosity NMA shows markedly worse cycling stability than both the uncalendared and 25% porosity cathodes.

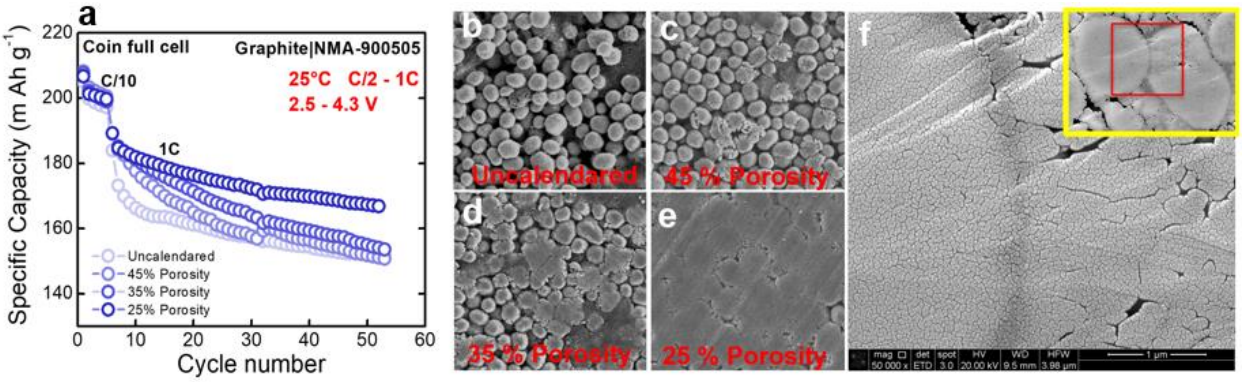

Figure II.4.E.4 (a) Cycling performance of NMA at various levels of porosity as obtained through calendaring, evaluated in coin-type full cells paired against graphite anode cycled between 2.5 and 4.3 V. Formation cycles are performed at a rate of C/10 and the main body of cycling is performed at C/2 charge rate and 1C discharge rate. (b-e) SEM images of NMA cathodes calendared to various levels of porosity. (f) Cross-sectional SEM image of NMA calendared to 35% porosity. Image is focused on the boundary between two secondary particles. The inset shows the zoomed-out image of the two particles, with the red box highlighting the boundary of interest.

The reason for this is thought to be due to increased surface area brought on by particle pulverization from calendaring (Figure II.4.E.4b-f). Even at moderate levels of calendaring, a meaningful portion of cathode particles are pulverized, significantly increasing surface area available for side reactions with electrolyte, depleting lithium inventory and causing capacity and voltage fade. Somewhat counterintuitively, this effect is not seen in the 25% porosity cathode because particle pulverization has occurred to an even greater extent. At this level of calendaring, nearly all surface particles have been essentially flattened (Figure II.4.E.4e). When the cathodes are calendared under sufficiently high pressures (e.g. 25% and 35% porosity), the particles are compressed to such an extent that the secondary particles appear to fuse at the interparticle boundaries (Figure II.4.E.4f). In the 25% porosity cathode, enough particles have been compressed to prompt the formation of near-continuous layer that may limit electrolyte penetration into the particle bulk, effectively lowering the surface area available for unwanted side reactions. The 35% porosity cathode, meanwhile, still has a significant portion of particles that did not undergo this fusing process and, therefore, does not receive as much benefit from it. As such, 25% porosity appears to be the optimal calendaring level, and we will apply this to electrode fabrication in future studies. The coin full-cells will continue cycling indefinitely, and pouch full-cells have been fabricated and will be cycled to at least 500 cycles to gauge the trends in long-term cyclability.

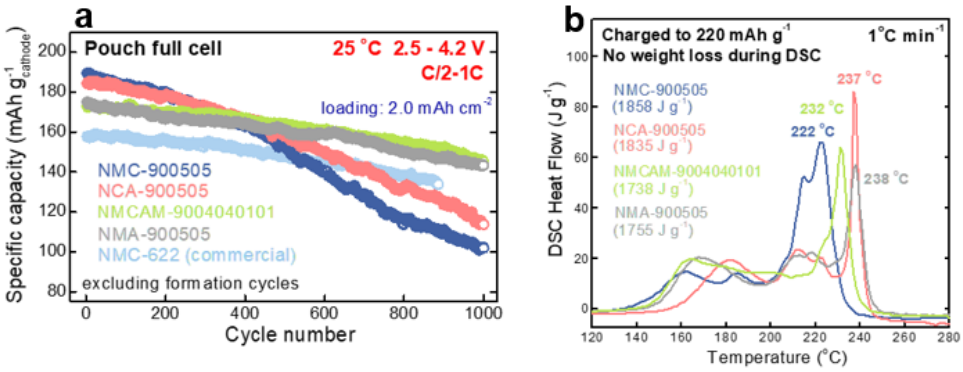

Figure II.4.E.5 (Left) Pouch cell cycling performance of various $LiNi_{0.90}M_xN_yO_2$ (where M = Mn or Mg, C = Co, and A = Al and x, y ≤ 0.05) with 90% Ni and commercial NMC-622 at 2.5 – 4.2 V; active material loading: 2.0 mAh cm^{-2}; single stack). (Right) Corresponding DSC curves for cathode materials displayed in cycling profile. Each material was charged to the same state- of-charge of 220 mAh g^{-1} before carrying out the DSC experiments.

In addition, the cycling performances and differential scanning calorimetry (DSC) curves of four in-house synthesized compositions with 90% nickel and a commercial NMC-622 are compared in in Figure II.4.E.5. The cobalt-free NMA-900505 outperforms both NCM-900505 and NCA-900505 in cyclability and nearly matches the performance of optimized NCMAM-9004040101. Furthermore, NMA exhibits a higher onset temperature of 238 °C for exothermic breakdown with a lower exothermic peak height in the differential scanning calorimetry plots in Figure II.4.E.5, indicative of improved thermal stability and safety. With further adjustments to composition and surface conditioning, we believe the cobalt-free NMA can become a competitive cathode for lithium-ion batteries.

We have also completed a study on the effect of synthesis oxygen pressure on the properties and performance of cobalt-free $LiNiO_2$. The cycling performances, Ni^{3+} content, and oxygen content of $LiNiO_2$ synthesized on various oxygen pressures between 1.0 and 2.0 atm are presented in Figure II.4.E.6. By applying a modest 1.7 atm of oxygen pressure during synthesis, the cyclability of $LiNiO_2$ is significantly enhanced. The baseline $LiNiO_2$ lasted 330 cycles with greater than 80% capacity retention. In contrast, $LiNiO_2$ synthesized under 1.7 atm of oxygen pressure lasts a remarkable 825 cycles before reaching 80% of its initial capacity, more than doubling the useful lifetime of the baseline $LiNiO_2$. Iodometric titration revealed a greater fraction of nickel in the 3+ valence state, as well as a higher oxygen content in the 1.7 atm $LiNiO_2$.

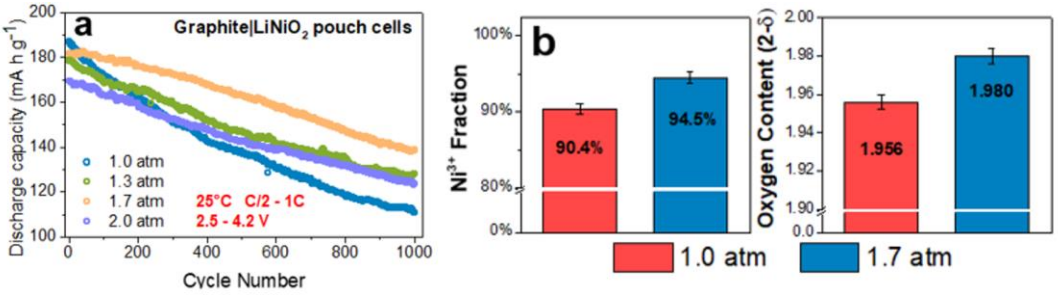

Figure II.4.E.6 (a) Long-term cycling performance of $LiNiO_2$ synthesized under various oxygen pressures (1.0, 1.3, 1.7, and 2.0 atm), evaluated in pouch-type full cells paired with graphite anode. Pouch cells were cycled between 2.5 and 4.2 V at a charge rate of C/2 and discharge rate of 1C. (b) Fraction of nickel in the Ni^{3+} valence state and oxygen contents in $LiNiO_2$ synthesized under 1.0 and 1.7 atm of oxygen pressure, as determined by iodometric redox titration.

The increased synthesis oxygen pressure improves the stability of Ni^{3+}, reducing the amount of Ni^{2+} and the number of oxygen vacancies formed during synthesis. This in turn produces a less defective, more stable structure that is better able to withstand mechanical degradation during extended cycling. Furthermore, the decrease in oxygen vacancy content contributes to a reduced surface reactivity in the 1.7 atm $LiNiO_2$, alleviating impedance growth and the consumption of active lithium in parasitic side reactions with electrolyte. This method of pressurized synthesis is simple means of improving the cyclability and stability of high-nickel cathodes without the need for exotic dopants or coatings. We believe the benefits of synthesis oxygen pressure are broadly applicable to all nickel-based layered oxide cathodes, and we will be testing this pressurized synthesis with other cobalt-free high-nickel layered oxides in the near future.

Conclusions

In Year 2, UT Austin has explored various low-cobalt and cobalt-free, high-nickel compositions prepared through co-precipitation of metal hydroxides. Based on the results, we have synthesized and delivered to Tesla Inc. ~ 1.7 kg of a low-cobalt, high-nickel layered oxide for fabrication of twenty-one 2 Ah pouch cells. Fourteen of these cells were delivered to INL for calendar life and cycle life evaluation. The 2 Ah cells performed well both at Tesla and INL. In addition, we have improved the performance of cobalt-free $LiNiO_2$ through co-doping with Mg and Cu as well as with increased synthesis oxygen pressure. We expect the technique of pressurized synthesis to broadly improve the performance of other high-nickel compositions. Also, with cobalt-free NMA, we have investigated the effects of electrode loading and calendaring to optimize our electrode fabrication processes for improved energy density and capacity retention. These results have built a strong foundation for our continuing efforts towards the development of low-cobalt and cobalt-free, high-nickel layered oxide cathodes for automotive batteries throughout this project.

Key Publications

Reports: Four reports have been submitted to the DOE at the end of each quarter.

1. W. Li, E. M. Erickson, and A. Manthiram, "High-nickel Layered Oxide Cathodes for Lithium-based Automotive Batteries," *Nature Energy* 5, 26–34 (2020).

2. W. Li, S. Lee, A. Manthiram, "High-Nickel NMA: A Cobalt-Free Alternative to NMC and NCA Cathodes for Lithium-Ion Batteries," *Advanced Materials* **2002718**: 1–6 (2020).

3. W. M. Seong and A. Manthiram, "Complementary Effects of Mg and Cu incorporation in Stabilizing the Cobalt-free $LiNiO_2$ Cathode for Lithium-ion Batteries," *ACS Applied Materials & Interfaces* **12**, 43653-43664 (2020).

4. Y. Kim, W. M. Seong, and A. Manthiram, "Cobalt-free, High-nickel Layered Oxide Cathodes for Lithium-ion Batteries: Progress, Challenges, and Perspectives," *Energy Storage Materials* **34**, 250-259 (2020).

5. A. Mesnier and A. Manthiram, “Synthesis of $LiNiO_2$ at Moderate Oxygen Pressure and Long-term Cyclability in Lithium-ion Full Cells,” *ACS Applied Materials & Interfaces* (accepted).

II.4.F Cobalt-Free Cathodes for Next Generation Li-Ion Batteries (Nexceris)

Neil Kidner, Principal Investigator
Nexceris, LLC
404 Enterprise Drive
Lewis Center, OH 43035
E-mail: n.kidner@nexceris.com

Peter Faguy, DOE Technology Development Manager
U.S. Department of Energy
E-mail: Peter.Faguy@ee.doe.gov

Start Date: October 1, 2018 End Date: December 31, 2020
Project Funding: $3,083,213 DOE share: $2,466,547 Non-DOE share: $616,666

Project Introduction

As the largest distributed source of CO_2 emissions, the transportation sector is currently experiencing a rapid transition to electric mobility and the adoption of electric (EV) vehicles, with 100-million EVs targeted by 2020. The increased demand for EVs will drive demand for battery materials. Current state-of-the-art lithium-ion batteries (LiBs) are based on cobalt-containing cathode chemistries. Speculation over a future global shortage of cobalt has led to a rapid increase in cobalt prices and renewed interest in increasing battery performance with reduced or cobalt-free cathode formulations. This provides an opportunity to reestablish U.S. dominance in batteries and prevent us from going from one dependency on oil to another in cobalt.

One of the most attractive approaches to improve battery energy density is to increase the battery voltage. There is, therefore, a need for next-generation, high-potential, and high-capacity cathode materials. The spinel formulation $LiNi_{0.5}Mn_{1.5}O_4$ (LNMO) is a very promising candidate based on its high specific energy (650 Wh/kg-cathode level) and cobalt-free formulation. Unfortunately, the adoption of this material has been limited by its poor cycle life, caused by oxidative decomposition of the electrolyte and a series of parasitic reactions occurring at the electrode-electrolyte interface, which prevents its commercial adoption.

Objectives

The project goal is to develop a next-generation LiB based on a cathode material that can meet the following specifications:

- Useable specific energy (cathode level) of at least 600 Wh/kg @ C/3
- 15 years of calendar life
- 1000 cycles (C/3 deep-discharge rate) with less than 20 percent energy fade
- Compatibility with cell cost of less than $100/kWh.

LNMO is an attractive candidate cathode material, which already satisfies two of the specifications. The goal of this project is to develop and validate a stabilized Ti-substituted lithium manganese nickel- oxide, $LiNi_{0.5}Mn_{1.2}TiO_{0.3}O_4$ (LNMTO) with improved cycle and calendar life. The cell chemistry, including electrode and electrolyte formulations, will be optimized for stable performance under aggressive high-voltage operating conditions. Technical feasibility will be demonstrated through the fabrication and testing of 2 Ah-cells. In FY19 the project focused on establishing a performance baseline for the LNMTO cathode derived from solid-state processing that will serve as a starting point for the LNMTO core/shell work. In FY20 alternative new wet-chemical synthesis approaches and core/shell advancements have been investigated to develop improved LNMO and Ti-substituted LNMTO cathode powders.

Approach

The proposed project approach is shown schematically in Figure II.4.F.1. The cycle and calendar life of high-voltage cathodes will be improved by developing a novel core-shell microstructure that enables the formation of a solid-electrolyte interface that effectively passivates the cathode surface. The microstructural enhancements of the cathode material focus on preferentially enriching the surface with titanium. In parallel, new, optimized electrode binder and electrolyte chemistries will be incorporated to address degradation mechanisms associated with high-voltage systems.

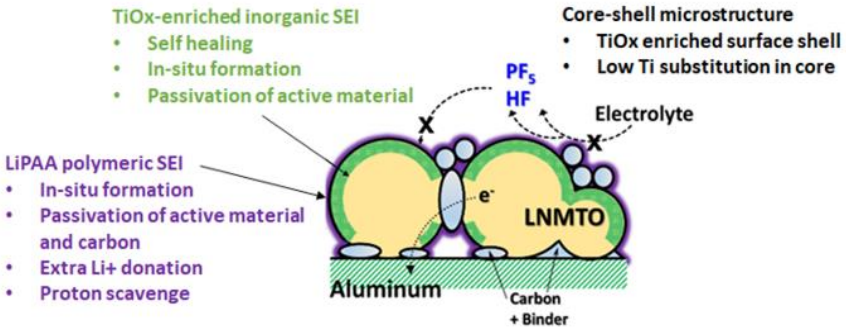

Figure II.4.F.1 Schematic of the technical approach for creating high-performance LNMTO Li-ion cathodes.

Commercially-practiced solid-state and chemical precipitation-based approaches will be used to scale-up the production of the LNMTO powder and demonstrate its performance in large-format 2-Ahr cells. In parallel, microstructural enhancement of the LNTMO powder will be completed to create novel core-shell structures where Ti is preferentially located at the surface to provide additional passivation and minimize capacity loss from Ti substitution in the bulk. Finally, to address additional degradation mechanisms associated with the operation of carbon conducting powders at high-voltages, advanced cell chemistries, including binder and electrolyte additives will be developed and optimized for the LNMTO cathode material.

In FY19 the project team focused on producing LNMTO (and LNMO) powders by conventional solid-state synthesis methods, fabricating LiB cells using these cathode materials, and testing these cells to establish baseline performance levels. Multiple large (2-Ahr) cells were successfully manufactured and fifteen (15) of these Project Progress Cells (PPCs) were delivered to Idaho National Laboratory (INL) for performance testing. In parallel, preliminary experiments were completed to demonstrate the feasibility of alternative co-precipitation synthesis and core/shell approaches.

In FY20 the project team has built on the Year 1 results and continued to improve the performance of the high voltage LNM(T)O cells. Core-shell cathode microstructures are being investigated to identify higher-performing cathode materials (maintain the stability provided with the TiO_2 enriched surface while increasing capacity with the LNMO core). The project team is also continuing electrolyte development with the goal of down-selecting intermediate promising cell chemistry for integration with the candidate core-shell LNMTO cathode and demonstration in 2 Ah cells at the end of 2020. This will allow the team to accurately assess their progress towards the overall project performance targets.

Results

Despite disruptions caused by the COVID-19 pandemic, the project team has been able to make significant progress in FY20. At the beginning of the year, 2-Ah PPCs were manufactured and tested. The down-select PPC cell chemistry was based on a solid-state homogeneous LNMTO cathode with LiPAA binder and 1 wt.% LiBOB electrolyte additive. Fifteen PPCs, manufactured at Navitas, were delivered to INL for testing based on a test protocol agreed between INL and the project team. In addition, another set of 2 Ah PPCs were manufactured and tested against 2 Ah cells made with the standard LNMO cathode powder. The down-select LNMTO PPCs show promising cell performance, as shown in Figure II.4.F.2. Initial capacity, ICL, and cycle life are all significantly improved compared to a control set of 2 Ah LNMO cells, illustrating the benefit of the

Ti-substituted LNMTO cathode in combination with the advanced cell chemistry, and providing baseline performance metrics that the project team has worked to advance over the remainder of FY20.

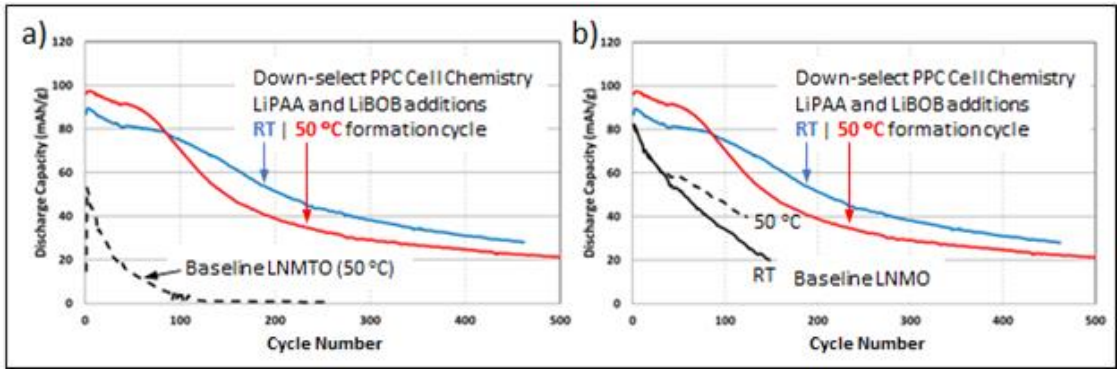

Figure II.4.F.2 2-Ah PPC cycle life performance comparing LNMTO cathodes with and without electrode binder and electrolyte additive modifications (left), and LNMTO versus LNMO cathodes (both with 1 wt.% LiBOB) (right). The figures also show the effect of aging T (RT, 50 °C) during the formation protocol. Testing procedure: 4.9 V - 3.5 V, -0.33C/0.33C

Comprehensive post-mortem characterization to understand the degradation mechanisms has been completed on the tested 2 Ah PPCs. No electrolyte was found during cell teardown (both electrodes and separator were dry) indicating severe electrolyte decomposition during cell testing. As shown in Figure II.4.F.4, the aged cathode maintained good adhesion to the Al current collector, while the aged graphite anode was mostly delaminated from the Cu current collector. Instead, the graphite anode adhered to the separator due to the thick SEI layers that grew between them (shown in the SEM image). Anode residue (Mn, Ni, Ti) was found on the separator, due to transition metal dissolution from cathode and migration to the graphite SEI. These degradation mechanisms were confirmed by XRD as shown in Figure II.4.F.4. Both aged cathode and anode shows a decrease in the peak intensities compared with their pristine counterparts, likely due to the formation of SEI and CEI layers. For the aged graphite anode, additional XRD peaks are observed at 21.6° and 24.1° which would be associated with the SEI products. In the case of the aged cathode, no extra peaks are found but there was a slight reduction of lattice parameters from a = 8.225 Å to 8.164 Å, which can be explained by transition metal dissolution from the spinel phases.

TGA analysis was performed to quantify the CEI and SEI layers. The mass loss during the heating can be attributed to specific thermal degradation modes which were indexed in Figure II.4.F.5.[1] The aged anode shows 9.87% mass loss corresponding to SEI breakdown occurring between 80-270°C(exothermic peak in the heat flow measurement). The aged cathode shows about 3.62% mass loss corresponding to CEI breakdown between 175-358°C. Beyond 358°C, oxygen evolution occurs from aged LNMTO spinel which may be delayed due to the CEI decomposition. The results agree well with the SEM images in Figure II.4.F.4 suggesting that the heavily deposited SEI layer occupied ~ 10 wt.% of the aged graphite anode.

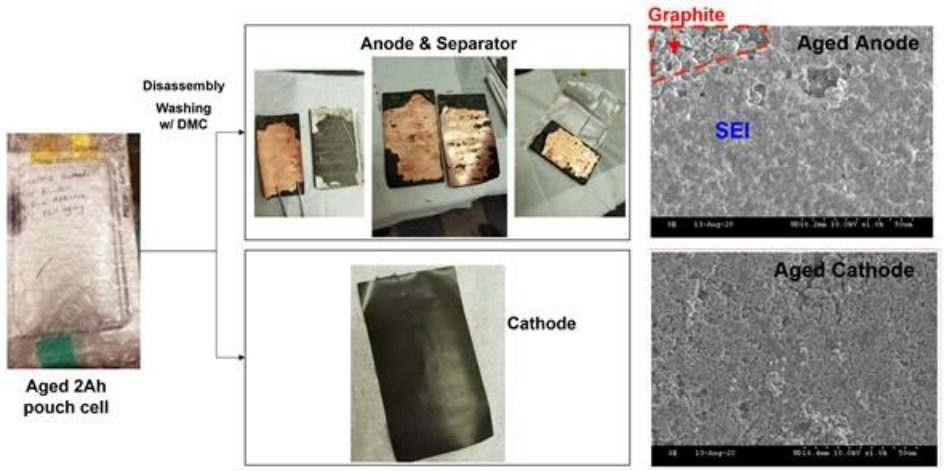

Figure II.4.F.3 Tear-down of 2 Ah pouch cells for the post-mortem analysis. (middle) Showing the photographs of anode, separator, and cathode. (right) SEM images from aged anode and cathode.

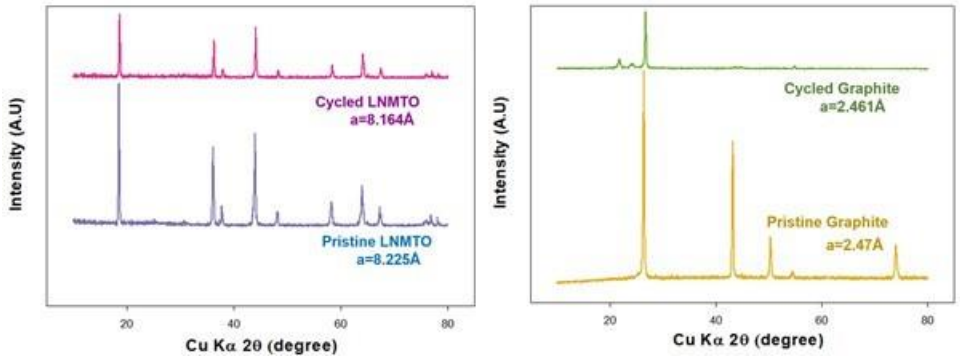

Figure II.4.F.4 XRD patterns and lattice parameters of pristine and cycled LNMTO (left) and graphite anode (right).

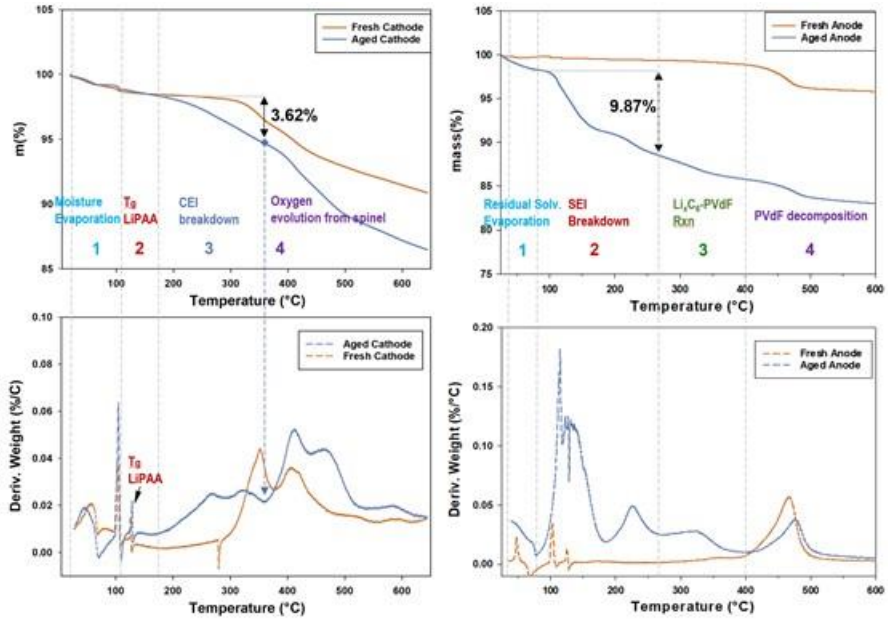

Figure II.4.F.5 TGA data from fresh and aged electrodes; LNMTO cathodes (left) and graphite anodes (right); mass loss (top) and derivative of weight (bottom) of electrodes.

The aged cathodes from cycled 2 Ah pouch cells were recovered, rinsed using DMC, and prepared as coin half-cells to characterize their electrochemical performances and residual lithium contents. Figure II.4.F.6 shows that all the aged cathodes (i.e., cells 1-3) delivered full charging/discharging capacity similar to that of fresh (i.e., baseline) LNTMO cathode. However, the aged cathodes delivered capacity retentions inferior to the fresh cathode due to larger cell impedances from the CEI. This result suggests that the LNMTO cathode did not have the lithium-loss during the cycling of 2 Ah pouch cells. The aged anodes could not be used for coin cells due to its severe delamination from Cu current collector.

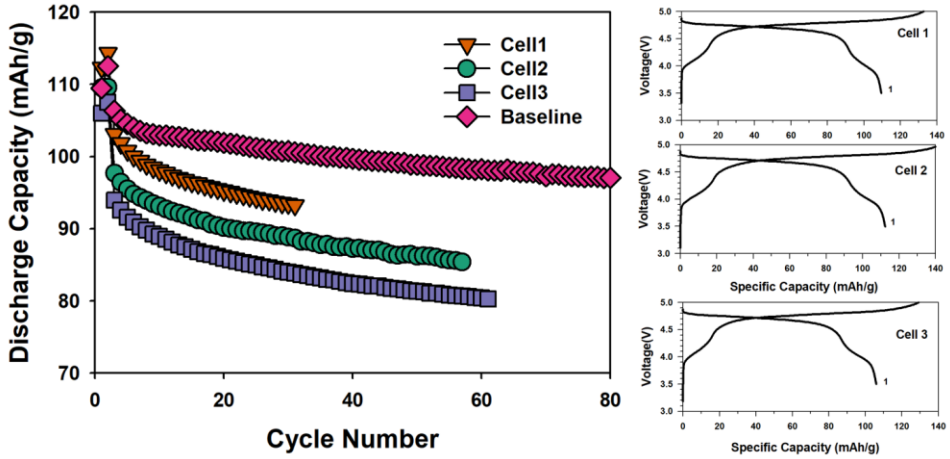

Figure II.4.F.6 Cycle life (left) and voltage profile at the 1st cycle of coin half-cells (right) made with aged cathodes recovered from the cycled 2 Ah pouch cells.

In FY19 Nexceris demonstrated improved cell performance with a co-precipitation-based synthesis process, that produced a compositionally more uniform powder that using solid-state processing. In FY20, motivated by the difficulty in scaling the co-precipitation process, and the expensive equipment required, Nexceris has pursued an alternative, low-cost, synthesis approach. The resulting two-step Hybrid Alternative Wet-Chemical Synthesis (HAWCS) process enables the same excellent compositional and particle morphology control achieved with co-precipitation without the strict process controls and associated expensive process equipment. Nexceris has demonstrated the feasibility of the HAWCS process by successfully synthesizing a highly uniform spherical LNMO cathode powder. The LNMO powder has a very narrow particle size distribution (Figure II.4.F.7), centered at d50 = 6 – 9 µm. In contrast, both the solid-state and co-precipitation processes produce fewer uniform powders with broader size distribution. Importantly, the particle size achieved with the HAWCS process can be well controlled and does not require post-calcination size reduction (i.e. attrition milling) which would destroy the preferred spherical morphology.

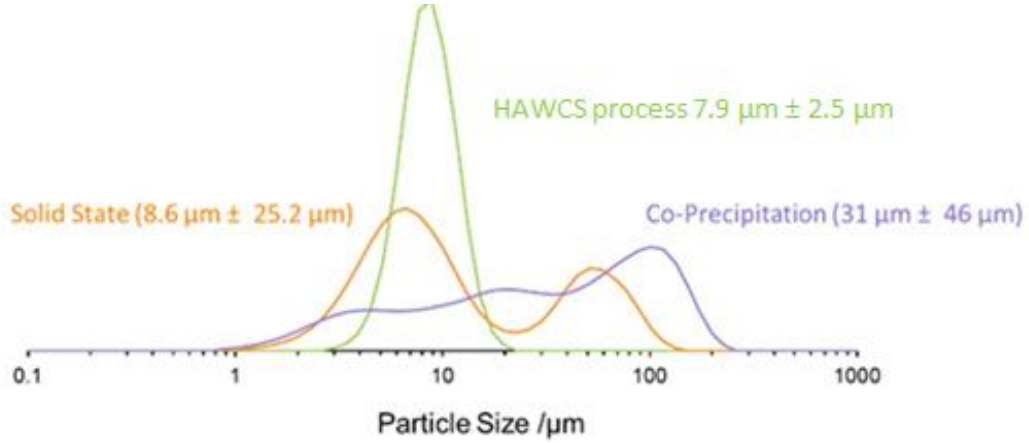

Figure II.4.F.7 Particle Size Distribution of LNMO powders synthesized using solid-state, co-precipitation, and HAWCS.

Through optimization of the process conditions, the level of impurity phases including Ni_6MnO_8, Li_2MnO_3, and rock-salt impurities has been successfully reduced. Rietveld refinement for HAWCS derived LNMO indicates the powder is extremely phase-pure (99.2-percent LNMO phase) with less than 1 percent impurities. This compares very favorably with Nexceris' highest purity solid-state LNMO which still showed ~ 5 percent impurity phases. The enhanced compositional and microstructural uniformity translates into enhanced cell performance. Figure II.4.F.8 shows the half-cell performance of LNMTO cathodes made by the down-select FY19 solid-state process compared to the latest HAWCS produced LNMO powder.

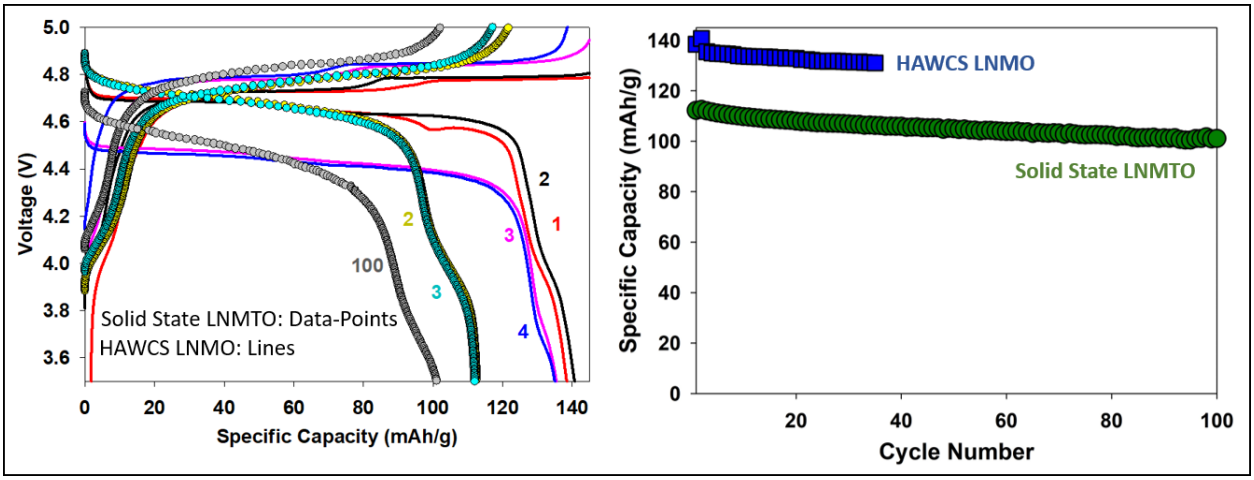

Figure II.4.F.8 Charge/Discharge-voltage profiles (left) and cycle performance (right) for coin-type half-cells at 25 °C with LNMTO and LNMO cathodes made with solid-state and HAWCS processes. Electrolyte 1 M LiPF6 in 1:1 wt. EC/EMC (no additive). Cycling conditions: Cycle 1: C/10 then C/5 (Ch) and C/2 (dis).)

In parallel to the development of the scalable HAWCS process Nexceris has advanced its core/shell hierarchical powder microstructure concept. Significant development has been completed to identify the most appropriate deposition approach and shell thickness, and how to integrate it within the HAWCS process. Figure II.4.F.9 shows the microstructure of LNMO core particles made by HAWCS and the corresponding LNMO/LNMTO core/shell powders. Figure II.4.F.10 shows the half-cell performance of the down-selected LNMO/LNMTO core/shell cathode powder versus the initial core/shell powder. The project team has been able to make a substantial improvement in the compositional and morphology uniformity of the core/shell powder which translates into improved cell performance

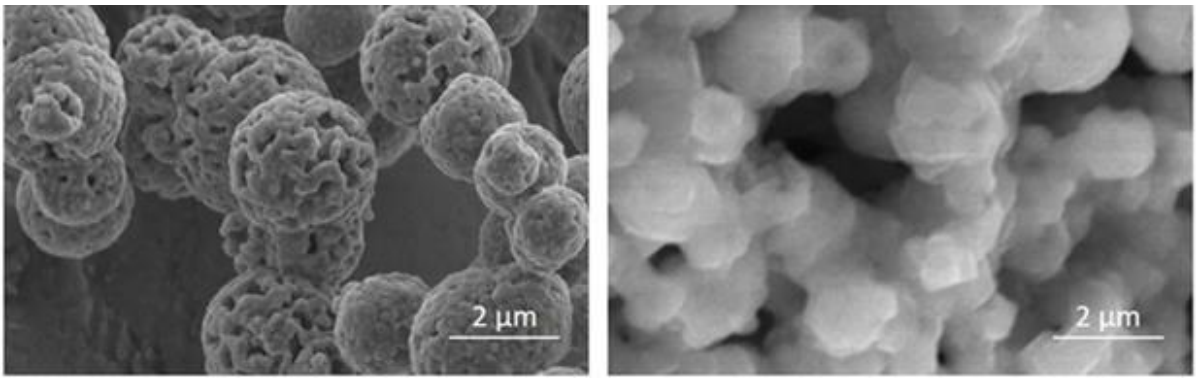

Figure II.4.F.9 Down-selected LNMO core powder (left), and LNMO/LNMTO core/shell powder (right).

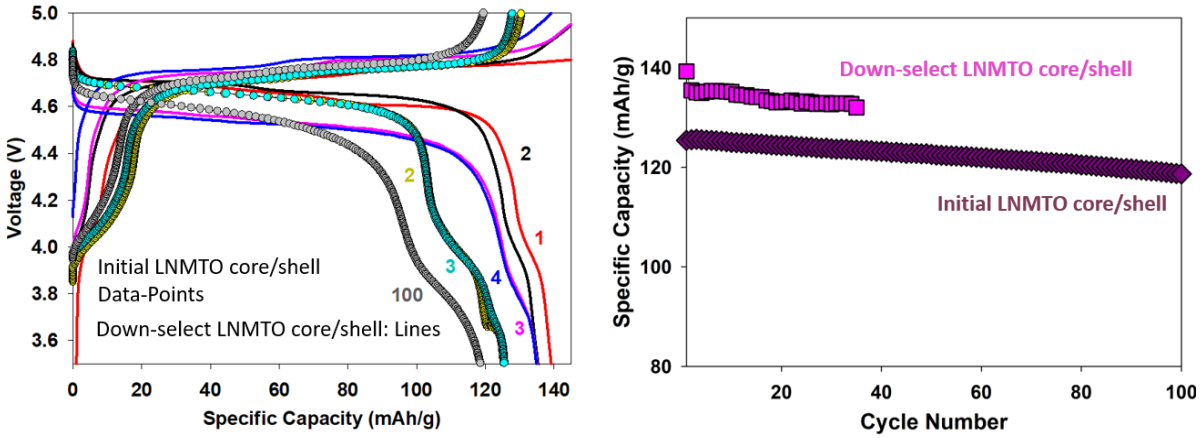

Figure II.4.F.10 Charge/Discharge-voltage profiles (left) and cycle performance (right) for coin-type half-cells at 25 °C with initial and down-selected LNMO/LNMTO core/shell cathodes made with solid-state and HAWCS processes. Electrolyte 1 M LiPF6 in 1:1 wt. EC/EMC (no additive). Cycling conditions: Cycle 1: C/10 then C/5 (Ch) and C/2 (dis).)

The HAWCS process enables Nexceris to produce cathode powder in ~ 1 kg batch size and a roadmap has been identified to scale this to larger batch sizes. Multiple batches of this down-selected LNMO/LNMTO core/shell powder have been produced to support single-layer pouch cell electrolyte development and optimization of the formation cycle to minimize gas-generation in the larger 2 Ah cells.

Conclusions

The post-mortem analysis of the 2 Ah PPCs indicated that capacity fading is primarily caused by electrolyte decomposition at high operating voltages (~ 4.7 Vvs. Li) of LNMTO cathodes as evidenced by (1) electrolyte depletion, (2) abnormally thick SEI (~ 10 wt.% of anodes), and (3) cathode CEI (~3.6 wt%). It is interesting to note that no Li-loss from the LNMTO cathode was detected, which is the main degradation mechanism of Ti-free LNMO cathodes.[2]–[4] In this regard, the project team is continuing to develop and implement high-voltage resistive electrolytes that are compatible with the LNMTO cathodes.

In parallel, Nexceris has successfully developed a new process (HAWCS) for producing high voltage LNMO powder and integrated this process with core/shell synthesis approaches to produce highly controlled and high-performing LNMO/LNMTO core/shell cathode powders.

References

1. H. Maleki, G. Deng, A. Anani, J. Howard, Thermal Stability Studies of Li-Ion Cells and Components, J. Electrochem. Soc. 146 (1999) 3224–3229.

2. J.-H. Kim, N.P.W. Pieczonka, Z. Li, Y. Wu, S. Harris, B.R. Powell, Understanding the capacity fading mechanism in LiNi0.5Mn1.5O4/graphite Li-ion batteries, Electrochimica Acta. 90 (2013) 556–562.

3. N.P. Pieczonka, Z. Liu, P. Lu, K.L. Olson, J. Moote, B.R. Powell, J.-H. Kim, Understanding Transition-Metal Dissolution Behavior in LiNi0.5Mn1.5O4 High-Voltage Spinel for Lithium-Ion Batteries, J. Phys. Chem. C. 117 (2013) 15947–15957.

4. J.-H. Kim, N.P.W. Pieczonka, L. Yang, Challenges and Approaches for High-Voltage Spinel Lithium-Ion Batteries, ChemPhysChem. 15 (2014) 1940–1954.

Acknowledgements

Nexceris would like to acknowledge the support of their project partners, Dr. Jung-Hyun Kim at The Ohio State University, and Navitas Systems. Dr. Kim's team has provided excellent technical guidance and support

for cell chemistry development and cell testing. Navitas Systems has provided feedback on the large-format cell manufacturing, and fabricated and tested the 2 Ah cells.

Nexceris would also like to thank the project's NETL manager, Adrienne Riggi for her project support and management, and Dr. Jack Deppe and Dr. Ahmad Pesaran for their technical guidance.

II.4.G High-Performance Low-Cobalt Cathode Materials for Li-ion Batteries

Donghai Wang, Principal Investigator
Department of Mechanical Engineering
The Pennsylvania State University
University Park, PA 16802
E-mail: dwang@psu.edu

Chao-Yang Wang, Principal Investigator
Department of Mechanical Engineering
The Pennsylvania State University
University Park, PA 16802
E-mail: cxw31@psu.edu

Jagjit Nanda, Principal Investigator
Chemical Sciences Division
Oak Ridge National Laboratory
Oak Ridge, TN 37831
E-mail: nandaj@ornl.gov

Chongmin Wang, Principal Investigator
Environmental Molecular Sciences Laboratory
Pacific Northwest National Laboratory
Richland, WA 99352
E-mail: chongmin.wang@pnnl.gov

Peter Faguy, DOE Technology Development Manager
U.S. Department of Energy
E-mail: Peter.Faguy@ee.doe.gov

Start Date: January 1, 2020 End Date: December 31, 2020
Project Funding: $850,329 DOE share: $680,263 Non-DOE share: $170,066

Project Introduction

The layer-structured $Li[Ni_xCo_yMn_{1-x-y}]O_2$ (NCM) cathode materials have been the best choice for increasing the driving distance per charge of electric vehicles.[1]-[3] The high Ni layered oxide represents successfully commercialized NCM cathodes (such as NCM622 [4] and NCA [5]) in lithium-ion batteries (LIBs) for EV applications due to their high energy density and acceptable cycling stability. The price of cobalt, a key element within LIBs for stability, has nearly tripled over the past few years due to increased demand from the cell phone industry, current materials shortage, increased adoption of electrical vehicle, and speculation for a future global shortage,[6]-[8] as mentioned in the DOE Funding Opportunity Announcement. To meet the requirement and sustainability of the next-generation long-range and low cost EVs, developing cathode materials with very low Co content to achieve higher energy density and lower cost is both essential and urgent.

Objectives

The overarching objective of this proposed work is to develop stabilized NCM cathode materials with low Co content (namely $LiNi_xCo_yMn_{1-x-y}O_2$, $y \leq 0.04$) so as to meet DOE's goal of reducing Co loading to below 50 mg Wh^{-1}, while maintaining energy density greater than 600 Wh kg^{-1} based on cathode material. The obtained NCM cathode paired with graphite anode shall deliver batteries with a high initial specific energy density of over 240 Wh kg^{-1} and low capacity fading rate of less than 20% in 1000 cycles under C/3 discharge rate.

Approach

To accomplish this goal, a multidisciplinary team with several co-investigators has been formed from three organizations: The Pennsylvania State University (PSU), Oak Ridge National Laboratory (ORNL), and Pacific Northwest National Laboratory (PNNL). The PI and co-investigators are Dr. Donghai Wang (PI) from PSU with expertise on synthesis of nanostructured materials and manipulation of interfacial properties of electrochemically active materials, Dr. Jagjit Nanda with substantial knowledge of and expertise in state-of-the-art cathodes from ORNL, Dr. Chao-Yang Wang with significant experience in advanced cell design and fabrication and cell diagnostics from PSU, and Dr. Chongmin Wang with world-wide known expertise of advance atomic scale characterization of electrode materials from PNNL. Furthermore, this project will leverage off and synergistically work with the current DOE-funded programs on battery materials at PSU and ORNL, and electrode materials characterization at PNNL.

Results

1. LFP-coated high-nickel NCM811/graphite pouch cells and single crystal NCM811 coating

In this year, we have been testing the 2.5 Ah pouch cells consisted of NCM811 cathode coated with 10wt% LFP and graphite anode, with the cathode loading of 17.5 mg/cm^2 and the N/P ratio of 1.1. These cells are cycled at 40ºC as well as room temperature, as shown in Figure II.4.G.1a. The cycling conditions are: C/3 CCCV to 4.2V till C/5, and aged cells are characterized at RPT condition every 200 cycles, i.e. C/3 CCCV to 4.2V till C/20. It can be seen that LFP coated NCM811 is very stable at room temperature, with the capacity retention at C/3 of 92.0% after 805 cycles. At 40ºC, the cell achieves 77.0% capacity retention after 805 cycles. The cell's capacity fade at elevated temperature is much faster than that at room temperature. That's due to low stability of cathode material at high temperature.

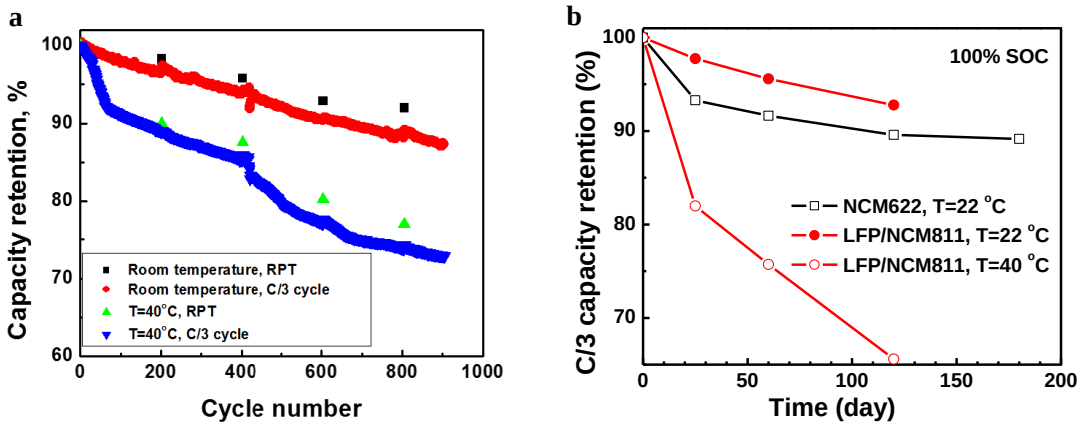

Figure II.4.G.1 a) Capacity retention of the LFP-coated NCM/graphite cells during C/3 cycling at room temperature and 40ºC. b) C/3 capacity retention of the LIBs using different cathode materials during storage at 22 ºC and 40 ºC, respectively.

The stability of LFP coated NCM811 is further investigated in calendar life tests, as shown in Figure II.4.G.1b. At 22 ºC and at 100% SOC (fully charged), LFP coated NCM811 is much stable than NCM622. C/3 capacity retention for NCM811 is 93.0% during storage at 22 ºC for 120 days, while the capacity retention for NCM622 is only 89.6% during the same storage temperature and time. LFP coated NCM811 shows fast capacity fade at an elevated temperature, as evidenced by a 65.3% capacity retention during storage at 40 ºC for 120 days. The result of calendar life tests agrees well with the cycle life test at different temperatures. C-rate performance was also measured as shown in Figure II.4.G.2. They can deliver 84% of cell capacity at 3C discharge rate and at room temperature.

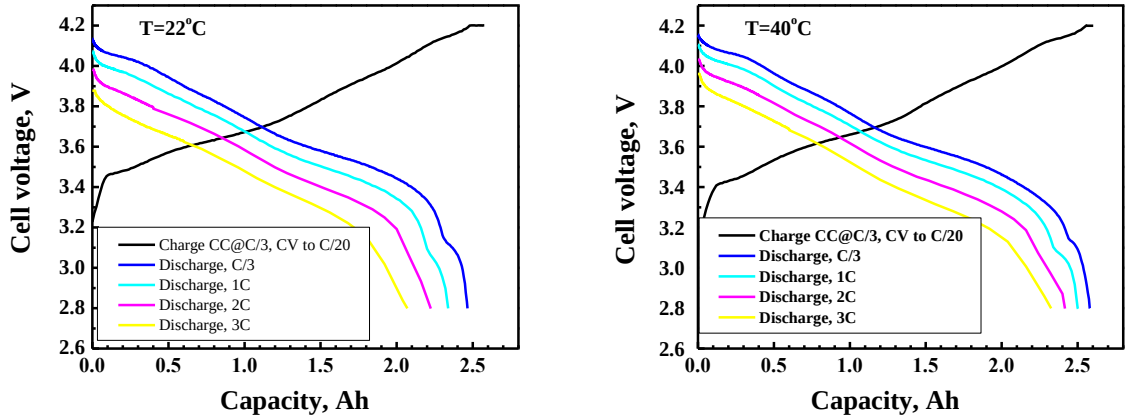

Figure II.4.G.2 C-rate performance of the LFP-coated NCM/graphite cell at different temperatures.

In addition to LFP-coated NCM811/graphite pouch cells, we have also tried to coat nano-oxides onto single crystal NCM811, which is exhibited in Figure II.4.G.3. The electrochemical performances of the coated materials are not as good as that of the bare sample. From the SEM images, it can be found that the nano-oxide particles agglomerate at the surface of the positive electrode material, which is considered to be the reason of the degraded electrochemical performance after nano-oxide coating.

In order to make the Al_2O_3 coating more uniform, the coated sample was sintered at 750°C for 4 hours (Figure II.4.G.4). From the SEM image, the Al_2O_3 coating of the sample after the second sintering is more uniform. For the electrochemical performance, the cycling stability of the material under the second sintering is better than that of the bare sample, and the coating amount of 1% alumina will be better than 2%.

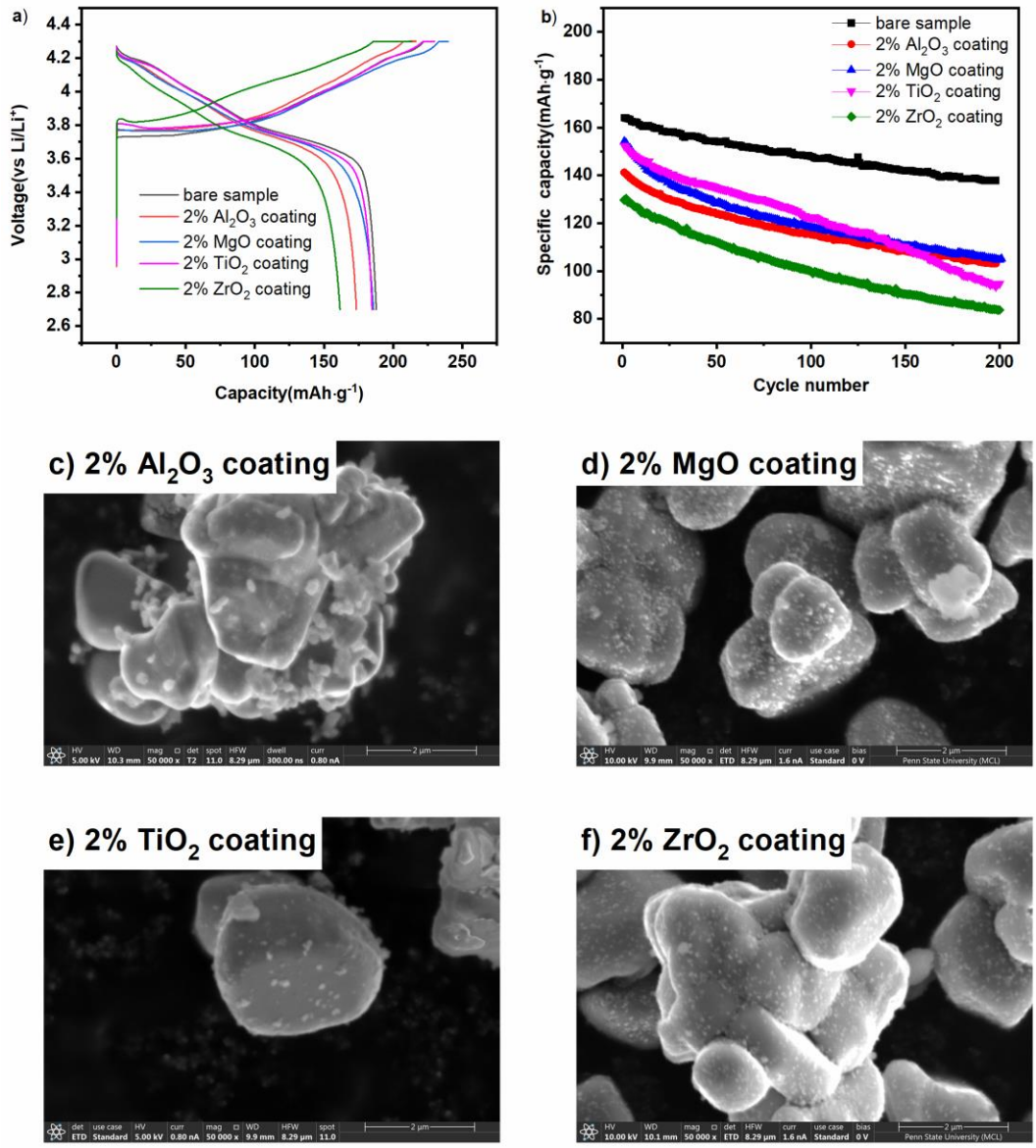

Figure II.4.G.3 a) Initial charge/discharge curves of bare and nano-oxide coated single crystal NCM811 at a rate of 0.1C. b) Cycling performance of bare and nano-oxide coated single crystal NCM811 at 1 C. c) - f) SEM images of different coated samples.

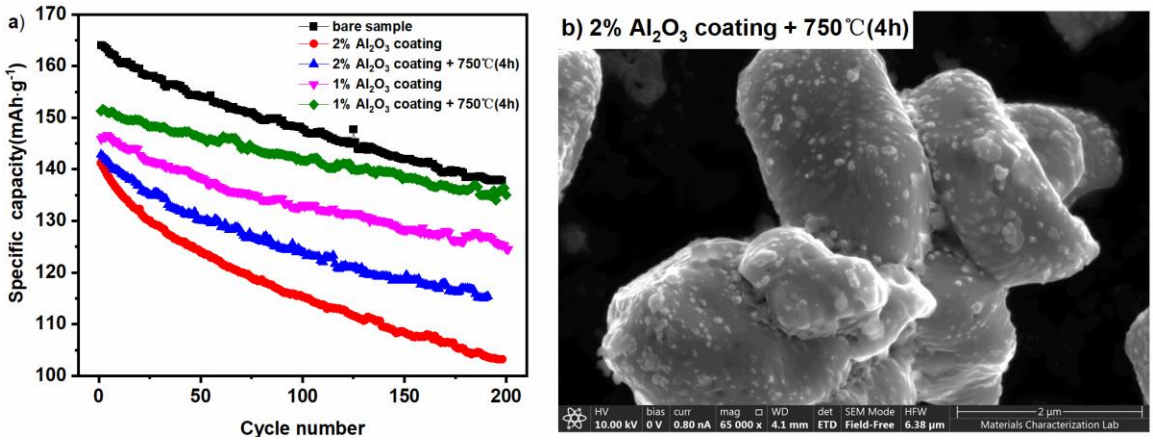

Figure II.4.G.4 a) Cycling performance of sample and Al_2O_3-coated samples with and without secondary sintering. b) SEM image of secondary sintered sample coated with 2% Al_2O_3

2. *Enhanced cycling stability of high-nickel low-cobalt cathode $LiNi_{0.92}Co_{0.055}Mn_{0.025}O_2$ by Al/Mo doping*

To increase the stability of high-nickel layered cathode material, cation doping has been considered as an efficient strategy. In particular, aluminum is one of the most valid dopants which has been reported that it can enhance the structure stability and elevate the thermal stability.

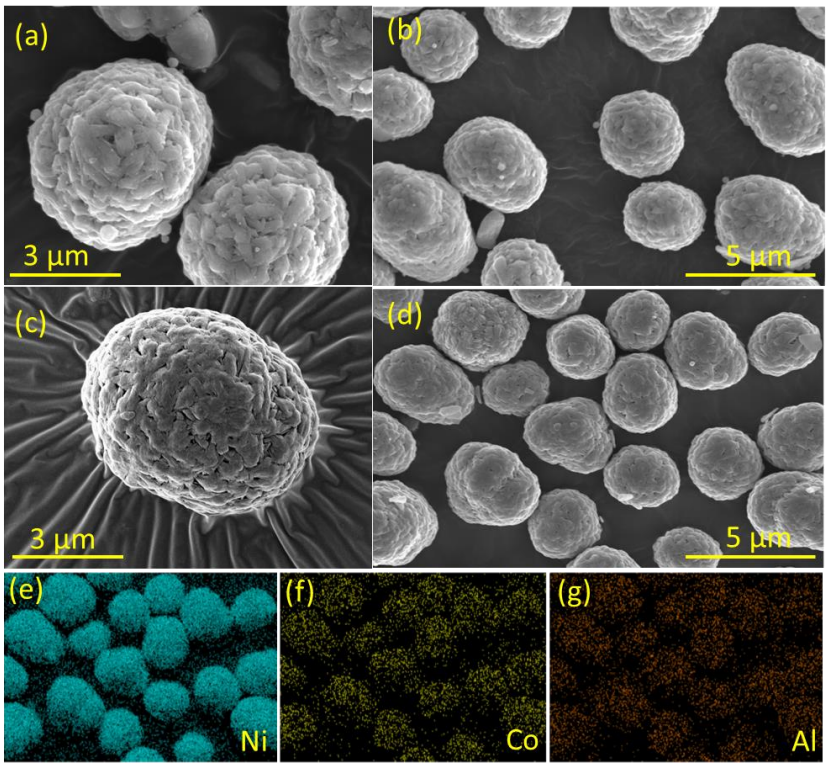

Figure II.4.G.5 SEM images of a) b) NCM_Al_2O_3. c) d) NCM_$Al(OH)_3$. e) - g) SEM EDS elemental mapping of the particle in d).

Figure II.4.G.5 shows the SEM images of $LiNi_{0.92}Co_{0.055}Mn_{0.025}O_2$ cathode with 1% Al_2O_3 (NCM_Al_2O_3) and 1% $Al(OH)_3$ (NCM_$Al(OH)_3$) dopants. The SEM and corresponding EDS images have been examined to

verify the uniform Al distribution on the precursor surface, and both materials consist of similar size secondary particles (around 3 to 5 µm). HAADF-STEM and corresonding EDS mapping in Figure II.4.G.6 has confirmed that Al in both cases has penetrated into the bulk strucutre and distributed uniformly through the lattice.

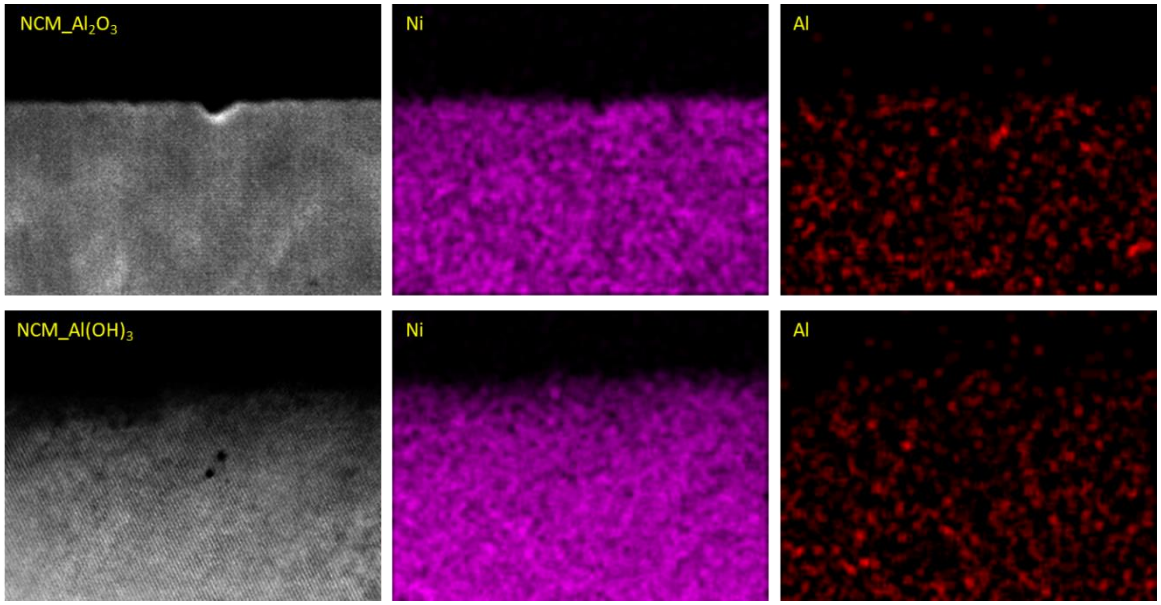

Figure II.4.G.6 HAADF-STEM image and corresponding EDS mapping of Al doped High Ni layered cathode. Upper: $NCM\_Al_2O_3$. Lower: $NCM\_Al(OH)_3$.

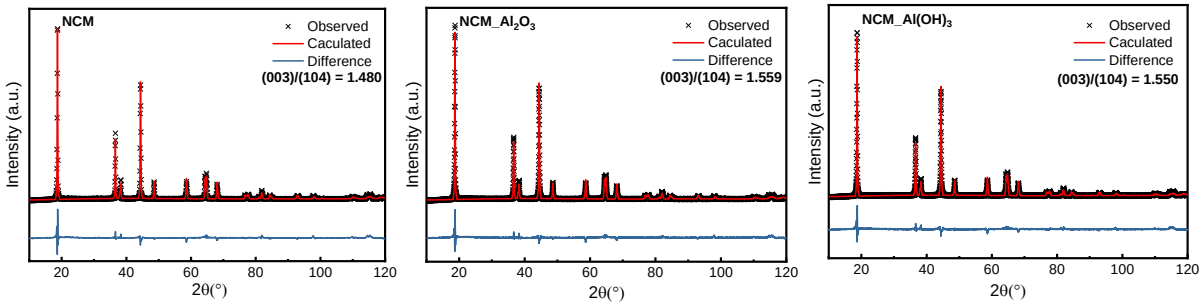

Figure II.4.G.7 XRD patterns and Rietveld refinement results of NCM_bare, $NCM\_Al_2O_3$ and $NCM\_Al(OH)_3$.

The XRD patterns and Rietveld refinement results in Figure II.4.G.7 and Table II.4.G.1 reveals that both $LiNi_{0.92}Co_{0.055}Mn_{0.025}O_2$ bare sample (NCM_bare) and Al doped NCM materials remain the rhomohedral α-$NaFeO_2$ structure (R-3m space group) without imupurity peak. The splitting of (006)/(102) indicates well-formed layer stuctures. The enhanced (003)/(104) ratio and Rietveld refinement results of the Al-doped NCM suggest lower level Li/Ni mixing after Al doping. The lattice parameters decline in the doped samples resulted from the Al^{3+} substitution with transition metal.

Table II.4.G.1 Lattice Parameters and Li/Ni Mixing of NCM, NCM_Al_2O_3 and NCM_$Al(OH)_3$

Samples	a(Å)	C(Å)	Li/Ni mixing
NCM	2.8841	14.2325	6.19%
NCM_Al_2O_3	2.8759	14.2225	5.96%
NCM_$Al(OH)_3$	2.8780	14.2293	5.16%

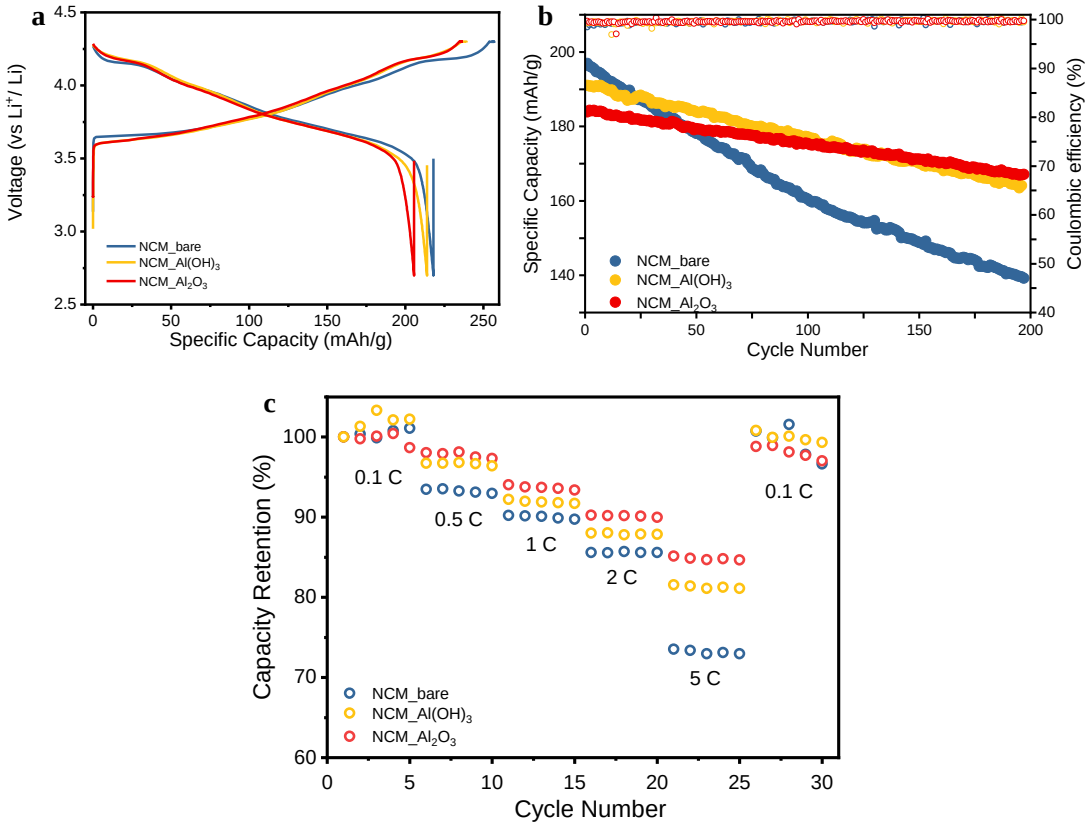

Figure II.4.G.8 Electrochemical performance of NCM_bare, NCM_Al_2O_3 and NCM_$Al(OH)_3$. a) Initial charge and discharge voltage profile at 0.1 C between 2.7-4.3 V. b) Cycling performance and coulombic efficiency at 1C for 200 cycles. c) Rate performance comparison from 0.1 C to 5 C.

Correspondingly, the cyclability for Al-doped materials is also greatly improved compared with the bare one (Figure II.4.G.8b). For NCM_bare, the capacity retention after 200 cycles is only 71%. After Al_2O_3 and $Al(OH)_3$ doping, such capacity retention can reach 91% and 86%, respectively. Although the initial discharge capacity of Al-doped materials is lowered, the slower capacity fading rate for doped materials leads to a higher capacity than that of bare NCM811 at around 25 cycles for NCM_$Al(OH)_3$ and 45 cycles for NCM_Al_2O_3. The improvement of cyclability is related to the suppression of Li/Ni mixing, as exhibited in Table II.4.G.1. Meanwhile, the rate performance has also boosted after doping since the doped Al stabilizes the structural stability (Figure II.4.G.8c).

Cross-section SEM was also utilized to investigate the stability of particle morphology. From Figure II.4.G.9, NCM_bare after 200 cycles has formed cavities and intergranular cracks from the center, while there is no obvious cracks or cavities within the Al-doped NCM cathodes.

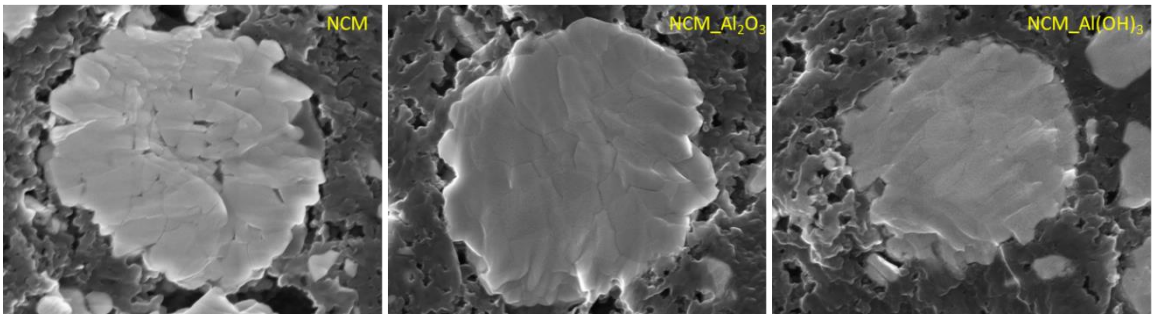

Figure II.4.G.9 Cross-section SEM images of NCM_bare, NCM_Al_2O_3 and NCM_$Al(OH)_3$ secondary particles after 200 cycles.

For High Ni layered cathode, phase transitions accompanied with oxygen evolution would occur at raised temperature. The charged NCM_bare exhibits an exothermic peak at 202.5°C while the Al doped NCM materials shift the peak to right (2.5°C and 10°C higher, Figure II.4.G.10). This result indicates that the Al-doped NCM has better resistance to phase transition and oxygen evolution reaction (OER). The improved thermal stability results from the stronger Al-O boding in the structure.

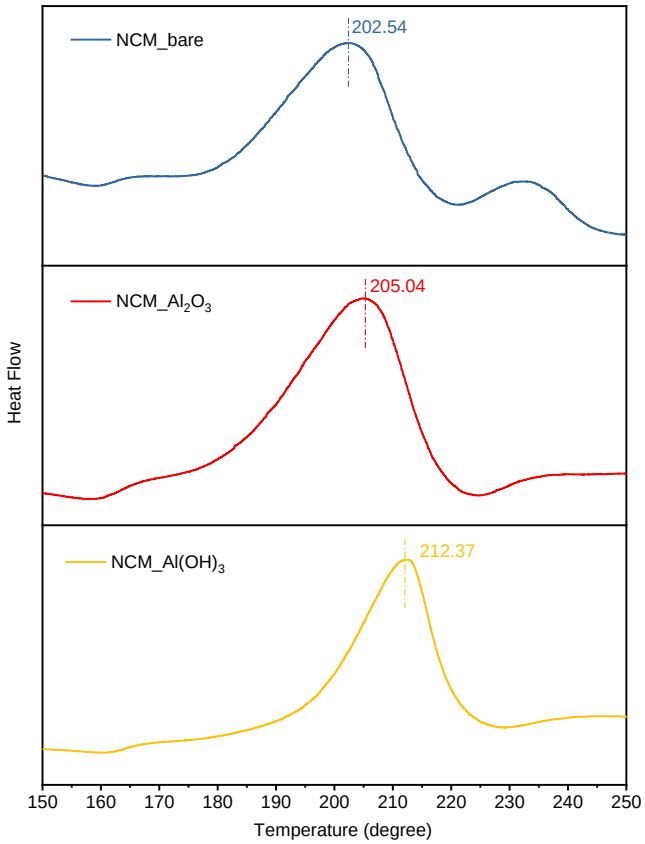

Figure II.4.G.10 DSC profiles of NCM_bare, NCM_Al_2O_3 and NCM_$Al(OH)_3$ charged initially to 4.3 V

The dQ/dV curves of the 1st cycle of NCM_bare, NCM_Al_2O_3 and NCM_$Al(OH)_3$ cells are given in Figure II.4.G.11. For Al-doped samples, the H2-H3 peak at around 4.17 V decreases compared with NCM_bare, indicating an inhibited H2-H3 phase transition process. This can explain why the capacity decay of Al-doped materials are suppressed, as H2-H3 phase transition can do harm to the structural stability.

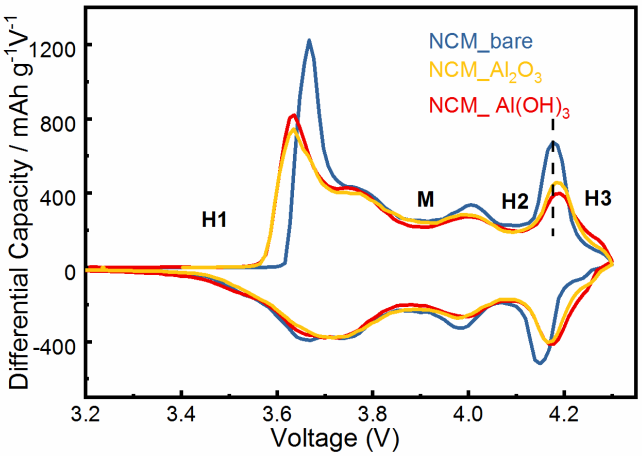

Figure II.4.G.11 The dQ/dV curves of the 1st cycle of NCM_bare, NCM_Al_2O_3 and NCM_$Al(OH)_3$ cells.

We have also tried different amount of Al dopants to observe the cycling stability evolution of $LiNi_{0.92}Co_{0.055}Mn_{0.025}O_2$. Cathodes with the nominal compositions $LiNi_{0.92(1-x)}Mn_{0.025(1-x)}Co_{0.055(1-x)}Al_xO_2$ (x = 0, 0.02, 0.05) were prepared by grinding the $NMC(OH)_2$ precursor with $LiOH{\bullet}2H_2O$ and $Al(OH)_3{\bullet}9H_2O$ followed by a two-stage heating process (500 °C for 4h and 725 °C for 12 h under flowing O_2). Figure II.4.G.12a shows X-ray diffraction (XRD) patterns of $LiNi_{0.92}Mn_{0.025}Co_{0.055}O_2$ powders with and without Al dopants. All materials were phase pure with α-$NaFeO_2$ layered structures (R-3*m* space group). SEM images in Figure II.4.G.12a and b show that the doped and undoped NMC powders had similar spherical morphologies. These findings indicate that this Al doping route preserved the cathode structure and morphology.

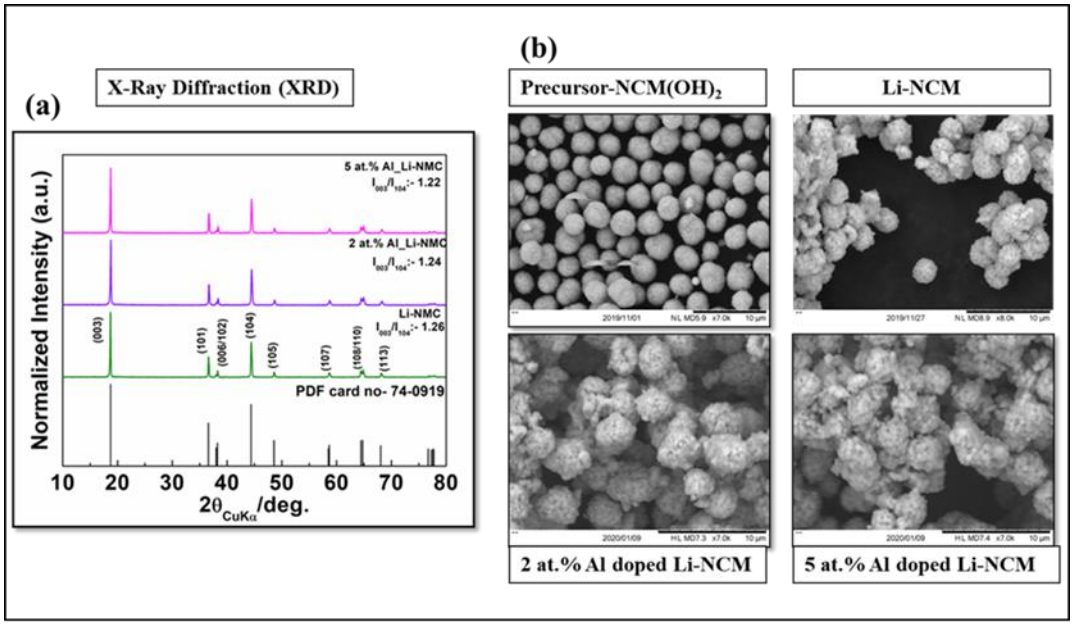

Figure II.4.G.12 Structural characterization of Li-NMC with and without 2 - 5 at.% Al dopant showing (a) Powder XRD patterns and (b) SEM images.

Neutron scattering experiments on the NOMAD beamline at the Spallation Neutron Source (SNS) was performed to understand the cationic distribution and the nature of cation present on lithium site. Figure II.4.G.13a-c shows the neutron diffraction pattern for $LiNi_{0.92(1-x)}\ Mn_{0.025(1-x)}\ Co_{0.055(1-x)}\ Al_xO_2$ (x = 0, 0.02,

0.05) for Bank 1 and it represent that with Al dopant the cation mixing slightly increases. Figure II.4.G.13d shows the cycling performance of Li-NMC, 2 at. % and 5 at. % Al doped Li-NMC cathode represents initial capacity of 220, 217, 211 mAh/g with the capacity retention of 82%, 81% and 91%, respectively.

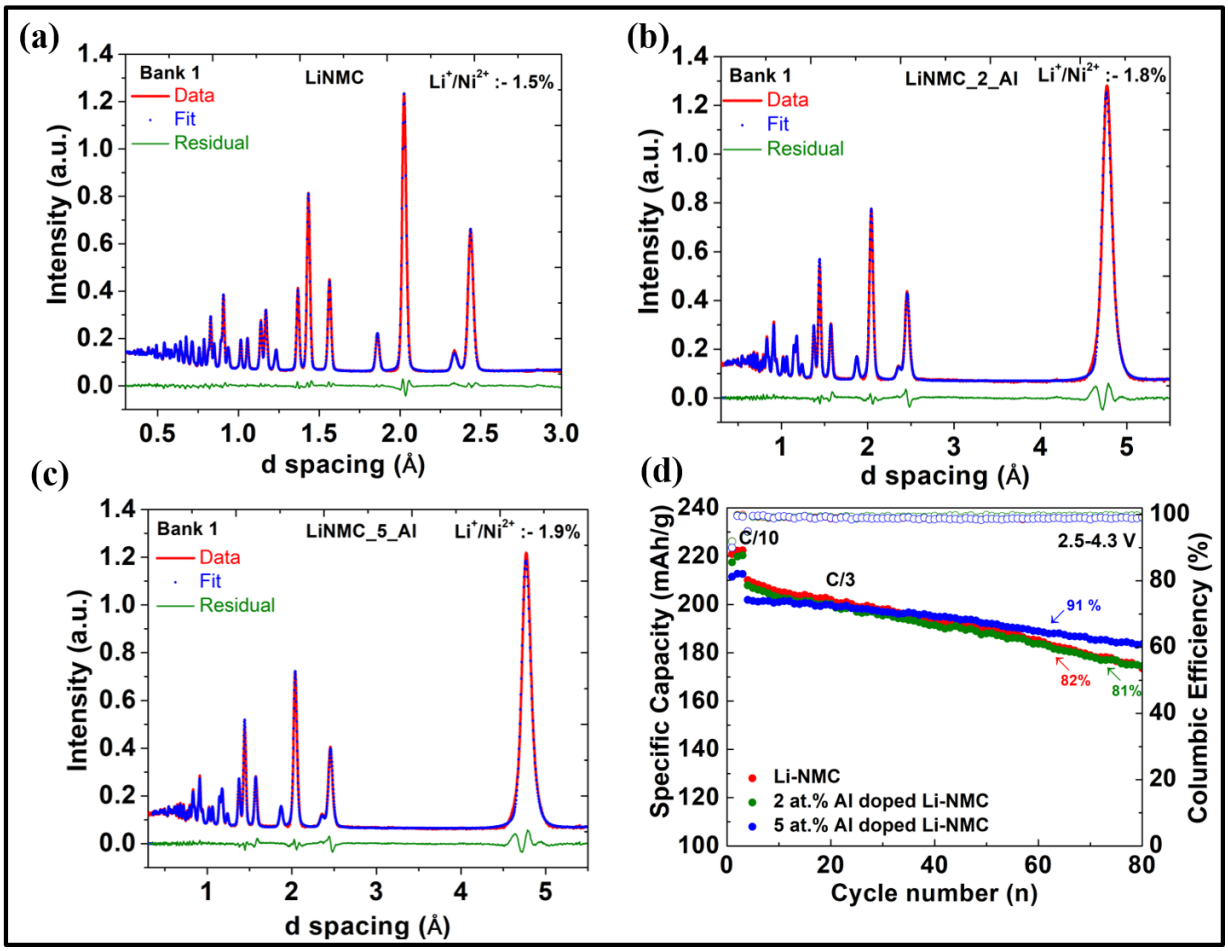

Figure II.4.G.13 Neutron diffraction studies for (a) $LiNi_{0.92}Mn_{0.025}Co_{0.055}O_2$ (Li-NMC) (b) 2 at.% Al doped Li-NMC (c) 5 at.% Al doped Li-NMC. (d) Electrochemical performance of half-cells for Li-NMC, 2 at.% and 5 at.% Al doped Li-NMC using constant current mode in the potential range of 2.5-4.3 V showing cycling stability at current rate of C/10 for first 3 cycle and rest of the cycle at C/3 rate. Capacity retention is calculated from 4th cycle where the coin cell cycles at the rate of C/3.

We have also conducted Mo doping to $LiNi_{0.92}Co_{0.055}Mn_{0.025}O_2$. Cathodes with the nominal compositions $LiNi_{0.92(1-x)}Mn_{0.025(1-x)}Co_{0.055(1-x)}Mo_xO_2$ (x = 0, 0.01) were prepared by grinding the $NMC(OH)_2$ precursor with $LiOH{\bullet}H_2O$ and $(NH_4)_6Mo_7O_{24}{\bullet}4H_2O$ followed by a two-stage heating process (500 °C for 4h and 725 °C for 12 h under flowing O_2). Figure II.4.G.14a shows X-ray diffraction (XRD) patterns of $LiNi_{0.92}Mn_{0.025}Co_{0.055}O_2$ (Li-NMC) powders with and without Mo dopant. All materials were phase pure with α-$NaFeO_2$ layered structures (R-3*m* space group). Galvanostatic charge/discharge performance of Li-NMC and Mo-doped Li-NMC cathodes are given in Figure II.4.G.14b-d. Although Mo doping had negligible impact on the voltage profile and initial reversible capacity (ca. 220 mAh/g at C/10), the doped cathode exhibited superior cycling stability with 85% capacity retention after 97 cycles at C/3 compared to 78% retention for the undoped Li-NMC.

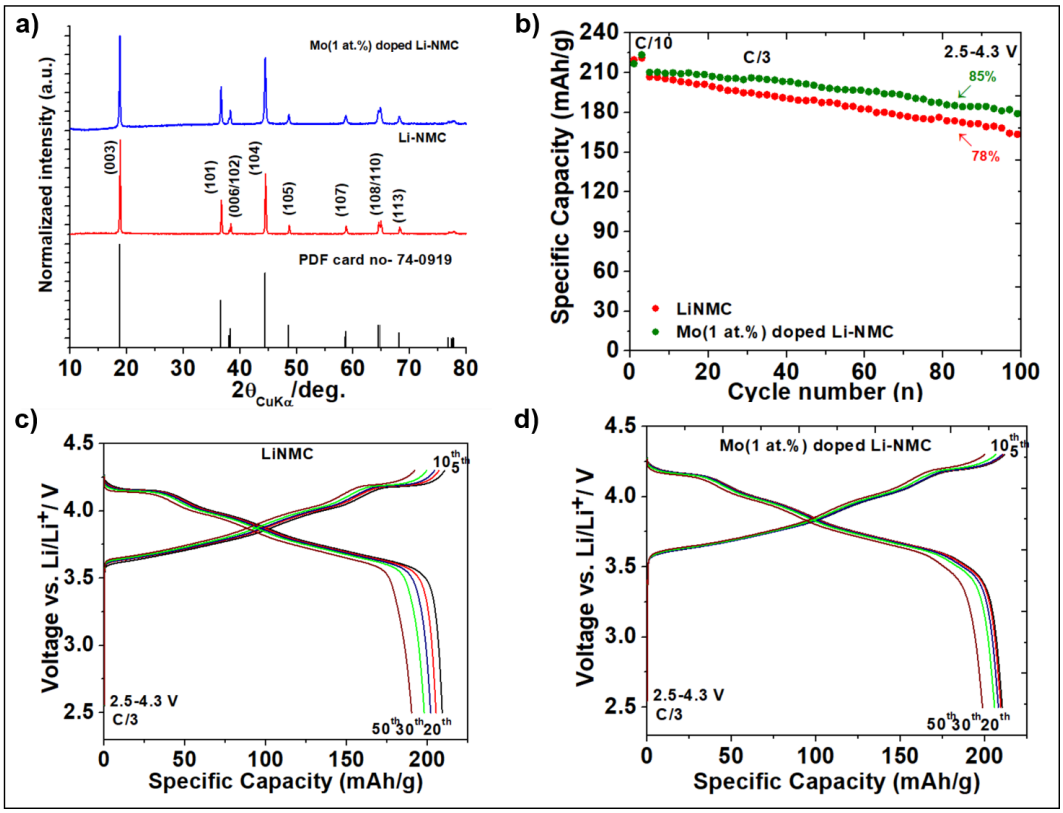

Figure II.4.G.14 Structural characterization and electrochemical performance of $LiNi_{0.92(1-x)}Mn_{0.025(1-x)}Co_{0.055(1-x)}Mo_xO_2$ (x = 0, 0.01) cathodes. (a) XRD patterns, (b) galvanostatic cycling performance in half cells, and (c-d) corresponding charge/discharge profiles for these materials. Capacity retention in (b) is calculated by normalizing the capacity to that obtained in the 4th cycle at C/3. Low levels of Mo cation dopants significantly improved the cycle life of Li-NMC.

3. *Phosphate/metaphosphate coating on $LiNi_{0.92}Co_{0.055}Mn_{0.025}O_2$*

In addition to doping, coating is also considered as an effective way to enhance the cycling stability of the high-nickel cathode materials, which is usually considered to be beneficial for protecting the cathode from electrolyte oxidation, tuning the CEI formation and inhibiting the particle decomposition. Here we have been working on phosphate coating on $LiNi_{0.92}Co_{0.055}Mn_{0.025}O_2$ in order to improve the electrochemical performance.

To synthesize $AlPO_4$ nanoparticles, $AlCl_3 \cdot 6H_2O$ and $NH_4H_2PO_4$ were mixed with $NH_3 \cdot H_2O$ together to form $AlPO_4$ precipitation, and then centrifuged and vacuum dried to obtain the final product. The particle size of the obtained AlPO4 is ~60nm, which is exhibited in Figure II.4.G.15a. Next the $AlPO_4$ nanoparticle was ball milled with the NCM precursor, and sintered with Li source to finish the synthesis. SEM and EDS mapping of the coated material (Figure II.4.G.15b-e) shows that the coating is quite uniform but there are still small clusters of $AlPO_4$ existed on the product.

Figure II.4.G.16 gives the electrochemical performance of the bare and 1%/2% $AlPO_4$ coated materials. The initial specific discharge capacity of 1% coated material is the same as the bare sample, and a 10 mAh/g specific capacity drop is observed for the 2% $AlPO_4$ coated material. The cyclability of 150 cycles increases from 74.6% (bare) to 80.5% (1% coated) and 84.3% (2% coated), respectively.

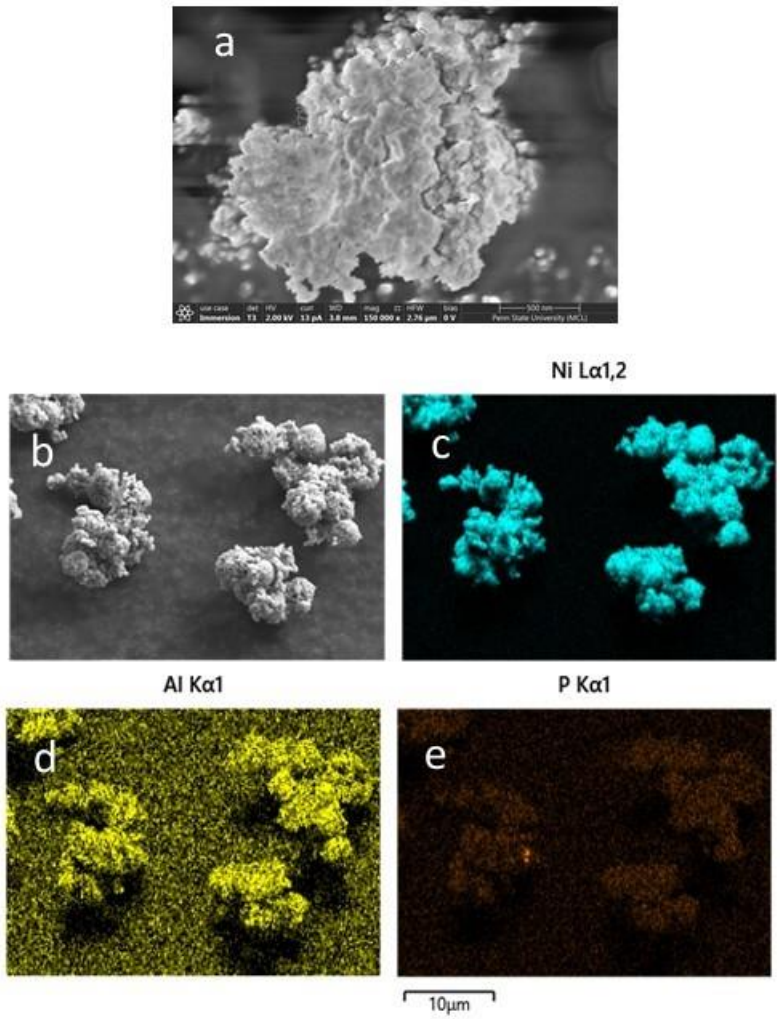

Figure II.4.G.15 SEM image of $AlPO_4$ nanoparticles. b) – e) SEM and EDS mapping of $AlPO_4$ coated $LiNi_{0.92}Co_{0.055}Mn_{0.025}O_2$.

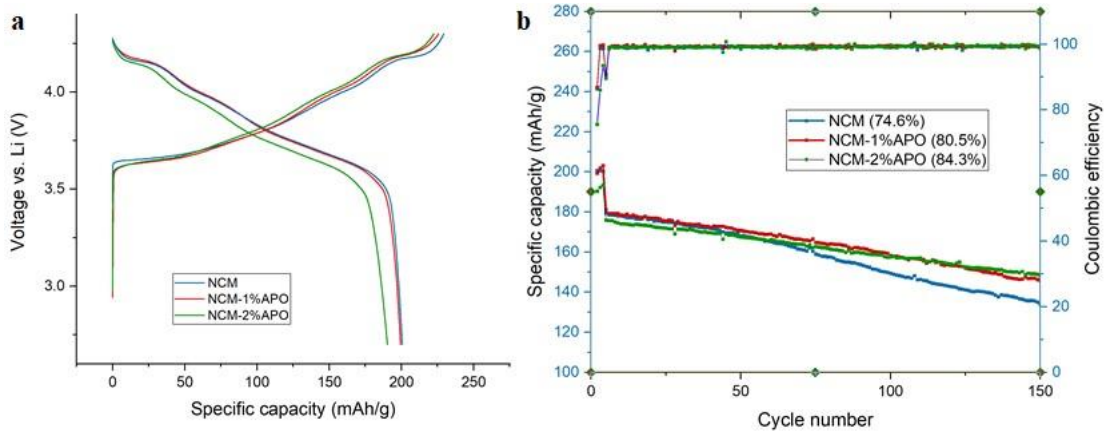

Figure II.4.G.16 a) Voltage profile of bare and coated NCM cathode (2.7 – 4.3 V, 0.1 C). b) Cycling performance of bare and coated NCM cathode (2.7 – 4.3 V, 0.1 C for the first 3 cycles, then 1 C). Capacity retention in b) is calculated by normalizing the capacity to that obtained in the 4th cycle at 1 C.

We have also obtained some preliminary results of $LiPO_3$ coating on $LiNi_{0.92}Co_{0.055}Mn_{0.025}O_2$. $LiPO_3$ is a lithium ion conductor and its coating can reduce side reactions at the interface between the cathode material

and the electrolyte. $LiPO_3$ was synthesized by solid-state method and decomposition method. XRD results (Figure II.4.G.17c) show that the syntheses by both methods are successful, and the SEM images (Figure II.4.G.17a and b) show that the particle size of the material synthesized by decomposition method is smaller. The SEM and EDS mapping results of the $LiPO_3$-coated material (Figure II.4.G.17d-f) show that $LiPO_3$ has good wettability to the cathode material. Electrochemical test will be conducted in the future.

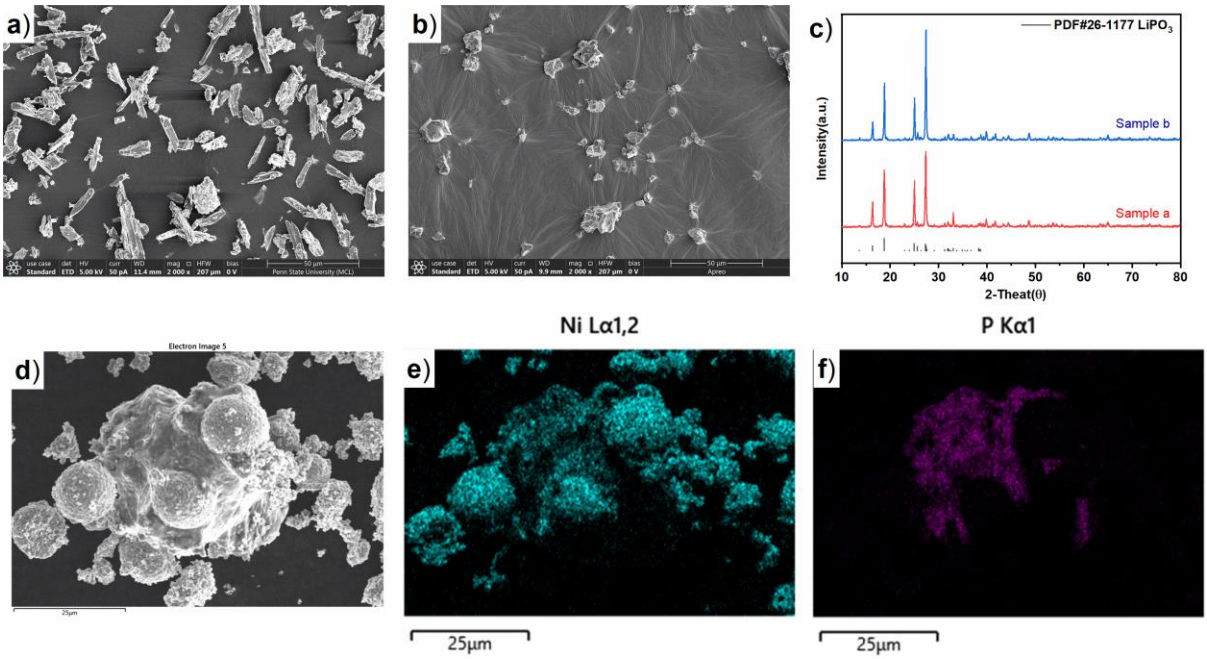

Figure II.4.G.17 a) b) SEM images of $LiPO_3$ prepared by solid-state method and decomposition method, respectively. c) XRD images of samples a) and b). d) - f) SEM and EDS mapping of the $LiPO_3$-coated material (coated with $LiPO_3$ synthesized by solid-state method)

4. Co-free $LiNi_{1/2}Mn_{1/2}O_2$ (LNMO) optimization and mechanism study

In FY2019, we have reported that Mo-doping is beneficial for the structural and cycling stability of co-free $LiNi_{1/2}Mn_{1/2}O_2$ material. This year we have been working on further optimization of the $LiNi_{1/2}Mn_{1/2}O_2$ system. $Mn_2P_2O_7$ was selected to be coated on the $LiNi_{0.495}Mn_{0.495}Mo_{0.01}O_2$ (LNMMO) cathode to further improve its stability. Besides, Ti and Zr doped $LiNi_{0.495}Mn_{0.495}M_{0.01}O_2$ cathodes (M = Ti and Zr) were also synthesized and tested. In addition to the optimization, the structural reconstruction in LNMMO was deeply studied by STEM HAADF, STEM ABF, and EELS.

LNMMO cathode powders were treated with a $Mn_2P_2O_7$ (MPO) coating to mitigate undesirable side reactions at the cathode/electrolyte interface. The coating was applied by dissolving stoichiometric amounts of $Mn(Ac)_2{\bullet}4H_2O$ and $NH_4H_2PO_4$ in deionized water followed by the addition of as-synthesized Mo-doped LNMO under continuous stirring. This suspension was dried at 60 °C to remove H_2O, and the resulting powder was heated at 300 °C for 5 h under ambient atmosphere to obtain the $Mn_2P_2O_7$-coated LNMMO. TEM images shown in Figure II.4.G.18a demonstrate that the 1.5 nm $Mn_2P_2O_7$ coating was amorphous and uniform on the particle surface. Figure II.4.G.18b shows galvanostatic cycling data (collected at 20 mA/g over 2.0-4.5 V vs. Li/Li^+) for the LNMO, Mo-doped LNMO, and the MPO coated cathodes over 100 cycles. The Mo-doped systems exhibited ~20% higher reversible capacity compared to LNMO (~180 vs. 150 mAh/g, respectively), and the $Mn_2P_2O_7$ coating improved the cathode's cycling stability considerably. After 100 cycles, the MPO coated cathode retained 78% of its initial capacity compared to only 65% capacity retention for the uncoated Mo-doped LMNO. The coated cathode also exhibited significantly better rate capabilities compared to the uncoated materials (Figure II.4.G.18c) which is attributed to the presence of a less resistive cathode/electrolyte interface.

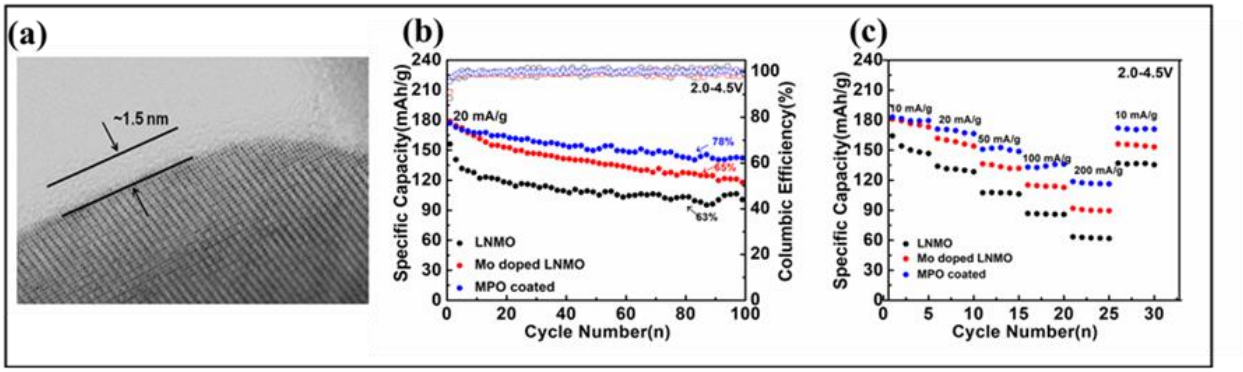

Figure II.4.G.18 (a) ABF-STEM images of Mo-doped LNMO ($LiNi_{0.495}Mn_{0.495}Mo_{0.01}O_2$) coated with $Mn_2P_2O_7$. (b-c) Galvanostatic cycling data collected between 2.0 – 4.5 V for half-cells containing Li anodes and the following cathodes: $LiNi_{0.5}Mn_{0.5}O_2$ (LNMO), Mo-doped LNMO, and Mo-doped LNMO coated with $Mn_2P_2O_7$ (MPO coated). (b) Cycling stability at 20 mA/g over 100 cycles and (c) rate capability data collected at specific currents of 10 - 200 mA/g.

$LiNi_{0.495}Mn_{0.495}M_{0.01}O_2$ cathodes (M = Ti and Zr) were prepared using a sol-gel reaction route. The cathodes' electrochemical properties were evaluated in half cells containing a Li metal anode and liquid carbonate electrolyte (1.2 M $LiPF_6$ in EC/EMC, 3/7 by weight). Figure II.4.G.19 shows the cathodes cycling performance collected at 20 mA/g between 2.0 – 4.5 V vs. Li/Li^+. Compared to undoped LNMO, 1 at. % Ti and Zr substitution did not improve initial reversible capacity (~140-155 mAh/g) but dramatically improved capacity retention for 1 at.% Ti (81 %),1 at.% Zr (71 %) vs. LNMO – (63 %).

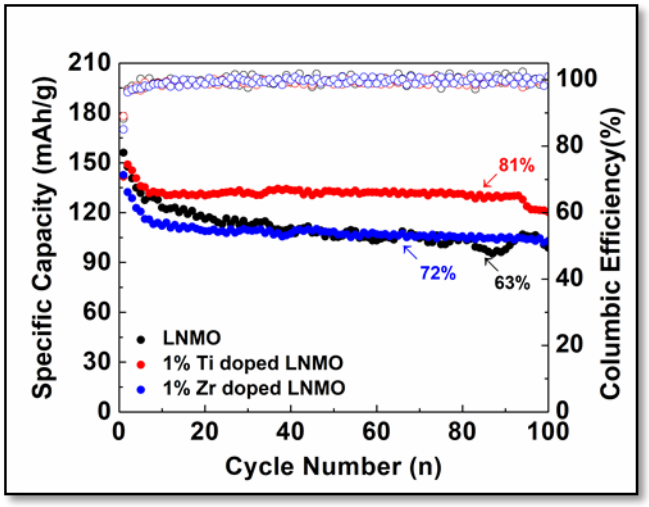

Figure II.4.G.19 Electrochemical performance of half-cells containing $LiNi_{0.5}Mn_{0.5}O_2$ (LNMO), 1 at.% Ti doped $LiNi_{0.5}Mn_{0.5}O_2$ and 1 at.% Zr doped $LiNi_{0.5}Mn_{0.5}O_2$ using constant current mode in the potential range of 2.0-4.5 V showing cycling stability at current density of 20 mA/g over 100 cycle.

In order to study the structural reconstruction in $LiNi_{0.495}Mn_{0.495}Mo_{0.01}O_2$ (LNMMO), characterizations such as STEM HAADF, STEM ABF, and EELS were conducted. The atomic structures of a nanoscale region below the surface of a pristine LNMMO particle are characterized by the STEM HAADF and ABF images as shown in Figure II.4.G.20d-f. In the HAADF image (Figure II.4.G.20d), the layered structure is clearly observed in almost the whole region, except for at the surface where 2-3 monolayers of rocksalt-like structures are formed. This feature has been generally documented for the pristine layered cathodes based on STEM HAADF imaging in which the reconstructed structures were found only within the very thin surface region and it was thus believed the layered structures were well preserved at the subsurface regions. Through ABF imaging, however, we reveal detailed fine structures that are hidden at the subsurface region. As shown by the ABF image of the same region (Figure II.4.G.20e) and the corresponding schematic (Figure II.4.G.20f), multiple

spinel-like nanoregions that are a few nanometers in width are observed within the layered matrices, forming discrete domains at the subsurface regions. Since the spinel-like structures are only evident in the ABF image but nearly invisible in the HAADF image, these structures should only involve a small number of TM atoms migrating into the Li layers and forming spinel-like patterns.

Our observation combining HAADF and ABF imaging have thus directly revealed the incipient states for the layered-to-spinel-like transformation, and we call them "incipient-spinel" structures. Our findings shed light on key structure/performance correlations in Co-free layered oxide cathodes, especially correlating Li ion transport and surface structure.

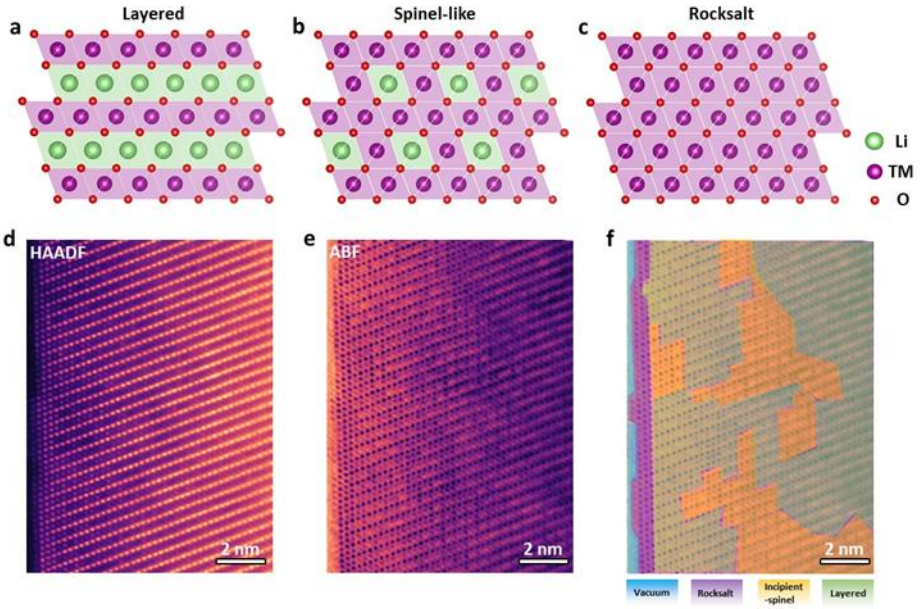

Figure II.4.G.20 Atomic structures of a pristine LNMMO particle. (a-c) Atomic models of layered (a), spinel-like (b), and rocksalt (c) LNMMO structures. (d) STEM HAADF image of a typical region containing surface and subsurface areas in the $LiNi_{0.495}Mn_{0.495}Mo_{0.01}O_2$ particle. (e) STEM ABF image of the same region. (f) Color schematic overlaid on the ABF image showing the distribution of different structures.

Formation of the surface reconstruction layer is associated with transition metal migration to Li layer, which is accompanied by valence change of both oxygen and transition metal. Therefore, we explore the valence state distribution of transition metal and oxygen near the surface of LNMMO, with a combination of STEM HAADF and ABF imaging.

STEM HAADF and ABF images of a magnified region below the surface containing the subsurface reconstruction are shown in Figure II.4.G.21a and b, respectively. The same ABF image with inverted contrast is shown in Figure II.4.G.21c. Image intensity profiles along the Li layers, as marked with "1" and "2" lines in the HAADF and inverted-ABF images, respectively, are averaged across multiple layers and plotted in Figure II.4.G.21d. From these intensity profiles, an arrangement of 2 monolayers of rocksalt structures at the outmost surface, followed by 3 monolayers of a transitional spinel-like structure, and then 5 monolayers of layered structures with strong cation mixing, and lastly a few monolayers of incipient-spinel structures, is deduced. Further inside, a gradual transition from the incipient-spinel structures to the layered structures with less cation mixing is observed.

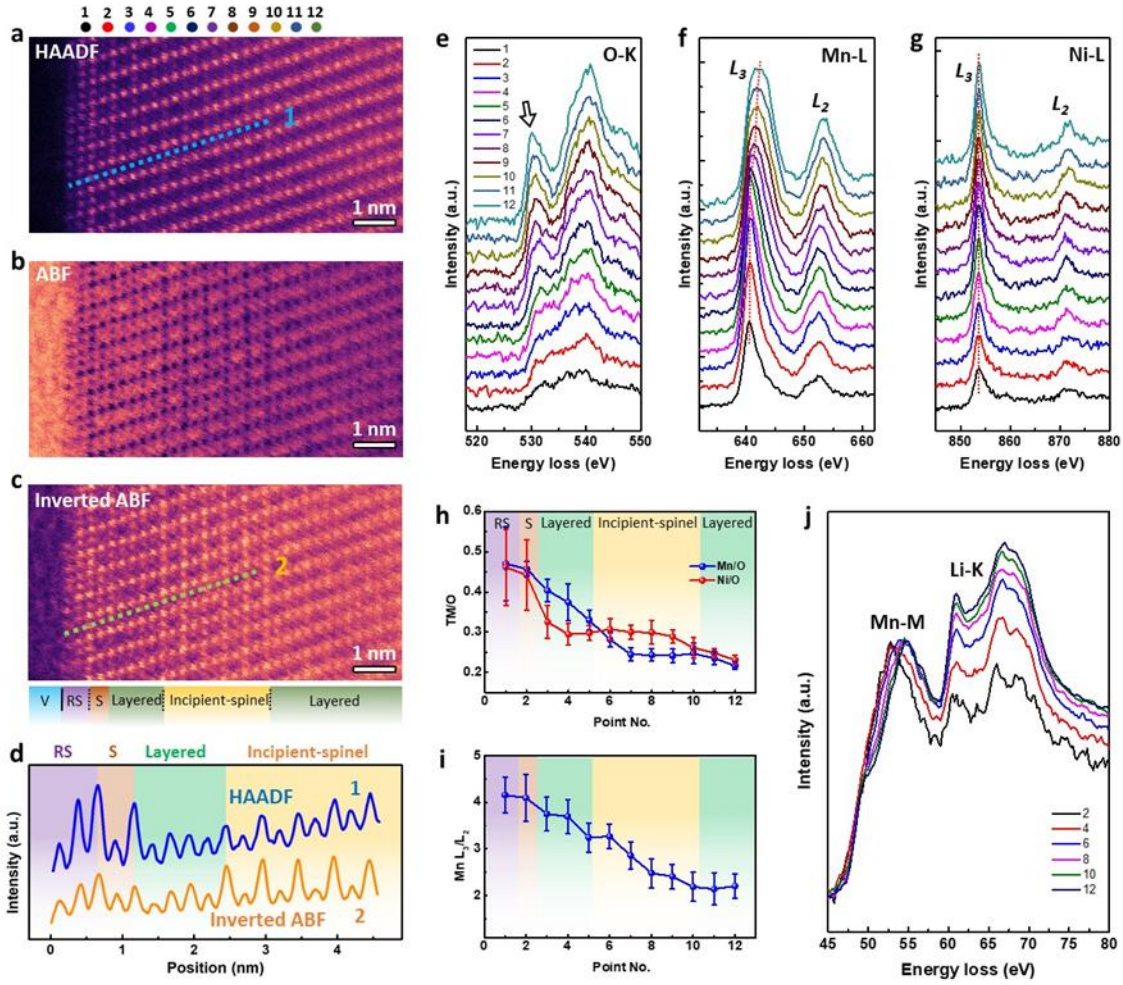

Figure II.4.G.21 Atomic structures, compositions, and oxidation states at a LNMMO surface with surface and subsurface reconstruction. (a-c) STEM HAADF (a), ABF (b), and inverted-ABF (c) images of the same LNMO surface. In (c), "V", "RS", and "S" are short for vacuum, rocksalt, and spinel, respectively. (d) Image intensity profiles along the Li layers as marked with "1" and "2" lines (a) and (c). The profiles are averaged across multiple Li layers. (e-f) EELS spectra of O K-edges and Mn and Ni L-edges collected at 12 different locations as marked in (a). The black arrow in (e) marks the O prepeaks. The dashed lines in (f) and (g) mark the L_3 peak positions. (h,i) Extracted composition ratios (i.e., Mn/O and Ni/O ratios) (h) and L_3/L_2 ratios of Mn (i) at these 12 different locations. In (h), "RS" and "S" are short for rocksalt and spinel, respectively. (j) Low-loss EELS spectra of Mn M-edges and Li K-edges collected at 6 different locations (even numbers marked in (a)), where the spectra are normalized with the Mn M-edges.

To explore the origin of such atomic rearrangements, EELS spectra of O *K*-edges and Mn and Ni *L*-edges are collected at 12 different locations (marked with numbers in Figure II.4.G.21a) below the surface (Figure II.4.G.21e-g). The extracted composition ratios (*i.e.*, Mn/O and Ni/O ratios) and L_3/L_2 ratios of Mn are plotted in Figure II.4.G.21h and i, respectively. Corresponding low-loss EELS spectra of Mn *M*-edges and Li *K*-edges are shown in Figure II.4.G.21j, where the spectra are normalized with the Mn *M*-edges. These EELS results clearly show some features that can be correlated to the structural transitions from the inner region to the outmost surface. First, the intensity of the O pre-peaks indicated by the arrow in Figure II.4.G.21e is gradually suppressed from the inner region to the surface, suggesting an increased accumulation of O vacancies. Second, the intensity of the Li *K*-edges is also gradually reduced from the inner region to the surface, indicating the formation of a local gradient distribution of Li, where the inner region is Li-retained and the surface is Li-depleted. Third, non-uniform distributions for both Mn and Ni are observed from the inner region to the surface (Figure II.4.G.21h), but these distributions present dramatically different features. Specifically, the Ni/O ratio starts to increase from the boundary between the innermost layered structures and the incipient-

spinel structures and then remains almost constant across the boundary between the incipient-spinel structures and the outer layered structures. From the outer layered structures to the outmost rocksalt structures, the Ni/O ratio increases again. In contrast, the Mn/O ratio starts to increase linearly from the middle of the incipient-spinel regions until the outmost rocksalt structures. As a result of these non-uniform composition gradient distributions, Ni becomes more than Mn within the incipient-spinel structures, and Mn is more than Ni in the outer layered structures. Last, a gradual increase in the Mn L_3/L_2 ratio (Figure II.4.G.21i) and a corresponding shift of L_3 peaks to lower energies (Figure II.4.G.21f) from the inner region toward the surface is observed, which corresponds to a decrease in oxidation state of Mn from Mn^{4+} to $Mn^{(4-x)+}$. The onset of such valence decrease locates at the boundary between the innermost layered region and the incipient-spinel region. In contrast, Ni remains at 2+ valence with its L_3/L_2 ratios and L_3 peak positions (Figure II.4.G.21g) showing no obvious variation from the inner region to the surface.

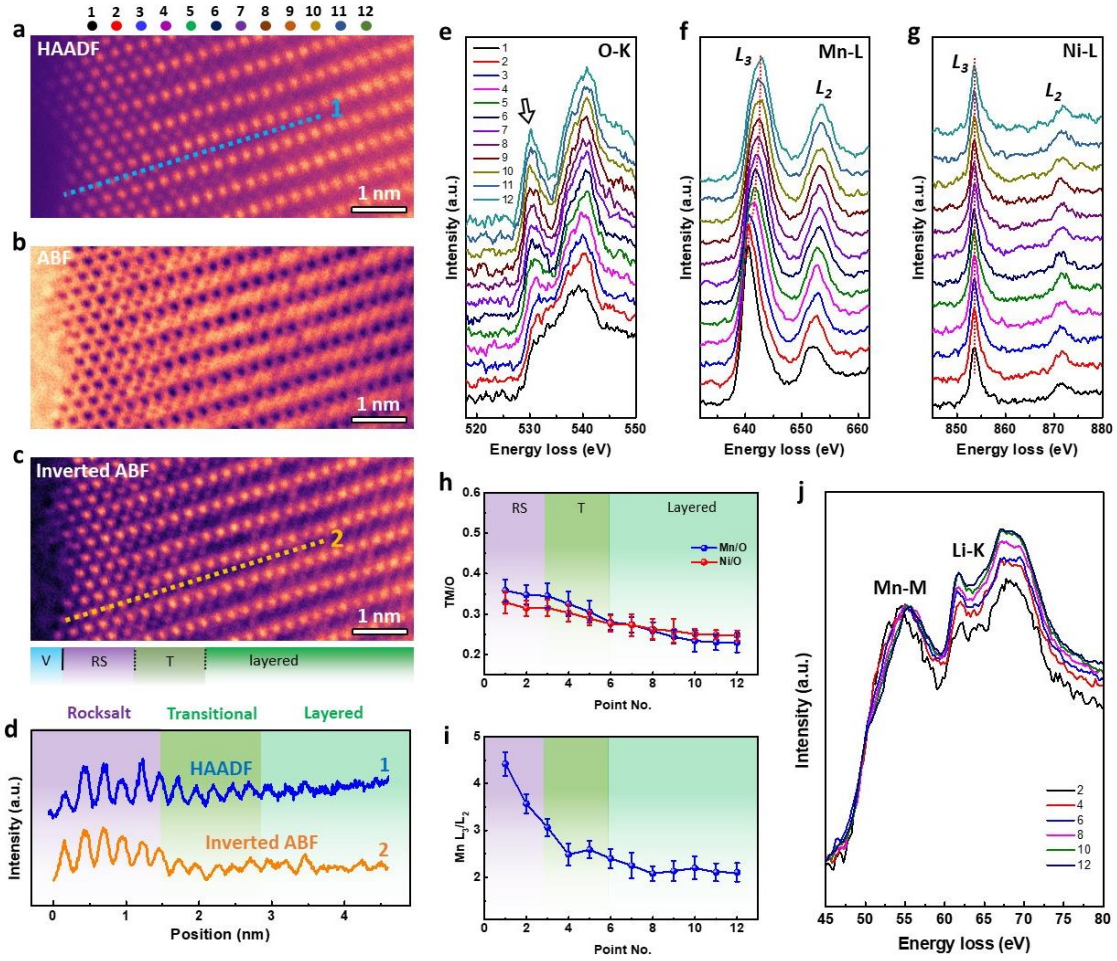

Figure II.4.G.22 Correlation of surface and sub-surface atomic structures, compositions, and oxidation states at a LNMMO: The case without a sub-surface reconstruction. (a-c) STEM HAADF (a), ABF (b), and inverted-ABF (c) images of the same LNMO surface. In (c), "V" and "RS", and "T" are short for vacuum, rocksalt, and transitional, respectively. (d) Image intensity profiles along the Li layers as marked with "1" and "2" lines (a) and (c). (e-f) EELS spectra of O K-edges and Mn and Ni L-edges collected at 12 different locations as marked in (a). The black arrow in (e) marks the O pre-peaks. The dashed lines in (f) and (g) mark the L_3 peak positions. (h, i) Extracted composition ratios (i.e., Mn/O and Ni/O ratios) (h) and L_3/L_2 ratios of Mn (i) at these 12 different locations. In (h), "RS" and "T" are short for rocksalt and transitional, respectively. (j) Low-loss EELS spectra of Mn M-edges and Li K-edges collected at 6 different locations (even numbers marked in (a)), where the spectra are normalized with the Mn M-edges.

So far, we have revealed the correlation of surface with the case of a subsurface fine structural features. Now we go on explore the surface that without a sub-surface structural feature in LNMMO with a combination of STEM HAADF and ABF imaging.

Figure II.4.G.22 shows the atomic structures and EELS analysis of a local region below the surface of a particle where the subsurface reconstruction is not observed. STEM-HAADF, ABF, and inverted-ABF images are shown in Figure II.4.G.22a-c, and corresponding image intensity profiles along the Li layers are shown in Figure II.4.G.22d. Here, a much simpler structure is observed, which contains only a few monolayers of rocksalt structures at the outmost surface, followed by a transitional region, and then the inner layered structures. EELS spectra of O *K*-edges and Mn and Ni *L*-edges collected at 12 different positions, the extracted composition ratios and L_3/L_2 ratios of Mn, and the corresponding EELS spectra of Mn *M*-edges and Li *K*-edges, are shown in Figure II.4.G.22e-j. The O and Li deficiency at the surface is also observed here in Figure II.4.G.22e and Figure II.4.G.22j, respectively. However, the changes of the spectra of the O *K*-edges and the Li *K*-edges from the inner region to the outmost surface are clearly reduced here, indicating a smaller gradient distribution of O and Li. Moreover, the difference between the gradient distributions of Mn and Ni is also much smaller. Both the Ni/O and Mn/O ratios increase linearly from the inner layered region to the outmost surface, and Mn is slightly more than Ni within both the transitional region and the rocksalt structures at the surface. As reflected by the L_3/L_2 ratio (Figure 1(i)) and L_3 peak positions (Figure II.4.G.22f), the valence of Mn remains almost unchanged in the inner layered structures and start to slightly decrease at the transitional region and then quickly reduces at the rocksalt surface. The valence of Ni also remains almost unchanged at 2+ from the inner region to the surface as indicated in Figure II.4.G.22g.

It is apparent that local oxygen and lithium concentration plays a key role for determining the local structural features. The surface structure plays key role for lithium ion transport and formation of solid electrolyte interphase layer. The present work provides insight in considering the surface structure and interfacial governed process in cathode.

5. The synthesis of Co-free, High-nickel $LiNi_xMn_{1-x}O_2$ cathodes (x = 0.90) at different temperature

In addition to the $LiNi_{1/2}Mn_{1/2}O_2$ system mentioned above, we have also been working on high-nickel Co-free cathodes. High-nickel (Ni=0.90) cathode were synthesis via sol-gel technique and optimize at different temperature. Figure II.4.G.23a shows the XRD of the $LiNi_{0.90}Mn_{0.10}O_2$ calcined from 730 °C to 770 °C for 12 hr in O_2 atmosphere. It shows no impure phase and the Bragg diffraction is indexed to the hexagonal layered structure of α-$NaFeO_2$ type belonging to R-3*m* space group. The cathode synthesis at 750 °C show higher I(003)/I(104) ratio of 1.20 vs. 1.06 and 1.13 for cathode calcined at 730 °C and 770 °C respectively indicates low cation mixing. The SEM images represents increase in the particle size with the temperature from 0.5 μm m to 2 μm shown in Figure II.4.G.23b. Figure II.4.G.23c shows cycling performance of the cathode heated 730 °C , 750 °C, 770 °C represents initial capacity of 189, 177, 194 mAh/g with the capacity retention of 44 %, 76% and 55% respectively after 100 cycle.

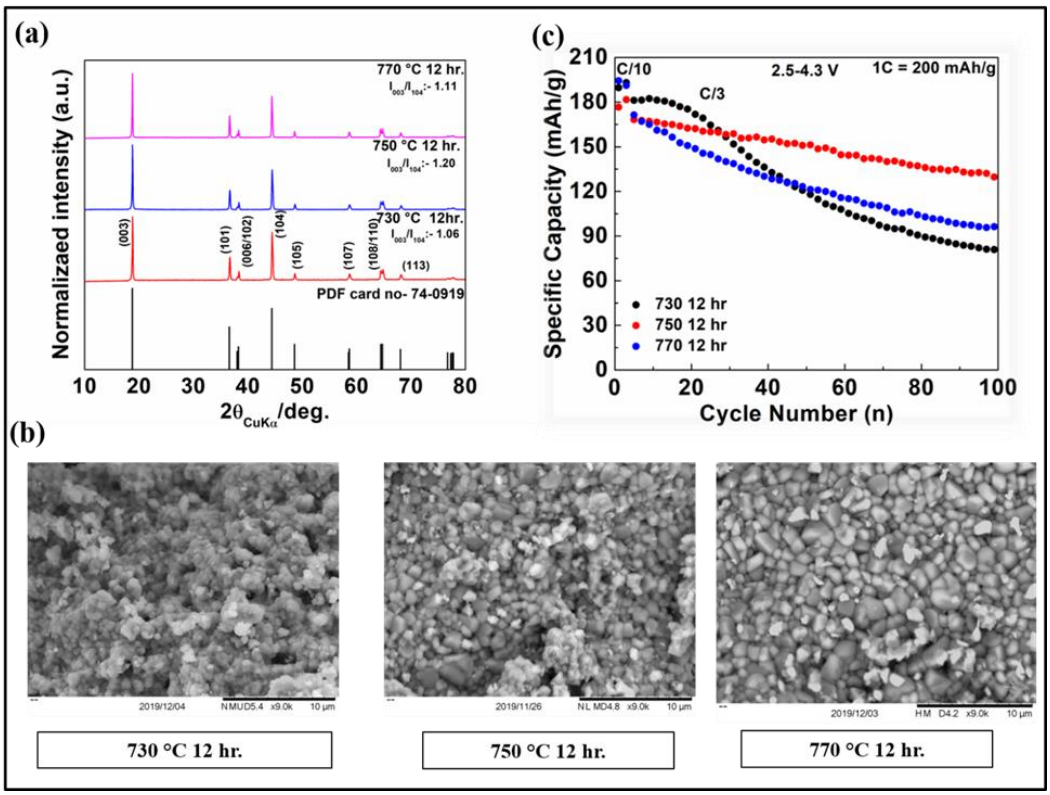

Figure II.4.G.23 Structural characterization, microscopy and electrochemical performances of $LiNi_{0.90}Mn_{0.10}O_2$ calcined at 730°C, 750°C and 770°C is performed and represented as (a) X-ray Diffraction and (b) Scanning Electron microscopy (SEM) image and (c) cycling performances in the potential range of 2.5-4.3 V showing cycling stability at current rate of C/10 for first 3 cycle and rest of the cycle at C/3 rate. Capacity retention is calculated from 4th cycle where the coin cell cycles at the rate of C/3.

Conclusions

In conclusion, this year we have worked on NCM811, $LiNi_{0.92}Co_{0.055}Mn_{0.025}O_2$, cobalt-free $LiNi_{1/2}Mn_{1/2}O_2$ and $LiNi_{0.9}Mn_{0.1}O_2$. We mainly focused on the optimization by coating/doping, and also deeply explored the structural reconstruction at the surface and subsurface of the particles.

The 2.5 Ah LFP-coated NCM/graphite cells is ultra-stable with the capacity retention at C/3 of 92.0% after 805 cycles. Besides, the C/3 capacity retention for NCM811 is 93.0% during storage at 22 °C for 120 days, which is much higher than that of NCM622.

For $LiNi_{0.92}Co_{0.055}Mn_{0.025}O_2$, we have found that Al doping can reduce H2-H3 phase transition upon cycling and inhibit the growth of cavities and intergranular cracks inside the secondary particles, and thus greatly improve the cycling stability. The thermal stability of Al-doped materials is also improved, which results from the stronger Al-O boding in the structure. In addition, Mo-doped $LiNi_{0.92}Co_{0.055}Mn_{0.025}O_2$ also exhibited superior cycling stability compared with the undoped one.

We have worked on phosphate/metaphosphate coating on $LiNi_{0.92}Co_{0.055}Mn_{0.025}O_2$, and $AlPO_4$ coating is proved to be effective on improving the cycling stability. $LiPO_3$ coating was also conducted, and the electrochemical test will be finished in the future.

For co-free $LiNi_{1/2}Mn_{1/2}O_2$ system, Mo/Ti/Zr doping and $Mn_2P_2O_7$ coating are all beneficial for improving the cyclability. Furthermore in Mo-doped $LiNi_{0.495}Mn_{0.495}Mo_{0.01}O_2$, and the structural reconstruction at the surface and subsurface was further studied. The layered-to-spinel-like structural reconstruction occurs at the subsurface, which plays a key role for lithium-ion transport and formation of SEI layer.

High-nickel cobalt-free $LiNi_{0.9}Mn_{0.1}O_2$ cathode was successfully synthesized via sol-gel technique and optimize at different temperature. The material shows a well-formed layered structure and the electrochemical performance was optimized by tuning the synthesis temperature.

Key Publications

1. Linze Li, Ethan C. Self, Devendrasinh Darbar, Lianfeng Zou, Indranil Bhattacharya, Donghai Wang, Jagjit Nanda, and Chongmin Wang, “Hidden Subsurface Reconstruction and Its Atomic Origins in Layered Oxide Cathodes”, Nano Lett. 2020, 20, 2756-2762.

2. Shanhai Ge, Yongjun Leng, Teng Liu, Ryan S. Longchamps, Xiao-Guang Yang, Yue Gao, Daiwei Wang, Donghai Wang, Chao-Yang Wang, A new approach to both high safety and high performance of lithium-ion batteries, *Science Advances* 6 (9), eaay7633 (2020). DOI: 10.1126/sciadv.aay7633

3. Devendrasinh Darbar, Ethan C. Self, Linze Li, Chongmin Wang, Harry M Meyers III, Jason R. Cory, Mahalingam Balasubramanian, Nitin Muralidharan, Ilias Belharouak, Indranil Bhattacharya, Jagjit Nanda, “Early Transition Metal d^0 Dopants and Manganese Pyrophosphate Coatings for Cobalt-free $LiNi_{0.5}Mn_{0.5}O_2$Cathodes”, *J. Power Source*, 479, 228591 (2020).

References

1. Bernhart, Wolfgang. "The Lithium-Ion Battery Value Chain - Status, Trends and Implications." In *Lithium-Ion Batteries*, edited by Gianfranco Pistoia, 553-65. Amsterdam: Elsevier, 2014.

2. Guilmard, M., C. Pouillerie, L. Croguennec, and C. Delmas. "Structural and Electrochemical Properties of Lini0.70co0.15al0.15o2." *Solid State Ionics* 160, no. 1 (2003/05/01/ 2003): 39-50.

3. Konarov, Aishuak, Seung-Taek Myung, and Yang-Kook Sun. "Cathode Materials for Future Electric Vehicles and Energy Storage Systems." *ACS Energy Letters* 2, no. 3 (2017/03/10 2017): 703-08.

4. Larcher, D., and J. M. Tarascon. "Towards Greener and More Sustainable Batteries for Electrical Energy Storage." *Nature Chemistry* 7 (11/17/online 2014): 19.

5. Myung, Seung-Taek, Filippo Maglia, Kang-Joon Park, Chong Seung Yoon, Peter Lamp, Sung-Jin Kim, and Yang-Kook Sun. "Nickel-Rich Layered Cathode Materials for Automotive Lithium-Ion Batteries: Achievements and Perspectives." *ACS Energy Letters* 2, no. 1 (2017/01/13 2017): 196-223.

6. Ren, Dong, Yun Shen, Yao Yang, Luxi Shen, Barnaby D. A. Levin, Yingchao Yu, David A. Muller, and Héctor D. Abruña. "Systematic Optimization of Battery Materials: Key Parameter Optimization for the Scalable Synthesis of Uniform, High-Energy, and High Stability $LiNi_{0.6}Mn0_{.2}Co_{0.2}O_2$ Cathode Material for Lithium-Ion Batteries." *ACS Applied Materials & Interfaces* 9, no. 41 (2017/10/18 2017): 35811-19.

7. Schipper, Florian, Evan M. Erickson, Christoph Erk, Ji-Yong Shin, Frederick Francois Chesneau, and Doron Aurbach. "Review—Recent Advances and Remaining Challenges for Lithium Ion Battery Cathodes: I. Nickel-Rich, $LiNi_xCo_yMn_zO_2$." *Journal of The Electrochemical Society* 164, no. 1 (January 1, 2017 2017): A6220-A28.

8. Vaalma, Christoph, Daniel Buchholz, Marcel Weil, and Stefano Passerini. "A Cost and Resource Analysis of Sodium-Ion Batteries." *Nature Reviews Materials* 3 (03/13/online 2018): 18013.

Acknowledgements

The work was supported by the Department of Energy, Office of Energy Efficiency and Renewable Energy (EERE), Vehicle Technology Office, under Award Number DE- EE0008447. We appreciated the support from NETL manager, Colleen Butcher, at National Energy Technology Laboratory.

II.5 Next-Gen Lithium-Ion: Diagnostics

II.5.A Interfacial Processes

Robert Kostecki, Principal Investigator
Lawrence Berkeley National Laboratory
1 Cyclotron Rd.
Berkeley, CA 94720
E-mail: r_kostecki@lbl.gov

Tien Duong, DOE Technology Development Manager
U.S. Department of Energy
E-mail: Tien.Duong@ee.doe.gov

Start Date: October 1, 2019 End Date: September 30, 2020
Project Funding: $440,000 DOE share: $440,000 Non-DOE share: $0

Project Introduction

Li-based batteries are inherently complex and dynamic systems. Although often viewed as simple devices, their successful operation relies heavily on a series of complex mechanisms, involving thermodynamic instability in many parts of the charge/discharge cycle and the formation of metastable phases. This paradigm of Li-battery system operation usually drives the battery toward irreversible physical and chemical conditions that lead to battery degradation and failure.

The requirements for long-term stability of Li batteries are extremely stringent and necessitate control of the chemistry at a wide variety of temporal and structural length scales. Progress towards identifying the most efficient mechanisms for electrical energy storage and the ideal material depends on a fundamental understanding of how battery materials function and what structural/electronic properties limit their performance. This in turn necessitates the development and use of new characterization tools to monitor these processes.

The design of the next generation of Li batteries requires a fundamental understanding of the physical and chemical processes that govern these complex systems. Although some significant advances have been made to prepare and utilize new materials efforts towards the understanding of their operation mechanisms and degradation modes have been insufficient and/or unsuccessful.

Instability and/or high resistance at the interface of battery electrodes limit electrochemical performance of high-energy density batteries. A better understanding of the underlying principles that govern these phenomena is inextricably linked with successful implementation of high energy density materials in Li-based cells for PHEVs and EVs. Pristine and cycled composite and thin film model electrodes are investigate using a variety of state-of-the-art techniques to identify, characterize and monitor changes in materials structure and composition that take place during battery operation and/or storage. This project constitutes an integral part of the concerted effort within the BMR Program and it supports development of new electrode materials for high-energy Li-metal based rechargeable cells.

Objectives

This collaborative project involves the development and application of advanced experimental methodologies to study and understand the mechanism of operation and degradation of high-capacity materials for rechargeable cells for PHEV and EV applications. The main objective of this task is to establish specific design rules toward the next generation of low impedance Li-metal rechargeable batteries that are capable of performing 1000 deep discharge cycles at CE > 99.9% and suppress lithium dendrites formation at high current densities (> 2 mA/cm^2). This project aims at the following:

1. Apply far- and near-field optical multifunctional probes and synchrotron-based x-ray techniques to obtain detailed insight into the composition, structure and mechanism of reactions at Li/electrolyte interfaces at an adequate spatial and temporal resolution.

2. Design new *in situ* diagnostic techniques and experimental methodologies that are capable of unveiling the function and operation of hidden or buried interfaces and interphases that determine material, electrode and battery cell electrochemical performance and failure modes.

3. Understand the mechanism of operation and degradation of high energy density materials for rechargeable Li-metal batteries for PHEV and EV applications.

4. Propose effective remedies to address inadequate Li-metal rechargeable batteries calendar/cycle performance for PHV and EV applications.

The other goal is development and application of far- and near-field optical probes and synchrotron-based advanced X-ray techniques to obtain insight into the mechanism of Li^+ transport and interfacial reactions in lithium/liquid model systems. Through an integrated synthesis, characterization, and electrochemistry effort, this project aims to develop a better understanding of lithium / liquid electrolyte interface so that rational decisions can be made as to their further development into commercially viable Li-metal cells.

Approach

- The pristine and cycled composite electrode and model thin-film electrodes were probed using various surface- and bulk-sensitive techniques, including FTIR, ATR-FTIR, near-field IR and Raman spectroscopy/microscopy, and SPM to identify and characterize changes in materials structure and composition.

- Novel *in situ / ex situ* far- and near-field optical multi-functional probes in combination with standard electrochemical and analytical techniques are developed to unveil the structure and reactivity at interfaces and interphases that determine materials electrochemical performance and failure modes.

Results

Lithium metal batteries (LMBs) are among the most promising candidates of high-energy-density devices for advanced energy storage. However, uncontrollable lithium dendrite growth induces poor cycling efficiency and severe safety concerns, dragging lithium metal batteries out of practical applications. We investigated a carbon-nitrogen modified stainless steel mesh (CNSSM), which favors homogeneous lithium-metal nucleation and growth of a dense lithium film when employed as an anode in lithium-metal battery characterized the surface structure and chemical composition of a carbon-nitrogen modified stainless steel mesh (CNSSM) with Raman and XPS. The morphology of plated lithium on CNSSM was investigated with X-ray tomography.

Figure II.5.A.1a shows the first-order Raman spectrum of the CNSSM. Two bands, at ~1345 cm^{-1} and ~1570 cm^{-1}, correspond to the D- and G-bands of carbon, respectively. The G-band originates from the in-plane vibrations of graphene sheets in graphitic carbons whereas D-band corresponds to the breathing motion of sp^2-hybridized carbon atoms in rings at edge planes and defects in the graphene sheet in disordered and amorphous carbons. The relatively high I_D/I_G ratio (0.37) in this case implies a relatively large ratio of disordering in the CNSSM outer layer, which may originate from nitrogen doping. The shoulder of the D-band (i.e., the D'-band at 1638 cm^{-1} in the inset), originates from an intra-valley double-resonance in the presence of nitrogen-induced defects.

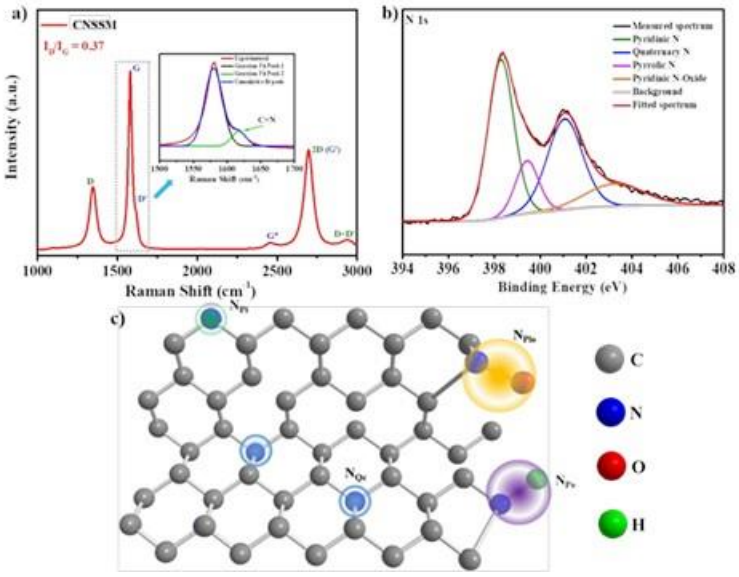

Figure II.5.A.1 (a) Raman spectrum of CNSSM; the inset shows the fitted peaks between 1500 cm^{-1} and -1700 cm^{-1}, (b) N1s XPS spectrum and the corresponding peak fitting, (c) schematic representation of the carbon structure with different types of nitrogen atoms doping (N_{Pi}: Pyridinic-N; N_{Po}: Pyrrolic-N; N_{Qc}: Quaternary-N (center); N_{Pio}: Pyridinic-N oxide).

Figure II.5.A.2 compares virtual cross-sections reconstructed from the nano-tomographic measurements for both a pristine CNSSM-Li composite and a CNSSM-Li composite after 2 h of lithium electrodeposition at 1 mA cm^{-2}. The bright areas in the lithium metal correspond to internal cracks, likely due to the manufacturing process of the CNSSM-Li composite. The stainless steel rod exhibits coaxial layers, in agreement with the SEM cross-sections. The external carbon-nitrogen coated layer, of ~1 µm in thickness can be seen, as can the unmodified residual (black) stainless steel at the core of the wire. Most importantly, it can be seen that a significant amount of lithium has been plated, and the mesh is fully embedded into the deposit.

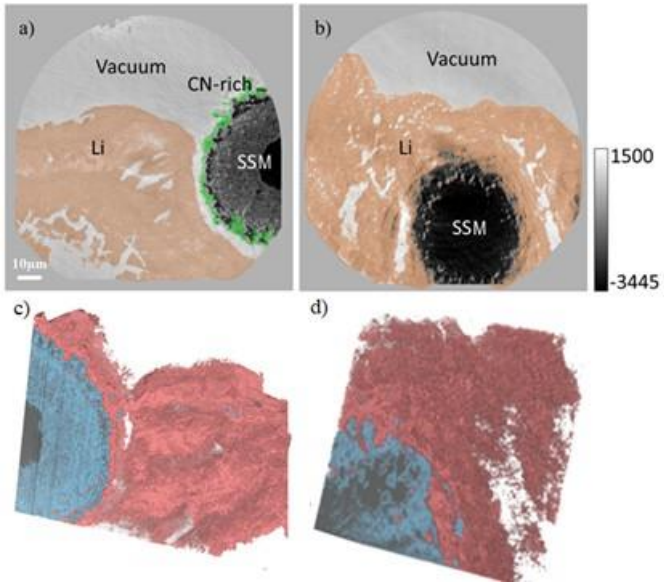

Figure II.5.A.2 Virtual cross-sections from X-ray holographic nano-tomography on (a) pristine CNSSM-Li composite, and (b) CNSSM-Li composite after 2 h of Li electrodeposition at 1 mA cm^{-2}. The scale bar of electro density applies to all panels. Rendering of the 3D tomographic reconstructed results from (c) pristine CNSSM-Li composite, and (d) CNSSM-Li composite after 2 h of Li electrodeposition at 1 mA cm^{-2}. Li: lithium metal (coral); CNSSM: carbon-nitrogen modified stainless steel (pale blue); SSM: stainless steel (dim gray).

We carried out a series of preliminary measurements of the molecular structure of a model graphene-solid state electrolyte interface at nano-scale spatial resolution. The measurements were performed with a unique combination of scanning probe microscopy and Fourier transform infrared spectroscopy (nano-FTIR). The infrared (IR) laser irradiation of the AFM tip generates a strong dipole at the tip apex, which extends a strong local evanescent wave which couples with the phonons in the sample. The single layer graphene (SLG) acts as an optical window and the electrode in direct contact with the solid-state electrolyte. The probing filed extends from the tip through the graphene window and interacts with specimens at the surface of the SLG electrode. This novel and unique experimental setup enables IR nano-probing of the interface C/electrolyte, which could enable *in situ* characterization of the C/electrolyte and Li/electrolyte interface at the close vicinity of the electrode.

Figure II.5.A.3 (a) Schematic illustration of the fabrication of the *in situ* cell with graphene window to study electrode/electrolyte interfaces. (b) FTIR absorption spectrum of PEO+ LiTFSI mixtures at EO/Li ratios of 10:1. (c) Scattered near-field IR amplitude image in a region where graphene window is in contact with the solid state electrolyte in the cell. (d) Nano-FTIR spectra collected at locations marked by blue and red dots mark points.

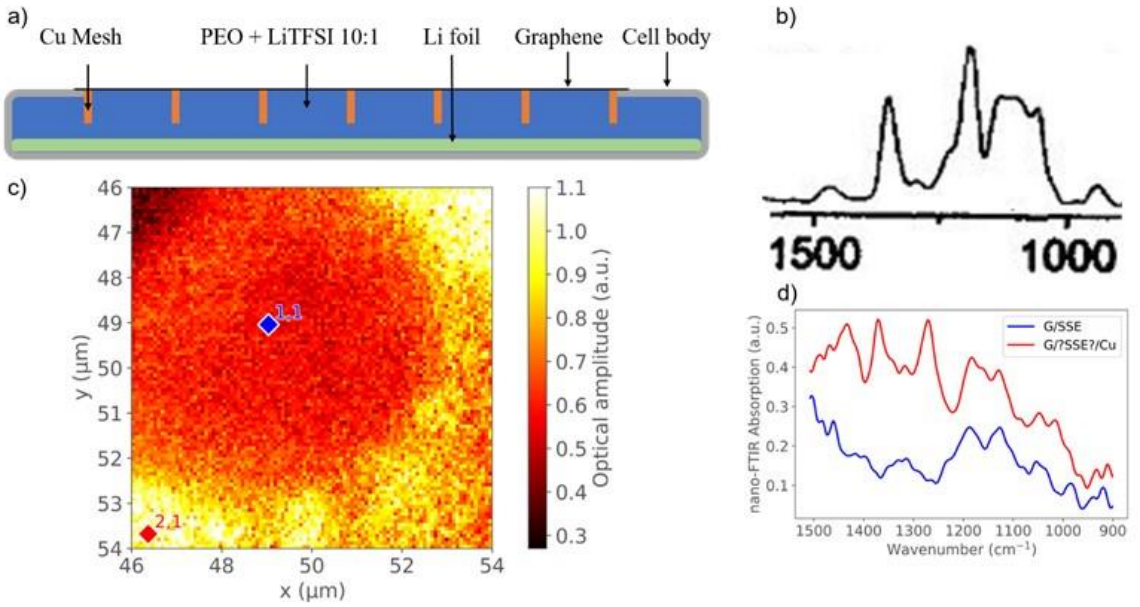

Figure II.5.A.3 (a) Schematic illustration of the fabrication of the in situ cell with graphene window to study electrode/electrolyte interfaces. (b) FTIR absorption spectrum of PEO+ LiTFSI mixtures at EO/Li ratios of 10:1. (c) Scattered near-field IR amplitude image in a region where graphene window is in contact with the solid state electrolyte in the cell. (d) Nano-FTIR spectra collected at locations marked by blue and red dots mark points.

Figure II.5.A.3 shows the experimental cell set-up for *in situ* nano-FTIR measurements. The mixture of PEO and LiTFSI was first filled in the cell and then sealed with copper mesh and single layer graphene window. Two representative points from the scattered near field IR amplitude image are selected for nano-FTIR measurements. Even with slightly shifts, the characteristic peaks in red area can fully match with the peaks shown in a standard FTIR spectrum of EO/Li (10:1). As the matter of fact, two sharp peaks at 1360 and 1215 cm^{-1}, and one broad peak at 1160 cm^{-1} are typically observed in the FTIR spectrum of EO/Li (10:1) composite. However, the blue area shows quite weak signal intensity and the peaks at 1360 cm^{-1} and 1215 cm^{-1} disappeared completely. This may be caused by inhomogeneous pressure and poor contact between copper mesh and graphene window, which could lead to the formation of a gap between solid-state electrolyte and graphene.

We then further optimized the experimental setup in order to obtain high quality IR signal from a model graphene-solid state electrolyte (SSE) interface at nano-scale spatial resolution. The measurements were performed with a unique combination of scanning probe microscopy and Fourier transform infrared spectroscopy (nano-FTIR). The single layer graphene (SLG) on copper mesh was replaced with a free standing SLG to perform as an optical window and simultaneously as the current collector for lithium deposition during the electrochemical polarization. The counter electrode consists of a copper foil on a flat silicon wafer, which provide good electronic conductivity and stable mechanical support for the SSE layer. Two electrodes were separated by a plastic spacer and the gap was filled with the solid electrolyte.

The near-field IR local probing of the electrode/SSE interface was accomplished by the SPM tip through the SLG window. This novel and unique experimental setup enables a direct IR probing of the interface of electrode/electrolyte at nanometer resolution, which enables *in situ* characterization of the active species adjacent to the electrode.

Figure II.5.A.4 (a) Schematic illustration of the fabrication of the modified cell with graphene window to study electrode/electrolyte interfaces. (b) Tomography image in a region where graphene window is in contact with the solid-state electrolyte (PEO+ LiTFSI mixtures at EO/Li ratios of 10:1) in the cell. (c). Nano-FTIR spectra collected with IR laser at locations of solid-state electrolyte and solid state electrolyte with graphene window. (d) Nano-FTIR spectra collected with synchrotron IR light source at locations of solid-state electrolyte with graphene window.

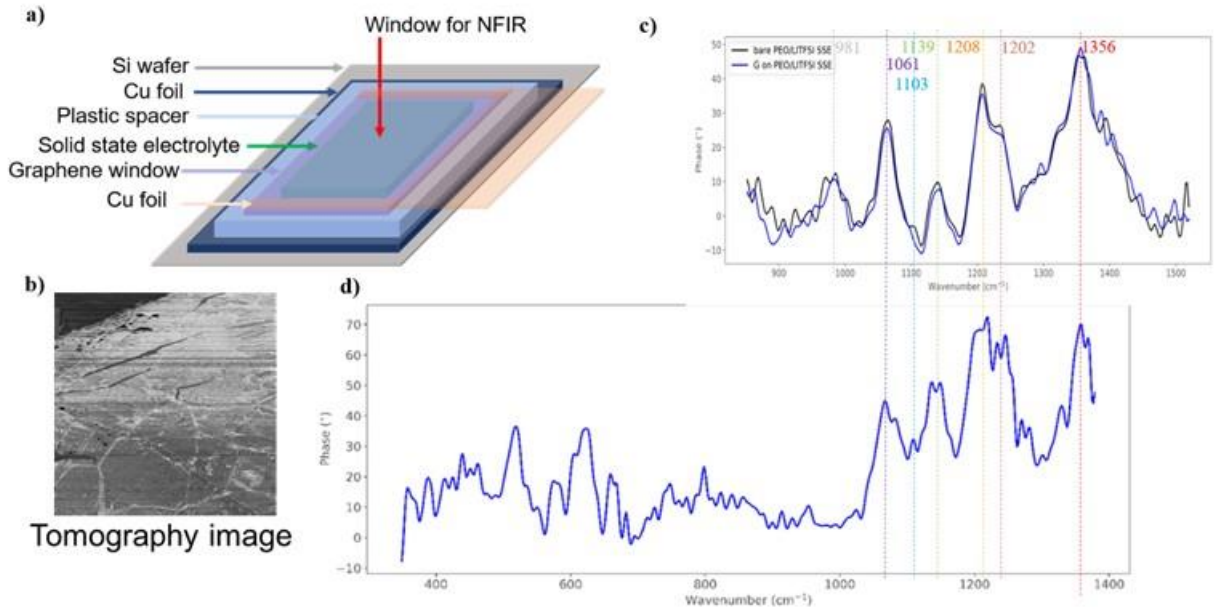

Figure II.5.A.4 (a) Schematic illustration of the fabrication of the modified cell with graphene window to study electrode/electrolyte interfaces. (b) Tomography image in a region where graphene window is in contact with the solid-state electrolyte (PEO+ LiTFSI mixtures at EO/Li ratios of 10:1) in the cell. (c). Nano-FTIR spectra collected with IR laser at locations of solid-state electrolyte and solid state electrolyte with graphene window. (d) Nano-FTIR spectra collected with synchrotron IR light source at locations of solid-state electrolyte with graphene window.

Figure II.5.A.4 shows the experimental cell set-up for *in situ* nano-FTIR measurements. The mixture of PEO and LiTFSI fills the space between two copper and SLG electrodes. The representative tomography image (Figure 1b) shows that the SSE is uniformly covered by the single layer graphene sheet without any defects or folding. The SSE under SLG and SSE sample were characterized by nano-FTIR measurement. We were able to observe IR bands characteristic for SSE through SLG, which fully match the spectrum of SSE recorded in direct contact with the nano-FTIR probe. The quality of spectra has been significantly improved when compared with previous results (through the copper mesh). In addition, similar spectrum could also be

observed from the data collected from synchrotron IR light source. As the detected wave range is much wider, which include the signal of lithium and its relevant compounds. These preliminary results constitute the proof of concept and foundation for future in situ studies of Li/SSE interfaces.

Conclusions

- Effective strategy to suppress lithium dendrite growth by surface modification of stainless steel current collector is demonstrated. X-ray tomography imaging provides a clear insight into the morphology and topology of the composite electrode components of pristine and cycled Li anodes
    - Pyridinic and pyrrolic carbon-nitrogen surface functional groups promote adsorb uniform nucleation and growth of metallic lithium
    - The 3D electrode architecture assures a uniform current density distribution, reduces the charge transfer resistance, and accommodates volume changes upon lithium plating/stripping
- Pioneered *in situ* near-field IR experiments to investigate Li/SSE interface at nanometer resolution
    - This preliminary study shows for the first time that near-field FTIR is uniquely suited to investigate electrode/electrolyte interfaces in rechargeable batteries at unprecedented surface selectivity and sensitivity

Key Publications

1. Miranda, Andrea; Li, Xiaoyi; Haregewoin, Atetegeb Meazah; Sarang, Kasturi; Lutkenhaus, Jodie; Kostecki, Robert; Verduzco, Rafael, ACS Applied Materials & Interfaces, DOI: 10.1021/acsami.9b13257
2. Laura Cabo-Fernandez, Alex Neale, Filipe Braga, Igor Sazanovich, Robert Kostecki, Laurence Hardwick, “Kerr gated Raman spectroscopy of a $LiPF_6$-based organic carbonate electrolyte for Li-ion batteries”, Physical Chemistry Chemical Physics, DOI: 10.1039/C9CP02430A
3. Lu, Yi-Hsien; Larson, Jonathan; Baskin, Artem; Zhao, Xiao; Ashby, Paul; Prendergast, David; Bechtel, Hans; Kostecki, Robert; Salmeron, Miquel, “Infrared Nanospectroscopy at the Graphene-Electrolyte Interface", Nano Letters, 2019, 19, 8, 5388-5393 DOI: 10.1021/acs.nanolett.9b01897
4. Haodong Liu, Zhuoying Zhu, Jason Huang, Xin He, Yan Chen, Rui Zhang, Ruoqian Lin, Yejing Li, Sicen Yu, Xing Xing, Qizhang Yan, Xiangguo Li, Matthew J. Frost, Ke An, Jun Feng, Robert Kostecki, Huolin Xin, Shyue Ping Ong, Ping Liu, “Elucidating the Limit of Li Insertion into the Spinel Li4Ti5O12”, A*CS Materials Lett,* 2019, 1, 1, 96-102, https://doi.org/10.1021/acsmaterialslett.9b00099
5. Erin B. Creel, Elizabeth R. Corson, Robert Kostecki, Jeffrey J. Urban, Bryan D. McCloskey, “Directing selectivity of electrochemical carbon dioxide reduction”, 70th Annual Meeting of ISE, August 4-9, 2019, Durban, South Africa
6. Ivana Hasa, Atetegeb Haregewoin, Hans Bechtel, Jinghua Guo, Philip N. Ross, Liang Zhang, Robert Kostecki, “In Situ and Ex Situ Studies of Interfacial Processes on Intermetallic Anodes”, Electrochemical Conference on Energy and the Environment Bioelectrochemistry and Energy Storage, July 21-26, 2019, Glasgow, Scotland
7. Robert Kostecki, “Probing Charge and Mass Transport Phenomena Across Interfaces and Interphases in Batteries”, Gordon Research Conference “Laser Diagnostics in Energy and Combustion Science” June 23-28, 2019, Les Diablerets, Switzerland (invited talk)

8. L. J. Hardwick, L. Cabo-Fernandez, R. Kostecki, I. Sazanovich, “Kerr Gated Raman Spectroscopy to Investigate Lithium-Ion Battery Interfaces”, 235th ECS Meeting, Dallas, TX, May 26-31, 2019

Acknowledgements

This work has been performed in close collaboration with:

- V. Battaglia: ABMR program leads
- ABMR Cathode and Anode Task Groups
    - ANL, LBNL, SUNY, UP, HQ, NREL and UU

(R-C. Lee, J. Franklin, G. Chen, V. Battaglia, M. Doeff, K. Persson, V. Zorba, W. Yang, C. Ban, N. Balsara, B. McCloskey)

- Advanced Light Source (H. Bechtel, E. Rotenberg, E . Crumlin)
- University College London (P. Shearing. J. Franklin)
- University of Liverpool (UK) (L. Hardwick)
- Central Laser Facility, Research Complex at Harwell (UK)
- University of California, Berkeley
    - Umicore, Farasis Energy, Inc.

II.5.B Advanced in situ Diagnostic Techniques for Battery Materials

Xiao-Qing Yang, Principal Investigator
Chemistry division, Brookhaven National laboratory
Bldg. 555, Brookhaven National Lab.
Upton, NY 11973
E-mail: xyang@bnl.gov

Seongmin Bak, Principal Investigator
Chemistry division, Brookhaven National laboratory
Bldg. 555, Brookhaven National Lab.
Upton, NY 11973
E-mail: smbak@bnl.gov

Tien Duong, DOE Technology Development Manager
U.S. Department of Energy
E-mail: Tien.Duong@ee.doe.gov

Start Date: October 1, 2019 End Date: September 30, 2020
Project Funding: $425,000 DOE share: $425,000 Non-DOE share: $0

Project Introduction

This project is focused on the development of advanced diagnostic characterization techniques for the following issues: obtaining in-depth fundamental understanding of the mechanisms governing the relationship between the structure and the performance of battery materials; providing guidance and approaches to improve the properties of battery materials. The approach of this project is the development and application of combined synchrotron based in situ X-ray techniques such as x-ray diffraction (XRD), pair distribution function (PDF), hard and soft x-ray absorption (XAS and SXAS), together with other imaging and spectroscopic tools such as transmission electron microscopy (TEM), scanning transmission electron microscopy (STEM), mass spectroscopy (MS), X-Ray fluorescence microscopy (XRF) and transmission x-ray microscopy (TXM), as well as neutron-based techniques, such as neutron diffraction and neutron PDF (NPDF). For advanced Li-ion battery technologies, the revolutionary approaches using new generation of materials for cathode, anode, electrolyte, and separator are in the horizon. The new generation of cathode materials such as Li-rich high energy density $Li_{1+x}(NiMnCo)O_2$ (NMC) composite materials, high Ni content NMC cathode materials, and high energy density S-based cathode materials, together with high energy density lithium metal anode materials will significantly increase the energy density of the advanced Li-ion and beyond lithium-ion battery systems . However, many technical barriers must be overcome before the large-scale commercialization of these new materials can be realized. This project uses the time-resolved x-ray diffraction TR-XRD and absorption (TR-XAS) developed at BNL to study the kinetic properties of these materials with structural sensitivity (TR-XRD) and elemental selectivity (TR-XAS). This project develops and applies the HRTEM, TXM and PDF techniques, as well as neutron diffraction and neutron PDF to study the mechanisms of capacity and performance fading of cathode and anode materials. Another important issue is the thermal stability of new cathode materials which is closely related to the safety of the batteries. This problem has been studied using the combined TR-XRD, TR-XAS with mass spectroscopy (MS). This project also develops a novel in situ and ex situ X-ray fluorescence (XRF) microscopy combined with X-ray absorption spectroscopy (XAS) technique, which will enable us to track the morphology and chemical state changes of the electrode materials during cycling. In summary, this project supports the goals of VTO, the Battery and Electric Drive Technologies, and BMR program by developing new diagnostic technologies and applying them to the advanced Li-ion as well as beyond lithium-ion (such as Li-metal, Na-ion, and Li-S) battery systems and by providing guidance for new material development.

Objectives

The primary objective of this project is to develop new advanced in situ material characterization techniques and to apply these techniques to support the development of new cathode, anode, and electrolyte materials with high energy and power density, low cost, good abuse tolerance, and long calendar and cycle life for the next generation of lithium-ion batteries (LIBs) and beyond Li-ion batteries (Li-metal, Na-ion, and Li-S) to power plug-in hybrid electric vehicles (PHEV) and electric vehicles (EV). The diagnostic studies have been focused on issues relating to capacity retention, thermal stability; cycle life and rate capability of advanced Li-ion and beyond Li-ion batteries

Approach

- Develop and apply advanced diagnostic techniques to study and improve the performance of high energy density LIBs and Li/S batteries.
- Using nano-probe beamline at NSLSII to study the elemental distribution of new solid electrolyte materials for Li-ion and Na-ion batteries
- Using hard X-ray fluorescence (XRF) imaging on the concentration gradient Ni-rich NCM cathode particles in a noninvasive manner with 3D reconstructed images through tomography scans to study the 3D Ni, Co, and Mn elemental distribution from surface to the bulk
- Using transmission X-ray Microscopy (TXM) studies on the concentration gradient Ni-rich NCM cathode particles with 3D reconstructed images through tomography scans.
- Using the S K-edge XRF imaging and XAS studies with examination of the reaction products on the sulfur cathode and Li-metal anode in high energy density Li/S cell.

Results

In FY2020, **BNL** has been focused on the development of new diagnostic techniques to study and improve the performance of high energy density LIBs and Li/S batteries. BNL team has developed a new synchrotron-based X-ray Photoelectron Spectroscopy (XPS) with depth-profiling functionality. Compared with the lab-based XPS, the synchrotron-based XPS offers the following advantages:

1. Capability to do experiments under ambient pressure (elevated gas pressure up to 10 torr) rather than must be done in UHV chamber for Lab-based XPS.
2. Quick data acquisition time
3. Tunable energy (probing different depth)
4. Good signal to noise ratio
5. Special sample transfer holder.

This new technique was used to study the surface chemistry and surface stability of high-nickel-content $LiNi_{0.92}Co_{0.06}Al_{0.02}O_2$ (NCA) cathode materials during storage with reaction with CO_2 and moisture. Li 1s, O 1s and Ni 2p XPS spectra of NCA were measured in the CO_2 environment. As shown in Figure II.5.B.1, compared with the data measured in UHV, Ni^{3+} peak in Ni 2p XPS collected at 1200 eV is still observed but with slightly decreasing intensity after reacting with CO_2. After increasing the energy to 1500 and 1800 eV to probe deeper and deeper from the outer surface, the Ni^{3+} peak increased significantly. Moreover, the

characteristic peaks of bulk Li and O still can be clearly observed even after reacting with CO_2. This result suggested that, Al doping may improve the stability of NCA by stabilizing the active oxygen on the surface.

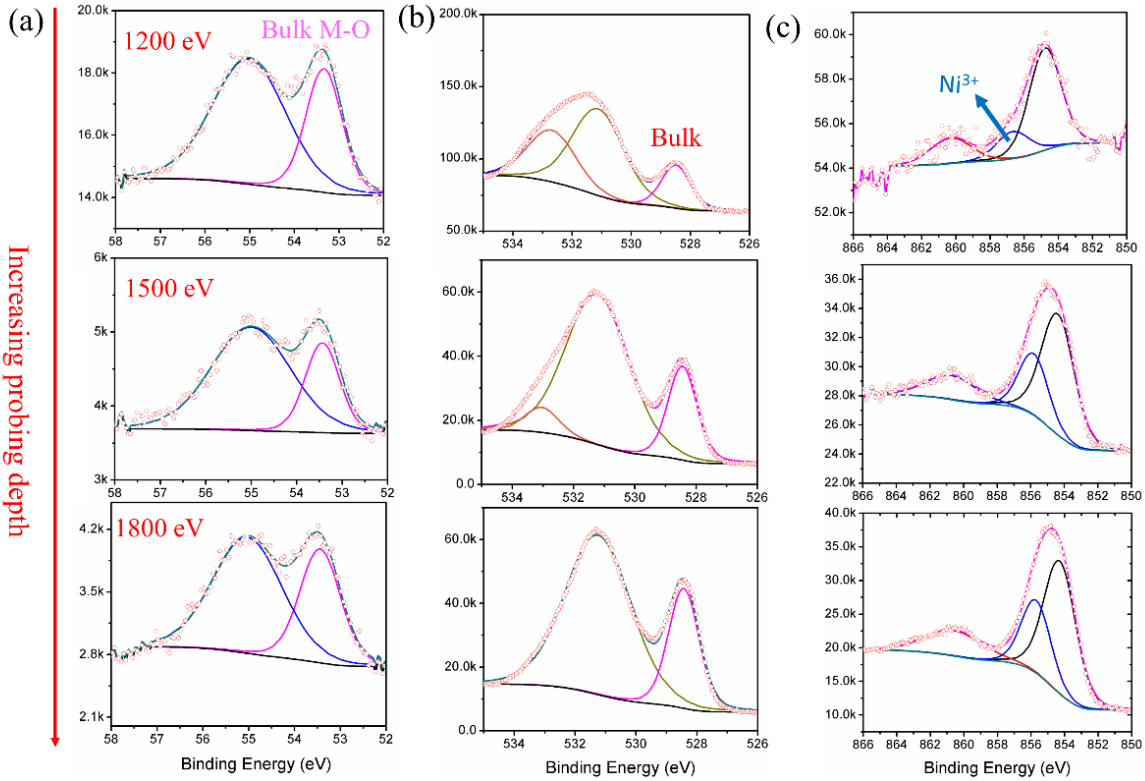

Figure II.5.B.1 Depth profile XPS spectra of as-synthesized NCA collected in the CO_2 environment (1.6 Torr). (a) Li 1S, (b) O 1S and (c) Ni 2p XPS spectra of NCA measured at 1200, 1500 and 1800 eV in the CO_2

BNL team has applied advanced hard X-ray fluorescence (XRF) imaging techniques with a high spatial resolution (down to 30 nm) and high probing sensitivity (under ppm level). This advanced imaging technique was used to study the structural stability of concentration-gradient Ni-rich NMC (CG-NMC) cathode particle in a noninvasive manner with 3D reconstructed images through tomography scans to study the 3D Ni, Co, and Mn elemental distribution. The ex-situ 2D XRF element mapping results are shown in Figure II.5.B.2a for pristine and cycled CG-NMC622. The line-scan from the 2D image revealed that the pristine CG-NMC622 has NMC701515 composition in the core and NMC442 at the shell with about 800 nm of concentration gradient layer from the surface. This compositional gradient structure was well maintained even after 100 cycles with 2.8-4.4 V (vs. Li/Li^+) voltage range and high voltage cycling (2.8-4.8V vs. Li/Li^+). This result is the first observation of the concentration gradient structure in a noninvasive manner without cross-sectioning the sample using focused ion beam. The clear feature of the Mn-rich shell structure shown in Figure II.5.B.2a was not observed from our previous studies using transmission X-ray microscopy (TXM). This demonstrated the power of high spatial resolution and high elemental selectivity of this nano-XRF imaging technique. Furthermore, the ex-situ 3D reconstructed XRF image (Figure II.5.B.2b) revealed that the secondary particle of CG-NMC622 didn't show a micro-crack generation at the particle core which is typically shown in similar composition Ni-rich NMC (Ni>70%) system. The quantitative composition analysis from the 3D XRF image shows clear evidence that the unique compositional gradient of this material is well kept even after 100 cycles. The results revealed that 1) the compositional gradient structure is stable over the long- and high-voltage cycling, 2) the Mn-rich surface of CG structure enhanced the structural stability at the secondary particle level. To further study the surface chemistry of the CG-NMC system, a combination of soft and hard X-ray absorption spectroscopy study will be carried out in the future.

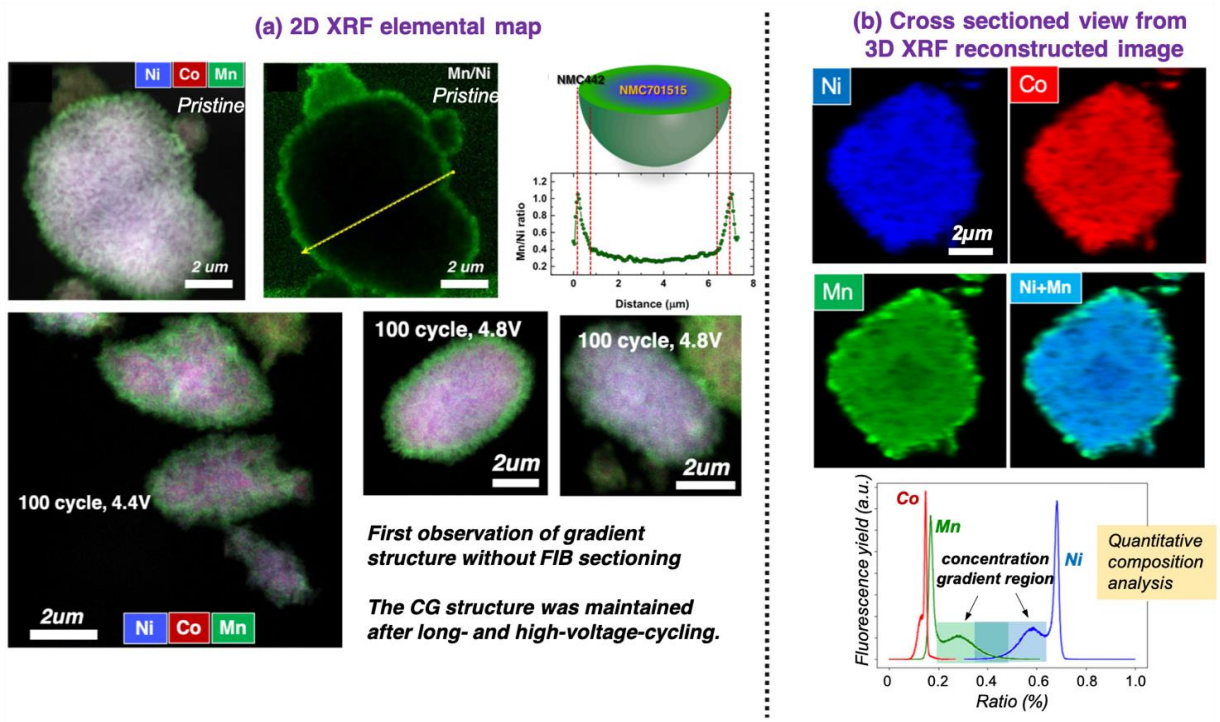

Figure II.5.B.2 (a) Schematic illustration of the fabrication of the modified cell with graphene window to study electrode/electrolyte interfaces. (b) Tomography image in a region where graphene window is in contact with the solid-state electrolyte (PEO+ LiTFSI mixtures at EO/Li ratios of 10:1) in the cell. (c). Nano-FTIR spectra collected with IR laser at locations of solid-state electrolyte and solid state electrolyte with graphene window. (d) Nano-FTIR spectra collected with synchrotron IR light source at locations of solid-state electrolyte with graphene window.

BNL team has applied advanced hard X-ray absorption spectroscopy (hXAS) and soft XAS (sXAS) on the concentration gradient Ni-rich NCM (CG-NCM) cathode particles to study the valence state changes of Ni, Co, Mn at the surface and bulk caused by multiple cycling. No noticeable differences were observed in both spectra of Ni and Mn K-edge hXAS after different number of cycles (Figure II.5.B.3a), which indicating the averaged valence state of Ni and Mn at the same state of charge were not changed much by cycling for both normal and CG-NCM622. The total electron yield (TEY) of Ni and Mn L-edge sXAS representing surface valence state and partial fluorescence (PFY) spectra reflecting bulk valence state of Ni and Mn are shown in Figure II.5.B.3b. The TEY spectra show clear cycle induced changes, while the PFY spectra show no cycling induced changes, similar as observed in hXAS spectra. More quantitative comparison using linear combination fitting (LCF) of the sXAS spectra are shown in Figure II.5.B.3c and d. The gradual reduction of surface Ni to Ni^{2+} was observed in the normal NMC622. It is commonly believed that the surface structural degradation are associated with the formation and propagation of inactive rock-salt structured NiO from the surface to the bulk. In contrast, the level of surface Ni valence state in the CG-NMC622 shows a gradual increase, rather than decrease, indicating the electrochemical active Ni^{3+} contribution was increased and reached to the average valence state (*ca.* $Ni^{2.7+}$) of the bulk (Figure II.5.B.3c). This result is originated from the valence state change of surface Mn. The LCF fit of TEY spectra for Mn L-edge reveals that the surface Mn was reduced from 4+ to 2+ in both normal and CG NMC cathode (Figure II.5.B.3d). Due to the large portion of surface Mn content in the shell of CG-NMC622 (surface shell composition: NMC442), Mn reduction from Mn^{4+} to Mn^{2+} lead to the increase of Ni valence state to keep the charge neutrality. In contrast, the effect of Mn reduction is much smaller in the normal NMC622 cathode, due to the low content of Mn at the surface. This result demonstrates that the Mn-rich surface of CG-NMC622 could suppress the formation of the inactive NiO phase with Ni^{2+} at the surface and improve the cycle performance.

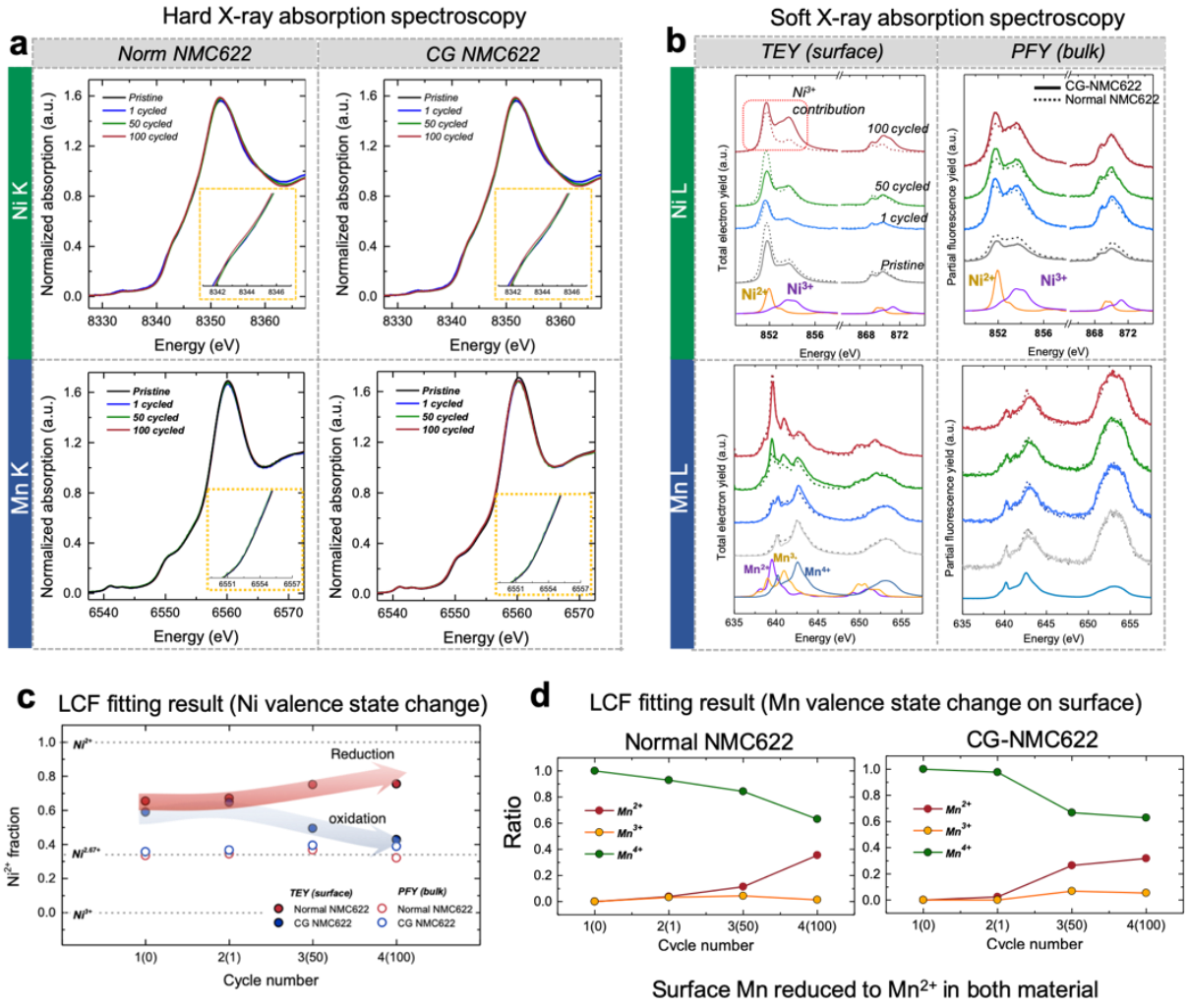

Figure II.5.B.3 (a) Ni and Mn K-edge hXAS spectra, (b) total electron yield (TEY) and partial fluorescence yield (PFY) of Ni and Mn L-edge sXAS, (c) linear combination fitting (LCF) results for TEY and PFY of Ni L-edge spectra, and (d) LCF results for TEY of Mn L-edge spectra.

BNL team carried out spatially resolved XAS at sulfur K-edge and imaging studies of sulfur-based chemical species using XRF on the Li-metal anode in a cycled high-energy Li/S pouch cell using electrolyte with $LiNO_3$ (LNO) comparing with electrolytes without LNO additives. The following conclusions were obtained from the results shown in Figure II.5.B.4a to Figure II.5.B.4d: (1). After adding LNO, TFSI decomposition was suppressed due to participation of NO_3^- in SEI formation, producing less Li_2S, SO_3^{2-}, and S-S species as confirmed by XAS and XRF results. (2). XRF images of Li metal anode cycled in TFSI-DOL/DME and FSI-DOL/DME electrolytes show different Li deposition morphology. XAS spectra show that TFSI and FSI salts have almost similar decomposition products but with different concentration. SO_3^{2-} cannot be detected from Li metal surface cycled in FSI based electrolyte. (3). Intensity of Li_2S formed in FSI-DX electrolyte is slightly higher than that formed in FSI-DOL/DME, indicating more FSI^- anion decomposed on Li metal anode.

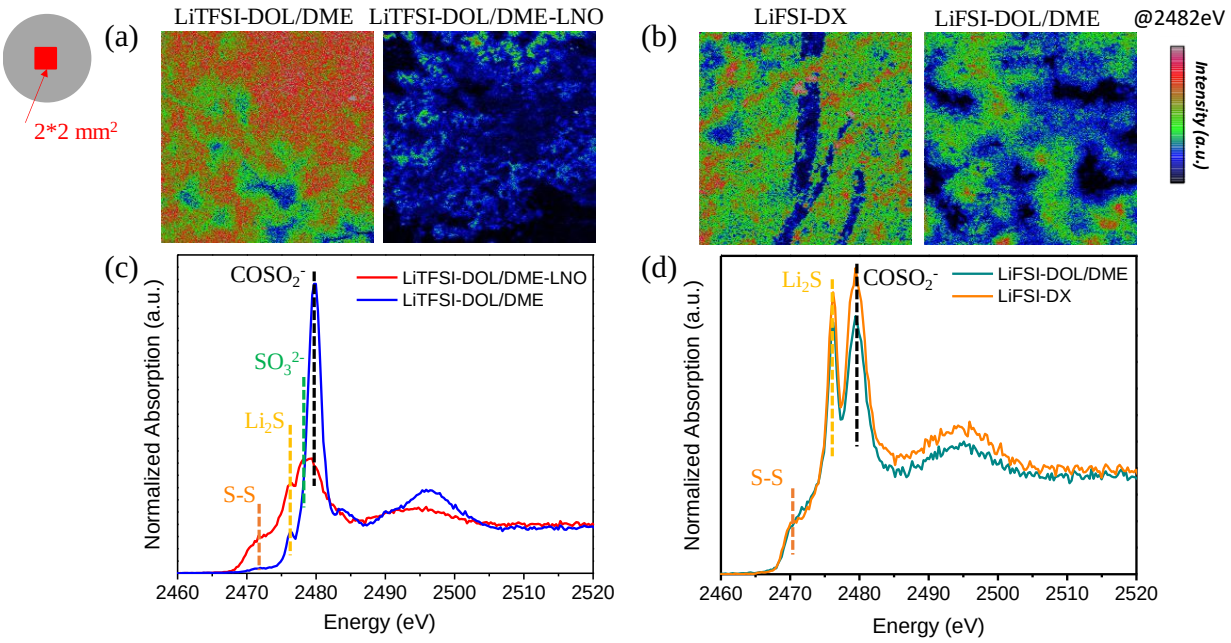

Figure II.5.B.4 XRF image of Li metal anodes cycled in (a) LiTFSI-DOL/DME, LiTFSI-DME/DOL-$LiNO_3$, and (b) LiFSI-DX, LiFSI-DME/DOL electrolytes after 10 cycles. Data were measured at an incident beam energy of 2480 eV. (c-d) (d) Normalized S K-edge XAS spectra measured from the selected area in a-b.

Conclusions

This project, Advanced in situ Diagnostic Techniques for Battery Materials (BNL), has been successfully completed in FY2020. All milestones have been completed. The publication records are very good. Extensive collaboration with other national labs, US universities and international research institutions were established.

Key Publications

Publications

1. Qiang Jiang, Peixun Xiong, Jingjuan Liu, Zhen Xie, Qinchao Wang, Xiao-Qing Yang, Enyuan Hu*, Yu Cao, Jie Sun, Yunhua Xu*, Long Chen*, "A Redox-Active 2D Metal-Organic Framework for Efficient Lithium Storage with Extraordinary High Capacity", *Angewandte Chemie* 132, 5311-5315, 2020 publication date (Web): March 23, 2020

2. Chunyu Cui, Xiulin Fan, Xiuquan Zhou, Ji Chen, Qinchao Wang, Lu Ma, Chongyin Yang, Enyuan Hu, Xiao-Qing Yang, and Chunsheng Wang, "Structure and Interface Design Enable Stable Li-Rich Cathode", J. Am. Chem. Soc. 2020, 142, 19, 8918–8927, DOI: 10.1021/jacs.0c02302, Publication Date (web): April 22nd, 2020.

3. Xuelong Wang, Xiulin Fan, Xiqian Yu, Seongmin Bak, Zulipiya Shadike, Iradwikanari Waluyo, Adrian Hunt, Sanjaya D. Senanayake, Hong Li, Liquan Chen, Chunsheng Wang, Ruijuan Xiao, Enyuan Hu, Xiao-Qing Yang, "The Role of Electron Localization on Covalency and Electrochemical Properties of Lithium-Ion Battery Cathode Materials", Advanced. Functional Materials, DOI: 10.1002/adfm.202001633, Publication Date: May 13, 2020.

4. Chao Luo, Enyuan Hu, Karen J. Gaskell, Xiulin Fan, Tao Gao, Chunyu Cui, Sanjit Ghose, Xiao-Qing Yang, and Chunsheng Wang, "A chemically stabilized sulfur cathode for lean electrolyte lithium sulfur batteries", PNAS, 2020 117 (26) 14712-14720, DOI: 10.1073/pnas.2006301117, Publication Date: June 17, 2020.

5. Zeyuan Li, Aijun Li, Hanrui Zhang, Ruoqian Lin, Tianwei Jin, Qian Cheng, Xianghui Xiao, Wah-Keat Lee, Mengyuan Ge, Haijun Zhang, Amirali Zangiabadia, Iradwikanari Waluyod, Adrian Hunt, Haowei Zhai, James Joseph Borovilasa, Peiyu Wang, Xiao-Qing Yang, Xiuyun Chun, and Yuan Yang, "Interfacial engineering for stabilizing polymer electrolytes with 4V cathodes in lithium metal batteries at elevated temperature", Nano Energy. Vol. 72, 104665, DOI: 10.1016/j.nanoen.2020.104655, Publication date: June 2020.

6. Lili Shi, Seong-Min Bak, Zulipiya Shadike, Chengqi Wang, Chaojiang Niu, Paul Northrup, Hongkyung Lee, Arthur Y. Baranovskiy, Cassidy S. Anderson, Jian Qin, Shuo Feng, Xiaodi Ren, Dianying Liu, Xiao-Qing Yang, Fei Gao, Dongping Lu*, Jie Xiao*, and Jun Liu*, "Reaction heterogeneity in practical high-energy lithium–sulfur pouch cells", Energy & Environmental Science (2020), DOI: 10.1039/d0ee02088e, Publication Date: September 4, 2020.

Presentations

1. Enyuan Hu, Zulipiya Shadike, Ruoqian Lin, Xiqian Yu, Seongmin Bak, Hung Sui Lee, Yijin Liu, Katherine Page, Jue Liu, Huolin Xin, Xuelong Wang, Yongning Zhou and Xiao-Qing Yang*, "Using X-ray and Neutron Multi-probe Spectroscopy Combined with TEM and TXM imaging Techniques to Study the New Cathode Materials for Batteries", presented at MEET, Muenster, Germany, October 10th, 2019**, Invited**.

2. Seong-Min Bak*, Youngho Shin, Xiao-Qing Yang, "Multi-modal and Multi-length-scale Characterization of Composition Graded Ni-rich Layered Oxide Cathode Materials", presented at TMS2020 annual meeting, San Diego, CA, February 24, 2020, **Invited**.

II.5.C Microscopy Investigation on the Fading Mechanism of Electrode Materials (PNNL)

Chongmin Wang, Principal Investigator
Pacific Northwest National Laboratory
902 Battelle Boulevard, Mail Stop K8-93
Richland, WA 99352
E-mail: Chongmin.wang@pnnl.gov

Tien Q. Duong, DOE Technology Development Manager
U.S. Department of Energy
E-mail: Tien.Duong@ee.doe.gov

Start Date: October 1, 2019 End Date: September 30, 2022
Project Funding: $300,000 DOE share: $300,000 Non-DOE share: $0

Project Introduction

The proposed project will focus on addressing the challenges related to the stability of anode, cathode, solid electrolyte and interfaces defined by the active components in rechargeable batteries. The work will establish the structure and property relationships for rechargeable batteries of both solid-state and liquid electrolytes. The project will gain critical insights regarding the structural and chemical evolution of interfaces and their effect on electrode stability, which will form the foundation for addressing the key challenges of rechargeable batteries. The outcome of the proposed study will feed back to the battery materials fabrication group to aid in designing better materials with enhanced battery performance.

Objectives

- Explore interfacial phenomena in rechargeable Li-ion batteries of both solid state and liquid electrolyte configuration,
- Identify the critical parameters that control the stability of interface and the electrodes as well as solid electrolyte.
- Establish correlations between structural-chemical evolution of active components of batteries and their properties.
- Provide insight and guidance to the battery materials development groups for developing high performance battery materials.

Approach

- Integrated advanced microscopic and spectroscopic techniques across different platform
- In-situ S/TEM, ex-situ S/TEM, environmental S/TEM
- Cryo-S/TEM, EDS and EELS, gaining chemical and electronic structural information.
- STEM-HAADF atomic level imaging and EDS and EELS will be used to probe the interface and bulk lattice stability.

Results

Developing in-situ TEM capability that enables the measurement of the growth force of lithium dendrite

It is generally believed that Li dendrite (whisker) formation in batteries is essentially a non-regulated Li plating process, where localized current concentrations give rise to localized Li deposition. Yet, the fundamental reason for Li whisker formation and its interaction with the separator remain far from clear, which may hold crucial insights for mitigating the Li dendrite problem and hence the safe operation of Li metal anode in

batteries. In order to measure the force that a growing lithium dendrite exerts on solid electrolyte, we developed a new capability to measure the growth force of lithium whisker. We integrate an atomic force microscopy (AFM) cantilever into a solid open-cell setup in environmental transmission electron microscopy, which enable us to directly in-situ grow lithium whiskers, observe their growth characteristics and at the same time to measure the force a growing lithium whisker will exert on a separator (Figure II.5.C.1).

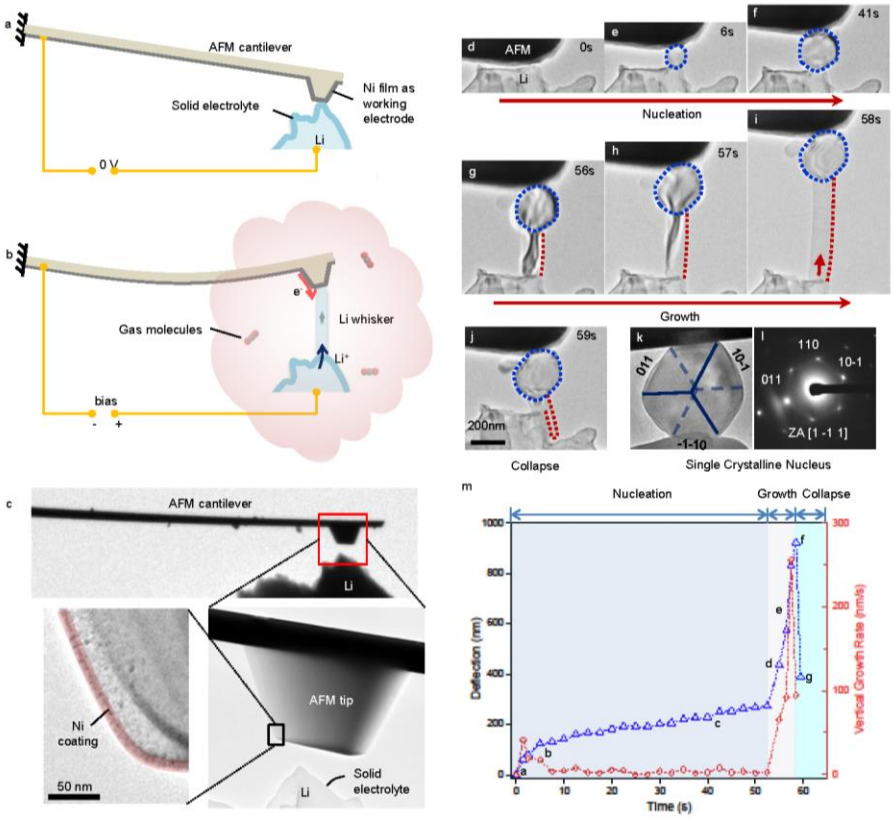

Figure II.5.C.1 The AFM–ETEM solid open-cell set-up for the in-situ study and Li whisker formation during electrochemical deposition of Li in a CO2 environment. a, Schematic of the experimental set-up before Li deposition. b, Schematic illustrating a growing Li whisker pushing the AFM cantilever, which leads to measurement of the force that the growing whisker can potentially exert on an obstacle. Note that the volume of the Li metal source is reduced as Li atoms are oxidized and contribute to the whisker growth. c, TEM images showing the in-situ solid cell in the ETEM. The Li deposition is driven by the electric potential added between the Ni-coated AFM tip and the native oxide layer on the Li metal. The gas environment controlled by the ETEM generates an SEI on the deposited Li surface. d–f, Sequential TEM snapshots of Li particle nucleation. g–i, Whisker growth process. j, Whisker collapse. The red arrow in i indicates that the Li whisker sprouts up from the whisker–electrolyte interface. Blue dotted lines indicate the nucleus. Red dotted lines highlight the side surface and shape of the Li whisker. m, Deflection of the AFM tip and vertical growth rate of the whisker during the process. k,l, Li particle in another nucleation case and corresponding electron diffraction pattern. The spring constant of the AFM cantilever is ~0.4 N m–1.

With this new in-situ capability, we directly captured the nucleation and growth behavior of Li whiskers under elastic constraint that mimics the effect of a separator. To mimic the interactions between a growing Li whisker and the separator in a battery, AFM cantilever with appropriate spring constant (0.1~2.0 $nN \cdot nm^{-1}$) was used for the test. The experiment was conducted in ~10^{-2} mbar CO_2 to form a SEI layer dominated by Li_2O and Li_2CO_3 on the deposited Li metal surface. A typical process of Li whisker formation, starting from nucleation (onset of Li deposition), whisker growth, to final "failure" by increasing compression. Upon applying a constant electric potential, Li deposition started with the formation of a Li nucleus at the interface between the solid electrolyte and the working-electrode. The Li nucleus is featured, morphologically, as a faceted particle. Diffraction analysis of the Li nucleus in a similar nucleation process demonstrates that the Li nucleus is single

crystalline body-centered cubic Li metal and terminated preferentially by {1 1 0} surfaces. Three types of interaction scenarios were revealed: buckling of the Li whisker; the ceasing of the Li deposition at the interface between the Li whisker and the solid electrolyte; and yielding of the Li whisker. Based on the force measurement, the engineering stress at the point of yielding is ~100 MPa, which is comparable to the yield strength of submicron-sized Li metal.

Revealing the intrinsic factors that control the formation of lithium dendrite

During the in-situ TEM deposition of Li metal, we found that under CO_2 gas environment, Li will grow as a whisker. However, when we change to N_2 gas, the Li deposits as large particles. Apparently, the SEI formed in CO_2 is dominated by carbonate species, which has a sluggish lithium ion transport, while for the case of N_2 gas, the SEI is dominated by Li_3N, a much better Li^+-conductor than Li_2CO_3 and Li_2O. These observations indicate that the localized Li deposition observed in CO_2 environment is tremendously attenuated in the case of N_2 environment, implying that the dendrite-free Li deposition is closely associated with the facile transport of Li in the initial SEI.

To validate the findings from the in-situ ETEM experiments described above in practical coin cells, we designed the following "electrolyte-poison" experiments and characterized the deposited Li by using SEM and Cryo-TEM. 1M lithium bis(fluorosulfonyl)imide (LiFSI) salt in dimethoxyethane (DME) solvent is used as the baseline electrolyte, which is well-documented to induce primarily the formation of large Li particles during deposition. Then, we intentionally added ethylene carbonate (EC) into the baseline electrolyte to reduce the ionic conductivity of the SEI. Due to the higher polarity of EC molecules compared to DME molecules, the EC molecules preferentially solvate the Li^+ ions. As the solvated Li^+ ions are driven by the electric field to the deposition site, the EC released there is expected to critically influence the deposited Li by reacting with the freshly deposited Li, generating dilithium ethylene dicarbonate (Li_2EDC)_ENREF_35 as the initial SEI_ENREF_29. Since the Li_2EDC has a low Li^+-conductivity, it is expected that the EC addition considerably reduces the Li deposition on the side surfaces, prompting whisker formation. Indeed, we observe that Li deposited in the baseline electrolyte is composed of pure monolithic morphology, while Li metal deposited in 0.2wt%-EC-poisoned electrolyte shows mixed morphologies of monolith and whisker. Increasing EC concentration to 2wt% leads to almost pure Li whiskers. A similar effect is also observed by poisoning the baseline electrolyte with ethyl methyl carbonate, the reduction of which on Li produces lithium alkyl carbonate.

These findings reveal the intrinsic cause and give a clear process on the formation and behavior of dendritic Li under stress, providing the much-needed insights for solving the Li whisker formation from the root cause rather than as currently containing it, and therefore potentially leading to the safe operation of Li metal anode in batteries.

In-situ liquid SIMS reveals molecular signature of SEI and fine features of SEI

The solid–electrolyte interphase (SEI) dictates the performance of most batteries, but the understanding of its chemistry and structure is limited by the lack of in situ experimental tools.

We used a newly developed in situ liquid secondary ion mass spectrometry (liquid-SIMS) technique to establish a dynamic picture of the SEI formation in lithium-ion batteries. The real-time formation of SEI at a copper electrode surface was monitored in an electrolyte that consisted of lithium bis(fluorosulfonyl)imide (LiFSI) dissolved in 1,2-dimethoxyethane (DME) at concentrations that ranged from dilute (1.0 M) to highly concentrated (4.0 M) regimes. We find that before any interphasial chemistry occurs (during the initial charging), an electric double layer forms at the electrode/electrolyte interface due to the self-assembly of solvent molecules. The formation of the double layer is directed by Li+ and the electrode surface potential. The structure of this double layer predicts the eventual interphasial chemistry; in particular, the negatively charged electrode surface repels salt anions from the inner layer and results in an inner SEI that is thin, dense and inorganic in nature. It is this dense layer that is responsible for conducting Li+ and insulating electrons, the main functions of the SEI. An electrolyte-permeable and organic-rich outer layer appears after the formation of the inner layer. In the presence of a highly concentrated, fluoride-rich electrolyte, the inner SEI layer has an elevated concentration of LiF due to the presence of anions in the double layer (Figure II.5.C.2) These real-time nanoscale observations will be helpful in engineering better interphases for future batteries.

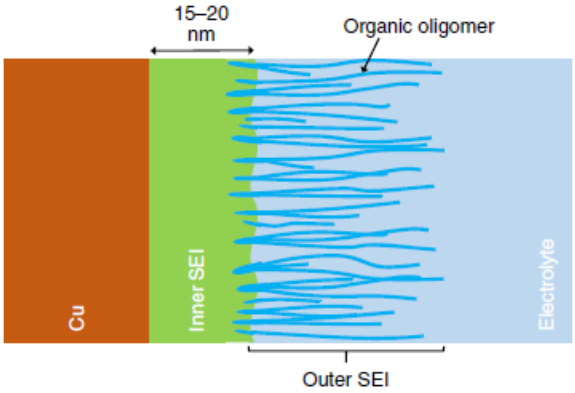

Figure II.5.C.2 An SEI model based on the observations in this work. The SEI can be divided into two parts: an inner SEI and an outer SEI. The inner SEI is continuous, dense and impermeable to electrolytes, and it is most probably composed of Li2O. The outer SEI is mainly composed of loose organic oligomers that result from the degradation of solvent molecules. The loose outer SEI is permeable to electrolytes

Revealing the correlation of current density on lithium morphology and SEI layer structure and chemistry

Current density has been perceived to play a critical rule for controlling Li deposition morphology and solid electrolyte interphase (SEI). However, the atomic level mechanism of current density on Li deposition and the SEI remains unclear. In this study, we explore the fundamental mechanism behind the current density effect on electrochemically deposited Li metal (EDLi) and SEI.

By applying high resolution Cryo-TEM, energy dispersive X-ray spectroscopy (EDS) and electron energy loss spectroscopy (EELS) techniques, we characterize the detailed structure and chemical distribution of EDLi and SEI layers with systematic control of current density, to establish the correlation between electrochemical performance (interfacial impedance) and current density induced structure and chemical evolution. The morphologies of EDLi and SEI are characterized in the electrolyte of 1.2 M $LiPF_6$/EC-EMC with VC additive under a systematically controlled variation of current density.

We found that both Li growth and SEI morphology/structure depend on the current density. As shown in Figure II.5.C.3, the EDLi whiskers formed at a very low current density (0.1 mA cm^{-2}) exhibit nonuniform distribution with various diameters. The EDLi formed at current densities of 2 to 9 mA cm^{-2} shows whisker-like configurations but with different density numbers, especially at high current density of 9 mA cm^{-2}. All whiskers are crystalline Li metal. We established that increasing current density leads to increased overpotential for Li nucleation and growth, leading to the transition from growth-limited to nucleation-limited mode for Li dendrite.

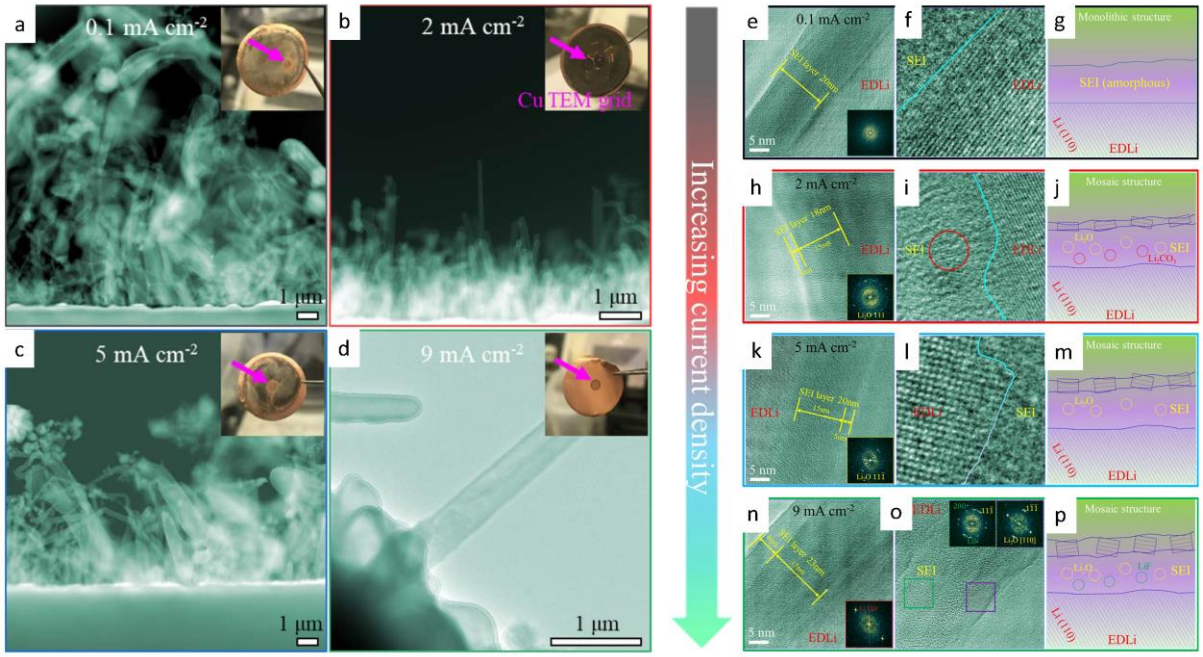

Figure II.5.C.3 Low magnification TEM images of Li deposits in 1.2 M LiPF6 in EC-EMC (3:7 by wt) electrolyte with 5% VC under current density of (a) 0.1 mA cm−2, (b) 2 mA cm−2, (c) 5 mA cm−2, and (b) 9 mA cm−2. Insets are digital photos of deposited Li. Atomic resolution TEM images of the SEI, interface structure between EDLi and SEI, and schematic of the observed SEI formed on Li at current density of (e–g) 0.1 mA cm−2 for 100 min, (h–j) 2 mA cm−2 for 5 min, (k–m) 5 mA cm−2 for 2 min, and (n–p) 9 mA cm−2 for 1.1 min. Insets, corresponding FFT patterns.

Conclusions

- Directly captured the Li whisker nucleation and growth processes under elastic constraint that mimics the effect of a separator.
- The growth mode and morphology of deposited Li can be critically related to the ionic conductivity of the initial SEI that is introduced by the basic reactions of freshly deposited Li metal with the surrounding gas molecules.
- Revealed that carbonate species in the initial SEI layer that is very adjacent to the developing Li metal plays a decisive role in the subsequent formation of Li with a whisker morphology
- In-situ liquid-SIMS reveal SEI has two layers: an inner layer that is dense, inorganic but LiF-depleted, whereas the outer layer, rich in organic species, is diffuse and permeable to the bulk electrolyte.
- Establish the correlation among Li deposition condition, dendrite growth kinetics, and SEI formation mechanism, shedding light on the optimization of the Li morphology and electrode-electrolyte interface.

Key Publications

1. Yaobin Xu, Haiping Wu, Yang He, Qingsong Chen, Ji-Guang Zhang, Wu Xu and Chongmin Wang, “Atomic to Nanoscale Origin of Vinylene Carbonate Enhanced Cycling Stability of Lithium Metal Anode Revealed by Cryo-Transmission Electron Microscopy”, **Nano Lett., 20, 418-425 (2020).**

2. Yaobin Xu, Haiping Wu, Hao Jia, Mark H. Engelhard, Ji-Guang Zhang, Wu Xu and Chongmin Wang, “Sweeping potential regulated structural and chemical evolution of solid-electrolyte interphase on Cu and Li as revealed by cryo-TEM”, **Nano Energy, 76, 105040 (2020).**

3. Yufan Zhou, Mao Su, Xiaofei Yu, Yanyan Zhang, Jun-Gang Wang, Xiaodi Ren, Ruiguo Cao, Wu Xu, Donald R. Baer, Yingge Du, Oleg Borodin, Yanting Wang, Xue-Lin Wang, Kang Xu, Zhijie Xu, Chongmin Wang and Zihua Zhu, "Real-time mass spectrometric characterization of the solid–electrolyte interphase of a lithium-ion Battery", **Nature Nanotechnology, 15, 2020, 224–230 (2020).**

4. Raymond R. Unocic, Katherine L. Jungjohann, B. Layla Mehdi, Nigel D. Browning, and Chongmin Wang, "*In situ* electrochemical scanning/transmission electron microscopy of electrode-electrolyte interfaces", **MRS Bulletin, 45, 738-745 (2020).**

5. Haiping Jia, Xiaolin Li, Junhua Song, Xin Zhang, Langli Luo, Yang He, Binsong Li, Yun Cai, Shenyang Hu, Xingcheng Xiao, Chongmin Wang, Kevin M. Rosso, Ran Yi, Rajankumar Patel and Ji Guang Zhang, "Hierarchical porous silicon structures with extraordinary mechanical strength as high performance, lithium-ion battery anodes", **Nature Communications, 11, 1474 (2020).**

6. Phung M. L. Le, Thanh D. Vo, Huilin Pan, Yan Jin, Yang He, Xia Cao, Hoang V. Nguyen, Mark H. Engelhard, Chongmin Wang, Jie Xiao, and Ji-Guang Zhang, "Excellent Cycling Stability of Sodium Anode Enabled by a Stable Solid Electrolyte Interphase Formed in Ether-Based Electrolytes", **Adv. Funct. Mater. 2001151 (2020)**.

7. Yan Jin, Yaobin Xu, Phung M. L. Le, Thanh D. Vo, Quan Zhou, Xingguo Qi, Mark H. Engelhard, Bethany E. Matthews, Hao Jia, Zimin Nie, Chaojiang Niu, Chongmin Wang, Yongsheng Hu, Huilin Pan, and Ji-Guang Zhang, "Highly Reversible Sodium Ion Batteries Enabled by Stable Electrolyte-Electrode Interphases", **ACS Energy Lett. 5, 3212-3220(2020).**

8. Xianhui Zhang, Lianfeng Zou, Yaobin Xu, Xia Cao, Mark H. Engelhard, Bethany E. Matthews, Lirong Zhong, Haiping Wu, Hao Jia, Xiaodi Ren, Peiyuan Gao, Zonghai Chen, Yan Qin, Christopher Kompella, Bruce W. Arey, Jun Li, Deyu Wang, Chongmin Wang, Ji-Guang Zhang, and Wu Xu, "Advanced Electrolytes for Fast-Charging High-Voltage Lithium-Ion Batteries in Wide-Temperature Range", **Adv. Energy Mater., 2000368 (2020).**

9. Yang He, Xiaodi Ren, Yaobin Xu, Mark H. Engelhard, Xiaolin Li, Jie Xiao, Jun Liu, Ji-Guang Zhang, Wu Xu and Chongmin Wang, "Origin of lithium whisker formation and growth under stress", **Nature Nanotechnology, 14, 1042-1047 (2019).**

Acknowledgements

Support from the U. S. Department of Energy (DOE), Vehicle Technologies Office, specifically from Tien Duong and David Howell is gratefully acknowledged.

II.5.D In-Operando Thermal Diagnostics of Electrochemical Cells (LBNL)

Ravi Prasher, Principal Investigator
Lawrence Berkeley National Lab
1 Cyclotron Rd
Berkeley, CA, 94720
E-mail: RSPrasher@lbl.gov

Tien Duong, DOE Technology Development Manager
U.S. Department of Energy
E-mail: Tien.Duong@ee.doe.gov

Start Date: October 1, 2019 End Date: September 30, 2022
Project Funding: $245,000 DOE share: $245,000 Non-DOE share: $0

Project Introduction

Characterizing electrochemical processes in Li-metal cells such as lithium deposition and dendrite growth at interfaces is of great significance for understanding and enhancing their electrochemical performance and reliability. In situ and operando 3-omega micro thermal sensors can provide significant information regarding the impact of buried interfaces as a function of time, material, voltage, current, and temperature, etc. Therefore, it is important to develop operando 3-omega micro thermal sensors and develop models relating those signals to electrochemical performance for beyond lithium ion cells. The physics-based model relating thermal and electrochemical properties based on these measurements can facilitate future design of Li metal batteries.

Objectives

Transport at various interfaces in beyond lithium ion cells will play a major role in electrochemical performance and reliability. It has not yet been possible to thermally profile a Li-metal cell during operation to provide a spatially resolved map of thermal transport properties throughout the cell. The objective of this research is to create a metrology capable of spatially resolved in operando thermal property profiling, and then relate thermal property to the quality of electrodes and interfaces, and use the developed thermal metrology to understand electrochemical processes in Li-metal batteries such as dendrite growth, interface kinetics, and ionic transport.

Approach

To accomplish project goals, the team will utilize an in-house adapted 3-omega technique to probe thermal properties of a Li-metal cell while it is in operation, without affecting the operation of the cell. The 3 omega sensors will be deposited and fabricated on Li-metal cells based on previous learning on 3-omega sensor fabrication. The characteristic depth of the thermally probed region is defined by the wave's "thermal penetration depth, $\delta = \sqrt{D/2\omega}$, where D is the sample's thermal diffusivity, and 2ω is the heating frequency of the thermal wave [1]. By depositing the project's 3ω sensors on the battery's outer surface and adjusting ω, the team controls δ to span the full range from the top to the bottom layer, thereby noninvasively probing the thermal transport in subsurface layers and interfaces within the bulk of the battery. Thermal transport can be related to quality of the interface. By doing concurrent thermal transport and electrochemical performance measurements, the team plans to relate thermal transport to electrochemical performance. As frequency based thermal measurement techniques provide excellent spatial resolution within the cell, the team also plans to study heat generation at the electrolyte – Li-metal interface and relate the thermal signals to the interface kinetics and ionic transport. The frequency dependence of heat generated due to transport resistance is different from that due to kinetic resistance. The team plans to utilize this difference to separate the contributions of kinetic and transport resistance at the interface, which will enable understanding of interface kinetics and transport at the Li-metal – SSE interface.

Results

The Prasher group is building operando 3ω micro thermal sensors and developing models relating thermal signals to electrochemical performance for beyond lithium ion cells. The anode-side 3ω sensor will be used to probe thermal properties of Li metal anodes and related interfaces. The group is also developing a general frequency based thermal metrology to probe the interface kinetics and transport.

In Q1, we performed sensitivity analyses for the anode-side 3ω measurements of thermal properties of Li metal anodes and interfaces and proposed that we will use the thermal interface resistance as a measure of morphology of the lithium at the interface [2]. In Q2, we developed the 3ω sensors for the symmetric cells and measured the thermal transport properties of the electrolyte (LLZO) using 3ω. The specific heat and thermal conductivity of LLZO were determined to be 720 J/kg-K and 1.33 W/m-K, respectively.

In Q3 and Q4, we worked on assembling the lithium symmetric solid-state cells with 3ω sensors, which we intend to cycle while simultaneously performing 3ω measurements to extract the anode-electrolyte thermal interface resistance and track its evolution as a function of the number of battery cycles. The cells assembled are circular and have a diameter of 15mm. They consist of 1mm thick LLZO pellets, 200μm thick Li-metal anode on both sides of the electrolyte and 20μm thick current collectors, with a 3ω sensor attached to one of the current collectors. The assembled cell, with different layers, is shown in Figure II.5.D.1(b), and the 3ω sensor is shown in Figure II.5.D.2(a). The 3ω sensor was attached to the copper current collector using an epoxy (SU-8). To form the assembly, the different layers were sandwiched together and heated to the melting point of the lithium (180.5°C). Both sides of the electrolyte and the side of the current collector adjacent to lithium were pre-coated with 20nm gold to facilitate lithium wetting and adhesion.

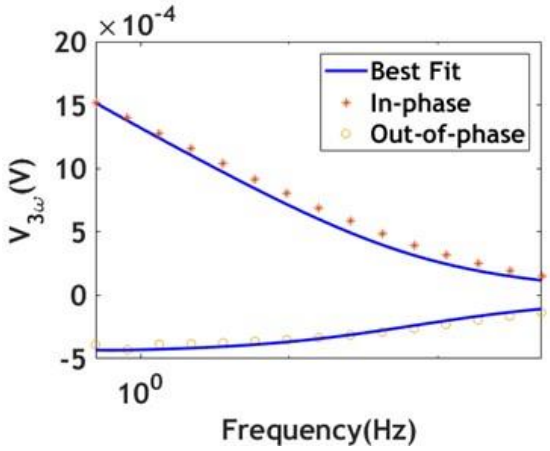

Figure II.5.D.1 3ω Fitting to determine LLZO thermal conductivity. The thermal conductivity of LLZO was measured to be 1.33W/mk.

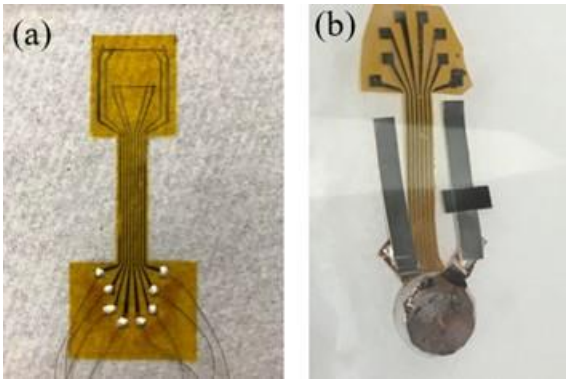

Figure II.5.D.2 (a) Anode side 3ω Sensor and (b) A lithium symmetric cell with an integrated 3ω Sensor.

Additionally, we are designing a new frequency dependent heat generation technique to study electrochemical processes related to the charge transport and reaction kinetics at electrode-electrolyte interfaces. We have completed the theoretical analysis, experimental design, and the experimental setup for this new frequency dependent thermal metrology. From our theoretical analysis, we have identified heat generation terms at different harmonics of the fundamental driving frequency of the current passed through the cell, and have quantitatively related these to important electrochemical parameters including the ionic conductivity of the solid state electrolyte, the transport resistance of the electrolyte-lithium metal interface and the exchange current density for the Li oxidation/reduction reaction at the electrode. Based on the fact that the technique utilizes the thermal signatures of the heat generated at multiple harmonics of the excitation current to extract the electrochemical properties, we have named this method Muti-harmonic ElectroThermal Spectroscopy (METS).

The heat generated at the 4ω and the 2ω frequencies contains information about the battery's kinetic and the charge transport, respectively. By performing a frequency sweep to vary the thermal penetration depth, we will in principle be able to isolate the location of the origin of the 4ω and the 2ω signatures, thereby non-invasively probing the kinetics and transport at the interfaces and the electrolyte. We have completed developing a full-scale combined electrochemical and thermal model that includes the effect of the applied frequency on the current distribution (capacitive vs. reactive), heat generation (4ω, 2ω and 1ω signatures) and the temperature rise at the sensors. To do so, we combined our frequency analysis of heat generation with the Feldman analysis [3] of frequency dependent temperature rise. With this combined electrochemical-thermal model, we performed a sensitivity analysis of the thermal signatures of the kinetic, transport, and capacitive processes in the interfaces and the electrolyte. The results are presented below in Figure II.5.D.3.

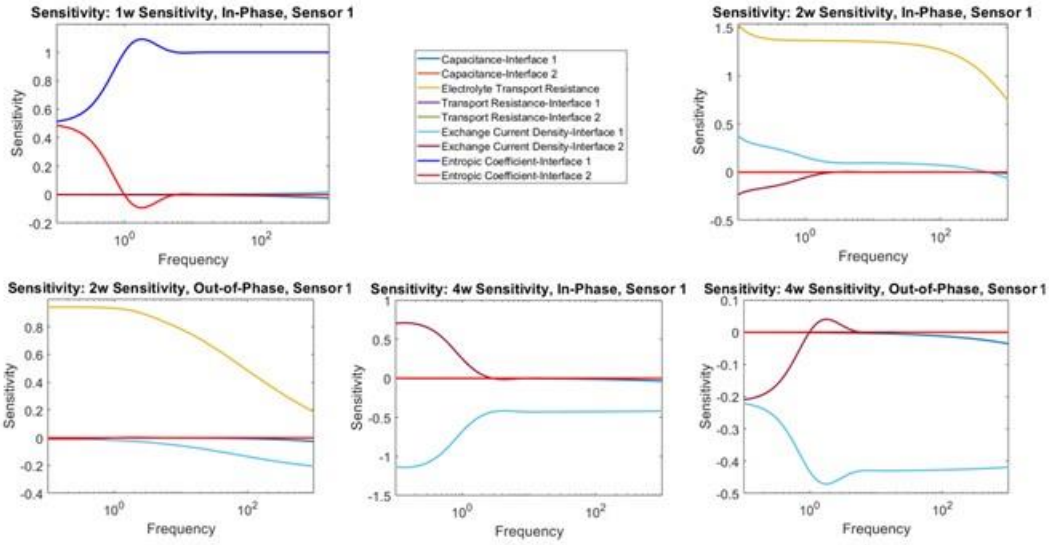

Figure II.5.D.3 Sensitivity of the temperature rise at different harmonics of the applied charging frequency (1ω, 2ω and 4ω) due to different electrochemical processes at the interfaces and the electrolyte. The 2ω temperature rise (both in-phase and out-of-phase) at low frequencies is the most sensitive to the ionic transport resistance in the electrolyte. The 4ω temperature rise (both in-phase and out-of-phase) at high frequencies is the most sensitive to the kinetics at the interface (exchange current density).

In order to verify the METS technique, we have designed an experiment to simultaneously measure the electrolyte transport resistance and the exchange current density in a symmetric cell using METS and Electrochemical Impedance Spectroscopy (EIS), so that we can compare the results from the two methods. The experimental cell setup for the verification consists of a redox coupled electrolyte Fc1N112-TFSI with symmetric platinum electrodes [4]. It is expected that the electrolyte will not react with Platinum, therefore eliminating any SEI –like compounds at the electrode. By doing so we will eliminate any SEI resistance, and the interface resistance obtained from EIS can be purely attributed to the charge transfer resistance or the

exchange current density. Then, we can directly compare the exchange current density and the electrolyte transport resistance obtained from EIS and METS to verify the METS technique. Figure II.5.D.4 shows a fabricated METS sensor we have designed to be used in the Pt- Fc1N112-TFSI-Pt cell for the verification experiment. The METS sensor also incorporates a 3ω sensor in the middle to simultaneously extract the thermal transport properties of the cell layers and interfaces, which can then be to relate the heat generation with the temperature rise.

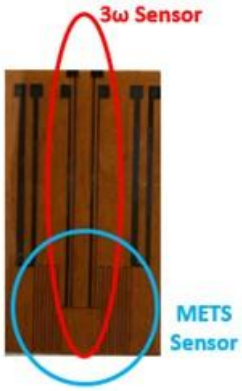

Figure II.5.D.4 A METS sensor with an integrated 3ω sensor. A 3ω measurement is performed first to extract the thermal properties, which are then used to relate the temperature rise detected by the METS sensor with the spatially resolved heat generation signatures of the separated-out electrochemical properties.

We have also completed the experimental setup for data acquisition. Shown in Figure II.5.D.5 is the setup for the METS experiment. It consists of a lock-in amplifier for frequency selective detection of the voltage (which corresponds to the temperature rise) from the METS sensor. The lock-in amplifier also provides an AC voltage/current source, which is used to generate the thermal signatures in the battery. The setup also consists of a custom-built circuit for signal conditioning and a current source to provide a DC sensing current through the METS sensor. The same setup can also work as a 3ω-system to acquire 3ω signals for the thermal properties of the cell.

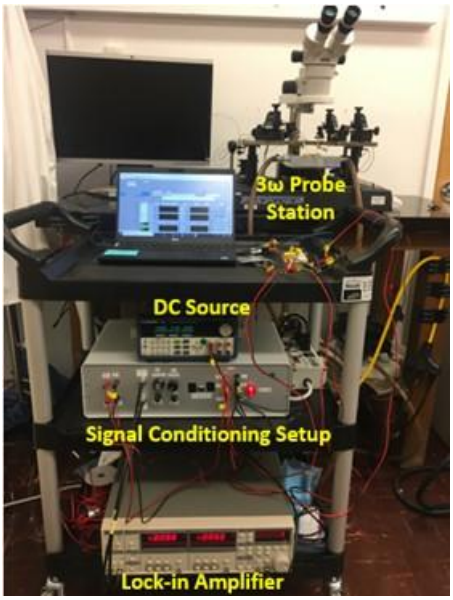

Figure II.5.D.5 Custom-Built METS and 3ω Data Acquisition System

Conclusions

In summary, we have been working on developing thermal sensors to study electrochemical and thermal phenomena in next generation solid state cells. We have formulated a complete model and experimental characterization scheme for the thermal interface resistance at the lithium metal-solid state electrolyte interface to study its evolution. We have fabricated the 3ω-sensors and have integrated them in the lithium symmetric solid-state cells in order to monitor the evolution of the interface. Next year, we will begin cycling the cells and obtaining *operando* 3ω measurements to study the morphology evolution of the interface.

Additionally, we have also worked on developing a frequency based thermal spectroscopy technique (Muti-harmonic ElectroThermal Spectroscopy—METS) to extract electrochemical parameters including kinetic and transport resistance at the interface, including spatial mapping. We have completed formulating the theory and performing the sensitivity analysis for a verification experiment of the METS technique. Finally, we have also completed building a custom data acquisition setup for METS and 3ω measurements.

References

1. Lubner, Sean D., Sumanjeet Kaur, Yanbao Fu, Vince Battaglia, and Ravi Prasher. 2020. "Identification and Characterization of the Dominant Thermal Resistance in Lithium-Ion Batteries Using Operando 3-Omega Sensors." Journal of Applied Physics 127 (10). https://doi.org/10.1063/1.5134459.

2. Wang, Michael, and Jeff Sakamoto. 2018. "Correlating the Interface Resistance and Surface Adhesion of the Li Metal-Solid Electrolyte Interface." Journal of Power Sources 377 (August 2017): 7–11. https://doi.org/10.1016/j.jpowsour.2017.11.078.

3. Feldman, Albert. 1999. "Algorithm for Solutions of the Thermal Diffusion Equation in a Stratified Medium with a Modulated Heating Source." In , 31:293–98.

4. Wei, Xiaoliang, Lelia Cosimbescu, Wu Xu, Jian Zhi Hu, M. Vijayakumar, Ju Feng, Mary Y. Hu, et al. 2015. "Towards High-Performance Nonaqueous Redox Flow Electrolyte via Ionic Modification of Active Species." Advanced Energy Materials 5 (1): 1–7. https://doi.org/10.1002/aenm.201400678.

Acknowledgements

We thank Divya Chalise, Dr. Yuqiang Zeng, Dr. Sean Lubner, Dr. Suman Kaur, Dr. Yanbau Fu, and Dr. Vince Battaglia for their help in carrying out the research in this project.

II.5.E In situ Diagnostics of Coupled Electrochemical-Mechanical Properties of Solid Electrolyte Interphases on Lithium Metal for Rechargeable Batteries (General Motors)

Xingcheng Xiao, Principal Investigator
General Motors Research and Development Center
30470 Harley Earl Blvd.
Warren, MI 48092-2031
E-mail: xingcheng.xiao@gm.com

Tien Duong, DOE Technology Development Manager
U.S. Department of Energy
E-mail: Tien.Duong@ee.doe.gov

Start Date: October 1, 2016 End Date: March 30, 2020
Project Funding: $1,815,845 DOE share: $1,452,676 Non-DOE share: $363,169

Project Introduction

Lithium (Li) metal-based batteries, including Li-air, Li sulfur batteries, and solid-state batteries, are among the most promising candidates of high energy density batteries, due to their ultrahigh capacity (3860 mAh g-1), lowest reduction potential (~3.04 V vs. S.H.E), and low density (0.534 g cm-3). However, Li typically goes through large volume expansion and contraction during stripping/plating processes, leading to coupled mechanical/chemical degradation at multiple length scales, including the formation of mossy structures and dendrite growth. The mossy structure leads to low cycle efficiency due to the continuous decomposition of electrolyte. Dendrite formation leads to current shortage and sometime catastrophic failure. Both failures are initiated from the damage of the solid electrolyte interphase (SEI).

The fundamental understanding of the coupled mechanical/chemical degradation of the SEI layer during lithium cycling will enable the project to identify the desirable mechanical properties on SEI/lithium as a system and the specific transport properties that enable the homogenous lithium stripping/plating while avoiding the mossy structure. Furthermore, it will allow the project to develop a highly impactful strategy to protect lithium metal and achieve dendrite-free high cycle efficiency, which can dramatically increase the energy density of lithium batteries for EV applications.

Objectives

The project objective is to develop a comprehensive set of in situ diagnostic techniques combined with atomic/continuum modeling schemes to investigate and understand the coupled mechanical/chemical degradation of the SEI layer/lithium system during lithium cycling. The goal of this understanding is to develop a new coating design strategy to achieve high cycle efficiency/dendrite free and extend the cycle life of high-energy-density batteries with lithium as the anode for EV applications.

Approach

Different in situ techniques, including AFM, nano-indentor, dilatometer, and stress-sensor, will be developed to investigate the mechanical compatibility between SEI and soft lithium and the relationship between surface morphology and current density distribution that results in an inhomogeneous lithium plating/stripping process. Multiple strategies will be developed to tailor the mechanical and transport properties of SEI and to properly engineer the protective coating/lithium interface.

Results

Stress evolution in protected Li metal electrode

Our previous results on LiF-protected sample show that the initial transient compressive stress we previously observed in samples without protection does not appear from 2nd ~ 5th cycle, as shown in Figure II.5.E.1. The initial transient stress from bare Au sample was a dominant stress trend, which was attributed to the surface phenomena associated with SEI formation reaction. With LiF protection, however, this initial transient stress is relatively small, and a steady-state, linear growth stress behavior is instead seen throughout the entire plating sequence. Figure II.5.E.1 further shows that with an artificial SEI protection, the dominant compressive stress that arises from reaction between Lithium and the liquid electrolyte can be suppressed, and the stress response becomes more "growth-stress dominant" from the plated lithium metal instead.

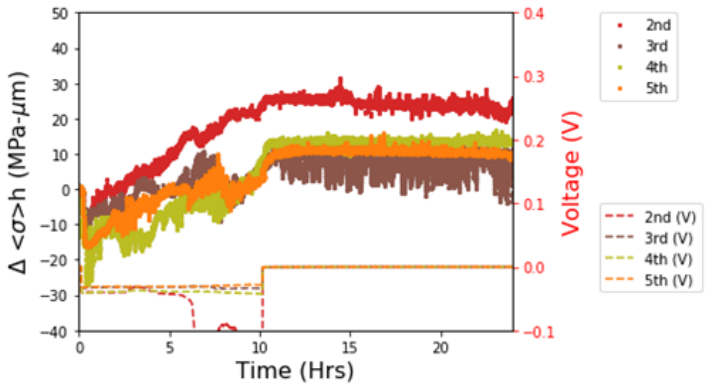

Figure II.5.E.1 Change in stress-thickness vs. time for respective cycles from the MOSS studies. Left plot is the response with soft (PEO) artificial layer. Right plot is the response with stiff (LiF) artificial layer.

To relate the stress effects on the overall coulombic efficiency of the cell, coin cells were made for both bare and LiF-protected samples. The current density of 0.25 mA/cm^2 with overall capacity of 1 mAh/cm^2 was plated during each cycle and stripped at the same current density with a voltage limit of 1V. The results are shown below in Figure II.5.E.2.

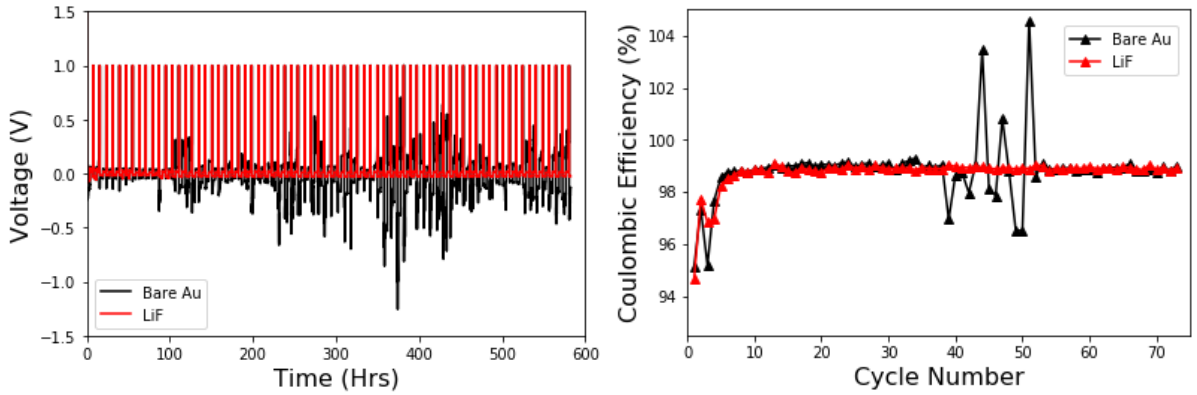

Figure II.5.E.2 Overall voltage profile and the respective coulombic efficiencies for both Bare Au vs. LiF-protected Au. Black lines indicate the Bare Au sample; Red lines indicate the LiF-protected sample.

As shown in the voltage profile plot, relatively smaller overpotential was observed for LiF-protected sample during plating sequence, as compared to the more erratic voltage profile observed in the bare-Au sample. This indicates that with the aid of LiF artificial layer, the overpotential stays relatively constant and stable as compared to the unprotected sample. The coulombic efficiency, however, show a similar behavior regardless of the voltage profile. Longer cycling will be required for better overall comparison of the coulombic efficiency, as the data is only indicative of 73 cycles for each sample. Nonetheless, the voltage profile for the protected sample shows much more favorable behavior, with smaller magnitude and better stability.

Mechanical properties of plated lithium electrode

From flat-punch indentation measurements, the Young's modulus (E) of bulk Li is determined to be ~7.8 GPa, which is consistent with the reported values by macroscopic tensile and nanoindentation measurements. The Young's modulus, E, of the mossy Li slightly increases from 1.6 to 2.6 GPa with increasing the maximum indentation load. The measured much smaller E of the mossy Li than bulk Li can be attributed to the highly compliant porous structure of the mossy Li, even though the SEI layer has a much higher modulus than lithium. Figure3 (a) shows that the creep depth (h_{creep}) of bulk Li during the holding period increases remarkably with the punch stress ($\sigma_{ind} = F_{max}/A$, where A is the projected area of the flat punch). Surprisingly, h_{creep} of the mossy Li is much smaller than that of bulk Li and increases slightly with increasing σ_{ind}.

The impression velocity, ν_c, during the holding period of flat punch indentation is shown in Figure 3(b). The steady-state creep velocity, ν_{ind}, determined as the expectation value of ν_c during the steady-state creep period using Gaussian distribution [Figure II.5.E.3 (c) and (d)]. As shown in Figure II.5.E.3(e), ν_{ind} of the mossy Li increases slightly as σ_{ind} increases from 5.04 MPa and 14.41 MPa. The average ν_{ind} (in the range between 0.25 ± 0.03 and 0.74 ± 0.23 nm/s) of the mossy Li is larger than the thermal drift rate limit of 0.05 nm/s. Under the same punching stress range between 4.93 and 5.76 MPa, ν_{ind} of the mossy Li is only one-thirtieth of that of bulk Li. Thus, mossy lithium is more creep resistant than bulk lithium which can have significant effects on the design and operation of Li metal electrodes, including the effects of the liquid electrolyte and current density as shown in Figure II.5.E.4.

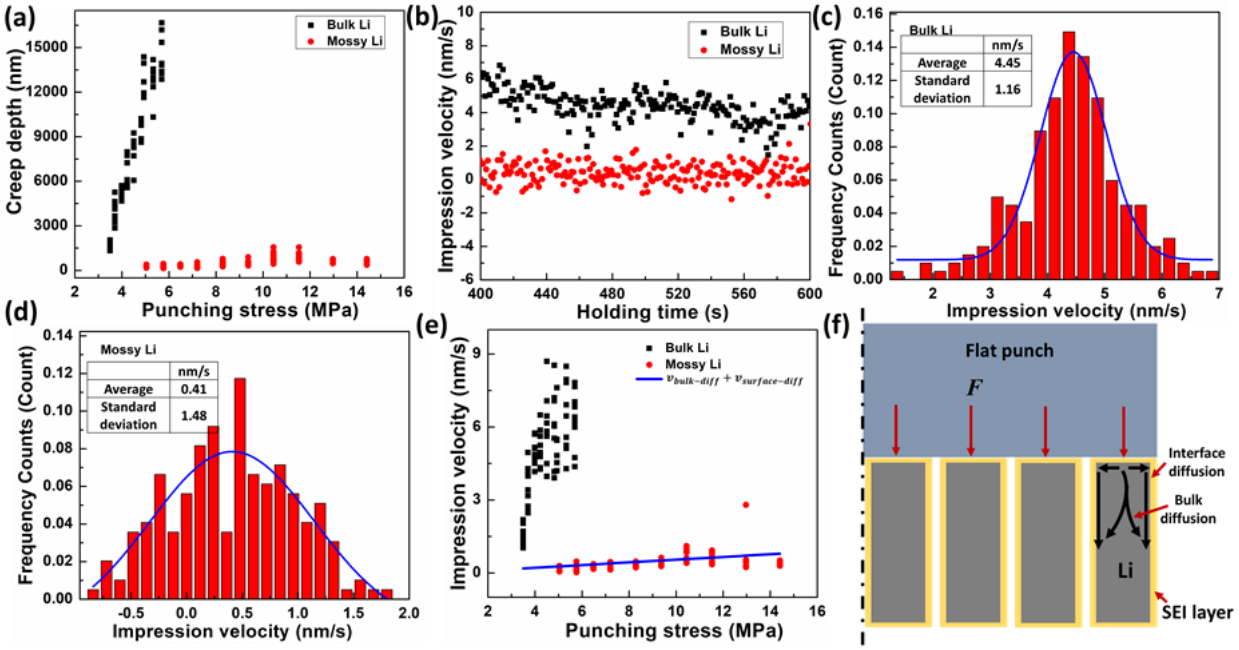

Figure II.5.E.3 (a) The creep depth-punching stress profiles of the mossy and bulk Li. (b) The impression velocity-holding time profiles of the mossy and bulk Li during the holding period between 400 and 600 s. (c) and (d) are the Gaussian distributions of the impression velocity of bulk and the mossy Li during the holding period between 400 and 600 s, respectively. The steady-state impression velocity is determined as the expectation value (the average value) of Gaussian distribution. (e) The impression velocity-punching stress profile of the mossy and bulk Li. The impression creep velocity of bulk Li caused by diffusion is also plotted in (e). (f) A schematic of the diffusion paths in Li dendrites.

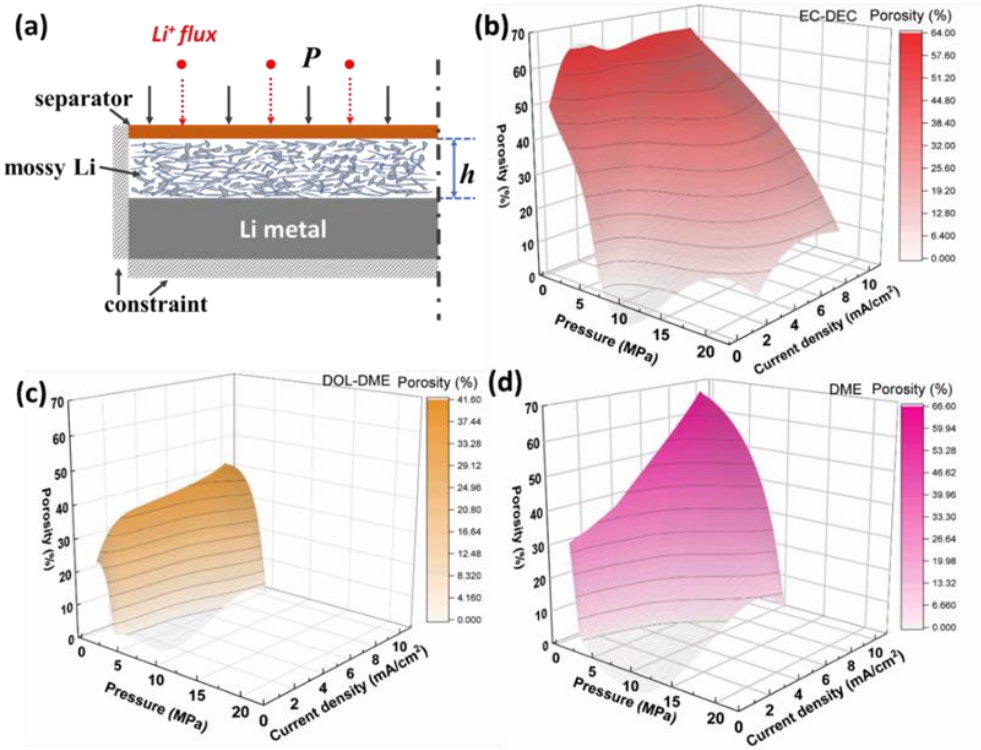

Figure II.5.E.4 (a) A schematic diagram of Li plating under a stack pressure of P. The bottom and the lateral side are constrained. The mossy Li can only be electroplated between the Li metal electrode and separator. (b)-(d) show the porosity profiles of mossy Li as a function of the current density and stack pressure in the EC-DEC, DOL-DME, and DME electrolytes at RT, respectively.

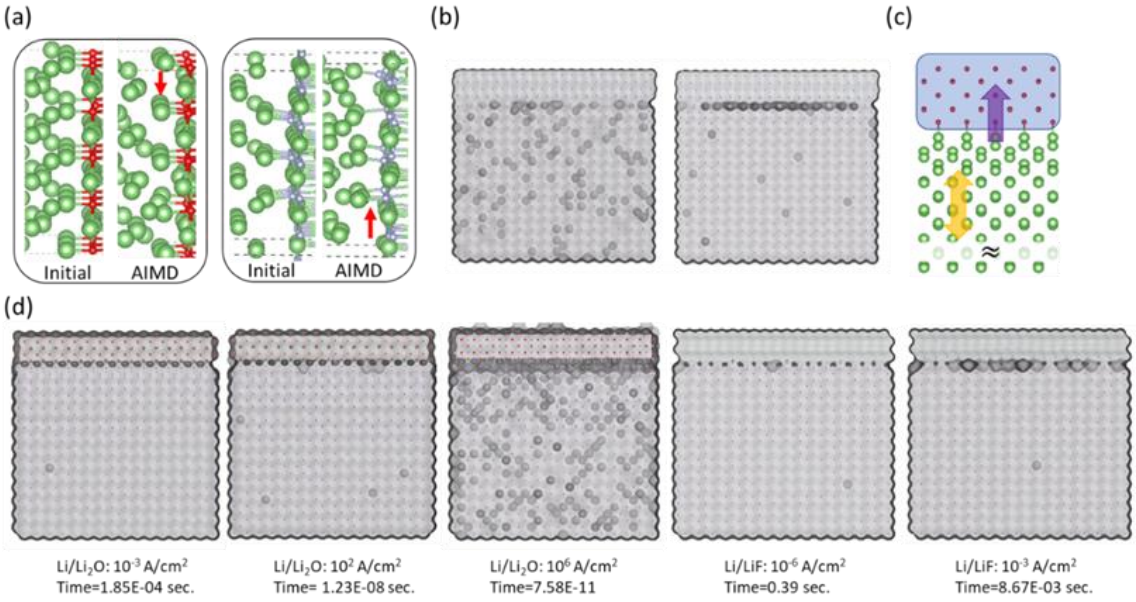

Figure II.5.E.5 (a) Left: number of Li-O bonds at Li/Li_2O interface and Right: number of Li-F bonds at Li/LiF interface before and after AIMD simulation. (b) KMC results of left: case I, reducing ΔETI_2->1 and of right: case II, increasing ΔETB_2<-1. (c) Illustration of KMC simulation incorporating Li delithiation (purple) and Li atom diffusion in the Li anode (yellow). (d) KMC results with different current density upon Li/Li2O (10^{-3}, 10^{2}, and 10^{6} A/cm^2) and Li/LiF (10^{-3} and 10^{-6} A/cm^2).

A stripping mechanism based on the KMC simulation

The Li atoms in the SEI layers are removed in the initial KMC structure to represent the Li sink for Li delithiation as shown in Figure II.5.E.5(c). k_s is the probability (per unit time) with which an Li atom leaves the interface. As shown in Figure II.5.E.5(d), the KMC results show that at the typical current density of 10^{-3} A/cm^2 the interface of Li/Li_2O has no vacancy. When the current density is at 10^2 A/cm^2, though some vacancies generated due to stripping submerged into the bulk, vacancies at the interface can be seen (3 vacancies at L1 out of 7 delithiated Li). When the current density is at 10^{-6} A/cm^2, we can clearly see vacancies occurring at the interfaces (101 vacancies at L1 out of 327 delithiated Li). On the other hand, even at the typical range of the current density (10^{-3} - 10^{-6} A/cm^2), the presence of vacancies can be seen at the interface, 41 vacancies at L1 out of 42 delithiated Li for the former current density. In sum, the tendency of Li diffusion toward the interface determines vacancy-free surface and is one atomistic mechanism behind lithiophilic surface.

New coating strategy to protect lithium metal electrode

Dendrite growth and low cycle efficiency, due to the unstable solid electrolyte interphase (SEI) formed on Li surface, have been the major bottleneck to the practical applications particularly for electrical vehicles (EVs). Protective coatings as the artificial SEI layer on Li metal have been extensively investigated to tackle those two issues. Due to the electrochemical and mechanical incompatibility between soft Li metal and protective coating, the cycling stability of the coated Li electrodes with targeted energy density still cannot meet the requirements for EV applications. In this new coating strategy, we applied a physical vapor deposition (PVD) process to coat fluorinated polymers on Li metal and form an artificial SEI layer by the defluorination reaction between the polymer and Li. In this process, the ionized C-F fragments from the radio-frequency plasma react with Li metal spontaneously upon reaching Li surface, resulting in a unique composite coating where nano-sized lithium fluoride crystals are embedded in carbonaceous matrix. The defluorination derived artificial SEI layer effectively suppresses the dendrite formation and mossy structure evolution during cycling. The cycle life is dramatically increased in both carbonate and ether-based electrolytes even under a harsh test condition (1 mA/cm2 of current density and 4 mAh/cm^2 of capacity equivalent to 20 μm Li).

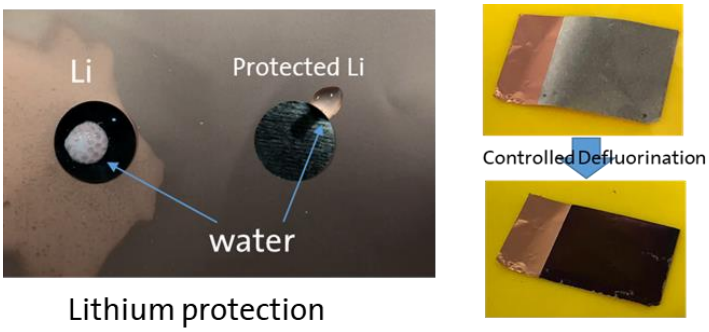

Figure II.5.E.6 The molecular of the polymer coating for protecting Li. The optical images show that the coating can protect Li reaction with water.

In addition, we developed a composite coating which consists of LiF and polymer matrix to protect Li metal electrode. The coating is derived from the defluorination reaction between Li metal and fluoropolymer which has –CF_3 functional groups such as FEP (fluorinated ethylene propylene), PFA (perfluoroalkoxy). Employing trifluoro (-CF_3) in the molecule structure of a SEI can significantly tune the orbital energies and the LUMO gap due to the strong electron-withdrawing property of -CF_3 functional groups. The fluorine based coating is hydrophobic, which effectively protects Li from water and moisture (Figure 6) It makes lithium handling much easier (no strict requirement such as dry room).The resulted coating can effectively protect Li metal electrode in both air and electrochemical environment, leading to extended cycle life for high energy density lithium batteries, as shown in full cell test (Figure II.5.E.7).

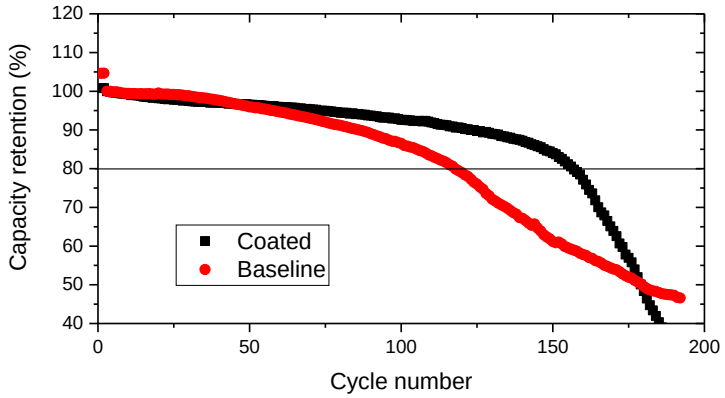

Figure II.5.E.7 The cycle performance of protected Li comparing with baseline. Testing condition: 1M $LiPF_6$ in EMC/FEC (4:1), C/10 charge & C/5 discharge, 20 μm Li electrode paired with NMC622 (4.4 mAh/cm^2)

Conclusions

- Further investigated the stress evolution of Li metal electrode with artificial SEI layer. It shows the dominant compressive stress that arises from reaction between Lithium and the liquid electrolyte can be suppressed, and the stress response becomes more "growth-stress dominant" from the plated lithium metal instead.

- The mechanical properties of Li metal is strongly correlated with its morphology. mossy lithium is more creep resistant than bulk lithium which can have significant effects on the design and operation of Li metal electrodes,

- Further developed a composite coating which consists of LiF and polymer matrix to protect Li metal electrode. The coating is derived from the defluorination reaction between Li metal and fluoropolymer which has –CF3 functional groups such as FEP (fluorinated ethylene propylene), PFA (perfluoroalkoxy). The resulted coating can effectively protect Li metal electrode in both air and electrochemical environment, leading to extended cycle life for high energy density lithium batteries.

Key Publications

1. Patent: B. Li, X. Xiao, In-situ Polymerization to Protect Lithium Metal Electrodes, P048616, 2019

2. Patent: X. Xiao, Methods for manufacturing electrode including fluoropolymer based solid electrolyte interface layers, P049559-US-NP, 2019

3. Patent: X. Xiao, Electrode including fluoropolymer based solid electrolyte interface layers and batteries and vehicles utilizing the same. P049933-US-NP, 2019

4. Yikai Wang, Dingying Dang, Ming Wang, Xingcheng Xiao, and Yang-Tse Cheng, Mechanical behavior of electroplated mossy lithium at room temperature studied by flat punch indentation, Appl. Phys. Lett. 115, 043903 (2019); https://doi.org/10.1063/1.5111150

5. Jung Hwi Cho, Xingcheng Xiao, Kai Guo, Yuanpeng Liu, Huajian Gao, Brian W Sheldon, Stress evolution in lithium metal electrodes, Energy Storage Materials (2019) DOI: 10.1016/j.ensm.2019.08.008

6. Guo, K.; Kumar, R.; Xiao, X.; Sheldon, B. W.; Gao, H., Failure progression in the solid electrolyte interphase (SEI) on silicon electrodes. Nano Energy 2020, 68, 104257.

Acknowledgements

The PI would like to acknowledge co-PIs: Prof. Brian W. Sheldon, Prof. Huajian Gao at Brown University, Prof. Yue Qi at Michigan State University, Prof. Yang-Tse Cheng at University of Kentucky, Dr. Qinglin Zhang at General Motors R&D Center, graduate students and postdocs: Dr. Binsong Li, Kai Guo, Yuxiao Lin, Yikai Wang.

The team would like to also acknowledge the support from Program Managers Tien Duong at DoE, Patricia Smith at NAVSEA-Carderock, and Aaron Yocum at NETL.

II.5.F Synthesis and characterization of polysulfone-based copolymer electrolytes : High Conductivity, Low Temperature Polymer Electrolytes for Li-Ion Batteries (LBNL)

Bryan D. McCloskey, Principal Investigator
Lawrence Berkeley National Laboratory and University of California, Berkeley
201-D Gilman Hall
Berkeley, CA 94720
E-mail: bmcclosk@berkeley.edu

Tien Duong, DOE Technology Development Manager
U.S. Department of Energy
E-mail: Tien.Duong@ee.doe.gov

Start Date: October 1, 2019 End Date: September 30, 2022
Project Funding: $218,000 DOE share: $218,000 Non-DOE share: $0

Project Introduction

Nonaqueous polyelectrolyte solutions, in which anion motion is slowed through their covalent attachment to a polymer chain, have attracted recent interest as potential high Li^+ transference number (t_+) electrolytes, which have been theorized to improve the efficiency of Li metal stripping and plating. However, fully characterizing liquid electrolyte properties (not just polyelectrolytes, but also traditional binary salt electrolytes) has been challenging from an experimental standpoint for reasons that are not entirely clear. Such transport characterization will be critical to develop an understanding of the influence of electrolyte properties on Li metal stripping/plating performance. In FY20, our project focused on developing capabilities that allow us to understand how molecular level ion dynamics impact macroscale transport properties typically considered relevant for battery performance and modeling. Ultimately, we would like to optimize these transport properties (e.g., create a high conductivity, high t_+ number electrolyte) to enable long-life Li metal batteries. We will continue to address our limited understanding of polyelectrolyte solution ion dynamics through the development of a combined experimental/ computational approach, where the experimentally observed transport properties will be explained by simulations at various time and length scales.

Objectives

This task aims to understand lithium plating and stripping in non-traditional electrolyte systems (specifically, polyelectrolyte solutions) that have been proposed to reduce dendrite formation during lithium stripping and plating due to their high Li^+ transference numbers (t_+). In FY20, we developed capabilities that allow us to understand how ion dynamics in these electrolytes impact macroscale transport properties and Li-metal plating and stripping.

Approach

To understand various aspects of lithium plating and ion transport in these systems, we developed diagnostic and computational modeling techniques. Model polyelectrolytes, based on a robust sulfonated polysulfone chemistry, were used as polyanions, as their properties can be easily tuned via changes in the polymerization chemistry. Solution parameters that can be varied for both polyelectrolyte solutions and concentrated electrolytes included solvent and salt composition, additive inclusion, and the aforementioned polymer properties, all of which can have a profound impact on electrostatic interactions between charged species in solution, as well as interfacial stability and reaction kinetics of the lithium electrode. We developed capabilities that allow an understanding of how molecular-level ion dynamics in these electrolytes impact macroscale transport properties and Li-metal plating and stripping. We optimized electrochemical methods for these electrolytes to evaluate relevant transport properties under the Concentrated Solution Theory framework, which has never been performed on liquid polyelectrolyte solutions. ^1H and ^{19}F nuclear magnetic resonance (NMR) diffusometry were also used to measure single-ion self diffusion coefficients without an applied

electric field; solution viscosity measurements using a state-of-the-art rotating sphere viscometer were performed under entirely air/water-free conditions.

Results

Understanding solvent's influence on transport in polyelectrolyte systems. We showed that Li^+-bearing polyelectrolyte solutions can achieve high conductivities and Li^+ transference numbers when the Li^+ is well-dissociated from the polymer-appended anions. Good dissociation was only observed in strong Lewis basic nonaqueous solvents (for example, dimethylsulfoxide (DMSO)). In order to further understand the role of solvent-backbone and solvent-ion interactions in the ultimate ion-transport properties of polyelectrolyte solutions, we studied the conductivity, viscosity and diffusion of model polysulfone-based polyelectrolyte solutions in DMSO and water (see Figure II.5.F.1 for the structure of the model polysulfone polymer). In both solvents, the polyion, sulfonated polysulfone, is readily soluble and the charged group is known to dissociate, but the neutral backbone polymer is only soluble in DMSO. Marked differences were observed in the transport behavior of polymer solutions prepared from the two solvents, particularly at high concentrations. Comparing this transport behavior to that of the monomer in solution demonstrates a larger decrease in lithium motion in DMSO than in water, even though the bulk viscosity in water increases far more rapidly. We found that the combination of poor backbone solvation with good ionic moiety solvation allowed improved ion dissociation while reducing polyanion mobility for polyelectrolyte solutions in water. This study suggests that tuning polymer backbone chemistry and therefore backbone-solvent interactions could help increase t_+ without sacrificing ionic conductivity. These results were published in Diederichsen et al., ***J. Phys. Chem. B*** (2019), listed under Publications. The team plans to further investigate these properties in the triflimide-based styrene and acrylate ionomer systems in FY21, which should provide model polymers with high degrees of ion dissociation in battery-relevant solvents (e.g., carbonates).

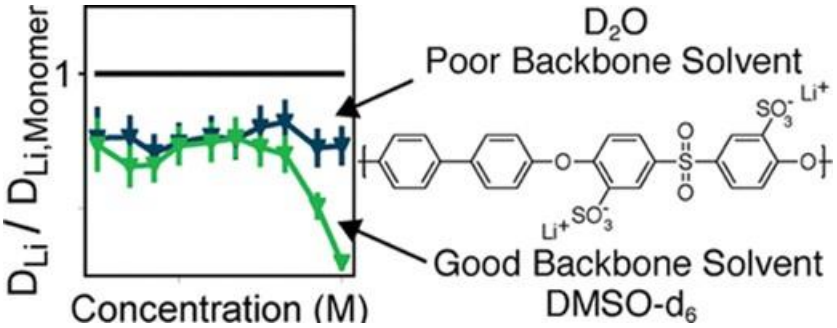

Figure II.5.F.1 Diffusion coefficient of Li^+ as measured via NMR normalized to the monomer diffusion coefficient of sulfonated polysulfone polyions in 2 different solvent system: DMSO and water. In DMSO where the backbone is well solvated, diffusion coefficients drop rapidly at high concentration, whereas this trend is not observed for the aqueous solutions where the polymer backbone is poorly solvated.

Measurement of transport properties of liquid electrolytes. Substantial effort in FY20 focused on understanding limitations in reliability of transference number measurements of liquid electrolytes via the Bruce-Vincent method. We specifically wanted to develop techniques that, when combined, reliably measured the complete transport coefficients, namely conductivity, total salt diffusion coefficient, thermodynamic factor and non-ideal concentrated solution transference number. We focused on implementing the Balsara-Newman method originally developed for polymer and glyme electrolytes. $LiPF_6$ in EC:EMC (3:7 w/w) was chosen as a benchmark due to availability of data on this electrolyte from the Hittorf method. Full transport property measurements were performed and consisted of concentration cell measurements to measure the open circuit potential as a function of solution concentration ($dU/dln(m)$), Bruce-Vincent steady state current measurements to capture ideal transference number (t_+^{id}), restricted diffusion measurements (D), and conductivity measurements (κ). The concentrated solution transference number (t_+^0) was calculated according to Equation 1 once all other parameters were measured.

$$t_+^0 = 1 - \sqrt{\frac{\frac{F^2 D \tau c}{\nu \kappa RT}\left(\frac{1}{t_+^{id}} - 1\right)}{1 + \frac{dln(\gamma_\pm)}{dln(m)}}} \qquad [1]$$

From Figure II.5.F.2, it is clear that significant uncertainty in the final calculated values of the concentrated solution Li^+ transference number, with an average uncertainty of 55% for solutions ranging in concentration from 0.05-1.5 M. We found that these uncertainties were exacerbated primarily by the instability of the lithium metal electrode in carbonate solutions, leading to large cell to cell variability in interfacial resistance. We turned to theory and modeling to understand the interfacial issues occurring during transference number measurements. In order to capture the evolution of the concentration gradients and electrolyte potential during these experiments, a simple 1-dimensional COMSOL model was created for a lithium symmetric cell similar to those used in our laboratory experiments. The concentrated-solution ion transport properties of $LiPF_6$ in EC:EMC (3:7 by wt.) were directly used from the COMSOL material library. At each lithium electrode, a film resistance was added to model the effect of interfacial resistance due to SEI formation. Values for this film resistance (~250 Ω cm^2 per electrode) were directly taken from EIS measurements on our typical Li|Li symmetric cells employing $LiPF_6$ in EC:EMC electrolytes. Potentiostatic polarization experiments with a typical 10 mV bias were modeled for a variety of electrolyte concentrations yielding both the concentration gradient across the cell along with the corresponding liquid electrolyte potential difference across the cell. From this data we observed that only small concentration gradients are achieved at this polarization, on the order of 5 mM for a 1 M electrolyte solution, which corresponds to less than 1 mV of potential drop across the electrolyte.

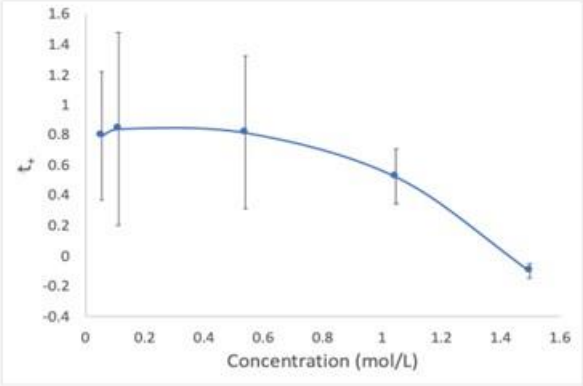

Figure II.5.F.2 Li^+ transference number as measured by the Balsara-Newman method for $LiPF_6$ in EC:EMC (3:7 w/w) as a function of $LiPF_6$ concentration. Error bars represent ± 1 standard deviation.

Looking at an applied voltage breakdown for this system from our COMSOL data, we can clearly see the majority of the applied voltage is used to drive ions through the SEI, with the desired Nernst potential representing less than 2% of the overall applied voltage (see Figure II.5.F.3). This is significant because the polarization experiments rely on our ability to induce a small but significant electrochemical potential gradient across the electrolyte. When the majority of polarization is lost to SEI resistance, it is easy to understand how even small shifts in the interfacial resistance at the electrodes would mask any other phenomena in the cell. The high variability of the results shown in Figure II.5.F.2 are a direct result of this issue: the interfacial resistance entirely dominates the total cell resistance, and hence measuring nuanced changes in the resistance due to the electrolyte's concentration gradient is challenging. This suggests the need to reduce the contribution of the interface through either cell redesign, different electrodes, or alternative non-electrochemical methods. Along these lines, our team has started to explore using lithium-based alloys for these polarization experiments, as well as using colligative properties as an alternative means to calculate the activity coefficient, both of which we will continue to study in FY21. We have initially observed that it is possible to achieve an order of magnitude lower interfacial resistance in Li-Al cells, however we have not yet been able to achieve sufficiently stable electrode potentials over the course of full polarization experiments.

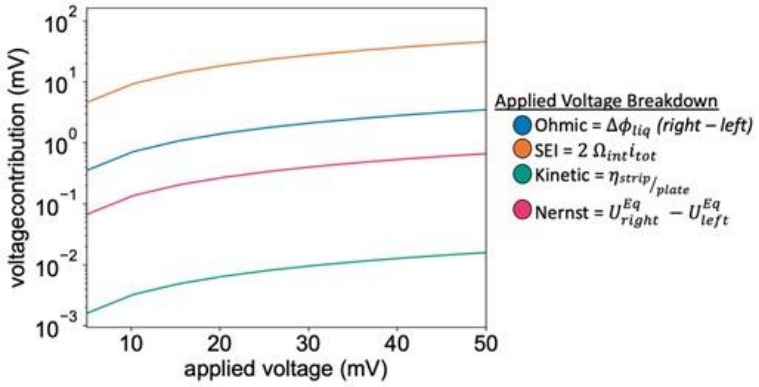

Figure II.5.F.3 Applied voltage breakdown for 1M $LiPF_6$ in EC:EMC (3:7 by wt.) as calculated in a lithium symmetric cell using COMSOL Multiphysics. Note the most significant contribution is from the SEI resistance (using a typical experimentally measured value), with the Nernst potential, the desired measured quantity, representing less than 2% of the applied voltage.

Importance of data fitting ranges in restricted diffusion. We found that diffusion coefficients measured via the restricted diffusion method were particularly sensitive to the data fitting range– with fits over the entire experiment time (>10 minutes) resulting in diffusion coefficients 2 orders of magnitude smaller than those reported in the literature. By restricting the fit window to the characteristic diffusion time for each cell according to the relationship $0.05l^2/D_{\pm} < t_{fit} < l^2/D_{\pm}$ where l is the separation distance between the planar electrodes, we can obtain more accurate salt diffusion coefficients. For example, Figure II.5.F.4 presents our results when fitting relaxation data using the timescale range above, or using an unbounded timescale range (*i.e.*, $t_{fit} > 0.05l^2/D_{\pm}$), compared to prior literature values for 1M $LiPF_6$ in 3:7 wt:wt EC:EMC. The drastic effect of bounding the fit indicates that at longer relaxation times, we are not actually measuring diffusive phenomena and instead likely are measuring surface phenomena related to the slow corrosion of lithium metal electrodes. Despite the new fitting procedure, at low Li concentration in the electrolyte, we still see slight deviation from the diffusion coefficients reported for the $LiPF_6$/EC/EMC electrolyte system. We believe that this deviation can be further reduced by inducing larger concentration gradients prior to measuring diffusion coefficients, effectively increasing the measurement signal to noise ratio. This knowledge is necessary for rigorous analysis of experimental data, but is not discussed in previous reports that characterize liquid electrolytes.

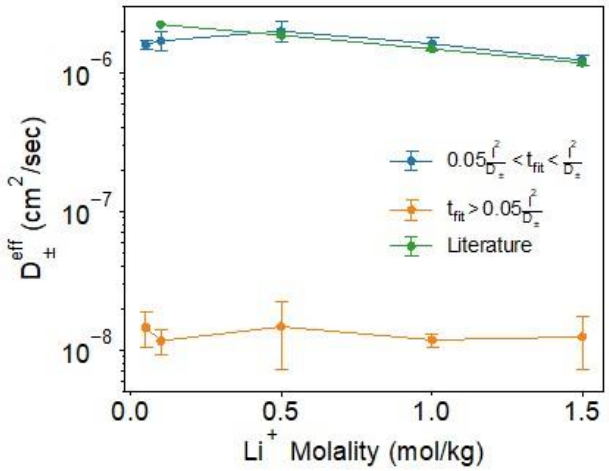

Figure II.5.F.4 Effective diffusion coefficients of $LiPF_6$ in 3:7 EC:EMC in Celgard 2500 as measured by the restricted diffusion method. Different curves represent different data fitting methods. We can observe that restricting the data fitting regime to the characteristic diffusion time (l^2/D) is essential to getting diffusion coefficients of the right order of magnitude. Literature values taken from Landesfield & Gasteiger., J. Electrochem. Soc., 2019, 166, A3079-A3097.

Additionally, we developed a 1D COMSOL model to provide important insight into the necessary fitting window for restricted diffusion experiments. We monitored open circuit voltage concentration and potential profiles in the COMSOL model after polarizing a cell at 10mV for 1 hour (see Figure II.5.F.5). We can see that the concentration profile is almost completely relaxed within 2 minutes of stopping polarization. This suggests that much of the change in OCV that we see at longer time scales is due to other undesirable phenomena, such as SEI formation on freshly plated lithium and surface corrosion. This again highlights the importance of experimental design with polarizations large enough to have induce a sufficiently large concentration gradient to have sufficient signal, but small enough to allow the approximation of local zero-order concentration dependence for transport coefficients.

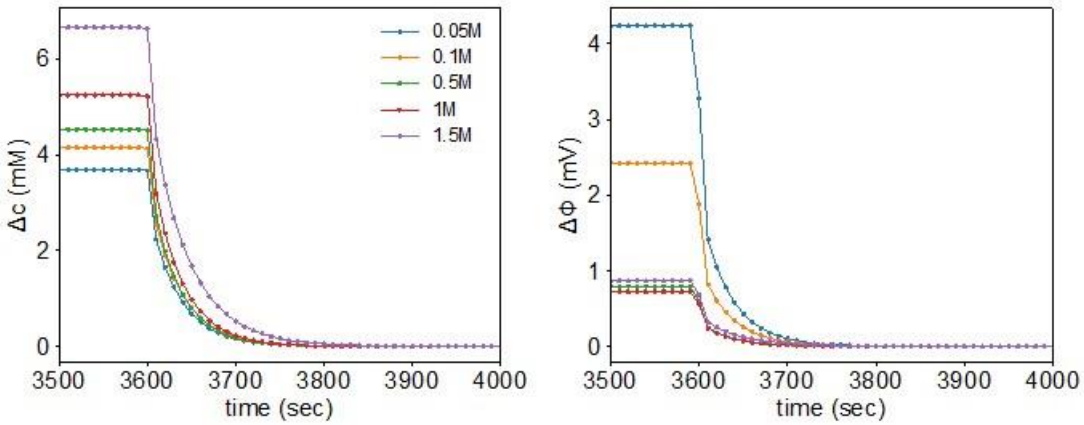

Figure II.5.F.5 Concentration gradient (Δc) and electrolyte potential (Δφ) relaxation across a 250μm lithium symmetric cell after 1 hour of polarization at 10mV for a range of LiPF6 in EC:EMC (3:7) concentrations as modeled in COMSOL Multiphysics.

Coarse grained modelling of polyelectrolyte solution transport properties. In FY20, we also developed coarse-grained molecular dynamics simulations of polyelectrolyte solutions to understand how various compositional effects impact transport behavior (see Fong *et al.*, ***Macromolecules*** (2020) in the Publications section). The simulations were performed using the classical Kremer-Grest bead-spring model and specifically evaluated transport as a function of chain length and concentration. The focus of the work was analysis of the Onsager transport coefficients of these polyelectrolytes, which provide insight into the ion correlations dictating ion motion and allow us to rigorously compute the cation transference number (t_+) of the solutions. Despite the intuitive expectation that these systems should yield high t_+ and the high t_+ predicted by the Nernst-Einstein equation (t_+^{NE}), none of the polyelectrolyte solutions studied exhibit t_+ greater than that of the conventional monomeric (binary salt) electrolytes (Figure II.5.F.6). The trends in t_+ are cleanly rationalized via the systems' strong anion-anion and cation-anion correlations, which the Nernst-Einstein assumption neglects. For long chain lengths and low concentrations, we observe negative cation transference number ($t_+ < 0$), making this work one of the first instances in which negative transference numbers — a contentious topic in the field of polymer-based battery electrolytes — have been rigorously computed using molecular dynamics. We attribute this phenomena of negative t_+ to the presence of long-lived negatively charged aggregates in solution, for example a single cation bound to a long polyanion. Importantly, we demonstrate that trends in cation-anion correlations cannot be predicted from static analysis of the fraction of ion pairs, as is conventional in the molecular dynamics literature, but rather must be understood through a dynamic analysis of ion pair residence times. Our work thus repudiates some of the intuitive assumptions typically made for understanding transport phenomena in polyelectrolytes.

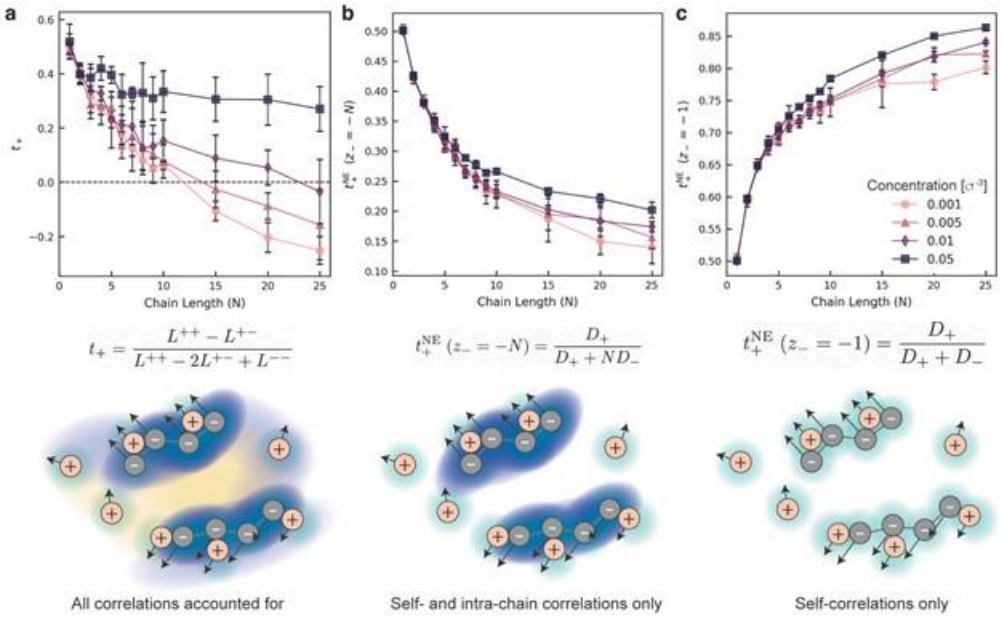

Figure II.5.F.6 Cation transference number as a function of chain length computed from coarse-grained molecular dynamics simulations. (a) Rigorously computed t_+ obtained from the Onsager transport coefficients and accounting for all ion correlations present in solution. (b) and (c) t_+^{NE}, the ideal solution transference number ignoring correlations between ions. (b) Treating entire polymer chains as the anionic species (z_- = -N) accounts for intra-chain correlations but ignores correlations between chains and between cations and anions. (c) Treating individual monomers as the anionic species (z_- = -1) ignores all ionic correlations. From Fong et al., **Macromolecules** (2020) 53, 9503.

We have also used the coarse-grained molecular dynamics model to investigate polymerized ionic liquids, i.e., polyelectrolyte solutions with no added solvent. We have derived the special theoretical considerations necessary for two-component systems, which dictate that the transference number is only a function of the ions' charge and molar masses. For the current model, this corresponds to a transference number of exactly 0.5 for all chain lengths. In these systems we also observe anti-correlated cation-anion motion, as has been previously observed in non-polymeric ionic liquids.

Although this work suggests that unentangled, short-chain polyelectrolyte solutions may not be useful as high t_+ alternatives to conventional LIB electrolytes, the insights we gained here suggest several avenues for more promising systems. It is possible that polyelectrolyte solutions or gel-like single-ion conductors may be able to attain high cation transference number if the chains are entangled or cross-linked such that the polymer is effectively immobile. The slow dynamics and complex structure of these systems precludes us from studying them with molecular dynamics, so we will focus on experimental characterization of these polymers in the coming quarter. We anticipate that while these systems may have higher transference number, they will also have lower conductivity; we will need to consider this trade-off when developing optimal electrolyte formulations.

Conclusions

The key conclusions from our research this year are:

1. When selecting a polyelectrolyte solvent, a combination of poor backbone solvation and good ion solvation allows improved ion dissociation while reducing polyanion mobility for polyelectrolyte solutions, thereby enhancing their Li^+ transference number.

2. When characterizing liquid electrolyte transport using polarization measurements involving planar Li electrodes, the interface overwhelms the overall cell resistance, such that any variability in the interfacial resistance is roughly of the same order of magnitude as the bulk electrolyte resistance. As a result, the development of low interfacial impedance electrodes is critical for such measurements, or entirely new

strategies to quantify the Bruce-Vincent transference number besides polarization measurements are needed.

3. When measuring salt diffusion coefficients, background Li metal corrosion can induce a transient voltage relaxation that impacts data fitting. We described a rational data fit time scale that should be implemented in any future analyses of such data.

4. Coarse-grained molecular simulations of polyelectrolyte solutions capture correlated ion motion to show that negative Li^+ transference numbers can occur at high polymer molecular weights. Our models suggest that polyelectrolyte solutions or gel-like single-ion conductors may be able to attain high cation transference number if the chains are entangled or cross-linked such that the polymer is effectively immobile.

Key Publications

1. Diederichsen, K. M.; Terrel, R. C.; McCloskey, B. D. "Counterion transport and transference number in aqueous and nonaqueous short chain polyelectrolyte solutions." ***Journal of Physical Chemistry B*** (2019), 123(50), 10858-10867.
2. Diederichsen, K. M.; McCloskey, B. D. "Additive engineering to enable nonaqueous polyelectrolyte solutions for lithium ion batteries." ***Molecular Systems Design and Engineering*** (2020), 5, 91-96.
3. Grundy, L. S.; Shah, D. B.; Nguyen, H. Q.; Diederichsen, K. M.; Celik, H.; DeSimone, J. M.; McCloskey, B. D.; Balsara, N. P. "Impact of frictional interactions on conductivity, diffusion, and transference number in ether- and perfluoroether-based electrolytes." ***Journal of the Electrochemical Society*** (2020), 167(12), 120540.
4. Fong, K. D.; Self, J.; McCloskey, B. D.; Persson, K. A. "Onsager Transport Coefficients and Transference Numbers in Polyelectrolyte Solutions and Polymerized Ionic Liquids." ***Macromolecules,*** (2020) 53, 9503.
5. Fong, K. D.; Bergstrom, H. K.; McCloskey, B. D.; Mandadapu, K. K. "Transport phenomena in electrolyte solutions: Non-equilibrium thermodynamics and statistical mechanics." ***AIChE Journal***, (2020), e17091.

Gordon Research Conference on Batteries, Ventura, California (February 16 – 21, 2020): "Li-Ion Transference Numbers in Nonaqueous Polyelectrolyte Solutions." (Poster); Kara Fong

7. The Electrochemical Society (ECS) PRiME 2020 (virtual, Oct. 4-9, 2020): "Characterizing Ion Transport in Non-Aqueous Electrolyte Solutions for Li-Ion and Li- Metal Batteries"; Helen Bergstrom
8. Battery Modeling Webinar Series (virtual, Oct. 6, 2020): "Transport Phenomena in Electrolyte Solutions: Non-Equilibrium Thermodynamics and Statistical Mechanics"; Kara Fong
9. American Institute of Chemical Engineers (AIChE) Annual Meeting, Orlando, Florida (November 10-15, 2019): "Influence of Backbone Solvation on Polyelectrolyte Solution Transport Properties"; Kyle Diederichsen.
10. American Institute of Chemical Engineers (AIChE) Annual Meeting, Orlando, Florida (November 10-15, 2019): "Charge Transport in Nonaqueous Polyelectrolyte Solutions for Li-Ion Batteries: Ion-Ion Correlations and the True Transference Number from Molecular Dynamics Simulations"; Kara Fong

Acknowledgements

B.D.M. gratefully acknowledges his colleagues- Kyle Diederichsen, Kara Fong, and Helen Bergstrom- who performed this work, as well as the fruitful computational collaboration with Prof. Kristin Persson and theory collaboration with Kranthi K. Mandadapu.

II.6 Next Generation Lithium-Ion Batteries: Modeling Advanced Materials

II.6.A Electrode Materials Design and Failure Prediction (Argonne National Laboratory)

Venkat Srinivasan, Principal Investigator
Argonne National Laboratory
9700 S. Cass Avenue,
Lemont, IL 60439
E-mail: vsrinivasan@anl.gov

Tien Q. Duong, DOE Technology Development Manager
U.S. Department of Energy
E-mail: Tien.Duong@ee.doe.gov

Start Date: October 1, 2019 End Date: September 30, 2020
Project Funding: $1,460,000 DOE share: $1,460,000 Non-DOE share: $0

Project Introduction

The largest bottleneck faced by the lithium ion batteries (LIBs) of the next generation are their limited energy densities and specific energies. It is hypothesized that adoption of lithium metal anodes can effectively help to improve the energy density of existing LIBs. However, Li metal demonstrates the formation and growth of dendrites, which can short the cell under moderate operating conditions. Solid electrolytes (SEs) are expected to stabilize the Li anodes through the suppression of these dendritic protrusions. In a true LIB, along with anode/electrolyte interface, there also exists the cathode/electrolyte interface, which is equally important to achieve good performance from these LIBs with solid electrolytes. In the present research, LLZO based oxide solid electrolytes are being studied due to their high modulus, desirable room temperature conductivity and good electrochemical stability against Li metal. Since NMC and LCO are two very widely used cathode materials used in present day LIBs, the interfacial aspects at the NMC/LLZO and LCO/LLZO cathode electrolyte interface will be investigated here. Interfacial delamination and interdiffusion of ions during the synthesis and operation are the two major bottlenecks experienced by the cathode/solid-electrolyte interfaces, which tends to increase the interfacial impedance. In the present work, difference in interfacial delamination experienced by NMC and LCO cathodes will be investigated. Impact of exchange current density on the delamination induced capacity fade will also be reported. Finally, how to minimize the delamination induced capacity fade by incorporating interfacial layers will be studied.

Since adoption of Li metal anodes can help to improve the energy density of present day LIBs substantially, further investigation has been conducted to understand the deposition of Li on top of the metal electrode during the charge process. A detailed computational methodology has been developed to investigate the nucleation and propagation of dendrites during Li deposition on top of Li electrodes.

There is growing interest in the development of Li-metal-based solid state batteries, driven by their promise in improving the energy density to satisfy electric vehicle requirements. Solid polymer electrolytes (SPEs) have been studied as one of the promising candidates for lithium metal batteries because of the advantages of the non-flammability and relatively higher mechanical properties than liquid electrolytes. Compared to existing batteries based on liquid electrolytes, solid polymer electrolytes still have limitations, such as low ionic conductivity under room temperature conditions, which can significantly hinder its application in EVs. Hence, research on next-generation solid polymer electrolyte is being conducted to improve its transport properties. In this project, by using a model-based approach, the status of the present-day solid polymer electrolyte battery is examined, and compared with the traditional batteries with liquid electrolyte, with a focus on EVs.

Objectives

The main objective of this project is to develop computational methodologies to capture the relevant degradation phenomena encountered by the next generation LIBs and devise strategies to mitigate them. For the cathode/solid-electrolyte interface, a mesoscale level computational methodology will be developed capable of capturing the extent of interfacial delamination during charge and discharge processes. The model will also be extended to predict the effectiveness of interphase layers in minimizing the detachment between the cathode and solid-electrolytes. Apart from the cathode/solid-electrolyte interface, further model development has been conducted as part of this project where the Li deposition phenomena has been investigated on top of a planar metal electrode. Since, deposition of Li happens through a nucleation and growth mechanism, the present model captures both the physical phenomena. Dependence of nucleation density and deposit size on the evolution of over-potential will also be investigated.

The main objective of the second part of this project is to evaluate the present status of state-of-the-art SPE's for EVs by comparing their performance to that of liquid electrolytes, the presently used electrolyte, using Li metal anode and lithium iron phosphate (LiFePO4) cathode. Here, we investigated $LiFePO_4$ (LFP) cathode/lithium metal anode batteries containing three different electrolytes, namely (1) a liquid electrolyte, (2) the polystyrene-b-poly(ethylene oxide) (SEO) block copolymer electrolyte, and (3) a single-ion conducting (SIC) block copolymer electrolyte, with the liquid electrolyte serving as the baseline for the comparison. We achieve these objectives by developing a mathematical model for Li-metal based SPEs (both with low and unity transference number) and verify the model's applicability with experimental data. A second objective of the project is to establish targets for these SPE's in order to make the performance of Li-metal/SPE/LiFePO4 all solid-state batteries comparable to equivalent liquid electrolyte batteries. Thus, this model is used to optimize the design (volume fraction of the different phases and thickness) to maximize the energy density while simultaneously allowing the power density requirements for EVs are satisfied.

Approach

In order to address the cathode/solid-electrolyte interphase problems mentioned earlier, a computational methodology have been developed, based on a combination of lattice spring method and finite volume method, that can capture the evolution of potential field and mechanical deformation within the SSEs. This technique has been used to predict the extent of delamination that occurs at the cathode/SSE interface. Butler-Volmer based reaction current have been assumed at the electrode/electrolyte interface for both cathode and anode. The impact of mechanical stress induced electrochemical potential on the reaction kinetics has also been taken into account.

For modeling the nucleation and growth of the Li deposits, the following computational scheme have been adopted. The results show the initial stages of reaction-limited growth during Li electrodeposition. It includes two processes - the formation of new Li nuclei and their subsequent growth. Appropriate rate expressions were developed using non-equilibrium thermodynamics. The growth mechanism is captured using Butler-Volmer reaction kinetics with a curvature term. The final governing equations are a system of coupled ordinary differential equations and were solved numerically using an in-house code.

To achieve the objectives mentioned in the second part of this project, physics-based models have been developed for three lithium metal anode batteries with different electrolytes: the liquid electrolyte, the SEO polymer electrolyte, and the SIC polymer electrolyte. When designing the cell, in practitioners modify on the thickness and volume fractions for each material set to obtain a unique design that takes advantage of each material's individual properties. Therefore, we mimic this iterative process by using the mathematical model. We first compare the three cells, fairly by setting them to the same electrode design. Subsequently, to identify the cell design that maximizes the specific energy, we obtain Ragone plots by changing the cathode thickness and porosity or polymer content to examine differences between the current SPEs-based cells and the liquid electrolyte-based cell in terms of specific energy and power. Finally, we present targets for improving the transport properties of transference number, ionic conductivity, and diffusivity for the current polymer or hypothesis polymer suggested in this work to achieve the performance level of the liquid electrolyte-based cell.

Results

Elucidate the difference in delamination mechanisms for NMC/LLZO and LCO/LLZO type cathode/solid-electrolyte interfaces. Due to the high elastic modulus and non-conformability of solid state electrolytes (SSEs), the interface between cathodes and SSEs are prone to rupture and detachment. During lithiation and delithiation process, the cathode particles expand or contract, which depends on the partial molar volume of lithium within the cathode material. As the cathode shrinks, tensile stresses evolve at the cathode/SSE interface because the solid electrolytes cannot change its shape easily to accommodate the volume change within the cathodes. If the magnitude of tensile stress exceeds its fracture threshold, delamination would occur at the interface of cathode and SSEs. Figure II.6.A.1(a) and Figure II.6.A.1(b) demonstrates the partial molar volume of lithium within NMC and LCO cathodes, respectively. In NMC, the partial molar volume of Li is positive, which means during charge as Li goes out, the cathode material shrinks and induces tensile stress at the interface. This eventually leads to delamination at the NMC/LLZO interface at the time of charge process. Whereas the partial molar volume of Li within LCO is negative for the voltage range of battery operation. Hence, the cathode expands as Li goes out during charge, and shrinks at the time of discharge process when Li ions move into the LCO lattice. As a result, tensile stress at the LCO/LLZO interface is observed at the time of discharge, and majority of the delamination occurs at that time.

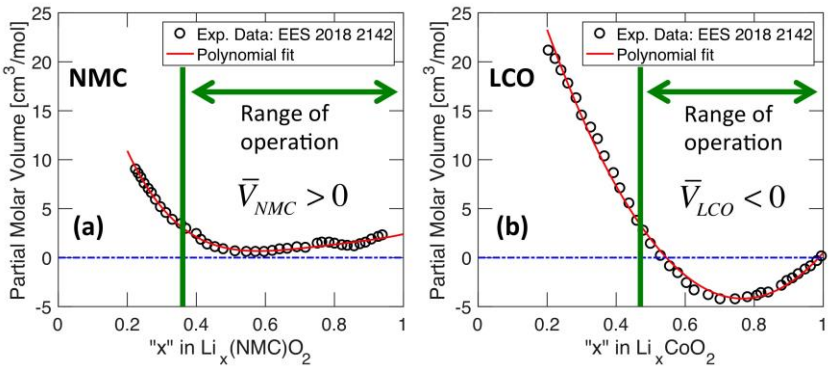

Figure II.6.A.1 (a) Concentration dependent partial molar volume of lithium within NMC cathodes. (b) Partial molar volume of Li within LCO cathodes. It is evident that within the range of operation, NMC and LCO demonstrate positive and negative partial molar volumes with respect to Li, which impacts their performance.

The charge discharge curve as observed in NMC and LCO cathodes with LLZO SSE is shown in Figure II.6.A.2(a) and Figure II.6.A.2(b), respectively. As mentioned earlier, major interfacial delamination occurs for NMC during charge, and for LCO during the discharge process. This interfacial delamination leads to increase in charge transfer resistance, and eventually, discharge capacity fade. Both the NMC and LCO cathodes have been operated under CCCV charge and CC discharge protocol under an applied current density of 1A/m^2. It has been argued that decreasing the LLZO grain size can help to minimize the delamination induced capacity fade. Accordingly, the capacity fade experienced by LCO and NMC cathodes with various LLZO grain sizes have been demonstrated in Figure II.6.A.2(c). For both NMC and LCO, adoption of smaller LLZO grains can minimize capacity fade. This analysis shows the correlation between the delamination induced capacity fade experienced by LCO and NMC cathodes.

Investigate impact of exchange current density on delamination-induced capacity fade. If effect is minor, use experimentally observed exchange current values. In the previous quarter we reported the difference in interfacial delamination experienced by the NMC and LCO type cathodes at the cathode/solid-electrolyte interface due to their difference in partial molar volumes with respect to lithium. In the present quarter, we investigated the impact of exchange current density on the interfacial capacity fade experienced by the NMC and LCO type cathodes while operating with solid-electrolytes. The exact magnitude of exchange current density at NMC/LLZO interface as well as LCO/LLZO is difficult to determine using experimental procedures. In the present context, the exchange current density between cathode and LLZO have been estimated from the interfacial charge transfer resistances (R_{ct}). A correlation between exchange current

density (i_0) and the charge transfer resistance can be estimated from the linearization of the Butler-Vomer equation: $i_0 = RT/(FR_{ct})$, where, R stands for universal gas constant, T indicates temperature, and F denotes Faraday's constant. A list of charge transfer resistance values, at NMC/LLZO and LCO/LLZO interfaces, reported by different experimental researchers, and corresponding exchange current densities, are provided in Table II.6.A.1.

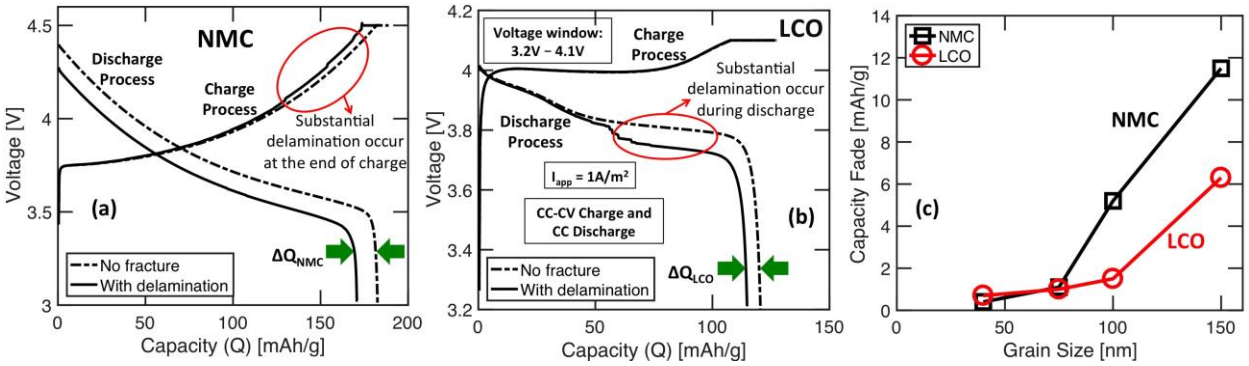

Figure II.6.A.2 (a) Performance curves demonstrated by NMC cathodes with LLZO electrolytes. Substantial delamination induced impedance rise observed during charge, which leads to capacity fade during discharge. (b) Charge/discharge performance curves experienced by the LCO cathodes with LLZO electrolytes. Major delamination induced impedance rise, and subsequent capacity fade, occurs during the discharge process. (c) LLZO grain size dependent discharge capacity fade experienced by NMC and LCO cathodes. Smaller grains help to minimize the delamination induced capacity fade in both the cathode materials.

Table II.6.A.1 Experimentally observed exchange current densities at the cathode/solid-electrolyte interface

Type of cathode electrolyte interface	Interfacial charge transfer resistance $(\Omega.cm^2)$	Exchange current density (A/m^2)	Reference
NMC/LLZO	2000	0.1284	ACS AMI (2019) 4954
LCO/LLZO	600	0.428	Chem. Mater. (2018) 6259
LCO/LLZO-Nb	170	1.51	JPS (2012) 332
LCO/LiPON	720	0.3566	JPS (2016) 342
LCO/LLZO	101	2.56	Joule (2018) 497

Please note that these exchange current densities are always affected by the presence of surface impurities, or other kind of solid electrolyte interphase layers. Following all these experimental observations, the exchange current density at the NMC/LLZO interface have been varied between 0.1A/m^2 and 5.5A/m^2, whereas the exchange current density of LCO/LLZO interface have been altered between 0.2 A/m^2 and 2.0A/m^2. DFT calculations revealed that the exchange current density at NMC/LLZO interface should be around 5.5A/m^2. Extent of interfacial delamination, and subsequent capacity fade, at the NMC/LLZO and LCO/LLZO interface has been demonstrated in Figure II.6.A.3(a) and Figure II.6.A.3(b), respectively. Since exchange current density does not influence the magnitude of stress generation, the amount of delamination is independent of i_0 for both NMC/LLZO and LCO/LLZO interfaces. However, increasing i_0 helps to minimize the interfacial potential drop, which leads to suppression in capacity fade. Since the change in capacity fade with i_0 is substantial, we will use the exchange current density obtained from DFT calculations, which is around 5.5A/m^2 for NMC/LLZO interface.

Develop continuum model for charge transport and mechanical degradation incorporating an interphase layer between LLZO electrolyte and NMC cathode. It has been demonstrated in the earlier quarters that substantial detachment occurs between the NMC cathodes and LLZO solid electrolytes during operation, which leads to loss of electrochemically active surface area, and subsequent increase in interfacial charge transport resistance.

It has been argued that incorporation of interphase layers, such as LBO (Li_3BO_3) and/or LBCO (Li_3BO_3-Li_2CO_3), can substantially help to mitigate the interfacial resistance growth. It has been experimentally demonstrated that LBCO can prevent the inter-diffusion of transition metal ions from the cathode to the electrolyte, and vice-versa, during synthesis as well as charge-discharge operation. Impact of LBCO coating layers on the extent of interfacial delamination has not been investigated yet. In the present quarter, we implemented an LBCO interphase layer between the NMC cathode and LLZO solid electrolytes. Single ion conduction behavior has been assumed within the LBCO interphase layers. Conductivity of LBCO has also been assumed to be two orders of magnitude smaller than the conductivity of LLZO ceramic sold electrolytes. Exchange current densities at NMC/LBCO and LBCO/LLZO interface has been assumed to be same as the NMC/LLZO interfacial region. Fracture energies at the NMC/LBCO and LBCO/LLZO interface have also been assumed to be 3 times and 2 times larger than the NMC/LLZO interface, respectively. These magnitudes of fracture energies have been obtained from the atomistic calculations. Figure II.6.A.4(a) and Figure II.6.A.4(b) demonstrates the NMC/LBCO/LLZO cathode/interphase-layer/solid-electrolyte microstructure with two different thicknesses of the interphase layer, 5 nm and 25 nm, respectively. Extent of fractional delamination with and without the LBCO interphase layer has been demonstrated in Figure II.6.A.4(c).

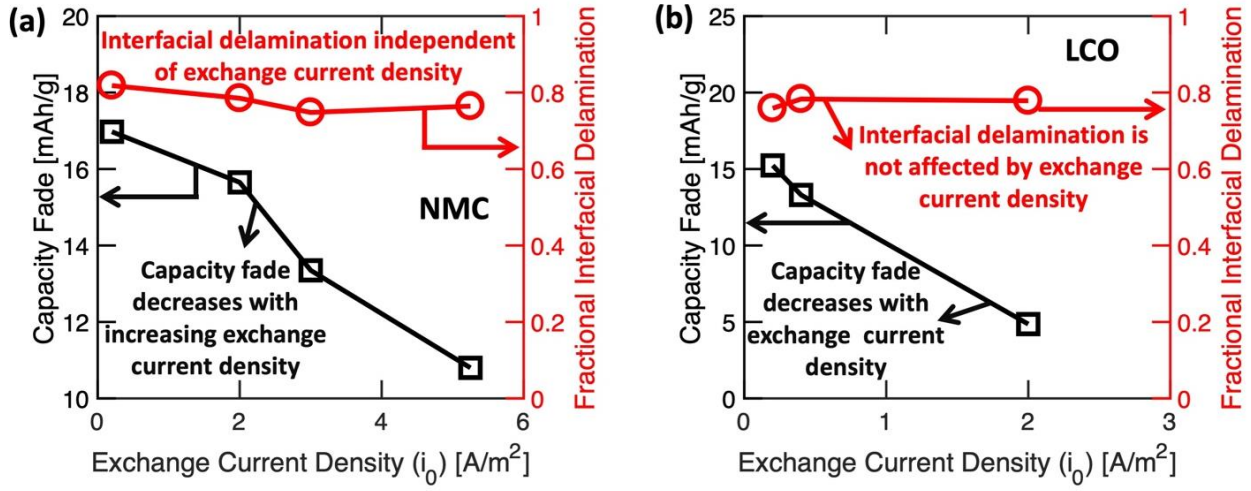

Figure II.6.A.3 Impact of exchange current density on the interfacial delamination and capacity fade. (a) NMC/LLZO interface. (b) LCO/LLZO interface. Applied current density is 1A/m^2. For both NMC and LLZO, extent of delamination is independent of exchange current. However, the capacity fade decreases with increasing exchange current density.

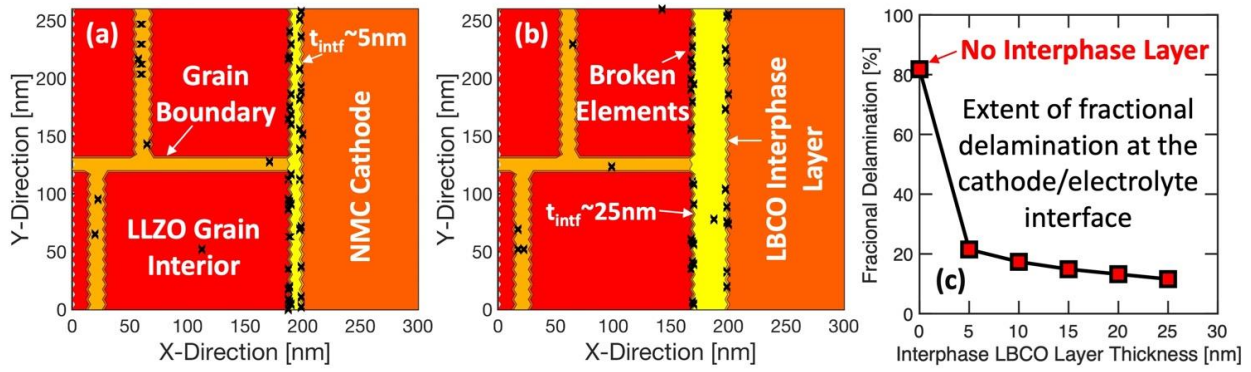

Figure II.6.A.4 (a) NMC/LLZO cathode electrolyte microstructure with a 5 nm thick LBCO interphase layer in between. (b) NMC/LBCO/LLZO cathode/interphase-layer/electrolyte microstructure with thickness of interphase layer being 25 nm. (c) Evolution of fractional delamination with increasing thickness of the LBCO interphase layer. Addition of interphase layer helps to minimize the delamination.

The voltage vs. capacity performance curves, with and without LBCO interphase layers, have been demonstrated in Figure II.6.A.5(a). The discharge capacities obtained with different thickness of the interphase layers has been depicted in Figure II.6.A.5(b). It is evident that addition of LBCO helps to improve discharge capacity, and prevents the increase in interphase resistance.

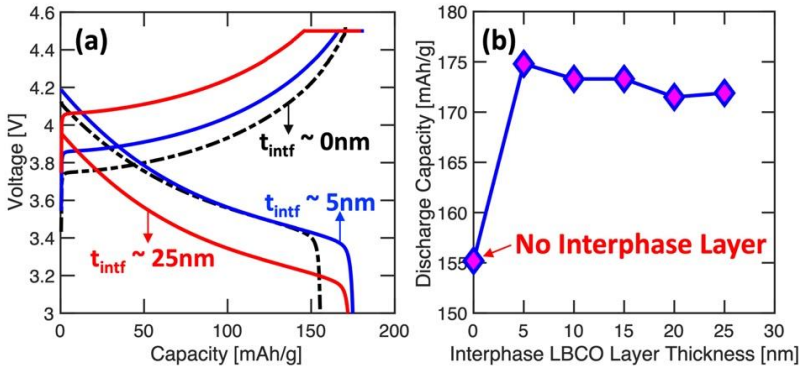

Figure II.6.A.5 (a) Voltage vs. capacity performance curves with interphase layer thickness 0 nm (black dashed line), 5 nm (blue line), and 25 nm (red line). (b) Discharge capacity with increasing thickness of the interphase layer. Addition of interphase layer helps to minimize delamination and enhances discharge capacity. Increasing thickness of interphase layer also increases the ohmic resistance.

Gain understanding of growth rate of electrodepositing lithium nuclei. Previous studies have shown that any nonuniformity at the lithium surface can trigger irregular unstable growth. When Li is electrodeposited on Li covered with a surface film or on another substrate, it does not immediately grow as a planar front. Such fresh deposition requires forming new contacts between fresh Li and preexisting surface, and in turn, it follows nucleation and growth dynamics. The depositing interface is nonuniform during this process, and we describe this dynamics using the Classical Nucleation Theory and Nonequilibrium thermodynamics for electrodeposition reaction. The electrode averaged current contributes to (i) nucleation – formation of new nucleation sites and (ii) growth – of the activated sites. For the current densities of interest and representative site density, N_0, values for substrates in contact with liquid electrolytes, all sites are activated almost instantaneously. And at subsequent times, these sites grow via electrodeposition. Figure II.6.A.6(a) plots overpotential evolution for galvanostatic deposition. Initially high overpotential is needed to activate the nucleation sites, and subsequently, the overpotential decays as growth progresses. Corresponding size evolution for each nucleus is shown in Figure II.6.A.6(b). If the growth remains reaction-limited, these individual nuclei will coalesce once they become large enough (comparable to the average separation between nucleation sites) and eventually form a uniform film. Note that the nucleation and growth dynamics plays out at very early times ~seconds as shown in Figure II.6.A.6.

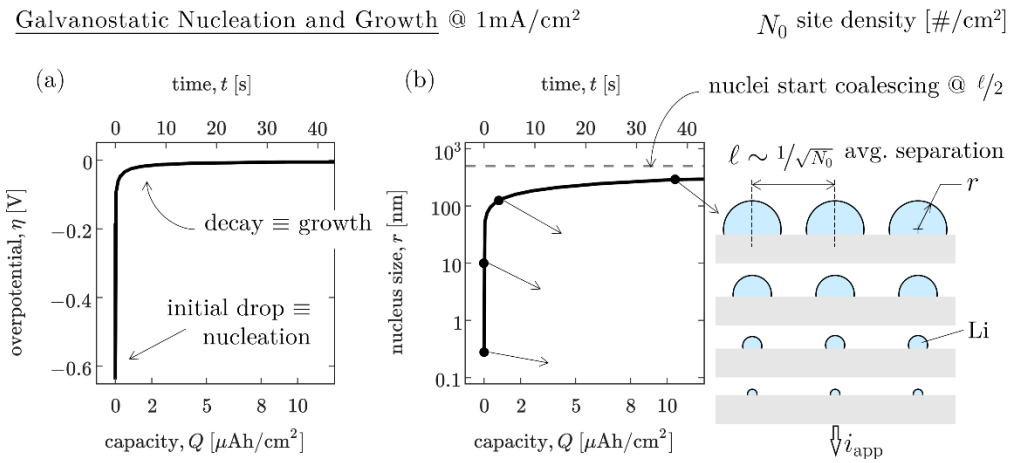

Figure II.6.A.6 Short-time electrodeposition is due to nucleation and growth. Accordingly, time evolution of (a) overpotential and (b) nucleus size are interrelated. The nuclei coalesce and form a film at late times.

For the same electrode average current, the current per nucleus scales with the site density. Hence, the nuclei grow faster and larger at smaller site densities as shown in Figure II.6.A.7(a). The nucleus size for different site density and the same amount of deposition (10 μAh/cm²) is shown in Figure II.6.A.7(b). Even if these initial stages represent fundamentally nonuniform growth, if the growth is reaction limited, the nuclei coalesce and transition to a uniform film (= stable growth). The nuclei need to grow more to coalesce at smaller site densities (Figure II.6.A.7(b)). This would indirectly allow more time for electrolyte concentration gradients to manifest which may cause unstable growth if mass transport becomes limiting. Thus, smaller site densities are more prone to unstable growth before the transition to the film growth can take place.

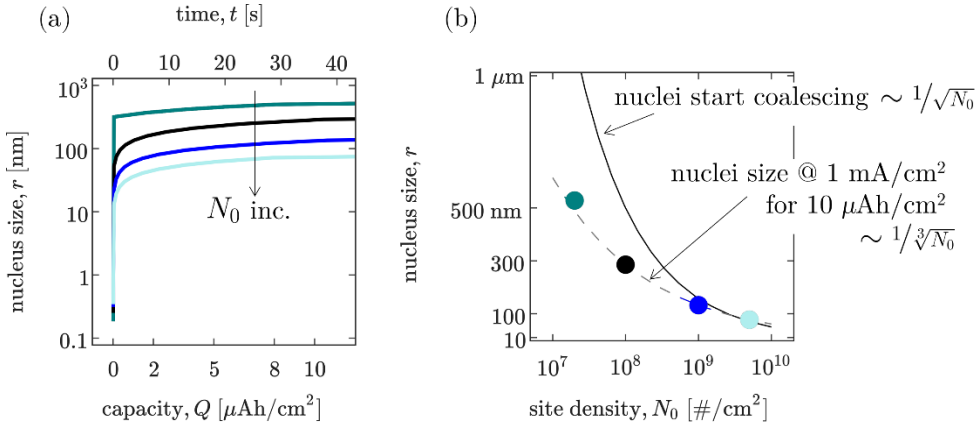

Figure II.6.A.7 When deposited at the same electrode averaged current density, the current per nucleus scales with the site density. (a) The size evolves faster at smaller site density. (b) Hence, at the same deposition capacity, larger nuclei form at smaller site densities.

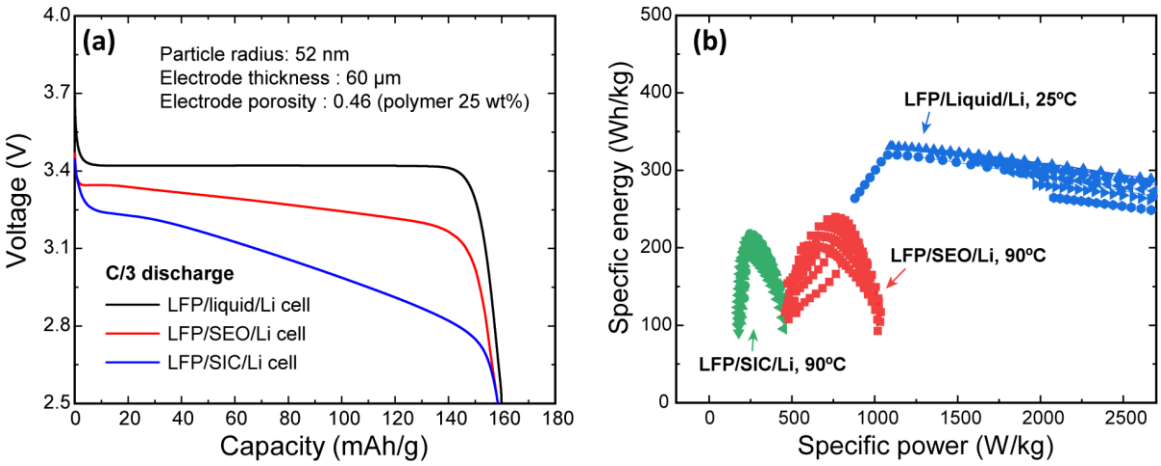

Figure II.6.A.8 (a) Modeling-based comparison of results of the three cells under the same electrode design: with electrode thickness of 60 μm, porosity of 0.46, particle size of 52 nm (radius), and other operating conditions. (b) Comparison of specific power vs specific energy (Ragone plot) following the DOE-USABC protocol to compare the status of the three cells.

Comparison of three cells under the same electrode design and optimization for the three cells: Figure II.6.A.8(a) shows the discharge behaviors of the three cells under the constant current density with C/3-rate. The capacities for all the three cells were about 160 mAh/g; the LiFePO4/liquid-electrolyte/Li has a lower voltage drop than those of the two other cells during the same span of time because of its higher ionic conductivity and smaller concentration gradient. In case of LiFePO4/SEO/Li cell, it can be seen that the voltage loss due to the concentration gradient is more dominant that the ohmic voltage loss caused by lower conductivity. Note that the voltage loss of the LiFePO4/SIC/Li cell is only from lower conductivity because there is no concentration gradient due to transference number being 1.0. The specific energy vs specific power plots for liquid, SEO and SIC electrolytes are compared in Figure II.6.A.8(b), and the optimum design conditions are selected in terms of electrolyte thickness and porosity. For optimization study, we estimated the specific energy and power of the three cells using the EV protocol provided by DOE-USABC. Following the USABC manual, the specific energy of the three cells was evaluated from the C/3 discharge until cell voltage reaches cutoff of 2.5 V and the specific power was determined from the 30 s discharge pulse at 1C rate at 80% depth of discharge (DOD) following the Peak Power Test (PPT). The optimized specific energy of the liquid electrolyte cell is about 330 Wh/kg, which is within 95% of the cell-level target point for EVs suggested by the USABC. The LiFePO4/SEO/Li cell has slightly better usable energy and power levels than the LiFePO4/SIC/Li cell; however, it is still significantly lower than those of the LiFePO4/liquid-electrolyte/Li cell.

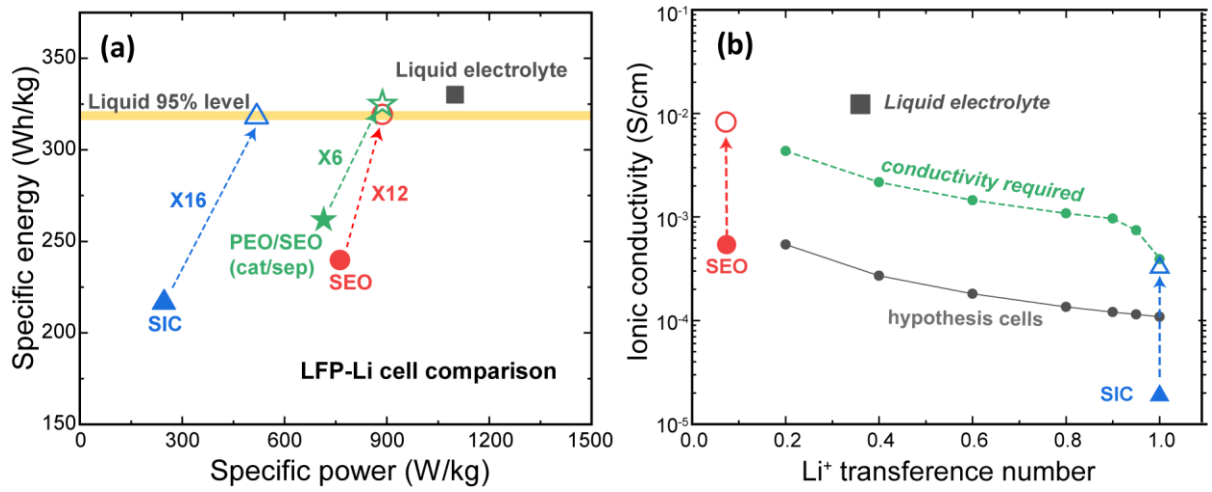

Figure II.6.A.9 (a) Comparison of increasing factor in which SPEs-based cells should be enhanced to reach specific energy levels of liquid electrolyte-based cells and (b) The trend of required ionic conductivity to satisfy the specific energy of the liquid-electrolyte-based cell as the transference number increases.

Targets for polymer electrolytes: The poor ionic conductivity for SPEs needs to be resolved before these cells can be expected to achieve the specific energy comparable to the liquid electrolyte-based cell. We investigated how much the ionic conductivity and diffusion coefficient of the SEO and SIC polymer electrolytes needs to be enhanced to reach the specific energy target. Figure II.6.A.9(a) shows the results of the specific energy for SPEs-based cells when the ionic conductivity increases. In order to reach a specific energy level within 95% of the level of the liquid-electrolyte-based cell, the ionic conductivity needs to improve by about 12 times for the SEO polymer and by about 16 times for the SIC polymer. To investigate the required ionic conductivity to satisfy the targeted specific energy level as the transference number improves, we simulated hypothetical cells having transference numbers from 0.2 to 1.0 as shown in Figure II.6.A.9(b). The results revealed that the required ionic conductivity, which enables a specific energy level as high as the level reached in a liquid electrolyte cell, decreases if the transference number increases. One interesting pattern is observed in the cells with a transference number greater than 0.9, where the required conductivity suddenly decreases. It should be noted that hypothetical cells with a transference number of less than 0.9 require about 8 times higher ionic conductivity. On the other hand, in cells with a transference number greater than 0.9, only 4 times higher ionic conductivity is needed to achieve the targeted specific energy. The result shows the importance of developing high transference number polymers to ensure that the conductivity targets are minimized. However, the advantages are significant only for transference numbers greater than 0.9.

Conclusions

A multiscale computational methodology has been developed capable of predicting the extent of delamination that can occur at the interface between cathode and solid state electrolytes. A mesoscale level computational model has been developed, where the continuum level mass, charge and momentum balance equations have been solved to capture the detachment between cathode and SSEs during charge and discharge operation. Two different cathode materials have been investigated, namely NMC and LCO. Lithium demonstrates positive magnitude of partial molar volume within NMC, whereas, in LCO, Li shows a negative magnitude of partial molar volume, at least within the potential window of operation. Due to this variation in the partial molar volume of Li within the cathode material, delamination at the NMC/LLZO interface occurs during the charge process, whereas detachment at the LCO/LLZO interface occurs at the time of discharge. Exchange current density at the cathode/solid-electrolyte interface, or in other words the interfacial resistance, shows negligible impact on the extent of delamination, but demonstrates influence on the amount of delamination induced capacity fade. Also, adoption of interphase layers can help to minimize the extent of delamination experienced by the cathode and solid-electrolytes. However, due to its lower ionic conductivities, adoption of interphase layers can lead to enhanced ohmic potential drop, and subsequently minimized energy densities of the cell.

To enable lithium metal anodes, it needs to electrodeposit uniformly such that a flat lithium - electrolyte interface is maintained. However, when Li deposits on Li covered with an SEI film or on another substrate, the initial electrodeposition is not uniform and manifests as individual growing nuclei. If the nucleation site density (# nuclei/ unit interface area) is large, these individual nuclei grow and coalesce to form a uniformly growing interface. Alternatively, when the nucleation site density is small, the nuclei grow independently. The individual growth represents a nonuniform interface which likely leads to unstable growth, and is a focus of the ongoing work.

Regarding the optimization of the solid polymer electrolytes, we conducted mathematical simulations to investigate polymer-based, solid-state batteries for EV application. A mathematical model was used to compare three cells, all with LiFePO4 composite cathode and lithium metal anode, but with different electrolytes: a conventional liquid electrolyte, a SEO polymer electrolyte, and a SIC polymer electrolyte. After model validation, an optimization procedure was implemented using the USABC protocol to maximize energy density with also satisfying the pulse power requirements for different battery designs. The findings are summarized below:

1. The optimized specific energy of the LiFePO4/liquid-electrolyte/Li cell is about 330 Wh/kg, however, the SPEs-based cells achieve less than 75% specific energy of liquid electrolyte-based cell.

2. SPEs' ionic conductivity needs to increase by about 12 times for the LiFePO4/SEO/Li cell and by about 16 times for the LiFePO4/SIC/Li cell. Note that if SEO were used as a separator, while PEO were used in the cathode composite, the required ionic conductivity only needs to increase by 6 times to reach the level of the LiFePO4/liquid-electrolyte/Li cell.

3. From the optimization study with increasing transference numbers, we found that increasing transference number allows lowering of the required conductivity, but significant changes only occur at transference numbers above 0.9.

These simulations, along with simulations on dendrite growth reported by our group, provide guidance to polymer scientists to ensure development of materials that can aid in developing solid polymer based solid state batteries for EV applications.

Key Publications

1. Pallab Barai, Anh Ngo, Badri Narayanan, Kenneth Higa, Larry A Curtiss, Venkat Srinivasan. The role of local inhomogeneities on dendrite growth in LLZO-based solid electrolytes. *Journal of the Electrochemical Society* 167, 100537 (2020).

2. H-K. Kim and V. Srinivasan. Status and Targets for Polymer-Based Solid-State Batteries for Electric Vehicle Applications. *Journal of the Electrochemical Society* (2020) **167** 130520.

Acknowledgements

This research is supported by the Vehicle Technologies Office (VTO), Department of Energy (DOE), USA, through the Battery Materials Research (BMR) program. Argonne National Laboratory is operated for DOE Office of Science by UChicago Argonne, LLC under the contract number DE-AC02-06CH11357. The work on cathode/solid-electrolyte interface was conducted by Pallab Barai, the work on lithium dendrite growth was done by Aashutosh Mistry, and the optimization work with liquid and polymer electrolytes were conducted by Hong Keun Kim, all employees of Argonne National Laboratory.

II.6.B Characterization and Modeling of Li-Metal Batteries: Model-system Synthesis and Advanced Characterization (LBNL)

Guoying Chen, Principal Investigator
Lawrence Berkeley National Laboratory
1 Cyclotron Road
Berkeley, CA 94720
E-mail: GChen@lbl.gov

Tien Duong, DOE Technology Development Manager
U.S. Department of Energy
E-mail: Tien.Duong@ee.doe.gov

Start Date: October 1, 2019 End Date: September 30, 2022
Total Project Cost: $500,000 DOE share: $500,000 Non-DOE share: $0

Project Introduction

Development of mitigating approaches and rational design of advanced functional materials require a better understanding of the relationships among structure, properties and functions. For Li-metal batteries employing a solid-state electrolyte (SSE), significant challenges, both at the materials level and systems level, prevent them from practical applications. It is well recognized that fundamental knowledge on the role of SSE microstructure in solid-state ion conduction and Li dendrite formation/propagation, performance-limiting processes and phase transition mechanisms in SSEs, and the dynamic evolution of the SSE/electrode interfaces are key to the development of high-energy Li-metal batteries with improved commercial viability. This project addresses these challenges in a systematic way, by synthesizing well-controlled SSE model systems and SSE/electrode model interfaces, obtaining new insights into the model materials and interfaces utilizing state-of-the-art analytical techniques, and subsequently establishing the correlations between specific property and function. The goal is to use these findings to rationally design and synthesize advanced SSE materials and interfaces with improved performance.

Objectives

This project will use a rational, non-empirical approach to design and develop SSE materials and interfaces for the next-generation Li-metal batteries. Combining a suite of advanced diagnostic techniques with carefully prepared model-system samples, the project will perform systematic studies to achieve the following goals: 1) obtain understanding on the role of SSE grain and grain boundaries on ion conduction and dendrite formation, 2) obtain fundamental knowledge on rate- and stability-limiting properties and processes in SSEs when used in Li-metal batteries, 3) investigate the reactivities between SSE and electrodes and gain insights on the dynamic evolution of the interfaces, and 4) design and synthesize improved SSE materials and interfaces for safer and more stable high-energy Li-metal batteries.

Approach

The project will combine model-system synthesis and advanced diagnostic studies to investigate ion conduction and interfacial chemistry of SSE in Li-metal batteries. Single crystalline, polycrystalline and amorphous model samples with various grain and grain boundary properties will be synthesized. Model interfaces between the SSE and electrodes with controlled properties will also be developed. Both bulk-level and single-grain level characterization will be performed. Global properties and performance of the samples will be established from the bulk analysis, while the single-grain-based studies will utilize time- and spatially-resolved analytical techniques to probe the intrinsic redox transformation processes and failure mechanisms under battery operating conditions.

Results

In order to understand the role of solid-state electrolyte grains, grain boundary chemistry and properties in ion conduction and interfacial behavior, it is important that SSE particles with well-controlled physical characteristics, particularly grain morphology and surface properties are used for the studies. In FY20, the feasibility of synthesizing high-quality grains of model SSEs was evaluated.

Because lithium lanthanum zirconium oxide (LLZO) has been well studied, it was selected as our first SSE model system. In our previous studies, molten-salt methods were used to produce single crystals of layered- and rocksalt-structured oxide cathode materials with well-defined properties. Here, a similar approach was adopted to synthesize LLZO single-grain samples. Upon heat treatment of the pre-mixed $La(OH)_3$, Li_2CO_3, ZrO_2 and Al_2O_3 precursors in a $LiNO_3$ flux at 1000 ^oC for 6 hrs, faceted Al-substituted LLZO ($LI_{6.75}Al_{0.25}La_3Zr_2O_{12}$, Al-LLZO) primary particles with an average grain size of ~ 40 μm were obtained (Figure II.6.B.1a and b). After exploring a variety of experimental conditions, uniform size distribution was achieved by maintaining the mole ratio between the flux and total metal precursors (defined as R) at 20. Due to the presence of excess Li in the flux, the as-synthesized Al-LLZO sample adopted a tetragonal phase, as shown in the XRD pattern in Figure II.6.B.1c. A simple proton exchange process was found to effectively convert the tetragonal phase to the cubic phase, which is more desirable due to its higher ionic conductivity. To facilitate the Li^+/H^+ exchange process in the garnet lattice, the tetragonal Al-LLZO powder was mixed with DI water in a hydrothermal autoclave and heated at 150 ^oC for 12 hrs, followed by annealing in air at 300 ^oC for 12 hrs to remove the protons. The final product was found to have the garnet cubic structure without any impurities (Figure II.6.B.1d), with the particle morphology fully retained.

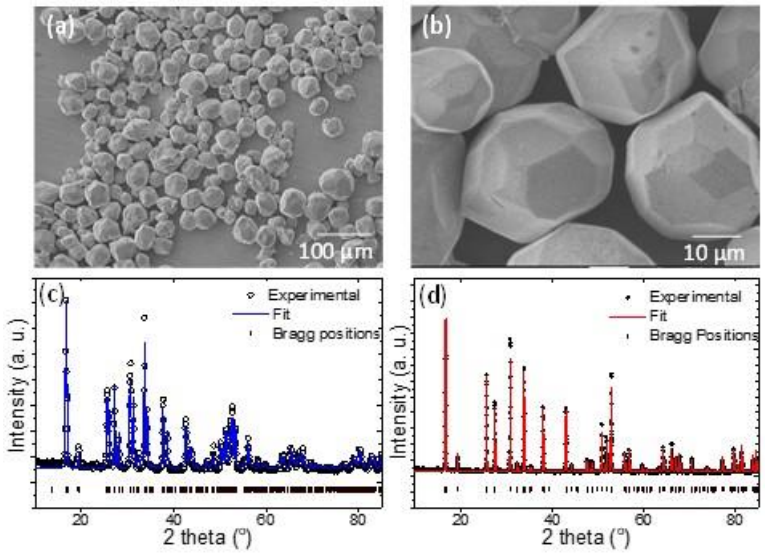

Figure II.6.B.1 (a, b) SEM images of Al-LLZO particles prepared using the molten-salt method and (c, d) refinement of XRD patterns collected on as-synthesized (garnet tetragonal phase) and proton exchanged Al-LLZO particle after annealing (garnet cubic phase).

Single-grain cubic Al-LLZO was also obtained by annealing pre-formed garnet phase in a $LiNO_3$ flux, which utilizes a recrystallization process. Figure II.6.B.2a shows the SEM image obtained on an Al-LLZO sample prepared by heating a commercially-available cubic Al-LLZO in a $LiNO_3$ flux at 1100 ^oC for 12 hrs, with the mole ratio between the oxide and flux maintained at 1:1. The as-synthesized sample showed a well-defined single particle morphology with an average particle size of ~ 4 μm, which is 10x smaller than that of the sample made by the molten-salt method. This suggests the feasibility in varying grain sizes through controlled synthesis. The cubic crystal structure remained even after the thermal treatment (Figure II.6.B.2c), as Li loss during the high-temperature process, which typically promotes the formation of tetragonal phase, was prevented by the presence of a $LiNO_3$ flux in this case. In the absence of the flux, on the other hand, large aggregated LLZO secondary particles were obtained. As shown in Figure II.6.B.2b, the sample obtained after

heating $La(OH)_3$, Li_2CO_3, ZrO_2 and Al_2O_3 precursors alone under the same conditions adopted a secondary particle morphology with an average size of ~ 20-40 µm. Obtaining the garnet cubic crystal structure was possible when an excess amount of Li_2CO_3 was used during the solid-state synthesis (Figure II.6.B.2c).

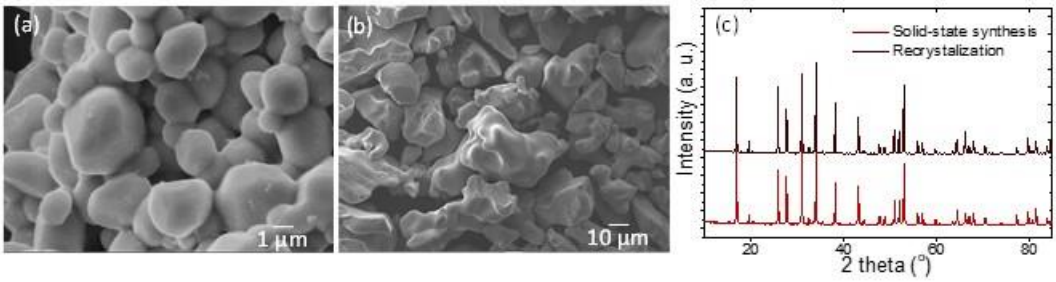

Figure II.6.B.2 (a, b) SEM images and c) XRD patterns of Al-LLZO samples obtained from the recrystallization process and solid-state synthesis method.

The synthesized Al-LLZO primary particles were then used to evaluate processing approaches suitable for varying grain and grain boundary characteristics in densified solid-state electrolyte pellets. Al-LLZO primary particles with an average grain size of 3-4 µm were further ball milled to reduce the size, with nearly 10x size reduction was achieved after milling at 300 rpm for 6 hr. Both samples before and after the ball milling (Al-LLZO_a and Al-LLZO_b, Figure II.6.B.3a and b) were sintered in air at 1100 ºC for 12 hr. Figure II.6.B.3c and d show the densified pellets prepared from the Al-LLZO_a and Al-LLZO_b particles, respectively. While large grains with defined grain boundaries were clearly observed in the former, denser pellets without obvious presence of grain boundaries were obtained in the latter. The reduction in particle size promotes grain growth during the sintering and enables more effective densification of the garnet electrolyte. We believe the process of particle size/morphology control followed by sintering can be adapted to tune grain and grain boundary properties of other SSE pellets besides garnets.

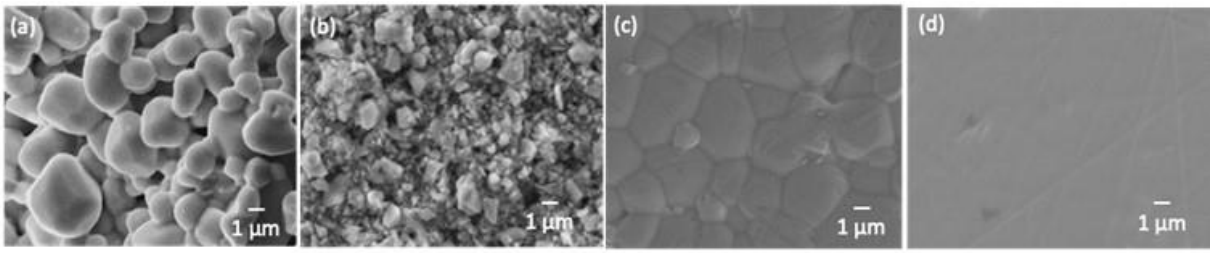

Figure II.6.B.3 SEM images of Al-LLZO particles before and after ball milling a, b) and sintered Al-LLZO pellets c, d) prepared from a) and b), respectively.

Changes in crystal structure after sintering were also investigated. While phase pure cubic structure maintained in the as-prepared pellet from Al-LLZO_a, a small amount of $La_2Zr_2O_7$ impurity was detected on the sintered Al-LLZO_b sample. This is likely a result of increased surface area in the latter which results in more Li loss at high temperatures. Gentle surface polishing with 4000 grit SiC paper was able to effectively remove the impurity. Figure II.6.B.4a compares the XRD patterns of the pellets after polishing. Phase-pure crystalline garnets with the cubic structure were obtained in both cases. The ionic conductivity of the pellets was compared by using electrochemical impedance spectroscopy (EIS). The measurements were performed based on the blocking electrode configuration where the SSE pellet is sandwiched between two Pt electrodes (shown in the schematics in Figure II.6.B.4b). EIS spectra were collected in the temperature window of room temperature to 80 ºC, at an increment of 10 ºC per measurement. The total ionic conductivity, including contributions from grains and grain boundaries, was determined based on the real component of impedance at the frequency when AC ion conduction migrates through the pellet. Figure II.6.B.4b shows the resulting Arrhenius plots from the EIS measurements. For the pellet made from large grain Al-LLZO_a, the activation energy was 0.32 eV, corresponding to a total ionic conductivity of $1.0x10^{-4}$ S cm^{-1} at room tempreature. On

the other hand, the denser pellet of Al-LLZO_b was found to have a lower activation energy of 0.28 eV, corresponding to a total ionic conductivity of 2.1×10^{-4} S cm^{-1}, which is 2 times higher than the former. The results suggest that the presence of defined grain boundaries negatively impact the conductivity of SSE seperators. Although the origin is unclear at this time, as it may relate to the resistance between the grains or the changes in chemistry/conductivities due to impurities at the grain bourndaries, it is expected that performing controlled studies by varying grain and grain boundary characteristics will provide further insights on the role of various physical properties in solid-state ion conduction as well as Li dendrite propagation.

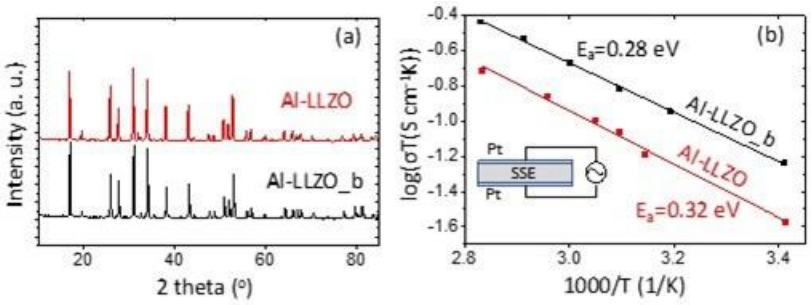

Figure II.6.B.4 a) X-ray diffraction patterns of polished pellets sintered from Al-LLZO_a and Al-LLZO_b samples and b) Arrhenius plots of the total ionic conductivity measured on the sintered pellets.

As LLZO belongs to oxide SSE family with grains that are intrinsically rigid and difficult to sinter, we also investigated a "softer" SSE model system, halide compounds with a general formula of Li_3MX_6 (M = Sc, Y, In, Er, X = Cl, Br), for comparative studies. This class of materials were recently shown to have a very high room-temperature ionic conductivity of up to 10^{-2} S/cm, a wide electrochemical stability window of up to 6 V, and good stability towards oxide cathode materials. Compared to the sulfide SSEs such as Li_3PS_4 (LPS), the halides are generally more stable towards air exposure as well as high voltage conditions at the cathode. On the other hand, halide SSEs have higher ionic conductivities and they are much easier to sinter compared to the oxide SSEs.

The feasibility of synthesizing Li_3InCl_6 (LIC) with different grain morphology and properties was evaluated. As shown in Figure II.6.B.5a, in $InCl_3$ chloride anions form a closed packed O3 lattice and occupy the octahedral sites. In Li_3InCl_6, Li^+ cations are located at the octahedral sites to form the layered *C*/2*m*-like structure with distinct Li layers (blue color in Figure II.6.B.5b). Most In^{3+} cations are located at the 2*a* sites while the rest at the 4*g* sites (Figure II.6.B.5c). By simply adjusting high-energy ball milling time, glassy Li_3InCl_6 with the same average size of ~ 20 μm but two types of grain morphologies were synthesized. Secondary particles composed of sub-micron primary particles and distinct grain boundaries (Figure II.6.B.6a and b) were obtained after 36h while large single grains in the absence of clear grain boundaries (Figure II.6.B.6c and d) were obtained after 24h. Room-temperature ionic conductivities of the Li_3InCl_6 samples were measured by using stainless steel (SS) blocking electrodes in EIS. The obtained values are slightly higher in the single-grain sample, at approximately 2.8×10^{-4} S/cm as compared to 2.5×10^{-4} S/cm for the secondary-particle sample.

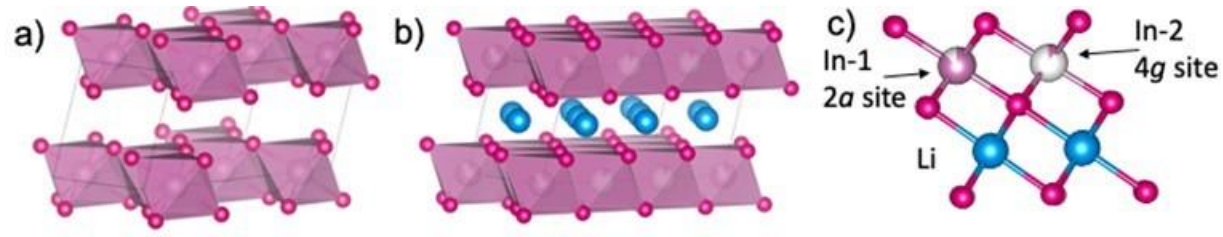

Figure II.6.B.5 Crystal structure of a) $InCl_3$ and b) Li_3InCl_6, c) atomic arrangement of In and Cl in Li_3InCl_6.

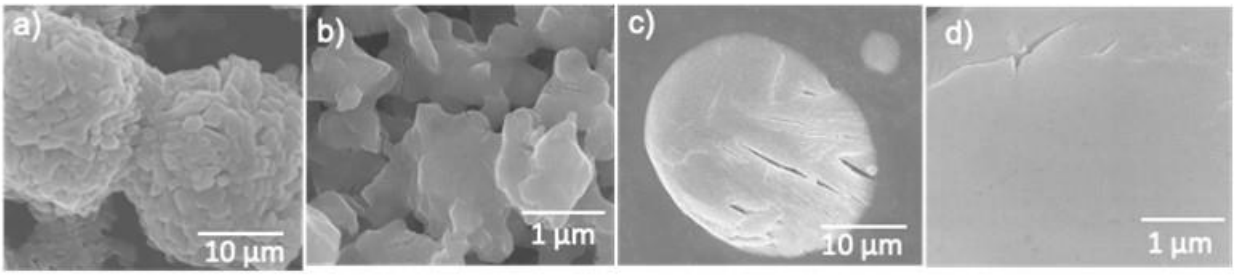

Figure II.6.B.6 SEM images of the secondary-particle Li_3InCl_6 sample (a, b) and single-grain Li_3InCl_6 sample (c, d) synthesized by mechanical ball milling under different conditions.

It is well-known that in softer sulfide SSEs such as LPS, crystallinity often plays a critical role in Li^+ transport, mostly due to the effect of chemical bonding and atomic arrangements on ion mobility. Here, we investigated the effect of crystallinity by annealing the synthesized secondary-particle Li_3InCl_6 sample in a vacuum-sealed quartz ampoule at 300 ^oC for 6h. Even at the relatively low heating temperature, annealing largely fuses the primary particles within the grains and increases sample crystallinity, as shown in the SEM images before (Figure II.6.B.7a) and after (Figure II.6.B.7b) annealing. Comparison on Nyquist plots obtained from blocking-electrode EIS measurements are also shown in Figure II.6.B.7c. The room-temperature conductivity of the secondary-particle Li_3InCl_6 sample increased from 2.5 x 10^{-4} to 1.5 x 10^{-3} S/cm after annealing, confirming the significant role of crystallinity and grain boundaries in Li ion conduction in halide SSEs.

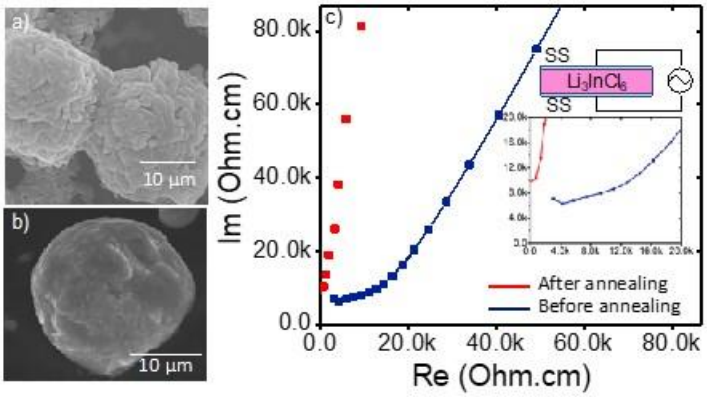

Figure II.6.B.7 SEM images of the secondary-particle Li_3InCl_6 sample before a) and after b) annealing, c) comparison of EIS Nyquist plots of the samples.

Figure II.6.B.8 compares the Rietveld refinement of XRD patterns collected on the as-synthesized glassy crystalline Li_3YCl_6 (LYC, Figure II.6.B.8a) and LIC (Figure II.6.B.8b). Structure wise, LYC adopts a hexagonal unit cell with an ABAB stacking anionic sublattice (*P*-3*m*1). While most Y cations are located at the 1*a* and 2*d* sites, a significant fraction of them also share the same sites with Li at the 6*g* and 6*h* sites. The atomic arrangement based on the refinement is shown in Figure II.6.B.8a. On the other hand, LIC adopts a monoclinic unit cell with an ABCABC stacking anionic sublattice (*C*2/*m*). Extensive cation mixing is also found between the Li and In sites, leading to the formation of rocksalt-type phase shown in the XRD pattern and the atomic structural arrangement in Figure II.6.B.8b.

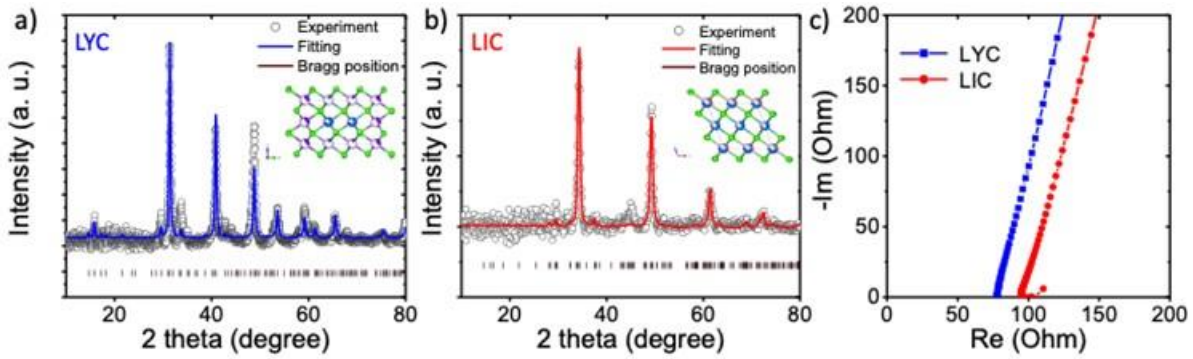

Figure II.6.B.8 Rietveld refinement of XRD patterns: a) LYC and b) LIC. The insets show atomic arrangements that highlights the disordering nature of Y and In, respectively, and c) comparison of EIS Nyquist plots of blocking-electrode cells with as-synthesized LYC and LIC.

Room-temperature ionic conductivities were measured by EIS using SS blocking electrodes (Figure II.6.B.8c). The obtained values for LYC and LIC were 0.43 and 0.29 mS/cm, respectively, suggesting that bulk LYC is slightly more conductive. EIS measurements were also carried out on symmetrical Li|LYC|Li and Li|LIC|Li cells under the open circuit voltage (OCV) conditions with an AC amplitude of 10 mV. The Nyquist plots in the frequency range of 1 MHz to 0.1 Hz collected on the as-assembled cells are shown in Figure II.6.B.9a. In general, the depressed semi-circle at the high frequency can be attributed to the interfacial impedance between Li and SSE. The measured diameters were ~ 2 and 100 Ohms for LYC and LIC, respectively, suggesting a much less resistive interface between LYC and Li metal. Figure II.6.B.9b and c further compares the evolution of interfacial impedance as a function of time. The EIS measurements were carried out for 10 cycles at an interval of 10 mins. While the impedance increased continuously in the LIC symmetrical cell (Figure II.6.B.9b), implying reactivities between LIC and Li metal, negligible changes were observed on the LYC cell (Figure II.6.B.9c). The lower initial impedance and higher stability indicates a better interface between LYC and Li electrode. Although LYC and LIC belong to the same family of halide SSEs with In and Y sharing the same oxidation state of +3, the observed differences on anode reactivities suggest the critical role of metal center in halide SSE behavior and the need for its optimization in future studies.

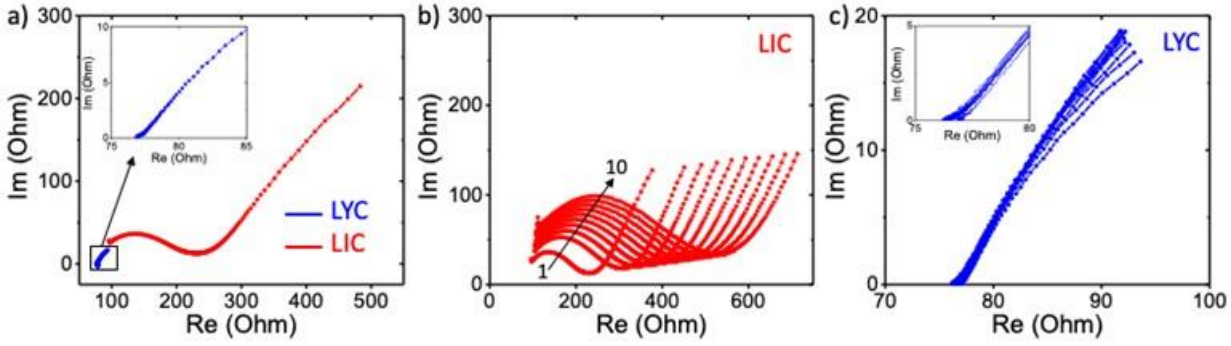

Figure II.6.B.9 a) Comparison of EIS Nyquist plot of as-assembled Li|LYC|Li and Li|LIC|Li symmetrical cells, b) and c) evolution of EIS as a function of time in Li|LIC|Li and Li|LYC|Li cells, respectively.

Conclusions

LLZO and the Li_3MX_6 series were selected as model oxide and halide SSE systems with grains that are of different hardness. Synthesis methods were developed to prepare particles with well-controlled physical properties, including size and morphology. The role of SSE grain chemistry, size and morphology in ion conduction and interfacial behavior was systematically investigated. In hard SSE like LLZO, it was found that grain size directly impacts ionic conductivities of the sintered electrolyte. In softer SSE like the halides, the metal center M was found to play a critical role in regulating conductivity, interfacial reactivities and

impedance. Our study suggests that proper SSE chemistry design and grain engineering are likely to lead to high-energy lithium-metal batteries with much improved performance.

Key Publications

1. D. Chen, J. Wu, J. K. Papp, B. D. McCloskey, W. Yang and G. Chen, "Role of Redox-Inactive Transition-Metals in the Behavior of Cation-Disordered Rocksalt Cathodes," *Small* 2000656 (2020). DOI: 10.1002/smll.202000656.
2. E. Yi, H. Shen, S. Heywood, J. Alvarado, D. Y. Parkinson, G. Chen, S. W. Sofie and M. M. Doeff, "All-Solid-State Batteries Using Rationally Designed Garnet Electrolyte Frameworks," *ACS Applied Energy Materials*, 3 (1), 170 (2020). DOI: 10.1021/acsaem.9b02101.
3. L. Zou, Y. He, Z. Liu, H. Jia, J. Zhu, J. Zheng, G. Wang, X. Li, J. Xiao, J. Liu, J.-G. Zhang, G. Chen and C. Wang, "Unlocking the passivation nature of the cathode-air interfacial reactions in lithium ion batteries," *Nature Communications* (2020). DOI: 10.1038/s41467-020-17050-6
4. H. Shen, E. Yi, S. Heywood, D. Y. Parkinson, G. Chen, N. Tamura, S. Sofie, K. Chen and M. M. Doeff, "Scalable Freeze Tape Casting Fabrication and Pore Structure Analysis of 3D LLZO Solid-State Electrolytes," *ACS Applied Materials & Interfaces* (2019). DOI: 10.1021/acsami.9b11780.
5. H. Shen, E. Yi, M. Amores, L. Cheng, N. Tamura, D. Y. Parkinson, G. Chen, K. Chen and M. M. Doeff, "Oriented Porous LLZO 3D Structures Obtained by Freeze Casting for Battery Applications," *Journal of Materials Chemistry A*, 7, 20861 (2019). DOI: 10.1039/C9TA06520B.
6. D. Chen, W. H. Kan and G. Chen, "Understanding Performance Degradation in Li-Rich Rock-Salt Cathodes," *Advanced Energy Materials* 1901255 (2019). DOI: 10.1002/aenm.201901255.
7. D Chen and G Chen, "Probing the Role of Redox-Inactive Transition-Metals in the Behavior of Cation-Disordered Rocksalt Cathodes via synchrotron X-ray Spectroscopy," 2020 SSRL/LCLS User Meeting, Menlo Park, CA, September 2020.
8. G. Chen, "Model System Diagnostics for High-Energy Cathode Development," 2020 Vehicle Technologies Office Annual Merit Review Meeting, Arlington, Virtual, June 2020.
9. D. Chen and G. Chen, "Understanding Performance Degradation in Cation Disordered Rock-Salt Cathodes," 2019 Bay Area Battery Summit, Berkeley, CA, November 2019.

II.6.C Design of High-Energy, High-Voltage Lithium Batteries through First-Principles Modeling (LBNL)

Kristin A. Persson, Principal Investigator
Lawrence Berkeley National Laboratory
1 Cyclotron Rd
Berkeley, CA, 94720
E-mail: kapersson@lbl.gov

Tien Duong, DOE Technology Manager
U.S. Department of Energy
E-mail: Tien.Duong@ee.doe.gov

Start Date: October 1, 2019 End Date: September 30, 2022
Project Funding: $500,000 DOE share: $500,000 Non-DOE share: $0

Project Introduction

This project supports VTO programmatic goals by developing next-generation, high-energy cathode materials and enabling stable cathode operation at high voltages through target particle morphology design, functional coatings, and rational design of electrolytes. We aim to provide fundamental insights into the atomistic mechanisms underlying surface reactivity and performance of Li-ion cathode materials and electrolytes with the ultimate goal to suggest improvement strategies, such as coatings, surface protection, novel electrolyte formulations, and particle morphology design. Transport modes as a function of solvent and salt concentrations will be clarified, and a data-driven reaction network framework will be designed and implemented to predict early SEI formation on lithium metal.

Objectives

The end-of-project goals include the following:

- Understanding of the factors that govern charge transport in nonaqueous, superconcentrated LEs.
- Critical surface and coating design and optimization strategies that will improve cycling of Li-ion battery cathodes by reducing cathode degradation from oxygen loss.
- Simulation and ML of the early formation of the SEI on Li-metal electrodes.

Approach

- First-principles calculations, both static and dynamic approaches, are used to model SSE material thermodynamics and kinetics. LEs are modeled through coupled classical MD and first-principles methods to accurately capture solvation structure as well as reactivity of the liquid system.
- Examine different transport models to study the electron and ion mobility through the amorphous coating layer.
- The reaction network is built on large-scale first-principles data, using graph theory and machine learning (ML) models.

Results

Due to the high level of correlations between the ionic species dissolved in solution, the use of dilute-limit descriptions for transport are precluded. Using classical molecular dynamics simulations to model the electrolytes LiBF4 in propylene carbonate (PC) and LiPF6 in propylene carbonate (PC), transport properties were investigated via residence time analysis.

In Figure II.6.C.1 (top), the residence time is plotted as function of concentration. The residence time increases as a function of salt concentration, which is generally expected due to the large increase in solution viscosity. In Figure II.6.C.1 (middle), the characteristic diffusion length $L^c = \sqrt{6D\tau^{res}}$ is shown as a function of concentration. For Li^+-PC, with both anions (PF_6^- and BF_4^-), L^c slightly decreases with concentration, implying a slight shift towards a more structural diffusion. However, here, the transport mode remains a mix of vehicular and structural diffusion since L^c is comparable to the size of the solvation shell. For the transport mode of Li^+ with respect to PF_6^- : the vehicular quality increases with concentration but is at all concentrations more structural than BF_4^-. This may be due to the stronger binding energy of Li^+ to BF_4^-. Li^+ with respect to BF_4^-, in contrast, although more vehicular at all concentrations, shows a shift towards more structural diffusion at higher concentrations. Figure II.6.C.1 (bottom) shows the ratio of the average time a Li^+ spends around at least one anion to the residence time (one specific anion), τ^{bound}/τ^{res} . A higher value of τ^{bound}/τ^{res} can be argued as a higher amount of ion hopping. Interestingly, although the ion hopping quality increases with concentration above 1.5 M, it is similar for both Li^+-PF_6^- and Li^+-BF_4^-.

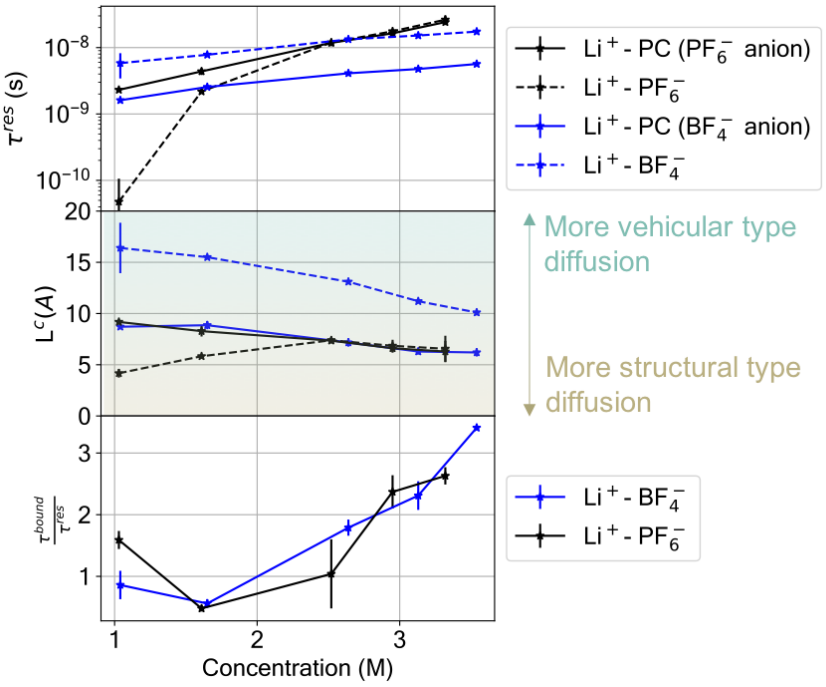

Figure II.6.C.1 (top panel) Residence time τ^{res} for various species and (middle panel) L^c as a function of concentration. (bottom panel) τ^{bound}/τ^{res}. Error bars, when smaller than the symbols for computed data, are not shown.

The second goal of the current BMR project is aimed towards identifying the Li diffusion bottlenecks in two known amorphous coating materials: Al_2O_3 and ZnO. We consider two different scenarios of Li diffusion in conformal coatings: (1) Electron conducting model, i.e. insert extra Li^0 into amorphous Al_2O_3 and ZnO to generate $Li_xAl_2O_3$ and Li_xZnO, respectively; (2) Electrolyte model, i.e. insert Li_2O as the coordination shells of Li^+ cations into amorphous Al_2O_3 and ZnO to generate $Li_{2x}Al_2O_{3+x}$ and $Li_{2x}ZnO_{1+x}$, respectively. Using ab-initio molecular dynamics simulations to model Li^+ and O^{2-} diffusions in amorphous Al_2O_3 and ZnO, the room temperature self-diffusion coefficients (D_{rt}) were obtained via Arrhenius relation.

In Figure II.6.C.2, the extrapolated D_{rt}^{Li} and D_{rt}^{O} are plotted as function of Li^+ concentration. The following observations can be made: (1) In general, D_{rt}^{Li} and D_{rt}^{O} increase with a higher Li^+ content. Also, Li^+ and O^{2-} diffuse much faster in ZnO than in Al_2O_3. Ion diffusion in amorphous structure is accompanied by a bond breaking/making process. Li^+ diffusion in ZnO is facilitated by the lower oxygen coordination. The slower O^{2-} diffusion in Al_2O_3 is rationalized by the stronger Al-O bond as compared to the Zn-O one, which can be demonstrated by crystal orbital Hamiltonian populations analysis. (2) In Al_2O_3, the electrolyte model has faster Li^+ transport than the electron conducting model. This suggests that the significantly impeded electron hopping in amorphous Al_2O_3 would impose a bottleneck for Li^+ diffusion. On the other hand, there is no major difference in D_{rt}^{Li} between the electron conducting and the electrolyte models in ZnO, which implies that the electron mobility in semiconducting ZnO is fast enough to support Li^+ diffusion. Indeed, the room temperature

electrical conductivity of ZnO is orders of magnitude higher than that of Al_2O_3. Furthermore, the electron conducting model promotes O^{2-} transport in Al_2O_3, which suggests that the reduced Al cations exhibit a weaker bond to oxygen, while Al cations remain 3+ state in electrolyte model. (3) Based on the obtained Li^+ and O^{2-} diffusivities, we find that Al_2O_3 provides a better conformal coating for high-voltage cathodes than ZnO. Al_2O_3 coating layer has facile Li^+ diffusion and also impedes O^{2-} transport. However, its coating thickness must be thin to avoid the coating layer from reducing Li-ion conductivity and rate capability of the electrode. (4) While the lithiated counterparts of Al_2O_3 and ZnO can achieve a higher Li^+ transport, they are not stable against delithiation and subsequent decomposition to Al_2O_3 and ZnO at a high charge state.

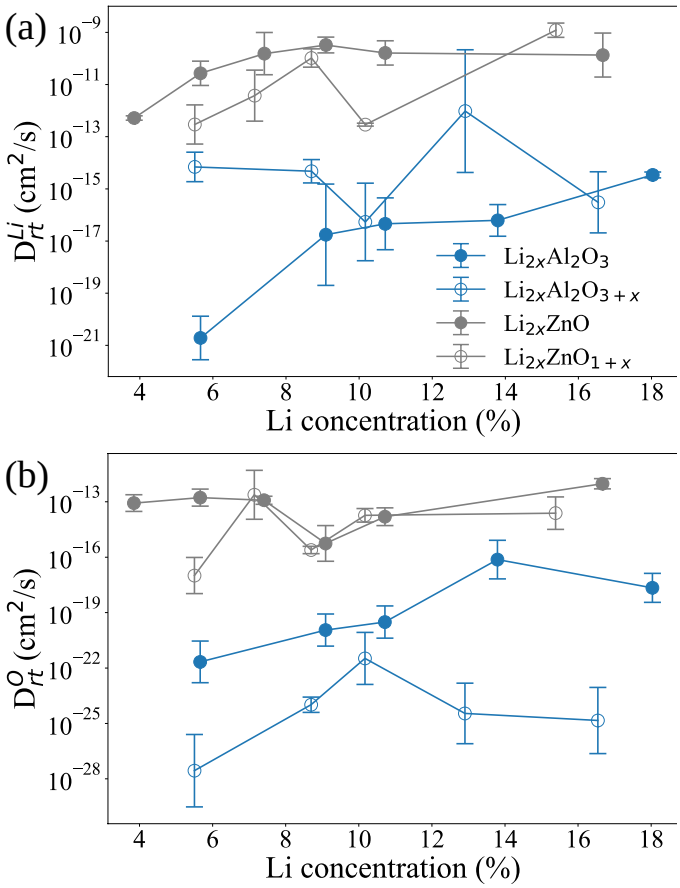

Figure II.6.C.2 Estimated room temperature self-diffusion coefficients of Li^+ (a) and O^{2-} (b) in Al_2O_3 and ZnO with varying Li^+ concentration.

The third goal of the current BMR project is aimed towards using a data-driven reaction network approach to identify reaction pathways responsible for the formation of important SEI component species. To that end, we have developed a high-throughput framework capable of simulating arbitrary molecules, including charged, open shell, solvated, and metal coordinated species with calculations completing successfully over 97% of the time. We leveraged these computational workflows to perform tens of thousands of calculations in order to construct a chemical reaction network describing $LiPF_6$/EC SEI formation on lithium metal including nearly 6000 species and 4.5 million reactions, orders of magnitude larger than any previously reported reaction network. We further developed a novel chemically consistent graph architecture to allow optimized pathfinding algorithms to be applied to general reaction networks for the first time in order to be able to tractably analyze such a massive network.

Lithium ethylene dicarbonate (LEDC) is thought to be the majority organic component of the $LiPF_6$/EC SEI and its formation pathways have been studied in depth for nearly two decades, making it an ideal candidate with which to test our approach. By applying optimized pathfinding algorithms to find the shortest path to LEDC in our chemical reaction network, we autonomously identify the five low cost formation pathways shown in Figure II.6.C.3. A key validation of our approach is that both previous prominent mechanisms, originally proposed through manual investigations - the two-electron path (purple) and the one-electron path (green) - are recovered as our shortest and 3rd shortest paths, respectively. The 2nd and 4th shortest paths (blue and red) are nearly equivalent to the shortest and 3rd shortest paths, respectively, with the blue path being another two-electron mechanism and the red path being another one-electron mechanism. However, both include a counterintuitive ring-opening step that has not been previously considered because it is slightly less thermodynamically favorable than the conventional ring-opening mechanism (-1.08 eV vs. -1.21 eV). Intuitively, a chemist would select the more favorable route at a given step, but in this case non-intuitive reactions could meaningfully contribute, and our reaction network approach will capture such mechanisms.

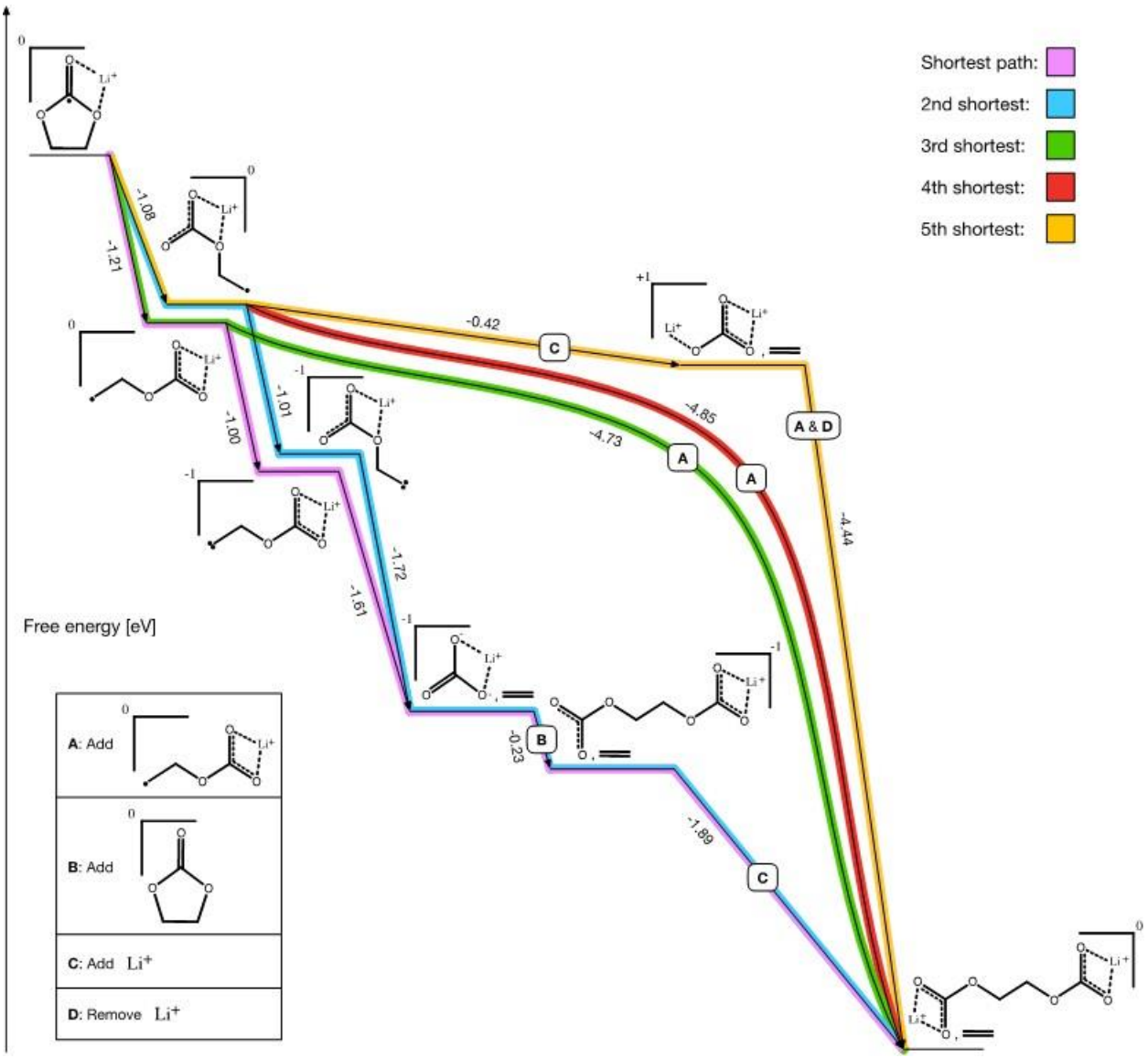

Figure II.6.C.3 LEDC five shortest paths autonomously identified from a reaction network with nearly 6000 species and 4.5 million reactions.

The 5th shortest path (gold) is entirely novel and leverages a transient lithium ion to decompose ring-opened Li^+EC^- exergonically. Note that decomposing ring-opened Li^+EC^- in isolation is slightly endergonic according to our calculations (+0.25 eV), which may be why it has not previously been reported. However, our procedure autonomously identified that the coordination of an additional lithium ion simultaneous with the decomposition yields a much more thermodynamically favorable reaction (-0.42 eV), perhaps making it competitive with the other mechanisms emerging from the network. The additional lithium ion can then dissociate simultaneously with the addition of another ring-opened Li^+EC^- to form LEDC (-4.44 eV), making it a transient participant in the gold pathway. This unexpected mechanism further demonstrates the ability of our approach to identify new and unintuitive reaction paths that may participate in SEI formation. We are now using our reaction network approach to identify the optimal formation pathways of lithium ethylene monocarbonate (LEMC), which a recent controversial paper suggested may be the true majority organic component of the SEI instead of LEDC.

Conclusions

- We find that the Li^+ mode of diffusion with respect to its surrounding propylene carbonate solvation shell is a mix of vehicular and structural diffusion at all studied concentrations, exhibiting a small increase toward structural diffusion in the superconcentrated regimes.

- The Li^+ ions associated with PF_6^- anions move in an increasingly vehicular manner as the salt concentration is increased, while the Li^+ ions associated with BF_4^- anions move in an increasingly structural manner.

- In general, a higher Li^+ content increases both Li^+ and O^{2-} diffusivities in both Al_2O_3 and ZnO. Also, Li^+ and O^{2-} diffuse much faster in ZnO than in Al_2O_3. However, neither Al_2O_3 nor ZnO is expected to retain a significant concentration of Li^+ at high charge. ZnO performs much more poorly in terms of O^{2-} blocking, and hence, Al_2O_3 is preferred for high-voltage cathode applications.

- We report a chemically consistent graph architecture using a novel multi-reactant representation and iterative cost-solving procedure. Leveraging our architecture, we construct the first ever electrochemical reaction network from first-principles thermodynamic calculations to describe the formation of the Li-ion solid electrolyte interphase (SEI), which is critical for passivation of the negative electrode.

Key Publications

1. Self, Julian, Kara D. Fong, and Kristin A. Persson. "Transport in Superconcentrated LiPF6 and LiBF4/Propylene Carbonate Electrolytes." ACS Energy Letters 4.12 (2019): 2843-2849.

2. Jianli Cheng, Eric Sivonxay, and Kristin A. Persson. "Evaluation of Amorphous Oxide Coatings for High-voltage Li-ion Battery Applications using a First-Principles Framework." ACS Appl. Mater. Interfaces, 2020, 12, 31, 35748–35756.

3. Samuel M. Blau, Hetal D. Patel, Evan Walter Clark Spotte-Smith, Xiaowei Xie, Shyam Dwaraknath, and Kristin A. Persson. "A Chemically Consistent Graph Architecture for Massive Reaction Networks Applied to Solid-Electrolyte Interphase Formation." *ACS Cent. Sci.* Submitted.

Acknowledgements

This work was intellectually led by the Battery Materials Research (BMR) program under the Assistant Secretary for Energy Efficiency and Renewable Energy, Office of Vehicle Technologies of the U.S. Department of Energy, Contract DE-AC02-05CH11231. This research used resources of the National Energy Research Scientific Computing Center, a DOE Office of Science User Facility supported by the Office of Science of the U.S. Department of Energy under Contract No. DE-AC02-05CH11231. This research also used the Lawrencium computational cluster resource provided by the IT Division at the Lawrence Berkeley National Laboratory (Supported by the Director, Office of Science, Office of Basic Energy Sciences, of the U.S. Department of Energy under Contract No. DE-AC02-05CH11231).

II.6.D First Principles Calculations of Existing and Novel Electrode Materials

Gerbrand Ceder, Principal Investigator
Lawrence Berkeley National Laboratory
1 Cyclotron Rd, MS: 33-146
Berkeley, CA, 94720
E-mail: gceder@berkeley.edu

Tien Duong, DOE Technology Development Manager
U.S. Department of Energy
E-mail: Tien.Duong@ee.doe.gov

Start Date: October 1, 2019 End Date: September 30, 2020
Project Funding: $350,000 DOE share: $350,000 Non-DOE share: $0

Project Introduction

Because of their superior safety and high energy density all-solid-state batteries are regarded as one of the most promising next-generation energy storage technologies. Commercial use of an all-solid-state battery requires the development of a solid-state electrolyte with 1) high ionic conductivity; 2) flexible and facile synthesis, and 3) good chemical/electrochemical stability against Li metal as well as against typical cathode materials [1], [2], [3]. No solid-state electrolyte satisfying all the aforementioned conditions has so far been developed yet [9], [10], [11].

In this BMR program we have investigated the alkali-ion diffusion in three important but distinct materials, so as to get a broader understanding on how one can design solids with very high ionic conductivity.
1) **Amorphous Li-P-S materials.** Sulfide electrolytes are of interest due to their high ionic conductivity [4], [5], [6] and ability to establish good contact with electrode materials due to their mechanical softness [7], [8]. Because of the lack of long-range ordering in amorphous structures, the structure of Li-P-S cannot be analyzed with typical experimental techniques such as X-ray diffraction. For this reason, we have applied Density Functional Theory calculations to model amorphous $Li_3PS_{4-\delta}$ structures and their Li-ion diffusivity.
2) **Na-argyrodites**. The Li variants of these materials are excellent conductors, but no related Na compounds have been developed. In the BMR work we investigated the potential stability and synthesizability of this potential class of Na-ion conductors. In addition, we investigated the chemical factors that influence the N-ion conductivity in them. 3) While **Li-titanate (LTO)** is an anode material, it displays extremely high Li-ion conductivity, and the mechanism of Li diffusion in these materials is likely to be applicable for the design of Li-ion solid-state electrolytes.

Objectives

Solid-state batteries are promising to achieve high energy density. The project objective is to determine the design principles needed to create SSEs with high Li-ion conductivity while also achieving stability against common Li-ion cathodes and Li-metal anodes.

Approach

High-throughput computations are used to screen compounds for high electrochemical stability and high ionic conductivity. Ionic mobility and diffusivity are calculated using the Nudged Elastic Band (NEB) and Ab-Initio Molecular Dynamics (AIMD). Density Functional Theory using the GGA or SCAN functional is used to calculate formation energies of compounds, elastic constants of materials, and surface energies. Thermodynamic interface stability is assessed from the *ab initio* computed grand potential phase diagrams in which the lithium voltage can be controlled. Kinetic limits for solid electrolyte decomposition are assessed by topotactic lithium insertion and removal from the solid electrolyte.

Results

Modeling of LPS Li mobility in amorphous state with variations of PS_4 structural units and composition

The anion building blocks in amorphous Li-P-S phase are regarded as important elements that control their ionic conductivity. Multiple building blocks such as PS_4^{3-}, $P_2S_6^{4-}$, $P_2S_7^{4-}$ and polysulfides have been reported [12], [13], and their relative fraction depends on atomic composition and synthesis method. To unambiguously elucidate the influence of each anion building on ionic conductivity we systematically constructed amorphous structures with various P-S groups while

To solve this problem, we theoretically generate amorphous structures with different ratio of building blocks maintaining the chemical composition. The glass formation was simulated using the AIMD simulated melt-quench method. Figure II.6.D.1a, shows how we systematically transform an amorphous structure with only PS_4 units into systems with some P_2S_7 or P_2S_6 groups. For each amorphous structure the conductivities at 300K are extrapolated from AIMD simulations (< 250 ps) at 5-7 temperatures (Figure II.6.D.1b). The conductivities of the amorphous structures with density 1.8 $g \cdot cm^{-3}$ are in the range of 10^{-4} to 10^{-2} $S \cdot cm^{-1}$, which agrees well with the experimental information [15]. The conductivities of the crystalline phases similarly match the literature data for these compounds [15], [16], supporting the validity of our approach. We find no strong correlation between the existence of particular anion blocks and the conductivity. But we do find that there is about an order of magnitude difference in conductivity among the structures that only consist of PS_4^{3-} anions. The "β-PS_4" and "r-PS_4", differ only in their position and orientation of tetrahedra. These results imply that there are likely to be other structural factors that influence the ionic conductivity, rather than the existence of a certain polyanion.

a)

	Amorphous (1.8 and 2.0 g cm^{-3})		Crystalline
Stoichiometry $Li_2S : P_2S_5$ = 75 : 25	$48Li^+ + 16PS_4^{3-}$ (from β-Li_3PS_4) $48Li^+ + 14PS_4^{3-} + P_2S_7^{4-} + S^{2-}$ $48Li^+ + 14PS_4^{3-} + P_2S_6^{4-} + (2S)^{2-}$ $48Li^+ + 12PS_4^{3-} + 2P_2S_7^{4-} + 2S^{2-}$ $48Li^+ + 16PS_4^{3-}$ (random)	β-PS_4 $1P_2S_7$ $1P_2S_6$ $2P_2S_7$ r-PS_4	α-Li_3PS_4 β-Li_3PS_4 γ-Li_3PS_4
Off-stoichiometry	$48Li^+ + 14PS_4^{3-} + P_2S_7^{4-} - 2e^-$ $48Li^+ + 14PS_4^{3-} + P_2S_6^{4-} - 2e^-$ $48Li^+ + 12PS_4^{3-} + 2P_2S_7^{4-} - 4e^-$ $48Li^+ + 12PS_4^{3-} + 2P_2S_6^{4-} - 4e^-$	$1P_2S_7$-S $1P_2S_6$ -2S $2P_2S_7$ -2S $2P_2S_6$ -4S	$Li_7P_3S_{11}$

b)

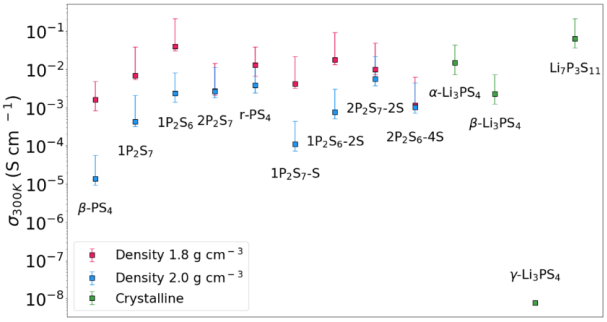

Figure II.6.D.1 a) The list of simulated phases, i.e. amorphous structures with different anion ratio and representative crystalline phases. b) The ionic conductivity extrapolated at 300K for the materials in the list.

Designing a sodium argyrodite solid electrolyte with high stability and ionic conductivity

We applied first-principle computational techniques to evaluate the potential of Na argyrodites for fast Na-ion transport. We studied different pnictogen (P or Sb), chalcogen (S or Se), and halogen (Cl, Br, or I) combinations and investigated the effect of varying site occupancies on the halogen site. Phase stability, electrochemical stability, and ionic conductivity of 48 types of Na argyrodites were investigated allowing us to identify promising Na argyrodites with reasonable stability and ionic conductivity. The thermodynamic stability of the possible Na argyrodites was evaluated by constructing the convex hull of the DFT total energy for all phases in the relevant chemical space. The calculated E_{hull} values for all the studied Na argyrodites are shown in the Figure II.6.D.2. Given that reported Li argyrodites typically have E_{hull} values of 20 meV/atom, we propose that many of the Na argyrodites considered here may be synthetically accessible. Na argyrodites are

generally electrochemically stable within the voltage range of 1-2 V. We predict that at higher voltage the chalcogen atom is susceptible to oxidation. Voltages below the stability window reduce the pnictogen atom. Ab initio molecular dynamics (AIMD) was used to investigate the ionic conductivity. Activation energies and estimated RT conductivities are obtained from an Arrhenius fit to the T-dependent data. Two major trends can be extracted from the distribution of conductivities. First, for all four chemical spaces, the $Na_5AB_4X_2$-type argyrodites generally exhibit higher conductivity than all the configurations with the Na_6AB_5X composition. Second, there is a significant variation in the ionic conductivity with the site occupancy in the sulfide systems. For selenide-based systems, the conductivities do not show a strong dependence on the halogen occupancy.

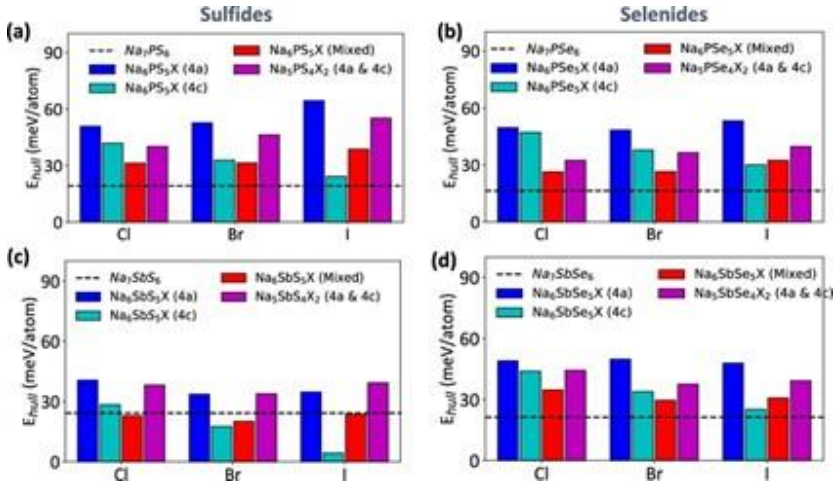

Figure II.6.D.2 Phase stability (energy above the hull, E_{hull}) of Na argyrodites in the (a) Na−P−S−X, (b) Na−P−Se−X, (c) Na−Sb−S−X, and (d) Na− Sb−Se−X compositional spaces.

Elucidating the Li-stuffing effect on the ionic conductivity in oxide materials

Li-stuffing has been suggested as a useful strategy for creating high ionic conductivity by exploiting the Li-Li repulsion to frustrate the Li energy landscape [18]. We chose the lithium titanate ($Li_4Ti_5O_{12}$) as a benchmark system for analyzing Li stuffing effect. Using first principles calculations and the nudged elastic band (NEB) method, we explored the energetics of Li-stuffing defects and their migration in representative low-energy intermediate $Li_{4+x}Ti_5O_{12}$ configurations. In these intermediate configurations, we discovered a large amount of highly distorted face-sharing Li that are involved in distinct Li+ ion migration pathways with substantially lower activation energy than the pathways in the end members. Figure II.6.D.3A shows the energy profile of the pathways in $Li_{4+\delta}Ti_5O_{12}$ (green), $Li_{5+\delta}Ti_5O_{12}$ (red), and $Li_{7-\delta}Ti_5O_{12}$ (blue) as a function of distance along the paths. The activation energies for Li+ ion migration in the lowest energy $Li_4Ti_5O_{12}$, and $Li_5Ti_5O_{12}$ and $Li_7Ti_5O_{12}$ configurations are ~343, ~216, and ~455 meV, respectively. Steps a to g in Figure II.6.D.3B illustrate an example migration pathway in one representative metastable $Li_{5+\delta}Ti_5O_{12}$ configuration. The black arrows show the migration direction of each step. The purple-colored face indicates the three-coordinated oxygen face through which the Li+ ions can migrate from a Li(8a) tetrahedron to a Li(16c) octahedron.

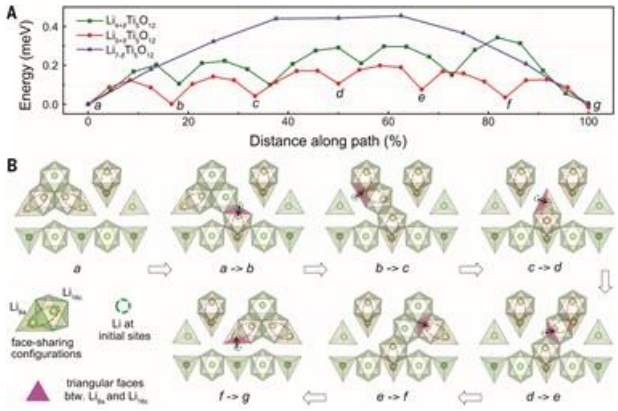

Figure II.6.D.3 Li^+-ion migration pathways and the corresponding energy barriers in the intermediates.

Along this path, although face-sharing Li^+ ions change position, the number of face-sharing Li^+ ions (three to four) remains nearly constant in the $Li_4Ti_5O_{12}$ (always two) and $Li_5Ti_5O_{12}$ (from three to four to three) pathways. In the higher-energy pathway in $Li_7Ti_5O_{12}$, however, the number of face-sharing Li^+-ions changes substantially, from zero to two and back to zero. The low migration barrier for Li^+ ions in the LTO system can be attributed to two important factors: (i) The number of face-sharing Li polyhedra is smaller in the transition state than in the initial and final states. The reduction in $Li^+ – Li^+$ repulsion in the transition state is likely to lower the activation barrier. (ii) Because local distortion helps to reduce the effective coordination number of Li, the change in Li coordination is minimized during Li^+-ion migration through the three-coordinated oxygen face, further lowering the activation barrier. This result is published in Science [19].

Conclusions

The effects of amorphization and Li-stuffing on the conductivity, which are believed to be important strategies for designing super-ionic conductors, have been studied using AIMD and NEB calculations. We have found that a frustrated Li energy landscape is conducive to high Li-ion conductivity. This is realized in amorphous Li-P-S compounds by the high Li content and the amorphous structure, whereas in LTO this is realized by the lithiation which introduces face-sharing Li-Li defects.

Key Publications

1. Zhang, W., Seo, D. H., Chen, T., Wu, L., Topsakal, M., Zhu, Y., ... & Wang, F. (2020). Kinetic pathways of ionic transport in fast-charging lithium titanate. *Science*, *367*(6481), 1030-1034.

2. Ji, H., Wu, J., Cai, Z., Liu, J., Kwon, D. H., Kim, H., ... & Balasubramanian, M. (2020). Ultrahigh power and energy density in partially ordered lithium-ion cathode materials. *Nature Energy*, *5*(3), 213-221.

3. Kwon, D. H., Lee, J., Artrith, N., Kim, H., Wu, L., Lun, Z., ... & Ceder, G. (2020). The Impact of Surface Structure Transformations on the Performance of Li-Excess Cation-Disordered Rocksalt Cathodes. *Cell Reports Physical Science*, *1*(9), 100187.

4. Jadidi, Z., Chen, T., Xiao, P., Urban, A., & Ceder, G. (2020). Effect of fluorination and Li-excess on the Li migration barrier in Mn-based cathode materials. *Journal of Materials Chemistry A*, *8*(38), 19965-19974.

5. Shi, T., Zhang, Y. Q., Tu, Q., Wang, Y., Scott, M. C., & Ceder, G. (2020). Characterization of mechanical degradation in an all-solid-state battery cathode. *Journal of Materials Chemistry A*, *8*(34), 17399-17404.

6. Xiao, Y., Wang, Y., Bo, S. H., Kim, J. C., Miara, L. J., & Ceder, G. (2020). Understanding interface stability in solid-state batteries. *Nature Reviews Materials*, *5*(2), 105-126.

7. Lun, Z., Ouyang, B., Kwon, D. H., Ha, Y., Foley, E. E., Huang, T. Y., ... & Huang, J. (2020). Cation-disordered rocksalt-type high-entropy cathodes for Li-ion batteries. *Nature Materials*, 1-8.

References

1. Wang, Y., Richards, W. D., Ong, S. P., Miara, L. J., Kim, J. C., Mo, Y., & Ceder, G. (2015). Design principles for solid-state lithium superionic conductors. *Nature materials*, *14*(10), 1026.

2. Richards, W. D., Miara, L. J., Wang, Y., Kim, J. C., & Ceder, G. (2015). Interface stability in solid-state batteries. *Chemistry of Materials*, *28*(1), 266-273.

3. Zhu, Y., He, X., & Mo, Y. (2016). First principles study on electrochemical and chemical stability of solid electrolyte–electrode interfaces in all-solid-state Li-ion batteries. *Journal of Materials Chemistry A*, *4*(9), 3253-3266.

4. Chen, S., Xie, D., Liu, G., Mwizerwa, J. P., Zhang, Q., Zhao, Y., ... & Yao, X. (2018). Sulfide solid electrolytes for all-solid-state lithium batteries: structure, conductivity, stability and application. *Energy Storage Materials*, *14*, 58-74.

5. Seino, Y., Ota, T., Takada, K., Hayashi, A., & Tatsumisago, M. (2014). A sulphide lithium super ion conductor is superior to liquid ion conductors for use in rechargeable batteries. *Energy & Environmental Science*, *7*(2), 627-631.

6. Kamaya, N., Homma, K., Yamakawa, Y., Hirayama, M., Kanno, R., Yonemura, M., ... & Mitsui, A. (2011). A lithium superionic conductor. *Nature materials*, *10*(9), 682.

7. Deng, Z., Wang, Z., Chu, I. H., Luo, J., & Ong, S. P. (2016). Elastic properties of alkali superionic conductor electrolytes from first principles calculations. *Journal of The Electrochemical Society*, *163*(2), A67-A74.

8. Sakuda, A., Hayashi, A., & Tatsumisago, M. (2013). Sulfide solid electrolyte with favorable mechanical property for all-solid-state lithium battery. *Scientific reports*, *3*, 2261.

9. Hayashi, A., Hama, S., Morimoto, H., Tatsumisago, M., & Minami, T. (2001). Preparation of Li2S–P2S5 amorphous solid electrolytes by mechanical milling. *Journal of the American Ceramic Society*, *84*(2), 477-79.

10. Zheng, F., Kotobuki, M., Song, S., Lai, M. O., & Lu, L. (2018). Review on solid electrolytes for all-solid-state lithium-ion batteries. *Journal of Power Sources*, *389*, 198-213.

11. Tian, F., Radin, M. D., & Siegel, D. J. (2014). Enhanced charge transport in amorphous Li2O2. *Chemistry of Materials*, *26*(9), 2952-2959.

12. Ohara, K., Mitsui, A., Mori, M., Onodera, Y., Shiotani, S., Koyama, Y., ... & Fukunaga, T. (2016). Structural and electronic features of binary Li 2 SP 2 S 5 glasses. *Scientific reports*, *6*, 21302.

13. Dietrich, C., Weber, D. A., Sedlmaier, S. J., Indris, S., Culver, S. P., Walter, D., ... & Zeier, W. G. (2017). Lithium ion conductivity in Li 2 S–P 2 S 5 glasses–building units and local structure evolution during the crystallization of superionic conductors Li 3 PS 4, Li 7 P 3 S 11 and Li 4 P 2 S 7. *Journal of Materials Chemistry A*, *5*(34), 18111-18119.

14. de Klerk, N. J., van der Maas, E., & Wagemaker, M. (2018). Analysis of diffusion in solid-state electrolytes through MD simulations, improvement of the Li-ion conductivity in β-Li3PS4 as an example. *ACS applied energy materials*, *1*(7), 3230-3242.

15. Kudu, Ö. U., Famprikis, T., Fleutot, B., Braida, M. D., Le Mercier, T., Islam, M. S., & Masquelier, C. (2018). A review of structural properties and synthesis methods of solid electrolyte materials in the Li2S− P2S5 binary system. *Journal of Power Sources*, *407*, 31-43.

16. Hori, S., Kato, M., Suzuki, K., Hirayama, M., Kato, Y., & Kanno, R. (2015). Phase Diagram of the Li4GeS4–Li3 PS 4 Quasi-Binary System Containing the Superionic Conductor Li10GeP2S12. *Journal of the American Ceramic Society*, *98*(10), 3352-3360.

17. Ouyang, B., Wang, Y., Sun, Y., & Ceder, G. (2020). Computational investigation of halogen-substituted Na argyrodites as solid-state superionic conductors. *Chemistry of Materials*, *32*(5), 1896-1903.

18. Ong, S. P., Mo, Y., Richards, W. D., Miara, L., Lee, H. S. & Ceder, G. (2013) Phase stability, electrochemical stability and ionic conductivity of the $Li_{10\pm1}MP_2X_{12}$ (M = Ge, Si, Sn, Al or P, and X = O, S or Se) family of superionic conductors, Energy & Environmental Sciences, 6(1), 148-156

19. Zhang, W., Seo, D. H., Chen, T., Wu, L., Topsakal, M., Zhu, Y., ... & Wang, F. (2020). Kinetic pathways of ionic transport in fast-charging lithium titanate. *Science*, *367*(6481), 1030-1034.

II.6.E Characterization and Modeling of Li-Metal Batteries: Force field theory and Li-S battery simulations (Lawrence Berkeley National Laboratory)

Lin-Wang Wang, Principle Investigator
Lawrence Berkeley National Laboratory
One cyclotron road, MS-66
Berkeley, CA, 94760
E-mail: lwwang@lbl.gov

Tien Duong, DOE Technology Development Manager
U.S. Department of Energy
E-mail: Tien.Duong@ee.doe.gov

Start Date: October 1, 2019 End Date: September 30, 2020
Total Project Cost: $225,000 DOE share: $225,000 Non-DOE share: $0

Project Introduction

Making the Li-S battery a commercial reality will have a major impact on society and also help to realize the VTO goal of 500 km per charge for EV. However, the nature of chemical reaction makes it different from the traditional intercalation-based Li-ion battery. The molecular nature of Li_2S_n also allows solvation in the electrolyte. To address these problems, it is essential to have fundamental studies and understandings of the underlying mechanisms. Theoretical simulations can play an important role in discovering and designing new cathode materials. However, traditional ab initio calculations are limited by their computational size, while the classical force field simulations are limited by their accuracy and the lack of adequate force field. The development of ML-FF can overcome these problems by bridging the size gap between the ab initio simulation and the real systems needed to be studied.

Objectives

The project objective is to develop force field based on ab initio calculations to study Li-S cathode and Li liquid electrolyte. It also includes designs for Li-S cathode systems for high gravimetric and volumetric capacities. Li diffusion in both liquid electrolyte in a confined space, and in Li-S cathode systems is a main focus of this sub-task. To enable the calculation of large systems, machine learning force field (ML-FF) trained on ab initio calculation data will also be developed. The success of this new approach will greatly expand the capability of the theoretical simulation for battery systems. Such ML-FF can also be used in combination with traditional classical force field to deal with the nonreactive parts of the system.

Approach

ML-FF will be developed by first running ab initio simulations, which can generate hundreds of thousands of data set. We have a unique capability of decomposing the total energy of a density functional theory (DFT) calculation into the energy of each atom. Compared to conventional DFT calculations, this increases the number of data by hundreds of time, an important requirement for ML model training. The dependence of the atomic energy to the local atomic bonding environment will be captured using ML methods. Three different ML approaches will be: linear fitting, neural network model, and Gaussian Process Regression (GPR) model. We will compare the efficacies of these models. In the meanwhile, we will also deal with the long rang Coulomb interactions existing in electrolyte system and the ionic species in the liquid electrolyte. The idea is to first fit the charge density of the system, and remove the long range electrostatic energy before the fitting of the local energy on each atoms. We will also design new Li-S, and Na-S cathode materials. In particular, we will design amorphous Li-S mixture, with some other materials (e.g., carbon nanotube, black carbon or electric conductive 2D materials). We will use our fixed potential electrochemistry calculation to study the electrolyte molecule decomposition near the surface of the anode.

Results

1. Long range Coulomb interaction in electrolyte

We have initiated a study of electrostatic potential calculation in Li electrolyte. This is for the machine learning (ML) force field (FF) development. As the current ML-FF model only describes the atomic energy dependence on the local atomic binding environment, it is incapable of describing any long range interaction. One major long range interaction is the Coulomb interaction. This will be a concern for the Li electrolyte, where the Li^+ ion and the counter anion (e.g, PF_6^-) can cause long range interaction. We have developed a way to fit the charge density around each atom. Using such charge density, the long range electrostatic interaction can be pre-calculated. Furthermore, this part of the energy can be taken out of the total energy expression of the DFT formalism. The hope is that, the remaining energy will be absent of such long range interaction. On the other hand, the fitted density part of the long range interaction can be presented in an analytical pair potential expression, which can be included in the force field calculation. Figure II.6.E.1 shows the original electrostatic potential versus the electrostatic potential after the removal of the fitted charge. One can see that after the removal of the fitted charge, the electrostatic potential is significantly smaller.

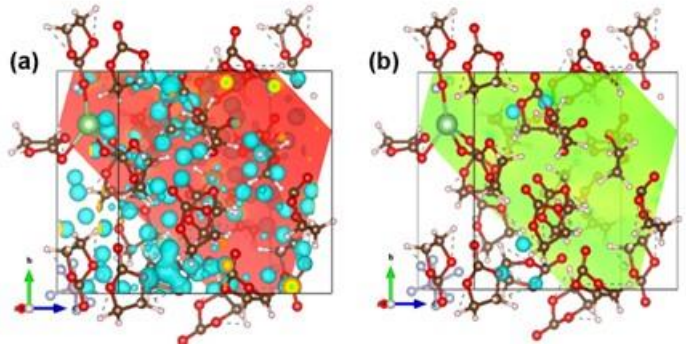

Figure II.6.E.1 the electrostatic potential in a Ethylene carbonate (EC) electrolyte with $LiPF_6$ salt. The Li^+ and PF_6^- can induce long range electric field. (a) is the full electrostatic potential, while (b) is the electrostatic potential after removing the fitting charge density electrostatic potential.

2. Force field for amorphous-S

We have developed machine learning force field (ML-FF) for S systems, this includes the S-S chain, and amorphous S. 100 atom amorphous S systems are first simulated under density functional theory (DFT) molecular dynamics simulations at different temperatures. We have generated atomic energy for each atom. These atomic energy together with their ab initio forces are used to train the ML-FF. This is different from other ML-FF effort where only the atomic forces are available, not the atomic energy. One of the purposes of this work is to test how well can the atomic descriptors (features) be used to describe the S systems when there are chemical interactions. We found it is particularly challenging to describe its interaction due to the chain like bonding structure in the system, which has some long range chemical bond propagation effects. We have also compared linear fitting scheme with a new scheme which includes derived features generated from the original features. These constitute different machine learning force field models to describe the system. We found such derived feature scheme can reduce the root mean square error of the energy prediction by a factor of 2 in some cases. We have used the developed ML-FF to carry out large system molecular dynamics simulations. Figure II.6.E.2 shows the typical amorphous S structure and the ML-FF predicted atomic energy versus the direct DFT calculated results.

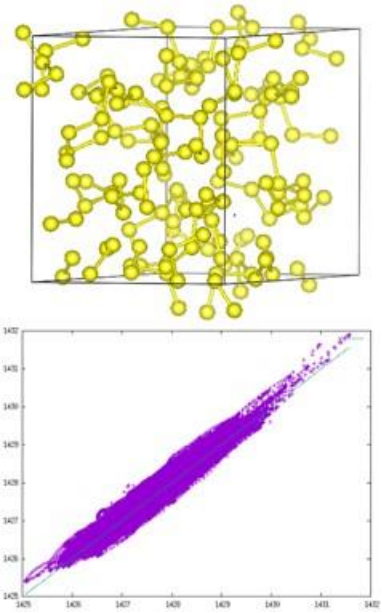

Figure II.6.E.2 upper panel: the amorphous S structure used for ML-FF training; bottom panel, the atomic S energy fitting, comparing the DFT results (horizontal axis, unit eV) with the ML-FF predicted results (vertical axis).

3. *Decomposition of electrolyte molecules near Li surface*

We have investigated the decomposition of ethylene carbonate near the surface of Li anode via a fix-potential method. The goal is to understand the mechanism for the formation of the solid electrolyte interface (SEI). At the high anode electrode voltage, it is known thermodynamically, the electrolyte molecule is unstable and can be reduced. The SEI can prevent such reduction process kinetically. Thus to understand the actual kinetic process of the reduction can shed some light on how the SEI is formed and perhaps help to design electrolytes for better protections. With Ab initio molecular dynamic simulation via the fix-potential method, we obtained two possible composition pathways during the decomposition of ethylene carbonate: $EC \rightarrow CO_3^{2-} + C_2H_4$ and $EC \rightarrow CO + OC_2H_4O^{2-}$ (as shown in Figure II.6.E.3). CO_3^{2-}, C_2H_4, CO, and $OC_2H_4O^{2-}$ are reported in the experimental literature. By analyzing these two decomposition pathways, we can find key factors, such as charge transfer and local atomic structures, which determine the decomposition process. Based on such knowledge, one can provide suggestions for how to control the decompositions. For this study, it is critical to be able to carry out fixed potential (grand canonical) ab initio molecular dynamics.

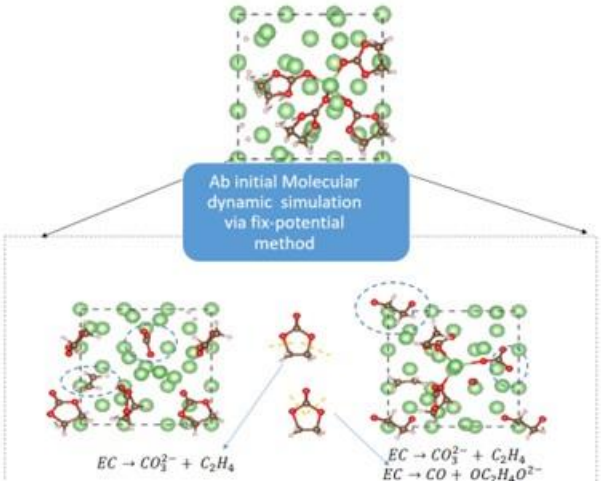

Figure II.6.E.3 the possible composition of solid electrolyte interface obtained via Ab initial molecular dynamic simulation under fix-potential method.

4. *Mixture of carbon nanotube with amorphous Li-S*

Carbon nanotube is wildly used as an additive in the cathode of Li-S battery due to its good electronic conductivity. How the carbon nanotube interact with S and Li-S system is largely unknown. We have tried to explore other roles beyond the electric conductivity that carbon nanotube plays in Li-S battery via *ab initio* molecular dynamics. In particular, we like to know in what cases, the system is stable upon repeated charging and discharging process. In Figure II.6.E.4, we show that, there is no obvious chemical interaction between an empty carbon nanotube and amorphous S. In that case, when Li is added in the system, the Li-S can crash the empty carbon nanotube, makes it forming additional bonds. Thus we propose that such a system can become unstable upon repeated charging and discharging. On the other hand, if the carbon nanotube can be filled with Li atom from the beginning, then the carbon nanotube maintains a good bonding topology during the discharging (lithiation) process, except the shape changes from circle into oval. After the charging process (removing the Li from Li-S), the carbon nanotube recoveries to its initial condition. Therefore, only when the carbon atom is filled with Li, the system is stable for charge/discharge process. This is a case for extremely fine grain mixing between the carbon nanotube and the Li-S system. The purpose of this simulation is to see whether it is possible to make stable carbon nanotube and S mixture to be used as S battery cathode. The carbon nanotube can make such bulk system electric conductive, overcoming of the obstacle for S cathode.

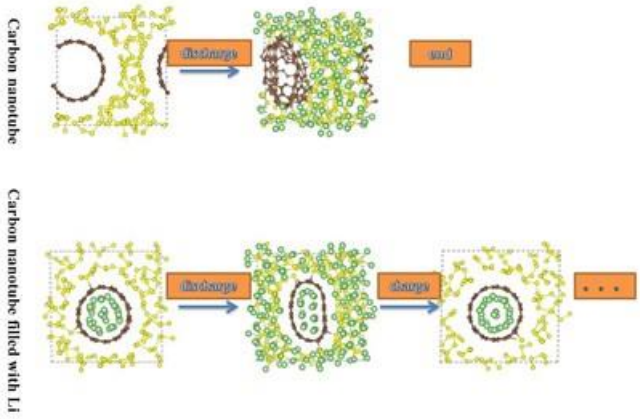

Figure II.6.E.4 the interaction of S and Li-S with Carbon nanotube with /without internal filling with Li.

5. *Vulcanization of conductive polymer as Li-S battery cathode*

We have proposed a practical approach to utilize the conductive polymer, poly (2-vinyl, 1, 4-phenylene sulfide), via vulcanization as a Li-S cathode (Figure II.6.E.5). Such an approach is to address the issue of conductivity, low S content, and short cycling performance in conventional polymer as cathode. Our theoretical investigation aims to answer the fundamental questions in such designs, including the limit of gravimetric and specific capacities, the structure stability, and electronic conductivity in such systems. We found that: (1) The unsaturated C=C bonds in the edge is the most active sites for vulcanization via crosslinking; (2) substituting one hydrogen of poly (1, 4-phenylene sulfide) with the vinyl group, the simplest S vulcanization sites with edge C=C bond, has almost no influence on the conductivity of the backbone; (3) the most stable S chains for vulcanization on the polymer are S6*; (4) the S content obtained in our approach is extremely high: if 1/3 of the vinyl groups are vulcanization, the S content is 49% in weight, and the value can reach to 69% while all the vinyl groups are vulcanization. (5) During the lithiation process, the Li atoms break down all the S-S bonds to form LixSτ clusters gradually. However, the LixSτ clusters are restricted by the polymers via the strong covalent C-S bonds, which suppress polysulfides shuttling phenomena effectively. (6) these polymer cathodes exhibit a unique redox process with only one discharge voltage plateau which corresponds to the single discharge product Li2S; (7) The maximum specific capacity and gravimetric energy densities for crosslinking polymers are 672 mAh/g and 1018 Wh/kg, respectively, which are more than twice the state-of-the-art Li-S value obtained by OXIS Energy Ltd(450 Wh/kg). (8) The dissolution energies in the crosslinking polymer case are positive throughout the whole discharge process, indicating the crosslinking polymer can restrict the shuttling effect efficiently in the whole discharge process. This means overall such conductive polymer substituted via vinyl group for vulcanization can be effective as Li-S cathode.

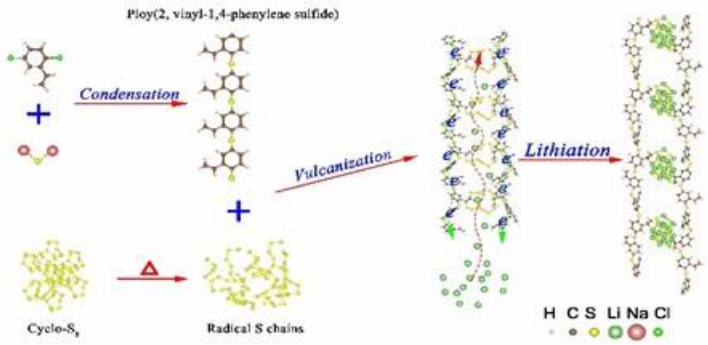

Figure II.6.E.5 Schematic illustration of the preparation of Li-S cathode with poly (2-vinyl, 1, 4-phenylene sulfide)

6. *Block copolymer as binder*

We have collaborated with experimental group to understand the function of the partially swellable block-copolymer as a binder for lithium-sulfur batteries (Figure II.6.E.6). The synthesized block-copolymers is consisted with both ethylene oxide unit and styrene unit, and it is utilized as binder for lithium sulfur batteries. The improved electrochemical performance is attributed to the synergistic effects contributed by different units of block-copolymer. Based on density functional theory calculations, we find that ethylene oxide unit is able to trap polysulfide which strongly bond with the intermediate lithium polysulfide, and enhance the transport of Li-ions to reach high capacity. The adsorption energy of lithium polysulfide is much stronger than that of PVdF by 2.2-3.2 times. Meanwhile, the styrene unit plays the role to maintain cathodes integrity by promoting the mechanical properties and elasticity

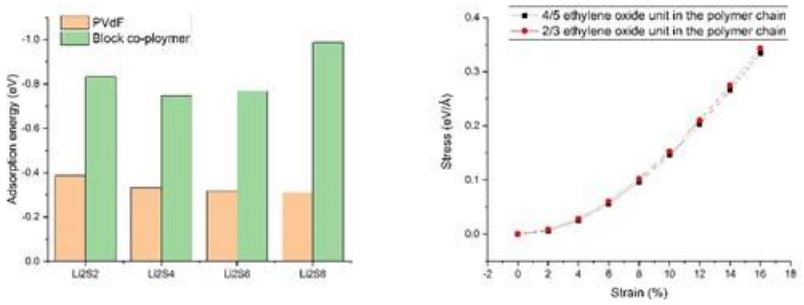

Figure II.6.E.6 (a) the adsorption energy of lithium polysulfide on PDvF and block co-ploymer, (b) the mechanical properties of co-ploymer with different enthylene ratio.

of the constructed block copolymer in order to accommodate the large volume changes. We also found that the optimized enthylene and stryrene ratio is 2:1 for the best mechanical properties

Conclusions

In conclusion, we have focused on two topics in the last year: the machine learning force field (ML-FF) development for electrolyte and S systems, and the Li-S cathode materials. For the ML-FF development, we have studied the long range Coulomb interaction effect. We have developed a method to fit the molecule charge density using spherical charge around the atom. When this fitted charge density is removed from the system, the remaining electrostatic potential is much smaller, hence the long range effect will be smaller. We have also tested different atomic descriptors for amorphous-S ML-FF. Different machine learning models are also used to test the accuracy of such ML-FF. For electrolyte stability, we have used the fixed potential grand canonical method and ab initio molecular dynamics to simulate the decomposition of ethylene carbonate. We found two different pathways for the decomposition, depending on the atomic micro environment. For the Li-S cathodes, we have studied the mixture of amorphous Li-S system and the carbon nanotube. We found that when the carbon nanotube is filled with Li, the system is stable. We have also studied gravimetric and volumetric capacities of vulcanized conductive polymer as the Li-S cathode material. We found that the cross linking vulcanization has larger capacities. Finally, in collaboration with experimental groups, we have studied the block copolymer as binder, and we have studies their binding energy with different Li-S clusters.

Key Publications

1. G. Zhou, A. Yang, Y. Wang, G. Gao, A. Pei, X. Yu, Y. Zhu, L. Zong, B. Liu, J. Xu, N. Liu, J. Zhang, Y. Li, L.W. Wang, H. Hwang, M. Brongersma, S. Chu, Y. Cui, "Electrotunable liquid sulphur mircodroplets", Nat. Comm. 11, 606 (2020).

2. B. Zhang, Z. Lin, H. Dong, L.W. Wang, F. Pan, "Revealing cooperative Li-ion migration in Li1+xAlxTi2-x(PO4)3 solid state electrolyte with high Al doping", J. Mat. Chem. A 8, 342 (2020).

3. G. Zhou, A. Yang, G. Gao, X. Yu, J. Xu, C. Liu, Y. Ye, A. Pei, Y. Wu, Y. Peng, Y. Li, Z. Yang, K. Liu L.W. Wang, Y. Cui, " Super-cooled liquid sulfur maintained in three-dimensional current collector for high-performance Li-S batteries", Sci. Adv. 6, eaay5098. (2020).

4. G. Gao, F. Zheng, L.W. Wang, " Design via Stacking 2D Conductive Microporous Coordination Polymers and Amorphous Li–S Layers ", Chem. Mat. 32, 1974 (2020)

5. G. Gao, X. Sun, L.W. Wang, “Inverse vulcanized conductive polymer for Li-S battery cathode”, J. Mat. Chem. A, 8, 21711 (2020).

6. X. He, Z. Liu, G. Gao, X. Liu, M. Swietoslawski, J. Feng, G. Liu, L.W. Wang, R. Kostecki, "Revealing the working mechanism of a multi-functional block copolymer binder for lithium-sulfur batteries", J. Energy Chem. 59, 1 (2021).

II.6.F Dendrite Growth Morphology Modeling in Liquid and Solid Electrolytes (MSU)

Yue Qi, Principal Investigator
Michigan State University
3509 Engineering Building
East Lansing, MI, 48824
E-mail: yueqi@egr.msu.edu

Tien Duong, DOE Technology Development Manager
U.S. Department of Energy
E-mail: Tien.Duong@ee.doe.gov

Start Date: January 1, 2017 End Date: June 30, 2020
Project Funding: $1,135,125 DOE share: $999,843 Non-DOE share: $135,282

Project Introduction

In this project, we will first develop a phase-field model to incorporate the electrochemical driving forces predicted from first principles simulations in liquid electrolytes and then incorporate mechanical driving forces to simulate dendrite growth in solid electrolytes with resolved microstructures. The μm-thick solid electrolytes will allow easier, direct comparison of modeling and experimental results, thus facilitating the validation of the electrochemical-mechanically driven Li-dendrite growth model. Last but not least, the computational model for solid electrolytes can also be applied to study and design nm-thin artificial SEI on Li metal surface. Therefore, this atomically-informed phase-field model will allow us to design the desired properties of artificial SEI coating to suppress dendrite growth in liquid-electrolyte and the microstructure of a solid-electrolyte to be dendrite-resistant during cycling. This model will enable the design of durable and safe Li-anodes for Li-S, Li-air, all-solid Li-ion batteries, as well as high energy density Li-ion batteries, lead to batteries that meet DOE's target for the high energy batteries cell density (>350 Wh/kg) for EV applications and cost below $100/kWh.

Objectives

The ultimate goal of this project is to develop a validated model to predict Li dendrite morphology evolution in both liquid and solid electrolytes during electrodeposition and stripping, in order to accelerate the adoption of Li metal electrodes in current and emerging battery technologies. To achieve this goal, the project has four objects:

1. formulate a general framework that captures the electrochemical-mechanical driving forces for Li morphology evolution;
2. consider the role of the nm-thin SEI in liquid-electrolytes as well as the microstructures of mm-thick solid-electrolytes for Li morphology evolution;
3. connect micron-scale phase-field models and atomic-scale DFT-based simulations via parameter- and relationship-passing in order to predict Li dendrite nucleation and growth kinetics and morphology; and
4. validate the key input parameters and main conclusions of the multi-scale model as new capabilities being developed step-by-step.

Approach

This project will develop a multi-scale model that connects micron-scale phase-field models and atomic-scale DFT-based simulations via parameter- and relationship-passing in order to predict Li-metal dendrite morphology evolution, in both liquid and solid electrolytes. The key innovation of this project is to capture the electrochemical-mechanical driving forces and incorporate the roles of nm-thin solid electrolyte interphase (SEI) in liquid electrolytes as well as of the microstructures of μm-thick solid electrolytes for all-solid-state

batteries. Our strategy to study Li dendrite morphology in both liquid and solid electrolytes allows us to share many similar governing equations and common mechanisms, to gradually increase the complexity of the model, and to validate the model step-by-step for its crucial input parameters and main conclusions through tailored experiments.

Results

This project successfully ended in June of 2020. In this project, we have formulated and implemented phase-field models to incorporate the electrochemical driving forces in liquid electrolytes and then incorporate mechanical driving forces to simulate dendrite growth in solid electrolytes with resolved microstructures. We have implemented two treatments for the SEI: an **explicit model** to include the microstructure of the SE or SEI in the phase field model and an **implicit model** to simulate the impact of nano-meter thick SEI in liquid electrolytes by varying the electrode/electrolyte interfacial properties. The key interfacial properties, including the electronic and ionic transport properties, the charge transfer reaction kinetics, and mechanical properties, were computed by DFT-based calculations. At the DFT-based model, a major advancement is to directly predict the charge transfer reaction kinetics at a complex Li/SEI/electrolyte interface by linking DFT with density functional tight binding (DFTB) calculations. As the main accomplishments, we have demonstrated two successful predictions in both solid electrolyte (Figure II.6.F.1 a) and liquid electrolyte (Figure II.6.F.1 b) based on this multiscale approach (as shown in Figure II.6.F.1). The predicted intergranular Li dendrite growth in LLZO (Figure II.6.F.1 a) revealed the importance of trapped electrons at internal interfaces in the microstructure of LLZO. The predicted electroplating morphology of mossy Li and faceted Mg (Figure II.6.F.1 b) agreed well with experiments.

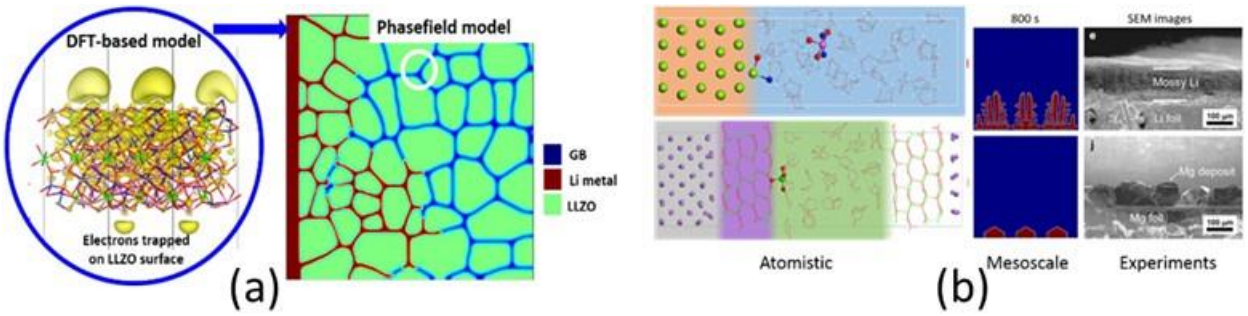

Figure II.6.F.1 (a) Demonstrating the excess electrons at the internal surfaces and grain boundaries in LLZO facilitate Li dendrite growth in solid electrolytes; (b) Revealing the difference in cation de-solvation-induced exchange current is mainly responsible for the dramatically different dendritic Li-plating and smooth Mg-plating.

An implicit multiscale dendrite morphology simulation method has been developed. In this formulation, the role of SEI is included implicitly via interfacial properties. We applied this model to simulate Li and Mg electrodeposition morphologies. The key input parameters for the phase field model were based on DFT and DFTB calculations, as listed in Table II.6.F.1. The model successfully captured the experimentally observed morphology difference: a mossy Li and a smooth faceted Mg (Figure II.6.F.1 b). The success of the model relies on the phase field model that captures the important electrochemical driving forces and the parameters developed from atomistic simulations. In particular, we have computed the cation desolvation energy barrier, ΔE_{de-sol}, in Li and Mg electrode systems (with different electrolytes) and linked it to the electrochemical reaction kinetics, Butler-Volmer equation, and the equilibrium exchange current density, as

1. $i_0^{Li} = B_0^{Li}(1-\theta)^{N_{sol}^{Li}} \exp\left(-\frac{\Delta E_{de-sol}^{Li}}{RT}\right)$ (Eq 1a)
2. $i_0^{Mg} = 2B_0^{Mg}(1-\theta)^{N_{sol}^{Mg}} \exp\left(-\frac{\Delta E_{de-sol}^{Mg}}{RT}\right)$ (Eq 1b)

While B_0 is a constant, $N_{sol}(\geq 1)$ is the number of available reaction sites that is related to the solvation shell radius (r_i) and the electrode surface structure; θ is the mean coverage fraction of the adsorbed solvated-cations onto the electrode surface; and ΔE_{de-sol} is the de-solvation energy.

Table II.6.F.1 Comparison of Li and Mg electrodeposition parametric inputs for bridging atomic calculations and phase-field modeling

Methods	Properties	$Li^+ + e^- \rightarrow Li^0$	$Mg^{2+} + 2e^- \rightarrow Mg^0$
Experiments	Morphology	More dendrite	More faceted
	SEI	Li_2CO_3, LiF, etc.	No-SEI
	Electrolyte	EC-DMC/$LiPF_6$	Mg-$(AlCl_2BuEt)_2$/LiCl/THF
Atomic Simulation	Surface energy (J m^{-2})	0.46 ~ 0.53 for Li (001), (011) and (111)	0.54 ~ 0.72 for Mg (0001), $(10\bar{1}0)$ and $(11\bar{2}0)$
	Lattice Constants a_i (nm)	0.34 (100) plane	0.32 (0001) plane
	Solvation structures	$Li(EC)_5$	$MgCl^+ \bullet (THF)_3$
	Cation Solvation energy (eV/atom)	5.2-5.5	19.71
	Chemical potential difference (eV/atom)	1.26 (thermo-cycle)	2.59 (thermo-cycle)
DFT results	Charge density (e nm^{-2}) on the electrode at $\eta = 0$	~ 0.50	~ 0.66
	Desolvation structure	$Li(EC)_2$	$MgCl^+ \bullet (THF)$
	Desolvation shell radius r_i (nm)	0.52	0.42
	Desolvation energy barrier ΔE_{de-sol} (eV) at $\eta = 0$	~ 0.41	~ 0.49
	mean coverage fraction θ	0.23	0.32
	solvation shell size parameter N_{sol}^M	4.29	3.20
Phase field Model Parameters	Charge of Cation n	1	2
	Average Surface Energy of metal κ_0 (J m^{-2})	0.49	0.73
	Crystallographic symmetry of metal ω	4	6
	2D Anisotropy of surface energy δ	0.04	0.09
	Exchange Current of electrodeposition i_0 (A m^{-2})	0.376	0.031

Inspired by the smooth morphology of Mg electrodeposition, we attempted to understand the key parameters that lead to the morphological differences between Mg and Li plating. In particular, a morphological evolution map (Figure II.6.A.2) was generated by controlling the most relevant parameters in the phase-field simulations, namely, the surface energy, anisotropy, and the exchange current. To demonstrate a transition between dendritic pattern and the as-observed dendrite-free morphology in Mg plating, we kept the 6-fold symmetry of Mg and the rest parameters from Li plating, and tuned each investigated property in a physical range covering most metal electrodeposition scenarios. By increasing the surface energy from 0.375 to 1 J m^{-2}, the secondary dendrite arms gradually vanish and the plating morphology becomes less mossy as shown in Figure II.6.A.2 a~ e. This is because the energy penalty for creating new surfaces increases and thus the secondary arms are eliminated to reduce the total energy. However, the remaining primary arms are still detrimental to battery safety due to the probability of separator penetration. By varying the anisotropy from 0 to 0.15, the splitting in dendrite's primary arms disappears while the tip growth rate increases slightly (Figure II.6.A.2 k ~ o). More

significantly, by decreasing the exchange current density from 2 times to 0.2 times of Li plating, the deposit morphology transforms notably from mossy dendrite ($2i_0^{Li}$) (Figure II.6.A.2j) to hexagonal faceted ($0.2i_0^{Li}$) (Figure II.6.A.2g). Moreover, when the exchange current is further decreased to $0.02i_0^{Li}$, the plating morphology starts to become spherical (Figure II.6.A.2f). This morphological variation demonstrates that the exchange current difference in Mg and Li is the main reason for the faceted morphology of the Mg deposit. Although the higher Mg metal surface energy, which originated from the stronger Mg-Mg bond strength at the atomic level, also contributes to the minimization of the total surface area, the lower exchange current of Mg plating is majorly responsible for the non-dendritic Mg deposit morphology. However, this does not mean Mg will never form dendrite during electrodeposition. Under specific experimental conditions (e.g. higher current density, larger overpotential, different electrolyte, poor initial surface condition, etc.), dendrite growth with Mg anodes is possible.

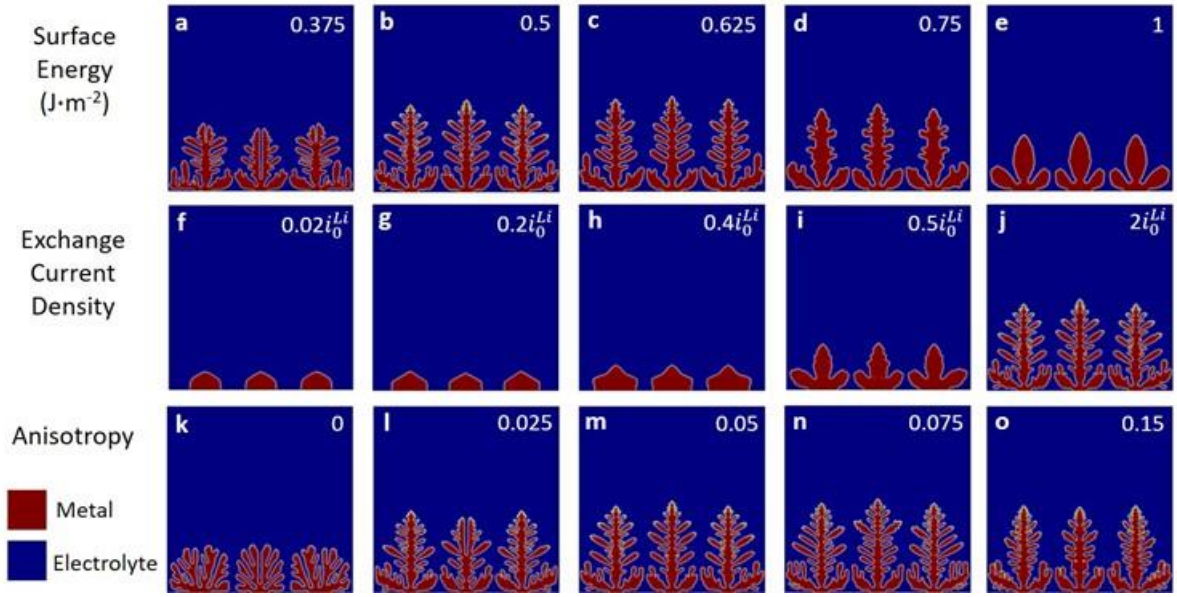

Figure II.6.F.2 (a) Metal electrodeposition parametric study. The plating morphology variation from systematic phase-field simulations by tuning the values of (a-e) surface energy, (f-j) exchange current, and (k-o) anisotropy. This work is currently under review by Cell Reports Physical Science.

Our model suggests that, under similar plating current and overpotential, the most effective approach to achieve dendrite free electrodeposition is lowering the intrinsic exchange current of electrodeposition reaction, I_0. This insight and Eq 1. suggests that a lower exchange current would be the most effective way to promote smooth surface electrodeposition. The DFT calculations revealed that the major factor responsible for the high desolvation energy for Mg is its multi-valence charge state and strong interaction with the solvent, including the anion addition of Cl^-. Therefore, electrolyte-engineering can be a promising approach to creating a dendrite-free smooth Li-plating surface. A number of experimental efforts have demonstrated that much less Li-dendrite formation can be related to the increase in ΔE_{de-sol}. For example, adding positive ions to create a shielding layer on the negative electrode surface was shown to increase ΔE_{de-sol} and lower i_0^{Li}. It should be pointed out that the current phase field model identified cation desolvation as the rate-limiting step and considered the impact of SEI on charge-transfer kinetics by modifying the effective parameters.

The explicit dendrite growth captures the impact of SEI microstructure on Li dendrite growth in liquid electrolyte turned its focus on the inhomogeneity at GBs or heterogeneous interfaces in the SEI, particular for the initial stage of dendrite nucleation at Li metal anode. Based on our study on electron trapping mechanism at GBs in solid electrolyte materials, it is anticipated the GBs in SEI are likely to serve as the electron conduction pathways, as the individual SEI components are wide bandgap insulators in their single crystalline. We have computed the electronic properties of representative grain boundaries of the main SEI components

(LiF, Li_2O, and Li_2S) on Li via DFT calculations. It was found that all the GB bandgaps were smaller than the corresponding bulk bandgap, with an order of amorphous GBs < Tilt GBs < Twist GBs < single crystal. Some GBs, such as the coherent Li_2S Tilt $\sum 3\ (\bar{1}2\bar{1})/[111]$ GB and the amorphous LiF GB showed empty electronic states lower than the Li^+/Li^0 depositing level. The isolated GB states can trap electrons from Li metal, leading to nucleation of metallic Li inside of the SEI and contributing to the Li dendrite growth. Structural analysis revealed that more under-coordinated atoms in the GBs caused larger bandgap drops and more excess electrons localization in the less dense GB regions. These insights suggested that dense SEI structures such as sharp interfaces and well-ordered GBs are preferred to design a fully electronically passivating SEI. Furthermore, an analytical model can be fitted to extrapolate the bandgaps of special GB structures based on the DFT-computable bulk and surface bandgaps to facilitate multiscale simulations.

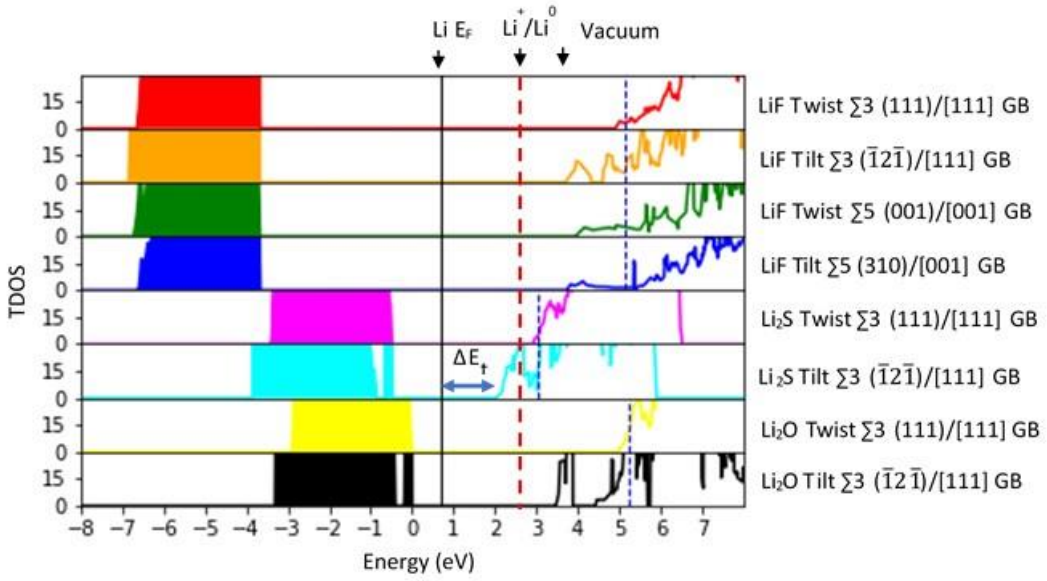

Figure II.6.F.3 Calculated TDOS for the eight GBs aligned with the vacuum level. The conduction band minimum (CBM) of bulk materials is labeled as the blue dash lines. The Fermi level of Li metal (Li E_F), the potential of the Li^+/Li^0 deposition and the vacuum level are marked by black arrows on the top of the figure. ΔE_t is the smallest tunneling barrier for electrons to transfer from the Li E_F to the lowest unoccupied GB states in the Li_2S Tilt $\sum 3\ (\bar{1}2\bar{1})/[111]$ GB.

The phase field model has been used to simulate SEI with different properties and microstructure (by explicit model) and provided guidance on the SEI Microstructure design. By varying exchange current, transport property of SEI (Figure II.6.A.4(a-d)) introducing porous structure (Figure II.6.A.4 (e-h)) and cracks (Figure II.6.A.4 (i-J) in SEI, and comparing SEI/Li interfacial adhesion properties,(Figure II.6.A.4 (k-l)), we have elucidated the impact of these factors on Li plating morphology. It can be seen that the most effective method to achieve a smooth plating surface, similar to those observed in Mg plating as shown in Figure II.6.A.4 (b)), was reducing the intrinsic exchange current, I_0. This can be achieved by increasing the de-solvation energy and/or increasing solvation shell size via electrolyte design, following the atomistic informed Butler-Volmer equation we developed. Another method to change the interface kinetics is to design a porous SEI with a high-zeta-potential sponge to change the concentration and current density profiles, which enabled dendrite-free plating/stripping of lithium (Figure II.6.A.4 (e-h)). Other structural failures, such as crack and delamination promoted dendrite growth.

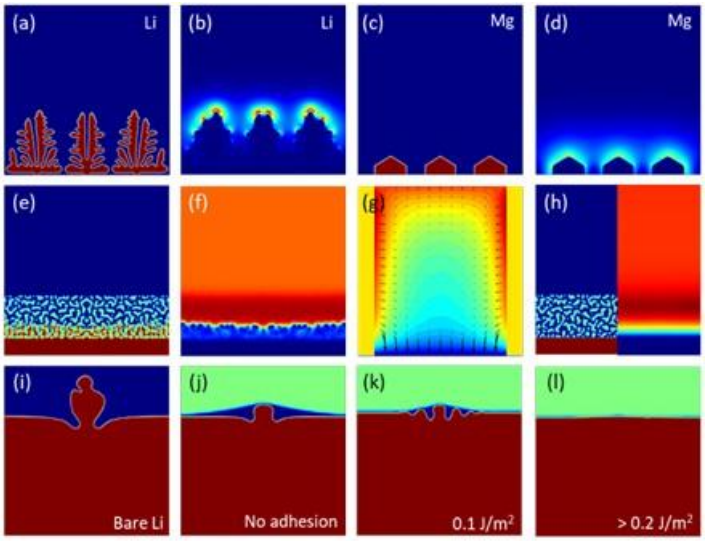

Figure II.6.F.4 Phase-field simulations on (a-d) Li and Mg plating morphologies using implicit SEI model; (e-h) Li dendrite suppression by Li+-affinity porous media at anode; (i-l) Li metal/coating interfacial adhesion impact on electrodeposition.

Conclusions

In summary, in this project, we have formulated and implemented phase-field models to incorporate the electrochemical driving forces in liquid electrolytes and then incorporate mechanical driving forces to simulate dendrite growth in solid electrolytes with resolved microstructures. We have implemented two treatments for the SEI: an **explicit model** to include the microstructure of the SE or SEI in the phase field model and an **implicit model** to simulate the impact of nano-meter thick SEI in liquid electrolytes by varying the electrode/electrolyte interfacial properties. The key interfacial properties were computed by DFT-based calculations. At the DFT-based model, one key advancement is to directly predict the charge transfer reaction kinetics at a complex Li/SEI/electrolyte interface by linking DFT with density functional tight binding (DFTB) calculations. The success of the model has been demonstrated.

Key Publications

1. B. Xu, Z. Liu, J. Li, X, Huang, B. Qie, T. Gong, L. Tan, X. Yang, D. Paley, M. Dontigny. K. Zaghib, X. Liao, Q. Cheng, H. Zhai, X. Chen, L.-Q. Chen, C-W Nan, Y.-H. Lin, Y. Yang, "Engineering interfacial adhesion for high-performance lithium metal anode", Nano Energy, 67 104242 (2020).

2. Z. Liu, Y. Li, Y. Ji, Q. Zhang, X. Xiao, Y. Yao, L-Q. Chen, Y. Qi, "Dendrite Free Li – Lesson Learned from the Li and Mg Electrodeposition Morphology Simulations", Submitted (2020).

3. J.G. Xu, B.S. Li, M. Wang, Q.L. Zhang, Y.Qi, X.C. Xiao, "Impact of Solid Electrolyte Interphases on Lithium Metal Plating and Stripping at Early Stages" to be submitted (2020)

Acknowledgements

The CoPIs for the project, Prof. Long Qing Cheng at Penn State University and Xingcheng Xiao and Qinglin Zhang at GM are acknowledged. Prof. Yan Yao from U. of Huston is acknowledged for the Li-Mg plating morphology work.

II.7 Next-Gen Li-ion: Low Temperature Electrolytes

II.7.A Ethylene Carbonate-Lean Electrolytes for Low Temperature, Safe Li-ion batteries (LBNL)

Bryan D. McCloskey, Principal Investigator
Lawrence Berkeley National Laboratory and University of California, Berkeley
201-D Gilman Hall
Berkeley, CA 94720
E-mail: bmcclosk@berkeley.edu

Mallory Clites, DOE Technology Development Manager
U.S. Department of Energy
E-mail: Mallory.Clites@ee.doe.gov

Start Date: October 1, 2019 End Date: September 30, 2022
Project Funding: $850,000 DOE share: $850,000 Non-DOE share: $0

Project Introduction

Conventional Li-ion battery electrolytes are comprised of lithium hexafluorophosphate ($LiPF_6$) dissolved in a mixture of linear and cyclic carbonates (e.g., 3:7 wt:wt ethylene carbonate (EC):ethyl methyl carbonate(EMC)), along with 1%–3 wt% of solid-electrolyte interface-stabilizing additives, such as fluorinated ethylene carbonate (FEC), vinylene carbonate (VC), or 1, 3-propane sultone (PS). While room-temperature viscosities and conductivities of these standard carbonate electrolytes are sufficiently high to allow good rate capabilities, the large volume fraction of ethylene carbonate, which is a solid at 25 ºC and relatively viscous even at slightly elevated temperature, is problematic at low temperatures.

Our strategy is to reduce (or entirely eliminate) the ethylene carbonate fraction and replace it with abundant solvents that possess lower melting temperature and viscosity, thereby enhancing transport properties of the electrolyte at lower temperatures. However, in doing so, three key challenges need to be addressed. First, EC is an important component in stable and low resistivity graphite SEI formation, and therefore stability and resistivity of the solid electrolyte interface at the graphite anode will need to be engineered in EC-lean/free compositions through the inclusion of appropriate additives. We note that high SEI resistivity has been observed to be limiting in conventional electrolytes at low temperatures in prior studies, making interfacial impedance an important parameter in our studies. Second, the volatility of low melting point additives will need to be counterbalanced by the incorporation of other constituents that increase the electrolyte's flash point and therefore maintain safety. Third, EC possesses a high dielectric constant, making it an excellent solvent that enables high salt dissociation. Solvents of similar dielectric strength will need to be added to maintain salt dissociation and conductivity. For these reasons, and we will study two solvent systems, carbonate/linear ester mixtures, and solvents where EC is partially or fully replaced by γ-butyrolactone (a cyclic ester), each with the stabilizing additives mentioned above (FEC, VC, and PS) that have been selected from a survey of the literature.

Objectives

Our overall 3-year project goal is to develop an EC-lean/free electrolyte that provides optimal transport and graphite interfacial properties to enable high capacity (70% of room temperature capacity) at modest rates (C/3) during low temperature discharge (-20 ºC) of graphite|NMC622 cells. Specific objectives include:

1. Understanding the key properties (e.g., interfacial stability, interfacial impedance, or electrolyte transport) that limit cell capacity and performance at low temperatures in EC-lean, ester/lactone-rich electrolytes.

2. Identification of additive compositions that provide low interfacial resistance and good cycle stability specifically in EC-lean, ester/lactone-rich electrolytes at low and moderate temperatures.

3. Studying and optimizing transport properties (conductivity, transference number, and salt diffusion) of these electrolytes for low-temperature battery performance.

4. Applying results obtained in Li|graphite half cells and coin cell sized graphite|NMC622 full cells to select an optimized electrolyte composition that provides the low-temperature performance listed above in 100 mAh graphite|NMC622 pouch cells.

Approach

We will use a systematic approach in which we characterize the transport and interfacial effects of incorporating a moderate to large fraction of low viscosity, low melting point linear ester solvents into the electrolyte. GBL-rich electrolytes will also be studied given GBL's high dielectric constant, wide liquid temperature range, and relatively low viscosity compared to EC. In FY20, our initial studies focused on ensuring that our baseline electrolyte composition (1 M $LiPF_6$ in 3:7 wt:wt EC:EMC, or LP57) provided reliable results across the PI's laboratories. Interfacial resistivity can be overcome through the inclusion of additives such as FEC, VC, PS, and LiFDOB. We will use the numerous capabilities developed by the project PI's at LBNL to guide selection of optimal additive and solvent composition. Our approach will start with cells on the order of 1-3 mAh scale but will move to larger cells as our understanding of the optimal electrolyte properties improves. Both full graphite|NMC622 cells and graphite|Li cells will be used to ensure validity of our data analysis. Li|Li symmetric cells will be used in the analysis of electrolyte transport properties, and graphite single particle studies will be used in relevant *in-situ* spectroscopic characterizations. In FY20, our approach focused on understanding low temperature behavior of our baseline electrolyte, LP57, with graphite and $Li(Ni_{0.6}Co_{0.2}Mn_{0.2})O_2$ (NMC622) electrodes provided by the Cell Analysis, Prototyping, and Modelling (CAMP) facility at Argonne National Laboratory. However, in future years, we will target 3 important solvent parameters initially and use knowledge gained in these initial studies to guide further development later in the project: **1.** *Varying additive composition* (2%-3% wt. % FEC, VC, PS, and LiFDOB) in an EC:EMC electrolyte **2.** *Varying EC/EA content* with 2%-3% wt. % FEC, and **3.** *Varying EC/GBL content* with 2%-3% wt.% FEC.

Results

Electrochemical baseline and protocol development for Li_xC_6|NMC622 cells. Although our project was delayed by COVID by roughly 2 quarters, we were still able to make good progress towards establishing techniques and protocols to study low temperature battery performance. This year we conducted electrochemical performance evaluations of two sets of electrode materials provided by Argonne National Lab and established a methodology for accelerating the acquisition of the Arrhenius plot of energy and coulomb capacity *versus* discharge temperature. The first anode/ cathode pair was from the CAMP Facility, library #A-A015 graphite (nominal 1C capacity at 25 ^oC of 1.87 mAh/cm^2), and #A-C022 NMC622 (nominal 1C capacity of 1.41 mAh/cm^2). Weights of the individually punched electrodes indicated a cell to cell variability of 1.6 % for the cathode and 1.1 % for the anode; the coupling of the two electrodes into a full cell resulted in an excess anode to cathode capacity on the average 41% with a variability of 6.0 %. Despite the cell-to-cell variability, the cells cycled very well at 30 ^oC with little-to-no capacity fade in the first 150 cycles.

The metric of interest in the project is the discharge capacity at C/3 and the pulse power capability when the cell's temperature has been lowered to -20 ^oC following a charge at 30 ^oC. In our approach to understanding the decline in accessible capacity at lower temperatures, we measured the discharge capacity at temperatures between -20 and 30 ^oC. However, to avoid warming the cell to 30 ^oC, charging it at that temperature, then cooling the cell down to another cold temperature, and discharging it at C/3 at the new temperature, we decided a more efficient approach would be to charge the cell once at 30 ^oC, discharge the cell at -20 ^oC to the lower cutoff voltage, heat the cell to the next lowest temperature, say -10 ^oC, let it sit for 5 hours to thermally equilibrate, then discharge the cell again to the lower cutoff voltage and add the additional discharge capacity

from this step to that measured in the subsequent discharge steps, and repeat, until the cell was fully discharged at 30 °C. The data for A-A015/A-C022 electrode pair, with a cell capacity of approximately 1.5 mAh/cm^2 at 30 °C, is provided in Figure II.7.A.1. LP57 is used as the electrolyte. Here the data is plotted in an Arrhenius fashion of natural log of the discharged capacity *versus* the inverse of the discharge temperature in degrees Kelvin. This plot shows a change in slope at around -4 °C. Differential Scanning Calorimetry (DSC) measurements by the McCloskey Group of the pure electrolyte indicate that this is around the temperature at which the ethylene carbonate (EC) begins to freeze in the electrolyte solution. As provided on the figure, the slope at temperatures below - 4 °C is -360 K and the slope above -4 °C is -230 K. These values, when multiplied by the gas constant of 8.3145 J/mol K, give activation energies of 3.0 and 1.9 kJ/mol, respectively.

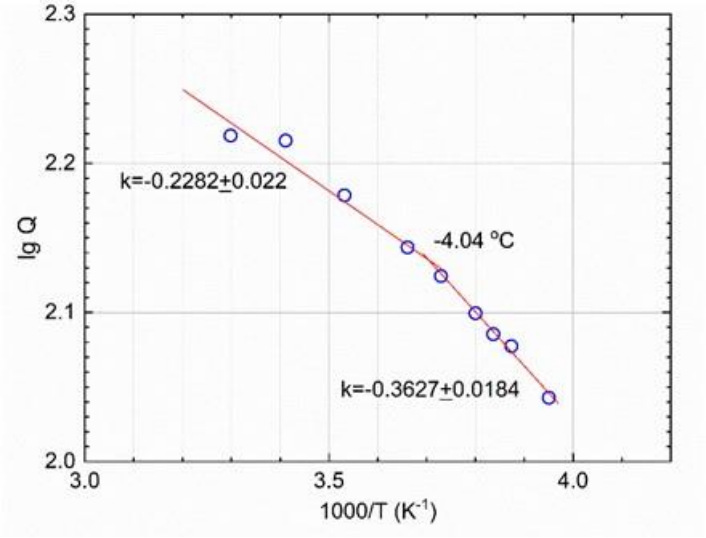

Figure II.7.A.1 Arrhenius plot of the natural log of discharge capacity versus the inverse of the discharge temperature for the first batch of electrodes with a capacity of 1.5 mAh/cm^2 at 30 °C. The values on the graph indicate the slope of the lines and the temperature at which the slope appears to shift.

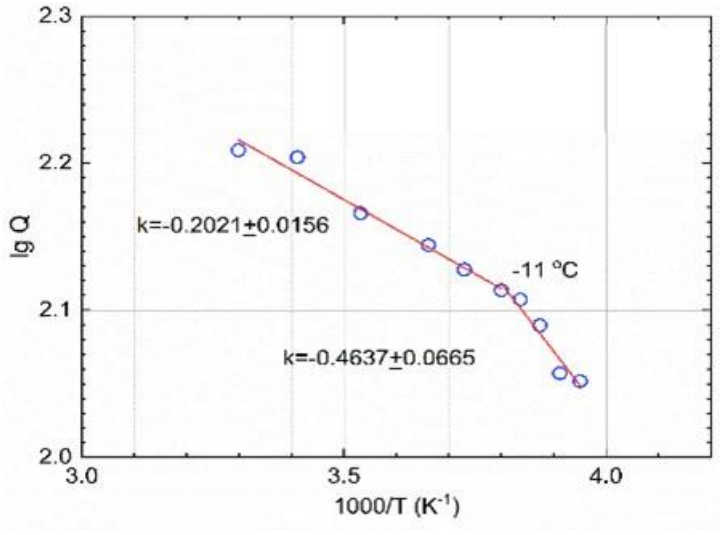

Figure II.7.A.2 Arrhenius plot of the natural log of discharge capacity versus the inverse of the discharge temperature for the second batch of electrodes with a capacity of 2.7 mAh/cm^2 at 30 °C. The values on the graph indicate the slope of the lines and the temperature at which the slope appears to shift.

Subsequently, we received a second batch of electrodes from Argonne, with a nominal graphite capacity of 2.9 mAh/cm^2 and a nominal NMC622 capacity of 2.5 mAh/cm^2, both at 25 °C. For this electrode pair, the capacity

of the full cells was around 2.7 mAh/cm^2, however, the cycle life was a little less consistent with capacity loss per cycle as high as 0.55 %. The Arrhenius plot of the capacity *versus* inverse of temperature is provided in Figure II.7.A.2. This figure is similar to the data in Figure II.7.A.1 for the lower loading electrodes with a low temperature activation energy of 3.9 kJ/mol and a higher temperature activation energy of 1.7 kJ/mol around a transition temperature of -11 ^{o}C.

Impedance and 3-electrode cell designs to understand origin of cell resistances. To understand the origin of resistive losses at low temperatures, we analyzed graphite|NMC622 cells with LP57 using two-electrode galvanostatic electrochemical impedance spectroscopy (GEIS) and a three-electrode cell (AuLi reference; ~0.32 V vs Li/Li$^+$) to monitor overpotential relaxation of the graphite and NMC electrodes. GEIS data was fit using an equivalent circuit that contained a porous electrode transmission line model, which was in series with an RC-circuit (to model the SEI resistance) and a series resistance (to model the bulk electrolyte resistance). Relevant resistances are extracted from our equivalent circuit and shown in Figure II.7.A.3. The results of the GEIS experiments, summarized in Figure II.7.A.3, indicate that the interfacial charge transfer resistance (R_{CT}) drastically increases with decreasing temperature (Figure II.7.A.3a) and its contribution to the total cell impedance also increases with decreasing temperature (Figure II.7.A.3b). At a temperature of -20^{o}C, this project's target for discharge performance, the R_{CT} contributes >85% of the full cell impedance. The charge transfer resistance is greatly influenced by the solvation environment of the Li$^+$ ions (i.e., the electrolyte composition), as well as the surface concentration of the Li$^+$ ions during the reaction, which is influenced by cell mass transport effects. Hence, a key outcome of this study is the need to understand ion solvation and its influence on interfacial kinetics, which we plan to study using molecular dynamics simulations in subsequent years.

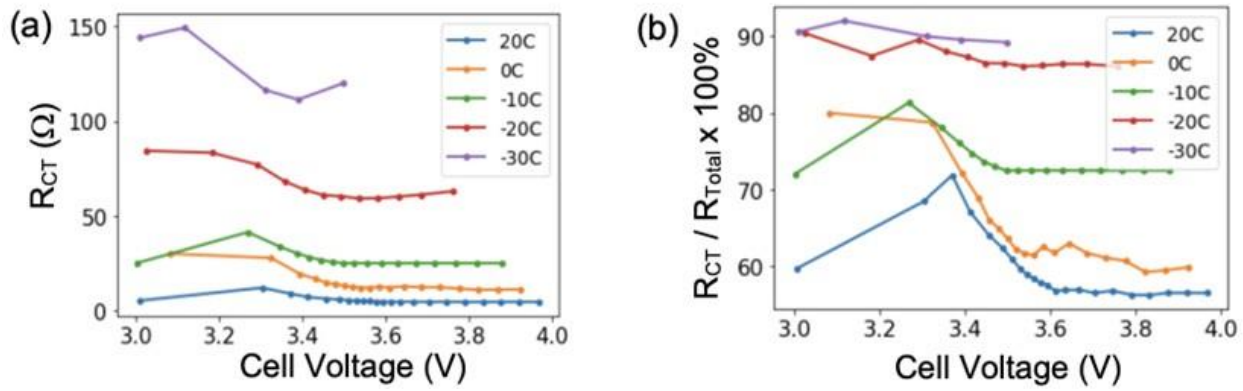

Figure II.7.A.3 The charge transfer resistance (R_{CT}) of an NMC/Gr coin cell with 1M $LiPF_6$ in EC:EMC (3:7 wt%; Gotion LP57) gathered during C/3 discharge at a range of temperature (a) and the percent contribution of the charge transfer resistance to the total impedance during the same discharges (b).

To understand the relative polarization at the anode and cathode during discharge, we monitored voltage relaxation in a three-electrode full cell after discharge in increments of 10% of capacity at a rate of C/3. Voltage was monitored during a 15 minute rest period after each increment. This was repeated at various temperatures—all with 30 ^{o}C charges after full discharge—and the magnitude of the total relaxation change was calculated for each electrode after each pulse. In other words, we calculate the voltage relaxation magnitudes as the difference in the voltage right at the end of the discharge and at the end of the 15 minute relaxation that immediately follows. A subset of these voltage relaxation magnitudes are summarized in Figure II.7.A.4. These results serve to estimate the relative overpotentials at each electrode during the entire discharge process at each temperature. At temperatures above -20^{o}C, the NMC622 cathode experiences much larger voltage relaxation magnitudes than the graphite anode at the end of the discharge, indicating overpotentials at the NMC622 limit the final achievable discharge capacity. However, at the target of -20^{o}C, the graphite electrode experiences the largest overpotentials throughout the discharge. Next steps for this work include gathering three-electrode full cell GEIS data to further elucidate the overpotential trends seen in Figure

II.7.A.4 and to determine which electrode is experiencing the largest fraction of the R_{CT} changes seen in Figure II.7.A.3. Subsequently, these techniques will be applied to inform the development of new electrolyte formulations that will show improved -20°C C/3 discharge performance compared to the baseline electrolyte.

T (°C)		1	2	3	4	5	6	7	8	9	10
20	Graphite	**28.2**	**23.3**	**23.4**	**25.8**	**28.9**	**28.0**	**27.7**	**28.6**	**62.0**	48.0
	NMC	18.1	18.1	17.7	17.3	17.0	18.2	18.8	22.6	28.7	**54.6**
0	Graphite	**55.0**	**47.5**	**47.0**	**50.8**	**58.5**	**62.2**	52.2	67.1	81.3*	----
	NMC	33.8	34.8	33.8	33.4	34.7	39.9	**58.2**	**122.3**	**266.2***	----
-20	Graphite	**167.0**	**193.5**	**208.8**	**229.6**	**220.5***	----	----	----	----	----
	NMC	102.9	95.6	98.7	114.8	144.0*	----	----	----	----	----

Figure II.7.A.4 The magnitude of the total relaxation (in mV) of the potential at both the graphite anode and the NMC622 cathode after 10% SOC pulses of C/3 at different temperatures. Bolded values indicate that this is the larger magnitude relaxation compared to the opposite electrode, starred (*) values indicate that the 3.0 V full cell voltage cutoff was reached before 10% of capacity was passed, and the dashed (----) entries indicate no pulses after 3.0 V.

Liquid electrolyte transport characterization using model electrolytes. We are in the process of developing capabilities to measure the full transport coefficients using the Newman-Balsara method. Given our prior experience with ether-based electrolytes, we first focused on fully characterizing a liquid electrolyte composed of lithium bis(trifluoromethanesulfonyl)imide (LiTFSI) salt dissolved in tetraethylene glycol dimethyl ether (tetraglyme) at varying salt concentrations. Fully characterizing the electrolyte consists of measuring conductivity, current fraction, salt diffusion coefficient, thermodynamic factor, and the transference number. Full characterization of liquid electrolytes can be difficult due to reaction between lithium electrodes and the electrolyte, potentially leading to inconsistent characterization of the electrolyte. LiTFSI/tetraglyme is a relatively stable liquid electrolyte system compared to conventional carbonate mixtures and is being used to refine the full characterization procedure and develop methods to check stability of the system, especially for low temperature conditions.

Conductivity values were measured in triplicate at 30 °C using a FiveEasy Conductivity Meter F30 and a two platinum pole conductivity probe from Mettler Toledo (Figure II.7.A.5). Conductivity increases as a function of salt concentration until a maximum is reached, after which conductivity decreases, as is expected. Current fraction, ρ_+ , also sometimes referred to as the ideal transference number, was measured at 30 °C using lithium-lithium symmetric coin cells with five layers of Celgard 2500, soaked in electrolyte. A constant dc polarization of ± 10 mV was applied to the cell and ac impedance data were collected every 20 minutes. The current fraction was calculated based on the following equation:

$$\rho_+ = \frac{I_{ss}}{I_\Omega}\left(\frac{\Delta V - I_\Omega R_{i,0}}{\Delta V - I_{ss} R_{i,ss}}\right)$$

where ΔV is the applied potential, I_{ss} is the steady state current, $R_{i,0}$ is the initial interfacial impedance, and $R_{i,ss}$ is the interfacial impedance at steady state. I_Ω is the initial current in the cell, determined via Ohm's law, assuming no concentration gradients prior to cell polarization.

$$I_\Omega = \frac{\Delta V}{R_T}$$

R_T is the total initial cell resistance before polarization, measured via ac impedance spectroscopy. Raw data are reported in Figure II.7.A.5. Over this salt concentration range, current fraction decreases up until a r value (the ratio of Li^+ concentration to ether oxygen concentration) of about 0.12, after which it appears to begin increasing.

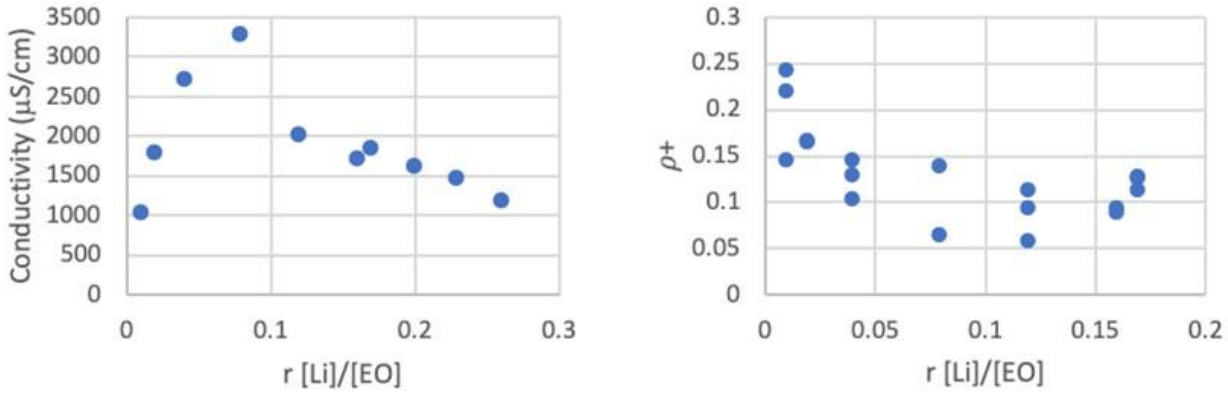

Figure II.7.A.5 Left panel: Conductivity of LiTFSI/tetraglyme of varying concentrations (averaged data). Right: Current fraction for LiTFSI/tetraglyme system at varying concentrations (non-averaged data).

Going forward, we will focus on finalizing full characterization of LiTFSI/tetraglyme at 30 °C and beginning characterization at lower temperatures, including 0 °C and -20 °C. After this, we will begin full characterization of a conventional carbonate based electrolyte, 3:7 vol:vol EMC:EC, both at room temperature and low temperature, with an emphasis on maintaining stability at the electrode-electrolyte interface to reliably characterize this electrolyte in lithium-lithium symmetric cells.

Molecular dynamics simulations to understand ion solvation and dynamics. We have used classical molecular dynamics simulations to characterize the baseline electrolyte, LP57, as a function of temperature from 25 to -20°C. These simulations employ the commonly-used optimized potentials for liquid simulations (OPLS) force field, which we have validated for this particular system by comparing to experimental conductivity data. By analyzing the structural and bulk transport properties of the electrolyte, we are working to understand the molecular-level processes which dictate the decreased performance of these systems at low temperatures. Intuitively, we might expect some combination of increased ion aggregation (fewer charge carriers), increased viscosity, and potentially decreased cation transference number to all contribute to greater concentration overpotentials during cycling at low temperature. We find, however, that ion pairing actually *decreases* at lower temperatures (Figure II.7.A.6). This is likely due in part to an increase in the dielectric constant at low temperature and further suggests that ion pairing may be entropically favorable, as it results in the release of free solvent molecules. Furthermore, we find that the cation transference number is relatively constant as a function of temperature. Thus, the main phenomenon leading to poor transport at low temperature is increased viscosity, which we indirectly quantify via each of the species' self-diffusion coefficients. These diffusion coefficients decrease as temperature decreases, approximately following an Arrhenius relation.

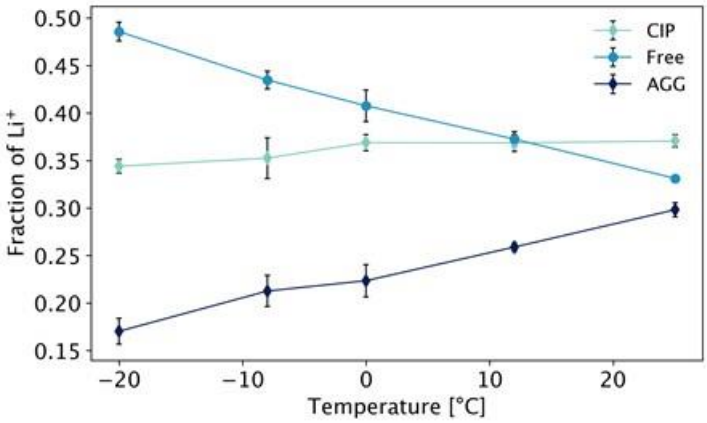

Figure II.7.A.6 Li-ion speciation as a function of temperature in the baseline electrolyte. As temperature decreases, the fraction of free ions increases while the fraction of contact ion pairs (CIP) and larger aggregates (>2 species in cluster, AGG) decreases.

In addition to properties of the bulk electrolyte, it is hypothesized that interfacial resistances, particularly those due to the large desolvation energy of the Li-ion, may be important in limiting low temperature battery

performance. While it is difficult to explicitly model interfacial phenomena using molecular dynamics, we propose using the ion-solvent residence times (the average time a given solvent molecule remains associated to a Li-ion before exchanging with another solvent molecular or an anion) as a proxy for the desolvation energy. We have characterized the residence times in the baseline electrolyte and have found that solvation shell residence times generally increase as temperature decreases, in accordance with the greater viscosity of the low temperature systems. Further, we find that the Li-EMC residence times are lower than those for Li-EC, as expected from the larger donor number of EC. We are currently working to develop a more rigorous understanding of how the thermodynamics and kinetics of ion residence times can be explicitly related to desolvation energy.

Finally, we have begun simulations of electrolytes which replace some fraction of the EC with gamma-butyrolactone (GBL). We find that while this low-viscosity co-solvent results in increased self-diffusion of all species, it also yields increased ion pairing (consistent with the fact that the dielectric constant of GBL is lower than that of EC). The competition between these two factors results in conductivity roughly equivalent to that of the baseline electrolyte. Our future work will focus on continuing simulations of these GBL-based electrolytes, specifically aiming to understand the effect of GBL on the aforementioned ion-solvent residence times.

Conclusions

The key conclusions from our research this year are:

1. When logarithm of discharge capacity is plotted against the inverse of discharge temperature, a slope change occurs around the observed freezing point of EC in LP57, indicating that its presence deleteriously impacts discharge capacity at low temperatures.

2. Charge transfer resistance was observed to dominate the cell resistance at sub-freezing (< 0 ^{o}C) temperatures.

3. At low temperatures, polarization at both the anode and cathode are significant, such that understanding how electrolyte composition impacts charge transfer resistance at both electrodes will be critical in subsequent years.

4. Molecular dynamics simulations show that ion pairing in LP57 actually decreases at lower temperatures due in part to an increase in the dielectric constant at low temperature. Thus, the main phenomenon leading to poor transport at low temperature is increased viscosity.

Acknowledgements

This section was coauthored by co-PIs Kristin Persson, Gao Liu, Nitash Balsara, Vincent Battaglia, Robert Kostecki, and Wei Tong, as well as Kara Fong, Alexandra Ringsby, David Brown, Dion Hubble, Yanbao Fu, and Triesha Singh. We also thank Bryant Polzin, Andrew Jansen, and their CAMP Facility colleagues for providing the graphite and NMC622 electrodes used in our studies.

II.7.B Fluorinated Solvent-Based Electrolytes for Low Temperature Li-ion Battery (ANL)

Zhengcheng (John) Zhang, Principal Investigator
Argonne National Laboratory
9700 S Cass Ave
Lemont, IL 60439
E-mail: zzhang@anl.gov

Peter Faguy, DOE Technology Development Manager
U.S. Department of Energy
E-mail: Peter.Faguy@ee.doe.gov

Start Date: October 1, 2019 End Date: September 31, 2022
Project Funding: $400,000 DOE share: $400,000 Non-DOE share: $0

Project Introduction

Electric vehicles require Li-ion batteries (LIB) that not only have high energy/power densities at low cost, but also can achieve superior performances at low temperature (LT) environment (< 0°C). However, current battery technology has not yet meet the satisfactory LT performance requirement, in large part due to the limitation in the electrolyte and the electrolyte-derived electrode/electrolyte interfaces. Particularly at LT, the electrolyte ionic conductivity is significantly reduced and the interface impedances are significantly increased, [1] severely limiting the energy/power of LIB and potentially causing undesired lithium plating. This project aims to improve the electrolyte performances at LT using fluorinated solvents.

Objectives

The objective is to develop electrolytes that enable LIB to deliver > 70 % of usable energy at -20°C compared to the normal battery operating temperature (30°C) at C/3 rate, and to achieve excellent cycling performances and calendar life at high temperatures (40~60°C).

Approach

Our first approach is to use fluorinated carbonates as co-solvents for the state-of-the-art (SOA) electrolyte. Due to the weaker polar-polar interaction in fluorine-containing groups, fluorinated carbonates are anticipated to show lower melting points than their non-fluorinated counterparts, which can be beneficial for LT application. Moreover, our previous studies demonstrated that fluorinated carbonates can significantly improve high temperature cycling performances of LIB. [2], [3], [4] Thus, incorporating fluorinated carbonates into the SOA electrolyte can potentially improve the performances of LIB at both low and high temperature.

Our second approach is to use fluorinated carboxylate esters as single solvents with solid-electrolyte interphases (SEI)-forming additives. Carboxylate esters generally have very low melting points, good dielectric constants, and low viscosities; thus, it is anticipated that carboxylate esters and its fluorinated derivatives can likely maintain excellent ionic conductivities at LT. Previous studies have reported the use of carboxylate esters or fluorinated carboxylate esters as co-solvents in the SOA electrolyte for LIB; [5], [6] however, their use as single solvents is less explored. The major challenge of using carboxylate esters is that carboxylate esters cannot form stable graphite SEI and thus SEI-forming additives are required.

Results

Gen 2 electrolyte, i.e. 1.2 M $LiPF_6$ in EC/EMC (30/70, w.t.%), has been widely used as the electrolyte for LIB working in the typical temperature range. To understand whether the $LiPF_6$ concentration in Gen 2 is optimal for LT application, we first investigated the effect of $LiPF_6$ concentration on the electrolyte ionic conductivity. The results are shown in Figure II.7.B.1a. Electrolytes with 0.6~1.2 M $LiPF_6$ showed similar ionic conductivities at 60~-20°C, but 0.6 M $LiPF_6$ had the highest ionic conductivities at -20°C, which is likely due to the reduced viscosity from its low salt concentration. 0.3 M $LiPF_6$ showed substantially decreased ionic

conductivities above 0°C and similar values to others below 0°C. This suggests that the low ionic conductivity from the low salt concentration is offset by the reduced viscosity at LT. 2.4 M $LiPF_6$ showed the lowest ionic conductivity among all electrolytes, likely due to its highest viscosity. Figure II.7.B.1b compares electrochemical cycling performances of Gr//NMC622 coin cells at -20°C using 0.6, 1.2, and 2.4 M $LiPF_6$ in EC/EMC (30/70, w.t.%), respectively. Cells were first cycled for three times at 25°C (rate = C/3), then cycled at a rate of C/20 once and at a rate of C/3 at -20°C, and finally C/3 for three times and C/20 for twice at 25°C. 0.6 M $LiPF_6$ showed the much higher specific discharge capacities and better capacity retention than 1.2 and 2.4 M $LiPF_6$, suggesting that the higher ionic conductivity of 0.6 M $LiPF_6$ at -20°C is beneficial for LT performances of LIB. Thus, 0.6 M $LiPF_6$ in EC/EMC (30/70, w.t.%), denoted as 0.6 M Gen 2, was selected as the baseline electrolyte for further study.

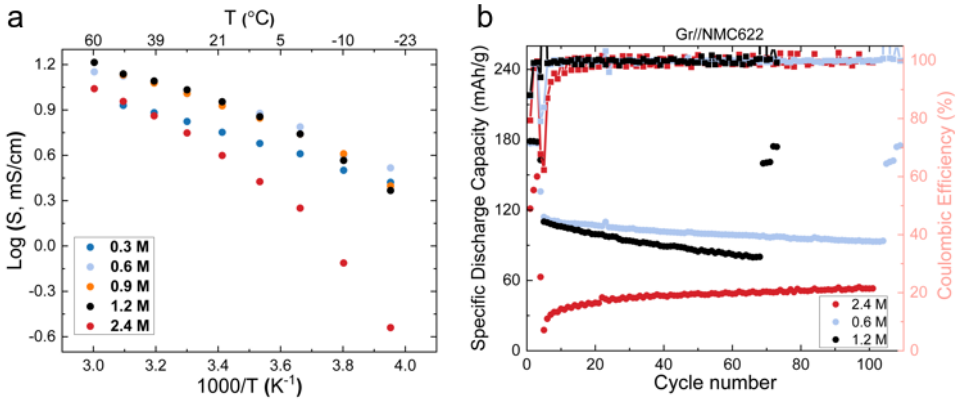

Figure II.7.B.1 (a) Ionic conductivities of electrolytes with different $LiPF_6$ concentration. The solvent is EC/EMC (30/70, w.t.%). (b) Electrochemical cycling performances of graphite//NMC622 coin cells using electrolytes with different $LiPF_6$ concentration. The lower and upper cut-off voltage is 2.7 and 4.2 V, respectively.

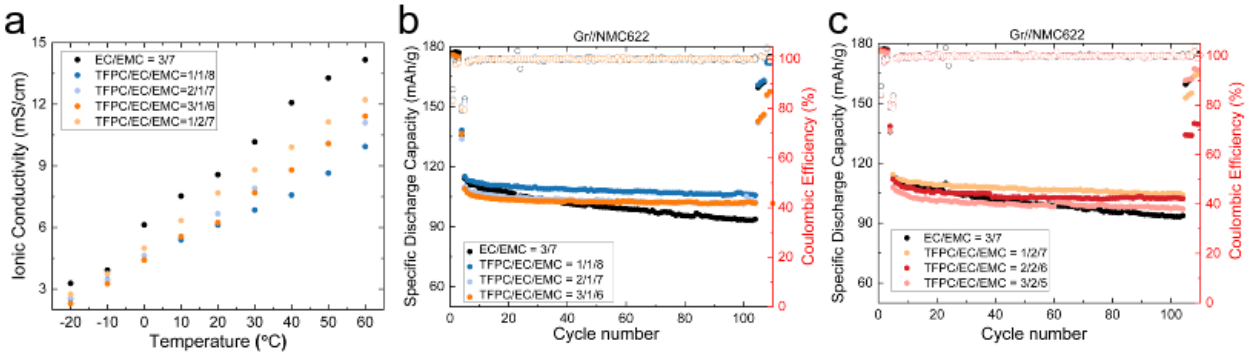

Figure II.7.B.2 (a) Ionic conductivities of 0.6 M $LiPF_6$ in EC/EMC (30/70, w.t.%) with TFPC co-solvent. (b) and (c) Electrochemical cycling performances of graphite//NMC622 coin cells with TFPC co-solvent. The lower and upper cut-off voltage is 2.7 and 4.2 V, respectively.

To further improve LT performances of Gr//NMC622 cells, 3,3,3-trifluoropropylene carbonate (TFPC) was added as the co-solvent (10~30 w.t.%) into 0.6 M Gen 2. Figure II.7.B.2a shows ionic conductivities of 0.6 M Gen 2 without and with TFPC co-solvents at -20~60°C. TFPC lowered electrolyte ionic conductivity at all studied temperatures. This is likely due to the larger viscosity of TFPC (4.82 cP) than EC (1.9 cP) and EMC (0.69 cP). Figure II.7.B.2b and Figure II.7.B.2c show electrochemical cycling performances of Gr//NMC622 coin cells at -20°C. Despite their lower ionic conductivities, electrolytes with 10 w.t.% TFPC showed higher

specific discharge capacities and better capacity retention than 0.6 M Gen 2. This improved performance is likely the result of an improved graphite SEI at LT that involves TFPC participation.

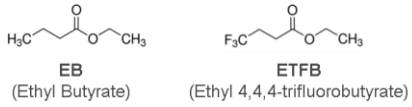

Figure II.7.B.3 Chemical structures of ethyl butyrate and ethyl 4,4,4-trifluorobutyrate

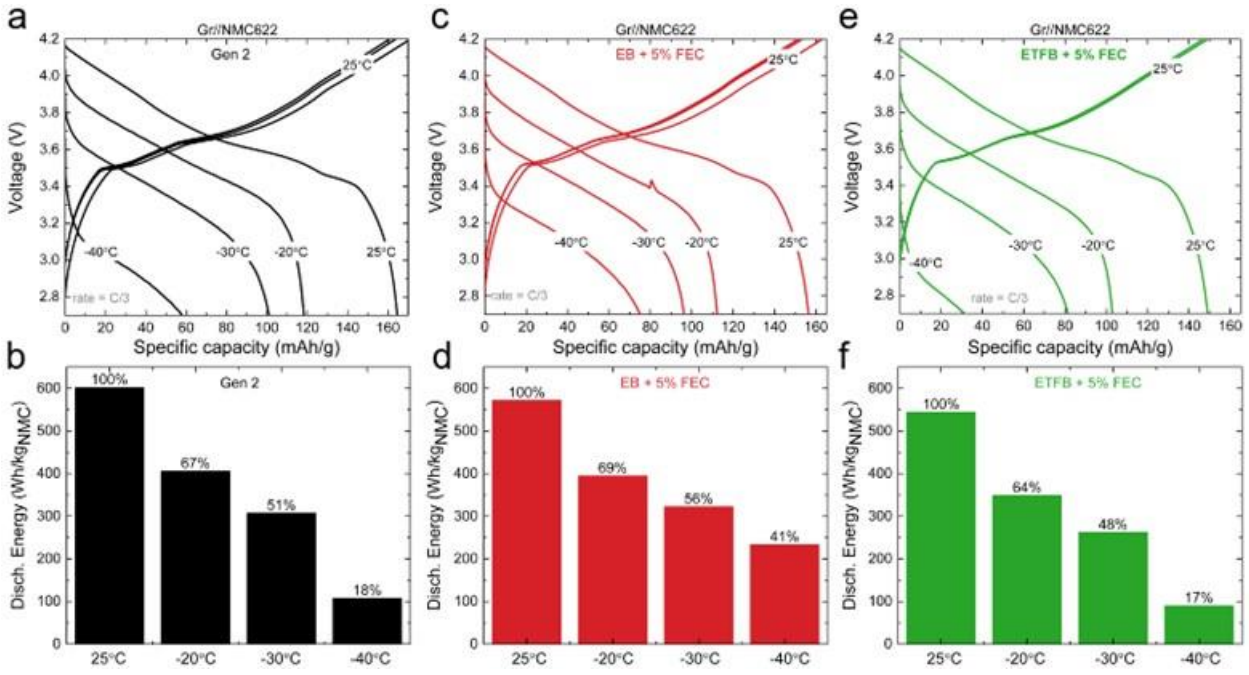

Figure II.7.B.4 Voltage profiles and the corresponding discharge energy densities of graphite//NMC622 coin cells with Gen 2 (a and b), 1 M $LiPF_6$ in EB + 5 w.t% FEC (c and d), and 1 M $LiPF_6$ in ETFB + 5 w.t% FEC (e and f) electrolyte, respectively. Cells were charged at 25 °C and then discharged at the indicated temperature with the same C/3 rate. The lower and upper cut-off voltage is 2.7 and 4.2 V, respectively. Discharge energy densities are normalized to active cathode material mass. Percentages of discharge energies over those at 25 °C are also indicated in b, d, and f.

Our second approach involves the use of fluorinated carboxylate esters. A fluorinated carboxylate ester, ethyl 4,4,4-trifluorobutyrate (ETFB, Figure II.7.B.3), was selected as the solvent and side-by-side compared to its non-fluorinated counterpart, ethyl butyrate (EB, Figure II.7.B.3), and the baseline Gen 2 electrolyte. For ETFB and EB-based electrolytes, 5 w.t.% fluoroethylene carbonate (FEC) was added as an additive in order to form stable graphite SEI. The discharge voltage profiles and energy densities of graphite//NMC622 coin cells at different temperatures are shown in Figure II.7.B.4. At 25°C, ETFB-based electrolyte showed lower discharge capacities (150 mAh/g) than EB-based electrolyte (158 mAh/g) and Gen 2 electrolyte (162 mAh/g). Reducing temperature to -20, -30, and -40°C led to significantly reduced capacities and discharge energies for all electrolytes, due to increased cell impedances at LT. At -20 and -30°C, the discharge capacity trend was the same: ETFB < EB < Gen 2. At -40°C, EB-based electrolyte showed the highest discharge capacity. In terms of discharge energy densities, ETFB-based electrolyte was the lowest in all temperatures; EB-based electrolyte had slightly lower energy density than Gen 2 at 25°C, very similar one to Gen 2 at -20 and -30°C, and higher than Gen 2 at -40°C. Moreover, EB-based electrolyte can deliver 69% of its room temperature energy at -20°C, which is higher than that of Gen 2 electrolyte (67%). These results suggest that using carboxylate esters as the solvent can be highly beneficial for LT application, especially below -40°C. Fluorinated carboxylate esters-based electrolyte suffers from low capacities/energies, the cause of which is currently under investigation.

Conclusions

In conclusion, low $LiPF_6$ concentration (0.6 M) can increase ionic conductivities of EC/EMC-based electrolyte and improve electrochemical cycling capacities and capacity retention at -20°C. Adding 10 w.t.% TFPC into 0.6 M $LiPF_6$ in EC/EMC (30/70, w.t.%) electrolyte can also be beneficial for the performances of graphite//NMC622 cells at -20°C. Fluorinated carboxylate esters, i.e. ETFB, show inferior capacity and energy density than carboxylate esters, i.e. EB, and the baseline Gen 2 electrolyte.

References

1. Zhang, S. S.; Xu, K.; Jow, T. R., Electrochemical impedance study on the low temperature of Li-ion batteries. Electrochimica Acta 2004, 49 (7), 1057-1061.

2. He, M.; Su, C.-C.; Feng, Z.; Zeng, L.; Wu, T.; Bedzyk, M. J.; Fenter, P.; Wang, Y.; Zhang, Z., High Voltage LiNi0.5Mn0.3Co0.2O2/Graphite Cell Cycled at 4.6 V with a FEC/HFDEC-Based Electrolyte. Advanced Energy Materials 2017, 7 (15), 1700109.

3. Tornheim, A.; Sahore, R.; He, M.; Croy, J. R.; Zhang, Z., Preformed Anodes for High-Voltage Lithium-Ion Battery Performance: Fluorinated Electrolytes, Crosstalk, and the Origins of Impedance Rise. Journal of The Electrochemical Society 2018, 165 (14), A3360-A3368.

4. Tornheim, A.; Sharifi-Asl, S.; Garcia, J. C.; Bareño, J.; Iddir, H.; Shahbazian-Yassar, R.; Zhang, Z., Effect of electrolyte composition on rock salt surface degradation in NMC cathodes during high-voltage potentiostatic holds. Nano Energy 2019, 55, 216-225.

5. Smith, K. A.; Smart, M. C.; Prakash, G. K. S.; Ratnakumar, B. V., Electrolytes Containing Fluorinated Ester Co-Solvents for Low-Temperature Li-Ion Cells. ECS Transactions 2008, 11 (29), 91-98.

6. Smart, M. C.; Ratnakumar, B. V.; Chin, K. B.; Whitcanack, L. D., Lithium-Ion Electrolytes Containing Ester Cosolvents for Improved Low Temperature Performance. Journal of The Electrochemical Society 2010, 157 (12), A1361-A1374.

Acknowledgements

Support from Peter Faguy and David Howell at Vehicle Technologies Office (VTO), Office of Energy Efficiency and Renewable Energy, U.S. Department of Energy is gratefully acknowledged. Argonne, a U.S. Department of Energy laboratory, is operated by UChicago Argonne, LLC under contract DE-AC02-06CH11357.

II.7.C Synthesis, screening and characterization of novel low temperature electrolyte for lithium-ion batteries (BNL)

Xiao-Qing Yang, Principal Investigator
Brookhaven National Laboratory
Bldg. 555, Brookhaven National Lab.
Upton, NY 11973
E-mail: xyang@bnl.gov

Mallory Clites, DOE Technology Development Manager
U.S. Department of Energy
E-mail: Mallory.Clites@ee.doe.gov

Start Date: October 1, 2019 End Date: September 30, 2020
Project Funding: $1,000,000 DOE share: $1,000,000 Non-DOE share: $0

Project Introduction

While the energy density and cost of batteries powering electric vehicles are becoming competitive with internal combustion engines, there are still several critical issues that need to be addressed. The low temperature performance of the batteries and the fast charge capability are two of them. Current lithium-ion batteries (LIB) experience a significant capacity drop down to about one fifth of its room temperature capacity at -30 °C. Current LIB electrolyte is almost exclusively based on ethylene carbonate (EC) as a major solvent component due to the high dielectric constant and formation of an excellent solid-electrolyte-interphase (SEI) on the graphite anode. Unfortunately, EC has a rather high melting point (37 °C), leading to significantly increased viscosity and severely decreased Li^+ conductivity at low temperatures. LIB also has high impedance at low temperature due to the sluggish Li^+ transport through SEI. These issues result in the much decreased capacity and poor cyclability at low temperature. Therefore, to improve the low temperature performance of LIB, it is critical to develop new electrolyte system that is low in viscosity, high in Li^+ conductivity, and is able to form stable and low-impedance interphase on both anode and cathode. This consortium, with team members of Brookhaven National Laboratory **(BNL**), Army Research Laboratory (**ARL**), University of Maryland (**UMD**), and University of Rhode Island (**URI**), address the low temperature electrolyte challenge through integrated approaches of theoretical calculation, electrolyte components design, synthesis, and testing, as well as advanced characterization.

Objectives

The project objective is to develop next generation electrolyte formulations that enable the Li-ion batteries to deliver >70% of room temperature energy at -20 °C, while still meeting the United States Advanced Battery Consortium (USABC) Operating Environment Conditions (-30 to +52 °C), fast charge capability, calendar life testing at 30, 40, 50, and 60 °C.

Approach

Up to date, most low temperature electrolyte development efforts have been focused on adjusting the combination of different commercially available solvents only, and a decent low-temperature performance can only be achieved by scarifying other properties such as high-temperature and high voltage performance. Keeping the goals of automobile application in mind, to achieve the desired low temperature performance while maintaining other performance, we need to design new electrolyte systems using an integrated approach starting from theoretical calculations of the new electrolytes, understanding the electrolyte-electrode interphases, to the synthesis of new solvents, salts, and additives, as well as advanced characterizations of the electrolyte systems in actual battery environments. Theoretical calculations have been used to predict the transport property, electronic structure and SEI formation mechanism to propose possible candidates that have high Li^+ conductivity, good stability, as well as low-impedance SEI. These candidates have been or will be synthesized and purified for experimental validation. The new electrolyte system is subject to a series of

electrochemical testing and diagnostic studies for performance evaluation and mechanistic studies. These knowledges provide feedback to the theoretical model for better understanding and more accurate predictions.

Solvent candidates to be explored include but are not limited to ethers, esters, nitriles and their fluorine-substituted derivatives. Salt candidates include lithium tetrafluoroborate ($LiBF_4$), lithium hexafluorophosphate ($LiPF_6$), lithium bis(fluorosulfonyl) imide (LiFSI), lithium bis(trifluoromethanesulfonyl) imide (LiTFSI), lithium bis(oxalato) borate (LiBOB), and lithium difluorooxalatoborate (LiDFOB) etc. Additive candidates include vinylene carbonate (VC), fluoro ethylene carbonate (FEC), phosphites, phosphates, sulfones, sultones, and sulfates.

New electrolyte systems are subject to a series of characterizations and theoretical calculations such as Infrared and Raman spectroscopies as well as x-ray and neutron pair distribution function (xPDF and nPDF) analysis. The results have been analyzed together with molecular dynamic (MD) calculations to understand the structure of the electrolyte. The SEI and cathode-electrolyte-interphase (CEI) components are subject to characterizations such as high energy x-ray photoelectron spectroscopy (HAXPES), resonant inelastic x-ray scattering (RIXS), x-ray absorption spectroscopy (XAS), x-ray photoemission electron microscopy (XPEEM), as well as cryo transmission electron microscopy (TEM) to obtain information such as structure, depth-profiling, and chemical distribution.

Results

In FY2020, significant progress has been made by this consortium. Different electrolyte systems with new solvents, new salts, and new additives have been tested, characterizes and screened. Several systems have been selected which show very promising electrochemical performance at a wide temperature range, especially at -20 °C.

1. Low-temperature electrolytes development at BNL

At **BNL**, isoxazole (IZ) is identified to be a promising solvent for low temperature application. As Figure II.7.C.1a and b suggest, IZ based electrolyte has superior lithium ion conductivity compared with conventional electrolyte. At -20 º C, IZ based electrolyte still has a conductivity of more than 10 mS/cm which is comparable to that of conventional electrolyte at room temperature. Encouraged by this result, electrolytes using the same solvent (IZ) but different salts are tested in a Li||graphite half-cell. As Figure II.7.C.1c suggests, when $LiPF_6$, LiFSI, and LiTFSI are used as salts, the cells cannot be charged and discharged, suggesting incapability of forming a stable SEI on graphite anode when IZ is used as the solvent. Interestingly, when LiDFOB is used as salt, the cell can be discharged and charged. The plateau at around 1.6 V corresponds to the decomposition of LiDFOB salt which has been reported in the literature. The plateau at around 1.1 V corresponds to the decomposition of IZ, suggesting that SEI needs to be further improved to present this from happening. Adding FEC as a co-solvent was able to address this issue as shown in Figure II.7.C.1d where the 1.1 V plateau is much suppressed. It also shows good reversibility for the Li||graphite half-cell.

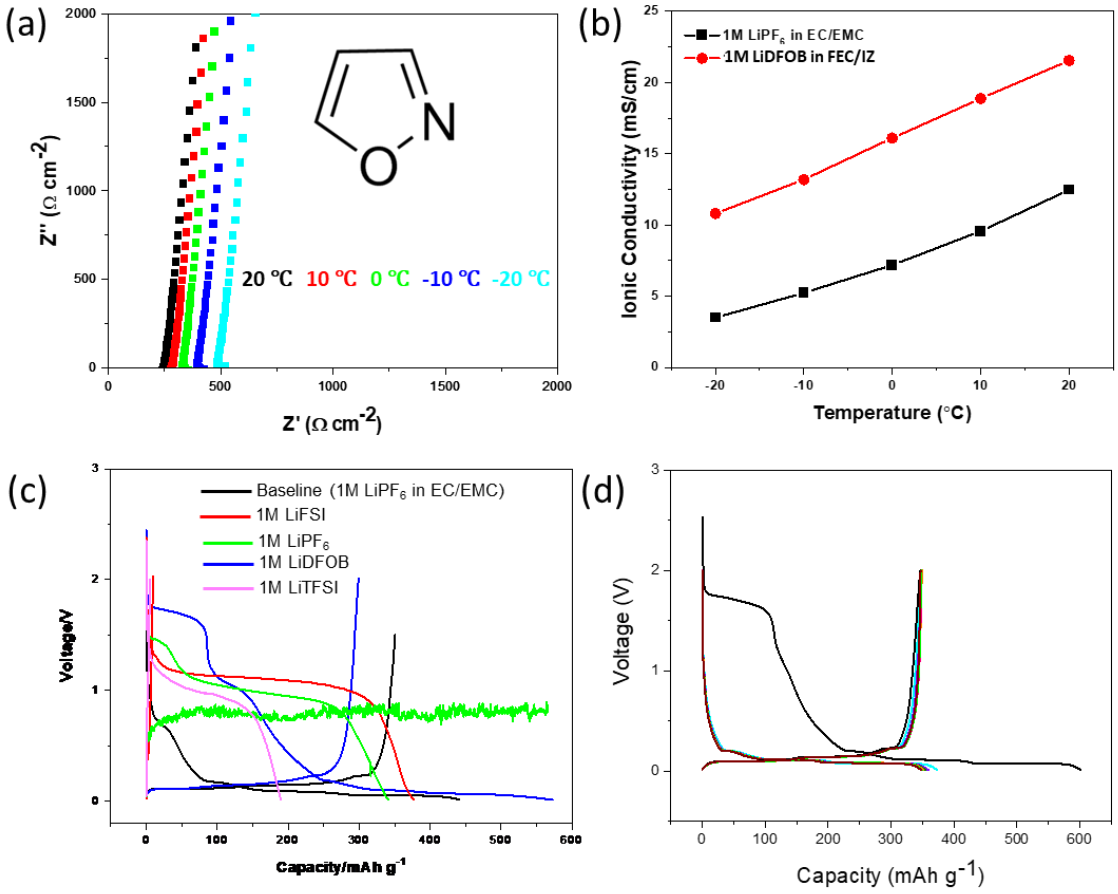

Figure II.7.C.1 (a) impedance measurement of 1M LiPF6 in IZ electrolyte at various temperatures. The inset graph shows the structure of IZ. (b) lithium ion conductivity of conventional electrolyte and IZ-based electrolyte. LiDFOB instead of $LiPF_6$ was used as the salt because the former is compatible with IZ. (c) the first cycle discharge-charge profile of Li||graphite cells with various electrolytes using the same solvent (IZ) and different salts. The result is compared with the profile of Li||graphite cell using conventional electrolyte. (d) the discharge-charge profile of the first 20 cycles for Li||graphite cell using 1M LiDFOB in FEC/IZ (1:9).

The possibility of using PC-based electrolyte has also been explored at **BNL**. PC has a low melting point of -49 ° C and high dielectric constant, both of which may be favored for low temperature electrolyte. However, it is well known that PC can be co-intercalated into graphite anode along with lithium ion, leading to exfoliation of graphite. This is also shown in Figure II.7.C.2a. Replacing $LiPF_6$ with a good SEI-forming salt such as LiDFOB did not change the irreversibility nature of PC (Figure II.7.C.2b). Interestingly, adding 10% FEC to the PC-based electrolyte enables reversible lithium intercalation into the graphite as shown in Figure II.7.C.2c. The performance can be further improved by using mixed salts of LiDFOB and LiFSI (2:8) as suggested by Figure II.7.C.2d, showing good cyclability.

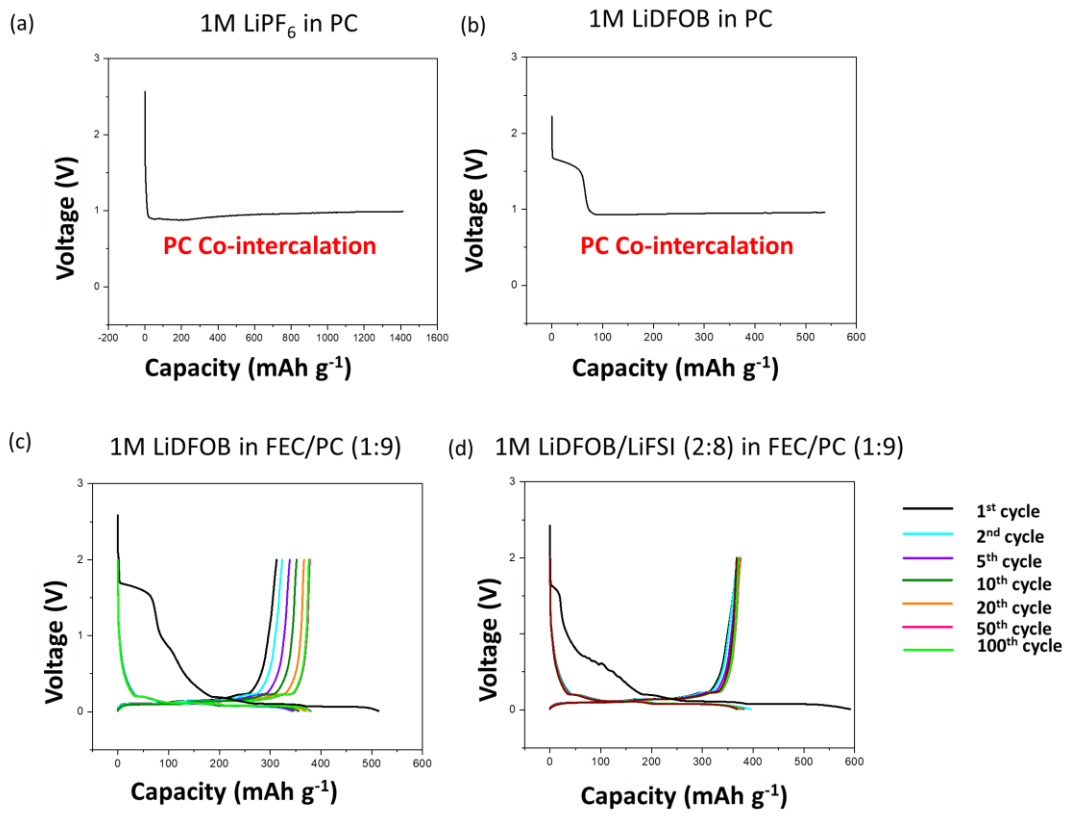

Figure II.7.C.2 (a) the first cycle discharge profile of Li||graphite cell using 1M LiPF6 in PC. (b) the first cycle discharge profile of Li||graphite cell using 1M LiDFOB in PC. (c) cycling performance of Li||graphite cells with 1M LiDFOB in FEC/PC (1:9). (d) cycling performance of Li||graphite cell using 1M LiDFOB/LiFSI (2:8) in FEC/PC (1:9).

2. *Electrochemical performance of graphite anodes and NMC811 cathodes in LiFSI- TTE-X Eelectrolytes Developed at UMD*

UMD team developed an all fluorinated carbonate electrolyte (1.28 M LiFSI in $FEC_{0.1}FEMC_{0.2}HFE_{0.7}$) that enable Li metal battery to operate at -80ºC (*Nature Energy, 4, 882–890(2019)*). However, this electrolyte has a huge over-potential for graphite anode at -20ºC. UMD team modified the electrolyte by removing FEC, replacing expensive FEMC by X solvent, and replacing low-boiling point HFE with TTE to enhance the performance in a wide temperature range. The electrochemical performance of graphite anodes in 2.0 M LiFSI-X-TTE and 3.0 M LiFSI-X-TTE electrolytes at low-temperatures were evaluated. As shown in Figure II.7.C.3a, graphite anodes provided a full capacity at -20ºC and provided >70% of room-temperature capacity at -40ºC at a current of 1/5C and 1/20C, respectively. The graphite anodes in 3.0 M LiFSI-X-TTE electrolyte shows similar performance as in 2.0 M LiFSI-X-TTE at 1/3C at -20ºC (Figure II.7.C.3b**)**. Figure II.7.C.3c shows that NMC811 cathodes in 3.0 M LiFSI X-TTE electrolyte at -20°C can deliver around 160 mAh/g at 1/3C, which is 80% of the capacity at room temperature. Therefore, the 3.0 M LiFSI-X-TTE electrolyte enables both graphite anodes and NMC811 cathodes to achieve high capacity at -20ºC.

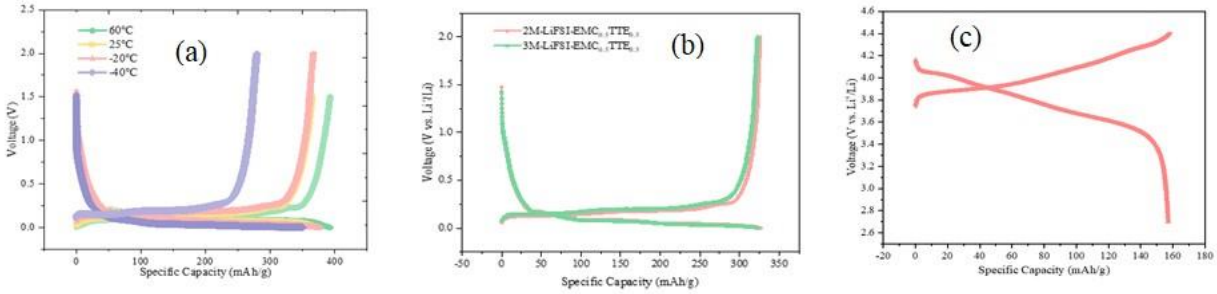

Figure II.7.C.3 (a) Charge-discharge profiles of graphite in 2 M LiFSI- X-TTE electrolyte at the rate of 1/5 C at 25oC, 60oC and -20 ℃ and 1/20C at -40 ℃. (b) charge-discharge profiles of graphite anode in 2.0 M and 3.0M LiFSI-X-TTE electrolytes at a current density of 1/3C at -20℃. (c) Charge/discharge behaviors of NMC811 cathodes in 3.0M LiFSI-X-TTE electrolytes at the rate of 1/3 C at -20℃

3. *Electrochemical performance of NMC811||graphite full cells in 3.0M LiFSI-X-TTE electrolytes developed at UMD*

As shown in Figure II.7.C.4, the NMC811||Graphite pouch cell at 25ºC in 3.0M LiFSI-X-TTE electrolytes delivers a full capacity at 1/3C with a high capacity retention of 80% after 100 cycles. In addition, the NMC811||Graphite pouch full cell at a low temperature of -20℃ can also deliver 75% capacity at -20℃ at the same rate of 1/3 C (Figure II.7.C.4c).

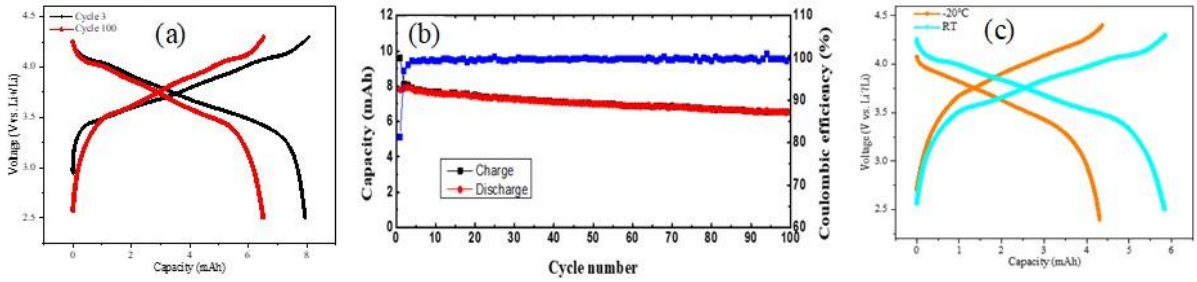

Figure II.7.C.4 (a) Charge–discharge and (b) cycling stability of NMC811||graphite full pouch cell with 3.0 M LiFSI-X-TTE electrolyte at a rate of 1/3 C at 25oC; (c) Charge/discharge behaviors of NMC811||graphite pouch cell in 3M LiFSI-X-TTE electrolytes at a rate of 1/3 C at -20℃. P/N capacity ratio=1.25, Area capacity: 0.8 mAh/cm2

4. *SEI characterization at URI*

In order to understand the improved cycling performance with IZ based electrolytes with LiDFOB salt, surface film on graphite electrodes at the end of cycling (room temperature formation+ post low temperature cycling at -10 º C) was investigated by X-ray Photoelectron Spectroscopy (XPS). C1s, O1s, F1s and B1s spectra of graphite surface film formed in cells containing 1.2 M LiPF6 in EC:EMC (3:7 v/v%) (STD), 1M LiDFOB in FEC:IZ (1:9 v/v%) and 1 M LiDFOB in EC:IZ (1:9 v/v%) are depicted in Figure II.7.C.5**.** The XPS spectra of the surface of the anodes cycled with LiDFOB electrolytes are significantly different from the XPS spectra observed for the cells cycled in STD electrolyte. A relatively thicker SEI is observed on graphite cycled in STD formulation compared to the SEI thickness in IZ based formulation which is evident by drastic decrease of magnitude of graphite peak at 285 eV in former, at the end of cycling. However, surface film generated with both 1M LiDFOB in FEC: IZ and 1 M LiDFOB in EC: IZ are very similar and are dominated by decomposition products of LiDFOB. In C1s spectra intense peaks at 286.7 eV (C-O) and 289.4 eV (C=O) are characteristics to the functional groups of oxalate species from the decomposition of LiDFOB in IZ based electrolytes while anode surface of the STD electrolyte is primarily consists of lithium alkyl carbonates (287 eV) and lithium carbonate (290 eV) from the decomposition of carbonate solvents. The O1s spectrum of all formulations consists of board peak centered around 533 eV, consistent with a mixture of C-O and C=O containing species. As depicted in Figure II.7.C.5 differences in F1s spectra are also observed. While a single asymmetric F1s peak is observed at IZ based formulation characteristics to LiF (685 eV) and a shoulder peak

at 687 eV for boron-fluorine decomposition products (B-F) , two separate peaks are observed for STD formulation at 685 eV for LiF and 688 eV for lithium fluorophosphates. Peaks at 687 eV and 688 eV are characteristic for B-F and C-F containing species in the cells cycles with IZ based and STD formulation and consistent with reduction of LiDFOB and $LiPF_6$ salts, respectively. Finally, the corresponding B1s spectra are presented for supporting the presence of LiDFOB decomposition products in IZ based formulation. Peaks observed at 193.5 eV corresponds to the decomposition products of LiDFOB.

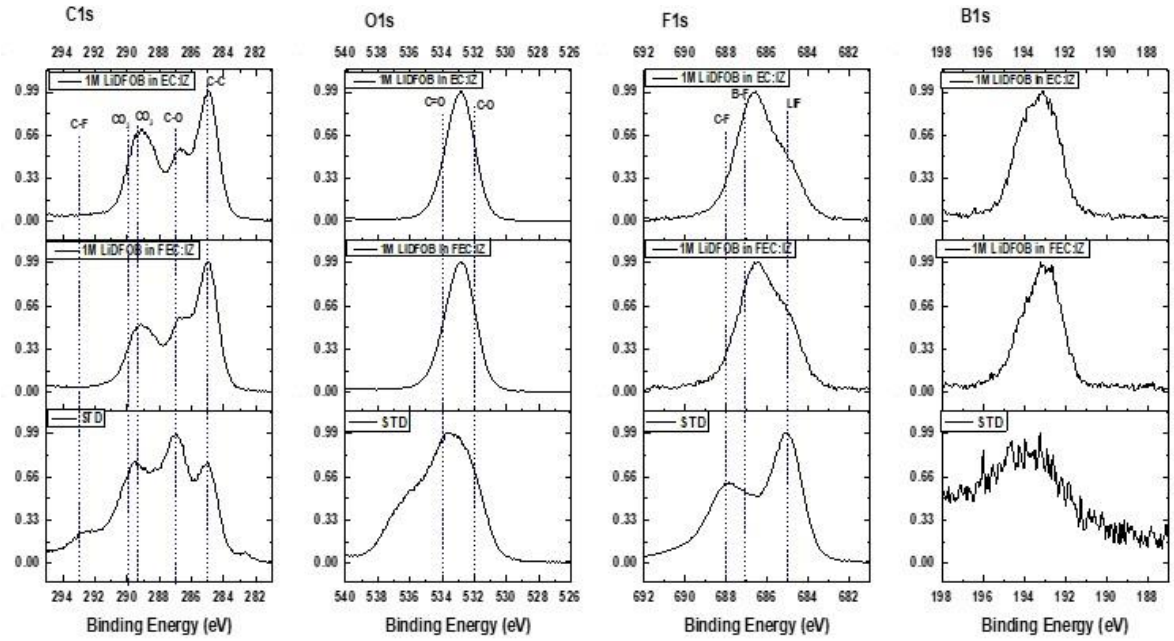

Figure II.7.C.5 C1s, O1s, F1s, and B1s spectra at the end of cycling of graphite electrodes in 1.2 M $LiPF_6$ in EC:EMC (STD), 1 M LiDFOB in FEC: IZ and 1M LiDFOB in EC: IZ.

Ex-Situ surface analysis of graphite electrodes extracted from cells cycled (room temperature formation+ post low temperature cycling at -10 ºC) in 1M $LiPF_6$ in FEC:EMC:TTE (5:45:50 v/v%) and 2 M LiFSI in FEC:EMC:TTE (5:45:50 v/v%) has been investigated by XPS. C1s, O1s, F1s and S2p spectra of anode surface films are presented in Figure II.7.C.6**.** As shown in Figure II.7.C.6, after cycling, in both electrolyte formulations relatively thinner SEI is observed which is evident by a small decease in the magnitude of graphite peak (285 eV) on C1s spectra. Surface film generated by both electrolytes are very similar and has similar peak shapes for C1s and O1s spectra. Both graphite electrodes have C-O (287 eV) and C=O (289.4 eV) features on C1s spectra characteristic to carbonate solvent decomposition along with an additional peak at 291 eV consistent for formation of poly-VC by decomposition of FEC. In O1s spectra broad peak centered around 533 eV is consistent with the mixtures of C-O and C=O functional groups from the electrolyte reduction products. F1s spectra of both anode surface has an intense peak for LiF (685eV) while a small shoulder peak present at 688 eV related to $Li_xPF_yO_z$ and decomposition products of LiFSI for $LiPF_6$ and LiFSI electrolytes, respectively. S2p spectra shown in Figure II.7.C.6**,** further supports the decomposition of LiFSI salt in SEI formation, in 2M LiFSI in FEC: EMC: TTE electrolyte. Peak detected at 170 eV corresponds to the degradation products of LiFSI; probably Li_2SO_4 or lithium alkyl sulfonate.

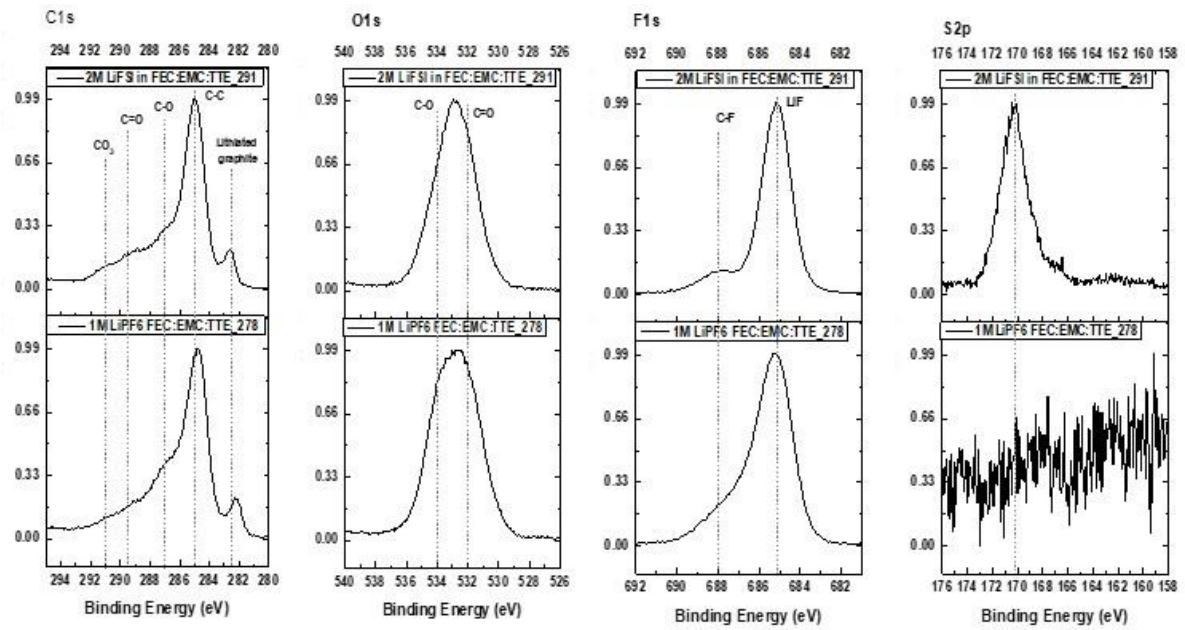

Figure II.7.C.6 C1s, O1s, F1s, and B1s spectra at the end of cycling of graphite electrodes in 1M $LiPF_6$ in FEC:EMC:TTE and 2M LiFSi in FEC:EMC:TTE.

5. Molecular dynamics (MD) simulation work at ARL

Molecular modeling efforts at **ARL** are aimed at understanding the electrolyte structure, transport and initial stages of the SEI formation. Many-body polarizable force field (APPLE&P) was chosen for molecular dynamics (MD) simulations because it allows direct parameterization based upon quantum chemistry calculations and unlike the non-polarizable force fields does not require any empirical scaling of charges to match ion transport. Quantum chemistry (QC) calculations were performed on the TTE, TTE/Li^+, FEC/Li^+, LiFSI and EC/DMC/Li^+/PF_6^- to validate ability of MD simulations predict baseline properties where ample experimental data are available for validation. Figure II.7.C.7 demonstrates an excellent ability of MD simulations using the revised APPLE&P force field to predict the Li^+ solvation shell composition, diffusion coefficients of all species and temperature dependence of conductivity. MD simulations of the TTE-based electrolytes are currently initiated based upon initial optimization performed by UMD.

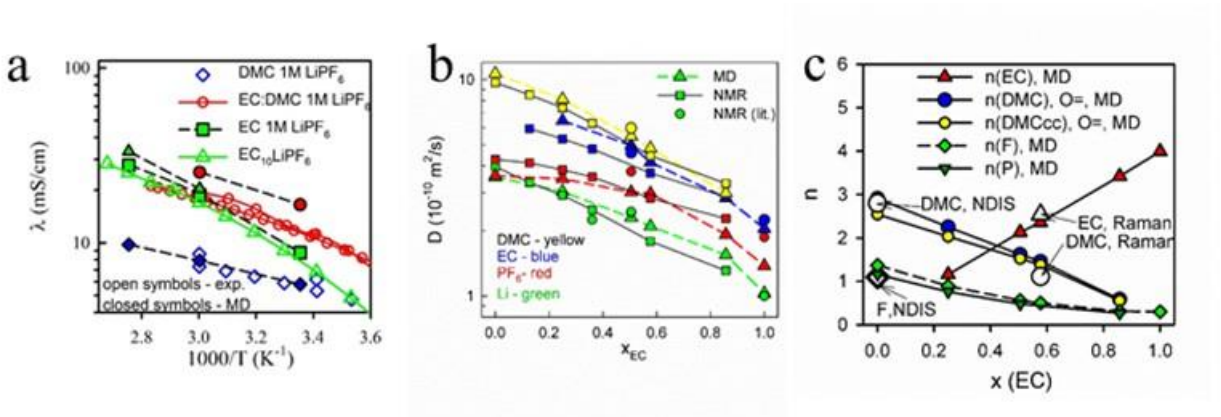

Figure II.7.C.7 Predictions of ionic conductivity (a), self-diffusion coefficients (b) and the Li+ coordination numbers (c) from MD simulations using polarizable APPLE&P force field and experiments.1,2 NDIS denotes neutron diffraction with isotopic substitution experiments. [1]

Conclusions

This project, "Synthesis, screening and characterization of novel low temperature electrolyte for lithium-ion batteries (BNL)", has been successfully completed in FY2020. All milestones have been completed.

References

1. Kameda, Y.; Saito, S.; Umebayashi, Y.; Fujii, K.; Amo, Y.; Usuki, T., Local structure of Li^+ in concentrated $LiPF_6$–dimethyl carbonate solutions. *J. Molec. Liq.* **2015,** *217*, 17-22.

2. Morita, M.; Asai, Y.; Yoshimoto, N.; Ishikawa, M., A Raman spectroscopic study of organic electrolyte solutions based on binary solvent systems of ethylene carbonate with low viscosity solvents which dissolve different lithium salts. *J. Chem. Soc.-Faraday Trans.* **1998,** *94* (23), 3451-3456.

II.8 Beyond Li-ion R&D: Metallic Lithium

II.8.A Composite Electrolytes to Stabilize Metallic Lithium Anodes (ORNL)

Nancy Dudney, Principal Investigator
Oak Ridge National Laboratory
PO Box 2008, MS6124
Oak Ridge, TN 37831
E-mail: dudneynj@ornl.gov

Xi (Chelsea) Chen, Principal Investigator
Oak Ridge National Laboratory
PO Box 2008, MS6124
Oak Ridge, TN 37831
E-mail: chenx@ornl.gov

Tien Duong, DOE Technology Development Manager
U.S. Department of Energy
E-mail: Tien.Duong@ee.doe.gov

Start Date: October 1, 2018 End Date: September 30, 2021
Project Funding: $400,000 DOE share: $400,000 Non-DOE share: $0

Project Introduction

A stable lithium anode is critical to achieve high energy density batteries with excellent safety, lifetime and cycling efficiency. This study will identify the key design strategies that should be used to prepare composite electrolytes to meet the challenging combination of mechanical and chemical and manufacturing requirements to protect and stabilize the lithium metal anode for advanced batteries. The composites are composed of two solid electrolytes, a ceramic component for high ionic conductivity and high elastic modulus plus a small volume fraction of a polymer electrolyte to provide processability of a very thin, light weight and flexible electrolyte membrane.

In previous years we limited the choice of electrolyte materials to those that were well characterized and readily available. This allowed us to focus on how to process and characterize the thin dense composite membrane, and more importantly, this strategy allowed us to determine what factors determine the control the ionic conductivity across the polymer-ceramic interface. This interface is critical for good performance of simple composite structures. The design rules and approaches from earlier studies are now being applied to composites using alternative and novel electrolyte materials which will improve the composite solid electrolyte performance. In recent work, we went beyond model polymers and ceramics to develop new composite electrolytes including ceramic-doped gel polymer electrolytes and composites with an interconnected ceramic structure. Both achieved significantly improved interfacial properties compared to the model composites studied previously with the feasibility of scaling up. While the interfaces between the polymer and ceramic electrolytes is still a key challenge, attentions are also directed towards cation transference number of the electrolytes as well as full cell making process. Success in this program will enable these specific DOE technical targets: 500-700Wh/kg, 3000-5000 deep discharge cycles, robust operation.

Objectives

The overall objective of this program is to prepare composites of polymer and ceramic electrolyte materials as thin membranes which have the unique combination of electrochemical and mechanical properties required to stabilize the metallic lithium anode while providing for good power performance and long cycle life. If successful, this composite electrolyte will help eliminate failure mechanisms including the formation of lithium dendrites, delamination of the lithium or cathode electrodes, and the gradual consumption of lithium due to side reactions or physical isolation.

In a solid-state Li metal battery built on a composite solid electrolyte, a number of interfaces need to be optimized to maximize performance. The interfaces include exterior interfaces (cathode/electrolyte and Li/electrolyte) and interior interfaces (polymer/ceramic and ceramic particle/ceramic particle). We aim to develop a fundamental understanding of ion transport across these interfaces and search for practical solutions to optimize them.

For the interior interfaces, we want to characterize and compare the ion transport between a variety of polymers with different ion transport mechanism and several model ceramics. This will allow design of new polymer systems capable of forming synergistic interfaces with the ceramic. At the same time, we aim to develop practical approaches to decrease the ceramic particle/particle contact resistance. While developing the composite electrolytes, we aim at using ready-to-scale-up processing techniques and making them into commercially relavent form factors (thin and large area).

At the cell level, we seek to understand how the chemical and mechanical properties of the electrolyte affects cell performance, failure mechanism and formation of Li filaments. We also seek solutions to reduce the interfacial resistance between the electrode and the electrolyte and undesired side reactions.

Approach

Our earlier approach was to spray coat a slurry containing the ceramic powder along with a Li salt and dissolved polyethylene oxide (PEO). This was subsequently dried and pressed to densify the film into a homogeneous membrane with high ceramic loading of discrete particles with polymer filling the interstices. Composites were also formed by hot-pressing the dry mixtures of the ceramic, Li salt and PEO as this provided a more rapid sample fabrication to shape. For either processing route, only when the PEO was plasticized with a small organic molecule was the ceramic-polymer interface sufficiently conductive for the composite to achieve our goal for an acceptable Li ion conductivity. The interface properties were carefully confirmed by using ideal laminated structures of the same materials used in the composites. Clearly other materials and methods were needed to further improve the composite electrolyte.

Alternatives for both the ceramic and the polymer phase are being explored with goals to: improve the percolated connectivity of ceramic, improve the Li ion conduction across polymer-ceramic interface, and enhance the Li ion transference number conductivity in polymer. Various polymer materials were synthesized and tested, including cross-linked and gelled polymer electrolytes and single ion conducting polymers with anions bound to the polymer structure. Impedance spectroscopy together with a host of other characterizations methods are used to determine the ion associations and polymer dynamics as they affect the Li^+ conductivity in both the neat polymer phase and in the ceramic composites. For ceramic phase, the processing methods and performance of thin sintered membranes is explored, initially with glass-ceramic LATP-based powders from Ohara Corporation, LICGC™, then with alternatives including the garnet LLZO. The sintering process is intended to ensure a fully 3D connected pathway of the ceramic phase across and along the membrane. The porosity in the ceramic membrane will then be filled with the polymer electrolyte. If Li^+ ion transport between the ceramic and polymer was facile, this would improve the overall homogeneity of Li ion current across the separator membrane. X-ray tomography and electron microscopy are used to determine the microstructure, and various dynamic and stress-strain tests to determine mechanical properties.

While the scientific goals are focused on addressing the composite electrolyte and interfaces, fabricating and cycling electrochemical cells is an important way to characterize the stability with Li and mechanical integrity of the electrolyte. We are seeking to identify practical processing routes to fabricate full batteries using the composite electrolytes with a composite cathode and thin lithium metal anode. The addition of a very thin single ion conducting layer, such for Lipon, may play an important role to eliminate the salt concentration polarization and provide a smooth interface for the lithium anode. These studies increase the complexity of the program, but are practical approaches to improve performance and advance our appreciation for challenges to come with implementation of the solid electrolyte and Li anode technology.

Results

Results are summarized for four topics: 1. Tape-cast three-dimensionally interconnected polymer/ceramic composite electrolyte. 2. Composite electrolytes with single-ion-conducting polymer matrix. 3. Overcharging and capacity fading in polymer electrolyte battery with excess Li. 4. Current response and relaxation of composite electrolytes during Li//Li DC polarization.

1. Tape-cast three-dimensionally interconnected polymer/ceramic composite electrolyte.

Last year we fabricated the composite electrolyte film with interconnected morphology through spray-coating followed by sintering and back-filling. The composite electrolyte thin film was supported by a substrate. This year, we fabricated a free-standing interconnected composite film consisting of LICGC™ ceramic and crosslinked PEO-based polymer electrolyte to assess and minimize the interface resistance with Li metal electrodes. The free-standing film was made using tape-casting method, instead of spray-coating, to provide access to both faces. The rest of the film preparation procedure was the same as described in Ref [1]. The physical appearance and a cross-sectional SEM image of the film are shown in Figure II.8.A.1a and b. The film was ~80 µm thick, with some flexibility. With the free-standing film, we achieved the same uniform interconnected ceramic morphology (Figure II.8.A.1b). We intentionally overfilled the ceramic so that there are two thin layers of polymer (~5 µm) protecting the surface of the ceramic. After being in contact with Li metal, the part of the composite with no surface polymer layer turned black (Figure II.8.A.1c), indicating that LICGC™ reacted with Li. With the surface polymer layer, reactions between LICGC™ and Li were prevented (Figure II.8.A.1d).

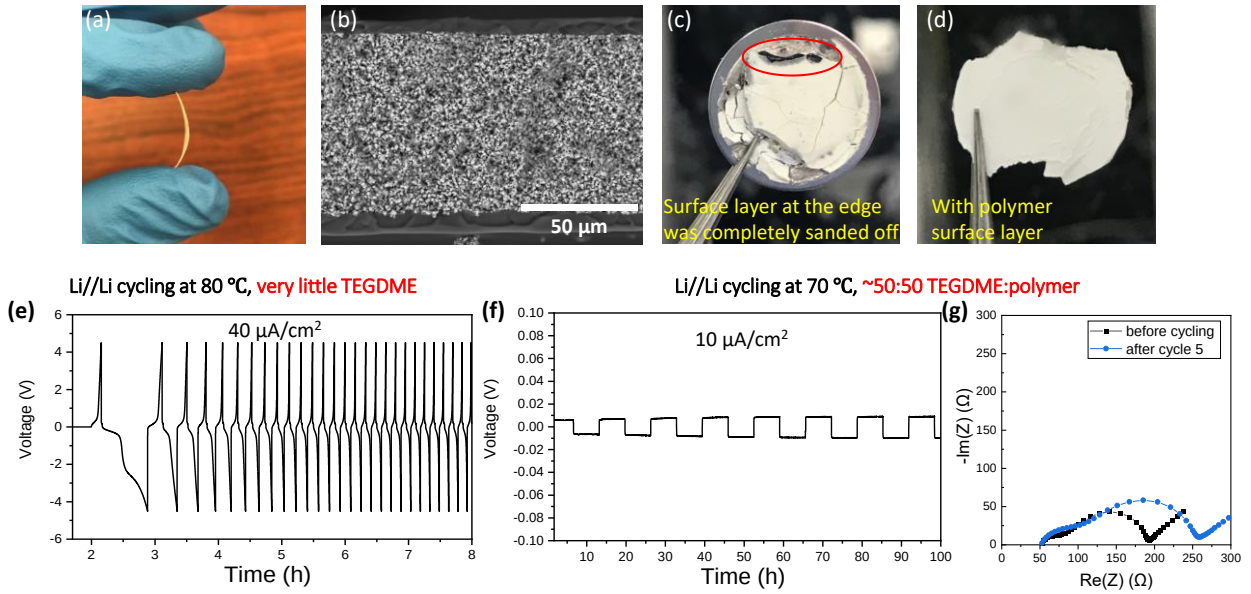

Figure II.8.A.1 (a) a free-standing interconnected composite film made of LICGCTM ceramic and crosslinked polymer electrolyte (TC composite). (b) a cross-sectional SEM image of the film. Note the presence of thin layers of polymer protecting both surfaces of the ceramic. (c,d) pictures of the composite electrolyte film after being in contact with Li. (c), the part where there was no surface polymer layer turned black; (d) with the surface polymer layer, no sign of ceramic reacting with Li was observed. (e-g) Li symmetrical cell cycling using the interconnected composite film: (e) cycling at 80 °C with very little plasticizer was in the film; (f) cycling at 70 °C with the polymer phase containing 50:50 TEGDME plasticizer/polymer by weight; (g) impedance spectra of the cell in (b) before cycling and after 5 cycles.

We performed Li symmetrical cell testing using the tape-cast composite film. With no or very little (a few microliters) TEGDME plasticizer, the cell could not cycle well. This is due a very large interfacial resistance between the polymer surface layer and Li. At room temperature, the interfacial resistance was approximately 13 KΩ·cm^2. At 80 °C, Li symmetrical cell cycling was possible, but a large overpotential was observed (Figure II.8.A.1e). We then filled the ceramic with 50:50 TEGDME:polymer (by weight) and repeated the Li symmetrical cell testing. This cell showed improved cycling performance at 70 °C, with overpotential < 0.01 V

(Figure II.8.A.1f). The interfacial resistance with Li, however, increased with further cycling (Figure II.8.A.1g). This indicates that the polymer electrolyte and/or the plasticizer is not stable with Li. The polymer phase's composition needs to be optimized towards better stability with Li. At room temperature, with 50% TEGDME, the interfacial resistance with Li decreased greatly, but it is still significant at approximately 5 KΩ·cm^2. Without the ceramic, the plasticized polymer electrolyte exhibited an interfacial resistance of 500 Ω·cm^2 with Li at room temperature.

2. Composite electrolytes with single-ion-conducting (SIC) polymer matrix.

In most of the studies concerning composite electrolytes, the polymer matrix used to form the composites are standard polymer electrolytes with lithium salts "freely" dissolved. Thus, the matrix has low Li^+ transference numbers. In contrast, Li^+-conducting ceramics are typically single ion conductors with a Li^+ transference number near 1. This transference number mismatch causes polarization at the polymer-ceramic interface. To date, composite electrolytes using SIC polymers as the host have largely been unexplored. In this work, we synthesized SIC polymers by crosslinking poly(ethylene glycol) dimethacrylate (PEGDMA) with ion-containing monomers including 4-styrenesulfonyl(trifluoromethylsulfonyl)imide (STFSI) and 4-vinylbenzenesulfonate (SS) (Figure II.8.A.2a). LICGC™ was used as the ceramic filler. We investigated the effects of LICGC™ on the physical, thermal, mechanical, ion transport and electrochemical properties of SIC composites in which the anions are covalently bound to the polymer chains. It is discovered that in the dry state, with the addition of ceramics, the intrinsic ionic conductivity of the SIC polymer increased. This is true even at high loadings of ceramic (> 50 vol%) (Figure II.8.A.2b). When the polymers and the composites were plasticized with TEGDME, the molar conductivity of the SIC composite electrolytes were up to 40% higher compared to the neat SIC polymer (Figure II.8.A.2c).

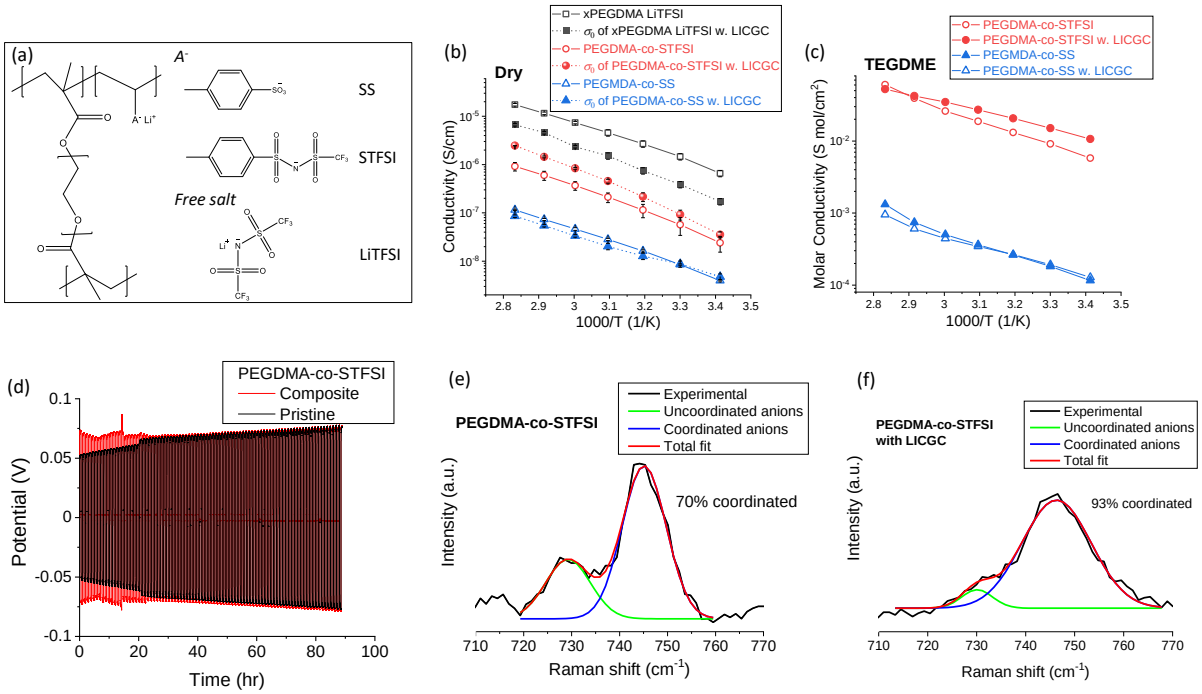

Figure II.8.A.2 (a) Chemical structure of polymer electrolytes synthesized in this work, (b) intrinsic conductivity of the polymer phase in the composite electrolytes as a function of inverse temperature, compared to the measured conductivity of the polymer electrolytes without ceramic. (c) Molar conductivity of single-ion conducting-polymers with and without LICGC™ particles. (d) Symmetrical cell cycling of Li/Li cells with composite and pristine xPEGDMA with LiTFSI. (e, f), Fitting of the Raman spectra of the TFSI breathing stretch for dry state (e) PEGDMA-co-STFSI, and (f) PEGDMA-co-STFSI with LICGC™ ceramic particles

Lithium symmetrical cell cycling with the SIC composites was evaluated. The overpotential and interfacial impedance with Li showed improved stability with the presence of LICGC™ ceramic, compared to the pristine

polymers (Figure II.8.A.2d). Raman spectroscopy revealed that STFSI anions in the SIC polymer can coordinate with the ceramic (Figure II.8.A.2e,f). This coordination led to increased Li^+ dissociation in single ion conductors, which is the root cause of the conductivity enhancement observed. Overall, our study shows that the addition moderate loadings (50 wt%, ~35 vol%) of Li^+-conducting ceramics into single-ion-conducting polymers is beneficial. They improve the conductivity of the polymers, improve the processability of the electrolyte films and cyclability. Using this strategy, the ceramic size, ceramic surface chemistry, morphology, and spatial distribution of SIC composites may be optimized to maximize the positive effects of these ceramics.

3. Overcharging and capacity fading in polymer electrolyte battery with excess Li.

We tested our dry, unplasticized polymer electrolyte and our ceramic-polymer composite electrolytes as full and packaged coin cells. The cathodes, supplied by an industrial collaborator, were high-quality and composed of $LiFePO_4$ in a dry polymer composite with a nominal 1.1 mAh/cm^2 capacity. It became necessary for us to step-back and study the coin cell assembly because of unexpected cycling behavior. We assembled cells with different sizes of Li anode, electrolyte and LFP cathode (Figure II.8.A.3). The line in each sub-figure indicates that cycle is controlled by the time instead of the charge voltage of 3.7 V. All the cells were tested at 80µA current. In Figure II.8.A.3a, the charge capacity vs. cycle number of three sets of Li(1/2)PE(5/8)LFP(1/2) are shown, where we see ~200% overcharge for three cells. Notably, the overcharge occurred earlier for the thinner electrolyte. In (b), two sets of tests are completed for a smaller area LFP and a consistent ~300% of overcharge is observed even though the onset of overcharge occurred at a different cycle. In (c), for a smaller Li, ~200% overcharge is shown with a thick electrolyte while little overcharge is shown with a 65 µm electrolyte test. In (d), we only have one set of data for the Li(1/2)PE(1/2)LFP(1/2) cell, due to the challenges in cell alignment with a small electrolyte layer. A Kapton washer is used to prevent unwanted electrical contact in the half inch cell. Figure II.8.A.3e shows that the discharge capacity for all types of cell are close to 1.1 mAh/cm^2, which is the theoretical capacity of the LFP cathode used in this study.

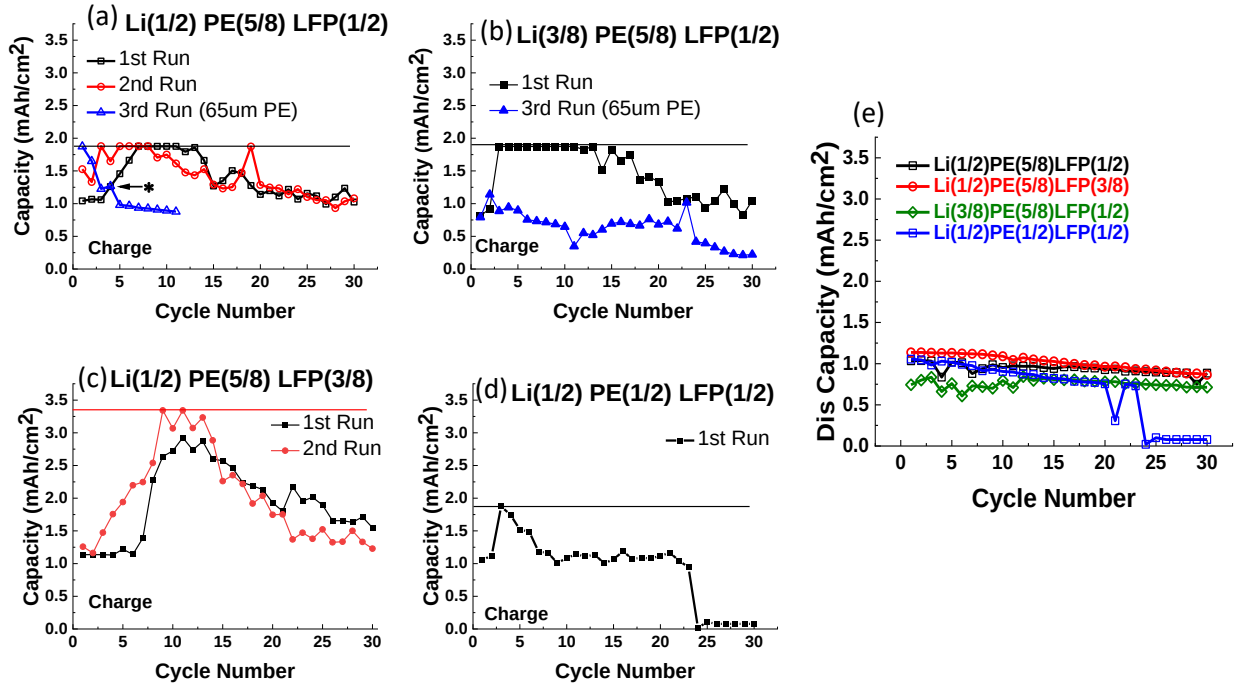

Figure II.8.A.3 Charge capacity as a function of cycle number for Li (1/2) PE (5/8) LFP (1/2) (a), Li (1/2) PE (5/8) LFP (3/8) (b), Li (3/8) PE (5/8) LF P (1/2) (c), Li (1/2) PE (1/2) LFP (1/2) (d) and their consistent discharge capacities for 30 cycles (e).

In ref [2], Homann et al. concluded that formation of micro-dendrites at the Li/PE interface is the cause of the noisy voltage and apparent overcharge capacities. Our observations suggest soft shorts may occur more frequently at electrode edges. There may be multiple causes for the overcharge in our test, including micro-dendrites, change in the structure of PE with cycling, PE-Cu contact and PE/cathode interface. These causes have been investigated thoroughly and a manuscript has been written.

4. Current response and relaxation of composite electrolytes during Li//Li DC polarization.

It is common to utilize the Bruce Vincent method [3] for approximating the transference number under Li//Li polarization. However, there are few attempts to analyze the relaxation kinetics of the chronoamperometric step for these cells, yet results differ for various electrolytes. We fabricated Li//Li symmetric cells with different layers of electrolyte as well as composite electrolytes with dispersed ceramic particles. The experimental results pertaining to the DC polarization of a series of composite electrolytes are shown in Figure II.8.A.4a-c. The matrix of the composite electrolyte was crosslinked poly(ethylene oxide), denoted as XPEO, with bis(trifluoromethane)sulfonimide lithium salt (LiTFSI). LICGC™ particles were dispersed in the polymer matrix as ceramic fillers. The composite electrolyte was plasticized with tetraethylene glycol dimethyl ether (TEGDME) to form the gel. Our goal remains to develop a fully-dry composite electrolyte, but completion of this work provides insight into the ion transport processes. The relaxation curves, shown in Figure II.8.A.4b and c, are under 10 mV voltage bias at 30°C. The relaxation of the current was recorded for 10 hours, and most samples equilibrated at much shorter times. In Figure II.8.A.4c, the same results are plotted as the current ratio normalized to the initial current (I_0) recorded at 5ms. Typical impedance spectra of the composite electrolyte before and after polarization is shown in Figure II.8.A.4a, with 50 wt% ceramic (dry weight). the steady current under 10 mV bias followed the order of CEM-50 > CEM-30 > XPEO >CEM-70.

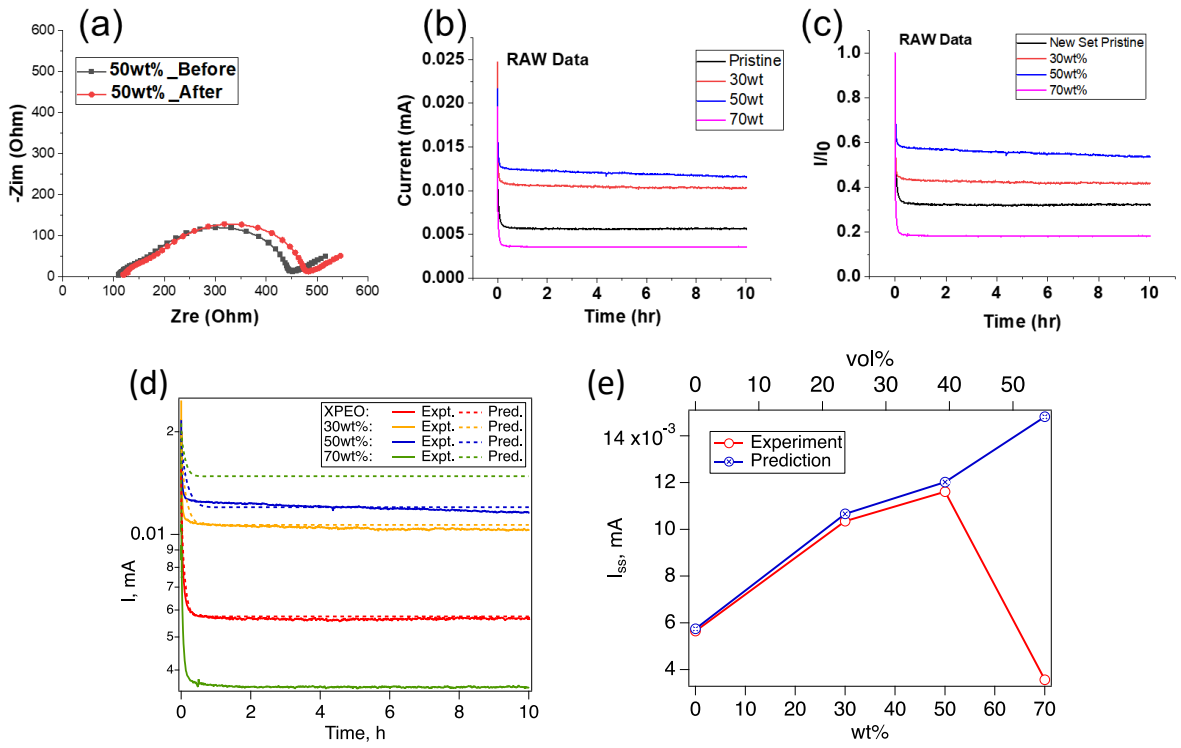

Figure II.8.A.4 Cycling of Li/LiFePO4 solid state cells with dry composite and polymer electrolytes. a, cells at cycle 10 with different thicknesses of excess Li, 0-120 μm; b, reduced polarization when thin PEO+salt fills interface between the cathode and electrolyte composites; c, one of the longest cycling cells with Lipon at the cathode interface.

Numerical modeling to predict the transient behavior and relaxation to steady state current was also conducted. Instead of applying electrolyte theory based on effective ionic conductivity and transference number, we use Nernst-Plank equations to directly trace the fluxes of anions and cations in the electrolyte due to diffusion and

mobility in electric field. The comparison between experimentally measured and predicted chronoamperometry curves is shown in Figure II.8.A.4d. In all cases a 10 mV bias was applied to the cell. In the model the ion diffusivity was taken as an average of the diffusivities in components of the composite using the corresponding volume fractions. The same approach was done to set initial concentrations of Li^+ and $TFSI^-$. As can be seen, the model significantly overpredicts the current in the case of 70 wt% loading of LICGC in the composite. This is further illustrated in Figure II.8.A.4e where the steady state current from experiments is compared to that from numerical prediction. This discrepancy is likely because the transport mechanism of the composite with high volume fraction of ceramic differs from the other composites and from that used in the model. The experimental data and modeling combined provide insight in the transference number and formation of concentration gradient of the composite electrolytes. We are working to interpret the data and to gain a deep understanding the ion transport process in these electrolytes.

Conclusions

- Using a tape-cast film, we successfully made a free-standing composite electrolyte with an interconnected ceramic structure. The backfilling of polymer provides thin surface layers that protects the ceramic from reacting with lithium metal. Li symmetric cell cycling at elevated temperatures and low rates was successful. Compared to the gel composite electrolyte with dispersed, unconnected ceramic particles, the interfacial resistance between Li and the electrolyte at room temperature is almost one order of magnitude larger. Given that the polymer phase's chemistry is identical between the two composite electrolytes, the large interfacial resistance seen in the interconnected composite must originate from other mechanisms – such as mechanical properties of the composite electrolyte. In FY21, efforts will be made to minimize the interfacial resistance and improve cycling performance, with a different ceramic (LLZO).

- We explored the performance of composite electrolytes formed from a single-ion-conducting polymer host with dispersed ceramic particles. We discovered that the main effect from the addition of ceramic particles is that the intrinsic ionic conductivity of the SIC polymer increased in the dry state. Raman spectroscopy suggests that the root cause of this effect is the immobilization of the anion by the ceramic surface, freeing up more Li^+ cations. Due to the intrinsically low conductivity of the SIC polymer, the improvement is only moderate. The low conductivity of the SIC is partly due to the low Li concentration in this polymer. It will be beneficial to evaluate the effect the ceramic fillers with increased Li concentration. This will be written into a white paper.

- We experienced an unexpected overcharging issue when testing dry polymer and composite electrolytes with $LiFePO_4$ cathode from a commercial source and Li metal anode. The overcharging capacity as a function of cycle number was investigated by systematically changing the diameters of the cathode, the electrolyte and the anode as well as the thickness of the electrolyte and the anode. Our observations suggest soft shorts may occur more frequently at electrode edges. There may be multiple causes for the overcharge in our test, including micro-dendrites, change in the structure of the polymer electrolytes with cycling, the polymer-Cu contact and polymer electrolyte/cathode interface.

- Attempts were made to understand the ion transport and concentration gradient formation processes by investigating the relaxation kinetics of the chronoamperometric steps during DC polarization of Li symmetric cells. Both layered electrolytes and composite electrolytes were investigated. Nernst-Planck equation was used to model the transient and steady state current of the relaxation process. The experimental data and modeling combined provide insight in the transference number and formation of concentration gradient of the composite electrolytes investigated. To gain a thorough understanding of the relaxation behavior, efforts will be continued into FY21.

Key Publications

Publications

1. Max Palmer, Sergiy Kalnaus, Marm Dixit, Andrew Westover, Kelsey Hatzell, Nancy Dudney, X. Chelsea Chen, *A Three-Dimensional Interconnected Polymer/Ceramic Composite as a Thin Film Solid Electrolyte*, Energy Storage Materials, 26, 242-249, **2020.**

2. Merrill, L. C., Chen, X. C.*, Zhang, Y., Ford, H. O., Schaefer, J. L., Dudney, N. J., *Polymer-Ceramic Composite Electrolytes for Lithium Batteries: A Comparison Between Single Ion Conducting Polymer Matrix and Its Counterpart,* ACS Applied Energy Materials, **2020**, 3, 9, 8871–8881.

Patents

1. X. Chen, Y. Zhang, T. Saito, F. M. Delnick, N. J. Dudney, M. Lehmann, Composite Gel Electrolyte Membrane for Lithium Metal Batteries, May 2020, Patent application pending. S-138,862.

References

1. M. J. Palmer, S. Kalnaus, M. B. Dixit, A. S. Westover, K. B. Hatzell, N. J. Dudney and X. C. Chen, "title" *Energy Storage Materials* **26** (2020): 242-249.

2. Evans, J.; Vincent, C. A.; Bruce, P. G., Electrochemical measurement of transference numbers in polymer electrolytes. *Polymer* **28** [13] (1987): 2324-2328.

3. Gerrit Homann, Lukas Stolz, Jijeesh Nair, Isidora Cekic Laskovic, Martin Winter, Johannes Kasnatscheew, "Poly(Ethylene Oxide)-based Electrolyte for Solid-State-Lithium-Batteries with High Voltage Positive Electrodes: Evaluating the Role of Electrolyte Oxidation in Rapid Cell Failure", Scientific Reports 10 (2020): 4390.

Acknowledgements

These researchers provided important insight and assistance with the program:

Laura Merrill, student of Prof. Jennifer Schaefer, Notre Dame

Marm Dixit, student of Prof. Kelsey Hatzell Vanderbilt University

Drs. Sergiy Kalnaus, Andrew Westover and Beth Armstrong, staff members at Oak Ridge National Laboratory

II.8.B Lithium Dendrite Prevention for Lithium Batteries

Wu Xu, Principal Investigator
Pacific Northwest National Laboratory
902 Battelle Boulevard
Richland, WA 99354
E-mail: wu.xu@pnnl.gov

Ji-Guang Zhang, Principal Investigator
Pacific Northwest National Laboratory
902 Battelle Boulevard
Richland, WA 99354
E-mail: jiguang.zhang@pnnl.gov

Tien Duong, DOE Technology Development Manager
U.S. Department of Energy
E-mail: Tien.Duong@ee.doe.gov

Start Date: October 1, 2018 End Date: September 30, 2021
Project Funding (FY20): $400,000 DOE share: $400,000 Non-DOE share: $0

Project Introduction

Lithium (Li) metal batteries (LMBs) have been regarded as the 'holy grail' for the next generation high-energy-density rechargeable batteries due to the use of Li metal anode (LMA) with extremely low redox potential (−3.040 V vs. standard hydrogen electrode), ultrahigh theoretical specific capacity (3860 mAh g^{-1}), and low density (0.534 g cm^{-3}). However, the applications of LMBs have been hindered by two main problems. One is the growth of Li dendrites during repeated charge/discharge processes, which can penetrate the separator and cause safety hazards. Another is the low Coulombic efficiency (CE) of Li plating/stripping because Li metal is thermodynamically unstable in organic electrolytes, causing the depletion of electrolyte and the consumption of LMA, thus shortening the cycle life of the batteries using LMA. In our previous works, the effects of Li salt mixtures, solvents, additives, and surface coating on polymer separators have been systematically studied. Those previous works mainly focused on liquid electrolytes. In FY20, our research have been extended to polymer electrolytes, including the effects of polymer electrolytes on oxidation stability, ionic conductivity, Li CE, Li anode morphology, battery performance and compatibility with $LiNi_xMn_yCo_zO_2$ (NMC) cathodes. Furthermore, the ex-situ protective coating for LMAs has also been studied. The findings will guide the development of polymer electrolytes and protection of LMAs to achieve higher Li CE and suppress Li dendrites.

Objectives

1. Development of nonflammable gel polymer electrolytes (GPEs).

2. Systematic investigation on the effects of various factors, including electrolyte additive, deposition current density, cutoff voltage, and deposition capacity, on the SEI compositions and Li deposition behavior.

Approach

The following approaches have been used to reach the objectives outlined above.

1. To achieve the first objective, an ionic liquid plasticized polymer-in-salt electrolyte and a nonflammable polymer matrix incorporating a nonflammable, high concentration liquid electrolyte were prepared and evaluated for their Li CE, Li deposition morphology, and battery cycling performance.

2. To achieve the second goal, conventional $LiPF_6$/carbonate electrolytes with and without vinylene carbonate (VC) additive were utilized to deposit Li metal on Cu substrates, and then the deposited Li samples were retrieved and analyzed by various characterization techniques to study the influence of various test conditions on the structure and composition of solid electrolyte interphase (SEI) on Li surface.

Results

1. Development of polymer-in-salt electrolytes (PISEs)

PISEs with reduced ratio of polymer can largely reduce the flammability of the electrolyte. PISEs were prepared using a solvent-free ball-milling process. As shown in Figure II.8.B.1a, with the decrease of O/Li ratio, the melting point of the $P(EO)_nLiFSI$ system decreases to the lowest in $P(EO)_4LiFSI$, then increases to highest in $P(EO)_1LiFSI$ and finally decreases to a slightly lower value again in $P(EO)_{0.5}LiFSI$. The ionic conductivities of the system exhibit opposite trend at various temperatures (Figure II.8.B.1b), which means the PISE with a lower melting point has a higher ionic conductivity. The ion conductivities of the PISEs increase with the increasing temperature (Figure II.8.B.1c). With the increase of salt concentration, the initial oxidation potential (defined as the voltage value when the current density is 0.3 μA cm^{-2}) first shifts to a more positive potential and then decreases at highest concentration. The oxidation voltages of PISEs with EO/Li=16, 2 and 1 are around 4.36 V, 4.52 and 4.48 V, respectively.

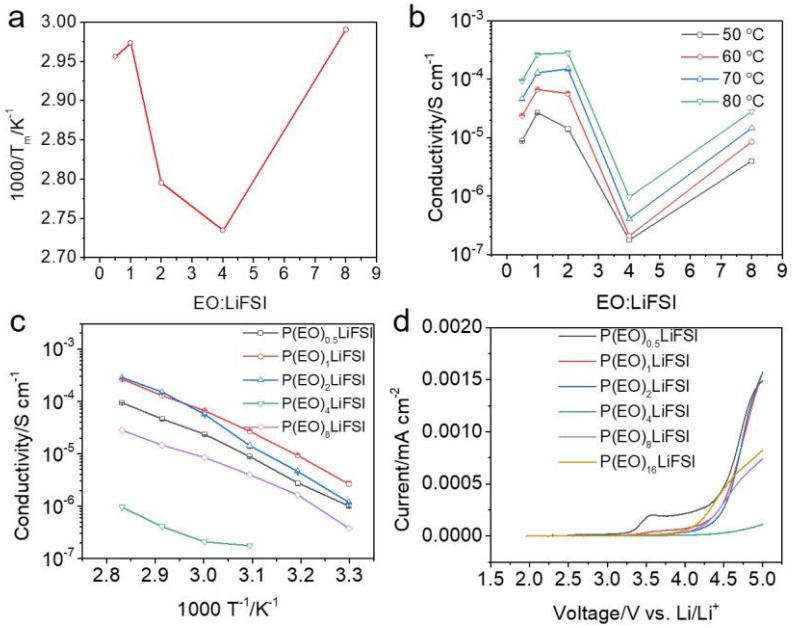

Figure II.8.B.1 (a,b) Variation of melting point (a) and ionic conductivity (b) of $P(EO)_nLiFSI$ with EO:Li mole ratio. (c) Temperature dependence of ionic conductivity and (d) electrochemical oxidation potential of $P(EO)_nLiFSI$ system.

Since the ionic conductivities of the PISEs are not high enough for battery testing, an ionic liquid Pyr14FSI was used to plasticize the PISEs. The conductivity of plasticized PISEs increases with the increase of Pyr14FSI ratio (Figure II.8.B.2a). $P(EO)_1LiFSI$-0.4Pyr14FSI is a gel-like electrolyte and has an ionic conductivity of 1.1×10^{-3} S cm^{-1} at 60 °C, which is suitable for battery operation. The average Li Coulombic efficiency (CE) of $P(EO)_1LiFSI$-0.4Pyr14FSI was tested in Li||Cu cells at 60 °C. A CE of 99.3% is obtained under a current density of 0.1 mA cm^{-2} and a capacity of 0.2 mAh cm^{-2}, but the CE decreases to 69.2% when both current density and capacity increase (at 0.5 mA cm^{-2} and 1.0 mAh cm^{-2}), indicating that $P(EO)_1LiFSI$-0.4Pyr14FSI doesn't have good rate capability due to its high viscosity. Polyimide nonwoven membrane was chosen as a framework to soak $P(EO)_1LiFSI$-0.4Pyr14FSI to make the composite electrolyte. Flammability test shows that the PISCE is difficult to ignite. Li||NMC333 cells with this PISCE exhibit stable cycling performance with a cut-off voltage up to 4.3 V (Figure II.8.B.2b).

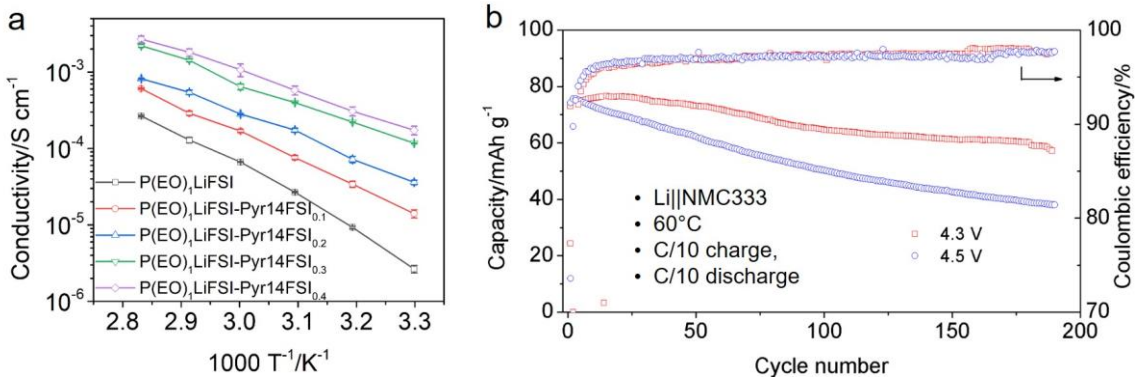

Figure II.8.B.2 (a) Temperature dependence of ionic conductivity Pyr14FSI-plasticized $P(EO)_1LiFSI$ system. (b) Cycling performance of Li||NMC333 cells with $P(EO)_1LiFSI$-0.4Pyr14FSI at C/10 rate and 60 °C.

2. Development of nonflammable polymeric electrolytes

Trimethyl phosphate (TMPa) is a widely used nonflammable solvent. High concentration LiFSI-nTMPa electrolytes are nonflammable, they also exhibit high CEs. LiFSI-1.1TMPa and LiFSI-1.3TMPa have CEs of 98.5% and 98.7% at 25 °C from Li||Cu cell tests, respectively. Increasing temperature reduces the Li CE, e.g., LiFSI-1.3TMPa has a Li CE of 96.4% at 60 °C, due to the accelerated side reactions between electrolyte and Li metal. A nonflammable organophosphate monomer was designed and synthesized according to literature.[1] ^{1}H NMR confirmed the success in synthesis of the monomer. Thereafter, the monomer was mixed with LiFSI-1.3TMPa electrolyte and polymerized under UV light to yield a transparent, self-standing gel polymeric electrolyte (GPE) (Figure II.8.B.3a). As shown in Figure II.8.B.3b, the GPE exhibits non-flammability even under constant butane flame blazing. Therefore, this GPE exhibits excellent flame resistivity. The Li CE of the flame-resistive GPE was measured in Li||Cu cells at 60 °C. Figure II.8.B.3c shows the voltage profiles of two parallel cells. The average Li CE was determined to be 81.3%. The deposition morphology of Li on Cu substrate was also evaluated, which shows a granular morphology of Li (Figure II.8.B.3d). Figure II.8.B.3e shows the voltage profile of a Li||NMC622 cell using the GPE at C/10 rate in the first charge/discharge cycle. The discharge capacity of the cell amounts to 157.1 mAh g^{-1} under such condition. The long-term cycling performance of the Li||NMC622 cells is currently under testing.

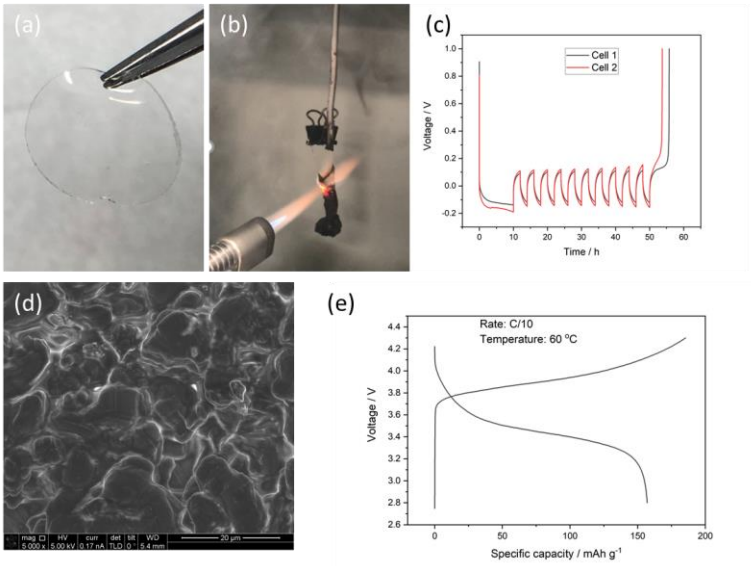

Figure II.8.B.3 (a) Photo of in-situ polymerized nonflammable GPE. (b) Flammability test on the GPE. (c) Voltage profiles of Li||Cu cells using the GPE during the CE evaluation. (d) Morphology of deposited Li using the GPE, (e) First cycle charge-discharge voltage profiles of Li||NMC622 cells using the GPE at C/10 rate 60 °C.

3. *Development of acetonitrile-based high concentration electrolytes*

In a separate effort, high concentration electrolytes (HCEs) based on acetonitrile (AN) solvent and vinylene carbonate (VC) additive, $LiFSI_x$-AN-VC_y system were investigated with x = 0.2 ~ 1.1 and y = 0.02 ~ 0.15 in molar ratio. Addition of VC in LiFSI-AN HCEs significantly stabilizes the compatibility of Li metal anode and the electrolyte, thus increasing Li CE to 99.2% for the optimal electrolyte of $LiFSI_{0.52}$-AN-$VC_{0.09}$ (LAV) with large granular Li deposition. The optimal LAV exhibits excellent stability with Li metal (Figure II.8.B.4a,b) and is also stable at 4.5 V vs Li/Li^+. It enables Li||NMC333 cells to stably cycle for more than 400 cycles in 2.7-4.3 V at 1.8 mA cm^{-2} or 250 cycles in 2.7-4.5 V at 3.6 mA cm^{-2} (Figure II.8.B.4c), and Li||NMC622 cells with high cathode loading (4.0 mAh cm^{-2}) to stably cycle over 200 times at 2.0 mA cm^{-2} in 2.7-4.4 V (Figure II.8.B.4d).

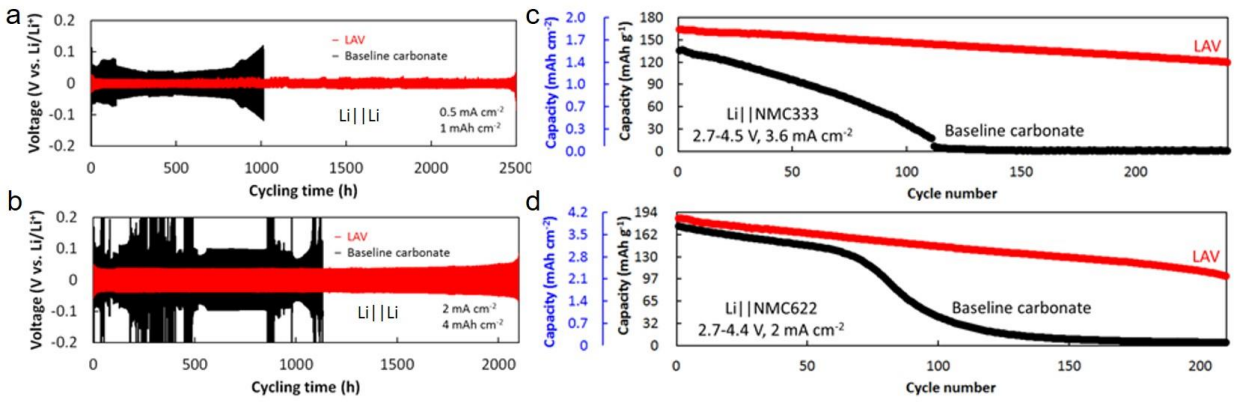

Figure II.8.B.4 (a,b) Cycling stability of Li||Li cells with , (e) First cycle charge-discharge voltage profiles of Li||NMC622 cells using GPE at C/10 rate 60 °C.

4. Evaluation of Mg-doped Li metal alloys as anode materials

In FY20, Mg-doped Li metal was also investigated as an anode for Li metal batteries. According to the density functional theory calculations, the surface energy of Li deposition substrate plays an important role in influencing the Li deposition behavior. The surface energy of Li can be altered by introducing small amount of Mg in the Li metal foil (Figure II.8.B.5a,b). The cycling performances of Li||NMC811 and Li-Mg||NMC811 coin cells using flooded electrolyte of LiFSi-1.2DME-3TTE are compared in Figure II.8.B.5c. It is seen that the Li-Mg5 (by weight ratio) based cells exhibit superior cycling stability and capacity retention to the pure Li based cells. A higher Mg doping in Li (e.g. Li-Mg10) deteriorates the cycling stability of the cells. The results indicate that small Mg doping may be a promising substitute to the pure Li metal as anode materials for the development of high energy density batteries. More cell testing and characterization are under way.

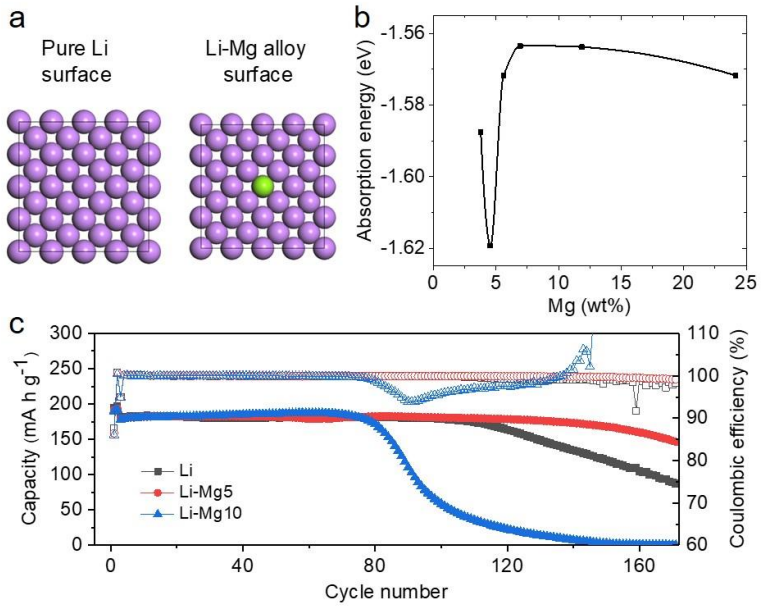

Figure II.8.B.5 (a,b) Simulation model of pure Li (a) and 4.5 wt.% Mg-doped Li surface. Li, purple ball; Mg, green ball. (c) Cycling performances of Li||NMC811 cells and Li-Mg||NMC811 cells with two Mg-doped Li anodes (Li-Mg5 and Li-Mg10), 4.2 mAh cm^{-2} NMC811 cathode, and lean electrolyte at 14 µL. Voltage window is 2.8~4.4 V. The batteries were tested at C/3 charge and discharge after two formation cycles at C/10.

5. Investigation of factors affecting SEI composition and Li deposition morphology

In the studies under the US-Germany Energy Storage Collaboration Program, effects of four factors — additive, deposition current density, cutoff voltage, and deposition capacity — were investigated on the morphologies of the electrochemically deposited Li (EDLi) films on Cu substrates and the compositions of SEI layers formed on these EDLi films in two electrolytes, 1.2 M $LiPF_6$/EC-EMC (3:7 by wt.) with and without 5 wt.% VC, by collaboration with Dr. Chongmin Wang's team using SEM, cryo-TEM, EDS and EELS. The VC-containing electrolyte results in a slightly oxidized Li with SEI being nanoscale mosaic-like structure comprised of organic species, Li_2O and Li_2CO_3, while the VC-free electrolyte leads to a combination of fully oxidized Li with Li_2O SEI layer and pure Li metal with multilayer nanostructured SEI. For EDLi deposited at different current densities, a fixed Li amount (0.167 mAh cm^{-2}) was used. With the increase of deposition current density from 0.1 to 9 mA cm^{-2}, the nucleation overpotential increased from 95 to 948 mV, and the growth overpotential increased from ~85 to ~550 mV. As shown in Figure II.8.B.6a-d, regardless of the current density variation, the EDLi exhibits whisker-like configuration with rough structure, indicating the uncontrolled growth of Li metal. The fine feature of EDLi varies as the current density changes. The number density of the whiskers decreases with increasing current density. In terms of chemical compositions, the EDLi and SEI layers at current densities from 0.1 to 5 mA cm^{-2} are mainly comprised of O and C (Figure II.8.B.6e), while at the high current density (9 mA cm^{-2}), the LiF content significantly increases. The SEI formed at 0.1

mA cm^{-2} exhibits a monolithic amorphous structure, while the SEIs formed at 2 to 9 mA cm^{-2} exhibit mosaic-like structures.

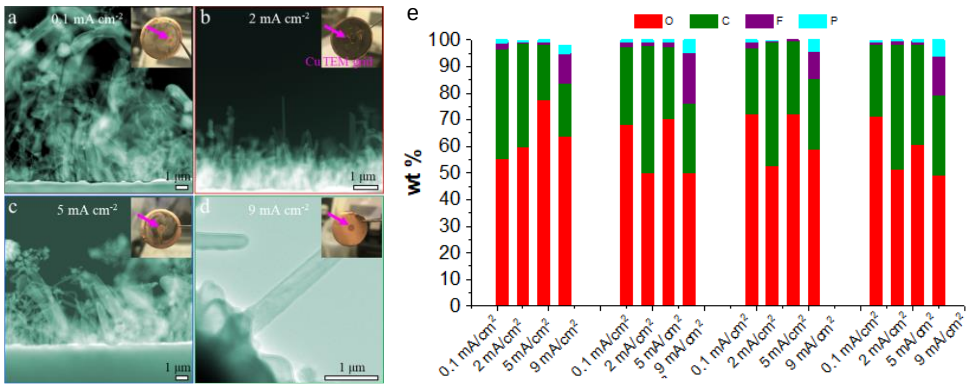

Figure II.8.B.6 (a-d) Low magnification TEM images of EDLi under current density of (a) 0.1 mA cm^{-2}, (b) 2 mA cm^{-2}, (c) 5 mA cm^{-2} and (b) 9 mA cm^{-2}. Insets: Digital photos of deposited Li. (e) Composition information acquired from EDLi interface between Li and SEI, SEI and the surface of SEI areas at different current densities.

For the influence of electrode potential (i.e. the cutoff voltage) on the morphology and composition of SEI formed on Cu substrate before and after Li deposition, it is found from Figure II.8.B.7 that in the conventional $LiPF_6$/EC-EMC electrolyte without VC additive, the SEI formed at 1.0 V exhibits a monolithic amorphous structure, which evolves to amorphous matrix embedded with crystalline Li_2O particles as the voltage decreases to 0 V where no Li deposition occurs. In the case of VC-containing electrolyte, crystalline Li_2O can be observed in the entire selected voltage range. The thickness of SEI formed on Cu foil increases with decreasing voltage. When Li deposition occurs, the composition of SEI further evolves whereas the SEI thickness remains almost unchanged. The results have confirmed that the SEI composition is highly dependent on the potential electrode.

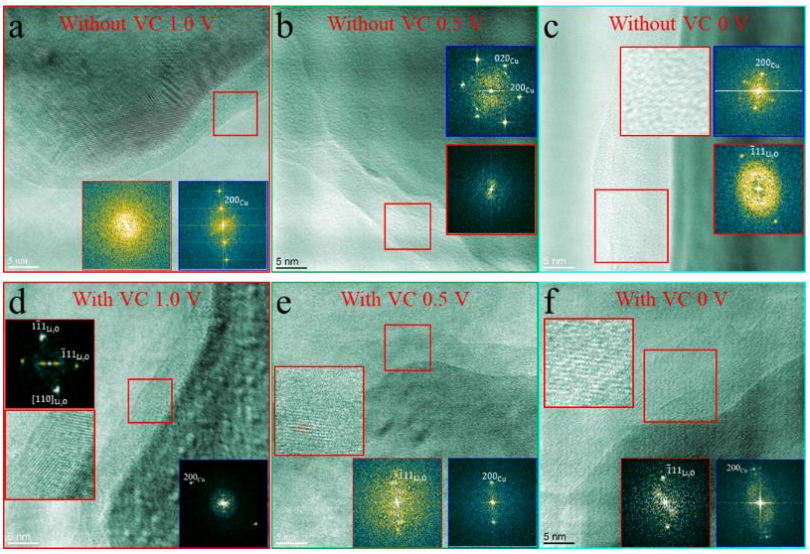

Figure II.8.B.7 Cryo-TEM images of SEI formed on TEM Cu foil in the electrolytes without and with 5% VC additive. (a-c) At different cut-off voltages of 1.0 V, 0.5 V and 0 V in the electrolyte without VC additive. (d-f) At different cut-off voltages of 1.0 V, 0.5 V and 0 V in the electrolyte with VC additive. Insets: FFT patterns from SEI (red) and Cu foil (blue).

When Li was deposited under the different areal deposition capacities (1, 2 and 4 mAh cm^{-2}) at the same current density of 0.1 mA cm^{-2}, the morphology of the EDLi slightly changes, from fine dendrites at 1 mAh cm^{-2} to slightly larger size dendrites at 2 mAh cm^{-2} and to some granular deposits at 4 mAh cm^{-2} (Figure II.8.B.8a). The compositions of the SEIs formed under different deposition capacities were studied by XPS (Figure II.8.B.8b). From the XPS, it can be confirmed that the species such as LiF, $LiPO_xF_y$, Li_2O, Li_2CO_3, $LiRCO_3$ and RCOOLi were detected in all the SEIs, but there was no clear difference in compositions. It can be concluded that the deposition capacity has a minimal influence on the SEI composition in VC-containing electrolyte.

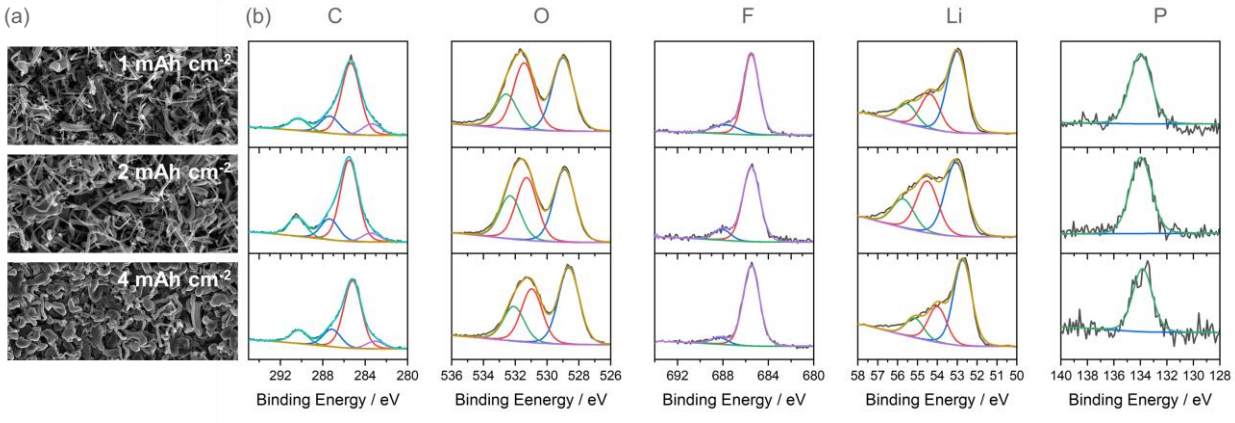

Figure II.8.B.8 (a) Morphologies of EDLi deposited on Cu at the current density of 0.1 mA cm^{-2} for different deposition capacities (b) X-ray photoelectron spectroscopy of the EDLi deposited at the areal capacities of 1, 2 and 4 mA cm^{-2} (top to bottom).

Conclusions

1. Solid-state polymer-in-salt electrolytes (PISEs) were developed through solvent-free ball-milling process. The melting points, ionic conductivities and oxidation potentials were evaluated. By plasticizing with an ionic liquid, the hybrid PISE could allow the Li||NMC333 cells to stably cycle to 200 cycles at 60 °C in the voltage range of 2.7-4.3 V.

2. A nonflammable gel polymer electrolyte (GPE) was fabricated by combining a nonflammable high concentration liquid electrolyte (LiFSI-1.3TMPa) and a nonflammable polymer matrix. This GPE exhibits excellent flame resistivity. The Li deposited in this electrolyte exhibits granular morphology. The application of this nonflammable GPE in Li||NMC622 cells is under testing.

3. High concentration electrolytes (HCEs) based on acetonitrile (AN) solvent and vinylene carbonate (VC) additive were developed for Li metal batteries. The optimal electrolyte of $LiFSI_{0.52}$-AN-$VC_{0.09}$ (LAV) shows high Li CE of 99.2%, lead to large granular Li deposition, and high voltage stability. The Li||NMC cells using this optimal LAV exhibit excellent stability at 4.5 V under high current density and high loading cathode.

4. Mg-doped Li alloys were studied for Li metal batteries by computational calculations and experimental tests. The preliminary results showed that 5 wt.% Mg doping (Li-Mg5) improves the cycling performance of NMC811 cells, compared with pure Li.

5. Effects of four factors — additive, deposition current density, cutoff voltage, and deposition capacity — were investigated on the morphologies of electrochemically deposited Li (EDLi) films and the compositions of SEI layers formed on these EDLi films in two conventional electrolytes with and without VC additive. The first three factors largely affect the SEI compositions but less on Li deposition morphologies, while the deposition capacity can change the Li deposition morphology but show less influence on the SEI compositions.

Key Publications

1. Y. Xu[#], H. Wu[#], H. Jia, M. H. Engelhard, J.-G. Zhang, W. Xu*, and C. Wang*, "Sweeping Potential Regulated Structural and Chemical Evolution of Solid-Electrolyte Interphase on Cu and Li as Revealed by Cryo-TEM", *Nano Energy*, 2020, **76**, 105040. DOI:10.1016/j.nanoen.2020.105040

2. Y. Xu[#], H. Wu[#], H. Jia, J.-G. Zhang, W. Xu*, and C. Wang*, "Current Density Regulated Atomic to Nanoscale Process on Li Deposition and Solid Electrolyte Interphase Revealed by Cryogenic Transmission Electron Microscopy", *ACS Nano*, 2020, **14** (7), 8766-8775. DOI:10.1021/acsnano.0c03344

3. Z. Peng, X. Cao, P. Gao, H. Jia, X. Ren, S. Roy, Z. Li, Y. Zhu, W. Xie, D. Liu, Q. Li, D. Wang,* W. Xu,* and J.-G. Zhang*, "High-Power Lithium Metal Batteries Enabled by High-Concentration Acetonitrile-Based Electrolytes with Vinylene Carbonate Additive", *Advanced Functional Materials*, 2020, **30** (24), 2001285. DOI:10.1002/202001285

4. Y. Xu[#], H. Wu[#], Y. He[#], Q. Chen, J.-G. Zhang, W. Xu*, and C. Wang*, "Atomic to Nanoscale Origin of Vinylene Carbonate Enhanced Cycling Stability of Lithium Metal Anode Revealed by Cryo-Transmission Electron Microscopy", *Nano Letters*, 2020, **20** (1), 418-425. DOI:10.1021/acs.nanolett.9b04111

5. W. Xu and J.-G. Zhang, "Lithium Dendrite Prevention for Lithium Batteries", *2020 DOE VTO Annual Merit Review Meeting*, Virtual, June 1-4, 2020.

6. H. Wu, Y. Xu, X. Ren, B. Liu, M. H. Engelhard, M.S. Ding, P. Z. El-Khoury, L. Zhang, Q. Li, K. Xu, C. Wang, J.-G. Zhang, and W. Xu, "Polymer in Quasi-Ionic Liquid Electrolytes for High-Voltage Lithium Metal Batteries", *2019 MRS Fall Meeting & Exhibit*, Boston, Massachusetts, December 3, 2019.

References

1. H. Jia, H. Onishi, R. Wagner, M. Winter, and I. Cekic-Laskovic, "Intrinsically safe gel polymer electrolyte comprising flame-retarding polymer matrix for lithium ion battery application", ACS Applied Materials & Interfaces, 2018, **10** (49), 42348-42355.

Acknowledgements

Key contributors Drs. Haiping Wu, Hao Jia, Chongmin Wang and Yaobin Xu are appreciated.

II.8.C Understanding and Strategies for Controlled Interfacial Phenomena in Li-Ion Batteries and Beyond (Texas A&M University, Purdue University)

Perla B. Balbuena, Principal Investigator
Texas A&M University
3122 TAMU
College Station, TX 77843
E-mail: balbuena@tamu.edu

Jorge M. Seminario, Principal Investigator
Texas A&M University
3122 TAMU
College Station, TX 77843
E-mail: seminario@tamu.edu

Partha P. Mukherjee, Principal Investigator
Purdue University
55 Purdue Mall
West Lafayette, IN 47907-2088
E-mail: pmukherjee@purdue.edu

Tien Duong, DOE Technology Development Manager
U.S. Department of Energy
E-mail: Tien.Duong@ee.doe.gov

Start Date: October 1, 2016 End Date: September 30, 2020
Project Funding: $ 1,333,335 DOE share: $1,200,000 Non-DOE share: $133,335

Project Introduction

This project focuses on elucidating the roles of the electrolyte and electrode on the formation and evolution of the SEI layer and cell electrochemical performance on silicon and on Li metal anodes. For Si nano/microstructures we evaluate lithiation, volume changes, reactivity, and chemo-mechanical transformations as functions of nanoparticle size, shape, presence of coatings, electrolyte composition, electron leakage to the electrolyte, and cycling. For Li metal anodes we provide a detailed analysis of the electrode and electrolyte effects on reactivity and as a function of microstructural evolution and underlying stochasticity as dendrites nucleate and grow. We thoroughly investigate and test how the chemistry of the various components of the electrolyte and the electrode architecture may affect the electrochemical reactions as well as cell degradation. The analysis of Si electrodes was reported in the previous years. This report focuses on Li metal anodes issues characterization and analyses.

Objectives

The knowledge gained by developing fundamental understanding of the issues associated with metal electrodeposition and stripping are aimed to elaborate strategies for solving practical issues associated with SEI instability, electrode expansion, and dendrite formation. These strategies emerge from electrolyte formulation and electrode morphology design.

Approach

A comprehensive multiscale modeling approach including first-principles ab initio static and dynamics, classical molecular dynamics, and coarse-grained mesoscopic models is used to characterize the roles of the electrolyte chemical, structural, and dynamical properties and of the electrode micro- and nanostructure on the formation and evolution of the SEI layer and associated electrochemical performance on silicon and on Li metal anodes. For Si nano/microstructures we evaluate lithiation, volume changes, reactivity, and chemo-

mechanical transformations as functions of nanoparticle size, shape, presence of coatings, electrolyte composition, electron leakage to the electrolyte, and cycling. For Li metal anodes we focus on a detailed analysis of the electrolyte effects on reactivity leading to solid electrolyte interphase formation, and as a function of electrode microstructural evolution and underlying stochasticity as dendrites are formed.

Results

A simple model to describe Li nucleation. The geometry and electronic structure of Li_x nanoclusters (x =2-20) were used to investigate nucleation and growth of lithium dendrites from an ab-initio perspective. Thermodynamic DFT calculations of reduction of Li ions on Li_x nanoclusters indicated that there is no directionality in the growth. We showed that kinetic processes have more control over non-uniform growth than thermodynamics processes. Based on this, we developed a Matlab code to describe Li nucleation of up to 2,000 atoms. The steps are explained in the next paragraph.

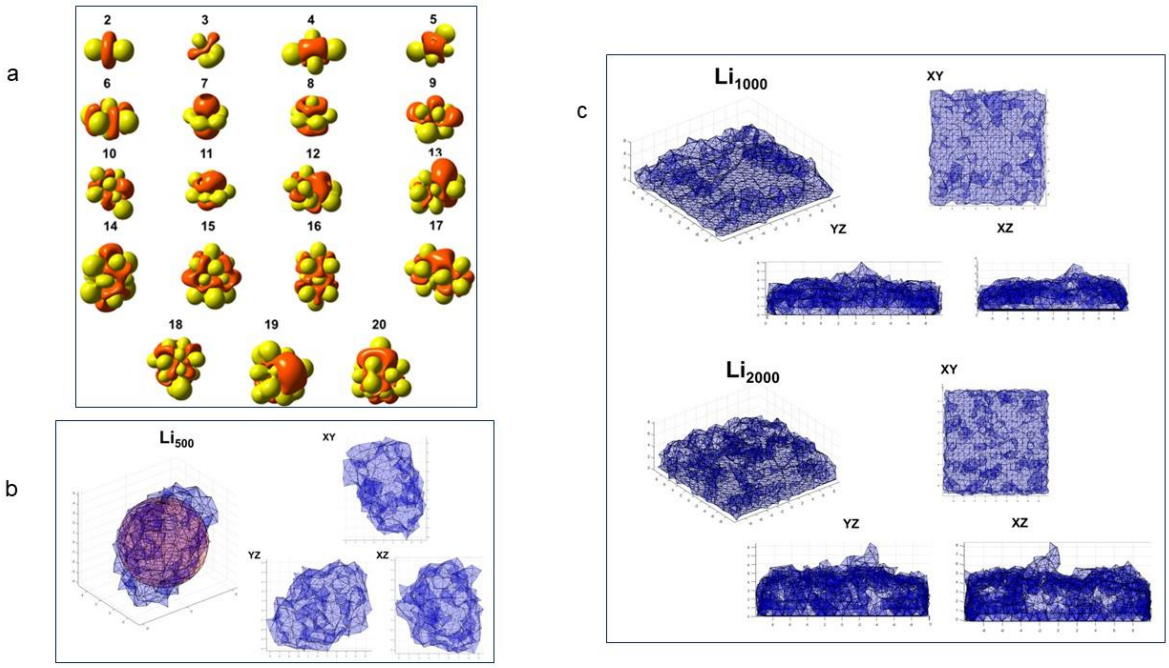

Figure II.8.C.1 a) Electrostatic potentials for Lix clusters. Orange is negative, Yellow is positive. Isosurface value of .008 au. b) Most acentric Li_{500} cluster. Blue is surface of cluster, orange is a unit sphere to provide perspective. c) The top structure shows the Li_{1000} electrode largest dendritic growth case. The bottom structure shows the Li_{2000} electrode largest dendritic growth case. (PCCP, Royal Society of Chemistry, 2020).

The important forces guiding the Li^+ ion in the range between bulk solvent and reduction distance will be electrostatic interactions which will come from two places: the electrostatic potential (ESP) and electric field from the electrode. Attractive interaction will force the Li^+ ion in a particular direction and once the ion is close enough reduction will occur. We first explored this concept by visualizing and quantifying the ESP of the Li nanoclusters (Figure II.8.C.1a). The negative parts of the ESP will be attractive to the Li^+ ion while the positive parts will be repulsive. Based on this model, the Li^+ ions will be reduced guided by the ESP. The shape of the ESPs of the clusters follows a general pattern such that the ESP is always repulsive over Li atoms and attractive over the rest of the cluster. Therefore, the ESP is attractive to the Li^+ ions at interstitial locations. Under an electric field, the general shape of the ESP is the same except some sides of the clusters are promoted over others. Based on this, we built an evolution model that is computationally inexpensive and allows for the growth of large Li clusters (# of Li ~5000 or less). T An internal program was created in Matlab to build or evolve Li clusters based on the assumption that a Li will always add to an interstitial site and that each interstitial site. Other assumptions are that the generalization of the ESP holds and that the energetics of these configurations are still similar in energy to the minimum energy configuration. Since we are interested in the

nucleation of dendrites, we characterized the configurations of lithium based on acentricity or the deviation from a spherical configuration. Our acentricity factor was defined by determining the variance in the radius of the outer Li atoms normalized by the number of total Li atoms. The more acentric the cluster is, the more interesting as a potential dendrite nucleation mechanism. The most acentric case for a Li_{500} is shown in Figure II.8.C.1b. We then tested growth on a surface, as shown in Figure II.8.C.1c where most of the lithium is added in a uniform manner but there are definite spikes or dendrite like structures that have started to form.

These simulations demonstrate that with very few rules based on the ESP from first principles simulations, dendritic structures are observed in the electrode-like starting structure. This gives important insight into the fundamentals of lithium dendrite nucleation and growth and mitigation strategies to counteract dendrites. Based on this model, solutions to changing how dendrites grow should focus on manipulating the electrostatic potential whether by insulating or ensuring homogeneity.

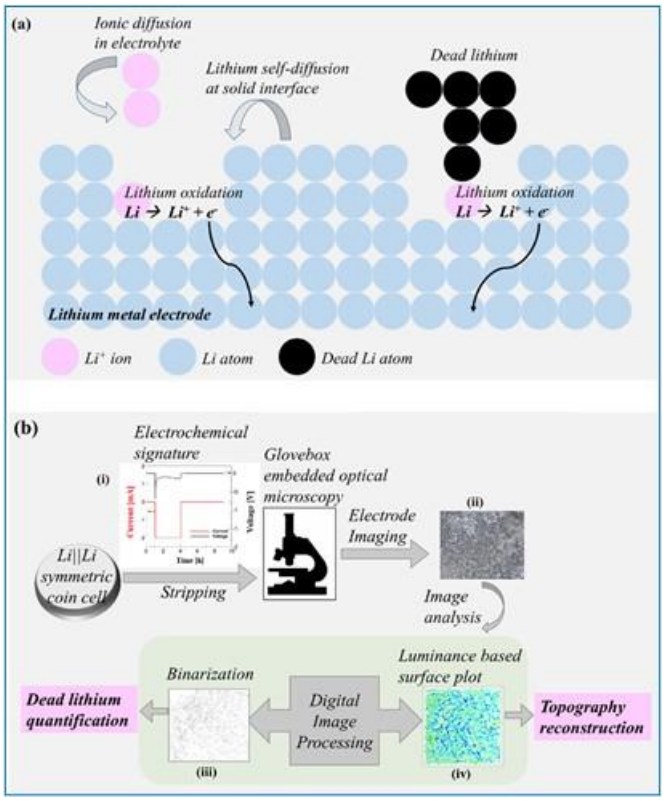

Figure II.8.C.2 (a) Mesoscale computational model includes diffusion of Li^+ in the electrolyte, surface diffusion of a Li atom on solid Li, and the oxidation reaction of Li at the interface. (b) Experimental method workflow include surface imaging and luminescence based surface plot . (JPCC, American Chemical Society, 2020).

Dead lithium formation. Interfacial morphology evolution during stripping impacts the dead lithium formed. When the interfacial morphology consists of finely connected ligaments or peaked structures above the height of the average interface, a greater amount of dead lithium is formed. On the other hand, when the interfacial morphology is nearly flat or pitted, a smaller amount of dead lithium is formed. The optical imaging of the lithium metal electrode inside the glovebox after an electrochemical stripping experiment and a mesoscale computational model (Figure II.8.C.2) reveal a connection between interfacial morphological features and the amount of dead lithium. The mesoscale computational model is used to study the physical mechanism affecting the formation of dead lithium. The ionic diffusion of lithium in the electrolyte, the self-diffusion of lithium at the solid interface, and the lithium oxidation electrochemical reaction at the interface are considered. More dead lithium is formed at a higher temperature and a lower overpotential. Changing the overpotential modifies the rate of oxidation reactions while changing the temperature modifies the diffusion kinetics of ions

in the electrolyte and lithium self-diffusion at the solid interface. So, the diffusive processes play a key role in the amount of dead lithium formed near the interface. Further studies reveal that between the two diffusive processes, the self-diffusion of lithium at the solid interface is more significant than ionic diffusion toward the formation of dead lithium. This study provides a link between the physical mechanisms (ionic and self-diffusion and oxidation reaction) active near the interface and evolution of the morphology of the interface and the amount of dead lithium formed. To minimize the amount of dead lithium, the stripping or discharging of the electrode should occur at a low temperature and higher overpotential or higher current density. This is in clear opposition to the recommended operating conditions of a high temperature and a low current density during plating or charging of the battery to reduce the likelihood of dendritic deposition at the lithium metal anode.

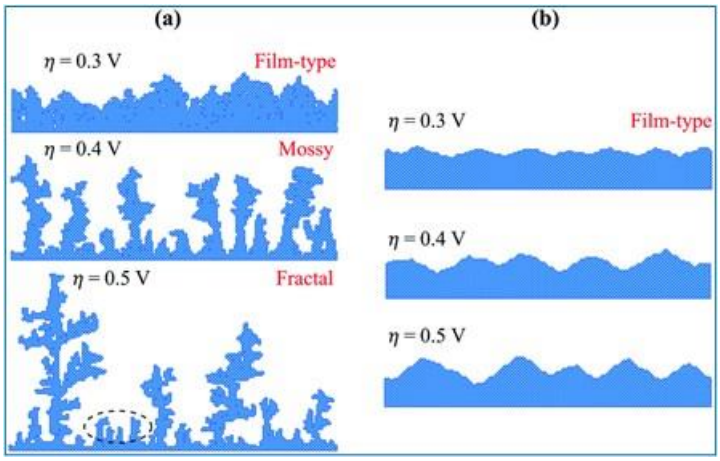

Figure II.8.C.3 Electrodeposition morphologies obtained at an overpotential of 0.3 V, 0.4 V and 0.5 V. Two specific conditions are set for the self-diffusion barriers: (a) E_{a1} = 0.15 eV and E_{a2} = 0.3 eV with E_{a3}-∞; (b) E_{a1} = 0.15 eV and E_{a3} = 0.3 eV with E_{a2} - ∞. (Royal Society of Chemistry, PCCP, 2020)

Effects of Li surface diffusion on dendrite growth. A mesoscopic model was developed to incorporate the effects of ionic surface diffusion and their impact on nucleation morphologies. The electrodeposition morphologies at various applied overpotentials (or deposition rates) are shown in Figure II.8.C.3. As illustrated in the first scenario, the growth mode undergoes two morphological transitions with an increase in overpotential, i.e. from film-type to mossy and from mossy to fractal. These morphological transitions arise from the competition between the surface self-diffusion kinetics and deposition rate. Three diffusion barriers are considered: E_{a1} = on a terrace; E_{a2} = away from a step; E_{a3} = descend from step.

Theoretically, it is desired to have a low barrier height for terrace diffusion and a large barrier height for diffusion away from a step. Morphology maps shown in Figure II.8.C.4 suggest that any improvement in the surface morphology (from the bottom to top corner) may be due to an increase in the barrier height for diffusion away from a step, while any deterioration can be attributed to an increase in the barrier height for terrace diffusion. On visual examination, the morphologies do not show any surface smoothening on going from the bottom to top corner at Z = 0.3 V and 0.5 V. Therefore, we conclusively deduce that any adverse impact on the surface morphology is due an increase in the barrier height of terrace diffusion. Figure II.8.C.4 (a) shows that at a relatively low deposition rate, the porosity of the film-type metal increases with an increase in the barrier height of terrace diffusion, due to a sluggish surface atoms transport. Physically, adatoms are incapable of diffusing to favorable sites before being pinned on the growth front by the arrival of newly deposited atoms. Besides, the fractal morphology exhibits two discrete features at a high deposition rate. First, nucleated islands on the electrode surface are not interlinked with each other, thereby impeding the formation of a film-type morphology.

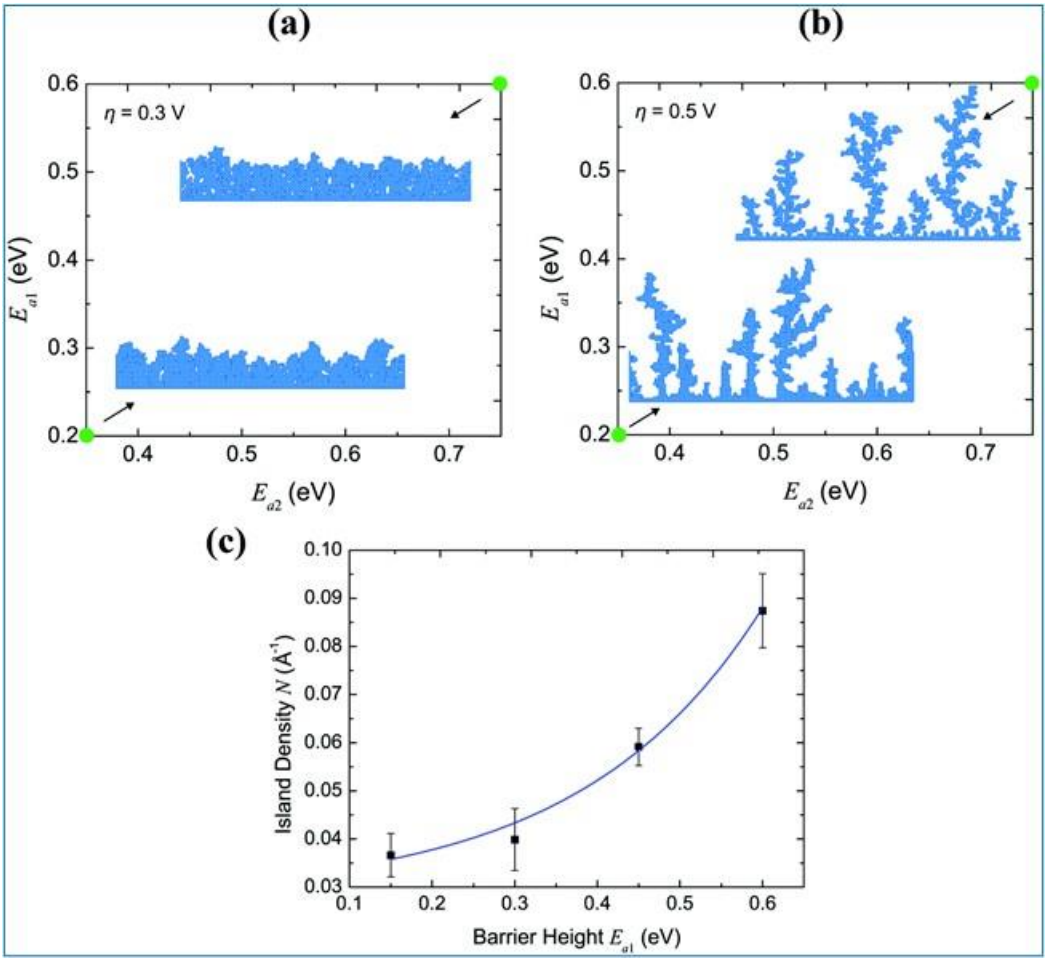

Figure II.8.C.4 Electrodeposition morphologies obtained at an overpotential of 0.3 V, 0.4 V and 0.5 V. Two specific conditions are set for the self-diffusion barriers: (a) E_{a1} = 0.15 eV and E_{a2} = 0.3 eV with E_{a3}-∞; (b) E_{a1} = 0.15 eV and E_{a3} = 0.3 eV with E_{a2} - ∞. (Royal Society of Chemistry, PCCP, 2020)

Figure II.8.C.4 (c) illustrates that the exponential increase of the island density with the height of terrace diffusion barrier. Initially, the deposited single atoms meet and form dimers. For low terrace diffusion barriers, newly deposited atoms diffuse rapidly on the surface and may fuse with those dimers to form larger islands. In addition, sluggish terrace diffusion of atoms facilitates nucleation of new islands, leading to a relatively large island density. Second, the branch thickness of the fractal metal contracts with decreasing surface diffusion rate, as depicted in Figure II.8.C.4 (b). However, based on Figure II.8.C.4 (a) and (b), we infer that though E_{a1} affects morphological features like porosity, nucleation density and branch thickness, it is unable to alter the nature of the electrodeposition morphology. In other words, the electrodeposit being film-like or fractal depends only on the overpotential or deposition rate in the absence of interlayer diffusion. Interestingly, these barriers that appear as parameters in the mesoscopic model, and others occurring during the series of events taking place during the approach of the solvated Li ion to the surface (including desolvation and diffusion) can be accurately obtained from first principles constrained molecular dynamics free energy simulations as recently demonstrated by the team. [1] Moreover, the Li dendritic morphology growth and their dependence on current rate and current protocols was carefully observed and analyzed using atomistic classical molecular dynamics simulations, [2] and the variation of the overpotentials for electrodeposition at interfaces were characterized by ab initio molecular dynamics simulations [3] reported by this team.

New tools for the analysis of complex interfaces. As we discover the interplay between multiple factors in these systems, new computational tools for their analysis are needed. For this purpose, analysis tools were implemented in the context of ab initio molecular dynamics simulations at interfaces under electric fields.

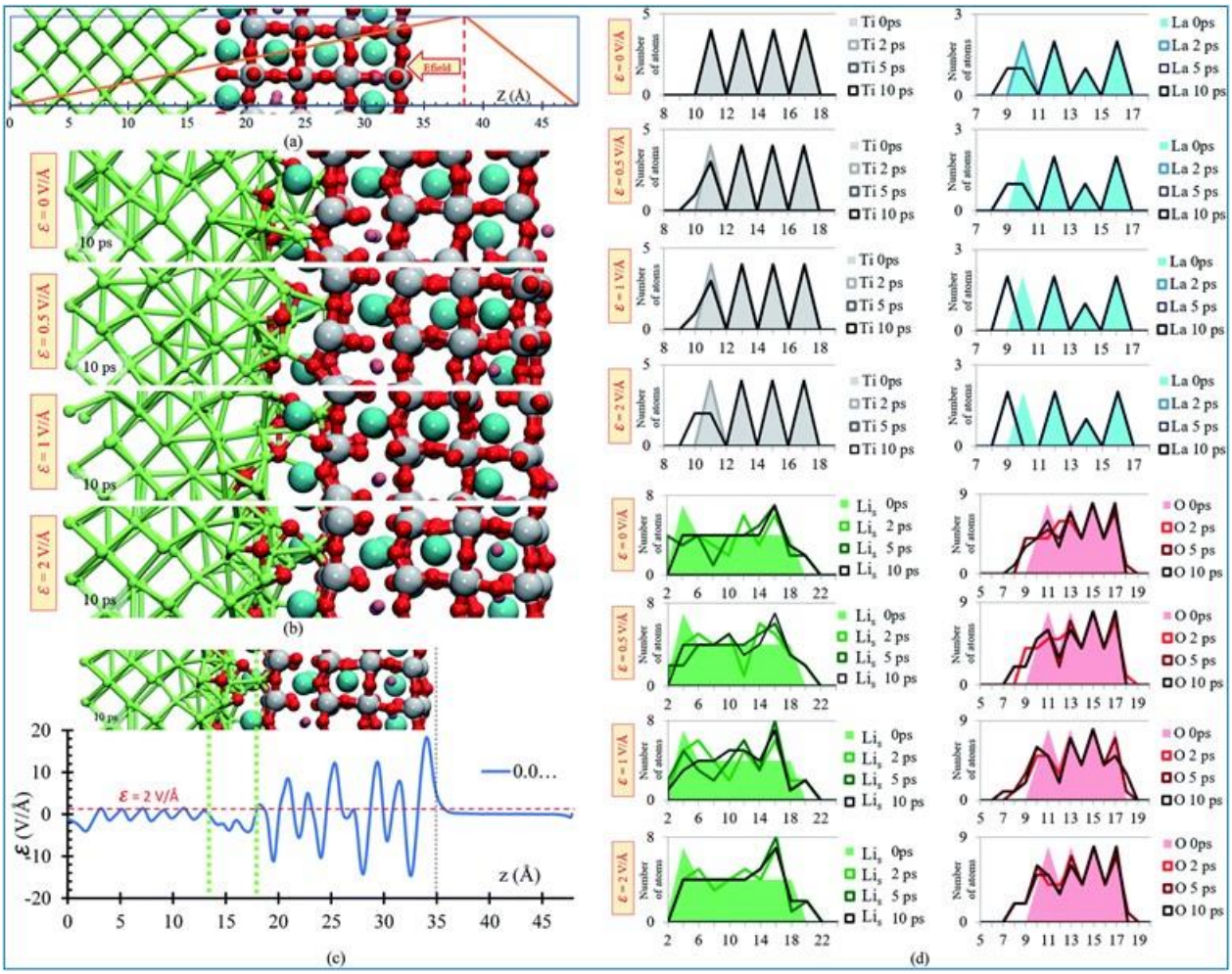

Figure II.8.C.5 (a) $Li_{0.29}La_{0.57}TiO_3$/Li-metal electrochemical cell under the application of a sawtooth external electric field. (b) Structural changes of the $Li_{0.29}La_{0.57}TiO_3$/Li-metal interface at 10 ps of applying external electric fields of ε = 0, 0.5, 1 and 2 V Å^{-1}. (c) Profile average of the electric field component in the drift direction of ion transport. (d) Atomic profile along the z axis at different times, for the four electric field cases, ε = 0, 0.5, 1 and 2 V Å^{-1}. (Royal Society of Chemistry, RSC Advances, 2020)

The system chosen for this tool development was the $Li_{0.29}La_{0.57}TiO_3$/Li-metal interface. Figure II.8.C.5a illustrates the electric field as a function of position. The direct bias part simulates an externally applied electric field. It is simply included to keep the periodicity of the potential, avoiding its growth from cell to cell. Therefore, the reverse bias region is left empty as any interaction in that region would correspond to unphysical effect not related to the system under study. Figure II.8.C.5b shows the structural changes at the interface. Atomic species (O, La, Ti) migrated from the solid electrolyte towards the Li-metal due to the application of the external electric field as shown also in Figure II.8.C.5d. Oxygen atoms originally belonging to the solid electrolyte are the first atomic species that reacts in contact with the Li-metal. The migration of O atoms to the metal anode increases as the applying external electric field increases. Shorter displacements are observed for the heaviest atoms in the electrolyte, Ti and La, moving towards the Li-metal phase. The migration of Ti and La to the metal anode increases as the applying external electric field increases. Likewise, some Li atoms from the Li-metal (Lis) diffuse towards the SSE. Based on the atomic profiles, the nascent interface is composed in its majority of O and Li atoms during the first 10 ps, and as the electric field

increases, the formation of a new interface is favored. The profile average of the internal electric field component in the drift direction of transport of ions reaches more than 10 V $Å^{-1}$ in the solid electrolyte region; however, at the interface (between the green dotted lines in Figure II.8.C.5c) all the values are under 2 V $Å^{-1}$. Therefore, that determines the upper limit of the range of fields needed to cross over and to analyze reactions on the interface. However, the electric field for a practical condition, i.e., in a real Li-ion battery, is much smaller, ~10^{-6} V $Å^{-1}$, but it may change a few orders of magnitude up or down according to the specific characteristics of the battery such as anode–cathode average distance, rate of charge, type of charging, conductivity of components, geometry of the cell, among several factors. This analysis will be repeated for other systems, especially liquid electrolytes, to determine the effects of the applied field on the electrodeposition behavior.

Conclusions

The results of this work provide new insights into the Li electrodeposition phenomena during Li-metal battery cycling. First, the formulation of a model for Li nucleation based on the pattern for Li ions reduction and deposition on ab initio-derived electrostatic potentials suggested that kinetic processes have more control over non-uniform growth than thermodynamics processes, and illustrates the initial stages of dendritic behavior. Including other dynamic processes such as surface diffusion on the growing Li nuclei, mesoscopic modeling proved the growth of the various morphologies observed experimentally. The competition between surface diffusion and overpotential for electrodeposition then determines under what conditions specific type of morphologies are observed. Finally, we demonstrate the performance of new tools that allow to elucidate atomistic details where degradation reactions compete with electrodeposition phenomena.

Key Publications

1. Ethan P. Kamphaus, Karoline Hight, Micah Dermott, Perla B. Balbuena, “Model Systems for Screening and Investigation of Lithium Metal Electrode Chemistry and Dendrite Formation,” *Phys. Chem. Chem. Phys.*, 22, 575-588, (2020). Selected as 2019 Hot PCCP Article.

2. Deepti Tewari, Sobana P. Rangarajan, Perla B. Balbuena, Yevgen Barsukov, and Partha P. Mukherjee, “Mesoscale Anatomy of Dead Lithium Formation,” *J. Phys. Chem. C*, 124 (12), 6502-6511, (2020).

3. Galvez-Aranda, D. E.; Seminario, J. M., “Solid Electrolyte Interphase Formation between the $Li_{0.29}La_{0.57}TiO_3$ Solid-State Electrolyte and a Li-Metal Anode: An Ab Initio Molecular Dynamics Study”, *RSC Adv.*, 10, 9000-9015, (2020).

4. Bairav S. Vishnugopi, Feng Hao, Ankit Verma and Partha P. Mukherjee, “Surface Diffusion Manifestation in Electrodeposition of Metal Anodes,” *Phys. Chem. Chem. Phys.*, 22, 11286-11295, (2020), 2020 Hot PCCP Article.

5. D. Tewari and P. P. Mukherjee, “Energetics Dictates Deposition at Metal/Solid Electrolyte Interfaces,” *J. Phys. Chem. C* (2020), DOI: 10.1021/acs.jpcc.0c05873.

References

1. S. Angarita-Gomez and P. B. Balbuena, “Insights into Lithium Ion Deposition on Lithium Metal Surfaces,” *Phys.Chem.Chem.Phys*., 22, 21369-21382, (2020).

2. L. A. Selis and J. M. Seminario, “Dendrite formation in Li-metal anodes: an atomistic molecular dynamics study,” *RSC Advances*, 9, 27835-27848, (2019).

3. D. E. Galvez-Aranda and J. M. Seminario, “Li-Metal Anode in Dilute Electrolyte LiFSI/TMP: Electrochemical Stability Using Ab Initio Molecular Dynamics”, *J. Phys. Chem. C*, 124, 40, 21919–21934, (2020).

II.8.D Engineering Approaches to Dendrite Free Lithium Anodes (University of Pittsburgh)

Prashant N. Kumta, Principal Investigator
University of Pittsburgh
815C Benedum Hall, 3700 O'Hara Street
Pittsburgh, PA, 15243
E-mail: pkumta@pitt.edu

Tien Duong, DOE Technology Development Manager
U.S. Department of Energy
E-mail: Tien.Duong@ee.doe.gov

Start Date: October 1, 2016 End Date: January 31, 2020
Project Funding: $1,562,500 DOE share: $1,250,000 Non-DOE share: $312,500

Introduction

Lithium (Li) cycling under normal temperature and pressure conditions (T = 298K and P= 1atm) in a lithium metal battery (LMB) experiences an uncontrollable growth of needlelike cellular structures and tree like dendrites of metallic lithium primarily contributing to poor performance, safety and reliability of LMBs [1], [2]. A safe and efficient operation of lithium anodes requires a planar front interface which is critical for determining the fate of next-generation energy storage systems involving rechargeable Li-air batteries, Li-sulfur batteries, and anode free Li metal batteries comprising high capacity Li containing intercalation cathodes. It is reported that Li metal/electrolyte planar front interface is stable only if the current density is sufficiently small, and/or the transference number (t_+) as well as/or chemical diffusivity of Li ion (D_L) in the electrolyte is sufficiently large [1], [2], [3], [4]. However, as complex and ubiquitous as it seems, the phenomenon of Li dendrite nucleation and growth are not very well-understood. Since the surface microstructures form a major link connecting the battery performance and charging/plating conditions, it is important to develop scientific understandings of how the Li metal plating conditions (charging condition), as well as the electrolyte and the current collector properties influence the resulting microstructures of the plated Li metal. This is important in order to predict, modify, and control the microstructure of the deposited Li metal by meticulously designing the appropriate battery components (e.g. current collector, electrolyte) as well as the Li metal plating conditions. Adding to this complexity and increasing enigmatic nature of LMBs is the formation of the solid-electrolyte interphase (SEI).

Objectives

The current project is thus, a scientific study of novel approaches undertaken and implemented to address the highly complex but ubiquitous problem of dendrite formation in LMBs, combined with electrolyte decomposition, and associated cell-failure. The goal is to systematically characterize the different approaches identified for the generation of dendrite-free Li-metal anodes while also providing an understanding of the scientific underpinnings, as well as evaluating the microstructure and electrochemical performance of the dendrite free Li metal anodes. Development of dendrite free high-performance Li anodes will enable the use of Li-free cathodes (e.g. Li-S, Li-air) opening up a myriad possibility pushing the envelope in terms of achieving the desired battery energy density (>350 Wh/kg) and cycle life (>1000 cycles) with cost ≤$100 $(kWh)^{-1}$.

Approach

To achieve the targeted objectives/goals, a major theoretical and experimental study was performed to understand the formation of the undesirable non-planar interface microstructure, which will ultimately determine the conditions needed to eliminate the probability of dendrite formation. In the present study therefore, a rigorous theoretical calculation based on mass transfer and charge transfer of Li ion under the combined influence of potential gradient (G_L), named as migration, and concentration gradient (G_c), named as diffusion, as well as the perturbation and dendrite growth theory of the electrode-electrolyte interface has been studied for the first time [4]. A major driving force for this study was to draw the uncanny analogy and

similarity between melt solidification principles and electrochemical deposition of metallic lithium. The ensuing morphological stability/instability criterion analysis similar to that developed for metal solidification was also formulated and developed herein based on the concept of "*the constitutional under-potential plating*" (CUP) occurring at the Li-metal/electrolyte interface to understand the driving force for the formation of the nonplanar interface microstructure very similar to constitutional supercooling concept developed in melt solidification by the pioneering work of Chalmers and his group [5], [6].

In addition to the driving force of perturbation, the Gibbs Thomson phenomenon or the capillarity effect, which is a measure of the resistance to perturbation has been addressed to understand the effect of interfacial energy/interfacial enthalpy with the current collector, a critical and extremely important criterion for the evolution of the ensuing morphological stability of the Li surface evolving at high current densities (Figure II.8.D.1). Finally, identification of suitable current collectors, has been proposed exhibiting desired interfacial enthalpy/capillarity with Li metal (high Gibbs Thomson parameter (Γ)) in line with the theoretical analyses, and as a result, offering a novel approach to dendrite-free anode less LMB system with improved cycle life. This is the basis of the three year program leading to the fundamental scientific reasons causing dendrites during electrochemical deposition and the rationale for identifying new current collectors that will eliminate dendrites completely heralding in a new class of current collectors for possible dendrite free and anode-free LMB. Accordingly, alloy design for suitable current collectors exhibiting desired interfacial enthalpy/capillarity as well as high wettability with Li metal has been performed to increase the energy required to perturb the interface with high curvature, and consequently, improve the cycle life of LMBs. It must be mentioned here that identification of suitable current collector exhibiting excellent wettability ($\theta < 30^{o}$, θ is wetting angle) with Li metal also improves the nucleation kinetics by minimizing the nucleation barrier and improving the nucleation rate to yield conditions for favoring dendrite free deposition of Li metal across the current collector. To determine the Li growth front morphology after significant crystal growth (~10-20μm thickness) of the nucleated Li, and study the long term cycling performance of the deposited Li metal at a charge density of 1mAh/cm^2-4mAh/cm^2, the Li metal plating/stripping was carried out at a current density of 0.5mA/cm^2-1mA/cm^2 for 1h-4h up to 100-300 cycles and tested in 1.8M LiTFSI+0.2M $LiNO_3$ in DOL:DME electrolyte.

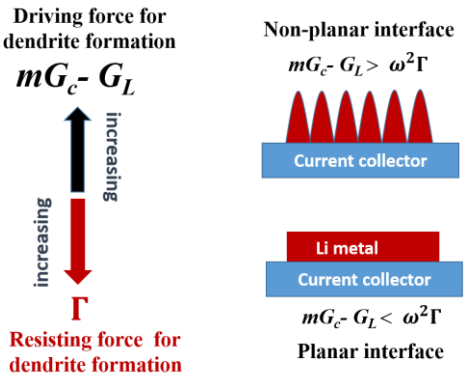

Figure II.8.D.1 The effect of the resisting deformation parameter (Gibbs Thomson effect,Γ) contributing to the evolution of the ensuing morphological stability of the Li surface evolving at high current densities.

Results

In the bulk electrolyte (away from the electrode) or in an electrolyte where concentration gradients are small and electric field gradients are high, the total mass transfer is primarily contributed by migration. The actual potential E_L in the electrolyte for different values of x is shown as the straight line in Figure II.8.D.2a. The interface stability and instability conditions occurring under the migrational Li ion flux derived from the perturbation analysis for planar and non-planar interface growth of Li metal is graphically represented in Figure II.8.D.2b. The figure also shows the relationship of the fractional rate of change of the amplitude $\left(\frac{\dot{\delta}}{\delta}\right)$ of the dendrite with the wave number,ω, of the shape of the perturbation given by, $x = \delta(t)\ sin\ (\omega y)$). In the

absence of diffusional flux of Li ion towards the electrode/electrolyte interface, the perturbation analysis (Figure II.8.D.2b) predicts that the planar interface is stable $\left(\frac{\delta}{\delta} < 0\right)$ under the positive potential gradient (G_L>0) by considering Li ion charge transfer due to only migrational movement [1].

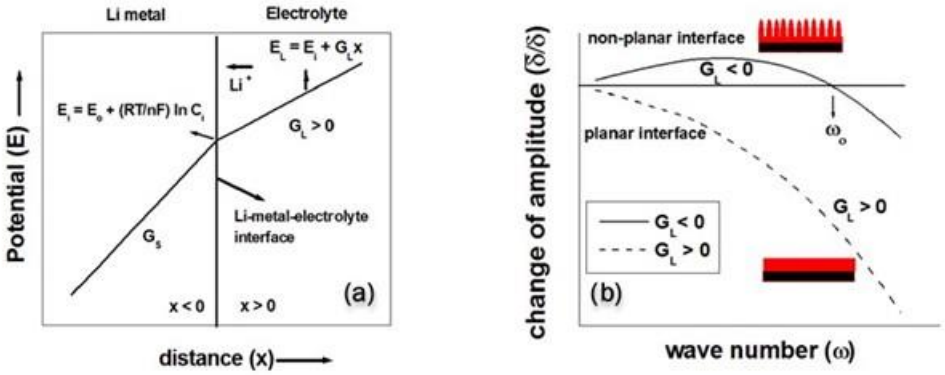

Figure II.8.D.2 Schematic diagram of (a) linear potential profile (E_L) and potential gradient (G_L) at the electrolyte and (b) Rate of change of amplitude $\left(\frac{\delta}{\delta}\right)$ of the perturbed interface as a function of perturbation wave number (ω). If the rate of change of amplitude is positive $\left(\frac{\delta}{\delta} > 0\right)$ for any value of ω, the interface is susceptible to perturbation. G_L> 0 planar interface is stable, G_L< 0 instability of planar interface ensues transforming to cell/dendrite morphology.

On the other hand, the concentration gradient at the electrode/interface (G_c) (Figure II.8.D.3a) which determines the diffusional flux at the electrode/electrolyte interface has a significant contribution to the formation of the undesired non-planar interface. The analysis conducted in the program predicts that if the equilibrium potential gradient ($G_{ei} = mG_c$) generated at the electrode/electrolyte interface arising due to concentration gradient at the interface is higher than the true potential gradient in the electrolyte ($mG_c > G_L$), the electrolyte in front of the interface will be in an underpotential region and as a result, a non-planar interface will be formed [4]. In the present study, this phenomenon is named as "*constitutional underpotential plating*" (CUP) very similar to constitutional supercooling in melt solidification as it arises due to the generation of a concentration variation at the interface. The equilibrium electrodeposition potential at the Li-metal/electrolyte interface is plotted in Figure II.8.D.3b and Figure II.8.D.3c for different transference number (t_+), and diffusivity (D_L) along with G_L = 1mV cm^{-1}. For a given current density (e.g. 1mA cm^{-2}) and potential gradients (e.g. 1 mV cm^{-1}), the planar interface could be maintained by developing a novel electrolyte which exhibits a high transference number t_+ and high diffusivity D_L as shown in Figure II.8.D.3b and Figure II.8.D.3c. The derived CUP criterion predicts the driving force (mG_c-G_L) needed for the creation and formation of a non-planar interface structure (Figure II.8.D.1).

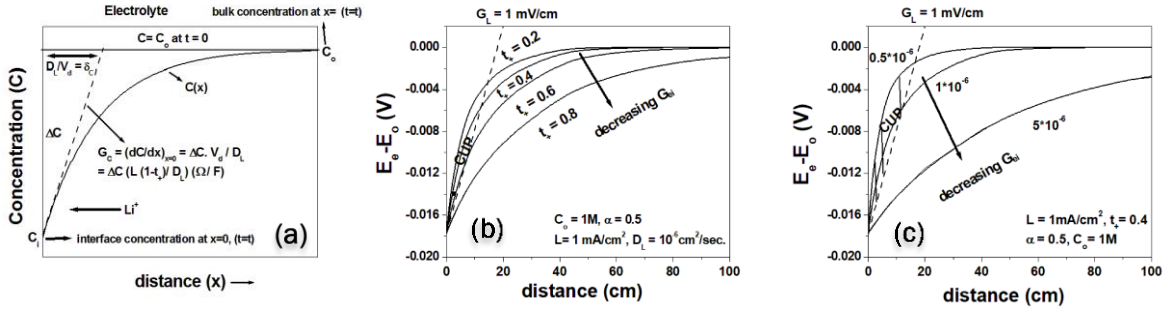

Figure II.8.D.3 Schematic diagram of (a) concentration profile [C(x)] and concentration gradient (G_c) in the electrolyte. Equilibrium electrodeposition/plating potential (E_e) of Li metal arises due to compositional variation at the Li-metal/electrolyte interface, illustrating the condition for constitutional underpotential plating (CUP), (b) with different transference number (t_+), and (c) Li ion diffusivity (D_L).

In order to stabilize the lithium-metal battery system, studies were focused on developing a flexible moving boundary high diffusivity and high transference number solid state electrolyte system to achieve planar growth of the lithium-metal on the current collector. The first approach involved development of a high diffusivity composite polymer electrolyte (CPE) which would control the concentration gradient at the interface and thus modify the deposition conditions thereby inhibiting the dendritic growth of Li. The CPE separators identified in this program were accordingly fabricated by electrospinning of polymer-blends, after which the electrospun mats were punched to yield the individual separators. The separators were then soaked in traditional liquid electrolyte (50:50 DOL:DME by volume, 1.0M LiTSFI, 0.1M $LiNO_3$) before assembling the symmetric Li/Li coin cells. Figure II.8.D.4a and Figure II.8.D.4b shows the potential-time curves generated for the two different CPEs (CPE III and CPE VI) after cycling at a current density of 1mA/cm^2 for 1h for ~300 cycles at an areal capacity of 1mAh/cm^2 in symmetric Li/Li cells. The SEM images collected on the lithium-metal foil before and after ~300 cycles indeed confirm the absence of any dendrites after cycling (Figure II.8.D.4c and Figure II.8.D.4d). Moreover, the images indicate the formation of uniform Li metal plating due to homogenous Li^+ diffusion that is afforded by the improved Li-ion conduction processes occurring in these composite polymer electrolytes (CPEs).

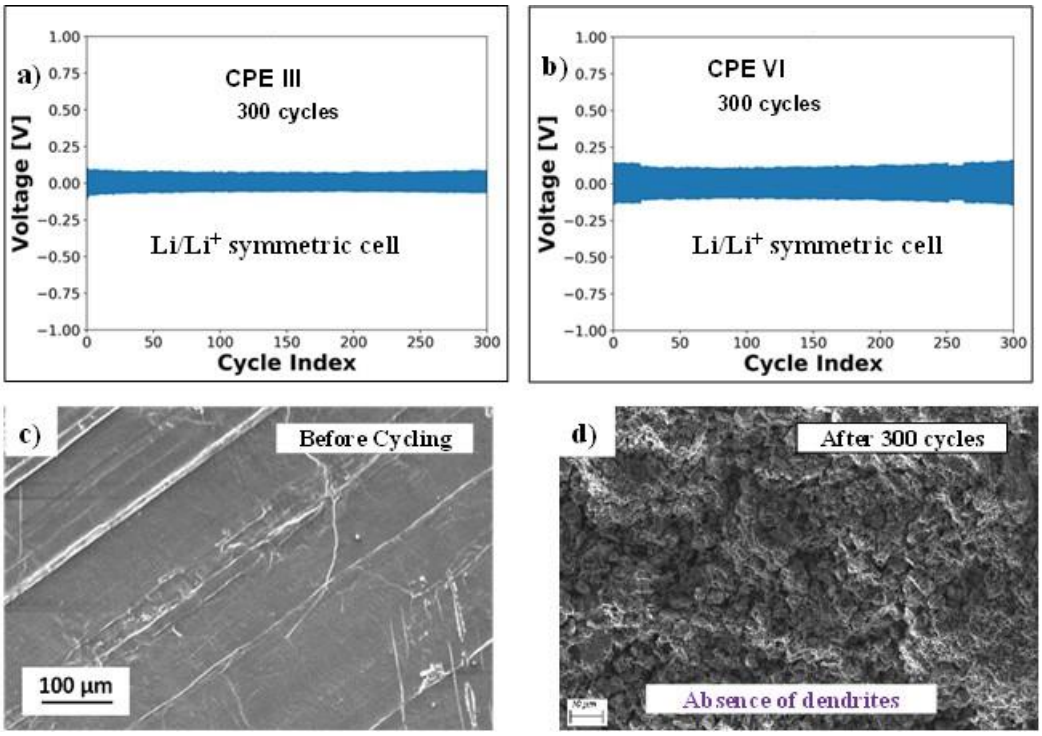

Figure II.8.D.4 Voltage-time curve for symmetric Li/Li cells using composite polymer electrolytes (CPE) a) CPE-III and b) CPE-VI (~300 cycles). SEM images of lithium-metal before and after cycling in symmetric Li/Li cells with c) CPE-III and d) CPE-VI after ~300 cycles with areal capacity of 1mAh/cm^2 showing absence of dendrites.

The simple criterion for interface stability developed above in this program based on the CUP condition of Li metal/electrolyte interface determines the driving force (*i.e.* $mG_C - G_L$) for interface perturbation. This has been derived considering only the diffusional mass and migrational charge transport phenomena without taking into account the contribution of any interfacial energy (surface tension) of the interface on stabilization of the perturbed interface, widely known as the capillarity or the Gibbs-Thomson effect. The increase in free energy arising due to perturbation occurring at the interface can be written as $G_{int} = 2\gamma\Omega K \cos\theta$ where γ is the interfacial energy between electrode and Li metal (J cm^{-2}), K is the curvature (cm^{-1}) of the perturbed interface and θ is the wetting angle. In addition to the driving force to perturbation (mG_c-G_L) parameter, the developed perturbation theory as well as dendrite kinetic theory successfully predicts the effect of interfacial energy (γ) or Gibbs Thomson parameter (Γ) as resistance to perturbation parameter on the formation of planar interface

structure. As shown in Figure II.8.D.5, the perturbation analysis reveals that the non-planar interface is stable within a range of wavelengths (λ_i - λ_a) wherein λ_i is the lower bound of possible instabilities called as the marginally stable interface. The critical perturbation wavelength, λ_i increases with increase in the value of the Gibbs Thompson parameter (GTP), Γ whereas the rate of change of amplitude decreases with increase in the value of Gibbs Thompson parameter, Γ which suggests that the resistance to perturbation of the planar interface increases with increase in the Gibbs-Thomson parameter or the interfacial energy. Consequently, guidelines are laid down for selection of an appropriate current collector that will result in dendrite free morphology for the electrodeposited Li metal enabling an anode-free LMB system. The detailed analysis of the studied CUP criterion, the perturbation analysis and dendrite kinetics [4] conducted in this program for the first time brings to the forefront the intricate connections between the concentration and the potential gradients with the current density such that one can predict, modify, and control the microstructure of the electrochemically deposited Li metal by designing appropriate current collector, electrolyte and cycling conditions to prevent the deleterious influence of formation of dendrites enabling an anode-free LMB system. This theory was hence, validated with use of known systems.

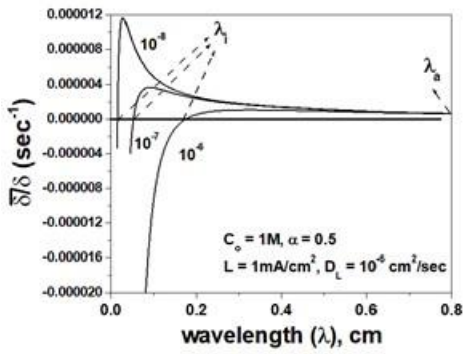

Figure II.8.D.5 Rate of change of perturbation amplitude $\left(\frac{\bar{\delta}}{\delta}\right)$ with different values of the Gibbs Thomson parameter (GTP) (10^{-6} to 10^{-8} V.cm) under the given growth conditions.

The theoretically calculated interfacial enthalpy or enthalpy of mixing of the promising metal current collectors along with the electronic conductivity of the current collectors is tabulated in Table II.8.D.1. The transition and non-transition metals with high negative enthalpy of mixing (e.g. Zn-Li, Si-Li) are generally subject to form intermetallics/intermediate phases or the so-called Zintl phases in Zn, Sn and Si resulting in different crystal structures due to large negative enthalpy of formation prior (above 0V of Li/Li^+) or during the Li metal plating (below 0V of Li/Li^+). As an example, the voltage profile of Li metal plating/stripping on pure Zn foil (enthalpy of mixing of Zn-Li = -26kJ/mole) obtained at a current density of $1mA/cm^2$ with a discharge specific capacity ~$0.5mAh/cm^2$ (Figure II.8.D.6a) clearly shows the effects of alloying and dealloying of Li on Zn leading to the formation of Zn-Li intermetallics during electrochemical cycling as expected. As shown, correspondingly in Figure II.8.D.6, the Li metal plating/alloying occurs at -150mV after 1st cycle whereas stripping/dealloying occurs at +180mV and +400mV. The Zn foil as a substrate also exhibits excellent Coulombic efficiency, CE (above ≥95%) at the 1st cycle as well as for subsequent cycles (Figure II.8.D.6b). The formation of intermetallics of different crystal structures than parent crystal structure is however, known and is subject to large volume expansion and contraction during the alloying and dealloying processes resulting in pulverization of the host metal/current collector (similar to Li-Sn and Li-Si) during repeated cycling (repeated alloying/dealloying) which is not suitable for long cycle life. The excellent CE and zero nucleation underpotential characteristic of Zn foil could make it as a promising nucleating agent for Li metal plating/stripping if however, the formation of intermetallics could be bypassed.

Table II.8.D.1 Interfacial Enthalpy and electrical conductivity of selected materials at T = 300K

System	Cu-Li	Fe-Li	Zn-Li	Si-Li
Interfacial Enthalpy (kJ/mol)	+110	+94	-26	-46
Electronic conductivity (ohm-1 cm-1)	$5.98 * 10^5$	$1 * 10^5$	$1.69 * 10^5$	$4 * 10^{-6}$

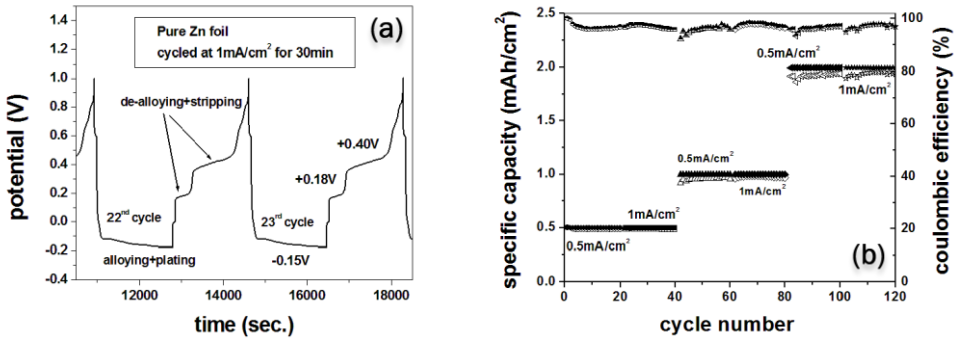

Figure II.8.D.6 (a) Variation of experimentally determined Li metal plating and stripping potential for 22nd and 23rd cycles of negative interfacial energy current collector showing formation of intermetallics cycled at a current density of 1mA/cm2 with plating areal capacity 0.5mAh/cm2 and stripping cut off voltage 1V. (b) Areal capacity and CE with cycle number of negative interfacial energy current collector.

By contrast, the transition metals exhibiting positive interfacial enthalpy/heat of mixing (e.g. Cu-Li, Fe-Li. in Table II.8.D.1) are indeed preferable for plating/stripping of Li metal because the formation of Li metal intermetallics/intermediate phases associated with the change in crystal structure is not thermodynamically feasible in addition to the favorable economics and commercial availability. However, the current collectors with positive interfacial enthalpy ($\Delta H_{mix} >> 0$) associated with poor wetting with Li metal indeed based on the theory presented above, is expected to have low Gibbs Thomson parameter (GTP) for resisting the interface perturbation. In addition, a large nucleation barrier is expected to show large nucleation underpotential and consequently, leading to dendrite growth due to poor wetting. The voltage profile of the Li metal plating/stripping on Fe foil as an anode free current collector at a current density of $1mA/cm^2$ with a discharge specific capacity $4mAh/cm^2$, displayed in Figure II.8.D.7(a), shows that Li metal nucleation occurs at an underpotential of -78 mV whereas the equilibrium growth potential of plating/stripping occurs at -0.27V/+0.27V. The cycle life performance and CE of Li metal plating/stripping on Fe foil at a current density of $1mA/cm^2$ with a discharge specific capacity $4mAh/cm^2$ in Figure II.8.D.7(b) shows the degradation of the cycling performance (e.g. CE and voltage profile) after 25 cycles validating the Gibbs Thomson parameter (GTP) concept.

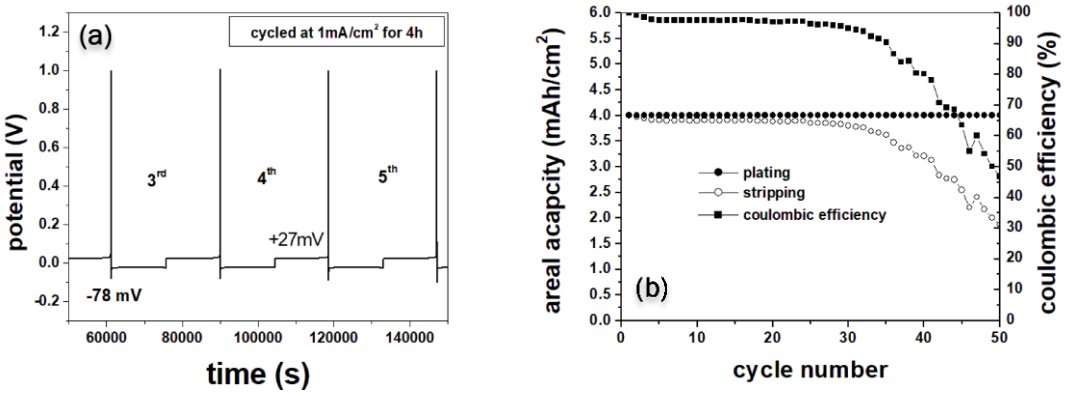

Figure II.8.D.7 (a) Variation of experimentally determined Li metal plating and stripping potential for 3rd -5th cycles of positive interfacial energy current collector showing large nucleation underpotential (-78mV) with growth potential of -27mV cycled at a current density of 1mA/cm² for 4h with plating areal capacity 4mAh/cm² and stripping cut off voltage 1V. (b) Variation of experimental plating and stripping potential with time for 50 cycles, and areal capacity with cycle number of positive interfacial energy current collector showing capacity fade after 25 cycles reflecting the poor cycle life validating the GTP concept.

Therefore, suitable alloy design of current collector exhibiting non-reactivity to Li metal along with high interfacial energy and excellent lattice registry as well as good wetting with Li metal is highly desirable. Several promising structurally isomorphous alloys (SIAs), and interface engineered Cu current collectors (IES) have been developed in this program keeping in mind the above aspects identified and generated conducive for realizing effective Li metal plating/stripping and consequently, achieving the desired microstructural control. The developed structurally isomorphous alloy (SIAs), and interface engineered substrate (IESs) with excellent Li metal lattice registry and large GTP in particular, serve as next generation current collectors displaying excellent cyclability obviating cellular or dendritic structure formation promoting long cycle life (Figure II.8.D.8 and Figure II.8.D.9).

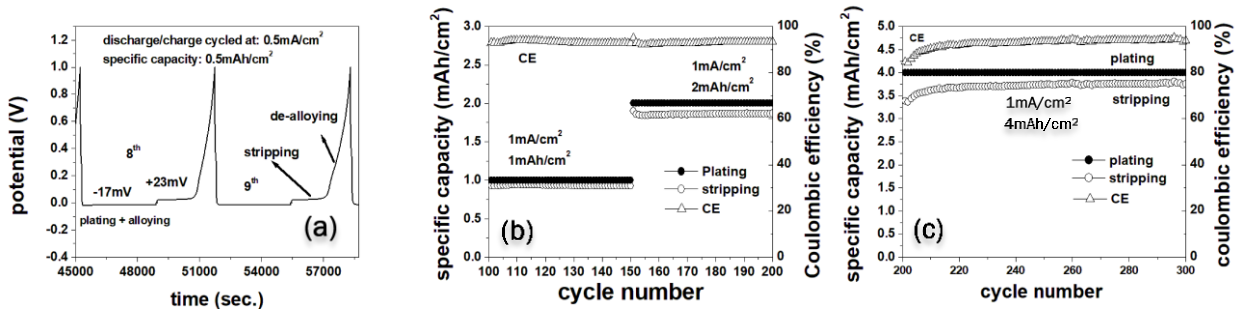

Figure II.8.D.8 (a) Variation of Li metal plating and stripping potential of 8th and 9th cycles of SIA cycled at a current density of 0.5mA/cm² with plating areal capacity 0.5mAh cm-2. (b) and (c) Variation of areal capacity with cycle number of SIA showing excellent cycle life. However, the SIA exhibits low CE due to the low Li ion diffusivity in the system.

The developed SIA alloys show the desired "zero nucleation underpotential" whereas the equilibrium growth potential of plating/stripping occurs at -0.17V/+0.23V. The SIA alloys also exhibit excellent cyclability upto 300 cycles with zero nucleation underpotential cycled at a current density of 1mA/cm² yielding an areal capacity ~1mAh/cm², 2mAh/cm² and 4mAh/cm² (Figure II.8.D.8). The plating/stripping behavior of Li metal using the novel "zero nucleation underpotential" SIAs (Figure II.8.D.8) shows a low coulombic efficiency <90% due to the low diffusivity of Li and solid-electrolyte interphase (SEI) formation of highly reactive SIAs with the electrolyte. A systematic theoretical study based on DFT calculation was performed to identify suitable alloying elements to improve the Li ion diffusivity in SIA alloys. Similarly, low Li-ion reactive IES coated Cu current collector shows excellent cyclability (Figure II.8.D.9). The IES is expected to act as a heterogeneous nucleating sites and effective grain refiner to inhibit dendrite growth. The variation of areal

capacity with cycling (Figure II.8.D.9a) up to 100 cycles of studied IES coated Cu foil tested at a different current density of 0.5mA/cm^2 with 0.5mAh/cm^2 areal capacity shows excellent cyclability with CE >99.5% after the10th cycle**.** Figure II.8.D.9b also shows absence of intermetallics formation during Li metal plating suggesting the realization of the desired Li ion non-reactivity of IES to form intermetallics or solid solution. Furthermore, the growth potential of Li metal (Figure II.8.D.9b), cycled at a current density of 0.5mA/cm^2 for 1h, show no significant growth potential change (~23 mV) with time or cycling, suggesting minimal potential hysteresis of IES coated Cu foil. The above results therefore clearly serve as a testament to the theoretical studies conducted in this program and suggest that the novel materials developed exhibiting high Li ion absorption (i.e. minimizing the driving force of perturbation) and high Gibbs Thomson parameter current collector are a promising way to improve the Li metal battery performance without formation of deleterious dendrites.

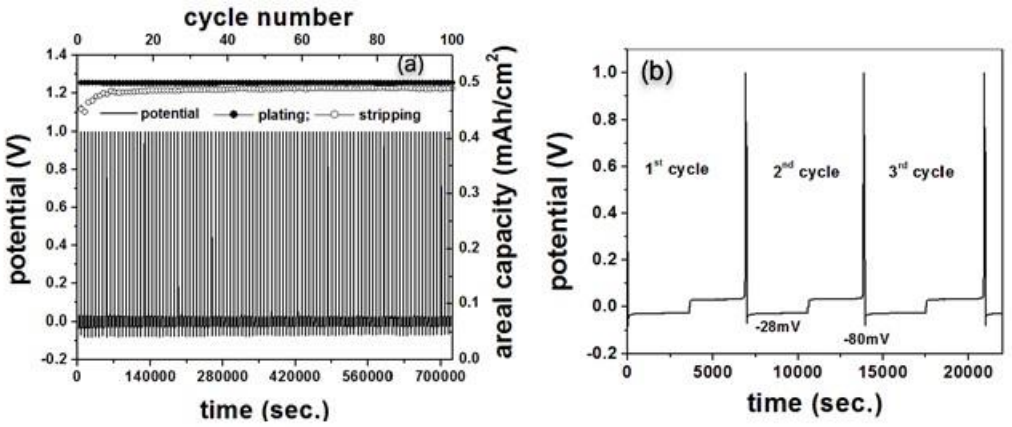

Figure II.8.D.9 (a) Variation of areal capacity with cycle number of grain refiner IES showing excellent cycle life with CE >99%. (b). Variation of nucleation and growth potential with time for IES coated on Cu current collector cycled at a current density of 0.5mA/cm^2 for 1h.

Conclusions

A novel detailed CUP criterion calculation conducted herein for the very first time establishes the relationship of battery operating conditions (*e.g.* current density, potential gradient) with the electrolyte properties (e.g. Li-ion transference number and chemical diffusivity) predicting the morphological stability condition at the interface. In addition to the driving force for interface perturbation, the capillarity effect or the Gibbs Thomson effect, a measure of the resistance to perturbation of the perturbed interface is also discussed for the very first time bringing together a unique and critical understanding of the interfacial energy/adhesion energy between the current collector and the deposited Li influence on the overall morphological stability of the Li/electrolyte interface, a critical criterion for overcoming the unwanted dendritic morphology. The current project was therefore successful in developing high diffusivity and transference number composite polymer electrolyte (CPE) and structurally isomorphous alloy (SIA) combined with interfacial engineered substrate (IES) exhibiting zero nucleation underpotential and no intermetallic formation with reversible plating and de-plating of Li metal. The developed alloys clearly suggest a novel engineering pathway to identifying next generation materials exhibiting high Li ion diffusivity (i.e. minimizing the driving force for perturbation) and high Gibbs Thomson parameter (GTP) current collectors that can be successfully generated together serving as a promising way to improve the Li metal battery performance without the formation of dendrites over long cycles (~300 cycles). The program has therefore led to establishment of fundamental theoretical rationale for the very first time laying the groundwork for important criteria contributing to dendrite formation. In doing so, pathways and rationale for engineering new systems to overcome dendrite formation was also established. These criteria have led to the identification of several new systems and strategies that show the potential for use as dendrite free current collectors enabling next generation anode free high energy density lithium metal batteries.

Key Publications

1. Moni K. Datta, Bharat Gattu, Ramalinga Kuruba, Pavithra Shanthi, and Prashant N. Kumta, "Constitutional Under-potential Plating (CUP) – New Insights for Predicting the Morphological Stability of Deposited Lithium Anodes in Lithium Metal Batteries", J. Power Sources 467 (2020) 228243.

2. Jampani, P.H., Shanthi, P. M., Gattu, B., Datta, M K, Velikokhatnyi, O.I., Kumta, P.N., "High capacity, air-stable, Structurally Isomorphous lithium Alloy (SIA), Multilayer Porous Foams (MPFs) and Composite Multilayer Anodes (CMAs) for dendrite-free lithium metal anodes for Li-ion batteries", U.S. Provisional Patent Appln. No. 62/529,588 (2017).

References

1. G. Zhang, W. Xu and W. A. Henderson, *Lithium metal anodes and Rechargeable Lithium metal batteries*, Springer Series in Materials Science, Springer International Publishing, Switzerland **2017**.

2. X. B. Cheng, R. Zhang, C. Z. Zhao, Q. Zhang, *Chemical Reviews* **2017**, 117, 10403.

3. R. Tao, X. Bi, S. Y. Yao, F. Wu, Q. Wang, C. Zhang, J. Lu, *ACS Appl. Mater. Interfaces*. **2017**, 9, 7003.

4. M. K. Datta, B. Gattu, R. Kuruba, P. Shanthi, and P. N. Kumta, *J. Power Sources*. **2020**, 467, 228243.

5. D. A. Porter, K. E. Esterling, M. Y. Sherif, *Phase Transformation in Metals and Alloys*, 3rd ed., CRC press, Taylor and Francis group, FL **2009**.

6. T. Nishinaga, *Handbook of Crystal Growth, Fundamentals: Transport and stability*, Vol. 1, 2nd ed, Elsevier, Oxford, UK, **2015.**

Acknowledgements

Authors acknowledge the support and guidance of Tien Duong, VTO, BMR Program Manager. Authors also acknowledge the funding from the U.S. Department of Energy VTO DE-EE0006825. Partial support from the Edward R. Weidlein Chair Professorship Funds, Nanomaterials for Energy Conversion and Storage Technology (NECST) Laboratories, and the Center for Complex Engineered Multifunctional Materials (CCEMM) from the Swanson School of Engineering, University of Pittsburgh is also acknowledged for assistance and help with procuring the electrochemical equipment and facilities used in this research work.

II.8.E Integrated Multiscale Modeling for Design of Robust 3D Solid-State Lithium Batteries (Lawrence Livermore National Laboratory)

Brandon C. Wood, Principal Investigator
Lawrence Livermore National Laboratory
7000 East Avenue
Livermore, CA 94550
E-mail: wood37@llnl.gov

Tien Q. Duong, DOE Technology Development Manager
U.S. Department of Energy
E-mail: Tien.Duong@ee.doe.gov

Start Date: November 1, 2018 End Date: October 30, 2021
Project Funding: $1,125,000 DOE share: $1,125,000 Non-DOE share: $0

Project Introduction

Architected 3D solid-state batteries have a number of intrinsic performance and safety advantages over conventionally processed 2D batteries based on liquid organic or polymer electrolytes [1]. Functionality and architecture of component materials in principle can be tuned for optimal energy and power density. In addition, the use of solid-state electrolytes offers increased safety and potential compatibility with higher-voltage and higher-energy-density electrode materials, which can further enhance capacity. Nevertheless, proper design of 3D solid-state batteries remains a formidable challenge. Solid-state batteries tend to suffer from high interfacial resistance arising from poor physical contacts [5], as well as the formation of intermediate phases at the often-unstable interface between the cathode and electrolyte. They also suffer from non-uniform mechanical responses that can promote stress cracking in response to lithium uptake during cycling. For 3D architectures, these issues can become even more problematic, since the complex morphologies tend to introduce additional non-uniformities in electric fields and current densities [2] at the numerous component interfaces. The use of 3D printing and other additive manufacturing methods offer the promise of directed engineering of architectures to improve structural and chemical integrity, but such approaches also introduce other difficulties, including microstructures that are notoriously difficult to control and vary widely according to the specific processing condition.

To realize the ultimate goal of designing and printing optimized 3D solid-state batteries, it is critical to understand the interfacial losses and instabilities that impede performance and promote failure at multiple scales. Validated modeling and simulation have a unique role to play in pursuit of this aim, since they can directly probe structure-property relations and provide guidance for optimizing function of component materials. In general, existing modeling strategies tend to suffer from one of two shortcomings. Some fail to address the multi-physics nature of the various processes active in 3D batteries, which range from electrical to chemical to mechanical responses that are often coupled. Others fail to address the multiscale nature of the battery materials and their integration, ignoring the fact that atomistic, microstructural, and cell-level processes must be considered to understand how processing and architecture affect performance. This project leverages advanced computational models to address these shortcomings and investigate diffusion kinetics limitations in ceramic 3D solid-state battery materials. This can be viewed as a first step towards enabling future optimization of 3D battery designs.

Objectives

This project is developing a multiscale, multi-physics modeling framework for probing the effects of materials microstructure and device architecture on ion transport within 3D ceramic solid-state battery materials, with the goal of enhancing performance and reliability. The project has three primary objectives: (1) integrate multi-physics and multiscale model components; (2) understand interface- and microstructure-derived limitations on ion transport; and (3) derive key structure-performance relations for enabling future optimization.

Approach

Our approach integrates simulations at three scales to predict ion transport limitations within the ceramic solid-state electrolyte $Li_{7-x}La_3Zr_2O_{12}$ (LLZO), as well as across the interface between LLZO and $LiCoO_2$ cathodes. A particular focus is on understanding the effects of microstructures and architectures resulting from processing of 3D solid-state batteries, as well as their mechanical and chemical evolution at different stages of cycling. Classical and ab initio molecular dynamics (AIMD) simulations are used to compute fundamental Li-ion diffusion within bulk solid electrolyte and cathode materials, along/across grain boundaries of the electrolyte, and along/across electrolyte/cathode interfaces. Next, phase-field simulations are used to generate digital representation of realistic microstructures of the materials, which are combined with the atomistic simulation results to parameterize mesoscale effective property calculations and to establish microstructure-property relationships for ion transport. Finally, these relationships inform a microstructure-aware model of experimental electrochemical impedance spectroscopy, which connects microscale features to macroscale properties in order to optimize the performance of ceramic 3D solid-state Li batteries based on LLZO solid electrolytes.

Results

Atomistic simulations of Li-ion diffusion at the LLZO grain boundaries

In collaboration with Prof. Adelstein's group at San Francisco State University, the team used molecular dynamics to compute Li-ion diffusivity at the grain boundaries of cubic LLZO. The high-angle grain boundary structures were modeled as a series of randomly disordered LLZO systems with variations in density and Li composition, from which the activation energies, E_a for Li-ion diffusion were computed. As shown in Figure II.8.E.1, the distribution of activation energy barriers for disordered LLZO exhibits a broad bimodal distribution spanning values, with average values that are significantly higher than for crystalline LLZO (0.28 eV). The bimodal shape of the E_a distribution reflects the simultaneous presence of "fast" and "slow" (trapped) conduction channels in the disordered regions. Overall, the predicted E_a values agree very well with existing literature (see tabulated comparison in Figure II.8.E.1). The team expects that this reported range of E_a encompass realistic ranges of parameters that could be achieved depending on processing conditions. These ranges were then used to explore the sensitivity of overall effective ionic conductivity to grain boundary mobility in the mesoscale models, as described below.

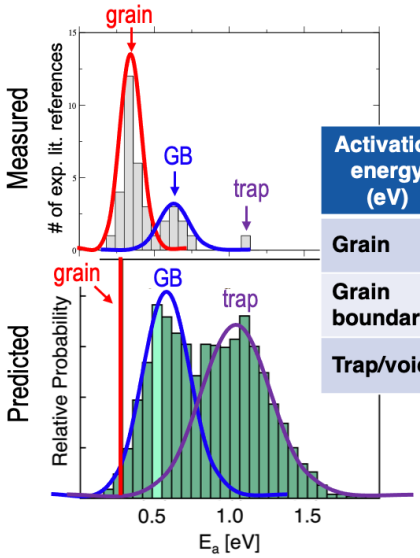

Activation energy (eV)	Exp. lit. avg.	Predicted avg.
Grain	0.32	0.28
Grain boundary	0.62	0.59
Trap/void	1.10	1.12

Figure II.8.E.1 Comparison of predicted activation energies for Li diffusion in polycrystalline LLZO against a compilation of reported literature values. Contributions from grains, grain boundaries, and traps are computed separately, with averages listed in the table [3].

Atomistic simulations of Li-ion diffusion at the LLZO/LCO interface

The team used AIMD simulations to probe the structural and chemical evolution at the LLZO/LCO electrolyte/cathode interface. Figure II.8.E.2(a) shows a snapshot of the LLZO/LCO interfacial structure during the AIMD run. The black dots indicate the positions of Li vacancies, which were used to identify interfacial diffusion pathways for neighboring Li^+ ions migrating into these vacancy sites. The activation energies for diffusion along these pathways were computed using the nudged elastic band method and are plotted as a histogram in Figure II.8.E.2(b). It was found that the activation energies for Li diffusion in this specific LLZO/LCO interfacial model span a broad range from 0.03 to 1.74 eV with an average of 0.63 eV, which is significantly higher than the activation energies for Li^+ diffusion (~0.3 eV) in bulk LLZO and LCO. In addition, Co interdiffusion into the Li layers is observed. As shown in Figure 2(c) and (d), the presence of Co at the Li layer further blocks Li diffusion from the surface of LCO to LLZO. The team speculates that the structural instability of the LCO surface caused by Co diffusion into adjacent Li layer is one of the factors that contributes to the sluggish Li-ion diffusion at the LLZO/LCO interfaces.

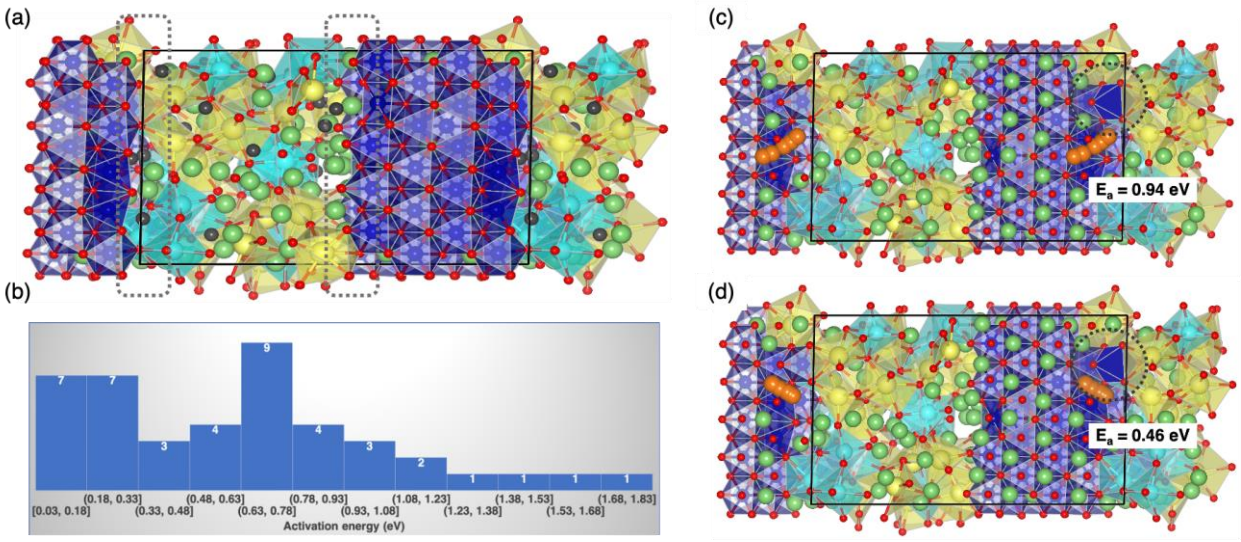

Figure II.8.E.2 Calculated activation energies for Li-ion diffusion at the LLZO/LCO interfaces. Li, La, Zr, Co and O atoms are shown as green, yellow, cyan, blue and red spheres in the structure representation of the LLZO/LCO interfacial model. The black dots in (a) indicate Li vacancy sites, from which the activation energies in (b) are computed for nearby Li atom migrating into these vacancy sites in the interfacial regions. The orange balls in (c) and (d) mark Li diffusion pathways within the Li layer near the surface of LCO, along which the activation energies are calculated.

Mesoscale modeling of Li transport through complex microstructures

Last year, the team established a workflow for connecting the atomic-scale simulations within a mesoscale framework to compute the effective ionic conductivity of a complex polycrystalline LLZO microstructure. The model incorporates microstructural parameters both at the atomistic scale (via grain boundary properties) and at the mesoscale (via grain structure and morphology). This year, the team applied the model to account for a wide range of microstructural features that are believed to be expressed in printed or conventionally processed LLZO. This allowed for a more complete analysis of microstructural effects on ionic conductivity by creating a "designability map" to connect the predictions to actual 3D microstructures and processing conditions. This map, shown in Figure II.8.E.3a, illustrates the quantitative impact of the atomistic and mesoscale microstructural parameters on the critical temperature at which the mechanism changes from grain-dominated to grain boundary-dominated ion conduction. The range of parameters for grain size and grain boundary width were derived from the atomistic simulations to cover the large potential variability of 3D printed microstructural features. These results can be used to correlate the processed microstructure to the battery operating conditions and determine the temperature window for which sensitivity of the ionic conductivity to microstructure is highest. The team also explored the impact of the grain shape to account for possible morphological control by the printing and thermal processing conditions. Figure II.8.E.3b compares the

anisotropy in computed diffusion properties for two limiting cases of grain morphology using phase-field simulations. Whereas **t**he equiaxed grain structure exhibits isotropic effective diffusion, it is anisotropic for the columnar grain structure, with the degree of anisotropy dependent on temperature. These results were submitted for publication (Heo et al. 2020).

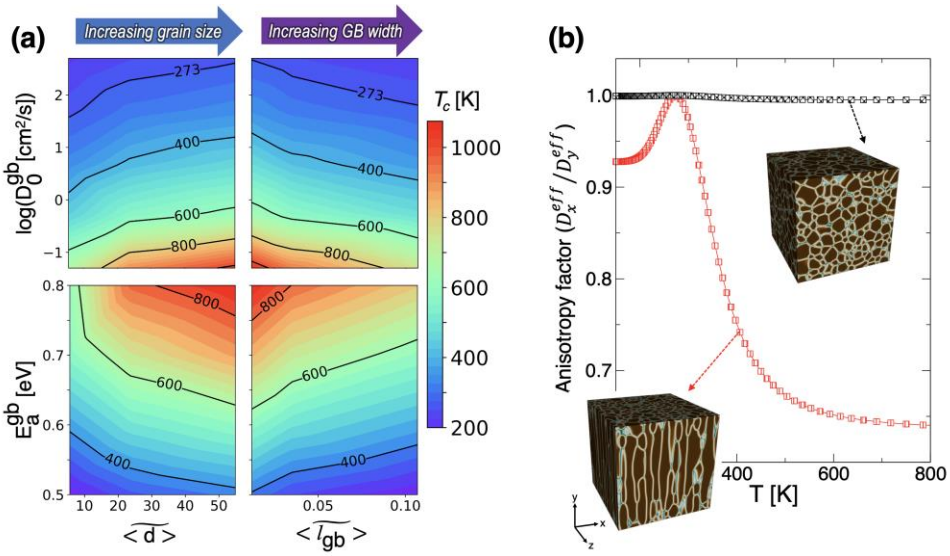

Figure II.8.E.3 (a) Designability map of the critical temperature T_c that determines the transition between bulk grain- and grain boundary-dominated ion conduction, based on engineering mesoscopic and atomistic microstructural features of polycrystalline LLZO. T_c is shown as a function of varying atomistic grain boundary diffusive prefactor and activation energy (D_0^{GB}, E_a^{GB}), as well as mesoscale grain size and grain boundary width (<d>,$<l_{GB}>$). (b) Computed anistropy factor as a function of temperature for two grain structures with different grain shapes.

Mesoscale modeling of internal stress distribution in LLZO

In addition to the impact of 3D printed microstructures on ionic transport, the team also investigated internal stress and its evolution in LLZO solid electrolytes under mechanical loading during operation. This is critical for co-optimizing the mechanical integrity of the processed electrolyte and the ionic conductivity. For input microstructures, the team generated digital representations of LLZO microstructures using phase-field simulations. They then parameterized the site-specific elastic moduli within these polycrystalline microstructures. By numerically solving the mechanical equilibrium equation with the microstructure-informed elastic modulus, the equivalent von Mises stress (σ_v) profile was obtained under the applied loading condition. The results indicate that the internal stress profile is sensitive to the grain size. For larger grains, the stress distribution is skewed toward lower σ_v compared with the small-grain counterpart, indicating less internal stress when larger grains are present. The team then defined stress "hot spots" using a simple criterion $\sigma_v > \sigma_Y$, where σ_Y is the yield strength of LLZO. Depending on the grain size, the LLZO microstructures were found to exhibit different spatial distributions of the hot spots, which can be correlated to the likelihood of mechanical failure and cracking. The evolution of the hot spot fraction under increasing applied strain was also monitored. For smaller grains, the hot spot fraction was found to be more sensitive to increasing strain, indicating that controlling grain size could be an effective way to reduce mechanical failure.

Modeling of microstructural effects on electrochemical impedance spectra

To bridge understanding of transport parameters and microstructure with experimentally measurable quantities, the team developed and demonstrated a mesoscale model to simulate the electrochemical impedance spectrum (EIS) of a polycrystalline solid electrolyte. Using the computed ionic conductivity and reference microstructure, the model can generate the impedance spectra and provide information on electric field localization and heterogeneity in ion transport kinetics that contribute to the overall impedance (Figure II.8.E.4). The team used the model to quantitatively demonstrate the influence of several material parameters on the simulated EIS: ionic conductivities and permittivities of the grain and grain boundary, grain size, and

grain boundary thickness. This analysis identifies parameters that have strong or weak effects on the overall impedance in order to inform experimental fabrication. The grain boundary permittivity was found to have a very weak effect, whereas the ionic conductivity of both the grain and the grain boundary have strong effects. The team is collaborating with partners at DLR, Germany to incorporate space-charge effects into the EIS model. They will also work to complete parameterization of the model for LLZO-cathode interfaces based on the calculated atomic-scale and mesoscale transport properties.

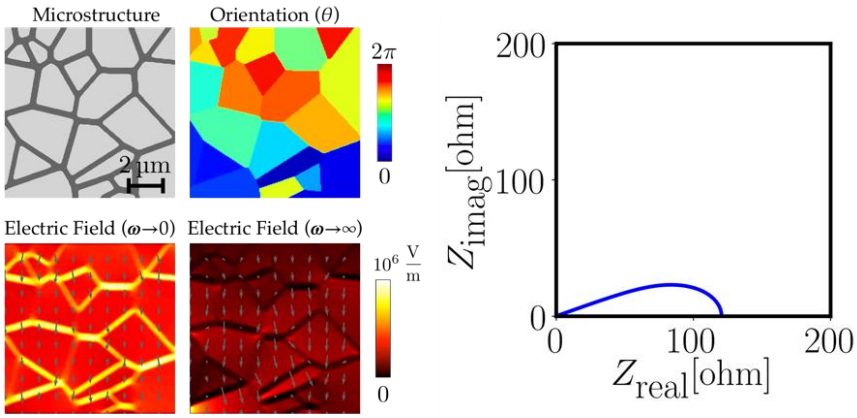

Figure II.8.E.4 Demonstration of an EIS model for polycrystalline LLZO. The grain boundary width is proportional to the misorientation between the adjacent grains. A sinusoidally varying voltage, with a varying frequency (zero to 108 Hz) is applied on the top edge and the bottom edge remains electrically grounded. Grain boundaries perpendicular to the direction of the current show the maximum electric field and contribute most to overall impedance at low frequencies, while the grains contribute most at high frequencies.

Conclusions

The team's activities this year were used to create a full correlation map of the atomic-scale grain boundary mobility, microstructure, and operating conditions to the mechanism of ionic conductivity. This map can be used to connect processed LLZO microstructures and compositions to the conditions for maintaining suitable ion transport. The team also demonstrated a framework for correlating the microstructure to the appearance of stress hot spots that can act as fracture initiation sites. This framework can be used to co-optimize ionic conductivity and mechanical robustness for microstructures generated with 3D printing. Progress is also being made on determining ranges of ion mobility barriers at heterogeneous interfaces cathode-electrolyte interfaces, which will be incorporated into the mesoscale effective transport models in future quarters. Finally, the team demonstrated the ability to simulate electrochemical impedance spectra from generated microstructures, facilitating a connection between materials properties and macroscale measurements that can accelerate the feedback cycle for electrolyte optimization.

Key Publications

1. T.W. Heo, A. Grieder, B. Wang, M. Wood, S.A. Akhade, L.F. Wan, L.-Q. Chen, N. Adelstein, and B.C. Wood, "Microstructural impacts on the ionic conductivity of garnet solid electrolytes: A combined atomistic-mesoscale approach," manuscript in review.

2. B.C. Wood, J.B. Varley, K.E. Kweon, P. Shea, A.T. Hall, A. Grieder, M. Ward, V.P. Aguirre, D. Ringling, E.L. Ventura, C. Stancill, and N. Adelstein, "Paradigms of frustration in superionic solid electrolytes," manuscript in review.

3. Z. Mehmedovic, V. Wei, A. Grieder, P. Shea, B.C. Wood, and N. Adelstein, "Disorder and correlated motion from increased vacancies improve Li^+ diffusion in solid-state battery electrolyte Li_3OCl," manuscript in review.

4. B.C. Wood, “Paradigms of structural, chemical, and dynamical frustration in superionic conductors,” Chicheley, United Kingdom, scheduled for March 2020 (invited talk; cancelled due to COVID-19).

5. A. Jana, T.W. Heo, M. Wood, J. Ye, L. Wan, B.C. Wood, “Microstructural effects on electrochemical impedance spectroscopy,” Gordon Research Conference on Batteries, Ventura, CA (February 2020).

6. A. Jana, T.W. Heo, M. Wood, J. Ye, L. Wan, B.C. Wood. “Microstructural effects on electrochemical impedance spectroscopy,” ACS Fall 2020 Virtual Meeting & Expo (August 2020).

7. B.C. Wood, “Integrated multiscale modeling for design of robust 3D solid-state lithium batteries,” Vehicle Technologies Office Annual Merit Review (June 2020).

8. T.W. Heo, A. Grieder, L.F. Wan, N. Adelstein, and B.C. Wood, “Impacts of microstructures on the ionic diffusivity of solid electrolytes: Mesoscale modeling,” 236th ECS Meeting, Atlanta, GA (October 2019).

9. L.F. Wan, T.W. Heo, A. Jana, and B.C. Wood, “Integrated multiscale model for design of robust 3-D solid-state lithium batteries,” PNNL Solid State Electrolytes Workshop, Richland, WA (October 2019).

10. V. Wei, Z. Mehmedovic, A. Grieder, A, Hall, N. Leclerc, A. Musaelian, L. Kahle, N. Marzari, B. Kozinsky, T.J. Udovic, P. Mehta, V. Stavila, O. Borodin, S. Akhade, P. Shea, K. Kweon, J. Varley, B.C. Wood, and N. Adelstein, “Comparison of correlated Li^+ diffusion from molecular dynamics of promising solid electrolytes,” 236th ECS Meeting, Atlanta, GA (October 2019).

11. A. Grieder, T.W. Heo, S. Akhehe, B.C. Wood, and N. Adelstein, “Effects of cell size and structure on Li^+ diffusion in LLZO,” 236th ECS Meeting, Atlanta, GA (October 2019).

References

1. Arthur, T. S., D. J. Bates, N. Cirigliano, D. C. Johnson, P. Malati, J. M. Mosby, E. Perre, M. T. Rawls, A. L. Prieto, and B. Dunn. 2011. "Three-dimensional electrodes and battery architectures." Mrs Bulletin 36 (7):523-531. doi: 10.1557/mrs.2011.156.

2. Hart, R. W., H. S. White, B. Dunn, and D. R. Rolison. 2003. "3-D microbatteries." Electrochemistry Communications 5 (2):120-123. doi: 10.1016/s1388-2481(02)00556-8.

3. Heo, T. W., A. Grieder, B. Wang, M. Wood, S.A. Akhade, L.F. Wan, L.-Q. Chen, N. Adelstein, and B.C. Wood. 2020. “Microstructural impacts on the ionic conductivity of garnet solid electrolytes: A combined atomistic-mesoscale approach,” manuscript in review.

4. Long, J. W., B. Dunn, D. R. Rolison, and H. S. White. 2004. "Three-dimensional battery architectures." Chemical Reviews 104 (10):4463-4492. doi: 10.1021/cr020740l.

5. McOwen Dennis, W., Shaomao Xu, Yunhui Gong, Yang Wen, L. Godbey Griffin, E. Gritton Jack, R. Hamann Tanner, Jiaqi Dai, T. Hitz Gregory, Liangbing Hu, and D. Wachsman Eric. 2018. "3D-Printing Electrolytes for Solid-State Batteries." Advanced Materials 30 (18):1707132. doi: 10.1002/adma.201707132.

Acknowledgements

This work was performed under the auspices of the U.S. Department of Energy by Lawrence Livermore National Laboratory under contract DE-AC52-07NA27344.

Collaborations. The LLNL computational modeling team includes Tae Wook Heo, Liwen Wan, and Aniruddha Jana. The project also collaborates with Prof. Nicole Adelstein from San Francisco State University

(atomistic diffusion modeling) and Dr. Jianchao Ye from LLNL (3D printing of solid-state battery materials). Through the U.S.-Germany partnership on solid-state battery research, we are also partnered with Dr. Arnulf Latz and Dr. Timo Danner from DLR (multiscale integration, EIS modeling, and incorporation of space-charge effects in interface models).

Impact: Completion of this project will lead to understanding of interfacial losses and instabilities that impede performance and promote failure of solid-state batteries. The multiscale and multi-physics modeling framework developed in this work will address shortcomings of existing modeling strategies that either lack coupling of the multi-physics nature of various processes active in 3D batteries or fail to incorporate processes at different length scales to understand function. Ultimately, the tools and understanding generated by this project can be utilized to realize optimization of interface-dominated 3D batteries.

Out-Year Goals. Future activities will focus on methods for extending the atomistic simulations of the cathode-electrolyte interfaces to longer time scales, connecting the atomic transport properties to the mesoscale models for the heterogeneous interface, and incorporating internal stress effects in the mesoscale effective diffusion models. The team will also continue to work with collaboration partners to refine and parameterize the EIS models, incorporate space-charge effects, and connect microstructures of 3D printed materials to experimental measurements.

II.8.F 3D Printing of All-Solid-State Lithium Batteries (LLNL)

Jianchao Ye, Principal Investigator
Lawrence Livermore National Laboratory
7000 East Avenue
Livermore, CA, 94550
E-mail: ye3@llnl.gov

Tien Duong, DOE Technology Development Manager
U.S. Department of Energy
E-mail: Tien.Duong@ee.doe.gov

Start Date: November 20, 2018 End Date: November 19, 2021
Project Funding: $1,125,000 DOE share: $1,125,000 Non-DOE share: $0

Project Introduction

Traditional batteries are composed of two-dimensional films that are stacked and/or rolled. Thin film batteries display high power density while their thick film counterparts show good energy density, but it has proven difficult to concurrently achieve both within these planar form factors. In addition, conventional Li-ion batteries based on liquid organic electrolytes or gel polymer electrolytes have raised severe safety concerns due to the intrinsic flammable properties of the organic electrolytes. They are also not ideal for the use of high energy density metallic lithium (Li) anodes due to Li dendrite growth, or sulfur cathodes due to shuttling effects that result in fast capacity fade. There is an urgent need to develop safe, high-performance solid-state batteries (SSBs) with advanced electrolyte and separator technologies. Although in recent years a series of superionic conductors have been developed for electrolytes and separators [1], [2], [3], their performance does not satisfy demanding criteria due to large impedance from poor solid electrolyte-electrode contact and questionable electrochemical and mechanical stability. Unlike the well-established roll-to-roll fabrication of conventional Li-ion batteries, the processing of SSBs is unique due to the brittleness of solid-state electrolytes (SSEs). The commercially available or lab-developed SSE discs are usually very thick (hundreds of micrometers to millimeters) to overcome their brittle nature, which unfortunately increases the cell impedance and accounts for the majority of the overall cell weight and volume, leading to dramatically decreased power and energy densities. [4]

In this project, we will investigate 3D printing techniques to overcome safety, fabrication, mechanical, and electrochemical issues in SSBs. 3D printing builds complex structures in a layer-by-layer fashion, which allows rapid production of hierarchical architectures, gradient and multi-material structures, and multi-component assemblies. 3D printing is an emerging area that could fundamentally transform energy storage devices. For example, 3D printing can produce batteries with arbitrary form factors to fit a product's specific volume requirements and can create interwoven electrode arrangements over a wide range of length scales to improve transport and increase power density for a given energy density. For SSBs, 3D printing may dramatically reduce the separator thickness from ~1 mm (by hydraulic pressing) to tens of micrometers or less. In addition, the interfacial contact area between the electrolyte and the electrode may be increased via 3D interdigitated designs. Hence, we expect a significant reduction of the overall cell impedance and enhancement of both energy and power densities of SSBs by harnessing an array of 3D printing technologies being developed at Lawrence Livermore National Laboratory (LLNL).

The major R&D challenge in 3D printing of batteries is to develop a fabrication scheme that exhibits good printability, processability, and compatibility while achieving the ideal 3D layouts and feature resolution necessary to improve properties and performance. Batteries are complex systems that typically involve assembly of multiple components—for example, active materials (anode and cathode), electrolyte, separator, electrically conductive additives, binders, current collectors, and packaging. To be economically viable, the assembled system must meet many stringent requirements, such as high weight percentage of active materials,

high ionic and electronic conductivities, and good mechanical and thermal properties. To print a battery, the feedstocks (e.g., inks, resins, powders, suspensions, etc.) must also meet certain process requirements, such as exhibiting proper flow characteristics (or rheology), being stable and predictable, or perhaps even being photocurable for some specific 3D printing approaches. In addition, the multi-material nature of batteries is a nontrivial problem for 3D printing, and aspects such as varied particle morphologies and surface chemistry place increased importance on properly tuning the feedstock properties. For the case of SSBs, the solid-state electrolyte (SSE) is included in three battery components, the anode, cathode, and separator, which increases the difficulty in the feedstock development as multiple interactions between different solid components (e.g., solid electrolyte, conductive filler, and active materials) need to be considered. In the case of extrusion-based 3D printing processes, such as Direct Ink Writing (DIW) and Fused Deposition Modeling (FDM), particle aggregation or agglomeration in the ink can limit the minimum feature size that can be achieved due to jamming and nozzle clogging, which hinders the enhancement of power characteristics in 3D batteries. To realize the full potential of 3D printing, feedstocks for each component must be created that are suitable for the particular printing approach, multi-material printing methods must be developed, and material compatibility during post-processing steps must be addressed. With respect to the latter, sintering is a typical post-processing method used to improve the ionic conductivity of SSE separators. Yet, co-sintering with active materials could facilitate undesired reactions that may increase the interfacial impedance. [5], [6] Furthermore, stresses that develop during post-processing due to dimensional changes and volume reductions could lead to cracking and fracturing. We aim to solve these materials, manufacturing, and processing challenges to create 3D multi-material batteries and will first focus on the printing of SSEs. In addition, we will strive to develop materials and 3D printing approaches for SSBs that eliminate the need for sintering steps.

Objectives

Objective 1: Tuning microstructures of 3D printed SSE separators

Objective 2: Process compatibility with cathode printing

Objective 3: 3D printing of sinter-free SSE separators.

Approach

The project will focus on 3D printing the solid-state electrolyte to tackle materials, manufacturing and processing challenges. In the first year, we will develop feedstock materials based upon state-of-the-art Li-ion conductors for SSBs. Next, we will explore a range of LLNL 3D printing methods to determine feedstock compatibility, complexity of 3D structure, and minimal feature size. We will focus on DIW, but other AM techniques will also be explored throughout the three-year timeline as long as budget allows. We will consider the scalability of these approaches and strive to develop high throughput methods that could be economically viable. In addition, material and processing compatibilities will be considered throughout the project. For example, we will verify the compatibility of our printed SSEs with typical SSB cathode materials during post-processing, specifically during sintering. Recognizing that sintering could be a limiting factor, both from a technological but also from a business standpoint, we will develop sintering-free feedstocks and 3D printing techniques to eliminate the possible compatibility issues during post-processing.

Results

In FY20, we finalized the study of ball milling effects on sintering densification, microstructure, and ionic conductivity. The sintering behavior of LLZTO pellets was investigated using in situ USAXS/WAXS, and the thermal stability of LLZTO and LLZTO/cathode composites was evaluated. In addition, we examined several LLZTO and NMC 622 ink recipes with different binders and solvents and co-sintered printed LLZTO/NMC 622 bilayers. Our detailed progress is described in the following subsections.

Powder feedstock development

In FY19, we demonstrated that ball milling in aprotic solvents with surfactant can effectively reduce the LLZTO particle size down to ~ 220 nm without Li loss, which lowers the sintering temperature by 100 °C.

Additional experiments were conducted to correlate particle size, sintering temperature, density, ionic conductivity, and activation energy, as shown in Figure II.8.F.1. [7] In general, for pellets made with both ball milled (~220 nm) and pristine (~7 µm) LLZTO powder, higher sintering temperature leads to higher density, higher ionic conductivity and lower activation energy. However, the transition to higher ionic conductivity and lower activation energy occurs at a lower temperature for the ball milled samples (between 900 and 950 °C) than the pristine samples (between 1000 and 1050 °C). To further investigate LLZTO sintering mechanisms, in situ synchrotron X-ray scattering experiments were carried out to determine morphological and chemical variations during thermal treatment. As shown in Figure II.8.F.2, an increase in feature size (pores and grains) and decrease in total pore volume were captured by the USAXS analysis, and these changes correlate to peak shifting of the LLZTO phase, formation and disappearance of the LZO phase (revealed from WAXS analysis), and the mass loss caused by H_2O and Li_2CO_3 removal (determined from TGA analysis).

Surface modification and additives to improve sintering kinetics and conductivity of printed LLZTO films

In addition to bulk ionic conductivity, charge transfer resistance is another obstacle for solid electrolytes. Although acid surface treatment greatly reduces the charge transfer resistance (to ~ 20 ohm cm^2) for samples sintered at high temperatures (≥1000 °C), it is still very large (~10^4 ohm cm^2) for samples sintered at low temperatures (e.g., 900 °C). By coating ball milled LLZTO powder with only one ALD cycle of Al_2O_3, we observed 10 times higher ionic conductivity (> 10^{-4} S/cm) and 100 times lower charge transfer resistance (< 100 ohm cm^2) at a sintering temperature of 900 °C for hydraulic pressed pellets (Figure II.8.F.3). The density at this temperature was still low, but could be improved by adding sintering agents such as Li_3BO_3.

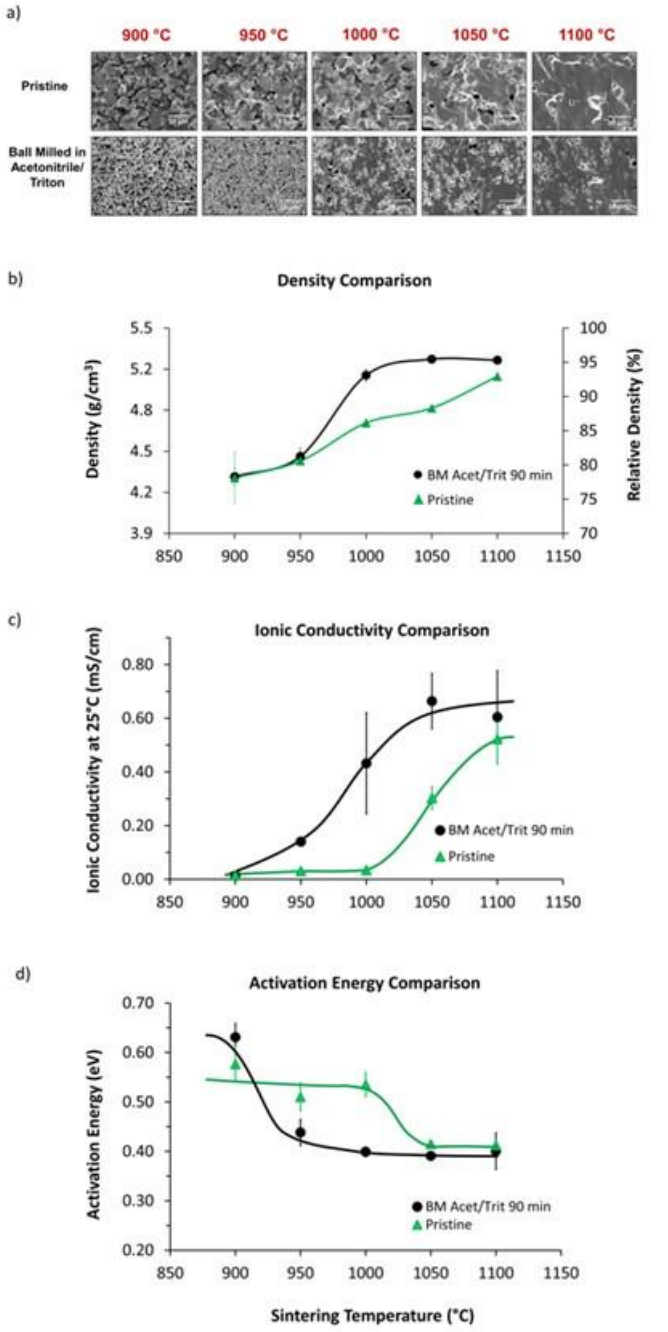

Figure II.8.F.1 Characterization of LLZTO pellets sintered at different temperatures. a) SEM cross-sections of pellets made with pristine powder (top row) and powder ball milled in acetonitrile/Triton for 90 min (bottom row) sintered at five different temperatures (from 900 °C to 1100 °C) for 6 h in argon. b) Density of each pellet measured by Archimedes' method using Fluorinert™ FC-40. c) Room temperature ionic conductivity and d) activation energy plotted as a function of sintering temperature for LLZTO pellets made with pristine powder (green markers) and powder ball milled in acetonitrile/Triton for 90 min (black markers). Lines are provided to guide the eye. Error bars on all plots represent the standard deviation for 3 samples.

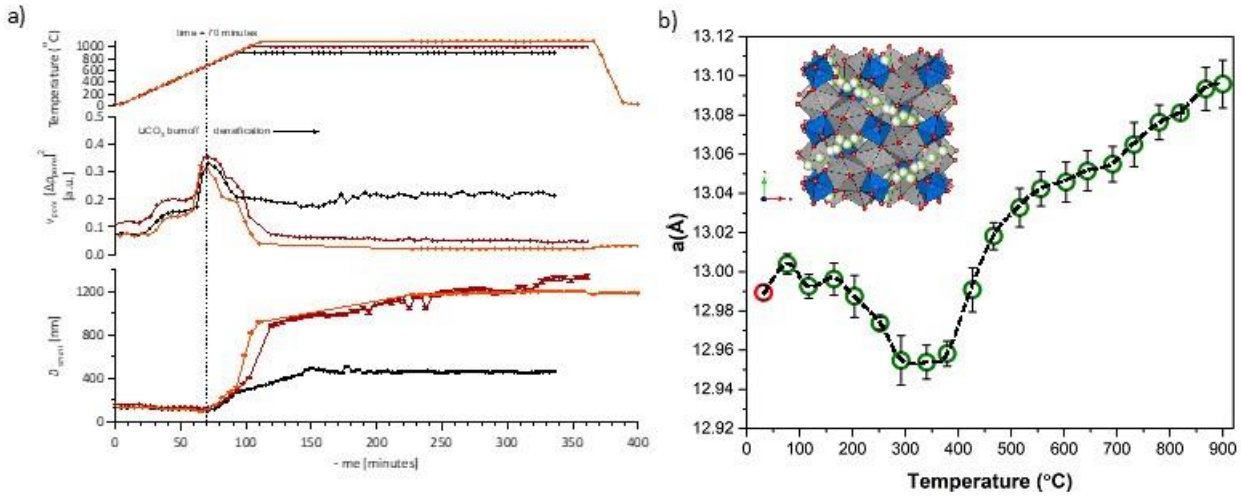

Figure II.8.F.2 In situ USAXS/WAXS studies on the sintering behavior of LLZTO pellet pressed from ball milled powders. a) Temperature profile (top), pore volume (middle), and pore diameter (bottom) evolution as a function of time. Black, brown, and orange colored plots are from three samples programmed to sinter at 900 °C, 1000 °C, and 1100 °C in Ar. b) Lattice constant calculated from WAXS spectra as a function of temperature.

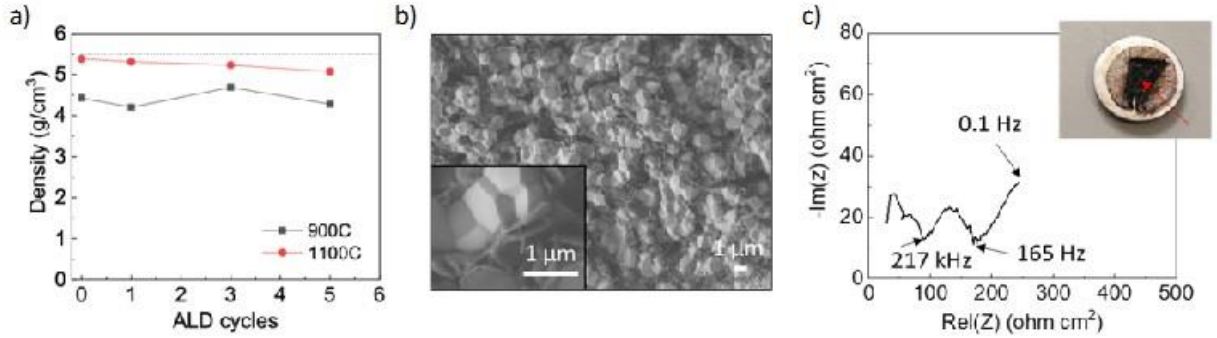

Figure II.8.F.3 (a)Density of LLZTO-Al pellets with different ALD cycles of Al_2O_3 coating after sintering at 900 °C (black) and 1100 °C (red). (b) SEM image of LLZTO-1Al with 1 cycle of Al_2O_3 sintered at 900 °C. Inset is a zoomed in image showing the existence of a low-z phase between LLZTO grains. (c) EIS of LLZTO-1Al sintered at 900 °C. Inset is an optical image of a disassembled Li/LLZTO-1Al/Li cell with the interface exposed. Arrow indicates the black color formed after contact between lithium and LLZTO-1Al above the Li melting point.

Printed LLZTO films show different thermal stability than hydraulic pressed pellets. Figure II.8.F.4(a) shows that while films made from pristine LLZTO powder (~7 µm particle size) are very stable up to 1100 °C in Ar, films made from ball milled powder show $La_2Zr_2O_7$ phase formation at or above 1000 °C. The addition of Li_3BO_3 and one ALD cycle of Al_2O_3 coating did not improve the thermal stability or reduce Li loss at high sintering temperatures (Figure II.8.F.4(b)). However, it did improve the density and eliminate $La_2Zr_2O_7$ phase formation at 900 °C. As a result of improved densification from Li_3BO_3 and chemical modification by Al_2O_3, good ionic conductivity and low charge transfer resistance was achieved in the printed thin film after pressureless furnace sintering at 900 °C (Figure II.8.F.4(c)).

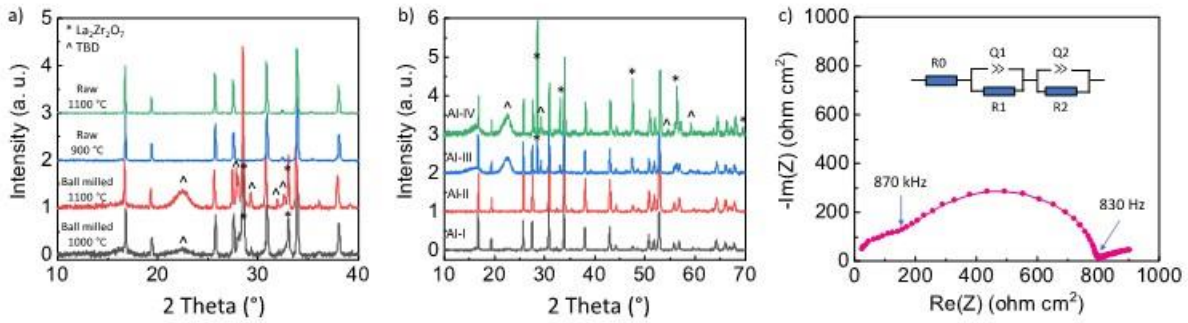

Figure II.8.F.4 XRD of sintered PuSL printed LLZTO films (a-b) and EIS of a LLZTO film with the addition of 5wt% Li_3BO_3 and one ALD cycle of Al_2O_3 (c). (a) bottom to top: LLZTO film made with ball milled powder, treated in Ar at 1000 °C (black) and 1100 °C (red); LLZTO film made with pristine (raw) powder, treated at 900 °C (blue) and 1100 °C (green). (b) bottom to top: LLZTO-5LBO-1Al film treated in Ar at 800 °C (black), 900 °C (red), 1000 °C (blue), and 1100 °C (green). (c) Room-temperature Nyquist impedance plot of a LLZTO-5LBO-1Al film sintered at 900 °C in Ar followed by air burning at 700 °C.

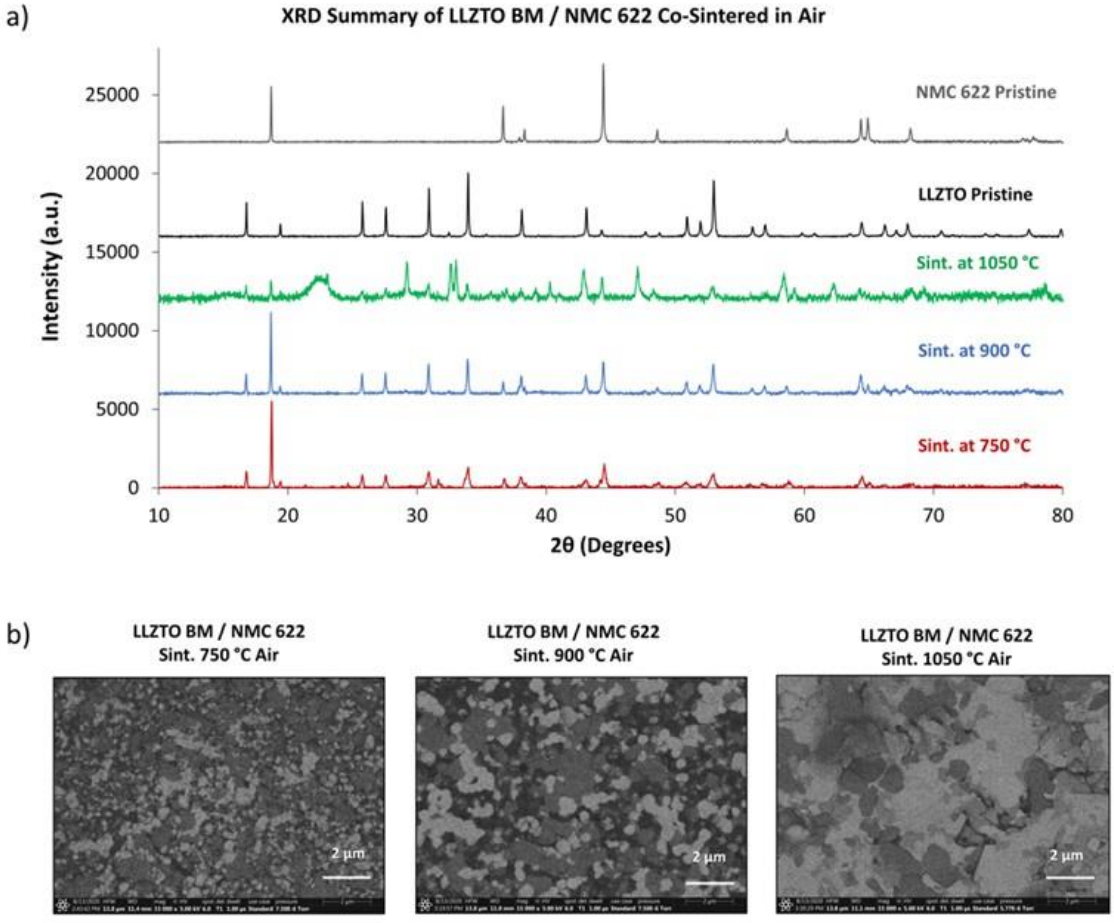

Figure II.8.F.5 XRD spectra a) and backscattered SEM cross-sections b) of LLZTO (ball milled) / NMC 622 pellets co-sintered at different temperatures for 2h with mother powder in air. Pellets were prepared by ball milling LLZTO and NMC 622 (both previously ball milled individually) together in a 1:1 wt ratio for 60 min with 3 mm YSZ beads. Note that the broad peak at ~22 degrees in the 1050 °C XRD spectrum is due to the paper that the XRD sample was mounted on.

Co-sintering stability studies

One way to improve the solid-solid contact between the cathode and LLZTO electrolyte is to co-sinter them together. However, the thermal stability during co-sintering is not well understood. Therefore, we evaluated the effect of sintering temperature and environment (air or Ar) on the densification and structural stability of pellets made with a 1:1 ratio of LLZTO and two different cathodes (NMC 622 and LCO). Three different LLZTO powders were used based on our previous sintering studies described above: ball milled, ball milled with 5 wt% Li_3BO_3, and ball milled with an ALD Al_2O_3 coating. These samples were sintered at three temperatures (750, 900, and 1050 °C) in both air and Ar. Figure II.8.F.5 and Figure II.8.F.6 show the XRD results and backscattered SEM images for the LLZTO/NMC 622 samples. We found that NMC 622 is relatively stable with LLZTO at or below 900 °C in air, and sintering in air generally leads to fewer reactions than sintering in Ar, though the solid-solid contact is poorer. Although a higher sintering temperature helps enhance the contact between LLZTO and NMC 622, secondary phases were clearly observed in the XRD spectra that could be detrimental to the electrochemical performance. The addition of Al_2O_3 or Li_3BO_3 does not affect thermal stability significantly and seems to be beneficial for densification. As we observed when sintering LLZTO by itself, the behavior of printed films could be very different from hydraulic pressed pellets due to the incorporation of polymer binder and possibly lower initial packing density. It is therefore important to evaluate the co-sintering stability of NMC 622 and printed LLZTO films in the future.

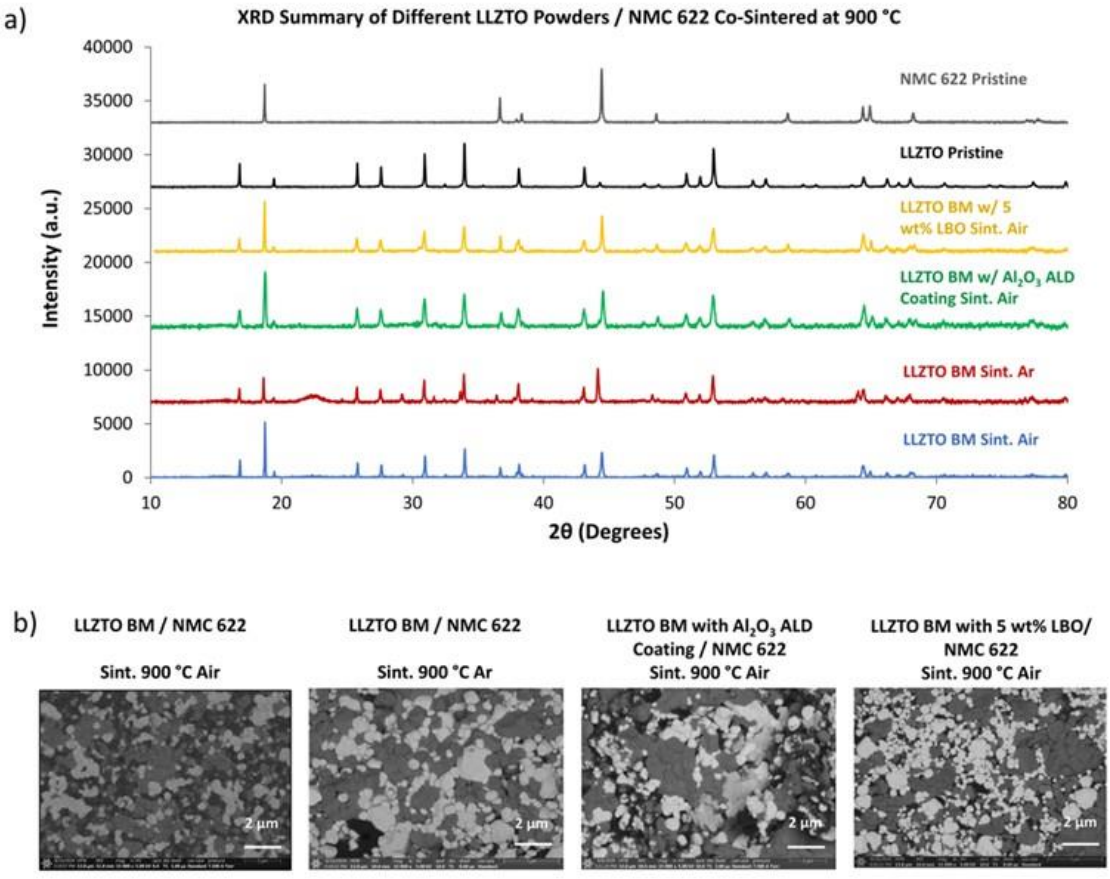

Figure II.8.F.6 XRD spectra a) and backscattered SEM cross-sections b) of pellets made with different LLZTO powders / NMC 622 co-sintered at 900 °C for 2h with mother powder in either air or argon. Pellets were prepared by ball milling LLZTO and NMC 622 (both previously ball milled individually) together in a 1:1 wt ratio for 60 min with 3 mm YSZ beads. Note that the broad peak at ~22 degrees in the XRD spectrum of the sample sintered in argon is due to the paper that the XRD sample was mounted on.

Co-printing and co-sintering of bilayer structures

Several ink recipes for direct ink writing of both LLZTO and NMC 622 layers were investigated. Binders, including polyvinyl butyral (PVB), cellulose, poly(ethylene glycol) diacrylate (PEGDA), polypropylene carbonate (PPC), and poly(ethylene oxide) (PEO), were tested with corresponding solvent systems for both pristine LLZTO and NMC 622 powders. It was found that although most binders work fine with pristine powders (several micrometer size), some strongly interact with ball milled powders, leading to accelerated degradation of ink properties. Figure II.8.F.7 (a) shows the co-printing of a log-pile NMC 622 structure followed by a uniform LLZTO layer based on a solvent recipe with PVB binder. Pristine powders (~7 μm) worked well for this approach. Co-sintering of the printed bilayer structure was conducted at different temperatures in both air and Ar environments (shown in Figure II.8.F.7 (b-d)). While possible thermal-induced reactions suggested by the color change are still under investigation, the geometry of the bilayer structure is well maintained after co-sintering. The structural integrity may be attributed to the very limited shrinkage and 3D interface, although the film is still porous leading to high resistivity. It is critically important to develop NMC and LLZTO inks with low-temperature densification capabilities and synchronized shrinking behavior to avoid thermally-induced strain mismatch. Proper binder systems with optimized solid content are under development to achieve good printability and mechanical and chemical compatibility during co-sintering.

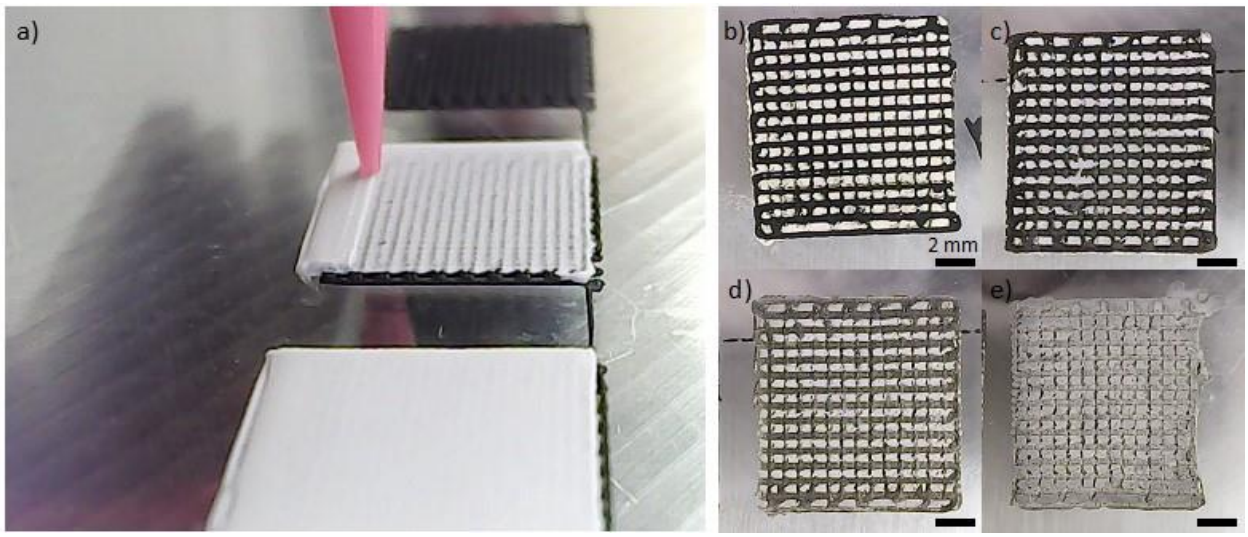

Figure II.8.F.7 a) Direct ink writing of a structured NMC 622 cathode followed by a uniform LLZTO layer. b)-e) The NMC 622/LLZTO bilayer co-sintered at 750 °C in Air, 750 °C in Ar, 900 °C in Ar, and 1050 °C in Ar, respectively. Note the color change with increasing temperature suggesting possible thermal-induced reactions.

Conclusions

LLZTO powder feedstocks were developed and evaluated for 3D printing. We found that the initial particle size, green film/body preparation method (pressing vs printing), and sintering conditions affect the thermal stability of both LLZTO itself and mixed LLZTO/NMC samples. In addition, our results show that sintering agents such as Al_2O_3 and Li_3BO_3 may facilitate sintering and co-sintering kinetics and enhance solid-solid contact. Additional work is necessary to develop inks that do not suffer from the observed reaction between ball milled LLZTO and certain binders. In order to realize co-sintering of 3D printed LLZTO/NMC structures while avoiding poor densification, warpage, cracking, and delamination, it is critically important to tune the ink compositions and sintering conditions in a more detailed study.

References

1. N. Kamaya, K. Homma, Y. Yamakawa, M. Hirayama, R. Kanno, M. Yonemura, T. Kamiyama, Y. Kato, S. Hama, K. Kawamoto, A. Mitsui, A lithium superionic conductor, Nat. Mater. 10(9) (2011) 682-686.

2. W.S. Tang, A. Unemoto, W. Zhou, V. Stavila, M. Matsuo, H. Wu, S. Orimo, T.J. Udovic, Unparalleled lithium and sodium superionic conduction in solid electrolytes with large monovalent cage-like anions, Energy Environ. Sci. 8(12) (2015) 3637-3645.

3. Y. Wang, W.D. Richards, S.P. Ong, L.J. Miara, J.C. Kim, Y.F. Mo, G. Ceder, Design principles for solid-state lithium superionic conductors, Nat. Mater. 14(10) (2015) 1026-1032.

4. Y. Kato, S. Hori, T. Saito, K. Suzuki, M. Hirayama, A. Mitsui, M. Yonemura, H. Iba, R. Kanno, High-power all-solid-state batteries using sulfide superionic conductors, Nat. Energy 1 (2016) 1-7.

5. Y. Ren, T. Liu, Y. Shen, Y. Lin, C.-W. Nan, Chemical compatibility between garnet-like solid state electrolyte Li 6.75 La 3 Zr 1.75 Ta 0.25 O 12 and major commercial lithium battery cathode materials, J. Materiomics 2(3) (2016) 256-264.

6. L. Miara, A. Windmüller, C.-L. Tsai, W.D. Richards, Q. Ma, S. Uhlenbruck, O. Guillon, G. Ceder, About the compatibility between high voltage spinel cathode materials and solid oxide electrolytes as a function of temperature, ACS Appl. Mater. Interfaces 8(40) (2016) 26842-26850.

7. M. Wood, X. Gao, R. Shi, T.W. Heo, J.A. Espitia, E.B. Duoss, B.C. Wood, J. Ye, , Exploring the Relationship Between Solvent-Assisted Ball Milling, Particle Size, and Sintering Temperature in Garnet-Type Solid Electrolytes, J. Power Sources (2020) Under Review.

Acknowledgements

I would like to acknowledge our team members including Marissa Wood, Joshua Hammons, Jose Ali Espitia, Erika Ramos, Siwei Liang, and Jean-Baptiste Forien, for their great contributions to the project. We also express our thanks to Brandon Wood, Rongpei Shi, Tae Wook Heo, Marcus Worsley, Eric Duoss and Tony Van Buuren for helpful discussions. This work was performed under the auspices of the U.S. Department of Energy by Lawrence Livermore National Laboratory under Contract DE-AC52-07NA27344.

II.8.G Advanced Polymer Materials for Li-ion (SLAC)

Zhenan Bao, Principal Investigator
Stanford University/SLAC
443 Via Ortega
Stanford, CA 94305
E-mail: zbao@stanford.edu

Yi Cui, Principal Investigator
Stanford University/SLAC
450 Serra Mall
Stanford, CA 94305
E-mail: yicui@stanford.edu

Tien Duong, DOE Technology Development Manager
U.S. Department of Energy
E-mail: Tien.Duong@ee.doe.gov

Start Date: October 1, 2019 End Date: September 30, 2020
Project Funding: $400,000 DOE share: $400,000 Non-DOE share: $0

Project Introduction

Lithium metal anode suffers from several instabilities during electrodeposition process in the battery charging. Specifically, lithium deposition leads to inhomogeneous coverage on the electrode substrate, resulting in concentration of electric field at the tip of these deposits, ultimately resulting in dendritic growth that shorts the battery. The high surface area metal deposition also causes faster parasitic reactions between the lithium metal and organic electrolyte that is responsible for the rapid fade of battery capacity. According to a conventional understanding, the primary sources of instabilities in electrodeposition is diffusion limitations in ion transport processes both in the bulk electrolyte and at the electrode-electrolyte interfaces. Consequently, many theoretical efforts have been focused on modeling the dendritic growth in a purely diffusion limited condition by varying the transport properties like ion conductivity, relative mobility of anions and cations (transference number) and studying their effect on electrolyte modulus or electrode geometry. Likewise, several experimental efforts have reported improved electrodeposition stability with electrolytes with high transference number, conductivity or modulus. While, the ion transport and mechanics are important determinants of morphological evolution of the metal electrode, other coupled parameters like electrochemical kinetics, electrostatic potential landscape can play a critical role. For example, several experimental findings have reported observation of fractal structures during electrodeposition of metallic lithium even at rates much below the diffusion limited current density. This further indicates that transport parameters in the electrolyte may not be the sole determinant of morphological stability. The relative effect of the electrochemical kinetics and ion transport is particularly important considering the metal electrode doesn't have a smooth surface, which is aggravated even at earlier stages of deposition. The physical perturbations on the metal surface results in abrupt enhancement of local electric field causing the ions to be preferentially directed towards the dendritic tips, ultimately leading to unstable growth. In addition, a major challenge in understanding this phenomenon is the fact that the transport and kinetics essentially rely for the same physical factors as ion concentration, viscosity, temperature among others. Here, we leverage ultrafast scanning voltammetry and pulse-field gradient NMR to decouple the effects of kinetics and transport, respectively. Based on these analyses, we design a polymer interface that stabilizes electrodeposition by maintaining a uniform ion flux to the electrode. Subsequently, we intend to utilize the polymer interface for improving lithium metal battery cycling both in Li||Cu and Li||NMC configurations.

The project uses soft polymer coatings with dynamic crosslinking to give the resulting polymers liquid-like rheological properties and stretchable and self-healing properties. In previous work, the project has shown that

such coatings resulted in uniform deposition/stripping of lithium metal and improved cycling stability of Li-metal electrodes. To understand the design rules for effective polymer coatings, the team chose a few representative polymers to systematically understand structure property relationships. Here, the team investigates the correction between surface energy of the polymer and exchange current for lithium deposition.

Objectives

This project will develop new polymer materials for batteries. The team will develop polymer coatings with specific mechanical properties that can accommodate the volume expansion and contraction of the Li-metal anode associated with deposition and stripping (charging and discharging).

Results

Molecular Simulations of Electrodeposition

In collaboration with the group of Jian Qin in Stanford, we used a three-dimensional coarse-grained Brownian dynamics model of lithium deposition under an applied voltage to understand the effect of the Damköhler Number (Da) on lithium morphology. This model accounts for both diffusive motion and drift driven by the electric field. The potential field is solved at every time step using the Poisson equation, with boundary conditions defined by the positions of the existing lithium deposits, in order to accurately represent the effect of lithium morphology on the local electric field. Further details are available in the Supporting Information. When lithium cations contact a lithium metal surface or the current collector, they have a probability p of depositing. This is analogous to the exchange current density for the reaction (i_o). In the limit of fast kinetics, p=1, growth is extremely dendritic and porous (Figure II.8.G.1). This is due to the electrostatic forces attracting ions to growing lithium tips. The uniformity of the deposits can be quantified by the ratio of deposited volume of lithium within the control volume to ideal close-packing for the same volume, defined as the normalized density. In the case of slow kinetics or low Da, growth is uniform, dense, and non-dendritic. Lithium is initially attracted to dendritic tips but diffuses away before the reaction occurs, leading to randomized deposition. The rate of lithium deposition decreases at low Da, as expected. Therefore, decreasing Da can lead to more uniform lithium deposition at the cost of a lower charging rate for the same applied potential.

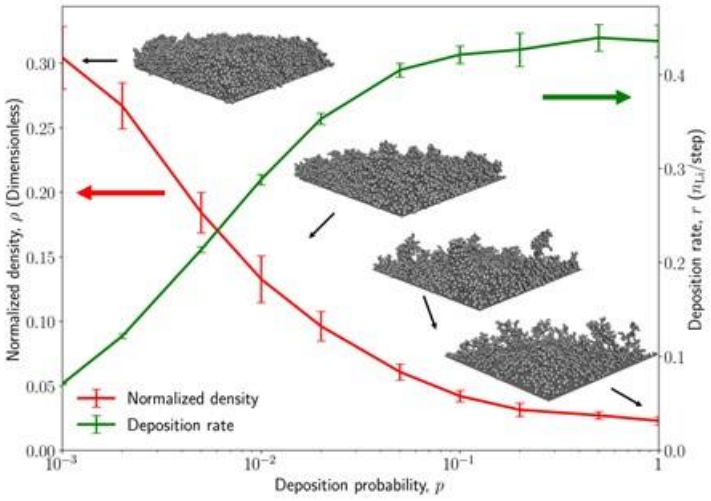

Figure II.8.G.1 Molecular dynamics simulations showing relationship between the rate and morphology with the deposition probability.

Polymer Coating Design

On the basis of aforementioned theoretical understanding, we propose a design strategy to stabilize lithium electrodeposition, without significantly altering the battery chemistry or architecture. Here, we incorporate a polymer interface based on crosslinked ionic networks between electrode and electrolyte. An ideal polymer

interface is hypothesized to have the following characteristics: 1) Chemically inert and unsusceptible to degradation by side reactions with lithium metal, 2) Insoluble and chemically resistant liquid electrolyte accessibility to the metal electrode, 3) Unhindered transport channels to facilitate high interfacial conductivity, 4) Regulate uniform charge transport on the electrode surface. The chemical design of the polymer network is shown in Figure II.8.G.2. Specifically, perfluoropolyether-dimethacrylate (PFPE-DMA) is used as polymer network backbone, pentaerythritol-tetrakis(3-mercaptopropionate) (PETMP) as the crosslinker and lithium-styrene-trifluoromethanesulfonyl-imide (Li-STFSI) is utilized as salt linker in different ratios. The PFPE polymer is known to be highly resistive to chemical corrosions, while the salt molecules are incorporated to facilitate ion transport. The variation in the salt content in the polymer is characterized using nuclear magnetic resonance (NMR) and infrared spectroscopy (FTIR). Figure II.8.G.2b shows the varying 1H NMR peak intensities of the polymers for the specific methyl groups labeled in Figure II.8.G.2b, where it is seen that as linkable Li-STFSI is increased in the feed, the immobilized salt content in the polymer network is progressively higher. We further analyzed the IR-spectra of the ionic polymer networks as shown in Figure II.8.G.2c, where we observe that upon crosslinking, the representing vibrational mode of the thiol group (-SH) at 2550cm^{-1} disappears for all the polymers synthesized here, thus we can conclusively say that all the PETMP linkers are reacted. Also, the vibration modes of the double bonds (1650cm^{-1}) in the styrene molecule present in the Li-STFSI monomers were compared for different cases and it is confirmed that increasing the Li-STFSI in the feed indeed leads to stronger intensity of this peak. Thus, we are able to systematically vary the immobilized salt content in the polymer network that can ultimately lead to fundamental understanding of the effect of ionic polymers in stabilizing electrodeposition.

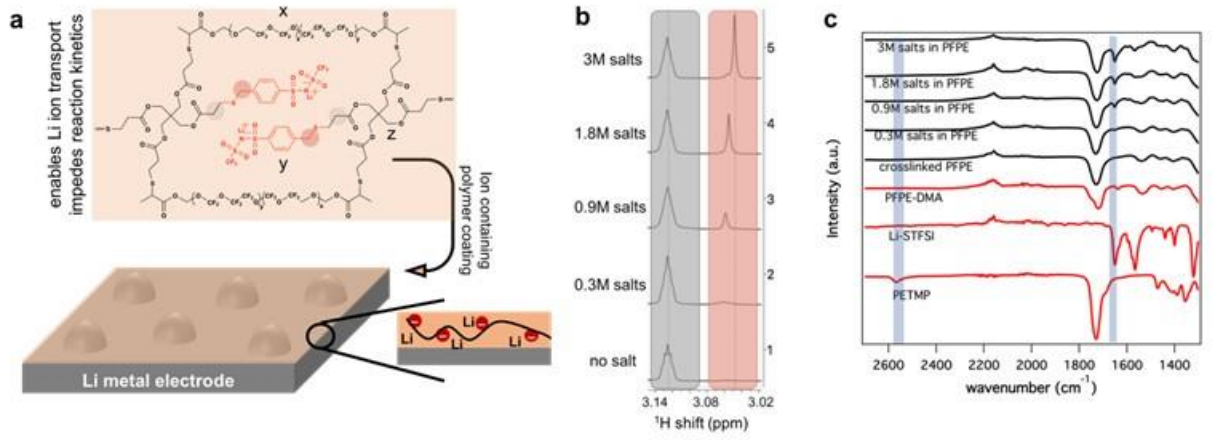

Figure II.8.G.2 Schematic showing the structure of ionic polymer coated on the lithium metal electrode. The ionic polymer comprises of x: PFPE-DMA backbone, y: PETMP crosslinker and z: STFSI-Li salts. (b) Comparison of peak heights obtained from 1H NMR measurements showing the relative content of the methyl groups in the polymer backbone and the tethered anions (spectra referenced to residual protons in CD3OD). (c) Infrared spectroscopy measurements for polymer networks with varying salt content. The shaded region at 2550cm^{-1}, indicates the –SH group in PETMP, while at 1650cm^{-1} is for C=C bond in Li-STFSI.

Ionic Properties of Polymer Coating

The lithium ion solvation environment and transport properties in these ionic polymer networks in presence of the solvent mixture ethylene carbonate/diethylene carbonate (EC/DEC) was analyzed using NMR. Figure II.8.G.3a shows the ^{7}Li NMR intensity profiles at different immobilized salt content. There are two important observations as the tethered salt content is varied: the peak intensity increases and also there is downfield (less-negative) shift. The progressive rise in the intensity indicates the increase in the tethered salt, while the downfield shift of ^{7}Li-NMR peak implies a reduction of the solvation energy of lithium ions. This finding agrees with previous study that as the salt content is increased the solvent molecules interact more with the anions rather than the lithium ions, thus Li experiences less ion pairing or a looser solvation shell. We further measured self-diffusion characteristics of lithium and grafted STFSI ions. Figure II.8.G.3b plots the lithium ion diffusivity in the left axis, measured using pulse-field gradient NMR, while the right axis reports the Li-

transference number (t_{Li}) for the corresponding ionic polymer networks. The Li diffusivity across the different salt concentration is relatively high compared to the diffusivity values of lithium salts reported in the literature and also are similar for all concentrations measured in this study. For comparison, the lithium diffusivity using the same method for 1M LiTFSI in EC/DEC is $1.41 \times 10^{-6} cm^2/s$. Thus, it can be asserted that the lithium ion mobility in the ionic polymer network is similar to that of liquid electrolyte which is essential to enable unhindered transport when used as polymer electrolyte or as electrode coating. The Li transference number in Figure II.8.G.3b is calculated using a simple formula: $t_{Li} = \frac{D_{Li}}{D_{Li}+D_F}$, where D_{Li}, D_F are the diffusivities obtained from the pulse field gradient NMR measurements. Owing to the immobilization of the STFSI anions, the t_{Li} > 0.5 (~0.7) for all the polymer networks as compared to t_{Li} = 0.49 for the liquid electrolyte (1M LiTFSI in EC/DEC). The higher transference number polymer electrolytes can essentially eliminate space charge formation due to ion polarization even at relatively high current densities as reported by several theoretical and experimental studies.

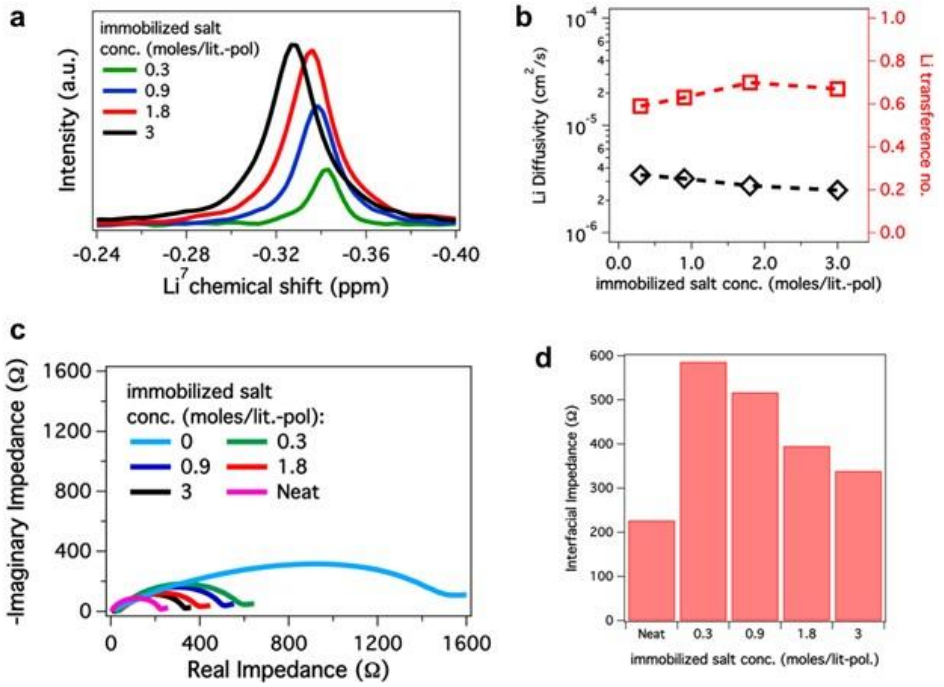

Figure II.8.G.3 (a) 7Li chemical shift measured for different ionic polymer networks, showing a downfield shift with increasing salt concentration. (b) Lithium diffusivity and transference number obtained from pulse field gradient NMR measurements. (c) Nyquist plot showing the impedance measurement in symmetric lithium cell, where the electrode was coated with and without polymer networks. (d) Comparison of the interfacial resistances measured using impedance spectroscopy of symmetric lithium cells. In part a and b, the solvent used was EC/DEC and in part c, d, the bulk liquid electrolyte utilized was 1M LiTFSI in EC/DEC.

We utilized the synthesized ionic polymer networks as an interfacial layer on the lithium metal electrodes in a symmetric cell configuration and analyzed the interfacial impedance using a bulk electrolyte, 1M LiTFSI in EC/DEC. Figure II.8.G.3c shows the Nyquist plots for various ionic polymer networks, while the interfacial resistance values are plotted in Figure II.8.G.3d for the corresponding measurements. The resistance value for the neat electrolyte (without any coating) is the lowest, as expected, while that of one with salt-free polymer coating is the highest. Specifically, the interfacial resistance increases by about ~8 times when the electrode is coated by the crosslinked PFPE layer (1µm thickness), implying that the coating significantly blocks the liquid electrolyte access to the metal electrode. Our group recently reported that mass transport limiting polymer interfaces can prevent continuous side reactions between the bulk electrolyte and lithium metal electrode that caused capacity fade in reactive metal batteries. While it is important to prevent or limit the electrolyte access to the lithium electrode, the electrode-electrolyte interface should maintain unperturbed ion transport. Our design strategy of incorporating tethered salt molecules in the polymer networks is useful to enable high

interfacial ion conduction. As seen in Figure II.8.G.3d, the interfacial resistance progressively decreases as the salt content in the network increases, in fact for the 3M salt containing polymer coatings, the resistance is under twice that of the bare electrodes. As previously observed using the NMR analysis, the ionic polymer networks can maintain high lithium ion mobility, thus the coatings facilitate transport from the bulk electrolyte to the Li electrode without significantly contributing to the interfacial resistance.

Coulombic efficiency measurements and morphological studies

We examine the effect of the synthesized polymer coatings on the electrode in a lithium metal battery. Figure II.8.G.4a shows the comparison of the coulombic efficiency for the neat electrolyte with that of polymer coated electrodes. It is seen with the electrolyte 1M LiTFSI in DME, there is successive improvement in the coulombic efficiency of lithium metal plating-and-stripping as the grafted salt conc. is increased in the polymer coating, which indicates that the ionic polymers suppress dendritic growth and chemical side-reactions of the lithium metal. It is further seen in Figure II.8.G.4a that the coulombic efficiency measured using 2M LiTFSI/DME shows similar behavior such that the ionic polymer coating outperforms the bare electrode. We analyzed the morphology of lithium deposits using scanning electron microscopy (SEM). In this experiment, we plated 25µm (5mAh/cm^2) of lithium onto a copper electrode with and without the polymer coating, thereafter stripped and re-plated the same amount, before disassembling the battery for the SEM analysis using the electrolyte 1M LiTFSI in DME. As shown in Figure II.8.G.4b, the electrodeposits without the polymer coating (bare) is fibrous and comprises of heterogenous shapes. However, the electrodeposition morphology with 1.5moles/kg grafted salts is significantly more stable. The long-term performance of the ionic polymer coatings in Li||Cu configuration was analyzed using the electrolyte 1M LiTFSI in DOL/DME (1wt.% $LiNO_3$) and plotted the coulombic efficiency at 1mA/cm^2 and 3mA/cm^2 current densities. We observe that the 3M immobilized salt containing polymer coatings significantly outperform the control cells.

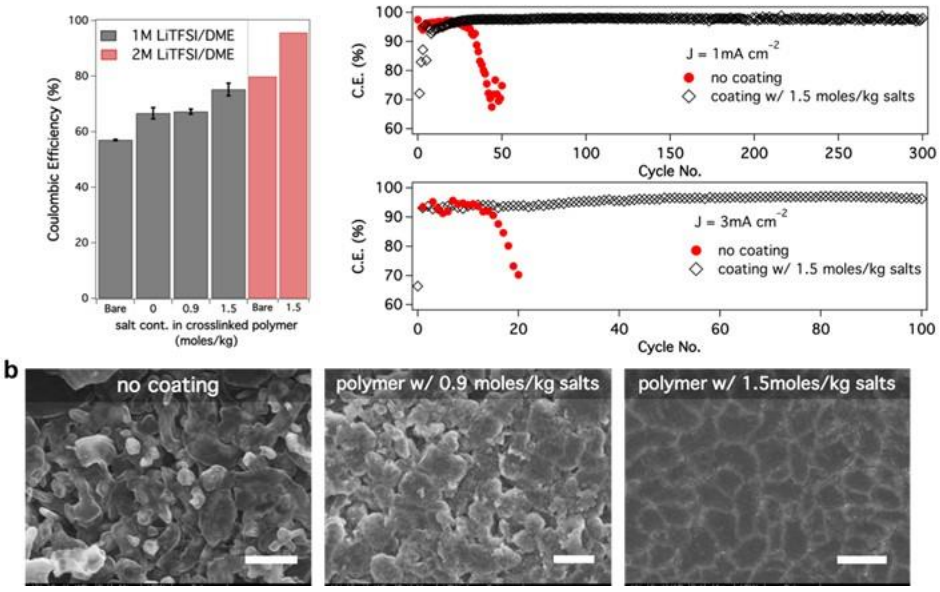

Figure II.8.G.4 (a) Comparison of coulombic efficiency measurements in Li||Cu configuration, where the copper is coated with or without different ionic polymers and the bulk electrolyte utilized is 1M LiTFSI in DME as well as 2M LiTFSI in DME. a) Comparison of lithium morphology on copper electrode after depositing and stripping 5mAh/cm^2 of lithium before re-depositing the same amount, using the electrolyte 1M LiTFSI in DME. The scale bars represent 5µm. (c) Long term coulombic efficiency measuring using a Li||Cu electrode for the polymer coated and bare copper cases at two different current densities of 1mA/cm^2 and 3mA/cm^2, with the plating time in both cases being 1 hour. The electrolyte utilized here is 1M LiTFSI in DOL/DME with 1wt.% $LiNO_3$.

Electrochemical analysis

The cycling stability of the ionic polymer coatings in Li||Cu configuration was analyzed using conventional electrolyte of 1M $LiPF_6$ in EC/EMC with 10% FEC. The coulombic efficiency comparison of the control (bare

electrode) and polymer coating is presented in Figure II.8.G.5a. It is seen that the ionic polymer coating shows improved performance for at least 150 cycles in comparison to the control that fails at about 50 cycles. Finally, the polymer coated thin 25µm lithium metal electrode (N = 5mAh/cm^2) was paired against LiNiMnCoO^2 cathode having capacity (P) 1.7mAh/cm2 and the batteries (N/P = 3) were cycled using the electrolyte 1M $LiPF_6$ in EC/EMC with 10% FEC. The corresponding capacity and coulombic efficiencies for the two different cases (with and without polymer coating) is plotted in Figure II.8.G.5b, while the overall efficiency, measured the formula, C.E.=100(1-N⁄(n×P)), where n is the cycle number until 80% fade, is plotted as bar chart in the inset. We observe that the polymer coating significantly enhances the lifetime of the full-cell, in agreement with the findings from the aforementioned electrochemical and electrodeposition results.

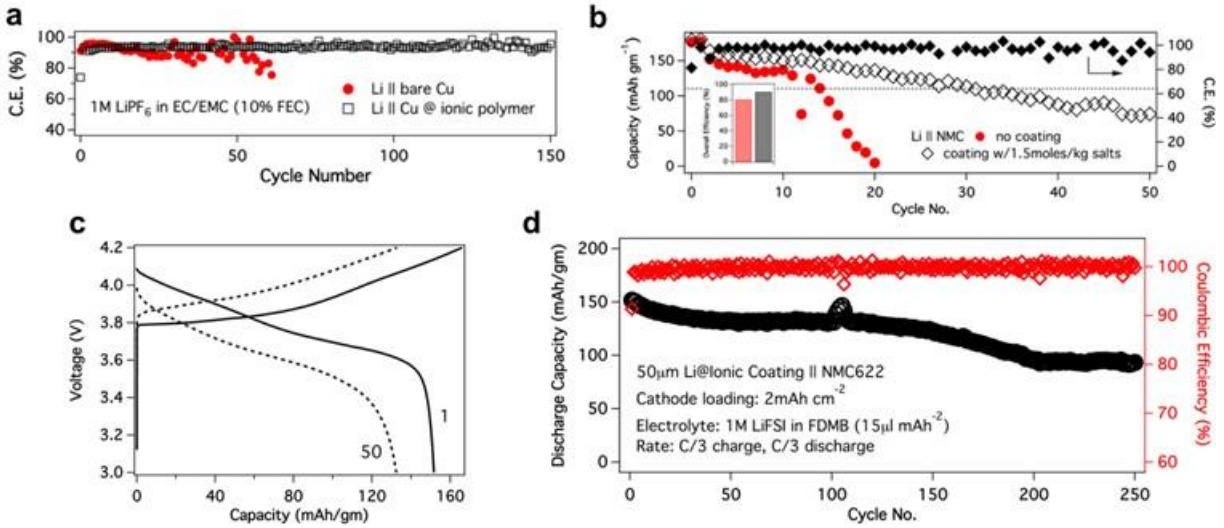

Figure II.8.G.5 (a) Cycling stability of lithium vs. copper cells, were the copper electrodes were either bare or coated with ionic polymers containing 1.5moles/kg of grafted salts. The bare electrode fails in 50 cycles, while that with coating showed enhanced stability. (b) Li||NMC full cell cycling using 25µm lithium and 1.7mAh/cm^2 NMC532, such that the anode (N) to cathode capacity (P) ratio is 3:1. The lithium metal utilized either bare or coated with the ionic polymer (1.5moles/kg of salts). The inset shows the comparison of the overall efficiency obtained using the formula: (1−N/ (n × P))100%. The electrolyte in all the subparts was 1M $LiPF_6$ in EC/EMC with 10% FEC. (c) Voltage profile in a lithium vs. NMC622 cathode for the first and 50th cycle. (d) Cycle life of the full cell upto 250 cycles. In part c and d: the electrolyte utilized was 1M LiFSI in FDMB and the volume was limited to 15µl/mAh. The lithium utilized was 50µm thick coated with ~1 µm thick layer ionic polymer (1.5 moles/kg of grafted salts). The cathode loading here is 2mAh/cm^2. The electrolyte utilized was 1M LiFSI in FDMB and the volume was limited to 15µl/mAh

Additionally, we believe that the ionic polymer coating utilized in this work is independent of the chemistry of electrolyte. Thus, we pair the polymer coated lithium with a high voltage cathode utilizing an electrochemically stable electrolyte that can enhance the high voltage performance as well as form a stable SEI on the lithium metal synergistically with the effect of the polymer interface. Specifically, efficacy of the coating in Li ||NMC full cells is examined using specific conditions to meet practically relevant parameters: ionic polymer coating was applied to a 50µm (10mAh/cm^2) thin lithium anode and paired against NMC622 with 2.0 mAh/cm^2 capacity. We maintain the electrolyte amount to be about 15µl/mAh. The electrolyte utilized was a high performing reported our group: 1M LiTFSI in FDMB. We find that this battery is able to cycle stably for at least 150 cycles (Figure II.8.G.5a-b). Here, we use a rigorous cycling rate of C/3 charge and C/3 discharge. Clearly, we find that the fluorinated electrolyte based on FDMB and the ionic polymer coating on lithium anode show a synergistic effect, enabling stability. In comparison to previous results involving Li||NMC full configurations, the cycling results show one of the highest reported improvement in the full-cell configuration.

Conclusions

We believe, the polymer design presented in this work can stabilize metal-electrolyte interfaces independent of the electrolyte and cathode chemistries, or even battery geometry. Thus, they provide a facile pathway towards energy-dense, yet stable lithium metal battery operation.

Key Publications

1. D. G. Mackanic, X. Yan, Q. Zhang, N. Matsuhisa, Z. Yu, Y. Jiang, T. Manika, J. Lopez, H. Yan, K. Liu, X. Chen, Y. Cui, Z. Bao, "Decoupling of mechanical properties and ionic conductivity in supramolecular lithium ion conductors", **Nature Commun.,** 10, 5384, 2019.

2. D. T. Boyle, X. Kong, A. Pei, P. E. Rudnicki, F. Shi, W. Huang, Z. Bao, J. Qin, and Y. Cui, "Transient Voltammetry with Ultramicroelectrodes Reveals the Electron Transfer Kinetics of Lithium Metal Anodes." **ACS Energy Letters** 5, 701-709, 2020.

3. C. V. Amanchukwu, Z. Yu, X. Kong, J. Qin, Y. Cui, and Z. Bao. "A new class of ionically conducting fluorinated ether electrolytes with high electrochemical stability." **Journal of the American Chemical Society** 142, 7393-7403, 2020.

4. D. G. Mackanic, T.-H. Chang, X. Huang, Y. Cui, Z. Bao, "Stretchable electrochemical energy storage devices", **Chem. Soc. Rev.**, 49, 4466-4495, 2020.

5. D. G. Mackanic, M. Kao, Z. Bao, “Enabling Deformable and Stretchable Batteries”, **Adv. Energy Mater**., 10, 2001424, 2020

6. Z. Yu, H. Wang, X. Kong, W. Huang, Y. Tsao, D.G. Mackanic, K. Wang, X. Wang, W. Huang, S. Choudhury, Y. Zheng, C. Amanchukwu, S.T. Hung, Y. Ma, E.G. Lomeli, J. Qin, Y. Cui, Z. Bao, “Molecular design for electrolyte solvents enabling energy-dense and long-cycling lithium metal batteries”, **Nature Energy**, 5, 526-533, 2020.

7. X. Kong, P. E. Rudnicki, S. Choudhury, Z. Bao, J. Qin, “Dendrite Suppression by a Polymer Coating: A Coarse-Grained Molecular Study”, **Adv. Funct. Mater.**, 30, 1910138, 2020.

8. Z. Yu, Y. Cui, Z. Bao, “Design principles of artificial solid electrolyte interphases for lithium-metal anodes”, **Cell Rep. Phys. Sci.,** 1, 100119, 2020.

Patents

1. Zhenan Bao, Zhiao Yu, Dawei Feng, Min Lee, Yi Cui, Allen Pei, U.S. Application No.: 62/740,785, PCT Patent Application No.: PCT/US2019/054298, Ion-conductive organic networks for battery.

2. Y. Cui, Z. Bao, Z. Yu, S. Choudhury, H. Wang “Liquid and Solid Electrolytes with Special Li-F Solvation Structure Enabling Practical Li-metal Batteries”, US provisional patent filed.

Acknowledgements

We acknowledge collaboration from Prof. Jian Qin and his group on modeling and simulation of lithium ion solvation structures and lithium metal deposition.

II.9 Beyond Li-ion R&D: Solid-State Batteries

II.9.A Improving the Stability of Lithium-Metal Anodes and Inorganic-Organic Solid Electrolytes

Dr. Nitash P. Balsara, Principal Investigator
Department of Chemical and Biomolecular Engineering
University of California, Berkeley
Berkeley, CA 94720
E-mail: nbalsara@berkeley.edu

Tien Duong, DOE Technology Development Manager
U.S. Department of Energy
E-mail: Tien.Duong@ee.doe.gov

Start Date: October 1, 2017 End Date: September 30, 2020
Project Funding: $300,000 DOE share: $300,000 Non-DOE share: $0

Project Introduction

Polymer electrolytes offer increased stability in lithium batteries in comparison to more widely used liquid electrolytes. Nanostructured electrolytes containing both soft, ion-conducting domains and rigid non conducting domains offer the opportunity to tune both mechanical and electrical properties separately. Such electrolytes are conveniently made by block copolymer self-assembly. Most of the block copolymer electrolytes studied thus far comprise organic polymer chains for both the conducting and rigid domains. The team hopes to synthesize new electrolytes that simultaneously have high transport properties and have greater stability against lithium in comparison to organic diblock copolymers. The project objective is to establish a new hybrid electrolyte that will be stable against cells with a Li-metal anode.

Objectives

The project will synthesize a new hybrid electrolyte that is designed to be stable against lithium metal. The materials are block copolymers wherein acryloisobutyl polyhedral oligomeric silsesquioxane (POSS) is covalently bonded to the chain. The second block is a conventional polymer electrolyte, PEO. Electrochemical characterization of this polymer will include measurement of all transport properties including conductivity, diffusion coefficient, and the transference number. The stability against lithium metal will be evaluated by cyclic voltammetry (CV), while its applications as an electrolyte will be evaluated and visualized using cycling X-ray tomography experiments on symmetric Li-hybrid-Li cells.

Approach

First, the team synthesized hybrid diblock copolymers by incorporating monomers that contain an inorganic component. Then electrolytes are prepared by mixing these diblock copolymers with salt. Electrochemical and mechanical characterization of these materials are performed before carrying out cycling X-ray tomography experiments. The combination of these approaches enables rational design of materials that exhibit improved stability against lithium metal.

Results

Synthesize a series of POSS-containing block copolymer electrolytes for electrochemical studies

A variety of diblock and triblock organic inorganic hybrid triblock copolymers were synthesized in order to compare their electrochemical properties. The polymers synthesized are poly(ethylene oxide)-*b*-polyhedral oligomeric silsesquioxane (PEO-POSS) diblock and polyhedral oligomeric silsesquioxane-*b*-poly(ethylene oxide)-*b*-polyhedral oligomeric silsesquioxane (POSS-PEO-POSS) triblock copolymers. The chemical structures are depicted in Figure II.9.A.1.

The polymerizations were carried out based on atom transfer radical polymerization (ATRP). Typically, POSS acrylate was polymerized from PEO-based mono or di-ATRP macro initiator using copper (I) bromide catalyst in toluene at 60°C for 24h. After the reaction, the cooled solution was passed through neutral alumina to get rid of the copper catalyst. Pure copolymer was obtained by multiple reprecipitation from cold diethyl ether. The incorporation of POSS units in the block copolymers was confirmed via NMR spectra and the purity was determined using GPC. Table II.9.A.1 summarizes the composition of all the polymers.

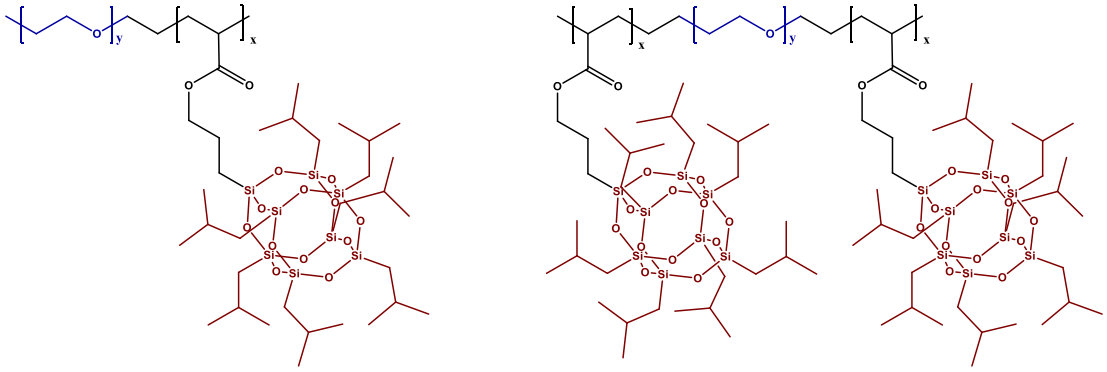

Figure II.9.A.1 Chemical structure of PEO-POSS diblock and POSS-PEO-POSS triblock copolymer

Table II.9.A.1 Composition of various PEO-POSS diblock and POSS-PEO-POSS triblock copolymers

PEO-POSS	POSS units	M_{PEO} (kg mol^{-1})	M_{POSS} (kg mol^{-1})
5-2	2	5	1.9
10-4	4	10	3.7
2-10-2	4	10	3.7
5-35-5	10	35	9.2

In addition, single ion organic inorganic triblock terpolymer (Figure II.9.A.2) was synthesized. These polymers were synthesized via nitroxide mediated polymerization (NMP) techniques. Typically, PEO-based macroalkoxamine initiator was copolymerized with both POSS acrylate and lithium-4-styrenesulfonyl(trifluoromethane sulfonyl) imide, in one pot, in dimethyl formamide at 120 °C for 24 h. After the reaction the polymer was first precipitated from diethyl ether. It was then dialysed against deionized water for 72 h and freeze dried to obtain the pure product. The composition of the polymer was determined by NMR spectra and is given in Table II.9.A.2. The composition was determined by NMR spectra. The *r* values denote the concentration of Li ion in the polymer and is given by *r* = [Li]/[EO].

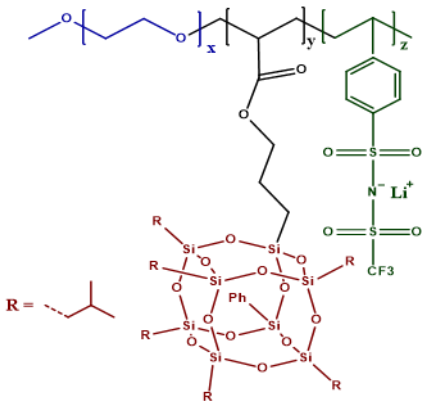

Figure II.9.A.2 Chemical structure of PEO-POSS-PSTFSILi

Table II.9.A.2 Composition of the triblock terpolymer PEO-POSS-PSTFSILi

PEO-POSS-PSTFSILi	M_{PEO} (kg mol^{-1})	M_{POSS} (kg mol^{-1})	$M_{PSTFSILi}$ (kg mol^{-1})	*r*
5-2-1	5	1.9	1	0.035
5-2-2	5	1.9	2	0.055
5-2-4	5	1.9	4	0.1
5-2-6	5	1.9	6	0.17
5-2-11	5	1.9	11	0.31

Create impurity-free lithium layers

Electrodes free of impurity layers were created by electrochemical filtering treatment. This to reduce the concentrations of impurity particles near the electrode−electrolyte interfaces in lithium symmetric cells. Lithium symmetric cells are fabricated with polystyrene-block-poly(ethylene oxide) (PS−PEO, or SEO) diblock copolymer/LiTFSI electrolytes using the method outlined in [1]. The electrolyte properties are summarized in Table II.9.A.3.

Table II.9.A.3 Properties of electrolytes used for lithium filtering study

SEO	M_{PS} (kg mol^{-1})	M_{PEO} (kg mol^{-1})	f_{EO} (kg mol^{-1})	PDI
(115-172)	115	172	0.59	1.10
(200-222)	200	222	0.51	1.08

In a newly fabricated cell, impurity particles lie at the lithium/electrolyte interface. Figure II.9.A.3a demonstrates a schematic of electrochemical filtering process carried out to remove lithium impurities. The blue blocks are lithium electrodes, the triangles are impurity particles, and brown strips are impurity-free lithium layers. At first, lithium is deposited on the bottom electrode at a constant current density. This create a layer free of impurity particles on the electrode. Next, by reversing the direction of current, lithium is plated from the bottom electrode onto the upper electrode, creating impurity-free layers on both electrodes. Figure II.9.A.3b demonstrates the current density and voltage of the treatment described in Figure II.9.A.3a during lithium deposition onto the bottom electrode, then lithium deposition onto the top electrode, as a function of time. Lithium was deposited on to the lower electrode at a low current density of 0.04 mA cm^{-2} for 43.75 hours and deposited back on to the upper electrode at the same current density for 8.75 hours. The thickness of lithium deposited on the lower electrode is 8.5 μm whereas that for the upper electrode is 1.7 μm.

Cells treated using the above method were imaged using hard X-ray microtomography. Figure II.9.A.3c shows a slice through a reconstructed volume of a symmetric cell after 14 conditioning cycles. No inhomogeneities were observed at the top nor the bottom lithium electrode/electrolyte interfaces. Figure II.9.A.3d shows slices through a reconstructed volume of the symmetric cell in Figure II.9.A.1c after an electrochemical filtering treatment. Yellow dashed lines differentiate deposited impurity-free lithium after the treatment from the original bulk lithium electrode. Impurity particles are visibly pushed away from the electrode−electrolyte interface, resulting in a void defect. Figure II.9.A.3e shows slices through a different area of the cell shown in Figure II.9.A.3c and Figure II.9.A.3d. Yellow dashed lines in this figure also indicate the calculated height of filtered lithium after the treatment. In this section, there are still impurity particles attached to the polymer electrolyte at both of the lithium−electrolyte interfaces.

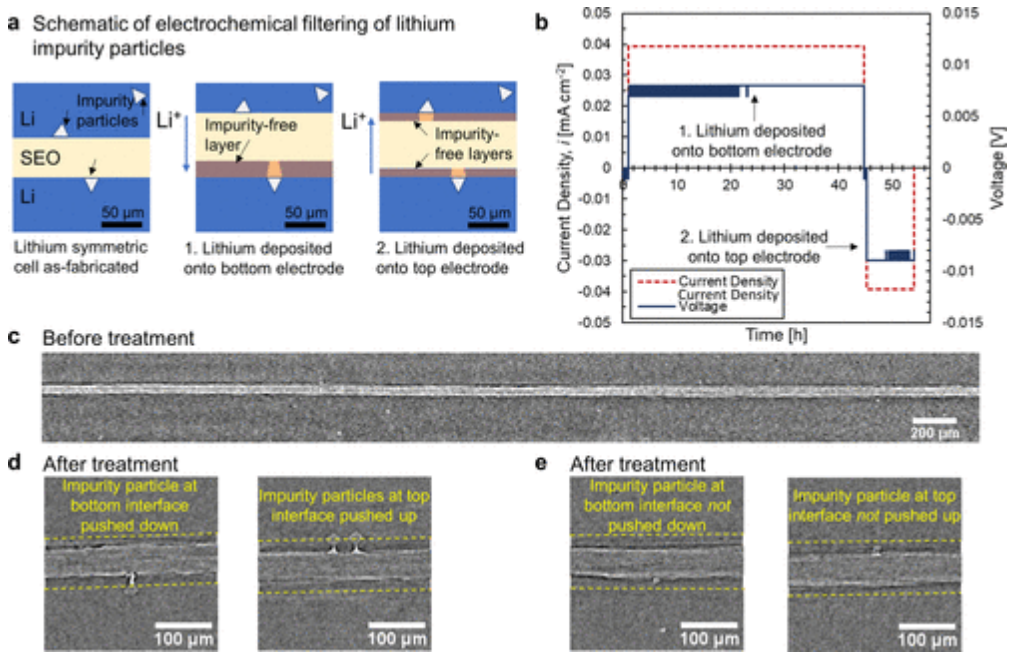

Figure II.9.A.3 Electrochemical filtering treatment to reduce the concentrations of impurity particles near the electrode/electrolyte interfaces in lithium symmetric cells. a) Schematic of electrochemical filtering of lithium impurities, b) current density and voltage of the treatment, c) slice through a reconstructed volume of a symmetric cell, d) slices through a reconstructed volume of the symmetric cell in c) after an electrochemical filtering treatment, e) slices through a different area of the cell after treatment showing impurity particles attached to the polymer electrolyte at both lithium/electrolyte interfaces. Adapted from [1].

Complete electrochemical characterization of POSS-containing block copolymer electrolytes

The polymers investigated in this study are PEO-POSS diblock and POSS-PEO-POSS triblock copolymers. All copolymers in the study have similar volume fraction of the conductive PEO block, between 0.76 to 0.80. Electrolytes are prepared by mixing PEO-POSS or POSS-PEO-POSS with lithium bis(trifluoromethanesulfonyl)imide (LiTFSI) salt.

We posit that the PEO block is the conductive phase in the copolymer whereas, the POSS block is nonconducting and provide mechanical rigidity to the electrolyte. Ionic conductivity is a complex function of both morphology of nanostructured block copolymers as well as the length of PEO block.

Figure II.9.A.4 summarizes the ionic conductivity of PEO-POSS/LiTFSI and POSS-PEO-POSS/LiTFSI mixtures. Figure II.9.A.4a shows POSS-PEO-POSS(5-35-5) ionic conductivity as a function of temperature alongside PEO(35 kg/mol) homopolymer and all organic poly(styrene)-b-poly(ethylene oxide)-b-poly(styrene) (SEOS) (5-35-5) triblock copolymer of comparable molecular weights at a salt concentration of r = [Li]/[EO] = 0.04 to 0.05. Conductivity of the hybrid organic-inorganic triblock copolymer is similar to the all-organic

triblock copolymer, and exhibits a similar trend with temperature above the melting transition of PEO block (~55 °C).

PEO-POSS(5-2), PEO-POSS(10-4), and POSS-PEO-POSS(5-35-5) ionic conductivity is plotted as a function of salt concentration and compared to PEO(10 kg/mol) homopolymer at 90 °C in Figure II.9.A.4b. The PEO domain is amorphous at this temperature and all the copolymers exhibit lamellar morphology in most of the salt concentrations. The three hybrid organic-inorganic polymer electrolytes also exhibit a similar trend, with a maximum in ionic conductivity in the proximity of r = 0.08. All block copolymers in the study exhibit ionic conductivity lower than that of the homopolymer. PEO-POSS(5-2), the lowest molecular weight copolymer, exhibits ionic conductivity below that of POSS-PEO-POSS(5-35-5) and PEO-POSS(10-4). This indicates ionic conductivity in POSS-containing block copolymers increases with overall molecular weight.

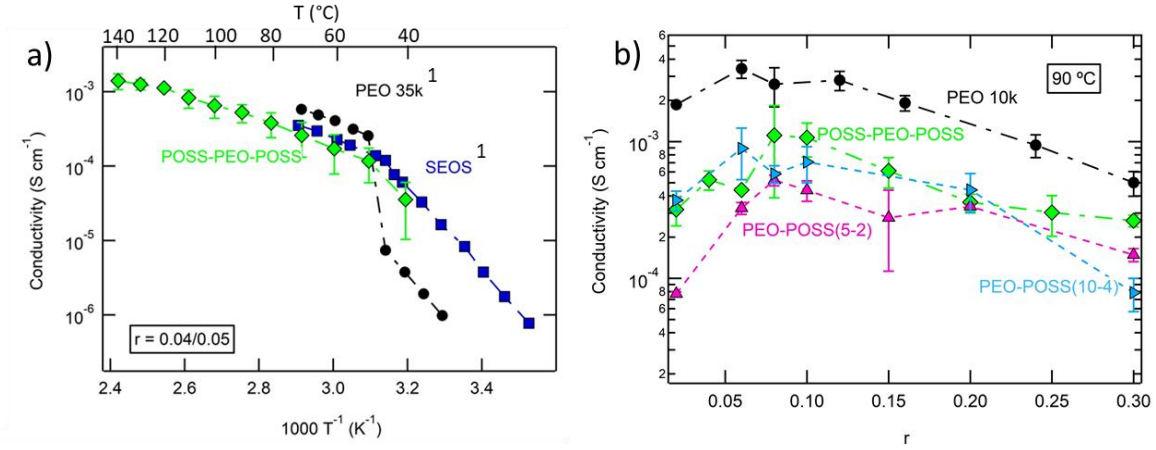

Figure II.9.A.4 Ionic conductivity of PEO-POSS, POSS-PEO-POSS/LiTFSI mixtures. a) POSS-PEO-POSS(5-35-5) ionic conductivity is plotted as a function of temperature alongside PEO(35 kg/mol)[2] and SEOS(5-35-5)[2] of comparable molecular weights at a salt concentration of r = [Li]/[EO] = 0.04 to 0.05. b) PEO-POSS(5-2), PEO-POSS(10-4), and POSS-PEO-POSS(5-35-5) ionic conductivity is plotted as a function of salt concentration and compared to PEO(10 kg/mol) at 90 °C.

Complete electrochemical characterization includes requires knowledge of two or more transport coefficients in addition to the ionic conductivity: diffusion coefficient (D) and cation current fraction (ρ_{+SS}) of the electrolytes. This allows for the prediction of salt concentration gradients across a battery electrolyte during polarization. Ideally, the electrolyte should have small salt concentration and potential gradients across the electrode at large current densities. Complete electrochemical characterization was carried out in PEO-POSS(5-2) diblock copolymer. The diffusion coefficient (D) and cation current fraction (ρ_{+SS}) calculated using ideal, dilute solution theory, are demonstrated in Figure II.9.A.5 and compared to an all organic analogous diblock copolymer, poly(styrene)-*b*-poly(ethylene oxide) (SEO) and PEO (5 kg/mol) at 90 °C. All three copolymers exhibit similar ρ_{+SS} and exhibit a similar trend with salt concentration. However, D, shown in Figure II.9.A.5b is about 2 orders of magnitude lower in PEO-POSS(5-2) than the other two polymers and exhibits weak salt concentration dependence over the salt concentration range.

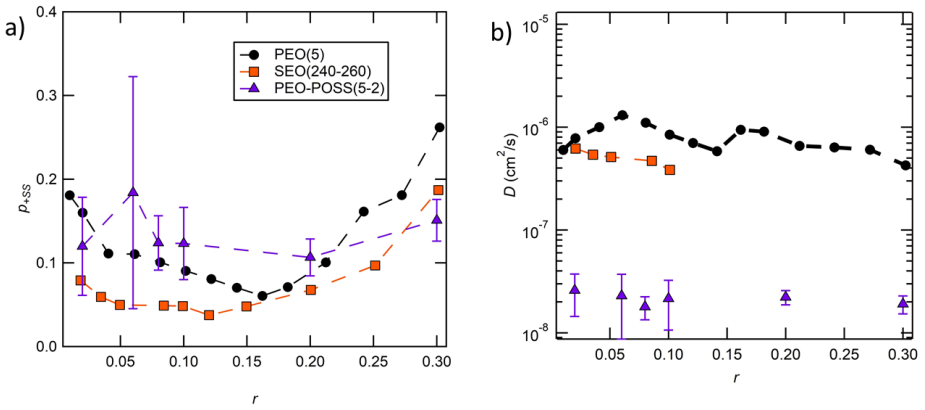

Figure II.9.A.5 Electrochemical characterization of PEO-POSS, PEO[2], and SEO[2]. a) diffusion coefficient (D), b) current fraction (ρ_{+SS}) as a function of salt concentration, r at 90 °C.

The thermodynamic factor (T_f), $1 + d\ln\gamma/d\ln m$, is calculated using the open-circuit voltage and the anion current fraction according to [4], where m is molality of salt and γ is the mean molal activity coefficient of the salt. T_f of PEO-POSS(5-2) is shown in

Figure II.9.A.6a, and increases with salt concentration. A similar trend is exhibited with PEO homopolymer [2], indicating that PEO-POSS/LiTFSI can be treated as a 2-component system. For an ideal system, T_f should be close to 1, indicating PEO-POSS is far from ideal. [4]

Figure II.9.A.6b demonstrates the full transference number, $t_{+,Ne}$ of lamellar PEO-POSS(5-2) alongside lamellar SEO of various molecular weight [3]. The two diblock copolymers exhibit $t_{+,Ne}$ between 0.20 and 0.70. While PEO-POSS exhibits a maximum at $r = 0.08$, SEO exhibits a maximum at $r = 0.30$. The results of the study show that the addition of an inorganic moiety to an organic, conductive, polymer chain does not drastically decrease $t_{+,Ne}$.

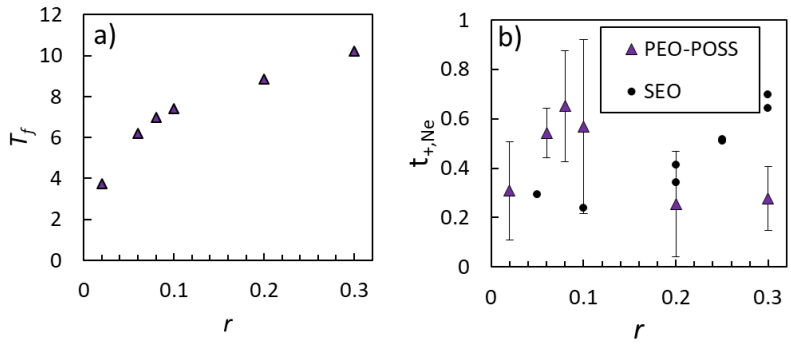

Figure II.9.A.6 a) Thermodynamic factor (Tf) and b) cation transference number (t+,Ne) in PEO-POSS(5-2) and lamellar SEO4 of varying molecular weights as a function of salt concentration, r, at 90 °C.

Cycling study for POSS-containing block copolymer electrolytes

Organic and inorganic-organic block copolymer electrolytes must account for current density effects on lithium dendrite growth when optimizing cell lifetime. One important measurement, thus, is the limiting current of the electrolyte. This measurement can be performed by electrodepositing lithium at different current densities and monitoring the current density at which the measured potential diverges.

The electrolyte in this study is a triblock copolymer, POSS-PEO-POSS (5-35-5) where the molecular weight of PEO block is 35 kg mol^{-1} and POSS block is 10 kg mol^{-1}. Three electrolyte membranes of thickness 25-30 μm were fabricated with the salt concentration of [Li]/[EO] = 0.02, 0.04, and 0.06.

Ionic conductivity using nonblocking electrodes, κ_{nb}, was measured in the three membranes by sandwiching the membrane between lithium electrodes and performing impedance spectroscopy. Temperature was varied from 70 to 110 °C. Figure II.9.A.7 demonstrates that the ionic conductivity increases with increasing temperature in all electrolytes following a Vogel- -Tamman-Fulcher type relationship, as typical with polymer electrolytes. Additionally, ionic conductivity increases with salt concentration in this salt concentration regime.

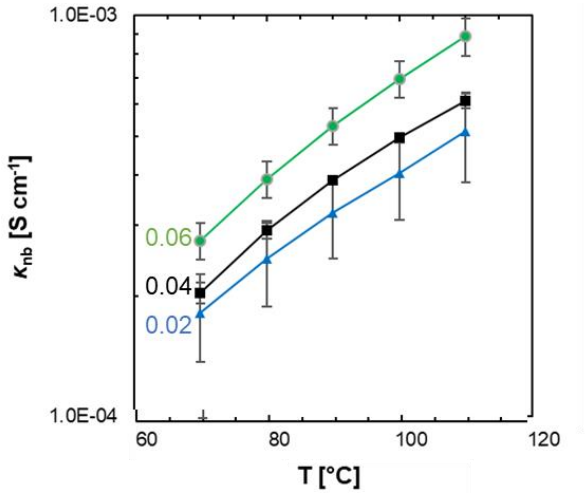

Figure II.9.A.7 Ionic Conductivity, κ_{nb}, as a function of temperature, T, in 3 POSS-PEO-POSS electrolytes at temperatures ranging from 70 °C to 110 °C.

Limiting current was measured in POSS-PEO-POSS Li-polymer-Li cells by sandwiching POSS-PEO-POSS membrane between two Li electrodes and cycling at different current densities. In Figure II.9.A.8, a routine used to test limiting current measurements is shown. The POSS-PEO-POSS hybrid triblock electrolyte showed an exceptionally high limiting current between 1.8 and 5.7 mA cm^{-2} for a membrane of 25-30 µm thickness within the experimental salt concentration regime, demonstrated in Figure II.9.A.9.

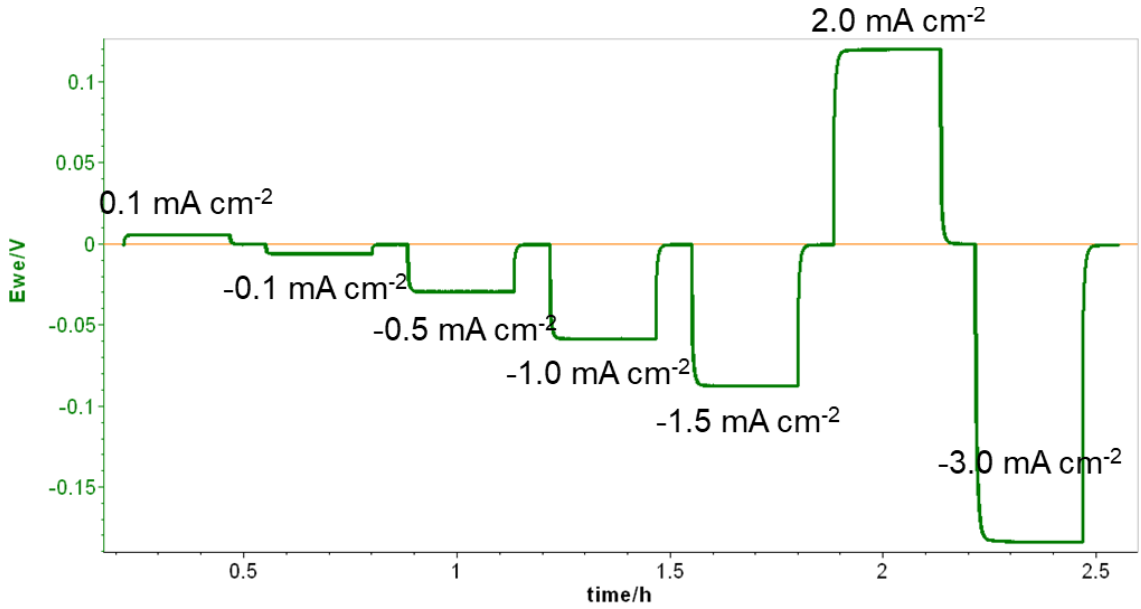

Figure II.9.A.8 Example of a routine used to test the limiting current of POSS-PEO-POSS (5-35-5) at salt concentration [Li]/[EO] = 0.04. This 30-micron thick solid hybrid organic-inorganic polymer electrolyte was sandwiched between two lithium electrodes and polarized to electrodeposit Li from one electrode to the other. The current density was increased systematically until the potential diverged or the cell short-circuited.

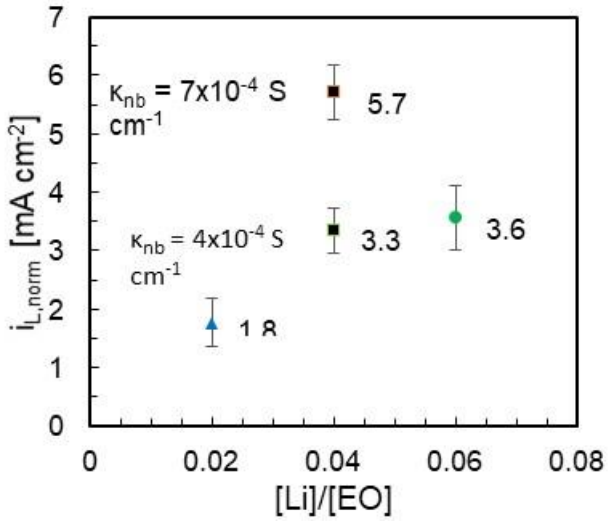

Figure II.9.A.9 Limiting current ($i_{L,norm}$) measurements in 3 POSS-PEO-POSS electrolytes. Error bars indicate standard deviation from 3 experiments. All measurements were performed at 90 °C. Ionic conductivity measured using non-blocking electrodes (κ_{nb}) is indicated on the left of data points of multiple batches at [Li]/[EO] = 0.04.

To ensure the lithium interface is stable during limiting current measurements, the interfacial resistance was measured before and after the experiment. The interfacial impedance doesn't change before and after limiting current measurements, as shown in Figure II.9.A.10.

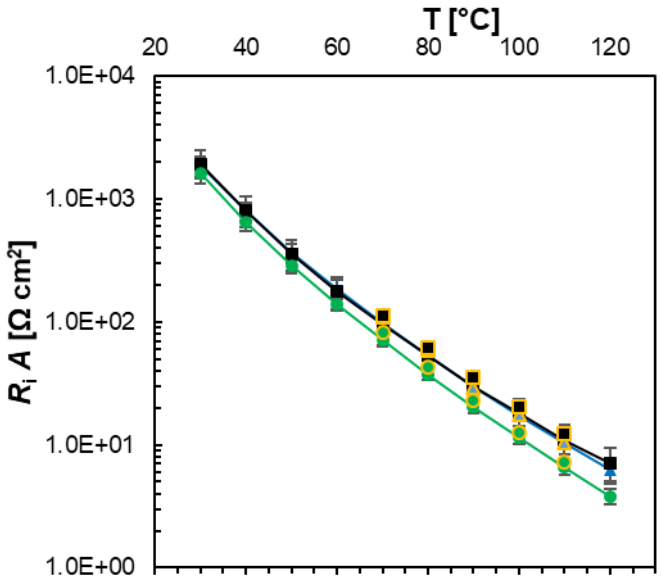

Figure II.9.A.10 Interfacial resistance multiplied by area (Ri*A) measurements in 3 POSS-PEO-POSS electrolytes before and after limiting current measurements, indicating a stable interface during measurements. Error bars indicate standard deviation from 3 experiments.

The POSS-PEO-POSS hybrid triblock electrolyte (r = 0.02 to 0.06) showed an exceptionally high limiting current between 1.8 and 6 mA cm^{-2} for a membrane of 25-30 µm thicknesses. Additionally, the polymers exhibit stability against lithium metal after cycling experiments. The operating current density is an important factor in the lifetime of lithium symmetric cells with solid polymer electrolytes.

Conclusions

In the present research, the stability of hybrid organic-inorganic copolymer electrolyte against lithium metal has been investigated. The major conclusions are summarized below:

1. A variety of diblock and triblock organic inorganic hybrid copolymers with different chain lengths and PEO volume fraction were synthesized successfully. Furthermore, we demonstrated the covalent incorporation of single ion conducting chains within such hybrid electrolytes.

2. The electrochemical filtering technique is employed to remove impurities from polymer/electrode interface. This is a simple procedure to plate planar clean lithium at a low current density to use the electrolyte to “filter” out impurity particles.

3. Complete electrochemical characterization of diblock PEO-POSS (5-2) was carried out.

4. The hybrid triblock electrolyte demonstrated an exceptionally high limiting current between 1.8 and 6.0 mA cm^{-2} for a membrane of 30 µm thickness and salt concentration of [Li]/[EO] = 0.02 to 0.06. For the first time, we were able to experimentally achieve the estimated limiting current of 4.5 mA cm^{-2} based on Monroe and Newman’s model.

Key Publications

1. Frenck, L., Sethi, G. K., Maslyn, J. A., Balsara, N. P. "Factors That Control the Formation of Dendrites and Other Morphologies on Lithium Metal Anodes". *Frontiers in Energy Research*, 2019. 7:115.

2. Maslyn, J. A., Frenck, L., Loo, W. S., Parkinson, D. Y., Balsara, N. P. "Extended Cycling through Rigid Block Copolymer Electrolytes Enabled by Reducing Impurities in Lithium Metal Electrodes". *ACS Applied Energy Materials*, 2019. 2, 8197-8206.

3. Chakraborty, S., Jiang, X., Hoffman, Z., Sethi, G.K., Balsara, N.P. and Villaluenga, I., 2020. “Reversible Changes in the Grain Structure and Conductivity in a Block Copolymer Electrolyte”. *Macromolecules*.

4. Maslyn, J.A., McEntush, K.D., Harry, K.J., Frenck, L., Loo, W.S., Parkinson, D.Y. and Balsara, N.P., 2020. “Preferential Stripping of a Lithium Protrusion Resulting in Recovery of a Planar Electrode.” *Journal of The Electrochemical Society*, *167*(10), p.10055

References

1. Maslyn, Jacqueline A., et al. "Extended Cycling through Rigid Block Copolymer Electrolytes Enabled by Reducing Impurities in Lithium Metal Electrodes." *ACS Applied Energy Materials* 2.11 (2019): 8197-8206.

2. Bouchet, R., et al. "Charge transport in nanostructured PS–PEO–PS triblock copolymer electrolytes." *Macromolecules* 47.8 (2014): 2659-2665.

3. Villaluenga, Irune, et al. "Negative Stefan-Maxwell diffusion coefficients and complete electrochemical transport characterization of homopolymer and block copolymer electrolytes." *Journal of The Electrochemical Society* 165.11 (2018): A2766.

4. Galluzzo, Michael D., et al. "Measurement of Three Transport Coefficients and the Thermodynamic Factor in Block Copolymer Electrolytes with Different Morphologies." *The Journal of Physical Chemistry B* 124.5 (2020): 921-935.

II.9.B Lithium Thiophosphate Based Solid Electrolytes and Cathode Interfaces

Jagjit Nanda, Principal Investigator
Oak Ridge National Laboratory
1 Bethel Valley Road
Oak Ridge, TN, 37831
E-mail: nandaj@ornl.gov

Tien Duong, DOE Technology Development Manager
U.S. Department of Energy
E-mail: Tien.Duong@ee.doe.gov

Start Date: October 1, 2019 End Date: September 30, 2020
Project Funding: $450,000 DOE share: $450,000 Non-DOE share: $0

Project Introduction

Advances in solid electrolytes (SEs) with superionic conductivity and stable electrode/electrolyte interfaces are key enablers for all solid-state batteries (SSBs) to meet the energy density and cost targets for next generation batteries for electric vehicles. Interfacial reactions between thiophosphate SE and cathode active materials in SSBs are not well-understood. Key deliverables of this project include: (i) synthesis of lithium thiophosphate solid electrolytes with high Li^+ conductivity using low temperature (<350°C) solvent-mediated routes and (ii) combine electrochemical measurements with complementary *in situ* and *ex situ* spectroscopy and microscopy to identify decomposition reaction products at the cathode/electrolyte interface. In this multi-year work, the team will investigate several solid electrolytes [e.g., Li_3PS_4 (LPS), $Li_{10}GeP_2S_{12}$ (LGPS), and $Li_{9.54}Si_{1.74}P_{1.44}S_{11.7}Cl_{0.3}$ (LSiPCl)] followed by fabrication and electrochemical performance evaluation of solid-state cells using different class of composite cathodes [e.g., $LiFePO_4$ (olivine), FeS_2 (sulfide-based conversion cathode), and $LiNi_xMn_yCo_{1-x-y}O_2$ (NMC, layered oxide)]. Ultimately, this work will enable a mechanistic understanding of factors that limit the rate performance and cyclability of SSBs.

Objectives

1. Identify synthesis, doping, and processing conditions to prepare Li_3PS_4 family of solid electrolytes with Li^+ conductivity exceeding 10^{-4} S/cm at room temperature.
2. Develop binder systems for Li_3PS_4 family of solid electrolytes for improving processability and stability at the Li metal and cathode interfaces.
3. Design, fabricate, and test solid-state cells using Li_3PS_4 family of solid electrolytes and composite lithium-ion cathodes.
4. Undertake spectroscopic and microscopic studies including cryo-TEM and solid-state NMR for characterizing Li_3PS_4 and cathode-Li_3PS_4 interfaces.

Approach

Low-temperature (< 350°C) solvent-mediated synthesis routes were used to prepare lithium thiophosphate solid electrolytes. The structures of key intermediates and final products (e.g., *ß*-Li_3PS_4) were characterized using a suite of methods including X-ray diffraction (XRD), vibrational spectroscopy, solid-state nuclear magnetic resonance (ssNMR) spectroscopy, and X-ray photoelectron spectroscopy (XPS). Standard AC/DC electrochemical methods were used to characterize the Li^+ conductivity of solid electrolytes, and an *in-situ* load cell was designed to monitor internal stresses generated during SSB charge/discharge cycling.

Results

Investigation of Complex Intermediates in Solvent Mediated Synthesis of Li-P-S Solid-State Electrolytes

Solvent mediated synthesis (also known as solvent suspension synthesis) of Li_2S-P_2S_5 glass and glass-ceramic superionic thiophosphates offers a means for high-volume, low-cost production of solid-state battery electrolytes. Typically, this synthetic approach utilizes organic solvents in which the reactants Li_2S and P_2S_5 are virtually insoluble. Nevertheless, milled/mixed slurries containing Li_2S and P_2S_5 yield solvent complexes of Li_3PS_4 and $Li_7P_3S_{11}$ superionic conductors through the precipitation of (PS_4^{-3}) anionic/polyanionic salts. The coupling, coordination, orientation and lattice disposition of these (PS_4^{-3}) tetrahedra are highly dependent on the ratio of the reactants (Li_2S and P_2S_5), the organic solvent, the mixing/milling protocol, and the subsequent thermal processing. The resulting wide variation in microstructure has led to a broad range (typically several orders of magnitude) of reported ionic conductivities for thiophosphate solid electrolytes prepared by solvent mediation. It has been reported that Li_2S : P_2S_5 mixtures (molar ratio 1:1) form soluble solvate complexes in acetonitrile (AN) and EP solvents, and these complexes react with excess Li_2S to precipitate the above (PS_4^{3-}) anionic/polyanionic salts. To reproducibly control the synthesis of highly conducting lithium thiophosphate solid electrolytes, we evaluated the role of the solvent and corresponding soluble intermediate solvate complexes during synthesis. We utilized various materials characterization methods including: (i) Raman spectroscopy to identify the soluble anionic/polyanionic solvate complexes and resulting insoluble anionic/polyanionic products after precipitation and thermal processing, (ii) XPS to establish changes in oxidation state and Li-P-S bonding environments, and (iii) XRD to evaluate the materials' crystallinity.

Figure II.9.B.1a shows Raman spectra of the solution phase Li_2S:P_2S_5 (molar ratio 1:1) solvate complexes in AN, MA, EA, EP, DME, TEGDME, and THF. Figure II.9.B.1a also shows the Raman spectra of solid precipitates in the DME and THF vials. Interestingly, all solvate complexes and solid precipitates exhibit the same primary Raman band centered at 391 ± 2 cm^{-1} with the same additional secondary peaks corresponding to the stretching and bending frequencies of the $P_2S_6^{2-}$ anion. We also note that solvation of this anion can only account for very small shifts in these characteristic frequencies. The Raman peaks corresponding to each solvent (not shown here) are generally are much weaker than those of the solvated $Li_2P_2S_6$.

Figure II.9.B.1b shows: a) the Raman spectra for the solution phase solvate complex in AN, b) the same complex vacuum dried at 140 °C for 24 h, (this complex still contained about 3 wt% strongly coordinated AN), c) the same complex heated to 270 °C to remove the remaining AN, and d) the Raman spectra of sample c) re-dissolved in AN. The Raman shift at 423 cm^{-1} is assigned to the symmetric stretch of the P-S-P-S ring for crystalline $Li_2P_2S_6$ (reported in the literature at 421 cm^{-1}). However, this band is also very close to the 422 cm^{-1} characteristic shift for PS_4^{3-}. Furthermore, the 390 cm^{-1} band shown in all solution phases complexes is very close to the 385 cm^{-1} characteristic shift for $P_2S_6^{4-}$ in $Li_4P_2S_4$. To ensure accurate assignment of the Raman bands, additional XRD and XPS measurements were performed.

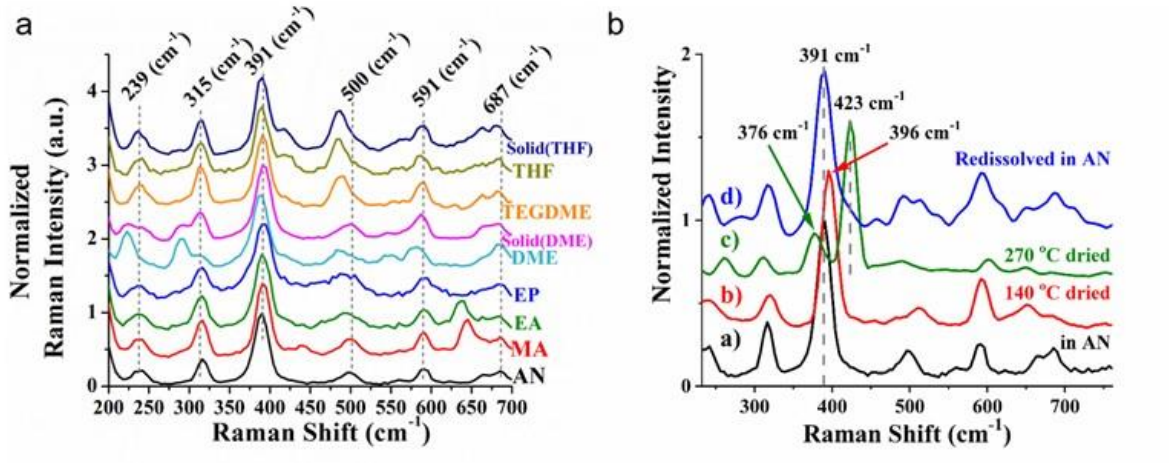

Figure II.9.B.1 (a) Raman spectra of the solution phase Li2S:P2S5 (molar ratio 1:1) solvate complexes in AN, MA, EA, EP, DME, TEGDME, and THF; and the solid precipitates in the DME and THF vials. Samples prepared in DME and THF contained two liquid phases in addition to the solid phases. For these samples, the Raman spectra are shown for the higher density of the two liquid phases. (b) Raman spectra of Li2S:P2S5 (molar ratio 1:1) reaction products mediated from an AN solution.

Figure II.9.B.2a shows XRD patterns of the same solvate complexes described in Figure II.9.B.1b. These results indicate that the solvate complex dried at 140°C was completely amorphous but heating this powder to 270°C induced crystallization of $Li_2P_2S_6$. Therefore, for the sample dried at 270 °C, the Raman shift at 423 cm^{-1} is assigned to the ν(P-S_b) stretch in the $P_2S_6^{2-}$ polyanion (S_b denotes a bridging sulfur atom). Figure II.9.B.2b and c show XPS spectra for the same solvate complexes. The P 2p and S 2p spectra were normalized with respect to the maximum intensity of each core level for ease of comparison. The P 2p and S 2p spectra were very similar for the samples processed at 140 °C and 270 °C. This result indicates that the S and P in the amorphous sample (140 °C) had similar local bonding environments compared to that of the crystalline $Li_2P_2S_6$ sample (270 °C), thus eliminating consideration of $Li_4P_2S_6$ as a reaction product.

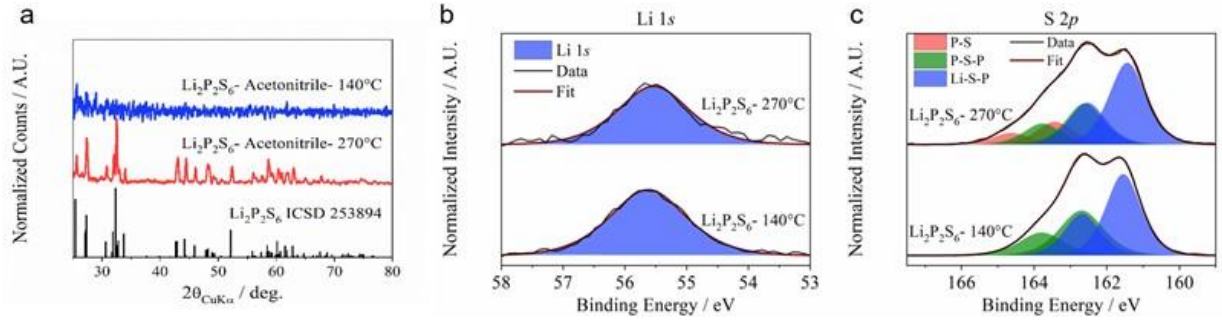

Figure II.9.B.2 (a) XRD patterns and (b-c) XPS spectra of $Li_2P_2S_6$ prepared from an AN solution and heated at 140°C (amorphous) and 270°C (crystalline) showing (b) Li 1s and (c) S 2p core-level spectra.

Overall, this work demonstrates that, over a large range of solvents, the mediated reaction of Li_2S and P_2S_5 proceeds through a single universal intermediate described as a lithotrophic tautomer of the $P_2S_6^{2-}$ anion and characterized by a primary Raman band at 391± 2 cm^{-1} in all solvents. This intermediate serves as the gateway to several key lithium thiophosphate glass and glass-ceramic superionic conductors (e.g., Li_3PS_4 and $Li_7P_3S_{11}$) as shown in Figure II.9.B.3.

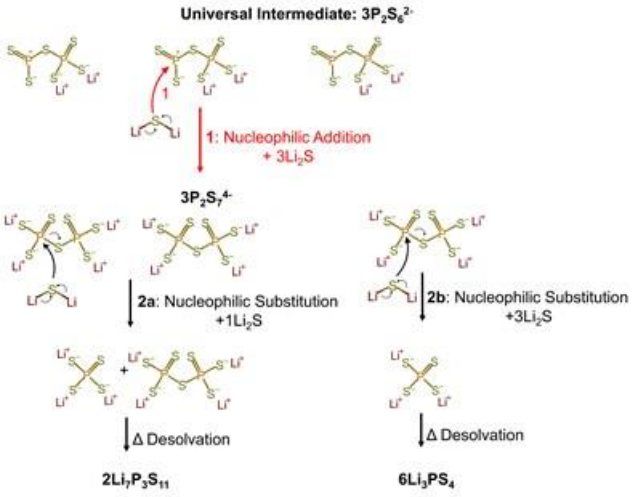

Figure II.9.B.3 Proposed reaction mechanism for solvent mediated synthesis of Li_2S-P_2S_5 glass and glass-ceramic solid electrolytes from a solvated $P_2S_6^{2-}$ intermediate. For graphic clarity and charge balance, we show the Li^+ cation and $P_2S_6^{2-}$, $P_2S_7^{4-}$, and PS_4^{3-} anions uncoordinated with solvent. Each reaction sequence is written to stoichiometric completion. However it is likely that several reactions can occur simultaneously in parallel and in series, and a distribution of products may result.

Synthesis and Characterization of Amorphous Li_3PS_4/PEO Composite Solid Electrolytes

To improve the processability of sulfide-based SEs, our team focused on development of Li_3PS_4/poly(ethylene oxide) (PEO) composites using a one-pot solvent-mediated synthesis route. Here, the Li_3PS_4 was synthesized *in-situ* by blending Li_2S, P_2S_5, and PEO (600 kDa) in AN followed by vacuum drying and thermal treatment steps. Li_3PS_4/PEO composites with 0.2 – 56 wt.% PEO were almost entirely amorphous even after annealing at temperatures up to 250°C as determined using XRD (results not shown). Cryo-TEM measurements in Figure II.9.B.4a confirmed that the composites contained no nanocrystalline ß-Li_3PS_4, but samples had small domains (<50 nm) indexed to trace crystalline Li_2S (see fast-Fourier transform (FFT) inset in Figure II.9.B.4a).

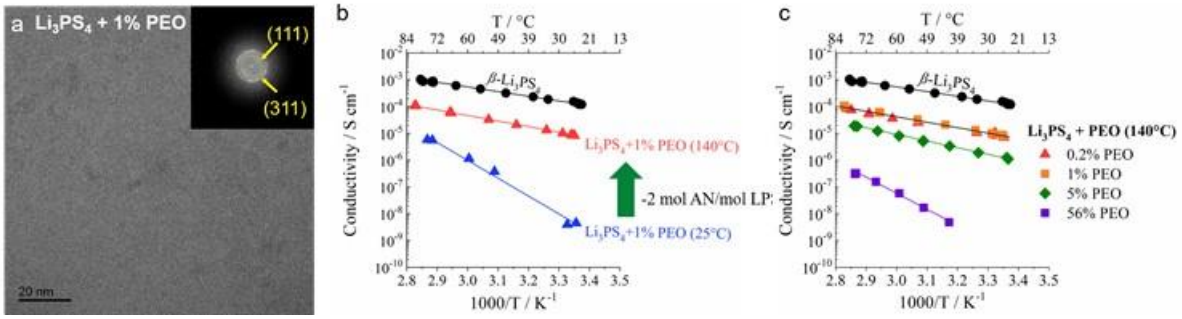

Figure II.9.B.4 (a) Cryo-TEM image of a composite solid electrolyte containing amorphous Li_3PS_4 + 1 wt.% PEO. (b-c) Li^+ conductivity measurements of ß-Li_3PS_4 and Li_3PS_4+PEO composites showing (b) Li_3PS_4 + 1 wt.% PEO dried at 25 and 140 °C and (c) Li_3PS_4 + PEO composites containing 0.2-56 wt.% PEO dried at 140°C.

The Li^+ conductivities of crystalline ß-Li_3PS_4 and amorphous Li_3PS_4 + PEO composites were evaluated in a blocking cell configuration using AC impedance spectroscopy. As shown in Figure II.9.B.4b, the crystalline ß-Li_3PS_4 exhibited high Li^+ conductivity (*e.g.*, 1.2 x 10^{-4} S/cm at room temperature) with an activation energy of 0.36 eV, values which are in good agreement with previous reports on the crystalline polymorph. In comparison, the ionic conductivity of the polymer/ceramic composites varied greatly depending on the thermal treatment. For instance, after drying under vacuum at 25 °C, the conductivity of Li_3PS_4 + 1% PEO was 5 orders of magnitude lower than that of ß-Li_3PS_4 (*e.g.*, 4.5 x 10^{-9} S/cm at room temperature) due to the presence of coordinated AN. After heating to 140 °C, the material evolved ~2 mol AN/mol Li_3PS_4 (corresponding to ~30 wt.% loss), and the ionic conductivity increased 3 orders of magnitude at room temperature (*i.e.*, from 4.5

x 10^{-9} to 8.4 x 10^{-6} S/cm). The higher conductivity coincided with a lower activation energy (1.37 vs. 0.45 eV for samples dried at 25 and 140 °C, respectively), indicating the coordinated AN hindered Li^+ mobility and provided a less favorable energy landscape for long-range Li^+ migration.

Figure II.9.B.4c shows the Li^+ conductivity of Li_3PS_4 + PEO composites heated at 140 °C as a function of polymer content. Samples with 0.2 and 1 wt.% PEO exhibited identical conductivities and activation energies within experimental error. Increasing the PEO content from 1 to 5 wt.% slightly decreased the conductivity (*e.g.*, 1.1 x 10^{-6} S/cm at room temperature) due to the insulating nature of PEO. As expected, higher PEO loading resulted in even lower conductivity, and the sample with 56 wt.% PEO could only be measured at elevated temperature (*e.g.*, 4.8 x 10^{-9} S/cm at 42 °C) due to its high resistance. Based on these findings, the polymer content in amorphous Li_3PS_4 + PEO composites should be limited to ca. 1 – 5 wt.% to ensure reasonable ionic conductivity while providing enough binder to facilitate processing. Overall, the solvent-mediated synthesis approach developed here can be applied to a wide range of composite sulfide-based SEs where the material structure and electrochemical properties can be tuned by modifying key processing variables (*e.g.*, solvent, mixing protocol, binder content, and thermal post-treatment).

A suite of materials characterization methods was employed to understand how different thermal treatments affected the local structure of Li_3PS_4-based solid electrolytes. Figure II.9.B.5a presents Raman spectra of *ß*-Li_3PS_4 and amorphous Li_3PS_4 + 1% PEO composites after thermal treatments up to 250 °C. As expected, the *ß*-Li_3PS_4 showed a single peak at 427 cm^{-1} which is assigned to a P-S stretch in the structure's isolated PS_4^{3-} tetrahedra. In comparison, the unheated composite showed several Raman-active bands in the range 100 – 600 cm^{-1}. The bands at 395 and 435 cm^{-1} are assigned to P-S vibrational modes of the $P_2S_6^{2-}$ and PS_4^{3-} polyanions, respectively. The Raman spectra of Li_3PS_4 + 1 wt.% PEO exhibited subtle changes in the range 390 – 430 cm^{-1} upon heating due to rearrangement of the polyanionic network. More specifically, heating at 140 – 200 °C resulted in a new band at 408 cm^{-1} (attributed to formation of $P_2S_7^{4-}$ polyanions) and increased intensity ~430 cm^{-1} (attributed to PS_4^{3-}). Compounds with these polyanionic structures (e.g., *ß*-Li_3PS_4 and $Li_7P_3S_{11}$) typically exhibit higher Li^+ conductivity compared to structures containing $P_2S_6^{2-}$ (e.g., $Li_2P_2S_6$) which was the predominant moiety in the unheated sample. This finding is consistent with the conductivity measurements (Figure II.9.B.4b and c) which showed that annealing Li_3PS_4 + 1% PEO at 140°C increased the material's Li^+ conductivity by several orders of magnitude.

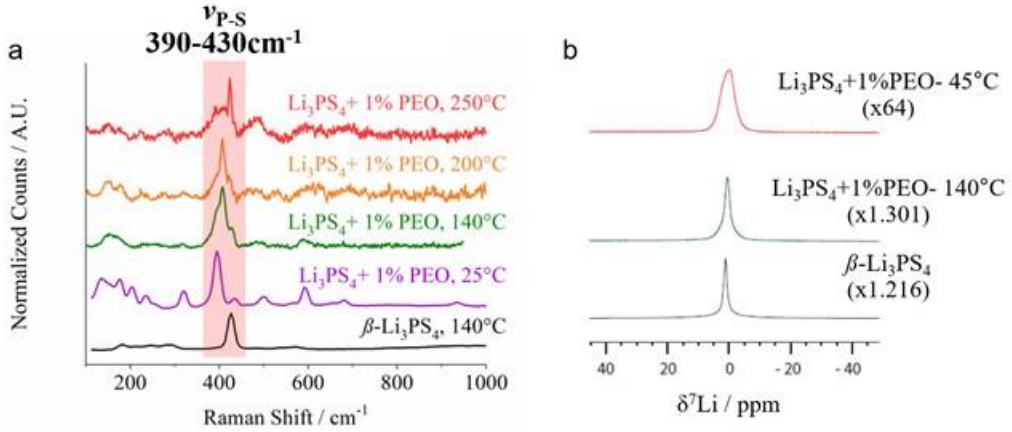

Figure II.9.B.5 (a) Raman spectra and (b) ^{7}Li ssNMR spectra of ß-Li_3PS_4 and amorphous Li_3PS_4+1% PEO solid electrolytes prepared through solvent-mediated routes. In (b), the materials exhibited significantly different peak intensities and thus have been linearly scaled to facilitate direct comparisons. All ssNMR spectra are referenced to lithium triflate (δ = 0 ppm).

To complement the Raman measurements in Figure II.9.B.5a, the near-surface structures of Li_3PS_4 + 1% PEO and *ß*-Li_3PS_4 were studied using XPS, and core-level S 2p, P 2p, and Li 1s spectra are provided in Figure II.9.B.6a, b, and c, respectively. The S 2p and P 2p spectra of *ß*-Li_3PS_4 showed doublets due to $2p_{1/2}$ and $2p_{3/2}$ spin-orbit splitting where the components were separated by 1.1 and 0.9 eV for S 2p and P 2p, respectively.

These features indicate a single type of P-S bonding environment was present in ß-Li_3PS_4 (*i.e.*, isolated PS_4^{3-} tetrahedra). In comparison, the amorphous Li_3PS_4 + 1% PEO samples showed significantly broader signal in the S 2p spectra with additional features at 162.6 – 163.7 eV which are assigned to $P_2S_6^{2-}$ and $P_2S_7^{4-}$ polyanion structures that contain bridging S atoms. Notably, the sample annealed at 140 °C contained more $P_2S_7^{4-}$ and less $P_2S_6^{2-}$ compared to the unheated sample which is consistent with the Raman findings. On the other hand, the P 2p spectra of the composites were very similar to that of the ß-Li_3PS_4 which may be due to similar 2p binding energies of phosphorus in different polyanion structures (*e.g.*, PS_4^{3-} vs. $P_2S_7^{4-}$), thus making it difficult to resolve these subunits. The Li 1s spectra of the composites were broader and shifted by +0.2 eV compared to ß-Li_3PS_4 which indicates the amorphous Li_3PS_4 contained a wider distribution of local Li-P-S bonding environments which led to their lower Li^+ conductivity as reported in Figure II.9.B.4b and c.

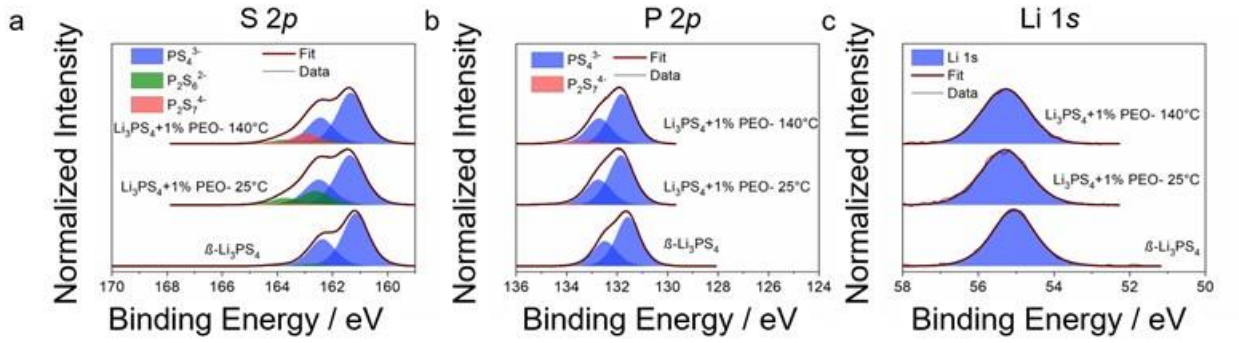

Figure II.9.B.6 XPS analysis showing core-level scans of (a) S 2p, (b) P 2p, and (c) Li 1s for ß-Li_3PS_4 and amorphous Li_3PS_4 + 1 wt.% PEO dried overnight at 25 and 140 °C. Compared to ß-Li_3PS_4, the amorphous composites contained a broad distribution of Li-P-S bonding environments which resulted in lower Li^+ conductivity.

The structure of several sulfide SEs developed in this program were also evaluated using ssNMR spectroscopy in collaboration with Prof. Steve Greenbaum's team at Hunter College. Figure II.9.B.5b shows ^7Li NMR spectra of crystalline ß-Li_3PS_4 and amorphous composites containing Li_3PS_4+1% PEO. All samples exhibited a single peak centered at 0 ppm. After annealing Li_3PS_4+1%PEO at 140°C to remove coordinated AN, the ^7Li peak width decreased substantially which correlates with higher Li^+ cation mobility. This finding is consistent with ionic conductivity measurements (Figure II.9.B.4b and c). $^7Li/^1H$ cross-polarization NMR measurements are underway to better understand the influence of coordinated solvent and PEO binder on the Li^+ dynamics and local bonding environment. These findings will be reported in FY21. Combining NMR measurements with other characterization methods (e.g., vibrational spectroscopy, X-ray/neutron scattering, and electrochemical testing) is critical to establish structure/function correlations for sulfide SEs produced via solvent-mediated routes.

SSB Fabrication and Testing

Our team developed an experimental setup to benchmark the performance of SSBs containing a ß-Li_3PS_4 solid electrolyte, Li metal anode (~45 µm thick on Cu foil), and $LiNi_{0.8}Mn_{0.1}Co_{0.1}O_2$ (NMC811) cathodes (with and without a 1 wt% $LiNbO_3$ coating). The cells were constructed by cold-pressing tri-layer Li|ß-Li_3PS_4|cathode pellets (diameter ½", thickness ~1 mm) in a PEEK cell. The SSBs were tested at room temperature using a stack pressure of 5 MPa, and internal stresses during cycling were monitored using an *in-situ* load cell. Figure II.9.B.7 shows galvanostatic charge/discharge curves for cells containing a Li metal anode and NMC811-based cathodes. When cycled in a conventional liquid electrolyte (Figure II.9.B.7a), the composite cathodes (80 wt% active material, 10 wt% carbon black, and 10 wt% PVDF binder) showed the expected performance (e.g., reversible capacities ~200 mAh/g, an average discharge voltage ~3.7 V vs. Li/Li^+, and coulombic efficiencies of 86 and >99.9% during the 1st and 2nd cycles, respectively). In comparison, SSBs containing composite cathodes (60 wt.% active material, 30 wt.% ß-Li_3PS_4, 8 wt% carbon black, and 2 wt.% carbon nanofibers) exhibited significantly lower capacity and efficiency as shown in Figure I.1.A.7b. During the first charge, an irreversible oxidative process occurred ~3-3.5 V vs. Li/Li^+ (attributed to ß-Li_3PS_4 decomposition) followed by

a sloping plateau to 4.3 V vs. Li/Li$^+$ (attributed to Li$^+$ deintercalation from NMC811). Although a high charge capacity was attained (~200 mAh/g), the reversible capacity was only ~100 mAh/g, corresponding to an initial coulombic efficiency ~50%. Subsequent cycles exhibited higher coulombic efficiencies (~95%) but suffered from gradual capacity fade and increasing voltage hysteresis. Application of a $LiNbO_3$ coating, which has been widely reported in the SSB literature, had little impact on the capacity and cyclability of the NMC811 cathode. Interestingly, the stack pressure systematically increased/decreased ($|\Delta P|/P \sim 0.15$) during charge/discharge due to internal stresses generated within the cathode and/or Li anode (results not shown here). The effect of different nominal stack pressures (e.g., 0.1 – 50 MPa) and cathode chemistries on the mechanical stress profile will be reported in FY21.

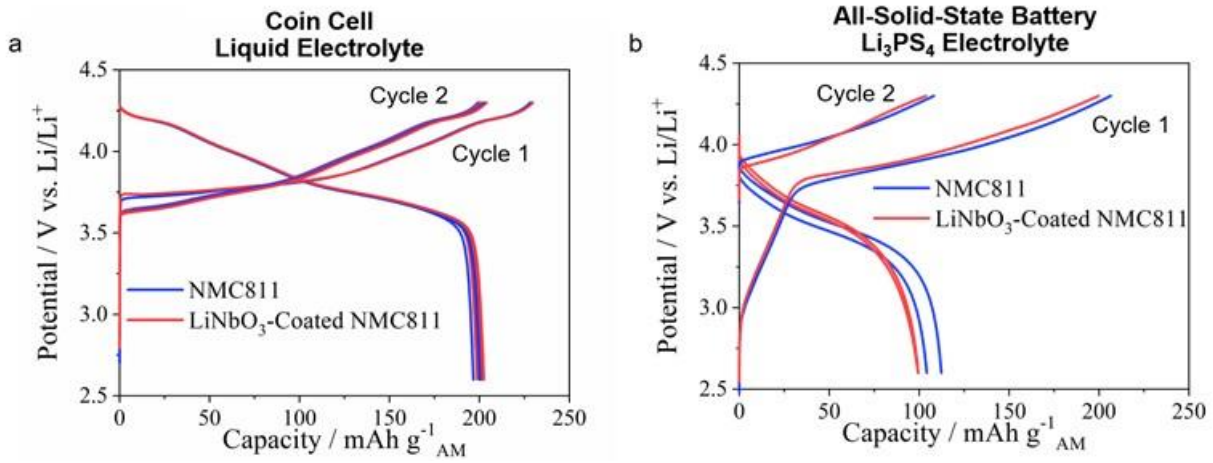

Figure II.9.B.7 Galvanostatic charge/discharge curves for the first 2 cycles of NMC811 with and without a 1 wt% $LiNbO_3$ coating in (a) coin cells containing a liquid electrolyte (1.2 M $LiPF_6$ in 3/7 EC/EMC w/w) and (b) SSBs containing a ß-Li_3PS_4 solid electrolyte using the setup shown in Figure II.9.A.10. The solid electrolyte and cathode active materials were obtained from NEI Corp. All cycling experiments were conducted at room temperature at a specific current of 10 mA/$g_{active\ material}$. The active material loading in (a) and (b) were 3.6 and 6.6 mg/cm^2, respectively.

Conclusions

Solvent mediated synthesis offers a means for high-volume, low-cost production of thiophosphate superionic conductors for SSBs. Historically, this synthetic approach has led to a wide range of electrolyte properties attributed to various reaction mechanisms and intermediates influenced by specific mediating solvents. This report demonstrates that, over a large range of solvents, the mediated reaction of Li_2S and P_2S_5 proceeds through a single universal intermediate described as a lithotrophic tautomer of the $P_2S_6^{2-}$ anion and characterized by a primary Raman band at 391± 2 cm^{-1} in all solvents. This intermediate serves as the gateway to several key lithium thiophosphate glass and glass-ceramic superionic conductors including Li_3PS_4 and $Li_7P_3S_{11}$.

Our team also investigated the effects of different solvents, polymer binders, and thermal treatments on the structure and Li$^+$ conductivity of Li_3PS_4 solid electrolytes prepared through solvent mediated synthesis routes. Conducting the synthesis in THF resulted in crystalline ß-Li_3PS_4 whereas AN led to amorphous Li_3PS_4. Annealing at 140 °C increased the Li$^+$ conductivity of an amorphous composite (Li_3PS_4 + 1 wt.% PEO) by 3 orders of magnitude (e.g., from 4.5 x 10^{-9} to 8.4 x 10^{-6} S/cm at room temperature) due to: (i) removal of coordinated solvent and (ii) rearrangement of the polyanionic network to form $P_2S_7^{4-}$ and PS_4^{3-} moieties. The PEO content in these composites should be limited to 1 – 5 wt.% to ensure reasonable Li$^+$ conductivity (e.g., up to 1.1 x 10^{-4} S/cm at 80 °C) while providing enough binder to facilitate scalable processing. The results of this study highlight a new strategy to suppress crystallization in sulfide-based solid electrolytes which has important implications for SSBs.

SSBs containing NMC811 cathodes, ß-Li_3PS_4 solid electrolyte, and Li metal anodes (~45 µm on Cu foil) were fabricated and tested. When tested at room temperature under moderate stack pressures (5 MPa), these SSBs

exhibited high initial charge capacities ~200 mAh/$g_{active\ material}$ but suffered from low coulombic efficiency (e.g., 50% during the first cycle) due to irreversible oxidation of *ß*-Li_3PS_4. Application of an interfacial buffer layer (1 wt.% $LiNbO_3$) to the cathode particles had little impact on the SSB cycling performance. Experiments in FY21 will explore various cathode compositions (e.g., different classes of active materials and solid electrolytes) to improve integration of sulfide SEs into high energy SSBs. Effects of key testing parameters (e.g., stack pressure and temperature) on cell performance will also be investigated. These fundamental electrochemical investigations will be paired with *in-situ* and *ex-situ* Raman and Kelvin-probe force microscopy measurements to identify how the cathode/SE interface and interphase layers evolve during cycling.

Key Publications

1. E. C. Self*, Z. D. Hood*, T. Brahmbhatt, F. M. Delnick, H. M. Meyer III, G. Yang, J. L. M. Rupp, J. Nanda, A New Class of Amorphous Sulfide-Based Solid Electrolytes: Synthesis, Characterization, and Electrochemical Properties, Chem. Mater. 2020, 32, 8789.

2. T. Brahmbhatt, G. Yang, E. Self, J. Nanda, Cathode-Sulfide Solid Electrolyte Interfacial Instability: Challenges and Solutions, Front. Energy Res. 2020, 8, 247.

3. F. M. Delnick, G. Yang, E. C. Self, H. M. Meyer III, J. Nanda, Investigation of Complex Intermediates in Solvent Mediated Synthesis of Thiophosphate Solid-State Electrolytes, J. Phys. Chem. C 2020 (Accepted).

* denotes co-first authorship

Acknowledgements

This research is sponsored by the United States Department of Energy through the Office of Energy Efficiency and Renewable Energy (EERE) and Vehicle Technologies Office (VTO, Program Manager: Tien Duong). Project team members include Drs. Ethan Self, Frank Delnick, Guang Yang and Prof. Steve Greenbaum - Hunter college, CUNY- NY. Collaborators - Dr. Zach Hood and Prof. Jennifer Rupp, MIT.

II.9.C Advancing Solid-Solid Interfaces in Li-ion Batteries (Argonne National Laboratory)

Sanja Tepavcevic, Principal Investigator
Argonne National Laboratory
9700 S Cass Ave
Lemont, IL 60439
E-mail: sanja@anl.gov

Larry A. Curtiss, Principal Investigator
Argonne National Laboratory
9700 South Cass Avenue
Lemont, IL 60521
E-mail: curtiss@anl.gov

Tien Duong, DOE Technology Development Manager
U.S. Department of Energy
E-mail: Tien.Duong@ee.doe.gov

Start Date: November 1, 2019 End Date: November 1, 2022
Project Funding: $1,480,000 DOE share: $1,480,000 Non-DOE share: $0

Project Introduction

One of the most important technological advances in sustainable energy harvesting and storage is the development of Li-ion battery technology. However, many challenges must be resolved in order to fully implement this technology, including: (i) development of high energy density cathode and anode materials (activity/cyclability); (ii) enhancement in the stability of electrode materials and the corresponding electrolytes; (iii) improvement in the selectivity of electrochemical interfaces, e.g., minimizing undesired side reactions at electrode surfaces; and (iv) eliminating many of the safety issues related to the high flammability of organic solvents and Li dendrite formation on the anode electrode. The focus of much research in the field of Li energy storage is centered on the development of methods that can enable Li metal anodes (required for high energy density Li-ion batteries) without dendrite formation and parasitic electrode-electrolyte interactions, as well as the replacement of flammable organic solvents with solid electrolytes.

Today, two methods have been introduced to address the safety/performance issues. The first method relies on the hypothesis that by shielding the Li metal anode with various types of "thin membranes" (either polymers or ceramics) Li dendrite formation will be significantly reduced relative to the bare Li anode along with the harmful side reactions. The second method regards the development of an all solid-state battery, composed of Li ion conductive solid electrolytes that connect metal Li anodes with high energy cathodes. "Hard" ceramic solid-state electrolytes have been developed with suitable ionic conductivities, but the stability of these materials must be improved to allow facile Li transport across the electrolyte while inhibiting dendrite formation. On the other hand, while "soft" polymer materials help to inhibit dendrite formation, none have ionic conductivities as high as liquid electrolytes (0.1 S cm^{-1}). Overall, both methods need further development to move Li-ion battery technology forward. Advances will require the application of knowledge, concepts, and tools from a variety of fields including materials science, physics, engineering, theory, and, in particular, interfacial electrochemistry.

Objectives

The project objectives are multifaceted, including the development of a mechanically / chemically stable and Li ion conductive (≥2 x 10^{-4} S/cm at 298K) solid electrolyte for a solid-state battery. The battery consists of a metal Li anode, a transition metal oxide cathode, and a nonflammable crystalline / amorphous solid electrolyte that operates at cathode potentials > 5V (denoted as a S_{Li}-S_{EL}-S_C system). We will develop and exploit a variety of ex-situ and in-situ experimental methods, including highly surface sensitive / electrochemical

probes, as well as computational techniques, to explore, optimize, and explain bulk and interfacial properties of the selected materials. The results will serve to unravel many of the puzzling bulk and interfacial properties of S_{Li}-S_{EL}-S_C systems, including various types of ceramic and glass materials.

Approach

Our approach is to use the interdisciplinary, atomic-/molecular-level insight obtained from integrating both experimental- and computational-based methodologies to define the landscape of parameters that control interfacial properties for new generations of Li-ion solid-solid battery systems. Our strategy will involve transferring the knowledge gained from well-characterized thin film materials to real-world materials. This strategy forms a closed loop in the sense that the knowledge gained from the model systems is used to design the more complex, real-world materials and vice-versa. The work will focus on utilizing existing in-house synthesis and characterization methods to enable the rapid transition from fundamental science to realistic cell.

Results

Effect of LLTO(hkl) orientation and crystallinity on the LLTO/Li interface

$Li_{0.33}La_{0.55}TiO_3$ (LLTO) is a perovskite solid electrolyte that crystallizes in a pseudo-perovskite structure with ordered La (A-site) vacancies along the c-axis in a tetragonal structure. To better understand the observed interfacial reactivity, it is important to investigate changes or the differences in chemical composition and structure in these films and their impact on real battery system. Our previous work on this system revealed that amorphous LLTO exhibits significantly enhanced chemical stability to contact with Li metal relative to crystalline systems, motivating additional studies to understand whether differences in intrinsic (e,g., Li diffusivity) or extrinsic (e.g., surface segregation, interfacial roughness) materials properties lead to improved stability. We performed neutron reflectometry studies on these systems, as neutron reflectometry is sensitive to interfacial reaction/roughening and/or variations in composition as a function of depth into the film, which can play an important role in understanding interfacial behavior. We started our neutron reflectivity study with bare LLTO epitaxial thin films grown by pulsed laser deposition (PLD). Due to the similarity in lattice parameters, the surface unit cell of $NdGaO_3$ (110) promotes the LLTO (001) orientation while $SrTiO_3$ (001) leads to the LLTO (100) orientation. Silicon substrates and room temperature deposition was conducted to promote the growth of amorphous LLTO. Characterization of amorphous LLTO thin film showed they are significantly less dense on average than crystalline LLTO (~70% nominal density). These results confirm that there are no differences in the strain-induced density and roughness of the LLTO films, regardless of crystallinity. Importantly, we also learned that amorphous LLTO films are highly uniform throughout their thickness with no surface layer formation, suggesting that the observed improvements in stability are likely intrinsic to the amorphous nature of the films. These measurements of bare LLTO thin films will serve us as a benchmark for later experiments with Li and as a comparison for the LLTO and cathode bilayers.

Effect of $LiCoO_2$/LLTO Crystallinity on Interfacial Structure and Li^+ Mobility

Of particular interest is the interface between the electrolyte and the cathode – here between thin films of LLTO and $LiCoO_2$ – to help determine if and how the surface of the LLTO film roughens after the deposition of $LiCoO_2$ and to understand the impact of interfacial structure on Li^+ kinetics. To do this, we synthesized several distinct crystalline interfaces by growing epitaxial thin films with different crystal orientations and crystallinity followed by growth of the $LiCoO_2$ cathode films. As stated above, LLTO is tetragonal, and the different orientations should differ in the rate of Li^+ transfer across the interface. For all crystalline films the $LiCoO_2$ overlayer is epitaxial; however, regardless of LLTO orientation $LiCoO_2$ films grow with the (104) orientation. Room temperature deposition yielded amorphous bilayer films of LLTO and $LiCoO_2$, and for another sample, this was repeated four times, effectively making an amorphous superlattice.

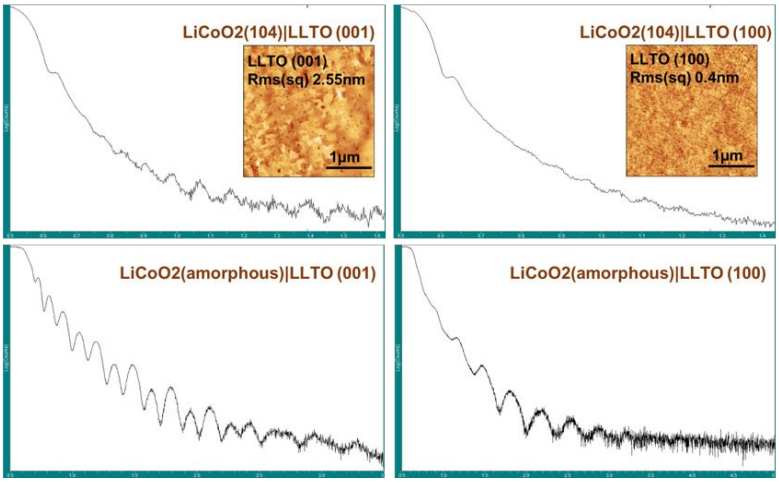

Figure II.9.C.1 (X-ray reflectivity (XRR) and atomic force microscopy (AFM) of LLTO films) AFM measurements on bare LLTO films for the (001) and (100) orientations are shown in the insets. XRR for crystalline LiCoO2/LLTO (hkl) are shown at the top and amorphous LiCoO2/LLTO (hkl) at the bottom.

Figure II.9.C.1 shows results from X-ray reflectivity (XRR) and atomic force microscopy (AFM). AFM on the (001)-oriented LLTO film gives a surface roughness of ~ 2.5 nm while that of the (100) film is only ~ 0.4 nm. Surprisingly, XRR measurements after depositing $LiCoO_2$ indicate the $LiCoO_2$ (104) / LLTO (100) interface is rougher than the $LiCoO_2$ (104) / LLTO (001) interface, despite the initially smoother film. As the scattering length densities of LLTO and $LiCoO_2$ differ by only 8% at 8048 eV (Cu Kα radiation), it is difficult to accurately measure the chemical width of the interface (and inter-diffusion). On the other hand, the neutron scattering length densities differ by 160%, making neutron reflectometry a much more sensitive probe for inter-diffusion. We therefore also performed neutron reflectometry studies at the SNS (ORNL) on these systems in collaboration with Suzanne te Velthuis (ANL), starting with measurements on the initial LLTO films to serve as benchmarks. We find a surface roughness of ~ 5 nm for LLTO (001) and ~ 3 nm LLTO (100), suggesting that the difference in the XRR can be just normal sample variation due to stochastic processes that occur during deposition. More importantly, neutron reflectivity allows a good measure of the atomic density profile. We find that both the LLTO (100) and (001) films have ~ 100% atomic density, as would be expected for epitaxial layers (Figure II.9.C.2).

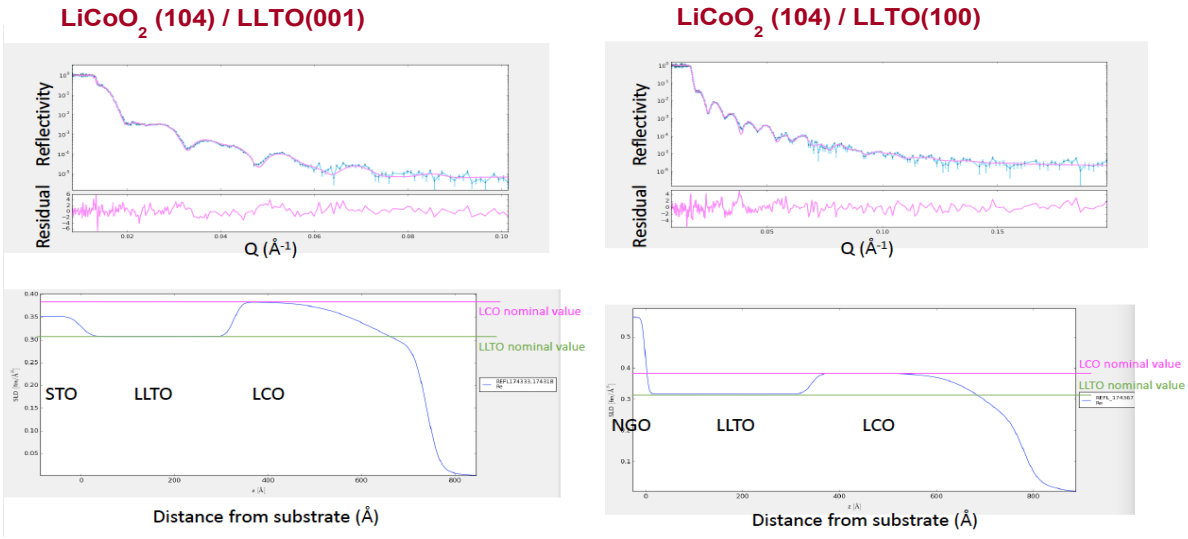

Figure II.9.C.2 (Neutron Reflectometry of $LiCoO_2$/LLTO Thin Films) Neutron reflectometry measurement on bilayer thin films of $LiCoO_2$ (104) / LLTO (hkl), where (hkl) is (100) for films grown of $SrTiO_3$ (001) and is (001) for films grown on $NdGaO_3$ (110).

$LiCoO_2$ layers, however, exhibit a relatively complex density profile, as shown in Figure II.9.C.2. The reflectivity must be modeled with two distinct $LiCoO_2$ layers: the layer near the surface is only ~ 50% dense on average, while the layer closest to the substrate is ~ 100% dense. This could indicate some loss of crystallinity in the $LiCoO_2$ during the PLD process. Regardless, the interface width between $LiCoO_2$ and LLTO remains very narrow – ~1 to 2 nm – despite the fact that deposition took place ~ 800°C. When the $LiCoO_2$ and LLTO films are grown at room temperature, the interfaces also remain relatively sharp (~ 1-2 nm), as shown in Figure II.9.C.4 (a, b), but the atomic densities of the films are lower than the bulk densities, ranging from 80% to 94% (Figure II.9.C.3 (c)). This is presumably due to greater free volume per atom in the amorphous structure. Although the film is amorphous, the superlattice structure still provides a diffraction peak at low angles, as shown in the X-ray reflectivity scan of Figure II.9.C.3 (a). We monitored the behavior of this "superlattice peak", which originates from the $LiCoO_2$ / LLTO superlattice, at elevated temperatures using a coherent X-ray beam at the APS to measure the activation energy for Li^+ inter-diffusion. We plot the results in the form of a two-time correlation function, as shown in Figure II.9.C.3 (d). By measuring this for different temperatures, we arrive at Figure II.9.C.3 (e), which is an Arrhenius plot showing the activation energy for Li^+ migration across the interface. The activation energy appears to be quite low ~0.05 eV – indicating that Li^+ mobility across the amorphous LLTO/LCO interface is facile and suggesting that Li^+ transport in amorphous materials may be comparable or even enhanced relative to their crystalline counterparts.

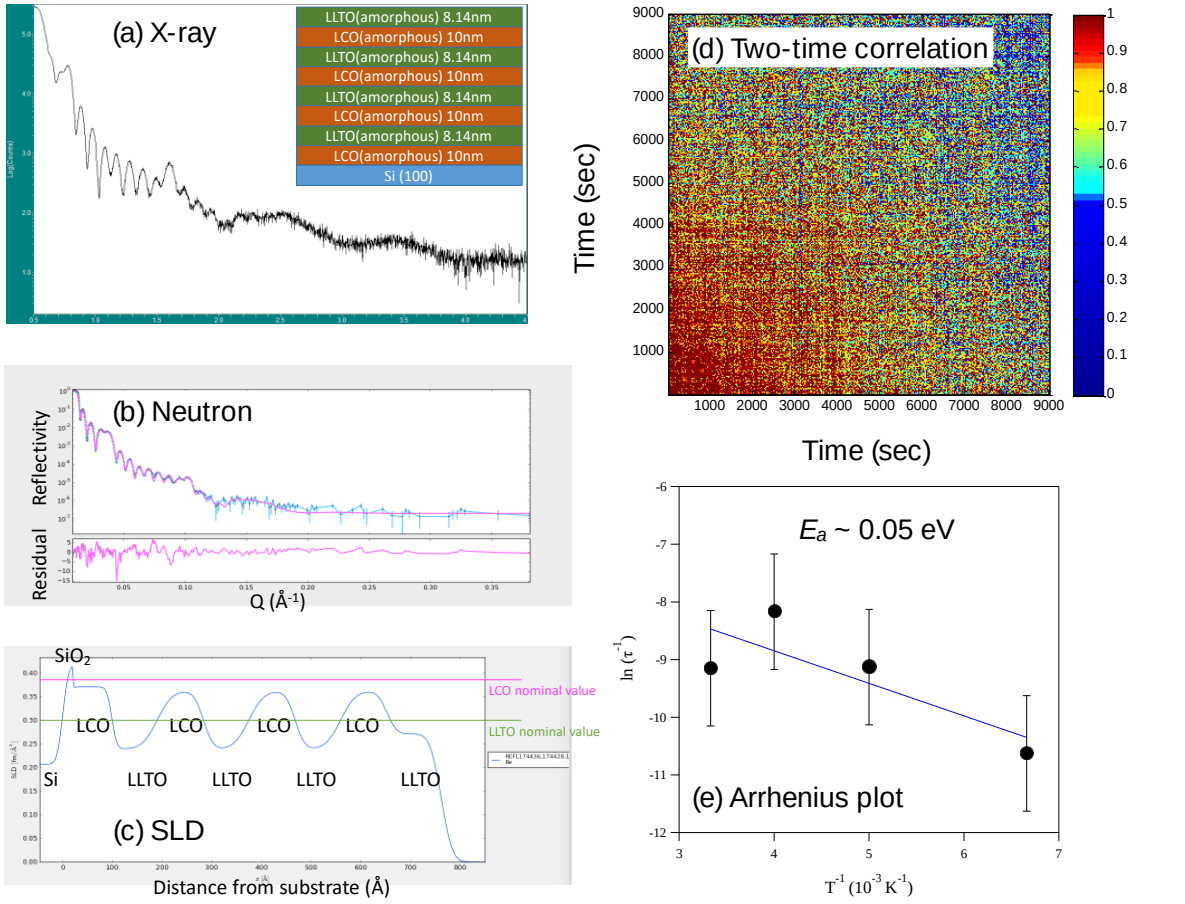

Figure II.9.C.3 (X-ray and Neutron Reactivity of $LiCoO_2$/LLTO Interface) (a) X-ray reflectivity and (b) neutron reflectivity, along with the fitted density profile for the amorphous $LiCoO_2$ / LLTO superlattice (c). (d) The two-time correlation function, as measured using a coherent X-ray beam at the APS. The results at different temperatures allow measurement of the activation energy for Li ion fluctuations across the interface (e).

Molecular Dynamics Modeling of Dopant Distribution in Undoped and Ta-doped LLZO

The dopant and Li distribution in the interfacial regions of LLZO play critical roles in stabilization of the high temperature (T > 630° C) cubic crystal phase (c-LLZO) and determine the properties of Li interactions with the material. Our previous work demonstrated significant driving forces for dopant segregation to LLZO surfaces, and we wanted to determine whether similar driving forces exist at grain boundaries within the material. MD simulations for a model internal interface in undoped and Ta-doped LLZO (LLZO and LLZT, respectively) were performed using the isothermal-isobaric ensemble to equilibrate interface structures obtained by bringing together surfaces initially terminated with Li, La and O in the (110) orientation and MD annealed at high temperature. The resulting structures were further simulated using the canonical ensemble, resulting in the formation of a ~2-nm-wide disordered region separating two crystalline regions, as shown in Figure II.9.C.4 (left). The LLZT and LLZO concentration profiles are shown in Figure II.9.C.4 (right and center, respectively). While the structure retains the highly ordered garnet structure in the crystalline regions, the interfacial region exhibits disorder, which appears to be more pronounced in case of LLZT. The average atomic density ratios, e.g. Li/Zr and Ta/Zr, in the disordered region are similar to the values for bulk materials. The distribution of Ta shown in Figure II.9.C.4 (left) shows higher ordering in the amorphous region close to the interface compared to the middle of the region, in contrast to the Zr distribution, which does not show such ordering in the amorphous region.

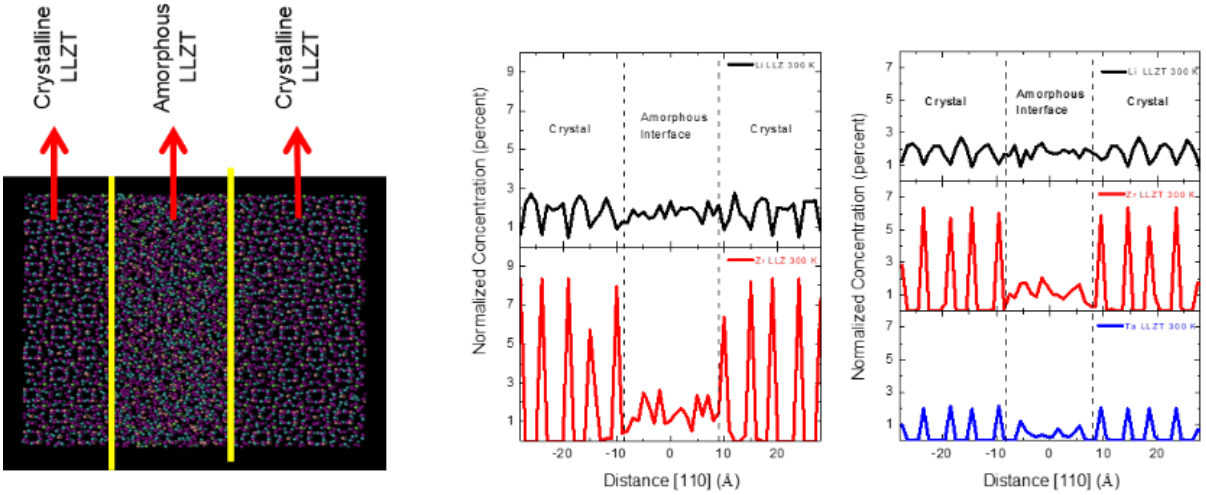

Figure II.9.C.4 (Molecular Dynamics of doped LLZO Interfaces) [(left) Amorphous interface was created using molecular dynamics with NPT simulation after bringing together two partially melted LLZT surfaces. Amorphous region is approx. 2 nm in width; Distribution of Li (black) and Zr (red) across internal interfaces in LLZO (center) and LLZT (left). Ta distribution is in blue (left).

Size Effect of Li Diffusivity in LLZO

We have used the structures described in Figure II.9.C.4 to calculate diffusivities in Figure II.9.C.5, Upon close examination of diffusivities in Figure II.9.C.5 (left) a surprising result was the absence of a change in slope for diffusivity vs inverse temperature for crystalline regions of undoped LLZO structure. Since this observation suggests the absence of a transition to tetragonal phase, we examined several possible reasons using MD simulations. It appears that the size limitation of crystalline regions to several nm with periodic boundary conditions resulted in suppression of the phase transition. We have examined the size effect by calculating the temperature dependence of diffusivities for LLZO and LLZT slabs with different thicknesses (1.8, 3.6, and 5.5 nm) bounded by Li, La and O terminated (110) surfaces. Both sides were identical in composition. The diffusivities of two slabs, 3.6 nm and 5.5 nm, are shown in Figure II.9.C.5 (right). No structural phase transition from cubic phase to tetragonal phase was observed for the 1.8 nm and 3.6 nm slabs of undoped material during cooling. A transition was observed for the 5.5-nm-thick slab, where the diffusivity shows a change in slope vs temperature that is associated with the phase transition. The size effect is partially attributed to a slight depletion in the bulk Li concentration caused by its migration to the interface in slabs with

thicknesses below 5.5 nm. This result indicates that stabilization of the cubic phase may be possible in nanocrystalline systems below a critical grain size.

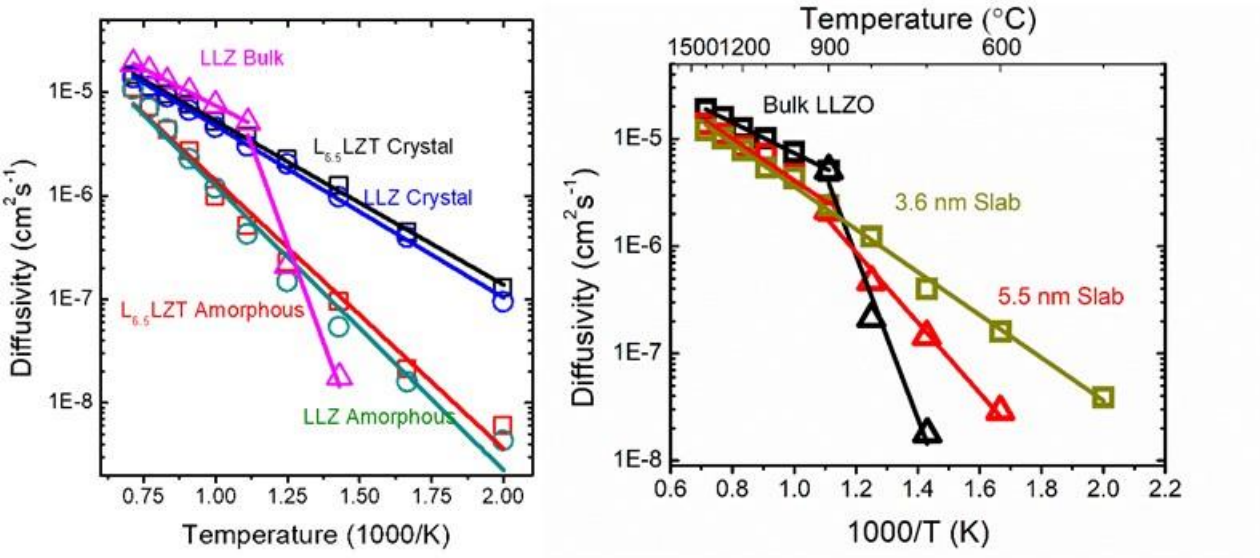

Figure II.9.C.5 (Li Diffusivities from Molecular Dynamics Calculations) (left) Li diffusivities from molecular dynamics calculations of in the interface regions of LLZO and LLZT. (right) Calculated Li Diffusivity as a function of temperature for undoped LLZO and two-dimensional slabs of thicknesses 3.6 nm and 5.5 nm.

Chemical Reactivity and Li⁺ Generation at Li/PEO Interfaces

In contrast to rigid, inorganic solid electrolytes, cells with polymer electrolytes and lithium metal anodes are able to cycle with no applied pressure, siginificantly simplifying the cell stack. However, as with inorganic electrolytes, polymer electrolytes suffer from issues of chemical reactivity with Li metal, as well as overall lower ionic conductivities, motivating the search for new systems and concepts to improve chemical stability and Li^+ transport. Polyethylene oxide (PEO) has been widely studied as a model system for polymer electrolytes due to its chemical simplicity. Thin films of PEO dimethyl ether (PEO with methyl terminals) was used as our primary test platorm, while oxygen-free polyethylene (PE) and carbon-free SiO_2 were used as two control samples. XPS data were acquired from all samples before and after Li metal deposition via electron-beam evaporation, and all Li-deposited samples were heated to 120ºC prior to XPS analysis. Note that this is the first study of PEO/Li interface with PEO thin films and vacuum deposited Li, and all experiments were done with the same ultrahigh vacuum transfer procedure used previously to understand Li reactivity with LLZO and LLTO surfaces. After Li deposition onto PEO samples, clear peaks corresponding to organolithium (LiCR, ~282 eV) and lithium alkoxide (LiOR, ~530 eV), were found (Figure II.9.C.6, left), which was not observed on the PE control sample. This evidence strongly suggests that PEO reacts with Li metal upon contact. Based on the XPS data, we propose that reactions take place between Li and PEO involving the breaking of C-C and C-O bonds with addition of Li from the surface. Soon after initial contact, the reaction initiates with Li atoms cleaving the ether bonds to form Li-OR and Li-R (Figure II.9.C.6, Step 1). The Li-R species are unstable and continue cleaving other ether bonds. To determine the validity of this proposed reaction scheme, density functional theory (DFT) calculations were performed for various Li-PEO fragments using glymes of various lengths as models for PEO, and Li atoms were assumed to come from the Li surface either by dissolution or by a surface reaction (Figure II.9.C.6, bottom right). Free energy calculations for Li reactions with O-H, C-H, C-O and C-C bonds indicate that the most favorable reaction is breaking of a C-O bond to form ethylene and an ionic Li^+ bound to the remaining ether fragment. This result is significant, as it indicates that it may be possible to generate free Li ions in the absence of any added salt simply through reaction of PEO with Li metal. The calculations further indicate that our proposed reactions are thermodynamically favorable, supporting the reaction scheme deduced from the XPS measurements of chemical reactivity.

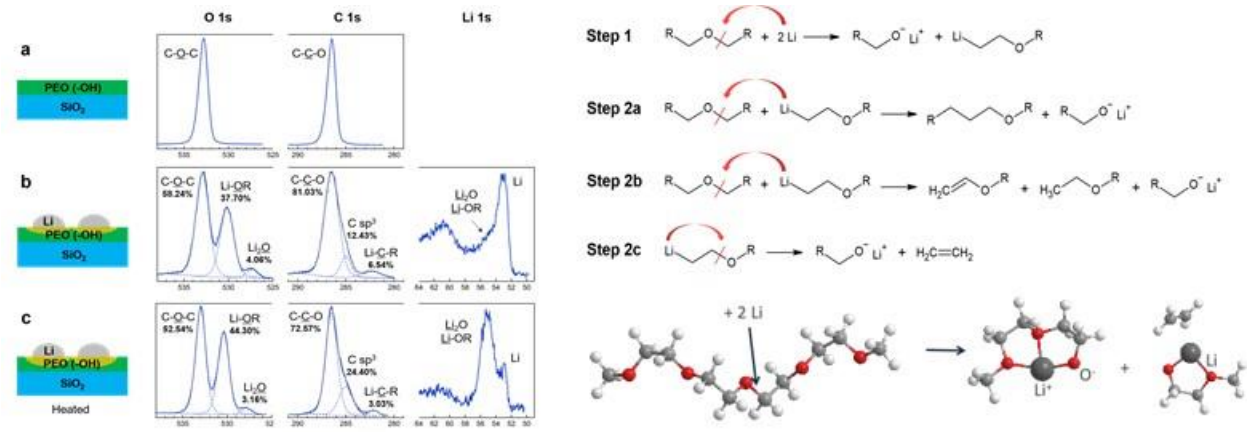

Figure II.9.C.6 (Chemical Reactivity of PEO/Li Interface) (left) XPS core levels of neat PEO (-OH) (a) before Li deposition, (b) after Li deposition, and (c) after 3 hours of heating (top right) Reactions proposed at PEO/Li interface (bottom right) DFT calculations of the most favourable reaction between PEO and mettalic Li.

Conclusions

Through the close integration of materials characterization and theory, we have significantly advanced our understanding of several technologically relevant interfaces between multiple solid electrolyte materials and both Li metal and oxide cathodes. Neutron reflectometry studies on LLTO and LCO thin films with different crystallinity and orientations indicates that amorphous LLTO films are highly uniform throughout their thickness with no surface layer formation, suggesting that the enhanced chemical stability of amorphous LLTO in contact with Li metal is intrinsic to the material and likely not related to surface segregation or roughness. We further demonstrated the ability to create epitaxial $LiCoO_2$(104) cathode layers on top of epitaxial LLTO(hkl) electrolyte films to study well-defined cathode/electrolyte interfaces. Using coherent X-ray photon correlation spectroscopy measurements at different temperatures, we were able to generate an Arrhenius plot showing that the activation energy for lithium ion migration across the amorphous LLTO/$LiCoO_2$ interface to be ~0.05 eV. This result suggests that Li^+ mobility in the amorphous material is not significantly reduced relative to crystalline LLTO. Calculated diffusivity for Ta-doped (LLZT) and undoped (LLZO) lithium garnets was simulated at a model grain boundary interface to understand inhomogeneous behavior within the material in addition to the surface phenomena identified previously. Amorphous regions show Li^+ diffusivities an order of magnitude lower than crystalline regions; while only small differences are observed between doped and undoped interfaces. Interestingly, calculations of Li^+ diffusivity as a function of material thickness in 3.6 nm thick LLZO shows no cubic/tetragonal transition in MD simulations, suggesting that the cubic phase may be possible to stabilize at the nanoscale without the need for dopants. Finally, we demonstrate that Li metal reacts with PEO, resulting in the breaking of C-C and C-O bonds. DFT shows the resulting Li-O bond is ionic (Li^+-O^-) and this may serve as a new mechanism by which to introduce free Li^+ without the need for additional salt.

Key Publications

Patents

1. **Interface Design For High Current Density Cycling Of Solid-State Battery** (Yisi Zhu, Sanja Tepavcevic, Justin Connell, Peter Zapol and Nenad Markovic, US 16/784543, applied)

2. **In-19-173 "Improved Ion Conductivity Of Polyethylene Oxide By In-Situ Lithium Salt Formation"** (Pei Liu, Yisi Zhu, Daniel Sharon, Paul F. Nealey, Sanja Tepavcevic, Larry A. Curtiss, Nenad Markovic, filed at ANL)

Publications

1. **Kinetic versus Thermodynamic Stability of LLZO in Contact with Lithium Metal** Connell, Justin, Till Fuchs, Hannah Hartmann, Thorben Krauskopf, Yisi Zhu, Joachim Sann, Regina Garcia-Mendez, Jeff Sakamoto, Sanja Tepavcevic and Jürgen Janek. *Chemistry of Materials* (2020) *Accepted.*

2. **Interface Design for High Current Density Cycling of Solid State Batteries** Sanja Tepavcevic, Yisi Zhu, Justin G. Connell, Peter Zapol, Pei Liu, John W. Freeland, Dillon D. Fong, Vojislav R. Stamenkovic, Regina Garcia-Mendez, Jeff Sakamoto, Larry A. Curtiss and Nenad M. Markovic, submitted (submitted)

3. **Comparison of chemical reactivity of amorphous LLTO to epitaxial films of different orientation towards metallic Li anode,** Zhu, Y., Zapol, P., Tepavcevic, S., Connell, J. G., Freeland, J. W., Fong, D. D., Curtiss, L. A., Markovic, N. M. (in preparation)

4. **Improved Ion Conductivity of Polyethylene Oxide by In-situ Lithium Salt Formation** Pei Liu, Yisi Zhu, Daniel Sharon, Larry Curtiss, Justin Connell, Sanja Tepavcevic, Shrayesh Patel, Nenad Markovic, Paul Nealey (in preparation)

Presentations

1. **S. Tepavcevic,** "Surface Science Approach to Solid-Solid interface" Virtual National Solid-State Battery Brainstorming Session, Oakridge National Laboratory, May 2020

2. **S. Tepavcevic** "Advancing Solid State Interfaces in Li-ion Batteries", Solid State Electrolytes Meeting, Pacific Northwest National Laboratory, October 2019.

3. Markovic, Nenad, Larry Curtiss, **Sanja Tepavcevic,** Peter Zapol, Yisi Zhu, Justin Connell, Dillon Fong, et al."Advancing Solid-Solid Interfaces in Li-Ion Batteries." Slide presentation at the 2020 DOE Vehicle Technologies Office Annual Merit Review, Washington, DC US, June 1, 2020 - June 4, 2020.

4. **J. G. Connell**, Y. Zhu, S. Tepavcevic, P. Zapol, J. W. Freeland, D. D. Fong, V. R. Stamenkovic, R. Garcia-Mendez, J. Sakamoto, L A. Curtiss, N. M. Markovic. "Coupling Interfacial Stability with Electrochemical Performance of Oxide Solid Electrolytes in Contact with Lithium Metal." (Poster) Batteries Gordon Research Conference, Ventura, CA, February 2020

Acknowledgements

The PIs are grateful to our collaborators Yisi Zhu, Justin G. Connell, Peter Zapol, John W. Freeland, Dillon D. Fong and Nenad M. Markovic for data collection and analysis and their valuable contributions to the project. We also thank Suzanne te Velthuis for help with neutron diffraction.

II.9.D Li Dendrite-Free Li_7N_2I-LiOH Solid Electrolytes for High Energy Lithium Batteries

Chunsheng Wang, Ph.D, Principal Investigator
Department of Chemical & Biomolecular Engineering
University of Maryland
Room 1223C Chemical & Nuclear Engineering Building
College Park, MD 20742-2115
E-mail: cswang@umd.edu

Tien Duong, DOE Technology Development Manager
U.S. Department of Energy
E-mail: Tien.Duong@ee.doe.gov

Start Date: October 1, 2019 End Date: September 30, 2021
Project Funding: $500,000 DOE share: $500,000 Non-DOE share: $0

Project Introduction

All-solid-state lithium batteries (ASSLBs) hold great potential to improve the safety and energy density of today's lithium-ion batteries by using non-flammable inorganic solid electrolytes. Solid electrolytes (SEs) are believed to prevent Li dendrite growth because of high mechanical strength and high Li^+ transference numbers. Significant advances in SE have been achieved, among which, $Li_7La_3Zr_2O_{12}$ (LLZO) and $Li_2S–P_2S_5$ (LPS) are the most promising SEs for bulk-type solid-state lithium batteries because of high ionic conductivities (>10^{-4} S/cm^2). However, in contrast to our expectations, the growth of lithium dendrites is not suppressed but is facilitated in LLZOs and LPSs regardless of dopants [1], porosity [2], and crystallinity [1], [3] of the electrolytes. Despite the unity Li transference number and over two-times of shear modulus than that of Li metal, the critical current densities for Li plating and stripping in these SEs are less than 1.0 mA cm^{-2}, which is one-fourth to one-tenth of that in liquid electrolytes at room temperature [4]. The incompatibility between LLZO and LPS with Li metal seriously limits the energy density of all-solid-state batteries.

The mechanism for lithium dendrite formation and growth in SEs are still disputable. Lack of understanding of the Li dendrite formation mechanism seriously impeded the development of solid-state lithium batteries. The development of the criterion for Li dendrite suppression is essential for the success of solid electrolyte lithium batteries. In this project, a criterion for Li dendrite suppression will be developed through thermodynamics and kinetics analysis of lithium dendrite nucleation/growth, which will guide the solid-state electrolyte design. Li_7N_2I-LiOH, Li_5NI_2-LiOH and Li_3YCl_6 solid electrolyte with high ionic conductivity and low electronic conductivity were used to validate the criterion for lithium dendrite suppression.

Objectives

The objective of this project is to research, develop, and test Li-metal-based batteries that implement solid Li-ion conductors (LICs) equipped with targeted solid electrolyte capable of achieving cell performance of 350 Wh/Kg energy density for 1000 cycle life with a cost of ≤ $100/kWh.

The main objective in the Budget Period 1, is to develop and optimize the targeted electrolytes. The tasks for the first budget period are (1) synthesis of targeted electrolytes with high ionic conductivity; (2) electrochemical properties of targeted electrolytes; (3) Li dendrite suppression capability; and (4) High Coulombic Efficiency (CE) for Li plating/stripping.

In year one, the project will synthesize, modify, and optimize the targeted electrolytes to achieve a high ionic conductivity to > 5×10^{-4} S/cm Critical Current Density (CCD) of > 2.0 mA/cm^2 at a capacity of > 2.0 mAh/cm^2. The team will focus on enhancing the CE for lithium anode to > 99%. The CE of the solid electrolyte is a powerful indicator of electrolyte stability and lithium dendrite growth. The mechanism of Li dendrite growth in the targeted solid-state electrolytes and thermodynamic Li dendrite suppression criterion will also be developed.

Approach

We will establish the relationship among interface energy, Li plating/striping overpotential, interface resistance, solid electrolyte stability with Li, and CCD. The dendrite suppression criterion will be developed based on the relationship. The dendrite suppression capability for the Li_7N_2I-LiOH pellet will be evaluated by testing the CCD.

Results

1. Synthesis, Characterization and Optimization of Li_7N_2I-LiOH, Li_5NI_2-LiOH and Li_3YCl_6 Electrolytes

Li_7N_2I-LiOH, Li_5NI_2-LiOH and Li_3YCl_6 were prepared through mild solid-state reaction and ball-milling. The Li_7N_2I-LiOH shows a high ionic conductivity of 0.14 mS/cm while that of Li_3YCl_6 is 0.48 mS/cm (Figure II.9.D.1a). The activation energy of the Li_7N_2I-LiOH pellet is measured to be 0.34 eV. The ionic conductivity of Li_3YCl_6 is quite close to the goal of 0.5 mS/cm and the activation energy of the Li_7N_2I-LiOH meets the requirement of 0.34 eV. To improve the ionic conductivity of the Li_7N_2I-LiOH, we optimized the ratio of Li_3N, LiI, and LiOH. As shown in Figure II.9.D.1b, the ionic conductivity of Li_5NI_2 can be significantly improved by doping LiOH. The Li_5NI_2-LiOH shows a high ionic conductivity of 0.8 mS/cm meeting the requirement of 0.5 mS/cm^2. Figure II.9.D.1d shows the cyclic voltammetry (CV) curve of Li| Li_7N_2I-LiOH-Li_3YCl_6| SS cells at a scan rate of 1 mV/s. The CV indicates that Li_7N_2I-LiOH/Li_3YCl_6 bi-layer solid-state electrolyte enables a wide voltage window of 0-5 V. In Figure II.9.D.1c, the electrochemical window Li_3YCl_6 is from 1.0V to 4.2V vs. Li^+/Li. Comparing to LPS, the electrochemical window of Li_7N_2I-LiOH/Li_3YCl_6 bi-layered electrolyte is significantly extended.

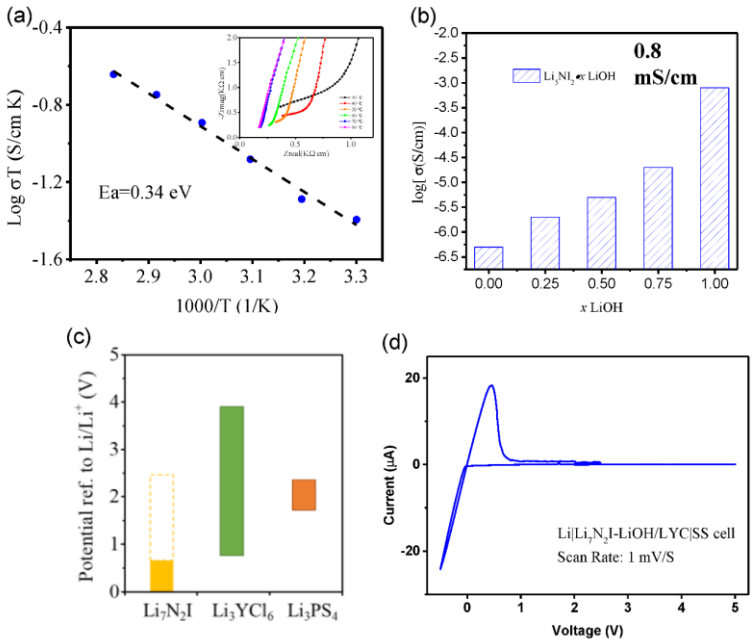

Figure II.9.D.1 (a) Ionic conductivity of Li_7N_2I-LiOH electrolyte at different temperatures from 25 to 80 °C. (b) ionic conductivity of Li_5Ni_2-xLiOH with different amount of LiOH. (c) Calculated electrochemical stability window of Li_7N_2I, Li_3YCl_6 and Li_3PS_4. (d). Electrochemical stability window of the Li_7N_2I-LiOH |Li_3YCl_6 solid-state electrolytes using the cycle voltammetry test of a Li|SSE|SS (SS=stainless-steel) at the scan rate of 1 mV/s.

The SEM of Li_3YCl_6 and Li_7N_2I-LiOH pellets and the cross-section of the Li_7N_2I-LiOH/Li_3YCl_6 bi-layer solid-state electrolyte is shown in Figure II.9.D.2. As we can see, the cold-pressed Li_3YCl_6 and Li_7N_2I-LiOH is rather dense. Moreover, Li_3YCl_6 and Li_7N_2I-LiOH in bi-layer electrolyte were close in contacted with each other.

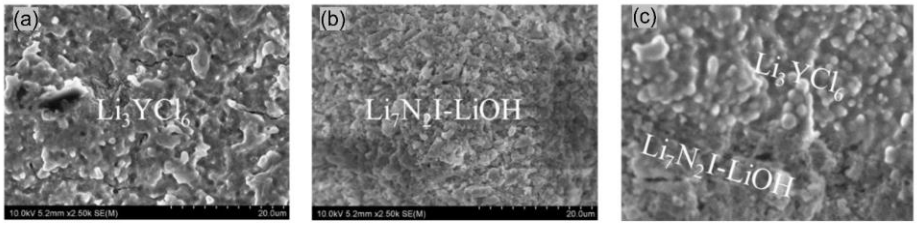

Figure II.9.D.2 SEM images of (a) Li_3YCl_6, (b) Li_7N_2I-LiOH and the cross section of the cold-pressed pellets.

2. *Reduction of Li/Li_7N_2I-LiOH / Interface Resistance and the Dendrite Suppression Capability of the Li|Li_7N_2I-LiOH|Li Symmetry Cell*

The Li_7N_2I-LiOH is thermodynamically stable with Li and has high interface energy, which causes large interfacial resistance. As shown in Figure II.9.D.3, molten metallic Li is not wetted with Li_7N_2I-LiOH pellet surface, exhibiting a large contact angle. By surface coating, the contact angle of Li on Li_7N_2I-LiOH pellet surface becomes smaller. We use this method to assemble the Li|Li_7N_2I-LiOH|Li symmetry cell to measure the Li dendrite suppression capability of the solid-state electrolytes.

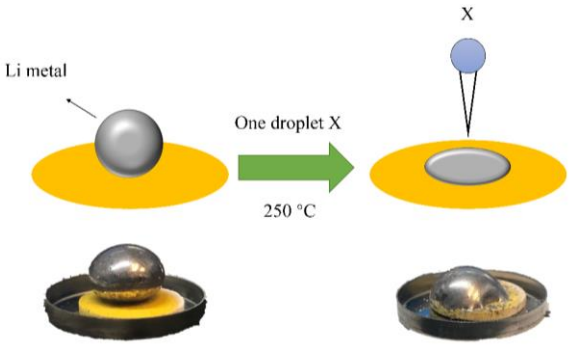

Figure II.9.D.3 Scheme and digital picture of molten metal lithium on Li_7N_2I-LiOH pellet surface with and without surface treatment.

The Li dendrite suppression capability of Li_3N-LiI-LiOH electrolytes was evaluated using the CCDs. As shown in Figure II.9.D.4, the critical currents for both Li_7N_2I-LiOH and Li_5NI_2-LiOH electrolytes are higher than 2.0 mA/cm^2 at a capacity of 2.0 mAh/cm^2. Figure II.9.D.4b demonstrates the cycle performance of Li|Li_7N_2I-LiOH|Li at a current density of 2.0 mA/cm^2 with a capacity of 2 mAh/cm^2. The overpotential slightly decreases at the first 5 cycles and becomes stable due to the penetration of Li metal into the porous of Li_7N_2I-LiOH electrolytes near the interface. Since the Li_7N_2I-LiOH electrolyte is thermodynamically stable and has high interface energy against Li, the Li penetration into porous Li_7N_2I-LiOH electrolyte is self-limited depending on the Li plating capacity. The Electrochemical Impedance Spectroscopy (EIS) plots of Li|Li_7N_2I-LiOH|Li before cycles, after the activation cycles, and after cycled at 2 mAh/cm^2 (Figure II.9.D.4c) demonstrate that the Li_7N_2I-LiOH does not short and the decrease in overpotential is attributed to self-limited Li penetration. The decrease in the resistance is attributed to the enhancement of the contact between Li electrode and electrolyte due to the Li penetration into electrolytes. Figure II.9.D.4d shows the cycle performance of Li|Li_5N_2I-LiOH|Li at a step-increased current density to 2.0 mA/cm^2 and capacity of 2 mAh/cm^2. The critical current of Li_5N_2I-LiOH is also higher than 2 mA/cm^2 at a capacity of 2.0 mAh/cm^2. The EIS of Li_5N_2I-LiOH electrolytes is shown in Figure II.9.D.4e. The goal for a high critical current density of 2

mA/cm^2 in the Budget Period I has been reached. The mechanism of self-limited Li penetration into Li_7N_2I-LiOH is illustrated in Figure II.9.D.4f.

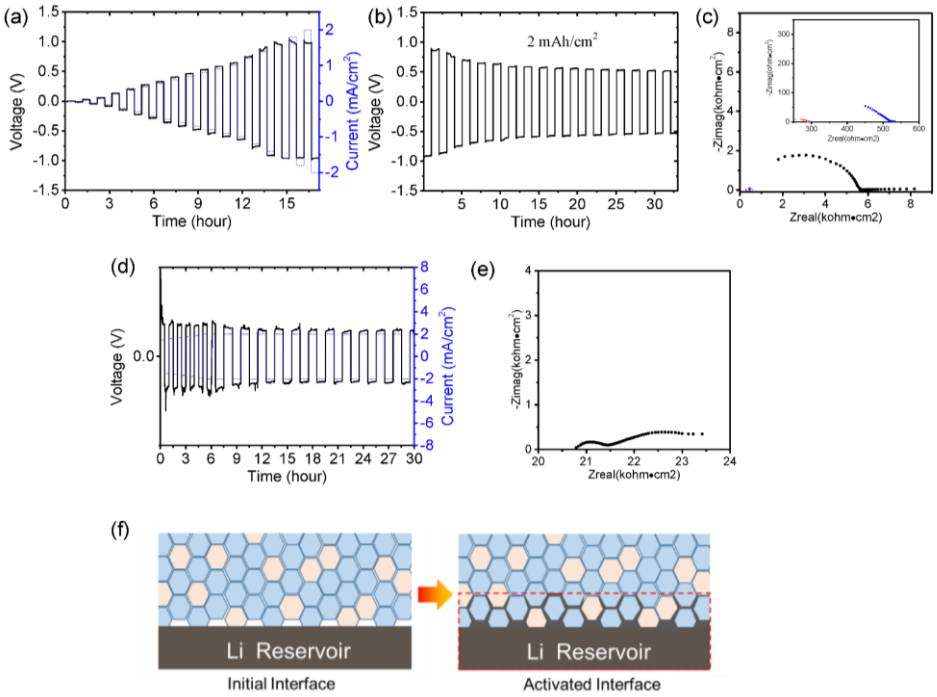

Figure II.9.D.4 Electrochemical behavior of Li|Li_7N_2I-LiOH|Li and Li|Li_5NI_2-LiOH|Li cell. The Li plating/stripping behavior for the Li| Li_7N_2I-LiOH |Li cells (a) at a step-increase current for 0.5h; (b) at a current of 2 mA/cm^2 and the capacity of 2 mAh/cm^2; and (c) the EIS plot before cycle (black circle), after activation (blue circle), and after cycled at 2 mAh/cm^2 for 16 cycles. The Li plating/stripping behavior for the Li|Li_5N_2I-LiOH |Li cells (d) at a step-increase current for 0.5 h and 6 cycles and then at 2 mAh/cm^2 for 1.0 hour and (e) the EIS plot before cycles. (f) Scheme for self-limited Li penetration into Li_7N_2I-LiOH process.

The CE of Li plating and stripping of the Li|Li_7N_2I-LiOH|Cu cells is still under testing. A high CE of 99% was achieved for the Li_3N-LiF protected LPS electrolytes, which is attributed to the electrochemical stability of Li_3N-LiF protective layer against Li (Figure II.9.D.5). We expected that CE of Li_3N-LiI-LiOH electrolyte should reach 99%. We will report the CE of Li_3N-LiI-LiOH electrolyte in the first-quarter report in Budget Period 2.

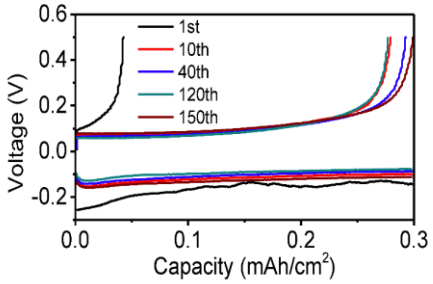

Figure II.9.D.5 Li plating/stripping CEs in Li/Li_3N–LiF/LPS/Li_3N–LiF/SS cell at a current of 0.3 mA/cm^2 and voltage cut-off of 0.5 V.

3. Development of Li dendrite suppression criterion for solid electrolytes

The Li dendrite nucleation and growth in SSEs depends on the energy landscape for Li deposition and stripping inside SSEs, which is represented by the Bulter-Volmer kinetics (Figure II.9.D.6a). The parabolas on the left designate reaction coordinate of Li deposition ($Li^+ + e^- \rightarrow Li$) and the parabola on the right designates

that of Li stripping ($Li \rightarrow Li^+ + e^-$). At an open-circuit after the SSE contacting with Li metal, the activation energy and the reaction rate for Li plating in SSEs is much larger than Li stripping in SSEs (blue dashes in Figure II.9.D.6a). The difference in activation energy between Li plating and stripping increases with the increasing of interface energy and decreasing of electronic conductivity of the SSEs. Once the Li plating starts, the electrolyte potential up-shifts by η, Li plating driving energy inside SSE moved up by Fη, which reduces the energy barrier for Li plating inside electrolyte ($\Delta G'_{Li^+ + e \rightarrow Li}$) but increase energy barrier for the Li stripping ($\Delta G'_{Li + e \rightarrow Li^+}$). When the Li plating current reach to a critical current, in which the potential shift (overpotential) reach to a critical value η∗ (critical overpotential), the activation energy of Li plating is the same as that of Li stripping in SSEs (red dashes in Figure II.9.D.6a). Li dendrite will be formed in SSE when the overpotential is larger than critical overpotential η* where the current is larger than the critical current (I*=η*/ASR). The critical current is high when the activation energy difference between Li plating and stripping at open-circuit is large and area specific resistance (ASR) is low. Therefore, the critical current density of SSEs increase with increasing of interface energy against Li, increasing of the ionic conductivity (reducing ASR), and decreasing of electronic conductivity. Since the high interface energy of SSE can provide large interface tension to prevent Li dendrite nucleation and growth in SSE, especially at void, defect and grain boundary, highly dense SSE is not required. However, if SSEs are lithophilic with a much low interface energy against Li, SSEs should have a high dense with less grain-boundary defects since the large interface tension force Li to penetrate into the grain-boundary, especially at grain boundary and defects.

The impact of thermodynamic stability, interface energy and electronic conductivity of SSEs on the Li dendrite formation was summarized in Figure II.9.D.6b. When the SSEs are stable with Li, electronic insulated and have low interface energy, Li dendrite grow from Li anode into grain boundaries (GBs) or hole of SSEs through mechanical Li infiltration due to the high interface tension and Li plating pressure. The mechanical Li dendrite growth mainly contributes to the intergranular growth, such as propagation in GBs, pores and cracks induced by Li growth (first row Figure II.9.D.6b). However, if the local electronic conductivity of SSEs is high, the Li chemical potential in SSEs will drop to a negative potential similar to the Li plating anode, so Li can even directly nucleate and grow inside SSE. (second row in Figure II.9.D.6b). Only if the SSEs are stable with Li have high interface energy against Li and insulated electronic conductivity, Li dendrite will not nucleate and grow inside SSEs, and not penetrate into SSEs because the high interface energy significantly increase the energy barrier of heterogeneous nucleation and the high interface tension between SSEs and Li also suppress Li propagation and penetration into SSEs (third row in Figure II.9.D.6b). If the SSEs are unstable with Li, and the formed interphases have a high electronic conductivity, the electrochemical reaction between Li and SSEs accelerate the Li dendrite nucleation and growth in SSEs. The Li dendrite growth in SSEs changes from mechanical pattern to electrochemical-mechanical pattern. (fourth row in Figure II.9.D.6b). The continuous side reaction between Li and electrolyte will unavoidably lead to high self-charge.

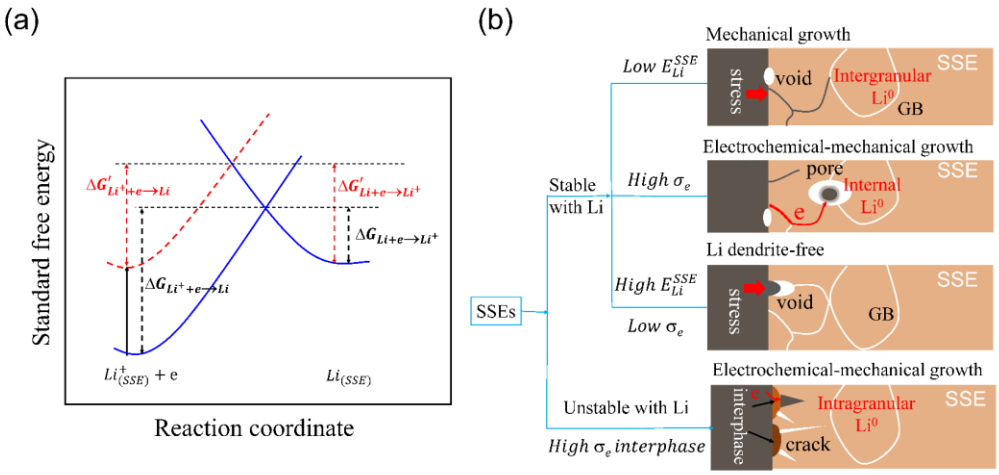

Figure II.9.D.6 Li dendrite formation mechanism in SSEs. (a) Illustration of Butler-Volmer model for Li plating in SSE; (b) Li dendrite formation and growth mechanism in SSE with different properties.

Conclusions

We systematically investigated the composition of Li_xN_yI-zLiOH electrolytes (x=5, 7, 10, y=2, 3, z=0.25, 0.5, 0.75, 1) by mixing with different amount of Li_3N with LiI and LiOH. Li_5NI_2-LiOH and Li_7NI_2-LiOH were selected for further investigation. In addition, by replacing LiI with LiF, Li_3N-LiF electrolytes were also developed to investigate the Li dendrite formation mechanism. The principles of designing Li dendrite-free solid-state electrolytes have been published in *Advanced Materials* in October, 2020. The main achievements are summarized below.

- Development of Li_5NI_2-LiOH and Li_3YCl_6 solid-state electrolytes with high ionic conductivities of 0.8 and 0.5 mS/cm, respectively, reaching the milestone of > 5×10^{-4} S/cm.
- Both Li_5NI_2-LiOH and Li_7N_2I-LiOH electrolytes show a high lithium dendrite suppression capability with a critical current density of 2.0 mA/cm^2 at a capacity of 2.0 mAh/cm^2; reaching the milestone of CCD of > 2.0 mA/cm^2 at a capacity of > 2.0 mAh/cm^2.
- The Li_3N-LiF electrolyte has reached the 99% of Coulombic efficiency [*Advanced Materials*, 2020, 2002741]. The CEs of Li|Li_7N_2I-LiOH|Cu and Li|Li_5NI_2-LiOH|Cu cells are under testing.
- The electrochemical stability window is 0.0 to 2.5 V for Li_7N_2I-LiOH electrolyte and 0.0 to 5.0 V for Li_7NI_2-LiOH/Li_3YCl_6 bi-layer solid-state electrolyte.
- A Li dendrite suppression criterion has been proposed and validated in Li_3N-LiF/Li_3PS_4 based all-solid-state battery.

Key Publications

1. X. Ji, S. Hou, P-F. Wang, X. He, N. Piao, X. Fan, C. Wang, Solid-State Electrolyte Design for Lithium Dendrite Suppression. *Advanced Materials*, 2020, 2002741.

References

1. X. Fan, X. Ji, F. Han, J. Yue, J. Chen, L. Chen, T. Deng, J. Jiang, C. Wang, Fluorinated solid electrolyte interphase enables highly reversible solid-state Li metal batter, *Science Advances*, **2018**, 4, eaau9245

2. J. Yue, X. Zhu, F. Han, X. Fan, L. Wang, J. Wang, C. Wang, A Long-Cycle Life All-Solid-State Sodium Ion Battery, *ACS Applied Materials & Interfaces*, **2018**, 10, 39645

3. R. Xu, F. Han, X. Ji, X. Fan, J. Tu, C. Wang, Interface engineering of sulfide electrolytes for all-solid-state lithium batteries, *Nano Energy*, **2018**, 53, 958

4. X. Fan,† J. Yue,† F Han, J. Chen, T. Deng, X. Zhou, S. Hou, C. Wang, High Performance All-Solid-State Na-S Battery Enabled by Casting-Annealing Technology, *ACS Nano*, **2018**, 12, 3360

II.9.E All Solid State Batteries Enabled by Multifunctional Electrolyte Materials

Pu Zhang, Principal Investigator
Solid Power Inc.
486 S Pierce Ave, Suite E
Louisville, CO 80027
E-mail: pu.zhang@solidpowerbattery.com

Tien Duong, DOE Technology Development Manager
U.S. Department of Energy
E-mail: Tien.Duong@ee.doe.gov

Start Date: October 1, 2019 End Date: September 30, 2022
Project Funding: $1,249,995 DOE share: $999,982 Non-DOE share: $250,013

Project Introduction

Solid Power is teaming with University of California San Diego (Prof. Shirley Y. Meng) to develop a high energy, long life, low cost, and safe all-solid-state-battery (ASSB). The battery is enabled by a multifunctional solid state electrolyte (SSE). The project will enable scalable production of large format solid state batteries required by the vehicle market and building domestic battery manufacturers as leaders in the global vehicle ASSB production.

Objectives

The project objective is to develop Li-metal solid batteries enabled by multifunctional SSEs for EV application. The ultimate goal is scalable production of large-format ASSBs able to deliver ≥ 350 Wh/kg specific energy, ≥ 1000 cycle life, and ≤ $100/kWh cost.

Approach

The project will develop a high-performance Li-metal solid-state cell enabled by a multifunctional SSE. The new SSE will: (1) have high conductivity (up to 10 mS/cm), (2) be stable against lithium metal and high-voltage cathode (0-4.5 V), (3) promote uniform lithium plating (enabling > 2C charge rate), and (4) be compatible with large-scale manufacturing processes. The specific cell chemistry to be demonstrated will be the SSE with Li-metal anode and high-nickel-content Li-metal oxide cathode. The solid-state cell will be assembled by scalable roll-to-roll processes developed by Solid Power.

Results

1. SSE material development

Solid Power's halogenated LPS material was used as a starting point. Li_2S, P_2S_5, a halogen and other selected dopants were ball-milled to form glassy sulfide electrolytes by using a mechanical ball mill. A subsequent heat-treatment was conducted to obtain glass-ceramic solid electrolytes. The multifunctional SSE materials have met the Year 1 performance targets on both Li ion conductivity and critical current density (CCD) against Li metal. The material status is shown in Table II.9.E.1.

Table II.9.E.1 Conductivity and CCD of the Multifunctional SSE Materials

Parameters	Year 1 Target	Year 1 Status
Li Ion Conductivity (mS/cm)	≥ 3.0	≥ 4.5
Critical Current Density (mA/cm²)	≥ 6.0	≥ 6.0

2. SSE film (separator) development

We have scaled up the SSE separator coating process at pilot scale. A separator slurry was prepared by mixing the SSE powder, a binder, and a solvent by using an industrial mixer. The slurry was then cast on a carrier film by using a pilot scale slot-die coater. Figure II.9.E.1 shows the "roll-to-roll" coated separator film and the flexibility of a free-standing film.

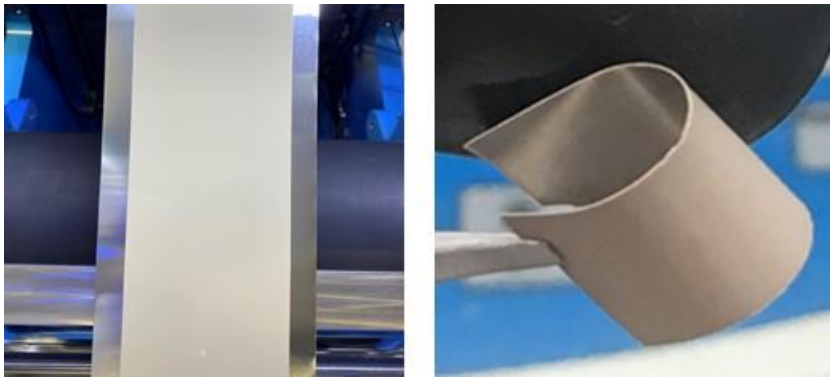

Figure II.9.E.1 (left) a separator film coated by a slot-die coater; (right) flexibility of the separator

3. Full cell demonstration

A single layer pouch cell (at 6 mAh) was assembled for performance demonstration. The cell contained a NMC 622 composite cathode (at 3 mAh/cm^2), a thin Li metal anode, and a SSE separator. The cell is designed to deliver a specific energy of 300 Wh/kg if scaled to 20 Ah. When tested at C/5 - C/5, 2.8 - 4.2V, and 70°C, the cell demonstrates 250 cycles with 80% capacity retention and 350 cycles with 75% capacity retention (Figure II.9.E.2). It exceeds the first year goal of 200 cycles.

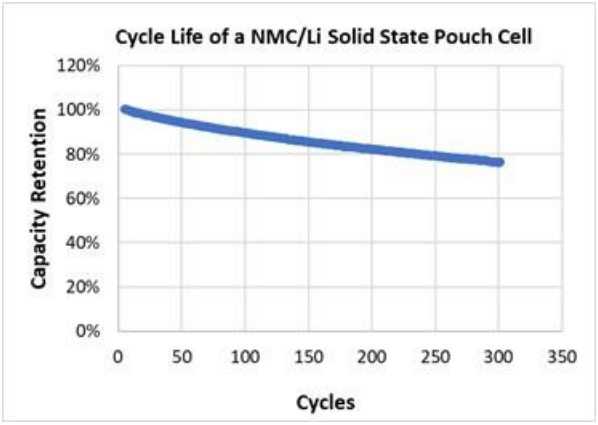

Figure II.9.E.2 Cycle life of an NMC/Li metal solid state pouch cell with the multifunctional SSE

Conclusions

Multifunctional SSE materials have been developed with high conductivity and stability. SSE separator films have been coated by using a roll-to-roll process. A solid state NMC-Li pouch cell containing the developed SSE has been assembled and tested. The cell cycle life of > 250 at 100% DOD has been demonstrated.

Acknowledgements

Colleen R. Butcher served as the NETL Project Manager for this project.

II.9.F Development of Thin, Robust, Lithium-Impenetrable, High-Conductivity, Electrochemically Stable, Scalable, and Low-Cost Glassy Solid Electrolytes for Solid State Lithium Batteries (Iowa State University of Science and Technology)

Steve W. Martin, Principal Investigator
Iowa State University
528 Bissell Rd
Ames, IA, 50011-1096
E-mail: swmartin@iastate.edu

Tien Duong, DOE Technology Development Manager
U.S. Department of Energy
E-mail: Tien.Duong@ee.doe.gov

Start Date: October 1, 2019 End Date: September 30, 2022
Project Funding: $1,252,595 DOE share: $1,000,000 Non-DOE share: $252,595

Project Introduction

The development of thin mixed oxy-sulfide-nitride (MOSN) mixed glass former (MGF) glassy solid electrolyte (GSE) films that yield superior performance in a safer, lower-cost, and Li-dendrite impenetrable form will be used to develop new solid-state lithium batteries (SSLBs). It is expected that high rate and long cycle life SSLBs can be achieved using thin-film MOSN GSEs. The new GSEs in SSLBs are anticipated to increase the energy density (anode basis) from ~ 300 mAh/g to ~ 4,000 mAh/g, enabling replacement of internal combustion engines in both light and heavy-duty vehicles. Each 20% reduction in the ~ 1.6 billion liters of gasoline used per day in the United States would reduce CO2 emissions by ~ 4 billion kg CO2 per day. The team will also increase scientific and engineering knowledge of thin-film GSEs in SSLBs.

Objectives

The objective of this project is to develop new high Li+-conducting MOSN GSE thin-films, < 50µm, that are impermeable to lithium dendrites, scalable through low-cost glass manufacturing, chemically and electrochemically stable, and will enable low-cost, high-energy-density SSLBs. It is expected that the SSLBs constructed from these new MGF MOSN GSEs will meet and exceed all program objectives: useable specific energy @ C/3 ≥ 350 Wh/kg, calendar life 15 years, cycle life (C/3 deep discharge with < 20% energy fade) 1,000, and cost ≤ $100/kWh.

Approach

The MOSN MGF GSEs have been prepared and developed in previous work in bulk glass form to exhibit the necessary thermal stability and ionic conductivity for successful use as a drawn thin-film GSE. In this new project, the glass chemistry will be further improved and optimized for even more desirable properties by investigating structure property relationships of these GSES and testing variations in glass chemistry. Optimized glass chemistries will be cast into large preforms, 10cm x 30cm x 1cm, and drawn into meters long thin-films, 50µm x 5 cm, and used for cell level testing.

Results

Compositional Optimization of MOSN MGF GSEs

Through our previous research on these MOSN MGF GSEs, it was determined that the materials must have a thermal stability between -20°C and 100°C, Li+ ion conductivity ≥ 1 mS/cm at 25°C, Li+ ion area specific resistance (ASR) of ≤ 100 Ohm-cm2, electronic ASR of > 0.1 M Ohm-cm2, electrochemical stability between 0 and 4.5 V versus Li/Li+, and no more than 1 wt% change in 45% relative humidity (RH) air over the period of a few hours.

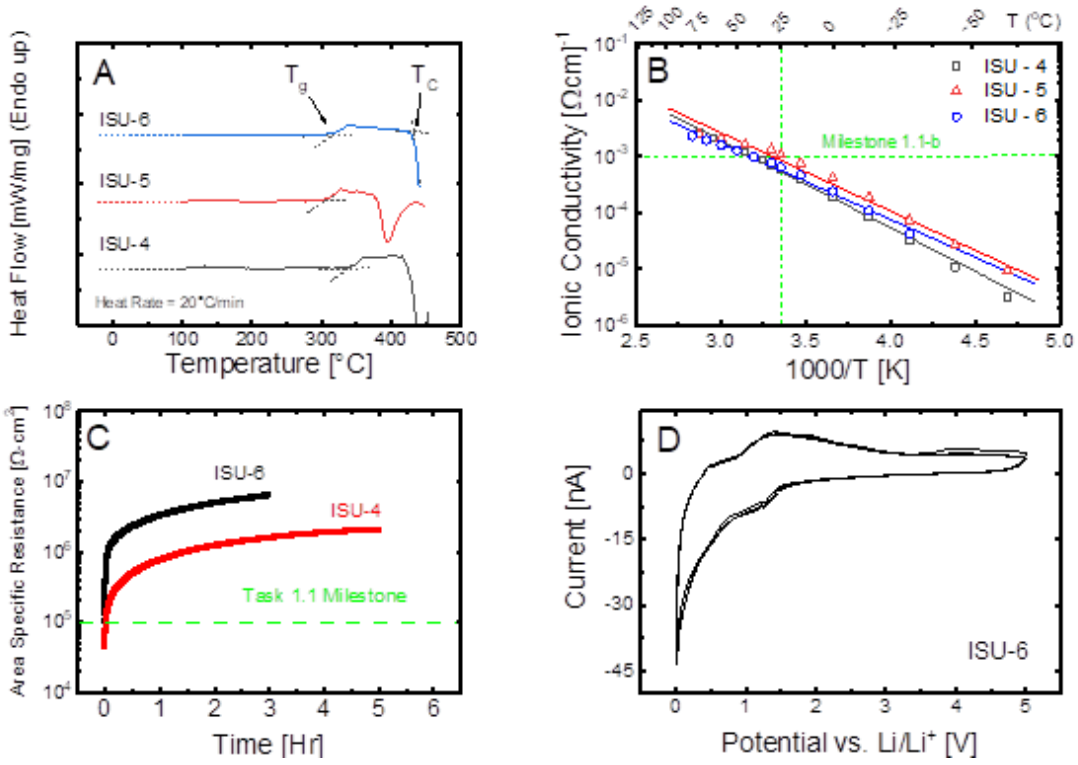

Figure II.9.F.1 (A) DSC Thermograms showcasing the thermal stability of ISU GSEs. (B) Arrhenius plot comparing the temperature dependent ionic conductivity for the three ISU GSEs, ISU-4, ISU-5, and ISU-6. (C) Area specific electronic resistance of ISU-4 and ISU-6 GSEs. (D) Cyclic voltammograms for the ISU-4, -5, and -6 GSEs over the range from 0 to 5V.

Figure II.9.F.1A shows that all GSEs are thermally stable from -20 to 100oC. The newest composition ISU-6, with the largest working range, was found to form a glass upon cooling in bulk pieces. The thermal events above 100oC correspond to the glass transition temperature (Tg) and crystallization temperature (TC). Our recent efforts have found that GSEs that possess a working range (ΔT = Tc -Tg) > 100oC are much easier to cast into preforms and draw into films and for this reason, this criterion is being used to select the final GSE composition Figure II.9.F.1B shows the temperature dependent ionic conductivity of the different ISU GSEs measured using impedance spectroscopy (IS). It can be seen that GSE ISU-6 has a 25oC Li+ ion conductivity of 0.7 mS/cm ± 0.4 mS/cm and GSE ISU-5 has a 25oC Li+ ion conductivity of 1 mS/cm ± 0.4 mS/cm. Shown in Figure II.9.F.1C, the electronic ASR of the different ISU GSEs was measured using the DC polarization technique. In these experiments, a static, 1V potential was applied for 3-5 hours across the cell with blocking Au sputtered electrodes while the responding electronic current was measured as a function of time. The data shows the evolution of the electronic ASR as the Li+ continue to pile up at the interface as a function of time. It was determined that the newest chemistry, ISU-6, demonstrates an electronic ASR of ~10 M Ω-cm2 after ~3 hours of polarization. Figure II.9.F.1D shows the results of cyclic voltammetry (CV) used to test oxidative stability on asymmetric cells, assembled as Li metal | GSE | stainless steel. No major oxidative peaks are present in each ISU GSE materials. The ISU-5 and ISU-6 compositions were found to be more stable than the previous ISU-4 composition as indicated by the consistently lower oxidative currents in the range of 1.5 to 3 V which we ascribe to polysulfide -S-S- reduction and oxidation. The lack of major oxidative peaks indicates that these glasses are largely stable in the potential window of 0 to 5 V vs. Li/Li+.

Nitrogen Analysis of MOSN MGF GSEs

The MOSN MGF GSE, ISU-4, was successfully prepared through the addition of a nitrogen containing precursor to the MOS MGF, ISU-3, base composition. The retention of nitrogen was confirmed with C/H/N/S combustion analysis and x-ray photoelectron spectroscopy (XPS).

The CHNS analysis confirmed the MOS, ISU-3, composition contained 0.00 wt% N, while the MOSN, ISU-4, composition had 0.155±0.001 wt% N. This value is slightly lower than the compositionally batched value of 0.254 wt% N. The N 1s XPS spectra confirms this finding, as shown in Figure II.9.F.2. The MOS ISU-3 composition is featureless in this region, while the MOSN ISU-4 composition and LiPON GSEs exhibit an XPS peak at ~399.5 eV. Mascaraque et al.[1] have assigned this peak to the trigonal coordinated nitrogen (Nt), see insert to Figure II.9.F.2. An additional peak is observed in the LiPON N1s XPS spectra at ~397 eV which has been assigned to the doubly bonded nitrogen (Nd) which appears to not be present in the MOSN glass[2].

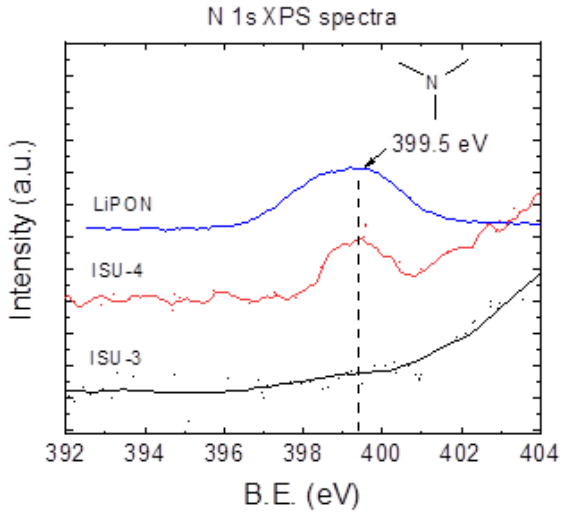

Figure II.9.F.2 N 1s XPS spectra of ISU-3 and ISU-4 GSEs.

Chemical Stability

TGA results shown in Figure II.9.F.3A reveal pure sulfide glass, Figure II.9.F.3B that reacts immediately compared to ISU-4 and ISU-5 GSEs Figure II.9.F.3C which remain stable for multiple hours. The new MOS GSE also show stability for multiple hours. The ISU GSEs exhibit the chemical stability required to be handled in a dry room environment for short periods of time with little degradation of the material.

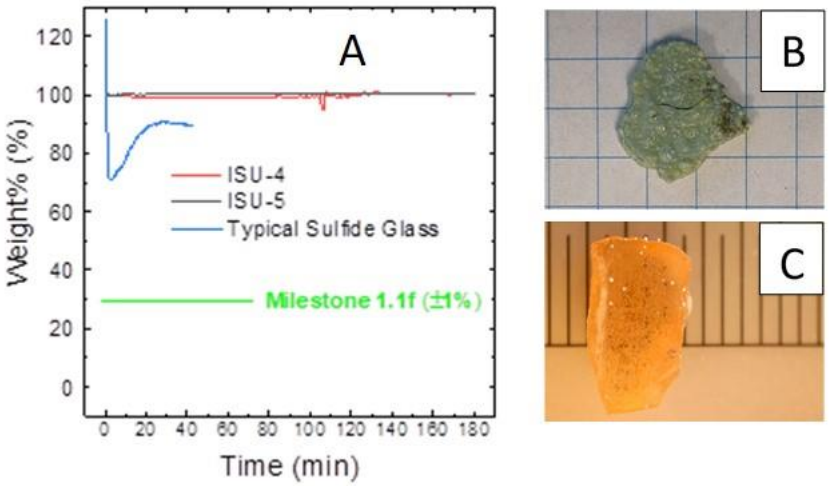

Figure II.9.F.3 (A) TGA results for a typical sulfide glass, that reacts violently with air, compared to the ISU-4 and ISU-5 compositions that do not react at all or react very little with air. (B) Photograph of a typical sulfide glass after exposure to atmosphere for an hour. (C) Optical micrograph of a MOS glass exposed to atmosphere for 3 hours.

Electrochemical Stability

Time-dependent EIS was conducted on symmetric Li | GSE | Li coin cells and in a second cell design with an approximate stack pressure of 5 MPa to determine the stability of the GSEs in contact with lithium metal. Any formation of a solid electrolyte interphase (SEI) can be seen in the Nyquist plots and the DC resistance can be determined using an equivalent circuit diagram. Figure II.9.F.4 demonstrates that the ISU-5 composition forms a stable interfacial layer after roughly four hours that generally tends to decrease with increasing time. This shows that the ISU-5 composition is stable against lithium metal at no applied potential, forming a slightly less conductive SEI that does not continue to grow over time.

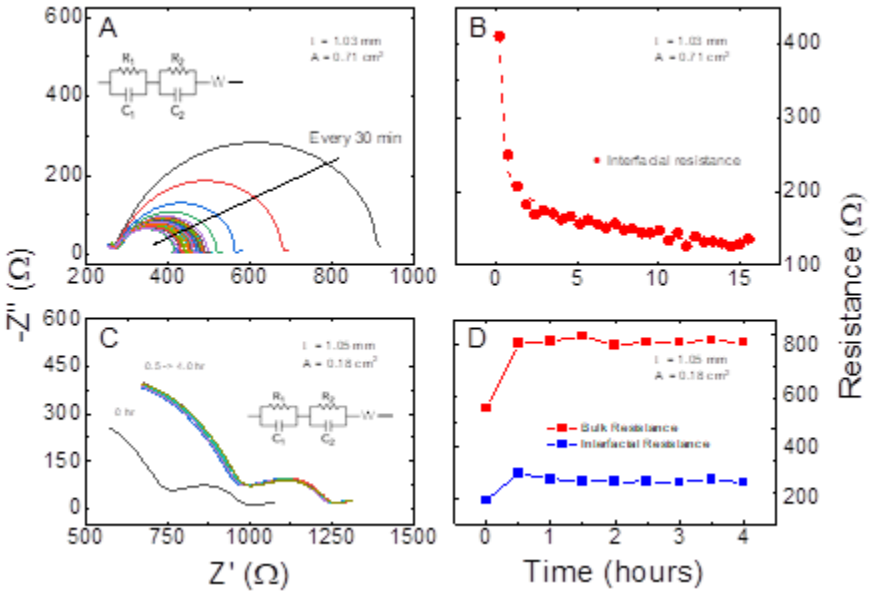

Figure II.9.F.4 (A) Nyquist plot of ISU-5 symmetric cell at approximately 5 MPa for 16 hours with EIS scans every 30 minutes. (B) Equivalent circuit fitted EIS data from (A) showing a decrease in interfacial resistance that plateaus at around 120 Ω. The dotted line is shown as a guide for the eyes. (C) Nyquist plot of ISU-5 symmetric coin cell. (D) Equivalent circuit fitted EIS data from (C) showing a slight increase in bulk and interfacial resistance in the first 30 minutes after which a plateau is seen.

Development of Thin-Film Glass Ribbon Processing Facility

Our team has developed the capability to draw thin-film glass ribbons in a high quality glovebox environment as shown in Figure II.9.F.4A-D. The initial drawing capability was achieved outside of the glovebox with a custom draw tower, as seen in Figure II.9.F.4A. Once the drawing conditions were determined, the draw tower was enchased in a large N2 glovebox, Figure II.9.F.4B, which is operated from an external scaffolding system. Figure II.9.F.4C shows the system used to lower GSE preforms into the furnace to initiate the film drawing process. Once the film drawing process has stared between 10 and 100 m of glass can be drawn into thin films of variable thickness. Figure II.9.F.4C demonstrates the continuous film drawing process during operation inside of the glovebox environment.

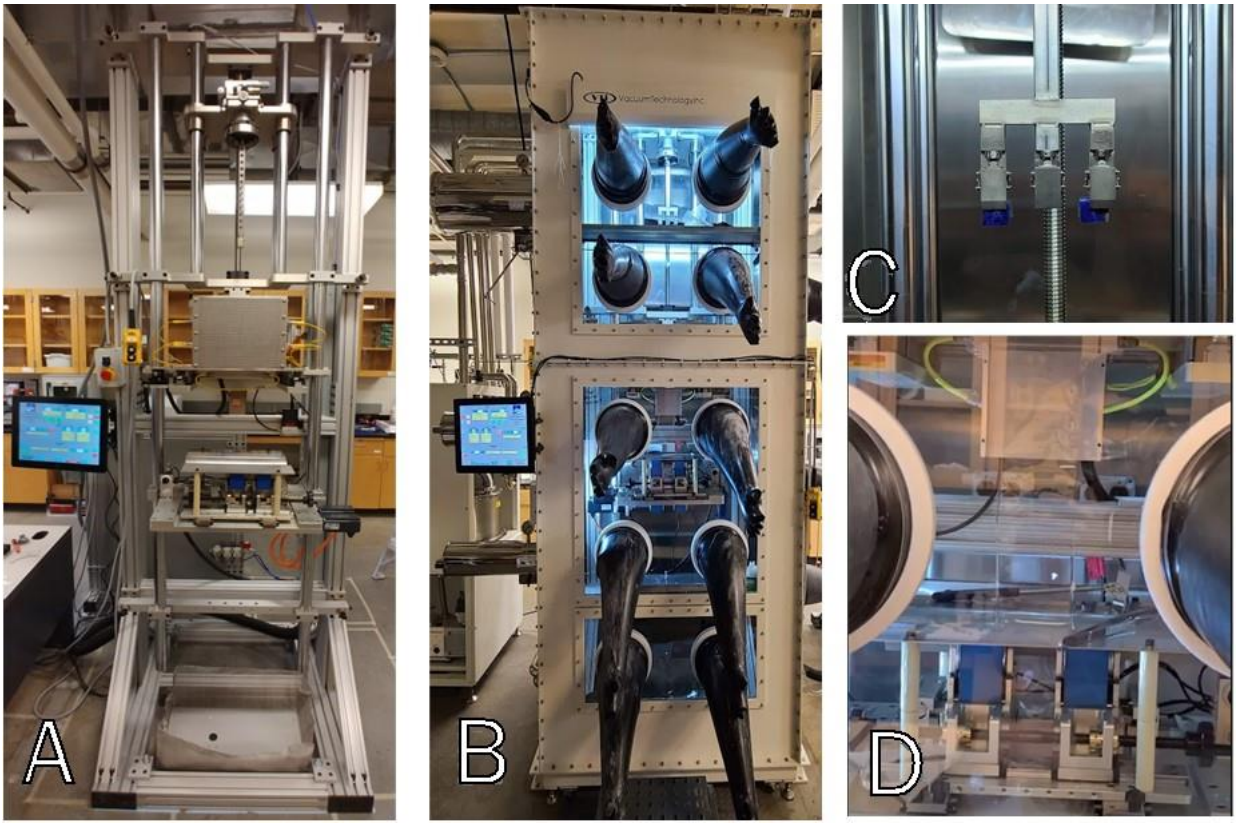

Figure II.9.F.5 (A) Inner assembly of the draw tower without the glovebox. (B,C) External views of the draw tower assembly in the glovebox. (D) Continuous film drawing of LiPO3 glass inside of the glovebox facility.

Develop Processing Conditions for the Production of Thin-Film MOSN MGF GSEs Ribbons

A large melting furnace and crucible were used to prepare 300+ g preforms of stable oxide glasses with similar properties to the planned MOSN GSE chemistries. The preforms were cast onto a temperature-controlled brass mold and then annealed through a slow cool thermal cycle for the specific chemistry. This consists of an isothermal hold near the Tg to remove mechanical stresses induced in the GSE preform during the casting and quenching process, followed by a slow cool to avoid thermal shock induced cracking of the GSE preform. This optimized process will allow for scale-up of chemistries selected based on initial property testing.

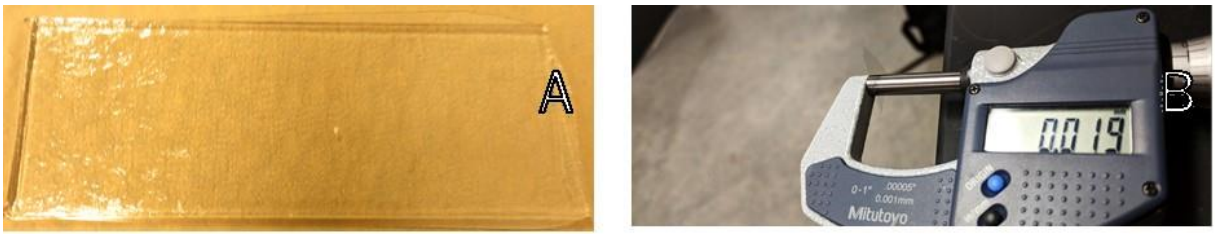

Figure II.9.F.6 (A) Full size preform (10cm x 30cm x 1cm) of LiPO3 glass (B) Drawn thin-film ribbon of LiPO3 glass thin-film (19 µm).

Prepared preforms were loaded into the draw tower assembly and lowered into a box furnace heated slightly above Tg. The glass becomes viscous enough to be slowly drawn, first by hand, then using a controlled conveyor. Temperature and draw speed were adjustable to control the film thickness. Pieces of the thin film were sectioned off and stored for future use. Most work has been done using stable oxide glasses to this point but adjusting the processing parameters for MOSN GSE chemistries will only require knowledge of basic material properties.

Fabricate and Test ASSLBs GSEs in Large Area Planar Formats.

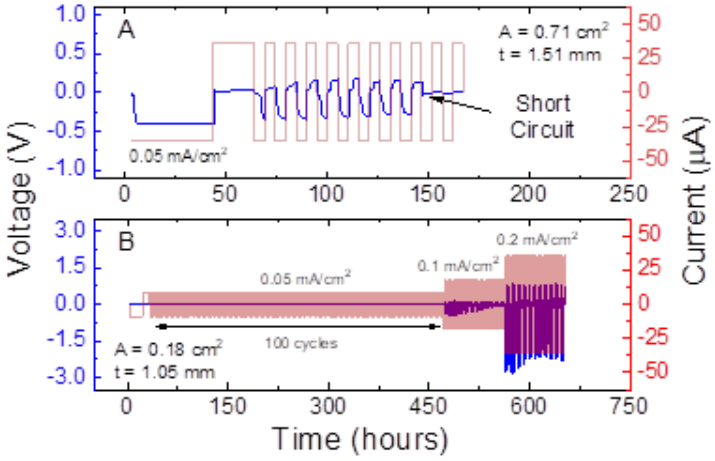

Figure II.9.F.7 A) Low current density symmetric cell cycling of ISU-4 composition showing unstable cycling for nine cycles prior to shorting. B) Low current density symmetric cell cycling of ISU-5 composition showing stable cycling for 100 cycles at low voltage. Cycling stability decreased as the current density increased until short circuiting after cycling at 0.2 mA/cm2

Select GSEs were tested in coin cells to determine cycling stability. In Figure II.9.F.7, the ISU-5 glass was cycled for 100 cycles at 0.05 mA/cm2 following which the current density was increased to 0.1 mA/cm2 for 20 cycles and then to 0.2 mA/cm2 until shorting occurred. The consistent low voltage of the cell during cycling at low current density indicates that the resistance of the cell does not increase significantly. At higher current densities, the cell begins to have a larger change in voltage than expected, indicating that some chemical reaction or surface alteration has occurred. Based on recent studies by Wang et al[3]., it is believed that this increase of resistance may be due to a lack of conformal lithium metal during stripping. Applied stack pressure is being investigated as a means to decrease this effect. The ISU-5 composition is considered to be stable against lithium dendrite formation at low current densities for more than 100 cycles.

Lithium meta-phosphate glass (LiPO3), with a low room temperature conductivity (~10-9 S/cm), were drawn into a thin film using the draw tower. Thin-film pieces of approximately 50 µm in thickness were fabricated into symmetric cells inside CR2032 coin cells and tested at low current density to determine cycling stability. It can be seen in Figure II.9.F.8 that at the low current densities necessary due to the poor conductance of the glass, stable cycling is possible for 100 cycles. These results indicate that higher conductivity glassy materials such as the ISU-6 composition will be very viable low-conductance solid electrolyte materials when drawn to into thin-films.

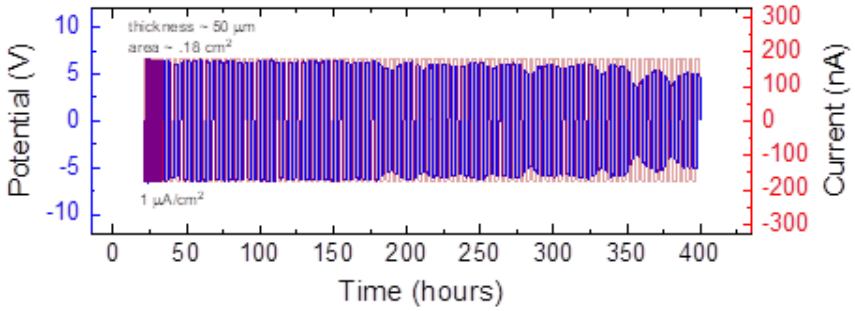

Figure II.9.F.8 Low current density symmetric cell cycling of the drawn thin-film lithium oxy-phosphate glassy electrolyte. Inconsistent voltage required in the range from 200-400 hours is partially due to temperature-related Arrhenius conductivity effects due to inconsistent laboratory room temperature varying from approximately 20-28°C.

Conclusions

In this first year of the project we have:

- Developed new MGF MOSN GSEs that have met all of the required milestone properties for the MGF MOSN GSEs in this project.
- Assembled the glass preform draw tower inside a high-quality glove box.
- Developed glass melting, casting, and annealing processes to produce high quality large glass preforms of the MGF MOSN GSEs
- Demonstrated drawing thin films of LiPO3 GSEs in multiple meter lengths and at < 20µm thickness.
- Demonstrated symmetric cell testing of thin film LiPO3 GSEs over hundreds of hours and hundreds of cycling.
- Demonstrated symmetric cell testing of bulk, < 1mm, MGF MOSN GSEs over hundreds of hours and hundreds of cycling.
- Published one paper, one paper in press, and submitted and under review three publications from this work.

Key Publications

1. "Glass Transition Temperature Studies of Planetary Ball Milled Na4P2S7-xOx, $0 \leq x \leq 7$, Oxy-Thio Phosphate Glasses", Adriana Joyce; Steven Kmiec, Steve W Martin, Journal of Non-Crystalline Solids, Vol. 551 pps120462, 2021.
2. "Anomalously Strong Viscosity Behavior In Mixed Oxy-Sulfide Na4P2S7Ox Invert Glasses," Steven Kmiec, Jacob Lovi, Adriana Joyce, Dmitriy Bayko, Steve W Martin, Journal of Non-Crystalline Solids, Manuscript number NOC-D-20-00706, In press.
3. "A New Amorphous Oxy-Sulfide Solid Electrolyte Material: Anion Exchange, Electrochemical Properties, and Lithium Dendrite Suppression via in situ Interfacial Modification," Ran Zhao, Guantai Hu, Steven Kmiec, Ryan Gebhardt, Alison Whale, Steve W. Martin, ACS Applied Materials and Interfaces, Manuscript number am-2020-09420a, Submitted May 23, 2020.
4. "A Study on the Improved Structure and Properties of Cation and Anion Double Doped Li10[SnySi1-y]P2S12-xOx Solid Electrolytes," Kim, Kwang-Hyun; Martin, Steve W., Chemistry of Materials, Manuscript ID: cm-2020-02499d, Submitted June 15, 2020.
5. "Investigations into Reaction between Sodium and Solid-State Sodium Electrolytes," Michael Lazar, Steven Kmiec, Adrian Joyce, Steve W. Martin, ACS Applied Energy Materials, Submitted April 21, 2020,

References

1. Mascaraque, N., et al., Thio-oxynitride phosphate glass electrolytes prepared by mechanical milling. Journal of Materials Research, 2015. 30(19): p. 2940-2948.
2. Zhao, S.l., et al., Study on structure and electrochemical properties of LiPON thin film. Cailiao Rechuli Xuebao, 2005. 26(4): p. 17-21.
3. Wang, M.J., R. Choudhury, and J. Sakamoto, Characterizing the Li-Solid-Electrolyte Interface Dynamics as a Function of Stack Pressure and Current Density. Joule, 2019. 3(9): p. 2165-2178.

Acknowledgements

Funding for this work was provided by the ARPA-E of the Department of Energy through contract number DE-EE0008852. Dr. Dapeng Jing of the Materials Analysis and Research Laboratory (MARL) of the Iowa State University Office of Biotechnology is thanked for his help with the collection of the XPS data. Dr. Sara Cady of the Chemical Instrumentation Facility (CIF) of the Iowa State University Chemistry Department is thanked for the collection and analysis of the CHNS combustion experiments.

II.9.G Physical and Mechano-Electrochemical Phenomena of Thin Film Lithium-Ceramic Electrolyte Constructs (University of Michigan)

Jeff Sakamoto, Principal Investigator
University of Michigan
Mechanical Engineering
2350 Hayward Ave.,
Ann Arbor, MI, 48109
E-mail: jeffsaka@umich.edu

Tien Duong, DOE Technology Development Manager
U.S. Department of Energy
E-mail: Tien.Duong@ee.doe.gov

Start Date: October 1, 2019 End Date: September 30, 2022
Project Funding: $1,250,000 DOE share: $1,000,000 Non-DOE share: $250,000

Project Introduction

While a small number of solid electrolytes exhibit high ionic conductivity (~1mS cm at 298K), few are stable against Li metal. The garnet-type solid electrolyte, based on the nominal formula $Li_7La_3Zr_2O_{12}$ (LLZO), is unique in that it is a fast ion conductor and – as we demonstrated in our recent project (DE-EE-00006821) – is stable against Li. Moreover, our former project successfully demonstrated a decrease in Li-LLZO interface resistance from 12,000 to 2 Ohms cm^2 and stable cycling at 1 mA cm^2 for 100 cycles (+ - 15 µm Li per cycle). Although the past project (DE-EE-00006821) demonstrated LLZO is a viable solid electrolyte for enabling batteries using metallic Li, the studies used thick pellets (1mm) and thick anodes (~500 µm). To achieve commercial relevance, performance must be demonstrated using substantially lower LLZO and Li thickness.

Objectives

The goal of this project is to understand the underpinning mechanisms that comprise these knowledge gaps to advance LLZO thin film technology. At the University of Michigan (UM), **Sakamoto-Dasgupta-Siegel** have an established history of research with LLZO, batteries, solid-state batteries, computation related to batteries, interface engineering, and the manufacturing research of batteries.

Approach

To achieve a step increase in technology readiness level (TRL), the same performance characteristics previously shown should be demonstrated in technologically relevant cells, for example, thin LLZO using thin Li electrodes.

Results

The first year of the project focused on designing, integrating, and optimizing relevant model thin film, solid-state prototype cells. The thin film constructs (TFC) consisted of LLZO and various forms of Li metal. Reference electrodes were integrated when certain studies required them. A summary of the activities, tasks, and milestones in FY 2020 is provided.

Milestone 1.1. (Due 2020 Q1) Milestone 1.1 was successfully completed. Using the reference electrode design criteria for thick film LLZO, the same approach was used to establish the reference electrode geometry and placement for the thin film constructs (TFC) to be used throughout the project. The design will guide fabrication and testing of reference electrodes in Milestone 1.2. and 2.1 where TFC are to be cycled with reference electrodes.

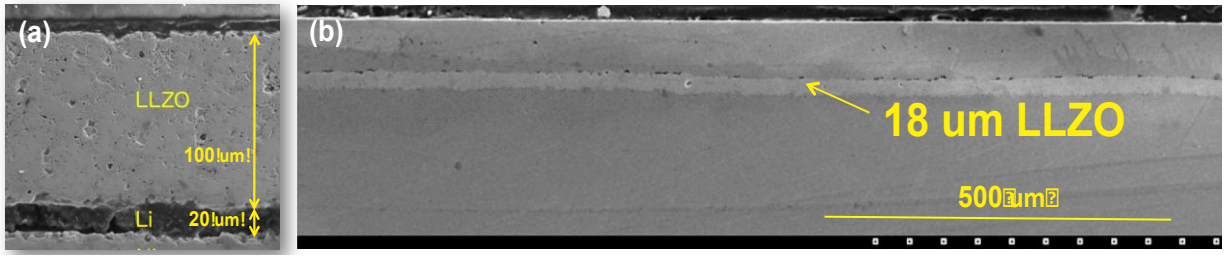

Figure II.9.G.1 Thin Film Construct and precision reference electrode manufacturing. (a) TFC consisting of 20 µm thick Li and 100 µm thick LLZO. (b) 18 µm tape cast and densified LLZO cast and polished in metallographic mounting epoxy.

Milestone 1.2. (Due 2020 Q2) Demonstrate manufacturing and preliminary cycling tests of TFC: Milestone 1.2 was successfully completed. A scale-able approach was used to manufacture thin (≤50 - 100µm) LLZO films with comparable microstructures and conductivities to bulk processed LLZO manufactured (Figure 2). This approach will guide the manufacturing of TFCs throughout subsequent milestones.

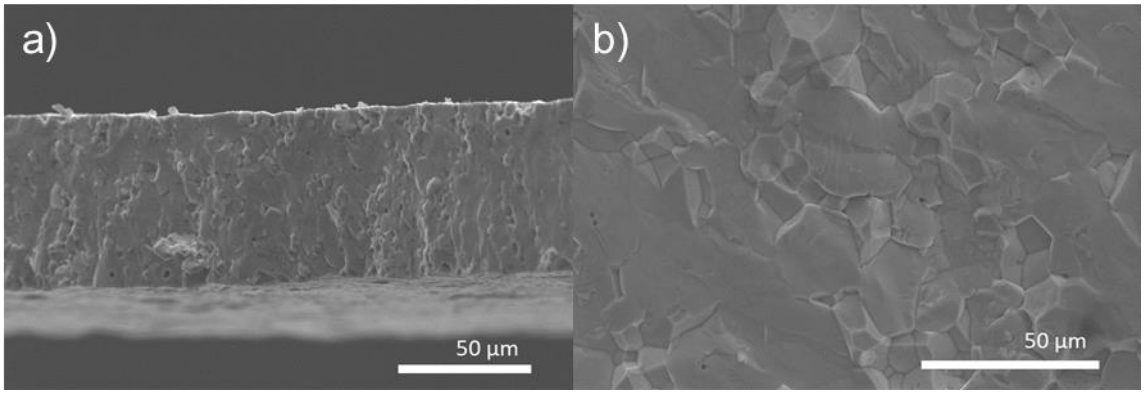

Figure II.9.G.2 Manufacturing of TFC with desired microstructure and thickness. (a) Fracture surface of a 70µm thick LLZO thin film, in comparison to the (b) fracture surface of a 1mm thick hot-pressed LLZO pellet.

Milestone 2.1. (Due 2020 Q3) Initial integration of precision micro reference electrodes with thin Li and thick LLZO: Milestone 2.1 was completed. Using a precision Li deposition technique, thin Li metal microelectrodes were integrated with thicknesses between 1 and 20µm. Precision micro reference electrodes were also deposited and tested successfully on thick LLZO membranes to serve as a baseline for measuring the critical current density (CCD) (Figure 3). The baseline cell with thin Li and thick LLZO will be compared against the CCD of TFC.

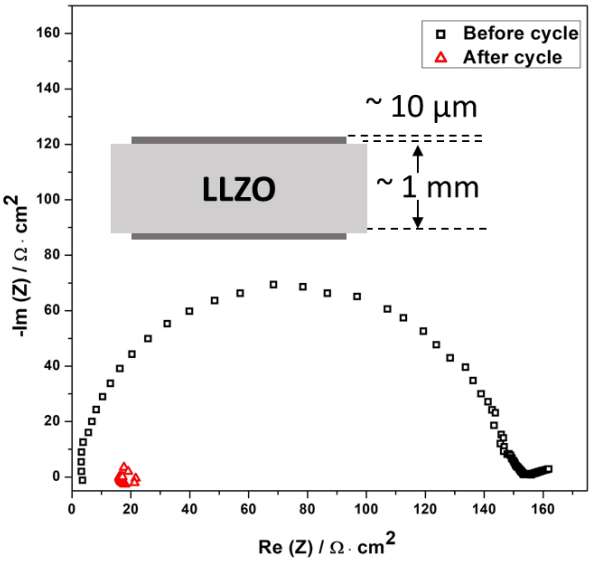

Figure II.9.G.3 Electrochemical impedance spectra of 1mm thick hot-pressed LLZO using 10µm thick precision working and reference electrodes.

Task 3: Mechanics of the Li-LLZO interface The goal of the Task 3 Milestone was to measure the CCDs of thin film constructs (TFC). Some of the data was acquired and is currently undergoing analysis. Because the laboratories were inaccessible for April and May, progress toward the Q3 milestone was slowed. However, the Sakamoto group was able to manufacture TFCs for delivery to the Dasgupta group for surface chemical analysis using X-ray photoelectron spectroscopy (XPS) (Figure 4). The XPS of as fabricated TFC indicated the LLZO surface was relatively clean and consistent through the top ~ 100 nm. There likely was some Li carbonate on the surface, but was only ~ 10 nm thick. After sputtering beneath 10 nm the LLZO composition was relatively constant. The impact of these analyses demonstrates that the surface of as fabricated TFC LLZO is clean on both the Li anode and Cathode interfaces. Because surface cleanliness directly correlates with interface resistance, these data indicate the interface resistances should be relatively low.

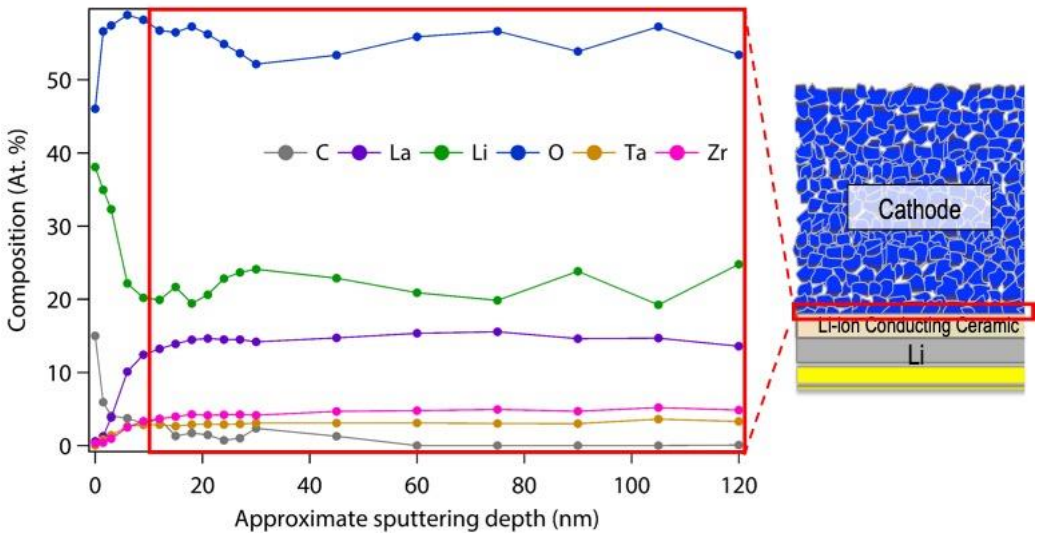

Figure II.9.G.4 XPS surface analysis of as densified TFC LLZO.

Task 4: Stability and Kinetics of the LLZO-Electrolyte Interface (Q4-2020 Completed) To study the behavior or TFC during cycling, cathode technology was developed. Previously, it was determine that state-of-the-art electrolytes react with the TFC to form a solid-electrolyte interphase. The interphase increase the

cell resistance with time. To eliminate the solid-electrolyte interphase reaction, a new cathode technology was developed. It was implemented to enable preliminary cycling studies of TFC.

Conclusions

The focus in the first year of this project was to systematically design, develop, manufacture, and optimize relevant model thin film constructs (TFC). The development of TFCs was successful, enabling the study of the physical and mechano-electrochemical phenomena in prototype cells representing commercially relevant solid-state batteries in years 2 and 3.

Key Publications

1. Sakamoto, Dasgupta, Postdoc Kazyak, and PhD Student Wang submitted an invited Perspective to Cell Press *Joule*; "Transitioning solid-state batteries from the lab to market: linking fundamental understanding with practical considerations". The Perspective leverages our strong connections with industrial leaders in automotive EV technology: Asma Sharafi, Andy Drew, and Ted Miller (**Ford**), Tim Arthur (**Toyota**), and Tobias Glossman (**Daimler-Benz**). Each group was specifically identified for their unique expertise and to represent diverse global perspectives on vehicle electrification enabled by solid-state batteries.

Acknowledgements

The PIs would like to acknowledge and also thank support from Patricia Smith (US Navy NSWC, Carderock). Adrienne Riggi served as the DOE NETL Program Manager for this project.

II.9.H Low Impedance Cathode/Electrolyte Interfaces for High Energy Density Solid-State Batteries (University of Maryland, College Park)

Eric Wachsman, Principal Investigator
University of Maryland
1206 Engineering Laboratory Building
College Park, MD 20742
E-mail: ewach@umd.edu

Yifei Mo, Principal Investigator
University of Maryland
1137 Engineering Laboratory Building
College Park, MD 20742
E-mail: yfmo@umd.edu

Tien Duong, DOE Technology Development Manager
U.S. Department of Energy
E-mail: Tien.Duong@ee.doe.gov

Start Date: October 1, 2019 End Date: September 30, 2022
Project Funding: $1,250,000 DOE share: $1,000,000 Non-DOE share: $250,000

Project Introduction

All-solid-state batteries using a ceramic fast Li-ion conductor as a solid-state electrolyte (SSE) have been proposed as a promising strategy to significantly increase the energy density of lithium batteries. Due to their high ion conductivity and excellent stability, Li-stuffed garnets exhibit the most promising physical and chemical properties for SSEs. However, the typical microstructure (thick (>100 μm) bulk electrolyte and simple planar electrode/electrolyte interfaces) combined with poor electrode wetting of the garnet resulted in excessively high area specific resistances (ASRs) that severely limited achievable current density and cell energy density. The key objective of this project is to develop composite cathode-garnet structures that enable high loading of advanced NMC cathodes with both low cathode/electrolyte interfacial impedance and high cyclability. Our approach is to extend our prior garnet trilayer architecture to an integrated high-conductivity garnet network with high-energy NMC cathodes to achieve low-interfacial impedance, using state-of-the-art ceramics synthesis, processing, and fabrication guided by computational materials design. This project will demonstrate the ability to make a high energy solid-state battery with a long cycle life using Li garnet as the solid electrolyte, Li metal anode, and NMC cathode by applying novel interfacial engineering and trilayer cell architectures. Moreover, this project addresses the key challenge in truly enabling an all-solid-state battery with Li metal and high-energy NMC cathode, as well as low electrode interfacial impedance, high rate, and good stability, leveraging developed technologies in the prior EERE BMR projects. The outcomes of this project can potentially revolutionize all-solid-state Li-metal battery technology for a wide range of applications.

Objectives

The project objective is to research, develop, and test Li-metal-based batteries that implement solid SSEs equipped with NMC cathodes integrated into the Li-metal/LLZ (Li7La3Zr2O12) tri-layer architecture. Specifically, the team will achieve the following: (1) identify and demonstrate interfacial layers to achieve low impedance and stable NMC/LLZ interfaces; (2) develop novel processing techniques to fabricate NMC/LLZ composite cathodes with low interfacial resistance; and (3) enable high-performance ASSBs with an energy density of 450 Wh/kg and 1400 Wh/L and negligible degradation for 500 cycles.

Approach

In this new EERE project, the team will build on their demonstrated expertise with garnet electrolytes and all-solid-state cells in an integrated computational and experimental approach to accomplish the following: (1) engineer interfaces to overcome high NMC/LLZ interfacial impedance and interfacial degradation; (2) develop processing and fabrication techniques to achieve high-loading NMC/LLZ composite cathodes with low resistance and high cyclability; and (3) integrate the NMC/LLZ cathodes into all-solid-state Li-metal/LLZ cells to achieve high-energy-density batteries.

Results

Computational studies based on first principles calculations were performed to evaluate the thermodynamic interface stability of LLZ solid electrolytes for cathode materials using the thermodynamic analysis demonstrated in our previous studies. As a test and benchmark of our current model, our theoretical calculations found that LLZ garnet has minor reaction with lithiated LiCoO2, and decomposes into a phase equilibria of La2O3, Li6Zr2O7, and Li5CoO4, with a small mutual reaction energy of –1 meV/atom. Moreover, LLZ garnet is less stable with delithiated Li0.5CoO2, decomposing into La2O3, La2Zr2O7, Li7Co5O12, with a reaction energy of –39 meV/atom. These formed products are consistent with previous computation studies and previous experimental studies, confirming the validity of our current computation models.

In addition, computational analyses based on the same method were performed to identify the interface stability between LLZ solid electrolytes with NMC cathode in comparison to LiCoO2 (Figure II.9.H.1 and Table II.9.H.1). The computational study found that Ni-rich cathode materials such as NMC exhibit mutual chemical reactions, suggesting a limited interface stability between LLZ garnet and NMC cathode materials. In addition, the delithiated NMC shows poor interface stability with LLZ garnet, indicating potential interface degradation during cycling or the charged state of the solid-state battery. We further analyzed the thermodynamic phase equilibria of the reaction products. The behavior of different transitions metals in the NMC cathodes were identified. In addition, we compared the interface stability of LLZ garnet with a range of different layered oxide cathodes, such as LiCoO2, LiNiO2, NMC111 and NMC in other compositions. The variation of materials stability was identified among these cathodes. It was found that higher Ni content in cathodes generally lead to poor stability.

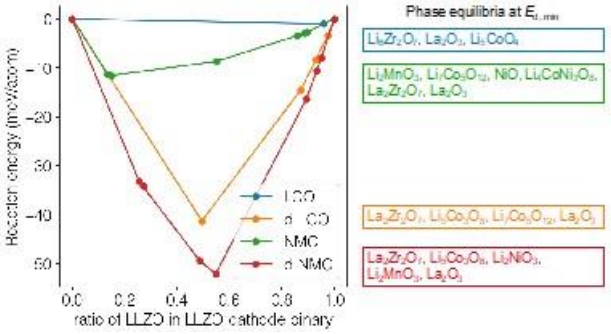

Figure II.9.H.1 Decomposition of LLZ with lithiated and delithiated (prefix "d-") LCO and NMC111. Phase equilibria of each reaction at the minimum decomposition energy for the pseudobinary of LLZO and cathode are written at right.

Table II.9.H.1 Decomposition energy and phase equilibria of LLZ with lithiated and delithiated (prefix "d-") LCO and NMC111 from thermodynamic analyses based on first principles data

	Ed (eV/atom)	Phase Equilibria
LCO	-0.0013	Li5Co04, La203, Li6Zr207
d-LCO	-0.039	La203, 02, Li7Co5012, La2Zr207
NMC111	-0.012	La203, Li2Mn03, Li4CoNi308, Ni0, La2Zr207, Li7Co5012
d-NMC111	-0.050	02, Li2Mn03, Li7Co5012, Li2Ni03, La2Zr207, La203

We also studied potential interfacial layers as a first step to identify the promising coating layers between LLZ-NMC interfaces. Using our thermodynamic scheme, we studied the interface stability of a wide range of lithium ternary oxides with commonly used cathode materials. Our analyses identified a wide range of coating materials that have been demonstrated in previous experimental studies, suggesting the validity of our approach and the promises in predicting new materials. In addition, we compared the materials stability with different cathodes, such as LiCoO2, LiNiO2, NMC111 (LiMn0.3Co0.3Ni0.3O2) and NCA (LiAl0.05Co0.15Ni0.8O2). The variation of materials stability was identified among these cathodes (Figure II.9.H.1). It was found that in all these cathodes, the delithiated states is generally less stable, and higher Ni content generally lead to poor stability with these coating materials. These results will be used for further detailed analyses to identify promising coating for LLZ-NMC interfaces.

Using demonstrated thermodynamic analyses for interface stability based on first-principles computation, we performed high-throughput screening to identify oxide materials that stabilize with LLZO-NMC interfaces. We performed a high-throughput systematic analysis of these coating materials by investigating the chemical stability of the cathode-LLZO interface, chemical stability of oxide coatings with NMC and LLZO and the electrochemical stability of the coated interfaces. The results of chemical and electrochemical stability of ternary oxides with lithiated and delithiated NMC and LLZO are shown in Figure II.9.H.2. Our results provide the stable oxide coating for LLZO-NMC interfaces and also the stabilization mechanisms. In general, LLZO is stable with coating layers with high Li content, likely because of the high Li content of LLZO. By contrast, NMC is stable with low-Li content coatings. Due to these differing requirements for Li content, many materials are not stable with both LLZO and NMC. In summary, the compositions with small chemical and electrochemical reactions with LLZO and NMC are identified as stable coating layers (Figure II.9.H.2). Notably, our analysis identifies several compositions that have been used experimentally to stabilize the LLZO-NMC or LLZO-LCO interface. For example, the Li-Si-O and Li-Nb-O systems have several compositions with low decomposition energies with LLZO and NMC, and these systems have also been widely used experimentally as coating layers. Our analysis also identifies the lithium Al, Ti, Sn, and Ta oxides as promising systems for coating layers with LLZO and NMC interfaces. This good agreement with experiments confirms the validity of our computation approach, and many promising coatings for the LLZO-NMC interfaces are predicted and will be further tested. In summary, we have successfully achieved our milestone and Go/No-Go of computationally determine the mechanism of interfacial stabilization and the appropriate compositions to stabilize the LLZ-NMC interface.

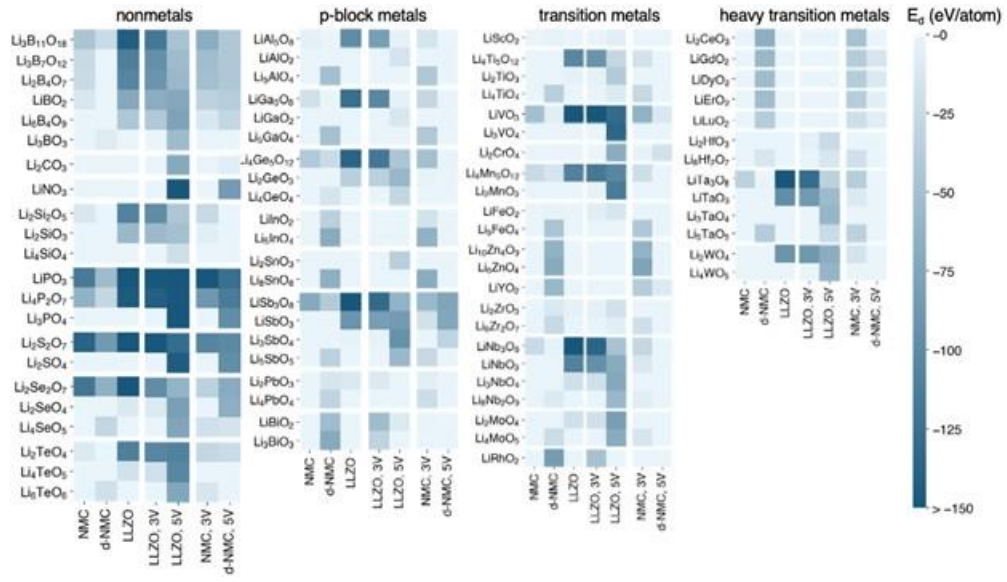

Figure II.9.H.2 Heatmap showing the chemical decomposition energy of NMC, delithiated NMC, and LLZO with lithium ternary oxide compounds, and the electrochemical decomposition energy of the coating-LLZO and coating-NMC interfaces at 3 V and 5 V.

While computational results were obtained without issue (above), experimental results were significantly delayed due to COVID-19 which shut down the university lab access for nearly 6 months and has just recently re-opened on a partial use basis.

XRD experiments were performed on composite pellets of Ta-doped LLZO (LLZTO) and cathode materials prepared by physical mixing, mold pressing and co-sintering at 700 °C for 3 hours. Cathode materials tested include NMC-111, LiMnO4(LMO), LiNi0.5Mn1.5O4(LNMO), and LiCoO2(LCO). The weight ratio of LLZTO and the cathode material in each pellet is 1:1. XRD results suggest that at 700 °C all the cathode materials investigated react with LLZTO with the reactivity increasing in the order of LCO<LNMO<LMO=NMC-111 (Figure II.9.H.3). This trend agrees with our computational studies reported above showing that higher nickel content in cathodes generally leads to poor stability with garnet. The reaction products, e.g., Li2MnO3 and La2Zr2O7, between LLZTO and NMC-111 detected by XRD have also been predicted by our previous computational studies. These consistent results demonstrate the efficacy of combining computation with experiment in facilitating understanding on garnet/cathode interfacial stability. We will proceed next to extend the experiment to include NMC in other compositions and LLZTO/cathode reactivities at other temperatures in the range of 600-1100°C to eventually complete our experimental investigation on determining thermochemical stability between LLZ and infiltrated NMC.

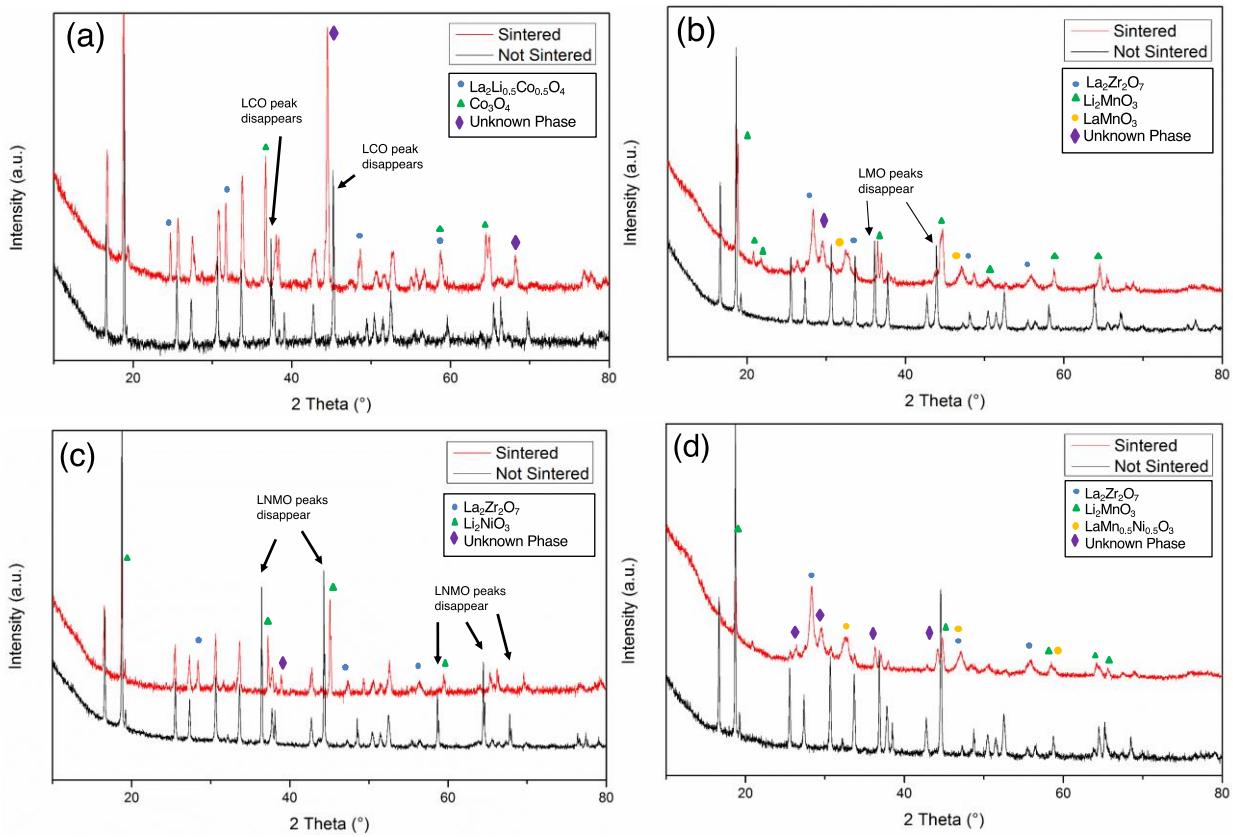

Figure II.9.H.3 XRD patterns of LLZTO and 50/50 w/w mixtures with various cathode materials before and after co-sintering at 700 °C. Cathode material for each figure is (a) LCO, (b) LMO, (c) LNMO, and (d) NMC-111.

XRD experiments were performed on composite pellets of Ta-doped LLZO (LLZTO) and cathode materials (1:1 in weight ratio) prepared by physical mixing, mold pressing and co-sintering at 500-1000 °C for 3 hours. Cathode materials tested include NMC-811, NMC-622 and LiMnO4(LMO). XRD results suggest that LMO can strongly react with LLZTO even at 500 °C (Figure II.9.H.4a). All NMCs are chemically compatible with LLZTO up to 600°C, after which minimal decomposition phases could be detected (Figure II.9.H.4b and c).

NMC-811 shows greater loss in peak intensity at 1000°C than NMC-622, indicating instability of high Ni content NMC with garnet.

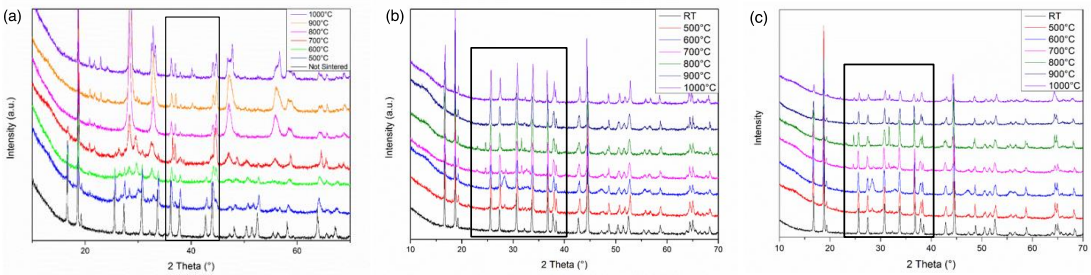

Figure II.9.H.4 XRD patterns of 50/50 w/w mixtures of LLZTO with various cathode materials before and after co-sintering at 500-1000 °C. Cathode material for each figure is (a) LMO, (b) NMC-622, and (c) NMC-811. The boxed regions are where the new peaks are appearing.

Conclusions

In this year, we have computationally determined interfacial stability between LLZ SSEs and NMC cathode, and our experiments determined thermochemical stability between LLZ and infiltrated NMC. In addition, our computational results have determined the mechanism of interfacial stabilization between LLZ and NMC through coating layers. We have achieved the Go/No-Go decision that we computationally determine appropriate compositions to stabilize the LLZ-NMC interface to achieve design capable of meeting performance requirements.

Key Publications

1. Adelaide M. Nolan, Yunsheng Liu, Yifei Mo*, “Solid-State Chemistries Stable with High-Energy Cathodes for Lithium-Ion Batteries”, ACS Energy Letters, 4, 2444-2451 (2019)

2. A. Nolan, Y. Liu, Y. Mo, “Solid-State Chemistries Stable with High-Energy Cathodes for Lithium-Ion Batteries”, ECS PRIME (10/2020) (Invited)

3. Y. Mo, “Data-Driven Discovery of New Materials for Solid-State Batteries”, ECS PRIME (10/2020)

II.9.I Molecular Ionic Composites: A New Class of Polymer Electrolytes to Enable All Solid-State and High Voltage Lithium Batteries (Virginia Polytechnic Institute and State University)

Louis A. Madsen, Principal Investigator
Department of Chemistry
Virginia Tech
319 Davidson Hall
1040 Drillfield Dr.
Blacksburg, VA 24061
E-mail: lmadsen@vt.edu

Feng Lin, Principal Investigator
Department of Chemistry
Virginia Tech
323 Davidson Hall
1040 Drillfield Dr.
Blacksburg, VA 24061
E-mail: fenglin@vt.edu

Tien Duong, DOE Technology Development Manager
U.S. Department of Energy
E-mail: Tien.Duong@ee.doe.gov

Start Date: October 1, 2019 End Date: December 30, 2020
Project Funding: $434,343 DOE share: $329,572 Non-DOE share: $104,771

Project Introduction

Based on a newly discovered class of solid polymer electrolyte materials, which we term molecular ionic composites (MICs), we are developing Li solid electrolytes targeted for use in transportation applications. MICs form a mechanically stiff (~ 1 GPa modulus), electrochemically stable, and highly thermally stable matrix that can resist dendrite formation with metal anodes, allow high voltage operation, provide robust safety against fire, and enable fast charging/discharging over a wide temperature range. The component molecules in MICs are inexpensive and MICs can be processed to yield a large area format at room temperature and generally in ambient atmosphere. Our team is advancing this class of polymer electrolytes to promote uniform lithium plating, inherent safety, and low reactivity against both lithium metal anodes and high voltage layered oxide cathodes.

Objectives

Based on a newly discovered class of solid PE materials, that is, molecular ionic composites (MICs), the overall objective is to develop solid-state lithium conductors targeted for use in transportation applications. MICs form a mechanically stiff, electrochemically stable, and thermally stable matrix. Specific objectives include the following: (1) development of robust MIC electrolyte thin films (~ 20 μm) to serve as simultaneous nonflammable separators and dendrite-blocking Li+ conductors, (2) electrochemical quantification of key performance metrics including electrolyte stability, interfacial reactions, and suitability/compatibility with a range of electrode materials, and (3) comprehensive investigation of ion transport mechanisms and electrode-electrolyte interfacial reactivity under practical operating conditions using NMR and synchrotron X-ray analyses.

Approach

MICs rely on a unique polymer that is similar to Kevlar® in its strength, stiffness, and thermal stability, but with densely spaced ionic groups that serve to form an electrostatic network that permeates mobile ions in the

MIC. The team can tailor the ion concentrations and types to yield MIC electrolyte films that are electrochemically compatible with Li-metal anode as well as a range of high-voltage layered cathodes. They are searching the composition space of lithium salts, electrochemically compatible ionic liquids, and polymer (PBDT) molecular weight to determine best composition windows for MIC electrolytes. The team is also investigating best methods for casting thin films in terms of temperature, solvent/evaporation conditions, and control over the initial liquid crystalline gel formation point. Concurrently, they are testing MIC films in various electrochemical cells, quantifying transport and structural/morphology parameters with NMR and X-ray techniques, and measuring key mechanical (dynamic mechanical thermal analysis, stress-strain) and thermal (DSC, TGA) properties.

Results

The team has so far generated solid MIC electrolyte films with uniform thickness and with areas up to 10 × 10 cm. These films contain the charged rigid-rod PBDT polymer along with mobile and non-volatile ions (lithium salt and ionic liquid). These films are non-flammable and flexible, and can conduct Li+ over a wide range of temperature. Figure II.9.I.1 shows the chemical components of our prototype films, a transparent and flexible large area film, and an SEM image showing a smooth film surface after Li-Li electrochemical cell cycling. Table II.9.I.1 shows the composition by weight of the three main components (PBDT, LiTFSI salt, and Pyr14TFSI) as well as the final film thickness and the ionic conductivity. We have generated robust and uniform films that are down to 40 μm thick and that show high room temperature ionic conductivity (up to 2.7 × 10-4 S/cm). Madsen (PI) and Lin (co-PI) are dividing the project in terms of film fabrication, thermal, mechanical, and NMR transport and morphology analyses by Madsen, and electrochemical, interfacial, and X-ray morphology and surface analyses by Lin.

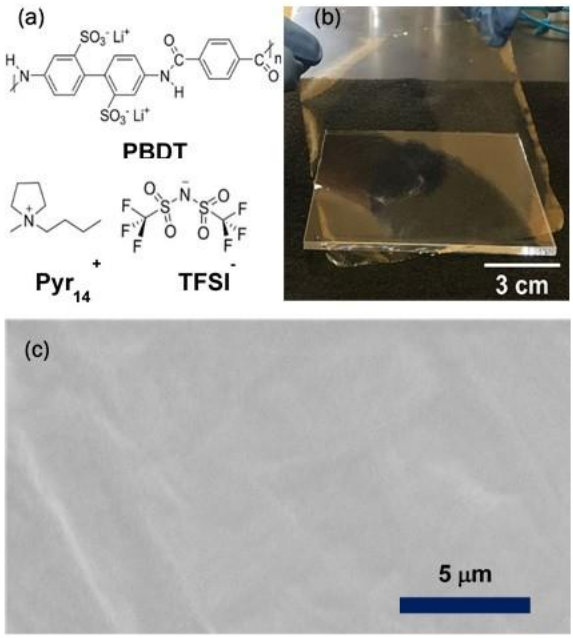

Figure II.9.I.1 Initial MIC electrolyte films. (a) Chemical structures of PBDT polymer and ionic liquid Pyr14TFSI. (b) Large area as-cast 80 mm thick MIC film. (c) SEM image of MIC film after Li-Li electrochemical cell cycling (pinhole free).

We are continuing to scan composition space and casting conditions to optimize the various film properties: conductivity, elastic modulus, and electrochemical stability with several electrode materials. We have discovered that a liquid crystalline gel forms during the casting process, as solvent evaporates. We are investigating the details of this phase formation with NMR and X-ray, which should lead to more rational control over the casting process. We are also beginning to measure conductivity over at least the range – 30°C to + 100°C, as well as DSC, TGA, and DMTA over a similar or wider temperature range.

Table II.9.I.1 Compositions by weight, final film thicknesses, and ionic conductivities of the three main components (PBDT, LiTFSI salt, and Pyr14TFSI)

Composition (PBDT-LiTFSI-Pyr14 TFSI, wt%)	Thickness (µm)	Conductivity (mS/cm) @ 25°C
10-10-80	86	0.22
10-15-75	82	0.27
15-10-75	69	0.23
15-15-70	75	0.080

Figure II.9.I.2 shows preliminary dynamic mechanical-thermal analysis (DMTA) on MIC films made using the current casting process. These initial films did not have Li salt included, and those tests are upcoming. The high modulus and thermal stability are evident in our initial tests.

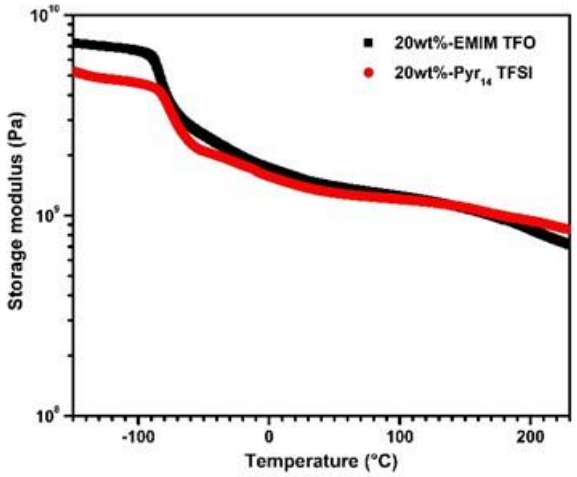

Figure II.9.I.2 Dynamic mechanical analysis of MIC electrolyte films. The red curve shows storage modulus for 20 wt% PBDT / 80% Py_{r14}TFSI electrolyte film and the black curve shows the same for 20 wt% PBDT / 80% EMIm TfO (an initial pilot material). Similar analysis of Li-loaded films is underway. These films have tensile storage modulus > 1 GPa over a wide temperature range and show no evidence of decomposition (also with TGA – not shown) to well above 200°C.

The team has also searched the composition space of Li salts, ionic liquids, and polymer (PBDT) molecular weight, as well as the relative concentrations of each component. The team has developed the baseline MIC electrolyte composition through variation of the component types and ratios, and then verified they can obtain robust films with maximal conductivity and chemically/electrochemically stability in the presence of Li metal and during Li|Li cell cycling. Figure II.9.I.3 shows the chemical structures and relative amounts of the solid electrolyte components, a photograph of a uniform and flexible MIC film, ionic conductivity versus temperature, and separate ion diffusion coefficients versus temperature.

An exciting frontier in this work is the ability to reversibly measure properties for these MIC electrolytes over a wide temperature range, at least from -50 to +200 °C. This opens possibilities for a range of Li-based batteries where a monolithic solid Li conductor electrolyte film can be employed with no thermal or mechanical degradation upon fast charging/discharging and/or when operating in extreme temperature environments. The team has explored such temperatures with ionic conductivity and NMR diffusometry experiments (Figure II.9.I.3, parts c and d), and will expand this work further.

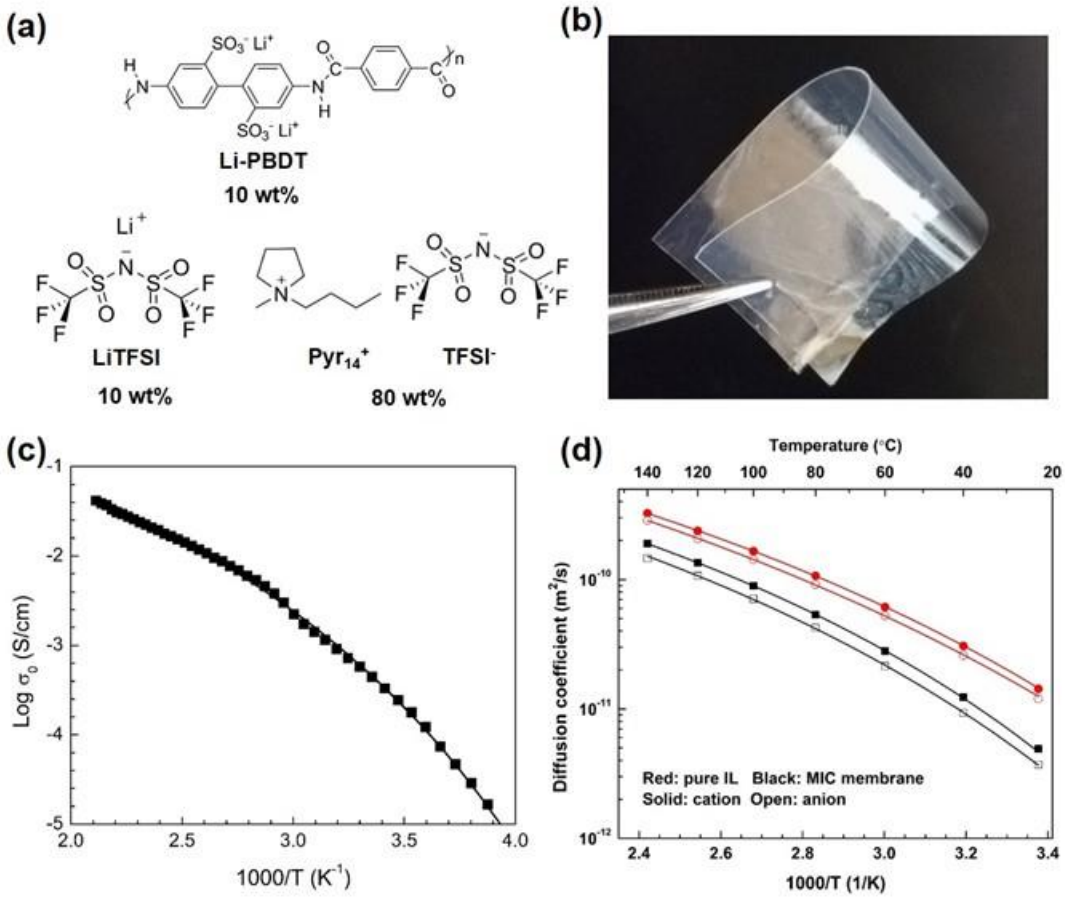

Figure II.9.I.3 Composition and transport properties of MIC electrolyte films. (a) Chemical composition of baseline-optimized MIC film with relative percentages of each component. (b) Photograph of MIC film with improved uniformity and flexibility. (c) Temperature dependence of ionic conductivity of the MIC film. (d) Separate diffusion coefficients of ionic liquid (IL) cation and anion in the film compared to the diffusion coefficients of pure IL. (Li+ diffusion coefficient measurements underway.) This composition enables robust electrolyte films down to 60 μm thickness that can reversibly thermally cycle from -50 to +200 °C.also with TGA – not shown) to well above 200°C. An article on this work has been submitted for publication.

Regarding the comparison of ionic conductivity and NMR diffusometry results in Figure II.9.I.3 parts (c) and (d), the team is working toward a model for prediction of conductivity from diffusion coefficients. Initial observations suggest that something about the interface (between electrolyte and electrode, be it stainless steel for conductivity or Li for cell cycling) is unduly influencing overall conductivity and Li|Li cell performance. We are investigating the possibility of a surface layer that develops during casting that is denser in PBDT polymer, thus reducing cell performance. The team expects to use this fundamental knowledge to be able to tune our relatively simple tape/solvent casting procedure (time, solvent removal, solvent composition) to alleviate this effect.

The team is pursuing more broad mechanical testing on these MIC films, including variable-temperature shear rheology and dynamic mechanical tensile measurements. Figure II.9.I.4 shows a tensile stress-strain curve for the present MIC film at room temperature, with mechanical results described in the caption.

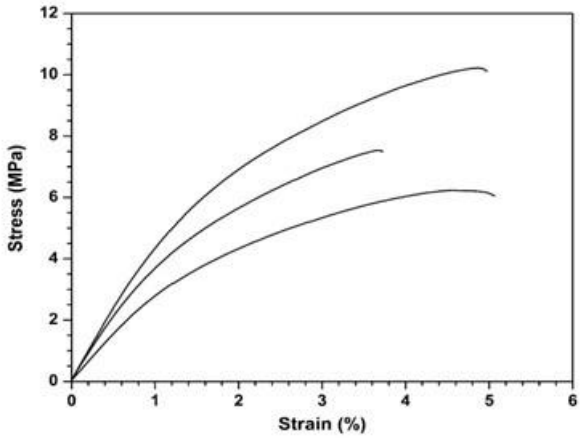

Figure II.9.I.4 Tensile stress-strain curve for MIC electrolyte film at room temperature. The three curves represent tests on dogbone samples cut from various locations spanning the as-cast film. The tensile modulus averages 400 MPa. These MIC films exhibit approximately 2× higher strain at break relative to non-Li-loaded MICs and comparable tensile modulus (see Q1 report dynamic mechanical analysis curves). Note that assembly under compression into (Li|Li symmetric) coin cells does not damage the film, as observed after disassembly. An article on this work has been submitted for publication.

The team has further investigated the compatibility between the MIC electrolyte and lithium metal anode through cyclic voltammetry (CV) and symmetric cell cycling. The team has also investigated the mechanisms of ion transport and the thermo-mechanical stability of the MIC electrolyte.

The team analyzed the formation of SEI layer between MIC membrane and lithium metal through CV characterization. Comparisons among CV curves for the MIC membrane and a liquid electrolyte composed of LiTFSI and Pyr14TFSI (Figure II.9.I.5), strongly indicates that side reactions come predominantly from the ionic liquid. In addition, reduction of $TFSI^-$ against lithium metal forms a stable SEI layer between the MIC membrane and lithium metal.

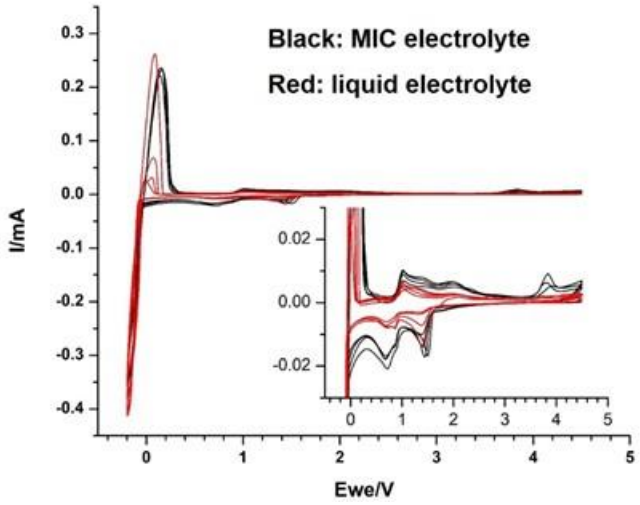

Figure II.9.I.5 Cyclic voltammetry (CV) of the MIC electrolyte membrane and a liquid electrolyte composed of LiTFSI and Pyr14TFSI in a 1:8 mass ratio. These CV measurements were recorded at room temperature using stainless steel as working electrode and lithium metal as counter and reference electrode with a scan rate of 0.1 mV s-1. The main peak near 0 V corresponds to lithium plating and stripping. The reductive peaks at 0.7 V and 1.5 V and oxidative peaks at 1.0 V and 2.0 V appear both in the MIC membrane and in the liquid electrolyte, suggesting they are caused by the IL. An oxidative peak at 3.9 V is evident only in the MIC membrane, indicating it is caused by either the polymer or an impurity.

The team has also tested the long-term compatibility of the MIC membrane electrolyte against lithium metal. This long-term test was conducted using lithium symmetric cells, with cell voltage monitored during multiple

stripping-plating cycles. Figure II.9.I.6 shows the voltage profiles for Li/MIC/Li symmetric cells cycled at 23 °C and 100 °C, in which the cells lasted for 800 and 700 hours, respectively, before cell failure. This result demonstrates that the MIC material is stable against lithium not only at room temperature but up to at least 100 °C. This is exciting because for many electrolyte systems their side reactions with lithium metal anode become more aggressive with increasing temperature, leading to rapid electrolyte consumption, SEI formation, and cell failure. This finding suggests that lithium batteries built using this MIC electrolyte can potentially work over a wide temperature range, which is crucial for applications such as electric vehicles where a cooling system is conventionally needed to maintain the temperature of the battery package within a restricted range.

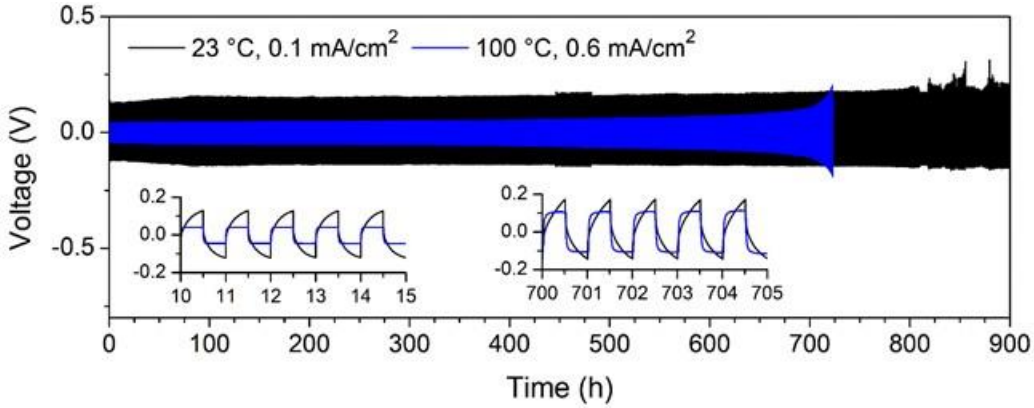

Figure II.9.I.6 Voltage profiles of Li/MIC/Li symmetric cells cycled at 23 °C using a current density of 0.1 mA/cm² and 100 °C using a current density of 0.6 mA/cm². The cells lasted for 800 and 700 hours, respectively, under these two conditions before cell failure, indicating durable compatibility between the MIC material and lithium metal over a wide temperature range. An article on this work has been submitted for publication.

The team has furthermore continued exploration of ion transport properties in this period. The lithium-ion transference number of the MIC membrane is measured (via the dc polarization method) to be 0.12 (Figure II.9.I.7 part a). To further investigate the mechanism of ion transport, dielectric relaxation spectra (DRS) have been analyzed and the α-segmental relaxation of the membrane has been identified from the frequency dependence of the imaginary dielectric modulus (Figure II.9.I.7 part c). The frequency of α-relaxation increases with temperature. The Arrhenius plot of this modulus relaxation frequency vs. temperature (Figure II.9.I.7 part d) shows that this relaxation is associated with the glass transition of the ionic liquid and salt in the membrane. The transport of ionic species in the membrane is thus decoupled from the glass transition (segmental dynamics) of the polymer, thus leading to the high ionic conductivity of the MIC. The team has also studied the thermo-mechanical stability of the MIC membrane via oscillatory shear rheology. As shown in Figure II.9.I.7 part b, the shear storage modulus (G′) of the MIC electrolyte demonstrates only a slight decay from 16.2 MPa at 25 °C to 10.5 MPa at 200 °C, demonstrating that the MIC remains solid to 200 °C.

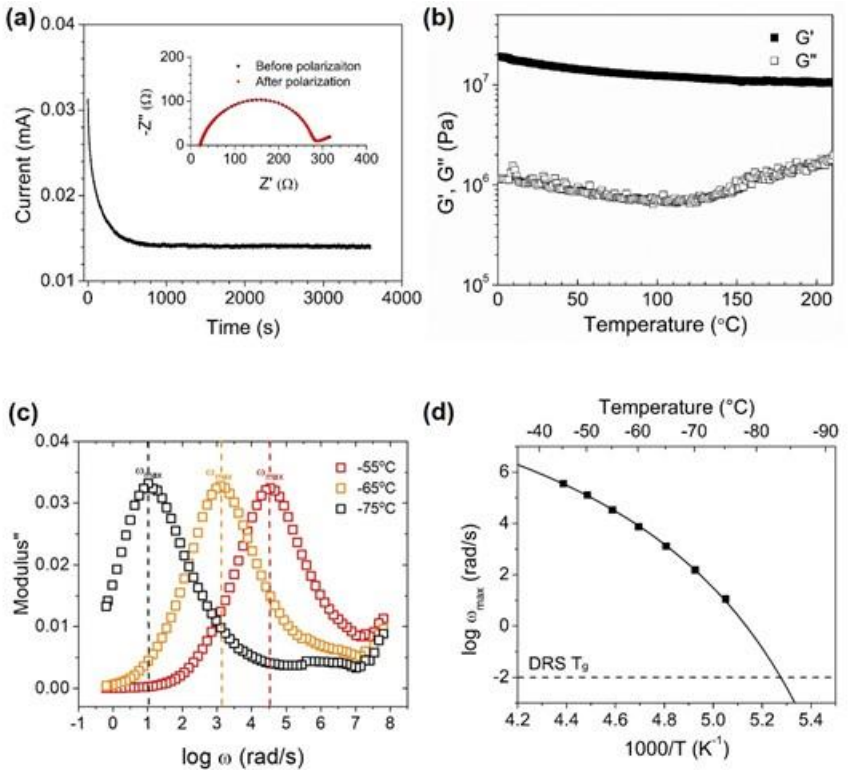

Figure II.9.I.7 (a) Lithium-ion transference number measurement of the MIC electrolyte through the dc polarization technique. Inset is the impedance spectrum before and after polarization. (b) Temperature dependence of the shear storage and loss moduli (G′ and G″) at heating rate = 5 °C min^{-1}. (c) Frequency dependence of imaginary modulus (M'') at varying temperature. The main peak is the α relaxation and the minor peak at higher frequency is the β relaxation. (d) Temperature dependence of the α relaxation frequency (ω_{max}) of the MIC electrolyte. An article on this work has been submitted for publication.

The MIC electrolyte has shown promising properties in terms of Li|Li cycling performance. As part of the project goals, the team will assemble MIC-based full cell batteries with various cathodes, thus motivating an exploration of the stability of the MIC electrolyte against layered cathodes. If there is any side reaction between the MIC electrolyte and the layered oxide cathode, the surface chemistry of the layered oxide cathode will be modified, such as lowering the transition metal oxidation states. Characterizing the surface chemistry of layered oxides is easier than characterizing the MIC electrolyte, so the team has studied how the surface chemistry of layered oxides may be influenced by contact with the MIC electrolyte. In order to mimic the chemical stability of the MIC against a given cathode, the team has used electrochemically delithiated NMC to produce a highly oxidized cathode (i.e., high nickel oxidation state) (Figure II.9.I.8 part a). Then, the electrochemically delithiated NMC electrode was cut into three pieces. The first piece was stored in an Ar glove box at room temperature. The second piece was sealed in Ar and stored at 60 °C. The third piece was in physical contact with a MIC film under high pressure and stored at 60 °C. After one month, examination by Ni L-edge soft XAS of the three electrodes (Figure II.9.I.8 part b) showed a minimal difference under the various storage conditions. This suggests that the MIC electrolyte shows high stability against layered oxide cathodes even in the charged state. This result is consistent with the robust oxidative stability of the MIC electrolyte as previously reported.

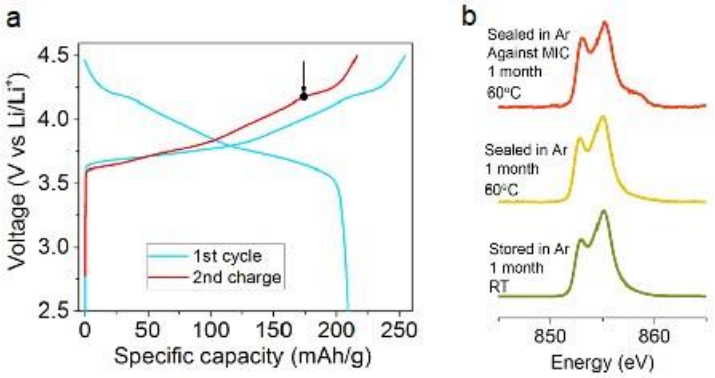

Figure II.9.I.8 (a) Charge/discharge profiles of a cell containing NMC as the cathode, 1 M LiPF6 in EC/EMC with 2 v.% VC as the electrolyte, and Li metal as the anode, the cell was cycled at C/10 within 2.5–4.5 V in the first cycle and then stopped at the charge 4.2 V. This charged cathode then serves as a testing platform to evaluate the stability of the MIC electrolyte. (b) The Ni L3-edge soft X-ray absorption spectra (XAS) in the TEY mode of the NMC811 electrode (charged to 4.2 V) after storing under various conditions. These spectra show that the MIC electrolyte is stable against layered cathodes.

The team has further studied Li-ion transport properties in MIC electrolytes and their compatibility with lithium metal over a wide temperature range through lithium symmetric cell cycling (Figure II.9.I.9). When cycled at 23 °C, the observed voltage increases slowly during the lithium stripping process, corresponding to establishment of a salt concentration gradient across the cell. The maximum voltage reached during one cycle increases monotonically with increasing current density. When the current density is increased to 0.2 mA/cm2, the voltage increases drastically to above 5 V, suggesting the concentration of Li-ion at the anode surface is approaching zero and the current density has approached the limiting current density. Since ionic conductivity increases with temperature, the maximum current density obtained from lithium symmetric cell cycling also increases with temperature. At 60 °C, the symmetric cell can be cycled steadily using a current density of 0.35 mA/cm2. The current density can be further raised to 0.6 and 1.8 mA/cm2 at 100 and 150 °C, respectively. It is encouraging that the symmetric cell can be cycled at 150 °C for 150 hours (Figure II.9.I.9 part b), further demonstrating the thermal and electrochemical stability of the MIC electrolyte at extreme temperatures.

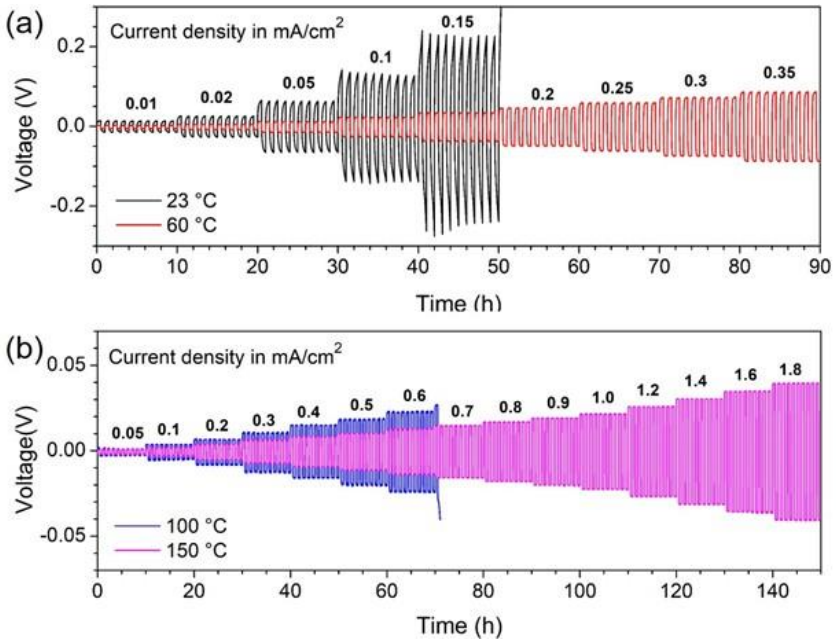

Figure II.9.I.9 Voltage profiles of lithium symmetric cells cycled at (a) 23 °C, 60 °C and (b) 100 °C and 150 °C in increasing steps of current density. The deposition and stripping time is 0.5 h respectively, and the current density (labeled above each step in mA cm-2) is changed every 10 cycles. An article on this work has been submitted for publication.

In addition to the above lithium symmetric cell tests, the team also studied the long-term cycling stability of the MIC electrolyte membrane in a Li/MIC/LiFePO4 cell at 23 °C using a C/10 charge/discharge rate (Figure Figure II.9.I.10). The specific capacity increases during the initial few cycles, probably resulting from the improved contact between the cathode and the electrolyte. The team is continuing to investigate this mechanism in more detail. The Coulombic efficiency is above 99.5 % in general during cycling, demonstrating that the MIC electrolyte is electrochemically stable. The team is working to further improve the Coulombic efficiency. The specific discharge capacity reaches a maximum of 150 mAh g-1, with a high retention of 94 % after 400 cycles, again signifying the strong stability of MIC membrane. The charge/discharge profile during cycling showed negligible change except for an increase in the ohmic resistance at a high state of charge, which is likely caused by the accumulation of side reaction products.

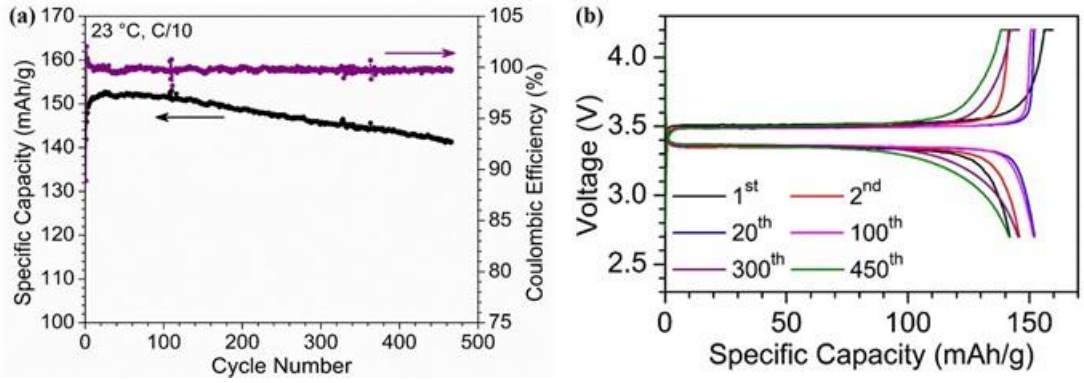

Figure II.9.I.10 Specific discharge capacity and Coulombic efficiency of Li/MIC/LiFePO4 over 470 cycles (a) and the charge/discharge profile during given cycle numbers (b). An article on this work has been submitted for publication.

In addition to using LiFePO4 cathode material, the performance of the MIC electrolyte using other cathode materials, such as layered oxides, was also investigated in this reporting period. Through systematic experiments, we found that it is necessary to include MIC electrolyte in the cathode formulation to obtain battery cycling (Figure II.9.I.11 part b inset, Li/MIC/NMC 811 catholyte cell). Essentially, the MIC electrolyte in the cathode, i.e., catholyte, facilitates ion transport in the cathode. In our earlier report, we showed that the MIC electrolyte is stable with layered cathodes. In this quarter, we discovered that the conventional PVDF/NMP combination can be replaced by the MIC precursor solution during the cathode formulation process, so that cathode particles are embedded in the ionically conductive polymer matrix. Our initial assessment has shown that the mechanical properties of the composite cathode are not impacted by building such a catholyte. The preliminary performance of the solid-state cell is shown in Figure II.9.I.11. When cycled at 23 °C using a C/20 charge/discharge rate, the solid-state cell with various cathode mass loadings all exhibit comparable specific capacity. This experiment shows: (1) the MIC electrolyte can replace PVDF in the cathode and improve ion transport in the cathode, and (2) the MIC electrolyte shows stability against layered oxide cathodes. Next, we will modulate the cathode mass loading and investigate the relationship between mass loading and battery performance. The target is to obtain practically meaningful loadings. Due to the added catholyte in our design, we expect to achieve a high cathode areal loading capacity. We will also perform battery testing at different temperatures to further evaluate the thermal stability and cell kinetics.

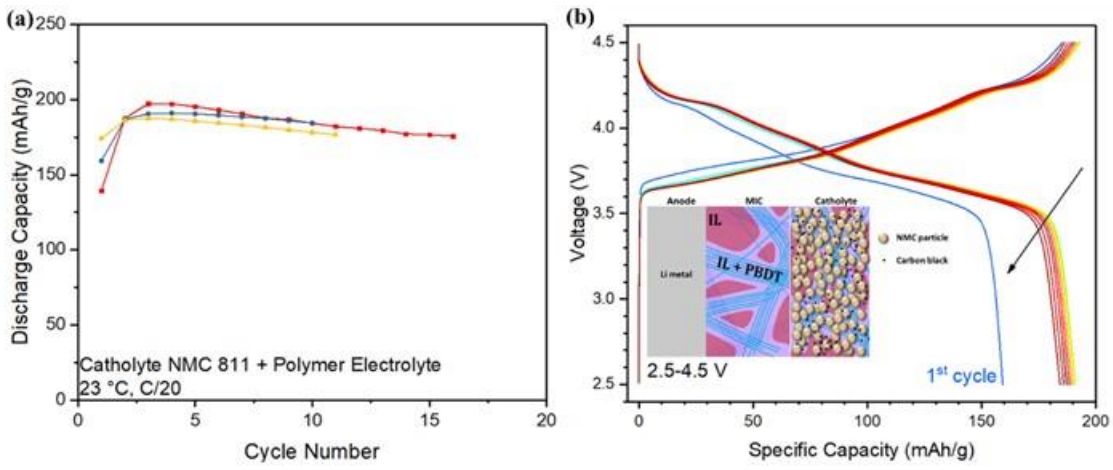

Figure II.9.I.11 (a) Three repetitions of specific discharge capacity testing of the Li/MIC/NMC 811 catholyte cell cycled at 2.5–4.5 V. (b) Corresponding charge–discharge profiles for 10 cycles at C/20 at room temperature, where the arrows indicate gradual capacity fading. The voltage profile of the first cycle is labeled. The voltage profiles are similar to those for the liquid electrolyte.

We also note that we requested and received a no-cost extension for three months (ending 12/31/20) due to the almost three month lab shutdown at Virginia Tech due to COVID-19. We are on track to complete the milestones for reporting period 1 before 12/31/20.

Conclusions

In summary, the team has verified the suitability of these new MIC solid electrolytes for use in solid state batteries. The materials creation, cell integration, and testing platforms have all been established. The milestones set for the current budget period have been completed. New research opportunities and strategies have been identified on track to testing our research hypotheses and achieving year-2 milestones.

Key Publications

1. "Ion Transport and Mechanical Properties of Non-Crystallizable Molecular Ionic Composite Electrolytes" Joshua E. Bostwick, Curt J. Zanelotti, Ciprian Iacob, Andrew Korovich, Louis A. Madsen, Ralph H. Colby. Macromolecules (2020) 53, 4, 1405-1414. doi: 10.1021/acs.macromol.9b02125.

Acknowledgements

The team acknowledges collaborations with T. J. Dingemans' group at University of North Carolina (UNC) Chapel Hill in which they are forming composites based on PBDT polymer and carbon materials such as graphene oxide, and are beginning to develop charged rigid-rod polymers building on PBDT. The team also acknowledges collaborations with Prof. R. H. Colby at PSU on shear rheology and broadband dielectric spectroscopy. The team also acknowledges collaborations with Dr. D. Nordlund and Dr. Y. Liu at SLAC National Accelerator Laboratory (SLAC), conducting synchrotron X ray studies on MIC films and composite electrodes

II.9.J Hot Pressing of Reinforced All-solid-state Batteries with Sulfide Glass Electrolyte (General Motors LLC)

Thomas A. Yersak, Principal Investigator
General Motors LLC
GM Global Research and Development
30470 Harley Earl Blvd.
Warren, MI 48092-2031
E-mail: thomas.yersak@gm.com

Tien Duong, DOE Technology Development Manager
U.S. Department of Energy
E-mail: Tien.Duong@ee.doe.gov

Start Date: October 1, 2019 End Date: December 31, 2020
Project Funding: $1,250,000 DOE share: $1,000,000 Non-DOE share: $250,000

Project Introduction

The performance of all-solid-state batteries (ASSBs) with sulfide solid-state electrolytes (SSEs) is limited because they are 10% - 20% porous. Porosity limits energy density of the composite cathode and provides a conduit for Li-metal deposits through the separator if operating specifications (*i.e.* current density, operating temperature, and pressure) are not strictly controlled. This project intends to demonstrate that hot press cell processing and appropriately formulated sulfide glass SSEs can eliminate porosity to enable Li-NCM ASSBs with energy density of $\geq$ 350 Wh/kg.

Objectives

The objective of this project is to research, develop, and test Li-NCM ASSBs capable of achieving program performance metrics by implementing appropriately formulated sulfide glass SSEs and hot press cell processing in a dry room environment. In the composite cathode, hot pressing eliminates porosity to increase energy density by enabling thick composite cathodes with high active material loading. In the separator, hot pressing eliminates porosity that may otherwise provide a conduit for Li metal deposits to short the cell. Unfortunately, hot press cell processing may cause a deleterious side-reaction between sulfide SSE and NCM active material even though sulfide SSEs are kinetically stable versus NCM at room temperature. For this reason, work conducted during this project's first budget period focused on enabling the hot press processing of composite cathodes with the objective of demonstrating a reversible capacity of > 120 mAh/g after hot pressing.

Approach

The sulfide SSE used in the composite cathode, otherwise known as the catholyte, will dictate the processing specifications for ASSB hot pressing. Thermal stability can be achieved by NCM passivation and proper catholyte formulation. Work conducted during this project's first budget period systematically evaluated different NCM coatings, catholyte formulations, and hot press cell processing conditions (*i.e.* temperature, time, and pressure). The performance of hot-pressed ASSBs was then compared to that of green baseline ASSBs and hot-pressed control ASSBs consisting of the β-Li_3PS_4 model SSE. In parallel, GM studied the NCM/SSE interface after hot pressing with electron microscopy to assess how hot pressing changes electrode microstructure and to elucidate guiding principles for thermal stability. GM aimed to characterize the interface across several length scales. At the micron scale, we used focused ion beam scanning electron microscopy (FIBSEM) cross sectioning and digital image analysis to quantify porosity and composite homogeneity. At the nano scale, we intend to use the cyro-high resolution transmission electron microscopy (cyro-HRTEM) to study the nature of the NCM/SSE interface.

Results

This section will be separated into three parts. In the first part we outline the development of a baseline ASSB, which provides a point of reference to determine how hot press cell processing affects cell performance. Next, we detail our systematic evaluation of thermally stable catholytes. We will conclude by describing our preliminary characterization of hot pressed ASSB using electron microscopy. We note that the progress of this project was impacted by delays associated with the COVID-19 pandemic. GM employees were issued a work from home directive starting March 16th, which was followed shortly thereafter by a Michigan State-wide shelter in place mandate. Lab work recommenced the week of May 18th, with full lab access granted 3 weeks later. Access to the University of Michigan's Center for Materials Characterization $(MC)^2$, where we conduct a majority our electron microscopy work, was regained in mid-September.

Development of a baseline ASSB considers the cathode active material, protective cathode coating, sulfide catholyte, composite cathode composition, and composite preparation method. This project utilizes $LiNi_{0.85}Co_{0.1}Mn_{0.05}O_2$ (NCM) as the cathode active material with an average particle diameter of less than 5 µm, which prior work found to be optimal for ASSB [1]. NCM was obtained from BASF without a proprietary surface coating since these coatings are optimized for conventional Li-ion batteries with liquid electrolyte and not for application in ASSB. Furthermore, it is crucial to fully understand the NCM passivating coating characteristics if GM is to rigorously study interfacial phenomena between NCM and sulfide SSE catholyte during hot pressing. To this end, GM successfully applied a baseline $LiNbO_3$ coating to NCM via a solution-based method [2]. In this method, NCM powders were mixed in an ethanol solution of Li and Nb alkoxides and dried under ultrasonic agitation. The recovered NCM powder was then annealed under oxygen flow at 400ºC for 1 hour. High-resolution TEM characterization of the resulting product found the coating thickness to be approximately 10 nm (Figure II.9.J.1), which agreed with previous reports using similar methods [2].

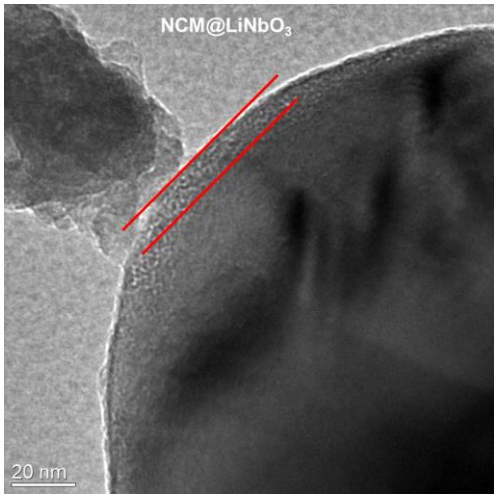

Figure II.9.J.1 High-resolution TEM image of NCM@$LiNbO_3$ powder. The $LiNbO_3$ coating is approximately 10 nm thick.

In addition to the $LiNbO_3$ coating, GM chose β-Li_3PS_4 for the baseline catholyte. The β-Li_3PS_4 SSE synthesized for this project had an ionic conductivity of 2×10^{-4} S/cm at room temperature and acceptable anodic stability against cathode active materials. GM then proceeded to examine the coating effect on the electrochemical performance of baseline SSBs. The hand ground composite cathode contained 70 wt.% NCM@$LiNbO_3$ and 30 wt.% β-Li_3PS_4. Carbon black was eliminated to avoid the possibility of accelerating the interfacial reaction [3]. Indium foil was selected as the anode material to guarantee a compatible anode-electrolyte interface since our main focus is NCM/catholyte compatibility for this budget period. The baseline cells (NCM@$LiNbO_3$ + β-Li_3PS_4/β-Li_3PS_4/Li_xIn) were cold pressed (25 °C) at 375 MPa for 10 minutes. Before cycling, electrochemical impedance spectroscopy (EIS) was conducted to assess impedance. As shown in Figure II.9.J.2a, the cell with uncoated NCM exhibited a larger impedance than that of the cell with NCM@$LiNbO_3$. A larger impedance led to a poor reversible specific capacity of 108 mAh/g and a 1st cycle

coulombic efficiency of 68.4% at a C/20 rate (Figure II.9.J.2b). On the other hand, the cell with NCM@$LiNbO_3$ delivered a higher reversible capacity of 163 mAh/g and 1st cycle coulombic efficiency of 80.7%. This significant improvement in the cell performance stresses the importance of using NCM@$LiNbO_3$ in the baseline and control cells.

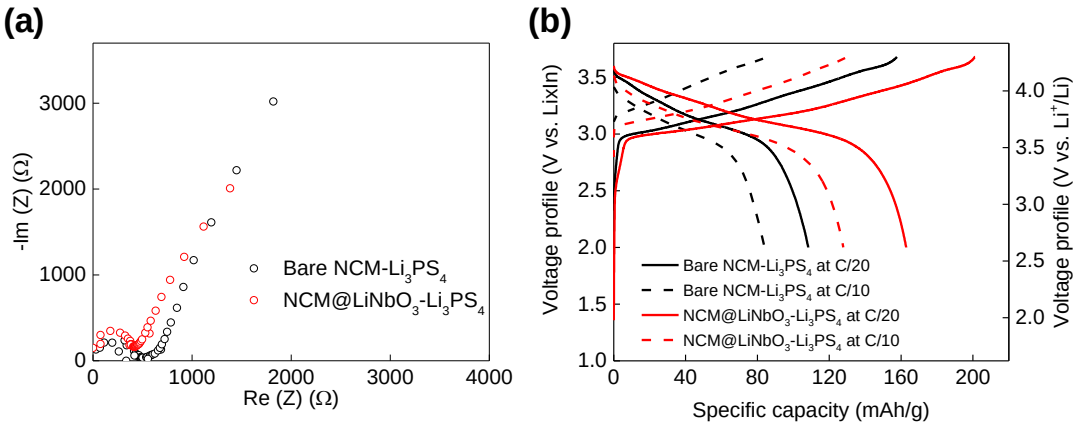

Figure II.9.J.2 Electrochemical performance of bare NCM+β-Li_3PS_4/β-Li_3PS_4/Li_xIn and NCM@$LiNbO_3$+β-Li_3PS_4/β-Li_3PS_4/Li_xIn cells at room temperature. (a) EIS spectra and (b) initial voltage profiles.

Having established the baseline coated NCM, GM next developed a low-energy ball-milling process to prepare composite cathodes. Ball-milling is a scalable mixing method, providing a pathway towards large-scale fabrication while promoting uniform particle distribution in the composite cathodes [4]. However, the milling procedure must be designed appropriately to avoid damage to NCM particles. Here, 70 wt.% NCM@$LiNbO_3$ and 30 wt.% β-Li_3PS_4 were ball-milled together. As shown in Figure II.9.J.3a, a hand-mixed composite cathode exhibited aggregated SSE particles and a poor ionic percolation network. This issue was mitigated by using ball milling to mix the composite as shown in Figure II.9.J.3b. To quantify the homogeneity of composite cathodes, we conducted FIBSEM and digital image analysis to calculate the average aggregated SSE area and average nearest neighbor distance (NND) as shown in Figure II.9.J.3c. The hand-milled composite cathode showed an average aggregated SSE area of 110.1 μm^2 and an average NND of 6.5 μm, while the ball-milled composite showed an average aggregated SSE area of 52.9 μm^2 and an average NND of 9.12 μm. A smaller aggregated SSE area and larger NND suggest that the ball milled composites were more homogenous. First-cycle voltage profiles at C/10 rate with different cathode loading are shown in Figure II.9.J.3d. GM successfully established the baseline cell with high areal capacity (> 3mAh/cm^2) with the aid of a ball milling process.

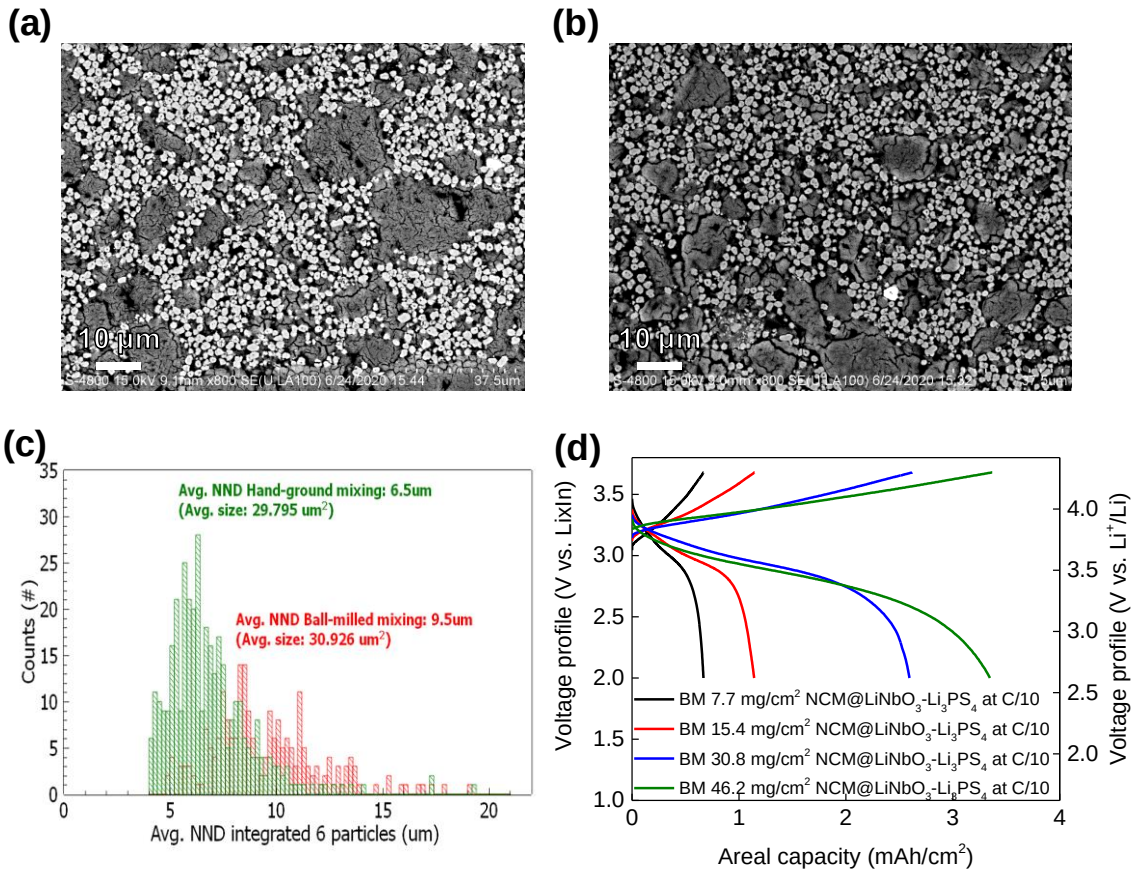

Figure II.9.J.3 Cross-sectional images of a baseline composite cathodes prepared by (a) hand mixing and (b) ball milling. (c) Chart depicting nearest neighbor distance for hand milled (green) and ball milled (red) composite cathodes as quantified by digital image analysis. (d) First-cycle voltage profiles for ball-milled NCM@$LiNbO_3$+ β-Li_3PS_4/β-Li_3PS_4/Li_xIn cells with different cathode loading at room temperature at C/10 C-rate.

With a baseline ASSB established, GM then systematically investigated the thermal stability of different composite cathodes. As we mentioned earlier, hot press cell processing may cause a deleterious side-reaction between sulfide SSE and NCM active material even though sulfide SSEs are kinetically stable versus NCM at room temperature. Therefore, it is crucial to examine the thermal stability of cathode composites. To tune the thermal stability of the composite cathode, the NCM coating and catholyte composition can be changed. We first evaluated the value of different NCM coatings. In addition to $LiNbO_3$, NCM was also coated with Li_3PO_4 [5] and Li_2O-ZrO_2 (LZO) [6]. Li_3PO_4 and LZO coatings were both deemed inferior to $LiNbO_3$ coatings based on electrochemical and differential scanning calorimetry (DSC) testing, respectively. A cold-pressed cell with NCM@Li_3PO_4 had worse performance than that of the baseline cell (Figure II.9.J.4a). Furthermore, a composite with NCM@LZO had an exothermic onset of 350 °C whereas a composite with NCM@$LiNbO_3$ had a higher exothermic onset of 380 °C (Figure II.9.J.4b). Therefore, $LiNbO_3$ coatings were carried forward for the rest of the work presented here.

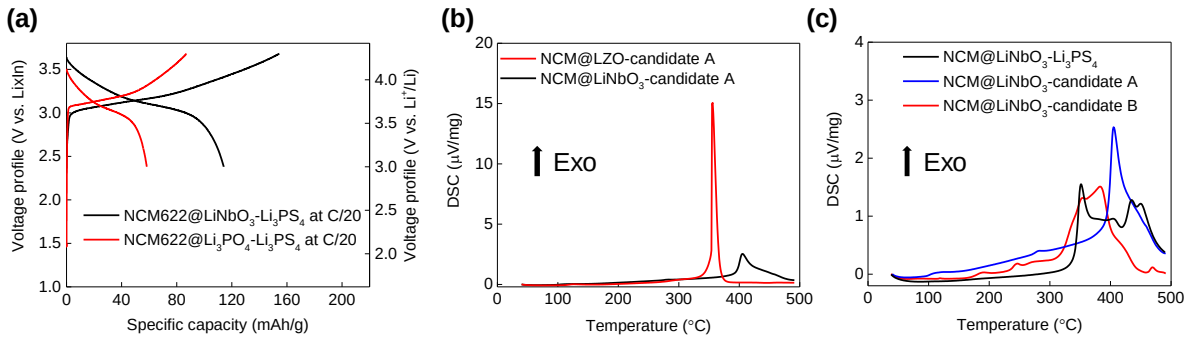

Figure II.9.J.4 (a) First cycle voltage profiles for test cells with either NCM622@$LiNbO_3$ or NCM622@Li_3PO_4 at room temperature and C/20 rate. (b) DSC of NCM cathode composites with catholyte Candidate A and either NCM@$LiNbO_3$ or NCM@LZO. (c) DSC of NCM composites with NCM@$LiNbO_3$ and different catholytes. The onset temperature for β-Li_3PS_4, Candidate A, and Candidate B are 333ºC, 380ºC, and 318ºC, respectively.

Next, thermal stability was evaluated as a function of catholyte composition using DSC and hot pressing trials. Two potential catholytes were evaluated in this study, referred to here as "Candidate A" and "Candidate B". Based on DSC, catholyte Candidate A was deemed thermally stable with a exothermic onset of 380 °C (Figure II.9.J.4c). Hot pressed SSBs were then fabricated and tested with three cathode composites composed of either baseline β-Li_3PS_4, Candidate A, or Candidate B catholytes. Kevlar fiber was mixed into the separators of these cells to enhance mechanical strength during hot pressing using methods described in our previous work [7]. All cells were uniaxially pressed at 375 MPa and 200ºC for 10 minutes. The EIS spectra and electrochemical performance of ASSBs based on these three cathode composites are shown in Figure II.9.J.5. The impedance of the hot pressed baseline cell is almost one order magnitude higher than that of the cells made with catholytes Candidate A and Candidate B (Figure II.9.J.5a). This result indicates that a severe reaction occurred at the NCM/β-Li_3PS_4 interface in the baseline cell during hot pressing. The hot pressed baseline cell showed poor performance with a first-cycle discharge capacity of only 58 mAh/g and a 1st cycle coulombic efficiency of 57% (Figure II.9.J.5b). On the other hand, the hot pressed cell made with Candidate B catholyte showed excellent electrochemical behavior with a first-cycle discharge capacity of 188 mAh/g and a coulombic efficiency of 75.9% (Figure II.9.J.5b) despite its low DSC onset temperature. The electrochemical performance correlated well with the EIS spectra as NCM-candidate B cell exhibited the best electrochemical performance and the lowest impedance (Figure II.9.J.5a). We are currently investigating the mechanism for candidate B's superior thermal stability. Work is underway to link electrochemical results to a fundamental mechanism by XPS analysis and cyro-electron microscopy. We posit that our catholyte formulations promote a thermally stable solid-state solid electrolyte interphase (SEI).

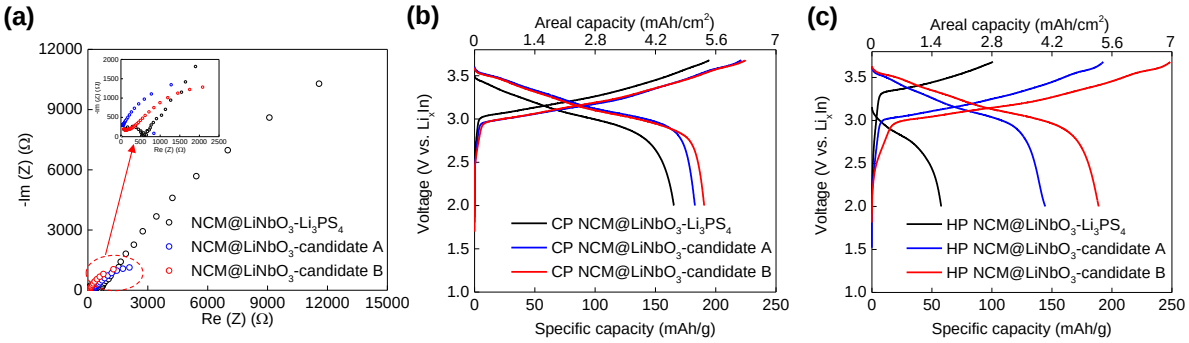

Figure II.9.J.5 Electrochemical performance of NCM-SSEs cells at room temperature at 0.05 C-rate. (a) EIS spectra. (b) First cycle voltage profiles of cold pressed (CP) ASSBs and (c) hot pressed (HP) ASSBs.

In parallel with the hot pressing trials discussed above, electron microscopy work is underway to characterize the cathode composites before and after hot pressing. To measure the porosity of the composites we used FIBSEM and digital image analysis (Figure II.9.J.6). A cold pressed composite cathode with Candidate A catholyte has a porosity of nearly 24%. The porosity of the composite cathode is substantially higher than that of a similarly cold pressed neat Candidate A pellet (~14% porosity). The higher porosity can be explained by the mismatch of mechanical properties between the stiff, ceramic NCM and the compliant sulfide SSE. The porosity of the cathode composite with Candidate A catholyte was reduced to less than 9% by hot pressing. Similarly, the porosity of the cathode composite with Candidate B was only 4.5%. When one considers that the cathode is the thickest component of a ASSB, it is understood that eliminating porosity here substantially improves cell energy density. Work to characterize the NCM/SSE interface with cyro-TEM is ongoing due to the delays associated with the COVID-19 pandemic.

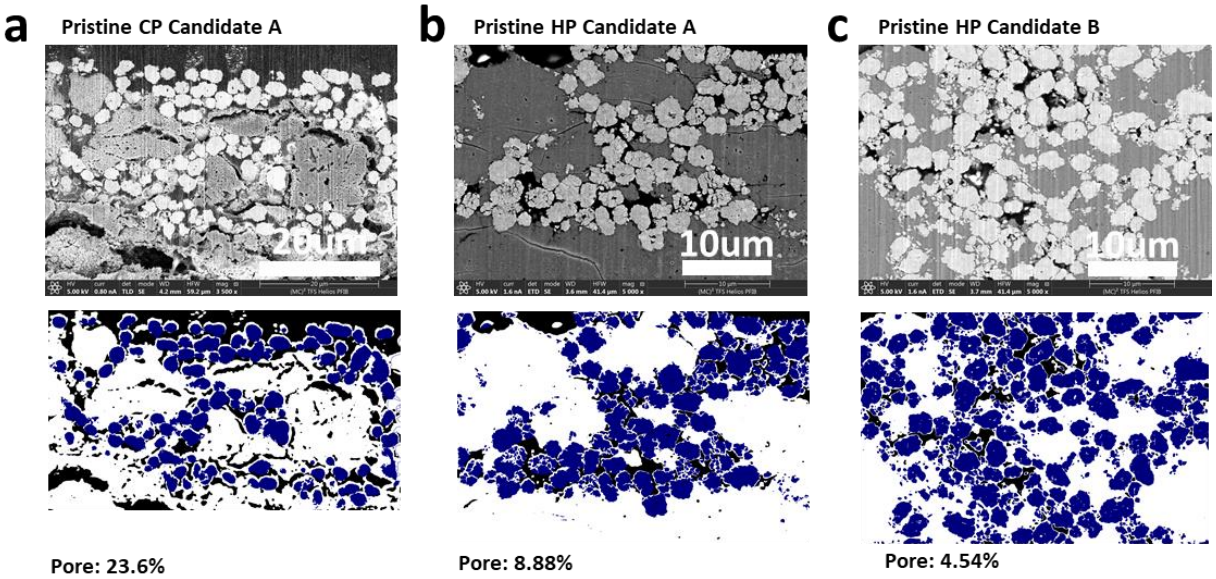

Figure II.9.J.6 Quantification of composite cathode porosity using FIBSEM and digital image analysis. Top row corresponds to SEM images of different composite cathode cross sections. Bottom row corresponds to processed images after digital image analysis (key: white = catholyte, blue = NCM, black = pore).

Conclusions

Our results suggest that suitable catholytes are available to enable the hot pressing of ASSB up to 200°C, ensuring that budget period deliverables will be met. Hot pressing eliminates porosity in both the cathode and separator. Importantly, we realized a reduction in porosity while maintaining electrochemical function. A hot pressed ASSB made with baseline β-Li_3PS_4 essentially failed, with failure attributed to an increase in cell impedance as a result of NCM/β-Li_3PS_4 interfacial instability. On the other hand, a hot pressed ASSB made with Candidate B catholyte retained its discharge capacity of 188 mAh/g. Work is underway to develop a scientific understanding for thermal stability. We posit that our catholyte formulations promote a thermally stable solid-state solid electrolyte interphase (SEI) to enable hot press cell processing.

References

1. Bielefeld, Anja, Dominik A Weber, and Jürgen Janek. "Microstructural Modeling of Composite Cathodes for All-Solid-State Batteries." *The Journal of Physical Chemistry C* 123, no. 3 (2018): 1626–34.

2. Ohta, Narumi, Kazunori Takada, Isao Sakaguchi, Lianqi Zhang, Renzhi Ma, Katsutoshi Fukuda, Minoru Osada, and Takayoshi Sasaki. "LiNbO3-Coated LiCoO2 as Cathode Material for All Solid-State Lithium Secondary Batteries." *Electrochemistry Communications* 9, no. 7 (2007): 1486–90.

3. Zhang, Wenbo, Thomas Leichtweiß, Sean P Culver, Raimund Koerver, Dyuman Das, Dominik A Weber, Wolfgang G Zeier, and Jürgen Janek. "The Detrimental Effects of Carbon Additives in Li10GeP2S12-Based Solid-State Batteries." *ACS Applied Materials & Interfaces* 9, no. 41 (2017): 35888–96.

4. Nagao, Motohiro, Akitoshi Hayashi, and Masahiro Tatsumisago. "High-Capacity Li 2 S–Nanocarbon Composite Electrode for All-Solid-State Rechargeable Lithium Batteries." *Journal of Materials Chemistry* 22, no. 19 (2012): 10015–20.

5. Tsukasaki, Hirofumi, Misae Otoyama, Yota Mori, Shigeo Mori, Hideyuki Morimoto, Akitoshi Hayashi, and Masahiro Tatsumisago. "Analysis of Structural and Thermal Stability in the Positive Electrode for Sulfide-Based All-Solid-State Lithium Batteries." *Journal of Power Sources* 367 (2017): 42–48.

6. Han, Fudong, Jie Yue, Xiangyang Zhu, and Chunsheng Wang. "Suppressing Li Dendrite Formation in Li2S-P2S5 Solid Electrolyte by LiI Incorporation." *Advanced Energy Materials* 8, no. 18 (2018): 1703644.

7. Yersak, T., J.R. Salvador, R.D. Schmidt, and M. Cai. "Hot Pressed, Fiber-Reinforced $(Li_2S)_{70}(P_2S_5)_{30}$ Solid-State Electrolyte Separators for Li Metal Batteries." *ACS Applied Energy Materials* 2, no. 5 (2019). https://doi.org/10.1021/acsaem.9b00290.

Acknowledgements

The PI (Thomas A. Yersak) and co-PI (James R. Salvador) would like to provide recognition to our NETL manager, Adrienne L Riggi. Special thanks is also given to Dr. Fang Hao and Dr. Chansoon Kang for their important contributions to the project.

II.9.K Developing Materials for High-Energy-Density Solid State Lithium-Sulfur Batteries (Penn State University Park)

Donghai Wang, Principal Investigator
Penn State University
134 Energy & Environmental Laboratory
University Park, PA 16802
E-mail: dwang@psu.edu

Tien Duong, DOE Technology Development Manager
U.S. Department of Energy
E-mail: Tien.Duong@ee.doe.gov

Start Date: October 1, 2019 End Date: September 30, 2020
Project Funding: $411,326 DOE share: $330,529 Non-DOE share: $80,797

Project Introduction

Lithium-sulfur (Li-S) all-solid-state battery (ASSB) is a promising candidate to replace existing Li-ion batteries for application in electric and plug-in hybrid electric vehicles (EVs and PHEVs) due to its high energy density and superior safety. Moreover, recent advances in improvement of ionic conductivities ($\approx 10^{-2}$ S cm^{-1}) of sulfide-based solid-state electrolytes (SSEs) put us one step closer to the practical application of Li-S ASSBs[1]. In Li-S ASSBs, the polysulfide shuttling and self-discharges in liquid-type Li-S batteries could be fundamentally resolved[2]. As added benefits, sulfide-based SSEs possess improved safety due to the absence of flammable organic electrolytes[3], [4]. Despite those encouraging characteristics of ASSBs, there are technological challenges such as low sulfur utilization and increased interfacial resistances due to poor contact, large volume expansion of sulfur upon cycling and unoptimized microstructure of sulfur-carbon-SSEs composites in solid cathode, poor charge/discharge rate due to low conductivity of SSEs, and SSEs' chemical instability against moisture and lithium/lithium alloy anodes. The challenges are fundamentally attributed to properties of the solid materials and their interfaces in electrodes.

In brief, we shall address the following three problems of Li-S ASSBs in this project. First, we aim to construct electron and ionic transport pathways in the cathode to improve sulfur utilization upon cycling and therefore boost overall energy density. Second, we target generating favorable interface between carbon-sulfur composite and solid-state electrolytes with novel solid additives or approaches. Third, we plan to develop new sulfide-based solid electrolytes with high ionic conductivity and improved stability against moisture and lithium alloys for all.

Objectives

The project objectives are to develop materials involving advanced S-C composite materials, solid additives, and sulfide-based SSEs, and to acquire knowledge for Li-S ASSBs. Li-S ASSBs with large areal sulfur loading ($\geq$ 5 mg cm^{-2}) and high sulfur content ($\geq$ 50 wt% in cathode), pairing with lithium or lithium alloy anode, shall deliver a high initial specific capacity of over 1200 mAh g^{-1} at high charge/discharge rate (> 0.3 C) for 500 cycles with over 80% capacity retention. The out-year goals are as follows: (1) develop new S-C materials, new cathode additives, and cation-doped solid electrolytes (ionic conductivity above 2 mS cm^{-1} at room temperature), (2) conduct characterization and performance tests on both material and electrode levels. The Go/No-Go Decision will be demonstration of all-solid-state sulfur cathode with over 1000 mAh g^{-1} discharge capacity at 0.3 C discharge rate and 50 wt% sulfur content for 50 cycles at 60°C.

Approach

The project goal will be accomplished through developing new materials, together with in-depth characterization of sulfur cathode. Specifically, approaches to realize the project objectives include: (1) development of new carbon material with unique structure, high surface area, and large pore volume; (2)

development of new S-C materials to facilitate electron/ion transport; (3) development of novel additives to tune interfacial behavior among components in the cathode; (4) development and optimization of new SSEs through cation and anion doping with superior properties such as high ionic conductivity, good moisture, and stability; and (5) diagnostics, characterization, and cell tests on the developed new material or advanced sulfur cathode.

Results

In budget period 1, we mainly focused on the following three aspects: (1) development of sulfide-based SSEs; (2) development of advanced carbon materials; (3) development of solid additives for sulfur cathode. At the meaning time, we also worked on acquiring knowledge of Li-S ASSBs using advanced characterization techniques to assist our research. In the following part, we shall elucidate our accomplishments that has been achieved so far.

1. Sulfide-based solid electrolyte development

Solid electrolyte is one of the key components that shall affect sulfur cathode performance in Li-S ASSBs. It is crucial to gain knowledge of its impacts and desired properties as well as developing solid electrolytes with high ionic conductivity at room temperature.

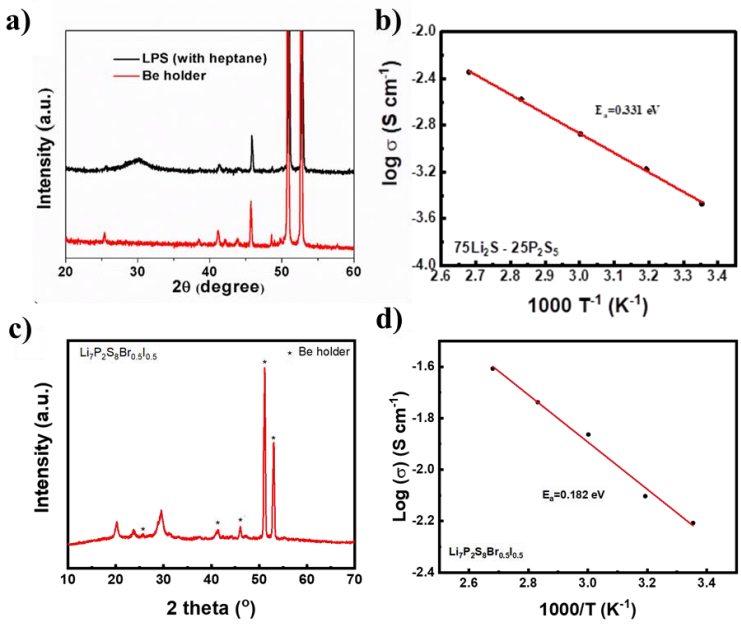

Figure II.9.K.1 XRD spectra and Arrhenius plot of a, b) LPS glass solid electrolyte, and c, d) $Li_7P_2S_8Br_{0.5}I_{0.5}$ glass-ceramic solid electrolyte.

To gain more knowledge of solid electrolytes, we have synthesized various glass and glass-ceramic solid electrolytes which includes $75Li_2S{\cdot}25P_2S_5$ glass solid electrolyte (LPS), Li_6PS_5Cl glass solid electrolyte, and $Li_7P_2S_8Br_{0.5}I_{0.5}$ glass-ceramic solid electrolyte. As a result, we could currently prepare basic sulfide solid electrolyte, LPS, with moderate ionic conductivity (3.8×10^{-4} S cm^{-1} at 25 °C) for fundamental study, as well as advanced glass-ceramic solid electrolyte, $Li_7P_2S_8Br_{0.5}I_{0.5}$, which possess high ionic conductivity at room temperature (6.2 mS cm^{-1} at 25 °C) which shall contribute to fabricating Li-S ASSBs with superior performance. The X-ray diffraction (XRD) spectra and Arrhenius plot of LPS glass and $Li_7P_2S_8Br_{0.5}I_{0.5}$ glass ceramic solid electrolytes are shown in Figure II.9.K.1. Besides synthsizing various solid electrolytes, we also investigated the impacts of different synthesis methods, namely, dry and wet ball milling process. More specifically, in dry ball milling process, only dry precursor powders (Li_2S, P_2S_5, etc.). While in wet ball milling process, heptane is additionally added. Both LPS and Li_6PS_5Cl glass solid electrolytes were

synthesized using wet ball milling process. The ionic conductivity of LPS synthesized through wet ball milling process (3.8×10^{-4} S cm^{-1}) is slightly higher than the LPS synthesized through dry ball milling process (3.2×10^{-4} S cm^{-1}). Besides the differences on ionic conductivity, the morphology of synthesized solid electrolytes was also characterized using scanning electron microscopy (SEM) and the results are shown in Figure II.9.K.2. It was found that by adding heptane, the agglomeration of solid electrolyte could be reduced and the particle size of either LPS or Li_6PS_5Cl glass solid electrolytes could be further reduced to 1 ~ 10 μm. In contrast, the particle size of the solid electrolytes synthesized using dry ball milling approach is relatively large. It is believed that smaller particle size of solid electrolyte is more favorable for both cathode performance and preparation of thin solid electrolyte membrane.

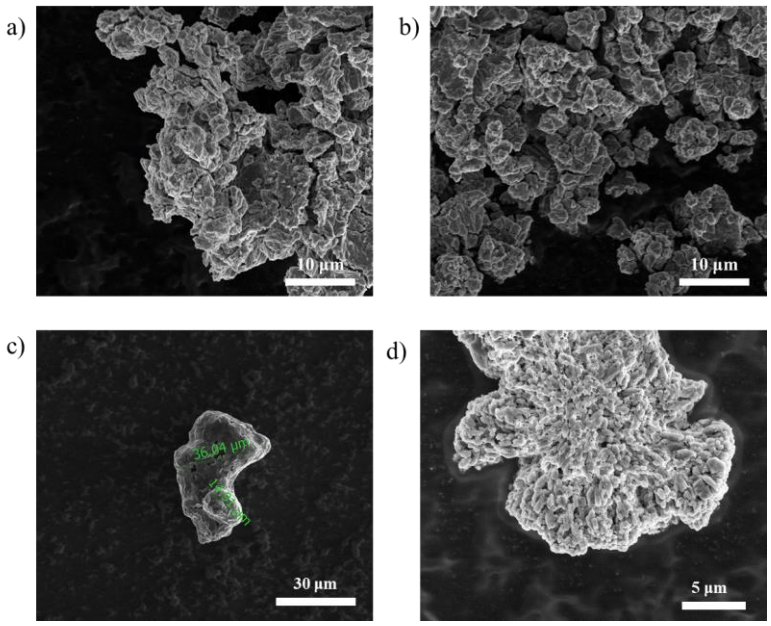

Figure II.9.K.2 SEM images of dry-ball-milling synthesized a) LPS and c) Li_6PS_5Cl glass solid electrolytes and wet-ball-milling synthesized b) LPS and d) Li_6PS_5Cl glass solid electrolytes.

Apart from gaining more knowledge of solid electrolytes that have already been developed in literature, we also tried to develop new sulfide based solid electrolyte with high ionic conductivity and superior electrochemical stability against lithium by incorporating nitrogen and aluminum. Initially, a series glass-ceramic solid electrolytes $75Li_2S$-$25P_2S_5$-$5Li_3N$-xAl_2S_3 (x=0, 1, 2, 3 and 4) were synthesized using dry ball milling method with post annealing at 300 ºC for 1 hour. The XRD spectra and Raman spectra of the synthesized glass solid electrolyte were summarized in Figure II.9.K.3. Several peaks representing Li_2S could be observed on the XRD spectra for all samples, while peaks standing for P_2S_5, Li_3N and Al_2S_3 were not observed. In Raman spectra, a peak at 421 cm^{-1} was observed for all samples which represents PS_4^{3-}. To get glass-ceramic solid electrolyte, these samples were further heated at 300 ºC for 1 hour. As shown in the XRD pattern for $75Li_2S$-$25P_2S_5$-$5Li_3N$-$4Al_2S_3$ in Figure II.9.K.4a, the thio-LISICON III analog phase is precipitated in the solid electrolyte while peaks representing Li_2S impurity could still be observed. The ionic conductivity of $75Li_2S$-$25P_2S_5$-$5Li_3N$-$4Al_2S_3$ glass-ceramic solid electrolytes was measured at different temperature and

was plotted in Figure II.9.K.4b. However, due to the existence of Li_2S impurities, the ionic conductivity at 25 ^oC is merely 0.08 mS cm^{-1} and activation energy is 0.27 eV.

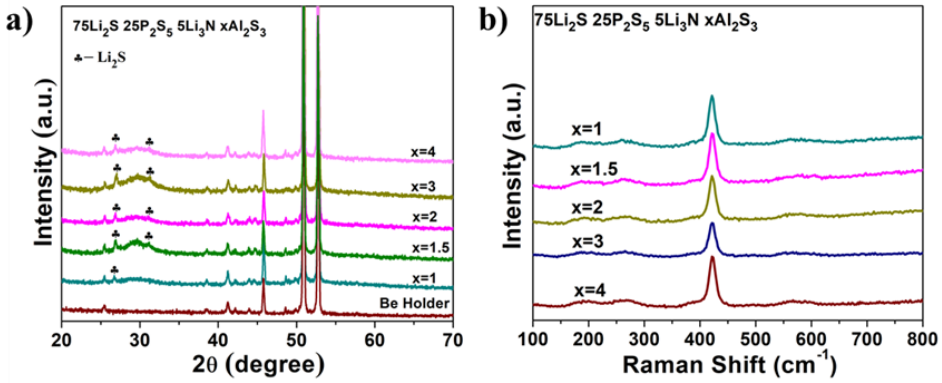

Figure II.9.K.3 a) XRD and b) Raman spectra of synthesized 75Li2S-25P2S5-5Li3N-xAl2S3 (x=0, 1, 2, 3 and 4) glass solid electrolytes.

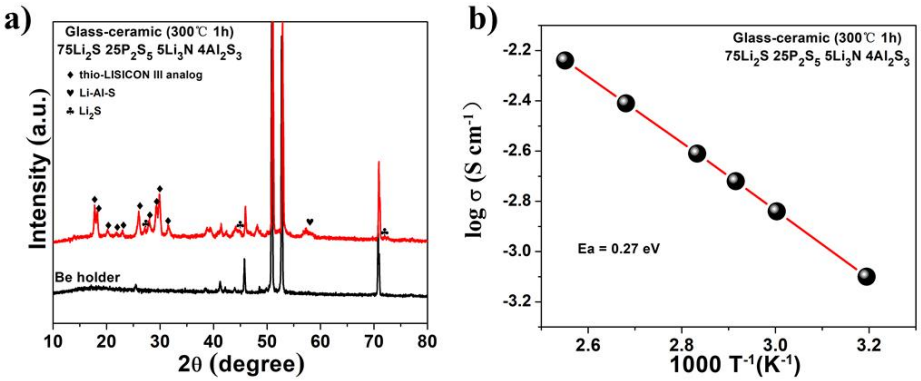

Figure II.9.K.4 a) XRD spectra and b) Arrhenius plot of 75Li2S-25P2S5-5Li3N-4Al2S3 glass-ceramic solid electrolytes.

To resolve the issues of Li_2S impurity and low ionic conductivity, we investigated a new solid electrolyte system, $65Li_2S$-$26P_2S_5$-$10Li_3N$-xAl_2S_3 (LPSNAl-x). The glass-type solid electrolyte was synthesized by conventional ball milling approach. The XRD spectra of the synthesized material is depicted in Figure II.9.K.5a. Peaks representing Al_2S_3 was observed only when x is above 14 and Li_2S impurity was not observed. As for the other compositions, no crystalline peaks were observed. The ionic conductivity of the synthesized glass-type solid electrolyte at 25 ^oC is summarized in Figure II.9.K.5b. Highest ionic conductivity of above 0.7 mS cm^{-1} was achieved when x=10. When x is above 14, significant ionic conductivity decay was observed due to the Al_2S_3 residuals. The synthesized glass-type solid electrolyte was further heated at 400 ^oC for 2 hours to obtain glass-ceramic solid electrolyte. According to XRD results in Figure II.9.K.6a, thio-LISICON III analog phase is precipitated and peaks representing Li-Al-S crystals were observed when x is between 1 and 12. The ionic conductivity of synthesized LPSNAl-x solid electrolytes at 25 ^oC is depicted in Figure II.9.K.6b. Among all synthesized glass-ceramic solid electrolytes, LPSNAl-12 demonstrated best ionic conductivity (5.19 mS cm^{-1} at 25 ^oC) and lowest activation energy (0.159 eV), and the Arrhenius plot for its measured ionic conductivity is shown in Figure II.9.K.7. Such high ionic conductivity meets our proposed milestone for synthesizing new solid electrolyte in budget period 1.

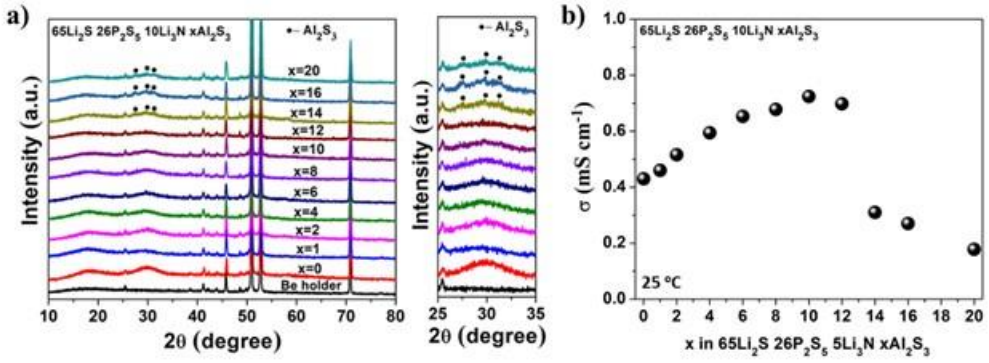

Figure II.9.K.5 a) X-ray diffraction (XRD) spectra and b) ionic conductivity at 25 °C and activation energy of various LPSNAI-x glass-type solid electrolyte (x=0 ~ 20).

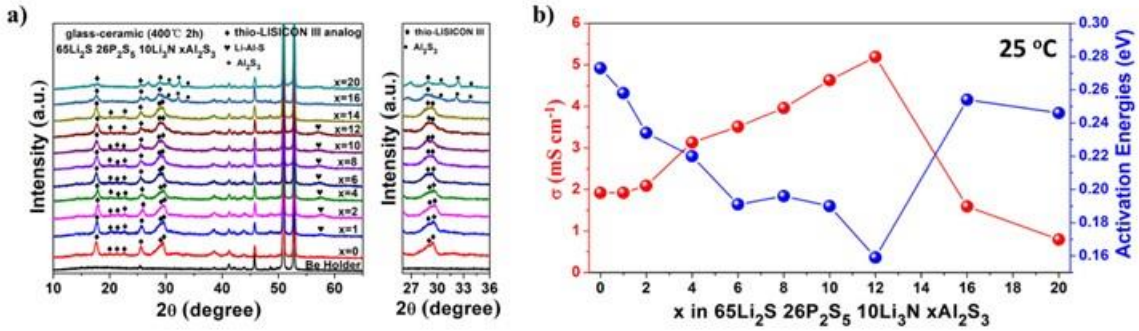

Figure II.9.K.6 a) X-ray diffraction (XRD) spectra and b) ionic conductivity at 25 °C and activation energy of various LPSNAI-x glass-ceramic solid electrolyte (x=0 ~ 20).

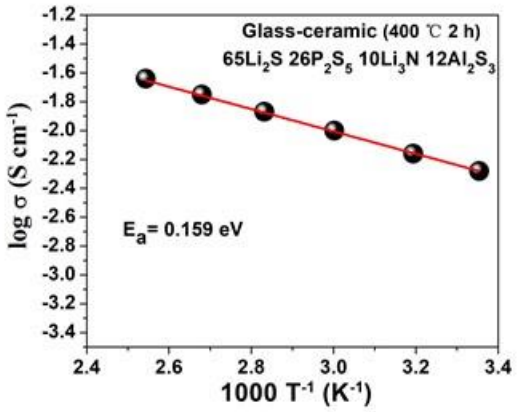

Figure II.9.K.7 The Arrhenius plot for the measured ionic conductivity of LPSNAI-12 glass-ceramic solid electrolyte.

Moreover, X-ray photoelectron spectroscopy (XPS) has also been employed to investigate the surface chemical environment of the synthesized material as shown in Figure II.9.K.8. It was observed that the incorporation of nitrogen andaluminum into the solid electrolyte framework by would lead to the formation of Li-Al-S bond, P-N bond and P=N bond. The formed bonds might contribute to the improvement of ionic conductivity of solid electrolyte.

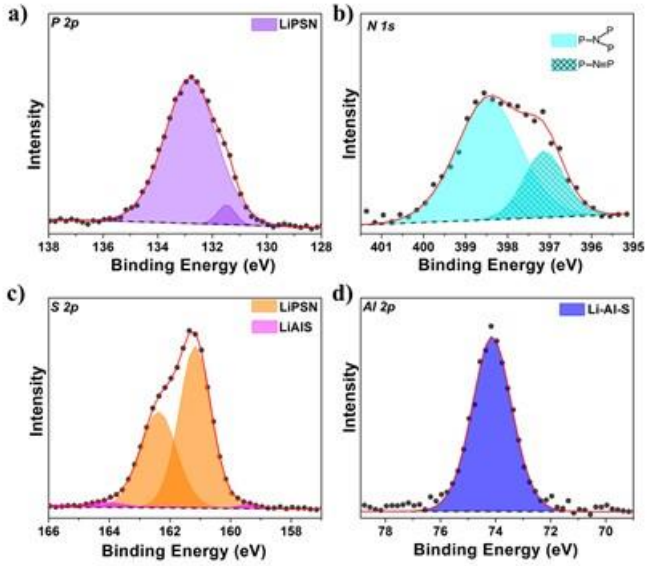

Figure II.9.K.8 XPS spectra of LPSNAl-12 glass-ceramic solid electrolyte.

The stability of the synthesized electrolytes against lithium metal has also been studied using Li/LPSNAl-x/Li symmetric cell test, and results are depicted in Figure II.9.K.9. And at 0.6 mA cm^{-2}, the polarization resistance (Rp) is merely 25 Ω cm^{-2}. And long-term stable cycling at 0.6 mA cm^{-2} and 0.6 mAh cm^{-2} of the symmetric cell for over 1000 hours have been achieved. All these superior properties demonstrate that the solid electrolyte we developed, LPSNAl-12, is a good candidate for future Li-S ASSBs.

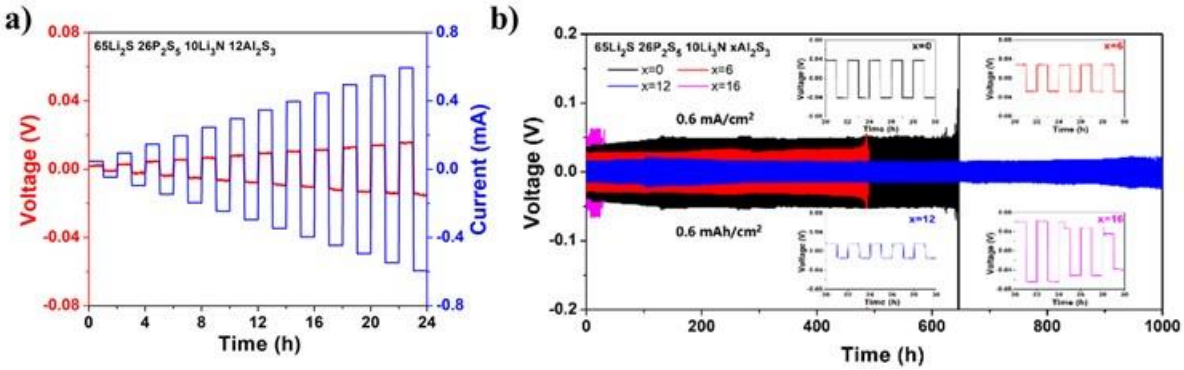

Figure II.9.K.9 a) A Li/LPSNAl-12/Li symmetric cell cycled at various current density. The duration time for each discharge/charge is 1 hour. b) Long term cycling of Li/LPSNAl-x/Li cell at 0.6 mA cm^{-2}, and 0.6 mAh cm^{-2}. All measurements were performed at room temperature.

2. Carbon materials for sulfur cathode

Constructing efficient electronic conductive network is quite significant in improving sulfur cathode performance. Choices of carbon materials, and preparation processes of sulfur-carbon-solid electrolyte composite are two key factors that determines the effectiveness of the electron pathway within sulfur cathode, and therefore were investigated. We have screened various carbon additives and found that sulfur cathode utilizing Ketjenblack EC600 JD (KB) demonstrated best performance. Moreover, we further optimized sulfur content in the cathode, cathode preparation process and conditions with KB as carbon additives. As an example, the rate performance of sulfur cathode with different sulfur content (around 39 wt% and 50 wt%) were compared using original cathode preparation process and optimized sulfur cathode process. The results and corresponding voltage profile are shown in Figure II.9.K.10. Before optimization, the discharge specific capacity of sulfur cathode is around 1200 mAh g^{-1} at 0.1 C at low sulfur content of around 39 wt%. After

optimization, the discharge capacity of sulfur cathode could reach over 1470 mAh g^{-1} at 0.1 C and 880 mAh g^{-1} at 0.5 C at high sulfur content of 50 wt%. Such superior performance meets our proposed milestone for optimizing carbon material for all-solid-state sulfur cathode. To be noted, LPS is used as solid electrolyte in all measurement. The improvement of specific capacity is attributed to better mixing of cathode components after optimization.

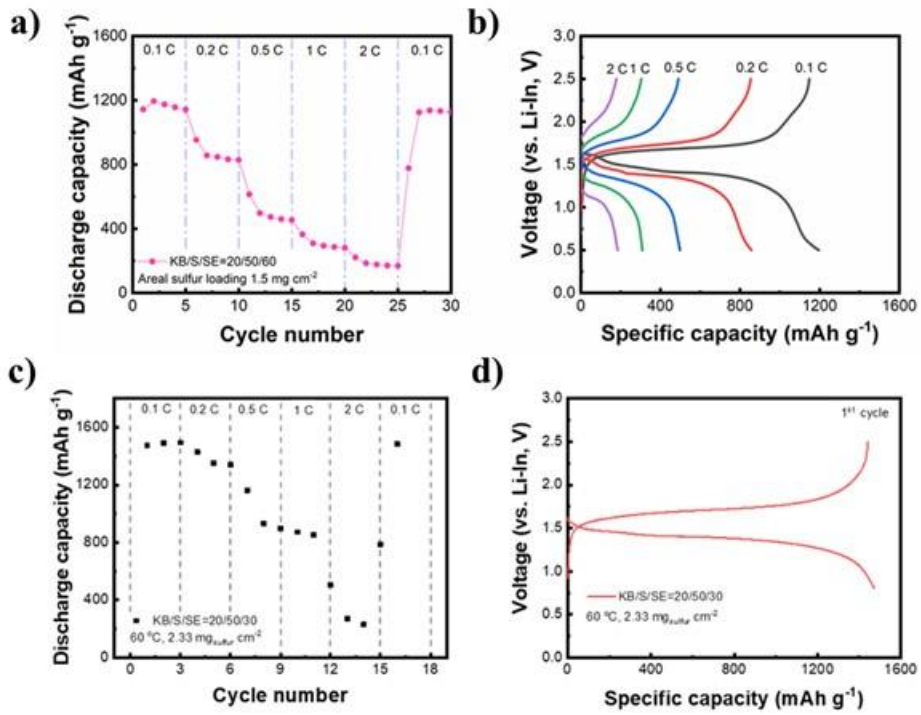

Figure II.9.K.10 Rate performance and corresponding voltage profile of sulfur cathode with compostion of a,b) KB/S/SE=20/50/60, and c, d) KB/S/SE=20/50/30. All measurements were performed at 60 °C.

3. *Solid additives for sulfur cathode*

We have found that the electrochemical active molecules (EAMs) solid additives could impact charge/discharge behavior and improve cathode performance. To identify potential solid additives for sulfur cathode and investigate their impacts, we worked on both inorganic and organic solid additives.

For inorganic solid additives, we picked TiS_2 for our study due to its unique electronic conductive properties and lithiation/delithiation feature upon cycling. We found that with TiS_2 addition (~ 0.38 wt% in the cathode) to replace solid electrolyte (LPS), rate performance and sulfur utilization of sulfur cathode was improved as shown in Figure II.9.K.11. It was found that with TiS_2 addition (~ 0.38 wt% in the cathode) to replace solid electrolyte (LPS), rate performance and sulfur utilization of sulfur cathode was improved. At 0.1 C, specific capacity of sulfur cathode could be increased from around 1200 mAh g^{-1} (Figure II.9.K.10a) to 1400 mAh g^{-1} after TiS_2 addition. The sulfur content of the cathode is around 39 wt% and the test was performed at 60 °C using LPS glass solid electrolyte.

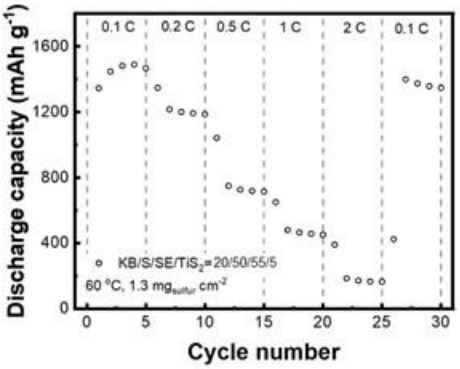

Figure II.9.K.11 Rate performance of sulfur cathode with TiS_2 additive.

Besides inorganic solid additives, we also investigated the effect of organic EAMs as additives on all-solid-state sulfur cathode. We found that with less than 5 wt% addition, the sulfur cathode discharge capacity could be significantly increased as shown in Figure II.9.K.12. Moreover, after adding EAMs as additive, the sulfur cathode with sulfur content of around 50 wt% and areal loading of around 1.5 mg cm^{-2} demonstrated high initial discharge capacity of over 1400 mAh g^{-1} and even after 50 cycles, the specific capacity could still retain above 1200 mAh g^{-1} at 0.3 charge/discharge rate at 60 ºC (Figure II.9.K.13). Li-In alloy was employed as anode and LPS glass type solid state electrolyte was employed as solid electrolyte membrane and electrolyte used in the cathode. Such superior performance fulfilled the EAMs additives demonstration milestone as well as the project progress cell demonstration target of Go/No Go decision for budget period 1. It is belived that the EAMs additive could contribute to generating favorable interface between carbon-sulfur composite and solid-state electrolytes.

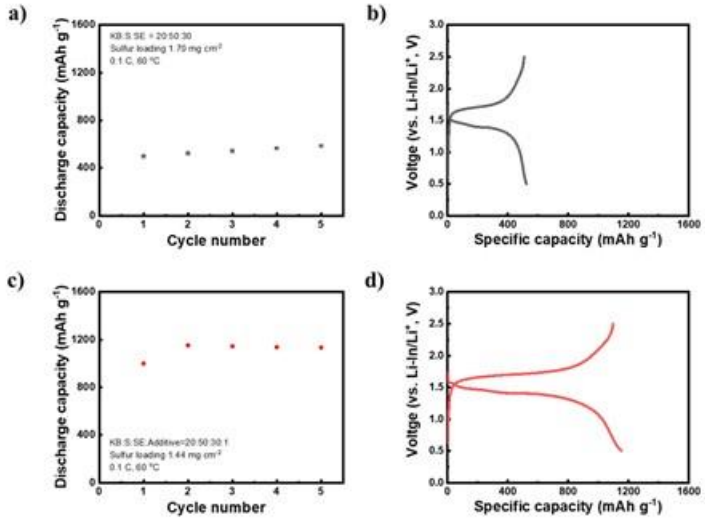

Figure II.9.K.12 a) Rate performance and b) corresponding 2nd-cycle voltage profile of sulfur cathode without additives. c) Rate performance and d) corresponding 2nd-cycle voltage profile of sulfur cathode with additives.

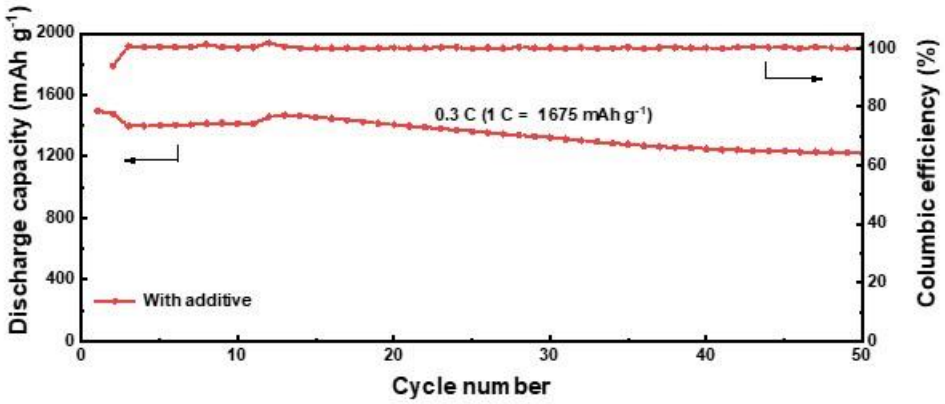

Figure II.9.K.13 Cycling performance of all-solid-state lithium-sulfur battery using EAM additive at 60 °C.

4. Advanced characterization techniques

Developing characterization techniques to acquire knowledge of all-solid-state sulfur cathode is helpful to understand the intrinsic problems and provide guidance for new material design and cathode fabrication. We have recently developed a tool to characterize the all-solid-state sulfur cathode using computed tomography (CT). The results could be seen in Figure II.9.K.14. We have found that upon discharge, sulfur cathode shall undergo volume expansion and form a dense layer. However, upon charging, the volume of the cathode would shrink, and inner cracks may generate within the cathode. Such behavior may lead to detachment of active material from conductive network, cathode structure degradation and therefore capacity decay upon cycling. The successful employment of CT characterization technique for Li-S ASSBs shall help us gain more in-depth understanding of the system, guide our future research, and contribute to the whole project.

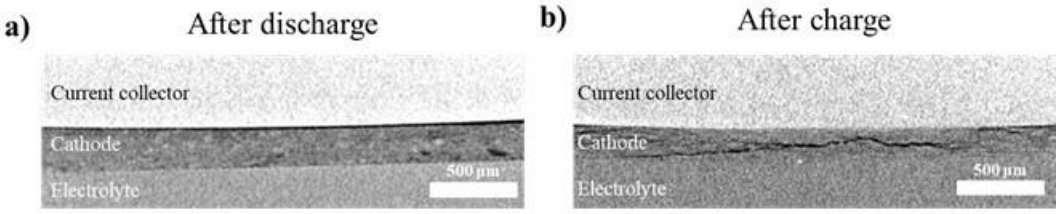

Figure II.9.K.14 Visulation of all-solid-state sulfur cathode after a) 1st discharge and b) 1st charge using CT.

Besides CT technique, we have also employed ex-situ XPS characterization, ex-situ Raman, transmission electron microscopy (TEM) and many other techniques for our research. We are working on developing ex-situ XRD and other advanced characterization techniques for sulfur cathode as well. All these efforts will contribute to the progress of the project and guide us developing advance new materials for all-solid-state Li-S batteries.

Conclusions

In summary, we have accomplished our goals and Go/no Go target for budget period 1 and obtained the following four main achievements. 1) We have synthesized various solid electrolytes and successfully developed a new glass-ceramic solid electrolyte, $65Li_2S$-$26P_2S_5$-$10Li_3N$-$12Al_2S_3$, which possesses high ionic conductivity of 5.19 mS cm^{-1} at 25 °C, low activation energy of 0.159 eV and superior stability against lithium metal. 2) We have screened various carbon materials and optimized the cathode preparation methods for Li-S ASSBs. Superior discharge specific capacity of over 1470 mAh g^{-1} has been reached using KB as carbon additives with high sulfur content of 50 wt%. 3) We have investigated the effects of both inorganic additive (TiS_2) and organic additive for sulfur cathode. As a result, stable cycling of sulfur cathode with specific capacity over 1200 mAh g^{-1} for 50 cycles at 0.3 C rate has been achieved using organic additives (< 5 wt% in

cathode). 4) We have developed various tools for the characterization of Li-S ASSBs which includes CT, XPS, ex-situ Raman, TEM etc.

Key Publications

1. Wang, Daiwei, Li-Ji Jhang, Shiyao Zheng, Atif AlZahrani, Tianhang Chen, Yue Gao, Donghai Wang. "Mixed ionic-electronic conductive lithium thiophosphate solid electrolyte for all-solid-state lithium-sulfur batteries with high sulfur utilization." *In preparation*.

References

1. Kamaya, Noriaki, Kenji Homma, Yuichiro Yamakawa, Masaaki Hirayama, Ryoji Kanno, Masao Yonemura, Takashi Kamiyama, Yuki Kato, Shigenori Hama, Koji Kawamoto, and Akio Mitsui. 2011. "A lithium superionic conductor." *Nature Material* 10: 682-686.

2. Hayashi, Akitoshi, Takamasa Ohtomo, Fuminori Mizuno, Kiyoharu Tadanaga, and Masahiro Tatsumisago. 2003. "All-solid-state Li/S batteries with highly conductive glass–ceramic electrolytes." *Electrochemistry Communications* 5, no. 8 (August): 701-705.

3. Inoue, Takao, and Kazuhiko Mukai. 2017. "Are All-Solid-State Lithium-Ion Batteries Really Safe? – Verification by Differential Scanning Calorimetry with an All-Inclusive Microcell." *ACS Applied Materials & Interfaces* 9, no. 2 (January): 1507-1515.

4. Tatsumisago, Masahiro, Motohiro Nagao, and Akitoshi Hayashi. 2013. "Recent development of sulfide solid electrolytes and interfacial modification for all-solid-state rechargeable lithium batteries." *Journal of Asian Ceramic Societies* 1, no. 1 (March): 17-25.

Acknowledgements

The work was supported by the Department of Energy, Office of Energy Efficiency and Renewable Energy (EERE), Vehicle Technology Office, under Award Number DE-EE0008862. We appreciate the support from Colleen Butcher at National Energy Technology Laboratory.

II.9.L Developing an In-situ Formed Dynamic Protection Layer to Mitigate Lithium Interface Shifting: Preventing Dendrite Formation on Metallic Lithium Surface to Facilitate Long Cycle Life of Lithium Solid State Batteries (University of Wisconsin-Milwaukee)

Deyang Qu, Principal Investigator
University of Wisconsin-Milwaukee
3200 N Cramer Street
Milwaukee, WI, 53211
E-mail: qud@uwm.edu

Tien Duong, DOE Technology Development Manager
U.S. Department of Energy
E-mail: Tien.Duong@ee.doe.gov

Start Date: October 18, 2019 End Date: October 17, 2022
Project Funding: $1,250,000 DOE share: $1,000,000 Non-DOE share: $250,000

Project Introduction

The next-generation battery innovations for EV without ICE will have to enable the vehicle to drive for long distances. Marginal improvements of state-of-art Li-ion technology cannot meet this challenge. Any "beyond Li-ion" technologies, which aim to achieve cell performance targets of ≥ 350Wh/Kg, over 1000 cycles at C/3 rate, 15 year shelf life and < $100/KWh cost, will need a metallic Li anode (~3862 mAh/g). Applications of Li anodes in batteries is hindered by dendrite formation during the battery operation leading to serious safety issues. Previous efforts to suppress dendrite formation on lithium metal anodes by altering the electrolyte, modifying the Li surface, or optimizing the cell structure fell short because they did not solve the root causes of dendrite formation during the interface shift of Li anodes during cycling. We propose to investigate interface shift, surface homogeneity and surface Li^+ concentration. Our work will focus on creating a dynamic protection layer during the interface shift to prevent dendrite formation throughout the battery operation, potentially enabling the commercialization of a safe metallic Li battery with a long cycle life. This is particularly important in a solid-state-electrolyte battery, since the interfacial changes between the Li anode and the electrolyte could create a physical gap which hinders the electrochemical reaction.

Objectives

The objective of this project is to research, develop, and test lithium metal-based batteries that implement solid lithium-ion conductors equipped with a formed dynamic protection layer. The proposed project aims to enable safe, long cycle Li anodes achieve cell performance targets of 400Wh/Kg, over 100 cycles, 15-year shelf life and < $100/KWh cost.

Our efforts are to contribute an *in-depth* understanding of the Li interface and dendrite growth prevention to the field of Li metal batteries, which will pave the way for the eventual development of high energy density, low cost and long-lasting Li batteries. This advancement could be a crucial selling point for the greater adoption of electric vehicles (EV). This project will make possible the translation of fundamental research into the practical implementation of high energy Li anodes, enabling the eventual achievement of the cell performance targets.

Approach

The novelty of our approach is that we intend to mitigate the dendrite problem by creating a dynamic protection layer during the interface shift to prevent dendrite formation throughout the battery operation. Four approaches will be explored: 1) Surface with homogeneous activity; 2) Artificial interface to "alloy" Li

dendrites; 3) Dissolution and re-deposition of Li through re-distribution of Li-carrier complex; 4) Control local Li concentration.

Results

FY 2020 has been a challenge one. Due to the pandemic of COVID-19, the PI's research labs in the university closed in March 2020 right after the university spring break and are only partially open in order to maintain social distance. But we managed to complete all milestones of FY2020.

During FY2020, we have accomplished three areas of research:

1. Designed and optimized *in-situ* electrochemical cells to observe a Li dendrite growth during a cell operation and to monitor the generation of gases during a cell formation.

2. Started testing the *in-situ* and *ex-situ* formation of the potential dynamic interfacial protective layers.

3. Set up a dedicated infrastructure for the solid-state-electrolyte research including materials synthesis, an Ar-filled glove box in a dry room, a double workspace glove box with temperature control chamber and static removal capability etc.

4. Designed and optimized a solid-state cell for cycling testing.

Design and optimization of in-situ MS-electrochemical cell. The apparatus for the *in-situ* electrochemical Mass Spectroscopy (MS) analysis was automated to conduct overnight experiments due to the nature of this research. Figure II.9.L.1 (I) shows the G1 design which was validated for the detection of gas generation real-time during the cycling of a battery. Figure II.9.L.2 (II) illustrated the G2 redesign of the gas collection chamber and automation using Labview . The gas formed during an cell operation can be identified by an in-line MS (Figure II.9.L.3 (III)), while the quantity of each gas can be measured at various stage of operation (Figure II.9.L.4 (IV).

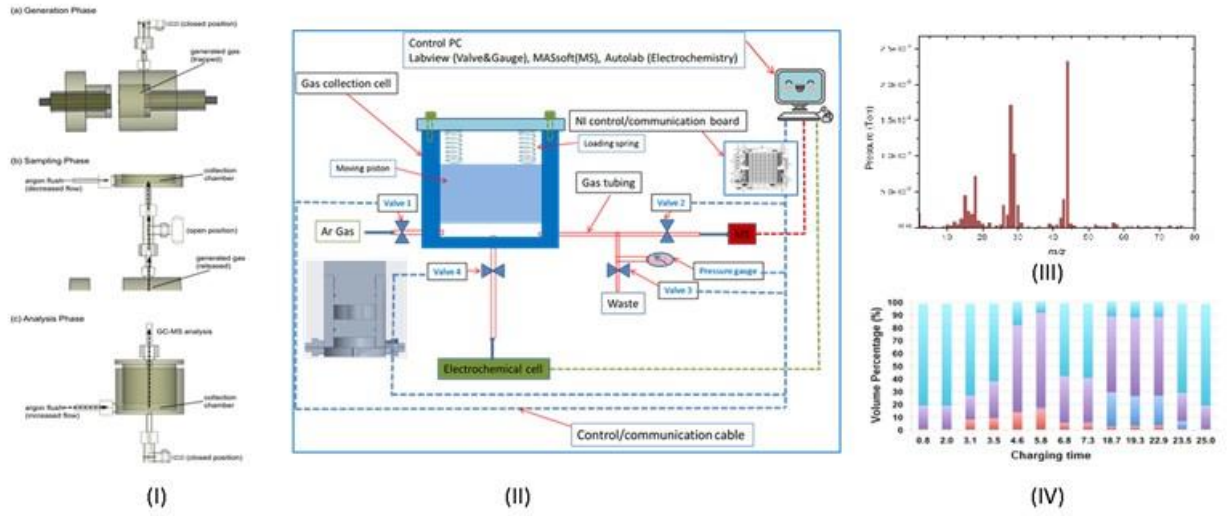

Figure II.9.L.1 Electrochemical cell for in-situ Mass Spectroscopic (MS) experiments (I). The gas generated during the cycling can be monitored real-time with a gas analyzer (MS). G2 manifold (collection chamber) design and automation design. G2 design of the in-situ cell eliminates the influence of the carry-over residual gases, so the gas amount and composition can be determined either at various voltage or various charging time (II). An example of analysis data is shown in (III) and (IV)

Design and optimization of in-situ optical-electrochemical cell. An optical electrochemical cell for the *in-situ* observation of a Li dendrite growth during the charge and the discharge of a cell is shown in Figure II.9.L.2 (i). The cell is designed to observe an electrode surface under a confocal 3D microscope shown in Figure II.9.L.2

(ii). Synchronized with an electrochemical test station, the dendrite growth under different electrochemical polarizations and at different DOCs can be manifested. Figure II.9.L.2 (iii) shows 3D images of the Li morphology observed at different electrolytes, different charge times and different surface treatments. Figure II.9.L.2 (iv) shows the G2 *in-situ* optical cell design for a real-time observation of Li/SS/cathode interface. The basic design was the same as the G2 cells for the performance tests shown in Figure II.9.L.3 , but with a window for an optical observation. The window is located right at the electrode/solid state electrolyte interface. The cell is assembled in a glovebox dedicated for the solid-state-electrolyte research. Either the assembled cell is then sealed in an airtight container with a transparent window for the tests at elevated temperature, or an O-ring sealed transparent window is attached to the cell body. The temperature in the box is kept at 60-70ºC with an inside heating element.

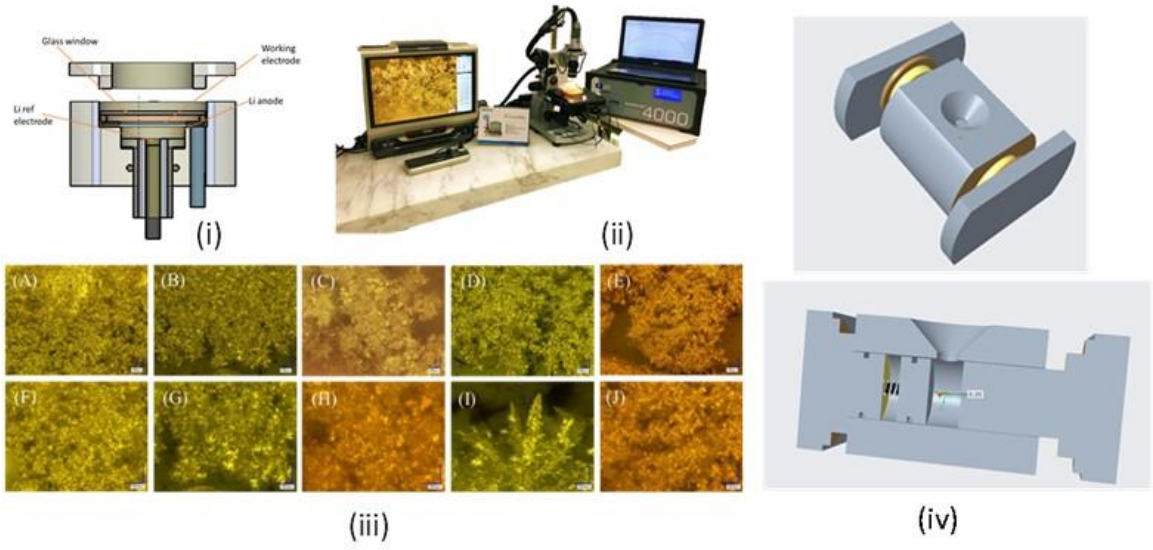

Figure II.9.L.2 (i) G1 optical electrochemical cell for in-situ electrochemical observations during the discharge and recharge of a Li anode; (ii) the photo of the set-up for the in-situ electrochemical optical experiments which includes laser confocal microscope, optical cell and electrochemical workstation. The surface morphology and dendrite growth can be observed real-time, examples are shown in (iii). G2 optical cell design for in-situ observation of Li/solid state interface.

Design and validation of the electrochemical cell for the Li/solid-electrolyte performance tests. Figure II.9.L.3 shows the G2 design of the cell used for the performance tests of a solid-state-electrolyte Li cell. A solid state electrolyte is pressed and formed in the cell using a pair of rods made by a harden steel. The cathode and the Li anode are then put on the both side of the solid state electrolyte, a set of Ti rods with O-ring seals are used as current collectors. A calibrated spring is used to ensure that a constant pressure can be maintained during testing. The cells are then tested at RT-60ºC. The impedance of a typical LPSCI electrolyte is also shown in Figure II.9.L.3 (ii).

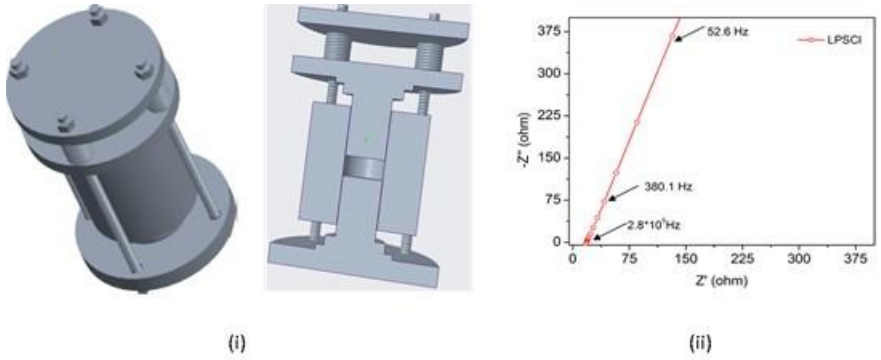

Figure II.9.L.3 G2 solid-state cell and the impedance of the formed solid state electrolyte (home synthesized LPSCl)

Dendrite growth prevention with a surface lamination. By mean of the *in-situ* optical electrochemical cell, new Li surface coatings were tested. The surface modification aims for a dynamic dendrite growth suppression. Figure II.9.L.4 shows an example of such modifications. In this particular example, dendritic Li reacted with the face layer forming a Li alloy, due to a small potential differential between the metal Li and the coating material. The Li in the alloy can be oxidized during a discharge at the similar potential to that of a metallic Li. In comparison with a pristine Li anode, no Li dendrite can be seen after five cycles. The modified Li demonstrated much longer cycle life than that of a pristine anode in a symmetric cell.

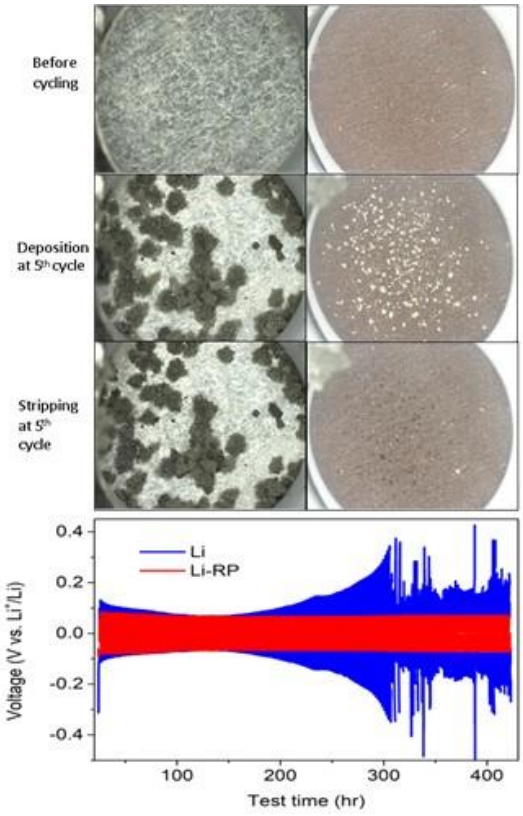

Figure II.9.L.4 in-situ observatins of a pristine Li andoe and a surface treated Li anode after 5 cycles and the comparision of the cycle performance of a pristine Li and a surface treated Li symmetric (Li/Li) cells.

Dendrite growth prevention with a surface self-assembled interfacial layer. Unlike the previous one, the dynamic interfacial layer was elastic, liquid electrolyte can be trapped in the layer through a strong bonding. The size of the layer can self-adjust to compensate the volume change of the Li anode during cycling to maintain a stable electrochemical interface. Figure II.9.L.5 shows the comparison of a pristine Li and a surface

modified Li created by the method. The electrodes were cycled at 2 mA cm^{-2} rate. The surface morphologies of the pristine and the modified anode surface are shown in the figures. Clearly, the dendrite growth and the "dead lithium formation" during cycling were substantially depressed on the modified Li surface. The artificial layer was not only formed *ex-situ*, but also can chemically "react" with Li dendrite *in-situ*. The artificial layer consisted of large conjugated system, which metallic Li can exchange electron with – one electron from a Li atom will be "dislocated" in the π conjugated system while Li^+ will become trapped in the matrix due to ion-ion interaction. It can be considered as the dissolution (not a chemical redox reaction) of Li dendrite in the interfacial layer. Therefore, regardless of the degree of an interfacial shift, as soon as a Li dendrite reaches the layer, Li dissolves in the layer. The Li trapped in the interface can eventually become oxidized during a subsequent discharge. Secondly with the artificial interface, the surface energy of Li anode can become more homogeneous, then the Li deposition would be more uniform. The preliminary results support these hypothesizes. The *ex-situ* formed artificial interface on Li anode could become an effective interface between Li anod and solid-state-electrolyte.

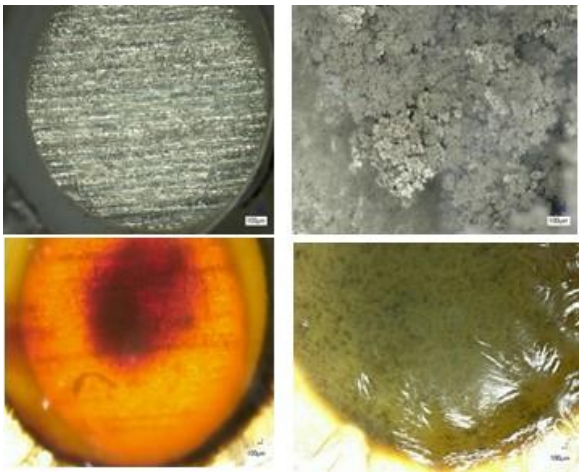

Figure II.9.L.5 Pristine Li surface (up right); pristine Li after five high rate cycles (up left; elastic surface coating (down right) and after five high rate cycles (down right). The comparison of coated and pristine Li anode

An organic cation, trisaminocyclopropenium (TAC) shown in the top of Figure II.9.L.6, was also tested to suppress dendrite growth on a metallic lithium anode. During the Li plating process, TAC cations with aliphatic chains can form a positively charged electrostatic shield around Li protrusions, repelling the approaching Li+ and thereby attaining a more uniform plating. A two times longer cycle life of 300 h at 1 mA cm^{-2} is achieved in a Li‖Li symmetric cell in comparison with the control. Eventually, the TAC molecular will be polymerized by attaching to a backbone or distributed in a polymer matrix. The objective is to form a dynamic interface between the Li anode and the solid-state-electrolyte.

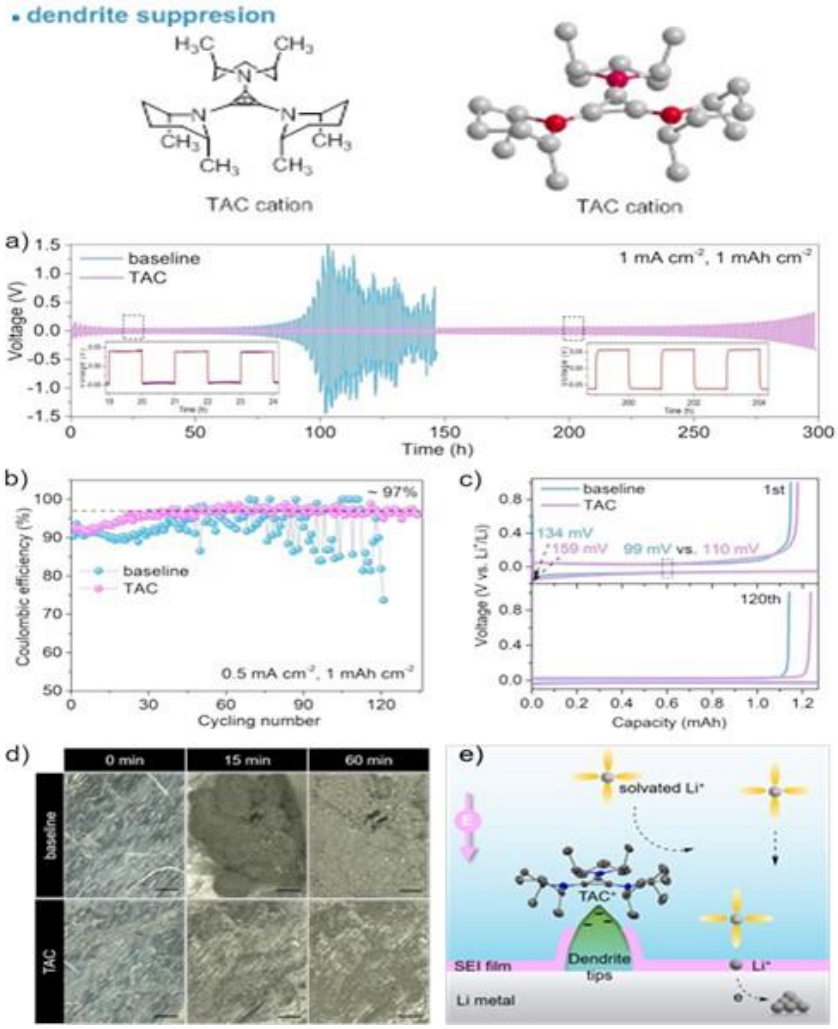

Figure II.9.L.6 (Top) Molecular structure of trisaminocyclopropenium (TAC). (bottom) Electrochemical performance of Li plating/stripping in TAC electrolyte. a) Voltage profiles of Li‖Li symmetric cells cycling at 1 mA cm-2 1 mAh cm-2; b) Coulombic efficiencies of Li‖Cu asymmetric cells cycling at 0.5 mA cm-2 1 mAh cm-2 and c) the voltage profiles of Li‖Cu cell at 1st and 120th; d) in-situ optical microscopic images during Li plating process at 4 mA cm-2, scale bar 200 μm; e) schematic illustration of a cation-shield mechanism. Note: the TAC is not drawn to scale. (The manuscript submitted and is under review.)

To investigate the role of TAC cation on dendrite suppression, the polarization profiles of Li‖Li symmetric cells were first cycled at 1 mA cm^{-2} rate for 1-hour duration. As displayed in Figure II.9.L.6 (a), the cell with TAC performs significant better than the baseline. In a baseline cell, Coulombic efficiencies (CEs) dropped below 90% after 49 cycles, while an average CE of 97% was preserved with TAC throughout 135 cycles (Figure II.9.L.6 (b)). The *in-situ* optical microscopic images were compared under a harsh Li plating condition of 4.0 mA cm^{-2}. As displayed in Figure II.9.L.6 (d), highly dendritic and mossy Li formed after 15 min in the baseline electrolyte and evolved into filament morphology after 60 min. These dead Li can lead to a poor CE and an increased cell impedance. In contrast, a relatively uniform Li deposition was observed in the TAC electrolyte throughout the test.

A cation-shield mechanism is proposed and illustrated in Figure II.9.L.6 (e). It is well established that the plating process can unavoidably generate protuberant tips on which electric charges tend to accumulate. The TAC cations can be absorbed on those tips without being reduced via electrostatic attraction. Thus, a lithiophobic protective layer can be formed due to its bulky scaffold with branched nonpolar groups. The

arriving Li^+ was repelled and deposited on the adjacent flat Li surface, thus generating a dendrite-free Li deposition.

Conclusions

1. The *in-situ* electrochemical cells were validated for the real-time identification of gas generation and observation of dendrite growth during the cell operation.

2. Preliminary results showed that the strategies of forming dynamic interfacial layer on the surface of Li anode can reduce dendrite growth during cycling.

3. A solid-state-electrolyte cell was validate for the performance test.

Key Publications

1. Weixiao Ji,, He Huang,, Dong Zheng, Xiaoxiao Zhang, Tianyao Ding, Tristan H. Lambert, Deyang Qu, “A Redox-Active Organic Cation for Safer Metallic Lithium-Based Batteries”, Energy Storage Material 32(2020)185-190.

Acknowledgements

The PI and associates in the University of Wisconsin Milwaukee are very grateful to Professor Tristan H Lambert and Dr. He Huang for providing the TAC compounds and fruitful discussions.

II.9.M Composite Solid Ion Conductor with Engineered Lithium Interface (Wildcat Discovery Technologies)

Kyler J. Carroll, Principal Investigator
Wildcat Discovery Technologies
6255 Ferris Square, Suite A
San Diego, CA 92121
E-mail: Kcarroll@wildcatDiscovery.com

Cam Peebles, Principal Investigator
Wildcat Discovery Technologies
6255 Ferris Square, Suite A
San Diego, CA 92121
E-mail: Cpeebles@wildcatdiscovery.com

Tien Duong, DOE Technology Development Manager
U.S. Department of Energy
E-mail: Tien.Duong@ee.doe.gov

Start Date: October 1, 2019 End Date: September 30, 2021
Project Funding: $1,529,792 DOE share: $1,223,833 Non-DOE share: $305,959

Project Introduction

Successful widespread commercialization of electric vehicles is contingent upon development of safe high energy density batteries capable of long cycle life. Lithium metal affords the highest theoretical capacity (3,860 mAh/g) and lowest electrochemical potential (-3.04V vs SHE), which offers the highest specific energy density of anode materials today. While Li-ion batteries are capable of delivering energy densities of 400-600 Wh/kg, the development of lithium metal batteries – such as Li-S and Li-air may boost this number up to 650 and 950 Wh/kg, respectively. However, significant progress towards the passivation of lithium metal must occur before the energy density benefit can be realized. Issues with lithium dendrite formation, anode volume expansion, and continuous solid electrolyte interphase (SEI) build-up often result in significant safety concerns, high cell resistance, and poor cycle life. The intrinsic high reactivity between lithium metal with conventional lithium ion electrolytes (organic carbonate-based solvents) makes it extremely difficult to overcome these problems. In this project, Wildcat seeks to perform focused, fundamental research and development on composite polymer/ceramic electrolytes and protected lithium metal anodes to develop an all solid state lithium metal battery that achieves the DOE requirements to enable commercialization. Wildcat will leverage its high throughput battery platform and explore a broad composite electrolyte compositional space. Additionally, Wildcat will screen thousands of inorganic and organic coatings for lithium metal protection using in situ liquid methods and translate the best results to all solid cells.

Objectives

The project objective is to develop a composite polymer/ceramic electrolyte and protected lithium metal anode for an all solid-state lithium metal battery that achieves the DOE requirements for performance and that enables the potential commercialization of this technology. Successful widespread commercialization of electric vehicles is contingent upon development of safe high energy density batteries capable of long cycle life. Lithium metal affords the highest theoretical capacity (3,860 mAh/g) and lowest electrochemical potential (-3.04V vs SHE) and offers the highest specific energy density of anode materials today. However, significant progress towards the passivation of lithium metal must occur before the energy density benefit can be realized. The intrinsic high reactivity between lithium metal with conventional lithium ion electrolytes (organic carbonate-based solvents) makes it extremely difficult to overcome these problems. The proposed composite polymer/ceramic electrolyte and a protected lithium metal anode will enable an all solid-state lithium metal

battery. It is expected that the outcomes from this effort will deliver a safe all solid-state lithium metal pouch cell with over 350 Wh/kg and over 1,000 cycles (C/3) with the cost estimate below $100/kWh.

Approach

The project approach involves (1) identifying a suitable combination of solid ion conductor, polymer, and additive that minimizes overall interfacial impedance between the polymer electrolyte and solid ion conductor, and (2) identification of stable Li-metal protection agent or combination of agents that show enhanced cycling performance (relative to a non-protected system) using the down-selected cell architectures.

Results

Synthesis of Ceramic Ion Conductors

Wildcat's High Throughout platform allows for the ability to synthesize many inorganic materials, in parallel, and measure their phase purity and ionic conductivity using X-ray diffraction and Electrochemical impedance spectroscopy, respectively. Figure II.9.M.1A shows an overview plot of ceramic ion conductors synthesized during the second quarter of the project and their ionic conductivity using gold blocking electrodes. During the second quarter Wildcat synthesized two types of ceramic ion conductors, garnet (LLZO) and NASICON (LATP), by solid-state methods. The LLZO and LATP diffraction patterns are shown in Figure II.9.M.1B. Based on the diffraction patterns we can see that phase pure materials were synthesized using Wildcat's high throughput platform. Due to the native oxide that forms on the LLZO surface, LATP was chosen as the ceramic test vehicle moving forward for the development of the trilayer sandwich cell.

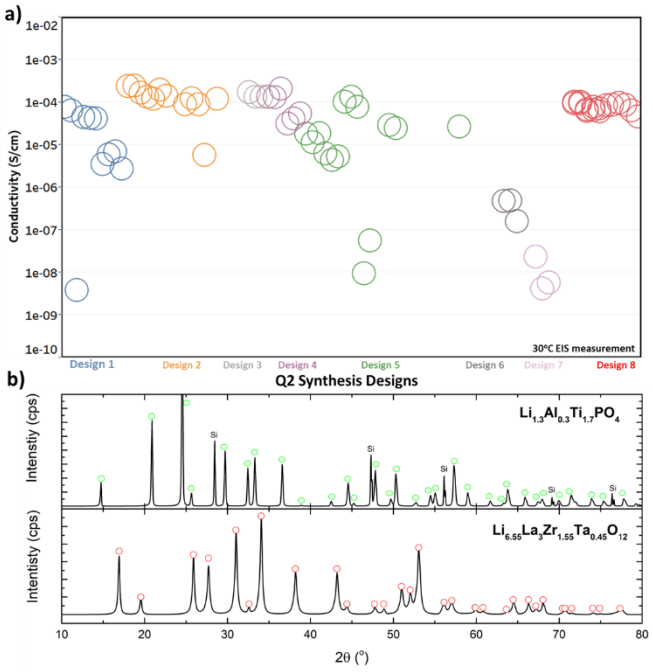

Figure II.9.M.1 a) EIS results for Au//Au blocking electrode results for Q2 ceramic ion conductor designs, b) XRD results for Wildcat synthesized LATP and LLZO powders.

Development of Composite Ceramic/Polymer Electrolyte

During the last year of the project Wildcat focused on 1) the development of a sandwich cell to screen the interfacial impedance between the polymer and ceramic, 2) demonstrating coupling agents that reduce the interfacial impedance, and 3) translating the screening results to free-standing composite ceramic/polymer solid state electrolytes. The first part of the project was developing a test vehicle to demonstrate the interfacial impedance between the polymer and ceramic components and Wildcat developed a trilayer sandwich cell. The baseline (Figure II.9.M.2A) consisted of a dense LATP ceramic pellet, previously developed by Wildcat,

sandwiched between two polymer electrolytes membranes. The cell architecture allowed for rapid screening using Wildcats High Throughput testing platform. The sandwich cells were characterized by AC impedance spectroscopy at various temperatures (30, 40, 50, and 60 ºC). The LATP ceramic pellet was measured using a gold blocking electrode while the polymer electrolyte was measured using a copper blocking electrode. Figure II.9.M.2B shows representative Nyquist plots of a LATP ceramic pellet, polymer electrolyte, and trilayer cell measured at 60 ºC. Temperature dependent conductivity values are calculated by fitting the data to an equivalent circuit model. If no interfacial impedance existed, the resistance of the trilayer sandwich cell would equal the sum of the LATP pellet and polymer electrolyte resistances. The area-specific resistance plot (Figure II.9.M.2C) shows that the trilayer sandwich cell deviates from the sum of the ceramic and polymer, indicating a larger interfacial impedance between the LATP and polymer. For the baseline polymer electrolyte and LATP, the $R_{interface}$ (Figure II.9.M.2D) was measured and shows a large interfacial resistance at room temperature (30 ºC).

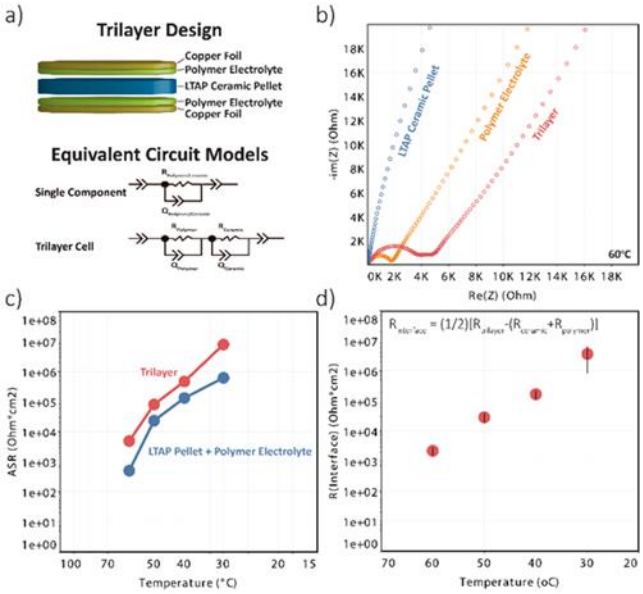

Figure II.9.M.2 a) Wildcats high throughput trilayer sandwich cell and equivalent circuit models for AC impedance fitting, b) Nyquist plots of LATP ceramic pellet, polymer electrolyte and trilayer cells, c) area-specific resistance of the trilayer cell and the sum of the LATP pellet and polymer electrolyte, and d) the calculated $R_{interface}$ for the trilayer cell.

The second focus was to use the above testing vehicle to screen thousands of coupling agents with various functional groups and polymer backbones which minimizes the interfacial impedance between the LATP and polymer electrolyte. Figure II.9.M.3A shows an overview plot of several coupling agent families tested at room temperature. In todal during the first three quarters of the project over 5200 EIS measurements were taken. As can be seen in the figure, several hits show low interfacial imepdance suggesting that the resistance between the ceramic LATP and PEO polymer were reduced or eliminated. Figure II.9.M.3B and Figure II.9.M.3C show a selected set of results where several familes have lower interfacial impedance and higher trilayer conductivities when compared to the control. Of the best coupling agents, Families A, C, and D show the lowested interfacial imepedance of all tested.

The third focus was to translate the results from the trilayer screening geometry to a free-standing composite polymer/ceramic electrolyte film with the coupling agent. Coupling agent family C was chosen as the preliminary additive to validate the process. The coupling agent was tested in two forms; one where the coupling agent was simply added to the slurry of the PEO, ceramic, salt, and solvent and then cast to make the composite electrolyte (non-functionalized) and the second where the coupling agent was first functionalized onto the surface of the LATP ceramic, then mixed with the PEO, salt, and solvent (Functionalized). Figure II.9.M.4 shows the preliminary results with 10wt% LATP for both functionalized and non-functionalized composites. From the figure you can see that the coupling agent increases the conductivity of the composite

ceramic/polymer over no coupling agent. The results show that the interfacial impedance between the PEO and ceramic is lowered by incorporating a coupling agent resulting in lithium ion conductivity moving through the ceramic phase.

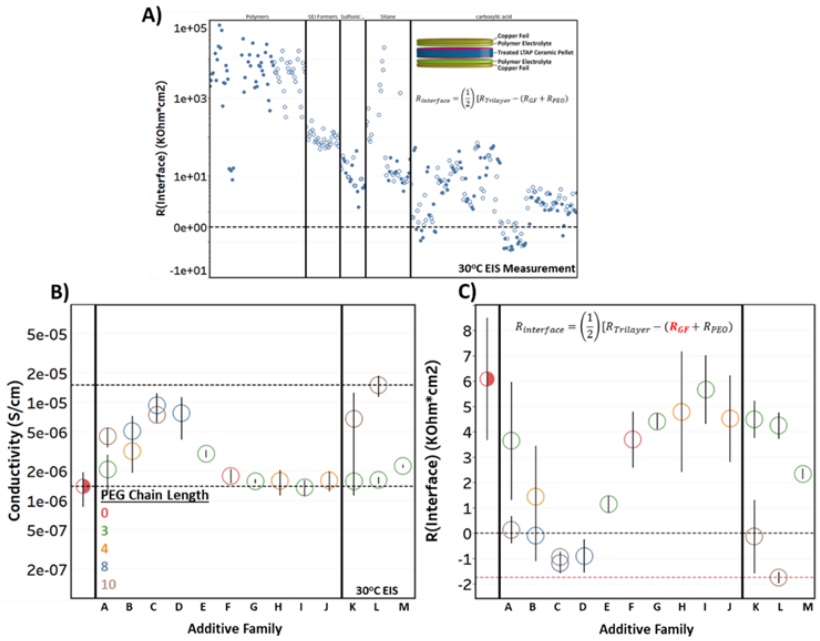

Figure II.9.M.3 A) Additive screening using Wildcats' HT trilayer cell geometry. Over 5200 EIS measurements ran in 3 quarters. B/C) Best hit families that show lowest interfacial impedance in tri-layer cell geometry. The baseline system is shown on the left-most panels of Figures B/C.

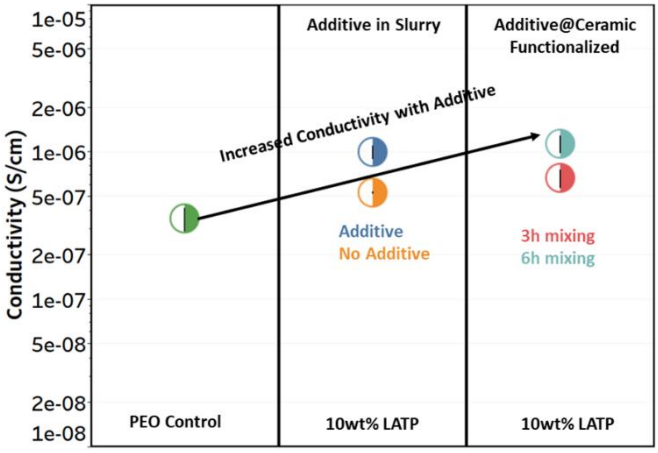

Figure II.9.M.4 Results of the PEO/Ceramic composite with and without the additive C. The results show that having the additive in the composite improves the ionic conductivity

Li Metal Screening

During the last year of the project Wildcat focused on 1) demonstrating enhanced Li/Li cell cycling using liquid electrolyte and 2) investigating the interface between lithium metal and solid state electrolyte materials (ie, ceramic and polymer). In the first focus, singular and combinations of lithium metal protection additives were screened with the goal of increasing the cycle life of Li/Li symmetric cells using a small voltage of carbonate-based electrolyte. Lithium metal was treated with specific singular additive (and later a combination of multiple additives) to assemble an artificial SEI (ASEI) that has properties of being both mechanically strong, elastic and ionically conductive. Figure II.9.M.5A shows the effect of single additive treatment on

lithium metal. Additives in the nitrate family, especially ASEI_58, was shown to be promising in enhancing Li/Li cell cycle life when a current density of 1.0 mA/cm2 for 1h plating and stripping was used. The additive responsible for ASEI_58 was then combined with other additives from several types of families (ie, anhydrides, chlorides, etc) in the hopes of further enhancing the beneficial effects of ASEI_58. The effect of this dual-additive lithium metal treatment is shown in Figure II.9.M.5B. Additives coming from both the polymer and inorganic salt family were able to enhance the performance of ASEI_58 dramatically (circled in green). These additive combinations will be further explored.

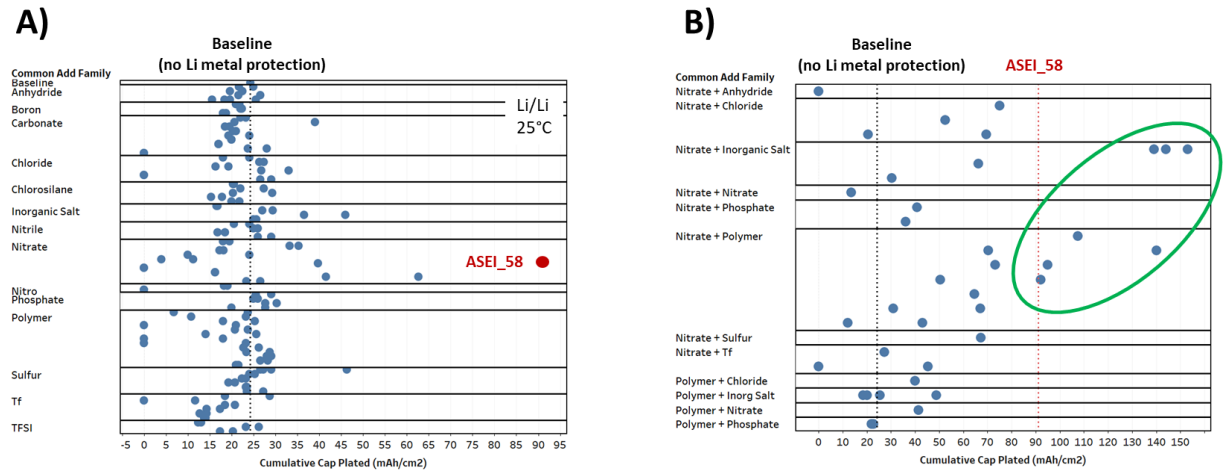

Figure II.9.M.5 . A) Performance of single additive ASEIs in Li/Li symmetric cells using liquid electrolyte. The baseline system (no lithium metal protection) is shown as a dashed black line. The cumulative capacity plated is calculated from cycle life (h) and plating current (mA). B) The additive responsible for ASEI_58 was then combined with various other additives to look for synergistic lithium metal protection effects and their performance is shown here. Promising two-additive ASEIs are circled in green.

The second focus of the third quarter was to explore the interface between lithium metal with $Li_{1.3}Al_{0.3}Ti_{1.7}(PO_4)_3$ (LATP), a ceramic commonly used to increase ionic conductivity in polymer composite electrolytes and provide mechanical strength, and with polyethylene oxide (PEO), a potential binder for polymer composite electrolytes. The goal was to begin investigating the Li/SSE interface to see how changes may occur upon aging. Additionally, stack anneal temperatures were investigated to see how the effect of heating lithium against a specific component would change its interfacial resistance. Li/Li symmetric cells were constructed and the resistance at either the Li/LATP or Li/PEO interface was monitored via EIS. Figure II.9.M.6A shows the interfacial resistance in Li/LATP/Li cells as a function of stack anneal from no stack anneal to high stack anneal temperatures (multiple cells are shown for each condition, these were all measured within a couple hours of cell building). In all cases only a single semi-circle is present with a small diffusion tail. Increasing the stack anneal temperature (the stack anneal time is maintained at 1h for all systems) leads to a small reduction in the width of the semi circles (this is small via the arrow). After the stack anneal was performed the cells were calendar aged for up to 20 days and the EIS was recorded intermittently (see Figure II.9.M.6B). Regardless of stack anneal condition the resistance increased dramatically from Day 0 to Day 6 (see the arrow that indicates this). From Day 6 to Day 12 the resistance increase for all systems was relatively smaller compared to the Day 0 to 6 increase. Interestingly, there was almost no change in resistance between Day 12 and Day 20 indicating that some form of passivation layer had been formed between Li and LATP that prohibited further resistance growth. Figure II.9.M.6C shows resistance growth changes in Li/PEO/Li systems when various stack anneal conditions are tested. Without any stack anneal the Li/PEO interface shows high resistance of ~350-400K ohms and only one semi-circle is present although there is a slight shoulder visible. When a stack anneal is applied to the interface the resistance becomes significantly lower with higher stack anneal temperatures. The reduction in interfacial resistance is understandable from a melting perspective – as the PEO polymer is melting it can create more intimate contact with the Li metal. At the high stack anneal temperature the resistance is on the order of ~10K ohms and there are also two semi-circles present. These

results suggest that a stack anneal is necessary to reduce the Li/PEO interface resistance and that upon being formed additional interfaces could be present. Regardless of stack anneal temperature the Li/PEO resistance grows upon calendar aging as shown in Figure II.9.M.6D. In combination with the Li/LATP/Li data this shows that a protection layer on the lithium metal will be required to reduce both the interfacial resistance and prevent SSE composition between the lithium metal and SSE.

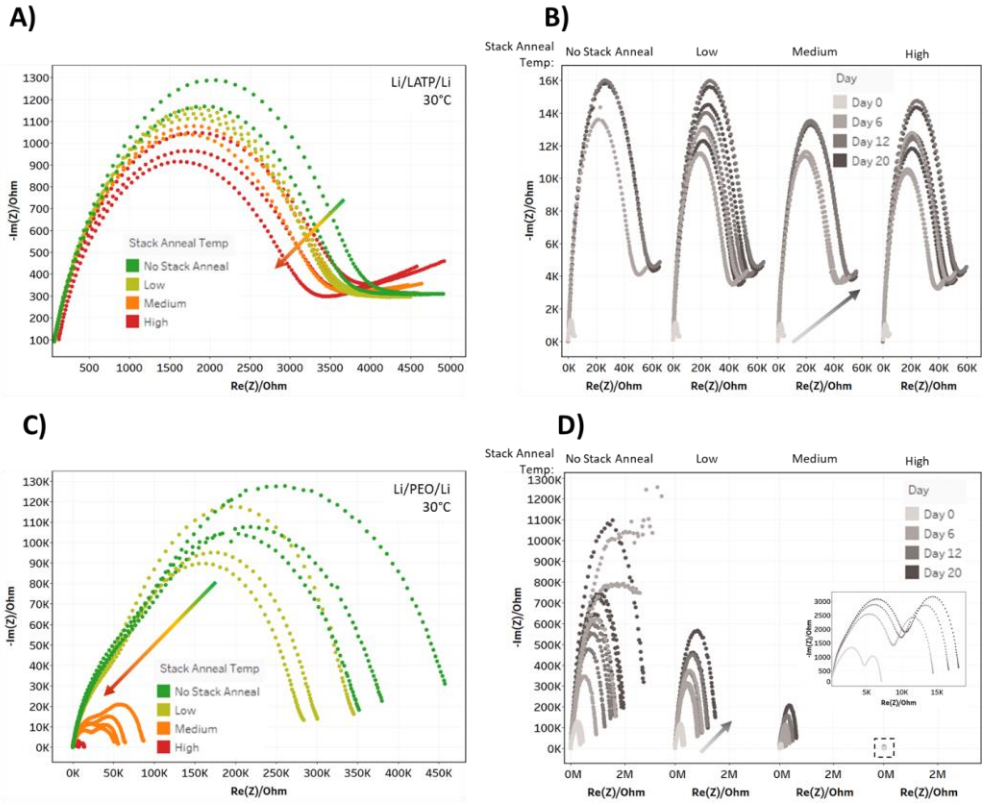

Figure II.9.M.6 A) Resistance due to stack anneals and calendar aging in Li/LATP/Li and Li/PEO/Li cells. A) and D) Stack anneal effects on Li/LATP/Li cells and Li/PEO/Li cells, respectively. B) and D) Calendar aging effects after stacking anneals on Li/LATP/Li cells and Li/PEO/Li cells, respectively.

During the upcoming year more effort will be placed on applying ASEIs to the LATP/Li interface to reduce resistance growth at that electrode. A similar screening will occur using the down-selected polymer from the other side of the project. Again, the idea is to investigate the interface between the polymer and the Li metal and decide how to best reduce resistance growth at the interface using ASEIs.

Conclusions

The trilayer sandwich cell developed at Wildcat allowed for the screening of coupling agents to minimize the interfacial impedance between the LATP and PEO interface using Wildcat's high throughput platform. Based on the best coupling agents free-standing composite films were made and show an improvement in ionic conductivity. The results show that the interfacial resistance is lowered and that the ionic transport is moving along the ceramic rather than the polymer. Current work is being conducted to improve the LATP loading and also the ionic conductivity of the free-standing composite ceramic/polymer solid state electrolyte. On the Li metal side of the project, Li/Li symmetric cells were initially used to test the viability of a protective artificial SEI (ASEI) coating to prevent decomposition of the Li metal. This test format in combination with Wildcat's high throughput platform allowed the screening of hundreds of materials in a short period of time. Subsequent work focused on optimizing the protective coating layer and investigating Li/ceramic interfaces. Ongoing work is focusing on Li metal protective coatings as they relate to the Li/ceramic interface.

II.9.N Fundamental Understanding of Interfacial Phenomena in Solid State Batteries (General Motors LLC)

Xingcheng Xiao, Principal Investigator
General Motors Research and Development Center
30470 Harley Earl Blvd.
Warren, MI 48092-2031
E-mail: xingcheng.xiao@gm.com

Tien Duong, DOE Technology Development Manager
U.S. Department of Energy
E-mail: Tien.Duong@ee.doe.gov

Start Date: October 1, 2019 End Date: March 30, 2023
Project Funding: $1,333,325 DOE share: $1,000,000 Non-DOE share: $333,325

Project Introduction

Solid-state batteries (SSBs) are considered the next generation battery technology for resolving the intrinsic limitations of current lithium-ion batteries, such as poor abuse tolerance, insufficient energy density, and short cycle life. However, the main hurdle for SSB in electric vehicle (EV) applications is the complexity caused by material interfaces, such as Li metal/solid electrolyte (SE) and SE/cathode interfaces, leading to increased impedance and shortened cycle life. Although interfaces in SSBs are one of the key factors, a clear understanding of their properties and functions is still unavailable, partly due to the difficulty in characterizing buried solid-solid interfaces and interphases formed during battery cycling.

Objectives

The project objective is to develop a comprehensive set of in situ diagnostic techniques combined with atomic/continuum modeling schemes to investigate and understand the coupled mechanical/chemical degradation associated with dynamic interfacial phenomena in SSBs. Specifically, in situ observations and characterizations of lithium plating-stripping processes, lithium dendrite formation, interphase formation, and the induced interfacial stresses, as well as the mechanical and electrochemical properties of interfaces and interphases, are paramount. The study will provide useful guidelines for optimizing cell structure design and engineering interfaces and interphases to enable SSBs. In addition, it will establish a critical guideline to design safe and durable SSBs with energy density > 500 wh/kg for EV applications.

Approach

The multiscale in situ diagnostic tools, including AFM, nanoindentation, dilatometer, stress sensors, and pressure cells, will be used to investigate mechanical behavior and microstructure evolution at interface/interphase during lithium plating and stripping. The information (along with Li-ion transport properties and microstructure evolution obtained using the advanced spectroscopic ellipsometry, and in situ TEM) will be correlated with electrochemical performance toward high cycle efficiency and dendrite-free SSBs. The goal of this understanding is to develop strategies for surface and interface engineering, apply them to commercially available SEs (including powder, pellets, and foils), and assemble SSBs for further validation and optimization, eventually extending cycle life for EV application.

Results

Developed the experimental capabilities for stress measurement of solid electrolyte during lithium Plating

During electroplating of lithium metal using garnet-based electrolyte such as $Li_7La_3Zr_2O_{12}$ (LLZO), two types of stress can be generated. First is the stress at the lithium metal/LLZO interface, which arises from inhomogeneous interfacial contact and volume change near the interface, and the electrode-electrolyte reaction layer. Second is the stress from the local defects inside the bulk solid electrolyte, which can cause current amplification and lithium metal penetration. The lithium metal penetration through the solid electrolyte (either bulk or grain boundary) can result in short circuiting, which is one of the main challenges that garnet-based solid electrolyte faces for a real-life application of all solid-state battery.

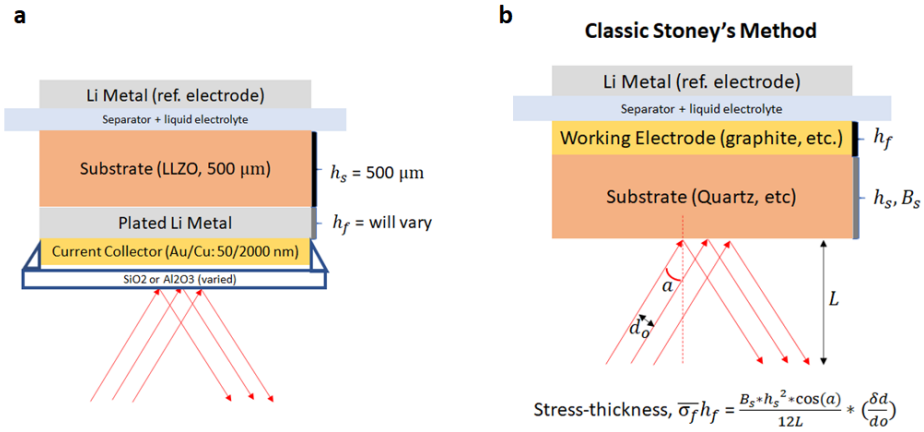

Figure II.9.N.1 a) Schematic of the MOSS sample using LLZO solid electrolyte with a reflective current collector for bending measurements. b) schematic of traditional MOSS electrode using classical Stoney's equation.

Both types of stress could make our solid electrolyte sample a measurable bending, which can be detected through multi-beam optical sensor (MOSS). With this measurable bending, we hope to relate the effect of stress on dendrite formation/penetration. Some information we intend to study are: 1) What kind of stress (tensile and compression) does the sample experience during plating at different current density? 2) What is the magnitude of stress experienced in LLZO and/or plated Li metal? 3) What drives the stress build-up in LLZO? To investigate these questions, LLZO pallet was prepared with reflective coating using e-beam deposition. A thin layer of copper (2um) and gold (50nm) current collectors were deposited directly onto the LLZO pallet to have a reflective surface and was capped with either SiO2 or Al2O3 (50nm) to improve the structural integrity of the current collector during plating. The schematic of the modified sample is shown below in Figure II.9.N.1a.

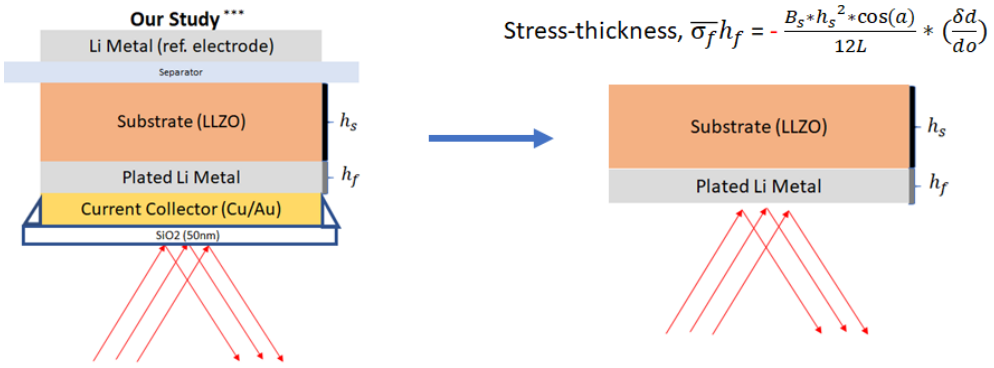

Figure II.9.N.2 Oversimplified approach of interpreting the bending measurements using LLZO. The resulting stress thickness equation is simply the negative value of classical Stoney's equation.

Lithium metal was used as a reference electrode, along with separator and liquid electrolyte to ensure good contact between lithium metal and the solid electrolyte during bending process. It is important to note that the bending measurement carried out with LLZO solid electrolyte differs from that of conventional electrode configuration used for classical Stoney's equation (Figure II.9.N.1b) to convert bending to stress-thickness. To assess our data accurately, it is essential that modeling work provides a way to interpret out curvature data. As an oversimplified approach (for now), we neglect the contributions from thin reflective current collectors and treat LLZO as the substrate, and the plated lithium metal as the working electrode. This will result in grossly oversimplified stress-thickness value as shown in Figure II.9.N.2.

Using the simplified interpretation, we can treat the measured curvature as a "membrane force," F, acting on the LLZO surface:

$$F(N/m) = \frac{Bs*Hs^2*\cos(a)}{12L} * -(\frac{\delta d}{do}) \quad (1)$$

Although this interpretation assumes that the stress is only generated by a thin Li film, we can look at these simplified data to determine the general trend of the bending during plating. Nonetheless, the results shown below are not expected to be valid, since the film is not sufficiently thin and there are other likely sources of stress as mentioned above.

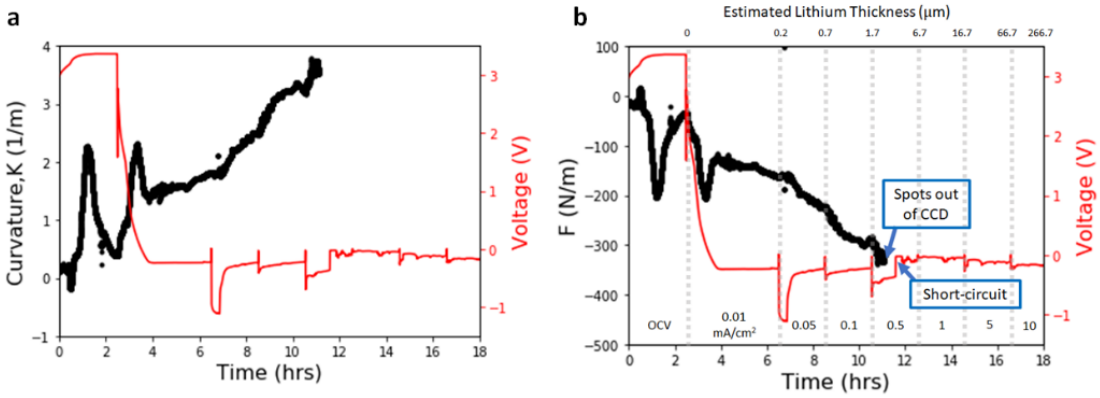

Figure II.9.N.3 a) Curvature and Voltage vs. Time measured by MOSS using LLZO solid electrolyte. b) Membrane force F and measured voltage vs. Time using oversimplified approach from Eq. (1).

As shown in Figure II.9.N.3b, an increase in compressive stress was observed prior to possible short-circuit feature in voltage profile. The stress values prior to short-circuiting is at around -150 MPa, which will need further analysis to evaluate. This large stress values we observed cannot be explained solely by the growth stress in lithium metal, which was previously reported to be around 0.2 MPa. The stresses we measured that are three orders of magnitude higher than the growth stress in lithium metal are most likely contributed by the stiff solid electrolyte prior to short-circuiting.

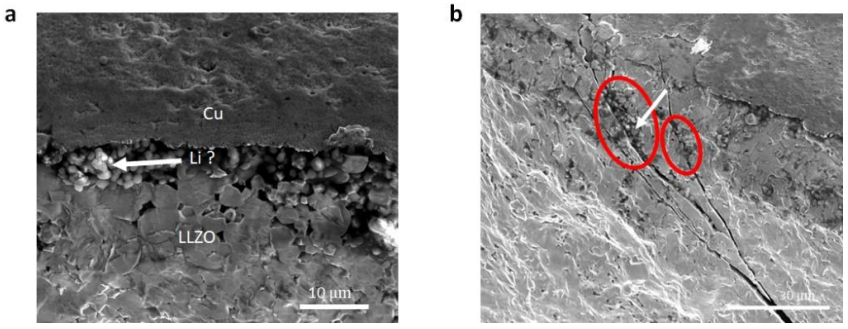

Figure II.9.N.4 a) Cross-sectional image of a fractured surface (near Cu side) after short circuiting. b) Li metal penetration through the LLZO solid electrolyte along the grain-boundary.

After the short-circuiting event, the LLZO pallet was then fractured and imaged using SEM. As shown in Figure II.9.N.4a and Figure II.9.N.4b, plating of lithium metal was observed both in Cu/LLZO interface and along the LLZO grain boundary. These post-mortem images will be essential in building the valid model that can describe the bending measurement accurately. A proof-of-concept experiment was carried out to investigate evolving stress when using garnet based LLZO solid electrolyte during plating. The schematic from Figure 1a using reflective current collectors showed that it is possible to measure curvature associated with stress in LLZO|Li electrode. However, further improvements are required in order to measure the curvature accurately throughout long time of plating. Hence, methods to improve the reflectivity of the LLZO|Li cell is paramount. Hence, a new schematic was carried out to improve the reflectivity of the samples by using a reflective quartz wafer. Details on the improve method and initial sets of measurement is presented.

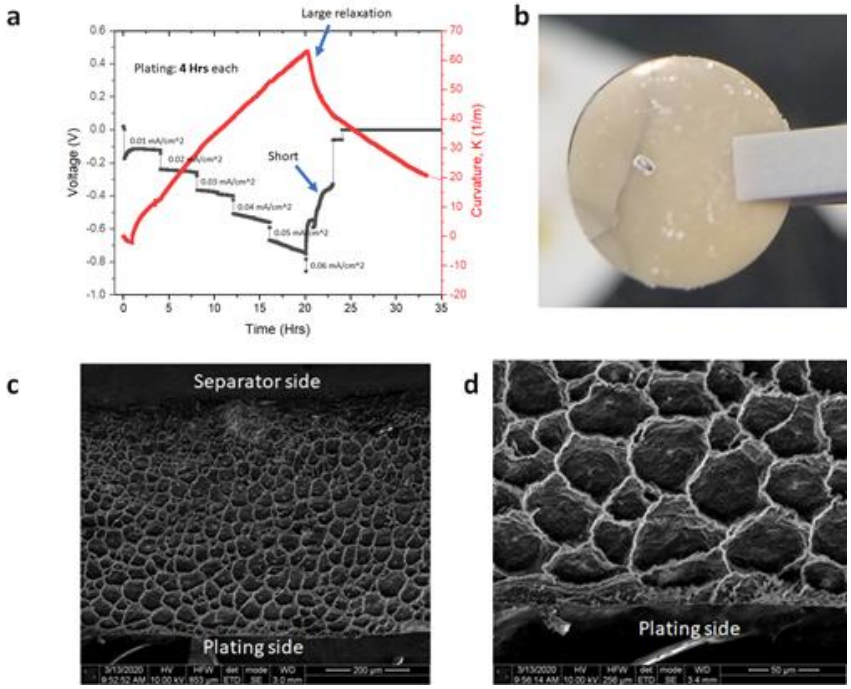

Figure II.9.N.5 a) Voltage & curvature vs. time of the LLZO/quartz electrode. Black and red lines indicate voltage and curvature profile, respectively. Plating current is applied as a stepwise increase of 0.01 mA/cm2 increments every 4 hours, starting at 0.01 mA/cm2. Both figures show a similar trend of linear increase in curvature prior to short-circuiting. b) Visible crack and fracture on the LLZO pallet after the shorting experiment presented in Figure 5a. c-d) Cross-sectional SEM image of the fracture surface after manually breaking the pallet along the crack.

With new and improved cell, galvanostatic plating was carried out with current density of 0.01 mA/cm^2 with stepwise increase in current density of 0.01 mA/cm^2 increments every 4 hours to correlate curvature evolution with LLZO's shorting phenomena. No stripping sequence was added in this experiment to ensure that the current was unidirectional at all times. The results are shown in Figure II.9.N.5a, which shows a large increase in curvature prior to the short-circuiting event. After either partial or complete short-circuit event has taken place, the curvature shows relaxation in the opposite direction. The curvature relaxation taking place right at the shorting event suggests that the linear increase in curvature during plating is indicative of stress evolved within the solid electrolyte prior to shorting. After the cell has shorted, the electrodes were taken apart in an Ar filled glovebox to for post-mortem imaging. As seen in Figure II.9.N.5b, the shorted pallets exhibit cracks that have propagated through the LLZO pallet. The pallet was mechanically broken apart by applying pressure near the cracks. After the shorting has taken place, Figure II.9.N.5c and Figure II.9.N.5d indicate that the crack is propagated via lithium metal plating along the grain boundaries of LLZO, which has been reported in the past. The curvature evolution before and after the shorting phenomena along with our post-mortem images suggest that lithium metal penetration through the solid electrolyte result in a stress build up in the LLZO pallet, which we demonstrate that it is detectable with in-situ curvature measurements.

Developed in situ nanoindentation technique to investigate the mechanical properties of Lithium Lanthanum Zirconium Oxide (LLZO)

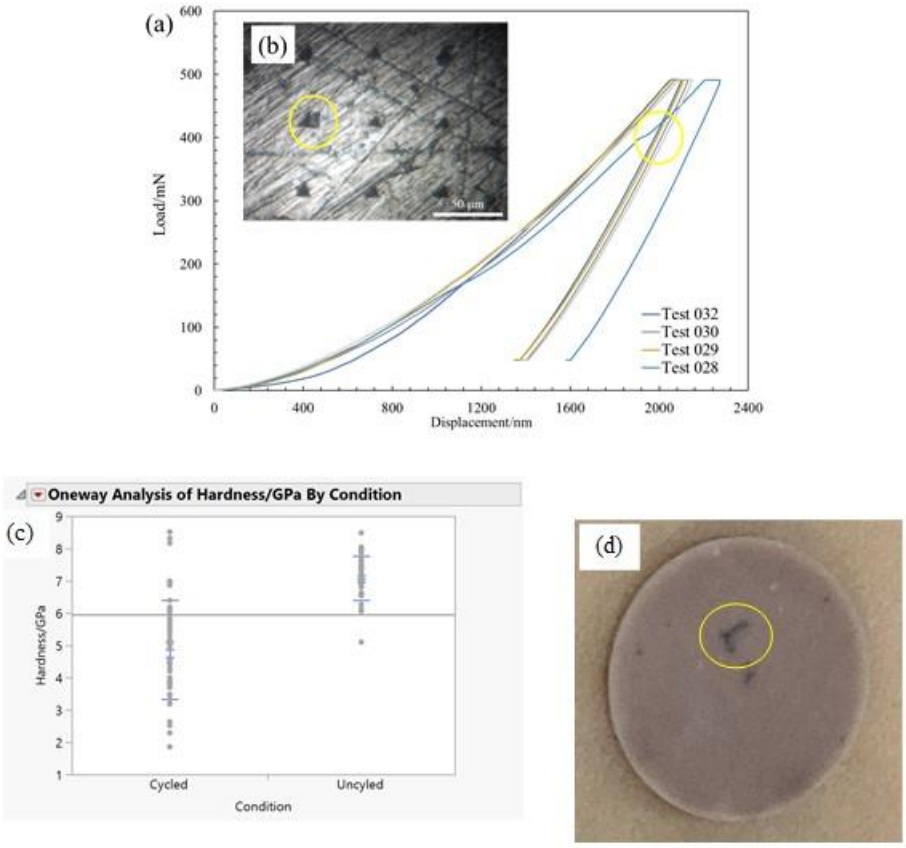

Figure II.9.N.6 (a) Load vs. Displacement curve for five indents into the uncycled LLZO pellet. (b) Microscope image post indentation of the uncycled LLZO surface, yellow circle highlights the chip in the surface. (c) Histogram results comparing the hardness of cycled vs. uncycled LLZO. (d) Photo of the cycled LLZO sample, dark spot highlighted by a yellow circle.

To help understand the mechanisms responsible for the degradation of the LLZO/electrode interfaces and interphases, we performed nanoindentation measurements on an uncycled and electrochemically cycled Ta doped LLZO pellet. The changes in mechanical properties after cycling may provide insight into these degradation mechanisms. For this initial study, a LLZO sample was placed between two lithium metal electrodes and cycled until failure at GM R&D Center. The failed cell was disassembled and the LLZO pellet was removed for indentation measurements at University of Kentucky. A dark spot was observed on the cycled LLZO pellet, Figure II.9.N.6(d). Because the cell short-circuited, we believe this dark spot contains lithium dendrites. For both samples, fifty indents were made in an array spaced out evenly to obtain a statistical average and to overcome any variation due to surface roughness. For the cycled sample, the array of indents was concentrated overtop of the dark spot. Indents were made to a maximum load of 490 mN then held at maximum load for 10 seconds before unloading. The load *vs*. displacement curves Figure II.9.N.6(a), were analyzed with the Oliver and Pharr method to extract the average Youngs Modulus and hardness. After using the JMP statistical software to identify and remove any outliers, histograms were created to obtain the mean and standard deviation for both Youngs modulus and hardness. The mean modulus and hardness for uncycled LLZO is 84.3 ± 4.4 GPa and 7.1 ± 0.7 GPa, respectively. For the cycled LLZO, the mean modulus and hardness was 80.2 ± 13.9 GPa and 4.9 ± 1.5 GPa, respectively. Because of the large standard deviation, a statistical significance t-test was performed comparing both the modulus and hardness of cycled *vs*. uncycled LLZO. The confidence level was set at 95%. With this test it was determined that there is no significant

difference between the two sample with regards to Youngs modulus. But, as shown in Figure II.9.N.6(c), there is a significant difference between the hardness.

The decrease in the hardness could be due to the presence of lithium dendrites in the cycled sample. However, the modulus value is affected little because the small volume fraction of the lithium dendrites even in the dark region. In addition, there are "jumps" in the load vs. displacement curves which are commonly associated with cracking or facture of the samples caused by the indenter. A "jump" can be seen in Figure II.9.N.6(a) on the uncycled LLZO for indent #28 circled in yellow. Post measurement microscope imaging reveals a chip on the surface, Figure II.9.N.6(b) circled in yellow, occurred during indent #28. Further investigation is needed to determine the fracture behavior of uncycled *vs*. cycled LLZO. Future work will also include studying the mechanical behavior of the Li metal electrode. Together, these studies will help reveal the degradation mechanisms at the Li/LLZO interface and/or interphase.

Explored the relationships between interfacial mechanical failure mechanisms and current density and pressure.

Optical spectroscopic ellipsometry measurements were conducted in the photon energy range of 1.2 – 5.9 eV on a lithium foil sample; its surface was prepared to a mirror-like finish before being transferred into the vacuum chamber for measurements. Experiments were conducted first in vacuum (i.e., ~10^{-7} Torr) before exposing the lithium to air. Measurements were taken every minute for 10 minutes to observe how the surface of lithium changed with exposure time. Analysis and modeling of the raw data, shown in Figure II.9.N.7(a), indicates a surface layer is present upon initial testing, about 40 nm thick. As seen in Figure II.9.N.7(b), this layer starts to quickly grow after 1 minute of exposure to air, then the rate of growth slowly decreases with time around 5 minutes. Although visually lithium looked very shiny and clean, a surface layer did exist on the lithium foil, which should be taken into consideration when studying lithium metal. This experimental result and analysis provide a baseline for future work studying the interface and interphase of lithium with materials such as solid electrolytes.

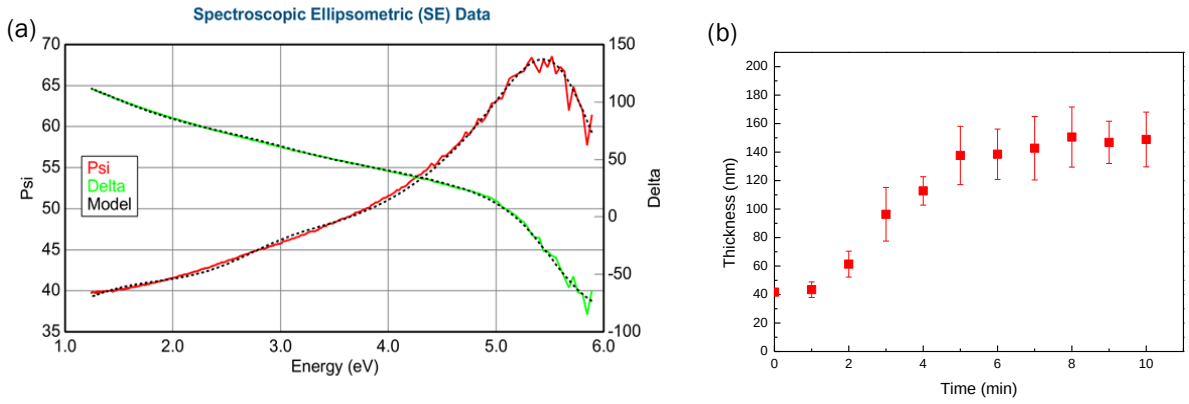

Figure II.9.N.7 Optical spectroscopic ellipsometry measurements and modeling of lithium metal (a) Psi and Delta vs. Energy. (b) Estimated surface layer thickness increasing in air exposure.

The energetics of Li vacancy formation and diffusion near a Li/SEI interface based on DFT calculations

Electroplating has been the main focus in mitigating the dendrite growth on Li-metal electrode; however, the stripping process is as critical, since the non-smooth Li surface during stripping will leads to non-uniform local current density, planting the seeds for dendrite growth. This year, we combined density functional theory (DFT) and Kinetic Monte Carlo (KMC) simulations to investigate the vacancy evolution in Li interfaced with different SEI/coating materials. It was found that lithiophilic interface, such as Li/Li_2O, repels vacancies into the bulk Li, so Li can quickly fill the Li vacancies near the Li/Li_2O interface and maintain a smooth Li surface. In contrast, lithiophobic interface, such as Li/LiF, traps Li vacancies toward the interface and the accumulated Li vacancies form voids and roughen the surface. The predicted critical stripping current density, below which a smooth Li surface will be maintained, is therefore much faster at the lithiophilic Li/Li_2O interface than that at

the lithiophobic Li/LiF interface. It was further revealed that the lithiophilicity at different SEI or coating materials can be ranked as Li/Li_2O > Li/LiPON > Li/Li_2CO_3 > Li/LiF based on the calculated interfacial adhesion and accumulation of electron density at the interface. This suggests that interface and coating design can be effective for maintaining a smooth Li surface during stripping process, another challenge to achieve a dendrite-free Li-metal electrode in both liquid and solid electrolytes.

Figure II.9.N.8a and Figure II.9.N.8b shows the relaxed structures of Li(001)/LiF(001) and Li(001)/Li_2O(110) interfaces, which have the lowest interfacial formation energies compared to other orientations. About 75% and 56% surface lithium atoms form direct bond (a bond length less than 2.2Å) with the O and F anions on the Li_2O and LiF surfaces, respectively. Figure II.9.N.8c and Figure II.9.N.8d show the vacancies formation and migration energies near the interface, especially in the first four layers (L1-L4) and reveal the vacancy interaction with the interface. The red dots are the DFT calculated vacancy formation energy profiles at each layer. The vacancy formation for bonded Li atoms is the highest at the Li/Li_2O interface but the lowest at Li/LiF interface (Figure II.9.N.8c and Figure II.9.N.8d). For the unbonded Li atoms, the Li vacancy formation becomes more possible at the Li/Li_2O interface, while is even more possible at the Li/LiF interface. This means, Li/Li_2O interface tends to repel Li vacancy, while Li/LiF interface attracts Li vacancy. The vacancy formation energies drop quickly from the interface to the bulk values. The black lines (connecting the red and blue solid circles based on DFT with NEB calculations) in Figure II.9.N.8c and Figure II.9.N.8d show the energy landscape during Li vacancy migration. It can be revealed that once a vacancy is present at the interface (due to the stripping), the vacancy is likely to migrate toward the bulk Li metal due to the repulsion in the Li/Li_2O interface, while is likely to be trapped at the Li/LiF interface, as the Li/LiF interface attracts Li vacancies.

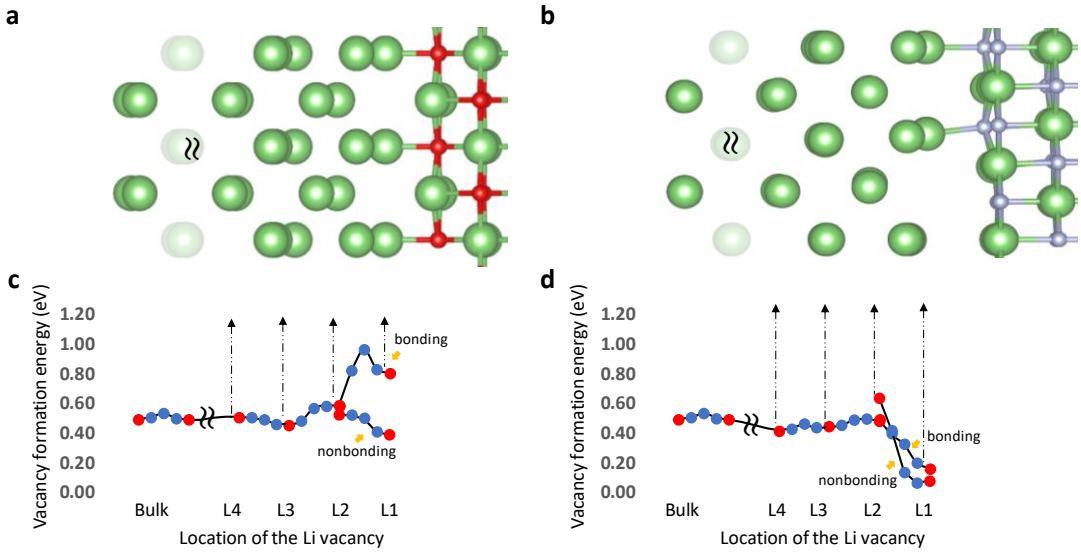

Figure II.9.N.8 Relaxed interfaces and the Li vacancy migration landscape. Sideview of the relaxed interfaces (partially shown) of (a) Li(001)/Li2O(110) and (b) Li(001)/LiF(001) interfaces. Vacancy formation energy profile and migration landscape for bonded Li atoms and non-bonded Li atoms at the interfaces of (c) Li(001)/Li2O(110) and (d) Li(001)/LiF(001) interfaces. Solid red circles represent the vacancy formation energy and solid blue circles represents Li diffusion path based on NEB technique. Note the diffusion of Li atom and Li vacancy is reverse (O in red, Li in green, and F in grey).

Vacancy accumulation and diffusion at different Li/SEI interfaces

KMC simulations with the rate constants computed from DFT calculated energy barriers were used to test if the diffusion process will fill the surface vacancies and maintain surface smoothness. In the beginning of the simulation, 23%–25% Li atoms within the first two layers (L1-L2) were removed randomly (Figure II.9.N.9b and Figure II.9.N.9c), mimicking an initial surface state created by stripping. Figure II.9.N.9a plots the average

distance of the vacancies from the interface and how it changes with KMC time. The vacancies at the Li/Li_2O interface quickly move away from the interface after $8.43x10^{-11}$ s, while in Li/LiF the vacancies barely move even after $1.60x10^{-06}$ s. Figure 9d further compares the distribution of vacancies after 10^5 KMC steps to the initial condition. For the Li/Li_2O interface, only 16% of the vacancies are at the interfaces, while 80% are distributed uniformly inside of the Li (Figure II.9.N.9e). For Li/LiF, the vacancies stay at the interface and connected to voids as shown in the final structures (Figure II.9.N.9f). The timestep in KMC model depends on the frequency of occurring events. In the Li/L_2O interface, the main events are the diffusion of Li vacancies, which occurs at a high frequency. In the Li/LiF interface, after the vacancies trapped at the interface, diffusion become a rare event, so the KMC step has a longer time span. This confirms that Li can fill the vacancies at the Li/Li_2O interface very quickly and reveals that this interface can withstand a higher current density without the presence of voids.

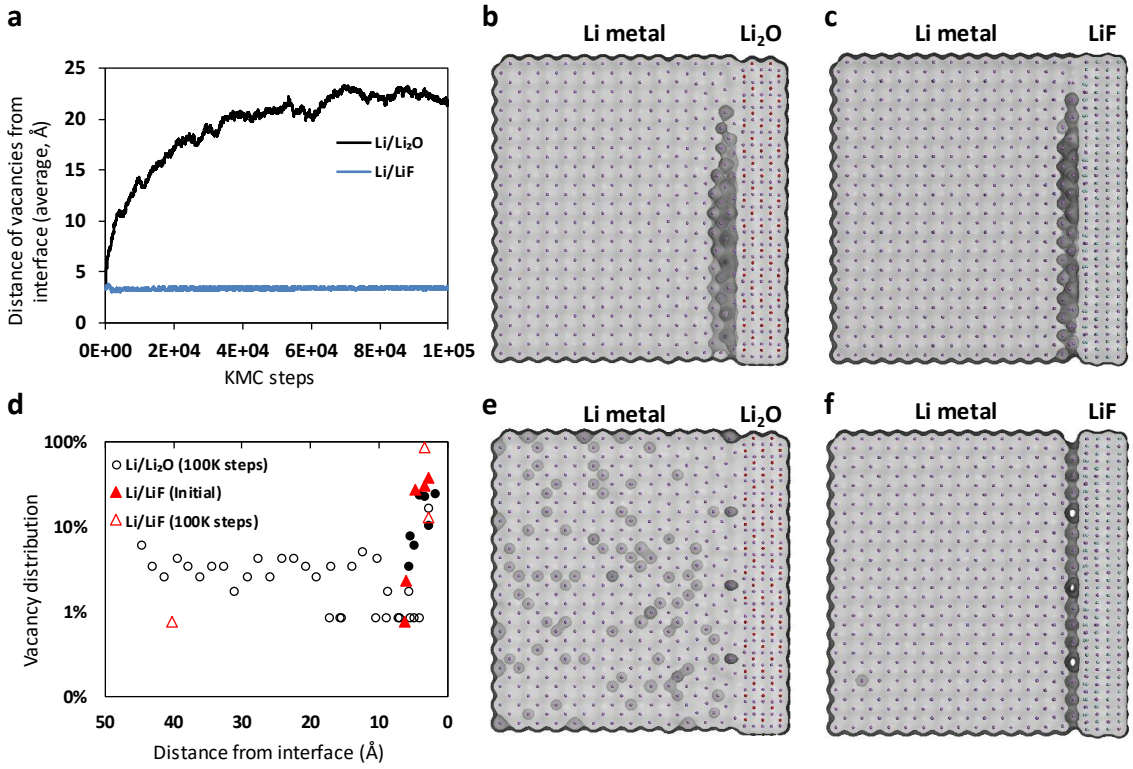

Figure II.9.N.9 KMC simulation of the vacancy evolution in the presence of interfacial vacancies at Li/Li_2O and Li/LiF interfaces. (a) The average distance of the vacancies from the interface variation versus KMC steps. The initial structures of (b) Li/Li_2O and (c) Li/LiF interfaces with vacancies on Li surface. (d) The vacancy distribution in the Li slab in the beginning and at 10^5 KMC steps. The final structures (at 10^5 KMC steps) of (e) Li/Li_2O at time of $8.43x10^{-11}$s and (f) Li/LiF at time of $1.60x10^{-06}$ s.

The critical delithiation current density to maintain a smooth Li surface

To evaluate how the surface roughness of Li electrode (vacancies formed and migrated) is impacted by the two different interfaces under the competition between Li diffusion and the stripping process, the stripping process was then incorporated in the KMC simulation. The stripping mechanism is mimicked by removing Li atoms from the lithium surface layer (L1) with a stripping rate (k_s), and the Li atoms in the SEI were removed to act as an infinite Li atom sink. Removing ~8 atomic layers in the Li-metal in one second (k_s~8 1/s) corresponds to a stripping current density of 1.0 mA/cm^2, which is a typical current density used in experiments.

The vacancy distribution as well as the surface roughness of the Li metal under the stripping current density (simulated by different k_s values) in the range of 10^{-6} – 10^{3} A/cm^2 for both interfaces. At the typical current density of 10^{-3} A/cm^2 the interface of Li/Li_2O has no vacancies, but the accumulation of the vacancies can be clearly seen at the Li/LiF interface (41 vacancies at L1 out of 42 delithiated Li). When the current density increased to 10^{1} ~10^{2} A/cm^2 (Figure II.9.N.10a and Figure II.9.N.10b, respectively), the Li/Li_2O interface shows a transition from a smooth Li surface at 10^{1} A/cm^2 with vacancies in the bulk to some trapped surface vacancies (3 vacancies at L1 out of 7 delithiated Li) at 10^{2} A/cm^2. The faster stripping rate of 10^{2} A/cm^2 is comparable to the Li atom toward the Li/Li_2O interface, so the vacancy filling events are limited. On the other hand, the accumulation of the vacancies at the Li/LiF interface at the of 10^{-3} A/cm^2 gradually disappear as the stripping rates decrease to 10^{-5} ~ 10^{-4} A/cm^2 (Figure II.9.N.10c and Figure II.9.N.10d, respectively). This means a critical current density (J_C), beyond which vacancies accumulate on the surface of Li, can be defined. To maintain a smooth Li surface, the applied stripping current density should be lower than the J_C which is material and interface sensitive. The simulation results seem to suggest J_C is on the order of 10~100 A/cm^2 and 0.01~0.1 mA/cm^2 for Li/Li_2O and Li/LiF, respectively. Kasemchainan reported the critical stripping current density, J_C, of 0.2 ~ 1.0 mAcm^{-2} under compression pressure for Li/Li_6PS_5Cl solid state cell. Without the compression pressure, the J_C values will be even lower. Thus, the predicted limiting current of Li/LiF interface is on the similar order of magnitude. If the J_C is on the order of 10~100 mA/cm^2 for Li/Li_2O, this stripping (discharge) current density will no longer a limiting factor for Li-metal applications. However, the current model assumes the interface is extremely flat, which is unlikely if the Li_2O is formed by oxidation of Li.

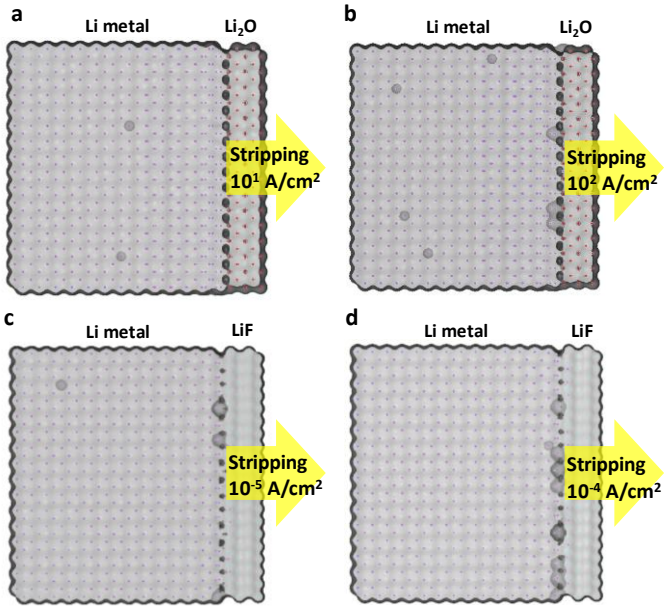

Figure II.9.N.10 KMC simulation, incorporating the stripping process and the Li atom diffusion, of the formation and evolution of vacancies near the interfaces at different current densities. Li/Li_2O: final structures upon current density at (a)10^{1} and (b)10^{2} A/cm^2 after 10^{5} KMC steps, corresponding to the time at 1.59x10^{-8} and 1.23x10^{-8}s, respectively. Li/LiF: final structures upon current density current density at (c)10^{-5} and (d)10^{-4} A/cm^2 at 10^{5} KMC steps corresponding to the time at 1.6x10^{-1} and 2.96x10^{-2}s. Note the numbers of stripped Li atoms in a-d are 3, 7, 5, and 13, respectively, during the simulation time.

Interface Design based on the electronic origin of Coating Materials

Since J_C is interface sensitive, KMC models further revealed that reducing $\Delta E_{2\to1}$ plays a major role in facilitating the void filling at the interface, since more vacancies migrated toward the bulk region. Therefore, it is important to find coating materials that repel Li vacancy away the interface and reduce the energy barrier for Li to move toward the interface, which can be evaluated based on DFT computable interfacial properties. The work of separation of Li(001)/Li_2O(110) is 1.11 J/m^2, and is 0.28 J/m^2 for Li/LiF. Therefore, Li/Li_2O is

lithiophilic and Li/LiF is lithiophobic. Understanding bonding nature and the electronic structures of these interfaces will help to guide our coating material design to maintain a smooth Li surface with high critical current density. A simple rationalization to explain the difference of Li/Li_2O and Li/LiF interface is that the Li_2O(110) surface exposes two-lithium under-coordinated O atoms and LiF(001) surface exposes one-Li under-coordinated F atoms. Although both have developed direct Li-O and Li-F bonds after interface relaxation, some O atoms of Li_2O(110) are still undercoordinated, so it can attract more Li, thus is lithiophilic. To quantify the bonding characteristics, the electronic structure origin of the lithiophilic and lithiophobic surfaces was analyzed. The (planar) charge density difference (CDD) was studied (Figure II.9.N.11). The electron density transferred from SEI materials to the interfaces, and more electron density accumulates at the Li/Li_2O interface than that at the Li/LiF interface. This enhanced electron density can attract more Li toward the interface, making Li/Li_2O interface lithiophilic, as well as creating a stronger interfacial adhesion.

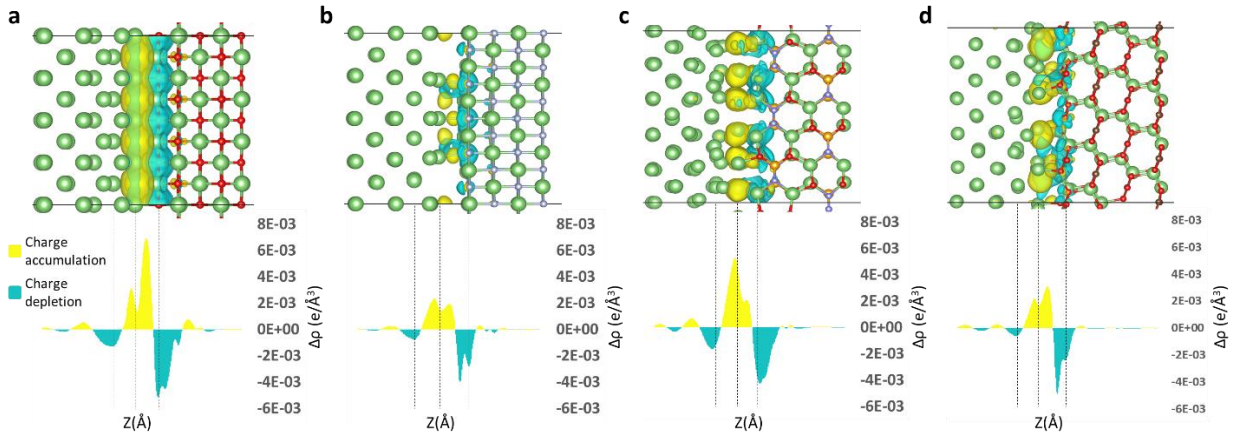

Figure II.9.N.11 Charge density difference (upper panel) and planar-averaged charge density difference (lower panel). (a)Li/Li_2O, (b)Li/LiF, (c) Li(001)/Li_2PO_2N(010) and (d) Li(001)/Li_2CO_3(001) (O in red, Li in green, F in grey, C in brown, N in light blue, and S in orange).

Conclusions

During past year, we have developed a series in-situ electrochemical-mechanical diagnostic tools to investigate the stress evolution and mechanical properties of solid electrolytes during lithium plating and stripping process. Particularly, we optimize the cell design the measure curvature evolution in the LLZO|Li cell and revealed that there is a linear increase in curvature during constant-current ramp up experiment. Once the short-circuit event has taken place, the curvature then relaxes in the opposite direction, indicating that the buildup in stress during the curvature increase is correlated with the stresses evolved that may relate to the lithium metal penetration in the LLZO solid electrolyte. In addition, the Li plating along the grain boundaries in solid electrolyte could significantly impact the mechanical properties such as modules and hardness.

We further combined DFT and KMC simulations to investigate the vacancy evolution in Li interfaced with different SEI/coating materials. It was found that lithiophilic interface, such as Li/Li_2O, repels vacancies into the bulk Li, so Li can quickly fill the Li vacancies near the Li/Li_2O interface and maintain a smooth Li surface. In contrast, lithiophobic interface, such as Li/LiF, traps Li vacancies toward the interface and the accumulated Li vacancies form voids and roughen the surface. Based on the calculated interfacial adhesion and accumulation of electron density at the interface, the lithiophilicity at these four interfaces can be ranked as Li/Li_2O > Li/LiPON > Li/Li_2CO_3 > Li/LiF.

Key Publications

1. Patent: Xingcheng Xiao, Mengyuan Chen, Qinglin Zhang, Mei Cai, A solution-based approach to protect lithium metal electrode, P053352, US patent application

2. Y. Wang, D. Dang, X. Xiao, Y.-T. Cheng, Structure and mechanical properties of electroplated mossy lithium: Effects of current density and electrolyte, Energy Storage Materials, Vol. 26, 2020, Pages 276-282.

3. C. Yang, Y. Lin; B. Li, X. Xiao, Y. Qi, The Bonding Nature and Adhesion of Polyacrylic Acid (PAA) Coating on Li-metal for Li Dendrite Prevention, ACS Appl. Mater. Interfaces 2020, 12, 45, 51007–51015

4. Cho, J. H.; Xiao, X.; Guo, K.; Liu, Y.; Gao, H.; Sheldon, B. W., Stress evolution in lithium metal electrodes. Energy Storage Materials 2020, 24, 281-290.

Acknowledgements

The PI would like to acknowledge co-PIs: Prof. Brian W. Sheldon, Prof. Yue Qi at Brown University and Prof. Yang-Tse Cheng, at University of Kentucky, Dr. Qinglin Zhang at General Motors R&D Center, graduate students and postdocs: Dr. Mengyuan Chen, Juny Choi, Andrew Meyer, Ming Yang.

The team would like to also acknowledge the support from Program Managers Tien Duong at DoE, Patricia Smith at NAVSEA-Carderock, and Adrienne L Riggi at NETL.

II.9.0 Multidimensional Diagnostics of the Interface Evolutions in Solid-State Lithium Batteries (University of Houston)

Yan Yao, Principal Investigator
University of Houston
4800 Calhoun Rd
Houston, TX 77004
E-mail: yyao4@uh.edu

Tien Duong, DOE Technology Development Manager
U.S. Department of Energy
E-mail: Tien.Duong@ee.doe.gov

Start Date: October 1, 2019 End Date: March 31, 2023
Project Funding: $1,250,000 DOE share: $1,000,000 Non-DOE share: $250,000

Project Introduction

The failure mechanism of a solid-state Li battery may be briefly attributed to two main causes: interfacial resistance increase and Li dendrites growth. The former may be further attributed to electrolyte decomposition and interfacial void formation (*i.e.* loss of physical contact). Electrolyte decomposition happens in two ways: oxidative decomposition at the cathode active material–electrolyte interface and reductive decomposition at the Li (including dendrites)–electrolyte interface. Void formation occurs at the same two interfaces. The complex origins of battery failure call for multidimensional diagnostics utilizing not one but a combination of tools that can quantify the formed void and dendrites, identify the chemical and mechanical natures of the Li dendrites and electrolyte decomposition products, and *in situ* monitor the evolution of the processes. The tools also need to cover a sufficiently large scale (up to ~100 μm), have spatial resolutions of a few nanometers, and be sensitive enough to detect subtle changes in chemical and mechanical properties. These considerations lead us to a toolset of FIB-SEM tomography, ToF-SIMS, and nanoindentation (inside SEM chamber, *i.e.* in-SEM nanoindentation) and atomic force microscopy (AFM; inside SIMS chamber, *e.g.* in-SIMS AFM)-based stiffness mapping for structural, chemical, and mechanical characterizations, respectively. We will acquire detailed information of interfaces and dendrites evolutions including but not limited to (1) real-time visualization of Li dendrites growth within the electrolyte layer, (2) chemical composition, mechanical property, and evolution of electrolyte decomposition products, including intermediate and metastable ones, at both cathode and anode interfaces, (3) potential correlation of the induction and propagation of Li dendrites with electrolyte decomposition, and, (4) quantitative correlation between electrolyte decomposition, void formation, and cell performance. These in-depth understandings will allow us to effectively predict and optimize the physical and chemical changes of components within solid-state Li batteries during charge and discharge.

Objectives

The project objective is to develop a platform in combination of FIB-SEM tomography, ToF-SIMS, and in-SEM nanoindentation-based stiffness mapping for structural, chemical, and mechanical characterizations in solid-state Li batteries. Assessment of the influence of cell design and testing conditions (external pressure, current density, temperature) on the evolutions of interfaces will be performed.

Approach

Space- and time-resolved structural, chemical, and mechanical characterizations of the cathode–electrolyte and anode–electrolyte interfaces will be performed on all-solid-state Li batteries using FIB-SEM, ToF-SIMS, in-SEM nanoindentation. Tasks include (1) development of solid-state cell thin stacks and test-cell configurations that are suitable for in-situ characterizations, (2) quantitative characterization and in-situ tracking of interfacial voids formation within composite cathode and electrolyte layer; (3) identification and in-situ tracking of the

chemical composition, spatial distribution, and mechanical properties of electrolyte decomposition products at the Li- and cathode-electrolyte interfaces; (4) visualization, chemo-mechanical properties detection, and in-situ tracking of Li dendrites grown within solid electrolyte layer.

Results

Thin-stack solid-state cells for structural-chemical-mechanical analysis have been developed. The cells consist of a solid-state composite cathode, a solid electrolyte layer, and a lithium metal anode. The composite cathode was prepared by coating a slurry consisting of NMC as the active material, Li_6PS_5Cl as the solid-solid electrolyte (LPSCl SSE), and a polymer binder on an aluminum foil. The SSE layer was prepared by coating a slurry of LPSCl and binder on a peal-able substrate. Finally, a lithium foil was stacked and pressed on the SE sheet for the full cell integration. Efforts have been focused on improving the reproducibility and stability of the thin-stack cells. The fabrication of tape-cast electrolyte thin films has been systematically studied. Traditional tape-casting uses a variety of methods to improve the resulting films and share a common theme of maximizing the solids content in the casting slurry as part of the development process. The solids loading is typically taken to a maximum value to obtain the best quality before the casting slurry becomes too viscous. We have therefore focused on optimizing solid content to improve the quality of the cast films.

Our initial study includes visually looking at the films prepared with different solids contents. When the solid content of the casting slurry of LPSCl is 45 wt% or less, obvious defects occur on the surface of the films, some of which are at the centimeter scale. Starting from 51 wt%, it is difficult to see the defects under normal lighting conditions (Figure II.9.O.1a). Therefore, we have visualized the films with backside illumination. Films cast with slurries containing 45–57 wt% have been visualized at a 5 × 5 cm^2 scale (Figure II.9.O.1c). Notable defects are observed even for those apparently defect-free films (*i.e.* films cast from slurries with 51–57 wt% solid content). The quality of the film may be quantified by the grayscale deviation of the images, which reflects the uniformity of the films. A large standard deviation of the grayscale of an image indicates poor film uniformity. Therefore, the film quality can be described by the reciprocal of the standard deviation of the grayscale. Figure II.9.O.1b shows that at a solid content of 54 wt%, the slurry produces the most uniform films.

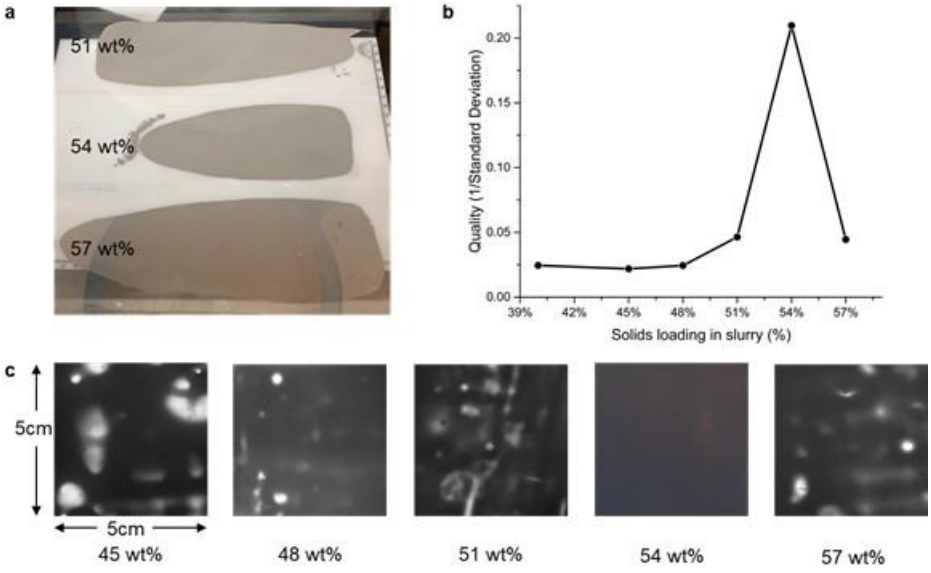

Figure II.9.O.1 Quality assessment of LPSCl thin films. **a**, Optical images of films cast with slurry containing 51–57 wt% of solid content. **b**, Correlation of film quality with solid content in the casting slurry. **c**, Optical images of back-illuminated films cast with slurry containing 45–57 wt% of solid content.

The optimized electrolyte thin films have enabled highly reproducible thin cells. The performance of a thin cell based on the optimized electrolyte film is shown in Figure II.9.O.2. The cell has an areal capacity of 1 mAh cm^{-2}. An initial capacity of 198 mAh g^{-1} is achieved, and 89% of the capacity is preserved after 50 cycles at C/10 at 60 °C. This performance is on par with that observed for bulk type solid-state cells. Therefore, diagnostics based the optimized thin cell will be representative of the behavior of NMC observed from typical studies.

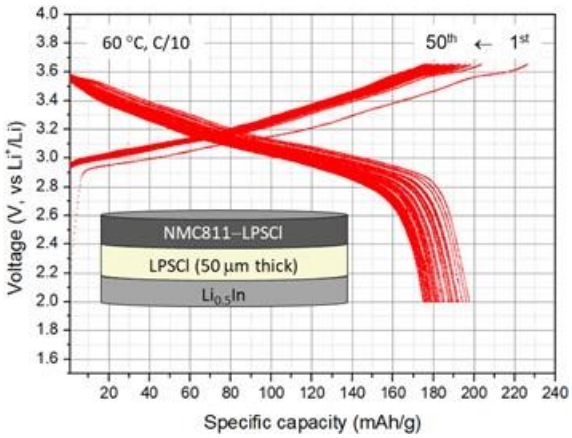

Figure II.9.O.2 Voltage profile of an NMC–LPSCl/LPSCl/$Li_{0.5}In$ thin cell.

After cell fabrication, the thin-stack cell was subjected to cross-section polishing to expose a flat cross section. Conventionally, ion polisher is suitable for milling a specimen composed of homogeneous materials. For a composite specimen, the ion milling-induced heating could result in voids due to the heat capacity differences. Measures have been taken to overcome this issue by using a cryogenic condition to reduce heat damage as shown in Figure II.9.O.3a. To alleviate the heat-induced damage to the cathode/SSE interfaces in the cathode, we have also developed a "step-protrude polishing" method where the protrusion of a specimen was broken down into small steps. Figure II.9.O.3b shows the polished cathode/SSE interfaces with suppressed void formation. The capability to produce a clean cross-section lays down the foundation for carrying out studies monitoring interface evolutions.

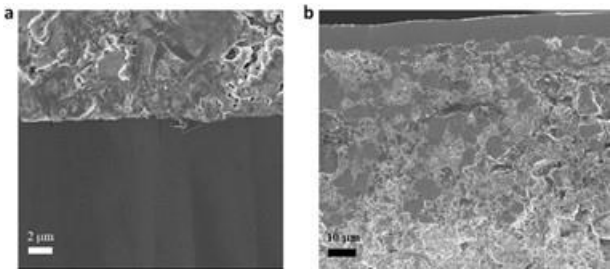

Figure II.9.O.3 Cross-section polishing result of a cell. **a**, Cryogenic polishing of a lithium metal anode. **b**, Cross-section of the cathode composite.

Micro-cell setups with the desired dimension for the proposed structural-chemical-mechanical microscopic and spectroscopic measurements have been explored based on thin-stack solid-state cells. The cells consist of a solid-state composite cathode/SSE/ metal anode trilayer structure with a typical combined thickness of <100 μm (illustrated in Figure II.9.O.4a). Figure II.9.O.4b shows the cross-section of such a thin-stack cell with a thickness of 90 μm.

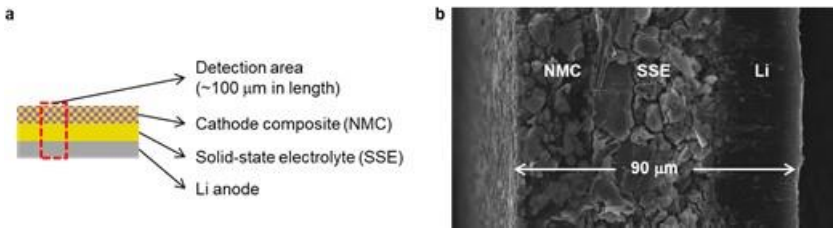

Figure II.9.O.4 Structure of a thin solid-state cell. **a**, A schematic illustration. **b**, Scanning electron microscopy image of the cross-section of the thin cell.

Operando characterization of micro-cells requires transferring a cell fabricated in a glove box to various analytical instruments without exposure to the air. Conventional transfer vessels for sample transferring are typically designed for use with a specific instrument, thus lacking the flexibility needed in this project for different instruments. Some diagnostic devices do not have any suitable transfer vessel options available. Therefore, an air-free transfer vessel has been developed to complement our micro-cell characterizations. Figure II.9.O.5 details the design and application of the transfer vessel. At the heart of the hermetically

sealable vessel sits a cell test platform (Figure II.9.O.5b). The cell test platform is equipped with a micro-cell mount where electrochemical tests is performed in situ. Heating and pressure applying/sensing modules are integrated in the platform. The air-tight vessel design allows transfer of the test platform, on which an air-sensitive all-solid-state cell is mounted, between different analytical instruments. For characterizations performed inside a chamber, such as focused ion beam techniques, the vessel is installed into the chamber with the cover closed (Figure II.9.O.5a). Once desirable atmosphere inside the chamber is reached, the cover of the vessel opens up via an electrically controlled motor. The test platform is lifted to an adjustable height according to the requirement of the measurement (Figure II.9.O.5d). Here we show an example of SEM observation of the cross-section of an NMC/LPSCl/Li-In thin-format cell mounted on the platform (Figure II.9.O.5e). For characterizations performed without a chamber, such as laser-based spectroscopy, the vessel is used directly with the cover closed. A window on top of the test platform allows analytical laser beams to strike through (Figure II.9.O.5c). Here an example of Raman spectroscopy measurement of the same thin-format cell used for SEM observation is presented. The optical image of the same area from the Raman spectrometer appears identical to the SEM image (Figure II.9.O.5g). Raman spectrum of the electrolyte layer reveals the chactacteristic peak attributable to the PS_4 tetrahedra (Figure II.9.O.5f). The results indicate the efficacy of the vessel in isolating the test platform from ambient atmoshpere without interfering analytical beams and signal collection.

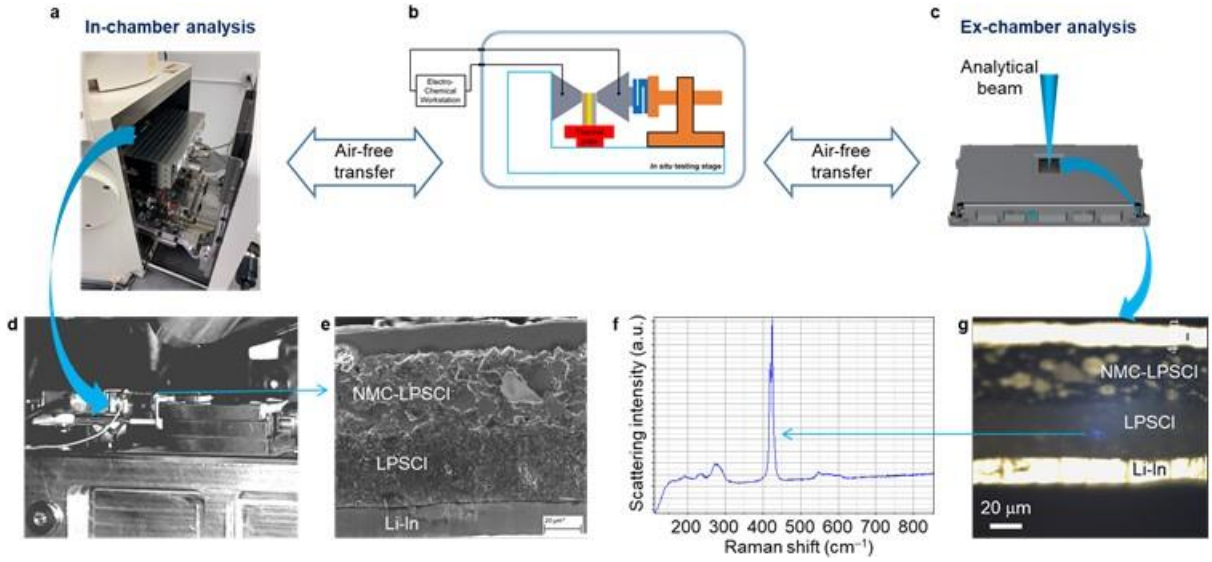

Figure II.9.O.5 Design and applications of an air-free transfer vessel with an in situ cell test platform built-in. **b**, Cell test platform equipped with micro-cell mount, heater, pressure applier, and sensor. **a**, Installation of the vessel in instruments where characterizations are performed inside a chamber (e.g. focused ion beam and SEM). **c**, Vessel remains closed when used with instruments without a chamber (e.g. laser-based spectrometers); analytical beams come in through a window in the vessel. **d**, The cover of the vessel opens up, revealing the test platform and lifting up towards the electron gun. **e**, SEM image of the cross-section of a thin cell obtained using the vessel. **f**, Raman spectrum of the LPSCl electrolyte obtained using the vessel. **g**, Optical image of the cross-section of a thin-format cell obtained with a Raman spectrometer using the vessel

The test platform for micro-cell tests has been optimized to deliver electrochemical performance akin to non-micro thin cells. Figure II.9.O.6a shows an NMC/LPSCl/Li-In micro-cell tested on the platform within the transfer vessel. The first discharge capacity approaches 200 mAh/g (based on the weight of NMC), which is comparable to results from thin cells. Initial efficiency, cycling stability, and rate capability are areas to be improved.

Both the heating and pressure-sensing modules have been preliminarily established. A temperature-sensing module was built into the system during the initial setup and validation stages so that the calibration of temperature was achieved. The heating power–cell temperature relationship has been determined after optimization of the placement of the heating module, rate of heating, and monitoring the delay between heating and the cell reaching stabilized temperatures. Figure II.9.O.6b shows that test temperatures ranging from room temperature to 63 °C that can be precisely controlled by adjusting the heating power from 0 to 0.90 W, and the degree of control is consistent in both heat-up and cool-down processes. The effectiveness of the applied elevated temperature has been confirmed in electrochemical tests. The electrochemical impedance of a Li/SSE/Li symmetrical micro-cell saw a decrease by almost an order of magnitude when the test temperature was raised from 25 to 45 °C, along with much less noisy spectra (Figure II.9.O.6c and d). A possible interpretation of the result is softening of the Li electrodes as a result of the elevated temperature, which improves the overall contact in the cell. The result does show a need for improvement of the micro-cell fabrication.

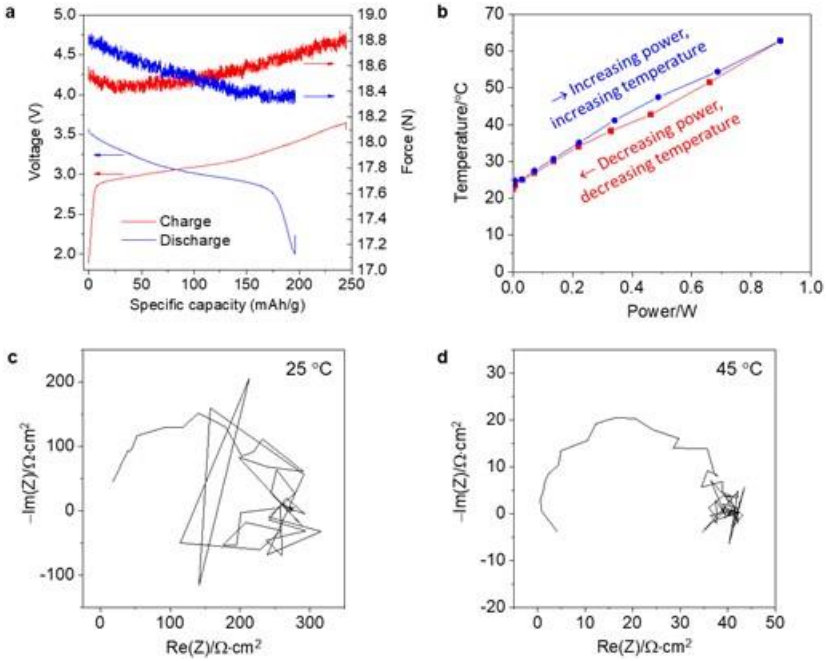

Figure II.9.O.6 Evaluation of the micro-cell setup. **a**, Voltage profile of an NMC/LPSCl/Li-In micro-cell for the first cycle tested in the transfer vessel and validation of the pressure module. Validation of the heating module in the micro-cell setup. **b**, Calibration curve for the heating power–temperature relationship. **c** and **d**, Nyquist plots for symmetrical Li/SSE/Li micro-cell tested at 25 (**c**) and 45 °C (**d**), respectively.

The pressure-sensing module has demonstrated its capability in an *in situ* micro-cell test. Figure II.9.O.6a shows that the pressure of an NMC/SSE/In micro-cell monotonously increased during charging, then monotonously decreased during discharging. Similar pressure changes have been reported in bulk-type solid-state Li cells and are attributed to the volume change of the anode which is the dominant volume change event in such cells. Here the volume change of the In anode is supposedly 50%–100%, compared with the 2%–6% for the NMC cathode. The pressure change is therefore dominated by the anode reaction.

Due to the imposed social distancing guidelines related to the COVID-19 pandemic, tasks M1.3 (Nano-cell development) and M1.4 (cell optimization and electrochemical benchmarking) have been delayed. Current budget period ending date has been extended by six months to March 31, 2021.

Conclusions

We have developed solid-state cells with a total thickness of less than 100 μm and electrochemical performance on par with their bulk-type counterparts. Custom platform and cell-milling procedures have been developed to fabricate and test micro-cells. The platform offers truthful reflection of electrochemical performance, precise temperature control, external pressure application, and pressure monitoring. It is proven effective in allowing spectroscopic measurements of the same cell across multiple techniques, either in vacuum or in ambient atmosphere. Nano-cells are being developed and on track toward completion by March 31, 2021.

Key Publications

Qing Ai, Qiyi Fang, Jia Liang, Xinyu Xu, Tianshu Zhai, Guanhui Gao, Hua Guo, Guifang Han, Lijie Ci, Jun Lou, Lithium-conducting covalent-organic-frameworks as artificial solid-electrolyte-interphase on silicon anode for high performance lithium ion batteries. Nano Energy, 104657, 2020

II.9.P First-Principles Modeling of Cluster-Based Solid Electrolytes (Virginia Commonwealth University)

Puru Jena, Principal Investigator
Virginia Commonwealth University
Department of Physics, Virginia Commonwealth University, 701, W Grace St
Richmond, VA 23284
E-mail: pjena@vcu.edu

Tien Duong, DOE Technology Development Manager
U.S. Department of Energy
E-mail: Tien.Duong@ee.doe.gov

Start Date: October 1, 2019 End Date: December 31, 2022
Project Funding: $991,335 DOE share: $793,040.00 Non-DOE share: $198,295

Project Introduction

The current modeling schemes to develop advanced solid electrolytes are focusing on materials in which the building blocks are individual atoms. Our theoretical approach is a paradigm shift in solid electrolyte design. Instead of atoms, we focus on clusters as the building blocks and model these solid electrolytes and their interfaces with electrodes, especially Li-metal anode, for their successful implementation in solid-state batteries. The advantage of using the cluster-ions to replace elemental-ions is that the size, composition, and shape of the former can be tailored to achieve higher superionic conductivity, electrochemical stability and charge transfer across solid-solid interfaces than conventional materials. Specifically, our proposed project includes: (1) Developing cluster-based solid electrolytes, where the halogen components are replaced by cluster-ions that mimic the chemistry of halogens but are characterized by additional degrees of freedom, including the size, shape, and composition. (2) Providing a fundamental understanding of the ionic conduction mechanism in the newly-developed cluster-based solid electrolytes; (3) Modeling the interfacial properties (i.e. structural, chemical and transport) between the cluster-based solid electrolytes and electrodes at the atomic level. For the cluster-based solid electrolytes incompatible with the Li-metal anode or cathode materials, potential candidates for interfacial coatings will be identified and studied. (4) Providing a theoretical framework towards optimizing critical parameters, such as current density, kinetic and mechanical stability, that will guide experimentalists to attain desired cathode-electrode interface for cluster-based solid electrolytes.

Objectives

The objective of the project is to use cluster-ions, which are stable atomic clusters that mimic the chemistry of individual atoms, as the building blocks of new solid electrolytes (SEs) for Li-ion batteries and the corresponding battery system. The advantages of using cluster-ions to replace elemental ions is that the size, shape, and composition of the former can be tailored to achieve higher superionic conductivity, electrochemical stability, and charge transfer across the solid-solid interfaces than the conventional materials. More specifically, the goal is to develop superior SEs based on cluster-ions and to model these SEs and their interfaces with electrodes, especially with the Li-metal anode, for successful integration into high performance SSBs for EVs. The team will model and screen cluster-based SEs that, compared to conventional SEs, have low activation energies, practical room-temperature ionic conductivities, wide electrochemical stability windows, and desired mechanical properties that, for example, can inhibit the Li-metal anode dendrite growth. They will provide a fundamental understanding of the ionic conduction mechanism in the newly developed, cluster-based SEs and identify means to further improve property metrics via chemical and defect engineering. The team will model the interfacial properties, such as the structural, chemical, electrochemical, and ion/charge transfer properties, between the cluster-based SEs and electrodes at the atomic level, as well as find the interfacial coating materials with desired properties. Based on accumulated data from modeling, they will establish links between the basic parameters of the cluster-ions and the bulk/interface properties, which can directly guide experiments. Meanwhile, the team will work closely with experimentalists in the BMR Program

to complement the project's theoretical efforts and to guide them in focused development of the predicted cluster-based SEs and the interfaces.

Approach

1. *Developing new cluster-based solid electrolyte materials using selected cluster-ions from the established database of clusters*

The possible crystal structures of the newly developed materials will be determined using structure prediction techniques, such as the particle swarm optimization and the evolutionary algorithm [1],[2]. The most stable phases that contain the cluster-ion from the search will be considered as the initial structures, subject to further investigation. Each cluster-based solid electrolyte material with the determined crystal structure will be fully optimized (for both the ion positions and lattice parameters) to its energy minimum using DFT calculations [3],[4]. The lattice dynamic stability of the structure will then be tested by phonon calculations based on the optimized structure; absence of imaginary frequency would define a stable structure. The formation energy of the lattice-dynamically stable cluster-based solid electrolyte material will be calculated. Its thermodynamic stability will be investigated by calculating the pair correlation function and the position correlation function using the structural data from MD simulations at different temperatures. For each cluster-based solid electrolyte that is thermally stable, possible defects involving Li^+ in the material will be studied by calculating their formation and binding energies. Next, for each cluster-ion based solid electrolyte, a supercell system with the relevant defect will be subjected to MD simulations with constant volume at different temperatures. MSD of the Li-ions will be calculated using our own programs. The diffusion coefficients and the ionic conductivity at different temperatures will be calculated from the MSD using the Nernst-Einstein relation. The room temperature ionic conductivity and the activation energy of the material will be obtained by fitting to the Arrhenius relationship. The relevant electronic properties, including the bandgap, the band edges and the electronic conductivity will be calculated using DFT. The hybrid functional (e.g. HSE [5]) or meta-GGA (e.g. mBJ [6]) will be applied. All the obtained results from the above process will be collected into a database.

2. *Modeling the ionic conduction mechanism in the cluster-based solid electrolyte materials*

To study the ionic conduction mechanism, we first investigate the channel size inside the solid electrolyte for Li^+ migration, created by different cluster-ions. Next, the migration routes of Li^+ in the presence of the chosen defect will be studied. Given the non-spherical nature of the cluster-ion, there are a number of inequivalent migration routes. The energy barrier for each of these will be calculated using the NEB method. The effect of the changing orientation of the cluster-ions on the ionic conductivity of the material will be studied by building a Boltzmann model for different orientational configurations and selective dynamic simulations. The pattern of Li^+ motions inside the cluster-based solid electrolytes will be investigated using statistical analysis, such as computing the distinct van Hove time correlation function in the modeled system. From the above studies, the dependence of the solid electrolyte performance on the size, shape (symmetry), internal charge distribution, electron affinity, as well as the dynamics of the cluster-ion will be established.

3. *Modeling and optimizing the chemical mixing and doping in the cluster-based solid electrolyte materials*

Different phases with mixed halides and clusters will be created via chemical mixing. Their structures with different ratio will be fully optimized using DFT energy calculations. Each optimized system will then be investigated using DFT calculations and MD simulations to reveal its formation energy, ionic conduction properties, electrochemical properties, and mechanical properties against the original phase. The ratio that can enable the highest ionic conductivity while maintaining merits in other aspects will be recorded in the database.

4. *Modeling and optimizing the defect formation and concentration*

Models will be built for the cation-doped cluster-based solid electrolyte systems with supercells that contain different concentrations of the Li-vacancy defects. The structure of these systems will first be energetically opimized using DFT calculations. Then, the structures will be studied using MD simulations at fixed

temperature. The ionic conduction properties of the resulting structures will be investigated. The defect concentration that can entail the highest ionic conductivity in the cluster-based solid electrolyte will be revealed.

5. Modeling the electrolyte-electrode interfaces

Given that many of the cluster-based solid electrolytes material are metastable, the possible equilibrium phases at the interfaces when the solid electrolyte is in contact with the electrode will be first identified by building lithium grand potential diagrams at different battery voltages (modeled by the lithium chemical potential) using the crystal data from the material database, e.g. the Materials Project [7]. Next, DFT calculations and MD simulations will be conducted to study the stability, electronic and ionic conduction properties of the obtained equilibrium phase at the interface. The interface between the cluster-based solid electrolyte and the equilibrium phase, or between the equilibrium phase and the electrode will be modeled using stacked slabs of the active materials. The local bonding reconstruction and charge transfer, as well as possible amorphization of the interface will then be studied using MD simulations. If the interface cannot form a Li-conducting layer, or will destroy the structure of the solid electrolyte through reaction, potential coating materials that are chemically/electrochemically stable, Li-conducting and having little lattice mismatch with the active materials, will be identified. The structural, electrochemical and transport properties of the coating materials will be studied using DFT calculations and MD simulations.

6. Modeling and optimizing the interface between the cluster-based solid electrolyte and the identified coating materials

Possible alloying phases between the cluster-based solid electrolyte and the coating material will be investigated using the cluster expansion method [8],[9]. The alloys that appear on or near the built convex hull will be selected as the stable phases and their relevant properties, e.g. the ionic conductivity, will be studied using DFT calculations and MD simulations. The alloying phase that can entail the highest ionic conductivity will serve as a good candidate for coating. The results regarding the identified coating materials and their possible alloying phases will be included in our database.

7. Establishing links between the key parameters of the cluster-ion and the bulk and interfacial properties of the cluster-based solid electrolyte materials

With the data accumulated in our database, links between the key parameters (such as the size, shape, composition, charge distribution, and electron affinity) of the cluster-ion and the cluster-based solid electrolyte as well as its interfaces can now be drawn by using machine learning techniques. The established links aim to guide experiments in terms of which cluster-ions to choose that can entail high-performance cluster-based solid electrolytes and interfaces with the electrodes, especially with the Li-metal anode. The PI and team at VCU will work in close collaboration and coordination (unfunded) with VTO-BMR (Vehicle Technology Office's Battery Materials Research) Program PIs working at multiple DOE National Laboratories on solid electrolyte modeling and interfaces and specifically with experimental groups working on synthesis and interfacial characterization of Li-based solid electrolytes.

Results

1. Structural studies of the designed cluster-based solid electrolyte materials with selected cluster-ions. (Q1, FY 2020; Completed, December 31, 2019)

Through extensive structure search and characterization, we have developed a number of new structures of cluster-based solid electrolytes for lithium-ion batteries using selected cluster-ions. The structures containing the clusters are searched using Particle Swarm Optimization (PSO) algorithm with first-principles energy calculations. After building the initial structures, they are subject to full optimization (in both lattice parameters and atomic positions) until certain convergence criteria are met. 60% of the optimized structures showing the lowest energies will form the next generation with newly generated structures according to symmetries. After 10-30 generations of optimization, structures with the lowest energies are picked as the candidates.

In most cases, the structures retain the original composition and geometry of the cluster-ions. There are several special cases, where the original composition of the used cluster-ion is slightly changed due to reaction with the existing elements in the lattice and new cluster-ions are formed in the lowest-energy bulk structure. Such cases often involve boranes $B_xH_x^-$ (x=6-9) or carboranes $CB_{x-1}H_x^-$ (x=6-9) clusters, where, in each case, hydrogen will be stripped from the cluster and form other units such as HS^- in the structure. These new cluster units formed in the bulk structures can result in interesting chemical and physical properties

2. *Property characterizations of stable cluster-based solid electrolyte materials. (Q2, FY 2020; Completed, March 31, 2020)*

The phonons and electronic structures of the low-energy structures obtained from the structure search are studied. As shown in Table II.9.P.1, in each case, we have managed to find out the cell size (Z) that contains the right number of formula units in order to make the periodic structure lattice-dynamically stable. By studying the phonons, we also identify the atomic vibrational modes, especially the ones corresponding to the motion of the cluster-ions as near rigid bodies, which are relevant to the ionic conductivity of the material. Table II.9.P.1 also shows the calculated bandgaps of the new materials which can serve as a measurement for the electrochemical stability of the material. The compositions of the electronic band structures are also studied. This can help to optimize the properties of the solid electrolyte materials via composition engineering.

The phonon calculations are carried out using density functional perturbation theory (DFPT), which avoids the use of large supercells. If imaginary frequencies are present for certain modes, its position in the reciprocal space can provide a hint on how to adjust the cell size in the lattice space to make the structure become lattice-dynamically stable. The phonon calculations are based on optimized structures with energy converged to 10^{-8} eV and force converged to 10^{-4} eV/Å. To obtain reliable bandgaps, meta-GGA functional (mBJ) and hybrid functional HSE06 are used. The calculations are based on the optimized structures with dense k-grids, a cutoff energy of 550 eV, energy converging to 10^{-6} eV and force converging to 10^{-3} eV/Å.

It is found that some cluster-based solid electrolyte materials must have large unit cell containing multiple formula units in order to be stabilized lattice-dynamically. Cluster-ions containing more atoms and having less regular shapes enable high population of low-energy phonon modes, which can result in high ionic conductivities. Nearly all the cluster-based solid electrolytes show larger bandgaps compared to their halogen counterparts. Sulfur is found to be the major contributor to the band edges of the materials, suggesting that the properties can be adjusted by replacing sulfur with the elements in same group, such as oxygen (O), selenium (Se) and tellurium (Te).

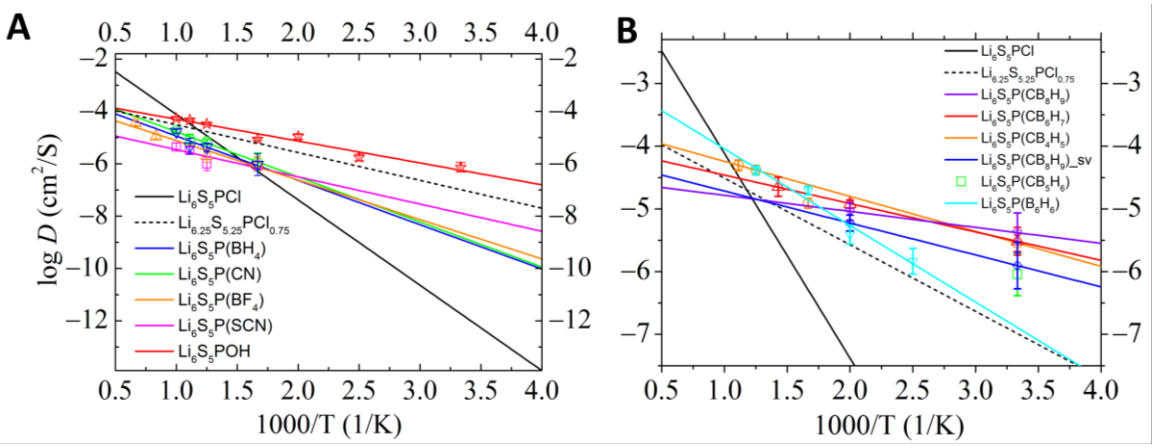

Figure II.9.P.1 (A) Calculated diffusivities of the newly developed argyrodite-alike solid electrolytes fitted by the Arrhenius relation. The diffusivity of stoichiometric Li_6PS_5Cl (in black) is used as a benchmark for comparison, with a poor room temperature (RT) ionic conductivity in the order of 10^{-7}-10^{-6} S/cm and a high activation energy between 5.0-6.0 eV. The new materials exhibit much (3 to 5 orders of magnitude) higher room temperature (RT) diffusivity than that of Li_6PS_5Cl. The corresponding ionic conductivities at RT are over 10^{-4}-10^{-2} S/cm with activation energies between 0.15-0.35 eV. (B) New electrolyte materials based on (C-doped) boranes. All these show ultra-high RT ionic conductivities in the order of 10-100 mS/cm and extremely low activation energy in the order of 0.05-0.1 eV. This is due to the dynamics and the multipolar moments of the polyatomic units as well as fragments present in the structures.

3. *Ionic conductivity characterization for cluster-based solid electrolyte materials and the ionic conduction mechanism. (Q3-Q4, FY 2020; Completed, September 30, 2020)*

We have conducted the molecular dynamics and data analysis for ionic conductivities of the newly developed cluster-based solid electrolyte materials. For each material, we have studied the ionic diffusion coefficients and conductivities at different temperatures. The diffusivity at room temperature (RT) and activation energy of each material are obtained by extrapolation using the Arrhenius relationship or direct calculation.

The *ab initio* molecular dynamics (AIMD) simulations are carried out for each material using a large supercell with its three sides well above 10 Å and containing hundreds of atoms. In each case, AIMDs are performed at 5 to 8 different temperatures. A typical AIMD lasts over 120 ps with a 2 fs time step, where 20 ps is allowed for the system to reach thermal equilibrium before the data are collected to calculate the mean squared displacements (MSD) for all the atomic species in the system. The diffusivity at each temperature is then calculated by linear fitting to the MSD. Those data points of the diffusivity will be discarded, if phase transitions or vibrational instabilities or fast-ion diffusion are spotted for elements other than Li at high temperatures. The remaining points are applied to the Arrhenius relationship to extrapolate to the RT and extract the activation energy.

As shown in Figure II.9.P.1 and Table II.9.P.1, the newly developed cluster-based solid electrolyte materials with the argyrodite composition exhibit very high RT ionic conductivities in the range of 10^{-4}-10^{-1} S/cm and low activation energies in the range of 0.05-0.35 eV. Some of these are especially intriguing, such as Li_6S_5POH and the solid electrolytes with carboranes. It is found that the presence of multiple polyatomic clusters or their combined fragments enable the high ionic conductivity, due to their different sizes, multipolar charge states and active dynamics (e.g. rotations) in the structures. For example, $Li_6S_5P(CB_6H_7)$ contains three types of polyatomic units, including $[CB_6H_6]$, $[PS_4]^{3-}$ and $[HS]^-$. $Li_6S_5P(CB_4H_5)$ contains polyatomic units, including $[PS_4]^{3-}$ and $[HS]^-$, as well as chain-like fragments formed by collision and fusion between the adjacent $[CB_4H_5]^-$ units. Such disordered fragments have been observed in some glassy electrolytes that exhibit ultra-high ionic conductivity and extremely low activation energy. This is due to the large multipolar moments provided by these large fragments, as well as the other polyatomic units with different shapes and charge states, facilitating the fast-ion diffusion.

Some of the new solid electrolytes with the antiperovskite composition also exhibit high ionic conductivities and low activation energies. Unlike the typical antiperovskite materials with (pseudo-)cubic structures, the newly developed materials do not need metal-vacancy defects to trigger the ionic conduction. Figure II.9.P.2A shows the calculated diffusivities of these materials at different temperatures. Other materials of the category are found to have little or no fast-ion conduction at RT and only exhibit very high ionic conductivities at high temperatures. Table II.9.P.1 lists the properties of these new solid electrolytes, including the RT ionic conductivity and the activation energy.

Materials in Figure II.9.P.2A exhibit RT ionic conductivities in the range of 10^{-4}-10^{-2} S/cm and activation energies in the range of 0.12-0.36 eV. Among them, $Li_3S(SCN)$ has the highest ionic conductivity of 0.079 S/cm at RT with the lowest activation energy of 0.124 eV. $Li_3O(SCN)$ and $Li_3S(B_8H_8)$ also exhibit high RT ionic conductivities above 0.01 S/cm and low activation energies. As shown in Table II.9.P.1, several materials are found to show fast-ion conduction only at high simulation temperatures in the range of 500-800 K. The Li^+ conductivities at the high temperatures are in the range of 0.1-1.0 S/cm. Diffusive phase transitions or partial melting is observed in the superionic phases of these materials, as demonstrated by the case of $Li_3S(B_6H_6)$ in Figure II.9.P.1B. Further chemical (e.g. doping) and defect engineering may reduce the phase transition temperatures of these materials and improve the ionic conductivity at RT. It is also found that the borane-based clusters in the studied materials show severe distortions from their gas-phase configurations, suggesting poor stabilities at high temperatures. However, such distortion can create large electric moments in these structures, which can enhance the ionic conductivity.

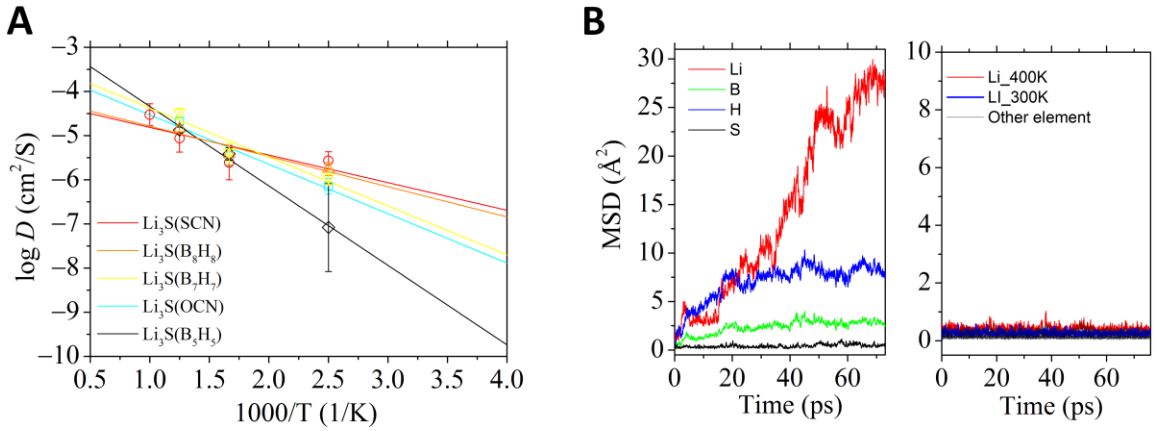

Figure II.9.P.2 (A) Calculated diffusivities of the newly-developed cluster-based solid electrolytes (SE) fitted by the Arrhenius relationship. The corresponding ionic conductivities at RT are in the order of 10^{-4}-10^{-2} S/cm with activation energies between 0.12-0.36 eV. Especially, the calculated RT conductivity of $Li_3S(SCN)$ reaches 0.079 S/cm with a low activation energy of 0.124 eV. (B) $Li_3S(B_6H_6)$ only exhibits fast-ion conduction at high simulation temperatures over 500 K, as shown by the calculated mean squared displacements (MSD) for different atomic species in the structure (left panel) with partial melting (blue and green lines). At simulation temperatures of 300 and 400 K, the material shows no superionic conductivity (right panel).

Conclusions

The major conclusions are:

1. A number of stable cluster-based solid electrolyte materials have been developed according to the chemical compositions of argyrodites and antiperovskites. Their stable bulk structures are found by structure search and first-principle calculations.

2. The newly-developed solid electrolyte materials exhibit superior properties, especially high (room-temperature) ionic conductivities and low activation energies. This is due to the multiple cluster units contained in their structures.

3. The newly developed cluster-based solid electrolyte materials are in fact prototype materials. Based on each of them, a number of nonstoichiometric (e.g. with Li-excess) or chemically altered (e.g. with group element substitutions) new solid electrolytes can be further developed. These can exhibit even better properties, especially higher ionic conductivities.

Table II.9.P.1 Cluster-ion based structures studied as candidates for electrolytes of lithium superionic conductors. "Z" stands for the number of formula units in the unit cell of the identified structure. "S" means stable and "INS" means unstable. "IC" means the calculated ionic conductivity at room temperature. "E_a" means the activation energy

Materials	Z	Lattice Dynamics	Bandgap (eV)	IC (mS/cm)	Ea (eV)
$Li_6PS_5(CN)$	1	S	2.14	0.23	0.342
$Li_6PS_5(OH)$	1	S	3.18	84	0.166
$Li_6PS_5(SCN)$	1	S	2.22	1.8	0.206
$Li_6PS_5(BH_4)$	1	S	2.25	0.18	0.336
$Li_6PS_5(BF_4)$	1	S	2.41	0.30	0.299
$Li_6PS_5(CB_6H_7)$	1	S	3.21	296	0.090
$Li_6PS_5(CB_4H_5)$	4	S	2.66	268	0.108
$Li_6PS_5(B_7H_7)$	4	S	2.32	melting	
$Li_6PS_5(CB_5H_6)$	1	S	3.05	78	--
$Li_6PS_5(B_6H_6)$	1	S	C	13	0.242
$Li_6PS_5(CB_7H_8)$	1	INS	—	--	--
$Li_6PS_5(B_8H_8)$	8	INS	—	--	--
$Li_6PS_5(B_9H_9)$	8	INS	—	--	--
$Li_6PS_5(CB_8H_9)$	1	S	1.85	103	0.101
$Li_6PS_5(CB_8H_9)$[a]	2	S	2.87	310	0.051
$Li_3O(SCN)$	1	S	2.50	12	0.222
$Li_3S(SCN)$	1	S	3.08	79	0.124
$Li_3S(CB_6H_7)$[b]	1	S	2.97	928 (800 K)	--
$Li_3S(CB_4H_5)$[b]	1	S	3.34	531 (600 K)	--
$Li_3S(B_7H_7)$	1	S	C	9.8	0.220
$Li_3S(CB_5H_6)$	1	S	3.52	0.0	--
$Li_3S(B_6H_6)$[b]	8	S	3.45	412 (500 K)	--
$Li_3S(CB_7H_8)$[b]	1	S	2.86	1185 (800 K)	--
$Li_3S(B_8H_8)$	1	S	C	36	0.136
$Li_3S(B_5H_5)$	8	S	1.40	0.37	0.357

[a] Isomeric structure in which one hydrogen in $CB_8H_9^-$ forms HS^- with S^{2-} and PS_3^{3-} are formed in the structure.
[b] Calculations show that these materials exhibit little fast-ion conduction at room temperature. In each of these cases, the Li^+ conductivity corresponds to the value at the simulated temperature specified in the parenthesis. The activation energy from the Arrhenius relationship is, therefore, unavailable.

Key Publications

1. Progress update presentation: First-principles modeling of cluster-based solid electrolytes, EERE Progress Meeting, 04/06/2020.
2. Progress update presentation: First-principles modeling of cluster-based solid electrolytes, EERE Progress Meeting, 08/25/2020.
3. Hong Fang and Puru Jena, Solid Electrolytes Based on Polyatomic Units with Liquid Ionic Conductivity, in preparation, 2020.
4. Hong Fang and Puru Jena, Argyrodite-Based Solid Electrolyte Materials Containing Multiple Clusters, in preparation, 2020.
5. Hong Fang and Puru Jena, Borane-Based Materials as Argyrodite Electrolytes, in preparation, 2020.
6. Collaboration with the Dr. J. Nanda's Oak Ridge National Laboratory group: Synthesis and Design Rules for Protiated Antiperovskites, in preparation, 2020.

References

1. Y. Wang, J. Lv, L. Zhu, Y. Ma, *CALYPSO: A Method for Crystal Structure Prediction*, Comput. Phys. Commun. **2012**, 183, 2063.
2. A. R. Oganov, C. W. Glass, *Crystal Structure Prediction Using Evolutionary Algorithms: Principles and Applications*, J. Chem. Phys. **2006**, 124, 244704.
3. S. J. Clark, M. D. Segall, C. J. Pickard, P. J. Hasnip, M. J. Probert, K. Refson, M. C. Payne, *First Principles Methods Using CASTEP*, Zeitschrift fuer Kristallographie. **2005**, 220, 567.
4. G. Kresse, J. Furthmueller, *Efficiency of Ab Initio Total Energy Calculations for Metals and Semiconductors Using a Plane-Wave Basis Set*, Int. J. Comput. Mater. Sci. Eng. **1996**, 6, 15.
5. A. V. Krukau, O. A. Vydrov, A. F. Izmaylov, G. E. Scuseria, *Influence of the Exchange Screening Parameter on the Performance of Screened Hybrid Functionals*, J. Chem. Phys. **2006**, 125, 224106.
6. J. Sun, A. Ruzsinszky, J. P. Perdew, *Strongly Constrained and Appropriately Normed Semilocal Density Functional*, Phys. Rev. Lett. **2015**, 115, 036402.
7. A. Jain, S. P. Ong, G. Hautier, W. Chen, W.D. Richards, S. Dacek, S. Cholia, D. Gunter, D. Skinner, G. Ceder, K.A. Persson, *The Materials Project: A Materials Genome Approach to Accelerating Materials Innovation*, APL Materials. **2013**, 1, 011002.
8. A. V. D. Walle, G. Ceder, *Automating First-Principles Phase Diagram Calculations*, J. Phase Equilib. **2002**, 23, 348.
9. A. V. D. Walle, M. Asta, G. Ceder, *The Alloy Theoretic Automated Toolkit: A User Guide*, Calphad. **2002**, 26, 539.

II.9.Q Predictive Engineering of Interfaces and Cathodes for High-Performance All Solid-State Lithium-Sulfur Batteries (University of Louisville)

Badri Narayanan, Principal Investigator
University of Louisville
332 Eastern Parkway
Louisville, KY, 40292
E-mail: badri.narayanan@louisville.edu

Tien Duong, DOE Technology Development Manager
U.S. Department of Energy
E-mail: Tien.Duong@ee.doe.gov

Start Date: October 1, 2019 End Date: September 30, 2022
Project Funding: $303,000 DOE share: $303.000 Non-DOE share: $0

Project Introduction

All solid lithium-sulfur battery (ASLSB) is a promising next-generation energy storage technology due to its high theoretical capacity (~1675 Ah/kg; ~5-6 times higher than state-of-the-art Li-ion batteries), high promised energy density (400 Wh/kg), safety, no polysulfide-shuttling, and natural abundance of sulfur. Sulfide (Li_2S-P_2S_5) solid electrolytes (SSEs) possess high Li-ion conductivity (~10^{-3} S/cm), good elastic stiffness (~30 GPa), good stability against Li metal, and low flammability. Such a collection of unique properties make them promising for use in long-lived, safe, high-capacity Li-S batteries for all-electric transportation. Despite this promise, ASLSBs (even using SSEs) remain far from commercialization due to unresolved issues at the electrode-electrolyte interfaces, including (a) poor contact, and high resistance to Li+ ion transport across the cathode/SSE interface, (b) poor ionic/electronic conduction within the cathode, and (c) dendrite growth at the Li/SSE interface. Most of these daunting challenges arise primarily from a lack of fundamental understanding of electrochemical/chemical and transport processes that occur at electrode/electrolyte interfaces, especially at atomic to mesoscopic scales.

Here, we propose to bridge this knowledge gap and address the interfacial issues by developing highly accurate materials models at atomic-to-mesoscopic length/time scales using data-centric and machine learning methods.. Successful development of these models will significantly advance the current state-of-the-art in fundamental understanding of reaction chemistry, kinetics, charge transfer, and dendrite growth at electrified solid-solid interfaces. Multi-scale simulations based on the newly developed models, alongside our wet-chemistry synthesis and advanced characterization will unravel novel strategies to mitigate interfacial resistance, enable precise control over the composition/morphology of solid electrolyte interphase (SEI) and design cathodes with high sulfur loading. Broadly, fundamental knowledge gained by this work will enable development of high-performance ASLSBs that meet DOE targets of specific energy (350 Wh/kg @C/3), sulfur loading (> 6 mg/cm^2), and high cycle life (1000).

Objectives

The primary goal of this project is to leverage data-driven methods and ML strategies to develop accurate multi-physics models for all-solid-state Li-S battery (ASLSB) materials that can capture electrochemical and transport phenomena over atomic-to-mesoscopic length/timescales; these models will be rigorously validated by synthesis and advanced characterization experiments. The team will leverage the predictive power of these models, alongside synthesis/characterization experiments and battery fabrication to address longstanding issues at the electrode/electrolyte interfaces in ASLSBs. The project's proposed technology involves the following: (1) halide-doped solid sulfide electrolytes that can concurrently provide high Li^+ ion conductivity and suppress dendrite growth; (2) novel mesoporous cathode composed of interconnected carbon nano-cages co-infiltrated with sulfur and sulfide electrolyte, which hold potential to allow high sulfur loading and optimal ion/electron

pathways; and (3) functionalization of sulfide electrolyte with ionic liquids to improve physical contact and minimize impedance at the cathode/electrolyte interface.

Approach

The project brings together innovative solutions in multi-scale materials modeling, electrolyte synthesis, fabrication of cathode architecture, and electrolyte functionalization to overcome the issues at electrode-electrolyte interfaces in ASLSBs. The central idea is to employ a data-driven and ML-based approach to develop accurate multi-physics battery models at atomic-to-mesoscopic scales. This approach overcomes critical problems with existing model development methods by foregoing need for pre-defined functional forms, introducing deep-learning technique to describe reactivity, and employing optimization methods that do not require human intuition. Multi-scale simulations based on the newly developed models will provide insights into electrochemical phenomena at electrode/electrolyte interfaces.

Results

1. *Design of new promising halide containing solid sulfide electrolytes for all solid state lithium sulfur batteries*

Aliovalent doping of lithium argyrodite sulfide electrolytes (SEs) with multiple halogens (X) provides an effective route to enhance Li-ion conductivity. Fluorine is particularly interesting as a dopant, since presence of LiF in solid-electrolyte interface (SEI) near the Li anode has been reported to inhibit dendrite formation during battery operation [1]. This opens up a a unique opportunity to concomitantly achieve enhanced Li^+ ion conduction, and a stable solid-electrolyte interface (SEI) by doping SE with F as well as using it as a co-dopant alongside other halogens (Cl/Br/I). Despite this promise, F containing SSEs have not been investigated till now. Here, we optimized the composition of F-containing SEs using density functional theory (DFT) calculations and ab initio molecular dynamics simulations (AIMD) to achieve both high Li-ion conductivity and interfacial stability. We found that doping Li_7PS_6 with equi-atomic amount of F and Cl (i.e., $Li_6PS_5F_{0.5}Cl_{0.5}$) provides the best combination of Li^+ ion conductivity and interfacial stability.

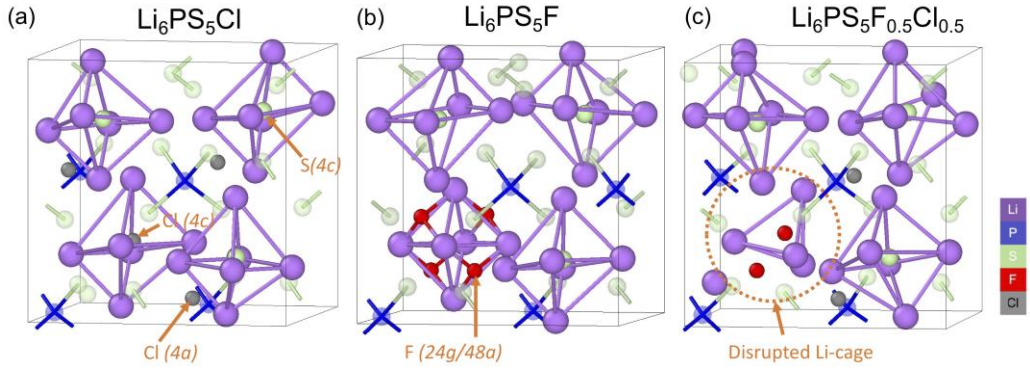

Figure II.9.Q.1 Thermodynamically stable crystal structure of halogenated argryrodites, namely (a) Li_6PS_5Cl, (b) Li_6PS_5F and (c) $Li_6PS_5F_{0.5}Cl_{0.5}$ obtained from density functional theory calculations. In all cases, the backbone of the structure is composed of PS_4 tetrahedra (P and S are shown as blue and green spheres). The lithium atoms (purple) occupy 24g or 48h crystallographic sites forming a cage-like arrangement around a central S or X atom in a 4c site. Regardless of composition, halogen doping introduces site-disorder in sulfur atoms that do not belong to the PS_4 tetrahedra. Addition of Cl/Br/I alone stabilizes S-X antisites; while F prefers to occupy 24g or 48h sites on the surface of the Li-cage. Co-doping with both F and Cl completely disrupts one of the Li-cages causing disorder in lithium sites.

A. *Structure and energetics of halogen doped sulfide electrolytes using DFT*

Halogen doped lithium argyrodites are structural derivatives of a parent sulfide Li_7PS_6 which possesses a cubic crystal (F-43m; space group: 216). The backbone of the structure is composed of PS_4 tetrahedra centered at *4b* sites with the remaining sulfur occupying *4a* sites (Figure II.9.Q.1). The lithium atoms are located at one-third of the available *24g* and *48h* sites exhibiting a cage-like arrangement surrounding a *4c* site containing sulfur. Upon aliovalent substitution of sulfur, the halogens can occupy *4a* and *4c* sites, without impacting the S

belonging to PS_4 tetrahedra. In a perfectly ordered structure, the added halogen atoms subsititute the S atoms placed at *4a* sites (i.e, corners and face centers) only, while the Li cage-centers (*4c*) remain occupied by S. Previous X-ray diffraction studies have shown that some X atoms can substitute the S at the cage-centers (4c) resulting in S-X antisite disorder. Co-doping with two halogens opens up a wide range of possible configurations for such disordered structures. We performed an extensive DFT-based search of the most stable atomic structure of halogen-doped Li_7PS_6 at various compositions. In all cases involving Cl/Br/I dopants, we find that the halogen disordered structures (containing S-X antisites) are energetically more stable than the ordered counterparts owing to the formation of new Li-X bonds than are stronger than Li-S. For instance, presence of one S-Cl antisite in Li_6PS_5Cl (Figure II.9.Q.1(a)) improves its stability by ~0.27 eV/u.f. as compared to the ordered structure owing to the formation of stronger Li-Cl bonds in place of Li-S bonds, as indicated by their bond dissociation energies (Li-S: 312 kJ/mol and Li-Cl: 469 kJ/mol). In SEs containing multiple halogens, the stability of the disordered structures is further enhanced; e.g., antisite in $Li_6PS_5Cl_{0.5}Br_{0.5}$ increases its stability by ~0.40 eV/u.f. Doping Li_7PS_6 with F yields an interesting behavior –unlike Cl/Br/I atoms that occupy *4c* or *4a* site, F prefers to occupy the empty *24g* and *48h* sites on the cage surface meant for lithium as shown in Figure II.9.Q.1(b). This behavior can be attributed to the small atomic radius of F (147 pm, compared to 175 pm for Cl) as well as high strength of Li-F bonds (567 kJ/mol). More interestingly, co-doping Li_7PS_6 with both F and Cl disrupts one of the S-centered Li-cages completely resulting in a thermodynamically stable structure with pronounced disorder in lithium sites (see Figure II.9.Q.1(c)). Such Li-disorder opens up possibility for achieving higher lithium-ion conduction in SEs containing multiple halogen dopants as compared to single halogen dopant type.

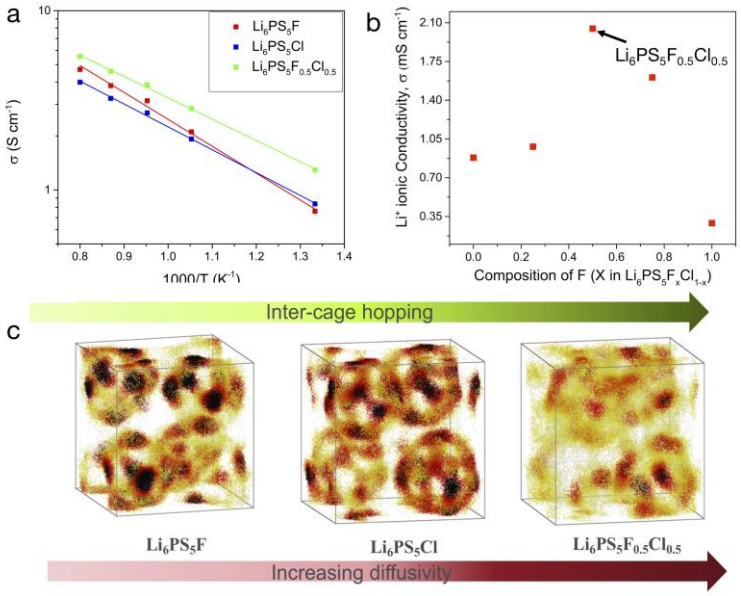

Figure II.9.Q.2 Ab initio molecular dynamics simulations to understand Li^+ ion transport in halogen doped lithium argyrodites. (a) Li-ion conductivity as a function of temperature for three representative electrolytes, namely, Li_6PS_5F (red), Li_6PS_5Cl (blue), and $Li_6PS_5F_{0.5}Cl_{0.5}$ (green), (c) Room temperature Li-ion conductivity as a function of F content in $Li_6PS_5F_xCl_{1-x}$ obtained by extrapolating diffusivity-temperature trends down to 300 K, and (d) Spatial density distribution of Li ions in the AIMD trajectory show enhanced inter-cage hopping for equimolar co-doped electrolyte as compared to the SSEs with single halogen dopant.

B. Effect of site-disorder on lithium ion conductivity in fluorine containing halogenated argyrodites using AIMD simulations

Our AIMD simulations clearly show that disruption of a lithium cage and consequent introduction of Li-disorder in $Li_6PS_5F_{0.5}Cl_{0.5}$ significantly enhances lithium ion conductivity; as compared to the counterpart single halogen doped cases (Figure II.9.Q.2(a)). In fact, under ambient conditions, the AIMD predicted Li^+ ion conductivity of $Li_6PS_5F_{0.5}Cl_{0.5}$ (2 mS/cm) is ~2.2 times higher than that in Li_6PS_5Cl (0.9 mS/cm), and ~6 times

that in Li_6PS_5F (0.3 mS/cm). Such increase in Li^+ conductivity is observed for any level of co-doping; however, the enhancement is most pronounced at equimolar dopant concentrations of the two halogens (e.g., see Figure II.9.Q.2(b)). To gain a fundamental understanding of this increased Li diffusion in co-doped cases, we plotted the probability density distribution of Li ions within the supercell during the AIMD simulations (Figure II.9.Q.2(c)). These distribution plots provide a clear visual depiction of the sites which the Li atoms prefer to occupy as they translate through the lattice with time. In the single halogen doping cases, the Li atoms remain largely restricted to cages composed of *24g* and *48h* sites surrounding a PS_4 tetrahedra ; while in $Li_6PS_5F_{0.5}Cl_{0.5}$, the density distribution shows only a weak cage-like structure. This clearly shows that in Li_6PS_5F and Li_6PS_5Cl, the dominant pathway for Li-ion diffusion remains hopping between adjacent *48h* sites confined within a cage (i.e., intra-cage hopping) with occasional hopping between neighboring cages. On the other hand, in the co-doped $Li_6PS_5F_{0.5}Cl_{0.5}$, the favorable energetics of Li-site disorder significantly enhance inter-cage hopping as illustrated by a more uniform spatial distribution of lithium probability density. This predicted trend is in excellent accordance with our experimental measurements (Figure II.9.Q.3).

C. *Wet chemistry synthesis and characterization of computationally optimized sulfide electrolyte*

Most of the SSEs are synthesized using solid-state methods that require high-temperature chemical reactions; these methods are typically not scalable, are expensive, and offer poor composition control. We recently developed a scalable, efficient, and economic solvent-based method to produce SSEs (Figure II.9.Q.3(a)). This technique employs a solvent-based approach, dissolving a stoichiometric mixture of Li_2S, Li_3PS_4 and LiX (X= Cl, Br, I) in anhydrous ethanol solvent; followed by evaporation and heat-treatment to achieve the desired halide doped SSE with prescribed composition. We extended this technique to introduce multiple halogens into Li_7PS_6 structure through a stoichiometric reaction between Li_2S, Li_3PS_4, LiF, and other LiX (X= Cl, Br, I) in ethanol solvent. Figure II.9.Q.3(b) shows the XRD patterns of Li_6PS_5F and $Li_6PS_5F{\cdot}LiF$ in comparison with Li_7PS_6. Fluoride doped argyrodites exhibit high crystalline while contain a small amount of LiF (2θ=38°), which may due to the poor solubility of LiF in ethanol. Li_6PS_5F shows a Li^+ ionic conductivity of 0.2 mS cm^{-1} at room temperature, higher than that of Li_7PS_6 (0.12 mS cm^{-1}). However, further increasing F content results in a lower ionic conductivity for $Li_6PS_5F{\cdot}LiF$. Beside F-doping, the effect of co-doping with F and Cl/Br/I ions on structure and conductivity of lithium argyrodites were studied. As shown in Figure II.9.Q.3(c), all co-doped sulfide electrolytes exhibit high crystalline and high phase purity without the observation of LiF. However, a new peak at 2θ=54° becomes stronger, which could be related to the enhanced S/X site disordering observed in our first-principles calculation. In comparison with Li_6PS_5F, the co-doped sulfide electrolytes show enhanced ionic conductivities as compared to single halogen counterparts, in excellent agreement with our theory predictions (Figure II.9.Q.3(d)). Similar to our AIMD simulations (Figure

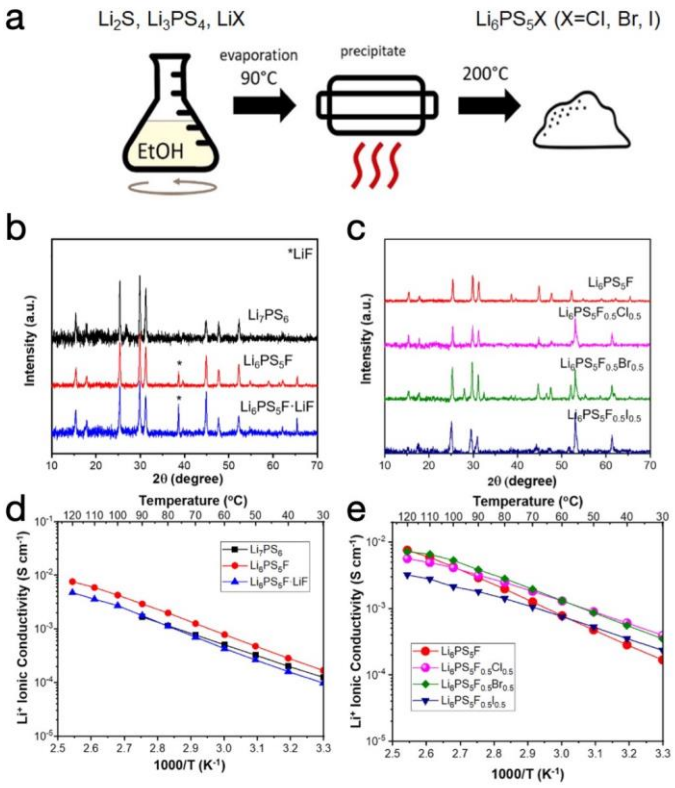

Figure II.9.Q.3 Liquid phase synthesis of lithium argyrodites solid electrolytes optimized by AIMD simulations. (a) Schematic representation of the solvent-based synthesis method. (b) XRD patterns of (a) F-doped lithium argyrodites and (b) F-Cl/Br/I co-doped lithium argyrodites, Arrhenius plots of (c) F-doped lithium argyrodites and (d) F-Cl/Br/I co-doped lithium argyrodites.

II.9.Q.2), our synthesized $Li_6PS_5F_{0.5}Cl_{0.5}$ exhibits the best conductivity of 0.4 mS/cm at room temperature (Figure II.9.Q.3(e)).

D. *Fundamental understanding of stability of anode/electroyte interface*

We performed AIMD simulations to track the structural evolution of anode/SSE interfaces for three electrolyte cases, namely (a) Li_6PS_5F, (b) $Li_6PS_5F_{0.5}Cl_{0.5}$, and (c) Li_6PS_5Cl at 300 K for 20 ps. For all the cases, we investigated the interface between the Li-anode and SSE oriented such that their crystallographic 001 directions are aligned normal to the interface (Figure II.9.Q.1); note this interface (i.e., Li (001) | Li_6PS_5X (001) | Li (001)) was chosen since the as-formed hetero-structure was nearly epitaxial (< 1% strain) for all electrolyte cases. In all the cases, we find three distinct atomic processes: (a) breaking of PS_4^{3-} structural units, (b) formation of new Li-P and Li-S bonds (forming Li_3P and Li_2S clusters), and (c) migration of halogens from SE into anode forming Li-X bonds (Figure II.9.Q.4).These observations are consistent with previous reports in the literature. However, the frequency of occurrence of the three processes is strongly governed by the composition of the electrolyte (Figure II.9.Q.4).

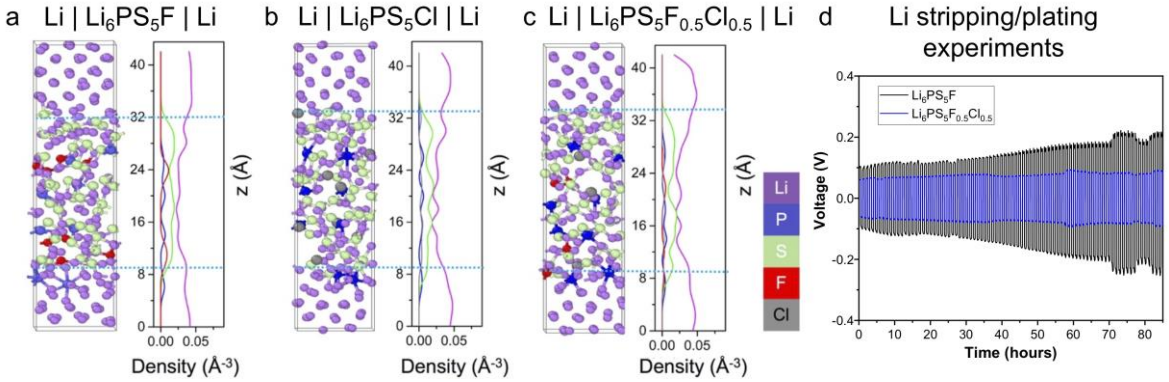

Figure II.9.Q.4 Electrochemical stability of the Li-anode/SSE interface using AIMD simulations and Li stripping/plating experiments on Li-symmetric cells. The equilibrated atomic structure of the interface between Li (001) and SSE (001) derived from room-temperature AIMD simulations are shown for three different electrolyte compositions, namely (a) Li_6PS_5F, (b) Li_6PS_5Cl, and (c) $Li_6PS_5F_{0.5}Cl_{0.5}$. The spatial distribution of Li (purple), P (blue), S (green), F (red), and Cl (grey) atoms (in terms of number density) are also shown in the direction normal to the interface. In panel d, experimentally measured cyclic performance of Li |SE | Li symmetric cells using F/Cl co-doped ($Li_6PS_5F_{0.5}Cl_{0.5}$) and Li_6PS_5F as SEs, respectively. Current density is set at 0.05 mA cm^{-2}

Careful analysis of the pair distribution functions (PDF) of Li-P, Li-S, Li-X, and P-S for the three electrolyte cases indicates new Li-P and Li-S bonds are most prevalent in Li | Li_6PS_5Cl | Li which is completely devoid of any fluorine (Figure II.9.Q.5(a,b)). Consistent with this observation, dissociation of P-S bonds is highest in Li | Li_6PS_5Cl | Li interface (Figure II.9.Q.5(d)). This finding can be attributed to the strong preference of Li to bind with F (as compared S/P/Cl), as illustrated by the significantly higher first neighbor peak for Li-F in Li | Li_6PS_5F | Li as compared to Li-Cl in Li | Li_6PS_5Cl | Li (Figure II.9.Q.5(c)). In all F-containing SSEs, nearly all F from SSE migrate to the anode/SSE interface coordinating with Li in a near-tetrahedral arrangement (Li-F shows an average coordination number is ~3.8). Note that this coordination number is significantly lower than that observed in rock-salt crystal of LiF (6); nevertheless, there is preponderance of new Li-F bonds near the interface. The co-doped electrolyte $Li_6PS_5F_{0.5}Cl_{0.5}$ clearly demonstrates clear energetic preference for Li-F bonds over Li-Cl bonds (the first peak for Li-F is nearly twice as high as Li-Cl). Interestingly, this co-doping also results in the highest number of surviving P-S bonds. These findings indicate that F-containing SSEs are more likely to form stable SEI owing to lower dissociation of P-S bonds. More importantly, our AIMD simulations indicate that SSE containing multiple halogen dopants (with high Li^+ ion conductivity) are at least similar to single-halogen counterparts in terms of stability against Li metal. Consistent with AIMD findings, our galvanostatic Li stripping/plating experiments showed a smooth and flat voltage profile, which indicates good stability of the Li/$Li_6PS_5F_{0.5}Cl_{0.5}$ interface (Figure II.9.Q.4(d)). On the other hand, the polarization voltage increases monotonically in Li_6PS_5F indicating deleterious reactions at the interface. X-ray

photoelectron spectroscopy (XPS) studies are currently underway to elucidate the electrochemical reactions at the Li/SSE interface and validate the AIMD predictions.

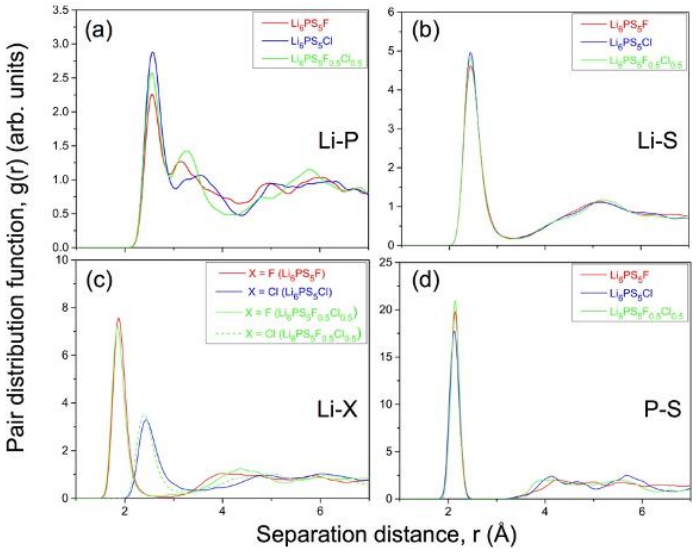

Figure II.9.Q.5 Partial distribution function of (a) Li-P, (b) Li-S, (c) Li-X, and (d) P-S pairs in equilibrated structure of the anode/SSE interfaces obtained from AIMD simulations. The PDF for the three electrolyte compositions Li_6PS_5F, Li_6PS_5Cl and $Li_6PS_5F_{0.5}Cl_{0.5}$ are shown as red, blue and green lines respectively. The PDFs are averaged over the last 3 ps.

2. Development of reactive interatomic potential for representative battery systems

We leverage large quantity of DFT data obtained during the first year of this project to develop a reactive interatomic potential (or force field FF) for SSE, which is capable of describing (a) chemical reactions (and their rates) at the cathode/SSE and Li/SSE interface; (b) effect of electrolyte composition on the formation, structure, composition, and mechanical properties of SEI; (c) ion/charge transport across the SEI, (d) decomposition reactions (of functional ILs or electrolytes), pathways, and rates, and (d) chemical segregation at interfaces. Since our optimized SSEs with desirable combination of Li+ conductivity and interface stability (Section 5.1) are derivatives of Li_7PS_6 prototype, we use Li-P-S ternary system as a representative system to develop the reactive FF. We attempted to develop a deep neural network based potential; however, due to lack of physics in DNNs, need for complex topologies required to describe the ternary system, and lack of training data (even 1000's of data points are too less) leads to gross over-fitting. While we continue to train DNNs, we decided to develop a reactive FF with well-defined functional form containing the necessary physics to describe the interfacial phenomena.

We employ a Tersoff-type bond-order potential (BOP), which is well known to capture the energetics and dynamics of a wide range of atomic configurations (see PI Narayanan's previous works [2]-[5]). To account for To account for the charge transfer between atoms at the interfaces, we employ the QeQ scheme to determine re-distribution of atomic charges with changes in local atomic configurations. We call this potential as Q-BOP. Briefly, the total energy of a system in the framework of Q-BOP can be written as sum of contributions from a short-range Tersoff potential and long-range shielded electrostatic interactions

$$E = \sum_{i=1}^{N} \sum_{j=i+1}^{N} \left[V_{ij} + C_{ij} \frac{q_i q_j}{\left(r_{ij}^3 + 1/\gamma_{ij}^3\right)^{1/3}} \right]$$

where V_{ij} is the the short-ranged Tersoff contribution arising from a pair of atoms i and j that are r_{ij} apart.

In the long-range electrostatic term, C_{ij} is a Taper constant, q_i and q_j are the instantaneous atomic charges whose values are provided by QeQ, and γ_{ij} is a shielding parameter. For Li-P-S ternary system, there are 80 independent parameters that need to be optimized.

We leverage our established machine learning framework to fit these parameters against a large dataset of DFT-properties (~1000) including energies of representative clusters, heat of formation, equation of state, and elastic constants of several known compounds in the Li-P-S ternary space at different stoichiometry. Atomic charges in a wide variety of structures are also employed in the training set to assure adequately diverse representation of charge states.

To assess the predictive power of the newly developed potential, we compared the predictions Q-BOP with values derived from DFT (Figure II.9.Q.6). The test set used to assess the performance of the potential was not used in training. Equations of state (energy-volume dependence) predicted by Q-BOP for the unary system are in remarkable agreement with DFT (< 1 meV/atom; Figure II.9.Q.6(a,b)). For the binary and ternary compounds, the difference between the Q-BOP and DFT values are within 10 meV/atom, which are still within the typical errors of DFT Figure II.9.Q.6(c-e) – let alone a classical potential such as Q-BOP. Figure II.9.Q.6(f) summarizes the errors in the predictions of Q-BOP for a variety of properties. Clearly, all the predicted energy (or heat of formation) values are within 10 meV/atom of DFT, elastic constants within 20% and structural properties (e.g., equilibrium volume) are within 3%. These errors are well within the accuracy that we targeted for the first year; and meet the requirements for completion of the Go/No-Go decision. We note that few shear elastic constants are associated with somewhat higher error; however, these could be improved by adding more data on the interfaces to the training set. Finally, the Q-BOP predicted atomic charges are in good agreement with the Bader charges derived from DFT.

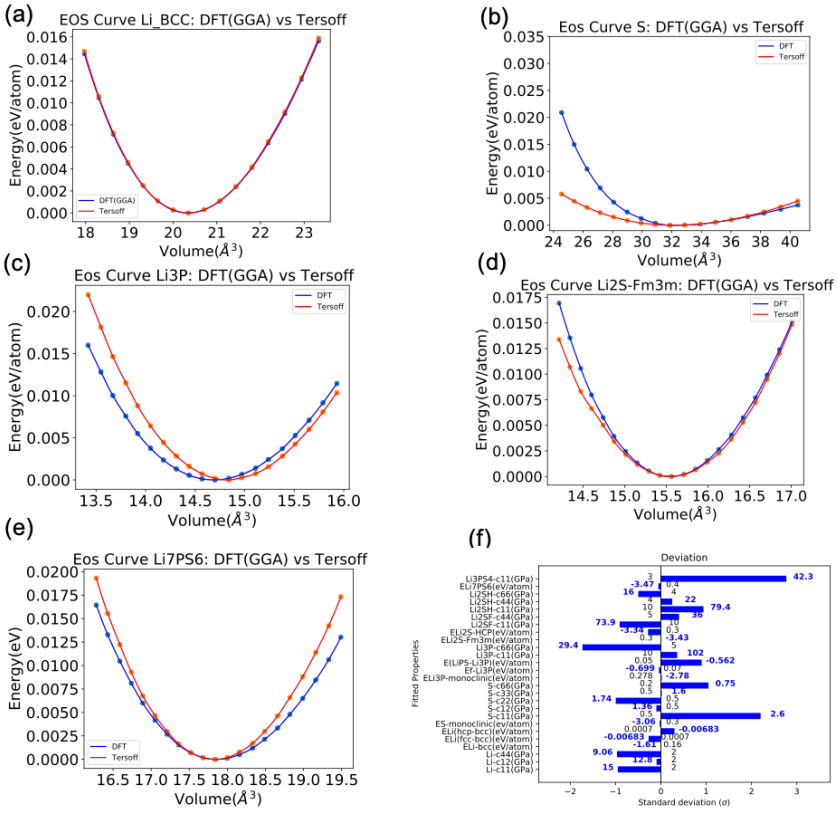

Figure II.9.Q.6 Predictive power of the newly developed Q-BOP potential for Li-P-S system. Comparison of the equation of state (EOS) between DFT and fitted Tersoff potential for (a) Li, (b) S, (c) Li-P, (d) LiS and (e) Li-P-S systems. (f) errors in the prediction of Q-BOP for a variety of materials properties. The energies in panels a-e are relative to the energy corresponding to equilibrium volume at a given level of theory.

3. *Fabrication of battery and characterization of electrode/electrolyte interface*

We synthesized a variety of morphologies of mesoporous carbon using our recently patented process involving thermolysis of sol-gel precursor consisting of nickel salt and carbon precursor, and templating on Ni nanoparticles. Using these mesoporous architectures (including carbon nanotubes, carbon nanocages, C65 nanoparticles, we prepared cathodes by mixing these different morphologies of carbon and sulfur at different weight ratios (33:67,50:50, 60:40 etc.) using ball milling. Then the C:S mixer was heated under vacuum at 115 ^{0}C for about 1 hour to allow sulfur to melt and infuse into carbon. Next, the C:S composite was mixed with water-based binder (carboxy-methyl cellulose (CMC)/Styrene-Butadiene rubber 5(SBR) wt. % in DI water) and Acetylene Black (AB) (92%, 3% and 5% weight ratio of CMC/SBR) to make a slurry and coated onto an Aluminum current collector using doctor blading technique (~100 micron thick). Finally, the cathode was vacuum annealed at 50 ^{0}C overnight. We used the water-based binder instead of state of the art, N-methyl-pyrrolidone (NMP) (as process solvent) in combination with polyvinylidene difluoride (PVdF) due to the high cost of NMP/PVdF. Further, water-based binders allow coating of the electrode material thicker and crack free. We were able to achieve cathodes with S-loading of 5 mg/cm^2.

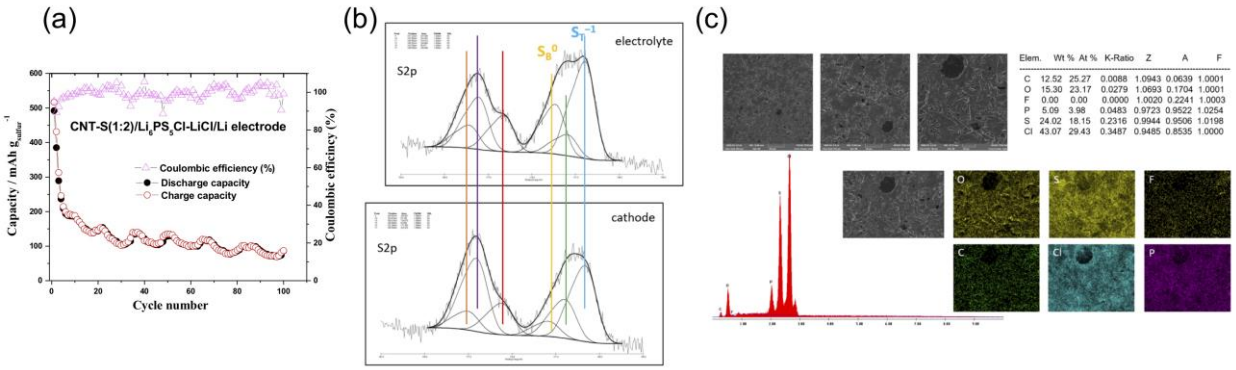

Figure II.9.Q.7 Fabrication ans characterization of solid state lithium sulfur battery. (a) Capacity versus cycle number of CNT-S (1:2) cathode electrode using SSE Li6PS5-Cl-LiCl at 0.1 C rate test. (b) High resolution XPS spectrum of sulfur at cathode/electrolyte interface taken from cathode and electrolyte surfaces, and (c) SEM and EDS characterization of the electrolyte at the end of 100 cycles.

To assemble the coin cell, first the cathode was punched and placed on a cap of the cell and few drops of ionic liquid were poured. Next SE was placed on the cathode. Finally, the anode comprising of Li pressed onto a stainless-steel mesh was placed on the other side of the SE. Figure II.9.Q.7(a) shows the charge and discharge capacities in the first 100 cycles of a CNT-S (1:2) cathode-based battery with Li_6PS_5Cl SE synthesized by our method, and Li anode at 0.1 C. It showed an initial capacity of ~ 500 mAh/g, but rapidly dropped to ~ 200 mAh/g within the first 5 cycles and retained a capacity of ~ 100 mAh/g after 100 cycles. To better understand the reactions occurring at the interface, high resolution X-ray photoelectron spectra (XPS) were collected for all the elements involved in the system. The S-*2p* XPS spectrum (Figure II.9.Q.7(b)) from cathode and electrolyte surfaces. show the same six components, grouped in two separate groups, one between 168 and 174 eV and the other one between 174 and 181 eV. The peaks of the first group originate from lithium sulfide and lithium polysulfides. The spectrum analysis yields three components, namely the lithium sulfide sulfur peak at around 162.4 eV,[6] and the peaks of terminal sulfur and bridging sulfur of lithium polysulfide (Li_2S_x with x > 1) at 161.6 and 163.3 eV, respectively [7],[8]. The analysis of the other group yields the S-*2p* peaks at around 166.5, 168.5 and 169.1 eV, which are typical binding energies for sulfite and sulfate groups, respectively. SEM and EDS characterizations were carried out to study the surface morphology and the distribution of all the elements. Results revealed the presence of sulfur and chlorine on the electrolyte interface. The analysis indicates also differences in the distribution of chlorine and phosphorous at the interfaces, which may indicate the decomposition of the Li_6PS_5Cl SE. We also tested charge-discharge performance of CNT-S (3:2) electrode-based Li-S battery using $Li_6PS_5F_{0.5}$-$Cl_{0.5}$ SE in the voltage range of 0.8 - 2.8V with a current of 0.05 C rate. The discharge curve shows a large flat plateau around 2.1-2.0 V with a high discharge capacity of 1271 mAh

g^{-1} but, the cell failed to charge. This is a stark difference between Li_6PS_5Cl and $Li_6PS_5F_{0.5}Cl_{0.5}$ solid state electrolytes. Future research work is planned to optimize the charging stability and understand the interface between the fluorine-based electrolyte and the cathode.

Conclusions

In summary, our DFT calculations revealed that novel disordered configurations can be obtained by doping argyrodite Li_7PS_6 SE with two dissimilar halogens, with one of them being fluorine. In particular, our AIMD simulations revealed that the fluorine-induced disorder in lithium sites significantly accelerates Li-ion diffusion in such co-doped argyrodites. In fact, enhancement in Li-ion conductivity for these co-doped electrolytes can be 2-6 times higher than their counterparts containing only one dopant type (i.e., Cl or F alone); the highest enhancement being at the equi-atomic doping, namely, $Li_6PS_5F_{0.5}Cl_{0.5}$. More importantly, our AIMD simulations showed that co-doping strategy also provides excellent stability of the anode/electrolyte interface owing to the formation of strong Li-F bonds; which, in turn, inhibits the dissociation of the backbone PS_4^{3-} network. Our theory predictions are firmly supported by our ionic conductivity and electrochemical characterization experiments. To enable simulation of large-scale systems (e.g., cathode-electrolyte interfaces, or ion/charge transport at grain boundaries in electrolytes), we have a reactive atomic interaction potential model (using Tersoff + Qeq formalism) for representative Li-P-S system using our established machine learning framework. Our newly developed interatomic potential (force field or FF) can accurately predict (a) structure (within ~2% of DFT), (b) heat of formation (~within 10 meV/atom of DFT), (c) elastic constants (within ~20% of DFT), and (d) atomic charges at interfaces. These FFs can provide key insights into (a) chemical reactions (and their rates) at the cathode/SSE and Li/SSE interface; (b) effect of electrolyte composition on the formation, structure, composition, and mechanical properties of SEI; (c) ion/charge transport across the SEI, (d) decomposition reactions, pathways, and rates, and (d) chemical segregation at interfaces.

On the synthesis and characterization front, we have developed a scalable, efficient, and economic solvent-based method to produce solid-state sulfide electrolytes; which provides much better composition control than state-of-the-art solid-state techniques. Our newly developed liquid-phase method also overcomes other key limitations of the existing solid-state methods, including need for high-temperature chemical reactions, non-amenability to scale-up, and high costs. We utilized this new method to synthesize a variety of halogen-doped argyrodites at various compositions, including the computationally optimized composition $Li_6PS_5F_{0.5}Cl_{0.5}$. Furthermore, we synthesized cathode architectures based on a variety of mesoporous carbon (including those with carbon nanotubes and carbon nanocages) with high sulfur loading (~5 mg/cm^2). Finally, using the cathodes and electrolytes synthesized in this work, we fabricated coin-cell batteries to perform baseline tests.

Key Publications

1. William Arnold, Dominika A. Buchberger, Yang Li, Mahendra Sunkara, Thad Druffel, and Hui Wang, “Halide doping effect on solvent-synthesized lithium argyrodites Li6PS5X (X= Cl, Br, I) superionic conductors”, Journal of Power Sources **464,** Article number 228158 (2020).

2. Yang Li, William Arnold, Jacek Jasinski, Arjun Thapa, Gamini Sumanasekera, Mahendra Sunkara, Badri Narayanan, Thad Druffel, and Hui Wang, “Interface stability of LiCl-rich argyrodite Li_6PS_5Cl with propylene carbonate boosts high-performance lithium batteries”, Electrochimica Acta 363, 137128 (2020).

References

1. Fan, Xiulin, Xiao Ji, Fudong Han, Jie Yue, Ji Chen, Long Chen, Tao Deng, Jianjun Jiang, and Chunsheng Wang. 2018. "Fluorinated solid electrolyte interphase enables highly reversible solid-state Li metal battery." *Science Advances* 4 (12), Article Number: eaau9245.

2. Chan, Henry, Badri Narayanan, Mathew J. Cherukara, Fatih G. Sen, Kiran Sasikumar, Stephen K. Gray, Maria K. Y. Chan, and Subramanian K. R. S. Sankaranarayanan. 2019. "Machine Learning

Classical Interatomic Potentials for Molecular Dynamics from First-Principles Training Data." *The Journal of Physical Chemistry C*, 123 (12), 6941-6957

3. Cherukara, MJ, B Narayanan, A Kinaci, K Sasikumar, SK Gray, MKY Chan, and SKRS Sankaranarayanan. 2016. "Ab Initio-Based Bond Order Potential to Investigate Low Thermal Conductivity of Stanene Nanostructures." *Journal of Physical Chemistry Letters* 7 (19): 3752-3759.

4. Narayanan, B, A Kinaci, FG Sen, MJ Davis, SK Gray, MKY Chan, and SKRS Sankaranarayanan. 2016. "Describing the Diverse Geometries of Gold from Nanoclusters to Bulk-A First-Principles-Based Hybrid Bond-Order Potential." *Journal of Physical Chemistry C* 120 (25): 13787-13800.

5. Narayanan, Badri, Kiran Sasikumar, Zhi-Gang Mei, Alper Kinaci, Fatih G. Sen, Michael J. Davis, Stephen K. Gray, Maria K. Y. Chan, and Subramanian K. R. S. Sankaranarayanan. 2016. "Development of a Modified Embedded Atom Force Field for Zirconium Nitride Using Multi-Objective Evolutionary Optimization." *The Journal of Physical Chemistry C* 120 (31): 17475-17483.

6. Xiong, Shizhao, Kai Xie, Yan Diao, and Xiaobin Hong. 2014. "Characterization of the solid electrolyte interphase on lithium anode for preventing the shuttle mechanism in lithium–sulfur batteries." *Journal of power sources* 246: 840-845.

7. Liang, Xiao, Connor Hart, Quan Pang, Arnd Garsuch, Thomas Weiss, and Linda F Nazar. 2015. "A highly efficient polysulfide mediator for lithium–sulfur batteries." *Nature communications* 6 (1): 1-8.

8. Fantauzzi, Marzia, Bernhard Elsener, Davide Atzei, Americo Rigoldi, and Antonella Rossi. 2015. "Exploiting XPS for the identification of sulfides and polysulfides." *RSC advances* 5 (93): 75953-75963.

Acknowledgements

This project involves three co-investigators: Dr. Hui Wang, Dr. Gamini Sumanasekera, and Dr. Jacek Jasinski at the University of Louisville. A part of this work was performed in collaboration with Dr. Anh Ngo at Argonne National Laboratory. This research used resources of the National Energy Research Scientific Computing Center, a DOE Office of Science User Facility supported by the Office of Science of the U.S. Department of Energy under Contract No. DE-AC02-05CH11231. Use of the Center for Nanoscale Materials was supported by the U. S. Department of Energy, Office of Science, Office of Basic Energy Sciences, under Contract No. DE-AC02–06CH11357. We also acknowledge generous computer time allocations at the Laboratory Computing Resource Center at Argonne National Laboratory

II.9.R Design of Strain Free Cathode – Solid State Electrolyte Interfaces Using Chemistry-Informed Deep Learning (ANL)

Hakim Iddir, Principal Investigator
Argonne National Laboratory
9700 South Cass Avenue
Lemont, IL 60439
E-mail: Iddir@anl.gov

Tien Duong, DOE Technology Development Manager
U.S. Department of Energy
E-mail: Tien.Duong@ee.doe.gov

Start Date: October 1, 2019 End Date: September 30, 2022
Project Funding: $300,000 DOE share: $300,000 Non-DOE share: $0

Project Introduction

Structure-property relationships are at the heart of most fundamental scientific approaches. However, the link between structure and property remains a challenge in the materials science of complex systems, such as the oxides that form battery components. **In particular, the chemical and mechanical stability of the cathode-SSE interface presents a challenge to the development of solid-state batteries**. High performance Density Functional Theory (DFT) calculations provide the necessary framework to understand such systems. Unfortunately, given the limited number of atoms and time scales accessible by the method and the myriad calculations required to achieve satisfactory results, the computational cost of simulating all the possible configurations of a multicomponent oxide is prohibitive. In this work, we augment the DFT data with Machine Learning (ML) – especially deep learning – techniques that allow us to access large system sizes and longer time scales necessary to build thermodynamic models. We focus on understanding the nature of benchmark $Li_{1-\alpha}Ni_{1-x-y-z}Mn_xCo_yM_zO_2$ structures (M dopant, α,x,y,z <1), their volume change with Li content, nature and concentration of the dopants, as well as the chemical stability of the SSE-cathode interface. The DFT and ML approach will provide new cathode compositions that will reduce the strain of the SSE-cathode interface and hence improve its mechanical and chemical stabilities

In this project we aim at developing a methodology that will allow us to explore and expand the configurational space using High-Performance Computing (HPC) approaches in a systematic and efficient way. The methodology will encompass, DFT, Ab-Initio Molecular Dynamics (AIMD), Molecular Dynamics, and ML. The methodology will also take advantage of the variety of software already developed at Argonne and at other DOE laboratories, such as BALSAM to automate, manage and control the large number of calculations needed to achieve our goal.

Objectives

Structure-property relationships are at the heart of most fundamental scientific approaches. However, the link between structure and property remains a challenge in the materials science of complex systems, such as the oxides that form battery components. **In particular, the chemical and mechanical stability of the cathode-SSE interface presents a challenge to the development of solid-state batteries**. High performance Density Functional Theory (DFT) calculations provide the necessary framework to understand such systems. Unfortunately, given the limited number of atoms and time scales accessible by the method and the myriad calculations required to achieve satisfactory results, the computational cost of simulating all the possible configurations of a multicomponent oxide is prohibitive. In this work, we augment the DFT data with Machine Learning (ML) – especially deep learning – techniques that allow us to access large system sizes and longer time scales necessary to build thermodynamic models. We focus on understanding the nature of benchmark $Li_{1-\alpha}Ni_{1-x-y-z}Mn_xCo_yM_zO_2$ structures (M dopant, α,x,y,z <1), their volume change with Li content, nature and

concentration of the dopants, as well as the chemical stability of the SSE-cathode interface. The DFT and ML approach will provide new cathode compositions that will reduce the strain of the SSE-cathode interface and hence improve its mechanical and chemical stabilities

In this project we aim at developing a methodology that will allow us to explore and expand the configurational space using High-Performance Computing (HPC) approaches in a systematic and efficient way. The methodology will encompass, DFT, Ab-Initio Molecular Dynamics (AIMD), Molecular Dynamics, and ML. The methodology will also take advantage of the variety of software already developed at Argonne and at other DOE laboratories, such as BALSAM to automate, manage and control the large number of calculations needed to achieve our goal.

Approach

All calculations will be performed by spin-polarized DFT as implemented in the Vienna Ab Initio Simulation Package (VASP).[1], [2] To make sure all the oxidation state of ions are correct, after geometry optimization within the DFT+U framework, electronic relaxation will be performed using a single point calculation with the hybrid functional HSE06.[3] For production calculations we will use the MPI parallelized version of VASP.

Exploration of the potential energy surface (PES) is needed to predict the structure of solid materials and interfaces. Such calculations are infeasible using MD or DFT calculations alone. Thankfully, the PES of a system can be represented by the sum of the energies of the local neighborhoods surrounding each atom. This enables the use of ML surrogate models trained with DFT calculations to capture the energies in local neighborhoods. The input to the ML surrogate must be a unique representation of the system under study. Consequently, the local environment of each ion is described using a local environment descriptor that renders the atomic configuration invariant to rotations, translations, and permutations of the atoms. In recent years, several different descriptors have come to prominence with advantages and disadvantages. Once the ML surrogate is trained, the total energy and forces over all the ions of any structural configuration can be determined. Such information can be used for atomistic simulations, namely, MD and Monte Carlo (MC).

In this project, we propose to use the open-source DeepMDkit python/C++ package to construct the ML PES and force fields. The promise of DeepMDkit in this work is to provide near-DFT accuracy at orders of magnitude lower computational expense, comparable to traditional molecular dynamic simulations. Efficiency in training is facilitated through integration with TensorFlow and MPI/GPU support.

One of the challenges of the development of a ML PES is achieving accurate predicted forces and energies across the entire configurational space, while minimizing the total number of calculations required for training. In recent years, active learning has been highlighted for its ability to target training examples most likely to improve the model quality or to achieve some other objective (i.e. maximizing a predicted material property). DP-GEN, an open source python package based on DeepMDkit, implements a similar active learning scheme with HPC support, and has been employed to construct a ML PES with accuracy approaching DFT and sometimes exceeding embedded atom potential for experimentally measured properties of interest.[4] In this work, we propose to leverage DeepMDkit and DP-GEN to efficiently generate ML-PESs for cathode-electrolyte systems including a variety of dopants.

Results

The scientific and technology challenge is illustrated in Figure II.9.R.1, which shows the relative change in volume for several known cathode materials as a function of Li content.[5] Contrary to most compositions, $LiCoO_2$ shows a different behavior, suggesting that volume change of the NMC materials can be controlled with dopants. In fact, the relative change in volume is reduced with increased Co content. This significant volume reduction is mainly due to the sudden collapse of the inter-layer spacing in these layered oxides as Li is removed, when accessing higher capacities. The shrinkage in the inter-layer spacing is itself the result of bulk phase transition that involves a change in the relative stacking of the oxide layers (H2 to H3) (see Figure II.9.R.2). To accurately capture this phase transition using DFT, we explored different DFT methods and

compared their abilities to capture the right physics, and hence the volume change. The results from our initial screening of these methods point to SCAN+rVV10[6], [7] as a viable option. The SCAN method avoids fixing the Hubbard potential U in DFT+U as Li is removed. SCAN+VV10 seems to better capture the binding between the TM layers in the absence or little Li content compared to SCAN without Van De Waals (VDW) or PBE (see Figure II.9.R.3).

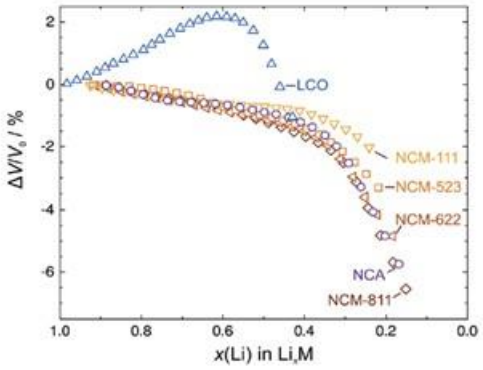

Figure II.9.R.1 The unit cell volume obtained from crystallographic data versus the state of lithiation of positive electrode materials.[5]

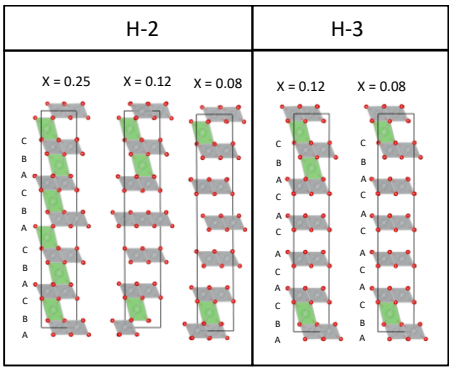

Figure II.9.R.2 Polyhedral representation of $LiNiO_2$ super cell at different lithium content (x) with oxygen stacking in the H-2 (ABC) and H-3 (AC) phases. Grey octahedrons represent Ni sites, green octahedrons represent Li sites, small red spheres represent oxygen atoms.

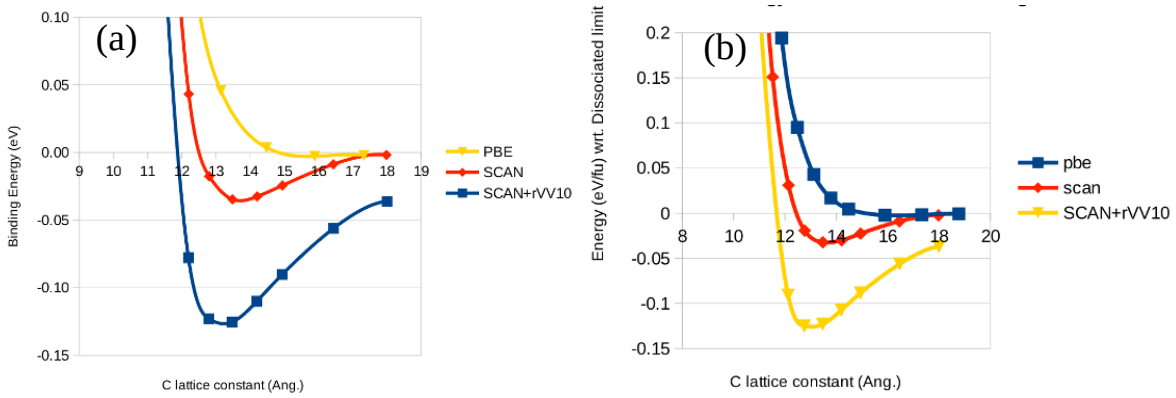

Figure II.9.R.3 Energy of the dissociated limit as a function of the interlayer spacing for PBE, SCAN and SCAN+rVV10 for NiO_2 (a) in O_1 stacking (b)in O3 stacking.

Before studying the response of the system to Li content during cycling, it is imperative to know the transition metal cation distribution within the material. For instance, for $LiNi_xMn_yCo_zO_2$ (NMC-xyz) materials, the distribution of Co and Mn within and across the transition metal layers determines the material properties. To get a better realistic cation distribution, a large simulation cell is necessary to allow the system to reproduce the local configurations that appear in the real system. Figure II.9.R.4a shows a top view of the super-cell used to model NMC-811, while Figure II.9.R.4b shows a side view of the whole supercell. The cell is composed of 432 atoms, which makes the structure optimization using DFT challenging.

The procedure used to screen for the configuration that minimizes the total energy of the system is summarized in Figure II.9.R.4c. First, a batch of randomly generated configurations is built. Second, a predictive model for the total energy, a machine learning approach is used to fit the DFT generated data. The fitted model is a feed-forward neural network as implemented in the AMP package.[8] Next, a new batch of random configurations is generated. The machine learning model is used to estimate the energies for each configuration. Using a Bayesian optimization procedure, a new set of configurations is selected. If the minimum energy criterion is not met, the new selected configurations are sent through the entire process again.

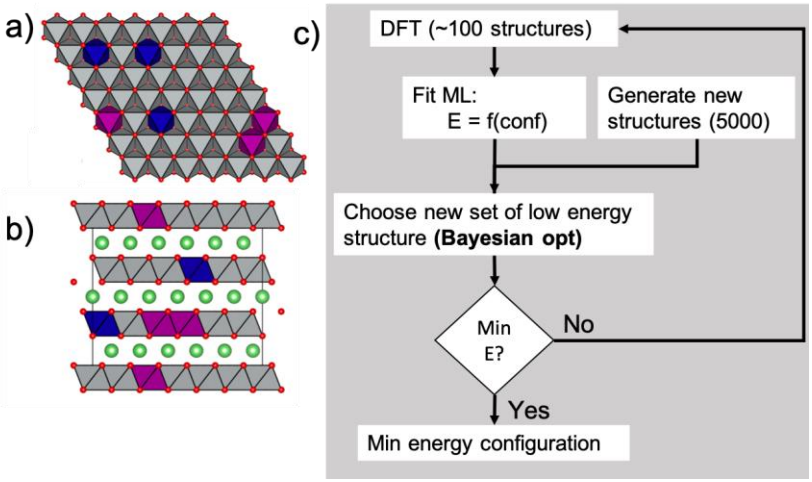

Figure II.9.R.4 Polyhedral representation of $LiNi_{0.8}Mn_{0.1}Co_{0.1}O_2$ (a) transition metal layer top view, (b) whole super-cell side view. Grey polyhedra represent Ni sites, blue polyhedral represent Co site, purple polyhedral represent Mn sites and green spheres represent Li ions. (c) Procedure to find minimal energy transition metal configuration.

The energies for the first and second round of DFT calculations are presented in Figure II.9.R.5c, where the configurations are sorted by total energies. The performance of the ML model (trained on round 1) is shown in Figure II.9.R.5a. An active learning scheme is employed to identify 50 additional structures (round 2) to

evaluate with DFT and improve the neural network model. Specifically, we employ a Bayesian optimization scheme with the lower confidence bound (LCB) acquisition function to select structures on the continuum of low predicted energies and high predicted uncertainties.[9] By probing this continuum we hope to minimize the number of DFT calculations necessary to construct an accurate neural network model. In practice, we used the bootstrapped NN model trained on all available training structures and predicted the energies (with uncertainty estimates) for 5000 random structures. The 50 most promising structures according to the batch LCB strategy were then selected and evaluated with further DFT calculations. Indeed, the new set of DFT results show lower energies than the initial random set (see Figure II.9.R.5c round 2). The new low energy configurations exhibit more uniform distribution of Co and Mn within the different transition metal layers and promote more of the NMC-111 domains (see Figure II.9.R.5d).

Additionally, we are validating the above neural network-based machine learning approach implemented in AMP with two other machine learning molecular dynamics potential generation formalisms. One, a gaussian process regression approach, called the Gaussian Approximation Potential (GAP), which has shown promising structural predictions for electronic materials.[10] Another, is DeepMD-kit, which is a neural network based approach that has shown promise in predicting properties of multi-component material systems.[11].

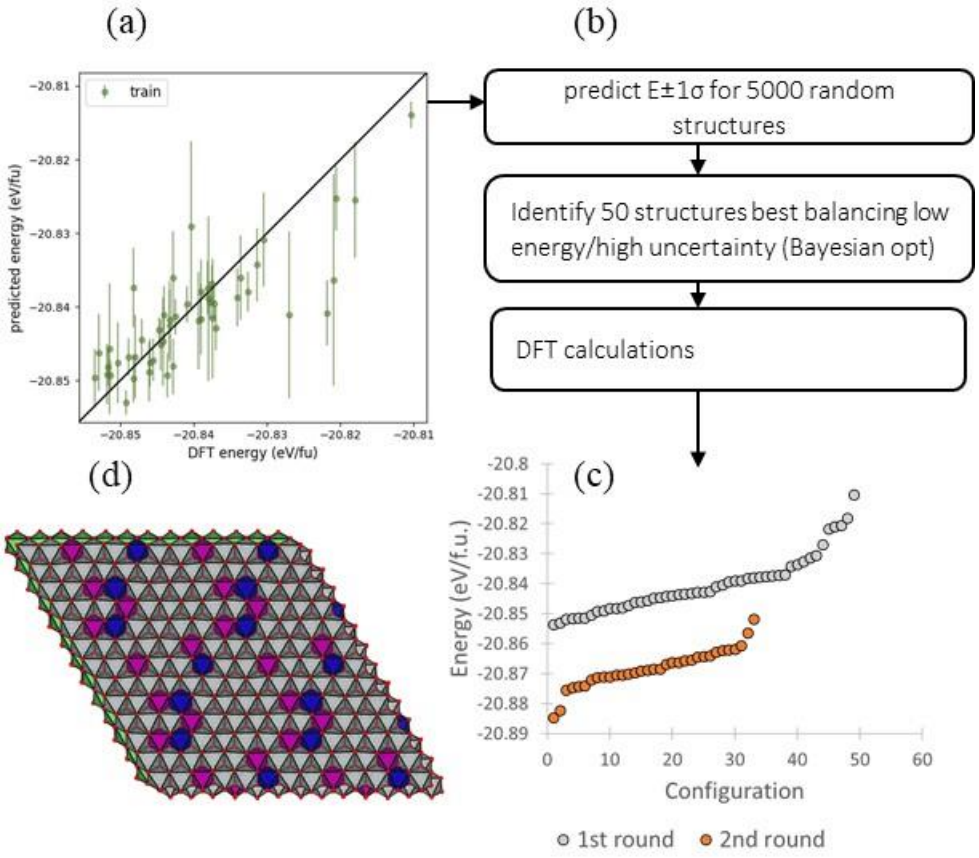

Figure II.9.R.5 (a) Neural network predicted versus DFT predicted energies. Additionally, 1-sigma uncertainty intervals are plotted for the neural network predictions. (b) Procedure to find minimal energy transition metal configuration. (c) DFT calculated energies for 50 configurations (round 1) where transitions metals are positioned randomly in the transition metal layers and energies after Bayesian optimization (round 2). (d) Transition metal layer top view polyhedral representation of $LiNi_{0.8}Mn_{0.1}Co_{0.1}O_2$. Grey polyhedra represent Ni sites, blue polyhedral represent Co site, purple polyhedral represent Mn sites and green spheres represent Li ions.

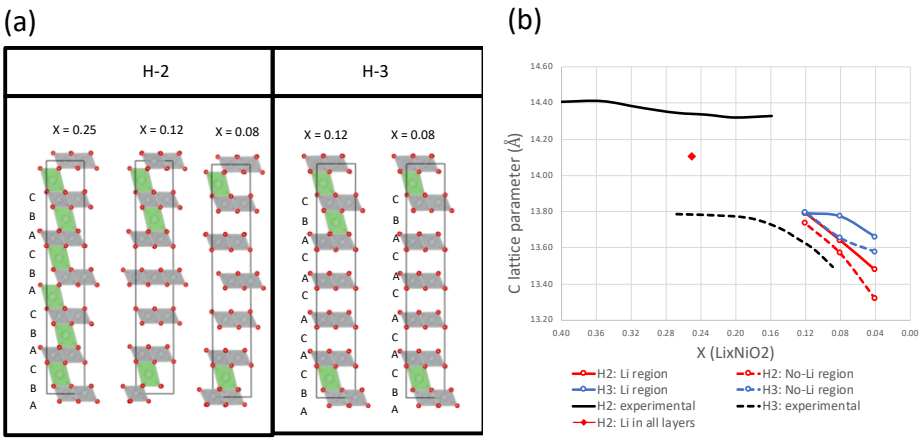

Figure II.9.R.6 (a) schematic representation of the Li_xNiO_2 structures used to model a "hybrid" cell where part of the cell can be lithiated while some layers are completely delitiated. Two different hexagonal structures were represented with different stacking sequences for the delithiated regions. Grey octahedrons represent Ni sites, green octahedrons represent Li sites and red spheres represent oxygen ions. (b) simulated c lattice parameter changes with Li content for LixNiO2. For compositions with less than x =0.25 some Li layers are completely empty (label as No-Li region) while some other layers have the same amount of Li as the x = 0.25 composition (label as Li region). All the DFT computed values used the optB86b-vdW functional.

The volume decrease of $LixNiO_2$ during charging causes significant stress and damage to $LiNiO_2$ during cycling. Understanding the volume change in the cathode is paramount for the design of cathode solid electrolyte interfaces. However, the physics of this volume change has caused some controversy. The more conventional theory attributes the change in oxygen stacking sequence to the collapse of the spacing between layers.[12] However, more recent evidence points to the electronic depletion around oxygen ions as the main cause of the decrease in the c-lattice parameter.[13] According to previous results for $LixNiO_2$, there are no stable Li distributions when $x < 0.25$[14]. Hence, for the region of interest in this project ($x < 0.25$), completely delithiated regions are thought to be formed at high state of charge (SOC), that might trigger a change in the oxygen stacking sequence (O3 to O1, i.e. H-2 to H-3). However, since the calculated energies for these two oxygens stacking sequences (O1 vs O3) are very similar, both stacking sequences could be present within the material. In order to mimic those local composition heterogeneities, a "hybrid" supercell was designed to accommodate different stacking sequences in the delithiated regions. Figure II.9.R.6a shows a schematic representation of the supercell used for the DFT calculations. The optB86-vdw functional was used to account for non-local interactions.[15] Figure II.9.R.6b shows the experimental and simulated c lattice parameters at high SOC in each region of the simulated domains. At $x = 0.25$ the simulated value underestimates the experimental value by about 0.2 Å. Furthermore, the experiment shows some H-3 phase already present at that composition. For even lower Li content the simulations predict a collapse in the c lattice parameter that mimics the experimental results. However, there is not a clear difference between the regions with and without Li and the different stacking sequences. Further investigation of this issue is underway.

Standard density functional theory does not include van der Waals' forces (VDW). Hence, it does not correctly estimate the interaction between Layers of NiO_2 in NiO_2 or the strong correlation of the Ni d electrons. We have tested several DFT functionals to discard spurious results given by the DFT methodology. The SCAN meta-functional has been shown to account for the strong correlation in $LiNiO_2$.[16] With the addition of van der Waals forces in the SCAN+rVV10 functional,[17] it is possible to account for strong correlation and van der Waals forces with no empirical terms. Issacs and Wolverton have shown that SCAN+rVV10 yields more accurate predictions of Li intercalation voltages in rechargeable battery cathode materials than PBE, optPBE-vdw, SCAN or SCAN+rVV10.[18] We have optimized the geometry of NiO_2 with PBE+U, SCAN and SCAN+rVV10 functional to demonstrate that VDW are indeed required to model the crystal structure of NiO_2. In going from PBE to SCAN and SCAN+rVV10 one increases the amount of VDW terms in the functional. PBE has no VDW terms. SCAN includes some VDW terms and SCAN+rVV10 includes all VDW terms. The

c lattice constant, which is equivalent to three times to interlayer spacing decreases as VDW terms are added. This is true for both O3 and O1 stacking of the layers of NiO_2. Note that the predicted c lattice constant of 13.33 Å compares well to the experimentally determined value of 13.039 Å for the H4 (O1 stacking) NiO_2 phase .[19] However, the predicted lattice constant for O3 stacking is 13.17, which is lower than the same distance in the predicted geometry for O1 stacking and experimentally measured distance for O3 (R3-NiO_2) stacking of 13.472 Å.[19] We believe that this difference is largely due to the presence Ni(II) between the NiO_2 layers in R3-NiO_2, which has stoichiometry of $Ni_{1.07}O_2$ in the experimental sample. A comparison of the binding energies O1 and O3 stacking relative to separated NiO_2 layers (large c distances) is shown in Figure II.9.R.7. We find the interlayer distances and binding energies for O1 and O3 stacking to be very similar. Although we are predicting that O3 stacking is a kJ/mol lower than O1 stacking, O1 could still have a lower energy than O3 stacking in reality because kJ/mol is likely to be less than the expected error in this calculation. We are planning to carry out RPA calculations for NiO_2 to get a more accurate estimate of the relative energy of the O1 and O3 stacking in NiO_2.[20]

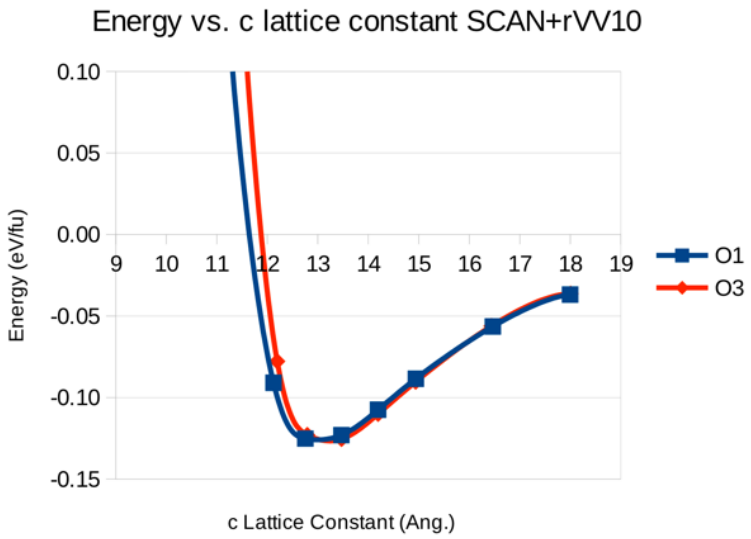

Figure II.9.R.7 Comparison of the Binding Energy of O1 and O3 stacking in NiO_2.

We also explored elemental segregation to surfaces. The transition metal configuration in the material might change with the presence of a surface or an interface. The appropriate description of the cathode solid electrolytes interfaces requires an accurate local composition to estimate interfacial properties. We followed the same procedure explained in the previous report to explore the potential energy surface using DFT and Bayesian optimization and propose the best candidates in a stepwise manner. Figure II.9.R.8 shows the energies of different configurations for the first and second round of calculations. The Bayesian optimization procedures found some lower configuration energies in the second round. Continuing this procedure, in the next quarter a “final” optimal configuration will be found.

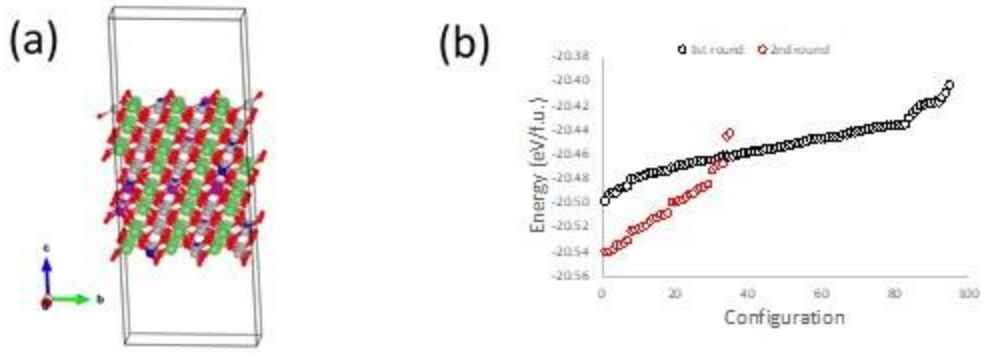

Figure II.9.R.8 (a) schematic representation of the NMC811 surface slab model. Green spheres represent Li, grey spheres represent Ni, blue spheres represent Co, purple spheres represent Mn and red spheres represent oxygen. (b) DFT calculated energies for 98 configurations (round 1) where transition metals are positioned randomly in the transition metal layers and energies after Bayesian optimization (round 2).

In Q4, the Argonne team began a transition from the open-source AMP Atomistic python package to DeepMDkit and DP-GEN ecosystem. AMP is a foundational package for ML fitting of atomistic potentials with flexibility in both ML modeling and local atomic environment descriptors. Unfortunately, as newer approaches have been developed and packages released, AMP has not received as frequent updates and the user community does not appear to be large. Furthermore, the Argonne team had difficulties with force training in AMP. In contrast, DeepMDkit is a more recently developed package with active support and demonstrated successes on both energy and force predictions in multicomponent systems. The Argonne team has some promising preliminary results in fitting force fields for diverse Li_xNiO_2 and NMC111 structures with high R^2 on the force and energy predictions. Example results for Li_xNiO_2, and NMC111 are shown in Figure II.9.R.9. We plan to add more training geometries from Artrith *et al* considering substituents for Ni.[21], [22] DeepMDkit and related software will be a strong choice moving forward as it will be well suited to run at scale on a variety of HPC resources, and shows signs of a rapidly growing user community. In one recent publication, DeepMDkit was shown to scale to a 113,246,208 atom Cu system at 1ns per day with a peak performance of 86 PFLOPS.[23]

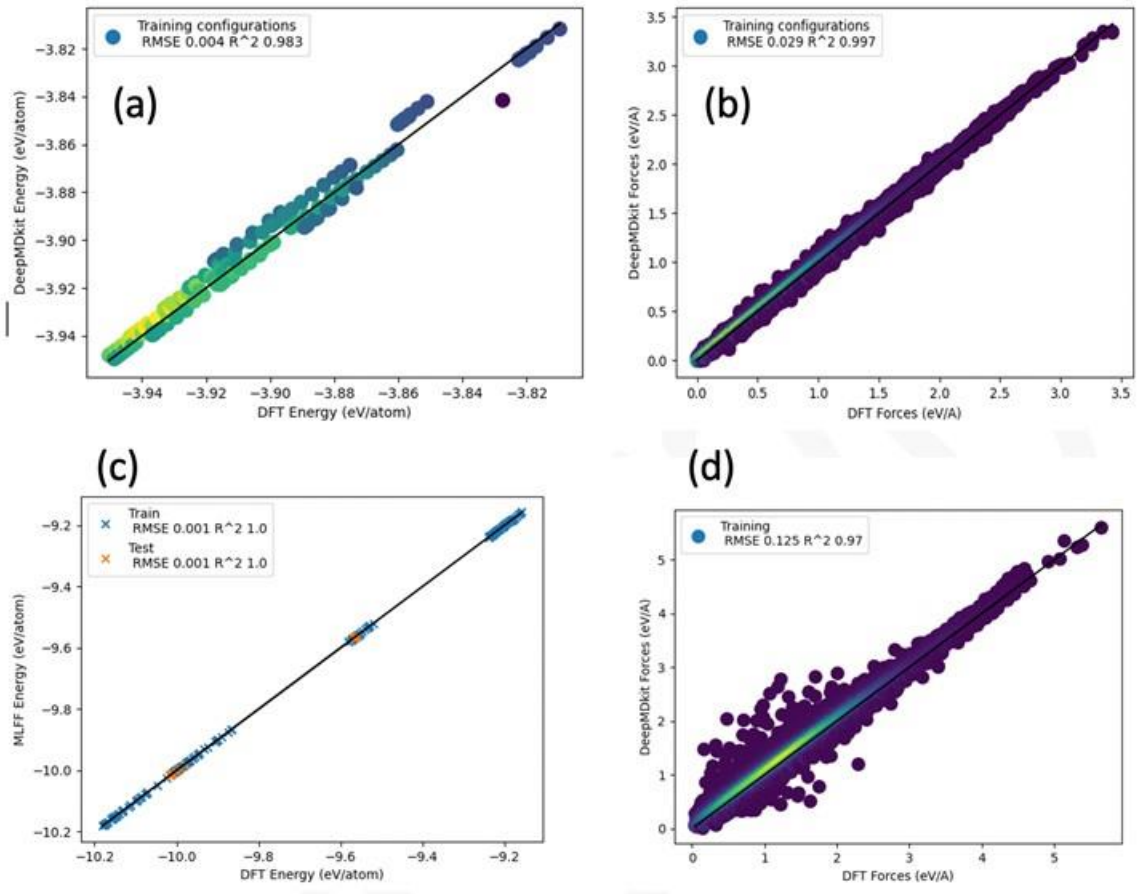

Figure II.9.R.9 DeepMDkit training (a) energy predictions and (b) force predictions for LixNiO2 structures compared with DFT training data (c) Training and test energy predictions and (d) training force predictions for NMC-111 structures compared with DFT training data.

DFT calculations are a powerful tool for predicting the electronic structure of elements and compounds at 0K. However, taking these predictions to finite temperatures is challenging, in principal due to difficulties in evaluating entropy. It was demonstrated by both experiments and computations that the free energy – which includes a temperature times entropy term – can change the relative stability of various phases at room or higher temperatures. In some cases, mixtures can be more stable than individual phases. The thermodynamics of $LiNiO_2$–NiO_2 pseudo-binary sub-system has been studied using the Calculation of Phase Diagram (CALPHAD) approach coupled with ab initio calculations and sublattice models of the O1, H1-3, and other O3 ordered and disordered phases.[24] The study concluded that LiNiO2 and NiO2 form an ideal solution. However, this result was obtained based on the calculated 0K enthalpy of mixing and the assumption that the entropy consists of an ideal configurational term. It is not surprising that the prediction was an ideal solution. Similarly, the relative stability of the O1, H1-3, and O3 phases was based on 0K results. In this project, we are evaluating all entropy terms (configurational, vibrational and electronic) and using the Gibbs free energy to predict finite temperature properties and stability of various phases. To that end, we are examining temperature effects using state of the art thermodynamic modeling that incorporates DFT, AIMD and ML results, for the particular case of the Li-Ni-M-O system, where M is a metal. The approach was developed by members of the team and was successfully applied to complex, non-stoichiometric oxides.[25] We estimate obtaining significant results during next two quarters.

Key Publications

Presentations:

1. Stan, Marius, Noah Paulson, Joseph Libera, Debolina Dasgupta, Joshua Gabriel, John Low, Juan Garcia, Hakim Iddir. "Intelligent Material and Process Design." (Invited) Northwestern University. July 20, 2020.

2. Gabriel, Joshua, Juan Garcia Sanchez, Noah Paulson, John Low, Marius Stan and Hakim Iddir. "Machine learning force fields for Li-ion cathodes." Atomistic Simulations for Industrial Needs, August 5, 2020-August 7, 2020.

References

1. G. Kresse and J. Furthmüller, “Efficiency of ab-initio total energy calculations for metals and semiconductors using a plane-wave basis set,” Comput. Mater. Sci., 1996, 6, 1, 15–50, doi: 10.1016/0927-0256(96)00008-0.

2. G. Kresse and J. Hafner, “Ab Initio molecular dynamics for liquid metals,” Phys. Rev. B, 1993, 47, 1, 558–561, doi: 10.1103/PhysRevB.47.558.

3. J. Heyd, G. E. Scuseria, and M. Ernzerhof, “Hybrid functionals based on a screened Coulomb potential,” J. Chem. Phys., 2003, 118, 18, 8207–8215, doi: 10.1063/1.1564060.

4. L. Zhang, J. Han, H. Wang, W. Saidi, R. Car, and W. E, “End-to-end Symmetry Preserving Inter-atomic Potential Energy Model for Finite and Extended Systems,” in Advances in Neural Information Processing Systems 31, S. Bengio, H. Wallach, H. Larochelle, K. Grauman, N. Cesa-Bianchi, and R. Garnett, Eds. Curran Associates, Inc., 2018, 4436–4446.

5. R. Koerver et al., “Chemo-mechanical expansion of lithium electrode materials – on the route to mechanically optimized all-solid-state batteries,” Energy Environ. Sci., 2018, 11, 8, 2142–2158, doi: 10.1039/C8EE00907D.

6. J. Sun, A. Ruzsinszky, and J. P. Perdew, “Strongly Constrained and Appropriately Normed Semilocal Density Functional,” Phys. Rev. Lett., 2015, 115, 3, 036402, doi: 10.1103/PhysRevLett.115.036402.

7. J. Sun et al., “Accurate first-principles structures and energies of diversely bonded systems from an efficient density functional,” Nat. Chem., 2016, 8, 9, 831–836, doi: 10.1038/nchem.2535.

8. A. Khorshidi and A. A. Peterson, “Amp: A modular approach to machine learning in atomistic simulations,” Comput. Phys. Commun., 2016, 207, 310–324, doi: 10.1016/j.cpc.2016.05.010.

9. J. Snoek, H. Larochelle, and R. P. Adams, “Practical Bayesian Optimization of Machine Learning Algorithms,” in Advances in Neural Information Processing Systems 25, F. Pereira, C. J. C. Burges, L. Bottou, and K. Q. Weinberger, Eds. Curran Associates, Inc., 2012, 2951–2959.

10. A. P. Bartók, M. C. Payne, R. Kondor, and G. Csányi, “Gaussian Approximation Potentials: The Accuracy of Quantum Mechanics, without the Electrons,” Phys. Rev. Lett., 2010, 104, 13, 136403, doi: 10.1103/PhysRevLett.104.136403.

11. L. Zhang, D.-Y. Lin, H. Wang, R. Car, and W. E, “Active learning of uniformly accurate interatomic potentials for materials simulation,” Phys. Rev. Mater., 2019, 3, 2, 023804, doi: 10.1103/PhysRevMaterials.3.023804.

12. M. Bianchini, M. Roca-Ayats, P. Hartmann, T. Brezesinski, and J. Janek, "There and Back Again—The Journey of LiNiO2 as a Cathode Active Material," Angew. Chem. Int. Ed., 2019, 58, 31, 10434–10458, doi: 10.1002/anie.201812472.

13. A. O. Kondrakov et al., "Charge-Transfer-Induced Lattice Collapse in Ni-Rich NCM Cathode Materials during Delithiation," J. Phys. Chem. C, 2017, 121, 44, 24381–24388, doi: 10.1021/acs.jpcc.7b06598.

14. M. E. Arroyo y de Dompablo, A. Van der Ven, and G. Ceder, "First-principles calculations of lithium ordering and phase stability on LixNiO2" Phys. Rev. B, 2002, 66, 6, 064112, doi: 10.1103/PhysRevB.66.064112.

15. J. Klimeš, D. R. Bowler, and A. Michaelides, "Chemical accuracy for the van der Waals density functional," J. Phys. Condens. Matter, 2009, 22, 2, 022201, doi: 10.1088/0953-8984/22/2/022201.

16. A. Chakraborty, M. Dixit, D. Aurbach, and D. T. Major, "Predicting accurate cathode properties of layered oxide materials using the SCAN meta-GGA density functional," Npj Comput. Mater., 2018, 4, 1, 1–9, doi: 10.1038/s41524-018-0117-4.

17. H. Peng, Z.-H. Yang, J. P. Perdew, and J. Sun, "Versatile van der Waals Density Functional Based on a Meta-Generalized Gradient Approximation," Phys. Rev. X, 2016, 6, 4, 041005, doi: 10.1103/PhysRevX.6.041005.

18. E. B. Isaacs, S. Patel, and C. Wolverton, "Prediction of Li intercalation voltages in rechargeable battery cathode materials: Effects of exchange-correlation functional, van der Waals interactions, and Hubbard U" Phys. Rev. Mater., 2020, 4, 6, 065405, doi: 10.1103/PhysRevMaterials.4.065405.

19. L. Croguennec, C. Pouillerie, and C. Delmas, "NiO2 Obtained by Electrochemical Lithium Deintercalation from Lithium Nickelate: Structural Modifications," J. Electrochem. Soc., 2000, 147, 4, 1314, doi: 10.1149/1.1393356.

20. J. Harl, L. Schimka, and G. Kresse, "Assessing the quality of the random phase approximation for lattice constants and atomization energies of solids," Phys. Rev. B, 2010, 81, 11, 115126, doi: 10.1103/PhysRevB.81.115126.

21. N. Artrith and A. Urban, "An implementation of artificial neural-network potentials for atomistic materials simulations: Performance for TiO2" Comput. Mater. Sci., 2016, 114, 135–150, doi: 10.1016/j.commatsci.2015.11.047.

22. A. M. Cooper, J. Kästner, A. Urban, and N. Artrith, "Efficient training of ANN potentials by including atomic forces via Taylor expansion and application to water and a transition-metal oxide," Npj Comput. Mater., 2020, 6, 1, 1–14, doi: 10.1038/s41524-020-0323-8.

23. D. Lu et al., "86 PFLOPS Deep Potential Molecular Dynamics simulation of 100 million atoms with ab initio accuracy," Comput. Phys. Commun., 2021, 259, 107624, doi: 10.1016/j.cpc.2020.107624.

24. K. Chang, B. Hallstedt, and D. Music, "Thermodynamic description of the LiNiO2–NiO2 pseudo-binary system and extrapolation to the Li(Co,Ni)O2–(Co,Ni)O2 system," Calphad, 2012, 37, 100–107, doi: 10.1016/j.calphad.2012.02.006.

25. Z.-G. Mei and M. Stan, "Pressure-induced phase transitions in UN: A density functional theory study," J. Alloys Compd., 2014, 588, 648–653, doi: 10.1016/j.jallcom.2013.11.143.

Acknowledgements

Juan Garcia, Noah Paulson, Joshua Gabriel, Jhon Low, Marius Stan, Jason Croy, Christopher Johnson and Eungje Lee. Support for High Performance Computing at ANL and NREL is gratefully acknowledged. Support from the U. S. Department of Energy (DOE), Vehicle Technologies Office is gratefully acknowledged

II.10 Beyond Li-ion R&D: Lithium Sulfur Batteries

II.10.A Novel Chemistry: Lithium-Selenium and Selenium-Sulfur Couple (ANL)

Khalil Amine, Principal Investigator
Argonne National Laboratory
9700 South Cass Avenue
Lemont, IL 60439-4837
E-mail: amine@anl.gov

Tien Duong, DOE Technology Development Manager
U.S. Department of Energy
E-mail: Tien.Duong@ee.doe.gov

Start Date: October 2013 End Date: Project continuation evaluated annually
Project Funding: $500,000/yr DOE share: $500,000/yr Non-DOE share: $0

Project Introduction

Lithium/sulfur (Li/S) batteries have attracted extensive attention for energy storage applications due to the high theoretical energy density (2600 Wh kg^{-1}) and earth abundance of sulfur.[1] Recently, selenium and selenium-sulfur systems have also received considerable attention as cathode materials for rechargeable batteries because of the high electronic conductivity (20 orders of magnitude higher than sulfur) and high volumetric capacity (3254 mAh cm^{-3}) of selenium.[2] Selenium-sulfur mixtures are miscible in a wide concentration range, and many Se-S composites can be prepared, including Se_5S, Se_5S_2, Se_5S_4, SeS, Se_3S_5, SeS_2, SeS_7, and even materials with a small amount of Se such as SeS_{20}.[2] These Se-S composites offer higher theoretical specific capacities than Se alone and improved conductivity compared to pure S. However, similar to Li/S batteries, two major obstacles resulting from lithium polysulfides/polyselenides shuttle and lithium dendrite formation remain huge challenges for long-life Li/Se-S batteries.[3] The former is due to the dissolution and migration of polysulfides/polyselenides intermediates in the conventional ether-based electrolytes, which could induce severe parasitic reactions with Li metal and hence formation of porous or mossy Li metal. The latter is originated from the parasitic reactions of lithium metal with the electrolytes, leading to the formation of fragile solid electrolyte interphase (SEI) on Li metal, further uncontrolled lithium dendrite growth and eventually dead lithium. These parasitic reactions are the direct cause for the rapid capacity fade and poor coulombic efficiency of Li/S and Li/Se-S batteries.

Via advanced diagnostic tools including synchrotron X-ray probes and computational modeling, the team led by Dr. Khalil Amine at Argonne National Laboratory (ANL) is focusing on the development of rational cathode structure designs and exploration of novel electrolytes to effectively eliminate these parasitic reactions and suppress simultaneously the shuttle effect and lithium dendrite formation during long-term cycling.

Objectives

The objective of this project is to develop novel Li/Se-S batteries with high energy density (500 Wh kg^{-1}) and long life (>500 cycles) along with low cost and high safety.

Approach

To prevent the dissolution of polysulfides and increase the active material utilization, S or Li_2S is generally impregnated in a conducting carbon matrix. However, this approach makes it difficult to increase the loading density of practical electrodes. It is proposed here to solve the above barriers by the following approaches: (1) partial replacement of S with Se, (2) confinement of the SeS_x in a porous conductive matrix with high pore volume, and (3) exploration of advanced electrolytes that can suppress shuttle effect and lithium dendrite growth.

COLLABORATIONS:

1. Materials and electrolytes development (Dr. Guiliang Xu (CSE), Rachid Amine (MSD) of ANL
2. Synchrotron X-ray characterization (Dr. Yang Ren and Dr. Chengjun Sun at APS of ANL)
3. Computational modeling (Dr. Larry Curtiss and Dr. Anh Tuan Ngo at MSD of ANL)

Results

Design and synthesis of new carbon host for Li/Se-S batteries

In this year, we prepared a metal-organic framework (MOF)-derived core-shell hollow (CSH) spheres as the host material to enhance the redox kinetics and suppress the shuttle effect of the Se-S cathode.

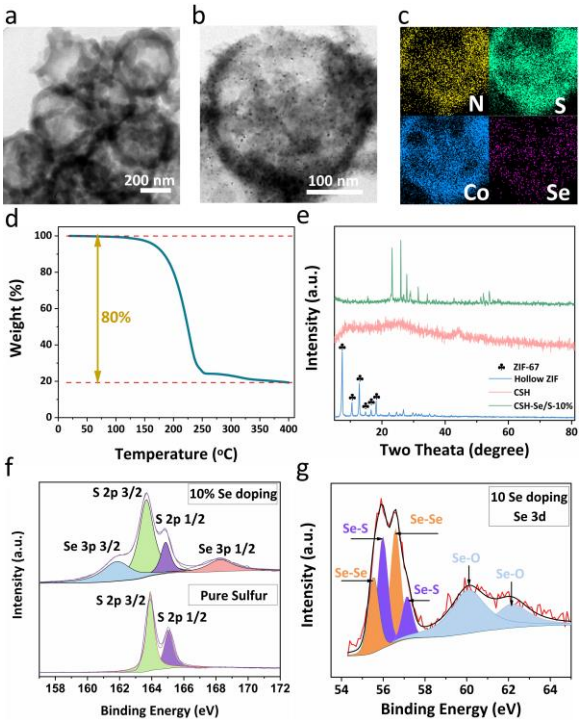

Figure II.10.A.1 Morphology and composition characterizations of cathode materials. (a) TEM image of CSH host material. (b, c) TEM image of CSH/S-Se cathode material and corresponding EDS mapping of N, S, Co, and Se. (d) TGA curve of CSH/S-Se-10% cathode. (e) XRD patterns of hollow ZIF, CSH, and CSH/S-Se-10%. (f) High-resolution XPS spectra of S 2p for CSH/S-Se-10% and CSH/S cathode materials. (g) High-resolution XPS spectrum of Se 3d of CSH/S-Se-10% cathode material.

As shown in the transmission electron microscopy (TEM) image of CSH spheres (Figure II.10.A.1a), a hollow core-shell structure with a diameter of 180 nm was obtained. TEM image (Figure II.10.A.1b) of CSH/S-Se revealed that Se-S particles can be identified within the hollow chamber, and the corresponding energy dispersive X-ray spectroscopy (EDS) mapping results (Figure II.10.A.1c) further confirmed the existence of Se and S inside the hollow chamber. In addition, uniformly dispersed Co atoms can be observed as well, which not only catalyzed the graphitization of carbon host to improve the electrical conductivity[4], but also acted as additional binding and catalyzing sites to effectively immobilize the dissolved polysulfides/polyselenides[5] and catalyze the subsequent reduction reaction[6]. The as-prepared cathode material is denoted as CSH/S-Se-*x*% (*x* is the weight ratio of doping Se in S-Se). The weight ratio of Se-S active material in the cathode composite was determined to 80 wt.% by thermogravimetric analysis (Figure II.10.A.1d). X-ray diffraction (XRD) characterizations (Figure II.10.A.1e) showed that, after Se-S infiltration, the XRD pattern of the as-prepared CSH/S-Se-10% cathode is different from that of S_8 (ICSD code: 63082), indicating the formation of a new phase after Se doping. X-ray photoelectron spectroscopy (XPS) results for the CSH/S-Se-10% and CSH/S

(insertion of pure sulfur into the CSH) further revealed that after doping with 10 wt.% Se, Se 3p 1/2 (168.0 eV) and Se 3p 3/2 (161.8 eV) bonding can be identified in the CSH/S-Se-10% cathode, while the CSH/S S 2p spectrum did not show the Se 3p bonding (Figure II.10.A.1f). Moreover, we fitted the Se 3d XPS spectrum and identified both Se-S (56.0 eV and 57.2 eV) and Se-Se (55.5 eV and 56.6 eV) bonds in the CSH/S-Se-10% cathode, confirming the formation of a new phase rather than a physical mixture of S and Se.

Electrochemical evaluation of the as-prepared Se-S cathode in conventional ether and fluorinated ether-based electrolytes

We evaluated the electrochemical performance of the as-prepared cathodes in conventional (DME-based) ether and fluorinated (HFE-based) ether based electrolytes. As shown in Figure II.10.A.2a, without Se doping, the cathode can deliver a specific capacity of only 600 mAh g^{-1} in HFE-based electrolyte.

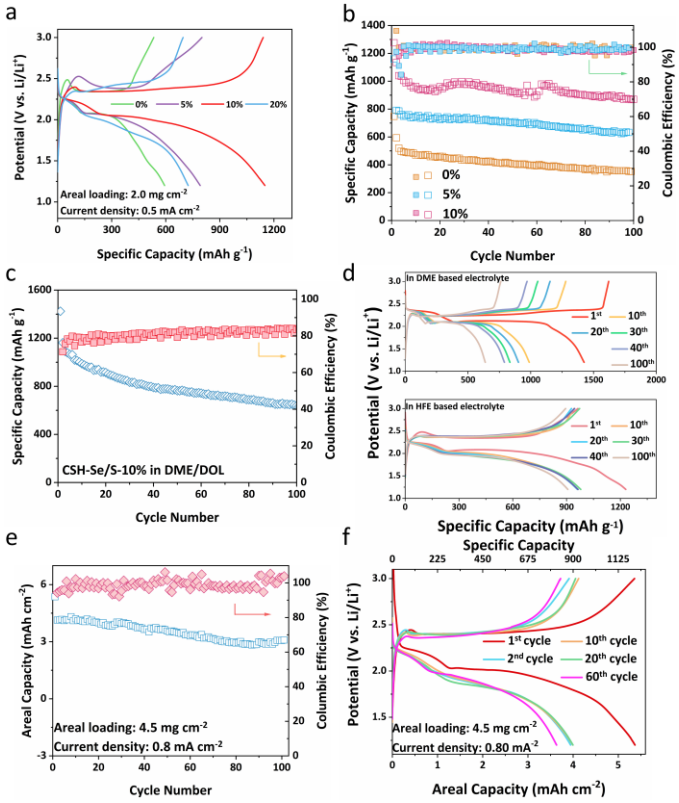

Figure II.10.A.2 Electrochemical characterizations of various cathode materials. (a) Voltage profiles and (b) cycle performance of CSH/S-Se-x% (x ranging from 0 to 20) cathode materials. (c) Cycling performance of CSH/S-Se-10% cathode in DME-based electrolyte. (d) Voltage profiles of CSH/S-Se-10% cathode in HFE- and DME-based electrolytes. (e) Cycling performance and (f) Charge/discharge curves of high areal loading cathode in HFE-based electrolyte.

After Se doping, it is striking to find that the reversible capacities dramatically increased, indicating that Se doping can significantly improve the S redox kinetics. As shown in Figure II.10.A.2b, the CSH/S-Se-10% cathode delivered a much higher capacity than the CSH/S and CSH/S-Se-5% cathodes within 100 cycles. The capacity retention was 84% with a high reversible capacity of 900 mAh g^{-1}. Nevertheless, they can all achieve stable cycling performance and high Coulombic efficiency (> 99.5%) during cycling, indicating that the HFE-based electrolytes can mitigate the shuttle effect.

The CSH/S-Se-10% cathode was cycled in the DME-based electrolyte as well for comparison. As shown in Figure II.10.A.2c and Figure II.10.A.2d, the Coulombic efficiencies of the cell in the DME-based electrolyte were very low (< 80%) during cycling, which can be attributed to the severe irreversible reactions between Li metal and dissolved polysulfides/polyselenides. As a result, the capacity retention rate of the CSH/S-Se-10% cathode in the DME-based electrolyte after 100 cycles was only 44.61%. We further characterized the cell

performance under a higher Se-S loading to increase the overall energy density. As shown in Figure II.10.A.2e and Figure II.10.A.2f, a thick cathode with Se-S loading of 4.5 mg cm^{-2} can achieve a high initial reversible areal capacity of 5.37 mAh cm^{-2} at 0.8 mA cm^{-2}. After cycling for 100 cycles, it can still maintain a high areal capacity of 3.33 mAh cm^{-2}, which is comparable to the typical areal capacity of state-of-the-art LIBs (3 mAh cm^{-2}).

Li stripping/plating reversibility comparison in conventional ether and fluorinated ether based electrolytes

Li metal plays an essential role in the cycling performance of Li/Se-S batteries especially in pouch-cell configuration. Thus, we further evaluated Li stripping/plating reversibility in two electrolytes by using Li|Cu cells and Li|Li symmetric cells. As evident in Figure II.10.A.3a-c, the Li stripping/plating Coulombic efficiency and cycling stability in Li|Cu cells improved remarkably in the HFE-based compared to DME-based electrolytes. At a current density of 1.0 mA cm^{-2}, the Li stripping/plating Coulombic efficiency in the HFE-based electrolytes improved to > 96.26% within 300 cycles (Figure II.10.A.3a and Figure II.10.A.3c). In contrast, the poor stability and the low Coulombic efficiency in the DME-based electrolyte (Figure II.10.A.3b and Figure II.10.A.3c) suggest severe parasitic reactions of the Li metal anode with the electrolyte. Therefore, although the polysulfide shuttle issue in the DME-based electrolytes could be addressed by rational cathode design, the intrinsic poor Li stripping/plating reversibility in the DME-based electrolytes would still cause rapid cell failure in the practical Li-S pouch cells.

Figure II.10.A.3d further compares the performance of Li|Li symmetric cells with an areal capacity of 1.0 mAh cm^{-2} at 1.0 mA cm^{-2} in two electrolytes. The Li|Li symmetric cell in the HFE-based electrolyte demonstrates a flat voltage plateau with a small polarization of around 33 mV, indicating a smooth and stable Li stripping/plating process in the HFE-based electrolyte. In contrast, the Li|Li symmetric cell in the DME-based electrolyte shows a rather unstable voltage profile, and its overpotential is much higher than that in the HFE-based electrolyte. We further increased the areal capacity of the Li|Li symmetric cell to 4.0 mAh cm^{-2}. As shown in Figure II.10.A.3e, even under such a high areal capacity, the Li|Li symmetric cell in HFE-based electrolyte can still attain excellent cycling stability for over 840 hours with a small polarization of 25 mV.

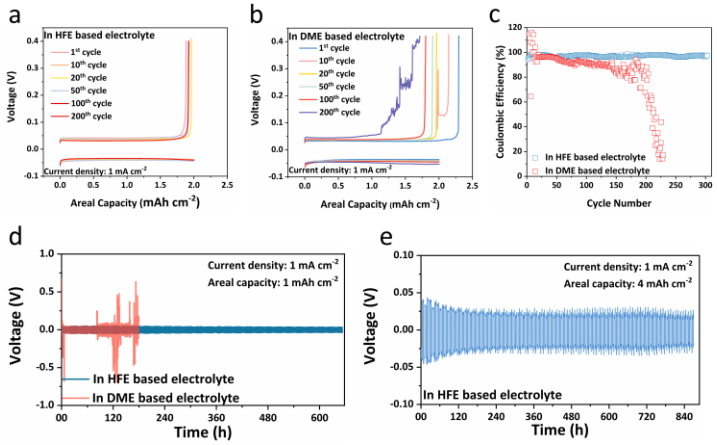

Figure II.10.A.3 Li stripping/plating in HFE-and DME-based electrolyte using Li|Cu and Li|Li cells. Li metal plating/stripping profiles of Li|Cu cells in (a) HFE-based electrolyte and (b) DME-based electrolyte. (c) Coulombic efficiencies of Li|Cu cells with HFE- and DME-based electrolytes. (d) Cycling performance of Li|Li symmetric cells with the areal capacity of 1 mAh cm^{-2} in HFE- and DME-based electrolytes under 1 mA cm^{-2}. e) Cycling performance of Li|Li symmetric cell with the areal capacity of 4 mAh cm^{-2} under 1 mAh cm^{-2} in HFE-based electrolyte.

Interface and morphology characterization

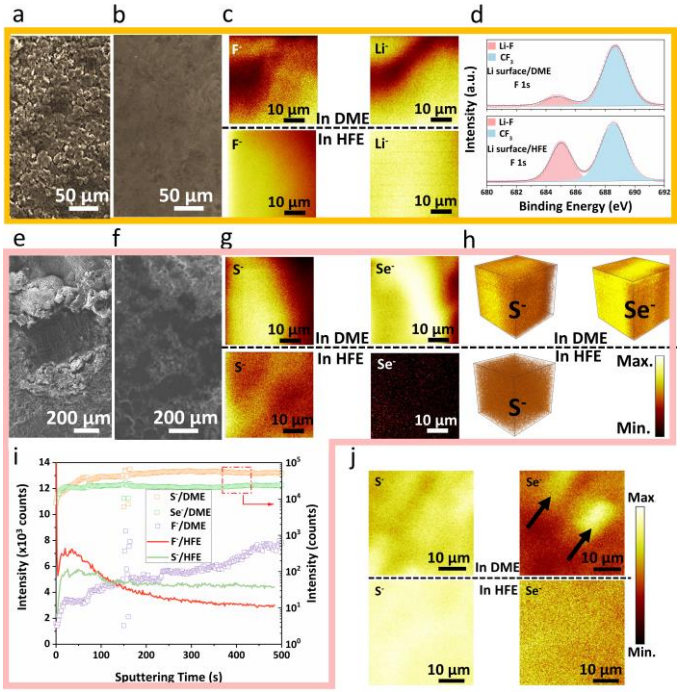

Figure II.10.A.4 Morphology and interphase analysis of cycled Cu foil, Li metal anode, and Se-S cathode. SEM images of cycled Cu foils of Li||Cu cells in (a) DME-based electrolyte and (b) HFE-based electrolyte. (c) ToF-SIMS mapping (F- and Li-) of cycled Cu foils for Li|Cu cells in two electrolytes. (d) High-resolution XPS F 1s spectra of cycled Li metal anode of Li|Cu cells in two electrolytes. SEM images of cycled Li metal anode of Li/Se-S cells in (e) DME-based electrolyte and (f) HFE-based electrolyte. (g) ToF-SIMS mapping, and (h) three-dimensional (3D) element reconstruction (S- and Se-) and (i) depth profile of cycled Li metal anode in Li/Se-S cells with two electrolytes. (j) ToF-SIMS elements mapping (S- and Se-) of cycled CSH/S-Se-10% cathode in two electrolytes.

To gain the underlying mechanism, we carried out XPS, scanning electron microscopy (SEM), and time-of-flight secondary ion mass spectrometry (ToF-SIMS) characterization to investigate the morphology and interphase properties of the cycled cathode and anode in both electrolytes. Figure II.10.A.4a and Figure II.10.A.4b show the morphologies of deposited Li on the surface of Cu foil in Li|Cu cells using DME- and HFE- based electrolytes, respectively. As shown, isolated metallic lithium dendrites were identified on the Cu foil surface after 100 cycles in the DME-based electrolyte (Figure II.10.A.4a). This morphology is caused by the continuous parasitic reaction between Li metal and the electrolyte molecules, resulting in the low Coulombic efficiency and poor cycling stability of the Li|Cu cell in DME-based electrolyte. In contrast, in the HFE-based electrolyte, the Cu foil has a dense and uniform surface without dendrite formation (Figure II.10.A.4b), suggesting a smooth and stable Li stripping/plating process in HFE-based electrolyte.

To analyze the distribution of the elements of the Li deposition process on the Cu surface along the thickness direction, ToF-SIMS characterizations were conducted on the cycled Cu foil in both electrolytes. As shown in Figure II.10.A.4c, the Li^- and F^- signals exhibit homogeneous distributions in the HFE-based electrolyte, further confirming the dendrite-free Li stripping/plating chemistry and the formation of a robust SEI layer. In contrast, metallic Li and non-uniform SEI layer were identified when cycled in DME-based electrolytes. We further analyzed the XPS F 1s and Li 1s spectra of cycled Li foil in both electrolytes to unravel the composition of their SEI. As shown in Figure II.10.A.4d, a much higher Li-F content SEI can be identified on the surface of the Li foil after cycling in the Li|Cu cell with HFE-based than the DME-based electrolyte.

We further carried out morphology and interphase analyses on the cycled anode and cathode from actual Li/Se-S cells. As shown in Figure II.10.A.4e, after cycling in the DME-based electrolyte, many irregular

deposition products were found on the surface of the cycled Li foil. Strikingly, in the case of HFE-based electrolyte, the cycled Li metal exhibited a uniform and homogeneous morphology (Figure II.10.A.4f). As further shown in Figure II.10.A.4g and Figure II.10.A.4h, a large amount of S and Se elements was found on the surface of the cycled Li foil in the Li/Se-S cell with DME-based electrolyte, corresponding to a severe shuttle effect. In contrast, in the HFE-based electrolyte, only a weak S^- signal was detected, and a Se^- signal could not be detected (Figure II.10.A.4g), confirming that the shuttle effect had been effectively eliminated. As clearly shown in the ToF-SIMS depth profiling of the cycled Li metal anodes (Figure II.10.A.4i), high S^- and Se^- intensities were observed on the cycled Li foil surface in the DME-based electrolyte. Nevertheless, Se^- was not found on the cycled Li foil surface in the HFE-based electrolyte, further confirming the shuttle-free chemistry of Se-S cathode in this electrolyte. Moreover, the higher F^- intensity on the outermost surface of cycled Li foil in HFE-based electrolyte confirmed the formation of a robust F-rich SEI layer, which does not appear on the Li foil surface in DME-based electrolyte. Figure II.10.A.4j shows the elemental mapping of S^- and Se^- on cycled cathode surfaces. Several isolated sulfur and selenium species were identified on the cycled cathode in DME-based electrolyte, which can be explained by the dissolution and deposition of polysulfides/polyselenides. In sharp contrast, in HFE-based electrolyte, both S^- and Se^- were uniformly and homogeneously distributed on the cathode, indicating no polysulfides/polyselenides were dissolved in the bulk electrolyte.

Conclusions

Electrolyte modulation has been reported to simultaneously suppress polysulfide shuttle effect and lithium dendrite formation of Li/S batteries. However, the sluggish S redox kinetics, especially under high S loading and lean electrolyte operation, has been intensively ignored, which dramatically limits the cycle life and energy density of practical Li/S pouch cells. We have demonstrated that a rational combination of cathode design and electrolyte modulation is necessary to simultaneously mitigate polysulfide shuttle and Li dendrite formation as well as poor cathode redox kinetics in Li/S batteries. As characterized by XPS and ToF-SIMS, ultra-stable Li stripping/plating and effective elimination of the shuttle effect were successfully enabled by the formation of a homogeneous and robust F-rich SEI layer on the surface of the Li metal anode and Se-S cathode. Moreover, due to the rational combination of Se doping and the hollow core-shell host structure, the Se-S cathode electrochemical kinetics was remarkably boosted. As a result, a shuttle- and dendrite-free Li/Se-S cell with high specific capacity has been successfully tested with high Se- S areal capacity loading (> 4 mAh cm^{-2}) and low E/S ratio (10 µL mg^{-1}), greatly improving the cycling stability, Coulombic efficiency, and safety of the Li/Se-S battery.

Key Publications

Publications/Patents

1. Zhao, C.; Xu, G. L.*; Zhao, T.*; Amine, K.*. Beyond Polysulfides Shuttle and Li Dendrite Formation: Addressing the Sluggish S Redox Kinetics for Practical High Energy Li-S batteries. *Angew. Chem. Int. Ed.* **2020**, 17634-17640.

2. Amine, R.; Liu, J.; Acznik, I.; Sheng, T.; Lota, K.; Sun, H.; Sun, C. J.; Fic, K.; Zuo, X.; Ren, Y.; EI-Hady, D. A.; Alshitari, W.; Al-Bogami, A. S.; Chen, Z.; Amine, K. * and Xu, G. L. *. Regulating the Hidden Solvation-Ion-Exchange in Concentrated Electrolytes for Stable and Safe Lithium Metal Batteries. *Adv. Energy Mater.*, **2020**, 2000901.

References

1. Z.W. Seh, Y. M. Sun, Q. F. Zhang, and Y. Cui. "Designing High-Energy Lithium-Sulfur Batteries." Chemical Society Reviews 45, no. 20 (2016): 5605-34. DOI:10.1039/c5cs00410a.

2. A. Abouimrane, D. Dambournet, K. W. Chapman, P. J. Chupas, W. Weng, and K. Amine. "A New Class of Lithium and Sodium Rechargeable Batteries Based on Selenium and Selenium-Sulfur as a Positive Electrode." Journal of the American Chemical Society 134, no. 10 (2012): 4505-08. DOI: 10.1021/ja211766q.

3. Y. Cui, A. Abouimrane, J. Lu, T. Bolin, Y. Ren, W. Weng, C. Sun, et al. "(De)Lithiation Mechanism of Li/SeS_x (X = 0-7) Batteries Determined by in Situ Synchrotron X-Ray Diffraction and X-Ray Absorption Spectroscopy." Journal of the American Chemical Society 135, no. 21: 8047-56. DOI: 10.1021/ja402597g.

4. J. Tang, R. R. Salunkhe, J. Liu, N. L. Torad, M. Imura, S. Furukawa, Y. Yamauchi, " Thermal Conversion of Core–Shell Metal–Organic Frameworks: A New Method for Selectively Functionalized Nanoporous Hybrid Carbon" Journal of the American Chemical Society 137, no. 4 (2015):1572-1580. DOI: 10.1021/ja511539a.

5. G. Zhou, S. Zhao, T. Wang, S. Yang, B. Johannessen, H. Chen, C. Liu, Y. Ye, Y. Wu, Y. Peng, C. Liu, S. P. Jiang, Q. Zhang, Y. Cui, " Theoretical Calculation Guided Design of Single-Atom Catalysts toward Fast Kinetic and Long-Life Li–S Batteries" Nano Letters 20, no. 2 (2020): 1252-1261. DOI: 10.1021/acs.nanolett.9b04719.

6. Z. Du, X. Chen, W. Hu, C. Chuang, S. Xie, A. Hu, W. Yan, X. Kong, X. Wu, H. Ji, " Cobalt in Nitrogen-Doped Graphene as Single-Atom Catalyst for High-Sulfur Content Lithium–Sulfur Batteries" Journal of the American Chemical Society 141, no. 9 (2019): 3977-3985. DOI: 10.1021/jacs.8b12973.

Acknowledgements

Support from Tien Duong of the U.S. DOE's Office of Vehicle Technologies Program is gratefully acknowledged. I would like to thank Dr. Guiliang Xu at ANL for the major contribution to this project.

II.10.B Development of High Energy Lithium-Sulfur Batteries (PNNL)

Dongping Lu, Principal Investigator
Pacific Northwest National Laboratory
902 Battelle Blvd.
Richland, WA 99354
E-mail: dongping.lu@pnnl.gov

Jun Liu, Co-Principal Investigator
Pacific Northwest National Laboratory
902 Battelle Blvd.
Richland, WA 99354
E-mail: jun.liu@pnnl.gov

Tien Duong, DOE Technology Development Manager
U.S. Department of Energy
E-mail: Tien.Duong@ee.doe.gov

Start Date: October 1, 2015 End Date: September 30, 2021
Project Funding: $400,0000 DOE share: $400,0000 Non-DOE share: $0

Project Introduction

Lithium-sulfur (Li-S) battery has a high theoretical energy (~2300 Wh kg^{-1}) coupled with an extremely low cost, making it one of the most promising battery technologies to meet the DOE target of < $80/kWh for vehicle electrification. Despite advances in materials research and mechanism study, deployment of the Li-S technology is still hindered by the low practical energy and limited cycle life. A crucial prerequisite for delivering a high energy Li-S battery is the integration of a high-loading sulfur cathode, a lean electrolyte amount, and a limited Li anode. For example, to reach a cell energy greater than 300 Wh/kg for a cell with a capacity of 2Ah, a cathode loading of > 4 mg S/cm^2 and an E/S (electrolyte volume/sulfur mass) ratio < 3 µL/mg are required. However, simultaneous application of these parameters often leads to the rapid deterioration of the cell performance. Fundamental mechanisms of the cell failure are still not very clear; materials that can fulfill both high energy density and long cycle life of the Li-S batteries are still a significant challenge. In our study of the high-loading sulfur cathode, electrode porosity was identified as one of the key parameters in cathode design, playing a significant role on both cell energy and cycle life. Compared to the dense NMC cathodes (20%–30% porosity), sulfur cathodes are much thicker and more porous (>65%) at the same areal capacity. This is due to the low density and porous structures of S/C cathode materials. This severely penalizes the cell energy level due to the significant weight contribution of electrolyte. More importantly, at a low E/S ratio (e.g. < 3 µL/mg), the majority of electrolyte injected into the cell fills the pores in the cathode. This leaves only a small portion of electrolyte available to support cell cycling and compensate the unavoidable electrolyte consumption. Therefore, conserving more electrolyte by reducing electrode porosity is critical for extending the lifespan of Li-S batteries at realistic conditions. However, this solution comes with complications: extremely low porosity reduces the sulfur conversion kinetics and the utilization rate as a result of the suppressed electrolyte transport inside the high tortuosity electrode. Therefore, a clear understanding of the effect that electrode porosity/tortuosity has on reaction kinetics and cell life through combined experimental and simulation approaches is critical for the rational design of a sulfur electrode. Approaches that can improve electrolyte permeability in a low-porosity cathode and maintain sufficient Li^+ conductivity under lean electrolyte conditions are desired for both improved cell energy and cycle life.

Objectives

- Realize S utilization rate at least 1000 mAh/g in highly dense (porosity≤40%) and high-loading (> 4 mg/cm^2) S electrodes through the control of materials and electrode architectures.

- Demonstrate >80 cycles in the highly dense S electrodes at extremely lean electrolyte conditions (E/S≤4 μL/mg).

Approach

1. Control the synthesis of S/C secondary particles for high-loading S electrode fabrication at a relevant scale (>4 mg S/cm^2).
2. Optimize electrode architecture to realize S utilization rate >1000 mAh/g in high-loading and dense S electrodes (S > 4 mg/cm^2, porosity≤50%).
3. Demonstrate >80 cycles (80% capacity retention) in the high-loading and dense S electrodes at lean electrolyte conditions (E/S≤4 μL/mg).
4. Enable S electrodes at extremely low E/S ratio of ≤3 μL/mg and scale up material synthesis for high-energy Li-S pouch cell fabrication.

Results

1. Controllable synthesis of IKB/S composite with particle size from 5 to 100 μm for high-loading S electrodes (>4 mg S/cm²)

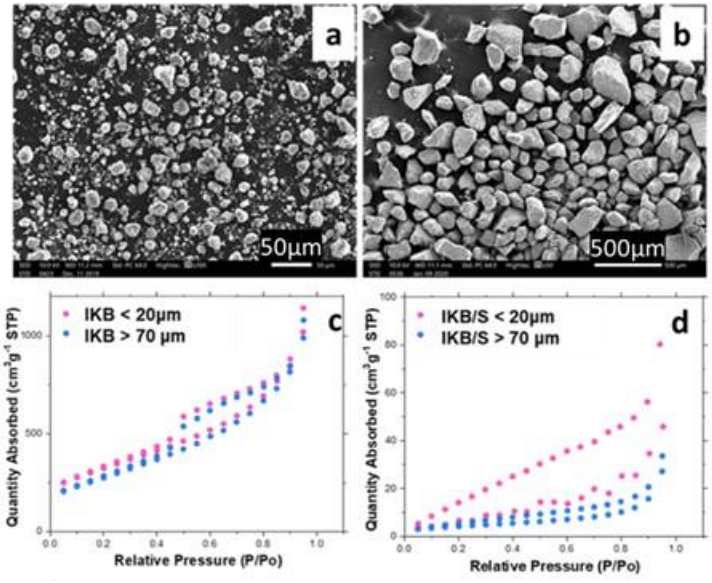

Figure II.10.B.1 SEM images of IKB particles with different particle sizes: (a) <20 μm and (b) >70 μm. BET absorption isotherms of (c) IKB and (d) IKB/S particles with different particle sizes.

Li-S pouch cells with practical energies >300 Wh/kg have been successfully demonstrated by using PNNL developed integrated Ketjen Black/sulfur (IKB/S) cathode materials. However, cycle life of the high-energy pouch cells is limited, mainly due to the electrolyte consumption and reaction heterogeneity of a high-loading electrodes under lean electrolyte conditions. The slow electrolyte diffusion/redistribution through the high-tortuosity electrode nanochannels is the root reason for low S utilization and subsequent reaction heterogeneity. This causes gradual electrode failure propagating from the center of the electrode to the edge, ultimately leading to the failure of cells. To address the electrolyte diffusion problems associated with the high-loading electrodes, electrode architecture should be optimized to enhance electrolyte permeability at a low porosity. The S/C material holds the biggest volume/mass proportion in S cathode; thus, its morphology plays a key role on the electrode tortuosity for a given electrode porosity. The IKB secondary particles with size ranging from 5 to 100 μm were synthesized and used as example materials to understand the correlation of electrode microstructure with the electrochemical properties. The particle was controlled through

stoichiometry of precursors and synthesis conditions. Figure II.10.B.1a and b show SEM images of the IKB particles with typical size of <20 μm and >70 μm, respectively. Typical morphologies of integrated secondary particles with irregular shapes were observed. The 70 μm powder has a tap density two-fold higher than that of 20 μm powder, which benefits improving the electrode energy density. Before loading S, the measured BET surfaces are 1155 m^2/g and 1001 m^2/g for 20 μm and 70 μm IKB powders, respectively (Figure II.10.B.1c). This means that the integration of particles does not cause a significant reduction in the electrode surface area, which ensures sufficient contact of S with conductive carbon. After S loading, the corresponding surfaces of IKB/S were reduced to 24 and 15 m^2/g, respectively. High-loading S electrodes (> 4 mg/cm^2) can be easily prepared with both types of particles and were calendered to 60 μm thick. The estimated electrode porosity is 44.7%, which is among the lowest porosities in a S cathode reported in the literature. The dense S electrodes with different size particles were used to study the effects of particle size on electrode structure and S reaction kinetics. Using a low-porosity electrode not only improves the cell volumetric energy density, but also conserves more electrolyte to support cell cycling, rather than filling the electrode pores.

2. *High S utilization rate (>1000 mAh/g) and improved cycle life of highly dense S electrodes (porosity ≤50%) at lean electrolyte conditions (E/S≤4 μL/mg).*

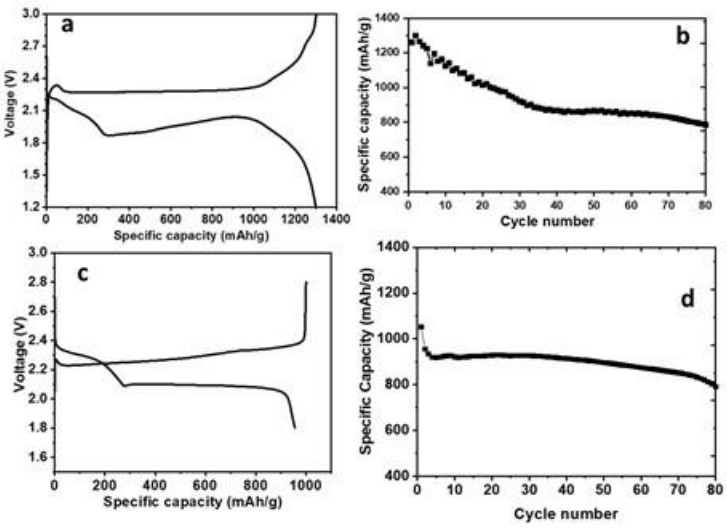

Figure II.10.B.2 Typical charge/discharge curves and cycling performance of S electrodes cycled in electrolytes with poor solubility for polysulfide (a, b) and liquid/polymer hybrid electrolytes (c, d). (Electrode: 4 mg S/cm^2, porosity <50%, and E/S = 4 μL/mg S, 0.05C for one formation cycle then 0.1C for cycling, at room temperature).

Lifespan of a Li-S cell highly depends on available liquid electrolyte especially for practical high-energy Li-S pouch cells. At lean electrolyte conditions, it is critical to utilize electrode structures featuring low porosity to reduce the volume of pore filling electrolyte, conserving the limited amount of electrolyte for cell cycling. It was found that dense electrodes composed of different size particles exhibit distinct cell performance. At the same level of porosity (e.g.<50%), the electrodes using >70 μm particles show much better performance compared to those using the < 20 μm particles. However, one remaining problem associated with the low porosity electrode is the accelerated cell decay at lean electrolyte conditions, potentially resulting from the stimulated polysulfide diffusion and physical loss. For a given electrode loading, higher Li polysulfide concentration gradient and shorter diffusion length (electrode thickness) are expected for dense electrodes with lower porosities and speed up the polysulfide diffusion, cross-over, and irreversible loss. Moreover, the increased tortuosity in the dense electrodes not only slows down the electrolyte diffusion, but also makes electrode passivation by Li sulfide deposits easier. To address this issue in high-loading and dense S cathodes, two approaches were used in our research. To suppress the polysulfide dissolution, new electrolytes with limited polysulfide solubility were prepared and tested (Figure II.10.B.2a and b). Compared to conventional 1M LiTFSI/DOL/DME electrolyte, the new electrolyte recipe enables much higher reversible capacities in the

dense S electrodes (4 mg/cm^2). Extremely high S utilization (~1300 mAh/g) was realized with the combination of dense electrode and new electrolyte recipe, indicating that suppressing polysulfide dissolution plays an important role in improving S utilization rate in the dense electrodes. After 80 cycles, the cell capacity drops from 1300 to 800 mAh/g, which is caused by consumption of the lean amount of electrolyte (E/S = 4 µL/mg). Inspired by the findings in the electrolytes with low solubility of polysulfide, we designed a new approach by integrating a second phase of polymer electrolyte into the electrode architecture. Thanks to the improved electrode wettability, the electrode porosity can be reduced further to < 40% without notably sacrificing the S reactivity. Figure II.10.B.2c shows typical charge/discharge curves of the dense S electrode (4 mg/cm^2, porosity < 40%) with the hybrid electrolytes. The reversible capacity stabilizes eventually at ~900 mAh/g at 0.1C after a formation cycle at 0.05 C. A much improved capacity retention was observed during the cycling, although the S utilization rate decreases slightly. After 80 cycles, a capacity of 792 mAh/g was obtained, which is 83% of the first cycle capacity (955 mAh/g) at 0.1 C. This means introduction of the polymer phase is helpful to enhance the cell capacity retention in very dense electrodes and at lean electrolyte conditions. A careful optimization of the electrode architecture and electrolyte composition is needed to take advantage of both low-polysulfide-soluble electrolytes and hybrid electrolyte design.

3. Impact of particle size on the electrochemical performance of dense S electrode

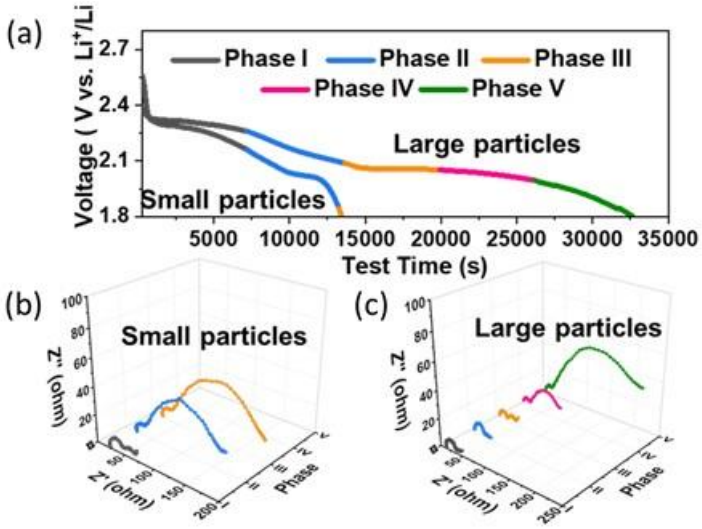

Figure II.10.B.3 (a) First discharging profiles and in-situ EIS of electrodes with (b) <20 µm and (c) >70 µm particles (Electrode: 45% porosity, 4 mg S/cm^2, and E/S = 4 µL/mg S, i=0.1C, room temperature, and electrolyte: 1M LiTFSI/DOL/DME+0.3 M $LiNO_3$).

To understand how particle size affects cell performance, dense S cathodes (porosity 45%) comprised of small (<20 µm) and large particles (>70 µm) were prepared and studied by using both characterization tools and electrochemical method. Figure II.10.B.3b and c show the in-situ electrochemical impedance spectroscopy (EIS) of these two types of electrodes. To decouple the interferences of Li metal while acquiring EIS spectra, a three-electrode cell configuration was used, where a tiny strip of LTO ($Li_4Ti_5O_{12}$) reference electrode was wrapped with polypropylene separator and placed in between the S working electrode and Li metal counter electrode. Figure II.10.B.3a shows the first discharge curves of the dense (45%) and high loading (4 mg/cm^2) electrodes at lean electrolyte conditions (4 µL/mg). EIS were acquired during the discharging of the cell in an interval of 7000 seconds. The dense electrode using large particles shows two typical discharge plateaus, which are comparable with highly porous S cathodes. Conversely, in the dense electrode comprised of small particles, only one discharging plateau with increased polarization was observed. Those distinct electrochemical behaviors were ascribed to the varied electrolyte infiltration and subsequent S reaction processes in different electrode architectures built on different size particles. Given the same materials and electrolyte, the EIS before cell cycling is an indicator of electrode wetting with electrolyte. Compared with the

small particle electrode, the large particle electrode shows much smaller resistances for both the bulk and the overall charge-transfer (R_{ct}). This suggests better electrolyte infiltration/distribution among the large particle electrode. Upon discharging, the overall R_{ct} of the large particle electrode decreased gradually from Phase I to Phase III. This is due to the generation of soluble polysulfides which lead to enhanced reaction kinetics. An increase of R_{ct} was observed only at the end of Phase IV and greatly enhanced during Phase V, which is due to the formation of solid Li_2S_2 and Li_2S_2 as well as their deposition on the carbon surface. However, for the small particle electrode, the overall resistance increased significantly at the end of Phase II to a value comparable to the R_{ct} in phase V of the large particle electrode (Figure II.10.B.3c). This means reactions of the small particle electrode were prematurely terminated by the end of Phase II, explaining its limited discharge capacity and large polarization. Despite the same levels of electrode mass loading and overall porosity, the pore structures and their tortuosity inside the electrodes were varied by using different particle sizes, leading to the different electrolyte permeability behaviors. Therefore, electrolyte diffusion, polysulfide solubility, and S reaction pathways are altered and result in different electrochemical performance. This was also supported by the detailed characterization of the electrodes with different particles, before and after cycling.

4. *Enabling highly dense S electrodes (porosity 40%) at extremely lean electrolyte conditions (E/S≤3 µL/mg) and material scaling up for high-energy Li-S pouch cells.*

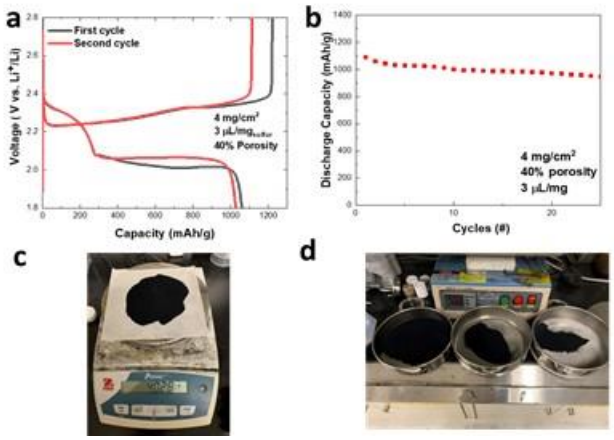

Figure II.10.B.4 (a) First and second charging/discharging curves and (b) cycling performance of dense S electrodes at extremely lean electrolyte conditions. (Electrode: 4 mg S/cm², porosity 40%, and E/S = 3 µL/mg S, 0.1C for cycling, at room temperature). (c and d) Scaling up synthesis of IKB/S composite with different particle sizes.

Approaches from materials design to electrode architecture control have been adopted to minimize the electrode porosity, without sacrificing the S utilization rate. At a porosity of ~50%, the S electrodes (>4 mg/cm²) can deliver a high specific capacity of >950 mAh/g at 0.1C and last for 80 cycles with a capacity retention of 80% at a very low E/S ratio of 4 µL/mg. To further push the limit of low E/S ratio, dense electrodes with porosity of ~40% were fabricated with large size particles (>70 µm). Figure II.10.B.4a shows the discharging/charging curves of the first (grey) and second (red) cycles. At an extremely low E/S ratio of 3 µL/mg, the dense S cathode still functions well and can deliver an initial discharge capacity as high as 1090 mAh/g. Although slightly high cell polarization was observed in the first cycle, the reaction kinetics recovered during the second and subsequent cycling. In the highly porous electrodes though, it is hard to obtain a reasonably high discharge capacity if E/S ratio is as low as 3 µL/mg. This suggests that use of dense electrodes is critical to enable the cell operation at extremely lean electrolyte conditions. It is important to note that a rational design of electrode structure is required to enable a uniform and adequate electrolyte wetting in the dense electrodes. Additionally, dense S electrodes with limited electrolyte (i.e. low E/S ratio) also benefit from minimized polysulfides shuttling and the resulting irreversible capacity loss. As shown in Figure II.10.B.4b, the dense S electrode exhibits a significantly improved capacity retention (87% after 25 cycles) without an obvious capacity drop in the initial cycles, which was often observed in the highly porous electrodes with

flooded electrolyte. This indicates that free diffusion and loss of polysulfides are significantly suppressed in the extremely dense electrode. Given the promising performance of the IKB/S materials, we scaled up the materials synthesis and supplied to Battery500 consortium for pouch cell demonstration. According to our research, the IKB/S particles with relative larger size have superiorities over small ones particularly for a low porosity S cathode under lean electrolyte conditions. Accordingly, the IKB/S materials with optimal particle size were prepared through the control of synthesis conditions and precursors. The IKB can be synthesized at a scale of 8 g per batch with desired particle size. Figure II.10.B.4c shows the weight of IKB/S composite cathode materials through one batch synthesis, which is feasible for large scale production via an amplified reactor design. With an additional sieving process (Figure II.10.B.4d), particles were further screened to ensure the batch consistency and thus electrode reproducibility. Such materials have been validated and supplied to Battery500 consortium for practical pouch cell fabrication.

Conclusions

1. IKB/S materials with controllable secondary particles from 5 to 100 μm were synthesized at a relevant scale and used for high-loading S electrode (>4 mg S/cm2) and high-energy Li-S pouch cell fabrication.

2. Particle size of IKB/S has an important impact on the electrode architecture and affects electrolyte permeability, polysulfide shuttling, and sulfur reaction pathways in high-loading and dense S electrodes.

3. High S utilization rate of >1200 mAh/g can be realized in dense S electrodes (S > 4 mg/cm2) at very lean electrolyte conditions (E/S ≤4 μL/mg) through electrode architecture control and electrolyte optimization.

4. At a lean electrolyte condition of E/S= 4 μL/mg, dense S electrode (S > 4 mg/cm2, porosity≤50%) can deliver 80 cycles with a capacity retention of 80%.

Key Publications

1. Shi L., Bak S., Shadike Z., Wang C., Niu C., Northrup P., Lee H., Baranovskiy A., Qin J., Feng S., Ren X., Liu D., Yang X., Gao F., Lu D., Xiao J., and Liu J., Reaction Heterogeneity in Practical High-Energy Lithium-Sulfur Pouch Cells, Energy & Environmental Science, Energy & Environmental Science, 2020, 13, 3620 - 3632.

2. Kang N., Li Y., Yang L., Lu D., Xiao J., Qi Y., Cai M. Cathode porosity is a missing key parameter to optimize lithium-sulfur battery energy density, Nature Communications, 10, 4597 (2019).

3. Lu D, Yu Z, Xiao J, and Liu J, Sulfide Based Solid Electrolyte for Lithium-sulfur Batteries, TMS 2020 Annual Meeting & Exhibition. February 23-27, 2020, San Diego, California, USA

4. Lu D and Liu J, Development of High Energy Li-S Battery, Department of Energy's (DOE) Vehicle Technologies Office (VTO) Annual Merit Review (AMR), virtually, June 1-4, 2020.

5. Lu D., Yu Z, Xiao J., and Liu J, Advancing High-energy Lithium-sulfur Battery: Challenges from Liquid-rich, Liquid-lean, to All-solid-state, International Battery Seminar, Florida, Virtual, July 28-30, 2020.

II.10.C Nanostructured Design of Sulfur Cathodes for High Energy Lithium-Sulfur Batteries (Stanford University)

Yi Cui, Principal Investigator
Stanford University
Department of Materials Science and Engineering, Stanford University
Stanford, CA 94305
E-mail: yicui@stanford.edu

Tien Duong, DOE Technology Development Manager
U.S. Department of Energy
E-mail: Tien.Duong@ee.doe.gov

Start Date: Oct. 1, 2019 End Date: Sep. 30, 2020
Project Funding: $500,000 DOE share: $500,000 Non-DOE share: $0

Project Introduction

Lithium-sulfur (Li-S) batteries are regarded as next-generation high-energy storage devices for portable electronics, electric vehicles, and grid-scale storage due to their high theoretical energy density (2500 Wh kg^{-1}). However, reaching the satisfactory performance of Li-S batteries has multiple challenges that include: 1) dissolved lithium polysulfides can be reduced at the lithium anode and diffuse back to the cathode, causing the "shuttle effect" and resulting in rapid capacity decay and low Coulombic efficiency. 2) the insulating nature of bulk sulfur and lithium sulfide leads to large polarization and sluggish reaction kinetics, requiring high activation voltages to drive the overall redox process. 3) sulfur and its reduced species are extremely sensitive to vacuum and electron beam irradiation, which limits the diagnostic tools one can use. Therefore, we systematically investigate the sulfur growth behaviors on different current collectors and correlate the results with their electrochemical performance. We develop high sulfur loading cathodes based on the understanding of liquid sulfur state. The liquid state of sulfur enables high mobility and fast phase transition, thus accelerating the redox chemistry and improving kinetics during the battery cycling. Using in situ sulfur K-edge X-ray absorption, we identify sulfur species and understand Li-S chemistry deeply in the liquid sulfur system. Finally, to simultaneously achieve high energy density and high safety Li-S batteries, we expand the research focus to solid polymer based all-solid-state Li-S batteries.

Objectives

The charge capacity limitations of conventional transition metal oxide cathodes are overcome by designing optimized nano-architectured sulfur cathodes. This study aims to enable sulfur cathodes with high capacity and long cycle life by developing sulfur cathodes from the perspective of nanostructured materials design, which will be used to combine with lithium metal anodes to generate high-energy Li-S batteries. In situ optical microscopy combined with ex situ analyses and density functional theory (DFT) calculations are used to systematically investigate and correlate the sulfur evolution on different current collectors with their electrochemical performance. Different sulfur growth behaviors are visualized in real time during battery operation. The batteries with liquid sulfur droplets deliver better reversible capacity, faster reaction kinetics, and longer cycling life as compared to solid sulfur. On the basis of the understandings of liquid sulfur formation, three-dimensional (3D) nickel (Ni)-based current collectors are designed to provide a large active surface area for sulfur/lithium sulfide (Li_2S) deposition, fast transport pathways for both electrons and lithium ions, and a route for lithium/sulfur transformation toward the development of high-energy and long-life Li-S batteries. Novel sulfur nanostructures as well as multi-functional coatings will be designed and fabricated to overcome issues related to volume expansion, polysulfide dissolution, and the insulating nature of sulfur in all-solid-state Li-S batteries.

Approach

The approaches refer to three main parts: (I) advanced nanostructured sulfur cathodes design and synthesis, including (1) engineer empty space into sulfur cathode to solve the problem of electrode volume expansion; (2) develop novel sulfur nanostructures with multi-functional coatings for the confinement of sulfur/lithium polysulfides to address the issues of active materials loss and low conductivity; (3) develop/discover optimal nanostructured materials that can capture the polysulfide dissolved in the electrolyte; (4) develop space efficiently packed nanostructured sulfur cathode to increase the volumetric energy density and rate capability; (5) identify the interaction mechanism between sulfur species and different types of oxides/sulfides, and find the optimal material to improve the capacity and cycling of sulfur cathode. (II) Structure and property characterization, including (1) ex-situ scanning electron microscopy; (2) XPS analysis; (3) in operando X-ray diffraction and optical microscopy. (III) Electrochemical testing including (1) coin cells and pouch cells; (2) A set of electrochemical techniques.

Results

Figure II.10.C.1A shows an optical cell for real-time imaging and monitoring of the sulfur evolution processes. Liquid sulfur droplets growing on the surface of 3D nickel (Ni) substrates during charging at room temperature are visualized. The liquid state of sulfur enables high mobility and fast phase transition, thus accelerating the redox chemistry and improving kinetics during the battery cycling (Figure II.10.C.1B).

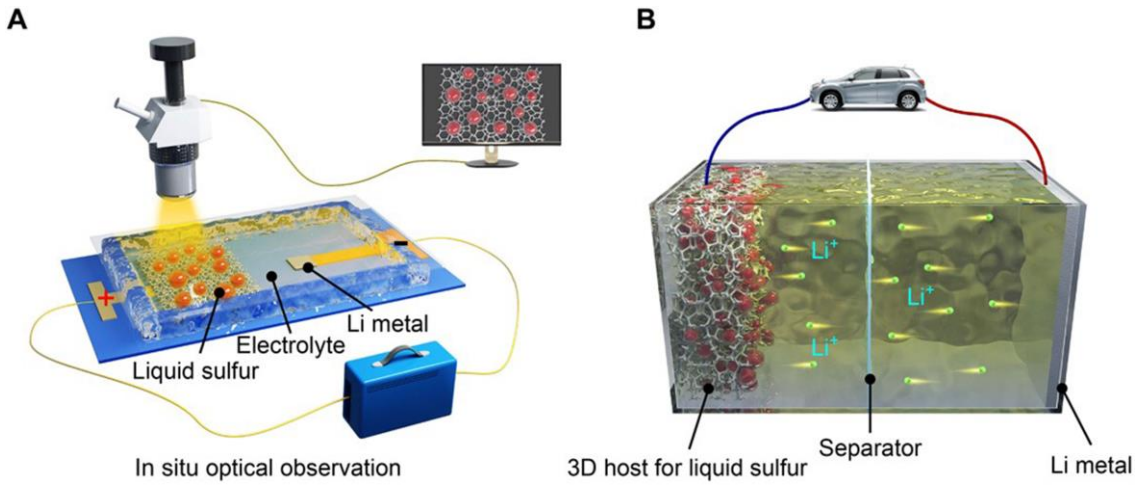

Figure II.10.C.1 **Supercooled liquid sulfur for Li-S batteries.** (A) In situ optical observation of sulfur evolution processes. (B) Design of three-dimensional (3D) electrodes for high-performance Li-S batteries.

To evaluate the effect of current collector materials on electrochemical performance, we chose Ni foam and carbon coated Ni foam as the 3D porous architecture to reveal the sulfur growth behavior and distinguish the battery performance. Ni foam can be employed as a template for the growth of graphene on its surface by chemical vapor deposition (CVD), thus enabling the comparison between 3D Ni foam and graphene-coated Ni (G/Ni) foam. Compared to the pristine nickel foam, wrinkled graphene layers adhered to the surface of Ni foam can be clearly observed after CVD growth (Figure II.10.C.2A). In order to obtain a more complete understanding of the reaction mechanism and to analyze the morphology change of sulfur on the 3D Ni foam and G/Ni framework, the transparent cell was used to monitor the sulfur evolution in real time under battery operation. Figure II.10.C.2B-D present optical images of a Ni foam electrode at initial, charged, and discharged states. Initially, the Ni foam was immersed in the polysulfides (Figure II.10.C.2B), and sulfur droplets were observed and grow large during the charging process. Two droplets touching with each other merged together and became a larger one (Figure II.10.C.2C). The sulfur droplets were gradually dissolved into the electrolyte, and completely disappeared at the end of the discharge process (Figure II.10.C.2D). The sulfur dissolution and reformation can be well controlled and repeated during tens of charge/discharge cycles. In contrast, the irregular sulfur crystals slowly grow and randomly distributed on the surface of G/Ni foam as

displayed in Figure II.10.C.2F-G. The sulfur crystals slowly dissolve into the electrolytes during discharge and finally disappeared upon discharging to 1.5 V (Figure II.10.C.2H). Notably, the liquid sulfur droplets grow faster than sulfur crystals at the constant voltage charging process, in which at the same charging time the Ni foam electrode produces more nuclei and faster growth of sulfur (Figure II.10.C.2I-L) than that of G/Ni foam (Figure II.10.C.2M-P), indicating the faster kinetics of liquid sulfur that is beneficial for fast charging.

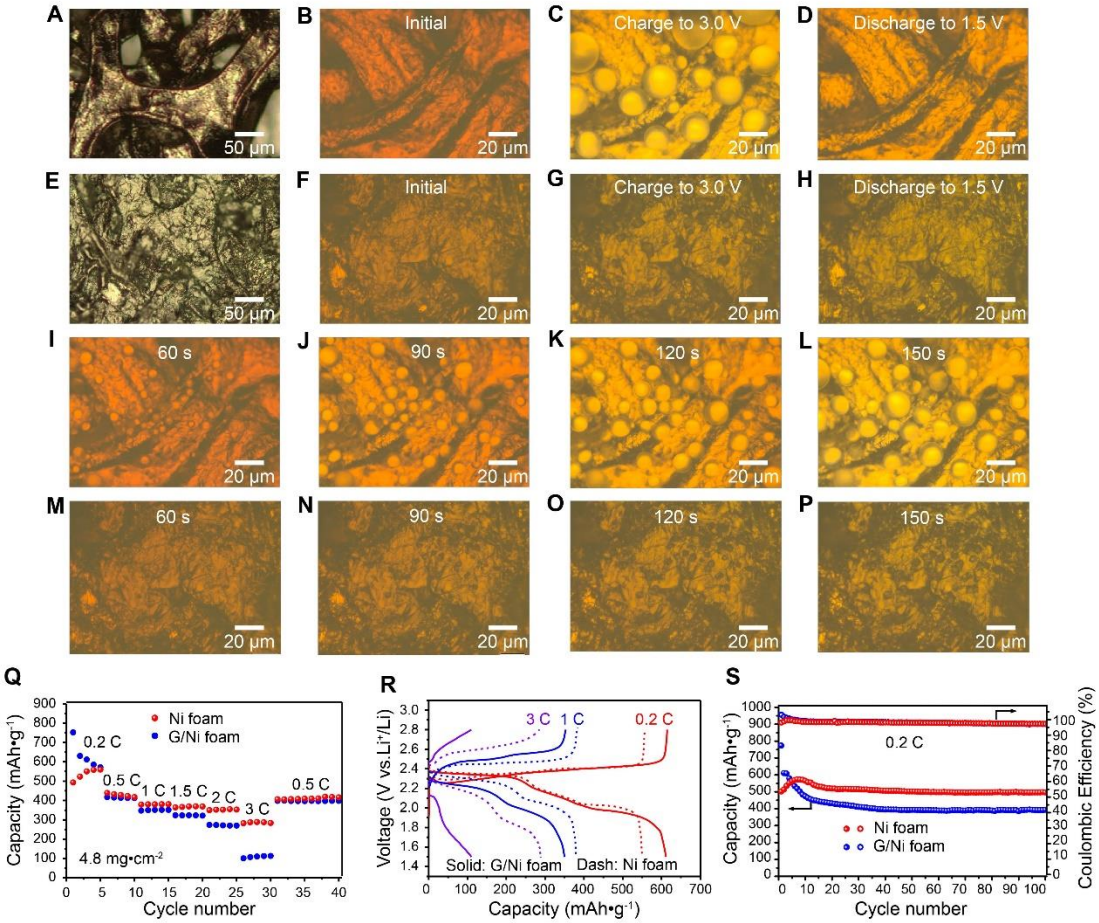

Figure II.10.C.2 In situ optical observation and electrochemical performance of the Ni foam and G/Ni foam electrodes in lithium polysulfide electrolyte. Optical images of (A) Ni foam, (E) G/Ni foam. Optical images of Ni foam in lithium polysulfide electrolyte (B) at initial state, (C) after charging to 3.0 V, and (D) discharging to 1.5 V. Optical images of G/Ni foam in lithium polysulfide electrolyte (F) at initial state, (G) after charging to 3.0 V, and (H) discharging to 1.5 V. Snapshots of the constant voltage charging process for Ni foam electrode at (I) 60s, (J) 90s, (K) 120s, (L) 150s. Snapshots of the constant voltage charging process for G/Ni foam electrode at (M) 60s, (N) 90s, (O) 120s, (P) 150s. (Q) Rate performance of the Ni foam and G/Ni foam electrodes at different current densities. (R) Charge/discharge voltage profiles of the Ni foam (dash line) and G/Ni foam (solid line) electrodes at 0.2C, 1C and 3C. (S) Cycling performance and Coulombic efficiency of the Ni foam and G/Ni foam electrodes at 0.2 C for 100 cycles.

To verify whether the liquid or solid state of sulfur affects the battery performance, the electrochemical properties of Ni and G/Ni foams were measured in coin cells. Figure II.10.C.2Q shows the rate performance of the cells at various current rates between 1.5 and 2.8 V. The 3D Ni foam electrode demonstrates good rate performance with capacities of around 360 and 300 mAh g^{-1} at 2C and 3C, respectively, whereas the cell with the G/Ni foam electrode only maintains capacities of 275 and 110 mAh g^{-1}. The corresponding charge-discharge profiles at 0.2C, 1C, and 3C for Ni and G/Ni foam electrodes are compared in Figure II.10.C.2R. It can be clearly seen that the voltage hysteresis between charge/discharge is much smaller for Ni foam compared to that of the G/Ni foam electrode, which shows large polarization. Moreover, the cell with the Ni foam electrode retains two distinct discharge voltage plateaus even at 3C, while there is almost no discharge plateau

for the G/Ni foam electrode at the same current density. Meanwhile, Ni foam also shows outstanding cycling stability and retains a capacity of 500 mAh g^{-1} over 100 cycles with a Coulombic efficiency of approximately 99% (Figure II.10.C.2S). The slight capacity increase in the first few cycles is possibly due to gradual wetting of some previously inaccessible areas in the Ni foam electrode. Conversely, the battery with the G/Ni foam electrode exhibits rapid capacity decay upon cycling with a capacity retention of only 50%, which is due to the weak polysulfide adsorption on the carbon surface leading to inevitable polysulfide dissolution into the electrolyte. The impressively improved cycle performance and rate capability of the Ni foam-based electrode as compared to that of the G/Ni electrodes arise from the chemisorption of polysulfides by the Ni framework, and the accelerated kinetics between liquid sulfur and liquid polysulfides on the surface of the Ni electrode.

To gain a deeper insight and understand the mechanism of why Ni-based electrodes show better battery performance as compared with carbon electrodes, we studied the decomposition of Li_2S on the Ni surface, graphene basal plane and graphene edge through DFT calculations. The overall Li_2S decomposition includes two elemental steps: one Li atom dissociates from Li_2S and the dissociated Li diffuses away from the LiS cluster. The barriers of these two elemental steps are obtained *via* the climbing-image nudged elastic band (CI-NEB) method as shown in Figure II.10.C.3A. It is well known that the reaction barriers are very sensitive to the adsorption energy of key intermediates. The adsorption energy of Li_2S (the key intermediate) on substrates is considered as an important parameter to explain and distinguish Li_2S decomposition behavior on Ni surface, graphene basal plane and graphene edge. The very strong interaction between Li_2S and the graphene edge (E_{ad} = -6.04 eV) promotes the Li_2S dissociation into Li and LiS, but hampers the lithium ion diffusion away from the edge with a barrier of 1.55 eV (Figure II.10.C.3B). On the other hand, the interaction of Li_2S with the graphene basal plane (E_{ad} = -0.78 eV) is too weak to activate the Li_2S dissociation. In addition, the dissociation intermediates (Li and LiS) is more unstable on graphene basal plane than that of Li_2S by 1.85 eV (Figure II.10.C.2C), indicating that the Li and LiS will be recombined into Li_2S automatically on graphene basal plane. Therefore, the ideal interaction between Li_2S and the substrate material for Li_2S decomposition should be between the range of -0.78 eV and -6.04 eV. The interaction of Li_2S on the Ni surface is relatively moderate (E_{ad} = -5.13 eV), and the rate-determining step of Li_2S decomposition exhibits a barrier of 1.07 eV (Figure II.10.C.2D). The theoretical calculations combined with the above experimental analysis explain the improved reversibility, active material utilization, and improved electrochemical reaction kinetics on the surface of Ni-based electrodes.

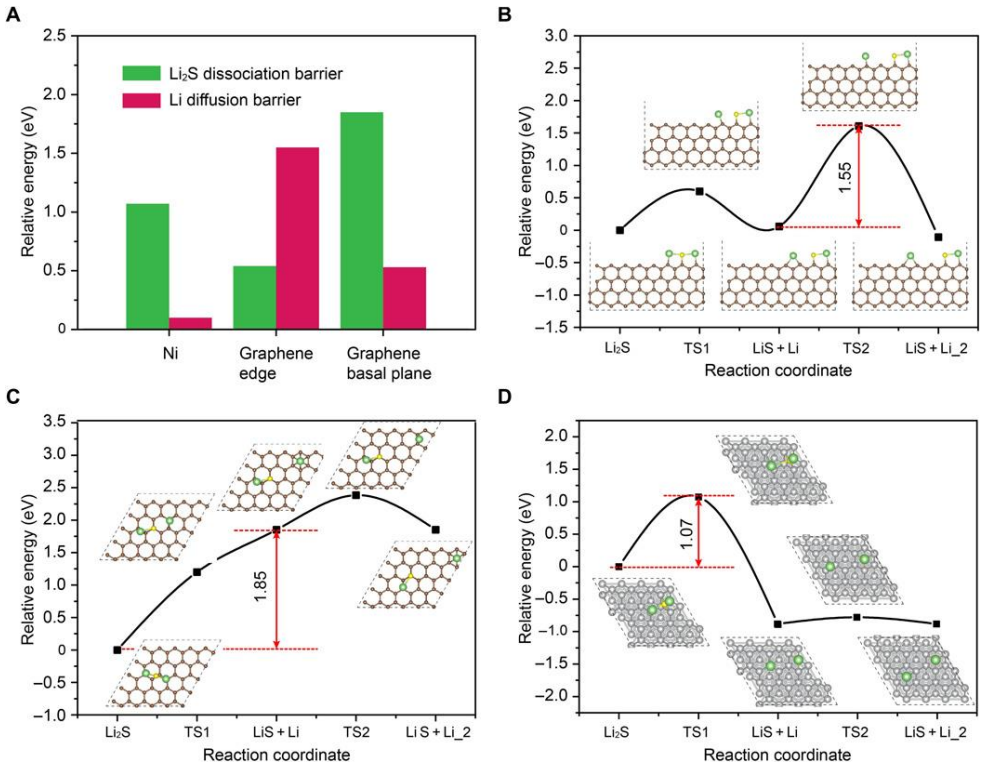

Figure II.10.C.3 **Li_2S decomposition and lithium ion diffusion barriers on the surface of nickel and graphene.** (A) Comparison of the Li_2S decomposition and lithium ion diffusion barriers on the surface of nickel, graphene basal plane, and graphene edge. Energy profiles for the decomposition of Li_2S cluster and lithium ion diffusion on the surface of (B) graphene edge, (C) graphene basal plane, and (D) nickel. Inset figures are top view schematic representations of the corresponding decomposition and lithium ion diffusion pathways for graphene edge, graphene basal plane, and nickel. Here, green, yellow, gray, and beige balls symbolize lithium, sulfur, nickel, and carbon atoms, respectively.

To better identify the state of sulfur species, we develop advanced characterizations including in situ Raman, in situ X-ray absorption, and cryogenic electron microscopy. We choose micron-scale two dimensional (2D) molybdenum disulfide (MoS_2) flakes as the sulfur growth substrates because they are crystalline-flat, amenable to microfabrication techniques, and can be easily integrated into devices and investigated by non-invasive optical microscopy. The in situ Raman spectroscopy confirmed the formation of sulfur on MoS_2 (Figure II.10.C.4A). Both the liquid and solid sulfur on MoS_2 show intramolecular Raman features at 150, 220 and 473 cm^{-1}, corresponding to asymmetric S-S bending mode, symmetric S-S bending mode and S-S stretching mode, respectively, and contain Raman signatures from MoS_2. The low frequency Raman spectra between 10 to 100 cm^{-1}, however, exhibit several modes for solid sulfur while only a Rayleigh wing feature for liquid sulfur. These different Raman features match that of commercial sulfur control and the molten sulfur, indicating that the generated solid sulfur is crystalline while the liquid sulfur is amorphous. To further confirm the composition of the liquid droplets, we performed in situ X-ray absorption spectroscopy (XAS) measurements (Figure II.10.C.4B). At open circuit voltage (OCV) ~ 2.4 V, the XAS spectrum of lithium polysulfides (Li_2S_x) exhibit two main absorption features near the sulfur K-edge, at 2471 eV due to the terminal sulfur atoms and 2473 eV due to the (x-2) internal atoms in the sulfur chain. When charged to 3.0 V, the absorption feature at 2471 eV disappears while the absorption feature at 2473 eV remains, matching that of the sulfur control, indicating the conversion of S_x^{2-} into elemental S. When discharged to about 2.0 V, the absorption feature at 2471 eV reappears, showing again the conversion of sulfur to S_x^{2-}. Combining in situ XAS and in situ optical microscopy measurements which unambiguously show the generation of liquid droplets, we can conclude that the generated liquid droplets are sulfur in composition. On the other hand, solid sulfur is sensitive to electron beam irradiation and can easily sublimate in high vacuum, therefore most reported work has sulfur encapsulated in carbon materials for TEM characterizations. Here, for the first time, we employ cryogenic electron microscopy (cryo-EM) to investigate the solid sulfur. We successfully obtained the electron diffraction patterns which demonstrate

a high degree of crystallinity (Figure II.10.C.4C and Figure II.10.C.4D), confirming that S_8 molecules in the solid sulfur have long-range order, consistent with the in situ Raman spectroscopy measurements.

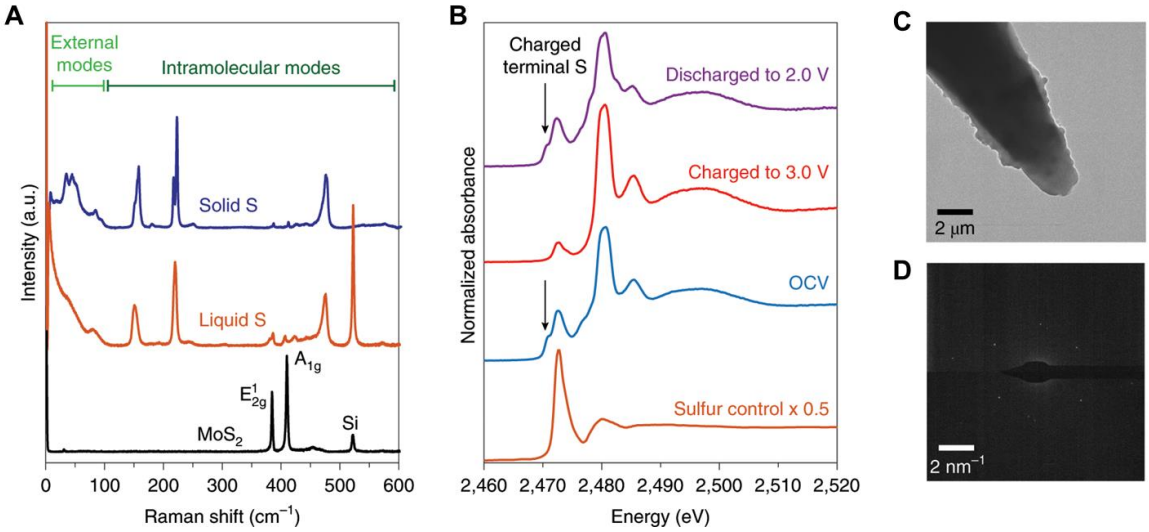

Figure II.10.C.4 **Advanced characterizations for understanding sulfur species in the liquid sulfur system.** (A) In situ Raman spectra of liquid and solid sulfur on molybdenum disulfide (MoS_2) both show intramolecular Raman modes of S_8 and contain signatures of MoS_2. In the low-frequency range, liquid sulfur shows a wing feature while solid sulfur shows distinct external modes. (B) In situ X-ray absorption spectroscopy (XAS) spectra confirming the composition of liquid sulfur. When charged to 3 V, the absorption feature at 2471 eV disappears, indicating the conversion of S_x^{2-} into elemental S (absorption feature at 2473 eV). (C) Cryogenic electron microscopy (cryo-EM) image and (D) selected area electron diffraction (SAED) confirming the crystallinity of solid sulfur.

Furthermore, to further develop high energy density and high safety Li-S batteries, we design a new strategy, by using thin-layered titanium disulfide (TiS_2) as an effective encapsulation for preventing polysulfides dissolving into solid polymer electrolytes in all-solid-state Li-S batteries (Figure II.10.C.5A-C). Li_2S cathodes are chosen because fully lithiated Li_2S is able to minimize structural damage compared to sulfur, and is compatible with anode-free cells. The TiS_2 encapsulated layer can efficiently trap polysulfides inside its shell because of a strong binding with Li_2S/Li_2S_x species. To test the hypothesis in Figure II.10.C.5C, $Li_2S@TiS_2$ particles were synthesized by directly converting 20% of the Li_2S on the surface into TiS_2. Scanning electron microscopy (SEM) image of Li_2S after TiS_2 coating reveals that the typical particle size of as-prepared $Li_2S@TiS_2$ is 1-5 μm with an average size of 2 μm (Figure II.10.C.5D). Transmission electron microscopy (TEM) image shows that Li_2S is encapsulated by a uniform layer with a thickness of ~20 nm (Figure II.10.C.5E). High resolution TEM image shows a spacing of 0.57 nm, which is consistent with the interlayer spacing of TiS_2 and verifies the crystalline structure of the TiS_2 layer (Figure II.10.C.5F).

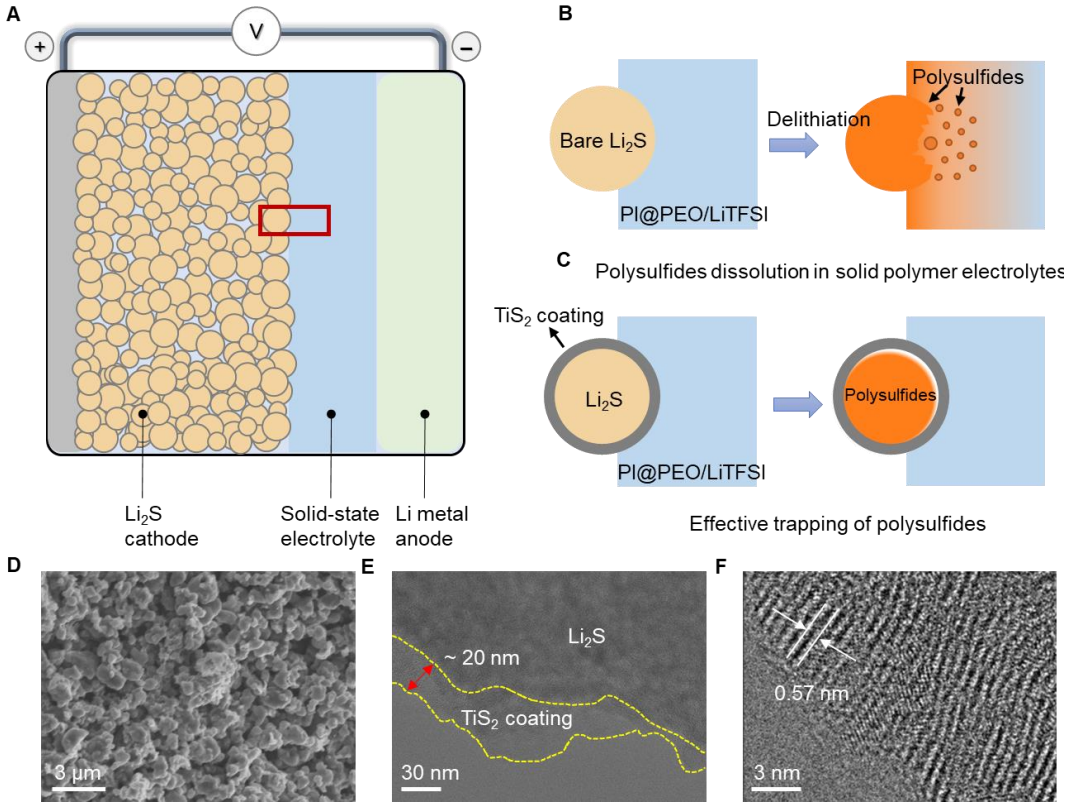

Figure II.10.C.5 **Design of encapsulated Li_2S cathodes for high energy density all-solid-state Li-S batteries (ASSLSBs).** (A) Schematic of the ASSLSBs architecture comprising of Li metal anode, nanoporous polyimide (PI) film filled with polyethylene oxide/lithium bis(trifluoromethanesulfonyl)imide (PI@PEO/LiTFSI) solid electrolyte, and Li_2S composite cathode. Zoomed-in schemes of the red rectangle in (B), to depict the interface between solid-state electrolyte and cathode during delithiation process for (B) bare Li_2S cathode and (C) Li_2S@TiS_2 cathode. Bare Li_2S particles undergo polysulfide dissolution upon delithiation, resulting in rapid capacity decay and low Coulombic efficiency. Li_2S@TiS_2 core-shell structure provides a structurally intact shell for effective trapping polysulfides, thereby avoiding the polysulfide dissolution into solid polymer electrolytes. Light yellow: Li_2S particles; Orange: polysulfide; Grey shell: TiS_2 coating. (D) SEM and (E) TEM image of Li_2S@TiS_2. The thickness of TiS_2 coating is about 20 nm. (F) High-resolution TEM image of TiS_2 coating.

Conclusions

In all, in the past one year, we have made great progress in understanding the mechanism and developing high energy Li-S batteries. In situ optical microscopy, in situ X-ray absorption combined with ex situ analyses and DFT theoretical calculations were used to systematically investigate and correlate the sulfur evolution on different current collectors with their electrochemical performance. Different sulfur growth behaviors were visualized in real time during battery operation: Solid sulfur crystals were produced on the carbon surface and supercooled liquid sulfur droplets formed on the Ni surface at room temperature. The batteries with liquid sulfur droplets deliver better reversible capacity, faster reaction kinetics, and longer cycling life as compared to solid sulfur. We explained the distinct battery performance from the aspects of sulfur adsorption binding energy, polysulfide conversion, Li_2S decomposition, and lithium ion diffusion energy barriers. The strong coupling between Ni and lithium polysulfides helps suppress polysulfide dissolution, improves the utilization of sulfur, and accelerates the kinetics of phase conversion, which are essential aspects of realizing stable and fast-charging Li-S batteries. On the basis of these fundamental understandings, 3D Ni-based interconnected architectures are designed to provide a large active surface area for sulfur/Li_2S deposition, fast transport pathways for both electrons and Li ions, and a route for Li_2S/sulfur transformation toward the development of high-energy and long-life Li-S batteries. Furthermore, we are also developing a new and promising approach by using thin-layered TiS_2 as an effective encapsulation for preventing polysulfides dissolving into solid polymer electrolytes in all-solid-state Li-S batteries for high energy density and high safety Li-S batteries.

Key Publications

1. G. Zhou, A. Yang, G. Gao, X. Yu, J. Xu, C. Liu, Y. Ye, A. Pei, Y. Wu, Y. Peng, Y. Li, Z. Liang, K. Liu, L.-W. Wang, and Y. Cui, "Supercooled liquid sulfur maintained in three-dimensional current collector for high-performance Li-S batteries" Science Advances (2020) DOI: 10.1126/sciadv.aay5098.

2. A. Yang, G. Zhou, X. Kong, R. A. Vila, A. Pei, Y. Wu, X. Yu, X. Zheng, C.-L. Wu, B. Liu, H. Chen, Y. Xu, D. Chen, Y. Li, S. Fakra, H. Y. Hwang, J. Qin, S. Chu, and Y. Cui, "Electrochemical generation of liquid and solid sulfur on two-dimensional layered materials with distinct areal capacities" Nature Nanotechnology (2020) DOI: 10.1038/s41565-019-0624-6.

II.10.D Mechanistic Investigation for the Rechargeable Li-Sulfur Batteries (U of Wisconsin)

Deyang Qu, Principal Investigator
University of Wisconsin Milwaukee
3200 N Cramer Street
Milwaukee, WI, 53211
E-mail: qud@uwm.edu

Enyuan Hu, Principal Investigator
Chemistry Division
Bldg. 555, Brookhaven National Lab.
Upton, NY 11973
E-mail: enhu@bnl.gov

Tien Duong, DOE Technology Development Manager
U.S. Department of Energy
E-mail: Tien.Duong@ee.doe.gov

Start Date: September 1, 2019 End Date: August 30, 2020
Project Funding: $300,000 DOE share: $300,000 Non-DOE share: $0

Project Introduction

Rechargeable lithium sulfur (Li-S) chemistry has attracted substantial attentions because it is considered as one of the potential candidates to replace state-of-art Li-ion batteries in EV applications. This is due to its high theoretical energy density (1672mAh*g^{-1}), safety, and low cost. However, there remain many obstacles to be overcome before a rechargeable Li-S battery could become practical. Those technical barriers include high self-discharge, low efficiency, low active material utilization and low cycle life. Most of challenges on the sulfur side are related to the polysulfide dissolution and the change of conductivity during cycling, while dendrite growth and "dead" Li formation on Li anode still remain as major technical difficulties.

In the past few years, we have successfully developed an *in-situ* electrochemical method, so the dissolved polysulfides during the battery operation can be qualitatively and quantitatively determined. The mechanisms for the sulfur redox reaction were revealed and the processes were better understood. The equilibrium reactions between dissolved polysulfides and elemental sulfur (polysulfide shuttle), are the major reason for the continuous decay of the capacity during cycling and high self-discharge during storage. This is especially true for the Li-S batteries with elemental sulfur as redox materials and lithium salts in organic solvents as liquid electrolytes. We also developed an *in-situ* electrochemical– microscopic technique for the real-time investigation of Li anode during cycling. Taking the advantages of the advancements of *in-situ* diagnostic technologies, the effectiveness of many potential inhibitors was investigated, the stability of cell components in polysulfide electrolyte was also studied, new anode materials were explored and polymerized sulfur compounds were synthesized and tested.

With these better understandings of the mechanisms for Li-S chemistry, through this collaborative project we will firstly, synthesize cross-linked polymerized sulfur compounds and sulfur composite material with inorganic anchors, in which sulfur is attached to the conductive backbone with covalent bonds and inorganic anchor sites,respectively, therefore the polysulfides can be localized within the conductive matrix; secondly, continue exploring the alternative anode materials which can cycle well and do not react with dissolved polysulfide and sulfur in the electrolyte, so "shuttle effect" can be mitigated; thirdly, develop synchrotron-based diagnostic tools to investigate the sulfur and polysulfide in the solid phase.

In addition, we will continue to engage in the fundamental *in-situ* electrochemical investigations of the sulfur redox mechanisms so more detail sulfur redox mechanisms can be revealed which will better guide the material and engineering designs. We will also continue optimize the alternative electrode fabrication processes.

Objectives

The primary objectives are:

- To continue conducting focused fundamental research on the mechanism of "shuttle effect" inhibition for rechargeable Li-S batteries.
- To continue developing the polymeric sulfur electrode, adequate anode and corresponding electrolyte to achieve high energy density, long cycle Li-S batteries.
- Carry out spatially resolved x-ray fluorescence (XRF) image and S-K edge x-ray absorption (XAS, including XANES and XAFS) studies of polymeric sulfur compounds.
- Investigate the alternative anode materials so they will not react with dissolved polysulfide ions.
- To continue develop and optimize creative electrode making processes to improve processability and aerial capacity, e.g. dry process and thick electrode.

The ultimate goal for the project is to develop a practical rechargeable Li-S battery to meet the challenges of power the next generation electric vehicles beyond Li-ion technologies.

Approach

1. *In-situ* High Performance Liquid Chromatography (HPLC)/Mass Spectroscopy (MS)-Electrochemical method was developed during the course of this project. It is the first and arguably the only reliable quantitative and qualitative analytical tool to monitor the change of polysulfide ions during the electrochemical and chemical reactions in real time.
2. *Ex-situ* X-ray diffraction (XRD) and X-ray photoelectron spectroscopy (XPS) to investigate the surface of the sulfur cathode and Li anode to elucidate the surface changes during the Li-S battery operation.
3. Development of a role-to-role prelithiation method for alternative anode.
4. Synthesis of polymer sulfur composite materials to limit the dissolved polysulfide ion migration.
5. Extended collaboration with other US and international academic institutions and US industrial partners.

Results

FY 2020 has been a challenge one. Due to the pandemic of COVID-19, the PI's research labs in the university closed in March 2020 right after the university spring break and are only partially open in order to maintain social distance. But we managed to complete all milestones of FY2020.

Different Li containing anode materials were continuously investigated in FY20. By means of the *in-situ* HPLC-MS electrochemical technique developed in the PI's lab, the chemical interaction between the potential alternative anode materials and dissolved polysulfide ion were investigated. As shown in Figure II.10.D.1, there is no change of the polysulfide distribution after one-hour exposure to an alternative anode. Figure II.10.D.1 B shows the comparison of the original distribution of polysulfide ions in an electrolyte and the distribution after one-hour exposure to a Li metal. From Figure II.10.D.1, two conclusions can be drawn:

1. *The "shuttle-effect" can be mitigated by the selection of alternative anodes which do react with dissolved polysulfides.*
2. *The short chain length polysulfide ions e.g. S_4^{2-} and S_5^{2-} are much less reactive than the longer chain polysulfide ions.*

With these information, we focused our research on the selection of alternative anode materials and limiting the dissolution of long chain polysulfide ions.

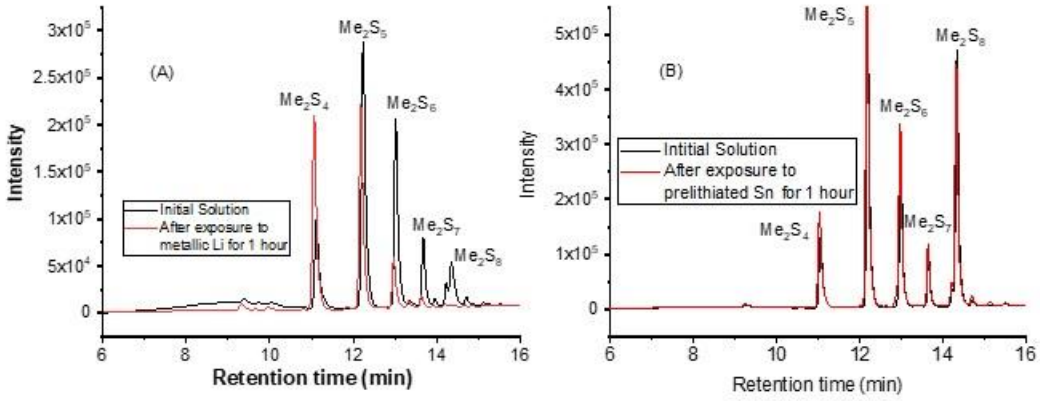

Figure II.10.D.1 Chemical reaction between dissolved polysulfide ions and metallic Li (A) and prelithiated Sn (B).

Alternative anode materials and pre-lithiation. In the FY19 report, we reported the success of using a prelithiated phosphouous material as an alternative anode in a P-Li/C-S/C full cell. A long and stable cycle life was demonstrated. However, due to the low cell voltage (1.2 V), the energy density was compromised. We also found that Sn or SnO_2 can be a good alternative anode candidate too. As shown in Figure II.10.D.1, the prelithiated SnO_2 anode demonstrates little reaction with the dissolved polysulfide ions. In the FY20, we have successfully pre-lithiated SnO_2. As shown in Figure II.10.D.2, the prelithiated Sn anode has high Li loading (500 mAh/g) and low active Li loss during cycling.

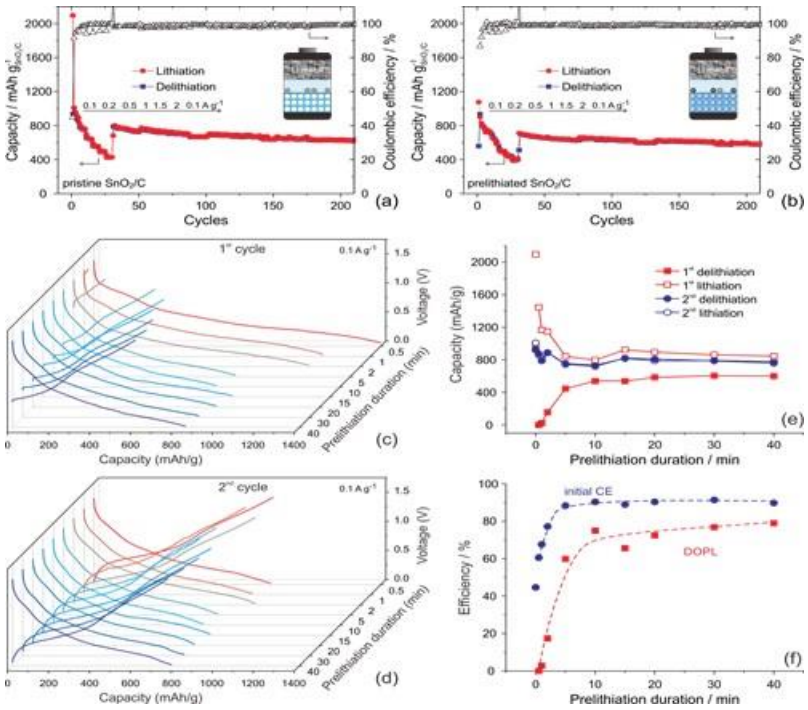

Figure II.10.D.2 Rate and cycling performance of the pristine (a) and prelithiated (b) SnO_2/C electrode. The 1st (c) and 2nd (d) cycle voltage profiles for prelithiated SnO_2/C electrodes with various prelithiation durations. The capacities (e) , initial CE and DOPL (f) of the pristine and prelithiated SnO_2/C electrodes. The half cell with the pristine SnO_2/C started with lithiation, while the half cells with the prelithiated SnO_2/C started with delithiation.

The prelithiated SnO_2/C electrodes were obtained by dipping the pristine SnO_2/C electrode into 1 M Li-Bp/THF solution. The prelithiated SnO_2/C electrodes were then immediately washed with anhydrous THF and dried under vacuum.

However, we still struggle to find an adequate electrolyte to accommodate both Sn(Li) anode and a sulfur or a polymeric sulfur cathode. To prove the effectiveness of the anode material, the prelithiated Sn anode was coupled with LCO cathode. Figure II.10.D.3 shows the performance of the cell. A good electrochemical performance was demonstrated.

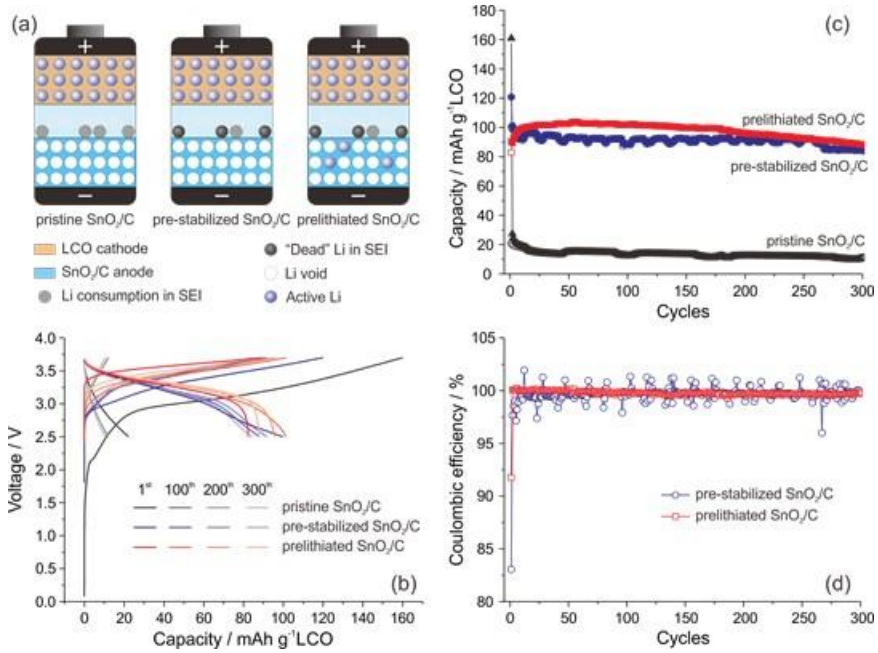

Figure II.10.D.3 (a) Schematic illustration of the full cells consisting of LCO cathode and different SnO_2/C anodes, respectively. Voltage profiles (b), cycling performance (c) and coulombic efficiency (d) of the full cells at 1C rate (1C = 140 mA g^{-1} of LCO).]

Restriction of polysulfide dissolution. To limit the dissolution of the polysulfide species formed during cycling. We experimented two approaches, to bond sulfide on polymer backbones and to entrap the polysulfides in a containment.

Polymeric Sulfur compounds. Altogether 26 polymeric sulfur compounds were synthesized through a route involving radicals. Various base monomers were selected. Polymeric sulfur compounds were synthesized through a sequence of heat treatment in which the sulfur and the ionomer can be linked through a radical assisting mechanism. All the monomers consisted of double bonds and were conjugated molecules. The characterization and testing of the materials are still in progress and will be reported later. Figure II.10.D.4 shows two examples of the electrochemical performance of the associated polymeric sulfur compounds. The polymeric sulfur compounds shown in A was synthesized with dicyclopentadiene monomer and subsequently treated at 270°C, while the polymer shown in C was synthesis through a different monomer. The respective cycle results are shown in (C) and (D). Even though it is not conclusive and more studies are to be done to understand the mechanism, it is apparent that if a one plateau discharge with voltage above 2.2 V instead of a two plateau discharge is shown, the cycle life can be improved. As we reported in the previous report (FY18), the high voltage plateau represented the electrochemical reaction and equilibrium among the longer chain length polysulfide ions, while the low voltage plateau represented that of the short chain length polysulfide ions.

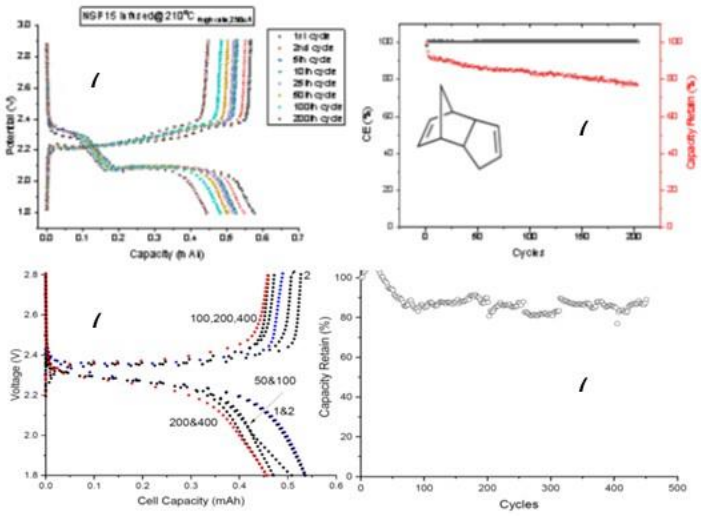

Figure II.10.D.4 The electrochemical performance of polymeric sulfur compound made with monomer (Dicyclopentadiene DCPC) shown in the inset (A)&(B). The polymer in (C)&(D) was synthesized differently.

Synthesis of sulfur containing materials with inorganic anchors. The overall performances of lithium-sulfur batteries are highly dependent on the structure and surface feature of carbon scaffolds as well as the architecture of sulfur cathodes. A series of semi-graphitic ordered mesoporous carbons with metal/nitrogen doping (Me-N-GOMCs; Me = Fe, Co, Ni, and Cu) were designed as sulfur hosts with abundant porosity and high electrical conductivity. It was revealed that the carbon capability of anchoring polysulfides can be remarkably enhanced through the synergistic effect of Fe and N doping.

DFT calculations were performed to reveal the corresponding adsorption energies and sites of Me-N-GOMCs towards sulfides. Compared with other samples, Fe-N-GOMC showed the most favorable surface tightly adhered to Li_2S, implying its strongest binding ability with LiPSs. The adsorption energies of Li_2S on the surfaces of Fe, Co, Ni, and Cu-N-GOMC are −3.01, −2.80, −2.15, and −1.48 eV, respectively. These values are much higher than those on the pure carbon (−0.3 eV) or nitrogen-doped carbon (−0.54 eV) reported in literature. The theoretical results reveal that Fe and N dopants can work synergistically to boost the anchoring ability of carbon materials towards sulfides, thus more effectively suppress the active sulfur loss and shuttle effect and eventually result in superior cycling stability.

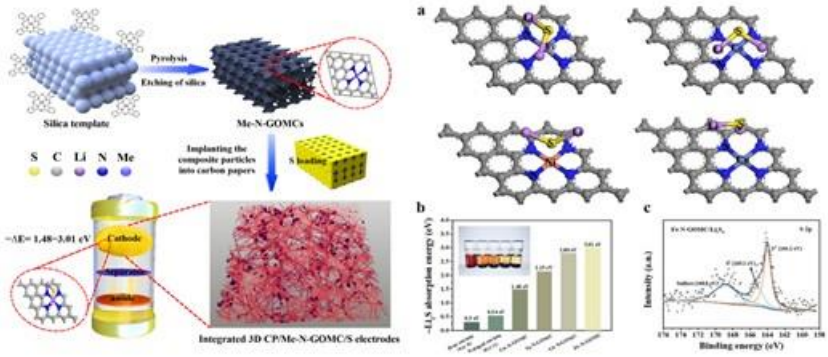

Figure II.10.D.5 Synthesis and characterization of the sulfur containing material with inorganic anchor.

Figure II.10.D.5 shows the schematic representation of the synthesis process the semi-graphitic ordered mesoporous carbons with metal and Nitrogen anchor to lock S within (left); Sulfide anchoring mechanism on Me-N-GOMCs. (a) Optimized geometries of most stable Li_2S on Fe/Co/Ni/Cu and N double-doped carbon framework surfaces. (b) Corresponding adsorption energies on different surfaces of framework and visual

adsorption tests of Li_2S_6 in DME by the various powders (from left, control, Ni-N-GOMC, Cu-N-GOMC, Co-N-GOMC and Fe-N-GOMC). (c) S 2p XPS spectra of Fe-N-GOMC/Li_2S_6(right).

Figure II.10.D.6 shows the electrochemical performance of the Me-N-GOMCs. Cyclic voltammetry, ac impedance, galvanostatic cycling and rate capability of all the materials are illustrated. The high areal loadings of 3 mg and 6 mg per cm^2 were tested. The Me-N-GOMCs were embedded in the void space of a carbon paper to construct the free-standing sulfur cathode. The electrochemical tests were done in a CR2016 coin cell with Li anode. The integrated 3D CP/Fe-N-GOMC/S electrode with a sulfur loading of ~3 mg cm^{-2} delivers a high initial capacity of 1473 mA h g^{-1} at 0.2 C and good cycling stability (a decay rate of 0.075 % per cycle over 500 cycles at 0.5C and a decay rate of 0.001 % per cycle over 120 cycles at 1C). Even at a sulfur loading of ~6 mg cm^{-2}, steady areal capacity (~5 mA h cm^{-2}) for over 120 cycles at 1C can still be attained.

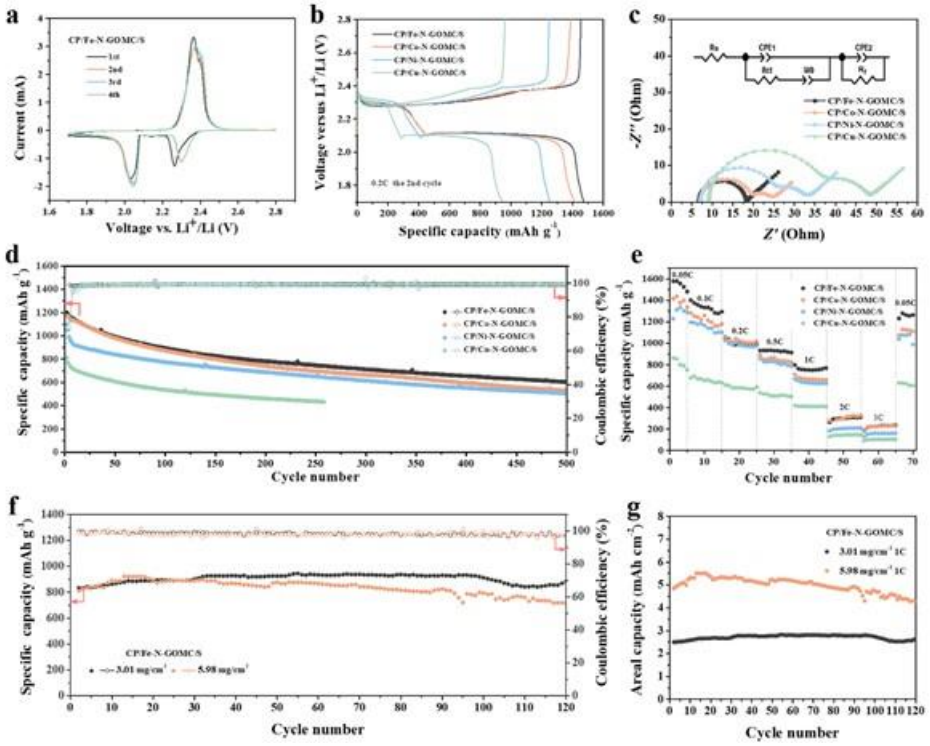

Figure II.10.D.6 Electrochemical performances for CP/Me-N-GOMC/S cathodes. (a) CV curves of the CP/Fe-N-GOMC/S electrode for initial several cycles at a scan rate of 0.05 mV s^{-1}. (b) Galvanostatic discharge-charge profiles of electrodes for the second cycle at 0.2 C. (c) Experimental Nyquist plots of electrodes after initial cycle of the cells as well as the fitting results (solid lines) based on the equivalent circuit shown in the inset. (d) Cycling performances of electrodes at 0.5 C and (e) rate capability of electrodes at various rates with a sulfur loading of ~3 mg cm^{-2}. (f) Cycling performances of CP/Fe-N-GMOC/S electrodes with different sulfur loading at 1 C and (g) the corresponding areal capacities.

Conclusions

1. Again it has been proven that the *In-situ* HPLC-MS electrochemical essays developed to quantitatively and qualitatively determine the polysulfide ions are very useful for Li-S investigation.

2. The short chain length polysulfide ions e.g. S_4^{2-} and S_5^{2-} are much less reactive than the longer chain polysulfide ions. Therefore if the long chain polysulfide ions can be restrained in the cathode matrix, the "shuttle effect" can be mitigated.

3. The "shuttle-effect" can be mitigated by the selection of alternative anodes which do react with dissolved polysulfides.

4. In order to restrain long chain polysulfide ions, various sulfur containing co-polymers and inorganic composites were synthesized and are being tested.

Key Publications

1. Zulipiya Shadike , Sha Tan , Qin-Chao Wang , Ruoqian Lin , Enyuan Hu , Deyang Qu , Xiao-Qing Yang, "Review on Organosulfur Materials for Rechargeable Lithium Batteries", Materials Horizons, *DOI: 10.1039/D0MH01364A*

2. Xiaoxiao Zhang, Huainan Qu, Weixiao Ji, Dong Zheng, Tianyao Ding, Dantong Qiu, Deyang Qu, "Roll-to-Roll Prelithiation of SiO Anodes with Organolithium Compounds for Lithium-Ion Batteries", J. Power Sources, 478(2020)229067

3. Feifei Li, Gongwei Wang, Dong Zheng, Xiaoxiao Zhang, Caleb J. Abegglen, Huainan Qu, Deyang Qu, Controlled Prelithiation of SnO2/Carbon Nanocomposite Anode for High Performance Lithium-ion Full Batteries, ACS Appl. Mater. & Interface 12(2020)19423-19430.

4. Hao Li, Dan Liu, Xinxin Zhu, Deyu Qu, Zhizhong Xie, Junsheng Li, Haolin Tang, Dong Zheng, Deyang Qu, "Integrated 3D electrodes based on metal-nitrogen-doped graphitic ordered mesoporous carbon and carbon paper for high-loading lithium-sulfur batteries", Nano Energy, 73(2020)104763.

5. Gongwei Wang, Feifei Li, Dan Liu, Dong Zheng, Caleb J. Abeggien, Yang Luo, Xiao-Qing Yang, Tianyao Ding, Deyang Qu, "High performance lithium-ion and lithium–sulfur batteries using prelithiated phosphorus/carbon composite anode", Energy Storage Materials, 24(2020)147-152.

II.10.E New Electrolytes for Lithium-Sulfur Battery (Lawrence Berkeley National Laboratory)

Gao Liu, Principal Investigator
Lawrence Berkeley National Laboratory
1 Cyclotron Rd.
Berkeley, CA
E-mail: gliu@lbl.gov

Tien Duong, DOE Technology Development Manager
U.S. Department of Energy
E-mail: Tien.Duong@ee.doe.gov

Start Date: October 1, 2019 End Date: September 30, 2022
Project Funding: $450,000 DOE share: $450,000 Non-DOE share: $0

Project Introduction

A strong demand for low-cost and high-energy-density rechargeable batteries has spurred lithium-sulfur (Li-S) rechargeable battery research. First, sulfur is an abundant and low-cost material. Second, the Gibbs energy of the lithium (Li) and sulfur reaction is approximately 2,600 Wh/kg, assuming the complete reaction of Li with sulfur to form Li_2S, more than five times the theoretical energy of transition metal oxide cathode materials and graphite coupling. With these advantages, Li-S batteries could be both high energy density and low cost, satisfying demand in energy storage for transportation application. The major obstacle is the loss of sulfur cathode material as a result of polysulfide dissolution into common electrolytes, which causes a shuttle effect and significant capacity fade. The polysulfide shuttle effect leads to poor sulfur utilization and fast-capacity fade, which have hindered widespread use of rechargeable Li-S batteries. This proposed work of electrolyte materials development in understanding the thermodynamics and kinetics of polysulfide dissolution and precipitation will yield new approaches for electrolytes of Li-S rechargeable batteries.

Objectives

The project objective is to develop new electrolytes, additives, and electrode compositions for Li-S battery with high ion-conductivity, stable toward polysulfide and promoting the polysulfide affiliation with the electrode substrate to prevent polysulfide dissolution.

Approach

This project aims to develop new electrolytes and additives for Li-S battery. The properties of the ideal electrolyte for sulfur electrode would be high ion conductivity, stable towards polysulfide, and promoting the polysulfide affiliation with the electrode substrate to prevent polysulfide dissolution. The project is designed to first understand the electrode substrate interaction with the polysulfides in different electrolytes. This will lead to better understandings of the polysulfide nucleation and precipitation mechanisms in common electrolytes. The second stage of the project will focus on chemically modifying the structures of the solvent and salt electrolyte molecules to increase electrolyte stability and ionic conductivity and to prevent polysulfide dissolution and promote polysulfides precipitation.

Results

I. Development of fluorinated electrolyte for suppressing polysulfide dissolution and lithium metal anode stabilization in Li-S battery

In order to address challenges central to practical implementation of Li-S battery such as low coulombic efficiency (CE) and polysulfide dissolution and shuttling, we have developed a fluorinated electrolyte additive with amphiphilic surfactant molecular design consisting of fluorocarbon chain moiety and ethylene oxide (EO) moiety. Polysulfide has a strong affiliation with electron donating EO groups in typical ether based electrolyte, which leads to the sulfur dissolution during cycling and serious capacity degradation. Figure II.10.E.1(a)

introduces the molecular structure of these synthesized fluorinated electrolyte additive molecules– denoted as F_8EO_4, F_4EO_2 and F_3EO_1. The electrolyte additives and lithium salts (LiTFSI or LiFSI) will self-assemble in the dilution electrolyte solvent 1,1,2,2-tetrafluoroethyl-2,2,3,3-tetrafluoropropyl ether (TTE) to form micelle-like solvation structure. This special electrolyte structure introduces benefits such as increasing electrolyte conductivity by forming special Li ions diffusion channels, increasing salt concentration while still maintaining a low viscosity, and facilitating Li anode stabilization. Most importantly, polysulfide dissolution is largely discouraged since electron donating sites of EO groups have been preoccupied by LiTFSI or LiFSI and the EO groups are surrounded by the fluorocarbon shells which adds accessing barrier for polysulfide as well.

One important effort of this work is to provide experimental evidence for formation of this self-assembly micelle structure. We choose small angle X-ray scattering (SAXS) to achieve this purpose as SAXS is often used to identify particle size and distribution for colloidal systems by probing response in electron density contrast of molecules or aggregates dispersed in solution.[1] The result of SAXS is summarized in Figure II.10.E.1(b) which shows complex aggregate size as a function of salt and HFE identity and (c) which reflects complex aggregate size change with LiTFSI salt concentration. As is displayed that salt identity plays a role in determining dimensions of the complex aggregates. Much larger size of aggregates are observed for LiFSI attributed to the participation of more LiFSI units in the formation of one single complex under the same salt concentration due to easier incorporation of the smaller anions. What's more, charge repulsion might have impact on the formation of larger LiFSI based aggregates due to more extensive ion pairing. Interestingly, it seems that the smaller HFE molecule (F_4EO_2) tends to form larger aggregates with the larger LiTFSI salt, while the larger HFE molecule (F_8EO_4) prefers LiFSI, which the underlying mechanism needs further investigation.

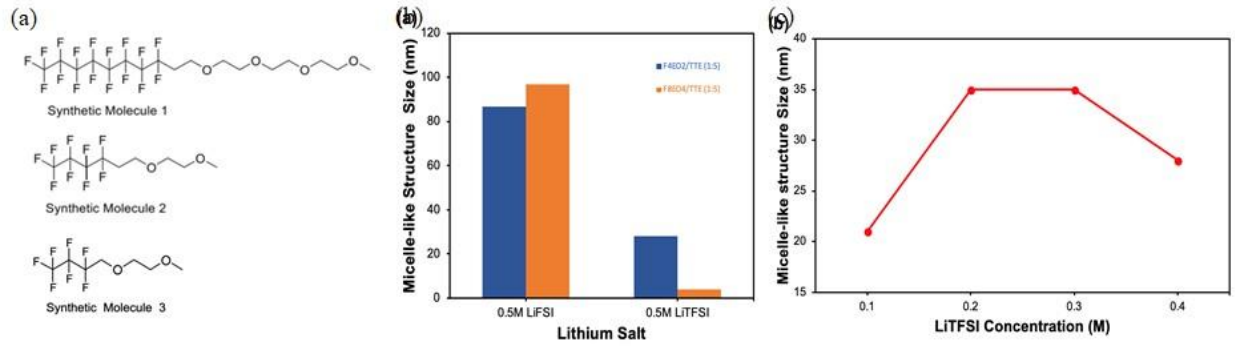

Figure II.10.E.1 (a) molecular structure of a class of synthesized fluorinated ether, denoted as F_8EO_4, F_4EO_2, and F_3EO_1 respectively. Size information extracted from SAXS measurement for (b) 0.5M salts dissolved in HFE/TTE 1:5 (v/v) as a function of salt and HFE additive identity. (b) Complex aggregate size as a function of LiTFSI salt concentration in F_4EO_2/TTE 1:5 (v/v).

The next effort of this work is focused on electrochemical performance of Li-S cell to demonstrate the suppression effect of polysulfide dissolution with the usage of these micelle electrolytes. The best CE and cycling performance of Li-S cell turns out to be the cells made by using the electrolyte-0.5M LiTFSI in F_3EO_1/TTE 1:5 (v:v), as shown in Figure II.10.E.2. The voltage profile exhibits several features in contrast to DOL/DME electrolyte which indicates polysulfide intermediates were significantly suppressed. First of all, the first plateau of discharging curves do not begin until 2.3V and percentage of this plateau is shortened, suggesting the dissolution of long chain polysulfides (Li_2S_n, $n \geq 6$) is alleviated in micelle electrolyte.[2] Secondly, both the second plateau of discharging curves and charging curves attenuates and sink to the lower volage with presence of increasing polarization. This is a quite common in sparingly-solvating electrolytes and indicates sluggish kinetics due to the increasingly solid-state nature of conversion. Thirdly, the cycling performance over 100 cycles shows significant improvement over the conventional ether based electrolytes. The Figure II.10.E.2(b) and (c) compares coulombic efficiency (CE) and cycling stability of various electrolytes. The CE remains constant around 99.9% for F_3EO_1/TTE 1:5 (v:v) electrolytes up to 100 cycles,

while it decays rapidly for baseline electrolyte and falls below CE line of F_3 electrolyte after only 30 cycles. The micelle electrolytes shows much superior cycling stability performance over baseline electrolyte. Again, F_3EO_1/TTE (1:5) electrolyte exhibits the optimum performance due to appropriate ionic conductivity and viscosity, while baseline electrolyte decays as a result of polysulfides dissolution and shuttling.

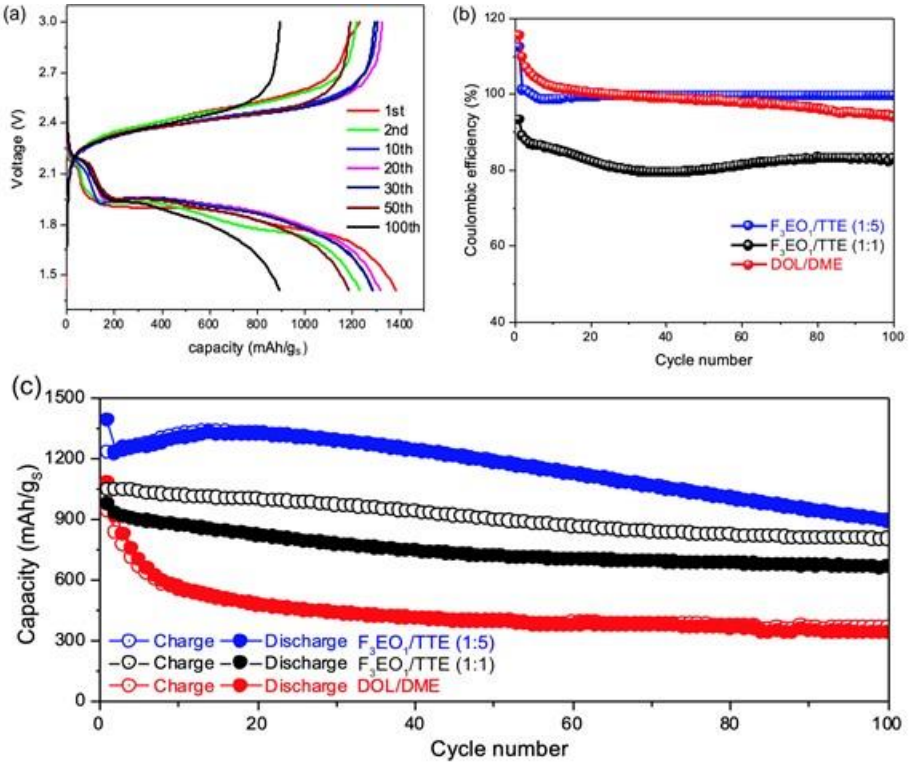

Figure II.10.E.2 voltage profile for F_3EO_1/TTE 1:5 (v:v) ; comparison of (b) coulombic efficiency and (c) cycling stability over 100 cycles between micelles electrolyte and DOL/DME electrolyte.

The other aspect of this work is on studying the stability of Li anode in micelle electrolyte by investigating Li platting/stripping behavior on Li-Cu cells. The fluorinated ether electrolyte is believed to have better chemical compatibility with lithium metal due to their rapid breakdown into passivating LiF. [3] The effect of various current rates was investigated to study rate capability of the cell. As displayed in Figure II.10.E.3, at 0.5mA/cm^2 current rate, initial CE was only about 90% but CE continuously increases with plating/stripping cycles after the Cu surface being passivated. Noted that more than 99.5% CE was observed after 200 cycles and likewise the polarization decreases with cycles, indicating micelle electrolyte is highly stable. A similar plating and stripping behavior was observed at 1.0mA/cm^2 and 2.0mA/cm^2 current rate. Though increased polarization appears, CE still remains above 99% after 100 cycles. This demonstrates good rate capability of cell by using micelle electrolyte. SEM images of deposition morphology were shown below the platting/striping curve for each current rate. Very smooth Lithium deposition surface was observed at 0.5 and 1.0 mA/cm^2 current rate. A relatively rough surface with lithium nodules formation appears at 2.0mA/cm^2 current rate. However, no the presence of lithium dendrite or dendritic growth was found on those surfaces indicating a good suppression of dendrite formation by using fluorinated additive electrolyte.

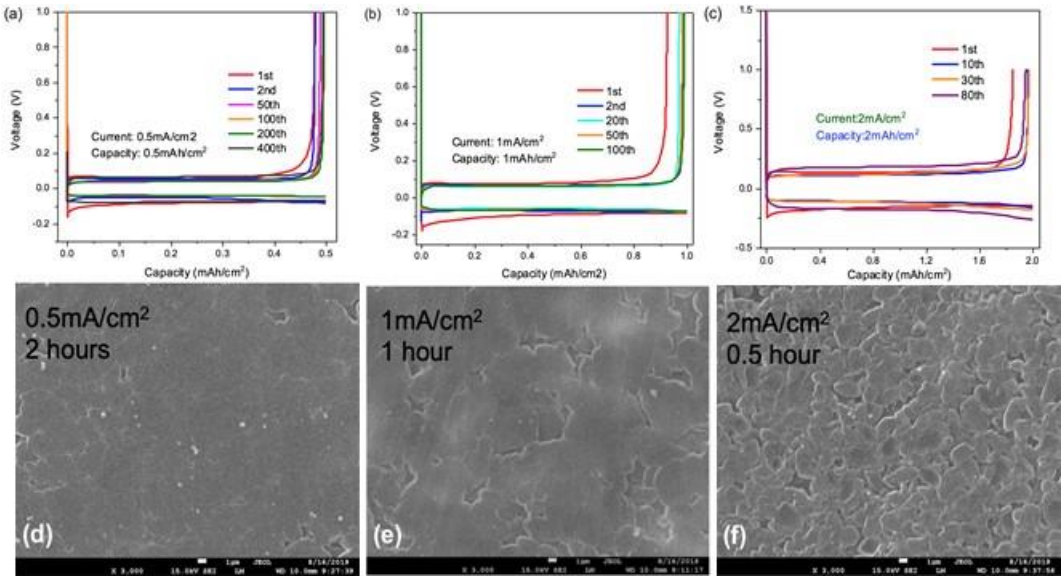

Figure II.10.E.3 Voltage profiles for Li plating/stripping test at various conditions: (a) 0.5mA/cm² current rate and 0.5mAh/cm² deposition capacity; (b) 1.0mA/cm² current rate and 1.0mAh/cm² deposition capacity (c) 2.0 mA/cm² current rate and 2.0 mAh/cm² deposition capacity; (d)-(f) SEM images (X3000 magnification) of deposition surface with 1.01.0mAh/cm² deposition capacity at various current rate.

II. Development of Alq3/Cu substrate for controlled Li deposition

Lithium metal is the most ideal anode material for next-generation high energy density batteries such as Li-S battery because of high theoretical charge capacity (3,860 mAh g^{-1}) and low redox potential (-3.04 V vs. standard hydrogen electrode).[4] In order to achieve uniform Li metal deposition, electrode surface modification is investigated to achieve the formation of controlled Li deposition.

Cu current collector is widely used in the battery fabrication because of high conductivity and low cost. However, it is reported that lithium deposits randomly on Cu due to the poor affinity with Li, leading to uncontrollable dendrite growth over long term cycling.[5] In order to address this issue, Al is coated onto Cu substrate due to good lithiophilicity, high conductivity, and low materials cost of metallic Al. Given the fact that Al can readily form Li-Al alloy, lithiophilic sites for lithium nucleation are provided on Al coating thus renders uniform deposition. However, there is one concern of Al coating – it is too brittle to remain intact in the process of alloying/dealloying,[6] which will incubate more aggressive dendrite growth from those fractured areas. In this thrust, we propose a strategy to avoid Al fracture situation by using a tris-(8-hydroxyquinoline) aluminum (Alq_3) coated copper substrate. Alq_3 is a widely used organometallic compound which the centered Al_3^+ ion is coordinated with hydroxyquinoline ligands. Al_3^+ is expected to be reduced to metallic Al during the initial Li deposition. Because of the unique chelate compound structure, Al source is stabilized, protected, and separated by organic ligands, which could provide uniformly scattered lithophilic nucleation sites for lithium deposition, reduce the nucleation overpotential, and enhance structural integrity. Our results show Alq_3 exhibits good conductivity and electrochemical stability and can modulate lithium metal growth on Cu surface. Lithium deposition morphology characterized by SEM is compared as a function of differing conditions (coating thickness, current density etc.). Figure II.10.E.4(a) and (b) show flat depositing morphology without aggressive growth of dendritic lithium on Alq_3/Cu-50 electrode at low current density (I=0.05 mA/cm²), while rod-like micro dendrites with uniform distribution appears at higher current density (I=1 mA/cm²). In addition, we've also demonstrated morphology control of deposited lithium by tuning variables such as current density and coating thickness. Optimal cycling stability and stable coulombic efficiency over 300 cycles are observed on the Li||Alq_3/Cu cell at 50 nm coating thickness (denoted as Alq_3/Cu-50). As revealed by Figure II.10.E.4(c), All exhibit CE retention in a reasonable range of 80%–90% as is typical for carbonate based electrolyte,[7] while Alq_3/Cu-50 electrode outperforms others with the highest 91% CE on average because of high surface area and superior conductivity. Finally, the time evolution voltage

curve as well as SEM images is used to study lithium dendrite growth on Cu, Al/Cu, Alq_3/Cu electrodes. In Figure II.10.E.4(d), voltage curve of each electrode demonstrates good consistency for the deposition process. Notably, Li-Al alloy formation occurs on Al/Cu electrode indicated by 0.25V potential shift. Both Alq_3/Cu and pure Cu electrode show a typical potential diagram of lithium platting. However, on Alq_3/Cu electrode, lithium deposition occurs with 8min delay because of reduction of Al^{3+} first. This sluggish kinetics also somehow indicates dendrite formation and growth was somehow suppressed.

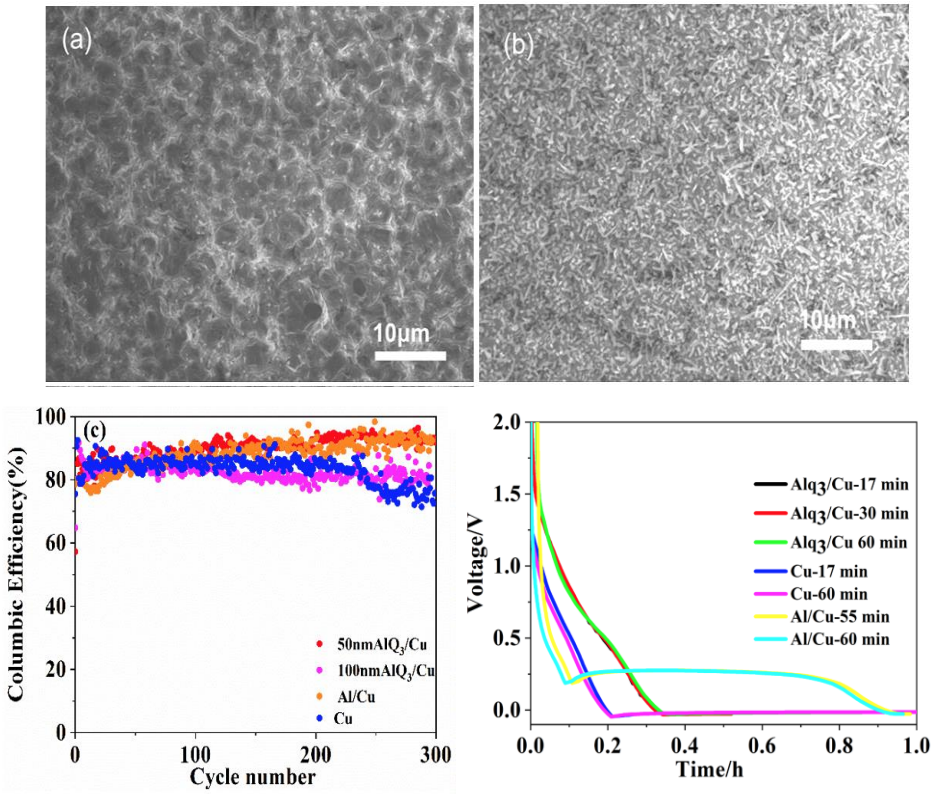

Figure II.10.E.4 SEM of Alq_3/Cu-50 substrate for 1h lithium deposition with various current density (a) 0.05 mA/cm^2; (b) 1 mA/cm^2; (c) CE over 300 cycles of Li plating/stripping process at 0.05 mA/cm^2 current rate; (d) Voltage profile for Li deposition at current density of 0.05 mA cm-2 as a function of substrates and deposition time.

Conclusions

A novel strategy to suppress polysulfide dissolution in Li-S cells utilizing fluorinated ether with a bi-functional structure (one lithiophilic section and one lithiophobic section) similar to that of amphiphilic surfactant was developed. The electrolyte used in this work was made by LiTFSI or LiFSI dissolved in HFE solvent at various concentrations with dilution of 1,1,2,2-tetrafluoroethyl-2,2,3,3-tetrafluoropropyl ether (TTE) solvent. Lithium salts dissolution follows a special solvation mechanism where dissociated lithium ions are readily coordinated with donating groups to form micelle-like complex, which was verified by small angle X-ray scattering. Superior cycling stability and higher coulombic efficiency was observed for Li-S cells fabricated with micelle electrolyte compared to those using benchmark DME/DOL electrolyte. The high coulombic efficiency together with decent polarization from Li-Cu cell plating/stripping tests also indicate good chemical compatibility of micelle electrolyte. In addition, dendrite formation was greatly reduced as only smooth surface morphology on deposited lithium was observed. Additionally, developed was a strategy to facilitate lithium deposition and prevent uncontrolled mossy dendrite growth by a conductive chelating compound Alq_3 as a surface modulation coating on copper current collector. The improved CE performance promising morphology results validate the use of Alq_3/Cu-50 as a favorable substrate for controlled lithium nucleation and deposition. Combining the effort of new electrolytes and electrode surface modification may lead to significantly improved Li-S rechargeable battery system in the near future.

Key Publications

1. Y. Zhao, C. Fang, G. Zhang, D. Hubble, A. Nallapaneni, C. Zhu, Z. Zhao, Z. Liu, J. Lau, Y. Fu, G. Liu, "A Micelle Electrolyte Enabled by Fluorinated Ether Additives for Polysulfide Suppression and Li Metal Stabilization in Li-S Battery", Front. Chem. 2020, 8, 484

2. H. Zhong, Y. Zhao, T. Zhang, G. Liu, "Controlled Lithium Deposition on Alq_3 Coated Substrate", Batteries & Supercaps, 2020, 3, 1-9.

References

1. Borchert, H.; Shevchenko, E. V.; Robert, A.; Mekis, I.; Kornowski, A.; Grübel, G.; Weller, H., Determination of Nanocrystal Size: A Comparison of TEM, SAXS, and XRD Studies of Highly Monodisperse CoPt3 Particles. *Langmiur* 2005, *21*, 1931-1936

2. Yin, Y. X.; Xin, S.; Guo, Y. G.; Wan, L. J., Lithium-sulfur batteries: electrochemistry, materials, and prospects. *Angew. Chem., Int. Ed. Engl.* 2013**,** *52* (50), 13186-13200.

3. Zhang, X.-Q.; Cheng, X.-B.; Chen, X.; Yan, C.; Zhang, Q., Fluoroethylene Carbonate Additives to Render Uniform Li Deposits in Lithium Metal Batteries. Advanced Functional Materials 2017, 27 (10).

4. Y. Guo, H. Li, T. Zhai, Reviving Lithium-Metal Anodes for Next-Generation High-energy Batteries eneration, *Adv Mater*. 2017, 29.

5. H. Ye, Z. J. Zheng, H. R. Yao, S. C. Liu, T. T. Zuo, X. W. Wu, Y. X. Yin, N. W. Li, J. J. Gu, F. F. Cao, Y. G. Guo, Guiding Uniform Li Plating/Stripping through Lithium-Aluminum Alloying Medium for Long-Life Li Metal Batteries, *Angew Chem Int Ed Engl*. 2019, 58, 1094-1099.

6. Y. Hamon, T. Brousse, F. Jousse, P. Topart, P. Buvat, D. M. Schleich, Aluminum negative electrode in lithium ion batteries, *J. Power Sources*. 2001, 97, 185-187.

7. H. Wu, Y. Cao, L. Geng, C. Wang, In Situ Formation of Stable Interfacial Coating for High Performance Lithium Metal Anodes, *Chem. Mater.* 2017, 29, 3572-3579.

II.10.F Multifunctional, Self-Healing Polyelectrolyte Gels for Long-Cycle-Life, High-Capacity Sulfur Cathodes in Li-S Batteries (University of Washington)

Alex K.-Y. Jen, Principal Investigator
University of Washington
Seattle, WA 98195
Email: ajen@u.washington.edu

Jihui Yang, Principal Investigator
University of Washington
Roberts Hall 315, Box 352120
Seattle, WA 98195
Email: jihuiy@uw.edu

Tien Duong, DOE Technology Development Manager
U.S. Department of Energy
E-mail: Tien.Duong@ee.doe.gov

Start Date: October 1, 2016 End Date: June 30, 2010
Project Funding: $1,388,888 DOE share: $1,250,000 Non-DOE share: $138,888

Executive Summary

The project aims to develop polyelectrolyte gels consisting of partially crosslinked ionomer, interpenetrated with self-healing/polysulfide-trapping chains and swelled with a mixture of room temperature ionic liquid (RTIL) and lithium salt. To our knowledge, no other sulfur-based cathode design has combined self-healing behavior, polysulfide containment, and lithium dendrite suppression into a single design. We have demonstrated the benefits of multifunctional ionomer gel polyelectrolytes / gel cathodes with self-healing properties, as well as chemical modification of mesoporous carbons for S/C composite cathodes. Success of the proposed program of study would have wide ranging impact on the electric vehicle industry and society as a whole. A Li-S battery system with the capability of doubling lithium-ion energy density would enable the production of lighter, longer range electric vehicles at a cost that is affordable to the average U.S. household. The availability of such vehicles should lead to wide-ranging adoption over the coming years which, in combination with increased renewable electricity generation, will drastically decrease carbon emissions across the country and reduce U.S. dependency on fossil fuel sources.

Project Introduction

Current electric vehicle (EV) battery market is dominated by lithium-ion batteries (LIBs). However, conventional LIBs based on lithium metal oxide cathodes and graphite anode have begun to reach their performance limits after progressive material and device optimization over the past two decades. In order to meet EV everywhere goals of 75% cost reduction and 50% weight reduction in electric vehicle batteries by 2022, radically new strategies must be employed.

One very promising solution is to look beyond traditional lithium-ion intercalation chemistry towards "beyond-lithium" systems such as the lithium-sulfur (Li-S) battery. A sulfur cathode has a theoretical gravimetric specific capacity of 1673 mAh/g at ~2V vs Li/Li+, rendering a theoretical energy density improvement of 500% as compared to the lithium metal oxide cathodes found in LIBs. This increase can be matched on the anode side by using lithium metal, which has an intrinsic theoretical gravimetric specific capacity of 3860 mAh/g – an order of magnitude higher than graphite. Additionally, sulfur is cheap and earth-abundant, making this redox couple highly attractive for EV battery use.

However, a commercially-viable Li-S battery has remained elusive due to technical challenges. Many of them stem from the formation of polysulfides (Li_2S_x, $3 \leq x \leq 8$) which are highly soluble in organic electrolytes,

leading to self-discharge, passivation of the lithium anode, low coulombic efficiency due to dissolution of polysulfides into the electrolyte, and voltage hysteresis from differences in forward and backward reaction mechanism. In addition, both the starting material (sulfur) and end products (Li_2S, Li_2S_2) are highly insulating, necessitating the use of a large amount of conductive carbon in the electrode. Furthermore, because the overall reaction is accompanied by a large volume change, this composite matrix is prone to cracking, resulting battery failure. Finally, on the anode side, lithium metal tends to form dendrites upon repeated stripping and plating, which puncture the cell separator and cause internal shorting.

Researchers have addressed these issues, to a certain degree of success, using a variety of strategies, introducing ionic liquid electrolytes, solid electrolyte interphase (SEI)-improving additives, mesoporous carbon hosts, advanced binders, and many others. Still, despite these myriad strategies, a safe Li-S battery with long cycle life based on scalable fabrication techniques remains elusive, as no single strategy or even combination of several has proven to be totally effective at both stopping efficiency/capacity loss due to dissolution of polysulfides and preventing lithium dendrite growth.

Objectives

The project objective is to develop self-healing and polysulfide-trapping polyelectrolyte gels containing room-temperature ionic liquid (RTIL) for the Li-S battery system. The Li-S battery will be capable of achieving gravimetric and volumetric energy densities of ≥ 800 Wh/kg and ≥ 1000 Wh/L, respectively.

The project will achieve the following performance targets (all cycles at C/10 rate unless otherwise specified):

- A cathode gravimetric specific capacity of ≥675 mAh/g after 10 charge/discharge cycles between 2.8 and 1.7 V vs Li/Li^+
- An average coulombic efficiency ≥99% for the 10th cycle through the 100th
- ≥90% capacity retention after 100 cycles as compared to the capacity of the 10th cycle.
- ≥30% capacity retention when cycled at a C/2 rate, as compared to the capacity at C/10
- Ability to operate at temperatures between -20°C and 50°C.

Approach

We have developed Li-S coin cells that utilize self-healing, interpenetrated ionomer gel electrolytes in both the cathode and separator. The team has synthesized necessary starting materials and fabrication procedures of components of these gels while testing their relevant electrochemical and mechanical properties. All components are combined into interpenetrating structures, which were tested both alone and in cell configurations. Device performance data have been collected and used to further optimize designs of both materials and cells, and to optimize Li-S battery design capable of doubling the energy density of traditional LIBs. Throughout the program, the team has focused on (1) design and synthesis of a variety of precursors for gel electrolytes, (2) fabrication and testing of both reference materials and novel materials made from these precursors, and (3) iterative validation and improvement of our design principles through both materials and device testing.

During Budget Period 1 (quarters 1-6), we have synthesized a series of starting materials for gel electrolytes and self-healing polymers, fabricated them into films both individually and together, and then tested their electrochemical/mechanical properties relevant to Li-S battery application. Additionally, we have synthesized a variety of sulfur/carbon (S/C) composites, utilizing mesoporous carbons with varying properties and molecular functional groups placed onto their surfaces. Organic synthesis includes naphthalene diimide (NDI) and pyrene (Py) containing materials, as well as monomers for the polyelectrolyte phase. Materials have been synthesized using established synthetic routes and characterized by nuclear magnetic resonance (NMR), gel permeation chromatography, and/or solution-phase cyclic voltammetry (CV). Synthesis of S/C composites was

achieved by mixing of sulfur and carbon at above the melting point of sulfur, and characterized by Brunauer–Emmett–Teller (BET) surface area and pore size analysis to confirm successful integration of sulfur into the pore structure. Surface functionality has been studied by thermal gravimetric analysis (TGA) and x-ray photoelectron spectroscopy (XPS).

Fabrication and testing of ionomer gels with varying ratios of ionic liquid (IL) and molecular starting materials have been performed. Basic electrochemical and mechanical properties of each gel composition have been tested and used to establish a structure-property relationship, then gel compositions with favorable properties were tested in detail on long-term interfacial stability with Li foil, Li dendrite suppression, and polysulfide diffusion. Conductivity and thermal properties of fabricated ionomer gels have been assessed by A/C impedance, TGA, and differential scanning calorimetry. Tensile stress tests were carried out to determine mechanical properties. Li/gel/Li symmetric cells have been constructed, and analyzed for development of interfacial resistance and lithium dendrite suppression using cyclic stripping/plating method. Polysulfide trapping ability were quantified by measuring UV-vis absorption spectra from a fixed-concentration solution.

Fabrication and testing of self-healing films, made from various structures and ratios of NDI and Py containing moieties, were performed. Mechanical and self-healing properties have been tested, as well as ionic conductivity. Static and dynamic mechanical testing have been carried out to determine tensile modulus, toughness modulus, and storage and loss modulus. Self-healing properties were characterized by slicing films in two pieces, contacting the pieces, and annealing at fixed temperature, followed by repeating tensile stress tests. This were followed by fabrication and testing of gel electrolytes containing both physically-crosslinked (self-healing) and chemically-crosslinked (ionomer) materials. All of the tests detailed above were performed in order to determine how the performance of individual components of the gel translates into an interpenetrated composite structures containing all components.

Parallel to materials development efforts, we undertook fabrication and testing of small-capacity coin cells utilizing a variety of cell design concepts, including organic electrolytes, IL electrolytes, non-self-healing polyelectrolyte gels, and interpenetrating gels in order to benchmark performance and demonstrate materials system capable of significantly improved performance. The test coin cells were cycled for short periods (≤100 cycles) at rates ranging from C/100 or C/50 to C/2. A/C impedance spectra have been collected at various points in order to observe the evolution of internal impedances during cell cycling. Voltages traces during charge and discharge were observed and correlated to internal processes such as polysulfide speciation and buildup of insulating Li_2S/Li_2S_2 deposits. The origins of undesirable cell performance were investigated using a combination of experimental techniques, including targeted cycling, CV mesurements, A/C impedance measurements, scanning electron microcopy, and x-ray diffraction (XRD).

During Budget Period 2 (quarters 7-13), we have continued synthesis of molecular components of gels and S/C composites from raw starting materials. All synthesis has been performed according to literature procedures, as well as working out necessary modifications in order to produce materials more efficiently. Testing of gel electrolytes containing both physically-crosslinked and chemically-crosslinked ionomer materials were continued, as well as development of self-healing polymer films based on physical-crosslinking. Basic electrochemical and mechanical (including self-healing) behavior have been characterized, and gel compositions with favorable properties were tested in more detail on long-term interfacial stability with Li foil, Li dendrite suppression, and polysulfide diffusion repeatedly. Systematic structural and compositional adjustments have been made to the gel electrolyte formulation based on cell performance data.

We have fabricated coin cells with sulfur-based cathodes and lithium metal anodes which utilize developed electrolyte materials in the cell structure, and studied their performance as a function of material design. Initially, low-mass-loading demonstration cells was constructed, followed by practical-loading cells. This task culminated directly in the production of deliverable 10 mAh Li-S cells for DOE testing. All of the experiments previously mentioned for cell testing have been performed as cell design was being optimized. We have utilized instrumentation at the Washington Clean Energy Testbeds on the University of Washington campus,

the University of Washington Molecular Analysis Facility, and NMR/microscopy instrumentation available at the Environmental Molecular Sciences Laboratory at the Pacific Northwest National Lab.

Results

Multifunctional Ionomer Gel Polyelectrolytes / Gel Cathodes

We have designed and optimized a synthetic procedure for producing crosslinked gel polyelectrolytes containing ionic liquid, which can be thermally cured using a radical initiator. In addition to using commercially available PEG dimethacrylate (PEGDMA), with an average molecular weight of 750Da, as a starting material, we also chemically synthesized PEGDMA with a higher molecular weight of ~3500Da, as well as an ionic-liquid-like monomer containing a pyrrolidinium cation and $TFSI^-$ counterion. We have become interested in "solvate" ionic liquids (SIL) in particular as a solvent for our gels, given their high Li^+ transference numbers (~0.5) relative to ternary pyrrolidinium$^+$:Li^+:$TFSI^-$ ionic liquids, as well as their facile synthesis and ability to be diluted with organic solvents for higher conductivity.

Using our procedure, we have successfully produced solvate ionogels (SIGs) containing varying ratios and structures of polymerizable components (Figure II.10.F.1a). All formulas produced transparent, freestanding films. We then measured the bulk ionic conductivity (κ) and lithium transference number (t_{Li+}) of each sample at 23°C, plus Li(G4)TFSI, a solvate ionic liquid itself as a control, using Electrochemical Impedance Spectroscopy (EIS) and/or potentiostatic polarization, as well as elastic modulus (E) using uniaxial compression with a 50N load cell. Following this, we have fabricated Li|Li symmetric cells using SIG films as separators, or Li(G4)TFSI/glass fiber as a control, and measured time-to-short-circuit (T_{sc}) under static polarization at 0.1 mA/cm^2. The results are summarized in Table II.10.F.1. Finally, Li|Li symmetric cells containing SIG separators (SIG 2 or SIG 5) were subjected to cyclic polarization test (period: 6 hr) at ±0.1 mA/cm^2, and the results compared to Li(G4)TFSI/glass fiber (Figure II.10.F.1b).

Table II.10.F.1 Composition/Properties of Five Novel SIGs in Comparison to Li(G4)TFSI

Formula	Components (vol% added)					Properties				
	P_{750}	P_{3500}	TEGMA	PyrTFSIMA	1,4-dioxane	Li(G4)TFSI	κ (mS/cm)	t_{Li+}	E (kPa)	T_{sc} (hr)
SIG 1	20%	0%	0%	0%	0%	80%	0.73	0.21	369	10.8
SIG 2	0%	20%	0%	0%	0%	80%	1.05	0.28	254	113.9
SIG 3	0%	10%	10%	0%	0%	80%	0.92	0.24	249	25.0
SIG 4	0%	10%	0%	10%	0%	80%	1.07	0.16	401	99.3
SIG 5	0%	20%	0%	0%	13.3%	66.6%	2.15	0.57	228	118.3
Li(G4)TFSI	0%	0%	0%	0%	0%	100%	1.08	0.13	n/a	10.6

We observed several distinct trends in electrochemical properties based on the SIG composition. Most notably, we found that formulas based on longer-chain P_{3500} produced uniformly higher conductivity values, in some cases even exceeding Li(G4)TFSI in its liquid state. Lithium transference number also increases with PEG molecular weight, with two outliers: SIG 4, in which t_{Li+} is decreased due to excess mobile anion content, and SIG 5, in which t_{Li+} is greatly increased due to the inclusion of 1,4-dioxane as a diluent. Finally, we found that suppression of/resistance to lithium dendrites (as measured by T_{sc}) also increases for samples with P_{3500}, although the variability between such samples is large. As seen in Figure II.10.F.1b, best-performing formulas SIG 2 and SIG 5 are able to strip and plate lithium reversibly, at low overpotential, for ≥600 hrs without any signs of short-circuit.

Following our investigation of basic SIG properties, we have developed a fabrication process for S/C composite cathodes with SIGs cured *in situ*, as well as a process for creating composite separators consist of SIGs cured into a porous polypropylene film (Celgard 2500) (Figure II.10.F.1c). We then assembled Li-S coin cells from these components and performed galvanostatic charge/discharge tests on them at C/10 rate. Representative cycling results are shown in Figure II.10.F.1d. We observed that capacity loss occurs gradually over the first 20 cycles, followed by recovery and stabilization at about 900 mAh/g. Coulombic efficiency averaged roughly 97% per cycle (note: no $LiNO_3$ or any other anode-passivating additives were present in this cell).

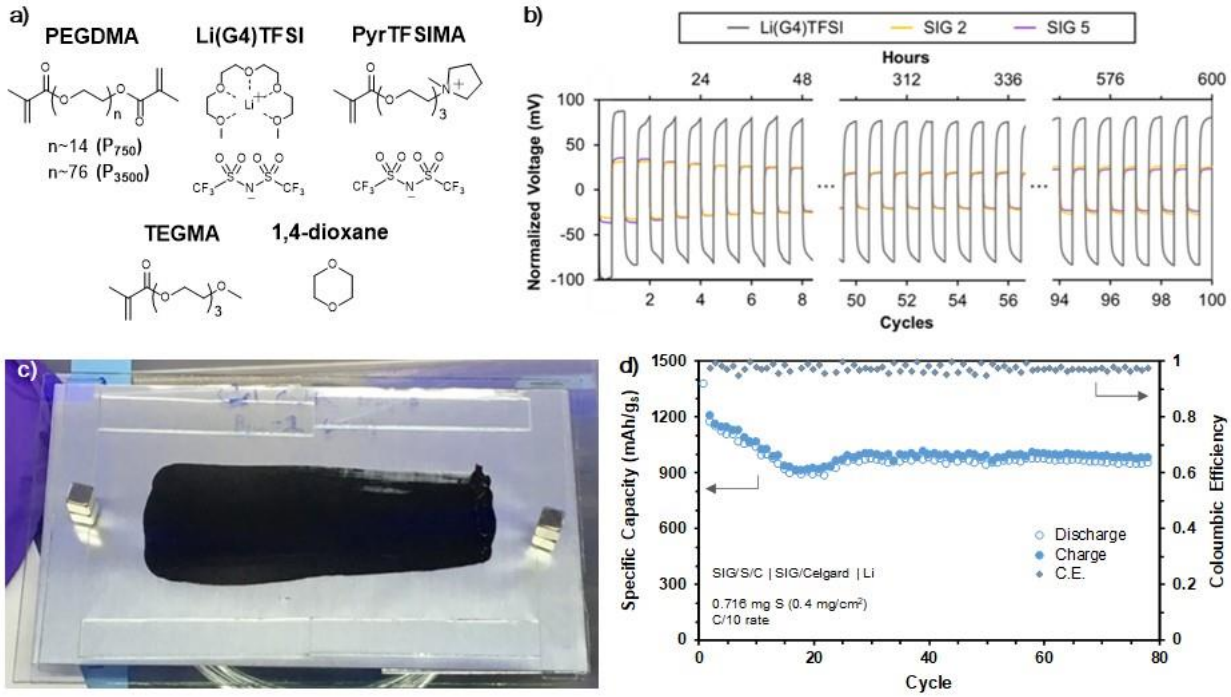

Figure II.10.F.1 a) Molecular structure of SIG components with their abbreviated names. b) Cycling data (0.1 mA/cm²) for Li|Li symmetric cells with SIG separators, along with Li(G4)TFSI/glass fiber for comparison. All cells completed 100 cycles (600 hrs) without developing short circuit. Cured SIG separators required less overpotential (normalized to separator thickness) for Li stripping/plating than the solvate ionic liquid alone. c) Photograph of a SIG/S/C cathode, where SIG is cured in situ within the pores of the electrode. d) Galvanostatic cycling data (theoretical C/10 rate) for an all-solid-state Li-S cell containing SIG in both the cathode and separator. Capacity retention (81%, 2nd → 75th cycle) and coulombic efficiency (~97%) are encouragingly high even without anode passivating additives (i.e. $LiNO_3$).

This quasi-solid-state cells showed excellent specific capacity and retention upon cycling at 23°C, but with a significant overpotential, and voltage features that are a typical of cells with organic electrolytes. We have developed improved formulations and fabrication procedures for our gel cathodes and composite separators, and also performed extensive testing on these materials (both in and outside of full-cell configurations) to gain insight into the origins of full-cell cycling behavior. Figure II.10.F.2a shows the capacity of Li-S concept cells (~1 mg_{sulfur}/cm^2) over 100 cycles at 30°C. At C/10 rate. We found that quasi-solid-state cells containing SIG showing better capacities than the control material system (PVdF binder + organic liquid electrolyte in Celgard 2500), but by a slight amount (~100 mAh/g), and exhibit long-term capacity fading at a similar rate. We have used 1,3-dioxolane (DOL) and 1,2-dimethoxyethane (DME) mixed solvents in 1:1 ratio as the organic liquid electrolyte. By contrast, cells of typical construction with Li(G4)TFSI electrolyte showed poorer initial capacity, but with reduced fading. Examining voltage profiles (3rd cycle) for these cells at varying rate revealed major differences between cell types (Figure II.10.F.1b-c). We found that the discharge overpotentials of SIG/SIL cells are consistently larger than the control electrolyte, especially during the low-voltage region that accounts for most of the cell capacity. The transition from higher to lower voltage also occurs more gradually

for these cells, although the voltage minimum at this transition point, characteristic of a polysulfide-induced "dip" in liquid electrolyte conductivity, is absent for the SIG cells. Similarly, overpotential for SIG/SIL cells during recharge is generally larger, and more sloped for SIG cells. Also notable is the maximum in voltage observed upon initiation of recharge, well-known to be associated with activation of solid Li_2S deposits. This "bump" is significant for the SIL case, but far less prominent in the SIG case and entirely absent from the control.

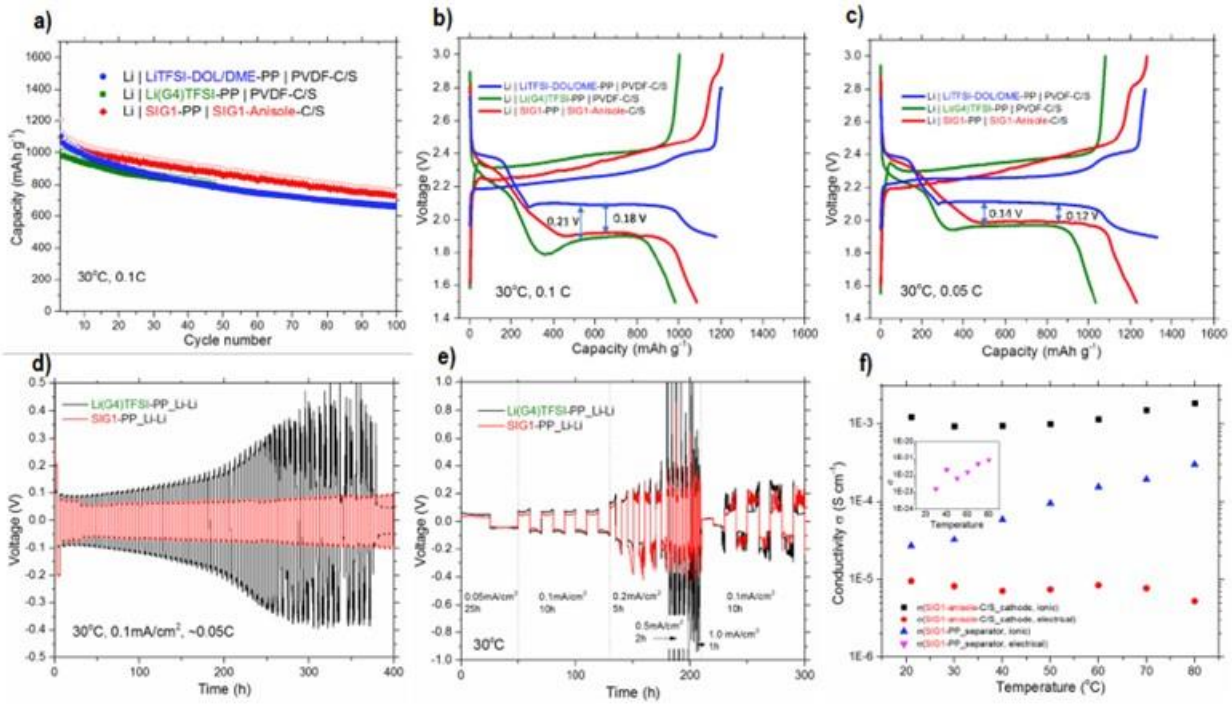

Figure II.10.F.2 a) Specific capacity (mAh/g_{sulfur}) for Li-S cells of indicated cell structure [anode |electrolyte-separator |binder/gel-cathode] during Galvanostatic cycling at C/10 (calculated based on 1672 mAh/G_{sulfur} theoretical capacity). b) 3rd cycle voltage profiles for indicated cells at C/10. c) 3rd cycle voltage profiles for indicated cells at C/20. d) Cycling of symmetric cells [electrolyte|separator |electrodes] at ±0.1 mA/cm^2 using a 6h cycle period. e) Cycling of symmetric cells [electrolyte |separator |electrodes] with varying current density and cycle period. f) Ionic/electrical conductivity vs temperature for gel cathodes and gel separators, extracted from frequency-dependent impedance between stainless steel blocking electrodes.

In order to gain further insight, we have fabricated Li|Li symmetric cells containing either SIG composite separators or Celgard 2500 wetted with a similar total volume of SIL. Cyclic stripping/plating at 30°C and 0.1 mA/cm^2 (Figure II.10.F.2d), roughly equivalent to the current density of the above cells at C/20, reveals consistently lower and more-stable overpotential for the SIG separators (~50mV vs. ~100mV). This trend roughly holds at larger current densities (Figure II.10.F.2e), although the potentials become erratic at 0.2 mA/cm^2 or higher, indicating unstable behavior that will eventually lead to dendrite-related short-circuiting. These differences at the anode/separator may explain the increased overpotential of full-cells with SIL electrolyte as compared to SIG, however they do not explain the differences of both compared to the control, even assuming the anode/separator resistance of the control cell is negligible. While many of these differences may instead relate to altered conversion chemistries in the cathode, a significant portion of the overpotential in the SIG cells may be due to poor electrical conductivity in the cathode as well. Impedance analysis of a typical gel cathode sample between blocking electrodes revealed a very poor through-film electrical conductivity of $<10^{-5}$ S/cm (Figure II.10.F.2f), corresponding to ~125mV cell polarization at C/10 rate.

Previously, we have noticed unique changes to the discharge voltage traces in QSS cells (less-distinct and lengthened upper plateau, downward shift of the lower plateau), and ruled out the influence of anode or

separator processes as being the primary source of these changes, leaving the cathode as the most likely source. However, it was still unclear whether the behavior we observed was due to overpotentials in the cathode – whether ohmic and/or state-of-charge-dependent – or a reflection of changes to the chemical pathways for sulfur conversion *i.e.* thermodynamic changes brought on by the SIG electrolyte.

In order to clarify the influence of these disparate factors on QSS cell behavior, we have performed Galvanostatic Intermittent Titration Technique (GITT) measurements on Li-S cells of varying design (Figure II.10.F.3a-f). This experiment allowed us to calculate the overpotential for each cell as a function of state-of-charge, and thus determine the open-circuit or "true" thermodynamic shape of the charge/discharge curves in each case. Since open circuit voltage depends solely on the chemical potentials of reactive species within the cell, this provides insight into the chemistry of our SIG cathodes, and also suggests areas of improvement within the design. For the sake of a clear comparison, we have marked the point of least overpotential during the lower discharge plateau of each cell. First, we may compare these discharge overpotentials amongst cell designs. Unsurprisingly, the control cell with organic electrolyte (Figure II.10.F.3a) requires the least overpotential, and the cell with a traditional cathode (S/C/PVDF) and limited volume of SIL (Figure II.10.F.3c) requires the most overpotential. This is due to significantly-increased charge transfer resistance at both the anode and cathode for the latter case, and highlights the limitations of "dropping in" a new electrolyte without considering its effects on the entire battery system. Adding a large excess of SIL electrolyte (Figure II.10.F.3b) alleviates this effect slightly, most likely due to improved wetting of the cathode and total capacity of the electrolyte to dissolve lithium polysulfides. On the other hand, replacing half of the volume of SIL with a SIG composite separator (Figure II.10.F.3d) gives a similar result without requiring an increase in total electrolyte volume. This is almost certainly related to decreased anode overpotential, as we have previously observed for SIG composite separators.

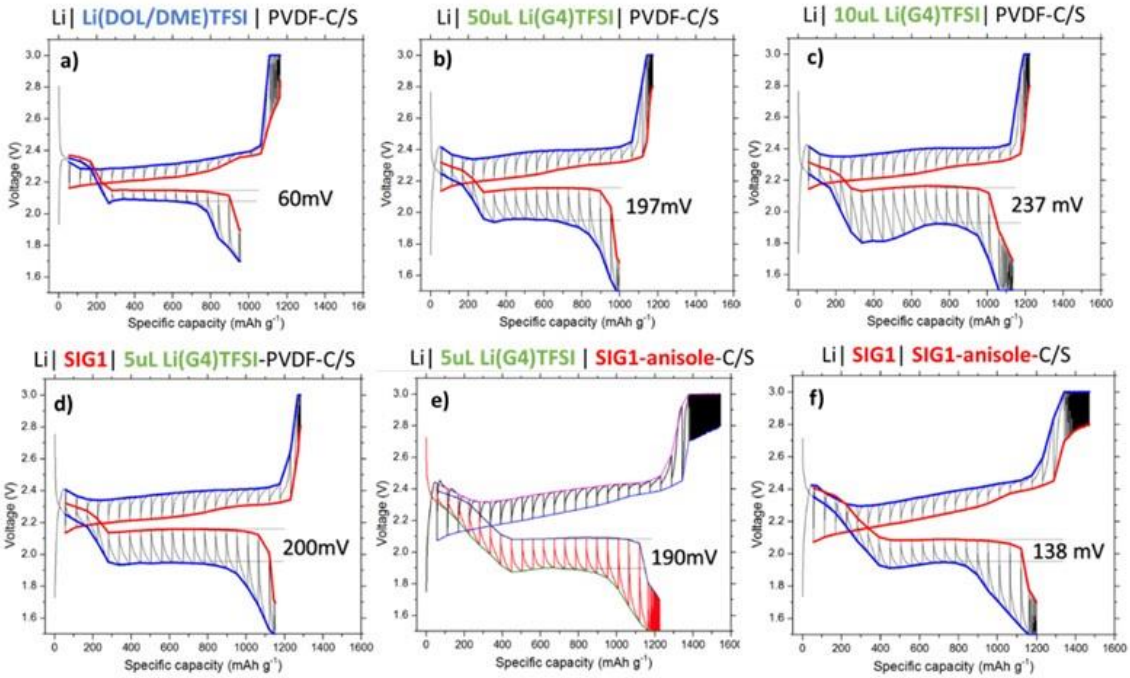

Figure II.10.F.3 GITT results for six different Li-S coin cell designs, with the cell structure indicated as Li | electrolyte | cathode. All data was collected at 30°C and C/10 rate (assuming 1672 mAh/g_S), with GITT being performed on the 3rd cycle. All cathodes have ~1 mg_S/cm^2 areal loading. The blue and red curves connect the current-applied voltages and open-circuit voltages, respectively, measured directly before current interruption and after a 1hr rest, respectively. Their difference represents the cell overpotential at that point of charge/discharge. The point of minimum overpotential during the lower discharge plateau of each cell is labeled on the corresponding graphs.

Cells containing SIG-based cathodes, on the other hand, outperform all cell designs based on S/C/PVDF cathodes and SIL electrolyte, with the lowest overpotential observed for the QSS cell (Figure II.10.F.3f). We can partially attribute this to the improved wetting of the cathode achieved by our fabrication technique, as well as the influence of polysulfide-solvating diluent anisole. Overall, this result indicates that the internal resistance of our QSS design can only partially explain its altered discharge characteristics. This implies that some fundamental change to the chemical pathway of discharge has also occurred in SIG-based cathodes. Comparing open circuit voltage traces (red curves in Figure II.10.F.3) further implicates this. We note that merely switching from an organic electrolyte to SIL electrolyte in the cathode has very little effect on the open circuit behavior, mostly manifesting as a slight decrease in the upper plateau voltage and less-sharp transition to the lower plateau. The differences in current-applied voltage between these cells can therefore mostly be attributed to overpotential. On the other hand, the open-circuit behavior of cells with SIG-based cathodes closely resembles their current-applied behavior, starting with a broad, extended, downward-sloping region that begins at a *higher* voltage than the upper plateau of traditional designs but ends at a *lower* voltage. This is followed by a lower plateau that is downward shifted by ~50mV from the other cells.

While we cannot yet identify the exact changes in cathode chemistry that cause these features, it seems safe to say that our SIG-based electrolyte has a dramatic effect on the sulfur conversion chemistry. These results also suggest that the increased overpotential associated with ionic liquid electrolytes in Li-S cells can be successfully mitigated to acceptable levels. We have accomplished this in our design through use of a solvating diluent (anisole), a cathode fabrication process which circumvents electrolyte wetting problems, and a gel composite separator that successfully restricts polysulfide migration without incurring large overpotentials or significant extra weight/volume. We have successfully fabricated test coin cells with higher cathode loadings ($\geq$4 mg_S/cm^2) based on these strategies and adjusted our design accordingly in order to retain favorable cycling characteristics whilst minimizing overpotential.

Furthermore, we have tested the robustness of our QSS design towards self-discharge, which Li-S batteries are particularly susceptible to. A reference cell, fabricated using PVDF binder in the cathode and liquid organic electrolyte (1M LiTFSI in DOL:DME 1:1 v/v + 1wt% $LiNO_3$), was also tested for comparison. After two "formation cycles" at C/20, cells were cycled at C/10 until the 7th discharge, at which point 300 mAh/g_S capacity was discharged, followed by a 100h rest. Discharge was then resumed, and cycling continued as normal. Figure II.10.F.4a depicts the results: the cell with organic electrolyte ("OE") lost 185 mAh/g_S (18.3%) to self-discharge relative to the previous cycle, while the QSS cell lost only 108 mAh/g_S (8.9%). Interestingly, the OE cell recovered 63 mAh/g_S in the following cycle, bringing the total two-cycle loss to 12.1%, while the QSS cell lost an additional 44 mAh/g_S for a similar total of 12.5%. However, the OE charge/discharge capacities rapidly diverged after this point, strongly suggesting an accelerated redox shuttle effect. The QSS cell did not exhibit this behavior, instead cycling its remaining capacity stably with a coulombic efficiency of ~98%. This result is especially encouraging given the lack of anode-passivating additives in the QSS system. Hence, while we have observed that both designs are similarly susceptible to irreversible capacity loss during self-discharge, we have found that the QSS system is more resistant to continued degradation caused by the redistribution of sulfur species during prolonged rest.

Examining the voltage profiles of each cell before, during, and after the self-discharge test (Figure II.10.F.4b and c) provides some insight into the cause of capacity loss. First, we found that the general shape and voltage of each discharge/charge region remains mostly unaffected following self-discharge; however, in each case, the irreversible capacity loss is mostly localized to the lower plateau, corresponding to the conversion of soluble polysulfides into insoluble Li_2S_2 and Li_2S. Prior literature suggests that the lower plateau capacity is often limited by the passivation of conducting surfaces with these insoluble products, rather than the total availability of reducible sulfur. Our GITT results also support this interpretation. In light of this, the capacity which is irreversibly lost by both cells following self-discharge may be related to the disproportionation of soluble polysulfides during the rest period, resulting in the production of insoluble sulfides and accelerated passivation of cathode surfaces. Further study is needed to confirm this mechanism and investigate its prevention.

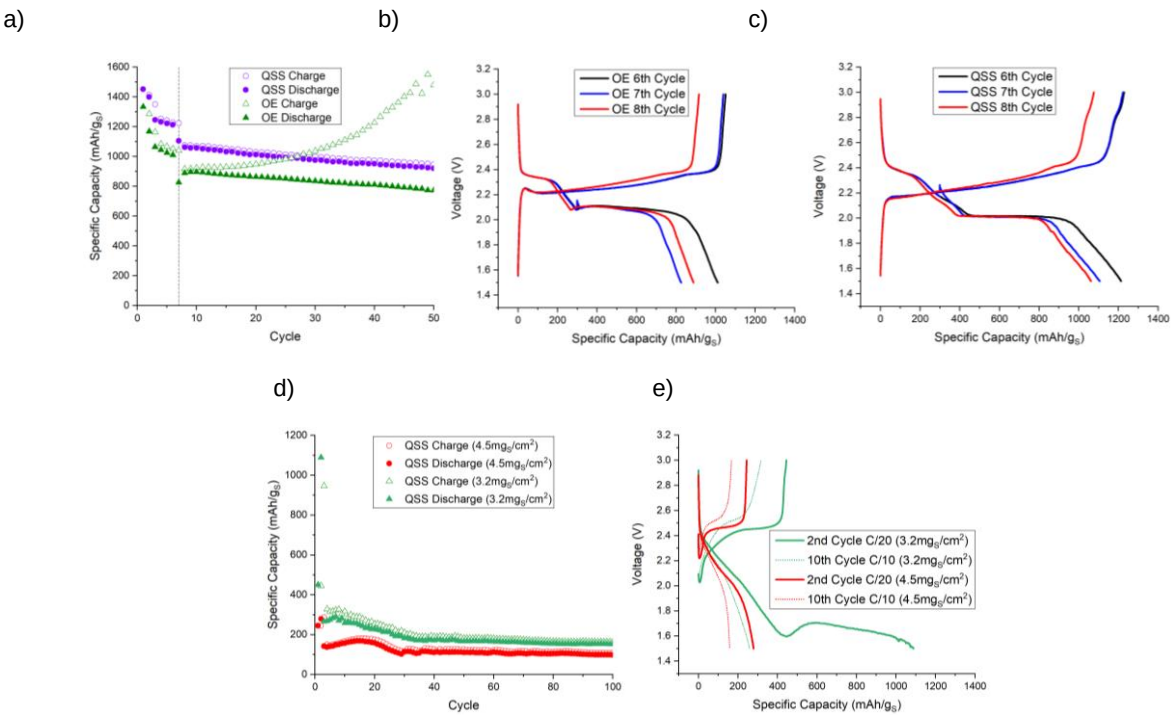

Figure II.10.F.4 a) Cycling performance of QSS and OE cells, with a 100h rest during 7th cycle discharge. Some irreversible capacity loss is observed for both designs, but the OE cell exhibits accelerated redox shuttling after the self-discharge test, while the QSS cell continues to cycle stably; b) OE voltage profiles for the 6th, 7th, and 8th cycles; c) QSS voltage profiles for the 6th, 7th, and 8th cycles; d) Cycling performance of two representative high-loading QSS cells. Available capacity is quite low at C/10 due to large internal resistance in the thick cathodes; e) 2nd and 10th voltage profiles for the representative high-loading cells. Increasing resistance during discharge prevents the cells from accessing their lower plateau capacity, especially at C/10.

We also focused significant effort on fabricating and testing QSS cells with higher cathode areal loadings, with the goal of attaining reasonable performance at 4-5 mg_S/cm^2. Since our gel cathodes are blade coated from a precursor-containing slurry, we were able to achieve increased loading simply by casting films at increased height. However, the downside of this "cure in place" method is that high loading cathodes were exceptionally thick – over 0.5mm in some cases. Predictably, this produced significant internal resistance in the final QSS cells. As shown in Figure II.10.F.4d, the capacity available during the initial two cycles at C/20 was commonly much larger than that available at C/10, which was generally 100-200 mAh/g_S in all cases. Examining the voltage profiles in Figure II.10.F.4e reveals that the cause of this low capacity is an inability to reach the lower plateau prior to the safety cutoff of 1.5V, due to rapidly growing internal resistance during the initial stages of discharge. We have also tested a number of improved gel cathode formulations with the goal of minimizing required thickness for high loading, and reducing the cathode charge transfer overpotential.

Higher-loading cathodes (>$3mg_S/cm^2$) were fabricated by increasing the coating thickness; however, these cathodes performed poorly due to their extreme thickness (approaching 1mm). In order to reduce the thickness of such cathodes without compromising their sulfur content, we have revised our SIG sulfur/carbon (S/C) slurry composition (Table II.10.F.2) to increase the overall solids content prior to the cure. To compensate for this, we also increased the amount of diluent solvent anisole relative to Li(G4)TFSI SIL in order to reduce viscosity of slurry and promote mixing. Much of the diluent was evaporated during the casting process and therefore acts merely as a processing solvent. The remaining anisole was meant to promote faster ion transport in the final cathode as a solvent diluent in the SIG electrolyte.

Table II.10.F.2 Composition of SIG/S/C slurry (and subsequent cathode) by weight. The demonstration cell formula was used for QSS cells with ~1 mg_S/cm^2 cathode loading, while the updated formula is intended for high-loading (4-5 mg_S/cm^2) cells

SIG/S/C Slurry Composition (1g basis)		
	Demonstration Cell Formula	**Updated High-Loading Formula**
Solid Components	**0.1g**	**0.2g**
S_8	117.5mg	133mg
MJ430	117.5mg	57mg
MWCNT	65mg	70mg
Liquid Components	**0.9g**	**0.8g**
PEGDMA (750Da)	153.4mg	143.9mg
Radical Initiator	3.1mg	2.9mg
Li(G4)TFSI	650.9mg	458.8mg
Anisole	92.6mg	195.5mg
(Addt'l Anisole, evap.)	9.3mg	219.6mg

This updated slurry composition did indeed produce cathodes with 4-5mg_S/cm^2 loading at ~400-500μm thickness. However, we found that casted cathode films from the composition were not mechanically robust and did not survive the die-cutting process without significant crumbling and/or delamination from the carbon-coated aluminum substrate. This is almost certainly due to the reduced amount of PEDGMA cross-linker relative to solids content. We have adjusted the ratio of liquid components in our slurry to produce a robust cathode with high loading and reduced thickness, as well as attempting to introduce our self-healing polymers into the slurry for additional robustness and electrochemical performance enhancement for deliverable test cells.

Self-Healing Materials

We have undertaken detailed study of the π-π interaction between NDI and Py, with the intent of designing a tunable self-healing materials system. We began this investigation by studying model compounds N,N'-dibutylnapthalene diimide (dbNDI) and Pyrene (Py) in dichloromethane solutions. UV-Vis analysis shows that upon addition of small amounts of dbNDI to a Py solution, a clear, broad absorption peak appears at 500nm. A second absorption peak at 514 nm becomes apparent upon increasing the ratio of dbNDI to Py, peaking at a ratio of 1:0.5 (Figure II.10.F.5). This suggests two different types of complex can be formed. NMR data also suggests complex formation of stoichiometry 1:1 (dbNDI:Py) and 2:1 (dbNDI:Py).

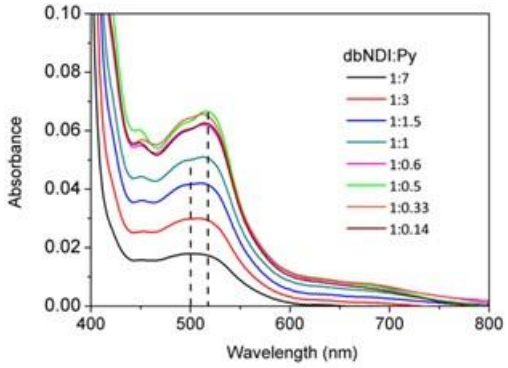

Figure II.10.F.5 UV-Visible spectra of dbNDI/Py solutions of varying ratios (constant total concentration) in dichloromethane, showing development of peaks in the visible region corresponding to complex formation.

Collecting UV-Vis spectra of these optimum stoichiometries while varying overall concentrations and applying Beer-Lambert Beer's law to the 500/514 nm peaks, we have calculated complexation free energies of

the complexes as -8.19 kJ/mol for the 1:1 dbNDI:Py complex and -16.49 kJ/mol for the 2:1 dbNDI:Py complex respectively. In the application of this interaction to polymeric systems, we have expected that varying the ratio between an NDI-containing polymer and a Py-containing cross-linker would result in changes in self-healing behavior, in accordance with the changing strength of the dominant π-π interaction modes. We have tested this approach to develop a novel polymeric material system for self-healing: PENDI-C6, a methacrylate polymer bearing NDI pendants with a six-carbon tail (as well as triethylene glycol methyl ether pendants for processability and ionic conductivity) and triPy, a three-arm branched polyethylene glycol (PEG) derivative terminated on each branch by pyrene units.

UV-Vis spectra of 1:1 (NDI:Py) mixtures produced the same 500 nm absorption peak observed for the small model molecules, confirming that the same non-covalent interactions occur between polymers. First, we have produced free-standing films of mixtures of these polymers corresponding to a 1:1 molar ratio of NDI to Py units (termed as PP-1), and tested their mechanical and self-healing properties. In order to adjust the dominant interaction mode in these materials without changing the relative amounts of polymer, we selectively the small model molecules dbNDI (PP-NDI) or Py (PP-Py) added into the films during fabrication, reinforcing either the 1:1 or 2:1 complexes to form according to Le Chatelier's principle. The self-healing behavior that we observed is summarized in Figure II.10.F.6. Changing the ratio of NDI to Py groups in the polymer composite does indeed produce large changes in behavior, allowing us to tune self-healing temperature from 30 °C-70 °C. Additionally, we observed that tensile modulus varied from 69MPa (PP-Py) to 219MPa (PP-NDI). These values are significantly higher than what has been reported for the vast majority of self-healing materials in literature.

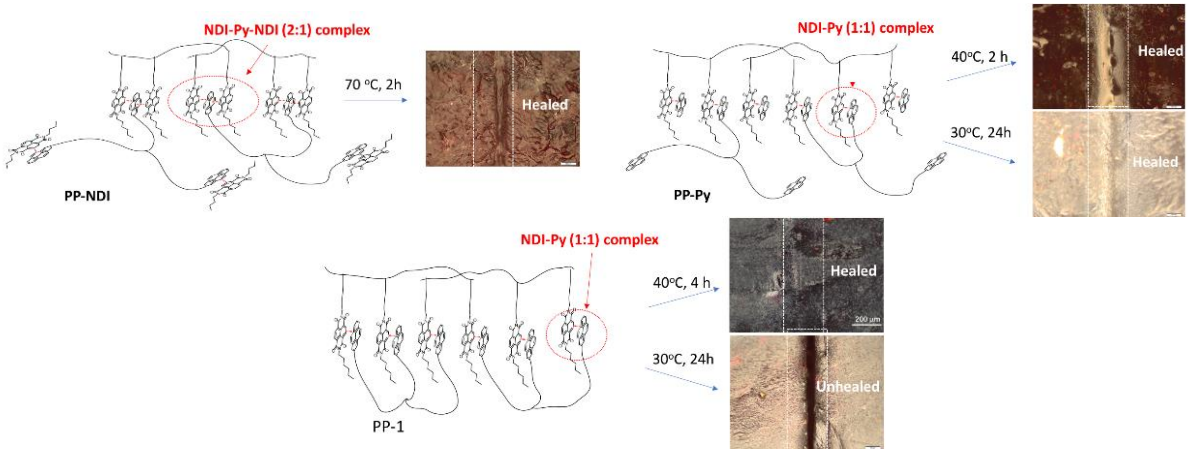

Figure II.10.F.6 Our novel polymeric materials form free-standing, self-healing films when mixed together in a 1:1 molar ratio of NDI to Py units. The self-healing temperature of these films can be adjusted over a wide range by doping small molecule NDI or Py compounds into the film, forcing formation of either 1:1 or 2:1 NDI:Py complexes, which have vastly different binding energies. Addition of these small molecules can also be used to "passivate" binding sites, adjusting the crosslinking density.

Finally, we have tested the ability of the PP-1 polymer composite to transport Li^+ ions by doping films with LiTFSI in a 20:1 [ethyleneoxy]:[Li^+] ratio during fabrication. Ionic conductivities of the films were measured between 10-55°C by A/C impedance measurements between stainless steel plates followed by fitting the data to a Debye impedance model with non-ideal interfacial capacitance. We found that the LiTFSI-doped composite had a conductivity in excess of 10^{-6} S/cm at 50 °C, which is in a similar range to other solid polymer electrolytes based on PEG derivatives.

Base on this material design approach, we have demonstrated a series of self-healing polymer composites PP-1, PP-Py, and PP-dbNDI with systematically varying self-healing temperatures. Extensive mechanical testing was carried out on these composites to demonstrate their tensile properties before and after healing also. Representative films were sliced in two, contacted under minimal pressure, and healed for 12 hours at 40-60°C, followed by stress-strain testing. As shown in Figure II.10.F.7, even after heat treatment at only 40°C, all healed materials still possess high Young's moduli (> 60 MPa). We also demonstrated good compatibility of solvate ionic liquid Li(G4)TFSI with PP-1, which swells well with up to 33wt% liquid to form a freestanding gel with bulk ionic conductivity ~10^{-5} S/cm at 25°C. Furthermore, the PP-1/Li(G4)TFSI gel showed complete self-healing ability at 40°C, lower than the polymer alone.

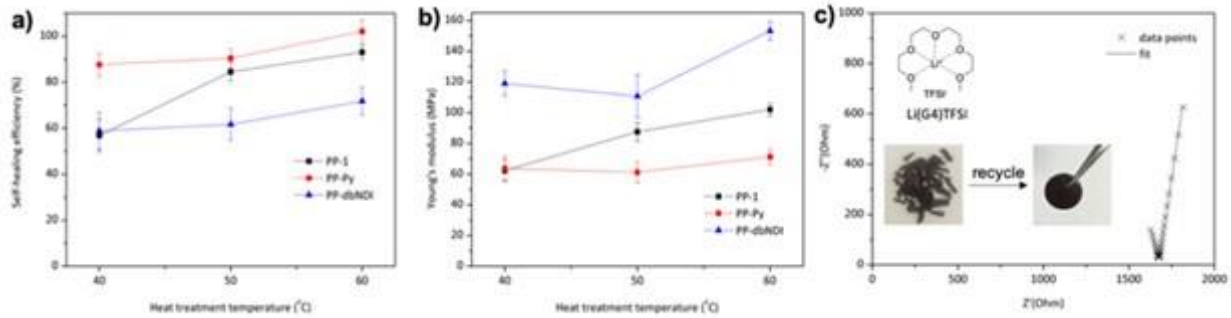

Figure II.10.F.7 a) Self-healing efficiency based on maximum tensile strength and, b) recovery of Young's modulus upon self-healing of composite films after heat treatment at different temperatures. c) Nyquist plots and curve fit of PP-1/Li(G4)TFSI at room temperature and recovery of PP-1/Li(G4)TFSI under 40 °C for 12 h.

Chemical Modification of Mesoporous Carbons for S/C Composite Cathodes

We have explored chemical surface modification of the starting carbon materials as an additional route to improve cathode performance further. Our procedure is based on well-studied diazonium chemistry, which attaches phenyl rings bearing customizable functional groups to carbon surfaces with unsaturated bonds. Functionalization was confirmed by pore shrinkage (determined by BET, as well as the appearance of nitrogen- or sulfur-associated peaks in XPS analysis and weight loss during TGA). The extent of functionalization, measured by %weight loss during TGA as compared to control samples, was easily varied by adjusting reaction conditions. We used this procedure to attach a variety of chemical functional groups to carbon surfaces, including primary amines, tertiary amines, and sulfides. In particular, we were interested in sulfide-based surface modifiers, as reversible covalent bonding between sulfide groups is well-known and has potential for containment of lithium polysulfides within the cathode pore structure. We have performed detailed study on S/C cathodes modified with phenylthiol functional groups by analyzing cell cycling data. Figure II.10.F.8 summarize data from this investigation.

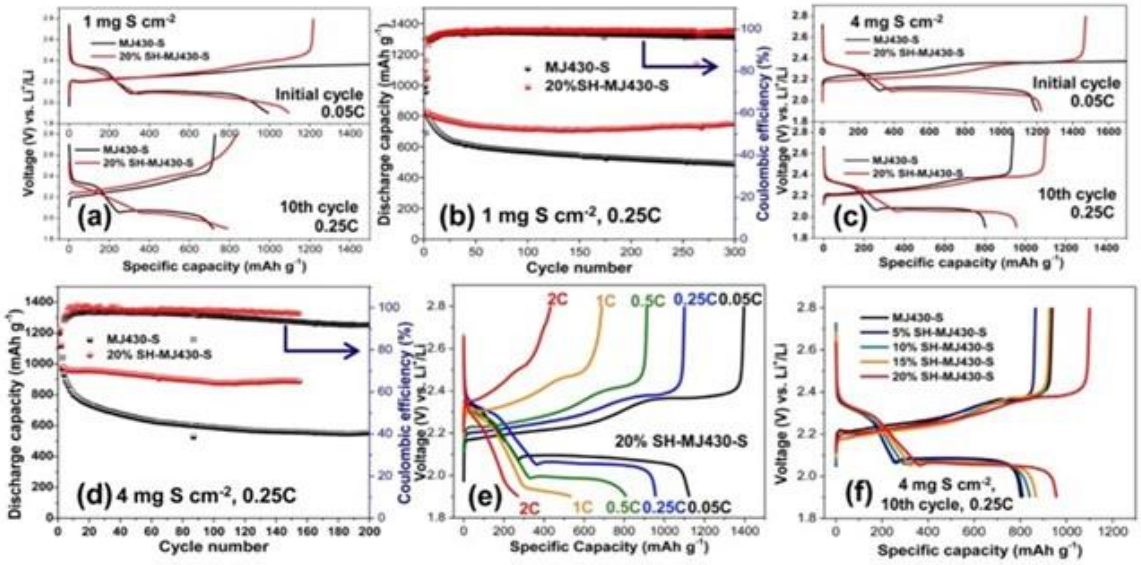

Figure II.10.F.8 a) The discharge/charge voltage profiles of the MJ430-S and the 20% SH-MJ430-S electrodes based on S loading of 1 mg cm-2 at initial activation cycle (0.05 C) and 10th cycle (0.25C). b) The corresponding cycling performance within the first 300 cycles. c) The discharge/charge voltage profiles, and d) the corresponding cycling performance of the MJ430-S and the 20% SH-MJ430-S electrodes based on S loading of 4 mg cm-2. e) The discharge/charge voltage profiles of the 20% SH-MJ430-S electrodes at various rate. f) The discharge/charge voltage profiles of a series [SH]-MJ430 with increasing weight percentage of thiol modifier, from 5% to 20%, controlled via reaction conditions. Thiol modification largely increases capacity retention.

We have noticed several important trends from the study. Firstly, the introduction of phenylthiol modifiers progressively inhibits the overcharging behavior at 2.37 V in the MJ430-S cathode (Figure II.10.F.9a and Figure II.10.F.9c), indicating an efficient protection of LiPS diffusion from the cathode to the Li anode, which is ascribed to the interaction of SH modifiers with LiPSs. In addition, Figure II.10.F.9b and Figure II.10.F.9d compares the long-term cycling performance of MJ430-S and 20% SH-MJ420-S cathodes with various S loading. As expected, the modified cathode displays an obvious improvement in capacity retention. The capacity of the unmodified MJ430-S decreased from 812 to 486 mAh g^{-1} at 0.25 C (C/4) (a capacity retention of 60%) after 300 cycles. Over the same number of cycles, the 20% SH-MJ430-S device shows a capacity retention of 89%, with the discharge capacity dropping from 838 to 745 mAh g^{-1}. Due to the additional challenges of a cathode with a high S loading (e.g. poor wettability and severe LiPS dissolution), the thick MJ430-S cells show a poor cycling retention of 56% at 0.25C, whereas the capacity retention in the 20% SH-MJ430-S cells remains at 89% (Figure II.10.F.9d). Upon close examination of the discharge curves of modified cells at various discharge rates, we found an increased polarization (Figure II.10.F.9e). The polarization could be gradually reduced as the concentration of SH modifier decreases (Figure II.10.F.9f).

The improved capacity retention of MJ430-S cathodes with SH modifiers is presumed to strongly correspond to the multifunctional surface interacting with solvated active materials in many ways, such as reversible covalent disulfide interactions and electrostatic lithium bonding. Such interactions were verified by solid-state magic angle spinning (MAS) NMR and XPS experiments (Figure II.10.F.9a-d). Although the surface interaction increased the charge transfer resistance and cell overpotential (Figure II.10.F.9e-h), these side-effects can be balanced by fine-tuning the modifier concentration. Additionally, the polar, nucleophilic surface induced by thiol modifiers can improve wetting of the electrode surface by the electrolytes due to the dipole-dipole interaction of SH groups with Li^+ from the electrolyte (Figure II.10.F.9a-b). The improved wettability can leads to enhanced utilization of active materials during cycling, since better access to the electrolyte within pores would aid in solvation and confinement of solvated LiPSs, while mainlining the tethering of solvated LiPSs to the cathode surface. In summary, we have correlated the alteration of surface chemistry with

electrochemical behavior of cycled cells. The fundamental insight on the thiol functionality suggests a further rational design of multi-functional interfaces to achieve better Li-S performance.

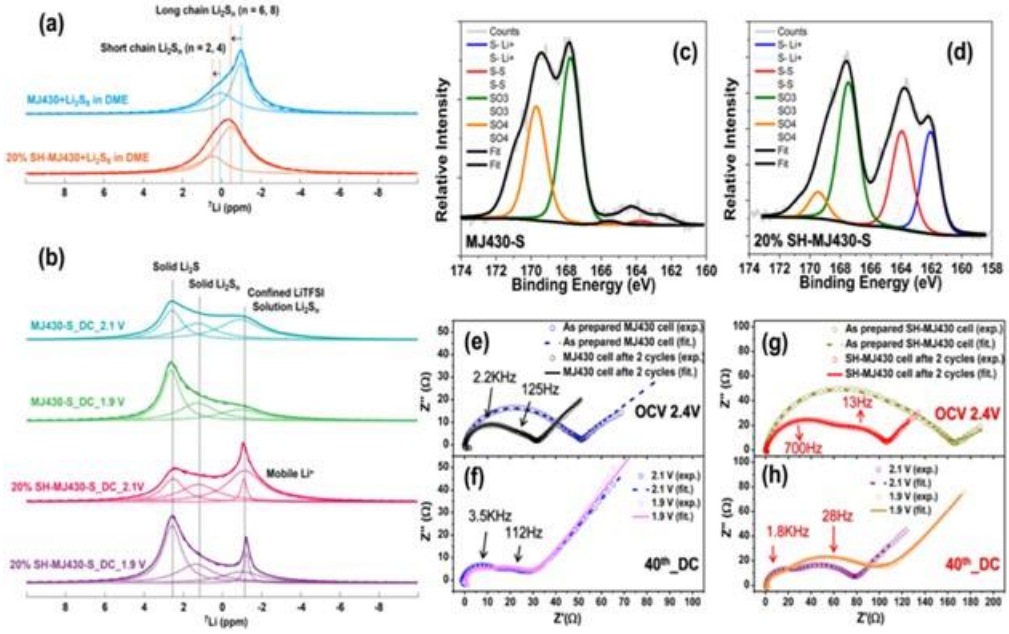

Figure II.10.F.9 . a) ^{7}Li MAS NMR spectra of the Li_2S_8 solution interacting with MJ430 and the 20% SH-MJ430. b) ^{7}Li MAS NMR spectra of the cathode materials with MJ430-S and 20% SH-MJ430-S from Li-S cells that are discharged to different voltages, with experimental data in solid lines, deconvolution peaks in dot lines, and the sum of deconvolution peaks in dash lines. High resolution S2p XPS spectra of c) the MJ430-S, and d) the 20% SH-MJ430-S cathodes, obtained from Li-S cells discharged to 1.9 V after 100 cycles. EIS analysis of (e-f) the MJ430-S and (g-h) the 20% SH-MJ430-S cells at different stages of discharge within 40 cycles.

Self-Healing Polymer Binders for S/C Composite Cathodes

Following basic characterization, we have tested the efficiency of PP materials on a Li-S battery system. We expected performance improvement from the two primary functions of PP: the polysulfide-trapping effect of naphthalene diimide (NDI) and PEG moieties, and resistance to cracks formed during cycling due to self-healing properties. In order to isolate the former effect, we have fabricated low-loading (~1 mg_S/cm^2) cathodes using either PVDF or various combinations of PENDI-350/triPy (latest generation of PP) as binders. The low loading ensures that mechanical stresses play a minor role in cell performance compared to cathode chemistry.

Cells were configured with Li metal anodes, Celgard 2500 separators, DOL:DME organic electrolyte, and C/S composite cathodes. The polymer binders made of up to 20 wt% of the cathode materials. We achieved best results using a PP binder with a 3:1 NDI:Py molar ratio (Figure II.10.F.10), which displayed >74% capacity retention after 100 cycles, as compared to less than 44% for the PVDF control. The charge/discharge rate capability of cathodes with the 3:1 PP binder formulation was also slightly better than the PVDF control, with almost no capacity loss observed up to 1C rate. To study the polysulfide-trapping properties of the PP binder separately, we added a saturated solution of Li_2S_8 (~10mM) in Li(G4)TFSI to powdered PVDF, PEO (M_w~1,000kDa), and PENDI-350, all of which are virtually insoluble in the ionic liquid, followed by dilution, stirring, and filtering to remove the polymers along with any absorbed polysulfides. We observed a much lighter colored solution from which had been in contact with PENDI-350 than either PEO or PVDF, indicating a strong interaction between PENDI-350 and Li_2S_x species, which tend to remove them from solution, *i.e.*, polysulfide trapping.

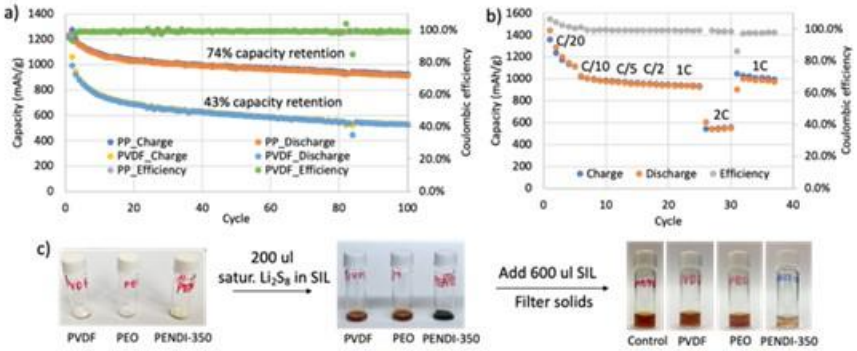

Figure II.10.F.10 a) Self-healing efficiency based on maximum tensile strength at C/20 and, b) recovery of Young's modulus upon self-healing of composite films after heat treatment at different temperatures, c) Nyquist plots and curve fit of PP-1/Li(G4)TFSI at room temperature and recovery of PP-1/Li(G4)TFSI under 40 °C for 12 h.

Following our characterization of the PENDI-350/triPy (PP) self-healing polymer system, we have continued our efforts to characterize the effects of this material in a Li-S battery system. The PP polymer when used as a binder for S/C composite cathode has shown to increase the capacity retention significantly from 43.5% to 74.2% after 100 cycles at C/20. The capacity retention reached close to 100% after 100 cycles at 1C, which demonstrated the polysulfide trapping property of the PP polymer. We have performed CV and UV-Vis studies of dibutyl-NDI (dbNDI) and Li_2S_8 as model compounds to understand the details of polysulfide-trapping mechanism. By simply mixing dbNDI with Li_2S_8 in DOL/DME, the color changed immediately from yellow of Li_2S_8 to black of mixture of polysulfide with various compositions (Figure II.10.F.11a). The color change suggests strong interaction/reaction between dbNDI and Li_2S_8. UV-vis studies were conducted of solutions with various ratio between dbNDI and Li_2S_8. As shown in Figure II.10.F.11b, dbNDI (red line) shows characteristic peak of neutral state at 379 nm. After adding Li_2S_8 with molar ratio of 1:1, the peak of the neutral dbNDI (379 nm) decreases slightly and a peak at 483 nm increases, which corresponds to the existence of dbNDI mono-anion. When the ratio of Li_2S_8:dbNDI increase to 2:1, more of the neutral dbNDI is reduced into dbNDI mono-anion. Meanwhile, the peak of $dbNDI^{2-}$ di-anion appears at 407 nm which increase rapidly with increasing Li_2S_8. In short, the NDI moiety enhance the capacity retention in two different ways: first, it can be reversibly reduced into NDI^{2-} di-anons which can trap polysulfides via strong ion-dipole interaction (Figure II.10.F.11d); second, it can also function possibly as a redox-mediator (Figure II.10.F.11e), which promotes the charge transfers to and from the active sulfur species and finally increases the utilization of sulfur during discharge process. Further characterization of this effect is ongoing in Li-S cell with practical loading of sulfur.

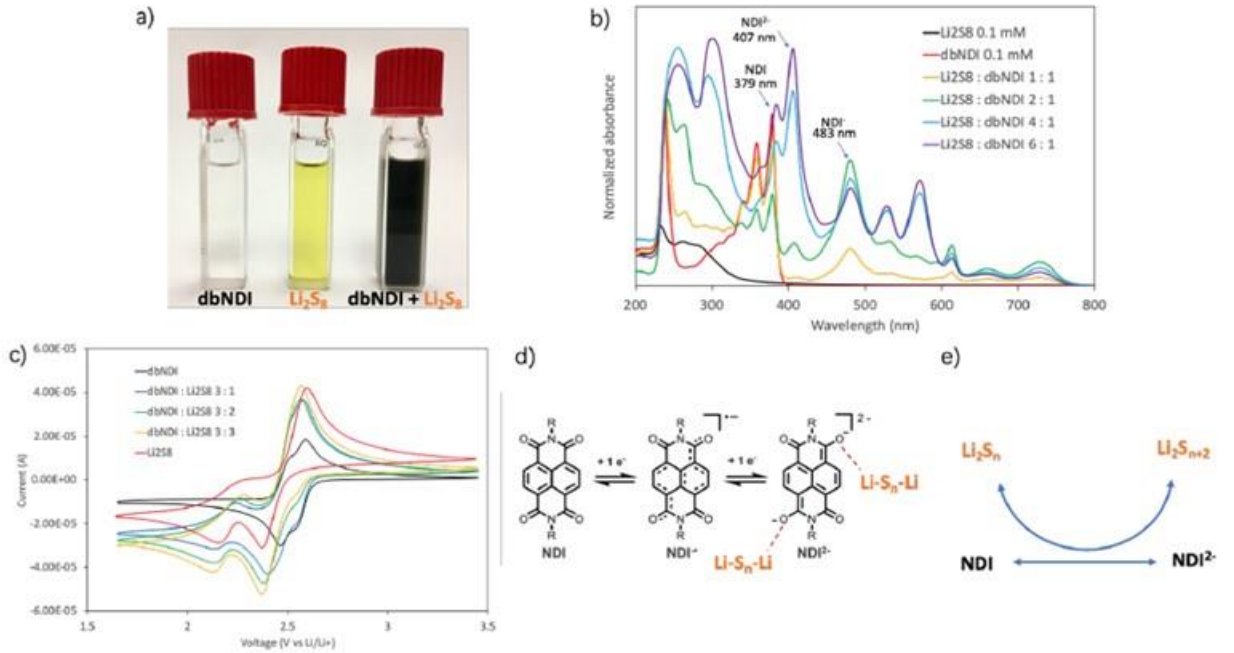

Figure II.10.F.11 a) Visual test of the reaction/interaction between Li_2S_8 (1 mM) in DOL/DME (1;1, v:v) with 1 M LiTFSI. b) UV-vis spectra of solutions with various ratio of dbNDI and Li_2S_8 in DOL/DME (1;1, v:v) with 1 M LiTFSI. The concentration of dbNDI was kept constant as 0.1 mM in the mixture. c) CV spectra of dbNDI (10 mM) and Li_2S_8 in DOL/DME (1;1, v:v) with 1 M LiTFSI (scan rate = 10 mV/s). d) Two-step reductions of NDI moiety and illustration of ion-dipole interaction between NDI moiety and polysulfides. e) Schematic illustration of redox-mediator effect of NDI moiety.

With the significant improvement of capacity retention at low S loading (around 1 mg/cm^2), we have focused our efforts on fabricating cathode with higher S loading (> 4 mg/cm^2). We have fabricated high loading S cathode via systematic design of the S cathode components, including current collector, ratio design between PENDI-350 and tri-Py, choose of carbon conductive additive, and the loading amount of S/C composite. Carbon coated Al foil was used as current collector which improves the adhesion between current collector with S cathode. Multi-wall carbon nanotubes were used as conductive additive to replace carbon black. The 1D structure of carbon nanotube is known to assist formation of interpenetrating conductive 3D network, which improves not only mechanical integration but also electrical conductivity of the cathode composite. The S ratio of S/C composite was improved to 70%. Using the new composition, we have fabricated cathodes with PP and PVDF as binder (Figure II.10.F.12a). After 40 cycles, the discharge capacity of cathode with PP binder retains as high as 1070 mAh/g (capacity retention of 92%). On the contrary, the capacity retention of cathode with PVDF binder after 40 cycles is about 76% (909 mAh/g). Meanwhile, we have noticed the decrease of coulombic efficiency, especially for cathode based on PVDF. We attributed this to the side reactions on the anode.

Besides, we have carefully optimized the ratio between PENDI-350 and tri-Py to achieve high loading S cathode considering efficient mechanical integration. As mentioned, a more robust binder system is needed to mitigate the increasing mechanical stress for S cathode with higher loading. As shown in Figure II.10.F.12b, the S cathode with PENDI-350:tri-Py ratio of 3:1 is prone to cracking as the S loading amount increases to around 4 mg/cm^2. After increasing the amount of tri-Py by changing the ratio to 1:1, a continuous S cathode was achieved even with S loading greater than 4.2 mg/cm^2. The cycling performances of cathode with PP binder (PENDI-350 : tri-Py = 1:1) with varying S loading is shown in Figure II.10.F.12c. The initial capacity of cathode with loading of 4.2 mg/cm^2 is around 800 mAh/g and remains almost constant within first several cycles. This implies the successful operation of S cathode with high S loading and good capacity retention. However, a sudden drop of capacity happens following the decrease of coulombic efficiency. The side reaction

on the anode can be a possible failure mechanism of S cathode with high S loading. We are investigating methods to protect the anode better.

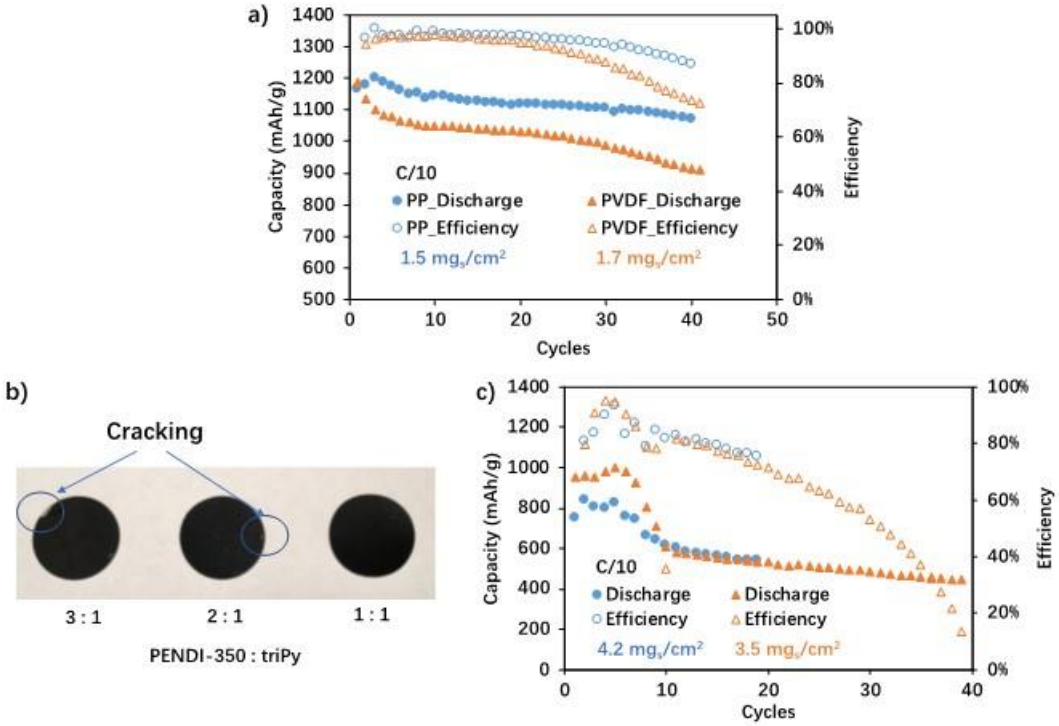

Figure II.10.F.12 a) Cycling performances of S cathodes with PP and PVDF as binder, respectively. b) S cathodes fabricated using PP binders with different ratio between PENDI-350 and tri-Py. c) Cycling performances of S cathodes with PP (PENDI-350: tri-Py = 1 : 1) binder with different loading amount of S.

As described above, although the cathode exhibited high and stable cycling capacity around 810 mAh/g in the first several cycles, sudden drop of capacity occurs in the following cycles. Therefore, we have focused our research on understanding the failure mechanism of cathode, including studies of lower coulombic efficiency and cathode cracking in this system. Coulombic efficiency is related to the dissolution of lithium polysulfides and therefore capacity retention. In our design, PENDI-350 is used to trap the polysulfides. First, pure PENDI-350 was used as binder to compare with reference binder PVDF. As shown in Figure II.10.F.13a, cathode with PENDI-350 as binder shows better capacity retention and much higher coulombic efficiency than case of PVDF. Specifically, the trends of capacity change are different. The dramatic capacity decrease in the first several cycles of cells with cathode using PVDF as binder implies the quick dissolution of the polysulfides into the electrolyte. Then the shuttle effect can become more significant, leading to constant decay of capacity and lowering of the coulombic efficiency. On the contrary, cells with cathode using PENDI-350 as binder has stable capacity around 1000 mAh/g in the first three cycles, which suggests effective trapping of the polysulfides. The coulombic efficiency stays constant around 98% even after around 60 cycles for the cell. The capacity stays almost constant after 30th cycles.

Therefore, we assumed these two cathodes have different capacity failure mechanism: cathode with PVDF as binder loses capacity due to the dissolution of the polysulfides; although cathode with PENDI-350 as binder traps polysulfides efficiently, cathode cracking can lead to the loss of sulfur by isolation. To prove this, SEM images of these cathodes were taken after cycling 20 cycles. As shown in Figure II.10.F.13b, cathode with PVDF binder showed continuous surface without significant cracking. However, there is cracking with width of 15 micron in the surface of cathode when PENDI-350 was used as binder, most likely due to its higher rigidity. Besides, the morphologies of the two film are quite different: in the case of cathode using PENDI-350 binder, the surface is smoother. This suggests better compatibility of PENDI-350 binder with carbon/sulfur

composite possibly resulting a layer of PENDI-350 film formation on the surface of cathode during the cycling process.

Second, due to the differences in failure mechanism, it is possible that the mechanical integration of electrode materials can be improved further by adding PVDF into PENDI-350. As shown in Figure II.10.F.13c, after adding PVDF (with weight ratio between PVDF and PENDI-350 as 1:3), the capacity retains around 962 mAh/g after 40 cycles with sulfur loading of 2.5 mg/cm^2. However, the coulombic efficiency was worse than pure PENDI-350. We think that although PVDF helps improve the mechanical integration, it may also interfere the interactions between PENDI-350 and PENDI-350 or between PENDI-350 and S/C composite. The SEM image of cathode with PENDI-350/PVDF as binder after 20 cycles is shown in Figure II.10.F.13c. It is found that the surface of cathode is less smooth than the cathode with pure PENDI-350 as binder. This suggests that less polymer film is formed on the surface of cathode, which means part of PENDI-350 may dissolved into the electrolyte. The lack of PENDI-350 may leads to the dissolution of the polysulfides and low coulombic efficiency.

Therefore, we have increased the thickness of sulfur cathode to alleviate the dissolution problem of PENDI-350. As shown in Figure II.10.F.13d, the cathode with sulfur loading of 3.7 mg/cm^2 and PENDI-350/PVDF as binder was fabricated. It shows stable capacity around 800 mAh/g after 32 cycles. And the coulombic efficiency was higher than 98%, which may due to the trapping effect of PENDI-350 and the physical blocking of thick cathode. In short, by improving the mechanical property and alleviating the dissolution of PENDI-350, high loading sulfur cathode with high capacity retention and coulombic efficiency has been achieved.

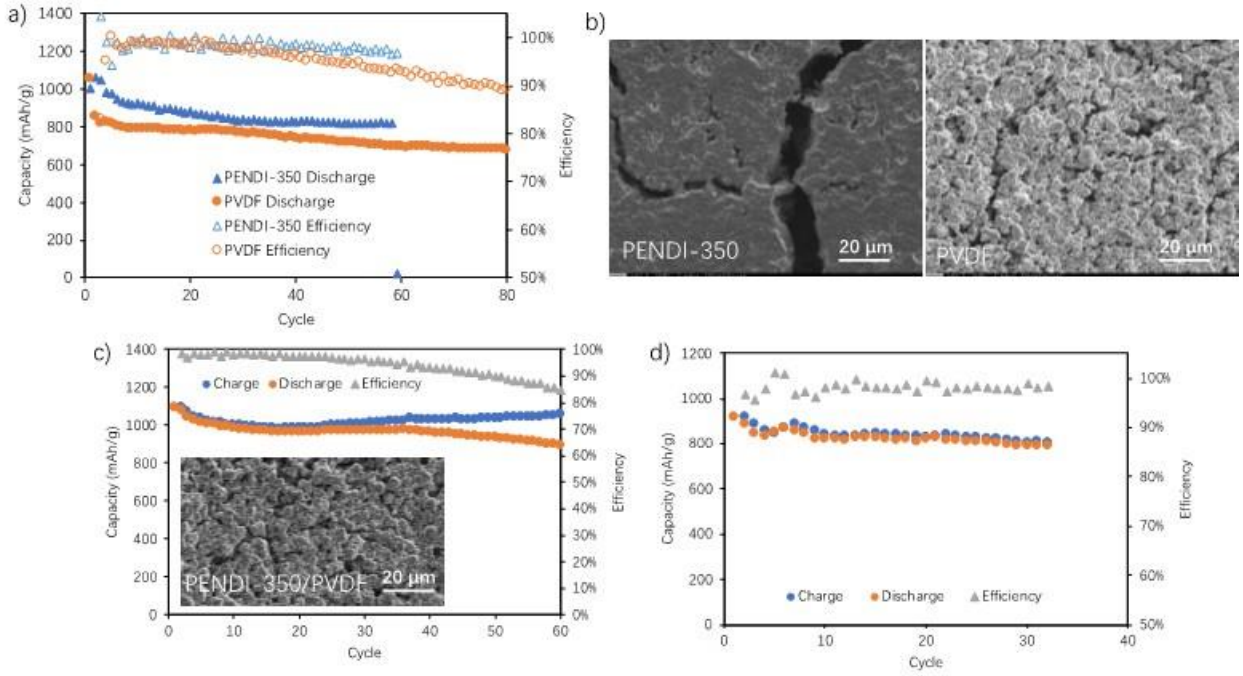

Figure II.10.F.13 a) Cycling performances of S cathodes with PENDI-350 (2.0 mgS/cm^2) and PVDF (3.1 mgS/cm^2) as binder, respectively. b) SEM images of cathodes with PENDI-350 and PVDF as binder after 20 cycles. c) Cycling performance of sulfur cathode with PENDI-350/PVDF as a binder and the SEM image of the cathode after 20 cycles. d) Cycling performance of sulfur cathode with PENDI-350/PVDF.

Although we have fabricated the cathode with S loading of 3.70 mgS/cm^2 by using PENDI-350/PVDF composite as a binder, the coulombic efficiency of the composite decreased quickly after around 30 cycles. We thought that PVDF may interfere with the interactions between PENDI-350 chains or between PENDI-350 and S/C composite. On the other hand, although we have demonstrated the effect of PENDI-350 on lithium

polysulfides trapping, and possible redox reaction between NDI units and the polysulfides, we thought a more detailed investigation of the reaction pathways of LiPS in the presence of such binder is necessary. Here, we have focused our efforts on stabilizing capacity retention of the cathode, understanding and modulating interactions between the polysulfides and NDI units of the binder to improve the performance further.

First, we have replaced PVDF with PEO to form a polymer blends of PENDI-350 and PEO as a binder for S/C cathode. As shown in Figure II.10.F.14a, we have fabricated test cells with S/C cathode using PENDI-350/PEO (weight ratio = 3:1) as binder with loading of 3.71 mgS/cm^2. It shows that the cell capacity remains at 718 mAh/g after 100 cycles at 1C. The capacity retention is as high as 91% (based on the 6th cycle with capacity of 789 mAh/g). We attribute the improved capacity retention to the flexibility of long-chain PEO (Mw = 1000 K) as well as its good compatibility with PENDI-350 functionalized with short-chain PEO groups resulting well dispersed polymer blends. To improve the mechanical properties further, we have added tri-Pyrene cross-linker forming reversibly crosslinked network structures with PENDI-350 *via* the quadrupolar aromatic π- π interactions between NDI and Pyrene units. In the PENDI-350/triPy/PEO (PPP binder) the flexible PEO chains from PENDI-350 and PEO could entangle to form inter-penetrating network structures. As shown in Figure II.10.F.14b, test cells with S/C cathode with a PPP (PENDI-350:triPy:PEO = 3 : 2 : 1 by weight) binder was fabricated with S loading of 2.91 mgS/cm^2. The capacity remains around 918 mAh/g after 30 cycles with relative capacity retention of 97% (based on 6th cycle with capacity of 954 mAh/g). We have also fabricated Li-S cells with the S/C cathode with relatively high loading of 5.04 mgS/cm^2 without cracking as shown in Figure II.10.F.14c.

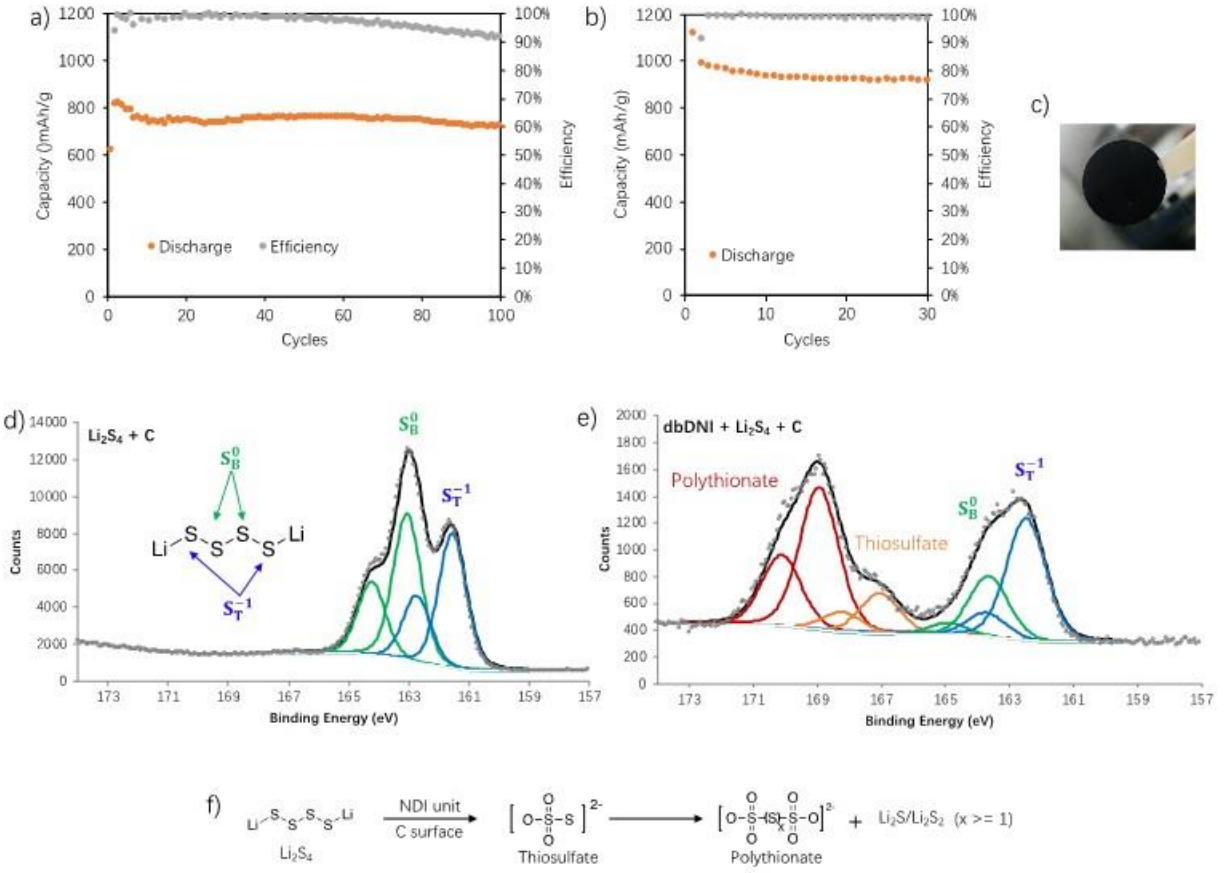

Figure II.10.F.14 Cycling performances of cells with S cathodes with a) PENDI-350/PEO as binder (3.71 mgS/cm^2) and b) PENDI-350/triPy/PEO (PPP) as binder (2.91 mgS/cm^2). All cells were cycled with C rate of C/10 in the first 5 cycles and then 1C in the remaining cycles. c) Image of S cathode using PPP as binder (5.04 mgS/cm^2). d) XPS spectrum of Li_2S_4 reacted with mesoporous carbon, and e) Li_2S_4 and dbNDI mixture reacted with mesoporous carbon. f) Possible reaction route of lithium polysulfides in the presence of NDI.

Meanwhile, we have performed series of XPS experiments to understand the interaction mechanism between the polysulfides and NDI units in more detail. Li_2S_4 was employed as a representative long-chain LiPS, which was synthesized by stoichiometric mixing of S_8 and Li_2S_2 in DME. Dibutyl-NDI (dbNDI) was used as a NDI model compound to react with Li_2S_4 before XPS test. Mesoporous carbon surface was functionalized with thiophenols using diazonium chemistry to enhance interactions with S species, and the mesoporous carbon was added into Li_2S_4 solution to mimic the cell operation condition. As shown in Figure II.10.F.14d, the XPS spectrum of Li_2S_4 interacted with the carbon shows two $S2p_{3/2}$ contributions at 161.6 and 130.0 eV with relative peak ratio of around 1:1, referred to as terminal (S_T^{-1}) and bridging (S_B^0) sulfur atoms. A typical XPS spectrum of Li_2S_4 from the test suggests that the existence of mesoporous carbon doesn't change the state of Li_2S_4. However, after adding dbNDI, as shown in Figure II.10.F.14e, XPS spectra show two more sulfur species. The new S2p3/2 peaks at 166.9 eV and 168.8 eV are in accord with the binding energy of thiosulfate and polythionate complex. As proposed in Figure II.10.F.14f, Li_2S_4 can be oxidized into polythionates and short chain polysulfides in the presence of NDI units in the binder. The additional electrochemical contribution of NDI can help to explain the exceptional performance enhancement of sulfur cathodes made of NDI containing PPP binder.

Despite the excellent cycling stability of cathode with PPP binder, the cathode needs additional improvement for a practical application. As shown in Figure II.10.F.15a, when the cathode was immersed in organic electrolyte for 48 hours, the cathode with PPP binder tends to break into pieces. Significant volume expansion stress during cycling would accelerate the dissociation NDI and Py units. We have designed and optimized the composites of PENDI-350/PEO/PVDF (PPPVDF) as binder for deliverable cells, which possesses following advantages; (1) the PENDI-350 impedes the diffusion of long chain lithium polysulfides (LiPS) via electrostatic trapping and redox mediation of NDI units, (2) PVDF helps to improve the film forming property of the binder system, and (3) long chain PEO improves electrolyte wettability and compatibility between PVDF and PENDI-350. Consequently, S loading higher than 6 mgS/cm^2 was achieved by using S/MJ430 (weight ratio = 7:3) as C/S composite.

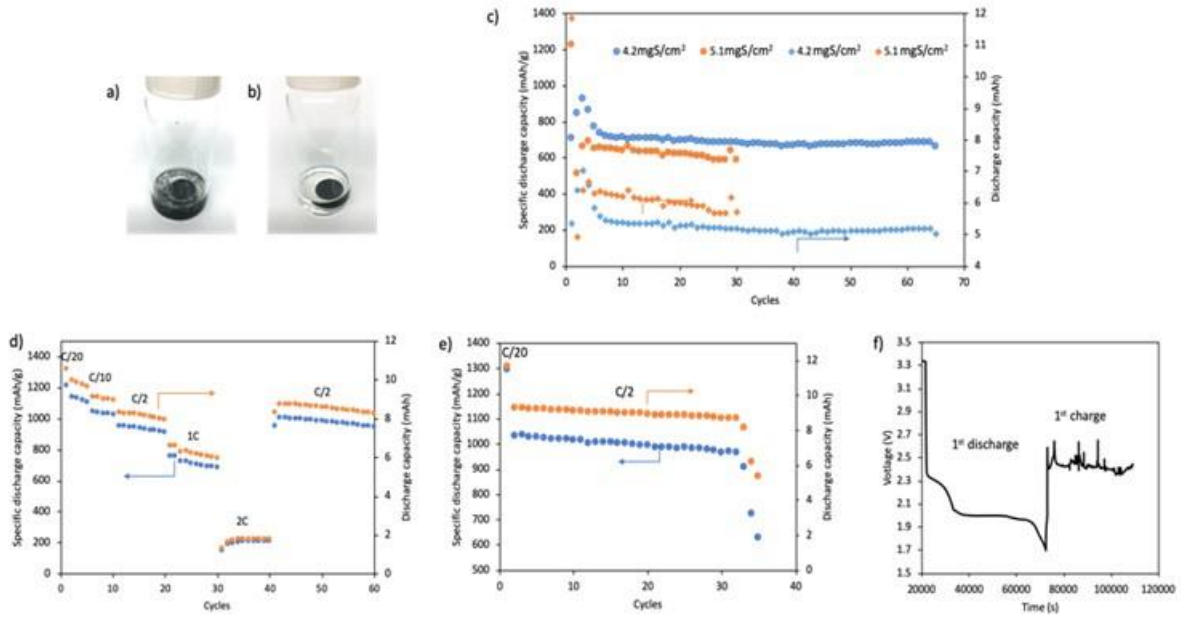

Figure II.10.F.15 a) Cathode with PPP binder immersed in organic electrolyte after 48 hours. b) Cathode with PPPVDF binder immersed in organic electrolyte after 48 hours. c) Cycling performances of cathodes with PPPVDF binder at different S loading (the cells were cycled at C/20 rate at 1st cycle and C/2 at remaining cycles). d) Cycling performances of cathodes with PPPVDF at different C rate (4.4 mgS/cm^2). e) Cycling performances of cathodes with PPPVDF with -SH surface modified carbon. f) The first discharge (at C/20 rate) and first charge (at C/2) performance of cathode with PVDF as binder.

Compared with PPP, cathode with the PPPVDF binder remain intact even after immersion in organic electrolyte (Figure II.10.F.15b). Composition of optimized PPPVDF binder used in the deliverable cells is a composite of PENDI-350:PEO:PVDF = 2:1:1 in weight ratio. Test cells with S loading of 4.4 mgS/cm^2 was fabricated. The specific discharge capacity stabilized in a low level of around 700 mAh/g (Figure II.10.F.15c), which implies low S utilization. Overall, the cells possess high capacity retention of 93% (from 10th cycle to 65th cycle). The utilization of S on the 10th cycle is lower than 50%. The specific capacity drops further after increasing the S loading amount to 5.1 mgS/cm^2. A thicker cathode composite layer could encumber the diffusion of electrolyte. Meanwhile, the insulating short chain LiPS formed during cycling may block the pores of mesoporous carbon and result in decrease of conductive surface. Therefore, we have employed two additional strategies to resolve the poor ion and electron conductivity issues at higher S loading: First, we have modified the surface of mesoporous carbon (MJ430) with -SH (thiol) functional groups. The polar, surface thiol groups resulted improved wetting of the electrode surface by the electrolyte due to the dipole-dipole interaction of the thiol groups with lithium ion in the electrolyte. Second, the weight ratio of S/C composite was adjusted from 70% to about 60%. Higher ratio of conductive mesoporous carbon would improve the conductive surface area and mitigate the blocking effect of insulating short chain LiPS.

As shown in Figure II.10.F.15d, the resulting cell was tested under different C rate. The cathode capacity is close to 10 mAh at C/20 rate. The specific discharge capacity is around 945 mAh/g even after 60 cycles at C/2 rate. Capacity retention higher than 90% was achieved when the cell is cycled at a C/2 rate, as compared to the capacity at C/10. As shown in Figure II.10.F.15e, at C/2 rate the cathode discharge capacity (C/20) is higher than 11 mAh in the first cycle. Even at C/2 rate, the cathode capacity remains at 8.7 mAh after 30 cycles. Meanwhile, the cathode capacity reminds high with specific discharge capacity of 967 mAh/g after 30 cycles. However, the cell failed suddenly after around 35 cycles. We attribute this to the failure of anode side. In the control cells using PVDF as a binder, the cells fail quickly due to shuttle effect especially for cells with higher S loading without LiPS trapping functionality. Figure II.10.F.15f shows the voltage profile of PVDF cathode with S loading of around 5.5 mgS/cm^2.

Deliverables

Composition of Deliverable Cells

The compositions of our final cell design are summarized in Table II.10.F.3. More specifically, the cathode layer consists of C-SH/S composite, binder, and conductive carbon (C-SH/S:binder:CNT = 70:25:5 by weight). The binder is formed by blending PENDI-350, PEO and PVDF in weight ratio of 2:1:1. Carbon-coated Al foil is used as cathode current collector. 2032 coin-type cells were assembled. PVDF was used as binder for in the control cells.

Table II.10.F.3 The key compositions of final cell, including cathode, separator, electrolyte and anode

Cathode	C-SH/S composite (70 wt%)	Mesoporous carbon (MJ430) was modified with thiol groups to form C-SH; C-SH was then mixed with S by melt-infiltrated method to form C-SH/S composite. The weight ratio of S in C-SH/S composite was estimated as 56% by TGA.
	Binder (25 wt%)	PENDI-350:PEO:PVDF = 2:1:1 (by weight)
	Conductive carbon (5 wt%)	Carbon nanotube (CNT)
Separator	Polypropylene (PP) Celgard2500	
Electrolyte	1 M lithium bis-(trifluoromethanesulfonyl)imide (LiTFSI) and 2 wt% $LiNO_3$ in 1,3-dioxolane (DOL) /1,2-dimethoxythane (DME) (v/v =1:1) as the electrolyte; 7mL of electrolyte was used for 1mg S.	
Anode	Li metal (0.25 mm in thickness)	

Suggested Testing Protocol for the Deliverable Cells

Protocol for testing the deliverable cells with 10 mAh nominal capacity and evaluation metrics for each cells are summarized below.

1. Cell Components and Construction

SS | Li Anode: Pure Li metal (Ø15.6mm, MTI Corp) pressed onto a SS304 disc (Ø15.5mm, MTI Corp).

Electrolyte: 1M LiTFSI dissolved in 1,3-dioxolane (DOL, Sigma-Aldrich) and 1,2-dimethoxyethane (DME, Sigma-Aldrich) in a 1:1 volumetric ratio, with 2wt% $LiNO_3$ (Sigma-Aldrich) added for anode protection.

S/C Cathode (Improved): A Ø16mm composite film of pure sulfur (powder, ≥99.8% trace metals basis, Sigma-Aldrich) melt-diffused into an equal or lesser weight of mesoporous carbon (MJ430, Toyo Tanso Co Ltd) which has been surface-modified with thiol functionality, held together by a novel mixture of polymer binders. The nominal capacity is 10 mAh.

S/C Cathode (Control): A Ø16mm composite film of pure sulfur (powder, ≥99.8% trace metals basis, Sigma-Aldrich) melt-diffused into an equal or lesser weight of mesoporous carbon (MJ430, Toyo Tanso Co Ltd), held together by poly(vinylidene difluoride) (PVDF, MTI Corp) as a binder. The nominal capacity is 10 mAh.

C/Al: Carbon-coated aluminum foil (Ø16mm, 0.018mm thick, MTI Corp) onto which the above composite film has been uniformly coated.

Cell Construction: The above components are assembled into CR2032 coin cells (Hohsen Corp), with the positive terminal contacting the large cap of the cell as following:

(SS | Li Anode | Electrolyte | S/C Cathode | C/Al)

2. Testing Protocol

It is recommended that cells be tested promptly after they are received. Electrochemical measurements should be performed on both Control Li-S Cells and Improved Li-S cells using an Arbin battery testing station or similar (LAND, Maccor, etc.) at room temperature (20-30°C). For constant-current cycling tests, cells should first be discharged at a fixed current of -0.5 mA cm^{-2} (corresponding to a C-rate of C/20) until the cells reach a lower voltage threshold of 1.8V, followed by a rest period of 10 min. This conditioning step should be considered the first cycle, after which the second cycle begins. Then, the cells may be charged and discharged at fixed currents (calculated from C-rate by assuming 10 mAh nominal capacity), between upper and lower voltage limits of 2.8V and 1.8V for charge and discharge, respectively. A rest step of 10 min should occur after each charge and discharge. It is recommended that cells be tested at both C/2 (±5 mA cm^{-2}) and C/10 (±1 mA cm^{-2}), although other rates may be acceptable. Test schedules should include a safety limit of 50 mAh capacity during each charge step, to halt the test in the case of an internal short-circuit due to redox shuttling of lithium polysulfides. Current should not exceed ±10 mAh.

3. Evaluation Metrics

Charge and discharge capacity may be converted to aerial capacity (mAh cm^{-2}) using cathode area (2.011 cm^2) or to gravimetric specific capacity (mAh/g) using the cathode weight table provided below. Coulombic efficiency is undefined for the first cycle, which consists solely of the first discharge; for the second cycle and beyond, it may be evaluated as the quotient of discharge capacity over charge capacity.

Table II.10.F.4 Test cell numbers and sulfur loading of deliverable test cells

	S/C Cathode Weights			
	Improved		Control	
Cell #	Total (mg)	Sulfur (mg)	Total (mg)	Sulfur (mg)
1	29.15	8.37	32.15	11.93
2	31.55	9.31	32.35	12.03
3	26.98	7.52	32.35	12.03
4	33.57	10.10	32.25	11.98
5	34.46	10.45	34.11	12.89
6	32.19	9.56	31.17	11.45
7	33.87	10.22	33.13	12.41
8	28.03	7.93	32.58	12.14
9	30.33	8.83	32.02	11.87
10	31.65	9.35	31.17	11.45
11	34.02	10.28	33.23	12.46
12	34.48	10.46	28.66	10.22

Deliverable Cell Test Performed at Idaho National Laboratory

As described, we have delivered 24 coin cells (12 improved cells and 12 control cells) for testing to DOE designated Idaho National Laboratory. We have received official release of deliverable cell test data via an e-mail on June 11, 2020. Results of the test is summarized in this section.

Deliverable test cells were divided into group A (3 improved cells and 3 control cells) for cycle life test at 0.1C rate and group B (3 improved cells and 3 control cells) for conditioning and cycle capacity tests with varying C rates of 0.1C and 0.5C (1C = 1675 mAh/g). Figure II.10.F.16 shows the test results in group A. The cells are denoted as AI2, AI4, AI5, AC2, AC3, AC5 ("A" refers to "group A", "I'' or "C" refers to "improved cells" or "control cells", the last number refers to their corresponding number listed in Table II.10.F.4. As shown in Figure II.10.F.16a, the initial discharge capacities of control cells (AC2 and AC5) are around 920 mAh/g and 1020 mAh/g at 0.1C rate, respectively. Due to the fact that, AC3 failed in the first cycle, there is no data point for AC3 in Figure II.10.F.16. Both AC2 and AC5 decay quickly and fail after 3-7 cycles. As mentioned previously, control cells were fabricated using PVDF as binder lacking LiPS trapping property. The Coulombic efficiencies of AC2 and AC5 are not only unstable but also generally lower than 75%, which suggests serious shuttle effect. On the contrary, the improved cells (AI2, AI4, AI5) deliver initial discharge capacities around 1020-1200 mAh/g, which are 100-200 mAh/g (10%–20%) higher than that of control cells. The cyclability is improved to 40 cycles for AI2. The improved cells also possess much more stable and higher coulombic efficiency.

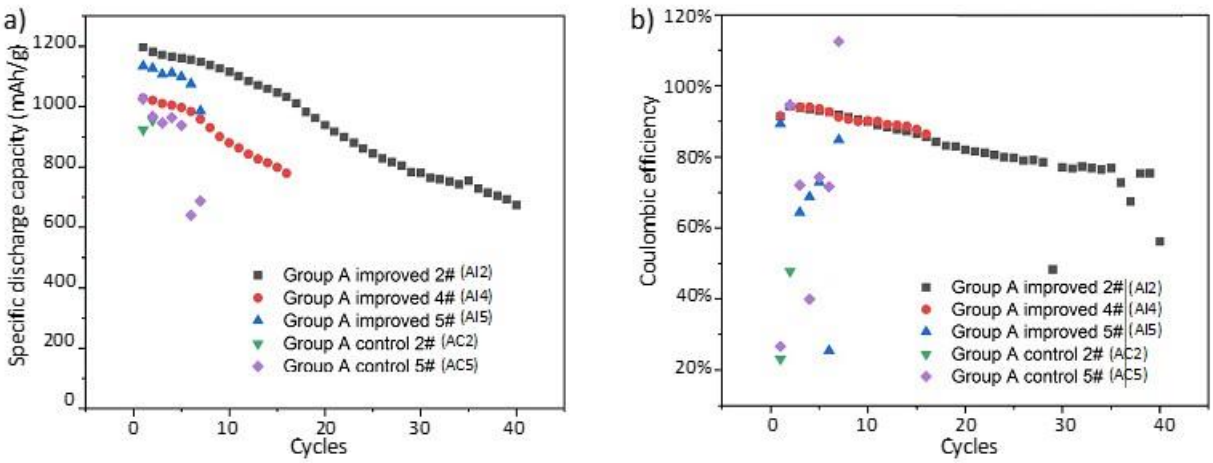

Figure II.10.F.16 Cycle capacity tests of improved and control cells in group A at 0.1C rate, including AI2 (4.67 mg_S/cm^2), AI4 (5.1 mg_S/cm^2), AI5 (5.2 mg_S/cm^2), AC2 (6.0 mg_S/cm^2), AC3 (6.0 mg_S/cm^2), AC5 (6.4 mg_S/cm^2). a) Specific discharge capacity and b) Coulombic efficiency of improved and control cells.

Figure II.10.F.17 summarize the test results of group B, including 6 cells denoted as BI7, BI11, BI12, BC7, BC8, BC11 ("B" refers to "group B", "I'' or "C" refers to "improved cells" or "control cells", the last one or two number refers to their corresponding number listed in Table II.10.F.4). In this group, cells were tested at 0.1C rate in the first three cycles and then followed by 9 cycles at 0.5C and 1 cycle at 0.1C alternately. As shown in Figure II.10.F.17a, the three control cells demonstrate similar initial discharge capacity to that of control cells in group A. However, their discharge capacities drop sharply to around 80 mAh/g at 0.5C and fail quickly. These suggest that control cells have poor C-rate performance. As for improved cells (BI7, BI12), they deliver discharge capacity around 860 mAh/g even at 0.5C rate. When the C rate changed back to 0.1C at 13^{th} cycle, they can still deliver discharge capacity around 990 mAh/g. The corresponding Coulombic efficiencies are stable and higher than 90%.

Overall, the improved cells possess much better performances in initial discharge capacity, cycling stability, and C-rate performance. We attribute the significantly improved cycling stability of cells to the multiple function of PENDI-350 which not only mediates transformation of soluble lithium polysulfides into insoluble polysulfides, but also traps dissolved polysulfides via strong ion-dipole interaction. The better initial discharge capacity and C-rate performances are contributed to the improved ionic conductivity and electrolyte wetting. EIS test shows that the Li ion conductivity of PENDI-350 ($1.4x10^{-2}$ mS/cm) reaches the same order of magnitude as amorphous PEO. The thiol groups surface modification of carbon also enhances the electrolyte wetting ability of cathode. All these advantages could enhance the cycling kinetics.

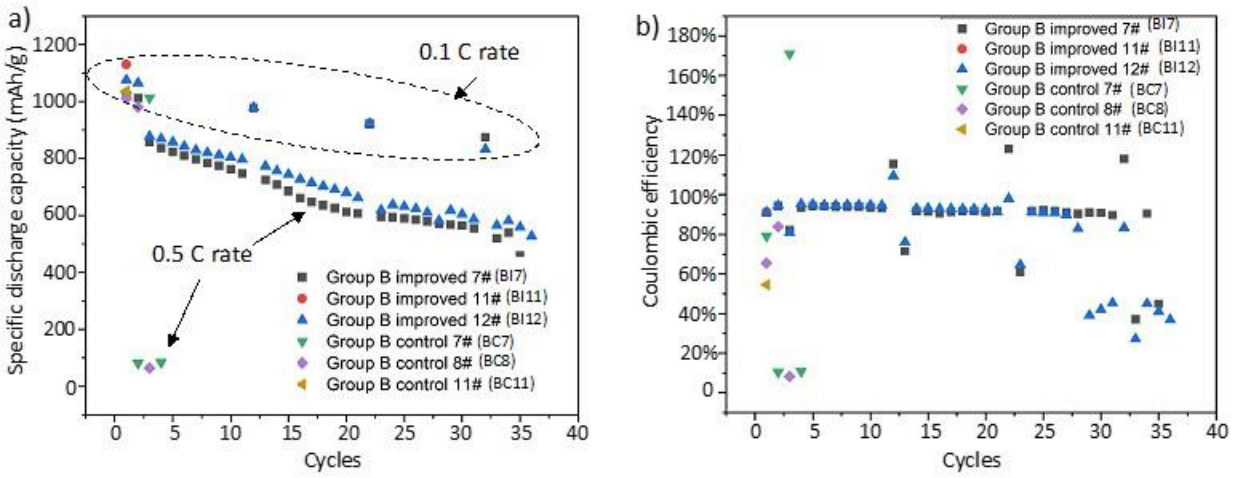

Figure II.10.F.17 Conditioning and cycle capacity tests of improved and control cells in group B at 0.1C rate, including BI7 (5.1 mg_S/cm^2), BI11 (5.1 mg_S/cm^2), BI12 (5.2 mg_S/cm^2), BC7 (6.2 mg_S/cm^2), BC8 (6.1 mg_S/cm^2), BC11 (6.2 mg_S/cm^2). a) Specific discharge capacity and b) Coulombic efficiency of improved and control cells.

Despite these improvements, the improved cells still suffer from capacity decay and shuttle effect. As discussed, the cracking issue has been a serious challenge for our PENDI binder system. As shown in Figure II.10.F.10 with low loading (1.0 mg_S/cm^2), the cracking issue is negligible which delivers improved cycling stability with high Coulombic efficiency (>99%). However, when we increase sulfur loading, the problem of cathode cracking and shuttle effect is revealed. Especially when we fabricated cells with high sulfur loading (4.7-5.2 mg_S/cm^2) in Figure II.10.F.16 and Figure II.10.F.17, the cathode cracking could be more prominent. Although LiPS could be transformed or trapped by PENDI, the cracks in cathode could lead to LiPS leaking into electrolyte. Therefore, to improve our design in the future, we need to improve the mechanical integrity of our binder system. Two possible ways should pay more attentions. First, design derivate polymers with higher flexibility and molecular weight. Second, the recipe of physical blending with other binders should be optimized further.

Conclusions

Multifunctional Ionomer Gel Polyelectrolytes / Gel Cathodes

- We have fabricated freestanding solvate ionogels with conductivity $>10^{-3}$ S/cm and lithium transference number >0.5, and demonstrated their utility as metallic-lithium-compatible electrolytes.
- We have developed fabrication procedures for all-solid-state Li-S cells containing solvate ionogel in both the cathode and separator, and demonstrated the potential of this system to produce good capacity retention and coulombic efficiency during galvanostatic cycling.
- Cyclic stripping/plating measurements revealed uniformly lower and persistent overpotential for the SIG separators. The differences at the anode/separator may explain the increased overpotential of full-cells with SIL electrolyte as compared to SIG.
- Increased overpotential associated with ionic liquid electrolytes in Li-S cells can be successfully mitigated to acceptable levels by using a diluent solvent (anisole), a cathode fabrication process which circumvents electrolyte wetting problems, and a gel composite separator that successfully restricts polysulfide migration without incurring large overpotentials or significant extra weight/volume.
- Unique changes to the discharge voltage traces in QSS cells (less-distinct and lengthened upper plateau, downward shift of the lower plateau) has studied in detail using GITT measurements on Li-S cells of varying design. Results indicated that the internal resistance of our QSS design can only partially explain

its altered discharge characteristics, and some fundamental change to the chemical pathway of discharge has also occurred in SIG-based cathodes.

- Robustness of the QSS design towards self-discharge has been tested and found that the system is more resistant to continued degradation caused by the redistribution of sulfur species during prolonged rest.

- A series of improved gel cathode formulations were tested with the goal of minimizing required thickness for high loading, and reducing the cathode charge transfer overpotential, as well as attempting to introduce our self-healing polymers into the slurry for additional robustness and electrochemical performance enhancement. This optimized slurry composition did indeed produce cathodes with 4-5mg$_S$/cm^2 loading at only ~400-500μm thickness.

Self-Healing Materials

- dbNDI and Py form non-covalent π-π complexes in either 1:1 or 2:1 molar ratios, respectively, depending on the concentration of dbNDI available relative to Py. The 2:1 complex is roughly twice as energetically favorable (-16.49 kJ/mol vs. -8.19 kJ/mol).

- We have designed polymers containing both NDI (PENDI-C6) and Py (triPy) moieties, which interact *via* the aforementioned π-π complexation to form non-covalently crosslinked films.

- These films are capable of self-healing following breakage, and the self-healing temperature can be tuned between 30-70 °C by introducing small molecule dbNDI or Py groups to adjust both the type of complex formed and the density of crosslinks. This "doping" with small molecules can also adjust tensile modulus of the films between 69-219MPa, which is significantly higher than most previously-reported self-healing materials.

- We have demonstrated recovery of mechanical strength upon self-healing in our PP polymer materials, as well as high swellability in solvate ionic liquid Li(G4)TFSI.

- We have fabricated low-loading Li-S cells using PP polymer formulations as binders, and demonstrated enhanced capacity retention after 100 cycles (>74%) compared to PVDF (<44%).

Chemical Modification of Mesoporous Carbons for S/C Composite Cathodes

- We have developed a procedure based on diazonium chemistry to covalently attach customizable functional groups to the surface of mesoporous carbons, and created S/C composites from both modified and unmodified samples.

- S/C cathodes based on phenylthiol-modified carbons display improved capacity and retention compared to unmodified samples. Voltage profiles exhibit significant changes upon modification, which may indicate covalent tethering of polysulfides to the carbon surface.

Self-Healing Polymer Binders for S/C Composite Cathodes

- Following the characterization of the PENDI-350/triPy (PP) self-healing polymer system, including its tunable mechanical/self-healing behavior and useful Li^+ conductivity, we have characterized the effects of this material as binder in a Li-S battery system.

- The PP polymer when used as a binder for S/C composite cathode has shown to increase the capacity retention significantly from 43.5% to 74.2% after 100 cycles at C/20. The capacity retention reached close to 100% after 100 cycles at 1C, which demonstrated the polysulfide trapping property of the PP polymer.

- We have performed CV and UV-Vis studies dibutyl-NDI (dbNDI) and Li_2S_8 as model compounds to understand the details of polysulfide-trapping mechanism. The NDI moiety in the PP polymer enhance

the capacity retention in two different ways: first, it can be reversibly reduced into NDI^{2-} di-anons which can trap polysulfides via strong ion-dipole interaction; second, it can also function as a redox-mediator, which promotes the charge transfer and finally increases the utilization of sulfur during discharge process.

- We have fabricated high loading S cathode via systematic design of the S cathode components, including current collector, ratio design between PENDI-350 and tri-Py, choice of carbon conductive additive, and the loading amount of S/C composite. Carbon coated Al foil was used as current collector which improves the adhesion between current collector with S cathode. Multi-wall carbon nanotubes were used as conductive additive to replace black carbon. The S ratio of S/C composite was improved to 70%. Based on the new composition, we have fabricated cathodes with PP and PVDF as binder. After 40 cycles, the discharge capacity of cathode with PP binder retains as high as 1070 mAh/g (capacity retention of 92%).

- Robust binder system is needed to mitigate the increasing mechanical stress for S cathode with higher loading. The S cathode with PENDI-350:tri-Py ratio of 3:1 is prone to cracking as the S loading amount increases to around 4 mg/cm^2. After increasing the amount of tri-Py by changing the ratio to 1:1, a continuous S cathode was achieved even with S loading amount greater than 4.2 mg/cm^2.

- In our binder, PENDI-350 is used to trap the polysulfides. Cathode with PENDI-350 as binder has stable capacity around 1000 mAh/g in the first three cycles, which implies the significant trapping of the polysulfides. The coulombic efficiency stays constant around 98% even after around 60 cycles. The capacity stays almost constant after 30^{th} cycles. Although cathode with PENDI-350 as binder traps polysulfides efficiently, cathode cracking can lead to the loss of sulfur by isolation.

- The dramatic capacity decrease in the first several cycles of cathode with PVDF as binder implies the quick dissolution of the polysulfides into the electrolyte. However, cathode with PVDF as binder showed continuous surface without significant cracking. It is possible that the mechanical integration of electrode materials can be improved by adding PVDF into PENDI-350.

- We have fabricated test cells with S/C cathode using PENDI-350/PEO (weight ratio = 3:1) as binder with loading of 3.71 mgS/cm^2. The capacity retention was as high as 91% (based on the 6^{th} cycle with capacity of 789 mAh/g). We attribute this improved capacity retention to the flexibility of long-chain PEO (Mw = 1000 K) as well as its good compatibility with PENDI-350 resulting well dispersed polymer blends. To improve the mechanical properties further, we have added tri-Pyrene cross-linker that can form reversibly crosslinked network structures with PENDI-350 *via* quadrupolar aromatic pi-pi stacking between NDI and pyrene units.

- In the PENDI-350/triPy/PEO (PPP binder) the flexible PEO chains could entangle to form inter-penetrating network structures. Test cells with S/C cathode with a PPP (PENDI-350:triPy:PEO = 3 : 2 : 1 by weight) binder was fabricated with S loading of 2.91 mgS/cm^2. The capacity remains around 918 mAh/g after 30 cycles with relative capacity retention of 97% (based on 6^{th} cycle with capacity of 954 mAh/g). We have also fabricated Li-S cells with the S/C cathode with relatively high loading of 5.04 mgS/cm^2 without cracking.

- We have designed and optimized the composites of PENDI-350/PEO/PVDF (PPPVDF) as binder for deliverable cells, which possesses following advantages; (1) the PENDI-350 impedes the diffusion of long chain lithium polysulfides (LiPS) via electrostatic trapping and redox mediation of NDI units, (2) PVDF helps to improve the film forming property of the binder system, (3) long chain PEO improves electrolyte wettability and compatibility between PVDF and PENDI-350. S loading higher than 6 mgS/cm^2 was achieved by using S/MJ430 (weight ratio = 7:3) as C/S composite.

- We have used mesoporous carbon (MJ430) modified with -PhSH (phenylthiol) functional groups on the surface. The polar, thiol groups resulted improved wetting of the electrode surface by the electrolyte due to the dipole-dipole interaction of the thiol groups with lithium ion in the electrolyte.

- The cathode capacity with the thiol modification was close to 10 mAh at C/20 rate with S loading of 4.4 mgS/cm^2. The specific discharge capacity is around 945 mAh/g even after 60 cycles at C/2 rate. Capacity retention higher than 90% was achieved when the cell is cycled at a C/2 rate, as compared to the capacity at C/10. At C/2 rate the cathode discharge capacity (C/20) is higher than 11 mAh in the first cycle. Even at C/2 rate, the cathode capacity remains at 8.7 mAh after 30 cycles. Meanwhile, the cathode capacity reminds high with specific discharge capacity of 967 mAh/g after 30 cycles.

Deliverable Cell Test Performed at Idaho National Laboratory

- We have delivered 24 coin cells (12 improved cells and 12 control cells) for testing to DOE designated Idaho National Laboratory. We have received official release of deliverable cell test data via an e-mail on June 11, 2020.

- Overall, the improved cells possess much better performances in initial discharge capacity, cycling stability, and C-rate performance. We attribute the significantly improved cycling stability of cells to the multiple function of PENDI-350 which not only mediates transformation of soluble lithium polysulfides into insoluble polysulfides, but also traps dissolved polysulfides via strong ion-dipole interaction. The better initial discharge capacity and C-rate performances are contributed to the improved ionic conductivity and electrolyte wetting.

- Despite these improvements, the improved cells still suffer from capacity decay and shuttle effect. The cathode cracking issue is negligible with low loading (1.0 mg$_S$/cm^2) which delivers improved cycling stability with high Coulombic efficiency (>99%). However, with increased sulfur loading (4.7-5.2 mg$_S$/cm^2) of the deliverable cells, the decay was more prominent. We propose two different ways to improve the mechanical integrity of our binder system further. First, develop derivative polymers with higher flexibility and molecular weight. Second, optimize blends with other binders with complementary mechanical properties.

Key Publications

1. Hubble D., Qin J., Lin F., Murphy I. A., Jang S.-H., Yang J., Jen A. K.-Y., “Designing Lithium Solvate Ionogels with Very High Conductivity and Lithium Transference Number.” *J. Mater. Chem. A*, **2018**, 6, 24100–24106. DOI: 10.1039/C8TA08808J.

2. Qin J., Lin F., Hubble D., Wang Y., Li Y., Murphy I. A., Jang S.-H., Yang J., Jen A. K.-Y., “Tuning Self-healing Properties of Stiff, Ion-conductive Polymers.” *J. Mater. Chem. A*, **2019**, *7*, 6773–6783. DOI: 10.1039/C8TA11353J.

3. Li Y.,* Murphy I. A.,* Chen Y., Lin F., Wang X., Wang S., Hubble D., Jang S.-H., Mueller K. T., Wang C., Jen A. K.-Y., Yang J., “A Multi-functional Interface Derived from Thiol-modified Mesoporous Carbon in Lithium-sulfur Batteries ” *J. Mater. Chem. A*, **2019**, 7, 13372-13381. DOI: 10.1039/C9TA02743B.

4. Lin, F. Design and Synthesis of Organic Functional Materials for Energy Conversion and Storage Applications (Ph.D. Thesis). University of Washington, Seattle, WA, September, **2019**.

5. Hubble, D. From Solvate to Cell: A Molecular Engineering Approach to the Li-S Battery (Ph.D. Thesis). University of Washington, Seattle, WA, November, **2019**.

Acknowledgements

Project team includes a senior research scientist Dr. Sei-Hum Jang, Ph.D. candidate students Dion Hubble, Jiaxu Qin, Ian Murphy, and Francis (Ray) Lin from the Jen group, as well as Dr. Shanyu Wang and Yun (April) Li from the Yang group. Special thanks to *PNNL personals.* Dion Hubble acknowledges government support under and awarded by the Department of Defense, Air Force Office of Scientific Research, National Defense Science and Engineering Graduate (NDSEG) Fellowship, 32 CFR 168a.

II.11 Beyond Li-ion R&D: Lithium-Air Batteries

II.11.A Rechargeable Lithium-Air Batteries (Pacific Northwest National Laboratory)

Ji-Guang Zhang, Principal Investigator
Pacific Northwest National Laboratory
902 Battelle Boulevard
Richland, WA 99354
E-mail: jiguang.zhang@pnnl.gov

Wu Xu, Principal Investigator
Pacific Northwest National Laboratory
902 Battelle Boulevard
Richland, WA 99354
E-mail: wu.xu@pnnl.gov

Tien Duong, DOE Technology Development Manager
U.S. Department of Energy
E-mail: Tien.Duong@ee.doe.gov

Start Date: October 1, 2015 End Date: September 30, 2021
Project Funding: $200,000 DOE share: $200,000 Non-DOE share: $0

Project Introduction

It is well known that the state-of-the-art (SOA) lithium (Li)-ion batteries are a mature technology and may reach their practical limit on specific energy (~300–350 Wh kg^{-1}) soon. Therefore, a worldwide effort has been made to explore new battery chemistries that may far exceed the specific energies of Li-ion batteries. Among the alternative energy storage systems, Li-air batteries have attracted worldwide research interest since the first report of a non-aqueous Li-air battery in 1996 due to their extremely high theoretical specific energy density (~5,200 Wh kg^{-1} when only the weights of Li and O_2 are included). However, before the commercialization of Li-air batteries, considerable challenges need to be overcome. These challenges include electrolyte instability, high overpotential, and severe corrosion of Li anodes. These problems cause poor round-trip efficiency and short cycle life in SOA Li-air batteries. To enable ultrahigh-energy-density Li-air batteries suitable for electric vehicle applications, it is critical to develop electrolytes that are more stable against reactive oxygen species and Li metal anodes, design alternative catalysts and carbon-based or carbon-free air electrodes, stabilize Li metal anodes, and seek new insights into the mechanisms of oxygen reduction/evolution reactions (ORR/OER).

Objectives

The objective of this project is to develop rechargeable Li-oxygen (Li-O_2) batteries (LOBs) with long-term cycling stability through in-depth research on more stable electrolytes and highly efficient catalysts for air electrodes, protect Li metal anodes, and have an in depth understanding on the ORR/OER mechanisms behind the electrochemical performance of Li-O_2 cells. In FY20, our main focus is to improve the stabilities of electrolytes and Li anode surface to enable long-term rechargeable LOBs.

Approach

Stability of Li metal anode (LMA) is very sensitive to the electrolyte used in LOBs, especially when Li is exposed to an oxygen-saturated electrolyte. The following approaches have been used to stabilize Li metal anode in LOBs:

- Develop a localized high-concentration electrolyte (LHCE) with a high activation energy to stabilize LMA against highly reactive singlet oxygen ($^1O_2$) species.

- Protect LMA with a polymer supported solid electrolyte interphase (PS-SEI) layer by combining PEO-based gel (PG) film coating on LMA and in-situ electrochemical pre-charging of Li-O_2 cells under O_2 atmosphere before regular cycling of the cells.

Results

Significant progress has been made in stabilization of LOBs with development of LHCEs and optimization of the polymer-supported SEI layer in FY20. The details are described below.

1. Develop stable electrolyte to minimize the parasitic reactions at the electrodes

The development of stable electrolytes is critical for practical application of LOBs as well as Li-air batteries (LABs) with long cycle life. We designed a localized high concentration electrolyte (LHCE) of LiTf in tetraglyme (G4) diluted by 1H,1H,5H-Octafluoropentyl 1,1,2,2-tetrafluoroethyl ether (OTE), and investigated its properties and battery performances in comparison with 1 M LiTf in G4 electrolyte and high concentration electrolyte (HCE, 2.8 M LiTf in G4). Density functional theory (DFT) simulations indicate that the activation energies of these three electrolytes against the $^1O_2$ exhibit the following order: LHCE (347.8 KJ mol^{-1}) > HCE (293.2 KJ mol^{-1}) > 1 M LiTf/G4 (238.0 KJ mol^{-1}). In general, a higher activation energy means a reaction is more difficult to occur. In other words, LHCE is much more stable against singlet oxygen. This prediction has been verified in our experiment as shown in Figure II.11.A.1.

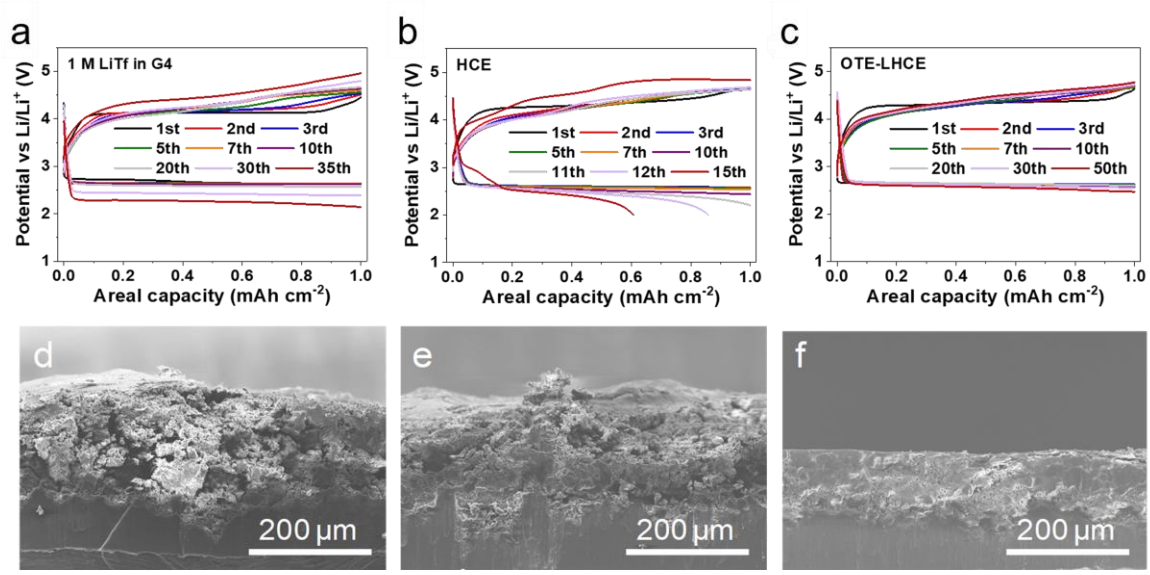

Figure II.11.A.1 (a-c) Voltage profiles of Li-O_2 cells with the three electrolytes at selected cycles at a current density of 0.2 mA cm^{-2} under a capacity limited protocol of 1.0 mAh cm^{-2}. (d-f) Cross-sectional SEM images of Li metal anodes from cycled Li-O_2 cells. (a,d) 1 M LiTf in G4, (b,e) HCE, and (c,f) LHCE.

Li||Li symmetric cell test demonstrates the excellent stability of LHCE with Li metal, significantly superior to HCE and 1 M LiTf/G4. Linear sweep scanning results also show that LHCE has higher oxidation potential than HCE and 1 M LiTf/G4. Therefore, Li-O_2 cells with LHCE and an air electrode composed of carbon paper without any catalyst can be cycled stably for more than 60 cycles under the capacity limited protocol of 1.0 mAh cm^{-2} at a current density of 0.2 mA cm^{-2}, while the similar cells with HCE and the 1 M LiTf/G4 electrolyte can only run for 16 and 36 cycles, respectively under the same conditions (Figure II.11.A.1a-c). In addition, scanning electron microscopy (SEM) images in Figure II.11.A.1d-f show that Li metal anode cycled in Li-O_2 cells using LHCE electrolyte can maintain their morphology well, but the serious corrosion on Li metal anode was observed when it was cycled in Li-O_2 cells using HCE and 1 M LiTf/G4 electrolyte. Another advantage of LHCE is its oxygen solubility which is almost twice as that in HCE and 1 M LiTf/G4. This advantage enables the Li-air batteries with LHCE have much higher discharge capacity and stable cycling than those using other two electrolytes under the same oxygen partial pressure. Using Zero Air gas (N_2 : O_2 = 79 :

21, volume ratio) which contains less than 3 ppm moisture, the capacity of Li-air cell using LHCE is about 9 mAh cm^{-2} which is much higher than those using 1 M electrolyte (0.353 mAh cm^{-2}) and HCE (0.004 mAh cm^{-2}). The Li-air cell using LHCE can be cycled for more than 27 times in zero air gas under a capacity-limited protocol of 1.0 mAh cm^{-2} at 0.2 mA cm^{-2}, but the Li-air cells using other two electrolytes can only cycle 1 time in the same gas. The above results demonstrate that the OTE-based LHCE is a very promising electrolyte for rechargeable LOBs and LABs thanks to its chemical/electrochemical stability, proper physical properties with low viscosity, and effective oxygen utilization due to its high oxygen solubility. Further development of novel electrolytes is necessary to stabilize Li metal anode against reactive oxygen species for more reversible and stable LOBs and LABs.

2. *Effects of diluents in LHCEs on cycling performance of LOBs*

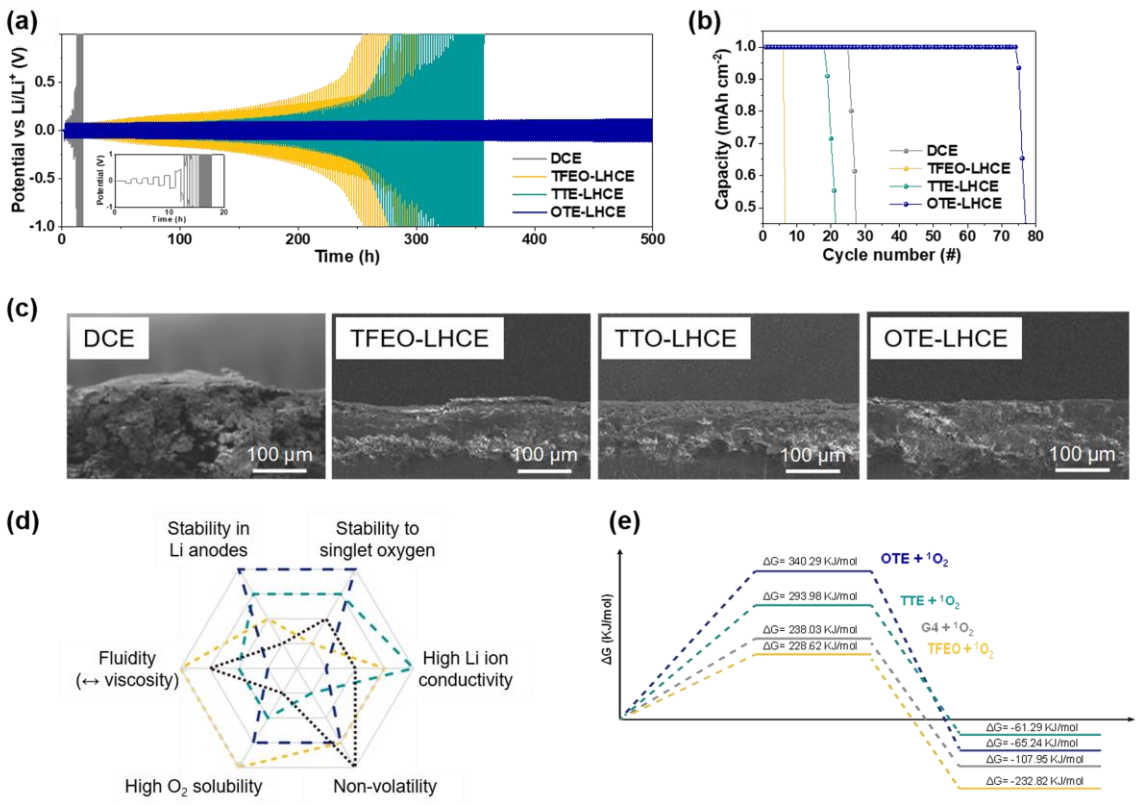

Figure II.11.A.2 (a) Voltage profiles of Li||Li symmetric cells cycling in different electrolytes at a current density of 1.0 mA cm^{-2} under a capacity limited protocol of 1.0 mAh cm^{-2}. (b) Cycle life of LOBs using different electrolytes at 0.2 mA cm^{-2} (200 mA g^{-1}) and capacity cutoff at 1.0 mAh cm^{-2} (1000 mA g^{-1}). (c) Cross-sectional SEM images of Li metal anodes in cycled LOB cells with DCE, TFEO-LHCE, TTE-LHCE, and OTE-LHCE after 10th cycles at a current density of 0.2 mA cm^{-2} with a capacity limited protocol of 1.0 mAh cm^{-2}. (d) The radar chart for the properties of the electrolytes in this study. (e) DFT calculation data about parasitic reaction energies of G4 solvent and three diluents with singlet oxygen.

The effects of diluent in LHCEs on the electrochemical performance of LOBs have been systematically investigated. Three diluents, Tris(2,2,2-trifluoroethyl)orthoformate (TFEO), 1,1,2,2-tetrafluoroethyl 2,2,3,3,-tetrafluoropropyl ether (TTE), and 1H,1H,5H-Octafluoropentyl 1,1,2,2-tetrafluoroethyl ether (OTE), were added in diluted concentration electrolyte (DCE, 1 M LiTf/G4) separately to for different LHCEs (TFEO-LHCE, TTE-LHCE, and OTE-LHCE) that have the same molar ratio of LiTf, G4, and diluent (1:1.75:3.5). Li||Li symmetric and Li-O_2 cell tests demonstrate much better stability of OTE-LHCE as compared to TFEO-LHCE, TTE-LHCE and DCE in LOBs as shown in Figure II.11.A.2a. Li-O_2 cells with OTE-LHCE and an air electrode composed of carbon paper without any catalyst can be cycled stably for 73 cycles under the capacity limited protocol of 1.0 mAh cm^{-2} at a current density of 0.2 mA cm^{-2}, while the cells with DCE, TFEO-LHCE

and TTE-LHCE can only run for 25, 6 and 17 cycles, respectively under the same testing conditions (Figure II.11.A.2b). Although DCE has a lower viscosity and volatility than LHCEs investigated in this work, other more important factors, such as stability of Li metal anode in the electrolyte lead to the early failure of LOB using DCE electrolyte. As shown in Figure II.11.A.2c, all of Li metal anodes removed from the cycled LOBs using LHCEs still exhibit well-maintained morphology after cycling, while the Li metal anode removed from the cycled LOB using DCE shows severe pulverization after cycling. The electrochemical performance of LOBs using different LHCEs also largely depend on diluent types. Thus, various physical and electrochemical properties of the electrolytes mentioned above (including their stability with Li anodes and $^1O_2$, fluidity/viscosity, conductivity, O_2 solubility and volatility) have been investigated to understand the key electrolyte parameters required for high performance LOBs. The results are summarized in Figure II.11.A.2d. Among these parameters, the activation energy of the diluents reacting with $^1O_2$ largely determined the electrochemical stabilities of the electrolytes in LOBs (Figure II.11.A.2e). As a result, LHCE containing the diluent (OTE) with the highest activation energy against $^1O_2$ demonstrates the best chemical and electrochemical stabilities and lead to the best long-term cycling stability of LOBs as shown in Figure II.11.A.2b.

3. Develop robust polymer-supported SEI layer for long-term cycling of LOBs

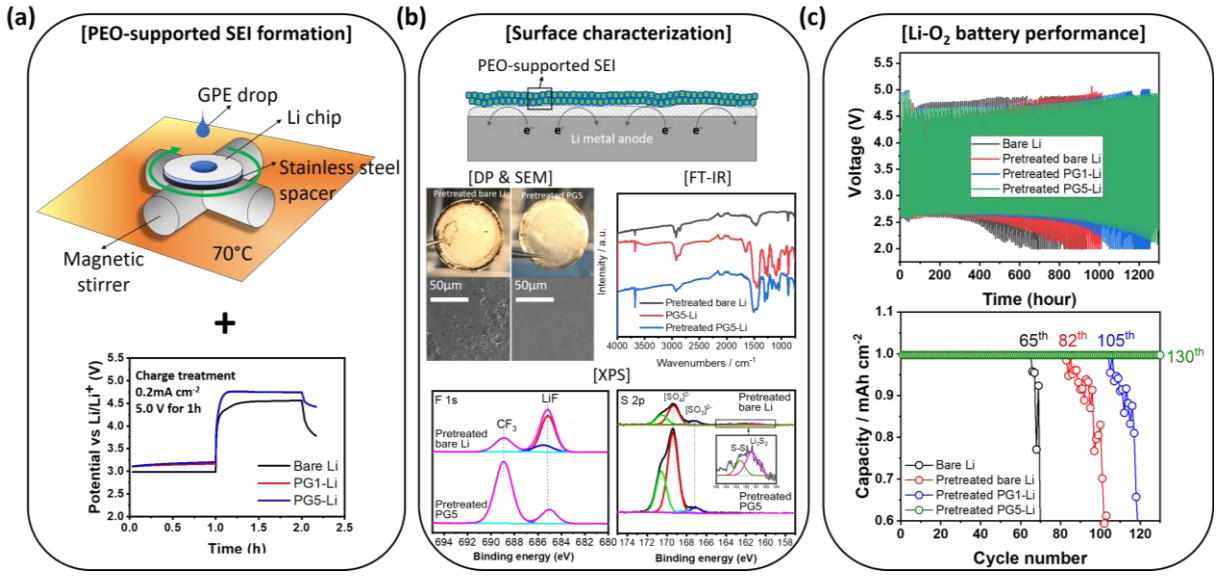

Figure II.11.A.3 (a) The formation process of PEO-supported SEI layer on the surface of Li metal anode by GPE coating and pre-charging to 5 V electrochemically. (b) Schematic illustration of the role of PEO-supported SEI layer and surface characterization results of Li metal surfaces after pre-charging step with and without pre-PG coating. (c) Voltage profiles of LOB cells with and without PEO-supported SEI layer cycling at a current density of 0.2 mA cm^{-2} under a capacity limited protocol of 1.0 mAh cm^{-2}. Cycling performance of LOBs corresponding to voltage profiles with repeated discharge and charge cycles at the same testing condition.

A new protection method has been developed to stabilize Li anode surface with a polymer-supported SEI (PS-SEI) layer for the long-term operation of rechargeable LOBs. A thin gel-polymer electrolyte (GPE) film containing polyethylene oxide (PEO-GPE, PG) was first coated on Li metal surface as an artificial SEI by spin coating method inside the glovebox filled with purified argon, then LOBs are assembled using such GPE precoated Li metal as anode and carbon paper as air electrode. After introducing O_2 into the containers with LOBs to be bested but prior to performing regular discharging/charging cycles of the LOBs, the cells were pre-treated at 5 V for 1 h in oxygen environment. A very thin and robust SEI layer was in-situ formed on Li metal surface during this electrochemical charging step (Figure II.11.A.3a). The surface characteristics of PS-SEI layer generated on Li metal surface were investigated (Figure II.11.A.3b) and compared with normal SEI layer generated by the same electrochemical charging step without PG coating. Digital photographs (DPs), SEM

images and FT-IR spectra indicate that the Li metal surface is very smooth with PS-SEI layer and PEO can be maintained without decomposition even after electrochemical pretreatment at 5 V for 1 h. X-ray photoelectron spectroscopy (XPS) results indicate that PEO-GPE layer contributes to the newly formed SEI film without severe electrolyte decomposition, while the pretreated bare Li metal has a rough surface consisting of LiF, S-S and Li_2S_2 resulting from severe decomposition of Li salt and solvent during pre-charging step. The performance of LOBs largely depends on the characteristics of SEI layers. The effect of PEO content (1 and 5 wt.%) in PS-SEI on LOB cell performance was also investigated. The higher PEO content leads to better LOB cell performance due to its better ionic conductivity and lower crystalline regions, which generates relatively dense and closely-packed SEI during the pretreatment step. The formation of PS-SEI layer with 5 wt.% of PEO significantly prolongs the cycle life (130 cycles) of LOBs under the capacity limited protocol of 1.0 mAh cm^{-2} at a current density of 0.2 mA cm^{-2}, while the cells with bare Li and pretreated bare Li anodes without PG supporting only reach 65 and 82 cycles, respectively under the same testing conditions (Figure II.11.A.3c). Thus, this novel strategy of constructing robust polymer-supported SEI layer on Li surface could be one of the effective solutions for the practical applications of rechargeable LOBs.

4. Optimize polymer-supported SEI layer with redox mediator to reduce cell overpotential

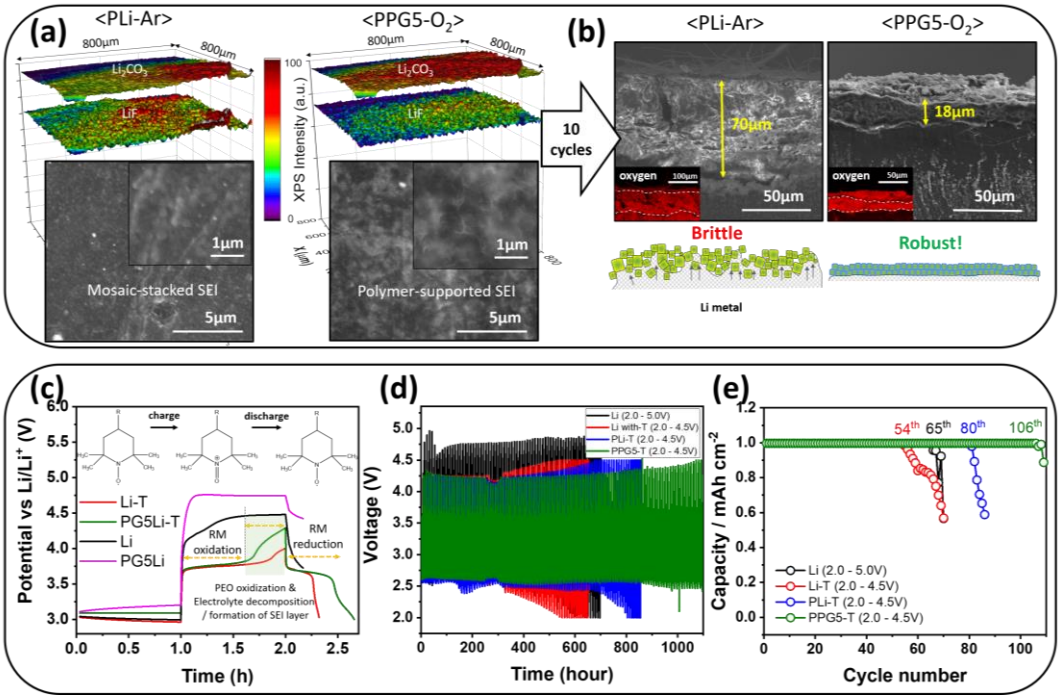

Figure II.11.A.4 Analysis of SEI layers: (a) XPS and SEM images (Li_2CO_3 and LiF) of Li metal surface with PPG5-O_2 (PEO-based gel polymer (PG) coating and electrochemical pre-treatment under O_2) and with PLi-Ar (without PG coating but with electrochemical pre-treatment under Ar). (b) Cross-sectional images and oxygen-EDX maps of Li metal anodes with PLi-Ar or PPG5-O_2 after 10 cycles at a current density of 0.2 mA cm^{-2} under a capacity limited protocol of 1.0 mAh cm^{-2} in the operation voltage range of 2.0 – 5.0 V and the corresponding illustrations for each SEM image. Electrochemical performance of Li-O_2 battery with redox mediator [(2,2,6,6-tetramethylpiperidin-1-yl) oxidanyl, TEMPO]: (c) Charging profiles of LOB cells with TEMPO, (d) charge/discharge curves and (e) cycling of LOB cells with different SEI layers at a current density of 0.2 mA cm^{-2} under a capacity limited protocol of 1.0 mAh cm^{-2} in the operation voltage range of 2.0 – 4.5 V.

The polymer-supported solid electrolyte interphase (PS-SEI) layers were generated to protect Li metal surface by a combination of *ex situ* and *in situ* methods. A redox mediator (RM) was further introduced reduce cell overpotential and energy efficiency of LOBs. After cycling, the characteristics of PS-SEI layer were systematically investigated by XPS, SEM and energy dispersive X-ray spectroscopy (EDX). XPS spectra shown in Figure II.11.A.4a indicate that PEO-based gel polymer (PG) layer promotes a uniform distribution of LiF and Li_2CO_3 components which enhanced mechanical strength of PEO coating layer during the pre-

charging step under O_2 due to the strong coordination chemistry of PEO chains with Li ions. SEM images reveal that the PS-SEI layer is a continuous film while the pristine Li has a brittle mosaic-stacked SEI consisting of particulate inorganic components. Li deposition with PS-SEI layer is much thinner (PPG5-O_2, about 18 µm) and more uniform than that of the pre-treated bare Li anode without PS-PEO layer (PLi-Ar, about 70µm) after 10 cycles (Figure II.11.A.4b). This is a clear indication that the PS-SEI layer can effectively prevent the side reactions on Li metal surface with 0.1 M (2,2,6,6-tetramethylpiperidin-1-yl) oxidanyl (TEMPO) as a RM (PPG5-T), consequently the prolonged cycle life was obtained in the cut-off voltage range of 2.0 – 4.5 V. The combination of the PS-SEI layer and the TEMPO RM led to the significant improvement of cycling stability (106 cycles) with a relatively low charging voltage, while bare Li (Li-T) and pretreated bare Li (PLi-T) anodes with TEMPO only reached 54 and 80 cycles under the same testing conditions, respectively (Figure II.11.A.4d and e). In other words, the PS-SEI layer with uniform distribution of strong inorganic components embedded in the flexible PEO phase is chemically and mechanically robust to stabilize Li metal anodes effectively against attacks of highly reactive species during LOB operations.

Conclusions

- OTE based localized high-concentration electrolytes (LHCEs) with a high activation energy were designed to stabilize the electrolyte system against highly reactive singlet oxygen ($^1O_2$) in an oxygen-rich environment, which enhances chemical/electrochemical stability, proper physical properties, and effective oxygen utilization.

- The physical and electrochemical properties of three diluents in LHCE were systematically investigated. PTE based LHCE exhibits the highest activation energy against $^1O_2$ and leads to the best long-term cycling stability of LOBs.

- A polymer-supported solid electrolyte interphase (PS-SEI) layer was developed to stabilize the Li metal surface for Li-O_2 batteries. These protective layers significantly improved the cycling stability of Li-O_2 cells (from 65 cycles to 130 cycles). The cell overvoltage during charge process was further reduced with the addition of redox mediator (TEMPO).

Key Publications

1. Won-Jin Kwak, Sujong Chae, Ruozhu Feng, Peiyuan Gao, Jeffrey Read, Mark H. Engelhard, Lirong Zhong, Wu Xu, and Ji-Guang Zhang, "Optimized Electrolyte with High Electrochemical Stability and Oxygen Solubility for Lithium-Oxygen and Lithium-Air Batteries", *ACS Energy Letters*, **2020**, 5, 2182-2190. DOI: 10.1021/acsenergylett.0c00809.

2. Won-Jin Kwak, Hyung-Seok Lim, Peiyuan Gao, Ruozhu Feng, Sujong Chae, Lirong Zhong, Jeffrey Read, Mark H. Engelhard, Wu Xu, and Ji-Guang Zhang, "Effects of Fluorinated Diluents in Localized High Concentration Electrolytes for Lithium–Oxygen Batteries", *Advanced Functional Materials*, **2020**, 2002927. DOI:10.1002/adfm.202002927.

Acknowledgements

Key contributors including Drs. Won-Jin Kwak and Hyung-Seok Lim are greatly appreciated.

II.11.B Lithium-Air Batteries (ANL)

Khalil Amine, Principal Investigator
Argonne National Laboratory
9700 S. Cass Ave
Lemont, IL 60439
E-mail: amine@anl.gov

Jun Lu, Principal Investigator
Argonne National Laboratory
9700 S. Cass Ave
Lemont, IL 60516
Email: junlu@anl.gov

Larry Curtiss, Principal Investigator
Argonne National Laboratory
9700 S. Cass Ave
Lemont, IL 60516
Email: curtiss@anl.gov

Tien Duong, DOE Technology Development Manager
U.S. Department of Energy
E-mail: Tien.Duong@ee.doe.gov

Start Date: October 1, 2019 End Date: September 30, 2020
Project Funding: $500,000 DOE share: $500,000 Non-DOE share: $0

Project Introduction

Lithium-oxygen batteries are of much interest because they offer, in principle, ten times the energy density of conventional lithium-ion systems. The inherent energy potential of lithium metal approaches that of gasoline, but there are challenges that remain to be able to unlock this potential. While today's lithium-ion batteries may provide acceptable power for hybrid electric vehicles and all-electric vehicles, they do not as yet provide sufficient energy for driving distances desired by consumers. A breakthrough in Li-oxygen battery technology would significantly increase the possibility of extending the electric range of these vehicles with the added advantages of reducing battery cost and weight.

The successful implementation of non-aqueous Li-air cells has been hampered because of severe materials problems that have limited electrochemical performance. These include (1) the non-aqueous electrolytes can be unstable under both the charge and discharge conditions, thereby seriously limiting cycle life; (2) during discharge, the solid and insoluble Li_2O_2 and/or other lithium oxide products are deposited on the surface or within the pores of the carbon cathode, thereby passivating the surface as well as clogging the pores and restricting oxygen flow; (3) degradation of the lithium anode due to oxygen crossover destroys the integrity and functioning of the cell; and (4) commonly used transition metal cathode catalysts, do not access the full capacity of the oxygen electrode or enable sufficiently high rates.

The team led by Dr. Khalil Amine, Dr. Larry Curtiss, and Dr. Jun Lu at Argonne National Laboratory is working on problems that limit the electrochemical performance of the Li-oxygen battery, including the stability of the organic electrolytes, development of new cathode catalysts, and the stability of the lithium anode under oxygen-crossover conditions. This effort will lead to the development of a reversible lithium oxygen battery that provides much higher energy density than state-of-the-art lithium ion batteries for electric vehicles.

Objectives

The objective of this project is to develop new cathode materials and electrolytes for Li-air batteries for long cycle life, high capacity, and high efficiency. Commonly used carbons and cathode catalysts do not access the full capacity of the oxygen electrode and can cause significant charge overpotentials, which lowers efficiency and limits cycle life. Therefore, there is a need for improved catalysts and how they can control the discharge product morphology, which affects the overpotentials. New more stable electrolytes are also needed to prevent gradual electrolyte decomposition that occurs in the presence of the reduced oxygen species. The goal is to obtain critical insight that will provide information on the charge and discharge processes in Li-air batteries to enable new advances to be made in their performance. This will be done using state-of-the-art characterization techniques combined with state-of-the-art computational methodologies to understand and design new materials and electrolytes for Li-air batteries.

Approach

The project is using a joint theoretical/experimental approach for design and discovery of new cathode and electrolyte materials that act synergistically to reduce charge overpotentials and increase cycle life. Synthesis methods, in combination with design principles developed from computations, are used to make new cathode architectures. Computational studies are used to help understand decomposition mechanisms of electrolytes and how to design electrolytes with improved stability. The new cathodes and electrolytes are tested in Li-O_2 cells. Characterization, along with theory, is used to understand the performance of materials used in the cell and to make improved materials.

Results

In this project, we have developed new cathodes for high energy efficiency and long cycle life, and investigated the effects of the anion and cation additives in Li-O_2 batteries.

A novel fabrication technique to construct noble metal-enabled oxygen electrode. Though the noble metal-based electrocatalysts may exhibit high activity, the synthesis process is often complicated and environmentally unfriendly. We herein develop a novel fabrication technique to construct noble metal-based cathode, which also solves the questionable key issue in Li-O_2 battery: the catalyst promotes the electrochemical reaction but spontaneously toward a wrong direction by enhancing the parasitic reactions, leading to the invalid of the electrochemical system.

As shown in Figure II.11.B.1**,** by using a thin film deposition technique, the reduction of catalyst dimensionality was easily realized by applying unique wettability of various metals. The dimension of catalyst is dramatically decreased from 3D, to 2D (wetting) and eventually 0D (de-wetting). By applying this to a typical lithium-oxygen cell, the cathode loading with dimensionally controlled catalyst exhibited a low charge potential with extended cycle life (Figure II.11.B.2). This dimensionally constrained catalyst layer is responsible for improving the areal energy and power density without any additional materials or complicated processes. More importantly, this technique provides much opportunity for further work via optimizing the electrolyte solvents and additives. The fabrication process is straight forward, low-cost and user-friendly with promising potential for industrialization.

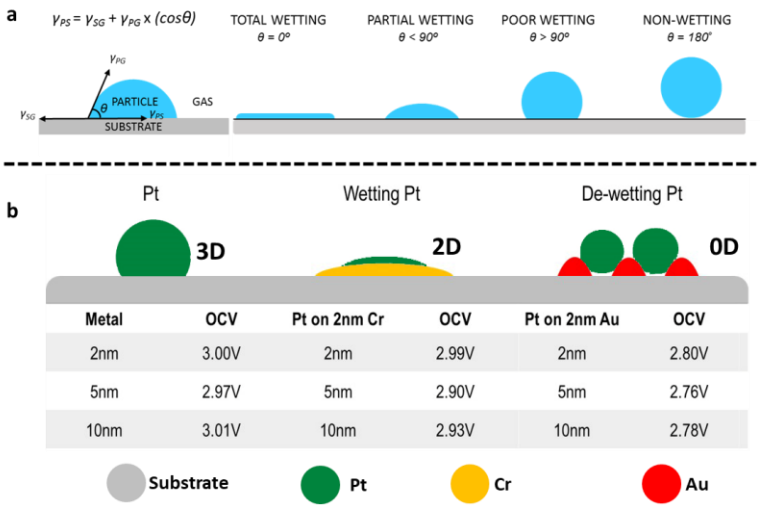

Metal	OCV	Pt on 2nm Cr	OCV	Pt on 2nm Au	OCV
2nm	3.00V	2nm	2.99V	2nm	2.80V
5nm	2.97V	5nm	2.90V	5nm	2.76V
10nm	3.01V	10nm	2.93V	10nm	2.78V

Figure II.11.B.1 Nano-engineering strategies for creating the ultra-small wetting and de-wetting dimensionality of reduced Pt catalysts on a substrate. (a) Definition of wetting and de-wetting in a typical metal-nonmetallic substrate system. (b) Formation of dimensionality reduced Pt with help of functional metal layers on a carbon black substrate for a lithium oxygen battery, and the related regular open circuit voltage (OCV) for each cell.

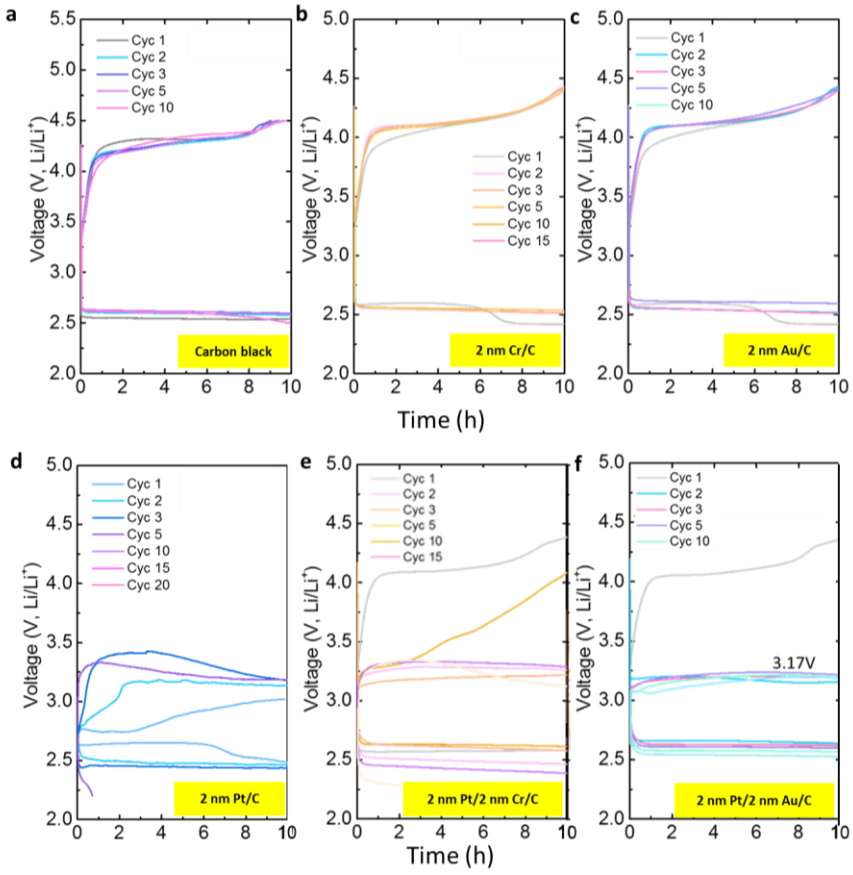

Figure II.11.B.2 Examples of galvanostatic charge/discharge profiles of Li-O_2 batteries with (a) carbon black, (b) Cr/C, (c) Au/C, (d) 3D Pt/C, (e) 2D Pt/Cr/C, and (f) 0D Pt/Au/C in the voltage range of 2.2 - 4.5 V vs. Li+/Li within a fixed capacity.

Optimized oxygen electrode combined with soluble for a Li-O_2 battery. Though solid electrocatalysts (Pd/carbon, Pt/Au/C) as reported above can deliver good electrocatalytic activity, combining them with soluble electrocatalyst may further enhance the electrochemical performance. Based on this idea, a biomass-derived activated carbon (ACs) with high specific surface area (1033 m^2/g) and decent porosity (0.52 cm^3/g) was prepared as the oxygen electrode, and LiI was added to the electrolyte to serve as the soluble catalyst. As shown in Figure II.11.B.3a, the hierarchical porous structure of ACs can promote the exposure of active sites, provide transport channels for oxygen and soluble catalyst LiI, and accommodate more discharge products without causing blockages. Compared with carbons (pyrolytic carbon materials without activation), ACs can deliver higher capacity due to its optimized structure, and an ultrahigh areal specific capacity of 7.95 mAh/cm^2 is achieved after combining ACs with soluble catalyst LiI (Figure II.11.B.3b).

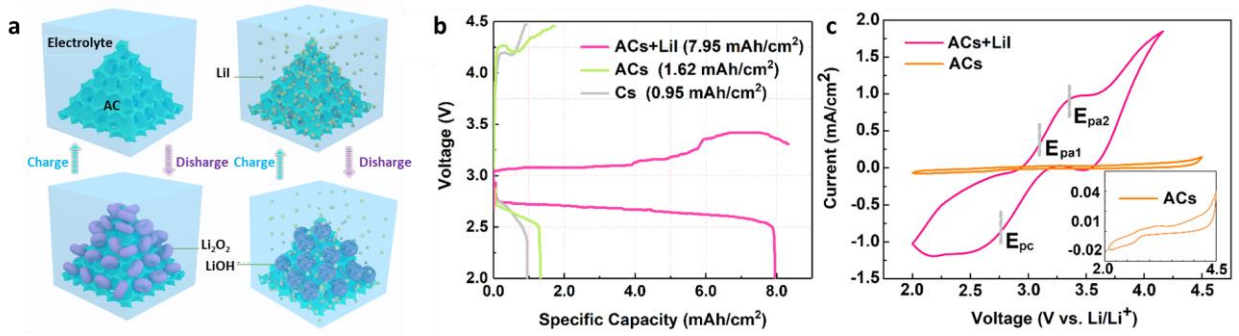

Figure II.11.B.3 Schematic illustration of the charge and discharge processes with or without the LiI in Li-O2 batteries using ACs electrodes (a). The initial discharge–charge voltage profiles of Li‖1M LiTFSI/TEGDME‖Cs-O2 cell, Li‖1 M LiTFSI/TEGDME‖ACs-O2 cell and Li‖1M LiTFSI/TEGDME+0.5 M LiI‖ACs-O2 cell at a current density of 0.02 mA/cm2 (b). The CV curves of Li‖1M LiTFSI/TEGDME‖ACs-O2 cell and Li‖1M LiTFSI/TEGDME+0.5 M LiI‖ACs-O2 cell within a voltage widow of 2.0~4.5 V at a scanning rate of 1 mv/s (inset: Enlarged CV curve of ACs) (c).

The greatly improved overall performance is mainly due to the synergetic effect of the novel designed oxygen electrode capable of mediating the soluble catalyst to trigger the ORR and OER processes. It should be noted that water is inevitably present in the system, and the addition of a small amount of water to aprotic Li-O_2 battery does not affect the formation of Li_2O_2 as the dominant product, but when LiI and water coexist, the formation mechanism of the discharge product will undergo complicated changes, and LiOH would be formed as the main discharge product. As shown in the Cyclic voltammetry (CV) curves (Figure II.11.B.3c): the positively shifted E_{pc} peak corresponds to the discharge plateau of 2.7 V, and E_{pa1} and E_{pa2} peaks are attributed to I^-/I_3^- and I_3^-/I_2 redox couples, and LiOH can be chemically oxidized by I_3^- to form O_2 and H_2O. The overall reaction should be: $4\,Li^+ + O_2 + 4e^- + 2H_2O \leftrightharpoons 4\,LiOH$.

Cation additive enabled rechargeable LiOH based Li-O_2 batteries. We have investigated cation additives to the electrolyte to optimize the reaction pathways and improve the electrochemical performance. Here, we used a simple strategy to achieve a reversible LiOH based Li-O_2 battery with the use of a cation additive, namely, sodium ions, to the lithium electrolyte. Without a LiI redox mediator in the cell, LiOH is detected as the sole discharge product and it charges at a low charge potential of 3.4 V. As shown in Figure II.11.B.4a-b, the addition of Na^+ can considerably reduces the charge potentials: for the electrolyte with 1 M Li^+ and 0.5 M Na^+, the charge voltage decreases to 3.4 V, exhibiting a low charge overpotential smaller than 0.5 V. Besides, the addition of Na^+ can also increase the discharge capacity and enhance the cyclability: the discharge capacity increases from 2.08 to 7.2 mAh cm^{-2} (Figure II.11.B.4c) and a low charge voltage over 30 cycles is maintained (Figure II.11.B.4d).

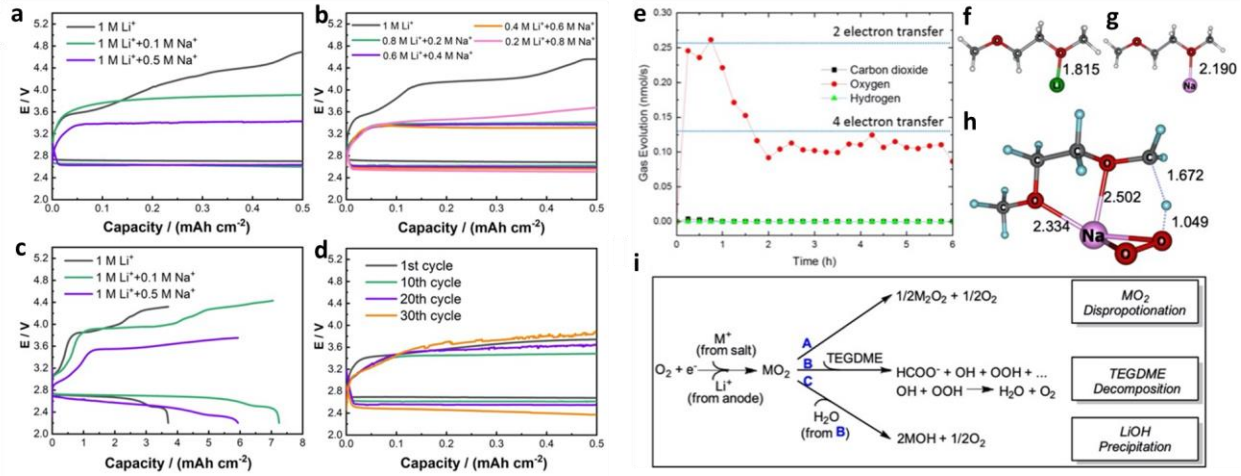

Figure II.11.B.4 Electrochemical results of Li-O_2 batteries. Voltage profiles (a) and deep cycles (c) in 1 M Li triflate/TEGDME electrolyte with 0, 0.1 and 0.5 M Na triflate, respectively. Voltage profiles (b) in TEGDME based electrolyte with a total concentration of 1 M metal triflate. Cycle life (d) in 1 M Li triflate and 0.5 M Na triflate. The current density for all the galvanostatic tests is 50 μA·cm^{-2}. DEMS measurement (e) of the charging process of the Li-O_2 battery in 1 M Li^+ + 0.5 M Na^+ electrolyte. The indication of the bond length of TEGDME binding to Na and Li ions (f, g). Optimized geometry of the transition state of C-H activation of TEGDME by NaO_2 (h). Illustration of possible reaction pathways of Li^+ and Na^+ during discharge. "M" denotes either Li or Na (i).

The discharge mechanism was investigated with density functional calculations. The calculated Na-O distance (2.19 Å) is longer than the Li-O distance (1.82 Å) in the complexes with TEGDME (Figure II.11.B.4f-g), indicating that surrounding the solvent molecules by Na^+ ions near the electrode could create a more gas-phase like environment, compared to Li^+ ions. The presence of Na-ions in the double-layer would enhance the "gas-phase like" environment near the electrode surface via the participation of NaO_2 in the formation of H_2O (Figure II.11.B.4i, Pathway B). As C-H activation of TEGDME by NaO_2 (Figure II.11.B.4h) has a lower barrier of 0.91 eV than that without NaO_2 (1.58 eV), it may be less favorable for LiO_2 to participate in these reactions (Figure II.11.B.4i, Pathway B). Thus, it is NaO_2 that mainly causes the formation of H_2O, which plays a critical role in MOH forming during discharge. As NaOH is more soluble than LiOH, any NaOH will remain in solution while LiOH will form a precipitate; therefore, the final product MOH should be LiOH. The charge mechanism is also studied via theoretical calculation and differential electrochemical mass spectrometer (DEMS), as shown in Figure II.11.B.4e, and the $4e^-/O_2$ process is confirmed to result from the oxidation of LiOH.

Lithium superoxide battery based on *ex-situ* formed Ir_3Li particles. Previously we **e**mployed iridium nanoparticles supported on rGO as a cathode material and demonstrated that lithium superoxide was the sole discharge product. The battery could be cycled for up to 40 cycles with low charge overpotentials (3.3-3.5 V). The lithium superoxide was characterized by various techniques and from DFT studies it was found that there was a good lattice match between LiO_2 and epitaxial Ir_3Li layers formed on the Ir nanoparticle surfaces. The Ir_3Li was found to be formed electrochemically on the Ir nanoparticle surfaces during discharge within the Li-O_2 system. The Ir_3Li alloy has been previously synthesized, but it has never been investigated as a cathode material for Li-O_2 batteries. In new work, we have demonstrated the first implementation of *ex-situ* synthesized Ir_3Li particles in an Li-O_2 battery. The Ir_3Li cathode catalyst led to the formation of superoxide discharge product nanoparticles during discharge in a Li-O_2 cell and cycling of the lithium superoxide.

The Ir_3Li synthesis was done using iridium powder and lithium foil sealed in a tantalum tube inside an argon atmosphere using a 3:1.1 molar ratio. The tantalum in quartz tube was heated to 800 °C for 8 days and then furnace-cooled to room temperature. The resulting Ir_3Li particles were put on an rGO substrate and used in a Li-O2 cell. The voltage profile is shown in Figure II.11.B.5a**.** The voltage profile shows a charge potential of

about 3.5 V vs Li/Li^+ that is gradually increasing. This charge potential is similar to results for the *in situ* formed $IrLi_3$ surfaces on Ir nanoparticles. The discharge product was characterized by titration with a $Ti(IV)OSO_4$ solution followed by UV-Vis of the titrant. It was also characterized by Raman spectroscopy. The UV-Vis absorbance curve and Raman spectra are shown in Figure II.11.B.5c and d, respectively. The absorbance value of 0.12 indicated that the presence of Li_2O_2 was negligible on the discharged cathode (< 0.1 mg). Raman spectra demonstrate strong LiO_2 characteristic peaks at 1125 and 1505 cm^{-1}, along with the characteristic rGO peaks at 1596 and 1328 cm^{-1}. These results indicate the LiO_2 was the dominant discharge product formed in the Li-O_2 cell the presence of $LiIr_3$ catalyst. These results both confirm that the Ir_3Li alloy is responsible for the lithium superoxide formation in the Li-O_2 battery using Ir-based cathodes, as well as opens the way for the use of other alloys that can provide lattice matches to stabilize formation of LiO_2 for use in development of closed Li-O2 systems.

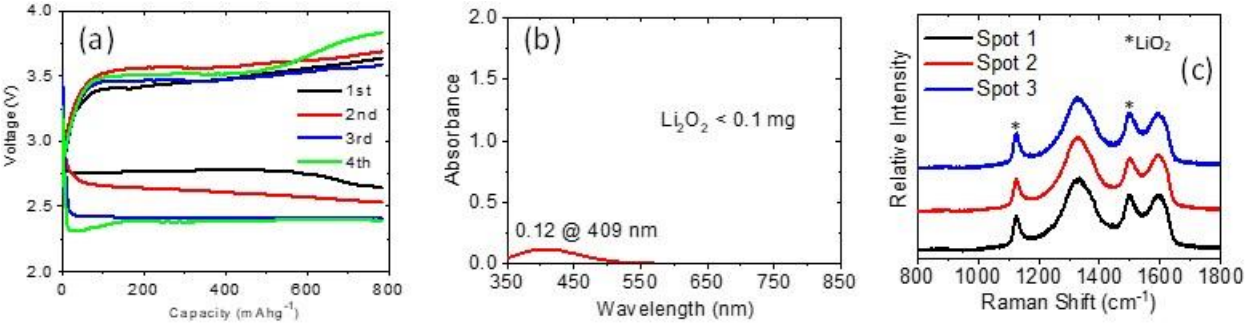

Figure II.11.B.5 (a) cycling voltage profile of Li-O2 cell with Ir3Li-rGO cathode (b) UV-Vis absorbance curve of titrant resulting from Li2O2 titration of discharged cell (c) Raman spectra of discharged Ir3Li-rGO cathode in Li-O2 cell.

Conclusions

In the project, we have developed effective cathode materials to achieve long cycle life and high energy efficiency of the lithium oxygen batteries. By rational designing the catalysts using a thin film deposition technique, Pt based Pt/Au and Pt/Cr catalysts are found to exhibit excellent catalytic performance, leading to a high energy efficiency. In addition, we have also used additives in the electrolyte to tune the cell chemistry. Biomass derived active carbon, along with LiI additive, can achieve ultrahigh discharge capacity and high energy efficiency, based on the formation of LiOH. The addition of sodium ions into the electrolyte enable the tuning of the solvation environment of the lithium ions, resulting in the reversible formation/decomposition of LiOH at a low charge potential. Finally, we have demonstrated the first implementation of *ex-situ* synthesized Ir_3Li particles in a lithium superoxide-based Li-O_2 battery. The catalyst design and the understanding of the additives in the electrolyte are critical for the development of highly efficient lithium oxygen batteries.

Key Publications

1. Bi, X.; Li, M.; Liu, C.; Yuan, Y.; Wang, H.; Key, B.; Wang, R.; Shahbazian-Yassar, R.; Curtiss, L.; Lu, J.; Amine, K. Cation Additive Enabled Rechargeable LiOH based Lithium-Oxygen Batteries. ***Angew. Chem. Int. Ed.*** 2020, DOI: 10.1002/ange.202010745.

2. Plunkett, S. T.; Wang, H.-H.; Park, S. H., Lee, Y. J.; Cabana, J.; Amine, K.; Al-Hallaj, Chaplin, B. P.; Curtiss, L. A. Charge Transport Properties of Lithium Superoxide in Li–O_2 Batteries. ***ACS Applied Energy Materials***, 2020, DOI: 10.1021/acsaem.0c02495.

3. Li, M.; Bi, X.; Amine, K.; Lu, J., Oxygen-Based Anion Redox for Lithium Batteries. ***Acc. Chem. Res.*** 2020, *53(8)*, 1436-1444.

4. Zhang, T.; Zou, B.; Bi, X.; Li, M.; Wen, J.; Huo, F.; Amine, K.; Lu, J., Selective Growth of a Discontinuous Subnanometer Pd Film on Carbon Defects for Li−O_2 Batteries. ***ACS Energy Lett.*** 2019, *4*, 2782-2786.

5. Ma, Z.; Cano, Z. P.; Yu, A.; Chen, Z.; Jiang, G.; Fu, X.; Yang, L.; Wu, T.; Bai, Z.; Lu, J. Enhancing Oxygen Reduction Activity of Pt-based Electrocatalysts: From Theoretical Mechanisms to Practical Methods. ***Angew. Chem. Int. Ed.*** 2020, *59*, 18334-18348.

6. Li, M.; Bi, X.; Wang, R.; Li, Y.; Jiang, G.; Li, L.; Zhong, C.; Chen, Z.; Lu, J. Relating Catalysis between Fuel Cell and Metal-Air Batteries. ***Matter*** 2020, *2(1)*, 32-49.

7. Wang, M.; Yao, Y.; Bi, X.; Zhao, T.; Zhang, G.; Wu, F.; Amine, K.; Lu, J. Optimization of oxygen electrode combined with soluble catalyst to enhance the performance of lithium–oxygen battery. ***Energy Storage Materials*** 2020, *28*, 73-81.

8. Bi, X.; Amine, K.; Lu, J. The importance of anode protection towards lithium oxygen batteries. ***J. Mater. Chem. A*** 2020, *8*, 3563-3573.

9. Li, M.; Liu, T.; Bi, X.; Chen, Z.; Amine, K.; Zhong, C.; Lu, J., Cationic and Anionic Redox in Lithium-ion based Batteries. ***Chem. Soc. Rev.*** 2020, *49*, 1688-1705.

10. Li, M.; Wang, C.; Chen, Z.; Xu, K.; Lu, J. New Concepts in Electrolytes. ***Chem. Rev.*** 2020, *120(14)*, 6783-6819.

II.11.C Lithium Oxygen Battery Design and Predictions (ANL)

Larry A. Curtiss, Principal Investigator
Argonne National Laboratory
9700 S. Cass Ave
Lemont, IL 60439
E-mail: amine@anl.gov

Amin Salehi, Principal Investigator
University of Illinois at Chicago
Department of Mechanical and Industrial Engineering
842 West Taylor Street, Chicago, IL 60607
Email: salehikh@uic.edu

Anh Ngo, Principal Investigator
Argonne National Laboratory
9700 S. Cass Ave
Lemont, IL 60516
Email: curtiss@anl.gov

Tien Duong, DOE Technology Development Manager
U.S. Department of Energy
E-mail: Tien.Duong@ee.doe.gov

Start Date: October 1, 2019 End Date: September 30, 2022
Project Funding: $1,350,000 DOE share: $1,350,000 Non-DOE share: $0

Project Introduction

Lithium(Li)-oxygen (O_2) batteries are considered as a potential alternative to Li-ion batteries for transportation applications due to their high theoretical specific energy. The high energy density of Li-O_2 batteries is made possible because of the formation of the Li_2O_2 product, which can store significantly higher amounts of energy compared to other energy storage systems because of the Li-O bonds. However, the challenge is that the decomposition of Li_2O_2 during the charge process requires charge transfer, which is difficult because of the large band gap of solid Li_2O_2 likely covering catalytic sites. This leads to a sluggish charge process requiring higher potentials for Li_2O_2 decomposition, which in turn reduces the energy efficiency of the battery and puts the electrolyte at risk of degradation. Additionally, the charge potential can depend on the morphology and size of Li_2O_2 product. The major issues with the existing Li-O_2 systems include degradation of the anode electrode, reactions with air components, clogging of the cathode, and electrolyte instability.

Objectives

The objective of this work is to develop new materials for Li-O_2 batteries that give longer cycle life and improved efficiencies in an air environment as well as high charge rates New electrolytes blends and additives are being investigated the can reduce clogging and at the same time can promote the cathode functionality needed to reduce charge overpotenials. The cathode materials are based on the 2-dimensional transition metal dichalcogenides (TMDCs) that we have found to be among the best oxygen reduction and evolution catalysts. The objective is to design and predict new electrolytes that work with these catalysts to give longer cycle life, high charge rates, good efficiencies, and high capacities needed to make scale up possible for these types of batteries.

Approach

The experimental strategy is to use cathode materials based on 2-dimensional transition metal dichalcogenides (TMDCs) that we have found to be among the best oxygen reduction and evolution catalysts.[1,2] These cathode

materials will be combined with new electrolyte blends and additives that can work in synergy to reduce charge potentials and increase the stability of the Li-air system. Density functional theory and ab initio molecular dynamics simulations are used to gain insight at the electronic structure level of theory of the electrolyte structure and function both in the bulk and at interfaces with the cathode, anode, and discharge product. Classical molecular dynamics are used to obtain understanding at longer length and time scales of processes occurring in the electrolyte and growth mechanisms of discharge products. Computations play a key role in the design and predictions of new electrolytes as well as characterization for understanding.

Results

Investigation of salts that work in combination with redox mediators

The effects of various salts in combination of a LiI redox mediator on the performance of a Li-O_2 battery has been investigated. Last year we reported that LiI in combination with $LiNO_3$ could lower the charge potential and increase cycle life in a Li-O2 battery. We found that the LiI serves as a redox mediator to reduce the charge potential and the $LiNO_3$ provides lithium anode protection to extend cycle life. We have subsequently investigated use of other salts in place of $LiNO_3$.

We investigated three salts, namely $LiClO_4$, LiTFSI and LiTF, for comparison with of $LiNO_3$ in an electrolyte composed of tetraethylene glycol dimethyl ether (TEGDME) and EMIM-BF_4 ionic liquid as well as LiI as the redox mediator. Figure II.11.C.1 shows the charge-discharge profiles for 1M LiI-1M $LiClO_4$ and 1M LiI-1M $LiNO_3$ after 100 cycles using the same electrolyte. The $LiClO_4$ discharge profile shows a plateau around 3.3 V in the beginning of discharge, which is not present in the $LiNO_3$ profile. The other two salts (LiTFSI and LiTF) also show a similar plateau. This has been ascribed to reduction of triiodide to iodide during discharge process leading to a decrease in the capacity due to Li_2O_2 formation. The results in Figure II.11.C.1 show that the Li_2O_2 discharge capacity retention after 100 cycles for $LiClO_4$ is around 65%, whereas using $LiNO_3$ 95% of Li_2O_2 capacity is retained. The capacity retention as a function of cycle number for the four salts is shown Figure II.11.C.1. The figure shows that $LiNO_3$ has much better capacity retention than the other three salts.

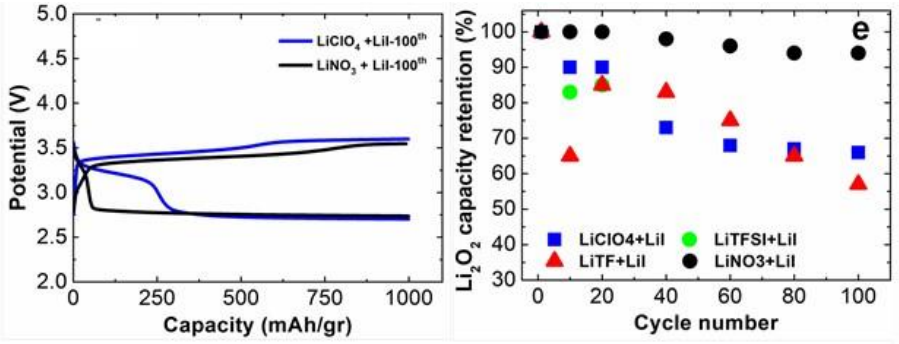

Figure II.11.C.1 (left) Charge and discharge profiles comparing $LiClO_4$ and $LiNO_3$ in the 100th cycle; (right) comparison of battery capacity retention with the four salts over 100 cycles.

These results raise the question as to what property of the LiI/$LiNO_3$ system reduces capacity loss observed during discharge compared to the other salts. One possible explanation is that the other three salts ($LiClO_4$, LITFSI, LITF) result in too slow utilization of the LiI_3 for the chemical decomposition of Li_2O_2 on charge and, thus, there is unused LiI_3 available during discharge. Our DFT calculations indicate that the reduction potential of LiI_3 is around 3.3 V so it could be what is reduced initially during discharge (the first plateau) and, therefore account for the lower capacity retention (occurring at 2.7 V) for the three salts ($LiClO_4$, LITFSI, LITF) in Figure II.11.C.1. The efficacy of the $LiNO_3$ salt system for LiI_3 utilization in contrast to the other three salts may be due to the protection of the Li anode by the reaction of $LiNO_3$ with the surface to form a protective coating. An amorphous coating containing 3:1 O:N has been detected on the lithium anode surface. This coating is able to reduce electrolyte decomposition and side reactions with the iodide species.

Domain formation in Li-O_2 battery electrolytes

We have carried out classical molecular dynamics (CMD) simulations and X-ray studies of the $LiNO_3$/LiI system to investigate the nature of the distribution of species in the electrolyte that may have important effect on how the Li-O_2 battery operates. The main result from the CMD simulations is that there are ionic and neutral domains in the electrolyte. The ionic domain contains largely the salts $LiNO_3$ and LiI with the EMIM-BF_4 ionic liquid. There is also a small amount of neutral solvent species (TEGDME) present in the ionic domain. The neutral domains contain largely TEGDME. These surprising results from computation suggesting the formation of different domains in the electrolyte was confirmed by x-ray studies of the electrolyte with variation of the salt content. The CMD simulations indicate the neutral domain will have a significantly higher O_2 concentration and faster O_2 diffusion rates than the ionic domain. The transport properties of O_2 in the IL/TEGDME along with the high oxygen reduction rate of the MoS_2 catalyst in this electrolyte may be factors in the high charge rates (0.5 mA/g) attainable in this system. Another interesting result of the CMD simulations is that in the presence of an electric field such as would be present in the battery, part of the ionic domain is found concentrated near the surface of the MoS_2. This concentration near the cathode surface may contribute to the efficacy of the discharge and charge reactions found for the LiI/$LiNO_3$ system and contribute to the large capacity retention. Further studies of domain formation in this electrolyte, as well as others are underway to understand this important finding in more detail.

Bifunctional redox mediators: $InBr_3$

We have investigated the $InBr_3$ bifunctional additive in a Li-O_2 battery for comparison with InI_3 that we previously found to give a low charge potential and a long cycle life. The results for the InI_3 additive are given in Figure II.11.C.2. for comparison with the new work on $InBr_3$.

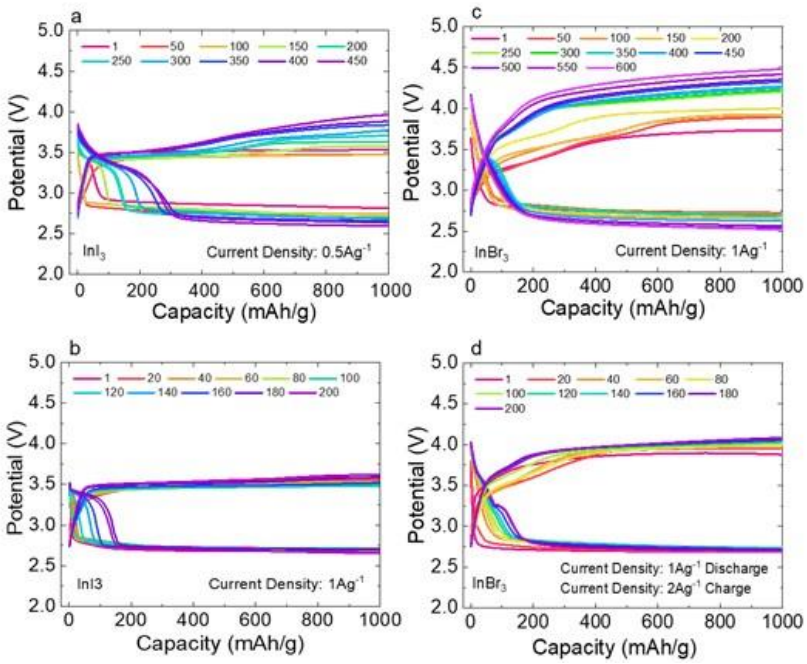

Figure II.11.C.2 Discharge/charge voltage profile. (a) 25mM InI_3 and current density of 0.5Ag^{-1}. (b) 25mM InI_3 and current density of 1Ag^{-1}. (c) 25mM $InBr_3$ and current density of 1Ag^{-1}. (d) 25mM $InBr_3$ and current densities of 1Ag^{-1} discharging and 2Ag^{-1} charging.

The battery with $InBr_3$ as the additive was run with the same cathode and electrolyte as for InI_3. The cell configuration was based on a molybdenum disulfide cathode in a hybrid electrolyte of 10% ionic liquid (EMIM BF_4) and 90% DMSO and 0.1 M LiTFSI. The additive was 0.025 M $InBr_3$. This composition enabled operation of the battery in a dry air environment with a capacity of 1000 mAh/g at a rate of 1 A/g up to 600 cycles as shown in Figure II.11.C.2c. The $InBr_3$ gives a polarization gap of less than ~1.0 for ~200 cycles and then the charge potential increased for the rest of the cycles. A higher charge rate of 2 A/g runs for ~200 cycles with a charge potential of ~4 V (**Figure II.11.C.2d**). Also, the capacity loss of the battery is less than 10% after more than 200 cycles. Different characterization techniques have been used to show the discharge product and all of them verify the presence of Li_2O_2 including Raman measurements

These results indicate that $InBr_3$ is not as good a redox mediator as the InI_3 as the gap in the latter case is ~0.7 V (Figure II.11.C.2a) compared to ~1 V for $InBr_3$ (Figure II.11.C.2a) for the same discharge/charge current

densities of 1 A/g. However, the $InBr_3$ additive enables a Li-O_2 cell with long life of ~600 cycle before failure at which point the charge potential has increased to ~4.4 V. In addition, the $InBr_3$ system can handle a higher current density as shown in Figure II.11.C.2d. In summary, this study has demonstrated that the $InBr_3$ bifunctional additive that can simultaneously improve the energy efficiency of the battery and enable long-term performance in a dry air atmosphere, similar to InI_3.

Characterization of the protective solid electrolyte interphase (SEI) that forms on the Li anode when InI_3 is used as a redox mediator

To characterize the SEI formed on the Li anode from the InI_3, SEM imaging was carried out on the pure Li anode and the Li surface after the 5th discharge cycle. The results should be representative for the InI_3 additive also. The electrolyte for the Li-O_2 cell was composed of 25mM InI_3, 0.1M LiTFSI, and a mixture of 9:1 by volume DMSO/EMIM-BF_4. The catalyst was MoS_2 nanoflakes. The results are shown in Figure II.11.C.3. Figure II.11.C.3a,b,c shows a top-view SEM image of the pristine and cycled anodes. Also, the top-view SEM-EDX composition mapping of the In element is shown in Figure II.11.C.3d,e These results indicate that In is incorporated into the anode surface. The cross-sectional SEM-EDX composition mapping of the anode reveals the presence of ~26 wt% In, shown by green color, in the surface region of the lithium. XPS was also carried out on the surface of cycled Li anode to identify the chemical compositions. Figure II.11.C.3f shows the distinctive peaks of the In 3d spectrum (at 444.2 eV and 451.7 eV), consistent with EDX characterization results. Moreover, electrochemical impedance spectroscopy (EIS) measurements were performed on the fresh and cycled (5, 10, 20 cycles) anodes to measure the charge transfer resistance upon the battery cycling Figure II.11.C.3g. The results indicate an increase in the charge transfer resistance from 21 ohms to 1315 ohms after 20 cycles, which is attributed to the incorporation of the In on the Li anode surface upon cycling. The mechanism by which InI_3 forms an SEI has been studied computationally and is described in the next section.

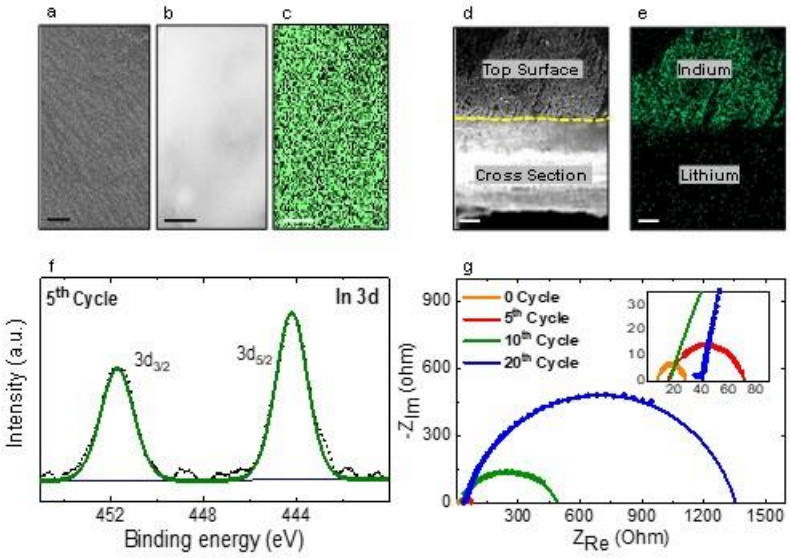

Figure II.11.C.3 Characterization of Li anode in the InI_3 system. (a) Top-view SEM image of fresh anode (Scale bar: 500nm). (b) Top-view SEM image of anode after the 5th discharge (Scale bar: 500nm). (c) Top-view SEM-EDX composition mapping of anode for In (Scale bar: 500nm). (d) Cross-sectional SEM image of anode after the 5th discharge (Scale bar: 10μm). (e) Cross-sectional SEM-EDX composition mapping of anode after the 5th discharge for In (green) showing it present on surface, but not in the interior. (Scale bar: 10μm). (f) XPS results of Li anode showing In 3d after the 5th discharge cycle. (g) EIS measurements and fitted data for fresh and cycled anode surface.

Computational studies on the protective interphase formed on Li by the InX_3 bifunctional additives

The mechanism by which the InX_3 (X = I, Br) forms a layer on the lithium surface was investigated by density functional theory (DFT). The calculated oxidation potentials of the InI_3 and $InBr_3$, including solvent effects, are 6.07 and 7.13 eV, respectively. This means that these species will not be oxidized at the anode during discharge, but rather chemically react as shown in the DFT calculations described below. Furthermore, the calculated reduction potentials of the InI_3 and $InBr_3$ (<2.6 eV) are less than the discharge potential so they will not likely be involved in the discharge process at the cathode. A possible chemical reaction between InX_3 and the lithium surface is given by:

$$InX_3 + Li(s) \rightarrow InLi(s) + 3LiX$$

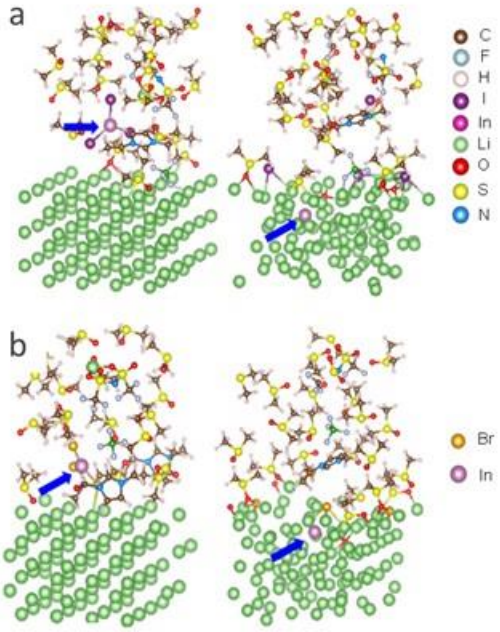

Figure II.11.C.4 AIMD simulation of Li(100) interface with DMSO/IL electrolyte with a InX_3 molecule added to the electrolyte. (a) initial (left) and optimized (right) structures for InI_3; arrow indicates the initial and final position of In atom; **(b)** initial (left) and optimized (right) structures for $InBr_3$; arrow indicates the initial and final position of In atom.

We investigated this chemical reaction for both InI_3 and $InBr_3$, with a (100) lithium surface using DFT periodic calculations. In these calculations, the halides are in a mixed electrolyte of 21 DMSO molecules, one EMIM-BF_4 (9:1 volumetric ratio), and LiTFSI salt. All molecules were initially randomly arranged in the simulation box. The results of ab initio molecular dynamics (AIMD) simulations at the electrolyte/anode interface are shown in Figure II.11.C.4. They indicate that for both InI_3 and $InBr_3$, the indium dissociates from the trihalide and moves into the Li surface with the halide ions reacting with the Li to form LiX species on the surface**.** When the InX_3 reacts and dissociates (shown by our DFT calculations) on the surface, the In^{3+} picks up three electrons from the Li anode because indium is more electronegative than the Li. Three Li from the surface can then form LiX where the Li^+ (formed by loss of the electrons to Indium) reacts with X^-The reaction of InX_3 with the Li surface is consistent with the experimental results from SEM, EDX, and XPS that there is indium on the lithium surface.

Conclusions

Our work this year has focused on understanding how redox mediators can work in concert with lithium anode protection to increase cycle life and lower charge potentials in Li-O_2 batteries. The effects of various salts in combination of a LiI redox mediator on the performance of a Li-O_2 battery has been investigated. We have compared $LiNO_3$ with three other salts ($LiClO_4$, LiTFSI and LiTF) and found that $LiNO_3$ work best. The efficacy of the $LiNO_3$ salt system for LiI_3 utilization in contrast to the other three salts may be due to the protection of the Li anode by the reaction of $LiNO_3$ with the surface to form a protective coating. This coating is able to reduce electrolyte decomposition and side reactions with the iodide species. We have also carried out classical molecular dynamics (CMD) simulations and X-ray studies of the $LiNO_3$/LiI system to investigate the nature of the distribution of species in the electrolyte that may have important effect on how the Li-O_2 battery operates. The main result from the CMD simulations is that there are ionic and neutral domains in the electrolyte. This concentration near the cathode surface may contribute to the efficacy of the discharge and charge reactions found for the LiI/$LiNO_3$ system and contribute to the large capacity retention.

We have investigated the $InBr_3$ bifunctional additive in a Li-O_2 battery for comparison with InI_3 that we previously studied. These results indicated that $InBr_3$ is not as good a redox mediator as the InI_3 as it has a

larger charge/discharge gap. However, the $InBr_3$ additive enables a Li-O_2 cell with long life of ~600 cycle with a charge potential has increased to ~4.4 V in a dry atmosphere. To characterize the SEI formed on the Li anode from the InI_3, SEM imaging was carried out on the pure Li anode and the Li surface. The results indicate the presence of In on the surface of the Li anode that serves to protect the anode during cycling. The mechanism by which the InX_3 (X = I, Br) forms a SEI on the lithium surface was investigated by density functional theory.

Key Publications

1. "Quasi-Binary Transition Metal Dichalcogenide Alloys: Thermodynamic Stability Prediction, Scalable Synthesis, and Application," Z. Hemmat, J. Cavin, A. Ahmadiparidari, A. Ruckel, S. Rastegar, S. N. Misal, L. Majidi, K. Kumar, S. Wang, J. Guo, R. Dawood, F. Lagunas, P. Parajuli, A. T. Ngo, L. A. Curtiss, S. B. Cho, J. Cabana, R. F. Klie, R. Mishra, and A. Salehi-Khojin, *Advanced Materials*, 1907041 (2020).

2. "A comparative study of redox mediators for improved performance of Li-Oxygen batteries," Chengji Zhang, Naveen Dandu, Sina Rastegar, Saurabh N. Misal, Zahra Hemmat, Anh T. Ngo, Larry A. Curtiss, Amin Salehi-Khojin, *Advanced Energy Materials*, June 2020, https://doi.org/10.1002/aenm.202000201

3. "A Lithium-Oxygen Battery that Operates in Dry Air with a Bifunctional InX_3 (X=Br,I) Electrolyte Additive," Sina Rastegar, Zahra Hemmat, Chengji Zhang, Samuel Plunkett, J. G. Wen, Naveen Dandu, Tomas Rojas, Leily Majidi, Saurabh Misal, Anh T. Ngo, Larry A. Curtiss, Amin Salehi-Khojin, submitted.

4. "Lowering Charge Potentials with Negligible Capacity Loss in High Rate Lithium Oxygen Batteries," Alireza Ahmadiparidari, Shadi Fuladi, Leily Majidi, Samuel Plunkett, Erik Sarnello, Zahra Hemmat, Sina Rastegar, Saurabh Misal, Paul C Redfern, Jianguo Wen**,** Tao Li, Anh Tuan Ngo, Fatemeh Khalili-Araghi, Larry A. Curtiss, Amin Salehi-Kojin, submitted.

References

1. "New Class of Electrocatalysts Based on 2D Transition Metal Dichalcogenides in Ionic Liquid," L. Majidi , P. Yasaei, R. E. Warburton, S. Fuladi, J. Cavin , X. Hu, Z. Hemmat, S. B. Cho, P. Abbasi, M. Vörös, L. Cheng, B. Sayahpour, I. L. Bolotin, P. Zapol, J. Greeley, R. F. Klie, R. Mishra, F. Khalili-Araghi, L. A. Curtiss, A. Salehi-Khojin, Adv Mater, **31,** 1804453 (2019).

2. "Lithium-Oxygen Batteries with Long Cycle Life in a Realistic Air Atmosphere," M. Asadi, B. Sayahpour, P. Abbasi, A. T. Ngo, K. Karis, J. R. Jokisaari, C. Liu, B. Narayanan, M. Gerard1, P. Yasaei, X. Hu, A. Mukherjee, K. C. Lau, R. S. Assary, F. Khalili-Araghi, R. F. Klie, L. A. Curtiss, Amin Salehi-Khojin, Nature, **555**, 502–506 (2018)

II.12 Beyond Li-ion R&D: Sodium-Ion Batteries

II.12.A Exploratory Studies of Novel Sodium-Ion Battery Systems (BNL)

Xiao-Qing Yang, Principal Investigator
Chemistry Division, Bldg. 555
Brookhaven National Laboratory
Upton, NY 11973
Email: xyang@bnl.gov

Enyuan Hu, Principal Investigator
Chemistry Division, Bldg. 555
Brookhaven National Laboratory
Upton, NY 11973
Email: enhu@bnl.gov

Tien Duong, DOE Technology Development Manager
U.S. Department of Energy
Email: Tien.Duong@ee.doe.gov

Start Date: October 1, 2019 End Date: September 30, 2020
Project Funding: $325,000 DOE share: $325,000 Non-DOE share: $0

Project Introduction

The next generation of rechargeable battery systems with higher energy and power density, lower cost, better safety characteristics, and longer calendar and cycle life need to be developed to meet the challenges to power electrified vehicles in the future. Na-ion battery systems have attracted more and more attention due to the more abundant and less expensive nature of Na resources. However, building a sodium battery requires redesigning battery technology to accommodate the chemical reactivity and larger size of sodium cations. Since Na-ion battery research is an emerging technology, new materials to enable Na electrochemistry and the discovery of new redox couples and the related diagnostic studies of these new materials and redox couples are quite important. This project uses the synchrotron based in situ x-ray diagnostic tools developed at BNL to evaluate the new materials and redox couples, to explore in-depth fundamental understanding of the reaction mechanisms aiming to improve the performance of these materials and provide guidance for new material developments. This project also focuses on developing advanced diagnostic characterization techniques for these studies. The synchrotron based in situ X-ray techniques (x-ray diffraction, x-ray pair distribution function, or PDF, and x-ray absorption XAS) will be combined with other imaging and spectroscopic tools such as transmission electron microscopy (TEM), scanning transmission electron microscopy (STEM), mass spectroscopy (MS), transmission x-ray microscopy (TXM), as well as neutron diffraction (ND) and neutron PDF (NPDF). In FY2019, this BNL team has performed several successful experimental studies at various beamlines of National Synchrotron Light Source II (NSLSII) such as (HXN) beamline, x-ray Powder diffraction (XPD), and ISS beamlines. By collaborating with Dr Huoling Xin, this team also has carried out studies using the 3d TEM tomography and STEM, EELS on the new cathode materials for Na-ion batteries. The BNL team has been closely working with top scientists on new material synthesis at ANL, LBNL, SLAC, and PNNL, with U.S. industrial collaborators.

Objectives

The primary objective of this project is to develop new advanced in situ material characterization techniques and to apply these techniques to support the development of new cathode, anode, and electrolyte materials with high energy and power density, low cost, good abuse tolerance, and long calendar and cycle life for the next generation of Sodium-ion batteries (SIBs) to power plug-in hybrid electric vehicles (PHEV) and electric

vehicles (EV). The diagnostic studies have been focused on issues relating to capacity retention, thermal stability; cycle life and rate capability of advanced Li-ion and beyond Li-ion batteries

Approach

- This project has used the synchrotron based in situ x-ray diagnostic tools developed at BNL to evaluate the new materials and redox couples to enable a fundamental understanding of the mechanisms governing the performance of these materials and provide guidance for new material and new technology development regarding Na-ion battery systems. These techniques include:
- Using nano-probe beamline at NSLSII to study the elemental distribution of new solid electrolyte materials for Na-ion batteries
- Using transmission x-ray microscopy (TXM) to do multi-dimensional mapping of cathode materials of Na-ion batteries
- Using A combination of time resolved X-ray diffraction (TR-XRD) and mass spectroscopy (MS), together with in situ soft and hard X-ray absorption (XAS) during heating to study the thermal stability of the cathode materials for Na-ion batteries
- Design and carry out three-dimensional (3D) STEM tomography experiments to study new cathode materials for Na-ion batteries at pristine state and after multiple cycling.

Results

In FY2020, **BNL** has been focused on studies of Ti, Cr, and S K-edge XAS for $NaTi_{1/3}Cr_{2/3}S_2$ cathode material at different state of charges (SOCs). Figure II.12.A.1a-c show a set of selected *in situ* XAS spectra for Ti, Cr, and S during the charge and discharge process of $NaCr_{2/3}Ti_{1/3}S_2$/Na battery cycled at C/10. It can be seen that during the whole charge process the Cr K-edge XAS is hardly changed, indicating that Cr ions do not participate in the electrochemical redox reactions. In contrast, the Ti K-edge XAS spectra change in the first stage: the 4977.8 eV peak shifts continuously toward high energy and finally reaches 4978.8 eV. The gradually increasing intensity of pre-edges at 4970 eV indicates the oxidation process from Ti^{3+} to Ti^{4+} in the first stage of charge, but no further oxidation reaction for Ti in later stages. The most significant spectral variations at different state of charge are found in the XAS spectra of sulfur K-edge: during the first stage, the S K-edge spectrum is hardly changed. In the second stage, the pre-edge located at ~2468 eV is gradually grown. Such a pre-edge is attributed to the hybridization between the Cr 3d and S 3p orbitals. The growth of a new peak appearing at 2470.7 eV can be clearly seen on the third stage of charging process, which is consistent with the changes previously reported for $NaCrS_2$. It corresponds to a newly-formed localized electronic states on sulfur, probably stand for S-S σ*, resulting from the occurrence of $2S^{2-}/(S_2)^{n-}$ ($n < 4$), i.e. the anionic redox process for charge compensation accompanied with the formation of S-S dimers.

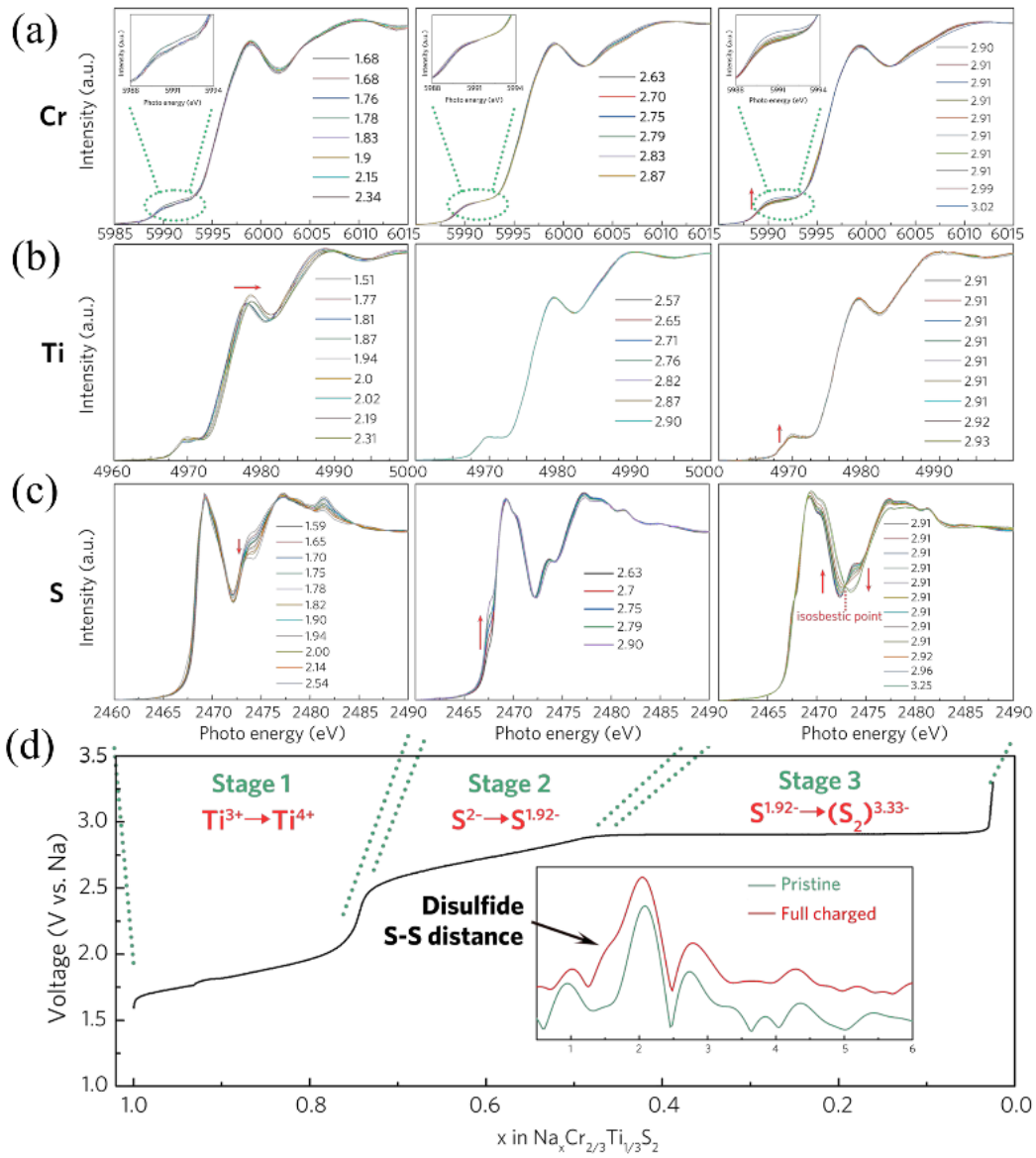

Figure II.12.A.1 In-situ X-ray absorption spectrum (XAS) of $NaCr_{2/3}Ti_{1/3}S_2$ at (a) Cr, (b) Ti and (c) S K-edges; (d) The corresponding voltage profiles for the first charge. The divided in situ XAS K-edge XAS spectra of three stages as marked in the bottom inset during the first charge process. The inset in the bottom part is converted R space of ex situ sulfur K-edge EXAFS for pristine and full charged samples.

BNL team also carried out synchrotron based XRD and PDF studies for NaCrSeS cathode material at different SOCs. Figure II.12.A.2a and b show the *ex situ* XRD and PDF data of pristine, charged, and discharged samples. Figure II.12.A.2a (XRD) indicates that the O'3 phase of the pristine material is changed to the O1 phase at charged state and back to the O'3 phase at the discharged state. In Figure II.12.A.2b (PDF), the intensity of G(r) peaks of charged and discharged samples are significantly reduced from that of the pristine sample, especially at the larger atomic pair distance (>50 Å), indicating that the charged and discharged samples have poorer crystallinity than the pristine sample. Figure II.12.A.2c and d show the fitted PDF patterns for pristine and charged samples respectively. Contribution from major atomic pairs are also shown. The structure models are obtained from density functional theory (DFT) calculation. In Figure II.12.A.2c, the first peak at 2.52 Å is related to the Cr-S/Se atomic pair and the second peak at around 2.92 Å is related to the Na-S/Se atomic pair. The broad and strong peak at 3.60 Å is attributed to the Cr-Cr (3.64 Å), S-S (3.60 Å) and Se-Se (3.60 Å) atomic pairs. After charging, the first and third peaks shift to lower positions of 2.44 and 3.36

Å, respectively, indicating the shortening of Cr-S/Se, Cr-Cr, S-S and Se-Se atomic pairs. More importantly, the peak related to the Na-S/Se correlation at 2.92 Å have essentially disappeared, indicating that the Na ions are fully extracted from the structure, which is consistent with the initial charge capacity of NaCrSSe.

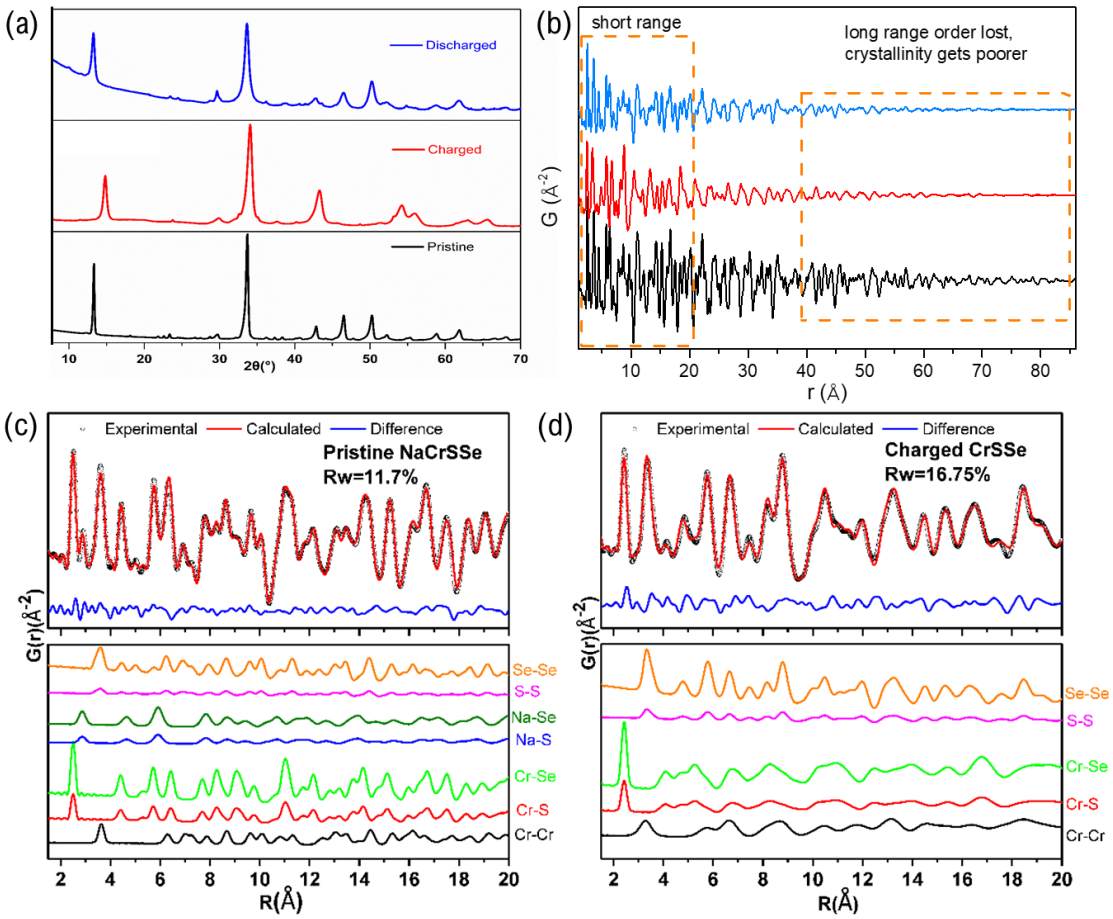

Figure II.12.A.2 (a) ex situ XRD data and (b) ex situ PDF data of pristine, charged, and discharged NaCrSSe; (c) PDF data of pristine sample and (d) PDF data of charged sample fitted using DFT calculated structural models. In both (c) and (d), contributions from major atomic pairs are also shown in the lower panels.

BNL team also carried out *Ex situ* XAS measurement at Cr K-edge to examine valance states of Cr at different charge/discharge states. As shown in Figure II.12.A.3a, no clear shifts of the Cr K-edge can be observed during charge/discharge processe indicating that the contribution of Cr ions in the charge compensation during the electrochemical process is very limited. A small reversible rise/drop in pre-edge should be attributed to the reversible distortion of Cr-S/Se octahedron, allowing the transition of electrons from Cr 1s to Cr 3d-t_{2g} and 3d-e_g, which is forbidden for the undistorted octahedral sysmetry. XAS spectra at Se K-edge at different charge/discharge stages are also measured. As shown in Figure II.12.A.3b, obvious changes in the Se K-edge XAS spectra can be observed during the charge and discharge processes, indicating the oxidation/reduction of Se. The peak A (red area in Figure II.12.A.3b) at ~12660eV could be assigned to the transition of 1s electron to unoccupied Cr 3d-Se 4p hybrid orbitals. The relative intensity of peak A also increases upon charging. This can be attributed to the increased population of the unoccupied valence 4p levels caused by the charging process, indicating the oxidization of Se ions. During discharge process, the intensity of peak A decreases, indicating that the redox of Se ions during the cycling is fully reversible. In addition, the broad peak B at ~12670 eV (blue area in Figure II.12.A.3b) caused by multiple scattering in the coordination sphere shifts to high energy and its intensity reduces upon charging. It shifts back to the pristine state after

fully discharge. All these changes demonstrate that the charge compensation is partly achieved by the redox of Se anions.

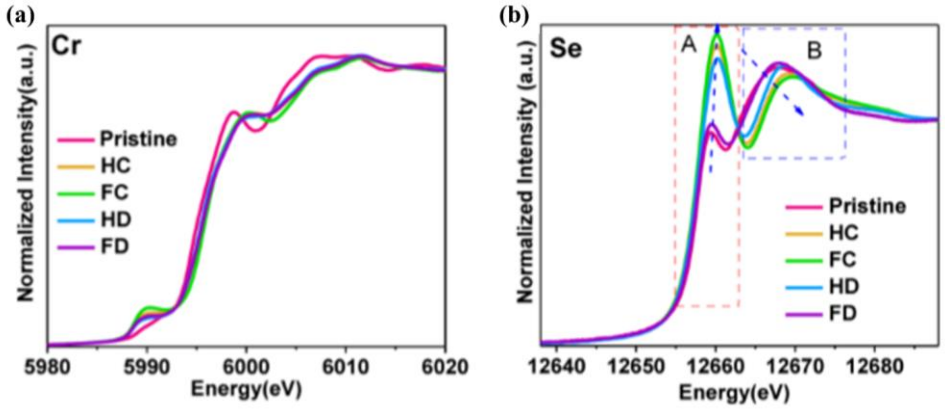

Figure II.12.A.3 Ex situ XAS of Cr (a) and Se (b) XANES spectra of NaCrSSe electrodes at various charge/discharge states which include pristine, half charged (HC, charged to a capacity of 70 mAh g^{-1}), full charged (FC, full charged to 3.3 V), half discharged (HD, discharged to a capacity of 70 mAh g^{-1} after full charged) and full discharged (FD, full discharged to 1.5 V after full charged).

BNL team also carried out synchrotron based XAS studies for NaCrSeS cathode material at different SOCs. *Ex situ* XAS spectra at S K-edge at different charge/discharge stages are shown in Figure II.12.A.4a**.** The relative intensity of peak A at ~2470eV (red area in Figure II.12.A.4a) varies greatly during the cycling and the evolution of peak B at ~2480eV (blue area in Figure II.12.A.4a) has the similar moving trend as that for Se K-edge. The peak A could be attributed to the transition of 1s electron to the unoccupied Cr 3d-S 3p hybrid orbitals. During the charge process, the emerging and growing of the shoulder peak located at ~2468 eV and addition peak formation at 2470.7 eV are clearly observed, corresponding to the formation of the holes of S and the dimerization of S/Se-S/Se respectively, and the process reverses upon discharge. These results suggest the reversible valence changes of S anions and the occurrence of S^{2-}/S^{n-} and $S^{2-}/(S_2)^{m-}$ redox couples during the cycling. The corresponding FT-EXAFS spectra of S are shown in Figure II.12.A.4b. Note that the FT-EXAFS spectra have not been phase-corrected so that the actual bond lengths could be ~0.4 Å longer. The peak at 2.1 Å for the pristine state in Figure II.12.A.4b is corresponding to the closest Cr ions to the core S, which shift to 2.0 Å after fully charged. During charge (desodiation), Cr-S/Se bonds shrink, also shown as the decrease in lattice parameters “a” and “b” obtained by XRD, caused by the contraction of the S and Se anion radii at higher oxidation states. These structural changes are in line with the mechanism of ‘normal unit cell breathing’.

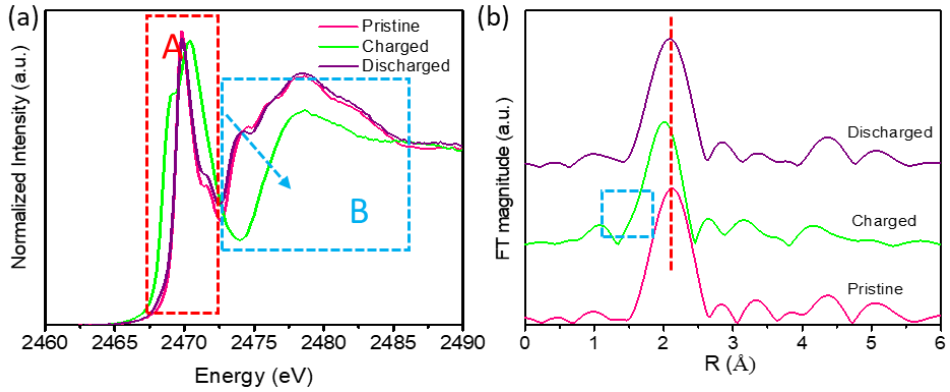

Figure II.12.A.4 (a) S K-edge XANES spectra and (b) corresponding FT-EXAFS spectra of NaCrSSe electrodes at various charge/discharge states which include pristine, full charged (charged to 3.3 V), full discharged (discharged to 1.5 V after full charged).

Conclusions

This project, "Exploratory Studies of Novel Sodium-Ion Battery Systems (BNL)", has been successfully completed in FY2020. All milestones have been completed. The publication records are very good. Extensive collaboration with other national Labs, US universities and international research institutions were established.

Key Publications

Publications

1. Tian Wang, Guo-Xi Ren, Zulipiya Shadike, Ji-Li Yue, Ming-Hui Cao, Jie-Nan Zhang, Ming-Wei Chen, Xiao-Qing Yang, Seong-Min Bak, Paul Northrup, Pan Liu, Xiao-Song Liu* & Zheng-Wen Fu*, "Anionic redox reaction in layered $NaCr_{2/3}Ti_{1/3}S_2$ through electron holes formation and dimerization of S–S", *Nature Communications*, 10, Article number: 4458 (2019), publication date (Web): October 1st, 2019.

2. Peng-Fei Wang, Yao Xiao, Nan Piao, QinchaoWang, Xiao Ji, Ting Jin, Yu-Jie Guo, Sufu Liu, Tao Deng, Chunyu Cui, Long Chen, Yu-Guo Guo, Xiao-QingYang, Chunsheng Wang, "Both cationic and anionic redox chemistry in a P2-type sodium layered oxide", Nano Energy. DOI: 10.1016/j.nanoen.2020.104474, Publication Date (web): January 10th, 2020

3. Ting Jin, Peng-Fei Wang, Qin-Chao Wang, Kunjie Zhu, Tao Deng, Jiaxun Zhang, Wei Zhang, Xiao-Qing , Lifang Jiao*, and Chunsheng Wang*, "Realizing Complete Solid-Solution Reaction in High Sodium Content P2-Type Cathode for High-Performance Sodium-Ion Batteries", Angewandte Chemie, DOI: 10.1002/ange.202003972, Publication Date (web): June 05th, 2020.

4. Peng-Fei Wang, Ting Jin, Jiaxun Zhang, Qin-Chao Wang, Xiao Ji, Chunyu Cui, Nan Piao, Sufu Liu, Jijian Xu, Xiao-Qing Yang, and Chunsheng Wang, "Elucidation of the Jahn-Teller effect in a pair of sodium isomer", Nano Energy. DOI: 10.1016/j.nanoen.2020.105167, Publication date (web): July 28th, 2020.

5. Liangtao Yang, Juan Miguel López del Amo, Zulipiya Shadike, Seong-Min Bak, Francisco Bonilla, Montserrat Galceran, Prasant Kumar Nayak, Johannes Rolf Buchheim, Xiao-Qing Yang, Teófilo Rojo, and Philipp Adelhelm, "A Co- and Ni-Free P2/O3 Biphasic Lithium Stabilized Layered Oxide for Sodium-Ion Batteries and its Cycling Behavior", Advanced. Functional Materials, DOI: 10.1002/adfm.202003364, Publication Date: August 21st, 2020.

II.12.B Development of Advanced High-energy and Long-life Sodium-ion Battery (ANL)

Khalil Amine, Principal Investigator
Argonne National Laboratory
9700 S Cass Ave,
Lemont, IL 60439
E-mail: amine@anl.gov

Christopher S. Johnson, Principal Investigator
Argonne National Laboratory
9700 S Cass Ave,
Lemont, IL 60439
E-mail: cjohnson@anl.gov

Tien Duong, DOE Technology Development Manager
U.S. Department of Energy
E-mail: Tien.Duong@ee.doe.gov

Start Date: January 1, 2019 End Date: September 30, 2021
Project Funding: $700,000 DOE share: $700,000 Non-DOE share: $0

Project Introduction

Considering the natural abundance and low cost of sodium resources, sodium-ion batteries (SIBs) have received much attention for large-scale electrochemical energy storage.[1] However, the larger ionic radius of Na^+ (1.02 Å) than Li^+ (0.67 Å) brings more challenges on the development of good Na-host materials with optimal electrochemical properties. On one hand, despite most SIBs cathode materials are either imitating or duplicating from lithium analogues, there are significant differences in the intercalation chemistries between sodiation and lithiation. The layered oxides cathodes deliver very high energy density, but undergo more complex phase transition during charge/discharge, resulting in severe capacity fade during prolonged cycling. [2] On the other hand, the absence of suitable anode materials has obstructed progress in the development of SIBs. Two of the most promising anode materials, graphite and silicon have limited sodium storage capability. Hard carbon can demonstrate reversible sodiation/de-sodiation, but the capacity is lower than 300 mAh g^{-1}, significantly limited the energy density of SIBs. [3],[4] Alloying anode materials such as phosphorus can deliver high capacity, but suffer from huge volume changes and severe parasitic reactions with the electrolytes, resulting in rapid capacity degradation during long-term cycling. [5]

Via advanced diagnostic tools including synchrotron X-ray probes and computational modeling, the team led by Dr. Khalil Amine and Dr. Christopher Johnson at Argonne National Laboratory (ANL) is focusing on the development of rational cathode materials, anode materials and electrolytes to develop long life and high energy SIBs with low cost and high safety.

Objectives

The project objective is to develop high-energy SIBs with long life, low cost and high safety. The energy density target is 200 Wh kg^{-1} and/or 500 Wh L^{-1}, wherein the anode and cathode capacity targets are 600 $mAhg^{-1}$ and 200 $mAhg^{-1}$, respectively.

Approach

In a team approach, the Na-ion battery group will create a versatile Na-ion battery chemistry with beneficial advantages such as low cost, safety, recycling, and sustainability of materials used. The team will work in a synergistic way so that the final design is the culmination of advances in phosphorus carbon composites mated with optimized lead or other highly dense metalloids, such as tin and/or antimony and derivatives thereof, for the recyclable anode. Synthesis and optimization of such blended composite anodes will be conducted in

parallel to diagnostic characterization of structures, phase formation, and cycling stability. Cathode work will begin at the end of the first year and will involve (1) gradient cathodes consisting of Fe-Mn compositions, and (2) intergrowths of layer stacking sequenced oxides. If resources allow, the team also will attempt to stabilize cathode surfaces using ALD methods, particularly for the benefit of staving off dissolution of manganese and iron/electrolyte reactivity.

Results

The second year of this project was focusing on the optimization of the developed anode materials and development of cathode materials. However, due to the impact of COVID-19, Argonne National Laboratory was operated under limited operation and mini-safe mode. This has slowed down our scheduled plan on the cathode efforts. Thus, here we summarized our progress on the anode materials and will report the progress of cathode materials in the coming quarterly report.

Understanding the excellent electrochemical performance of black phosphorus based anodes

In previous year, we reported a hierarchical micro/nanostructured black phosphorus/Ketjenblack-multiwalled carbon nanotubes (BPC) composite anode for sodium-ion batteries, which can deliver a high specific capacity of > 2000 mAh/g and good cycle life. However, the cost of making black phosphorus is high, which prevents the commercialization of this anode. Nevertheless, the underlying mechanism of its excellent electrochemical performance is valuable for the design of novel lost-cost phosphorus anodes, such as red phosphorus based anodes. In FY 2020, we used a series of techniques to characterize its sodiation/de-sodiation process.

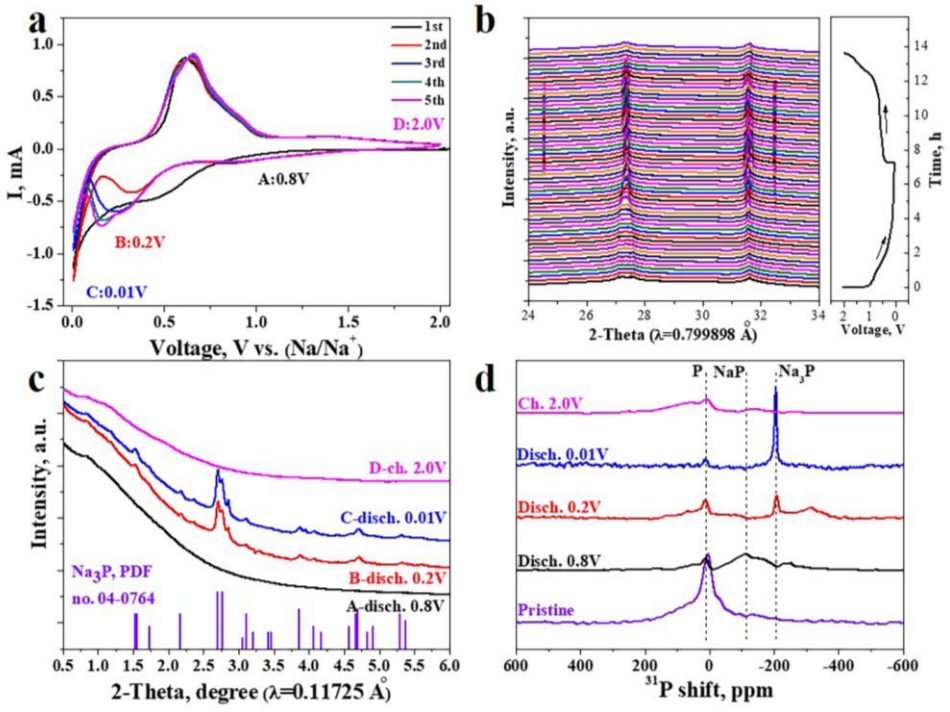

Figure II.12.B.1 (a) Cyclic voltammogram at 0.1 mV s^{-1} and (b) in-situ HEXRD in the 1st cycle at 0.1 C of BPC anode, (c) ex-situ HEXRD and (d) ^{31}P NMR spectra of BPC anode at different charge/discharge states.

Figure II.12.B.1a illustrates cyclic voltammetry data for the first five cycles of the BPC anode, which is almost overlapped after the first two cycles, indicating high sodiation/de-sodiation reversibility. In-situ synchrotron HEXRD was further used to investigate the phase changes of the BPC anode. As shown in Figure II.12.B.1b, no crystalline phase is present at the beginning of discharge, indicating the reaction intermediate at this stage is in an amorphous state. When the cell was discharged to around 0.3 V, crystalline Na_3P phase first appeared, and its intensity gradually increased with sodiation. During the de-sodiation process, the Na_3P intensity

gradually decreased and completely disappeared at about 1.4 V. The HEXRD patterns at the beginning of discharge and at the end of charge are quite similar, confirming the highly reversible sodiation/de-sodiation process of the BPC anode. This result was further confirmed by ex-situ HEXRD characterization on the BPC electrode at different charge/discharge states (Figure II.12.B.1c). To further reveal the structures of sodiation/de-sodiation intermediates and/or products, especially those in amorphous states, we conducted solid-state ^{31}P magic angle spinning (MAS) NMR spectroscopy. Figure II.12.B.1d shows the mass-normalized ^{31}P MAS NMR spectra of the BPC anode at different charge/discharge states. The result illustrated that the BP nanocrystalline was transformed to crystalline Na_3P through an amorphous NaP intermediate during the sodiation process, and then converted back to amorphous phosphorus with a small amount of amorphous NaP remaining during the de-sodiation process. Considering the volumetric expansion of forming Na_3P is up to around 500%, our result implies that an effective integration of nanostructured composite can be a practical solution to develop high capacity and high energy density metallic anode.

To further confirm the excellent performance of our BPC anode, we further applied our BPC anode in full cell study using a P2 type Zn-doped $Na_{0.66}Ni_{0.26}Zn_{0.07}Mn_{0.67}O_2$ cathode. As shown in Figure II.12.B.2, the assembled $Na_{0.66}Ni_{0.26}Zn_{0.07}Mn_{0.67}O_2$/BPC full cell demonstrate excellent cycle and rate performance. The specific capacity of the BPC/NNZMO cell is currently limited by the cathode. When the BPC composite anode is coupled with other sodium cathode materials with higher specific capacity, the specific energy of the corresponding full cell could be further increased.

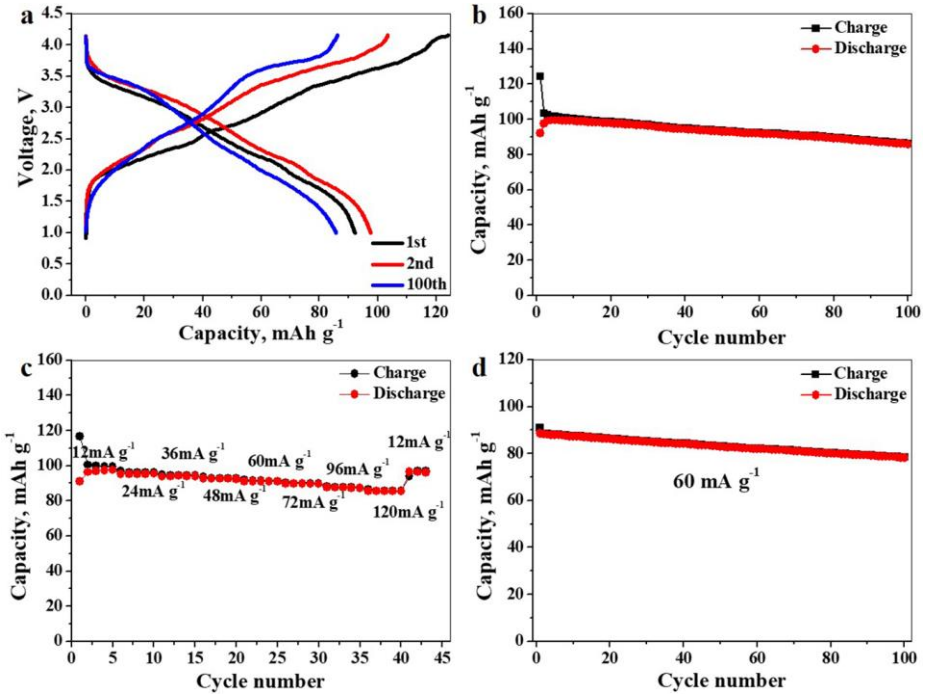

Figure II.12.B.2 Representative charge/discharge curves, (b) cycle performance at 12 mA g^{-1}, and (c, d) rate performance of a $Na_{0.66}Ni_{0.26}Zn_{0.07}Mn_{0.67}O_2$/BPC cell with electrolyte of 1 M $NaPF_6$/PC with 2 vol.% fluorinated ethylene carbonate additive.

Development and characterization of high-capacity/low-cost red phosphorus anode materials

The mechanistic understanding on BPC anode showed that our structure design strategy could significantly accommodate the huge volume changes of phosphorus anode during charge/discharge and thus enable a highly sodiation/de-sodiation process. Therefore, we further used this strategy to develop a new high-capacity and low-cost red phosphorus anode material.

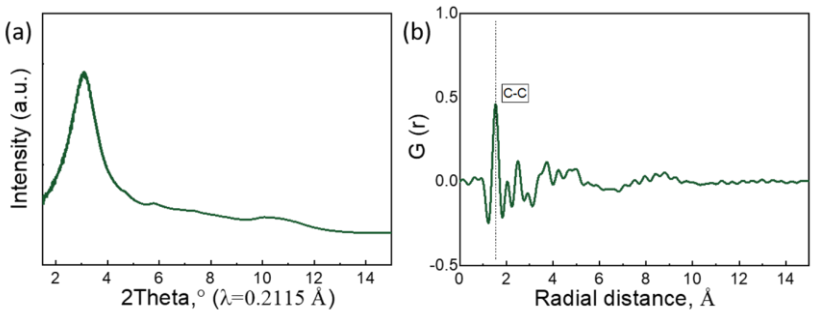

Figure II.12.B.3 (a) High-resolution X-ray diffraction and (b) pair distribution function data for RPC composite.

We prepared a red phosphorus/Ketjenblack-MWCNTs (RPC) composite anode with a red phosphorus loading of 70 wt.% by using similar high-energy ball milling (HEBM) process. X-ray diffraction (XRD) was carried out to investigate their crystal structures. As clearly shown in Figure II.12.B.3a, RPC anode exhibit amorphous structures, indicating that RP have very small particle sizes and are homogeneously distributed in the carbon matrix after HEBM. In addition, the pair distribution function (PDF) was investigated for the RPC anode, as the PDF can provide both local and long-range structural information as a histogram of all atom-atom distances within a system, independent of crystallinity. As shown in Figure II.12.B.3b The RPC only show oscillations in the low radical distance range (<6 Å), which confirms their amorphous structure and reveals that the coherent domain size of RP is smaller than 6 Å.

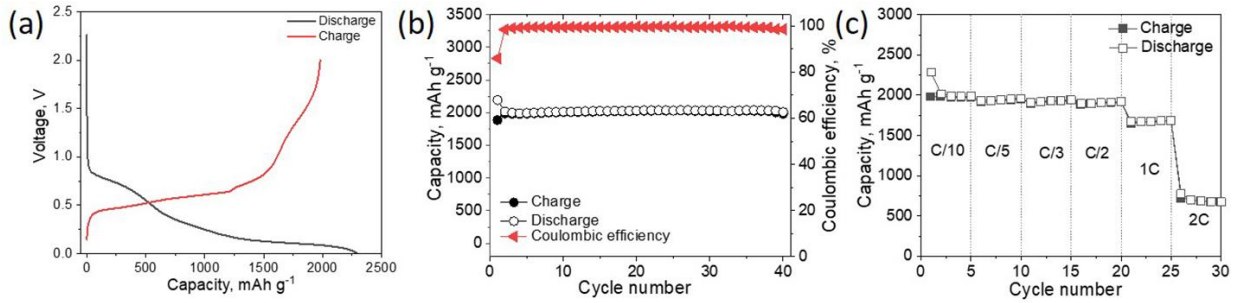

Figure II.12.B.4 (a) The 1st charge/discharge curve of RPC anode at C/10 (1C=2600 mA/g). (b) cycling performance of RPC anode at C/3. (c) Rate capability of RPC anode.

Figure II.12.B.4a shows the voltage profiles of the RPC anode at C/3 within 0.02-2.0 V in the conventional carbonate-based electrolytes (1M $NaPF_6$/ Propylene carbonate (PC)+2 vol.% Fluoroethylene carbonate (FEC)). As shown, two main voltage plateaus can be observed at about 1.0-0.5 V and below 0.5 V during the sodiation process, corresponding to the sodiation process from P to Na_xP and eventually Na_3P. In the desodiation process, the charge curves consist of a sloping region at 0.02-0.4 V and an inclined plateau at 0.4-1.0 V followed by a sloping region up to 2.0 V. The initial discharge and charge capacities of RPC at C/10 were measured to be 2285.6 and 1979.5 mAh g^{-1}, manifesting a high ICE of ~ 86.6% and a high phosphorus utilization of 76% compared to the theoretical capacity of RP (2596 mAh g^{-1}). The initial irreversible capacity loss (~14%) was mainly attributed to the decomposition of electrolytes to form the SEI on the surface of RPC. Compared to other reported RP-based anodes, the irreversible electrolyte decomposition has been remarkably suppressed, which led to the observed high ICE.

RPC anode demonstrates good cycle stability, as illustrated in Figure II.12.B.4b, which can still maintain a high reversible capacity of 1981.8 mAh g^{-1} (i.e., 1386.8 mAh $g^{-1}_{composite}$) after 40 cycles at C/3. The tap density of RPC composite was measured to be ~0.7 cc g^{-1}, which thus leads to a high volumetric capacity of 970.7 mAh cc^{-1} (1386.8 mAh $g^{-1}_{composite}$X 0.7 cc g^{-1}) based on the mass of RPC composite. To the best of our knowledge, such a high volumetric capacity has been rarely reported in anodes for SIBs.

Figure II.12.B.4c further shows the rate capabilities of RPC. RP_{70}/C_{30} can deliver high specific capacities at low rates (C/10 to 1C). However, the specific capacity at 2C drops to ca. 800 mAh g^{-1}, which is only 40% of that at C/10. This is because of the low electronic conductivity of red phosphorus, which will be further improved by doping in the next step.

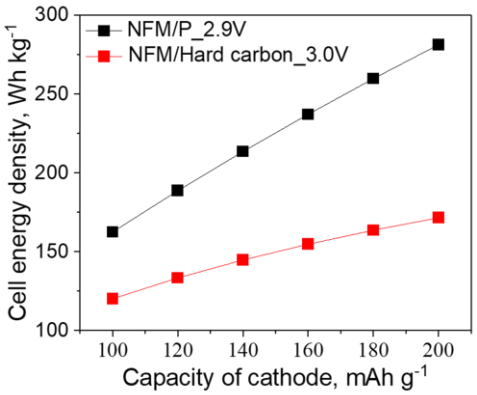

Figure II.12.B.5 Estimated cell energy density of sodium-ion batteries with different anode materials using BatPaC.

We further used the Argonne Battery Performance and Cost (*BatPaC*) model, which is a public spreadsheet tool for estimating battery performance and cost, to compare the energy density of SIBs at the cell level using different anode materials. As shown in Figure II.12.B.5, compared to hard carbon, our RP-based anodes can significantly increase the cell specific energy of SIBs.

Intrigued by the extraordinary sodium storage performance of RPC composites, we further conducted a comprehensive characterization to gain an understanding of the underlying mechanism of their excellent structural and interface stability.

To probe the volume changes of RPC during sodiation/de-sodiation, we carried out in situ morphological observations of single-particle charges/discharges using focused ion beam scanning electron microscopy (FIB-SEM). The detailed experimental set-up can be seen in our previous report.[6] Different from the widely used solid Li_2O/Na_2O electrolytes in the in situ TEM characterization of alloying-based anodes. We used ionic liquid electrolytes during charge/discharge, which can better reflect their electrochemical reaction process. Figure II.12.B.6a shows the 1st charge/discharge curve of a single RPC particle during charge/discharge within 0.2-2.0 V at 500 pA using Na-based ionic liquids, which exhibited similar sodiation/desodiation features as that in coin cells. The morphologies of RPC particles during charge/discharge were captured and shown in Figure II.12.B.6b-d. As shown, the pristine RPC particle is a micrometer-sized secondary particle, which further consists of nanometer-sized secondary-like nanoparticles. After being discharged to 0.2 V, the particle expanded slightly due to the insertion of Na. When charged back to 2.0 V, it can be seen that the particle can almost overlap the pristine particle. Given the volume expansion of P to Na_3P is estimated to be 499%, the volume expansion of P to Na_xP when discharged to 0.2 V was thus estimated to be 319%. As a comparison, the volume expansion of our RPC anode when discharge to 0.2 V was suppressed to 156%, which can serve as strong evidence for its robust mechanical integrity during charge/discharge.

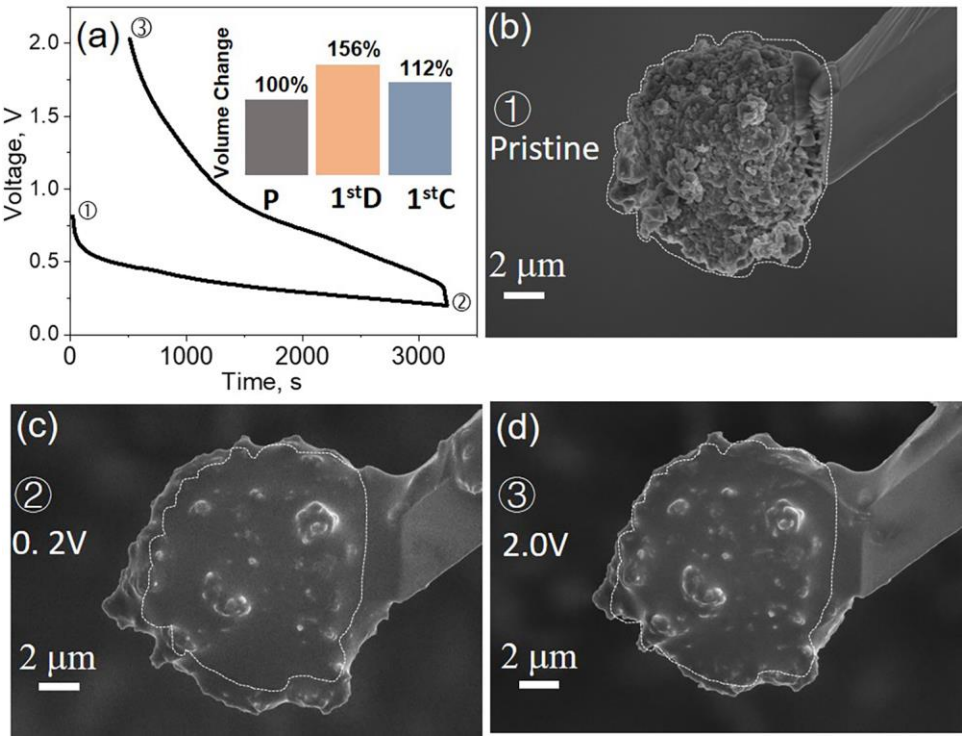

Figure II.12.B.6 (a) Voltage profile and (b-d) corresponding SEM images of single RPC particle during charge/discharge at 500 pA with Na metal anode; inset of (a) shows the estimated volume changes during charge/discharge.

Figure II.12.B.7a shows the P2p XPS spectra of RPC electrode during charge/discharge in the carbonate electrolytes. As shown, the pristine RPC electrode shows two major peaks at 129.0 eV and 130.0 eV, which can be assigned to the $P2p_{3/2}$ and $P2p_{1/2}$ doublet of the element P. In addition, a weak P-O peak at 133.2 eV can be observed, which is due to the partial oxidation of RPC during laminate fabrication under ambient atmosphere. When the cell was discharged to 0.02 V, two new peaks appeared at 136.9 eV and 126.8 eV. The peak at 126.8 eV is attributed to the formation of Na_3P, which leads to a significant decrease of the P2p peaks at 130 eV and 129 eV. The peak at 136.9 eV is assigned to $Na_xPF_yO_z$, which is due to the decomposition of $NaPF_6$ salt, resulting in the simultaneous increase of the P-O peak at 132.8 eV due to the deposition of PO_4^{3-}. After charging back to 2.0 V, the $Na_xPF_yO_z$ and PO_4^{3-} peaks remained stable, while the P2p peaks of RP were recovered along with the disappearance of the Na_3P peak due to the desodiation of Na_3P to P during charge. The identification of the Na_3P and P2p peaks of RP during charge/discharge in the XPS clearly demonstrates that the SEI layer on the RPC is very thin (<10 nm due to the penetration depth limit of XPS). In order to probe the decomposition of solvents and additives, we further measured the C1s XPS spectra. As shown in Figure II.12.B.7b, the C1s spectrum of pristine RP_{70}/C_{30} consists of four components, which can be assigned to C-C (284.8 eV), C-O (286.3 eV), and O-C-O (288.5 eV) from Na alginate binder, as well as the sp2 carbon peak from Ketjenblack or conductive carbon black (283.3 eV). After being discharged to 0.02 V, the intensities of all the peaks significantly decreased except the C-C peak at 284.8 eV. When charged back to 2.0 V, the intensity of C-C decreases, which is accompanied with the increase of the other three peaks. Such a result indicates that a thin film comprising C-C or C-H was formed and decomposed during the discharge/charge process. Note that the decomposition of propylene carbonate (PC, the main solvent of carbonate-based electrolytes) would lead to a large amount of sodium alkyl carbonates and sodium carboxylates, which will cause the increase of the C-C, C-O, and O-C-O peaks rather than a decrease. Therefore, PC decomposition was significantly reduced during the discharge of RP_{70}/C_{30} anode. In addition, sp2 carbon can be detected as well during discharge/charge, which is another evidence of thin SEI formation. Taken together, we can infer that the formed thin SEI film is mainly derived from the decomposition of the fluoroethylene carbonate (FEC) additive and $NaPF_6$ salt in our electrolytes, which significantly suppress the decomposition of PC solvent. The F1s

spectra (Figure II.12.B.7c) result has well confirmed our hypothesis. It exhibits F1s XPS peaks of Na_xPF_yOz, PF_6^-, and NaF, which are the main decomposition products of FEC and $NaPF_6$, rather than PC solvent.

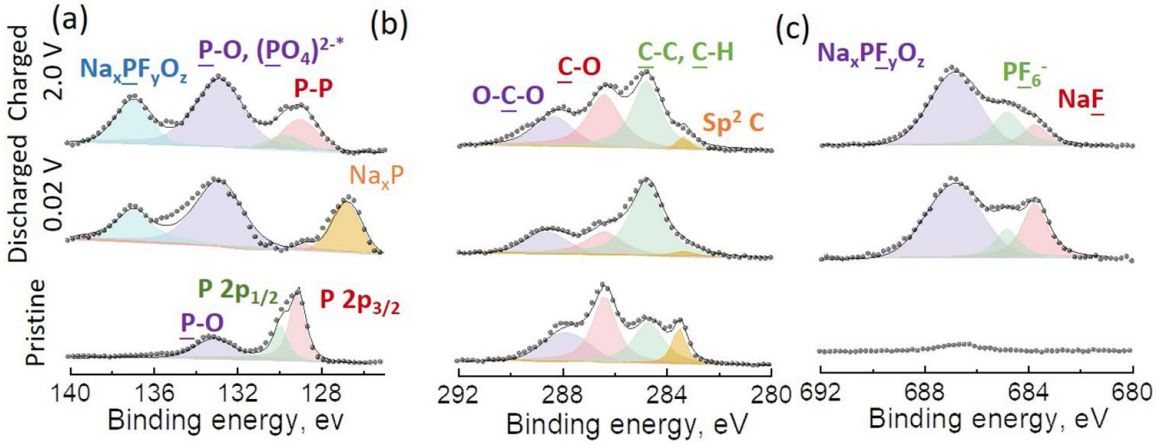

Figure II.12.B.7 (a) P2p XPS spectra; (b) C1s and (c) F1s XPS spectra of RPC anode during charge/discharge in the carbonate-based electrolytes.

Performance comparison of Pb-O-C nanocomposite anode in Na and Li cells

In previous year, we reported the synthesis of the Pb-O-C nanocomposite anode material. A unique nanocomposite structure of Pb@PbO core-shell nanoparticles in a carbon matrix was obtained by a facile high-energy ball milling method using the low-cost starting materials, PbO and carbon black. Its electrochemical sodium reaction performance showed decent volumetric capacity and cycle stability, but room for further improvement as well particularly in specific capacity and rate capability. For example, the reversible specific capacity is less than 300 mAh/g, which is lower than the value expected from its theoretical reactions:

$$Pb + 3.75Na \rightarrow Na_{3.75}Pb \qquad (485\ mAh/g)$$

$$PbO + 5.75Na \rightarrow Na_2O + Na_{3.75}Pb \qquad (690\ mAh/g)$$

In contrast, the Pb-O-C nanocomposite demonstrates excellent electrochemical lithium reaction properties. The initial reversible capacity is 610 mAh/g and 98.4% of the capacity is maintained after 100 cycles (Figure II.12.B.8). This performance is the highest among the Pb-based anode materials previously reported in the literature (Table II.12.B.1); it appears that the nanocomposite design is highly effective for lithium storage.

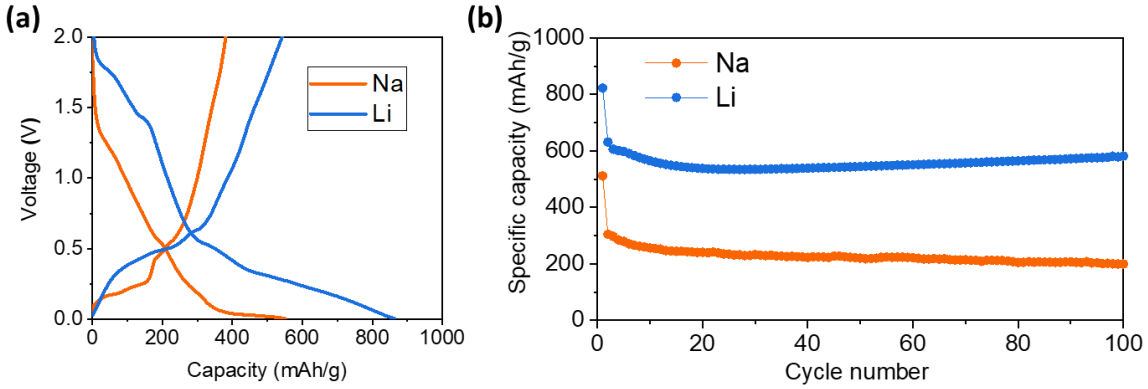

Figure II.12.B.8 (a) Initial voltage profiles and (b) cycle performance of Pb-O-C nanocomposite anode in Na and Li cells.

Table II.12.B.1 Summary of Previously Reported Pb-based Anode for Lithium-ion Batteries

Year	Material	Synthesis method	1st lithiation capacity / 2nd capacity	Reversible capacity	Addition of FEC	Ref
1971	Metallic Pb	N/A	N/A	N/A	No	[7]
1986	Metallic Pb powder	N/A	N/A	N/A	No	[8]
2001	PbO film	Spray pyrolysis technique	~260 mAh/g / ~305 mA/g	500 mAh/g at 40 cycles	No	[9]
2002	PbO powder	N/A	~740 mAh/g / ~200 mAh/g	20 mAh/g at 25 cycles	No	[10]
2003	Pb/PbO	Aqueous precipitation	~130 mAh/g / ~14 mAh/g	50 mAh/g at 15 cycles	No	[11]
2006	PbO-C nanocomposite	Spray pyrolysis technique	~660 mAh/g / ~260 mAh/g	100 mAh/g at 50 cycles	No	[12]
2015	PbO-C nanocomposite	Solvothermal synthesis	~620 mAh/g / ~420 mAh/g	250 mAh/g at 100 cycles	No	[13]
2016	Metallic Pb powder	N/A	~425 mAh/g	N/A	Yes	[14]
2019	Graphene oxide-coated PbO	Solution-based carbon coating	~550 mAh/g / ~420 mAh/g	240 mAh/g at 200 cycles	Yes	[15]
2020	Pb-O-C nanocomposite	Carbothermal synthesis	~430 mAh/g / ~429 mAh/g	400 mAh/g at 400 cycles	Yes	[16]
2020	**Pb@PbO-C nanocomposite**	**High-energy ball milling**	**~864 mAh/g / ~610 mAh/g**	**600 mAh/g at 100 cycles**	**Yes**	**This work**

Na and Li reaction mechanism

To compare the lithium and sodium storage mechanisms of the Pb-O-C nanocomposite anode, the Pb redox reaction and local structural change were investigated by ex situ X-ray absorption spectroscopy (XAS) measurements (Figure II.12.B.9). The XANES spectrum for the pristine Pb-O-C nanocomposite is located at a slightly lower energy than that of the lead(II) oxide reference, reflecting the average valence state of PbO and Pb. The XANES spectrum during the initial discharge process shows an edge shift toward lower energy, according to the conversion reaction during which Pb^{2+} (PbO) reduces to zero-valent Pb (metallic Pb). In the following alloying reaction region, the XANES spectra show a surprisingly large degree of edge shifts toward the lower absorption energy (Figure II.12.B.9a and b). This was quite an unexpected observation because it indicates that Pb continues to reduce even during the Na-Pb and Li-Pb alloying reaction. The observed change in the half-height edge energy corresponds to the Pb valence of approximately Pb^{-4} at the end of the reaction. Such a large degree of edge shift has never been reported in other alloying-reaction-based anode materials (e.g., Si, Ge, Sn). It is evident from our data that Pb acts like an anion in the Na-Pb and Li-Pb alloying process and the wide-range Pb redox is the basis for the large capacity of the Pb-O-C nanocomposite material. A clear distinction between the Na-Pb and Li-Pb alloying reactions was found in the EXAFS analysis. After the dissociation of the Pb-O bond in Pb oxide due to the conversion reaction, the Na-Pb data in Figure II.12.B.9c shows an evolution of a strong peak at around 3.2 Å. In accordance with the large negative charge of Pb in the Na_xPb phases, this intensified new peak likely corresponds to the Pb-Pb cluster in a *Zintl* phase. However, in Figure II.12.B.9d, the EXAFS data for the Li_xPb phases doesn't show a similar Pb-Pb peak in the alloying region suggesting different phase transition pathways for the Na-Pb and Li-Pb intermediates.

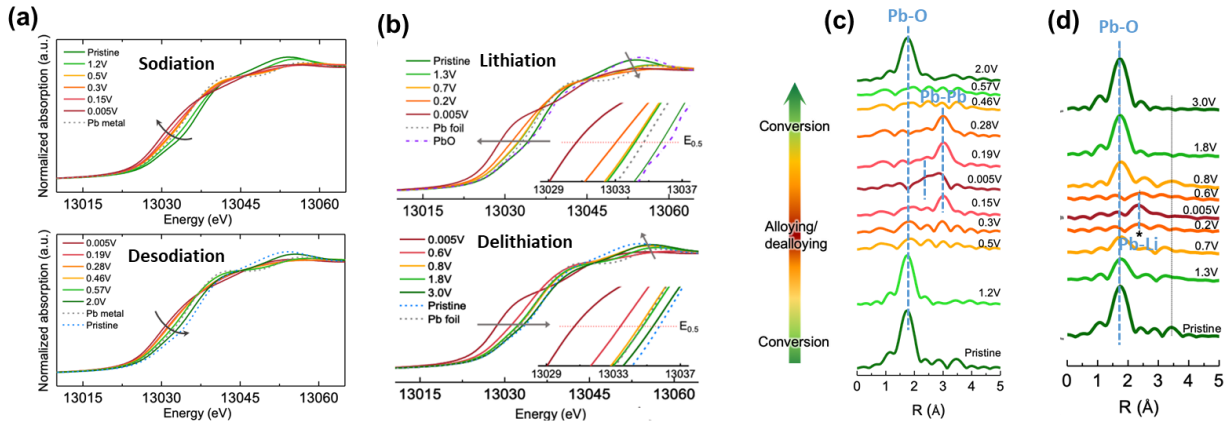

Figure II.12.B.9 (a, b) Ex situ XANES and (c, d) EXAFS data collected at various states of (a, c) sodium and (b, d) lithium reactions.

The operando XRD analysis was conducted to compare the phase evolutions during the electrochemical sodiation and lithiation processes (Figure II.12.B.10a). In contrast to the room temperature lithiation and sodiation of other group 14 metals that exhibit amorphous intermediate phases during the entire (Si and Ge) or significant regions (Sn) of the reaction pathways, the Pb-O-C follows the thermodynamic equilibrium pathways forming crystalline intermediate structure. Interestingly, the NaPb phase is stabilized as the tetragonal *Zintl* structure (*I4₁/acd*) while LiPb is formed as a cubic metallic alloy phase (*Pm-3m*). The formation of the tetragonal *Zintl* structure, which comprises tetrahedral Pb_4 clusters, corresponds to the EXAFS data that shows the evolution of the Pb-Pb bond during the sodium reaction (Figure II.12.B.10b). The strong covalent character of the Pb_4 *Zintl* clusters adversely affects the electronic conductivity (Figure II.12.B.10c) and thus limits the electrochemical performance of the Pb-O-C anode in sodium cells. This is the first experimental demonstration of the dynamic transition to *Zintl* structures during an electrochemical sodium reaction with Pb.

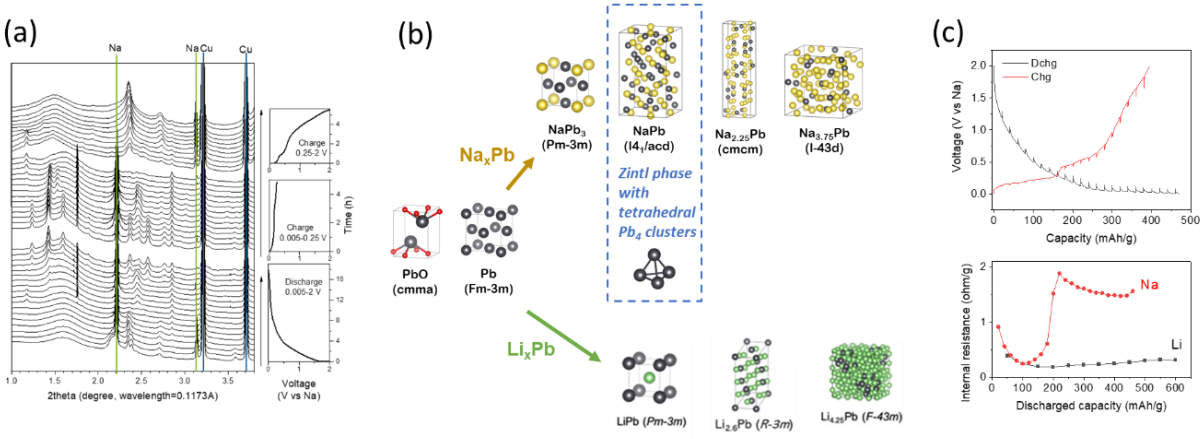

Figure II.12.B.10 (a) Operando XRD of the Pb-O-C nanocomposite anode during sodium cycling, the comparison of (b) phase evolution and (c) internal resistance change during the electrochemical sodium and lithium reaction.

Synthesis and electrochemistry of the cation substituted Pb-M-O-C nanocomposite

Of the various synthesis parameters tested, such as milling time, the choice of lead oxide starting materials, and carbon content, the Pb-O-C nanocomposite synthesized via 6h of high-energy ball milling with 30% carbon black has shown the most promising electrochemical properties. In order to explore the further improvement, a series of Pb-M-O-C nanocomposite materials have synthesized with an additional element M (Sn, Sb, Fe, Mn, or Ni) and tested in both sodium and lithium cells using carbonate-based electrolytes.

Anode powder samples were prepared by the high-energy ball milling of PbO, carbon black, and a source of the additional element, M. The starting materials for the additional element M were Sn, SnO, Sb, Fe_2O_3, Mn_2O_3, and NiO. The synthesis conditions were determined from previous studies which showed nanoscale pulverization and carbothermal reduction of the PbO starting material. Figure II.12.B.11 shows the XRD patterns of the $Pb_{1-x}M_x$-O-C nanocomposite samples where x = 0.3 and 0.5. All samples clearly exhibit strong peaks indexed to metallic Pb structure, suggesting that the additional materials react well with PbO forming a Pb-based metallic alloy as the major phase. The broad hump at 28° is attributed to the PbO minor phase that is formed as a result of surface oxidation of the metallic Pb nanoparticles up on air-exposure. A careful examination of the XRD patterns for the Fe, Mn, or Ni added samples further reveals a trace amount of unreacted impurity phases such as Fe_2O_3, Mn_2O_3, or NiO, respectively. In contrast, the Sn or Sb addition doesn't form an apparent impurity phase up to 30% addition. The additional peaks corresponding to metallic Sn or Sb structure is only observed for the 50% Sn or Sb added samples.

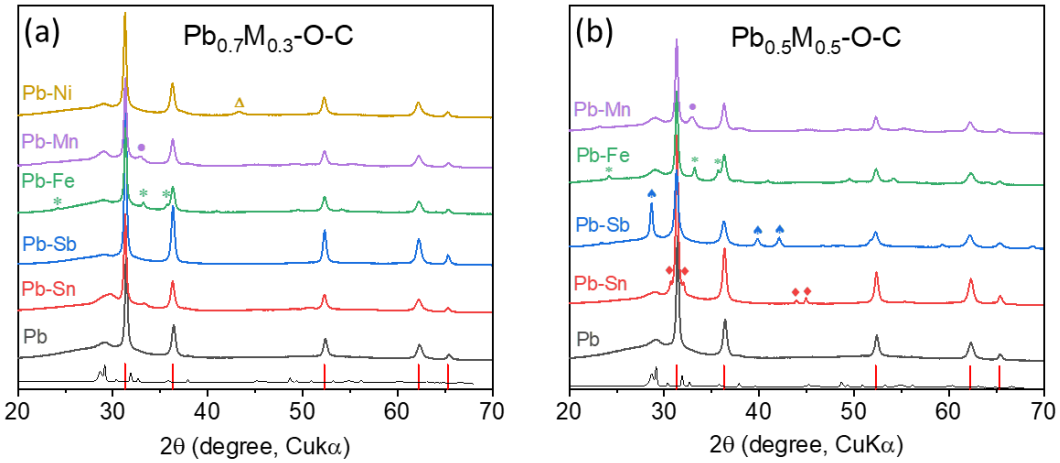

Figure II.12.B.11 X-ray diffraction patterns for the (a) Pb0.7M0.3-O-C and (b) Pb0.5M0.5-O-C nanocomposite materials prepared by high energy ball mill of PbO, carbon and the additional elements, M (Sn, Sb, Fe, Mn, or Ni). The marked impurity phases are Sn (♦), Sb (♠), Fe2O3 (*), Mn2O3 (•), and NiO (Δ).

Figure II.12.B.12 compares the initial specific capacity of the $Pb_{1-x}M_x$-O-C nanocomposite anodes cycled in sodium and lithium half-cells. While the addition of Fe, Mn, or Ni does not have a beneficial effect on the electrochemical performance of sodium cells, the $Pb_{1-x}Sn_x$-O-C and $Pb_{1-x}Sb_x$-O-C anodes show an improvement in the specific capacity, first cycle efficiency, and cycle stability. The advantage of the additional elements is more significant when the electrodes are tested in lithium cells. For instance, the specific discharge capacity of $Pb_{0.7}Sn_{0.3}$-O-C is ~100 mAh/g higher than that of the Pb-O-C baseline, and the $Pb_{0.7}Sb_{0.3}$-O-C anode shows a significantly improved coulombic efficiency and cycle stability. The highest specific capacity of ~800 mAh/g is achieved by 50% Sb addition and is attributed to the synergistic effect of the coexistence of both $Pb_{1-y}Sb_y$ and Sb phases as shown in Figure II.12.B.12b. The marginal performance improvements in sodium cells, which contrast with the significant effects of the M addition in lithium cells, corroborate our previous observations that suggest the improvement of interface kinetic and intermediate structure is of critical importance for the high energy Pb-O-C nanocomposite anode for sodium-ion batteries.

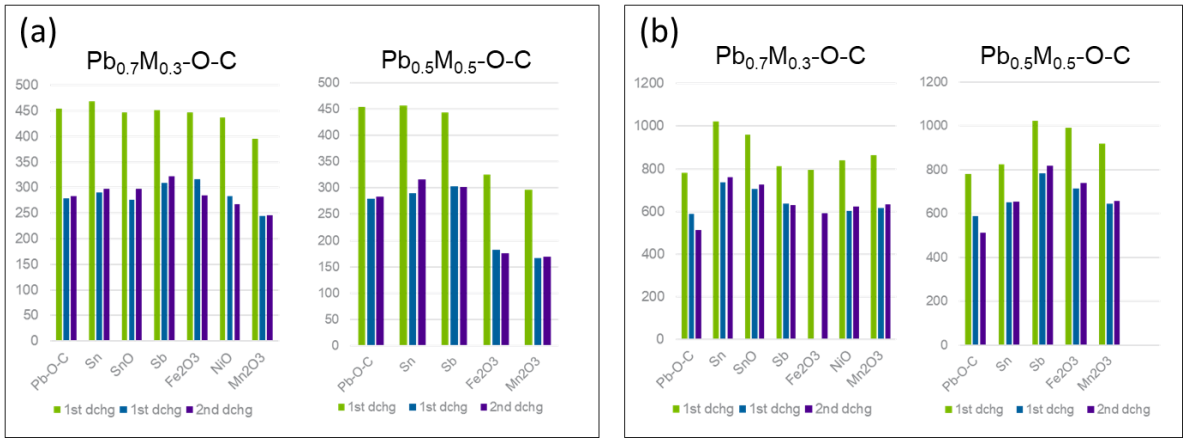

Figure II.12.B.12 The initial specific capacity of the Pb1-xMx-O-C nanocomposite anodes tested in (a) sodium and (b) lithium half-cells (Voltage = 0.005 – 2.0 V vs. Na and 0.005 – 3.0 V vs. Li; Current density = 100 mAh/g; Electrolytes = 1M NaPF6 in EC/DEC w/ 2% FEC for Na cells, 1.2M LiPF6 in EC/EMC w/ 10% FEC for Li cells).

Conclusions

We have reported a hierarchical micro/nanostructured Sb-doped red phosphorus/Ketjenblack-MWCNTs composite as a practical anode material of sodium-ion batteries fabricated via a scalable high-energy ball milling process. Complementary characterization has clearly revealed that such unique structure design could not only enable fast electronic and ionic transport, but also could mitigate large volume changes and suppress parasitic reactions, leading to excellent structural integrity and favorable SEI formation. Our strategy has provided a good solution for the practical anode development of low-cost and high-energy sodium-ion batteries.

New Pb-based nanocomposite anode materials, which are characterized by core@shell Pb@PbO nanoparticles homogeneously embedded in a carbon matrix, exhibit excellent electrochemical performance in lithium cells while their sodium reaction performances have room for further improvement. Synchrotron X-ray diffraction and absorption spectroscopy analysis revealed the unique lithium and sodium storage mechanism of this material, which is based on charge compensation by a wide-range Pb redox (between Pb^{2+} and Pb^{-4}) and the associated structural evolution of Zintl-type phases. The lower sodium storage performance in comparison with that of lithium storage is associated with the larger volume expansion and higher ionic character of the Na-Pb *Zintl* phase that lead to both lower electronic conductivity and brittle characteristics.

Key Publications

Patent

1. G-L. Xu, X. Liu, and K. Amine. “Electroactive Materials for Secondary Batteries.” IN-19-0160, U. S. Patent application. Filed.

Publications

1. R. Amine, A. Daali, X. Zhou, X. Liu, Y. Liu, Y. Ren, X. Zhang, L. Zhu, S. Al-Hallaj, Z. Chen, G. L. Xu, and K. Amine. “A practical phosphorus-based anode material for high-energy lithium-ion batteries.” *Nano Energy* 74 (2020): 104849. https://doi.org/10.1016/j.nanoen.2020.104849.

2. J. Han, J. Park, S-M. Bak, S-B. Son, J. Gim, C. Villa, X. Hu, V. P. Dravid, C. C. Su, Y. Kim, C. Johnson, and E. Lee. “New High-Performance Pb-Based Nanocomposite Anode Enabled by Wide-Range Pb Redox and Zintl Phase Transition.” *Advanced Functional Materials* (2020): 2005362, https://doi.org/10.1002/adfm.202005362.

3. Z. J. Liu, A. Daali, G. L. Xu, M. H. Zhuang, X. Zuo, C. J. Sun, Y. Liu, Y. Cai, M. D. Hossai, H. W. Liu, K. Amine, and T. Luo. “Highly Reversible Sodiation/Desodiation from a Carbon-Sandwiched

SnS_2 Nanosheet Anode for Sodium Ion Batteries." *Nano Letters* 20 (2020): 3844-3851. https://doi.org/10.1021/acs.nanolett.0c00964.

4. B-Q. Xiong, X. Zhou, G-L. Xu, Y. Liu, L. Zhu, Y. Hu, S-Y. Shen, Y-H. Hong, S-C. Wan, X-C. Liu, X. Liu, S. Chen, L. Huang, S-G. Sun, K. Amine, and F-S. Ke. "Boosting Superior Lithium Storage Performance of Alloy-Based Anode Materials via Ultraconformal Sb Coating-Derived Favorable Solid-Electrolyte Interphase." *Advanced Energy Materials* 10 (2020): 1903186. https://doi.org/10.1002/aenm.201903186.

5. Su, H.; Guo, G.; Ren, Y.; Yu, X.; Zhang, X.; Ma, T.; Lu, Y.; Zhang, Z.; Ma, H.; Sui, M.; Li, H.; Sun, C.; Chen, Z.; Xu, G.-L; Zhang, R.; Amine, K. and Yu, H. Local spring effect in titanium-based layered oxides. Energy & Environmental Science 2020, https://doi.org/10.1039/D0EE02313B.

Presentations

1. C. Johnson, "Na-Ion Batteries: The Best Option for Beyond Li-Ion Batteries?" Center for Electrochemistry Workshop, UT, Austin, Texas, February 22–23, 2020.

2. C. Johnson, "Performance and (de)lithiation mechanism of lithium-lead (Pb) anode for Li battery," ECS PRiME 2020, Virtual conference, October 4-9, 2020.

3. "Challenges and strategies to advance sodium-ion battery towards higher energy density", Gui-Liang Xu and Khali Amine, 2019 ICNaB, Naperville, IL, USA, Nov 4-7, 2019

References

1. N. Yabuuchi, et al., Chemical Reviews 114 (2014):11636-11682.

2. M. Han, et al., Energy & Environmental Science 8 (2015):81-102.

3. Y. Wen, et al., Nature Communications 5 (2014): 4033.

4. S. Huang, et al., Adv. Mater. 30 (2018):1706637.

5. H. Kang, et al., Journal of Materials Chemistry A 3 (2015):17899-17913.

6. B. Xiong, et al. Advanced Energy Materials 10 (2020): 1903186.

7. A. Dey. *Journal of The Electrochemical Society* 118 (1971): 1547.

8. L. Peraldo Bicelli, et al., *Journal of Power Sources* 18 (1986): 63.

9. M. Martos, et al., *Electrochimica Acta* 46 (2001): 2939.

10. F. Lipparoni, et al., *Ionics* 8 (2002): 177.

11. M. Martos, et al., *Electrochimica Acta* 48 (2003): 615.

12. S. H. Ng, et al., *Journal of The Electrochemical Society* 153 (2006): A787.

13. C.-H. Li, et al., *RSC Advances* 5 (2015): 50245.

14. S. M. Wood, et al., *Journal of The Electrochemical Society* 163 (2016): A1027.

15. A. Guo, et al., *ACS Applied Energy Materials* 2 (2019): 3017.

16. J. A. Weeks, et al., *Journal of The Electrochemical Society* 167 (2020): 060509.

Acknowledgements

Support from Tien Duong of the U.S. DOE's Office of Vehicle Technologies Program is gratefully acknowledged. I would like to thank Dr. Guiliang Xu and Dr. Eungje Lee at ANL for the major contribution to this project.

II.12.C High capacity, Low Voltage Titanate Anodes for Sodium Ion Batteries (LBNL)

Marca Doeff, Principal Investigator
Lawrence Berkeley National Laboratory
1 Cyclotron Road
Berkeley, CA 94720
E-mail: mmdoeff@lbl.gov

Tien Duong, DOE Technology Development Manager
U.S. Department of Energy
E-mail: Tien.Duong@ee.doe.gov

Start Date: January 1, 2019 End Date: September 30, 2021
Project Funding: $300,000 DOE share: $300,000 Non-DOE share: $0

Project Introduction

Cost and supply security issues with lithium [1] are compelling reasons to develop sodium-ion batteries as potential alternatives to the better-known lithium-ion analogs. Identification of a suitable anode material for sodium-ion cells remains the critical challenge to further progress, as graphite (the anode material used in lithium ion batteries) does not intercalate sodium to an appreciable extent. Recently, several sodium titanates[2],[3],[4] have been found to undergo reversible sodium intercalation processes at potentials much lower than 1V vs. Na+/Na, making them attractive candidates for use as anodes in sodium ion systems. These materials have stepped layered structures but show very different electrochemical behaviors depending on composition and step size. Work on this project is directed towards understanding these differences through an array of synthetic, electrochemical, and structural characterization techniques, and overcoming practical impediments to their use, such as the high first cycle coulombic inefficiencies that are currently observed. The ultimate goal of the project is to produce a 200-250 mAh/g anode that cycles reversibly. Such a material would be an enabling technology for a practical high-energy sodium ion battery.

Objectives

The planned work is conceived to overcome the main obstacle to the practical realization of sodium-ion batteries; the lack of a suitable anode material. Experiments are designed to improve the practical reversible capacities and overcome the high first cycle coulombic inefficiencies of promising low voltage sodium titanates, as well as to assess the stabilities of the sodiated (partially and fully discharged) products of the electrochemical reactions. Some effort is devoted to consideration of electrolytes and understanding of the electrolyte/anode interface, which must go hand-in-hand with anode development. The ultimate goal is to produce a high capacity (200-250 mAh/g), stable, and reversible low voltage anode material suitable for use in a sodium-ion battery configuration.

Approach

Candidate stepped layered titanates are synthesized by appropriate routes (hydrothermal, solid state routes, etc.). Materials are then characterized electrochemically and physically. Structure-function relationships are built to correlate the effect of changing structure (for example, step size) on electrochemical properties. Synchrotron methods such as soft and hard X-ray absorption spectroscopy and XPS are used to probe electronic structures and particle surfaces of pristine and cycled materials. Various electrolytic solutions are prepared from commercially available materials and studied in cells to understand the effect on coulombic efficiency.

Results

The structures of the titanates under study for this project are shown in Figure II.12.C.1. “Sodium nonatitanate” or NNT ($NaTi_3O_6(OH)\cdot 2H_2O$) in the as-made state (before dehydration) is shown on the left, and lepidocrocite-type titanate on the right. Both are comprised of TiO_6 octahedra connected by edges and, in the

case of NNT, corners, to form stepped layers, with cations and sometimes water between the layers. In lepidocrocite-type titanates, the step size is one (i.e., the layers are corrugated). For NNT, the step size is six. Both types of materials were found to undergo reversible sodium intercalation at low potentials in our previous work [3], [4].

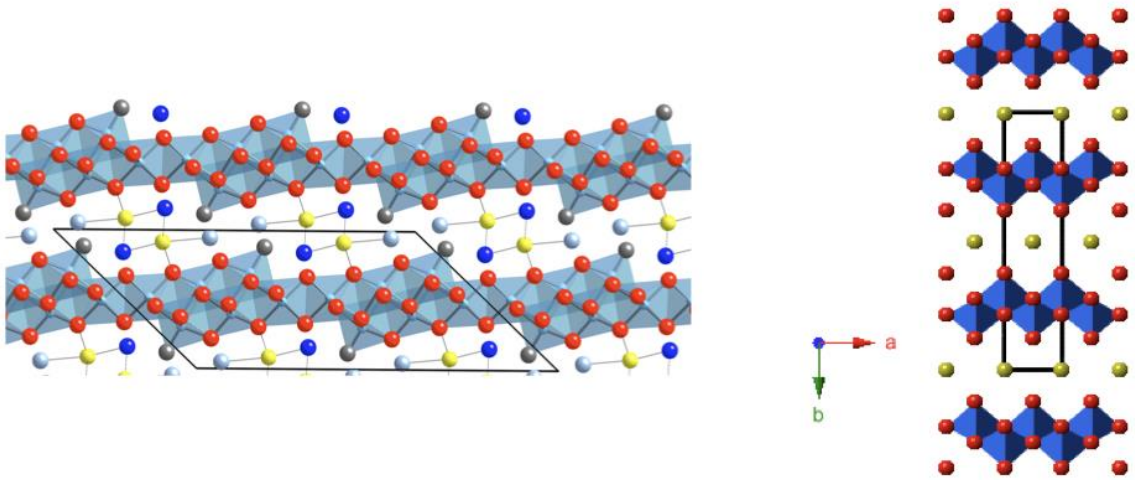

Figure II.12.C.1 Structure of "sodium nonatitanate" or NNT ($NaTi_3O_6(OH)\cdot H_2O$) is shown on the left, with TiO_6 octahedra in light blue and interlayer species (sodium ions and water shown as spheres. On the right is a representation of a lepidocrocite-type titanate with TIO_6 octahedra in dark blue and interlayer cations represented by spheres.

In FY19 and early FY20, most of our work was directed towards improving the electrochemistry of NNT using both materials and electrode engineering. We found that dehydration at 600°C caused the *c*-axis to contract 12% and sodium ions to rearrange, resulting in the formation of O-Na-O bridges and a quasi-tunnel like structure. An investigation of the electrochemistry of NNT thermally treated at different temperatures revealed that the highest capacity and best cycling was obtained for the material dried at 500°C rather than 600°C, however. When combined with carbon coating and a CMC binder instead of PVdF, the full theoretical capacity of 200 mAh/g could be obtained at moderate discharge rates. The results of these experiments are summarized in a recent publication [5]. The dehydrated NNT reached our goal of a reversible 200-250 mAh/g capacity at a low average potential of about 0.3V vs. Na/Na^+.

For most of FY20, we concentrated on a set of lepidocrocite-structured titanates derived from the $Cs_xTi_{2-y}\square_yO_4$ system, where $\square$ represents a vacancy. Our previous work on a related system [6] indicated that the presence of either vacancies or mobile cations in the titanium-containing layer is necessary to achieve high capacity at reasonable rates. The parent compounds can be readily made by solid-state reactions, with pure solid solutions obtained for values between about x=0.71-1 and y=0.179-0.25 ($Cs_{0.71}Ti_{1.821}\square_{0.179}O_4$ to $CsTi_{1.75}\square_{0.25}O_4$). The phase-pure materials could be exchanged under mild conditions to form the sodium-containing analogs, and materials with compositions between $Na_{0.74}Ti_{1.815}\square_{0.179}O_4$ to $NaTi_{1.75}\square_{0.25}O_4$ were studied electrochemically. Figure II.12.C.2 shows typical results on one of these materials in a sodium half-cell. A capacity in excess of 230 mAh/g could be obtained on the second cycle, with an average discharge potential of about 0.6V. Even though the cell is not optimized, relatively good capacity retention is observed over 40 cycles.

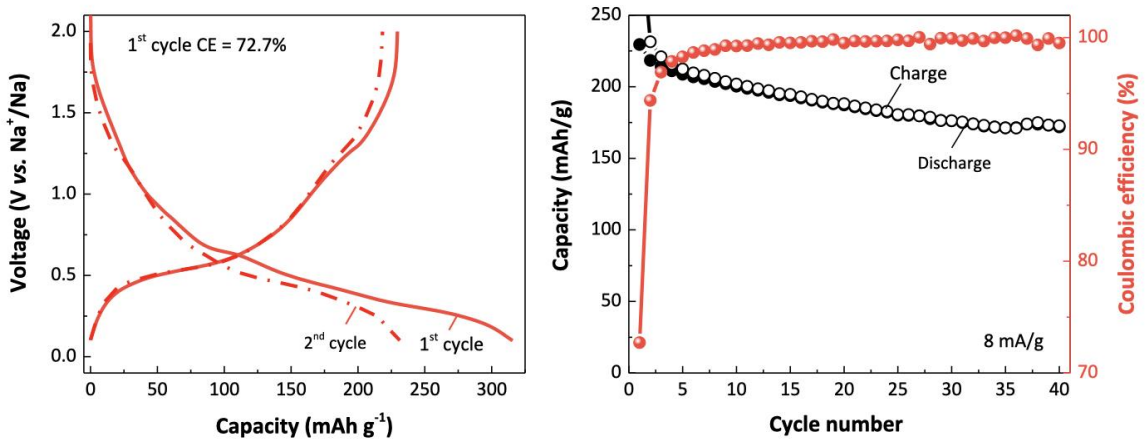

Figure II.12.C.2 (Left) first and second cycles of a sodium half-cell containing a $Na_{0.74}Ti_{1.815}\square_{0.185}O_4$ electrode at charge and discharge rates of 8 mA/g . (Right) Cycling data for the same cell, including coulombic efficiency (CE) as a function of cycle number.

There is a weak dependence of practical capacity on titanium content in this system, which might be expected (Figure II.12.C.3). However, because some of the interlayer sites are already occupied by sodium ions in the as-made materials, the theoretical capacity is expected to be site-limited rather than titanium-limited. Interestingly, the practical capacities are higher than expected if only the interlayer sodium sites are considered. In fact, practical capacities match fairly well with the sum of the available interlayer sites and vacancies. Another possible explanation for the excess capacity is pseudo-capacitative storage on surface sites. To investigate this possibility, an analysis of cyclic voltammetry (CV) data was performed (Figure II.12.C.4). There are two sets of reversible peaks in the CVs of the half-cells; a main feature near 0.5V, labeled O1/R1 and a smaller one above 1V, labeled O2/R2. The dependence of current (i) on scan rate (ν) gives information on the redox mechanism according to the power law, $i=a\nu^b$. Diffusion-controlled processes such as intercalation give b values of 0.5, while purely pseudo-capacitative processes give values of 1 [7]. For O1/R1, b is 0.69, but it is 0.92 for O2/R2, indicating that the higher voltage process is primarily surface-related. Half-cells containing carbon-free electrodes (not shown) still exhibited the O2/R2 feature, indicating that this process is attributable to the titanate and not the high surface area carbon in the electrodes. The surface process contributes about 25% of the capacity.

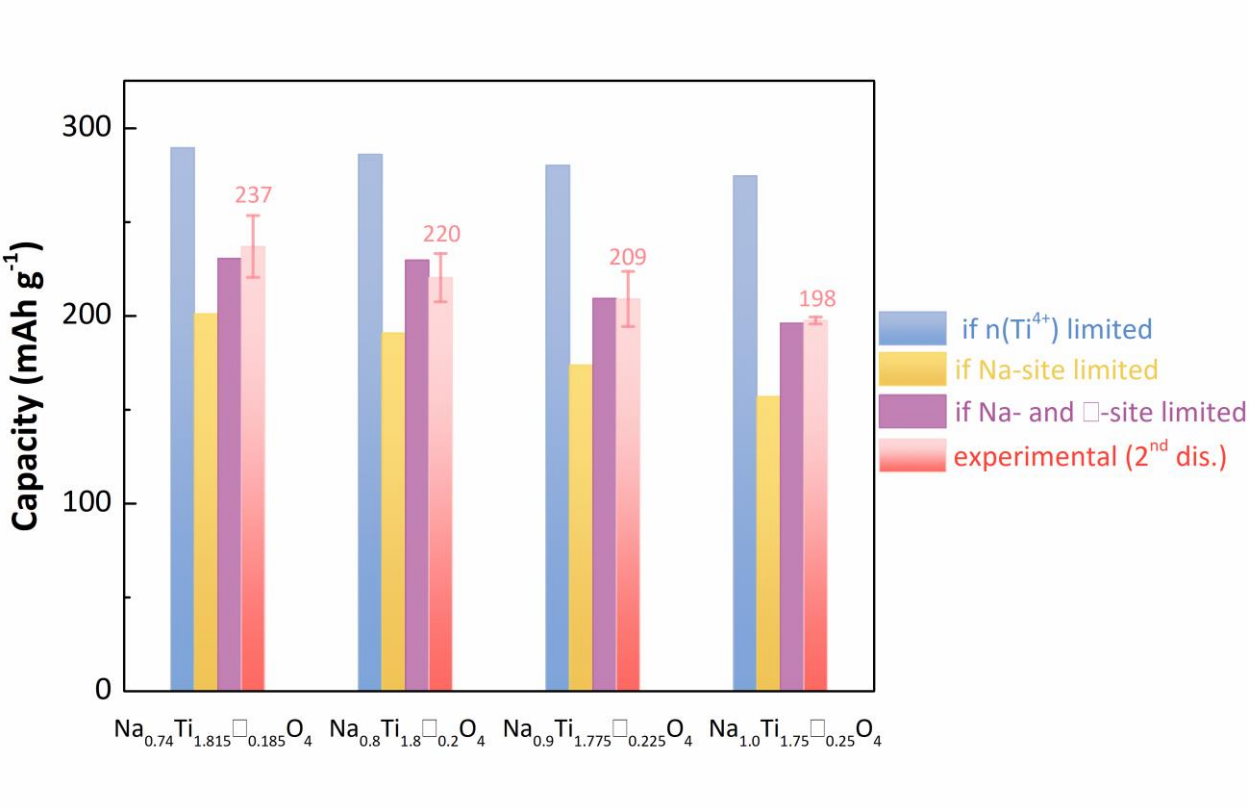

Figure II.12.C.3 Theoretical and practical capacities of $Na_xTi_{2-y}\square_yO_4$ electrodes as a function of composition. The blue column indicates the maximum possible reversible capacity assuming all Ti is redox active. The yellow column assumes capacity is limited by the number of interlayer sites that are available. The purple column includes both interlayer sites and vacancies in the titanium-containing layers. The pink column shows the practical capacity that was obtained.

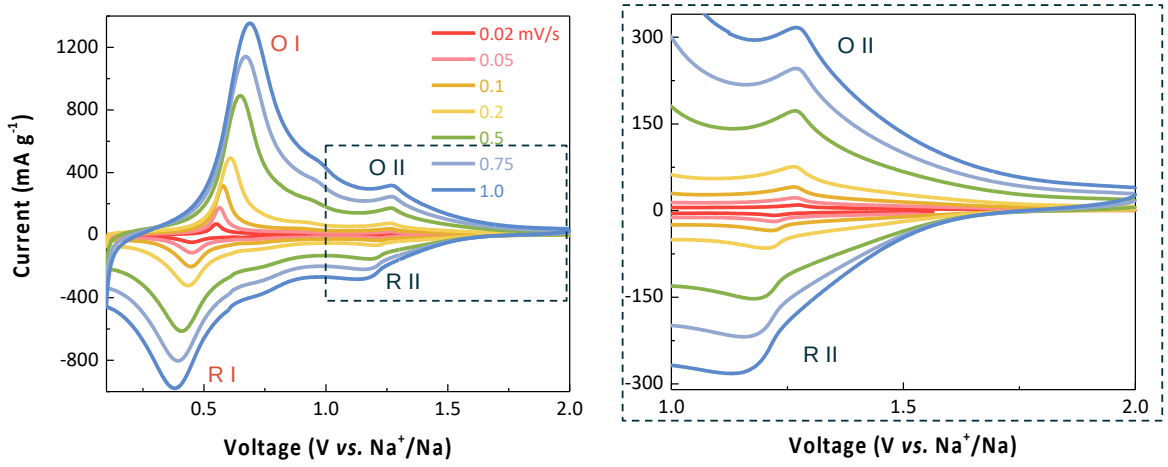

Figure II.12.C.4 (Left) Cyclic voltammograms on a sodium half-cell containing a $Na_xTi_{2-y}\square_yO_4$ electrode, carried out at different scan rates. On the right is a detail of the high voltage process.

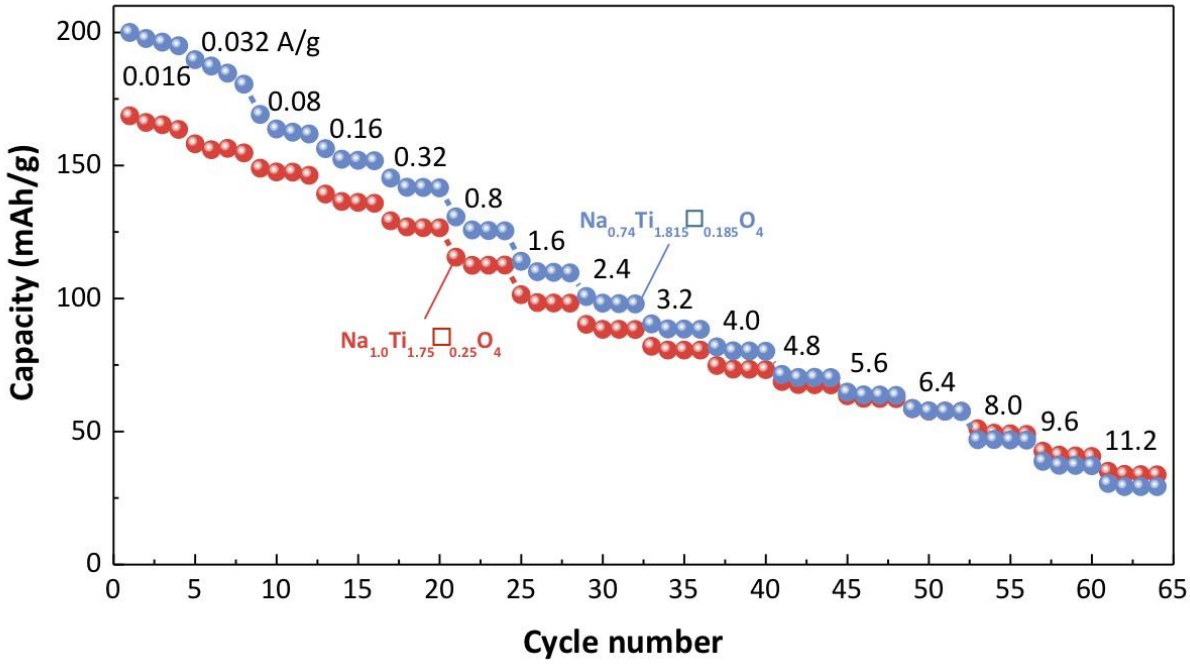

Figure II.12.C.5 Capacity as a function of discharge rate for half cells containing either $Na_{0.74}Ti_{1.815}\square_{0.185}O_4$ (in blue) or $NaTi_{1.75}\square_{0.25}O_4$ (in red).

A comparison of the rate capabilities of half cells containing two electrodes with different vacancy concentrations is shown in Figure II.12.C.5. The material with higher titanium content ($Na_{0.74}Ti_{1.815}\square_{0.185}O_4$) but fewer vacancies has higher capacity at low rates but the rate capability is inferior to that of the electrode with more vacancies ($NaTi_{1.75}\square_{0.25}O_4$). The vacancies in the titanium layers provide additional diffusional pathways for sodium ions [6].

The first cycle coulombic efficiencies (CE) of cells containing these electrodes are low, although efficiencies improve markedly upon subsequent cycles. This is behavior typical of electrodes that are redox-active at low potentials, like graphite, and indicates that a solid electrolyte interphase (SEI) is formed. First cycle CEs for cells containing the lepidocrocite vary considerably depending on the electrolytic solution that is used (Table II.12.C.1) and can be further improved by electrode engineering. Cells with binder-free electrodes have first cycle CEs of 94.7%, suggesting side reactions involving binders may be responsible for some of the irreversibility on the first cycle. The $Na_xTi_{2-y}\square_yO_4$ electrodes are also very hygroscopic. Rigorously dried electrodes exhibit better behavior in half cells than those that have been exposed to air for even a short period of time. A survey of the electrochemical behavior of cells with electrodes containing three different types of binders (PVDF, PTFE, or CMC/SBR) indicate that best results are obtained when carefully dried electrodes containing CMC binders are used. In these types of cells, first cycle CEs as high as 81.8% can be obtained.

Differential Electrochemical Mass Spectrometry (DEMS) experiments are currently being carried out with the McCloskey group to give some insight into how water contributes to inefficiencies in cells with electrodes that had not been fully dried.

Table II.12.C.1 Coulombic Efficiencies (CE) for Sodium Half Cells containing $Na_xTi_{2-y}\square_yO_4$ Electrodes as a Function of Electrolytic Solution Composition

Electrolyte	1st cycle CE
1M $NaPF_6$ in PC	29.1%
1M Na PF_6 in EC/DEC	57.9%
0.5M $NaPhB_4$ in DEGDME	70.2%
1M $NaPF_6$ in DEGDME	56.5%
1M NaFSI in EC/DEC	52.7%
0.5M NaTFSI in DEGDME	61.8%
0.5M $NaClO_4$ in EC/DEC	70.8%

The presence of water also affects the electrochemical properties of the lepidocrocite titanate electrodes. In rigorously dried electrodes, a third reversible feature appears at intermediate potentials (labeled O3/R3 in Figure II.12.C.6). Values of b derived from the power law analysis described above are 0.67 for O1/R1, 0.77 for O2/R2 and 0.76 for O3/R3, a value intermediate between a purely Faradaic and a pseudo-capacitive process. The first two values are lower than what is obtained for hydrated electrodes, suggesting that surface water contributes somewhat to the pseudo-capacitive component of these features in hydrated electrodes.

Dehydrated electrodes do not cycle as well that have not been as carefully dried, although the effect is rather modest. An analysis of capacities as a function of cycle number in cyclic voltammetry experiments show that fading in the 1.0-2.0V region is more apparent than at lower voltages regardless of whether electrodes are completely dried or not. The rate of loss, however, is not as great for the hydrated electrodes (Figure II.12.C.7). This suggests that restricting the upper voltage limit would result in better cycling behavior, although it would come at the expense of somewhat lower overall capacity.

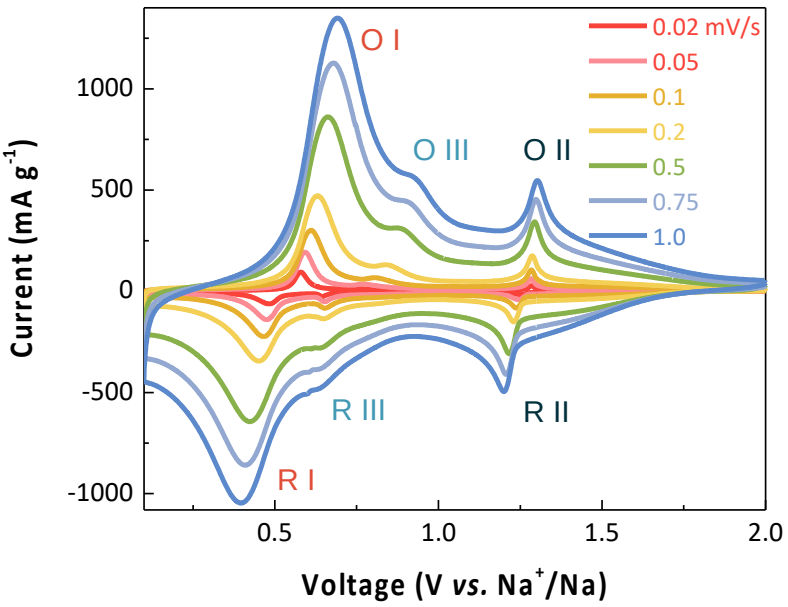

Figure II.12.C.6 Cyclic voltammograms on a sodium half-cell containing a rigorously dehydrated $Na_xTi_{2-y}\square_yO_4$ electrode, carried out at different scan rates. Compare to Figure 4, where the electrode was not as carefully dried.

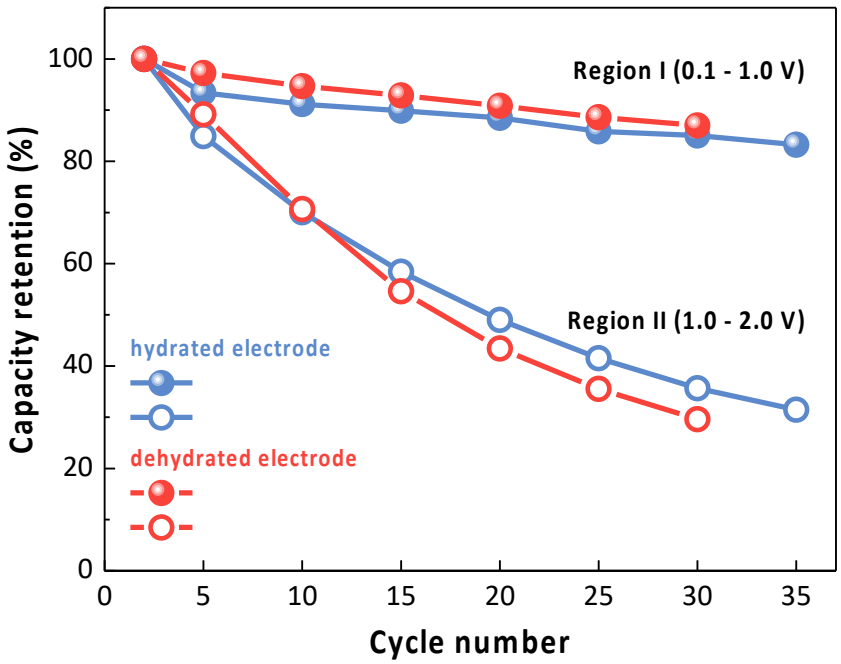

Figure II.12.C.7 Analysis of capacity retention as a function of voltage region for cells containing hydrated and dehydrated $Na_xTi_{2-y}\square_yO_4$ electrodes.

Conclusions

The electrochemical properties of a series of lepidocrocite-structured titanates in the $Na_xTi_{2-y}\square_yO_4$ system in sodium half-cells were intensively studied. Practical capacities were dependent on titanium content, with over 230 mAh/g at an average potential of about 0.6V obtained for the end member $Na_{0.74}Ti_{1.815}\square_{0.185}O_4$ at low rates. Although electrodes with lower titanium content deliver lower capacities, their rate capabilities are somewhat better, presumably due to the presence of more vacancies in the titanium layer, which provide additional diffusional pathways for sodium ions. An analysis of the electrochemical properties show that pseudo-capacitance contributes to redox processes above 1.0V, particularly in electrodes that had not been completely dried, while intercalation is primarily responsible for the main process centered around 0.5V. The electrodes are hygroscopic in nature, and rigorous drying is necessary to reduce first cycle coulombic inefficiency. This, however, comes at the expense of marginally poorer cycling. The removal of water slightly changes the electrochemical properties of the electrode, with another redox process observed below 1.0V, which is intermediate in behavior between purely diffusional and pseudo-capacitive. Electrode and cell engineering were used to improve first cycle coulombic efficiencies to 81.8% in cells. An analysis of cycling results shows that the main contributor to capacity fade is the process above 1.0V, suggesting that limiting the upper voltage cutoff is the easiest way to improve capacity retention in these cells. The high practical capacity, low operating potential, and good reversibility of these electrodes make them excellent candidates for use as anodes in sodium-ion cells.

Key Publications

1. Alvarado, J., Barim, G., Quilty, C. D., Yi, E., Takeuchi, K. J., Takeuchi, E.S., Marschilok, A. C., and Doeff M. M. “Optimization of Nonatitanate Electrodes for Sodium-ion Batteries” J. Mater. Chem. A, 8, (2020):19917-19926.

References

1. Vaalma, C., Buchholz, D., Weil. M., and Passerini, S., “A Cost and Resource Analysis of Sodium-Ion Batteries” Nature Rev. Mater. 3, (2018): article number 18013.

2. Senguttuvan, P., Rousse, G., Seznec, V., Tarascon, J.-M., and. Palacin, M. R, “$Na_2Ti_3O_7$; The Lowest Voltage Every Reported Oxide Insertion Electrode for Sodium Ion Batteries” Chem. Mater., 23, (2011): 4109-4111.

3. Shirpour, M., Cabana, J., and Doeff, M., “New Materials based on a Layered Sodium Titanate for Dual Electrochemical Na and Li Intercalation Systems” Energy & Environ. Sci., 6, (2013): 2538-2547.

4. Shirpour, Mona, Cabana, Jordi, and Doeff, Marca “Lepidocrocite-type Layered Titanate Structures: New Lithium and Sodium Ion Intercalation Anode Materials”, Chem. Mater. 26, (2014): 2502-2512.

5. Alvarado, J., Barim, G., Quilty, C. D., Yi, E., Takeuchi, K. J., Takeuchi, E.S., Marschilok, A. C., and Doeff M. M. “Optimization of Nonatitanate Electrodes for Sodium-ion Batteries” J. Mater. Chem. A, 8, (2020):19917-19926.

6. Markus, Isaac M., Engelke, Simon, Shirpour, Mona, Asta, Mark, and Doeff, Marca “Experimental and Computational Investigation of Lepidocrocite Anodes for Sodium-Ion Batteries” Chem. Mater., 28 (2016): 4289-4291.

7. Optiz, Martin, Yue, Junpei, Wallauer, Jens, Smarsly, Bernd, and Roling, Bernhard “Mechanisms of Charge Storage in Nanoparticulate TiO_2 and $Li_4Ti_5O_{12}$ Anodes: New Insights from Scan Rate-Dependent Cyclic Voltammetry” Electrochim. Acta 168 (2015):125-132.

Acknowledgements

We acknowledge the contributions of members of the Molecular to Mesoscale Over Time (m2m/t) Energy Frontier Center for part of the work described in the nonatitanate paper listed under key publications. These are Calvin Quilty, Ken Takeuchi, and Esther Takeuchi of the State University of New York at Stonybrook.

II.12.D Electrolytes and Interfaces for Stable High-Energy Sodium-ion Batteries (PNNL)

Ji-Guang Zhang, Principal Investigator
Pacific Northwest National Laboratory
902 Battelle Boulevard
Richland, WA 99354
E-mail: jiguang.zhang@pnnl.gov

Tien Duong, DOE Technology Development Manager
U.S. Department of Energy
E-mail: Tien.Duong@ee.doe.gov

Start Date: October 1, 2018 End Date: September 30, 2021
Project Funding: $430,000 DOE share: $430,000 Non-DOE share: $0

Project Introduction

The sodium (Na)-ion battery (NIB) is regarded as one of the most promising alternative power sources for lithium-ion batteries due to the natural abundance of sodium in the earth's crust and similarities between the electrochemical properties of Na^+ and Li^+ ions. However, practical performance of NIBs largely depends on the properties of electrode materials and electrolytes. In recent years, a series of potential electrode materials (both anode and cathode) have been developed with good capacity and electrochemical windows, but the electrochemistry of NIBs, especially the stability of electrode-electrolyte interfaces in these batteries, is still not fundamentally understood. One of the essential challenges for NIBs is to understand the electrode/electrolyte interphases formed on the electrode materials and design a functional, stable interface for long-term cycling of NIBs. The Na^+-ion diffusion kinetics in electrode materials also need to be improved for enhanced coulombic efficiency (CE) and power rate of NIBs. In this regard, design of advanced electrolytes is critical to enable the formation of an effective solid electrolyte interphase (SEI) and cathode electrolyte interphase (CEI), especially during the initial cycles of NIBs. A stable SEI/CEI layer will determine the long-term cycling stability and the rate capability of the NIBs. In FY20, our work focused on new electrolyte design to enable high electrode material utilization and stable and safe cycling of NIBs, and fundamental studies on the physicochemical properties of electrolytes and their relationship to the performance of NIBs. The results obtained in this work will guide electrolyte optimization and stabilize both anode and cathode, and thereby enable high energy and stable cycling of NIBs.

Objectives

- Establish a fundamental understanding on the correlation between electrolyte/electrode interface and electrochemical performance of NIBs and guide the electrolyte development.
- Design new electrolytes and compatible to enable high electrode material utilization and stable and safe cycling of NIBs.

Approach

- Na based localized high concentration electrolytes (LHCE) were developed to improve the cycling stability of NIB full cells. New electrolyte additives (including both salt and solvent additive) were identified to further stabilize hard carbon anode and cathode interphase to improve coulombic efficiency (CE) and cycling stability of NIBs.
- The SEI composition of hard carbon anode and cathode of NIBs in selective phosphate electrolytes were investigated and the relationship between electrolyte components and SEI composition are studied. Finally, the optimized electrolytes are used to enable high capacity and long cycle life of NIBs.

Results

1. *Development of non-flammable localized high concentration electrolytes (LHCE) for NIBs*

The composition of nonflammable phosphate based LHCE is optimized by studying the molar ratio among NaFSI salt, solvent, and diluent. Layered Na‖O3-$NaCu_{1/9}Ni_{2/9}Fe_{1/3}Mn_{1/3}O_2$ (Na-CNFM) cells were used to evaluate the triethyl phosphate (TEP)-based electrolytes (Na-CNFM weight ratio in cathode: 93.5%, mass loading: 13-16 mg cm^{-2}). All the cells were cycled at 0.1 C for the first 3 cycles and 0.2 C for the later cycles (1 C = 100 mAh g^{-1}). First, we evaluated the effect of the NaFSI salt concentration in TEP solvent (Figure II.12.D.1a and b). As the NaFSI/TEP molar ratio increased from 1:1.8 to 1:1.3, the cycling stability and CE of Na||Na-CNFM cells changes significantly. The highest solubility of NaFSI salt in TEP solvent is when NaFSI/TEP molar ratio reached 1:1.3, but the CE of the cells using this electrolyte was not stable, possibly due to high viscosity and low ion conductivity of the electrolyte as shown in Figure II.12.D.1b. The capacity retention of the Na||Na-CNFM cell using this electrolyte is only 57.1% after 100 cycles as shown in Figure II.12.D.1a. When the salt to solvent ratio was reduced to 1:1.5 and 1:1.8, the capacity retention and CE of the cells improved significantly. After 100 cycles, the discharge capacity of the Na||Na-CNFM cells with a NaFSI/TEP molar ratio of 1:1.5 and 1:1.8 was 102.4 and 100.1 mAh g^{-1}, respectively. Because higher concentration of the electrolyte is more favorable for the formation of a stable SEI/CEI layers, the electrolyte with a NaFSI/TEP molar ratio of 1:1.5 (instead of 1:1.8) was chosen as the baseline to further optimize localized high concentration electrolytes.

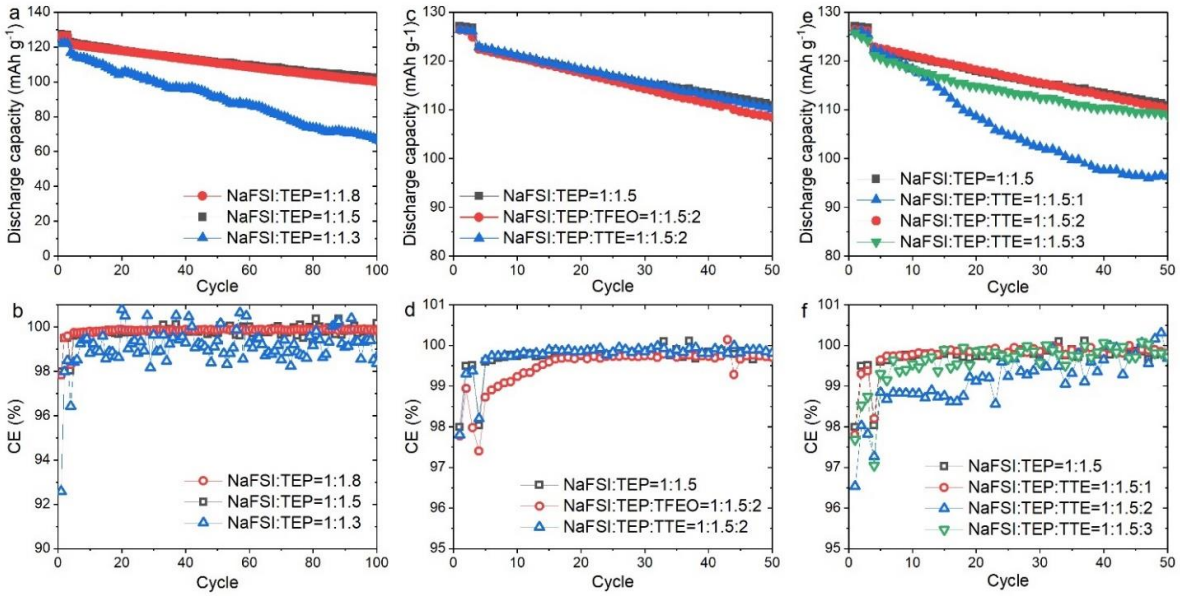

Figure II.12.D.1 (a) Cycling stability and (b) CE of Na‖O3-$NaCu_{1/9}Ni_{2/9}Fe_{1/3}Mn_{1/3}O_2$ cells with the electrolyte with different molar ratio of NaFSI:TEP. (c) Cycling stability and (d) CE of Na‖O3-$NaCu_{1/9}Ni_{2/9}Fe_{1/3}Mn_{1/3}O_2$ cells using the electrolytes with different diluents but the same NaFSI:TEP ratio (1:1.5). (e) Cycling stability and (f) CE of Na‖O3-$NaCu_{1/9}Ni_{2/9}Fe_{1/3}Mn_{1/3}O_2$ cells using the electrolytes with different amount of TTE diluent but the same NaFSI:TEP ratio (1:1.5).

Although high concentration electrolyte can lead to the formation of stable SEI/CEI layers on anode and cathode, the high viscosity and high cost may hinder its real application. Therefore, a non-solvating diluent was added to high concentration electrolyte to form LHCE which can still retain Na ion-solvation structure, but the overall molar concentration of the electrolyte will be much lower. Two fluorinated solvents were used as diluent. One is 1,1,2,2-tetrafluoroethyl-2,2,3,3-tetrafluoropropyl ether (TTE) and the other is tris(2,2,2-trifluoroethyl)orthoformate (TFEO) (Figure II.12.D.1c and d). By comparing the cycling performance of Na-CNFM cells in HCE and LHCE, it was found that the CE of the cells using TTE diluent is better than those using TFEO diluent, especially during the initial cycles. The CE of the cells at the 10^{th} cycles was 99.74% (NaFSI:TEP=1:1.5), 99.78% (NaFSI:TEP:TTE=1:1.5:2), and 99.23% (NaFSI:TEP:TFEO = 1:1.5:2). The

discharge capacity after 50 cycles is 110.9 (NaFSI:TEP=1:1.5), 110.1 (NaFSI:TEP:TTE=1:1.5:2), and 108.4 (NaFSI:TEP:TFEO=1:1.5:2). In addition, we also tested Na||Na-CNFM cells using the LHCE electrolytes with the same NaFSI:TEP ratio but different amount of TTE diluent to optimize electrochemical performance of the cells. It is found that the cell using a LHCE electrolyte with a NaFSI:TEP:TTE molar ratio of 1:1.5:2 exhibits the best capacity retention and CE (Figure II.12.D.1e and f).

Effects of additives in the baseline LHCE electrolyte (NaFSI:TEP:TTE (1:1.5:2 in molar ratio)) have been further investigated as shown in Figure II.12.D.2a-f. $NaBF_4$ salt were used as additives in the baseline LHCE to replace part of NaFSI (NaFSI: $NaBF_4$:TEP:TEGDME:TTE (0.95:0.05:1.3:0.2: 2 in molar). The Na||Na-CNFM cells using the electrolytes with $NaBF_4$ additive exhibit a capacity retention of 86.10% (107.8 mAh g^{-1}) after 100 cycles as compared with 78.11% (96 mAh g^{-1}) for those using the LHCE electrolyte without $NaBF_4$ additive (Figure II.12.D.2a). The CE of the cells using both LHCE and LHCE+$NaBF_4$ were stable around 99.8-99.9% (Figure II.12.D.2b). When tested in Na||HC cells, the capacity retention of the cells after 400 cycles was 96.67% (252.3 mAh g^{-1}) for LHCE and 101.38% (249.7 mAh g^{-1}) for LHCE+$NaBF_4$ (Figure II.12.D.2c). The CE for both LHCE and LHCE+$NaBF_4$ were higher than 99.9% (Figure II.12.D.2d). Therefore, $NaBF_4$ salt was a beneficial electrolyte additive which can enhance electrochemical performance of NIBs.

In addition to the additives for the LHCE electrolytes, effects of additives to carbonate electrolyte (1M $NaClO_4$ in EC:PC:DMC (1:1:1 in vol.), named as E1) was also investigated in Na ‖ $NaCu_{1/9}Ni_{2/9}Fe_{1/3}Mn_{1/3}O_2$ cells 2 wt% VC additive was added into baseline electrolyte. The capacity retention of the cells after 100 cycles was improved from 33.1% (39.4 mAh g^{-1}) in E1 to 85.7% (105.7 mAh g^{-1}) in E1+ 2% VC (Figure II.12.D.2e). The initial CE was increased from 74 % in E1 to 96% in E1+ 2% VC. The long cycling CE in the electrolyte with additive was also increased to 99.6%–99.7% compared with 97%–99% in baseline electrolyte (Figure II.12.D.2f).

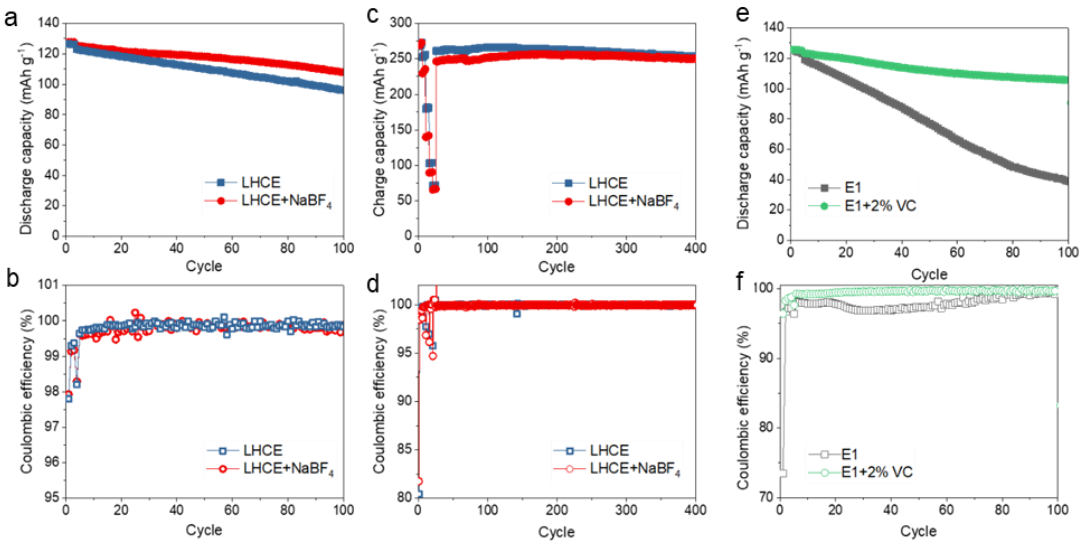

Figure II.12.D.2 Electrolyte additive effect (a) Cycling stability and (b) CE of Na ‖ $NaCu_{1/9}Ni_{2/9}Fe_{1/3}Mn_{1/3}O_2$ cells in phosphate electrolyte with/without $NaBF_4$ additive. (c) Cycling stability and (d) CE of Na ‖ Hard carbon cells in phosphate electrolyte with/without $NaBF_4$ additive. (e) Cycling stability and (f) CE of Na ‖ $NaCu_{1/9}Ni_{2/9}Fe_{1/3}Mn_{1/3}O_2$ cells in carbonate electrolyte with/without VC additive.

2. *Understanding the electrode/electrolyte interphase in LHCE*

The electrode/electrolyte interphase has been studied by X-ray photoelectron microscopy (XPS) to understand stable electrochemical performance of both cathode and anode in LHCE (NaFSI-TEP/TTE (1:1.5:2 in mole)) compared with baseline electrolyte (BE)(1 M $NaPF_6$ in EC/DMC (1:1 in weight)). The cathode electrolyte interphase (CEI) formed in BE was dominated by organic species as shown in Figure II.12.D.3a. The C1s

peaks indicate the existence of C-C/C-H, C-O, and poly(CO_3) groups in the CEI layer originated from the decomposition of the organic carbonate solvent (Figure II.12.D.3a). F1s (Figure II.12.D.3b) and P2p (Figure II.12.D.3c) peaks suggest the decomposition of $NaFP_6$ salt. While for the CEI formed in LHCE, in addition to the C-C/C-H, C-O, C=O peak, substantial C-SO_x and C-F peaks were also found (Figure II.12.D.3d), indicating possible TTE and NaFSI decomposition. The F1s spectrum showed much higher F contents, including S-F/C-F and NaF (Figure II.12.D.3e). S2p spectrum also showed the components from NaFSI salt decomposition (Figure II.12.D.3f). The high inorganic composition, and higher F and S based components in the CEI layer formed in the NaFSI-TEP/TTE electrolyte enable the fast Na^+ transport at the cathode/electrolyte interphase, providing stable cathode electrochemical performance.

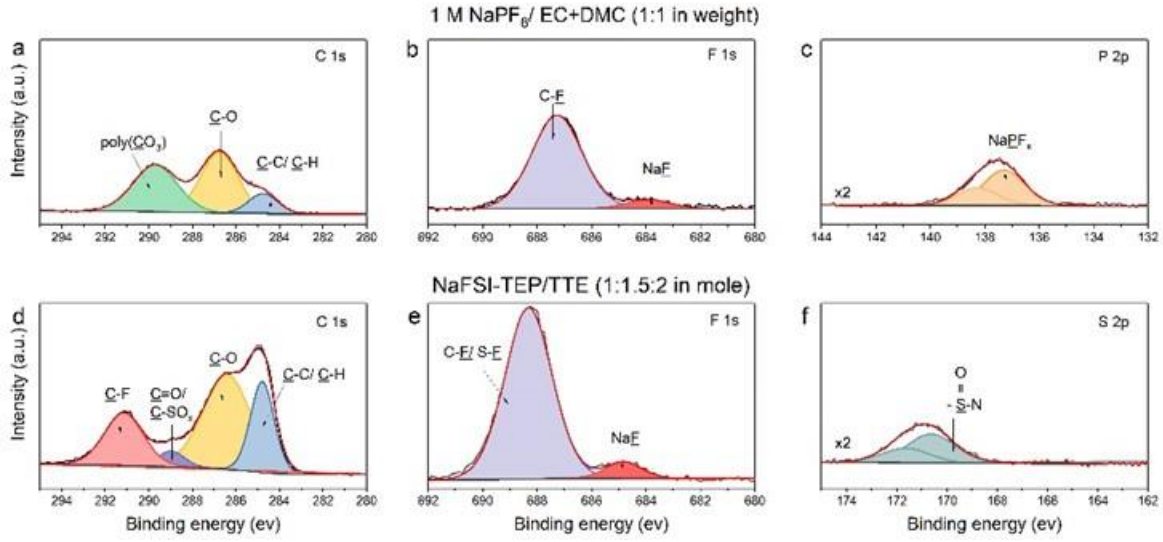

Figure II.12.D.3 XPS characterization of the CEI components on Na-CNFM ($NaCu_{1/9}Ni_{2/9}Fe_{1/3}Mn_{1/3}O_2$) cathodes after 10th cycles in different electrolytes. a, d) C 1s spectra, b, e) F 1s spectra, c) P 2p spectra and f) S 2p spectra for 1 M $NaPF_6$/EC+DMC (1:1 in weight) electrolyte (a-c) and NaFSI-TEP/TTE (1:1.5:2 in mole) electrolyte (d-f).

Figure II.12.D.4 shows the XPS analysis on solid electrolyte interphase (SEI) formed on HC in different electrolytes. C1s of a pristine HC electrode showed strong sp2 carbon and sp3 carbon/C-H peaks in Figure II.12.D.4a. After cycling in the BE (Figure II.12.D.4b), the main C1s peaks in the HC electrode were dominated by C-C/C-H, C-O, C=O groups, revealing carbonate solvent decomposition. F1s peaks of NaF and P2p peaks of $NaPF_x$ in the SEI layer are probably from the decomposition of $NaPF_6$ salt (Figure II.12.D.4e and 4g). While in LHCE, the C1s peak intensity significantly decreased as compared to BE (Figure II.12.D.4c), suggesting greatly reduced solvent decomposition. In addition to the C-C peak from the HC, the C-SO_x peak was formed due to the decomposition of the NaFSI salt (Figure II.12.D.4c). NaFSI salt decomposition also resulted in F1s spectra with more NaF (Figure II.12.D.4f), S2p peaks (Figure II.12.D.4h) from sodium sulfur oxynitride (NaSON), $Na_2S_2O_5$, and N1s peaks (Figure II.12.D.4i) from NaSON. Inorganic dominated SEI layer on HC anode formed in the LHCE ensures a robust SEI layer and excellent cycling stability of Na||HC cells.

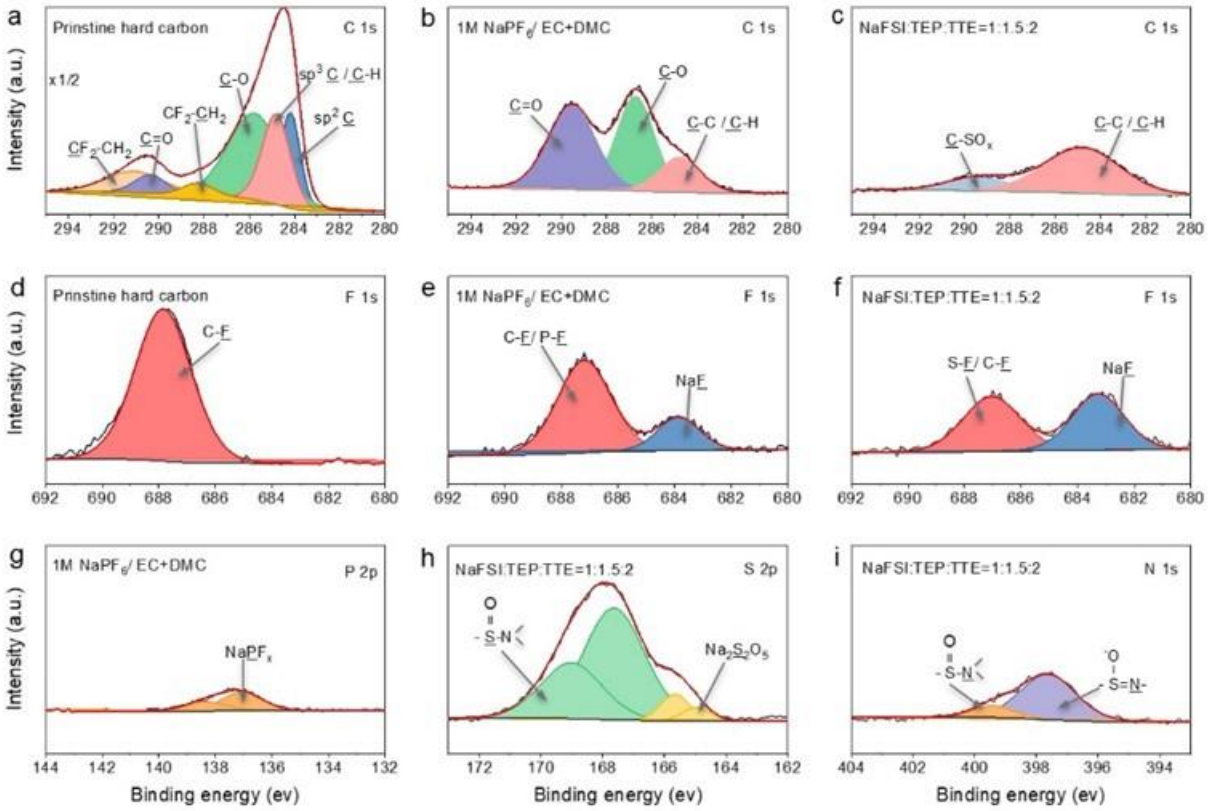

Figure II.12.D.4 Characterization of the SEI components on pristine and cycled hard carbon (HC) electrodes by XPS. a-c) C 1s, d-f) F 1s, g) P 2p, h) S 2p and i) N 1s XPS profiles of the pristine HC anode (a, d) and the HC anode after 20 cycles in 1 M $NaPF_6$/EC+DMC (1:1 in weight) electrolyte (b, e, g) and NaFSI-TEP/TTE (1:1.5:2 in mole) electrolyte (c, f, h, i).

3. Na-ion full cells with long cycling stability and CE higher than 99%

Na ion full cells have been tested in non-flammable localized high concentration electrolyte (LHCE: NaFSI-TEP/TTE (1:1.5:2 in mole)) and compared with those tested in baseline electrolyte (BE:1 M $NaPF_6$/EC+DMC (1:1 in weight)). The electrochemical performance of full cells using $NaCu_{1/9}Ni_{2/9}Fe_{1/3}Mn_{1/3}O_2$ (Na-NCFM) as the cathode and pre-sodiated HC as the anode is shown in Figure II.12.D.5. Three formation cycles at 0.1 C were conducted for better electrode-electrolyte interphase formation before long-term cycling at 0.2 C. HC||Na-NCFM full cells in both electrolytes show similar discharge capacity during the initial formation cycle, i.e. 118.2 mAh g^{-1} for the NaFSI-TEP/TTE electrolyte and 117.8 mAh g^{-1} for the baseline carbonate electrolyte (Figure II.12.D.5a). Note the capacity calculation for the full cell was based on the mass of cathode active material. However, the long-term cycling stability of the HC||Na-NCFM full cells differs significantly in these electrolytes.

In the conventional carbonate electrolyte, the capacity of the full cell decayed quickly with a low capacity retention of 48.4% after 200 cycles (Figure II.12.D.5a). This is consistent with the CE of 99.6% (see Figure II.12.D.5b). Dramatic overpotential increase and capacity decrease during cycling were observed in the NIB full cells using the baseline electrolyte as shown in Figure II.12.D.5c. This indicates the increased interfacial resistance and quick capacity fade during cycling. In contrast, in the nonflammable NaFSI-TEP/TTE electrolyte, the NIB full cell shows greatly improved cycling performance with a highly reversible capacity of 97.5 mAh g^{-1} and capacity retention of 82.5% after 200 cycles (Figure II.12.D.5a and d). The CE of the NIB full cell reached 99.93% during cycling due to both the high quality CEI layer formed on the Na-NCFM cathode, and the SEI layer formed on the HC anode in the NaFSI-TEP/TTE electrolyte. The charge and

discharge curves of the NIB full cell with NaFSI-TEP/TTE electrolyte exhibit minimal changes over 200 cycles (Figure II.12.D.5d). Therefore, the electrode-electrolyte interphase formed at both the cathode and anode are very stable in NaFSI-TEP/TTE electrolyte during long-term cycling.

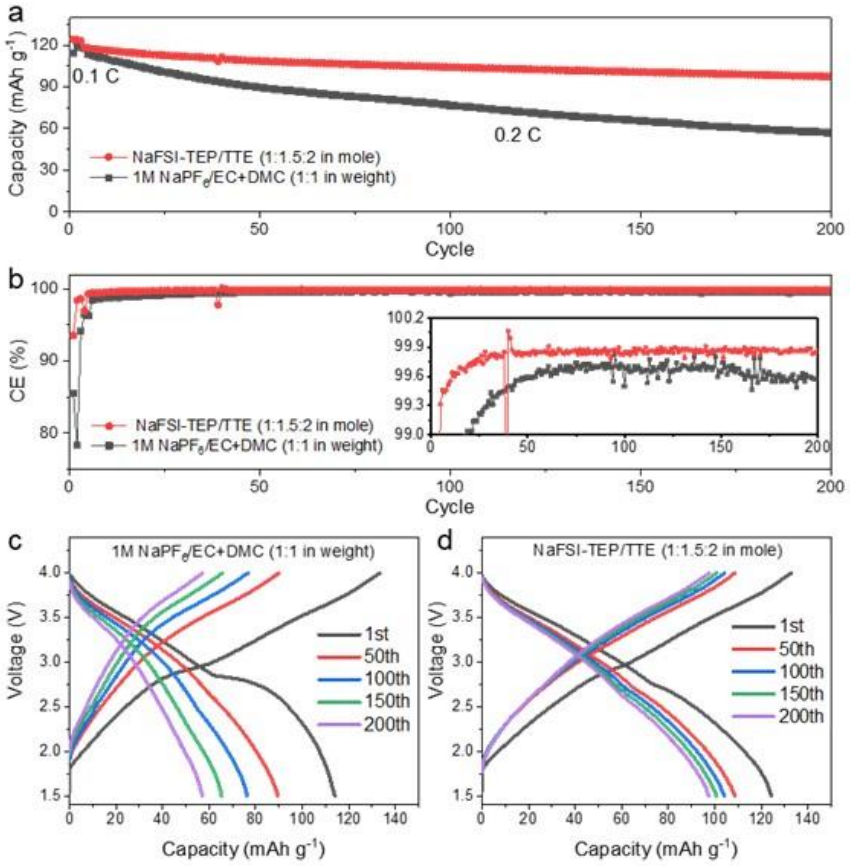

Figure II.12.D.5 Electrochemical behaviors of HC||Na-CNFM full cells. a) Cycling performance and b) Coulombic efficiency of the full cells using nonflammable NaFSI-TEP/TTE (1:1.5:2 in mole) electrolyte and conventional 1 M $NaPF_6$/EC+DMC (1:1 in weight) electrolyte. c-d) Selected charge–discharge voltage curves for the full cells using 1 M $NaPF_6$/EC+DMC (1:1 in weight) (c) and NaFSI-TEP/TTE (1:1.5:2 in mole) (d) electrolyte.

4. *Porous carbon anode with capacity > 480 mAh g^{-1}*

A novel carbon-based anode material with sealed porosity has been developed for sodium ion batteries (SIBs). This material is consisted of carbon and pores in which 1) carbon particles are interconnected and 2) closed pores exist inside the overall carbon structure.

Figure II.12.D.6 shows the morphology and structure of the carbon. TEM images in Figure II.12.D.6a shows a clear core/shell structure. The amorphous carbon shell of ~20 nm thickness is observed on surface while a different feature inside. This outside coating layer can effectively prevent diffusion of electrolyte from entering the inner pores of the porous carbon, therefore minimize the side reaction between Na and electrolyte and extend the cycle life of SIBs. A high magnification TEM image in Figure II.12.D.6b reveals the porous nature of the core. The size of these pores is around 1-2 nm. When the carbon is used in SIBs, sodium ions insert into carbon shell first and then diffuse into pores in porous core.

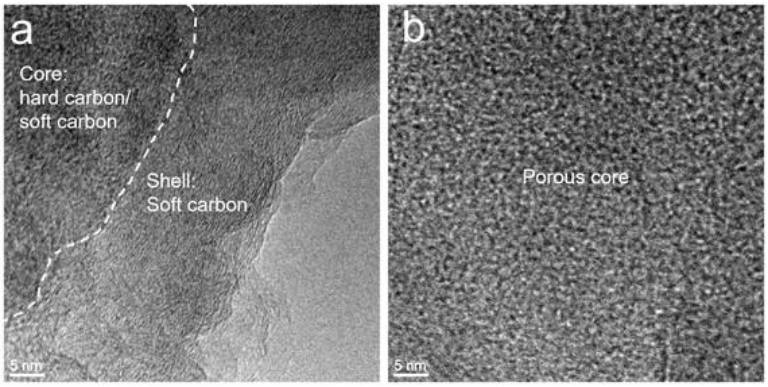

Figure II.12.D.6 (a) TEM and (b) STEM images of the porous carbon.

The true density of the carbon is measured to be 1.48 g/cm^3 by a helium pycnometer, corresponding to 36% of closed porosity inside the carbon. The surface area measured by nitrogen sorption is below 10 m^2 g^{-1}, consistent with the high closed-porosity and the low true-density.

Figure II.12.D.7 shows the electrochemical performance of the carbon anode in sodium half-cell. The anode is tested in a coin cell with sodium metal as counter electrode and an electrolyte of 1 M $NaPF_6$ in EC-DMC (1:1 by weight). The cell is charged/discharged within a voltage window from 0.005 to 2.0V with 0.1C (1C = 450 mA/g). The first cycle coulombic efficiency is 85%, with the 1st de-sodiation capacity of 487 mAh/g as shown in Figure II.12.D.7a. The cell retains 97% capacity after 80 cycles in (Figure II.12.D.7b). The cycling coulombic efficiency increases to 99.8% in 15 cycles and remains at this level afterwards (Figure II.12.D.7c), indicating stable SEI formation. Figure II.12.D.7d shows the rate capability. A high de-sodiation capacity of 435 mAh/g can be delivered even at 2C. The ratio of capacity at 2C to 0.1C is about 89%, demonstrating its great high rate capability.

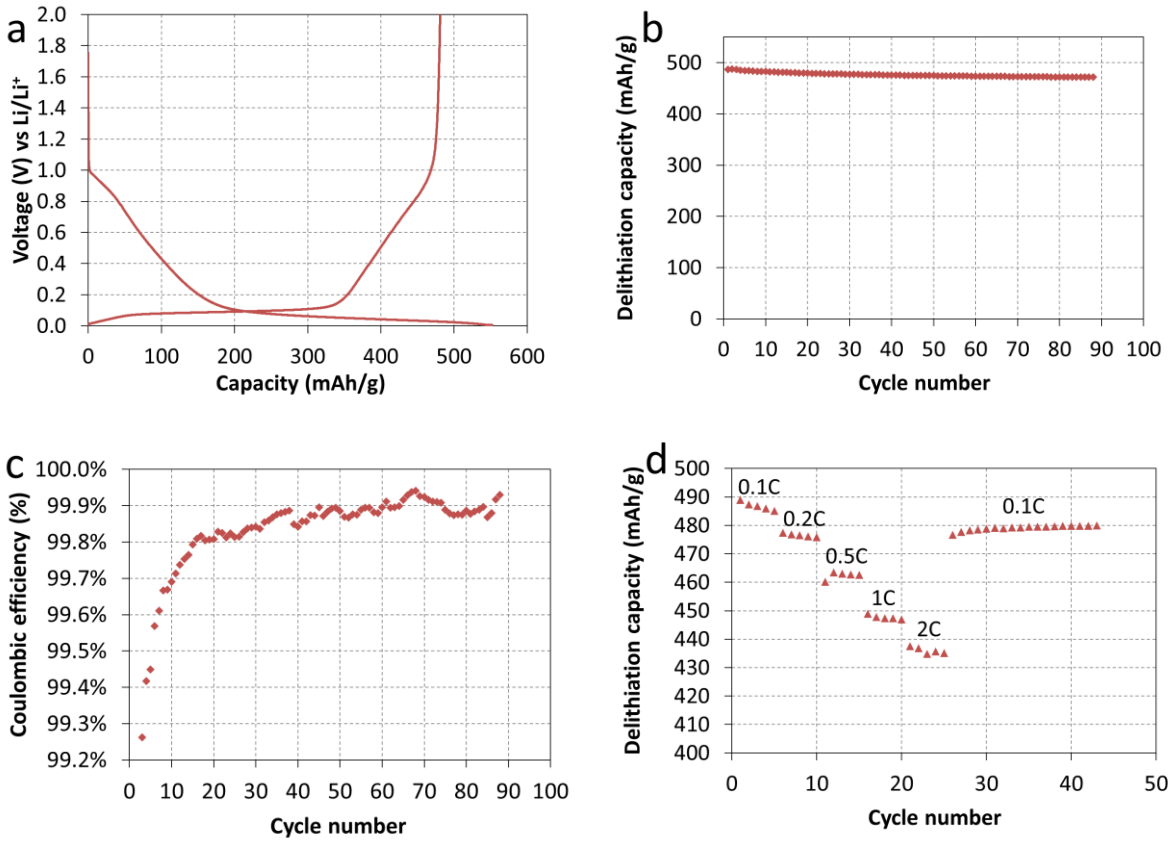

Figure II.12.D.7 Electrochemical performance of the carbon in sodium half-cell. (a) first cycle voltage profile. (b) Cycling stability as a function of cycle number. (c) Coulombic efficiency as a function of cycle number. (d) Cycling stability at different rates as a function of cycle number.

Conclusions

- Non-flammable localized high concentration electrolytes (LHCE) has been optimized with a salt:solvent:diluent of NaFSI:TEP:TTE=1:1.5:2. HC||Na-NCFM full cell using this electrolyte demonstrates 82.5% capacity retention after 200 cycles with a CE of 99.93%.

- Relationship between the composition of the SEI/CEI layers and electrochemical performance of NIBs was identified. The inorganic (F and S) rich SEI and CEI layers formed in LHCE (NaFSI-TEP/TTE)

minimize the interactions between the hard carbon anode and the electrolyte, block the dissolution of transition metals from the cathode and lead to excellent cycling stability of NIBs.

- A novel carbon anode with soft carbon surface and porous core shows a high de-sodiation capacity >480 mAh g^{-1} with good cycling stability (97% capacity after 80 cycles) and rate performance (435 mAh g^{-1} delivered even at 2C).

Key Publications

1. P. M Le, T. D Vo, H. Pan, Y. Jin, Y. He, X. Cao, H.V Nguyen, M. H Engelhard, C-M. Wang, J. Xiao, J.-G. Zhang*. "Excellent cycling stability of sodium anode enabled by a stable solid electrolyte interphase formed in ether-based electrolytes," Advanced Functional Materials, 2020, 30, 2001151.

2. Yan Jin, Yaobin Xu, Phung M. L. Le, Thanh D. Vo, Quan Zhou, Xingguo Qi, Mark H. Engelhard, Bethany E. Matthews, Hao Jia, Zimin Nie, Chaojiang Niu, Chongmin Wang, Yongsheng Hu, Huilin Pan,* and Ji-Guang Zhang*, "Highly Reversible Sodium Ion Batteries Enabled by Stable Electrolyte-Electrode Interphases", ACS Energy Letters, 2020, 5, 3212.

3. Ji-Guang Zhang*, Ran Yi, Phung M Le, Thanh D Vo, Yan Jin. "Electrolytes and Interfaces for Stable High-Energy Na-Ion Batteries", 2020 DOE VTO Annual Merit Review.

Acknowledgements

Key contributors include Dr. Yan Jin, Dr. Phung Le, Thanh Vo, and Dr. Ran Yi.

II.13 Beyond Li-ion R&D: Battery500

II.13.A Battery500 Innovation Center (PNNL)

Jun Liu, Principal Investigator
Pacific Northwest National Laboratory
902 Battelle Boulevard
Richland, WA 99354
E-mail: jun.liu@pnnl.gov

Yi Cui, Principal Investigator
Stanford University/SLAC
450 Serra Mall
Stanford, CA 94305
E-mail: yicui@stanford.edu

Tien Duong, DOE Technology Development Manager
U.S. Department of Energy
E-mail: Tien.Duong@ee.doe.gov

Start Date: October 1, 2019 End Date: September 30, 2020
Project Funding: $8,000,000 DOE share: $8,000,000 Non-DOE share: $0

Project Introduction

Lithium (Li)-ion batteries play a critical role in modern day technologies, but their specific energy (Wh/kg) and energy density (Wh/L) are approaching the maximum practically achievable values based on existing technology with the conventional cathode and anode materials. The large-scale deployment of electric vehicles and ever-increasing demand of modern technologies require further increase in cell energy and cost reduction. Rechargeable Li-metal batteries are regarded as "Holy Grail" of high-energy-density systems because Li metal has an ultrahigh theoretical specific capacity (3860 mAh/g), an extremely low redox potential (-3.040 V vs. standard hydrogen electrode), and a very low gravimetric density (0.534 g/cm). However, the practical application of Li metal anode (LMA) still faces several big challenges, including safety concerns due to Li dendrite growth, limited cycle life because of low Li Coulombic efficiency (CE), and infinite volume change during Li stripping and redeposition if a two-dimensional (2D) flat Li foil is used. In addition, developing the next generation rechargeable Li metal batteries with a specific energy higher than 300 Wh/kg, up to 500 Wh/kg, is still a significant challenge. Many groups are focusing on the fundamental breakthroughs in electrode materials and control the unnecessary side reactions in such new battery concepts. Solid-state Li batteries using solid electrolytes have recently received wide attention due to the inherent high safety and decent energy. There have been intense efforts to improve the bulk conductivity, interfacial charge transport and stability for the manufacturing of the solid-state cells. A very desirable strategy is to take advantage of the electrode materials that are commercially or nearly commercially available and introduce the least perturbation to the cell configuration and manufacturing process of the current technologies. Based on these considerations, two battery chemistries, high nickel content lithium nickel-manganese-cobalt oxide (high-Ni $LiNi_xMn_yCo_zO_2$ (NMC), Ni>60%), coupled with LMA, and Li-sulfur (S) chemistry, with the potential to achieve a specific energy higher than 500 Wh kg^{-1} are selected for this Battery500 innovation center project.

Objectives

The Battery500 Consortium aims to develop commercially viable Li battery technologies with a cell level specific energy of 500 Wh/kg through innovative electrode and cell designs that enable the extraction of the maximum capacity from advanced electrode materials. In addition, the project aims to be able to achieve 1000 cycles for the developed technologies.

Approach

The Battery500 Consortium will utilize first class expertise and capabilities in battery research in the United States and develop an integrated and multidisciplinary approach to accelerate the development and deployment of advanced electrode materials in commercially viable high energy batteries. The LMA combined with compatible electrolyte systems and two types of cathodes—one high-Ni NMC and another S—will be studied and developed to reach high specific energy. The project focus is to design novel electrode and cell architectures to meet the 500 Wh/kg goal. The Consortium will work closely with R&D companies, battery/materials manufacturers and end-users/OEMs to ensure that the developed technologies are aligned with industry needs and can be transferred to production. The out-year goals for FY2020 include: (1) Deliver pouch-cell design and pouch-cell parameters for over 400 Wh/kg pouch cells; (2) Develop new 3D anode structures; test and validate such using coin-cell standard protocols; (3) Fabricate and test 350 Wh/kg Li-S pouch cells with over 50 stable cycles; and (4) Fabricate and test a pouch cell capable of 400 Wh/kg and 100 cycles. All of these goals have been successfully achieved in FY2020.

Results

1. Keystone project 1: Materials and interfaces

I.1 High Ni content Cathode and Li Metal Anode

In FY 2020, the consortium focused on developing further understanding of the SEI layer to inform further conception of advanced electrolyte systems, electrode design, and interfacial engineering and to support efforts on improving current pouch cell performance to reach the project goal of 500 Wh/kg specific energy.

In the FY2020, **Binghamton University** team has been continuously working on the development of a Li-Nb-O coating on NMC 811 with improved electrochemical performance, including a reduced first cycle loss. since the coating did not improve the thermal stability of the material because NMC 811 has a strong tendency to form a lithium-rich layer on the surface due to reactivity with the environment, a Li-free precursor was investigated which could simultaneously form a protective layer and scavenge the residual lithium species. In the initial studies, the Nb-O coating showed a better thermal stability than pristine 811. Furthermore, the coating effectiveness was found to be a function of annealing temperature (Figure II.13.A.1). Intermediate temperatures of 400 - 500°C resulted in the highest first cycle coulombic efficiency, with higher temperatures showing shifts in lattice parameters due to Nb doping. Extended cycling is now underway with optimized coating.

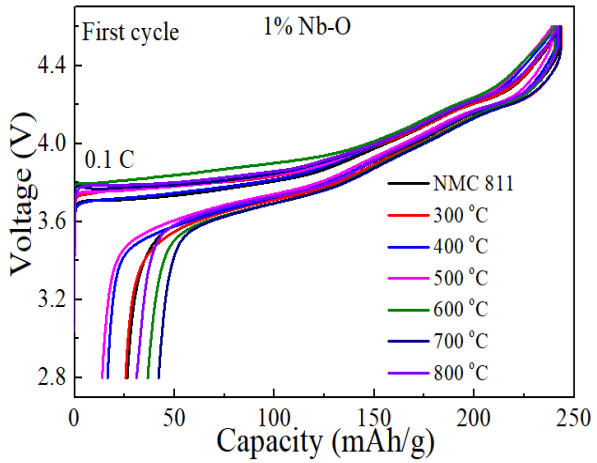

Figure II.13.A.1 Charge/discharge curves of pristine NMC 811 and Nb-O modified NMC 811 heated from 300 to 800 °C.

They further investigated relative merits of surface modification vs. bulk substitution for improved cathode stability. Their previous work showed that a surface coating using a Li-Nb-O solution on NMC 811 meatballs reduces the 1st cycle capacity loss and improves the rate performance. Surface coating plus surface substitution occurs when the Li-Nb-O/NMC material is fired at 400-500°C, whereas when the firing occurs at ≥ 700°C the niobium diffuses into the bulk of the material. Both thermal treatments gave improved capacity retention over the untreated 811, as shown in Figure II.13.A.2a; however, bulk substitution showed the best performance. It is believed that surface coating protection suppresses the side reactions with electrolyte, and the bulk Nb-substitution enhances the structural stability during cycling. Figure II.13.A.2b-d shows that both coating and substitution reduces the change in the dQ/dV 4V peaks relative to untreated 811. This may be associated with suppression of the H2 to H3 transition or converting it into a single-phase region. Therefore, there is a need for both a coating to protect the surface and substitution to stabilize the lattice. Phosphate, borate and Al-O species have been extensively studied for the layered oxides, and more work will be done to look at different species for the coating and for substitution, for example by coating an aluminium substituted material. In addition, more investigation will be done to replace NMP in the preparation of NMC 811 electrodes by the greener solvent-Cyrene. However, under ambient conditions it is unable to satisfactorily dissolve the PVdF binder and the coating crumbled in use. Other opportunities for replacing NMP will be studied.

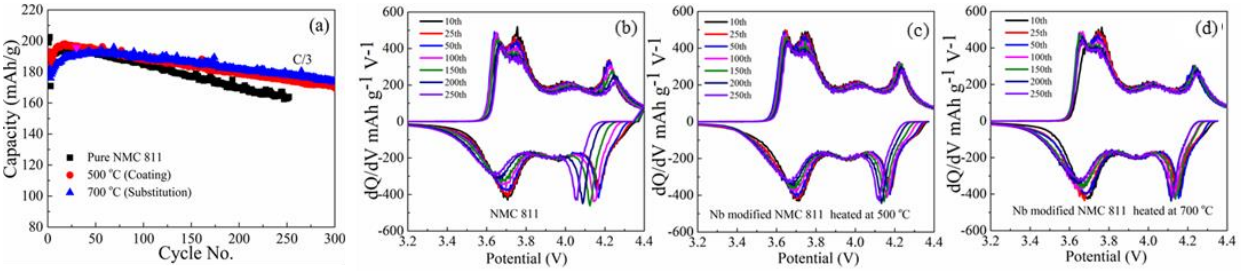

Figure II.13.A.2 Cycling performance of NMC 811 and Nb modified NMC 811 at 500°C (mainly coating) and 700°C (mainly substitution). Cycled 2.8 ~ 4.4 V at C/3. dQ/dV vs V curves of (b) NMC811, (c) Nb modified NMC 811 at 500 °C and (d) Nb modified NMC 811 at 700 °C for cycles 10, 25, 50, 100, 150, 200 and 250.

Previously, **Binghamton University** reported that the slow in-diffusion of lithium ions at high lithiation levels is the main contributor to the 1st cycle capacity loss for NMC811 cathode. Even when only 10 mAh/g Li was extracted, the insertion was severely limited at 21°C, as shown in Figure II.13.A.3 (left). In FY2020, the researchers compares NMC811 with LCO (Figure II.13.A.3 (right)), when both were charged to remove 120 mAh/g. The 1st cycle loss for the LCO is much less, and is not much impacted by raising the temperature to 45°C. In contrast, much of the 1st cycle loss of the NMC811 can be eliminated at 45°C, again indicating kinetic limitations. However, this required small increase of temperature suggests that lattice substitution should be able to have the same effect.

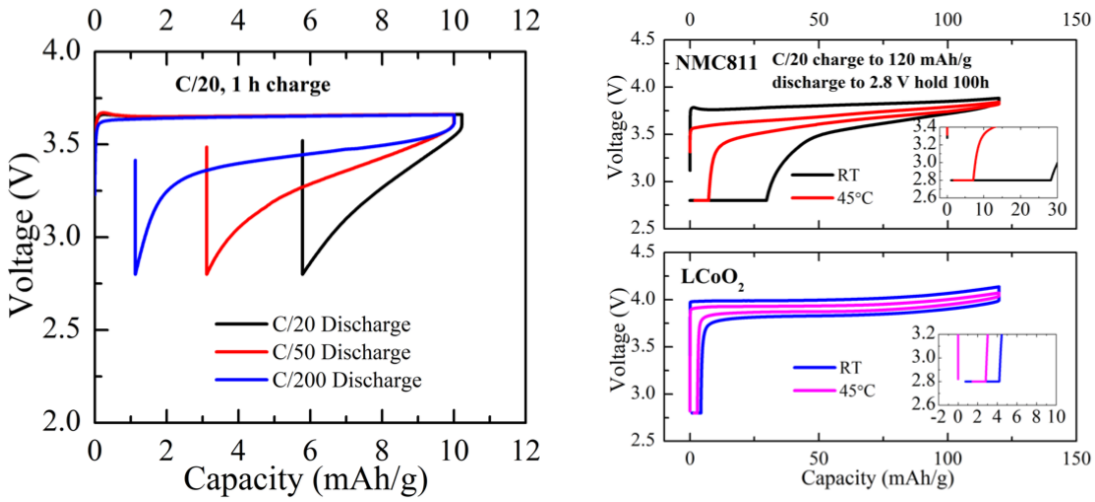

Figure II.13.A.3 (left) 1st cycle of ECOPRO NMC811 vs. Li with 1h charge at C/20 and then discharged to 2.8 V with different current rates: C/20, C/50 and C/200. (right) Comparison of NMC811 with LCO charged to 120 mAh/g Li removal.

A second approach the researchers have found to reduce the 1st cycle loss is surface coating (and partial substitution) the NMC811. Figure II.13.A.4. shows that for each of three low charging levels, the 1st cycle loss is less for the Nb treated NMC811. They conclude that modification of the NMC to make it more like LCO is a viable method to mitigate the 1st cycle loss; this might be accomplished by substitution. The optimum coating/substitution must now be found.

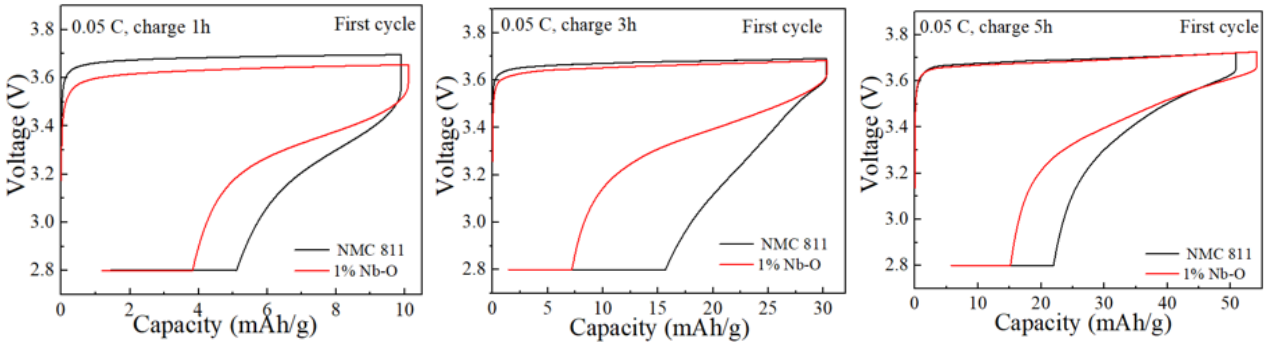

Figure II.13.A.4 Reduction of 1st loss of NMC811 by a niobium treatment for three charge levels.

University of Austin (UT Austin) team used a conductive polymer polyaniline (PANI) with numerous benefits as an additive/binder in ultrahigh-nickel, NMC900505 cells. In order to fully delineate its effect on the cathode performance during long-term cycling, pouch full cells with a graphite anode were assembled to avoid cell failure due to lithium-metal anode. When PANI was mixed with PVDF in a 5:1 ratio as a binder for both the electrodes, capacity retention improved remarkably from 47% to 81% after 1,000 cycles (Figure II.13.A.5). The cells also showed improved average coulombic efficiency (99.5% vs 98.5%) and discharge voltage (3.6 V vs. 3.2V at 1,000 cycles). Unlike other modifications such as dopants and coatings, which can often sacrifice capacity to improve cycle life, conductive PANI maintains the same capacity at C/2 rate and further improves the rate capability (200 $mAhg^{-1}$ vs. 180 $mAhg^{-1}$ at 3C rate). Even when applied to only one electrode, the cell stability is greatly enhanced.

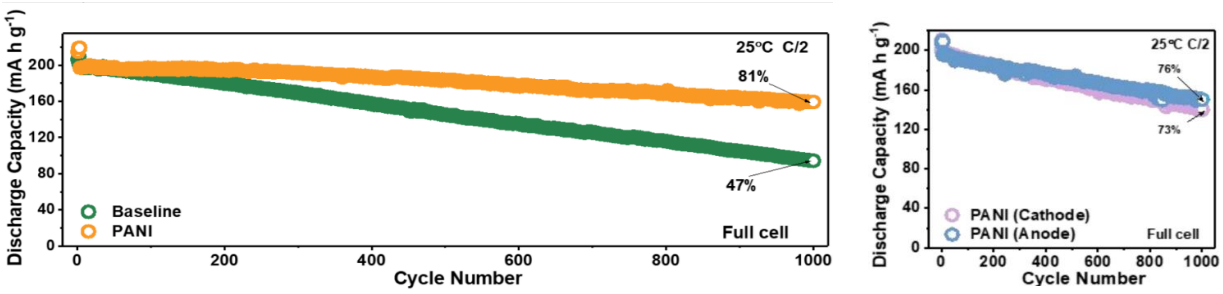

Figure II.13.A.5 Cycling stability of a cell with PVDF-only binder (baseline) and a 5:1 PVDF:PANI binder blend (left) in both the cathode and anode and (right) in the cathode only or anode only.

PANI's ability to function when applied to either electrode is due to its role as an HF scavenger. HF generated *via* $LiPF_6$ decomposition can leach transition-metal ions from the cathode particle, generating resistive spinel and rock-salt phases, releasing reactive oxygen from the lattice, and causing crossover that can damage the anode SEI. PANI in its deprotonated phase can react with and consume HF in the electrolyte, drastically reducing HF attack. Within only a few seconds of HF exposure, a blue sheet of deprotonated PANI protonates and becomes green, visually demonstrating its capability. In addition, time-of-flight secondary ion mass spectrometry (TOF-SIMS) on cycled electrodes (both anode and cathode) show substantially reduced signal from deposited transition-metal fluorides.

TOF-SIMS is also able to reveal information regarding PANI's effect on the cathode-electrolyte interface (CEI). The depth of the maximum NiO^- yield is much lower in the PANI-modified sample, indicating a much thinner CEI (Figure 4). Additionally, the CEI is simplified into a two-layer structure with an outer layer composed of phosphorous compounds and an inner layer composed of organic species from electrolyte decomposition, as well as CNO^- from PANI itself. A third layer heavy in dissolved and re-deposited transition-metal compounds is found only in the baseline sample without the HF scavenging effect. The combined effects of the HF scavenging and stable-CEI formation protect the cathode, leading to much-improved crystallinity after cycling as indicated by *ex-situ* x-ray diffraction (Figure II.13.A.6).

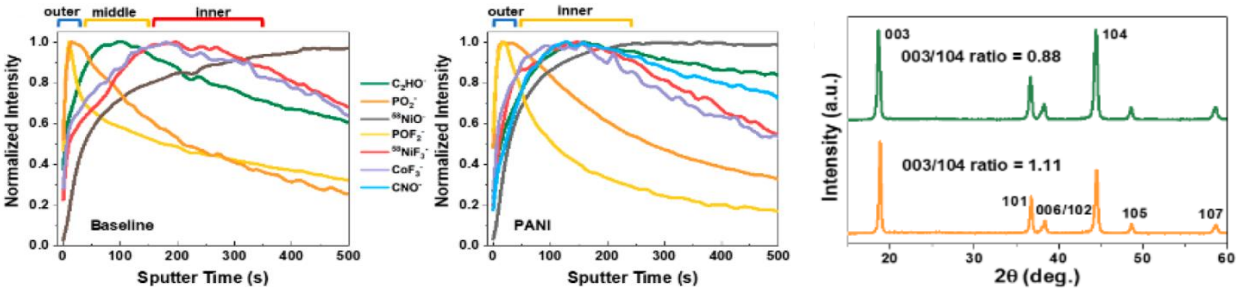

Figure II.13.A.6 Cathode TOF-SIMS data with normalized signal intensities for cells with (left) no PANI and (middle) PANI after 1,000 cycles. (Right) Ex-situ XRD patterns of the cathode (top) without PANI and (bottom) with PANI after 1,000 cycles. Both the TOF-SIMS and XRD characterizations were performed on pouch cell electrodes.

UT Austin team also assembled coin cells by pairing ultrahigh-nickel $LiNi_{0.9}Mn_{0.05}Co_{0.05}O_2$ (NMC900505) cathode with graphite anode as well as with lithium-metal anode. Three-electrode electrochemical impedance spectroscopy (EIS) was performed periodically during cycling to track changes in the cathode impedance, with an aim to understand whether decomposition species from the lithium-metal anode would crossover and affect the cathode. Figure II.13.A.7 shows the EIS data after 1, 20, and 100 cycles. As can be seen, cathode impedance for the cell paired with lithium-metal anode is remarkably higher than that for the cell paired with graphite anode even after just one cycle, which was confirmed with duplicate cells. However, cathode impedance growth on extended cycling appears comparable between the two cell types. The data suggest that anode-to-cathode crossover in NMC | lithium-metal cells occurs predominantly during formation cycles. In the first cycle, pristine lithium reacts particularly aggressively to form SEI and other soluble decomposition

products. In addition, the cathode has not yet formed its own protective SEI and may be more vulnerable to the attack or deposition of these crossover products. The finding suggests anode-to-cathode crossover as another contributor to failure in lithium-metal batteries.

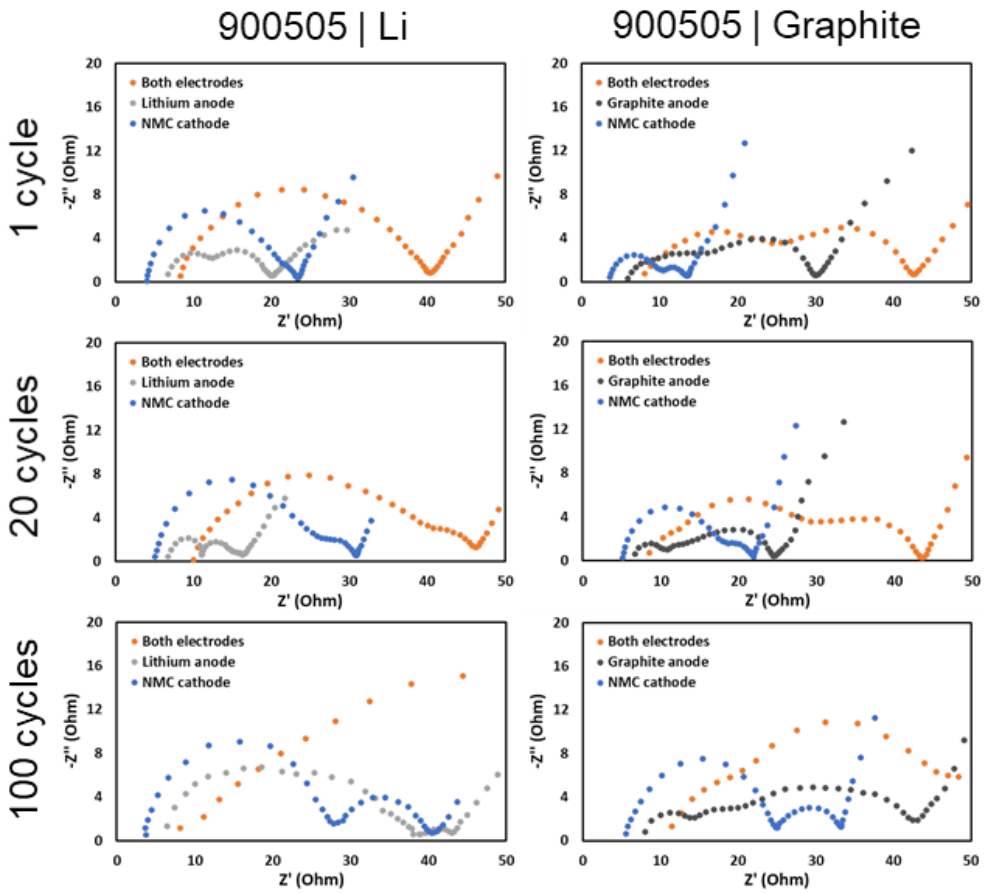

Figure II.13.A.7 Nyquist plots showing the electrode-level and whole-cell impedances for NMC900505 cathodes cycled with lithium-metal (left) and graphite (right) anodes as a function of cycle number.

In collaboration with UT Austin, **Brookhaven National Lab. (BNL)** team focused on applying synchrotron based XAS, 3-dimensional (3D) XANES tomography, as well as synchrotron-XPS with depth-profiling functionality to do comparison studies on nickel-rich $LiNi_{0.94}Co_{0.06}O_2$ (NC) and $LiNi_{0.92}C_{o0.06}Al_{0.02}O_2$ (NCA) cathodes. It was found that during high-voltage cycling, many micro-cracks were developed and propagated through the $LiNi_{0.94}Co_{0.06}O_2$ particles (Figure II.13.A.8). In contrast, for the $LiNi_{0.92}C_{o0.06}Al_{0.02}O_2$ particles, no such cracks were developed after 70 cycles at a cut-off voltage of 4.8 V. In addition, the distribution of Ni valence states in $LiNi_{0.92}C_{o0.06}Al_{0.02}O_2$ looks much more homogeneous than in $LiNi_{0.94}Co_{0.06}O_2$ particles. These results provide valuable insights on the origin of superior performance after doping.

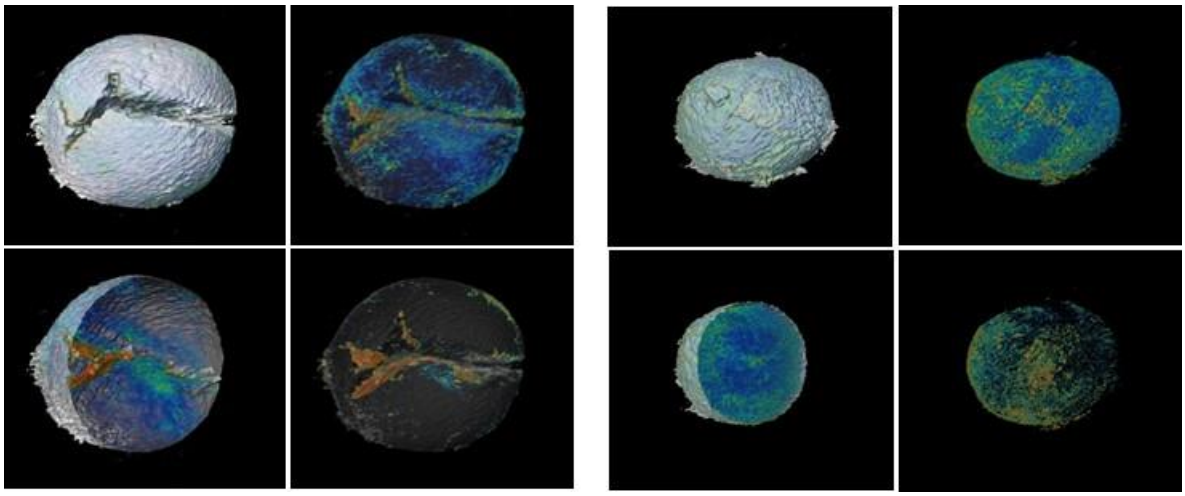

Figure II.13.A.8 3-dimensional XANES tomography of (left) $LiNi_{0.92}Co_{0.06}O_2$ (NC) and (right) $LiNi_{0.92}Co_{0.06}Al_{0.02}O_2$ (NCA) after 70 cycles at a cut-off voltage of 4.8 V.

Researchers from **Brookhaven National Laboratory** performed neutron powder diffraction data to examine the defect fraction in a variety of NMC cathodes. In order to realize the maximal performance achievable using NMC layered cathodes, it is necessary to optimize not just the cathode composition but also the concentration of defects within the cathode material, as these defects have the potential to modify both the electronic and ionic conductivity of the cathode. While it has long been recognized that anti-site defects are present in layered NMC compounds, to date it has not been possible to elucidate structure-properties relationships due to the difficulty of accurately quantifying defect compositions. To address this unmet need, **BNL** team carried out a comprehensive study of more than a dozen NMC compounds using the highest quality of synchrotron and neutron powder diffraction data attainable in this country. Using this data along with new analysis methods that we developed, we have been able to independently determine defect concentrations using the x-ray and neutron data with an agreement of 0.1% (absolute), a sensitivity to defects that appears to be unprecedented both for these compounds and for the entire field of powder diffraction. This sensitivity to defects exceeds that of traditional chemical methods. From the defect compositions refined in this manner, it has been proved that the dominant defect for almost all NMC compositions is paired anti-site (PAS) defects of Ni_{Li} and Li_{Ni} (Figure II.13.A.9). It was previously assumed that PAS defects occur due to the similar sizes of Ni^{2+} and Li^{+}. If this is the case, the defect formation energy should be independent of the sample composition, something that can be now tested using our high-precision measurements of defect concentration to calculate defect formation energies through the Boltzmann relationship. It can be clearly seen that (1) the defect formation energy is not composition-independent, (2) thermodynamic and not kinetic considerations primarily determine the defect concentration, and (3) the defect formation energy is non-zero even for NMC compositions which lack Ni^{2+}. It is concluded that the composition-dependence is due to variation in the average size of octahedra in the transition metal layer (which continuously increases as the Ni^{2+} fraction increases). Furthermore, our derived relationship between chemical composition and defect formation energy can be used to predict the defect concentration for any NMC composition and any synthesis temperature.

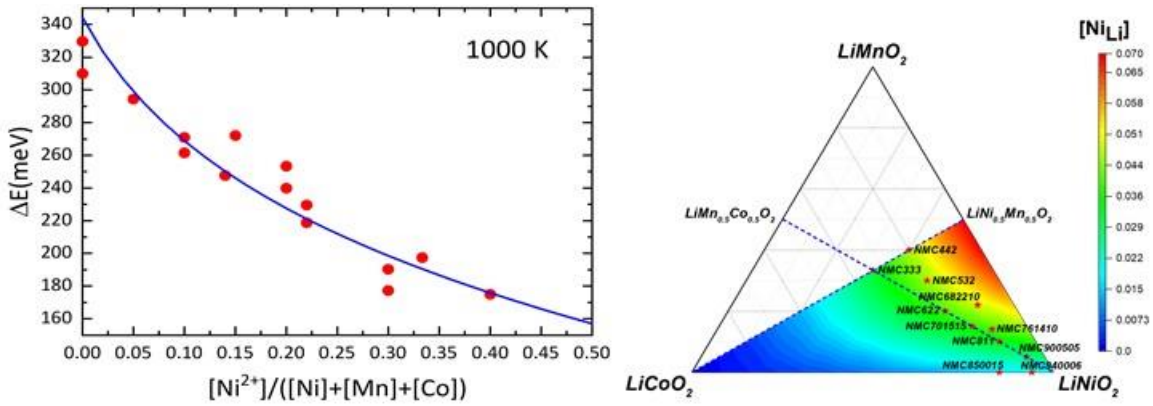

Figure II.13.A.9 Left: Energy of PAS defect formation is found to depend on the total concentration of NI^{2+} in NMC phase. Right: Predicted PAS defect composition as a function of NMC composition. For the range of experimentally measured samples (symbles), predictions are accurate within ~0.5% (absolute).

University of California at San Diego UCSD team has been studying the deposition of lithium metal. It is qualitatively believed that increased uniaxial stack pressure can help to alleviate Li dendrite formation and improve Coulombic efficiency (CE) and cycling performance of Li metal batteries. Quantitatively understanding the role of stack pressure on Li nucleation, growth and dissolution, and building the pressure-morphology-performance relationship will open up new opportunities to rationally solve issues regarding Li metal anodes in high-energy Li metal batteries. In this study, researchers at **UCSD** used a custom-designed split cell with a load cell to precisely control the stack pressure applied to the battery during cycling, with a pressure measurement resolution of 0.1 psi. Figure II.13.A.10a shows the first cycle CE of Li-Cu cells as a function of applied stack pressure under current densities up to 2 mA/cm^2, using an advanced ether-based electrolyte. At 0 psi, the CE deceased from 92.5% at 1 mA/cm^2 to 85.5% at 2 mA/cm^2. When slightly increasing the stack pressure to 5 psi, the CE at 2 mA/cm^2 significantly increased to 92%; the CE also increased from 87% to 92.5% at 1.5 mA/cm^2. A gradual increment of CE at three current densities was observed when gradually increase the stack pressure to 20 psi. At 20 psi, the CE was boosted to 97.5%, 96.5% and 96% at 1, 1.5 and 2 mA/cm^2, respectively. Further increasing the stack pressure from 20 psi to 50 psi, the CE remains almost unchanged. For the electrochemical performance testing, the pressure was set as the on-set value. Two representative pressure (0 and critical pressure) were selected to study the deposited Li morphology using cryo-FIB-SEM. A high current density of 2 mA/cm^2 was applied for the morphological study. At 0 psi, highly porous and whisker-like Li deposits were formed even using advanced ether-based electrolyte, as shown in Figure II.13.A.10b (top view) and 5d (cross-section). This type of morphology is highly similar to the one formed in commercial carbonate electrolyte using coin cells with internal stack pressure of ~30 psi. When applying a critical pressure, the Li deposits become highly close-packed (Figure II.13.A.10c). The cross-section morphology (Figure II.13.A.10e) shows that the Li deposits form a perfect columnar structure with large granular diameter of ~4 µm, near-theoretical thickness of ~10 µm and minimum electrode-level porosity, indicating that pressure plays an important role in tuning Li deposition morphology. The researchers predicted in their previous study that the columnar Li deposits may help to improve the CE of Li metal by mitigating the isolated metallic Li formation. This study proves that the columnar Li deposits can be achieved by optimizing stack pressure, in combine with ether-based electrolytes. The role of pressure during the stripping process will be studied.

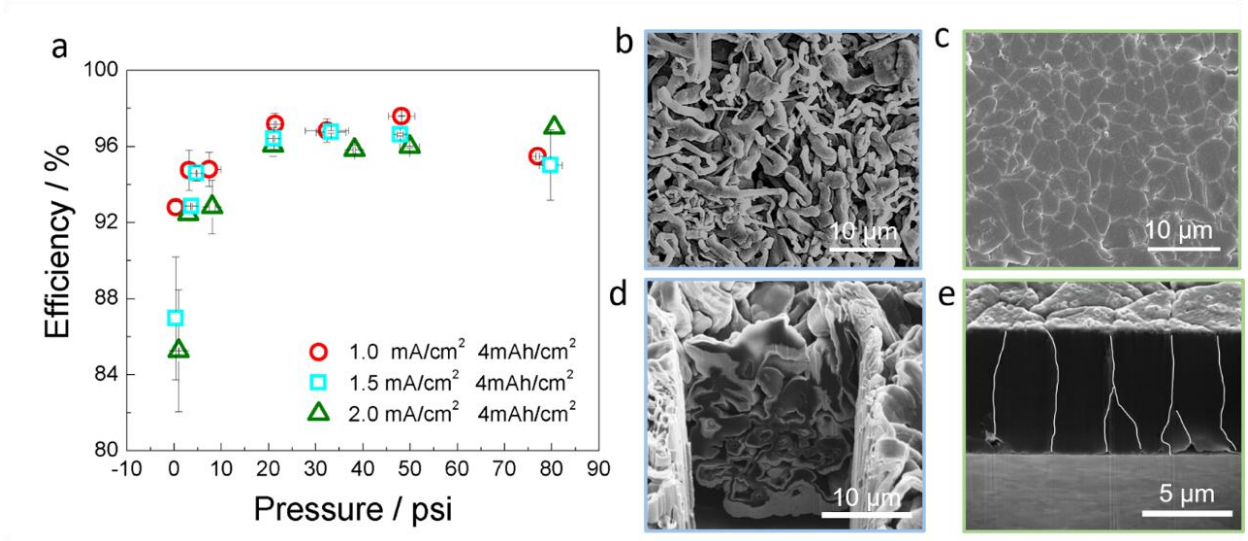

Figure II.13.A.10 (a) Coulombic efficiency as a function of stacking pressure under various current densities. (b, d) top view and cross-section view of deposited Li morphology formed under no pressure. (c, e) top view and cross-section view of deposited Li morphology formed under critical pressure. The Li in (b-e) was deposited at 2 mA/cm² for 1 hour

I.2 New electrolte additives and electrolyte systems

Stanford University team has developed a novel method to synthesize a new class of fluorinated ether electrolytes (Figure II.13.A.11) with combined high ionic conductivity and high oxidative stability in a single molecule. Structure–property relationship was obtained through varying the length and type of the ether group, as well as the length of the fluorinated segment. They show that the molecules (although in liquid state at room temperature with low molecular weight) actually have glass transitions rather than the melting transitions of typical ethers. For compound in this class with different structures, the Ionic conductivity is higher for those with longer ether groups combined with a shorter fluorinated segment. It is demonstrated that ion conductivities as high as 2.7×10^{-4} S/ cm can be obtained, which is very close to the typical ethers such as tetraglyme, but the lithium transference numbers is higher than that (Figure II.13.A.12a-d). In addition to the high ionic conductivity, these compounds also have high oxidative stabilities up to 5.6 V, which is at least 1.4 V greater than tetraglyme or a tetraglyme:TTE mixture, as shown in Figure II.13.A.12e. These results demonstrated the great advantages of these compounds with a combination of high ionic conductivity and high oxidative stability originated from the covalently attached ether segment and fluorinated segment respectively.

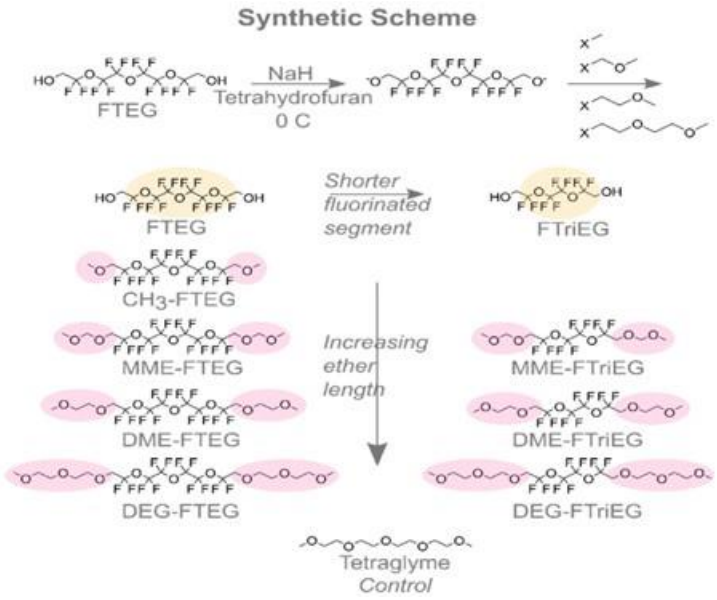

Figure II.13.A.11 Covalently attaching an ether to the hydrofluoroether allows for both high ionic conductivity and oxidative stability (our approach). Synthesis of fluorinated ethers through deprotonation of fluorinated tetraethylene glycol (FTEG) and fluorinated triethylene glycol (FTriEG) and subsequent addition of varying alkoxy halides

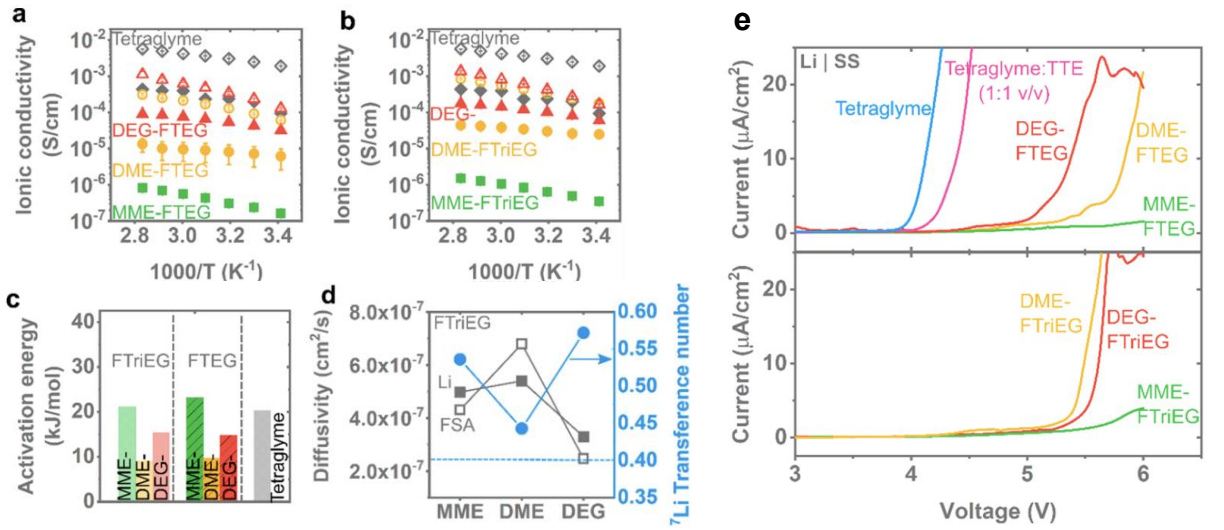

Figure II.13.A.12 Ionic transport and conductivity. Ionic conductivity as a function of LiFSA salt content (closed symbol: 0.1 M, open symbol: 1 M) for (a) FTEG compounds and (b) FTriEG compounds with tetraglyme as the control in both. (c) Activation energy obtained from Arrhenius fits of conductivity versus temperature for 0.1 M LiFSA salt concentration. (d) ^{7}Li

Stanford University team has been pursuing a new electrolyte approach to enable lithium metal anodes. They demonstrated a design strategy for electrolytes that enable anode-free Li metal batteries with single-solvent single-salt formations at standard concentrations (*Nature Energy* 2020). Rational incorporation of –CF2– units yields fluorinated 1,4-dimethoxylbutane (FDMB) as the electrolyte solvent. Paired with 1 M lithium bis(fluorosulfonyl)imide, this electrolyte possesses unique Li–F binding and high anion/solvent ratio in the solvation sheath, leading to excellent compatibility with both Li metal anodes (Coulombic efficiency ~ 99.52% and fast activation within five cycles) and high-voltage cathodes (~6V stability). Unlike typical transparent and colorless electrolytes, 1 M LiFSI/FDMB is brownish in color as shown in Figure II.13.A.13a**.** Fifty-µm-thick Li|NMC batteries retain 90% capacity after 420 cycles with an average Coulombic efficiency of 99.98%.

Industrial anode-free pouch cells achieve ~325 Wh/kg single-cell energy density and 80% capacity retention after 100 cycles.

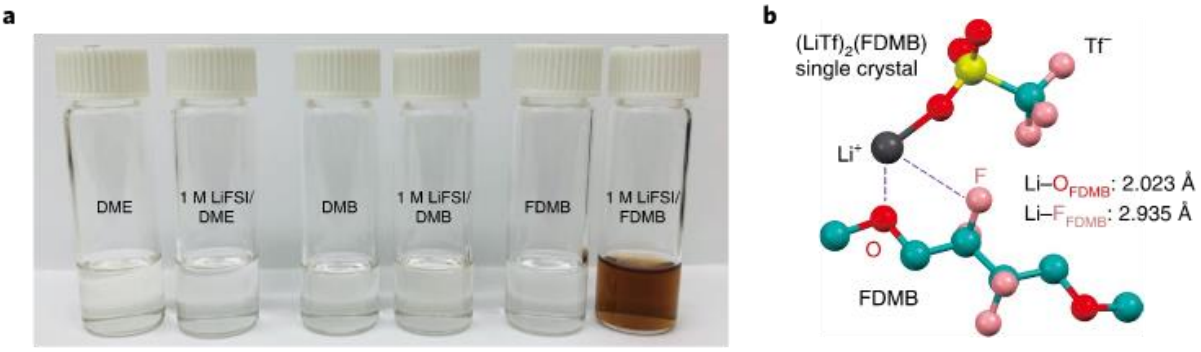

Figure II.13.A.13 (a) Optical image of three liquids and their 1 M LiFSI electrolytes. (b) Single crystal of LiTf/FDMB showing Li–F interactions. For clarity, only one LiTf and one FDMB are shown.

The Stanford University team investigated Li metal morphology and SEI structure of new electrolytes developed by their team. Figure II.13.A.14 shows the design concepts of the synthesized solvents. The Li metal deposition morphology and SEI nanostructure are carefully studied as shown in Figure II.13.A.15. When the 1 M LiFSI/DME or 1 M LiFSI/DMB is applied in Cu|NMC532 anode-free cells after 10 cycles, the Li structure on Cu is dendritic and porous (Figure II.13.A.15a, b). By contrast, with the 1 M LiFSI/FDMB electrolyte, the 2.7 mAh cm^{-2} Li deposited on Cu (~14 μm thick theoretically while ~20 μm observed) shows densely-packed, flat and large grains even after 70 cycles (Figure II.13.A.15c, d). The morphology is highly beneficial to reducing the surface area for SEI growth as well as suppressing "dead Li" formation, leading to an ideal cycling performance. Furthermore, cryogenic transmission electron microscopy (cryo-TEM) is utilized to characterize the SEI structure. In 1 M LiFSI/DME, the SEI layer is relatively thick (~10 nm) and nonuniform; however, an ultra-thin (~6 nm) and amorphous SEI is observed on Li when 1 M LiFSI/FDMB is applied (Figure II.13.A.15e and f). Instead of containing wrinkles or nonuniform domains as the SEI observed in 1 M LiFSI/DME or other conventional electrolytes, the SEI in 1 M LiFSI/FDMB exhibits extraordinary uniformity according to the fast Fourier transform (FFT, Figure II.13.A.15e and f insets). This is also one of the thinnest SEIs observed to date. This feature can effectively reduce the Li consumption from SEI formation during each cycle, thus improving the CE. The F 1s spectra of X-ray photoelectron spectroscopy (XPS) further supports this argument (Figure II.13.A.15g). The peaks assigned to LiFSI (~688 eV) in 1 M LiFSI/FDMB have similar intensities throughout the depth profiling, indicating uniform SEI, while those in 1 M LiFSI/DME show large variation with sputtering.

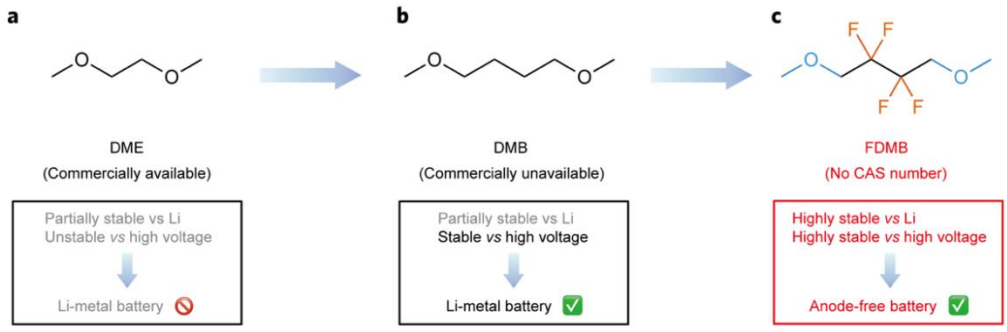

Figure II.13.A.14 Design concepts of solvent molecules studied in this work. a-c, Design scheme and molecular structures of three liquids studied in this work: DME (a), DMB (b), and FDMB (c)

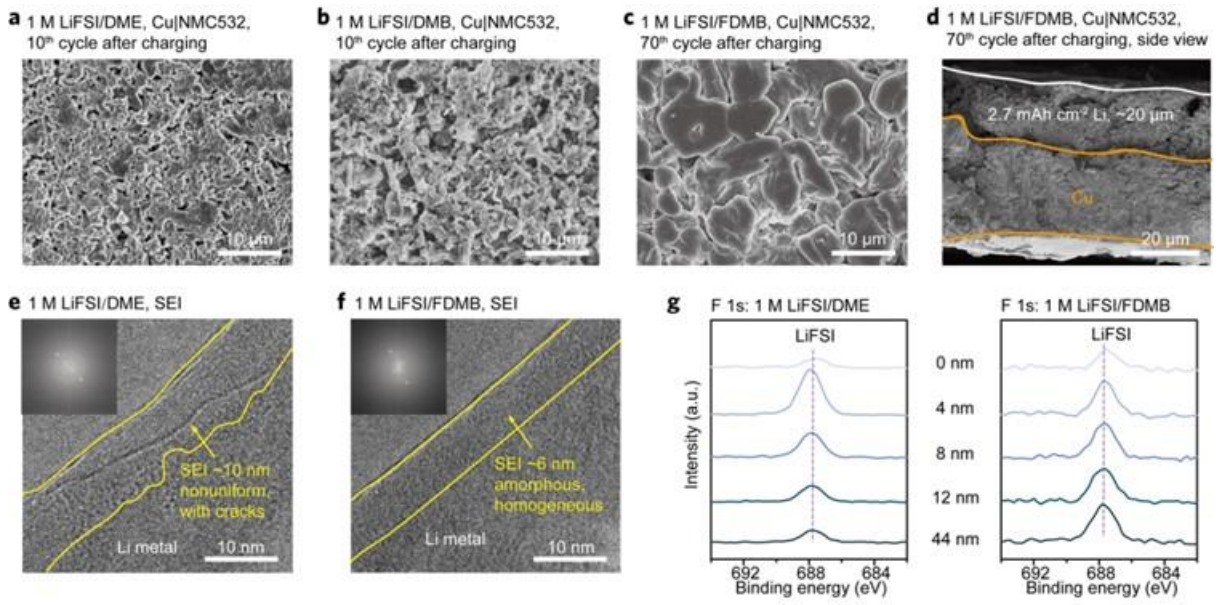

Figure II.13.A.15 Li metal morphology and SEI. a-d, Li morphology in anode-free Cu|NMC532 (2.7 mAh cm^{-2}) coin cells using 1 M LiFSI/DME after 10 cycles (a); 1 M LiFSI/DMB after 10 cycles (b), and 1 M LiFSI/FDMB after 70 cycles (c) and (d); Cryo-EM showing the SEI of 1 M LiFSI/DME (e) and 1 M LiFSI/FDMB (f). Insets in € and (f); the fast Fourier transform (FFT) of SEIs. (g); F 1s XPS depth profiles of Li metal surface in 1 M LiFSI/DME (left) and 1 M LiFSI/FDMB (right)

The Pacific Northwestern National Lab. (PNNL) team has been systematically studying the effects and mechanisms of four different model solvent molecules (carbonate, sulfone, phosphate and ether) in LHCEs for 4.4 V Li||NMC811 cells. Electrochemical tests and electron microscopies show largely different cathode/electrolyte and anode/electrolyte stabilities with the solvents selected. Among the four LHCEs, the DME-LHCE demonstrates the best capabilities to stabilize both the LMA and the Ni-rich cathode. XPS analysis proves both the salt and the solvent in the LHCEs are involved in the reactions at the electrode/electrolyte interfaces. Further theoretical analysis reveals that the strong interactions between the salt and the solvent in the inner solvation sheath of the LHCEs greatly influence their individual reactivities. Their intermolecular proton/charge transfer processes are likely the key steps for the interfacial reactions. This work provides new crucial insights in understanding the electrolyte solvation structure and its implications on the electrode/electrolyte interfacial chemistry.

The PNNL team systematically studied different types of fluorinated solvents, including fluorinated ethers (BTFE, TTE), fluorinated carbonate (BTFEC), fluorinated borate (TFEB), and fluorinated orthoformate

(TFEO) as diluents for localized high concentration electrolytes (LHCEs). Significant differences were observed in the LHCEs (based on LiFSI-1.2DME high concentration electrolyte (HCE)) with these diluents. Among them, BTFEC coordinates with Li^+ in a second solvation shell beyond the first solvation with DME and FSI^-, which partially damages the high-concentration coordinated clusters in the HCE by forming a pseudo-LHCE; thus, the favorable features of HCE are lost in BTFEC-LHCE. BTFE, TTE, TFEB, and TFEO maintain the high-concentration salt clusters while the overall LiFSI concentration decreases in the electrolytes. In addition to the crucial role of the FSI^- anion in the SEI and CEI properties in LHCEs, the diluent molecules also make great contributions to the interfacial chemistries on both the cathode and the anode. TFEB significantly accelerates oxygen release in the Ni-rich NMC811 material and causes fast cathode decay because of its electron-deficient nature. BTFE-, TTE-, and TFEO-based LHCEs demonstrated high Li CEs of 99.4%, 99.5%, and 99.5%, respectively (Figure II.13.A.16a). For these three LHCEs, the high-voltage Li||NMC811 cell performance was determined by the cathode electrolyte interphase (CEI) chemistries under the testing conditions. The capacity retention of Li||NMC811 with the tested LHCEs follows the order TFEO-LHCE>TTE-LHCE> BTFE-LHCE> BTFEC-LHCE> SOA electrolyte> TFEB-LHCE. These results reveal the

selection rules for diluents to achieve stable cycling of high-voltage LMBs. The cycled cathodes were also characterized by annular bright-field scanning transmission electron microscopy (ABF-STEM) and high-angle annular dark-field (HAADF)-STEM. The significant amount of LiF found on these cathode primary particles supports previous findings on the critical role of LiF in CEI for effective interfacial protection. With the enhanced protection of a LiF-rich layer, no apparent transition metal (represented by Ni) dissolution and transport to the cycled LMA is observed in these electrolytes. In TFEO-LHCE, a thicker SEI of 5 nm is obtained on the NMC cathode, which successfully suppresses the cation-mixing phase transition. For the LHCEs studied in this work, the CEI thickness and LiF crystallinity follow the order of BTFE < TTE < TFEO, and the suppression of cation-mixing transformation follows the same order (Figure II.13.A.16b-f), which is also in good agreement with the cell capacity retention trend shown in Figure II.13.A.16a.

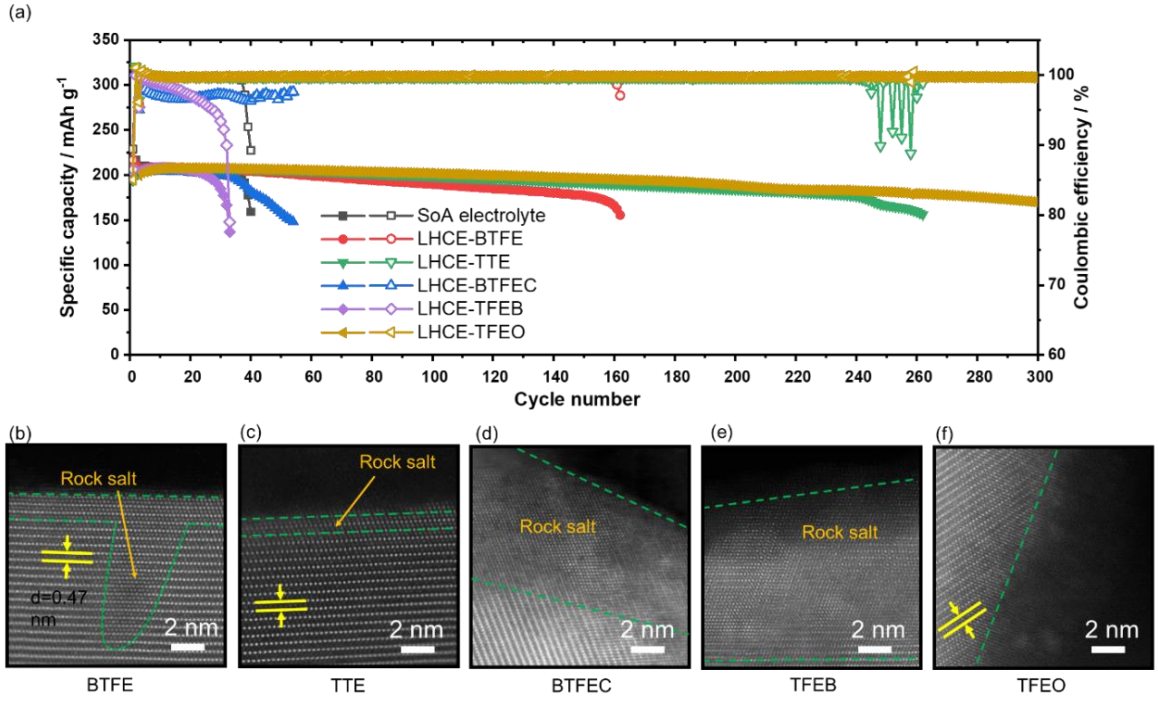

Figure II.13.A.16 (a) **Cycling** performance of the Li||NMC811 cells. (b-e) The ABF-TEM images of NMC811 cathodes after 100 cycles in LHCEs with different diluents (b) BTFE, (c) TTE, (d) BTFEC, (e) TFEB and (f) TFEO . The Li||NMC 811 cells were cycled at C/3 after two formation cycles at C/10 with 1.5 mAh cm^{-2} NMC811, 50 µm Li and 75 µL electrolyte

The UT Austin group investigated the capacity retention of an array of high-nickel-content compounds in lithium half cells, to validate their use in high energy density lithium-metal batteries. It was confirmed that layered-oxide cathodes with a nickel content > 90% can achieve > 220 mAh g^{-1} at C/3 rate when paired with lithium anodes, while operated at room temperature and without any constant voltage steps Figure II.13.A.17a). However, without extrinsic modifications, the cycle life of these materials does suffer. $LiNi_{0.94}Co_{0.06}O_2$ (NC9406) reaches a maximum capacity of 228 mAh g^{-1} and is projected to reach 80% capacity retention after 95 cycles. $LiNiO_2$ (LNO) reaches a maximum capacity of 223 mAh g^{-1} and reaches 80% capacity retention after 97 cycles. $LiNi_{0.95}Co_{0.02}Mn_{0.015}Al_{0.01}Mg_{0.005}O_2$ (NCMAM95) reaches a maximum capacity of 218 mAh g^{-1}, slightly below 220 mAh g^{-1}, and is projected to reach 80% capacity retention after 121 cycles. $LiNi_{0.9}Mn_{0.05}Co_{0.05}O_2$ (NMC900505) is substantially below 220 mAh g^{-1} at 208 mAh g^{-1}, but is projected to reach 80% capacity retention after 176 cycles. It is worth noting that capacity does not have to directly correlate to nickel content. By adjusting calcination parameters, such as temperature and oxygen pressure, pure-nickel LNO can give superior capacity retention compared to NC9406, though at the cost of reduced capacity. To improve the stability of the cathodes, a typical localized high-concentration electrolyte (LHCE), LiFSI-DME-TTE in a molar ratio 1:1.2:3 (Figure II.13.A.17b) was investigated. Aluminum-clad cell cases were used to prevent the corrosion of the LiFSI salt. By comparing the normalized capacity of these cells

to other cells subjected to the same temperature spike (Figure II.13.A.17c), it is clear that the capacity retention of the LHCE cells is dramatically higher than their counterparts employing a typical carbonate-based electrolyte (3:7 EC:EMC by volume, 1 M $LiPF_6$, 2% VC by mass). In addition, the LHCE cells with LNO cathodes deliver a capacity only a few mAh g^{-1} lower than the same cathode in the baseline electrolyte, and can still attain > 220 mAh g^{-1} at C/3 rate.

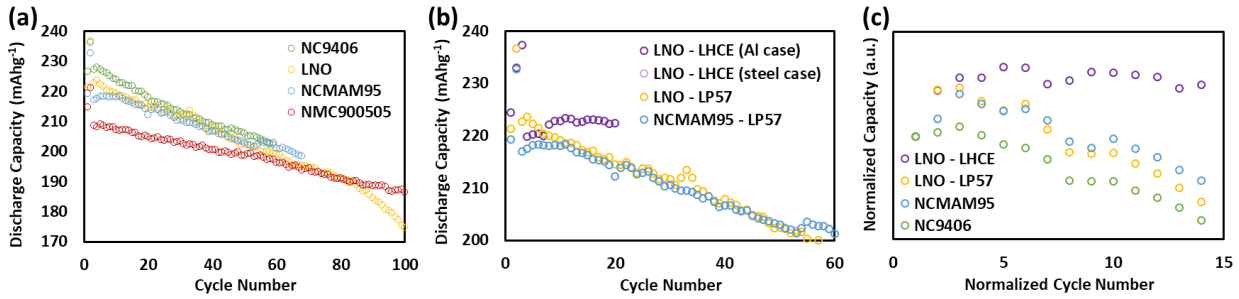

Figure II.13.A.17 Cycling performance of high-nickel cathodes. (a) Performance of cathodes with various compositions with the baseline electrolyte. (b) Comparison of cells with an LNO cathode and baseline electrolyte to those with a localized high-concentration electrolyte. (c) Capacity of cells immediately before and after an ambient temperature spike. Capacities and cycle numbers are normalized to the cycle immediately before the spike

The University of Washington (UW) team synthesized mesoporous N-doped hard carbon (mN-HC) as a potential alternative for high-energy-density Li battery anodes. mN-HC prepared via the Stöber method exhibits high specific capacity and high surface area. The as-obtained mN-HC exhibits a uniform spherical morphology with a diameter of ~500 nm (Figure II.13.A.18a). The X-ray diffraction (XRD) pattern reveals the amorphous, hard carbon nature of the as-obtained product. The d-spacing value of (002) is 0.408 nm, much larger than that of graphite (0.334 nm), which will facilitate Li insertion/extraction between the carbon planes. N 1s X-ray photoelectron spectroscopy (XPS) spectrum of the sample confirmed the doping of N in the hard carbon. The introduction of N could enhance the electronic conductivity of carbon and lower the polarization during Li insertion. The pore size distribution indicates a high portion of mesopores with a pore width of ~15 nm. The electrochemical performance of the mN-HC was tested in the localized high-concentration electrolyte (LHCE) (1.54M LiFSI in DME/TTE (1.2:3 by mol)). Figure II.13.A.18b displays the cycling performance of the mN-HC_{Li}/$LiNi_{0.8}Mn_{0.1}Co_{0.1}O_2$ (NMC811) and Li/NMC811 batteries in LHCE with an N/P ratio of 0.4 (1.6/4). The full cell with Li anode (1.6 mAh cm^{-2}) exhibits obvious capacity deterioration after 30 cycles, implying continuous Li loss during repeated Li plating/stripping. In comparison, the full cell with mN-HC_{Li} anode (1.6 mAh cm^{-2}) shows a capacity retention of 87.3% after 100 cycles with an average CE of 99.8%, indicating high lithiation/delithiation reversibility of the mN-HC_{Li}. In addition, the mN-HC_{Li}/NMC811 battery exhibits lower polarization than that of the Li/NMC811 at the same cycles. This pre-stored Li could compensate for the inevitable Li consumption, and hence improve the cycle performance.

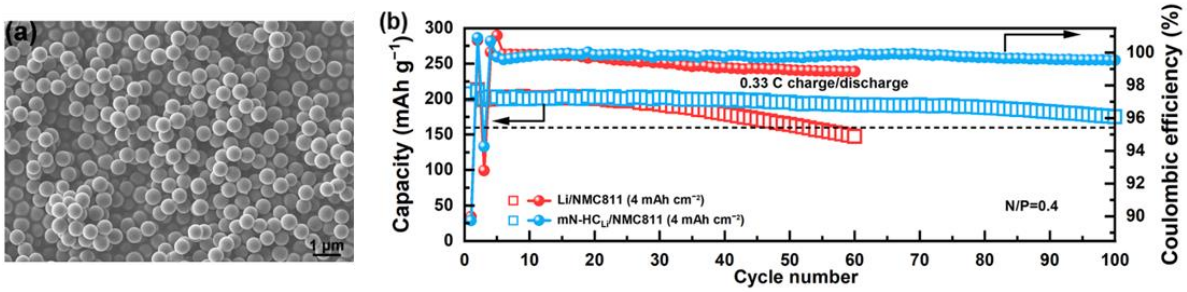

Figure II.13.A.18 (a) SEM image of the mN-HC materials. (b) Cycling performance of Li/NMC811 and mN-HCLi/NMC811 batteries in LHCE

2. Keystone project 2: Electrode architectures

UCSD team demonstrated that Sulfurized polyacrylonitrile (SPAN) is a promising cathode due to limited polysulfide dissolution in carbonate electrolytes arising from the physical confinement of the small molecular sulfur in the conductive polymer network which provides a high specific capacity of > 550 mAh g^{-1} and an average discharge potential of ~ 1.8 V. However, the Li metal Coulomb efficiencies (CEs) in carbonate electrolytes are still unsatisfied yet. Although ether electrolytes provide much better Li metal CEs, the SPAN is known to cycle poorly in common ether-based electrolytes due to the generation of soluble polysulfides, in which the reaction mechanism resembles that of elemental sulfur with poor cycling stability. The Liu group discovered a novel ether electrolyte, which is compatible with both Li metal and SPAN. The cycling performance of thin SPAN electrodes (1mAh cm^{-2}) in different electrolytes were compared. When cycled in the novel ether electrolyte, the Li||SPAN cell displayed a capacity of 579 mAh g^{-1}, and excellent cycling performance. As displayed by the voltage profiles where no capacity decay was observed over 1200 cycles (5000 hours of testing). In order to achieve a Li||SPAN pouch cell with energy density of > 250 Wh kg^{-1}, the areal capacity of the SPAN electrode should be larger than 5 mAh cm^{-2}. By increasing the areal mass loading of SPAN material to 10 mg cm^{-2}, the reversible capacity of SPAN electrode reaches 5.8 mAh cm^{-2} (Figure II.13.A.19a). The Li||SPAN cells were cycled using 1M $LiPF_6$ in EC/EMC (vol. ratio 1:1) at C/5 between 1.0 and 3.0 V. The Li||SPAN cell with high SPAN loading showed fast degradation (Figure II.13.A.19b). After 90 cycles, the capacity of the Li||SPAN cell with 10 mg cm^{-2} of SPAN degraded from 5.98 mAh cm^{-2} to 2.43 mAh cm^{-2}, which remains only 40.6% of its original capacity. As a comparison, the Li||SPAN cell using the novel ether electrolyte showed much better capacity retention with little capacity decay, which maintained a high capacity of 4.43 mAh cm^{-2} (Figure II.13.A.19c). These Li/SPAN coin cell results will enable us to reach 250 Wh/kg energy density in 2 Ah pouch design.

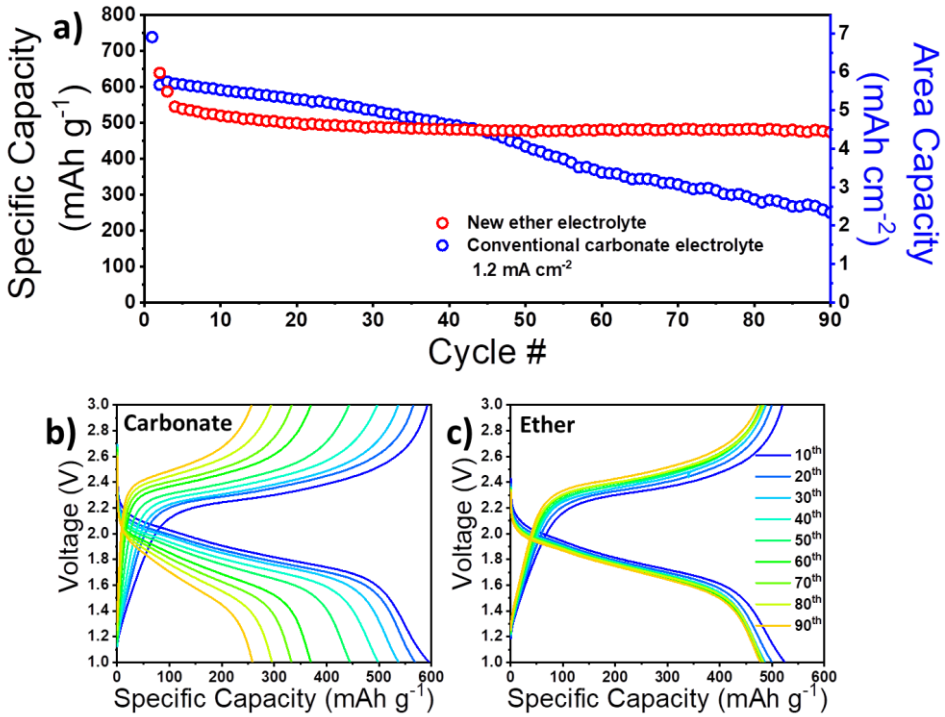

Figure II.13.A.19 The comparison of cycling performance of SPAN electrodes in different electrolytes. (a)-(c) Thick SPAN electrode with areal capacity loading of 6 mAh cm^{-2}, at 1.2 mA cm^{-2} (C/5). (b) Voltage profiles of thick SPAN electrode in conventional carbonate electrolyte. (c) Voltage profiles of thick SPAN electrode in novel ether electrolyte.

UCSD team used STEM EELS to probe the bonding environment evolution of Nitrogen (N), Sulfur (S) and Carbon (C) in SPAN cathode fabricated by UCSD at the pristine, discharged and charged states, providing

insight information about the interaction between Li and SPAN during cycling. *N K-edge*. The Figure II.13.A.20a shows the N K-edge at three different states. In the pristine state, two peaks that are associated to 1s to π*, and 1s to σ*, transitions are seen, which suggests that N exists in mostly the sp^2-hybridization state. After discharge, the N K-edge shows a decrease in the σ* peak intensity compared to the π* peak. This change potentially indicates that N is actively participating in the electrochemical reaction between Li and SPAN. After charging, the σ* peak was recovered to a similar intensity as the pristine state. The reversibility of the σ* peak intensity in N K-edge suggests that N plays an active reversible role in the electrochemical reaction. *C K-edge***.** Figure II.13.A.20b shows the C K-edge during cycling. In the pristine state, the C K-edge shows two peaks that are associated with 1s to π* and 1s to σ* transitions, which suggests that the C is also in a sp^2-hybridization state. The C K-edge and N K-edge show similar near edge structures at the pristine state, which indicates that C and N are in similar electronic environment and form an aromatic ring structure, consistent with existing literature. After discharge and charge, the most noticeable change happens in the relative peak intensity of the π* bonding peak. To better illustrate the change in the peak intensity, an intensity ratio π*:σ* is listed in Figure II.13.A.20d, which shows that the ratio changed from 0.9135 at pristine state to 0.7180 after discharge and then back to 0.7770 after charge. This peak intensity change shows that there is less degree of reversibility in the C bonding environment during cycling after the first discharge. *S L-edge*. As shown in Figure II.13.A.20c, for the S L-edge, the peaks at 165.7 and 228.7 eV corresponding to the S $L_{2,3}$ edge and S L_1 edge confirms the presence of S in the pristine SPAN. While there is no clear feature in the S L-edge after discharge, the S $L_{2,3}$ edge reappeared after charge, which shows a possible reversibility of S in SPAN. The S $L_{2,3}$ edge for Li_2S is also simulated by FEFF9. The simulated spectrum shows two characteristic peaks at 173.2eV and 180.9eV, which are not obvious in the measure S $L_{2,3}$ edge from both discharged and charged states. The lack of Li_2S signals in the cycled SPAN might explain why SPAN material shows an excellent stability during cycling, due to material losses into the electrolyte bulk caused by Li_2S oxidation to form polysulfides.

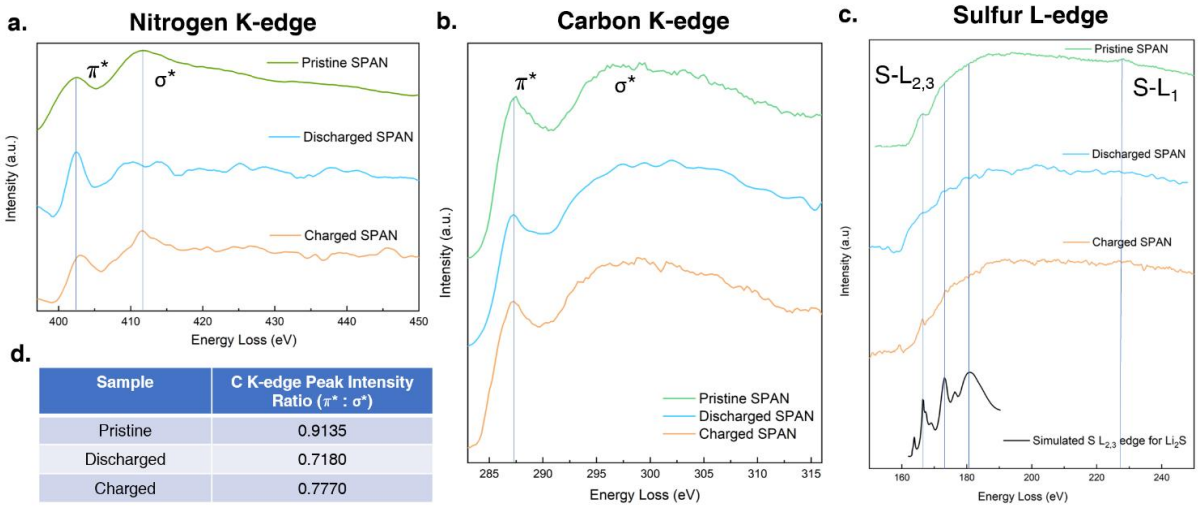

d.

Sample	C K-edge Peak Intensity Ratio (π* : σ*)
Pristine	0.9135
Discharged	0.7180
Charged	0.7770

Figure II.13.A.20 STEM EELS spectrum of a) Nitrogen K-edge; b) Carbon K-edge; c) Sulfur L-edge in Pristine, Discharged and Charged SPAN. d) table of C K-edge peak intensity ratio (π*: σ*).

BNL team (in collaboration with **UCSD** team) applied synchrotron-based diagnostic tools to understand why addition of $LiNO_3$ can enable stable cycling of SPAN in ether-based electrolyte (DME/DOL). This is important because only ether-based electrolyte can be compatible with lithium metal anode. By using spatially-resolved x-ray fluorescence (XRF) microscopy combined with x-ray absorption spectroscopy (XAS), it was found that in pure DME/DOL electrolyte, the Li_2S_x that forms on the cathode side after one discharge-charge cycle shuttles to the Li side, resulting in the fast capacity degradation (Figure II.13.A.21). After adding $LiNO_3$, the Li_2S_x in the SPAN cathode is retained via the formation of a robust cathode electrolyte interphase (CEI) layer, leading to dramatic improvement in the cyclability of SPAN in ether electrolyte. Based on the

knowledge learned from detailed XRF/XAS and electrochemical study, **UCSD** team has successfully demonstrated the stable cycling of SPAN cathode with high areal loading (>6.5 mAh cm^{-2}) with lean electrolyte, showing promising Li-SPAN cell performance under practical conditions (Figure II.13.A.22).

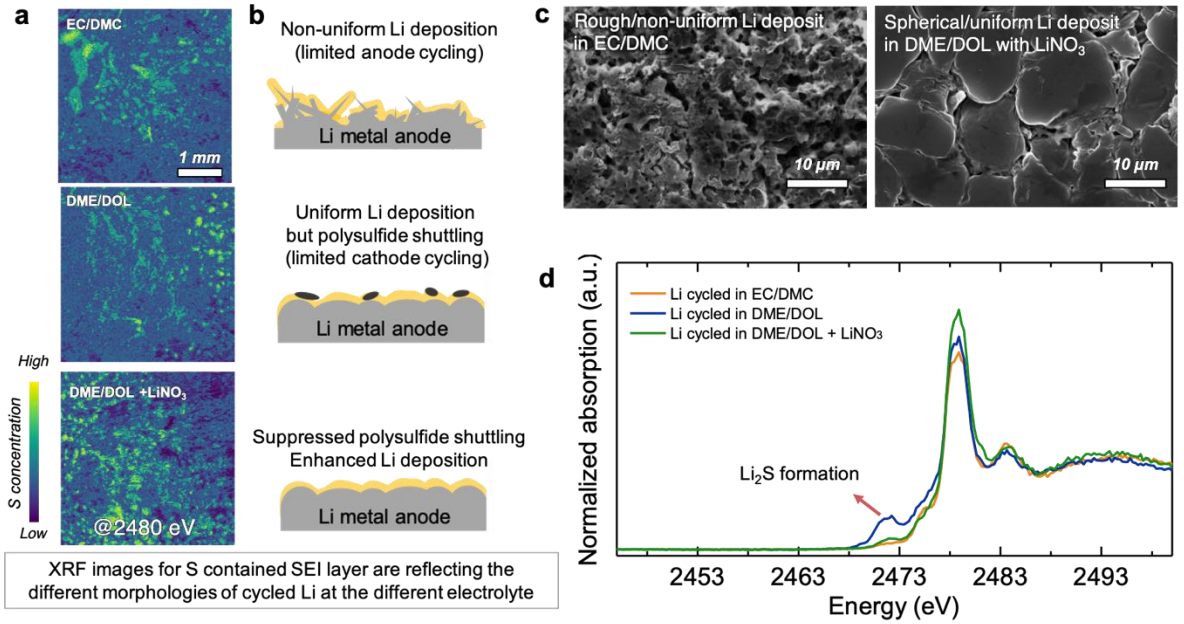

Figure II.13.A.21 (a) XRF image of Li metal anodes cycled in EC/DMC, DME/DOL, and DME/DOL with LiNO3, measured at an incident beam energy of 2480 eV. (b) Corresponding schematic sketch of a cross-section view of Li metal anode for each case and (c) SEM images for Li metal anode after 100 cycled in EC/DMC and DME/DOL with LiNO3. (d) Normalized S K-XANES measured from the selected area from (a).

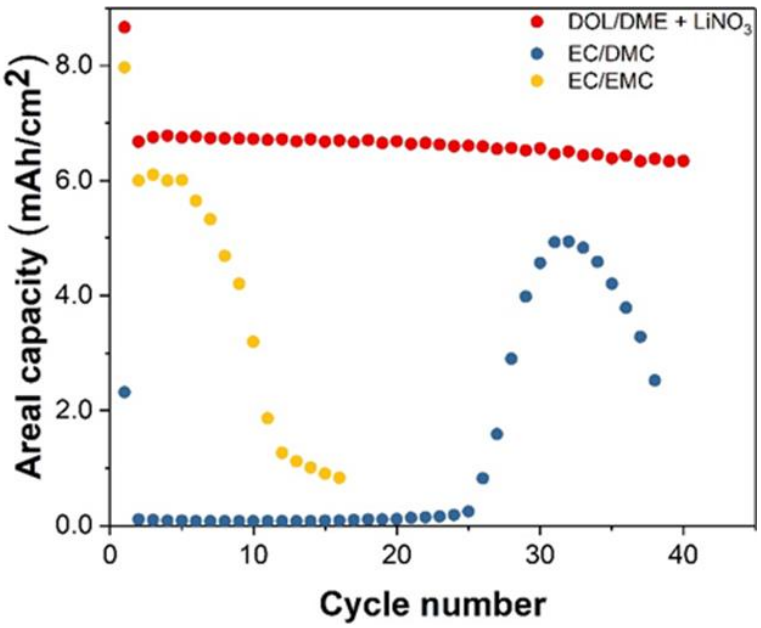

Figure II.13.A.22 Lean electrolyte (3g/Ah) cycling performance of thick SPAN electrode in Carbonates and DME/DOL with LiNO3 (azure blue dots).

PNNL evaluated the long-term cycling performance of Li||SPAN coin cells with DME-based LHCE and $LiPF_6$/EC-EMC+VC control electrolyte, in which the high areal loading (>6.5 mAh cm^{-2}) SPAN cathode (from Liu's group at UCSD), medium-thick (250 µm) Li and flooded electrolyte (75 µL) were used. As shown in Figure II.13.A.23, the discharge areal capacity in LHCE reaches 6.1 mAh cm^{-2} after initial activation and maintains at 5.3 mAh cm^{-2} after 400 cycles at C/5 under 25 °C (1C = 6.0 mAh cm^{-2}), corresponding to a capacity retention of 86.9%. Moreover, with LHCE, the Li||SPAN cell exhibits an average coulombic efficiency (CE) ~100% during the 400 cycles, indicating inhibited side reactions on the SPAN cathode and the Li anode and limited resistance growth during cycling. By comparison, although the Li||SPAN cell with Control exhibits higher capacities during both the formation and the following first 10 cycles than the cell with LHCE, it suffers from a rapid capacity drop after only about 15 cycles at C/5, and the remained capacity after 50 cycles is negligible. The evaluation of Li||SPAN cells with DME-LHCE under practical conditions will be performed.

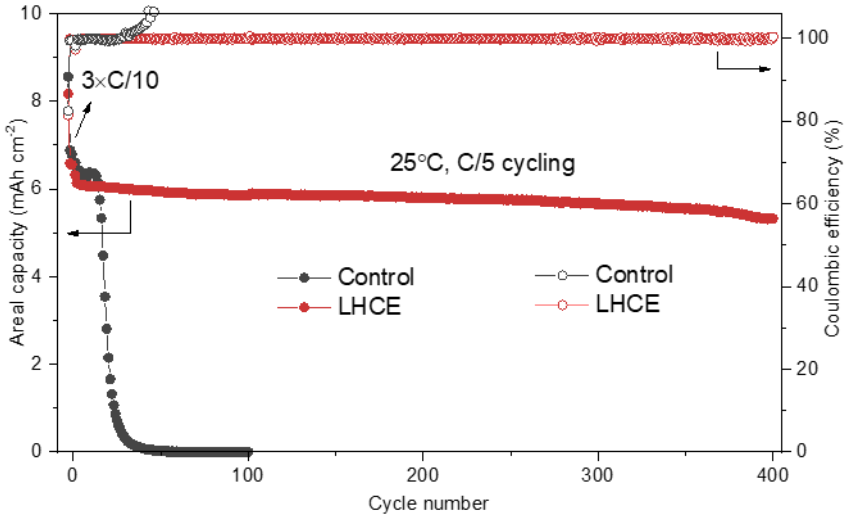

Figure II.13.A.23 Cycling performance of Li||SPAN coin cells with two different electrolytes of Control and LHCE at C/5 (1.2 mA cm^{-2}) between 1.0-3.0 V.

PNNL team has made significant progress in understanding the electrolyte distribution along the large-size and porous electrode during cell cycling. A multi-physics simulation coupling Darcy porous flow and species transportation was performed. The reaction rate was estimated based on the electrolyte amount and the cycle life of the Li-S pouch cell. The electrolyte transfer process was modeled by solving the time-dependent diffusion equation for the spare volume. For electrolyte diffusion in the porous cathode and separator, an effective diffusion coefficient considering porosity and tortuosity was adopted. For simplicity, one quarter of the cathode area (Figure II.13.A.24a) was simulated and the corresponding results are depicted in Figure 6. After electrolyte injection and upon a long rest period (24 hr), the electrolyte diffuses through the interconnected nanopores to wet the nanosized domains of the electrode (Figure II.13.A.24b). The excess portion of electrolyte is stored along the edge area after vacuum sealing the cell. Upon cell cycling, electrolyte depletion starts because of the unavoidable side reactions on both the cathode and Li anode. According to Lewis' theory, as driven by electrolyte concentration gradient, the electrolyte will redistribute to replenish the electrolyte loss. However, such diffusion is hindered by the high tortuosity of the nano-porous electrodes, especially when stacking pressure is applied. Note that the 100% electrolyte content means that all the pores are filled with electrolyte. As long as the content is less than 100%, the electrode may suffer from electrolyte deficiency; i.e., pores are not fully wetted by electrolyte. Simulation results indicate that the electrolyte content maintains >95% of its original volume and is sufficient to promote the S reaction in the first 50 hours of cycling (Figure II.13.A.24c), which agrees well with the high S utilization rate in the first cycle as reported earlier. During the 100–150 hours of cycling (2–3 cycles) (Figure II.13.A.24d and Figure II.13.A.24e), the electrolyte amount keeps decreasing with a steeper electrolyte concentration gradient. Because of the low

current density, the decreasing electrolyte will not yet cause significant cell polarization at such low rates and few cycles. However, after 200 hours of cycling, the continuous electrolyte consumption triggers the electrolyte deficiency emerging from the center (Figure II.13.A.24f). More than half of the electrodes (65%) have an electrolyte content less than 85% (Figure II.13.A.24g and Figure II.13.A.24h). The electrolyte distribution inhomogeneity deteriorates over time and imposes electrochemical polarization on S conversion, and eventually discontinues the electrochemical reactions starting from the center regions. This is supported by the experimental observation that the exaggerated energy decay was observed starting during the 6th cycle (reported earlier and not shown here). The electrolyte distribution inhomogeneity is attributed to the competition between the electrolyte diffusion across the nano-porous electrode and the chemical consumption. Therefore, if the electrolyte diffusion during cycling is enhanced, the electrolyte inhomogeneity problem will be significantly reduced.

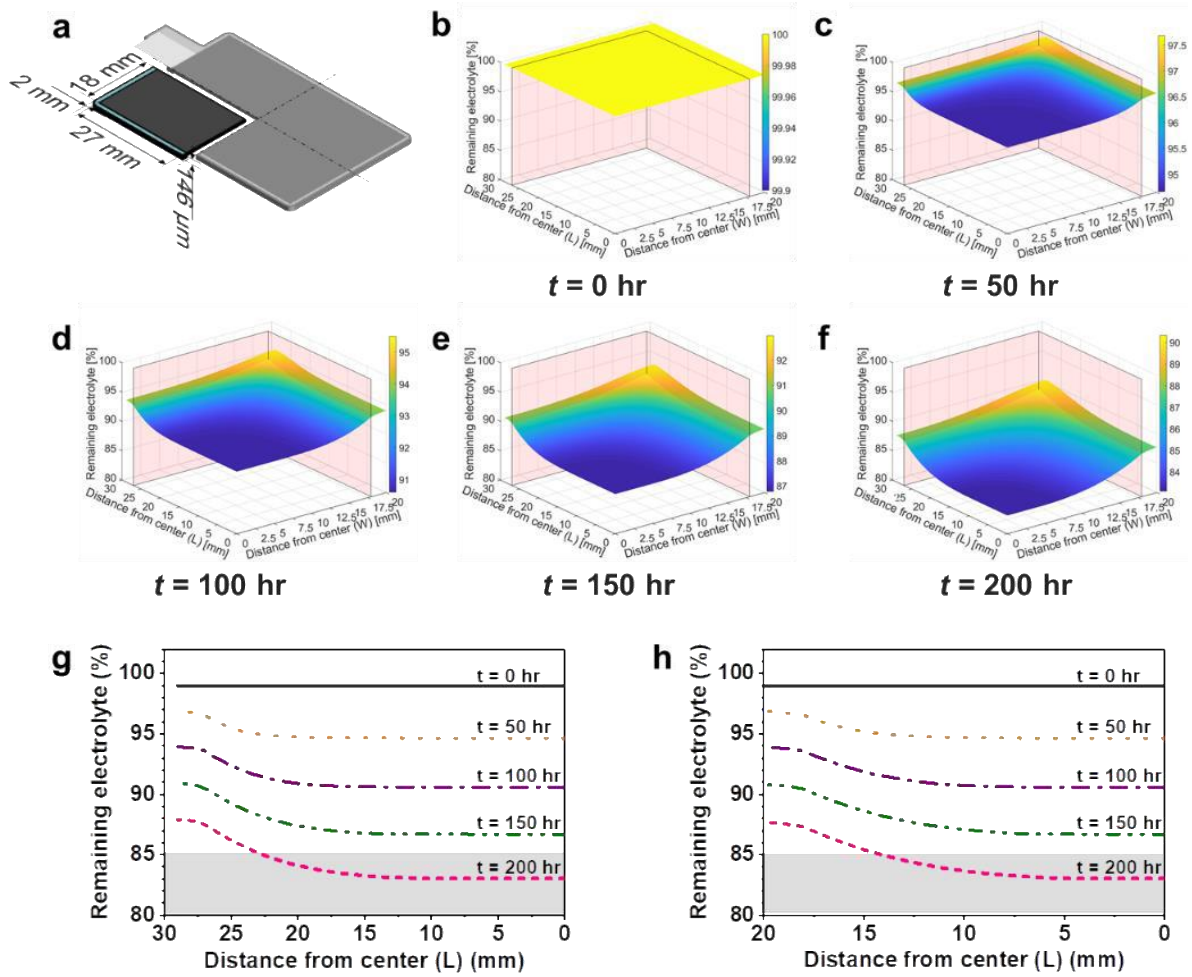

Figure II.13.A.24 **The transient simulation of electrolyte diffusion and redistribution in a large-size pouch cell upon cycling.** **(a)** Schematic illustration of the electrode dimension selected for the simulation with an electrolyte diffusion coefficient of 1 × 10-10 m2 s-1. Electrolyte distribution at half of the electrode thickness (0.073 mm) after different reaction time. **(b)** t = 0 hr. **(c)** t = 50 hr. **(d)** t = 100 hr. **(e)** t = 150 hr. **(f)** t = 200 hr. Electrolyte content (%) variation at different times and locations: **(g)** at long line of (x, 0 mm, 0.073 mm); **(h)** at short line of (0 mm, y, 0.073 mm).

UW modeling group successfully developed a two-dimensional (2D) moving boundary model to study the 2D nature of transport in the electrolyte and the resulting deposition profile on the Li anode. The key inputs to this model are applied current density, design parameters, transport parameters for the liquid phase, and exchange current density on the anode. The model provides the two-dimensional distribution of the concentration, anode

potential, deposition profile, and rate of deposition as the outputs. This model and pressure aware model can be used to study how charging rate, anode length, separator length and thickness, and cycling influence the deposition profile on the anode. As a comparison to the 1D model developed previously, the voltage obtained using the 1D and 2D models for 10 cycles at charging rates of 1C and C/3 shown in Figure II.13.A.25. Voltage trends observed by the 2D model does not seem to be captured by the 1D model. This can be attributed to the fact that the 1D model cannot capture 2D transport, and the resulting distribution in concentration and liquid phase potential along the x direction. This further highlights the importance of using 2D model to study performance of lithium metal anode.

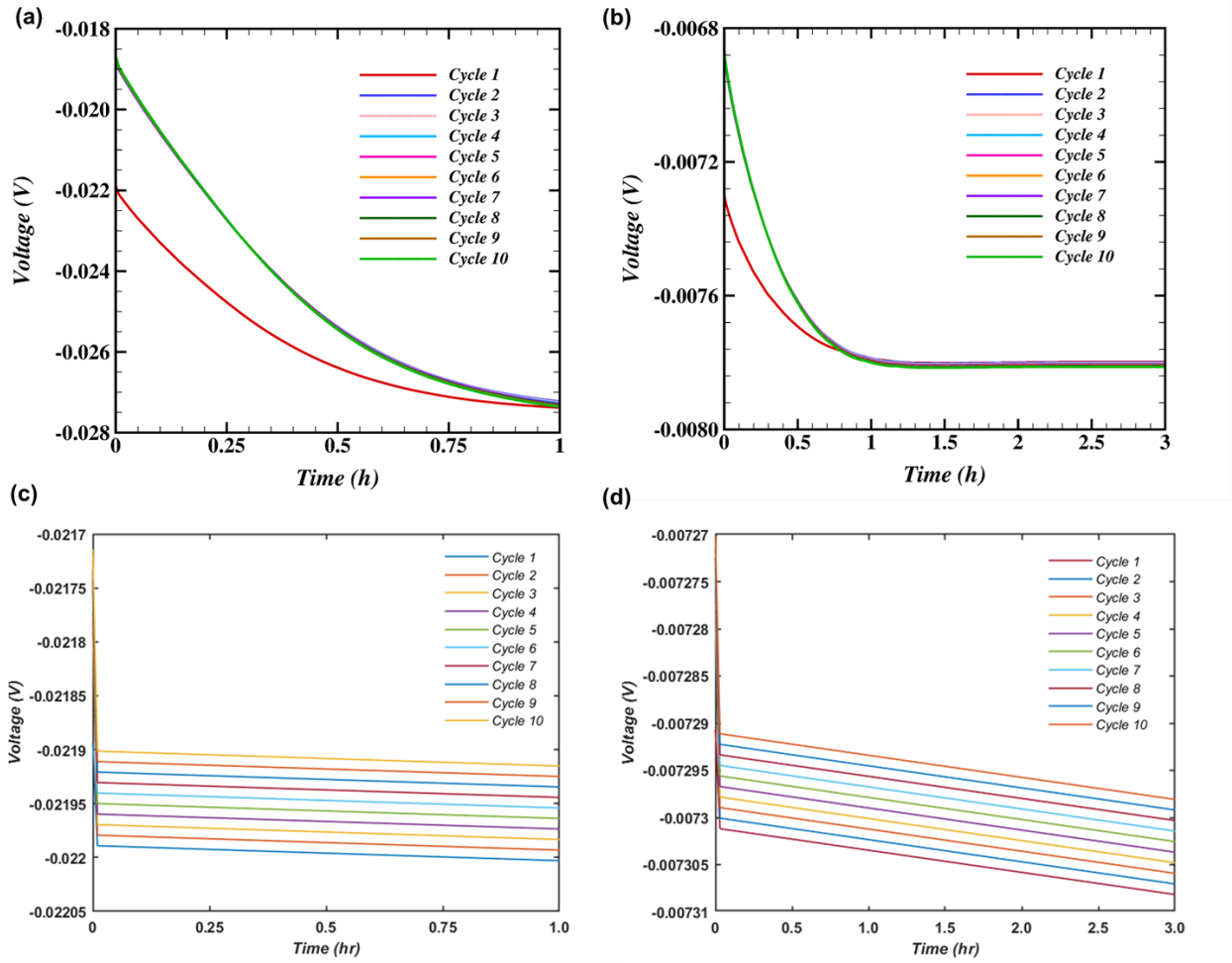

Figure II.13.A.25 Voltage versus time for 10 cycles (a) 2D model 1C rate (b) 2D model C/3 rate (c) 1D model 1C rate (d) 1D model C/3 rate

UW team revealed in the past that both surface coating and doping on NMC811 can reduce polarization and improve cycling performance. However, a long activation period is needed for the coated cathode because the low-conductivity coating layer reduces the electron-transfer rate between particles. In FY2020, they try to resolve this issue by direct coating on cathodes without disrupting the inter-particle electronic/ionic pathways. Figure II.13.A.26a shows the initial charge–discharge curves of the pristine and LATP($Li_{1.3}Al_{0.3}Ti_{1.7}(PO_4)_3$)-coated Al-NMC811 (Al-doped NMC 811) electrodes. The Al-NMC811 cathode exhibits an initial reversible capacity of 222.2 mAh g^{-1} with a Coulombic efficiency of 89.7% at 0.1 C between 2.8 V and 4.4 V, similar to those of LATP-coated Al-NMC811 electrode (223.2 mAh g^{-1}, 89.5%). After the formation cycles, both Al-NMC811 and LATP-coated Al-NMC811 cathodes deliver similar discharge capacities and Coulombic efficiencies at 0.33 C (Figure II.13.A.26c). Figure II.13.A.26b displays the charge–discharge curves of both

electrodes at the 50th cycle. The two curves are almost overlapped, indicating the two electrodes show similar reversible capacity and polarization. These results demonstrate that direct LATP coating on Al-NMC811 electrodes will not affect their electrochemical.

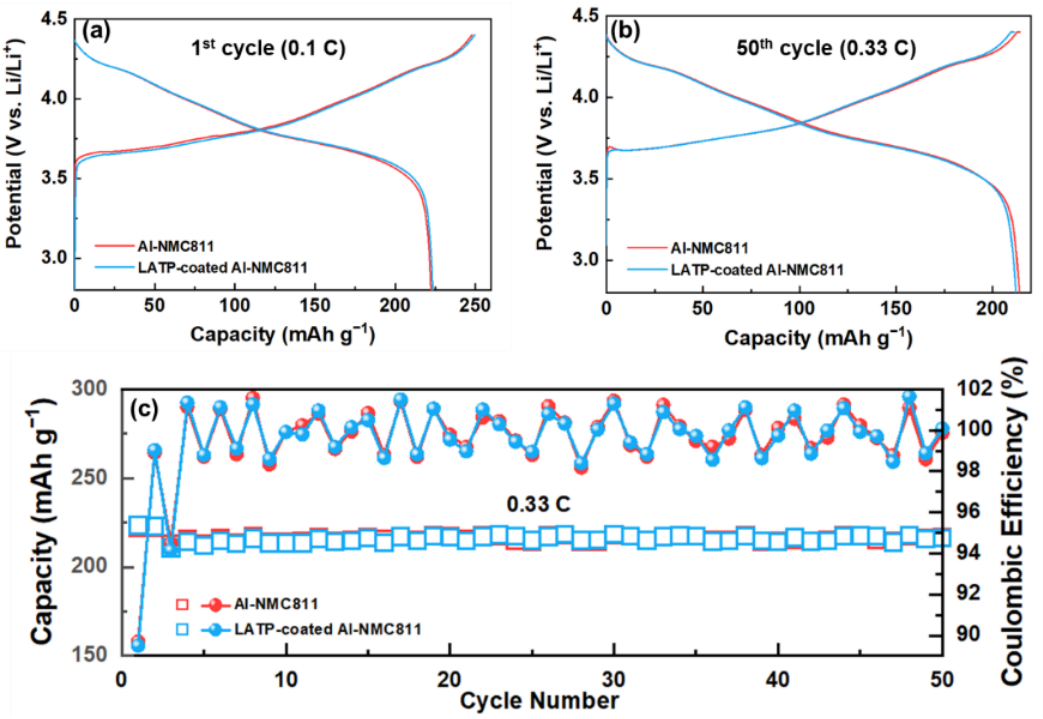

Figure II.13.A.26 (a) Initial and (b) the 50th charge–discharge curves of pristine and LATP-coated Al-NMC811 electrodes. (c) Cycling performance of pristine and LATP-coated Al-NMC811 electrodes

UW team developed ion conductive coatings on the polymer separator to regulate lithium deposition. They have focused on minimizing the thickness of the coating using nanomaterials. In this regard, the polyethylene (PE) separator was coated with a nano-size LATP (Li-Al-Ti phosphate) by a doctor blade coating method. The average thickness of the separator is directly measured by a micrometer caliper and it shows that the thickness of bare PE and LATP-coated separator is 15.7 μm and 17.1 μm, respectively (Figure II.13.A.27a and Figure II.13.A.27b). Therefore, the thickness of the coating layer is only 1.4 μm. They also used SEM to measure the thickness of the coating layer. As shown in Figure II.13.A.27c. the thickness of the LATP coating layer is ~2.6 μm, thinner than those of previous coated separators (~5 μm) based on micron meter-sized LATP particle.

Figure II.13.A.27 Photograph of the recorded thickness of (a) PE and (b) LATP-coated PE separator by a micro-meter calliper. (c) SEM image of the cross-section of the LATP-coated PE separator.

Stanford University team discovered that tortuosity is a critical parameter affecting the morphology and electrochemical performances of hosted Li anodes. They synthesized three types of hosts: vertically aligned (VGA), horizontally aligned (HGA), and random reduced graphene oxide (rGO) (RGA) electrodes with

tortuosity of 1.25, 4.46, and 1.76, respectively. They show that high electrode tortuosity causes locally higher current density on the top surface of electrodes, resulting in thick Li deposition on the surface and degraded cycling performance. Low electrode tortuosity in the vertically aligned rGO host enables homogeneous Li transport and uniform Li deposition across the host, realizing greatly improved cycling stability (Figure II.13.A.28). Using this principle of low tortuosity, the designed electrode shows through-electrode uniform morphology with anodic Coulombic efficiency of 99.1% under high current and capacity cycling conditions Figure II.13.A.29).

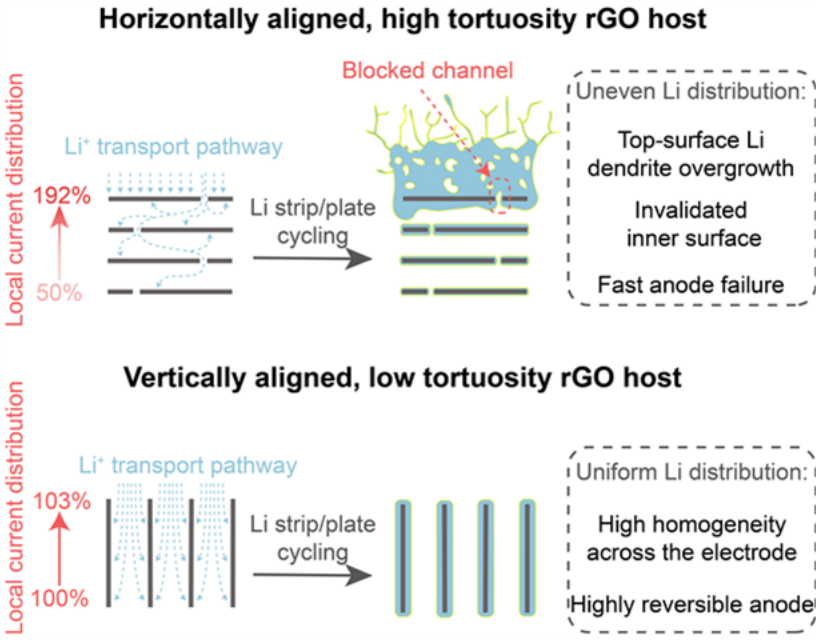

Figure II.13.A.28 The tortuosity of reduced graphene oxide as a lithium host has a profound impact on lithium deposition. Vertically aligned host with minimal tortuosity results in more uniform lithium deposition in the host.

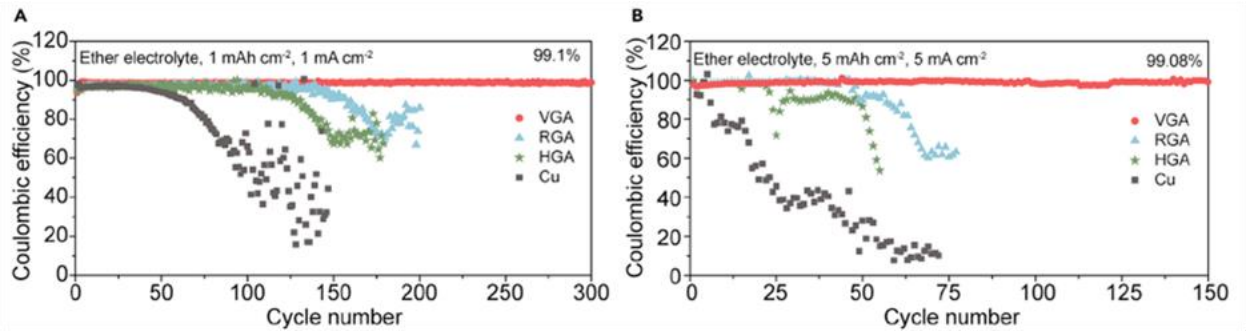

Figure II.13.A.29 In an ether electrolyte (1M of LiTFSI in 1:1 v/v DOL/DME with 1% $LiNO_3$), VGA clearly outperforms RGA and HGA due to its low tortuosity. LiTFSI: Lithium bis(trifluoromethanesulfonyl)imide; DOL: dioxalane; DME: Dimethoxyethane.

UCSD team explored a 3D host based on porous copper (Cu) obtained from dealloying Cu-Fe alloys to examine the effects of key physical properties, such as the surface area, pore size and tortuosity, on the Li plating morphology and cycling performances. By tuning the melting method and the atomic percentage (at%) of Cu during the synthesis, four types of Cu current collectors with a variety of pore sizes have been synthesized: 30Arc (30at% of Cu with Arc-melting), 20Arc, 10Arc and 30Furnace (30at% of Cu with Furnace-melting). The three key physical parameters (surface area, pore size, tortuosity) of the porous Cu films mentioned above were quantified by laboratory X-ray microscale computed tomography (micro-CT). With spatial resolutions of 0.7834µm or 1.07µm depending on the pore size of the sample, the 3D tomography of

each porous Cu film was obtained from the micro-CT (Figure II.13.A.30d, e). With the high-resolution 3D tomography, post measurement analysis was performed by Amira-Avizo software to calculate pore size distribution, tortuosity and surface area of the porous copper films. The pore size distribution in each porous Cu film is shown in Figure II.13.A.30a. Because of the high at% of Cu and the fast melting rate, 30Arc gives the smallest pore size, which averages at around 8μm. For the Arc-melting samples, as the at% of Cu decreases in the Cu-Fe alloy, the average pore size of the resulting porous copper films increases. Because of the weak structure of the 10Arc, furnace was used to make the porous Cu film (30Furnace) with the largest pore size, which has an average pore size of 25μm. The tortuosity was obtained from the Centroid Path Tortuosity module in the Amira-Avizo which computes the centroid of each plane and the corresponding path length between the centroids along the z-axis (electrode thickness) to determine the tortuosity. With the smallest average pore size (~8μm), 30Arc shows the highest tortuosity, which ranges from 1.9 to 2.05 as the thickness increases to 100μm (Figure II.13.A.30b). With the increased pore size in the 20Arc (~11μm), the resulting tortuosity decreases since the larger pores provide a transport pathway for ions with less obstacles. As the pore size further increases in the 10Arc (~20μm), tortuosity further decreases to around 1.10 with a thickness of 100μm. However, when the melting method was changed to make the 30Furnace samples, because of the higher at% of Cu, the tortuosity slightly increases to 1.25 in these porous copper films. The effective surface area for each porous copper films with 7mm diameter is listed in Figure II.13.A.30c. With the smallest pores, 30Arc shows the highest effective surface area of 29.49 cm^2 in a 7mm diameter piece, which is 76 times larger than that of the Cu foil with the same diameter. The effective surface area decreases as the pore size increases in the porous Cu. Nonetheless, the porous Cu with the highest pore size, 30Furnace, still has almost 10 times higher surface area than the Cu foil does.

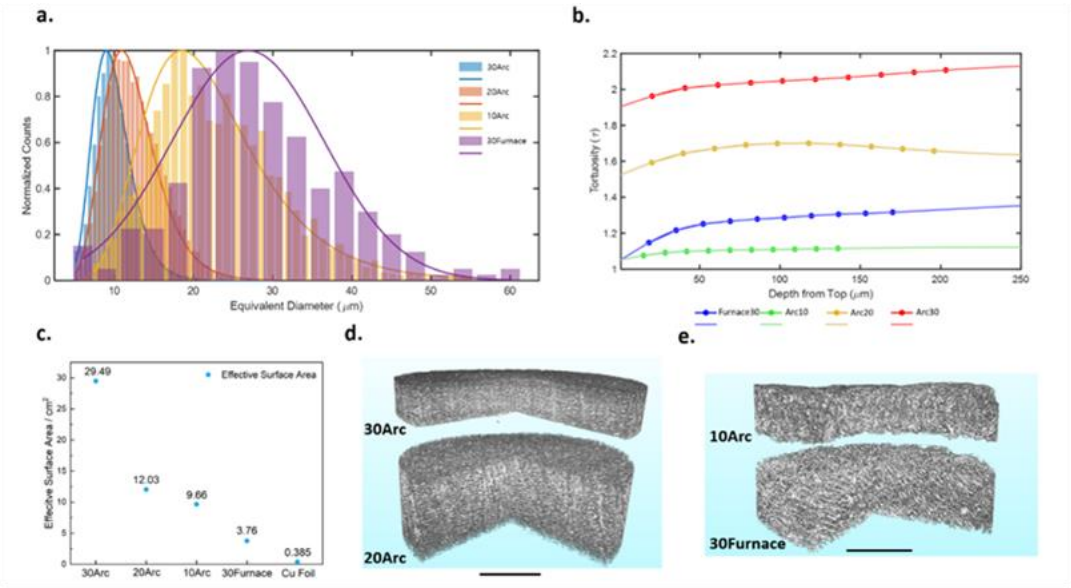

Figure II.13.A.30 a) histogram of the pore size distribution of the porous copper; b) tortuosity of the porous copper as a function of depth; c) effective surface area in the porous copper; d) the 3D tomography of 30Arc and 20Arc with resolution of 0.7834μm; e) the 3D tomography of 10Arc and 30Furnace with resolution of 1.07μm; the scale bar indicates 200μm.

After obtaining the tortuosity of each porous copper sample with different pore sizes, tortuosity of the 3D current collector was systematically studied by **UCSD** team to understand its influence on the Li metal deposition distribution. The effect of tortuosity was studied by cross-section SEM imaging of the deposited lithium within the porous copper. Figure II.13.A.31 shows the distribution of the deposited lithium in the porous coppers after being plated for 20 hours at 1mA/cm^2. The Back-Scattered Electron (BSE) images (Figure II.13.A.31e-h) give a clear view of how lithium is distributed across the whole porous copper: the brighter region is copper and darker region is lithium. The boundary between vacuum and lithium is marked by white lines for reference. Schematic illustrations were also made to better illustrate the lithium deposition's

spatial distribution and morphology in the different samples. With the smallest pore diameter (~4 µm) and the highest z-directional tortuosity (1.95), the 30Arc samples showed the greatest inhomogeneity of deposited lithium (Figure II.13.A.31a, e, i). Most of the deposited lithium accumulated near the top surface of the porous copper. The space under the surface, where the lithium was desired to be deposited, was devoid of lithium deposition. This inhomogeneous distribution of deposited lithium can be attributed to the fact that the complex structure of porous copper with small pores and high tortuosity will block the incoming lithium from entering the empty space inside the structure. As a result, most of the lithium deposited near the top surface while the extra surface/pores that was provided in the 3D structure was not utilized. As the pore size was increased to 10 µm, a decrease in the z-directional tortuosity to 1.60 was observed (from 1.95). The distribution of the deposited lithium in the porous copper changed dramatically (Figure II.13.A.31b, f, j). More lithium was found to be deposited inside the pores of the porous copper instead of on the top surface. The high utilization of the empty pores can help to increase the contact area between lithium and the copper, which would lower the local effective current density and result in a more uniform morphology. Upon further increase in the pore size (~20 µm) and decrease in the tortuosity (1.08), more lithium was found to grow further inside the pores (Figure II.13.A.31c, g, k). The deposited lithium grew in a bulky and cluster-like morphology inside the porous copper, which is less homogenous compared to the 10 µm pore sized porous sample. Using porous copper with the largest pore size (~25 µm), the distribution of the deposited lithium is similar to the previous 10Arc sample. However, the increase of the pore size also led to the decrease in specific surface area. Therefore, the morphology of the deposited lithium changed from bulky chunk type to whisker-like (Figure II.13.A.31d, h, l). This change of morphology would eventually lead to the formation of inactive metallic lithium and cause the decrease in coulombic efficiency. Based on the observations above, the effect of the tortuosity can be summarized as follows: 1) The narrow and tortuous structures, such as the case in the 30Arc sample (with a tortuosity of 1.95), would largely hinder the diffusion of lithium ions, leading to an inhomogeneous distribution of the deposited lithium. 2) The inhomogeneous distribution would also under utilize the empty space and surface area provided by the 3D structure and possibly lead to the formation of lithium whiskers after the top surface is fully covered by deposited lithium.

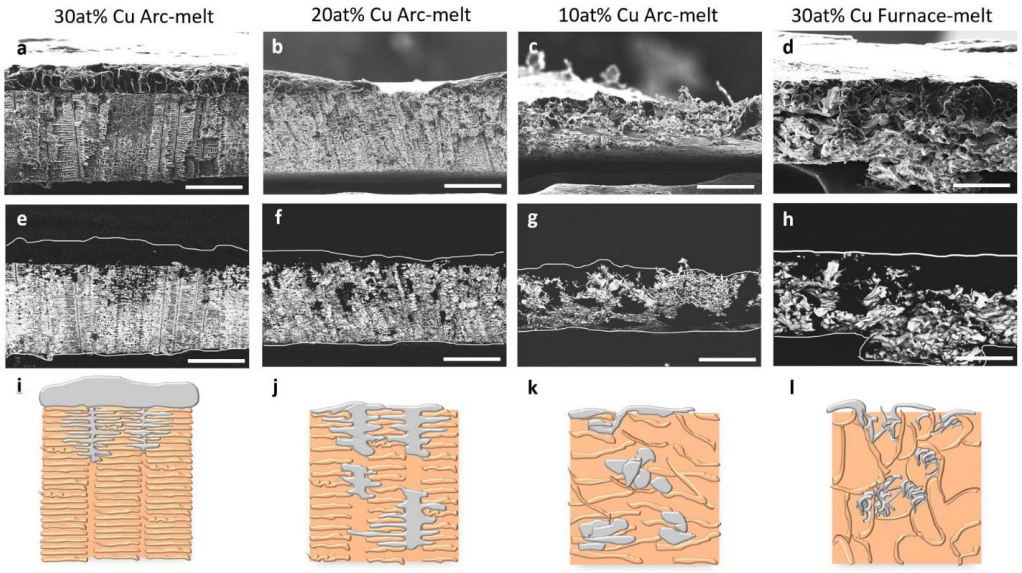

Figure II.13.A.31 a-d) SEM Cross section images, e-h) Back-Scattered Electron images and i-l) schematic illustration of lithium distribution in the cross-section of the porous copper with lithium deposited within different parts of the structure. All samples were plated to 20mAh/cm^2. The scale bars indicate 50µm in all images.

3. Keystone project 3: Cell fabrication, testing and diagnosis

With the significant increase in research associated with lithium metal batteries it has become more important for researchers to understand the safety related issues for all stages of the research and development. **PNNL** and **Idaho National Lab. (INL)** team consolidated knowledge on the use of lithium metal for preparation,

testing, disposal of battery cells and cell materials. As shown in Figure II.13.A.8 several different types of possible safety risks were identified throughout the research procedures from personnel training to materials handling and testing. Key recommendations include the proper tools and materials to be used to handle lithium metal and to disassemble cells. Personnel trainings needed prior to start research for new researchers and appropriate measures and methods for disassembly and disposal of used cells. In addition to this published paper, the lessons learned, and knowledge gained were shared within the Battery500 consortium through several discussions involving both senior and junior researchers. This is very critical to achieve the development of new high energy battery technologies.

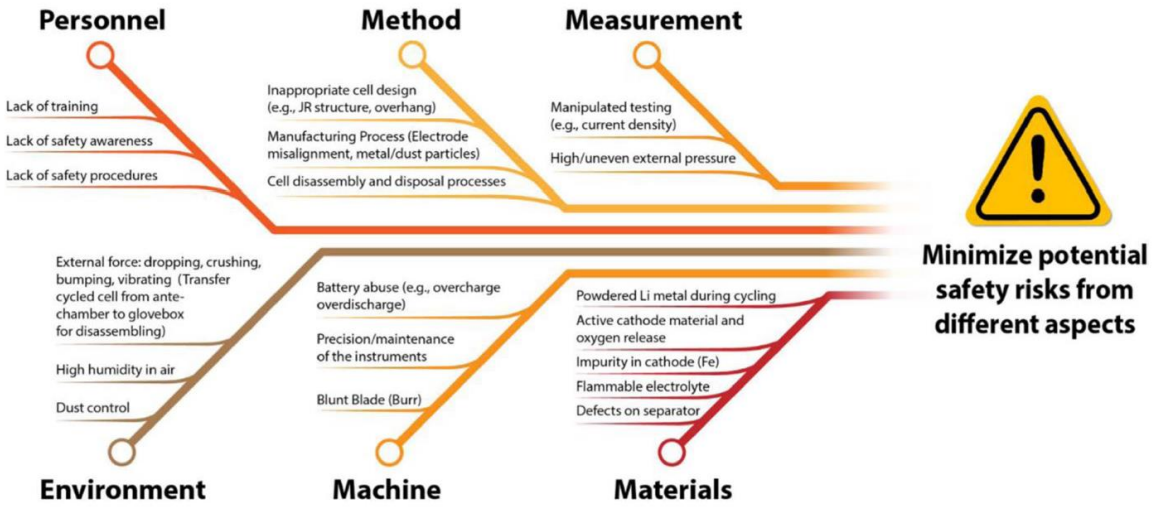

Figure II.13.A.32 Schematic showing different types of risk associated with lithium metal use, preparation of lithium metal batteries, and cycling of lithium metal batteries. From reference.

In work related to increasing the understanding of Li-S batteries experiments looking at characterizing and identifying the failure of different S cathode support structures was also undertaken. INL used a modified Pechini method to synthesize an assortment of porous carbon host materials that included core-shell structured NiO@Ni/Ni_3S_2@Ni materials on the carbon surfaces. The work helped identify key differences in the electrode kinetics. As shown in Figure II.13.A.33 without the Ni-based core-shell materials, the performance is rather poor. With the addition of the core-shell structures, electrode kinetics was significantly improved, and higher capacity was gained in the cathode. The inclusion of the core-shell structures also reduces the rate of capacity fade of the cell. To better understand the difference in the performance of the electrodes which were all tested using lean electrolyte more direct analysis of the charge and discharge profiles (Figure II.13.A.33b) was performed. The Ni_3S_2-carbon cathode exhibits a much lower polarization compared with the NiO-carbon cathodes, demonstrating that the surface transformation from NiO to Ni_3S_2 in cathode design significantly enhances the kinetics and reversibility of the electrochemical redox reaction of sulfur, which is consistent with the voltammetry results in Figure II.13.A.33c. While both the Ni_3S_2@Ni -carbon and the NiO@Ni-carbon cells produced similar coulombic efficiencies, the Ni_3S_2@Ni-carbon cells had a significantly lower fade rate of 0.18% per cycle. To further investigate the cause for the enhanced performance of the Ni_3S_2@Ni-carbon cell, the discharge curves were separated into an upper and lower regime, where the upper regime corresponds to the reduction of S_8 to Li_2S_4 and the lower regime corresponds to lithium polysulfides being transformed to Li_2S. In both regions, Ni_3S_2@Ni-carbon cell displays less significant capacity fade highlighting increased, prolonged utilization of the sulfur in the cathode. Using DFT analysis it becomes evident that the binding energies with Ni_3S_2 are significantly stronger suggesting better wetting and ultimately enhanced sulfur utilization. Combining these methods provide a better performance analysis to guide cell design and to quantify the performance fade for Li-S cells.

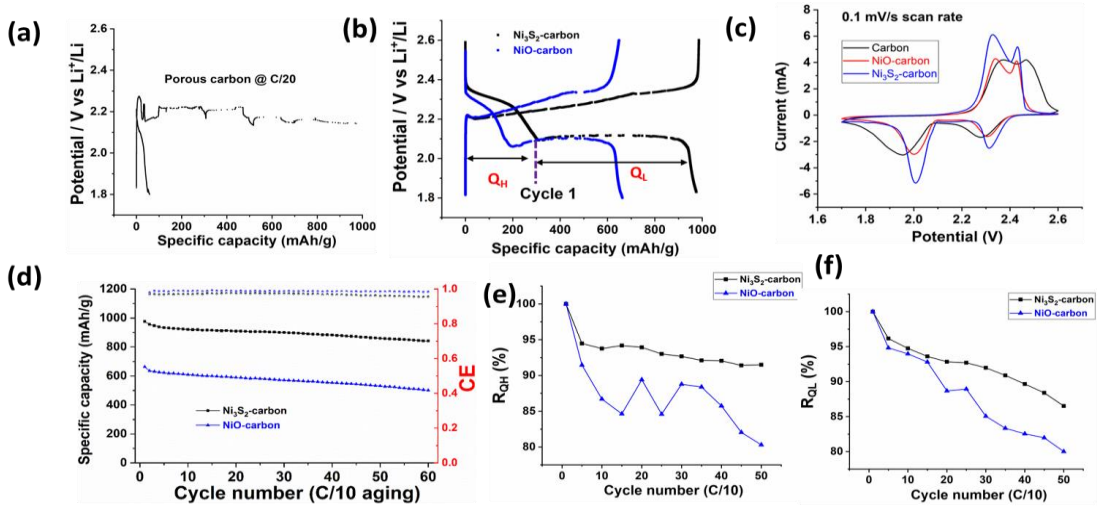

Figure II.13.A.33 (a) shows that the cells using carbon-only cathode cannot reach the upper cutoff potential and only delivers a very limited amount of discharge capacity under the lean electrolyte condition even during C/20 formation. (b) shows the discharge/charge profiles of NiO-carbon and Ni_3S_2-carbon materials at the first cycle under the lean electrolyte condition, and their discharge capacities are 690 and 1128 mAh/g, respectively. (c) includes CV curves shown for the various cathode materials. In (d) cycling performance is shown while (e) and (f) show the retention (normalized to discharge capacity of first aging cycle) of capacities for upper-plateau (Q_H) and lower-plateau (Q_L) regions of the NiO@Ni-carbon and Ni_3S_2@Ni-carbon cells.

Directing the morphology of lithium metal deposits during electrodeposition is crucial to the development of safe, high energy density batteries with robust cycle life. Towards this end, mechanistic insight into the correlation between various electrolyte components or cycling conditions and different lithium morphologies is imperative. Recently, **SLAC** team have used a standard carbonate-based electrolyte while systematically adding water (ppm levels) in Li||Cu cells to study the links between electrolyte composition, initial solid electrolyte interphase (SEI) formation, and morphology of electroplated lithium metal using electrochemical characterization, X-ray scattering, X-ray photoelectron spectroscopy, and electron microscopy techniques. Under certain conditions (e.g. electrolyte with 100 ppm added HF and an applied constant current of 0.5 mA/cm^2) this system yields electrodeposited lithium metal with a highly monodisperse columnar morphology. Systematic experimental investigation of the HF reduction process, nanostructure of the initial SEI, and crystallographic texture of electrodeposited lithium metal enable insights to be drawn concerning the underlying mechanisms of columnar lithium formation, as illustrated in Figure II.13.A.34. The columnar morphology arises from an SEI layer comprising crystalline LiF deposits, formed through preferential reduction of HF, embedded in an amorphous matrix of solvent reduction products. This interphase structure contains fast lithium ion diffusion pathways which lead to a high nucleation density and uniform growth of lithium metal deposits. This mechanistic understanding will help to inform future electrolyte additive design and rational cycling protocols for lithium metal batteries. The current phase of this work includes investigating the combined effects of an additive which promotes columnar growth and applied external pressure. We hypothesize that the two variables will synergistically combine to result in an "anode-free" lithium metal cell with large, uniform lithium metal deposits with preferred texture, and enhanced Coulombic efficiency due to a decrease in both "dead" lithium and SEI formation during cycling.

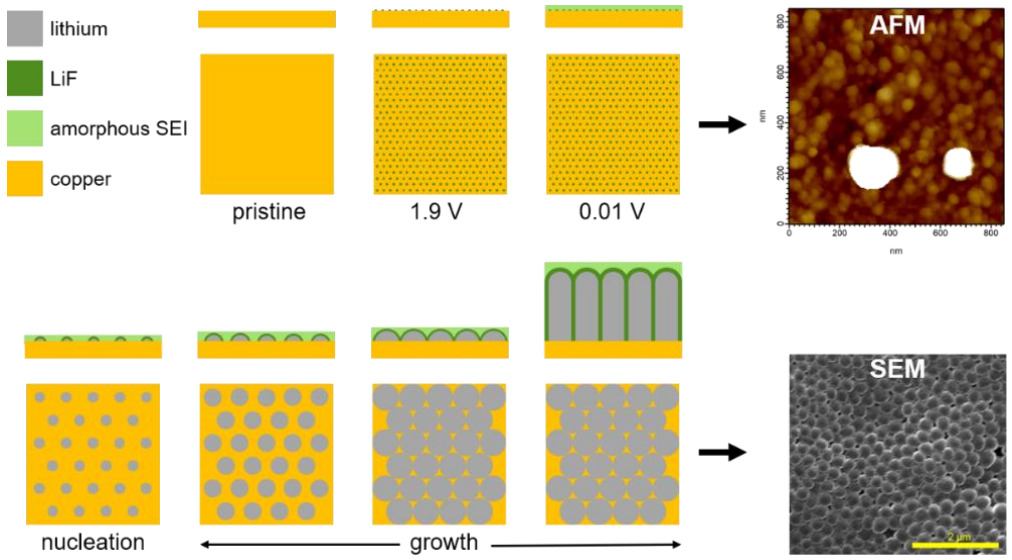

Figure II.13.A.34 Proposed mechanism and correspond data for the initial nucleation and growth of Li metal deposits in electrolyte that contains HF.

INL team refined their efforts to understand signatures from reduced lithium inventory. Figure II.13.A.35 includes the incremental capacity (IC) variations in a Li | LiFSI/DME-TFEO | NMC-811 cell over 350 cycles. The analysis provides insight into the transitions from H1, M, H2 to H3 phases in NMC-811. These transitions index the capacity — lattice structure correspondence. In Figure II.13.A.35, the IC peak near 3.7 V is quite dominant. The sharp rise in IC implies a distinct phase transition from H1 to monoclinic (M) phase. A secondary IC peak is also observed, of which the origin is not clear at the present time (see Area ①). Over cycle aging, the distinct H1-M transition IC peak retreated from Cycle 50 to 350, and the primary IC peak gradually disappeared, survived with the secondary peak. This retreat is however not the result of increasing polarization, but due to the shortage of Li supplies, as shown in Area ②. In Area ③, the IC peak marked by the H2-H3 transition drastically reduced/disappeared after 150 cycles. The congruent disappearance of the H1-M primary peak and the H2-H3 peak seems to suggest that these two might be related; yet, with limited data, it is difficult to confirm. This observation by ICA allow us to correlate the cell performance with NMC cathode materials characterization and understanding. The methods developed will continue to be further integrated with both Keystone 1 and 3 to enhance efforts for materials development and full cell cycling analysis and optimization. The team also focused on further refining the computational modeling of cells. A 2D moving boundary model was successfully developed to study two-dimensional nature of transport in the electrolyte and the resulting two-dimensional deposition profile on the anode. The key inputs to this model are applied current density, design parameters, transport parameters for the liquid phase, and exchange current density on the anode. The model provides the two-dimensional distribution of the concentration, anode potential, deposition profile, and rate of deposition as the outputs. This 2D model and pressure aware model can be used to study how charging rate, anode length, separator length and thickness, and cycling influence the deposition profile on the anode.

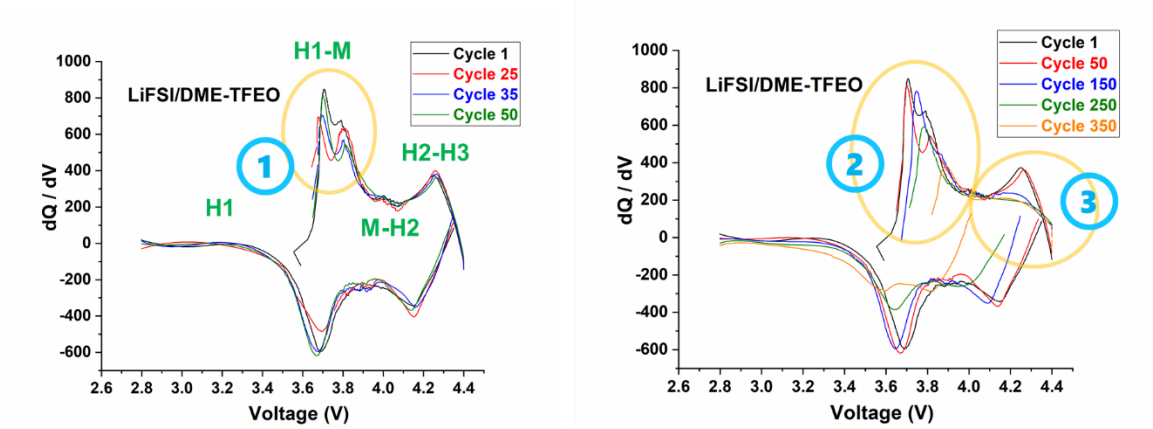

Figure II.13.A.35 Incremental capacity analysis (dQ/dV) of Li||NMC-811 performance and capacity fading with a LiFSI/DME-TFEO diluted high-concentration electrolyte-containing cell. Incremental capacity variations associated with phase transitions (H1-M-H2-H3) are identified and quantified.

The Li-S electrochemical modeling team at the **UT Austin** used a detailed one-dimensional model (1-D model), a Tanks-in-Series methodology to generate a computationally efficient model which retains adequate physical detail while facilitating extensive parametric studies and parameterization against experimental data. Model comparisons of the Tank Model with the full 1-D model are shown in Figure II.13.A.36. For the Base Case parameters and discharge rates considered, the 1-D model indicates negligible transport limitations in the Li-S cell. That means species concentration profiles and partial currents are relatively uniform across the electrode thickness, reducing the underlying cause of deviations between the Tank Model and the 1-D model. In this limiting case, the Tank Model almost exactly matches the 1-D model, as seen in Figure II.13.A.36(a). Convergence between two independent models under appropriate limiting conditions is reasonable evidence for computational accuracy. To further examine the Tank Model averaging and flux assumptions, the diffusion coefficient was varied over two orders of magnitude, which resulted in different transport effects on the solution. For the voltage curves in Figure II.13.A.36(a), the Base Case diffusion coefficient of $1x10^{-10}$ m^2/s was used in the Tank Model and the 1-D model. An analysis of characteristic time scales suggests that the Base Case parameters correspond to a kinetically limited cell with negligible transport resistances. Other workers have found that by changing the ionic diffusion coefficients by one to two orders of magnitude, the model was able to predict experimental data more accurately under varying rates. For the simulations in Figure II.13.A.36(b), a reduced diffusion coefficient of $1x10^{-11}$ m^2/s is used to induce additional transport limitations in the cell. At 0.2C and 0.5C rates, the difference in predictions between the 1-D and Tank Models is negligible. The simulations at 1C indicate the overall voltage response is closely matched until the end of discharge, where increased concentration overpotentials produce deviations. For Figure II.13.A.36(b), a diffusion length parameter $\delta = \frac{1}{3}$ is found to produce the least error compared to the 1-D model.

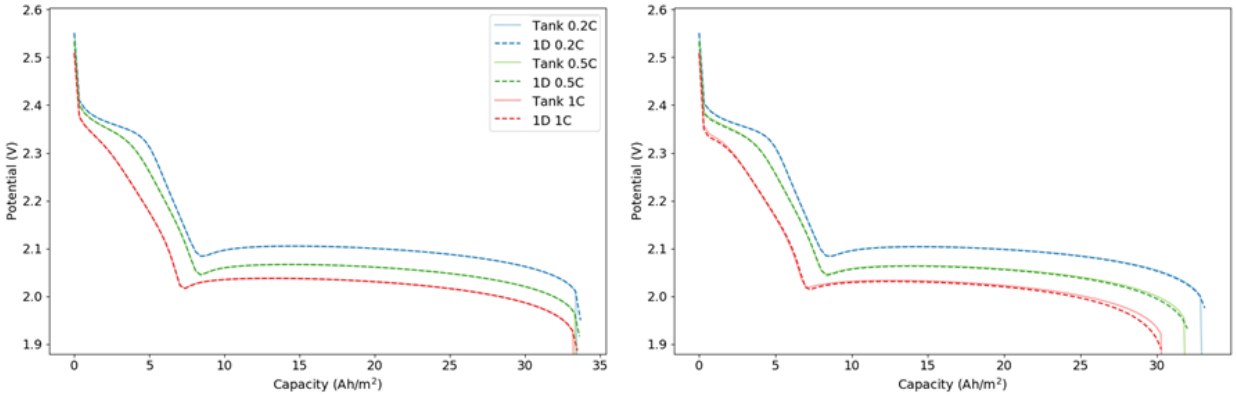

Figure II.13.A.36 Comparison of tank-in-series model (dashed) and 1-D model (solid) predictions at rates of 0.2C (blue), 0.5C (green), and 1C (red) (left) with the Base Case diffusion coefficient of 1 x 10-10 m2/s and (right) with diffusion coefficient of 1 x 10-11 m2/s where transport limitations are introduced and some variation is introduced at the end of discharge.

The seedling team at **University of Maryland at College Park** synthesized and demonstrated a chemical bonding-stabilized high-capacity carbon/small sulfur composite as an improved cathode for Li-S battery using lean electrolyte. The strong chemical bonding of C–S and O–S groups in the CPAPN–S composite is confirmed by the Raman spectroscopy, FTIR, XPS, and PDF characterizations. The PDF characterization was carried out by **BNL** team. The PDF analysis was adopted to analyze the activation mechanism as it is ideal for analyzing complicated structure without crystallinity. It is possible to directly monitor the evolution of bonds of interest during electrochemical cycling. Figure II.13.A.37A shows the PDF data of pristine sulfur and CPAPN–S. The PDF of S8 is used as control. The puckered ring structure of S8 is illustrated in the inset graph. It indicates that peaks 1 through 5 in sulfur PDF can be directly correlated with S–S atomic pairs within the S8 molecule and between the molecules. Similarly, the PDF data of CPAPN–S show the presence of S–O (1.42 Å), S–C (1.76 Å), and S–S (2.07Å) bonds in the material which are in good agreement with previous XPS studies. It is noted that the S–S bond length in CPAPN–S is very similar to that in the pure sulfur (2.06 Å, peak 1 in sulfur PDF). Figure II.13.A.37B shows the ex situ PDF data of CPAPN–S during the first cycle. It clearly indicates that upon lithiation the bond lengths of S–O, S–C, and S–S generally increase during discharge and decrease during charge. As illustrated by the arrows, the bond lengths generally show partially reversible change during the first cycle, suggesting the success of the proposed modification strategy by introducing the functional groups. A more detailed comparison between PDF data of the pristine material and the charged sample (Figure II.13.A.37C) indicates that the S–O peak intensity decreases and the S–S peak intensity increases after the first cycle. This is very likely caused by the breakage of some of the S–O bonds and more availability of the S–S bond. Interestingly, the second cycle electrochemical profile shows more capacity above 1 V, which is very likely contributed by lithium bonded to S–S parts. A schematic illustration (Figure II.13.A.37D) for the synthetic process of CPAPN–S is presented based on the material characterizations and XPS and PDF results. When the mixture of sulfur, PAN, and PTCDA is annealed at 600 °C, the ring-structured S8 is vaporized and dissociated into small sulfur molecules such as S2 and S3, while PAN and PTCDA are carbonized to oxygen- and nitrogen containing carbon matrix at the same time. Then, the small sulfur molecules bond with -C and -O groups in CPAPN to provide the chemical bonding-stabilized high-capacity SSCCs. The resulting SSCCs are promising cathode materials for high energy lean electrolyte LSBs.

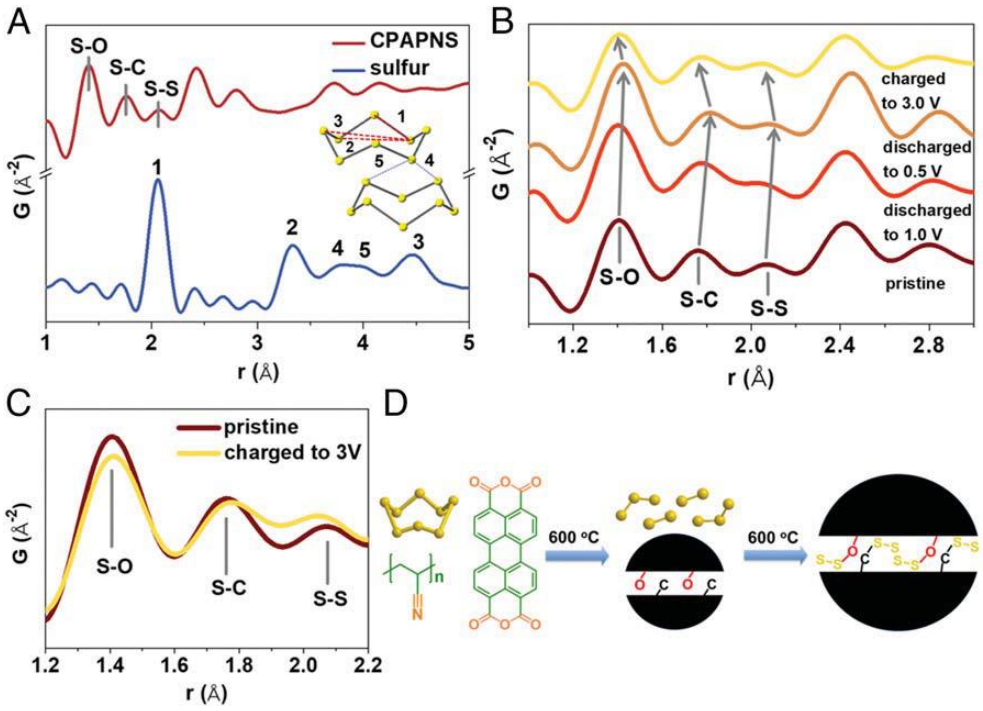

Figure II.13.A.37 PDF analysis and schematic illustration of the synthetic process of CPAPN-S. (A) PDF data of sulfur and CPAPN-S. Characteristic bonds and their corresponding PDF peaks are labelled; (B) PDF data of pristine and ex situ CPAPN-S electrodes in the 1st cycle, indicating that S-O, S-C, and S-S bond lengths generally increase during discharge and decrease during charge; (C) PDF data of charge-to-3V electrode overlaid on the pristine data (without offset), showing the decrease of S-O peak and increase of S-S peak after 1st cycle. (D) A schematic illustration of the formation of chemical bonding stabilized carbon-small sulfur composite.

PNNL team has developed *Li Batt Design App*, a "Machine learning-assisted lithium metal battery design software package". (https://www.pnnl.gov/technology/li-batt-design-app), using machine learning to help battery developers and researchers easily and rapidly design lithium-metal-based pouch cells. The *Li-Batt Design App* helps researchers quickly obtain all possible combinations of design parameters, including those for different cathode materials and pouch cell dimensions, to achieve desired energy density.

PNNL team developed approaches for large-scale preparation of sulfur electrodes with integrated nano-structured sulfur/carbon (S/C) materials and identified the key challenges for the long-term cycling of high energy Li–S pouch cells at realistic conditions. High mass-loading S electrodes at 4-6 mg cm^{-2} have been prepared in large scale at PNNL's Advanced Battery Facility (ABF) and used for multiple-layer Li–S pouch cell fabrication (Figure II.13.A.38a). The S/C composites and high loading electrodes were supplied to other Battery500 teams upon request for benchmark or validation research. Key parameters affecting the practical energy of the Li–S battery were investigated using the Li–S pouch cell as a platform. It is found that reducing the electrolyte content while increasing the active S amount are the two important approaches for substantial cell-level specific energy improvement. A steady increase in cell level specific energy with increased cathode areal capacity is only feasible when electrolyte and inert weight are tightly controlled. For a S cathode with loading of at least 4 mg cm^{-2}, the amounts of electrolyte and Li need to be strictly controlled to reach a high specific energy of 350 Wh kg^{-1} in a practical pouch cell. Following cell design, practical pouch cells with different E/S ratios were fabricated and tested (Figure II.13.A.38d). The lifespan of Li–S pouch cells is highly dependent on the amount of electrolyte used, i.e. electrolyte volume/Sulfur mass ratio (E/S in unit mLg^{-1}). To clearly understand the effects of E/S ratio on cell cycling life, the cumulative specific discharge capacities (the total discharge capacities delivered in the lifespan) are plotted versus applied E/S ratio (Figure II.13.A.38e). The cumulative specific discharge capacity decreases almost linearly with the E/S ratio indicating that Li–S pouch cell cycling mainly dominated by the electrolyte amount. To extend cell cycle life at high cell level specific energy, S electrodes with improved S utilization and electrode density are under development to

reduce the requirements for excessive thick electrodes and high S loading in order to increase the amount of available electrolyte.

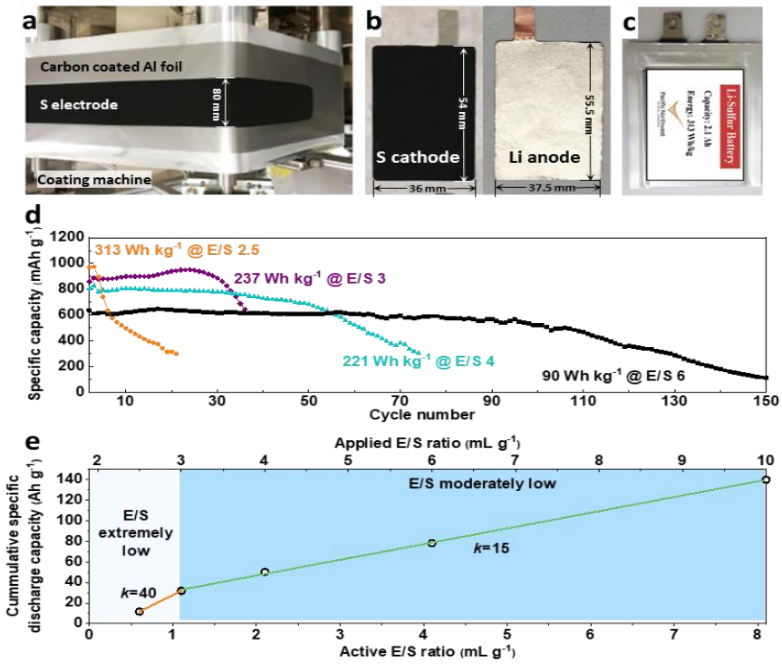

Figure II.13.A.38 High-energy Li–S pouch cell. (a) Digital photograph of the large-area S electrode on a coating machine. (b) Digital photographs of punched S cathode and Li anode (thickness = 50 μm) for pouch cell. (c) Digital photograph of the high energy pouch cell. (d) Cycling performances of Li–S pouch cells with different energy densities and E/S ratios (mL g^{-1}). (e) Relationship of the cumulative specific discharge capacity and applied E/S ratio and active E/S ratio of pouch cells in (d).

INL team studied the formation and aging of Li-S batteries at different cycling rates and temperatures with the aim to better understand guidance on cycling use and implications to future cell designs. Assorted temperatures for formation ranging from 10-45°C and cycling rates C/2-C/20 were investigated. A distinct change in performance was observed when using intermediate temperatures. The capacity retention and aging cycling performance at C/10, C/5 and C/2 C-rates (25ºC C/20 formation) suggests a competition between polysulfide shuttle and electrode utilization. Advanced analysis is currently underway following similar procedures we used for Li-NMC cells using Battery500 electrolytes and formation process. In work on Li-NMC, INL has expanded the electrochemical methods that can uniquely show the interplay between cell-level thermodynamic and kinetic aspects including Kinetic Polarization Hinderance (KPH) for Li-NMC cells [1],[2]. The origin of this KPH effect could include mass transport in the porous media of the electrode, the charge transfer rate at the electrode-electrolyte interface, or the Li diffusion in the lattice of NMC; etc. By comparing the capacity ration measured at a *C/n* rate of polarization ($QR_{C/n}$) with the theoretical capacity ration (QR_T) it is possible to obtain the NMC utilization efficiency ($\varepsilon_{C/n}$) at the *C/n* rate at a specific SOC and cycle number. Further derivation can provide the degree of the KPH effect (η_{KPH}) based on $\eta_{KPH} = QR_{KPH} / QR_{C/n}$. The values of QR_{KPH} are calculated by the incremental amount of $QR_{KPH} = \Delta Q_{KPH} / \Delta SOC$. The quantifications as shown in Figure II.13.A.39 are very useful to identify and quantify the effects that affect the materials utilization and capacity loss (reversible or irreversible) with clear separation of the origin of the attributes. Such information will become more critical and quantitative to effectively established a quantitative measure to improve the specific energy and cycle life.

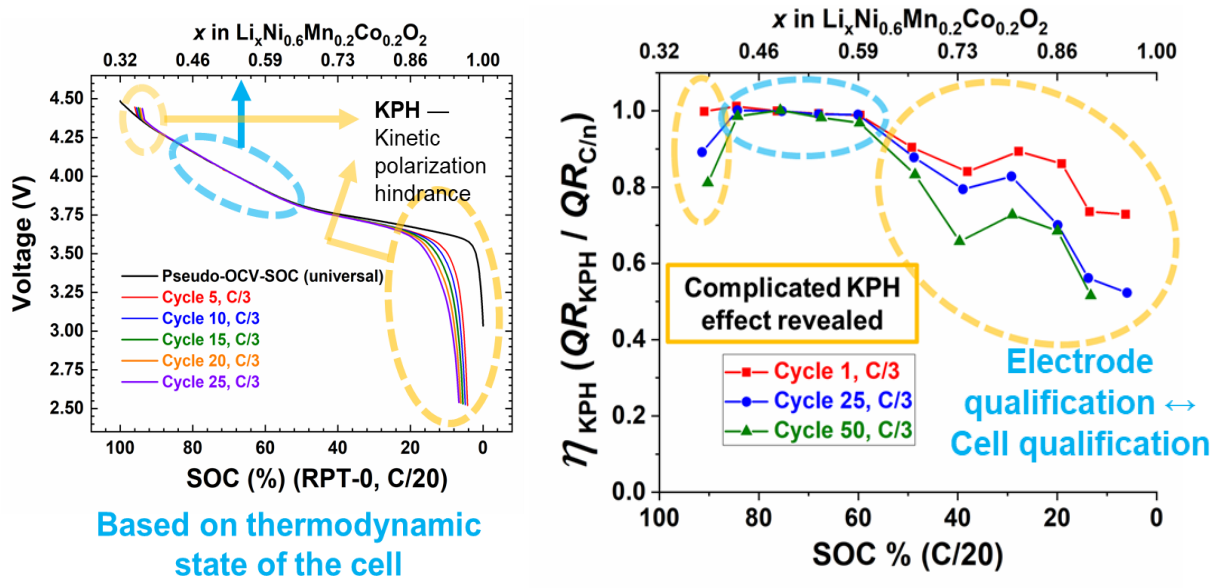

Figure II.13.A.39 INL's electrochemical analytic diagnosis (eCAD) technique can transform a typical charging-discharging curve into a cell IR-free voltage versus SOC (which corresponds to the Li content in NMC cathode composition) curve to separate the thermodynamic and kinetic effect attributes. (Left) The transformed curves show regions where NMC potential versus Li content in the NMC composition (pseudo-OCV vs. x in Li_xNMC) correlation and the IR-free voltage versus SOC ($V_{IR\text{-}free}$ vs. SOC) correlation are compared. (Right) The effect from an electrode's kinetic polarization hindrance (KPH) can then be derived from the charging-discharging curves as "the degree of KPH effect" ($\eta_{KPH} = QR_{KPH} / QR_{C/n}$) as a function of SOC and cycle number.

Modeling team **at UW and UTA** has developed a coupled electrochemical-thermal model for Li-S batteries, while also highlighting many of the key challenges that remain in multi-scale battery models including moving boundaries and mechanical aspects that prevail in Li-NMC and Li-S batteries [1]. The Li-S electrochemical model developed was based on the model developed by Kumaresan et al [2]. In this model, the overall potential is set by the thermodynamics of individual electrochemical reactions and their overpotentials. The anode is modeled as a constant source of lithium ions. The model explores how the battery dynamics change over the one-dimensional regions of the cathode and the separator. The thermal model was developed by extending porous electrode models for Lithium-ion batteries. The temperature is a function of ohmic heating and heat due to the electrochemical reactions. For this work, the researchers have developed a single sandwich model, and for our future work, we will be considering more layers to depict thermal behavior more accurately. To understand the rate dependence of the thermal behavior, three different rates were compared with low natural convection ($h=1\ W/m^2K$). All variables are compared on a capacity basis. As the rate increases, there is increased polarization, and these losses result in depressing the voltage curve and capacity loss at the end of discharge. As expected, the temperature rise increases with increase in rate. The temperature rise is greatest initially with another increase at the point of inflection between the two plateaus. To understand the heat sources, the heats have been included. As shown in Figure II.13.A.40, Ohmic heating increases dramatically at the transition between the two plateaus and decreases until another steep increase at the end of discharge, indicating the conductivity is lowest during those rises. The heat generation from the reactions is about an order of magnitude larger than ohmic heating. The reversible heating is larger than the irreversible heat during the first plateau, and then the irreversible heat increases steadily until the end of discharge, indicating the overpotentials are larger in the second half of discharge. For the ohmic heating and the reaction heats, the increase in rate accompanies a similar increase in the heating terms Q.

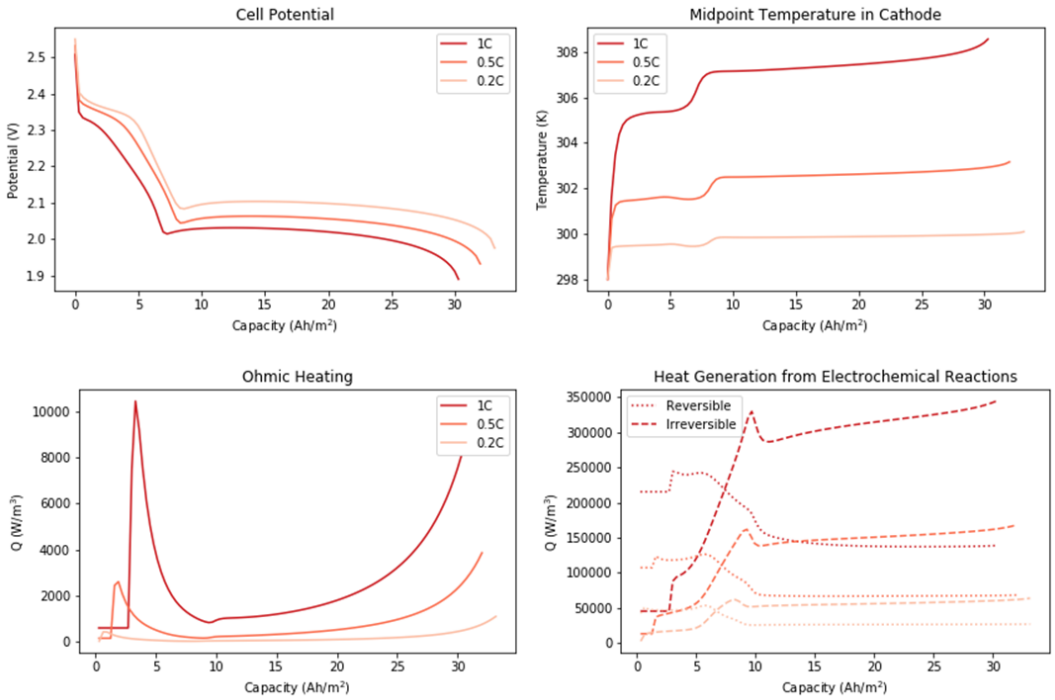

Figure II.13.A.40 Thermal profiles for assorted rates associated with low convection.

Conclusions

This project has been successfully completed in FY2020. All milestones have been completed. The publication records are very good: 4 US patent applications were filed by the Battery500 team member institutions. 52 peer reviewed papers were published, and more than 77 invited presentations were delivered in FY2020. Extensive collaboration within the consortium and with seedling teams, as well as other national Labs and US universities has been well established and achieved very fruitful results.

Key Publications

Patents

1. Ping Liu, from **UCSD**, “A Scalable 3D Lithium Metal Anode”, US patent application No. 62/905,971, filed on September 25, 2019.

2. Xia Cao, Ji-Guang Zhang, and Wu Xu from **PNNL**, " Electrolyte for stable cycling of rechargeable alkali metal and alkali ion batteries", U.S. patent filed in November 2019.

3. Boryann Liaw, Yulun Zhang, Qiang Wang, from **INL,** “Electrochemical analytic diagnosis for battery cell qualification.” US patent application, No. 62/961,096, filed on January 14, 2020.

4. Bin Li, from **INL** “Fast Diagnosis of Failure Mechanisms and Prediction on Lifetime of Li Metal Batteries Using Anode-free Batteries”, US patent application No. 62/981,433, filed on February 25th, 2020.

5. Jason Zhang, from **PNNL**, “High Efficiency Electrolytes for Silicon-Based Lithium Ion Batteries”, US patent application, No. 62/959,051, filed on January 09, 2020.

6. Wu Xu from **PNNL**, “Electrolytes for Lithium Ion Batteries With Graphite Anodes and/or Nickel-Rich Cathodes”, US patent application No. 62/970,651, filed on February 05th, 2020.

7. Xia Cao, Ji-Guang Zhang, Wu Xu, from PNNL, “Electrolytes for rechargeable metal-sulfur batteries”, U.S. Patent Application No. 16/904,376. Filed on June 17, 2020.

8. J. Yang, Yao, Liu, X. Wu, X. Jiang, and J. Liu, "High Energy Lithium Batteries with Lean Lithium Metal Anodes and Methods for Prelithiation", 63/046,918, June 30, 2020.

Publications

1. Bingbin Wu, Yang Yang, Dianying Liu, Chaojiang Niu, Mark Gross, Lorraine Seymour, Hongkyung Lee, Phung M. L. Le, Thanh D. Vo, Zhiqun Daniel Deng, Eric J. Dufek, M. Stanley Whittingham, Jun Liu, and Jie Xiao, “Good Practices for Rechargeable Lithium Metal Batteries”, *J. Electrochem. Soc*., 2019, 166: A4141-A4149. DOI: 10.1149/2.0691916jes, Publication date (Web): December 19, 2019

2. J. Xiao*, “How Lithium Dendrites Form in Liquid Batteries”, Science, 2019, 366, 426, Publication date (Web):

3. Zhixin Dong, Qi Wang, Ruibo Zhang, Natasha A. Chernova, Fredrick Omenya, Dongsheng Ji and M. Stanley Whittingham, “The Reaction Mechanism of Sn_2Fe Anode in Lithium-Ion Batteries”, *ACS Omega*, 2019, 4: 22345-22355. 10.1021/acsomega.9b02417. Publication date (Web): December 18, 2019.

4. Yu Zheng, Fernando A. Soto, Victor Ponce, Jorge M. Seminario, Xia Cao, Ji-Guang Zhang, and Perla B. Balbuena, “Localized high concentration electrolyte behavior near a lithium–metal anode surface,” *J. Mater. Chem. A*, 2019,7, 25047-25055. Publication date (Web): October 14, 2019.

5. Yang He, Xiaodi Ren, Yaobin Xu, Mark H. Engelhard, Xiaolin Li, Jie Xiao, Jun Liu, Ji-Guang Zhang, Wu Xu & Chongmin Wang "Origin of Lithium Whisker Formation and Growth under Stress." *Nature Nanotechnology* 14, no. 11:1042-1047. Publication date (Web): October 14, 2019.

6. Q. Xie, W. Li, A. Dolocan, and A. Manthiram, “Insights into Boron-based Polyanion-tuned High-nickel Cathodes for High-energy-density Lithium-ion Batteries” *Chemistry of Materials* **31**, 8886-8897 (2019). DOI: 10.1021/acs.chemmater.9b02916, Publication date: October 3, 2019.

7. L. Luo, J. Li, and A. Manthiram “A Three-dimensional Lithiophilic Mo_2N-modified Carbon Nanofiber Architecture for Dendrite-free Lithium-metal Anodes in a Full Cell,” *Advanced Materials* **31**, 1904537 (2019). **DOI:** 10.1002/adma.201904537, Publication date: November 25, 2019.

8. J. Li and A. Manthiram “A Comprehensive Analysis of the Interphasial and Structural Evolution over Long-term Cycling of Ultrahigh-nickel Cathodes in Lithium-ion Batteries,” *Advanced Energy Materials* **9**, 1902731 (2019). DOI: 10.1002/aenm.201902731, Publication date: December 6, 2019.

9. J. Li, C.-H. Chang, and A. Manthiram “Towards Long-life, Ultrahigh-nickel Layered Oxide Cathodes for Lithium-ion Batteries: Optimizing the Interphase Chemistry with a Dual-functional Polymer,” *Chemistry of Materials* DOI: 10.1021/acs.chemmater.9b04102, Publication date (Web): December 31, 2019.

10. Akshay Subramaniam, Jerry Chen, Taejin Jang, Natalie R. Geise, Rober M. Kasse, Michael F. Toney, and Venkat R. Subramanian, "Analysis and Simulation of One-Dimensional Transport Models for Lithium Symmetric Cells", *Journal of The Electrochemical Society*, 2019, 166(15): A3806-A3819, DOI: 10.1149/2.0261915jes, publication date (Web): November 15, 2019.

11. Akshay Subramaniam, Suryanarayana Kolluri, Caitlin D. Parke, Manan Pathak, Shriram Santhanagopalan, and Venkat R. Subramanian, "Properly Lumped Lithium-ion Battery Models: A Tanks-in-Series Approach", *Journal of The Electrochemical Society*, 2020, 167(1): 013534, DOI: 10.1149/2.0342001jes, publication date (Web): December 19, 2019.

12. Hansen Wang, Yayuan Liu, Yuzhang Li and Yi Cui, “Lithium Metal Anode Materials Design: Interphase and Host”, *Electrochemical Energy Reviews*, 2(4), 509-517. Publication Date (Web): October 12, 2019.

13. David G. Mackanic, Xuzhou Yan, Qiuhong Zhang, Naoji Matsuhisa, Zhiao Yu, Yuanwen Jiang, Tuheen Manika, Jeffrey Lopez, Hongping Yan, Kai Liu, Xiaodong Chen, Yi Cui andZhenan Bao, "Decoupling of mechanical properties and ionic conductivity in supramolecular lithium ion conductors" *Nature Communications* 10.1 (2019): 1-11. Publication Date (Web): November 26, 2019.

14. Yu-Ting Weng, Hao-Wen Liu, Allen Pei, FeiFei Shi, Hansen Wang, Chih-Yuan Lin, Sheng-Siang Huang, Lin-Ya Su, Jyh-Ping Hsu, Chia-Chen Fang, Yi Cui and Nae-Lih Wu "An ultrathin ionomer interphase for high efficiency lithium anode in carbonate based electrolyte" *Nature Communications* 10.1 (2019): 1-10. Publication Date (Web): December 20, 2019.

15. Guangmin Zhou, Shiyong Zhao, Tianshuai Wang, Shi-Ze Yang, Bernt Johannessen, Hao Chen, Chenwei Liu, Yusheng Ye, Yecun Wu, Yucan Peng, Chang Liu, San Ping Jiang, Qianfan Zhang, and Yi Cui, "Theoretical calculation guided design of single-atom catalysts towards fast kinetic and long-life Li-S batteries" *Nano Letters* (2019). Publication Date (Web): December 30 2019.

16. Yulun Zhang, Qiang Wang, Boryann Liaw, Shrikant C. Nagpure, Eric J. Dufek, Charles C. Dickerson, “A quantitative failure analysis on capacity fade in rechargeable lithium metal cells.” J. Electrochem. Soc., 2019, 167, 090502. DOI:10.1149/1945-7111/ab6cf4 Publication date (web): January 7 ,2020

17. Abhi Raj, Charles C. Dickerson, Shrikant C. Nagpure, Sangwook Kim, Chaojiang Niu, Jie Xiao, Boryann Liaw, Eric J. Dufek, “Communication—Pressure evolution in constrained rechargeable lithium-metal pouch cells.” J. Electrochem. Soc. 167 (2020) 020511. DOI: 10.1149/1945-7111/ab6439 Publication date (web): January 2, 2020

18. David T. Boyle, Xian Kong, Allen Pei, Paul E. Rudnicki, Feifei Shi, William Huang, Zhenan Bao, Jian Qin, and Yi Cui, "Transient Voltammetry with Ultramicroelectrodes Reveals the Electron Transfer Kinetics of Lithium Metal Anodes." ACS Energy Letters 5.3 (2020): 701-709. Publication Date (Web): February 03, 2020.

19. Yi Cui, Jiayu Wan, Yusheng Ye, Kai Liu, Lien-Yang Chou, and Yi Cui, "A Fireproof, Lightweight, Polymer–Polymer Solid-State Electrolyte for Safe Lithium Batteries." Nano letters 20.3 (2020): 1686-1692. Publication Date (Web): February 05 2020.

20. David Sichen Wu, Guangmin Zhou, Eryang Mao, Yongming Sun, Bofei Liu, Li Wang, Jiangyan Wang, Feifei Shi, and Yi Cui, "A novel battery scheme: Coupling nanostructured phosphorus anodes with lithium sulfide cathodes." Nano Research (2020): 1-6. Publication Date (Web): March 02 2020.

21. William Huang, Hansen Wang, David T. Boyle, Yuzhang Li, and Yi Cui, "Resolving Nanoscopic and Mesoscopic Heterogeneity of Fluorinated Species in Battery Solid-Electrolyte Interphases by Cryogenic Electron Microscopy." ACS Energy Letters (2020). Publication Date (Web): March 16 2020.

22. Xin-Yang Yue, Jian Bao, Si-Yu Yang, Rui-Jie Luo, Qin-Chao Wang, Xiao-Jing Wu, Zulipiya Shadike, Xiao-Qing Yang, Yong-Ning Zhou, “Petaloid-shaped ZnO coated carbon felt as a controllable host to construct hierarchical Li composite anode”, Nano Energy. DOI: 10.1016/j.nanoen.2020.104614, Publication Date (web): February 13th, 2020

23. Liang Yin, Zuo Li, Gerard S. Mattei, Jianming Zheng, Wengao Zhao, Fredrick Omenya, Chengcheng Fang, Wangda Li, Jianyu Li, Qiang Xie, Evan M. Erickson, Ji-Guang (Jason) Zhang, M. Stanley Whittingham, Y. Shirley Meng, Arumugam Manthiram, and Peter G. Khalifah, “Thermodynamics of

anti-site defects in layered NMC cathodes: systematic insights from high-precision powder diffraction studies", Chem. Mater., 32, 1002-1010 (2020). DOI: 10.1021/acs.chemmater.9b03646, [ACS "Editor's Choice" manuscript, January 30, 2020].

24. Hao Liu, Zhuo Li, Antonin Grenier, Gabrielle Kamm, Liang Yin, Gerard S. Mattei, Monty R. Cosby, Peter G. Khalifah, Peter J. Chupas and Karena W. Chapman, "Best Practices for Operando Depth-Resolving Battery Experiments", J. Appl. Cryst., J. Appl. Cryst., 53, 133-9 (2020). DOI: 10.1107/S1600576719016315, Publication date: Feb, 2020.

25. Jie Xiao, Qiuyan Li, Yujing Bi, Mei Cai, Bruce Dunn, Tobias Glossmann, Jun Liu, Tetsuya Osaka, Ryuta Sugiura, Bingbin Wu, Jihui Yang, Ji-Guang Zhang and M. Stanley Whittingham, "Understanding and Applying Coulombic Efficiency in Lithium Metal Batteries", Nature Energy, DOI: 10.1038/s41560-020-0648-z , Publication date (web): June 25 ,2020

26. Chibueze V. Amanchukwu, Zhiao Yu, Xian Kong, Jian Qin, Yi Cui*, and Zhenan Bao*. "A new class of ionically conducting fluorinated ether electrolytes with high electrochemical stability." Journal of the American Chemical Society 142.16 (2020): 7393-7403. DOI: 10.1021/jacs.9b11056, Publication Date (Web): April 01, 2020.

27. Chen, Hao, Allen Pei. Jiayu Wan, Dingchang Lin, Rafael Vilá, Hongxia Wang, David Mackanic, Hans-Georg Steinrück, William Huang, Yuzhang Li, Ankun Yang, Jin Xie, Yecun Wu, Hansen Wang, Yi Cui*. "Tortuosity Effects in Lithium-Metal Host Anodes." Joule (2020). DOI: 10.1016/j.joule.2020.03.008. Publication Date (Web): April 08, 2020.

28. Hansen Wang, Xia Cao, Hanke Gu, Yayuan Liu, Yanbin Li, Zewen Zhang, William Huang, Hongxia Wang, Jiangyan Wang, Wu Xu, Ji-Guang Zhang, Yi Cui, Improving Lithium Metal Composite Anodes with Seeding and Pillaring Effects of Silicon Nanoparticles, ACS Nano, 2020, 14(4), 4601-4608. DOI: 10.1021/acsnano.0c00184. Publication date: April 28, 2020.

29. Hao Chen, Guangmin Zhou, David Boyle, Jiayu Wan, Hongxia Wang, Dingchang Lin, David Mackanic, Zewen Zhang, Sang Cheo Kim, Hye Ryoung Lee, Hansen Wang, Wenxiao Huang, Yusheng Ye, Yi Cui*, "Electrode Design with Integration of High Tortuosity and Sulfur-Philicity for High-Performance Lithium-Sulfur Battery." Matter (2020). DOI: 10.1016/j.matt.2020.04.011. Publication Date (Web): May 08, 2020.

30. Guangmin Zhou, Ankun Yang, Guoping Gao, Xiaoyun Yu, Jinwei Xu, Chenwei Liu, Yusheng Ye, Allen Pei, Yecun Wu, Yucan Peng, Yanxi Li, Zheng Liang, Kai Liu, Lin-Wang Wang, and Yi Cui*, "Supercooled liquid sulfur maintained in three-dimensional current collector for high-performance Li-S batteries." Science Advances 6.21 (2020): eaay5098. DOI: 10.1126/sciadv.aay5098. Publication Date (Web): May 22, 2020

31. Xin Gao, Xueli Zheng, Jingyang Wang, Zewen Zhang, Xin Xiao, Jiayu Wan, Yusheng Ye, Lien-Yang Chou, Hiang Kwee Lee, Jiangyan Wang, Rafael A. Vilá, Yufei Yang, Pu Zhang, Lin-Wang Wang, and Yi Cui*, "Incorporating the nanoscale encapsulation concept from liquid electrolytes into solid-state lithium-sulfur batteries." Nano Letters (2020). DOI: 10.1021/acs.nanolett.0c02033 Publication Date (Web): June 09, 2020.

32. Zhiao, Yu, Hansen Wang, Xian Kong, William Huang, Yuchi Tsao, David G. Mackanic, Kecheng Wang, Xinchang Wang, Wenxiao Huang, Snehashis Choudhury, Yu Zheng, Chibueze V. Amanchukwu, Samantha T. Hung, Yuting Ma, Eder G. Lomeli, Jian Qin, Yi Cui* and Zhenan Bao*, "Molecular design for electrolyte solvents enabling energy-dense and long-cycling lithium metal batteries." Nature Energy (2020): 1-8. Publication Date (Web): June 22, 2020.

33. D. G. Mackanic, M. Kao, Z. Bao*, “Enabling Deformable and Stretchable Batteries”, Adv. Energy Mater., DOI 10.1002/aenm.202001424. Publication date: June 24, 2020.

34. S. Kim, A. Raj, B. Li, E.J. Dufek, C.C. Dickerson, H.Y. Huang, B.Y. Liaw, G.M. Pawar, “Correlation of electrochemical and mechanical responses: Differential analysis of rechargeable lithium metal cells” J. Power Sources, 463 (2020), 228180. DOI: 10.1016/j.jpowsour.2020.228180. Publication date (web): Apr. 29, 2020.

35. Y. Zhang, Y. Lin, L. He, V. Murugesan, G.M. Pawar, B.M. Sivakumar, H. Ding, D. Ding, B.Y. Liaw, E.J. Dufek, B. Li, ”Dual functional Ni3S2@Ni Core-shell Nanoparticles Decorating Nanoporous Carbon as Cathode Scaffolds for Lithium-Sulfur Battery with Lean Electrolytes” ACS Appl Energy Materials, 3 (2020), 4173. DOI: 10.1021/acsaem.0c00568. Publication date (web): May 5, 2020.

36. M.J. Hossain, G. Pawar, B. Liaw, K.L. Gering, E.J. Dufek, A.C.T. van Duin, “Lithium-electrolyte solvation and reaction in the anode/electrolyte interface of a lithium ion battery: A ReaxFF reactive force field study.” J. Chem. Phys. 152 (2020) 184301DOI: 10.1063/5.0003333. Publication date (web): May 8th, 2020.

37. E. M. Erickson, W. Li, A. Dolocan and A. Manthiram, “Insights into the Cathode-electrolyte Interphases of High-energy-density Cathodes in Lithium-ion Batteries,” ACS Applied Materials and Interfaces 12, 16451-16461 (2020). DOI: https://doi.org/10.1021/acsami.0c00900, Publication date: March 17, 2020. (this paper was published in FY2020Q2, but was not listed in our FY2020Q2 report).

38. Qiang Jiang, Peixun Xiong, Jingjuan Liu, Zhen Xie, Qinchao Wang, Xiao-Qing Yang, Enyuan Hu*, Yu Cao, Jie Sun, Yunhua Xu*, Long Chen*, “A Redox-Active 2D Metal-Organic Framework for Efficient Lithium Storage with Extraordinary High Capacity”, Angewandte Chemie 132, 5311-5315, 2020 publication date (Web): March 23, 2020, (this paper was published in FY2020Q2, but was not listed in our FY2020Q2 report).

39. Xuelong Wang, Xiulin Fan, Xiqian Yu, Seongmin Bak, Zulipiya Shadike, Iradwikanari Waluyo, Adrian Hunt, Sanjaya D. Senanayake, Hong Li, Liquan Chen, Chunsheng Wang, Ruijuan Xiao, Enyuan Hu, Xiao-Qing Yang, “The Role of Electron Localization on Covalency and Electrochemical Properties of Lithium-Ion Battery Cathode Materials”, Advanced. Functional Materials, DOI: 10.1002/adfm.202001633, Publication Date: May 13, 2020.

40. Chao Luo, Enyuan Hu, Karen J. Gaskell, Xiulin Fan, Tao Gao, Chunyu Cui, Sanjit Ghose, Xiao-Qing Yang, and Chunsheng Wang, “A chemically stabilized sulfur cathode for lean electrolyte lithium sulfur batteries”, PNAS, 2020 117 (26) 14712-14720, DOI: 10.1073/pnas.2006301117, Publication Date: June 17, 2020.

41. Xia Cao, Lianfeng Zou, Bethany E. Matthews, Linchao Zhang, Xinzi He, Xiaodi Ren, Mark H. Engelhard, Sarah D. Burton, Patrick Z. El-Khoury, Hyung-Seok Lim, Chaojiang Niu, Hongkyung Lee, Chunsheng Wang, Bruce W. Arey, Chongmin Wang, Jie Xiao, Jun Liu, Wu Xu, Ji-Guang Zhang, “Optimization of fluorinated orthoformate based electrolytes for practical high-voltage lithium metal batteries,” Energy Storage Materials, Volume 34, 2021, Pages 76-84, ISSN 2405-8297, https://doi.org/10.1016/j.ensm.2020.08.035. Publication date (web): September 4, 2020.

42. J. Xiao, Q. Li, Y. Bi, M. Cai, B. Dunn, T. Glossmann, J. Liu, T. Osaka, R. Sugiura, B. Wu, J. Yang, J.-G. Zhang, M S. Whittingham, “Understanding and Applying Coulombic Efficiency in Lithium Metal Batteries”, Nature Energy, 2020, 561-568. Publication date (web): June 5, 2020.

43. L. Shi, S.-M. Bak, Z. Shadike, C. Wang, C. Niu, P. Northrup, H. Lee, A. Y. Baranovskiy, C. S. Anderson, J. Qin, S. Feng, X. Ren, D. Liu, X.-Q. Yang, F. Gao, D. Lu, J. Xiao,M. Stanley

Whittingham, , J. Liu, “Reaction Heterogeneity in Practical High-Energy Lithium-Sulfur Pouch Cells”, Energy & Environmental Science, 2020, DOI:10.1039/D0EE02088E, Publication date (web): Sep 4, 2020.

44. X. Wang, G. Pawar, Y. Li, X. Ren, M. Zhang, B. Lu, A. Banerjee, P. Liu, E.J. Dufek, J.G. Zhang, J. Xiao, J. Liu, Y.S. Meng, B.Y. Liaw, “Glassy Li metal anode for high-performance rechargeable Li batteries” Nature Materials (2020), DOI:10.1038/s41563-020-0729-1. Publication date (web): July 27, 2020.

45. Y. Zhang, Q. Wang, B.Y. Liaw, S.C. Nagpure, E.J. Dufek, C.C. Dickerson, “Cell degradation quantification – a performance metric-based approach” J. Phys. Energy, 2 (2020) 034003, DOI:10.1088/2515-7655/ab979b. Publication date (web) July 3, 2020.

46. Fengxia Xin and M. Stanley Whittingham, “Challenges and Development of Tin Based Anode with high Volumetric Capacity for Li-ion Batteries”, Electrochem. Energy Reviews, 2020, on-line. DOI: 10.1007/s41918-020-00082-3, Publication date (web) October 1st, 2020.

47. S. Nanda and A. Manthiram, “Lithium Degradation in Lithium-Sulfur Batteries: Insights into Inventory Depletion and Interphasial Evolution with Cycling,” Energy & Environmental Science 13, 2501 – 2514 (2020). Publication date (web): July 3, 2020.

48. Q. Xie and A. Manthiram, “Long-life, Ultrahigh-nickel Cathodes with Excellent Air-storage Stability for High-energy-density Lithium-based Batteries,” Chemistry of Materials 32, 7413–7424 (2020). Publication date (web): August 4, 2020.

49. W. Li, X. Liu, Q. Xie, Y. You, M. Chi, and A. Manthiram, “Long-term Cyclability of NCM-811 at High Voltages in Lithium-ion Batteries: An In-depth Diagnostic Study,” Chemistry of Materials 32, 7796-7804 (2020). Publication date (web): August 27, 2020.

50. Akshay Subramaniam, Suryanarayana Kolluri, Shriram Santhanagopalan, and Venkat R. Subramanian. “An Efficient Electrochemical-Thermal Tanks-in-Series Model for Lithium-Ion Batteries”, Journal of The Electrochemical Society, 2020, 167, 113506. DOI: 10.1149/1945-7111/aba700, Publication Date: July 29, 2020

51. Krishna Shah, Akshay Subramaniam, Lubhani Mishra, Taejin Jang, Martin Z. Bazant, Richard D. Braatz, and Venkat R. Subramanian. “Editors’ Choice—Perspective—Challenges in Moving to Multiscale Battery Models: Where Electrochemistry Meets and Demands More from Math”, Journal of the Electrochemical Society, 2020, 167, 133501. DOI: 10.1149/1945-7111/abb37b, Publication Date: September 24, 2020.

52. R.M. Kasse, N.R. Geise, J.S. Ko, Johanna Nelson Weker, H.-G. Steinrück, M.F. Toney, “Understanding additive controlled lithium morphology in lithium metal batteries”, J. Mater. Chem. A 8, 16960-16972 (2020) DOI: 10.1039/d0ta06020h, Publication Date (web): July 30, 2020.

Invited Presentations

1. M. Stanley Whittingham, ***Nobel Lecture**, “The Origins of The Lithium Battery”, Stockholm, Sweden, December 8th, 2019.

2. M. Stanley Whittingham, “The Origins of The Lithium Battery (From an Idea to Domination of Energy Storage)”, Uppsala University, Uppsala, Sweden, December 13th, 2019. **Invited.**

3. M. Stanley Whittingham, “What are the Ultimate Limitations of Intercalation-Based Cathodes for Lithium (or Sodium) Batteries” ABAA, Ulm, Germany, October 9th 2019. **Invited.**

4. M. Stanley Whittingham, “Beta Alumina - Prelude to a Revolution in Solid State Electrochemistry”, ECS Fall Meeting, Atlanta, GA, October 16th, 2019. **Invited**

5. M. Stanley Whittingham, “From an Idea to Domination of Energy Storage” A long but satisfying journey”, Scialog, Tucson, AZ. November 16th, 2019. **Invited**

6. M. Stanley Whittingham, “From an Idea to Domination of Energy Storage”, Materials Science, Univ. of Washington, WA. November 19th 2019. **Invited**

7. Ji-Guang Zhang, "Li Metal Batteries." Presented in University of Washington, Seattle, Nov. 5, 2019, **Invited**.

8. Cao X., W. Xu, and J. Zhang, “New Electrolyte for Lithium-Metal Batteries with High-Voltage NMC811 Cathode,” 2019 MRS Fall Meeting & Exhibit. , Dec. 4, 2019, **Invited**.

9. Cao X., X. Ren, W. Xu, and J. Zhang. "Orthoformate (TFEO)-based Localized High Concentration Electrolytes for Li Metal Batteries." Presented by J. Zhang at ABAA 12, Ulm, Germany. 10/07/2019, **Invited**.

10. Wu Xu, Ji-Guang Zhang, Xiaodi Ren, Xia Cao, Shuhong Jiao, “Enabling High-Energy Lithium Metal Batteries through Electrolyte Strategy”, Presented by Wu Xu at 236th ECS Meeting, Atlanta, GA, Oct. 14, 2019. **Invited**.

11. Jie Xiao, “Lithium Metal Anodes: Origin of Lithium Dendrites and their Implications in Rechargeable Lithium Metal Batteries”, Seminar at Sustainable Power and Energy Center at UC San Diego, San Diego, October 2nd, 2019, **Invited**.

12. Jie Xiao, “Materials Science and Electrochemistry in Li-S Batteries”, Seminar at University of Washington, Seattle, November 19th, 2019, **Invited**.

13. Jie Xiao, “Effective Cathode Thickness in High-Energy Li-ion Batteries”, International Conference for Advanced Cathodes in Lithium&Sodium Ion Batteries, Souel, South Korea, November 13th, 2019, **Invited**.

14. Jie Xiao, “Understanding Lithium Sulfur Batteries at Different Scales”, 236th ECS Fall Meeting, Atlanta, October 15th, 2019, **Invited**.

15. Jie Xiao, “Battery500 Consortium: Addressing the Fundamental Challenges to Enable Next-generation Battery Technologies”, Advanced Lithium Batteries for Automobile Applications (ABAA) 12, Ulm, Germany, October 8th, 2019, **Invited**.

16. A. Manthiram, “Next-generation Battery Technologies,” Missouri University of Science and Technology, Rolla, MO, October 21, 2019 (**Invited**).

17. A. Manthiram, “Electrical Energy Storage: Near-term and Long-term Perspectives,” Clark Doctoral Fellows Distinguished Speaker Series, University of Maryland, College Park, MD, October 18, 2019 (**Invited**)).

18. A. Manthiram, “Where are We Headed with Electrical Energy Storage?” World University Forum on Materials Science & Engineering Leadership, Wuhan, China, October 9 – 12, 2019 (**invited keynote talk**).

19. A. Manthiram, “Where are we Headed with Battery Technologies?” Energy@UT Research Expo, Energy Institute, University of Texas at Austin, Austin, TX, October 2, 2019 (**Invited**).

20. MF Toney, “Processing & operation under extreme conditions: insights from in situ x-ray scattering & spectroscopy”, 236th Electrochemical Society Meeting, Atlanta, Ga, Oct 15, 2019, (**Invited**).

21. MF Toney, “X-rays Show Operating Principles of Energy Storage Materials”, University of Houston. Materials Science Colloquium, Oct 11, 2019, (**Invited**).

22. Venkat R. Subramanian "Model-based Battery Management System,” VIPER rover development, Johnson Space Center, Huston, TX, October 23, 2019. (**Invited**).

23. John B. Goodenough, ***Nobel Lecture**, “Designing Lithium-ion Battery Cathodes,” Delivered by Arumugam Manthiram, Stockholm, Sweden, December 8th, 2019.

24. Yi Cui, “Lithium Metal Anodes: Materials Design, Interface and Characterization” the 12th International Conference on Advanced lithium Batteries for Automotive Applications (ABAA12), Ulm, Germany, Oct. 6-9, 2019, (**Invited Plenary**)

25. Yi Cui, “Materials and Interface Design of Lithium Metal Anodes” 236th Electrochemical Society (ECS) Meeting, Atlanta, GA, on Oct. 13-17, 2019, **(Invited).**

26. Yi Cui, “Materials and Interface Design for Batteries” UCLA, Materials Science Seminar, Oct. 25, 2019, **(Invited seminar)**

27. Yi Cui, “Materials and Interface Design for Batteries” University of Washington, Materials Science Seminar, Oct. 29, 2019, **(Invited seminar)**

28. Yi Cui, “Materials and Interface Design for Batteries” University of Technology Sydney, Nov. 19, 2020, **(Invited seminar)**

29. Yi Cui, “In-situ and Cryogenic Electron Microscopy for Energy Materials” The Second International Symposium on Advanced Electron Microscopy and Spectroscopy (SAEMS), Dec. 9-11, 2019, University of California, Irvine, **(Invited)**

30. Y. Zhang, B. Liaw, "From battery failure analysis to safety mitigation." Battery Safety Council Forum #8, Washington, DC, November 19-20, 2019, **(Invited).**

31. B. Liaw, "Lithium metal electrode — Understanding its characteristics." Department of Chemistry Seminar, Temple University, Philadelphia, PA, November 11, 2019, **(Invited).**

32. Manthiram, “Battery Technologies for India,” Battery India – 2020, Bengaluru, India, January 10 – 12, 2020 (invited keynote talk).

33. Manthiram, “Lithium Battery Chemistry,” Battery India – 2020, Bengaluru, India, January 10 – 12, 2020 (invited tutorial talk).

34. Manthiram, “Understanding the Limits and Failure Mechanisms of Layered Oxide Cathodes,” Gordon Research Conference, Ventura, CA, February 16 – 21, 2020 (invited talk).

35. Manthiram, “Battery Technologies for Electric Mobility,” Workshop on Emerging Technologies and Trends in Electric Mobility, Kolkata, India, March 2, 2020 (invited talk).

36. Manthiram, “Energy Storage: Battery Technologies for Grid Storage and E-Mobility,” India Smart Grid Forum, New Delhi, India, March 3, 2020 (invited short course).

37. Manthiram, “Battery Technologies for Grid Storage and E-Mobility,” India Smart Grid Forum, New Delhi, India, March 4 – 5, 2019 (invited plenary talk).

38. Boryann Liaw, “Lithium Metal Electrode—Stability, Reversibility, and Durability.” Li Metal Electrode Characterization and Modeling Workshop, University of California San Diego, La Jolla, CA, February 13, 2020.

39. Boryann Liaw, “From Battery Failure Analysis to Life Prediction.” Presented in the Battery Innovation Summit, NAATBatt Annual Meeting and Conference 2020, Pasadena, CA, February 12, 2020.

40. Jihui Yang, January 2020. Materials Science and Engineering Department Seminar, University of Michigan, Ann Arbor, MI, USA: “Solid State Batteries – from Interfaces to High Energy Density”. (Invited)

41. Yi Cui, “Nanomaterials Design for Energy and Environment” International Conference on Nanoscience and Nanotechnology 2020 (ICONN 2020), Feb. 9-13, 2020, Brisbane, Australia. (Plenary, online talk due to COVID-19)

42. Yi Cui, “Materials and Interface Design for Batteries” UIUC Materials Science Seminar, Feb. 17, 2020. (Invited)

43. Yi Cui, “Nanomaterials Design for Energy and Environment” Rice University, Feb. 20, 2020, (Invited)

44. Yi Cui, “Nanomaterials Design for Energy and Environment” University of Houston, Feb. 21, 2020, (Rockwell Lectureship)

45. Whittingham, “Trends for the Future of High Energy Density Battery Technology”, NAATBatt Annual Meeting, February 11th, 2020. M. Stanley Whittingham (Chief Scientific Officer) (by internet)

46. Whittingham, “The Origins of the Lithium Battery and Future Chemistry and Materials Challenges”, Applied Materials, Santa Clara, CA, February 28th 2020.

47. Whittingham, “The Origins of the Lithium Battery and Future Challenges”, ICESI, Sydney, Australia, March 2nd, 2020. M. Stanley Whittingham. Plenary Lecture (by internet)

48. Whittingham, “The Li-Ion Battery and its Global Impact”, Battery Materials Supply Chain, Toronto, Canada, March 2nd 2020, Keynote Lecture.

49. Michael Toney, “X-rays Show Operating Principles of Energy Storage Materials”, Prisker School of Molecular Engineering Colloquium, University of Chicago, Feb 25, 2020, (invited)

50. Michael Toney, “X-rays Show Operating Principles of Energy Storage Materials”, Chemical Engineering Colloquium, University of Colorado at Boulder, Jan 23, 2020, (invited)

51. Y. Shirley Meng, invited talk, “Probing and Understanding the Electrochemical Interfaces and Interphases by Combining Advanced Characterization with Computation Modeling”, Gordon Research Conference (GRC) on Electrochemistry, Ventura, CA, January 6th, 2020, (Invited)

52. M. Stanley Whittingham, “The Origins of the Lithium Battery and Future Challenges/Opportunities”, Stanford Energy Storage International On-line Symposium, May 2nd, 2020. Invited

53. M. Stanley Whittingham, “Batteries”, Lindau Nobel Laureates Meetings (on-line), June 29th 2020. Invited.

54. Yi Cui, Elsevier “From Innovation to Commercialization for Materials, Energy and Environment” April 3, 2020. Invited online webinar

55. Yi Cui, American Chemical Society, “Facial Masks during COVID-19: Disinfection, Homemaking and Imaging” May 14, 2020. Invited online webinar

56. Yi Cui, MIT InnoTherm Symposium, “Thermal Effects on Battery Materials and Chemistry” Jun 17, 2020. Invited online webinar.

57. Jie Xiao, “Integrating Materials Science, Electrochemistry and Engineering in Energy Storage Technologies”, Virtual Seminar for Clean Energy Institute, University of Washington

58. A. Manthiram, “Rechargeable Battery Chemistry,” National Science Foundation – Industry-University Cooperative Research Center Conference, Austin, TX, April 7, 2020 (invited plenary talk).

59. A. Manthiram, “High-nickel Cathodes for Lithium-ion Batteries,” NASA Decadal Plan – Energy Storage Needs, Austin, TX, May 25, 2020 (invited talk).

60. A. Manthiram, “Intricacies of High-energy Cathodes for Lithium-ion Batteries,” Electrochemical Society Webinar, Austin, TX, June 17, 2020 (invited talk).

61. A. Manthiram, “A Perspective on Next-generation Battery Chemistries,” A virtual Workshop on Rechargeable Batteries, University of Texas at Austin, Austin, TX, June 25, 2020 (invited talk).

62. Y. Shirley Meng, invited talk, “Energy Storage Solutions from -80 ℃ to +100 ℃: From Liquified Gas Electrolytes to Solid State Electrolytes”, 2020 StorageX International Symposium, July 17th, 2020

63. Y. Shirley Meng, keynote talk, “Advanced Diagnostic Tools for Characterizing Lithium Metal Batteries and Solid- State Batteries”, 2020 Israel National Research Center for Electrochemical Propulsion, Sept. 15th, 2020

64. M. Stanley Whittingham, “The Li Battery: From Its Origin to Enabling an Electric Economy”, Florida Battery Symposium (on-line), July 28th, 2020.

65. M. Stanley Whittingham, “Lithium Batteries: From an Idea to Domination. What’s Next?”, ISE Meeting, Belgrade (on-line), August 31st, 2020.

66. M. Stanley Whittingham, “The Origins of the Lithium Battery and Future Challenges/Opportunities”, MSE Seminar, Iowa State University, September 14th, 2020.

67. M. Stanley Whittingham, Nobel Lecture, “The Origins of the Lithium Battery and Future Challenges/Opportunities”, Israel National Research Center for Electrochemical Propulsion, September 16th 2020.

68. M. Stanley Whittingham, “The Origins of the Lithium Battery and Future Challenges/Opportunities”, Inaugural Lecture, Diamond Jubilee, IIT New Delhi, India, September 17th, 2020.

69. M. Stanley Whittingham, “The 2020s – The Decade of Energy Storage: Cleaning the Environment and Mitigating Global Warming”, World Energy Storage Day Conference and Expo, September 22nd, 2020.

70. M. Stanley Whittingham, “The Origins of the Lithium Battery and Future Challenges/Opportunities”, General Motors, September 22nd, 2020.

71. M. Stanley Whittingham, “Lithium Batteries: From an Idea to Domination. What’s Next?”, TESTA - Int. Electric Vehicle Technology Conference and Exhibition, Taiwan, September 24th, 2020. .

72. M. Stanley Whittingham, “Lithium Batteries: From an Idea to Domination. What’s Next?” 2020 Advanced Lithium-ion Battery and Fuel Cell Conference, Taiwan, September 29th, 2020.

73. M. Stanley Whittingham, “Why Materials?”, IMDD-MRSEC Launch Celebration, UC San Diego, September 29th, 2020.

74. A. Manthiram, “Battery Technologies and Charging Characteristics,” Online Training Program on Electric Mobility & Charging Infrastructure, India Smart Grid Forum, New Delhi, India, July 4, 2020

75. A. Manthiram, “Oxide Cathode Chemistry for Batteries: Richness and Complexities,” StorageX International Symposium, Stanford, CA, July 24, 2020.

76. A. Manthiram, “Electrical Energy Storage: A Materials Chemistry Perspective,” Indian Institute of Technology Madras Webinar, Chennai, India, August 14, 2020.

77. A. Manthiram, “Next Generation Battery Chemistries,” International Advanced Research Centre for Powder Metallurgy and New Materials (ARCI), Chennai, India, August 28, 2020.

References

1. K. Shah et al., *J. Electrochem. Soc.*, **167**, 133501 (2020).

2. K. Kumaresan, Y. Mikhaylik, and R. E. White, *J. Electrochem. Soc.*, **155**, A576

Acknowledgements

The Battery500 consortium sincerely appreciate the guidance, help, and support provided by NETL manager, Colleen Butcher, the advisory board, and executive committee of Battery500.

II.13.B Battery500 Seedling Projects (NAVSEA)

Patricia Smith, Report Coordinator
NAVSEA, Carderock Division
9500 MacArthur Blvd
West Bethesda, MD 20817
E-mail: patricia.h.smith1@navy.mil

Tien Duong, DOE Technology Development Manager
U.S. Department of Energy
E-mail: Tien.Duong@ee.doe.gov

Start Date: October 1, 2017 End Date: March 31, 2021
Project Funding: $11,992,025 DOE share: $10,374,194 Non-DOE share: $1,617,831

Project Introduction

The Battery500 Consortium is a multi-institution program working to develop next-generation Li-metal anode cells. Although the Consortium has made significant progress developing novel cell materials and integrating these materials in industry relevant pouch cells, the demanding goals of ≥500 Wh/kg and 1,000 cycles have not been reached. Additional time and support are required.

Objectives

Eleven seedling or proof-of-concept projects seek to support the Battery500 Consortium Program by exploring high-risk, high-payoff concepts. Their goal is to provide an infusion of novel technology into the program.

Approach

The seedlings are taking various approaches to jump-start several emerging technologies. These include:

Design, Processing, and Integration of Pouch-Format Cells for High-Energy Lithium-Sulfur Cells. (Mei Cai, General Motors)

This effort seeks to develop the design, processing, and integration methodology for Li-S batteries to achieve the desired energy density and cycle life goals. The sulfur cathode will be optimized to obtain the desired loading and porosity. Novel electrode fabrication processes will be developed to provide continuous cathode production and the electrolyte formulation will be modified and tuned to further improve the electrochemical performance. The developed technology will be demonstrated in a pouch-format cell (e.g., ≥ 2 Ah).

Electrochemically Stable High-Energy-Density Lithium-Sulfur Batteries (Prashant N. Kumta, University of Pittsburgh)

This project is a scientific study to obviate the primary problems of: (a) low overall electrode capacity (mAh/g active material) occurring due to low electronic conductivity of sulfur, (b) poor cycling stability owing to polysulfide dissolution, (c) voltage drop due to polysulfide transport across and deposition at lithium anode, and (d) poor Coulombic Efficiency (CE). Efforts will focus on developing approaches to effectively prevent polysulfide dissolution into the electrolyte. One method will be to generate framework confinement materials to effectively trap polysulfide species within the electrode. The second approach exploits the chemical interactions of polysulfides with effective catalysts identified by density functional theory (DFT) involving transition metal oxides and other systems to enhance conversion as well as trapping of sulfur in porous carbon structures. A third approach involves use of composite polymer electrolytes (CPEs) to enhance transport and prevent lithium metal dendrite formation. Finally, utilization of CPE's in confinement systems to enhance transport and enable improves cycling and CE will be investigated.

Highly Loaded Sulfur Cathode, Coated Separator, and Gel Electrolyte for High-Rate Lithium-Sulfur Batteries (Yong L. Joo and Jin Suntivichi, Cornell University, Trung Nguyen, EIC Laboratory)

The key features of this project's approach are the development of: (a) a highly loaded sulfur cathode by alternating sulfur-impregnated mesoporous carbon and graphene layers, (b) a thermally stable polymer/ceramic hybrid separator coated with graphene, and (c) a safe gel-electrolyte based on ceramic crosslinker for Li-S battery systems with improved performance at high rates. Rigorous abuse tests of Li-S batteries will provide insight into the safety of Li-S batteries.

Controlled Interfacial Phenomena for Extended Battery Life (Perla Balbuena and Jorge Seminario, Texas A&M University)

First principles computational tools will be used for selection of electrolytes compatible with the Li-metal anode and high-voltage NMC cathode electrodes. The study will characterize strengths and weaknesses associated with the electronic and molecular structure of electrolytes at the electrode/electrolyte interfaces and their effects on Li-metal plating/stripping phenomena, SEI, and cathode electrolyte interphase (CEI) formation. In addition, first-principles computational tools will be used for elucidation of the effects of anode surface morphology and chemistry on performances of the electrolytes. The study will include characterization of lithium nucleation, interactions with the electrolyte, and SEI formation and stability on various anode surface morphologies.

3D Printed, Low Tortuosity Garnet Framework for Beyond 500 Wh/kg Batteries (Eric Wachsman and Liangbing Hu, University of Maryland)

This project will fabricate controlled 3D porous solid-state electrolyte structures that are ordered and act as electrode supports, facilitating fast ion transport within the electrodes. It will enable higher battery C-rates and thicker electrodes for higher loading. The 3D structures can also increase the mechanical strength of the solid-state battery. In parallel, 3D solid-state ionic and electronic transport models will be developed to determine achievable C-rates as a function of structure. With this information, high-performance Li-S and Li-NMC batteries will be fabricated using the 3D solid state electrolyte structures.

Composite Cathode Architecture for Solid-State Batteries (Marca M. Doeff, Lawrence Berkeley National Laboratory, Guoying Chen Lawrence Berkeley National Laboratory, Stephen Sofie, Montana State University, Tobias Glossmann, Mercedes-Benz Research and Development, North America)

Freeze tape-casting techniques will be utilized to produce porous scaffolds of LLZO (variants of $Li_7La_3Zr_2O_{12}$) solid electrolyte and then infiltrate the pores with the other components needed to make composite electrodes. Freeze tape casting allows unparalleled control of porosity by changing processing variables such as slurry loading, solvent, and temperature at selected thicknesses (hundreds of microns thick or less) during continuous production. The unidirectional pores of the scaffolds will then be infiltrated with Ni-rich NMC powders and a conductive additive such as carbon (with or without binder) to form thick (100-150 μm) composite cathodes, which ultimately can be used in all solid-state battery configurations. Porous/dense bilayer LLZO structures will also be fabricated by combining the porous structure with a dense layer of LLZO electrolyte, with lithium foil added to complete the solid-state cell. Another configuration of interest is that of a trilayer, in which the dense layer is sandwiched between two porous layers, one of which contains cathode material and the other an anode material such as lithium metal, to form the device. Some effort will also be devoted to fabrication of NMC scaffolds and infiltration of LLZO into these structures, essentially the reverse of the procedure discussed above.

High-Energy Solid-State Lithium Batteries with Organic Cathode Materials (Yan Yao, University of Houston)

The project will research, develop, and demonstrate a cobalt and nickel-free, multi-electron organic insertion material (OIM) for solid-state lithium batteries to meet the Battery500 goals. It is divided into two parts: (a) exploring strategies to achieve a favorable microstructure of the OIM-electrolyte composites, and (b) identifying OIMs with higher specific energy than those previously developed.

Solvent-Free and Non-Sintered 500 Wh/kg All-Solid-State Battery (Michael Wixom, Navitas; Chunsheng Wang, University of Maryland; David Wood, Oak Ridge National Laboratory)

A solid state battery will be developed using a highly conductive stable solid electrolyte, a composite high-energy cathode, a surface-protected lithium anode, and a roll-to-roll film fabrication process. It will address both material limitations and process challenges facing large-format SSB production. At present, sulfide solid state electrolytes have two major limitations to be solved before being adopted for large-scale battery production: (1) low (electro)chemical stability against air and common cathode materials, and (2) lack of scalable fabrication processes. This project will address the first by modifying the sulfide structure to improve its stability and will address the second challenge by adopting and scaling a dry process electrode fabrication technology developed successfully at Navitas.

Multifunctional Lithium-Ion Conducting Interfacial Materials for Lithium-Metal Batteries (Donghai Wang, Pennsylvania State University)

The project will research, develop, and demonstrate multifunctional LIC interfacial materials as a protective layer for Li-metal anodes in Li-ion batteries, enabling Li-metal anodes to cycle with a high efficiency of ~ 99.5% at high electrode capacity (> 6 mAh/cm^2) and high current density (> 2 mA/cm^2) for over 500 cycles. The project will demonstrate Li-metal battery cells with an energy density of ≥ 500 Wh/kg and a ≥ 80% capacity retention over 500 cycles using Li-metal anodes with this protective layer.

Advanced Electrolyte Supporting 500 Wh/kg Lithium-Carbon/NMC Batteries (Chunsheng Wang, University of Maryland)

This project will research, develop, and demonstrate a unique Li-C/NMC battery system supported by novel all-fluorinated and ionic liquid electrolytes as well as a micro-sized Li/C composite anode capable of achieving an energy density ≥ 500 Wh/Kg while achieving a 1,000-cycle life. By optimizing the salts, solvents, and the compositions in electrolytes, the team aims to form a lithiophobic LiF SEI and a lithiophilic substrate for the lithium anode, as well as a LiF-rich CEI on cathodes. The stable SEI and CEI during charge/discharge cycles will ensure a high cycling efficiency and long cycle life.

Results

Design, Processing, and Integration of Pouch-Format Cells for High-Energy Lithium-Sulfur Cells. (Mei Cai, General Motors)

Single layer Li-S pouch cells were developed and evaluated. The cell contained a cathode with a mass loading of 4 mg cm^{-2} per side and a 100 µm lithium anode. The cathodes utilized a carboxyl cellulose polymer binder (30 wt%) and were calendared to a porosity of ~55 %. TiO_2/C@Al_2O_3 coated polypropylene separators were used with the 80 wt% TiO_2/C coating facing the sulfur cathode. An excessive amount of electrolyte was used due to the dead volume inside the pouch case.

The impact of a dual-phase electrolyte, consisting of both liquid-phase electrolyte and solid-phase electrolyte, on lithium cycling stability was investigated. Repetitive plating/stripping tests of lithium using asymmetrical Li|Cu cells with different dual-phase electrolytes and a traditional liquid electrolyte were conducted. The cell configurations of Li|Cu cells with different types of electrolytes are shown in the insets of Figure II.13.B.1. The cycling efficiency of Li|Cu cell using traditional liquid electrolyte was ~ 96% in the first 70 cycles, fading quickly afterwards. In contrast, the cycling efficiency of the cell using the Generation 1 (Gen 1) dual-phase electrolyte increased to ~ 98% and was maintained over 100 cycles, indicating the ability of a dual-phase electrolyte to efficiently protect the lithium metal.

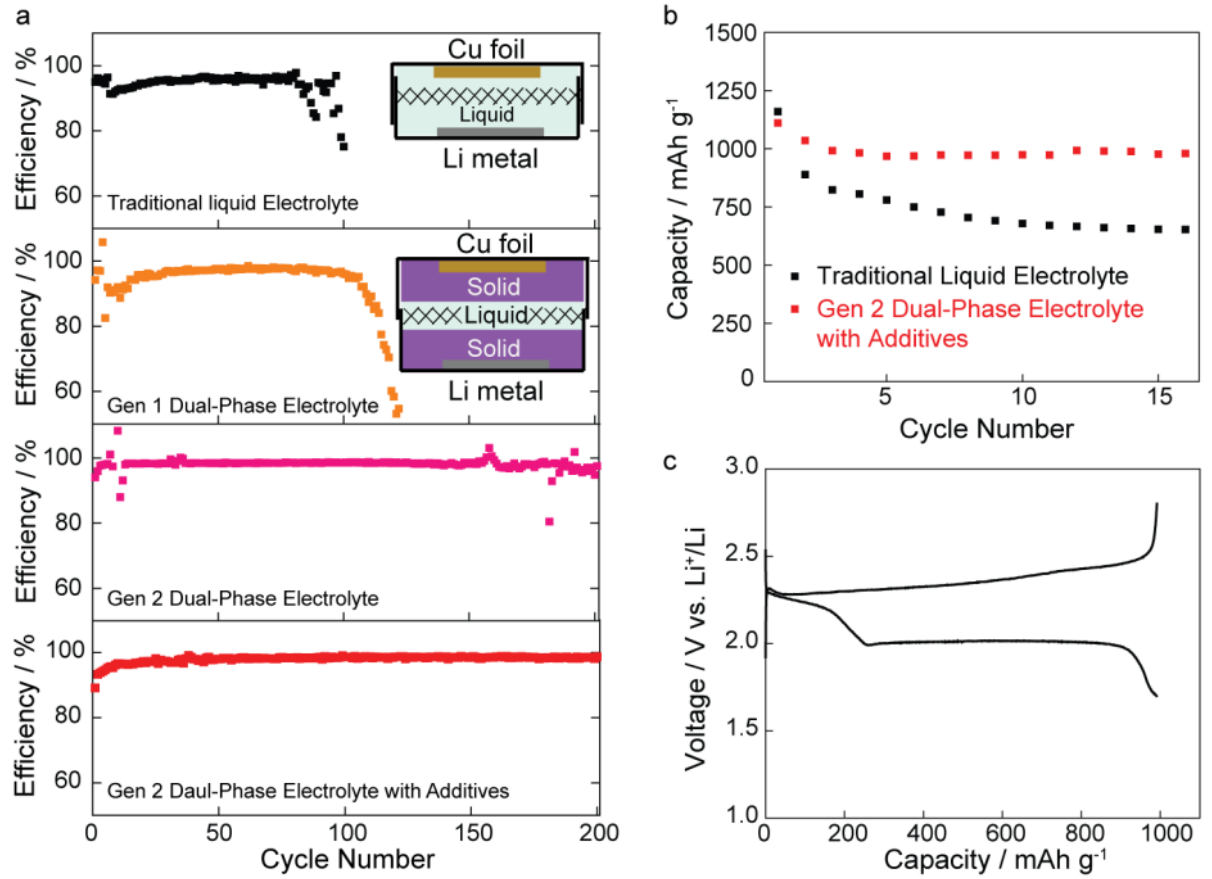

Figure II.13.B.1 Electrochemical behavior of Li-metal anode and Li-S cell in different dual-phase electrolytes. (a) Coulombic efficiency of Li-metal plating/stripping at the current density of 1 mA cm^{-2} with a deposition capacity of 1 mAh cm^{-2} using Li|Cu cells in a traditional liquid electrolyte and different dual-phase electrolytes. The Inset shows the schematic of Li-Cu cells using traditional liquid electrolyte and a dual-phase electrolyte. (b) Cycling stability of Li-S cells in traditional liquid electrolyte and the Gen 2 dual-phase electrolyte, respectively, at the current density of 50 mA g^{-1}. (c) Typical galvanostatic voltage profile of a Li-S cell with Gen 2 dual-phase electrolyte at the current density of 50 mA g^{-1}.

The cycling efficiency of Li|Cu cell using 2nd generation (Gen 2) dual-phase electrolyte was dramatically enhanced to ~ 99% and was stable to more than 150 cycles (Figure II.13.B.1a). Addition of a new electrolyte ingredient maintained the same cycling efficiency but extended the number of cycles to more than 200 (Figure II.13.B.1a). This improvement could be explained by the ability of the additive to form a better protective robust solid electrolyte interphase layer; the mechanism study is in progress. Finally, studies of operating the Li-S cell in the Gen 2 dual-phase electrolyte showed excellent cycling stability. As shown in (Figure II.13.B.1b), the cell released an initial capacity of ~ 1100 mAh g^{-1} and was stabilized at ~ 1000 mAh g^{-1} from the 2nd cycle. The charge-discharge voltage profiles of this cell shows the typical two plateaus during discharge and one plateau during charge without large voltage hysteresis (Figure II.13.B.1c).

Based on the collected evidence, the team concludes that dendrite-free lithium deposition and dramatically enhanced cycling performance can be achieved for the lithium plating/stripping in dual-phase electrolyte, enabling a significantly improved cycling stability of Li-S full cell. Going forward, the mechanism study and optimization of dual-phase electrolytes will continue to achieve longer cycling life of Li-S full cells.

Electrochemically Stable High-Energy-Density Lithium-Sulfur Batteries (Prashant N. Kumta, University of Pittsburgh)

One of the efforts in this last year involved developing high sulfur loading (~10-18 mg/cm^2) electrode architectures exploiting methods to directly deposit sulfur combined with in-situ generation of coatings of polysulfide trapping agents over the directly deposited sulfur architectures (DDSA-PTA). Figure II.13.B.2 shows the cycling performance of the PTA coated DDSA electrodes (DDSA-PTA). The DDSA-PTA electrode 1 (sample 1) exhibits an initial capacity of ~1188 mAh/g (~14.62 mAh/cm^2 areal capacity) with stable capacity of ~870 mAh/g (~10.71 mAh/cm^2 areal capacity) after 100 cycles at 0.1 C rate. The DDSA-PTA electrode 2 (sample 2) shows an initial capacity of ~1152 mAh/g (~14.06 mAh/cm^2 areal capacity) and a stable capacity of ~925 mAh/g (~11.29 mAh/cm^2 areal capacity) after 100 cycles at 0.1C rate when tested under lean electrolyte (4µl/mg-S) testing conditions.

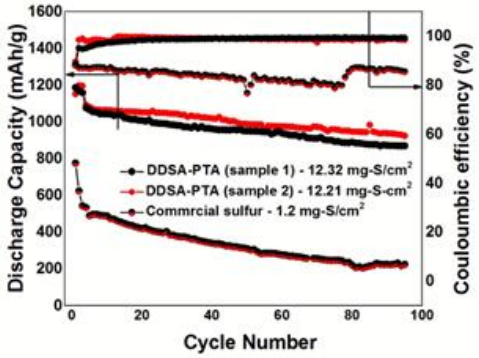

Figure II.13.B.2 Electrochemical cycling performance of the DDSA-PTA electrodes.

XPS analysis on cycled separators and electrodes after 100 cycles showed effective trapping of polysulfide species. In line with the goals of the project, studies were conducted utilizing DFT based computer simulation to identify prospective functional catalysts to enable rapid polysulfide species conversion to Li_2S and back to Li+S. The DFT studies have shown six different inorganic functional catalysts (IFC) favoring both reactions 1 and 2 (defined in Figure II.13.B.3) on the IFC surface. The figure also shows that IFC 1, 3 and 5 have the best reaction kinetics favoring both reactions. Theoretical simulation studies were continued and five other IFC systems were also identified favoring reactions 1 and 2 on the IFC surface. Efforts are underway to incorporate these IFC systems into experimental electrode architectures to demonstrate efficacy.

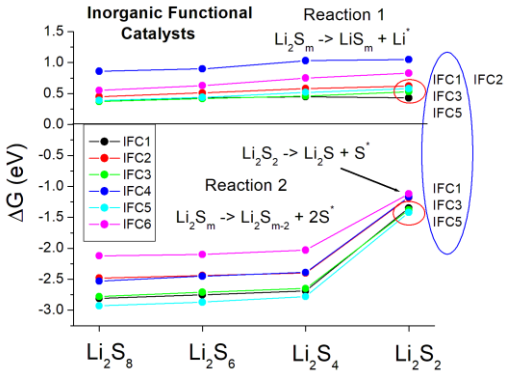

Figure II.13.B.3 Free energies of reactions 1 and 2 for different inorganic functional catalysts (IFCs) and their efficacies for formation of polysulfide species.

Studied continued on lithium-ion conductor (LIC) coated complex framework materials (CFMs) with high sulfur loadings to achieve maximum sulfur utilization and the targeted areal capacity (4mAh/cm^2) and an energy density of 500 Wh/kg. To maximize sulfur utilization, strategies were explored to optimize electrode thickness and porosity. Figure II.13.B.4 shows cycling tests of an optimized S electrode with a thickness of 90 µm (calculated porosity ~51%) and a S loading of 5.71 mg/cm^2. An initial discharge specific capacity of ≈ 900 mAh/g is observed at 52 wt. % S utilization when cycled at C/20 rate with a 7.24 mg sulfur cathode loading stabilizing to ≈ 650 mAh/g capacity at C/10 rate after 7 cycles.

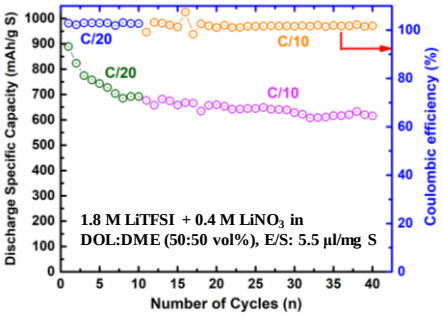

Figure II.13.B.4 Coin cell test results of LIC-CFM-S electrode with optimized porosity of 51.0 % and 90 µm thickness.

Continuing with the above studies of generating LIC-coated CFMs of high sulfur loadings and demonstrating the ability to effectively trap polysulfide species by creating sulfur-CFM chemical linkages in coin cells, the system was further explored in single layer pouch cells. Accordingly, single layer Li-S pouch cells were fabricated and tested with an optimized sulfur electrode of thickness 150 µm (calculated porosity ~66 %) and a S loading of 6.26 mg/cm^2 under lean electrolyte (4 µl/mg) following Battery500 protocol conditions. The results are shown in Figure II.13.B.5. An initial discharge specific capacity of ≈ 900 mAh/g is observed at C/20 rate stabilizing to ≈ 650 mAh/g capacity at 0.1C rate after 5 cycles. The energy density of the pouch cell is ≈ 200 Wh/kg at 0.1C rate (neglecting the mass of pouch case and tabs). Other single layer pouch cells fabricated with various mass loading of sulfur also displayed similar behavior (Figure II.13.B.5**)**. Tests are on-going to determine the effect of calendaring on the fabrication of the sulfur electrode in addition to long term electrode performance cycling, and failure analysis. The success of single layer pouch cells was also extended into fabricating stacked multilayer pouch cells. The results indicate very similar response and are currently being studied for their long term cycling performance. Finally, bi-functional IFC promoting polysulfide conversion and decomposition were added to CFM. The CFM containing a bi-functional catalyst derived by a simple and scalable solid state approach, created high surface area/pore volume and likely provides high activity for polysulfide trapping, conversion and decomposition. To study their initial response, 2032 coin cells were fabricated and cycled utilizing the optimized IFC containing CFM sulfur electrode of 107 µm thickness, porosity 63 % and sulfur loading, 3.71 mg/cm^2. The cells show an initial capacity ≈ 700 mAh/g, stabilizing at~ 730 mAh/g at C/20 rate after 2 cycles indicating promise. Process optimization of IFCs and conductive additives to improve polysulfide trapping and cycling stability of this system are on-going.

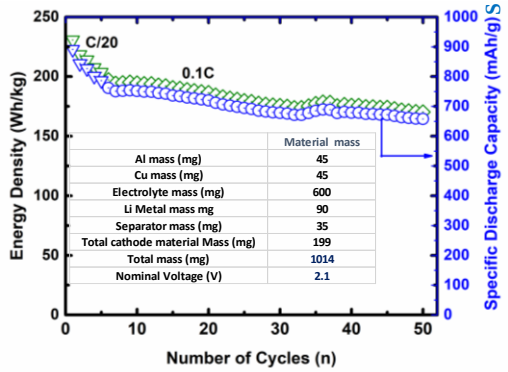

Figure II.13.B.5 Single layer pouch cell utilizing LIC-CFM-S electrode tested under lean electrolyte conditions of 4 µl/mg.

Highly Loaded Sulfur Cathode, Coated Separator, and Gel Electrolyte for High-Rate Lithium-Sulfur Batteries (Yong L. Joo and Jin Suntivichi, Cornell University; Trung Nguyen, EIC Laboratory)

Efforts focused on utilizing air-controlled electrospray and polysulfide transport modeling to develop a high sulfur-loaded cathode, a coated separator and a gel electrolyte for high-rate capable Li-S batteries.

Air-controlled (AC) electrospray was applied to alternatively layer sulfur impregnated mesoporous carbon (MPC) and graphene (Gr), and incorporate graphene nanoribbons (GNR) to increase the capacity and rate capability of a Li-S cell. This double layer approach was applied to high sulfur-loaded systems (3 - 5 mg S/cm^2), demonstrating the potential to increase sulfur utilization and capacity retention. The effect of Gr layer and GNR on capacity (Figure II.13.B.6) is highly pronounced at high C rates of 1C and 2C. Future efforts will extend double layers to multi-layers for high loading systems.

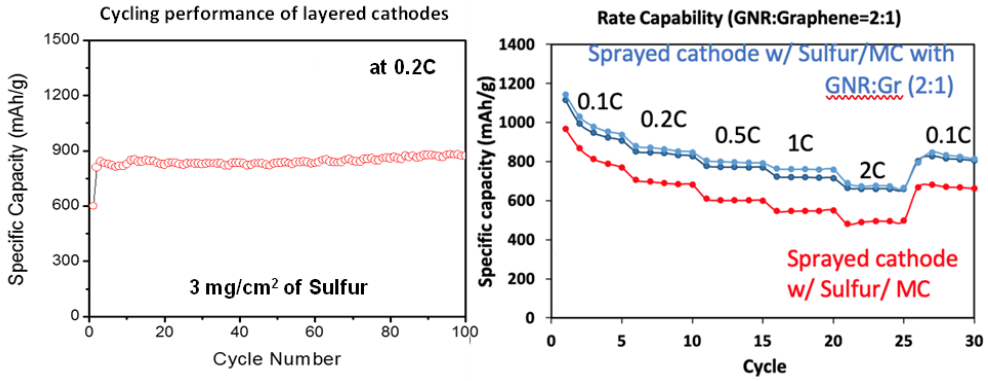

Figure II.13.B.6 Cycling performance and rate capability of highly loaded sulfur cathode with alternating layers of sulfur/mesoporous carbon and graphene or graphene/graphene nanoribbons (GNR)

A polymer (polyimide, PI)/ceramic (polysilsesquioxane, PSSQ) hybrid separator was shown to improve cell performance at high rates (Figure II.13.B.7). Nanofibers of polybenzoimidazole (PBI) and alumina were investigated to replace PI and PSSQ, respectively for further enhanced mechanical properties, electrochemical stability as well as safety. Coating of graphene on polymer/ceramic separator will be applied to highly loaded sulfur cathodes.

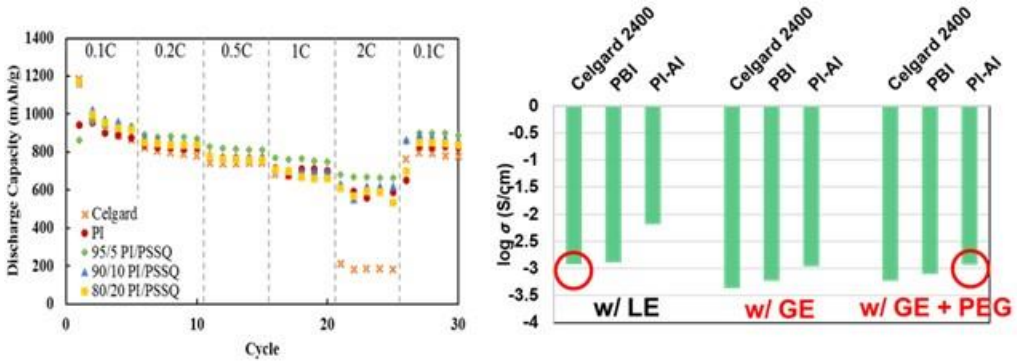

Figure II.13.B.7 Improved rate capability of polymer-ceramic hybrid separators and enhanced ionic conductivity of polymer/ceramic hybrid separators with gel electrolyte/PEG.

Ceramic gel electrolyte were shown to offer improved capacity retention and rate capability, and also effectively mitigates polysulfide shuttling (Figure II.13.B.8). Inclusion of PEG to ceramic gel electrolyte enhances the ionic conductivity and cell performance. Gel electrolyte will be combined with highly loaded S cathodes and polymer/ceramic separators in the future.

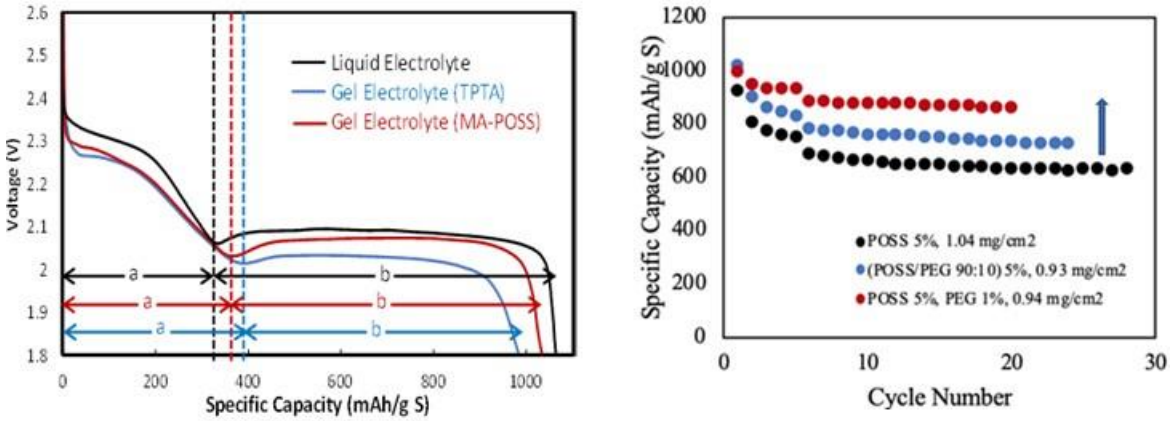

Figure II.13.B.8 Mitigation of soluble polysulfides by gel electrolyte over liquid electrolyte in Li-sulfur batteries, and improved cell performance with gel ceramic electrolyte (GE) by inclusion of PEG

Controlled Interfacial Phenomena for Extended Battery Life; Perla Balbuena and Jorge Seminario, Texas A&M University

Electrolyte structure and interfacial reactivity.

Li^+ coordination behavior with FSI^- anions triggers the formation of a 3-D solution structure in high concentrated electrolytes (HCE), Figure II.13.B.9a. In LHCE electrolytes, a diluent weakly interacting w/Li^+ does not alter the HCE 3-D structure, and Li-centered complexes appear as islands (Figure II.13.B.9b). Our ab initio molecular dynamics analysis identifies the most and less stable molecules at anode and cathode. At the cathode, our method predicts that high coordinated molecules are the most stable having the lowest oxidation levels, whereas the low coordinated molecules have the highest oxidation levels, i.e. the less stable. The CEI is predicted to result from decomposition of low coordinated molecules. Analysis of the reduction levels at the anode indicates that high coordinated molecules are easier to be reduced, and low coordinated molecules are more stable. Therefore, the SEI is predicted to arise from decomposition of high-coordinated molecules. The SEI and CEI components are identified.

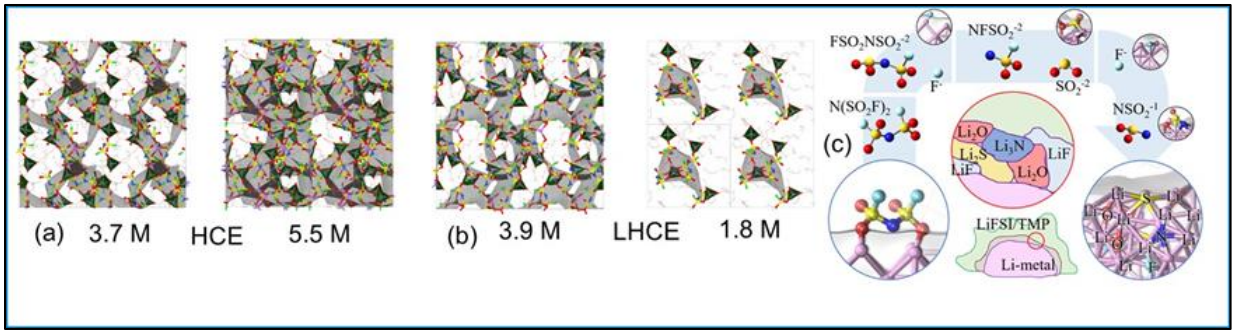

Figure II.13.B.9 Structure from AIMD simulations. (a) HCE electrolytes of 3.7 and 5M LiFSI in DMC. Dark tetrahedral regions are Li-ion centered complexes, usually coordinated with O from 3 anions and one solvent. Shaded regions are 3-D networks of connected complexes. Empty (white) regions have uncoordinated molecules. (b) LHCE electrolytes with less (3.9M) and more diluent (1.8M). Formation of islands is clear in the 1.8M solution. (Chem. Mater. 32, 5973-5984 (2020)). (c) SEI formation by anion decomposition on the Li metal anode in contact with a solution of LiFSI in trimethyl phosphate (TMP) solvent. J. Phys. Chem. C, 124, 21919–21934, (2020).) Color code: Li: purple, S: yellow, N: blue, O: red, F: light blue.

Electrolyte dynamics

AIMD and classical MD simulations of LHCE electrolytes under an electric field revealed the drifting ion dynamics and ion transport mechanisms. The most important feature is the changing nature of the first solvation shell of the ion. The ionic motion is dominated by a hopping mechanism. When the ion is coordinated to O atoms from solvent or anion, the ion transport is slower. However, when the diluent enters into the solvation shell, since the ion-diluent interaction is weaker, the ion motion is faster. Thus, Li+ ions jump between aggregated islands built mainly from FSI- anions via diluent zones (shown as white regions in Figure II.13.B.9b.

Electric field effects on reactivity

DFT and AIMD analysis performed on Li metal anode surface models in contact with electrolyte under applied fields showed that the activation barriers for the reactions decrease as the electric field strength increases, and the reaction energy becomes thermodynamically more favorable. Reaction mechanisms of the solvent and salt reductions do not change under the applied field. Lithium salts are very prone to decompose in either charged or uncharged interfaces. Yet, the extent of reduction is higher when the interfaces are charged. Initial bond-breaking steps for the salt anion reduction are found to be consistent throughout all the electrolyte mixtures. The structure of the nascent SEI layer resulting from our AIMD simulations of charged interfaces resembles a combination of the mosaic (nucleating components) and coulombic interaction (agglomeration of charged fragments) models. (J Power Sources, 472, 228449, 2020)

Nanobattery models

Fully atomistic models accounting for the presence of two electrodes in the cell characterize cell energetics, voltage drops, different charge protocols, SEI evolution during charge and discharge. Figure II.13.B.10 shows that the energy difference $\Delta E = E_{cathode} - E_{anode} = -3.86$ eV without any external electric field (blue curve in Figure II.13.B.10) yields the open-circuit voltage (OCV = 3.86 V) of this nanobattery, consistent with most of commercial Li-ion battery voltages ranging from 3 to 4.1 V. During discharge, the battery spontaneously yields a discharging external current of electrons from anode to cathode as soon as a load (resistance) is connected to the two electrodes. Simultaneously and internally, Li-ions travel from anode to cathode (same direction as electrons). During charge (red curve in Figure II.13.B.10), an external field is needed to at least counteract the OCV plus an additional potential to regulate the amount of current. Based on our previous work, we estimated that an external electric field of $\mathscr{E} = 0.75$ V/Å would be enough to charge nanobatteries in an acceptable computational time. The model provides many new insights into atomistic events occurring during charge and discharge. (PCCP, 2020, DOI: 10.1039/D0CP02851G).

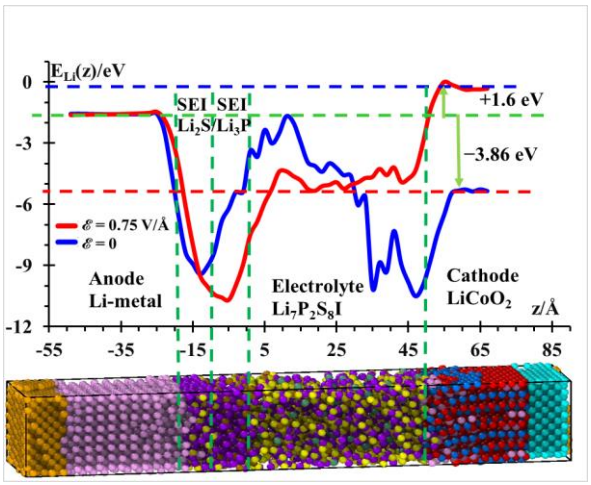

Figure II.13.B.10 Li+ potential energy profile along the longitudinal z-axis calculated from MD simulations for $\mathcal{E}$ = 0 (blue) and for $\mathcal{E}$ = 0.75 V/Å (red), at 300K.

Ion deposition

Constrained AIMD simulations used to evaluate barriers for the Li ion during its motion from the electrolyte phase to the surface, elucidate events such as desolvation, dissociation from the ion-pair, diffusion through the electrolyte phase, and ion deposition and reduction on pristine or SEI-covered surface, for various electrolyte chemistries and concentrations. A suggested inverse correlation between the barriers for ion desolvation and diffusion, and time for dendrite formation requires the barriers for each of the step in the ionic motion. This method allows us to characterize the ability of a given electrolyte to oppose inhomogeneous Li metal nucleation. (PCCP, 22, 21369-21382, (2020))

SEI nucleation and growth

MD simulations used to characterize SEI nucleation and morphology due to oxidation of Li metal in contact with a liquid electrolyte, allows identifying evolution of Li metal expansion and formation of a porous phase where the SEI components start to nucleate (Figure II.13.B.11). LiF nucleation is relatively easy to follow with classical MD simulations due to its fast kinetics. These simulations demonstrated for the first time many details regarding Li metal oxidation and SEI formation evolution.

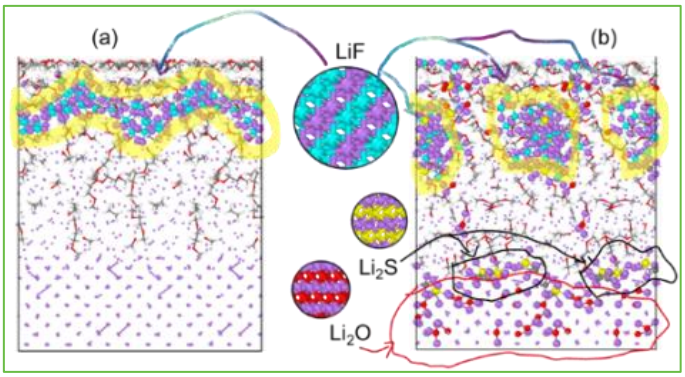

Figure II.13.B.11 Li oxidation and SEI morphologies in 2M solutions. (a) LiPF6 in DME: well-developed top layer of LiF nucleation observed at the top. The bottom of the Li slab keeps Li metal density after 20 ns, and a low-density Li region contains DME fragments and some intact DME molecules. (b) SEI structure and composition obtained from $LiCF_3SO_3$ in DME. (J. Mater. Chem. A, 8, 17036-17055, (2020))

3D Printed, Low Tortuosity Garnet Framework for Beyond 500 Wh/kg Batteries (Eric Wachsman and Liangbing Hu, University of Maryland)

Numerous column and grid LLZO structures were 3D printed on dense/porous sintered LLZO creating trilayer architectures consisting of a controlled porous LLZO structure on the cathode side of a thin dense LLZO separator layer, supported on the bottom by a random porous LLZO layer (Figure II.13.B.12). A major focus of research was developing the ink formulations and printing procedures necessary to obtain these unique 100-200 µm height controlled structures.

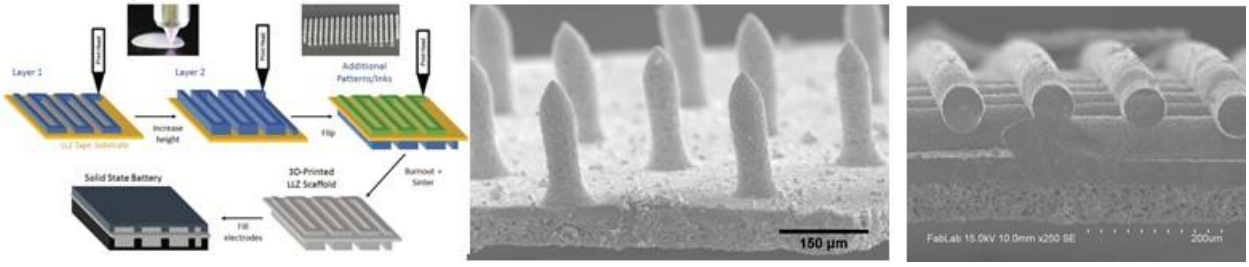

Figure II.13.B.12 3D printing of controlled architecture LLZO electrolyte structures as cathode ion-conducting path, on top of dense/porous bilayer LLZO structures; (middle) 200 µm high columns and (right) 100 µm high grid structures.

Transport models were developed to predict cell performance using these controlled architectures using known material properties and thermodynamic quantities with estimates of interfacial impedance. Calculations examined the effect of feature size (diameter and height) and spacing on electrode utilization at a fixed porosity for column and grid structures. These models not only provide ability to predict energy density as function of structure, but since based on transient transport equations also provide as function of C-rate (Figure II.13.B.13).

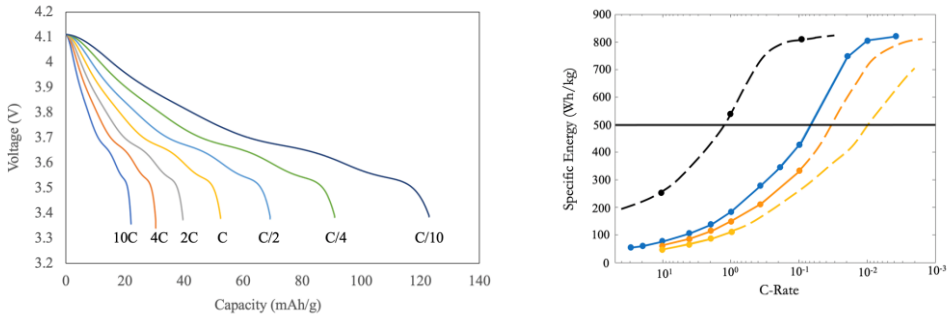

Figure II.13.B.13 Model calculations for solid-state battery performance; (left) voltage-capacity curves using 150 µm high LLZO columns, 40 µm in diameter at 100 µm spacing between columns, filled with NMC, and (right) specific energy as function of C-rate for various solid-state battery architectures to predict structure needed to achieve 500 Wh/kg energy density at desired C-rate.

Full cells were produced by filling 3D printed column and grid pores with NMC and sulfur, respectively. The random porous structure on the opposite side was filled with Li-metal. Figure II.13.B.14 shows NMC filled columns and sulfur filled grids.

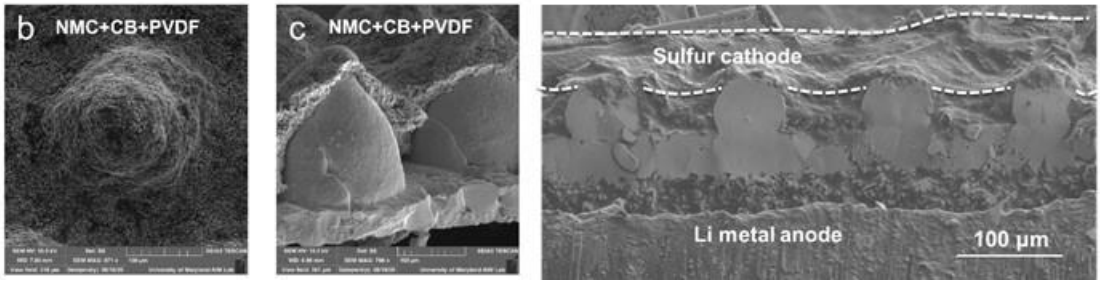

Figure II.13.B.14 SEMs of full cells; NMC filled columns (left) and sulfur filled grids (right).

Cell performance was determined at room temperature and elevated temperature. Figure II.13.B.15 shows cell results for columns filled with NMC at 60°C (left) and grids filled with sulfur at 25°C (right). These initial results are promising, but additional work is needed to reduce the cathode/electrolyte interfacial impedance, which is an area of continued research.

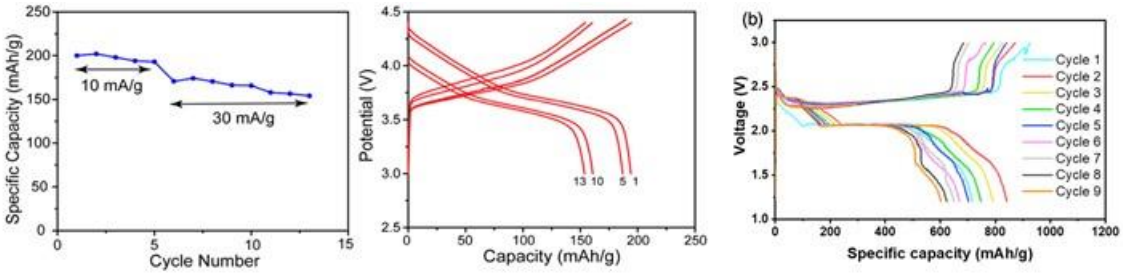

Figure II.13.B.15 Representative full cell performance; NMC filled columns at 60°C (left and middle) and sulfur filled grids at 25°C (right).

Composite Cathode Architecture for Solid-State Batteries (Marca M. Doeff, Lawrence Berkeley National Laboratory, Guoying Chen Lawrence Berkeley National Laboratory, Stephen Sofie, Montana State University, Tobias Glossmann, Mercedes-Benz Research and Development, North America)

The Team made progress in diversifying porous/dense bilayer and porous/dense/porous trilayer LLZO architectures by investigating lower LLZO vol% slurries and testing alternative ceramic processing methods for engineering the Li/LLZO interface. Additionally, the causes of early failures of the solid-state batteries constructed last year were identified and alternative approaches were explored to address the issue.

They expanded the vol. % range of the freeze-tape-castable LLZO slurry down to 5 vol% through optimizing slurry formulations. Lower LLZO loadings of 5 and 7.5 vol%, compared to the standard formulation of 10 vol%, were achieved by increasing the thickening agent fraction to obtain viscosities suitable for casting. Figure II.13.B.16 compares the sintered porous/dense LLZO bilayers produced using freeze-tape-cast green tapes using 5, 7.5, and 10 vol% LLZO slurries. The pore region noticeably increases with reducing vol% of LLZO. This permits higher areal loading of active materials which will be key to obtaining high energy density solid state batteries.

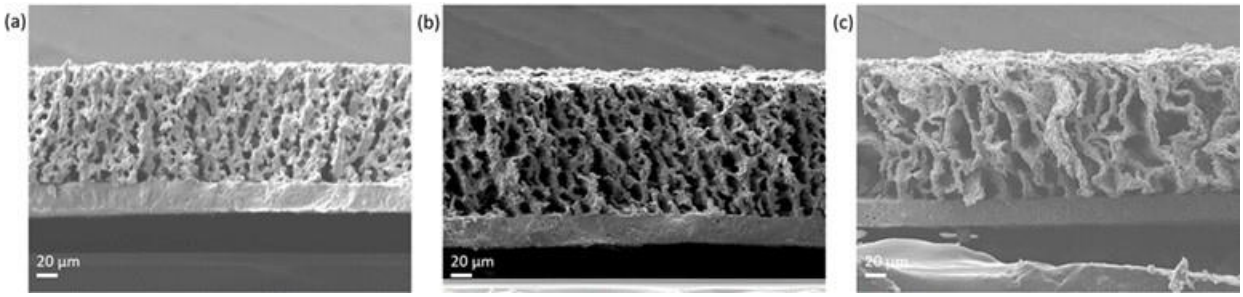

Figure II.13.B.16 Sintered bilayers using (a) 10 vol % (b) 7.5 vol %, and (c) 5 vol % freeze tape cast LLZO

Sol-gel coating of a ZnO interfacial layer was investigated in order to facilitate wetting of lithium on LLZO surfaces. This was to replace the Au coating layer with a lower cost, scalable alternative. Typical processes involved dispensing a precursor solution containing Zn and gently heating to burn off the organics (Figure II.13.B.17a). The sol-gel derived ZnO coating layer successfully aided the melt bonding of Li foil as shown in Figure II.13.B.17b where Li and LLZO are bonded seamlessly. We also investigated an application of a thin porous LLZO layer onto the dense LLZO layer to increase the specific interfacial area between LLZO and Li anode. This should permit cycling at higher current densities with minimal specific energy drop compared to using freeze-tape-cast derived LLZO anolytes at thicknesses of 80-120 µm. Figure II.13.B.17c shows a coated porous LLZO layer with a thickness to <10 µm by controlling the processing parameters.

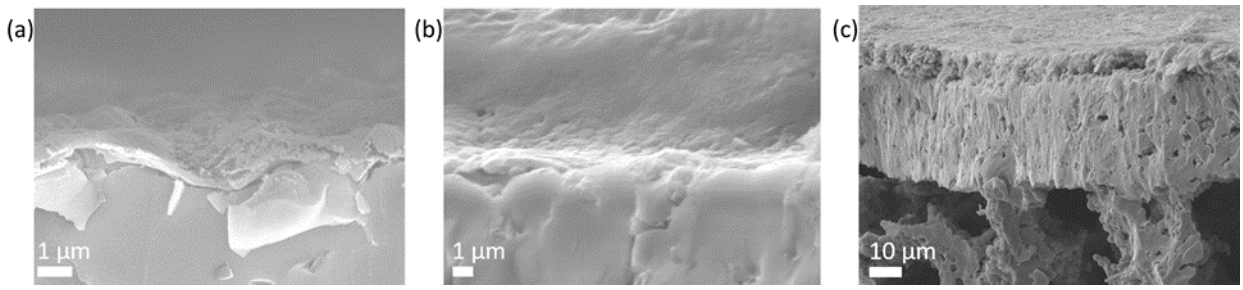

Figure II.13.B.17 (a) LLZO with 200 nm ZnO coating. (b) Seamless Li/LLZO interface aided by ZnO coating layer. (c) Porous LLZO coating layer (<10 µm) on dense LLZO.

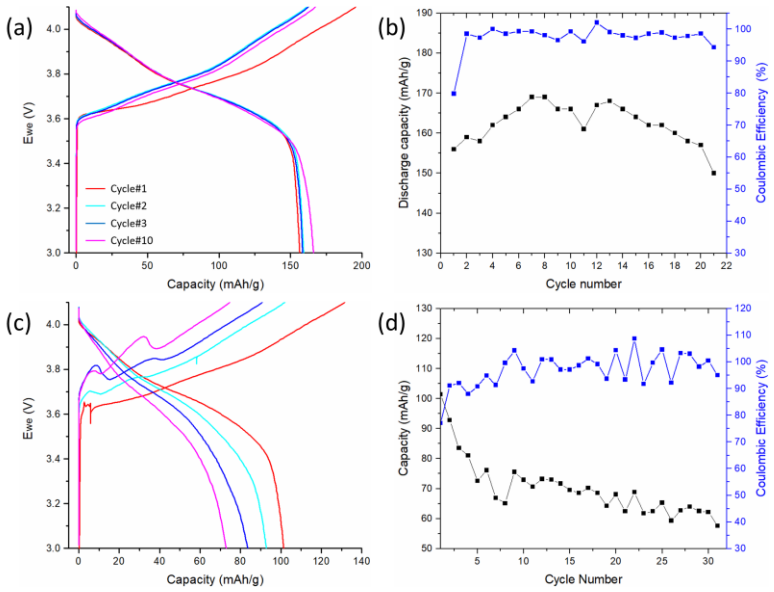

Figure II.13.B.18 (a)/(b) Cycling performance of solid-state battery using NMC cathode at C/10 in trouble-shooting configuration. (c)/(d) Cycling performance of solid-state battery using NMC cathode at C/10.

Solid state cells that use conventional tape cast NMC/C/PVDF cells were constructed for trouble shooting purposes. The porous layer was filled with plastic crystal electrolyte and the tape cast NMC cathode was attached on top. These cells performed very well as shown in Figure II.13.B.18a/b, suggesting that solvent exposure of LLZO during previous bilayer cell construction likely degrades the LLZO surface resulting in early cell failures. Spontaneous reactions of LLZO with common organic solvents have been recently reported. The Team initiated screening of usable organic solvents for NMC slurry infiltration to the porous layer and improved cell cycle life, compared to earlier cells as shown in Figure II.13.B.18c/d. More work is needed to formulate stable dispersions of NMC/C in order to improve the cell capacity. The Team will continue to narrow down optimal processing conditions/parameters for building LLZO based solid state batteries.

High-Energy Solid-State Lithium Batteries with Organic Cathode Materials (Yan Yao, University of Houston)

The Team previously reported a ceramic electrolyte-based organic-lithium battery with a material-level specific energy of 828 Wh kg–1. Pyrene-4,5,9,10-tetraone (PTO) served as the cathode and demonstrated a dynamically stable cathode-electrolyte interface and utilization of 99.5%. This high material utilization was, however, only achievable at a low mass fraction of PTO in the cathode (fPTO=20 wt%). In FY2020, the mass fraction was improved to 50 wt% by microstructure engineering of the cathode.

All solid-state lithium batteries (ASSLBs) were assembled with a cell configuration of PTO:Li_6PS_5Cl:C/Li_3PS_4/Li. PTO possesses a high theoretical specific capacity of 409 mAh g−1 from the redox reaction of four carbonyl groups (C=O ⇌ C-O−). The composite cathodes were prepared by dry-mixing process (DP), where PTO, Li_6PS_5Cl and conductive carbon. The ingredients were mixed in a mortar followed by uniaxial compaction (Figure II.13.B.19a). As fPTO increases from 20 to 50 wt%, CPTO and PTO utilization decrease from 323 to 134 mAh g−1 and from 80% to 32.8%, respectively.

To identify the origin of low PTO utilization, the microstructure of composite cathode was investigated. By exposing the cross-section via focused ion beam (FIB), a "sea-island"-type microstructure was observed. (Figure II.13.B.19b) — Li_6PS_5Cl "islands" with size between 2 to 15 μm were surrounded by a "sea" of PTO. Such a distribution of Li_6PS_5Cl and PTO is unfavorable for Li+ transport. The Team rationalize the undesired microstructure was the result of greater deformation of PTO than that of Li_6PS_5Cl, owing to its higher ductility.

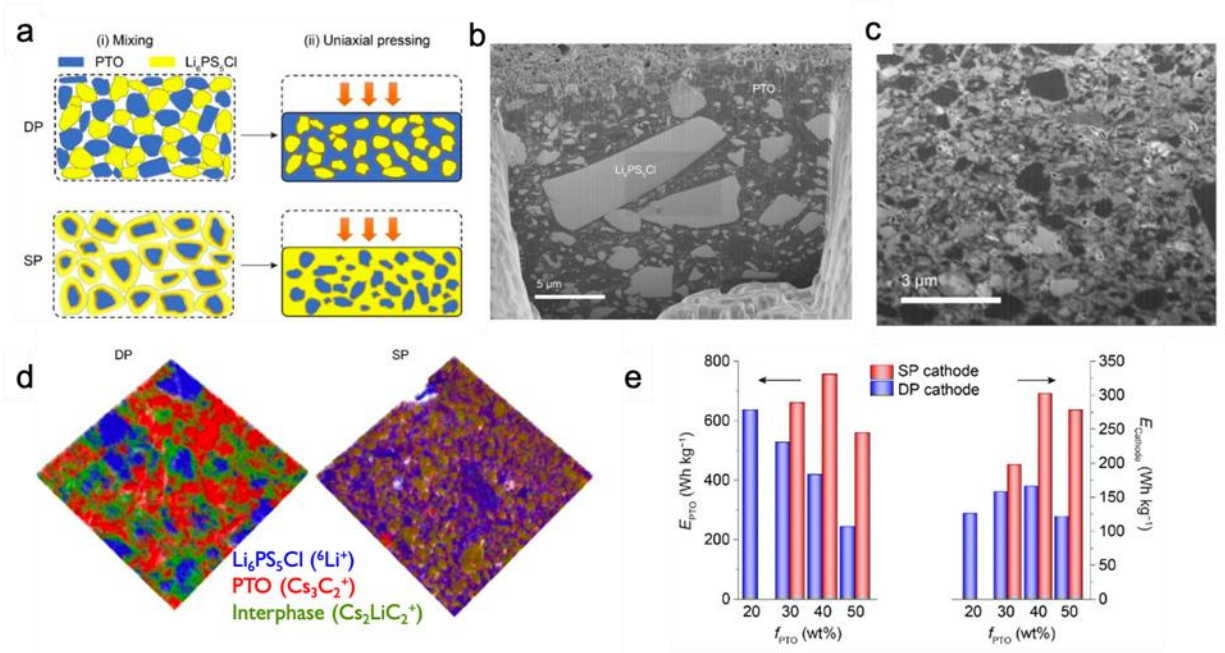

Figure II.13.B.19 Solution process regulates the microstructure of cathode to improve electrochemical performance of a Li-PTO solid-state cell. a, The two-step preparation for DP and SP cathodes. (i) Mixing PTO and Li^6PS_5Cl powders in dry or solvent-assisted fashion. (ii) Powder compaction by uniaxial pressing. b-c, FIB-SEM images on the cross-section of a (b) DP and (c) SP cathode (fPTO = 40 wt%). d, Reconstructed TOF-SIMS images of DP and SP cathodes, showing the distribution of PTO (red), Li_6PSCl (blue) and interphase (green) species. e, Specific energy of DP vs. SP cathodes at various PTO mass fraction. EPTO and ECathode represent specific energy based on the mass of PTO or the whole electrode, respectively.

A solution process (SP) to overcome this challenge as shown in Figure II.13.B.19a was designed. The objective was to preform "core-shell" structured particles, where a PTO core is surrounded by a Li_6PS_5Cl shell. The Team hypothesize by preforming the "core-shell" particles, the deformation of PTO during uniaxial pressing could be confined to reverse the "sea-island"-type microstructure. Cross-section of a SP composite cathode (fPTO = 40 wt%) (Figure II.13.B.19c) shows that the phase separation is clearly reversed: Li_6PS_5Cl domain (gray) forms a continuous network with PTO (black) embedded.

ToF-SIMS correlates the chemical information with spatial distributions. Figure II.13.B.19 shows the distribution of PTO ($Cs_3C_2^+$, red) and Li_6PS_5Cl ($6Li^+$, blue), in agreement with the morphology observed from the FIB-SEM. Reconstructed ToF-SIMS images illustrate the percolating network within cathodes – Li_6PS_5Cl domains are poorly connected in the DP cathode while SP cathode exhibits a well-connected Li_6PS_5Cl network, resulting an increased utilization of PTO. Figure II.13.B.19e summarizes EPTO and ECathode of DP and SP cathodes. Clearly, SP cathodes outperform DP cathodes, exhibiting ECathode of 302 Wh kg−1.

In summary, the Team demonstrated the impact of microstructure engineering on solid-state lithium battery performance. They developed a solution process to regulate the microstructure for ductile organic materials. As the result, the mass fraction of active materials was increased to 50 wt%. Cathode-level specific energy of 302 Wh kg−1 is on par with inorganic cathodes with better cycling stability.

Solvent-Free and Non-Sintered 500 Wh/kg All-Solid-State Battery (Michael Wixom, Navitas; Chunsheng Wang, University of Maryland; David Wood, Oak Ridge National Laboratory)

Large-scale fabrication of solid state batteries will require electrolytes that are stable in a production environment (e.g. an industrial dry room). Research efforts focused on extending the stability of LPS- P_2O_5-CaO electrolyte exposed to dry air conditions. The impedance of the most promising electrolyte material synthesized to date was shown to increase by 12% after 8 hours exposure in a dry room environment. To further test the electrochemical performance of the SE after air exposure, a Li-$LiCoO_2$ cell with LPS-P_2O_5-CaO electrolyte that was exposed to dry air for 8 hours was evaluated and compared to a cell not exposed to dry air. As shown in the voltage profiles of LCO/LPS-P_2O_5-CaO/Li cells (Figure II.13.B.20), cells can achieve an initial discharge capacity of 106.3 mAh/g after exposure to dry air. This corresponds to 83% of the initial discharge capacity of SSE cells not exposed to air. After two cycles, the cycling efficiency reached to a high value of 98.4% compared to 98.5 for cells whose electrolytes were not exposed to air.

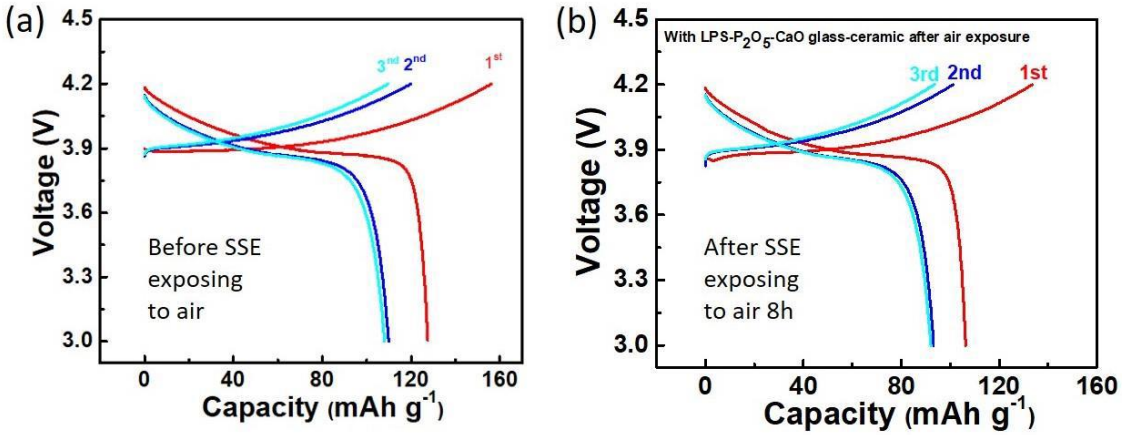

Figure II.13.B.20 Charge-discharge profiles of the LCO/LPS-P2O5-CaO/Li cell for the first 3 cycles (a) before and (b) after LPS-P_2O_5-CaO was exposed in dry air for 8 hours. It was measured at 3.0-4.2 V and at 0.1 C, 60°C.

The pouch cell and cell stack processes require a large amount of SE. Except for the solid-state electrolyte film, the cathode also contains 25-40 wt% solid electrolyte. Previous development efforts were based on a ~ 8 g/batch small-scale LPS synthesis (Prof. Wang's group) using a small ball mill, which is far less than the quantity demanded for the large-scale dry process. The team optimized several electrolyte parameters independently, including the ball milling speed, milling time, rest time between milling, weight ratio of balls and chemicals, ball size and numbers, etc. Employing the knowledge gained from all partners, a new process allows the synthesis of up to 32 g/jar and 128 g/batch, eliminating the bottleneck of the large-scale preparation of SSE film and cathode composite.

Multifunctional Lithium-Ion Conducting Interfacial Materials for Lithium-Metal Batteries (Donghai Wang, Pennsylvania State University)

A novel self-assembled monolayer of electrochemically active molecules (EAM) on current collectors was developed to regulate the nanostructure and composition of the SEI and deposition morphology of Li metal anodes. This enabled superior performance of Li metal batteries at low temperatures (−15 °C). Along with this EAM regulated SEI strategy for low temperature, a new surface-functionalized carbon host strategy was developed to achieve a uniform Li growth on the surface of the functionalized carbon host and in a dendrite-free manner at low temperature. The functionalized carbon host enabled dendrite-free Li deposition even when Li deposition amounts were 12 and 16 mAh cm^{-2} at -15 °C. To understand the uniform Li deposition behavior in the presence of functionalized carbon host, a systematic characterization study was conducted to reveal the mechanism.

Advanced Electrolyte Supporting 500 Wh/kg Lithium-Carbon/NMC Batteries (Chunsheng Wang, University of Maryland)

All-Fluorinated electrolytes (F-262A) and ionic liquid electrolytes were designed to support Li anodes and NMC811 cathodes. The 0.1Ah NMC811 pouch cell with F-262A under 2.0 MPa stacking pressure shows stable cycling with a negligible increase of surface resistance (Figure II.13.B.21a), thus maintaining 85% of capacity after 150 deep cycles with no apparent cell swelling (Figure II.13.B.21b). We also demonstrated the high cycling Coulombic efficiency of >99.9% for Li anode in Li||Cu coin cell at 0.5 mA cm^{-2} and 1.0 mAh cm^{-2} with a lean electrolyte (3g electrolyte/Ah), which is highest and never reported before. No obvious loss of reversibility was observed when anode capacity was increased to 2.0 and 3.0 mAh cm^{-2} (Figure II.13.B.22a). The ionic liquid electrolyte is also compatible with the high energy NMC 811 cathodes. Li-free NMC 811 || Cu cell with 2 mAh cm^{-2} cathode loading and lean electrolyte demonstrates over 80% capacity retention after 160 cycles (Figure II.13.B.22b). The exceptional performance of Li-free NMC 811 || Cu coin cell was validated in single layered pouch cell (electrode dimension= 4×4 cm) with a lean electrolyte and 2 mAh cm^{-2} cathode loading. The Li-free NMC 811 || Cu pouch cell shows a highly reversible charge and discharge behavior (Figure II.13.B.22c) with 200 stable cycles (Figure II.13.B.22d). The increase of capacity at the initial cycle is probably due to less efficient wetting process in pouch cell, which still needs to be optimized. The disruption of capacity at 50th cycle in Figure II.13.B.22d was caused by power-off in the Lab. We are testing Li-free NMC 811 || Cu pouch cells with areal capacity of 4.5-5.0 mAh cm^{-2} to approach an energy density of 500 Wh kg^{-1} at cell level.

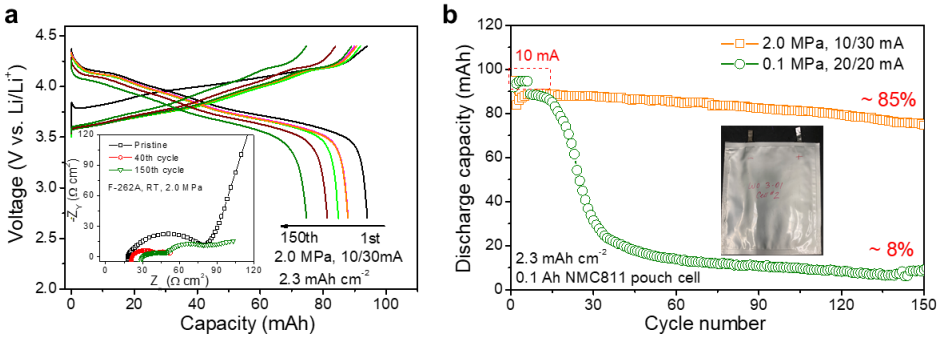

Figure II.13.B.21 Performances of 0.1 Ah Li||NMC 811 pouch cell with all-fluorinated electrolyte (F-262A) and 2.3 mAhcm^{-2}: (a) charge/discharge profiles of the cell under a high stacking pressure of 2.0 MPa, the inset shows Nyquist spectra of the pouch cell in cycling. (b) Cycling stability of NMC811 pouch cells under different stacking pressure conditions (2.0/0.1 MPa).

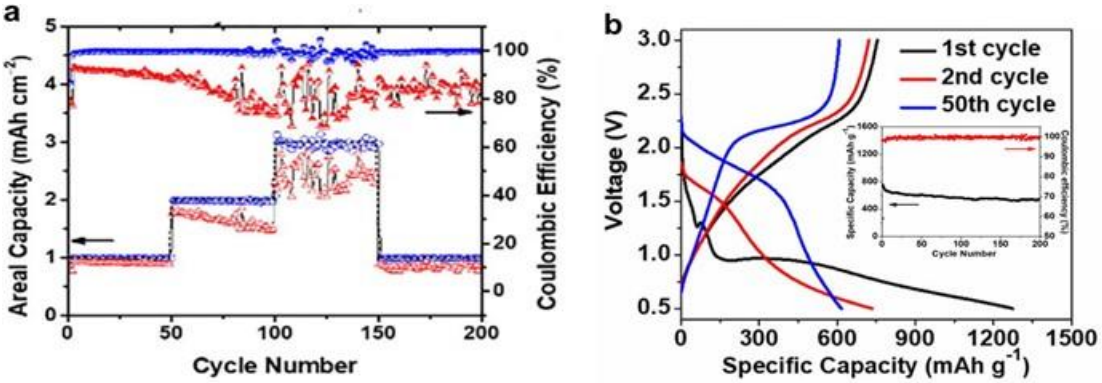

Figure II.13.B.22 Behavior of Li metal anode and NMC 811 cathode in the ionic liquid electrolyte. (a) The CE of Li deposition and stripping in Li|| Cu coin cell at lean electrolyte condition with different capacities. (b) The CE and capacity retention of NMC 811||Cu coin cell with 2mAh cm^{-2} cathode loading and lean electrolyte condition at 0.5 mA cm^{-2}. Inset is the cycling curve of NMC 811|| Cu coin cell at the same condition. (c). The cycling curve of NMC 811|| Cu pouch cell with 2mAh cm^{-2} cathode loading with lean electrolyte condition operated at 0.2C. (d) The CE and capacity retention of NMC 811||Cu pouch cell with 2mAh cm^{-2} cathode loading with lean electrolyte condition operated at 0.2C

Alternatively, we also developed a 1.0 M $LiPF_6$ in THF/2-methyl THF (mix-THF) electrolyte that enable a high Li plating/stripping CE of 99.83% on Bi and graphite (Bi-Gr) coated Cu at 0.5 mA cm^{-2} and 1.0 mAh cm^{-2}, and 99.5% at 3 mAh cm^{-2} (Figure II.13.B.23a). A Li-free Bi/Gr-LFP full cell (cathode loading =2 mAh cm^{-2}) tested with the same substrate and electrolyte shows stable cycling with 100% CE for 100 cycles.

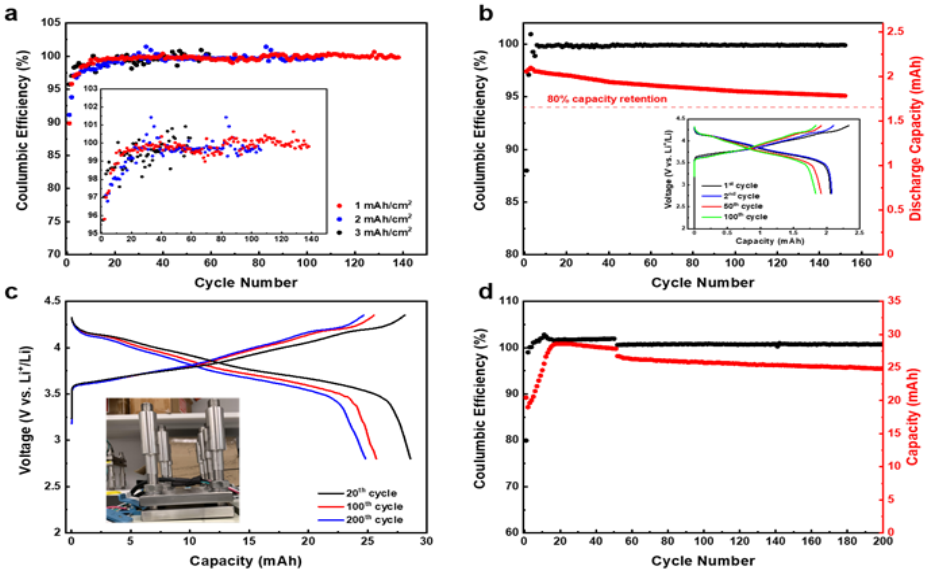

Figure II.13.B.23 (a) Li-metal plating/stripping CE on Bi-Gr coated copper current collector in 1M $LiPF_6$ mixTHF electrolyte at 0.5 mA cm^{-2} current density with different areal capacity (1.0-3.0 mAh cm^{-2}); (b) The galvanostatic charge and discharge curves at 50 mA·g^{-1}/0.5 mA cm^{-2} in all-fluorinated 1M $LiPF_6$ in FEC:FEMC:HFE lean electrolyte. (Inset) Delithiation capacity and CE versus cycle number in all-fluorinated 1M $LiPF_6$ in FEC/FEMC/HFE lean electrolyte. (Note: the specific capacity is calculated based on the total weight of C/S composite with an area mass loading of ~10 mg·cm^{-2})

In addition to intercalation cathode, Li-sulfur system was also investigated as the candidate for high energy battery. Quasi-solid-state LSBs, where sulfur is encapsulated in the micropores of carbon matrix and sealed by in situ formed solid electrolyte interphase, can operate under lean electrolyte conditions, but a low sulfur loading in carbon matrix (<40 wt %) and low sulfur unitization (<70%) still limit the energy density in a cell level. We significantly increased the sulfur loading in carbon to 60 wt % and sulfur utilization to ~87% by dispersing sulfur in an oxygen-rich dense carbon host at a molecular level through strong chemical interactions of C–S and O–S. In the all-fluorinated organic lean electrolyte, the C/S cathode experiences a solid-state lithiation/delithiation reaction after the formation of solid electrolyte interphase in the first deep lithiation (Figure II.13.B.23b), completely avoiding the shuttle reaction. The chemically stabilized C/S composite retains a high reversible capacity of 541 mAh·g−1 (total weight of the C/S composite) for 200 cycles under lean electrolyte conditions, corresponding to a high energy density of 974 Wh·kg^{-1} (Figure II.13.B.23b). The superior electrochemical performance of the chemical bonding-stabilized C/S composite renders it a promising cathode material for high energy and long-cycle-life LSBs.

Conclusions

Several emerging technologies were explored that have the potential to assist the Battery500 Team in meeting cell performance goals. The Consortium team members are in the process of validating the most promising electrode materials/architectures, electrolytes and cell designs.

Key Publications

Design, Processing, and Integration of Pouch-Format Cells for High-Energy Lithium-Sulfur Cells. (Mei Cai, General Motors)

1. S. Chen, F. Dai, M. Cai, “Opportunities and challenges of high energy lithium metal batteries for electrical vehicle applications”, ACS Energy Letter, 5, 10, 3140–3151, 2020.

Electrochemically Stable High-Energy-Density Lithium-Sulfur Batteries (Prashant N. Kumta, University of Pittsburgh)

1. Shanthi, P. M., R. Kuruba, O. I. Velikokhatnyi, P. J. Hanumantha, B. Gattu, M. K. Datta, S. D. Ghadge, and P. N. Kumta. "Theoretical and Experimental Strategies for New Heterostructures with Improved Stability for Rechargeable Lithium Sulfur Batteries." Journal of the Electrochemical Society 167 (2020): 040513.

2. Datta, M. K., B. Gattu, R. Kuruba, P. M. Shanthi, and P. N. Kumta. "Constitutional Under-Potential Plating (CUP) – New Insights for Predicting the Morphological Stability of Deposited Lithium Anodes in Lithium Metal Batteries." Journal of Power Sources 467 (2020): 228243.

Highly Loaded Sulfur Cathode, Coated Separator, and Gel Electrolyte for High-Rate Lithium-Sulfur Batteries; Yong L. Joo and Jin Suntivichi, Cornell University; Trung Nguyen, EIC Laboratory

1. Shebert, G. L., S. Zamani, C. Yi, and Y. L. Joo. "Polysulfide Entrapment and Retardation in Gel Electrolyte Li-S Batteries: Experiments and Modeling." Journal of Materials Chemistry A 8 (2020): 4341–4353.

Controlled Interfacial Phenomena for Extended Battery Life; Perla Balbuena and Jorge Seminario, Texas A&M University

1. Ponce, V., and J. M. Seminario. "Sulfur−Graphene Cathode Model using Reactive Force Field Molecular Dynamics Simulations." Journal of the Electrochemical Society 167 (2020): 100555.

2. Beltran, S. P., X. Cao, J-G. Zhang, and P. B. Balbuena. "Localized High Concentration Electrolytes for High-Voltage Lithium-Metal Batteries: Correlation between the Electrolyte Composition and its Reductive/Oxidative Stability." Chemistry of Materials. In press.

3. Camacho-Forero, L. E., and P. B. Balbuena. "Effects of Charged Interfaces on Electrolyte Decomposition at the Lithium Metal Anode." Journal of Power Sources. Invited contribution. In press.

4. Kamphaus, E. P., S. Angarita-Gomez, X. Qin, M. Shao, and P. B. Balbuena. "Effects of Solid Electrolyte Interphase Components on the Reduction of LiFSI over Lithium Metal." ChemPhysChem 21 (2020): 1310–1317.

Composite Cathode Architecture for Solid-State Batteries (Marca M. Doeff, Lawrence Berkeley National Laboratory, Guoying Chen Lawrence Berkeley National Laboratory, Stephen Sofie, Montana State University, Tobias Glossmann, Mercedes-Benz Research and Development, North America)

1. Yi, E., Shen, H., Heywood, S., Alvarado, J., Parkinson, D. Y., Chen, G., Sofie, S., Doeff, M. M., "All-Solid-State Batteries Using Rationally Designed Garnet Electrolyte Frameworks", ACS Appl. Energy Mater., 3 (2020): 170-175

High-Energy Solid-State Lithium Batteries with Organic Cathode Materials; Yan Yao, University of Houston

1. Yanliang Liang, Hui Dong, Doron Aurbach, Yan Yao, Current Status and Future Directions of Multivalent Metal-ion Batteries. Nature Energy, 5, 646-656, (2020).

2. Fang Hao, Yanliang Liang, Ye Zhang, Zhaoyang Chen, Jibo Zhang, Qing Ai, Hua Guo, Zheng Fan, Jun Lou, Yan Yao, High-Energy All-Solid-State Organic–Lithium Batteries, ACS Energy Letters, in revision.

Solvent-Free and Non-Sintered 500 Wh/kg All-Solid-State Battery; Michael Wixom, Navitas; Chunsheng Wang, University of Maryland; David Wood, Oak Ridge National Laboratory

1. Li, B., R. Sosik, and M. Wixom. Compositions and Methods for Electrode Fabrication. U. S. Patent Application # 62/984,144. March 2020.

Multifunctional Lithium-Ion Conducting Interfacial Materials for Lithium-Metal Batteries; Donghai Wang, Pennsylvania State University

1. Gao, Y., et al. "Low-Temperature and High-Rate-Charging Lithium Metal Batteries Enabled by an Electrochemically Active Monolayer-Regulated Interface." Nature Energy (2020). doi: 10.1038/s41560-020-0640-7.

Advanced Electrolyte Supporting 500 Wh/kg Lithium-Carbon/NMC Batteries; Chunsheng Wang, University of Maryland

1. S. Liu, X. Ji, N. Piao, J. Chen, N. Eidson, J. Xu, P. Wangm L. Chen, J. Zhang, T. Dengm S. Hou, T. Jin, H. Wan, J. Li, J. Tu, C. Wang. Inorganic-rich Solid Electrolyte Interphase for Advanced Lithium Metal Batteries in Carbonate Electrolytes. Angew. Chem. Int. Ed., 2020, https://doi.org/10.1002/anie.202012005.

2. J. Chen, X. Fan, Q. Li, H. Yang, M.R. Khoshi, Y. Xu, S. Hwang, L. Chen, X. Ji, C. Yang, H. He, C. Wang, E. Garfunkel, D. Su, O. Borodin, C. Wang, Electrolyte Design for LiF-rich Solid-Electrolyte Interfaces to Enable High-performance Microsized Alloy Anodes for Batteries. Nature Energy, 2020, https://doi.org/10.1038/s41560-020-0601-1.

3. C. Luo, E. Hu, K. J. Gaskell, X. Fan, T. Gao, C. Cui, S. Ghose, X-Q. Yang, C. Wang, A Chemically Stabilized Sulfur Cathode for Lean Electrolyte Lithium Sulfur Batteries. Proc. Natl. Acad. Sci. USA, 2020, 117, 14712-12720.

4. C. Cui, X. Fan, X. Zhou, J. Chen, Q. Wang, M. Lu, C. Yang, E. Hu, X-Q. Yang, C. Wang, Structure, and Interface Design Enable Stable Li-Rich Cathode. J. Am. Chem. Soc., 2020, 142, 8918-8927.

5. J. Chen, Q. Li, T. P. Pollard, X. Fan, O. Borodin, C. Wang, Electrolyte design for Li metal-free Li batteries, Mater. Today, 2020, 39, 118-126.

6. C. Cui, C. Yang, N. Eidson, J. Chen, F. Han, L. Chen, C. Luo, P. Wang, X. Fan, C. Wang. A Highly Reversible, Dendrite-Free Lithium Metal Anode Enables by a Lithium-Fluoride-Enriched Interphase. Adv. Mater., 2020, 1906427.

7. S. Liu, X. Ji, J. Yue, S. Hou, P. Wang, C. Cui, J. Chen, B. Shao, J. Li, F. Han, J. Tu, C. Wang, High Interfacial-Energy Interphase Promoting Safe Lithium Metal Batteries. J. Am. Chem. Soc. 2020, 142, 5, 2438-2447.

8. X. Fan, X. Ji, L. Chen, J. Chen, T. Deng, F. Han, J. Yue, N. Piao, R. Wang, X. Zhou, X. Xiao, L. Chen, C. Wang, All-temperature batteries enabled by fluorinated electrolytes with non-polar solvents, Nature Energy, 2019, 4, 882.

II.13.C Battery500 Seedling: Composite Cathode Architecture for Solid-State Batteries (LBNL)

Marca M. Doeff, Principal Investigator
Lawrence Berkeley National Laboratory
1 Cyclotron Road
Berkeley, CA 94720
Email: mmdoeff@lbl.gov

Guoying Chen, Principal Investigator
Lawrence Berkeley National Laboratory
1 Cyclotron Road
Berkeley, CA 94720
Email: gchen@lbl.gov

Stephen Sofie, Principal Investigator
Department of Mechanical and Industrial Engineering
Montana State University
Bozeman, MT 59717
Email: ssofie@montana.edu

Tobias Glossmann, Principal Investigator
Mercedes-Benz Research and Development, North America
12120 Telegraph Road
Redford, MI 48239
E-mail: tobias.glossmann@daimler.com

Tien Duong, DOE Technology Development Manager
U.S. Department of Energy
E-mail: Tien.Duong@ee.doe.gov

Start Date: April 1, 2019 End Date: March 31, 2021
Project Funding: $660,000 DOE share: $600,000 Non-DOE share: $60,000

Approach

We utilize freeze tape-casting techniques to produce porous scaffolds of LLZO (variants of $Li_7La_3Zr_2O_{12}$) solid electrolyte and then infiltrate the pores with the other components needed to make composite electrodes. Freeze tape casting allows unparalleled control of porosity by changing processing variables such as slurry loading, solvent, and temperature at selected thicknesses (hundreds of microns thick or less) during continuous production.[1] The unidirectional pores of the scaffolds are then infiltrated with Ni-rich NMC powders and a conductive additive such as carbon (with or without binder) to form thick (100-150 μm) composite cathodes, which ultimately can be used in all solid-state battery configurations. Porous/dense bilayer LLZO structures are also fabricated by combining the porous structure with a dense layer of LLZO electrolyte, with lithium foil added to complete the solid-state cell. Another configuration of interest is that of a trilayer, in which the dense layer is sandwiched between two porous layers, one of which contains cathode material and the other an anode material such as lithium metal, to form the device. Some effort is also devoted to fabrication of NMC scaffolds and infiltration of LLZO into these structures, essentially the reverse of the procedure discussed above.

Results

We were awarded an R&D100 award this year for our invention entitled “Solid Lithium Battery Using Hard and Soft Solid Electrolytes” that came about from the previous year’s research in this program.

This year, we made progress in diversifying porous/dense bilayer and porous/dense/porous trilayer LLZO architectures by investigating lower LLZO vol% slurries and testing alternative ceramic processing methods for engineering the Li/LLZO interface. Additionally, the causes of early failures of the solid-state batteries constructed last year were identified and alternative approaches were explored to address the issue.

We expanded the vol.% range of the freeze-tape-castable LLZO slurry down to 5 vol% through optimizing slurry formulations. Lower LLZO loadings of 5 and 7.5 vol%, compared to the standard formulation of 10 vol%, were achieved by increasing the thickening agent fraction to obtain viscosities suitable for casting. Figure II.13.C.1 compares the sintered porous/dense LLZO bilayers produced using freeze-tape-cast green tapes using 5, 7.5, and 10 vol% LLZO slurries. The pore region noticeably increases with reducing vol% of LLZO. This permits higher areal loading of active materials which will be key to obtaining high energy density solid state batteries.

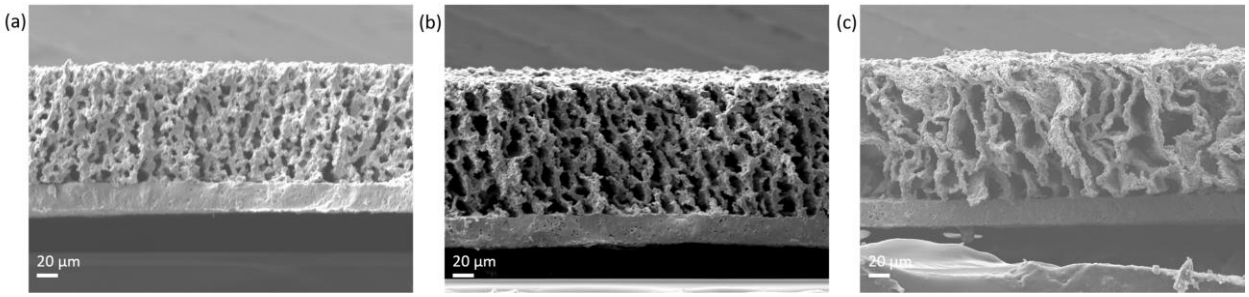

Figure II.13.C.1 Sintered bilayers using (a) 10 vol % (b) 7.5 vol %, and (c) 5 vol % freeze tape cast LLZO

Sol-gel coating of a ZnO interfacial layer was investigated in order to facilitate wetting of lithium on LLZO surfaces. This was to replace the Au coating layer with a lower cost, scalable alternative. Typical processes involved dispensing a precursor solution containing Zn and gently heating to burn off the organics (Figure II.13.C.2(a)).[2] The sol-gel derived ZnO coating layer successfully aided the melt bonding of Li foil as shown in Figure II.13.C.2(b) where Li and LLZO are bonded seamlessly. We also investigated an application of a thin porous LLZO layer onto the dense LLZO layer to increase the specific interfacial area between LLZO and Li anode. This should permit cycling at higher current densities with minimal specific energy drop compared to using freeze-tape-cast derived LLZO anolytes at thicknesses of 80-120 µm. Figure II.13.C.2(c) shows a coated porous LLZO layer with a thickness to <10 µm by controlling the processing parameters.

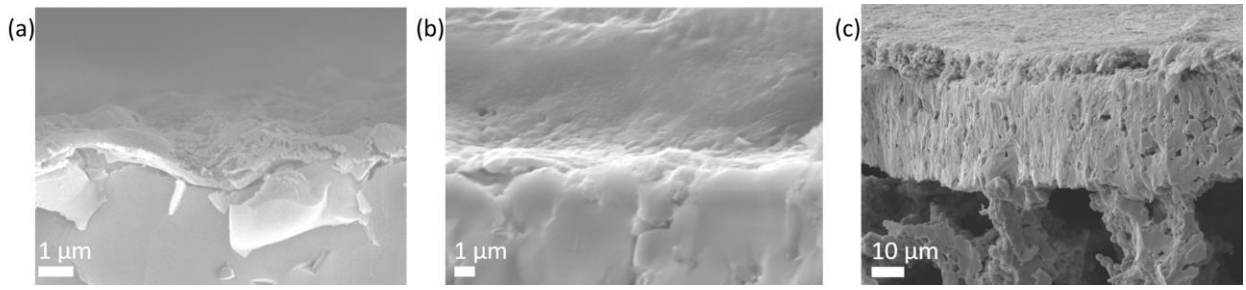

Figure II.13.C.2 (a) LLZO with 200 nm ZnO coating. (b) Seamless Li/LLZO interface aided by ZnO coating layer. (c) Porous LLZO coating layer (<10 µm) on dense LLZO.

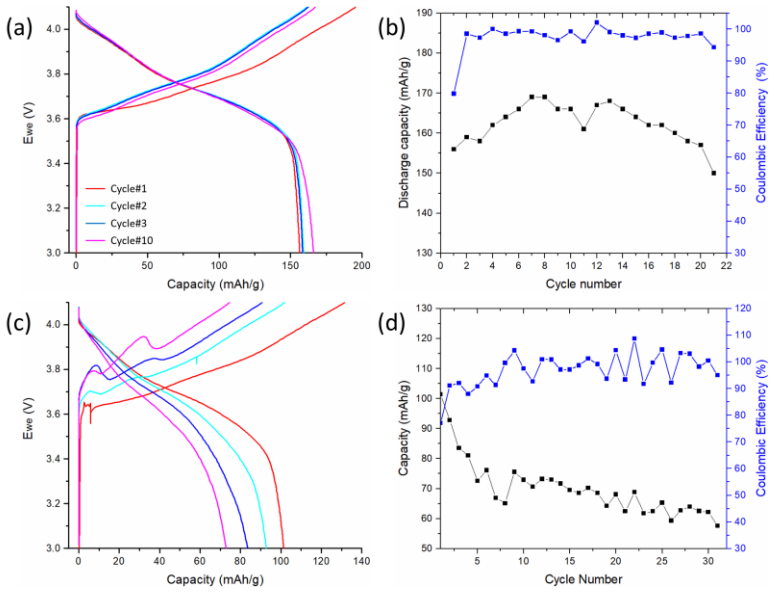

Figure II.13.C.3 (a)/(b) Cycling performance of solid-state battery using NMC cathode at C/10 in trouble-shooting configuration. (c)/(d) Cycling performance of solid-state battery using NMC cathode at C/10.

Solid state cells that use conventional tape cast NMC/C/PVDF cells were constructed for trouble shooting purposes. The porous layer was filled with plastic crystal electrolyte and the tape cast NMC cathode was attached on top. These cells performed very well as shown in Figure II.13.C.3(a)/(b), suggesting that solvent exposure of LLZO during previous bilayer cell construction likely degrades the LLZO surface resulting in early cell failures. Spontaneous reactions of LLZO with common organic solvents have been recently reported.[3] We initiated screening of usable organic solvents for NMC slurry infiltration to the porous layer and improved cell cycle life, compared to earlier cells as shown in Figure II.13.C.3(c)/(d). More work is needed to formulate stable dispersions of NMC/C in order to improve the cell capacity. We continue to narrow down optimal processing conditions/parameters for building LLZO based solid state batteries.

Conclusions

Porous/dense LLZO bilayers using a range of freeze tape cast LLZO green tape have been successfully produced. ZnO coating layer produced by wet chemical coating aids seamless bonding between Li and LLZO when melt bonded. Thin, porous LLZO layer attached to dense LLZO layer can be produced by simple drop-casting and calcination. We also find solvent selection is crucial for active materials infiltration due to easy reactivity of LLZO.

Key Publications

1. Yi, E., Shen, H., Heywood, S., Alvarado, J., Parkinson, D. Y., Chen, G., Sofie, S., Doeff, M. M., "All-Solid-State Batteries Using Rationally Designed Garnet Electrolyte Frameworks", *ACS Appl. Energy Mater.*, 3 (2020): 170-175

2. Shen, H., Yi, E., Heywood, S., Parkinson, D. Y., Chen, G., Tamura, N., Sofie, S., Chen, K., Doeff, M. M., "Scalable freeze tape casting fabrication and pore structure analysis of 3D LLZO solid-state electrolytes", *ACS Appl. Mater. Interfaces*, 12 (2020): 3494-3501

3. Doeff, M. M., Yi, E., "All-Solid-State Batteries Using $Li_7La_3Zr_2O_{12}$ Garnet Electrolyte Framework", PRiME2020, Oct. 4-9, 2020 (Invited)

4. Doeff, M. M., Yi, E., "Composite Cathode Architectures Made by Freeze-Casting for All Solid-State Lithium Batteries", 2020 DOE Vehicle Technologies Office Annual Merit Review

References

1. Sofie, S. W., "Fabrication of Functionally Graded and Aligned Porosity in Thin Ceramic Substrates With the Novel Freeze–Tape-Casting Process" *J. Am. Ceram*., 90 (2007): 2024-2031

2. Adl, A. H., Kar, P., Farsinezhad, S., Sharma, H., Shankar. K., "Effect of sol stabilizer on the structure and electronic properties of solution-processed ZnO thin films" *RSC Adv.* 5 (2015): 87007-87018

3. Gupta, A., Kazyak, E., Dasgupta, N. P., Sakamoto, J., "Electrochemical and Surface Chemistry Analysis of Lithium Lanthanum Zirconium Tantalum Oxide (LLZTO)/Liquid Electrolyte (LE) Interfaces" *J. Power Sources*, 474 (2020): 228598

(This page intentionally left blank)

U.S. DEPARTMENT OF ENERGY

Office of ENERGY EFFICIENCY & RENEWABLE ENERGY

For more information, visit:
energy.gov/eere/vehicles

DOE/EE-2332 • June 2021